ISHPMIE 2024

Napoli, Italy

15th International Symposium on Hazards, Prevention and Mitigation of Industrial Explosions
Naples, Italy | June 10 – 14, 2024

Proceedings

Authors:

Aakervik Espen
Abid Said
Acha Esther
Adamus Wojciech
Alauddin Mohammad
Allason Daniel
Almodovar Christopher
Amez Isabel
Amouzou Seyth
Amyotte Paul
Andreozzi Roberto
Andrews Gordon
Andriani Giuseppe
Angerler Theresa
Arbizu- Milagro Julia
Armstrong Adam
Arntzen Bjørn
Arntzen Bjørn Johan
Arulappan Dilip
Askar Enis
Atkinson Graham
Aube Aurélie
Auvray Alexandre
Axani Katherine
Barbu Bogdan
Baumann Florian
Bauwens C. Regis L.
Bauwens Luc
Bauwens Regis
Becker Dominik
Benke Alexander
Berger Frank
Bernard Stephane
Bernardy Christopher
Beyer Michael
Bi Mingshu
Bi Sheng
Binotto Ghislain
Birk Albrecht Michael
Birk Albrecht Mickael
Bjerketvedt Dag
Blanchard Robert John
Blanchetiere Vincent
Boeck Lorenz
Boeck Lorenz R.
Bond Nicole
Bordes Arnaud
Brandell Daniel
Bratek Dominik
Brennan Sile
Brunzendorf Jens
Bunse Roland
Burnett MIles
Calabrese Marcella
CALERO MATHIEU
Camplese Davide
Cao Kai-Quan
Capone Guido
Castells Blanca
Castillo-Ruiz Francisco J.
Chandran Sheela
Chang Ho-Jan
Chang Li
Chanut Clement
Chanut Clément
Charrondière Stéphane
Chaumeix Nabiha
Cheevers Kevin
Chen Jenq-Renn
Chong Tao
Christ Thomas
Ciccarelli Gaby
Cirrone Donatella
Cloney Chris
Cowling Nick
Cozzani Valerio
Danzi Enrico
Daragan Freyja Galina
Daubech Jérôme
Davis Branson
De Leo Elena
De Liso Benedetta
de Persis Stéphanie
De Rosa Filippo
D'Hyon Sebastian
Di Benedetto Almerinda
Dobashi Ritsu
Donner Marcel
Dorofeev Sergey
Dorofeev Sergey B.
Douasbin Quentin
Dounia Omar
Dueñas Santana Julio Ariel
Dufaud Olivier
Dutertre Antoine
Dworschak Rene
Dyduch Zdzislaw
Dymke Jessica
Eberwein Robert
Ebne-Abbasi Hazhir
El Gadha Chayma
Endo Takuma
Engelmann Frank
Essmann Stefan
Eyssette Roland
Farzana Nafi
Flemming Friederike
Fossan Ingar
Fossum Hannibal
Fouchier Charline
Franchini Fausto
Friedrichova Romana
Fu Hua
Furlong Andrew
Gabel Dieter
Gao Wei
Garnier Félicia
Garrido Ceca Ignacio
Gehle Nicole
Gellersen Frauke
Gerbeit Marco
Ghaffari Maryam
Giacopinelli Pablo
Gill Jason
Gluschitz Peter
Goedde Markus
Gorzelnik Tomasz
Grasse Dennis
Grobert Steffen
Grosshans Holger
Habib Karim
Hahn Alexander
Hajhariri Aliasghar
Hamzah Nur Faazila
Han Xu
Hau Michael
Herbst Sabrina
Herniksen Mathias
Heudier Laure
Heymes Frederic
Heymes Frédéric
Hilbert Michael
Hildershavn Andrine
Hilliger André
Himstedt Matthias
Hisken Helene
Hohenberger Michael

Höltkemeier-Horstmann Jacqueline
Hosoi Jin
Huang Chen
Huang Po-Hsun
Huang Yi-Peng
Hughes Robin
Hynynen Jonna
Ishikawa Takehiko
Islas Montero Alain
Jambut Romain
Jan Karl
Jankuj Vojtech
Janovsky Bretislav
Janovsky Prokop
Jantac Simon
Jaravel Thomas
Jian Wang
Jiang Haipeng
Jocher Agnes
Johnson Douglas Michael
Johzaki Tomoyuki
Kallestad Stople Vegard
Kant Hanjo
Kao Ting-Chia
Kapahi Anil
Karl Jan
Karlsson Anna
Kashkarov Sergii
Kazemi Mina
Kia Samira
Kianfar Amiriman
Kim Wookyung
Kim Yangkyun
Kirillov Igor
Kluge Martin
Knudsen Ørjan
Kraft Stefan
Krause Ulrich
Krentel Daniel
Krietsch Arne
Kuhlmann Karsten
Kuracina Richard
Kuwana Kazunori
Laamarti El Mehdi
Lach Agnieszka W.
Le Roux Benjamin
Lebas Alexandre
Lecocq Amandine
Lecocq Guillaume
Lee Minhyeok
León David
Leprette Emmanuel
Li Bei
Li Tao
Li Yanchao
Liang Bo
Limbacher Bernd
Lin Yuan-Chen
Lipatnikov Andrei
Liu Pandeng
Liu Wangchen
Lopez-Urionabarrenechea Alex
Lövström Cecilia
Lu Zhengkang
Lucas Melodia
Maas Ulrich
Makarov Dmitriy
Mansfield Duncan
Markus Detlev
Marlair Guy
Marmo Luca
Marotta Raffaele
Mathieu Laurent
MdKasmani Rafiziana
Medic Ljiljana
Melguizo-Gavilanes Josue
Methling Ralf
Meziat Ramirez Francis Adrian
Mikami Masato
Minotti Stefano
Mocellin Paolo
Möckel Dieter
Mogi Toshio
Mohanty Shuvam
Molkov Vladimir
Montagne Pierre
Moran Madeleine
Moreno Amets
Mos Antoine
Mousse Rayaleh Ayan
Mynarz Miroslav
Nagendra Karthik
Nakamura Yuji
Naudet Valérie
Ngai Eugene Y.
Nguyen Trung Thanh
Nie Baisheng
Norman Frederik
Orchini Alessandro
Osborne David
Otremba Frank
Ozler Gizem
Pan Chuanyu
Pan Yangyue
Pandal Adrian
Papalexandris Miltiadis
Paquet Frederick
Paquet Mario
Paredes Roberto
Pegg Michael
Pekalski Andrzej
Peng Hsiang-Ching
Perbal Roald
Perrin Laurent
Perrone Luca Pakj
Peschel Inka
Phylaktou Herodotos
Piao Junxiu
Pietraccini Matteo
Pio Gianmaria
Plaksin Vadim
Planötscher Kajetan
Poinsot Thierry
Porowski Rafal
Portarapillo Maria
Postacchini Alessio
Prodan Maria
Proust Christophe
Puig Gamero María
Putier Fabrice
Quartieri Eugenio
Radulescu Matei
Rakotoarison Willstrong
Raupenstrauch Harald
Regler Danny
Rossin Stefano
Russo Danilo
Russo Paola
S. Raghuram
S. Rangwala Ali
Saad Al Hadidi Farès
Saeki Rinrin
Salaün Nicolas
Salzano Ernesto
Sanchirico Roberto
Sandsta Nelly
Sandstå Nelly
Scarponi Giordano Emrys
Schalau Bernd
Schanner Richard

Schierding Carola
Schmelter Sonja
Schmidt Martin
Schrader Anton
Schroeder Johannes
Schüler Niklas
Schulze Marcel
Scott Alison
Seeber Henrik
Seidlitz Holger
Semenova Aleksandra
Serrano Jose
SERRANO José
Serrer Marc-André
Shen Jinghua
Shepherd Joseph
Shu Bo
Siegle Leo
Skjold Trygve
Skrinsky Jan
Snoeys Jef
Spijker Christoph
Spitzer Stefan
Spitzer Stefan H.
Spörhase Stefanie
Stankejevas Erikas
Strange Benjamin
Sun Yi
Sun Yuanxiang
Szabova Zuzana
Tanwar Nikhil
Tascón Alberto
Thedens Martin
Tokumitsu Seiji
Toman Adrian
Toraldo Gerardina
Tosolini Elia
Truchot Benjamin
Tsai Hsiao-Yun
Ubaldi Sofia
Uber Carsten
Ueda Akihiro
Uhrlandt Dirk
V. Raghavan
Vagner Gaathaug André
Vågsæther Knut
van der Prijt Jeroen
Van Laar Gerard
van Norden Paul
Van Wingerden Kees
van Wingerden Mattheus
van Wingerden Matthijs
Vasudevan Vaishakh
Velasco Manuel
Vermorel Olivier
Vianello Chiara
Vignes Alexis
Wade Robin
Wang Xishi
Wang Xueying
Wang Yanshu
Wickham Neil
Wiklund Jo
Wilkins Brian
William-Louis Mame
Willmann Christophe
Willstrand Ola
Wilms Christoph
Wooldridge Margaret
Xu Wenchao
Yang Hongxia
Yang Hui-Ning
Yang Ming-Hsuan
Yazaki Shigetoshi
Yeh Li-Yu
Yu Chunkan
Yu Haoshen
Yu Xiaozhe
Zakel Sabine
Zangene Farzane
Zhang Mengying
Zhang Zongling
Zhao Fengyu
Zhong Shenjung

Citation Template:

Author 1, Author 2, ... : "Title of article", pp. n1 - n2 . In: "Proceedings of the 15th International Symposium on Hazards, Prevention and Mitigation of Industrial Explosions (ISHPMIE 2024)", Naples, Italy, 2024. DOI: 10.5281/zenodo.12515711

Summary

Plenary Lectures

Session 1: Risk Management (Chair: A. Krietsch)

Session 2: AI & databasing applied to explosions (Chair: D. Russo)

Session 3: Battery Safety (Chair: G. Lecocq)

Greetings from the Local Organizing Committee Chair

Dear Colleagues and Friends,

We are pleased to welcome you to the **15th International Symposium on Hazards, Prevention and Mitigation of Industrial Explosions (ISHPMIE)** and to Naples.
The event is organized by the University of Naples Federico II, in collaboration with the National Research Council, the University of Rome, the University of Bologna and the Polytechnic University of Turin. I would like to thank the International Organizing Committee for giving us the opportunity to meet at the 15th Symposium in Naples.

We are glad to host in Naples around 200 Researchers and Scientists coming from all over the World. We would like to thank you all for your outstanding contributions! We are privileged to have a diverse array of fascinating papers from around the globe, covering a wide range of significant topics.

Here's what to expect:

- Plenary Lectures: Leading scientists will share their insights and the challenges they face on current topics.
- Technical Sessions: These sessions are organized into parallel tracks with three or four presentations each, focused on specific subjects and chaired by experts in the field.
- Poster Session: Join us during the coffee breaks: results from various research projects will be discussed and preliminary results from ongoing research projects are showcased.

We look forward to your participation and the enriching discussions!

In addition, we have organized an intensive social program and we hope you will enjoy our beautiful city. I wish all participants an interesting conference week with many contacts and fruitful discussions.

Almerinda Di Benedetto
Local Organizing Committee Chair

Foreword of the Proceeding Editors

It is our pleasure to present the proceedings of the 15th International Symposium on Hazards, Prevention, and Mitigation of Industrial Explosions (ISHPMIE).

We are happy to compile proceedings consisting of 111 high-quality papers that demonstrate the continuous advancements in the scientific knowledge of safety also related to emerging risk issues due to energy transition.
All articles in this volume have been subjected to a peer-review process administered by the Proceeding Editors. We are thankful to all the referees who guaranteed the professional and scientific standards expected of ISHPMIE.

After the conference, Elsevier will publish selected papers from the 15th ISHPMIE in a special issue of the Journal of Loss Prevention in the Process Industries.

We strongly believe that Naples will inspire stimulating and high quality scientific exchange between participants.

Symposium Committees

International Organizing Committee

T. Skjold, Norway, Chair

P. Amyotte, Canada

M. Beyer, Germany

R. Dobashi, Japan

W. Gao, P. R. China

U. Krause, Germany

M. Nifuku, Japan

M. Pegg, Canada

I. Sochet, France

J. R. Taveau, USA

Honorary members

R. Klemens, Poland

K. Lebecki, Poland

Local Organizing Committee

A. Di Benedetto, University of Naples Federico II, Symposium Chair

L. Marmo, Polytechnic University of Turin, Co-Chair

P. Russo, University of Rome La Sapienza, Co-Chair

E. Salzano, University of Bologna, Co-Chair

E. Danzi, Polytechnic University of Turin

G. Pio, University of Bologna

M. Portarapillo, University of Naples Federico II

D. Russo, University of Naples Federico II

R. Sanchirico, STEMS-CNR

Program Committee

A. Di Benedetto, University of Naples Federico II, Symposium Chair

M. Portarapillo, University of Naples Federico II

Why Do Dust Explosions Happen?

Paul Amyotte

Dalhousie University, Canada

Dust explosions are an ever-present threat wherever bulk powders are handled, not only in the chemical process industries but in numerous other applications throughout industrial practice. A dust explosion must not, however, be viewed as the inevitable outcome of processing a combustible dust in an industrial scenario. Normalization of deviance in such a manner ignores the strong evidence that the principles of process safety have been proven to be effective in dust explosion prevention and mitigation.

In this presentation, we will explore the reasons for the occurrence of dust explosions from a variety of perspectives. We will begin with the scientific and engineering underpinning provided by the familiar explosion pentagon, and will quickly move on to lessons drawn from the management and social sciences. Explosion causation factors that will be examined include: (i) placing a singular emphasis on occupational health and safety concerns (such as respirable dust concentrations), (ii) overreliance on procedural safety and use of personal protective equipment (PPE), (iii) ignoring warning signs of potential incidents, (iv) accepting safety management system deficiencies, and (v) adherence to a number of erroneous and outdated beliefs concerning the dust explosion problem. The overall goal of the presentation is to demonstrate that dust explosions do not happen because we do not have appropriate technology to prevent them. There are deeper, more systemic reasons for the occurrence of dust explosions.

Understanding the Limitations of Using K_{St} to Define the Reactivity of Large-Scale Dust Explosion Tests

C. Regis L. Bauwens, Lorenz R. Boeck & Sergey B. Dorofeev

FM Global, Norwood, USA

E-mail: carl.bauwens@fmglobal.com

Abstract

While dust explosions present a significant hazard to buildings and personnel, these events can often be mitigated through the appropriate use of explosion protection techniques. To determine the level of protection required, and the most effect mitigation strategy for a given scenario, it is critical to understand the reactivity of the specific dust present. Historically, the primary measure used to assess the reactivity of a combustible dust is a deflagration index, K_{St}. It is important to note, however, that K_{St} is an empirical parameter determined in a standard test apparatus under specific initial conditions. In this work, a new dust explosion test setup was used to decouple the dust injection process from the turbulence generation process to create a consistent level of initial turbulence while varying the type of dust, and dust loading. The pressure transients measured in these tests are compared with equivalent experiments performed in a 20-L sphere that was used to obtained K_{St} values for the same dusts, across a similar range of dust loadings. A comparison of the experimental results shows that the relative ranking of K_{St} did not correspond to the maximum rate of pressure rise observed in the large-scale experiments. A previously developed two-parameter dimensionless model was then used to interpret both the large-scale and 20-L sphere results. It was also found that the model could reproduce the experimental pressure time-histories in both the 20-L and 2.42-m^3 tests, and that the value of one parameter, χ, was similar between both. These results illustrate the limitation of using K_{St} to fully characterize the reactivity of large-scale explosion tests, and the need for improved measures to quantify dust reactivity.

Keywords: *explosion mitigation, dust explosions, dust reactivity, large-scale testing*

Introduction

Dust explosions are one of the most common explosion hazards in industrial facilities. These events can often produce significant loss of life and catastrophic damage to buildings and equipment. Despite the severity of dust explosions, the effective use of protection measures, such as explosion venting, suppression, and isolation, can mitigate the vast majority of these events. The proper application of these protection measures, however, need to account for the inherent reactivity of the dust, which have been shown to vary significantly between different dusts (Bartknecht, 1989, Eckhoff , 2003).

There is a significant challenge in characterizing the reactivity of a dust, as the severity of a dust explosion varies with both the level of turbulence present (Amyotte et al. 1988, Tamanini, 1998), which often determine the overall severity of the dust explosion, and the specific properties of a given dust, such as particle size distribution (Di Benedetto et al., 2010). As a result, efforts to quantify fundamental reactivity parameters for dusts, such as a laminar burning velocity (Bradley, 1989, Van Wingerden et al., 1996, Goroshin et al., 1996, Julien et al., 2015), have not produced parameters that are commonly used in industrial safety applications.

Due to the lack of fundamental reactivity properties that can be used to characterize combustible dusts, standardized empirical tests have been developed to measure the reactivity of a specific dust sample. These tests impose a set initial turbulent condition, with a specified ignition delay, in a specific apparatus with a specified injection system, and a specified ignition strength. Using this setup, the reactivity of a dust is defined by a dust deflagration index, K_{St}, which is calculated from the maximum rate of pressure rise, $(dP/dt)_{\max}$ in a closed volume, V, in a standard 1-m^3 or 20-L vessel (Bartknecht 1989, ASTM E 1226):

$$K_{\mathrm{St}} = \left(\frac{dP}{dt}\right)_{\max} V^{1/3}. \tag{1}$$

While this method provides a consistent basis for assessing the relative hazard presented by a combustible dust, it should be noted that the severity of an actual explosion event is often entirely determined by the specific dispersion and initiating event, which can significantly affect the level of initial turbulence present. As a result, K_{St} alone has been shown to have significant limitations in characterizing actual dust explosion events (Eckhoff , 2015).

These limitations create challenges when trying to use K_{St} to describe the reactivity of a specific test and the conditions at which it was performed. This is important, as a consistent reactivity measure is needed to characterize the conditions at which large-scale dust explosion tests are performed as these tests are used to develop engineering guidelines and the protection requirements for enclosures and to evaluate the performance of explosion protection devices. In these tests, the level of initial turbulence is commonly varied, by changing the delay between dust injection and ignition, to examine a range of explosion severities. In general, these experiments are characterized by an effective deflagration index, which we will refer to as K_{eff}, which is evaluated using Eq. (1), for a specific test condition. It is important to recognize, however, that K_{eff} still only represents the rate of combustion at a single time, typically late in the combustion process when the flame approaches the vessel walls. As a result, experiments performed with similar values of K_{eff} can still produce significantly different rates of pressure rise at the critical early phase where explosion protection measures are most effective.

Discrepancies have been found between values of K_{St} obtained in the 20-L and 1-m^3 standard sphere (Proust et al., 2007), where differences as high as to 80% were observed for some dusts. Those tests illustrate the potential for significant differences in small and larger-scale dust explosion reactivity, even using standardized test methods. Furthermore, it has been found that the dust injection process itself can vary between different dusts and dust loading in the standard 20-L sphere (Skjold, 2003), which could also impact the universality of the methodology in characterizing dust reactivity.

To account for these limitations, a two-parameter model was developed in previous studies (Bauwens et al., 2020, 2022), to characterize the full pressure time-history that develops during a closed vessel dust explosion. This model characterizes the reactivity of the dust explosion using two parameters, $S_{\mathrm{T},R}$, which is an effective burning velocity of the leading edge of the flame, and a dimensionless parameter χ, which compares the characteristic time of flame propagation with a characteristic consumption time of the dust within the flame.

In this work, a 2.42-m^3 dust explosion test setup was used, specially designed to decouple the dust injection process from the turbulence generation process, to create consistent levels of initial turbulence. This setup was used to examined dust reactivity for a range of dusts, and dust loadings, under well controlled initial conditions. These results are then compared with data obtained from 20-L sphere testing of the same dusts, both for the standard reactivity parameter K_{St}, and for the new reactivity values obtained using the two-parameter model.

1. Experimental setup

In this study, two different experimental setups were used to characterize the reactivity of six dusts over a range of dust loadings, ρ_{DL}. These setups include a standard 20-L sphere, described in Section 1.1, and a larger-scale 2.42-m^3 vessel described in Section 1.2.

1.1. Standard 20-L sphere test apparatus

To perform the testing to obtain standard values of K_{St}, a commercial Siwek 20-L sphere apparatus, shown in Fig. 1, (Cesana AG, 2016) was used in accordance with ASTM E 1226. The standard test procedure performs three repeat tests for the three dust loadings (in 0.25 kg/m^3 increments) that produce the highest overall rates of pressure rise dp/dt. In this setup, a 0.6-L reservoir was loaded with a prescribed mass of dust, m_d, to achieve the target dust loading, $\rho_{\mathrm{DL}} = m_{\mathrm{d}}/V$, which was then pressurized to 20 bar (gauge). Prior to dust injection, the vessel was evacuated to 0.4 bar. The test sequence starts with the injection and dispersion of the dust into the vessel through a rebound nozzle. Following a 60-ms ignition delay, timed from the start of dust injection, two 5-kJ Sobbe EBBOS ChZ pyrotechnic ignitors, centrally located within the sphere, are used to ignite the mixture. Two Kistler piezoelectric pressure transducers, sampling at a rate of 2.5 kHz, are used to capture the internal pressure.

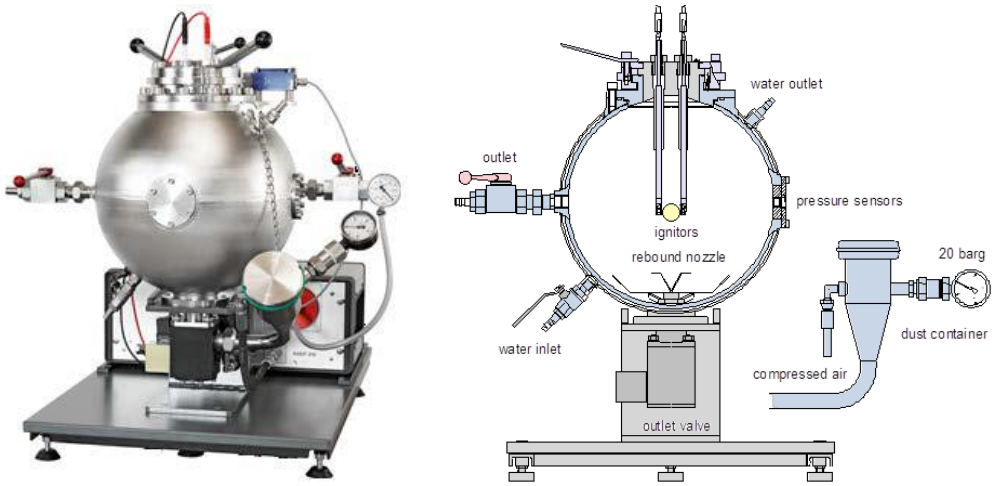

Fig. 1. *Standard 20-L sphere apparatus (Cesana AG, 2016)*

1.1.1. Dust injection effects

While the dust storage reservoir was not instrumented to record pressure during the dust injection process, the internal vessel pressure transient generated by dust injection can be used to examine whether dust injection and the turbulence generation process was affected by the specific dust tested and the dust loading. Figure 2a shows the internal pressure as a function of time during the dust injection process for different dusts, all with a dust loading $\rho_{\mathrm{DL}} = 0.75$ kg/m^3, which clearly shows how different dusts can affect the ignition delay, and resulting level of initial turbulence, in the 20-L sphere. Certain dusts, like cellulose fiber, and Irganox MD 1024 appear to inject faster, resulting in a longer delay between the end of dust injection and ignition. Conversely, Durez 32580 was found to inject noticeably slower than the other dusts, producing a shorter ignition delay. Furthermore, the dusts with a slower injection rate also produced slightly lower initial pressures.

In addition, Fig. 2b illustrates how the dust loading of an individual dust, in this case Durez 32580, can also significantly affect the rate of dust injection and the level of initial turbulence in the 20-L sphere. This is consistent with previous studies in a 20-L sphere, which saw similar behavior in lycopodium and silgrain dusts (Skjold, 2003).

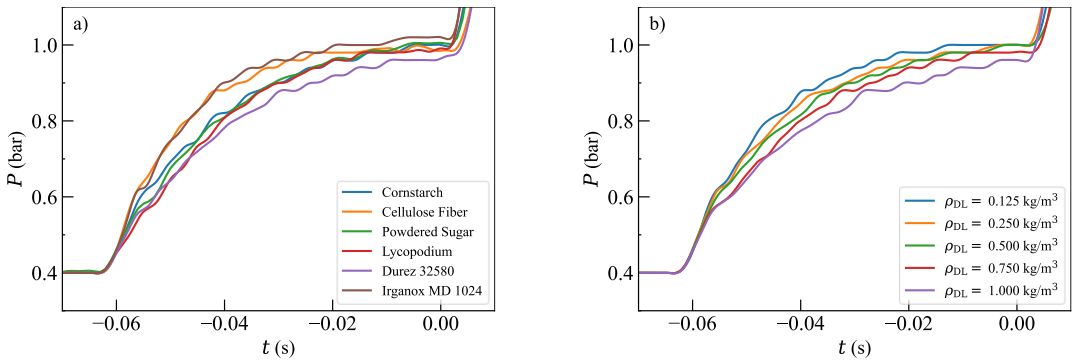

Fig. 2. *Comparison of injection profiles from the 20-L sphere, (a) across different dusts with* $\rho_{DL} = 0.75$ *kg/m*^{3}*, and (b) across different dust loadings for Durez 32580.*

1.2. Large-scale 2.42-m^3 test apparatus

A total of 155 tests were performed in a 2.42-m^3 vessel with a height to diameter ratio of 1.45, as shown in Fig. 3a. Unlike the standard 20-L tests, where a single 60-ms ignition delay is used, the ignition delay between dust injection and ignition was varied to produce different levels of initial turbulence in this setup. To provide a uniform comparison between different dusts and dust loadings at a given ignition delay, a new dual-air cannon dust injection system developed to eliminate these effects.

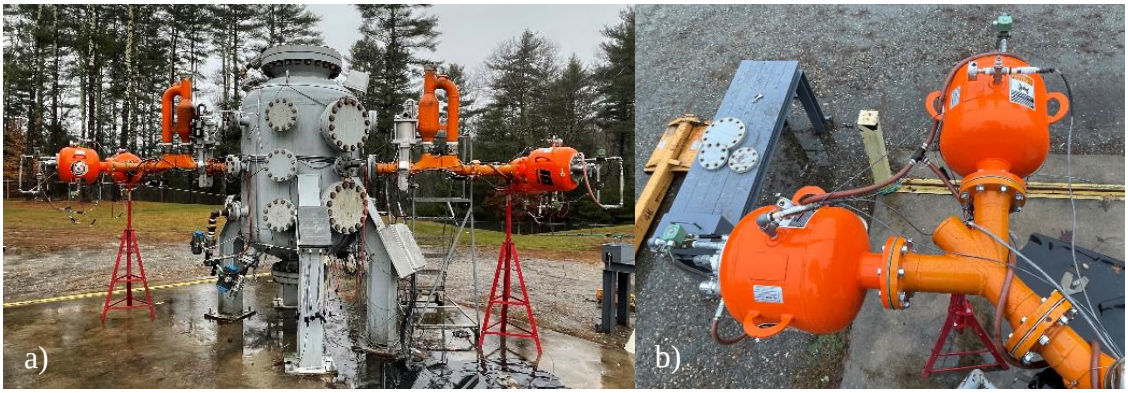

Fig. 3. *Photographs showing (a) the 2.42-m^3 test vessel setup and (b) the dual air cannon configuration.*

1.2.1. Dust injection system

Dust was injected into the vessel immediately prior to ignition using two counterflow injection systems, each comprised of two air cannons, a sealed dust hopper, an explosion isolation valve, and an internal dispersion nozzle. For each injector, two Martin® Hurricane 35-L air cannons, Fig. 3b, pressurized to 8.3 bar (gauge), were used to independently inject dust and generate turbulence. These air cannons were timed to fire in series with a prescribed 1.0-second delay, such that the first cannon fully dispersed the dust into the vessel before the second cannon injected air to generate the initial turbulence.

This dual air cannon arrangement was found to significantly reduce the variability in air injection times, relative to a single cannon, from a variation of 75 ms between the different dusts examined, Fig. 4a, for a dust loading $\rho_{\mathrm{DL}} = 0.5$ kg/m^3, to less than 5 ms, Fig. 4b. This variability in injection time was significant, since the range of ignition delays used in this test vessel was only on the order of 200 – 400 ms. It can be noted that the dusts that injected fastest in the 20-L sphere, cellulose fiber and Iraganox MD 1024, ultimately injected the fastest in the 2.42-m^3 system, and that the dust that injected the slowest in the 20-L sphere, Durez 32850, was also the slowest to inject in the 2.42-m^3 setup.

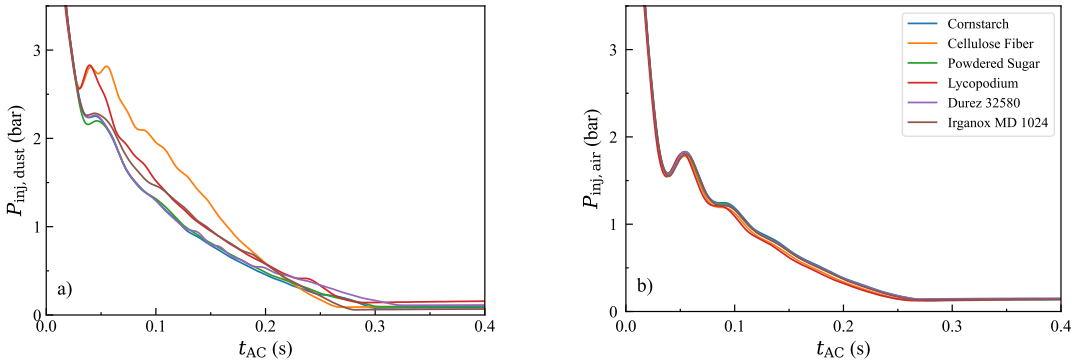

Fig. 4. *Comparison of dust injection profiles (a) and air injection profiles (b) from the dual air cannon injection system in the 2.42-m^3 vessel sphere, across the different dusts with $\rho_{DL} = 0.75$ kg/m^3.*

1.2.2. Test procedure

Prior to each test, the hoppers were loaded with a prescribed mass of dust, m_d, to achieve the target dust loading, ρ_{DL}. Next, the vessel was evacuated to a specified pressure, ~ 0.5 bar, that was varied slightly to account for initial gas temperature in order to produce an initial pressure, P_0, of 1.00 ± 0.02 bar following dust and air injection. A timed sequence, with an accuracy on the order of 1 ms, was used to trigger the ignition system after a prescribed ignition delay, t_{ign}, measured from the firing of the air cannons used for turbulence generation.

In these experiments, the mixture was ignited at the center of the vessel by two 5-kJ Sobbe EBBOS ChZ pyrotechnic ignitors. Internal pressure was measured at three vertical locations within the vessel, using Kistler 4260A 0-10 bar piezoresistive pressure transducers sampled at a rate of 20 kHz.

1.3. Dusts examined

In this study, six dusts were examined in both the 20-L sphere and 2.42-m^3 vessel, selected to cover a wide range of material properties, including bulk density, ρ_{bulk}, melting point, T_{melt}, and median particle size, d_{50}, as shown in Table 1. Values for K_{St} were those obtained using the 20-L sphere, in accordance with ASTM E 1226, and values for d_{50} were obtained from external laboratory testing using a Malvern MS 3000 particle analyzer.

Table 1. *Properties of the dusts examined.*

Dust	**Type**	**K_{St} (bar m/s)**	**ρ_{bulk} (kg/m^3)**	**T_{melt} (°K)**	**d_{50} (µm)**
Cornstarch	Food material	160	610	530	13.6
Cellulose fiber	Building insulation	75	140	538	74.1
Powdered sugar	Food material	57	657	458	17.0
Lycopodium	Theatrical pyrotechnic	141	320	-	29.8
Durez 32580	Phenolic resin	198	433	367	14.9
Irganox MD 1024	Phenolic antioxidant	268	350	502	68*

*d_{50} for Irganox MD 1024 was obtained from sieve analysis.

The dusts examined in this study cover a wide range of sizes and morphologies, as illustrated by SEM imaging shown in Fig. 5. The cellulose fiber and Irganox MD 1024 dusts had the largest overall size, with high aspect ratios. The Durez 32580 and powdered sugar samples both exhibited relatively wide particle sizes distributions, which were roughly equivalent to one another. Both cornstarch and

lycopodium samples had narrow particle size distributions, with the lycopodium being larger, and more consistent in size.

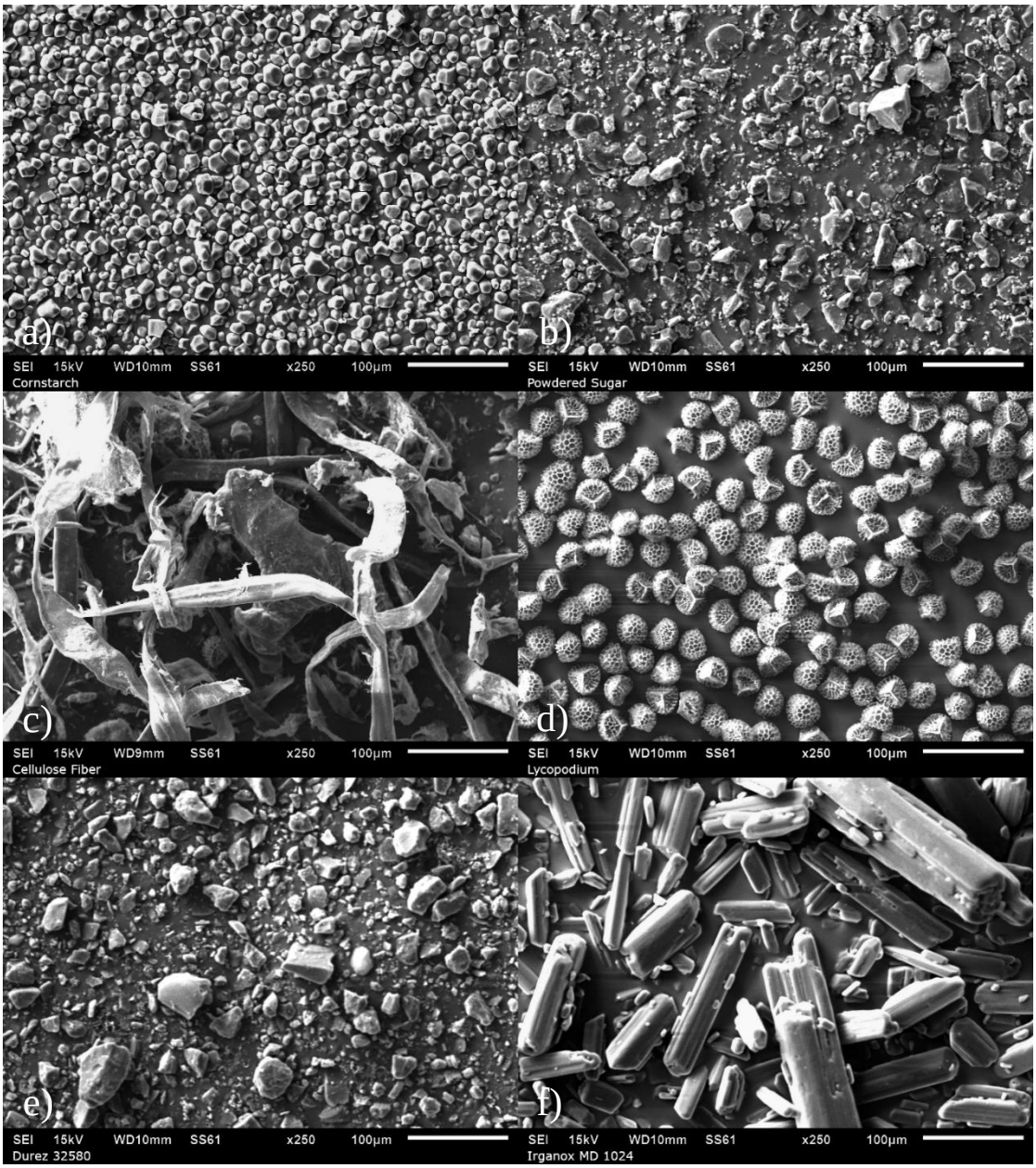

Fig. 5. *Scanning Electron Microscope (SEM) images of the six dusts a) cornstarch, b) powdered sugar, c) cellulose fiber, d) lycopodium, e) Durez 32580, f) Irganox MD 1024, at 250x magnification.*

2. Dust reactivity model

In addition to the use of K_{eff} to characterize the reactivity of an individual dust explosion, a recently developed two-parameter model (Bauwens et al., 2020, 2022) was used to compare the 20-L and 2.42-m^3 results. This model provides a comprehensive characterization of dust reactivity, considering the entire pressure time-history of an explosion event, rather than just the time of maximum pressure rise. An abbreviated description of the model is provided in this section.

The two-parameter dust combustion model approximates turbulent dust-flame propagation by using two simple assumptions. First, the dust within the flame region is consumed over a finite time. The model assumes that the propagation of the leading edge of the flame front is governed by turbulent mixing, which entrains a mixture of unburned dust/air into the flame region. Within this region,

characterized by an effective flame radius, r_f, the unburned mixture is not consumed instantaneously, and a mixture of burned and unburned dust is present. As the optimal dust concentration that maximizes the severity of a dust explosion is heavily fuel-rich, the reaction time within the flame region is modeled by considering the consumption rate of the oxidizer using a simple mass balance. The general model formulation is similar to that proposed by Tamanini, 1993.

The model is derived considering mass and energy conservation, consistent with previously developed models for gaseous flames (Chao et al., 2015, Boeck et al., 2021), where the rate of combustion is evaluated on a mass basis. The mass fraction of oxidizer is split into three quantities that are individually tracked: the unburned fraction upstream of the flame, x_u; the unburned fraction within the flame region, $x_{f,u}$; and the burned fraction that has been consumed within the flame region, $x_{f,b}$. As the total mass of oxidizer is conserved in a closed volume, the overall mass balance is given by:

$$1 = x_u + x_{f,u} + x_{f,b}, \tag{2}$$

and the internal state of the vessel can be expressed exclusively in terms of x_u and $x_{f,b}$.

Assuming spherical flame propagation, the rate unburned mass enters the flame region is given by:

$$\frac{dx_u}{dt} = -\frac{3r_f^2 S_T \rho_u^*}{R^3}, \tag{3}$$

where S_T is the turbulent propagation velocity of the leading edge of the flame, ρ_u^* is the gas density of the oxidizer in the unburned region, normalized by the initial gas density, and R is the effective radius of the vessel, $R = (3V/4\pi)^{1/3}$. The propagation velocity of the leading edge of the flame is assumed to be governed by turbulent mixing at the scale of the flame radius and is proportional to the turbulent fluctuation velocity at this scale. For a Kolmogorov cascade, this yields an increase of S_T with flame radius due to the increased range of turbulent length scales present as the flame grows:

$$S_T = S_{T,R}\left(\frac{r_f}{R}\right)^{1/3}, \tag{4}$$

where $S_{T,R}$ represents a characteristic turbulent burning velocity when $r_f = R$, and depends on the level of initial turbulence and the rate of thermal expansion of the dust flame.

For conditions typically present in a dust explosion, it can be shown that both the Taylor and Kolmogorov scales of turbulence significantly exceed the dust particle radii, and the local transport of fuel and oxidizer in the vicinity of the particle are in the laminar regime. As a result, it is assumed that the consumption rate of the oxidizer is governed by molecular diffusion and this rate is proportional to both the dust concentration and the molecular diffusion coefficient:

$$\frac{dx_{f,b}}{dt} = \frac{1}{\tau}\frac{T_f^{*1.75}}{P^*}\left(1 - \frac{x_{f,b}}{1-x_u}\right), \tag{5}$$

where τ is the characteristic consumption time of oxidizer in the flame region; $P^* = P/P_0$, the internal pressure of the vessel, P, normalized by the initial pressure, P_0; and $T_f^* = T_f/T_0$, the average temperature within the flame region, T_f, normalized by the initial temperature, T_0. It was found that the ratio between a characteristic flame propagation time, $R/S_{T,R}$, and the characteristic consumption time, τ, provides a dimensionless property, χ, that characterizes the pressure at which the maximum rate of pressure rise occurs, as shown in Fig. 6.

Using this model, the entire dust explosion process can be effectively characterized by the parameters $S_{T,R}$ and χ. Previous studies (Bauwens et al., 2020, 2022) have found that χ is relatively constant over a wide range of dust loadings, ignition delays, and vessel volumes, and appears to be a property of the dust.

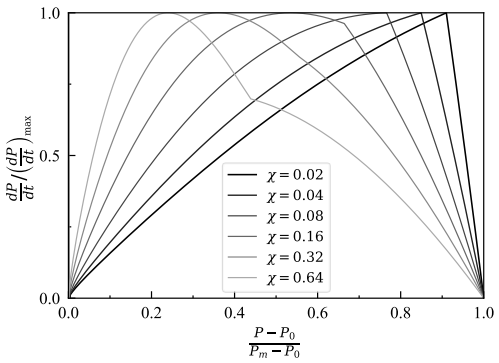

Fig. 6. *Generalized model results as a function of normalized pressure over a range of the dimensionless parameter, χ (Bauwens et al., 2022).*

Values of χ and $S_{T,R}$ are obtained for each individual experiment using an automated fitting routine. For each test, the experimental data were normalized and resampled in dimensionless terms, equivalent to that shown in Fig. 6, and the fitting routine obtains the value of χ that minimizes the absolute difference between the normalized results. The routine then finds a best fit value for $S_{T,R}$ through a comparison of the rate of pressure rise in dimensional terms. Using this methodology, values of $S_{T,R}$ and χ can be fit to the experimental pressure time-history of each test in an unbiased and unambiguous manner.

2.1. Model performance

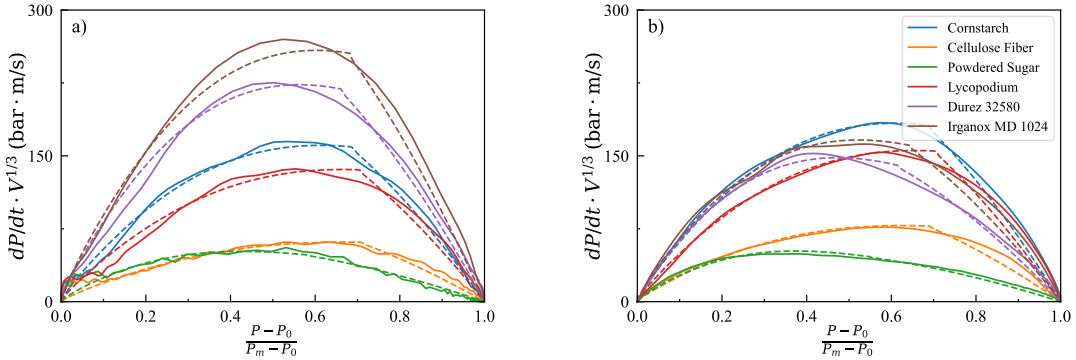

Fig. 7. *Experimental (solid) and modeled (dashed) rate of dimensionless pressure rise for representative experiments performed in a) the 20-L sphere and b) the 2.42-m^3 vessel.*

Figure 7 illustrates the overall quality of the model fits across a series of representative tests performed in the 20-L sphere and the 2.42-m^3 vessel for the optimal dust loading to maximize K_{St} for each dust, with an ignition delay of 330 ms in the large-scale tests. This figure shows that the two-parameter model accurately reproduces dP/dt throughout the entire combustion process for both the 20-L and 2.42-m^3 results. The figure also illustrates how the different dusts exhibit a maximum rate of pressure rise at different dimensionless pressures. When comparing the results between the 20-L sphere and the 2.42-m^3 vessel, it is clear that the maximum rate of pressure rise, normalized by $V^{1/3}$, is significantly different for some of the dusts, and these differences will be discussed in Section 3.

A comparison of pressure as a function of time, in dimensional terms, is shown in Fig. 8, where the model results were shifted in time to match the experiments in order to account for any variability in the initial flame propagation due to ignition effects. Overall, these curves also demonstrate the ability of the model to capture the pressure profile throughout the explosion event for both the 20-L sphere and 2.42-m^3 vessel. In general, only a slight deviation in pressure can be seen at later times. This is likely due, in part, to heat loss effects when the flame front reaches the vessel walls, which is not considered by the model but is clearly evident in the experimental results, where the pressures decrease after achieving a maximum value.

It is interesting to note that the early pressure rise is much closer together in time in the 20-L sphere results, likely due to the strong ignition source relative to the size of the vessel. This is most noticeable for the powdered sugar results, which shift considerably relative to the other dusts.

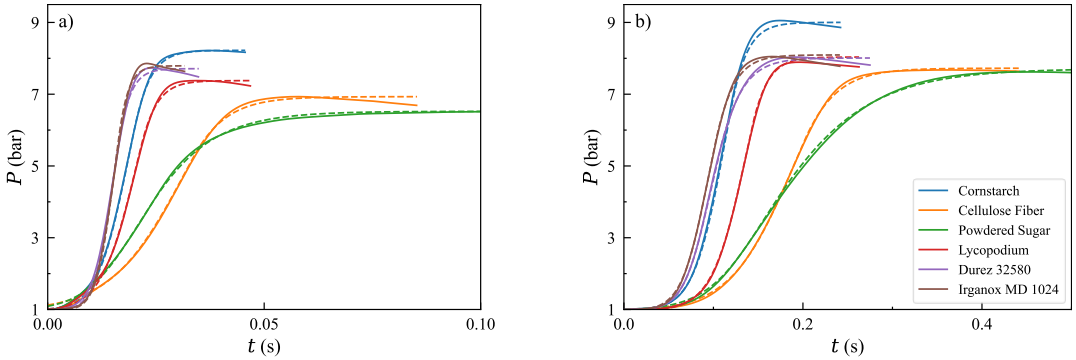

Fig. 8. *Experimental (solid) and modeled (dashed) pressure as a function of time for representative experiments performed in a) the 20-L sphere and b) the 2.42-m^3 vessel.*

2.2. Applicability of the two-parameter dust reactivity model to the 20-L sphere configuration

It should be noted that the model formulation considers a point source ignition at the center of the vessel, and spherical flame propagation. In the 20-L sphere, the strong ignition source relative to the vessel volume is likely a significant departure from this assumption. The observation that the model can reproduce the 20-L sphere results is interesting and was unexpected. A possible explanation is that the strong ignition source provides a large number of ignition kernels that are distributed throughout the vessel volume. The model can be readily modified to consider spherical flame propagation from an arbitrary number of evenly spaced ignition kernels. To consider this assumption, Eq. (3) simply becomes:

$$\frac{dx_{\mathrm{u}}}{dt} = -\frac{3r_{\mathrm{f}}^2 N S_{\mathrm{T}} \rho_{\mathrm{u}}^*}{R_N^3}, \tag{6}$$

where N is the number of ignition kernels and R_N is roughly half of the average spacing between kernels. The rest of the model is largely unaffected by this change, except that the value of the turbulent propagation velocity, $S_{\mathrm{T},R}$, develops a very weak dependence with N, becoming $S_{\mathrm{T},R} = S_{T,R_N} \cdot N^{1/9}$, where S_{T,R_N} is the local propagation velocity of each kernel. The value of N could potentially be determined through a comparison of 20-L sphere tests performed with a spark ignition source with tests performed with the standard chemical ignitors, however, this is outside the scope of the present study.

Ultimately, since the level of initial turbulence in large-scale tests are typically calibrated by tuning the ignition delay, rather than directly matching a turbulence intensity, the use of an effective value of $S_{\mathrm{T},R}$ that assumes a point source ignition does not necessarily create a problem with interpreting the results. Nevertheless, it is likely that the strong ignition source is responsible for at least some of the differences between the 20-L sphere and 2.42-m^3 results presented in Section 3.

3. Results and discussion

Figure 9 shows how the various reactivity parameters examined vary with ρ_{DL} for the standard ignition delay of 60 ms in the 20-L sphere and a 330-ms ignition delay in the 2.42-m^3 vessel. For each point, a minimum of three tests were performed and the standard deviation of these points are presented as uncertainty bars. As the 20-L sphere test procedure followed the standard ASTM E 1226 protocol, only the three ρ_{DL} producing the highest values of K_{eff} were evaluated. A wider range of tests are included for the 2.42-m^3 tests.

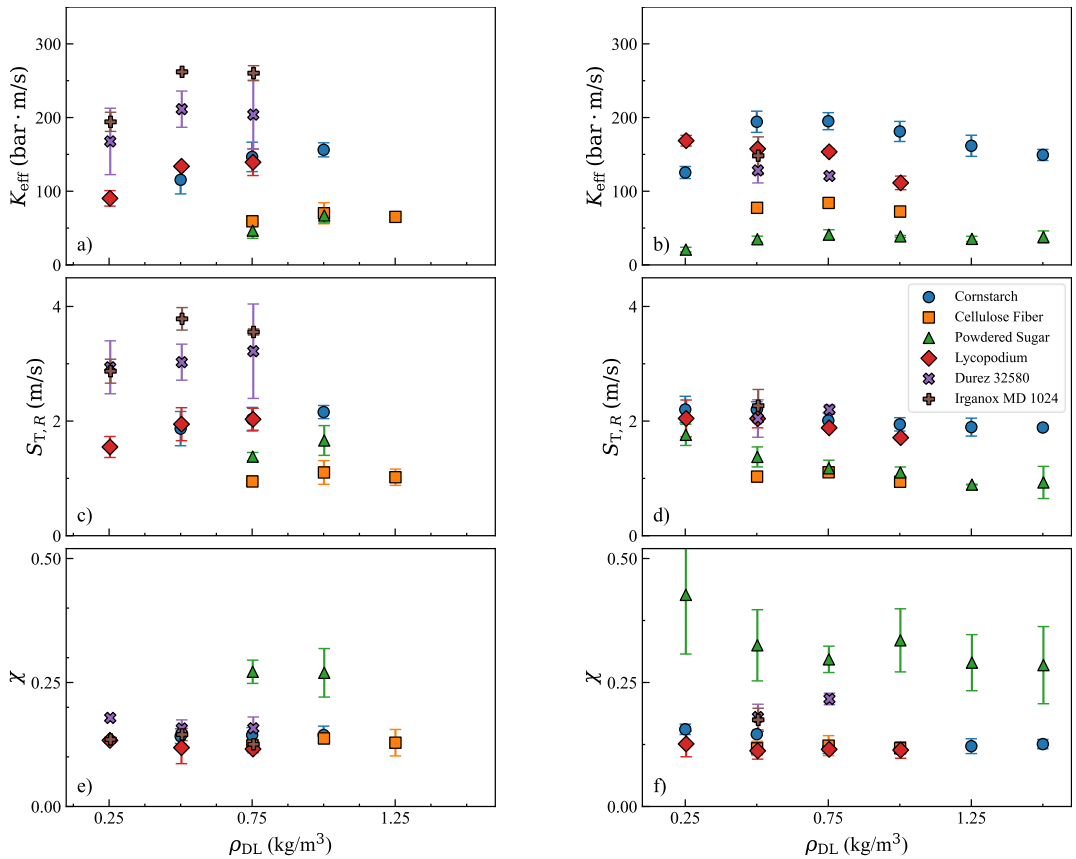

Fig. 9. *Variation of K_{eff}, $S_{T,R}$, and χ with ρ_{DL} in the 20-L sphere and the 2.42-m^3 vessel.*

Considering the results for K_{eff}, Figs 9a and 9b, it can be clearly seen that the relative ranking of the dusts is not preserved between the two test setups. Irganox MD 1024 and Durez 32580 produced the maximum values of K_{eff} in the 20-L sphere, while cornstarch was the most reactive dust in the 2.42-m^3 vessel. Aside from the Irganox MD 1024 and Durez 32580 results, the relative ranking of the remaining four dusts do appear to roughly correspond to the same relative ranking between both test setups.

When examining the variation of $S_{T,R}$ between the different dusts, Figs 9c and 9d, a similar trend is observed, where $S_{T,R}$ for Irganox MD 1024 and Durez 32580 are significantly higher in the 20-L sphere, relative to the 2.42-m^3 vessel. The relative ranking of the dusts appears to be closer, however, with some consistency between both setups. For χ, Figs 9e and 9f, it can be seen that the values are relatively consistent across the different dusts between the 2.42-m^3 vessel, and the 20-L sphere, however, χ is slightly lower for Durez 32580 and Irganox MD 1024 in the 20-L sphere.

When the 2.42-m^3 results for K_{eff} are normalized by the overall value of K_{St} obtained in the 20-L sphere, Fig 10a, two rough groupings of results are clearly visible. If the relative rankings of K_{St} obtained in the 20-L sphere was consistent with the 2.42-m^3 vessel results, then at some ignition delay all of the points should have collapsed to a value of one. Instead, we see that the cornstarch, cellulose fiber, and lycopodium results appear to collapse to a value of one at an ignition delay of 400 ms, while the Durez 32580, Irganox MD 1024, and powdered sugar results collapse to a value of one at an ignition delay of 200 ms. It is interesting to note that these two groups correspond to dusts with lower values of χ, and dusts with higher values of χ.

When comparing χ between the two test setups, Fig 10b, it can be seen that, with the exception of Irganox MD 1024, the values of χ obtained at each scale are within the standard deviation of the measurements. This suggests that the 20-L sphere data may provide some indication of the large-scale χ values of the dusts. For the Irganox MD 1024 results, it is unclear why the 20-L sphere produces a lower value of χ. One possible explanation is that the dispersion of dust through the

rebound nozzle in the 20-L sphere could be affecting the particle size distribution. Further research is planned to examine the variation of χ for a single dust over a range of particle size distributions.

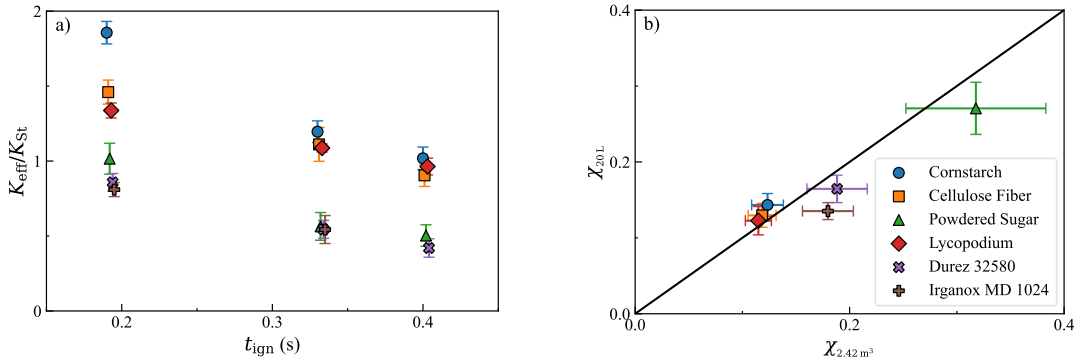

Fig. 10. *Plots of a) the ratio of K_{eff}, measured in the 2.42-m^3 vessel, and K_{St}, obtained from the 20-L sphere, as a function of ignition delay in the 2.42-m^3 vessel and b) a comparison between average χ values obtained in the 20-L sphere and 2.42-m^3 vessel.*

4. Summary and conclusions

In this work, the reactivity of six dusts were evaluated in the standard ASTM E 1226 20-L sphere and were compared with large-scale experiments performed in a 2.42-m^3 vessel. It was found that, in terms of the deflagration index, K_{St}, the relative ranking of dust reactivity varied significantly between the 20-L sphere and the 2.42-m^3 vessel. When the test results were examined using a previously developed two-parameter dust reactivity model, it was found that the model could characterize both the 20-L and 2.42-m^3 experimental setups. It was also found that dusts with higher χ parameters, which produced higher rates of pressure rise earlier in the process, behaved like one another, and the relative ranking of K_{St} was preserved between the two test setups. Furthermore, dusts with lower values of χ also behaved similarly to one another. The main discrepancy between the 20-L and 2.42-m^3 results was due to a shift between these two groups, where dusts with higher χ appear to be less reactive at large-scale than would be indicated by the 20-L sphere results. Further work is needed to determine what parameters control χ, and the minimum vessel volume required to produce representative dust reactivities at large-scale.

Acknowledgements

The work presented in this paper was funded by FM Global and performed within the framework of the FM Global Strategic Research Program on Explosions and Material Reactivity. The technical assistance of Kevin Mullins, Thomas Lapierre, and Joseph Marte in preparing and conducting the tests is greatly appreciated.

References

Amyotte, P.R., Chippett, S. and Pegg, M.J., 1988. Effects of turbulence on dust explosions. Progress in Energy and Combustion Science, 14(4), pp.293-310.

ASTM E 1226, 2020. Standard Test Method for Explosibility of Dust Clouds.

Bartknecht, W., 1989. Explosions-course, prevention, protection, Springer, New York.

Bauwens, C.R., Boeck, L.R., & Dorofeev, S.B., 2020. A simple dust combustion model for characterizing reactivity in large-scale experiments. 13th ISHPMIE, Braunschweig, Germany.

Bauwens, C.R., Boeck, L.R., & Dorofeev, S.B., 2022. Characterizing the Reactivity of Large-Scale Dust Explosions Using a Dimensionless Two-Parameter Combustion Model. 14th ISHPMIE, Braunschweig, Germany.

Boeck, L.R., Bauwens, C.R. and Dorofeev, S.B., 2021. Modeling of explosion dynamics in vessel-pipe systems to evaluate the performance of explosion isolation systems. Journal of Loss Prevention in the Process Industries, 71, p.104477.

Bradley, D., Chen, Z. and Swithenbank, J.R., 1989, January. Burning rates in turbulent fine dust-air explosions. In Symposium (International) on Combustion (Vol. 22, No. 1, pp. 1767-1775). Elsevier.

Cesana AG, 2016. KSEP 7.1 Manual for 20L Apparatus.

Chao, J., Lee, J.H., Bauwens, C.R. and Dorofeev, S.B., 2015. Laminar burning velocities of various silanes. Journal of Loss Prevention in the Process Industries, 36, pp.471-477.

Di Benedetto, A., Russo, P., Amyotte, P. and Marchand, N., 2010. Modelling the effect of particle size on dust explosions. Chemical Engineering Science, 65(2), pp.772-779.

Eckhoff, R.K., 2003. Dust explosions in the process industries, Third edition, Gulf Professional Publishing, Amsterdam.

Eckhoff, R.K., 2015. Scaling of dust explosion violence from laboratory scale to full industrial scale–A challenging case history from the past. Journal of Loss Prevention in the Process Industries, 36, pp.271-280.

Goroshin, S., Fomenko, I. and Lee, J.H.S., 1996. Burning velocities in fuel-rich aluminum dust clouds. In Symposium (International) on Combustion (Vol. 26, No. 2, pp. 1961-1967).

Julien, P., Vickery, J., Goroshin, S., Frost, D.L. and Bergthorson, J.M., 2015. Freely-propagating flames in aluminum dust clouds. Combustion and Flame, 162(11), pp.4241-4253.

Proust, C., Accorsi, A. and Dupont, L., 2007. Measuring the violence of dust explosions with the “20 l sphere” and with the standard “ISO 1 m3 vessel”: Systematic comparison and analysis of the discrepancies. Journal of Loss Prevention in the Process Industries, 20(4-6), pp.599-606.

Skjold, T., 2003. Selected aspects of turbulence and combustion in 20-litre explosion vessels: development of experimental apparatus and experimental investigation (Master's thesis, The University of Bergen).

Tamanini, F., 1993. Characterization of mixture reactivity in vented explosions. 14th International Colloquium on the Dynamics of Explosions and Reactive Systems (pp. 1-6). Coimbra, Portugal: University of Coimbra.

Tamanini, F., 1998. The role of turbulence in dust explosions. Journal of loss prevention in the process industries, 11(1), pp.1-10.

Van Wingerden, K., Stavseng, L. and Bergen, N., 1996. Measurements of the laminar burning velocities in dust-air mixtures. VDI-Berichte, 1272, pp.553-564.

Advances in Hydrogen Storage Technologies

Vladimir Molkov

Hydrogen Safety Engineering and Research Centre (HySAFER), Ulster University, Jordanstown, Shore Road, Newtownabbey, BT37 0NL, Northern Ireland, UK

E-mail: v.molkov@ulster.ac.uk

Abstract

Gaseous hydrogen storage is the most mature technology for fuel cell vehicles. The main safety concern is the catastrophic consequences of tank rupture in a fire, i.e. blast waves, fireballs, and projectiles. This paper summarises research on the development and validation of the breakthrough microleaks-no-burst (μLNB) safety technology of explosion-free in any fire self-venting Type IV tanks that do not require a thermally-activate pressure relief device (TPRD). The invention implies the melting of the hydrogen-tight liner of the Type IV tank before the hydrogen-leaky double-composite wall loses load-bearing ability. Hydrogen then flows through the natural microchannels in the composites and burns in microflames or together with resin. The unattainable to competitive products feature of the technology is the ability to withstand any fire from smouldering to extreme impinging hydrogen jet fires. Innovative 70 MPa tanks made of carbon-carbon, carbon-glass, and carbon-basalt composites were tested in characteristic for gasoline/diesel spill fires with a specific heat release rate of HRR/A=1 MW/m^2. Standard unprotected Type III and IV tanks will explode in such intensity fire. The technology excludes hydrogen accumulation in naturally ventilated enclosures. It reduces the risk of hydrogen vehicles to an acceptable level below that of fossil fuel cars, including underground parking, tunnels, etc. The performance of self-venting tanks is studied for fire intervention scenarios: removal from fire and fire extinction by water. It is concluded that novel tanks allow standard fire intervention strategies and tactics. Self-venting operation of the 70 MPa tank is demonstrated in extreme jet fire conditions under impinging hydrogen jet fire (70 MPa) with huge HRR/A=19.5 MW/m^2. This technology excludes tank rupture in fires onboard trains, ships, and planes, where hazard distances cannot be implemented, i.e. provides an unprecedented level of life safety and property protection.

Keywords: *hydrogen safety, composite hydrogen storage tank, microleaks-no-burst technology, self-venting (TPRD-less) tank, intervention strategies and tactics, fire test, hydrogen impinging jet fire*

Introduction

The rupture of high-pressure hydrogen storage tanks must be excluded in any fire to eliminate hazards and associated risks from blast waves, fireballs, and projectiles at an incident scene. This would reduce the risk of hydrogen cars, trains, plains, and maritime vessels below that of fossil fuel vehicles. The use of an explosion-free in fire self-venting tank without thermally-activated pressure relief devices (TPRD) provides an unprecedented level of life safety, property, and environment protection.

The technology does not require TPRD which is known to be unreliable in localised fires. The European FireComp project suggests a 50% TPRD failure probability in localised fires. The explosions of CNG composite tanks equipped with TPRDs were reported in the USA. The catastrophic failure of a tank with TPRD is possible even in an engulfing fire, e.g., with conformable tanks. Indeed, the time to rupture such tanks with thinner walls (due to decreased diameter) in a fire is about 2 min. This is comparable to or even shorter than TPRD activation time in a fire (reported TPRD activation time is up to 3.5 min in an engulfing fire (Molkov et al., 2024). The innovative safety technology provides the microleaks-no-burst (μLNB) performance of Type IV tanks in a fire.

There is a range of fire scenarios. They extend from low-temperature smouldering fires, through the vehicle tyre fires and gasoline/diesel fires, to severe scenarios of impinging hydrogen jet fires, e.g. from nearby storage tanks. Self-venting tanks demonstrate their safe performance in fires of different intensities up to a specific heat release rate of HRR/A=19.5 MW/m^2, which any standard tank cannot withstand. Protection of tanks by intumescent pain is thought cannot protect them from rupture in such high-intensity hydrogen jet fire with momentum jet able to erode the paint.

The quantitative risk assessment (QRA) of scenarios with onboard tank rupture in a fire for hydrogen-powered vehicle incidents in the open atmosphere (Dadashzadeh et al., 2018) and in the tunnels (Kashkarov et al., 2022) was carried out. It is shown that the risk is unacceptably high for currently used standard tanks with the fire resistance ratings (FRR), i.e. time to rupture in a fire, of a few minutes, e.g., 4-6 min in typical for traffic incidents gasoline/diesel spill fires with specific heat release rate of HRR/A=1-2 MW/m^2. To achieve an acceptable level of risk the FRR of the compressed hydrogen storage system (CHSS) should exceed, for example, 50 min for London roads and 90 min for the Dublin tunnel, respectively. The situation in real-life conditions is aggravated by the fact that the GTR#13 fire test protocol (UN ECE, 2023) has reduced localised fire intensity of HRR/A=0.3 MW/m^2, and engulfing fire intensity of 0.7 MW/m^2, i.e. below HRR/A=1-2 MW/m^2 characteristic for gasoline/diesel spill fires.

This paper summarises the results of research carried out in the last decade and the conclusions of a recent series of our three papers published in 2023-2024. The detailed concept and initial experimental validations of the technology for several carbon-carbon and carbon-glass double-composite wall μLNB tank prototypes of nominal working pressure NWP=70 MPa and 7.5 L volume are described in our first paper (Molkov et al., 2023a). The second paper in a series (Molkov et al., 2024) is focused on experimental validation of μLNB tank performance in conditions of fire intervention. The third in a series paper (Molkov et al., 2023b) proved an extraordinary safety performance of self-venting (TPRD-less) tanks in extreme conditions of impinging hydrogen jet fire from 70 MPa storage with a specific heat release rate of HRR/A=19.5 MW/m^2.

1. The safety issue of the standard fire test for hydrogen storage in composite tanks

The FRR is defined as a time to rupture in a fire for a storage tank or CHSS with failed to be activated TPRD, e.g., in smouldering or localised fire, or TPRD blocked in incident from a fire. Figure 1 shows the results of previous studies on the dependence of FRR as a function of HRR/A (thick blue strip).

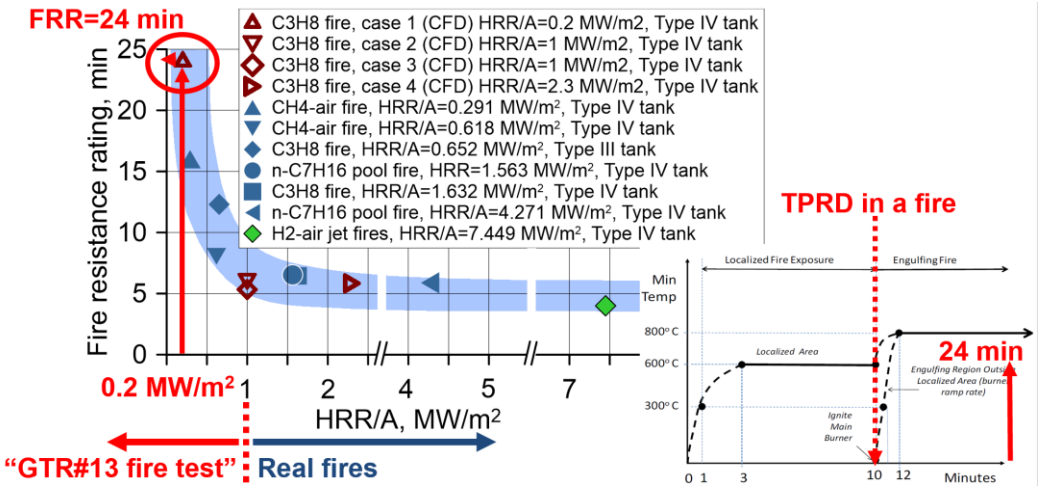

Fig. 1. *Dependence of FRR on HRR/A demonstrating that in a fire of low-intensity HRR/A=0.2 MW/m^2 the FRR is 24 min, i.e., longer than the localised fire duration of 10 min (Molkov et al., 2024)*

The FRR decreases with HRR/A and is practically constant for HRR/A≥1-2 MW/m^2. Regulation GTR#13 (UN ECE, 2023) requires fire testing of CHSS following the protocol. Unfortunately, the prescribed by regulation values of HRR/A are below of many real fires such as gasoline/diesel spill

fires and impinging hydrogen jet fires. The reason is as follows. Figure 1 demonstrates that lower intensity fire, e.g. HRR/A=0.2 MW/m^2, would provide FRR=24 min. This is longer than the duration of localised fire of 10 min and thus, after switching to the engulfing fire stage of the fire test, there is sufficient time for initiation of TPRD that would allow to pass the fire test without rupture.

The situation changes drastically if the same tank is in a fire of higher intensity, e.g., a gasoline/diesel spill fire of HRR/A=1-2 MW/m^2. Figure 2 shows that in such fire the tank could rupture in 5-6 min, i.e., before the TPRD is affected by the engulfing fire (see the insert at the bottom right corner of Figure 2). This creates unacceptable hazards and risks for life and property in high-intensity fires. Thus, the fire test protocol of GTR#13 could have serious real-life safety implications, especially for the first responders, and must be amended to include fires of lower (smouldering) and higher intensity.

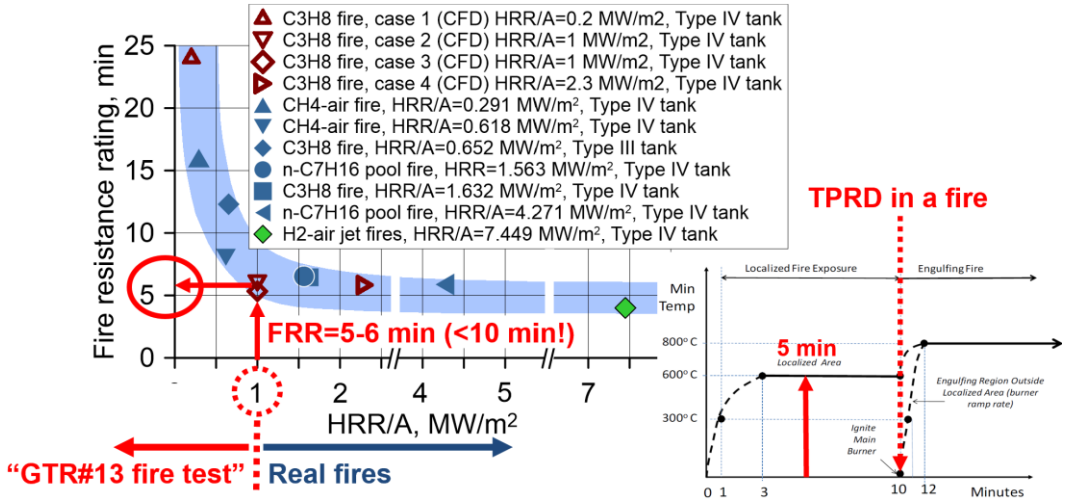

Fig. 2. *Dependence of FRR on HRR/A demonstrating that in a fire of intensity of HRR/A=1 MW/m^2 the FRR is 5-6 min, i.e. shorter than the localised fire duration of 10 min (Molkov et al., 2024)*

This analysis demonstrates that the fire test protocol of GTR#13 should be changed to include fires of any intensity to underpin the safety of hydrogen storage tanks in real-life conditions such as spill fires of fossil fuel during a traffic incident or impinging jet fire from hydrogen storage tank nearby.

2. The concept of self-venting (TPRD-less) tanks

The technology of self-venting tanks is the intellectual property (IP) of Ulster University (Molkov et al., 2018). Fig. **3** shows the structure of the µLNB Type IV tank and its performance in a fire.

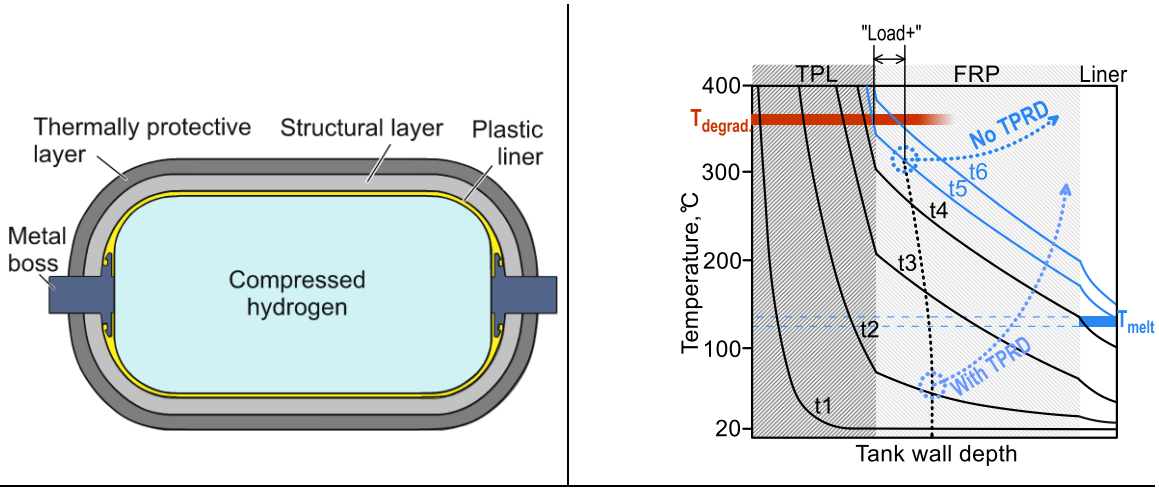

Fig. 3. *Left: Structure of µLNB tank. Right: Performance of µLNB tank in fire (Molkov et al., 2023a)*

Figure 3 (left) shows that a self-venting tank consists of a plastic liner (yellow colour), metal bosses (dark blue colour), the structural fibre-reinforced polymer layer (FRP, light grey colour), and the outside thermal protection layer (TPL, dark grey colour) with lower heat conductivity or intumescent paint layer. The use of intumescent paint has disadvantages. It would require an excessive amount of protection material which implies an increase in tank size, weight, and cost of a CHSS. The wear resistance of intumescent paint to refuelling cycling and weather operating conditions is not reported and can be unacceptable. Finally, likely, it would not stand high-momentum hydrogen impinging fire.

Figure 3 (right) demonstrates the tank wall depth (x-axis) and the temperature distribution through the wall (y-axis) for six different moments (a detailed explanation can be found in Molkov et al., 2023a). On the left-hand side of the TPL, the heat flux from a fire is applied. On the right-hand side, the liner is in contact with compressed hydrogen. The liner limits hydrogen permeation to the regulated level and is not a load-bearing layer. The TPL and FRP are not hydrogen-tight. The liner must melt at least in one location through its entire thickness to initiate hydrogen leak through the wall's naturally existing microchannels. The double-composite wall keeps its load-bearing ability before the liner melts. The black and blue curves descending from the left to the right across the wall are the temperatures. The elevation of the curve at each next moment demonstrates the temperature increase. The temperature range corresponding to the resin decomposition temperature is shown with the red horizontal stripe. The temperature range covering the melting of the liner lies significantly lower than and is denoted by the blue horizontal stripe. The difference between the actual non-degraded composite wall thickness and the minimum wall thickness required to bear the increasing in fire pressure load at the moment when the liner melts is named “Load+” (distance between red stripe and the location of minimum load-bearing wall thickness shown by black dotted curve in Figure 3, right). The wall thickness fraction that is sufficient to bear the load, and its relationship with the safety factor, i.e. the ratio of the actual burst pressure to the NWP regulated as 2.20-2.25. The composite wall thickness fraction that can bear the load (black dotted curve) “bends” to the left in time due to increasing in fire pressure inside the tank. Once the microleaks are initiated after the liner melts, the pressure in the tank starts dropping until it is equal to the atmospheric pressure. It is represented with the blue dotted curve labelled “No TPRD” bending to the right. This means that the minimum wall thickness fraction needed to bear the hydrogen pressure load without tank rupture decreases quickly following the pressure drop as the result of microleaks. The curve labelled “With TPRD” shows the decrease of the load-bearing wall thickness fraction in the case when there is a TPRD installed on the tank. The TPRD could be installed on the μLNB tank if wanted, yet it could have a significantly smaller release orifice compared to TPRD on a standard tank to eliminate problems with release in confined space, e.g. the pressure peaking phenomenon. The TPRD is initiated at the time “t2” (Figure 3, right). This, however, is not the case for a localised or smouldering fire affecting the composite wall, but not the sensing element of TPRD.

3. The first validation of the technology for carbon-carbon and carbon-glass systems

The first series of self-venting tank prototypes was designed using a “carbon-carbon” (CC) combination of composites (Molkov et al., 2023a). Two carbon fibres of different thermophysical and mechanical properties were used. They had different fibre/resin ratios. Four prototypes of composite overwrapped pressure vessels (COPV) with the same high-density polyethylene (HDPE) liner were fire-tested (see ***Table 1***). Prototype COPV#CC-4 had a wall thickness of the original tank.

Table 1. *Parameters of a series of μLNB tanks with carbon-carbon fibre combination*

Tank No.	Liner	Layer No.1	Layer No.2	Outside D increase
COPV#CC-1	HDPE	CFRP#1	CFRP#2	1.3%
COPV#CC-2	HDPE	CFRP#1	CFRP#2	0.3%
COPV#CC-3	HDPE	CFRP#1	CFRP#2	0.2%
COPV#CC-4	HDPE	CFRP#1	CFRP#2	0.0%

The pressure and temperature transients inside the self-venting tank during the fire tests are shown for COPV#CC-4 in Figure 4. The initial pressure and temperature of hydrogen in the tank at the beginning of the fire test, pressure in the tank when microleaks start, as well as the time of leak initiations and time of leak durations are shown in Table 2. The initial pressure in all four tests was almost equal to the tank's NWP=70 MPa and the initial temperature was in the range 10.9-23.1°C. The tanks started to leak at times from 4 min 26 s to 6 min 2 s when the pressure increased in the range 74.11-76.57 MPa. It should be noted that the hydrogen temperature shown in Figure 4 is below the temperature of the liner (not shown) due to the heat flux from the fire through the tank wall to hydrogen. The shortest blowdown time of hydrogen from a tank duration was 12 min 35 s and the longest was 14 min 31 s.

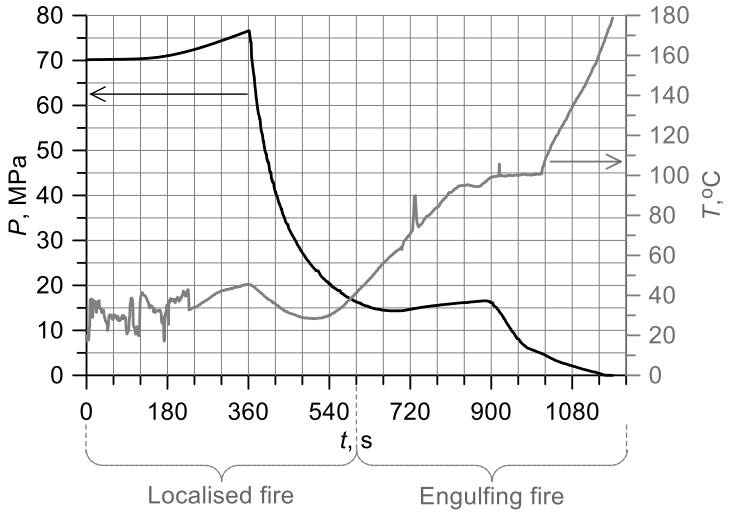

Fig. 4. *Pressure and temperature transients inside the μLNB tank prototypes COPV#CC-4 during the fire tests with HRR/A=1 MW/m²*

Table 2. *Results of fire testing of the series of μLNB tanks with carbon-carbon combination*

Tank No.	*P* initial	*T* initial	*P* at leak	Leak start time	Leak duration
COPV#CC-1	70.02 MPa	10.9°C	76.39 MPa	5 min 36 s	12 min 35 s
COPV#CC-2	70.09 MPa	20.7°C	74.11 MPa	4 min 26 s	12 min 40 s
COPV#CC-3	70.22 MPa	23.1°C	76.34 MPa	5 min 44 s	14 min 31 s
COPV#CC-4	70.17 MPa	19.8°C	76.57 MPa	6 min 2 s	13 min 24 s

The simulations using the developed and validated HySAFER model demonstrated that at the moment of COPV#CC-4 leak start at 6 min 2 s (see ***Table***), the total amount of energy transferred to the liner from the composite minus energy transferred from the liner to hydrogen, increases the liner's temperature to 128°C. This falls within the range of HDPE melting temperature of 110-130°C. This is supported by the observed pressure and temperature drop inside the tank at 6 min 2 s (Figure 4).

The start of the pressure drop in Figure 4 identifies the beginning of microleaks. The decrease in pressure is associated with the observed decrease in hydrogen temperature due to gas expansion. Hydrogen temperature rises at the end of microleaks when the pressure inside the tank drops to the atmospheric pressure. The pressure transient in the test with COPV#CC-4 has a plateau. This plateau is the result of tank contraction with the pressure decrease and either a decrease in size or even closure of some of the microchannels. Then, the hydrogen temperature continues to grow and at about 100°C (close to the melting temperature of 110-130ºC of the HDPE liner) the microleaks intensify and promote pressure drop to atmospheric pressure.

The non-adiabatic blowdown model (Kashkarov et al., 2022) was used to process experimental pressure and temperature transients in a fire test with COPV#CC-4. Figure 5 (left) shows experimental and simulated pressure dynamics inside the tank (left y-axis), and the numerically derived diameter of the equivalent orifice which would have a cross-section area equal to the total

effective cross-section area of the microleaks in the tank wall (right y-axis). The equivalent to microleaks orifice diameter was defined by the inverse problem method using in-house programmes with the "orifice" as a design parameter to match experimental pressure (and temperature, if available). Figure 5 (right) compares experimental and simulated temperature transients in the tank.

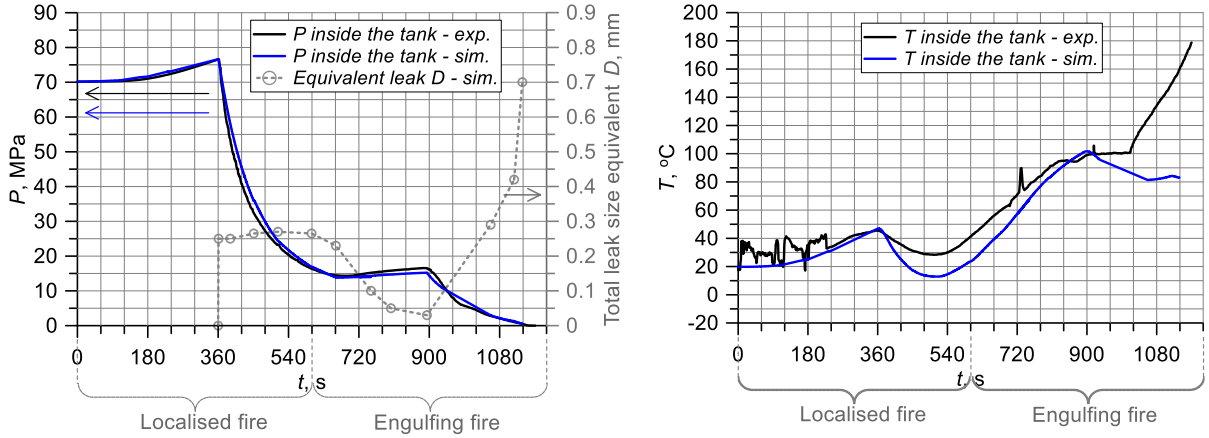

Fig. 5. *Experimental and simulated pressure (left, left y-axis), temperature transients (right) inside COPV#CC-4, and equivalent microleaks diameter (left, right y-axis)*

Figure 5 shows that the pressure and temperature are reproduced with good accuracy by the model. The grey dashed curve with circular symbols represents the changing equivalent diameter of the "orifice" with a cross-section area equal to the total effective cross-section area of microleaks. The "orifice" diameter is equal to 0.25 mm at the start of microleaks (6 min 2 s). This diameter remains almost constant until 10 min. The pressure drops from the initial 76.57 MPa at 6 min 2 s to below 15 MPa at 10 min, i.e., more than 5 times in 4 min. The wall contraction is thought to be the main factor that is evidenced by the decrease of cumulative area of microleaks from an initial 0.25 mm at the start of the hydrogen escape through the wall to only 0.03-0.04 mm at the end of the plateau. Then the pressure starts to drop again after 15 min down to atmospheric. This is due to further decomposition of resin in the composite and associated formation of new microchannels and/or increase of cross-section area of existing microchannels. The cumulative area of microleaks grows after 15 min and reaches 0.7 mm at the end of the blowdown. This is the reason for the simulated temperature decrease after 900 s (faster gas expansion). However, the experimental temperature increases after 900 s. This "discrepancy" between the experiment and simulations is thought due to fire products penetrating through the wall composed only of fibres after the decomposition of resin (this is not a simulated phenomenon). The pressure inside this 7.5 L tank decreased by more than 5 times at 10-15 min to that when microleaks started. The wall thickness needed to bear the load is significantly thinner compared to the original, i.e., by about the same 5 times and multiplied by the safety factor. The decrease of cumulative microleaks area after about 9 min due to tank wall contraction, and other mentioned factors, changes the balance between hydrogen cooling and heating in favour of heating (see Figure 5, right). The increase in temperature afterwards is further supported by switching to the engulfing fire mode when the whole tank surface is subject to fire.

Let us estimate the largest diameter of a microchannel assuming the maximum hydrogen flame length (ignoring resin combustion) of about 15 cm as evidenced by the experiments at the leakage start. Then, the dimensionless flame length correlation (Molkov, 2012) gives the microchannel diameters of about 100 μm (in the assumption of pressure at the exit of the microchannel of about 10 MPa abs, while it is about 75-80 MPa inside the tank). This is of the order of carbon fibre size of 7 μm. Not all microleaks can sustain microflames. The lowest leak possible to sustain a flame from a miniature burner configuration is reported as 3.9-5.0 μg/s, which is the quenching limit (Lecoustre et al., 2010).

Three fire tests were performed for carbon-glass tanks. The initial pressure, the pressure at the start of microleaks, the microleaks start time, and the microleaks duration are shown in ***Table*** 3. The scatter of microleaks start time and its duration is defined by the difference in thicknesses of carbon and

glass layers. Using the model (Kashkarov et al., 2022) it was estimated, that similarly to the carbon-carbon prototypes, the initial overall leak flow rate in carbon-glass prototypes was 2 g/s. All prototypes leaked in a fire with HRR/A=1 MW/m^2 and pressure dropped to the atmospheric pressure.

Table 3. *Testing outcomes for COPVs with carbon-glass composite layers combination*

Tank No.	*P* initial	*T* initial	*P* at leak	Leak start time	Leak duration
COPV#CG-1	70.99 MPa	N/A	80.98 MPa	9 min	17 min
COPV#CG-2	70.76 MPa	N/A	85.35 MPa	12 min	25 min
COPV#CG-3	70.69 MPa	N/A	71.22 MPa	3 min 30 s	5 min

4. Validation of the technology for fire intervention conditions

In the study (Molkov et al., 2024) we expanded the validation domain for this innovative safety technology of explosion-free in a fire self-venting (TPRD-less) tanks to scenarios of intervention at the fire scene by the first responders. To address the safety concerns of firefighters, the localised and engulfing parts of the fire test were carried out at HRR/A=1 MW/m^2 which is characteristic of realistic gasoline/diesel spill fires. This value is above the unreasonably decreased specific heat release rate as per the GTR#13 (UN ECE, 2023) fire test protocol of HRR/A=0.3 MW/m^2 and HRR/A=0.7 MW/m^2 for localised and engulfing fires, respectively.

Six μLNB tank prototypes were tested in two different fire intervention scenarios within the research programme of the HyTunnel-CS (https://hytunnel.net/) project coordinated by Ulster University: (a) removal from a fire (an experiment where only the burner is turned off without spraying water), and (b) water supply to tank in the fire. Two grades of HDPE liner (L1, L2), two carbon fibre-reinforced polymers (CFRP#1, CFRP#2), and one basalt fibre-reinforced polymer (BFRP) as a TPL (and load-bearing composite) were used to design and manufacture the tank prototypes.

Figure 6 shows a comparison of pressure and temperature dynamics for carbon-basalt tanks COPV#CB-2 (left) and COPV#CB-3 (right) for scenarios with water jets supplied to the tank from above. Both tanks had the wall thickness of the original tank. The only difference in tanks' design is the grade of liner. The order of actions in the tests was as follows. The burner was ignited when the pressure in the tanks was equal to NWP=70 MPa. Tank COPV#CB-2 started to leak after melting liner L2 after 4 min 45 s when pressure inside the tank increased to 78 MPa, while liner L1 in COPV#CB-3 melted faster at 3 min 50 s when pressure raised to only 74.5 MPa.

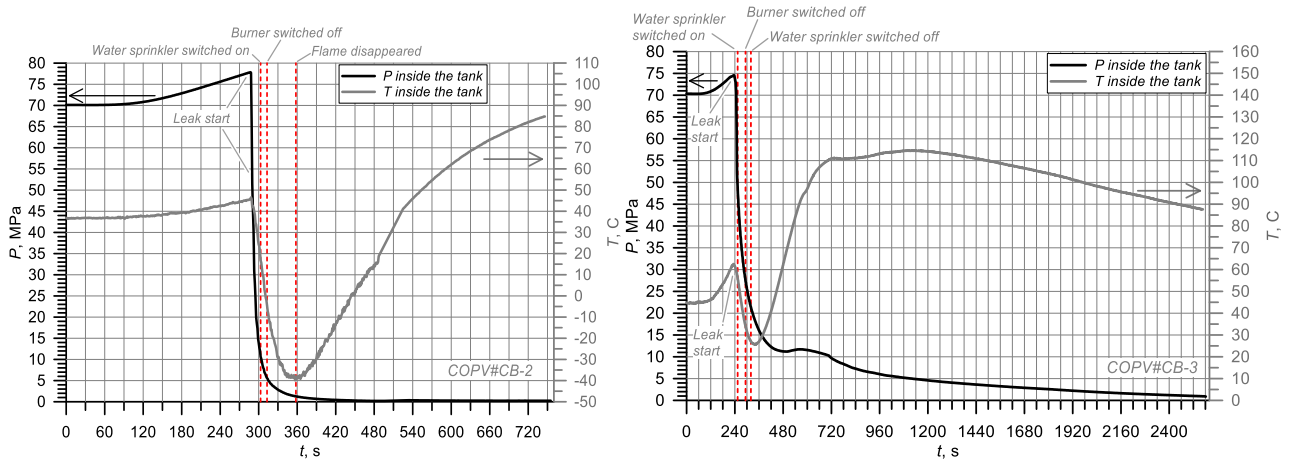

Fig. 6. *Pressure and temperature transients measured inside μLNB tank prototypes during the fire tests: COPV#CB-2 with liner L2 (left), COPV#CB-3 with liner L1 (right)*

The rate of pressure rise in the closed tanks was the same in both tanks but in test COPV#CB-3 liner L1 melted earlier. The deeper drop of pressure in the test with tank COPV#CB-2 is responsible for the larger decrease of hydrogen temperature from 45ºC down to -38ºC (decrease by 83ºC), while the

smaller rate of pressure decrease in tank COPV#CB-3 with the pressure plateau resulted in a temperature decrease from 62ºC to 26ºC (decrease by only 36ºC).

In about 10 s after the start of microleaks, the sprinkler was switched on and water sprays were applied to the top of the burning tank surface. Then in 10-20 s, the burner was switched off. Then the two tests proceeded differently. While in the test with tank COPV#CB-2, the water supply continued to the test end, in the test with tank COPV#CB-3 the water supply was switched off in 20 s after the burner was switched off. This is thought to contribute to the larger temperature drop in the test with COPV#CB-2. The visible flames on the tank surface disappeared in both tests after the water supply.

5. Performance of the technology for extreme conditions of impinging hydrogen jet fire

In the work (Molkov et al., 2023b) we expanded the validation domain of the technology further to the most extreme but realistic scenario of the NWP=70 MPa self-venting tank being impinged by the under-expanded hydrogen jet fire from nearby 70 MPa storage. The μLNB tank prototype experimentally tested in the impinging hydrogen jet fire in this study was designed at the HySAFER Centre using as the basis the original 7.5 L Type IV tanks with NWP=70 MPa produced by our USA partner. The prototype COPV#CB-1 was made of carbon fibre-reinforced polymer (CFRP) and basalt fibre-reinforced polymer (BFRP). The wall thickness of the self-venting prototype was equal to that of the original tank made of CFRP (making it cheaper not only by avoiding TPRD purchase but substituting the expensive and deficient on-the-market carbon fibres with cheaper basalt fibres).

The use of the "Jet parameters model" tool of the freely available online e-Laboratory of Hydrogen Safety (https://elab.hysafer.ulster.ac.uk/) allows calculation of the hydrogen mass flow rate from 70 MPa tanks through 0.71 mm diameter orifice as 13.51 g/s. Multiplication of this mass flow rate by the hydrogen heat of combustion in air of 119.96 MJ/kg gives the total heat release rate of such jet fire of HRR=1.62 MW. The specific heat release rate, HRR/A, is defined as the ratio of the total fire HRR and the area of the fire source, A. Determination of the HRR/A of such impinging jet fire source is not a trivial task. With the jet fire, it is unclear what to choose as the fire source area, e.g., it could be the release orifice area, the tank projection area, or the cross-section area of the jet fire near the tank. In the case of the release orifice of 0.71 mm diameter used in the experiment performed at the Health and Safety Executive (UK), the orifice area was $A=3.96^{-7}$ m^2. That would result in the tremendously large HRR/A=1.62 MW/3.96×10^{-7} m^2 = 4.09×10^6 MW/m^2=4.09 TW/m^2. It was considered more reasonable to use the tank projection area A=0.083 m^2 as the area of the fire source, especially in the conditions of the impinging jet with a diameter near the tank practically equal to the tested tank diameter. This resulted in still extremely high fire testing conditions with HRR/A=19.5 MW/m^2. This is the highest specific heat release rate ever applied and reported in fire testing of CHSS.

Figure 7 shows the transients of parameters measured during this fire test at extreme conditions and simulated using our in-house non-adiabatic blowdown model.

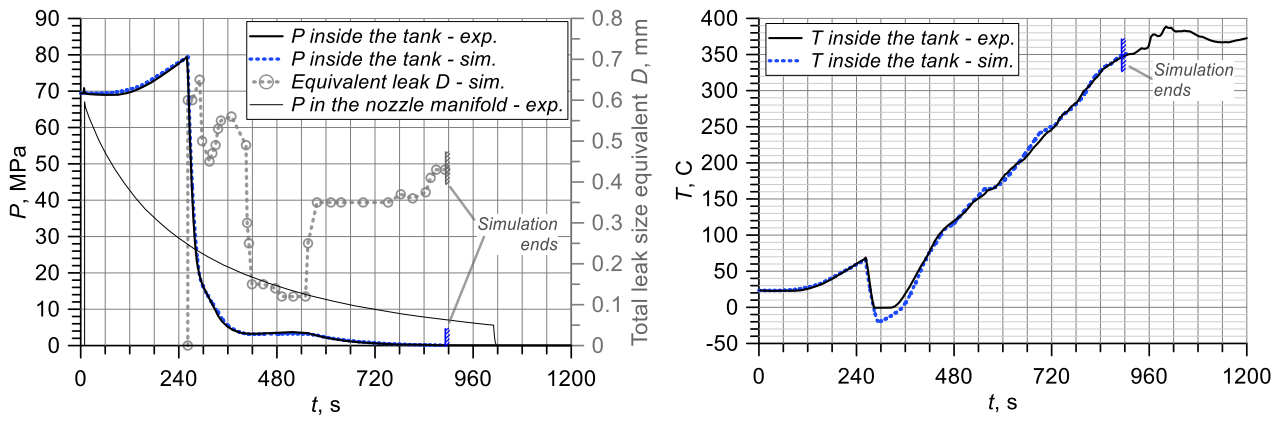

Fig. 7. *Hydrogen pressure in the tank and manifold (left) and temperature (right) transients inside the carbon-basalt μLNB tank*

The inverse problem method was used to define changes in time of the equivalent diameter of microleaks as a sought parameter. Figure 7 (left) shows the experimental pressure in the tank (thick solid curve), experimental pressure in the nozzle releasing hydrogen jet (thin solid curve), simulated pressure in the tank (dashed curve) and defined by the inverse problem method the changing in time diameter of an "equivalent area orifice" with the area equal to the cumulative areas of microleaks through the tank wall (grey dash curve with circular symbols). Figure 7 (right) compares the experimental (solid curve) and simulated (dashed curve) hydrogen temperature in the tank.

The initial pressure in the tank of 69.4 MPa grows in the closed tank due to heat transfer from the fire. The liner melts at 4 min 12 s. The pressure inside the tank has increased at this moment by 10 MPa to 79.4 MPa and the hydrogen temperature has reached 65ºC (43ºC above its initial temperature of 23ºC). The microleaks reduce the pressure in the tank which causes the temperature to drop to almost -20ºC due to expansion. The decrease in hydrogen temperature does not stop its release. Cooled hydrogen can "solidify" the resin of the composite at the corresponding thickness as the glass transition temperature varies in the range of 75-135ºC, and the decomposition temperature is 370-380ºC (Molkov et al., 2023b). There should be some heating of hydrogen due to the Joule-Thomson effect during the throttling of the gas through the microchannels which to some extent compensates cooling of hydrogen inside the tank due to expansion with the pressure drop.

The contraction of the wall and decrease of temperature are followed by a plateau of measured pressure at about 6 min 30 s. It is shown in the paper (Molkov et al., 2023a) that even though the total equivalent area of microleaks reduces at the plateau, the release of hydrogen continues but with a smaller flow rate. This conclusion is confirmed in the study (Molkov et al., 2023b). The strong heat transfer from the high-temperature hydrogen impinging jet fire continues and is responsible for the increase of hydrogen temperature inside the storage tank. The start of the secondary pressure drop after the plateau corresponds to a hydrogen temperature increase to about 150ºC sufficient to melt the entire liner. In addition to this, the jet fire continues to decompose the composite resin that could support the creation of new microchannels in the wall with continuously decreasing thickness fraction required to bear a pressure load. The pressure in the tank drops to atmospheric at time 15 min after the fire test starts. Because the impinging jet fire was affecting the tank afterwards, the temperature inside the tank continues to grow and is "stabilised" at 360-390ºC which corresponds to the resin decomposition temperature. Hydrogen temperature cannot exceed this temperature unless the impinging jet erodes the tank wall and directly penetrates the tank. This was not the case in the test. The impinging jet fire was terminated at 21 min 47 s and the temperature in the tank began to decrease.

Figure 7 (left) shows the dynamically changing equivalent leak diameter defined in simulations. The orifice varies from about 0.60-0.65 mm at the start of the leakage. Then, due to composite shrinkage with pressure drop, the equivalent orifice diameter reduces to 0.15 mm and then to its minimum of 0.12 mm. The diameter varies within these values for about 2 min. The equivalent orifice diameter never drops below 0.12 mm, i.e., there are microleaks even when the pressure plateau is observed.

Figure 8 presents snapshots of the extreme condition hydrogen impinging jet fire with HRR/A=19.5 MW/m^2. It is seen that at time 4 min 13 s when hydrogen starts to leak through microchannels of the composite wall (after melting the liner) the combustion intensities. This increase in heat release rate could, in principle, accelerate the melting of the resin of the composite inside the wall and decompose fibres on the tank's surface.

Figure 9 shows a photo of the tank after the extreme fire testing by impinging hydrogen jet fire. Not only is the resin of the external basalt composite layer decomposed but also several plies made of basalt fibres. It is worth mentioning that the decomposition temperature of basalt fibres is about 900ºC, i.e., higher than that for carbon fibres 540-620ºC. This underpins the use of basalt fibres in composite Type IV tanks for safety and economic reasons.

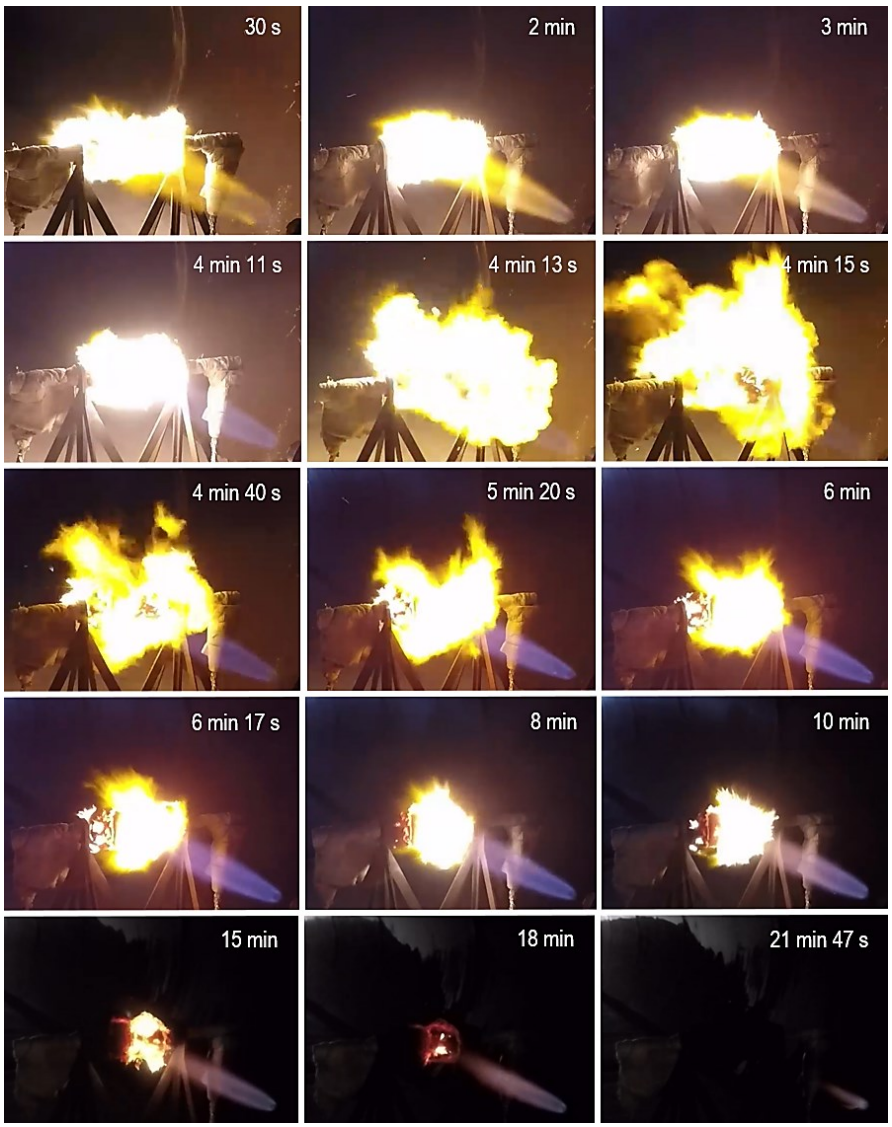

Fig. 8. *Snapshots showing the progression of the impinging hydrogen jet fire test*

Fig. 9. *Photo of the tank after the impinging hydrogen jet fire test*

6. Conclusions

The *originality* of this review paper is in the presentation of breakthrough safety technology of explosion-free in fire self-venting (TPRD-less) Type IV tanks, based on the microleaks-no-burst (μLNB) concept. The technology is tested at realistic fire conditions beyond the unexplainable limits of the fire test protocol of GTR#13 (UN ECE, 2023). Different intervention strategies of the first responders to control fire were investigated, i.e., the removal of the vehicle from a fire scene with fire re-ignition, and scenarios of continuous and temporary extinction of the fire by water supply on the tank surface. The study revealed that the proper choice of HDPE liner grade could further improve the performance of the technology and eliminate the low-pressure plateau. The originality of this work is further supported by using numerical and experimental methods to demonstrate the reliability of the design of self-venting (TPRD-less) tanks at extreme but realistic conditions of impinging hydrogen jet fire from 70 MPa hydrogen storage system located nearby with highest ever used in fire test HRR/A=19.5 MW/m^2.

The *significance* of this work is in the development and validation of the storage tank designs that exclude rupture in a fire, including extreme conditions of impinging high-momentum 70 MPa hydrogen jet fire. The μLNB self-venting tanks eliminate blast waves, fireballs, projectiles (including the largest projectile which is a vehicle itself), long flames from TPRD, the destructive pressure peaking phenomenon in storage enclosures, the formation of flammable cloud that could deflagrate after delayed ignition, and ultimately the loss of life and property from tank rupture in a fire. The reduction of carbon fibre amount in the double-composite wall μLNB tank is possible by using cheaper fibres, e.g. glass and basalt. The significance of this work is in the demonstration that self-venting (TPRD-less) tanks could have the same size as original tanks but exclude rupture in any fire. The use of μLNB tanks reduces hazards and associated risks for first responders when dealing with fires of hydrogen transport and fires in storage enclosures onboard road vehicles, trains, marine vessels, planes at airports and hydrogen storage infrastructure at hydrogen refuelling stations. The technology closes safety concerns for confined spaces like tunnels, underground parking, etc. Testing of μLNB tanks confirmed that the fire extinction does not interrupt hydrogen release through microleaks, i.e., firefighters can conduct their interventions at an incident scene following current strategies and tactics. The work demonstrates that there is an advanced technology for hydrogen storage in self-venting tanks that can withstand fire of any intensity without rupture and does not require the use of TPRD to avoid associated issues like localised and smouldering fires, blockage at incident scenes, etc. The technology validation creates the basis for the improvement of the regulation and fire test for extreme yet realistic fire conditions like impinging hydrogen jet fire. The existence of technology underpins and widens the public acceptance of hydrogen transport and infrastructure.

The *rigour* of this study is in the experimental validation of the technology for carbon-carbon, carbon-glass and carbon-basalt fibre designs and “matching” resins in the composite tanks of NWP=70 MPa. The μLNB tanks are tested in localised and engulfing fires, and at realistic specific heat release rates from HRR/A=1 MW/m^2 to HRR/A=19.5 MW/m^2, in which many standard tanks will rupture already at the localised fire stage when their TPRD is not yet affected by the fire. The unique Ulster models were applied to analyse the changing in time cumulative area of microleaks. Simulations successfully reproduced the experimental pressure and temperature transients and gave insights into the underlying physical phenomena. The pressure inside the μLNB tank drops to atmospheric at the end of the fire. This facilitates safer procedures and dealing with hydrogen storage tanks after the fire incident. The rigour of this research is underpinned further by the experimental validation of the μLNB tank design done by unique models developed at Ulster University. All numerically designed tanks successfully passed fire tests, including extreme test, as predicted by this innovative technology.

Acknowledgements

The author gratefully acknowledges the research collaboration on this technology with colleagues from the HySAFER Centre, namely Dr Dmitriy Makarov and Dr Sergii Kashkarov, and collaborators

in the listed below national and European projects. The research on explosion free in fire self-venting (TPRD-less) tanks was co-funded by the UK EPSRC grant "SUPERGEN Hydrogen and Fuel Cells Challenge: Safety Strategies for Onboard Hydrogen Storage Systems" (EP/K021109/1), EPSRC grant "UK National Clean Maritime Research Hub" (EP/Y024605/1), Invest Northern Ireland (NI) grant Proof of Concept PoC 629 "Composite tank prototype for onboard compressed hydrogen storage based on novel leak-no-burst safety technology" and PoC Plus "Optimisation of explosion free in a fire composite cylinder to industrial requirements", Invest NI Centre for Advanced Sustainable Energy (CASE) "Breakthrough safety technologies for hydrogen vessels from Northern Ireland" project, Innovate UK Clean Maritime Demonstration Competition (CMDC2) "Hydrogen Fuel Cell Range Extender", Fuel Cells and Hydrogen 2 Joint Undertaking (now Clean Hydrogen Joint Undertaking) through the HyTunnel-CS "Pre-normative research for safety of hydrogen driven vehicles and transport through tunnels and similar confined spaces", SH2APED "Storage of hydrogen: alternative pressure enclosure development" and HyResponder "European Hydrogen Train the Trainer Programme for Responders" projects. The HyTunnel-CS project has received funding under grant agreement No. 826193, the SH2APED project under grant agreement No. 101007182, and the HyResponder under grant agreement No. 875089. This Joint Undertaking receives support from the European Union's Horizon 2020 research and innovation programme, Hydrogen Europe, and Hydrogen Europe Research. The author is grateful to tank manufacturers and testing laboratories around the globe who contributed to these advancements in gaseous hydrogen storage systems.

References

Dadashzadeh, M., Kashkarov, S., Makarov, D., Molkov, V., 2018. Risk assessment methodology for onboard hydrogen storage. Int J Hydrog Energy, 43, 6462–75. https://doi.org/10.1016/j.ijhydene.2018.01.195

Kashkarov, S., Dadashzadeh, M., Sivaraman, S., Molkov, V., 2022. Quantitative Risk Assessment Methodology for Hydrogen Tank Rupture in a Tunnel Fire. Hydrogen, 3, 512–30. https://doi.org/10.3390/hydrogen3040033

Lecoustre, V.R., Sunderland, P.B., Chao, B.H., Axelbaum, R.L., 2010. Extremely weak hydrogen flames. Combust Flame, 157, 2209–10.

Molkov V. 2012. Fundamentals of Hydrogen Safety Engineering. www.bookboon.com, free download e-book.

Molkov, V., Makarov, D., Kashkarov, S., 2018. Composite Pressure Vessel for Hydrogen Storage. WO 2018/149772 A1.

Molkov, V., Kashkarov, S., Makarov, D., 2023a. Breakthrough safety technology of explosion free in fire self-venting (TPRD-less) tanks: The concept and validation of the microleaks-no-burst technology for carbon-carbon and carbon-glass double-composite wall hydrogen storage systems. Int J Hydrog Energy, 48 33774-33785. https://www.sciencedirect.com/science/article/pii/S0360319923024448

Molkov, V., Kashkarov, S., Makarov, D., 2023b. Explosion free in fire self-venting (TPRD-less) Type IV tanks: Validation under extreme impinging 70 MPa hydrogen jet fire conditions. Int J Hydrog Energy, 48, 40117-40126. https://doi.org/10.1016/j.ijhydene.2023.09.020

Molkov, V., Kashkarov, S., Makarov, D., 2024. Explosion free in fire self-venting (TPRD-less) composite tanks: Performance during fire intervention. Int J Hydrog Energy, 50, 804-814. https://www.sciencedirect.com/science/article/pii/S0360319923034821

UN ECE, 2023. Global technical regulation on hydrogen and fuel cell vehicles. Addendum 13: Global technical regulation No. 13. Global Registry, https://unece.org/sites/default/files/2023-07/ECE-TRANS-180-Add.13-Amend1e.pdf. [accessed 17 February 2024].

Teaching process safety in the twenty-first century

Trygve Skjold
University of Bergen, Norway
E-mail: trygve.skjold@uib.no

Abstract

Knowledge and competence related to process safety is relevant for a broad range of systems in industry and society where loss of containment of hazardous materials, fires, and explosions represent a hazard to people, property, and the environment. Process safety is an interdisciplinary subject, as well as an applied discipline that evolves with the development of industry and society, and it may not be straightforward to decide which topics to include in a curriculum on process safety, what level of detail to cover, and how courses and teaching should be organized to maximize learning outcomes and relevance for future employment. This paper summarises results from a survey targeting practitioners of process safety, from academia and various branches of the labour market. The main objective of the study was to explore global trends, practices, and priorities related to process safety, with a view to promote sharing of knowledge and best practices between stakeholders. Overall, the responses from academia and the labour market are reasonably aligned, and the results reflect the global efforts to replace fossil fuels with renewable energy sources in conjunction with energy carriers such as hydrogen, ammonia, and batteries.

Keywords: *process safety, teaching, knowledge, competence, research, energy transition*

1. Introduction

1.1. Process safety

Process safety is a discipline that emphasises prevention and mitigation of accidents in chemical process plants or other facilities where hazardous materials are produced, handled, stored, transported, or consumed (Mannan, 2012; Crowl & Louvar, 2019). It entails applying good design principles, engineering, and operating and maintenance practices to manage the integrity of systems and processes. As such, process safety is relevant for a broad range of systems in industry and society where loss of containment of hazardous materials, fires, and explosions represent a hazard to people, property, and the environment (MKOPSC, 2011; Mannan *et al.*, 2015).

1.2. Global trends

Chemical engineering and process safety are applied disciplines that evolve with the development of industry and society (Aris, 1977; Kletz, 2000; Mannan *et al.*, 2015; Kletz and Amyotte, 2019; Guerrero-Pérez, 2023; Qian *et al.*, 2023, Abedsoltan *et al.*, 2024), and many of the principles for achieving safe operation in the process industry apply equally well to coal mines, nuclear facilities, and emerging technologies for the production, storage, transport, and use of energy carriers such as hydrogen, ammonia, and batteries (MKOPSC, 2011). In this perspective, it is relevant to explore how practitioners of process safety perceive the implications of the technological and scientific development, emerging energy technologies, sustainability and circular economy, artificial intelligence (AI), development in regulations, codes, and standards (RCS), and lessons learnt from major accidents.

1.3. Curriculum

Chemical engineering and process safety are interdisciplinary subjects, comprising elements from thermodynamics, fluid mechanics, heat and mass transfer, chemical kinetics, unit operations, material science, risk analysis, toxicology, electrostatics, fire and explosion protection, RCS, psychology,

sociology, and so on (Aris, 1977; Kouwenhoven, 2021). As such, a comprehensive syllabus in process safety should cover a wide range of topics, from basic physical and chemical phenomena and unit operations to complex and increasingly automated systems, designed and operated by humans (Mannan *et al.*, 1999; Leveson, 2011; Sanders, 2013; Kouwenhoven, 2021).

The global nature of the process industry implies a need for standardising the process safety curriculum (ISC/MKOPSC, 2013). However, the time allocated to process safety varies significantly between universities and study programs (Mkpat *et al.*, 2018), and the competence and experience of the academic staff, including research activities and cooperation with industry, is also likely to influence teaching practices and priorities. Finally, since the process industry in a country or region is likely to reflect its natural resources and the level of technological development, teaching of process safety may also vary between academic institutions and study programs in different parts of the world. In this perspective, it is not straightforward to decide which topics to include in a curriculum on process safety, what level of detail to cover, and how the courses should be organized and delivered to maximize learning outcomes and relevance for future employment (Mannan *et al.*, 1999; Amyotte, 2013; Forest, 2018; Vaughen, 2019; Amyotte *et al.*, 2019; Tighe *et al.*, 2021).

1.4. Safety and risk

The overall aim of process safety is to avoid major accidents that can cause serious harm to people, property, and the environment. In broad terms, safety implies control over hazards that can result in losses, and the purpose of a risk assessment is to increase the knowledge about a system or an activity, and thereby support decisions that may entail difficult economic, ethical, or political deliberations. As such, process safety, risk assessment, and risk management are inherently linked. Whereas conventional approaches to risk analysis tend to treat risk as an expectation value (Rasmussen, 1981; Weinberg, 1981), there is increasing awareness of the importance of uncertainty in risk assessments (Flage & Aven, 2009, Aven, 2010; Aven, 2013). To this end, it is relevant to explore whether the practices and trends in the teaching of process safety reflects the development in risk science.

1.5. Research priorities

Research on process safety is generally of an applied nature, and it often entails collaboration between academia and the labour market (Aris, 1976; MKOPSC, 2011; ISC/MKOPSC, 2013). Hence, it is also of interest to explore the experience from such collaboration from different stakeholders.

1.6. Prosa21

Process safety in the twenty-first century (Prosa21) is an initiative from the University of Bergen (UiB). The topic, title, and acronym are motivated by a series of strategies for the twenty-first century initiated by various ministries in Norway:

- *Energi21* – Strategy for research and development on new energy technologies.
- *Prosess21* – Strategy for reducing greenhouse gas emissions from the process industry.
- *Transport21* – Strategy for research, development, and innovation in the transport sector.
- *Maritim21* – Strategy for research, development, and innovation in the maritime industry.
- *OG21* – Strategy for developing the oil and gas technologies.

Whereas these strategies are national, the challenges addressed are global. A common denominator is the implementation of sustainable energy technologies in industry and society. To this end, safe implementation will require new knowledge and competence that must developed through state-of-the-art research, education, and training on process safety and related topics.

Prosa21 also addresses selected aspects of process safety from other strategy documents on process safety in the twenty-first century (MKOPSC, 2011; ISC/MKOPSC, 2013). Since process facilities and the energy infrastructure are potential targets for malicious attacks, the focus areas for Prosa21 comprise energy, safety, and security. In a longer perspective, the aim is to establish a research centre and collaborative research projects that can address critical knowledge gaps identified in the survey.

1.7. Objectives

This paper summarises the responses from $N = 165$ respondents to a survey distributed to practitioners of process safety and related areas, in academia and relevant branches of the labour market. The main objective was to explore global trends, practices, and priorities, and hence promote sharing of knowledge and best practices between stakeholders.

2. The survey

This section describes the structure and distribution of the survey.

2.1 Target audience

A premise for the content and structure of the survey was that knowledge and competence in process safety are relevant for a broad range of systems in industry and society where loss of containment of hazardous materials, fires, and explosions represent a hazard to people, property, and the environment. As such, the survey targeted practitioners of process safety and related areas, including:

- *Conventional process industries*: oil and gas, petrochemicals, food and feed, metals, etc.
- *Energy-related safety and security*: nuclear, hydrogen, ammonia, batteries, mining, etc.
- *Transport-related safety and security*: road, rail, maritime, aviation, etc.
- *Academia and research organisations*: researchers, lecturers, etc.
- *Other stakeholders*: consultants, providers of fire and explosion protection, model developers, regulators, insurance companies, standard development organisations (SDOs), etc.

2.2 Structure

The survey consisted of six sections, and a combination of multiple-choice and open-ended questions. Table 1 summarises the structure and number of questions in the survey. The multiple-choice questions were mandatory, and the open-ended questions optional. The response to selected questions were used to activate further questions, such as specific questions for respondents from academia or the labour market (based on current or most recent primary employment related to process safety).

Table 1. Structure of the survey and number of main questions by category.

Section	**Questions for academia**		**Questions for the labour market**	
	Multiple-choice	*Open-ended*	*Multiple-choice*	*Open-ended*
1. Experience	4	0	5	0
2. Collaboration	3	3	2	4
3. Priorities	2	2	2	2
4. Trends	3	1	3	1
5. Practice	5	4	1	0
6. Interactions	4	1	4	1
Sum:	**19**	**11**	**17**	**8**

2.3 Distribution and response

The survey was set up in the SurveyXact tool from Ramboll. It was a self-generating survey, i.e. respondents accessed the survey via a link. The original survey invitation was distributed by e-mail to corresponding authors of published papers on process safety and related topics registered in Web of Science over the period 2000-2024, as well as selected contact persons from various projects and networks. Table 2 summarises the distribution and response to the survey.

Table 2. Survey distribution and response.

Distribution			**Response**	
E-mails sent	Not delivered	Assumed delivered	Of e-mails sent	Of assumed delivered
3 600	**789** (21.9 %)	**2 811** (78.1 %)	**165** (4.6 %)	**165** (5.9 %)

Figure 1 summarises the countries of current or most recent primary employment related to process safety or related areas for the $N = 118$ respondents that completed the survey. Other countries ($n \leq 2$) include Brunei, Greece, Iran, Netherlands, Taiwan, Brazil, Colombia, Cyprus, Czech Republic, Finland, Mexico, Slovenia, South Africa, Sri Lanka, and Venezuela.

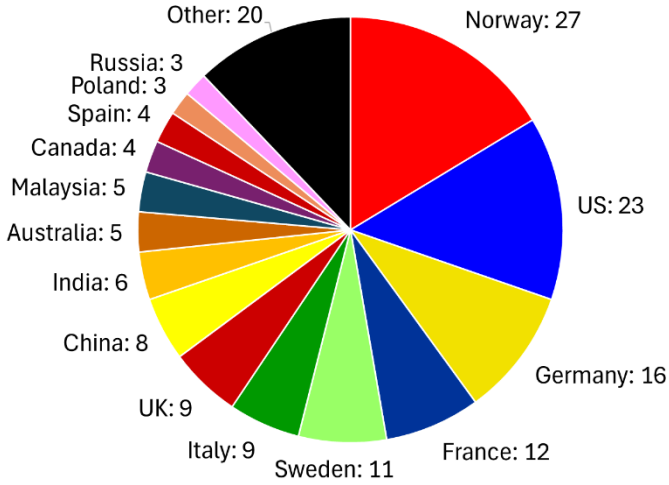

Figure 1. Country of current or most recent primary employment of the N = 165 respondents.

Figure 2 summarises the registered response duration, i.e. the time from a respondent accessed the online questionnaire and until the response was submitted. Since all respondents may not have been active during the entire period, the values indicated provide a conservative estimate of the time used for completing the survey.

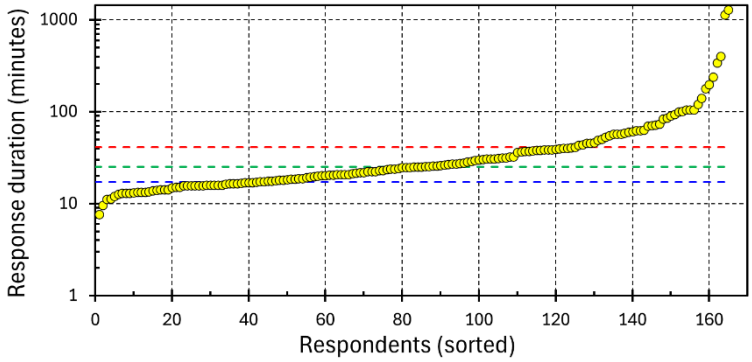

Figure 2. Response duration for the N = 165 completed responses. The first quartile (Q1), median (Q2), and third quartile (Q3), indicated by the blue, green, and red dashed lines, are 17.2, 25.3, and 41.2 minutes, respectively.

2.4 Data processing

All personal information was anonymised prior to the processing of the data. The responses to the open-ended questions were sorted by Microsoft Copilot (GPT-4) prior to manual editing supported by close reading of the responses.

3. Results

3.1 Experience

This part of the survey explored the experience related to process safety of the $N = 165$ respondents. Figure 3 shows the distribution according to type of organisation, specified as current or most recent primary employer. Other ($n \leq 2$) includes commercial software development, insurance, nuclear safety, vehicle manufacturer, industry trade consortium, and the Center for Chemical Process Safety (CCPS). The response to this question activated questions specific to *"academia only"* ($n = 68$) or *"labour only"* ($n = 165\text{-}68 = 97$) in other sections of the survey.

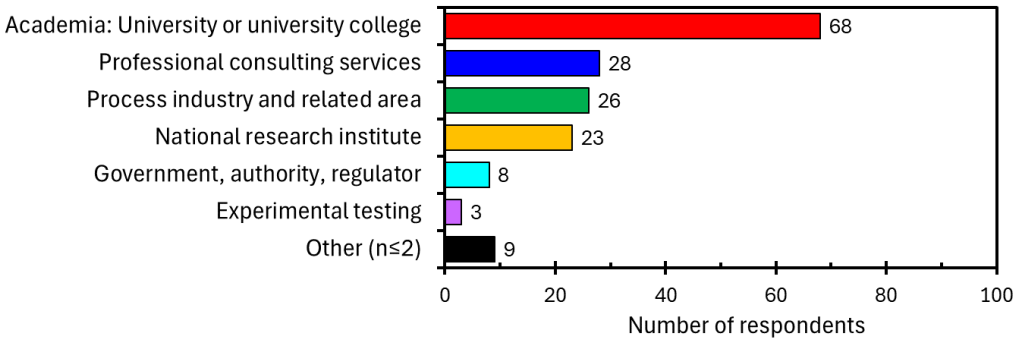

Figure 3. Type of organisation, current or most recent primary employer (N = 165).

Figure 4 summarises the experience of the respondents from process safety or related work.

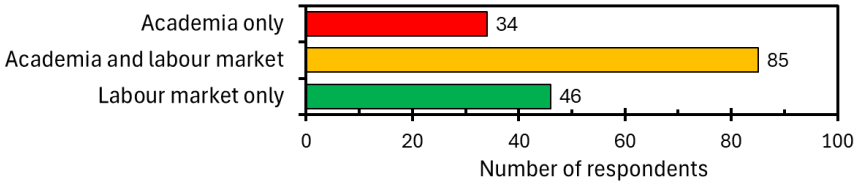

Figure 4. Accumulated professional experience from process safety or related work (N = 165).

Figure 5 summarises the personal experience of the respondents from process safety or related work, measured in years normalised to full time, based on the categories defined in Figure 4. Most of the respondents had more than ten years of experience.

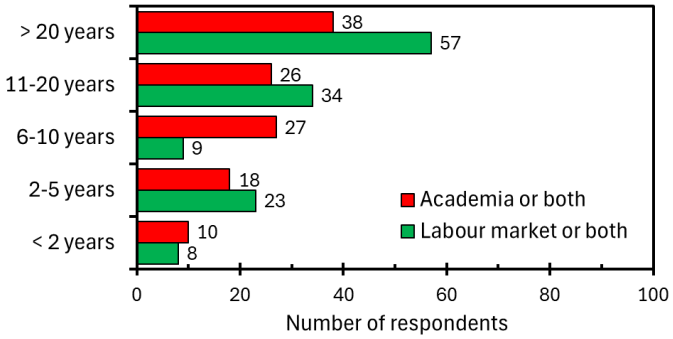

Figure 5. Years of personal experience from process safety or related work (n_1 = 119 & n_2 = 131).

Figure 6 summarises the experience of the respondents from teaching process safety in academia, including supervision (multiple answers possible). Examples of other experience include guest lectures post-graduate courses.

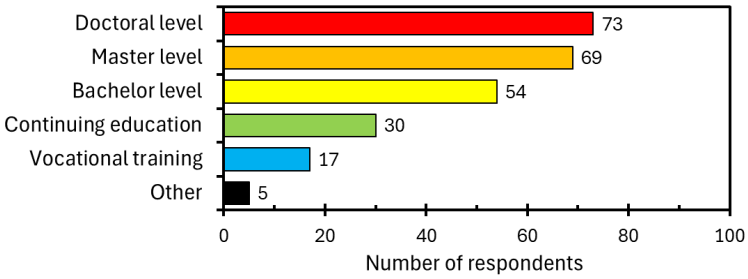

Figure 6. Personal experience from teaching process safety in academia (n = 119).

Figure 7 summarises the experience of the respondents from various branches of the labour market (n = 131, multiple answers possible). Examples of other branches include industry association, insurance, water company, vehicle manufacturer, project management, forensic engineering, and accident investigation.

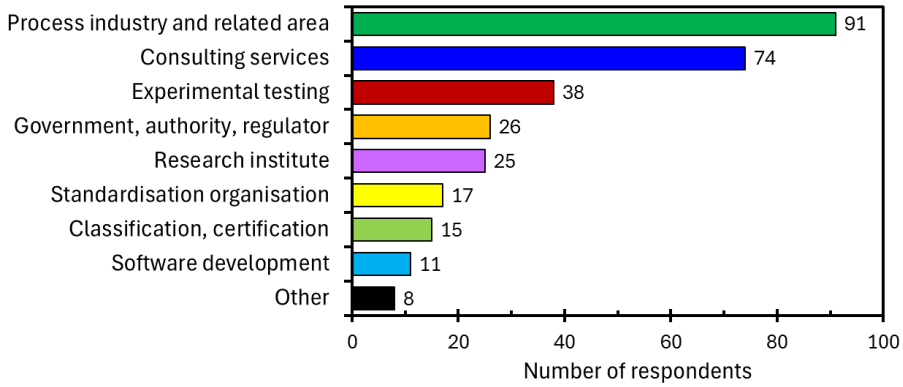

Figure 7. Experience from branches of the labour market (n = 131).

Figure 8 summarises the distribution of the respondents' experience from specific branches of the process industry (n = 91, multiple answers possible). Other branches ($n \leq 2$) include pipeline transport, geothermal energy, and agriculture.

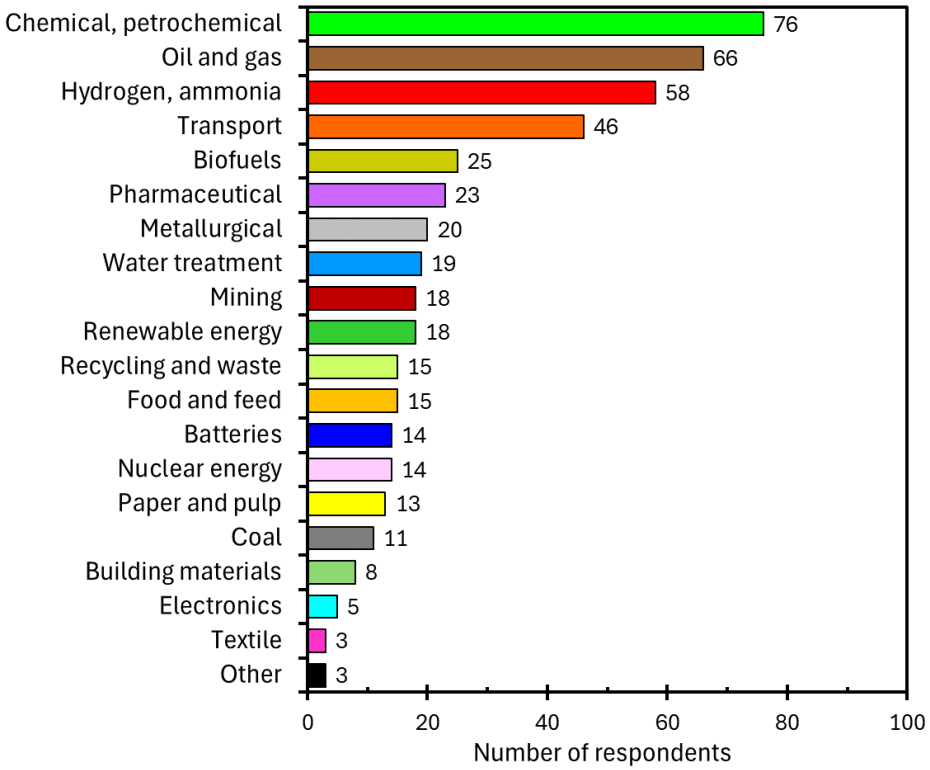

Figure 8. Experience from branches of the process industry (n = 91).

Although the respondents have significant experience from academia and relevant branches of the labour market, the limited numbers of respondents, and over-representation of respondents from certain countries (Figure 1), imply that the results from the survey are not suitable for exploring variation in trends, practices, and priorities between different countries and regions.

3.2 Collaboration

This part of the survey explored collaboration among stakeholders.

3.2.1 Multiple-choice questions

Figure 9 summarises the response to a question concerning cooperation with branches of the labour market addressed to representatives from academia (n = 68, multiple answers possible).

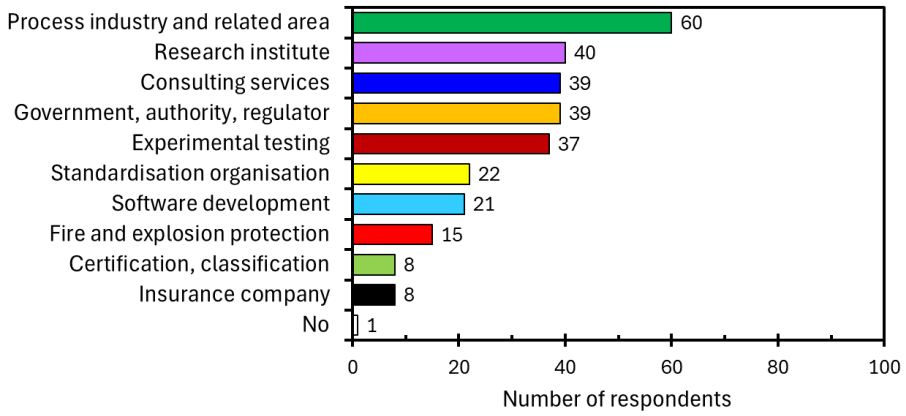

Figure 9. Collaboration with branches of the labour market, reported by academia (n = 68).

Figure 10 shows the branches of the process industry selected by the respondents with experience from process industry in Figure 9 ($n = 60$, multiple answers possible). Other ($n \leq 2$) includes pipeline transport and aeronautics.

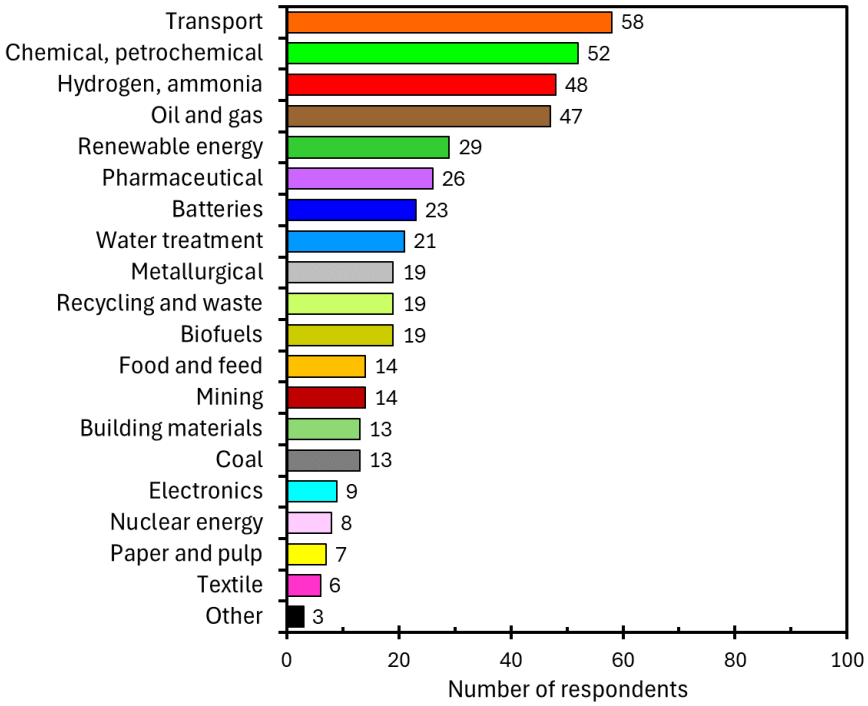

Figure 10. Collaboration with branches of the process industry, reported by academia (n = 60).

Figure 11 summarises the response to a question concerning the type of collaboration with the labour market addressed to representatives from academia ($n = 68$, multiple answers possible).

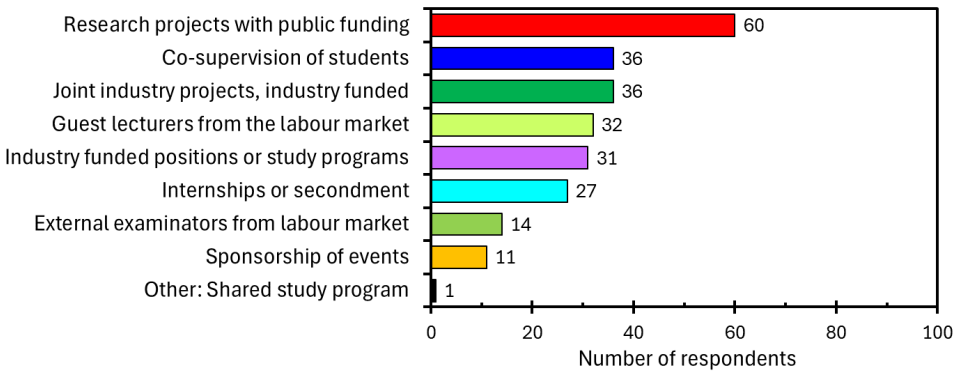

Figure 11. Type of collaboration with the labour market, reported by academia (n = 68).

From the n = 97 respondents from the labour market, 68 (70 %) were aware of active collaboration related to process safety between the company/organisation and academia. Figure 12 summarises the types of collaboration (n = 68, multiple answers possible). Other types of cooperation include scientific cooperation without financial transactions, expert reports, annual prices for students, and networking in associations. The results are reasonably consistent with the categories reported by representatives from academia (Figure 11).

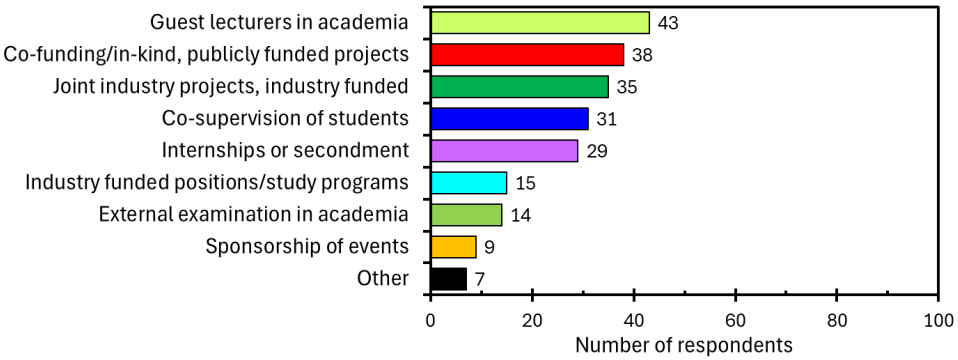

Figure 12. Type of collaboration with academia, reported by labour market (n = 68).

The results indicate extensive cooperation between academia and various branches of the labour market, reflecting the applied nature of process safety as a discipline.

3.2.2 Open-ended questions

The responses to an open-ended question concerning what the labour market had achieved from collaboration with academia highlighted (n = 97, optional):

- *Knowledge acquisition and innovation*: new knowledge; fresh ideas; access to resources.
- *Research and development*: development of numerical schemes and physical models.
- *Workforce development and recruitment*: access to candidates for employment.
- *Networking and visibility*: publications.

The responses to an open-ended question addressed to all respondents concerning the main benefits of cooperation between academia and the labour market focused on (N = 165, optional):

- *Relevance and applicability of research*: ensuring academic work has applicability to industry and the real world; getting in touch with the labour market.
- *Knowledge and exchange of experience*: sharing knowledge and experience; real case studies that benefit and enhance learning for students; exchange of ideas and challenges.
- *Preparation for the labour market*: preparing students for the labour market; previewing students for possible employment; introducing students and academics to potential roles outside academia.
- *Addressing real-world problems*: working on problems of practical importance; addressing important issues related to process safety.
- *Collaboration benefits*: achieving common goals by combining resources; financing projects.
- *Practical training and experience*: integration of fundamental knowledge with practical experience; bringing field experience to classrooms.
- *Access to resources*: access to specialist knowledge, publications, graduate students, etc.
- *Advancement of process safety*: looking at ‘big picture’ aspects of process safety; understanding the requirements of process safety; advancing the field of process safety.

Another open-ended question addressed to all respondents was concerned with the main challenges for successful cooperation between academia and the labour market (N = 165, optional):

- *Funding and resource constraints*: securing financing for larger projects; difficulties in attracting funding from industry for research; resource constraints (funding, time, personnel).
- *Communication and understanding*: a communication gap between academia and the labour market; need for a common language to exchange information; mutual understanding.
- *Different objectives and expectations*: common ground (long-term projects vs. quick practical solutions); aligning expectations (research papers and rigour vs. practical results).
- *Intellectual property and confidentiality issues*: Intellectual property rights (IPR) vs. publications; non-disclosure policies.
- *Alignment of schedules*: timeline for labour market vs. timeline for students.
- *Cultural differences and trust*: academic ideas perceived as expensive and not very practical.

The last open-ended question in this section addressed criteria for successful cooperation between academia and the labour market (N = 165, optional). The responses highlighted:

- *Communication and understanding*: common language; open bidirectional communication.
- *Alignment of goals and expectations*: aligning expectations and priorities.
- *Mutual respect and trust*: mutual respect and trust established from previous collaborations.
- *Resource availability and management*: competent personnel and sufficient time and resources.
- *Collaboration and partnership*: project collaboration; fostering long-term partnerships.
- *Benefit and value creation*: public benefit; clear and tangible value creation and positive impact for both academia and the labour market (win-win situation).

The responses to the open-ended questions in this section are somewhat redundant, and some of the questions should be combined or omitted if a similar survey will be conducted in the future.

3.3 Priorities

This part of the survey focused on teaching priorities and relevance for the labour market.

3.3.1 Multiple-choice questions

Figure 13 summarises how the respondents from academia perceive the prioritisation of various physical phenomena in the curriculum on process safety (n = 68, mandatory), and Figure 14 summarises to what extent the respondents from the labour market consider knowledge and understanding of the same physical phenomena relevant for their work (n = 97, mandatory).

The responses from representatives from academia and the labour market concerning physical phenomena are reasonably consistent (Figure 13 and Figure 14). The categories with the highest priority are gas explosions in enclosures, vapour cloud explosions (VCEs), flammability limits, source models for releases (loss of confinement), jet fires, dispersion in confined systems, and deflagration-to-detonation-transition (DDT) and detonations.

Compared to academia, representatives from the labour market tend to put *less emphasis* on fires involving solid organic materials, such as wood, paper, and plastic, and *more emphasis* on:

- Gas and spray/mist explosions in enclosures, e.g. vessels and buildings.
- DDT and detonations.
- Harm criteria for explosion scenarios: blast waves, fragments, etc.
- Dispersion in confined environments, such as vessels and buildings.

Figure 15 summarises how the respondents from academia perceive the prioritisation of selected aspects of process safety in the curriculum (n = 68, mandatory), and Figure 16 summarises to what extent respondents from the labour market consider knowledge and understanding of the same aspects relevant for their work (n = 97, mandatory).

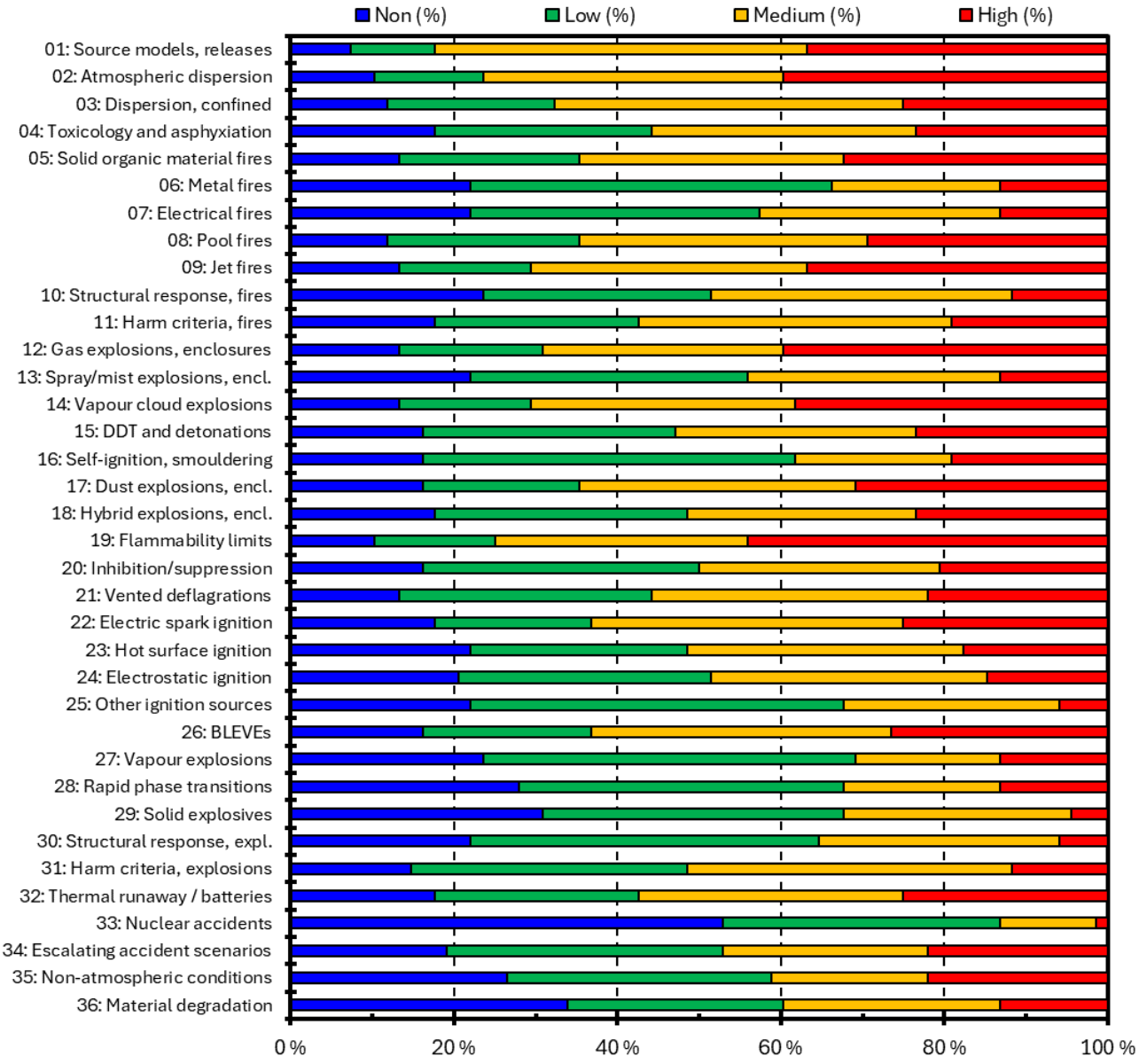

Figure 13. Physical phenomena prioritised by responders from academia (n = 68).

The responses from representatives from academia and the labour market are also reasonably consistent concerning the different aspects of process safety (Figure 15 and Figure 16). The categories with the highest priority are risk analysis and risk assessment, case histories, risk awareness, uncertainty in risk assessments, inherently safer design, and unit operations (process design). Compared to academia, representatives from the labour market put *less emphasis* on laboratory safety, and *more emphasis* on:

- Uncertainty in risk assessments.
- Plant siting and layout.
- Regulations, codes, and standards (RCS).

3.3.2 Open-ended questions

The responses to an open-ended question concerning the main knowledge gaps related to physical phenomena in process safety focused on (N = 165, optional):

- *Risk assessment and modelling*: awareness of the uncertainty in risk assessments; uncertainty in consequence modelling; the ability to model the consequences of liquid leaks with the same

accuracy as gaseous leaks (dispersion, ignition, fire, and explosion); predictive models for flame acceleration in partially congested and partially premixed atmospheres.

- *Understanding material behaviour*: material behaviour for specific materials and scenarios, e.g. hydrogen embrittlement in high-strength steel.
- *Ignition phenomena*: especially relevant for hydrogen, including spontaneous ignition and delayed ignition of jet releases.
- *Dispersion and explosion phenomena*: gas dispersion; self-heating; dust explosions; mist explosions; deflagration-to-detonation-transition (DDT) in unconfined congested spaces.
- *Artificial intelligence (AI) and advanced technologies*: computational fluid dynamics (CFD) modelling of complex phenomena in congested environments; technological disasters triggered by natural phenomena (NaTech).
- *Education and awareness*: public awareness; understanding what process safety is and how it can impact people, property, and the environment.

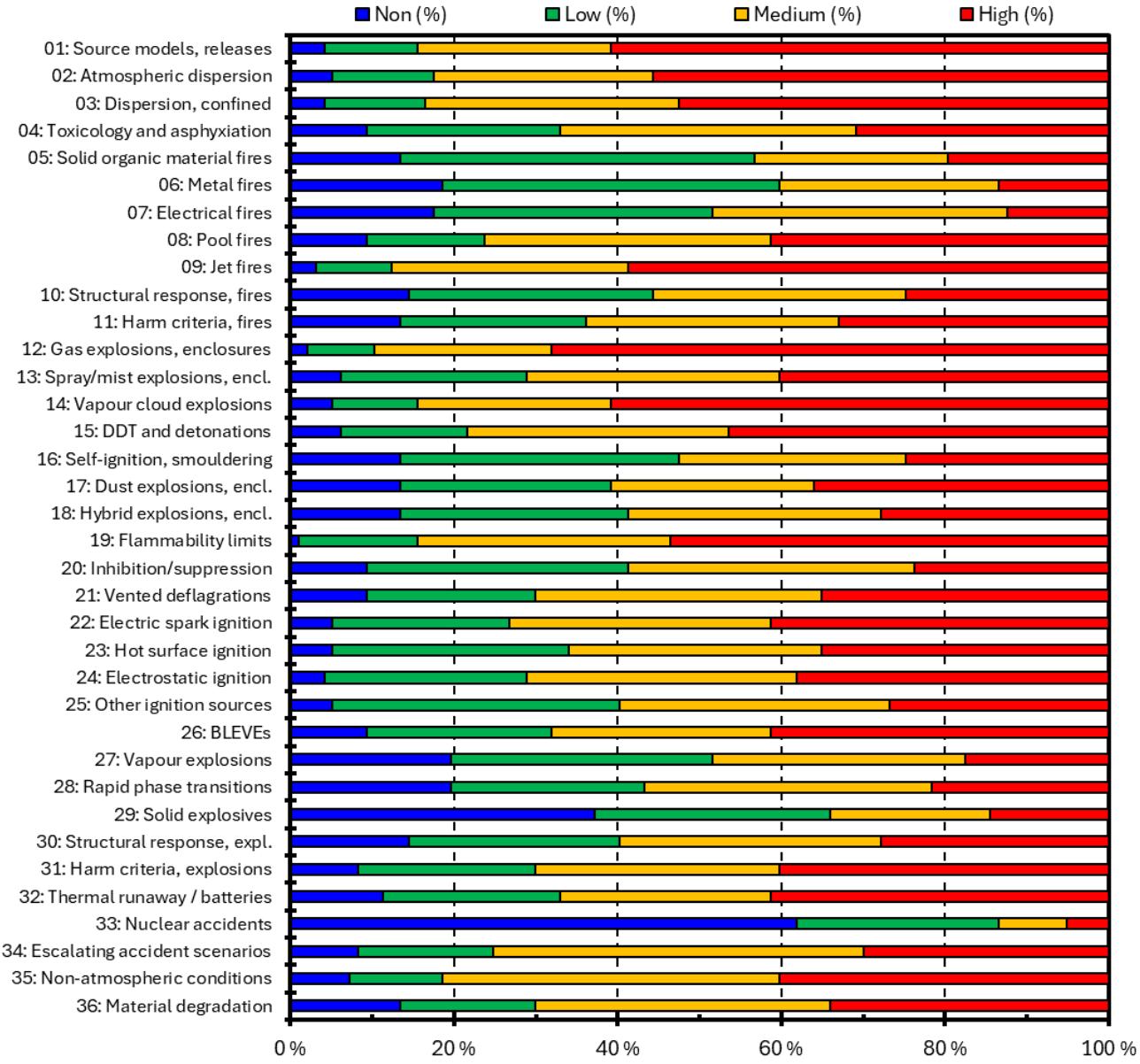

Figure 14. Physical phenomena prioritized by responders from the labour market (n = 97).

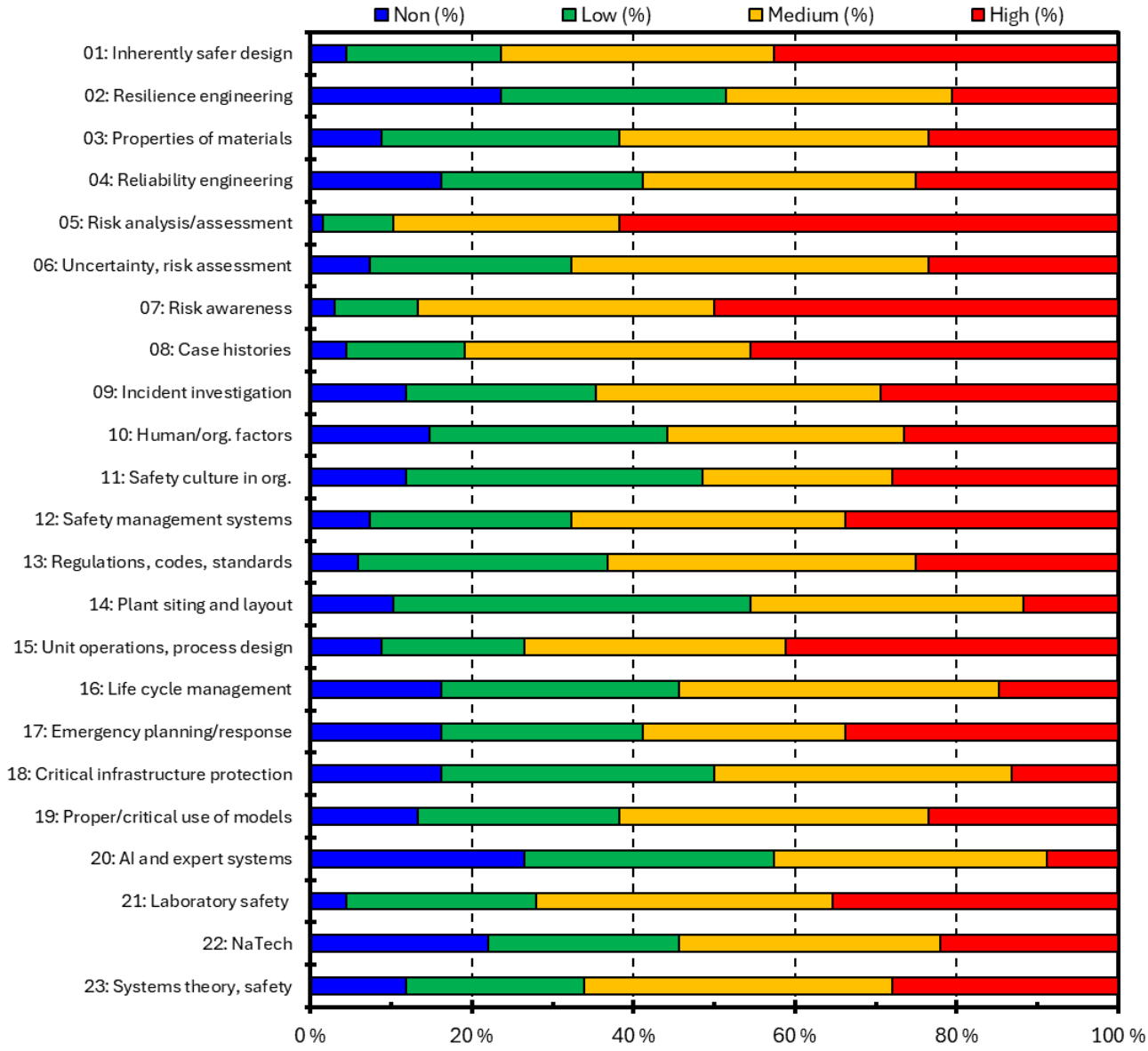

Figure 15. Aspects of process safety prioritised by responders from academia (n = 68).

The responses to an open-ended question concerning the main knowledge gaps in process safety in the twenty-first century can be summarised as follows ($N = 118$, optional):

- *AI and advanced technologies*: use of AI in risk assessments; implications for safety of the use of AI for processing: responsible use of digitalisation and AI throughout the safety lifecycle.
- *Risk assessment and management*: preventing hazards by risk-based preventive maintenance; advancing the development of risk assessment models; risk associated with hydrogen-based energy carriers (H_2, NH_3).
- *Human factors and safety culture*: risk awareness; strength of knowledge; safety culture in organizations; not forgetting the human in the sea of technological advancements; creating a sense of vulnerability in operations, maintenance, and design.
- *Data and information management*: establishing worldwide databases for recording accidents and failure rate data.
- *Process design and control*: inherently safe processes and design; more efficient and intelligent systems and devices for monitoring and control; fail-safe design of products and processes.

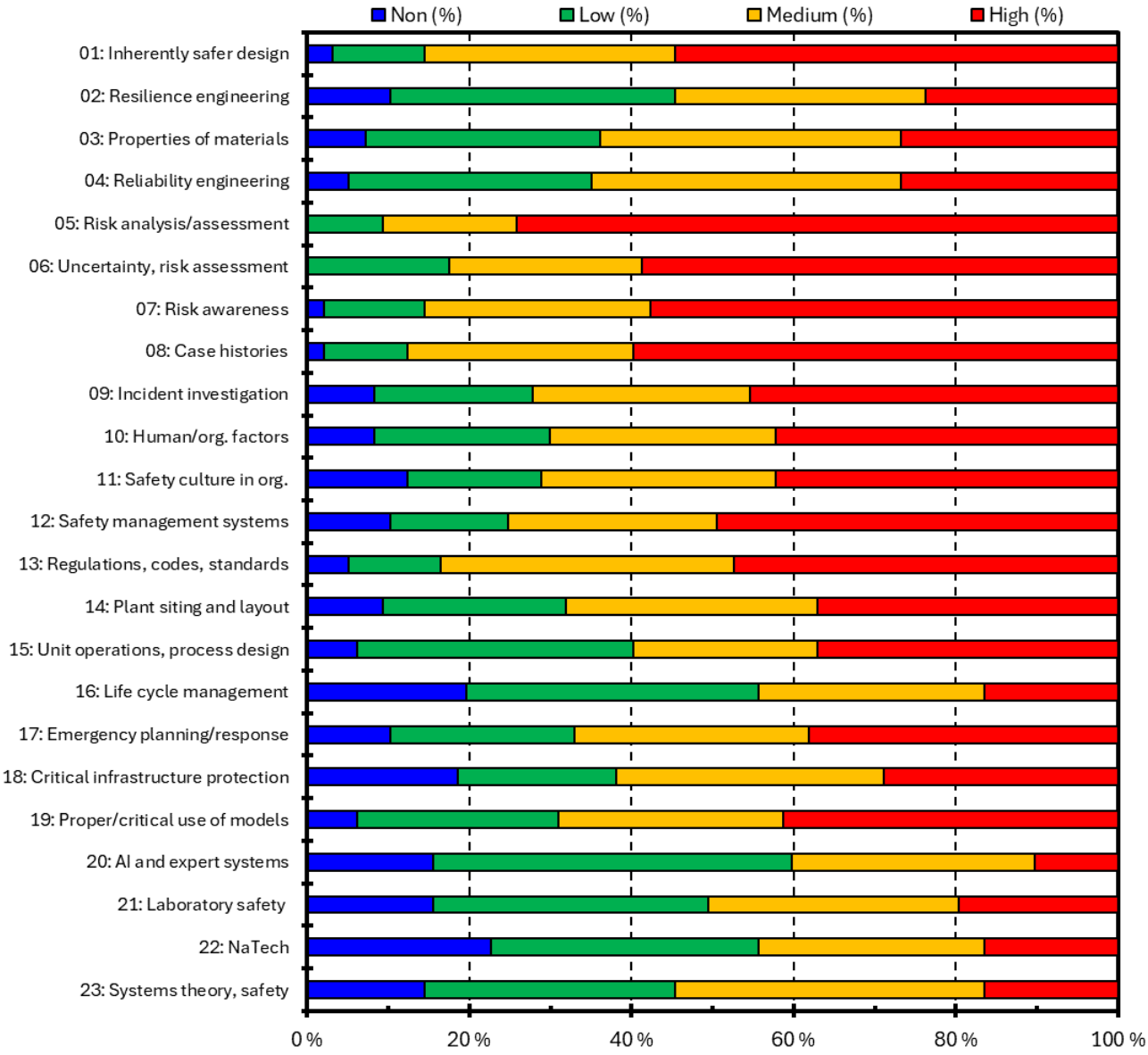

Figure 16. Aspects of process safety prioritised by responders from the labour market (n = 97).

Overall, the responses to the open-ended questions collaborate the responses to the multiple-choice questions. The focus on uncertainty and strength of knowledge in risk assessments is in line with the development in risk science mentioned in section 1.4.

3.4 Trends

This part of the survey explored global trends in process safety and the process industries.

3.4.1 Multiple-choice questions

Figure 17 summarises the expectations of the respondents concerning the development of selected industries in their country or region towards 2050 (N = 165, mandatory). The results suggest a significant increase in industries related to the global energy transformation, including renewable energy and associated energy carriers such as hydrogen, ammonia, and batteries, as well as recycling and waste. The largest reduction is expected for coal, followed by oil and gas, and the mining industry.

Figure 18 and Figure 19 summarise experienced, from 2000 to 2024, and expected, for 2025 to 2050, changes, respectively, in the teaching of process safety at the academic institutions in response to various factors (n = 68, academia only, mandatory).

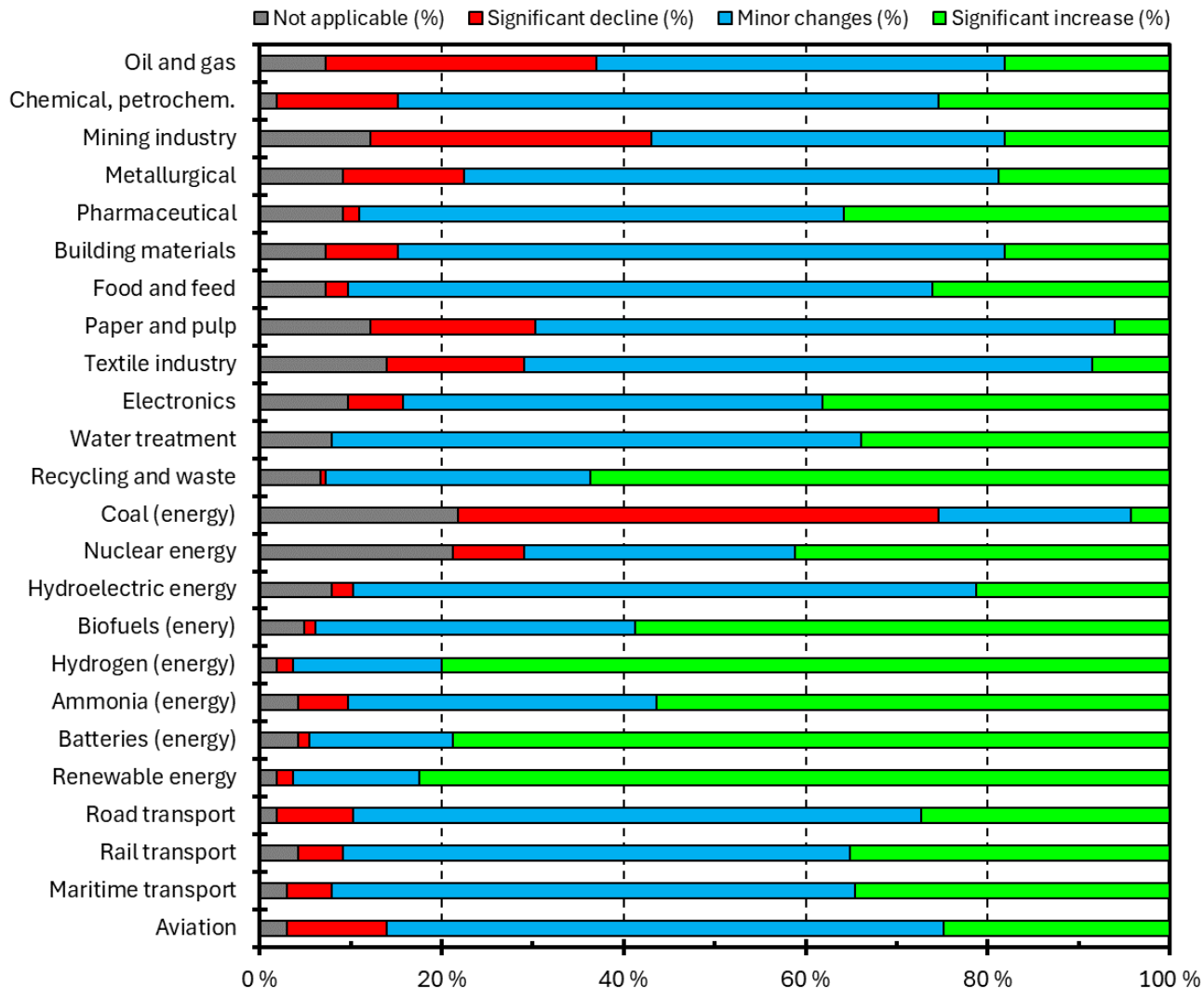

Figure 17. Expected development of selected industries towards 2050 (N = 165).

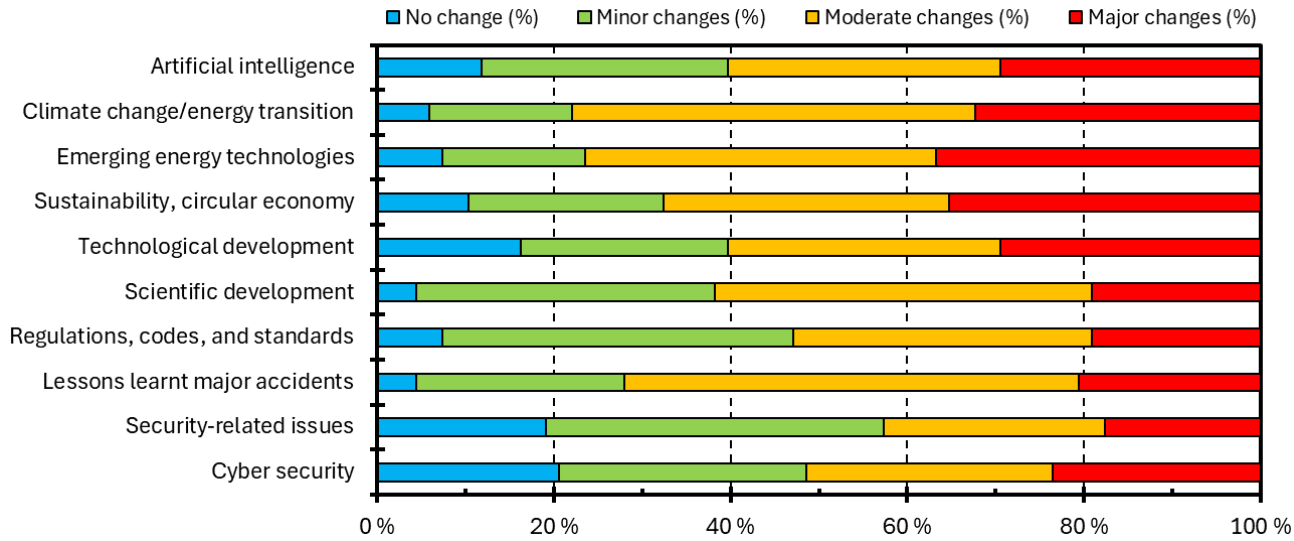

Figure 18. Experienced changes in the teaching of process safety in response to various factors (n = 68).

Figure 20 and Figure 22 summarise experienced, from 2000 to 2024, and expected, for 2025 to 2050, changes, respectively, in the activities related to process safety in the labour market in response to various factors (n = 63, labour market only, mandatory).

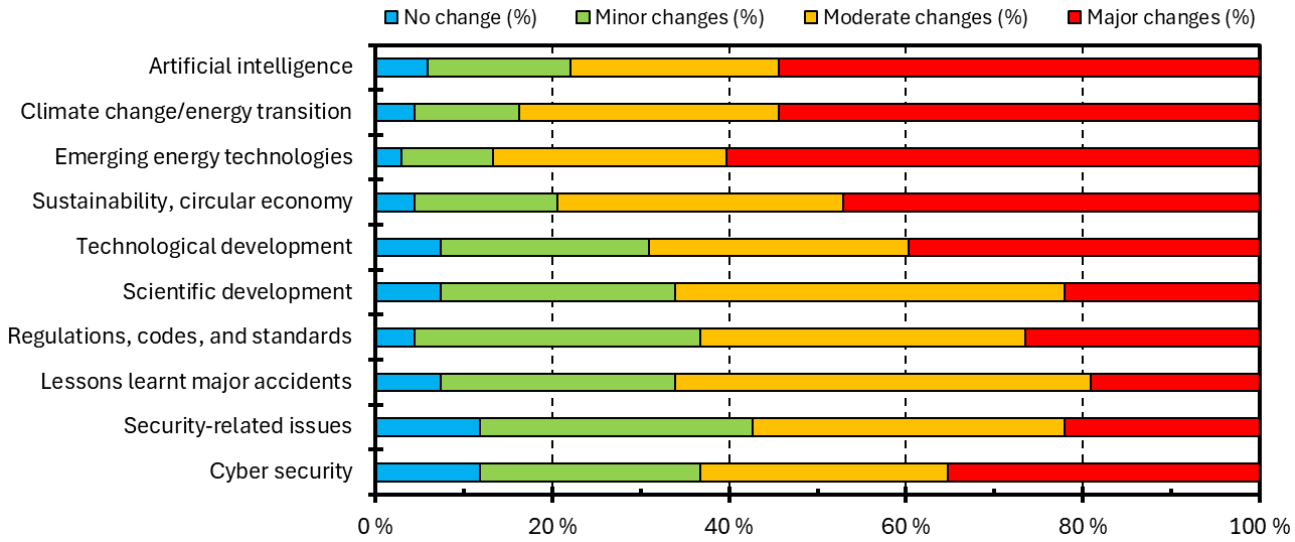

Figure 19. Expected changes in the teaching of process safety in response to various factors (n = 68).

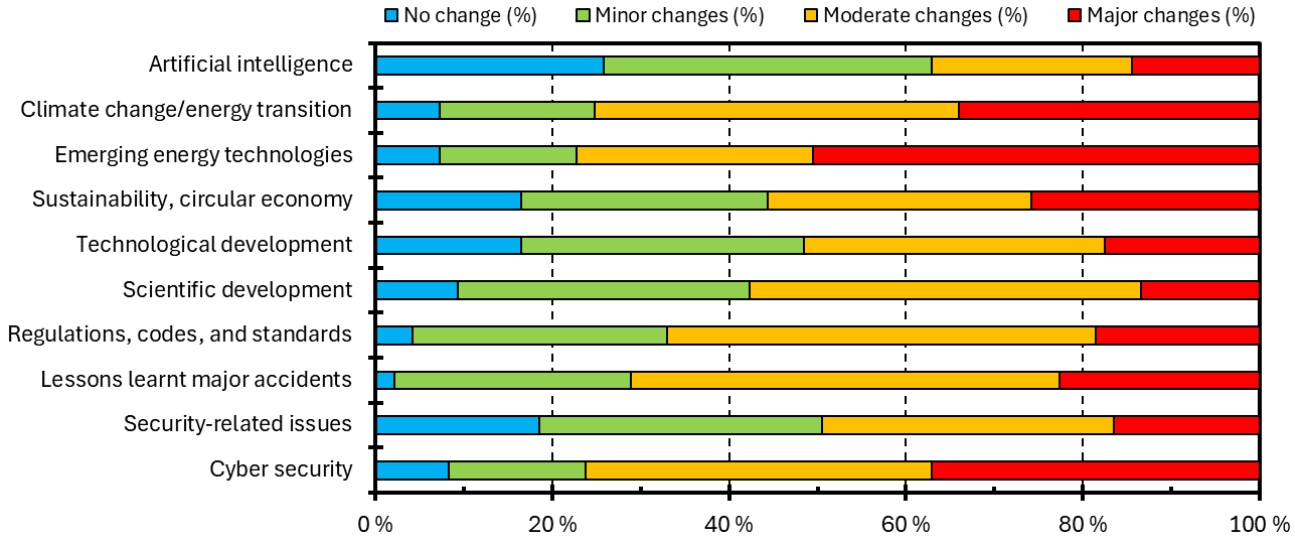

Figure 20. Experienced changes to process safety in response to various factors (n = 97).

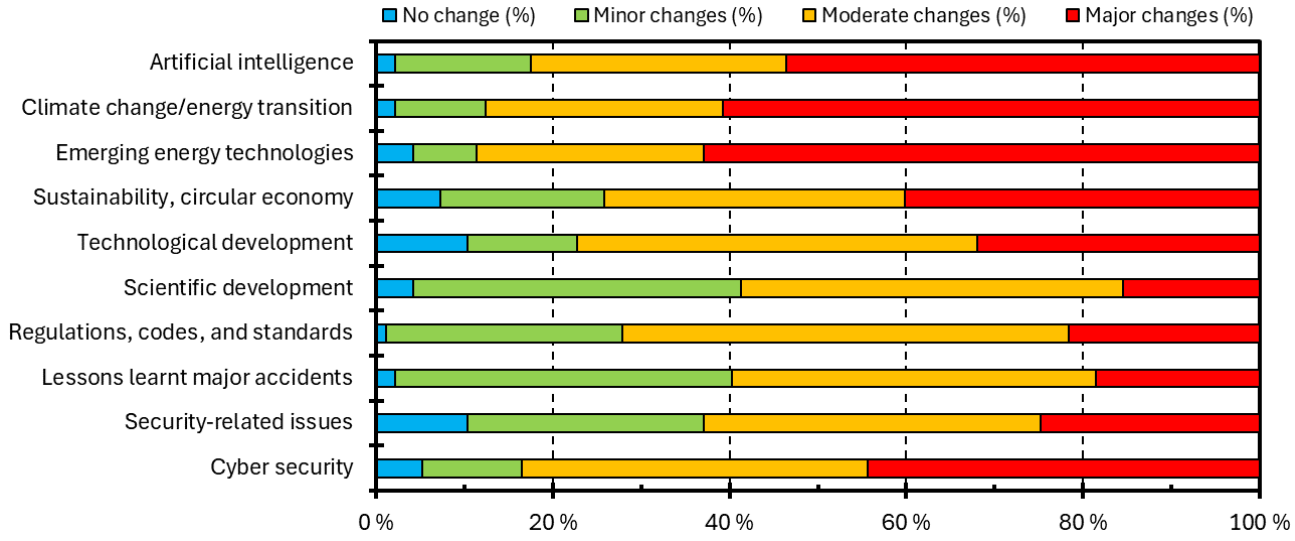

Figure 21: Expected changes to process safety in response to various factors (n = 97).

The largest changes, both experiences and expected, are related to emerging energy technologies, such as hydrogen, ammonia, and batteries, followed by climate change and the global energy transition, sustainable use of natural resources (circular economy), cyber security and AI.

Compared to academia, representatives from the labour have experienced somewhat fewer changes in response to AI, but the expectations for future changes are similar.

3.4.2 Open-ended questions

The responses to an open-ended question addressed to all respondents concerning the factor that will have the greatest impact on process safety in the twenty-first century, and why, can be classified into the following themes ($N = 165$, optional):

- *Artificial intelligence (AI) and digitalization*: many responders highlight the impact of AI, machine learning, and digitalization on process safety – these technologies may provide new ways of predicting and preventing safety issues, but they can also introduce new challenges and risks if they are not well understood or properly managed.
- *Energy transition and emerging technologies*: the shift towards new energy sources and energy technologies, such as wind, solar, hydrogen, and ammonia.
- *Climate change*: an increased risks of extreme weather events, damage to infrastructure, and the need for adaptation measures can all pose significant challenges for the process safety.
- *Cybersecurity*: the risk of cyber threats increases with the digitalisation of processes, making cybersecurity a critical factor in process safety.
- *Workforce issues*: issues related to the workforce include loss of knowledge and skills, and the need for management commitment to process safety.
- *Regulations and political factors*: regulations, legislation, and sanctions can influence the direction of the industry and create challenges for process safety.
- *Other factors*: this category included responses concerning global competition and the need for international collaboration on health, safety, climate protection, environment protection, and poverty reduction.

Given the frequency of the terms mentioned by the respondents and the potential impact on process safety, AI and digitalisation, as well as energy transition and emerging technologies, appear as the most important categories. Climate change and cybersecurity are also crucial, follows by workforce issues, regulations, and political factors.

3.5 Practice

This part of the survey addressed study programs, teaching practices, and sources of information.

3.5.1 Multiple-choice questions

Figure 22 and Figure 23 summarise the levels and types of education in process safety offered, and how process safety is taught, at the academic institutions, respectively.

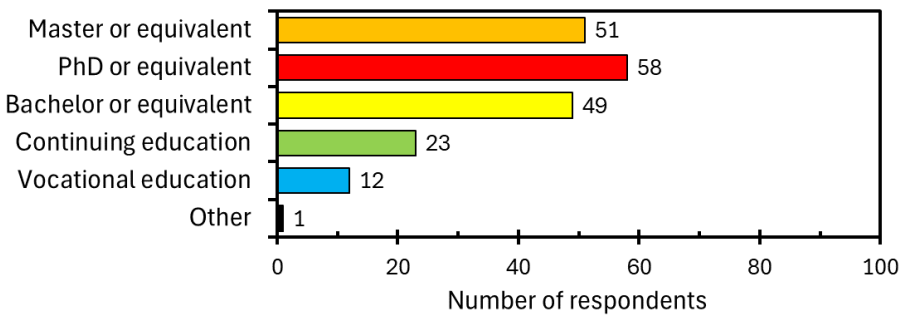

Figure 22. Levels of education offered by the academic institutions of the respondents (n = 68).

Figure 24 summarises the methods or activities used in the teaching of process safety or related topics (academia only, n = 68, mandatory, multiple answers possible). The results indicate a significant spread in teaching practices between academic institutions. Almost 60 % of the respondents rely on conventional lectures, but various other methods of teaching are also practiced.

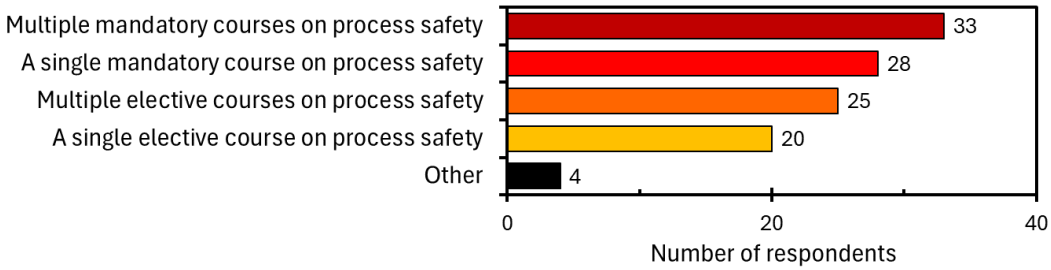

Figure 23: How process safety is taught at academic institutions (n = 68).

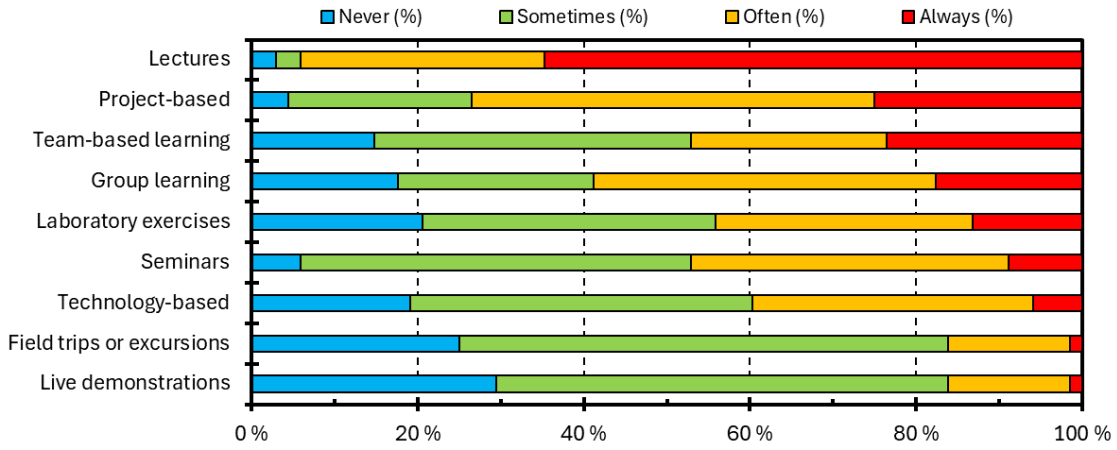

Figure 24: Methods or activities used in the teaching of process safety or related topics (n = 68).

Figure 25 and Figure 26 summarise the responses to question concerning books, including book chapters or extracts, and other material, respectively, uses in the process safety curriculum (academia only, n = 68, mandatory, multiple answers possible). The most frequently used textbook is *Chemical Process Safety* by Crowl & Louvar (2019). However, the respondents mention a variety of other books used in the curriculum on process safety.

Other books in English (n≤6): *Dust explosion dynamics* (Ogle), *Fire hazards in industry* (Thomson), *Hydrogen safety for energy applications* (Kotchourko & Jordan, eds.), *Explosions* (Bartknecht), *Hydrocarbon process safety* (Jones), *Safety and security review for the process industries* (Nolan), *Offshore risk assessment* (Vinnem & Røed), *Fundamentals of risk management for process industry engineers* (Hassall & Lant), *Process systems risk management* (Cameron & Raman), *An introduction to combustion* (Turns), *Towards process safety 4.0 in the factory of the future* (Laurent), *Ignition handbook* (Babrauskas), *Evaluation of the effects and consequences of major accidents in industrial plants* (Casal), *Natech risk assessment and management* (Krausmann, et al.), *Explosion dynamics* (Rangwala & Zalosh), *Industrial fire protection* (Zalosh), *Fundamentals of fire engineering* (Quintiere), *Dust explosion* (Barton), *Gas explosion handbook* (Bjerketvedt et al.), *Purple book* (TNO). Other non-English books (n≤6): *Prozess und Anlagensicherheit* (Hauptmanns), *Vådautsläpp av brandfarliga och giftiga gaser och vätskor* (FOA, 1998), *Seguridad industrial en atmosferax explosivas* (Garcia-Torrent), *Chemical Process Safety* in Chinese, *Sécurité des procédés chimiques* (Laurent).

Reports and videos from U.S. Chemical Safety and Hazard Investigation Board (CSB) and reports from UK Health and Safety Executive (HSE) are the main sources of additional material in the process safety curriculum.

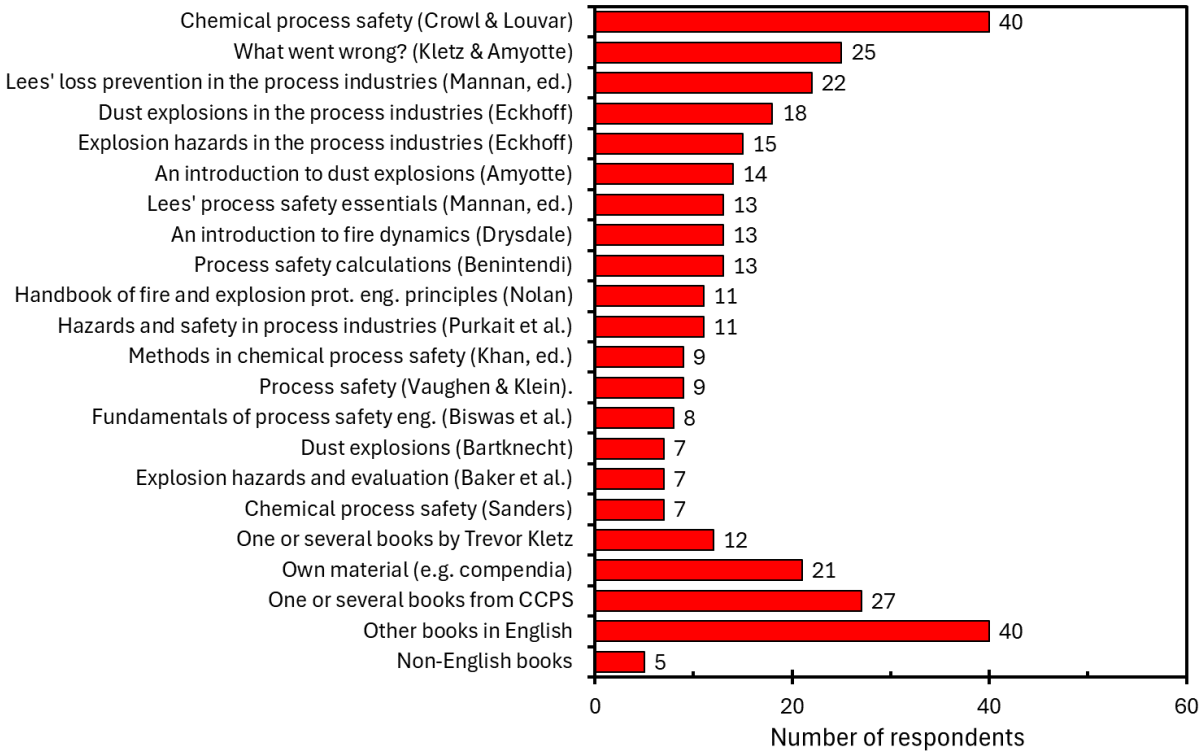

Figure 25: Books, including book chapters or extracts, used in the process safety curriculum (n = 68).

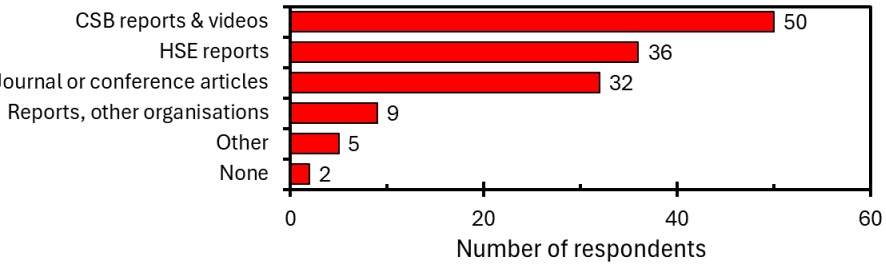

Figure 26: Other material used in the process safety curriculum (n = 68).

Figure 27 summarises the responses from the labour market concerning books or other resources used in the daily work (mandatory, n = 97, labour market only, multiple answers possible). Here, journal articles are the most frequently used resource, followed by material from CSB and HSE, and several of the textbooks mentioned by responders from academia (Figure 25).

Other books in English (n≤6) include *Hydrogen safety for energy applications* (Kotchourko & Jordan, Eds.), *An introduction to dust explosions* (Amyotte), *Handbook of fire and explosion protection engineering principles* (Nolan), *Chemical process safety* (Sanders), *Process safety* (Vaughen & Klein), *Dust explosion dynamics* (Ogle), *Fire hazards in industry* (Thomson), *An introduction to fire dynamics* (Drysdale), *Hazards and safety in process industries* (Purkait *et al.*), *Safety and security review for the process industries* (Nolan), *Process safety calculations* (Benintendi), *Fundamentals of process safety engineering* (Biswas *et al.*), *Methods in chemical process safety* (Khan, Ed.), the 'coloured books' (Yellow, Green, Red, Purple) from TNO, and various books on combustion science.

Other sources mentioned include reports from organisations such as Sandia National Laboratories and NIOSH (USA), INERIS and BARPI (France), TNO (Netherlands), VDI/VDE (Germany), PSA/HAVTIL and NORSOK (Norway), RISE (Sweden), as well as the *Annual Combustible Dust Incident Reports* from Dust Safety Science, the Process Safety Beacon from CCPS, various regulations, codes, and standards (RCS), results from joint industry projects (JIPs), open databases, and various reports, podcasts, and best practice guidelines from various branched of the process industry.

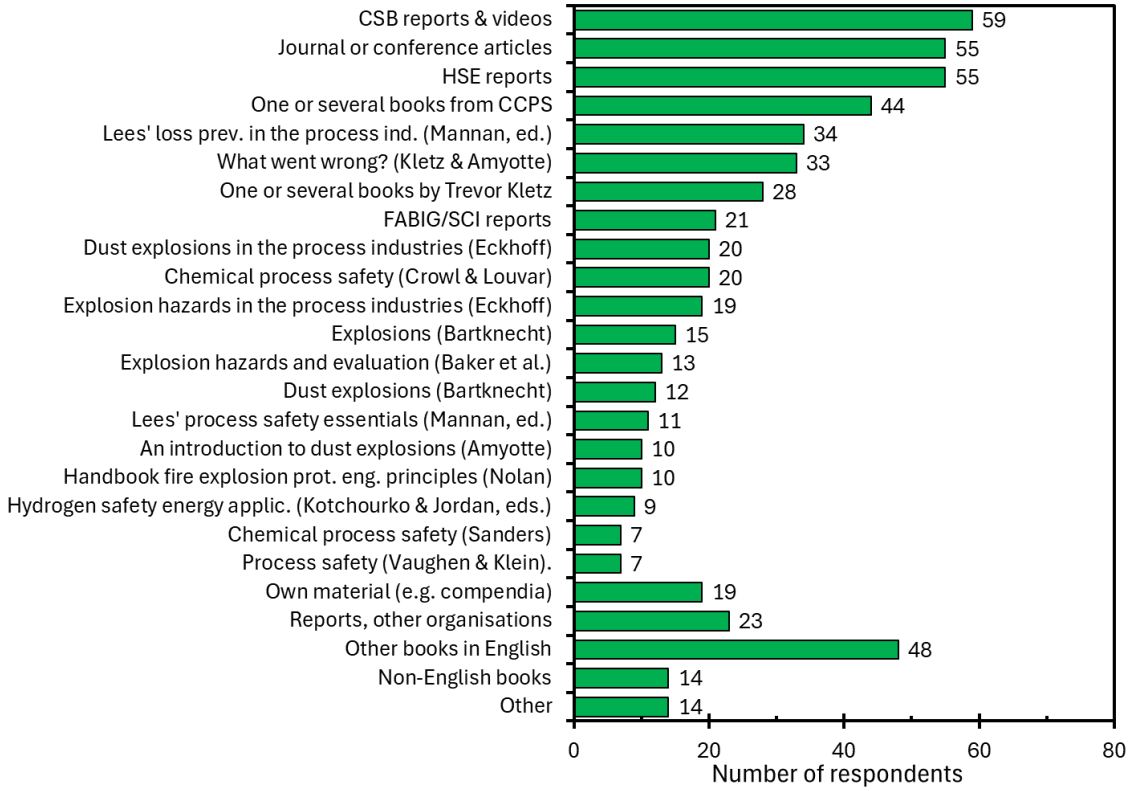

Figure 27. Books or other resources used in your daily work (n = 97).

3.5.2 Open-ended questions

The responses to an open-ended question concerning study programs related to process safety offered by the institution can be classified into the following themes (academia only, $n = 68$, optional):

- *Undergraduate programs*: this category includes bachelor's degrees in topics such as chemical engineering, fire safety engineering, and chemical safety engineering.
- *Master's programs*: this category includes various master's programs related to process safety, such as energy and process technology, process safety and loss prevention, and process safety.
- *PhD programs*: several respondents mentioned PhD programs related to process safety.

The responses to a follow-up question concerning examples of specific courses on process safety offered by the institution reveal a variety of courses with different degree of specialisation (academia only, $n = 68$, optional):

- *General process safety*: chemical process safety, safety in chemical processes, process plant safety, technical management of process safety, design for process safety, process safety and loss prevention, process safety engineering, safety in industrial operations and design, introduction to occupational safety, major accident prevention.
- *Focus on risk and reliability*: risk analysis, hazards and risk analysis, risk management, hazard risk assessment, hazard identification and risk analysis, process risk analysis, reliability and safety in the process industry, reliability and maintainability engineering, safety and reliability analysis, principles and methods of risk analysis, industrial risks,
- *Focus on toxicology:* toxicology and industrial hygiene.
- *Focus on fire and explosion hazards*: structural fire safety of industrial buildings, fire protection systems, fire chemistry, industrial fire protection, fire and explosion engineering, explosion risk in working environment, explosion hazards in the process industries, dust explosions in the process industries.
- *Focus on human factors*: human factors for process safety, human behaviour & human error.

- *Miscellaneous courses*: technical safety, technical safety systems, consequence calculations, lab safety, chemical handling, maintenance management.

The responses to an open-ended question concerning recommendations for teaching methods or approaches can be classified into the following themes:

- *Group-based learning*: project-based group work fosters teamwork, collaboration, critical thinking, problem-solving and communication skills, and creativity; groups of students can analyse accidents or incidents; team-based learning (TBL).
- *Case studies and incident analysis*: Presenting major accidents that have occurred in the chemical industry, including root causes, and demonstrating to students how the accidents could have been prevented; case studies accompanied by simulations.
- *Experiential learning* (i.e. learning by doing): field trips allow students to experience first-hand applications; live demonstrations.
- *Lectures and presentations*: lectures by faculty members, complemented with guest lectures from industry or videos.

The responses to an open-ended follow-up question on teaching material the respondents would recommend for colleagues in other universities or university colleges can be categorised as follows:

- *Books and articles*: Chemical Process Safety by Crowl & Louvar provides comprehensive and detailed fundamental knowledge on process safety; recent review articles can be very useful, especially when the textbook has not been updated for some time.
- *Videos*: several respondents recommended the videos from U.S. Chemical Safety and Hazard Investigation Board (CSB)
- *E-Learning*: can be integrated into courses.

These responses to the open-ended questions are in line with the results from the multiple-choice questions. Overall, the results indicate a larger variation in teaching materials compared to a survey on process safety education conducted by AIChE EdDiv in the US and Canada (Ford, 2023).

3.6 Interaction

This part of the survey addressed networking and dissemination.

3.6.1 Multiple-choice questions

Figure 28 summarises the responses to a question addressing membership or active participation in organisations or networks ($N = 165$, multiple answers possible). The category for other organisations ($n \leq 6$) included Institute for Dynamics of Explosions and Reactive Systems (IDERS), UK Explosion Liaison Group (UKELG), European Process Safety Centre (EPSC), Design Institute for Emergency Relief Systems (DIERS), American Petroleum Institute (API), Fire and Security Association of India (FSAI), European Safety and Reliability Association (ESRA), Society of Fire Protection Engineers (SFPE), Association of German Engineers (VDI), German Association for Electrical, Electronic & Information Technologies (VDE), and Canadian Society for Chemical Engineering (CSChE).

Figure 29 summarises the responses to a question concerning presentation of one or several papers at international conferences over the last ten years ($N = 165$, multiple answers possible). The category for other conferences ($n \leq 6$) includes International Symposium on Fire Safety Science (IAFSS) AIChE Global Congress on Process Safety (GCPS), UKELG meetings, and European Conference on Safety and Reliability (ESREL).

Figure 30 summarises the responses to a question concerning authorship of one or several papers in international peer-reviewed scientific journals the last ten years ($N = 165$, multiple answers possible). Other journals ($n \leq 6$) include *Progress in Energy and Combustion Science (6); Shock Waves (6); Flow, Turbulence and Combustion (4), Journal of Safety Research (4), Workplace Health & Safety*

(3), Journal of Electrostatics (2), Fuel (2), Reliability Engineering and System Safety (2); Risk Analysis (2); Fire Technology (2); and various journals mentioned only once.

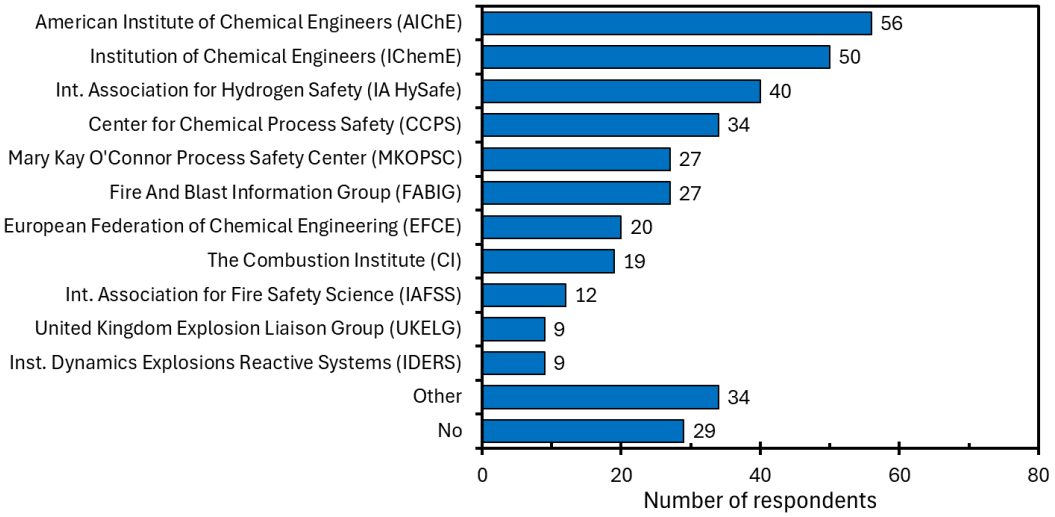

Figure 28. Membership or participants in organisations or networks (N = 165).

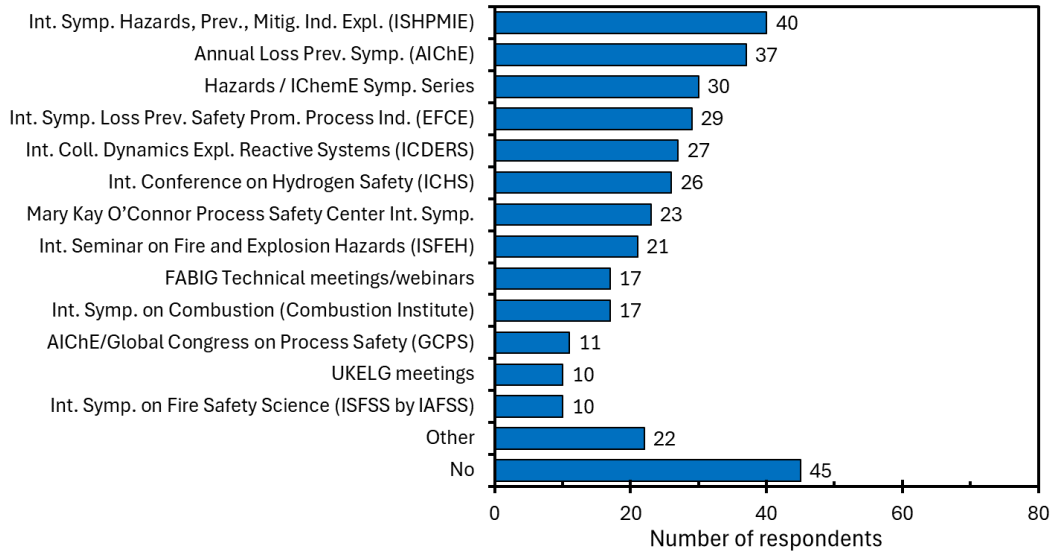

Figure 29. Papers presented at international conferences over the last ten years (n = 165).

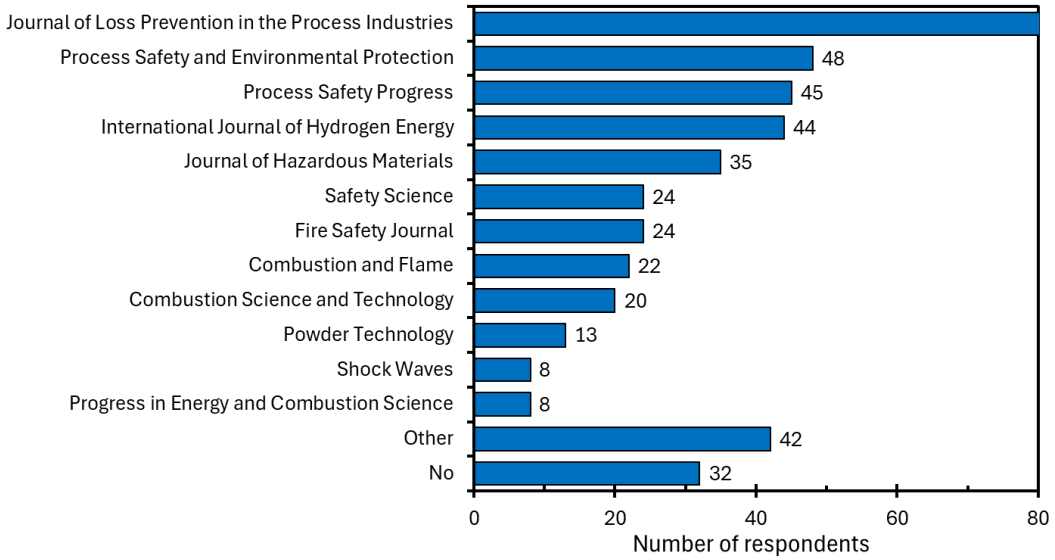

Figure 30. Publications in international peer-reviewed scientific journals over the last ten years (N = 165).

3.6.2 Open-ended questions

Of the N = 165 respondents, 110 (67 %) confirmed involvement in the development of RCS on process safety or related areas. Figure 31 summarises the most frequently mentioned standard development organisations (SDOs) mentioned in response to an open-ended follow-up question. Other SDOs (n ≤ 2) includes OSHA, API, VDI/VDE, SAE, IPS, NEN, BSI, NEK, BIS, and UNE.

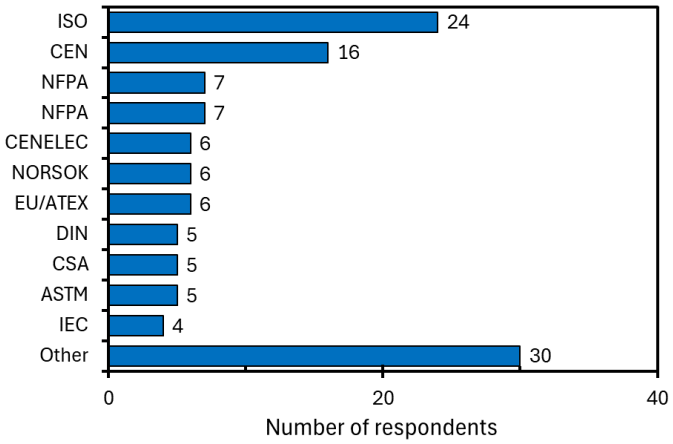

Figure 31. Involvement in standard development organisations (n = 110).

The responses to the final open-ended question concerning *"any final comments or suggestions"* included general feedback and inquiries for copies of the final results, and justified comments concerning the length of the survey. One respondent emphasised the importance of facilitating and maintaining learning about process safety in undergraduate and graduate education, and Louisa A. Nara sheared her *Rules for Great Process Safety* (reproduced with permission):

1. *Understand the hazards!*
2. *Keep it in the pipes!*
3. *Manage the risks!*
4. *Keep a sense of vulnerability!*
5. *Make a positive impact every day!*

4. Conclusions and further work

This paper summarises the results from a survey targeting practitioners of process safety, from academia as well as various branches of the labour market. The main objective of the study was to explore global trends, practices, and priorities related to process safety, with a view to promote sharing of knowledge and best practices between stakeholders.

The N = 165 respondents had significant experience from academia and relevant branches of the labour market. However, the limited numbers of respondents and over-representation of contributions from certain countries imply that the results are not suitable for exploring variations in trends, practices, and priorities between different countries and regions.

Overall, the responses from academia and the labour market are reasonably aligned, and the results reflect the global efforts to replace fossil fuels with renewable energy sources in conjunction with energy carriers such as hydrogen, ammonia, and batteries. Highlighted knowledge gaps include DDT and detonations in unconfined congested spaces, NaTech, risk awareness and uncertainty in risk assessments, implications of the use of AI in risk assessments, material behaviour for specific materials and scenarios, inherently safer processes design, and safety culture in organizations.

Further work may entail a more comprehensive analysis of the complete results from the survey, including comparisons of trends, practices, and priorities between different categories of respondents. It is also relevant to monitor the development over time by distributing updated versions of the survey that incorporate some of the observations and lessons from the present study.

Acknowledgements

The author gratefully acknowledges the time and efforts spent by the responders to the survey, as well as the financial support of Prosa21 from the University of Bergen and Vestland County Council.

References

Abedsoltan, H., Abedsoltan, A., Zoghi, Z., 2024. Future of process safety: Insights, approaches, and potential developments. *Process Safety and Environmental Protection*, 185, 684-707.

Amyotte, P.R. (2013). Process safety education determinants. *Process Safety Progress*, 32, 126-130.

Amyotte, P.R., Khan, F.I., Irvine, Y., 2019. Continuous improvement in process safety education. *Chemical Engineering Transactions*, 77, 409-414.

Aris, R., 1976. Some thoughts on the nature of academic research. *Chemical Eng. Edu.*, 10, 2-5.

Aris, R., 1977. Academic chemical engineering in an historic perspective. *Industrial & Engineering Chemistry Fundamentals*, 16, 1-5.

Aven, T., 2010. *Misconceptions of risk*. Wiley.

Aven, T., 2013. Practical implications of the new risk perspectives. *Reliability Engineering & System Safety*, 115, 136-145.

Crowl, D.A., Louvar, J.F., 2019. *Chemical process safety: Fundamentals with applications*. Pearson.

Flage, R., Aven, T. (2009). Expressing and communicating uncertainty in relation to quantitative risk analysis. *Reliability: Theory & Applications*, 4: 9-18.

Ford, L.P. (2023). *How we teach: Process safety*. AIChE Annual Meeting, 5-10 November, Orlando.

Forest, J.J, 2018. Risk based process safety in chemical engineering curriculum. *Chemical Engineering Education*, 52, 287-293.

Guerrero-Pérez, J., 2023. Imperative of integrating process safety education in chemical engineering curricula. *ACS Omega*, 8, 47318-47321.

ISC/MKOPSC, 2013. *Process safety for the 21st century and beyond*. IChemE Safety Centre (ISC) & Mary Kay O'Connor Process Safety Center (MKOPSC).

Kletz, T. 2000. *By accident – a life preventing them in industry*. PFV Publications, London.

Kletz, T., Amyotte, P., 2019. *What Went Wrong?* Elsevier/Butterworth-Heinemann, Oxford, UK.

Kouwenhoven, P., 2021. Process safety education: A comparative study. *Education for Chemical Engineers*, 36, 128-142.

Leveson, N., 2011. *Engineering a safer world: Systems thinking applied to safety*. MIT Press.

Mannan, M.S. (Ed.), 2012. *Lees' loss prevention in the process industries*. Elsevier.

Mannan, M.S., Akgerman, A., Anthony, R.G., Darby, R., Eubank, P.T., Hall, K.R., 1999. Integrating process safety into ChE education and research. *Chemical Engineering Education*, 33, 198-209.

Mannan, M.S., Sachdeva, S., Chen, H., Reyes-Valdes, O., Liu, Y., Laboureur, D.M., 2015. Trends and challenges in process safety. *AIChE Journal*, 61, 3558-3569.

MKOPSC, 2011. *Process safety research agenda for the 21st century*. Mary Kay O'Connor Process Safety Center (MKOPSC), Texas A&M University System, College Station, Texas.

Mkpat, E., Reniers, G., Cozzani, V., 2018. Process safety education: A literature review. *Journal of Loss Prevention in the Process Industries*, 54, 18-24.

Qian, Y., Vaddiraju, S., Khan, F., 2023. Safety education 4.0 – A critical review and a response to the process industry 4.0 need in chemical engineering curriculum. *Safety Science*, 161, 106069.

Rasmussen, N.C., 1981. The application of probabilistic risk assessment techniques to energy technologies. *Annual Review of Energy*, 6: 123-138.

Sanders, R.E., 2013. Keep a sense of vulnerability: For safety's sake. *Process Safety Progress*, 32, 119-121.

Tighe, C.J., Maraj, M.P., Richardson, S.M., 2021, Sharing good practice in process safety teaching, *Education for Chemical Engineers*, 36, 73-81.

Vaughen, B.K., 2019. An approach for teaching process safety risk engineering and management control concepts using AIChE's web-based concept warehouse. *Process Safety Progress*, 38, e12010 (18 pp.).

Weinberg, A.M. (1981). Reflections on risk assessment. *Risk Analysis*, 1, 5-7.

The SAFEN ignition probability model for hydrogen

Ingar Fossan[a], Kees van Wingerden[b], Ørjan Knudsen[c], Jo Wiklund[d], André Vagner Gaathaug[e]

[a]Safetec Nordic (Trondheim, Norway)
[b]Vysus Group (Bergen, Norway)
[c]Gexcon (Bergen, Norway)
[d]Proactima (Oslo, Norway)
[e]Equinor (Porsgrunn, Norway)

E-mail: ingar.fossan@safetec.no

Abstract

There are significant gaps in our understanding of risk drivers in the hydrogen industry. Knowledge gaps implies more caution in the safety design potentially leading to cost-driving solutions, or worse, materialisation of unforeseen accidental costs. The SAFEN JIP (Safe Energy Carriers) was established to address fire and explosion safety design knowledge gaps. SAFEN Phase 1 delivered models for leak frequencies and ignition probabilities. The SAFEN ignition probability model for hydrogen is presented with its basis comprised of our current knowledge basis on ignition mechanisms and incident data. The model objective is to enable estimation of ignition probability for use in quantitative risk analysis for facilities handling hydrogen. Principally, factors affecting model parameters fall into two categories: 1) the physical properties of the released fluid (*e.g.*, composition, pressure, temperature) and its ignitability (*e.g.*, MIE and AIT), and 2) the properties of the objects exposed to the fluid including ignition mechanisms caused by interaction between the fluid and the object. Any object must possess an ignition mode (a mode where an ignition mechanism will materialise if exposed to combustible fluid) to initiate ignition. Objects and equipment intended for use in explosive atmospheres (Ex rated) shall only possess an ignition mode if the equipment is faulty. For objects not intended for use in explosive atmospheres (Non-Ex equipment), modes that facilitate ignition may be present when the object possesses its normal function. SAFEN has reviewed available knowledge and theories on hydrogen ignition mechanisms and derived models for estimation of ignition probability given exposure to both Ex rated and Non-Ex equipment. Important ignition mechanisms are hot surface ignition, mechanically generated sources, static electricity and adiabatic compression and shock waves. The SAFEN model is tailored in line with the state-of-the-art ignition probability model for oil and gas facilities ((Lloyd's Register Consulting (2018)). The model is tested for a refuelling station demonstrating results according to the model target set based on our current knowledge basis. The model will be improved in SAFEN Phase 2 based on an experimental campaign and additional incident data.

Keywords: *hydrogen, ignition mechanism, ignition probability, ignition control, risk analysis*

1. Introduction

Hydrogen (H2) plays a crucial role in the decarbonization of the world's energy consumption. H2 is one of the energy carriers that will enable the transition to a more renewable energy system, provided that green or blue hydrogen is used. H2 is more prone to ignition than most other gases (such as hydrocarbons), which implies a higher probability for fires and explosions in case of accidental leaks. At present, there is a significant knowledge gap on understanding ignition mechanisms for H2 leaks. Consequently, more caution needs to be taken in the safety design. This may at one hand lead to overly conservative and thereby costly design solutions – for example an excessive safety zone around the facility. On the other hand, the lack of knowledge may lead to inadequate safety design allowing for materialisation of intolerable accidents in the long run. This threatens successful implementation of the renewable energy solutions, which was demonstrated by the fire and explosion at the hydrogen refuelling station in Sandvika in June in 2019 (Hansen, O.R (2019)).

The SAFEN (Safe Energy Carriers) Joint Industry Project was established to address and close knowledge gaps in risk management in the climate friendly energy sector. The first phase ending Q4 2023 delivered models for leak frequencies and ignition probabilities. The models were presented at

the 106th FABIG Technical Meeting 18th and 19th October 2023 (see www.fabig.com). In this paper, the SAFEN ignition probability model for hydrogen is presented with its basis comprised of our current knowledge basis on ignition mechanisms and incident data. The model objective is to enable estimation of ignition probability for use in Quantitative Risk Analysis (QRA) for facilities handling hydrogen. The presented model will be further developed in a research and innovation project partly funded by the Norwegian Research Council. This project is denoted HICON – Hydrogen Ignition CONtrol. The planned research in HICON will mitigate the uncertainties in the presented SAFEN Phase 1 ignition probability model through an experimental campaign and further compilation of incident data.

The SAFEN and HICON projects are headed by Safetec. The technical work is executed by Safetec, DNV, Proactima, Vysus Group and Gexcon in partnership with Vår Energi, Equinor, Gen2Energy, Gassco, Storegga, Swagelok Norway, Yara, Aker Horizons, Origin Energy, Hyds, Lloyd's Register, Energy Institute, GreenH, The Norwegian Maritime Authority, RIVM (National Institute for Public Health and Environment in Netherlands), World Class Maintenance and DSB (Norwegian Directorate for Civil Protection). With the key category of stakeholders included in the project – including authorities enforcing risk-based regimes – the SAFEN project facilities an effective environment for obtaining a broad industry consensus on how to solve the challenges faced by the hydrogen industry.

2. Modelling principles

The SAFEN project concluded to recommend the MISOF (Modelling of Ignition Sources on Offshore oil and gas Facilities) framework for ignition modelling (Lloyd's Register Consulting (2018)). Principally, factors affecting model parameters fall into two categories: 1) the physical properties of the released fluid (e.g., composition, pressure, temperature) and its ignitability (e.g., MIE and AIT), and 2) the properties of the objects exposed to the fluid including ignition mechanisms caused by interaction between the fluid and the object. Any object must possess an ignition mode (a mode where an ignition mechanism will materialise if exposed to combustible fluid) to initiate ignition. Objects and equipment intended for use in explosive atmospheres (Ex rated) shall only possess an ignition mode if the equipment is faulty. For objects not intended for use in explosive atmospheres (Non-Ex equipment), modes that facilitate ignition may be present when the object possesses its normal function. SAFEN has reviewed available knowledge and theories on hydrogen ignition mechanisms and derived models for estimation of ignition probability given exposure to both Ex rated and Non-Ex equipment. Important ignition mechanisms are hot surface ignition, mechanically generated sources, static electricity and adiabatic compression and shock waves.

The MISOF model is based on that ignition of leaks is governed by ignition mechanisms materialised by interaction between the combustible mixture and the exposed object(s) facilitating initiation of the combustion process. The mechanism could for instance be heat transfer due to excessive temperature of the object or the object releasing electrostatic discharges due to potential differences between component parts. The most recent version of the MISOF ignition model was developed by Lloyd's Register and Lilleaker Consulting AS on behalf of Equinor (Lloyd's Register Consulting (2018)). The MISOF model is also recommended for use at land-based oil and gas facilities, but with some adjustments and additional parameter values (Safetec (2022)).

In MISOF, the ignition probability, $P(I)$, is the product of two probabilities: the probability for exposure of a live ignition source to a flammable atmosphere, $P(E)$, and the ignition probability given such exposure, $P(I\ given\ E)$. The ignition probability, $P(I)$, then becomes

$$P_{Ignition} = P(I) = P(E) \cdot P(I\ given\ E) \qquad (1)$$

Both $P(E)$ and $P(I\ given\ E)$ possess a time dependent behaviour.

The SAFEN ignition probability model incorporates required adjustments of $P(I\ given\ E)$ relative to hydrocarbon facilities making the MISOF model applicable to facilities processing, storing, or

distributing hydrogen. $P(E)$ is not part of the ignition model but is critical for the obtained accuracy of the ignition probability estimation. It is referred to Chapter 4, 5 and 6 in the MISOF report (Lloyd's Register Consulting (2018)) for further description on the modelling principles and guidelines.

The MISOF model does not explicitly differentiate between gas and liquid leaks. It is the resulting volumetric distribution of the explosive atmosphere generated by the leak that matters.

On a high level, the ignition model consists of the following main categories

- Immediate ignition: probability for ignition before a flammable gas cloud has been formed. This is a special case where the ignition mechanism is related to the properties of the object that the release originates from and/or the fluid that is released.
- Delayed ignition: probability of ignition due to exposure of objects that constitute a potential source of ignition if exposed to flammable atmospheres. Ignition will in this case take place after start of the release and a flammable atmosphere has formed.

These two groups are further broken down to a few categories dependent on the type of equipment and ignition mechanism. For the group "immediate ignition", there is two categories:

- Generic immediate ignition is ignitions that occur immediately upon start of the leak originating from any type of equipment except pumps
- Pump immediate ignition only applicable to leaks stemming from pumps

The equipment categories under the delayed ignition group are as follows:

- Rotating equipment intended for use in explosive atmosphere (Ex-rated equipment)
- Electrical equipment intended for use in explosive atmosphere (Ex-rated equipment)
- Other equipment intended for use in explosive atmosphere (Ex-rated)
- Objects not intended for use in explosive atmosphere (Non-Ex equipment) such as Non-Ex electrical equipment, conventional vehicles, gas turbines, transformers, hot work activity etc.

Modelling of the ignition probability given exposure to Ex-rated equipment can be done in two ways, but the most used way is to apply the generic parameter "Ignition sources in the area" (λ_i). λ_i is the expected number of ignitions per volume unit. Hence, it is a volumetric parameter representing the likelihood of having an effective potential ignition source in a classified area.

Based on general classification of the actual physical ignition mechanisms, the following two types of idealized ignition mechanisms are established in the ignition model:

- Continuous ignition mechanisms cover ignition mechanisms that are present continuously (such as a flame or a hot surface) and ignites the flammable atmosphere upon first exposure.
- Discrete ignition mechanisms are an effective ignition source only at distinct moments in time. A discrete ignition source can be an electric spark due to static electricity or generated by a switch being turned on or off. Another example is ignition sources introduced by activities performed by personnel (*e.g.*, operation of equipment). The personnel may be present initially or they could enter the scene of the incident after the onset of the leak.

The modelling of the exposure probability ($P(E)$ in equation (1) for these two idealized ignition mechanisms are different, which must be reflected in the time-dependant exposure model.

3. Uncertainties and varying practice in hydrogen ignition modelling

Identified models for ignition probability quantification are shown in Fig. 1. The documentation of the various model's basis and limitations is generally scarce. For example, if generic probabilities suggested by the model is derived from incident data captured from oil and gas facilities with strict ignition source control, it is unlikely to be valid in areas with much hot work without habitat and use of vehicles classified areas. Depending on the facility at hand, one model may be more relevant and therefore applicable than another. Since the validity and limitations for each model is not well described, it seems fair to say that current practice varies substantially and that ignition modelling in

QRA is not consistent. Differences between QRA's arise from analysts choosing different models that appear equally relevant or valid.

Moosemiller, M. and B. Galindo (2014) discuss the divergence in opinions and experiences on ignition probabilities. The paper includes a literature review with examples and the overall evaluation is that there is limited knowledge available from data enabling estimation of the ignition probability related to hydrogen leaks. This is indirectly supported by Sandia National laboratories in developing the HyRAM+ model as they did not identify relevant statistics to develop an ignition model (Ehrhart, B.D (2022)). HyRAM+ is therefore derived from the model for hydrocarbons presented in Cox, A.W. et.al. (1990). The ignition probability model in Cox, A.W. et.al. (1990) is based on statistical data covering oil and gas blowouts at the Norwegian Continental Shelf (SINTEF (1983)). The model in HyRAM+ is obtained by adjusting the proposed probabilities in Cox, A.W. et.al. (1990) according to the expected size of a gas cloud resulting from a gaseous hydrogen leak compared to a hydrocarbon leak (due to molecular weight and flammability range). Consequently, the fundament for the HyRAM+ model is weak in terms of the relevance for facilities handling hydrogen.

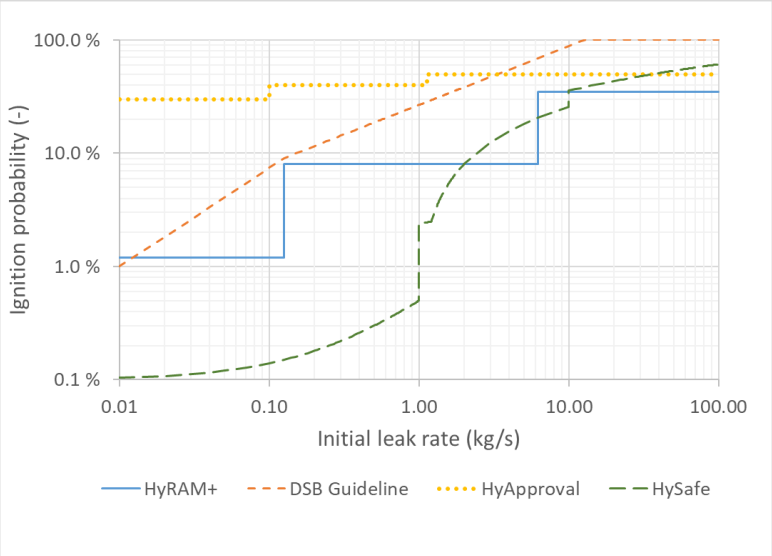

***Fig. 1**. Various ignition models used in industry (Ehrhart, B.D (2022), HyApproval & DNV (2008), HySafe (2007), Vysus Group (2021). The results for HySafe are based on an assumed flammable gas cloud.*

4. Key factors affecting the ignition probability

In general, ignition is caused by energy transferred from the ignition source (the object possessing an ignition mode) to the flammable atmosphere exposing the ignition source. Ignition occurs when an initiating combustion process in a flammable atmosphere is sustainable without external supply of energy. Each chemical substance possesses unique physical properties. In principle, a given ignition mode of an object causing ignition of combustible atmosphere consisting of mixture of hydrocarbons at certain state (e.g., concentration, pressure, temperature, and velocity) may not be able to ignite a slightly different mixture of hydrocarbons. When deriving the parameters in MISOF, the effect of the difference in ignitability between various mixtures of hydrocarbons has been disregarded. Important arguments supporting this are that the minimum ignition energy (MIE) and the autoignition temperature (AIT) of the gaseous hydrocarbons (C1 through C4) are quite similar (MIE in the range 25-30 mJ and AIT in the range 405-580 ^{O}C). The most important argument is however that the ignition modes related to the objects are assumed to generate more than enough energy to ignite any of the possible hydrocarbon mixtures.

Based on the above, when evaluating the difference across industries, the questions to answer are (1) whether the objects at facilities in various industries possess different ignition modes and (2) whether the relevant ignition modes possess the same capability to ignite the relevant types of combustible atmosphere. We know that hydrogen is more prone to ignition than hydrocarbons (see chapter 6

through chapter 9), but the relative effect the elevated ignitability of H2 has on the ignition probability estimated for facilities handling oil and gas is hard to evaluate without data on the spectra of ignition modes. Since the potential for ignition modes includes effects related to fundamental ignition control design requirements and operational inspection and maintenance schemes it is a considerable challenge to assess the ignition probability for various facilities handling hydrogen unless having representative statistical data at our disposal for benchmarking of the level of the ignition probability.

5. The expected level of the ignition probability

The intention in this section is to derive the interval where we believe that the underlying ignition probability associated with hydrogen leaks larger than 0.01 kg/s reside. We do not know, so we argue for our conclusion by a list of quantitative and qualitative statements regarding what we know about the ignition probability level.

1) We know that the average ignition probability associated with process leaks > 0.1 kg/s at offshore and onshore oil and gas facilities are about 0.25% (Lloyd's Register Consulting (2018) and Safetec (2022))
2) We know that the ignition probability associated with small and moderate gaseous hydrogen leaks are very low (most likely zero) if no object is exposed, and the diffusion ignition mechanism cannot materialize downstream the leak point. This we know from experimental work (for example Proust (2019) and incident data gathered as part of the SAFEN project).
3) We have very limited knowledge on the scalability of the ignition probability. There have been very few large leaks of hydrogen and experiments do generally not include large leaks. This is to some extent the situation for hydrocarbon leaks as well. There have been few large leaks in the oil and gas industry also, and the uncertainty associated with modelling of the ignition probability for large leaks is therefore also prominent. Although we know that the ignition probability associated with large hydrocarbon leaks in the oil and gas industry is much lower than 30% (based on overall statistics from process, riser, pipeline (exclusive buried pipelines) and blowout leaks (Lloyd's Register Consulting (2018), Safetec (2022), Vysus Group (2021), Vysus Group (2023) and Energy Institute (2006)), we are not entirely confident whether there are any interdependencies between the rate and the materialisation of ignition mechanisms that could undermine the current modelling approach for large leaks in the oil and gas industry. The current modelling approach for hydrocarbon leaks does only reflect the correlation between leak rate and size of the generated explosive atmosphere. It might be that there are other factors than size of the combustible cloud that drives the proportionality with leak rate size.
4) Most of the recorded ignited hydrogen leaks can be explained by concrete sources of ignition facilitating the ignition mechanism, such as diffusion ignition, hot surface ignition, electrostatic discharges, presence of Non-Ex equipment or presence of activity in the area. This is line with what is observed in experiments and our understanding of the ignition mechanisms associated with hydrogen leaks. This is also in accordance with what we observe in the oil and gas industry. Concrete sources of ignition not designed for exposure to flammable atmosphere totally dominate the historical fire and explosion risk picture.
5) We have examples of recorded hydrogen leaks generating large hydrogen clouds in classified areas that did not ignite (*e.g.*, two examples at refineries (0.5 kg/s and about 10 kg/s) and one hydrogen leak due to rupture of tubing in a container).
6) Due to certain ignition mechanisms associated with hydrogen leaks, we know that hydrogen leaks are much more likely to ignite than hydrocarbon leaks. The following ignition

mechanisms are considered to be special for hydrogen, and forms the basis for the ignition model parameters discussed in chapter 6 through chapter 9: (a) Ignition by hot surfaces, (b) Ignition by mechanically generated sources, (c) Ignition by static electricity and (c) Adiabatic compression and shock waves (diffusion ignition).

Based on above, our understanding of the magnitude of the hydrogen ignition probability as follows:

> *The overall ignition probability associated with the full spectrum of hydrogen leaks with an initial leak rate larger than 0.01 kg/s released in industrial environments is much higher than equivalent hydrocarbon leaks and much lower than 100%. Hydrogen is more prone to ignition due to a few special ignition mechanisms. Although not having firm quantitative support in data, we postulate that the expected average ignition probability across all leak rates is in the region 1% to 10% if the leaks are released in environments where the objects are designed for exposure to combustible atmosphere (i.e., the objects designed according to the ATEX directive or equivalent requirement) and cannot be exposed to Non-Ex equipment. With effective ignition sources at site, such as Non-Ex equipment (e.g., electrical tools with motors with brushes), vehicles and hot work activity, that could be exposed to flammable atmosphere, the ignition probability can be much higher than 10%.*

The established level of the average ignition probability is used as a benchmark for setting the model parameters for hydrogen leaks. The adjusted model is tested with respect to the target in Chapter 11.

6. Ignition by hot surfaces

Hot surface ignition occurs by local heating of a flammable mixture to the point where a sufficiently large volume reaches the ignition temperature, and the combustion reaction is initiated. The capability of a hot surface to cause ignition depends on the type, temperature, pressure, and concentration of flammable mixture. Moreover, the temperature that triggers ignition depends on the size and shape of the heated body, on the concentration gradient in the vicinity of the surface, the flow velocity and turbulence of the flammable atmosphere around the hot surface and, to a certain extent, also on the surface material.

Results from Proust & Daubech (2019) indicate that hydrogen-air temperature and flow speed across the hot surface do not significantly affect ignition. This is contrary to what has been seen *e.g.*, in Bartknecht (1989) and Laurendeau (1982), and should be investigated further. However, the results Proust & Daubech (2019) indicate that much smaller hot surfaces can ignite H2 opposed to natural gas for the same surface temperature. The reduction in ignitability with increasing flow speed across the surface could be due to shorter induction time of H2. Calculated and measured induction times for hydrogen and methane are demonstrated by Liberman et.al. (2018). The general relative difference between hydrogen and methane induction time constitutes about a factor of 10 but varies with gas concentration.

Although uncertain, there are historical hydrogen leaks that possibly was ignited by hot surfaces – for example the incident at Herøya in 1985 where an overheated pump was believed to be the source of ignition (Bjerketvedt, D and Mjaavatten (2005)). It is however considered likely that ignition would have resulted also in a hypothetical incident identical to the Herøya incident where a different combustible substance, such as natural gas, were released. Nevertheless, due to the uncertainty related to ignition of hydrogen exposed to hot surfaces, it is concluded to increase the ignition probability parameters reflecting hot surface ignition for hydrocarbons in MISOF with a factor of 3. See Table 2 in Chapter 11 for resulting parameter values).

Experiments investigating hot surface ignition of hydrogen are not prioritized in the HICON project. Nonetheless, we believe that experiments ought to be executed to close knowledge gaps on

the effect of low speed and the properties of the hot surface for varying H2 mixtures and may be incorporated into later phases of the SAFEN project.

7. Ignition by mechanically generated sources

7.1 Mechanical impact ignition mechanisms

A large hydrogen release may cause larger particles or objects (*e.g.*, debris, gravel, tools/equipment) to be drawn along by the flow and being slung against other objects in the path of the hydrogen jet. This may cause direct ignition of the jet. Objects may also be torn loose as part of the failure of equipment. At the impact point, instantaneously short duration high temperature may exist. Moreover, mechanical sparks may be generated. Furthermore, hydrogen handling facilities may contain rotating equipment where due to a failure in the equipment friction may arise. There are also several other processes which may result in friction including transport systems and moving people. Friction processes convert mechanical energy primarily into thermal energy, which results in a temperature increase potentially up to temperatures allowing for hydrogen-air mixtures to ignite.

Experiments performed with different types of steel show that every ignition of hydrogen-air mixtures with stainless steel was caused by a hot surface. Mixtures of 10 % hydrogen in air with mild steel were ignited by sparks, while at 30 % hydrogen the hot surface was exclusively responsible for the ignition (Weltzel (2011)).

Experiments with single impacts between two objects show that ignitions of hydrogen-air mixtures are especially caused by hot surfaces generated at the impact location. This accounts for both stainless and mild steels (Holländer 2016). The thermal conductivity of the material was shown to play an important role for the ignition probability. Single impact sparks may be important during accident scenarios where objects are blown away by the release itself (including gravel) or by a rupture of equipment. (Askar 2023) recently showed that also soft metal parts when impacting on a concrete plate can cause ignition.

Beyer, M. and Markus, D. (2011) concludes with the following: "*The ignition temperatures for 1000 um particles are, even for hydrogen, above the onset temperature for mechanical sparks. Therefore, it is highly improbable that single non-burning particles separated during mechanical wear processes are capable of igniting explosive vapour atmospheres*". Hence, the particles that ignite are those that burn. For hydrogen the concentration where mechanical sparks are most likely to ignite is at 10 % hydrogen. At higher concentrations there is less oxygen and the particles do not burn anymore.

Mechanical sparks are one of the theories for ignition at Sandvika in 2019 (Hansen, O.R (2019)) – parts of gravel base near leak point may have been accelerated by the leak and generated burning particles upon impingement with objects nearby. Another possible example is the event in Diamond, California, in 2018. A release from a tube trailer was ignited where impact between the dislodged vent tubing, handhold bar, and the rear door of the trailer possibly caused the ignition (HIAD 2.0 ID 885). No such ignition mechanisms have been recorded at offshore oil and gas installations in the North Sea or Norwegian land-based facilities processing oil and gas (Lloyd's Register Consulting (2018) and Safetec (2022)).

7.2 Ignition model for mechanical impacts

Despite the lack of clear evidence from incidents it is concluded to supplement the MISOF model with a term that accounts for that hydrogen more easily ignite due to mechanical sparks. This mechanism is probably materialized within a very short time window after start of the leak. The likelihood for the generation of impacts causing ignition is likely to be proportional to the impulse of the leak. To reduce the model complexity, the model is only based on leak rate (*e.g.*, pressure is disregarded). It should be noted that the ignitability caused by burning particles decreases with

increasing gas concentration of the atmosphere they pass through. This is due to the reduced oxygen content in rich concentration hampering combustion of the burning particle. Experiments have demonstrated that the ignitability of burning particles is optimal at a concentration of 10 vol% hydrogen and decreases for increasing concentration (Weltzel (2011)). This effect will counteract the trend with leak rate as the volume of concentration of gas above 10 vol% increases with the leak rate. On the other hand, for the short duration hot surface at the impact point, optimal conditions for ignition are at stoichiometric concentration.

Without any concrete quantitative basis to define the model, the following model is suggested

$$P_{event,impact} = \frac{1}{200} \cdot Q_{1s}^{\frac{1}{4}} \quad (2)$$

that is distributed uniformly over the first 5 seconds of the leak. Q_{1s} is the average leak rate in kg/s over the first second after start of the leak (this is to truncate the initial peak leak rate for very small reservoirs where the release rate decreases rapidly in the very initial phase of the leak). As the probability are to be distributed uniformly over the first five seconds, the model captures that a significant explosion can be generated due to this ignition mechanism. This potential was exemplified by the explosion at the refuelling station at Sandvika in 2019, which generated a significant explosion within a few seconds. The leak rate has been assessed to be in the range 0.3 – 1 kg/s and the equivalent stoichiometric gas has been estimated to be around 20 m^3 (Hansen, O.R. (2019)).

This model, which must be considered very uncertain, will be reassessed in the HICON project based on new knowledge generated by the results from two types of experiments:

- Experimental investigation ignition due to friction
- Experimental investigation of ignition due to single impact

8. Ignition by electrostatic discharges

8.1 Electrostatic discharge ignition mechanisms

There are three main types of electrostatic discharge to consider: spark discharges, brush discharges and corona discharges. Ignition of explosive hydrogen atmospheres by electrostatic discharges has been demonstrated in multiple experimental setups. The governing factor is the low MIE of hydrogen. The smallest spark visible to the human eye releases an energy amount 10 times higher than the MIE of Hydrogen (at optimal H2 concentration). It is however important to underline that it is for concentrations above 10 vol% that the difference between MIE for hydrocarbons and hydrogen starts to grow large (up to a concentration of 62 % of hydrogen in air).

If objects are appropriately grounded according to standards and best industry practice, electrostatic discharges should be rare. However, the MIE of H2 for concentrations above 10 vol% are very low, and it is hard to eliminate potential differences that could generate sparks with sufficient energy. For example, differences in electrical potential generated by conducting objects separated by isolating material (*e.g.*, door in typical car or humans working in the area). In addition, sharp edges in the area could facilitate corona discharges –particularly in weather conditions facilitating ionization of the air.

It is hard to find evidence that electrostatic discharges have caused ignition in incidents. Typically, one suspect this to be ignition mechanism if no other explanation is found reasonable. No incidents are recorded in oil and gas incident data that we clearly believe were due to electrostatic discharges.

8.2 Ignition model for electrostatic discharges

The low MIE of H2 calls for a parameter in MISOF reflecting the elevated potential for electrostatic discharges causing ignition of hydrogen leaks compared to hydrocarbon leaks. It is found reasonable

that materialization of the phenomena scales with the leak rate as it is for concentrations above 10 vol% that the MIE for H2 becomes significantly higher than for hydrocarbons. Both the fraction of high concentrations within the cloud and the overall size of the gas cloud scale with the leak rate.

If idealizing the phenomena as a spark that occur randomly with time at any point in the area, it is reasonable to argue that the parameters quantifying discrete sources in MISOF should be ramped up. However, it could be that ignition due to electrostatic discharge materializes upon the first exposure of the object to combustible gas. This because there is a repeated (or even continuous) electrostatic discharge phenomenon on-going at the exposed object (*e.g.*, corona discharge at a specific edge of an equipment), which implies that the mechanism described by continuous mechanism also should be ramped up to cater for the difference with respect to hydrocarbons.

It could also be argued that ignition due to electrostatic charges are related to the leak itself due to the generation of electrical potential (triboelectric charging). In this case, the ignition point is expected to be quite near the leak source and take place quite quickly after the start of the release.

Based on the above, it is suggested to increase both idealized mechanisms (continuous and discrete) in the MISOF model for hydrogen leaks. In addition, it is concluded to include a term reflecting ignition within a short time window after start of the leak.

It is suggested set the parameter value reflecting the continuous mechanism so that total contribution from the continuous mechanism is doubled. The discrete ignition mechanism is suggested to be elevated with a factor around 30 as we believe that the relative difference to hydrocarbons is considerable (*i.e.*, very small discharges may ignite hydrogen). It must be noted that the uncertainty related electrostatic discharges is prominent, which also must be accounted for when setting the parameter values of the model (see Table 2 for resulting parameter values).

The following model is suggested for electrostatic discharges causing ignition in the immediate vicinity of the leak (the leak affects generation of the sparks). This gives a contribution twice the contribution from mechanical impact presented in the previous chapter as we believe electrostatic discharges are more important. The suggested model is

$$P_{event,electrostatic} = \frac{1}{100} \cdot Q_{1s}^{\frac{1}{4}} \quad (3)$$

that is distributed uniformly over the first 5 seconds of the leak. Q_{1s} is the average leak rate in kg/s over the first second after start of the leak (this is to truncate the initial peak leak rate for very small reservoirs where the release rate decreases rapidly in the very initial phase of the leak).

This model will be reassessed in the HICON project based on the knowledge harvested from the experimental campaign investigating electrostatic ignition. Releases are suggested in which high-momentum, turbulent hydrogen jet releases, occurring near gravel- or sand-covered surfaces, are used to provoke electrostatic charging of non-grounded/non-earthed metal objects located in the path of the release in the open/unconfined and uncongested areas.

9. Adiabatic compression and shock waves (diffusion ignition)

9.1 Diffusion ignition mechanism

This ignition mechanism is documented to take place in geometrical situations where pressurized H2 above about 15 barg is released immediately into a closed geometry with oxygen/air. This has been studied in detail for venting of hydrogen into a vent line from high reservoir vessels protected by bursting discs. The vent line allows for an optimal reflection of shock waves towards the centre of the vent line causing local high temperatures (Wolanski, P., & Wojcicki, S. (1972)).

We do not possess knowledge from experiments or incidents where hydrogen released in other geometrical situations can be confidently explained by diffusion ignition. Hence, it is judged that materialization of this phenomenon is an unlikely case considering typical failure mechanisms leading to external leaks. We understand that the geometrical properties of the flow path from the reservoir to the external environment is decisive for the ignition mechanism to occur. Real life examples are blowout of a part of a gasket in a flange or a missing NPT plug in a valve body. However, we cannot rule out that impingement of the leak/pressure wave immediately downstream the hole could facilitate the ignition mechanism. This applies in particular if the pressure is very high.

9.2 Ignition model for diffusion ignition

To account for that there exist failure states of equipment leading to external leaks that could facilitate the diffusion ignition phenomenon, a model reflecting the pressure and hole size is suggested. Based on discussions at the FABIG TM106 in London 18th and 19th October 2023, we got the impression that we should be careful about ruling out this mechanism for high pressures (Proust C. (2022)). It is judged that the average probability for diffusion ignition across all conditions (leak failure mechanisms) could be around 1%. The probability is set to 0% if the reservoir pressure is less than 15 barg. The ignition mechanism is disregarded for liquified hydrogen. The following mathematical model is proposed:

$$P_{event,diffusion}(P,d) = \frac{\ln(P)}{5000} \cdot (\ln(d+1) + 10) \qquad (4)$$

where

d *is the hole diameter* in mm
P *is the pressure in bar gauge* $(barg)$

This model will be reconsidered as part of the HICON project based on experiments to be executed on sudden rupture of a reservoir with high pressure hydrogen. The experimental set-up will be a high-pressure reservoir connected to a mechanical release mechanism simulating a failing gasket.

10. Exposure to equipment not certified for use in explosive atmosphere

For Non-Ex equipment, there could be a wider range of ignition modes associated with the equipment. In addition, it is a sound risk management principle to apply risk models that drive design towards safer solutions. Hence, the ignition probability model should respond negatively to application of Non-Ex equipment at locations possibly exposed to combustible atmospheres.

We find it reasonable to infer that several ignitions in the hydrogen industry have been due to exposure to Non-Ex equipment. This is one of the several candidates for mechanisms causing ignition of the leak at the Sandvika refuelling station in Oslo in 2019 (Hansen, O.R. (2019)). It is our understanding the industry practice for definition of hazardous zones do not reflect the extent of flammable gas in credible accident scenarios. Extended zones for ignition source control are therefore recommended. Practice for Norwegian offshore installations are to apply Ex-rated equipment for all outdoor areas (at least where feasible). Standards should, as a minimum, recommend control of ignition sources extended to the area that can be exposed to flammable gas in accidental situations.

The use of Non-Ex equipment must be evaluated specifically in each case. The risk analysis should describe the units and their properties alongside an evaluation of possible ignition modes and whether these modes are present continuously or intermittently. To enable estimation of the contribution from Non-Ex equipment, ignition model parameters based on the possibility for gas ingress according to the IP protocol have been proposed (see Table 1). These parameters may not provide an adequate idealization of the conditional ignition probability associated with the specific component, but the

figures given are considered to give a reasonable effect of the risk of using Non-Ex equipment. The values are derived from the values for Non-Ex equipment exposed to hydrocarbons presented in Safetec (2022). The parameters for hydrocarbons are increased with a factor 3 for immediate exposure ($\lambda_{C,IP,j}$) and a factor of 30 for the time-dependant part ($\lambda_{D,IP,j}$). This in line with the factor 3 for hot surfaces presented in chapter 6 and the relative contribution added for electrostatic discharges presented in section 8.2. It should be noted that the hydrocarbon parameter values for other type of Non-Ex objects, such as vehicles (both conventional with combustion engines and with electrical drive), presented in Safetec (2022) is also recommended to be somewhat elevated if exposed to hydrogen. That part of the SAFEN ignition probability model is not covered in this paper.

Table 1. *Ignition model parameters for electrical equipment for varying ingress protection compared with Ex n protection type.*

Solid particle protection	$\boldsymbol{\lambda_{C,IP,j}}$ **(per component)**	$\boldsymbol{\lambda_{D,IP,j}}$ **(per component per second)**
Ex n [1)]	$1.5 \cdot 10^{-4}$	$7.2 \cdot 10^{-8}$
≥ IP64	$4.5 \cdot 10^{-4}$	$5.4 \cdot 10^{-5}$
≥ IP54	$9.0 \cdot 10^{-4}$	$1.1 \cdot 10^{-4}$
≥ IP44	$4.5 \cdot 10^{-3}$	$5.4 \cdot 10^{-4}$
<IP44	$4.5 \cdot 10^{-2}$	$5.4 \cdot 10^{-3}$

1) Basis for Ex n failure rate is presented in Lloyd's Register Consulting (2018)

The total probability for ignition related to the Non-Ex are to be calculated using the following equation assuming that the ignition probability can be approximated by a Poisson process:

$$P = P(1\ or\ more\ ignitions) = 1 - P(zero\ ignitions) == 1 - e^{-(\lambda_{C,IP,j} + \lambda_{D,IP,j} \cdot t)} \quad (5)$$

where t is the exposure time. The resulting probability versus exposure time is shown in Fig. 2. The results demonstrates that the model generate substantial ignition probabilities in case of exposure to Non-Ex equipment.

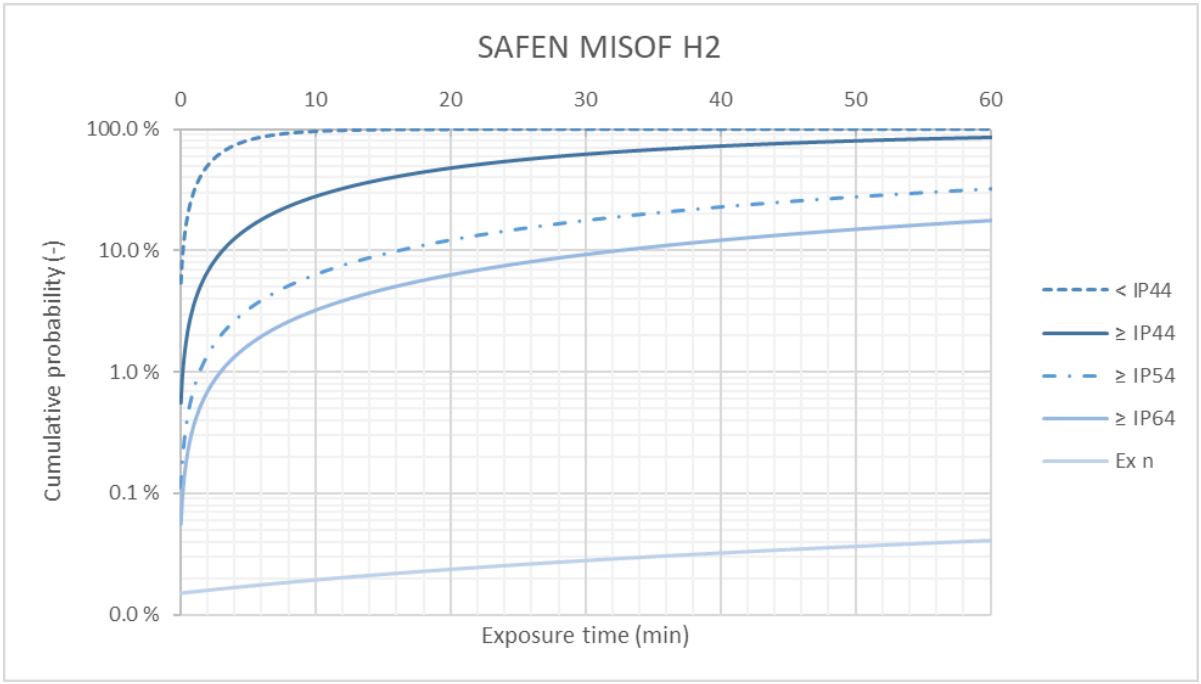

Fig. 2*. SAFEN ignition model for exposure to single Non-Ex equipment exposed to flammable H2 compared with exposure to Ex-rated equipment with protection type Ex n.*

11. Test of the SAFEN ignition probability model

A simple test case has been run with the SAFEN hydrogen parameters presented in Table 2 and according to the algorithm including guidelines described in the MISOF report (Lloyd's Register Consulting (2018)). The objective has been to test the results with respect to the targeted level of the ignition probability established in chapter 5. In order to run the model, a set of transient gas clouds when varying the leak rate is required. In addition, to reflect ignition due to diffusion ignition, the relative distribution in terms of operational pressure is required. For simplicity it is assumed that the system components are distributed uniformly in three categories: 30 barg, 175 barg and 350 barg. The gas cloud transients for the six investigated leak rates (0.01 kg/s, 0.1 kg/s, 1 kg/s, 10 kg/s, 100 kg/s, 1000 kg/s) are shown in Fig. 3. The three largest rates are expected to be irrelevant in most practical cases (pipe dimensions are usually quite small at refuelling stations).

The results in Fig. 4 show that the model generates results in line with the target. The dominant ignition mechanisms for leaks less than 1 kg/s are immediate ignition due to diffusion ignition and ignition within the first 5 seconds after start of the release due to electrostatic discharges. For leaks larger than 1 kg/s, also ignition due to mechanical impact (burning particles generated from impacts) becomes prominent. The contribution from delayed ignition due to faulty Ex-rated equipment (ignition sources in the area – see chapter 2) is quite small due to small size of the area. The reason for that is that the potentially exposed amount of equipment within 100 m^3 of process area is rather limited. For a larger area, the contribution from delayed ignition would become dominant due to more potential ignition sources within the area (the number of units is typically proportional to the gross volume of the area) and because a larger gas cloud could be contained within the area. The contribution from delayed ignition is dominated by ignition due to electrostatic discharges idealized by the discrete ignition mechanism and hot surfaces idealized by the continuous ignition mechanism.

Table 2. *SAFEN hydrogen ignition model parameters for Ex-rated equipment compared with MISOF for hydrocarbons.*

Ignition model parameter description			**SAFEN, hydrogen**	**MISOF, hydrocarbons**
Generic immediate ignition			0.07%	0.07%
Diffusion ignition, event			See equation (4)	NA
Mechanical impact, event			See equation (2)	NA
Electrostatic discharges, event			See equation (3)	NA
Delayed ignition Ignition sources in the area	Continuous mechanism	Rotating equipment	$1.1 \cdot 10^{-5}\ m^{-3}$	$3.7 \cdot 10^{-6}\ m^{-3}$
		Electrical equipment	$5.4 \cdot 10^{-6}\ m^{-3}$	$1.8 \cdot 10^{-6}\ m^{-3}$
		Other	$1.8 \cdot 10^{-6}\ m^{-3}$	$6.0 \cdot 10^{-7}\ m^{-3}$
		Electrostatic discharges	$2.0 \cdot 10^{-5}\ m^{-3}$	NA
		Total	$3.82 \cdot 10^{-5}\ m^{-3}$	$6.10 \cdot 10^{-6}\ m^{-3}$
	Discrete mechanism	Rotating equipment	$1.5 \cdot 10^{-9}\ m^{-3} \cdot sec^{-1}$	$1.5 \cdot 10^{-9}\ m^{-3} \cdot sec^{-1}$
		Electrical equipment	$1.5 \cdot 10^{-9}\ m^{-3} \cdot sec^{-1}$	$1.5 \cdot 10^{-9}\ m^{-3} \cdot sec^{-1}$
		Other	$1.2 \cdot 10^{-8}\ m^{-3} \cdot sec^{-1}$	$1.2 \cdot 10^{-8}\ m^{-3} \cdot sec^{-1}$
		Electrostatic discharges	$4.0 \cdot 10^{-7}\ m^{-3} \cdot sec^{-1}$	NA
		Total	$4.15 \cdot 10^{-7}\ m^{-3} \cdot sec^{-1}$	$1.50 \cdot 10^{-8}\ m^{-3} \cdot sec^{-1}$

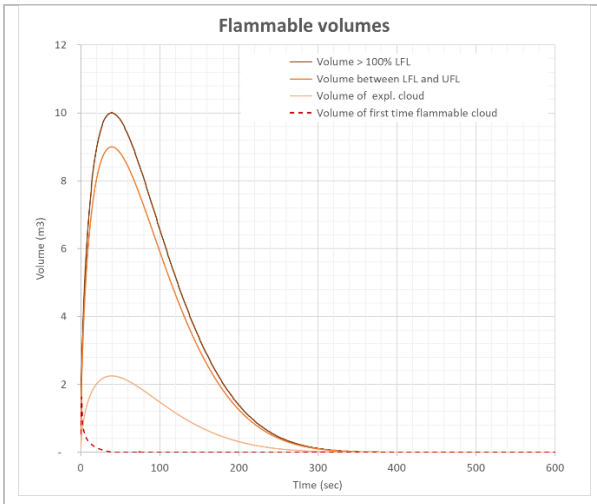

0.01 kg/s H2 – fuelling station

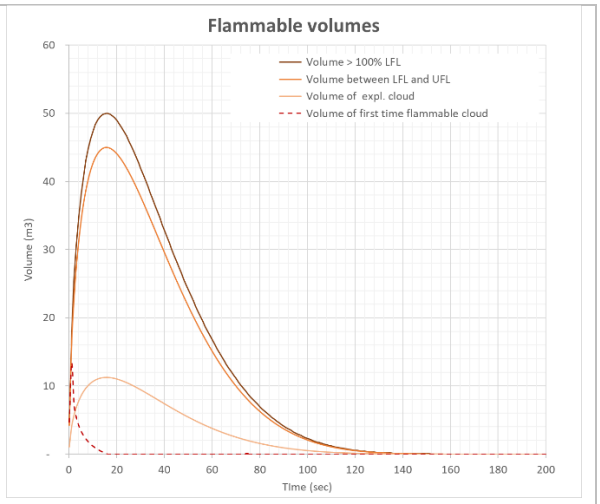

0.1 kg/s H2 – fuelling station

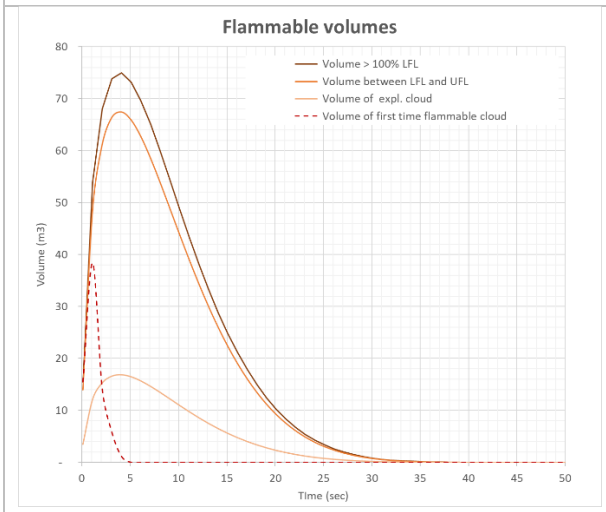

1 kg/s H2 – fuelling station

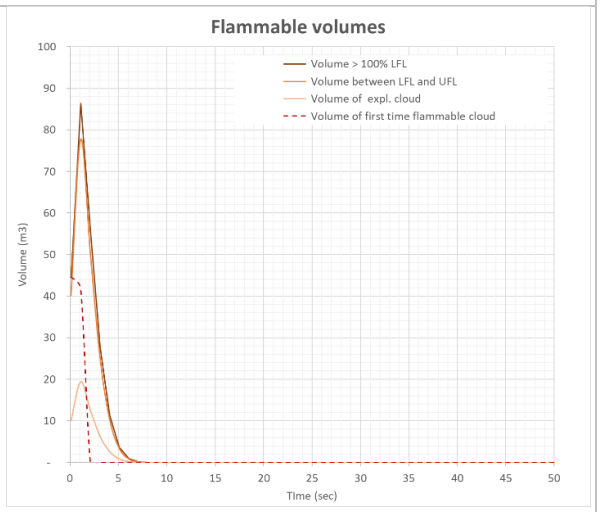

10 kg/s H2 – fuelling station

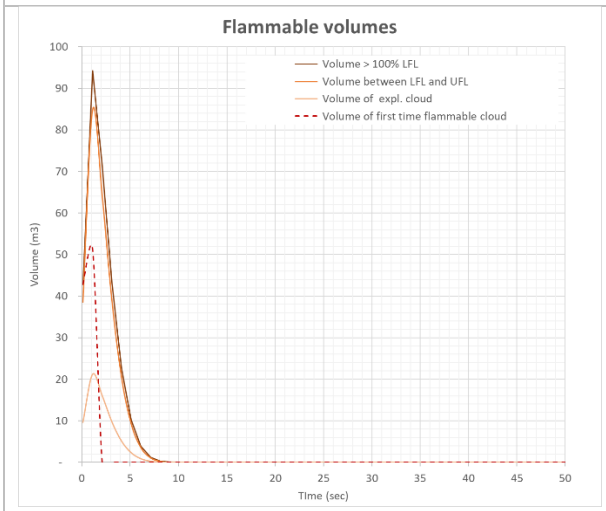

100 kg/s H2 – fuelling station

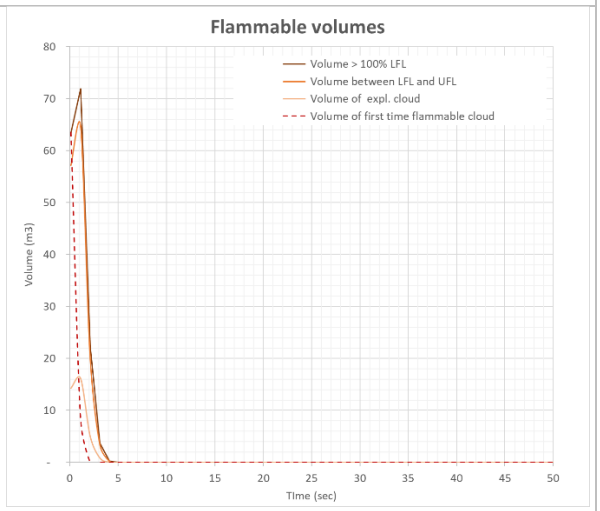

1000 kg/s H2 – fuelling station

***Fig. 3**. Assumed gas cloud transients for refuelling station.*

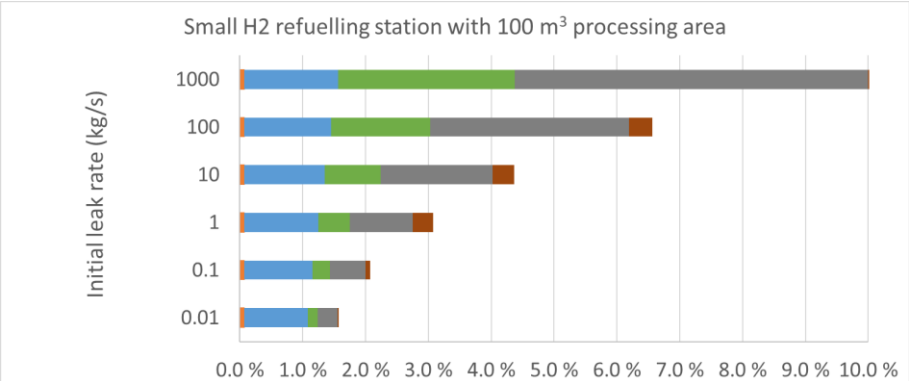

	0.01	0.1	1	10	100	1000
Generic immediate ignition	7.0E-04	7.0E-04	7.0E-04	7.0E-04	7.0E-04	7.0E-04
Diffusion ignition, event	1.0E-02	1.1E-02	1.2E-02	1.3E-02	1.4E-02	1.5E-02
Mechancial impact, event	1.6E-03	2.8E-03	5.0E-03	8.9E-03	1.6E-02	2.8E-02
Electrostatic discharges, event	3.2E-03	5.6E-03	1.0E-02	1.8E-02	3.2E-02	5.6E-02
Delayed, total	1.5E-04	7.0E-04	3.2E-03	3.5E-03	3.7E-03	2.8E-03

***Fig. 4**. Car refuelling case: overall results.*

12. Conclusions

A model enabling estimation of ignition probability for use in quantitative risk analysis for facilities handling hydrogen is presented in this paper. The model was delivered by the first phase of the SAFEN (Safe Energy Carriers) JIP project. The model parameters are derived from current industry knowledge basis on ignition mechanisms and incident data captured in the SAFEN project. The model is sensitive to ignition mechanisms that we believe are driving for ignition of hydrogen leaks: (1) Ignition by hot surfaces, (2) Ignition by mechanically generated sources, (3) Ignition by static electricity and (4) Adiabatic compression and shock waves (diffusion ignition).

The SAFEN ignition model incorporates a specific model for Non-Ex equipment that we believe is crucial for the ignition probability at facilities with such equipment. According to current industry practice, Non-Ex equipment may be found at facilities handling hydrogen due to that the method for definition of hazardous zones do not reflect the extent of flammable gas in credible accident scenarios.

The test of the ignition model demonstrated results in line with the established target stating that the overall ignition probability for hydrogen leaks in industrial environments is expected to be in the range 1 to 10%.

It must be emphasized that the uncertainty associated with the proposed SAFEN ignition model is considerable, and an experimental campaign is launched in the HICON project to provide basis for reassessment of the proposed model. Note also that the first version of the model does not incorporate special ignition mechanisms related to liquified hydrogen released into/onto water, which is believed to be a case that needs special attention. A revised model will be delivered according to updated knowledge late 2025. Nevertheless, the proposed model is considered to be the best available ignition probably model for estimation of ignition probability associated with hydrogen leaks in industrial environments.

Acknowledgements

The authors gratefully acknowledge the financial contribution from Vår Energi, Equinor, Gen2Energy, Gassco, Storegga, Swagelok Norway, Yara, Aker Horizons, Origin Energy, Hyds, Lloyd's Register, Energy Institute, GreenH, The Norwegian Maritime Authority, RIVM (National Institute for Public Health and Environment in Netherlands), World Class Maintenance and DSB (Norwegian Directorate for Civil Protection).

References

Beyer, M. and Markus, D. (2011), *Ignition of explosive atmospheres by small hot particles: Comparison of experiments and simulations*, Sci. Tech. Energetic Materials, Vol. 73, No. 1, 2012.

Bjerketvedt, D and Mjaavatten (2005), A, *A hydrogen explosion in a process plant: A case history*, Proceedings First International Conference on Hydrogen Safety, Pisa, Italy, 2005.

Cox, A.W., Lees, F.P. & Ang, M.L. (1990), *Classification of Hazardous Locations*, IIGCHL, IChemE.

Ehrhart, B.D (2022), et al., *HyRAM+ Hydrogen Plus Other Alternative Fuels Risk Assessment Models*, Version 5.1 Technical Reference Manual, SAND2023-14224, December 2023, Sandia National Laboratories.

Energy Institute (2006), *Ignition probability review, model development and look-up correlations*, ISBN 978 0 85293 454 8, January 2006.

FABIG TM 106 18th & 19th October (2023), *Ignition mechanisms for high pressure hydrogen technologies*, Christophe Proust – INERIS.

Hansen, O.R. (2019), *Hydrogen Safety: Kjørbo-incident, overview and perspectives*, MoZEES workshop, Oslo, October 2019 (https://mozees.no/wp-content/uploads/2019/10/Hansen_Hydrogen-safety_Kjoerbo-incident-overview-and-perspectives.pdf).

HyApproval & DNV (2008), *Summary of Quantitative Risk Assessment performed for a Hydrogen Refuelling Station with on-site production*, HyApproval WP4 by Det Norske Veritas (DNV), Deliverable 4.9 Appendix IV Version 2.0, 14th of April 2008.

HySafe (2007), *An Ignition Probability Model Methodology for Hydrogen Risk Analysis*, Deliverable No 71, Contract No SES6-CT-2004-502630, Document version: Draft 1.0, 01.06.2007.

Holländer, L., Grunewald, T., Grätz, R., *Influence of Material Properties of Stainless Steel on the Ignition Probability of Flammable Gas Mixtures due to Mechanical Impacts*, Chemical Engineering Transactions, 48, 307-312, 2016.

Lloyd's Register Consulting (2018), *Modelling of ignition sources on offshore oil and gas facilities- MISOF*, Date: November 2018, Report No: 107566/R2, Rev: Final

Michael Liberman, Cheng Wang, Chengeng Qian & JianNan Liu (2018): *Influence of chemical kinetics on spontaneous waves and detonation initiation in highly reactive and low reactive mixtures*, Combustion Theory and Modelling, DOI: 10.1080/13647830.2018.1551578.

Moosemiller, M. and B. Galindo (2014), Hydrogen ignitions—Wildly differing opinions, and why everyone could be right, 10th Global Congress on Process Safety, Loss Prevention Symposium, New Orleans, Louisiana, March 30–April 2, 2014.

Safetec (2022), *Modelling of ignition sources on land-based oil and gas facilities*, Doc. No. ST-16542-1, Rev. 7.0, Date 22.12.2022.

SINTEF (1983), *Risk of oil and gas blowout on the Norwegian Continental Shelf*, SINTEF Report STF 88A82062, 1983.

Proust, C. (2019), *Fire and Explosion Safety in Hydrogen Containing Processes: State of the Art and Outstanding Questions*, 9th International Seminar on Fire and Explosion Hazards, April 21-26, 2019, Saint Petersburg.

Proust, C. (2022), *Ignition likelihood of a sudden hydrogen release*, Proceedings of the Tenth International Seminar on Fire and Explosion Hazards (ISFEH10), Oslo, May 2022.

Proust, C., & Daubech, J. (2019), *Hot surface ignition in flowing streams of hydrogen air mixtures*, Sorbonne Universities, INERIS.

Vysus Group (2021), *Guidelines for quantitative risk analysis of facilities handling hazardous substances*, Report No. PRJ1110026033/R1, Rev.: Final report, Date: 19 November 2021.

Vysus Group (2023), *2023 version of Blowout and well release frequencies based on SINTEF Offshore Blowout Database 2022*, Report No. 19101001-8/2023/R3, Rev. 02, Date: 14 March 2023.

Welzel, F., Beyer, M., Klages, C.-P. (2011), *Limiting values for the ignition of hydrogen/air mixtures by mechanically generated ignition sources*, Proc. 23rd ICDERS colloquium, Irvin, 2011.

Wolanski, P., & Wojcicki, S. (1972). *Investigation into the mechanism of the diffusion ignition of a combustible gas flowing into an oxidizing atmosphere*. Proceedings of the Combustion Institute, 14, 1217–1223.

Ex-LOPA method for the assessment of explosion risks in hazardous areas

Roald Perbal [a], Paul van Norden [b] & Jeroen van der Prijt [c]

[a] SABIC (Process Risk Assurance & Assessment, Sittard, The Netherlands)
[b] FrieslandCampina (Global Engineering & Standardisation, Amersfoort, The Netherlands)
[c] Bilfinger Tebodin (Engineering & Consultancy, Elsloo, The Netherlands)

E-mail: roald.perbal@sabic.com

Abstract

"Can the LOPA method be used for assessing explosion risks in hazardous areas?" In the Platform ATEX 153 and SIL Platform, under governance of the Royal Netherlands Standardization Institute (NEN), there was a growing interest in having a semi-quantitative approach for explosion risk assessment in designing process installations. This resulted in the development of a so-called explosion layer of protection analysis (Ex-LOPA) method, complementary to the conventional PHA-LOPA, which allows for a consistent assessment of explosion risks in hazardous areas. In hazardous areas (Ex-Zones), the frequency of the occurrence of an explosive atmosphere can be expected at least once per year or more during normal operation, i.e. within the Safe Operating Limits, and is regarded as an enabling condition for an explosion to happen. Hence, in Ex-LOPA the deviating initiating event under normal operation becomes the occurrence of potential ignition sources. The likelihood that the identified potential ignition sources become active and effective was estimated from international standards for use of equipment in hazardous areas and the modelling of ignition sources on offshore oil and gas facilities under real conditions. Different types of measures of explosion prevention and protection can be considered as independent protection layers (IPLs), for which Risk reduction factors (RRFs) are suggested. Practical application of the Ex-LOPA method demonstrates the difference between the risk of ignition in a hazardous area and the overall assessment of explosion risks. The sensitivity with respect to different level of protection of Ex-equipment (i.e. Zone 2 versus Zone 1) decreases with a lower proportion of critical failure modes, while the likelihood of the occurrence of an explosive atmosphere increases. Hence, the resulting overall ignition hazard frequency appears to be independent of the Ex-Zone and typically ranges between 10^{-3} and 10^{-4} per year. Additional measures may still be necessary to reduce the explosion risk of hazardous explosive atmospheres to acceptable or tolerable levels.

Keywords: *explosion risks, hazardous areas, layer of protection analysis, ignition sources*

1. Introduction

European Directive 1999/92/EC (ATEX 153) deals with the safety and health protection of workers potentially at risk from explosive atmospheres. The employer shall comply with the minimum requirements set out in this Directive for workplaces and work equipment where potentially explosive atmospheres may occur. It requires an overall assessment of explosion risks and provision of measures to eliminate, prevent or protect against explosions, taking account of:

- the likelihood that explosive atmospheres will occur and their persistence,
- the likelihood that ignition sources will be present, become active and effective,
- the installations, substances used, processes, and their possible interactions,
- the scale of the anticipated effects.

Every company may use its own risk matrix and risk tolerance criteria to assess and evaluate risks from potentially explosive atmospheres.

An overview of the different types of explosion risk assessment methods is shown in Figure 1.

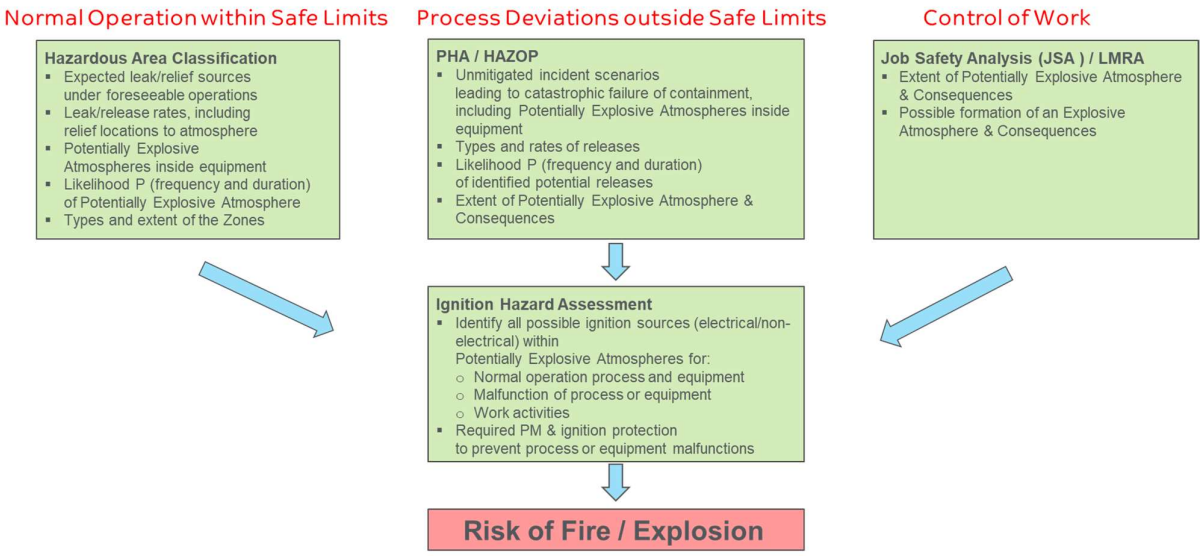

Fig. 1. *Different types of explosion risk assessment methods*

The formation of potentially hazardous explosive atmospheres should preferably be avoided inside process equipment as well as leakages or venting of flammable/combustible materials to the atmosphere. Measures should be taken that reduce the Ex-Zone to preferably a Non-Hazardous Area or Zone 2/22, i.e. reduction of the likelihood of an explosive atmosphere being present.

In PHA-LOPA studies the risks of credible explosion scenarios associated with processes and operations, as identified in Process Hazard Analysis (PHA), are assessed for unintended process deviations (causes/initiating events) outside the Safe Operating Limits (API RP 584) that may result in catastrophic failure of equipment.

On the other hand, the explosion layer of protection analysis (Ex-LOPA) is developed for normal operations within the Safe Operating Limits, which allows for a consistent risk assessment of explosion scenarios in hazardous areas. The presented Ex-LOPA method is especially intended for:

- analysis of possible explosion scenarios in Hazardous Areas (especially Zones 1/21 and 0/20), which depends on the likelihood (i.e. frequency and duration) of an explosive atmosphere;
- identifying effective explosion prevention and protection measures in enclosed areas where an explosion overpressure can be expected;
- evaluating risks from credible explosion scenarios with potential fatal consequences.

This Ex-LOPA method is not applicable for risk assessment of mist explosions or dust explosions originating from dust layers, such as secondary dust explosions.

2. Ex-LOPA Methodology

2.1. Presence of Explosive Atmospheres and Explosion Risks

The Ex-LOPA method distinguishes between the risk of ignition in a hazardous area and the assessment of explosion risks. Hazardous areas can be classified, based on the likelihood (i.e. frequency and duration) of occurrence of an explosive atmosphere, in accordance with standards IEC 60079-10-1 and IEC 60079-10-2. In Hazardous Areas (Zones) the frequency of the occurrence of an explosive atmosphere can be expected under normal operation (i.e. within the Safe Operating Limits) at least once per year or more, which is typically a high-demand mode, as is illustrated in Figure 2. The frequency ($F_{Ex} \geq 1$/yr.) of the occurrence and duration (T_{Ex}) of an explosive atmosphere may be taken from codes (Energy Institute, 2015) relating to specific industries or applications.

A convenient quantitative definition of the zone types in terms of the total duration that an explosive atmosphere would be expected to be present in a year (~10,000 hours) is:

- Zone 0/20: $T_{Ex} > 1000$ hours
- Zone 1/21: 10 hours $< T_{Ex} \leq 1000$ hours
- Zone 2/22: $T_{Ex} \leq 10$ hours

This results in the calculation of the probability of an explosive atmosphere being present (P_{Ex}):

$$P_{Ex} = T_{Ex}/10{,}000 \quad (1)$$

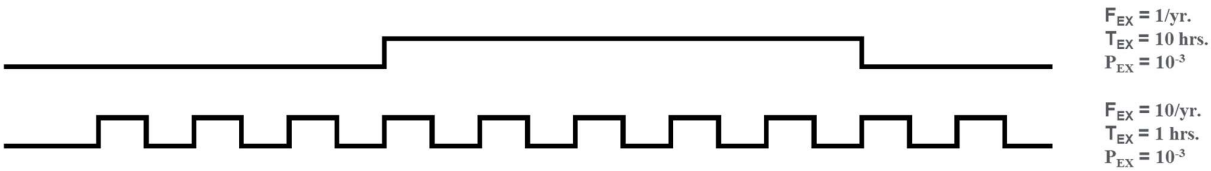

Fig. 2. *Difference between frequencies (F_{Ex}) and probability (P_{Ex}) of explosive atmospheres for Zone 2/22*

Layer of Protection Analysis (LOPA) is a semi-quantitative risk assessment for evaluating each single cause-consequence pair of a typical explosion scenario with independent protection layers (IPLs), based on the principles of explosion prevention and protection, as presented in Figure 3 (Perbal et al., 2006). Elimination or minimization of explosion risk can be achieved by taking additional technical and/or organizational measures appropriate to the nature of the operation, in order of priority and in accordance with the following basic principles:

1. preventing the formation of explosive atmospheres;
2. preventing potential ignition sources;
3. mitigating the consequences of an explosion, where necessary combined with additional measures against propagation of explosions.

Different types of technical and/or organizational measures of explosion prevention and protection can be considered as independent protection layers (IPLs). An IPL is defined as a device, system or action that is capable of preventing the scenario from proceeding to its undesired consequence, independent of the initiating event or the action of any other layer of protection associated with the scenario.

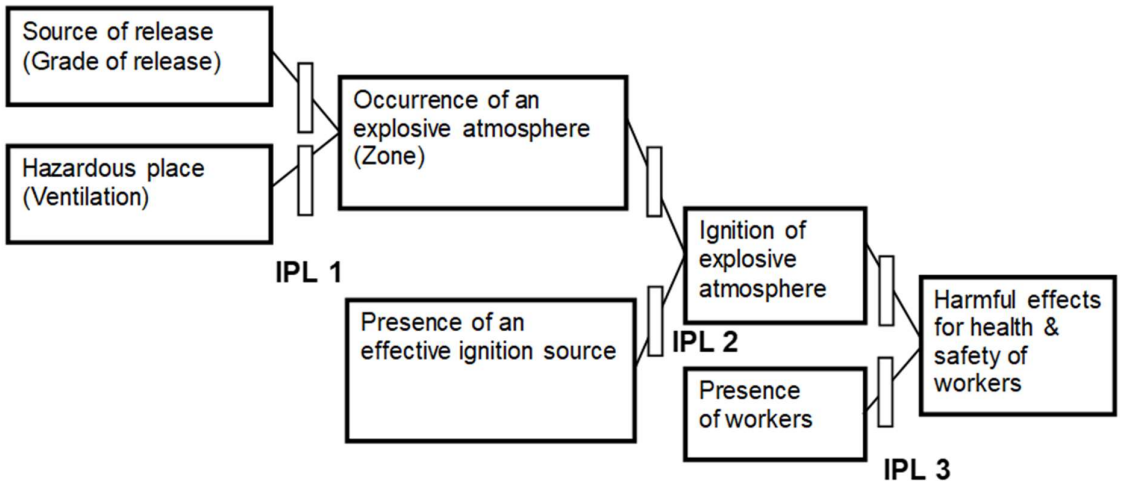

Fig. 3. *Typical explosion scenario with independent protection layers (IPLs)*

In Ex-LOPA the frequency of an explosion scenario or Explosion Hazard Frequency (EHF) can be quantified:

$$EHF = IHF \times P_{CM} \times (\prod_1^3 P_{IPL}) \qquad (2)$$

In which:

P_{CM} = Probability for Conditional Modifiers (see 2.4)
P_{IPL} = Probability of failure on demand for an Independent Protection Layer (see 2.5)

To be able to calculate the Ignition Hazard Frequency (IHF), it is necessary to both know the frequency and the duration of the effective ignition source as well as that of the occurrence of a potentially explosive atmosphere. In Figure 4 two example time scales are shown to indicate the statistical element of coincidence for Zone 1 and Zone 2 (Pieters et al., 2011).

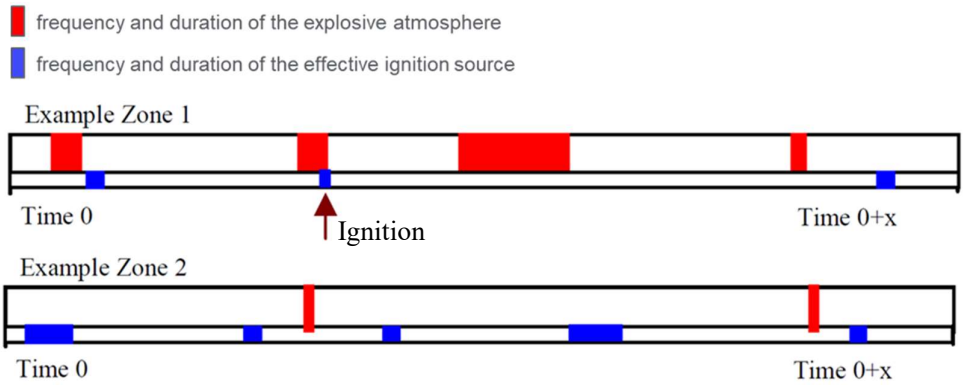

Fig. 4. *Simultaneous independent occurrences of an explosive atmosphere and effective ignition source*

An ignition of an explosive atmosphere will occur when the red time periods (frequency and duration of the explosive atmosphere) coincide with the blue time periods (i.e. occurrence of an effective ignition source). The ignition hazard frequency (IHF) can be estimated for simultaneous but independent occurrences of an explosive atmosphere and that of an effective ignition source (in case $P_{Ig} = F_{Ig} \times T_{Ig} \leq 0.1$):

$$IHF = F_{Ig} \times P_{Ex} + F_{Ex} \times P_{Ig} = F_{Ig} (P_{Ex} + F_{Ex} \times T_{Ig}) \quad \text{per year} \qquad (3)$$

The variables influencing the Ignition Hazard Frequency (IHF) are:

F_{Ig} = Frequency of an effective ignition source
T_{Ig} = Duration of the ignition source being effective
F_{Ex} = Frequency of occurrence of a potentially explosive atmosphere
T_{Ex} = Duration of the potentially explosive atmosphere
P_{Ig} = Probability of an effective ignition source being active ($P_{Ig} = F_{Ig} \times T_{Ig} \leq 0.1$)
P_{Ex} = Probability of the explosive atmosphere being present ($P_{Ex} = F_{Ex} \times T_{Ex} \leq 0.1$)

When $F_{Ex} \times T_{Ig} << P_{Ex}$ (or $T_{Ig} \leq 0.1\ T_{Ex}$), a simplified formula can be used for estimation of the Ignition Hazard Frequency (IHF):

$$IHF \approx F_{Ig} \times P_{Ex} \quad \text{per year} \qquad (4)$$

with the initiating event frequency (F_{Ig}) of an effective ignition source.

The more likely the occurrence of a hazardous explosive atmosphere is, the higher the extent of measures against effective ignition sources shall be and vice versa. Effective independent protection layers (IPLs) shall be specified to demonstrate that the residual explosion risk as per design intent is achieved.

2.2. Initiating Event Frequency

2.2.1. Occurrence of potential ignition sources

In Ex-LOPA the deviating initiating event under normal operation is the occurrence of potential ignition sources. There are 4 main types of initiating events that can cause ignition:

1. Equipment failure
2. Process related
3. Human related
4. External events

Ignition Hazard Assessment (IHA) shall be conducted for all possible ignition sources present in each hazardous area that could occur during normal operations or in case of (rare) malfunctions. The 13 types of possible ignition sources, as defined in EN 1127-1, shall be systematically evaluated, and compared with the ignition properties of the specified potentially explosive atmospheres. Subsequently, the likelihood that the identified potential ignition sources become active and effective shall be estimated.

2.2.2. Equipment failure

The unmitigated frequency (F_{Ig}) of occurrence of effective ignition sources without application of any additional measures and the required explosion protection of (non-)electrical Ex-equipment for safe use in the different zone types is indicated in Table 1. This table is based on the Hardware Fault Tolerance (HFT) requirements for equipment related to the occurrence of effective ignition sources, with reference to the standards ISO 80079-37 and IEC/TS 60079-42. The required additional risk reduction measures, with risk reduction factors (RRF) for IPLs presented in Table 1, will then result in the Category of the Ex-equipment for use in the applicable Zone. Equipment that has no own potential sources of ignition needs also to be assessed for the intended operation in accordance with the European Directive 1999/92/EC (ATEX 153).

The Ignition Hazard Frequency (IHF) of Ex-equipment can be estimated from Table 1:

$$IHF = (F_{Ig}/RRF) \times P_{Ex} \qquad (5)$$

Table 1. *Unmitigated ignition frequencies and IPL requirements for equipment in different zones*

Unmitigated Potential Sources of Ignition (IEC 60079-0 / ISO 80079-36)				
Likelihood	**(F_{Ig} > 0.1/yr.)** Effective ignition sources to be expected during normal operation frequently or for long periods (T_{Ig} > 10 hrs.)	**(F_{Ig} ≤ 0.1/yr.)** Effective ignition sources only to be expected during single expected malfunctions	**(F_{Ig} ≤ 0.01/yr.)** Effective ignition sources only to be expected due to a combination of two independent expected malfunctions or during one rare malfunction	**(F_{Ig} = 0/yr.)** Not Relevant No own potential sources of ignition when operated as intended, including during any malfunctions
Zone 2/22 **(P_{Ex} ≤ 0.01)**	1 IPL: RRF ≥ 10	--- Detection of arising faults within 1 shift (T_{Ig} ≤ 10 hrs.)*	--- Detection of arising (rare) faults during weekly visits (T_{Ig} ≤ 100 hrs.)*	ATEX 153
Zone 1/21 **(P_{Ex} ≤ 0.1)**	2 IPL's: RRF ≥ 100	1 IPL: RRF ≥ 10	a Self-revealing (rare) faults (T_{Ig} ≤ 1 hrs.) or automatic detection of arising rare faults	
Zone 0/20 **(P_{Ex} ≤ 1)**		2 IPL's: RRF ≥ 100	1 IPL: RRF ≥ 10 In the event of two independent faults occurring independently of each other	

* *Continuous Supervision (IEC 60079-17)*

--- *No Safety Requirements / Protection Layer is not needed*

a *No Special Safety Requirements (Unclassified Safeguard since PFD > 0.1) / Protection Layer is probably not needed*

For non-electrical Ex-equipment, failure rate data are often not available and depend strongly on the application and conditions in use (Sherwen, 2009). It is noted that the ignition frequency of electrical Ex-equipment suited for Zone 0/20 in Table 1 is believed to be high compared to real evidence. Unfortunately, manufacturers usually do not specify dangerous failure rate data in their specifications of Ex-equipment.

In situations where insufficient or no failure rate data are available, Table 1 can be used as a worst-case approach.

In Table 2 the failure frequencies for electrical equipment resulting in a sufficiently strong ignition source for different types of Ex-protection were estimated from modelling of ignition sources on offshore oil and gas facilities under real conditions (van Wingerden, 2010). The suggested failure frequencies have been verified and confirmed for a limited number of electrical equipment approved for use in potentially explosive gas atmospheres. If more substantiated data are available, these may be used instead. For convenience in the calculations, a year can be assumed to have ~10,000 hours.

Table 2. *Estimated failure frequency (hr^{-1}) for electric equipment in explosive gas atmospheres that may result in a potential ignition source for different types of Ex protections (van Wingerden, 2010).*

Type of protection	Use in Zone	Normal failure rate (hr^{-1})	Failure rate harsh environment (hr^{-1})
Ex ia	0	$3.3x10^{-8}$	$1.0x10^{-7}$
Ex ma	0	$3.3x10^{-8}$	$1.0x10^{-7}$
Ex ib	1	$3.3x10^{-7}$	$1.0x10^{-6}$
Ex mb	1	$3.3x10^{-7}$	$1.0x10^{-6}$
Ex d, only sparking	1	$1.0x10^{-7}$	$1.0x10^{-7}$
Ex d, sparking and hot surfaces	1	$3.3x10^{-7}$	$1.0x10^{-6}$
Ex e	1	$3.3x10^{-7}$	$1.0x10^{-6}$
Ex p	1	$3.3x10^{-7}$	$1.0x10^{-6}$
Ex n	2	$3.3x10^{-6}$	$1.0x10^{-5}$
Ex s*	0-2	$3.3x10^{-6}$	$1.0x10^{-5}$

* *Assumed equal to Zone 2 equipment Ex n (IEC 60079-15) by Ex sc (IEC 60079-33) unless Zone Category is given*

All technical requirements for electrical equipment with the types of protection:
- flameproof enclosure "d" (IEC 60079-1)
- pressurized enclosure “p” (IEC 60079-2)

also apply to non-electrical equipment. Hence, the dangerous failure rates would be identical for these protection concepts (see ISO 80079-36: Annex G).

The following types of protection can be used for Ex-equipment in potentially explosive dust atmospheres:

- intrinsic safety “i” (IEC 60079-11)
- encapsulation “m” (IEC 60079-18)
- pressurized enclosure “p” (IEC 60079-2)
- enclosure “t” (IEC 60079-31)

Electrical equipment can initiate dust explosions by electrical sparks or by thermal ignition from hot surfaces. For electrical equipment with types of protection “i” (IIIA/IIIB), “m”, and “p”, there will be no differences in failure mechanisms, whether used in explosive gas or dust atmospheres. Hence, the ignition frequency (F_{Ig}) of an explosive dust cloud due to malfunction can be assumed to be identical as the estimated failure frequencies for these types of electrical equipment in Table 2, without the use of a Conditional Modifier for ignition source effectiveness. Unfortunately, for equipment with protection by enclosure "t" no generic failure rate data are available. In case of dust layers the failure mechanisms of the equipment may be different, for which Table 2 cannot be used but Table 1 may still be applicable under the European Directive 2014/34/EU (ATEX 114).

2.2.3. Process related

For potential process related ignition sources (e.g. high temperatures) to be expected during normal operation frequently or for long periods (high-demand mode scenarios), the Basic Process Control System (BPCS) shall prevent the occurrence of an effective ignition source in hazardous areas. In case of a BPCS failure a typical initiating event frequency F_{Ig} = 0.1/yr. is chosen in practice.

2.2.4. Human related

In case the potential ignition source is related to activities or presence of personnel in a hazardous area, the initiating event frequency (F_{Ig}) needs to be estimated, taking into account the effectiveness of administrative control measures to prevent ignition sources. For the use of dissipative clothing, footwear and permit-to-work system typically a RRF = 4-10 can be expected (HSE RR226, 2002).

2.2.5. External events

External events include natural phenomena such as lightning strikes. IEC 62305-2: is applicable to risk assessment for a structure due to lightning flashes to earth. Its purpose is to provide a procedure for the evaluation of such a risk. The number of lightning flashes influencing the structure depends on the dimensions and the characteristics of the structure, on the environmental characteristics of the structure, as well as on lightning ground flash density in the region where the structure is located (IEC 62858). In Ex-LOPA a typical frequency of lightning strikes $F_{Ig} = 10^{-3}$/yr. is assumed.

2.3. Enabling Condition

2.3.1. Definition and Characteristics

In Ex-LOPA there may be so-called Enabling Conditions that are neither failures nor protection layers, An Enabling Condition is a condition or operating phase that does not directly cause or initiate the scenario, but which must be present or active in order for the scenario to proceed to a hazardous event, expressed as a dimensionless probability. In hazardous areas (Ex-Zones), the probability of the occurrence of an explosive atmosphere (P_{Ex}) that can be expected during normal operation within the Safe Operating Limits, is regarded as an enabling condition for an explosion to happen.

2.3.2. Time at risk for different zone types

A typical Enabling Condition is the so-called time at risk (or hazard presence factor) is the fraction of time the hazard is present in the process. In Ex-LOPA the Enabling Condition is determined by the grade of a release source resulting in the likelihood of an explosive atmosphere being present. In order to use the time at risk factor, the risk has to be proportional to the duration that the hazard exists; an initiating event with a random frequency supports the use of time at risk.

If the initiating event (effective source of ignition) can occur prior to the hazardous time fraction without being detected, e.g. by a safety device, or continuous supervision (IEC 60079-17), then the error is only revealed during the hazardous time fraction and the time at risk factor (P_{Ex}) as Enabling Condition does not apply.

If the likelihood of a potentially explosive atmosphere is proportional to the frequency of occurrence of a potential ignition source (e.g. due to equipment failure), then the time at risk is not appropriate and a probability of 1 shall be assumed. For example, in the case that occurrence of potential ignition sources (e.g. auto-ignition, hot surface, electrostatic discharge, or shockwave) is not independent from the leakage or release of a flammable substance.

The maximum probabilities of a potentially explosive atmosphere (P_{Ex}) being present can be related to the different Ex-Zones:

Zone 0/20: $P_{Ex} = 1$
Zone 1/21: $P_{Ex} = 10^{-1}$
Zone 2/22: $P_{Ex} = 10^{-2}$ (see 3.1)

For a Non-Hazardous Areas (NHA) the likelihood of an explosive atmosphere is assumed:

$P_{Ex} \leq 10^{-5}$ per annum.

Artificial ventilation may result in Zone reduction. In case artificial ventilation has not already been credited in the Zone of the Hazardous Area Classification, then a risk reduction factor for artificial ventilation can be included as IPL1 from Table 3.

2.3.3. Inerting

Where specific measures such as inerting are used, the interior of equipment containing flammable substances may not need to be classified as a hazardous area or may be assigned a less onerous zone. In such cases the reliability of the inerting system should be proportional with the reduction in hazardous area that is determined for the interior of the equipment. The required safeguarding of the inerting system is determined by the risk reduction factor (RRF) for IPL1 in Table 3.

2.4. Conditional Modifiers

2.4.1. Definition and Characteristics

Conditional Modifiers are probabilities (P_{CM}) included in scenario risk calculations, when risks are expressed in consequences (e.g. explosion, fatalities) instead of initiating event terms (e.g. equipment failures, ignition sources). Conditional Modifiers include, but are not limited to probability of personnel presence potentially at risk from explosive atmospheres, probability of injury or fatality, and probability of equipment damage or other financial impact. Conditional Modifiers in Ex-LOPA, if applicable, are described below.

2.4.2. Probability that initiating event (dangerous failure) causes an effective ignition

Normally, in Ex-LOPA the likelihood estimation of the initiating event is already the occurrence of an effective ignition source (F_{Ig}). In that case, the probability of ignition (P_{Ig}) cannot be used as a Conditional Modifier. However, the suggested Ex-equipment failure rates in Table 2 seem also to include failure modes that do not actually become an effective source of ignition in outdoor classified areas for Zone 1 and Zone 2. In reality, the results show that the number of hazardous failure modes (in terms of modes that actually cause an effective ignition) is not more than 2% of the equipment failure modes that may result in a potential ignition under outdoor conditions (Fossan et al., 2018). Hence, in outdoor classified areas for Zone 1 and Zone 2 a Conditional Modifier $P_{CM} = 0.02$ could be used in case of gas detection combined with automatic isolation of electrical ignition sources (HSE RR1123, 2017). In all other situations, including dust explosion hazards, $P_{CM} = 1$ shall be used.

Dust explosions are generally more difficult to initiate than gas/air explosions. Hence, the outcome of the Ex-LOPA calculations – the expected frequency of the incident – may be higher than expected in practice. This may be due to the fact that the probability that a failure in Ex-equipment leading to an effective ignition (which is a Conditional Modifier) has been set at 1. However, numerous tests with powders have shown that dust clouds do not ignite with every spark. Therefore, the true ignition hazard frequency in dust zones will probably be lower than calculated.

2.4.3. Probability of Personnel Presence

This Conditional Modifier is to provide supporting realistic estimation of personnel presence in the effect area potentially impacted by an explosion or fire scenario. Credit may be taken for time that personnel is not present in the effect area if the hazard may result in injury or fatality consequences.

This probability (P_{CM}) is to distinguish between areas that is normally occupied against areas that are normally unoccupied or significantly less occupied. In case the potential ignition source is related to the presence of people, no credit can be taken and $P_{CM} = 1$. Personnel presence should also not be credited if it is included in the determination of the severity of consequences.

2.4.4. Probability of Injury or Fatality

The probability (P_{CM}) that, given a person is within the effect area, a serious injury or fatality would actually occur. This conditional modifier cannot be determined independently of the probability of personnel presence, since it will be affected by the criteria chosen for calculating the effect area (e.g. heat radiation and blast effects) potentially impacted by the scenario, e.g. for a flash fire, jet fire, pool fire, or a (confined) gas explosion. The probability of a fatality $P_{CM} = 1$ in case a person is outdoors:

- inside the contour of the Lower Flammable Limit (LFL) at the time of ignition, or
- exposed to heat radiation ≥ 35 kW/m^2 (exposure ≥ 20 s), or
- exposed to an explosion peak overpressure ≥ 0.3 barg.

This Conditional Modifier should not be credited if it is already included in the determination of the severity of consequences. Under certain conditions it might also be possible to avoid the hazard in case of a timely escape or evacuation and a $P_{CM} \geq 0.1$ may be considered, e.g. after a gas alarm generated by detection of the formation of a potentially hazardous explosive atmosphere.

2.5. Independent Protection Layers

2.5.1. Definition and Characteristics

An Independent Protection Layer (IPL) is a device, system, or action that is capable of preventing a scenario from proceeding to the undesired consequence without being adversely affected by the initiating event or the action of any other protection layer associated with the scenario. While IPLs are extrinsic safety systems, they can be active or passive systems:

Active IPL: An active IPL is a device or system that changes from one state into another, in response to a change in process activity. For example, a pressure relief device is an active IPL that opens when there is an abnormal change in the pressure inside a vessel and remains open until the pressure in the vessel reduces to a value below the settings in the pressure relief device.

Passive IPL: A passive IPL can achieve its risk reducing function without the requirement to take any action or change the state of the system. For example, detonation arresters and blast-walls are passive IPLs that reduce the risk.

Human IPL: Human IPLs involve the dependency on operators or other staff to take action to prevent an undesired consequence, in response to alarms or following a routine check of the system.

2.5.2. Basic concepts for explosion protection

Explosion prevention and protection systems can be distinguished in the following order of priority (Pekalski et al., 2005):

IPL1: Explosive Atmospheres Prevention Measures

In Table 3, IPL1 may only be applied if these have not already been credited in the Ex-Zone of the Hazardous Area Classification. It is recommended that risk reduction by means of artificial ventilation, including (start-up) conditions, are identified as IPL1.

IPL2: Ignition Prevention Measures

Examples are safety-instrumented-systems to prevent ignition source formation, end of line flame arresters, grounding and bonding (see Table 4). RRF for electrostatic bonding via conductive solid metal bolt/flange connections will be dependent on conductivity of flange connections (e.g. presence of corrosion, paint or coating).

IPL3: Explosion Protection Measures

For example, explosion vent panels and explosion suppression systems. A model for calculation of the residual risk of failure of explosion protection systems to mitigate an explosion on an industrial process plant for specific configurations may be used (Date et al., 2009). However, for reasons of simplicity the RRF values in Table 5 may be used instead.

Based on data in literature (Markowski, 2007), expert insights, and information from manufacturers, the following Risk Reduction Factors (RRF) for IPL1, IPL2, and IPL3 are suggested in Tables 3, 4, and 5, where:

$$P_{IPL} = 1/RRF \quad (6)$$

It is assumed that the equipment is well designed, installed, inspected, tested and maintained in accordance with applicable standards and manufacturers recommendations. If more substantiated data are available, these may be used instead.

Table 3. *Explosive atmospheres prevention measures (IPL 1): Risk Reduction Factors (RRF)*

Measures to prevent the occurrence of potentially explosive atmospheres	**Standards**	**RRF ***
Gas tight/fluid resistant physical barriers	IEC 60079-10-1	1000
Dust tight/ physical barriers/zone boundaries	IEC 60079-10-2	1000
Blind flange/leakage clamp to prevent formation of explosive atmospheres	IEC 60079-10-1	100
Safety Instrumented System (SIL 1) to prevent explosive atmospheres	IEC 61511	1/PFD
Safety Instrumented System (SIL 2) to prevent explosive atmospheres	IEC 61511	1/PFD
Safety Instrumented System (SIL 3) to prevent explosive atmospheres	IEC 61511	1/PFD
Restriction orifice to prevent formation of explosive atmospheres	ISO 5167-2	100
Preventing ingress of explosive gas atmospheres by internal overpressure	IEC 60079-10-1	10
Opening Type B	IEC 60079-10-1	10
Opening Type C	IEC 60079-10-1	100
Opening Type D	IEC 60079-10-1	1000
Continuous local artificial ventilation (to be present during normal operation)	IEC 60079-10-1	10
Continuous local artificial ventilation (with automated monitoring and alarm)	IEC 60079-10-1	100
Continuous local artificial ventilation (with interlock/automated backup)	IEC 60079-10-1	1000
Fair inerting/purging system (well designed and expected to be present during normal operation)	NFPA 69 CEN-TR 15281	10
Good inerting/purging system (well designed and good availability with adequate safeguarding)	NFPA 69 CEN-TR 15281	100
Displacement/evaporation suppression in enclosures/spaces by foam systems	NFPA 11	10
Non-Return Valve (single/double check valve in clean non-plugging service)	EN 16767 API 594	10/100
Single/Double Mechanical Seal	API 682 API 617	10/100
Liquid/Water Seals to prevent air ingress / to protect against air infiltration	API 521	10

* Estimates

Table 4. *Ignition prevention measures (IPL 2): Risk Reduction Factors (RRF)*

Measures to prevent the presence of effective ignition sources	**Standards**	**RRF ***
Safety Instrumented System (SIL 1) to prevent ignition sources	IEC 61511	1/PFD
Safety Instrumented System (SIL 2) to prevent ignition sources	IEC 61511	1/PFD
Safety Instrumented System (SIL 3) to prevent ignition sources	IEC 61511	1/PFD
End of Line flame arrester	IEC/ISO 80079-49 CEN/TR 16793	100
Fluid tight/fluid resistant thermal insulation with visible Ex warning	ASTM C1696-20	10
Fluid tight resistant thermal insulation with visible Ex warning (sealed & periodic inspection)	ASTM C1696-20	100
Lightning Protection System	IEC 62305 NFPA 780	10
Electrostatic grounding detection with interlocking	IEC/TS 60079-32-1	100
Electrostatic bonding (via conductive solid metal bolt/flange connections)	IEC/TS 60079-32-1	10-100
Additional electrostatic bonding via separately mounted cable	IEC/TS 60079-32-1	10
Ioniser (passive/active/radioactive)	IEC/TS 60079-32-1	10
Insulating flange for preventing dangerous stray currents	IEC/TS 60079-32-1	100
Spark extinguishing system	VdS 2106	10

* Estimates

Table 5. *Explosion protection measures (IPL 3): Risk Reduction Factors (RRF)*

Measures to mitigate the consequences of explosions	**Standards**	**RRF ***
Explosion-pressure-resistant/explosion pressure shock-resistant equipment	EN 14460	1000
Inline deflagration/detonation arresters	IEC/ISO 80079-49 CEN/TR 16793	100
Explosion suppression system Extinguishing barrier	EN 14373 EN 15233 EN 15089	100
Explosion pressure relief systems/Explosion venting devices on enclosures	ISO 80079-50 EN 14797 EN 14994	100
Highly reliable bursting plates	EN 14491 EN 16009 NFPA 68	1000
Tanks with weak roof-to-shell seam/joint (frangible roof)	API 650/ NFPA 30	100
Flame front diverters (passive)	EN 16020 EN 15089 NFPA 69	100
Passive explosion isolation system/passive flap valves	EN 16447 NFPA 69	10
Active explosion isolation system	EN 15089 NFPA 69	10
Rotary valve	EN 15089 NFPA 69	100
Screw conveyor/product receiver (material chokes for explosion isolation)	EN 15089 CEN-TR 17838	10
Remotely Operated Emergency Isolation Valve (ROEIV) Shut-Off Valves (ROSOVs)	API RP 553 HSG 244	10

* Estimates

3. Calculations and discussion

3.1. Ignition Hazard Frequency

For the different Ex-Zones, the IHF values in Table 6 can be calculated with Formula (3) for the different frequencies and durations of effective ignition sources. For convenience of calculations, a year is assumed to have ~10,000 hours. If the simplified Formula (4) for Ex-LOPA is consistently being used for Zone 2/22, then $P_{Ex} = 10^{-2}$ shall be used to achieve the comparable residual IHF = 10^{-3}/yr. for an expected $F_{Ig} = 10^{-1}$/yr. in Zone 2/22.

Table 6. *IHF values for different Ex-Zones depending on frequencies and durations of ignition sources*

Zone	F_{Ex} (1/yr.)	T_{Ex} (hrs.)	P_{Ex}	F_{ig} (1/yr.)	T_{Ig} (hrs.)	IHF (1/yr.)
2/22	1	10	10^{-3}	10^{-1}	10*	$2x10^{-4}$
2/22	10	1	10^{-3}	10^{-1}	10*	$1.1x10^{-3}$
2/22	10	1	10^{-3}	10^{-2}	100*	$1.01x10^{-3}$
1/21	100	10	10^{-1}	10^{-2}	0	$1x10^{-3}$
1/21	10	100	10^{-1}	10^{-2}	1	$1.1x10^{-3}$
1/21	100	10	10^{-1}	10^{-2}	1	$1.1x10^{-3}$
0/20	10	1000	1	10^{-3}	0	$1x10^{-3}$
0/20	10	1000	1	10^{-3}	1	$1.001x10^{-3}$
0/20	100	100	1	10^{-3}	0	$1x10^{-3}$
0/20	100	100	1	10^{-3}	1	$1.01x10^{-3}$

* Continuous Supervision (IEC 60079-17)

From Table 6 it can be concluded for Ex-equipment that is suited for the applicable Zone, the worst-case ignition hazard frequency (IHF) appears in all cases to be typically in the range between 10^{-3} and 10^{-4} per year. Hence, additional measures may be necessary to reduce the explosion risk of hazardous explosive atmospheres to acceptable or tolerable levels, depending on the company's risk policy.

3.2. Example of Ex-LOPA

The hazardous area classification of the potentially explosive vapour phase inside a vessel is Zone 1. The mechanical shaft seal of the agitator is intended for use in Zone 1 (Cat.2), but will in case of seal overheating due to rare malfunctioning result in an effective ignition source. The consequent vapour explosion inside the vessel may result in catastrophic failure with a potential fatality.

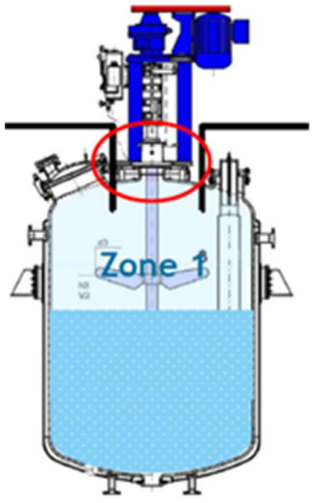

Fig. 4. *Ex-LOPA example: mechanical shaft seal of an agitator in Zone 1*

The Ex-LOPA calculation for the above described explosion scenario would become:

LOPA target value for a fatality: $\leq 10^{-5}$/yr.
F_{Ig} for rare malfunction of shaft seal (Cat.2): $\leq 10^{-2}$/yr.
P_{Ex} for presence explosive atmosphere (Zone 1): $\leq 10^{-1}$/yr.

Additional explosion prevention and protection measures will be required:

IPL1 prevention of explosive atmosphere by inerting: $\leq 10^{-2}$/yr.; or
IPL3 explosion protection by installing venting device: $\leq 10^{-2}$/yr.

4. Conclusions

The Ex-LOPA method is complementary to PHA-LOPA and allows for a consistent risk assessment of explosion scenarios in hazardous areas. The sensitivity with respect to different level of protection of Ex-equipment (i.e. Zone 2 versus Zone 1) decreases with a lower proportion of critical failure modes, while the likelihood of the occurrence of an explosive atmosphere increases. Hence, the resulting overall ignition hazard frequency appears to be independent of the Ex-Zone and typically ranges between 10^{-3} and 10^{-4} per year. Additional measures may still be necessary to reduce the explosion risk of hazardous explosive atmospheres to acceptable or tolerable levels, depending on the company's risk policy. The failure frequencies for Ex-equipment are based on general data from literature, but may be better for specific Ex-equipment in practice. This Ex-LOPA method is not applicable for risk assessment of mist explosions or dust explosions originating from dust layers.

References

Date P. et al. (2009). Modelling the risk of failure in explosion protection installations. *Journal of Loss Prevention in the Process Industries 22*.

Energy Institute (2015). Model code of safe practice Part 15: Area classification code for installations handling flammable fluids. *4th ed., London*.

Fossan I., Hansen O.R. (2018). Modelling of ignition sources on offshore oil and gas facilities. *Lloyd's Register Report No. 107566/R2*.

HSE RR226 (2002). Development of a method for the determination of on-site ignition probabilities.

HSE RR1123 (2017). Fixed flammable gas detector systems on offshore installations: optimization and assessment of effectiveness.

Markowski A.S. (2007). exLOPA for explosion risks assessment. *Journal of Hazardous Materials 142*.

Pekalski A.A. et al. (2005). A Review of Explosion Prevention and Protection Systems Suitable as Ultimate Layer of Protection in Chemical Process Installations. *Process Safety and Environmental Protection, Volume 83, Issue 1*.

Perbal, R., Fernie L. (2006). Implementation of the ATEX Directive 99/92/EC and a practical methodology for explosion risk assessment in existing plants. *2nd International Conference on Safety & Environment in Process & Power Industry Naples*.

Pieters P., Perbal R. (2011). Quantitative "ATEX" Risk Assessment - An alternative method for (parts of) rotating equipment. *Petroleum and Chemical Industry Conference Europe*.

Sherwen S. (2009). Quantifying the tolerability of potential ignition sources from uncertified mechanical equipment installed in Hazardous Areas. *IChemE Hazards XXI Symposium Series 155*.

Wingerden K. van (2010). Electrical equipment on offshore facilities: residual risk for ignition. *CMR GexCon AS Project No. 44162*.

Unravelling Explosion Risk Assessment: Insights from Driven Parameters and Case Studies

Filippo De Rosa [a *], Gerardina Toraldo [a], Pablo Giacopinelli[a] & Alexandre Lebas[a]

[a] MES (Leatherhead, UK)

* E-mail: *filippo.derosa@mes-international.com*

Abstract

Explosions pose a significant risk across various industrial settings, needing methodologies for risk quantification, prevention and mitigation. This paper provides an in-depth exploration of the Explosion Risk Assessment (ERA) methodology, with a specific focus on the application of Computational Fluid Dynamics (CFD) modelling techniques, and their pivotal role in understanding and mitigating explosion risk.

The ERA methodology involves a systematic approach encompassing hazard identification, quantitative risk assessment, and strategic mitigation planning. By systematically examining variables such as leak frequencies, ignition probabilities, environmental conditions (e.g., ambient temperature, wind speed) and geometrical effects (e.g., congestion and confinement), it is possible to quantify both likelihood and severity of explosion events. Through some case studies, we demonstrate the nuanced effects of certain variables on ERA analysis. Variation in leak frequencies, changes in ignition probabilities, alterations in process conditions and geometry configurations can significantly affect the assessed risk levels. These case studies provide valuable insights into the dynamic nature of explosion risk, enabling stakeholders to tailor preventive strategies and enhanced safety protocols.

This session aims to deepen the understanding of the ERA methodology, highlighting the significance of CFD-driven studies in assessing and managing explosion risk within industrial environments with the use of binning approach. By leveraging with case studies, attendees will gain valuable insights into how different variables impact ERA outcomes, refining preventive strategies and fortifying safety measures.

Keywords: *Explosion Risk Assessment (ERA), Computational Fluid Dynamics (CFD), Quantitative Risk Analysis, Process Safety, Risk Reduction, Risk Mitigation*

Introduction

In a risk-based approach, it is accepted that the risk of harm is inevitable, and risk is calculated as the probability of the event occurring and multiplied with the severity of the outcome. The risk would reduce to a level that would be deemed as acceptable by either reducing the event likelihood, the severity of the consequence, or both. A consequence based assessment considers the most severe outcome, disregarding the estimation of the event likelihood, thus the idea of an acceptable risk. A risk-based approach represents a more solid way to look at potential harm as it considers both the extent of the consequence but also the probability of these consequences to happen.

Quantitative Risk assessment is therefore a powerful technique used in the Oil and Gas industry to help both in the design of the facility itself (Risk Prevention) and in minimising impact on environment, people (population or workers), asset and reputation of a business in case of a Major Accident Hazard (MAH). MAHs typically include events like Toxic Dispersion, Jet Fire, Flash Fire, Explosion (deriving from vapour / 2-phase release) and Pool Fire (from liquid release).

The present work will focus on the Explosion Hazard and how it can be used for design purposes targeting the two areas of the risk:

- Consequence deriving from an explosion event: calculated from CFD simulations and typically summarised via Overpressure, Pressure Impulse, Drag.
- Frequency of an explosion event: calculated using databases for an estimation of the loss of containment frequency and ignition probability as per recognised international standards like IOGP 434-01 (2019), API 580 (2023), NORSOK Z-013 (2010) and IOGP 434-06 (2019).

Each of these variables is dependent on a number of different parameters which will be discussed during the article, highlighting the effect of the main ones on the final outcome of the risk assessment.

A case study will also be presented to show the difference between confined explosion and partially confined explosion. Results will be shown in terms of exceedance curves and Design Accidental Loads (DALs) (i.e Overpressure values at specific exceedance frequency).

1. Methodology

Risk is defined as (Frequency of a specific event) x (Magnitude of the consequence arising from such event). The main steps carried out during an ERA are reported in **Fig. 1**.

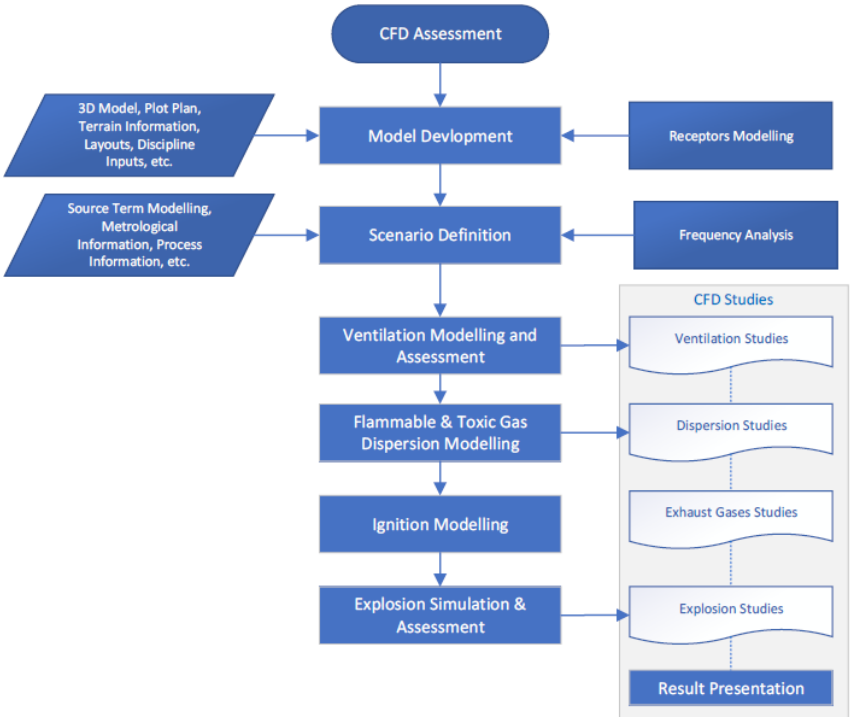

Fig. 1. *Main Parameters involved in risk calculation.*

A typical exceedance analysis will go through the following steps:

- 3D mode construction.
- Screening of the scenarios with the potential for explosion hazard.
- Calculation, via dispersion simulations, of flammable cloud sizes.
- Calculation of the explosion frequency associated to each scenario.
- Calculation of overpressure detected at each target of interest.
- Summary of the results (Exceedance curves / Design Accidental Loads).

2. Consequence Assessment

An explosion is a sudden and rapid increase in volume and release of energy, usually accompanied by the generation of high temperatures (flames) and release of high-pressure gases (blast wave). This phenomenon happens when a flammable cloud is ignited in a relatively confined and congested area. Therefore, in order to compute the right overpressure at targets, initial dispersion simulations need to be carried out to calculate the flammable mass that can accumulate in an area of interest.

Congestion (i.e., high density of small objects such as piping, cable trays, supports etc.) is in fact responsible for increasing the turbulence of the front of flame, which further accelerates generating higher turbulence levels as it interacts with the congestion in the area. To compute the right explosion magnitude, it is therefore necessary to estimate both the right levels of congestion and of flammable volume.

In order for a MAH to happen, a release of hazardous material into the atmosphere has to take place. Typically, a release (flammable or toxic) from a pressurised vessel is referred to as Loss of Containment (LOC), leading to the formation of a dangerous cloud in the atmosphere. Although clouds can be both flammable and toxic, only flammable clouds are assessed in the present paper.

2.1. Loss of Containment and release rate

Loss of containment can be due to a number of different reasons (e.g., corrosion, vibration, dropped objects, faulty welding, lack of maintenance, etc.). This paragraph will focus on the modelling of different release rates while the estimation of the frequency of occurrence will be discussed in Paragraph 3.

Because of the aleatory nature of a loss of containment, it is not possible to foresee when or the extent of such release. Therefore, a standard set of release rates is modelled as suggested in IOGP 434-06 (2019).

Release rate through an orifice due to a differential pressure is calculated from Bernoulli equation assuming incompressible flow as detailed in Perry (1984):

$$q_m = CA_2\sqrt{2\rho(p_{int} - p_{amb})} \qquad \text{Eq. (1)}$$

This calculation is performed using specific consequence modelling software, allowing the calculation of the release rates from a pressurised release of given Temperature and Pressure from different leak sizes.

This exercise is performed for any pressurised release, to which the right material composition is associated. The outcome of this process is the calculation of all of the possible releases from a given facility (e.g. offshore platform, etc).

2.2. Release Velocity

Given the pressurised release, it is important to predict the right velocity of the jet. Considering Eq. (1) (as described in Paragraph 2.1) and the mass balance for flow in pipes:

$$q_m = \rho u A_2 \qquad \text{Eq. (2)}$$

It is possible to calculate the exit velocity of the jet by sampling combining Eq. (1) and Eq. (2) to calculate the velocity u.

Velocity is another crucial parameter into the estimation of the right cloud properties. Jets with lower velocity (i.e., being released by a lower pressure or with a higher molecular weight) will be subject to a fast dilution due to interaction with the wind. This will result into smaller flammable cloud volume and lower value of the overpressure at targets.

2.3. Material

Based on the nature of the chemical processes, every part of the plant will handle different types of materials (e.g., a de-butaniser will produce LPG from the top of the column and C5+ cut from the bottom). Computing the right material properties is essential as different flammable mixtures will have different values for burning velocities, flammability limits, molecular weights, etc; all parameters that can affect explosion overpressure values at different targets.

Different materials (e.g., Methan, Ethane, Propane) being released with the same velocity will create two different clouds. In fact, materials with a higher molecular weight will have a higher density and therefore, on equal velocity, will be released at a higher flowrate than material with lower molecular weight.

For our case study, three materials were considered and a release was setup. The pressure vessel was calibrated to consider:

- Leak size of 150 mm in diameter
- Methane release temperature at 20°C
- Methane release rate at 1 kg/s

An initial exit velocity was calculated at 85 m/s for such release. The same simulation has been carried out using ethane and propane and the release was tuned to keep a velocity of 85 m/s as it was calculated for the methane simulation.

Results were collected and they are presented in **Table 1** where it is shown that on equal release velocity, methane was released with a flowrate of 1kg/s, Ethane was released at 1.87 kg/s while propane was release with a flowrate of 2.75 kg/s.

***Table 1**. Impact of different material on released flow given constant velocity.*

Component	Mw	T	Flow	Area	Density	Velocity
	[kg/kmol]	[°C]	[kg/s]	[m^2]	[kg/m^3]	[m/s]
Methane	16	20	1.00	0.018	0.67	85
Ethane	30	20	1.87	0.018	1.25	85
Propane	44	20	2.75	0.018	1.83	85

Flowrates increases with molecular weight because of the increase in density. Also, because of the molecular weight, light clouds will disperse more easily compared to dense clouds creating, on equal set of all other process parameters, smaller flammable clouds. Therefore, different molecular weights (i.e. different materials) have an impact on the cloud volume as higher flowrates/ higher molecular weight can generate bigger flammable clouds leading to higher overpressures.

2.4. Wind

Wind is crucial for the prediction of the right flammable cloud size. It is a local property and therefore every assessment has a different distribution of wind intensity and directions (i.e., coming from). All information relevant to the wind are found in the local wind rose. Conventionally, 0 degrees is associated with wind coming from north and counted clockwise (i.e., 90 degrees is associated with wind coming from east, etc.)

An example of local wind rose is reported in **Fig. 2**

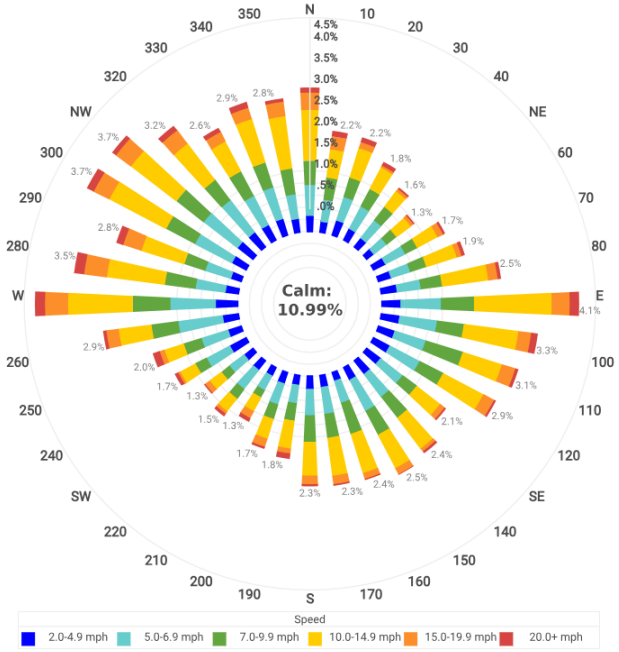

Fig. 2. *Example of local wind rose.*

Typically, the wind is modelled considering the combination of a Pasquill stability class and a wind speed.

Pasquill Classes are a system to categorise the atmospheric turbulence into six stability classes named A, B, C, D, E and F, with class A being the most unstable or most turbulent class, and class F the most stable or least turbulent class as described in Pasquill F. (1961).

Given the information provided in the wind rose, the wind velocity range is broken down into intervals (a typical set of velocities used in exceedance study is 2 / 5 / 10 m/s). Each of these velocities is associated with a Pasquill stability class in accordance with information provided in **Fig. 3**.

Table 3. Guidelines for determining Pasquill-Gifford stability classes

Surface wind speed (ms^{-1})	Day with insolation			Night	
	Strong	Moderate	Slight	Overcast or $\geq 4/8$ low low cloud	$\leq 3/8$ cloud
2	A	A–B	B	–	–
2–3	A–B	B	C	E	F
3–5	B	B–C	C	D	E
5–6	C	C–D	D	D	D
6	C	D	D	D	D

Fig. 3. *Guideline to selection of Pasquill Stability Class (*Pasquill F. (1961).

Wind affects the dispersion of the cloud. Different stability classes and wind speeds provide different levels of turbulence and therefore local mixing affecting the dilution of the cloud with air and so the flammable cloud size.

Considering the Methane scenario as detailed in **Table 1**, CFD simulations using FLACS v22.2 have been carried out considering 2 wind conditions (i.e. 2F and 5D) and 3 wind directions (i.e. along wind – 180 degrees, cross wind – 270 degrees, against wind - 0 degrees). Summary of the Run ID is reported in **Table 2**

***Table 2**. Run ID for Methane Release*

Run ID	Material	Leak Direction	Wind Direction		Weather
			-	[degrees]	[-]
200000	Methane	North (+Y)	Along Wind	180	2F
200001	Methane	North (+Y)	Along Wind	180	5D
200002	Methane	North (+Y)	Cross Wind	270	2F
200003	Methane	North (+Y)	Cross Wind	270	5D
200004	Methane	North (+Y)	Against Wind	0	2F
200005	Methane	North (+Y)	Against Wind	0	5D

Findings are presented in **Fig. 4** in terms of flammable cloud (isosurfaces between LFL value of 0.05 v/v and UFL value of 0.14 v/v) and **Table 3** in terms of flammable volumes.

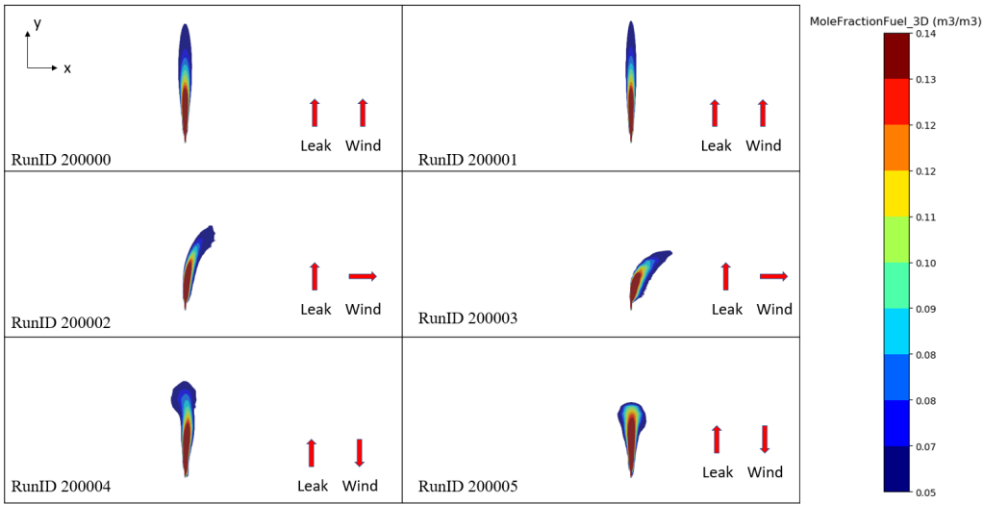

***Fig. 4.** 3D Flammable iso-surfaces for methane release under different wind conditions*

***Table 3**. Flammable cloud volumes from methane release for different weather conditions*

Run ID	Material	Leak Direction	Wind Direction		Weather	Flammable Volume
				[degrees]	[-]	[m^3]
200000	Methane	North (+Y)	Along Wind	180	2F	24
200001	Methane	North (+Y)	Along Wind	180	5D	15
200002	Methane	North (+Y)	Cross Wind	270	2F	23
200003	Methane	North (+Y)	Cross Wind	270	5D	10
200004	Methane	North (+Y)	Against Wind	0	2F	70
200005	Methane	North (+Y)	Against Wind	0	5D	40

Results presented in **Table 3** confirm that in general, on equal wind direction, the 2F cloud is bigger than the 5D cloud, this is due to the higher mixing of the outer layers of the LFL cloud (for 5D compared to 2F). In terms of wind direction, wind acting against the leak direction generate considerably bigger clouds than "along wind" and "cross wind" cases. This is due to air entrainment diluting higher concentrations of the cloud (higher than the UFL) generating larger flammable volumes.

CFD analysis is able to correctly predict the amount of flammable gas (i.e. gas mass between LFL and UFL) compared to integral models where it is not possible to model different combinations of release directions and wind directions. Most software developed on integral models can only in fact model along wind scenarios underpredicting the flammable clouds and therefore the explosion extent.

2.5. Duration of the release

Not all the pressurised vessels hold the same amount of hazardous material. For small volumes, in fact the pressure will decrease a few seconds after the release and therefore the release rate will also drop. On the other hand, big inventories can sustain a constant flowrate for a long duration. Based on the above, some releases can be strongly dependent on time and therefore require a time varying modelling to calculate the right size of the cloud. Therefore, the longer the release, the bigger the flammable cloud that will result from the LOC.

2.6. Explosion Extent

Once the dispersion simulations have been finalised and all flammable masses are correctly computed and calculated at each of the congested areas, the explosion consequence modelling is carried out.

As per software guidelines FLACS-CFD v22.2 (2023), it is recommended to use homogeneous stoichiometric fuel mixtures and idealized gas clouds of rectangular shapes for which the software has been validated against experimental data. This method is conservative as it assumes all flammable gas (between LFL and UFL) is mixed with air (by the turbulence generated during the explosion) to a stoichiometric concentration before being completely burnt, hence releasing the maximum amount of energy. An example of 3D flammable cloud for explosion simulation is reported in **Fig. 5**.

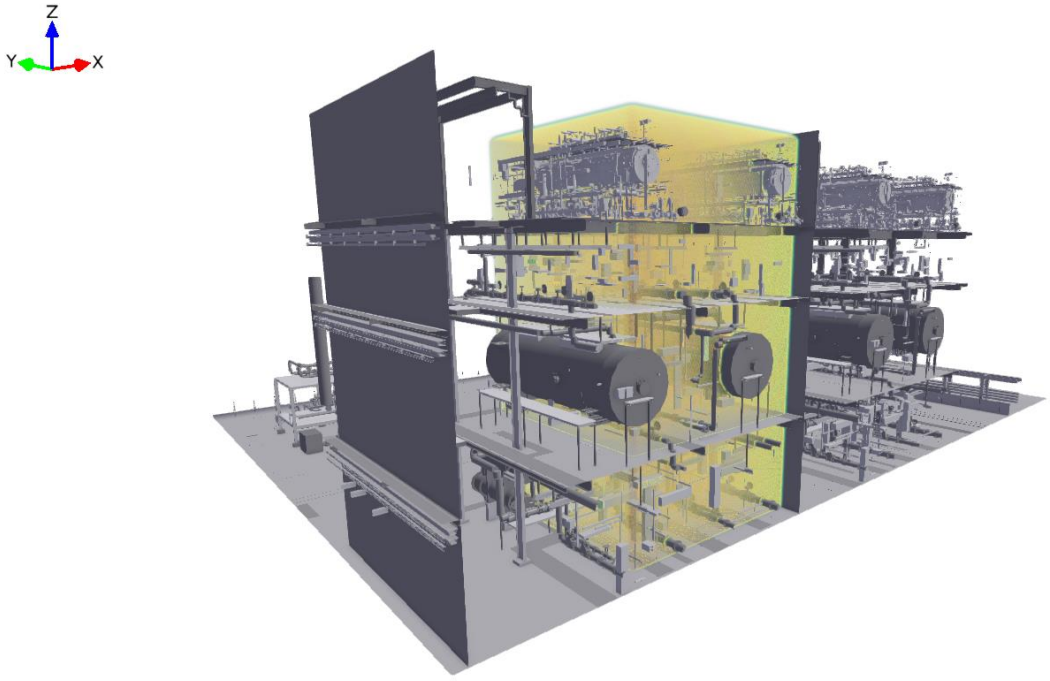

Fig. 5. *3D Flammable cloud for an explosion simulation using FLACS-CFD*

Different ignition points were also considered for each gas cloud size and location. Ignition points were selected with the aim of assessing likely worst-case scenarios. Edge / corner and central ignitions are primarily considered to ensure the inclusion of maximum potential flame development and speed-up cases.

Placing an ignition source near the edge / corner of the gas cloud will allow the flame front to travel further. In a congested environment, this will allow the flame front to accelerate over a greater distance as it interacts with the surroundings due to the so-called 'positive feedback loop' causing acceleration due to turbulence. Consequently, these scenarios are more likely to generate higher explosion overpressures. However, other parameters such as localised confinement also play a significant role in the generation of overpressures. The central ignition point is also modelled to provide a wider spread set of ignition sources. A central ignition point would likely occur from an intermittent source, whereas an ignition point located near the cloud edge would likely occur from a constant source. Overpressure values for the cloud reported in **Fig. 5** are shown in **Fig. 6** for two different ignition points.

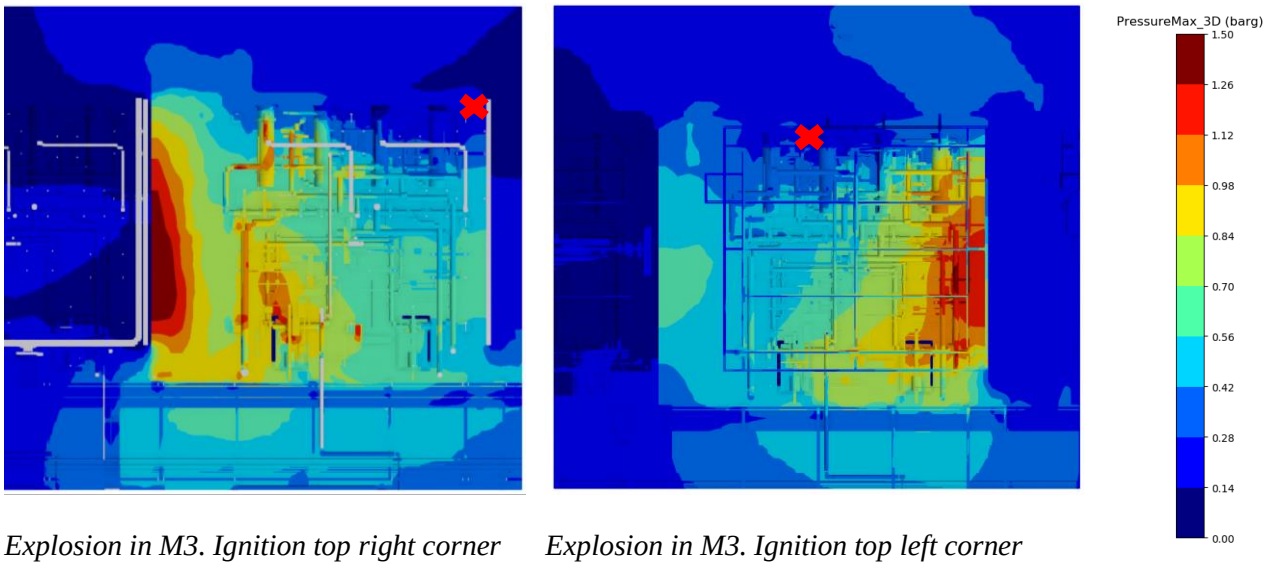

Explosion in M3. Ignition top right corner *Explosion in M3. Ignition top left corner*

Fig. 6. *3D Overpressure values for different ignition points (top view)*

Fig. 6 shows that the front of flame accelerates on the diagonal of the cloud creating the highest overpressure on the opposite corner from where it started. Considering that for the same cloud the two different ignition points create peak overpressures in two different areas of the facility, it is important to compute more than one ignition per cloud to collect enough data for the statistics to be reliable.

3. Frequency Assessment

3.1. Leak Frequency

In carrying out risk analysis it is necessary to select a set of representative hole sizes for the purpose of evaluating the consequences of the release as explained in Paragraph 2.1.

Each of these ranges is associated with a representative leak size that can be calculated in different ways. According to IOGP 434-01 (2019) it is statistically meaningful to consider one of the options as detailed in **Table 4**.

The standard set of leak sizes as reported in IOGP 434-01 (2019) is detailed in **Table *4***.

Table 4*. Breakdown of leak ranges into representative leak sizes*

Hole diameter Range [mm]	Upper Limit of the Range [mm]	Arithmetic Mean (Hole diameter [mm])	Arithmetic Mean (Hole Area [mm^2])	Geometric Mean (Hole diameter [mm])
1 to 3	3	2	2.2	1.7
3 to 10	10	6.5	7.4	5.5
10 to 50	50	30	36.1	22.4
50 to 150	150	100	111.8	86.6

The leak frequency is calculated in a systematic manner. Let us assume we have a control domain as shown in **Fig. 7** and the interest is to calculate the leak frequency of the system.

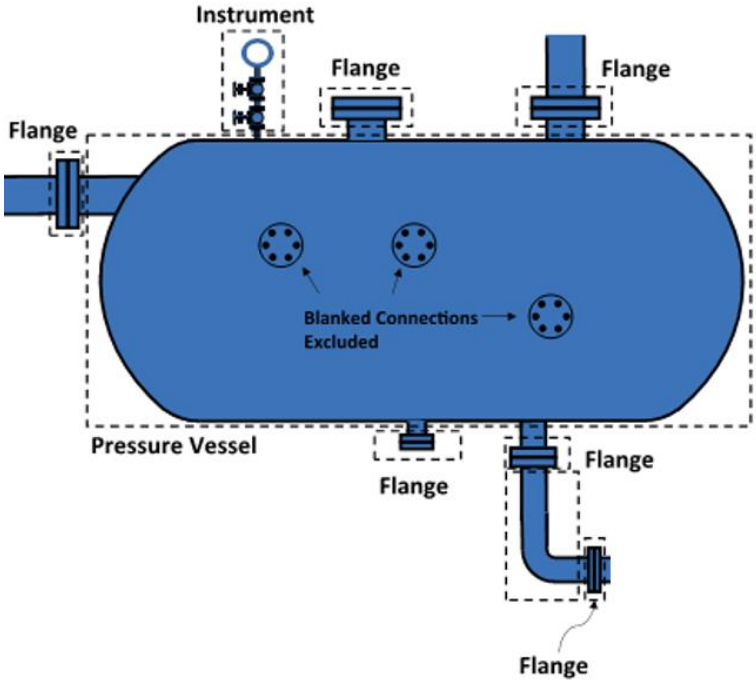

Fig. 7. *Control domain for leak frequency,* IOGP 434-01 (2019)

The 1st step is to calculate the number of items. For the domain considered we can count the number of:

- No 5 flanged joints
- No 1 instrument connection
- No 1 pressure vessel

Each of these items will have a specific leak frequency based on the applied standard and based on real leak events which have been counted and summarized. International standards also give fitting equations to break down the frequency into the selected leak sizes as detailed in **Table 4**.

The final outcome of the process is to calculate the leak frequency (per leak size) for the system detailed in **Fig. 7** broken down into the selected leak sizes expressed in leaks per year or simply year^{-1}.

The final process can be summarized in the few steps as detailed in **Fig. 9**

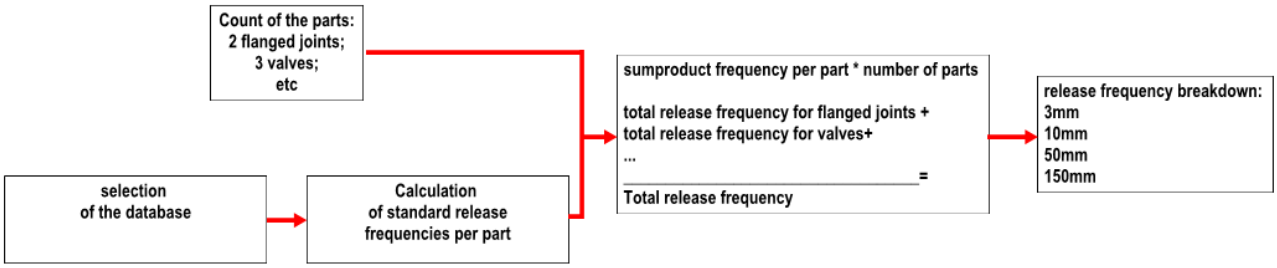

Fig. 8. *Parts Count and release frequency calculation schematics*

3.2. Ignition Probability

Because the main focus of the paper is related to the explosion phenomena, it is necessary to quantify the probability that a specific release event (release of hazardous material from a specific leak size) could ignite with a certain probability of delayed ignition as reported in IOGP 434-06 (2019).

The probability of ignition is dependent on the flowrate (therefore leak size) and type of facility (i.e. LPG process plant will have different ignition probability compared to methanol handling process etc).

3.3. Wind Distribution

As already mentioned in Paragraph 2.4, wind direction has an important effect on the calculation of the cloud size however, the probability of wind coming from a specific direction should also be taken into consideration while performing an exceedance study.

4. Exceedance Analysis

Use of exceedance curves is widely used in the process industry to quantify the blast load for the design of occupied buildings close to process areas or design separation walls. The exceedance curves purpose and construction is detailed in (Glynn, 2011)

This paragraph will describe a project case study (hereinafter referred to as project) focusing on the steps that have led to the exceedance analysis.

The scope of the project was to carry out an exceedance analysis to calculate the design conditions for the separation walls at specific exceedance values (i.e. 1E-04 per year with ALARP Demonstration for 1E-05 per year, see (Glynn, 2011)). Specifically, exceedance curves were plotted and receptors were designed to withstand minimum 1E-04 explosion overpressure impairment frequency such that no harm or injury to personnel occurs., or does not lead to failure of Escape, Evacuation, and Rescue (EER) measures. ALARP demonstration was therefore performed for 1E-05 explosion overpressure impairment frequency.

The project consisted of four modules of gas separation, handling mixture with different ranges of C1-C4 hydrocarbons separated by blast walls 40 meters tall (whole elevation of the structure) as shown in **Fig. 9** (2D) and **Fig. 10** (3D).

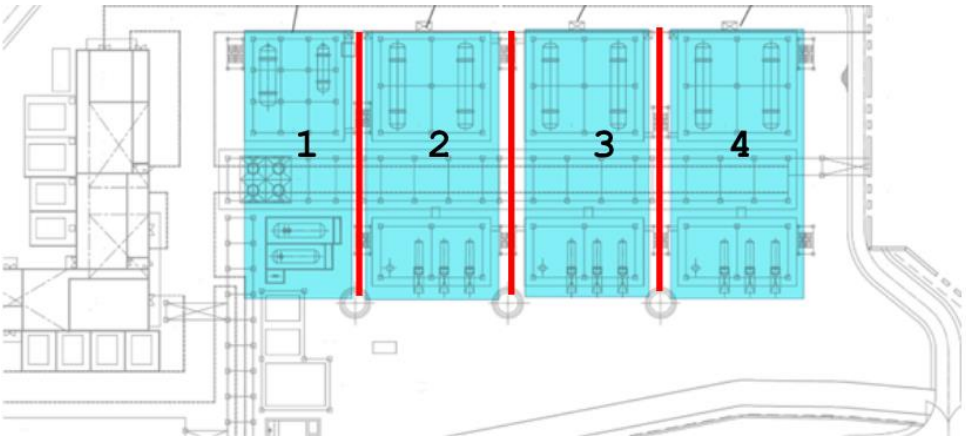

Fig. 9. *Plot Plan for the four project modules*

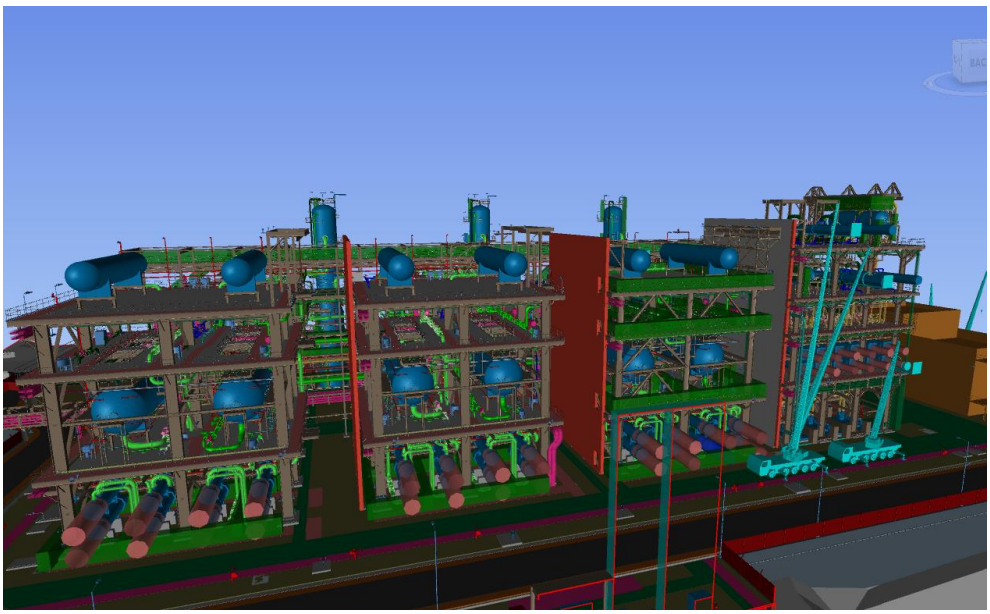

Fig. 10. *3D model of the project modules*

The project was modelled using 20 failure cases. Each failure case was represented by its own material and modelled using three release sizes (e.g., 25 mm, 100 mm, 150 mm) and two release directions (specifically selected to maximise the flammable cloud inside each module.

Two weather conditions were considered for the exceedance analysis (2F and 5D) for two wind directions: Wind coming from north (0 degrees) and wind coming from south (90 degrees).

The total number of dispersion simulations run was therefore:

20(FailureCases)*3(leakSizes)*2(LeakDirections)*2(WeatherConditions)*2(WindDirections)
= 480 Dispersion Simulations

Each flammable cloud has been considered as a potential explosion cloud.

Six (6) different percentage filled (binning) scenarios (3%, 6%, 12%, 25%, 50%, and 100% of the PESs) were considered for each identified PES. Each % of filling (stoichiometric gas cloud) has been modelled with 4 ignitions as a minimum.

In reality, an infinite number of release locations and jet orientations are possible, resulting in an infinite number of gas cloud locations and sizes similar to those predicted. Therefore, gas clouds were positioned around each congested area to account for different release directions, locations, and wind conditions. Positions were selected with the aim of assessing likely worst-case scenarios. The big advantage of this methodology is that it allows to run explosion simulations and dispersion simulations independently minimizing the number of explosion cases (one single explosion can in fact represent more than one dispersion scenario if such dispersions generate similar flammable clouds in terms of percentage of filling - binning).

Therefore, the total number of explosions modelled and breakdown into binning levels and ignitions is detailed in ***Table 5***:

***Table 5**. Explosion Simulation Count*

Binning	Number of Cloud Locations	Number of Ignitions	Total Number of Simulations
3	32	4	128
6	16	4	64
13	8	4	32
25	4	4	16
50	2	4	8
100	1	4	4
Total			252

Within the limit of the assumptions made (i.e. 6 binning levels, 4 ignition per cloud) the maximum number of explosion simulations to be carried for this analysis was 252. This represents all of the possible overpressure profiles at any target in the domain. Therefore, any dispersion cloud can be associated to one binning level (and all relevant cloud locations). This helps reducing the number of explosion simulations to be undertaken.

A normal 1to1 approach would have considered 480 dispersions (each associated to one dedicated cloud) * 4 ignitions; with the need to run 1920 explosion cases.

This point is crucial in the optimisation of the scenarios because any future modification to the Project requiring additional dispersion cases will not require any additional explosion modelling as the explosion profile has already been determined. While on a 1 to 1 approach, for each of the new potential dispersion cases, the relevant 4 explosion cases should be run.

Once consequence modelling was conducted, the exceedance construction followed. Detailed steps are discussed in (Glynn, 2011)

To draw the exceedance, the following steps were followed:

- Several targets were selected to assess the explosion risk.
- For each explosion scenario, the overpressure detected at the targets was extracted.
- Each explosion simulation was associated to the relevant explosion frequency (i.e., dispersion frequency * 0.25 to account for four ignition points). The overpressure values at targets were sorted in a descending order and the relevant frequency (associated accordingly) was added up to generate a cumulative distribution.

For each simulation, the explosion frequency was calculated as:

Explosion Frequency = Leak Frequency * Delayed Ignition Probability * Weather Condition Probability * Wind Direction probability * Leak Direction Probability

Therefore Module 3 (M3) and Module 4 (M4) were selected to prove the effects of confinement on the clouds in terms of exceedance and design accidental loads (DALs).

The total explosion frequency was calculated to be 8E-04 per year for both M3 and M4.

5. Results and discussion

Flammable clouds in each module were extracted from the CFD software for each simulation. Maximum and average flammable gas accumulation is reported for each module in **Fig. 11**.

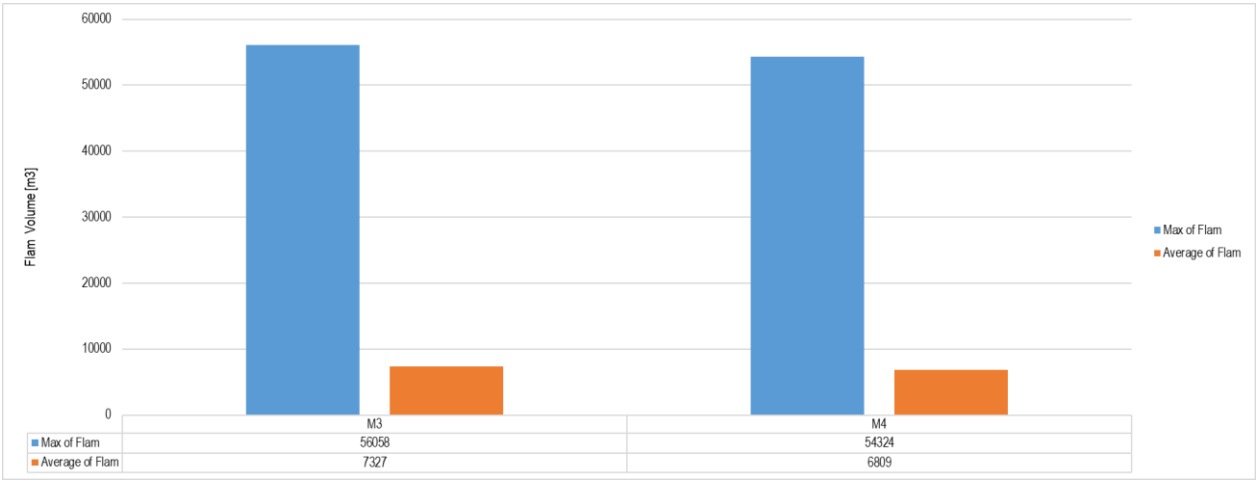

Fig. 11. *Maximum and average cloud size at each of the congested areas assessed*

The 2 modules show a comparable accumulation although M3 is confined and M4 is partially confined. Ventilation in fact has a small effect providing a reduction of flammable gas accumulation between M3 and M4 by a factor 1.03 for the maximum flammable gas cloud and 1.07 for the average.

Moreover, for all failure cases modelled, the flammable gas accumulation has been plotted against the cumulative explosion frequency (flammable volumes were sorted in a descending order and the relevant frequency was added up to generate a cumulative distribution) for M3 and M4 and reported in **Fig. 12**.

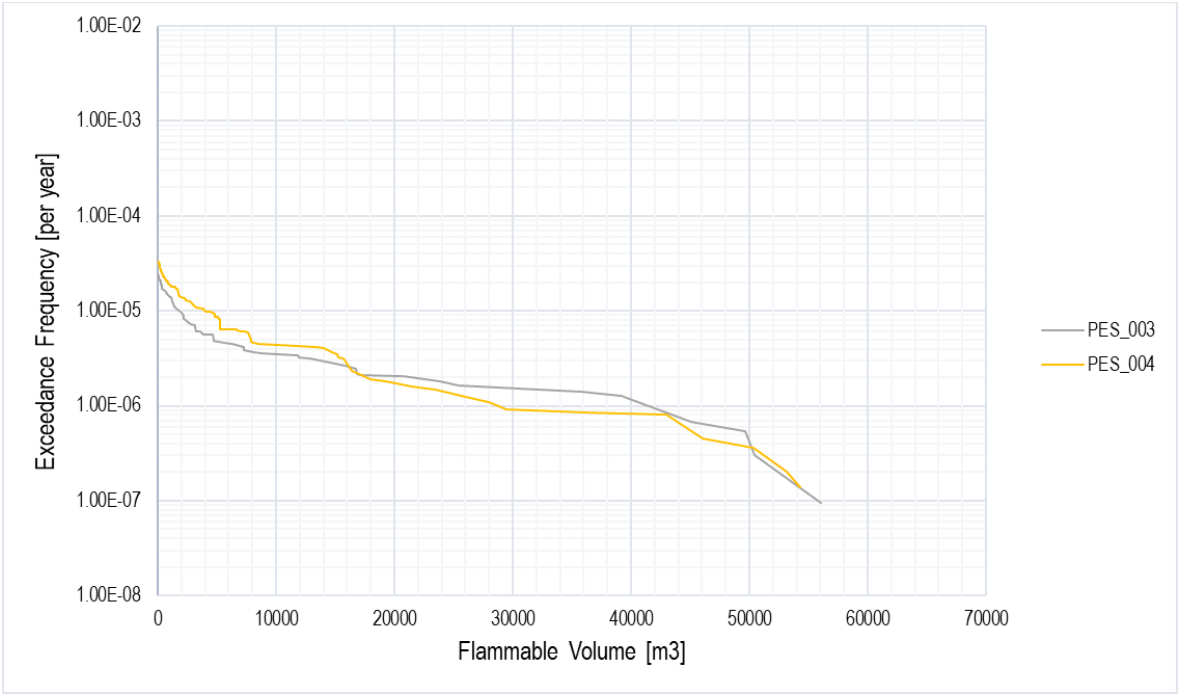

Fig. 12. *Accumulation of flammable gas clouds in congested areas M3 and M4*

The curves show that the accumulation of the flammable cloud is comparable. However, for high exceedance frequency (greater than 2E-06 per year) accumulation in module 4 is generally higher than accumulation in module 3, while this consideration is reversed for exceedance frequencies lower than 2E-06 per year which is due to a more effective ventilation in module 4.

One of the targets assessed was the separation wall between modules 3 and 4 (M3M4). It should be noted that the contributors to the exceedance overpressure at the separation wall are respectively from M3 (west side) and M4 (east side).

The exceedance curve derived considering overpressure values from ignition of flammable clouds distributed as per **Fig. 12** are reported in **Fig. 13** (in blue M3M4_West and in orange M3M4_East).

It should be noted that smaller flammable clouds contributed to higher exceedance values, and bigger flammable clouds contribute to lower exceedance values (being the exceedance curve a decreasing function of the overpressure).

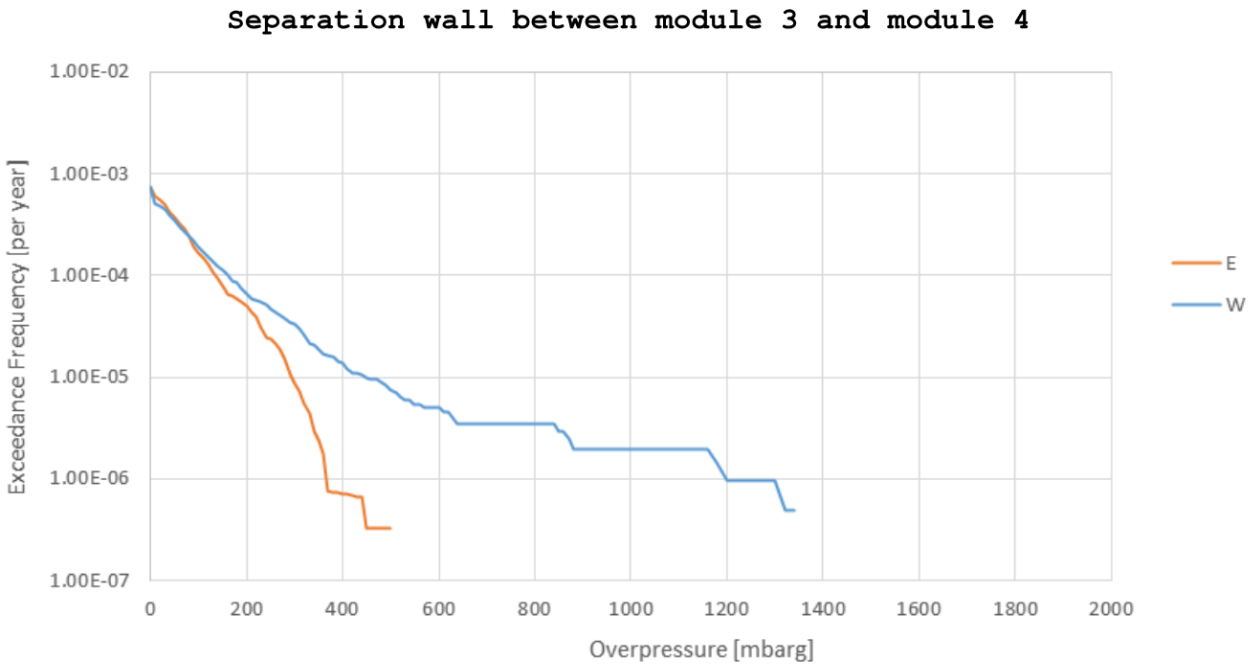

Fig. 13. *Accumulation of flammable clouds in congested areas 3 and 4*

DALs represent the overpressure that the blast wall M3M4 should withstand in the event of an explosion. They are typically (but not limited) referred to 1E-03/1E-04/1E-05/1E-06 per year and they are based on corporate criteria. In general, different companies have different tolerability criteria, which applicability/discussion is not part of the present paper.

Based on the Exceedance curves, DALs were calculated and reported in ***Table 6***:

Table 6*. Design accidental loads for east and west side of the blast wall M3M4*

Target	**Design Accidental Loads [mbarg]**		
	1E-04 per year	**1E-05 per year**	**1E-06 per year**
East side of M3M4	120	300	360
West side of M3M4	160	450	1200

The following can be extracted from the plot:

- The top of the exceedance curve (exceedance value at 0 mbarg) is the same for M3M4_East and M3M4_West and it represents the total explosion frequency for the modules.
- The bottom of the exceedance curve represents the maximum overpressure value that can be generated in the module, namely 500 mbarg for M3M4_East and 1350 mbarg for M3M4_West. This is due to the confinement provided both on east and west of M3 while M4 is partially confined only on the west side. On similar distribution of the flammable clouds, the partial confinement has reduced the overpressure by a factor of 2.7.
- The 2 curves nearly overlap for the higher frequencies (>1E-04 per year) therefore, for smaller clouds the confinement is not able to reflect the overpressure and therefore M3M4_East and M3M4_West have the same exceedance values.
- Considering the flammable gas clouds exceedance reported Fig. 12 is comparable between M3M4_East and M3M4_West, the overpressure values should also be comparable. However, as reported in Fig. 13, overpressure exceedance curves diverge for exceedance frequencies lower than 1E-04 per year recording higher exceedance values on M3M4_West. This can be explained due to the confinement of the cloud on M3 enhancing the overpressure at M3M4_West.
- DALs represent the overpressure that the blast wall M3M4 should withstand in the event of an explosion, the lower the exceedance frequency the higher the gap between M3M4_East and M3M4_West.

6. Conclusions

ERA is a study based on the combination of consequence and frequency of occurrence of explosion events that provides indications (through exceedance curves and DALs) about the risk to asset or people aiming to give recommendations based on the comparison between DALs and corporate tolerability criteria.

Different parameters were highlighted to affect both the consequence and the probability of occurrence.

A case study has been presented to show the approach of the exceedance analysis considering a 3D geometry highlighting the effects of confined (module M3) and partially confined (module M4) explosions.

CFD dispersion and explosion simulations were conducted using FLACS-CFD v22.2. Due to the aleatory nature of the exceedance study, a large number of simulations is needed to guarantee a statistical meaning to the final results, this number can be optimised using the binning approach.

Specifically for the case study presented the following scenarios were assessed:

- 480 dispersion simulations (considering several leak sizes, leak directions, wind directions, weather conditions).
- 256 explosion simulations (considering different ignition points per flammable cloud).

Frequency analysis confirmed that the overall explosion frequency for M3 and M4 is 8E-04 per year.

Dispersion analysis showed that for M3 and M4 the flammable gas accumulation was similar with slightly bigger accumulation in M3 due to confinement leading to a less efficient ventilation and therefore less dilution of flammable clouds with air. This trend is confirmed both by the maximum (reduction by a factor 1.03) and the average accumulations (reduction by a factor 1.07).

Explosion analysis has been carried out and overpressures at the separation blast wall M3M4 was computed from explosion events coming from east (M4 partially confined) and from west (M3 confined). Results were reported in terms of exceedance curves and DALs.

It was shown that for smaller clouds the exceedance curves relevant to M3M4_East and M3M4_West were comparable as the confinement was not affecting the overpressure at the target (for an exceedance frequency around 1E-04 per year), while for lower exceedance frequency the effect of the confinement started affecting the overpressure values and therefore the 2 curves diverged.

From the exceedance curves, DALs were derived and based on the tolerability criteria selected they provided a structural design to the blast wall (Note that tolerability criteria was not part of the present discussion).

While blast walls are crucial to avoid escalation of a MAH between one module to another, they also introduce confinement that can increase the design overpressure up to a factor of 2.7.

In conclusions, a statistical approach based on binning is still able to correctly predict the behaviour of the explosion profile via association of a dispersion case with the most similar binning level. This is able to optimise the number of explosion simulations.

References

API 580. (2023). *Risk Based Inspection (RBI)*. www.nationalarchives.gov.uk/doc/open-government-licence/,

FLACS-CFD v22.2. (2023). *FLACS-CFD v22.2 User's Manual*.

Glynn, K. J. (2011). *Use of the Exceedance Curve Approach in Occupied Building Risk Assessment*.

IOGP 434-01. (2019). *IOGP, 434-01 - Process Release Frequencies*.

IOGP 434-06. (2019). *IOGP, 434-06 - Ignition Probabilities*.

NORSOK Z-013. (2010). *NORSOK STANDARD, Z-013, Edition3 October 2010, Risk and emergency preparedness assessment*.

Pasquill F. (1961). *Pasquill, F. (1961). The estimation of the dispersion of windborne material, The Meteorological Magazine, vol 90, No. 1063, pp 33-49.*

Perry, R. H. G. D. W. (1984). *Perry, Robert H.; Green, Don W. (1984). Perry's Chemical Engineers' Handbook (Sixth ed.). McGraw Hill.*

ML enhanced measurement of the electrostatic charge distribution of powder conveyed through a duct

C. Wilms[a,b], W. Xu[a], G. Ozler[a,b], S. Jantač[a], S. Schmelter[c] & H. Grosshans[a,b]

[a] Physikalisch-Technische Bundesanstalt (PTB), Braunschweig, Germany
[b] Otto von Guericke University of Magdeburg, Institute of Apparatus and Environmental Technology, Magdeburg, Germany
[c] Physikalisch-Technische Bundesanstalt (PTB), Berlin, Germany

E-mail: *christoph.wilms@ptb.de*

Abstract

The electrostatic charge acquired by powders during transport through ducts can cause devastating dust explosions. Our recently developed laser-optical measurement technique can resolve the powder charge along a one-dimensional (1D) path. However, the charge across the duct's complete two-dimensional (2D) cross-section, which is the critical parameter for process safety, is generally unavailable due to limited optical access. To estimate the complete powder charge distribution in a conveying duct, we propose a machine learning (ML) approach using a shallow neural network (SNN). The ML algorithm is trained with cross sectional data extracted from four different three-dimensional direct numerical simulations of a turbulent duct flow with varying particle size. Through this training with simulation data, the ML algorithm can estimate the powder charge distribution in the duct's cross-section based on only 1D measurements. The results reveal an average L^1-error of the reconstructed 2D cross-section of 1.63 %.

Keywords: *industrial explosions, powder processing, electrostatics, measurement, simulation, shallow neural network (SNN), machine learning (ML)*

1 Introduction

Pneumatic conveying is widely applied in industry to transport material, in most cases powders and particulate materials, by fluids like air as a conveying medium. Such transport systems are superior to mechanical conveyors regarding automation, maintenance and installation cost, and layout flexibility (Lim et al., 2006). However, electrostatic charging can cause a severe hazard in operation as a discharge can ignite a dust explosion (Ding et al., 2024). Hence, pneumatic conveying systems need to be well-controlled to counteract this risk. Therefore, at least two issues are crucial: (a) knowledge about the boundaries for save operation as a function of material properties, ambient conditions, etc., and (b) precise monitoring to assess if the system is within the safety conditions.

At the moment, the charge of particles Q can be measured non-invasive using Faraday pails or by grounding the conveying duct, resulting in an electric current caused by the charge transfer when particles passes the measurement section (Matsusaka and Masuda, 2006, Ndama et al., 2011). Even though these principles are simple and cheap, they report only the average charge of the particles, which can significantly differ from the actual charge. For example, the charge of bipolar particles would cancel out, leading to a close to zero Faraday reading. In terms of safety, however, this would lead to a fallacy since a local and instantaneous charge extremes can cause a discharge. To address this problem, a spatially resolved measurement of the particle charge distribution would be necessary. Xu et al. (2023) presented a new technology which can measure the time-averaged particle charge distribution on a one-dimensional (1D) path oriented in wall-normal direction. To this end, multiple particles are illuminated and tracked within a two-dimensional (2D) slice of a finite thickness. In the second step, a homogeneous electric field is applied by two transparent electrodes on opposite sides of the duct. Charged particles respond to the applied electric field with an increased response for stronger charged particles. By subtracting the time-averaged measurements of the particle velocity

and particle acceleration without electric field, the mean forces of the fluid on the particles cancel out, allowing us to determine the electric charge of particles.

The disadvantage of the laser-based charge measurement is effort required to quantify the charge in the complete cross-section. The system cannot measure a cross-section in one step. Instead, the laser plane must be offset to scan the section by several measurements. Such an effort seems unfeasible in industrial applications, especially since it requires large optical access to the flow.

To enhance the method by Xu et al. (2023), this paper proposes a data-driven approach that predicts the entire streamwise-normal charge distribution based on a single line measurement. Computational fluid dynamic (CFD) simulations of a particle-laden turbulent duct flow provided the necessary training data. In the following, the developed machine learning (ML) algorithm is presented, and its potential is evaluated. This procedure prepares the laser-based particle charge measurement for industrial application and contributes to reducing hazards when operating pneumatic conveying systems.

2 Method

This section describes, in 2.1, the setup of the duct flow simulations and, in 2.2 and 2.3, the ML algorithm for predicting the particle charge distribution.

2.1 CFD simulation

The training and validation data was extracted from four direct numerical simulations of a turbulent duct flow at a bulk Reynolds number of

$$Re = \frac{h^* u_\mathrm{b}^* \rho_\mathrm{f}^*}{\mu^*} = 2700 \tag{1}$$

with half duct height h^*, bulk velocity u_b^*, fluid density ρ_f^*, and dynamic viscosity μ^*. The * marks dimensional quantities. The friction Reynolds number amounts to

$$Re_\tau = \frac{h^* u_\tau^* \rho_\mathrm{f}^*}{\mu^*} = 180 \tag{2}$$

with the friction velocity u_τ^*. The particles have a material density of $\rho_\mathrm{p} = \rho_\mathrm{p}^*/\rho_\mathrm{f}^* = 1150/1.2$, a coefficient of restitution $e = 1.0$, and a number density of $N_\mathrm{p} = 800h^{-3}$ with $h = h^*/h^*$. The size of the particles was varied between $D_\mathrm{p} = D_\mathrm{p}^*/h^* = 2.5 \cdot 10^{-3}$, $5 \cdot 10^{-3}$,$7.5 \cdot 10^{-3}$, and $1 \cdot 10^{-2}$ in the four simulations.

The simulations were performed using the open-source solver *pafiX* (Grosshans et al., 2020). The motion of the gaseous phase is described by the Navier-Stokes equations and the electrostatic field by Gauss law, both in an Eulerian framework. The particles' motion is calculated using Newton's law of motion in a Lagrangian framework. The coupling between both phases is four-way, meaning that the fluid acts on the particles, the particles on the fluid, and the particles between each other and the walls, see Grosshans and Papalexandris (2017). The resolution of the Eulerian grid amounted to $256 \times 144 \times 144$ grid points in x^*, y^*, and z^* direction, corresponding to $\Delta x^+ = 8.44$, $\Delta y_\mathrm{c}^+ = \Delta z_\mathrm{c}^+ = 3.93$ in the duct's center, and $\Delta y_\mathrm{w}^+ = \Delta z_w^+ = 0.05$ at the wall. The $^+$ indicates wall units which are achieved by normalization with u_τ^* and kinematic viscosity $\nu^* = \mu^*/\rho_\mathrm{f}^*$. The coordinates are normalized with h^*. The computational domain had a size of $12h^* \times 2h^* \times 2h^*$ with cyclic boundary conditions in the streamwise direction and walls in the spanwise directions. In total, $7 \cdot 10^4$ time steps were computed. This covers the time until the particles reach a predefined saturation charge of $Q_\mathrm{sat}^* = 50\,\mathrm{fC}$. In the following, the particle charge Q^* is displayed in normalized form as $Q = Q^*/Q_\mathrm{sat}^*$, see figure 1(a) and 1(c).

2.2 ML algorithm

This section describes the data extraction from the simulation and the ML model based on a neural network.

Figure 1(a) shows the particles with their charge for a streamwise-normal slice with a thickness of $h = 3/8$ while subfigure (c) renders all particles within the duct. Snapshots of the Lagrangian particle field were saved every 1000 time steps of the simulation, corresponding to $\Delta t^+ \approx 0.52\,\mathrm{s}$. In total, this results in 70 snapshots per simulation. For each snapshot, the result fields were mapped on a regular equidistant Cartesian grid with $128 \times 21 \times 21$ grid points. The mapping was performed by determining a distance-weighted mean of the nearest 10 particles for each grid point. In the next step, 128 equidistant slices in streamwise direction were extracted. Figure 1(b) depicts an instantaneous particle charge field mapped on a regular grid. To mimic the temporal averaging, which is necessary for the experimental measurement setup, spatial averaging in flow direction was applied, resulting in a single slice per time step, see figure 1(d). These slices created the database for the ML. Hence, the database consisted of 280 two-dimensional slices with a resolution of 21×21 grid points.

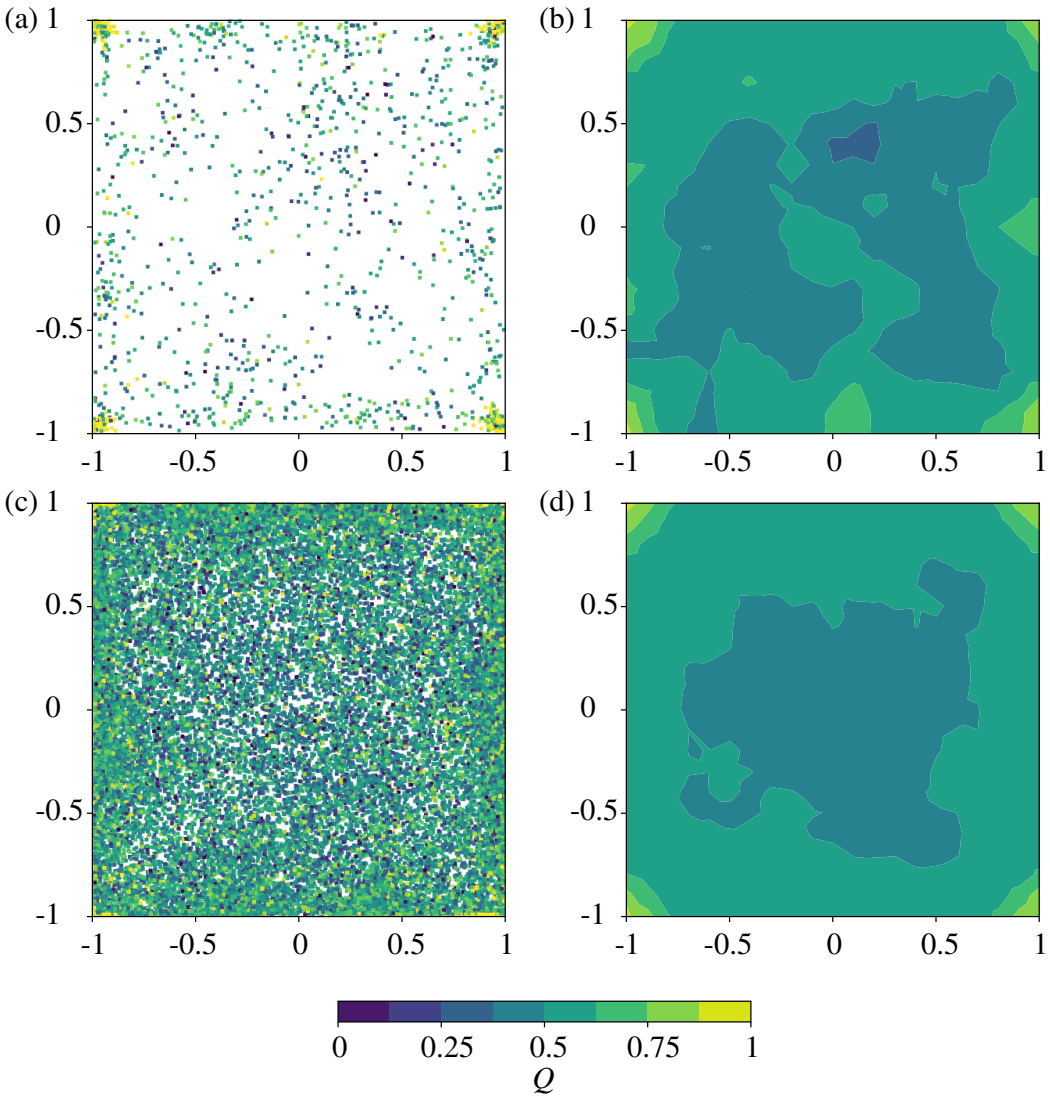

***Fig. 1**: Particles colored according to their charge for (a) a streamwise-normal slice with a thickness of $h = 3/8$ and (c) of all particles within the duct. The mapping of the particles in (a) to a regular grid is depicted by (b), and (c) corresponds to (d).*

The objective of the ML algorithm is to predict a 2D field based on the single path data. For this purpose, Erichson et al. (2020) developed a ML algorithm based on a shallow neural network (SNN), which is applied in the following. The same neural network architecture has also been used by Wilms et al. (2024) to predict the velocity field and volumetric flow rate of a disturbed pipe flow based on a single path measurement. Compared to a deep neural network, the advantages of a SNN are a smaller training dataset, faster training, and a smaller risk of overfitting.

The network decodes the input of the 1D path over two fully connected hidden layers to an output of the 2D field. The first hidden layer consisted of 40 neurons, followed by 45 in the second hidden layer. The algorithm was implemented in Python 3.10 (Van Rossum and Drake, 2009) based on pytorch (Paszke et al., 2019). For further details, the reader is referred to Erichson et al. (2020) and Wilms et al. (2024). To improve the prediction, the neural network was operated on normalized datasets. Therefore, standard normalization based on the 1D path was applied to the 1D input and 2D output field. The normalization was grounded on the 1D path to be able to re-normalize the output data after prediction. For each trained model, bootstrapping with 20 repetitions of the training with new initial conditions of the neuron weights was applied to improve the robustness.

2.3 Training and validation data

The training and validation data for the SNN were extracted from the four simulations described above. At the start of the simulation, uncharged particles were seeded homogeneously distributed in a fully developed turbulent duct flow. Due to triboelectricity, the average charge of all particles increased over time until it reached the predefined saturation charge of $Q_{\mathrm{sat}} = 1$, see figure 2. Particles with a smaller size reach the saturation charge faster. Three different versions of the SNN were trained to validate its performance. Therefore, the training data was varied, while the validation data was the same for all models. The validation data consists of all time steps from the case with a particle size of $D_{\mathrm{p}} = 1 \cdot 10^{-2}$ as well as specific time steps from the other three simulations, namely $t_{v_{1\ldots6}} = 5.68$, 10.85, 16.02, 21.19, 26.36, and 31.53. This data was excluded from the training data of the three models.

The first model $M1$ was trained on all available time steps ($0 \leq t^+ \leq 36.17$), the second model $M2$ was trained with a smaller training dataset containing the latest 35 time steps ($18.09 \leq t^+ \leq 36.17$), and the third model $M3$ was trained on the first 35 time steps ($0 \leq t^+ \leq 18.09$) excluding three validation time steps. Hence, $M1$ was validated on an interpolation task concerning the particle sizes $D_{\mathrm{p}} = 2.5 \cdot 10^{-3}$, $5 \cdot 10^{-3}$, and $7.5 \cdot 10^{-3}$ while $M2$ and $M3$ had to deal with some extrapolation in the validation and less training data. The case with a particle size of $D_{\mathrm{p}} = 1 \cdot 10^{-2}$ was an extrapolation for all three models.

For the training, from each slice, two 1D paths were extracted (at $x = 0$ and $z = 0$). Hence, $M1$ was trained on 384 data pairs and $M2$ and $M3$ on 192 data pairs. In the validation step, the 1D path was taken at the same positions which resulted in 176 one-dimensional validation paths (1 case with 140 paths and 3 cases with each 12 paths).

The reconstructed fields of the SNN were quantified by the L^1- and $\overline{Q}$-error:

$$L^1\text{-error} = \left(\sum_{i=1}^{n} \left| 1 - Q_{\mathrm{ref},i} / Q_{\mathrm{rec},i} \right| \right) / n \quad ; \quad \overline{Q}\text{-error} = \left| 1 - \overline{Q_{\mathrm{ref}}} / \overline{Q_{\mathrm{rec}}} \right| \tag{3}$$

where n represents the number of points on the 2D grid, Q_{ref} the ground truth 2D field and Q_{rec} the reconstructed field. The bar $(\bar{\cdot})$ represents an spatial average. The latter metric can be compared to the state-of-the-art measurements, which supports the reliability in practical application.

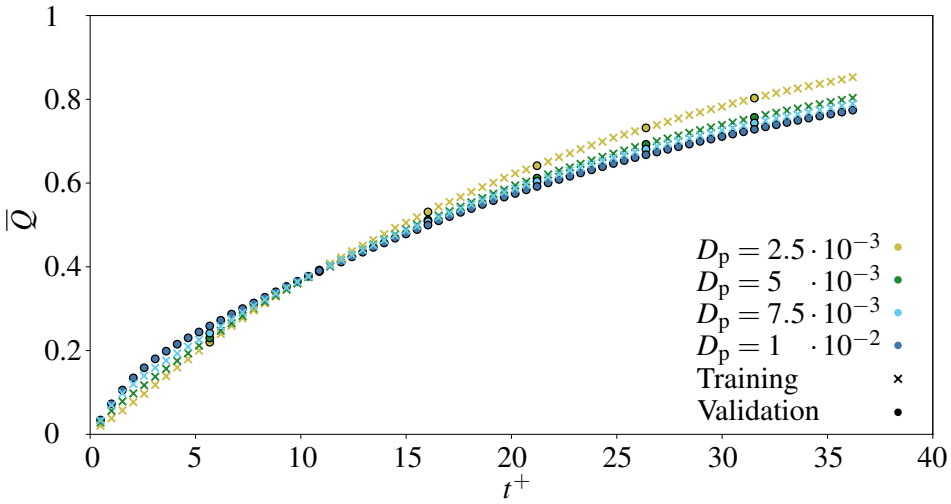

***Fig. 2**: Evolution of the mean particle charge $\overline{Q}$. The marked positions (circles) represent the time steps excluded in the training and used for validation.*

3 Results & Discussion

In the first step, we analyzed the abilities of the SNN visually by comparing the reconstructed profile with the ground truth. Figure 3 displays the results for the 1D profile extracted at the center of the duct ($y = 0$) for all six validation time steps of the simulation with a particle size of $D_p = 5 \cdot 10^{-3}$ and the three models ($M1$, $M2$, $M3$). In addition, the relative error is plotted. The analysis of the reconstructions reveals a more accurate reconstruction of the particle charge field for later time steps, independent of the model. For time steps later than t_{v_2}, every predicted point of the 2D field results in a smaller relative error than 20 % and for $t > t_{v_4}$ of less than 5 %. The largest relative errors for the first time step occur in the corners of the cross-section. An explanation for this lies in the physical principle of particle charging and information transport. The charging process starts predominantly in the corners of the duct. In such early time steps, there seems to be only a weak correlation between the initiated charging process and the charge distribution on the duct center line. Hence, it is almost impossible for the SNN to predict the corners precisely as the information is not diffused to the center.

Figure 4 expands the analysis to a statistical comparison of the different models for all available validation data. Therefore, the L^1-error per particle sizes is plotted over time t^+. First, the trend of smaller errors for larger time steps (higher particle charges) is confirmed independent of the particle size. The later time steps are easier to predict due to smaller gradients over the entire field. Thus, the field is more homogeneous and covers not several decades of charge compared to the first time steps.

The comparison between the three different models reveals that the model $M3$ performs overall best with an average L^1-error across all validation data of 1.63 %, followed by $M1$ (2.26 %) and $M2$ (2.44 %). The low error of $M3$ is astonishing as it was trained only on the first half of the time span ($0 \leq t^+ \leq 18.09$). Even in the second half of the time span ($18.09 \leq t^+ \leq 36.17$), where $M3$ was not trained at all, the error of $M3$ is the smallest ($M1$: 0.98 %, $M2$: 1.02 %, $M3$: 0.63 %). Thus, this period is a pure extrapolation for $M3$ (for $D_p = 10^{-2}$ it is even an extrapolation for two parameters). Based on the training data, $M2$ should be optimized for this time span. An explanation for the good results of $M3$ might be its training on more noisy data as the charging process just started. Additionally, this period features higher charge gradients reducing the risk of overfitting.

Averaging of the received particle charge fields allows a comparison to conventional Faraday pails, which improves the trustworthiness. It has to be noted that the results are only directly comparable when the particle distribution is homogeneous, otherwise a weighted average would be necesassary. Figure 5 plots the deviation of $\overline{Q}$ as absolute error over time for the different validation cases. In general, the observations of the L^1-error are confirmed. However, due to the averaging, all errors are approximately halved. The $M1$ model achieves an average error of 1.04 %, $M2$ results in 1.04 % and $M3$ in 0.94 %.

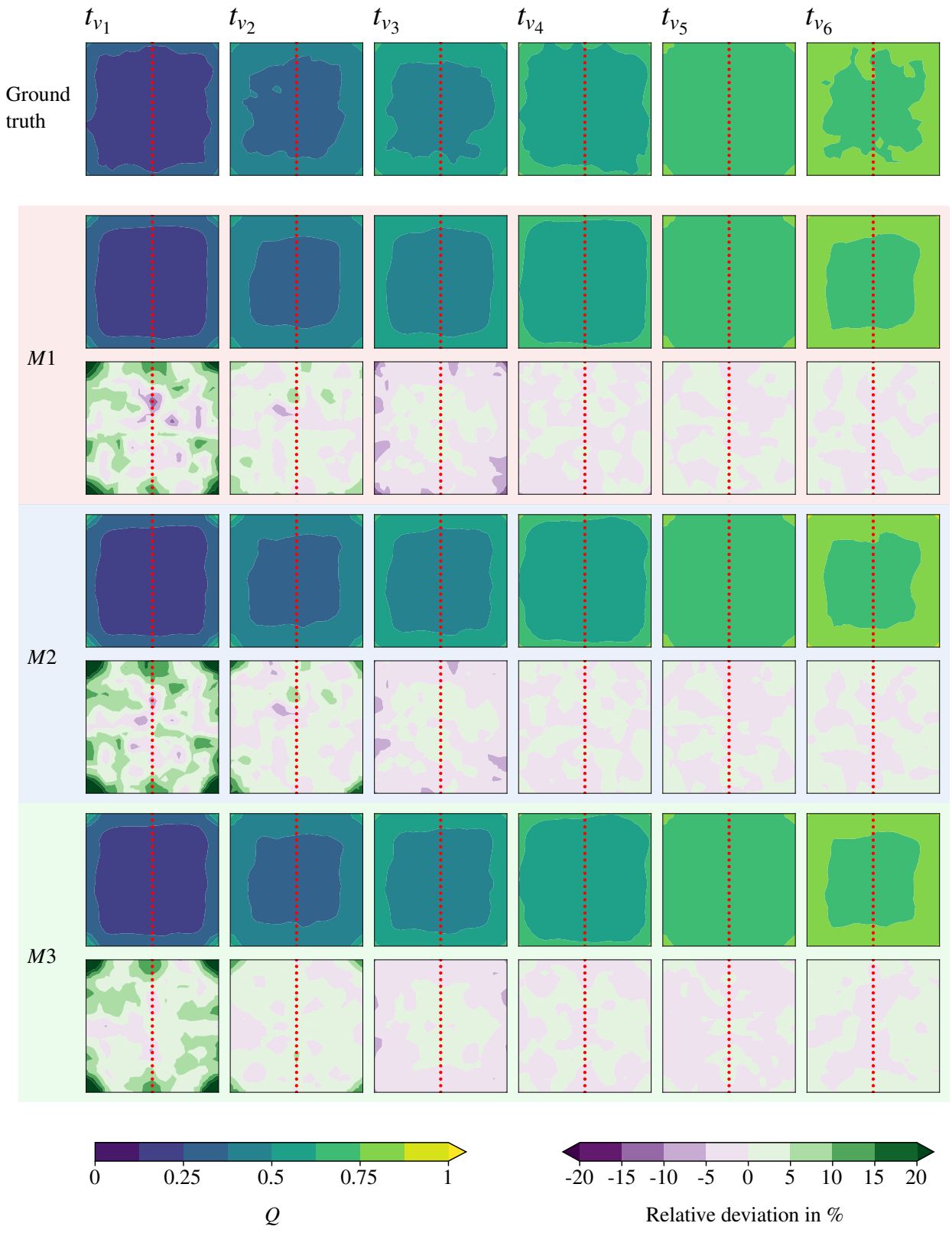

***Fig. 3**: Contour plots of the ground truth particle charge fields (Q_{ref}) for all validation time steps with a particle size of $D_p = 5 \cdot 10^{-3}$. The reconstructions (Q_{rec}) of the three models is shown below the first row including a contour plot of the relative deviation in the range of $\pm 20\,\%$. The red dots indicate the location of the 1D path.*

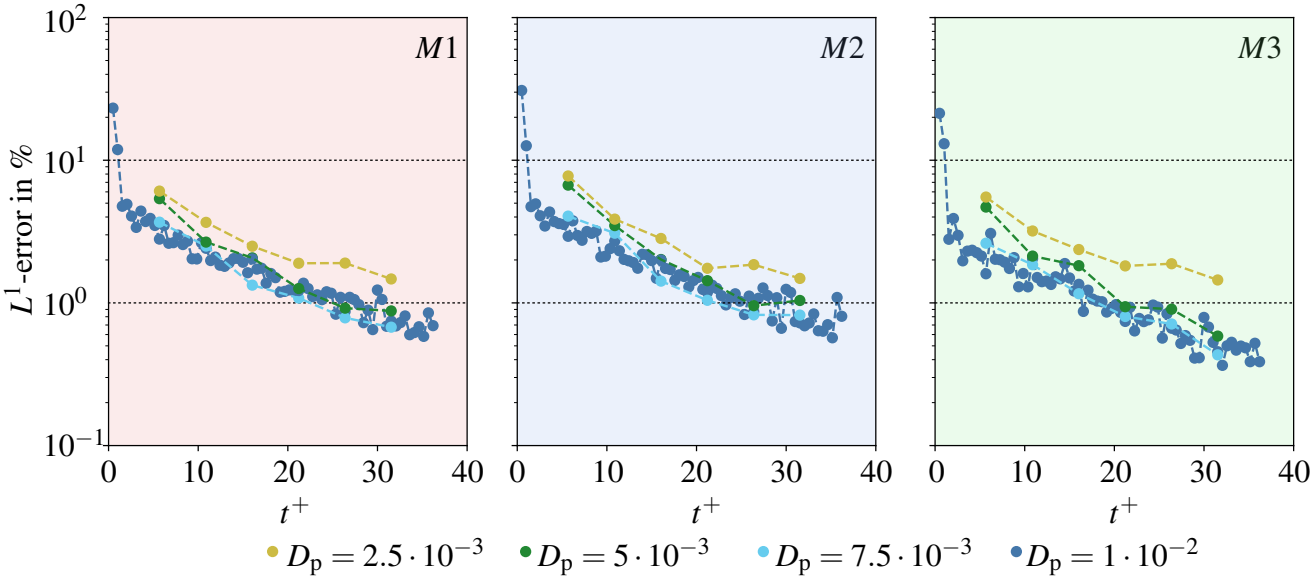

***Fig. 4**: L^1-error plotted for all validation data over time. Depicted are the results for the three trained models M1, M2, and M3.*

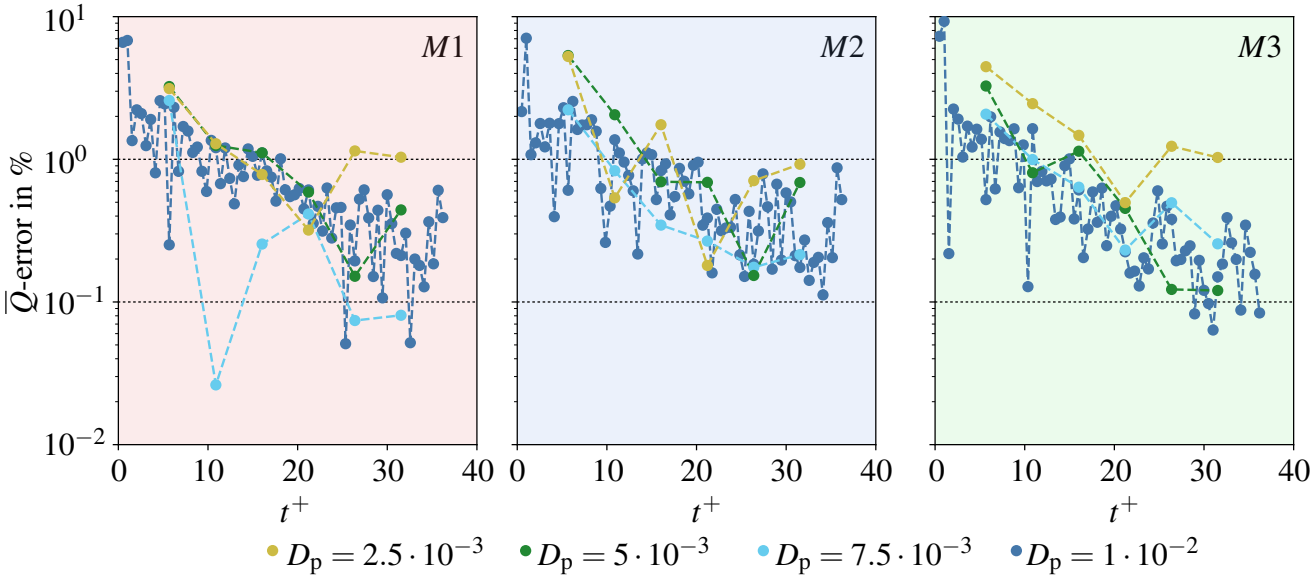

***Fig. 5**: $\overline{Q}$-error plotted for all validation data over time. Depicted are the results for the three trained models M1, M2, and M3.*

3.1 Training on a quarter of the field

The simulations of this study model a monopolar charging process leading to a statistically symmetric particle charge field. Hence, all four corners of the duct feature the same distribution. If such preknowledge exists also in the practical application, it is wise to incorporate it. Therefore, this section studies the effect of averaging the particle charge distribution over all four corners and trains the neural network on the achieved quarter. The obtained prediction was replicated and transformed four times to obtain the full field.

Figure 6 compares the L^1-error of the base $M1$ model with a $M1$ model that is trained on a quarter of the field. One could observe a reduction of the mean L^1-error from 2.26 % to 1.63 %, which equates to a reduction of 28 %. This reduction seems independent of the particle size and the time step. Nonetheless, the error fluctuation across different time steps rises slightly with the latter model. As

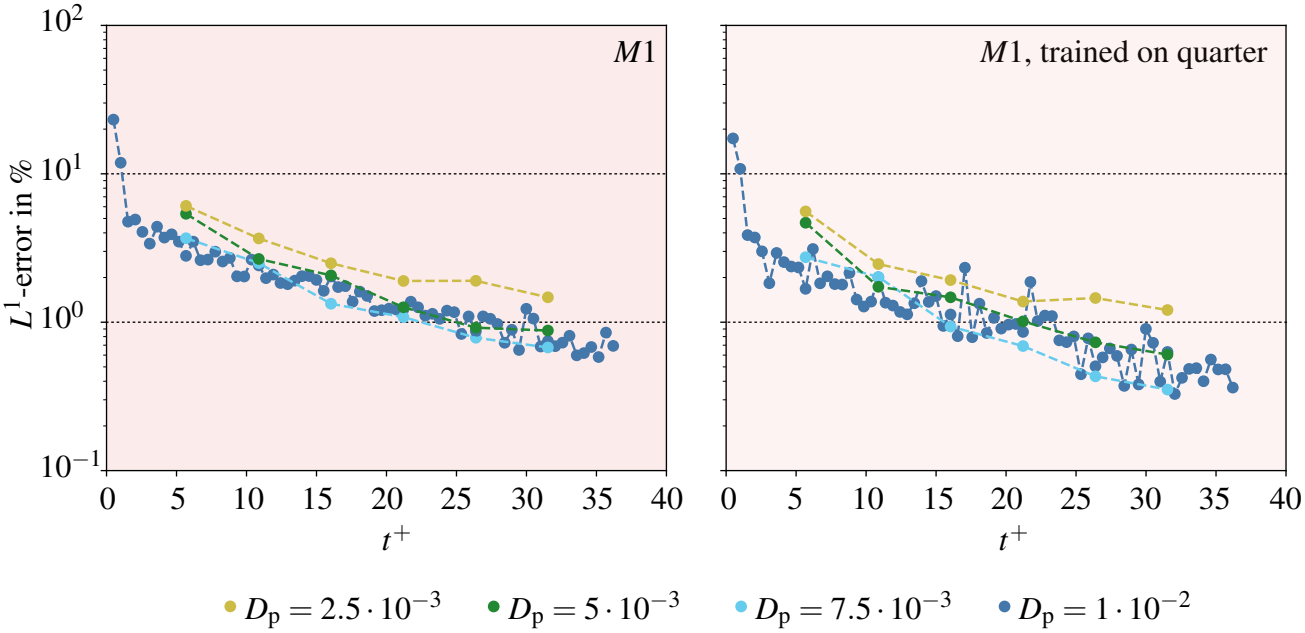

***Fig. 6**: L^1-error plotted for all validation data over time. Depicted are the results for (left) the base version of $M1$ and (right) a version of $M1$ trained on a quarter of the field.*

introduced before, the error reduction could be expected for two reasons: (a) the contour plots of the data are smoother due to the additional averaging step, and (b) the model is faced with a smaller decoding task. The base $M1$ model scales 21 data points from the 1D path up to 441 points on the 2D field, which corresponds to a factor of 21. The model which operates only on a quarter of the channel exhibits an upscale factor of 11 (11 points on the 1D path to 121 on the 2D field).

3.2 Incorporating particle velocity

Another possibility to improve the algorithm's predictions is to incorporate further information on the 1D path. The measurement principle of Xu et al. (2023) directly provides the particle velocity. Hence, an additional neural network has been developed which includes as the last layer a convolution layer to combine the multiple input channels (different physical fields) to a single output channel, in this case, the particle charge.

Figure 7 compares the L^1-error of the base $M1$ model with a modified version of $M1$ that includes the particle velocity. The additional information reduces the L^1-error by 27 % on average. This improvement is independent of the particle size. However, the error fluctuations increase slightly, similar to the training on a quarter of the field. The reduction of the error proves that the particle velocity gives additional information that is not directly correlated to the particle charge. This might change with the particle acceleration, which is necessary for the experiment to determine the particle charge, as it is directly correlated to the particle velocity.

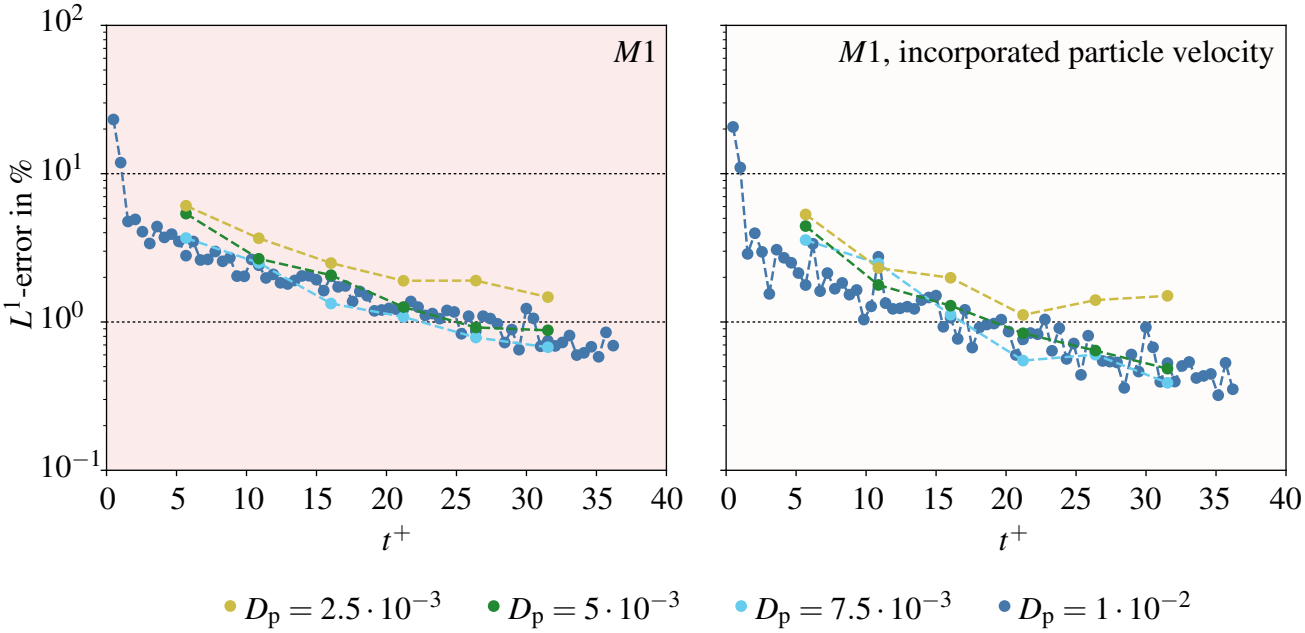

***Fig. 7**: L^1-error plotted for all validation data over time. Depicted are the results for (left) the base version of $M1$ and (right) a version of $M1$ which incorporates the particle velocity.*

4 Conclusion & Outlook

This paper contributes to improving the safety of pneumatic powder conveying, an industrial transport operation. It builds upon a new measurement technology that can evaluate the particle charge distribution on a single line but not on an entire cross-section of a pipe or duct. To achieve this, we developed an algorithm to predict the 2D particle charge field based on the 1D line measurement. The algorithm's abilities were demonstrated based on simulation data, where a mean L^1-error of 1.63 % was achieved with the standard configuration. This corresponds to a mean error of 1.04 % of $\overline{Q}$. By incorporating the particle velocity, the L^1-error could be reduced additionally by 27 %. Considering that until now only the mean charge could be measured, this is a significant step forward in safe pneumatic conveying. The ML model can be further improved by increasing the training database to cover a larger parameter space and increase robustness. In addition, the particle density distribution could be incorperated to calculate a weighted average charge, which would be directly comparible to a Faraday measurement. The presented algorithm is one example of how the rise of ML can shape the future of measurement technologies impacting explosion protection.

Acknowledgements

This project has received funding from the European Research Council (ERC) under the European Union's Horizon 2020 research and innovation program (Grant Agreement No. 947606 PowFEct).

References

Ding, J., Qi, C., Yan, X., Lv, X., Zhang, S., Liang, H., Fan, T., Yu, J. (2024). *Effect of airflow velocity on flame propagation and pressure of starch dust explosion in a pneumatic conveying environment*. Powder Technology, 433:119147. doi:10.1016/j.powtec.2023.119147.

Erichson, N. B., Mathelin, L., Yao, Z., Brunton, S. L., Mahoney, M. W., Kutz, J. N. (2020). *Shallow neural networks for fluid flow reconstruction with limited sensors*. Proceedings of the Royal Society A: Mathematical, Physical and Engineering Sciences, 476(2238):20200097. doi: 10.1098/rspa.2020.0097.

Grosshans, H., Bissinger, C., Calero, M., Papalexandris, M. V. (2020). *The effect of electrostatic charges on particle-laden duct flows*. Journal of Fluid Mechanics, 909:A21. doi:

10.1017/jfm.2020.956.

Grosshans, H., Papalexandris, M. V. (2017). *Direct numerical simulation of triboelectric charging in particle-laden turbulent channel flows*. Journal of Fluid Mechanics, 818:465–491. doi: 10.1017/jfm.2017.157.

Lim, E. W. C., Zhang, Y., Wang, C.-H. (2006). *Effects of an electrostatic field in pneumatic conveying of granular materials through inclined and vertical pipes*. Chemical Engineering Science, 61(24):7889–7908. doi:10.1016/j.ces.2006.07.045.

Matsusaka, S., Masuda, H. (2006). *Simultaneous measurement of mass flow rate and charge-to-mass ratio of particles in gas–solids pipe flow*. Chemical Engineering Science, 61(7):2254–2261. doi: 10.1016/j.ces.2005.05.006.

Ndama, A. T., Guigon, P., Saleh, K. (2011). *A reproducible test to characterise the triboelectric charging of powders during their pneumatic transport*. Journal of Electrostatics, 69(3):146–156. doi:10.1016/j.elstat.2011.03.003.

Paszke, A., Gross, S., Massa, F., Lerer, A., Bradbury, J., Chanan, G., Killeen, T., Lin, Z., Gimelshein, N., Antiga, L., Desmaison, A., Kopf, A., Yang, E., DeVito, Z., Raison, M., Tejani, A., Chilamkurthy, S., Steiner, B., Fang, L., Bai, J., Chintala, S. (2019). *Pytorch: An imperative style, high-performance deep learning library*. In *Advances in Neural Information Processing Systems 32*, pages 8024–8035. Curran Associates, Inc.

Van Rossum, G., Drake, F. L. (2009). *Python 3 Reference Manual*. CreateSpace, Scotts Valley, CA. ISBN 1441412697.

Wilms, C., Ekat, A.-K., Hertha-Dunkel, K., Eicher, T., Schmelter, S. (2024). *Enhanced flow rate prediction of disturbed pipe flow using a shallow neural network*. submitted.

Xu, W., Jantač, S., Matsuyama, T., Grosshans, H. (2023). *Spatially resolved measurement of the electrostatic charge of turbulent powder flows*. Experiments in Fluids, in press. doi: 10.48550/arXiv.2306.06970.

Enhancing real-time metal dust concentration monitoring through a machine learning-based Kalman Filtering algorithm

Fengyu Zhao, Wei Gao, Mingshu Bi, Haipeng Jiang*

[a] *State Key Laboratory of Fine Chemicals, Department of Chemical Machinery and Safety Engineering, (Dalian University of Technology, Dalian 116024, China)*

E-mail: *jhp@dlut.edu.cn*

Abstract

The aim of this paper is to investigate the application of machine learning for concentration detection in the field of metal dust, which is essential for reducing dust hazards and establishing effective dust reduction and removal facilities. The traditional prediction methods are affected by the nonlinear system and the environmental noise of the practical application, with low prediction accuracy and poor robustness. To quickly and accurately detect high concentrations of dust. In this study, the research on the detection of aluminum dust with concentrations of (94.55-349.g/m3) was carried out by using an electrostatic sensor combined with a Kalman filter algorithm based on the machine learning GRU model. The results show that the KFGRU method is superior to the traditional linear filtration method, with a large fluctuation time of less than 4s, and is capable of real-time online detection of dust concentration. In terms of prediction accuracy, compared with the Kalman filtering algorithm 0.516, the sliding average method 0.643, median filtering method 0.667 (the smaller the discrete value, the higher the prediction accuracy), the KFGRU method handles the curve with a dispersion of only 0.313. The accuracy is significantly higher than the other three algorithms. This study provides a comprehensive and innovative method for dust concentration monitoring in dust and explosion suppression systems, which meets the real-time requirements and also makes important progress in explosion safety management. This will provide more reliable and advanced technical support for dust control and safety in industrial production processes.

Keywords: *High-concentration dust detection; Machine learning; Explosion prevention*

1. Introduction

Combustible dust has a dual identity as both a product and a by-product in industry. During the production and processing of industrial metal products, especially when performing processes such as cutting and grinding, large amounts of combustible dust particles are generated. It poses a serious threat to the environment and human health (Taveau et al., 2018). To reduce the risk of explosions triggered by normal operations or unusual events, dust generation needs to be minimized and the formation of dust clouds and dust layers needs to be considered. In particulate dispersions, the Minimum Explosive Concentration (MEC) is an important parameter. When the dust concentration in the air is kept below the MEC of the material, the fuel component of the fire triangle can be effectively eliminated, thus theoretically preventing dust explosions from occurring (Amyotte, 2019). Therefore, monitoring changes in the actual ambient concentration and removing them promptly through dust concentration detection technology is an effective way to reduce dust concentration.

The choice of dust concentration detection techniques is highly dependent on the specific work environment and requirements. Common dust detection techniques include vibrating balance, optical,

beta-ray, and electrostatic induction methods (Wang et al., 2023). Each of these techniques has some specific challenges and limitations in high-concentration dust environments. The vibrating balance method usually requires frequent replacement of the filter membrane because the deposition of large amounts of dust tends to clog the membrane, reducing the accuracy of the measurement. Optical methods are susceptible to airway obstruction and contamination of the detection unit in high-concentration environments, thus requiring frequent maintenance and cleaning (Widiatmojo et al., 2015). β-ray methods, while more adaptable, have a slower response time and usually provide hourly averages, which is not suitable for situations where real-time monitoring is required (Huang et al., 2022). Compared to the other three methods, the electrostatic induction method has multiple advantages, including a wide measurement range, adaptability, and durability (Gajewski, 2013). The detection unit of the electrostatic induction method is not susceptible to bonded dust, making it the technique of choice for the detection of highly concentrated dust.

However, the openness of the experimental environment makes the range of variation of dust concentration large, and there are a variety of electromagnetic interference factors around [15]. These factors will have an impact on the dust concentration detection technique based on the electrostatic induction method, resulting in a relatively noisy sensing signal, which affects the stability and accuracy of the detection results [16-18]. These interference noises exist objectively and are difficult to be solved individually by sensor circuit design. In addition, the instability of the dust flow in the working environment and the large changes in concentration also increase the noise of the sensing signal. Machine learning is used as a mainstream data-driven method (Schmidhuber, 2015). It has gained attention in the field of sensors due to its high computational speed and ability to automatically find and learn features from data.

Therefore, in this study, a real-time dust concentration detection method (KFGRU) based on Kalman filtering algorithm with the gated recursive unit (GRU) is proposed based on machine learning to cope with the inefficiency of the Kalman filtering algorithm execution in large-scale applications, such as high-concentration dust environments. The method aims to increase the concentration detection speed, shorten the data processing time, and more efficiently satisfy nonlinear systems with high real-time requirements. For the fast and accurate detection of highly concentrated aluminum powder dust, this method provides new ideas and solutions.

（1) The KFGRU method is introduced, which integrates a gated recirculation unit (GRU). The KFGRU method is excellent in data processing and provides new insights for real-time dust concentration detection.

(2) The KFGRU method is more accurate than the KF, sliding filter method and median filter method.

2. Experiments

2.1. Dust Detection Laboratory System

This integrated system consists of four main components designed to enable efficient monitoring and measurement of dust concentrations. These components include the powder spraying system, the sensor detection system, the standard concentration sampling system, and the data acquisition system. The powder spraying system is the core part of the system and its main task is to precisely regulate the release of aluminum powder. This process is accomplished through precision air cylinders and pressure-reducing valves to ensure that the pressure in the air is accurately controlled during the powder release process. The sensor detection system employs an electrostatic induction sensor, a highly sensitive sensor designed to monitor the movement of aluminum powder in the air in real-time. The standard concentration sampling system targets the dust within a certain spatial area near the sensor probe through a sampler. This system utilizes suction to deposit a portion of the dust onto a filter membrane. By measuring the ratio of the mass of dust deposited on the filter membrane to the volume of the sampler, the actual concentration of dust can be accurately calculated. The standard

concentration sampling system is designed to obtain reliable dust concentration data to ensure the credibility of the system's monitoring results. The data acquisition system uses equipment such as Yokogawa oscilloscopes to convert the induced currents generated by the sensors into voltage signals. The conversion and recording of these signals allow changes in dust concentration to be visualized, as well as permit data to be recorded and analyzed over time.

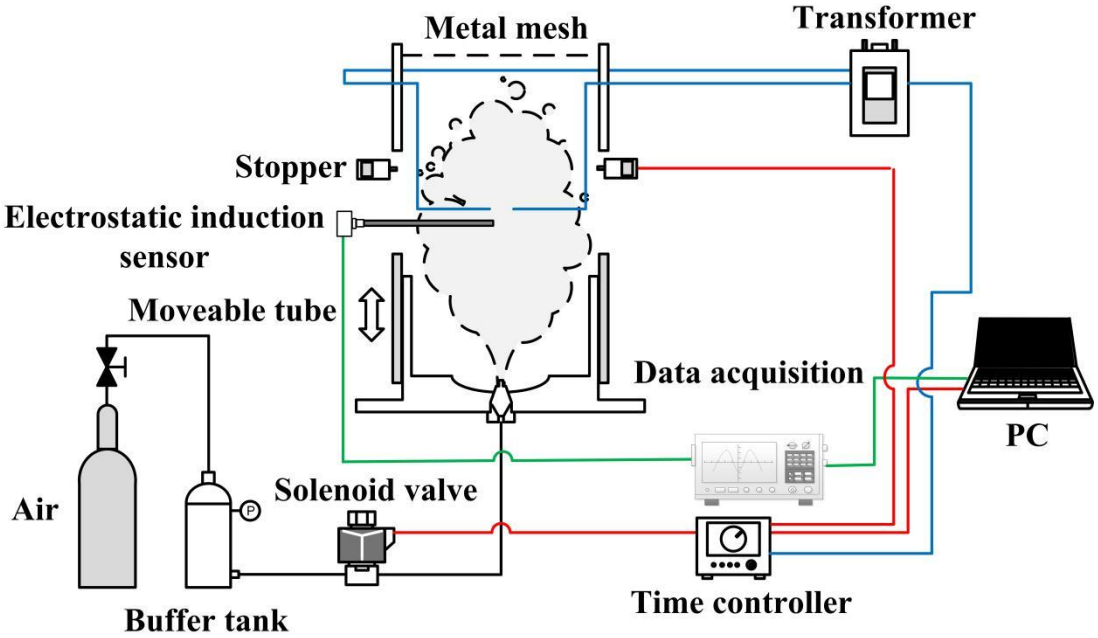

Fig. 1. *Dust detection experimental platform.*

2.2. Experimental materials Electrostatic induction sensor

Aluminum powder (AL-5) with 5 μm particle size was purchased from Angang Industry Microfine Aluminum Powder Co. The particle size distribution and morphology are shown in Figure 2, and the morphology is mostly ellipsoidal, resulting in a median particle size d50 of 8.287 μm.

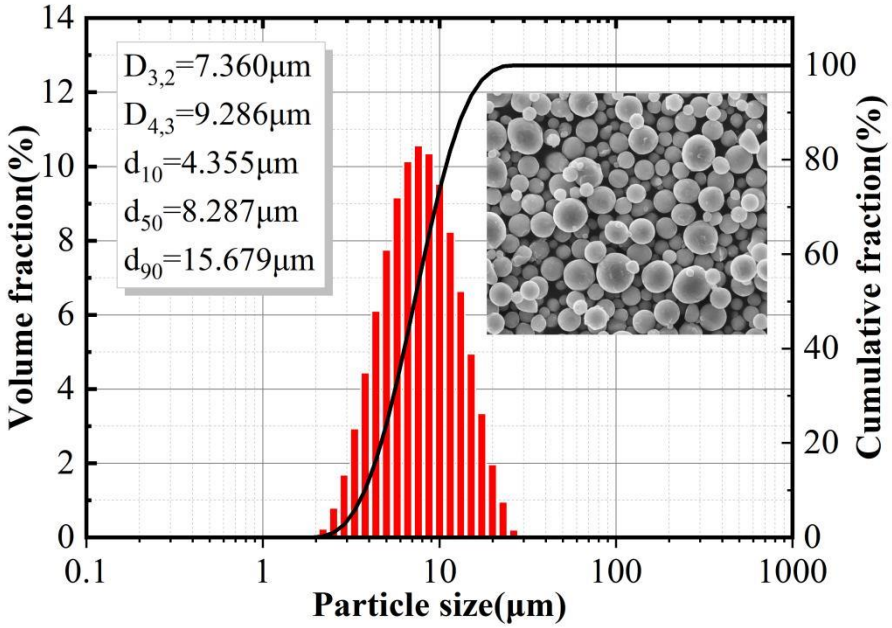

Fig. 2. *Dust particle size distribution*

2.3. Dust Detection Laboratory System

The specific dimensions of the sensor are labeled as shown in Fig. 3, and the units of the labeled dimensions in Fig. 3 are all in (mm).

The principle of operation of the sensor is based on the electrostatic induction method, where fluctuations in the sensed signal are generated by analyzing the changes in the distribution of the induced charge on the surface of the electrodes, reflecting the level of dust concentration in the surroundings (Kamm et al., 2023; Peng et al., 2008)). In this process, dust cloud particles traverse the sensing electrode region of the sensor due to gravity or external forces. Since the particles themselves are electrically charged, electrostatic induction causes them to sense on the surface of the detection electrode producing charge changes as they approach and move away. This periodic process results in the generation of alternating current signals at the electrodes and their changing characteristics are used to analyze and quantify the dust concentration around the electrodes (Roach et al., 2023; Ning et al., 2019). As shown in Fig. 3, the sensor is connected to the data collector via a data cable, and the digital collection transforms the alternating current signals into voltage signals displayed on the display and stored in the hard disk for subsequent processing.

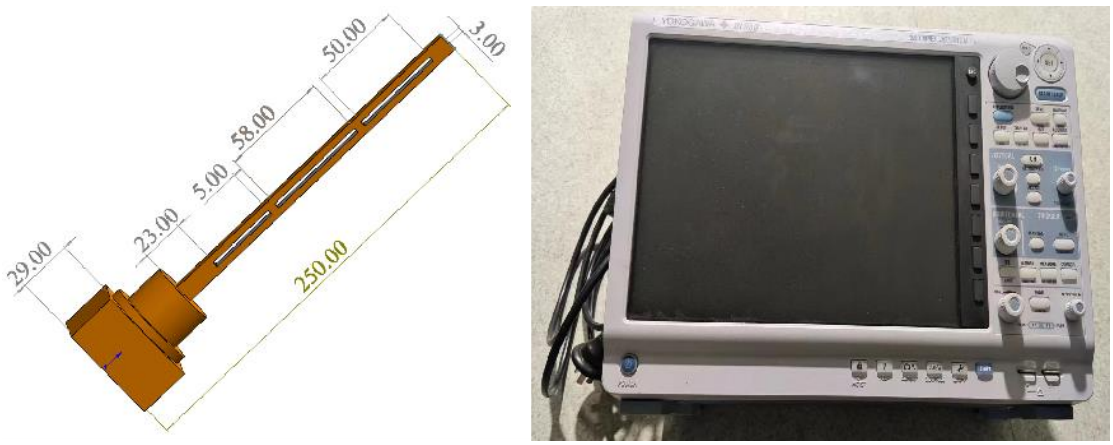

Fig. 3. *Schematic of a rod-shaped electrostatic dust detector and data collector.*

3. The proposed KFGRU method

3.1. The proposed KFGRU method

Kalman filtering is a mathematical and computationally based method for state estimation of dynamic systems (Welch and Bishop, 1995). The core principle lies in the synthesis of previous state estimates and current measurement data, and the estimation of the target state is continuously updated recursively by taking into account the statistical properties of the system and the measurement noise, to obtain as accurate a state estimate as possible. This algorithm is supported by mathematical principles such as linear systems theory and Bayesian filtering theory.

3.2. Kalman Filter Algorithm Combining Machine Learning Ideas

Kalman filter algorithm is a prediction-based method for motion target detection and tracking, however, its tracking effect is limited, and its real-time performance and accuracy cannot meet the demand of nonlinear systems. Incorporating the machine learning model GRU into the framework of the Kalman filter algorithm can better deal with the relationship between time series and significantly

improve the data processing performance. At the same time, the machine learning Kalman filter algorithm has adaptive system dynamics, real-time adjustment to adapt to system changes. The main equations are as follows (Revach et al., 2022).

Firstly, The GRU model we use contains two gating units: the update gate and the reset gate. The update gate, we compute the update gate Zt for the time step using the following equation (Zhu et al., 2023):

$$z_t = \sigma(w_u[H_{t-1}, x_t]) \tag{4}$$

σ is the sigmoid function, through which the data can be transformed into numerical values in the range of 0-1 to act as a gating signal. When Xt is fed to the network cell, he is multiplied by his weight wu. For H_{t-1}, it keeps the information of the first t-1 unit. These two results add together and then apply the sigmoid activation function to compress the results between 0 and 1

The second is the reset door, which is essentially used by the model to determine how much information about the past is forgotten.

$$r_t = \sigma(w_r * [H_{t-1}, x_t]) \tag{5}$$

This formula is the same as the update gate, except for the weight and the use of the gate. As to how exactly these gates affect the final output. First, starting with the use of reset doors, we introduce new memory content that will use reset doors to store relevant information from the past.

$$\tilde{H}_t = \tanh(W \cdot [r_t * H_{t-1}, x_t]) \tag{6}$$

As a final step, the network needs to compute Ht (which is a vector that holds the current unit information and passes it to the network). For this purpose, it is necessary to update the gate, which determines the collected content from the current memory content xt', as well as the collected content from the previous step H_{t-1}.

$$H_t = GRU(X_t) = (1 - z_t) * H_{t-1} + z_t * \tilde{H}t \tag{7}$$

The machine learning algorithm focuses on optimizing the Kalman gain coefficients and the detailed process is as follows:

The initial values are set by a model trained against an existing dataset:

$$y_{predict[0]} = X_{measure[0,1]} \tag{8}$$

Where: $y_{predict[0]}$ denotes the first element of the initialized prediction result array, $X_{measure[0,1]}$ indicates the actual standard deviation value calculated from the initial window data.

Continue the prediction using the predicted and true values from the previous moment:

$$temp = predict(t_{prev}, y_{predict[i-1]}) \tag{9}$$

Where: *temp* denotes the output prediction value of the GRU model, $predict$ represents the treatment of the prediction result of the previous moment by the GRU model, t_{prev} denotes the time value corresponding to the previous moment, and $y_{predict[i-1]}$ denotes the prediction value of the previous moment;

The deviation values are then obtained by further processing:

$$bias_{predict} = \exp(temp - \overline{X}_{measure,1:i}) \tag{10}$$

$$bias_{measure} = \exp(X_{measure[i:1]} - \overline{X}_{measure,1:i}) \tag{11}$$

where, $X_{measure[i:1]}$ denotes the standard deviation value at moment *i*, $\overline{X}_{measure,1:i}$ denotes the cumulative mean of standard deviations of all windows up to moment *i*. $bias_{predict}$ denotes the bias value of the GRU output, $bias_{measure}$ denotes the bias value of the actual measurement result.

The role of $bias_{predict}$ and $bias_{measure}$ is to combine the outputs of neural networks and Kalman filtering algorithms for predicting the mean of the standard deviation:

$$y_{predict[i]} = \frac{X_{measure[i:1]} \cdot bias_{predict}}{bias_{predict} + bias_{measure}} + \frac{temp \cdot bias_{measure}}{bias_{measure} + bias_{predict}} \tag{12}$$

After training the GRU model, the traditional Kalman filter coefficients KG are updated with the coefficients K. When integrated with the GRU network model, it is defined as:

$$k_G = \frac{(F \cdot P_{t-1|t-1} \mathrm{F}^{\mathrm{T}} + \mathrm{Q}) H^T}{H(F \cdot P_{t-1|t-1} \mathrm{F}^{\mathrm{T}} + \mathrm{Q}) H^T + R} \overset{GRU\ traning}{\Rightarrow} \frac{bias_{predict}}{bias_{predict} + bias_{measure}} = K \tag{13}$$

Substituting *K* into the equation gives:

$$y_{predict[i]} = K \cdot X_{measure[i:1]} + (1-K) temp \tag{14}$$

Machine learning is used to correct the Kalman gain coefficients and construct a machine learning-assisted Kalman filtering algorithm to achieve a real state prediction curve.

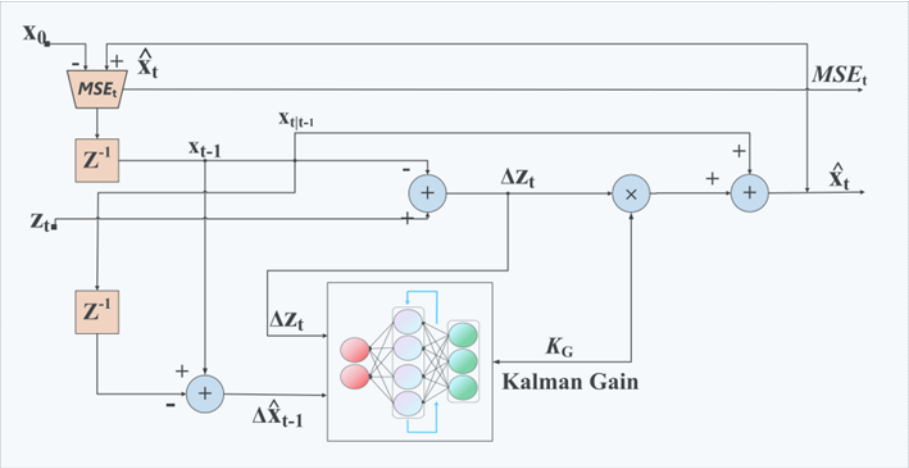

Fig. 4. *Kalman filter algorithm incorporating machine learning ideas.*

4. Method specification and comparison

4.1. Method specification

The sensing signal of the dust concentration sensor is demonstrated in Fig. 5. By observing the image, the sensing signal curve of the measured data has a large fluctuation in the curve at the initial time, which is due to the fluctuation of the data caused by the change of dust concentration due to the turbulent movement between the dust particles and the effect of gravity. The impunity of gradual stabilization of the standard deviation values over time can be attributed to two main factors. First, the dust state gradually smoothed out and no longer experienced significant fluctuations, indicating that the system gradually entered a more balanced state. Secondly, as more data is accumulated, we can obtain more reliable statistical analyses, which further helps to minimize the effects of noise. By accumulating data, we can effectively average out the effects of some random noise, thus more accurately describing the trend of dust concentration.

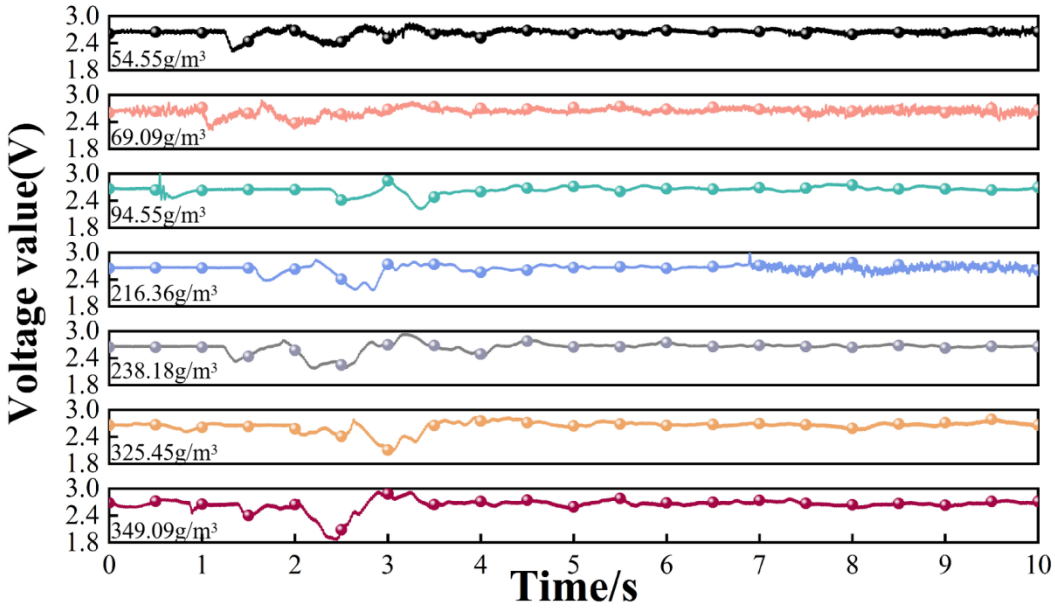

Fig. 5. *The statistical curve of sensed signals for 5μm aluminum powder under different dust concentration conditions.*

Under high concentration conditions, the interaction between aluminum powder particles of 5um particle size increases significantly, accompanied by electromagnetic interference and turbulent motion between the particles, and the level of interference to the electrostatic induction signal rises significantly. This situation leads to a significant increase in the noise level and range of fluctuations faced by the electrostatic induction signal. To meet this challenge, the KFGRU algorithm was used to process the standard deviation of the induction signals generated by 5um particle size aluminum powder dust at different dust concentrations (including 94.55g/m^3, 154.55g/m^3, 216.36g/m^3, 281.82g/m^3, 325.45g/m^3, and 349.09g/m^3). The processing results are shown in Fig. 6. After the Kalman filter processing of machine learning, the predicted standard deviation curves separated from the actual measured standard deviation curves and converged to the neighborhood of the mean value at a faster time. Subsequently, it fluctuates around the mean standard deviation. This high degree of consistency indicates that the algorithm successfully reduces the uncertainty of the estimated values and brings them closer to the actual measured values. This excellent performance is supported by the powerful ability of machine learning to efficiently extract useful information in high noise and high interference environments, leading to more accurate predictions.

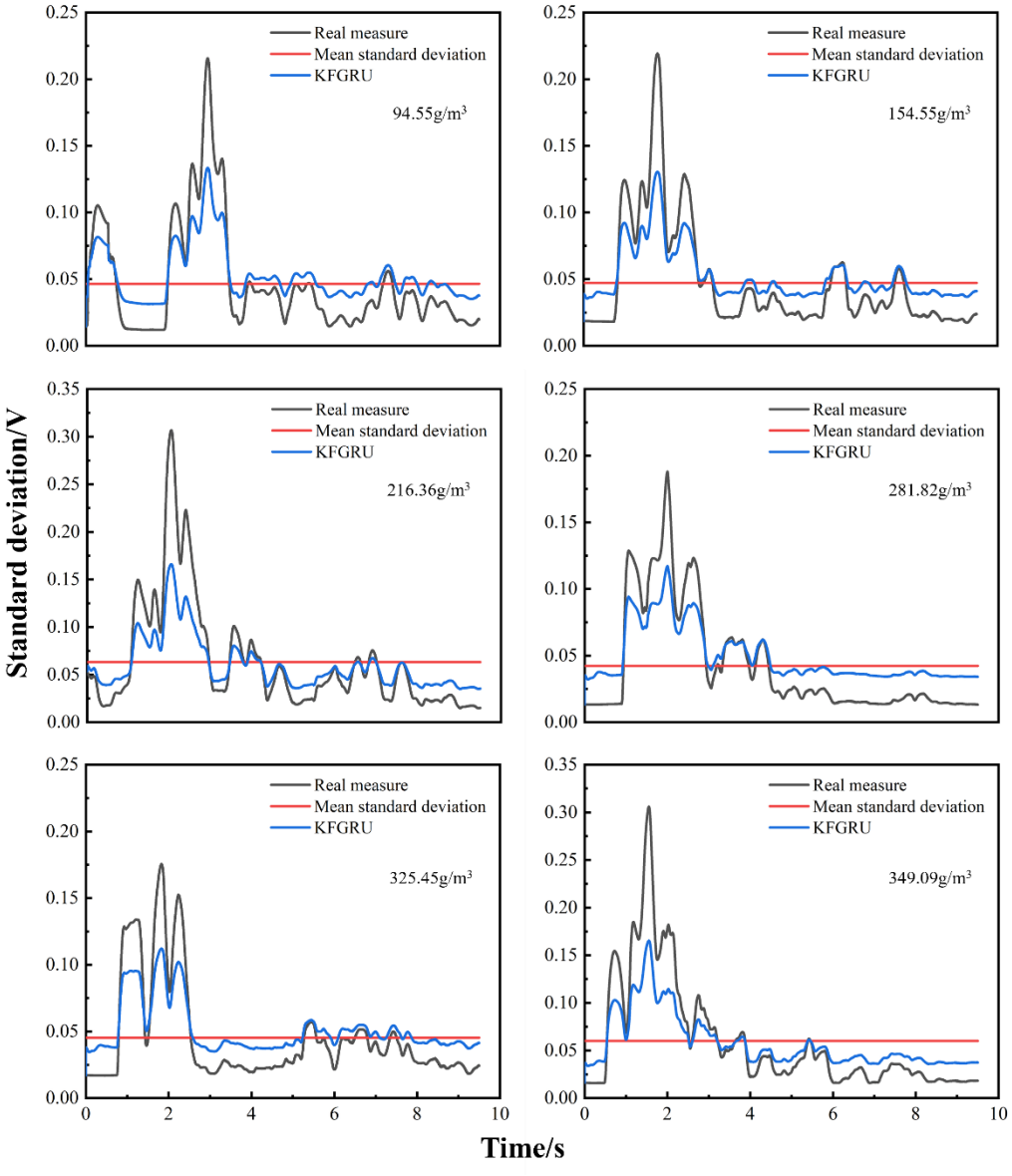

Fig. 6. *The curve processed by KFGRU with different dust concentrations.*

Overall, the KFGRU curves consistently converge to near the actual deviation mean in about 4 seconds, gradually leveling off or showing small fluctuations as the data accumulate. These findings highlight the fast convergence rate of the algorithm in processing dust-induced signals, allowing it to reach a relatively stable state in a relatively short period. Furthermore, the results highlight the effectiveness of the KFGRU algorithm in meeting the challenges of dust-induced signals and demonstrate its fast convergence and stability under dynamic environmental conditions.

4.2. Comparison

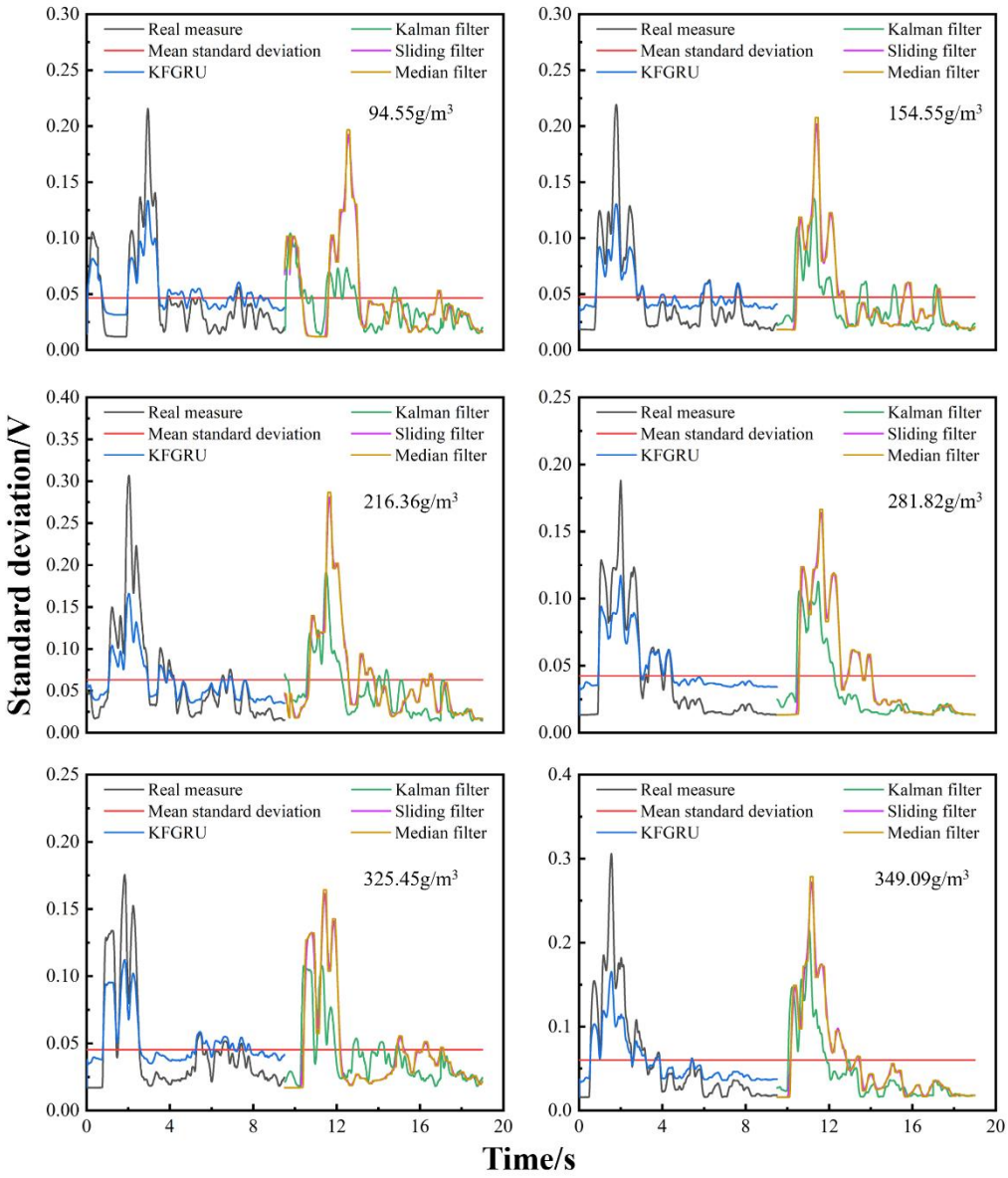

Fig. 7. *Comparison of Kalman filter, sliding average algorithm, median algorithm, and KFGRU.*

In this study, a comprehensive test was conducted using a benchmark test dataset to evaluate the algorithmic performance of the KFGRU method by comparing the dispersion of the traditional Kalman filter, median filter, and sliding average algorithms. Figure 6 visualizes the capability of the different methods in processing the data. It is worth noting that the sliding average, median filter, and traditional Kalman filter require an initial data collection period of nearly 10 seconds before processing, whereas the KFGRU method exhibits faster convergence to the eigenvalues. This speedup is attributed to the use of curves supported by the comprehensive dataset, which allows KFGRU to be updated in parallel with new data and to make predictions based on existing models. In addition,

we define the degree of discretization, which is used to evaluate the accuracy of the algorithm. A relative degree of dispersion is obtained by differencing each point of its curve from the mean and absolute, then summing and normalizing by dividing by the area below the mean. The final result is shown in Fig. 8. By comparing the average dispersion of each method, we evaluated the accuracy performance of their algorithm performance. The results show that KFGRU has a dispersion of XXX, which is significantly smaller than Kalman filter (0.312), moving average (0.646) and median filter (0.661). The dispersion of the methods fluctuated as the concentration increased, but the dispersion of the KFGRU method was always lower than that of the remaining three methods. This indicates that KFGRU exhibits superior robustness and can adapt to changes in concentration faster. Overall, it appears that the KFGRU method significantly improves the real-time accuracy and precision of dust concentration detection. The results of this study emphasize the potential benefits of integrating the GRU model into Kalman filtering applications, providing strong support for accurate and real-time measurements in online environments.

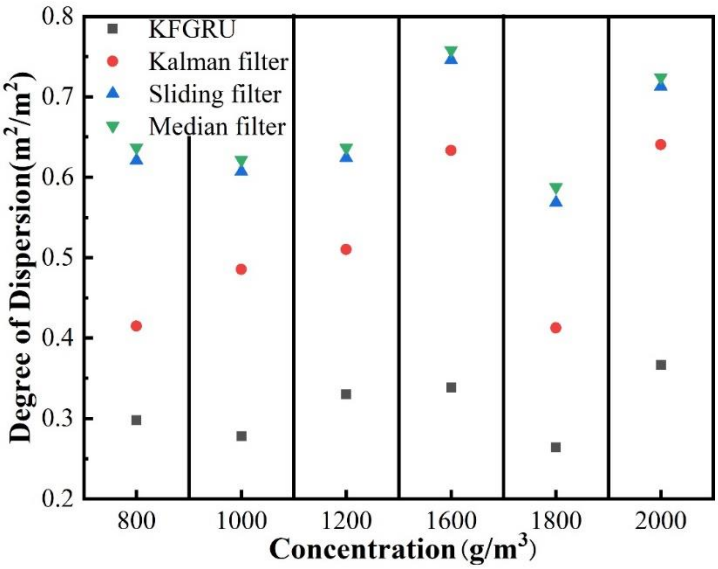

Fig. 8. *Comparison of Kalman filter, sliding average algorithm, median algorithm, and KFGRU.*

Although the KFGRU method shows superior performance compared with the traditional Kalman filtering method, there are still some limitations of our proposed KFGRU method. Currently, the KFGRU method proposed in this paper is only applicable to laboratory environment working conditions. In this case, the variation affected by the noise interference signal is small. Therefore, it cannot directly visualize the simulation of nonlinear system industrial environment. The scale from laboratory to industrial environment changes the environmental factors to which our proposed method is subjected. Our proposed KFGRU is one of the data-driven methods for real-time detection of concentration, and we are modeling the detection of concentration directly using data. This type of data detection comes from the laboratory system itself, and the performance of the developed model will be impaired if the network configuration is changed. In addition, further work in the future will extend the method's baseline dataset for significant training of the model, aiming to improve the method's ability to handle anomalies. The dataset includes not only common environmental situations, but also a variety of possible anomalies, enhancing its ability to handle anomalies and take proactive measures to cope with their uncertainty.

5. Conclusions

Aiming at the complex problems of long detection time and low accuracy, the paper proposes an innovative method that combines the gated recirculation unit (GRU) with the traditional Kalman filtering algorithm to realize real-time on-line rapid detection of dust concentration in a high-

concentration dust environment. The real-time and interpretability of the method is verified through experiments, and the following conclusions are drawn:

(1) Compared with the traditional linear filtering method, the new method proposed in this study successfully reduces the data acquisition time and can effectively improve the real-time rapid detection of dust concentration.

(2) The algorithm shows excellent performance in terms of robustness and practical results after concentration detection experiments in a highly concentrated metal dust environment, and the validation of concentration changes further proves the excellence and reliability of the results of the KFGRU algorithm.

The KFGRU method provides a feasible solution for metal dust concentration detection by the electrostatic induction method. The algorithm can accurately estimate the state of the system, making the measurement results more stable and reliable. This provides important technical support for high-concentration dust monitoring and environmental protection in workplaces, as well as new ideas and directions for further research and application in related fields.

Acknowledgments

The authors appreciate the financial supported by the National Natural Science Foundation of China (No. 52374185).

References

Al-Shabi, M., Gadsden, S. A., Habibi, S. R., 2013. Kalman filtering strategies utilizing the chattering effects of the smooth variable structure filter. Signal Processing, 93(2), 420-431.

Amyotte, P. R., Pegg, M. J., & Khan, F. I. (2009). Application of inherent safety principles to dust explosion prevention and mitigation. Process Safety and Environmental Protection, 87(1), 35-39.

Andersson, M., Streb, M., Ko, J. Y., Klass, V. L., Klett, M., Ekström, H., Mikael Johansson., Lindbergh, G., 2022. Parametrization of physics-based battery models from input–output data: A review of methodology and current research. Journal of Power Sources, 521, 230859.

Barber, E. L., Garg, R., Persenaire, C., Simon, M., 2021. Natural language processing with machine learning to predict outcomes after ovarian cancer surgery. Gynecologic oncology, 160(1), 182-186.

Chen, J., Nie, Z., Zhao, F., Jiang, H., Zhu, L., 2023. Improving the stability of electrostatic induction dust concentration detection using kalman filtering algorithm aided by machine learning. Process Safety and Environmental Protection, 174, 882-890.

Dong, Y., Zhao, B., Yang, J., Cao, Y., Cao, Y., 2023. Two-stage convolutional neural network for joint removal of sensor noise and background interference in lock-in thermography. NDT & E International, 137, 102816.

Guo, X., Wang, Y., Mei, S., Shi, C., Liu, Y., Pan, L., Li K., Zhang B., Wang J.,Zhong Z., Dong, M., 2022. Monitoring and modelling of PM2. 5 concentration at subway station construction based on IoT and LSTM algorithm optimization. Journal of Cleaner Production, 360, 132179.

Gajewski, J.B., 2013. Accuracy of cross correlation velocity measurements in two-phase gas–solid flows. Flow. Meas. Instrum. 30, 133–137. https://doi.org/10.1016/j. flowmeasinst.2013.01.001.

Huang, Y., Liu, X., Wang, Z., Jiang, M., Zhou, Z., Xu, M., Han J., Yang B., Fan, X., 2022. On-line measurement of ultralow mass concentration particulate based on light scattering

coupled with beta ray attenuation method. Fuel, 329, 125461.

Han, X., Liu, Y., Gao, H., Ma, J., Mao, X., Wang, Y., Ma, X., 2017. Forecasting PM2. 5 induced male lung cancer morbidity in China using satellite retrieved PM2. 5 and spatial analysis. Science of the Total Environment, 607, 1009-1017.

İnan, R., Aksoy, B., Salman, O., 2023. Estimation performance of the novel hybrid estimator based on machine learning and extended Kalman filter proposed for speed-sensorless direct torque control of brushless direct current motor. Engineering Applications of Artificial Intelligence, 126, 107083.

Jiang, Z., Zeng, F., Wang, Y., 2021. Research status and prospect of dust pollution control in typical working places during mining and transportation of metal mines in China. Metal Mine, 50, 135.

Jwo, D. J., & Wang, S. H., 2007. Adaptive fuzzy strong tracking extended Kalman filtering for GPS navigation. IEEE Sensors Journal, 7(5), 778-789.

Jordan, M. I., Mitchell, T. M., 2015. Machine learning: Trends, perspectives, and prospects. Science, 349(6245), 255-260.

King, D. E., 2009. Dlib-ml: A machine learning toolkit. The Journal of Machine Learning Research, 10, 1755-1758.

Khayyam, H., Shahkhosravi, N. A., Jamali, A., Naebe, M., Kafieh, R., Milani, A. S., 2023. GMDH-Kalman Filter prediction of high-cycle fatigue life of drilled industrial composites: A hybrid machine learning with limited data. Expert Systems with Applications, 216, 119425.

Khani, M., & Abdel-Qader, I., 2023. Machine learning based asynchronous computational framework for generalized Kalman filter. Concurrency and Computation: Practice and Experience, 35(6), 1-1.

Kamm, S., Veekati, S. S., Müller, T., Jazdi, N., Weyrich, M., 2023. A survey on machine learning based analysis of heterogeneous data in industrial automation. Computers in Industry, 149, 103930.

Kuang, X., Sui, X., Liu, Y., Chen, Q., Guohua, G., 2017. Single infrared image optical noise removal using a deep convolutional neural network. IEEE photonics Journal, 10(2), 1-15.

Kowalska, M., Skrzypek, M., Kowalski, M., Cyrys, J., Ewa, N., Czech, E., 2019. The relationship between daily concentration of fine particulate matter in ambient air and exacerbation of respiratory diseases in Silesian Agglomeration, Poland. International Journal of Environmental Research and Public Health, 16(7), 1131.

Li, B., Hu, H., Long, Y., Zhan, S., Zhang, Z., Li, W., Li j., Gong, J., 2022. Dust transport behaviour in the Nanwenhe extra-large stepped underground metal mine stope. Journal of Cleaner Production, 372, 133699.

Li, Q., Li, R., Ji, K., Dai, W., 2015. Kalman filter and its application. In 2015 8th International Conference on Intelligent Networks and Intelligent Systems (ICINIS) (pp. 74-77). IEEE.

Ning, P., Shi, H., Niu, P., Lu, T., Wang, W., 2019. Electric field analysis of auxiliary electrode in needle-free electrostatic spinning. Ferroelectrics, 548(1), 60-71.

Peng, L., Zhang, Y., Yan, Y., 2008. Characterization of electrostatic sensors for flow measurement of particulate solids in square-shaped pneumatic conveying pipelines. Sensors and Actuators A: Physical, 141(1), 59-67.

Ribeiro, M., Grolinger, K., Capretz, M. A., 2015, December. Mlaas: Machine learning as a

service. In 2015 IEEE 14th International Conference on machine learning and applications (ICMLA) (pp. 896-902). IEEE.

Revach, G., Shlezinger, N., Ni, X., Escoriza, A. L., Van Sloun, R. J., Eldar, Y. C., 2022. KalmanNet: Neural network aided Kalman filtering for partially known dynamics. IEEE Transactions on Signal Processing, 70, 1532-1547.

Roach, L., Rignanese, G. M., Erriguible, A., Aymonier, C., 2023. Applications of machine learning in supercritical fluids research. The Journal of Supercritical Fluids, 106051.

Schmidhuber, J. (2015). Deep learning in neural networks: An overview. Neural networks, 61, 85-117.

Taveau, J., Hochgreb, S., Lemkowitz, S., Roekaerts, D., 2018. Explosion hazards of aluminum finishing operations. Journal of Loss Prevention in the Process Industries, 51, 84-93.

Vashist, A., Li, M. P., Ganguly, A., PD, S. M., Hochgraf, C., Ptucha, R., Kwasinski A., Kuhl, M. E., 2021. KF-Loc: A Kalman filter and machine learning integrated localization system using consumer-grade millimeter-wave hardware. IEEE Consumer Electronics Magazine, 11(4), 65-77.

Wang, M., Yao, G., Sun, Y., Yang, Y., Deng, R., 2023. Exposure to construction dust and health impacts–a review. Chemosphere, 311, 136990.

Widiatmojo, A., Sasaki, K., Sugai, Y., Suzuki, Y., Tanaka, H., Uchida, K., Matsumoto, H., 2015. Assessment of air dispersion characteristic in underground mine ventilation: Field measurement and numerical evaluation. Process Safety and Environmental Protection, 93, 173-181.

Wagstaff, K., 2012. Machine learning that matters. arXiv preprint arXiv:1206.4656.

Welch, G., Bishop, G., 1995. An introduction to the Kalman filter.

Xu, Y., Hu, M., Zhou, A., Li, Y., Li, S., Fu, C., Gong, C., 2020. State of charge estimation for lithium-ion batteries based on adaptive dual Kalman filter. Applied Mathematical Modelling, 77, 1255-1272.

Gas release from lithium-ion batteries and mitigation of potential consequences

Ola Willstrand [a,b], Jonna Hynynen [a], Anna Karlsson [a] & Daniel Brandell [b]

[a] RISE Research Institutes of Sweden, Borås, Sweden
[b] Department of Chemistry – Ångström Laboratory, Uppsala University, Sweden

E-mail: ola.willstrand@ri.se

Abstract

Lithium-ion batteries are used in a wide range of applications, from small consumer products and electric vehicles to large stationary energy storage systems and electrically propelled ships. The increased use of lithium-ion batteries for energy storage systems has put an emphasis on battery safety. Upon battery failure, e.g. due to external heating or an internal short circuit, material decomposition and accelerated exothermic reactions may result in a thermal runaway. Thermal runaway in lithium-ion batteries generally means the production of large amounts of flammable gas which poses an explosion risk. To mitigate explosions and to enable safety evaluation and design of appropriate and rightfully dimensioned safety features, such as ventilation, the gas release characteristics are of great importance. In this paper, gas characteristics from thermal runaway in lithium-ion battery cells are evaluated. The gas characteristics, such as the gas production rate, gas volumes and chemical composition are evaluated for more than 80 battery cell tests. The chemical composition was analyzed using multiple techniques to assess the consistency of the obtained data. The main components formed during thermal runaway are carbon dioxide, carbon monoxide, hydrogen and various hydrocarbons. The total volume of gas produced, normalized to the rated electrical energy of the cell, varies typically between 0.1 and 0.7 L/Wh. Results show that the cell type, cell size, state-of-charge and even the thermal runaway trigger method influence the gas characteristics. Furthermore, explosion mitigation strategies for large battery systems focusing on ventilation and ventilation strategies are presented. Finally, safety aspects related to the battery cell and system design, such as choice of cell chemistry, thermal barriers, and routes for safe evacuation of thermal runaway vent gas are discussed.

Keywords: *lithium-ion battery, thermal runaway, gas composition, gas production rate, ventilation, explosion*

1. Introduction

Lithium-ion batteries (LIBs) are used in a wide range of applications, from small consumer products and electric vehicles (EVs) to large stationary energy storage systems and electrically powered ships. The increased use of LIBs in energy storage systems has put an emphasis on battery safety. Especially from a personal safety perspective, where the more severe potential consequence of a failure is an explosion. Explosions due to battery failure are rare, but in applications where large quantities of battery cells are used or stored, the consequences of a battery failure can be severe. Some major incidents are briefly discussed in section 1.1.

The use of flammable organic electrolytes in LIBs enable production of large amounts of flammable gas upon battery failure. The specific combination of battery materials determines the potential rate and extent of decomposition reactions and the vast number of material compositions used in LIBs also reasons the large differences of failure behaviour within the family of LIBs. When a LIB cell is heated, e.g. due to an external heating source or an internal short circuit, material decomposition and accelerated exothermic reactions typically leads to thermal runaway (TR). TR implies that the self-heating reactions are out of control and non-reversible. In recent years, several reviews have covered the fundamentals of TR behaviour of LIBs and potential causes and consequences, e.g. (Chen et al., 2021; Duh et al., 2021; Jindal & Bhattacharya, 2019; Wang et al., 2019).

A key aspect that enables safety evaluation of LIBs is the gas release characterisation during TR. The potential consequences of a TR will heavily depend on both the gas production rate and gas composition. The gas composition varies but the main components formed during TR are carbon dioxide (CO_2), carbon monoxide (CO), hydrogen (H_2) and hydrocarbons such as methane (CH_4) and ethene (C_2H_4) (Baird et al., 2020; Willstrand et al., 2023). Furthermore, the proportion of each compound will shift based on the state of charge (SOC). At low SOC, inert CO_2 dominates, and at higher SOC, both the proportion and total volume of flammable gases increases drastically, especially for H_2 and CO. Koch et al., (2018) studied the gas composition and volumes of gas for different LIB cells in different sizes, and they observed that the total volume of gas could be correlated to the cell capacity and the energy density of the cell. However, there was no correlation between gas composition and cell capacity. Comparative studies that include large test series are, however, still relatively rare. In a recent and extensive meta-analysis by Rappsilber et al., (2023) it was concluded that results differentiated by cell type is vastly complex and coarse-meshed due to the diversity of test methodologies used.

An important aspect of the gas composition is the lower flammability limit (LFL), also referred to as the lower explosive limit (LEL). It denotes the lowest volume fraction of a flammable gas, in air, which could ignite in the presence of an ignition source such as an arc, flame and hot surface. The LFL will vary depending on the gas compositions, and thereby also for different SOC levels. For gases produced during TR, the LFL typically lies between 5 and 12 percent (Baird et al., 2020; Li et al., 2021). The proportion of H_2 will significantly affect the LFL, as well as the laminar burning velocity and ignition time (Nilsson et al., 2023).

This paper presents work on how the SOC, battery cell size and TR trigger methods affect the gas composition, gas production rate and volumes of gas generated. To enable analysis of a broad range of chemical compounds, a range of analysis techniques were used including gas chromatography (GC) with flame ionization detector (FID) and mass spectrometer (MS), as well as nondispersive infrared (NDIR) and Fourier-transform infrared (FTIR) spectroscopy. The consistency between the different analysis methods was also verified. Further, the consequences due to the gas release, and especially the risk of gas explosion, are analysed and discussed based on the results from two recently completed projects; where (1) focused on battery room ventilation strategies on fully electric ships (Ramachandra et al., 2023), and (2) focused on general installation safety guidelines for stationary battery energy storage systems (BESS) (Grönlund et al., 2023).

1.1. Explosion incidents

Data on LIB incidents are relatively scarce. Some data have been gathered regarding EVs, but explosions are rare (Hynynen et al., 2023). For stationary systems, the BESS Failure Event Database (EPRI, 2024) reports 75 BESS failures between 2011 and 2023 which have led to fires and a few explosions. This data is based on publicly available information. Additional explosion incidents reported in the news media recently include, for example, a private home BESS explosion in Germany (Enkhardt, 2023), a BESS container explosion in Martinique (Leonce, 2023), and a couple of EV explosions where vented gas was released into the driver's compartment or into a small garage (StacheD Training, 2024). A few explosion incidents which have resulted in a fire investigation report are summarized shortly below.

In 2019, a fire and an explosion occurred at the McMicken Energy Storage Unit facility in Arizona, USA. Three hours after the first cell experienced TR, firefighters opened the door to the facility and a few minutes later an explosion occurred, injuring several firefighters. Lessons learned from this incident include: the importance of cell quality and thermal propagation protection between cells and modules, the need for a response plan accessible from outside the BESS space, education for firefighters and hazmat teams, design of the ventilation system to handle vent gases from TR, the need for pressure relief panels, the need for appropriate detectors as well as the need for continuous feedback from inside the BESS space (Hill, 2020; McKinnon et al., 2020).

In 2021, a short circuit caused thermal runaway in a 25 MWh BESS facility in central Beijing, China. The released gases reached another building through a cable trench. Explosions occurred in both buildings, resulting in three fatalities and one injured firefighter. Shen et al., (2023) provide more details and overpressure calculations for this incident.

Also in 2019, a fire broke out in the battery room on the electric hybrid ferry MF Ytterøyningen, Norway. In the evening it was announced that the fire was under control and the following morning the rescue service decided to open the hatch to the battery room to ventilate the space. The temperature began to rise and about two hours later there was a large explosion which caused extensive damage to the ferry. The incident report concludes that a LIB incident in a closed space poses a major explosion risk (Josdal, 2019). A similar incident occurred in 2021 when a fire started in the battery room of MS Brim in Vallø, Norway. In this case, the rescue service managed to prevent major consequences by purging the battery room with nitrogen gas when ventilating the space. This was a previously untested method on ships that appears to have effectively prevented a potential gas explosion during the intervention (Helle et al., 2021).

2. Lithium-ion battery cell tests

The results and analysis presented and discussed below are based on existing literature and on test series conducted at RISE. One of the RISE conducted test series (test series 1 in Table 1) has previously been published in detail (Willstrand et al., 2023) while others have been partially published (Willstrand et al., 2024). Detailed description of the test setups and test procedures can be found in these publications. For the purpose of this paper, only tests conducted in inert atmosphere are presented. This was performed in an 80 L pressure vessel, see Figure 1, and enabled analysis of produced flammable gases. The volume of gas produced was determined using the ideal gas law and by measurements of the gas temperature and pressure increase.

For the gas composition analysis, several instruments were used including an *Agilent 490* Micro-GC, *X-STREAM* and *BINOS 100* instruments including a paramagnetic oxygen analyzer and NDIR sensor for CO, CO_2 and CH_4, and a *HY-ALERTA 500* hydrogen sensor. Additionally, FTIR spectroscopy was performed using a *BRUKER Matrix-MG* with a MCT detector, 0.2 L heated gas cell (180 °C) and a spectral resolution of 0.5 cm^{-1}. In addition, some samples were collected in gas sampling bags and were further analyzed using GC-FID and GC-MS to detect different hydrocarbons.

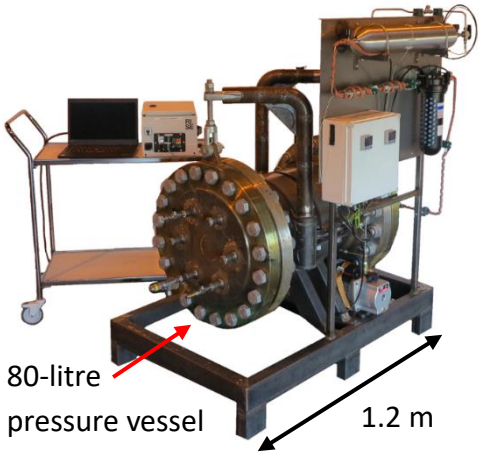

Fig. 1. *Pressure vessel setup used for tests in inert atmosphere.*

3. Results and discussion

3.1. Gas composition

Gas composition data is presented in Figure 2, including both literature data and results from performed test series. The number of tests in inert atmosphere and battery cell information are found in Table 1. For the literature data, most tests are conducted at 100% SOC, and results for other SOC levels are based on 3 to 7 tests at each level. Error bars in the figure show one standard deviation. Note that no clear trends were found for the literature data sorted on cell type, why the literature data is presented as means of all tests. As can be seen, H_2 and CO increase with SOC, while CO_2 decreases. The total amount of hydrocarbons (THC) shows no clear SOC dependency. The high energy density NMC811/C cell tested indicates a much higher CO/CO_2 ratio compared to the literature data, showing the same effect as when increasing the SOC. For H_2 there is no such difference between the tested NMC811/C cell and the literature data. However, production of H_2 is typically associated with lithium reacting with binders while production of CO and CO_2 is associated with electrolyte decomposition and release of oxygen from the cathode (Wang et al., 2019), which might explain the different trends for SOC versus cell chemistry for the different compounds. Overall, the different test series conducted show similar results (Figure 2). Test series 2 and 3 mainly utilizes a local heater as the TR triggering device, which initiates TR in one end of the cell without pre-heating the rest of cell. Test series 1 utilizes several different TR triggering methods. Since there are larger differences in Figure 2 between test series 1 and the other test series as compared to test series 2 and 3 mutually, the triggering method seems to have a larger influence on these results compared to the difference in cell size between test series 2 and 3.

***Table 1**. Number of tests and battery cell type for the performed test series and in the collected literature data.*

Data source	Number of tests	Type of cell(s)
Test series 1	15	NMC811/C, 157 Ah
Test series 2	5	NMC811/C, 70 Ah
Test series 3	3	NMC811/C, 157 Ah
Literature[a]	63	LFP/NMC/NCA/LMO/LCO, 0.5-130 Ah

[a]reference list is found in (Willstrand et al., 2023)

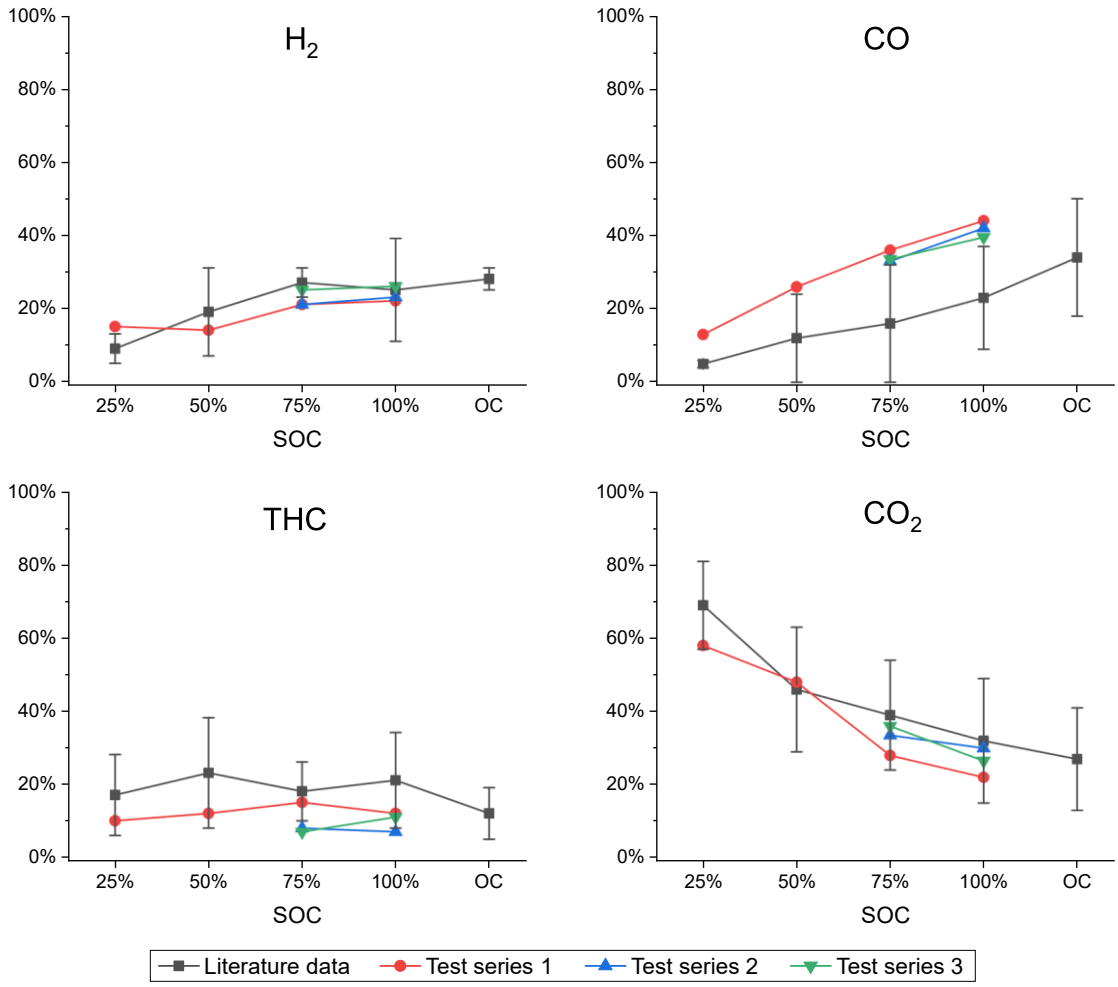

***Fig. 2.** Mean concentrations of H_2, CO, CO_2 and THC in TR vent gas from performed test series as well as from literature. OC means overcharge.*

In Figure 3, gas composition data from four tests in test series 2 and 3 are presented. Here, the gas samples were analyzed using several analysis techniques. In general, the data is consistent. However, using FTIR and GC-FID indicates a higher amount of THC originating from detection of ethene (C_2H_4). This is also evident in the GC-FID data shown in Figure 4. In addition, for NDIR, detection of methane seems to have been influenced by the larger hydrocarbons for measurements at 75% SOC. The FTIR measurements seems to have overestimated the CO/CO_2 ratio. Note that the battery cell vent gas was diluted before analysis by FTIR and that the results were normalized to CO_2 data from NDIR measurements.

Figure 4 shows detailed THC data analyzed by GC-FID and GC-MS (for the carbonates) for four tests in test series 2 and 3. Methane and ethene are the main compounds and larger hydrocarbons are detected only in small quantities. It can be noted that an increase of methane is followed by a decrease in ethene and that this seems to be dependent on SOC as well as on the battery cell size.

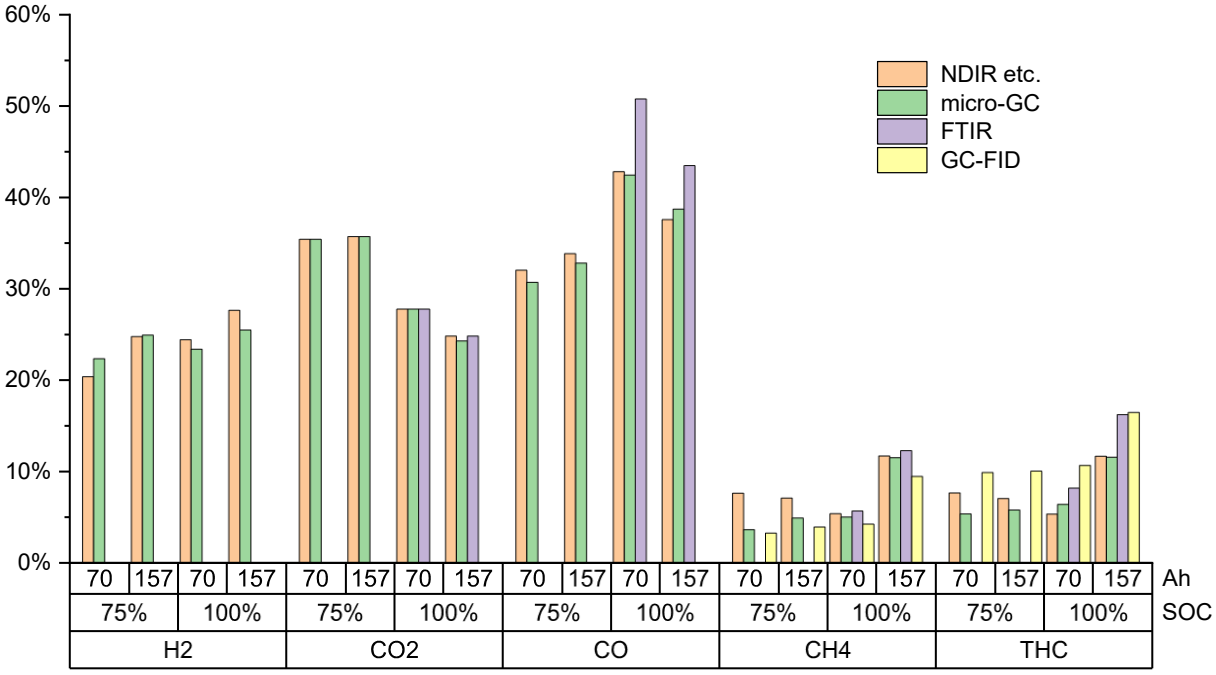

Fig. 3. *Concentration of gas components from test series 2 and 3, analysed using different analysis instruments.*

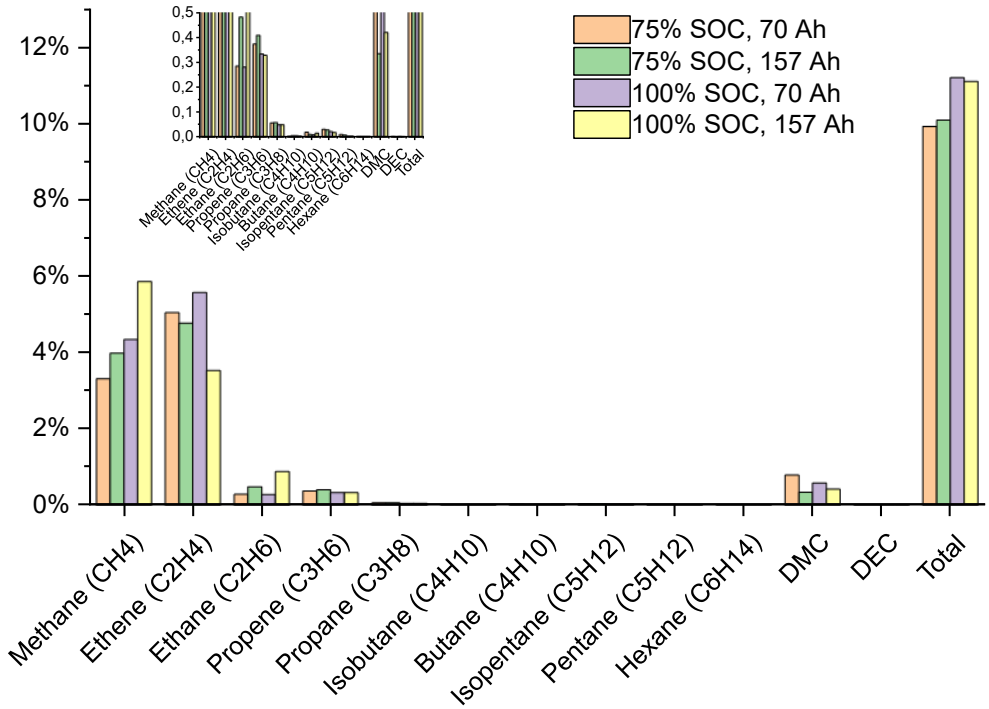

Fig. 4. *THC from four tests in test series 2 and 3.*

3.2. Gas production

The total volume of gases produced during TR in inert atmosphere is presented in Figure 5, including both literature data and the results from performed test series. The gas volume presented is at normal temperature and pressure (NTP) and normalized to the rated electrical energy of the tested cell. For the literature data, most tests are conducted at 100% SOC. The total gas production increases with SOC, except for the LFP cells where this trend is less evident. As for the gas composition, the difference in test procedure between test series 1, and test series 2 and 3, had a small influence on the gas production as seen in the figure. In contrast to gas composition, cell size also appears to influence the total gas production and is most prominent at 100% SOC.

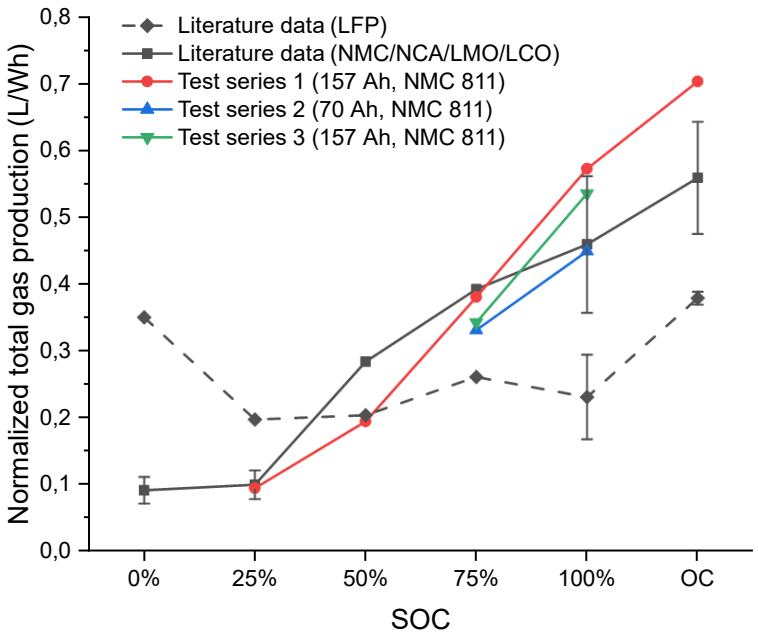

Fig. 5. *Total gas production, normalized to the rated electrical energy of the cell, during TR in inert atmosphere from performed test series as well as literature. OC means overcharge.*

For risk assessment purpose, a consistency of the normalized gas production during TR, for different LIBs, is of importance to be able to estimate the risk for different scenarios. Figure 5 shows that, without specific test results, a value of, e.g., 0.5 L of battery gas per Wh of installed electrical energy provide a good, still conservative, estimate of the total amount of gas that can be produced. However, it is always recommended that tests are performed for a specific battery installation to obtain reliable data.

4. Explosion risk mitigation

The maritime industry has always prioritized safety, so also for electrically powered ships. Two recent projects investigated the design of a fully electric roll-on/roll-off (ro-ro) passenger ship intended to operate between Sweden and Denmark (Ramachandra et al., 2023; Willstrand et al., 2021). The anticipated size of the battery system is approximately 60 MWh. The first project, from 2021, concluded that a fully electric ro-ro passenger ship is both technically viable and a realistic alternative to conventional ship design, but the risk analysis also identified further research needs such as design of ventilation systems and explosion protection. These aspects were further studied in the second project which was completed in 2023.

Battery systems come in a variety of designs, which complicates the composition of a general safety installation guideline. A crucial design parameter is the presence of an off-gas duct or similar solution connected to the battery modules, which prevent gases produced during TR to enter the battery room. That is generally a good safety measure which reduces the risk of gas explosion in the battery room in the event of a single battery cell failure. However, the size of the off-gas duct is typically dimensioned for TR in one cell only, why TR propagation protection between cells is also very important. TR propagation may result in duct rupture leading to release of gases into the battery room. An important conclusion from the project (Ramachandra et al., 2023) is that the room ventilation design must consider the risk of flammable gases released into the room despite battery system design, e.g. despite presence of an off-gas duct. There are several reasons for this:

- Test procedures does not test for all existing failure modes, especially where several cells might experience TR at the same time, e.g. due to mechanical impact, submersion or coolant leakage.
- A successful TR propagation test at cell level does not guarantee that TR propagation can be hindered for all possible scenarios. Several parameters affect the outcome, such as TR triggering method, triggered cell location, electrical connections (parallel/serial), and battery aging effects.
- Off-gas ducts are typically designed for single cell failures and therefore not designed to handle larger volumes of gas following a TR propagation.

To further improve safety, it is suggested to implement thermal barriers, not only on cell level, but also on module and system level, as well as to design off-gas ducts that can handle TR in e.g. a whole module. During TR, a significant amount of gas (see Figure 5) could typically be released within seconds. If TR propagation cannot be prevented, slowing down the TR propagation is of great importance to mitigate extensive gas release in short time frames.

Without ventilation, a small module of e.g. 10 kWh could generate 5000 L volume of gas (assuming 0.5 L/Wh), resulting in a flammable air-gas mixture of 100 m^3 (assuming a LFL of 5 % battery gas in air). Therefore, the gas explosion risk is difficult to eliminate even with high ventilation rates. An additional safety measure could be to design deflagration vent panels or similar protection to handle overpressure in the battery room in case of an explosion event (Grönlund et al., 2023).

Another important factor is to connect the ventilation and explosion design with the choice of fire suppression system. There are pros and cons with all the different suppression systems available, where e.g. gaseous systems will require that the ventilation is shut off. Furthermore, extinguishment of flames may introduce an explosion hazard, while the presence of flames may accelerate TR propagation and fire spread.

4.1. Forced ventilation

To avoid gas explosion, forced ventilation as a safety measure could be effective but it requires that the battery design limits the maximum gas production rate during TR. Further, ventilation strategies must consider that intake of fresh air may increase the rate of fire spread and potentially increase the risk of explosion, in case the ventilation rate cannot match the gas production rate.

The ventilation rates needed will depend on the cell type, battery design, SOC, size of the battery enclosure/room as well as on the anticipated scenarios (worst case as well as most probable scenario). Some ventilation rate recommendations for worst-case scenarios range between 0.1 and 0.3 $Ls^{-1}Wh^{-1}$, focusing on the size of the battery, or between 6 and 50 acph (air changes per hour), focusing on the size of the battery room (Grönlund et al., 2023). For the time being, ventilation strategies should be developed for each specific installation, based on possible ventilation rates and anticipated scenarios.

In the project focusing on battery room ventilation strategies on fully electric ship (Ramachandra et al., 2023) some general recommendations were developed. The battery room ventilation capacity should be divided into three categories: (1) basic, (2) preventive, and (3) casualty ventilation. For basic ventilation, 6 acph could be seen as a minimum as it is often required by authorities for this type of ship enclosures. At any type of failure detection that may lead to TR the ventilation capacity should be increased to preventive level, ensuring that off-gas from a single battery cell does not create an explosion hazard. When an off-gas duct is present, the room ventilation rate should still be increased as a precautionary measure. Finally, upon detection of flammable gases in the battery room the casualty ventilation should be started and increase the ventilation rate to its desired capacity. The actual ventilation rates in the different modes is dependent on the free volume of the battery room and shall be calculated on a case-to-case basis.

For some cases it might be better to shut off the ventilation. For example, in case of confirmed fire, since forcing oxygen into the room will feed the fire; or when the production rate of flammable gases is too high such that the LFL is reached. Detection and feedback from the battery room is crucial, not only initially but throughout the event. LFL detectors in the ventilation outlet, visual feedback (e.g., video surveillance) and information from the battery management system (BMS) are of great importance to understand the event inside the room and assist in decision making. If the feedback communication fails or at any sign of fire development (also after fire suppression system is activated), it could be the safest strategy to turn off the ventilation, even if that means that flammable gases may accumulate in the room. It is essential to have a well-defined plan on how to safely release these flammable gases after an incident, such that an explosion does not occur as in previous incidents (see section 1.1).

4.2. BESS installation guidelines

In the other recently finished project focusing on general installation guidelines for stationary BESS (Grönlund et al., 2023), the guidelines divide BESS into three different application categories associated both with expected battery size as well as user responsibilities. These are BESS in single-family homes, BESS in multi-dwelling blocks or businesses, and BESS for large-scale commercial applications. For details on the guidelines the reader is referred to the published guideline document (Grönlund et al., 2023). Here, the most important aspects related to gas release and explosion risk are shortly mentioned:

- BESS spaces should not be located such that battery gases affect the building's main evacuation strategy. A rule of thumb may be to not place BESS within an evacuation route or in spaces that are directly connected to the evacuation route. BESS spaces should also be distant from sleeping areas.
- Forced ventilation can be used to prevent a gas mixture from reaching LFL and causing an explosion during TR in a single cell or a few cells. The ventilation should only serve the space

that contains the BESS and connect directly to the outside. This ensures that ventilation can continue even if fire dampers were to activate in the building. Additionally, a negative pressure environment mitigates gas leakage through doors or other leakage points in the room. Explosion classification or spark resistant fan might increase safety, but the battery cells themselves will always be a potential ignition source during TR.

- The fire and rescue service should be able to evacuate the fire gases without opening doors that connect the space with the rest of the building. Preferably, this should be possible from a remote and safe location. Pressure relief systems such as deflagration vent panels reduce the damage in case an explosion occur.

Finally, as already mentioned, the battery cell and battery system design are crucial to limit the gas production rate and limit the consequences of a battery failure event. System design includes aspects such as choice of cell chemistry, thermal barriers between cells/modules/racks, internal distances between modules/racks, and routes for safe evacuation of TR vent gas.

5. Conclusions

To mitigate explosions due to battery failure and to enable safety evaluation and design of appropriate and rightfully dimensioned safety features, such as ventilation, the gas release characteristics during TR in LIBs are of great importance. The gas production rate, gas volumes, and gas composition are key factors. Carbon dioxide, carbon monoxide, hydrogen, and various hydrocarbons are the main components formed during thermal runaway where all except carbon dioxide are flammable. The total volume of gas produced, normalized to the rated electrical energy of the cell, typically varies between 0.1 and 0.7 L/Wh. Cell type, cell size, SOC and TR trigger method influence TR vent gas characteristics, typically important to consider in test procedures, test standards and battery design.

Cell level characteristics will of course influence battery system design, but for battery user applications it is the latter that is of greatest importance. The gas production rate of a single cell can be high, but it will be TR propagation characteristics that determine the maximum limits of the gas production rate, important for the design of ventilation safety measures. Implementing thermal barriers and increasing internal distances inside the battery system are important safety aspects as well as establishing safe evacuation routes for TR vent gas.

Ventilation strategies are important for explosion risk reduction but must consider both fire and non-fire scenarios, including the design of a fire suppression system. Other important safety measures include proper placement of the battery system, information feedback from affected areas/systems, and to facilitate fire and rescue service intervention.

Acknowledgements

The authors gratefully acknowledge the financial contribution from the Swedish Energy Agency (project no. 51787-1), the Swedish Transport Administration through LIGHTHOUSE – the Swedish Maritime Competence Centre, and FORMAS – a Swedish Research Council for Sustainable Development (grant no. 2022-02015). We also acknowledge support from Batteries Sweden (grant no. Vinnova-2019-00064), and STandUP for Energy.

References

Baird, A. R., Archibald, E. J., Marr, K. C., & Ezekoye, O. A., 2020. Explosion hazards from lithium-ion battery vent gas. Journal of Power Sources, 446. https://doi.org/10.1016/j.jpowsour.2019.227257

Enkhardt, S., 2023. German home destroyed by 30 kWh battery explosion. https://www.pv-magazine.com/2023/10/13/german-home-destroyed-by-30-kwh-battery-explosion/, accessed 2024-01-26

EPRI, Electric Power Research Institute, 2024. BESS Failure Event Database, https://storagewiki.epri.com/index.php/BESS_Failure_Event_Database, accessed 2024-01-26.

Grönlund, O., Quant, M., Rasmussen, M., Willstrand, O., & Hynynen, J., 2023. Guidelines for the fire protection of battery energy storage systems.

Hill, D., 2020. McMicken Battery Energy Storage System Event - Technical Analysis and Recommendations.

Hynynen, J., Quant, M., Pramanik, R., Olofsson, A., Li, Y. Z., Arvidson, M., & Andersson, P., 2023. Electric Vehicle Fire Safety in Enclosed Spaces.

Josdal, A., 2019. Evalueringsrapport - Brann i MF Ytterøyningen.

Koch, S., Fill, A., & Birke, K. P., 2018. Comprehensive gas analysis on large scale automotive lithium-ion cells in thermal runaway. Journal of Power Sources, 398, 106–112. https://doi.org/10.1016/j.jpowsour.2018.07.051

Leonce, F., 2023. Fire on a Saint-Esprit poultry site in Martinique: more than 1 million euros in estimated losses. https://euro-dayfr-com.cdn.ampproject.org/c/s/euro.dayfr.com/trends/amp/943555, accessed 2024-01-26.

Li, W., Rao, S., Xiao, Y., Gao, Z., Chen, Y., Wang, H., & Ouyang, M., 2021. Fire boundaries of lithium-ion cell eruption gases caused by thermal runaway. IScience, 24(5). https://doi.org/10.1016/J.ISCI.2021.102401

McKinnon, M., DeCrane, S., & Kerber, S., 2020. Four Firefighters Injured in Lithium-Ion Battery Energy Storage System Explosion -- Arizona. https://doi.org/10.54206/102376/TEHS4612

Nilsson, E. JK., Brackmann, C., & Tidblad, A. A., 2023. Evaluation of combustion properties of vent gases from Li-ion batteries. Journal of Power Sources, 585(233638). https://doi.org/10.1016/j.jpowsour.2023.233638

Ramachandra, V., Karlsson, A., Willstrand, O., Hägg, M., & Schreuder, M., 2023. Battery Fire Safety Ventilation for Fully Electrical Vessel.

Rappsilber, T., Yusfi, N., Krüger, S., Hahn, S. K., Fellinger, T. P., Krug von Nidda, J., & Tschirschwitz, R., 2023. Meta-analysis of heat release and smoke gas emission during thermal runaway of lithium-ion batteries. Journal of Energy Storage, 60. https://doi.org/10.1016/j.est.2022.106579

Shen, X., Hu, Q., Zhang, Q., Wang, D., Yuan, S., Jiang, J., Qian, X., & Yuan, M., 2023. An analysis of li-ion induced potential incidents in battery electrical energy storage system by use of computational fluid dynamics modeling and simulations: The Beijing April 2021 case study. Engineering Failure Analysis, 151(107384). https://doi.org/10.1016/j.engfailanal.2023.107384

StacheD Training, 2024. Electric Car Explosions Worldwide. https://www.youtube.com/watch?v=aLtkTp4GVuE, accessed 2024-01-26

Wang, Q., Mao, B., Stoliarov, S. I., & Sun, J., 2019. A review of lithium ion battery failure mechanisms and fire prevention strategies. Progress in Energy and Combustion Science, 73, 95–131. https://doi.org/10.1016/J.PECS.2019.03.002

Willstrand, O., Pushp, M., Andersson, P., & Brandell, D., 2023. Impact of different Li-ion cell test conditions on thermal runaway characteristics and gas release measurements. Journal of Energy Storage, 68, 107785. https://doi.org/10.1016/j.est.2023.107785

Willstrand, O., Pushp, M., Ingason, H., & Brandell, D., 2024. Uncertainties in the use of oxygen consumption calorimetry for heat release measurements in lithium-ion battery fires. Fire Safety Journal, 143(104078). https://doi.org/10.1016/j.firesaf.2023.104078

Willstrand, O., Ramachandra, V., Evegren, F., Hägg, M., Ramne, B., Li, Z., Thies, F., Ringsberg, J., & Julià Lluis, E., 2021. Electric Light - Lightweight and electrically propelled Ro-Pax ships.

Effects of Heating Rate on Thermal Runaway of LFP Lithium-ion Batteries: Vent Gas Quantification and Composition Analysis

Christopher A. Almodovar, Lorenz R. Boeck & C. Regis L. Bauwens

FM Global, Research Division
Norwood, MA, USA

E-mail: lorenz.boeck@fmglobal.com

Abstract

This study examines the effects of heating rate on cell venting, thermal runaway (TR), and related gas generation. Measurements of characteristic temperatures, the amount of gas released, and quantitative composition analysis of the TR products were performed using a sealed 20-L sphere setup, examining 18650 form-factor LIB cells with lithium iron phosphate ($LiFePO_4$ or LFP) cathodes and carbon anodes. The gas generation process was observed to occur in two phases: the first when the internal cell pressure exceeds the burst pressure of the safety vent and the second during the rapid onset of TR. The characteristic temperatures and number of moles released from the cells were found to increase with heating rate between 10 and 80 °C/min. Samples of thermal runaway gas (TRG) at different heating rates were collected and composition analysis was performed, revealing significant amounts of hydrogen (H_2), small chain hydrocarbons, and oxygenated volatile organic compounds (OVOCs).

Keywords: *lithium-ion batteries, thermal runaway, gas analysis, heating rate*

1. Introduction

The use of lithium-ion batteries (LIBs) for energy storage applications is rapidly increasing in both residential and industrial settings. Such energy storage systems (ESSs) are typically composed of a series of battery modules that each contain an array of unit cells. These systems can present new fire and explosion hazards, however, as LIBs have the potential to undergo thermal runaway (TR) – an uncontrolled rise in temperature due to runaway internal chemical reactions that can release significant quantities of flammable gases (Wang et al., 2012). When a single cell undergoes TR, adjacent cells and modules are at risk of entering TR due to heat transfer from the initiating cell. Predicting the propagation of TR through modules and systems, and the resulting release of flammable gas, requires a detailed understanding of the TR dynamics of individual cells, including thermal and electrochemical effects, the gas venting process, and heat transfer between cells. Ignition of the released flammable gases may significantly enhance the heat transfer to adjacent cells, intensifying TR propagation, and pose an explosion hazard. In order to accurately analyze and predict the fire and explosion risks of LIB systems, and develop engineering recommendations to prevent and mitigate potential loss, it is critical to study the TR behavior of individual cells, modules, and systems.

This work examines aspects of single-cell TR, quantifying the amount and composition of released thermal runaway gases (TRGs) over a range of heating rates. An experimental methodology was developed to provide a consistent method to force 18650 form-factor LIBs into TR via thermal abuse under constant heating rates. While previous works in other apparatuses, such as accelerating rate

calorimeters (ARCs), typically provide low heating rates on the order of ~5 °C/min, experimental analysis has revealed that heating rates as high as several hundred °C/min can occur during cell-to-cell TR propagation (Said et al., 2020). The experimental setup developed in this work enables a wide range of heating rates and was used to measure the characteristic temperatures of the TR process for LIB cells with lithium iron phosphate ($LiFePO_4$ or LFP) cathodes and carbon anodes, and quantify the amount and composition of the TRG released.

2. Literature

Select studies that provide TRG quantity and composition measurements for LFP LIBs are summarized in Table 1. While earlier works mostly focused on cylindrical form-factor cells (*i.e.*, 18650 and 26650), the research focus has shifted more recently toward prismatic cell geometries. Quantitative TRG composition analysis has been performed primarily by gas chromatography (GC) coupled with thermal conductivity detectors (TCD), flame ionization detectors (FID), or mass spectrometers (MS). Several studies utilized Fourier transform infrared spectrometers (FTIR), ion chromatography (IC), or solid-state gas sensors for H_2 and O_2. Total moles of TRG released are commonly normalized by the capacity rating of the LIB under test.

Reported values of total moles of TRG released range from 22.2 to 55.5 mmol/Ah and show significant variability between studies, even between studies conducted by the same authors for the same cell type. Such variability is quite common among LIB TR experiments, including cell chemistries other than LFP (Baird et al., 2020). Gas composition measurements show similar variability between studies. While Table 1 includes major gas components detected across all studies, it is important to note that some studies were also able to detect additional species. Overall, even for the major components of H_2, CO_2, CO, CH_4, C_2H_4 and C_2H_6, significant variability is seen between studies, which may be due to differences in the tested batteries and their electrochemical, thermal, and mechanical properties, due to differences in experimental procedures, or related to the capabilities and uncertainties of the gas analysis methods used.

Table 1. TRG quantity and composition measurements from select literature

Ref.	Cell type	TR method	Gas analysis	TRG quantity (mmol/Ah)	H_2 (%)	CO_2 (%)	CO (%)	CH_4 (%)	C_2H_4 (%)	C_2H_6 (%)
Golubkov et al. (2014)	18650	Overheat	GC-TCD	45.5	30.9	53.0	4.8	4.1	6.8	0.3
Golubkov et al. (2015)	18650	Overheat	GC-TCD	28.2-55.5	2.7-34	48.3-93.5	1.8-9.1	0.7-6.4	0.7-7.2	0.7-1.0
Fernandes et al. (2018)	26650	Overcharge	GC-TCD; GC-MS; FTIR	29.3	9.0	18.0	1.9	0.6	3.9	0.2
Yuan et al. (2020)	26650	Overheat	GC	38.7	24.3	25.4	4.5	5.9	3.3	1.3
Wang et al. (2022)	Prismatic	Overheat	GC	22.2	36.2	25.2	7.4	6.4	15.2	2.4
Yang et al. (2022)	Prismatic	Overheat	GC	53.0	42.6	26.0	10	6.2	11.7	1.3

3. Methodology

3.1 Experimental setup

Figure 1 shows a schematic of the experimental setup developed in this work, including a 20-L spherical vessel that serves as a gas-tight containment for the LIB under test, and the heater control and data acquisition systems. The LIB was mounted at the center of the test vessel inside a cylindrical heater assembly, consisting of a coiled 24 AWG nichrome 80 wire use as the heating element sandwiched between two layers of Cotronics ceramic paper and a wrapping of fiberglass tape. Power to the heater was supplied by a 24 V DC power supply and was varied using 25 Hz pulse-width modulation (PWM) controlled by a PID loop that used the LIB surface temperature as feedback. Heater voltage and current were measured to determine the instantaneous and time-averaged heating power.

The internal pressure of the test vessel was measured with piezoresistive pressure transducers (Omega PX409). Two type-K 30 AWG thermocouples (TCs) were spot-welded onto the LIB shell to measure surface temperature, where one TC provided feedback to the heater control. Two additional TCs were used to measure the internal gas temperature in the sphere. Prior to each experiment, two purge-vacuum cycles were performed with nitrogen, before a final evacuation of the 20-L sphere for the tests performed under vacuum conditions. While most experiments were conducted under vacuum to produce undiluted gas samples that can be used for further reactivity testing, a smaller number of tests were conducted in a nitrogen environment at ambient initial pressure.

In this study, LFP batteries with 18650 form-factor and manufactured by K2-Energy were examined. A C7400 C-series battery analyzer was used to determine the state-of-health (SOH) and set the state-of-charge (SOC) for each LFP LIB cell to 100% prior to each experiment.

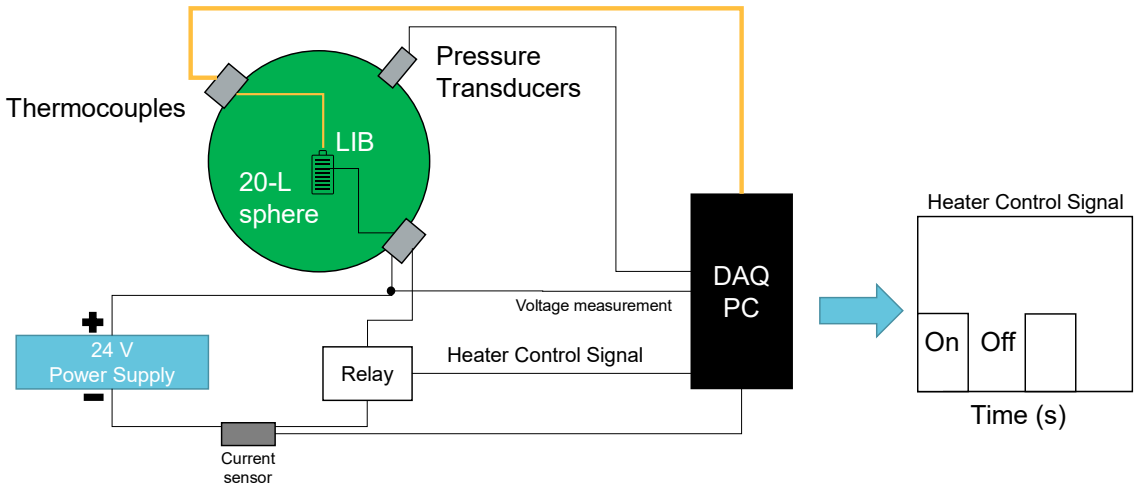

Fig. 1. *Schematic of experimental setup including data acquisition and heater control*

Figure 2 shows an example of measurements taken during a typical experiment. The top panel includes the heater power determined through measurements of current and voltage. The instantaneous power, in light blue, is not resolved in the figure since the power was modulated by the PID-PWM signal but provides an indication of when heating was being applied. A time-averaged power signal is shown in the envelope of the power signal and is representative of the heater's power

output. The red curve (right axis) of the top panel shows TC signals measuring the surface temperature of the LIB.

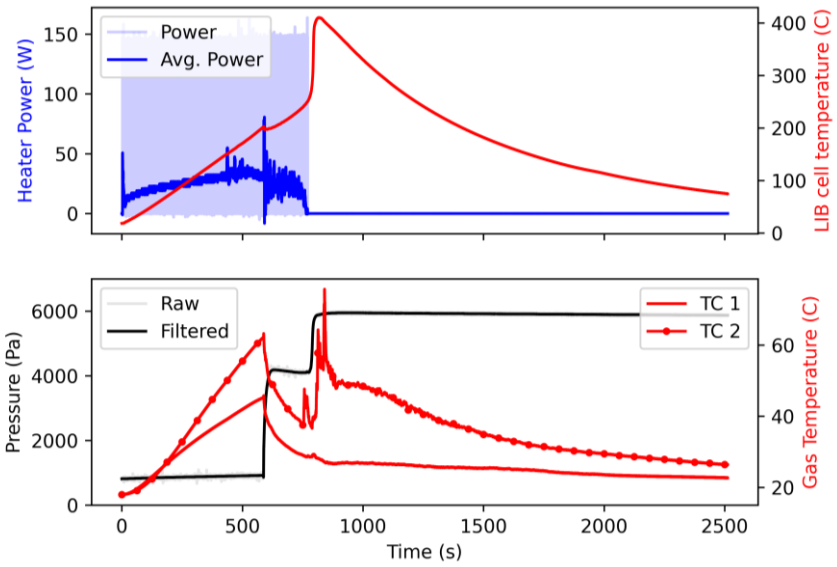

Fig. 2. *Representative measurements for an LIB TR experiment with a 20 °C/min heating rate under vacuum conditions*

The bottom panel of Figure 2 shows the measured internal pressure of the 20-L vessel and TC measurements of the gas volume. There are two regions distinguished by rapid pressure changes. The first rise at about 600 s occurs due to the rupture of the LIB's safety vent and is referred to as initial venting. The second pressure rise at about 800 s occurs during TR and corresponds to a rapid rise in temperature of the LIB.

TC 1 is located below the LIB, and TC 2 is located above the vented top of the 18650 LIB. Prior to the venting of the cell, the temperature rise of each TC is due to radiative heat transfer from the heater. After initial venting, convective heat transfer dissipates heat from the TC surfaces, but TC 2 remains significantly affected by the radiative heat transfer from the hot surface, particularly once TR occurs.

3.2 Vent gas composition analysis

Samples of TRG were collected and analyzed by an external laboratory using GC, FTIR, and CO_2 detector tubes. The GC was coupled with either TCD, FID, or a discharged ionization detector (DID), depending on the molecular target. The uncertainties of these measurements were 5.8%, 3.3%, and 3.1% for GC-DID, GC-FID, and FTIR, respectively. The analysis returned the mole fractions of hydrogen, oxygen, carbon monoxide, carbon dioxide, hydrocarbons, and oxygenated volatile organic compounds (OVOCs).

A gas sampling manifold and sampling cylinders were connected to the 20-L sphere. Before any TR experiment, the manifold and cylinders were purged with UHP N_2 and evacuated. During the TR experiment, the 20-L sphere remained isolated from the manifold. After completion of TR and an equilibration period, the sphere was pressurized with UHP N_2 to 200 kPa and the sampling cylinders were filled from the sphere. Gas composition measurements were corrected by accounting for the dilution by N_2 used to pressurize the 20-L sphere prior to sampling, using pressure and temperature measurements taken before and after pressurization with N_2.

4. Results

4.1 Characteristic temperatures and moles released

The results of 30 experiments performed in vacuum are summarized in Figure 3 (filled symbols), where characteristic LIB surface temperatures (a) and measured moles of gas released from the LIB (b) are plotted against heating rates varied from 10 to 80 °C/min. Table 2 summarizes the data shown in Figure 3. Figure 3(a) shows three characteristic temperatures. The temperature at venting, T_{vent}, defined as the temperature recorded when the pressure derivative is 25% of its peak during the initial venting event. The temperature at the onset of TR, T_{onset}, defined as the temperature where a line tangent to the temperature profile at the peak temperature derivative intersects with a projection of the imposed heating rate prior to TR. The maximum temperature, T_{max}, measured during the TR event. Each data point is the average of two simultaneous temperature measurements taken at the LIB surface, and the vertical error bars represent the maximum and minimum values of these measurements. The plotted heating rate (x-axis) is the average of linear fits to the temperature measurement versus time. Horizontal error bars represent the maximum and minimum heating rates (*i.e.*, the slope of the linear fit) up to venting inferred from the two surface-temperature TCs.

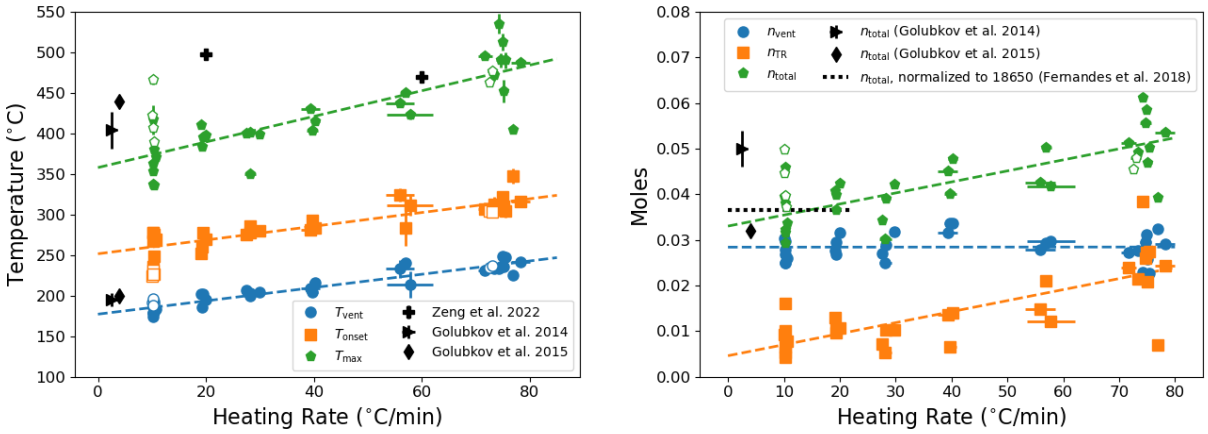

(a) (b)

Fig. 3. *The effects of heating rate on characteristic temperatures (a) and moles (b) released during different stages of TR*

The measured characteristic temperatures generally increased with heating rate. Linear regression was performed on each of the characteristic temperatures versus prescribed heating rate. If one considers a null hypothesis of slope equaling zero, the alternative hypothesis for a non-zero slope returns p-values $\leq 10^{-6}$ for each fit, indicating that the slope is non-zero with a high level of significance. Furthermore, the coefficients of determination, R^2, were 0.90, 0.74, and 0.65 for T_{vent}, T_{onset}, and T_{max}, respectively.

The open symbols near 10 and 80 °C/min represent six experiments performed in an inert nitrogen environment at 102 kPa initial pressure. There are subtle differences between the filled and open symbols, but the observed trends established with the vacuum data are preserved. While there is little change in T_{vent} between filled and open symbols across heating rates, on average, T_{onset} is 37 °C lower for the experiments in the nitrogen environment and T_{max} is 55 °C higher for the experiments in nitrogen at 10 °C/min. For the experiments at 80 °C/min, the differences between the vacuum and

nitrogen environments are within the standard deviations of the collected data. Additional experiments are needed at intermediate heating rates in the nitrogen environment to fully establish a comparison between vacuum and nitrogen environments.

Table 2. *Average results of experiments performed at various heating rates and initial environments. ± ranges represent the standard deviations*

Heating Rate (°C/min)	**Exp. No.**	T_{vent} (°C)	T_{onset} (°C)	T_{max} (°C)	n_{vent} (mmol)	n_{TR} (mmol)	n_{total} (mmol)
				Vacuum			
10.3±0.2	7	181.9±6.1	264.6±16.0	365.3±28.1	27.2±2.1	8.5±3.9	35.7±5.7
19.3±0.3	4	196.5±8.0	265.0±11.0	396.8±10.8	28.9±2.1	10.9±1.4	39.9±2.4
27.9±1.2	4	203.1±2.9	279.8±4.7	387.2±25.2	28.2±2.9	8.3±2.5	36.5±5.3
38.5±0.9	3	210.2±5.9	285.7±6.6	416.3±13.7	32.9±1.2	11.4±4.3	44.3±3.8
54.2±1.5	3	228.9±13.8	306.4±21.1	436.6±13.3	28.9±1.0	15.9±4.5	44.8±4.7
74.8±1.3	9	237.2±7.7	315.3±13.2	482.2±37.2	27.6±3.4	24.1±8.2	51.7±6.6
				Inert N_2			
10.2±0.1	4	191.2±3.6	227.0±3.3	420.9±33.2	--	--	42.9±5.6
73.1±1.1	2	235.8±2.2	303.5±1.0	470.2±9.8	--	--	46.7±1.8

Literature values for characteristic TR temperatures measured at the sidewalls of LFP cells are also shown in Figure 3(a). T_{max} and T_{vent} reported by Golubkov et al. (2014; 2015) for LFP LIBs with 100% SOC were measured in an apparatus similar to the present work but in an inert atmospheric environment. Despite similar procedures and heating rates, their two studies report T_{max} values that differ by 36 °C, highlighting the inherent variability in LIB TR studies. However, the T_{vent} values show reasonable agreement with trends observed in this work. Zeng et al. (2022) reported T_{max} values for heating inputs of 20.4 and 34.1 W which correspond to about 20 and 60 °C/min heating rates at the LIB surface, respectively. The result at 20 °C/min exceeds the results of this study while the value near 60 °C/min is closer to the trendline. Zeng et al. applied heat to 18650 LIBs with a Fire Propagation Apparatus (FPA) that uses infrared heaters for the entire duration of the experiment, and an inert atmosphere is maintained by a nitrogen co-flow during the experiment. The methodology differs from that of the present study, which could account for the differences in observed T_{max}.

Figure 3(b) shows the moles released during the initial venting (n_{vent}), during TR (n_{TR}), and the sum of the two (n_{total}). In all experiments except for one near 80 °C/min, $n_{vent} > n_{TR}$. At higher heating rates, the distinction between venting and TR is less pronounced. As a result, the initial venting process may not be complete before gas generation due to TR begins. Linear regression was performed on n_{vent}, n_{TR}, and n_{total} versus the prescribed heating rate. Like the characteristic temperature regression, the null hypothesis is a zero slope, and the alternative hypothesis is a non-zero slope. For the n_{vent} regression, the p-value and R^2 value are 0.984 and 0.000, respectively, *i.e.*, n_{vent} is independent of heating rate. There is a stronger correlation between the heating rate and n_{TR} (p-value = 0.0002, R^2 = 0.548), so these results indicate that the increase in n_{total} is primarily dependent on the heating rate through the correlation with n_{TR}. Open symbols near 10 °C/min represent n_{total} for experiments performed in a nitrogen environment at 102 kPa. The average value for n_{total} in nitrogen experiments differs from n_{total} measured in the vacuum environment by about

7 mmol at 10 °C/min and 5 mmol at 80 °C/min. Additional measurements are needed to ascertain this trend across the entire range of heating rates.

Literature values in Figure 3(b) represent total gas moles released from LFP cells, n_{total}. Values from Golubkov et al. (2014; 2015) show reasonable agreement with the present measurements; between their studies, however, results differ significantly but no reason for the difference is given. The dotted line represents the value reported by Fernandes et al. (2018) for a 26650 form-factor LFP cell. The value shown is normalized by the 18650 form-factor mass as an approximation. In their study, TR was induced through overcharge, and the values of observed heating rates during the process ranged from 0 to 22 °C/min. Regardless of the differences in methodology, the present measurements of total moles released, and the value reported by Fernandes et al., are in good agreement.

4.2 Gas composition analysis

TRG samples from a preliminary set of eight experiments at nominal heating rates of 10 and 80 °C/min and initial pressures of 700 Pa and 104 kPa were collected and analyzed, resulting in four distinct cases. Cases 1 and 2 are for initial pressure of 700 Pa with nominal heating rates of 80 and 10 °C/min, respectively. Cases 3 and 4 are for initial pressure of 104 kPa with nominal heating rates of 80 and 10 °C/min, respectively. Table 3 presents the average composition results (in mole fraction) of the four cases. Case 1 consists of three experiments, Case 2 and Case 3 consist of two experiments each, and Case 4 consists of one preliminary experiment. The composition results show similar mole fraction distributions of the measured gas species across each case. Notable differences are the increased OVOC produced in Case 2 experiments and the increased H_2 produced in Cases 3 and 4.

Table 3. *Summary of measured composition (in mole fraction)*

	Case 1	Case 2	Case 3	Case 4
Nominal Heating Rate (°C/min)	80	10	80	10
Initial Pressure (kPa)	0.7	0.7	104	104
Number of samples	3	2	2	1
Oxygen	0.010	0.0010	0.011	0.008
Carbon Monoxide	0.022	0.013	0.022	0.029
Carbon Dioxide	0.106	0.058	0.081	0.117
Hydrogen	0.311	0.274	0.389	0.388
Volatile Hydrocarbon Content (VHC)	0.164	0.136	0.150	0.174
Oxygenated Volatile Organic Compounds (OVOC)	0.213	0.264	0.211	0.239

Figure 4 shows the mole fractions of the detected components for each of these experiments. For a given case, the composition breakdowns show similar distributions across repeated experiments. Also included in Figure 4 are the breakdowns of OVOC and VHC groups. Certain larger hydrocarbon species such as Toluene and Benzene were detected and grouped in the OVOC category by the external lab and have been kept in those categories for convenience. Over 80% of the OVOC detected is assigned to the unknown OVOC category. This means that the gas analysis methods used by the external lab could not identify the vast majority of OVOC present in the sample. In Cases 1, 3, and 4, speciated hydrocarbons with 5 or fewer carbon atoms account for about 50% of the measured VHC, and C_{6+} hydrocarbons account for the rest of the detected VHCs. In Case 2 experiments, about 80% of the detected VHCs are in the C_{6+} category.

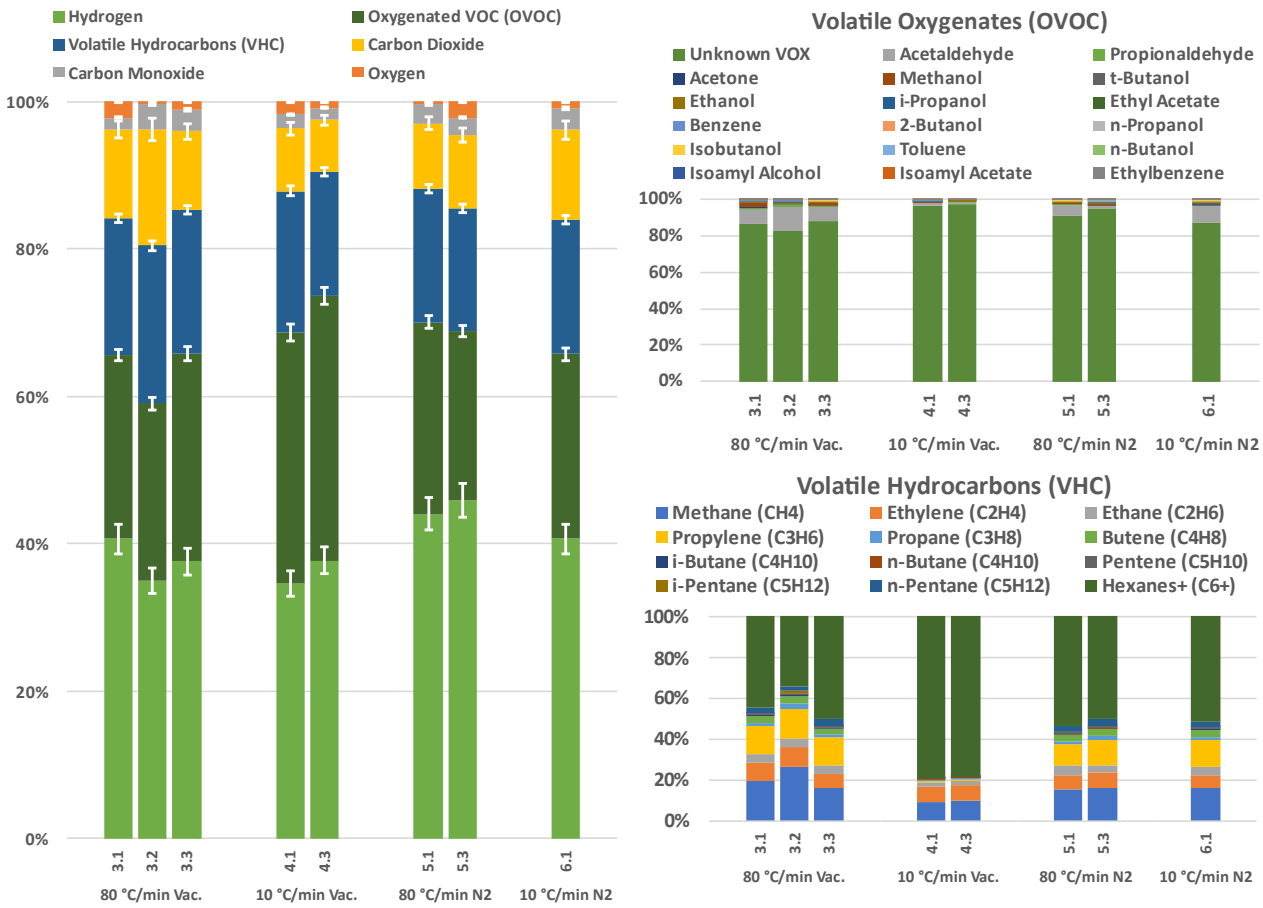

Fig. 4. *Summary of TRG composition analysis*

LIB electrolyte typically consists of a mixture of ethylene carbonate (EC, $C_3H_4O_3$), ethyl methyl carbonate (EMC, $C_4H_8O_3$), dimethyl carbonate (DMC, $C_3H_6O_3$), and/or propylene carbonate (PC, $C_4H_6O_3$) (Golubkov et al., 2015; Fernandes et al., 2018; Sturk et al., 2019). The composition breakdown of VHC and OVOC in Figure 4 shows the presence of C_5 and C_6+ molecules. The source of these larger volatile molecules is unclear, but the solid electrolyte interface (SEI) formed at the graphite anode of the LIB is suspected to include an organic polymer with the formula $C_6H_4O_6$ (Golubkov et al., 2015).

Figure 5 shows the number of moles assigned to each species based on the composition analysis and the measurements of moles released, providing an absolute perspective of the quantities of different gases released. The top (yellow) portion of the bar chart shows the unassigned moles (the discrepancy between cumulative moles of all species detected in gas analysis and the gas quantity measurement using pressure/temperature measurements at the 20-L sphere) that could represent errors in composition measurement or species not identified by the gas composition analysis.

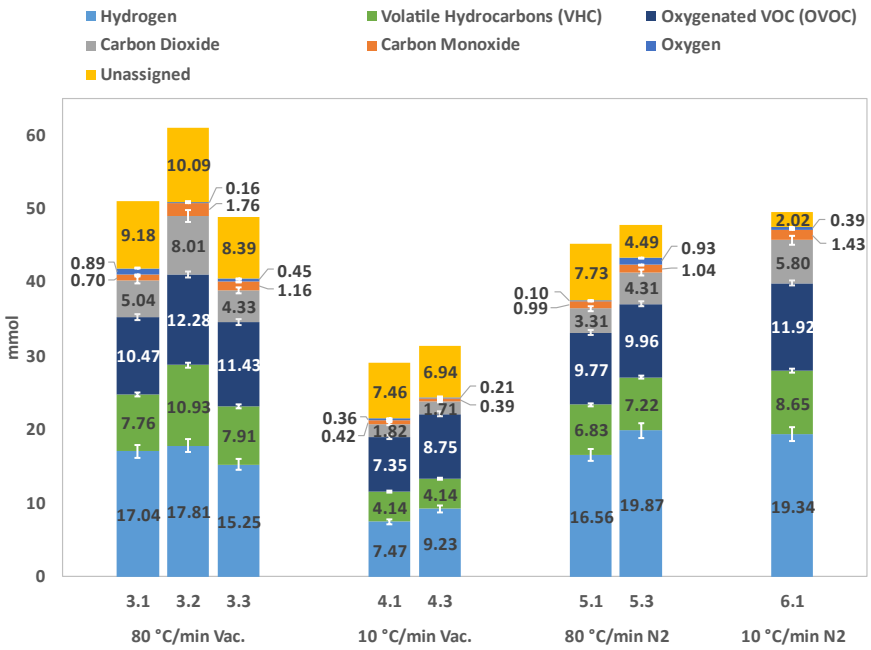

Fig. 5. *Molar distribution based on gas composition analysis*

5. Conclusions

In this study, thermal runaway (TR) experiments were conducted on 18650 form-factor lithium-ion batteries (LIBs) with lithium iron phosphate ($LiFePO_4$ or LFP) cathodes and carbon anodes, to support the development of risk assessment methods and loss prevention/mitigation recommendations for LIB fires and explosions. LIBs were forced into TR by external heating, and the effects of the heating rate was examined on the quantity and composition of the released thermal runaway gases (TRGs), both in vacuum and inert environments.

This study found that the heating rate influences the amount of TRG released and the characteristic temperatures of the LIB when TR occurs under vacuum conditions. Most notably, the amount of TRG increased linearly with heating rate in the investigated range from 10 to 80 °C/min. A limited number of additional experiments were conducted in nitrogen environments at initial atmospheric pressure, which indicated a comparable trend of increasing TRG quantity over heating rate.

A limited number of experiments with TRG composition analysis confirmed the presence of small gas species previously reported in the literature, such as H_2, CO_2, CO, and CH_4. While some larger molecular species were also identified and quantified, a significant quantity of unknown species were detected and could only be classified as oxygenated volatile organic compounds (OVOCs). This was consistent with FTIR analysis from the literature, which suggests that OVOCs may originate from the LIB electrolyte. Normalized gas compositions reveal similar distributions of gas species across all investigated heating rates. Additional experiments are needed to confirm this observation, using expanded gas analysis capabilities that allow for quantifying the currently unknown OVOCs.

Overall, the present results show that the amount of gas released from LFP LIBs during initial venting and TR increases with heating rate, whereas preliminary gas analysis suggests that the relative composition of the released gas may be insensitive to heating rate. From a loss prevention perspective, the present results are significant, suggesting that realistic heating rates would need to be applied in TR experiments with single LIB cells to obtain realistic values of the released gas quantity. Such heating rates would need to replicate the conditions expected during cell-to-cell TR propagation

within LIB modules and systems. Experiments performed at unrealistically low heating rates may result in an under-prediction of potential gas release, and therefore in under-conservative risk evaluations and under-designed mitigation systems including ventilation and fire/explosion protection.

Future work is planned to examine different LIB cell chemistries and form factors in order to quantify their amounts and composition of vent gases for fire and explosion risk assessment. These experiments will utilize new in-house gas analysis methods that allow for quantifying the gas composition more comprehensively, and apply realistic heating conditions that occur during TR in LIB modules and systems.

References

Baird, A.R., Archibald, E.J., Marr, K.C., Ezekoye, O.A., 2020. Explosion hazards from lithium-ion battery vent gas. Journal of Power Sources, 446, 227257

Fernandes, Y., Bry, A., de Persis, S., 2018. Identification and quantification of gases emitted during abuse tests by overcharge of a commercial Li-ion battery. Journal of Power Sources, 389, 106-119.

Golubkov, A.W., Fuchs, D., Wagner, J., Wiltsche, H., Stangl, C., Fauler, G., Voitic, G., Thaler, A., Hacker, V., 2014. Thermal-runaway experiments on consumer Li-ion batteries with metal-oxide and olivin-type cathodes. Rsc Adv, 4, 3633-3642.

Golubkov, A.W., Scheikl, S., Planteu, R., Voitic, G., Wiltsche, H., Stangl, C., Fauler, G., Thaler, A., Hacker, V., 2015. Thermal runaway of commercial 18650 Li-ion batteries with LFP and NCA cathodes – impact of state of charge and overcharge. Rsc Adv, 5, 57171-57186.

Said, A.O., Lee, C., Stoliarov, S.I., 2020. Experimental investigation of cascading failure in 18650 lithium ion cell arrays: Impact of cathode chemistry. Journal of Power Sources, 446, 227347.

Sturk, D., Rosell, L., Blomqvist, P., Ahlberg Tidblad, A., 2019. Analysis of Li-ion battery gases vented in an inert atmosphere thermal test chamber. Batteries, 5, 61.

Wang, Q., Ping, P., Zhao, X., Chu, G., Sun, J., Chen, C., 2012. Thermal runaway caused fire and explosion of lithium ion battery. Journal of Power Sources, 208, 210-224.

Wang, H., Xu, H., Zhang, Z., Wang, Q., Jin, C., Wu, C., Xu, C., Hao, J., Sun, L., Du, Z., Li, Y., Sun, J., Feng, X., 2022. Fire and explosion characteristics of vent gas from lithium-ion batteries after thermal runaway: A comparative study. eTransportation, 13, 100190.

Yuan, L., Dubaniewicz, T., Zlochower, I., Thomas, R., Rayyan, N., 2020. Experimental study on thermal runaway and vented gases of lithium-ion cells. Process Safety and Environmental Protection, 144, 186-192.

Yang, X., Wang, H., Li, M., Li, Y., Li, C., Zhang, Y., Chen, S., Shen, H., Qian, F., Feng, X., Ouyang, M., 2022. Experimental Study on Thermal Runaway Behavior of Lithium-Ion Battery and Analysis of Combustible Limit of Gas Production. Batteries, 8, 250.

Zeng, D., Gagnon, L., Wang, Y., 2022. Cell-level hazard evaluation of 18650 form-factor Lithium-ion battery with different cathode materials. Proceedings of the Combustion Institute, 39, 3822-3831.

Thermal Runaway of Lithium-Ion Batteries in Flameproof Enclosures: Effect of Internal Surface and Gas Mixture

Freyja Galina Daragan [a,b], Stefanie Spörhase [a], Amiriman Kianfar [a], Bernd Limbacher [c], Alexander Hahn [b], Stefan Essmann [a]

[a] Physikalisch-Technische Bundesanstalt, Braunschweig, Germany
[b] Institute for Particle Technology, Technische Universität Braunschweig, Braunschweig, Germany
[c] R.STAHL AG, Waldenburg, Germany

E-mail: stefan.essmann@ptb.de

Despite their excellent properties as electrochemical energy storage devices, lithium-ion-batteries (LIBs) are potentially hazardous due to the possibility of thermal runaway (TR). TR can be particularly dangerous in explosive atmospheres such as those found in mines. To mitigate the consequences, flameproof enclosures according to IEC 60079-1 can be used to house the LIBs. In order to quantify the material stress, TR experiments were performed by overheating a LIB (18650 format, NMC-811) in a flameproof enclosure, recording the explosion pressure and temperature. The parameters of internal surface and gas mixture (propane, hydrogen) were modified. By varying the volume of the enclosure, a direct proportionality between volume and explosion pressure was observed. This was due to the increase in internal surface area accompanied by a reduction in volume, resulting in improved heat transfer. In particular, the increase in surface area resulting from the use of expanded metal grids as internal pressure relief confirmed the surface dependance with a pressure reduction of 49 %. Furthermore, a linear relationship was established between the system energy, consisting of the energy released by the cell and the chemical energy of the gas atmosphere, and the pressure energy after TR.

Keywords: *thermal runaway of lithium-ion batteries, flameproof enclosures, explosion pressure relief, gas explosion, internal surface area, heat transfer*

Introduction

Lithium-ion batteries (LIB) are widely used as a flexible and efficient energy storage technology. Due to their high energy and power density and long lifespan, they can be used in a wide range of applications (Rahimi, 2021). In general, LIBs are a safe way of storing energy, which is reflected in the estimated failure probability of $<1:10^6$ (Larsson, 2017). Due to the many areas of application, the quantity of LIBs worldwide is growing at a high rate. As a result, the number of incidents associated with thermal runaway (TR) is also rising. Between 2016 and 2022, for example, the incidents in Vancouver increased fivefold (Little, Karamali, 2022). The TR describes the exothermic reactions between different components of the LIB, resulting in mechanical, thermal and chemical loads for the periphery (Essl et al., 2020). This poses a particularly high risk if the gas atmosphere surrounding the LIB contains a flammable or explosive mixture. A TR in such an environment, for instance a mine, can lead to the ignition of the entire surrounding combustible atmosphere due to the energy released and thus to a massive increase in the damage caused (Dubaniewicz, DuCarme, 2013; 2014). In hazardous areas, the standard IEC 60079-0 therefore provides further measures in the form of several types of ignition protection, including the "flameproof enclosure" (International Electrotechnical Commision, 2014). This type of protection involves an enclosure surrounding the LIB, which serves to protect the environment from the consequences of the TR. Flameproof enclosures are characterized, amongst other parameters, by thick walls, enabling them to withstand high material loads (Spörhase et al., 2022). The material stress caused by the TR is directly dependent

on the free gas volume of the encapsulation. Small volumes in particular lead to high pressures (Dubaniewicz et al., 2022). It is unclear whether the material stress can be reduced by simply increasing the volume, or whether there are other factors whose lack of consideration could result in a critical material stress. The case of the simultaneous occurrence of a gas explosion of a surrounding fuel-air mixture and the TR is also of interest, as the coincidence of both phenomena happening must be considered in potentially hazardous areas. In this work, the enclosure volume, the inner surface and the composition of the gas atmosphere are therefore varied. The effects on the resulting material stress are analyzed using mechanical and energetic variables.

1. Experiments

All tests were carried out in the "CUBEx" flameproof enclosure (type: 8264, Company: R.STAHL AG, 480x340x360 mm) according to the test arrangement shown in Fig. 1. The measured variables temperature (red), static pressure (blue) and material strain on the outer wall of the enclosure (green) were recorded.

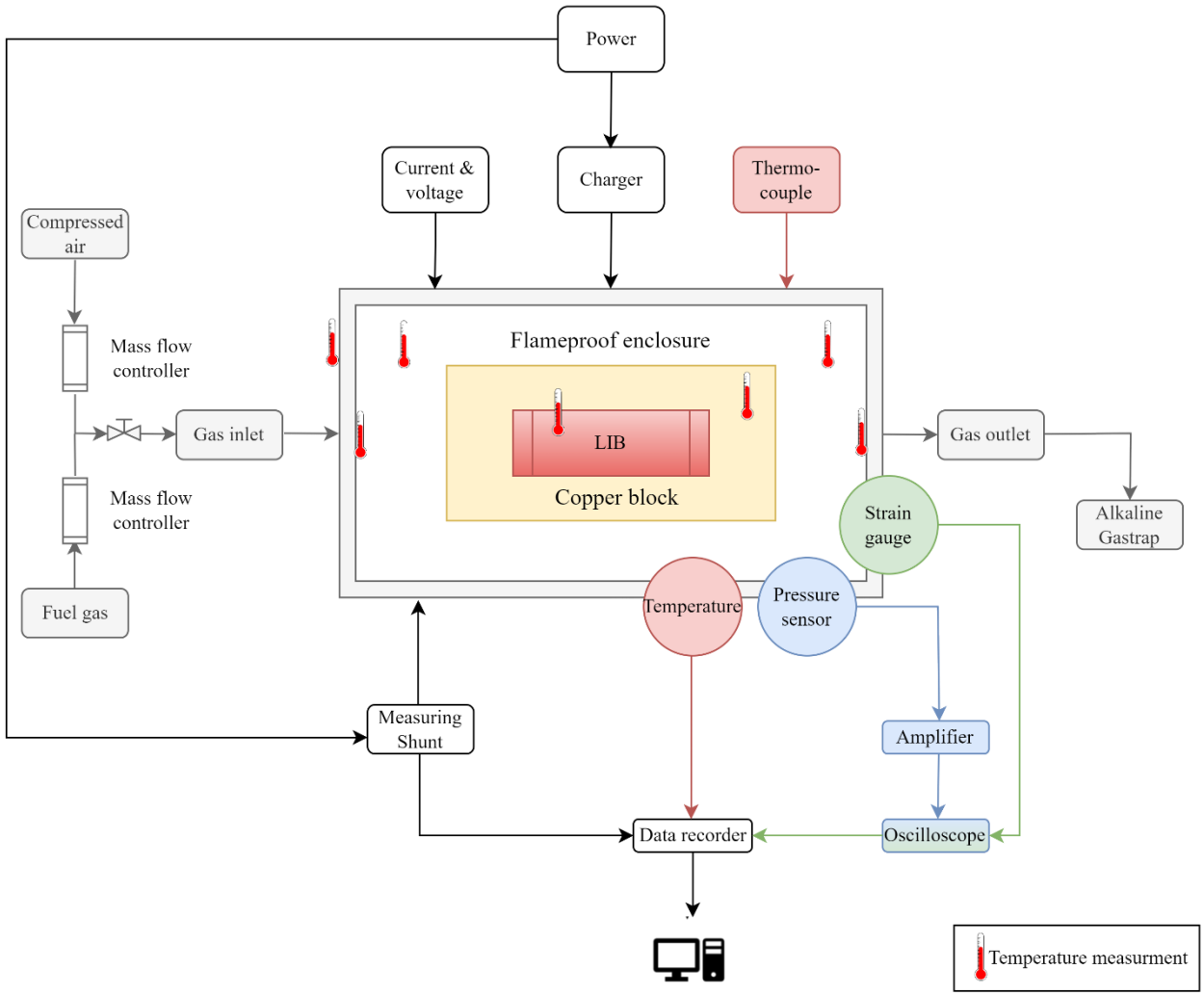

Fig. 1. Schematic representation of the experimental setup

An oscilloscope (type: DL850, company: Yokogawa) and a data acquisition system (type: 34970A Data Acquisition/Switch Unit Family including 20-channel multiplexer 34901A, company: Keysight Technologies/Agilent) were used to acquire the measurement data. The material strain was used to verify the measured maximum pressure, which is why the measured strain is listed in Table 4 but will not be discussed in detail. The temperature measuring points are labelled with thermometers. In addition, an explosive atmosphere was created by adding different fuel gases using

mass flow controllers and purging with the gas mixture until the gas volume in the housing was exchanged five times. Due to the deposition of particles from the TR events on the enclosure walls, it was not possible to check the composition of the mixture. Overheating at a constant temperature rate was selected as the misuse mechanism in all tests. As can be seen in Fig. 1, the cell was placed on a copper block which featured a heating element on the inside (type: MFH14 or a high-temperature ceramic heating element, company: Paul Rauschert Steinbach GmbH).

1.1. Assessment of the material stress

The material strain recorded using a strain gauge was utilized to assess the material stress. The material load and strain are proportional to each other in case of static load and dynamic load due to a gas explosion (Spörhase et al., 2022). Two methods are used to further understand why the measured maximum strains ε_{max} occur. According to the standard IEC 60079-1, the maximum pressure p_{max} and the pressure rise time (PRT, defined between 10 % – 90 % of p_{max}) represent comparative parameters (International Electrotechnical Commision, 2014). Furthermore, an energetic analysis of the measurement data was carried out.

The flameproof enclosure is not isolated from the periphery. Hence a continuous exchange of energy and power occurs. Furthermore, mass can be transferred into the periphery through leaks. To understand this in more detail, a simplified energy balance is used (see Fig. 2). Energy inputs are shown in green and power losses in red. The gas volume inside the flameproof enclosure serves as the control volume. The mixture of energies and powers is chosen to express the fact that the total energy built up in the system is suddenly reduced due to different power losses. The instantaneity is emphasized by the time-dependent representation of the energy loss.

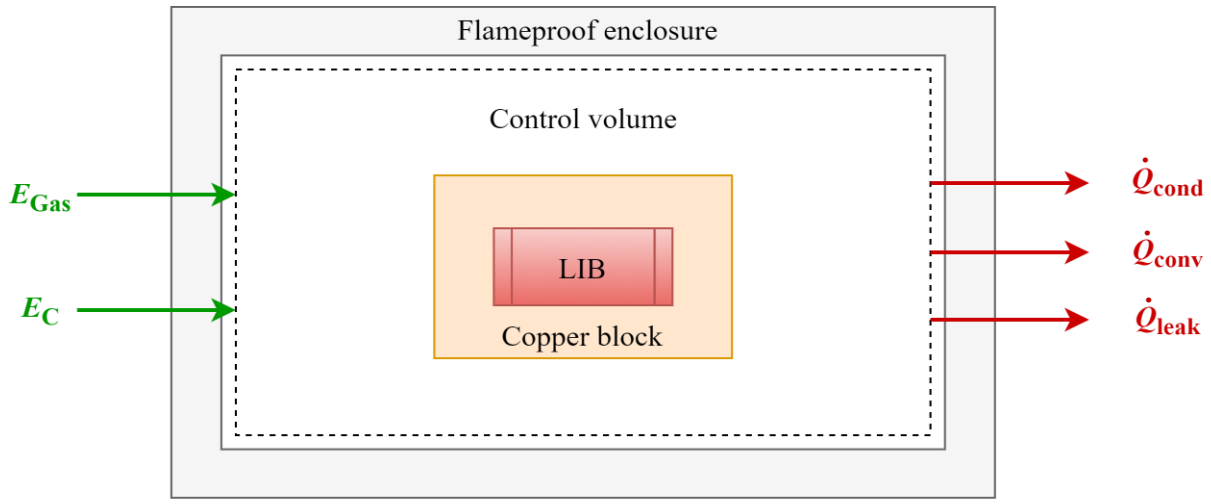

Fig. 2. Schematic representation of the control volume (dashed line)

The progressive heating due to various exothermic reactions during the TR releases energy through the cell (E_C). E_C is defined according to equation (1), where m_C and c_C denote the mass and specific heat capacity of the cell, T_{max} the maximum temperature on the cell surface and T_{TR} the temperature at the beginning of the TR (Jiang et al., 2021).

$$E_C = m_C \cdot c_C \cdot (T_{max} - T_{TR}) \qquad (1)$$

If an explosive atmosphere is provided in the housing, the combustion of the gas introduces additional energy into the system (E_{Gas}). This intake can be calculated using equation (2), where m_{Gas} is the mass of the fuel in the gas volume, ΔH_{Gas} is its lower heating value and η_{Gas} is the associated empirical explosion efficiency. For the latter, a value of 8.5 % is assumed as the mean value from the literature data 2 - 15 % (Chi et al., 2021). As the literature values regarding the empirical explosion efficiency

differ greatly from each other, this value is only an estimate and is not considered in the measurement uncertainty of the chemical energy of the fuel gases.

$$E_{\mathrm{Gas}} = m_{\mathrm{Gas}} \cdot \Delta H_{\mathrm{Gas}} \cdot \eta_{\mathrm{Gas}} \qquad (2)$$

Due to the lack of thermal insulation, energy can be released to the environment through thermal conduction ($\dot{Q}_{\mathrm{cond}}$), convection ($\dot{Q}_{\mathrm{conv}}$) and radiation ($\dot{Q}_{\mathrm{rad}}$). Equation (3) is used to calculate the conductive heat transfer, which takes into account the thermal conductivity of the material λ, the surface under consideration A, its thickness d_{A} and the temperatures of the inner and outer walls of the housing T_{i} and T_{o} (Incropera et al., 2007). The following thermal conductivities apply to the materials stainless steel and aluminum: λ_{S} = 15 W·m·K^{-1} and λ_{A} = 140 W·m·K^{-1} (Xometry Europe GmbH, 2021).

$$\dot{Q}_{\mathrm{cond}} = \lambda \cdot A/d_{\mathrm{A}} \cdot (T_{\mathrm{i}} - T_{\mathrm{o}}) \qquad (3)$$

The calculation of the convective heat transfer furthermore requires the temperature of the free gas volume T_{∞} and the heat transfer coefficient α (Incropera et al., 2007). The heat transfer coefficient is estimated at a value of 5 W·m^{-2}·K^{-1}, which corresponds to the value range for free convection (García et al., 2022).

$$\dot{Q}_{\mathrm{conv}} = \alpha \cdot A \cdot (T_{\infty} - T_{\mathrm{i}}) \qquad (4)$$

Heat transfer by radiation is neglected, as the contribution is small compared to that of conduction and convection (Incropera et al., 2007). The inherent property of flameproof enclosures of lacking gas tightness can also lead to a loss of mass to the environment. The leakage rate $\dot{Q}_{\mathrm{leak}}$ according to equation (5) depends on the enclosure volume V and the pressure difference Δp over a time interval Δt (DIN Deutsches Institut für Normung e. V., 2018).

$$\dot{Q}_{\mathrm{leak}} = V \cdot \Delta p/\Delta t \qquad (5)$$

For a summarized view of the most important influencing parameters in the energy balance, the system energy E_{S} and power loss P_{L} are defined according to equations (6) and (7). P_{L} incorporates material-specific parameters as well as various temperatures and the pressure inside of the enclosure. It should be noted that all loss mechanisms contained in P_{L} occur simultaneously.

$$E_{\mathrm{S}} = E_{\mathrm{C}} + E_{\mathrm{Gas}} \qquad (6)$$

$$P_{\mathrm{L}} = \dot{Q}_{\mathrm{cond}} + \dot{Q}_{\mathrm{conv}} + \dot{Q}_{\mathrm{leak}} \qquad (7)$$

In order to further create the possibility of relating E_{S} to the energy resulting from pressure, the relative pressure energy $E_{\mathrm{P,rel.}}$ is introduced according to equation (8). It can be determined using the pressure difference between the maximum explosion pressure p_{max}, the initial pressure at the start of the experiment p_0 and the enclosure volume V (Baehr, Kabelac, 2016).

$$E_{\mathrm{P,rel.}} = (p_{\mathrm{max}} - p_0) \cdot V \qquad (8)$$

1.2. Key data of the used LIB

The key data of the selected LIB are listed in Table 1. All cells are initially overcharged to a voltage of 4.62 V with a current of 3 A (1 C rate) before the start of the test. This procedure serves to intensify the TR due to the additional amount of charge (Essl et al., 2020). The subsequent voltage dip after the end of the overcharging process results in a state of charge (SoC) range of 90-105 % at the start of the test. The SoC was determined by using the coulomb counting method.

***Table 1**. Key data of the cell used (Jiang et al., 2021; LG Chem, 2015)*

Cell	**INR18650HG2**
Manufacturer	LG Chem
Format	18650
Cell chemistry	$LiNi_{0.8}Mn_{0.1}Co_{0.1}O_2$
Maximum weight / g	48
Nominal capacity / Ah	3.00
Cut off voltage / V	4.20
Specific heat capacity / $J \cdot kg^{-1} \cdot K^{-1}$	1020

1.3. Variation of the experimental setup

In the course of the experiments, two test parameters are changed: the free volume of the flameproof enclosure and the composition of the gas atmosphere it contains.

1.3.1. Variation of the free volume

Four test configurations are analyzed, which are designated SAV-xx-xx on the basis of their surface-to-volume-ratio (*SA*/*V*-ratio) and the free volume *V*. The corresponding free volumes, inner surfaces *A* and the *SA*/*V*-ratio are listed in Table 2. Various aluminum components and expanded metal grids (used for internal pressure relief) are placed inside the housing to vary the volume.

***Table 2.** Key data for the different enclosure configurations (R.STAHL, 2015)*

Description	***V* / l**	***A* / m²**	***SA*/*V*-Ratio / m^{-1}**
SAV-339-5	4.7 ± 1.7	1.60 ± 0.0088	339 ± 121
SAV-38-22	21.6 ± 1.0	0.83 ± 0.0005	38 ± 2
SAV-275-37[a]	37.3 ± 1.0	10.24 ± 0.0004	275 ± 7
SAV-18-38[b]	38.1 ± 1.0	0.68 ± 0.0004	18 ± 1

[a]including expanded metal grids

[b]This volume corresponds to the empty volume of the housing including all permanently installed test setups, such as the gas inlet and outlet.

1.3.2. Fuel-air mixtures

An ignitable atmosphere is generated in mixture compositions in accordance with the standard IEC 60079-1 in a ratio of (31.0 ± 1.0) vol.-% for hydrogen (H_2) and (4.6 ± 0.3) vol.-% for propane (C_3H_8) with air (International Electrotechnical Commision, 2014). The gases were selected on the basis of their properties with regard to the maximum explosion pressure, which is particularly high for C_3H_8 (see Table 3), and the pressure rise time (PRT), which is particularly short for H_2 (EC-Project SAFEKINEX, 2006). Table 3 provides an overview of the relevant parameters of both gases, listing the lower heating value ΔH_{Gas}, the maximum absolute explosion pressure p_{max} and the autoignition temperature (AIT). Only the test configuration SAV-18-38 (maximum volume) is used to analyze the influence of the gas atmosphere.

***Table 3.** Properties of the fuel gases (at p_0 = 1 bar, T_0 = 20 °C) (Database BAM-Project CHEMSAFE, 2016; Lendt, B., Cerbe, G., 2016)*

Fuel gas	**ΔH_{Gas} / kJ·kg^{-1}**	**p_{max} / bar**	**AIT / °C**
H_2	119972	8.3	560
C_3H_8	46354	9.4	459

2. Results and discussion

In the following sections, the results are discussed using the mean values from three tests in each case. For all measured variables except the PRT, only the maximum values over the TR are considered and the mean values are calculated from these. Table 4 provides an overview of all relevant mean values, whereby the tests labelled G-xx refer to the variation of the gas atmosphere (see section 1.3.2). In all tests, the pressure is proportional to the strain and therefore to the material stress. This observation is consistent with data on gas explosions (Spörhase et al., 2022). The energy input is used as a measure of the thermal load.

Table 4. Overview of all relevant test data

Description	p_{max} / bar	ε_{max} / µm·m^{-1}	PRT / ms	E_C / kJ	E_{Gas} / kJ	E_S / kJ	P_L / kW
SAV-339-5	4.1 ± 0.3	176 ± 20	22 ± 6	6 ± 2	/	6 ± 2	299 ± 178
SAV-38-22	4.7 ± 0.3	241 ± 18	81 ± 27	10 ± 1	/	10 ± 1	106 ± 22
SAV-18-38	5.3 ± 0.4	299 ± 32	113 ± 16	14 ± 5	/	14 ± 5	32 ± 2
SAV-275-37	3.0 ± 0.1	122 ± 10	117 ± 30	12 ± 1	/	12 ± 1	385 ± 42
G-air	5.8 ± 0.9	307 ± 48	121 ± 30	17 ± 3	/	17 ± 3	70 ± 5
G-H2	8.0 ± 0.1	406 ± 12	7 ± 1	16 ± 1	11 ± 0	27 ± 1	31 ± 3
G-C_3H_8	8.2 ± 0.0	423 ± 5	43 ± 6	14 ± 2	14 ± 0	28 ± 2	84 ± 19

2.1. Influence of the free volume and inner surface area

The gas development resulting from exothermic reactions inside of the cell during the TR leads to an increase in pressure, which is measured and used as a comparative value between the test configurations in the form of the maximum absolute pressure p_{max}. Fig. 3 shows the experimentally determined values and data according to Dubaniewicz et al. (2022) for p_{max} as a function of the free volume V (left) and the inner surface area A (right).

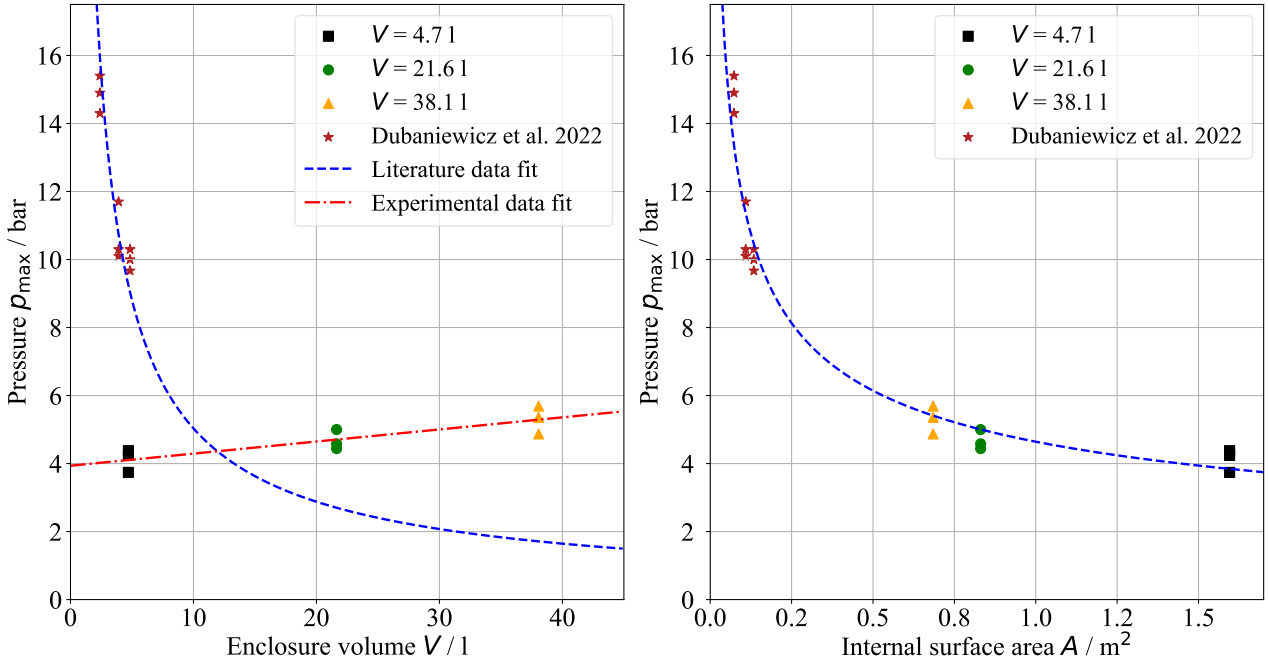

Fig. 3. Maximum pressure p_{max} as a function of enclosure volume V and inner surface A (Dubaniewicz et al., 2022; Dubaniewicz, 2023)

As can be seen from Fig. 3 (left, red), an increase in volume in the case of the data collected here results in an increase in p_{max}, while an increase in surface area leads to a reduction in pressure. An eightfold increase in volume accompanied by a reduction in surface area by a factor of approx. 2.4 from SAV-339-5 to SAV-18-38 leads to an increase in maximum pressure of 29 %. In contrast,

according to Dubaniewicz et al. (2022), both an increase in volume and in surface area resulted in a reduction of p_{max}. With regard to the influence of volume, there is consequently a contradiction between the current literature and the experimental data recorded here. The background to this contradiction is the inversely proportional behavior of volume and surface area in the present work, which is caused by the type of volume reduction resulting from the addition of aluminium components. The additional components in the housing lead to an increase in the internal surface area. In contrast, these variables behave proportionally to each other in the experiments by Dubaniewicz et al. (2022) (self-similarity). This results in varying behavior with regard to the energy exchange between the housing and the periphery. However, as the enclosure volume also has an influence on the material load and stress, the *SA*/*V*-ratio is considered as a comparative value in the following.

2.1.1. Energy balance of the TR

The energy of the system E_S increases due to the gas development during the TR of the cell. The larger the free volume V or the smaller the *SA*/*V*-ratio, the higher the E_S in the experimental setup used becomes (Fig. 4, left). This is a direct consequence of the amount of oxygen in the gas volume, which is decisive for the exothermic oxidation of the cell's electrolyte and thus the release of energy in the form of heat (Feng et al., 2018). An eightfold increase in the enclosure volume results in an increase in E_S by a factor of approx. two. The energy input and with it the thermal load on the material increases with the volume, provided the gas atmosphere in the housing contains additional oxygen and the amount of oxygen increases with the volume. The surface dependence of the maximum pressure is in turn a consequence of the heat transfer behavior. As equations (3) and (4) show, both heat conduction and convection are influenced by the surface area. The increase in the internal surface area leads to enhanced heat transfer and, as a result, a rise in power loss P_L (see Fig. 4, right).

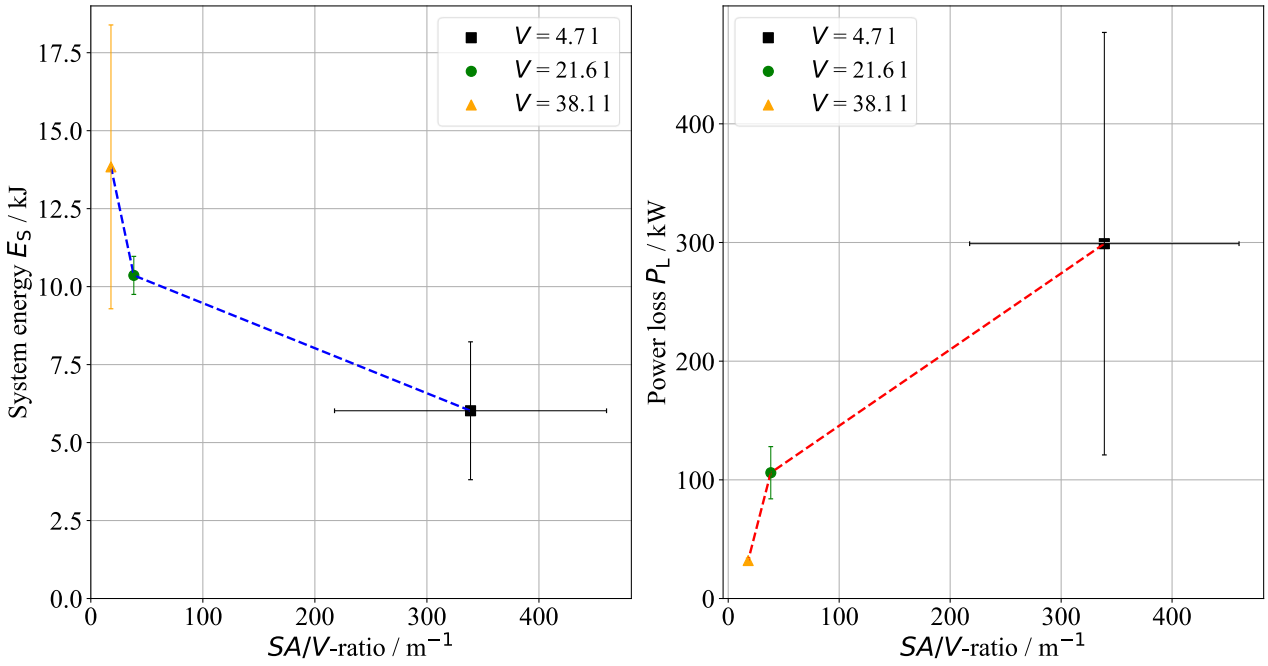

Fig. 4. System energy E_S and power loss P_L as a function of the SA/V-ratio

Increasing the surface area from 0.68 m^2 to 1.60 m^2 results in a growth in P_L by a factor of nine. The energy input is therefore inversely proportional to the power loss and the *SA*/*V*-ratio. The enclosure configuration with the smallest surface area and correspondingly smallest *SA*/*V*-ratio therefore has the highest E_S. There is a linear dependency between E_S and the maximum pressure p_{max} or the maximum strain ε_{max}. The smaller the *SA*/*V*-ratio, the greater the material stress that occurs. Accordingly, the material stress can be reduced by using expanded metal grids (SAV-275 37). These act as internal pressure relief. The grids can be used to increase the internal surface area by a factor of 15 to 10.2 m^2 compared to the SAV-18-38 configuration. Due to the increase in surface area, a rise

in P_L and consequently a reduction in system energy can be observed. This results in a halving of the maximum pressure. The internal pressure relief is therefore capable of reducing the thermal load and material stress caused by the TR of a LIB. The results thus show that the material stress cannot solely be estimated on the basis of the free volume as the inner surface has a more significant influence. The statements made by Dubaniewicz et al. (2022) cannot be generalized, but are valid for the case of self-similar enclosures (proportionality between free volume and inner surface).

2.1.2. Severity of TR

As can be seen from the PRT values in Table 4, an increase in the free volume *V* from SAV-339-5 to SAV-18-38 results in a fivefold increase in PRT. This corresponds to a reduction in the severity of the TR (International Electrotechnical Commision, 2014), which is in contrast to the conclusions drawn from section 2.1.1. However, since the measured pressure values could be verified using the strain measurement values, the assessment of the strength of the TR of a LIB and the resulting material stress based on the maximum pressure is the more meaningful way. In conclusion the material stress increases with increasing volume or decreasing inner surface area (decreasing *SA*/*V*-ratio) in the case of an inverse proportionality between volume and surface area.

2.2. Influence of explosive gases

In all the tests that included a fuel gas/air atmosphere in addition to the TR of the LIB, the latter was ignited by the TR. Since the AIT (see Table 3) are only reached in the case of G-C_3H_8, ignition probably occurs via sparks and the ejection of hot particles by the LIB and not due to the surface temperature of the cell or the copper heating block. An increase in pressure due to the fuel gas was observed for all fuel gas/air mixtures analyzed. This is discussed below.

2.2.1. Superposition of gas explosion and TR

The addition of a fuel-air atmosphere results in an additional energy input E_{Gas} (see Fig. 5, left). C_3H_8 contributes more energy to the system than H_2, which is why G-C_3H_8 has the highest system energy E_S. Due to the linear relationship between E_S and p_{max}, the highest pressure follows for G-C_3H_8 (see Fig. 5, right).

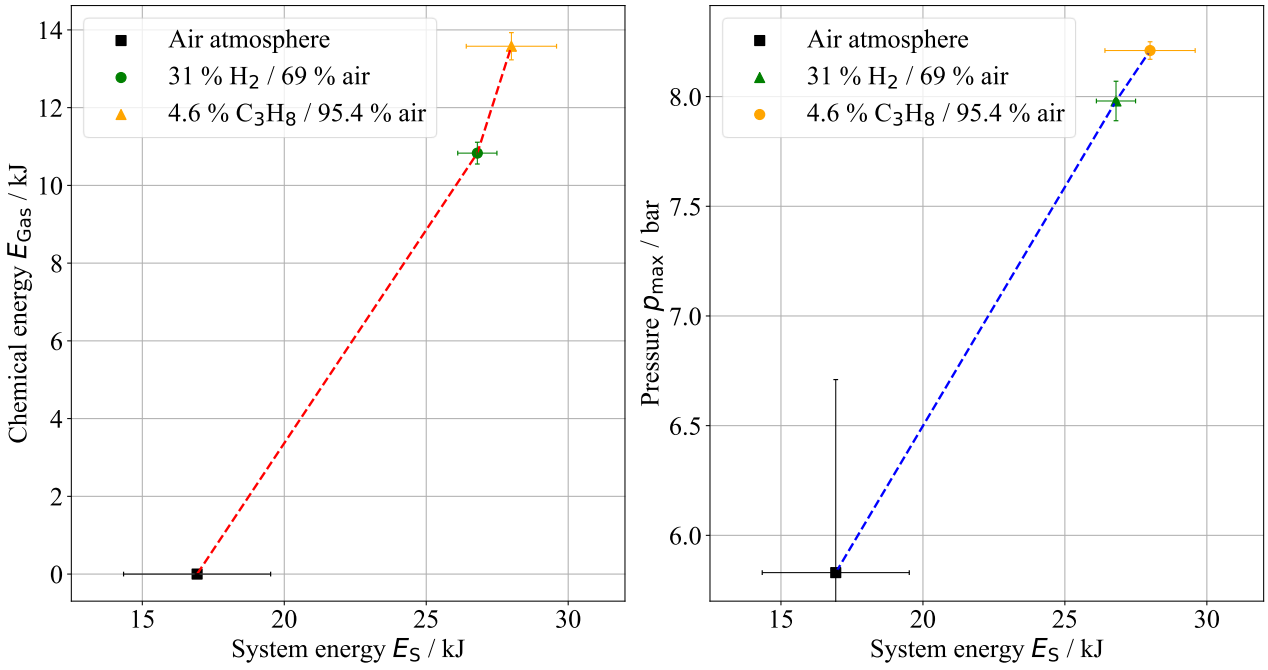

Fig. 5. Energy input by the fuel gas E_{Gas} and the pressure p_{max} as a function of the system energy E_S

Regardless of the gas used, the superposition of TR and gas explosion leads to a higher pressure than a pure air atmosphere (G-air) and thus to increased material stress. This is consistent with data according to Dubaniewicz and DuCarme (2013; 2014) on methane-air explosions and simultaneous TR, in which the additional gas explosion also led to an increase in pressure. The thermal load due to the energy released by the cell E_C assumes the highest values for G-air, as the amount of oxygen present is greatest there compared to G-H_2 and G-C_3H_8. The speed of the TR is determined by the properties of the fuel gas, as can be seen from the PRT (see Table 4). G-H_2 produces the fastest pressure rise, whereas G-air has the highest PRT. According to the standard IEC 60079-1, the highest material stress results for G-H_2. However, the material strain also shows that the material stress should be assessed on the basis of p_{max} and therefore G-C_3H_8 has the highest stress.

2.2.2. Influence of the LIB on the material stress in case of combined phenomena

The influence of the TR of a LIB with a capacity of 3 Ah on the maximum pressure is low. This can be shown by means of tests of gas explosions without TR (V-C_3H_8 and V-H_2). The additional TR results in an approx. 11 % higher pressure in the case of H_2 and a 5 % higher pressure in the case of C_3H_8 than was achieved in the tests where only a gas explosion was present. The material stress for small cell capacities is therefore determined by the gas explosion. Within the scope of the measurement uncertainty, the additional TR in an H_2-air-atmosphere does not lead to any change in the PRT. However, a decrease of the PRT due to the TR can be observed between G-C_3H_8 and V-C_3H_8. The superposition of both phenomena thus leads to a faster pressure rise. The properties of the respective fuel gas also come into play here. H_2 is generally characterized by a faster pressure rise than C_3H_8 (see section 1.3.2). However, both fuel gases represent the faster process compared to the TR of a LIB. Depending on how much time the gas explosion itself takes, the influence of the TR on the duration of the combined behavior of the gas explosion and the TR changes.

2.3. Overview of all experiments

Using the relative pressure energy $E_{P,rel.}$ (see equation (8) resp. $\Delta p \cdot V$) and the system energy E_S (see equation (6)), a final comparison of all experiments can be made between the energy input and the resulting energy due to the pressure, as shown in blue in Fig. 6.

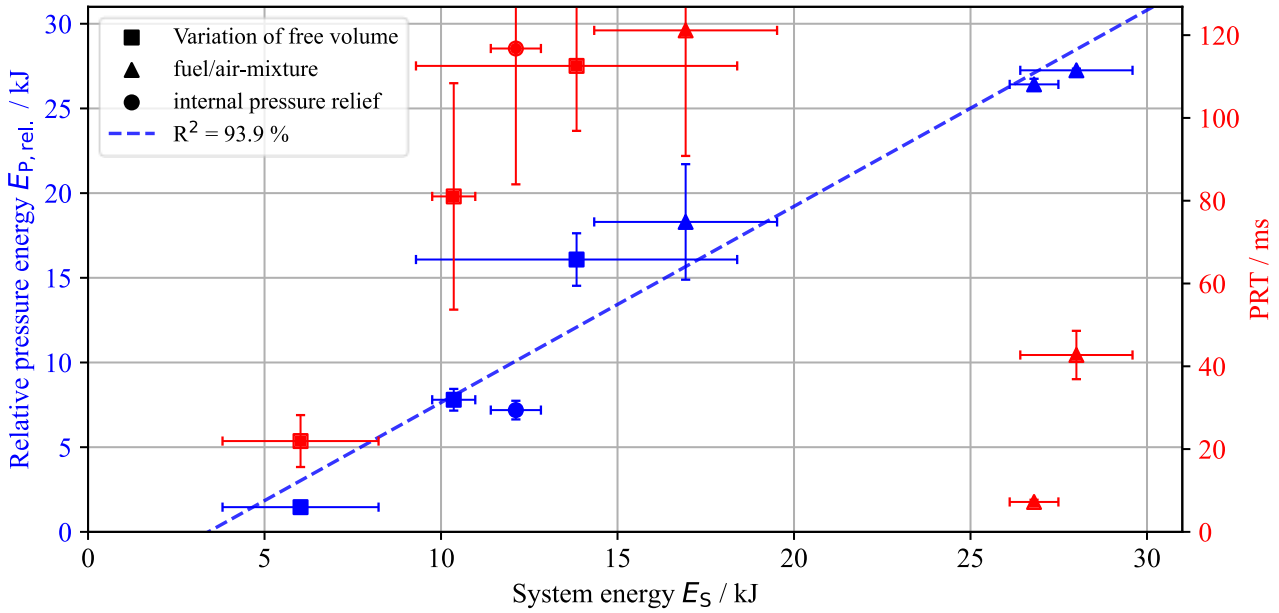

Fig. 6. Overview of the relative pressure energy $E_{P,rel.}$ (blue) and the PRT (red) of all experiments as a function of the system energy E_S. Each measurement series is symbolically marked.

As can be seen, there is a linear dependency between the system energy and the relative pressure energy regardless of the measurement series. A high system energy results in a high relative pressure

energy and therefore a high material stress. The lowest values are achieved for the test configuration SAV-339-5, whereas the highest values are obtained by the additional provision of a fuel gas-air atmosphere (in particular C_3H_8). As can be seen by plotting the PRT as a function of the system energy (see Fig. 6, red) a statement about the material stress using this variable is not meaningful (see section 2.1.2). Overall, the system energy increases by almost 400 % (approx. 22 kJ) between these limits, which results in an increase in the relative pressure energy of almost 2000 % (approx. 25 kJ). Fig. 6 demonstrates the validity of the data analysis based on the system energy, as developed in this work, for a wide range of test scenarios. A consideration of the system energy therefore enables the comparison of various conditions and the estimation of the effect of a TR on the enclosure.

3. Conclusions

The TR of a LIB was experimentally investigated in a flameproof enclosure whilst varying the free volume and the composition of the gas atmosphere inside the enclosure. The increase in the free volume with a simultaneous reduction in the internal surface area caused an increase in maximum pressure. This rise in pressure was the result of the increased system energy and reduced power loss. An increase in the internal surface area consequently leads to pressure relief. This can be confirmed in particular by the significant reduction in pressure due to the enlarged surface area of the internal pressure relief. Extrapolation of the material load and stress based solely on the free volume is therefore not possible in general. However, an increase in the free volume in an air atmosphere created a bigger thermal load. The superposition of the TR and a gas explosion resulted in a growth in the maximum pressure. C_3H_8 led to the highest pressure among the gases analyzed, whereas H_2 showed the fastest increase in pressure (PRT). If the energy of the fuel gases is also taken into account in the system energy term, a linear relationship is found between system energy and maximum pressure. Comparative tests without TR showed that the additional TR of a LIB with a capacity of 3 Ah was only accompanied by a slight increase in pressure. The gas explosion was therefore decisive for the maximum pressure. A linear relationship between the system energy and the resulting pressure energy was observed across all experiments. It is therefore possible to describe various test scenarios using a simplified energy balance. The correlations determined here between the material stress and the volume as well as the inner surface area have shown that the latter must be taken into account to predict the pressure triggered by the TR. As a result the dependencies according to Dubaniewicz et al. (2021) and Dubaniewicz et al. (2022) cannot be generalized. In the future, such a general quantification of the material stress as a function of the housing geometry and the LIB should be sought. Furthermore, both individual LIB and battery packs should be examined in the future.

Acknowledgements

The authors gratefully acknowledge funding by the German Ministry of Economics and Climate Action (grant no. 03TN0038A).

References

Baehr, H. D., Kabelac, S. (Ed.), 2016. Thermodynamik: Grundlagen und technische Anwendungen. Springer Vieweg: Berlin.

Chi, M., Jiang, H., Lan, X., Xu, T., Jiang, Y., 2021. Study on Overpressure Propagation Law of Vapor Cloud Explosion under Different Building Layouts. ACS omega 6 (49), 34003–34020. 10.1021/acsomega.1c05332.

Database BAM-Project CHEMSAFE, 2016. Recommended Safety Characteristics and Classifications of Flammable Gases and Gas Mixtures.

DIN Deutsches Institut für Normung e. V., 2018. DIN EN 13184:2001-07: Non-destructive testing - Leak test - Pressure change method. DIN Deutsches Institut für Normung e. V: Berlin 19.100.

Dubaniewicz, T. H., 2023. Innere Abmaße des experiementellen Aufbaus. E-Mail.

Dubaniewicz, T. H., Barone, T. L., Brown, C. B., Thomas, R. A., 2022. Comparison of thermal runaway pressures within sealed enclosures for nickel manganese cobalt and iron phosphate cathode lithium-ion cells. Journal of Loss Prevention in the Process Industries 76, 104739. 10.1016/j.jlp.2022.104739.

Dubaniewicz, T. H., DuCarme, J. P., 2013. Are lithium ion cells Intrinsically Safe? IEEE Transactions on Industry Applications (6), 1–10. 10.1109/IAS.2012.6374075.

Dubaniewicz, T. H., DuCarme, J. P., 2014. Further study of the intrinsic safety of internally shorted lithium and lithium-ion cells within methane-air. Journal of Loss Prevention in the Process Industries 32, 165–173. 10.1016/j.jlp.2014.09.002.

Dubaniewicz, T. H., Zlochower, I., Barone, T., Thomas, R., Yuan, L., 2021. Thermal Runaway Pressures of Iron Phosphate Lithium-Ion Cells as a Function of Free Space Within Sealed Enclosures. Mining, Metallurgy & Exploration 38 (1), 539–547. 10.1007/s42461-020-00349-9.

EC-Project SAFEKINEX, 2006. Report No. 8: Report on the experimentally determined explosion limits, explosion pressures and rates of explosion pressure rise - Part 1: methane, hydrogen and propylene.

Essl, C., Golubkov, A. W., Fuchs, A., 2020. Comparing Different Thermal Runaway Triggers for Two Automotive Lithium-Ion Battery Cell Types. J. Electrochem. Soc. 167 (13), 130542. 10.1149/1945-7111/abbe5a.

Feng, X., Ouyang, M., Liu, X., Lu, L., Xia, Y., He, X., 2018. Thermal runaway mechanism of lithium ion battery for electric vehicles: A review. Energy Storage Materials 10, 246–267. 10.1016/j.ensm.2017.05.013.

García, A., Monsalve-Serrano, J., Sari, R. L., Martinez-Boggio, S., 2022. Influence of environmental conditions in the battery thermal runaway process of different chemistries: Thermodynamic and optical assessment. International Journal of Heat and Mass Transfer 184, 122381. 10.1016/j.ijheatmasstransfer.2021.122381.

Incropera, F. P., Dewitt, D. P., Bergman, T. L., Lavine, A. S., 2007. Fundamentals of heat and mass transfer, 6th ed. John Wiley: Hoboken NJ.

International Electrotechnical Commision, 2014. IEC 60079-1.: Explosive Atmospheres - Part 1: Equipment Protection By Flame Proof Enclosures “d”.

Jiang, K., Gu, P., Huang, P., Zhang, Y., Duan, B., Zhang, C., 2021. The Hazards Analysis of Nickel-Rich Lithium-Ion Battery Thermal Runaway under Different States of Charge. Electronics 10 (19), 2376. 10.3390/electronics10192376.

Larsson, F., 2017. Lithium-ion Battery Safety: Assessment by Abuse Testing, Fluoride Gas Emissions and Fire Propagation. Dissertation: Göteborg.

Lendt, B., Cerbe, G. (Ed.), 2016. Grundlagen der Gastechnik: Gasbeschaffung – Gasverteilung – Gasverwendung, 8th ed. Carl Hanser Verlag: München.

LG Chem, 2015. Product Specification Rechargeable Lithium Ion Battery: Model: INR18650HG2 3000mAh.

Little, S., Karamali, K., 2022. Vancouver firefighters issue warning amit five-fold increase in battery fires. https://globalnews.ca/news/8827482/vancouver-battery-fire-warning/. Accessed 27 February 2024.

R.STAHL, 2015. Ex d Enclosure System Made of Light Metal or Stainless Steel, "Flameproof Enclosure": Series 8264 CUBEx.

Rahimi, M., 2021. Lithium-Ion Batteries: Latest Advances and Prospects. Batteries 7 (1), 8. 10.3390/batteries7010008.

Spörhase, S., Brombach, F. M., Eckhardt, F., Krause, T., Markus, D., Küstner, B., Walch, O., 2022. Untersuchungen zur Vergleichbarkeit der statischen und dynamischen Überdruckprüfung von druckfesten Kapselungen. Forsch Ingenieurwes. 10.1007/s10010-022-00604-z.

Xometry Europe GmbH, 2021. Data sheet: Stainless Steel 316 l / 1.4404 / X2CrNiMo17-12-2.

Explosivity of nanomaterials for lithium-ion battery electrodes

Sofia Ubaldi [a], Ghislain Binotto [b], Amandine Lecocq [b], Guy Marlair [b], Aurélie Aube [b], Arnaud Bordes [b] & Paola Russo [a]

[a] Department of Chemical Engineering Materials Environment, Sapienza University of Rome, Rome, Italy
[b] INERIS, Verneuil-en-Halatte, France

E-mail: paola.russo@uniroma1.it

Abstract

As the European Union tries to develop important LIB production capacity by supporting the development of many gigafactories, new materials are under investigation to enhance the Lithium-ion batteries (LIBs) performances. A promising way onwards seems to be the optimization of the chemical composition of LIBs using nanomaterials (NMs). NMs most frequently used as active materials for the anode are silicon, lithium titanate oxide (LTO) and graphite. In addition, carbon black (CB) is used as an additive to increase the conductivity and the electrical performance of LIBs. Even if NMs are beneficial for LIB performances, the reduction of the particle size might induce an explosive behaviour of the powder used during manufacturing. For this reason, a study on crucial NMs safety was conducted to evaluate both physicochemical characteristics and relating explosivity risks of those NMs to ensure their safe production, handling and use, including in the gigafactories under construction all over Europe. Firstly, the characterization of the pristine NMs was performed (i.e., median particle size (d_{50}), and specific surface area (SSA)). Then, explosion parameters were assessed (i.e., minimum explosible concentration (MEC), maximum explosion pressure (P_{max}) and deflagration index (K_{st})) according to the standards. For LTO materials, no explosivity is observed due to the lack of combustibility and absence of any explosion-prone chemical group. A rise in the explosion's parameters was noted with the material's reduction in size from micro to nanoscale. In general, for the NMs, a smaller concentration of combustible dust mixed with air is needed for a deflagration to occur. This deflagration leads to higher maximum pressure values that in addition are set faster. For example, the micro-C exhibited no explosive behaviour, while the nano-C showed weak explosive severity (K_{max} = 63 bar m/s). Consequently, the utilisation of nanomaterials in the production of LIBs necessitates that the risk assessment be conducted with due consideration of the heightened explosion risk that is due to their use.

Keywords: *nanomaterials, NMs, Lithium-ion batteries, LIBs, explosion, P_{max}, $K_{st.}$*

Introduction

The available active powder materials for the anode and the cathode are limited by pore size and volume density. The current electrode active materials have micro-sized dimensions that limit the intrinsic diffusivity of the Li-ion intercalation in the solid state on the anode and that can pass through the separator. To enhance both the intercalation/deintercalation and the charge/discharge rates, the micro powders used as active materials can be substituted with either the same or different materials, thereby achieving nano-scale driven performance (Jiang, Hosono, and Zhou, 2006). Nanomaterials (NMs) have a smaller size, resulting in a shorter diffusion length and a higher contact area between active materials and electrolyte (Corcione and Frigione, 2012). This can enhance the performance and energy storage capacity of batteries while reducing their dimensions. Table 1 reports the different NMs currently under investigation for use as materials for the positive or negative electrode. NMs can take on various morphologies, including nanoparticles (NPs), nanotubes (NTs), nanowires (NW),

hollow nanosphere, and porous nanostructure. They can be used as pure materials, after mixing with other substances or as a coating for other materials.

***Table 1**. A summary of the NMs under investigation, with the relative application and reference*

Material	Application	Reference
Si	Anode	Wang et al., 2015
Si	Anode	Chen et al., 2012
Carbon coating on the Si surface	Anode	Wang et al., 2015
Core-shell amorphous silicon-carbon	Anode	Sourice et al., 2016
Mixing Si with C-based	Anode	Chen et al., 2012
Mixing Si with C-based	Anode	Chen et al., 2017
Si with polymer and chemical bonding	Anode	Erk et al., 2013
Si with polymer and chemical bonding	Anode	Assresahegn and Bélanger, 2017
Hybrid 0D and 1D Si	Anode	Pinilla et al., 2020
SiO_2	Anode	Al Ja'farawy et al., 2021
$Li_4Ti_5O_{12}$	Anode	Hudak, 2014
Carbon black (CB)	Anode additive	Hu, Zhong and Yan, 2021
$LiFePO_4$	Cathode	Hudak, 2014

Table 1 shows that the research in the field of the NMs is mainly focused on the anode materials. The two main possibilities for NMs as anode active material are titanium (Ti) (Hudak, 2014) and silicon (Si) (Eshetu et al., 2021). Additives, such as the carbon black, have also been evaluated for their ability to enable fast charging of batteries when added to the anode composition. The principal form is the $Li_4Ti_5O_4$, but various form of TiO_2 can also be used. The cycling mechanism of $Li_4Ti_5O_{12}$ is quite similar to that of $LiFePO_4$. The process relies on Li^+ insertion due to the formation of $Li_7Ti_5O_{12}$ at 1.55 V versus Li/Li^+ . This leads to a theoretical capacity of 175 mAh/g and a high degree of reversibility. Lithium titanate spinel is used in a nanocrystalline or nanoparticulate state to achieve a higher charging rate and extended cycle life compared to the same material in micro-size. In literature, most studies focus on developing materials made of or with Si, to replace graphite (C) powder as an innovative anode. Silicon nanoparticles (Si-NPs) are chosen due to their higher gravimetric and volumetric capacity, which surpasses that of all other elements currently considered or studied for this purpose (Qi et al., 2017). This results in lighter batteries being produced. Si-NPs are an attractive option due to their abundance, low cost, and high theoretical capacity of 3579 mAh g^{-1}. When reacting with lithium, they form the alloy Li_xSi, where $0 < x < 3.75$. However, Si-NPs have two significant drawbacks. Firstly, they undergo a volume change during lithiation and de-lithiation, expanding and contracting by about 300 % in volume. Secondly, they have an unstable solid electrolyte interphase (SEI) (Li et al., 2023). The significant quantity of lithium results in substantial structural changes, which are expressed in volume and can reach up to 300 %. This expansion in volume represents the primary drawback of silicon NMs, which leads to an irreversible loss of capacity due to the continuous SEI formation and a poor retention capacity due to the pulverization of the active material, Si-NPs (Sun et al., 2022). For this reason, Si is not considered as an active material alone but is often coupled with other species, such as Si-NPs. Si-NPs act as a coating for carbon particles, and the mixing of Si-NP with C-based NM help to reduce the pulverization of Si by improving its electronic conductivity and structural stability (Enotiadis et al., 2018). As a cathode, $LiFePO_4$ is one of the most developed NMs (Hudak 2014). The material has several advantages, including low ionic and electronic conductivity, high theoretical capacity for full de-lithiation (170 mAh/g), and a degree of reversibility (between $LiFePO_4$ and $FePO_4$) due to the cycling mechanism.

The performance achievement must be benchmarked against subsequent safety characteristics, particularly of explosivity behavior of the pristine NMs. While the explosivity behavior of micro-sized materials is well-known, this potential hazard must be re-evaluated for NMs due to the

significant change in particle size distribution (Johnston, Mansfield, and Smallwood, 2017). The reduction in particle size results in an increase in specific surface area (SSA), which increases sensitivity to explosions and significantly rises their severity (Bouillard, 2015). For a better understanding of how the sensitivity and explosion severity of powders vary with particle size distribution from the micro to the nano range, please refer to Assresahegn and Bélanger (2017).

Various parameters can be used to express the explosivity and severity of an explosion. These parameters can be evaluated by lab-scale standardized explosivity tests, such as the minimum explosible concentration (MEC), the maximum pressure (P_{max}) and the deflagration index (K_{st}). The MEC and the explosivity factors, P_{max} and K_{max}, can be evaluated by conducting experiments inside a 20-L sphere apparatus, according to ISO/IEC 80079-20-2. This test describes the test methods for combustible dust and the determination of the explosive characteristics of dust clouds according to EN 14034. Part 1 determines the maximum explosion pressure (P_{max}) of dust clouds; part 2 determines the maximum rate of explosion pressure rise ((dp/dt)max) of dust clouds; and part 3 determines the lower explosion limit (LEL) of dust clouds. The deflagration index (K_{st}), can be calculated from the cube-root law in Equation (1) (Bartknecht et al., 1989):

$$K_{st} = \left(\frac{dp}{dt}\right)_{max} * V^{1/3} \quad (1)$$

where V is the volume of the vessel (m^3), t is the time (s), and $\left(\frac{dp}{dt}\right)_{max}$ is the maximum rate of pressure rise (bar/s).

Equation (1) provides the size-normalized maximum rate of pressure rise for a constant-volume explosion. The severity of the explosion can be classified as follows: a value of 0 indicates no explosion, values between 1 and 200 indicate a weak explosion, values between 201 and 300 a strong explosion, and values higher than 300 indicate a very strong explosion.

Although MEC, P_{max}, and $(dp/dt)_{max}$ can be easily determined, it is important to note that they are strongly dependent on material characteristics, such as particle size or SSA (Khudhur, Ali, and Abdullah, 2021). Previous studies dating back a decade have shown an increase in the ignitability and explosivity of combustible powders when shifting from a micro to a nano particle size distribution (PSD) range (Dufaud et al., 2011). The MEC of the NP material is lower compared to the micro-scale material and is directly proportional to the bulk density. According to Dufaud et al. (2011), the explosion severity of Al powder tends to increase as the SSA decreases, before reaching a peak for 1 µm particle size. Therefore, the nanosized sample ignites at lower ignition energies and significantly lower dust amounts than is the micrometric sample.

The objective of this work is to assess the risk of explosivity associated with critical nanometric materials that are used to enhance the performance of the new LIBs. The comparison in this study includes both micro and nano sized materials to evaluate the change in explosivity properties between these particle size ranges. The materials selected for the study included Si, C, and LTO, which are under investigation for the anode of LIBs. Additionally, CB was selected as the main additive. The explosivity parameters were evaluated using the standard test, ISO/IEC 80079-20-2. Physical properties characterization was conducted for all selected materials to correlate explosivity-related parameters with their physical properties. These assessments can improve the safety assessment of dust explosions in process industries, including the gigafactories currently under construction throughout Europe (Eckhoff, 2003).

1. Materials and Methods

1.1. Materials

As a general rule in material selection, chemically similar materials were supplied at both micro and nanoscales. Dedicated use for the Li-ion battery field was a selection criterion, especially for NMs.

Regarding the micrometric reference materials, the selection process was less strict. Sometimes, the choice was not based solely on their proven use in batteries but also on the interest in accessing well-characterized micro powder materials for larger applications. For example, micro LTO ($Li_4Ti_5O_{12}$) for has a registration dossier available on the European Chemical Agency (ECHA) website.

The selection process concluded by gathering the following materials: the related PSD data extracted from the corresponding material safety data sheet (MSDS), as shown in Table 2.

***Table 2**. List of the materials considered in this work*

Materials	Purity (%) and PSD	Producer	References
Natural Graphite (C) Nanopowder/Nanoparticles	purity: 99.9 %, PSD: 400 nm - 1.2 µm	MTI Corporation	-
MesoCarbon MicroBeads (MCMB) graphite powder for Li-ion battery anode	purity: 99.96 % PSD: 8.087 µm – 33.080 µm	MTI Corporation	-
Lithium Titanate Oxide powder for Li-ion battery anode	purity: > 98 % PSD: 0.2 µm – 34 µm	MTI Corporation	-
Lithium Titanate Oxide	PSD: 2.26 µm	-	ECHA dossier (LTO, ECHA)
Carbon black Monarch 1300®	PSD: 13 nm	Cabot Corporation	Vignes et al., 2023
Carbon black	PSD: 17 µm	-	ECHA dossier (Carbon Black, ECHA)
Silicon powder	purity: 99+ % PSD: 50-100 nm	IolitecNanomaterials	Vignes et al., 2023
Silicon	PSD: 13.5 µm	-	ECHA dossier (Si, ECHA)

The physical and explosivity properties of both micro and nano materials have been characterized.

1.2. Methods

The explosivity behaviour is closely linked to the physical properties of selected powders. Therefore, a first characterization of materials was performed at both micro and nano levels to correlate the obtained data in our work.

1.2.1. Characterization of the pristine materials

The main characteristics to be evaluated for the pristine NMs are PSD, SSA and the density. For all these measurements, there are standards that can be applied to unify the data obtained.

The particle size distribution measurements were evaluated according to ISO 13320 (ISO, 2020). The tests were performed with a HELOS-KR instrument equipped with Quixel or Rodos dispersing units (Sympatec). For the analysis, the test material was first dispersed in a solution of water and octylphenoxypolyethoxyethanol, a non-denaturing detergent (IGEPAL®, Merck), and further shaken at ultrasonic frequency of 40 kHz, to maximize dispersion. The SSA of porous solids was measured by physical adsorption of nitrogen gas according to the Brunauer, Emmett and Teller (BET) method, following ISO 9277 (ISO, 2010). The SSA tests were performed with a 3-Flex (Micromeritics) instrument. Finally, the (skeletal) density was evaluated with helium gas according to ISO 12154:2014. Density tests were performed using an Accupyc II 1340 (Micromeritics).

1.2.2. Explosivity of the materials

The parameters that define the explosivity severity of a material are MEC, P_{max}, K_{st}. These parameters have to be evaluated from specific tests according to the ISO/IEC 80079-20-2 (ISO, 2016). The tests were performed inside a 20-L sphere (Kuhner), where the ignition source, placed in the center of the sphere, triggers an energy of 10 kJ for the evaluation of P_{max}, K_{st} or 2 kJ for the determination of MEC.

2. Results and discussion

The physical properties and explosivity hazards of the materials, both at the micro and nanoscale levels, have been evaluated using the same standard procedures in order to highlight any significant differences induced by the three orders of magnitude change in size studied.

2.1. Characterization of the pristine materials

A multi-criteria physical characterization of the pristine materials was carried out, even if some information was already available in the MSDS, in order to confirm the reported values. The PSD can be qualified according to various size-related parameters related to number, weight or surface based criteria. d_{50}, which reflects the median particle size distribution (50% of the total particles are smaller and 50 % are larger) was primarily used here for comparison.

The results for the nano-graphite (nano-C) are reported and discussed here in detail, while the results for the other materials are summarised in Table 3. In particular, the PSD curve for the nano-C is shown in Figure 1.

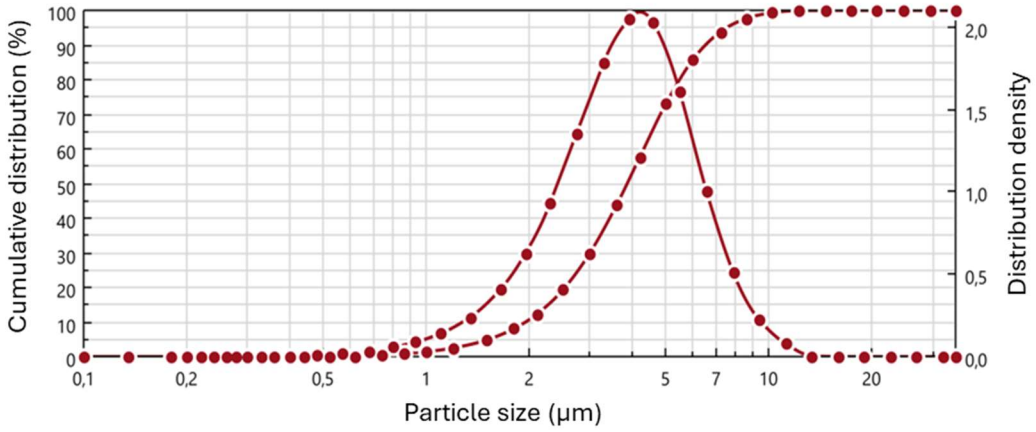

Fig. 1. *Size distribution curve of the nano-C*

The distribution appears to be monodispersed, centered around the value of 4 µm, close to the d_{50} value (3.86 µm). From the cumulative distribution curve, the so called d_{10} and d_{90} parameters, which fix 10 % and 90 % of the cumulative particle size distribution in the test powder, can be easily determined as 1.94 µm and 6.63 µm, respectively. Corresponding data can then further be used to qualify the particle size metric range more globally. The values indicate that the supplied "nano-C" nanomaterial appears to be in the micrometric particle range, in contrast to the data given in the relevant MSDS issued by the manufacturer. This is indicated by the fact that more than 50% of the particles have a size greater than the 1-100 nm range indicated by the European Commission. In fact, the European Commission has standardized the terms in the 10th Commission Recommendation of June 2022: this text defines that *Nanomaterials means solid particles where 50 % or more of the particles in the number-based size distribution of one or more external dimensions are in the size range 1 nm to 100 nm* (European Commission, 2020).

This ambiguity in the interpretation of results is due to the extrinsic properties of NMs, which tend to agglomerate, especially when dispersed in solution, such as IGEPAL®, resulting in larger agglomerates. In order to reduce the ambiguity in the classification of the NMs a new parameter can be mathematically evaluated, which is the volume specific surface area (VSSA). This parameter is obtained by the combination of two physical parameters, the density and the SSA of the materials. The VSSA, expressed in m^2/cm^3, can be calculated according to Equation (2) (Dazon et al., 2020):

$$VSSA = SSA * \rho \quad (2)$$

where SSA is the specific surface area (expressed in m^2/cm^3) and ρ is the density (expressed in g/cm^3).

If the result of Equation (2) is higher than 6 m^2/cm^3, the material under investigation can be considered as a nanoscale material (CEU, 2019). Therefore, this parameter can be used as an alternative method to assess whether the material is a nanomaterial or not (Bau et al., 2021).

For the NM under investigation the ρ is equal to 2.4 g/cm^3, while the SSA is equal to 9.7 m^2/g. So, applying the Equation (2), the VSSA for the nano-C under investigation is 23.3 m^2/cm^3, which is higher than the limit of 6 m^2/cm^3. The materials can therefore be defined as NMs, although the PSD curve would suggest a different interpretation.

Physical profiles of the other materials of interest in the research are summarized in Table 3.

***Table 3**. Physical properties of various micro- and nanoscale materials, either collected from related MSDS or obtained experimentally*

Material	PSD from MSDS	Size (d_{50})	ρ (g/cm^3)	SSA (m^2/g)	VSSA (m^2/cm^3)
Micro-CB	n.a.	17 µm	n.a.	n.a.	n.a.
Nano-CB	n.r.	13 nm	n.r.	377	n.r.
Micro-C	1.07 µm – 60.26 µm	17.79 µm	2.3	0.7	1.7
Nano-C	400 nm- 1.2 µm	3.86 µm	2.4	9.7	23.3
Micro-LTO	n.a.	2.46 µm	n.a.	n.a.	n.a.
Nano-LTO	200 nm – 34 µm	1.13 µm	3.6	4.6	16.6
Micro-Si	n.r.	13.5 µm	n.r.	1.3	n.r.
Nano-Si	50 nm – 100 nm	-	0.36	18.6	6.7

n.a.: data not available from ECHA web site. n.r.: not reported.

From the data presented in Table 3, there are some difficulties in making a detailed comparison of the granulometry ranges of the two selected sets of materials (micro and nano), either obtained from MSDS or reflected by their d_{50} as measured in our work. Again, this may be because the powders and the relative dusts of NMs may be difficult to fully disperse into primary particles, leading to the particles behaving as if they were coarser. This could results in a higher measured d_{50} values than those intrinsically associated with an ideal dispersion of corresponding NPs. However, this issue can be resolved by basing the identification of the metric range of the test materials on the VSSA parameter, as explained above for nano-C. This alternative method, appears to eliminate inconsistencies in the classification of test materials within the micro or nano range, according to their respective MSDS. For example, both graphite materials have a d_{50} of micro (17.79 µm for micro-C and a lower value of 3.86 µm for nano-C), the results still leave some doubts as to whether nano-C is a true nanomaterial. Nevertheless, a comparison of the VSSA values provides a more distinct differentiation between these materials. In fact, the VSSA for micro-C is equal to 1.7 m^2/cm^3 while the VSSA for nano-C is equal to 23.3 m^2/cm^3. In other words, the first VSSA value is well below 6 m^2/cm^3, while the second VSSA value is well above 6 m^2/cm^3. This confirms the nano range in the second case and micro range in the first one, in accordance with the material designation. Similarly, the value of VSSA calculated for the nano-LTO and e nano-Si confirms their classification as NMs.

From previous results it can be concluded that analytical techniques, specifically laser diffraction, can be used to evaluate the particle size distribution, but it is not necessarily an adequate technique for the nanometric range of PSD, especially since it has not been developed specifically/exclusively for this range of particles. It can certainly give a general trend, but the results needs to be confirmed by e.g. dynamic light scattering (DLS) or transmission electron microscopy (TEM). Indeed, if the particles are not fully dispersed, the results obtained may be somewhat biased by particle agglomeration, depending on the particle morphology. For instance, cylindrical morphology may lead to interpretation problems. Therefore, it can be concluded that at the moment the mathematical evaluation by VSSA is the most effective technique to confirm the nano-size dimension of the materials, as defined in the NanoDefine project (Mech et al., 2020). An unique classification method of the NMs must be drawn up in order to obtain a uniform classification.

These assessments are of fundamental importance for the correct characterisation of the materials during the production steps, such as quality control. Thay are also of great significance in terms of safet, as they enable the assessment of the risk of explosivity.

2.2. Explosivity of the pristine materials

The explosivity tests were carried out according to the relative standard procedures on all the pristine materials, however only the results for the nano-C are reported in detail, while for the other materials the results are reported in Table 4. The key parameters that qualify the sensitivity and severity of a potential ATEX generated by the nano-C, are shown in Figure 2.

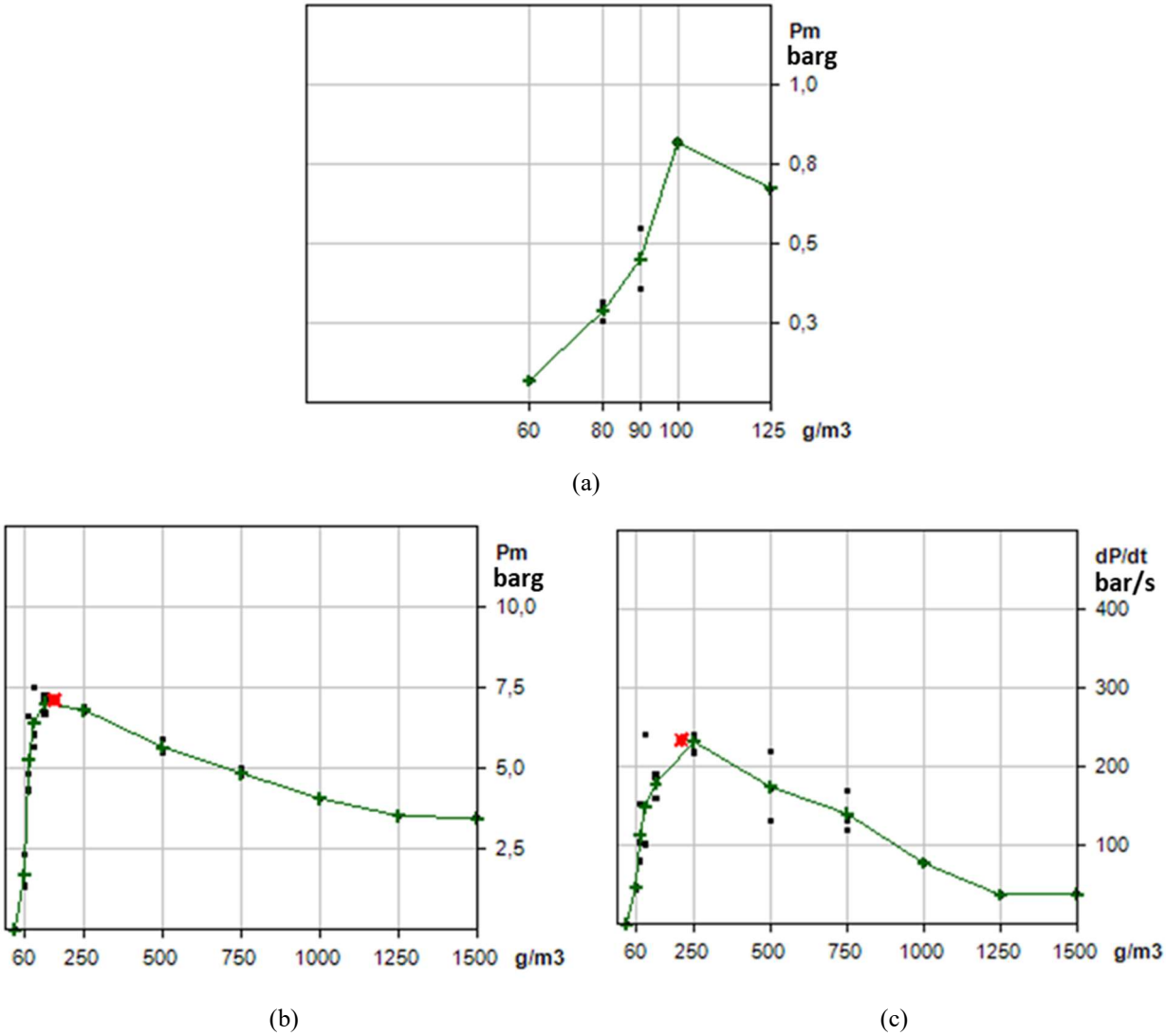

Fig. 2. *Graphs of the explosivity parameters of nano-C: (a) MEC, (b) P_{max}, (c) $(dp/dt)_{max}$*

From Figure 2a it is possible to determine the MEC, which for the nano-C is equal to 80 g/m^3. This result indicates that is from this value of concentration the nano-C can generate an ATEX. In fact, by examining the profile over the whole concentration range (Figure 2b), P_{max} is found to be of the order of 7.1 barg. The maximum rate of explosion pressure rise $(dp/dt)_{max}$ of nano-C dust is found to be around 234 ± 47 bar/s (Figure 2c). From this last parameter the explosivity severity can be quantified according to Equation (1) and by the associated criteria. The resulting K_{st} is 63 ± 13 bar m/s which corresponds to a weak explosion.

The same parameters for the other materials at different size ranges are reported in Table 4.

***Table 4**. Explosivity parameters for the various micro- and nanoscale materials*

Material	MEC (g/m³)	P_{max} (barg)	$\left(\frac{dp}{dt}\right)_{max}$ (bar/s)	K_{st} (bar m/s)	Explosivity severity
Micro-CB	125	3	n.a.	6	Weak
Nano-CB	70	7.8	337	91	Weak
Micro-C	0	*	*	*	Nil
Nano-C	80	7.1	234	63	Weak
Micro-LTO	n.a.	n.a.	n.a.	n.a.	n.a.
Nano-LTO	0	*	*	*	Nil
Micro-Si	n.r.	7.8	170	46	Weak
Nano-Si	135	7.9	249	68	Weak

*n.a.: not available in the ECHA dossier. n.r.: not reported. *: not conducted, due to the MEC = 0.*

From a first comparison of the data presented in Table 4 reveals a consistent trend across the parameters, with the exception of LTO. It can be observed that downscaling the PSD of the materials, from micro to nano, results in an increase in the sensitivity or severity of the explosion. Specifically, the MEC value decreases with decreasing dimensions, while for P_{max} and $K_{st,}$ an increase in these parameters occurs when the dimensions of the materials decrease. In general, therefore, for NMs, a lower concentration of dust is required for a deflagration to potentially occur, and this deflagration leads to higher pressure values and faster rate of pressure rise. Finally, the evaluation of the explosivity severity resulting from the application of Equation (1) and the associated criteria is given in Table 4.

The most significant difference in terms of explosivity parameters is obtained by comparing the micro-C and nano-C materials. In fact, the micro-C dispersed inside the 20-L sphere does not generate an ATEX (MEC = 0 g/m³), whereas the nano-C material can cause an explosion at a concentration at least equal to the MEC value (80 g/m³). The other explosivity parameters, i.e., $(dp/dt)_{max}$ and P_{max}, for the micro-C were not available due to the non-explosivity of the materials. So, the explosivity severity of the micro-C can be classified as nil (K_{st} = 0 bar m/s), while that of nano-C is classified as weak.

Both Si and CB also exhibit , albeit to a lesser extent than C, an increase in explosivity behavior as the particle size range shifts from micro to nano. With regard to CB, the MEC obtained passes from 125 g/m³ for the micro-CB to 70 g/m³ for the nano-CB, representing a reduction of one order of magnitude. In any casee, the difference in the P_{max} obtained for the two sizes is not significantly different (3 barg for micro-CB vs 7.8 barg for nano-CB). The resulting K_{st} values for both dimensions are included in the range between 1 and 200 bar m/s, indicating that the explosivity severity of micro and nano CB is classified as weak.

In the case of Si, the differences between the various explosiveness parameters are not significantly different, which lead to the same final classification. Consequently, both Si materials lead to a weak explosion. Thus, for the Si and the CB, the transition from the micro to the nanoscale shows a decrease in MEC, but since K_{st} remains in the same order of magnitude on both metric scales, i.e. less than 100 bar m/s, a weak explosion severity is both cases.

Finally, the comparison between the micro-LTO and the nano-LTO remains complex due to lack of data for the micro material (no data available on the ECHA website for this material). As regards the LTO material, the explosion risk is indeed practically non-existent, whatever the PSD. The explanation lies in two facts: according to the chemical formula of LTO, the material does not have any significant combustibility property, thus suppressing any dust explosion hazard. In addition, this material does not contain any explosion-prone chemical group, which therefore cannot explode per se. A similar trend has been observed for the nano-LTO, which, when dispersed in air, does not generate an explosive atmosphere as the MEC is zero and even the ignition temperature is higher than 1000 °C indicating the thermal stability of the LTO material.

These assessments are of great importance for the increased awareness of the explosion risk of powders used in process industries, such as the gigafactories under construction around the world and in Europe. Conventional processing for the production of a lithium-ion cell consists of three steps: (1) electrode production, (2) cell assembly, and (3) cell formation (Örüm Aydin et al., 2023). The phase that is most affected by the variation of the material size and its relative explosivity is that of the electrode production. In fact, in this phase, the different pure powders of the active material and the conductive agent, previously dosed, are placed inside the mixer and added to the electrode slurry, the so-called binding solution. Subsequently, the mixture is degassed and then pumped out so as to obtain a uniform, homogenous coating over the current collector. Finally, several drying steps are conducted in the oven. The proposed procedure is general, as each manufacturer then applies different operating conditions and/or different treatments. In any case, the transition from micro-materials to NM requires an update of the technical procedure and/or instruments used. In particular, the tools used during the mixing of pure NMs must be adapted to the pressure and must avoid the generation of an ATEX atmosphere within the plant at any stage of the process.

3. Conclusions

On the anode side, to improve the performance of LIBs, nano-Si, nano-LTO and nano-C are the most studied active materials, while nano-CB can be used as additive to enhance the conductivity. The increase in the performance is accompanied by a potential increase in explosivity risk during the manufacturing phases, which is strongly correlated with the decrease in particle size.

Firstly, a characterization of the materials, both at micro and nano size, was carried out to obtain more detailed information on the granulometry of the particle in the powder, i.e., d_{50}. Anyway, in the case of NMs the evaluation of this parameter can be affected by an error, since the powders and relative dusts of NMs can be difficult to disperse completely into primary particles and therefore behave as coarser particles. So, the classical analytical technique, such as laser diffraction, needs additional confirmation by DLS or TEM. An alternative mathematically method, based on the determination of the VSSA, has been developed to observe the real differences in the PSD of the materials and to confirm the classification of selected materials as NMs (VSSA > 6 m^2/cm^3). By this mathematically method the ambiguity between the experimental data and the data given in the relevant MSDS issued by the manufacturer were solved.

In terms of explosion risk, the key parameters, i.e., MEC, P_{max} and K_{st}, were evaluated according to the relevant standard procedures. By reducing the size of the material, from micro- to nano-size, an increase in explosion severity for all the NMs, except for LTO, was observed. This behaviour is increasingly evident from nano-CB to nano-Si up to the extreme case of nano-C. In fact, regarding the graphite, the micro-C does not show any explosive behaviour (MEC = 0 g/m^3) while the nano-C shows a weak explosive severity (K_{st}=63 bar m/s) associated to a MEC of 80 g/m^3. Finally, both nano and micro LTO showed zero risk of explosion due to the non-combustible nature of the material. In conclusion, the increase in the risk of explosivity, due to the size reduction, is confirmed in terms of sensitivity and severity of explosion by the determination of the explosivity parameters.

These assessments are fundamental both for a correct characterization of the materials during the production and assembly phase of the cells and for a greater awareness of the risk of explosion of the NMs used in the process industries such as the gigafactories under construction all over the world as in Europe.

A future application of this work could be to consider not only the pristine single materials but also the coupled NMs, such as Si and CB together in the same formation ratio used in the Li-ion cell anode. In fact, the anode will not consist of a single NM, but of the coupling of two or more NMs and additives to achieve the best possible performance.

Acknowledgements

The study received funding from the SAF€RA 2022 joint call for proposals in the year 2022 for the project entitled "Safety evaluation of nanomaterials in Novel EES materials and LIBs (Nano-SaNE)".

References

Al Ja'farawy, M.S., Hikmah, D.N., Riyadi, U., Purwanto, A. & Widiyandari, H. (2021). A Review: The Development of SiO2/C Anode Materials for Lithium-Ion Batteries. *Journal of Electronic Materials,* 50(12): 6667–87.

Assresahegn, B.D. & Bélanger, D. (2017). Synthesis of Binder-like Molecules Covalently Linked to Silicon Nanoparticles and Application as Anode Material for Lithium-Ion Batteries without the Use of Electrolyte Additives. *Journal of Power Sources,* 345: 190–201.

ASTM. 2022. "ASTM B923-22 Standard Test Method for Metal Powder Skeletal Density by Helium or Nitrogen Pycnometry." https://www.astm.org/b0923-22.html.

Bartknecht, W., Bartknecht, W. & Bartknecht, W. (1989). *Dust Explosions: Course, Prevention, Protection*. Berlin Heidelberg: Springer.

Bau, S., Dazon, C., Rastoix, O. & Bardin-Monnier, N. (2021). Effect of constituent particle polydispersion on VSSA-based equivalent particle diameter: Theoretical rationale and application to a set of eight powders with constituent particle median diameters ranging from 9 to 130 nm. *Advanced Powder Technology*, 32(5): 1369–1379.

Bouillard, J.X. (2015). Fire and Explosion of Nanopowders. In *Nanoengineering*, 111–48. Elsevier.

Chen, S., Gordin, M.L., Yi, R., Howlett, G., Sohn, H. & Wang, D. (2012). Silicon core–hollow carbon shell nanocomposites with tunable buffer voids for high capacity anodes of lithium-ion batteries. *Physical Chemistry Chemical Physics*, 14(37): 12741.

Chen, S., Shen, L., Van Aken, P.A., Maier, J. & Yu, Y. (2017). Dual-Functionalized Double Carbon Shells Coated Silicon Nanoparticles for High Performance Lithium-Ion Batteries. *Advanced Materials,* 29(21): 1605650.

CEU. (2019). Identification of nanomaterials through measurements :points to consider in the assessment of particulate materials according to the European Commission's Recommendation on a definition of nanomaterial. *Joint Research Centre*, LU: Publications Office. Available online: https://data.europa.eu/doi/10.2760/7644

Chen, S., Gordin, M.L., Yi, R., Howlett, G., Sohn, H. & Wang, D. (2012). Silicon Core–Hollow Carbon Shell Nanocomposites with Tunable Buffer Voids for High Capacity Anodes of Lithium-Ion Batteries. *Physical Chemistry Chemical Physics,* 14(37): 12741.

Corcione, C. & Frigione, M. (2012). Characterization of Nanocomposites by Thermal Analysis. *Materials*, 5(12): 2960–80.

Dazon, C., Fierro, V., Celzard, A. & Witschger, O. (2020). Identification of Nanomaterials by the Volume Specific Surface Area (VSSA) Criterion: Application to Powder Mixes. *Nanoscale Advances,* 2(10): 4908–17.

Dufaud, O., Vignes, A., Henry, F., Perrin, L. & Bouillard, J. (2011). Ignition and Explosion of Nanopowders: Something New under the Dust. *Journal of Physics: Conference Series,* 304: 012076.

ECHA. Carbon Black: Echa Dossier. Available online: https://echa.europa.eu/ro/registration-dossier/-/registered-dossier/16056/1/1. (Accessed on March 4, 2023).

ECHA. LTO: ECHA dossier. Available online: https://echa.europa.eu/ro/registration-dossier/-/registered-dossier/5366/1/1. (Accessed March 4, 2023).

Eckhoff, R.K. (2003). *Dust Explosions in the Process Industries*. 3rd. ed. Amsterdam: Gulf professional publ.

Enotiadis, A., Fernandes, N.J., Becerra, M.A., Zammarano, M. & Giannelis, E.P. (2018). Nanocomposite Electrolytes for Lithium Batteries with Reduced Flammability. *Electrochimica Acta,* 269: 76–82.

Erk, C., Brezesinski, T., Sommer, H., Schneider, R. & Janek, J. (2013). Toward Silicon Anodes for Next-Generation Lithium Ion Batteries: A Comparative Performance Study of Various Polymer Binders and Silicon Nanopowders. *ACS Applied Materials & Interfaces,* 5(15): 7299–7307.
Eshetu, G.G., Zhang, H., judez, X., Adenusi, H., Armand, M., Passerini, S. & Figgemeier, E. (2021). *Nature Communications*, 12(1).
European Commission. (2020). The NanoDefine methods manual. *Joint Research Centre,* LU: Publications Office, 2020. Available online: https://data.europa.eu/doi/10.2760/79490
European Standard (EN) (2011). BS EN 14034-3:2006+A1:2011 Determination of Explosion Characteristics of Dust Clouds Determination of the Lower Explosion Limit LEL of Dust Clouds. Available online: https://www.en-standard.eu/bs-en-14034-3-2006-a1-2011-determination-of-explosion-characteristics-of-dust-clouds-determination-of-the-lower-explosion-limit-lel-of-dust-clouds/.
Hu, J., Zhing, S. & Yan, T. (2021) Using carbon black to facilitate fast charging in lithium-ion batteries. *Journal of Power Sources*, 508(230342).
Hudak, N.S. 2014. Nanostructured Electrode Materials for Lithium-Ion Batteries. *Lithium-Ion Batteries*, 57–82. Elsevier. https://doi.org/10.1016/B978-0-444-59513-3.00004-2.
Iolitec Nanomaterials. Silicon NM-0020-HP. Available online: https://nanomaterials.iolitec.de/index.php/en/products/metals/NM-0020-HP. (Accessed February 13, 2024)
ISO (2010). ISO 9277:2010 Determination of the Specific Surface Area of Solids by Gas Adsorption — BET Method. Available online: https://www.iso.org/standard/44941.html.
ISO (2016). ISO/IEC 80079-20-2:2016 Explosive Atmospheres — Part 20-2: Material Characteristics — Combustible Dusts Test Methods. Available online: https://www.iso.org/standard/66564.html.
ISO (2020). ISO 13320:2020 Particle Size Analysis — Laser Diffraction Methods. Available online: https://www.iso.org/standard/69111.html.
Jiang, C., Hosono, E. & Zhou, H. (2006). Nanomaterials for Lithium Ion Batteries. *Nano Today,* 1(4): 28–33.
Johnston, L., Mansfield, E. & Smallwood, G.J. (2017). Physicochemical Properties of Engineered Nanomaterials. In *Metrology and Standardization of Nanotechnology*, edited by Elisabeth Mansfield, E., Kaiser, D.L., Fujita, D. & Van De Voorde, M. 99–114. Weinheim, Germany: Wiley-VCH Verlag GmbH & Co. KGaA.
Li, Y., Li, Q., Chai., J., Wang, Y., Du, J., Chen, Z., Rui, Y., Jiang, L. & Tang, B. (2023). Si-based Anode Lithium-Ion Batteries: A Comprehensive Review of Recent Progress. *ACS Materials Letters*, 5(11): 2948-2970.
Khudhur, D.A., Ali, M.W., & Tuan Abdullah, T.A. (2021). Mechanisms, Severity and Ignitability Factors, Explosibility Testing Method, Explosion Severity Characteristics, and Damage Control for Dust Explosion: A Concise Review. *Journal of Physics: Conference Series,* 1892 (1): 012023.
Mech, A., Rauscher, H., Babick, F., Hodoroaba, V., Ghanem, A., Wohlleben, W., Hans, Marvin, Weigel, S., Brungel, R., Friedrich, C.M., Kirsten, Rasmussen, Loeschner, K. & Gilliland, D. (2020). The NanoDefine Methods Manual. Available online: https://publications.jrc.ec.europa.eu/repository/handle/JRC117501. (Accessed May 10, 2024).
MTI Corporation. Li4Ti5O12 Powder for Li-Ion Battery Anode, 200g/Bag - EQ-Lib-LTO. Available online: https://www.mtixtl.com/Li4Ti5O12PowderforLi-ionbatteryanode200g/bag-EQ-Lib-LTO.aspx. (Accessed July 19, 2023).
MTI Corporation. MCMB (MesoCarbon MicroBeads) Graphite Powder for Li-Ion Battery Anode, 250g/Bag - EQ-Lib-MCMB. Available online: https://www.mtixtl.com/MCMBMesoCarbonMicroBeadsGraphitePowderforLi-ionBatteryAnode250g.aspx. (Accessed July 19, 2023).
Nanographenex. Natural Graphite (C) Nanopowder/Nanoparticles, Purity: 99.9% Size: 400 Nm-1.2 Um. Available online: https://nanographenex.com/natural-graphite-c-nanopowder-nanoparticles-

purity-99.9-size-400-nm-1.2-um-nanoparticles?search=carbon&description=true&category_id=60&sub_category=true. (Accessed July 19, 2023).
Örüm Aydin, A., Zajonz, F., Günther, T., Dermenci, K., Berecibar, M. & Urrutia, L. (2023). Lithium-Ion Battery Manufacturing: Industrial View on Processing Challenges, Possible Solutions and Recent Advances. *Batteries,* 9(11): 555.
Pinilla, S., Park, S.-H., Fontanez, K., Márquez, F., Nicolosi, V. & Morant, C. (2020). 0D-1D Hybrid Silicon Nanocomposite as Lithium-Ion Batteries Anodes. *Nanomaterials,* 10(3): 515.
Qi, W., Shapter, J.G., Wu, Q., Yin, T., Gao, G. & Cui, D. (2017). Nanostructured Anode Materials for Lithium-Ion Batteries: Principle, Recent Progress and Future Perspectives. *Journal of Materials Chemistry A,* 5(37): 19521–40.
Sourice, J., Bordes, A., Boulineau, A., Alper, J.P., Franger, S., Quinsac, A., Habert, A., Leconte, Y., De Vito, E., Porcher, W., Reynaud, C., Herlin-Boime, N. & Haon, C. (2016). *Journal of power Sources*, 328: 527-535.
Sun, L., Liu, Y., Shao, R., Wu, J., Jiang, R. & Jin, Z. (2022). Recent Progress and Future Perspective on Practical Silicon Anode-Based Lithium Ion Batteries. *Energy Storage Materials,* 46:482–502.
Vignes, A., Dutouquet, C., Aube, A., Laurent, M., Bressot, C., Bouillard, J., Pohl, A., Ribalta, C. & Fonseca, S. (2023). Draft of the operational methodology for the use of dustiness for risk assessment of NMs and HARNs explosion risk in industrial scenario to support ATEX safety assessment, Deliverable D1.15, NanoHarmony H2020 EU Project, Grant agreement ID: 885931. Available online: https://ec.europa.eu/research/participants/documents/downloadPublic?documentIds=080166e505fe1678&appId=PPGMS.
Wang, L., Gao, B., Peng, C., Peng, X., Fu, J., Chu, P.K. & Huo, K. (2015). Bamboo Leaves Derived Ultrafine Si Nanoparticles and Si/C Nanocomposites for High-Performance Li-Ion Battery Anodes. *Nanoscale,* 7(33): 13840-13847.

Fluid Motion and Heat Transfer in Autoignition Testing

Branson Davis[a] & Charline Fouchier[a,b] & Joseph Shepherd[a]

[a] Graduate Aerospace Laboratories, California Institute of Technology, Pasadena, CA, USA
[b] von Karman Institute for Fluid Dynamics, Sint Genesius Rode, Belgium

E-mail: *bdavis@caltech.edu*

Abstract

In this study, experimental measurements and three-dimensional numerical simulations were used to characterize the flow field inside our laboratories' Autoignition Temperature (AIT) facility based on the ASTM-E659 standard. Within the flask, small surface temperature differences, along with the downward movement of air through the center of the neck, create a single dominant toroidal vortex that transports fluid upwards along the walls and downward along the center line. Increasing the height of the flask holder caused the average temperature to increase and the magnitude/frequency of fluctuations to decrease. Studies of fuel-air mixing of ethene (C_2H_4), n-hexane (nC_6H_{14}), and n-dodecane ($nC_{12}H_{26}$) found that the lighter fuels more readily diffuse into air whereas the heavier fuels are more strongly influenced by buoyancy effects and take longer to mix. Further, in some cases the mixing time will be comparable to the time to ignition and long ignition times may result in significant quantities of fuel molecules escaping from the open top of the flask.

Keywords: *Thermal Ignition, Standardized Tests, Heat Transfer, Fluid Mechanics, Safety*

1 Introduction

The minimum autoignition temperature (AIT) of a fuel in hot air is used to evaluate the flammability and fire hazards of combustible gases and liquids. Early work to create standardized tests (Setchkin, 1954, Zabetakis et al., 1954)) has led the test methods which have evolved into the modern day ASTM-E659 (2005) standard in North America and its current international equivalent, ISO/IEC (2017). During an ASTM-E659 test, a small quantity of liquid fuel is injected into 500 mL flask containing hot air at atmospheric pressure. The AIT temperature is the minimum temperature for which ignition is observed within a limited time period in a series of trials varying the fuel amount and flask temperature following the procedure set out in the standard.

Many authors have since used the ASTM-E659 standards to characterize AITs for various liquid fuels. The reported AITs from extensive testing are tabulated in combustion safety databases, such as the Chemical Hazard Response Information System (CHRIS) and CHEMSAFE (Guard, 1999, Zakel et al., 2019). Recent experimental results of Martin and Shepherd (2021) emphasized that a wide range of ignition behaviors can occur, which could be categorized into at least four distinct modes. Measured AITs are also found to be sensitive to the specifics of the measurement technique, with variability often exceeding the precision of published data.

Recent experiments with our own ASTM-E659 apparatus indicate that the transient heat transfer and fluid motion inside the flask could significantly impact AIT measurements. The focus of this study is to investigate the effect various experimental setups conforming to the ASTM-E659 standards could have on the flow field inside the flask and temperature measurements used to report AITs. The temperature profile along the axis of symmetry inside the flask was characterized experimentally and compared with three-dimensional, unsteady numerical simulations. The influence of the mixing zone between outside air and the flask interior was identified as a key factor in determining the mean and fluctuating temperature profile in the flask. Numerical simulations of fuel-air mixing studies were conducted to characterize the transient mixing process that takes place after fuel is introduced into the flask.

2 Experimental Methods

For our study, we adapted the experimental setup used by Martin et al. for the characterization of the AITs for Jet A and surrogate jet fuels (Martin and Shepherd, 2021, Martin, 2023). This apparatus was constructed following the ASTM-E659 (2005) standard. Figure 1 shows a picture and a cross-section drawing of the setup.

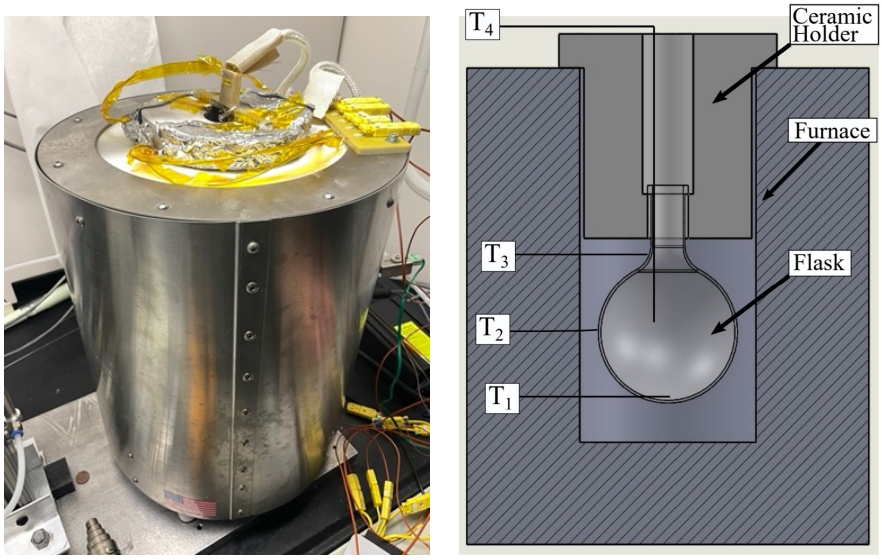

***Fig. 1**: Experimental apparatus*

The apparatus is composed of a Mellen CV12 crucible furnace with a 133 mm diameter and 200 mm deep cylindrical volume, which controllably heats up a 500 mL round bottom, borosilicate flask up to 1250 °C with a PID controller (Love Controls series 16B) system accurate to 1 °C. The flask is suspended in the furnace by a ceramic holder molded from silica-based Cotronics Rescor 750. The flask and ceramic holder are covered by aluminum foil to reflect the radiation inside the flask and reduce heat loss.

The temperature of the flask surface is measured with three 34 gauge, type K thermocouples inside a mineral-insulated metal sheath, set at positions T_1, T_2, and T_3 (see Figure 1). The thermocouple conventionally used to measure the air temperature, T_4, in ignition experiments was removed and replaced with a 36 gauge, type K thermocouple attached to a Velmex slide (NEMA 17, 155 mm travel) capable of precise vertical resolution. This allowed temperature measurements to be taken at various heights within the apparatus. The temperature variation is recorded with a NI 9213 16-channel, 24-bit, 75 Hz thermocouple data acquisition module from National Instruments, connected to a cDAQ-9171 CompactDAQ Chassis. We sampled each height for 120 s and waited an additional 120 s between measurements to allow unsteadiness effects caused by the movement of the internal thermocouple to dampen.

3 Numerical Methods

The transient, three-dimensional fluid motion, heat transfer, and mixing were numerically simulated by solving the Navier-Stokes equations of a multi-component ideal gas mixture. The equations of motion Eqn. (1)-(4), boundary and initial conditions were implemented in OpenFOAM using the PISO algorithm. We only considered non-reacting flow and did not attempt to model chemical reactions or the actual autoignition process in this study.

3.1 Geometric Model and Meshing

The flask and ceramic holder of the ASTM setup shown in Figure 1 were carefully measured and modeled in Solidworks to provide a suitable framework for simulation. The interior geometry was then meshed in three dimensions using the OpenFOAM tool, snappyHexMesh, prioritizing uniform hexahedral cells. A grid-independent solution, as determined from a statistical analysis of the unsteady flow, could be achieved for a grid of 6 million cells resulting in cell sizes of approximately 600 μm. In addition to modeling the flask and ceramic holder, a rectangular region above the flask (not shown in Figure 2) with open boundaries was included to model the exchange of gas between the flask and the surrounding atmosphere.

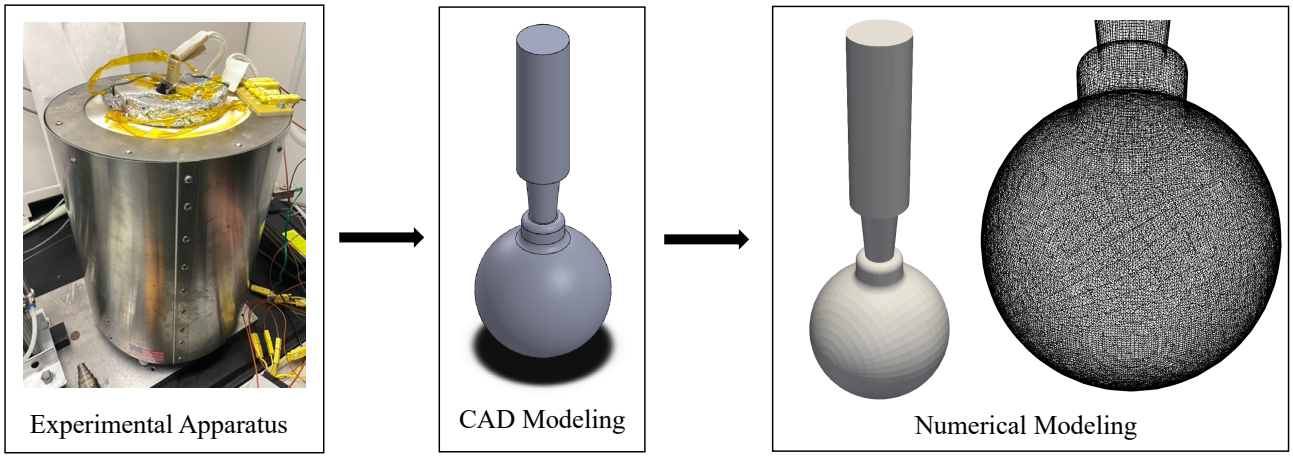

***Fig. 2**: Numerical Modeling of the ASTM apparatus*

3.2 Governing Equations

The governing equations we simulated were the variable-density Navier-Stokes equations for a Newtonian fluid with temperature-dependent transport properties and buoyancy forces in the momentum equation.

$$\frac{\partial \rho}{\partial t} + \nabla \cdot (\rho \mathbf{u}) = 0, \tag{1}$$

$$\frac{\partial}{\partial t}(\rho \mathbf{u}) + \nabla \cdot (\rho \mathbf{u}\mathbf{u} + p\mathbf{I}) = \nabla \cdot \tau + \rho \mathbf{g}, \tag{2}$$

$$\frac{\partial}{\partial t}(\rho Y_i) + \nabla \cdot (\rho Y_i \mathbf{u}) = -\nabla \cdot (\rho Y_i \mathbf{V}_i) \quad i = 1, 2, \ldots, K, \tag{3}$$

$$c_P \frac{\partial}{\partial t}(\rho T) + c_P \nabla \cdot (\rho \mathbf{u} T) = -\nabla \cdot (\lambda \nabla T) - \rho \nabla T \cdot \sum_{i=1}^{K} c_{P,i} Y_i \mathbf{V}_i, \tag{4}$$

where t is time, ρ is the mixture density, p is the pressure, u is the velocity, g is the acceleration due to gravity, T is the temperature, c_P is the specific heat at constant pressure, λ is the mixture thermal conductivity, Y is the mass fraction, $\mathbf{V}$ is the correction diffusion velocity, and τ is the viscous stress tensor written as:

$$\tau = \mu(\nabla \mathbf{u} + (\nabla \mathbf{u})^T) - \frac{2}{3}\mu(\nabla \cdot \mathbf{u})\mathbf{I} \tag{5}$$

where $\mathbf{I}$ is the identity matrix. The subscript, i, indicates the individual species, and K is the total number of species. For simulations in air, the species conservation equation and mass diffusion term

in the energy equation were omitted. The ideal gas equation of state was used to calculate the density of the mixture.

The diffusion velocities are calculated according to Chapman and Cowling (1990) using Fick's law, including a contribution by thermodiffusion (Soret effect) as:

$$\mathbf{V_i} = -\frac{D_i}{Y_i}\nabla Y_i - \frac{D_i \Theta_i}{X_i}\frac{1}{T}\nabla T \tag{6}$$

where X_i is the mole fraction, and Θ_i is the thermodiffusion ratio of species i. The individual-species mixture-averaged diffusion coefficients, D_i, are calculated according to Curtiss and Hirschfelder (1949) as:

$$D_i = \frac{1 - Y_i}{\sum_{j \neq i}^{N} \frac{X_i}{D_{ji}}} \tag{7}$$

where D_{ji} are the binary diffusion coefficients. To ensure the conservation of mass, a correction diffusion velocity is applied to $\mathbf{V}_i$ in Eqs (3) and (4) as described by Coffee and Heimerl (1981) as:

$$\mathbf{V}_i^C = \mathbf{V}_i + \mathbf{V}_C \, . \tag{8}$$

3.3 Initial and Boundary Conditions

Figure 3 shows the temperature boundary condition on the flask and holder as a function of height. A piece-wise linear profile in height z was imposed on the surface of the flask and was assumed constant in the holder section due to the large ceramic mass being held inside the furnace. These temperatures correspond to experimentally measured flask surface temperatures T_1, T_2, and T_3. A no-slip condition was imposed on the walls.

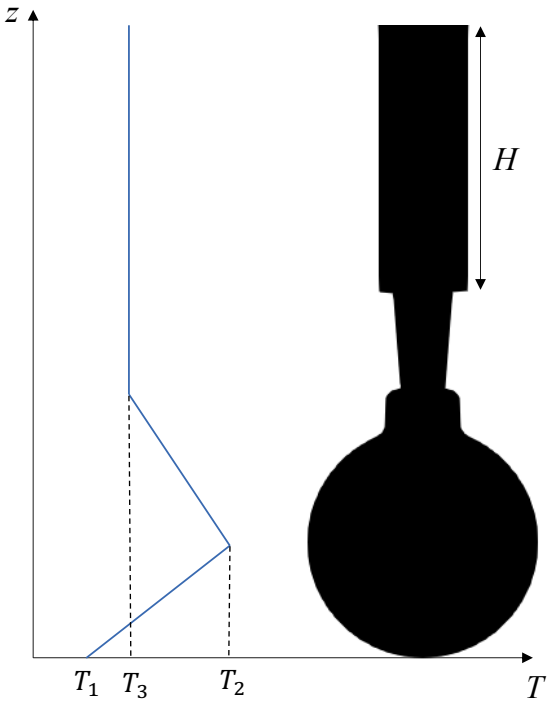

***Fig. 3**: Height-varying temperature boundary condition*

The simulations were initiated from rest at room temperature and continued until the temporal flow field became statistically stationary. Flow characterization and mixing simulations used this resultant flow field as an initial condition.

3.4 Test Conditions

The initial and boundary conditions were used to characterize a dry air flow field for various height ceramic holder pieces within the specs of the ASTM-E659 standard, which are summarized in Table 1. The inner diameter for all holders was 38.1 mm.

***Table 1**: Geometric holder configurations*

Case	Holder Height H (mm)
A	57.15
B	114.3
C	228.6

Case B corresponds to the dimension of the ceramic holders used in our laboratory and was used to numerically examine fuel mixing within the flask for gaseous ethene (C_2H_4), n-hexane (nC_6H_{14}), and n-dodecane ($nC_{12}H_{26}$). The ASTM-E659 standard with an open flask is intended for liquid or solid substances. Ethene was examined in order to investigate the effect of lighter, more diffusive fuels on the mixing process and efflux. Although the ASTM standard uses a closed flask for gas testing, the ISO/IEC (2017) international standard allows the testing of gas in an open flask similar to the ASTM liquid apparatus. The syringe injection process was not simulated, but instead, a 15 mm ball of fuel was initialized into a fully established flow field at the internal flask temperature. The resulting evolution of the composition (without reaction) was characterized as a function of time and space.

4 Results and discussion

4.1 Experimental Validation

To validate the numerical model, temperature measurements were digitally recorded and temporally averaged for a series of points on the vertical center line of the experimental apparatus and compared with values from the equivalent numerical simulation of case B. The position 0 mm corresponds to the bottom of the flask. Figure 4 (left) compares the average temperature between the experiment and the simulation. The vertical dashed lines indicate the top of the lower, spherical part of the flask (98 mm) and the upper neck of the flask (159 mm). A variation of 4 K was seen across the lower portion of the flask. Through the neck, a more significant 75 K temperature variation was seen due to the mixing region at the exit of the flask and within the ceramic holder. Above the flask, the temperature decreases with increasing height, approaching the value of the cold ambient air above the setup.

Comparing the average temperature between the simulation and the experiment within the lower part of the flask, the maximum deviation was only 1.5 K for any measured position. However, larger deviations in the temperature profile inside the ceramic holder can be observed. The surface temperature profile within the ceramic holder was not measured and was assumed to be spatially uniform in the simulation. This assumption is likely the source of discrepancy between simulation and experiment in this region.

Computed and observed temporal temperature fluctuations are shown in Figure 4 (right) at heights of 9, 47.1, and 159.5 mm along the flask center line. These heights correspond to the bottom, middle, and region immediately above the top of the flask. In the simulations, fluctuations up to 5 K are observed at the bottom of the flask and up to 12 K at the center of the flask. Immediately above the top of the flask, the flow is very unsteady. Fluctuations up to 80 K are observed with durations of approximately 0.1 s. The experimentally measured fluctuations for all heights are significantly less than those simulated, only 20 K at most above the flask in the ceramic holder. This difference is due to the slow response time of the thermocouple used for the measurements, estimated to have a characteristic step response time of $\tau = 1$ s to reach 67% of the final value. This is at least an order of magnitude slower than the fluctuations observed in the simulations and accounts for the observed differences.

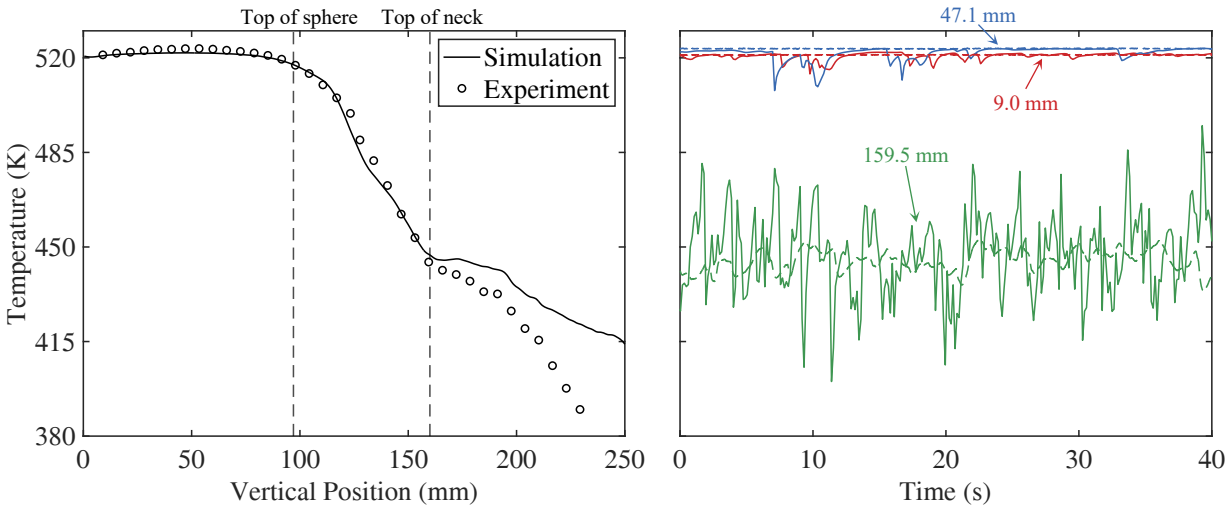

***Fig. 4**: (Left) Average temperature along the vertical center line of the flask, comparing simulation and experiment. (Right) Comparison of temperature fluctuations at selected heights between the simulation (solid lines, –) and experiment (dashed lines, - -)*

4.2 Effects of holder height

The ASTM standard allows users flexibility in the construction of the apparatus and in particular, the dimensions of the ceramic holder and the location of the flask within the furnace. We examined the influence of the three insulating holder heights shown in Table 1 on the fluid motion. The motion was simulated for 50 seconds after stationary statistics were achieved that were independent of start-up behavior. Figure 5 plots on a vertical cross-section through the center line the average temperature field and projected (surface) streamlines. For all three cases, a toroidal vortex is observed within the bottom of the flask. The flow is in the unsteady but laminar regime with an estimated Reynolds number (based on flask diameter and maximum center line gas velocity) of $Re \approx 120$. Flow is driven by both the temperature distribution in the flask and, more importantly, the flow of colder, more dense air penetrating down the ceramic holder through the center of the flask and an upward counterflow of hot air circulating from the bottom portion of the flask upward along the hot walls. Circulation cells commonly observed in natural convection flows within nonuniformly heated slots or cavities are observed above the flask within the ceramic holder. As the holder height is increased, the number of cells increases, from 2 to 10. The averaged flows are approximately axisymmetric but evidence of the three-dimensional motion and symmetry-breaking can be observed in the surface streamline patterns.

Examining the average temperature field, an unstable vertical stratification is apparent within the holder, with temperature decreasing with increasing height, as shown in Figure 6 (left). Modest variations in temperature can be observed within the round portion of the flask, case A was on average 7 K lower than case C. The temperature variations within the neck of the flask decrease with the increasing height of the ceramic holder. This is due to the increased mixing and longer residence time of the cold ambient gas as it plunges down through the longer holders into the flask. The cold air above the furnace has to travel further to reach the flask in case C compared to case A. The average downward velocity, Figure 6 (right), is lower in case C than in case A leading to a longer mixing time and greater heat transfer. Therefore, larger average temperatures are observed as the holder height increases. Transverse velocities along the center line (not shown) are two orders of magnitude smaller than the vertical component.

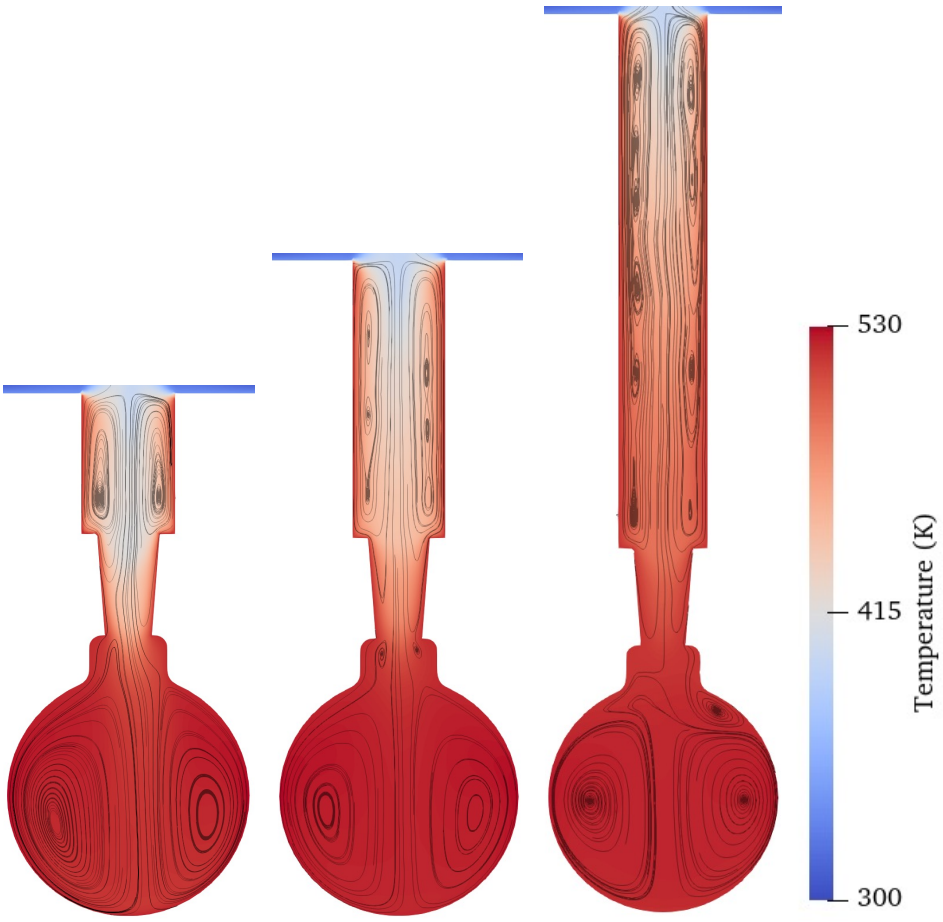

Fig. 5*: Average temperature field and surface streamlines along a vertical cross-section of the domain for the three holder heights*

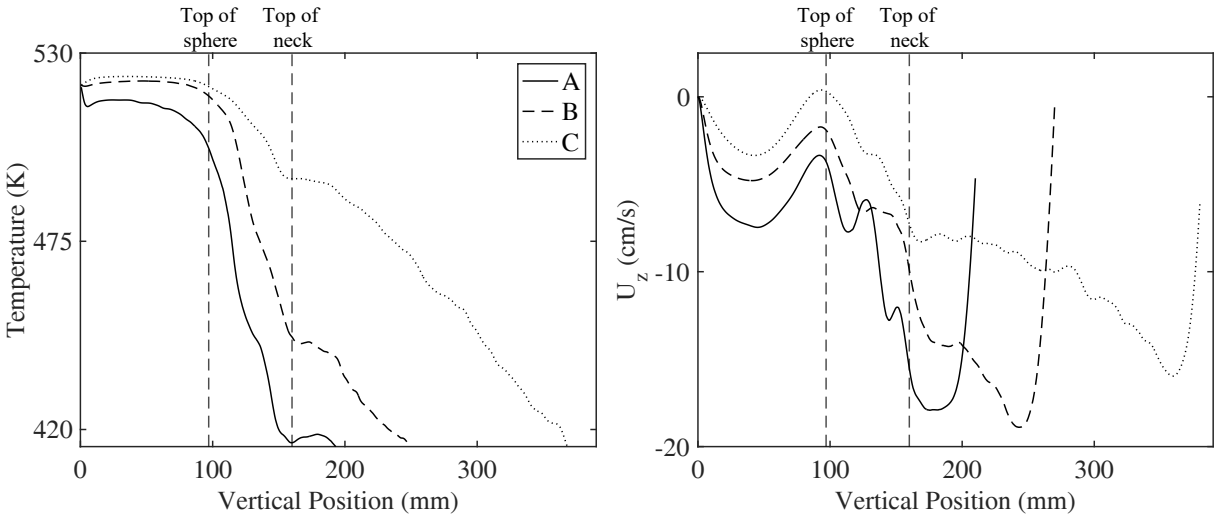

Fig. 6*: (Left) Average temperature profile and (Right) Average vertical velocity along the vertical center line for the three holder heights*

While averages can be informative about the large-scale features of the flow, temperature fluctuations[1] are important for unsteady reactive flow problems since reaction rates strongly depend on temperature.

[1] Correlations between temperature and composition and conditional averages of reaction rates are also important but we only examined non-reacting aspects of the flow in this study.

Table 2 gives the temporal temperature statistics in the center of the flask. This location is consistent with the nominal location of thermocouple T_4, used by the ASTM-E659 standard to monitor and characterize the temperature within the flask during ignition experiments. Case A had the largest temperature standard deviation (8 K) and largest absolute fluctuation size (38 K), while case C had the smallest standard deviation (0.9 K) and absolute fluctuation size (3 K). This is expected since the residence times of downward moving cold air are smaller in the shorter flask holder as compared to the taller holders.

***Table 2**: Statistical analysis of temperature at the center of the flask for the three holder heights*

Case	T_{avg} (K)	T_{std} (K)	T_{min} (K)	T_{max} (K)
A	515.6	8.00	477.2	522.1
B	520.6	3.30	494.3	523.6
C	522.8	0.90	519.7	524.1

The temporal average temperature was computed for all cells within the spherical portion of the flask. A histogram was obtained by binning the average temperature field. This is directly related to the probability distribution as the computational volumes are essentially identical in size and uniformly distributed. Figure 7 plots the distributions for the three holder heights. The location of the temperature at the center of the flask, T_4, is indicated with vertical lines. For the shortest holder, case A, the distribution is broadest, spanning 15 K, whereas cases B and C are narrower, spanning 9 and 8 K, respectively. These trends are consistent with the fluctuations reported in Table 2. With decreasing holder height, the flow fields become less steady and more cold air enters the flask, broadening the temperature probability distribution. For all holders, T_4 is on the left tail of their respective distributions with values of T_4 up to 5 K less than the median temperature. The implications for the reported AIT are discussed in Section 5.

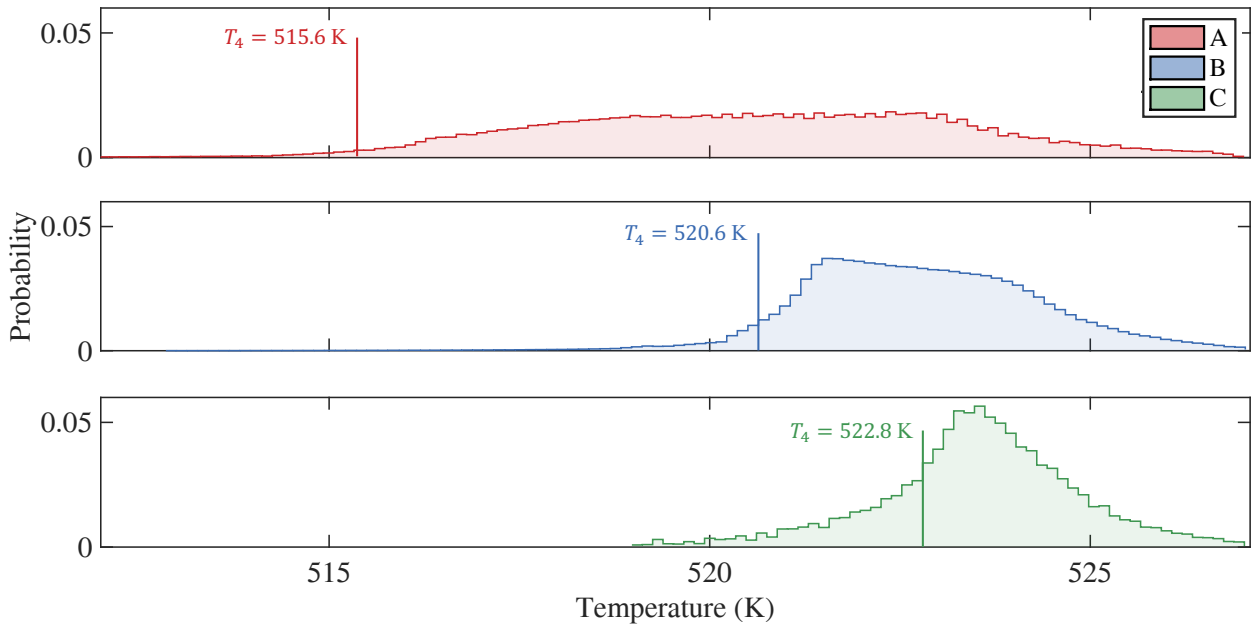

***Fig. 7**: Flask average temperature probability distributions for the three holder configurations. Flask center temperatures, T_4, are also indicated.*

4.3 Fuel Mixing

During an ignition experiment, fuel is injected from a syringe through a thin needle into the flask. Depending on the temperature, ignition can occur at a range of times following injection and with different extents of mixing depending on the fuel density and diffusivity. Understanding how the fuel distribution evolves within the flask following injection is also relevant to explaining the various modes of ignition that have been observed (Martin and Shepherd, 2021).

To study the effect of mixing, a ball of fuel in its gaseous phase was initialized near the bottom of the flask in an established dry air flow field. The temperature of the fuel sphere was set to be equal to the local air temperature at the time of injection. We acknowledge that a more complicated situation exists for liquid fuels, with droplets and two-phase mixtures emerging from the needle. The flow momentum, droplet vaporization, impact on the flask surface, and droplet dynamics, including the Leidenfrost effect, will influence the mixing behavior. Chemical reactions will also begin to take place concurrent with the mixing process. We have drastically simplified the problem to enable a preliminary analysis.

The evolution of fuel concentration over time was computed for three fuels of very different sizes and molecular weights. Figures 8 and 9 plot the mole fractions of C_2H_4 and nC_6H_{14} on a vertical cross-section through the center of the flask over time. The color bar is updated at every instance in time so that the mixing characteristics can be visualized. For the C_2H_4 case, the fuel initially rises slightly before being fully mixed in the flask within 30 seconds. The nC_6H_{14} and $nC_{12}H_{26}$ (not shown) cases mix very differently than C_2H_4. For the heavy molecules, the fuel initially sinks to the bottom of the flask before diffusing upwards and becoming fully mixed over a much longer period, 100-200 s.

The effect of varying the fuel molecular weight can be characterized by the density of the fuel sphere, ρ_F, the Froude number based on peak center line speed U, flask diameter d, and density normalized density difference $\Delta\rho/\rho_F = (\rho_F - \rho)/\rho_F$ between the fuel volume and surrounding air

$$Fr = \frac{U}{\sqrt{gd|\Delta\rho|/\rho_F}} \cdot \text{sign}(\Delta\rho_F)\,,$$

and the Schmidt number based on the mixture viscosity μ and fuel diffusivity D_F in the surrounding fuel-air mixture

$$Sc = \frac{\mu}{\rho D_F}\,.$$

Representative values for each fuel are shown in Table 3. Because all the cases were initialized at the same temperature and pressure, the initial density of the ethene sphere is slightly smaller than the ambient air density (0.69 kg·m^{-3}) and the initial density of the n-hexane and n-dodecane spheres are larger than ambient. As a consequence, Ethene is slightly buoyant with $Fr < 0$ and the flow is dominated by convection. The unstable fuel sphere is convected throughout the flask and the distorted volume rapidly mixes by diffusion. The n-hexane and n-dodecane are dominated by buoyancy with $1 \gg Fr > 0$. The initial negative buoyancy results in the fuel spheres settling to the bottom of the flask and then slowly diffusing upward with a stable interface between the fuel-air mixture and air.

***Table 3**: Molecular weight, Lennard-Jones parameter, fuel sphere density, Schmidt number, and Froude numbers for the three tested fuels*

Fuel	W_F [kg· kmol^{-1}]	σ_F [nm]	ρ_F [kg·m^{-3}]	Sc	Fr
C_2H_4	28	0.39	0.65	0.93	-0.27
nC_6H_{14}	86	0.59	2.00	1.8	0.059
$nC_{12}H_{26}$	170	0.76	3.95	2.6	0.053

The degree of "mixedness" can be studied to quantitatively assess how quickly the fuels mix within the flask. The intensity of segregation can be defined in terms of the coefficient of variation as described

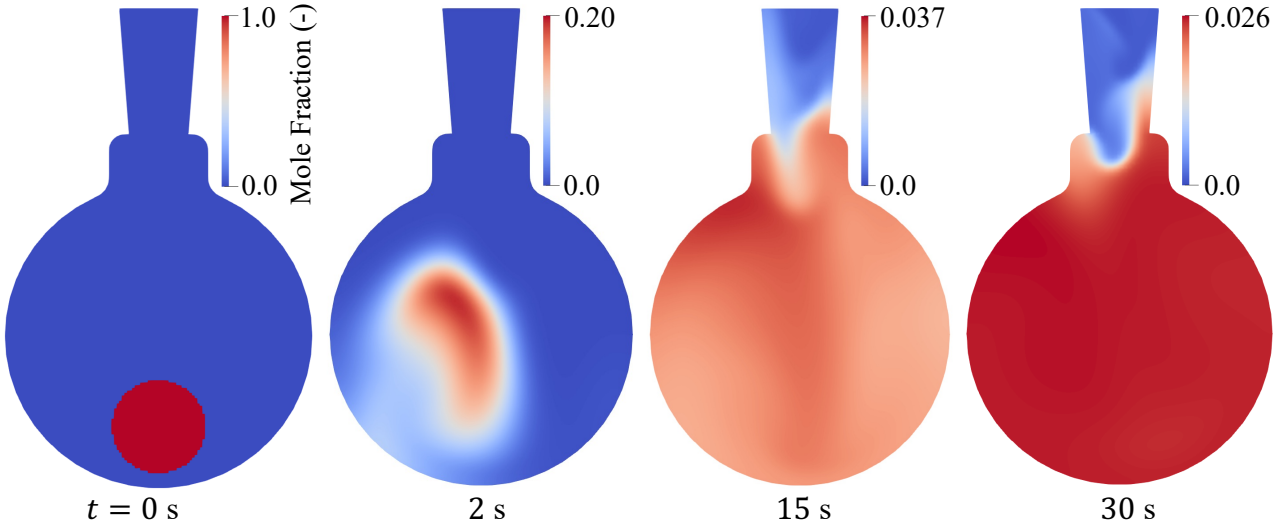

***Fig. 8**: C_2H_4 mole fraction temporal evolution on a vertical cross-section within the flask*

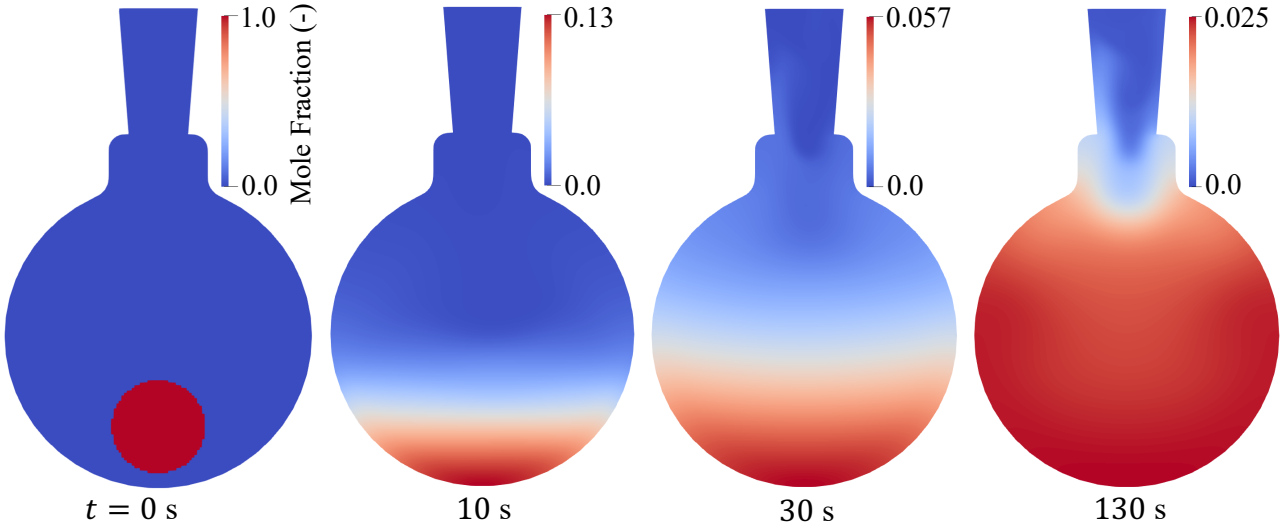

***Fig. 9**: nC_6H_{14} mole fraction temporal evolution on a vertical cross-section within the flask*

in Kukukova et al. (2009) as:

$$c_v = \sqrt{\frac{1}{N}\sum_{i=1}^{N}\left(\frac{X_i - \overline{X}}{\overline{X}}\right)^2} \tag{9}$$

where X_i is the fuel mole fraction for a given computation cell, $\overline{X}$ is the volume average fuel mole fraction, and N is the total number of cells in the domain. The coefficient of variation, c_v, can be normalized by the initial $c_v(0)$ to obtain a value between 0 and 1. Given that c_v computes the standard deviation over the mean, the value is largest for a perfectly unmixed state and will decay to 0 for a completely homogeneous mixture. As c_v is dimensionless, it can be readily compared between the different fuel cases. Figure 10 plots c_v against time for the three fuels. In very early times, the mixedness of n-hexane and n-dodecane decays more rapidly than ethene. This is caused by the strong buoyancy force that immediately drives the heavier fuels to the bottom of the flask. However, as time continues, ethene c_v reaches a steady value near zero significantly faster than for n-hexane and n-dodecane.

The effect of diffusivity on mixing can be understood by examining the estimated Schmidt numbers,

Sc, in Table 3. The increase in *Sc* with increasing fuel molecular weight is primarily due to the decrease in diffusivity with increasing fuel molecule size, although there is a small contribution (15%) from the difference in mixture kinematic viscosity. For example, consider how the binary diffusion coefficient (Kee et al., 2005) depends on both the molecular weights W_i and effective collision cross sections σ_{FA}^2

$$D_{FA} \propto \frac{1}{\sigma_{FA}^2}\sqrt{\frac{1}{W_F}+\frac{1}{W_A}}$$

where $\sigma_{FA} = (\sigma_F + \sigma_A)/2$ and σ_A = 0.35 nm. The increase in molecular size σ_F and decrease in diffusivity for the larger fuel molecules results in an increase in the time to mix, all other factors being the same. This accounts for the differences in the mixing rate of n-hexane and n-dodecane.

Taking a 5% level of c_v conventionally used in industry to characterize mixing time, the time to mix was = 11, 59, and 104 s for C_2H_4, nC_6H_{14}, and $nC_{12}H_{26}$, respectively. Previous work from Martin (2023) shows that nC_6H_{14} and $nC_{12}H_{26}$ can ignite before these times in some ASTM test conditions. In those cases, it is probable that ignition occurs before the fuel is fully mixed inside the flask.

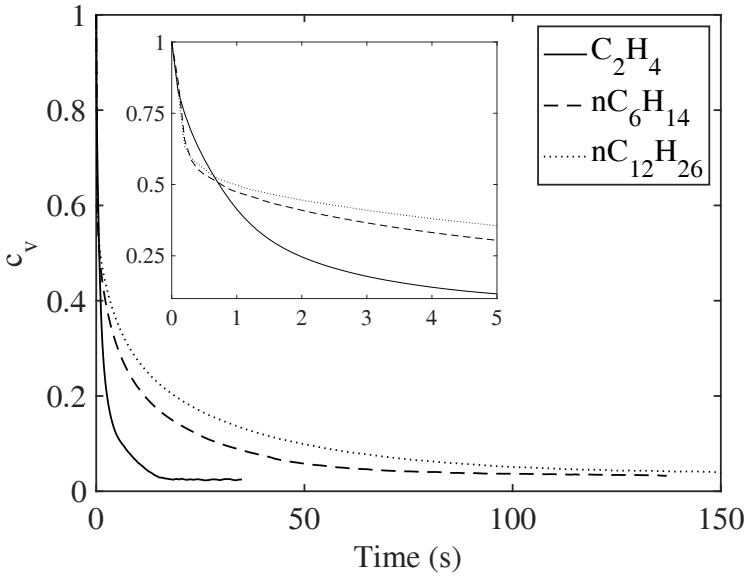

***Fig. 10**: Coefficient of variation (9) over time for C_2H_4, nC_6H_{14}, and $nC_{12}H_{26}$*

The number of fuel moles, *n*, within the flask can also be tracked over time by integrating spatially over the number of cells. This is shown in Figure 11. Since the same volume, pressure, and temperature were initialized, *n* is initially the same for all three cases. After 3 seconds, ethene molecules begin leaving the flask and the number of moles rapidly decreases over the next several seconds. After 26 s, 10% of the fuel has escaped into the holder and ambient air above. For n-hexane and n-dodecane cases, a 10% loss of fuel takes significantly longer at 117 and 173 s, respectively. The much slower loss of the larger, heavier fuel molecules is a consequence of the stable stratification, resulting in a much longer time for the fuel-air interface to reach the top of the flask, diffuse into the neck of the flask, and, ultimately, escape. For all cases, the time to lose 10% of the fuel molecules is longer than the time for the intensity of segregation to drop below 5%. Thus, the fuel molecules remain mostly within the flask prior to complete mixing, even for the smaller, lighter C_2H_4 case. Martin (2023) observed ignition of n-hexane and n-dodecane up to approximately 70 and 170 seconds, respectively. It's probable that less than 10% of the fuel leaves the flask before he observed ignition.

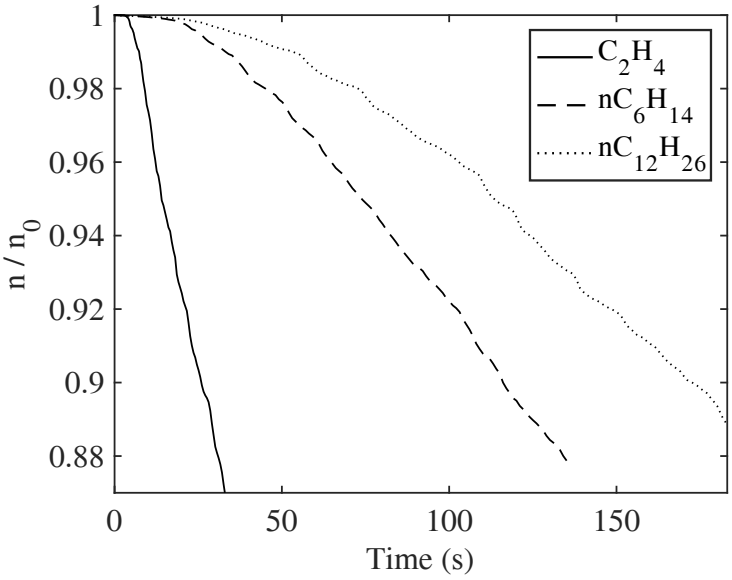

***Fig. 11**: Number of fuel moles normalized by the initial value within the flask over time*

5 Implications for AIT experiments

Our results (Figure 7) indicate that various setups, all conforming to the ASTM-E659 standard, can have significantly different temperature distributions. A range of temperatures can exist within the flask and will not be captured by the single point of measurement at T_4. Further, the size of fluctuations and general unsteadiness are different for the three cases we considered. This indicates that investigation and consideration of variations between apparatus construction is needed when evaluating reported results. The existence of a range of temperatures within the test flask indicates that care is needed in interpreting the values of AIT based only on the measurements of T_4.

We observe that fuel dispersion inside the flask is affected by the flow field and the fuel's physical properties, such as the density and diffusion coefficient. For short-duration tests, ignition could occur in a poorly mixed atmosphere before the fuel is perfectly dispersed, while for long-duration tests, loss of fuel could influence the AIT. Competing mixing and chemical timescales could cause AIT comparisons between different fuels to be misleading unless these factors are taken into account.

6 Conclusions

Experimental measurements and three-dimensional numerical simulations with realistic transport properties were used to characterize the flow field inside our ASTM E659 Autoignition Temperature (AIT) facility. Within the test flask, small surface temperature differences along with downward movement of air through the center of the neck create a single dominant toroidal vortex that transports fluid upwards along the walls and downward along the center line. Temperature measurements were made along the vertical center line in our AIT facility and were compared to a numerical simulation of the same geometry. A maximum variation of 4 K (0.7%) was observed in the average temperature within the flask. Above the flask, larger deviations between the simulation and experiment were observed due to the isothermal boundary condition used on the numerical model. For all measured locations, experimental temperature fluctuations were significantly smaller than those seen in the simulation at the same location, These discrepancies are attributed to the the slow response time of the thermocouple used in the experimental measurements.

A parametric study of the ceramic holder heights was carried out numerically to observe the effect on the resultant flow field. While the same toroidal vortex was seen within the bottom of the flask for all cases, the flow into the flask decreased and the number of convective cells seen on average increased with holder height. As a result, the average temperature for any given location along the vertical center line increased with increasing holder height. At the center of the flask, the average temperature for case A (shortest) was 7 K lower than for case C (tallest). Similarly, the absolute fluctuation size

decreased from 8 K with the shortest holder to 0.9 K for the tallest holder.

A parametric study was carried out to observe the effect of varying fuel molecule size and molecular weight on the mixing process within the flask. For the smallest molecule, ethene, complete mixing can occur in only 11 s due to minimal buoyancy effects and small Schmidt number. Heavier fuels, such as n-hexane and n-dodecane, consequently have much smaller, positive Froude numbers. Therefore, gravity initially plays a dominant role in forcing the fuel to the bottom of the flask. With significantly larger Schmidt numbers, these fuels diffuse much more slowly in air with mixing times of 59 and 104 s respectively, compared to ethene. A 10% loss of fuel molecules was observed after 25, 119, and 180 s for ethene, n-hexane, and n-dodecane, respectively. Therefore for all fuels studied, significant loss of fuel from the flask only occurs after complete mixing is obtained.

Our study has identified a number of factors that are important to consider in interpreting AIT data from the ASTM-E659 apparatus. We observe that both the construction of the apparatus (with the allowable specification of the standard) and the fluid motion induced by buoyancy can have a significant influence of gas inside the flask prior to ignition. The observed variability in temperature and fuel concentration may have an influence the measured autoignition temperatures and ignition delay times with implications for application to hazard assessment.

Acknowledgements

This research was carried out in the Explosion Dynamics Laboratory of the California Institute of Technology. This work was supported by The Boeing Company through a Strategic Research and Development Relationship Agreement CT-BA-GTA-1 and C. Fouchier was supported by the European Union through a Marie Sklodowska-Curie Fellowship.

References

ASTM-E659 (2005). *Standard test method for autoignition temperature of liquid chemicals*. American Society for Testing and Materials.

Chapman, S., Cowling, T. G. (1990). *The mathematical theory of non-uniform gases: an account of the kinetic theory of viscosity, thermal conduction and diffusion in gases*. Cambridge university press.

Coffee, T., Heimerl, J. (1981). *Transport algorithms for premixed, laminar steady-state flames*. Combust. Flame, 43:273–289.

Curtiss, C. F., Hirschfelder, J. O. (1949). *Transport properties of multicomponent gas mixtures*. J. Chem. Phys., 17(6):550–555.

Guard, U. C. (1999). *Chemical hazard response information system (chris)-hazardous chemical data*. Commandant Instruction, 16465.

ISO/IEC (2017). *ISO/IEC 80079-20-1: Explosive atmospheres - Part 20-1: Material characteristics for gas and vapor classification-test methods and data*. Technical report, International Organization for Standardization.

Kee, R. J., Coltrin, M. E., Glarborg, P. (2005). *Chemically reacting flow: theory and practice*. John Wiley & Sons.

Kukukova, A., Aubin, J., Kresta, S. M. (2009). *A new definition of mixing and segregation: Three dimensions of a key process variable*. Chemical engineering research and design, 87(4):633–647.

Martin, C. D. (2023). *Experiments in Thermal Ignition: Influence of Natural Convection on Properties of Gaseous Explosions*. Ph.D. thesis, California Institute of Technology.

Martin, C. D., Shepherd, J. E. (2021). *Low temperature autoignition of jet a and surrogate jet fuel*. Journal of Loss Prevention in the Process Industries, 71:104454.

Setchkin, N. P. (1954). *Self-ignition temperatures of combustible liquids*. Journal of Research of the National Bureau of Standards, 53(1):49.

The Open Foam Foundation (2023). *OpenFOAM*. `https://www.openfoam.org/`.

Zabetakis, M. G., Furno, A. L., Jones, G. W. (1954). *Minimum spontaneous ignition temperatures of*

combustibles in air. Industrial & Engineering Chemistry, 46(10):2173–2178.
Zakel, S., Brandes, E., Schröder, V. (2019). *Reliable safety characteristics of flammable gases and liquids–the database chemsafe*. Journal of Loss Prevention in the Process Industries, 62:103914.

Small Scale Pool Fires: the Case of Toluene

Benedetta Anna De Liso[a], Gianmaria Pio[a], Ernesto Salzano[a,*]

[a] Department of Civil, Chemical, Environmental and Materials Engineering, Alma Mater Studiorum - University of Bologna, Bologna 40131, Italy (IT)

E-mail: ernesto.salzano@unibo.it

Abstract

Recently, the industrial applications adopting toluene as a solvent have been largely extended, including some solutions within the framework of the energy transition and energy storage technologies. The potential use of this flammable compound in a different set of operative conditions and compositions requires a comprehensive and complete knowledge of its fire behaviour. To this scope, an experimental campaign devoted to the quantification of the mass burning rate and the heat release rate derived by a small-scale pool fire was carried out for the case of toluene. An innovative procedure was developed for this scope and implemented at different boundary conditions. More specifically, the specimen was exposed to air and heat fluxes between 7 – 50 kW/m^2, at a constant sample surface of 0.01 m^2, an initial sample thickness of 0.01 m, and a distance between the sample and the horizontally oriented conical-shaped heater of 0.025 m. Measurements were compared with data from the current literature, when available. The collected data were, then, further utilized to obtain the most relevant safety parameters. Specific insights were provided on the formation of the main products, including soot tendency. Based on the collected data a simplified kinetic model suitable for the computational fluid dynamics was proposed to reproduce the chemistry of the system.

Keywords: Pool fire; Toluene; Soot; Solvents; Mass burning rate; Heat release rate.

1. Introduction

The use of hydrocarbon-based solvents has been largely adopted for several industrial processes either to control the temperature within reactors or to separate undesired substances from the main products. Among the others, toluene is intensively adopted in industrial processes (Pich et al., 2006). In addition, toluene has been largely considered as a component for surrogate mixtures suitable for the numerical and experimental characterization of traditional and bio-based fuels, including gasoline, diesel, and biodiesel (Pio et al., 2019). More recently, the use of this compound has been also suggested within the hydrogen supply chain because of the implementation of the liquid organic hydrogen carrier (LOHC) strategy (Niermann et al., 2019) within the framework of energy transition. Besides, the physical and chemical properties of toluene have promoted its inclusion as an additive in liquid electrolytes for the development of innovative energy storage solutions (Choi et al., 2008).

Toluene is a toxic and flammable compound, having a boiling temperature of 110.6 °C and a flash point of 4 °C (Luning Prak et al., 2022). Therefore, the use of toluene in several industrial processes as well as a component of surrogate mixtures for fossil- and bio-derived fuels requires an accurate evaluation of the safety aspects involving an accidental release in the atmosphere. Nevertheless, most of the available literature has explored the evaluation of mixtures containing toluene, with a limited set of data for the characterization of the flame behaviour of pure toluene (Liaw et al., 2022).

Considering thermodynamic properties and the overall reaction rate of toluene in air, a pool fire represents the main concern in the case of accidental release excluding the environmental impacts and the dispersion of its vapour in the atmosphere. From a phenomenological point of view, pool fires are heterogeneous reactive scenarios resulting in diffusion flames characterized by buoyancy flow, chemical reactions, convective mixing, and turbulence, as described in detail elsewhere (Babrauskas, 1983). Typically, the evaluation of safety aspects of a pool fire is based on the characterization of the mass burning rate (MBR) and the heat release rate (HRR) of the analysed fuel. Generally speaking, these parameters can be assessed starting from the chemical and physical properties of the investigated fuels together with boundary conditions representative of the analysed scenarios. Among the others, the effects of the atmospheric conditions and the pool size are worth to be mentioned. The former is particularly relevant to assess fire shape and tilt angles, typically evaluated by well-established correlations (Hu, 2017), whereas the latter significantly affects the combustion regime as well as the MBR, as reported in a pioneering study by Hottel (Hottel, 1959). In this sense, a recent tendency is to consider bench scale tests providing a trade-off between the measurability of the desired parameters, the techno-economic requirements, and the repeatability of the experimental campaign, as testified by the recent analysis on heptane-toluene mixtures (da Silva et al., 2023). Besides, a pool diameter ranging from 2 cm to 10 cm is typically associated with a transition from a laminar-dominated to a turbulent-dominated flow regime, allowing for the evaluation of peculiar phenomena associated with fire dynamics (Drysdale, 2011). From a thermal point of view, this range of pool diameter includes also the transition from a conduction-controlled to a convection-controlled heat feedback mechanism (Tu et al., 2016).

Regardless of the investigated size of the initial pool, a recent literature review collecting the current methodology and understanding of the dynamic of pool fires has indicated the evaluation of the soot formation as one of the main challenges to tackle shortly for a correct and robust evaluation of the flame properties (Chen et al., 2023). In this sense, it is worth mentioning that the chemical structure of toluene makes the system prone to producing soot precursors and particles (Blanquart et al., 2009). Hence, based on the combustion properties of toluene (Dobashi et al., 2000), proper quantification of the soot tendency and production rate shall have beneficial impacts on the estimation quality of the abovementioned safety parameters (Guo et al., 2023). However, most of the available literature covering the characterisation of mixtures containing toluene is oriented toward the assessment of the impact of its presence within exhaust gases on the environment or the normal operation of diesel engines as well as the chemistry of liquid blends with other hydrocarbons (e.g., heptane, dodecane) in the view of surrogate mixtures (Zhou et al., 2017).

For these reasons, an experimental campaign devoted to the characterization of the main flame properties of an ignited pool of toluene was carried out. A modified procedure was developed to allow the utilization of a cone calorimeter test for the characterization of the fire behaviour of liquid species at a bench scale. Different boundary conditions were tested. Results were compared with the existing literature including experimental and numerical analyses and correlations.

2. Methodology

In this work, a pool of toluene (≥ 99%), having dimensions Length x Width x Height equal to 10 cm x 10 cm x 1 cm, was exposed to different external heat fluxes (i.e., 7, 15, 25, 35, and 50 kW/m^2) and immediately ignited with an electrical sparkler at 10 kV. Several physical and chemical properties were monitored during the tests, including the heat release rate (HRR), smoke production rate (SPR), mass burning rate (MBR), and the composition of exhaust gas. More specifically, the HRR is calculated based on oxygen depletion, in compliance with the methodology described within the ASTM E 1354/ISO 5660 standards (ISO 5660-1, 2019). A load cell was adopted to measure the mass profile during the test. The time evolution of the sample mass was used for the evaluation of the MBR. The exhaust gases were conveyed in a dedicated duct with a constant flow of 24 L/s. The amount of oxygen, carbon monoxide, and carbon dioxide within the gaseous stream were detected by paramagnetic and IR analysers, whereas a laser photometer beam (He-Ne beam) was adopted for a qualitative assessment of the presence of particulate matter. In this view, the optical density was calculated according to Burgers' law for light attenuation (Equation 1)

$$D = \log\left(\frac{I_0}{I}\right) = \exp(-kL) \qquad 1$$

where the overall light intensity (I, [-]), the initial overall light intensity (I_0, [-]), and the extinction coefficient (k, [m^{-1}]) derived from direct measures, whereas the length of the light beam (L, [m]) was 0.11 m. In addition, the temperature profile within the liquid was monitored during the test through K-type thermocouples. For the sake of completeness, the adopted experimental system is reported in Figure 1.

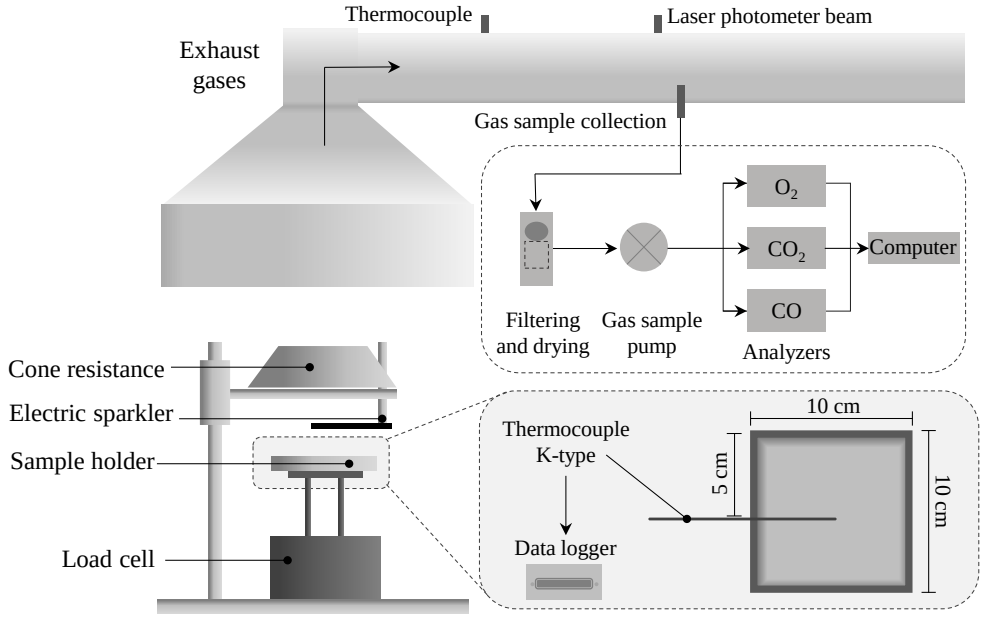

Fig. 1. *Overall schematic configuration of cone calorimeter apparatus.*

Considering the investigated phase, the characterization of the liquid-vapour transitions is paramount to guarantee accurate and robust evaluations of the consequences. Therefore, the collected data were adopted for the evaluation of the boiling transition time (BTT) under direct evaluation and different assumptions for indirect assessment. BTT is defined as the time between the exposure of the sample to the onset of boiling phenomena. This parameter is typically visually individuated and associated with an inflection point in the mass burning rate profile versus time (DiDomizio et al., 2021). Conversely, in this work, the combination of visual inspections and direct measurements of the temperature profile within the liquid phase was adopted for the determination of BTT at the investigated conditions.

The collected data were also adopted for the development and quantification of a simplified kinetic mechanism, which includes the total oxidation of toluene (Equation 2), the partial oxidation of toluene to CO and H_2O (Equation 3) and the production of soot and H_2 (Equation 4). For the sake of simplicity, the chemical composition of soot was assumed as C, in agreement with the approach reported by McGrattan (McGrattan, 2006).

$$C_7H_8 + 9\ O_2 \rightarrow 7\ CO_2 + 4\ H_2O \quad (2)$$

$$C_7H_8 + 11/2\ O_2 \rightarrow 7\ CO + 4\ H_2O \quad (3)$$

$$C_7H_8 \rightarrow 7\ C_{(s)} + 4\ H_2 \quad (4)$$

The extent of reactions for the first two reactions were derived from the direct measures of CO_2 and CO, whereas the value corresponding to the last reaction was calculated based on the measured profile of the sample mass, assuming a complete conversion of toluene. The HRR potentially deriving from the quantified kinetic mechanism (HRR_c) was compared with the measured values (HRR_m) to assess the validity of the posed assumptions. To this scope, the required thermodynamic properties were calculated based on dedicated databases (NIST, 2024).

3. Results and discussion

In light of the experimental findings, the following section presents a comprehensive analysis of the results obtained, elucidating the key observations and insights derived from the conducted experiments. Figure 2 shows the measured heat release rate (HRR_m) and mass burning rate (MBR) profiles experimentally obtained in this work as a function of time for different external heat fluxes.

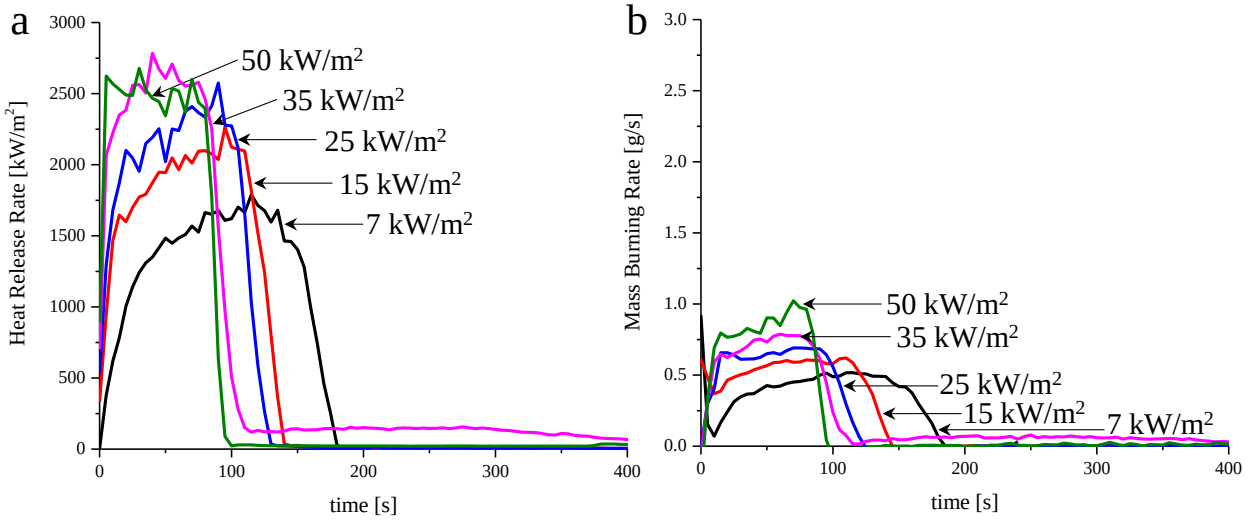

Fig. 2. *Measured heat release rate (a) and mass burning rate (b) of toluene obtained at different external heat fluxes (7, 15, 25, 35, and 50 kW/m²).*

Regardless of the adopted heat fluxes, three phases can be distinguished in the power production of toluene pool fire: growth, pseudo-steady state, and decay. At first, an abrupt increase of HRR can be observed, due to the low flash point temperature (4 °C) (NIST, 2024) and the presence of an ignition source. After the initial heating phase, where the enrichment of the atmosphere in terms of the vapour fraction of toluene leads to an increasing phase, a pseudo-steady state emerges. Subsequently, the HRR exhibits a gradual decay, resulting in a complete extinction of the flame. Throughout the experiment, fluctuations in the HRR profile can be observed. These fluctuations denote the dynamic nature of the combustion and may be attributed to variations in the availability of oxygen, boil-over phenomena regarding the liquid sample, changes in the fuel-air mixture, or the combined effects of local turbulence and combustion kinetics. Similar trends and observations can be applied also to the measured profiles for the mass burning rate.

On the contrary, the temperature measurements within the liquid exhibit minimal susceptibility to scattering or fluctuations. This occurs because the liquid state represents a more controlled environment, mitigating the impact of the turbulence-induced perturbations. It is worth mentioning that during the pseudo-steady state phase, the liquid surface temperature reaches an almost constant temperature in proximity to the boiling point. In a broader context, it was observed that the vaporization rate increases with the temperature of the liquid, and this relationship persists even with higher external heat fluxes. Besides, the obtained results indicate that the entire volume of fuel heats rapidly, causing a sequential transition from ignition to boiling, to flame extinction as the fuel is consumed. This chain of events is typical of the thin-layer behaviour described by (DiDomizio et al., 2021).

The combination of the measured profiles can be used to generate further insights on the phenomenological aspects as well as on the main parameters to be considered for numerical simulations of toluene pool fire. Considering that this work is mostly focused on the characterization of safety aspects related to the investigated scenario, particular emphasis will be provided to the growth and pseudo-steady state phases. More specifically, the former will be analysed in terms of the dynamic of liquid-vapour transitions and peak in power production, whereas the latter will be characterized in terms of duration, averaged HRR, MBR, and product composition.

At first, the collected data were adopted for the evaluation of the bulk boiling phase time span (BBP) and transition based on inflection point of mass burning rate as well as the measured temperature, as reported in Table 1.

Table 1. *Measured bulk boiling phase time span (BBP), boiling transition time obtained by thermocouples (BTT_T), boiling transition time obtained by the inflexion point of mass burning rate profile (BTT_{MBR}), time of the peak of HRR (tpHRR) and time of steady-state phase (t_{ss}).*

Heat flux [kW/m^2]	**BBP, [s]**	**BTT_T, [s]**	**BTT_{MBR}, [s]**	**tpHRR, [s]**	**t_{ss}, [s]**
7	33	134	155	115	65
15	29	123	120	95	65
25	24	108	95	90	65
35	20	88	75	40	60
50	16	78	70	30	60

The boiling transition times obtained from mass burning rate profiles (BTT_{MBR}) were compared with boiling times measured by thermocouples (BTT_T). The comparison underscores a good agreement between the two values, discouraging the use of a visual inspection as a qualitative procedure for the determination of the boiling transition time. In addition, the realization of a sooty flame, as in the case

of toluene, can have a detrimental effect on visual inspection. Therefore, it is possible to conclude that this approach has larger uncertainties and possible inconsistency if compared with strategies based on direct measurable parameters such as MBR and temperature profiles. It is worth noting that the time of the peak of HRR (tpHRR) is significantly affected by the external heat flux provided to the sample, whereas the duration of the pseudo-steady state phase (t_{ss}), identified by mass burning rate profiles to limit the experimental fluctuations, is less sensitive to the external heat flux. From the conducted tests, it was possible to visually observe the development of phenomena such as boiling and boilover under different thermal flow conditions, noting the progression of a flame characterized by different shapes and dynamics depending on the specific condition of interest, as depicted in Figure 3.

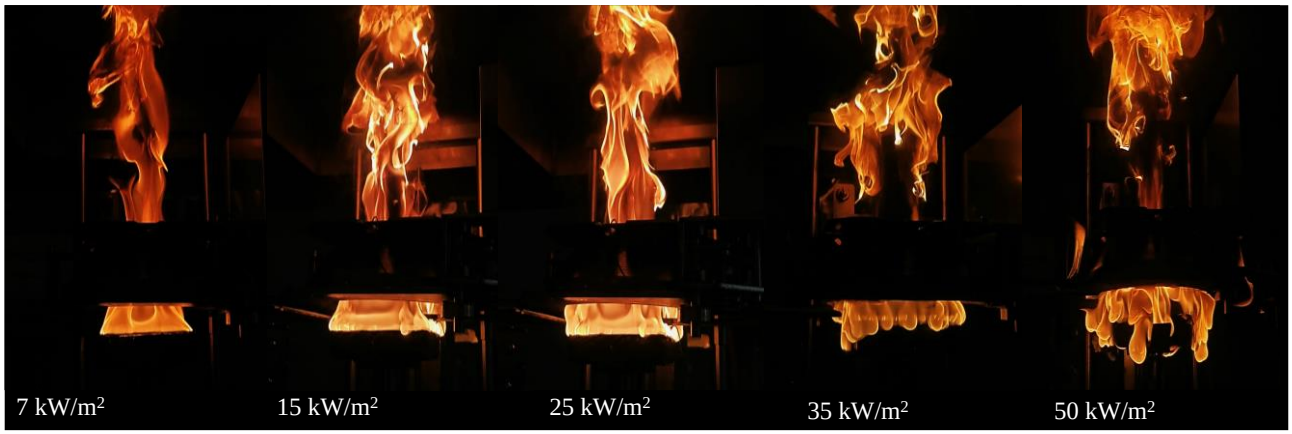

Fig. 3. *Toluene pool fires by cone calorimeter at different heat fluxes (7, 15, 25, 35, 50 kW/m^2).*

Subsequently, the key parameters obtained under stationary conditions are detailed in Table 2, in order to analyze the reactivity and efficiency of toluene within the studied framework.

Table 2*. The peak of Heat Release Rate (pHRR), Effective Heat of Combustion (EHC), and Mass Burning Rate (MBR) obtained in this work at steady-state conditions for different heat fluxes.*

Heat flux	**7 kW/m^2**	**15 kW/m^2**	**25 kW/m^2**	**35 kW/m^2**	**50 kW/m^2**
pHRR (kW/m^2)	1788	2264	2575	2784	2677
EHC (kJ/g)	33.9	34.9	35.5	37.4	29.6
MBR (g/s)	0.47	0.59	0.66	0.76	0.85

An increase in the external heat flux provided to the sample leads to a larger MBR, in compliance with expectations for liquid hydrocarbon fuels (Rantuch et al., 2019), where an increase in the external heat flux accelerates pyrolysis/evaporation/boiling, enhancing the availability of flammable compounds in the vapour phase. This phenomenon may suggest an increase in the combustion kinetics, resulting in heightened reactivity and increased power production. However, this trend is not representative of the peak of heat release rate (pHRR), which experiences consistent growth until 35 kW/m² where a maximum value is reached. Similarly, the effective heat of combustion (EHC) shows a proportional rise in heat flux with a decrease at 50 kW/m^2. This discrepancy can be attributed to a facilitated and more complete breakdown of toluene molecules once larger thermal energy is provided. Under this assumption, a reduced production of small oxidized species and a larger amount of long-chain compounds shall be expected. Therefore, to corroborate this explanation, Table 3 shows the averaged values of CO_2 and CO yields obtained experimentally at the steady-state phase. Based on the kinetic mechanism reported in the methodological section, soot yield was calculated from the

measured values of yields and MBR. For the sake of completeness, the optical density, the measured and calculated HRR at the steady state were also reported.

Table 3. *Mass yield of CO_2 (Y_{CO2}), mass yield of CO (Y_{CO}), mass yield of soot (Y_{soot}), smoke optical density (D), experimental mean heat release rate (HRR_{exp}) and numerical heat release rate (HRR_{num}) obtained in this work at steady state conditions.*

Heat flux [kW/m^2]	Y_{CO2} [kg/kg]	Y_{CO} [kg/kg]	Y_{soot} [kg/kg]	D [-]	HRR_{exp} [kW/m^2]	HRR_{num} [kW/m^2]
7	2.64	0.10	0.17	0.83	15.80	15.73
15	2.80	0.10	0.14	0.88	20.93	20.84
25	2.61	0.09	0.18	0.83	22.83	21.74
35	2.39	0.08	0.22	0.68	25.22	22.99
50	2.34	0.11	0.24	1.08	25.39	25.16

The conjugated π bond system in the aromatic ring, characterized by resonance stabilization, provides enhanced stability to the molecule, making it less prone to bond cleavage during the combustion process. Consequently, toluene exhibits a notable preference for undergoing complete combustion, leading to a substantial production of carbon dioxide. Interestingly, also the carbon monoxide yield (Y_{CO}) exhibits almost constant values throughout the range of heat flux levels during toluene combustion. This trend aligns with the chemical composition of the liquid, which appears to restrain the formation of CO. The intriguing behaviour of soot yields, especially the peak observed at 35 kW/m², can be linked to the complex pathways associated with the scission of the benzene ring. This scission process may lead to the formation of polycyclic aromatic hydrocarbons (PAHs), which are precursors to soot. The subsequent decrease at 50 kW/m² is, therefore, associated with a shift towards enhanced soot production, highlighting the intricate interplay between combustion kinetics and the influence of the chemical structure (Shukla and Koshi, 2011).

The comparison between the measured and estimated HRRs indicates a satisfactory agreement between the adopted approaches. Indeed, except for the tests conducted at 25 kW/m2 and 35 kW/m2, the developed model almost perfectly matches the experimental data, having a discrepancy within the 1 %. Conversely, for the abovementioned fluxes, the model tends to underestimate the HRR with a deviation from the measured values of 4.7 % and 8.8 %, respectively. On the one hand, the observed discrepancies can be attributed to the potential presence of additional exothermic reactions not fully captured by the simplified reaction pattern considered in the numerical approach. On the other hand, the assumption that soot is composed of pure carbon can have a detrimental effect on the accuracy of the estimated heat release rate, especially at intermediate temperatures where partially oxidized hydrocarbon structures can be representative of the chemical composition of the produced soot (Peña et al., 2017). The optical density (D) shows a trend in line with the estimated soot yield. Furthermore, the determined soot yields show an outstanding match with data reported in the current literature for the medium-scale pool fire of toluene (Węgrzyński and Vigne, 2017). The combination of these aspects confirms the robustness of the adopted kinetic mechanism, reducing the impacts related to the possible neglect of side reactions.

Based on the collected information it is possible to confirm that the increase in the external heat flux promotes a less effective combustion, which reduces the heat release rate although an increased availability of flammable vapours. Hence, the utilization of physical and chemical properties deriving from experimental characterization of liquid species at elevated external heat flux cannot be considered as aprioristically as a conservative assumption. Eventually, despite the adopted simplifications, the oxidation process of toluene and the soot production is well captured by the reaction pathway assumed.

4. Conclusions

The widespread adoption of toluene in industrial applications, particularly within the realms of energy transition and storage technologies, necessitates a thorough understanding of its fire behaviour under different operational conditions. The experimental tests conducted in this work provided a direct assessment of critical parameters such as mass burning rate, heat release rate, combustion effectiveness, and soot tendency. The pool fire tests under different heat fluxes revealed distinctive phases in the combustion process, offering insights into growth, steady-state, and decay stages. In particular, toluene behaves as a thin liquid under the investigated conditions, producing a large amount of soot and by-products in its combustion process. Notably, this work delved into the production of soot particles, a critical aspect often overlooked in the available literature. A novel procedure was developed and implemented, considering a simplified pathway of reaction to describe the oxidation mechanism of toluene and quantify the soot yield in the process. The observed behaviour of soot yields, particularly the peak at 35 kW/m², sheds light on the complex pathways associated with the scission of the aromatic ring in toluene. An average yield of 0.19 kg/kg in soot was obtained for sample burning, besides being a result in agreement with other limited studies in the literature, this value is an important key input parameter for most fire scenario simulation software. The comparison of the obtained values suggests that an increase in the external heat flux adopted for the experimental characterization of liquids does not imply that the collected data can be considered conservative on the safe side. Indeed, a combination of physical and chemical phenomena affects differently the combustion efficiency and the availability of flammable vapours in the atmosphere.

References

Babrauskas, V., 1983. Estimating large pool fire burning rates. Fire Technol. 19, 251–261. https://doi.org/10.1007/BF02380810

Blanquart, G., Pepiot-Desjardins, P., Pitsch, H., 2009. Chemical mechanism for high temperature combustion of engine relevant fuels with emphasis on soot precursors. Combust. Flame 156, 588–607. https://doi.org/10.1016/j.combustflame.2008.12.007

ISO 5660-1 : 2015 + A1 : 2019 — Reaction-to-fire tests — Heat release , smoke production and mass loss rate, 2019.

Chen, Y., Fang, J., Zhang, X., Miao, Y., Lin, Y., Tu, R., Hu, L., 2023. Pool fire dynamics: Principles, models and recent advances. Prog. Energy Combust. Sci. 95, 101070. https://doi.org/10.1016/j.pecs.2022.101070

Choi, J.-W., Cheruvally, G., Kim, D.-S., Ahn, J.-H., Kim, K.-W., Ahn, H.-J., 2008. Rechargeable lithium/sulfur battery with liquid electrolytes containing toluene as additive. J. Power Sources 183, 441–445. https://doi.org/10.1016/j.jpowsour.2008.05.038

Da Silva, R.M., Lang, R., Thion, S., Nmira, F., Consalvi, J.L., 2023. Experimental study of the thermal and burning characteristics of 15 cm pool fires fueled by heptane-toluene mixtures. Int. J. Therm. Sci. 193, 108454. https://doi.org/10.1016/j.ijthermalsci.2023.108454

DiDomizio, M.J., Ibrahimli, V., Weckman, E.J., 2021. Testing of liquids with the cone calorimeter. Fire Saf. J. 126, 103449. https://doi.org/10.1016/j.firesaf.2021.103449

Dobashi, R., Kong, Z.W., Toda, A., Takahashi, N., Suzuki, M., Hirano, T., 2000. Mechanism of smoke generation in a flickering pool fire. Fire Saf. Sci. 255–264. https://doi.org/10.3801/IAFSS.FSS.6-255

Drysdale, D., 2011. Spontaneous Ignition within Solids and Smouldering Combustion, in: An Introduction to Fire Dynamics. https://doi.org/10.1002/9781119975465.ch8

Guo, Y., Xiao, G., Wang, L., Chen, C., Deng, H., Mi, H., Tu, C., Li, Y., 2023. Pool fire burning characteristics and risks under wind-free conditions: State-of-the-art. Fire Saf. J. 136, 103755. https://doi.org/10.1016/j.firesaf.2023.103755

Hottel, H.C., 1959. Review of Certain Laws Governing Diffusive Burning of Liquids. Fire Res. Abstr. Rev. 1.

Hu, L., 2017. A review of physics and correlations of pool fire behaviour in wind and future challenges. Fire Saf. J. 91, 41–55. https://doi.org/10.1016/j.firesaf.2017.05.008

Liaw, H.-J., Hsu, W.-C., Lakzian, K., 2022. Exploration of two types of maximum–minimum flash point behavior of ternary mixtures. J. Loss Prev. Process Ind. 80, 104915. https://doi.org/10.1016/j.jlp.2022.104915

Luning Prak, D., Hamilton, M., Banados, R., Cowart, J., 2022. Density, viscosity, speed of sound, flash point, bulk modulus, and surface tension of mixtures of military jet fuel JP-5 and biodiesels dataset. Data Br. 41, 107849. https://doi.org/10.1016/j.dib.2022.107849

McGrattan, K.B., 2006. Fire dynamics simulator (version 4). Gaithersburg, MD. https://doi.org/10.6028/NIST.SP.1018

Niermann, M., Beckendorff, A., Kaltschmitt, M., Bonhoff, K., 2019. Liquid Organic Hydrogen Carrier (LOHC) – Assessment based on chemical and economic properties. Int. J. Hydrogen Energy 44, 6631–6654. https://doi.org/10.1016/j.ijhydene.2019.01.199

NIST, 2024. NIST Chemistry WebBook 69, National Institute of Standards and Technology, URL https://webbook.nist.gov/chemistry/. Access: 31/01/2024.

Peña, G.D.J.G., Raj, A., Stephen, S., Anjana, T., Hammid, Y.A.S., Brito, J.L., Shoaibi, A. Al, 2017. Physicochemical properties of soot generated from toluene diffusion flames: Effects of fuel flow rate. Combust. Flame 178, 286–296. https://doi.org/10.1016/j.combustflame.2017.01.009

Pich, A., Schiemenz, N., Boyko, V., Adler, H.J.P., 2006. Thermoreversible gelation of biodegradable polyester (PHBV) in toluene. Polymer (Guildf). 47, 553–560. https://doi.org/10.1016/j.polymer.2005.11.070

Pio, G., Carboni, M., Salzano, E., 2019. Realistic aviation fuel chemistry in computational fluid dynamics. Fuel 254, 115676. https://doi.org/10.1016/j.fuel.2019.115676

Rantuch, P., Blinová, L., Bartošová, A., Martinka, J., Wachter, I., 2019. Burning process characterization of biodiesel pool fires. J. Fire Sci. 37, 3–17. https://doi.org/10.1177/0734904118807627

Shukla, B., Koshi, M., 2011. Comparative study on the growth mechanisms of PAHs. Combust. Flame 158, 369–375. https://doi.org/10.1016/j.combustflame.2010.09.012

Tu, R., Zeng, Y., Fang, J., Zhang, Y., 2016. Low air pressure effects on burning rates of ethanol and n -heptane pool fires under various feedback mechanisms of heat. Appl. Therm. Eng. 99, 545–549. https://doi.org/10.1016/j.applthermaleng.2016.01.044

Węgrzyński, W., Vigne, G., 2017. Experimental and numerical evaluation of the influence of the soot yield on the visibility in smoke in CFD analysis. Fire Saf. J. 91, 389–398. https://doi.org/10.1016/j.firesaf.2017.03.053

Zhou, C.W., Simmie, J.M., Somers, K.P., Goldsmith, C.F., Curran, H.J., 2017. Chemical Kinetics of Hydrogen Atom Abstraction from Allylic Sites by 3O2; Implications for Combustion Modeling and Simulation. J. Phys. Chem. A 121, 1890–1899. https://doi.org/10.1021/acs.jpca.6b12144

ASTM E659 Standardized Test Analysis and Results for Synthetic Paraffinic Kerosene

Charline Fouchier[a,b] & Joseph Shepherd[a]

[a] Graduate Aerospace Laboratories, California Institute of Technology, Pasadena, CA, USA
[b] von Karman Institute for Fluid Dynamics, Sint Genesius Rode, Belgium

E-mail: *charline@caltech.edu*

Abstract

Improvements on ASTM E659 apparatus are used to investigate autoignition (AIT) of a Synthetic Paraffinic Kerosene (SPK). The apparatus injection system has been automated, and the temperature acquisition system has been improved to reduce variability due to human factors. The SPK was compared with a Jet A standard, POSF4658. The two fuels have a similar range of combustion behaviors but the SPK shows a lower AIT and lower effective activation energy than Jet A. A statistical analysis is proposed to quantify the likelihood of ignition for a range of injected fuel volumes and types of ignition events. We observe that luminous ignition (Mode I) and non-luminous cool flame (Mode III) both result in a vigorous reaction and comparable peak temperatures. This highlights the importance of using the temperature signal to detect ignition instead of relying only on flame visualization. Surveys of the temperature distribution inside the hot vessel demonstrate that a single point measurement is not sufficient to characterize the temperature and that subtle changes in the assembly of the apparatus can significantly alter the temperature distribution and the measured AIT.

Keywords: *Thermal Ignition, Flammability, Standardized Tests, Synthetic Paraffinic Kerosene, Safety*

1 Introduction

The ignition of flammable gases, combustible liquids, or powders in a hot air atmosphere is a critical safety concern in many industries such as power generation, petroleum, automotive, chemical, and aerospace. In order to evaluate the hazard of ignition, standardized tests have been developed to determine a temperature threshold, the autoignition temperature (AIT). The AIT is defined as the minimum temperature required to initiate self-sustaining combustion in the absence of an external source of ignition such as a spark or flame (NFPA, 1991). The AIT, as defined by standardized tests, is widely used to define maximum safe operating temperatures for surfaces in the presence of flammable or combustible substances.

However, the standard AIT test is not a hot surface test but examines the case of a hot flammable atmosphere surrounded by a hot surface in a confined geometry. While this is an important test for hazard evaluation, particularly the classical self-heating or thermal runaway condition (Semenoff, 1929, Frank-Kamenetskii, 2015), many hazards involve hot surfaces surrounded by a cold atmosphere with an unconfined geometry (Jones and Shepherd, 2021) and the ignition threshold surface temperatures in the latter case can be much higher (500-600°C) than the standard test AIT values. In the present study, we focus exclusively on the self-heating aspect of autoignition in a confined hot atmosphere within a hot vessel.

The most widely used methodologies for determining AIT are ASTM-E659 (2005) standard and the international standard (ISO/IEC (2017)). In our study, we have used the ASTM apparatus. The protocol consists of injecting a small fuel quantity into a 500 mL rounded bottom flask heated at a constant temperature in a furnace and observing for 10 minutes the presence or absence of flame. Following a specific procedure for varying the temperature and fuel volume in the test, a minimum temperature at which the ignition occurs is used to specify the AIT.

The current standardized test apparatus and protocols evolved from substantial prior work in the twentieth century. Setchkin (1954) *et al.* developed an early version, gave results for various fuels,

and provided a comprehensive summary of testing methods being used at that time. They highlighted important parameters affecting the AIT, which have been the focus of many studies since that time. They found that the AIT becomes lower with increasing vessel size, and the ratio of the combustible substance to air was a significant factor. Setchkin also emphasized the importance of temperature uniformity inside the flask and the difficulties in observing the flame during ignition in some cases, advising the analysis of the temperature signal rather than purely visual observation.

Other factors known to influence the AIT include the shape of the flask, the rate and duration of heating, and the flask material (NFPA (1991)). Recent studies have examined further the effect of the combustion vessel and the influence of increased pressure and nitrogen dilution levels on the AIT (Hirsch and Brandes, 2005, Brandes et al., 2018). The effect of the flask material has been highlighted by Chen and Hsieh (2010) where the AIT of ethanol measured inside a quartz flask was found to be 20 °C higher than the one measured in a borosilicate flask. The same authors investigated the effect of the ambient temperature and found a quadratic relation between the AIT and the ambient temperature, where the AIT showed an increase of around 10 °C for an increase of 25°C on the ambient temperature. The cleanliness of the flask was also reported to affect the AIT (Martin (2023)), where a flask used multiple times can lead to higher AIT readings.

While the ASTM standard defines ignition with the presence of a flame, it has been frequently reported that ignition could lead to a weak flame that can be invisible to human eyes. Many authors recommend detecting ignition based on the temperature signal rise instead of the flame visualization (Affens et al., 1961, Johnson and Mashuga, 2023, Setchkin, 1954). This difference in definition leads to significant variation in the reported AIT value. Over time, different ignition modes have appeared, such as the four ignition modes used by Martin and Shepherd (2021), and can be used to qualitatively take into account the complexity of ignition. The ASTM standard does not describe the injection rate and height of injection, while the evaporation rate has been shown to have a non-negligible effect on the AIT (Swarts and Orchin (1957)). Finally, fluid motion and mixing have been shown to affect the autoignition (Mastorakos et al., 1997, Martin, 2023). The standard states that the flask temperature should be uniform, but measuring the temperature distribution and quantifying uniformity is not part of the standard.

The main objectives of this work are to report some improvement in the apparatus, provide data on a new fuel, a synthetic paraffinic kerosene, to raise awareness about the challenges of using the ASTM protocol when characterizing a new fuel, and propose some new statistical methods of analyzing test data to account for a range of compositions. Tests have been conducted under conditions similar to the standard protocol, and we identified some limitations as well as proposed improvements to reduce the measurement uncertainties. The paper is organized as follows. Section 2 gives the experimental details, including modifications to the ASTM apparatus, the experimental procedure, and the tested fuels. Two fuels are tested in the present project: Jet A POSF-4658, also tested by Martin and Shepherd (2021), and a representative Synthetic Paraffinic Kerosene (SPK). Section 3 gathers the experimental results. The first subsection discusses the test repeatability. The second subsection gives the ignition maps and compares results for the two fuels. The difference between Mode I (flame) and Mode III (no flame) ignition is discussed. The third section investigates the ignition characterization, including an estimation of the effective activation energies of the two fuels, and the maximum temperature measured during ignition. The ignition transition is discussed in the fourth section, while the fifth section gives a statistical analysis of this transition. The sixth subsection discusses the ASTM apparatus and how to estimate a more accurate AIT. Finally, a conclusion and recommendations are given.

2 Experiments

2.1 Experimental setup

The apparatus used by Martin et al. for the characterization of the AIT of Jet A and surrogate jet fuels (Martin and Shepherd (2021), Martin (2023)), constructed based on the ASTM-E659 (2005)

standards, was adapted for this work. Figure 1 is a photograph and a cross-section drawing of the ASTM setup.

The apparatus is composed of a Mellen CV12 crucible furnace with a 133 mm diameter and 200 mm deep cylindrical volume, which heats up at a controlled temperature a 500 mL round bottom borosilicate flask up to 1250°C with a PID controller (Love Controls series 16B) system accurate to 1°C. The flask is suspended in the furnace by a ceramic holder molded from silica-based Cotronics Rescor 750. The flask and the bottom part of the ceramic holder are covered by aluminum foil to reflect the radiation inside the flask and reduce heat loss. A 50 mm diameter mirror is positioned above the apparatus's opening at a 45° angle to allow the user to visualize the flames inside the flask. The fuel injection is made with a 500 μL hypodermic syringe with a 6-inch long (152.4 mm) 26 gauge needle.

The temperature of the flask surface is measured with three thermocouples type K, gauge 34, from Omega, inside a mineral-insulated metal sheath, set at position T1, T2, and T3 (see Figure 1 right). The air temperature is measured with a thermocouple type K, gauge 36, inside a 3 mm diameter ceramic sheath set at T4 in the middle of the flask. The temperature T4 is used as the reference temperature, and has an uncertainty of 0.75 %, with a minimum of 2.2 °C (value provided by the manufacturer).

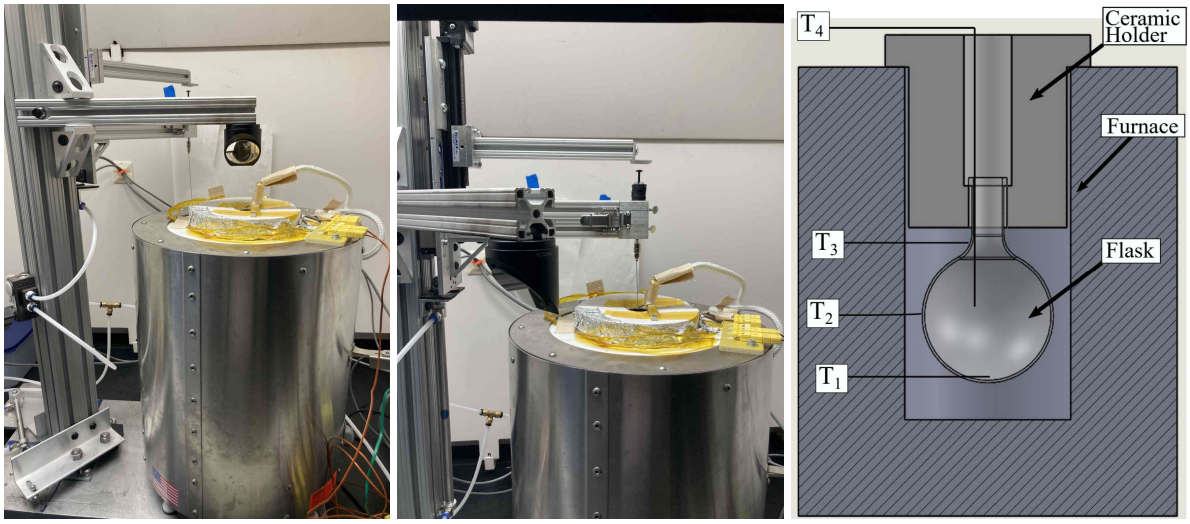

Fig. 1*: (Left) ASTM-E659 test apparatus in visualization mode. (Middle) Apparatus in injection mode with a closer look at the injection system. (Right) Cross-section schematic of the internal heated region with thermocouple locations highlighted.*

The temperature of the flask is not homogeneous and depends on the setup configuration. Two configurations have been used during this project. The two are very similar, with the only difference being that the aluminum foil of Configuration 1 has a discontinuity (gap) between the flask and the ceramic holder, while Configuration 2 does not. A drawing to illustrate the two configurations is given in Figure 2. The gap in the foil increases the flow of hot air in the ceramic holder opposing the counterflow of cold air falling downward toward the flask. This leads to a different temperature profile inside the flask between the two configurations.

The vertical temperature profile over the flask centerline when T4 = 235°C is given in Figure 3 for the two configurations. The temperature has been acquired at 75 Hz for 120 seconds and averaged for each position. A pause of 60 seconds has been made between each position change. The position 0 mm corresponds to the bottom of the flask. Half of the flask's approximate dimensions have been represented in the figure for illustration purposes. In Configuration 1, the temperature increases with height until the middle of the flask neck, after which it decreases. This is due to natural convection, where hot air can circulate around the flask's rounded part and neck. In Configuration 2, the flask temperature is nearly constant up to the 2/3 height of the flask and decreases near the end of the flask

round portion. The flask neck is suspended in the ceramic holder, and the absence of hot air circulation around it leads to a decrease in temperature. Values of the mean temperature over the profile, the difference between the temperature given by T4 and the mean temperature, and the difference between T4 and the profile extrema are given in Table 1. Only points inside the round (bottom) portion of the flask are considered, as ignition occurs in this area. The difference in fluid motion and influence on the temperature profiles is analyzed in detail in a companion publication (Davis et al., 2024). Most of the results discussed in this paper come from Configuration 1, and a few data have been taken in Configuration 2 for comparison purposes.

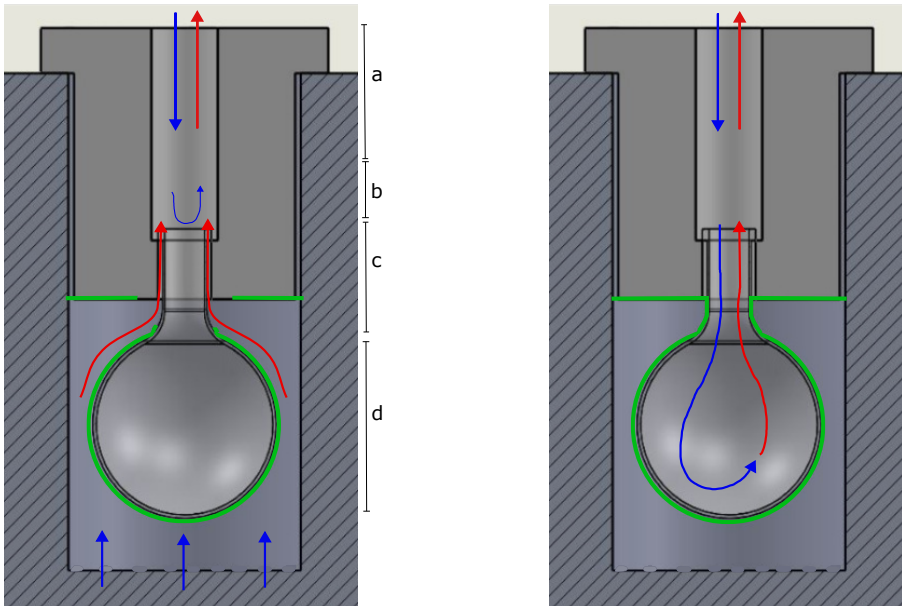

***Fig. 2**: Configuration 1 (Left) and Configuration 2 (Right). Highlighted features: (a) cold and hot air entering and leaving the furnace through the ceramic holder neck, (b) cold air back-flow created by the hot air flowing along the flask neck due to the aluminum foil (green) opening (c), leading to different atmosphere conditions inside the flask (d) compared to Configuration 2.*

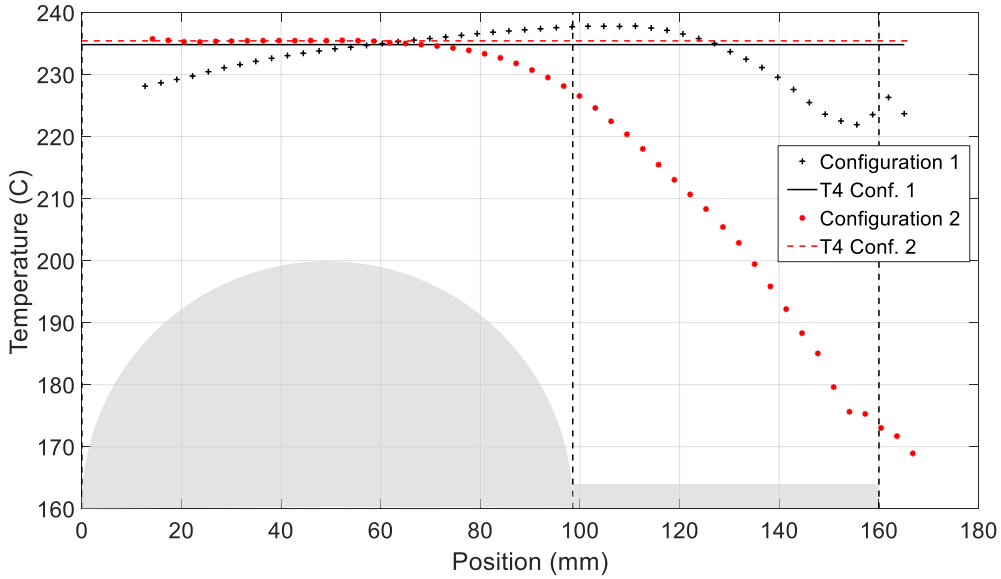

***Fig. 3**: Temperature profile inside the flask for the two configurations, T4 = 235°C*

***Table 1**: Comparison of T4 with flask temperature*

Configuration	T4	T_{mean}	$(T_{mean} - T4)/T4$	$(T_{max} - T_{min})/T4$
Conf. 1	234.8°C	234°C	0.34%	2.8%
Conf. 2	235.4°C	234°C	0.59%	3.8%

The apparatus has been modified from the original design for the sake of the study. First, the temperature variation is recorded with a 16-channel, 24-bit, 75 Hz thermocouple acquisition module (NI 9213) from National Instruments, connected to a cDAQ-9171 CompactDAQ Chassis. The module has one internal autozero channel, 1 internal cold-junction compensation channel, and 16 thermocouple channels. This system allows a higher resolution in time compared to a 1 Hz recorder usually used.

Efforts have been made to improve the fuel injection repeatability and control key parameters, such as the injection velocity, height, and duration. Instead of the manual injection described in the ASTM standards, injection is automated with a Velmex slide (NEMA 17, 115 mm travel) connected to a computer. A vertical stand mounted on a rotating platform holds the syringe and a mirror, allowing the user to switch from the injection to the observation with a 45° rotation. Tests are conducted in Pasadena, California, United States, 260 m above sea level, and the pressure is nominally at 1 atm with small day-to-day variations.

2.2 Experimental methods

The test procedure is as follows. The flask is set at the desired temperature, and thermal stability is reached before each test (variation less than 0.5°C/min). A temperature sample of 30 seconds from T4, in the middle of the flask, is recorded just before the injection, and the average is used as the initial test temperature. Once the measurement is completed, the syringe is lowered to a specified location inside the flask using an air-actuated cylinder. The fuel is injected into the lower part of the flask using the Velmex translation stage to actuate the plunger, the syringe is raised with the air cylinder, and the vertical stand holding the syringe is rotated 45° to place the mirror over the flask opening. The temperature acquisition begins at the same moment as the fuel injection. A test lasts 10 minutes, during which the temperature is recorded, and the presence or absence of flame is observed. After each test, the flask is flushed using a heat gun and an aluminum cylinder. It takes approximately 30 minutes between each test to reach thermal stability.

After a number of tests, particularly with non-ignition events, deposits accumulate on the flask walls, which tends to increase the AIT value (Martin, 2023). The flask is frequently visually inspected and, if necessary, cleaned via a thermal cycle (600°C for 2 hours) or replaced. Examples of flasks used for aviation fuel tests are shown in Figure 4. The left one is an unused flask. The middle one is a flask used for around ten tests with the SPK; this one can be cleaned with a thermal cycle. The right one is a flask used many times with Jet A, and after several thermal cleaning cycles, this one needs to be replaced.

Fuel volumes between 25 to 600 μL ($\pm 5\mu$L) are tested with temperatures T4 from 190 to 280°C ($\pm$2.2°C). Two fuels are examined: a representative Synthetic Paraffinic Kerosene (SPK) and a JetA standard, POSF-4658. The two fuels are described in Section 2.3. The SPK has been tested most extensively using a range of fuel volumes and temperatures. Tests using Jet A fuel have been limited to a few values for comparison with the results of Martin and Shepherd (2021) in order to validate the improved apparatus.

***Fig. 4**: New (left), used (center), heavily used (right) flasks after testing with aviation fuels*

The ignition behaviors are classified into four distinct modes, as used by Martin and Shepherd (2021): (I) Ignition, (II) Cool Flame, (III) Non-Luminous Cool Flame, and (IV) Rapid Reaction. They are defined based on visual observations and temperature variations measured in the middle of the flask (T4). The description of each mode is given in Table 2. The classification is very similar to the one used by Affens et al. (1961), with the addition of Mode II characterized by a small luminosity flame and a small temperature rise. In the present study, this mode is not observed as it primarily occurs in compounds with higher ignition temperatures (>400°C, Martin and Shepherd (2021)).

***Table 2**: Classifications of ignition modes observed in ASTM-E659*

Ignition Mode	Name	Luminosity	Temperature Rise
I	Ignition	Large [a]	Large
II	Cool Flame	Small	Small
III	Non-Luminous Cool Flame	None [b]	Large
IV	Rapid Reaction	None	Small
-	Non-Ignition	None	< 15°C

[a] Associated with a weak to intense explosion sound

[b] None or faint glow only visible to the naked eye, and small puff of smoke

The temperature signals are processed by extracting the maximum temperature recorded and the ignition delay time. The maximum temperature used in this project is measured by the thermocouple T4. It does not represent the flame temperature, which might be higher. Even though the thermocouple is small (36 gauge, 0.127 mm diameter), its size and thermal mass result in a response time that is too slow to capture the flame temperature accurately. However, the thermocouple response is repeatable between tests, and the temperature trace is used as a comparison tool in this work. The ignition delay time corresponds to the moment when the temperature increases the fastest. It is extracted using the peak of the signal second derivative, as illustrated by Figure 5.

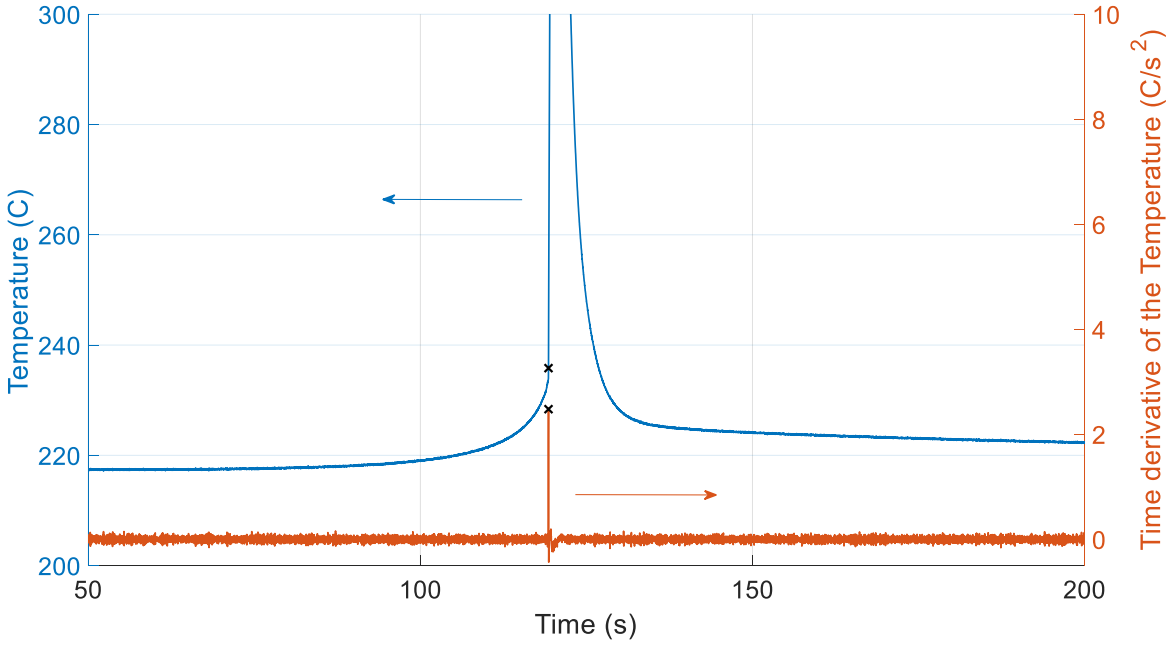

***Fig. 5**: Detection of the ignition beginning using the second derivative of the signal. The ignition delay time is represented by a black cross*

2.3 Tested fuels

Two fuels are used in this work: Jet A POSF-4658, identical to the one used by Martin and Shepherd (2021), and a representative Synthetic Paraffinic Kerosene (SPK). The flask point of the two fuels has been measured following the standard ASTM-D56 (1999) at 46°C for Jet A, and 40°C for the SPK. An AccuTOF™ GC-Alpha (JEOL, Inc.) Gas Chromatography-Mass Spectrometer (GC-MS) was used to investigate and compare the composition of the two fuels. The GC (Model 8890, Agilent Technologies) was fitted with a Restek Rxi-5ms column with dimensions of 30 m × 0.53 mm i.d. × 1.5 μm film thickness. The GC front inlet temperature was 250°C, and the total He flow was 1 mL/min. 1 μL of sample was injected onto the column with a split ratio of 200 for Field Ionization (FI) MS and 250 for Electron Ionization (EI) MS. The GC run started at 40°C with a 1-minute hold, then raised to 150°C with a gradient of 2°C/min and 30°C/min up to 300°C with a 1-minute hold. The total analysis time was 62 minutes. During the last two minutes of each run, an Octamethylcyclotetrasiloxane standard (Aldrich, m/z = 281.05114) was introduced into the ion source for mass-scale drift compensation. Mass spectra were acquired by Field Ionization (FI), which generates molecular ions, and Electron Ionization (EI), which generates diagnostic fragment ions allowing full characterization of the sample components. The FI signals of the SPK and Jet A are given respectively in Figures 6 and 7. Each peak can be associated with a particular molecule by combining the FI and the EI signals. This analysis has been done automatically with the msFineAnalysis AI software (msFineAnalysis, 2023) for all the detected peaks. Some molecules have been added to the figures to highlight the differences and similarities between the two fuels. All stronger peaks are due to linear alkanes for Jet A, and linear and iso-alkanes for SPK. SPK does not have any aromatic molecules, Jet A has multiple peaks associated with aromatic and cyclic species, consistent with the known typical composition of aviation kerosene.

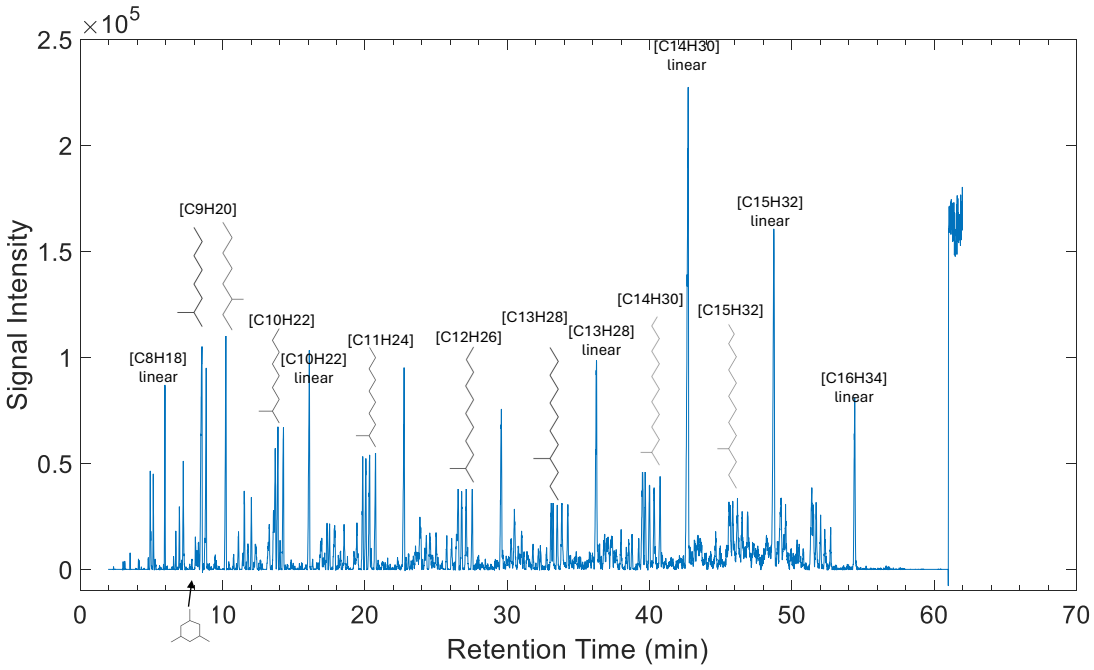

***Fig. 6**: Field ionization signal of SPK*

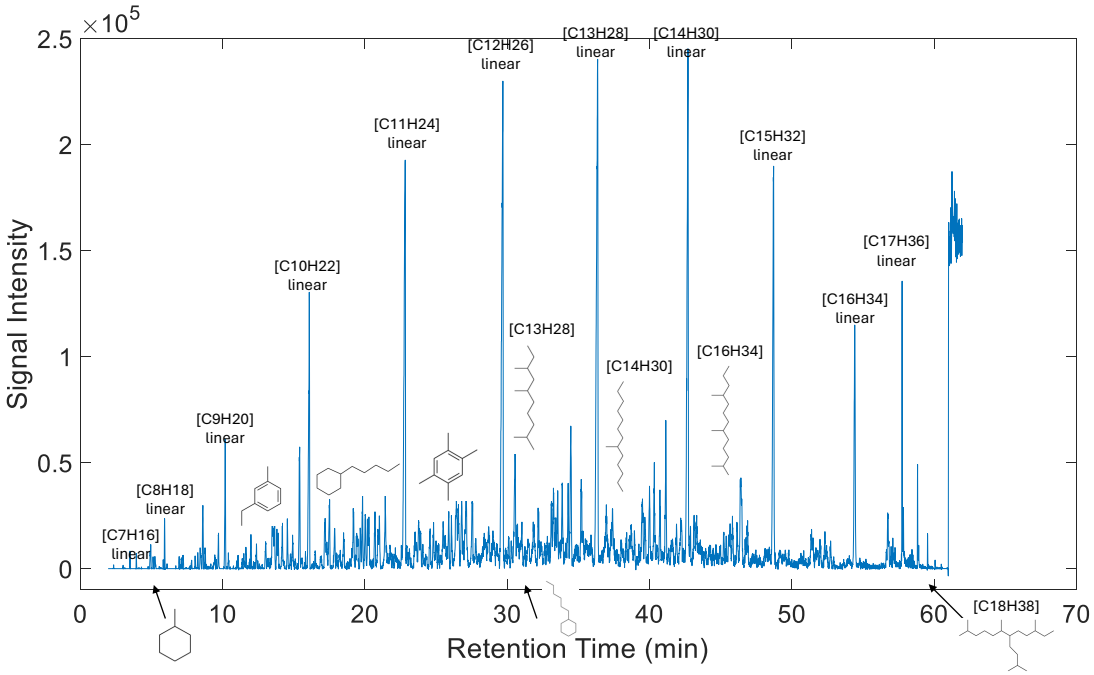

***Fig. 7**: Field ionization signal of Jet A*

A Kendrick Mass Defect (KMD) analysis was conducted on the field ionization (FI) signals using the Mass Mountaineer v7.1.13.0 software to reach a global visualization of the fuels composition. Outcomes provide the relative abundance of the different molecular families composing the tested fuels. The resulting Kendrick plots of Jet A and SPK are compared in Figure 8. Each dot corresponds to one group of molecules with a given KMD value (y-axis), directly linked to the molecular family, and a molecular mass (x-axis). The amplitude of the dot represents the sum of the signal amplitudes from

the FI data of the molecules included in the group. Each molecule group has its own KMD value and can be recognized in the plot. The observed ion intensities do not reflect absolute concentrations because of differences in the ionization efficiencies among the various classes of hydrocarbons. Standard calibration plots could not be made for each molecule identified in the analysis. Therefore, the results cannot provide absolute values of molecule concentration, but they provide a good relative comparison when two fuels are analyzed under the same experimental conditions. The molecule families detected in each fuel are gathered in Table 3. It appears from the KDM plots that Jet A and SPK share a very similar composition regarding the alkanes. The SPK contains only alkanes and a few cyclic alkanes and alkenes. Jet A contains a more diverse range of molecules. The SPK has carbon molecules up to C16, while Jet A has carbon molecules up to C19 with temperature programs used in the GC.

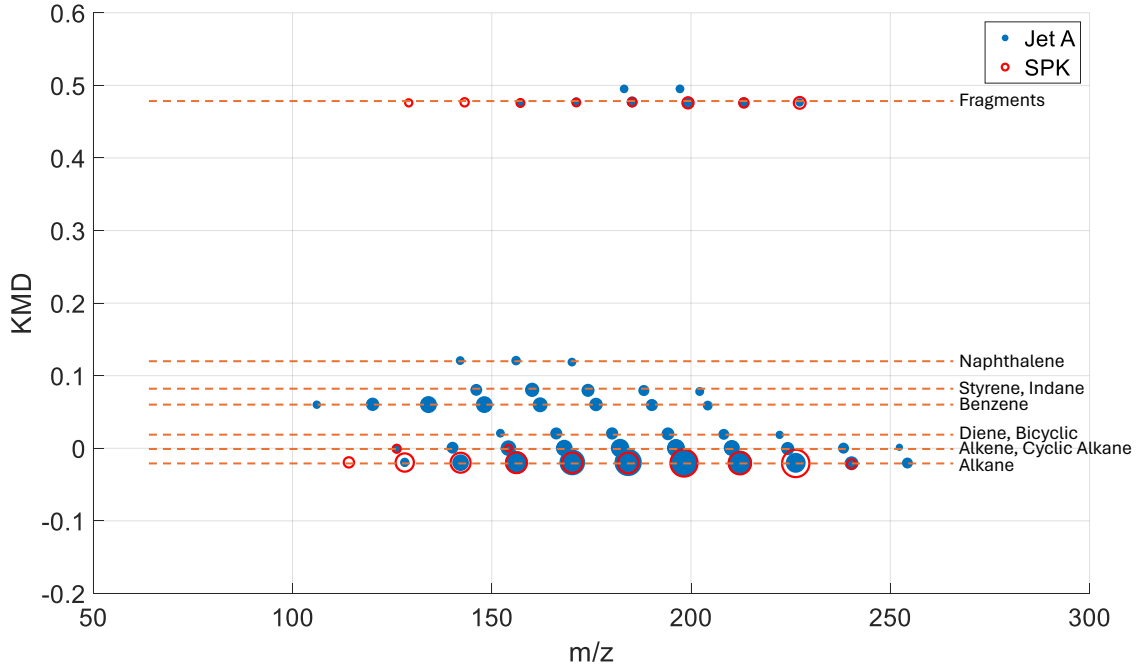

***Fig. 8**: Kendrick mass defect plots of Jet A and SPK*

***Table 3**: Relative abundances of the different molecule families, obtained with the Kendrick Mass Defect method*

Molecule Family	**POSF-4658**	**SPK**
Alkane	Presence	Presence
Alkene, Cyclic Alkane	Presence	Presence
Diene, Bicyclic	Presence	-
Benzene	Presence	-
Styrene, Indane	Presence	-
Naphthalene	Presence	-

3 Results and discussion

3.1 Test Repeatability

AIT test repeatability is assessed by conducting ignition tests at experimental conditions that are as similar as possible from one to the other. The temperature signals from T4 can be separated into two phases: the first few seconds of the signal during the fuel injection and the later temperature peak during ignition. Results are illustrated by three Mode I ignition tests at 217°C with 75 μL of SPK injected. Details of the temperature signals are given in Figure 9 and 10 for the ignition and the injection phase, respectively. The exothermic reaction starts at the same moment for the three tests, at around 115 s, where a faster temperature increase can be seen. The temperature increases similarly for all tests until the ignition, which appears between 127 and 133 seconds after injection. The shape of the temperature signal is similar for the three cases. To highlight the similarities, the integral of the signal has been calculated from 115 and 150 s. Results of the signal processing are gathered in Table 4. Repeatability of the injection is challenging, even with an automatic injection system, as shown in Figure 10. The temperature variation observed at the beginning is due to the cold needle entering and leaving the flask and does not appear to be primarily caused by vaporization as observed by other authors (Chen and Hsieh (2010), Johnson and Mashuga (2023), Setchkin (1954)). The temperature of the flask is affected by the injection and takes 3 to 60 seconds to stabilize after injection.

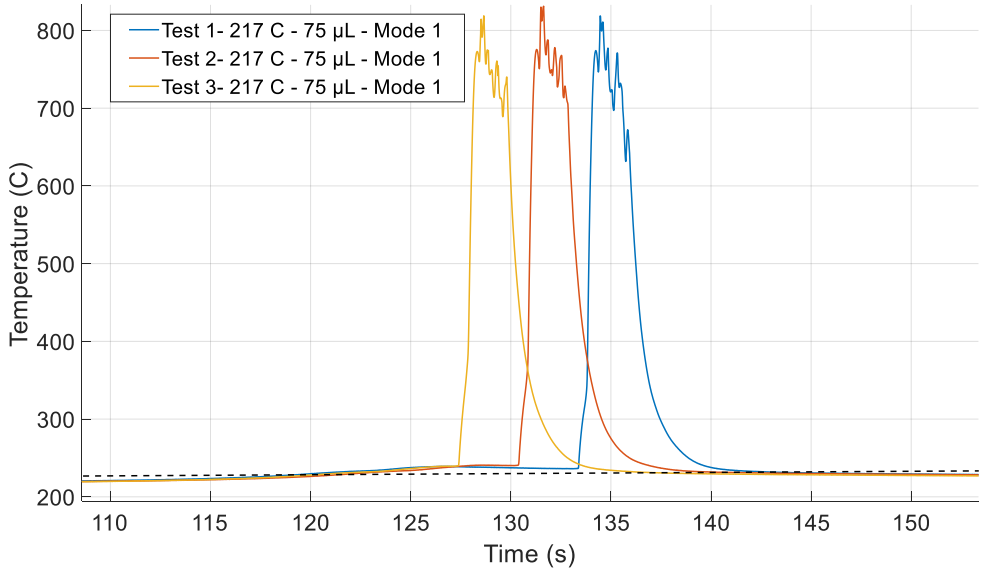

***Fig. 9**: Test sensitivity and repeatability, temperature signals during the ignition - SPK*

***Table 4**: Characteristics of ignition tests at 217°C, 75 µL, SPK*

Test	Ignition time	Maximum temperature	Integral temperature peak
1	133.4 s	818.7°C	1.06e4 C·s
2	130.4 s	831.1°C	1.06e4 C·s
3	127.4 s	818.8°C	1.05e4 C·s

3.2 Ignition Testing Results

The ignition test results for the SPK and Jet A are shown in Figures 11 and 12. Configuration 1 of the ASTM test (see Section 2.1) was used for the SPK data, which were all acquired during the present

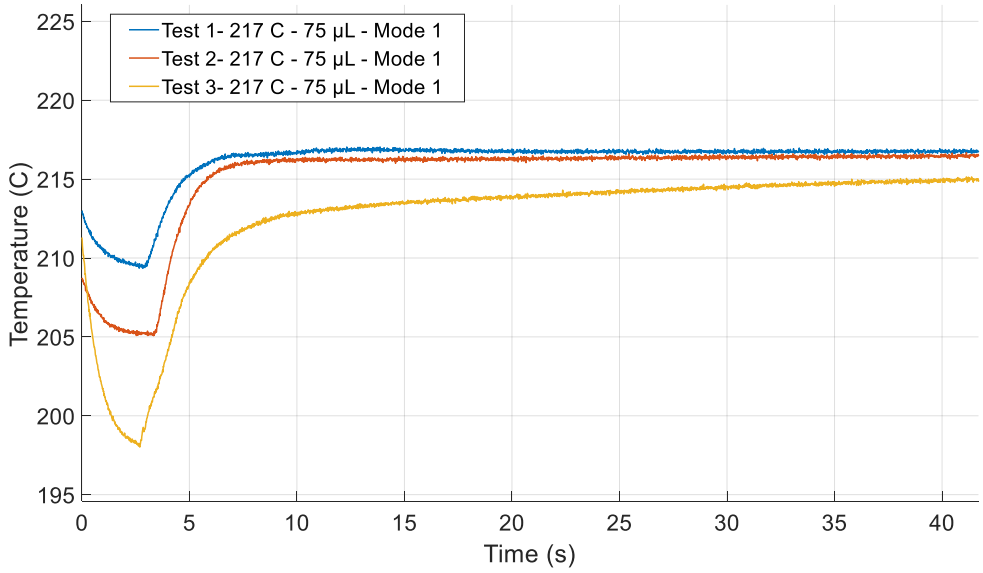

***Fig. 10**: Test sensitivity and repeatability, temperature signals during the injection - SPK*

study. The difference between the ignition maps obtained with Configurations 1 and 2 is discussed in Section 3.6. No flame was visible in Mode III ignition when testing the SPK fuel. However, a noticeable flow from the vessel and a small puff of smoke was observed at the time of ignition. Jet A results from the present study and those of Martin and Shepherd (2021) are plotted together. Consistency is observed between the two sets of measurements.

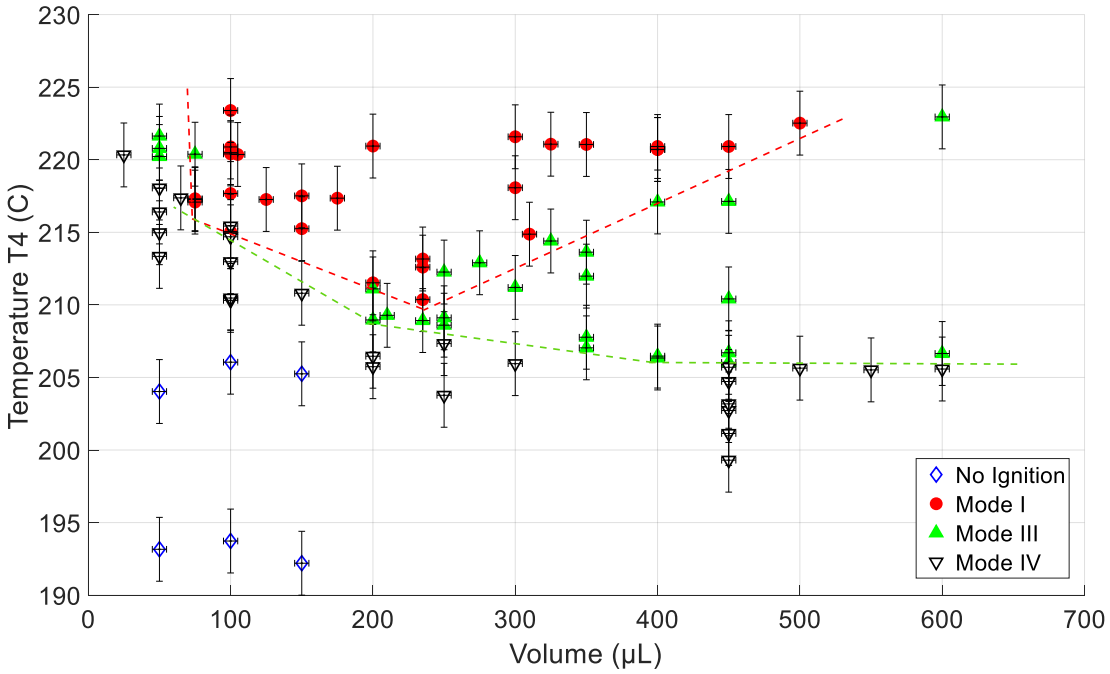

***Fig. 11**: SPK ignition testing results - Configuration 1*

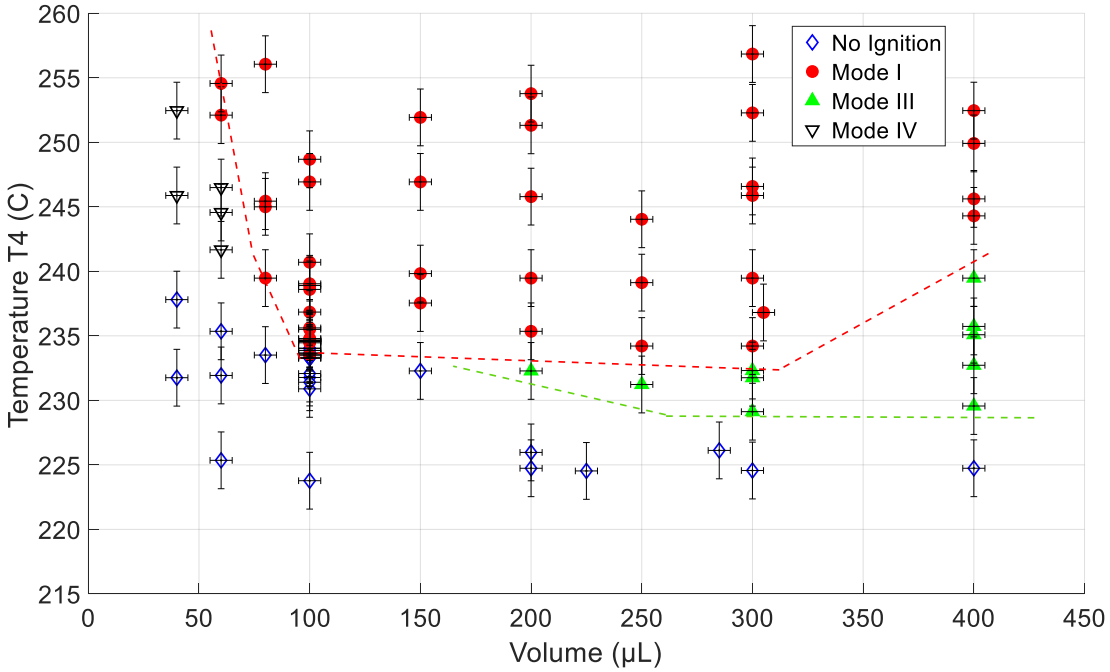

***Fig. 12**: Jet A ignition testing results. Ten tests from the present study (Configuration 1) are shown together with the data from Martin and Shepherd (2021).*

Three ignition modes are observed for both fuels. Figure 13 gives examples of T4 temperature signals obtained from Mode I, III, and IV at various experimental conditions for SPK. While Mode III presents the absence of a visible flame, compared with Mode I, the temperature signals cannot be distinguished between these two modes. However, temperature signals observed during Mode IV event are very different from Modes I and III, with much lower temperature rises and larger ignition delay times. Figure 14 gives the maximum temperature recorded from T4 during the tests, as a function of the initial temperature. The different modes are represented by different markers and colors. White dots have been added to the markers representing the data from Configuration 2. A clear demarcation is observed between Mode IV and Mode III. However, the transition between Mode III and Mode I is smooth, with an overlap between the two modes in a specific temperature range.

Our observations lead to the conclusion that the modes can be separated into two groups - the non-ignition group, with Mode IV and No ignition, where the temperature rise during the chemical reaction is negligible compared to the initial air temperature, and the ignition group, with Mode III and Mode I, where the temperature rise is large enough to create potential hazards by initiating a propagating reaction. The similarities between Mode I and Mode III have already been discussed in the past (Martin and Shepherd, 2021, Johnson and Mashuga, 2023). Based on the experimental observations, we propose to characterize the AIT of a tested fuel based on temperature signals and not flame luminosity and use the Mode III and I ignition events to define the AIT instead of just Mode I.

Dashed lines on Figures 11 and 12 represent the approximate low limits of Modes I and III. The minimum of the two boundaries occurs at different injected volumes and temperatures. It was observed for both fuels that the lower limit of Mode III occurs at higher fuel volumes. A minimum in the lower limit of the Mode III region has not been determined in our tests. Tests at larger fuel volumes will be necessary to investigate if such a minimum exists.

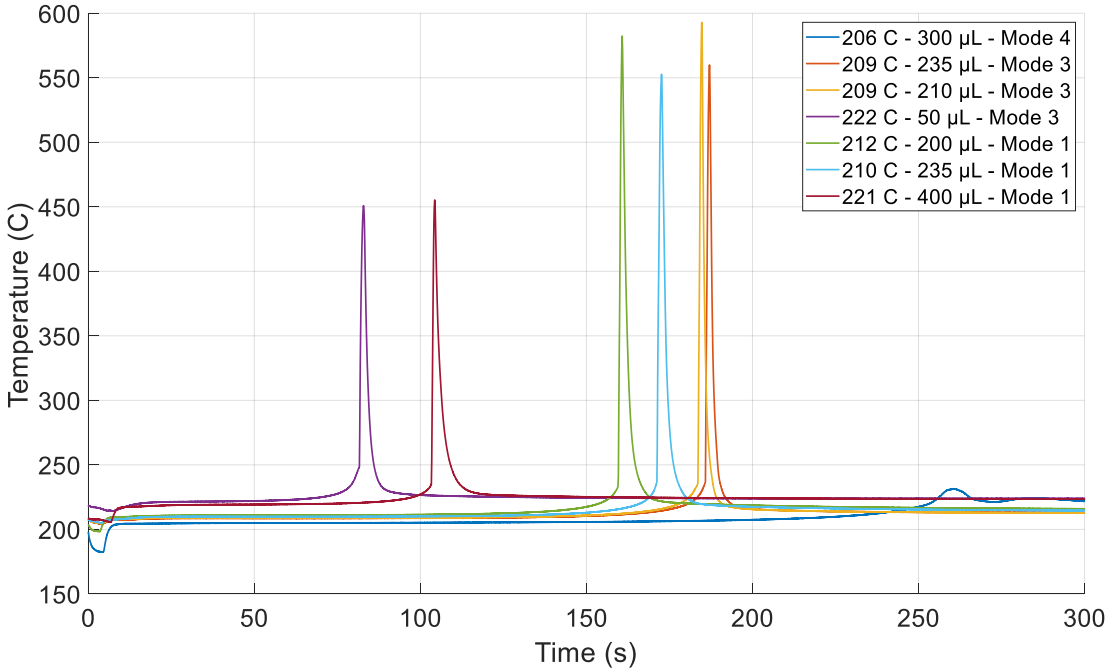

***Fig. 13**: Temperature signals for different ignition modes - SPK*

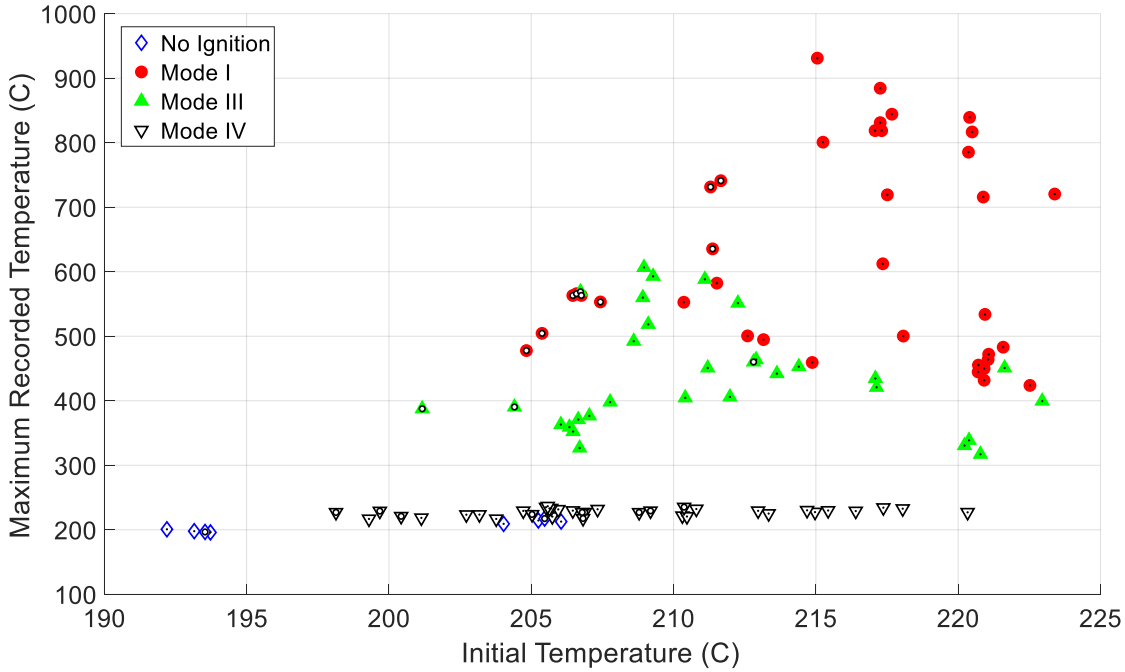

***Fig. 14**: Maximum temperature recorded as a function of the initial test temperature - SPK*

Lines between the different Modes allow better visualizations of the ignition limits but can be deceptive. The transition between no ignition and ignition is not a straight line and can spread over a temperature interval. This phenomenon is discussed in more detail in Sections 3.4 and 3.5.

3.3 Ignition Characteristics

The ignition delay time has been investigated as a function of the initial temperature of T4. The time is plotted in logarithmic scale as a function of the inverse of the initial temperature in Figure 15 for SPK. All the tested fuel volumes are represented for ignition modes I and III. The two ASTM configurations have been used in this study. The markers with a white dot represent data from Configuration 2. The others are from Configuration 1.

A linear correlation can be found by using the Arrhenius plot of the logarithmic value of the ignition time and the inverse of the initial temperature for the two sets of data. While the ignition delay time for these tests is known to depend on the mixture composition (Babrauskas, 2003), our measured ignition delay times appear to depend primarily on the initial temperature. The slopes of the two linear correlations are very similar, and only a small shift in the intercept is observed. An overlap of the curves is obtained when the reference temperature of Configuration 2 is shifted by 2°C. The experimental ignition delay time τ_i can be modeled as:

$$\tau_i = ae^{b/T}, \tag{1}$$

with a and b empirical constants obtained by carrying out linear regression for $\ln \tau_i$ vs T^{-1}. The values are $b = 1.4\times10^4$ K^{-1}, and $a = 4.3\times10^{-11}$ s for Configuration 1; $a = 3.85\times10^{-11}$ s for Configuration 2 and b has the the same value as Configuration 1.

Our results are consistent with a simple Arrhenius form of a one-step model reaction and the Semenov/Frank-Kamenetskii model for the ignition delay time (Babrauskas, 2003):

$$\tau_i \propto e^{Ea/(\tilde{R}T)}, \tag{2}$$

where Ea is the effective activation energy of the tested fuel, and $\tilde{R}$ the universal gas constant.

The effective activation energy of the tested SPK can be computed from the constant b of the regression analysis and is equal to:

$$Ea_{\mathrm{SPK}} = 116\ \mathrm{kJ\cdot mol^{-1}} \quad \text{or} \quad 28\ \mathrm{kcal\cdot mol^{-1}}. \tag{3}$$

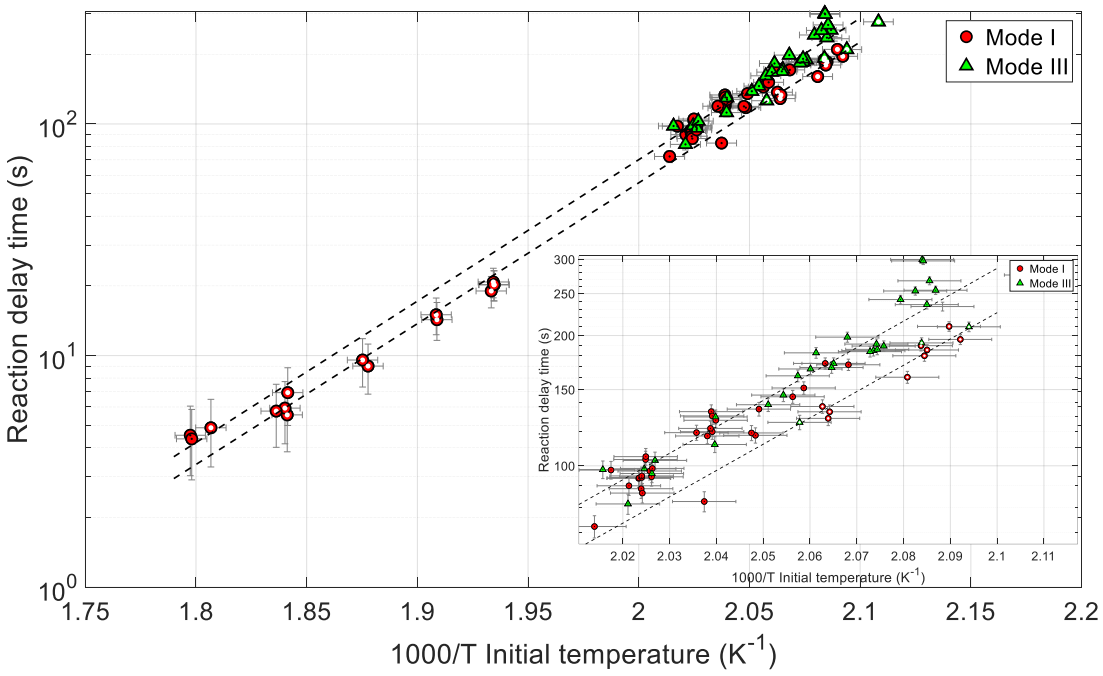

***Fig. 15**: Reaction delay time as a function of initial temperature - SPK*

The same analysis has been conducted with Jet A. The data are gathered in Figure 16. The effective activation energy of the tested Jet A is estimated as:

$$Ea_{\text{Jet A}} = 141\ \text{kJ}\cdot\text{mol}^{-1} \quad \text{or} \quad 34\ \text{kcal}\cdot\text{mol}^{-1}\,. \tag{4}$$

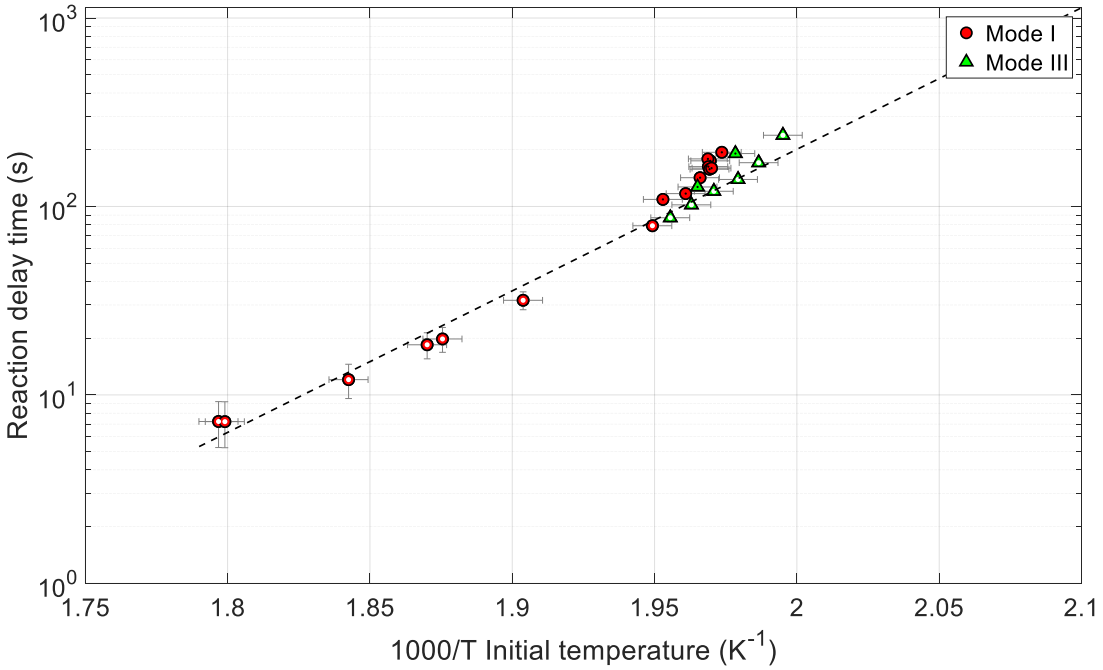

***Fig. 16**: Reaction delay time as a function of initial temperature - Jet A*

A common feature of reaction delay time data is that the Arrhenius plots are not linear, and the effective activation energy depends on the temperature and pressure. A general trend (Babrauskas, 2003) is that Arrhenius plots for autoignition exhibit at least two slopes, i.e, two effective activation energies; one at high temperature (with $Ea \approx 50$ to 90 kJ·mol^{-1}) and one at low temperature (with $Ea \approx 140$ to 190 kJ·mol^{-1}). The low-temperature range of values is consistent with our experimental results and similar in magnitude to the range of values reported in the literature (Goodger and Eissa, 1987, Lefebvre et al., 1986, Babrauskas, 2003) for paraffin-based fuels.

The effective activation energy is a useful way to summarize the fuel ignition delay and is widely used in simplified models of ignition. However, the value obtained is highly dependent on the testing environment and fuel type and is not a true measure of chemical reactivity but depends on the many complex phenomena involved before and during ignition, such as heat transfer, turbulence, and fuel vaporization, and does not account for composition changes during combustion. The value is qualitative and can be carefully compared for different fuels only tested in the same environment.

The variation of the maximum temperature recorded during ignition has been studied as a function of the injected fuel volume. Figure 17 gathers the collected data for SKP. White dots highlight data from ASTM Configuration 2. The other markers are from the ASTM Configuration 1. The temperature dependence regarding the fuel volume is not apparent for the non-ignition and Mode IV cases. Mode I and III ignitions present a temperature peak at around 100 μL. Ignition with that specific fuel volume leads to the most violent combustion reactions with the highest temperature. It is suspected that 100 μL represents a volume near the stoichiometric conditions. Mode I and Mode III cannot be distinguished regarding their behaviors. The same trend is observed for Jet A. Data for Jet A are gathered in Figure 18.

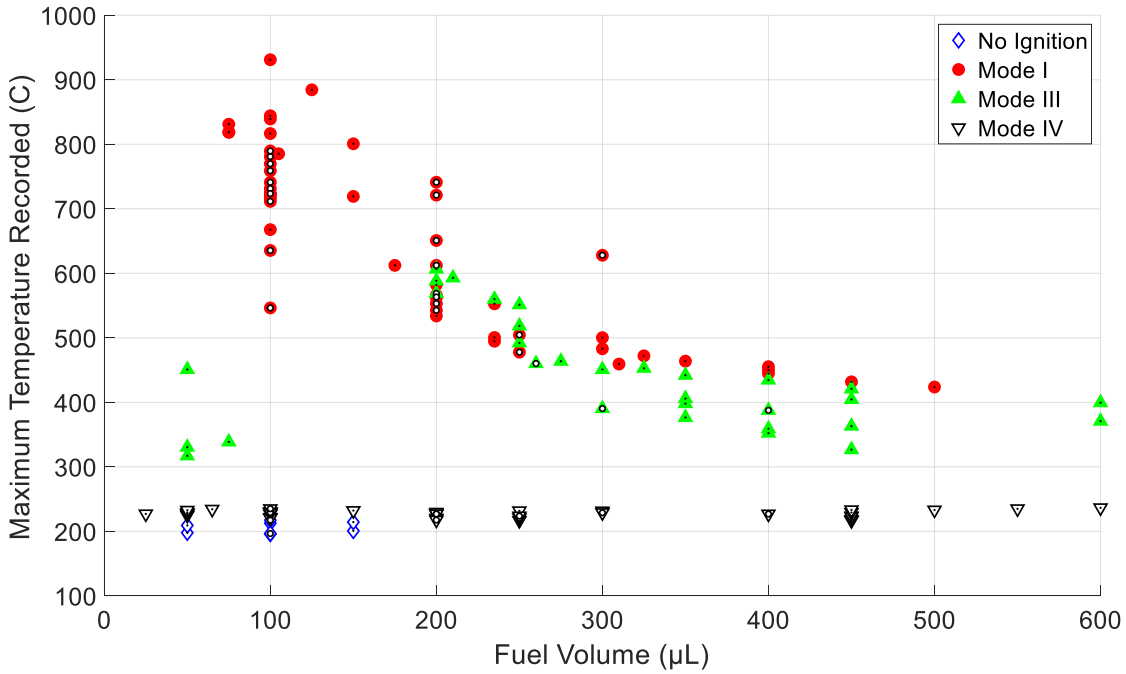

***Fig. 17**: Maximum temperature recorded as a function of the injected fuel volume - SPK*

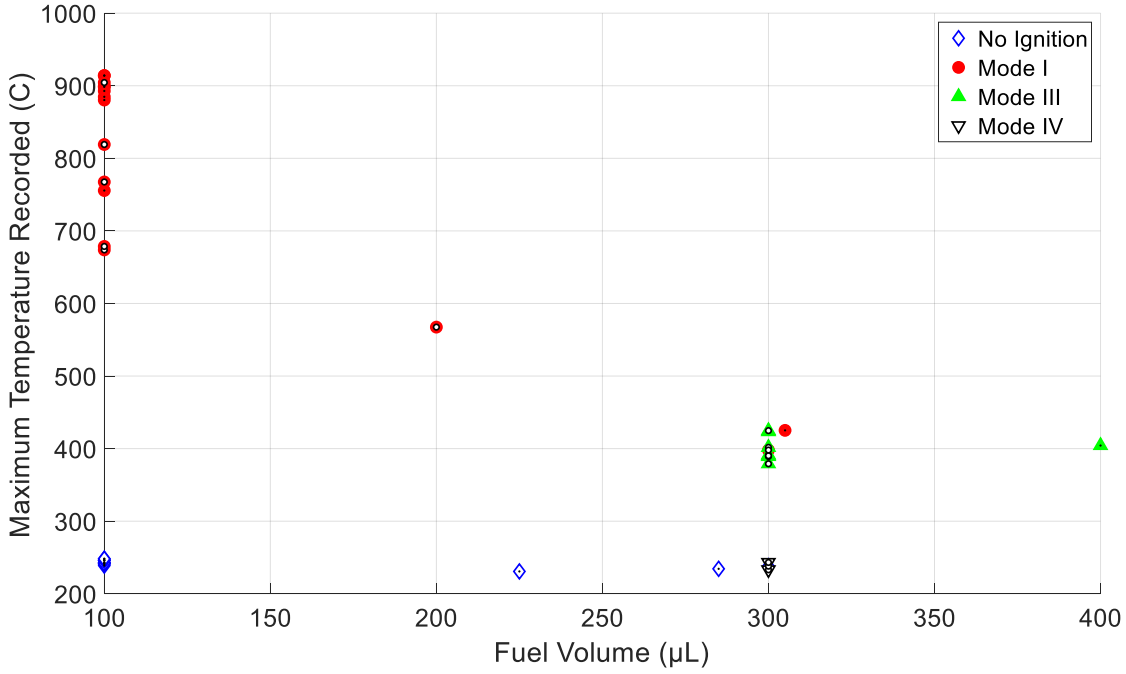

***Fig. 18**: Maximum temperature recorded as a function of the injected fuel volume - Jet A*

3.4 Ignition Transition

The transition between the different ignition modes is investigated by analyzing the different temperature signals at different temperatures for an equal fuel volume. Figures 19 and 20 give the temperature signals of 50 μL and 450 μL of SPK, respectively. When a small amount of fuel is injected (here 50 μL), the temperature signal at a temperature just before the transition between no-ignition (Mode

IV) and ignition (Mode III) is composed of one smooth temperature bump (see signal at 218°C, 50 μL). More complex phenomena occur when the injected volume increases, where multiple peaks can be seen (see signal at 206°C, 450 μL). It was observed that the ignition occurs at the second or third temperature peak (see signal 207°C, 450 μL). This two to three-stage reaction seems typical to some transportation fuels, as it was also observed in the very first ASTM-style tests by Setchkin (1954) when testing Motor Gasoline. Contrary to his observations, the multiple-stage reaction depends here on the tested fuel volume and happens in rich atmospheres. Once the temperature is high enough, the signal is only composed of one peak, as for the lower fuel volume cases.

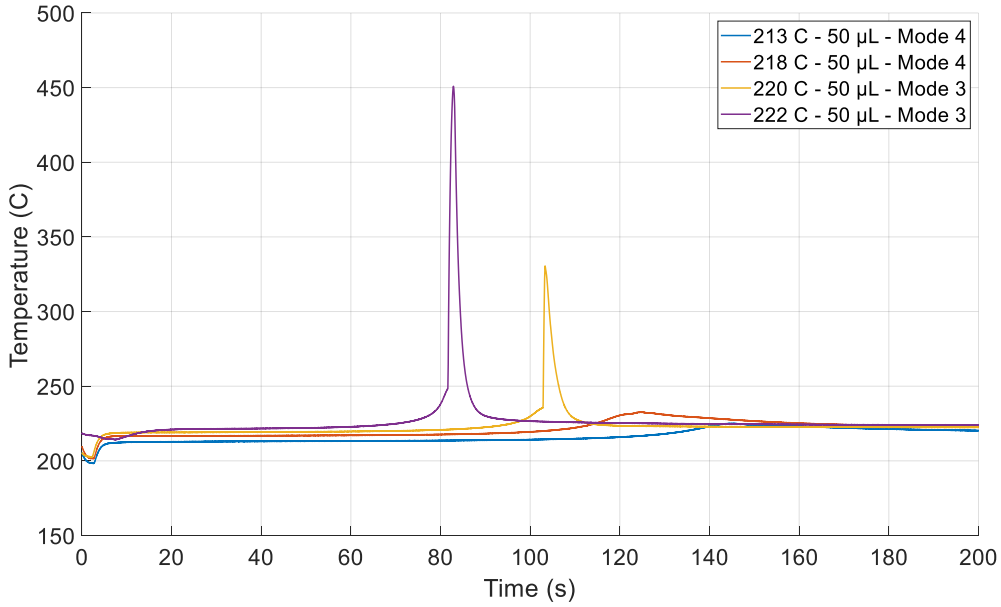

***Fig. 19**: Transition between Mode III and Mode IV, SPK, 50 µL*

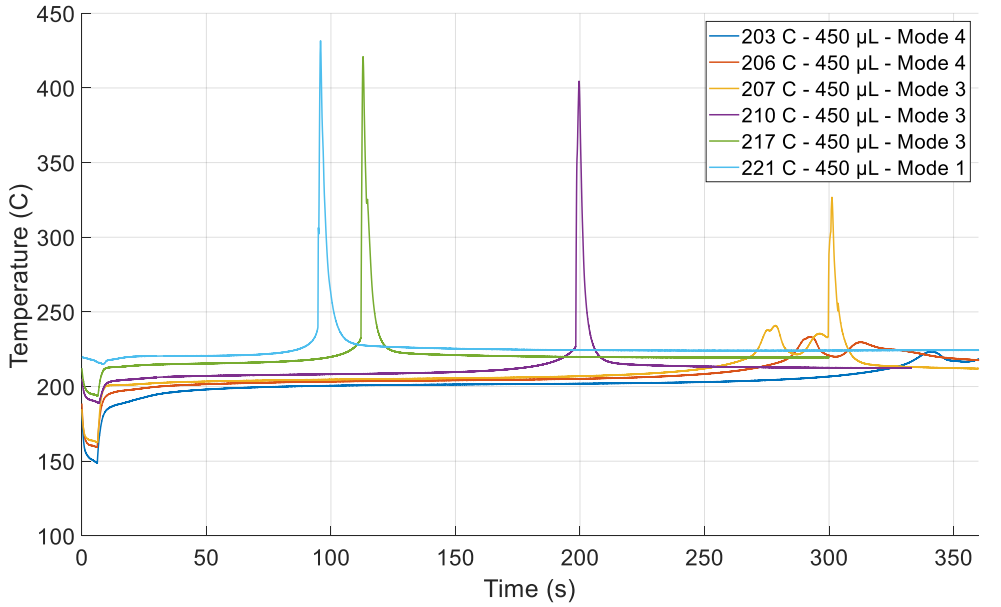

***Fig. 20**: Transition between Mode I, Mode III, and Mode IV, SPK, 450 µL*

Figure 21 examines the transition between non-ignition and ignition, showing a close-up comparison

of two tests conducted at the same temperature for two different fuel volumes. Interestingly, the two temperature signals present a similar temperature increase at the beginning of the exothermic reaction just after 150 seconds. A switch occurs several seconds later when the 200 μL ignites while the 150 μL does not.

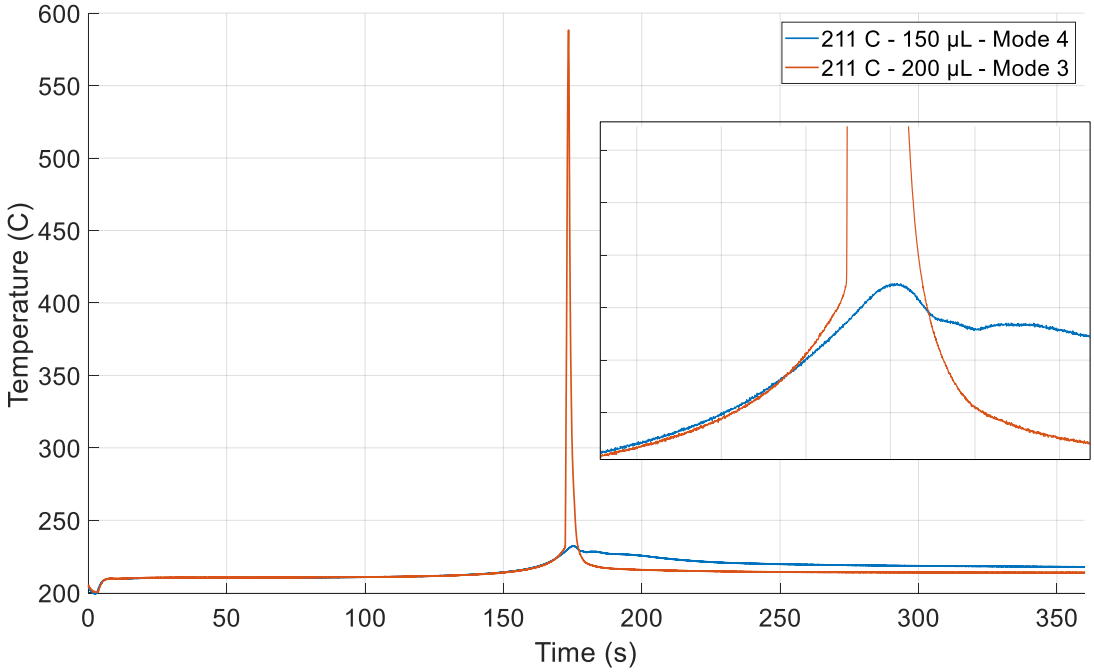

***Fig. 21**: Transition between Mode IV and Mode IV, SKP*

As discussed by Martin (2023), and similarly to dust cloud ignition (Danzi et al., 2018) or spark ignition (Bane et al., 2013), the transition between no ignition and ignition of a fuel in a hot atmosphere is not a sharp line and a zone where both cases can occur exist. The nature of this transition region is discussed in the next section.

3.5 Ignition Statistical Analysis

The statistical methodology of logistic regression (Hosmer and Lemeshow, 2000) was applied to two data sets, one from the Jet A testing and the other from SPK testing. The data from the previous testing series (Martin, 2023) used Configuration 2; data from the present tests used Configuration 1. In this study, we consider both Mode I and Mode III as ignition events.

A total of 80 results for a standard sample (POSF 4658) of aviation kerosene were analyzed with the logistic regression technique. The majority (70) were from previous testing series (Martin and Shepherd, 2021), and 10 were added from the present round of testing. The results are shown in Figure 22 (right) as a plot of the outcomes y_i vs. the temperature T at the center of the test vessel. For clarity, the data points have been randomly displaced from the ignition (y = 1) and non-ignition (y = 0) axes. The confidence intervals were computed in terms of the stimulus $x(\pi)$ using confidence limits in the logit function for a particular value of $\hat{\pi}$

$$\frac{1}{\hat{\beta}_1}\left(\hat{g}(x) \pm z_{\alpha/2}\hat{\sigma}_{\hat{g}(x)} - \hat{\beta}_0\right) = x(\hat{\pi}) \pm \frac{1}{\hat{\beta}_1} z_{\alpha/2}\hat{\sigma}_{\hat{g}(x)} \tag{5}$$

using the approach discussed in Hosmer and Lemeshow (2000). The symbol π denotes the probability of ignition and x corresponds to the temperature $T4$. Symbols with a hat, such as $\hat{\pi}$, $\hat{\beta}$, etc., are expected values computed using the maximum likelihood method.

Note that this analysis uses the aggregate of all test conditions, which spans a range of 50 to 400 μL in fuel volume in addition to the range of temperatures shown. This approach introduces additional factors, fuel volume and ignition mode, which could be included in the regression analysis, but we lack sufficient points at each volume and mode to discriminate between these factors. We elected to focus on temperature as the most important variable. We acknowledge that this differs from the procedure of ASTM-E659 (2005), but as the fuel concentration is unknown in most hazard situations, we propose that this method enables an assessment of ignition threshold that includes variability in fuel concentration and only includes modes with a significant temperature rise as an ignition.

A total of 61 data points are located in the overlap region between 229 and 246°C. The uncertainty limits shown on each datum are ±2.2°C which is the stated accuracy uncertainty of the type K thermocouple used in the apparatus. The precision is much greater, the standard error of the mean is on the order of ±0.1°C and limited by signal fluctuations and record lengths used to obtain mean values.

A useful way to summarize the results with a single statistic is the temperature where $\hat{\pi} = 0.5$, the temperature T_{50} that corresponds to 50% likelihood of ignition. From the logistic analysis, the stimulus at a particular value of expected probability is

$$x(\hat{\pi}) = \frac{1}{\hat{\beta}_1}\left[\ln\left(\frac{\hat{\pi}}{1-\hat{\pi}}\right) - \hat{\beta}_0\right].$$

The value of $T_{50} = -\hat{\beta}_0/\hat{\beta}_1$ for the Jet A data in Figure 22 is 233.4°C and the 95% confidence interval is 5.7°C.

The effect of temperature measurement uncertainty was assessed by carrying out a Monte Carlo study of the effect of random variation of the measured temperatures on the computed value of T_{50}. Random deviates were sampled from a normal distribution with a standard deviation of 2.2°C and added to each temperature in the data series. Random sampling, perturbation of the temperatures, and logistic analysis was repeated 5000 times. The frequency of T_{50} values was recorded, see Figure 23 and analyzed. The distribution is approximately normal, the peak frequency is 233°C and 95% of the data are within ±1.1°C, which is substantially smaller than the confidence interval obtained from the logistic regression on the original data set.

A total of 71 results from the ASTM E659 tests for a sample of synthetic paraffinic kerosene (SPK) were analyzed with the same logistic regression technique as used for Jet A. The results are shown in Figure 22 (left). A total of 47 data points are located in the overlap region between 206 and 220°C. The value of T_{50} for the SPK data in Figure 22 is 207.9°C and the 95% confidence interval is 7.8°C. The effect of temperature measurement uncertainty was assessed by carrying out a Monte Carlo study of the effect of random variation of the measured temperatures on the computed value of T_{50}. The frequency of T_{50} values are shown in Figure 23. The distribution is approximately normal, the peak frequency is at 207.9°C and 95% of the data are within ±5.9°C, which is somewhat larger than the confidence interval obtained from the logistic regression on the original data set.

Results from another sample of Jet A, POSF10325, obtained by Martin and Shepherd (2021), are shown to illustrate the range of AIT results possible with different batches of Jet A. The T_{50} temperatures are slightly lower (227.8°C) and the 95% confidence interval (13.5°C) is approximately twice as large. The results of the Monte Carlo study are consistent with these values.

All the results are summarized in Table 5. The temperature for a 50% likelihood of the new SPK is lower than Jet A (POSF4658), and no overlap was observed between the two fuel data sets. These observations highlight a lower, about 20°C, autoignition temperature for the SPK compared to Jet A (POSF4658). Even though the overlap regions where both ignition and no ignition cases can occur have a similar width, Jet A (POSF4658) has a much sharper T_{50} distribution, where the 95% of the Monte Carlo data interval is almost 6 times smaller than the SPK. It is not yet known if this observation is due to the physical properties of the fuel or the distribution of the tested experimental condition. More work is needed to draw a final conclusion on this behavior.

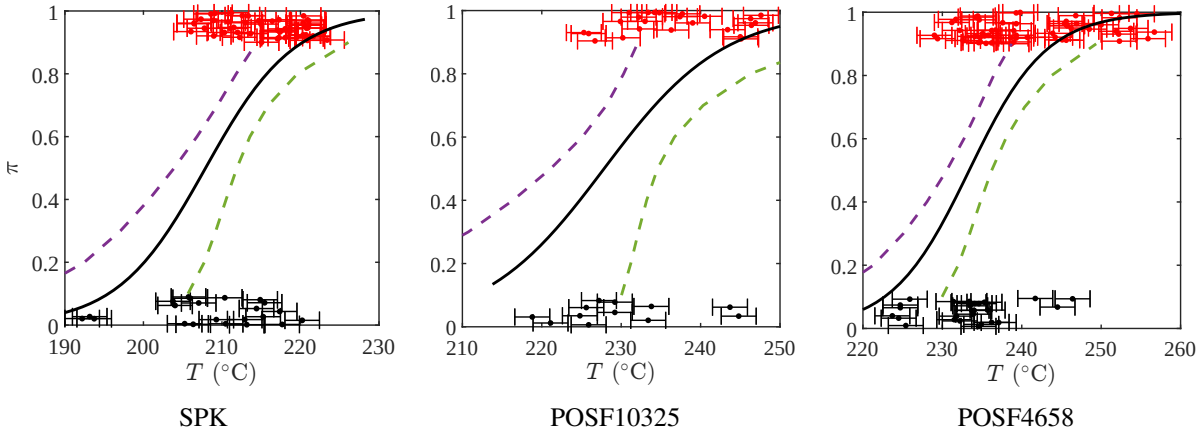

***Fig. 22**: Logistic analysis of ASTM E659 test results for a synthetic paraffinic hydrocarbon (SPK) and Jet A (POSF10325, POSF4658). The solid line is the MLE estimate of probability and the dashed lines are the 95% confidence interval.*

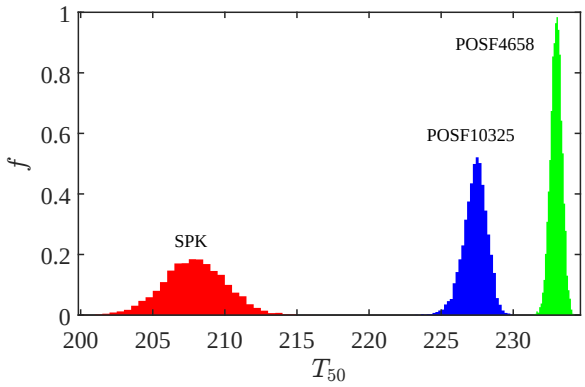

***Fig. 23**: Frequency of T_{50} values computed from 5000 logistic analyses of SPK and Jet A data simulating the effect of uncertainty in measured temperature.*

3.6 Effect of the ASTM Apparatus and Estimation of an AIT Value

The ignition map for SPK was initially generated with Configuration 1 of the ASTM apparatus (see Section 2.1). Results from Configuration 2 have been added on Figure 24 for SPK. The new data are highlighted by white dots and the uncertainty bars of only the new data have been kept on the graph to enable visibility.

The new data shows a shift a few degrees down compared to the old data. Users shouldn't interpret these results as indicating a lower AIT or a lack of repeatability but rather as an issue with characterizing the temperature inside the flask. The ASTM protocol uses one-point measurement as the temperature reference. One key issue is the use of this temperature reference to directly estimate the AIT temperature temperature directly. The measurement of the temperature profile inside the flask for the two configurations (Figure 3) shows that a small apparatus modification can lead to a significant difference in temperature distribution. In the presented case, a variation of 3% between T4 and the temperature over the vertical profile was estimated for the two configurations. This variation represents a difference of more than 6°C, which is slightly higher than the shift observed on the new ignition map. This observation is consistent with the idea that T4 is inadequate at characterizing the initial temperature conditions inside the flask and that more accurate AIT measurements could be reached with a better temperature reference. In order to have better accuracy in the AIT estimation, the temperature distribution inside the flask needs to be characterized accurately and a standardized temperature uniformity needs to be defined, which is not yet the case in the standardized protocol.

***Table 5**: Summary of the logistic regression and Monte Carlo analyses*

Fuel	Overlap Region	Overlap Width	T_{50}	95 % Confidence Interval	MC Peak Frequency T_{50}	95 % of the MC Data
SPK	[206 220]°C	14°C	207.9°C	7.8°C	207.9°C	±5.9°C
POSF10325	[225 245]°C	20°C	227.8°C	13.5°C	227.4°C	±2.2°C
POSF4658	[229 246]°C	17 °C	233.4°C	5.7°C	233°C	±1.1°C

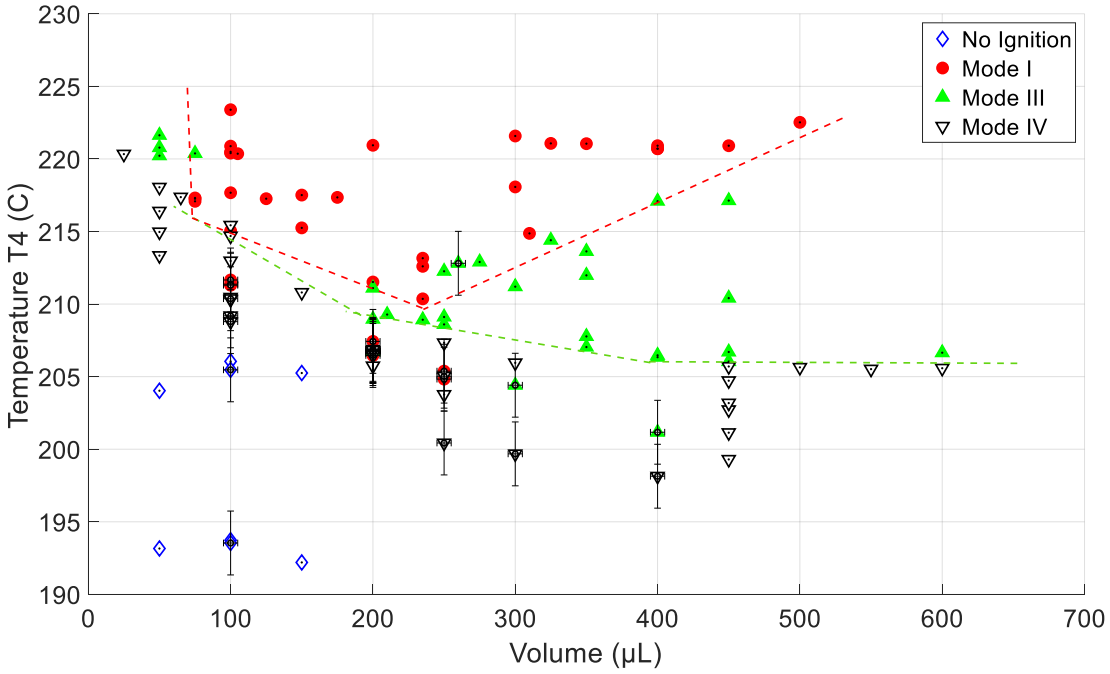

***Fig. 24**: SPK ignition testing results for two configurations. Configuration 1 data are without error bars, Configuration 2 are with error bars and white dots in markers.*

Another key issue is that AIT values given in the literature are associated with a particular temperature distribution, which is usually not reported. In our case, the temperature profile of Configuration 1 provides an estimation of a variation of temperature inside the flask of 3%. This is under the assumption that the temperature inside the whole flask is represented by its centerline profile and that this variation is consistent over the range of test conditions. Further analysis needs to be conducted to investigate the temperature distribution inside the flask and its variation compared to the value given by T4 in order to estimate the AIT of the tested fuels with more confidence.

4 Conclusions

The ASTM-E659 standard has been used to investigate the autoignition of two fuels: Jet A-POSF4658 and a representative Synthetic Paraffinic Kerosene (SPK). The two fuels present a similar composition regarding the alkanes but unlike Jet A, the SPK is mainly composed of alkanes, with just a few alkenes and cylco-alkanes, and no aromatics. An automatic injection system has been used to improve the repeatability of the tests. A higher resolution for temperature acquisition than the one used in the ASTM standard has also been used so that the reaction delay times of the two fuels could be investigated as a function of the initial temperature. The results were fitted to a simple Arrhenius model, and an effective activation energy was computed.

The ignition maps of the two fuels have been given and discussed. Results highlight the importance of using the digital recording of the small gauge thermocouple to detect and quantify ignition instead of

relying only on flame visualization, as suggested by the standard. Mode III ignition (no flame) appears as vigorous (comparable temperature excursion) as Mode I (flame) but often occurs at a lower initial temperature. For this reason, in our statistical evaluation, we consider both Mode I and Mode III to be ignition events.

Autoignition testing under the ASTM protocol aims to define a sharp limit between no-ignition and ignition corresponding to the AIT. Our results show the existence of a temperature interval where both ignition and no-ignition events can happen. In our study, ignition occurs in a temperature interval of 15-20°C and can be characterized by the 50% probability of ignition and a confidence interval.

The autoignition temperature of our SPK sample was found to be 20-25°C lower than Jet A using either statistical or conventional methods to define the ignition threshold temperature. The ignition processes were very similar in the two fuels, with the absence of Mode II ignition, the presence of multiple peaks for large tested fuel volumes, and the general aspect of the ignition maps.

The temperature distribution inside the flask was found to influence the outcome of autoignition testing. We observed that a slight modification of the ASTM apparatus can significantly change the temperature distribution. Using a single thermocouple in the middle of the flask without considering the temperature distribution can lead to erroneous estimations of the AIT and its associated uncertainty. An effort has been made in this project to distinguish the temperature measured by the thermocouple T4 from the AIT value. Future studies are planned to characterize the effect of temperature distribution on ignition thresholds and the implications of reporting AIT values.

Acknowledgements

This research was carried out in the Explosion Dynamics Laboratory of the California Institute of Technology. This work was supported by The Boeing Company through a Strategic Research and Development Relationship Agreement CT-BA-GTA-1 and C. Fouchier was supported by the European Union through a Marie Sklodowska-Curie Fellowship. The authors thank Mona Shahgholi, Manager of The Mass Spectrometry Facility at the Chemistry and Chemical Engineering department of Caltech, for her support and essential help on the fuel composition analysis.

References

Affens, W., Johnson, J., Carhart, H. (1961). *Effect of chemical structure on spontaneous ignition of hydrocarbons.* Journal of Chemical and Engineering Data, 6(4):613–619.

ASTM-D56 (1999). *Standard test method for flash point by Tag closed tester*. American Society for Testing and Materials.

ASTM-E659 (2005). *Standard test method for autoignition temperature of liquid chemicals*. American Society for Testing and Materials.

Babrauskas, V. (2003). *Ignition handbook: Principles and applications to fire safety engineering, fire investigation, risk management and forensic science*. Fire science publishers.

Bane, S., Ziegler, J., Boettcher, P., Coronel, S., Shepherd, J. (2013). *Experimental investigation of spark ignition energy in kerosene, hexane, and hydrogen*. Journal of Loss Prevention in the Process Industries, 26(2):290–294.

Brandes, E., Hirsch, W., Stolz, T. (2018). *Zündtemperaturen in anderen oxidationsmitteln als luft*. PTB-OAR.

Chen, C.-C., Hsieh, Y.-C. (2010). *Effect of experimental conditions on measuring autoignition temperatures of liquid chemicals*. Industrial & engineering chemistry research, 49(12):5925–5932.

Danzi, E., Bibbona, E., Di Benedetto, A., Sanchirico, R., Di Sarli, V., Marmo, L. (2018). *A statistical approach to determine the autoignition temperature of dust clouds*. Journal of loss prevention in the process industries, 56:181–190.

Davis, B., Fouchier, C., Shepherd, J. E. (2024). *Fluid motion and mixing in the ASTM E659 apparatus*. 15th International Symposium on Hazards, Prevention and Mitigation of Industrial Explosions, Naples, Italy, July 10-14, 2024.

Frank-Kamenetskii, D. A. (2015). *Diffusion and heat exchange in chemical kinetics*. Princeton University Press.

Goodger, E., Eissa, A. (1987). *Spontaneous ignition research - review of experimental data*. Journal of the Institute of Energy, 60(443):84–94.

Hirsch, W., Brandes, E. (2005). *Zündtemperaturen binärer gemische bei erhöhten ausgangsdrücken*. Physikalisch-Technische Bundesanstalt, Braunschweig und Berlin.

Hosmer, D. W., Lemeshow, S. (2000). *Applied Logistic Regression*. Wiley Series in Probability and Statistics. Wiley, New York, 2nd ed edition.

ISO/IEC (2017). *Iso/iec 80079-20-1: Explosive atmospheres - part 20-1: Material characteristics for gas and vapor classification-test methods and data*. Technical report, International Orgnization for Standardization.

Johnson, C., Mashuga, C. V. (2023). *Reconsidering autoignition in the context of modern process safety: Literature review and experimental analysis*. Journal of Loss Prevention in the Process Industries, 81:104963.

Jones, S. M., Shepherd, J. E. (2021). *Thermal ignition by vertical cylinders*. Combustion and Flame, 232:111499. Preprint, published version available at `https://doi.org/10.1016/j.combustflame.2021.111499`.

Lefebvre, A. H., Freeman, W. G., Cowell, L. H. (1986). *Spontaneous ignition delay characteristics of hydrocarbon fuel-air mixtures*. Nasa contractor report 175064, NASA.

Martin, C. D. (2023). *Experiments in Thermal Ignition: Influence of Natural Convection on Properties of Gaseous Explosions*. Ph.D. thesis, California Institute of Technology.

Martin, C. D., Shepherd, J. E. (2021). *Low temperature autoignition of jet a and surrogate jet fuel*. Journal of Loss Prevention in the Process Industries, 71:104454.

Mastorakos, E., Baritaud, T., Poinsot, T. (1997). *Numerical simulations of autoignition in turbulent mixing flows*. Combustion and Flame, 109(1-2):198–223.

msFineAnalysis (2023). *Jeol Software, Peabody, MA, USA*. `https://www.jeol.com/`.

NFPA (1991). *Fire protection guide to hazardous materials*. National Fire Protection Association, 10th edition.

Semenoff, N. (1929). *Kinetics of chain reactions.* Chemical Reviews, 6(3):347–379.

Setchkin, N. P. (1954). *Self-ignition temperatures of combustible liquids*. Journal of Research of the National Bureau of Standards, 53(1):49.

Swarts, D. E., Orchin, M. (1957). *Spontaneous ignition temperature of hydrocarbons*. Industrial & Engineering Chemistry, 49(3):432–436.

Explosion properties of iron dust in pure oxygen at elevated pressure

Emmanuel Leprette [a], Christophe Proust [a,b] & Valérie Naudet [c]

[a] Institut National de l'Environnement Industriel et des Risques, Verneuil-en-Halatte, France
[b] University of Technology of Compiègne, France
[c] Air Liquide Campus Innovation Paris, Jouy-en-Josas, France

E-mail: emmanuel.leprette@ineris.fr

Abstract

A 50 L explosion vessel was purposely designed and manufactured to investigate the explosion properties of iron dust in oxygen at elevated pressure. Pressurized oxygen was injected into the vessel through a perforated tube to blow the iron dust deposited at the bottom of the vessel. This technique has been calibrated to create a homogenous and turbulent flammable dust cloud. The flammable cloud was ignited with a pyrotechnic match delivering 60 J. During the first series of tests, the influence of the initial O_2 pressure and mass of iron were investigated. As expected, the maximum pressure and maximum rate of pressure rise increase when the initial pressure or the ratio mass Fe / mass O_2 increases. However, when the iron mass increased, a spontaneous ignition occurred at the beginning of oxygen injection, resulting in a violent jet fire that perforated the 25 mm thick wall of the vessel. Further investigations are required to explain this observation. The spontaneous ignition could be caused by friction between the iron particles and the steel walls or by electrostatics. The influence of ferric oxide Fe_2O_3 mixed with iron dust was also studied It resulted in rapid combustion with a high pressure increase quite different from the one caused by a dust explosion.

Keywords: *dust explosion, self-heating, iron, oxygen*

1. Introduction

The use of oxygen is widespread in many industrial applications like combustion, steel production, aerospace industry... Oxygen is usually stored and transported at high pressure. Such conditions promote fast oxidation reactions of metallic and non-metallic materials, which can result in unwanted ignition and severe accidents. Many accidents involving fires and explosions in oxygen-enriched atmosphere were reported in the past (Dicker & al., 1988), sometimes resulting in catastrophic failure and devastating consequences (Saha & al., 2011; Chowdhury, 2011).

Some of them involve metal particle deposits which may be blown in pipework and equipment conveying oxygen and create a flammable dust cloud. The most common ignition mechanisms in such situations are mechanical friction between mechanical parts or between particles, impact of metallic particles on walls, adiabatic compression, electrical arcing, electrostatics (Benson, 2015). Especially friction and impact can generate hot spots with very high temperature which may exceed the auto-ignition temperature of the material. Professional safety rules are implemented by industrial operators (EIGA, 2020) to prevent the risk of ignition. Prevention is usually based on the selection of materials (metallic and non-metallic) compatible with oxygen, geometrical design (to avoid sharp angles) and limitation of the conveying velocity. The American Society for the Testing of Materials (ASTM) have developed many guidelines and standardized test methods to characterize the ignition sensitivity of metallic and non-metallic materials in enriched-oxygen atmospheres (ASTM G63, G72, G74, G86, G88, G94, G124) which can be used for the design of high-pressure oxygen installations.

In addition, if one wants to design protection barriers to mitigate the explosion effects, like an explosion resistant enclosure, it is required to characterize the explosion pressure and pressure rise

during such events. Whereas explosion properties of metal dusts in air have been extensively investigated (Cashdollar, 2007), very limited data are available concerning the explosion properties of iron dust in pure oxygen.

The present work aims at producing experimental data on the explosion properties of iron dust in oxygen at elevated pressure. The testing conditions are selected to represent the pressure, velocity and turbulence level which are present in some oxygen production unit equipment like filters where iron dust can accumulate in operation. Tests are conducted in a similar way than the standardized tests usually performed to determine maximum explosion pressure and maximum rate of pressure rise (EN 14034-1 and -2). The influence of the initial pressure and iron dust concentration are investigated, as well as the effect of the addition of iron oxide dust to the iron dust. A secondary objective is to observe if the test conditions may result in a spontaneous ignition.

2. Experiments

2.1. Description of the experimental setup

An explosion vessel was purposely designed and manufactured for the project (Fig. 1). The vessel is a 50 L steel cylinder made of a 25 mm thick tube welded at the bottom to a steel cap and closed on the top by a steel flange. It is designed to withstand at least 150 bar. Two 5 L reservoirs pressurized with oxygen are connected through the upper flange to a vertical perforated tube into the vessel. The iron dust is placed in an aluminum cup at the bottom of the vessel. Due to the high combustion temperature, the aluminum cup melts and burns during the test and must be replaced at each test. It is assumed that the combustion of this aluminum cup does not interact with the dust cloud explosion as the combustion durations are not of the same order.

A fast-acting valve is mounted on the oxygen injection line. When it opens, oxygen is discharged into the vessel through the multiple holes of the perforated tube and blows the dust to create a flammable dust cloud. The flammable cloud is ignited close to the top flange by a pyrotechnic igniter delivering 60 J. The air initially present in the vessel is not evacuated before oxygen injection, so a small volume of nitrogen (about 40 L at atmospheric pressure) remains in the vessel during the test. When the initial pressure equals 30 bar, this represents about 2,5% of the total gas volume in the vessel. It is assumed to be negligible compared to the quantity of oxygen injected.

Fig. 1. *View and scheme of the experimental setup of the explosion vessel*

Attention is paid to the design of the perforated tube. It is inspired from the perforated ring used for standardized explosion tests described in EN 14034-1. This injection technique produces several high-speed jets at each hole of the tube. When the jets impact the vessel walls, the flow velocity is converted into recirculation velocity which allows both homogenous mixing of the dust and production of isotropic turbulence (Dyduch & al., 2016). Actually, the turbulence parameters in the

vessel mostly depend on the number and diameter of the holes (Proust et al., 2007). An additional issue comes from the high density of the iron dust.

An engineering tool based on the jet theory (Proust et al., 2009) is used to calculate the number and the diameter of holes on the perforated tube which are required to produce the desired turbulence intensity.

There is not any available technique to measure turbulence in the explosion vessel in oxygen-enriched atmosphere at high pressure. Consequently, to calibrate the system and validate the design of the perforated tube, it is first tested at smaller scale in a 7 L transparent vessel with pressurized nitrogen injection (Fig. 2) The transparent vessel is illuminated by a laser sheet and filmed. Video post processing is used to assess the turbulent velocity in the vessel (Bozier and Veyssière, 2005) and compare the results to the calculations (Fig. 3). As expected, the turbulence intensity is not constant during the gas injection. It drops with the discharge pressure and falls to 0 very quickly after the end of injection. Therefore, the initial injection pressure and the final injection pressure are set so that the turbulence intensity at the end of injection is about 2 m/s as it is in the standard 1 m^3 vessel (Proust et al., 2007). A good agreement is achieved between prediction and measurements. Then it is assumed that the design rules can be upscaled to the 50 L explosion vessel without any further verification.

Finally, the design parameters of the perforated tube are: tube diameter 4 mm, with one 2 mm axial hole at the bottom and fourteen (2 x 7) 1 mm radial holes homogenously distributed along the tube length. The initial pressure in the O_2 reservoirs depends on the expected initial pressure in the explosion vessel. The typical duration of oxygen injection is 2 s.

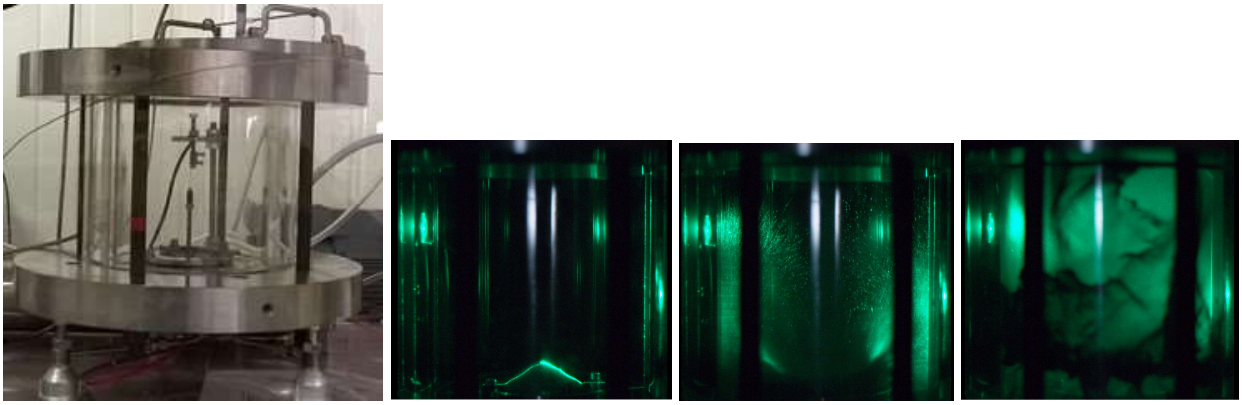

Fig. 2. *7 L transparent vessel used for calibration of the dust injection system setup*

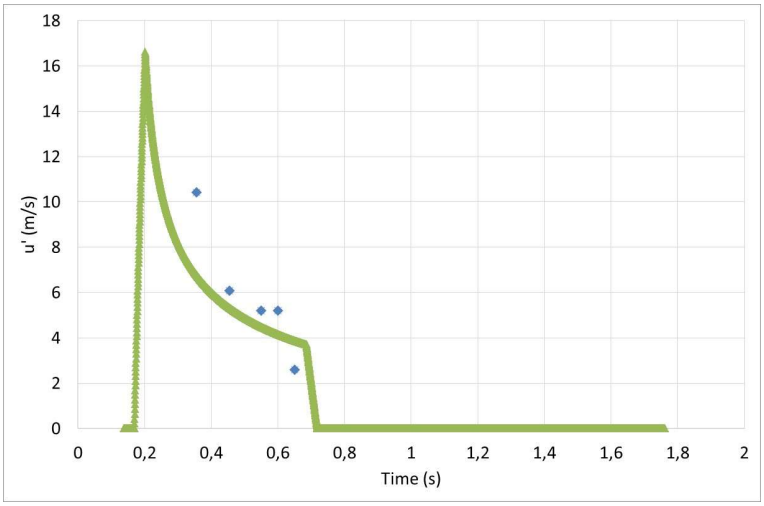

Fig. 3. *Turbulence intensity in the transparent 7L calibration vessel – comparison of calculation (green curve) and measurements (blue dots) – Nitrogen injection pressure 130 bar*

Ignition and injection valve closing are triggered simultaneously, so that there is no jet velocity anymore, whereas the turbulence is still present.

The dust is selected so that it can be easily dispersed, and it remains in suspension during the combustion. The fluidized bed theory (Davidson and Harrison, 1985) mentions that the first requirement is fulfilled when the particle diameter is larger than 20 to 40 µm. At the opposite, the free fall speed must be lower than the turbulent velocity assumed to rank a few m/s: for dense particles like iron, this happens when particle diameter remains below 100 µm. Finally, tests are conducted with iron dust (purity 99%) with a maximum particle size of 60 µm (Table 1).

***Table 1**. Particle size distribution (in µm)*

Dust	Dv(10)	Dv(50)	Dv(90)
Fe	20.8	34.9	55.6
Fe_2O_3	1.1	9.8	29.4

The explosion pressure is measured with a piezoresistive pressure sensor Kistler 0-200 bar. The sensor is remotely connected to the injection pipe rather than directly to the vessel, so that it is protected from the very high combustion temperature in the vessel. A few calibration tests are first carried out with a reference case (hydrogen-air explosion) in order to check that the pressure measurement is not disturbed by any acoustic effect in the injection tube.

All the tests are remotely controlled and monitored with a HD camera to detect any unexpected events.

2.2. Theoretical predictions

Preliminary calculations are performed with the CIRCE software (Liu & al.,) to estimate the explosion pressure depending on the initial ratio of iron mass and oxygen mass. A Monte-Carlo method is used to calculate the final equilibrium by minimization of the Gibbs energy. The reactants are solid iron (Fe) and oxygen (O_2). The remaining species after combustion are Fe (solid, liquid and gas), O, O_2 (gas), and stable solid iron oxides FeO, Fe_2O_3, Fe_3O_4 which result from the following reactions:

$$Fe + O \rightarrow FeO$$

$$2\ Fe + 3/2\ O_2 \rightarrow Fe_2O_3$$

$$3\ Fe + 2\ O_2 \rightarrow Fe_3O_4$$

Note that two mechanisms are in competition during the combustion process: on the one hand, the gaseous oxygen is consumed and converted into solid oxides, so that in the event of complete combustion there would be no more gas after combustion and therefore no pressure in the vessel. On the opposite, the very high combustion temperature partially vaporizes iron and heats the gases, which increases the pressure. Finally, the maximum explosion pressure (about 166 bar) would be reached when there is an excess of oxygen compared to the initial mass of iron (Table 2) i.e. when the molar ratio equals 15% mol Fe/mol O_2. The corresponding mass ratio is about 0.3, much lower than the stoichiometric concentration. The final composition of iron oxides depends on the initial molar ratio of iron and oxygen.

***Table 2**. Explosion properties calculated with CIRCE (initial conditions 30 bar, 10°C)*

Molar ratio (%mol Fe / mol O_2)	Mass ratio (kg Fe / kg O_2)	Maximum adiabatic temperature (°C)	Maximum explosion pressure (bar)	% Solid after explosion (mol/mol)	Combustion products
60	1.05	3662	57	80	FeO
50	0.87	3284	95	66	FeO
40	0.7	2758	127	49	FeO
30	0.52	2226	143	34	FeO
20	0.35	2041	157	17	Fe_2O_3 + FeO
15	0.26	1901	166	9	Fe_2O_3
10	0.17	1292	134	5.5	Fe_2O_3

3. Results and discussion

Twelve tests are performed in total. The first series (tests n° 1 to 4) aims at investigating the influence of the initial pressure, from 5 bar to 30 bar which is the common service pressure in oxygen operating units. The second test series (tests n°5 to 8) addresses the influence of the iron/oxygen mass ratio. Finally, the third test series addresses the influence of the addition of ferric oxide Fe_2O_3 to the iron dust. Tests conditions and main results are presented in Table 3.

***Table 3**. Test conditions and main results*

Test n°	Initial pressure P_{init} (bar)	Mass Fe (g)	Mass ratio Fe_2O_3 (g) / Fe (g)	Concentration (kg Fe / kg O_2)	Maximum explosion pressure P_{max} (bar)	P_{max}/P_{init}	Maximum rate of pressure rise (dP/dt)
1	5	114	0	0.3	16.5	3.2	38
2	10	228	0	0.3	32.3	3.2	149
3	20	456	0	0.3	67	3.3	182
4	30	683	0	0.3	76.7	2.6	78
5	30	341	0	0.15	41.7	1.4	8
6	30	1366	0	0.6	107.5	3.6	213
7	30	2730	0	1.2	136.6	4.6	490
8	*30*	*5640*	*0*	*2.4*	*Spontaneous ignition*		
9	30	341	1	0.15	35.7	1.2	0.3
10	30	1366	1	0.6	38	1.3	0.6
11	30	1366	0.5	0.6	64	2.1	6.4
12	30	1366	0.25	0.6	66.5	2.2	14.5

Some pictures of a typical test (Test 7) are shown on Fig. 4. After all tests a rust deposit is visible on the internal vessel walls and on the injection tube. This color is characteristic from Fe_2O_3 production. There is no visible trace of the other iron oxides (FeO, Fe_3O_4) in any test. The Fe_2O_3 deposit can be easily cleaned before each new test at the beginning, but after many tests there is always a thin oxide layer which sticks to the wall. Moreover, melt iron which does not participate to the combustion also accumulates in the bottom of the vessel after test. Unlike iron oxide it is almost impossible to remove this iron layer before each new test because it is “welded” to the vessel.

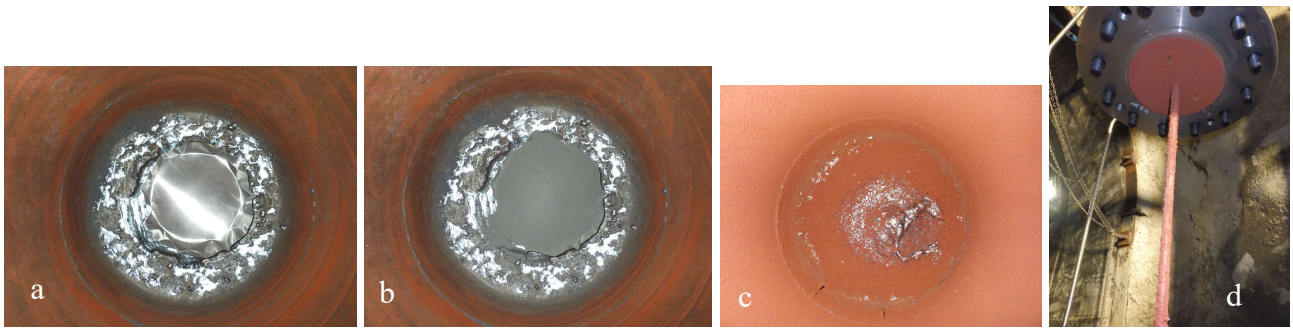

Fig. 4*: Pictures of Test 7 – a, b, c : bottom of the vessel – a: aluminum cup (empty); b: cup filled with iron dust ; c: iron oxide dust (from combustion, after the test); d: iron oxide deposit on the injection tube*

3.1. Influence of the initial pressure

A first series of tests is performed to investigate the influence of the initial oxygen pressure from 5 bar to 30 bar. Pressure curves are plotted on Fig. 5. They are typical of a dust explosion with a pressure rise duration lower than 500 ms. Tests are carried out at the theoretical optimum mass ratio which should result in the maximum P_{max}. As expected, the maximum explosion pressure P_{max} increases when the initial pressure P_{init} increases as well, and the ratio P_{max}/P_{init} is constant (Fig.6). However, the P_{max} value is much lower than the calculated value (see Table 2): with P_{init} = 30 bar one gets only P_{max}= 76.7 bar, whereas the expected value is about 160 bar.

Cashdollar & Zlochower (2007) performed an extensive testing program with metal dusts in the 20- L sphere at atmospheric conditions. They also observed a large difference between the experimental P_{max} and the theoretical predictions in adiabatic conditions. For two different iron dust samples with different particle size distribution, the measured P_{max} was 40% to 60% lower than the adiabatic P_{max}. The same observation was made for the maximum measured temperature T_{max} which was also 40% lower than the calculated adiabatic T_{max}. They noticed that the prediction was better for very fine particles (mean diameter ~4 µm) than for coarser ones (mean diameter ~45 µm) because the former are totally vaporized, whereas the latter volatilize only partially.

Then, the gap between the experimental and calculated values of P_{max} may come from the adiabatic hypothesis (the explosion vessel is not adiabatic), the particle size which influences the volatilized fraction of dust, and last but not least, the efficiency of the dust dispersion, especially at high concentration.

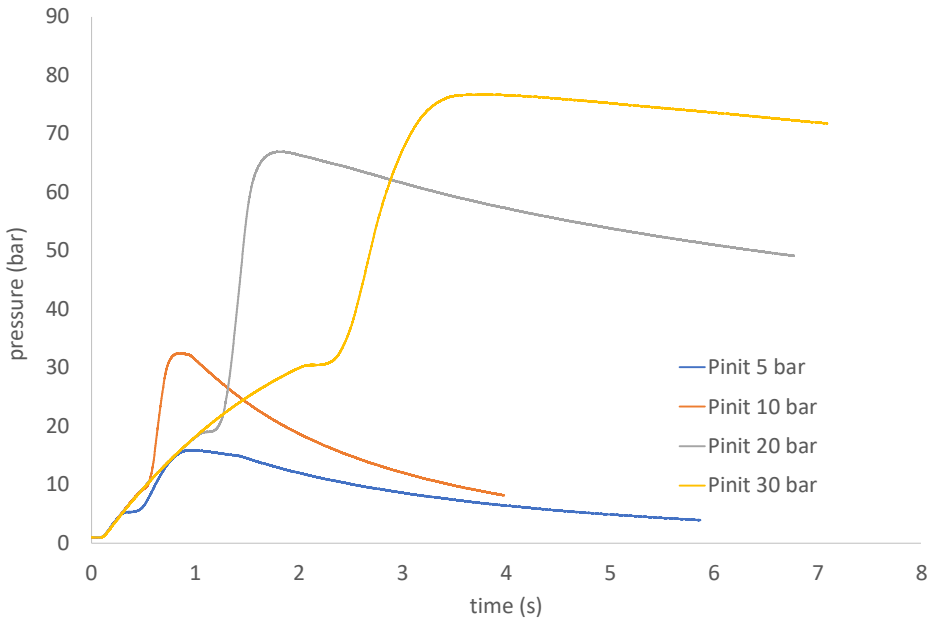

***Fig. 5**: Pressure-time curves for Tests 1 to 4 – Influence of P_{init}. Oxygen injection starts at t=0 – Injection duration, and therefore ignition time, vary with P_{init}*

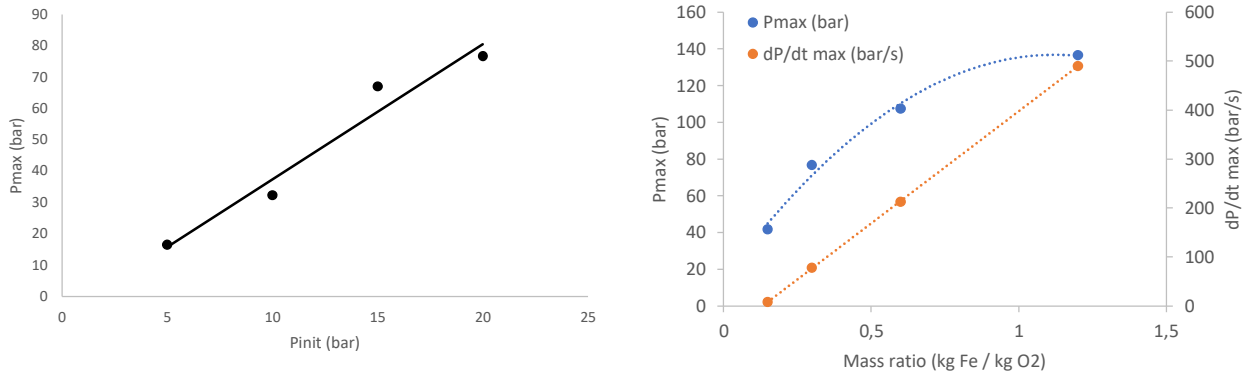

***Fig. 6**: Left : Dependency of P_{max} on P_{init} for kgFe/kgO_2=0.3– Tests 1 to 4*
Right: Dependency of P_{max} and dP/dt_{max} on mass ratio – Tests 4 to 7

3.2. Influence of iron mass

The next series (Tests 4 to 8) is performed at P_{init} = 30 bar with variation of the mass ratio Fe/O_2. Pressure-time curves are plotted on Fig. 7, and the influence of the mass ratio Fe/O_2 on P_{max} and dP/dt is plotted on Fig. 6. In all the tests O_2 injection starts at t=0 and ignition occurs at t = 2.1 s. At 0.15 kg Fe/kg O_2 (Test 5), the dust cloud does not ignite immediately, and the very low pressure increase is attributed to a delayed combustion of the dust. Test 8, with a mass ratio closed to stoichiometry, is discussed in the next chapter. It seems that the maximum pressure during Test 7 (P_{max} = 136.6 bar) with a mass ratio of 1.2 kg Fe/kg O_2 is closed to the calculated worst case (P_{max} = 166 bar – see Table 1), with. The corresponding K_{st} value, calculated as $(dP/dt).V^{1/3}$ with the vessel volume, reaches 180 bar.m/s. If we compare this value to the K_{st} of iron dust in air at atmospheric conditions, the iron dust looks much more reactive in oxygen than in air. The available databases (Cashdollar & Zlochower; 2007; Staubex database) mention that iron is classified as a ST1 dust with a typical K_{st} value of 30 to 40 bar.m/s. The initial elevated pressure also plays a role.

However, if we focus on the mass ratio which results in the maximum explosion pressure, the experimental mass ratio (1.2 kg Fe/kg O_2) is much higher than the calculated value (0.3 kg Fe/kg O_2).

Again, we suspect that the adiabatic hypothesis does not fully apply, but also that the dust dispersion is not fully efficient when the dust mass exceeds ~1kg in the vessel, and that a significant part of the dust may not contribute to the explosion. According to Cashdollar & Zlochower (2007), it could be highly dependent on the fraction of dust which vaporizes during the combustion. This assumption is difficult to verify in our experimental setup. It can only be noticed that at high concentration, part of the iron melts and accumulates at the bottom of the vessel.

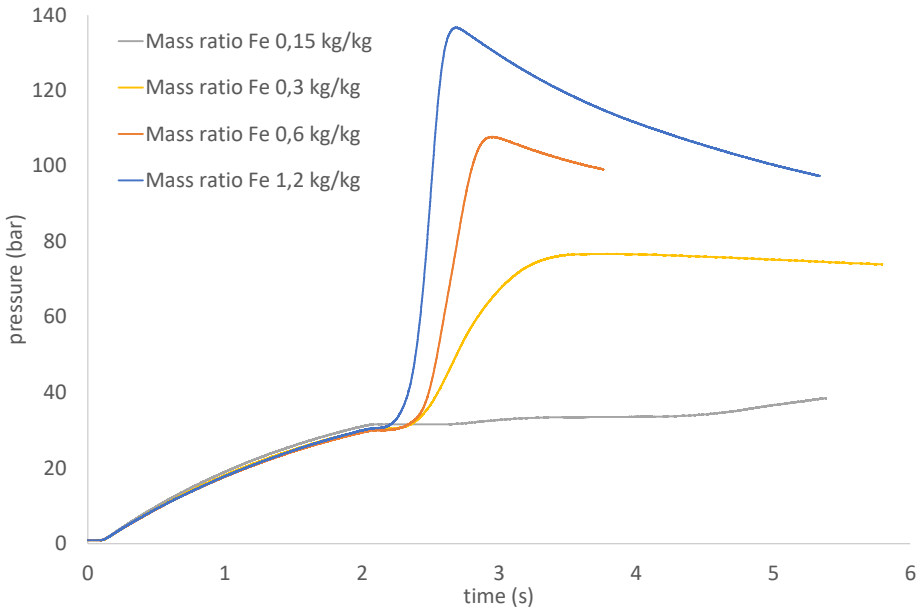

***Fig.** 7: Pressure-time curves for Tests 4 to 7 – Influence of mass ratio Fe/O_2. Oxygen injection starts at t=0 – Ignition at t = 2.1 s*

3.3. Spontaneous ignition

Test n°8 was performed with an increased mass of iron (5460 g) and an oxygen initial pressure of 30 bar. This test condition (mass ratio 2.4 kg Fe / kg O_2) is very close to the stoichiometric conditions since only Fe_2O_3 is formed (mass ratio 2.3 kg Fe / kg O_2). However, a spontaneous ignition occurred 250 ms after oxygen began to fill the vessel. The pressure started to increase immediately like in a dust explosion, but 100 ms later the 25 mm thick wall of the vessel was perforated. These events are visible on the pressure-time curve of Fig. 9. The test resulted in a violent phenomenon characterized by a flame jet outside the vessel (Fig. 8). The jet stopped at the end of oxygen injection. The oxygen injection tube completely disappeared during the test, and a 2 cm diameter hole was created in the vessel wall.

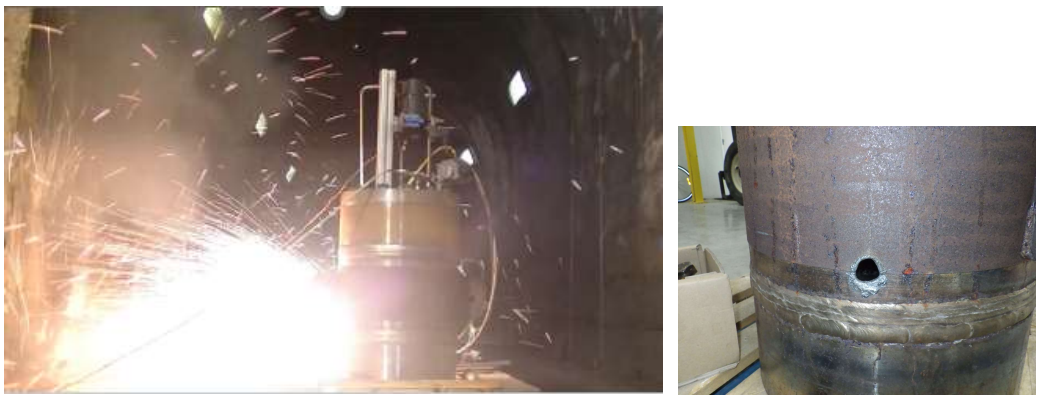

***Fig. 8.** View of test 8 after the vessel has been perforated*

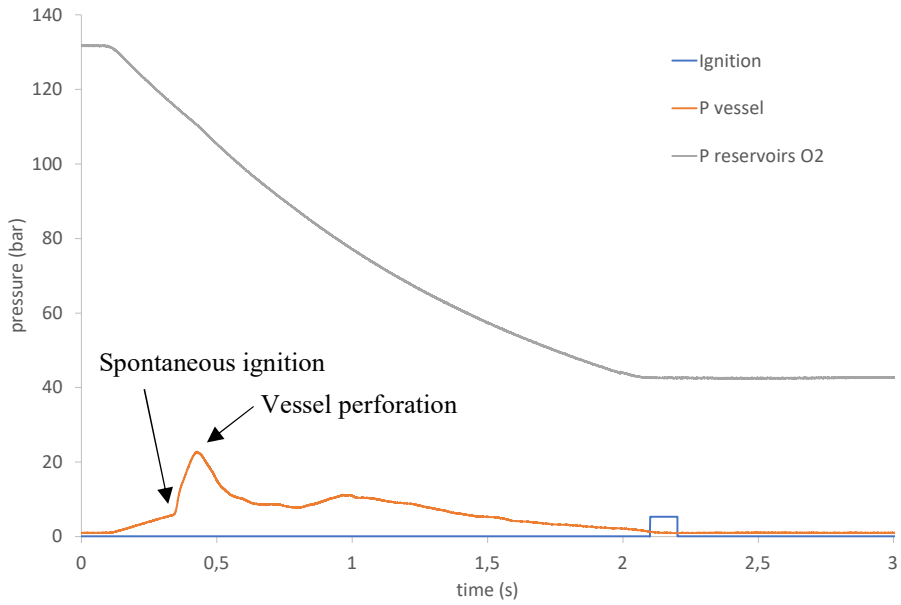

Fig. 9. *Pressure-time curve in Test 8 - spontaneous ignition*

There is no evidence about the ignition mechanism involved. The dust ignites spontaneously, before the ignition source is activated. This test is characterized by a large quantity of iron particles, which promotes friction and many shocks between particles and many impacts of particles on the internal steel walls. Mechanical impact or friction can generate very hot spots, especially at the beginning of oxygen injection, when the particles momentum is the highest.

Adiabatic compression can be excluded because the ignition occurs when the oxygen pressure is only 6 bar in the explosion vessel, and the corresponding temperature increase is not sufficient to cause auto-ignition.

The last explanation could be an electrostatic discharge. The iron dust is conductive so it cannot accumulate charges, but iron oxide particles are present on the vessel walls from the previous tests and may be blown from the walls and accumulate electric charges. Then electrical arcing could occur and ignite the dust cloud. Further investigations are required to understand the spontaneous ignition mechanism and in which conditions it occurs, as the present experimental setup has only a very limited instrumentation.

The mechanism of perforation of metallic pipes was investigated by Dieguez & al (1988) who set-up an experiment to investigate the risk of perforation of a “hollow vessel” containing an oxygen flow. The experiment aimed at assessing the resistance to ignition of metals and alloys used in oxygen pipes and equipment. It was carried out as follows: a constant flow of oxygen at a given speed (5 cm/s) , pressure and temperature is supplied to a section of pipe (the so-called “hollow vessel”, 1 m long and 80 mm diameter). A capsule containing a small quantity of iron dust (less than 200 g) and an electrical igniter is placed on the wall of the pipe. When the igniter is triggered, it causes the combustion of the iron dust on the internal surface of the wall. More than 600 parametric tests were performed. Depending on the initial conditions (oxygen purity, pressure, temperature), pipe material and pipe wall thickness, the combustion can propagate and burn more or less the pipe wall. Sometimes the pipe is totally perforated. Then the pipe is analyzed, the hole is characterized and the time between ignition and perforation of the wall is measured. Many interesting results were obtained. First of all, for a given initial pressure and wall thickness, the probability of perforation depends on the mass of iron dust in the capsule. For instance at 30 bar, a mass of iron dust of 150g is required to perforate a 10 mm thick carbon steel pipe, and the perforation takes about 25 s. Secondly, the iron dust capsule ignited spontaneously when the oxygen temperature was higher than 300°C.

In our experiment, the perforation went much faster and made a hole in 100 ms after ignition. This observation is not consistent with the results from Dieguez & al. However, our experiment is characterized by a high flow velocity in the vessel, which was not the case in the Dieguez & al experiment. Therefore, the hole in the vessel may result from the impingement of a large oxygen jet produced by the degradation of the injection tube. In such case, the ignition might have occurred close to the injection pipe, rather than on the vessel wall.

3.4. *Influence of iron oxide*

After Test 8 the vessel was repaired and a new injection tube was manufactured. Then the last test series was performed with addition of fine iron oxide dust Fe_2O_3 mixed to the iron dust. Tests 10 to 12 were carried out with the same mass ratio Fe/O_2 (0.6 kg Fe / kg O_2) and the mass ratio Fe_2O_3/Fe varying from 0.25 to 1. The pressure time curves are plotted on Fig. 10 together with the result of Test 6 which was performed with 0.6 kg Fe / kg O_2 but without any oxide addition. When oxide is added, a very different behavior is observed with a low but continuous pressure rise, which takes several seconds to reach the maximum pressure. This is definitely not a dust explosion. It looks like a rapid combustion with a high temperature rise which heats the gaseous phase and increases the pressure, similarly to what happens during a self-heating phenomenon.

This observation questions the way the combustion begins in the vessel. Obviously, even if the dust cloud is ignited by the pyrotechnic igniter, the flame does not propagate in the cloud because it is inerted by the presence of iron oxide dust. Then the ignition does not turn into an explosion. However, the combustion reaction starts. Is it due to the presence of very hot particles produced by the igniter which falls on the iron deposit? Or is it spontaneous ignition? It would be interesting to repeat the same tests without any igniter.

Unsurprisingly, the maximum pressure and the pressure rise increase when the amount of oxide dust decreases. Different mechanisms are in competition: on one side, oxygen is consumed so that gas is converted into solid oxide. On the other side, the very high temperature (about 2000 K) heats the excess of oxygen and may also vaporize part of the iron, which is responsible for the pressure increase. Once watching at the monitoring video, one can hear distinctly a “boiling noise” which could be attributed to a liquid pool of iron boiling at the bottom of the vessel.

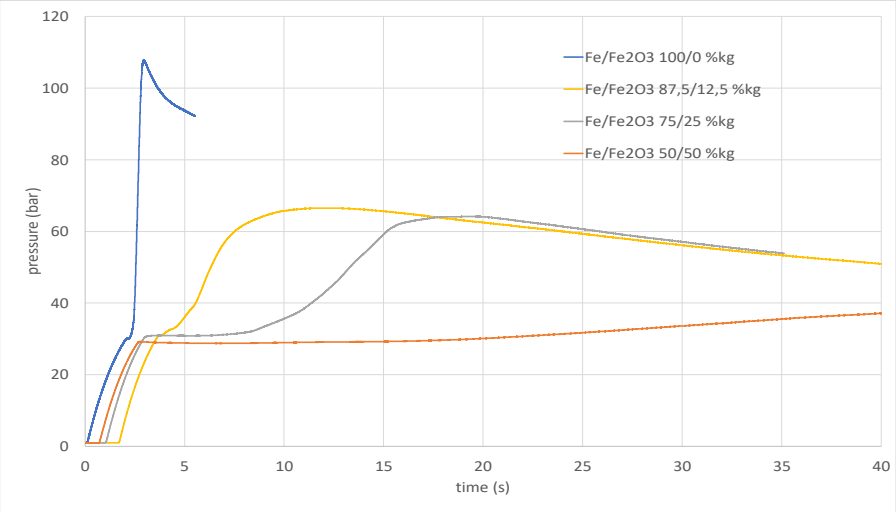

Fig. 10. *Pressure-time curves for Tests 4 to 7 – Influence of iron oxide concentration*

4. Conclusions

This work highlights three different behaviors when iron dust is dispersed in oxygen at elevated pressure:

- A classical “dust explosion” behavior but with an increased reactivity of iron dust compared to atmospheric conditions in air;
- A rapid combustion behavior similar to self-heating, which cannot be considered as an explosion, but can generate significant overpressure and very hot temperatures.
- Spontaneous ignition which might be promoted by mechanical friction and shocks between particles, and/or electrostatic discharges. We assume that spontaneous ignition could occur either in a dust cloud or in a dust deposit, and could be activated more easily when iron oxide was present.

This work gives interesting perspectives for the safety of oxygen operation units. First, the iron dust looks much more reactive in oxygen than in air. These new data must be considered for designing an explosion resistant equipment. Secondly, the rapid combustion phenomenon is probably correlated with a high and long temperature increase of the vessel walls. It could cause at the same time a loss of mechanical resistance of the walls, and a significant pressure rise in the vessel. Finally, the spontaneous ignition must be investigated further to be prevented because if it happens, it could result very quickly in a catastrophic failure, with very limited possibilities to mitigate the consequences.

Acknowledgements

The authors gratefully acknowledge Laurent Mathieu and Stéphane Charrondière for performing the tests.

References

ASTM G63-15 (2023) Standard guide for evaluating non-metallic materials for oxygen service

ASTM G72/G72M-24 (2024) Standard test method for autogeneous ignition temperature of liquids and solids in a high-pressure oxygen-enriched environment

ASTM G74-13 (2021) Standard test method for ignition sensitivity of non-metallic materials and components by gaseous fluid impact

ASTM G86-17 (2021) Standard test method for determining ignition sensitivity of materials to mechanical impact in ambient liquid oxygen and pressurized liquid and gaseous oxygen environments

ASTM G88-21 (2021) Standard guide for designing systems for oxygen service

ASTM G94-22 (2022) Standard guide for evaluating metals for oxygen service

ASTM G124-18 (2018) Standard test method for determining the combustion behaviour of metallic materials in oxygen-enriched atmospheres

C. M. Benson, 2015. Investigation into incidents involving the kindling chain of materials in high-pressure oxygen atmospheres, PhD thesis, London South Bank University

Bozier, O., Veyssière, B., 2006. Influence of suspension generation on dust explosion parameters, Combustion Science and Technology, 178: 1924-1955

K. Cashdollar, I. Zlochower, 2007. Explosion temperatures and pressures of metals and other elemental dust clouds, Journal of Loss Prevention in the Process Industries, 20: 337-348.

K. Chowdhury, 2011. “Fire in High Pressure Oxygen Filter: Analysis of an Accident in a Steel Plant.” Journal of ASTM International 8, no. 7 (n.d.): JAI103762-

Davidson, J.F, Harrison, D., 1985. Fluidization, Academic Press, ISBN 10 : 0122055527 ISBN 13 : 9780122055522

D.W.G. Dicker, R.K. Wharton, 1988: A review of incidents involving the use of high-pressure oxygen, from 1982 to 1985 in Great Britain, in Flammability and Sensitivity of Materials in Oxygen-Enriched Atmospheres, vol. 13, ASTM STP 986, D.W. Schroll ed.

Dieguez, J. M., Bothorel, L., de Lorenzo, A., Faupin, A., 1988: Ignition Testing of Hollow Vessels Pressurized with Gaseous Oxygen, Flammability and Sensitivity of Materials in Oxygen-Enriched Atmospheres: Third Volume, ASTM STP 986, D. W. Schroll, Ed., American Society for Testing and Materials, Philadelphia 1988, pp. 368-388.

Z. Dyduch, A. Toman, W. Adamus, 2016. Measurements of turbulence intensity in the standard 1 m^3 vessel, Journal of Loss Prevention in the Process Industries 40 (2016) 180e187

EIGA, 2020: Oxygen pipelines and piping systems, European Industrial Gases Association report Doc 13/20.

EN14034-1, 2011: Determination of explosion characteristics of dust clouds

Qi Liu, Ch. Proust, F. Gomez, D. Luart, Ch. Len, 2020: The prediction multi-phase, multi reactant equilibria by minimizing the Gibbs energy of the system: Review of available techniques and proposal of a new method based on a Monte Carlo technique, Chemical Engineering Science 216 (2020) 115-433.

Ch. Proust, A. Accorsi, L. Dupont, 2007: Measuring the violence of dust explosions with the ‘’20 L sphere’’ and with the standard ‘‘ISO 1m3 vessel’’ Systematic comparison and analysis of the discrepancies, Journal of Loss Prevention in the Process Industries 20 599-606.

Ch. Proust, J. Daubech, E. Leprette, 2009: Differentiated routes for the simulation of the consequences of explosions, Journal of Loss Prevention in the Process Industries 22 (2009) 288-294

A. Saha, A. S. Kartha, K. Chowdhury, 2011. Analysis of and Explosion in an Oxygen Pressure Reducing Station in a Steel Plant, Flammability and Sensitivity of Materials in Oxygen-Enriched Atmospheres, vol. 15, ASTM STP 1626, Th. Steinberg & G. Chiffoleau eds.

STAUBEX, Database Combustion and explosion characteristics of dusts, Institut für Arbeitsschutz der Deutschen Gesetzlichen Unfallversicherung, https://www.dguv.de/ifa/gestis/gestis-staub-ex

Investigation of the hot gas kernel expansion caused by a contact-break discharge during a hydrogen/air mixture ignition

Dominik Bratek [a], Carsten Uber [a], Niklas Schüler [a], Bogdan Barbu [b], Ralf Methling [c], Detlev Markus [a], Stefan Essmann [a], Dirk Uhrlandt [c], Frank Berger [b], Michael Hilbert [a]

[a] Physikalisch-Technische Bundesanstalt, Braunschweig, Germany
[b] Technische Universität Ilmenau, Germany
[c] Leibniz Institute for Plasma Science and Technology, Greifswald, Germany

E-mail: dominik.bratek@ptb.de

Abstract

Contact-break discharges that are generated, for example, by unplugging an electrical connector under voltage, represent an ignition source in explosive atmospheres. The discharges occur under certain conditions at, for instance, a voltage of 30 V and a current of 60 mA. A model is being developed for a user-oriented solution to predict ignitions caused by this kind of discharge. This requires the individual process steps from the contact-break discharge to the hot gas kernel expansion to be thoroughly analyzed, including their correlations.
In this article, the hot gas kernel expansion formed around the discharges is investigated using schlieren imaging. The observed discharges show a typical length of approximately 150 µm to 200 µm and a duration of approximately 200 µs to 1000 µs. The experimental results of the hot gas kernel expansion will be further investigated along with the numerical findings of 1D simulations with INSFLA and 2D simulations in COMSOL. The 1D simulations in INSFLA allow the calculation of the gas kernel expansion, including the thermochemical reaction, but without taking the influence of electrodes into account. The 2D simulations in COMSOL represent the hot gas kernel with an estimation of the energy losses caused by the electrodes but do not consider the thermochemical reaction.
The experiments show a critical radius (hemisphere) of the hot gas kernel of approximately 650 µm (at max. 30 V, 60 mA const., disk cathode and wire anode), while the simulations show lower values. Measurements with higher current values result in a comparable critical radius with a shorter ignition delay time. The correlations and loss estimations as well as an initial characterization of the hot gas kernel expansion will be discussed in the following.
Keywords: *electrical contact discharge, gas kernel, schlieren imaging, critical radius*

1. Introduction

Contact-break discharges are an ignition source in explosion hazardous areas and are therefore still in the focus of explosion protection. They are in practical use in the spark test apparatus for intrinsic safety testing, based on the international standard IEC 60079-11:2023 (2023). Discharges can occur when connectors are unplugged, or contacts are opened under voltage. Many authors like Slade (2014) and Zborovsky (1974) have mostly studied such contact-break discharges at relatively high currents and voltages, while Babrauskas (2003) has mentioned minimum currents of 30 mA for the formation of discharges. Therefore, this paper considers currents in the range of 60-80 mA and a maximum voltage of approximately 30 V to study ignitions close to the ignition limit. The goal of the project on which this paper is based, is to create a multiphysical model to describe ignition processes. Compared to previous studies (Barbu et al., 2022; Uber et al., 2021), a more advanced contact test

apparatus was used in this study and schlieren images were taken at a rate of 50000 frames per second to enhance the temporal resolution.

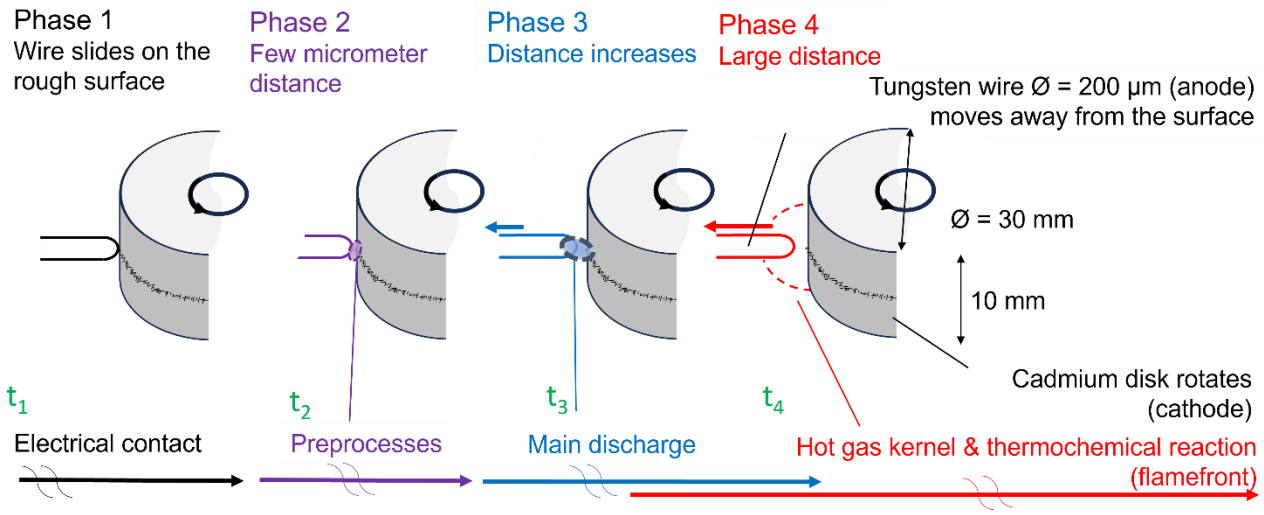

Fig. 1. *Schematic representation of the processes of a slow contact-break in the experimental contact device (cf. (Uber et al., 2019)).*

Figure 1 schematically shows the progress of a contact-break discharge, divided into four phases. Each phase is shown with an image of the disk-shaped cadmium cathode (right) and the wire-shaped tungsten anode (left). Voltage is applied to the electrical contacts and the cathode performs a continuous rotary movement while the wire stays at a fixed position. Thus, the wire slides across the rough surface of the cathode. A preconditioned surface is favorable to achieve a higher ignitability (Uber, 2019). The wire is slowly raised to a distance of a few micrometers from the cathode. This process is supported by the surface morphology. At this point, phase 2 begins and the so-called preprocesses start. The discharges that are now forming occur at a very small electrode gap and cannot lead to ignition but contribute to the formation of larger discharges (Uber, 2019). Only in the third phase, when the anode is moved further away from the cathode, can a main discharge form. These main discharges typically reach a length in the range of 150 to 200 µm, over a period of approximately 200 µs to 1 ms. The radiation of the plasma forming at the beginning of the discharge is strongly dominated by the cathode material cadmium and these discharges are therefore assumed to be metal vapor discharges (Uber, 2019). A further study of the optical emission spectrum indicates that these types of discharges are in thermal non-equilibrium (Methling et al., 2023). In the fourth phase, a hot gas kernel finally forms around the main discharge and an ignition of the fuel/air mixture can occur (self-sustaining thermochemical reaction).

Lintin and Wooding (1959) showed a correlation between the size of a spherical hot gas kernel and the ignition of a fuel/air mixture as a criterion for the ignitability of a discharge. The expansion of the hot gas kernel does not differ between igniting and non-igniting discharges until a critical radius is reached. The critical radius is thus defined as the radius of the hot gas kernel above which a distinction can be made (Lintin and Wooding, 1959). The thermochemical reaction can only continue in a self-sustaining manner if the critical radius is exceeded. When the critical radius is reached, the energy input can for the first time compensate the heat losses at the surface of the gas kernel due to the chemical reaction inside the volume (Zborovszky, 1969). The critical radius therefore depends on both the kinetics and the transport properties of the fuel/air mixture. In practice, additional effects due to the experimental setup, such as geometric conditions and heat sinks (electrodes), influence the above-mentioned interrelations.

Kakizawa (2023) and Kelley (2009) found that for energies close to the ignition limit, the propagation velocity of the hot gas kernel boundary has a minimum when the critical radius is reached. Near the ignition limit, this critical point can only be transcended when the chemical reaction becomes

dominant, and the flame propagation continues in a self-sustaining manner. This applies only to energies close to the ignition limit.
It has to be noted that there is a delay between the time when sufficient energy is supplied to the system and the actual start of a self-sustained flame propagation. This delay is known as the ignition delay time or induction time (Steen, 2000). It can be determined by a change in concentration of distinctive radicals of a chemical reaction. In the example of the hydrogen combustion, these would be the OH radicals whose concentration increases rapidly at the start of the combustion (Essmann, 2019).
In order to understand the ignition process, it is of crucial importance to investigate the expansion of the hot gas kernel in more detail. Therefore, schlieren images in the critical phase of the hot gas kernel expansion will be presented and analyzed in the following. Estimations of the critical radius will also be made. Such estimations will then be compared to theoretical findings with simulations in INSFLA (with a focus on chemical reactions) and in COMSOL (with a focus on electrode losses).

2. Experiments and simulations

2.1. Experimental setup

In these experiments, the hot gas kernel was measured by means of the schlieren method in a contact device specifically designed for this purpose. In the schlieren method, parallelized light is passed through the gas in the explosion chamber and through a lens system. Temperature changes in the gas cause changes in its density. This leads to localized changes of the refractive index. Changes in the gas density can also be induced by changes in pressure, but this is neglected for the processes under consideration. Applying a sharp knife edge creates light and dark areas in the image so that changes in temperature, especially strong gradients as distinct edges, can be analyzed qualitatively (Schardin, 1942; Toepler and Witting, 1906).

For the schlieren examination, the laser driven light source EQ-99X-FC-S by Hamamatsu Photonics was used as the light source. The image recordings were taken with a Photron Fastcam SA-5 at a frame rate of 50000 fps, meaning that one image was taken every 20 µs. The electrical parameters discharge current and voltage over the electrodes were recorded by means of a Yokogawa DLM5058 oscilloscope. Current and voltage were supplied by a constant current source with voltage limitation (Uber et al., 2022b).

The contact device used here consisted of a 200 µm diameter tungsten wire anode and a 30 mm diameter cadmium disk cathode. The contact-breaking movement was performed by a linear motor that moved the wire to a distance of 200 µm in about 1 ms. The cathode was continuously rotated at a speed of about 0.02 m/s at the outer radius.

The gas mixture used was a mixture of hydrogen and air with a volume fraction of 21 vol.% hydrogen, based on the international standard IEC 60079-11:2023 (2023).

2.2. Simulations with INSFLA

The first part of the simulations was performed with the 1D simulation program INSFLA (Maas and Warnatz, 1988). It uses a one-dimensional system equation for unsteady laminar flames. The conservation equations for mass, momentum and energy were solved with the method of lines. The necessary spatial discretization was carried out by means of the finite difference method. INSFLA uses a comprehensive transport model and chemical kinetics for simulation.
The gas is considered to be a homogeneous mixture of hydrogen/air with a volume fraction of 21 vol.% hydrogen. Its initial temperature and pressure are set to 298 K and 1 bar. The overall size of the vessel was configured as a sphere with a radius of 50 mm. The energy of the simulated discharge was applied as constant power over a fixed period of 200 µs within 100 µm, by adding a source term to the energy conservation equation (Dreizler et al., 2000). The size and duration of the energy coupling were chosen to simulate a fast discharge observed in the experiments.

As results, time- and 1D location-dependent solutions of temperature and concentration of different species can be obtained (Maas and Warnatz, 1988). The electrodes and losses related to their presence were not considered in the simulations. This allows the isotropic expansion of the hot gas kernel. Cadmium in the gas phase was not taken into account in these simulations.

2.3. Simulations with COMSOL

To estimate the expansion of the hot gas kernel, including the electrode losses and the metal vapor content in the hydrogen/air mixture, a rotationally symmetric 2D heat conduction model was implemented in COMSOL Multiphysics (Barbu et al., 2022). However, chemical reactions and gas diffusion are not considered in this model.

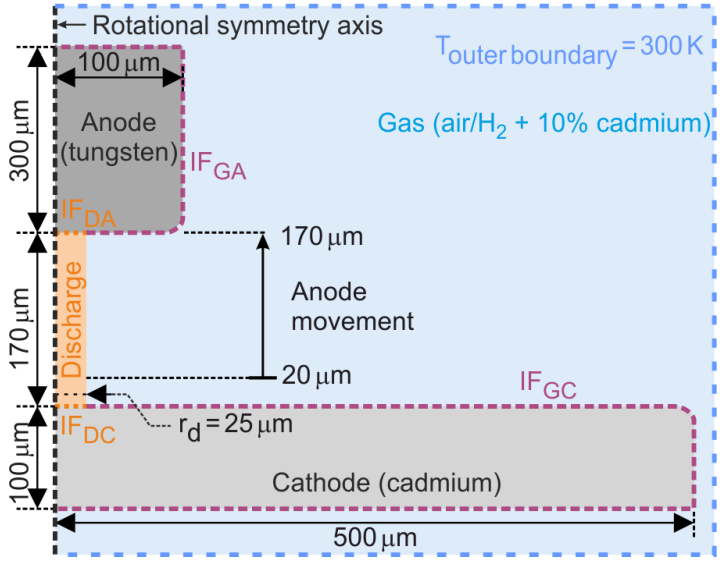

Fig. 2. *Heat transfer model geometry and boundary conditions of the COMSOL simulations.*

The model geometry and the boundary conditions are shown in Fig. 2. The cathode (at the lower part of the figure) has a fixed position during the entire simulation interval, while the anode (at the upper left part of the figure) is moved upwards starting from 20 µm to 170 µm above the cathode surface. The discharge radius is set at a constant value of 25 µm. The entire simulation domain has a size of 1000 µm × 1000 µm. Local thermodynamic equilibrium is assumed for the calculation of both the discharge and the surrounding gas area. For the gas, the hydrogen/air mixture with 21 vol.% hydrogen was used. Additionally, based on the absolute intensities of the atomic line emission observed in spectroscopic experiments a rough estimation of the partial pressure of cadmium atoms could be made. This resulted in 20 vol.% cadmium metal vapor for the gas in the discharge and a proportion of 10 vol.% cadmium metal vapor for the surrounding gas. The material properties for the two domains are set according to the cadmium percentage and are variable with temperature.
The power input has a non-linear increase over time to approximately 1.3 W at 1000 µs, similar to (Uber et al., 2022a). When computing the power input, energy losses over the electrode discharge interfaces (IF_{DA}, IF_{DC}) were estimated by the column voltage drop, i.e. the sheath layer voltage drop was subtracted. The heat transfer coefficients h_{elc} at the gas-cathode interface (IF_{GC}) and at the gas-anode interface (IF_{GA}) are subsequently calculated using the thermal conductivity of the gas $\lambda(T)$ and the height of the thermal boundary layer δ_T (Incropera et al., 2011; Uber et al., 2022a):

$$h_{elc} = \frac{\lambda(T)}{\delta_T}$$

Due to the very small gap between the electrodes, it is estimated that the magnitude of the thermal boundary layer is in the same range as the discharge height. For this reason, the thermal boundary

layer height is considered as half of the distance between the electrodes, that is, $\delta_T = d_{elec}/2$ (Baehr and Stephan, 2016; Uber et al., 2022a). An average temperature in the gas area was assumed for the calculation of the thermal conductivity.

3. Results and discussion

3.1. Experimental results

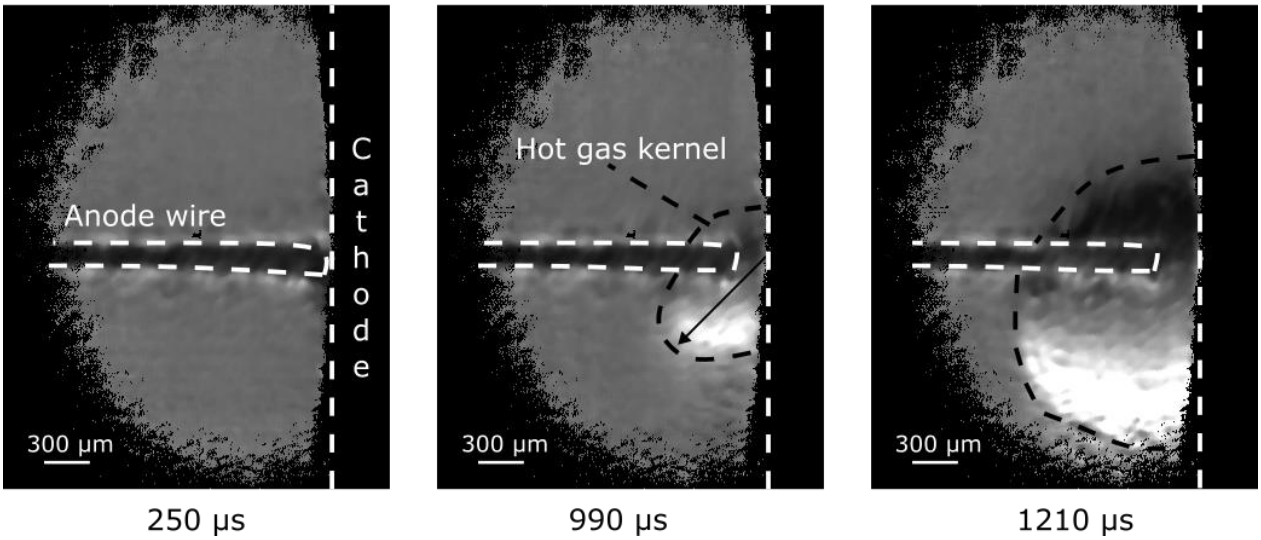

Fig. 3. *Expansion of the hot gas kernel using selected schlieren images. The edge of the cathode on the right of each image and the horizontal anode wire can be seen. The displayed time below each image corresponds to the time scale in Fig. 4. The arrow in the second image is an example of the intensity profiles taken at an angle of 45° to the cathode.*

The sequence of images in Fig. 3 shows an example of the expansion of a hot gas kernel by means of the schlieren method. In the images, the edge of the cathode, on the right, and the horizontal anode wire can be seen. As the sequence of images progresses, the anode wire is constantly moved further away from the cathode. Then the discharge is formed between the anode and the cathode. However, the discharge is not visible, since its intensity is negligible compared to the background lighting. At the same time, the hot gas kernel is formed in the gap between the anode and the cathode. The hot gas kernel is shown in the images with a dashed black line and limited to a hemisphere due to the geometric arrangement of the cathode and the anode. It can also be seen that the hot gas kernel in this example expands unsymmetrically. The expansion occurs on the lower side much earlier than on the upper side. This is assumed to be due to the discharge forming on the lower side of the anode. Hence, for the estimation of the radius of the hot gas kernel, only the lower profile of the hot gas kernel was considered. The images are postprocessed using a python script, and the radius of the hot gas kernel was determined with an extremum in the derivative of the intensity profiles (Xu et al., 2014). The intensity profiles were taken along a 45° line starting from the discharge center on the cathode surface in order to get the most undisturbed edge of the hot gas kernel. This is marked with an arrow in the second image of Fig. 3. Due to the blocking of the anode wire, only values for the hot gas kernel above 400 µm could be measured.

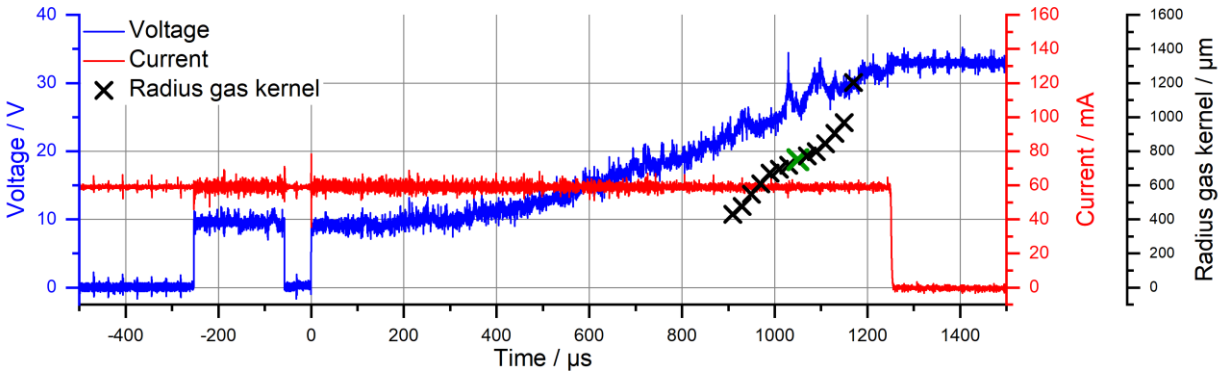

Fig. 4. *An example of the current and the voltage curve of an igniting discharge. The corresponding expansion of the hot gas kernel is also shown. The critical radius is marked with a green cross.*

The parameters of the igniting discharge that lead to the hot gas kernel expansion in Fig. 3 are shown in Fig. 4. It shows the current (red) and voltage (blue) curves of the discharge as well as the corresponding expansion of the lower part of the hot gas kernel (crosses). There is initially an electrical contact between the anode and the cathode (up to 0 µs). Therefore, the measured voltage is approximately 0 V. In Fig. 4, this is temporarily disrupted by the morphology of the cathode surface. As soon as a voltage jump up to approximately 10 V occurs, the preprocesses phase starts. At approximately 400 µs, the wire is further removed from the cathode surface, and as the current is kept constant, the voltage continues to rise during phase 3 as the distance between the anode and the cathode increases. At about 1250 µs, the voltage reaches its maximum of about 30 V and the discharge ends as the voltage provided by the power supply is no longer sufficient to sustain the discharge. The current then drops to 0 mA.

The radius of the hot gas kernel is also plotted in Fig. 4 (black crosses). The first image of the hot gas kernel expansion can be observed at around 900 µs. Initially, the gas kernel expands rapidly, driven by the discharge. The speed of this propagation decreases steadily, until a minimum is reached. This minimum is estimated at a gas kernel radius of about 750 µm (green cross). The propagation velocity then shows a sharp increase and finally attains a constant velocity. Averaged over the experiments, this yields a critical radius of approximately 650 µm. This is, however, only a first result and the accuracy of this value has to be verified in further measurements.

3.2. Simulations with INSFLA

In the simulations with INSFLA, the expansion of the hot gas kernel was calculated as a function of time. In Fig. 5 a), examples of the temperature profiles of the simulation with an input energy of 29 µJ are shown as a function of the radius for different time steps. A local minimum of the temperature profile gradient was used as a criterion for the edge of the hot gas kernel. This is marked with a dot for every time step. The temperature starts at about 1000 K after 15 µs and rises to about 1900 K within 200 µs. After 200 µs, the external energy source is turned off and the temperature in the center of the hot gas kernel decreases to about 1700 K, while the hot gas kernel expands steadily (dashed lines). This indicates that an ignition has occurred, and the flame is propagating outwards. Figure 5 b) shows the expansion of the hot gas kernel over time according to the simulation results for different input energies that are applied within the first 200 µs. The hot gas kernel has an initial radius of 100 µm corresponding to the size of the energy coupling. It then expands, mainly due to thermal conduction up to 10 µm, until the gas mixture ignites. The ignition delay time is followed by a self-sustaining flame propagation and the expansion of the hot gas kernel proceeds more rapidly. In the data, a jump in radius of the hot gas kernel from about 110 µm to about 200 µm is observed. This is due to the formation of the flame front on the outer part of the hot gas kernel and the chosen criterion for the hot gas kernel.

For 80 µJ, the increase in the radius can be observed at approximately 25 µs. For 39 µJ, this increase starts at approximately 75 µs. It can therefore be recognized that the ignition delay time decreases when the energy input is increased. In other words, the delay time at which the self-sustaining flame propagation starts is shorter. The ignition delay times of the hydrogen/air ignition were determined in INSFLA by means of the temporal change in the concentration of the OH radicals. For low energies in the range of 30 µJ, the ignition delay time lies at approximately 160 µs. For increasing energies, the ignition delay time decreases exponentially. This correlation can also be found in (Steen, 2000) and allows a prediction of the start of combustion.

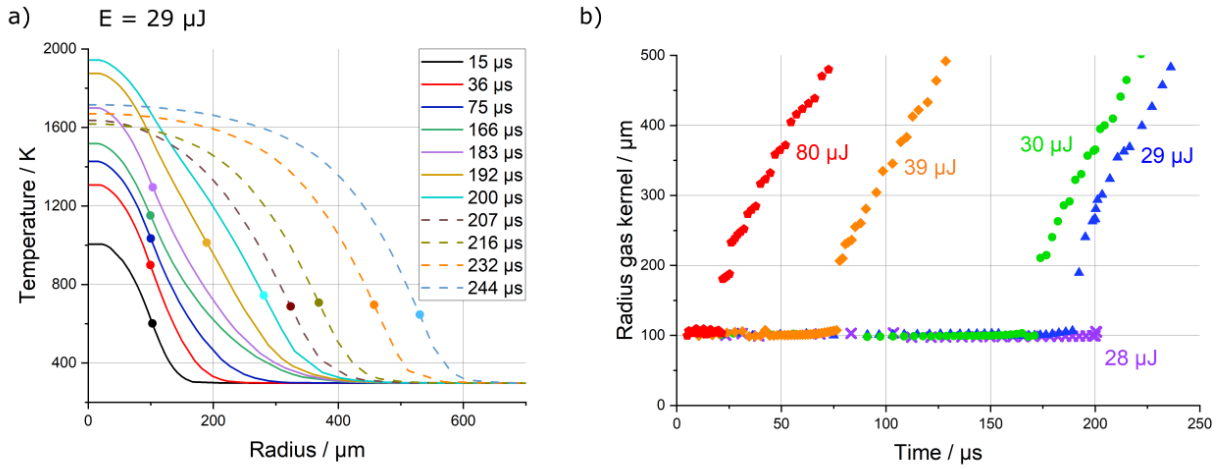

Fig. 5. *a) Development of the temperature profile over radius of the INSFLA simulation with an energy of 29 µJ for different time steps. The maximum gradient (criterion for the gas kernel radius) is marked with a dot for every time step. After 200 µs, the external energy input is turned off and the hot gas kernel expands only due to the thermochemical reaction (dashed lines). b) Expansion of the hot gas kernel over time for different simulated energies.*

The simulation with an energy of 28 µJ (violet crosses), where no ignition occurred, also shows an initial radius of about 100 µm due to the energy coupling. Contrary to the other simulated input energies, when the energy coupling ends after 200 µs, no self-sustained flame propagation is observed. Since the chemical reaction is not able to compensate for the losses mainly due to heat conduction, the temperature in the hot gas kernel decreases until it reaches the ambient temperature.

3.3. Simulations with COMSOL

The simulation in COMSOL can be used to calculate the temperature distribution over a period of time and with the specified geometry. Selected points in time are shown in Fig. 6 a). In Fig. 6 a), the geometry with a disk cathode (bottom of the image) and an anode wire (top left of the image) can be recognized. The discharge forms between the two electrodes, where the highest temperature develops. The radius of the hot gas kernel was determined by computing the minimum of the temperature gradient along a line placed at an angle of 45° to the cathode (L_1 in Fig. 6). Due to the blocking of the anode wire in the earlier simulation phase, values for the radius of the hot gas kernel could only be acquired starting from 750 µs.

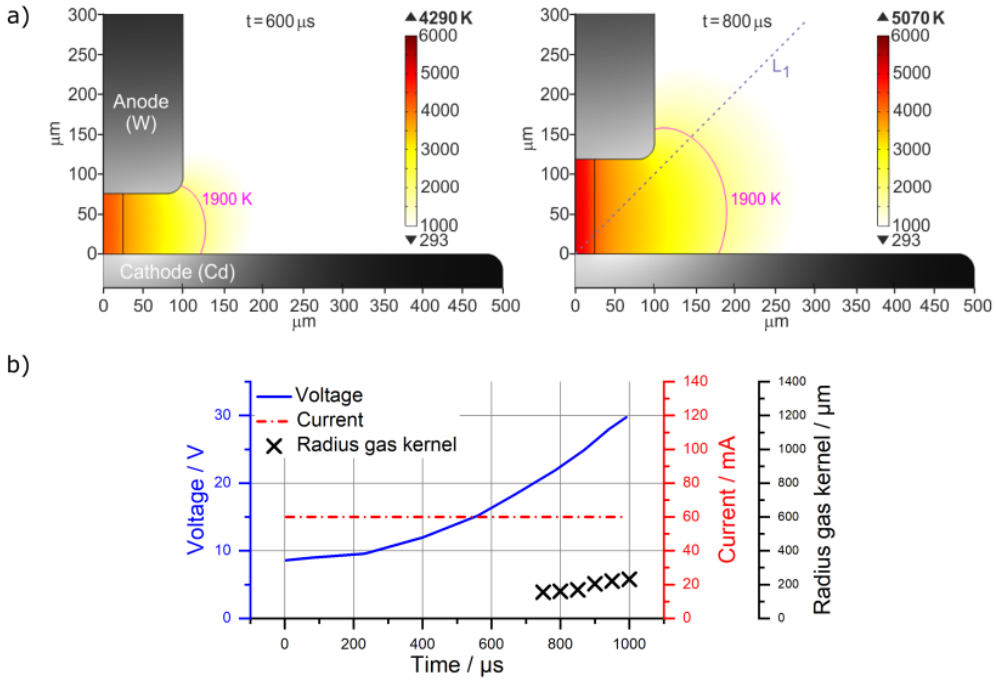

Fig. 6. a) Visual comparison of the hot gas kernel radius for different times and b) the corresponding discharge current and voltage curves and the hot gas kernel expansion over time.

Figure 6 b) shows the simulated discharge power input in terms of voltage and constant current along with the computed expansion of the hot gas kernel over time. At 750 µs, the hot gas kernel has expanded to a radius of about 150 µm and reaches about 230 µm at the end of the simulation. However, it is not possible to make a statement about a critical radius because no minimum of the propagation velocity is visible, and no chemical reaction is considered. A self-sustaining flame propagation of the gas kernel can therefore not occur.

3.4. Discussion of experiment and simulations

When compared, the values of the radius of the hot gas kernel from the simulations are significantly smaller than the critical radius determined experimentally. This is due to the necessary assumptions of the simulations. An assessment of these assumptions can be found in Table 1. In the INSFLA simulations, it is not possible to map the electrode losses. Heat conduction losses and the influence on the propagation of the gas kernel are therefore not considered. In addition, the influence of the cadmium metal vapor, in particular the influence of this metal vapor on the chemical reactions and thermodynamic influences, is not taken into account. In contrast, thermal conduction with the electrodes is considered in the COMSOL simulations, but the effect of the chemical reactions is neglected. The expansion of the hot gas kernel is also influenced by the geometry, similar to the experiments, so that only a hemispherical hot gas kernel is formed. Both in the experiments and in the COMSOL simulations, the power input is variable over time, whereas INSFLA only considers a constant power input over time.

Table 1. *Listing of parameters in the experiment and the simulations.*

	Experiment	INSFLA (1D)	COMSOL (2D)
Geometry	Disk cathode and wire anode influence the gas kernel expansion, hemispherical hot gas kernel	No electrodes, spherical hot gas kernel	Disk cathode and wire anode influence the gas kernel expansion, hemispherical hot gas kernel
Chemical reactions	Combustion H_2, possible catalytic effects of Cd, possible combustion of Cd	Combustion of H_2	No chemical reactions considered
Power input	Temporal variable, power input according to discharge length	Temporally constant power input	Temporally variable power input
Energy losses	Various losses to the electrodes	No electrode losses	Losses at electrodes according to heat conduction

4. Conclusions and outlook

In order to develop a comprehensive model for predicting ignitions caused by contact-break discharges, detailed knowledge regarding the expansion of the hot gas kernel is essential. For this purpose, schlieren measurements of the hot gas kernel correlated with electrical curves of current and voltage of the discharges were presented and analyzed in this article and compared to simulation results.

For contact-break discharges generated with the contact device presented in Fig. 1, the estimated critical radius, which must be exceeded for a self-sustaining thermochemical reaction is on average approximately 650 µm. The critical radius was determined by using a minimum of the propagation velocity of the hot gas kernel, and this applies to the observed hemispherical hot gas kernels.

Simulations with INSFLA show that, for the described energy coupling and without external losses to the electrodes, only an energy of approximately 29 µJ is necessary to ignite the gas mixture under consideration. The radius of the hot gas kernel formed in the simulations was determined with a minimum of the temperature gradient. The hot gas kernel expands to approximately 110 µm, until the flame propagation starts.

The simulations with COMSOL reveal that, without considering chemical reactions, a hot gas kernel with a size of approximately 230 µm is formed within 1000 µs. Based on an experimental discharge, the power input is chosen to be temporally variable. Additionally, the geometry of the experimental setup was fully considered. Furthermore, the influence of cadmium metal vapor in terms of heat conduction in and around the discharge was also included in the analysis.

The results presented here show the correlations for a basic contact-break discharge with constant current at the ignition limit. Possible extensions of the presented work include investigations with varying hydrogen/air compositions and varying mixtures (e.g. methane/air), in order to investigate their influence on the gas kernel expansion. Further, parameters like flame stretch and flow velocities could be considered in future investigations. On the modeling side, the next steps are to further improve the simulation models by adding diffusion to the COMSOL model and a time-variant energy input for the INSFLA model. Additional investigations are planned for a better understanding of the influences of the metal vapor. To this end, the expansion of the hot gas kernel is also to be further

investigated with other materials. Investigations considering different electrical power supplies with different characteristics are also planned, to enable an evaluation of intrinsic safe circuits.

Acknowledgements

This project has been funded by the German Research Foundation (DFG) - project number 411446115.

The authors would like to express their thanks to Robin Abraham, Lia Benedix, Rilana Rohde and Steffen Franke for their support in the experimental work as well as to Ulrich Johannsmeyer, the employees of Department 3.6 at PTB, and all those who supported this article with stimulating discussions and equipment.

References

Babrauskas, V., 2003. Ignition handbook: principles and applications to fire safety engineering, fire investigation, risk management and forensic science. Fire Science Publishers, Issaquah (WA, USA).

Baehr, H.D., Stephan, K., 2016. Wärme- und Stoffübertragung, 9th ed. Springer Vieweg, Berlin Heidelberg.

Barbu, B., Uber, C., Berger, F., 2022. Investigating the influence of additional inductivity in electrical circuits during ignition caused by contact break discharges, in: 14th International Symposium on Hazards, Prevention and Mitigation of Industrial Explosions (ISHPMIE), Proceedings. https://doi.org/10.7795/810.20221124

Dreizler, A., Lindenmaier, S., Maas, U., Hult, J., Aldén, M., Kaminski, C.F., 2000. Characterisation of a spark ignition system by planar laser-induced fluorescence of OH at high repetition rates and comparison with chemical kinetic calculations. Applied Physics B: Lasers and Optics 70, 287–294. https://doi.org/10.1007/s003400050047

Essmann, S., 2019. Experimentelle Untersuchung der Zündung durch elektrostatische Entladungen geringer Energie (PTB-Bericht Ex-11, PhD Thesis). Karlsruher Institut für Technologie (KIT), Braunschweig.

IEC 60079-11:2023 Explosive atmospheres - Part 11: Equipment protection by intrinsic safety “i”, 2023.

Incropera, F.P., DeWitt, D.P., Bergman, T.L., Lavine, A.S., 2011. Fundamentals of heat and mass transfer, 7th ed. Wiley, Hoboken, NJ.

Kakizawa, T., Hirano, Y., Mukoyama, T., Morii, Y., Nakamura, H., Maruta, K., 2023. Effects of repetitive spark discharges with milliseconds intervals on the ignition-to-flame propagation transition for lean n-heptane/air and iso-octane/air mixtures, in: 29th International Colloquium on the Dynamics of Explosions and Reactive Systems (ICDERS), Proceedings. SNU Siheung, Korea.

Kelley, A.P., Jomaas, G., Law, C.K., 2009. Critical radius for sustained propagation of spark-ignited spherical flames. Combustion and Flame 156, 1006–1013. https://doi.org/10.1016/j.combustflame.2008.12.005

Lintin, D.R., Wooding, E.R., 1959. Investigation of the ignition of a gas by an electric spark. Br. J. Appl. Phys. 10, 159–166. https://doi.org/10.1088/0508-3443/10/4/302

Maas, U., Warnatz, J., 1988. Ignition processes in hydrogen - oxygen mixtures. Combustion and Flame 74, 53–69. https://doi.org/10.1016/0010-2180(88)90086-7

Methling, R., Franke, S., Uber, C., Barbu, B., Berger, F., Hilbert, M., Uhrlandt, D., 2023. Investigation of a cadmium dominated discharge utilized in explosion protection by means of optical emission spectroscopy, in: Proceedings XXIII International Conference on Gas Discharges and Their Applications. Greifswald, pp. 362–365.

Schardin, H., 1942. Die Schlierenverfahren und ihre Anwendungen, in: Ergebnisse Der Exakten Naturwissenschaften. Springer Berlin Heidelberg, Berlin, Heidelberg, pp. 303–439. https://doi.org/10.1007/BFb0111981

Slade, P.G., 2014. Electrical contacts: principles and applications, 2nd ed. CRC Press, Boca Raton, Fla.

Steen, H., 2000. Handbuch des Explosionsschutzes. Wiley-VCH, Weinheim New York.

Toepler, A.J.I., Witting, A., 1906. Beobachtungen nach einer neuen optischen Methode: Ein Beitrag zur Experimentalphysik, Ostwalds Klassiker der exakten Wissenschaften. W. Engelmann.

Uber, C., 2019. Charakterisierung elektrischer Kontakt-Entladungen im Bereich niedriger Spannungen im Zündgrenz-Bereich von Wasserstoff-Luft-Gemisch (PhD Thesis). TU Ilmenau, Ilmenau.

Uber, C., Franke, S., Barbu, B., Hilbert, M., Berger, F., Uhrlandt, D., Lienesch, F., 2022a. Correlation between the electrical power of a slow contact break discharge and the ignition of an H2/air mixture. Journal of Loss Prevention in the Process Industries 74, 104620. https://doi.org/10.1016/j.jlp.2021.104620

Uber, C., Franke, S., Hilbert, M., Uhrlandt, D., Lienesch, F., 2021. Untersuchung des Übergangs von elektrischen Kontaktöffnungsentladungen zur Flammfront eines H2-Luft-Gemisches. tm - Technisches Messen 88, 633–639. https://doi.org/10.1515/teme-2021-0040

Uber, C., Runge, T., Brunzendorf, J., Kurrat, M., Gerlach, U., 2019. Electrical discharges caused by opening contacts in an ignitable atmosphere – Part II: Spectroscopic investigation and estimation of temperatures. Journal of Loss Prevention in the Process Industries 61, 213–219. https://doi.org/10.1016/j.jlp.2019.05.010

Uber, C., Schüler, N., Franke, S., Hilbert, M., Uhrlandt, D., 2022b. Schlieren imaging investigations of hot gas kernel expansion caused by slow contact break discharges, in: 14th International Symposium on Hazards, Prevention and Mitigation of Industrial Explosions, Proceedings. Physikalisch-Technische Bundesanstalt (PTB), Braunschweig, Germany, pp. 477-486 (734). https://doi.org/10.7795/810.20221124

Xu, D.A., Shneider, M.N., Lacoste, D.A., Laux, C.O., 2014. Thermal and hydrodynamic effects of nanosecond discharges in atmospheric pressure air. Journal of Physics D: Applied Physics 47. https://doi.org/10.1088/0022-3727/47/23/235202

Zborovsky, Z., Cotugno, L.A., 1974. Evaluation of the cadmium disc breakflash in testing electrical circuits safety in explosive atmospheres. a comprehensive study of intrinsic safety criteria. Open file report (No. PB-253589; BM-OFR-68-76), Bureau of Mines Open File Report No. 68-76. Denver Research Inst., Washington, DC.

Zborovszky, Z., 1969. Ignition Criteria and Flame Kernel Development between Breakflash Electrodes in Explosive Gas Mixtures (PhD Thesis). University of Surrey (United Kingdom).

Assessing the Degree of Pyrophoricity for Gases

Ming-Hsuan Yang [a], Kai-Quan Cao [a], Trung Thanh Nguyen [a], Jenq-Renn Chen [a], Hsiao-Yun Tsai [a], & Eugene Y. Ngai[b]

[a] Department of Safety, Health and Environmental Engineering, National Kaohsiung University of Science and Technology, Kaohsiung, Taiwan

[b] Chemically Speaking LLC, Whitehouse Station, New Jersey 08889, United States

E-mail: jrc@nkust.edu.tw

Abstract

A pyrophoric gas is defined as a flammable gas having an autoignition temperature (AIT) below 54 ºC. However, determining AIT below ambient temperature is difficult. On the other hand, pyrophoric gases, such as silane, when releasing steadily into ambient air with a velocity above a critical flow velocity may lead to delayed ignition in which the ignition is delayed indefinitely. The Vc is found to be a function of the vent size (D). A simple critical shear rate, defined as 8Vc/D, is considered a potential useful indicator for assessing the relative degree of pyrophoricity. Monochlorosilane (SiH_3Cl), a pyrophoric gas with reported AIT of < 20°C is used as an example and results of steady release tests are compared with those of silane and disilane. The results are surprising. Degree of pyrophoricity for the three gases are: disilane > silane > monochlorosilane. Lower degree of pyrophoricity implies lower reactivity towards air and thus delayed ignitions and vapor cloud explosions are favoured. The critical shear rate required to quench the autoignition kernel will be a useful indicator for assessing the hazards of pyrophoric gases.

Keywords: *pyrophoricity, silane, disilane, monochlorosilane, VCE*

Introduction

Silane (SiH_4) or monosilane is the most important silicon source gases for semiconductor manufacturing processes. It is also a well-known pyrophoric gas which is defined as a flammable gas that is capable to ignite spontaneously in air at a temperature of 54 ºC or below. In common practice, a pyrophoric gas has an autoignition temperature (AIT) below 54 ºC. On the other hand, it is generally difficult to determine AIT below ambient temperature owing to difficulties to mix the pyrophoric gases with air without premature ignition. This is evident as the AIT for typical pyrophoric gases such as silane has not yet been properly determined. Reported AIT for silane is scattered and can vary depending on source of data. For example, Baratov et al. (1969) had reported autoignition of silane in air down to -162 ºC. Most safety datasheet reported AIT of -50ºC.

Silane has been known to cause significant injuries and fatalities (Chen, et al., 2006; Chang et al., 2007; Peng et al., 2008). In particular, silane vapor cloud explosion, instead of fire, was considered as the major factor that contributed to the fatality. The mechanism for silane vapor cloud explosion has been studied extensively (Ngai et al., 2007; Tsai et al., 2010; Ngai et al., 2015; Tsai et al., 2017b). The main factor leading to vapor cloud explosion, even in air and unconfined, is attributed to the fact that direct silane release into air normally leads to delayed ignition rather than prompt ignition. A critical flow velocity (V_c) for the delayed ignition has been determined from steady release tests by Tsai et al. (2010) and Tsai et al. (2017a). The V_c is a function of vent sizes, moisture in the air and fluid temperature. A typical example of V_c in ambient air for a 4.32 mm diameter vent is 4.43 m/s which is a relatively small value compared to typical gas leak flow rate in the order of 100~300 m/s. For a small vent size such as 2.032 mm, V_c is only 0.324 m/s. The delayed ignition is always followed

by an ignition when flow stopped or ended. Thus, the silane release provided not only the flammable cloud but also the ignition source rendering the vapor cloud explosion (VCE) is a favourable event.

Disilane (Si_2H_6) is another important silicon source gas compared to monosilane for deposition of thin films because it requires lower process temperature that may protect the film's quality from damage. Disilane has a boiling point of -14.3°C which is much higher than the -111.5°C of silane, and is usually liquefied under pressure during storage. Like silane, disilane is also noted for its pyrophoric nature. There is however no reported AIT for disilane and thus it is difficult to compare the relative degree of pyrophoricity of silane and disilane.

Although the utilization of disilane has been increased dramatically, incidents involving disilane were considered to be far less than those of silane. There was a typical accident occurring at a semiconductor parts factory in Tateyama, Chiba, Japan, 1995 (Itagaki & Tamura, 1995). In that case, air leaked into the exhaust piping system and reacted with residual disilane resulting in a fire that injured four workers. There is no report of disilane VCE incident.

Nguyen et al. (2022) performed extensive experimental studies on the flammability limits and ignition behavior of disilane. The critical exit velocity of pure disilane release through an 0.762 mm I.D. tube was determined to be 49.6 m/s. The LFL of disilane/air mixture was measured to be 0.42 vol.%. The values of P_{max} and K_G of 1.9 vol.% disilane/air were determined to be 5.7 bar and 627 bar-m/s, respectively which are close to those of a stoichiometric H_2 explosion. The mixture of higher disilane/air concentrations ($\geq$ 2 vol.%) was metastable and automatically ignited in a certain delay. LFL of silane is however determined to be 1.4 vol.%, and the values of P_{max} and K_G of 3.7 vol.% silane/air were determined to be 7 bar and 452 bar-m/s according to Tamanini et al. (1997).

The extreme reactivity of disilane with air compared to silane may be derived from the weaker Si-H bonds and the presence of Si-Si bond in the disilane structure. Goumri et al. (1993) determined the dissociation enthalpy of Si-H bond in disilane of 373.7 kJ/mol, which is slightly lower than that in monosilane (384.1 kJ/mol) (Seetula et al., 1991). In addition, bond dissociation energy of Si-Si bond in disilane was determined to be 340.2 kcal/mol (Steele and Stone, 1962), which is smaller than that of Si-H bond. Therefore, it is much easier for O_2 to attack the weaker Si-Si bond instead of the stronger Si-H bond. With a very low LFL and very high V_c, in the case of disilane leaks, there is higher probability that prompt ignition with smooth fire may occur instead of explosion as compared to a leak of silane.

In summary, the above review on silane and disilane flammability studies suggests that V_c can be a good indicator for pyrophoricity. To further validate the concept, monochlorosilane (SiH_3Cl), a pyrophoric gas with reported AIT of <20°C, is used as an example and experimental results of flammability limits and ignition behavior of are monochlorosilane compared with those of silane and disilane. A new indicator based on global shear rate at the vent stub is proposed for assessing the pyrophoricity of gases.

1. Materials and methods

1.1. Monochlorosilane

Monochlorosilane (MCS) is rarely used in CVD or other semiconductor processing. It is an intermediate product for manufacturing silane (Alcántara–Avila et al. 2015) or used for the synthesis of trisilylamine (Burg & Kuljian, 1950). Semiconductor grade MCS with a liquid purity of >97%, silane <1%, and dichlorosilane (DCS) <1% was supplied from REC Silicon in a cylinder. MCS has a boiling point of -30.4°C and is liquefied under pressure during storage in cylinder. Vapor MCS is drawn out from cylinder with a pressure regulator. Thus, the concentration of vapor MCS would vary depending on the liquid content of cylinder as silane would vaporized first, followed by MCS, and then DCS. Our GC-TCD analysis suggested that actual vapor concentration of MCS varied between 97 to 99 vol.%.

1.2. Steady release tests

The system and procedure used was similar to the steady-state release configuration as Tsai et al. (2010) and Tsai et al. (2017a) and is shown in Fig. 1. The flow rate of MCS and nitrogen could be controlled accurately by using a set of mass flow controllers (MFC). A four-way switching valve was used to establish a parallel, steady flow of MCS into a wet scrubber and nitrogen into the release line. When switched, the MCS flowed steadily at the desired flow rate through the stainless-steel vent stub of 1/4-in Swagelok port connectors with inner diameters of 4.32 mm. The port connector was changed for every test. The ignition behaviour and flame kernel were recorded directly by using a high-speed video camera with a recording rate of 5000 frames/second.

The steady release tests were carried out at an ambient air temperature of 28.8 ± 0.8 °C. The MCS source temperature in the cylinder was 24.1 ± 0.8 °C owing to evaporative cooling. The relative air humidity was 65 ± 4%. Further tests were also carried out by placing the vent stub inside a partially open chamber with continuous flow of zero-grade air similar to Tsai et al.(2017a). The zero-grade air is a blend of pure nitrogen and oxygen and thus has a very low moisture content with a dew point of less than -50°C. Tests with zero-grade air avoid the interference from moisture in the air. This is particular important as some of the pyrophoric materials are also water-reactive.

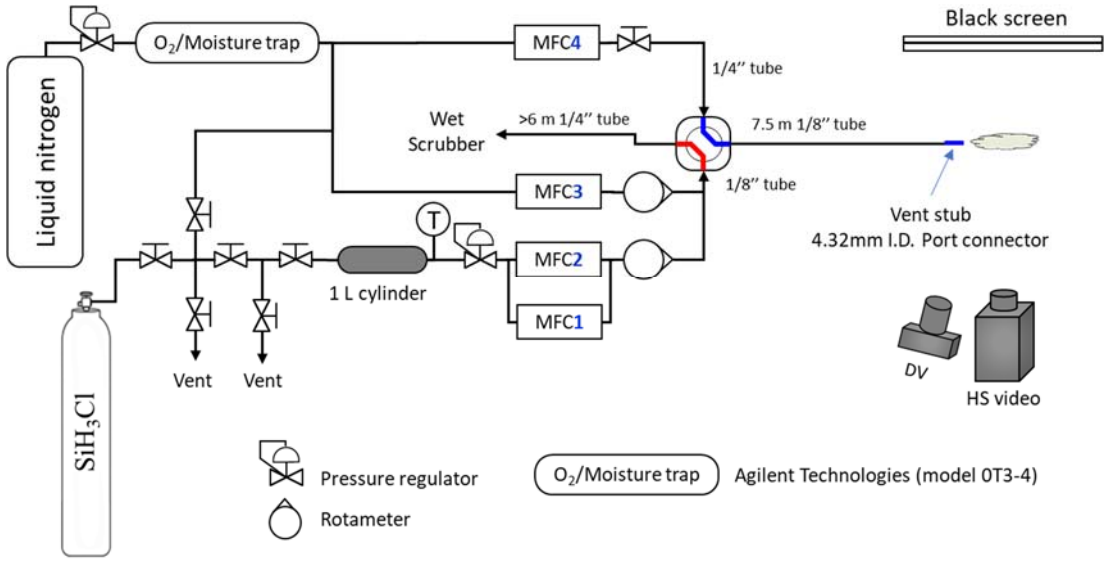

Fig. 1. *Setup for steady release tests*

1.3. Flammability limit measurement

The LFL and other explosion severity parameters including overpressure (P_{max}), and rate of maximum pressure rise $(dP/dt)_{max}$ were determined using a standard 20-L sphere apparatus from Kühner AG. A water bath maintained at temperature of 28 °C was circulated through the jacket of the sphere to maintain a constant test temperature of 27 ± 0.5 °C inside the sphere. A permanent electric spark igniter with an energy of 10 J installed at the centre of the test chamber was used as the ignition source. Bottom of the sphere has an inlet port and a rebound nozzle for dust dispersion and dust explosion measurement. The port was sealed and the nozzle was removed giving a clean sphere for gas measurement.

To have premixed MCS/air without premature ignition, the steady release rig was used to control the flow of MCS into the sphere at a velocity above V_c. To assist mixing after feeding MCS, a second four-way switching valve was used to allow air flow into the sphere as shown in Fig. 2. Both ambient air from compressor and zero-grade air with very low moisture were used as the air source.

The 20-L sphere was purged by air for 2 cycles (from 13 to 1000 mbar) and then evacuated to the designated pressure of 500 mbara by a vacuum pump. Pure MCS was fed into the sphere for a duration of 40~90s with a velocity of 2.3-3.0 m/s depending on the required concentration. At the end of MCS

flow, 4-way valve #1 was switched to nitrogen for 5 second, followed by switching 4-way valve #2 to air until the pressure in the sphere reached 1000 mbara. The mixture was then left for 10 min to allow mixing with natural convection and diffusion prior to ignition. Pressure measurement and high-speed video were used to monitor the ignition results. The criteria for flammability are based on a pressure rise of ≥7 % above the initial pressure in accordance with ASTM standard ASTM E918−19 (2020) and ASTM E2079−19 (2019). Recorded flame propagation from the sight glass and formation of powder inside the sphere can also be good indicators for confirming combustion. The sphere was cleaned after every trial.

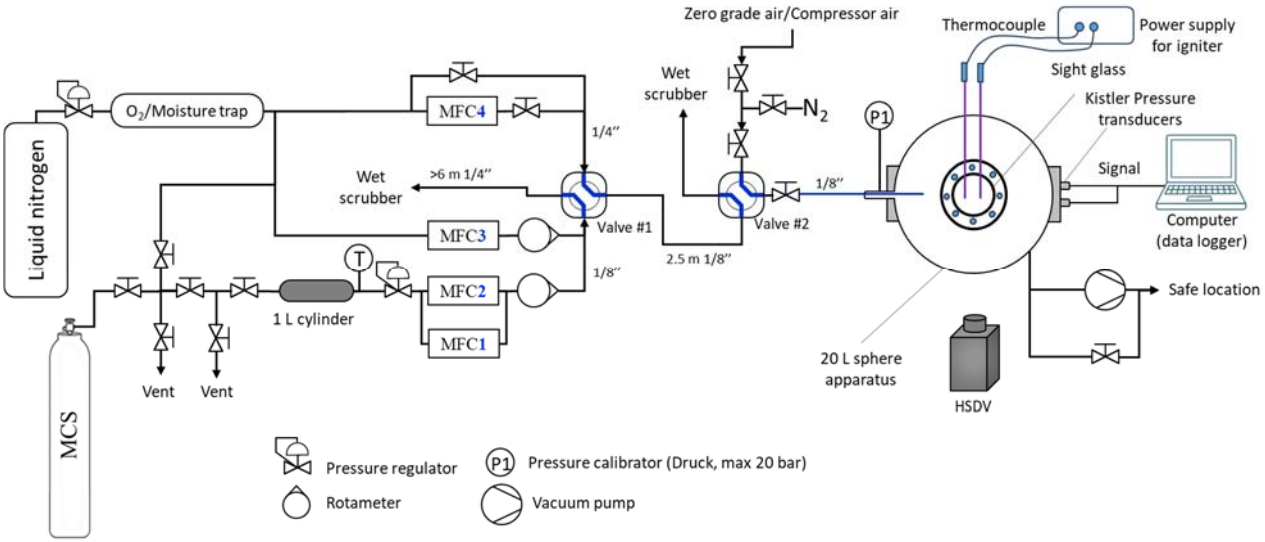

Fig. 2. *Setup for flammability limit measurement*

2. Results and discussion

2.1. Critical velocity for delayed ignition

The definition of prompt ignition in steady release test is given by ignition within 5 s after release into air. The exact time of release into air can be found from fuming near the vent stub. Fuming is a result of MCS react with moisture in the air. If there is no ignition in a long period of time (i.e. >5s) after release or fuming, it is classified as a delayed ignition. It is possible that premature ignition occurred in certain vent tests with higher velocities owing to contamination in the vent line or in the ambient air. Critical velocity (V_c) for delayed ignition is defined as the lowest possible flow velocity that gives delayed ignition. The V_c of MCS in air is found to be relatively low compared to other pyrophoric gases such as silane and disilane. As V_c increase with increasing vent size, the largest 4.32 mm ID port connectors were used to ensure prompt ignition occurred in the minimum flowrate range of the mass flow controller. Fig. 3 shows the typical results of high-speed video clips of delayed and prompt ignitions with release velocities of 0.437 m/s and 0.129 m/s, respectively. Contrary to those of silane, most prompt ignitions took place right at the vent stub giving zero ignition distance as shown in Fig. 3. V_c is determined to be 0.144 m/s which is about 1 order of magnitude smaller than that of silane.

The overall results are shown in Fig. 4 and 5 for ambient air and zero-grade dry air. An additional surprise is that V_c for both ambient air and zero-grade dry air are very close, 0.144 vs. 0.16 m/s, respectively. Note for silane with a vent sub of 3.5 mm ID, V_c for ambient air and zero-grade dry air are 1.79 vs. 9.17 m/s, respectively. This is a surprised result as MCS is expected to have higher water-reactivities than that of silane owing to its silicon-chlorine bond. The possible reason is that MCS has a much lower reactivity towards oxygen such that the effect of water reactivity is negligible.

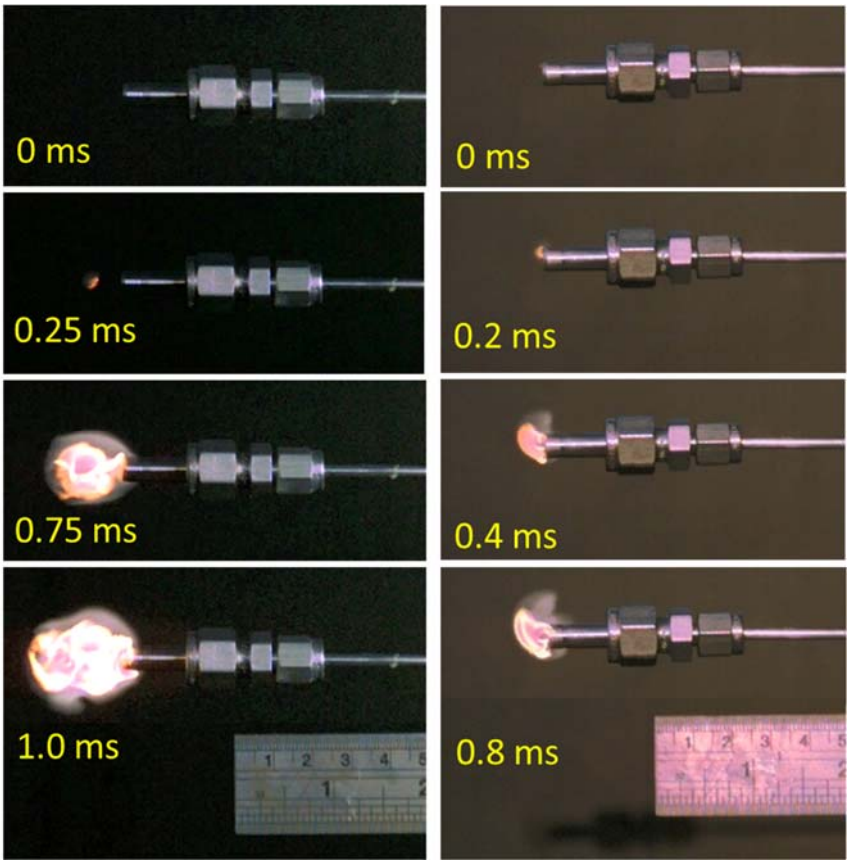

Fig. 3. *Results of high-speed video clips of delayed (left) and prompt (right)ignitions with release velocities of 0.437 m/s and 0.129 m/s, respectively*

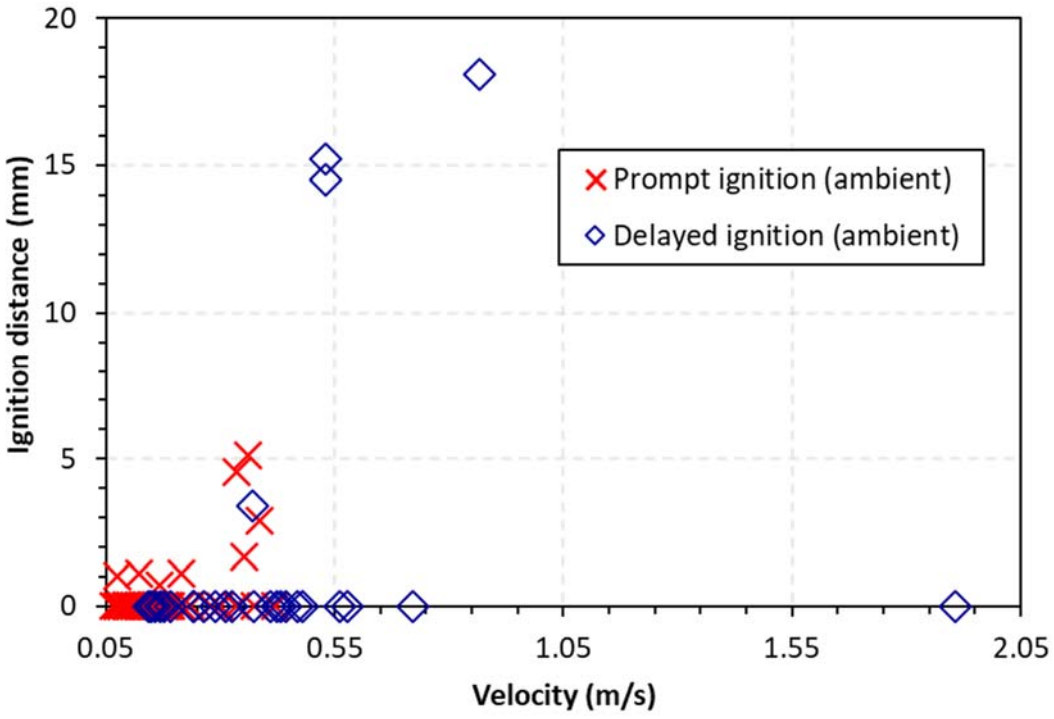

Fig. 4. *The steady flow test results for ambient air*

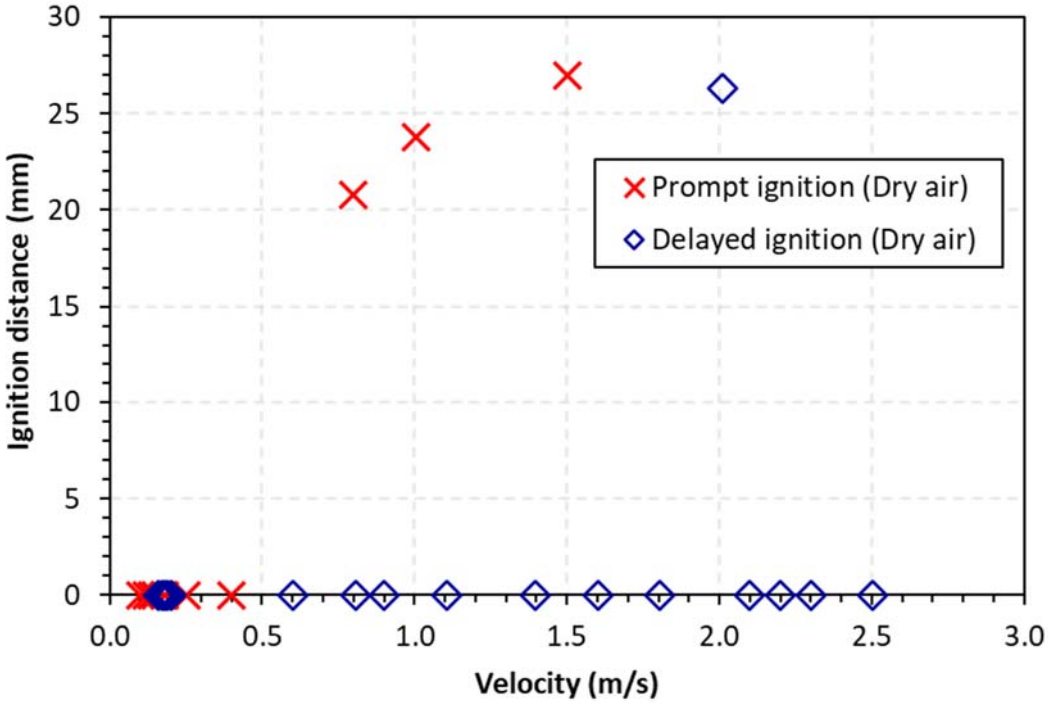

Fig. 5. *The steady flow test results for zero-grade dry air*

2.2. Lower flammability limits

There is very little flammability information on MCS according to Britton (1990) and it is reasonable to assume its AIT is intermediate between that of silane and dichlorosilane (DCS). Britton (1990) has determined the LFL and AIT of DCS are 4.7±0.1 vol.% and 47±3°C in dry air. MCS supplier REC Silicon gave an LFL of 4.6-4.8 vol.% (REC Silicon, 2011). Thus, tests were carried out from 4 vol.%. The results of 20-L sphere apparatus are shown in Fig. 6-8 for both ambient air from compressor and dry, zero-grade air. LFL in both airs are similar. When MCS concentration is higher than 2 vol.%, there is a sharp increase in overpressure and pressure rise rate. This is accompanied by white powder deposit on the inner wall of the sphere as shown in Fig. 9. The powder deposit is additional evidence of MCS combustion in addition to pressure measurement. Even the lowest flammable concentration of 2.11 vo.%, powder deposit was roughly uniform on the ignitor rods and inner surface of the 20-L sphere. Below 2 vol.%, the ignition did not lead to any noticeable pressure rise. There was also no sign of powder formation even with compressor air that contained approximately 0.5 vol.% moisture. High-speed video taken from the sight glass however did not show a clear flame but the spark was turning into orange colour with increasing MCS concentration as shown in Fig. 10. According to ASTM 819, LFL of MCS was determined to be average of the lowest of flammable concentration, 2.11 vol %, and highest of non-flammable concentration of 1.94 vol.%, which is equal to 2.03±0.12% vol.%, in both compressor air and zero-grade air. The determined LFL lies right between 1.37 vol.% of silane and 4.7 vol.% of DCS.

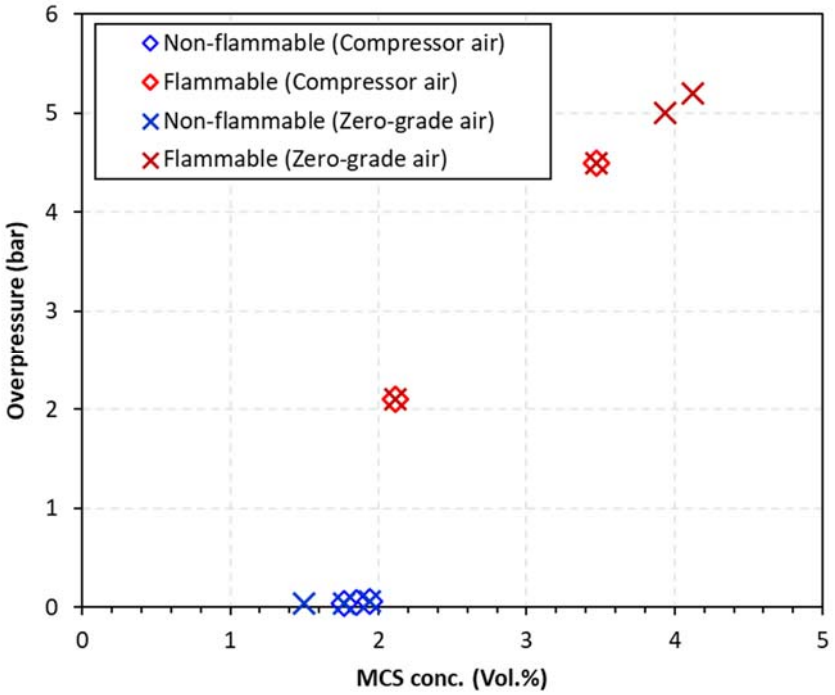

Fig. 6. *Overpressure data for MCS with compressor air and dry air*

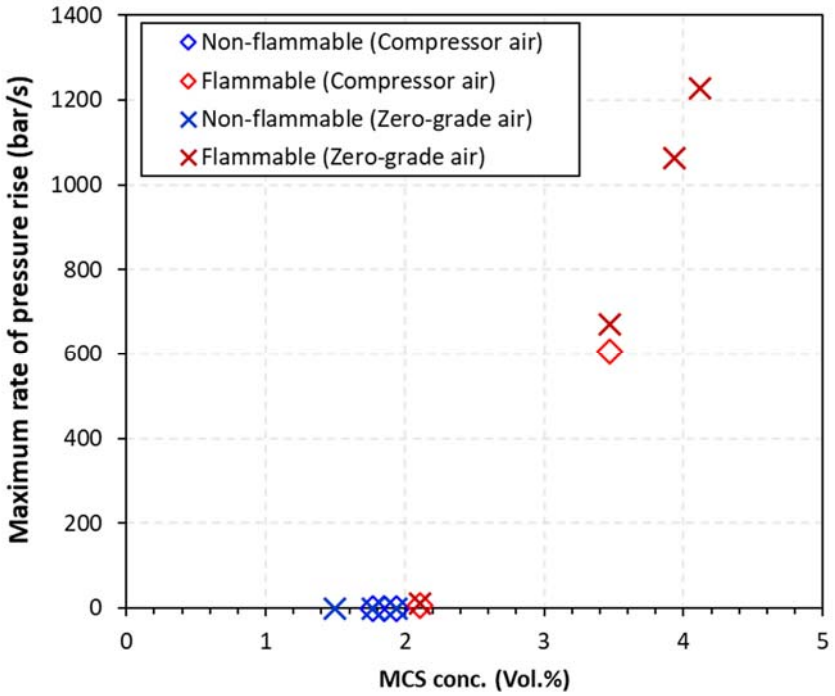

Fig. 7. *Data on maximum pressure rise rate for MCS with compressor air and dry air*

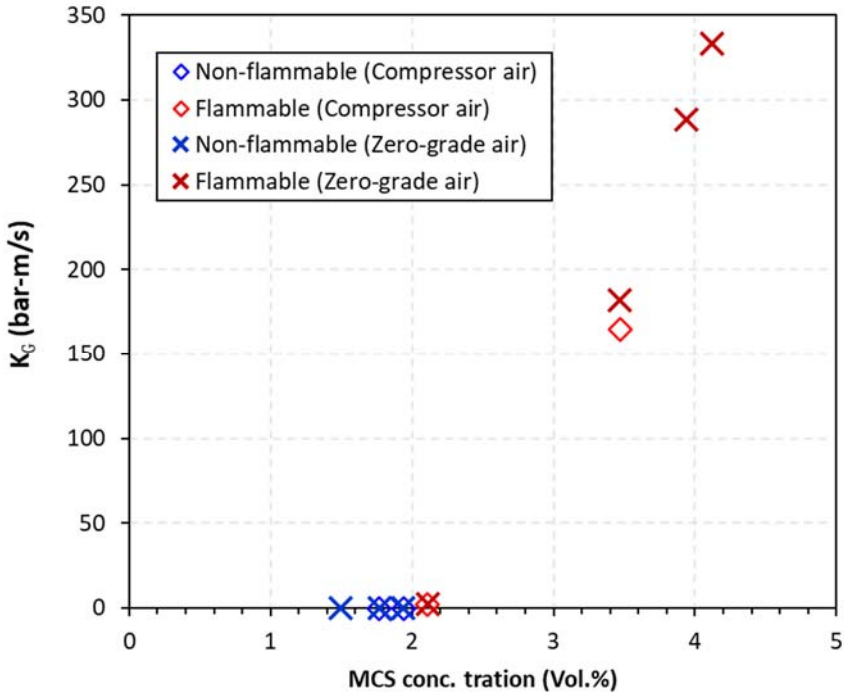

Fig. 8. *Calculated deflagration index for MCS with compressor air and dry air*

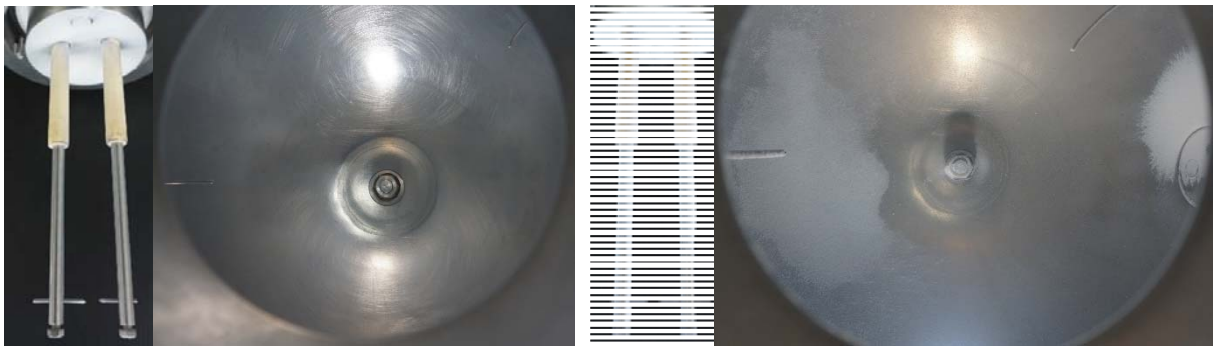

Fig. 9. *Results of powder deposit on ignitor rods and inner surface of 20-L sphere. Left: MCS 1.94 vol. % in compressor air; right: MCS 2.11 vol. % in compressor air*

Fig. 10. *High-speed video clip of ignition. Left: MCS 1.94 vol. %; central: MCS 2.11 vol.; right: MCS 3.47 vol.%, all with compressor air*

2.3. Critical shear rate

The steady release test produced a laminar or turbulent jet of the pyrophoric gas into air. It is known that the delayed ignition of the jet was caused by ignition kernel quenched by shear rate of the flow or scalar dissipation between the release gas and the ambient air (Tamanini et al., 1996; Tsai et al., 2010). For a fuel jet released into air, the scalar dissipation or flow strain at the fuel jet/air surface near the origin is so large that reactive kernel will be quenched. Downstream of the jet, the scalar dissipation or flow strain between the jet and surrounding air weakens and the ignition is a result of competition between the reactive kernel and scalar dissipation or flow strain. Further downstream in the jet, the reactive kernel is diminished along with reduced fuel concentration and autoignition is impossible. Thus, for silane and disilane, prompt ignition always takes place at downstream of the vent tube. For MCS, the reactive kernel is clearly weak and quenched easily with very low jet velocity. For unquenched flow, prompt ignition take place very close to the vent stub as shown in Fig. 3.

Although the V_c is a good indicator for pyrophoricity, it is also a function of vent diameter. Thus, a proper indicator would be the critical shear rate at the vent stub, defined by $8V_c/D$. Additional complication was the moisture in the air. Moisture has a strong effect on silane V_c. Thus, separate data are shown for dry air and ambient air. The only exception is disilane, in which V_c was not determined in dry air. Table 1 shows the summary of critical shear rate and other properties for three pyrophoric gases: disilane, silane and MCS. The critical shear rate is shown for average value and standard deviation for different vent sizes. Despite the data scattering from vent sizes, there are significant differences in the critical shear rate for the three pyrophoric gases, differs by at least one order of magnitude. A gas with a higher critical shear rate implies that the ignition kernel is highly active and thus a higher degree of pyrophoricity. On the other hand, a gas with a lower critical shear rate has a lower degree of pyrophoricity and lower reactivity towards air and thus delayed ignitions and VCE are favoured. Thus, the degree of pyrophoricity of the three gases are: disilane > silane > MCS. Also shown in Table 1 are the LFL, flash point, boiling point, critical temperature, and deflagration index (K_G) at a known concertation. None of the data correlates with the ranking of pyrophoricity except the LFL.

Certainly, the formation a VCE will also depend on amount of gas accumulation, gas release gas rate, etc., but the medium degree of pyrophoricity of silane in comparison of disilane do play a key role in numerous silane explosion incidents. Disilane has a relatively high boiling point and low vapor pressure to give a smaller flowrate in case of accidental leak. In combining with its high degree of pyrophoricity, it is less likely to form VCE for disilane. MCS has a medium boiling point and vapor pressure, and the lowest degree of pyrophoricity. It also has the lowest K_G at a relative high concentration of 4.12 vol.%. Thus, a MCS leak would most likely result in a delayed ignition but the intensity of VCE is expected to be much lower than that of silane.

***Table 1**. Summary of critical shear rate and other properties for three pyrophoric gases*

Gas		Disilane	Silane	MCS
Formula		Si_2H_6	SiH_4	SiH_3Cl
MW		62.219	32	66.56
Boiling point (°C)		-14.3	-111.5	-30.4
Critical temperature (°C)		159	-3.4	123
Flash point (°C)		<40	-	-90
LFL (vol. %)		0.5	1.38	2.03
Critical Shear rate (1/s)	Ambient air	520,735	3,532±2,870	267
	Dry air		25,189±5,920	296
K_G (bar·m/s)		627 @ 1.9 vol.%	452 @ 3.7 vol.%	333 @ 4.12 vol.%
Ranking of pyrophoricity		1	2	3

3. Conclusions

Experimental results of flammability limits and ignition behavior of monochlorosilane (MCS) are presented and compared with those of silane and disilane. Critical velocities for delayed ignition were determined to be 0.144 m/s and 0.16 m/s for MCS release from a vent stub of 4.32 mm into ambient air and dry air, respectively. LFL of MCS in ambient air and dry air are determined to be the same value of 2.03 vol.% A new indicator based on critical shear rate at the vent stub is proposed for assessing the pyrophoricity of gases. Degree of pyrophoricity for the three gases are: disilane > silane > monochlorosilane. Disilane has the highest reactivity towards air and thus a jet fire instead of VCE will be the most likely result upon accidental release. MCS on the other hand has lowest reactivity towards air and lowest K_G at a relative high concentration of 4.12 vol.%. Thus, a MCS leak would most likely result in a delayed ignition but the intensity of VCE is expected to be much lower than that of silane. Silane, with its intermediate reactivity towards air and high vapor pressure, will have the highest likelihood of VCE upon release. It is expected that critical shear rate will be useful to access the VCE hazards of all pyrophoric gases. This is of particular importance in the safety of semiconductor fabrications and related industries where increasing pyrophoric gases are used.

Acknowledgements

Eugene Y. Ngai, one of the key authors that contributed significantly to this work and other specialty gas safety, passed away in July 2023. This article is dedicated to him.

References

Alcántara–Avila, J. R., Sillas–Delgado, H. A., Segovia–Hernández, J. G., Gómez–Castro, F. I., & Cervantes-Jauregui, J. A., 2015. Silane production through reactive distillation with intermediate condensers. Computer Aided Chemical Engineering, 37, 1037-1042.

American Society for Testing and Materials, 2020. Standard Practice for Determining Limits of Flammability of Chemicals at Elevated Temperature and Pressure, ASTM E918−19.

American Society for Testing and Materials, 2019. Standard Test Methods for Limiting Oxygen (Oxidant) Concentration in Gases and Vapors, ASTM E2079−19.

Baratov, A. N., Vogman, L. P., & Petrova, L. D., 1969. Explosivity of monosilane-air mixtures. Combustion, Explosion and Shock Waves, 6, 592–594.

Britton, L. G., 1990. Combustion hazards of silane and its chlorides. Plant/Operations Progress, 9, 16–38.

Burg, A. B., & Kuljian, E. S., 1950. Silyl-Amino Boron Compounds1. Journal of the American Chemical Society, 72(7), 3103-3107.

Chang, Y. Y., Peng, D. J., Wu, H. C., Tsaur, C. C., Shen, C. C., Tsai, H. Y., Chen, J. R., 2007. Revisiting of a Silane Explosion in a Photovoltaic Fabrication Plant, Process Safety Progress, 26 (2), 155-157.

Chen, J. R., Tsai, H. Y., Chen, S. K., Pan, H. R., Hu, S. C., Shen, C. C., Kuan, C. M., Lee, Y. C., Wu, C. C., 2006. Analysis of a Silane Explosion in a Photovoltaic Fabrication Plant," Process Safety Progress, 25 (3), 237-244.

Itagaki, H., & Tamura, M., 1995, Fire of special material gas come into contact with air in exhaust piping at a semiconductor factory.
http://www.shippai.org/fkd/en/cfen/CC1200087.html

Ngai, E. Y., Huang, K. P. P., Chen, J. R., Shen, C. C., Tsai, H. Y., Chen, S. K., Hu, S. C., Yeh, P. Y., Liu, C. D., & Chang, Y. Y., 2007. Field tests of release, ignition, and explosion from

silane cylinder valve and gas cabinet, Process Safety Progress, 26(4), 265-282.

Ngai, E.Y., Fuhrhop, R., Chen, J.R., Chao, J., Bauwens, C.R., Mjelde, C., Miller, G., Sameth, J., Borzio, J., Telgenhoff, M., Wilson, B., 2015. CGA G-13 Large-Scale Silane Release Tests – Part II. Unconfined Silane-Air Explosion, Journal of Loss Prevention in the Process Industries, 36, 488-496.

Nguyen, T.T., Cao, K.Q., Yang, M.H., Chen, J.R., Tsai, H.Y., Gordon, M. & Ngai, E.Y. (2022). Experimental Studies on Ignition Behavior of Pure Disilane and Its Lower Flammability Limit, Chemical Engineering Transactions, 90, 199-204.

Peng, D. J., Chang, Y. Y., Wu, H. C., Tsaur, C. C., Chen, J. R., 2008. Failure Analysis of a Silane Gas Cylinder Valve: A Case Study, Engineering Failure Analysis, 15 (4), 275-280.

REC Silicon, 2011. Monochlorosilane Material Safety Data Sheet, May 24.

Tamanini, F., Chaffee, J. L., Jambor, R. L., 1998. Reactivity and ignition characteristics of silane/air mixtures. Process Safety Progress, 17, 243–258.

Tsai, H.Y., Wang, S.W., Wu, S.Y., Chen, J.R., Ngai, E.Y., Huang, K.P.P., 2010. Experimental Studies on the Ignition Behavior of Pure Silane Released into Air, Journal of Loss Prevention in the Process Industries, 23(1), 170-177.

Tsai, H. Y., Hung, H. L., Wu, S. Y., Ku, C. W., Chen, J. R., Fomin, P. A., Fedorov, A. V., 2017a. Effects of Temperature and Moisture on the Ignition Behavior of Silane Release into Air, Combustion, Explosions and Shock Waves, 53(3) 276–282.

Tsai, H. Y., Lin, Y. J., Chang, Y. C., Lin, J. S., Chen, J. R., Ngai, E. Y., 2017b. Unconfined Silane-Air Explosions, Journal of Loss Prevention in the Process Industries, 49B, 700-710.

Reproduction of the pressure load due to the thermal runaway of an NMC cell in a flameproof enclosure by gas explosions

Inka Peschel [a], Stefanie Spörhase [a], Amiriman Kianfar [a], Detlev Markus [a] & Stefan Essmann [a]

[a] Physikalisch-Technische Bundesanstalt (PTB), Bundesallee 100, 38116 Braunschweig, Germany

E-Mail: *stefanie.spoerhase@ptb.de*

Abstract

Lithium-ion batteries usage is rapidly growing due to their superior performance compared to other battery chemistries. However, they involve the risk of thermal runaway, which can cause catastrophic accidents. A large number of studies investigated the behaviour of cells undergoing thermal runaway. In hazardous areas, lithium-ion batteries may be used under specific conditions, for example in flameproof enclosures. However, there are few studies on this topic, limiting the information on how flameproof enclosures must be designed to contain a thermal runaway event and mitigate the risk. Notified bodies conducting type tests of flameproof enclosures usually do not have the capability to work with lithium-ion batteries in thermal runaway. However, gas explosions are regularly employed to test the enclosure`s ability to withstand pressure. In order to replace the lengthy destructive tests with batteries in the future, it is envisioned to reproduce the pressure load due to the thermal runaway of an NMC cell on the flameproof enclosure by a gas explosion. This work is the first step towards this goal. To this end, the temporal pressure development inside a flameproof enclosure during a thermal runaway of an NMC811 cell is reproduced by gas explosions. The cell was heated to thermal runaway in an air-filled flameproof enclosure and the resulting pressure was measured as a function of time. Various combustibles in air were the ignited in the same flameproof enclosure without the cell. The maximum pressure and the pressure rise time were varied by the type of combustible and its concentration in air. The gases used were hydrogen, methane, propane, ethylene and acetylene in different concentrations. The results show that the pressure evolution due to the thermal runaway of the NMC cells can be reproduced by gas explosions.

Keywords: *thermal runaway, lithium-ion batteries, flameproof enclosures, gas explosions*

Introduction

One of the biggest global challenges nowadays is to enable an energy transition towards a sustainable future. Lithium-ion batteries make a contribution in e-mobility and the storage of sustainable energy. They are increasingly being used in potentially explosive areas such as mining and the chemical industry. Lithium-ion batteries contain a combination of high-energy electrode materials and highly flammable electrolytes. This poses a risk of thermal runaway (TR), which can result in the explosive destruction of the battery (Korthauer, 2018). Even though a TR is an unlikely event, the rapid growth in the number of lithium-ion batteries worldwide means that this risk is increasing. This is further exacerbated by the continuous increase in energy density. In potentially explosive atmospheres, this risk is of particular importance. This is where explosion protection becomes relevant, which is concerned with preventing explosions and limiting their effects on the environment. The flameproof enclosure as one type of protection is aimed at shielding the explosion from the environment by encapsulation within an enclosure (Dubaniewicz et al., 2021; Spörhase et al., 2023). Flameproof enclosures must fulfil the requirements of IEC 60079-0 and IEC 60079-1. A part of the tests required is the test of ability of the enclosure to withstand pressure. This test can be carried out with a static

load (e. g. water pressure) or a dynamic load (gas explosion). Yet, it is unclear how the load due to the TR of a Lithium-ion battery would be tested experimentally. To avoid the handling of Lithium-ion batteries and overcome issues due to limited repeatability of TR, destructive testing using fully functional batteries could be replaced by tests using burnable gas/air mixtures. These will allow for simpler testing, eliminate toxic hazards, and save considerable time and resources. The replacement tests are intended to simulate the characteristic pressure curve of the battery during TR by means of a burnable gas-air explosion. Depending on the concentration of the burnable gas in the air, the exothermic reactions occur at different speeds which influence the pressure rise rate and the maximum pressure. The aim of this work is to find a burnable gas-air mixture that replicates the battery tests as closely as possible using the replacement tests. In order to determine the optimum mixture composition, a typical pressure trace to be reproduced is first selected from the available battery test data and defined as the target pressure curve. This is based on a theoretical analysis of possible mixture compositions. These are then tested experimentally on a suitable test bench, analysed and discussed.

1. Experiments

1.1. Safety characteristics

Under certain conditions (e. g. certain mixture ratio) mixtures of a burnable gas and air can explode. The burnable gas/air mixtures have different characteristic explosion properties which are described via safety characteristic data. The determination of these data is standardised. The “CHEMSAFE” database provides detailed and reliable tabulations of the properties of a wide range of burnable gases (PTB & BAM, 2024). In the following, the safety characteristics that will be used in this paper, are introduced briefly.

The lower and upper explosion limits define the range in which a burnable gas/air mixture is explosive (Hattwig et al., 2004). They include the minimum required and maximum possible concentration of fuel in air to allow for an explosive reaction. These limits depend on the specificity of the substance and the ambient conditions of pressure, temperature and relative humidity (Bjerketvedt et al., 1997).

The maximum explosion pressure ($p_{ex\ max}$) is the overpressure generated in the enclosure above the outlet pressure and describes the maximum of the pressure curve over time (Hattwig et al., 2004). Fig. 1 shows an exemplary pressure curve over time in blue. The maximum explosion pressure depends on the burnable gas concentration in the air. For most fuels, it is obtained at a composition slightly above stoichiometry. Mixture compositions far from stoichiometric will result in a lower explosion pressure.

The pressure rise time (*PRT*) is a measure of the rate of reaction and therefore the severity of the explosion (Hattwig et al., 2004). It is determined according to the IEC 60079-1 (2014) standard by measuring the time between reaching 10% and 90% of the maximum explosion pressure, as shown in green in Fig. 1.

The parameter rate of pressure rise (*RPR*) is given in two ways for this work. The first definition is the average gradient between reaching 10% and 90% of the maximum explosion pressure ($RPR_{10\%\text{-}90\%}$) as shown in red in Fig. 1. The second definition is the maximum gradient of the pressure curve (RPR_{max}) reached in a certain infinitesimally small section of the curve (Zhang, 2014). For both *RPR*, there is a strong dependence on the enclosure volume, which is described by the cubic law. The K_G value considers this and is a concentration-dependent, substance-specific quantity that is also tabulated in databases (Hattwig et al., 2004).

The pressure duration describes the length of a time interval during which a given pressure is maintained and gives an indication of the static load. In this work, the time interval between the first time half the maximum explosion pressure is reached and the second time after the pressure drops

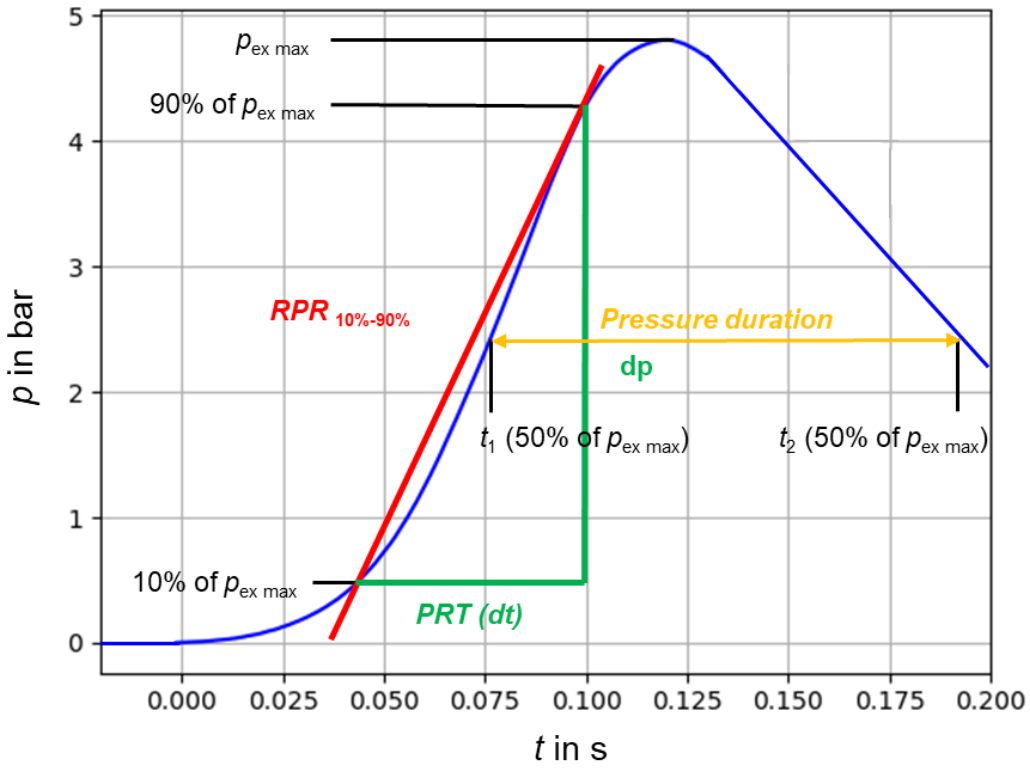

Fig. 1. *Illustration of explosion characteristics according to IEC 60079-1 on a typical pressure trace.*

below half the maximum value is used, as shown by the yellow line in Fig. 1. The pressure duration is not a standardised explosion characteristic.

1.2. Reference experiments with Lithium-ion batteries

The thermal runaway of a lithium-ion battery describes the rapid and uncontrolled exothermic reaction of the cell which can lead to the destruction of the entire system (Chen et al., 2021; Feng et al., 2018; Korthauer, 2018). This reaction can be triggered by both external abuse and internal system faults. External misuse includes deformation of the battery, creation of an external short circuit, overcharging, and excessive heating. Internal triggers include metallic impurities, anode or cathode instability and faulty separators. Furthermore, lithium deposits and dendrite formation can occur, which grow as metallic needles from the anode to the cathode. Contact with the cathode leads to complete self-discharge and a short circuit in the battery cell. The TR of a lithium-ion battery starts with an increase in cell temperature, regardless of the type of trigger. This leads to the decomposition of various cell components, which creates a self-accelerating cycle of further heat generation that can lead to cell fire. In addition, electrolyte decomposition also leads to the formation of gases. According to the ideal gas law, as the temperature rises, the pressure inside the cell increases and there is a risk that the cell will open, releasing the gases formed. These can then form an explosive atmosphere with air.

The TR of lithium-ion batteries has been investigated through previous destructive tests in flameproof enclosures (Spörhase et al., 2023). At the start of the test, the battery to be tested was charged to 110 % of final charge voltage. This constitutes a critical state for a lithium-ion battery. The battery was then placed on a heatable copper block inside the enclosure and continuously heated to TR. In this way, a range of cylindrical batteries with different electrode materials and capacities were tested. The electrode materials studied were LCO (2,55 Ah), NCA (3 Ah), LFP (3 Ah) and NMC811 (3 Ah and 3.5 Ah). Figure 2 shows the aggregated results of these experiments. The points represent single tests. The mean values plus minus the standard deviation are shown in the form of transparent boxes. In accordance with Wang et al. (2022), the evaluation of the tests showed that cells with the electrode

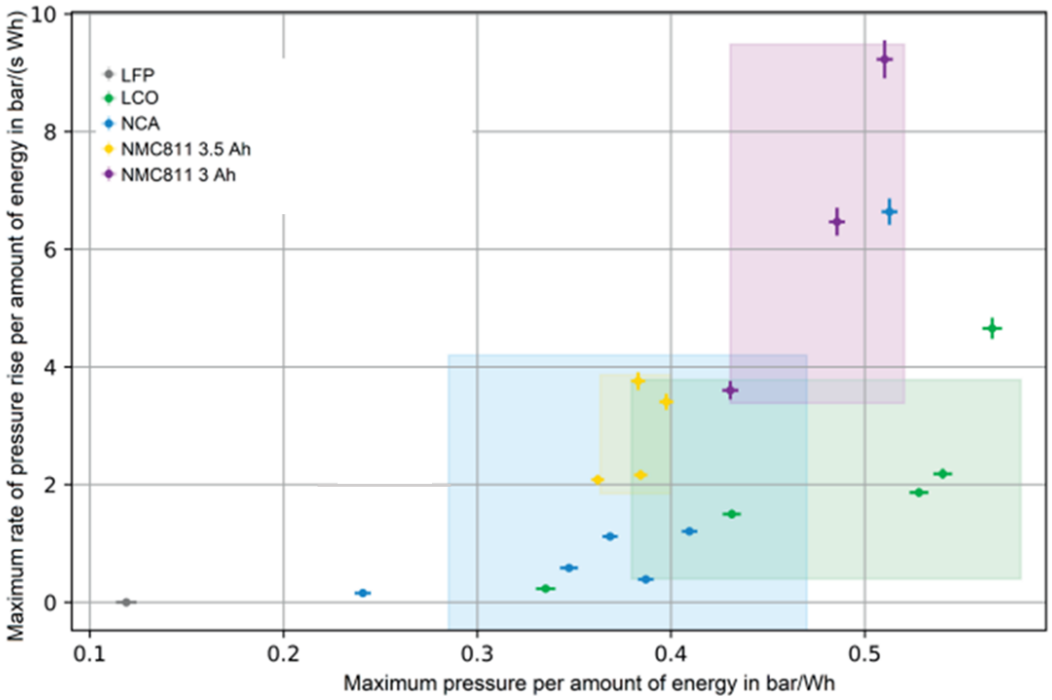

Fig. 2. *Maximum rate of pressure rise and maximum pressure during TR per amount of energy for different cell chemistries (Spörhase, 2023).*

materials LCO and NMC in a molar ratio of 8:1:1 (NMC811) had the greatest effect on TR per amount of electrical energy stored in the battery. Reproducibility was better with the NMC811 batteries than with the LCO batteries. For this reason, the pressure traces of the NMC811 batteries are selected as the target curves for the reproduction using the substitute test with burnable gas-air mixtures.

1.3. Gas explosions

In principle, the test setup from the battery tests (Spörhase et al., 2023) was retained for the experimental investigation in this work, with a few adjustments. The schematic test setup is shown in Fig. 3. The flameproof enclosure used in this work (series 8265, R. STAHL AG) is made of light metal. Its volume and mass are 19.7 ± 0.6 liter and 28.8 kg. The enclosure was equipped with a piezoelectric dynamic pressure sensor (Kistler Type 6031). The pressure signal was recorded via a charge amplifier (Kistler LabAmp 5167 Ax0) on an oscilloscope (Yokogawa DL850). The burnable gas/air mixture was prepared using mass flow controllers (Bronkhorst EL-FLOW) and checked via an oxygen analyser (Servomex OxyExact 2200). The enclosure was purged with the burnable gas/air mixture until the concentration reading on the oxygen analyser remained constant at the desired value. A spark plug close to the gas inlet valve was used to ignite the mixture. The five burnable gases hydrogen (H_2), methane (CH_4), propane (C_3H_8), ethylene (C_2H_4), and acetylene (C_2H_2) were used at different equivalence ratios. The experiments were recorded with a high-speed camera for visualization purposes. The initial conditions were ambient pressure and temperature (1 bar abs. and 20°C).

1.3.1. Measurement uncertainties

The uncertainty in mixture preparation is determined by the calibrated oxygen analyser. The oxygen analyser has known systematic uncertainty factors for the various burnable gases, which were corrected for. The residual uncertainty of the oxygen analyser is < 0.02 % O_2 (absolute error). As only one fifth of the mixture is tested (concentration of oxygen in air), this uncertainty has to be multiplied by five and an estimated drift of 0.001 % has to be added. For the uncertainty of the burnable gas concentration, this gives an estimated residual error of ± 0.2 vol.-% for all burnable gases used. For the pressure measurement chain consisting of pressure sensor, charge amplifier and oscilloscope, the combined uncertainty is 1.5 %.

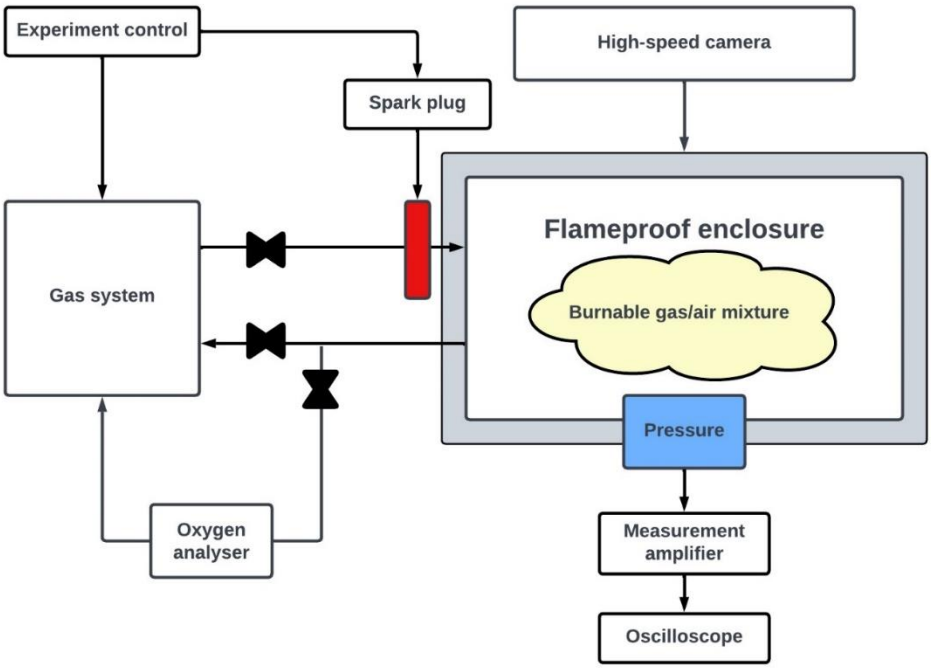

***Fig. 3**. Schematic of test setup*

2. Results and discussion

The explosion characteristics are analysed separately for each burnable gas with the primary objective of achieving an agreement between the pressure evolution of gas explosions and the average pressure evolution of the battery tests. In this work, a good agreement is defined if the explosion pressure characteristic of the gas explosions is within the 1 σ pressure range of the battery tests. Qualitatively, there is a difference in the pressure traces of TR and gas explosion. In the case of a gas explosion, the pressure rises steadily at the beginning, whereas in the case of a TR, there is a sudden rise in pressure at the beginning of the explosion. In the following, pressure is always given as a relative pressure, which is defined as the pressure differential with respect to the ambient atmospheric pressure.

In the first part of evaluation, the focus was on the agreement of the maximum explosion pressure, pressure rise time and rate of pressure rise between 10% and 90%. In the following parts the RPR_{max} and K_G value will also be analysed, which takes into account the dependence of an explosion on the enclosure volume. The pressure duration and a comparison with literature are also included.

2.1. Agreement with maximum explosion pressure, pressure rise time, and rate of pressure rise

For the three parameters maximum explosion pressure ($p_{ex\ max}$), pressure rise time (PRT), and rate of pressure rise ($RPR_{10\%-90\%}$), the reproduction of the battery tests is fulfilled for a total of three gas tests: the 5.1 vol.-% ethylene-air mixture as well as the 4.3 vol.-% to 4.6 vol.-% acetylene-air mixtures. The results of these gas and battery tests are given in table 1 and the pressure traces are shown in Fig. 4. Here, all pressure traces have been shifted in time so that half of the maximum pressure occurs at the same time. However, these tests do not agree well with RPR_{max} of the battery tests, i.e., the point in the pressure curve with the greatest gradient. This is due to the mentioned difference at the start of the reaction. In the TR event, the pressure rises abruptly at the beginning, whereas in the gas explosions there is a steady increase.

It is also important to clarify the issue of the reproducibility of the tests. As can be seen from the green curves of the battery test, they show a high scatter. In contrast, the gas tests are well repeatable, and the scatter is very small. The only exception is the testing of hyper-stoichiometric acetylene/air mixtures, due to the very strong soot production in these explosions.

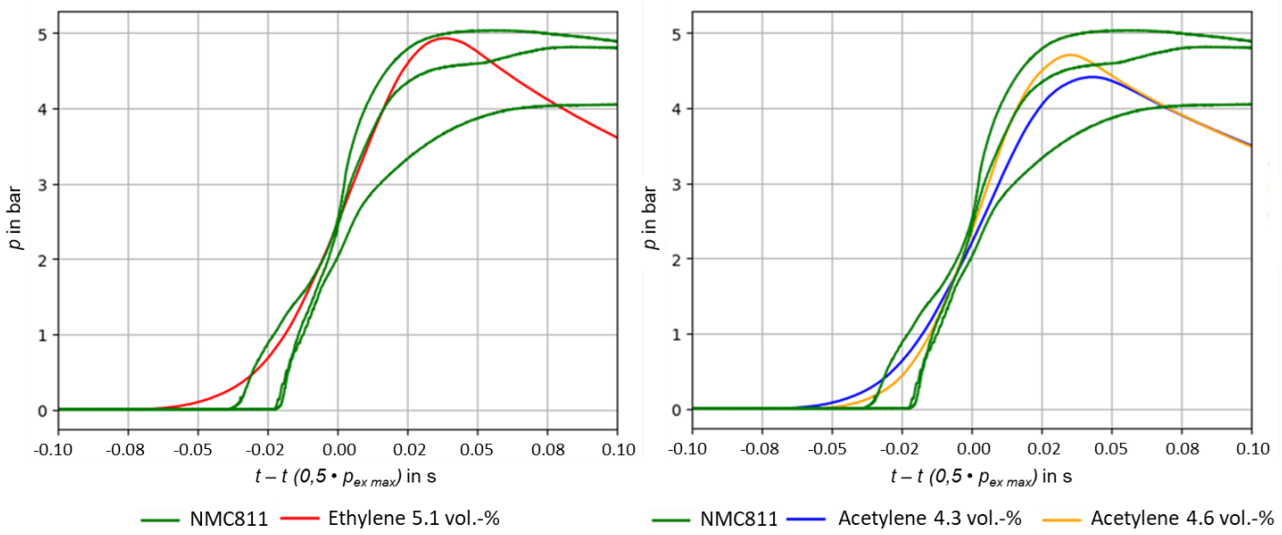

Fig. 4. *Pressure traces of the reference TR events and the gas explosion tests with best agreement.*

Table 1. *Test data of the TR of NMC811-batteries and the gas tests with best agreement*

TEST	$p_{ex\,max}$ **in bar**	***PRT*** **in ms**	$RPR_{10\%-90\%}$ **in bar/s**	RPR_{max} **in bar/s**
NMC811 (1)	4.9 ± 0.1	43 ± 1	90.6 ± 1.7	184.6 ± 1.0
NMC811 (2)	5.1 ± 0.1	49 ± 1	82.9 ± 1.5	232.9 ± 1.1
NMC811 (3)	4.2 ± 0.1	56 ± 1	57.8 ± 1.3	134.2 ± 6.3
Ethylene 5.1 vol.-%	4.9 ± 0.1	52 ± 1	75.9 ± 1.4	97.7 ± 0.1
Acetylene 4.3 vol.-%	4.4 ± 0.1	54 ± 1	65.7 ± 1.2	84.4 ± 0.1
Acetylene 4.6 vol.-%	4.7 ± 0.1	44 ± 1	86.0 ± 1.6	111.6 ± 0.2

2.2. RPR_{max}

Fig. 5 shows the maximum explosion pressure plotted against the RPR_{max}. The three battery tests are shown as green dots and their 1σ and 2σ surroundings are shown as a green area around them. This rectangular representation of the probable battery test values is used to examine which gas explosion test is closest to the TR of the tested batteries. None of the gas test fall into the 1σ surrounding. Acetylene 4.7 vol.-% is the only gas test in the 2σ surrounding, which is the closest simulation of TR in terms of this evaluation method. Overall, Fig. 5 shows that the gas tests with an appropriate mean maximum explosion pressure of 4.72 bar have lower RPR_{max}. In table 2 all gas test data is listed.

2.3. Pressure duration

The pressure duration, i.e., how long the enclosure is exposed to the high pressure, is also decisive. The pressure duration *MPD* thus describes the static pressure influence of the explosion. For the battery tests, the average pressure duration is 1015 ms and is therefore at least 900 ms longer compared to the stoichiometric gas explosions. The pressure duration varies depending on the proportion of burnable gas in the mixture. With a burnable gas content of 6.9 vol.-% propane is the only burnable gas to achieve similar pressure duration. However, in this case the maximum explosion pressure to be withstood is lower at 3.76 bar than in the battery tests. All other burnable gases have a lower pressure duration.

Table 2. *Overview of all gas test data*

Gas	Concentration in vol.-%	$p_{ex\ max}$ in bar	RPR_{max} in bar/s	K_G value in bar·m/s	*PRT* in ms	*MPD* in ms
Ethylene	3.4 ± 0.2	No explosion				
	4.5 ± 0.2	4.5 ± 0.1	60.7 ± 0.1	16 ± 1	76 ± 1	273 ± 1
	4.7 ± 0.2	4.6 ± 0.1	70.4 ± 0.1	19 ± 1	-	
	4.8 ± 0.2	4.7 ± 0.1	78.0 ± 0.1	21 ± 1	61 ± 1	
	5.0 ± 0.2	4.8 ± 0.1	86.0 ± 0.1	23 ± 1	57 ± 1	
	5.1 ± 0.2	4.9 ± 0.1	97.7 ± 0.1	26 ± 1	52 ± 1	
	6.6 ± 0.2	6.4 ± 0.1	276.5 ± 0.1	75 ± 2	26 ± 1	
	10.2 ± 0.2	6.0 ± 0.1	136.9 ± 0.1	37 ± 1	47 ± 1	
	11.3 ± 0.2	5.4 ± 0.1	74.0 ± 0.1	20 ± 1	80 ± 1	
	12.4 ± 0.2	4.9 ± 0.1	47.6 ± 0.1	13 ± 1	115 ± 1	
	12.9 ± 0.2	4.7 ± 0.1	38.5 ± 0.1	10 ± 1	139 ± 1	
	14.6 ± 0.2	No explosion				
Hydrogen	12.6 ± 0.2	2.7 ± 0.1	37.0 ± 0.1	10 ± 1	71 ± 1	126 ± 1
	13.6 ± 0.2	3.0 ± 0.1	53.4 ± 0.1	14 ± 1	54 ± 1	
	15.7 ± 0.2	3.6 ± 0.1	106.1 ± 0.1	29 ± 1	33 ± 1	
	19.7 ± 0.2	4.4 ± 0.1	304.4 ± 0.2	82 ± 3	15 ± 1	
	20.7 ± 0.2	4.8 ± 0.1	384.2 ± 0.2	104 ± 3	13 ± 1	
	21.8 ± 0.2	4.8 ± 0.1	475.5 ± 0.1	128 ± 4	11 ± 1	
	29.5 ± 0.2	6.0 ± 0.1	1198.6 ± 1.3	324 ± 11	6 ± 1	
	31.0 ± 0.2	5.9 ± 0.1	1211.7 ± 2.3	327 ± 11	5 ± 1	
	40.1 ± 0.2	5.7 ± 0.1	1187.8 ± 1.0	321 ± 11	5 ± 1	
	45.2 ± 0.2	5.4 ± 0.1	925.2 ± 0.3	250 ± 8	6 ± 1	
	50.3 ± 0.2	4.9 ± 0.1	680.4 ± 0.1	184 ± 6	8 ± 1	
	52.7 ± 0.2	4.7 ± 0.1	560.1 ± 0.1	151 ± 5	9 ± 1	
	71.0 ± 0.2	No explosion				
Methane	6.6 ± 0.2	No explosion				
	7.7 ± 0.2	4.0 ± 0.1	33.0 ± 0.1	9 ± 1	115 ± 1	109 ± 1
	8.3 ± 0.2	4.4 ± 0.1	49.6 ± 0.1	13 ± 1	89 ± 1	
	9.0 ± 0.2	4.8 ± 0.1	71.2 ± 0.1	19 ± 1	69 ± 1	
	9.5 ± 0.2	5.0 ± 0.1	78.1 ± 0.1	21 ± 1	64 ± 1	
	10.1 ± 0.2	5.0 ± 0.1	84.5 ± 0.1	23 ± 1	60 ± 1	
	11.2 ± 0.2	4.9 ± 0.1	66.7 ± 0.1	18 ± 1	74 ± 1	
	11.6 ± 0.2	4.7 ± 0.1	55.9 ± 0.1	15 ± 1	82 ± 1	
	11.9 ± 0.2	No explosion				
Propane	3.5 ± 0.2	No explosion				
	3.8 ± 0.2	5.5 ± 0.1	104.7 ± 0.1	28 ± 1	56 ± 1	1303 ± 1
	4.0 ± 0.2	5.7 ± 0.1	131.3 ± 0.1	35 ± 1	48 ± 1	
	4.6 ± 0.2	5.8 ± 0.1	149.1 ± 0.1	40 ± 1	41 ± 1	
	4.9 ± 0.2	5.8 ± 0.1	141.6 ± 0.1	38 ± 1	43 ± 1	
	5.3 ± 0.2	5.6 ± 0.1	127.2 ± 0.1	34 ± 1	48 ± 1	
	5.9 ± 0.2	5.3 ± 0.1	67.9 ± 0.1	18 ± 1	82 ± 1	
	6.5 ± 0.2	4.6 ± 0.1	35.6 ± 0.1	10 ± 1	148 ± 1	
	6.9 ± 0.2	3.8 ± 0.1	23.5 ± 0.1	6 ± 1	231 ± 1	
	7.5 ± 0.2	No explosion				
Acetylene	2.3 ± 0.2	No explosion				
	4.3 ± 0.2	4.4 ± 0.1	84.4 ± 0.1	23 ± 1	54 ± 1	125 ± 1
	4.5 ± 0.2	4.7 ± 0.1	107.9 ± 0.1	29 ± 1	44 ± 1	
	4.6 ± 0.2	4.7 ± 0.1	111.6 ± 0.1	30 ± 1	44 ± 1	
	4.7 ± 0.2	5.0 ± 0.1	138.5 ± 0.1	37 ± 1	37 ± 1	
	7.8 ± 0.2	7.3 ± 0.1	923.2 ± 0.1	249 ± 8	9 ± 1	
	11.7 ± 0.2	8.0 ± 0.1	1125.5 ± 0.1	304 ± 10	8 ± 1	
	16.8 ± 0.2	7.6 ± 0.1	348.3 ± 0.1	94 ± 3	24 ± 1	
	21.9 ± 0.2	6.6 ± 0.1	496.7 ± 0.1	134 ± 4	39 ± 1	
	22.9 ± 0.2	6.5 ± 0.1	408.5 ± 0.1	110 ± 4	24 ± 1	
	28.6 ± 0.2	No explosion				

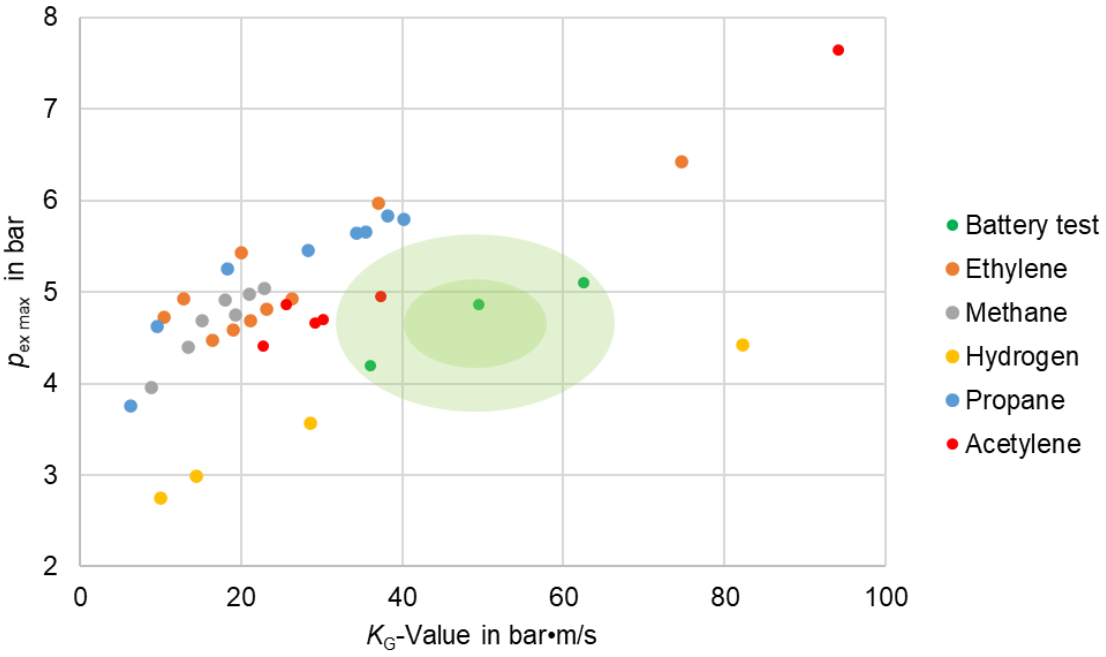

Fig. 5. *$p_{ex\ max}$ as a function of the K_G value for all tests.*

2.4. Comparison with "CHEMSAFE" Database

The test data obtained are compared with values from the "CHEMSAFE" database in Fig. 6. This is done using the maximum explosion pressure for gases hydrogen, ethylene, and methane in a wide range of burnable gas concentrations. For propane and acetylene, only the maximum explosion pressure of the stoichiometric mixture composition is considered, as no distribution curves are available in the database. The distribution curves of the test data and literature values in Fig. 6 show a similar trend. However, the test data give lower maximum explosion pressures than the literature values. For hydrogen they are consistently about 1 bar lower, for ethylene and methane the difference is greater at about 2 bar. For propane and acetylene, the maximum explosion pressure of the stoichiometric composition differs most from the CHEMSAFE database at > 2 bar. According to the database, a propane explosion results in a higher maximum pressure than a hydrogen explosion (8.4 bar and 7.1 bar, respectively). In the gas explosion test performed in this work, both fuels have a similar maximum explosion pressure. The suspected causes of the deviations described are the influences of the enclosure geometry (cubic as opposed to spherical) and the ignition location (close to a wall as opposed to central) on gas explosions.

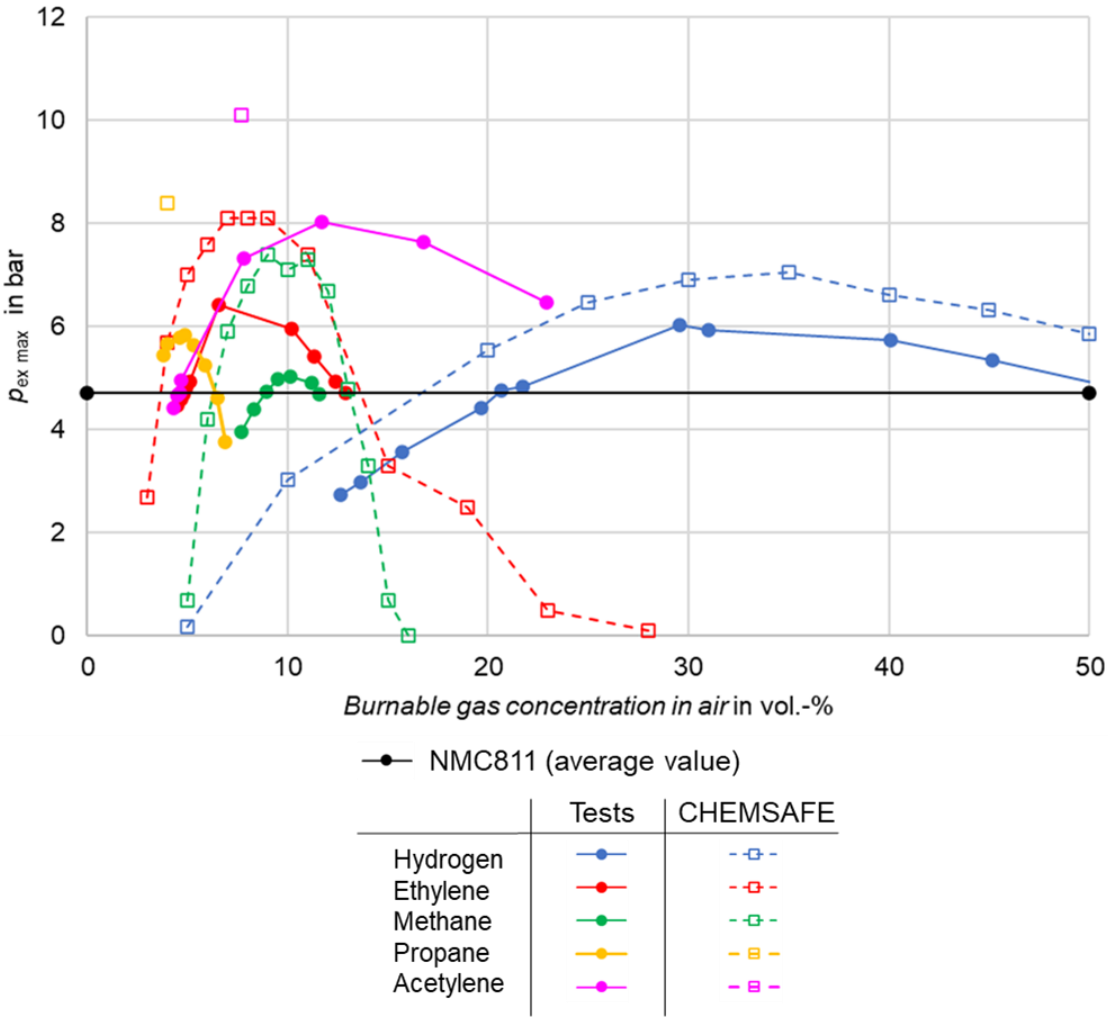

Fig. 6. *Comparison of $p_{ex\ max}$ experimental data with values from the CHEMSAFE database (PTB & BAM, 2024).*

3. Conclusions

In summary, this work has succeeded in reproducing the effects of TR of lithium-ion batteries through gas explosions. This applies to the explosion characteristics maximum explosion pressure, *PRT* and $RPR_{10\%\text{-}90\%}$. In contrast to the battery tests, the reproducibility of the gas test is satisfactory, so the parameters mentioned have low scatter. In this work a characteristic parameter of the gas explosion was considered to be in agreement with the battery test if it was within the 1σ-surrounding of the battery tests. In this respect, the target values obtained from the battery tests can be reproduced by a 5.1 ± 0.2 vol.-% ethylene/air mixture. The same target values are achieved with an acetylene concentration range of 4.3 ± 0.2 vol.-% to 4.6 ± 0.2 vol.-%. However, these suitable gas explosions have a different pressure duration and RPR_{max}. The acetylene/air mixture with 4.7 ± 0.2 vol.-%, which is very close to the concentration range mentioned above, provides a suitable RPR_{max} at a good agreement of the maximum pressure. Furthermore, the thermal load in a gas explosion at the appropriate maximum pressure is generally lower than in the battery tests. With regard to pressure duration, it should be noted that the static load is also tested in another test of the IEC 60079-1 standard. Therefore, it does not necessarily need to be included in the reproduction of the effects of TR with gas explosions.

The following extensions and improvements exist for future research. Firstly, there is a need in battery research to find a clear prediction the pressure load as a function of time during a TR of a lithium-ion battery. This would allow for a reduction of the observed scatter, enabling a more precise reproduction

of the load using gas explosions. Secondly, only one enclosure volume was analysed in this work. Due to the volume dependency of gas explosions, the validity of the results for other volumes should be determined. Thirdly, all experiments were limited to air at atmospheric pressure as the oxidiser. Future work could investigate to what extent a variation of the oxygen or nitrogen content provides a better match in terms of the maximum pressure rate or pressure duration.

Acknowledgements

The authors gratefully acknowledge funding by the German Ministry of Economics and Climate Action (grant no. 03TN0038A).

References

Bjerketvedt, D., Bakke, J. R., & van Wingerden, K. (1997). Gas explosion handbook. *Journal of Hazardous Materials*, *52* (1), 1–150. DOI: 10.1016/S0304-3894(97)81620-2

Chen, Y., Kang, Y., Zhao, Y., Wang, L., Liu, J., Li, Y., Liang, Z., He, X., Li, X. Tavajohi, N. & Li, B. (2021). A review of lithium-ion battery safety concerns: The issues, strategies, and testing standards. *Journal of Energy Chemistry*, *59*, 83–99. DOI: 10.1016/j.jechem.2020.10.017

Dubaniewicz, T. H., Zlochower, I., Barone, T., Thomas, R., & Yuan, L. (2021). Thermal Runaway Pressures of Iron Phosphate Lithium-Ion Cells as a Function of Free Space Within Sealed Enclosures. *Mining, Metallurgy & Exploration*, *38* (1), 539–547. DOI: 10.1007/s42461-020-00349-9

Feng, X., Ouyang, M., Liu, X., Lu, L., Xia, Y., & He, X. (2018). Thermal runaway mechanism of lithium ion battery for electric vehicles: A review. *Energy Storage Materials*, *10*, 246–267. DOI: 10.1016/j.ensm.2017.05.013

Hattwig, M., & Steen, H. (2004). *Handbook of explosion prevention and protection*. Weinheim: Wiley-VCH. ISBN: 978-3-527-30718-0

IEC 60079-1 (2014). *Explosive atmospheres – Part 1: Equipment protection by flameproof enclosures "d"*.

Korthauer, R. (2018). *Lithium-Ion Batteries: Basics and Applications*. Berlin, Heidelberg: Springer Berlin Heidelberg. DOI: 10.1007/978-3-662-53071-9

PTB & BAM (2024). Chemsafe: Database for safety characteristics in explosion protection. Retrieved from www.chemsafe.ptb.de

Spörhase, S., Brombach, F. M., Eckhardt, F., Krause, T., Markus, D., Küstner, B., & Walch, O. (2023). Untersuchungen zur Vergleichbarkeit der statischen und dynamischen Überdruckprüfung von druckfesten Kapselungen. *Forschung Im Ingenieurwesen*, *87* (2), 605–616. DOI: 10.1007/s10010-022-00604-z

Spörhase, S., Kianfar, A., Daragan, F. G., Essmann, S. & Markus, D. (2023). Thermal Runaway of Lithium-Ion Batteries in Flameproof Enclosures. *The 13th Annual Battery Safety Summit*. Tysons Corner

Wang, H., Xu, H., Zhang, Z., Wang, Q., Jin, C., Wu, C., Xu, C., Hao, J., Sun, L., Du, Z., Li, Y., Sun, L. & Feng, X. (2022). Fire and explosion characteristics of vent gas from lithium-ion batteries after thermal runaway: A comparative study. *ETransportation*, *13*, 100190. DOI: 10.1016/j.etran.2022.100190

Zhang, Q., Ma, Q. & Zhang, B. (2024). Approach Determining Maximum Rate of Pressure Rise for Dust Explosion. *Journal of Loss Prevention in the Process Industries*, 29, DOI: 10.1016/j.jlp.2013.12.002.

Experiments and Simulations of Hydrogen Dispersion in a 6-meter-long Channel

Mathias Henriksen [a], Hannibal Fossum [b], Espen Åkervik [b], Dag Bjerketvedt [a]

[a] Faculty of Technology, Natural Sciences and Maritime Sciences, University College of Southeast Norway, Kjølnes Ring 56, Porsgrunn, 3901, Norway
b Norwegian Defence Research Establishment (FFI), Oslo, Norway

E-mail: mathias.henriksen@usn.no

Abstract

Hydrogen has become increasingly popular as an alternative fuel and for storing energy. However, its wide flammability range and low ignition energy pose significant safety challenges, requiring a thorough understanding of its behavior in confined spaces. This study investigates hydrogen dispersion in a 6-meter-long channel by means of experimental and numerical simulations. The experimental setup involved twenty-nine hydrogen sensors to monitor dispersion at various mass flow rates. The data collected aimed to validate Computational Fluid Dynamics (CFD) models, particularly the OpenFOAM software's buoyantReactingFoam solver. From the experimental results, a quasi-steady state concentration was reached within 30 seconds of the release, and a slight variation between parallel experiments was seen. Furthermore, the experiments revealed a consistent increase in hydrogen concentration with increased mass flow rates, as expected. The CFD simulations were compared qualitatively with averaged concentration plots and quantitatively with a statistical comparison of all sensors. Both comparisons showed that the solver predicted the hydrogen concentration was in good agreement with the experimental results. The numerical simulations complemented the experiments, addressing limitations in sensor coverage and providing insights into hydrogen dispersion patterns. This research contributes to hydrogen safety. It offers a comprehensive dataset for CFD model validation and demonstrates the CFD solver's applicability to industrial explosion scenarios.

Keywords: *Hydrogen, Dispersion, OpenFOAM, CFD, Gravity Current*

1. Introduction

Over the past decade, hydrogen (H_2) has gained popularity as a clean alternative to fossil fuels. It is used in technologies like fuel cells and electrolysis, particularly for decarbonizing heavy-duty vehicles, the shipping industry, and metal and ammonia production (Hassan et al., 2023). However, hydrogen presents safety challenges due to its wide flammability range (4% to 75% hydrogen in air) and low ignition energy (0.02 mJ) (Cheikhravat et al., 2012; Ono et al., 2007). Being the least dense gas, hydrogen's accidental or planned release requires careful consideration. In hydrogen accidents, immediate ignition may lead to a jet fire scenario, while delayed ignition can result in combustible hydrogen-air clouds. Understanding hydrogen dispersion in confined spaces is crucial for effective safety measures and to reduce risk (Henriksen et al., 2017; Yang et al., 2021).

Lacome et al. (Lacome et al., 2011) studied the dispersion of helium and hydrogen in an 80 m³ chamber with a small opening, observing a clear stratification of hydrogen in the upper part of the room for sub-sonic releases. De Stefano et al. (De Stefano et al., 2019) studied hydrogen dispersion in a closed chamber with varying release points, rates, and durations, finding that the release rate significantly impacts the mixing of hydrogen and air. Similar experiments and observations were found by Denisenko et al. (Denisenko et al., 2019, 2009). Liu et al. (Liu et al. 2023) studied the

dispersion of helium with natural and forced ventilation in a channel open at both ends, noting a concentration gradient from the jet to the opening with natural ventilation. The height of the gravity current of helium also showed a concentration gradient.

This paper presents an experimental and numerical study of hydrogen dispersion in a 6 m-long channel at various mass flow rates. Twenty-nine hydrogen sensors were mounted inside the channel to characterize hydrogen dispersion. The main goal of this experimental campaign was to generate a broad range of quantitative data on large-scale naturally ventilating hydrogen dispersion that was well-suited for validating far-field dispersion prediction of CFD models. With a validated CFD model, the numerical results can give great insight into dispersion, which could not be explained adequately with experimental measurements due to a limited number of sensors. The hydrogen inlet was placed at the top of the channel, releasing the hydrogen downward into the channel. Although a downward jet is uncommon in release and dispersion studies, it is not an unrealistic leakage scenario, considering that pipelines in infrastructure, industrial plants, and ships are typically mounted in the ceiling. The number of sensors relative to the size of the channel, a downward-facing jet, the natural ventilation of hydrogen (and not helium), and the use of open-source CFD software make these experimental and CFD results unique.

2. Experiments

This section is divided into two sub-sections: the experimental setup and the OpenFOAM numerical setup.

2.1. Experimental Setup

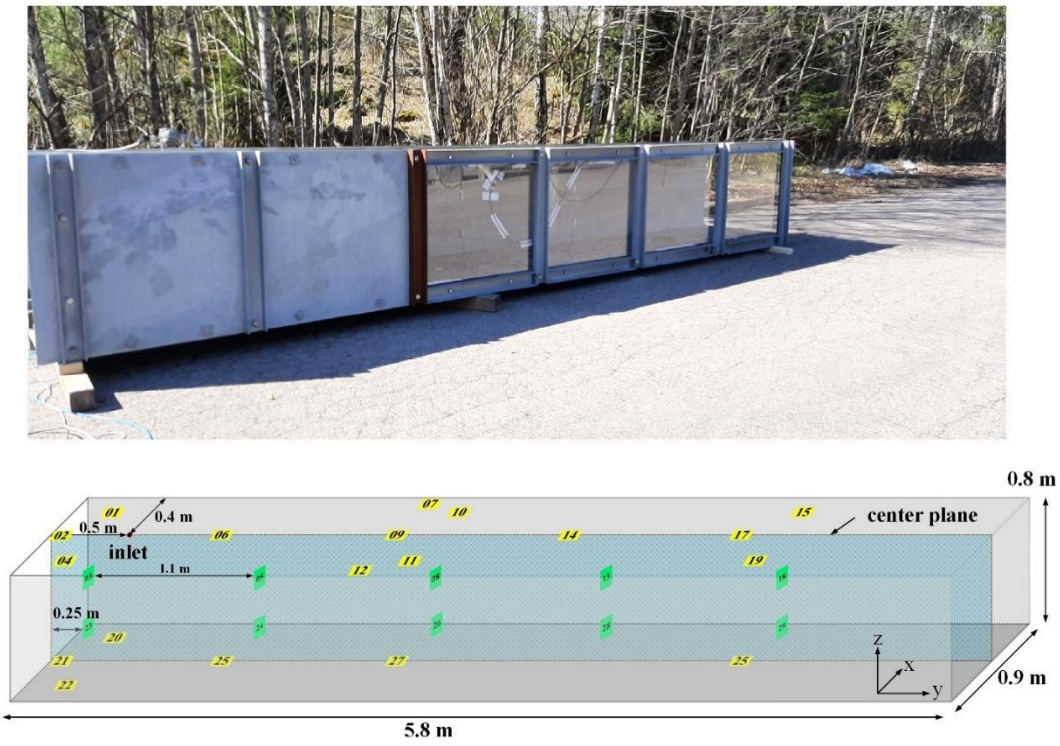

Figure 2-1. A photo and illustration of the 6-meter-long channel, including the placement of the hydrogen sensors.

Figure 2-1 shows a photo and an illustration, which includes the placement of the hydrogen sensors of the 6 m long steel channel used in the experiments. The channel has also been described in a previous study by Åkervik et al. (Åkervik et al., 2021). Inside the channel, the dimensions were as follows: length (y-axis) of 5.8 meters, width (x-axis) of 0.9 meters and height (z-axis) of 0.8 meters. Hydrogen was injected from the top, 0.5 meters away from the closed end and 0.4 meters from the

side wall, and the circular inlet had a diameter of 4.6 mm. A Bronkhorst Coriolis mass flow meter measured and controlled the hydrogen mass flow rate. The hydrogen release lasted from 30 to 120 seconds, depending on the time it took for the hydrogen concentration to stabilize. We calculated the average hydrogen concentration using data from the last 30 seconds of the release. Remarkably, this short duration aligns well with the overall release period, making it consistent for assessing mass flow rates. Table 1 lists the experiments with the average hydrogen mass flow rate.

A total of 29 hydrogen concentration sensors (XEN-5320 Xensors) were strategically placed in the channel, each with an accuracy of ±1% and a logging frequency of 3 Hz. Specifically, 13 sensors were on the channel ceiling, five of which were along the center plane. Additionally, ten sensors were positioned along the centerline: five at 0.52 meters from the bottom and the remaining five at 0.27 meters from the bottom. Finally, six sensors were located on the channel floor, with four of them aligned with the centerline.

Table 1. List of Experiments and CFD case, with Test ID, average mass flow rates, standard deviation of the mass flow, Corresponding CFD cases, and the mass flow rate in the CFD simulation

Test ID	Release duration (s)	Average Hydrogen Mass Flow Rate (g/s)	Standard Deviation (SD) of the Mass Flow Rate (g/s)	Corresponding CFD Case	Hydrogen Mass flow Rate in the CFD Case (g/s)
Test 01	60	0,48	0,002	Case 01	0.47
Test 02	120	0,48	0,001	Case 01	0.47
Test 03	30	0,48	0,002	Case 01	0.47
Test 04	60	0,36	0,010	None	[-]
Test 05	60	0,74	0,007	Case 02	0.72
Test 06	60	0,58	0,003	None	[-]
Test 07	60	0,58	0,003	None	[-]
Test 08	60	1,27	0,002	Case 03	1.25

2.2. OpenFOAM, Numerical Setup

The buoyantReactingFoam solver, which is part of the OpenFOAM v10 software (Greenshields, 2022; Weller et al., 1998) official release, was used for all simulations. The buoyantReactingFoam solver is suited for transient multi-species turbulent compressible flow and includes an enhanced treatment of buoyancy.

The time integration was discretized using the first-order forward Euler scheme. For the gradient and Laplacian/diffusion terms, the second-order linear scheme was used. Furthermore, two different second-order schemes were used for the advection schemes, Linear-Upwind Stabilized Transport (LUST) for momentum transport and limited-linear for all other scalar transport equations. The discretized equations are solved using the PIMPLE algorithm, which combines PISO (Pressure Implicit with Splitting Operators) and SIMPLE (Semi-Implicit Method for Pressure-Linked Equations).

The sub-grid LES turbulence model WALE, published by Nicoud and Ducros (Nicoud and Ducros, 1999), was used. The WALE turbulence model is based on the square of the velocity gradient tensor and has a near-wall scaling function without requiring a dynamic procedure. Moreover, the Sutherland equation (Sutherland, 1893) and the JANAF/NASA polynomial (McBride et al., 1993)

equations were used for modeling the transport and thermodynamic properties. The transport and thermodynamic model coefficients were generated using the *mech2Foam* code (Henriksen and Bjerketvedt, 2021) and the reaction mechanism by GRI-Mech 3.0 (Smith et al., 1999)

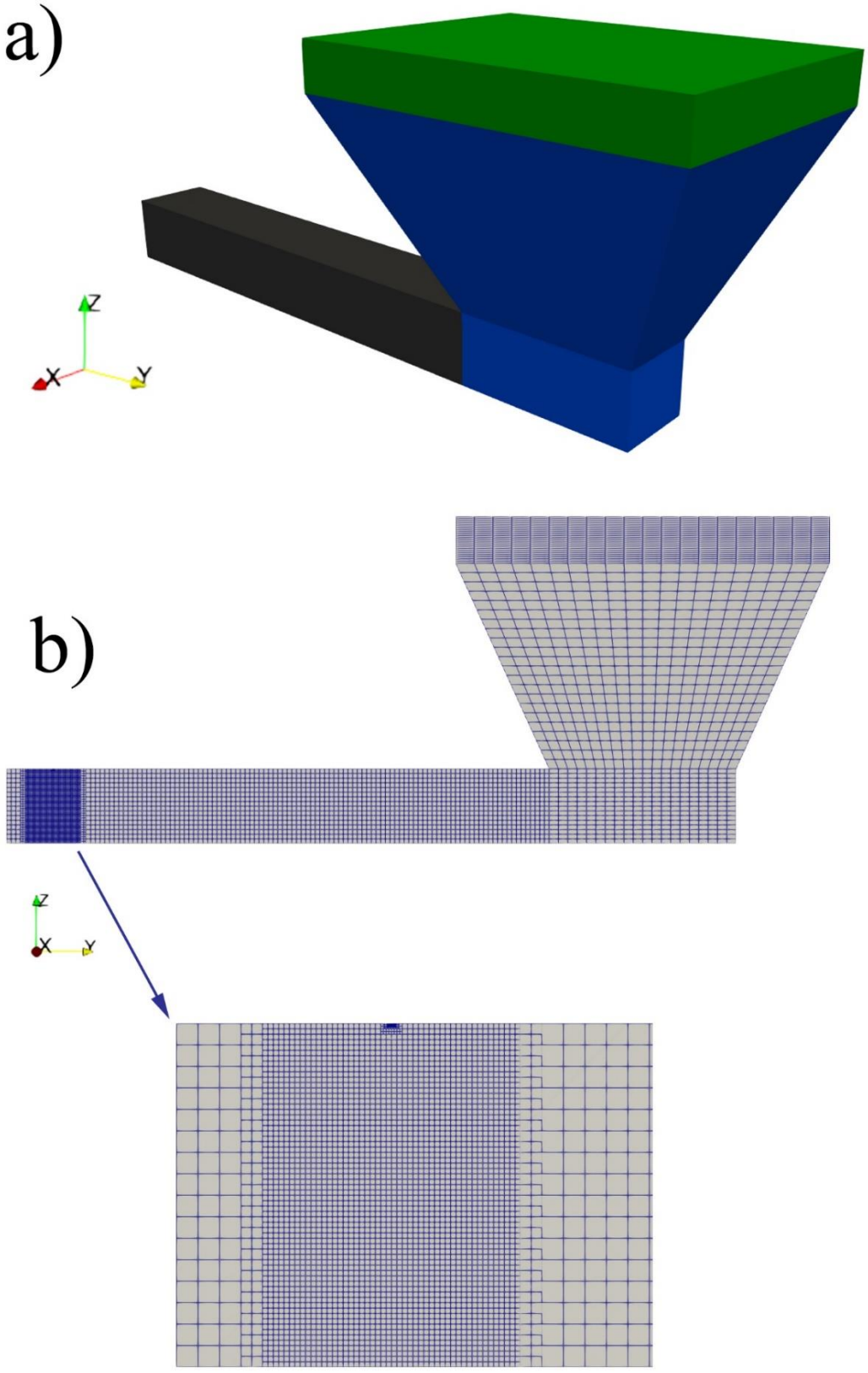

Figure 2-2. Images of the computational domain used in the simulations. a) The top-front view shows the three main regions in the mesh. b) Two x-plane slices of the computational domain.

Figure 2-2 shows three images of the geometry and computational domain. Figure 2-2 a) illustrates that the computational domain was divided into three main sections: the channel, still atmosphere, and wind atmosphere. The channel section represents the physical channel, with wall boundaries and the same dimensions as described in sub-section 2.1. In the channel section, the hexahedral cell sizes vary from 0.39 mm (near the inlet) to 50 mm (far from the inlet). A smaller cell size was used near the hydrogen inlet to better resolve the actual inlet surface area. The still atmospheric section has open boundaries, where the initial velocity zero. In contrast, the wind atmospheric section has an air inlet condition with a velocity of 1 m/s in the positive x direction. This wind atmospheric section was included to vent at the hydrogen of the internal domain, thus avoiding the accumulation of hydrogen in the upper part of the atmospheric section.

Finally, six CFD cases were simulated with different mass flow rates. Other than changing the inlet conditions, mass flow rate, and kinetic energy, all other initial conditions, boundary conditions, numerical mesh, schemes, and matrix solvers were identical. Table 2 summarizes the initial and boundary conditions used in all the simulations.

Table 2. List of variables with the applied wall and open boundary conditions.

Variable	Inlet Conditions	Wall boundary	Open boundary
species Air	fixed value (0 - H_2 inlet) fixed value (1 - "wind" inlet)	zero gradient	zero gradient outlet; fixed value inlet of (1)
species H2	fixed value (1 - H_2 inlet fixed value (0 - "wind" inlet)	zero gradient	zero gradient outlet; fixed value inlet (0)
Velocity (U)	constant mass flow rate (H_2 inlet), constant velocity ("wind inlet")	zero velocity at the wall (noSlip)	zero gradient outflow flux inlet value based on flux normal to the boundary surface
Temperature (T)	fixed value (293 K)	fixed value (293 K)	zero gradient outlet; fixed value inlet (273 K)
Pressure (p)	constant total pressure (101.3 kPa)	calculated based on hydrostatic pressure	calculated based on hydrostatic pressure
Static Pressure (p_rgh)	fixed value (0)	set pressure gradient according to velocity boundary conditions	calculated based on hydrostatic pressure
Subgrid turbulent kinetic energy (k)	Fixed value (Case dependent value)	zero gradient	zero gradient outlet; fixed value inlet
Turbulent viscosity (nut)	calculated based on the turbulent kinetic energy	calculated based on velocity using Spalding's Law	calculated based on the turbulent kinetic energy
Turbulent thermal diffusivity (alphat)	calculated based on the turbulent viscosity	calculated based on the turbulent viscosity for compressible flow	calculated based on the turbulent viscosity

3. Results and discussion

3.1. Experimental Results

Figure 3-1 shows an example (Test 06) of the experimentally measured time history of the hydrogen concentration in the channel's centerline. As the concentration profiles in Figure 3-1 show, a quasi-steady concentration is reached early in the release, approximately after 20-30 seconds, which was the case in all the experiments. Therefore, using the last 30 seconds of release to evaluate the average sensor concentrations and flow rates is justified by the concentration profile and the low fluctuations in mass flow rate (low SD in Table 1) during the release.

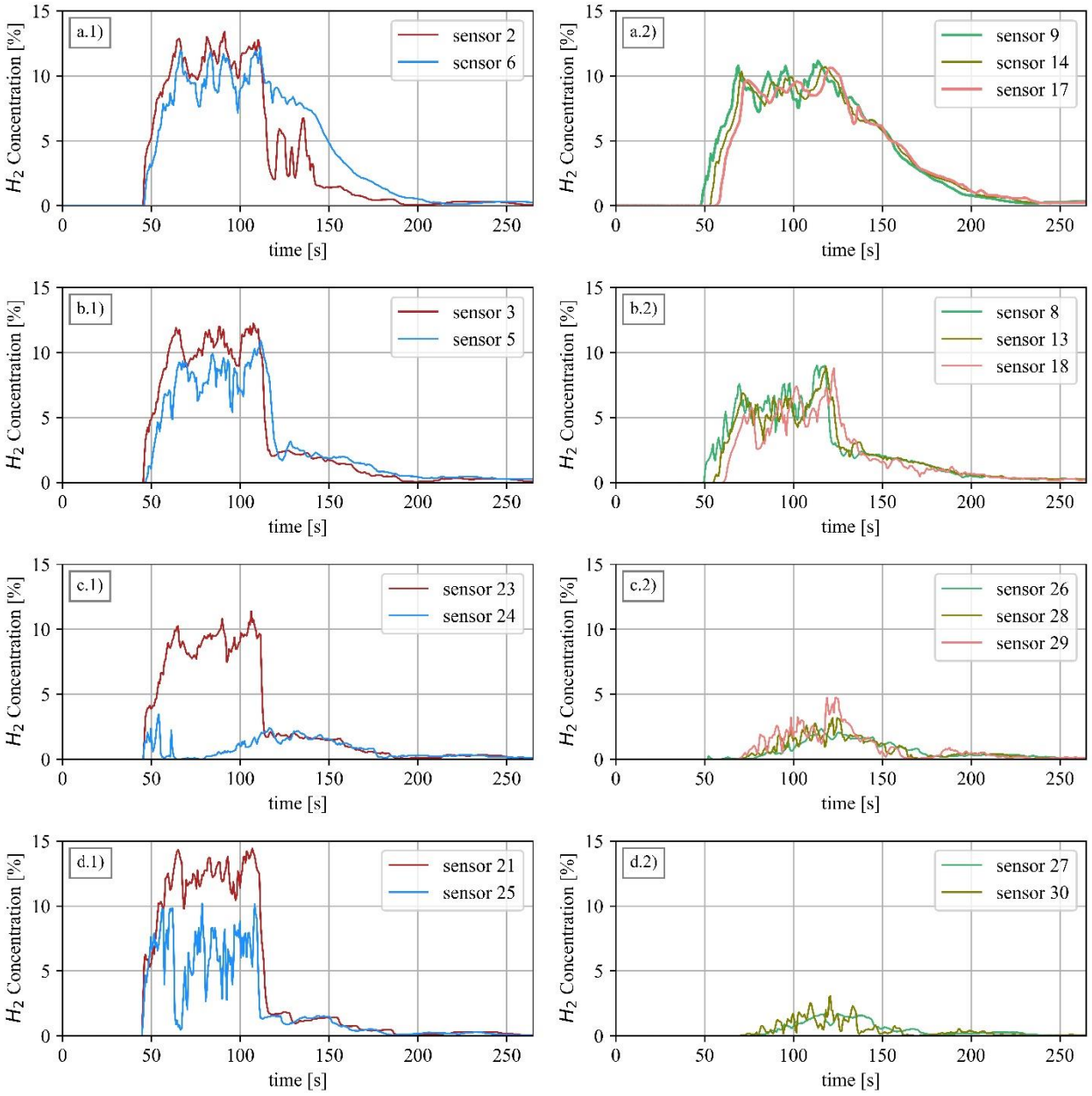

Figure 3-1. Hydrogen concentration as a function of time. a.1): Top sensors in the inner zone; a.2): Top sensors in the outer zone, b.1): mid-high sensors in the inner zone; b.2): mid-high sensors in the outer zone, c.1): mid-low sensors in the inner zone; c.2): mid-low sensors in the outer zone, d.1): bottom sensors in the inner zone; d.2): bottom sensors in the outer zone

The left column in Figure 3-1 (a.1 to d.1) represents the inner zone where most mixing occurs, resulting in a more uniform hydrogen concentration in the z-direction. This can be seen by comparing sensors 2, 3, 23, and 21 which are placed in descending height. The right column in Figure 3-1 (a.2

to d.2) represents the outer zone, and shows a distinct concentration gradient in the z-direction but similar concentrations at the same height (at equal x and y axis). Based on the concentration measurements alone, it is not clear where the interface between the inner and outer zones is located somewhere in between. Analyzing the CFD results showed that the inner and outer zone interface is measured to be within 0.7 m and 1.3 m from the closed end of the channel, depending on the mass flow rate.

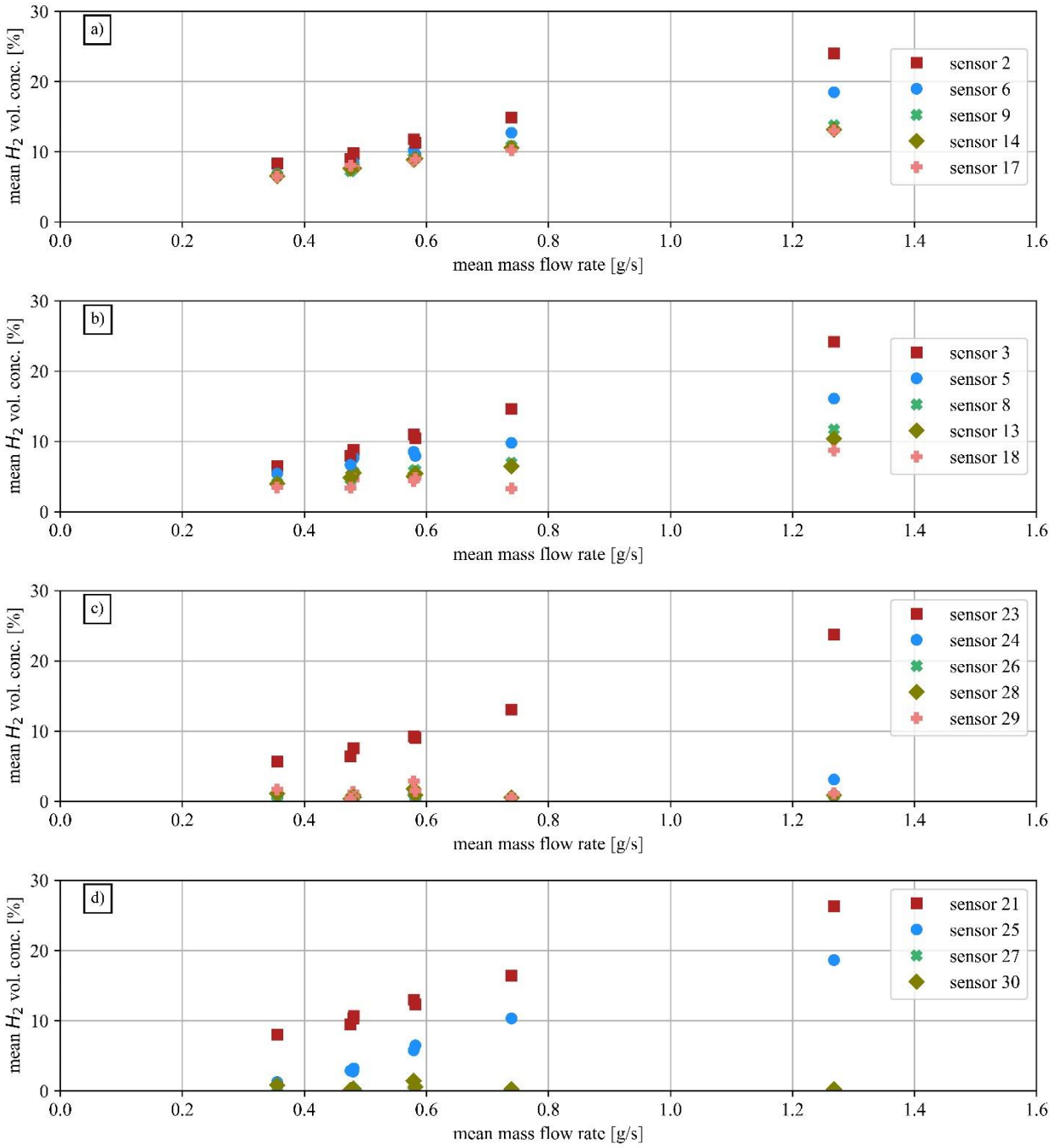

Figure 3-2 The averaged centerline hydrogen concentrations as a function of each experiment's averaged mass flow rate. a): Top sensors, b): mid-high sensors, c): mid-low sensors, d): bottom sensors

Figure 3-2 shows the average centerline hydrogen concentration as a function of each experiment's average mass flow rate. The sensor position in the y-direction for each graph is plotted in order, closest to the back wall (red square marker) and outwards of the channel (light coral plus marker). Some of the concentration measurements are below the hydrogen sensor accuracy of ±1\%. If those

are removed measurements, the remaining sensors have an average standard deviation of the mean of 0.67% (maximum 2.96%). This relatively low standard deviation on the hydrogen concentration measurement indicates that the hydrogen concentration did not fluctuate too much in the time frame in which the average hydrogen concentration for each experiment was evaluated.

A drawback in these experiments is that the wind conditions in effects were uncontrolled. The experiments were performed in calm to light air wind conditions, but some degree of gustiness was observed by means of a hand-held wind sensor. These gust events most probably affected the sensors closest to the open end of the channel. Signs of wind in the hydrogen measurements can be seen as small valleys in the upper sensors and peaks in the lower sensors. The dip in hydrogen concentration seen in sensor 18 for Test 05 (mass flow rate = 0.74 g/s) in Figure 3-2 b) is caused by a gust.

The overall low standard deviation and the hydrogen sensors' capability to capture the transient behavior inside the channel with a logging frequency of 3 Hz make this data set highly suitable for validating CFD models. Although some wind can be observed in some of the experiments, its effect is usually easy to detect and only slightly influences two out of 29 sensors. Furthermore, several parallel experiments are also used to test the accuracy and validity of the experimental setup. Figure 3-2 shows that there is minimal variation between parallel experiments.

As expected, hydrogen concentration increases as the mass flow increases. However, as the mass flow increases above 0.6 g/s, the concentration gradient in the y-direction increases in the inner zone, while the concentration gradient in the outer zone is still relatively constant in the y-direction. Furthermore, the difference in concentration between the inner and outer zones also increases significantly, which results in a factor two difference in concentration between the innermost roof sensor (sensor 2) and the three outermost sensors (9, 14, and 17) in the high mass flow rate experiment (Test 08 with 1.27 g/s). In this well mixed configuration, the innermost region can be thought of as a reservoir that fuels a gravity current that ventilates the channel (Sommersel et al., 2009). This high concentration of hydrogen near the source of a leak can cause severe damage if the gravity current finds an ignition source.

3.2. Numerical Results

Figure 3-3 shows the qualitative comparison of the centerline concentration in the experimental (colored markers) and numerical results (hollow black markers). Equal marker shapes represent the same sensors in the experiments and the CFD cases, and as in Figure 3-2, the markers are ordered from closest to the end wall and outwards. Figure 3-3 shows that the overall concentration trend in the numerical results agrees well with the experimental results. However, apparent discrepancies between the numerical and experimental results can be seen when comparing specific sensors. For example, for mass flows above 0.7 g/s, there is a relatively large discrepancy in the concentration at sensors 6, 5, and 24 when comparing the numerical and experimental results. These three sensors are located near the interface or transition from the inner and outer zones, which may not be in the position in the simulation and the experiments. The different positions of the transition from the inner mixing zone to the outer ventilation zones between the experiments and simulations are possibly due to the hydrogen jet and mixing not being adequately resolved. In order to accurately predict the far-field dispersion of hydrogen, our limited computational resources meant that we had to sacrifice the resolution in the mixing zone near the hydrogen jet. If we were to do it the other way around and focus on resolving the jet, we would have to decrease the resolution in the outer part of the domain. This would lead to excess numerical diffusion and poor performance in terms of overall concentration predictions.

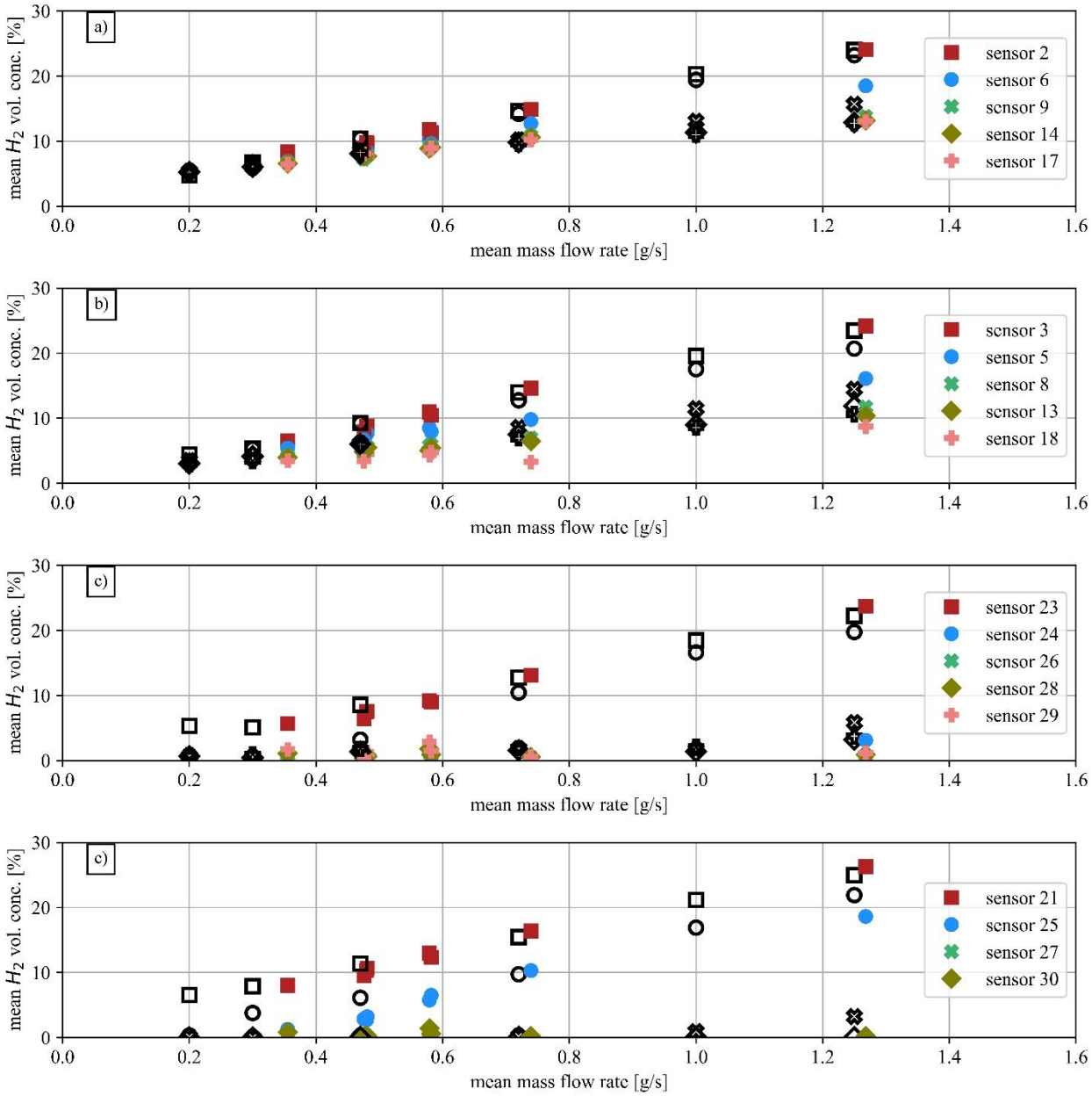

Figure 3-3. A comparison of the averaged centerline hydrogen concentrations as a function of the averaged mass flow rate, a): Top sensors, b): mid-high sensors, c.1): mid-low sensors; d): bottom sensors

For a quantitative comparison of the numerical and experimental results, the mean geometric bias (MG) and the mean geometric variance (VG) were computed for all the averaged concentrations for each experiment with a corresponding CFD case (Chang and Hanna, 2004; Hanna et al., 1993). Figure 3-4 shows that most of the simulations are within or close to the recommended criteria of MG between 0.5 and 2 and VG below 1.6. Only Test 03 is well above the VG criteria of 1.6. Surprisingly, Test 03 is one of the three parallel experiments at 0.47 g/s, and the two other parallel experiments (Test 01 and Test 02) are well within the recommended model performance criteria. The total release time of 30 seconds and the average time frame of 10 seconds in Test 03 is shorter than in all the other experiments. Since the numerical results agree well with Test 01 and 02, which have the same mass flow rate as Test 03, it is most likely that Test 03 has not reached a quasi-steady state in the entire channel. Thus, deviating from the numerical results.

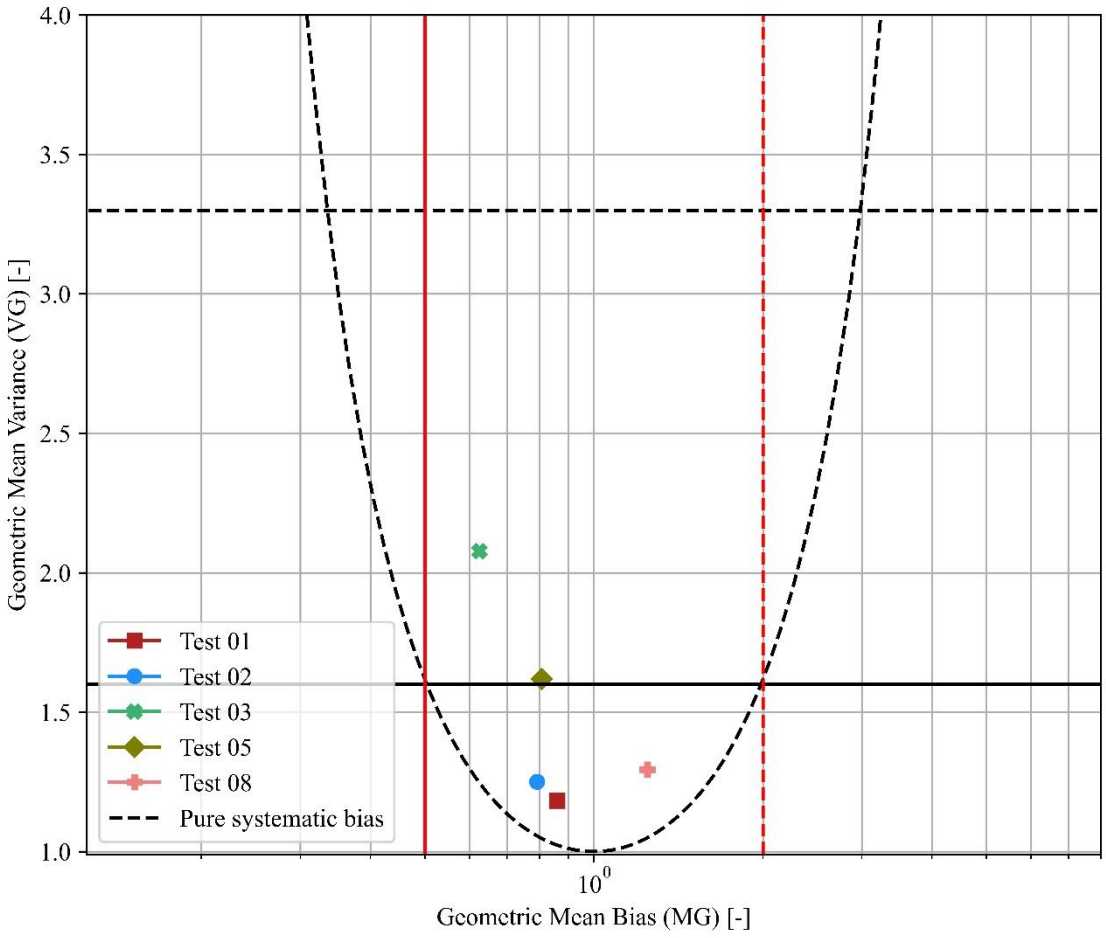

Figure 3-4 The mean geometric bias (MG) and the mean geometric variance (VG) for the hydrogen concentration for all sensors in each experiment and the corresponding CFD Case.

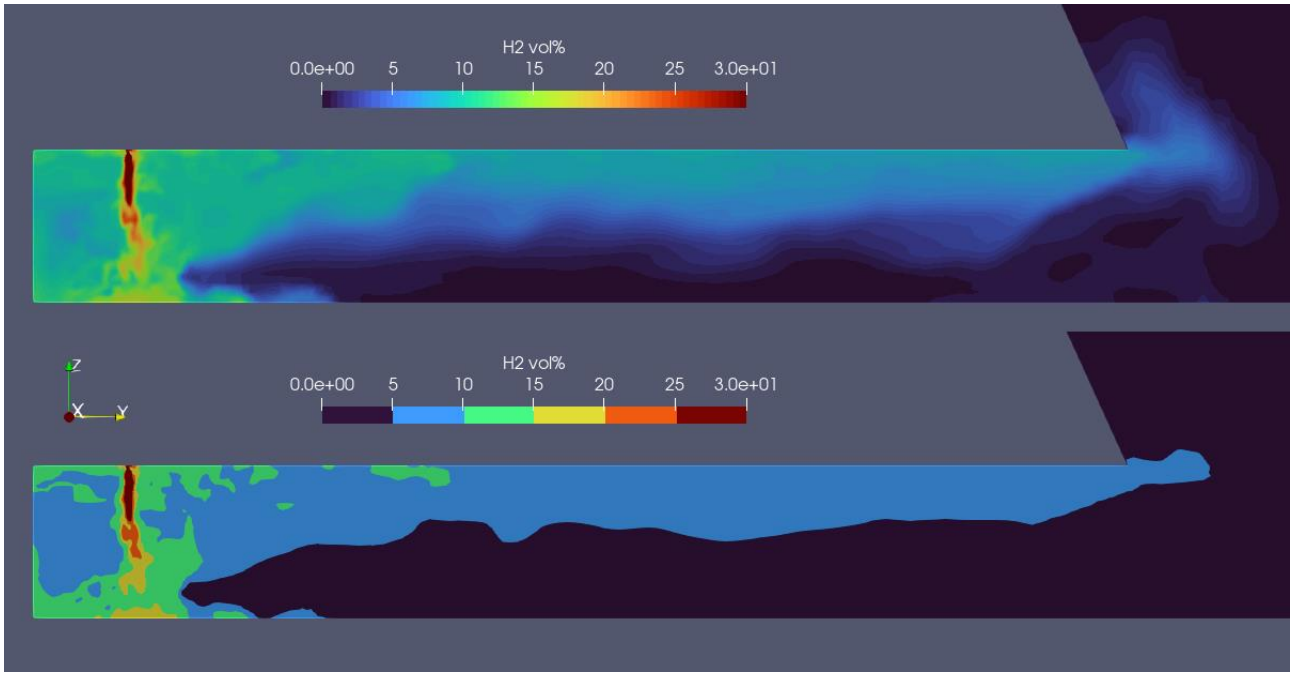

Figure 3-5. Two images of the same CFD simulations, with different discretization of the color gradients of the hydrogen concentration.

Figure 3-5 shows two images of the CFD simulation of Test 06, with a mass flow rate of 0.58 g/s, 120 seconds after the release was initiated. The difference between the two images is only the color discretization of the hydrogen concentration. In the upper image, the color discretization is set to 60, resolving the concentration at 0.5%. The lower image has a color discretization of 6, resolving the concentration in the range 0 to 30% vol. at 5%. Figure 3-5 shows that hydrogen is vented out of the top of the channel as a light fluid gravity current, which approximately fills half the channel's height (Gröbelbauer et al., 1993; Sommersel et al., 2009). Moreover, Figure 3-5 also shows that the overall concentration is higher in the inner and outer zones. These results agree well with what we can deduce from the sensor measurements shown in Figure 3-1 and Figure 3-2.

Finally, as earlier discussed, the discrepancies between simulation and experimental results for sensor 24, especially seen in the largest mass flow rate in Figure 3-3. This sensor is close to the pocket of air that stretches towards the hydrogen jet. Within the proximity of the air pockets crests, the hydrogen concentration varies significantly depending on the direction, with a very steep gradient towards the jet. The variation in hydrogen concentration in this region is much higher locally than in other places in the channel. Slight differences in the placement of this concentration gradient can cause significant deviations between numerical and experimental results, which most likely leads to the discrepancy with sensor 24.

4. Conclusions

In this study, hydrogen dispersion in a 6-meter-long channel at various mass flow rates has been analyzed numerically and experimentally. The eight experiments provide valuable quantitative data on hydrogen dispersion at various mass flow rates, which is crucial for CFD model validation. Overall, the numerical results were in good agreement with the experimental results. However, discrepancies in sensor readings near the interface or transition between the inner and outer zones suggest that not all the characteristics are captured. In dispersion simulations, it is difficult to accurately resolve both the near and far field characteristics, such as the hydrogen jet and gravity current.

This work contributes to the broader understanding of hydrogen safety by providing a dataset that captures the transient behavior of hydrogen dispersion and shows that the buoyantReactingFoam solver represent an appropriate tool for these types of scenarios. Furthermore, the validity of the experimental setup is tested through parallel experiments, ensuring the results' reliability when compared with CFD simulations. The insights gained from this research are essential in implementing safety measures and risk assessment for hydrogen infrastructure, thereby supporting the safe adoption of hydrogen as a clean energy carrier.

Acknowledgments

This work was performed within MoZEES, a Norwegian Centre for Environment-friendly Energy Research (FME), co-sponsored by the Research Council of Norway (project number 257653) and 40 partners from research, industry and public sector.

References

Åkervik, E., Fossum, H.E., Henriksen, M., Bjerketvedt, D., 2021. Measurements of hydrocarbon flame propagation in a channel (Technical No. 21/00790). Norwegian Defence Research Establishment.

Chang, J.C., Hanna, S.R., 2004. Air quality model performance evaluation. Meteorol Atmos Phys 87. https://doi.org/10.1007/s00703-003-0070-7

Cheikhravat, H., Chaumeix, N., Bentaib, A., Paillard, C.-E., 2012. Flammability Limits of Hydrogen-Air Mixtures. Nuclear Technology 178, 5–16. https://doi.org/10.13182/NT12-A13543

De Stefano, M., Rocourt, X., Sochet, I., Daudey, N., 2019. Hydrogen dispersion in a closed environment. International Journal of Hydrogen Energy 44, 9031–9040. https://doi.org/10.1016/j.ijhydene.2018.06.099
Denisenko, V.P., Kirillov, I.A., Korobtsev, S., Nikolaev, I.I., 2009. Hydrogen-Air Explosive Envelope Behaviour in Confined Space at Different Leak Velocities. Presented at the International Conference on Hydrogen Safety.
Denisenko, V.P., Kirillov, I.A., Korobtsev, S.V., Nikolaev, I.I., 2019. Hydrogen Distribution in Enclosures: On Distinction Criterion Between Quasi-Homogeneous Mixing and Stratification Modes. Presented at the International Conference on Hydrogen Safety.
Greenshields, C., 2022. OpenFOAM v10 User Guide. The OpenFOAM Foundation, London, UK.
Gröbelbauer, H.P., Fanneløp, T.K., Britter, R.E., 1993. The propagation of intrusion fronts of high density ratios. J. Fluid Mech. 250, 669–687. https://doi.org/10.1017/S0022112093001612
Hanna, S.R., Chang, J.C., Strimaitis, D.G., 1993. Hazardous Gas Model Evaluation with Field Observations. Atmospheric Environment 27A, 2265–2285. https://doi.org/10.1016/0960-1686(93)90397-H
Hassan, Q., Algburi, S., Sameen, A.Z., Jaszczur, M., Salman, H.M., 2023. Hydrogen as an energy carrier: properties, storage methods, challenges, and future implications. Environ Syst Decis. https://doi.org/10.1007/s10669-023-09932-z
Henriksen, M., Bjerketvedt, D., 2021. mech2Foam - Generating transport, combustion, and thermodynamic properties for the CFD solver XiFoam. https://doi.org/10.23642/USN.13721134.V4
Henriksen, M., Bjerketvedt, D., Vaagsaether, K., Gaathaug, A.V., Skjold, T., Middha, P., 2017. Accidental hydrogen release in a gas chromatograph laboratory: A case study. International Journal of Hydrogen Energy 42, 7651–7656. https://doi.org/10.1016/j.ijhydene.2016.05.299
Lacome, J.M., Jamois, D., Perrette, L., Proust, C.H., 2011. Large-scale hydrogen release in an isothermal confined area. International Journal of Hydrogen Energy 36, 2302–2312. https://doi.org/10.1016/j.ijhydene.2010.10.080
Liu, H., Salehi, F., Abbassi, R., Lau, T., Heng Yeoh, G., Mitchell-Corbett, F., Raman, V., 2023. Experimental and numerical analysis of low-density gas dispersion characteristics in semi-confined environments. Journal of Loss Prevention in the Process Industries 105184. https://doi.org/10.1016/j.jlp.2023.105184
Ono, R., Nifuku, M., Fujiwara, S., Horiguchi, S., Oda, T., 2007. Minimum ignition energy of hydrogen–air mixture: Effects of humidity and spark duration. Journal of Electrostatics 65, 87–93. https://doi.org/10.1016/j.elstat.2006.07.004
Smith, G.P., Golden, D.M., Frenklach, M., Moriarty, N.W., Eiteneer, B., Goldenberg, M., Bowman, C.T., Hanson, R.K., Song, S., Jr, W.C.G., Lissianski, V.V., Qin, Z., 1999. GRI-MECH 3.0.
Sommersel, O.K., Bjerketvedt, D., Vaagsaether, K., Fannelop, T.K., 2009. Experiments with release and ignition of hydrogen gas in a 3m long channel. International Journal of Hydrogen Energy 34, 5869–5874. https://doi.org/10.1016/j.ijhydene.2009.02.058
Weller, H.G., Tabor, G., Jasak, H., Fureby, C., 1998. A tensorial approach to computational continuum mechanics using object-oriented techniques. Comput. Phys. 12, 620. https://doi.org/10.1063/1.168744
Yang, F., Wang, T., Deng, X., Dang, J., Huang, Z., Hu, S., Li, Y., Ouyang, M., 2021. Review on hydrogen safety issues: Incident statistics, hydrogen diffusion, and detonation process. International Journal of Hydrogen Energy 46, 31467–31488. https://doi.org/10.1016/j.ijhydene.2021.07.005

Numerical modelling and validation for a methane leak from a buried pipeline

Shuvam Mohanty, Sile Brennan & Vladimir Molkov

Hydrogen Safety Engineering and Research Centre (HySAFER), University of Ulster, Shore Road, Newtownabbey, BT37 0QB, Northern Ireland, UK

E-mail: s.mohanty@ulster.ac.uk

Abstract

The release of methane from buried pipelines poses potential risks to humans and the environment. Prediction of the flammable methane-air envelope from a buried leak is important for safety recommendations and the estimation of hazard distances for pipelines. This work describes the development and validation of a computational fluid dynamics model capable of simulating an underground gas pipeline leak. Three-dimensional, unsteady, incompressible flow of methane through a sand layer to the atmosphere was simulated. The sand was considered as a porous medium. A species transport model was used for methane diffusion in sand. The dispersion of a buried methane, leak from a 4 mm and 2 mm diameter leak hole, and pipeline pressure of 300 kPa is presented. Validation of the model against experimental data for the initial stages of the leak is demonstrated. The numerical simulations of the first 60 s of the leak demonstrate a high degree of accuracy in capturing the transient behaviour of methane dispersion when compared with experiment. The model offers insights into the factors influencing the spread and dilution of the flammable cloud, thus serving as a reliable predictive tool for hazard distance estimation. The innovative aspect of this model lies in its unique portrayal of the flammable cloud development that is often overlooked in current modelling approaches. The model can be used to underpin inherently safer design of buried pipelines and devising emergency response procedures to gas leaks.

Keywords: *natural gas, underground pipeline leakage, diffusion range, leakage rate*

1. Introduction

In recent times, the worldwide need for natural gas has risen markedly, driven by its environmentally friendly attributes, high reliability and efficiency (Rui et al., 2017). As a more environmentally responsible choice, natural gas produces less carbon dioxide than coal and oil, thereby playing a vital role in the shift to a low – carbon economy. Transportation is a key aspect of the natural gas industry, with the majority of gas being moved through an extensive network of pipelines installed beneath the ground. However, leakage incidents from these pipelines have garnered attention for their possible detrimental effects on public health, environmental integrity and economic stability. Any size of gas leak can change soil characteristics, release combustible gases into the air and in extreme cases, lead to disastrous outcomes (Brand, 2006; EGIG, 2018). Buried leaks from the distribution network typically occur at pressures which are unlikely to cause cratering of the ground. Instead, the leak has potential to track beneath the ground surface. Buried leaks of this nature are the focus of this study.

Atkinson et al. (2019) conducted an analysis involving eight distinct generic flow regimes including methane, hydrogen, and propane–air mixtures, representing various scenarios under both open and covered surfaces. Their primary focus was on determining the distance travelled by the flammable cloud, particularly exploring how this distance changes when substituting hydrogen for methane. This information proved essential in the development of a quantitative risk assessment (QRA) for hydrogen supply. In uncovered environments, through the duct at P=0.0075 MPa, gauge, hole

diameter 12 mm and at a depth of 600 mm, both hydrogen and methane tend to disperse within a few meters of the release point. However, the results have shown that for a leak of 12 mm diameter, the substitution of NG by hydrogen extends the hazard distance for pressures of 50–300 Pa. It is important to note that the experimental data provided by the authors is qualitative, it lacks quantitative measured values for model validation. Indeed, there is an absence across the literature of quantifiable data for model validation, when considering buried leaks. Recently, Liu et al. (2021) investigated minor leaks from buried gas pipelines considering 100% methane. They estimated the leakage flow rate and the range of methane diffusion outside the pipeline. Thus, these experiments are chosen for validation of the developed CFD model. Zhu et al. (2023) experimentally investigated hydrogen-blended natural gas in buried pipelines at high pressure. The diffusion of hydrogen blended natural gas was measured and it was found that the leakage behaviour varies with the proportion of the hydrogen in the mixture. These findings helped in understanding the dispersion behaviour of hydrogen-blended natural gas from small leak holes; however, there is a lack of clarity on the type of soil used and its moisture content.

The progression of computational fluid dynamics (CFD) has been instrumental in accurately predicting gas dispersion dynamics in diverse environments. Ebrahimi-Moghadam et al., (2016, 2018) advanced this field with two dimensional approach for urban gas pipeline leak estimation and later enhanced it with 3D models for buried pipelines, achieving an error margin of ±7%. Bezaatpour et al. (2020) examined gas leaks from low pressure buried pipelines using three dimensional steady state simulations in COMSOL Multiphysics, considering soil as a layered and anisotropic porous medium. Their findings emphasized the significance of soil layer properties and gradients on leakage dynamics. Liu et al. (2021) conducted CFD simulations to develop correlations for estimating methane and air leakage rates from underground pipes across various pressure, considering soil as an isotropic porous medium. Their investigation revealed the influence of factors like pressure, hole diameter, soil depth and porosity, with the simulations aligning closely with experimental results, showing a numerical error range of 7% to 15%. Bagheri and Sari (2022) conducted a parametric study using CFD, considering a range of influential factors including pipeline pressure (0.2-10 MPa gauge), pipe diameter (4-56 *inches*), leak hole diameter (2-40 mm), and different soil types. Their scenarios are representative of both distribution and transmission pipeline systems; however, it is important to note that validation for all the simulations against experimental data was not provided. Overall, there is limited data in the literature quantifying gas dispersion from a buried leak in the gas network. There is a need for a validated numerical model which can be applied to simulate buried leaks.

This study enhances existing CFD model by introducing a novel combination of three-dimensional, unsteady simulations compared against new experimental data, with a detailed analysis of leak hole impacts on gas dispersion. Our approach advances previous methodologies by enabling more precise predictions of hazard distance, thus potentially improving safety protocols for natural gas pipelines.

2. Problem description

This study aims to develop and validate a numerical model capable of simulating leaks from buried pipelines typical of those found in the natural gas distribution network. This models built upon established physical principles and calibrated with experimental data to accurately represent the interaction between methane and its surrounding environment. The validated model can be used to predict gas dispersion, flammable cloud formation, and hence hazard distances. The experimental data by Liu et al. (2021) have been used to validate the model. Liu et al. (2021) present experimentally determined concentration values, for the initial stages of a methane leak from a buried pipeline through a sand filled tank to air. The concentration measurements presented by Liu et al. (2021) are for a 4 mm diameter leak orifice, pipeline pressure of 300 kPa, and sand layer depth of 0.1 m for times up to a maximum of 60 s. It should be noted that all pressures referred to in this paper are gauge. Specifically, Liu et al. (2021) present gas concentrations at three locations: horizontally along the tank centreline on the sand-air interface for 50 s, vertically above the leak up to a distance of 2 m for

60 s, and at positions offset from the leak to a maximum height of 0.8 m for 20 s. The experimental data captures the initial stage of the leak development only, thus the CFD analysis was extended to a flow time of 10 minutes in order to understand the point at which the leak reaches a quasi-steady state. The flammable envelope formed by the leak is a maximum at the point at which a quasi-steady state is reached. The simulated leak and geometry (Section 3) were chosen to allow comparison with experimental data. In the experiment used for validation (Liu et al. 2021), the leaking pipe is buried in a sandy soil specimen, described as brown loam. Material properties are described in Section 3.3.

3. Model and numerical details

This section outlines the physical and mathematical models of the problem and introduces the governing equations. Subsequently, an in-depth description of the numerical simulation employed for determining the leakage parameters is provided.

3.1 Mathematical model and governing equations

To simplify the model in the study, several assumptions have been adopted:

- The soil was considered an isotropic, homogeneous porous medium.
- There was no chemical interaction between the gas and the surrounding soil.
- The presence of moisture within the soil was not considered, the pores were air filled.

The pressure within the pipe is assumed to be constant throughout the leakage. Given these hypotheses, and use of ANSYS Fluent (ANSYS 2020R2) as computational engine, the governing equations for this problem are adopted from ANSYS Fluent in this study to simulate the buried leak.

3.1.1 Governing equations for porous media section

The soil was considered as a homogeneous porous media (Bagheri, M. and Sari, A. 2022). The governing equations for the soil mass section are as follows. The continuity equation:

$$\frac{\partial(\varphi\rho)}{\partial t} + \frac{\partial}{\partial x_i}(\varphi\rho u_i) = 0, \tag{1}$$

where φ is the soil porosity, ρ is the density and u_i is the velocity component. The momentum conservation equation in porous media of the soil mass is similar to its standard form with addition of the source term, S_i:

$$\frac{\partial(\varphi\rho u_i)}{\partial t} + \frac{\partial}{\partial x_j}(\varphi\rho u_i u_j) = -\frac{\partial(\varphi p)}{\partial x_i} + \frac{\partial \bar{\tau}_{ij}}{\partial x_j} + \frac{\partial}{\partial x_j}\left[\mu\left(\frac{\partial(\varphi u_i)}{\partial x_j} + \frac{\partial(\varphi u_j)}{\partial x_i} - \frac{2}{3}\frac{\partial u_k}{\partial x_k}\delta_{ij}\right)\right] + \varphi\rho g_i + S_i \tag{2}$$

In porous media, the stress divergence term $\frac{\partial \bar{\tau}_{ij}}{\partial x_j}$ is modified to account for the interaction between the fluid and solid matrix. It includes both the viscous stress components as in the standard fluid flow and additional resistive forces that arise from the presence of the solid matrix. Here g_i is the component of gravitational vector. The resistive forces are represented by the source term (S_i) in case of homogeneous porous media is:

$$S_i = \left[\frac{\mu}{\alpha}u_i + \frac{1}{2}C_2\rho|u|u_i\right], \tag{3}$$

where μ is the turbulent dynamic viscosity, α is the soil permeability, u_i is the superficial velocity across the CV and C_2 is the soil inertial resistance factor and ρ is the density of the medium, $|u|$ is

the magnitude of the velocity vector. The first and second terms on the right-hand side of equation (3) represent viscous and inertial losses, respectively.

To determine the values of the terms from equation (3), Ergun equation (Ergun, 1952) was employed which is a semi-empirical formula that has proven effective across steady and unsteady flows in porous media and packed-beds (Langer, 1993). This equation was articulated by Ergun and is acknowledged within the ANSYS software documentation (ANSYS 2020R2). The permeability and inertial loss coefficients are calculated as (ANSYS 2020R2):

$$\frac{1}{\alpha} = \frac{150\mu}{D_p^2}\frac{(1-\varphi)^2}{\varphi^3}, \tag{4}$$

$$C_2 = \frac{3.5\rho}{D_p}\frac{(1-\varphi)}{\varphi^3}, \tag{5}$$

where D_p is the mean particle diameter of sand and φ indicates the sand porosity which is a fraction of the control volume that is occupied by pores.

Energy equation: The only difference between the energy equation for the gas and porous media is related to the flux heat conduction and the effective thermal conductivity:

$$\frac{\partial(\rho E)}{\partial t} + \frac{\partial}{\partial x_i}\left(u_i(\rho E + p)\right) = \frac{\partial}{\partial x_j}\left[k'_{eff}\frac{\partial T}{\partial x_j} + u_i(\mu + \mu_t)\left(\frac{\partial u_i}{\partial x_j} + \frac{\partial u_j}{\partial x_i} - \frac{2}{3}\frac{\partial u_k}{\partial x_k}\delta_{ij}\right)\right], \tag{6}$$

where k'_{eff} is the effective thermal conductivity in the porous media and it is evaluated as:

$$k'_{eff} = \varphi k_{eff} + (1-\varphi)k_s, \tag{7}$$

where k_{eff} and k_s are effective thermal conductivity of gas and solid phase thermal conductivity. The values of density, thermal conductivity, and specific heat capacity of the solid phase in the soil mass are 1311.3 kg/m^3, 5.2138 W/m-k, 879 j/kg-K, respectively (Liu et al. 2021).

3.2 Simulation domain and mesh

Figure 1 shows the geometry of the computational domain. The domain comprises a tank within an ambient space. The tank contains a sand layer with the leak hole located at the centre of the solid base of the tank. The dimensions of the tank are L×H×W=4×0.15×4 m. The origin of the XYZ coordinate system was established at the bottom corner of the tank. Figure 1 demonstrates that the central point of the leakage was located at coordinates X,Y,Z=(2,0,-2) m. The calculation domain was 12×6×6 m. The gas release rate is primarily influenced by the pressure just beneath the leak hole (Lu et al. 2014; Bezaatpour et al. 2020). The computational focus was restricted to encompass only the region downstream of the leak, enabling a concentrated study of the gas behaviour and the immediate surrounding area, without incorporating the upstream piping system into the simulation model. The leak hole is located at depth of 0.1 m from the sand surface.

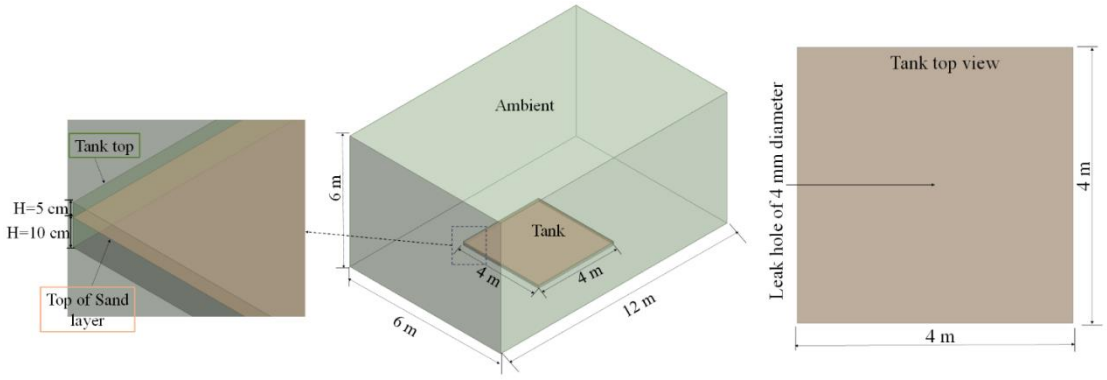

(a) (b)

Fig. 1. *Computational domain for simulation showing ambient, zoomed view of tank and sand layer (a), and top view of the tank showing leak located at the centre (b).*

A structured hexahedral mesh was generated using ANSYS mesh. Three mesh resolutions were considered initially coarse (86k control volumes), medium (460k CVs) and fine (2250k CVs). It was found that all three meshes has average orthogonality close to 0.98 and average skewness less than 0.066, which represents reasonable quality of the meshes. The medium mesh was found to give good results without the computational expense of the fine mesh. Full details of the grid independence study are not presented here. For the mesh of 86k, 460k and 2250k CVs the computation time for 20 second of flow time was approximately 49 hours, 240 hours and 389 hours, respectively, on a 512 core AMD Opteron CPU running at 2.3 GHz. Thus, simulations with the 460k CV mesh strike a balance between accuracy and efficiency, thus the medium grid was used for all simulation results presented in Section 4. The leak orifice of 4 mm diameter was approximated by a square of the same area, and this square was resolved by 10×10, 68×68, and 150×150 square cells respectively for coarse, medium, and fine grids.

3.3 Initial and boundary conditions

A predefined set of initial and boundary conditions are specified. The domain is initialised at a temperature of 300 K. Pressure at the leakage point is prescribed between 10 to 300 kPa, whereas the porous medium and ambient conditions are set to atmospheric pressure conditions at 101.325 kPa. The species transport model was used, where mole fraction of methane was defined as 1 indicating pure methane release from leak hole. The oxygen mole fraction was defined as 0.2073 and the mole fraction of carbon dioxide and water vapour set to zero. The soil was modelled as a porous medium characterised by its porosity, viscous resistance and inertial resistance. The parameters for inertial and viscous resistances within this soil medium, as quantified in the experiment have been adopted for this study (Table 1).

Table 1. *Soil properties (Liu et al., 2021).*

Properties	Value	Unit
Type of soil	Brown loam	– – –
Density (ρ)	1311.3	Kg/m^3
Porosity (φ)	0.6	– – –
Viscous resistance (μ)	2.45e+11	1/m^2
Inertial resistance (I)	5.02e+05	1/m

The leak point was treated as a pressure inlet, interfaces were used to represent soil boundaries, the top of the computational domain was treated as a pressure outlet. The tank was modelled as a stationary wall with no – slip condition.

3.4 Numerical details

Numerical simulations were conducted using the SIMPLE algorithm in ANSYS Fluent. A pressure based solver was used for the incompressible flows. The second-order upwind scheme was used for momentum, turbulent kinetic energy and dissipation rate equations. The momentum equation, turbulent kinetic energy and dissipation rate were discretised using the second order upwind method and are solved numerically using a pressure-based solver. Simulations were considered accurate with residuals converging to 1e-5. Simulation results were compared with experiments for a 460k grid for time step sizes, ranging from 1E-4 s to 0.25E-7 s. Whilst results are not shown here, minimal variation in predicted methane concentrations were observed as the time step size was reduced from 1E-6 to 0.25E-7 s. Thus, a time step size of 1E-7 s was used for the simulations presented in Section 4. To maintain the numerical stability and ensure the physical accuracy of the simulations, the time step was carefully chosen to comply with the Courant-Friedrichs-Lewy (CFL) condition, with a CFL number maintained below 1 throughout the analysis.

4. Results and discussion

In Section 4.1 validation of the model against experimental data for the initial stages of a buried methane leak is presented. Experimental data is available in the work of Liu et al. (2021) for the first 60 s of a buried leak from 300 kPa through a 4 mm diameter only. Nonetheless, the experimental data demonstrate that the flammable cloud expands beyond 60 s. Thus, the validated model has been applied to extend the analysis for a flow time of 10 minutes, as discussed in Section 4.2.

4.2 Model validation

As noted in Section 2, Liu et al. (2021) present gas concentration data at three locations for a buried leak from 300 kPa through a 4 mm diameter leak hole. 1: Discrete concentration values, and the growth of the distance to both 1.25% and 2.5% methane have been measured for 50 s vertically along the leak centreline using sensors positioned up to a height of 2 m. 2: Methane concentration data has been measured at discrete times up to 60 s at positions offset from the leak to a maximum height of 0.8 m. 3: Methane concentration data is presented for 20 s, measured horizontally on the tank centreline along the sand-air interface. Validation against each of these three data sets is discussed in turn in sections 4.2.1 – 4.2.3.

4.2.1 Vertically measured concentrations along the leak centreline: first 60 s of a release

As methane migrates from the soil to the atmosphere and interacts with air, it has the potential to reach flammable concentrations. In the case of methane, the lower flammability limit is typically taken as 5%. Sensors or alarms are typically designed to trigger at fractions of the LFL i.e., before a flammable cloud is established. Liu et al. (2021) reported the vertical distance to methane concentrations of 1.25% (25% LFL) and 2.5% (50%) over the first 50 s of a buried leak from 300 kPa through a 4 mm diameter leak hole. They calculated this distance using measurements taken along the vertical centreline above the leak. A comparison of the experimental and simulation values is given in Figure 2, alongside a schematic demonstrating the positions at which concentrations were measured in experiments. The positions at which the methane concentration reached 1.25% can be considered as a threshold for the first-level warning radius. Similarly, the boundary where the methane concentration hits 2.5% can be considered as the second-level warning radius. The simulation data shows excellent agreement with the experimental values. Moreover, the presented data confirm that the vertical distance to the two warning levels continues to increase at 60 s. Thus, in order to inform safety guidance, there is clear benefit to investigating the scenario for a longer flow time.

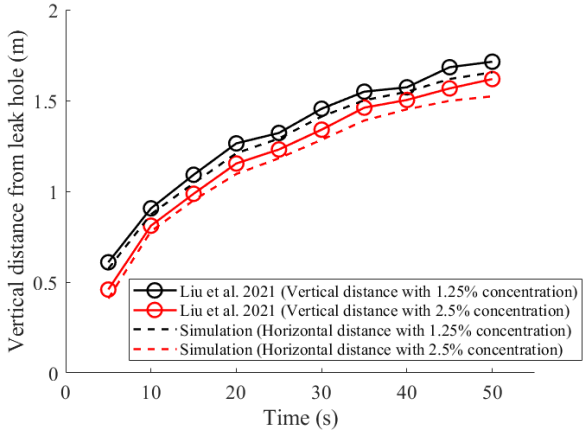

Fig. 2. *Comparison of experimental and simulated values of vertical distance to 1.25% and 2.5% methane with time for the first 50 s of a buried leak through a 4 mm diameter leak hole from a pipeline pressure of 300 kPa.*

In addition to estimating the distance to 1.25% and 2.5%, Liu et al (2021), presented methane concentration values along the leak centreline at different heights from the leak. The data is for the first 50 s of the leak, recorded at 10 s intervals. Figure 3 (left) shows a comparison of experimental and simulated results at times of 10, 20, 30, 40 and 50 s. The schematic on the right if Figure 3 indicates the height at which concentration measurements were taken. Again, it can be seen that the simulation results closely align with the experimental data.

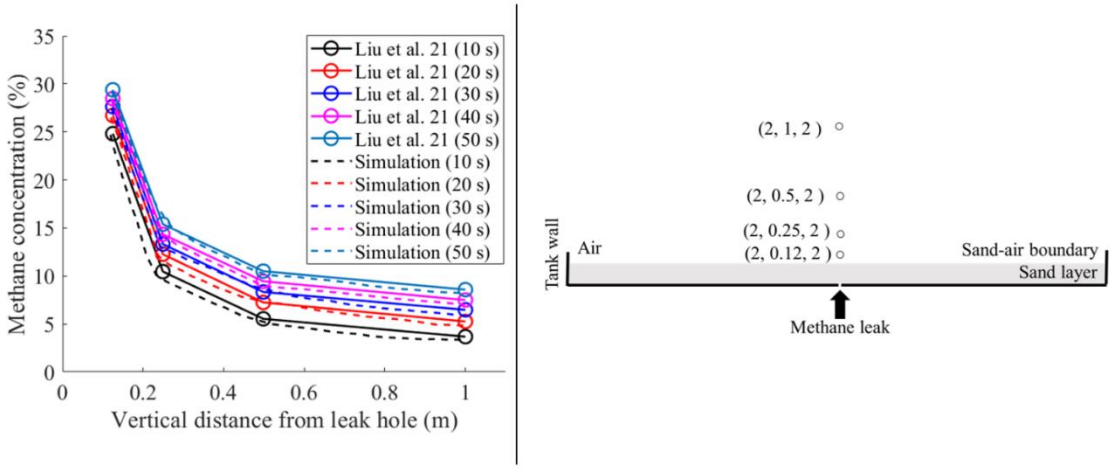

Fig. 3. *Methane concentration variation along vertical distance over the sand-air boundary for a 4 mm leak hole and inlet pressure of 300 kPa (left), schematic of the tank showing the monitoring points location (right).*

4.2.2. Methane concentration at sensor points above the sand layer: first 60 s of a release

Methane concentration was measured by Liu et al. (2021) over a matrix of six points, above the sand layer, at positions offset from the leak centreline. This enables us to capture a multidimensional profile of methane concentration over time. Each sensor's placement and its corresponding data point provide insights into the vertical and horizontal spread of methane which is critical for assessing safety and mitigation strategies. The data was once again for a buried leak through a 4 mm diameter hole and pipeline pressure of 300 kPa. The leak and sensor coordinates are given in Table 2. A schematic of the sensor positions (labelled a-f) is shown in Figure 4.

Table 2. Coordinates of leak and sensor points.

Locations	Leak point	a	b	c	d	e	f

X, m	2	1.4	1.7	1.85	1.925	2	2.2
Y, m	0	0.8	0.4	0.2	0.1	0.2	0.15
Z, m	-2	-2	-2	-2	-2	-1.85	-2

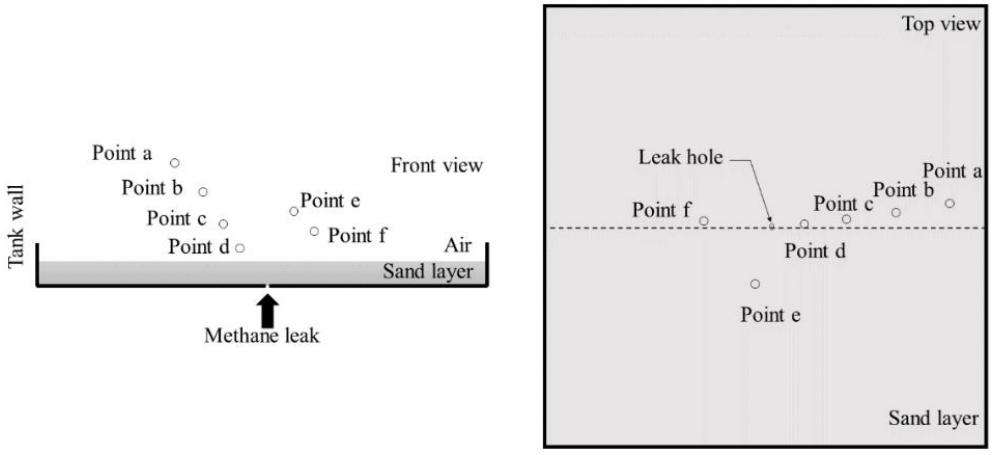

Fig. 4. *Schematic of monitoring points location.*

Figure 5 shows the comparison of the measured and simulated concentrations at the sensor points. The simulated concentrations show excellent agreement with the experimental values further validating the model. Furthermore, the data reveal ongoing growth in concentration levels at 60 s, marking the conclusion of the experiment. As expected, concentrations are highest closest to the leak source with point “a” showing the highest concentration and point “f” the lowest. The methane concentration at points “c”, “e”, and “f” are nearly identical over 60 s.

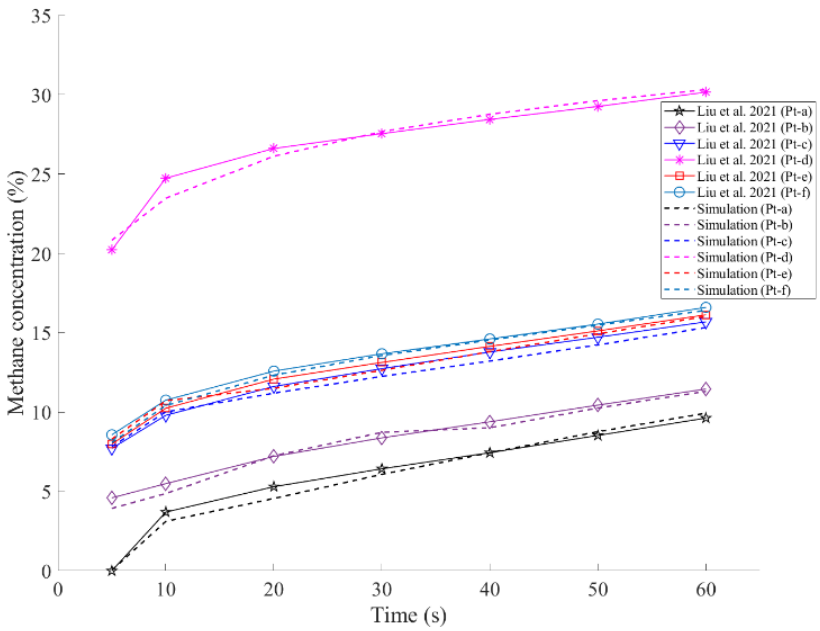

Fig. 5. *Comparison of experimental and simulated methane concentrations at monitored points (a - f) for pipe pressure 300 kPa during 60 s.*

4.2.3 Methane concentration along the sand-air boundary: first 20 s of a release

The final data considered for validation were methane concentration measurements taken along the centreline of the tank, measured horizontally along the sand-air boundary. As before the data, taken from the work by Liu et al. (2021) was for a buried leak from a 4 mm leak hole and pipeline pressure of 300 kPa.

A comparison of experimental and simulation data is given in Figure 6. The graph demonstrates the concentration of methane plotted against the horizontal distance from the tank wall along the sand–air boundary. The data is included for flow times of 5, 10, 15 and 20 s. The profile of methane concentration forms a bell shape, peaking close to the tank wall and decreasing towards the edge of the monitored line. This suggests a higher concentration of methane near the leak source which gradually diffuses as the distance increases. Once again, the simulations show good agreement with the experimental data, further supporting the model validation.

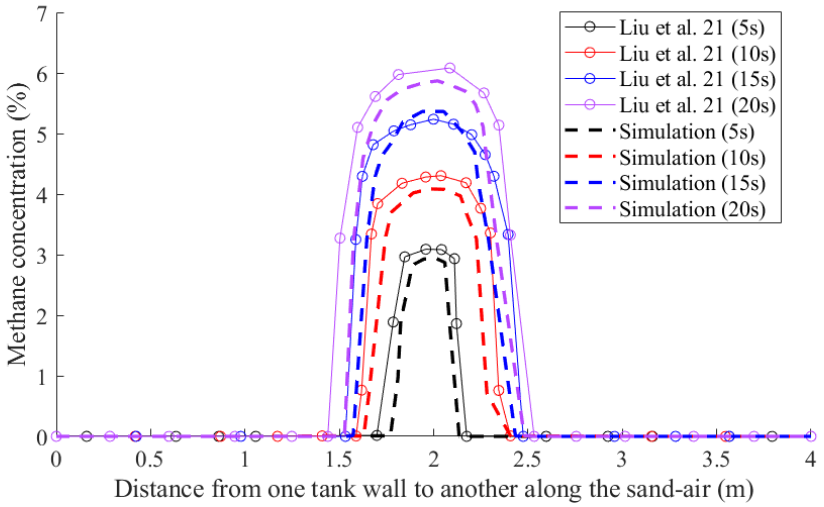

Fig. 6. *Distribution of methane concentration at sand-air boundary at time 5, 10, 15 and 20 s after leak start for a 4 mm hole and pressure of 300 kPa.*

It is clear from Figure 6, that as in sections 4.1.1 and 4.2.2. that the methane cloud is still growing at the point at which the experiments were concluded. Thus, the validated model has been applied to provide insight to the flammable cloud formation, over a longer period of time and the simulation results are presented in the next section (4.2).

4.3 The maximum extent of the flammable cloud (hazard distance)

The lower flammability limit (LFL) for methane is the minimum concentration of methane in air below which the mixture is too lean to support combustion. As noted in Section 4.2, the LFL for methane is approximately 5%. Below this limit the air-methane mixture is too lean to burn; above it, up to the upper flammability limit (UFL) of 15%, the mixture is ignitable. Knowledge on the maximum extent of the flammable cloud formed by a buried leak is essential to inform safety procedures and emergency response.

In Section 4.2 validation of the numerical model for a buried lead was described. Excellent agreement was demonstrated between simulation results and experimental measurements for the initial stages of a leak through a 4 mm diameter hole from a pipeline pressure of 300 kPa. However, the experimental data is available up to a maximum flow time of 60 s, and it is clear from the data that the methane cloud is still growing at this time. Thus, the validated model has been applied to simulate cloud development for a flow time an order of magnitude greater than experiments. Simulation of the leak has been completed for a flow time of 10 minutes (600 s) at which point it can be seen that a quasi-steady state has been reached.

Figure 7 shows the development of the flammable cloud with time up to 10 minutes. It can be seen that the plume slows in growth after approximately 8 min, stabilising at a height of 1.824 m from the leak point. The spread of the methane radially through the sand is also evident from the contour plots.

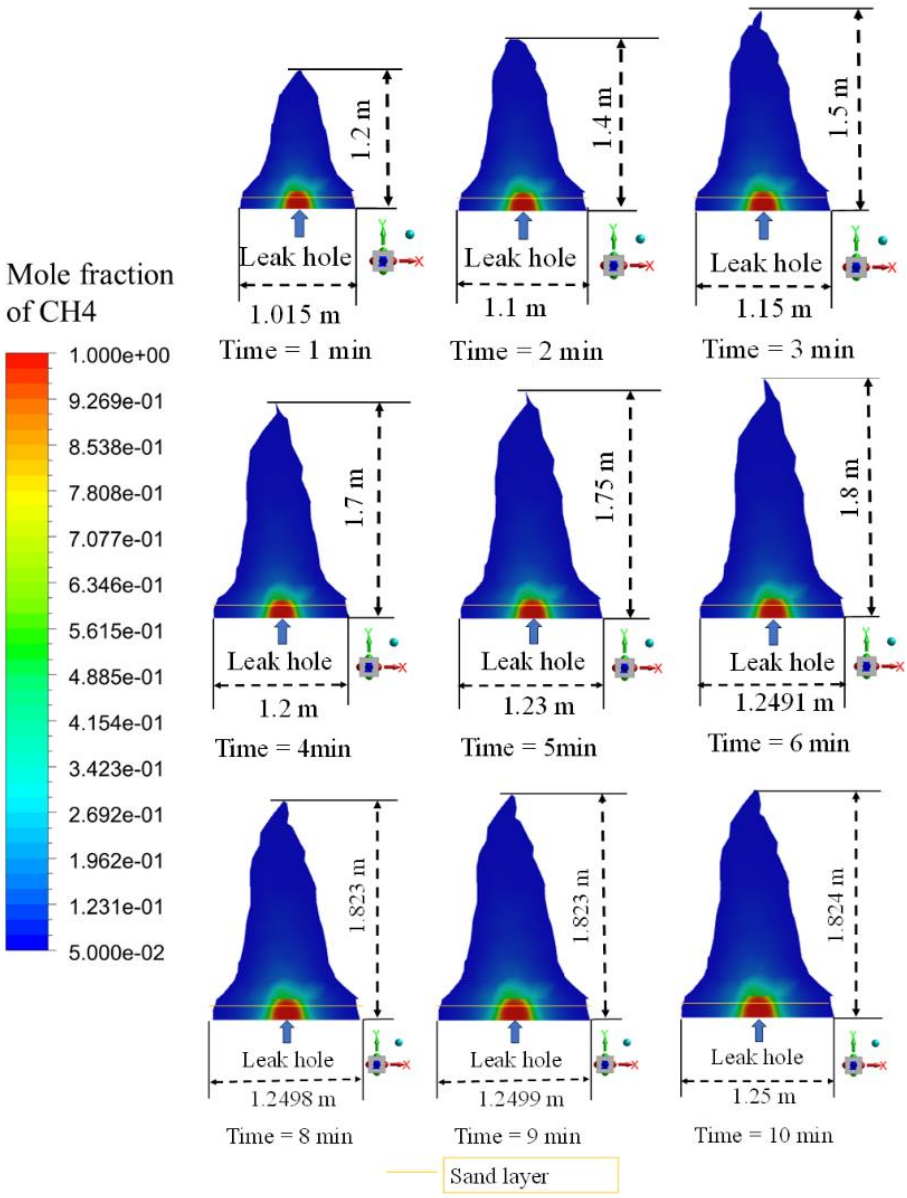

Fig. 7. *Development of flammable 5% methane-air cloud from a 4 mm buried leak hole at an inlet pressure of 300 kPa from 1 min to 10 min of simulation.*

As demonstrated above, the validated model can thus be applied to predict hazard distances and the dynamic development of the flammable cloud formed by a buried methane leak. For this particular scenario (300 kPa pipeline, 4 mm leak hole at a depth in sand of 0.1 m), it can be seen that the hazard distance does not grow any further after a matter of minutes. This demonstrated the potential impact of the model as a tool to predict both the maximum extent of the flammable cloud, and the time taken to reach it for a buried leak. This information can be used to inform safety strategies and leak response guidance.

Similarly, Figure 8 shows the spread of methane from a 2 mm diameter leak hole at different time intervals (20 s to 6 min). The vertical and horizontal distances from the leak hole increases over time, illustrating the dispersion pattern of gas. The vertical and horizontal distances increase gradually, reaching a maximum height of 0.54 m and a maximum horizontal distance of 0.55 m. It can be observed that the vertical expansion of methane plume slows down after 3 min, stabilising at a height of 0.26 m from the leak point. The horizontal spread of the methane through the sand layer is also clearly depicted in the contour plots, with the methane extending horizontally to a maximum distance of approximately 0.55 m.

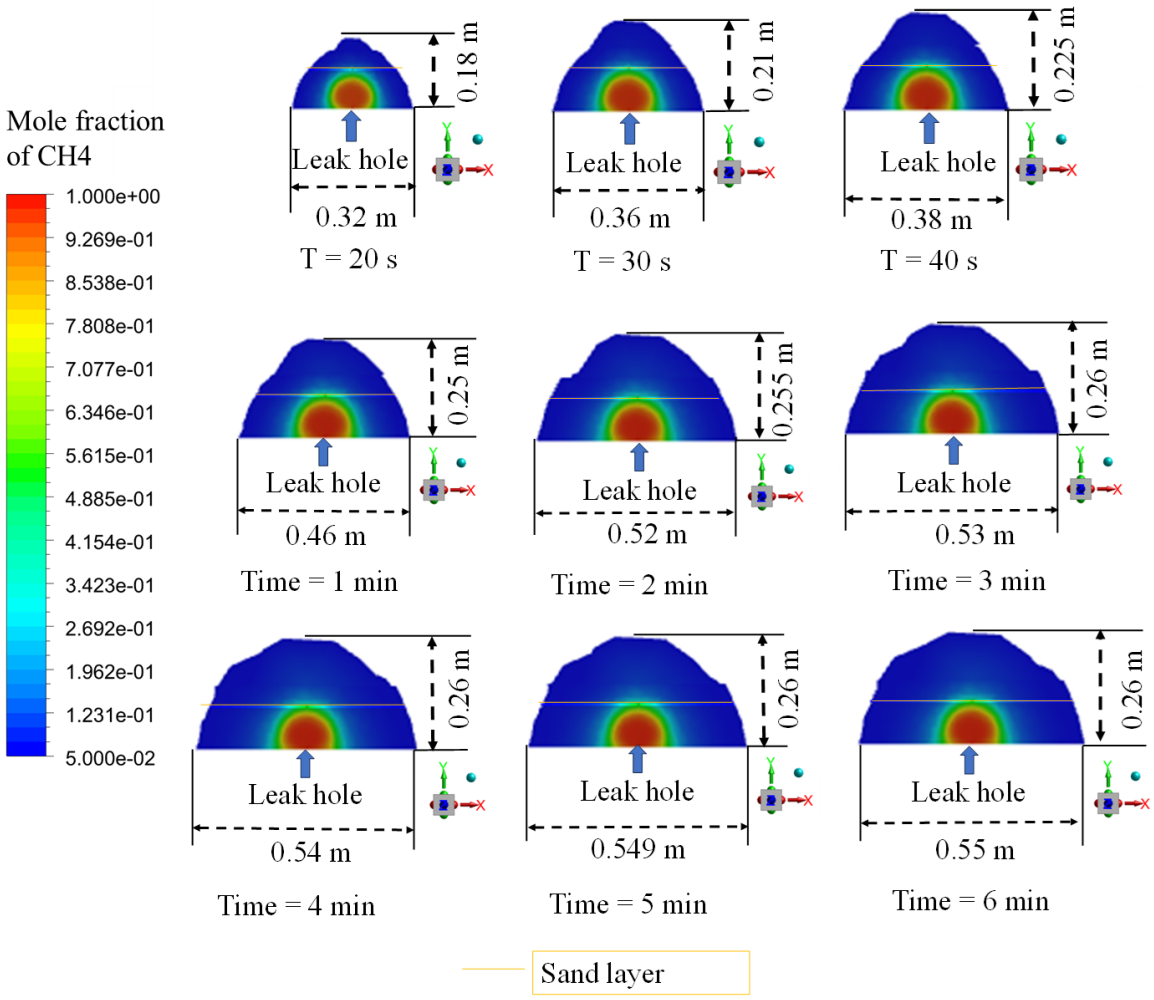

Fig. 8. *Development of flammable 5% methane-air cloud from a 2 mm buried leak hole at an inlet pressure of 300 kPa from 20 s to 6 min of simulation.*

In Figures 7 and 8, we observe the effects of different sizes on methane dispersion. The dispersion patterns from the 2 mm and 4 mm leak holes shows that the larger the leak size results in a faster and wider spread of methane, reaching higher concentration at increased distance in both the vertical and horizontal directions. The 4 mm leak exhibits a more pronounced and rapid methane cloud development, reaching a greater vertical and horizontal extent within the same time frame compared to the 2 mm leak. The difference underscores the influence of orifice size on the rate of dispersion and the extent of hazard zones, critical for designing safety protocols and emergency response measures.

5 Conclusions

In this study, numerical analysis of a methane leak from a buried pipeline through a sand layer is presented. Three-dimensional computational models, have been applied and validated to provide insight to a methane leak from both 4 mm and 2 mm diameter hole and pipeline pressure of 300 kPa through a sand layer of 0.1 m. The rigour of the of the work is in the validation of the model against experimentally measured concentration data from the literature for the initial stage of the release. Excellent agreement is demonstrated between the simulated and measured concentration data in 3 different regions of the domain.

The originality of the work is in the application of the validated model to provide insight to the development of the flammable cloud over an extended flow time, until it can be seen that a quasi-steady state is reached. The results of this study are significant, as they show that the model can be

used as a predictive tool to estimate hazard distances from buried methane leaks. This data is necessary for establishing safety zones around leaks in underground pipelines, and for underpinning technically informed safety guidance.

Acknowledgements

This work is supported by the Centre for Advanced Sustainable Energy (CASE). CASE is funded through the Department for the Economy NI's Green Innovation Challenge Fund and aims to transform the sustainable energy sector through business research.

References

ANSYS® Fluent Theory Guide, Release 2020 R2; ANSYS, Inc.: Canonsburg, PA, USA, 2020.

Atkinson, G., et al., 2019. Flow of Hydrogen from Buried Leaks. Report No. EA/18/35, HSE's Health and Safety Laboratory.

Bagheri, M., Sari, A., 2022. Study of natural gas emission from a hole on underground pipelines using optimal design-based CFD simulations: Developing comprehensive soil classified leakage models. J. Nat. Gas Eng. 102, 104583.

Bezaatpour, J., Fatehifar, E., Rasoulzadeh, A., 2020. CFD investigation of natural gas leakage and propagation from buried pipeline for anisotropic and partially saturated multilayer soil. J. Clean. Prod. 277, 123940.

Brand, D., Kutrowski, K. H., 2006. Safety in European gas transmission pipelines EGIG: European gas pipeline incident data group. In Proceedings of the 23rd World Gas Conference, Amsterdam, The Netherlands. 5-9.

EGIG (European Gas Pipeline Incident Data Group), 2018. 10th Report of the European Gas Pipeline Incident Data Group (period 1970-2016). 1–50.

Ebrahimi-Moghadam, A., Farzaneh-Gord, M., Deymi-Dashtebayaz, M., 2016. Correlations for estimating natural gas leakage from above-ground and buried urban distribution pipelines. J. Nat. Gas Eng. 34, 185-196.

Ebrahimi-Moghadam, A., Farzaneh-Gord, M., Arabkoohsar, A., Moghadam, A.J., 2018. CFD analysis of natural gas emission from damaged pipelines: Correlation development for leakage estimation. J. Clean Prod. 199, 257-271.

Ergun, S., 1952. Fluid flow through packed columns. Chemical engineering progress, 48, p.89.

Langer, M., 1993. The role of engineering geology for planning and construction of underground openings: Introduction of the symposium 19-3 "engineering geology in the utilization of underground space", 29th Int. geological congress, Kyoto, Japan 1992. Engineering Geology, 35, 143-147.

Liu, C., Liao, Y., Liang, J., Cui, Z., Li, Y., 2021. Quantifying methane release and dispersion estimations for buried natural gas pipeline leakages. Process Saf. Environ. Prot. 146, 552-563.

Rui, Z., et al. (2017). A new model to evaluate two leak points in a gas pipeline. J. Nat. Gas Eng. 46, 491-497.

Zhu, J., Pan, J., Zhang, Y., Li, Y., Li, H., Feng, H., Chen, D., Kou, Y., Yang, R., 2023. Leakage and diffusion behavior of a buried pipeline of hydrogen-blended natural gas. Int. J. Hydrog. Energy. 48, 11592-11610.

Research on Jet Structure and the Virtual Nozzle Model for High-pressure Hydrogen Leakage from Rectangular Nozzles

Jinghua Shen, Wei Gao*, Yi Sun

State Key Laboratory of Fine Chemicals, Department of Chemical Machinery and Safety Engineering, Dalian University of Technology, Dalian, Liaoning 116024, PR China

E-mail: *gaoweidlut@dlut.edu.cn*

Abstract

Due to the complex shock wave structure after high-pressure hydrogen gas leakage, simulating it is challenging. Currently, only a virtual nozzle model for circular leakage is used to simplify the shock wave structure, while a simplified model for rectangular nozzles is lacking. This study utilizes OpenFOAM to investigate the characteristics of high-pressure rectangular nozzle hydrogen leakage with pressures up to 70 MPa. A real gas model and a new thermophysical model are adopted to better demonstrate the shock wave structure of the jet under high pressure. The study examines the characteristics of jet structures after leakage from rectangular nozzles with different pressures, aspect ratios, and diameters. The critical conditions for forming Mach disks in rectangular jets are proposed, and an empirical relationship for the position of Mach disks is summarized. By combining the isentropic expansion equation, mass conservation, momentum conservation, energy conservation, and shock wave relationship before and after, a virtual nozzle model for rectangular nozzles is proposed. The large-scale diffusion of hydrogen leakage is simulated using the virtual nozzle model and compared with experimental data, showing good conformity. This model can provide boundary conditions for large-scale numerical simulations and theoretical calculations, simplifying the computational process.

Keywords: *hydrogen leakage, rectangular jet, jet structure, the virtual nozzle mode*

1. Introduction

Hydrogen, heralded as the "fuel of the future" boasts numerous advantages that position it as a key player in the global transition towards clean energy. As a versatile energy carrier, hydrogen offers a sustainable alternative to traditional fossil fuels, with the potential to significantly reduce greenhouse gas emissions and combat climate change(Yue et al.,2021). Its high energy density, renewability through electrolysis, and ability to produce only water vapor as a byproduct make it an attractive option for a wide range of applications worldwide. The utilization of hydrogen is increasingly prevalent across various sectors, reflecting its growing importance in achieving carbon neutrality goals. However, alongside its environmental benefits, hydrogen safety considerations cannot be overlooked. Guo et al.(2024) have noted that, owing to the intrinsic properties of hydrogen, safety throughout its production, transportation, storage, and utilization processes represents a pivotal concern. Currently, the primary method of hydrogen storage is high-pressure gaseous storage(Usman et al.,2022). However, the high storage pressure brings about a high risk of leakage. Once a leak occurs, due to its fast diffusion speed and wide flammability range, hydrogen is extremely prone to

causing explosions. Therefore, it is imperative to conduct research on the leakage and diffusion of hydrogen under high-pressure conditions.

Existing studies often simplify the leak orifice as circular, where high-pressure hydrogen leakage from storage tanks or pipelines forms an axially symmetric underexpanded jet(Okabayashi et al.,2019; Kobayashi et al.,2019; Takeno et al.,2017). Previous research has primarily focused on the structure and concentration distribution of the jet. The Mach disk is a characteristic feature of high-pressure underexpanded jets, and current research on Mach discs includes their distance from the leak orifice and diameter. Crist et al.(1966) conducted jet experiments with various gases, normalizing the Mach disc distance using the leak orifice diameter, and found that this dimensionless parameter is directly proportional to half of the stagnation pressure ratio, resulting in an empirical formula for Mach disc distance. Velikorodny et al.(2012) summarized the relationship between Mach disc diameter and the specific heat ratio of the gas. In terms of concentration distribution, Han et al.(2013,2014) found that the average concentration and velocity along the jet centerline after the Mach disk are inversely proportional to the dimensionless distance from the leak point, with the radial concentration distribution following a Gaussian pattern. Tang et al.(2018) discovered significant turbulence-induced oscillations in the instantaneous concentration along the jet centerline. Due to the complex shock structure of underexpanded jets, a virtual nozzle model is commonly employed to simplify the jet structure. Building upon the isentropic expansion theory, Brich et al.(1984) introduced the concept of a virtual nozzle and transformed the underexpanded jet into a free jet by combining mass and momentum conservation equations. Ewan et al.(1986) improved the Brich et al.(1984) model by setting the flow temperature at the virtual nozzle equal to the nozzle exit temperature. Based on the actual shock structure of high-pressure expansion jets, Harstad et al.(2006) proposed a virtual pipe model, assuming that the virtual nozzle is located behind the Mach disk. Subsequently, Molkov et al.(2012) introduced real gas state equations to enhance the accuracy of the model.

However, in actual leakage scenarios, the shape of the leak orifice is not limited to circular, and there is currently limited research on rectangular leak orifices. Li et al.(2019) found that after the jet exits a rectangular nozzle, there is an axis-switching phenomenon in the flow field, leading to differences in the diffusion rates of the jet on different planes of the nozzle, with a significantly faster diffusion rate on the short edge plane compared to the long edge plane. Makarov et al.(2013) pointed out that the similarity law formulas for centerline concentration decay in one-dimensional and two-dimensional planar jets may not be suitable for predicting hydrogen jet flows with finite aspect ratios. The relationship between the position of the Mach disc in rectangular jet flows and the leak pressure, leak diameter, and aspect ratio has not been explored. As for virtual nozzle models, Stewart et al.(2020) employed the Ewan et al.(1986) virtual nozzle model to simulate releases from rectangular nozzles, but the simulated outcomes significantly deviated from the actual results. Therefore, there is a need for research on virtual nozzle models for rectangular nozzles.

In this paper, a numerical simulation method is employed to investigate the effects of different hydrogen storage pressures, nozzle equivalent diameters, and aspect ratios on the leakage of hydrogen from rectangular nozzles. The study focuses on the near-field region of the jet, revealing the structural characteristics of the rectangular nozzle jet, the position of the Mach disk, and axial conversion phenomena. Based on the structural characteristics of the rectangular nozzle jet, in conjunction with the virtual nozzle model proposed by previous researchers for circular leak orifices, a virtual nozzle model applicable to rectangular nozzles was established. The research results of this paper provide a

new simulation method, which simplifies the complex shock wave structure at the leak port, can solve the problems of slow calculation speed and high computing resource consumption during high-pressure hydrogen leakage simulation, and can save time for the prediction and judgment of the combustible area when the hydrogen leakage accident occurs.

2. Modeling

2.1 Numerical methods

In this paper, The governing equations solved are the continuity, momentum, enery, and transport equations.

$$\frac{\partial \rho}{\partial t}+\frac{\partial \rho u_i}{\partial x_i}=0 \tag{1}$$

$$\frac{\partial \rho u_i}{\partial t}+\frac{\partial (\rho u_i u_j)}{\partial x_j}=-\frac{\partial p}{\partial x_i}+\mu \frac{\partial}{\partial x_j}(\frac{\partial u_i}{\partial x_j}+\frac{\partial u_j}{\partial x_i}-\frac{2}{3}\frac{\partial u_i}{\partial x_i}\delta_{ij}) \tag{2}$$

$$\frac{\partial \rho E}{\partial t}+\frac{\partial [u_j(\rho E+p)]}{\partial x_j}=\frac{\partial (k\nabla T)}{\partial x_j}+\frac{\partial}{\partial x_i}\mu u_j(\frac{\partial u_j}{\partial x_i}+\frac{\partial u_i}{\partial x_j}-\frac{2}{3}\frac{\partial u_i}{\partial x_i}\delta_{ij}) \tag{3}$$

$$\frac{\partial \rho Y_i}{\partial t}+\frac{\partial (\rho u_j Y_j)}{\partial x_j}=\frac{\partial}{\partial x_j}(\mu \frac{\partial Y_i}{\partial x_j})+R_{Y_i} \tag{4}$$

where ρ is density, u is the velocity, p is the pressure, μ is the dynamic viscosity coefficient. The total energy E is equal to $e+\frac{|u_i|^2}{2}$, the term e is the specific internal energy which is calculated by $C_V T$. Y and R_Y are the concentrations and diffusion coefficients of each of the components. The governing equations are solved by myRhoCentralFoam, which is developed based on rhoCentralFoam in OpenFOAM v7. Multiple species transport and multicomponent diffusion are added in the myRhoCentralFoam solver to study the diffusion process of hydrogen. The kOmegaSST turbulence model is a combination of the standard kEpsilon model and the kOmega model, which is chosen for solving the high Reynolds number and flow separation problems in this simulation.

For the chosen solver, there is a lack of appropriate thermophysical models for handling non-ideal gases under high-pressure conditions. As a result, a novel combination of thermophysical models has been developed. The Peng-Robinson equation of state has been selected due to its effectiveness across a broad spectrum of thermodynamic scenarios. The PR EoS(Peng et al.,1976) is expressed as follows:

$$p=\frac{RT}{v-b}-\frac{a}{v(v+b)+b(v-b)} \tag{5}$$

where a and b are the EOS model parameters. The pure component parameters can be calculated by

$$a=0.46\frac{R^2T_C^2}{P_c}\alpha(T) \tag{6}$$

$$b = 0.078\frac{RT_c}{P_c} \tag{7}$$

$$\alpha(T) = [1 + m(\omega)(1 - \sqrt{\frac{T}{T_c}})]^2 \tag{8}$$

$$m(\omega) = 0.375 + 1.542\omega - 0.270\omega^2, \omega \le 0.49 \tag{9}$$

$$m(\omega) = 0.380 + 1.485\omega - 0.164\omega^2 + 0.017\omega^3, \omega > 0.49 \tag{10}$$

To enhance the precision of assessing the thermophysical characteristics of substances, this study employs NASA polynomials (Mcbride et al.,1993) in the thermodynamic and transport models. Transport property coefficients are given for viscosity, and thermal conductivity, which are generated by a least-squares fit to the following form:

$$\left.\begin{matrix}\ln\mu \\ \ln k\end{matrix}\right\} = A\ln T + \frac{B}{T} + \frac{C}{T^2} + D \tag{11}$$

Thermophysical parameters such as heat capacity, enthalpy, and entropy are provided, computed using empirical equations.

$$\frac{C_P^0(T)}{R} = a_1 + a_2T + a_3T^2 + a_4T^3 + a_5T^4 \tag{12}$$

$$\frac{H^o(T)}{RT} = a_1 + a_2\frac{T}{2} + a_3\frac{T^2}{3} + a_4\frac{T^3}{4} + a_5\frac{T^4}{5} + \frac{b_1}{T} \tag{13}$$

$$\frac{S^o(T)}{R} = a_1\ln T + a_2T + a_3\frac{T^2}{2} + a_4\frac{T^3}{3} + a_5\frac{T^4}{4} + b_2 \tag{14}$$

2.2 Modelling establishment

Figure 1 illustrates the schematic diagram of the computational domain, taking the example of a rectangular nozzle with an equivalent diameter of 2mm. The main objective of this simulation is to analyze the jet structure in the near-field region. Therefore, a specific small area has been chosen for detailed investigation. In this paper, the aspect ratio, defined as the ratio of the long side to the short side, is adopted to describe the shape of the rectangular nozzle. The study investigates hydrogen leakage under different leak pressures (10MPa, 35MPa, 70MPa), various aspect ratios (AR2, AR4, AR8), and different leak diameters (2mm, 4mm, 6mm). Due to significant differences between operating conditions, different sizes of computational domains are employed. The largest computational domain mainly consists of a box of size 1000×1000×600 mm in x-, y-, and z-directions, respectively. High-pressure hydrogen is introduced through the "Inlet", traversing the nozzle and entering the internal field area, which contains air at standard temperature and pressure.

To assess grid independence in simulating leakage from the rectangular nozzle at 70MPa pressure, three different grids are employed. In the coarse mesh configuration, the leak port is divided into 400 cells, yielding an approximate total grid count of 2.8 million. For the medium mesh, the leak port consists of 1024 cells, resulting in a total grid count of 3.5 million, while the fine mesh divides the

leak port into 1296 cells, leading to a total grid count of 3.9 million. The distribution of the Mach number along the centerline of the jet after leakage from the AR4 nozzle at 70 MPa pressure is shown in Figure 2 for three different grids. The results obtained from the medium and fine grids exhibit uniform Mach disc positions and maximum Mach numbers. In contrast, the outcomes from the coarse grid significantly diverge from those of the medium and fine grids in these respects. Considering both accuracy and cost-effectiveness, the Medium grid has been chosen for this study.

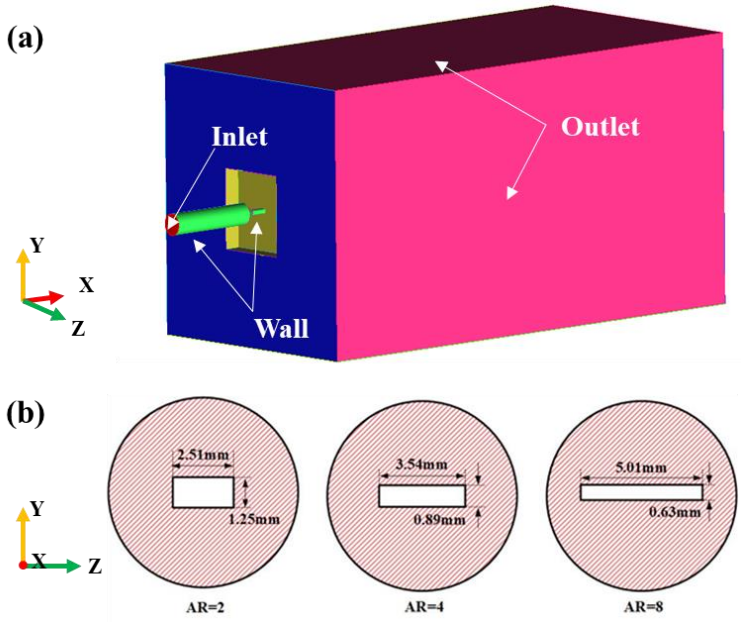

Fig. 1. *Schematic of the computational model. (a) Schematic of the computational domain, (b) Schematic diagrams of nozzles with different aspect ratios*

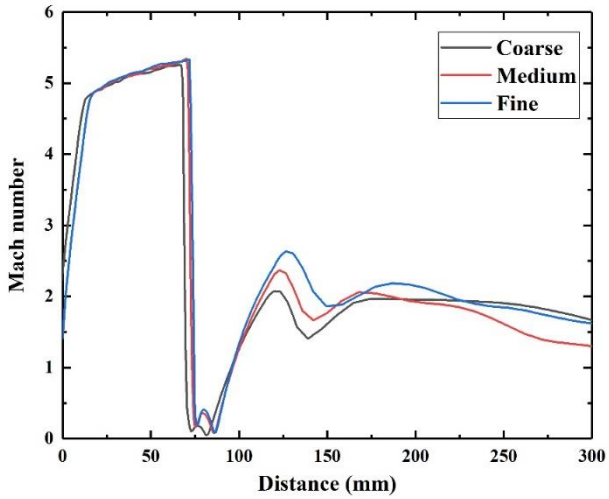

Fig. 2. *Mach number distribution along the centerline of jet flow for three different grids*

3. Result

3.1 Jet structures

Figure 3 illustrates the Mach number distribution of nozzles with different aspect ratios and an equivalent diameter of 4mm after leakage under a pressure of 10MPa. As a result of the pressure gradient across the nozzle, the hydrogen jet undergoes expansion into the ambient medium upon discharge. The expanded fan, which extends radially from the outlet of the nozzle, interacts with the

jet. These interactions lead to compression waves forming at the periphery of the jet, eventually converging downstream from the nozzle outlet to generate barrel-shaped shockwaves. In the AR2 nozzle, the hydrogen gas flow velocity shifts from supersonic to subsonic upon crossing shock waves. Conversely, in AR4 and AR8 nozzles, the hydrogen flow velocity diminishes post-shock waves, yet the Mach number remains above 1. The strength of the direct shock waves exceeds that of the oblique shock waves, leading to a clearer distinction in flow parameters before and after interacting with the planar shock wave. Consequently, the decrease in Mach numbers for the flow from the AR4 and AR8 nozzles is relatively insignificant.

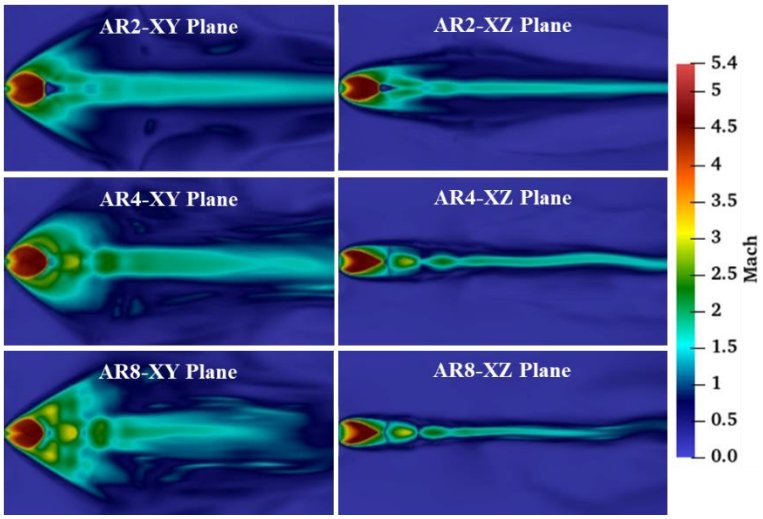

Fig. 3. *The Mach number distribution of nozzles with different aspect ratios and an equivalent diameter of 4mm after leakage under a pressure of 10MPa*

Statistical analysis of the data from all operating conditions reveals that, under all pressures and diameters, hydrogen leakage from the AR2 nozzle consistently leads to the formation of a direct wave, known as the Mach disk. On the other hand, hydrogen leaking from the AR8 nozzle always forms an oblique shock wave. However, the situation is rather unique for the AR4 nozzle. Figure 4 illustrates the Mach number distribution of the AR4 nozzle with a 4mm diameter under different leakage pressures. It is evident that under pressures of 35MPa and 70MPa, the hydrogen leakage also results in the formation of a direct wave, and the subsonic region expands with increasing pressure. Therefore, the formation of a Mach disk by the jet from a rectangular nozzle is related to the leak pressure and aspect ratio. Simulations are conducted for hydrogen leakage from the AR4 nozzle within the 10 MPa to 35 MPa range at 5 MPa intervals. The study find that a Mach disk can be formed when the pressure is equal to or greater than 20 MPa.

The angle between the shock wave and the direction of airflow is called the shock wave angle. For a normal shock wave, the shock wave angle is 90°, while for an oblique shock wave, the shock wave angle is less than 90°, as shown in Figure 5(a). The changes in airflow parameters after passing through an oblique shock wave need to be determined using the shock wave angle, hence requiring measurement of the shock wave angle. The shock wave angles of the AR8 nozzle at different pressures and nozzle diameters are shown in Figure 5(b). It can be observed that, for the same diameter, the shock wave angle decreases with increasing pressure, indicating that the shock wave angle is not simply linearly related to the nozzle diameter.

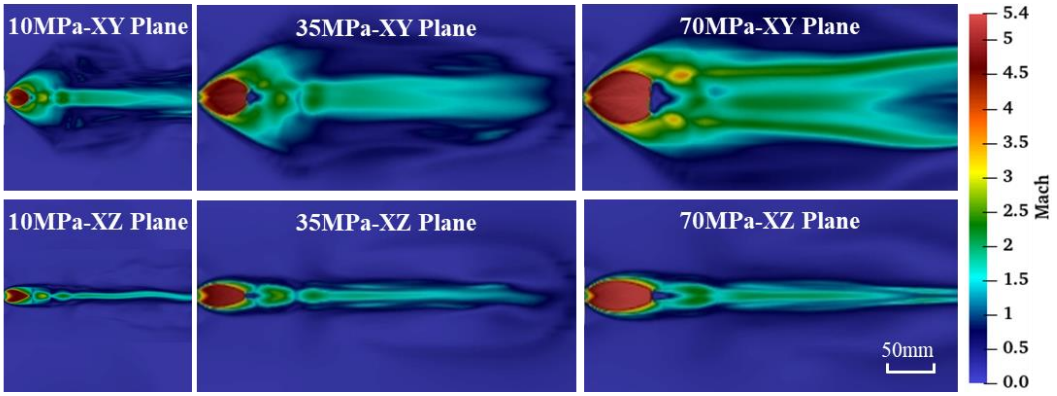

Fig. 4. *The Mach number distribution of the AR4 nozzle with a 4mm diameter under different leakage pressures*

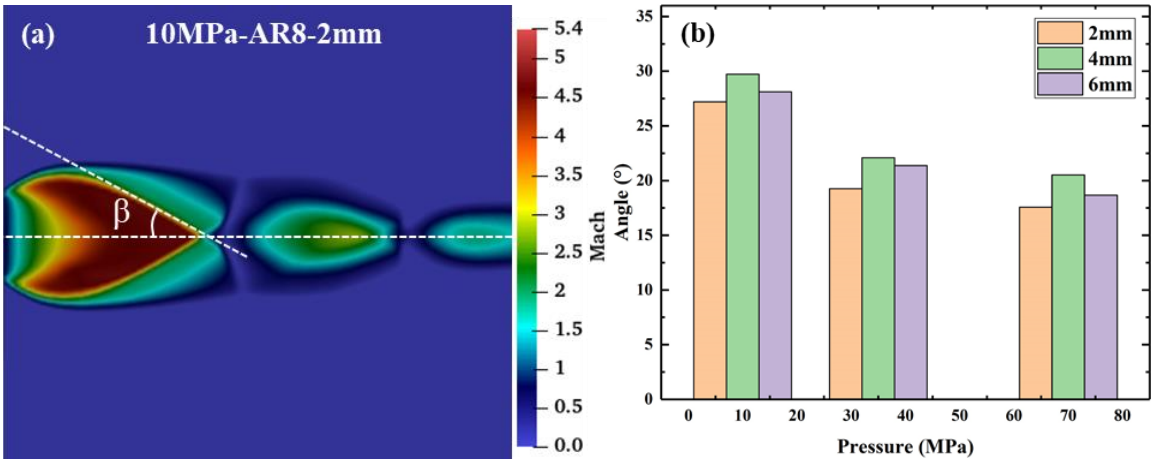

Fig. 5. *The shockwave angle. (a) Schematic diagram of an oblique shock wave angle, (b) The angle of oblique shock wave for the AR8 nozzle at different pressures and nozzle diameters*

The position of the shock wave is also studied in this paper. Anaclerio et al.(2023) introduced a linear relationship based on a semi-empirical formula for the Mach disk position to make it applicable to rectangular nozzle jets. This approach is adopted in this study, and the modified expression is shown below:

$$\frac{H_{disk}}{d} = E(AR)\sqrt{\frac{P_s}{P_a}} \tag{15}$$

where H_{disk} represents the shock wave location, P_s denotes the stagnation pressure, P_a signifies the ambient pressure, d is the equivalent diameter of a rectangular nozzle. E(AR) represents the linear function introduced, where the aspect ratio serves as the independent variable, producing diverse function outputs across different pressure levels. The linear relationship between E(AR) and AR under different pressures is shown in Figure 6. It can be observed that the ratio of E(AR) to AR for nozzles leaking at the same pressure but with different equivalent diameters tends to approach a constant line, indicating that the shock wave position adheres to the aforementioned expression. Additionally, as the aspect ratio increases, the shock wave position gradually moves closer to the nozzle exit.

The distribution of the 300kPa pressure contour after the leakage of the rectangular nozzles at 10MPa pressure is illustrated in Figure 7. With the augmentation of the aspect ratio, there is an exacerbation

in the reduction of pressure along the x-axis, consequently leading to a gradual shift of the Mach disk position towards the nozzle exit.

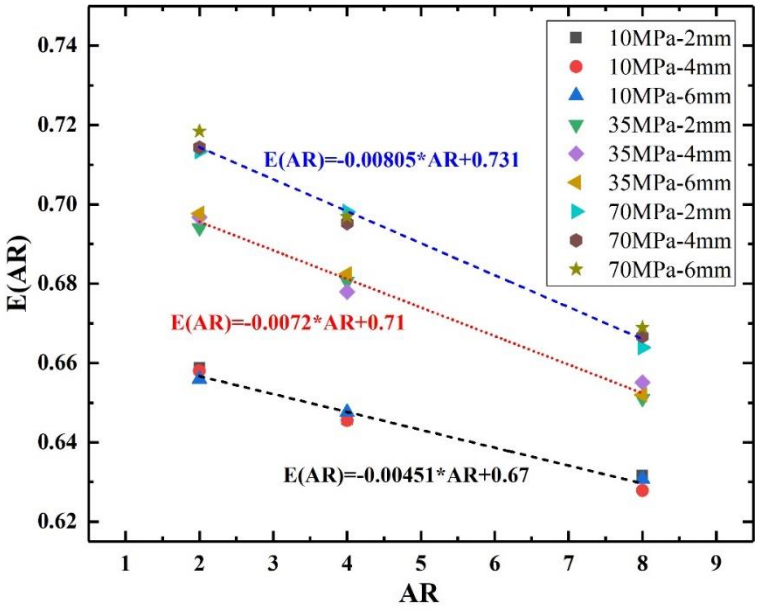

Fig. 6. *Linear relationship of E(AR) under different pressures*

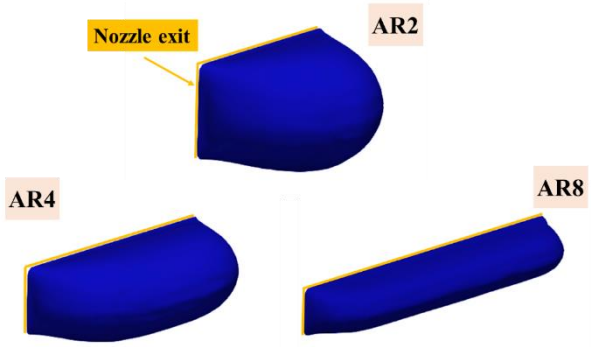

Fig. 7. *The distribution of pressure isosurfaces at 300 kPa after the leakage of the rectangular nozzles under a pressure of 10 MPa*

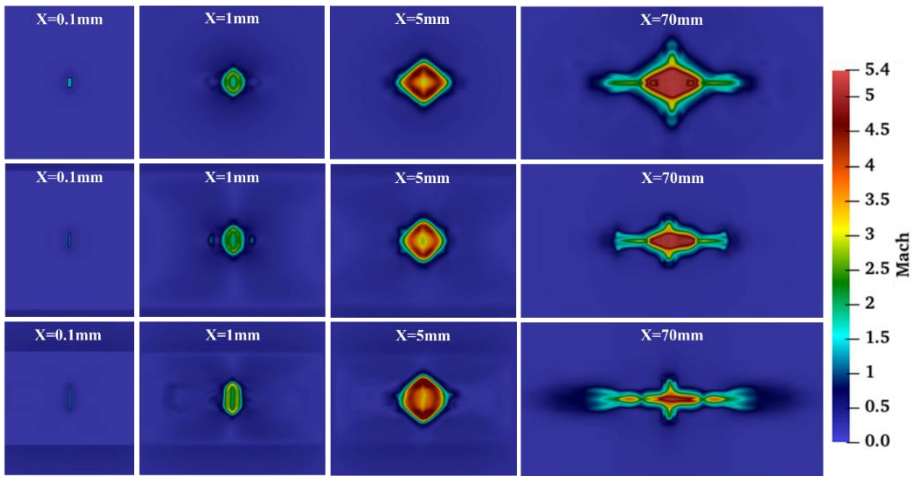

Fig. 8. *Cross-sectional slice of the Mach number flow field at 70MPa pressure*

Hydrogen gas leaking from nozzles with equivalent diameters of 4mm at various aspect ratios under pressure of 70MPa exhibits Mach number distributions parallel to the nozzle cross-section, as shown

in Figure 8. The phenomenon of axis conversion is also observed. As the jet travels downstream, its boundary rapidly expands. This is due to the greater vorticity magnitude at the centre of the jet edges, resulting in a faster expansion rate at the edge centres and a slower rate at the vertices, leading to deflection. At three different aspect ratios, the positions of the shock waves are 75.2mm, 73.1mm, and 70.4mm, respectively. Axis conversion is essentially completed before these positions.

3.2 The virtual nozzle model

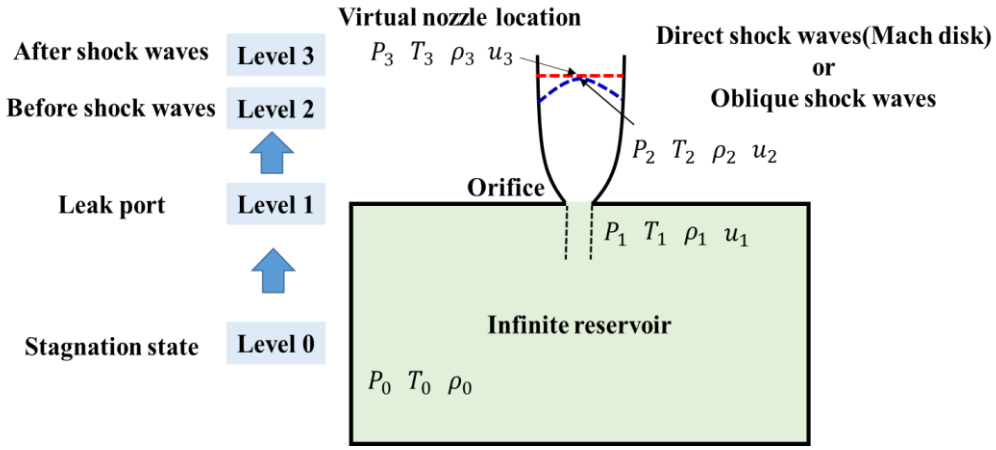

Fig.9. *Schematic diagram of the virtual nozzle model*

For the computational analysis of high-pressure shock structures, there is a proposition to model high-pressure shock structures using a virtual nozzle to simplify computations. This virtual nozzle is conceptualized as an imaginary leakage source with an equivalent gas mass flow rate to the real leakage and a gas pressure approximately equal to atmospheric pressure. This concept aims to simplify the intricate shock structures found in high-pressure underexpanded jets, treating them akin to traditional low-pressure leaks. Currently, there is no established virtual nozzle model for high-pressure hydrogen leakage from rectangular nozzles. This paper, based on the jet structure from rectangular nozzles, enhanced the existing virtual nozzle model. A schematic representation of the dummy nozzle model is illustrated in Figure 9. The process of high-pressure hydrogen release involves four states, namely:

Level 0 - the conditions inside the reservoir;

Level 1 - the conditions at the orifice;

Level 2 - the conditions before the Mach disk;

Level 3 - the conditions after Mach disk.

Assuming the virtual nozzle is positioned at Level 3, after the passage of the Mach disk. The gas undergoes isentropic expansion from stagnation conditions to the orifice. Parameters at the orifice can be computed using the gas state equation and isentropic expansion relations. The gas from the orifice to the dummy nozzle position satisfies mass conservation, momentum conservation, and energy conservation, expressed by the following relationships:

$$\rho_1 u_1 A_1 = \rho_3 u_3 A_3 \tag{16}$$

$$P_1A_1 + \rho_1 u_1^2 A_1 = P_3A_3 + \rho_3 u_3^2 A_3 \tag{17}$$

$$\rho_1 u_1 A_1 (c_P T_1 + \frac{u_1^2}{2}) = \rho_3 u_3 A_3 (c_P T_3 + \frac{u_3^2}{2}) \tag{18}$$

The symbol u_3 denotes the flow velocity behind the Mach disk, and its expression is given by:

$$u_3 = Ma_3 \sqrt{\gamma R_g T_3} \tag{19}$$

The relationship between the Mach numbers before and after the shock wave is expressed as

$$Ma_3^2 = \frac{Ma_2^2 + \frac{2}{\gamma - 1}}{\frac{2\gamma}{\gamma - 1} Ma_2^2 \sin^2 \beta - 1} + \frac{Ma_2^2 \cos^2 \beta}{\frac{\gamma - 1}{2} Ma_2^2 \sin^2 \beta + 1} \tag{20}$$

The β in the formula represents the angle between the shock wave and the hydrogen flow. For a normal shock wave, the shock angle is $\beta = 90^\circ$, while for an oblique shock wave $\beta < 90^\circ$. The relationship between stagnation pressure and Mach number holds during the expansion process of the airflow from the nozzle exit to the position before the Mach disk:

$$\frac{P_0}{P_2} = (1 + \frac{\gamma - 1}{2} Ma_2^2)^{\frac{\gamma}{\gamma - 1}} \tag{21}$$

When the hydrogen passes through a normal shock wave, the pressure before and after the shock wave satisfies the relationship:

$$\frac{P_3}{P_2} = \frac{2kMa_2^2}{k+1} - \frac{k-1}{k+1} \tag{22}$$

After the normal shock wave, the ambient pressure is present, meaning $P_3 = P_\infty$. Combining equations (21) and (22), the Mach number ahead of the normal shock wave is:

$$\frac{P_0}{P_\infty} = \frac{(1 + \frac{\gamma - 1}{2} Ma_2^2)^{\frac{\gamma}{\gamma - 1}}}{\frac{2\gamma}{\gamma + 1} (\mathrm{Ma}_2 - 1) + 1} \tag{23}$$

The simulation results indicate that the Mach numbers ahead of the Mach disk for all rectangular nozzles are nearly identical. Therefore, the Mach number ahead of the oblique shock wave is also calculated using equation (23). Substituting equation (19) into equations (16)~ (18), which include three unknowns T_3, ρ_3, A_3, the equations become closed, allowing for a solution.

When conducting large-scale hydrogen leak dispersion simulations, this model can be utilized to simplify the complex shock wave structures near the leak source. The specific implementation method is as follows: based on the known leak pressure and length-to-diameter ratio, it is determined whether a Mach disk is formed. The model is then used to calculate parameters such as mass flow

rate, temperature, velocity, and area at the virtual nozzle location. The mass flow rate obtained from the model serves as the inlet condition for numerical simulations, while the Mach disk/central shock wave position is used as the entrance location of the model. The calculated A3 is employed as the entrance area, taking into consideration that the axis transformation has already occurred before the Mach disk. It should be noted that when modelling, the leak source needs to be rotated 180°. Further research is needed for the application and validation of this model. In future studies, the effectiveness of the virtual nozzle model will be verified. A complete numerical simulation of the leakage process and a simplified simulation using the virtual nozzle model will be performed under the same operating conditions. The effectiveness of the virtual nozzle model will be verified by comparing the results of two simulations, such as concentration distribution and velocity distribution.

4. Conclusion

Numerical simulation based on OpenFOAM is employed to investigate hydrogen leakage from rectangular nozzles. The main conclusions are as follows:

(1) Under all operating conditions investigated in this paper, the AR2 nozzle forms a Mach disk after leakage, while the AR8 nozzle only generates oblique shock waves without forming a Mach disk. When the hydrogen storage pressure exceeds 20MPa, the AR4 nozzle also produces a Mach disk. Empirical formulas for the position of the Mach disk/shock wave are summarized.

(2) Based on the characteristics of the jet structure formed after the release from rectangular nozzles, an improved virtual nozzle model is proposed. The virtual nozzle assumes mass conservation, momentum conservation, and energy conservation from the nozzle to its position after the Mach disk. By integrating the equations before and after the shock wave, the parameters at the virtual nozzle position are solved.

(3) The virtual nozzle model is only suitable for rectangular nozzle leak simulations where the leak pressure, diameter, and aspect ratio are known. In addition, the model is based on a constant leakage pressure, and the prediction may be conservative when the pressure becomes smaller during the leakage.

Acknowledgements

The authors appreciate the financial support by the National Key R&D Program of China (No. 2021YFB4000902).

References

Yue M, Lambert H, Pahon E, Roche R, Jemei S, Hissel D,2021. Hydrogen energy systems: A critical review of technologies, applications, trends and challenges. RENEW SUST ENERG REV.146,111180.

Usman,MR.,2022.Hydrogen storage methods: Review and current status. Renewable and Sustainable Energy Reviews. 2022;167:112743.

Guo, L., Su,J., Wang,Z., Shi,J., Guan,X., Cao,W., Ou,Z.,2024. Hydrogen safety: An obstacle that must be overcome on the road towards future hydrogen economy, INT J HYDROGEN ENERG.51,1055-1078.

Okabayashi,K.,Tagashira,K.,Kawazoe,K.,Takeno.K,Asahara,M.,Hayashi,AK.,2019.Non-steady characteristics of dispersion and ignitability for high-pressurized hydrogen jet discharged from a

pinhole. INT J HYDROGEN ENERG.44,9071-9.

Kobayashi,H.,Naruo,Y., Maru,Y., Takesaki,Y., Miyanabe,K. ,2018.Experiment of cryo-compressed (90-MPa) hydrogen leakage diffusion. INT J HYDROGEN ENERG. 43,17928-37.

Takeno,K., Okabayashi,K., Kouchi,A., Misaka,N., Hashiguchi,K.,2017. Concentration fluctuation and ignition characteristics during atmospheric diffusion of hydrogen spouted from high pressure storage. INT J HYDROGEN ENERG. 42,15426-34.

Crist,S.,D.R.Glass,and P.M. Sherman,1966. Study of the highly underexpanded sonic jet. 68-71.

Velikorodny, A., Kudridkov,S.,2012.Numerical study of the near-field of highly underexpanded turbulent gas jets. INT J HYDROGEN ENERG.37(22),17390-17399.

Han,SH., Chang,D., Kim,JS.,2014. Experimental investigation of highly pressurized hydrogen release through a small hole. INT J HYDROGEN ENERG. 39,9552-61.

Han,SH., Chang,D., Kim,JS.,2013. Release characteristics of highly pressurized hydrogen through a small hole. INT J HYDROGEN ENERG. 38,3503-12.

Tang,X., Dzieminska,E., Asahara,M., Hayashi,AK., Tsuboi, N.,2018. Numerical investigation of a high pressure hydrogen jet of 82 MPa with adaptive mesh refinement: Concentration and velocity distributions. INT J HYDROGEN ENERG. 43,9094-109.

Birch,AD., Brown,DR., Dodson,MG., Swaffield,F.,1984. The Structure and Concentration Decay of High Pressure Jets of Natural Gas. c. 36,249-61.

Ewan,BCR., Moodie,K.,1986. Structure and Velocity Measurements in Underexpanded Jets. COMBUST SCI TECHNOL. 45,275-88.

Harstad,K.,Bellan,J.,2006. Global analysis and parametric dependencies for potential unintended hydrogen-fuel releases. COMBUST FLAME. 144(1-2), 89-102.

Molkov,V., 2012. Hydrogen safety engineering: The state-of-the-art and future progress. Compr Renew Energy.4,77-109.

Li,X.,Chen,Q.,Chen,M.,He,Q., Christopher,DM.,Cheng,X.,2019. Modeling of underexpanded hydrogen jets through square and rectangular slot nozzles. INT J HYDROGEN ENERG. 44,6353-65.

Makarov,D., Molkov,V.,2013. Plane hydrogen jets. INT J HYDROGEN ENERG. 38,8068-83.

Stewart,JR.,2020. CFD modelling of underexpanded hydrogen jets exiting rectangular shaped openings. PROCESS SAF ENVIRON. 139,283-96.

Peng,D., Robinson. DB.,1976. A New Two-Constant Equation of State. Industrial & Engineering Chemistry Fundamentals. 15,59-64.

Mcbride,BJ., Gordon,SD., Reno,MA.,1993. Coefficients for calculating thermodynamic and transport properties of individual species.

Anaclerio,G.,Capurso,T.,Torresi,M.,2023. Gas-dynamic and mixing analysis of under-expanded hydrogen jets: effect of the cross section shape. J FLUID MECH.970.

Calibrated Tracer-LIF Spectra for Experimental Investigation of Ignition Processes

J. Brunzendorf, V. Vasudevan, D. Markus

Physikalisch-Technische Bundesanstalt (PTB), Bundesallee 100, 38116 Braunschweig, Germany

E-mail: *Jens.Brunzendorf@PTB.de*

Abstract

Temperature distributions, gas concentrations, mixing processes and oxygen concentrations are key parameters in ignition and explosion processes e.g. by electrostatic discharges, hot free gas jets or hot surfaces. Knowledge of these quantities enables the definition of safe operating limits in the process industry and a proper design of explosion protected equipment. Accurate measurements are necessary to avoid large safety margins or explosions hazards. In recent decades, laser-induced fluorescence (LIF) has developed into an established method for measuring the 2D distribution of temperatures and gas concentrations with high spatial and temporal resolution. Knowledge of the emitted LIF spectrum is required to interpret the LIF signal. These spectra cannot be calculated, they have to be measured. Most of the available high quality LIF spectra are included in the tracer-sim database. However, even with the most common LIF tracers such as acetone, there are substantial deviations in the spectral shape; the relative intensities can differ by a factor of two or more. The number and position of the maxima also differ considerably from author to author. In this work we present intensity- and wavelength-calibrated LIF spectra for various suitable tracers (such as toluene, anisole, acetone, 2-butanone, 2-pentanone, 3-pentanone, cyclopentanone, cyclohexanone, acetophenone, ethyl acetate, 1,3-dimethoxybenzene) measured at room temperature and ambient pressure. There is a good overall agreement with previous publications, although the spectra in this work have both a higher spectral resolution and signal-to-noise ratio. This will allow for explosion and combustion experiments with lower uncertainties than previously possible.

Keywords: *laser-induced fluorescence, tracers, spectroscopy, calibration, explosion, visualization*

Introduction

Under what conditions do ignition processes take place? This question is just as important for explosion protection as it is for ensuring stable combustion processes, for example in burners or engines. One way of answering this question is to investigate the physico-chemical conditions, in particular the spatial and temporal temperature distributions, the gas concentrations, the mixing processes and the oxygen concentrations. Knowledge of these variables enables the definition of safe operating limits in the process industry and the appropriate design of explosion-proof equipment. Accurate measurements are necessary to avoid large safety margins or explosion hazards.

A common method for the determination of these quantities are laser-induced fluorescence (LIF) measurements. This non-invasive technique allows high-resolution two-dimensional investigations of chemical reactions, gas mixing and temperature fields. The fundamentals have been described excellently in the books by Eckbreth (1996) and Kohse-Höinghaus & Jeffries (2002) and references therein and shall not be repeated here.

During the last decades, LIF has become one of the established fundamental techniques in ignition and combustion research (Deguchi 2019). In tracer LIF, a suitable tracer gas is added which produces the LIF signal when exited. However, the interpretation of the detected LIF signal is not straightforward, because the shape and total intensity of the LIF spectrum does not only depend on

the concentration of the tracer gas, but also on other influence quantities like the laser excitation wavelength and pulse energy, gas temperature and pressure, as well as the remaining gas components (especially quenchers like oxygen and water). For quantitative results, these influence factors must be quantified. This applies in particular to the evaluation of signal ratios such as in two-color thermometry or other multispectral techniques (e.g. Thurber, Grisch & Hanson 1997, Thurber & Hanson 2001, Schulz & Sick 2005, Lind et al. 2016).

These dependencies cannot be calculated analytically; suitable models rely on several simplifications and free parameters which must be calibrated by fitting the model onto reference spectra. For meaningful results, these reference spectra should be both wavelength- and intensity-calibrated. Recently, UV-sensitive scientific CMOS cameras entered the market, which have a much higher resolution than the common image intensifier cameras, a near-perfect linearity, a large detector area and no sensitivity degradation by light. This, in combination with the unique calibration facilities at PTB, are good prerequisites for accurate LIF spectra measurements traceable to the SI system.

In this work, we present intensity and wavelength calibrated LIF spectra for various suitable tracers: ketones (acetone, 2-butanone, 2-pentanone, 3-pentanone, cyclopentanone, cyclohexanone, aceto-phenone), aromatic compounds (toluene, anisole, 1,3-dimethoxybenzene), and ester (ethyl acetate). Usually, the LIF spectra were measured in three different carrier gases: nitrogen, hydrogen and synthetic air at room temperature and ambient pressure. Some of these tracers are already common in explosion protection research, others are possible LIF alternatives and/or integral components of biofuels which can be used as integrated tracers. The spectra of several known LIF-active substances were not measured: Benzene was considered too carcinogenic, diacetyl even destroys PTFE hoses and seals, and others proved to have too weak LIF signals for meaningful measurements.

There is a good overall agreement with previous publications, although the spectra in this work have both a higher spectral resolution and signal-to-noise ratio. This will allow for concentration measurements with lower uncertainties than previously possible. Thus, this work promotes the detailed experimental investigation of ignition and explosion processes.

1. Experimental Setup

The experimental setup essentially consists of a 266 nm Nd:YAG laser, a quartz cell containing the tracer gas and a spectrometer with CMOS camera. The principal components are shown in Fig. 1.

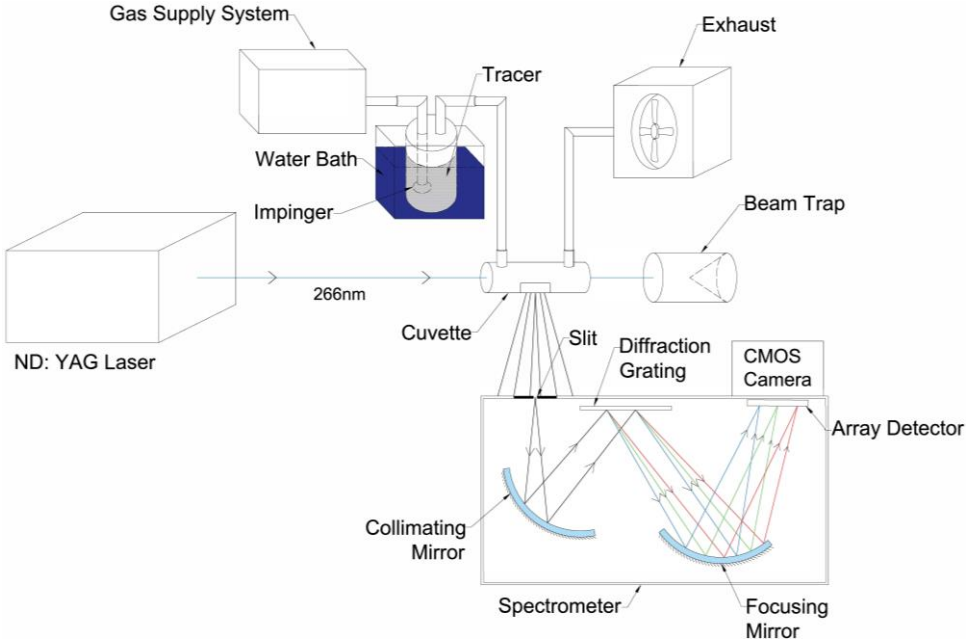

Fig. 1. *Principal components and light path. A 266 nm laser beam passes through a gas cell containing the tracer gas produced in a bubbler. The LIF signal is recorded with a grating spectrometer + CMOS camera.*

The 266 nm laser light is produced by an Innolas Spitlight 2500 (up to 200 mJ per pulse with 7 ns pulse length and a repetition rate of 3 Hz). The laser beam passes a cylindrical quartz glass gas cell of type Hellma 120-QS (Fig. 2). An 8 mm aperture directly in front of the gas cell (Fig. 2) removes incoming stray light and defines the laser beam.

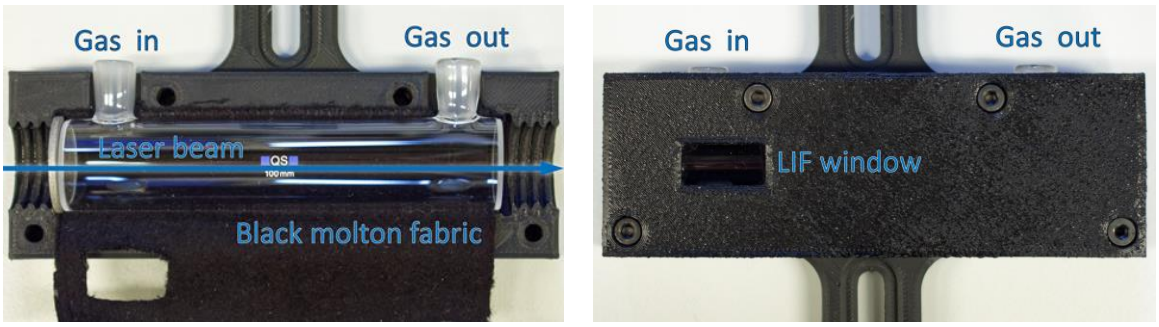

Fig. 2. *Quartz cuvette for LIF detection (Left: open housing, Right: final configuration). Laser beam and gas flow directions: left → right. Black molton wraps cuvette, LIF window below gas entrance.*

For further stray light absorption and removal, the gas cell is completely wrapped in black molton, with the exception of the laser entrance and exit windows and a side window 2×1 cm² just below the gas entrance.

The cell is purged with the carrier/tracer gas mixture, which is produced in a temperature-stabilized Drechsel gas wash bottle with filter disk containing the liquid tracer. This bubbler is purged with either nitrogen, hydrogen or dry air from gas bottles at a flow rate of 1 liter/min, corresponding to a gas velocity within the gas cell of 6 cm/s. This velocity ensures that the gas in front of the window is renewed between two laser shots. The temperature of the whole lab is kept at 22°C, i.e. above the bubbler water bath temperature of 19 °C to avoid tracer condensation.

The spectrometer entrance axis is aligned perpendicular to the laser beam axis entrance and centred to the gas cell side window. The distance between the laser beam axis and the slit entrance is 5 cm. To avoid various possible problems in the intensity calibration, there is deliberately no optical element between the gas cuvette and the spectrometer, neither a light-collecting optic nor a bandpass filter. This excludes all influences of the filter, the light-collecting optics or any anti-reflection coating on the calibration process. Note that the emission spectrum of a calibration lamp is different at different points of the lamp and optical elements can either focus on the hottest part of the tungsten wire or the cooler housing, thus changing the measured spectrum. The fact that no bandpass filter is used must be taken into consideration during the data evaluation: strong LIF signals in the 300 nm region might cause a (much fainter) artificial second order signal at exactly twice the wavelength. One major advantage is that a much broader spectral range can be measured simultaneously.

The spectra are measured with a conventional Czerny-Turner with 320 mm focal length (Acton Research SpectraPro-300i), a grating with 150 lines/mm and a blaze wavelength of 300 nm. An extra aperture is inserted between the last mirror and the detector for additional stray light removal. The spectra were recorded by a scientific CMOS camera containing a Gpixel GSENSE 400BSI sensor with 22×22 mm² area and 11 µm pixel size (2048×2048 pixels, backside-illuminated). Thus, a spectral range from 200 nm to 670 nm is simultaneously covered with a pixel resolution of 0.24 nm/pixel and a measured spectral FWHM resolution of better than 1 nm. With this type of sensor, nonlinearities are not an issue, and readout noise is less than 2 e-/pixel (sensor temperature -25 °C). The UV quantum efficiency exceeds 30 % above 200 nm.

Great care was taken to avoid LIF-active substances in the setup and to remove all reflections, including within the spectrometer. The surfaces of the setup are painted with black non-fluorescent paint or covered with black molton fabric. An additional housing shields the experiment from ambient light. More details are given in Brunzendorf et al. (2024).

2. Wavelength and Intensity Calibration

The calibration of the wavelength axis is based on the emission lines of a mercury vapor lamp of type Newport Spectral Calibration Lamp, Hg (Ar), Model 6035. The positions of the emission lines were taken from the metrological NIST atomic database. The sCMOS sensor is oriented so that the emission lines are parallel to the x-axis, while the wavelength axis follows the y-axis. A linear fit between the emission line wavelengths and the corresponding y positions of the lines provides the wavelength calibration with an uncertainty of less than 0.2 nm.

For the determination of the spectral response of the setup (intensity calibration), the gas cell is removed and a PTB calibration lamp is placed at a distance of 50 cm from the entrance slit of the spectrometer. All non-black parts outside the light path between lamp and entrance slit were covered with black molton fabric to suppress stray light. After the stated burn-in time is passed, the spectrum is measured. Calibration is performed both with a tungsten and a deuterium lamp. Both lamps were calibrated at PTB, the spectral irradiance is traceable to the International System of Units SI. The wavelength-dependent irradiance of both calibration lamps is shown in Fig. 3 (left), and the measured signal intensities are given in Fig. 3 (right).

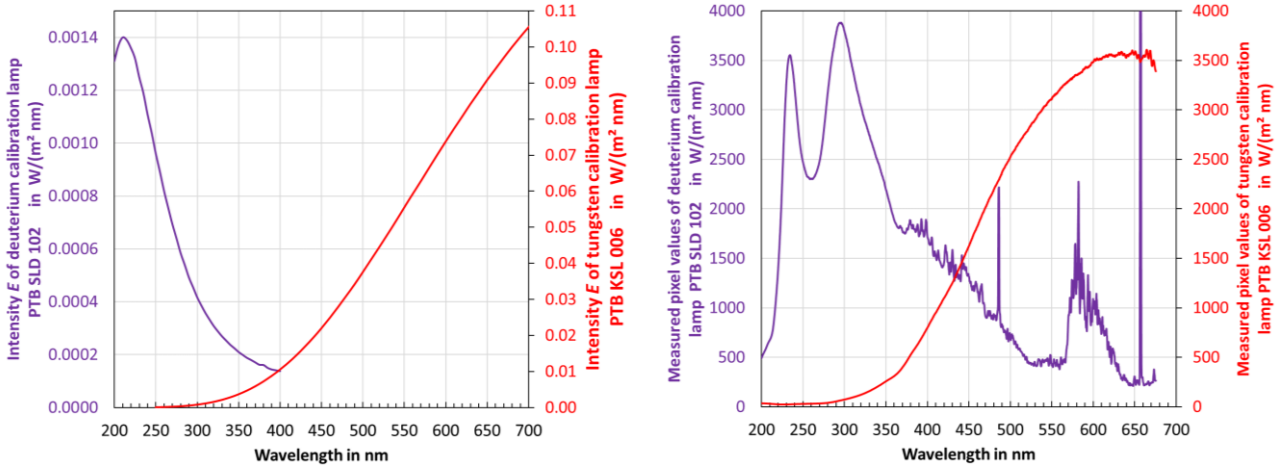

Fig. 3. *Intensity calibration.* ***Left:*** *Spectral irradiance of the Deuterium lamp PTB-SLD-102 (200…400 nm, violet) and tungsten lamp PTB-KSL-006 (250+ nm, red).* ***Right****: Corresponding measured pixel intensities.*

The shape of the signal intensities is determined by the product of lamp intensity, grating efficiency and sensor sensitivity. The significant drop in the measured signal intensity between the two peaks at 240 nm and 300 nm is due to a known local minimum in the sensor sensitivity.

The spectral irradiance of the deuterium lamp was traceably calibrated in the range from 200 nm to 400 nm, that of the tungsten lamp from 250 nm.

The tungsten signal below 350 nm is too weak for reliable calibration. On the other hand, the deuterium spectrum above 370 nm has emission lines that make intensity calibration difficult. Therefore, the determination of the spectral response was split in two: up to 360 nm it is based on the deuterium spectrum, whereas at longer wavelengths it is based on the tungsten spectrum. The relative response of the system for a given wavelength is equal to the ratio between the measured signal and the spectral irradiance of the lamp. The resulting relative response (sensitivity) of the spectrometer/camera system is shown in Fig. 4. Further details can be found in Brunzendorf et al. (2024).

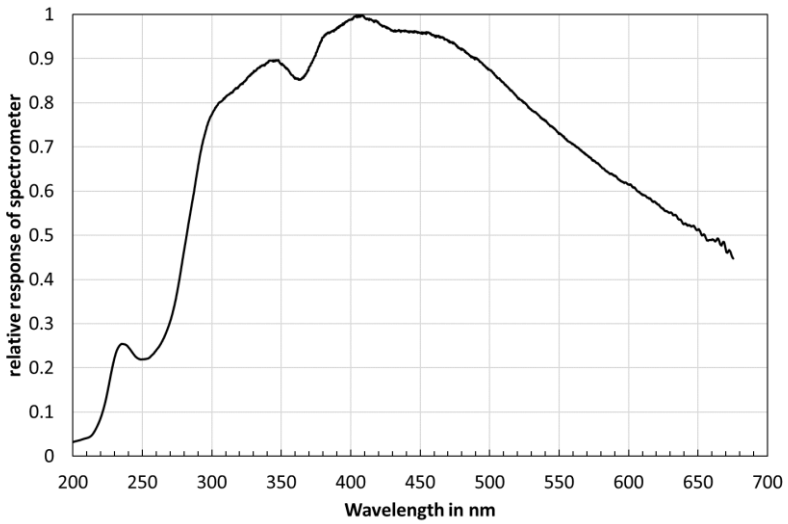

Fig. 4. *Resulting sensitivity curve of the spectrometer/camera system. Note that the data are not smoothed.*

3. Measurements

The measurements required to determine the LIF spectra were carried out in the following steps: (0) thorough cleaning and flushing of the whole setup if necessary, (1) measurement of the cuvette signal with 266nm laser light, but without tracer gas, (2) if a LIF signal is visible, proceed with step 0, otherwise (3) flushing the cuvette with the tracer gas in N_2 for at least 5 min, (4) switching on laser light, waiting for stabilization, (5) 100+ images of the 2D spectrum were taken (at most 700 images, depending on signal intensity), (6) repetition of steps 3-5 with carrier gas H_2, synthetic air, and again N_2, (7) repetition of step 1, (8) measurement of the signal with laser light switched off (dark frames). The integration time and detector gain had to be adjusted to the LIF intensity to avoid overexposure. The maximum exposure time was five seconds – at this exposure time the dark noise of the sCMOS detector becomes as high as the read-out noise.

The search for residual LIF signals in the absence of a LIF tracer is crucial to minimize the background signal and to produce reliable results. Prior to the actual measurements, the empty cuvette was illuminated with 266 nm laser light, which was passed through both windows. The images taken with an ordinary color camera showed a conspicuous, ubiquitous blue light that should not be present (Fig. 5, left image). Suprasil is known to be non-fluorescent. Although the cuvette was taken from a freshly purchased sealed box bought directly from Hellma Analytics, it already showed the LIF glow. However, blue LIF signals can also be generated by possible cleaning residues or organic substances. Fingerprints are also a known source of blue LIF signals (Saitoh & Akiba, 2005).

The search for the origin of the significant blue LIF glow of the original Hellma cuvettes and its elimination proved to be much more complicated, time-consuming and surprising than expected. The authors began with typical gentle cleaning procedures such as rinsing with triple distilled water, ultra-pure isopropanol and ethanole as well as Hellmanex III, but to no avail; the LIF signal persisted. Stronger chemicals such as acetone, H2O2, ethyl acetate and even KOH showed no discernible effect. In the third step, a mixture of warm Hellmanex III and isopropanol as well as hot KOH + isopropanol were tried. The effect was rather negative, as the hot KOH increased the blue glow, possibly due to the aggressive substance damaging the surface of the cuvette. The use of the above-mentioned chemicals in combination with an ultrasonic bath was also rather counterproductive, as it also increased the blue glow. Finally, a heat gun was used to generate hot air at temperatures of up to 800 °C (1070 K). Most organic substances burn at these temperatures. The cuvette became red-hot in the air stream. It was then rinsed with triple distilled water and ultra-pure isopropanol to remove any residue. The blue glow was weaker than ever before, but had not disappeared. In the end, the authors bought an old, used Hellma cuvette of the same type after learning that Hellma had changed the manufacturing process and the type of quartz glass about 6 years ago. This old cell had to be cleaned,

after which only a red LIF glow could be seen at those parts of the windows that were directly hit by the laser beam. The main part of the cell showed no fluorescence (Fig. 5, right). LIF emission at the windows is insignificant, as it cannot enter the spectrometer, and the red LIF emissions are in a different spectral range than the blue LIF of the ketones and aromatics.

Fig. 5. *266 nm laser light through Hellma cuvettes:* ***Left****: new cuvette claimed to be made of suprasil (QS), but shows a significant blue LIF signal,* ***Right:*** *old second-hand Hellma cuvette without blue LIF signal. The red spots at the windows are laser light LIF signals caused by the cleaning procedure and are insignificant.*

The final measurements were carried out with a measured laser intensity at the position of the cell of 60 mJ per shot, i.e. a fluence of 1.3 mJ/mm², with a 1 σ shot-to-shot stability of better than 3 %.

4. Data Reduction

According to the sensitivity curve (Fig. 4), the spectrometer has its highest sensitivity in the range from 260 nm, and the calibration applies up to a maximum of 650 nm. This range is exactly the relevant range for LIF measurements based on an excitation wavelength of 266 nm.

For all LIF spectra it was checked whether the LIF intensity or the LIF spectrum changed over time, i.e. over the sequence of frames. A drift or other change would indicate some kind of instability or chemical reaction. However, in no case an intensity or shape change of the LIF spectrum was detected.

Hence, all 100+ frames of a LIF measurement were evaluated: (1) Each frame was corrected for cosmic ray hits, (2) extraction of the central 171×2048 pixels (Czerny-Turner spectrographs are sharpest near the optical axis), (3) averaging of all 171 pixels at the same wavelength, resulting in a spectrum with a length of 2048 pixels. Finally, the 100+ spectra were averaged. Then, the dark spectrum (processed in exactly the same way) was subtracted from the light spectrum.

The LIF intensity is calibrated by dividing by the relative response. For each intensity calibrated LIF spectrum, the total intensity is derived, which is needed for the determination of quenching effects. In addition, each spectrum was normalized to the maximum intensity above 270 nm (the 266 nm laser line is not part of the LIF spectrum and must be excluded) to simplify the comparison of the spectral shapes.

Note that the laser lines at 266 nm and 532 nm (caused by scattered laser light) are not removed to indicate these two regions and the intensity of the laser signal. These regions should be considered as unreliable due to the superimposition of a non-LIF-signal. Initially, a removal of the laser lines was planned. For this purpose, no-tracer-spectra were taken just before and after the LIF measurements (same setup, but no LIF tracer in the cell, just the carrier gas). However, the intensities of the 266 nm and 532 nm laser lines were significantly different between LIF spectra and no-tracer-spectra. Partially, this is due to the different Rayleigh scattering cross sections of the different molecules. Another contribution comes from adsorption and photolysis, which increase laser light scattering. Therefore, the 266 nm and 532 nm regions should be discarded.

5. Results and discussion

The measured and peak-normalized irradiance spectra of several LIF tracers are shown in Fig. 6 to 8. Note that the data are not smoothed and the FWHM resolution is better than 1 nm. As this is an ongoing project, some follow-up measurements are planned to confirm the measured spectra and to evaluate previously undetected contributions to the uncertainty budget, such as long-term drift, cleaning effects, ageing and weathering of the cell.

Common LIF tracers are acetone and 3-pentanone. Their LIF spectra as well as those of two related ketones (2-butanone and 2-pentanone) are presented in Fig. 6. All four ketones have similar smooth, bell-shaped LIF-spectra with a maximum intensity in the blue region (415 nm for acetone and 3-pentanone, and 430 nm for 2-butanone and 2-pentanone). Despite the exceptionally high signal-to-noise ratio, there is no detectable influence of the carrier gas (N_2, H_2, or synthetic air) on the shape of the LIF tracer spectra: The three curves lie directly on top of each other. For 2-butanone, the spectra in H_2 and air were omitted because they were too noisy due to a drop in laser intensity.

Several 266 nm acetone LIF spectra under ambient conditions have already been published in the literature. The position of the acetone LIF intensity maximum was found to be at 385 nm (Schulz & Sick 2005), near 400…410 nm (Grisch, Thurber & Hanson 1997, Bryant, Donbar & Driscoll 2000, Rossow 2011) with a possible secondary maximum near 370 nm (Rossow 2011), at (408±2) nm (this work) or at 450 nm (Yu et al. 2019). The acetone spectra determined in this work match the literature values well (Brunzendorf et al. 2024). In general, the literature values show considerable noise, which is due to the use of image intensified cameras and is considerably higher than in the present work.

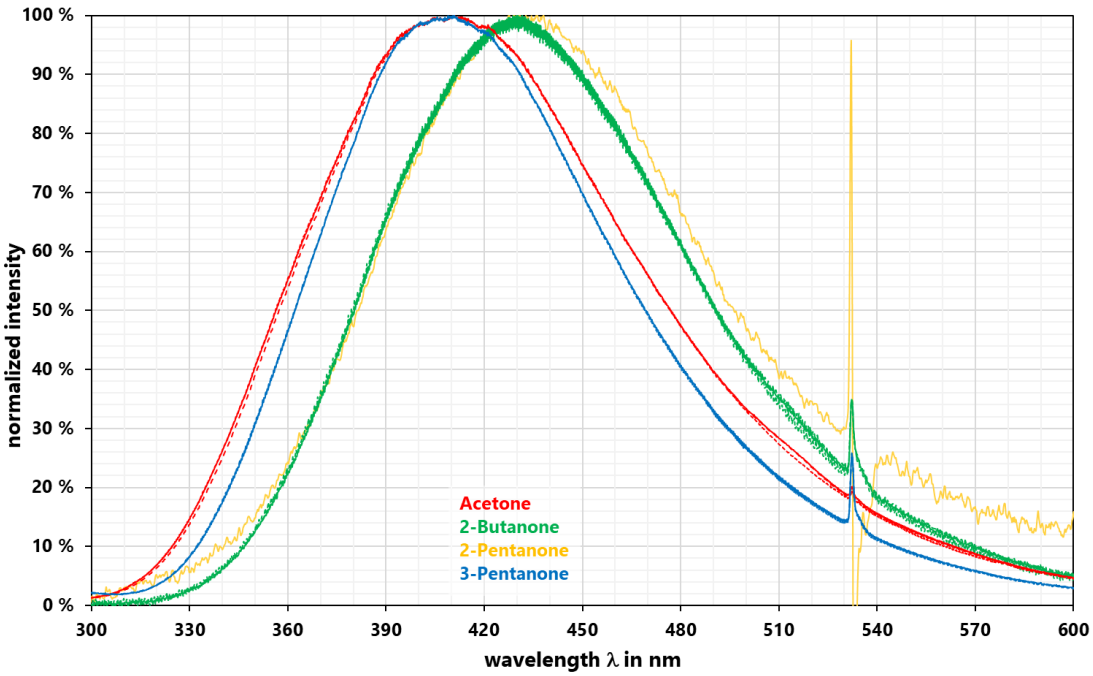

Fig. 6. *266 nm ketone LIF spectra: Peak-normalized intensities of acetone (red), 2-butanone (green), 2-pentanone (orange), and 3-pentanone (blue) at ambient conditions in N_2 (solid lines), H_2 (dashed lines) and synthetic air (dotted lines) as carrier gas. Note that the lines of each gas are practically superimposed.*

The LIF spectrum of 3-pentanone is similar to that of acetone, but somewhat narrower. The LIF spectra of 2-butanone and 2-pentanone are also similar. There is no evidence of band structures. The conspicuous laser line at 532 nm must be ignored as it is not part of the LIF spectrum. It was not removed because the LIF spectrum in this range is unusable. The position of the 532 nm laser line is an indicator of the quality of the wavelength calibration, as it must always be at 532 nm.

It shall be noted that for all four ketones – acetone, 2-butanone, 2-pentanone and 3-pentanone – the integral LIF intensity is independent of the carrier gas (N_2, H_2, synthetic air) within the measurement uncertainty (2% due to laser instabilities). There is no evidence of oxygen quenching. Hence, these ketones are well-suited for concentration measurements, even in the presence of oxygen.

Among the usual LIF-active aromatics, benzene was not measured because it is too carcinogenic, but toluene and anisole were. Their 266 nm LIF spectra are shown in Fig. 7. The strong 266 nm peak due to scattered laser light shall be ignored. The peak-normalized LIF spectra are consistent with the literature (TracerSim-Dat 2022, Yu et al. 2019). As expected, the LIF spectra in N_2 and H_2 agree, while synthetic air causes an apparent shift of the peak-normalized spectrum toward longer wavelengths. This effect is due to the strong oxygen quenching, which is more pronounced at shorter wavelengths. Due to the oxygen quenching, the total LIF intensity above 270 nm decreases by a factor of 17 (anisole) or 14 (toluene). It should be noted that the energy density of the laser triggers significant self-quenching of toluene (Fuhrmann et al. 2017). Although the synthetic air was always taken from the same gas bottle, the LIF spectra in synthetic air show some fluctuations, as shown by the second measurement in synthetic air (hence the two dotted lines in each figure). These results were confirmed by several follow-up measurements. The LIF spectra of both anisole and toluene show significant band structures.

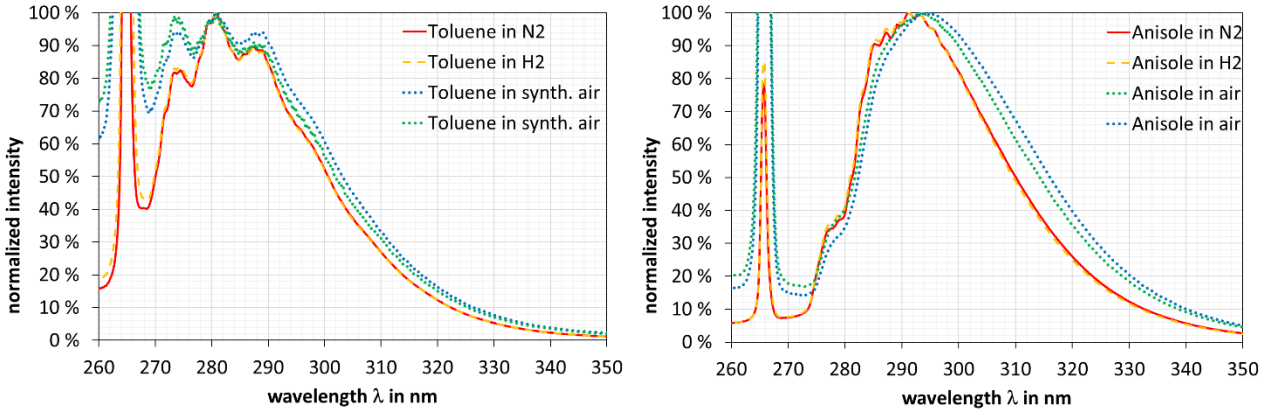

Fig. 7. *266 nm LIF spectra of toluene (**Left**) and anisole (**Right**) in N_2 (solid lines), H_2 (dashed lines) and synthetic air (dotted lines). The LIF spectra in N2 and H2 are practically superimposed, whereas the LIF spectra in synthetic air are significantly different, as are the total intensities of the LIF spectra in air compared to N_2 and H_2. Note that the 266 nm laser line is not removed, this region has to be ignored.*

In this study, further organic liquids were also examined for their suitability as LIF tracers. Because the LIF intensities are rather weak (up to a factor of 100000 weaker compared to anisole), the signal-to-noise ratio is not as good as for the common LIF tracer molecules. However, depending on the application, different LIF emission ranges are desirable to avoid interference with other measurements and problems in the transmission, reflectivity and sensitivity range of the experimental setup. In addition, these LIF tracers could be of relevance in combustion laser diagnostics if they are a natural fuel component (e. g. in biofuels).

Diacetyl was excluded as it proved to be too aggressive a chemical for the Teflon seals. Formaldehyde (37wt. % in water), glyoxal (40wt. % in water) and 2,4-pentadione provided too low a LIF signal and were therefore not pursued further. Several other substances tested produce a noticeable LIF signal: Fig. 8 shows the 266 nm LIF spectra in N_2 for acetophenone, cyclopentanone, cyclohexanone, ethyl acetate and 1,3-dimethoxybenzene. Here too, the 532 nm laser line is not part of the LIF spectrum and should be ignored.

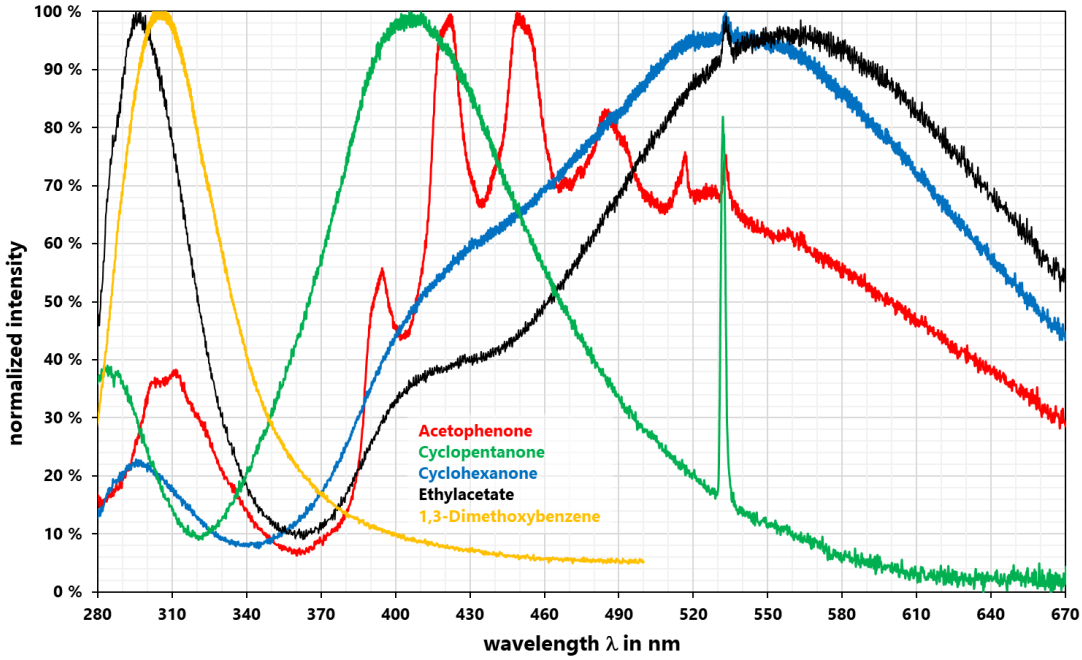

Fig. 8. *266 nm LIF spectra of further hydrocarbons at ambient conditions in N_2 as carrier gas.*

For 1,3-dimethoxybenzene, the LIF spectrum is intentionally cut off at 500 nm, as only the 2nd order signal of the grating spectrometer was visible at higher wavelengths. Although the grating is blazed at 300 nm, a 2nd order signal occurring at twice the wavelength of the original signal is not completely suppressed. Such signals can either be avoided by limiting the measurement to the range of the 1st order signal, e. g. by using bandpass filters (but then only a limited range can be measured simultaneously and intensity calibration can be trickier), or they can be taken into account when examining the LIF spectra, as in the present work.

Acetophenone shows LIF in a broad wavelength range from UV to IR and a distinct band structure. The LIF spectrum of 1,3-dimethoxybenzene is bell-shaped like that of the ketones, but has its maximum in the UV at the same wavelength as that of OH-LIF. The LIF spectra of cyclopentanone and cyclohexanone are surprisingly different, and the ester ethyl acetate shows a combination of a bell-shaped UV peak and a second broad LIF emission region in the visible range peaking in the orange region. Since the chemicals presented have vastly different LIF spectra, they significantly expand the palette of usable LIF tracers.

6. Conclusions

This work presents high-accuracy LIF spectra of several ketones (acetone, 2-butanone, 2-pentanone, 3-pentanone, acetophenone, cyclopentanone, cyclohexanone), aromatics (toluene, anisole, 1,3-dimethylbenzene) and ester (ethyl acetate) at ambient conditions with a FWHM resolution of 1 nm and an unprecedented signal-to-noise ratio. By using a large UV-sensitive sCMOS camera instead of an image intensified camera, many issues like low resolution, high noise, nonlinearity, varying sensitivity, vignetting, etc. were significantly improved.

The spectra of aromatics and ketones are fundamentally different, when excited at 266 nm: aromatics emit the LIF signal in the 270-340 nm range, whereas ketones only emit the LIF signal from 320 nm to over 500 nm. In aromatic compounds that also contain a keto group, the LIF signal from the keto group dominates.

The LIF signal of the aromatic compounds partially overlaps with the OH-LIF signal, which is in the range of 310-325 nm. If simultaneous OH-LIF measurements are to be carried out, aromatics are only suitable as LIF tracers to a limited extent. Aromatic compounds like anisole and toluene have a strong

oxygen quenching effect (difference of more than a factor of 10 between nitrogen and air as carrier gas). Both toluene and anisole show some variations in the shape of their LIF spectra in air that should be taken into account.

Ketones have a smooth, bell-shaped LIF spectrum with no recognizable band features, which simplifies data reduction when using bandpass filters. Both the shape of the spectrum and the total intensity of the LIF signal are insensitive to oxygen quenching. Ketones are therefore recommended for concentration measurements in the presence of oxygen.

The 266 nm LIF spectra of several other chemical substances were measured; they show very different curves and structures. These substances thus considerably expand the range of usable LIF tracers.

This paper reports on an ongoing project. Further measurements are planned, including different tracers, laser energies and excitation wavelengths, oxygen concentrations, higher temperatures and spectral resolution. Special attention was paid to a metrologically correct calibration of the setup.

References

Brunzendorf, J., Höltkemeier-Horstmann, J., Markus, D., 2024. 266 nm Laser-Induced Fluorescence Reference Spectra of Ketones and Aromatic Compounds, Combust. Sci. Technol., submitted.

Bryant, R.A., Donbar, J.M., Driscoll, J.F., 2000. Acetone laser induced fluorescence for low pressure/low temperature flow visualization, Exp. Fluids 28, 471-476.

Deguchi, Y., 2019. Industrial Applications of Laser Diagnostics, Taylor & Francis Ltd., ISBN 978-0367445928.

Eckbreth, A.C., 1996. Laser Diagnostics for Combustion Temperature and Species, 2nd Edition, Routledge, ISBN 978-9056995324.

Fuhrmann, D., Benzler, T., Fernando, S., Endres, T., Dreier, T., Kaiser, S.A., Schulz, C., 2017. Self-quenching in toluene LIF, Proc Combust Inst, 36 (3), 4505-4514.

Grisch, F., Thurber, M.C., Hanson, R.K., 1997. Mesure de température par fluorescence induite par laser sur la molécule d'acétone, Revue Scientifique et Technique de la Defense 4, 51-60.

Kohse-Höinghaus, K., Jefferies, J.B. (eds.), 2002. Applied Combustion Diagnostics, Taylor & Francis Inc., ISBN 978-1560329381.

Lind, S., Zigan, L., Trost, J., Leipertz, A., Will, S., 2016. Simultaneous two-dimensional measurement of fuel–air ratio and temperature in a direct-injection spark-ignition engine using a new tracer-pair laser-induced fluorescence technique, Int J Engine Research, 17 (1), 120-128.

Rossow, B., 2011. Processus photophysiques de molécules organiques fluorescentes et du kérosène applications aux foyers de combustion : applications aux foyers de combustion, Thèse de doctorat dirigée par Gauyacq, Dolorès Chimie physique Paris 11, https://www.theses.fr/2011PA112176.

Saitoh, N., Akiba, N., 2005. Ultraviolet Fluorescence Spectra of Fingerprints, The Scientific World Journal 5, 355–366. DOI: 10.1100/tsw.2005.43

Schulz, C. & Sick, V., 2005. Tracer-LIF diagnostics: quantitative measurement of fuel concentration, temperature and fuel/air ratio in practical combustion systems, Prog Energy Combust Sci 31, 75-121.

Thurber, M.C., Grisch, F., Hanson, R.K., 1997. Temperature imaging with single- and dual-wavelength acetone planar laser-induced fluorescence, Opt. Lett. 22(4), 251-253.

Thurber, M.C. & Hanson, R.K., 2001. Simultaneous imaging of temperature and mole fraction using acetone planar laser-induced fluorescence, Exp. Fluids 30, 93-101.

TracerSim-Dat, 2022. Open Database for Tracer-LIF Datasets, http://www.tracer-sim.com, viewed 03 February 2022.

Yu, X., Chang, G., Peng, J., Dong, H., Yu, Y., Gao, L., Cao, Z., Yan, B., Luo, Y., Qu, T., 2019. Oxygen Concentration Distribution Measurement of the Nozzle Flow Field by Toluene/Acetone Planar Laser-Induced Fluorescence, Front. Phys. 7, 205-213, DOI: 10.3389/fphy.2019.00205.

Systems Thinking for Explosion Safety Management

Julio Ariel DUEÑAS SANTANA [a*], Ernesto SALZANO [b] & Almerinda DI BENEDETTO [c]

[a] Scuola Superiore Meridionale. School for Advanced Studies. University of Naples Federico II. Largo S. Marcellino, 10, 80138, Napoli, Italia.

[b] Dipartimento di Ingegneria Civile, Chimica, Ambientale e dei Materiali, Università degli studi di Bologna, Via Terracini 28, 40131, Bologna, Italia.

[c] Dipartimento di Ingegneria Chimica, dei Materiali e della Produzione Industriale, Università degli Studi di Napoli Federico II, P.le Vincenzo Tecchio 80, 80125, Napoli, Italia.

E-mail: julioariel.duenassantana-ssm@unina.it or julio.duenas94@gmail.com

Abstract

The increasing prominence of hydrogen and its mixture with methane needs a comprehensive understanding of the complex interactions linked with industrial explosion risks and mitigation strategies. Systems thinking and system dynamics approaches are used to deal with complex systems This research explores the application of a Systems Thinking approach in the context of explosion management, specifically focusing on safety considerations associated with hydrogen, methane, and their mixtures. A Causal Loop Diagram is proposed for providing a holistic view of the complex interdependencies linked to the hydrogen enrichment implementation. A System Dynamics-based model is developed for computing the effects of hydrogen addition on the explosion risk and considering the dynamic behaviour of the interdependencies involving storage conditions, infrastructure design, and emergency response protocols. Furthermore, by adopting this holistic perspective, this research aims to identify leverage points and potential vulnerabilities in the explosion safety management associated with each gas and its mixtures. Using the developed models, it is possible to quantify and compare the risk profiles associated with H_2 and CH_4/H_2 mixture handling, providing valuable insights for designing effective explosion management strategies. By using the Systems Thinking approach, this work contributes to a better understanding of the multiple challenges in explosion management, leading to informed decision-making and advancements in safety practices.

Keywords: *Systems thinking, System dynamics, complexity, gas explosions, safety management.*

1. Introduction

One of the most crucial challenges nowadays in the energy sector is the hydrogen economy. In this regard, hydrogen enrichment represents one of the most efficient practices for sustainable hydrogen energy (Capocelli and De Falco, 2016). In other words, adding hydrogen to a mixture of other fuels is a ready alternative that can be a pathway toward a hydrogen economy in the near term. Hydrogen contributes only about 5-7% of the total heat of combustion but enables the exploitation of all the existing infrastructures and conversion technologies with improved results considering the efficiency and emission with respect to pure methane (Middha, 2016).

However, the hydrogen enrichment implementation brings a considerable additional complexity which needs to be explored. This complexity relies on the interdependencies among the adoption using CH_4/H_2 mixtures, their environmental impact, the technology efficiency, the hydrogen economy, the connection with renewable energy (RE) pathways, the public acceptance, and the explosion risk.

One of the most effective frameworks for capturing this complexity is a Systems Thinking paradigm because this offers a holistic view of a given complex system (Dueñas Santana et al., 2024). Precisely this research aims to capture the complexity linked to the hydrogen enrichment practice by using a Systems Thinking approach.

2. Methodology

This section contains the methodology proposed in this research study which consists of six main stages (Fig. 1.). The first stage aims to analyse the main characteristics as well as advantages and disadvantages related to the hydrogen enrichment (HE) of methane. This is crucial in order to understand and identify the main causalities associated with the HE. Secondly, a Systems Thinking framework is proposed for capturing the complexity linked to the previously identified causalities and interdependencies. The third stage consists of building a Causal Loop Diagram (CLD) for providing a holistic view of the complex interdependencies linked to the HE implementation. Then, the fourth stage focuses on developing a System Dynamics (SD) model for computing the effects of hydrogen addition on the explosion risk. The fifth stage aims to analyse the complexity of the HE by causal tracing and simulations for decision-making purposes. Finally, future research lines and challenges are outlined.

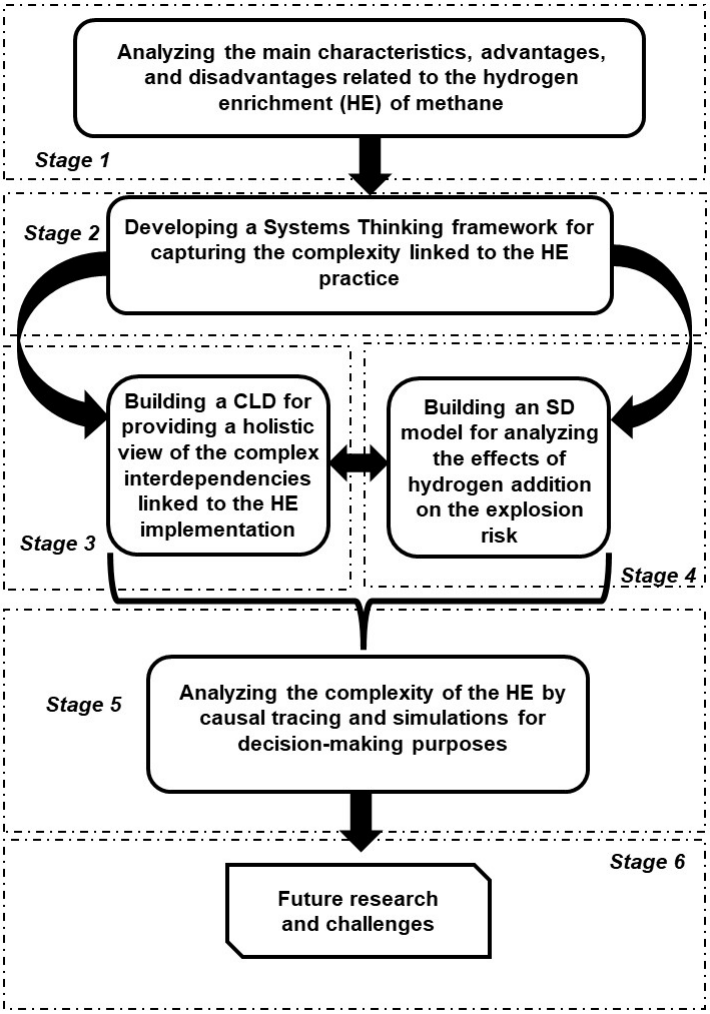

Fig. 1. *Proposed methodology in this research framework*

2.1- Conceptual framework for adopting a Systems Thinking approach

In general, there is a tendency to interpret the experience as a series of events, which means that every event has a cause, which is turned into an effect. This is defined in the literature as the event-oriented, or open-loop worldview, in which the assessment of the current state is given by a comparison between it and the goal; and then, the gap between the desired situation and the perceived state defines the problem (Ball & Wietschel, 2009).

However, there are certain elements related to the dynamic complexity that need to be included such as feedback effects, time delays, stocks, and flows. The problem is that complex and real systems react to our interventions, and these modify the environment. Therefore, there is feedback which means the results of the actions define the new situation in the future. Then, this new state alters the assessment of the problem and the possible effective policies needed to solve it. Additionally, there are some side effects which can emerge in an unanticipated way (Sterman, 2002). Understanding this is crucial because often policy resistance arises because of misunderstanding of the full range of feedback operating in the system. Hence, yesterday's solutions transform into today's problems, which implies that without a clear understanding of the feedback processes which trigger the possible system outcomes, (generally as a consequence of the taken policies) it is possible to create new crises (Garcia, 2009).

Systems Thinking and SD approaches are used to deal with complex systems. Systems Thinking is related to qualitative modelling, and it aims to develop a conceptual model for capturing the dynamic interaction between system components. SD approach refers to quantitative modelling, and it aims to build a simulation model for computing the dynamic interactions among different components (Sterman, 2002).

Moreover, the adoption of a Systems Thinking approach allows the development of models after a really careful assessment of the elements of the complex system and its interconnections and interdependencies. Using an SD approach, the internal logic of the model can be extracted and knowledge then can be gained for a long-term dynamic evolution of the system. The key issue for the model construction is the analysis of the internal logic and the structural relationships within the system. Therefore, the main application of SD is in the field of complex defined environments. (Dueñas Santana et al., 2024).

There are three main elements of a SD-based model: reinforcing loops, balancing loops, and delays. Reinforcing loops (RLs) generate growth, amplify deviations, and reinforce change. These are positive feedback loops and can lead also to the collapse of the system, and extreme changes as well. Balancing loops (BLs) change the current value of a system variable or a desired or reference variable using some actions. It corresponds to a negative feedback loop in control theory and it tends to be self-regulating. The third basic element is a delay, which is used to model the time that elapses between cause and effect. Delays make it difficult to link cause and effect (dynamic complexity) and could lead to unstable system behaviour, increasing the tendency of systems to oscillate. Real-life systems contain both types of loops, and the ultimate behaviour will depend on the dominant type at any particular time. Hence, it is important to understand how the structure of a given system affects their behaviour. Each CLD is associated with qualitative dynamic behaviour (Haraldsson & Sverdrup, 2021).

For developing the SD-based model in this research it is assumed that the *Explosion Risk Level* can be computed by using the equation (1) as follows:

$$Explosion\ Risk\ Level = \int_0^t (Explosion\ Risk\ Inflow - Explosion\ Safety\ Management)dt$$

3. Results and discussion

This section exposes the main obtained results and the developed conceptual models in this research framework. It is divided into five main sub-sections considering the stages proposed in the methodology: (1) advantages and disadvantages of hydrogen enrichment, (2) Systems Thinking approach for capturing the complexity linked to the HE, (3) a new conceptual model (CLD) for HE practice, (4) an SD-based model for computing the explosion risk of HE, and (5) future research and challenges.

3.1- Hydrogen enrichment of methane. Advantages and disadvantages (Stage 1)

Hydrogen enrichment implementation brings several advantages to the hydrogen economy (Makaryan et al., 2022). Notwithstanding, it triggers some negative effects, especially for the increased explosion risk and therefore less public acceptance (Groth and Al-Douri, 2023). Table 1 shows some of the most relevant advantages and disadvantages of the HE practice according to the reports in the literature(De Santoli et al., 2017; Judd and Pinchbeck, 2015; Middha et al., 2011).

Table 1. *Advantages and disadvantages of the hydrogen enrichment*

Factor	Advantages	Disadvantages
Economic impact.	Increase in the efficiency of the hydrogen economy.	Capital investments and new infrastructures (especially with higher hydrogen concentrations).
Environmental impact.	Decrease the emissions of carbon dioxide, carbon monoxide, and methane. In general, it brings much more environmental benefits compared to methane.	It could increase the emissions of nitrogen oxides.
Societal impact.	Works on public acceptance should be implemented by investing in safety.	Public acceptance could be decreased if an explosion occurs.
Safety management.	Stricter safety regulations are needed triggering more efficient safety management procedures.	Increased explosion risk.

3.2- Systems Thinking approach for hydrogen enrichment (Stage 2)

A Systems Thinking approach provides a holistic view of a given complex system (Sterman, 2002). It helps to visualize the complex interdependencies among the following variables: (1) adoption rate for using hydrogen/methane mixtures, (2) hydrogen enrichment practice, (3) technology efficiency, (4) environmental benefits, (5) efficiency of the hydrogen economy, (6) public acceptance, (7) failure probability, (8) explosion risk, (9) RE production and integration, (10) investment in safety, (11) explosion event, (12) domino effect propagation, and (13) major explosion consequences. These variables are linked by analysing the feedback loops which include them. Additionally, the role of effective safety management procedures, the gap between the actual and the perceived risk level, the human expertise, the innovation and development advancements, and the inherent safety are linked to the explosion risk by developing a system dynamics-based model.

3.3- A new conceptual model (CLD) for hydrogen enrichment (Stages 3-5)

A new conceptual model (CLD) is proposed for capturing the complexity related to the HE (Fig. 2.)

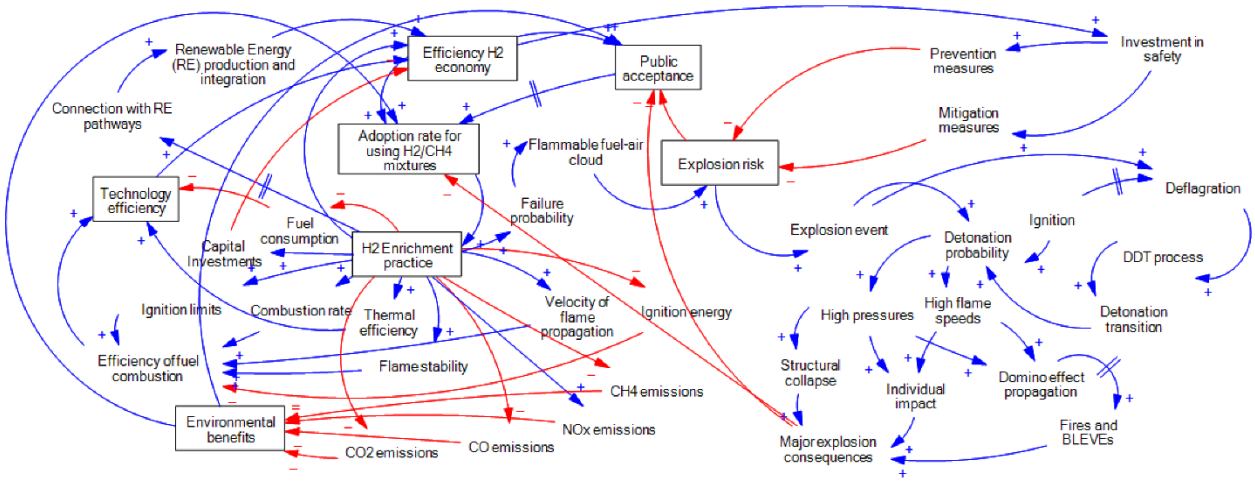

Fig. 2. *CLD for analysing the hydrogen enrichment implementation*

This CLD was built according to six main feedback loops (Table 2), considering the interdependencies among the model variables. Figures 3, 4, and 5 show the causal tracing for the variables: (1) adoption rate, (2) hydrogen enrichment practice, and (3) public acceptance. This analysis brings the remark that the hydrogen enrichment implementation is a high-interconnected complex system itself, where the main variables influence each other, triggering a huge number of new feedback loops.

Table 2*. Integrated feedback loops (FL) in the CLD for analysing the adoption of hydrogen enrichment to methane fuel gas*

No.	Feedback loop	Loop description
01	H_2 enrichment (HE) reinforced by technology efficiency.	The HE practice has several advantages from a technological point of view such as (1) a decrease in fuel consumption, (2) an increase in ignition limits, (3) a higher combustion rate, (4) higher thermal efficiency, (5) better flame stability, (6) an increase in the velocity of the flame propagation. These characteristics linked to the addition of H_2 to methane brings more efficient fuel combustion, leading to higher technology efficiency. In other words, this promotes a more efficient hydrogen economy, reinforcing the adoption of HE.
02	HE reinforced by environmental benefits.	The adoption of HE brings some positive impacts on the environment such as the reduction in CO_2, CO, and CH_4 emissions. However, there are some studies which support the idea that the HE can lead to more NO_x emissions. Despite this, in general, the HE reduces the pollutant gases, helping to meet the decarbonization objectives of the European Union. This positive environmental impact reinforces the public acceptance of the HE practice, and therefore the adoption of the HE itself.
03	HE linked to renewable energy (RE) production and integration, and to the hydrogen economy.	If the hydrogen used for the HE practice is produced from RE sources, this reinforces the integration of RE production leading to more forces on the HE itself. At the same time, when more hydrogen is required, more pressure will be established on green and/or blue hydrogen, making more efficient the current hydrogen economy.

04	HE practices linked to the explosion risk and the public acceptance.	HE can lead to a higher failure probability (due to the addition of H_2 phenomena such as hydrogen embrittlement). After a loss of containment, a flammable fuel-air cloud increases the explosion risk. This risk itself can decrease the public acceptance of HE usage. An explosion event can occur via a detonation (with direct ignition, but less probable) or deflagration phenomenon (with a delayed ignition, and much more probable). The major consequences came from a detonation rather than a deflagration. However, the hydrogen presence brings an additional complex issue in this regard, due to the deflagration-to-detonation transition (DDT), which can cause real severe damage. The high pressures due to a detonation can provoke structural damage, loss of life, and additional fires and/or BLEVEs. These major explosion consequences, decrease the public acceptance of the HE practice, balancing its adoption.
05	Efficiency of H_2 economy linked to the explosion safety management.	The implementation of the HE can lead to a more efficient hydrogen economy, one of the most crucial challenges nowadays. Part of this profits must be used for investing in safety management. The investment in mitigation measures as well as in prevention procedures will reduce the explosion risk, reinforcing the HE implementation.
06	Public acceptance of the HE practice.	The public acceptance of the HE implementation can be reinforced due to the environmental benefits and the efficiency of the hydrogen economy. On the other hand, public acceptance is balanced by the increased explosion risk and the possible major explosion consequences. Public acceptance itself can bring a certain delay to promote the adoption of the HE practice.

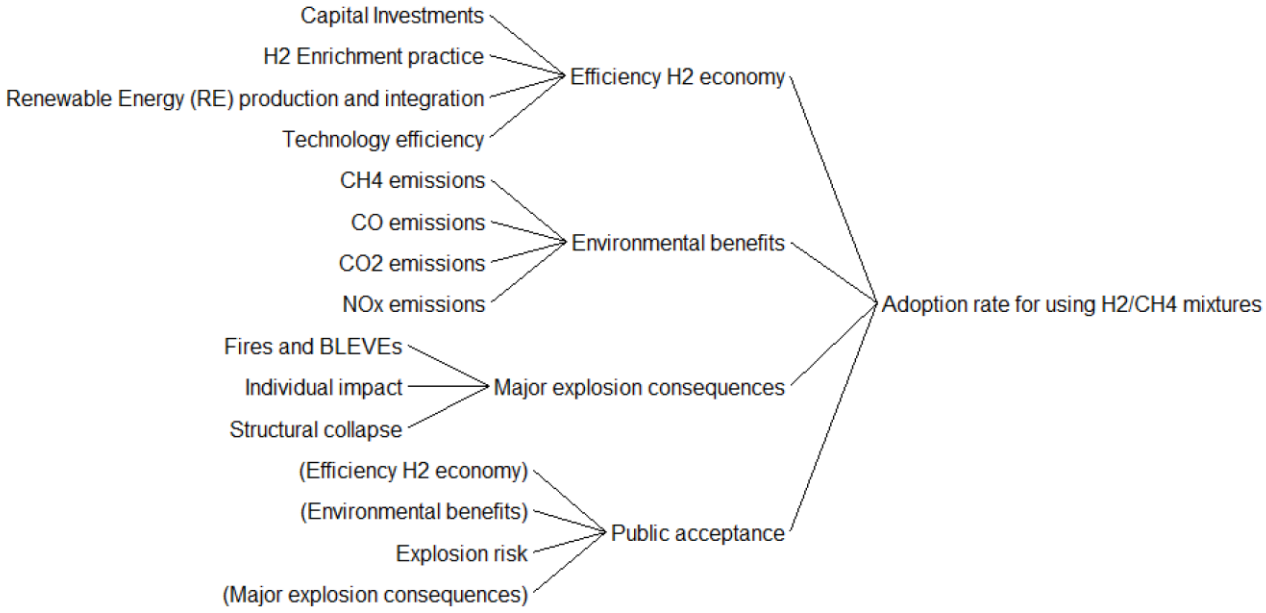

Fig. 3. *Causal tracing for the adoption rate for using H_2/CH_4 mixtures*

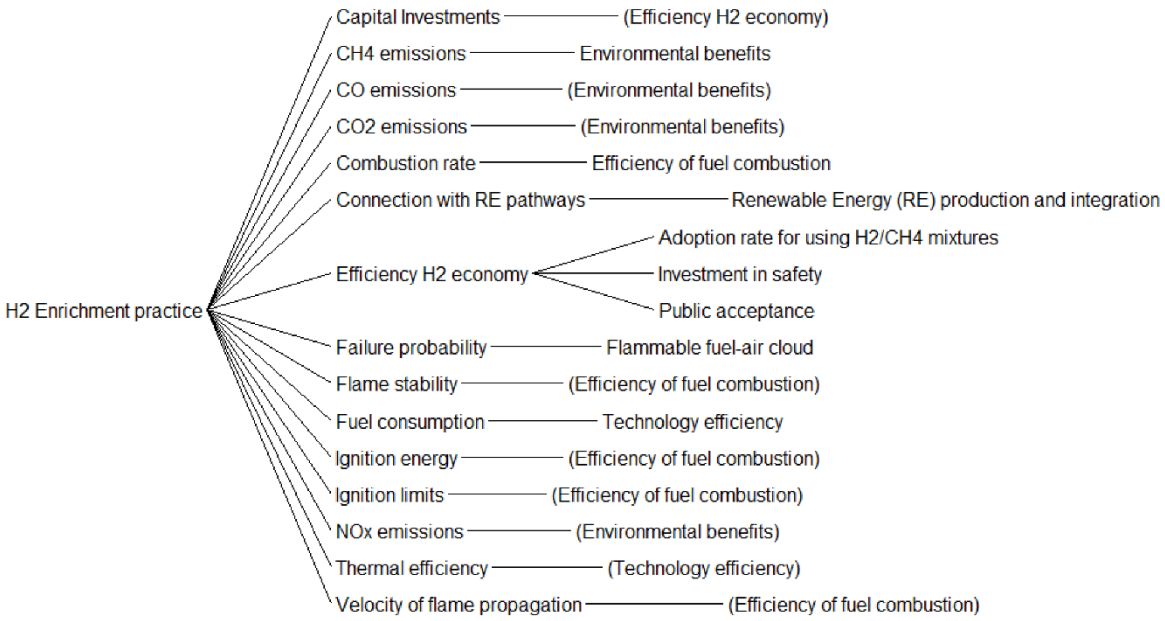

Fig. 4. *Consequences of the hydrogen enrichment practice*

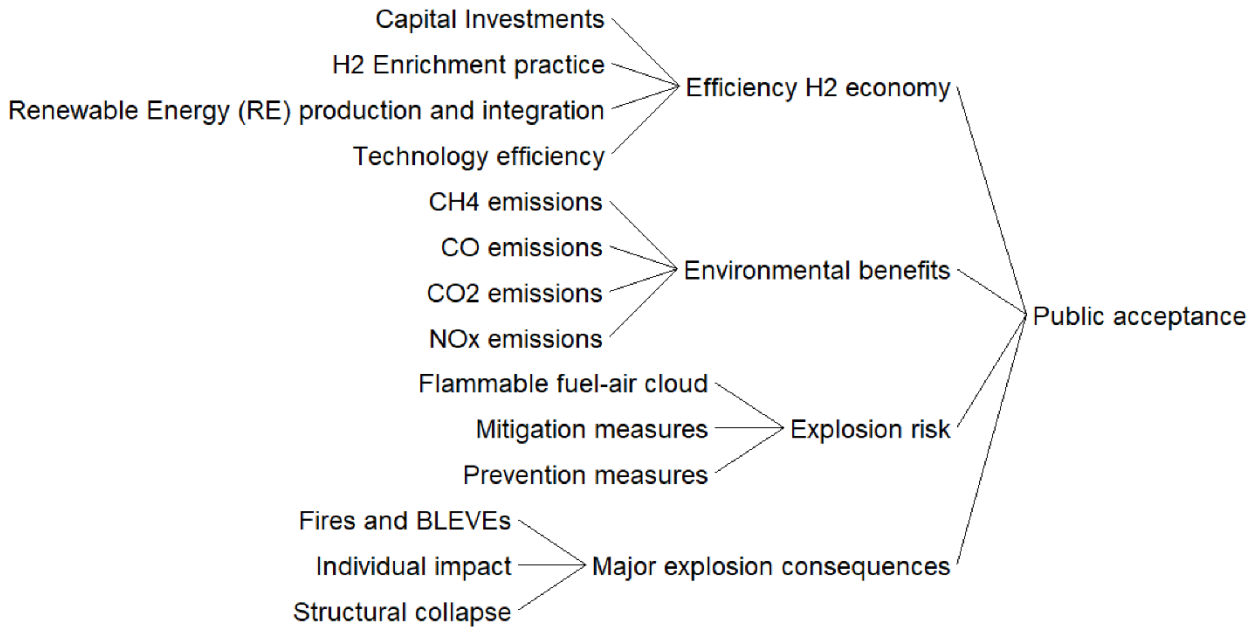

Fig. 5. *Causal tracing for the public acceptance of the hydrogen enrichment practice*

These huge number of new feedback loops appear as a consequence of the emerging complexity of the hydrogen enrichment implementation. Figure 6 shows the number of loops and the maximum observed loop length starting from the main model variables.

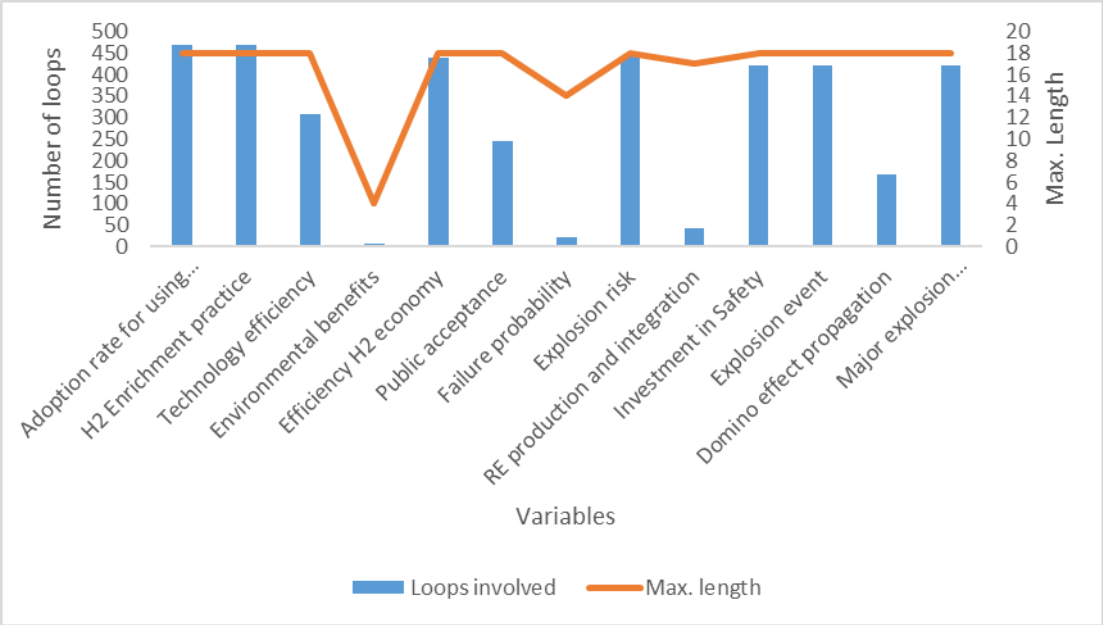

Fig. 6. *Loops involved and max. length for the main model variables*

The maximum number of feedback loops is observed starting from the variables adoption rate and H_2 enrichment practice, with 469 loops, and the maximum length is 18, which means that 18 out of the 40 variables are involved at least in one of these loops (45%). After that, the third most interconnected variable is the explosion risk (441 feedback loops-18 max. length), followed by the efficiency of the hydrogen economy (440 feedback loops-18 max. length), the investment in safety, and the explosion event (420 feedback loops-18 max. length, each one). Hence, the explosion risk plays a crucial role in the hydrogen enrichment implementation which is additionally studied in the following section.

3.4- An SD-based model for explosion risk related to hydrogen enrichment (Stages 4-5)

This section focuses on developing a System Dynamics-based model (Fig. 7.) for computing the explosion risk considering different percentages of hydrogen enrichment.

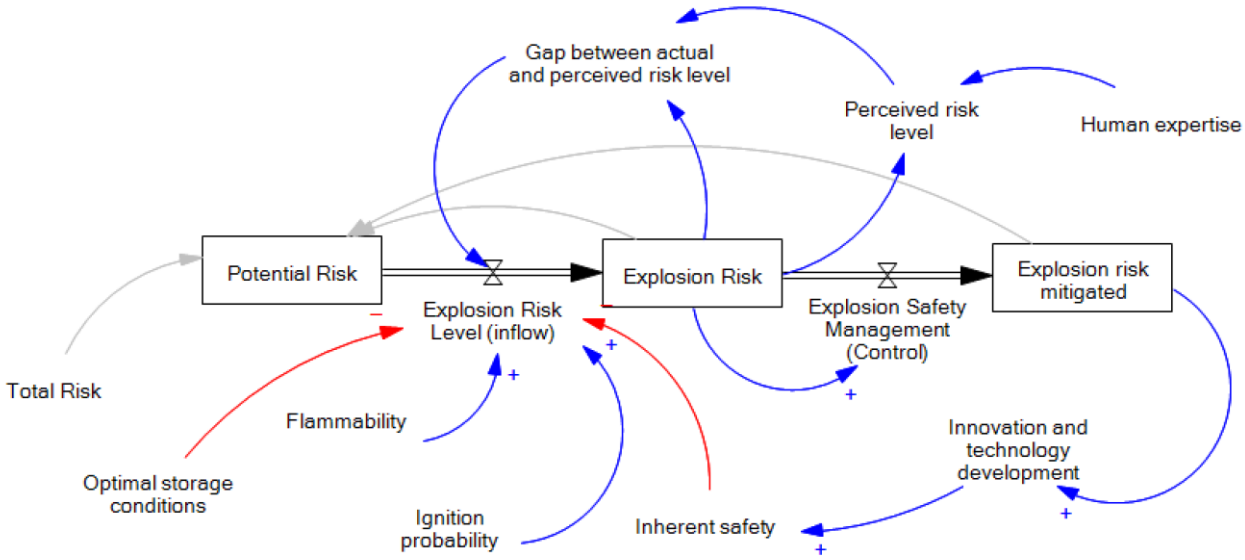

Fig. 7. *SD-based model for explosion risk linked to hydrogen enrichment*

This SD-based model complements the previously developed CLD by adding the following variables: (1) explosion safety management, (2) innovation and technology development, (3) inherent safety, (4) optimal storage conditions, (5) gap between actual and perceived risk level, and (6) human expertise.

For simulation purposes, the flammability in this model is taken as the difference between the flammability limits of different hydrogen compositions in the gas mixture according to Table 3 (adapted from the study of Atzori, 2023)

***Table 3**. Data for SD-based model simulations*

Molar Hydrogen Percentage	Lower Flammability Limit (LFL) (% vol.)	Upper Flammability Limit (UFL) (% vol.)	Flammability range (% vol.)
0	4.4	16.5	12.1
20	4.4	17.9	13.5
30	4.3	19.5	15.2
40	4.2	24.0	19.8
100	4.0	75.0	71.0

Figure 8 shows the dynamic evolution of the explosion risk profiles considering different hydrogen compositions (Table 3).

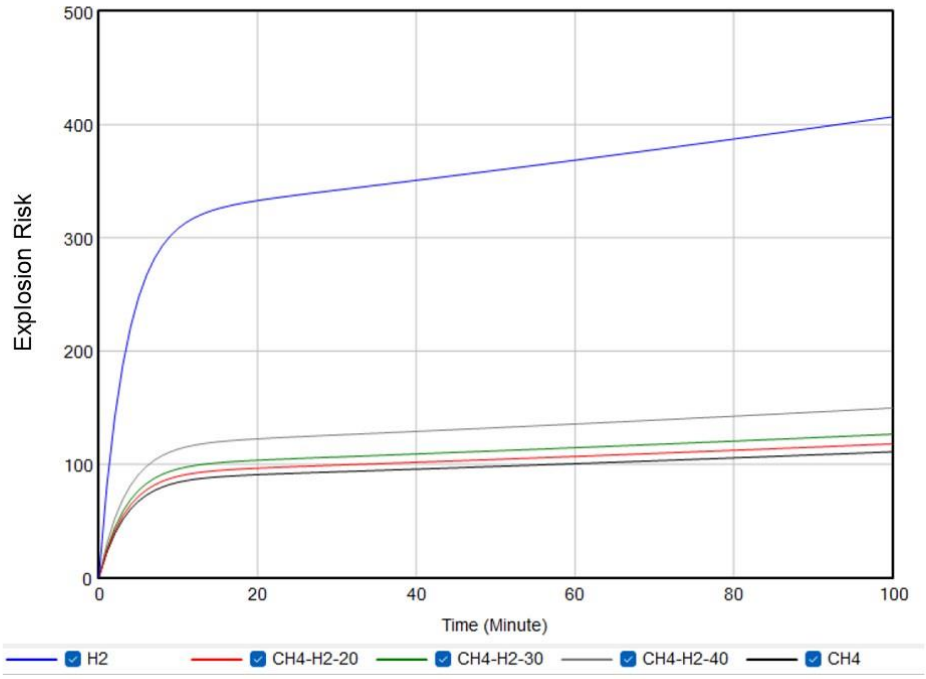

***Fig. 8.** Dynamic evolution of the explosion risk profiles linked to the hydrogen enrichment*

In general, it is observed an exponential growth in the first 5 minutes after a gas release for all the fuel mixtures, after that a slow increment of the explosion risk is captured due to the effect of the safety control measures. Despite that, this increment tendency is much higher for pure hydrogen than for the mixtures with methane. Similar tendencies are obtained for hydrogen compositions of 20% and 30% with regard to pure methane, however, the explosion risk is slightly higher. For hydrogen composition, 40% higher differences are observed compared to pure methane, but the explosion risk is still much lower than that of pure hydrogen. Therefore, this reinforces the idea that hydrogen enrichment explosion risk, although not negligible, can be managed effectively in the same way that the methane explosion risk for hydrogen molar compositions below 30%. These results are similar to those reported in the literature (Messaoudani et al., 2016; Molnarne and Schroeder, 2019).

3.5- Future research and challenges (Stage 6)

Future research can be performed by transforming the proposed conceptual model (CLD) into System Dynamics-based models. For this purpose, data about the public acceptance of hydrogen enrichment and the connection of this with renewable energy production and storage will be needed, challenging the simulation of these models. Computation of different expert criteria by Fuzzy logic could offer a solution in this regard. Moreover, the developed SD-based model for computing the explosion risk can be extended and applied to other fuels by considering specific safety management procedures and their effectiveness.

4. Conclusions

This research proposes a Systems Thinking framework for analysing the complex interdependencies linked to the hydrogen enrichment of methane. Two models were developed, the first one for capturing the interrelations related to the adoption rate of the hydrogen enrichment, and the second one for computing the explosion risk linked to different hydrogen concentrations in the gas mixture. The advantages of using the developed models and future research lines are as follows:

(1) The CLD can be further transformed into a Forrester Diagram, and in this way, it will be possible to quantify the adoption rate using real data.

(2) The SD-based model can be used in the presented form for assessing and comparing other fuel explosion risks.

(3) These two models can be used and extended for developing a unified framework for Risk Assessment and Safety Management in the chemical industry and the energy sector by considering the complex interdependencies among the economy, the environment, and society.

Overall, by considering a Systems Thinking framework, it is possible to capture the emerged complexity and the interaction among the analysed variables linked to the hydrogen enrichment practice.

Acknowledgements

The authors gratefully acknowledge the financial contribution from the *Scuola Superiore Meridionale* and the University of Naples Federico II.

References

Atzori Andrea, 2023. Risk Assessment of Uncontrolled Releases of Hydrogen and Methane Mixtures in Existing Methane Distribution Pipelines using CFD Simulations and Analytical Calculations. Politecnico di Milano, Milano.

Ball, M., & Wietschel, M. (Eds.), 2009. The hydrogen economy: Opportunities and challenges. Cambridge University Press.

Capocelli, M., De Falco, M., 2016. Enriched Methane: A Ready Solution for the Transition Towards the Hydrogen Economy. In: De Falco, M., Basile, A. (eds) Enriched Methane. Green Energy and Technology. Springer, Cham. https://doi.org/10.1007/978-3-319-22192-2_1

De Santoli, L., Paiolo, R., Lo Basso, G., 2017. An overview on safety issues related to hydrogen and methane blend applications in domestic and industrial use, in: Energy Procedia. Elsevier Ltd, pp. 297–304. https://doi.org/10.1016/j.egypro.2017.08.224

Dueñas Santana, J.A., Di Benedetto, A., González Gómez, O., Salzano, E., 2024. Towards sustainable hydrogen production: An integrated approach for Sustainability, Complexity, and Systems Thinking in the energy sector. J Clean Prod 449, 141751. https://doi.org/10.1016/j.jclepro.2024.141751

Garcia, J. M., 2009. Theory and practical exercises of system dynamics. MIT Sloan School of Management.

Groth, K.M., Al-Douri, A., 2023. Hydrogen safety, risk, and reliability analysis, in: Hydrogen Economy: Processes, Supply Chain, Life Cycle Analysis and Energy Transition for Sustainability. Elsevier, pp. 487–510. https://doi.org/10.1016/B978-0-323-99514-6.00012-1

Haraldsson, H. V., & Sverdrup, H. U., 2021. Systems science and system thinking in practice: How to develop qualitative and numerical models for evolving understandings of challenges and responses to complex policies. Swedish Environmental Protection Agency (Naturvårdsverket).

Judd, R., Pinchbeck, D., 2015. Hydrogen admixture to the natural gas grid, in: Compendium of Hydrogen Energy: Hydrogen Use, Safety and the Hydrogen Economy: Volume 4. Elsevier, pp. 165–192. https://doi.org/10.1016/B978-1-78242-364-5.00008-7

Makaryan, I.A., Sedov, I. V., Salgansky, E.A., Arutyunov, A. V., Arutyunov, V.S., 2022. A Comprehensive Review on the Prospects of Using Hydrogen–Methane Blends: Challenges and Opportunities. Energies (Basel). https://doi.org/10.3390/en15062265

Messaoudani, Z. labidine, Rigas, F., Binti Hamid, M.D., Che Hassan, C.R., 2016. Hazards, safety and knowledge gaps on hydrogen transmission via natural gas grid: A critical review. Int J Hydrogen Energy. https://doi.org/10.1016/j.ijhydene.2016.07.171

Middha, P., 2016. Explosion Risks of Hydrogen/Methane Blends. In: De Falco, M., Basile, A. (eds) Enriched Methane. Green Energy and Technology. Springer, Cham. https://doi.org/10.1007/978-3-319-22192-2_13

Middha, P., Engel, D., Hansen, O.R., 2011. Can the addition of hydrogen to natural gas reduce the explosion risk? Int J Hydrogen Energy 36, 2628–2636. https://doi.org/10.1016/j.ijhydene.2010.04.132

Molnarne, M., Schroeder, V., 2019. Hazardous properties of hydrogen and hydrogen containing fuel gases. Process Safety and Environmental Protection 130, 1–5. https://doi.org/10.1016/j.psep.2019.07.012

Sterman, J.D., 2002. SYSTEM DYNAMICS: SYSTEMS THINKING AND MODELING FOR A COMPLEX WORLD.

Some questions related to CFD modeling of pressurized tank burst in road tunnels

Guillaume Lecocq [a], Laure Heudier [a], Benjamin Truchot [a], Antoine Mos [b]& Christophe Willmann [b]

[a] INERIS (Verneuil-en-Halatte, France)
[b] CETU (Bron, France)

E-mail: guillaume.lecocq@ineris.fr

Abstract

The current paper focuses on high-pressure reservoirs and the consequences of their potential burst, related to scenarios of thermal or mechanical aggressions, in tunnels.

CFD (Computational Fluid Dynamics) modeling can be used to account for the effects of such scenarios. An intrinsic advantage of such an approach consists in integrating the specific geometrical effects (tunnel walls, presence of vehicles) on the pressure wave propagation.

To meet such an objective, experimental data are required to offer an opportunity for validation. Data from the literature and new ones from INERIS are detailed in this paper, with their strengths and weaknesses to identify relevant test cases for CFD.

Phenomenological tools are tested against experimental cases of bursting tank in a free field to evaluate their prediction capability for pressure. These tools could be used along with CFD in a global modeling framework.

CFD is tested against fictitious free-field cases, investigating the effect of the thermodynamic model on the results. The numerical method for propagating the pressure wave in realistic tunnels is also studied.

Keywords: tank burst, pressure effects, CFD, phenomenological tools

Introduction

To meet the objective of reducing the transportation impact on the global warming, car manufacturers currently develop new technologies. According to this change, the propulsion of vehicles crossing tunnels is expected to be more and more varied in a next future with Batteries, Fuel Cells or spark-ignition engines using either Natural Gas or Hydrogen. Currently, those two gases, Hydrogen and Natural Gas, are stored at a gaseous state under high pressure, up to 700 bar. The presence of such reservoirs in tunnels raises new risks that should be finely considered by technical experts and regulators.

A first specificity of such bursts in confined geometries is the existence of a reflection zone, close to the bursting capacity, leading to the formation of a planar pressure wave. The intensity of this latter decays much more slowly than in free field. Also, vehicles can be present and influence the pressure wave propagation.

As CFD intrinsically accounts for geometrical effects, this method appears attractive for dealing with these scenarios. Nevertheless, confronting CFD computations to reference test cases is needed to define a modeling strategy. Available experimental data are first listed and described. Phenomenological tools are then tested against some points of the database. These tools could be used along with CFD for getting a reference solution for example. CFD computations are also compared with free-field and tunnel burst tank cases.

1. Experimental data

1.1. Tunnel cases

The data of the literature produced in the framework of experimental campaigns in tunnels is given in the Table below. They are mainly the measurements from Kudriakov et al. (2022) in a disused 507 m long road tunnel. Original data obtained by INERIS in its test tunnel are also supplied. This tunnel cross section is about 10 m² and its length of about 80 m.

***Table 1**. Dataset for the tank burst in tunnel. The tests performed at INERIS are in italics. Reference [1] stands for (Blanc-Vannet et al., 2019), [2] for (Kudriakov et al., 2022) with second pressure peak in brackets, [3] for (Ruban et al., 2012) and [4] for (INERIS, 2012)*

Gas	Bottle type	Aggression mode	Volume (L)	Initial pressure (bar)	Rupture pressure (bar)	Brode energy (ideal gas law) (MJ)	Pressure measurements	Ref.
N2	*IV*	*Fire*	*19*	*700*	*706*	*3.3*	*At 5m: 220mbar*	*[1]*
N2	*IV*	*Fire*	*19*	*700*	*715*	*3.4*	*At 5m:287mbar*	*[1]*
N2	*IV*	*Fire*	*36*	*700*	*749*	*6.7*	*At 5m: 433mbar*	*[1]*
N2	*IV*	*Fire*	*36*	*700*	*716*	*6.4*	*At 5m: 399mbar*	*[1]*
N2	*IV*	*Fire*	*19*	*525*	*585*	*2.8*	*At 5m: 399mbar*	*[1]*
N2	*IV*	*Fire*	*19*	*700*	*714*	*3.4*	*At 5m: 377mbar*	*[1]*
He	IV	Detonation belt	78	650	650	7.7	At 30 m: 98 mbar / 50m: 85 mbar 80 m: 72 mbar / 110m: 68 mbar 140 m: 61 mbar / 170 m: 55 mbar	[2]
H_2	IV	Detonation belt	78	520	520	10.1	At 30 m: 207 mbar (271 mbar) 50m: 180 mbar (243 mbar) 80 m: 160 mbar / 110m: 205 mbar 140 m: 202 mbar / 170 m: -	[2]
H_2	IV	Detonation belt	78	610	610	11.9	At 30 m: 187 mbar (218 mbar) 50m: 180 mbar (225 mbar) 80 m: 151 mbar (204 mbar) 110m: 205 mbar (336 mbar) 140 m: 301 mbar / 170 m: 179 mbar	[2]
He	*IV*	*Fire*	*36*	*350*	*378*	*2.1*	*At 30 m: 187 mbar*	*[3]*
He	*IV*	*Fire*	*36*	*700*	*703*	*3.8*	*At 30 m: 248 mbar*	*[3]*
He	*III*	*Fire*	*17*	*718*	*881*	*2.3*	*At 19 m: 140 mbar / 24 m: 159 mbar / 29 m: 152 mbar*	*[3]*
He	*IV*	*Mechanical impact*	*2.4*	*698*	*698*	*0.25*	*At 1 m: 150 mbar / 5 m: 50 mbar*	*[4]*
He	*IV*	*Mechanical impact*	*2.4*	*693*	*693*	*0.25*	*At 2 m: 142 mbar / 5 m: 67 mbar*	*[4]*

A CFD method for modeling high-pressure tank bursts should be regarded on cases with increasing physical complexity for validation purpose. Then, a modeling work should first address the burst of non-reacting gas tanks. Indeed, the fireball was proved to contribute to the pressure effects (Molkov et al., 2015). Furthermore, the aggression mode is of importance as it impacts the discharge of the pressure wave. In free field, most reservoirs of the literature contain hydrogen and are thermally aggressed, making these cases hard to address with CFD. A CFD method was nevertheless previously proposed by Molkov et al. (2021) for such cases.

The results obtained recently by Kudriakov et al. (2022) are interesting as the way the pressure discharge is obtained is partially controlled, non-reacting gases are used, and numerous measuring

points were exploited. Nevertheless, there are no pressure measurements around the tank (between the tank and the first wall met by the pressure wave for example).

When the purpose is to assess the behavior of modeling tools, it is wished to check they could reproduce the pressure field from the source to an observer location. Some campaigns show only one measurement point, making them difficult to be used for validating tools.

The graph below is built from the data of Table 1. It plots the peak pressure versus the reduced distance λ, which writes: $\lambda = r/m_{TNT}^{1/3}$. r is the distance between the pressure source and the sensor and m_{TNT} is the TNT equivalent. This latter is deduced from E, the tank rupture energy, closed with the expression of Brode (1959): $E = \Delta p.V/(\gamma - 1)$. V is the tank volume, Δp is the rupture pressure and γ is the heat capacity ratio of the stored gas. An ideal gas behavior is assumed in this formula.

A free-field pressure decay is computed with the PROJEX tool (Heudier, 2013), relying on the Multi-Energy method abacus (Van der Berg, 1984). The severity is then set to 10 and the explosion energy is calculated with the Brode formula. The comparison shows that for a given explosion energy, the available experimental data describe either the spherical pressure wave expansion or the planar wave propagation, but not the whole propagation process.

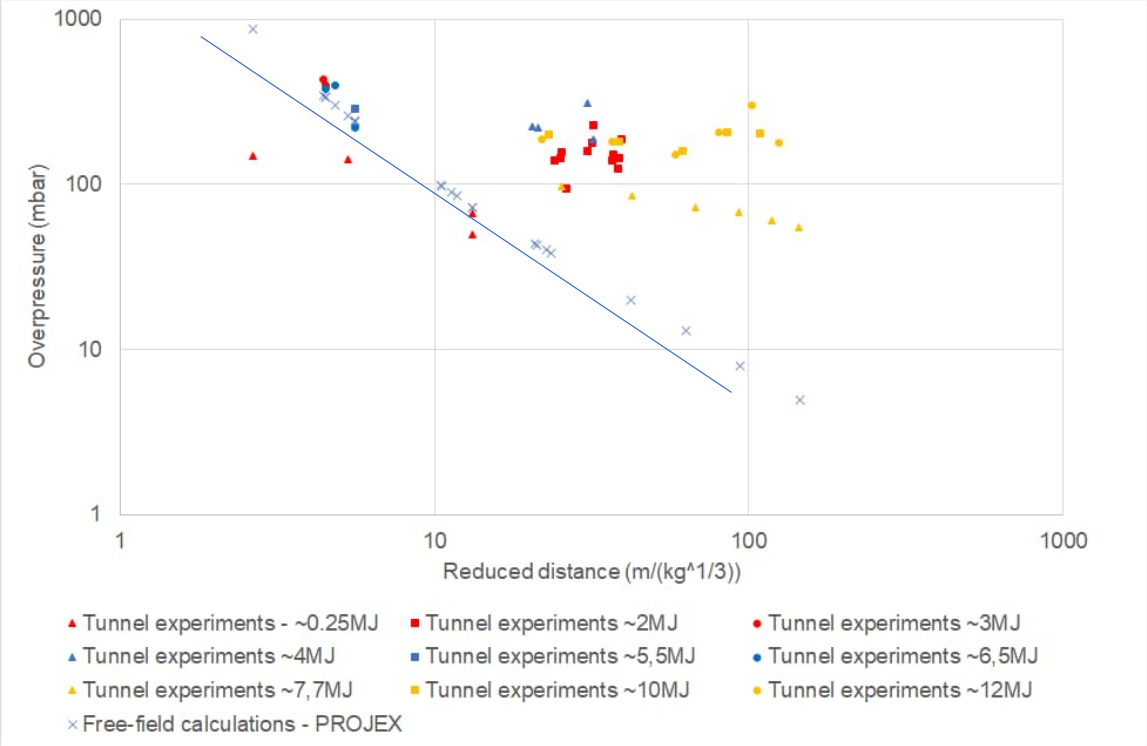

Fig. 1. *Overpressure peaks in case of tank burst in tunnel (experiments) and in free field (calculations). The blue line approximates the PROJEX results.*

The database is not sufficient for testing CFD. Tank burst cases in free field are then regarded in the next section.

1.2. Free-field cases

The data found in the literature related to tests of high-pressure tanks bursting in free field are detailed in Table 2. This latter contains also original data produced by INERIS.

The overpressure measurements in Fig. 2 show that several values of overpressure peaks can be retained, depending on the analysis of the measured signal. That's why, in Table 2, for some tests,

several values of overpressure peaks are indicated for the same sensor. For this reason, it is preferable to have the overpressure signals and not only the peak values when trying to assess the performance of modeling tools such as phenomenological or CFD based ones.

***Table 2**. Dataset for the tank burst in free field. For the data [(1)], the bottle was surrounded by four concrete walls that could have impacted the measured value. Furthermore, the bottle moved when bursting making it difficult to know the real distance between the sensor and the bottle. The tests performed at INERIS are in italics. Reference [1] stands for (Zalosh et al., 2005), [2] for (Shen et al., 2018), [3] for (Tamura et al., 2006), [4] for (Chaineaux, 2000), [5] for (INERIS, 2010) and [6] for (Blanc-Vannet et al., 2019)*

Gas	Bottle type	Aggression mode	Volume (L)	Initial pressure (bar)	Rupture pressure (bar)	Pressure measurements	Ref.
H_2	IV	Fire	72.4	343	357	On the bottle axis, at 4.2m: 650 mbar On the normal axis, at 1.9m: 3 bar / 4.2 m: 830 mbar, 6.5m: 410 mbar	[1]
H_2	III	Fire	165	350	440	No pressure measurement. Bottle projected 200 m away	[2]
H_2	IV	Fire	35	700	945	At 5 m: 1.1 bar / 10 m: 234 mbar	[3]
H_2	III	Fire	36	700	995	At 5 m: 743 mbar / 10 m: 234 mbar	
H_2	*N/A*	*Detonating cord*	*9*	*700*	*700*	*Axis 1, at 10 m: 96 mbar / 15 m: 58 mbar Axis 2, normal to axis 1: at 10 m: 110 mbar / 15 m: 64 mbar*	*[4]*
H_2	*IV*	*Fire*	*2.4*	*481*	*600*	*At 5 m: 58-68 mbar / 10 m: 30-36 mbar*	*[5]*
H_2	*IV*	*Fire*	*2.4*	*525*	*673*	*At 5 m: 58-75 mbar / 10 m: 32 mbar*	
H_2	*IV*	*Fire*	*2.4*	*700*	*827*	*At 5 m: 61-69-78 mbar / 10 m: 38 mbar*	
H_2	*IV*	*Fire*	*2.4*	*700*	*854*	*At 5 m: 71-80-104 mbar / 10 m: 41-53 mbar*	
N_2	*IV*	*Fire*	*19*	*700*	*722*	*At about 1 m: 1 bar[(1)]*	*[6]*
N_2	*IV*	*Fire*	*19*	*467*	*488*	*At about 1 m: 2.5 bar[(1)]*	
He	*IV*	*Fire*	*19*	*700*	*730*	*At about 1 m: 4.5 bar[(1)]*	
He	*IV*	*Fire*	*19*	*467*	*506*	*At about 1 m: 2.5 bar[(1)]*	
H_2	*IV*	*Fire*	*19*	*700*	*713*	*At about 1 m: 450 mbar[(1)]*	
H_2	*IV*	*Fire*	*19*	*467*	*483*	*At about 1 m: 6-7 bar[(1)]*	

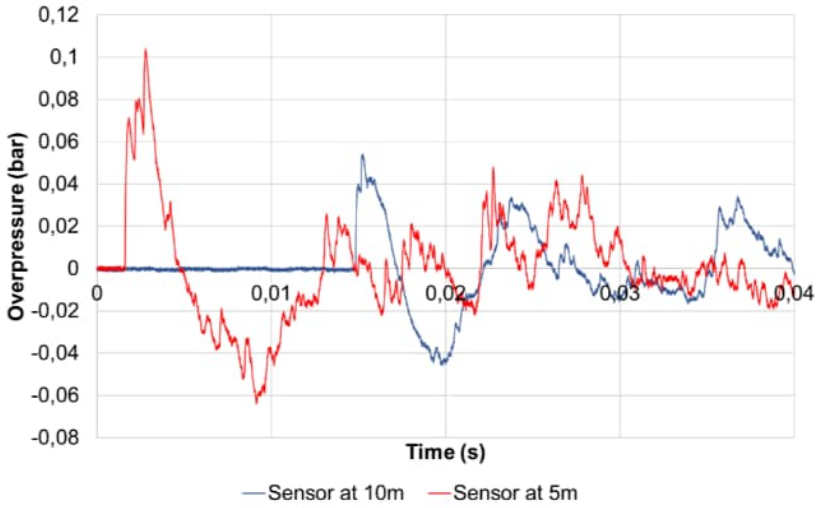

Fig. 2. *Pressure signals measured for the burst of a 2.4 L bottle containing 700 bar of hydrogen. Red: at 5 m. Blue: at 10 m.*

Again, a campaign only supplies a single measurement, which is not enough for testing the codes. This measurement can also be disturbed by the surrounding walls. The data coming from (INERIS, 2010) presents several tests and two measuring points. The first pressure rise is followed by several pressure peaks. This may notably be explained by a progressive pressure discharge, which is tricky to address through numerical modelling. The first part of the signals of Zalosh et al. (2005) and Tamura (2006) (not shown) is closer to the typical shock wave shape, with a single peak followed by a pressure decay. Some data obtained for non-reacting gases could greatly improve the database, when thinking of modeling tool assessment.

2. Modeling burst tank cases

2.1 Phenomenological tools for free-field bursting tanks

As experimental data appear to miss to provide a complete validation database for CFD dedicated to bursting tanks, some phenomenological tools are regarded. Indeed, if they are accurate enough, they could be used to complete experimental dataset with extra points.

The considered tools are PROJEX, the TNT equivalent (TM5 1300, 1969) and the Baker methods (Baker et al., 1983). Also, the Brode energy upon which PROJEX and the TNT equivalent method rely can be quantified with the ideal gas law and with a real gas law, such as the Able-Nobel one (Molkov et al., 2015). The dataset provided by Zalosh and Tamura is used to test the phenomenological approaches (see Tables 3 and 4). All approaches are employed for a charge located on the ground and do not account for chemical effects related to a fireball generation.

***Table 3**. Phenomenological tools results compared to Zalosh measurements (Zalosh et al., 2005). The Baker method results are from Molkov et al. (2015). Computations made for a TNT equivalent of 4.57 MJ/kg.*

Location	Exp. data	PROJEX (6.46 MJ)	PROJEX A-N (5.33 MJ)	TNT Eq. (1.41 kg)	TNT Eq. A-N (1.16 kg)	BAKER A-N (9.4 MJ)
at 1.9 m orthogonally to the bottle axis	3 bar	2.35 bar	2.05 bar	4.2 bar	3,6 bar	3,19 bar
at 4.2 m on the bottle axis	650 mbar	441 mbar	403 mbar	740 mbar	650 mbar	608 mbar
at 4.2 m orthogonally	830 mbar					
at 6.5 m orthogonally	410 mbar	222 mbar	205 mbar	336 mbar	302 mbar	284 mbar

***Table 4.** Phenomenological tools results compared to Tamura measurements (2006).*

	Location	Exp. data	PROJEX (8.3 MJ)	PROJEX A-N (5.8 MJ)	TNT Eq (1.81 kg)	TNT Eq. A-N (1.27 kg)
35 L type IV bottle	at 5 m orthogonally to the bottle axis	1.1 bar	390 mbar	320 mbar	618 mbar	500 mbar
	at 10 m orthogonally to the bottle axis	234 mbar	138 mbar	116 mbar	196 mbar	165 mbar
		Exp. data	PROJEX (8.95 MJ)	PROJEX A-N (6.3 MJ)	TNT Eq. (1.96 kg)	TNT Eq. A-N (1.37 kg)
36 L type III bottle	at 5 m orthogonally to the bottle axis	743 mbar	402 mbar	331 mbar	650 mbar	520 mbar
	at 10 m orthogonally to the bottle axis	234 mbar	142 mbar	120 mbar	204 mbar	172 mbar

For the Zalosh database, all the methods recover the proper orders of magnitude. Nevertheless, the most accurate methods seem to be the TNT Equivalent method with a real gas law and the Baker method. Concerning the Tamura cases, PROJEX and the TNT equivalent method underestimate the peak about 1 bar, 5 m from the first bottle. Overall, the best results are obtained with the TNT equivalent method.

According to the results, the phenomenological methods give most of the time the proper orders of magnitude when compared with the chosen experiments but are not necessarily accurate. These methods can help to assess a result obtained with CFD but do not give strict reference results.

2.2 CFD

The CFD approach is regarded in modeling the fictitious case of the burst of a 78 L reservoir containing air at a pressure of 610 bar. The CFD tool is OpenFoam (Weller, 1998). The solver *rhoCentralFoam* is chosen. It solves the Euler equations with the convective numerical scheme of Kurganov and Tadmor (2000). The time derivatives are discretized with the Euler scheme. The basic solver does not account for transport equations for the chemical species, meaning the gas in the bottle and in the environment is the same. By default, also, the user can only rely on an ideal gas law. The specific heat at constant pressure can be set to a constant or a JANAF table can be used to introduce a law $C_p = C_p(T)$.

Developments were carried out to add the transport equations for chemical species and enable to account for a real gas law such as the Peng-Robinson one. A recent work (Ghasemi, 2020) gives elements to perform the coding.

Several CFD computations are performed for a regular mesh, the cell width being 5 cm. In a volume equal to the tank one, a pressure of 610 bar is initially imposed. The discharge is then implicitly modeled as the instantaneous disappearance of the tank walls. The results of the CFD computations for several parametrizations are given in the Table below, as well as results obtained with phenomenological tools. It can be seen these latter tools provide the same orders of magnitude from 5 to 30 m from the pressure source, the TNT equivalent overpredicting the PROJEX results. In the previous part, the TNT equivalent gave the best results for similar bursting cases. The CFD computation based on a resolution of the chemical species transport equations and a real gas law gave the closest results to the TNT equivalent ones. It should be nevertheless noted that in the previous part, the regarded cases involved a fireball, that potentially contributed to pressure effects and not the current one.

***Table 5**. Pressure effects at several distances related to a fictitious case of a bursting 78 L reservoir containing 610 bar of air. Several computing methods are used.*

	Distance (m)					
Modeling method	5	10	15	20	25	30
PROJEX (E=12.2 MJ)	472 mbar	162 mbar	93 mbar	65 mbar	51 mbar	41 mbar
TNT equivalent (m=2.67 kg)	795 mbar	238 mbar	133 mbar	91 mbar	70 mbar	55 mbar
CFD with ideal gas law and constant Cp coefficients	168 mbar	69 mbar	38 mbar	25 mbar	21 mbar	19 mbar
CFD with transport equations for chemical species, an ideal gas law and JANAF tables	1550 mbar	320 mbar	189 mbar	154 mbar	124 mbar	90 mbar
CFD with transport equations for chemical species, a real gas law (Peng-Robinson) and JANAF tables	823 mbar	237 mbar	155 mbar	109 mbar	94 mbar	84 mbar

Finally, first CFD computations of a case of the Kudriakov et al. campaign is performed. The Helium case is addressed as it is theoretically the simplest as no fireball is generated at the tank rupture. The computational domain is 3D and 120 m long. It is decomposed into cubic cells with a characteristic width of 5 cm.

It was chosen to work with relatively small cells instead of using an Automatic Mesh Refinement (AMR) method. Indeed, the criterion that is used by default is the normalized pressure gradient meaning only the first pressure wave will be refined. This may be fine for dealing with free field cases but not necessarily tunnel cases for which the reflection zone involving numerous pressure waves is of importance.

Two CFD simulations are performed, both with the transport of the chemical species and JANAF tables for computing the Cp coefficients. The first CFD relies on the ideal gas law, the other on the Peng-Robinson law.

The Figure 4 shows the results obtained 30 m away from the pressure source and the measured pressure signal. It should be pointed out the experimental signal presented in the Kudriakov et al. paper has been treated with a low-pass filter and a cut-off frequency of 100 Hz to suppress acoustic effects. This signal as well as the unfiltered one are given in the Figure. It can be seen the shocks disappeared with the filtering procedure. The CFD results are very similar between them. The impact of the gas law can be noticed, as the real gas law leads to lower pressure magnitude but remains moderate. The CFD pressure waves have a higher intensity than the experimental one and are quicker. These computations are first attempts in order to assess their potential, but extra work is needed to address properly free field cases.

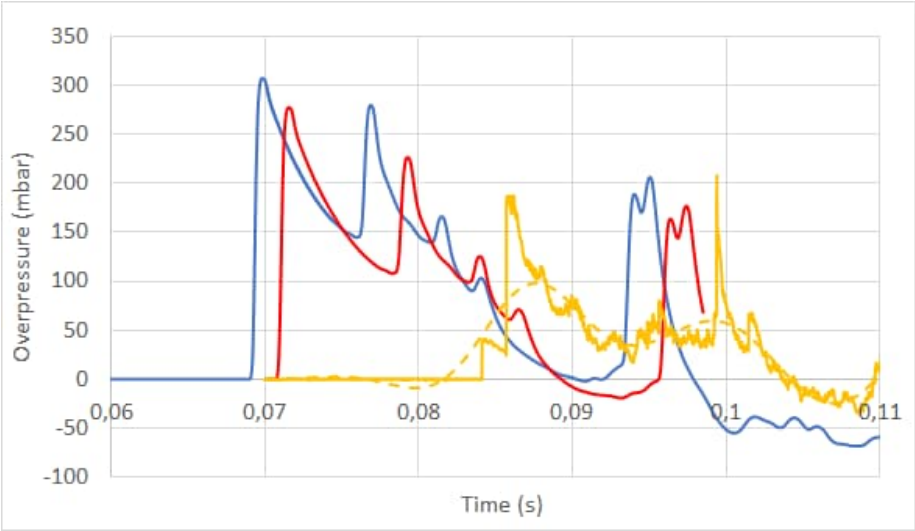

Fig. 3. *Experimental (yellow) raw (line) and filtered (dash line) signal measured at 30 m after bursting of a 78 L Helium bottle under 650 bar in the Mortier tunnel (Kudriakov et al., 2022). CFD modelling with an ideal gas law (blue) and a real gas law (red).*

3. Conclusions

A CFD approach is studied for dealing with high-pressure tank burst in tunnels. Reference tests are needed to propose a CFD strategy. Most tests are physically complex as they correspond to a thermal aggression of a hydrogen tank. These tests do not permit to quantify the part of pressure effects related to the fireball and the other one related to gas expansion.

Tests in tunnels were performed but the available data remain too limited to design and validate step by step a CFD modeling strategy. A promising experimental campaign could consist in provoking tank burst in free field for one or two non-reacting gas and for hydrogen, for the same tank volume and the same initial pressure. Burst could be generated by a detonating cord to control the discharge mode (initial pressure and surface discharging pressure). Repeatability tests would be needed. The same tests could be performed in a gallery or in a tunnel. The locations of the pressure probes should be the same in both types of tests and chosen in order to detect in tunnel, the reflection zone, the planar zone and the transition between the two of them.

Phenomenological tools were tested against some free field results. These models recover orders of magnitude for the pressure magnitude but their accuracy may vary. The way the pressure energy is quantified for high pressure cases may impact the results.

Some CFD was performed in free field and in tunnel. Some modeling choices for thermodynamics seem to be preferable nevertheless, the results obtained in the tunnel overestimate the experimental results. Extra work is needed based on the analysis of the projected experimental campaign mentioned above. This latter could also be beneficial for checking the behavior of already existing CFD strategies for modeling hydrogen tank bursts (Molkov et al., 2021).

Acknowledgements

The authors wish to thank Sergey Kudriakov for providing the unfiltered pressure signal related to the Helium tank rupture in the Mortier tunnel.

References

Kudriakov, S. et al., 2022. Full-scale tunnel experiments: Blast wave and fireball evolution following hydrogen tank rupture. Int. J. Hydrogen Energy 47(43), pp. 18911-18933

Blanc-Vannet, P. et al., 2019. Fire tests carried out in FCH JU Firecomp project, recommendations and application to safety of gas storage systems, Int. J. of Hydrogen Energy 44(17), pp. 9100-9109

Ruban, S. et al., 2012. Fire risk on high-pressure full composite cylinders for automotive applications, Int. J. of Hydrogen Energy 37 pp. 17630-17638

INERIS test campaign, 2012 (no publication)

Molkov, V. et al., 2015. Blast wave from a high-pressure tank rupture in a fire: Stand-alone and under-vehicle hydrogen tanks, Int. J. of Hydrogen Energy 40, pp. 12581-12603

Molkov, V.V. et al., 2021. Dynamics of blast wave and fireball after hydrogen tank rupture in a fire in the open atmosphere. Int. J. Hydrogen Energy 46(5), pp. 4644-4665

Brode, H.L., 1959. Blast waves from a spherical charge. Phys Fluids 2, pp. 217-29

Heudier, L., 2013. Les éclatements de capacité. Phénoménologie et modélisation des effets. Rapport Omega 15. www.ineris.fr.

Van den Berg, A.C., 1984. The Multi-Energy method – a framework for vapour cloud explosion blast prediction, TNO-PML Report 1984-C72

Zalosh, R. et al., 2005. Hydrogen Fuel Tank Fire Exposure Burst Test. SAE 2005-01-1886

Shen, C. et al., 2018. Consequence assessment of high-pressure hydrogen storage tank rupture during fire test. J. Loss Prev. in the Process Ind. 55, pp. 223-231

Tamura, Y. et al., 2006. Fire exposure burst test of 70MPa automobile high-pressure hydrogen cylinders. Society of Automotive Engineers of Japan Annual Autumn Congress

Chaineaux, J. et al., 2000. Sûreté des dispositifs de stockage de l'hydrogène sous haute pression équipant des véhicules routiers. Final report. EURO-QUEBEC HYDRO-HYDROGENE Project.

INERIS test campaign, 2010 (no publication).

TM5 1300, 1969. Department of the Army, the Navy and the Air Force. Structures to resist the effects of accidental explosions. Technical Manual, NAFVAC-P397 / AFM88

Baker, W.E., Cox, P.A., Westine, J.J., Kulesz, R.A., Strehlow, P.S., 1983. Explosion hazards and evaluation, Elsevier editions.

Weller, H.G, Tabor, G., 1998. A tensorial approach to computational continuum mechanics using object-oriented techniques. Computational Physics 12, pp. 620-631.

Kurganov, A. et al., 2000, New High-Resolution Central Schemes for Nonlinear Conservation Laws and Convection–Diffusion Equations, Journal of Computational Physics 160, pp. 241-282

Ghasemi, K.A., 2020. Release of high-pressure hydrogen into the air, Master's Thesis, University of South-Eastern Norway

BIOMASS MINIMUM IGNITION TEMPERATURE PREDICTION THROUGH DIFFERENTIAL STUDY OF THERMOGRAVIMETRIC ANALYSIS

Roberto Paredes[a], Isabel Amez[a,b], David León[a,b] & Blanca Castells[a,b]

[a] E.T.S. Ingenieros de Minas y Energía, Universidad Politécnica de Madrid (UPM), Madrid, Spain

[b] TECMINERGY - Laboratorio Oficial J.M. Madariaga (LOM), Universidad Politécnica de Madrid (UPM), Madrid, Spain

E–mail: r.pgallo@upm.es

With the global goal of minimising energy dependence on fossil fuels, biomass is taking on a crucial role, not only as an energy source, but also as a means of reducing greenhouse gas emissions and incorporating the use of new biofuels. However, the storage of processed biomass in dust form introduces several inherent hazards, e.g. the formation of fires due to self-ignition or the deposition of this powdery material on hot surfaces, thus reaching the minimum ignition temperature of dust layer. These hazards are not only observed in the industrial safety area but are also associated with the process of generating energy from biomass in controlled environments. In order to quantify these critical risks, this study focuses on correlating the devolatilisation temperature ranges of the main polymers of biomass from the differential analysis of thermogravimetric curves (DTG) to obtain a prediction of the minimum ignition temperature of dust layer. This parameter has been experimentally determined according to UNE - EN ISO/IEC 80079-20-2:2016. Six samples of lignocellulosic biomass of different origin and provenance were studied. The Fraser-Suzuki deconvolution method was used to determine the percentage of hemicellulose, cellulose, and lignin in order to establish a correlation between the composition and the flammability tendency of the samples. The results of the study underline the effectiveness of differential analysis of thermogravimetric curves as a fast and accurate tool for predicting the minimum ignition temperature of dust layer in lignocellulosic biomasses. This novel method, which requires only 60 mg and has an average error of 1.10% compared to experimental temperatures, improves the understanding of the combustibility of lignocellulosic biomasses by providing a more complete thermal record than that reported by international standard test methods. Therefore, its implementation would provide an improvement in terms of preventive and environmental risk management strategies related to combustible dust accumulation.

Keywords: Biomass, Thermogravimetric Analysis, Minimum Ignition Temperature of Dust Layer, DDTG, Industrial Explosions

1. INTRODUCTION

Recent studies indicate an increase in global carbon dioxide (CO_2) emissions due to, among other factors, technological improvements in the industrial sector and associated energy demand. The predominant use of fossil fuels intensifies greenhouse gas (GHG) emissions, notably CO_2 and methane (CH_4), contributing to global warming and climate change. This increase in CO_2 emissions triggers not only climate instability, but also impacts on the ecosystem and the quality of human life. This factor leads to an escalation of energy demand and thus to an increase in the carbon footprint and environmental consequences. Faced with this problem, during the COP21, the Paris Agreement was signed by several countries with the aim of keeping the global temperature increase below 2 ºC (Scarlat et al., 2015).

In line with the goal of reducing greenhouse gas emissions caused by the widespread use of fossil fuels, the production of biofuels has intensified and with it the transition to alternative energy sources. Despite the potential of biomass and lignocellulosic materials in terms of renewable energy production, the implementation of the process to obtain biofuels is characterised by high associated costs. However, this limitation draws attention to areas of opportunity that have not yet been fully explored. The wide scope for improving economic efficiency, strategic selection and cost optimisation

in pre-treatment processes suggests a promising future for biomass and lignocellulosic materials as valuable renewable alternatives that have yet to be fully exploited (Abbas Azeez & Al-Zuhairi, n.d.).

These lignocellulosic materials and biomasses can be treated by various conversion processes depending on the final product required. These processes, depending on the type of process applied, can be divided into thermochemical and biochemical processes. The first group of processes includes combustion, gasification, and pyrolysis, while biochemical processes include anaerobic digestion and fermentation (Mckendry, n.d.).

The recent rise in the use of these types of biofuels raises several risks related to industrial safety, triggering an increase in the number of accidents due to spontaneous combustion or smouldering processes, among others (Torero et al., 2020). Specifically, these two processes must be taken into account when addressing facilities industrial safety design and, in addition, when these processes are combined with dust deposition on a hot surface, they can serve as a source of ignition for future events (Salamonowicz et al., 2012; Tureková & Marková, 2020).

For this reason, accredited notified bodies have established certain tests that can experimentally predict the temperature at which a quantity of dust deposited on a hot surface will ignite. This parameter is known as the minimum ignition temperature of dust layer (MIT_L) and is standardised in the UNE – EN ISO/IEC 80079-20-2:2016 standard (Explosive Atmospheres—Part 20–2: Material Characteristics—Combustible Dusts Test Methods, 2021).

In order to understand the combustion process of powdery biomasses deposited on a hot surface it is crucial to understand the thermal profiles. Advance knowledge of these thermal profiles predicts potential future problems in terms of industrial and process safety. These thermal profiles are obtained by thermogravimetry (TGA) and differential analysis of their curves (DTG and DDTG) (Barzegar et al., 2020). By analysing these curves, critical parameters can be obtained, such as the ignition induction temperature (IT) (Castells et al., 2023a), burnout temperature (T_b) (Lu & Chen, 2015), maximum weight loss temperature (MWT_L), known as the temperature at which the three representative polymers of the biomass (hemicellulose, cellulose, and lignin) reach their maximum decomposition (Castells et al., 2023a).

In aiming to analyse the composition of the polymers mentioned above, the deconvolution technique using the Fraser Suzuki method was employed, representing an accurate method for this purpose. The technique was applied to data collected through thermal profiling extracted from TGA to provide accurate estimates of the hemicellulose, cellulose, and lignin content in lignocellulosic biomasses. (Perejón et al., 2011).

Due to the above, the main objective of this study is to introduce a new method never reported before to determine the minimum ignition temperature of dust layer from thermogravimetry. In addition, the relationship between sample composition by Fraser-Suzuki and ignition tendency has also been investigated. This innovative method provides accurate values of the minimum ignition temperature of dust layer compared to the data obtained from the experimental test, with a consequent reduction of time, sample quantity and toxic vapours emissions.

2. MATERIALS AND METHODS

2.1. Samples

The study presents the results obtained from the analysis of six biomass samples with different compositions and origins. These samples are categorized as different parts of the olive, various types of pellets and organic dusts. Their origins and identification are shown in Table 1.

Table 1: Samples identification

Material	*Origin*	*Identification*
Olive pomace	Portugal	BPA
Almod shell	Portugal	BCA

Olive leaves	Córdoba, Spain	BHO
Wood pellets	Gipuzkoa, Spain	BPM
Wheat straw	Sweden	BP
Soja dust	Huesca, Spain	BPS

Olive pomace and olive leaves are by-products of the industrial olive oil extraction process. While the remaining samples were obtained through different processes and origins. The samples were milled using an IKA-WEKE M20 mill and sieved through a 1 mm sieve.

Particle size distribution was analysed using laser diffraction (Mastersizer 2000, Malvern, UK), while the moisture content was assessed by measuring the reduction in mass when heating a sample to 105°C using a Mettler Toledo HB43-S halogen analyser. Table 2 displays the particle size characteristics and the moisture (MS) content.

Table 2: Samples particle size distribution and moisture content parameters

Sample	*d10 (µm)*	*d50 (µm)*	*d90 (µm)*	*MS (%)*
BPA	141.49	509.50	1190.13	5.04
BCA	69.23	534.24	1260.72	7.45
BHO	188.44	518.60	1167.03	6.22
BPM	51.88	167.51	653.89	7.92
BP	9.59	135.31	1008.83	6.87
BPS	338.21	769.14	1409.92	7.35

2.2. Thermogravimetric Analysis

Thermogravimetric analysis (TGA) is based on measuring changes in mass when a continuous, variable, or constant heating rate is applied. In this case, the Mettler Toledo TG-DSC T50 apparatus and 70 µL alumina crucibles were used. The experiments were carried out under three heating rates - β - (3, 5, and 7 K/min) and under a gaseous atmosphere that simulates the approximate composition of air (79% N_2 - 21% O_2), with a flow rate of 5 mL/min, simulating a combustion process. The amount of sample used for thermogravimetric tests has been 20 ± 1.5 mg.

By analysing TGA curves, it is possible to obtain the first derivative (DTG) to effectively interpret the analysis results. In the case of biomass samples, these curves typically exhibit three different phases. First, there is an initial drying phase and intramolecular moisture release, occurring approximately between ambient temperature and 120 ºC. Second, a biomass degradation phase takes place roughly between 120 ºC and 500 ºC, primarily involving the devolatilisation of hemicellulose and cellulose. Finally, there is an oxidation phase of the carbonaceous residue, which occurs at temperatures approximately between 500 ºC and 800 ºC.

Moreover, both TGA and DTG curves provide valuable information for determining key temperature points during degradation, as shown in Figure 1. These include the temperature at which the degradation rate reaches its maximum, known as the maximum weight loss temperature (MWLT), the temperature at which reactions accelerate, referred to as the induction temperature (IT), determined according to Castells et al., 2023a, and the burnout temperature (T_b), determine according to Lu & Chen, 2015. Furthermore, this parameter can also be determined by identifying the moment just before the reaction ceases when the rate of weight loss reaches 1% per minute (Lu & Chen, 2015).

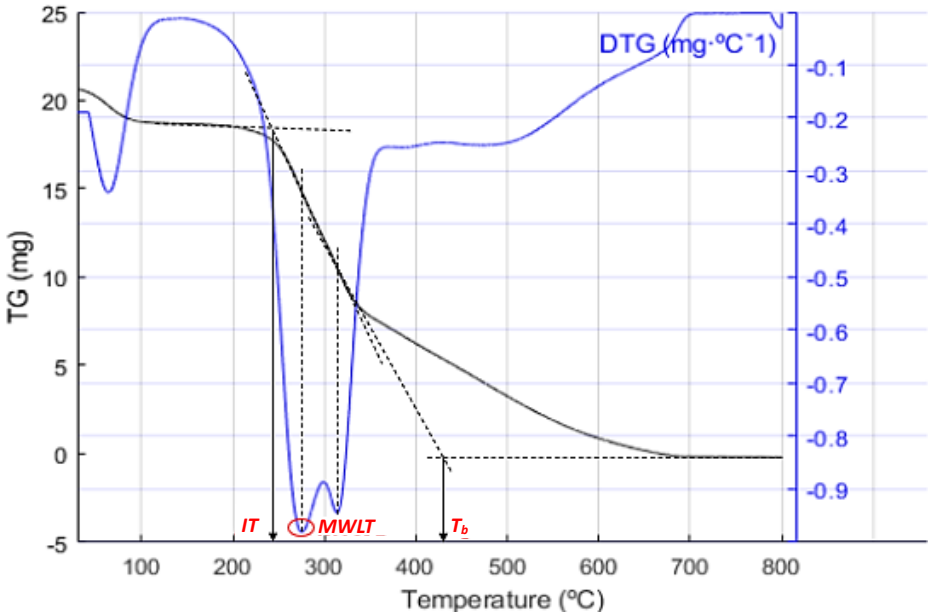

Figure 1: TG and DTG representative points

Additionally, it is possible to obtain the second derivative (DDTG) to properly address the results of the decomposition analysis. The DDTG curve allows to define the decomposition range and identify the maximum decomposition points for hemicellulose, cellulose, and lignin, as depicted in Figure 2. Specifically, (I) denotes the thermal decomposition range primarily associated with hemicellulose (though lignin is also present), locating the peak temperature of hemicellulose devolatilisation (H - as indicated on the DDTG curve). (II) encompasses the thermal decomposition range predominantly attributed to cellulose (with some lignin content), identifying the peak temperature of cellulose devolatilisation (C - referenced on the DTG curve). Lastly, (III) represents the thermal decomposition range encompassing lignin and carbonaceous residue, with the peak temperature of lignin devolatilisation (L - as marked on the DDTG curve) (Fonseca et al., 2022) (Gu et al., 2023).

2.3. Fraser-Suzuki Deconvolution

Lignocellulosic biomass is a complex material comprising three key components: lignin, cellulose, and hemicellulose. After moisture has been eliminated, the degradation of the sample primarily involves the volatilization of these three polymers. Therefore, it becomes possible to estimate the composition of lignocellulosic samples by applying deconvolution to the DTG curve and calculating the area under each individual component curve (Castells et al., 2020; Morgan et al., n.d.). Among the various available methods for curve deconvolution, the Fraser-Suzuki method has been chosen for its exceptional accuracy and reliability in this context (Castells et al., 2023b; Varela et al., 2023). Equation 1 presents the mathematical model used to perform these calculations.

$$y = \sum_{i=1}^{n} h_i \cdot exp\left[-\frac{ln2}{s_i^2} ln\left(1 + 2s_i \frac{T-p_i}{w_i}\right)^2\right] \quad (1)$$

In the context of this equation, it is important to define the various parameters involved: 'Y' represents the deconvoluted curve, while 'T' denotes the temperature, 'h_i' corresponds to the weight assigned to the ith curve in relation to the overall curve, 's_i' characterizes the skewness or asymmetry of the i-th curve, 'p_i' signifies the mean value of the i-th curve, and 'w_i' represents the width of the ith curve.

Furthermore, the parameter 'n' assumes a pivotal role as it indicates the number of pseudocomponents derived from the deconvolution process. As conventionally practiced, a value of 3 is typically chosen to discern hemicellulose, cellulose, and lignin components. However, it is noteworthy that in some

cases, samples may exhibit the formation of a carbonaceous residue or char as the reaction progresses, necessitating the consideration of a fourth component (Castells et al., 2023b; Varela et al., 2023). For the purposes of this particular study, three pseudocomponents are determined.

2.4. Minimum Ignition Temperature of Dust Layer

The Minimum Ignition Temperature of Dust Layer (MIT_L) has been determined at the Laboratorio Oficial José María de Madariaga (LOM), Universidad Politécnica de Madrid, in accordance with the standard UNE – EN ISO/IEC 80079-20-2:2016 standard (Explosive Atmospheres—Part 20–2: Material Characteristics—Combustible Dusts Test Methods, 2021). The hot surface consists of a circular metal surface providing at least a working area of 100 mm radius and a thickness of not less than 20 mm. The plate is electrically heated using glow resistors and controlled by thermocouples. This surface must be able to reach a maximum temperature, without dust layer, of 400 °C and must be constant with an accuracy of ± 5 K throughout the test process.

The test is carried out until dust layer is found to have ignited or to have heated above the temperature of the plate without igniting (self-heating) and is subsequently cooling. Ignition is considered to have occurred if one of the following phenomena is produced: a visible glow or flame is observed, a temperature of 450 °C is measured in the dust layer or a temperature rise of 250 K above the heated plate temperature is measured in the dust layer. This test enables the determination of the minimum temperature at which a 5 mm layer of the sample can ignite, produce sparks, or catch fire.

2.5. Minimum Ignition Temperature Approach Analysis

Numerous researchers have delved into the configuration of thermocouples in the minimum ignition temperature of dust layer test (Tureková & Marková, 2020), yet only a restricted few have developed numerical or computational methodologies to gauge this parameter (Li et al., 2020; Salamonowicz et al., 2012). Consequently, it is proposed to establish a correlation between the temperature that delimits the end of hemicellulose devolatilisation (the shoulder) and the start of cellulose devolatilisation. This temperature point aligns with the local minimum that immediately precedes the maximum absolute value on the DDTG curve, thereby serving as an estimation of the minimum ignition temperature of dust layer, as illustrated in Figure 2.

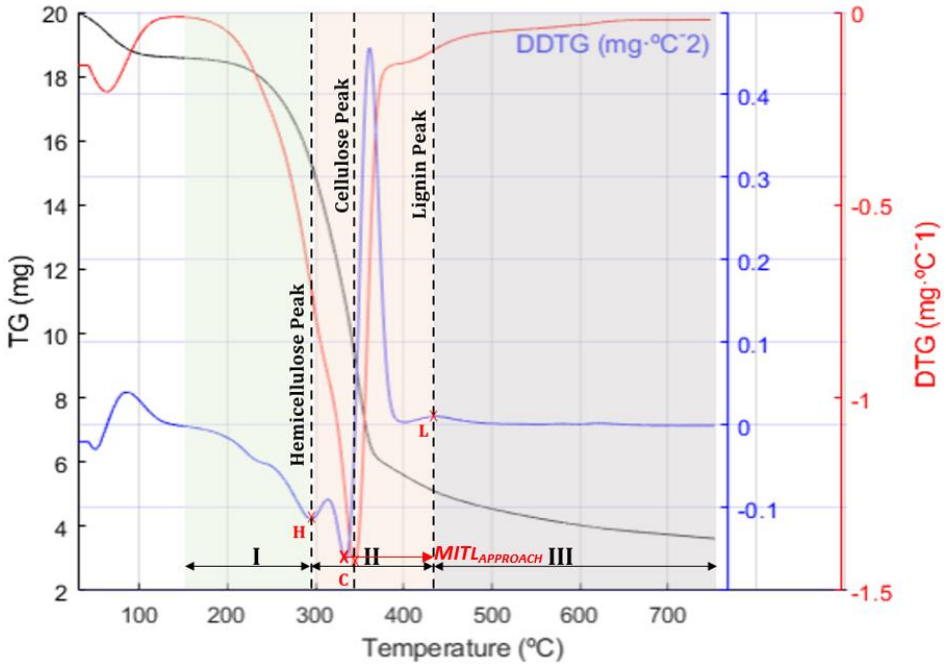

Figure 2: Thermal decomposition zones of biomass polymers analysed using TG, DTG and DDTG and Minimum Ignition Temperature of Dust Layer Approach Point

3. RESULTS AND DISCUSSION

3.1. TGA Results

The results of the thermogravimetric analysis are detailed in Table 3 and Figure 3, which includes the characteristic points for each curve. The outcomes of the IT and T_b parameters are presented from the thermogravimetric curve (TG), the MWLT parameter obtained from the derivative of the thermogravimetric curve (DTG), and, finally, the peak temperatures of the three main polymers extracted from the second derivative of the thermogravimetric curve (DDTG).

The detailed analysis of the data reveals significant patterns in the thermal responses of various biomasses to variations in the heating rate. A clear upward trend is observed in the ignition temperatures (IT) and burnout temperatures (T_b) as the heating rate increases. This phenomenon indicates a higher susceptibility of biomasses to ignition and more complete combustion at higher heating rates. However, it is crucial to note the disparities among the different samples, highlighting their uniqueness in response to rapid heating.

Similarly, the maximum weight loss temperature (MWLT) exhibits a parallel tendency with the heating rate. The escalation of the heating rate corresponds to a proportional increase in the MWLT value, indicative of enhanced efficiency in decomposition or combustion processes at elevated heating rates. Comparing the samples, it is observed that those originating from the olive tree (BPA and BHO) together with BPM present higher MWLT values than the other samples.

This is attributed to the higher content of hemicellulose in these, which shifts the curve to the right. Consequently, the temperature of maximum weight loss also shifts, coinciding with the temperature of maximum decomposition of the cellulose present in the sample.

The temperatures of maximum decomposition for the three polymers (hemicellulose, cellulose, and lignin) increase proportionally with the applied heating rate. However, as the heating rate increases, the associated shoulders become less evident. This is because, at higher speeds, the decomposition of polymers occurs simultaneously. Specifically, in sample BCA, it is impossible to clearly distinguish the lignin decomposition peak at any rate, as well as the hemicellulose peak at 7 K/min.

This phenomenon is also evident in sample BPM, where the hemicellulose devolatilisation peak is not totally clear. Similarly, this indicates that hemicellulose decomposition occurs concurrently with cellulose. In other words, holocellulose undergoes volatilization within a narrow temperature range, making it challenging to clearly distinguish between the polymers.

When comparing the graphs in Figure 3, a common trend is evident: as the heating rate increases, the peaks become higher and more pronounced. Similarly, with the increase in this parameter, it is observed that in the BCA and BP samples at 7 K/min, it is no longer possible to distinguish the peaks related to the devolatilisation of hemicellulose.

Although both BPA and BHO are samples originating from olive, it is noted that BPA results presented in this study are slightly higher than those reported by Castells et al., 2023b. However, the BHO sample more closely matches the results reported by the same study.

Comparing the BCA, BPM and BP samples with the results presented by García Torrent et al., 2016, it is observed that in the BCA and BPM samples the temperatures of the analysed parameters are lower than those reported in the current study. However, when comparing the wheat straw sample, BP, the values presented are remarkably similar to those calculated in this study.

As for the soybean dust sample, BPS, the values are consistent with parameters reported by other authors (Costella et al., 2016; Ramírez et al., 2010).

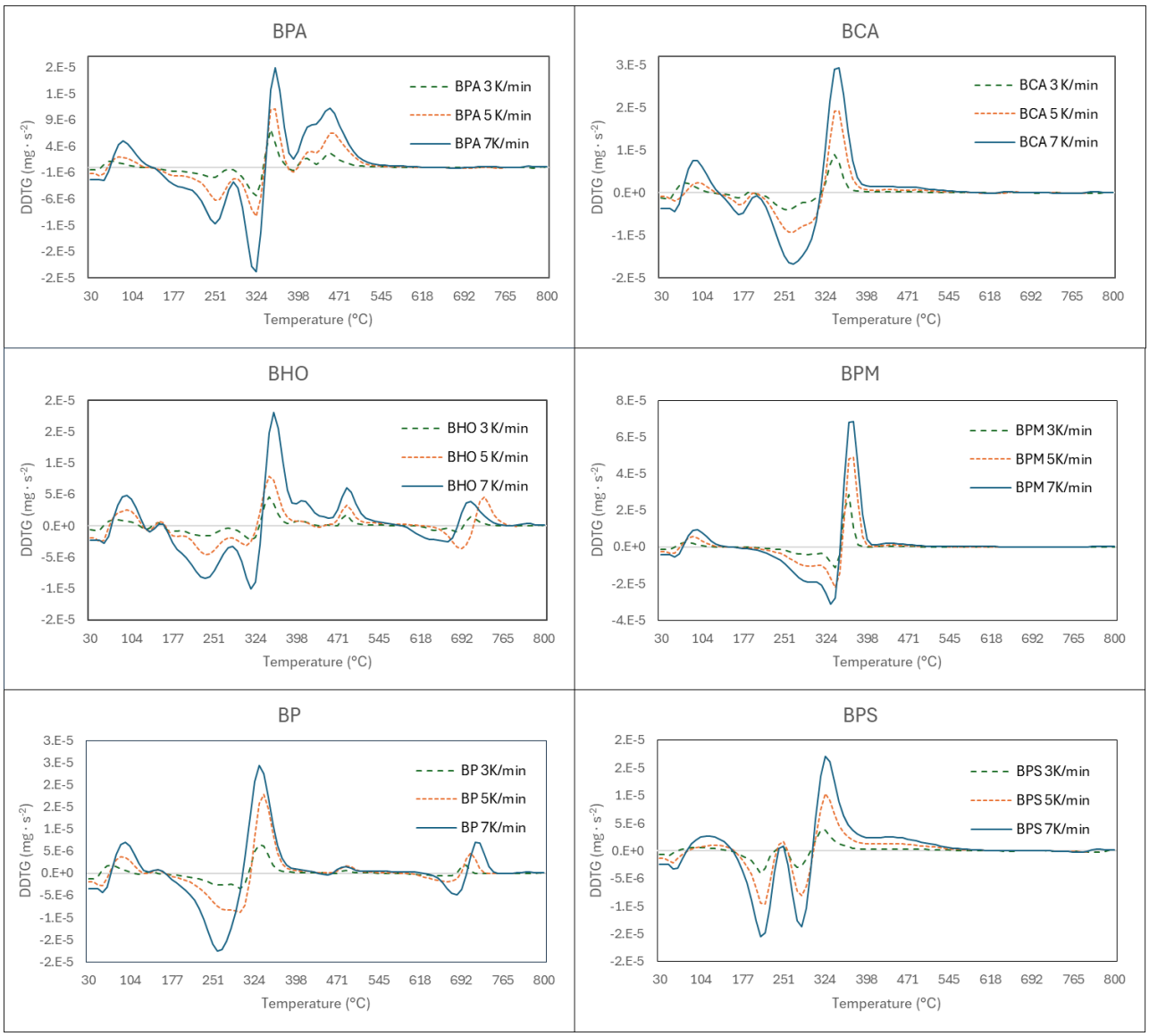

Figure 3: DDTG curves

Table 3: TGA parameters results

Sample	*Heating rate (K/min)*	*TG (ºC)*		*DTG (ºC)*	*DDTG (ºC)*		
		IT	*T_b*	*MWLT*	*H-Peak*	*C-Peak*	*L-Peak*
BPA	3	267.0	435.8	327.3	239.7	327.3	399.6
	5	270.3	446.3	333.2	248.8	333.2	411.8
	7	275.9	452.0	341.1	251.1	341.1	427.2
BCA	3	243.3	348.2	309.6	249.4	309.6	NAP*
	5	254.0	357.4	316.0	258.9	316.0	NAP
	7	260.6	365.0	318.7	NAP	318.7	NAP
BHO	3	235.4	384.8	322.9	229.6	322.9	394.8
	5	238.0	405.0	324.7	233.5	324.7	406.1
	7	251.7	407.1	338.5	234.9	338.5	411.6
BPM	3	298.6	357.7	341.3	285.2	341.3	423.4
	5	302.0	369.1	348.9	291.0	348.9	434.8
	7	308.7	376.6	352.9	NAP	352.9	467.5
BP	3	251.2	341.4	305.0	257.6	305.0	471.0

	5	262.0	359.1	312.6	269.6	312.6	481.4
	7	257.6	368.3	314.2	307.6	314.2	487.5
BPS	3	219.6	354.7	290.4	204.2	290.4	434.2
	5	222.0	368.3	300.5	209.9	300.5	468.0
	7	234.2	370.6	304.2	212.4	304.2	470.6

NAP: Not Appreciable Peak.

3.2. Fraser-Suzuki composition model results

As previously discussed, we employed the Fraser-Suzuki deconvolution method with a parameter value of $n = 3$ to precisely estimate the content of hemicellulose, cellulose, and lignin. Understanding the temperature-dependent degradation behaviour of these polymers is crucial for the aim of the study. Hemicellulose is the first to undergo degradation, typically occurring within a temperature range of 200 °C to 320 °C. Subsequently, cellulose follows suit, with its devolatilisation occurring in the temperature range of 300 °C to 400 °C. In contrast, lignin is the most thermally stable polymer and requires considerably higher temperatures for full degradation, spanning a wide devolatilisation temperature range from 200 °C to 800 °C (Maestri et al., 2019).

Based on the aforementioned temperature degradation ranges, we assigned pseudocomponent 1 (PS1) to represent hemicellulose, pseudocomponent 2 (PS2) for cellulose, and pseudocomponent 3 (PS3) for lignin. The mean values obtained for each polymer, accompanied by the R^2 fitting parameter, are presented in Table 4. However, the standard deviation is also provided and as it does not exceed 5% in any of the samples, the average of the three calculated heating ratios is considered as the data to be evaluated.

The values presented indicate that the samples related to the olive, BPA and BHO, exhibited a completely different distribution if compared to the other samples. This is due to their cellulose content, which is the lowest of the analysed samples, at 16.41% and 19.13%, respectively. BHO showed the lowest R^2 value, suggesting that the fitting method may lack accuracy. However, the BCA sample showed a hemicellulose percentage similar to that of BPA and BHO (27.52% and 25.36%, respectively), but in this case, the cellulose content is much higher at 39.61%.

The results indicate that the predominant polymers in samples not related to the olive are cellulose and lignin. The BP sample has the highest cellulose percentage, followed by the BPS sample. Regarding lignin, it is observed that the sample with the highest percentage of this polymer is BPA, followed by BHO, the only samples with olive origins.

Comparing results with data collected from the literature, it is noted that the BPA sample is similar to the data provided by Danzi et al., 2021. Regarding the two samples of olive origin, the composition is very similar, as can be seen in Table 4. The BCA sample shows similarities regarding the hemicellulose content reported by Vidal et al., 2019 for the sample tested from the US, but the cellulose and lignin content reported in this study is higher.

The BPM sample only slightly matches the percentage of lignin determined by Sobek & Werle, 2020. This may be explained due to the several possible origins for wood pellets, as the type of wood, the origin, etc., influence the composition.

The BP and BPS samples contain similar percentages of hemicellulose. However, only the cellulose content of the wheat straw sample is consistent with that reported by Baltierra-Trejo et al., 2016, while no relevant data were found in the literature for comparison with the soybean sample.

On the other hand, the correlation between the hemicellulose content and the minimum ignition temperature of dust layer was analysed, as shown in Figure 4. As it can be seen, there is a direct relationship: the lower the hemicellulose content, the lower the minimum ignition temperature of dust layer. This relationship may mean that hemicellulose, being the polymer that devolatilises at a lower temperature, may be the precursor of the reaction that triggers ignition. Therefore, with a higher content of this polymer, the energy and temperature required for its volatilisation is higher.

Table 4: Fraser-Suzuki deconvolution

Sample	PS1 (%)	σ_{PS1}	PS2 (%)	σ_{PS2}	PS3 (%)	σ_{PS3}	R^2
BPA	27.52	0.43	16.41	0.59	56.07	1.01	0.99
BCA	21.00	2.42	39.61	3.42	39.39	1.02	0.99
BHO	25.36	2.13	19.13	1.84	55.51	3.73	0.93
BPM	32.80	1.63	34.96	1.64	32.24	0.29	0.99
BP	18.53	0.86	47.83	0.52	33.64	0.37	0.98
BPS	12.83	1.96	44.00	4.12	43.17	3.52	0.98

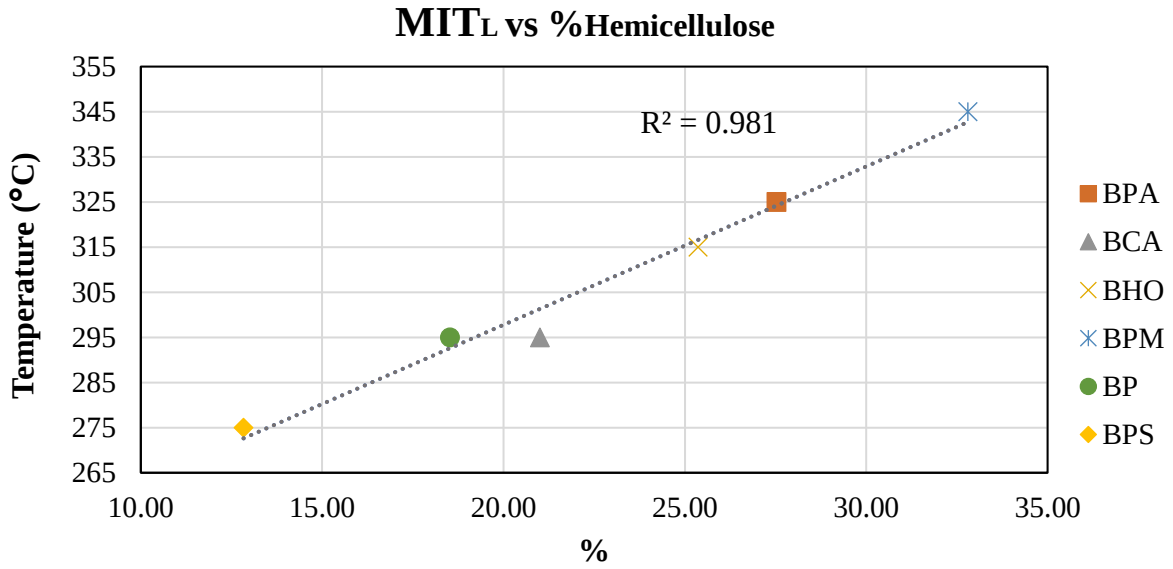

Figure 4: MITL vs %Hemicellulose

3.3. Minimum Ignition Temperature of Dust Layer Results

In order to compare the experimental results with the proposed approximation, the results of the Minimum Ignition Temperature of Dust Layer test (MITL) are shown in Figure 5. In all conducted tests, a consistent layer thickness of 5 mm has been maintained.

sample of soybean powder exhibits the lowest value at 270 °C, which means higher ignition sensitivity if compared to other samples. Following closely are almond shell and wheat straw, both registering a MITL value of 290 °C. This analysis suggests that, under conditions of deposition on a hot surface from this temperature onwards, soybean powder is the most prone to ignition, while the least flammable is the wood pellet sample and the samples originating from the olive.

When comparing the results presented with those compiled in the literature, it is observed that the BPA sample in this study has a value of 320 °C, contrasting with the 300 °C reported by Fernandez-Anez & Garcia-Torrent. Similarly, the BPM sample shows a MITL higher than that presented in the aforementioned study but lower than the MITL value for the BP sample. On the other hand, referring to the same article, the MITL value for the BCA sample remains unchanged.

3.4. Minimum Ignition Temperature Approach Results

In Table 5 and Figure 5, the results obtained through the new method to determine the minimum ignition temperature of dust layers are presented. In Figure 5, it is observed that only the upper limit has been depicted. The aim of solely representing this limit is to establish a safety margin in relation to the ignition temperature, as referred to in the experimental test. It is observed that these results

follow the same trends described in the previous section regarding the flammability of the samples. Sample BPS exhibits the highest flammability, while sample BPM is the least flammable.

Upon examining Table 5, it is noteworthy that the maximum error occurred in sample BPS at a heating rate of 7 K/min. Extrapolating this error to the other results, we can conclude that the highest percentage of error occurs in most samples at this heating rate. This phenomenon is due to the fact that, as mentioned in Section 3.1, the decomposition of polymers occurs more simultaneously as the heating rate increases. This is why, in samples BCA and BP at 7 K/min, it has not been possible to appreciate the point related to the parameter approximation.

On the other hand, it is observed that only sample BPS at heating rates of 5 and 7 K/min is outside the ignition range. This means that, in principle, the minimum ignition temperature of dust layer is determined with an accuracy of 5 K between the no-ignition temperature and the ignition temperature. Therefore, if this temperature is outside this range, it is because $MIT_{L_{approach}}$ > Ignition Temperature.

It is highlighted that the average error at heating rates of 3 and 5 K/min is similar, with values of 1.22% and 1.23%, respectively. The average error at 7 K/min cannot be verified because in samples BCA and BP, the peak determining the minimum ignition temperature of dust layer is not observed according to this new model. However, the average of the temperatures results in the value closest to the experimental, with an average error of 1.10%, thus establishing this temperature as $MIT_{L_{approach}}$ as Equation 2. This equation shows the average of the values obtained for each evaluated point of the DDTG curve for heating rates of 3, 5 and 7 K/min because at higher heating rates, it does not make sense to evaluate the resulting data, as there are several peaks that are not appreciable.

$$MIT_{L_{approach}} = \frac{\sum_{\beta=(3,\,5,\,7)|_{k\cdot min^{-1}}} MIT_{L_{approach_\beta}}}{length\,(\beta)} \tag{2}$$

Table 5: Minimum Ignition Temperature of Dust Layer Approach Results

Sample	*Heating rate (K/min)*	MIT_L *(ºC)*	$MIT_{L_{approach}}$ *(ºC)*	*Error (%)*	*In range?**
BPA	3	320	313.78	1.94	Yes
	5		318.06	0.61	Yes
	7		322.79	0.87	Yes
	Average		**318.21**	**0.56**	**Yes**
BCA	3	290	286.81	1.10	Yes
	5		289.7	0.10	Yes
	7		NAP	-	-
	Average		**288.26**	**0.60**	**Yes**
BHO	3	310	308.63	0.44	Yes
	5		305.68	1.39	Yes
	7		319.93	3.20	No
	Average		**311.41**	**0.46**	**Yes**
BPM	3	340	331.2	2.59	Yes
	5		335.67	1.27	Yes
	7		336.1	1.15	Yes
	Average		**334.32**	**1.67**	**Yes**
BP	3	290	292.19	0.76	Yes
	5		294.39	1.51	Yes
	7		NAP	-	-
	Average		**293.30**	**1.13**	**Yes**

BPS	3	270	268.69	0.49	Yes
	5		276.76	2.50	No
	7		282.03	4.46	No
	Average		**275.83**	**2.16**	**No**

In range?: Yes, if $MIT_{Lapproach} < MIT_L + 5$ K; No, if $MIT_{Lapproach} > MIT_L + 5$ K

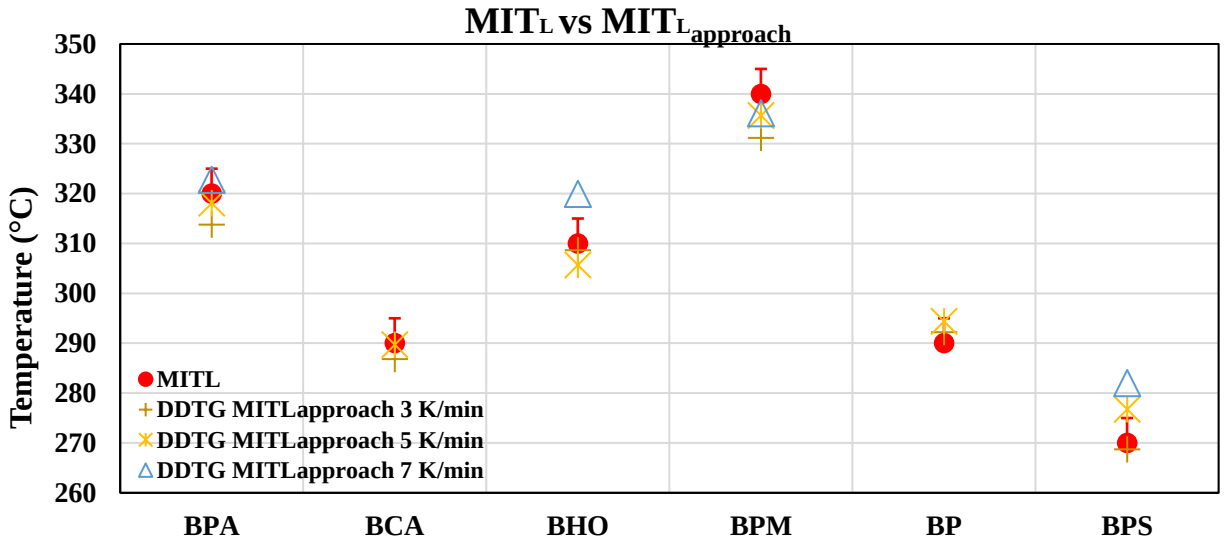

Figure 5: MIT_L vs $MIT_{Lapproach}$

4. CONCLUSIONS

The aim of this research has been the inclusion, validation and verification of a new model, which based on thermogravimetric curves (TGA), allows obtaining the minimum ignition temperature of dust layer from lignocellulosic biomass with an average error of 1.10%. Additionally, our objective was to evaluate the relationship between the percentage of each polymer in its composition, obtained through Fraser-Suzuki deconvolution via thermogravimetric analysis, with the flammability of the different biomasses reported in this study.

When applying thermogravimetric techniques, it is crucial to define the heating rate correctly, as it was proved that an increase in the heating rate led to thermal lag, higher induction temperatures, and higher maximum weight loss temperatures. Furthermore, depending on the lignocellulosic biomass, it is possible that at a heating rate above 5 K/min, the volatilization of hemicellulose and cellulose may not be distinguishable adequately to observe the temperature of the new method for obtaining MIT_L.

A direct correlation has also been found between the amount of hemicellulose and the minimum ignition temperature of dust layer. The lower the hemicellulose content, the lower the minimum ignition temperature of the dust layer. This relationship suggests that hemicellulose, being the polymer that volatilises at lower temperatures, could be the precursor of the reaction that triggers ignition. Therefore, the higher the content of this polymer, the more energy and the higher the temperature required for volatilisation to occur.

On the other hand, experimental tests for MIT_L determination have provided revealing data to clarify the flammability trend of different samples. Highlighting the BPS sample as the most flammable under these conditions, presenting the lowest MIT_L, and BPM as the least flammable.

The study of all these parameters together leads to the thermal characterization of a sample under dust layer conditions on a hot surface and confirms that the new method proposed to predict the minimum ignition temperature of dust layer through the differential analysis of thermogravimetric curves is a reliable, fast, and accurate alternative.

Future studies should consider investigating spontaneous combustion through TGA to observe possible relationships between this temperature and that exposed by the model.

5. REFERENCES

Abbas Azeez, R., & Al-Zuhairi, F. K. (n.d.). Biofuels (Bioethanol, Biodiesel,and Biogas) from Lignocellulosic Biomass :A Review. In *Journal of University of Babylon for Engineering Sciences* (Issue 28).

Baltierra-Trejo, E., Silva-Espino, E., Marquez-Benavides, L., & Sanchez-Yañez, J. (2016). Wheat straw liginin degradation induction to aromatics by Aspergillus spp and Penicillium chrysogenum. *Jorunal Selva Andina Research Society*, *7*, 10–19.

Barzegar, R., Yozgatligil, A., Olgun, H., & Atimtay, A. T. (2020). TGA and kinetic study of different torrefaction conditions of wood biomass under air and oxy-fuel combustion atmospheres. *Journal of the Energy Institute*, *93*(3), 889–898. https://doi.org/10.1016/j.joei.2019.08.001

Castells, B., Amez, I., Medic, L., & Torrent, J. G. (2020). Particle size influence on the transport classification labels and other flammability characteristics of powders. *Applied Sciences (Switzerland)*, *10*(23), 1–14. https://doi.org/10.3390/app10238601

Castells, B., Varela, A., Castillo-Ruiz, F. J., Calvo, L. F., Medic, L., & Tascón, A. (2023a). Ignition and explosion characteristics of olive-derived biomasses. *Powder Technology*, *420*. https://doi.org/10.1016/j.powtec.2023.118386

Castells, B., Varela, A., Castillo-Ruiz, F. J., Calvo, L. F., Medic, L., & Tascón, A. (2023b). Ignition and explosion characteristics of olive-derived biomasses. *Powder Technology*, *420*, 118386. https://doi.org/10.1016/j.powtec.2023.118386

Costella, M. F., Pilz, S. E., & Bet, A. (2016). Método de coleta e análise de amostras de poeira para avaliação de riscos de explosões de pós em suspensão em unidades de recebimento e armazenagem de grãos. *Gestão & Produção*, *23*(3), 503–514. https://doi.org/10.1590/0104-530x1324-15

Danzi, E., Di Benedetto, A., Sanchirico, R., Portarapillo, M., & Marmo, L. (2021). Biomass from winery waste: Evaluation of dust explosion hazards. *Chemical Engineering Transactions*, *86*, 301–306. https://doi.org/10.3303/CET2186051

Explosive Atmospheres—Part 20–2: Material Characteristics—Combustible Dusts Test Methods. (2021).

Fernandez-Anez, N., & Garcia-Torrent, J. (2019). Influence of Particle Size and Density on the Hot Surface Ignition of Solid Fuel Layers. *Fire Technology*, *55*(1), 175–191. https://doi.org/10.1007/s10694-018-0782-3

Fonseca, F. G., Anca-Couce, A., Funke, A., & Dahmen, N. (2022). Challenges in Kinetic Parameter Determination for Wheat Straw Pyrolysis. *Energies*, *15*(19). https://doi.org/10.3390/en15197240

García Torrent, J., Ramírez-Gómez, Á., Fernandez-Anez, N., Medic Pejic, L., & Tascón, A. (2016). Influence of the composition of solid biomass in the flammability and susceptibility to spontaneous combustion. *Fuel*, *184*, 503–511. https://doi.org/10.1016/j.fuel.2016.07.045

Gu, J., Chong, C. T., Mong, G. R., Ng, J. H., & Chong, W. W. F. (2023). Determination of Pyrolysis and Kinetics Characteristics of Chicken Manure Using Thermogravimetric Analysis Coupled with Particle Swarm Optimization. *Energies*, *16*(4). https://doi.org/10.3390/en16041919

Li, B., Li, M., Gao, W., Bi, M., Ma, L., Qin, Q., & Shu, C. M. (2020). Effects of particle size on the self-ignition behaviour of a coal dust layer on a hot plate. *Fuel*, *260*. https://doi.org/10.1016/j.fuel.2019.116269

Lu, J. J., & Chen, W. H. (2015). Investigation on the ignition and burnout temperatures of bamboo and sugarcane bagasse by thermogravimetric analysis. *Applied Energy*, *160*, 49–57. https://doi.org/10.1016/j.apenergy.2015.09.026

Maestri, D., Barrionuevo, D., Bodoira, R., Zafra, A., Jiménez-López, J., & Alché, J. de D. (2019). Nutritional profile and nutraceutical components of olive (Olea europaea L.) seeds. *Journal of Food Science and Technology*, *56*(9), 4359–4370. https://doi.org/10.1007/s13197-019-03904-5

Mckendry, P. (n.d.). *Energy production from biomass (part 2): conversion technologies*.

Morgan, P. A., Robertson, S. D., & Unsworth, J. F. (n.d.). *Combustion studies by thermogravimetric analysis. 1. Coal oxidation*.

Perejón, A., Sánchez-Jiménez, P. E., Criado, J. M., & Pérez-Maqueda, L. A. (2011). Kinetic analysis of complex solid-state reactions. A new deconvolution procedure. *Journal of Physical Chemistry B*, *115*(8), 1780–1791. https://doi.org/10.1021/jp110895z

Ramírez, Á., García-Torrent, J., & Tascón, A. (2010). Experimental determination of self-heating and self-ignition risks associated with the dusts of agricultural materials commonly stored in silos. *Journal of Hazardous Materials*, *175*(1–3), 920–927. https://doi.org/10.1016/j.jhazmat.2009.10.096

Salamonowicz, Z., Wolinski, M., Kukfisz, B., Salamonowicz, Z., Półłka, M., Woliński, M., & Kukfisz, B. (2012). *Ignition of a dust layer on a hot surface*. https://www.researchgate.net/publication/320556365

Scarlat, N., Dallemand, J. F., Monforti-Ferrario, F., Banja, M., & Motola, V. (2015). Renewable energy policy framework and bioenergy contribution in the European Union - An overview from National Renewable Energy Action Plans and Progress Reports. In *Renewable and Sustainable Energy Reviews* (Vol. 51, pp. 969–985). Elsevier Ltd. https://doi.org/10.1016/j.rser.2015.06.062

Sobek, S., & Werle, S. (2020). Kinetic modelling of waste wood devolatilization during pyrolysis based on thermogravimetric data and solar pyrolysis reactor performance. *Fuel*, *261*, 116459. https://doi.org/10.1016/J.FUEL.2019.116459

Torero, J. L., Gerhard, J. I., Martins, M. F., Zanoni, M. A. B., Rashwan, T. L., & Brown, J. K. (2020). Processes defining smouldering combustion: Integrated review and synthesis. In *Progress in Energy and Combustion Science* (Vol. 81). Elsevier Ltd. https://doi.org/10.1016/j.pecs.2020.100869

Tureková, I., & Marková, I. (2020). Ignition of deposited wood dust layer by selected sources. *Applied Sciences (Switzerland)*, *10*(17). https://doi.org/10.3390/APP10175779

Varela, A., Castillo-Ruiz, F. J., Arbizu-Milagro, J., & Tascón, A. (2023). The influence of moisture on the sieving performance of lignocellulosic biomass. *Biofuels, Bioproducts and Biorefining*, *17*(6), 1708–1723. https://doi.org/10.1002/bbb.2541

Vidal, R. V., García, R. V., Martínez, A. F., & Santos Estébanez, Fco. J. D. los. (2019). Activated Carbon from Almond Shells for Water Treatment: A Mini Review. *Agricultural Reviews*, *40*(04). https://doi.org/10.18805/ag.r-132

Sustainable Alternatives to Reduce Emissions and Sound Pressure Level of Flash Powder

David León [a,b], Isabel Amez [a,b], Roberto Paredes[a] & Blanca Castells [a,b]

[a] E.T.S.I Minas y Energía, Universidad Politécnica de Madrid (UPM), Madrid, Spain
[b] TECMINERGY - Laboratorio Oficial J.M. Madariaga (LOM), Universidad Politécnica de Madrid (UPM), Madrid, Spain

E-mail: david.leon.ruiz@upm.es

Abstract

Flash powder, an explosive compound widely used in flash bangers and pyrotechnic shells, among others, has emerged as a critical point in discussions about the negative effects of its use. Currently, fireworks present significant challenges due to their adverse impacts on the environment and the generation of acoustic disturbances in residential and urban areas due, among other compounds, to flash powder. This powder, mainly composed of potassium perchlorate and metallic compounds such as aluminium or magnesium, is crucial to achieve the opening and bursting of pyrotechnic devices. Therefore, it is necessary to develop alternatives that solve the flash powder associated problems to give a sustainable future to the pyrotechnic sector. This study proposes possible alternatives to reduce emissions and sound pressure levels, whit the intention of ensuring suitable performance for these pyrotechnic articles. F2 category flash bangers from different manufacturers were collected. The operation of these bangers was compared in different tests, by adding inert materials such as sodium bicarbonate ($NaHCO_3$) and recycled glass, at 10% and 20%(w/w), and by replacing the flash powder with nitrocellulose ($[C_6H_7(NO_2)_3O_5]n$), with a nitrogen percentage of less than 12.6%. The samples were subjected to sound pressure level measurements according to EN 15947-4:2015 standard, but also CO and CO_2 emissions were evaluated. It was observed that the alternatives studied could lead to a significant reduction in both pollutant emissions and the noise level generated by the pyrotechnic articles. After studying the explosion pressure generated for their substitution in pyrotechnic shells, it is concluded that the addition of inert compounds can be a real alternative, while nitrocellulose with a higher nitrogen content must be studied in order to achieve a correct operation.

Keywords: *flash powder, emissions, sound pressure level, explosion pressure*

1. Introduction

The attractiveness of pyrotechnic shows, which in several cultural traditions and celebrations can be considered as a base root, is now facing challenges due to the environmental impact (Chen et al., 2022; Gonzalez et al., 2022a; Greven et al., 2019; Nasir & Brahmaiah, 2015) and acoustic disturbances (Lombera et al., 2023). The widespread use of flash powder, one of the main components in pyrotechnic devices, has been identified as a significant contributor to these challenges, which leads to the need to explore sustainable alternatives. As several studies point out (Moreno et al., 2010; Sijimol & Mohan, 2014), the adverse effects emphasise the urge to mitigate the impacts associated with pyrotechnic events.

Flash powder is primarily composed of potassium perchlorate and metallic compounds (Russell, 2009), and plays the main role in achieving the spectacular sound effects of pyrotechnic shows. However, its association with environmental pollutants and high sound pressure levels requires innovative solutions for the continued viability of the pyrotechnic sector. In recent years, different

alternatives have been studied (Azhagurajan et al., 2019; M. Rajendran et al., 2021) and visual shows have even been designed with other types of technologies (Vergouw et al., 2016), but lacking the essence of pyrotechnics.

Nitrogen-rich compounds could be a solution. In the past years, the use of nitrocellulose in the pyrotechnic sector has increased significantly, especially in some devices that are currently using nitrocellulose as their main component. Based on the use of nitrocellulose as a propellant for different types of ammunition (Yolhamid et al., 2018), pyrotechnic devices such as fountains or table bombs, intended for indoor use, use nitrogen-rich compounds in their composition, according to the standard (EN 15947-4, Pyrotechnic Articles - Fireworks, Categories F1, F2, and F3 - Part 4: Test Methods, 2015). The use of nitrocellulose in pyrotechnic devices presents significant advantages that establish nitrocellulose as a viable substitute for flash powder. The most notable advantage lies in its potential to reduce environmental impact compared to traditional explosive compounds like flash powder, mainly because it removes metal compounds. According to toxicological research, it has been shown many of the metalliferous particles in fireworks smoke are reactive and can affect human health (Moreno et al., 2007). Additionally, nitrocellulose presents a cleaner combustion (Espinoza & Thornton, 1994; MacCrehan et al., 2002), generating less particle emissions and potentially lowering the overall environmental footprint of pyrotechnic shows. Still, the environmental advantages are tempered by challenges associated with nitrocellulose, as the production process of nitrocellulose involves the use of nitric acid and other nitrogen compounds (Jamal et al., 2020; Mattar et al., 2020), which present environmental implications, raising concerns about pollution. The content of nitrogen is an essential parameter in nitrocellulose pyrotechnic devices, as it directly influences their performance and safety. With a nitrogen content below 12.6%, nitrocellulose is more stable and less explosive (Chai et al., 2020), making it suitable for pyrotechnic applications such as fireworks, providing rapid combustion and vibrant colours without compromising safety (Dejeaifve et al., 2018).

Therefore, while nitrocellulose presents potential benefits for reducing some of the most important environmental impacts during pyrotechnic events, a comprehensive assessment of its use as a substitute needs to be carried out in order to determine if the environmental challenges are properly addressed and correct performance of the devices is achieved. Furthermore, the substitution of flash powder with nitrocellulose may require adjustments to the formulation to achieve comparable sound and visual effects.

Because of that, this study endeavours to address these concerns by proposing alternative device designs that not only maintain the performance standards of pyrotechnic articles but also significantly reduce emissions and noise levels. In addition to nitrocellulose, the implementation of inert compounds in flash powder is being studied for this purpose. The storage of pyrotechnic material can pose a high risk of accidents if the necessary measures are not taken (León et al., 2023). Therefore, the addition of these compounds presents safety improvements for explosive dust, as it is an effective way to reduce the risk of explosion and sensitivity to ignition (Amez et al., 2023; Bu et al., 2020). Furthermore, inert materials reduce the environmental emissions generated in the combustion of different fuel compounds (Guerrero et al., 2021; Hudák et al., 2021). The present research focuses on F2 category flash bangers from various manufacturers as representative samples. The test methodology focuses on involving the addition of inert materials and the substitution of flash powder with nitrocellulose, to study whether it is possible to optimize the composition of pyrotechnic devices without losing the visual and sound effects but reducing their negative impact.

The evaluation criteria extend beyond conventional sound pressure level measurements, encompassing the assessment of CO and CO_2 emissions. Carbon monoxide (CO) and carbon dioxide (CO_2) are two of the main combustion products of pyrotechnic compositions and can have significant adverse effects on air quality and human health. CO is a toxic gas that can cause poisoning when inhaled in high concentrations (Huzar et al., 2013), while CO_2 is a greenhouse gas that contributes to global warming and climate change (Edenhofer, 2015). Another key factor of flash powder is the pressure it generates inside the container, which allows the release of a shock wave with sufficient energy to cause the explosion or opening of the pyrotechnic device (A. J. Rajendran & Thanulingama, 2008). If the overpressure achieved by the combustion of the explosive powder is not sufficient, the pyrotechnic device will not work correctly. In this case, the application of these alternatives in pyrotechnic shells, a ubiquitous element in displays, would not be feasible, because this device needs to achieve a correct opening in the air to trigger the desired visual effect (Russell, 2009). Addressing this critical requirement, which also involves the achievement of optimal opening heights, the measurement of explosion wave pressure and establish a preliminary relationship between Net Explosive Content (NEC) – Explosion pressure are the main objectives.

2. Materials and Methods

The data collection process encompassed meticulous recording of CO and CO_2 emissions, sound pressure levels, and shockwave pressures for each busting charge type. All the equipment used in the study belongs to the Laboratory of Gas Detectors of the TECMINERGY - Laboratorio Oficial J.M. Madariaga (LOM) and is correctly calibrated, verified and in optimum condition for use at the time of the tests.

2.1. Samples

The objective of this study is to conduct a comprehensive comparative analysis of traditional flash powder commonly employed in pyrotechnic applications and possible alternatives. To achieve this objective, a meticulously designed experimental setup was utilized to analyse gas emissions, sound pressure levels, and overpressures generated by each bursting charge type. The investigated compositions comprised flash powder, consisting of a mixture of perchlorate and Al/Mg, nitrocellulose-based charges, and flash powder by adding inert compounds, such as recycled glass and sodium bicarbonate, with concentrations of 10% and 20% (w/w). The main fireworks using flash powder are flash bangers and shells (Kosanke & Weinman, 2012). Due to the complexity of the shells and their large NEC, all these compositions have been studied in three different F2 category bangers, as described in Table 1.

***Table 1**. Samples of category F2 flash bangers.*

Samples	Type of article	Composition	Category	NEC (g)
A	Banger	Perchlorate/metal	F2	0.08
B	Banger	Perchlorate/metal	F2	0.1
C	Banger	Perchlorate/metal	F2	0.2

In order to test the compositions under study in the three different bangers, it was necessary to remove the initial composition and fill it with the target composition and the same load. The new banger charge is now called New Net Explosive Content (NNEC). For this purpose, one of the gypsum plugs is removed from the container tube, which will be rebuilt after the tube has been filled. It is necessary to test the compositions inside these bangers because the pressure generated inside the tube by the

gases released during the combustion of the powder is responsible for the opening of the tube and thus the bursting effect. The different compositions under study can be seen in Table 2.

***Table 2**. Composition of bursting charges tested.*

Abbrev.	Type	Composition
FP	Flash powder	Perchlorate / metal
YN	Nitrocellulose	Yellow Nitrocellulose
WN		White Nitrocellulose
10B	Flash powder with inerts	10% Sodium Bicarbonate
20B		20% Sodium Bicarbonate
10G		10% Glass
20G		20% Glass

A certain flash powder composition, with 80% $KClO_4$ and 20% Al, is tested as a reference. In addition, two different types of nitrocellulose with different qualities are compared, white nitrocellulose has fewer impurities than yellow one. Finally, different concentrations of inert compounds are added to the reference flash powder. In particular, sodium bicarbonate with less than 300 μm and recycled glass with less than 700 μm are used, with concentrations of 10 and 20% (w/w). $NaHCO_3$ is one of the most studied and commercially available inert materials and recycled glass contributes to the circular economy of glass, promoting sustainability and minimizing waste and emissions.

2.2. Assessment of CO and CO_2 emissions

Some of the most polluting and harmful compounds in pyrotechnic mixtures are perchlorates and metalliferous particles (Steinhauser & Klapötke, 2008). In addition, other important levels that directly or indirectly influence the greenhouse effect must be considered (Ambade, 2018). Gas emission analysis was conducted using an Emerson XStreamIR continuous gas analyser,capable of accurately measuring CO_2 emissions in % vol. and CO emissions in parts per million (ppm) from an inlet flow rate.

Bursting compositions were ignited within a controlled environment to facilitate the capture and subsequent analysis of gas emissions. In order to have a verification of accuracy, before carrying out the tests, the values measured by the analyser were checked using a 300 ppm CO gas bottle and a 20 % vol. CO_2 gas bottle.

Two tests were conducted for each composition and sample, each involving one banger, to ensure accurate measurements. Samples are placed inside a 10L reactor, and once the fuse of the pyrotechnic article is ignited, the reactor is sealed before gas release begins. This ensures that gases generated by the devices remain inside the reactor. These gases include emissions from both the combustion reaction of the banger and the protruding fuse, although the latter's contribution is minimal compared to other emissions. The gas analyser's inlet flow is connected to the sealed reactor by a suction tube and the gases are extracted thanks to the analyser's pump through this tube. A valid measurement of CO and CO_2 is determined once stabilization occurs. Notably, the inlet flow to the analyser also includes gases trapped in the reactor's closed atmosphere, simulating real-life conditions where pyrotechnic devices are discharged in open environments. To prevent measurement interference, the reactor is opened and cleaned with an air compressor after each test, and analyser measurements are held until returning to the initial zero value.

2.3. Sound pressure level measurements

Fireworks, mainly those using flash powder, reach sound pressure levels that, although within the safety limits of human hearing, can be annoying to urban residents (Kukulski et al., 2018). Sound pressure levels produced by the different bursting charges mentioned above were measured. The sound level meter used in the tests is the Brüel & Kjaer model 2250-L portable analyser. This equipment complies with the IEC 61672-1 standard, as it belongs to class 1 and has a 4950-type open field microphone. It is also equipped with a ZC-0032 preamplifier. These measurements were taken following established pyrotechnic EN 15947-4:2015 standard, ensuring compliance with prescribed distances for F2 category articles (8 m), on a concrete surface and using a digital anemometer to measure wind speed and ambient temperature. The sound level meter is placed on a tripod so that it is stable and at a height of 1 m above ground level, as can be seen in Figure 1.

Fig. 1. *Sound pressure level test setup.*

The sound level measurement scale is the one used in fireworks measurements. The A-weighted scale and the maximum impulsive level are used, resulting in measurement values in dB (AImax). In order to carry out these tests and to obtain greater reliability, 5 bangers are fired with each of the compositions under study, which means a total of 35 samples for each banger. For these tests, as for the assessment of emissions, silicone is used to reconstruct the sealing plug of the container tube once it has been filled with the composition under study.

2.4. Explosion pressure analysis

The compositions studied must not only reduce pollutant emissions and sound pressure levels to be viable alternatives but also ensure the proper functioning of pyrotechnic devices. For this reason, shockwave pressures generated by the bursting charges were meticulously assessed using specialized pressure sensors. These sensors were strategically placed within a flame proof enclosure which would not allow the gases generated to escape, as can be seen in Figure 2. In addition, the equipment was installed in a testing tank to accurately capture and record shock wave pressures. The bangers were fired within these controlled environments, and pressure data were meticulously recorded for subsequent analysis.

For these tests, again two bangers are fired for each of the different compositions and samples. The difference with the bangers tested so far is that this time, it is necessary to remove the protruding fuse. The fuse is replaced by an electric igniter because the analytical equipment is designed to send an electrical signal when the measurement is initiated. Moreover, due to the delay of the fuse, it is unfeasible to use this means of ignition, since the explosion of the banger would occur outside the measuring range captured by the equipment. Furthermore, to adapt the banger with the new

compositions to real situations and thus be able to study their possible use as a substitute for flash powder, the plugs were rebuilt with gypsum.

Fig. 2. *Design of explosion pressure analysis tests*

3. Results and discussion

3.1. CO and CO_2 concentration of the released gases

The measurements made during the combustion of the different compositions studied allow a comparison of the emissions of carbon monoxide and carbon dioxide generated by each of them using the same amount of charge. Figure 3 shows the results recorded by the gas analyser.

Samples A

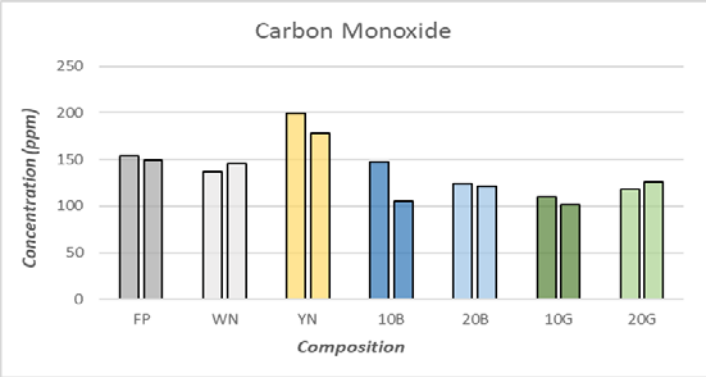

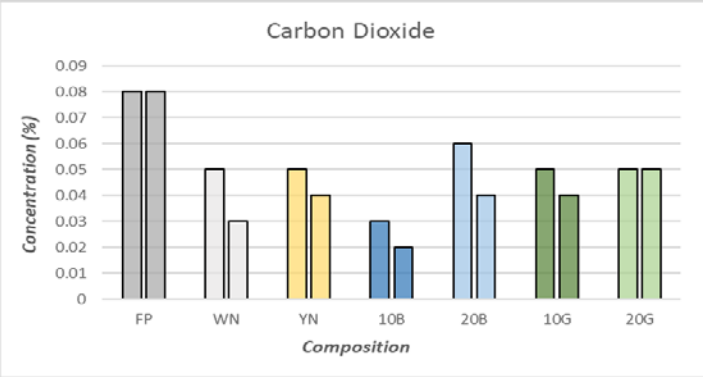

Samples B

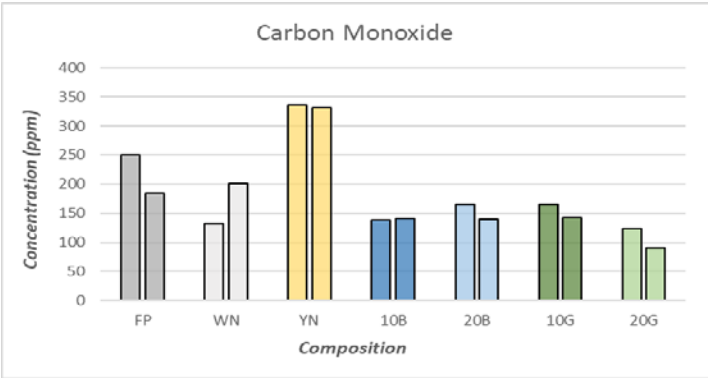

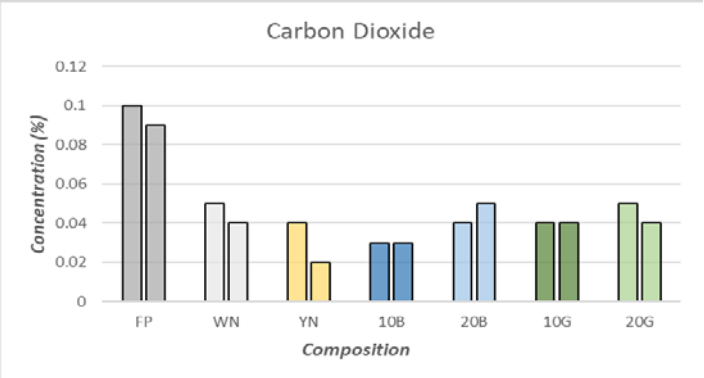

Samples C

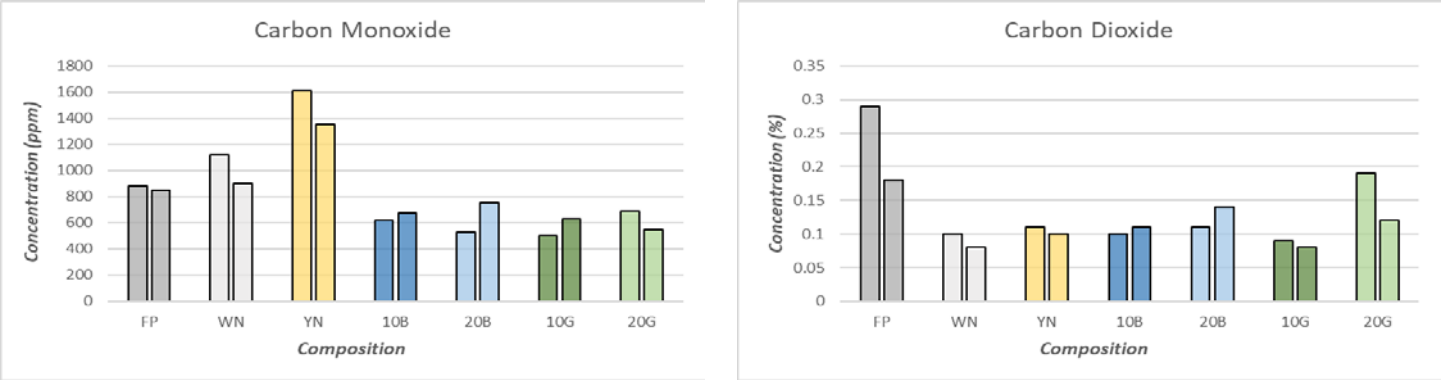

Fig. 3. *Emission test results*

These results offer remarkable conclusions about the emissions of gases such as CO and CO_2 released by flash powder and their possible alternatives studied. According to previous studies about firework emissions (Gonzalez et al., 2022b; Karuppasamy et al., 2024; Pathak et al., 2013), it is observed that as the NNEC contained in the banger increases, the emissions of both gases also increase. For samples A, which have 0.08 g of NNEC, the maximum concentrations reached are 199 ppm CO for the yellow nitrocellulose composition and 0.08% vol. CO_2 for the original flash powder composition. The maximum values for the B samples are obtained at the same compositions, but in this case, since 0.1 g of NNEC is used, the measured values are 336 ppm and 0.10% vol. of CO and CO_2 respectively. Finally, for the samples C using 0.2 g of NNEC, the highest concentrations of both gases are obtained. Again, the maximum carbon monoxide value appears in the yellow nitrocellulose, but this time with 1612 ppm. On the other hand, 0.29% vol. CO_2 is the maximum concentration of this gas reached for the original flash powder. As shown, the emissions released after the combustion of the different compositions are directly related to the NNEC amount used in the bangers.

Comparing each of the compositions used in the different samples (A, B and C), it can be seen that the three different types of bangers follow the same trend. Focusing on the carbon monoxide emissions released, this is one of the main products of nitrocellulose combustion (Dauerman & Tajima, 1968; Finnerty et al., 1992). It is clear that yellow nitrocellulose generates higher concentrations of this gas. White nitrocellulose, which has a higher purity, burns cleaner and more efficiently, so carbon monoxide emissions are lower and comparable to those of flash powder. According to the values recorded, yellow nitrocellulose emits 35-80% more CO than flash powder and white nitrocellulose. Moreover, nitrocellulose has been extensively studied and previous research has found that the use of this compound produces nitrogen oxides, a by-product that was not found in flash powder compositions (Guidotti, 1980; Szostak & Cleare, 2000). Nitric oxides cause significant environmental problems, such as acidification, eutrophication and toxicity, among other effects (Van Vuuren et al., 2011). By adding inert compounds such as sodium bicarbonate and recycled glass, a decrease in CO emissions is observed. This decrease was foreseeable, since by adding inert and still using the same total amount of mass inside the banger (NNEC), the amount of NEC decreases. Values close to 50% of the emissions generated by the reference powder can be observed. Forecasts indicated that the higher the amount of inert material, the lower the emissions should be, but this is not always the case. Concentrations from the combustion of compositions with 20% (w/w) recycled glass are observed to generate higher emissions than those with 10% (w/w). The same fact applies to sodium bicarbonate. This could be due to the loss of moisture and carbon dioxide that has been observed in previous studies during the thermal decomposition of inert (Ball et al., 1986). Further studies should consider carry out a larger number of tests with these compositions and to see average values, as these punctual deviations may also be due to the protruding fuse emissions or to residues of the initial composition in the container tube.

When looking at carbon dioxide emissions, it can be seen that in this case, traditional flash powder is the one that generates the highest concentrations of this gas. By adding inert and reducing the NEC, as with CO emissions, carbon dioxide emissions decrease. The resulting CO_2 emissions for such compositions are even lower than 50% of the flash traditional powder in some cases. In contrast to carbon monoxide emissions, nitrocellulose (both yellow and white) also generates less carbon dioxide emissions than flash powder. This is one of the great advantages of this compound, because although carbon monoxide emissions may be higher if low-quality nitrocellulose is used, carbon dioxide emissions are always reduced. It is important because CO_2 has a direct influence on climate change, while CO only has an indirect influence and has a much shorter residence time in the atmosphere (Liu et al., 2021). However, the most important advantage of this compound is the elimination of residues derived from perchlorate, the most harmful compounds in pyrotechnics (Wilkin et al., 2007), metalliferous particles contained in the flash powder and the removal of soot generated by traditional powder (Munroe, 1896; Petty, 1969), thereby achieving greater clarity in the pyrotechnics effects (Dejeaifve et al., 2018).

3.2. Sound pressure level

As previously pointed out, one of the great concerns of today's society in relation to fireworks is the annoyance caused by the sound pressure levels resulting from the bursting effects. Because of that, these tests measure the sound pressure level reached by the different compositions under study, in order to check if it is possible to reduce it while maintaining the correct performance of the pyrotechnic devices. As mentioned before, each test was repeated 5 times, therefore the mean values obtained for the sound pressure levels of each of the bangers and compositions under study are shown in Figure 4.

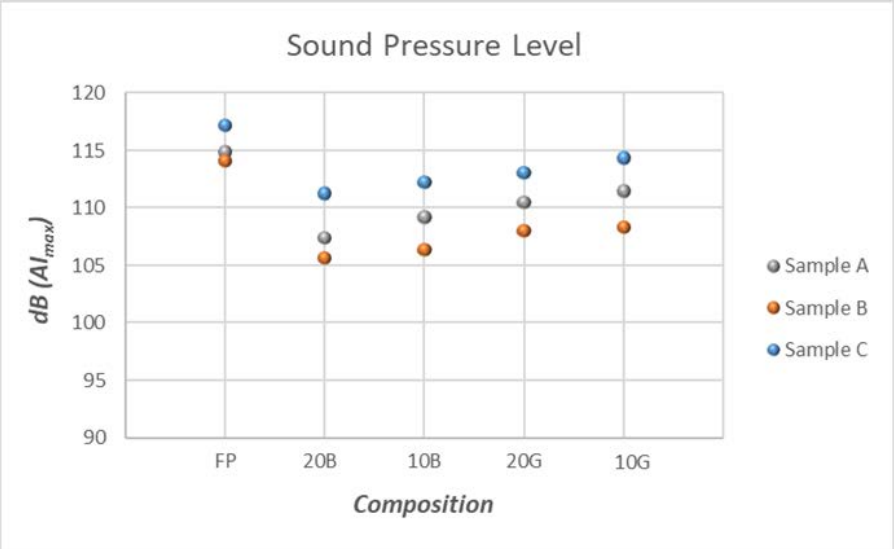

Fig. 4. *Sound pressure level test results*

As can be seen in the results obtained, the highest sound pressure level values are obtained for bangers using traditional flash powder. For sample A, the mean obtained is 114.85 dB (AImax). Sample B, which has a higher NNEC, reaches an average sound level of 114.03 dB (AImax). Finally, sample C, with an NNEC of 0.2 g per banger, reaches a mean value of 117.13 dB (AImax). It is shown that the sound pressure level does not depend only on the NNEC contained in the banger, since sample A with a lower NNEC than sample B achieves higher noise levels. This trend in noise levels continues for all the tested compositions of bangers A and B, so it is proved that other factors such as the design, bursting strength of the paper used for the container tube or the compression generated by the gases released also have a great influence on the sound levels reached (A. J. Rajendran & Thanulingama, 2008).

For each of the bangers tested, it is shown how the addition of inert compounds such as sodium bicarbonate and recycled glass reduces the sound pressure level reached. Sodium bicarbonate is found to be more effective in reducing the bursting noise generated by the banger. This differs from results obtained by other researchers. According to (Castells et al., 2024), both inert compounds show similar effectiveness when comparing their influence on the thermal properties of biomasses. This shows that the explosion pressure and the generated sound effect are not necessarily directly related to the thermal properties. Furthermore, as expected, noise levels are lower when using inert concentrations of 20 % (w/w) instead of 10 % (w/w). The lowest sound pressure level is recorded for each of the bangers when testing the composition composed of flash powder and 20 % sodium bicarbonate. A mean of 107.37 dB is recorded for sample A. Sample B gives an average of 105.61 dB and the average sound pressure level for sample C is 111.24 dB. With this type of composition, the noise level is reduced by 5-7%. As the decibel scale measures the sound pressure level on a logarithmic scale of base 10 (Roberts, 1984; Young, 1971), this decrease in decibels actually means a very important reduction in the perception of the ear. The decibel reductions achieved for the 20% sodium bicarbonate compositions are close to 10 dB, which represents a reduction in hearing response of about half. In other words, concentrations of 20% sodium bicarbonate reduce the perceived sound by approximately 50%.

For the two types of nitrocellulose (white and yellow) tested in the three different bangers, a correct performance is not achieved. In all of them, the banger does not break the cardboard that makes up the container tube, and therefore, the desired bursting effect does not occur. The nitrocellulose reacts but releases the gases generated by the silicone plug instead of breaking the cardboard. This is because nitrocellulose does not react as violently as flash powder. Flash powder is mainly composed of a strong oxidiser together with a reducing agent, such as aluminium powder. These ingredients react very quickly when ignited, resulting in instantaneous combustion and rapid energy release (Chapman & Howard, 2010; Kosanke & Weinman, 2012). On the other hand, nitrocellulose burns more slowly compared to flash powder (Oxley, 1993; Zel'dovich, 1942). To estimate the influence of the material used as a plug in the container tube, further tests should be carried out with gypsum plugs in an attempt to withstand the generated overpressure and to analyse whether in this way the nitrocellulose bangers would succeed in breaking the cardboard tube.

3.3. Explosion pressure analysis

The explosion pressure generated by bursting charges is one of their main characteristics. This powder is characterised by a high reaction speed and high temperatures due to the metallic compound (Kosanke & Weinman, 2012). This quickly generates a large quantity of gases that increase the pressure inside the container until it breaks and the explosion occurs. Therefore, it is possible to represent the phenomena as an explosion pressure (kPa) - time (ms) curve as shown in Figure 5. It can be seen that there is a sudden pressure increase reaching a maximum pressure in just 0.2 ms.

The pyrotechnic shells have a small container with flash powder inside. Once the desired height is reached, the flame communicates with this flash powder and the device opens, transmitting the flame to the main effects of the shell (coloured stars, cracker, sound effects, etc.) (Lancaster, 1998). Thus, it is noted that the aim of the flash powder is different when used in bangers or shells. Therefore, in order to be able to apply the alternatives studied in pyrotechnic shells, it is necessary to analyse the explosion pressure, to be able to study whether it is feasible to achieve the opening of the device. The results of the explosion pressure measurement tests are shown in Table 3.

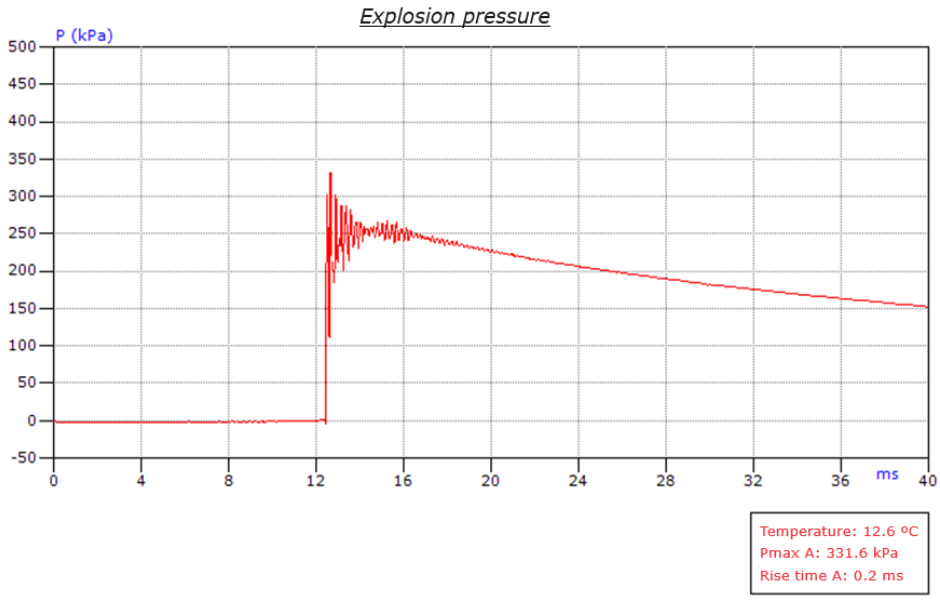

Fig. 5. *Explosion pressure curve generated by a banger*

Table 3*. Maximum explosion pressure registered (kPa).*

	Sample A	**Sample B**	**Sample C**
FP	320.0	512.0	555.9
FP	331.6	476.4	589.9
WN	14.4	--	--
WN	27.5	--	--
YN	--	--	--
YN	--	--	--
20G	228.6	353.6	497.3
20G	239.5	240.8	539.6
10G	311.2	404.2	542.3
10G	291.5	411.7	533.4
20B	132.7	297.8	466.4
20B	234.7	284.1	423.2
10B	272.1	427.3	520.8
10B	257.1	369.8	508.6

According to the results obtained, some of them are discarded due to failure or malfunctioning of the banger. In particular, for all the nitrocellulose bangers tested (except WN in sample A), the powder is flamed but does not break the carboard tube, as noticed in previous tests. This is because they do not react as violently and instead of achieving a bursting effect by breaking the cardboard, a more continuous effect is achieved as the gases are gradually released through the plug. Although the bursting effect is achieved for the WN of the A samples, it is noted that the pressures achieved are very low compared to traditional flash powder. This is again due to the release of the gases generated. In the flash powder example in Figure 5, a rise time of 0.2 ms is observed (resulting in a strong explosion), whereas in this case, the rise time is 14 to 17 ms. Increasing the nitrogen content of

nitrocellulose would result in a higher reaction rate and an increase in the heat of the reaction (ΔH) and thus a more explosive character (Cieślak et al., 2021), but its safety conditions would be worsened, due to the decline of the thermal stability (Chai et al., 2020; Pourmortazavi et al., 2009) and the critical explosion temperature (Tb) (Chai et al., 2019). However, previous research already reported improvements in nitrocellulose thermal stability by increasing the moisture content (Wei et al., 2018).

For bangers composed of the original flash powder and the samples with inert composition, a correct performance is achieved. As can be seen, generally the explosion pressure generated increases as the NNEC also increases. However, its relationship is not directly proportional. Using average values measured for the flash powder samples, it can be seen that sample A (0.08 g NEC) generates an explosion pressure of 325.8 kPa. Sample B, which contains 0.1 g of NEC, releases an explosion pressure of 494.2 kPa. Finally, sample C, which has twice the NEC of sample B, only generates 16% more pressure, i.e. 572.9 kPa. This shows that the NNEC is not the only factor influencing the explosion pressure. Other factors such as design, tube material or volume of the container also influence this pressure (A. J. Rajendran & Thanulingama, 2008), as was noticed when addressing the noise level tests.

Samples with inert are compared. The trend observed indicates that by adding a certain inert composition to the flash powder, the explosion pressure generated decreases. It can be seen that this reduction is greater in sample B than in sample A or C. Comparing the values obtained for sodium bicarbonate and recycled glass, it is again observed that bicarbonate is more effective and reduces the explosion pressure to a greater extent than recycled glass using the same concentration. This difference is even more accentuated in the C samples, where variations of approximately 75 kPa between compositions 20G and 20B are seen when comparing mean values. Predictably, the higher the concentration of inert, the lower the pressure obtained should be. This is confirmed by the results obtained. Compositions using 20% inert in their concentration generate a lower pressure than those using 10% inert. This is due to the fact that by using more inert, the amount of flash powder is reduced. Moreover, the addition of inert powder reduces the ignition sensitivity of the composition (Amez et al., 2023) and, according to (Dai et al., 2020), the explosion pressure of the mixture decreases as the concentration of inert dust increases.

When comparing the reductions obtained in sound pressure level and explosion pressure for the samples using inert, specifically those using a 20% concentration of sodium bicarbonate, it is observed that a greater sound reduction (close to 50%) than explosion pressure reduction (between 23% and 43% depending on the sample) is achieved. The reduction in explosion pressure due to the addition of inert materials to the flash powder could be compensated for by adding a higher charge to the banger. If it were possible to achieve similar explosion pressures in this way, such compositions could be used as alternatives to reduce emissions and noise.

In order to establish a relationship between Net Explosive Content (NEC) and explosion pressure, due to the other influencing factors, further tests must be performed analysing different container tube designs, waste paper and composition percentages. The same applies to nitrocellulose. In order to be able to use this type of composition as a substitute for flash powder, a higher energy release during combustion is required for correct functioning. Therefore, further tests must be performed analysing nitrocellulose with a higher nitrogen content.

4. Conclusions

Flash powder is a widely used compound due to its explosive characteristics. It is one of the main pyrotechnic mixtures, mainly used in bangers and pyrotechnic shells, and therefore, one of those responsible for the social difficulties to which this sector is currently exposed. Problems such as the disturbances in residential and urban areas caused by the noise levels or the emissions released into the atmosphere can be reduced if sustainable alternatives to this type of composition are studied.

Nitrocellulose ($[C_6H_7(NO_2)_3O_5]n$) or the addition of inert compounds such as sodium bicarbonate ($NaHCO_3$) and recycled glass, are possible alternatives to this type of explosive composition. Comparisons in the gas analyzer show that these compositions studied significantly reduce CO_2 emissions, the main greenhouse gas contributing to climate change. Moreover, the addition of inert compounds allows a reduction in carbon monoxide emissions. This gas is not directly related to the greenhouse effect but contributes to the formation of other gases that are connected to it. In addition, these compounds prevent the release of perchlorate derivatives and metalliferous particles, two of the most harmful pollutants in fireworks.

However, nitrocellulose does not achieve a correct functioning of the banger, since it does not release enough energy to achieve the opening of the container tube. This fact makes its implementation in pyrotechnic shells impossible, since the opening of the shell would not be achieved and, therefore, the desired visual effects would not be obtained. The explosiveness of nitrocellulose is directly related to its nitrogen content, so increasing this from the 12.6% that is used in the compositions used in pyrotechnics, it may be possible to achieve the desired performance.

On the other hand, the addition of inerts is a viable solution to reduce emissions and sound pressure levels. According to the results obtained, sodium bicarbonate is more effective and reduce sound pressure levels by about 50% when using a 20% concentration of sodium bicarbonate. Although the addition of inerts also reduces the explosion pressure generated, a greater decrease in sound than in pressure is observed. This makes its use in pyrotechnic shells viable, since by increasing the total charge, the same explosion pressure would be obtained and, therefore, the correct opening of the shell, reducing in turn the sound pressure level.

Although more tests are required to establish a Net Explosive Content (NEC) - Explosion pressure relationship, due to the influence of other factors such as design, material or percentages of each composition, it can be concluded that the addition of inerts to flash powder is a real alternative that would reduce its emissions and sound pressure level.

References

Ambade, B. (2018). The air pollution during Diwali festival by the burning of fireworks in Jamshedpur city, India. *Urban Climate*, *26*, 149–160.

Amez, I., Castells, B., León, D., García-Torrent, J., & Medic, L. (2023). Experimental study on inert products, moisture, and particle size effect on the minimum ignition energy of combustible dusts. *Journal of Loss Prevention in the Process Industries*, *81*, 104968.

Azhagurajan, A., Prakash, L., & Jeyasubramanian, K. (2019). Prevention of explosion accidents by employing boron instead of aluminium in flash powder. *Process Safety and Environmental Protection*, *131*, 160–168.

Ball, M. C., Snelling, C. M., Strachan, A. N., & Strachan, R. M. (1986). Thermal decomposition of solid sodium bicarbonate. *Journal of the Chemical Society, Faraday Transactions 1: Physical Chemistry in Condensed Phases*, *82*(12), 3709–3715.

Bu, Y., Li, C., Amyotte, P., Yuan, W., Yuan, C., & Li, G. (2020). Moderation of Al dust explosions by micro-and nano-sized Al2O3powder. *Journal of Hazardous Materials*, *381*, 120968.

Castells, B., Amez, I., Fernandez-Anez, N., León, D., & Tascón, A. (2024). Biomass Inertization to Increase Minimum Ignition Temperature. *Journal of Loss Prevention in the Process Industries*, 105345.

Chai, H., Duan, Q., Cao, H., Li, M., & Sun, J. (2020). Effects of nitrogen content on pyrolysis behavior of nitrocellulose. *Fuel*, *264*, 116853.

Chai, H., Duan, Q., Jiang, L., Gong, L., Chen, H., & Sun, J. (2019). Theoretical and experimental study on the effect of nitrogen content on the thermal characteristics of nitrocellulose under low heating rates. *Cellulose*, *26*, 763–776.

Chapman, D., & Howard, K. (2010). Defining Flash Compositions: Modifications to UN Time/Pressure Test. *Journal of Pyrotechnics*, *29*, 32.

Chen, S., Jiang, L., Liu, W., & Song, H. (2022). Fireworks regulation, air pollution, and public health: Evidence from China. *Regional Science and Urban Economics*, *92*. https://doi.org/10.1016/j.regsciurbeco.2021.103722

Cieślak, K., Gańczyk-Specjalska, K., Drożdżewska-Szymańska, K., & Uszyński, M. (2021). Effect of stabilizers and nitrogen content on thermal properties of nitrocellulose granules. *Journal of Thermal Analysis and Calorimetry*, *143*(5), 3459–3470.

Dai, L., Hao, L., Kang, W., Xu, W., Shi, N., & Wei, H. (2020). Inhibition of different types of inert dust on aluminum powder explosion. *Chinese Journal of Chemical Engineering*, *28*(7), 1941–1949.

Dauerman, L., & Tajima, Y. A. (1968). Thermal decomposition and combustion of nitrocellulose. *Aiaa Journal*, *6*(8), 1468–1473.

Dejeaifve, A., Fantin, A., Monseur, L., & Dobson, R. (2018). Making Progress Towards «Green» Propellants. *Propellants, Explosives, Pyrotechnics*, *43*(8), 831–837. https://doi.org/10.1002/prep.201800026

Edenhofer, O. (2015). *Climate change 2014: mitigation of climate change* (Vol. 3). Cambridge University Press.

EN 15947-4, Pyrotechnic Articles - Fireworks, Categories F1, F2, and F3 - Part 4: Test Methods (2015).

Espinoza, E. O., & Thornton, J. I. (1994). Characterization of smokeless gunpowder by means of diphenylamine stabilizer and its nitrated derivatives. *Analytica Chimica Acta*, *288*(1–2), 57–69.

Finnerty, A. E., Bowers, S. A., Schroeder, M. O., & D, A. R. L. A. B. A. P. G. M. (1992). *Ignition of Nitrocellulose in Various Atmospheres*.

Gonzalez, A., Boies, A., Swanson, J., & Kittelson, D. (2022a). Measuring the effect of fireworks on air quality in Minneapolis, Minnesota. *SN Applied Sciences*, *4*(5), 142. https://doi.org/10.1007/s42452-022-05023-x

Gonzalez, A., Boies, A., Swanson, J., & Kittelson, D. (2022b). Measuring the effect of fireworks on air quality in Minneapolis, Minnesota. *SN Applied Sciences*, *4*(5), 142.

Greven, F. E., Vonk, J. M., Fischer, P., Duijm, F., Vink, N. M., & Brunekreef, B. (2019). Air pollution during New Year's fireworks and daily mortality in the Netherlands. *Scientific Reports*, *9*(1), 5735.

Guerrero, F., Arriagada, A., Muñoz, F., Silva, P., Ripoll, N., & Toledo, M. (2021). Particulate matter emissions reduction from residential wood stove using inert porous material inside its combustion chamber. *Fuel*, *289*, 119756.

Guidotti, T. L. (1980). The higher oxides of nitrogen: unintended products of technological progress. *Environment International*, *3*(1), 69–77.

Hudák, I., Skryja, P., Bojanovský, J., Jegla, Z., & Krňávek, M. (2021). The Effect of Inert Fuel Compounds on Flame Characteristics. *Energies*, *15*(1), 262.

Huzar, T. F., George, T., & Cross, J. M. (2013). Carbon monoxide and cyanide toxicity: etiology, pathophysiology and treatment in inhalation injury. *Expert Review of Respiratory Medicine*, *7*(2), 159–170.

Jamal, S. H., Roslan, N. J., Shah, N. A. A., Noor, S. A. M., Ong, K. K., & Yunus, W. M. Z. W. (2020). Preparation and characterization of nitrocellulose from bacterial cellulose for propellant uses. *Materials Today: Proceedings*, *29*, 185–189.

Karuppasamy, M. B., Natesan, U., Giridharan, K. S., & Ravi, R. V. (2024). Environmental Assessment of Toxic Gases and Particulate Matter (PM2. 5) Monitoring During Fireworks Episodes (Diwali Festival) in Chennai Metropolitan, Southern India. *Sustainable Chemical Engineering*, 169–181.

Kosanke, K. L., & Weinman, L. (2012). As Defined by Regulation, What Is Fireworks Flash Powder? *Encyclopedic Dictionary of Pyrotechnics:(And Related Subjects)-B&W*, *113*.

Kukulski, B., Wszołek, T., & Mleczko, D. (2018). The impact of fireworks noise on the acoustic climate in urban areas. *Archives of Acoustics*, *43*(4), 697–705.

Lancaster, R. (1998). *Fireworks: Principles and Practice. 3rd edition*. Chemical Publishing Company.

León, D., Castells, B., Amez, I., Casín, J., & García-Torrent, J. (2023). Experimental Quantification of Fire Damage Inside Pyrotechnic Stores. *Applied Sciences*, *13*(10), 6181.

Liu, L.-J., Liu, L.-C., & Liang, Q.-M. (2021). Common footprints of the greenhouse gases and air pollutants in China. *Journal of Cleaner Production*, *293*, 125991.

Lombera, E. N., Bori, G., & Vergara, R. O. (2023). Assessment of noise pollution of fireworks during Christmas and New Year in the city of Buenos Aires: comparison with a different management strategy applied to the city of Santiago de Chile. *Discover Environment*, *1*(1), 19. https://doi.org/10.1007/s44274-023-00020-2

MacCrehan, W. A., Reardon, M. R., & Duewer, D. L. (2002). A quantitative comparison of smokeless powder measurements. *Journal of Forensic Science*, *47*(6), 1283–1387.

Mattar, H., Baz, Z., Saleh, A., Shalaby, A. S., Azzazy, A. E., Salah, H., & Ismail, I. (2020). Nitrocellulose: Structure, synthesis, characterization, and applications. *Water Energy Food Environ. J*, *3*, 1–15.

Moreno, T., Querol, X., Alastuey, A., Amato, F., Pey, J., Pandolfi, M., Kuenzli, N., Bouso, L., Rivera, M., & Gibbons, W. (2010). Effect of fireworks events on urban background trace metal aerosol concentrations: is the cocktail worth the show? *Journal of Hazardous Materials*, *183*(1–3), 945–949.

Moreno, T., Querol, X., Alastuey, A., Minguillón, M. C., Pey, J., Rodriguez, S., Miró, J. V., Felis, C., & Gibbons, W. (2007). Recreational atmospheric pollution episodes: inhalable metalliferous particles from firework displays. *Atmospheric Environment*, *41*(5), 913–922.

Munroe, C. E. (1896). ON THE DEVELOPMENT OF SMOKELESS POWDER. *Journal of the American Chemical Society*, *18*(9), 819–846.

Nasir, U. P., & Brahmaiah, D. (2015). Impact of fireworks on ambient air quality: a case study. *International Journal of Environmental Science and Technology*, *12*(4), 1379–1386. https://doi.org/10.1007/s13762-014-0518-y

Oxley, J. C. (1993). Non-traditional explosives: Potential detection problems. *Terrorism and Political Violence*, *5*(2), 30–47.

Pathak, B., Bharali, C., Biswas, J., & Bhuyan, P. K. (2013). Firework induced large increase in trace gases and black carbon at Dibrugarh, India. *Journal of Earth Science and Engineering*, *3*(8), 540.

Petty, C. S. (1969). Firearms injury research: The role of the practicing pathologist. *American Journal of Clinical Pathology*, *52*(3), 277–288.

Pourmortazavi, S. M., Hosseini, S. G., Rahimi-Nasrabadi, M., Hajimirsadeghi, S. S., & Momenian, H. (2009). Effect of nitrate content on thermal decomposition of nitrocellulose. *Journal of Hazardous Materials*, *162*(2–3), 1141–1144.

Rajendran, A. J., & Thanulingama, T. L. (2008). Sound level analysis of firecrackers. *Journal of Pyrotechnics*, *27*, 60–76.

Rajendran, M., Ramanathan, R., Ganesan, P., & Shanmugavel, R. (2021). Experimental analysis of tamarind seed powder-based flash powder composition for eco-friendly firecrackers. *Journal of Thermal Analysis and Calorimetry*, *143*, 3009–3021.

Roberts, B. L. (1984). The Decibel Scale. *Department of Physics Boston University*, 2–5.

Russell, M. S. (2009). *The chemistry of fireworks*. Royal Society of Chemistry, Cambridge, UK.

Sijimol, M. R., & Mohan, M. (2014). Environmental impacts of perchlorate with special reference to fireworks—a review. *Environmental Monitoring and Assessment*, *186*, 7203–7210.

Steinhauser, G., & Klapötke, T. M. (2008). “Green” pyrotechnics: a chemists’ challenge. *Angewandte Chemie International Edition*, *47*(18), 3330–3347.

Szostak, R., & Cleare, K. (2000). Emissions related to munitions firing: A case study of nitrogen oxides, volatile organic compounds, and energetic residue from detonable munitions. *Federal Facilities Environmental Journal*, *11*(3), 87–104.

Van Vuuren, D. P., Bouwman, L. F., Smith, S. J., & Dentener, F. (2011). Global projections for anthropogenic reactive nitrogen emissions to the atmosphere: An assessment of scenarios in the scientific literature. In *Current Opinion in Environmental Sustainability* (Vol. 3, Issue 5, pp. 359–369). https://doi.org/10.1016/j.cosust.2011.08.014

Vergouw, B., Nagel, H., Bondt, G., & Custers, B. (2016). Drone technology: Types, payloads, applications, frequency spectrum issues and future developments. *The Future of Drone Use: Opportunities and Threats from Ethical and Legal Perspectives*, 21–45.

Wei, R., He, Y., Zhang, Z., He, J., Yuen, R., & Wang, J. (2018). Effect of different humectants on the thermal stability and fire hazard of nitrocellulose. *Journal of Thermal Analysis and Calorimetry*, *133*, 1291–1307.

Wilkin, R. T., Fine, D. D., & Burnett, N. G. (2007). Perchlorate behavior in a municipal lake following fireworks displays. *Environmental Science & Technology*, *41*(11), 3966–3971.

Yolhamid, M. N. A. G., Ibrahim, F., Zarim, M. A. U. A. A., Ibrahim, R., Adnan, S., & Yahya, M. Z. A. (2018). The Novel Usage of Nitrocellulose as a Propellant of 5.56 mm Bullet. *Solid State Phenomena*, *280*, 361–367.

Young, R. W. (1971). Decibel, a unit of level. *Journal of the Audio Engineering Society*, *19*(6), 512–516.

Zel'dovich, Y. B. (1942). On the theory of combustion of powders and explosives. *Zh. Eksp. Teor. Fiz.*, *12*(11/12), 498–525.

Investigation of the flash pyrolysis of biomass dusts: is there really a correlation between MIT, volatile point and LFL of the pyrolysis gases?

Maria Portarapillo[a*], Matteo Pietraccini[b], Roberto Sanchirico[c],

Almerinda Di Benedetto[a] and Olivier Dufaud[b]

[a] Department of Chemical, Materials, and Production Engineering, University of Naples Federico II, P.le V. Tecchio 80, 80125 Naples, Italy

[b] Université de Lorraine, CNRS, LRGP, F-54000 Nancy, France

[c] Istituto di Scienze e Tecnologie per l'Energia e la Mobilità Sostenibili (STEMS), Consiglio Nazionale delle Ricerche (CNR), Piazzale Tecchio 80, 80125, Napoli, Italy

E-mail: maria.portarapillo@unina.it

Abstract

The prediction of the parameters characterising the probability and severity of an organic dust explosion requires experimental and theoretical approaches to find an optimal compromise between reality and modelling time. Moreover, in the case of organic dusts, several simultaneously occurring phenomena must be taken into account, since the presence of a hybrid mixture of the dust itself and its pyrolysis gases is mandatory. As far as the flammability characteristics are concerned, there are several key parameters that can be taken into account when assessing the probability of explosion, such as the minimum ignition temperature of the dust cloud (MIT), the flash point of the dust itself (the so-called volatile point, VP), but also the assessment of the lower flammability limit (LFL) of the gases released by the pyrolysis of the dust due to the increase in temperature. This LFL will be expressed in this work in terms of temperature and called “fastVP” since it will be obtained through fast pyrolysis tests. The answer to the "simple" question "Is there really a correlation between MIT, flash point and LFL of generated gases?" is anything but obvious. To reformulate this question, it would need to understand which of these parameters is the most conservative and closest to reality, which in the case of organic dusts should be evaluated in any case to allow an adequate assessment and design of preventive safety measures. To answer this question, flash pyrolysis of various organic powders (lignocellulosic components such as cellulose, hemicellulose, lignin and oak, Douglas fir) was carried out. A Godbert-Greenwald furnace was used for the experiments to mimic the basic characteristics of a dust explosion: high heating rate of the particles and reaction temperature, and short residence times (Pietraccini et al., 2023). The applied methodology, including auxiliary chemical, physical and thermal characterisations, led to significant results that also show a correlation between the lignocellulosic components and the investigated dust.

Keywords: *pyrolysis; biomass powders; dust explosion; flammability parameters*

1. Introduction

Prevention and mitigation of potential hazards, particularly those from organic matter explosions, is a major challenge. Navigating this complex landscape requires a synergy of experimental and theoretical efforts, seeking a delicate balance between realism and computational efficiency (Amyotte et al., 2019). Islas et al. (2022, 2023) proposed a three-layer method to study biomass dust explosions (Islas et al., 2023, 2022) based on the combination between the CFD simulation of the dispersion process in the standard 20 L and 1 m^3 vessels, the ignition and the flame propagation steps, the experimental tests and the general knowledge of the chemical mechanisms involved. However,

modeling a dust explosion means considering a significant number of phenomena, some occurring in parallel, others in series, and all subject to complex interactions.
Explosions of organic matter present a unique conundrum because of the confluence of factors. Unlike their inorganic counterparts, which can undergo heterogeneous oxidation, organic dust particles form a hybrid mixture consisting of the suspended particles and the pyrolysis gases. To understand the ignition properties of such explosions, the key parameters are the minimum ignition temperature of the dust cloud (MIT), the volatility point (VP) defined by (Sanchirico et al., 2018), and the lower flammability limit (LFL) of the pyrolysis gases.
In this myriad of parameters, however, a fundamental question looms: is there a correlation between MIT, volatile point and the LFL of the gases generated? The apparent simplicity of the question belies its inherent complexity, requiring a deeper understanding of which parameter is the most conservative and reliable indicator. Such discernment takes on greater significance in the world of organic dust, where the need for rigorous evaluation goes beyond mere academic curiosity and supports the formulation of robust safety protocols and preventive measures. In the case of organic dust, which mainly contribute to flame ignition and propagation though the generation of volatiles (Di Benedetto and Russo, 2007), an intrinsic relation among these parameters should be present.
The aim of the present work is to get insights into the fundamental relation among the flammability parameters affecting the likelihood of ignition, to eventually derive a criterium for classifying the hazard. To this end, flash pyrolysis experiments were performed, covering a spectrum of organic powders from cellulose to lignin, oak to Douglas fir, through flash pyrolysis tests in a modified Godbert-Greenwald furnace (Pietraccini et al., 2023). We decided to consider the LFL of the pyrolysis gases in terms of temperature, i.e., the temperature at which the gases generated by the dust are mixed with air and their composition is equal to LFL. Since the composition of the produced gases was obtained through flash pyrolysis test, we called this new parameter “fastVP”. In contrast to VP, that is a ‘static’ parameter, MIT and fastVP are ‘dynamic’ parameters, i.e. they change as a function of the hydrodynamic of the dust cloud and the apparent heating rate.
Chemical, physical and thermal characterizations were performed for all samples, along with the evaluation of the volatile point and minimum ignition energy. In addition, the evaluation of the burning velocity based on the combustion of gaseous products developed by devolatilization was carried by means of a previously developed theoretical model (Portarapillo et al., 2023). The increasing heterogeneity and complexity of the five samples used in this study was intended to compare the fast pyrolysis of a pure component (such as cellulose, hemicellulose/xylan and lignin) with that of lignocellulosic materials (woods like oak and fir).

2. Materials and Methods

Biomass is known to be chemically complex due to the numerous interactions between its three main components: cellulose, lignin and hemicellulose. These three constituents represent approximately 85 to 90 % of lignocellulosic biomass, the remaining elements being organic extractives and inorganic minerals, whose contribution will be neglected here. Therefore, the powders chosen were cellulose (Avicel pH 101, CAS 9004-34-6), xylan from beechwood (CAS 9014-63-5) as it is the main component of hemicellulose, alkali lignin (CAS 8068-05-1), oak (hardwood from the Haut-Beaujolais - France) and Douglas fir (softwood from the Haut-Beaujolais - France). The wood samples were first chopped into small pieces, without the bark, followed by grinding with a cutting mill (Retsch SM 300) at 1500 rpm. The pulverized samples were then sieved for 5 minutes in an AS 200 vibrating shaker (Retsch) with 180 and 56 µm sieves, when necessary. The specific surface area (SBET) was determined via N_2 adsorption at −196 °C starting from $P/P0 = 5 \times 10^{-6}$ using a Quantachrome Autosorb-1C instrument (Quantachrome, Anton Paar Italia, Rivoli, Italy), after degassing the samples at 120 °C for 4 h.

2.1. Chemico-physical and thermal characterization

The Particle Size Distribution (PSD) of the samples was determined by a Malvern Mastersizer 3000 equipped with an aero-dispersion unit (2 bar compressed air). Scanning electron microscopy (SEM) (JEOL JSM-649-LV) was used and the images were acquired using different magnifications. Proximate analysis was performed, determining their moisture content (MC), volatile matter (VM), fixed carbon (FC) and ash content, following the standard procedure (ASTM D7582-15, 2009). In order to assess the thermal behaviour, thermogravimetric analysis (TG) and Differential Scanning Calorimetry (DSC) were carried out using a TA Instrument Q600SDT. Finally, elemental analysis was performed on the powders, employing a Vario MICRO cube CHNOS elemental analyser (Elementar).

2.2. Volatile point, Minimum Ignition Temperature and Flash pyrolysis

The volatile point was measured with the same apparatus used for flash point (FP), the Setaflash Series 3 Plus. The device is a closed-cup instrument capable of measuring FP/VP for liquid/solid samples according to international standards over the range of ambient temperature to 300 °C (ASTM E502-07, 2010). The solid sample was put into a vessel heated at a rate of 20 °C/min with an ignition delay time equal to 6 minutes. For the determination of the Minimum Ignition Temperature (MIT) of a dust cloud, experiments were carried out in a Godbert-Greenwald (G-G) furnace, usually employed according to the standard (ASTM E1491-06, 2019). The original G-G furnace was modified to provide the ability to capture the products generated by pyrolysis as described by (Pietraccini et al., 2023). The gaseous products were collected in a collapsible Tedlar bag for analysis. Pyrolysis gases were analyzed by micro gas chromatography (SRA 3000 µGC equipped with a TCD detector, 3 ways). Permanent gases (CO, CO_2, CH_4, H_2, O_2 and N_2) were measured, as well as some aromatics (benzene, toluene and xylene isomers) and some light hydrocarbons (C_2H_2, C_2H_4 and C_2H_6).

2.3. Theoretical model

During an organic dust explosion and from a particle perspective, the following successive steps occur: heating, pyrolysis and combustible gases oxidation. If heat transfer can be limiting for coarse particles, pyrolysis is often the rate-limiting step for small organic particles. In this case, it is interesting to relate the VP to the explosion kinetics of the explosion, especially with the laminar flame speed S_u. A preliminary evaluation of S_u was performed with Portarapillo et al. (2023) correlation (Portarapillo et al., 2023), which is especially applicable to dust-air mixtures whose combustion is dominated by volatile flames. The theoretical derivation is based on a three-layers Mallard-Le Chatelier model (Glassman and Yetter, 2008) and is represented by the following equation:

$$S_u = \frac{\rho_{dev} S_l Cp_{gas,II}(T_{ign} - VP)}{\rho_{dust+air}(Cp_{dust+air}(VP-25)+\Delta H_{dev})} \quad (1)$$

Where ΔH_{dev} is the devolatilization heat, ρ_{dev} is the density of unburnt gases, S_l is the laminar burning velocity of the gaseous mixture with air, $Cp_{gas,II}$ is the specific heat of the unburnt gases, T_{ign} is the autoignition temperature of the generated gases, VP is the volatile point of the dust, $\rho_{dust+air}$ is the particles density mixed with air, $Cp_{dust+air}$ is the specific heat of the combustible dust mixed with air.

3. Results

3.1. Chemico-physical and thermal characterization

In **Fig. 1**, the scanning electron microscopy (SEM) images are shown for all investigated substances at magnification x150. SEM images of lignin (B) and hemicellulose (C) show that the samples are composed of smooth prismatic particles. SEM image of cellulose (A) shows that the particles have non-spherical particles tending to a slight agglomeration. The fibrous character conferred by the

cellulose chain to Douglas fir and oak results in elongated particles, in which the characteristic length for heat and mass transfer is most probably half the thickness.

***Table 1**. Characteristic PSD diameters, polydispersity index and specific surface area.*

Sample	Dx (10) (µm)	Dx (50) (µm)	Dx (90) (µm)	σ_D	D [3,2] (µm)	D [4,3] (µm)	SSA (m^2/kg)
Avicel pH 101 (Cellulose)	21	59	140	2.01	41	71	97
Kraft Lignin (56<Φ<180 µm)	37	93	173	1.46	61	100	98
Xylan (Hemicellulose)	25	102	200	1.71	32	109	187
Oak wood (56<Φ<180 µm)	76	164	352	1.68	132	212	45
Douglas fir (56<Φ<180 µm)	86	186	400	1.68	156	238	39

As is well known (Eckhoff, 2003), the granulometric distribution strongly influences the explosion behavior. Details of the percentile diameters (Dx(10), Dx(50) and Dx(90)), surface and volume averaged diameters (D[3,2] and D[4,3], respectively), polydispersity index (or span) σ_D and the specific surface area (SSA) of dusts are given in **Table 1**. Lignin, oak and Douglas' particle size distribution were selected using 180 and 56 µm sieves, but it should be kept in mind that sieving fibrous particles is not compatible with strict compliance with cut-off diameters. Douglas fir is the sample characterized by the highest values of Dx(90) and volume averaged diameters. With a span slightly greater than 2, cellulose is the most heterogeneous sample in terms of particle size, while lignin presents the highest homogeneity (σ_D = 1.46). Xylan shows the highest specific surface area value, i.e. the exposed surface of the particle to external air, followed by the other lignocellulosic components while the woody dusts are characterized by low values of SSA. Such trend can be explained mainly in the light of changes in Dx(10).

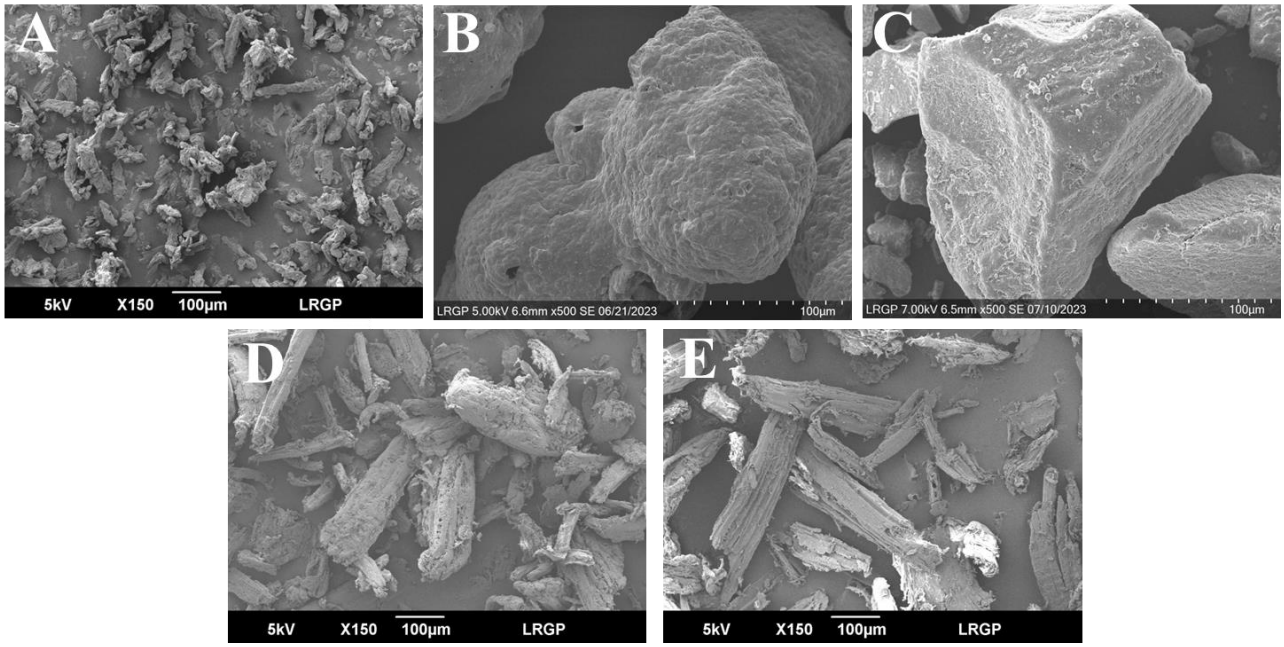

Fig. 1. *SEM images of the samples: Cellulose (A), Lignin (B), Hemicellulose (C), Oak wood (D) and Douglas fir (E).*

Table 2 reports the results of further characterizations such as proximate analysis, ultimate analysis, lignocellulosic components content and the evaluation of some properties useful for the application of the theoretical model for flame propagation. Variations in volatile matter (VM) and fixed carbon (FC) depend on the composition and content in lignin, cellulose and hemicellulose (Pu et al., 2013; Zoghlami and Paës, 2019). In the case of pure lignocellulosic components, the ratio VM/FC is reduced from 12.1 to 1.9 shifting from cellulose to lignin. In the case of woody dusts, the ratio is about 5, due to the presence of the different components and their interactions. This ratio is consistent with those shown by (Ulusal et al., 2021) for different types of woods and is, as expected, greater for fir than for oak (Taş and Yürüm, 2012). Cellulose is the most present component in both the woody samples while hemicellulose is more present in oak wood. Such trend is confirmed by literature data, even if the cellulose content of oak wood (table 2) is significantly higher than that determined by Ulusal et al. (2021), i.e. 39.3 wt%. Moreover, the elemental analysis shows that C, H and O contents vary relatively little, expect for xylan whose oxygen content reaches more than 55% (Ulusal et al., 2021). The heat capacity values for oak wood and douglas fir were obtained through DSC analysis. In the case of oak wood, the resulting value is slightly lower than the value found in the literature (2000 J/kg K, (Material Properties, 2024)). In the case of Douglas, the value is in agreement with literature (Zhang et al., 2019).

Table 2*. Summary of proximate, ultimate and lignocellulosic components analysis and properties of all the samples.*

	Avicel pH 101 (Cellulose)	***Kraft Lignin***	***Xylan (from beechwood)***	***Oak wood***	***Douglas fir***
			Proximate analysis		
Moisture (%)	5.3	4.4	3.7	6.1	6.7
Volatile matter (%)	87.4	59.1	85	77.5	78.9

Fixed carbon (%)	7.2	30.4	14	16.2	14.4
Ash (%)	0.1	6.1	0	0.3	0.1
Elemental analysis					
C (% daf)	44	47.4	39.3	47.3	49.4
H (% daf)	6.2	4.6	5.3	6.1	6.1
O (% daf)	49.4	48.0	55.3	46.6	44.5
Lignocellulosic components					
Hemicellulose (% daf)	-	-	100	34	29
Cellulose (% db)	100	-	-	51	44
Lignin (% db)	-	100	-	24.2	34.4
Properties					
Density (kg m^{-3})	700	1300	1314	907	545
Thermal analysis					
T_{onset} (°C)	305	220	200	264	292
T_{offset} (°C)	360	415	340	400	400
Exo/Endo-thermic reaction?	Endo	Eso (charring)	Eso (charring)	Endo	Endo
Heat of devolatilization (J/kg)	$1.9 \cdot 10^5$	$-1.97 \cdot 10^5$	$-3.05 \cdot 10^5$	$1.05 \cdot 10^5$	$1.3 \cdot 10^5$
Heat capacity (J kg^{-1} K^{-1})	1757	1100	1305	1600*	1500*

*DSC measurements

3.2. Volatile Point, Minimum Ignition Temperature and Flash pyrolysis in the G-G furnace

From the analysis of the pyrolysis gaseous products generated at temperatures ranging from 500 to 900°C (**Fig. 2**), CO, CO_2, H_2 and CH_4 were the most abundant compounds during the pyrolysis step. Other compounds, such as ethylene and aromatics, were sometimes present as traces but are neglected here. The main components of the syngas (H_2 and CO) generally increased with temperature and reached a maximum concentration of 78 mol%, 67 mol%, 50 mol%, 68 mol% and 72 mol% of the pyrolysis gases for cellulose, lignin, hemicellulose, oak and Douglas fir, respectively. The low content of syngas generated by xylan should be noted as this parameter influences the ignition sensitivity of the pyrolysis gases. The large amounts of carbon dioxide generated at low temperatures narrows greatly the explosion region of the gaseous mixtures. Moreover, it should be kept in mind that the micro-GC analyses cannot identify the water vapor inevitably generated during pyrolysis. Considering this additional gas will also reduce the explosion domain.

H_2/CO (**Fig. 3**) ratio showed linear increase and a decrease at 900 ◦C for lignin, oak and Douglas fir, while the trend is monotonically increasing for xylan, but quite constant for cellulose. CO_2/CO (**Fig. 3**) ratio decreases significantly due to higher CO content at increased reactor temperature. In the case of xylan, the trend is quite constant and the content in carbon dioxide is always very high (at least 40 mol%) as also confirmed in the literature (Zhao et al., 2017).

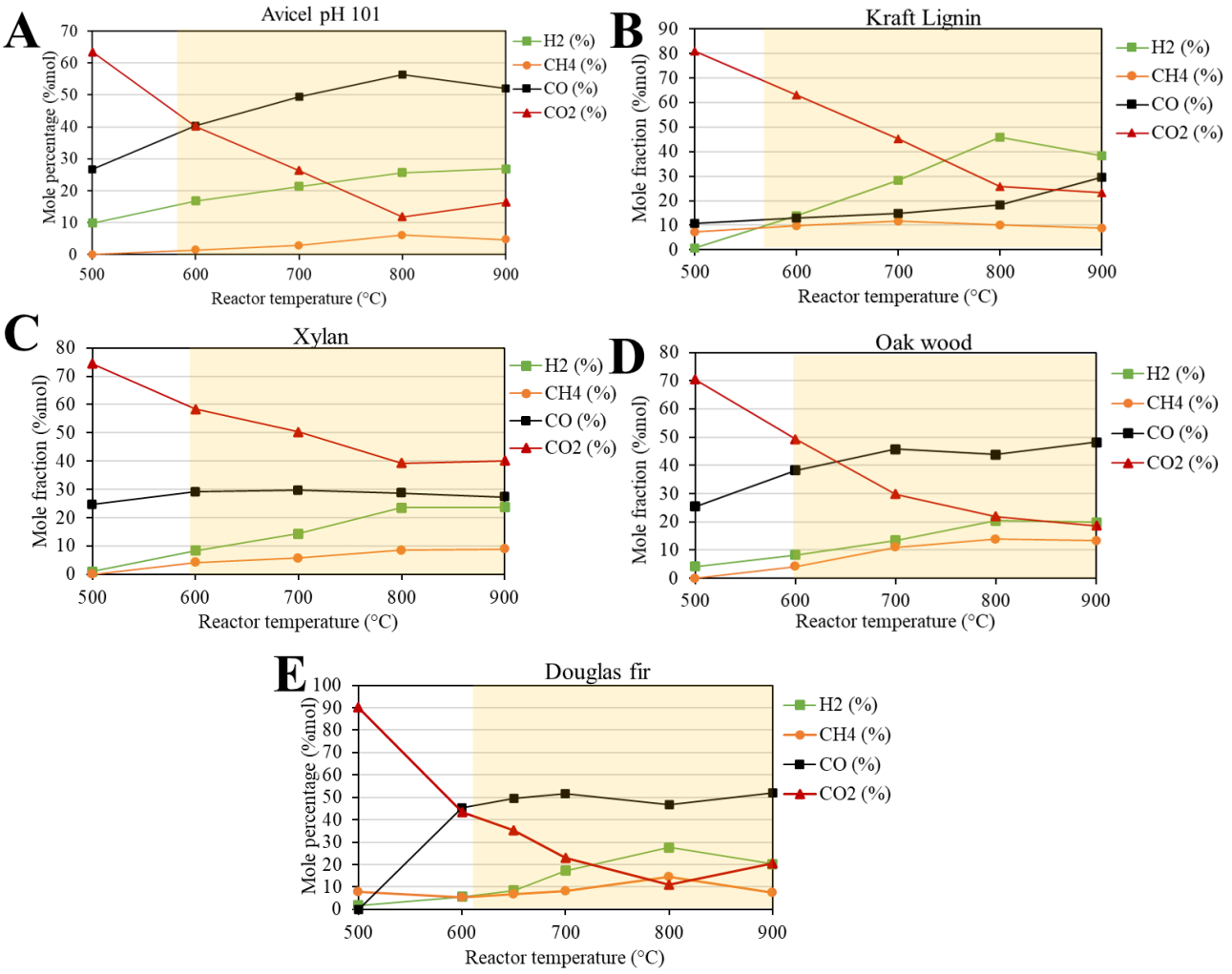

Fig. 2. *Pyrolysis gases composition as a function of the powder nature and G-G furnace temperature: Cellulose (A), Lignin (B), Hemicellulose (C), Oak wood (D) and Douglas fir (E).*

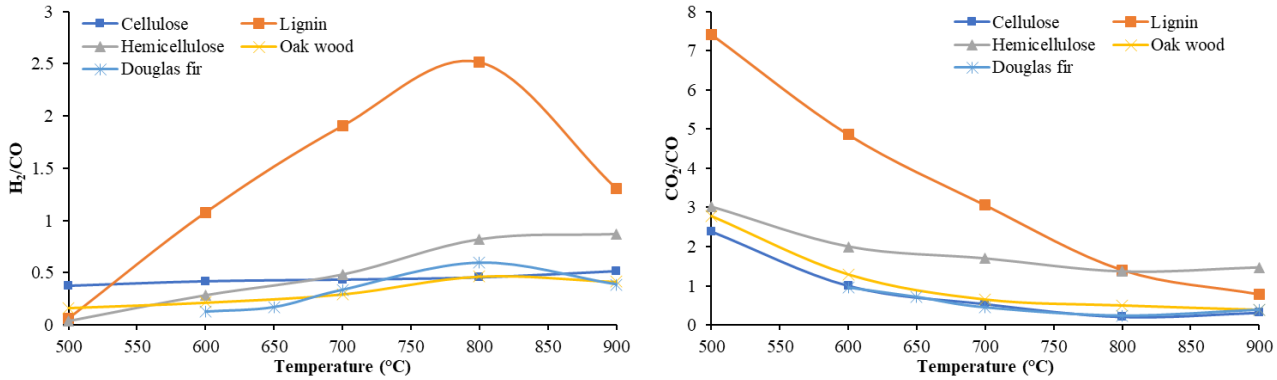

Fig. 3. *CO_2/CO and H_2/CO ratios as a function of the powder nature and G-G furnace temperature.*

By knowing the composition of the gas phase in the case of fast pyrolysis, it was possible to evaluate a fast volatile point (fastVP) based on the flammability of the gases produced using two criteria: the composition-related criterion, i.e., the volume fraction greater than or equal to the LFL, evaluated with Le Chatelier rule (Le Chatelier, 1891), and the thermal criterion, i.e., the GG oven temperature higher than the mixture ignition temperature, again evaluated with Le Chatelier rule.

Regarding the first criterion, it can be seen in **Table 3** that the lowest value of fastVP is represented by lignin, due to the high hydrogen concentration shown in **Fig. 2**, while the highest value is represented by Douglas fir. For the second criterion, a temperature range is tentatively indicated, while the point evaluation will be possible with some future additional tests. The comparison with typical standard thermal parameters such as VP and MIT is also given in **Table 3.** As for the volatile point, which was assessed with an ignition delay time of 6 minutes, the lowest value was measured for cellulose, while the other samples had a VP temperature of over 300 °C, the limit temperature of the standard device used (ASTM E502-07, 2010). Regarding the minimum cloud ignition temperature determined with the GG furnace in its standard configuration (ASTM E1491-06, 2019), cellulose has the lowest temperature (440 °C), followed by wood dusts, while the other two pure lignocellulosic components have the highest values (580-590 °C). If the values obtained for cellulose and wood powders are in satisfactory agreement with literature data, the MIT of lignin appears to be significatively higher than that determined by BGIA (1997) i.e. 470°C. However, the mean diameter of lignin from literature was much lower (18 µm) than that of the sample used here (93 µm) (BGIA, 1997).
As can be seen from **Table 3,** the fastVP, which is evaluated using the composition criterion, is always much higher than the standard parameters and lies in the temperature range between 600 and 700 °C. With regard to the fastVP evaluated with the thermal criterion, it can be seen that the temperature value in the case of lignin and hemicellulose is quite comparable to the minimum cloud ignition temperature, while in the case of cellulose and wood dust the fastVP is above the MIT. This similarity can be attributed to the fact that wood dust mainly consists of cellulose, as well as to the similar shape, which, compared to spherical particles, modifies the dispersion in the furnace and the mass transfer. Castells et al. (2021) demonstrated that, if the influence of lignin content on the ignition sensitivity is rather low, the hemicellulose-xylan/cellulose ratio plays a significant role: the Minimum Ignition Energy (MIE) decreasing when this parameter increases. Nevertheless, this trend seems to be the opposite in the present case (Castells et al., 2020). Lastly, the larger deviation from MIT may also be related to the larger contribution of the flame propagation path in the heterogeneous phase in the case of these fibrous powders, which are characterized by lower values of specific surface area.

Given the obtained results, it is possible to say that in order to answer the question regarding the existence of a correlation between VP, MIT, and LFL of the produced gases, investigations regarding the influence of the physical parameters of the analyzed powders are necessary. In general, it is possible to reiterate that as expected, VP is always the most conservative, obligatory parameter to be considered in the case of handling and storage of combustible materials. The temperature evaluated in the case of fast pyrolysis called here fastVP may be comparable to MIT but also deviate probably due to effects due to dispersion, specific area exposed and shape of the dust that may change the predominant path of flame propagation from predominantly homogeneous to mixed homogeneous-heterogeneous. Finally, another notable difference between VP, and MIT or fastVP lies the apparent heating rate of the samples: as VP is determined over an extended period of time, MIT and fastVP greatly depend on the temperature difference applied over the short residence time of the powder in the G-G furnace.

***Table 3**. VP measured following the standard (ASTM E502-07, 2010), MIT following the standard* (ASTM E1491-06, 2019) *and fast VP assessed using fast pyrolysis data.*

Sample	VP (°C)	MIT (°C)	FastVP (°C) Criterion $T > T_{ign}^{mix}$	FastVP (°C) Criterion $y > LFL$
Avicel pH 101 (Cellulose)	[260-270 °C] 265 °C	440	583	[600-700 °C]
Kraft Lignin (56<Φ<180 µm)	>300 °C	590	573	[600-700 °C]
Xylan (Hemicellulose)	>300 °C	580	593	[600-700 °C]
Oak wood (56<Φ<180 µm)	>300 °C	470	597	[600-700 °C]
Douglas fir (56<Φ<180 µm)	>300 °C	490	605	[650-700 °C]

3.3. Theoretical model

In **Fig. 4**, the dust laminar burning velocity obtained by the theoretical model calculations are shown starting from the volatile compositions at 700, 800 and 900 °C in the case of fast pyrolysis. Literature data obtained with different experimental rigs and concentration are also reported (Pietraccini, 2023).

As can be seen, depending on the powder analyzed, after the characterization of the evolved gas phase by fast pyrolysis and the application of the selected theoretical model, the range of the flammable powder concentration is larger in the case of experiments as in the case of the model. Such discrepancy is notably due to both lower experimental conversion leading to higher explosive concentrations, and the fact that the presence of char and especially tar is neglected in the theoretical analysis. The widest flammability range in terms of dust concentration is presented by cellulose (200-1600 g/m^3), while the narrowest range is formed by lignin (200-1100 g/m^3). The lignin content in the woody powders limits the flammability range to 200-1000 g/m^3.

In terms of flame velocity values, the highest S_u are obtained for lignin and cellulose (range 0.1-0.7 m/s). Hemicellulose (here xylan) appears to be characterized by maximum values lower than 0.5 m/s as in the case of woody powders. This may be caused by a high carbon dioxide content in the pyrolysis gases, even at low temperature, and the low percentage of combustible gases (Zhao et al., 2017). Such trend is in line with the high oxygen content of xylan determined by elemental analysis: the presence of oxygen tends to promote an oxidative pyrolysis which leads to more oxidized, and thus less flammable compounds.

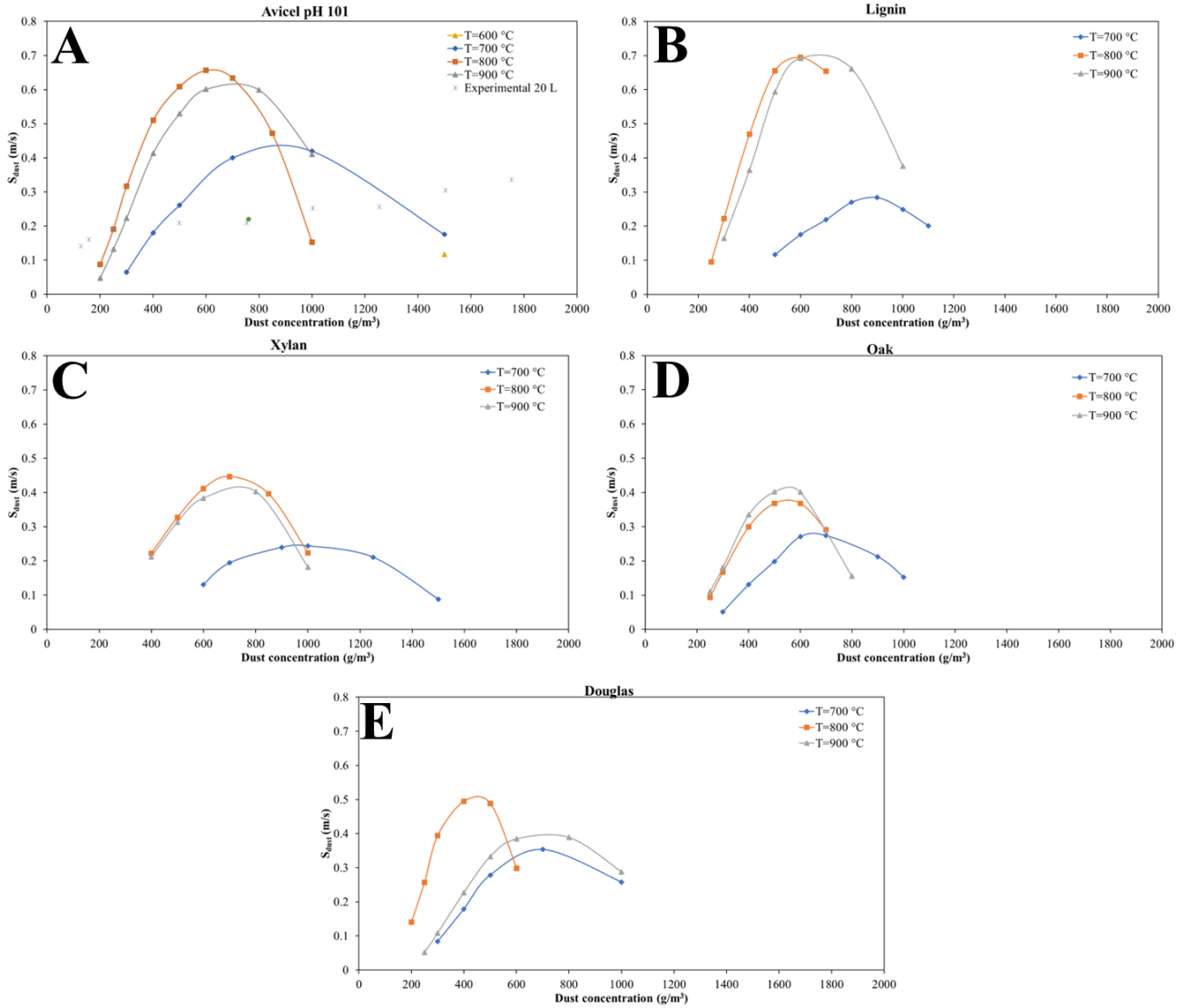

Fig. 4. *S_{dust} as function of samples concentration as computed at pyrolysis temperature at 700 °C, 800 °C and 900 °C: Cellulose (A), Lignin (B), Hemicellulose (C), Oak wood (D) and Douglas fir (E).*

4. Conclusions

This research includes a thorough exploration of the combustion behavior and properties of different lignocellulosic materials. A preliminary investigation of particle morphology and size distribution by SEM imaging revealed distinctive features between cellulose, lignin and hemicellulose particles. In particular, cellulose particles showed a non-spherical shape with a tendency for slight agglomeration, while lignin and hemicellulose particles looked like smooth prismatic entities. Further analysis of the particle size distributions showed that cellulose was the most heterogeneous, in contrast to the remarkably high homogeneity of lignin. Subsequent studies examined the chemical composition and properties of the samples, revealing both proximate and final analyses and characterization of lignocellulose components. It became clear that the presence of cellulose, lignin and hemicellulose played a central role in influencing parameters such as volatiles, fixed carbon and elemental composition, with woody samples closely resembling cellulose in atomic content.

Theoretical modeling of flame propagation provided valuable insights into the flammability properties of the samples. In particular, cellulose showed the widest flammability range in terms of dust concentration, while lignin showed the narrowest range. Flame velocity values varied among the samples, with lignin and cellulose showing the highest values. Furthermore, the analysis of pyrolysis

gases provided insight into the composition and behavior of evolved gases during thermal decomposition. Mainly hydrogen (H_2) and carbon monoxide (CO) emerged as the primary components, whose concentrations fluctuated with temperature and sample type. Finally, an exploration of the relationship between VP, minimum ignition temperature (MIT) and lower flammability limit (LFL) highlighted how important it is to consider the physical parameters of the analyzed powders. VP emerged as the most conservative parameter, with fast VP showing variability that was possibly influenced by dispersion effects, specific surface area and particle shape. In summary, the extensive characterization and analysis in this study offer valuable contributions to the understanding of the combustion behavior of lignocellulosic materials. Further research into the complex interaction between particle properties and combustion parameters is warranted to increase knowledge in this area.

Acknowledgement

The authors acknowledge Mr. Andrea Bizzarro for his excellent technical support.

References

Amyotte, P.R., Clouthier, M.P., Khan, F.I., 2019. Dust explosions: An overview, in: Methods in Chemical Process Safety. Elsevier. https://doi.org/10.1016/bs.mcps.2019.03.004

ASTM D7582-15, 2009. Standard Test Methods for Proximate Analysis of Coal and Coke by Macro Thermogravimetric Analysis. ASTM Int. West Conshohocken, PA.

ASTM E1491-06, 2019. Standard Test Method for Minimum Autoignition Temperature of Dust Clouds. ASTM Int. West Conshohocken, PA 1–10.

ASTM E502-07, 2010. Standard Test Method for Selection and Use of ASTM Standards for the Determination of Flash Point of Chemicals by Closed Cup Methods. ASTM Int. West Conshohocken, PA 1–6. https://doi.org/10.1520/E0502-07E01.priate

BGIA, 1997. Combustion and explosion characteristics of dusts (BIA-Report 13/97) and Gestis Database. Sankt Augustin, Germany.

Castells, B., Amez, I., Medic, L., Garcia-torrent, J., 2020. Preliminary Study of Lignocellulosic biomass ignition properties estimation from Thermogravimetric Analysis 434–445. https://doi.org/10.7795/810.20200724

Di Benedetto, A., Russo, P., 2007. Thermo-kinetic modelling of dust explosions. J. Loss Prev. Process Ind. 20, 303–309. https://doi.org/10.1016/j.jlp.2007.04.001

Eckhoff, R.K., 2003. Dust Explosion in the Process Industries. Gulf Professional Publishing, Boston.

Glassman, I., Yetter, R.A., 2008. Combustion-Fourth edition. Elsevier.

Islas, A., Fernández, A.R., Betegón, C., Martínez-Pañeda, E., Pandal, A., 2023. Biomass dust explosions: CFD simulations and venting experiments in a 1 m3 silo. Process Saf. Environ. Prot. 176, 1048–1062. https://doi.org/10.1016/j.psep.2023.06.074

Islas, A., Fernández, A.R., Betegón, C., Martínez-Pañeda, E., Pandal, A., 2022. Computational assessment of biomass dust explosions in the 20L sphere. Process Saf. Environ. Prot. 165, 791–814. https://doi.org/10.1016/j.psep.2022.07.029

Le Chatelier, H.L., 1891. Note sur le dosage du grisoupar les limetes de'inflammabilite. Ann. des mines 19, 388–395.

Material Properties, 2024. Oak Wood – Density – Strength – Melting Point – Thermal Conductivity

[WWW Document]. URL https://material-properties.org/oak-wood-density-strength-melting-point-thermal-conductivity/

Pietraccini, M., 2023. Mechanisms involved in the fast combustion of organic powders: application to dust explosions. Universitè de Lorraine.

Pietraccini, M., Badu, P., Tait, T., Glaude, P.A., Dufour, A., Dufaud, O., 2023. Study of flash pyrolysis and combustion of biomass powders using the Godbert-Greenwald furnace: An essential step to better understand organic dust explosions. Process Saf. Environ. Prot. 169, 458–471. https://doi.org/10.1016/j.psep.2022.11.041

Portarapillo, M., Sanchirico, R., Luciani, G., Di Benedetto, A., 2023. Flame propagation of combustible dusts: A Mallard-Le Chatelier inspired model. Combust. Flame 251. https://doi.org/10.1016/j.combustflame.2023.112737

Pu, Y., Hu, F., Huang, F., Davison, B.H., Ragauskas, A.J., 2013. Assessing the molecular structure basis for biomass recalcitrance during dilute acid and hydrothermal pretreatments. Biotechnol. Biofuels 6, 1–13. https://doi.org/10.1186/1754-6834-6-15

Sanchirico, R., Di Sarli, V., Di Benedetto, A., 2018. Volatile point of dust mixtures and hybrid mixtures. J. Loss Prev. Process Ind. 56, 370–377. https://doi.org/10.1016/j.jlp.2018.09.014

Taş, S., Yürüm, Y., 2012. Co-firing of biomass with coals : Part 2. Thermogravimetric kinetic analysis of co-combustion of fir (Abies bornmulleriana) wood with Beypazari lignite. J. Therm. Anal. Calorim. 107, 293–298. https://doi.org/10.1007/s10973-010-1281-z

Ulusal, A., Apaydın Varol, E., Bruckman, V.J., Uzun, B.B., 2021. Opportunity for sustainable biomass valorization to produce biochar for improving soil characteristics. Biomass Convers. Biorefinery 11, 1041–1051. https://doi.org/10.1007/s13399-020-00923-7

Zhang, Y., Zhang, L., Shan, Z., Wang, L., Liu, W., 2019. Thermal responses of woods exposed to high temperatures considering apparent thermo-physical properties. J. Renew. Mater. 7, 1093–1108. https://doi.org/10.32604/jrm.2019.07335

Zhao, C., Jiang, E., Chen, A., 2017. Volatile production from pyrolysis of cellulose, hemicellulose and lignin. J. Energy Inst. 90, 902–913. https://doi.org/10.1016/j.joei.2016.08.004

Zoghlami, A., Paës, G., 2019. Lignocellulosic Biomass: Understanding Recalcitrance and Predicting Hydrolysis. Front. Chem. 7. https://doi.org/10.3389/fchem.2019.00874

Quantitative risk assessment of aqueous formate for hydrogen storage: scale-up

Marcella Calabrese [a,b], Danilo Russo [a] , Guido Capone [b], Roberto Andreozzi [a], Raffaele Marotta [a] & Almerinda Di Benedetto [a]

[a] Department of Chemical Engineering, Materials, and Industrial Production, University of Naples Federico II, P.le V. Tecchio 80, 80125, Naples, Italy

[b] Plant & Process Technology, Saipem SpA, Via Luigi Russolo, 20138 Milano MI

E-mail: marcella.calabrese2@unina.it

Abstract

The renewed interest of the scientific community in hydrogen has led to the search for innovative production and storage solutions. An alternative and safe way for hydrogen storage is possible through the formate/bicarbonate catalytic interconversion cycle in aqueous solution. This paper presents a preliminary quantitative risk analysis for a train-feeding system. The formate storage system is compared to the case of storage of compressed hydrogen at 350 bar. For both system, frequency and consequences analysis is presented in order to build risk maps. In addition, societal risk is also analyzed, and it is represented in a FN-curve, which displays the probability of having N or more fatalities per year, as a function of N. Both isoharzard and F-N curves show that aqueous formate storage is safer than compressed H_2 storage. In addition, formate storage system is intrinsically safer in a large percentage of cases, this is evident not only considering a small scale but also for a train-feeding system considered. This is due to the presence of water in the system and the mild operating conditions required in the storage tank. In particular, in the case of aqueous solution of formates/bicarbonates a vapor cloud explosion is prevented.

Keywords: *Hydrogen storage; formate/bicarbonate storage; green hydrogen fuels; hydrogen safety; hydrogen train; risk analysis, chemical engineering.*

1. Introduction

The use of fossil fuels, coal, and natural gas as main energy sources has been and still is at the basis of the world economy resulting in greenhouse gas emissions and global warming. The European Union (EU) has promoted a plan that aims at reducing emissions by 2030 and a complete decarbonization by 2050 defined as "NZE: net zero emission" (Vivanco-Martín and Iranzo, 2023). Hydrogen is one of the main sectors of this change, as it is considered an important vector of the energy transition. IRENA declares that hydrogen could contribute to 10% of the mitigation of temperature increase and to 12% of final energy demand (Renewable Energy Agency and Trade Organization Agency, 2023). To achieve the objectives, it is necessary to increase the production, storage, transport, and diffusion of green hydrogen (Di Nardo et al., 2024; Megia et al., 2021).

However, many challenges must be faced. One of the main issues is H_2 storage, due to its physico-chemical properties, i.e. low energy density by volume, lowest minimum ignition energy (0.02 mj), widest flammability range (about 4.0 - 75.0 mol% in air), and highest diffusivity among known fuels. Another important problem of hydrogen technologies is related to the safety of both traditional and innovative storage systems (Faye et al., 2022; Nazir et al., 2020; Russo et al., 2022) .

Cryogenic and compressed systems, as well as more mature systems, still have many safety issues that are mostly related to the combination of intrinsic gas properties and extreme storage conditions, i.e. T = - 252°C and P = 350 -700 bar. Chemical methods, despite their innovation, are often based on the adoption of materials that are toxic and harmful to the environment and people, and do not guarantee a storage density, efficiency, and/or stability that is comparable to the present benchmark (Hassan et al., 2021; Ratnakar et al., 2021).

In recent years, there has been a growing interest in the development of new hydrogen vectors capable of releasing it at near-ambient conditions. One new method is aqueous solution of formic acid salts, formate (HCOOM), prepared through catalytic hydrogenation of bicarbonate ions. Based on the literature survey, the future goal of this system is the improvement of the cyclic formate/bicarbonate interconversion in order to meet the requirements of the industrial and automotive sector. The reactive cyclic formate/bicarbonate in aqueous solutions, is an interesting and effective way for the safety and economical storage of hydrogen (Calabrese et al., 2023). The reactive cycle is described below:

$$HCOOM + H_2O \leftrightarrow H_2 + MHCO_3 \quad Eq.\ 1$$

Where M = Na^+, K^+, NH_4^+ is the positive countercation.

Formates dehydrogenation and bicarbonates hydrogenation enable, respectively, the release and uptake of hydrogen through the catalytic cycle. This reactive cycle requires an appropriate catalyst to enable reactions to be carried out at near-ambient conditions, in the case of the dehydrogenation reaction, i.e. T = 50-90, P = 2 - 10 bar; while for hydrogenation it is necessary to increase the pressure up to a few tens of bars, working in a safer range than mature storage technologies such as compressed hydrogen (Treigerman and Sasson, 2019).

In this work, the objective is to highlight the safety aspects of this system compared to a traditional storage technique, i.e. compressed hydrogen. The risk assessment of a single aqueous formate vessel and comparison with traditional compressed hydrogen at 350 bar was presented in a recent work of Russo et al. (Russo et al., 2024). With this paper, risk assessment of a scaled-up case is analyzed by considering the amount of hydrogen necessary to feed a train. Particular attention will be paid to the occurrence of a vapour cloud explosion (VCE) as an incidental scenario and the occurrence of domino effects that can be generated from jet-fire and/or fireball coming from only one of the tanks considered.

Figure 1 shows the catalysed reactive cycle: during the hydrogenation reaction, bicarbonate is converted to formate for H_2 storage; instead, during the dehydrogenation reaction the formate is

converted again to bicarbonate for the release of hydrogen and this phase is necessary to power the train. The figure is simplified and useful for assessing the potential of this technology.

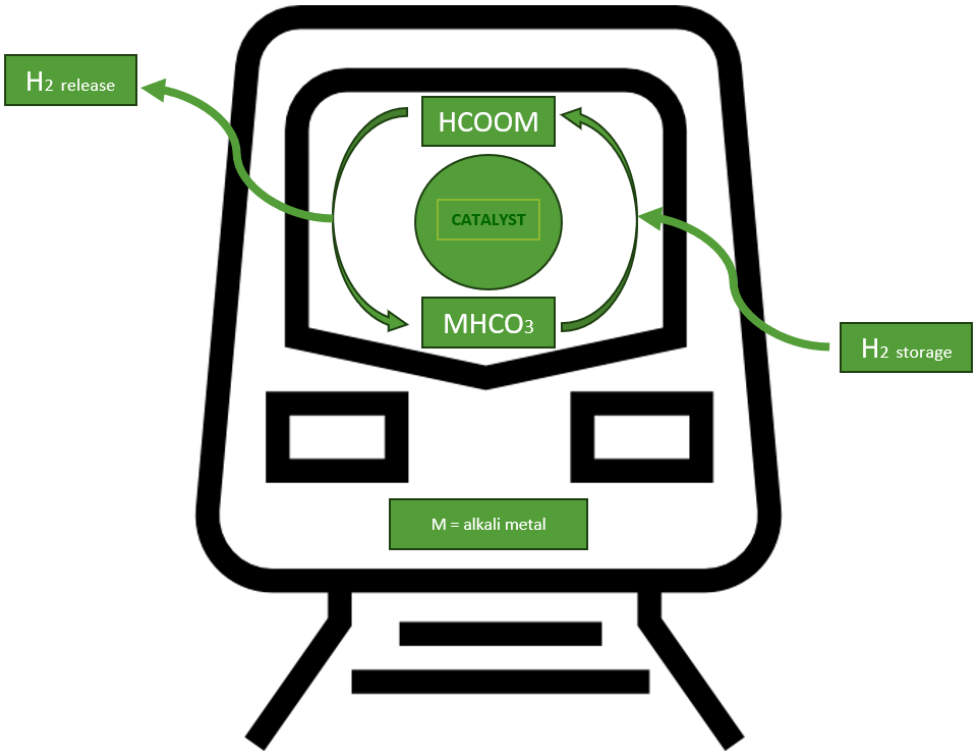

Figure 1 - Hydrogenation/dehydrogenation reactions for the storage and release of hydrogen in a vehicle.

2. Accidental Scenario description

In this work, we start from the same initiating event of our previous work (Russo et al., 2024) . More in details, as initiating event, the presence of an external fire is considered.
The consequence is the tank temperature and pressure increase. In the case of proper operation of the safety valve at $P = P_{set}$ this results in a continuous release of hydrogen that, if immediately ignited, determines a jet fire. In the case of delayed ignition, depending on the degree of mixing of the flammable substance with air, the expected outcome is a Vapour Cloud Explosion (VCE). In the case of malfunction of the safety valve, the tank pressure can reach the burst value (assumed at $P_{burst} = 2\ P_{set}$) and the catastrophic rupture may occur. In this case, a VCE or a fireball may occur, depending on the ignition. For a single vessel (4.7 kg of H_2), VCE was not considered since the H_2 amount was not sufficient for sustaining the flame propagation in unconfined environment.

In this work, we perform the risk analysis for 20 cylinders of H_2 at 350 bar necessary to ensure autonomy and efficiency of a train and for a storage tank for a formate system containing the same amount of hydrogen (Nqodi et al., 2023). All tanks are equipped with a safety valve activated at the set pressure P_{set} (Zheng et al., 2012). In the case of hydrogen-powered trains, two possible initiating events should be considered: a railway accident and/or an external fire. Analysing both accidents - in the case of compressed hydrogen - a domino effect is expected that affects the 20 pressurized tanks,

leading to the loss of the entire fuel. When performing the scale-up the H_2 amount is increased up to 20 times and then also the VCE has to be considered.
Figure 2 illustrates a train that will be analysed in this paper; however, the green circle indicates the wagon where both the storage and the supply of hydrogen occurs. In addition, an incidental scenario is shown to highlight one of the possible tragic events that could happen if a fault/accident is recorded.

Figure 2 - Train fuelled with hydrogen and possible accident scenario

3. Methods

The probability of occurrence of accidental scenarios was calculated through the event tree, as the product of the initiating event frequency multiplied by the probability of occurrence of event leading to the outcome (Laird, 2012). The spatial/temporal concentration distribution was computed by using the Pasquill-Gifford model.

The magnitude of the consequences has been evaluated by means of the models available in the literature. For the jet fire, the point source model (Point Source Model) (Díaz and Rigby, 2022) is used for a more conservative assessment of the thermal flux obtained. In the case of fire and explosions we have two different methods used: for the fireball and thermal fluxes were evaluated according to semi-empirical models and the physical explosion (Laird, 2012); therefore, in order to assess the damage from overpressure the equivalent TNT method is used.

The consequence has been evaluated as a function of the distance from the source point, using a probabilistic approach (Effect Model), based on Probit functions, (table 1)

Table 1 - Probit functions

jet fire, fireball	Death due to thermal radiation	$Y = -36.38 + 2.56 \ln(I^{4/3} \cdot t)$	(Hanley et al., 2018)
jet fire, fireball	I-degree burns due to thermal radiation	$Y = -39.83 + 3.0186 \cdot \ln(I^{4/3} \cdot t)$	(Pérez et al., 2010a; Shen et al., 2018a, 2018b)
VCE, physical explosion	Pulmonary haemorrhages due to overpressure	$Y = -77.1 + 6.91 \cdot \ln(P_0)$	(National technical information, 1975)
VCE, physical explosion	Structural damage	$Y = -23.1 + 2.92 \cdot \ln(P_0)$	(National technical information, 1975)

Starting from the analysis conducted on a single tank, 20 tanks of compressed hydrogen are considered as fuel for a train and the corresponding storage tank for the system formates/bicarbonates.

From the quantity of hydrogen contained in the system under analysis, the distances where LFL and UFL are reached have been estimated. The approach followed is the most conservative: for a continuous release, pure hydrogen release was considered for both storage systems. In fact, even in the case of tanks with formates, significant water evaporation is prevented by the high pressure in the vessel and gas stratification in the tank is likely to occur. In the event of a catastrophic failure of the storage tank at high temperature, water is suddenly released at high temperature to ambient pressure, and, as a result, a hydrogen/steam mixture will be obtained where the water acts as an inert, reducing the flammability range. For the assessment of gas flow, model proposed in the literature and the isentropic expansion through a hole were considered (Laird, 2012).

It was therefore possible to evaluate the thermal flux values for the two systems as a function of the distance from the point of release through the probit equations. A target of lethality or damage of 50% has been set, so distances are identified where a pressure wave, or an energy flow, can cause the expected effect.

Impact zones of the incidental outcomes were represented through the isorisk curves. In order to trace the isorisk curves, we assume the simplified hypothesis that in the region enclosed by the isorisk curve we have 100% of fatality, while outside 0%. As a result, the risk contour of each outcome is a circumference of radius equal to the effect zone identified with the probit equations.

4. Results

The evaluation of the VCE consequence was performed using the models given in Table 2. For the study of the result VCE was taken into account the case of 20 tanks of H_2 compressed to 350 bar, the H_2 in the tanks was released instantly resulting in the generation of a puff. The same amount of hydrogen was analyzed for a system containing a formates solution. In this case, the inertizing effect of H_2O, observed in the case of a single tank, is also expected: in case of a cloud formation, water can limit or even avoid the VCE as an incidental scenario.

Table 2 - data for the scale-up system and VCE results generated from 20 H_2 tanks at 350 bar

N° 20 TANKS AT 350 BAR			
VARIABLE	**VALUE**	**MODEL**	
Total mass of H_2 [kg]	$m_{H_2} = 94.4$	Real Gas Law	(Myslikova and Gallagher, 2020)
H_2 mass in the flammability range [kg]	$m_E = 83.11$	Van Buijtenen model	(Van Buijtenen, 1980)
Equivalent mass of TNT [kg]	$m_{TNT} = 214.42$	Model of equivalent TNT	(Shen et al., 2018c)
Distance limits for flammability [m]	$x_{LFL} = 184.4584$ $x_{UFL} = 625.3108$	Pasquill-Gifford model	(Laird, 2012)
Effect zone extension (50% lethality) [m]	48	Probit equation	(Pérez et al., 2010b)

In Figure 3, the effect of H_2O on the H_2 flammability limits is shown. The flammability range is significantly reduced by the presence of water, up to disappear at H_2O concentration above 60%.

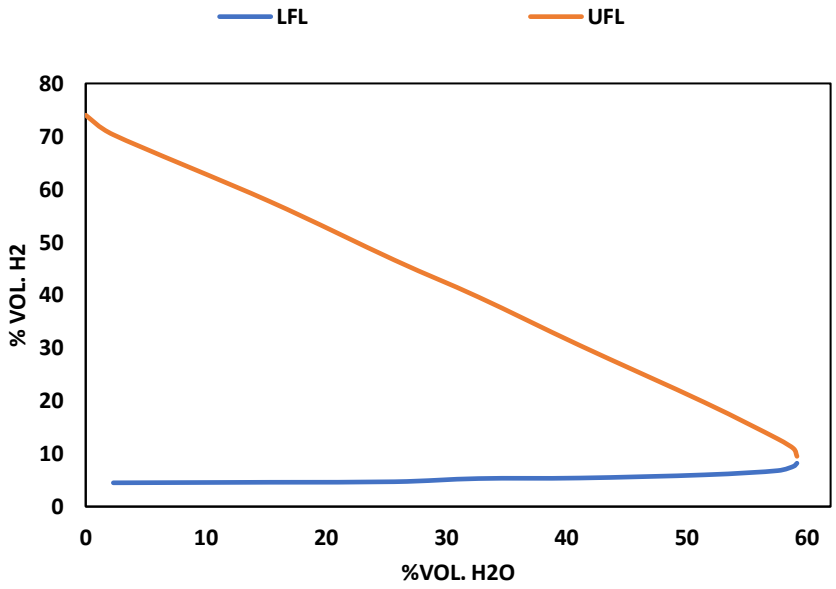

Figure 3 - Nose diagram for hydrogen at different inert percentage (H_2O)

This result suggests that the cloud formation could be not flammable, when the salt concentration up to 6.5 mol/L (Russo et al., 2024), thus ensuring the formate storage an intrinsically safe system with respect to VCE.

From these considerations it is clear that the system consisting of pressurized cylinders represents, in fact, a serious safety issue: if the isorisk curve for the VCE would be traced, the effect zone (centred at the trigger point) would be significantly expanded, while in the case of the formate solution system, the iso-hazard curves related to the VCE will be completely absent, as shown in Figure 4.

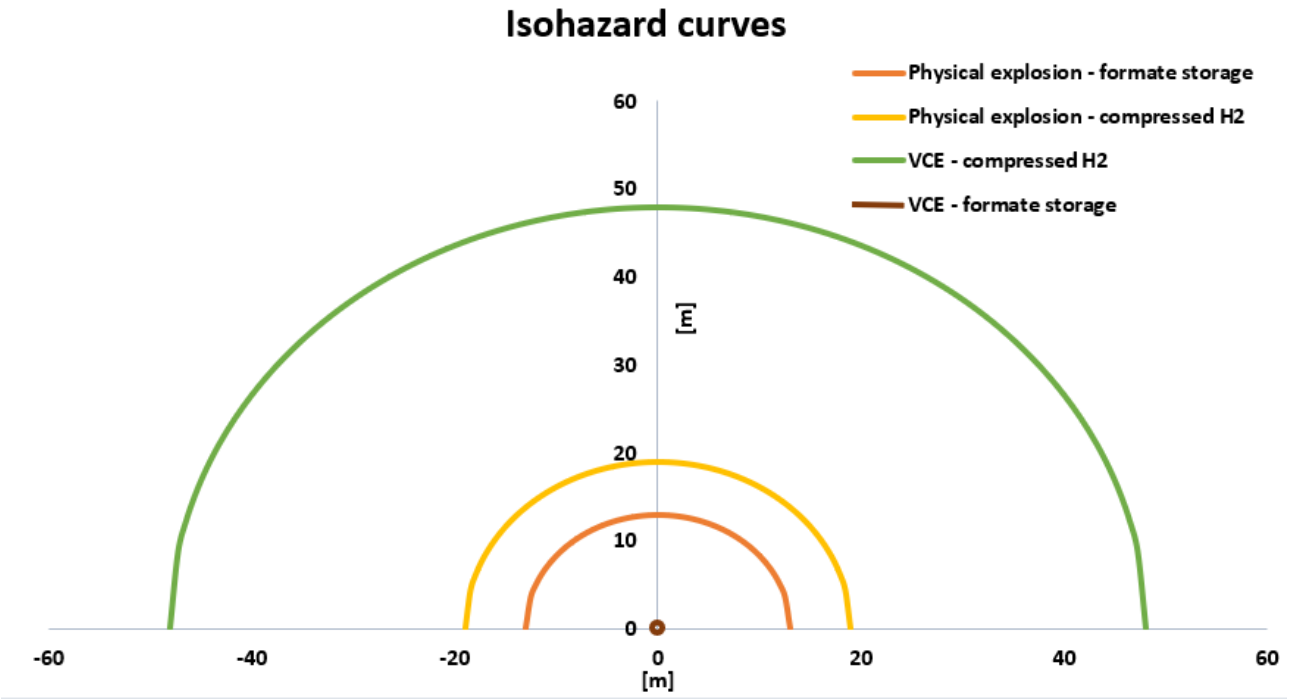

Figure 4 – Isorisk curves for physical explosion and VCE both in the case of compressed H_2 and formates

For the scenario that foresees the VCE is interesting to estimate the curve F-N. It is considered that the release of H_2 on the train happens while it is traveling in open country. Near the point of release, it has been hypothesized the presence of a small city centre of about 30,000 inhabitants with an extension of 775000 m^2, and it is considered that in the built-up area the cloud is triggered. Imagining for simplicity a homogeneous distribution of the population, a Fatality number for the VCE was estimated equal to about 26 people.

Table 3 shows the information obtained and the F-N curve in the case of VCE:

Table 3 - fatality number e FN value for compressed hydrogen (20 tanks)

FATALITY NUMBER (N)	***OUTCOMES***	***F_N [year^{-1}]***
N ≤ 26	*VCE*	*2E-6*
N > 26	*/*	*0*

Figure 5 shows the trend of the F-N curve in the case of compressed hydrogen, compared to the Dutch threshold, which is the most conservative (De Bruijn et al., 2010), however, a slight exceedance occurs. This could be much more marked if we consider other incidental scenarios with their domino effects. Such analysis will be further investigated. In the case of the formate/bicarbonate system, the F-N curve for this accidental scenario is not present; this is because the formed cloud is rich in water and therefore outside the flammability conditions of the solution and the VCE is not expected. As one can see from the results obtained, the storage of H_2 in formate solutions has a great potential.

This is even more evident when considering a real application of this type in which the volumes of H_2 considered are greater.

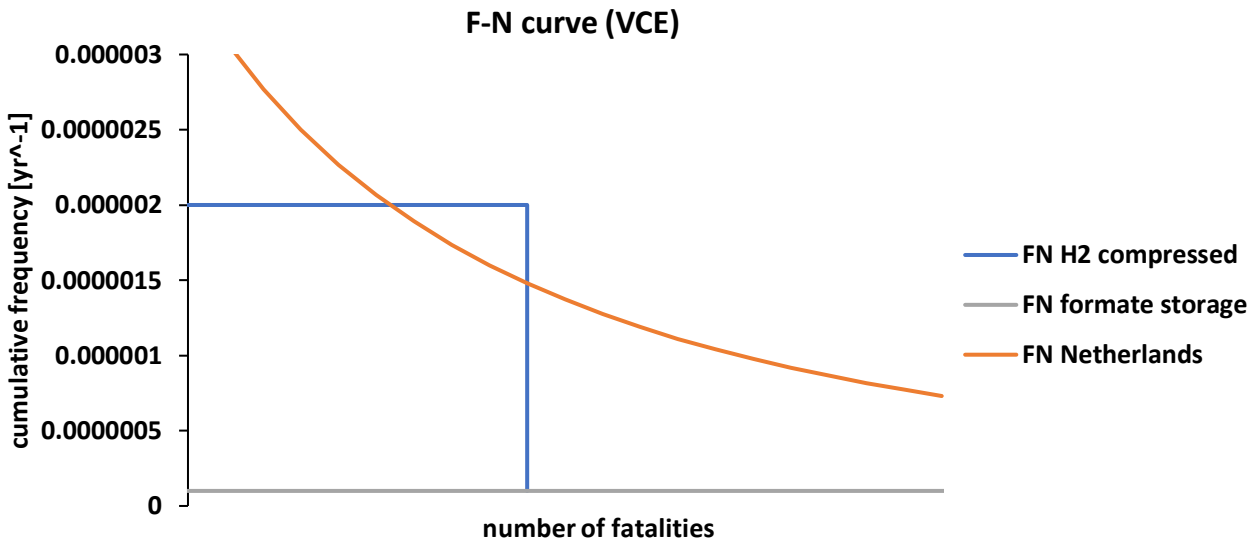

Figure 5 - F-N curve in case of VCE as outcome

Vehicles are vulnerable to catastrophic accidents due to the storage and the transport of flammable/ explosive materials, and this is even more evident when the hydrogen is the stored gas. Among all the most common incidental scenarios, there are fires and explosions, and these are interactive events, so they can generate a "domino effect", especially in processes where units are located within a limited distance. There is high complexity and uncertainty about the study of domino effects as it is not easy to analyze the interaction between various parts of the process. This paper aims to conduct a preliminary and simplified study on the domino effect from some hypotheses: (i) the initiating event is an increase in temperature in one of the tanks; (ii) the reactor is equipped with a safety valve that is operated and releases hydrogen continuously with the formation of a plume; and (iii) the most likely outcomes considered are jet-fire and fireball from a single vessel.

These hypotheses are in a range of conditions treated in the previous paper by Russo et al.(Russo et al., 2024).It is therefore possible to evaluate the threshold values for thermal flux and compare them with the literature values (Lynch et al., n.d.) of sufficient thermal radiation to cause damage to the process equipment and to melt plastics, shown in Table 4.

Table 4 - general effects of thermal radiation and relative distance for both storage systems

Radiation Intensity [kW/m^2]	**Impact**	**Jet-Fire compressed H_2 distance [m]**	**Jet-fire Formate distance[m]**	**Fireball compressed H_2 distance [m]**	**Fireball Formate distance [m]**
12.6	Minimum level to melt plastics	65	7	37	-

35.0	Damage to process equipment	28	2.5	22	-

As evident, the distances in the case of formates are considerably smaller than those obtained in the case of compressed hydrogen. However, in the event that the tanks are sufficiently close, the domino effect cannot be avoided in either system. Instead, if we consider the results of the thermal flux from the fireball, given the evaporation of water and the mixing with H_2, the critical values are never reached, and the fireball is an intrinsically safer result.

5. Conclusion

The storage of H_2 in aqueous formate solutions is an alternative and effective solution not only to traditional storage techniques but also to innovative and recent storage methods. In fact, within the category of LOHC, formates pose less severe safety issues. The results obtained in this study showed that the system of interest represents a real turning point for the safety of H_2 storage especially on a large scale, considering that the presence of inerting water can mitigate or completely prevent the occurrence of cloud explosions, contrary to compressed hydrogen. Moreover, the domino effects generated by fires from a single vessel have a higher probability of occurrence when considering the case of compressed hydrogen. Indeed, considering a comparison of risk areas for both systems, it is clear that the risk area for compressed hydrogen was significantly larger than the risk area for formate storage; Formate storage technology finds one of the main strengths in the highest levels of safety in accordance with current legislation and the targets set for the hydrogen economy in the near future.

Nevertheless, for an effective scale-up of the storage system with a formate solution, the frequency of occurrence of the outcomes can be reduced by introducing further and adequate safety functions and mitigating measures. The knowledge necessary for the transition of this system from the laboratory scale to that of industrial applications can be generated by increasing experimental data, and transferring the acquired knowledge acquired to a pilot scale.

Acknowledgements

This research received no funding.

Bibliography:

AD-A015 245 VULNERABILITY MODEL. A SIMULATION SYSTEM FOR ASSESSING DAMAGE RESULTING FROM MARINE SPILLS ENVIRO CONTROL, INCORPORATED PREPARED FOR COAST GUARD, 1975.

Calabrese, M., Russo, D., di Benedetto, A., Marotta, R., Andreozzi, R., 2023. Formate/bicarbonate interconversion for safe hydrogen storage: A review. Renewable and Sustainable Energy Reviews. https://doi.org/10.1016/j.rser.2022.113102

De Bruijn, K., Beckers, J., Van Der Most, H., 2010. Casualty risks in the discussion on new flood protection standards in The Netherlands. WIT Transactions on Ecology and the Environment 133, 73–83. https://doi.org/10.2495/FRIAR100071

Di Nardo, A., Portarapillo, M., Russo, D., Di Benedetto, A., 2024. Hydrogen production via steam reforming of different fuels: thermodynamic comparison. Int J Hydrogen Energy 55, 1143–1160. https://doi.org/10.1016/j.ijhydene.2023.11.215

Díaz, J.S., Rigby, S.E., 2022. Blast wave kinematics: theory, experiments, and applications. Shock Waves 32, 405–415. https://doi.org/10.1007/s00193-022-01089-z

Faye, O., Szpunar, J., Eduok, U., 2022. A critical review on the current technologies for the generation, storage, and transportation of hydrogen. Int J Hydrogen Energy. https://doi.org/10.1016/j.ijhydene.2022.02.112

Hanley, E.S., Deane, J.P., Gallachóir, B.P.Ó., 2018. The role of hydrogen in low carbon energy futures–A review of existing perspectives. Renewable and Sustainable Energy Reviews. https://doi.org/10.1016/j.rser.2017.10.034

Hassan, I.A., Ramadan, H.S., Saleh, M.A., Hissel, D., 2021. Hydrogen storage technologies for stationary and mobile applications: Review, analysis and perspectives. Renewable and Sustainable Energy Reviews. https://doi.org/10.1016/j.rser.2021.111311

Laird, T., 2012. Chemical and process safety. Org Process Res Dev. https://doi.org/10.1021/op3003322

Lynch, C.J., Kumar, R.M., Breedina, R.J., Durrani, M.N., n.d. A Critical Technical Review of Six Ilazard December 1975 Assessment Models A. ".

Megia, P.J., Vizcaino, A.J., Calles, J.A., Carrero, A., 2021. Hydrogen Production Technologies: From Fossil Fuels toward Renewable Sources. A Mini Review. Energy and Fuels. https://doi.org/10.1021/acs.energyfuels.1c02501

Myslikova, Z., Gallagher, K.S., 2020. Mission Innovation is mission critical. Nat Energy. https://doi.org/10.1038/s41560-020-00694-5

Nazir, H., Muthuswamy, N., Louis, C., Jose, S., Prakash, J., Buan, M.E., Flox, C., Chavan, S., Shi, X., Kauranen, P., Kallio, T., Maia, G., Tammeveski, K., Lymperopoulos, N., Carcadea, E., Veziroglu, E., Iranzo, A., Kannan, A.M., 2020. Is the H2 economy realizable in the foreseeable future? Part II: H2 storage, transportation, and distribution. Int J Hydrogen Energy. https://doi.org/10.1016/j.ijhydene.2020.05.241

Nqodi, A., Mosetlhe, T.C., Yusuff, A.A., 2023. Advances in Hydrogen-Powered Trains: A Brief Report. Energies (Basel) 16. https://doi.org/10.3390/en16186715

Pérez, J.F.S., Ferradás, E.G., Alonso, F.D., García, D.P., Cano, M.V.M., Cotorruelo, J.Á.B., 2010a. New Probit equations for the calculation of thermal effects on humans. Process Safety and Environmental Protection 88, 109–113. https://doi.org/10.1016/j.psep.2009.11.007

Pérez, J.F.S., Ferradás, E.G., Alonso, F.D., García, D.P., Cano, M.V.M., Cotorruelo, J.Á.B., 2010b. New Probit equations for the calculation of thermal effects on humans. Process Safety and Environmental Protection 88, 109–113. https://doi.org/10.1016/j.psep.2009.11.007

Ratnakar, R.R., Gupta, N., Zhang, K., van Doorne, C., Fesmire, J., Dindoruk, B., Balakotaiah, V., 2021. Hydrogen supply chain and challenges in large-scale LH2 storage and transportation. Int J Hydrogen Energy. https://doi.org/10.1016/j.ijhydene.2021.05.025

Renewable Energy Agency, I., Trade Organization Agency, W., n.d. International trade and green hydrogen: Supporting the global transition to a low-carbon economy.

Russo, D., Andreozzi, R., Calabrese, M., Marotta, R., Di Benedetto, A., 2024. Quantitative risk assessment of aqueous formate for hydrogen storage.

Russo, D., Calabrese, M., Marotta, R., Andreozzi, R., Di Benedetto, A., 2022. Thermodynamics of the cyclic formate/bicarbonate interconversion for hydrogen storage. Int J Hydrogen Energy 47, 31370–31380. https://doi.org/10.1016/j.ijhydene.2022.07.033

Shen, C., Ma, L., Huang, G., Wu, Y., Zheng, J., Liu, Y., Hu, J., 2018a. Consequence assessment of high-pressure hydrogen storage tank rupture during fire test. J Loss Prev Process Ind 55, 223–231. https://doi.org/10.1016/j.jlp.2018.06.016

Shen, C., Ma, L., Huang, G., Wu, Y., Zheng, J., Liu, Y., Hu, J., 2018b. Consequence assessment of high-pressure hydrogen storage tank rupture during fire test. J Loss Prev Process Ind 55, 223–231. https://doi.org/10.1016/j.jlp.2018.06.016

Shen, C., Ma, L., Huang, G., Wu, Y., Zheng, J., Liu, Y., Hu, J., 2018c. Consequence assessment of high-pressure hydrogen storage tank rupture during fire test. J Loss Prev Process Ind 55, 223–231. https://doi.org/10.1016/j.jlp.2018.06.016

Treigerman, Z., Sasson, Y., 2019. Separation of Formate Ion from a Catalytic Mixture after a Hydrogenation Process of Bicarbonate Ion and Generation of Formic Acid—The Last Stage of the Formic Acid Cycle. Am J Analyt Chem 10, 296–315. https://doi.org/10.4236/ajac.2019.108022

Van Buijtenen, C.J.P., 1980. CALCULATION OF THE AMOUNT OF GAS IN THE EXPLOSIVE) REGION OF A VAPOUR CLOUD RELEASED IN THE ATMOSPIERE, Journal of Hazardow Materi&&. Elaevier Scientific Publishing Company.

Vivanco-Martín, B., Iranzo, A., 2023. Analysis of the European Strategy for Hydrogen: A Comprehensive Review. Energies (Basel). https://doi.org/10.3390/en16093866

Zheng, J., Bie, H., Xu, P., Liu, P., Zhao, Y., Chen, H., Liu, X., Zhao, L., 2012. Numerical simulation of high-pressure hydrogen jet flames during bonfire test. Int J Hydrogen Energy 37, 783–790. https://doi.org/10.1016/j.ijhydene.2011.04.061

Hydrogen safety for systems at ambient and cryogenic temperature: a comparative study of hazards and consequence modelling

Donatella Cirrone [a], Dmitriy Makarov [a] & Vladimir Molkov [a]

[a]HySAFER Centre, Ulster University, Newtownabbey, Northern Ireland, BT37 0QB, UK

E-mail: d.cirrone@ulster.ac.uk

Abstract

Transport and storage of hydrogen as a liquid (LH_2) is being widely investigated as a solution for scaling up the supply infrastructure and addressing the growth of hydrogen demand worldwide. While there is a relatively well-established knowledge and understanding of hazards and associated risks for gaseous hydrogen at ambient temperature, several knowledge gaps are yet open regarding the behaviour in incident scenarios of cryogenic hydrogen, including LH_2. This paper aims at presenting the models and tools that can be used to close relevant knowledge gaps for hydrogen safety engineering of LH_2 systems and infrastructure. Analytical studies and computational fluid dynamics (CFD) modelling are used complementarily to assess relevant incident scenarios and compare the consequences and hazard distances for hydrogen systems at ambient and cryogenic temperature. The research encompasses the main phenomena characterising an incident scenario: release and dispersion, ignition, and combustion. Experimental tests on cryogenic hydrogen systems are used for the validation of correlations and numerical models. It is observed that engineering tools originally developed for hydrogen at ambient temperature are yet applicable to the cryogenic temperature field. For a same storage pressure and nozzle diameter, the decrease of hydrogen temperature from ambient to cryogenic 80 K may lead to longer hazard distances associated to unignited and ignited hydrogen releases. The potential for ignition by spark discharge or spontaneous ignition mechanism is seen to decrease with the decrease of hydrogen temperature. CFD modelling is used to give insights into the pressure dynamics created by LH_2 vessels rupture in a fire using experimental data from literature.

Keywords: *hazards, hydrogen safety, releases, jet fires, explosions*

Introduction

The growth of hydrogen demand and novel applications has led to the need for scaling up the supply infrastructure. One of the potential solutions is the transport and storage of hydrogen as a liquid (LH_2) owe to the larger densities and increased efficiencies compared to its gaseous form. Knowledge of phenomena associated to safety of gaseous hydrogen at ambient temperature is well settled. However, a deep understanding of the hazards and risks associated with cryo-compressed and LH_2 systems is yet needed in order to ensure an inherently safer LH_2 infrastructure. Several studies have been conducted within the European project PRESLHY (www.preslhy.eu) on pre-normative research for the safer use of LH_2 in non-industrial settings, addressing the knowledge gaps and open issues associated with LH_2 behaviour in accidental conditions. However, a methodical approach is yet needed to assess the whole range of incident's consequences and underpin the development of prevention and mitigation strategies. The present research aims at providing a set of engineering tools and numerical models for a systematic assessment of the potential consequences from relevant incident scenarios involving LH_2 applications. Main object of the research is the safety of cryo-compressed releases as representing the most likely events during safety operations of LH_2 operations, such as the venting from LH_2 storage systems to avoid a dangerous pressure build-up and

worst-case scenario of a catastrophic rupture of the storage tank. The systematic assessment first analyses the consequences deriving from unintended hydrogen releases. In this case the major safety concern is associated with the potential ignition of the formed flammable cloud and associated hazard zones. The study then investigates how the potential for ignition occurrence varies with the change of temperature of the hydrogen-air mixture or hydrogen storage. In the case of ignition, pressurised hydrogen releases are likely to ignite and form a jet fire with associated thermal hazards. The circumstances of a delayed ignition or ignited release in an enclosure with limited ventilation can also lead to the occurrence of significant pressure loads. Where possible application of engineering tools and correlations originally developed for hydrogen at ambient temperature is expanded to the field of cryogenic conditions. Otherwise, novel models are proposed and validated to address the knowledge gaps and open issues associated with cryogenic hydrogen behaviour in accidental conditions. More complex incident scenarios may present characteristics that could differ from the assumptions used in reduced models. Thus, computational fluid dynamics (CFD) modelling is also used to investigate and provide insights into the underlying phenomena characterising such incident scenarios.

The focus of the research is posed on the comparison of relevant hazards and consequences magnitude for hydrogen systems at ambient and cryogenic temperatures. To this scope, four representative scenarios are selected with storage pressures of 100 and 350 bar, as maximum pressure indicated in (DOE, 2006), and nozzle diameter of 1 and 2 mm. The final goal is to integrate the models into guidelines for inherently safer design of LH_2 infrastructure and equip stakeholders with tools to perform professionally hydrogen safety engineering.

1. Release and dispersion

1.1. Assessment of hydrogen releases

1.1.1. Steady-state hydrogen releases

The storage pressure for cryo-compressed hydrogen can reach 350 bar for optimum gravimetric performances (DOE, 2006). In case of an unintended leak or release from a pressure relief valve, an under-expanded jet is formed as the pressure at the nozzle is higher than atmospheric. Cirrone et al. (2023b) expanded applicability of the under-expanded jet theory by (Molkov et al., 2009) to cryogenic releases with storage pressure up to 5 bar and temperature down to 46 K. It was shown that the Abel-Noble Equation of State (EoS) well represents cryogenic releases for storage pressures up to 6 bar, whereas the high-accuracy Helmholtz energy formulations (NIST) shall be used for larger pressures. Fig. 1 presents calculations by the under-expanded jet theory in (Molkov et al., 2009), showing that for a given storage pressure (P_s), the calculated mass flow rate significantly increases with the decrease of temperature. As an example, mass flow rate for P_s=5 bar increases from 0.241 g/s at T_s=300 K to 0.597 g/s at T_s=48 K. The variation in mass flow rate is more pronounced for lower temperatures and higher pressures as consequence of the density change in the storage tank.

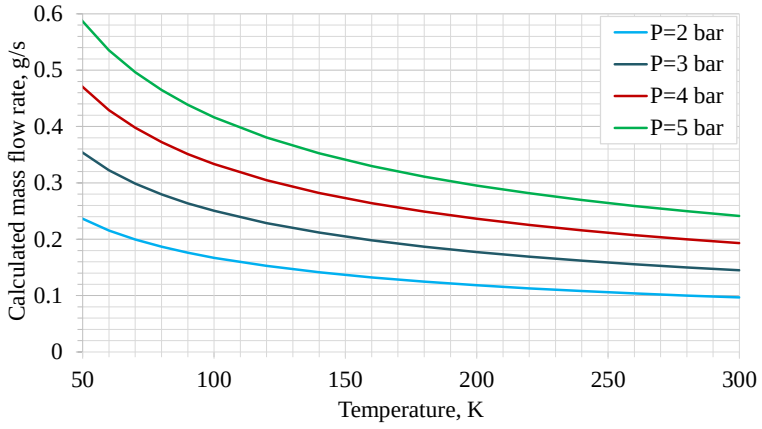

Fig. 1. *Calculated hydrogen mass flow rate as function of storage temperature for P_s=2-5 bar and d=1.0 mm.*

1.1.2. Transient hydrogen releases

A realistic incident scenario may involve a transient release during blowdown of a hydrogen storage. An accurate estimation of the blowdown dynamics is essential to assess the time changing release mass flow rate and characteristics, and thus magnitude and duration of the associated hazards. Heat transfer through a tank wall can play an important role in the model accuracy, especially when dealing with cryogenic hydrogen storages. Furthermore, research in (Cirrone et al., 2022b) highlighted the importance of taking into account heat transfer through a discharge pipe exposed to ambient air to correctly estimate mass flow rate for cryo-compressed hydrogen releases. A non-adiabatic blowdown model taking into account heat transfer through the tank and discharge pipe walls, and NIST EoS was proposed in (Cirrone et al., 2023a). The non-adiabatic blowdown model was seen to well reproduce the storage pressure and temperature dynamics in sixteen tests performed within PRESLHY project at initial pressure 5-200 bar and temperature 80-310 K, through release nozzle diameter of 0.5-4.0 mm. Fig. 2 shows the comparison of calculated storage pressure and temperature dynamics against experimental measurements for the tests at same initial storage pressure P_0=200 bar and release diameter d=1.0 mm, but different initial storage temperature T_0. It is possible to observe that the model well reproduces experiments throughout the blowdown duration. The pressure decay in the hydrogen storage is seen to have a similar behaviour for both ambient and cryogenic tests during the first stage of the release (<10 s). Beyond this time, the cryogenic test presents a slower pressure decay, resulting in a doubled release duration. The temperature dynamics (see Fig. 2, right) presents an initial decrease up to about 8 s due to the tank blowdown. Afterwards, temperature presents a more stable and slower increase due to heat transfer through a tank wall.

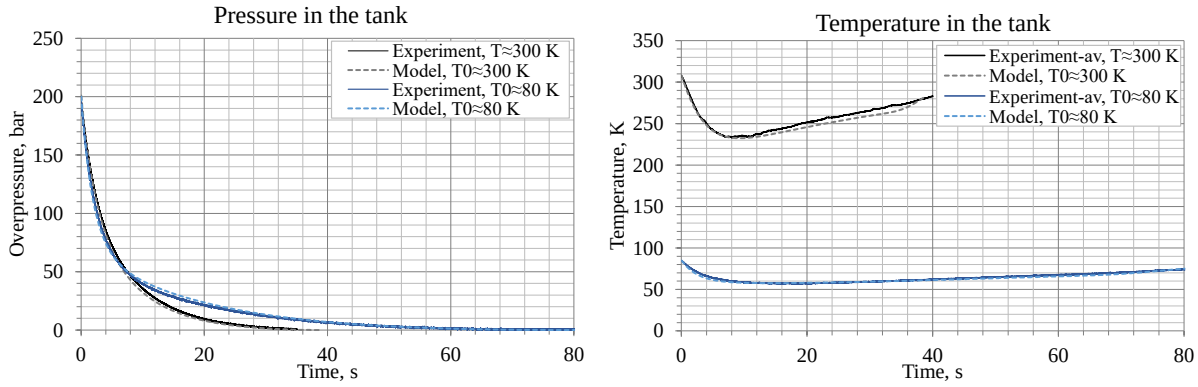

Fig. 2. *Effect of initial hydrogen storage temperature (T_0) on non-adiabatic blowdown dynamics of storage pressure and temperature for P_0≈200 bar and d=1.0 mm: calculations versus experiments.*

1.2. Assessment of hydrogen dispersion

The main hazards associated with hydrogen releases is given by the formation of a flammable cloud that could ignite producing thermal and pressure hazards. The knowledge of the flammable cloud extent is therefore of utmost importance to determine appropriate hazard distances. The similarity law for under-expanded jets allows to calculate axial hydrogen concentration decay in momentum-dominated hydrogen jets (Molkov, 2012):

$$C_{ax} = 5.4\sqrt{\rho_N/\rho_s}\ (d/x),$$

where ρ_N is the density of hydrogen at the nozzle exit (calculated using the under-expanded jet theory discussed in Section 1.1.1), ρ_s is the density of the surrounding air, d is the nozzle diameter and x is the distance from the release point. The similarity law was validated against a wide range of experiments on hydrogen under-expanded jets with storage temperature as low as 50 K, see (Cirrone et al., 2023b; Molkov, 2012). The similarity law can be used to calculate and compare the hazard distances associated with the lower flammability limit (LFL) to assess the extent of the flammable hydrogen-air mixture at different storage temperature. Table 1 reports calculations for the

representative scenarios selected for the consequences comparison. Let us consider a hydrogen storage tank with P_s=100 bar and d=1.0 mm. The hazard distance to the LFL is calculated as 3.7 m for temperature of the storage T_s=300 K, whereas the distance increases to 6.6 m when T_s=80 K. In general, it can be concluded that for a same storage pressure and nozzle diameter, the decrease of hydrogen temperature from ambient to cryogenic leads to longer hazard distances associated to unignited hydrogen releases. The engineering tool used for calculations in Table 1 is available on the e-Laboratory of Hydrogen Safety platform developed within Net-Tools and expanded during HyResponder (https://elab.hysafer.ulster.ac.uk/).

***Table 1**. Comparison of hazard distances to LFL for hydrogen releases at ambient and cryogenic temperature*

Case	P_s, bar	d, mm	Hazard distance to LFL, m	
			T_s=80 K	T_s=300 K
1	100	1.0	6.6	3.7
2	100	2.0	13.3	7.5
3	350	1.0	10.1	6.5
4	350	2.0	20.2	12.9

The similarity law proved to be an accurate tool to rapidly assess a hydrogen jet concentration decay. More complex scenarios may present different characteristics from the tool assumptions, e.g. impinging jets, releases in a confined space, etc. Thus, a CFD approach is developed to model cryogenic hydrogen releases and complement the similarity law engineering tool.

1.2.1. A CFD approach for modelling cryogenic hydrogen unignited releases

The CFD model is based on a Reynolds-averaged Navier–Stokes (RANS) approach with realizable κ-ε model for simulating the turbulent hydrogen jet. To validate the proposed CFD model, simulations were compared to experiments conducted at the Sandia National Laboratories (Hecht and Panda, 2019). The five experimental tests selected for the CFD model validation have storage temperature included in the range 51-61 K, storage pressure up to 5 bar abs, and nozzle diameter in the range 1.0-1.25 mm (see Table 2). The steady state hydrogen release source in simulations is modelled as a notional nozzle with conditions calculated through the under-expanded jet theory by (Molkov et al., 2009), since it was seen to well reproduce the mass flow rate in cryogenic hydrogen releases. Table 2 shows the temperature, velocity and diameter of the notional nozzle used as input to computations.

***Table 2**. Experimental tests selected for the validation of the CFD approach with notional nozzle parameters used as input to numerical simulations*

Test	Nozzle d, mm	Exp. mass flow rate, g/s	Storage		Notional Nozzle		
			P, bar	T, K	T, K	u, m/s	d, mm
1	1	0.334	3	56	46.67	519.09	1.25
2	1	0.585	5	50	41.67	490.49	1.61
3	1.25	0.334	2	61	50.83	541.76	1.27
4	1.25	0.546	3	51	42.5	495.37	1.56
5	1.25	0.706	4	54	45	509.73	1.80

The numerical domain reproduces the experimental set-up including a hood for the extraction of the combustion fumes with velocity calculated to be in the range 2-8 m/s. The hexahedral domain is rectangular with size 1.2 m x 1.2 m x 2.0 m. Given the symmetry of the problem, only a quarter of the domain was considered to reduce calculation time. The cell size varied from the notional nozzle size to about 10 cm in the far field. Ansys Fluent is used as a platform for numerical simulations.

Results and discussion

Results of numerical simulations performed for the tests described in Table 2 were compared to experimental measurements on hydrogen distribution along the jet axis and radius. Fig. 3 shows that

numerical simulations for Test N.3 (T_s=61K, P_s=2 bar and d=1.25 mm) well reproduce experimental measurements along the entire jet axis. Numerical simulations were performed for the minimum and maximum co-flow velocity of the experimental range v=2-8 m/s, finding that results were not affected by the variation of co-flow velocity (Fig. 3, left). The distributions of hydrogen concentration and temperature normalised to the centreline along the radial distance normalised to the axial distance for Test N.3 are shown in Fig. 4. The comparison confirms the capability of the CFD model to capture the hydrogen and temperature distribution throughout the cryogenic hydrogen jet. Overall, the developed CFD approach is found to well agree with the experimental measurements of hydrogen axial concentration for all the set of tests with accuracy within ±10%. An exception is given by test N.1 where the maximum relative difference between simulated hydrogen concentration and the more unstable experimental measurements was recorded to be 13.6%.

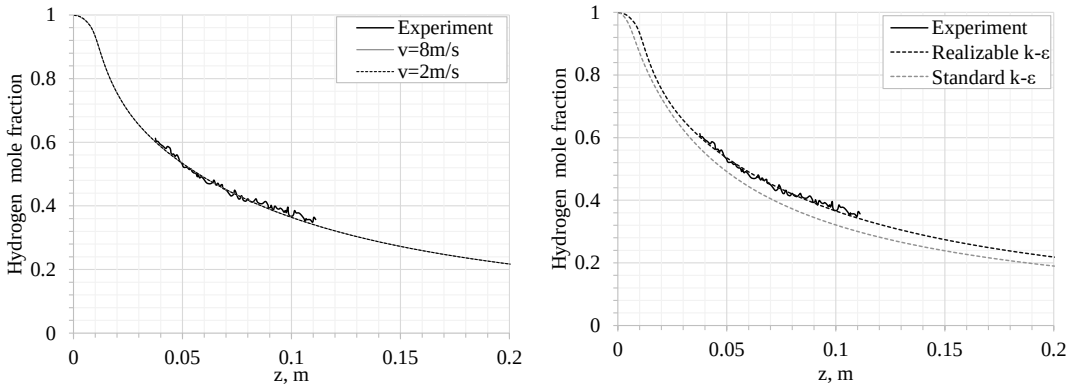

Fig. 3. *Results of CFD simulations versus experimental data for cryo-compressed hydrogen releases: hydrogen concentration along the jet axis for the Test N.3 with T_s=61 K, P_s=2 bar and d=1.25 mm.*

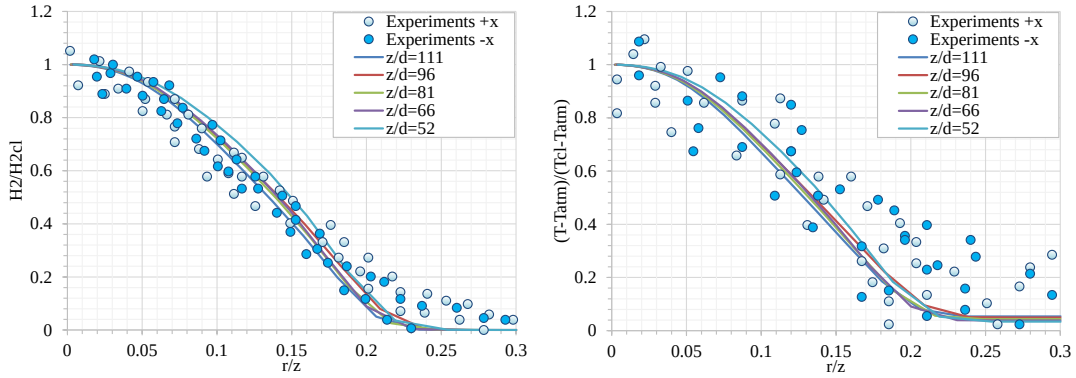

Fig. 4. *Results of CFD simulations versus experimental data for cryo-compressed hydrogen releases: normalised hydrogen concentration (left) and temperature (right) on the normalized radial distance for the Test N.3 with T_s=61 K, P_s=2 bar and d=1.25 mm.*

Further analyses are performed to assess the effect of numerical features of the CFD model on simulation results. Fig. 3 (right) compares the hydrogen axial distributions simulated by the realizable κ-ε and standard κ-ε turbulence sub-models. Simulation results are affected by the turbulence sub-model and the effect increases with distance from the release nozzle. Realizable κ-ε is observed to better predict the hydrogen concentration distribution, confirming the improved capability of such turbulence model to reproduce axisymmetric jets (ANSYS Inc, 2016).

2. Ignition

Ignition and combustion of hydrogen in air is considered more hazardous compared to other fuels due to the lower minimum ignition energy (MIE) and the wider flammability range. This section aims at analysing the effect of cryogenic initial temperature on the MIE and thus ignition potential of the

hydrogen-air mixture. The theoretical model developed in (Cirrone et al., 2023) allows to calculate the MIE in hydrogen mixtures with air for arbitrary concentration and temperature as follows:

$$E_{min} = \frac{1}{6}\pi d^3 \rho_u c_{p,u}(T_b - T_u).$$

where d is the critical flame kernel diameter, ρ_u is the density, $c_{p,u}$ the specific heat at constant pressure, T_u is the temperature for the unburnt mixture and T_b is the temperature of the burnt mixture. The theoretical model does not rely on experimental measurements for the critical kernel diameter, but this is estimated as $d = 2.5\delta_L$, with δ_L being the laminar flame thickness. The definition by Blint (Poinsot and Veynante, 2005) is used to assess the laminar flame thickness and requires the calculation of the laminar burning velocity S_u. To avoid any dependence on experimental data availability, S_u is calculated using Chemkin software or correlations, and accounts for effect of flame stretch and preferential diffusion, as the latter were found to have a strong effect in lean hydrogen-air mixtures. The model was validated in (Cirrone et al., 2023) against experimental tests for hydrogen mixtures with in air at temperature in the range 123-298 K. The theoretical model is applied to assess the MIE curve for variable hydrogen concentration in air and temperature. Results of calculations are shown in Fig. 5. Theoretical MIE for *T*=298 K is evaluated as 13 μJ for the stoichiometric mixture, which conservatively reproduces experimentally measured 17 μJ. As expected, MIE increases with the decrease of temperature to 43 μJ at *T*=173 K and 108 μJ at *T*=123 K for the near to stoichiometric mixtures. The largest increase of MIE with the decrease of temperature is observed for the leaner hydrogen-air mixtures. However, it should be highlighted that cryogenic lean-hydrogen mixtures could be more affected by flame instabilities associated with the flame stretch and preferential diffusion, which could result in a more conservative assessment of MIE.

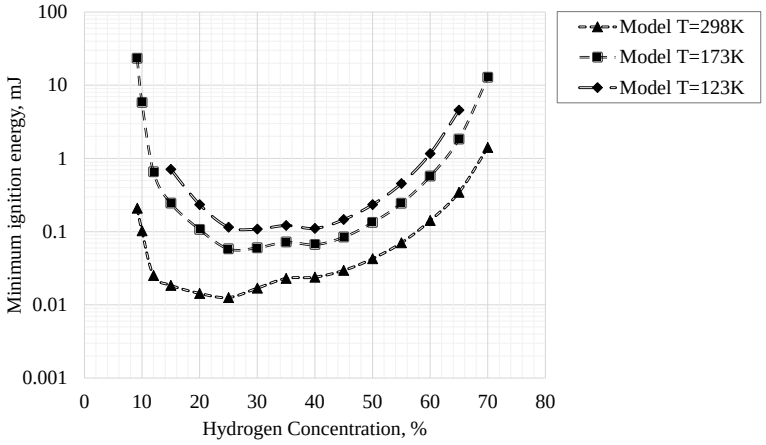

Fig. 5. *Theoretical evaluations of MIE for hydrogen-air mixtures at temperature 298 K, 172 K and 123 K.*

A CFD approach has been developed to complement the theoretical model developed in (Cirrone et al., 2023) and investigate the occurrence of larger flame instabilities for leaner hydrogen-air mixtures at cryogenic temperature, as hinted via the theoretical modelling. The CFD model employs detailed chemical mechanisms employing 13 chemical species and 37-step reduced chemical reactions. Fig. 6 (left) shows the flame kernel development for a stoichiometric hydrogen-air mixture at T=288 K and numerically calculated *MIE*=15 μJ, which well estimates experimental *MIE*=17 μJ. It is possible to observe that at 45 μs the high temperature zone is mainly located in the spark channel, while it starts to expand and develop at 100 μs as signalled by the more pronounced presence of hydroxyl (OH) radical. Fig. 6 (right) shows the flame kernel development for a stoichiometric hydrogen-air mixture at *T*=173 K and numerically calculated *MIE*=30 μJ. The flame kernel spherical expansion has a trend similar to ambient temperature hydrogen-air mixtures. However, it is possible to observe the appearance of disturbances of the flame front that could indicate the enhancement of flame instabilities for cryogenic hydrogen-air mixtures, confirming the observations drawn via the theoretical modelling and explaining the lower MIE calculated via numerical simulations.

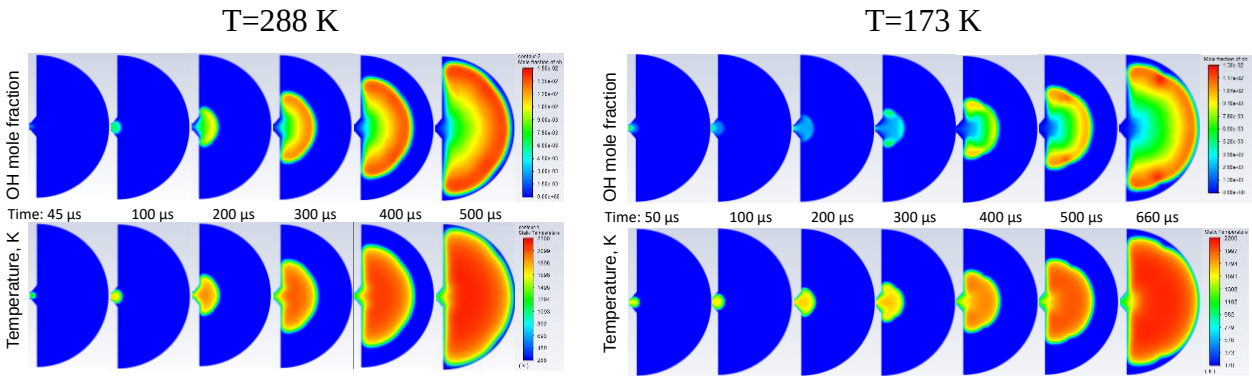

Fig. 6. *Flame kernel growth for T=288 K, H_2=30% by vol. in air, MIE=15 µJ (left) and for T=173 K, H_2=30% by vol. in air, MIE=30 µJ (right).*

Another potential ignition mechanism relevant for sudden releases of cryogenic hydrogen is the so-called "diffusion ignition" mechanism. The numerical research in (Cirrone et al., 2022c) assessed the effect of hydrogen storage temperature decrease from 300 K to 80 K by using a CFD model previously validated against ambient temperature tests. The analysed release system was represented by a T-shaped channel system where the cryo-compressed hydrogen was initially separated from the air by an inertial burst disk (diaphragm). The numerical research found that the pressure limit leading to spontaneous ignition increased from 2.9 MPa to 9.4 MPa when hydrogen temperature decreased from 300 K to 80 K. Thus, cryogenic hydrogen presents a minor potential than hydrogen at ambient temperature to trigger by diffusion ignition mechanism for the selected system configuration.

3. Combustion

Unintended hydrogen releases are likely to ignite and produce a jet fire leading to harmful conditions in its surroundings. Thermal hazards of a jet fire include the flame length itself, the presence of high temperature combustion products, elevated thermal radiative heat fluxes and thermal dose.

3.1. Assessment of potential thermal hazards

The dimensionless correlation for hydrogen jet flames in (Molkov, 2012) allows to calculate the flame length knowing the storage conditions and release nozzle diameter. The correlation was originally validated against ambient temperature releases and validation range was expanded to cryogenic hydrogen jet fires in (Cirrone et al., 2023b). Table 3 compares the calculated flame length for the example scenarios selected for the study. It is possible to observe that for a given storage pressure and release nozzle diameter, the decrease of storage temperature leads to longer hydrogen flame lengths L_f. Longer flames lead also to longer "no harm" distances along the jet axis corresponding to the temperature of 70°C for any exposure duration (LaChance, 2010), which is calculated as $3.5L_f$. The engineering tool used for calculations in Table 3 is available on the e-Laboratory of Hydrogen Safety platform (https://elab.hysafer.ulster.ac.uk/).

Table 3*. Comparison of calculated flame lengths and "no harm" hazard distance by temperature for hydrogen jet fires at ambient and cryogenic temperature*

Case	P_s, bar	d, mm	Flame length, m		"No harm" distance, m	
			T_s=80 K	T_s=300 K	T_s=80 K	T_s=300 K
1	100	1.0	2.6	1.5	9.3	5.4
2	100	2.0	5.3	3.1	18.5	10.8
3	350	1.0	3.9	2.6	13.7	9.0
4	350	2.0	7.8	5.2	27.4	18.0

Hazard distances along the jet axis defined by temperature may be shorter for horizontal hydrogen jet fires in comparison to vertical jets. CFD study in (Cirrone et al., 2022b) observed a positive effect of buoyancy on rising up of combustion products and thus reduction of hazard distances defined by temperature criteria for horizontal jets. Nevertheless, hazard distances defined by thermal radiation resulted to be longer to those defined by temperature. Thus, it is important that all harm criteria modes are considered for a thorough assessment of hazard distances. Numerical models to assess thermal hazards by radiative heat flux were validated in (Cirrone et al., 2022b; Cirrone et al., 2018).

3.1.1. An analytical approach to assess radiative heat flux from cryogenic hydrogen jet fires

Despite the great accuracy achieved by the numerical models, reduced tools for the estimation of thermal radiation are needed to overcome the calculation time and complexity required by CFD applications. An analytical model is proposed here for the assessment of the radiative heat flux in the surroundings of hydrogen jet fires from vertical and horizontal releases of hydrogen at ambient and cryogenic temperature. The analytical approach is based on the weighted multi source flame radiation model developed by (Hankinson and Lowesmith, 2012) and further expanded by (Ekoto et al., 2014). The model is hereby adapted to include evaluation of flame length and width through the dimensionless correlation in (Molkov, 2012). The radiative heat flux prediction at a given location requires evaluation of the radiant fraction χ according to (Molina et al., 2007):

$$q = \frac{VF}{A_f} \cdot S \cdot \tau \,, \qquad \text{with} \quad S = \chi \cdot \dot{m} \cdot \Delta H_c,$$

where *VF* is the flame view factor, A_f is the surface of the flame, τ is the atmospheric transmissivity, *S* is the surface emissive power, ΔH_c is the gas heat of combustion ($\Delta H_{c,H2O} = -119\ MJ\ /kg$) and $\dot{m}$ is the mass flow rate of hydrogen calculated as per the under-expanded jet theory mentioned in Section 1.1.1. The weighted multi source model in (Hankinson and Lowesmith, 2012) consists in the decomposition of the jet flame axis in N emitting points having a different contribution on the final balance of the heat flux. In the current model, the weighting of the points assumes a linear increase of source emitter contribution if located between the point of release and $0.6L_f$, corresponding to the flame maximum temperature as per the experimental data gathered in (Molkov, 2012), and a linear decrease if the point is located in the remaining part of the jet flame axis. Experiments on cryogenic hydrogen jet fires by (Breitung et al., 2009; Panda and Hecht, 2017) are used for validation of the extended analytical model. The experimental tests have storage pressure within the range 2-20 bar and storage temperature in the range 48-290 K.

Results and discussion

The analytical model results are compared against the radiative heat flux measurements on the side of jet fires up to a distance of 1.25 m. Here only results for five out of the nine tests selected for the CFD model validation are reported. Fig. 7 shows that the modelled radiative heat flux well predicts the experimental radiative heat flux measured in SNL tests (Panda and Hecht, 2017) in the first portion of the jet fire. Measurement at the furthest sensor from the release point is generally unpredicted. The furthers sensor coordinate is approximately the same of the flame length and given that it is very close to the jet axis (0.2 m), it may lead to an inaccurate view factor estimation when the weighted multi source model is applied. The overestimation of the maximum experimental radiative heat flux for Test 4 is due to the absence of modelling of the hood extracting combustion products at a given velocity. This effect is proven by CFD modelling previously validated against SNL experiments in (Cirrone et al., 2018) for hood velocity equal to 0 m/s, which well reproduces the maximum calculated by the engineering tool.

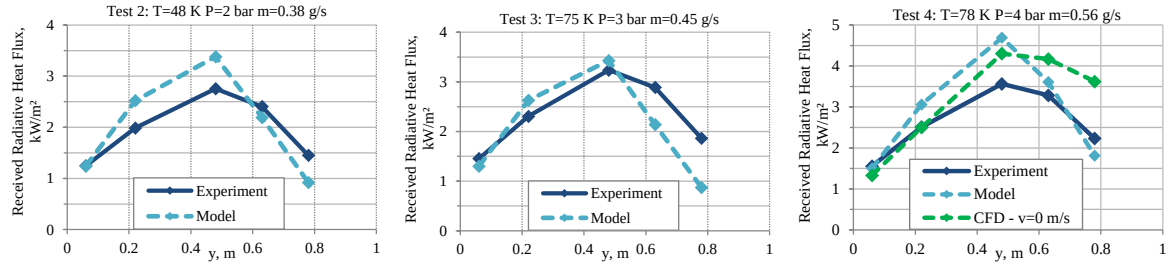

Fig. 7. *Validation of the model: calculated versus experimental radiative heat flux for SNL Tests 2-4.*

Fig. 8 shows the comparison of analytical calculations of radiative heat flux against measurements from two of the five tests carried out by Breitung et al. (2009) on jet fires with ambient and cryogenic storage temperature. Nine sensors were located on three lines parallel to the jet axis at distances *z*=50, 75 and 125 cm. Experiments are well reproduced by the engineering tool, whereas other tests presented a conservative estimation possibly due to overestimation of flame length up to about 20%.

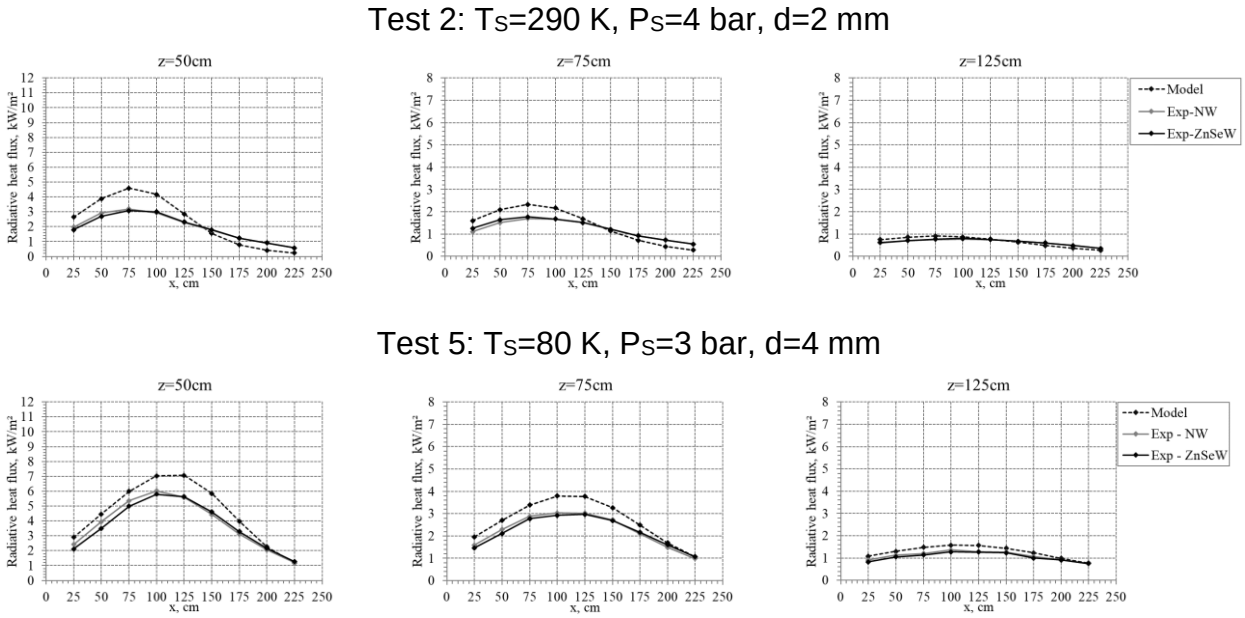

Fig. 8. *Validation of the model: calculated versus experimental radiative heat flux for KIT Tests 2 and 5.*

3.2. Assessment of potential pressure hazards

The delayed ignition of under-expanded hydrogen jets may generate strong overpressures that could harm people or damage properties. Authors in (Cirrone et al., 2022a) found that a unique conservative correlation can be used to assess the generated overpressure for both ambient and cryogenic hydrogen jets by knowing only the storage pressure, temperature and release nozzle diameter. The correlation is used to assess hazard distances according to the typical harm criteria outlined in (Cirrone et al., 2022a) and results for the example scenarios at different storage temperature are compared in Table 4. Cryogenic releases generally result in larger hazard distances and the effect of storage temperature on the calculated hazard distances increase with the storage pressure and nozzle diameter.

Table 4*. Comparison of calculated hazard distances from the release nozzle for delayed ignition of hydrogen releases at ambient and cryogenic temperature*

Case	P_s, bar	d, mm	"No harm" distance, m		Injury distance, m		Fatality distance, m	
			T_s=80 K	T_s=300 K	T_s=80 K	T_s=300 K	T_s=80 K	T_s=300 K
1	100	1.0	3.1	3.1	1.1	1.1	0.7	0.7
2	100	2.0	6.7	6.2	2.7	2.2	1.8	1.3
3	350	1.0	4.7	4.4	2.0	1.7	1.4	1.0
4	350	2.0	9.4	8.7	4.0	3.3	2.8	2.1

In the event of a hydrogen release in an enclosure with limited ventilation, the produced pressure dynamics may present a distinctive peak exceeding the steady-steady pressure level. This event is defined as pressure peaking phenomenon and increases in magnitude for ignited hydrogen releases. The main parameters affecting the pressure peak are the hydrogen release rate, enclosure volume and vent dimensions. The numerical assessment in (Cirrone et al., 2022) investigated the effect of hydrogen storage temperature on the overpressure dynamics in the enclosure. It was observed that for a same storage pressure, the pressure peaking phenomenon for cryogenic hydrogen releases is more pronounced than for ambient temperature releases producing a twice larger overpressure peak due to the larger mass flow rate released.

3.3. Hazards associated to BLEVE of LH_2 storage systems

Liquid hydrogen tanks are generally equipped with pressure relief device (PRD) which are aimed at venting the stored hydrogen and avoiding pressure build-up in incidental conditions, such as presence of a surrounding fire. In case of a PRD failure or loss of the tank structural integrity, the hydrogen storage tank may fail with consequent blast wave, fireball and projectiles, as per catastrophic rupture of high-pressure hydrogen storage tanks at ambient temperature (Molkov et al., 2021). Numerical investigations in (Cirrone et al., 2023c) and analysis of BMW experimental tests concluded that the maximum blast wave overpressure is mainly produced by the gaseous phase. Combustion energy was observed to contribute to the strength of the blast wave. The pressure peak associated to the boiling liquid expanding vapour explosion (BLEVE) was found to have a smaller magnitude and to follow the peak associated to the gaseous phase.

4. Conclusions

The significance of this research is given by the provision of models and tools that can be used to close relevant knowledge gaps for hydrogen safety engineering of LH_2 systems and infrastructure. Analytical studies and CFD modelling are used complementarily to assess the hazards and calculate hazard distances for relevant incident scenarios involving hydrogen release and dispersion, ignition, and combustion.

The rigour of the research is established by the thorough validation of models against experiments from literature and the PRESLHY project (www.preslhy.eu). It is observed that the similarity law for hydrogen concentration decay in momentum-dominated jets, the dimensionless correlation and numerical models for hydrogen jet flames for ambient temperature releases are also applicable to determine hazard distances for cryogenic jets. The originality of the study is given by the development of novel models where found to be missing to obtain a systematic analysis of the relevant hazards.

The developed models are used synergistically to assess selected incident scenarios starting from an initiating event to compare the consequences and hazard distances for hydrogen systems at ambient and cryogenic temperature. It is observed that for a same storage pressure and nozzle diameter, the decrease of temperature in the hydrogen storage from ambient to cryogenic 80 K may lead to longer hazard distances associated to unignited and ignited hydrogen releases. Both analytical and numerical modelling show a slight increase of minimum ignition energy for decreasing temperature of the hydrogen-air mixture, confirming the trend observed in experiments.

CFD modelling is further used to give insights into those phenomena with limited availability of experimental data and knowledge for cryogenic hydrogen applications. The results of BLEVE rethinking allowed to understand and explain the pressure dynamics created by LH_2 vessels rupture in a fire using experimental data from literature.

Acknowledgements

This research has received funding from the Fuel Cells and Hydrogen 2 Joint Undertaking (now Clean Hydrogen Partnership) under the European Union's Horizon 2020 research and innovation programme under grant agreement No. 779613 (PRESLHY), No.736648 (NET-Tools) and No.

101101381 (ELVHYS). ELVHYS project is supported by the Clean Hydrogen Partnership (CHP) and its members. University of Ulster in Horizon Europe Project ELVHYS is supported by UKRI grant number 10063519. Funded by the European Union. Views and opinions expressed are however those of the authors only and do not necessarily reflect those of the European Union or the CHP. Neither the European Union nor the CHP can be held responsible for them.

References

ANSYS Inc, 2016. ANSYS Fluent - Theory guide.

Breitung, W., Stern, G., Veser, A., Friedrich, A., Kutznetsov, M., Fast, G., Oechsler, B., Kotchourko, N., Travis, J.R., Xiao, J., Schwall, M., Rottenecker, M., 2009. Final Report:Experimental and theoretical investigations of sonic hydrogen discharge and jet flames from small breaks, KIT / Research Center Karlsruhe.

Cirrone, Donatella, Makarov, D., Friedrich, A., Grune, J., Takeno, K., Molkov, V., 2022a. Blast Wave Generated by Delayed Ignition of Under-Expanded Hydrogen Free Jet at Ambient and Cryogenic Temperatures 433–449.

Cirrone, Donatella, Makarov, D., Kashkarov, S., Friedrich, A., Molkov, V., 2023a. Physical model of non-adiabatic blowdown of cryo-compressed hydrogen storage tanks. Int. J. Hydrogen Energy. https://doi.org/10.1016/j.ijhydene.2023.05.182

Cirrone, Donatella, Makarov, D., Kuznetsov, M., Friedrich, A., Molkov, V., 2022b. Effect of heat transfer through the release pipe on simulations of cryogenic hydrogen jet fires and hazard distances. Int. J. Hydrogen Energy 47, 21596–21611. https://doi.org/10.1016/j.ijhydene.2022.04.276

Cirrone, D., Makarov, D., Lach, A.W., Gaathaug, A.V., Molkov, V., 2022. The pressure peaking phenomenon for ignited under-expanded hydrogen jets in the storage enclosure: experiments and simulations for release rates of up to 11.5 g/s. Energies 15, 1–20.

Cirrone, Donatella, Makarov, D., Molkov, V., 2023b. Safety of liquid and cryo-compressed hydrogen: overview of physical and CFD models developed at Ulster University. Chem. Eng. Trans. 105, 55–60. https://doi.org/10.3303/CET23105010

Cirrone, Donatella, Makarov, D., Molkov, V., 2023c. Rethinking "BLEVE explosion" after liquid hydrogen storage tank rupture in a fire. Int. J. Hydrogen Energy 48, 8716–8730. https://doi.org/10.1016/j.ijhydene.2022.09.114

Cirrone, Donatella, Makarov, D., Molkov, V., 2022c. Spontaneous ignition of cryo-compressed hydrogen in a T-shaped channel system. Hydrogen 3, 348–360. https://doi.org/10.3390/hydrogen3030021

Cirrone, D, Makarov, D., Proust, C., Molkov, V., 2023. Minimum ignition energy of hydrogen-air mixtures at ambient and cryogenic temperatures. Int. J. Hydrogen Energy 1–15. https://doi.org/10.1016/j.ijhydene.2023.01.115

Cirrone, D.M.C., Makarov, D., Molkov, V., 2018. Thermal radiation from cryogenic hydrogen jet fires. Int. J. Hydrogen Energy 44, 8874–8885. https://doi.org/10.1016/j.ijhydene.2018.08.107

DOE, 2006. Technical Assessment: Cryo-Compressed Hydrogen Storage for Vehicular Applications.

Ekoto, I.W., Ruggles, A.J., Creitz, L.W., Li, J.X., 2014. Updated jet flame radiation modeling with buoyancy corrections. Int. J. Hydrogen Energy 39, 20570–20577. https://doi.org/10.1016/j.ijhydene.2014.03.235

Hankinson, G., Lowesmith, B.J., 2012. A consideration of methods of determining the radiative characteristics of jet fires. Combust. Flame 159, 1165–1177. https://doi.org/10.1016/j.combustflame.2011.09.004

Hecht, E.S., Panda, P.P., 2019. Mixing and warming of cryogenic hydrogen releases. Int. J. Hydrogen Energy 44, 8960–8970. https://doi.org/10.1016/j.ijhydene.2018.07.058

LaChance, J.L., 2010. Progress in risk assessment methodologies for emerging hydrogen applications, in: Sixth International Short Course and Advanced Research Workshop "Progress

in Hydrogen Safety – Regulations, Codes and Standards." Belfast, Northern Ireland, UK.

Molina, A., Schefer, R.W., Houf, W.G., 2007. Radiative fraction and optical thickness in large-scale hydrogen-jet fires. Proc. Combust. Inst. 31 II, 2565–2572. https://doi.org/10.1016/j.proci.2006.08.060

Molkov, V., 2012. Fundamentals of Hydrogen Safety Engineering I.

Molkov, V., Makarov, V., Bragin, M. V., 2009. Physics and modelling of underexpanded jets and hydrogen dispersion in atmosphere. Phys. Extrem. States Matter 146–149.

Molkov, V. V., Cirrone, D.M.C., Shentsov, V. V., Dery, W., Kim, W., Makarov, D. V., 2021. Dynamics of blast wave and fireball after hydrogen tank rupture in a fire in the open atmosphere. Int. J. Hydrogen Energy 46, 4644–4665. https://doi.org/10.1016/j.ijhydene.2020.10.211

Panda, P.P., Hecht, E.S., 2017. Ignition and flame characteristics of cryogenic hydrogen releases. Int. J. Hydrogen Energy 42, 775–785. https://doi.org/10.1016/j.ijhydene.2016.08.051

Poinsot, T., Veynante, D., 2005. Theoretical and Numerical Combustion, Second Edition, Second. ed, Decision Support Systems. R.T. Edwards, Inc., P.O., Philadelphia, PA, USA. https://doi.org/10.1016/j.dss.2003.08.004

Explosion and Ignition behaviour of NH_3/H_2 mixtures

Dieter Gabel [a], Danny Regler [a] & Ulrich Krause [a]

[a] [l]Otto-von-Guericke University, Magdeburg, Germany

E-mail: dieter.gabel@ovgu.de

Abstract

Ammonia is one of the possible future energy carriers for transporting (green) hydrogen or it will be used as fuel directly. In both cases mixtures of NH_3 and H_2 in air can occur during normal operation or accidental release. To ensure the uphold of the explosion protection principles the explosion and ignition behavior of such mixtures need to be known.

In this project the ignition limits and explosions characteristics of mixtures of Ammonia and Hydrogen in air were systematically determined in the 20-l-sphere. Unlike the standard procedure (DIN EN 1839) all measurements were conducted in a closed vessel, recording the time sequence of the pressure rise.

The advantage of the closed setup is that in all cases a release of Ammonia into the environment can be avoided. Therefore, the operation procedure was adapted in a way that mixtures that could not be ignited were forced to react in a second step. This is possible by either adding addition fuel or Oxygen (air) and force an ignition before releasing the exhaust gases.

The aim of the project is to finally get a complete triangle diagram für NH_3/H_2/Air, not only showing the ignition limits but the explosions pressures and pressure rise velocities in the ignitable region, too.

Additionally, the 20-l-sphere enables to test for different conditions and ignition sources. Besides the quiescent mixture with electrical spark ignition test in turbulent mode will follow, comparable to the dust explosion standard (DIN EN 14034). In addition, the influence of the ignition source is will be tested by applying pyrotechnical igniters with 2 kJ and 10 kJ.

Starting with the pure substances, first the LELs were determined and found be comparable to the standard concentration. Next, all combinations along the non-ignition line were measured in steps of 1% until the LEL of NH_3 and H_2 were reached. Additional points inside the explosion region were measured as well to get an insight of the development of the explosion pressure and the pressure rise velocity. Next, the region of the UEL of the mixtures will be tested, if the suggested procedure holds to be sufficiently safe.

Keywords: *Ammonia, Hydrogen, ignition, explosion, LEL, UEL*

Introduction

In 2021, Germany committed to become greenhouse gas neutral by 2045 by reducing greenhouse gas emissions and offsetting the remaining emissions through appropriate sinks. The use of renewable electricity plays a crucial role because it offers high potential for avoiding GHG emissions. (Riemer, 2022)

Green hydrogen, which is produced from renewable electricity through electrolysis, is viewed as a key technology worldwide. Due to limited production potential in Europe, some green hydrogen will probably have to be imported, especially from sunny and windy regions outside Europe.

However, transporting hydrogen is challenging due to its physical properties. Therefore, various carrier media for hydrogen transport are being discussed. (Riemer, 2022)

Ammonia is a suitable hydrogen carrier because it does not contain carbon and can be stored comparatively easily due to its low vapor pressure of 8.58 bar at 20°C. (Nigbur, 2021)

However, using ammonia as a hydrogen carrier implies special risks. Ammonia is known for its toxic, corrosive and potentially explosive properties, which can pose significant risks to both human health and the environment. (TRAS110, 2021) In addition, the risks of Ammonia-Hydrogen-Air mixtures have so far been little investigated.

This work examines the explosion dangers of ammonia as a hydrogen carrier. A modified test stand was set up to enable a safe investigation of ammonia-hydrogen-air mixtures and safety-relevant key figures will be determined.

1. Ammonia and its safety properties

Ammonia is the second most commonly produced inorganic chemical worldwide (Nigbur, 2021) and is one of the seven basic chemicals from which numerous products are made. (Riemer, 2022)

It consists of one nitrogen and three hydrogen atoms and is formed according to the following formula:

$$3H_2 + N_2 \rightarrow 2NH_3$$

At ambient temperature and atmospheric pressure, it exists as an acutely toxic gas with a pungent odor. Ammonia has a variety of advantages over pure hydrogen and others chemical hydrogen storage possibilities. In contrast to many other chemical hydrogen storage ways, ammonia does not contain Carbon because the hydrogen atoms are bound to nitrogen. Consequently, no carbon dioxide is produced during the reverse reaction. Thus, ammonia has the potential for CO_2 neutral hydrogen transport. (Riemer, 2022)

Ammonia is not only much easier to liquefy than hydrogen, but in liquid form it contains 1.7 times the number of hydrogen atoms per cubic meter than liquid hydrogen. It is also significantly more difficult to ignite. (Riemer, 2022)

A comparison of the properties is shown in Table 1.

Table 1. Comparison of properties of Ammonia and Hydrogen (Chemsafe/ GisChem)

Property	Ammonia	Hydrogen
Minimum ignition energy	14 mJ	0.017 mJ
Melting point	-77.7 °C	-259 °C
Boiling point	-33 °C	-253 °C
Ignition temperature	630 °C	560 °C
Lower explosion limit	15.4% by volume	4% by volume
upper explosion limit	33.6% by volume	77% by volume
Density	0.771 kg/m3	0.090 kg/m3
Density ratio to air	0.6	0.07

Furthermore, ammonia has already been extensively researched and has been produced and transported for decades. This means that appropriate infrastructures are already in place and simply need to be expanded. There are also tried-and-tested handling procedures and safety regulations for ammonia.

The newly built LNG infrastructure can also be converted for ammonia. A respective project is already planned for the LNG terminal in Brunsbüttel that could be switched to Ammonia. (Riemer, 2022)

1.1. Safety measures

In Germany, plants in which ammonia is produced and processed are subject to strict regulations. These include technical tightness requirements to prevent ammonia leakage, as well as the installation of technical ventilation and gas measuring and warning devices. Likewise, fault and warning signals must be forwarded automatically and emergency measures triggered.

Ignition sources are strictly prohibited in the system area, including smoking, open flames and sparks from impact and friction. Work that poses a potential risk of ignition, e.g. welding, requires written approval.

It must be ensured that water sprinkling is possible using a sprinkler system, as water binds ammonia and can thus reduce the danger area. (Kojima, 2024) Contaminated water should be collected as it has a severe impact on the environment. Direct jets of water should not be directed at ammonia leaks because ammonia reacts with water in an exothermic reaction that results in a highly alkaline and corrosive liquid.

1.2. Existing literature of explosion characteristics

The search for existing studies on the explosion range of ammonia-hydrogen-air mixtures shows that this has so far been little researched. In contrast, the explosion ranges of the individual Ammonia-Air and Hydrogen-Air mixtures have been widely studied in detail. The explosions range is given in ternary diagrams created with data from Molnárné (2003) and shown in Figure 1.

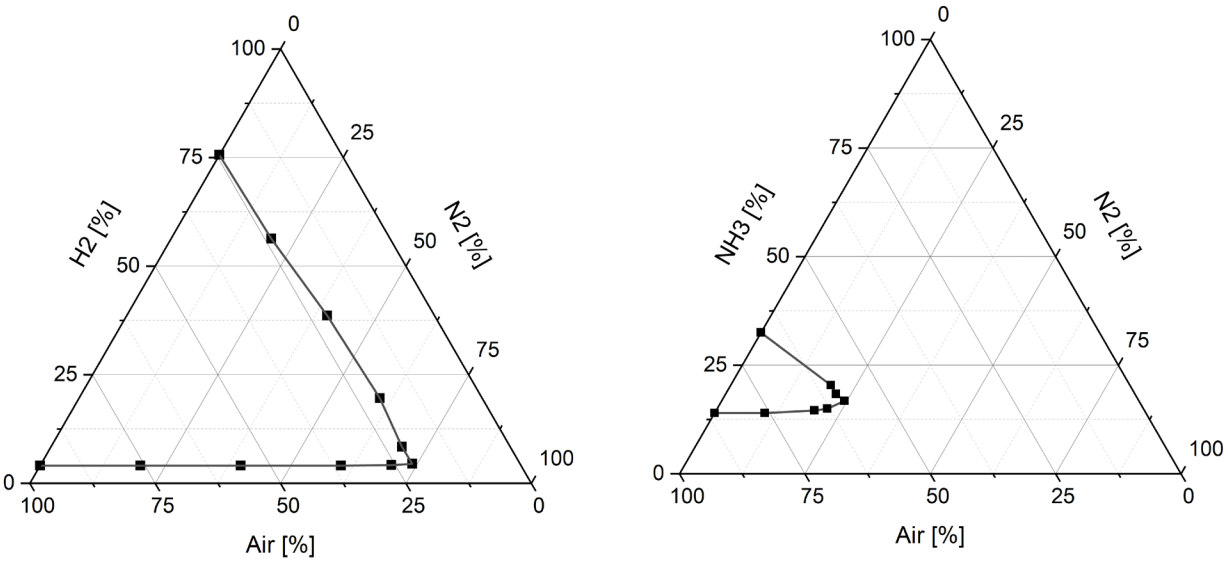

Fig. 1. *Explosion rages of H_2(left) and NH_3(right) in Air*

During the research, two studies were found that depict the entire explosion or ignition range of ammonia-hydrogen-air mixtures.

In 1926, Jorisson and Ongkiehong (Jorissen,1926) published their studies on the explosion limits of Ammonia-Hydrogen-Oxygen and Ammonia-Hydrogen-Aixygen. Their results are shown in Figures 2 and 3.

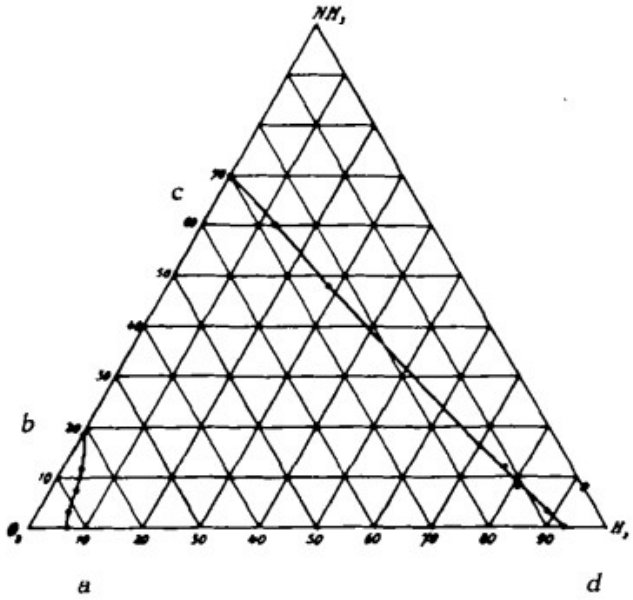

Fig. 2. *Explosions range of Ammonia/Hydrogen/Oxygen mixtures (Jorissen,1926)*

Furthermore, the lower ignition range was shown as a function of the Ammonia concentration. (Ciccarelli, 2005) The LEL is depicted in Figure 4. An illustration of the entire ignition range depending on the concentration of the individual components was not given.

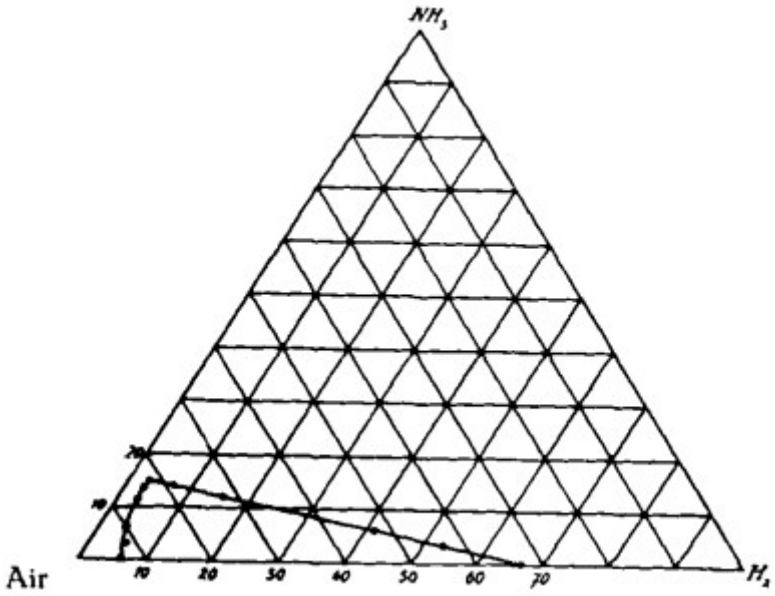

Fig. 3. *Explosions range of Ammonia/Hydrogen/Air mixtures (Jorissen,1926)*

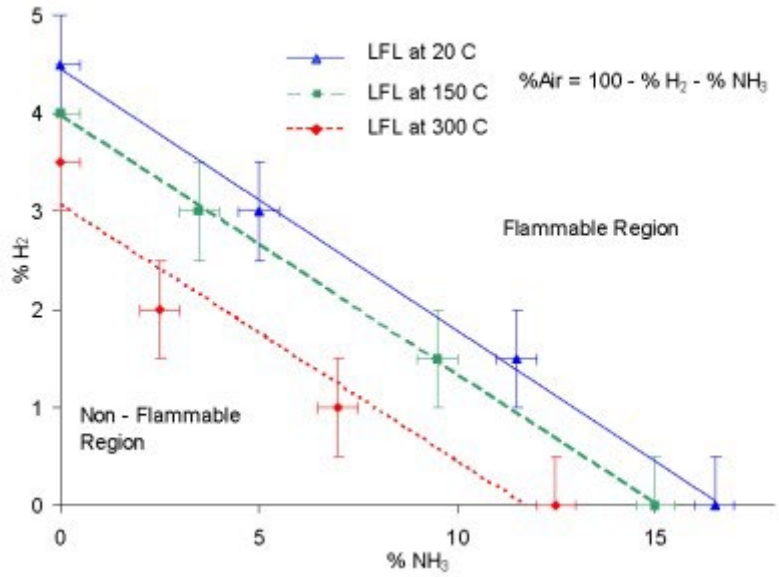

Fig.4. *Temperature dependency od the LEL of Ammonia/Hydrogen mixtures (Ciccarelli, 2005)*

Consequently, the project aims at systematically measure the explosions pressures and pressure rise velocities of the complete explosions range of all Ammonia-Hydrogen-Mixtures in Air.

2. Experimental Setup and Problems

In this project the ignition limits and explosions characteristics of mixtures of Ammonia and Hydrogen in Air were systematically determined in the 20-L-sphere in adoption of the setup described in (DIN EN 14034). The procedure is equivalent to the bomb method in a bigger volume. The test were conducted at 15 °C (active water cooling of the sphere) and 1 bar pressure.

All possible mixtures within the ignition range are tested, applying a 5% step width. Closer to the lower ignition limits intervals of 1% are used. Finer intervals are not justified due to the accuracy limit of the mixing method.

Additionally, the setup allows to test in turbulent mode as well as with other ignition systems than the electric spark, namely pyrotechnical igniters. Changes in the initial pressure would be possible, too with certain limits.

For a safe handling an unintended release of Ammonia is to be avoided. Therefore, all outlets were connected to the ventilation system. The experimental procedure was extended by the following steps:

- Flushing with compressed air for 3 minutes after each experiment to remove the condensed water
- For non-ignitions at the LEL additional H_2 was added and the mixtures was ignited to react the NH_3
- For non-ignitions at the UEL additional Air was added and the mixtures was ignited to react the NH_3

Unfortunately, the experiments could not be executed as intended. The main pressure sensor failed during the first series of experiments and could not be replaced immediately. The second pressure sensor had problems with the very low reaction velocity, as the recording time was limited to one second. As shown in Figure 5 the measured values did not reach the maximum within the given time. Thus, the complete measurement setup had to be redesigned and is not yet validated again.

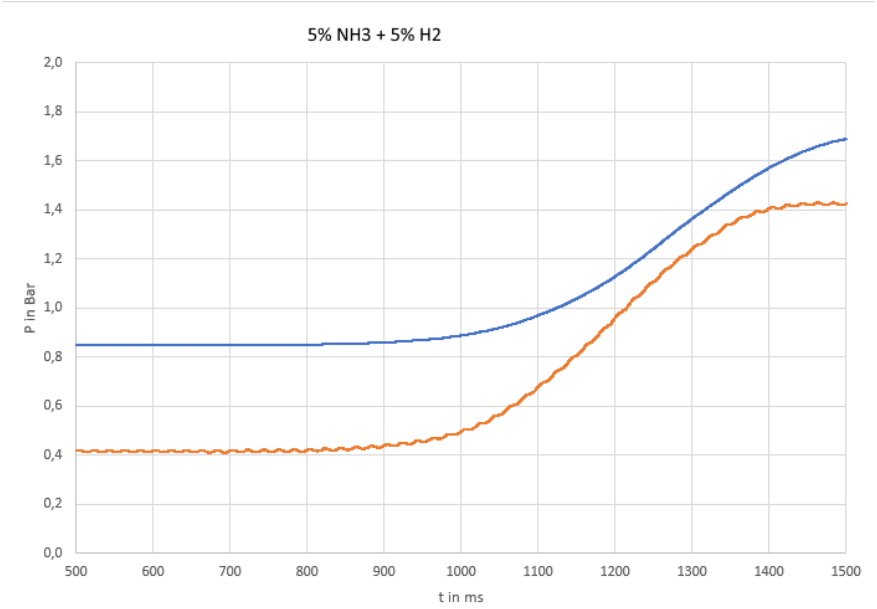

Fig.5. *Pressure curve of al slow reacting NH_3/H_2 mixture*

Nonetheless, the values obtained up to now allow a prove of concept and trustable measurement values will follow, soon.

3. Results and Plans

So far only the combinations close to the LEL of Ammonia and Hydrogen and pure NH_3/Air mixtures given in Figure 6 have been tested.

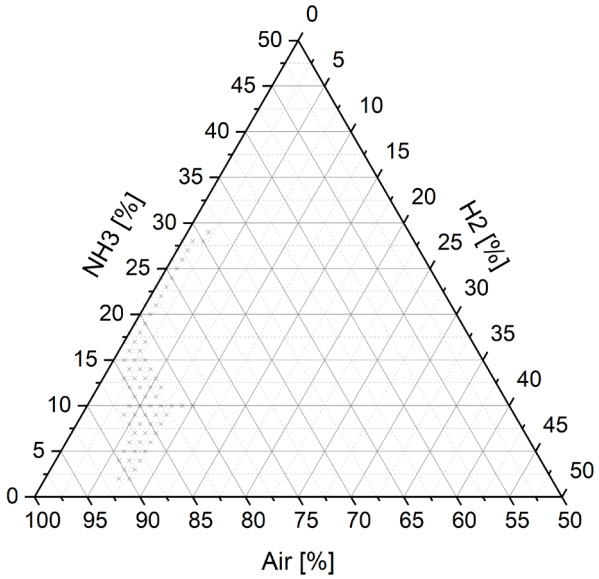

Fig.6. *Measured combination of NH3 and H2 in air (axes are cut to 50%!)*

Table 2 summarizes the measurement data for the lower explosion limit. These data represent the average of the results of the three tests carried out at the edge of the explosion zone. The data was collected from the pressure sensor at the outlet of the sphere because the internal pressure sensor failed during work. Consequently, the values are lower than expected.

Table 2. Comparison of properties of Ammonia and Hydrogen (Chemsafe/ GisChem)

	No Ignition		Ignition	
NH_3 [Mol%]	H_2 [Mol%]	P_{max} [bar]	H_2 [Mol%]	P_{max} [bar]
1	6	1,06	7	1,16
2	6	1,13	7	1,23
3	5	1,13	6	1,36
4	5	1,08	6	1,27
5	5	1,1	6	1,36
6	4	1,01	5	1,21
7	4	1,08	5	1,38
8	3	1,05	4	1,19
9	3	1,13	4	1,37
10	3	1,14	4	1,62
11	2	1,4	3	1,27
12	1	1,01	2	1,16
13	1	1,03	2	1,3
14	1	1,01	2	1,64
15	0	1,01	1	1,38

16	0	1,01	1	1,86

The representation in Figure 7 shows that LEL is well within the expected range. As postulated in Ciccarelli (2005) LeChatelier´s mixing rule seems to hold true. Up to now only the LEL of Hydrogen is slightly overpredicted in the experiments.

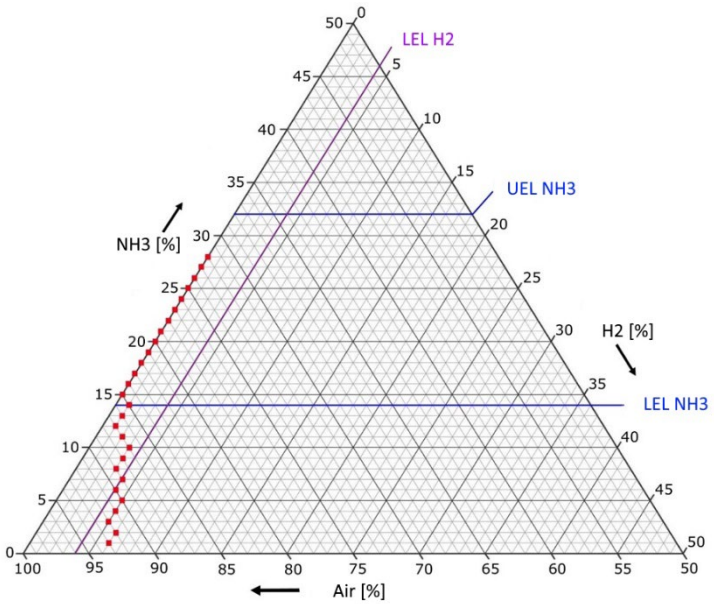

Fig.7. *Measured LEL and literature values for the pure gases*

The final aim of the project is to present the maximum explosions pressure and explosion rise velocity for the whole explosion range as ternary contour plots. With the data available so far, such a plot is of no real sense as represented in Figure 8. To give the reader an impression what the final result could look like Figure 9 is added with expected data.

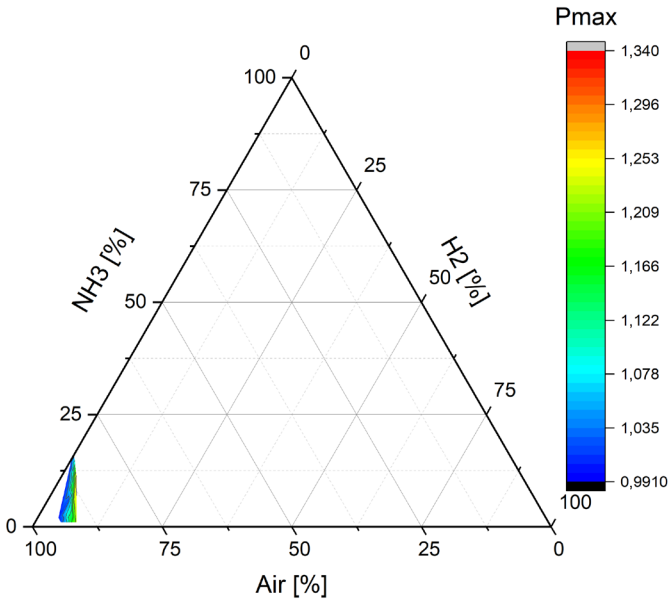

Fig.8. *Ternary contour plot with the available measured data points*

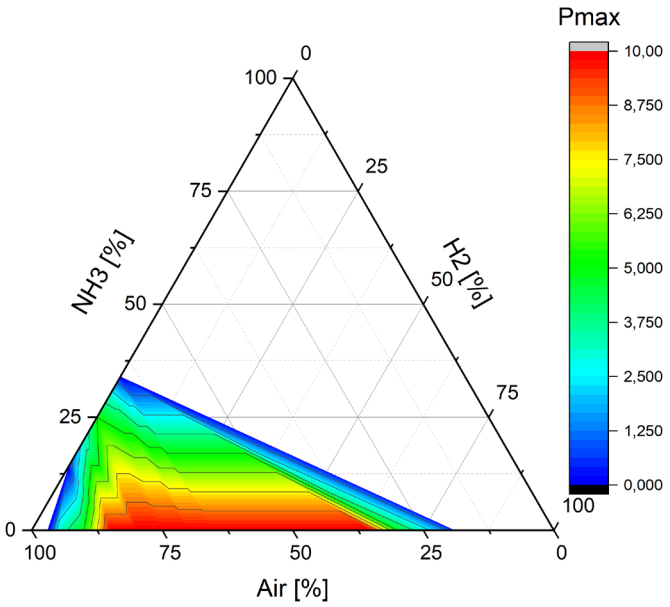

Fig.9. *Expected ternary contour plots for the maximum explosions pressure*

4. Conclusions

Ammonia is a potential component of the decarbonation of our energy system. The experience of decades of Ammonia production in other fields should make an extended use easier than the implementation of totally new systems. The knowledge of the explosion behavior of all possible Hydrogen/Ammonia Mixtures in Air will be helpful to design the right safety measurements. The versatility of the 20 Liter Sphere allows for safe testing and possible different conditions than implemented in the gas testing standards so far. More data will follow in the next months. Up to now the implementation of an adopted procedure to avoid Ammonia releases and thus ensure a safe handling is the major outcome of the project.

References

Ciccarelli, G. ; Jackson, D. ; Verreault, J.: Flammability limits of NH3–H2–N2–air mixtures at elevated initial temperatures. In: Combustion and Flame 144 (2006), Nr. 1-2, S. 53–63. http://dx.doi.org/10.1016/j.combustflame.2005.06.010. – DOI 10.1016/j.combustflame.2005.06.010. – ISSN 00102180

Jorissen, W. P. ; Ongkiehong, B. L.: Explosion regions, VIII: The explosion regions of hydrogen-ammonia-air and hydrogen-ammonia-oxygen mixtures. In: Recueil des Travaux Chimiques des Pays-Bas 45 (1926), 224–231. https://doi.org/10.1002/recl.19260450312

Kojima, Yoshitsugu: Safety of ammonia as a hydrogen energy carrier. In: International Journal of Hydrogen Energy 50 (2024), S. 732–739. DOI 10.1016/j.ijhydene.2023.06.213. ISSN 03603199

Molnárné, Maria ; Schendler, Thomas ; Schröder, Volkmar: Sicherheitstechnische Kenngrößen: Band 2: Explosionsbereiche von Gasgemischen. Bremerhaven : Wirtschaftsverl. NW, Verl. für Neue Wiss, 2003. – ISBN 3–89701–746–6

Nigbur, Florian E.: Ammoniak-Cracker zur Brenngasversorgung von Brennstoffzellen: Experimentelle und simulative Untersuchungen. Göttingen : Cuvillier Verlag, 2021. ISBN 9783736964976

Riemer, Matia ; Wachsmuth, Jakob ; Isik, Volkan ; Köppel, Wolfgang ; GermanEnvironment Agency (Hrsg.): Kurzeinschätzung von Ammoniak als Energieträger und Transportmedium für Wasserstoff. https://www.umweltbundesamt.de/sites/default/files/medien/479/dokumente/uba_kurzeinschaetzung_von_ammoniak_als_energietraeger_und_transportmedium_fuer_wasserstoff.pdf; Version: 2022. – last viewed 05.03.2024

TRAS 110: Bundesministerium für Umwelt, Naturschutz und nukleare Sicherheit: Bekanntmachung einer sicherheitstechnischen Regel der Kommission für Anlagensicherheit (TRAS 110 – Sicherheitstechnische Anforderungen an Ammoniak-Kälteanlagen): BAnz AT 03.11.2021 B7. https://www.kas-bmu.de/tras-endgueltige-version.html. Version: 3. November 2021

DDT in narrow channels for up to five step schemes

Luc Bauwens[a] & Josue Melguizo-Gavilanes[b]

[a] University of Calgary, Alberta, Canada
[b] Shell Global Solutions B.V., Major Hazards Management, Energy Transition Campus, 1031 HW Amsterdam, The Netherlands

E-mail: *bauwens@ucalgary.ca*

Abstract

There is evidence that the DDT process may be quite sensitive to details in the kinetic scheme. Thus overly simple schemes may not be truly meaningful. Complex schemes claim realism. However in some situations they may not reproduce experimental detonation results such as cells either. Furthermore, while stiff integration schemes ensure absolute stability, they do not do miracles. Indeed they do not actually resolve steps too fast to be resolved. Scheme complexity also may stand in the way of a proper physical interpretation. To gain understanding on the role of kinetics, we consider a range of increasingly complex simplified schemes, including up to five steps and two parallel chemical paths. We use these in a one-dimensional simulation relying on experimental flame acceleration data. This allows us to focus upon and resolve the DDT process. One might expect that the DDT process occurs when and where one of the eigenvalues of the chemical Jacobian matrix, initially all negative, first becomes positive. For both the three and the five step schemes under consideration here, the independent term in the characteristic equation is positive-definite, so that no eigenvalue is ever zero. Instead, transition occurs as a Hopf bifurcation, where a complex pair sees its real part go through zero. However in the schemes under consideration, because that independent term is small, the range over which the eigenvalues is complex is so narrow that, apart from producing significant oscillations when transition occurs, it is mostly not noticeable in the results.

1 Introduction

When simulating detonation processes including cell structure or deflagration to detonation transition (DDT), one is faced with a choice of kinetic scheme. Simpler schemes lead to smaller simulations, but they clearly cannot be fully realistic (Bykov *et al.*, 2022). While an appropriate complex scheme ought to be realistic, current schemes in the literature will likely have been developed focusing on other situations and while they may predict some features (Taileb *et al.*, 2020), they still do not seem to yield detonation cells matching experimental data (Taylor *et al.*, 2013). Likewise, complex schemes invariably feature an extreme range of scales, leading to the stiffness issue, which follows from an absolute stability requirement. So-called stiff schemes will allow for absolute stability to be retained for time steps much larger than those associated with the fastest modes in the kinetic matrix. However they do not truly resolve the fastest modes. In other words, even if a code used for the kinetics includes a full complex scheme, the simulation will truly include only the modes consistent with the resolution used. Finally, complex schemes are often used as a black box, and evaluating or analyzing how specific details affect the process under study may be challenging. Using simpler schemes of increasing complexity will allow to investigate how the various steps interact with each other and affect the results.

The focus here is on the DDT process in a straight tube. While a significant part of that process is the initial flame acceleration phase (Kuznetsov *et al.*, 2005, Gamezo *et al.*, 2007), we elected to avoid having to deal with that, and to rely upon experimental data instead, which include the approximately one-dimensional measured front position, versus time, using the methodology in Melguizo-Gavilanes & Bauwens (2022). This allows to focus fully on the DDT itself, and to restrict ourselves to a detailed and well-resolved one-dimensional model.

As to kinetic models, we focused upon three- and five step model. The former was a chain-branching model originally proposed by Kapila (1978) and widely used in the past (Liang & Bauwens, 2005, Bauwens *et al.*, 2009). Two closely related five steps models were studied. The first, proposed by Liang *et al.* (2007), features a second, competing path, in addition to the combination initiation-chain branching-termination as in the three step model. That scheme features a quadratic termination step, hence termination tapering to a very slow process at the end, which resulted in some issues when evaluating the eigenvalues of the Jacobian of the kinetic matrix. More importantly, that rate differed significantly from the linear termination in the three step scheme. For that reason, in addition to the original five step scheme, a nearly identical one was also considered, but with linear termination, and with termination pre-multiplier value suitably adjusted.

This article is organized as follows. First, the physical model is described, including the various kinetic schemes. Next numerical results are presented. An analysis of the Jacobian of the kinetic schemes and its eigenvalues follows, and their role in the numerical results is discussed.

2 Physical model

We solve the inviscid non-conducting one-dimensional reactive compressible equations. The domain is divided into two regions, separated by a reactive propagating front. The front separates a fully reacted region from an initially non-reacted one, and in which little reaction takes place because temperature is low. Front motion is imposed based upon the experimental data of Melguizo-Gavilanes *et al.* (2020). Across the front the full compressible Rankine-Hugoniot equations are solved, based upon a fully compressible extension of the front model in Bauwens *et al.* (2009). Such a model is needed because at least initially the front moves relatively slowly in comparison with the speed of sound, so that the front sits in the same computational cell for a relatively long time. For gas dynamics, the same well-validated ENO solver is used as in Bauwens *et al.* (2009).

The tube is closed at the end where ignition takes place and open at the other end. Initial conditions assume a front position very close to the closed end, preceded by the small amplitude pressure wave due to the impulsive start of the front. In the experimental data used for the front motion, DDT takes place before the leading pressure wave, reinforced by front acceleration, reaches the open end, so that in contrast with Bauwens *et al.* (2009), reflection at the open end does not play a role.

The kinetic scheme based upon Liang *et al.* (2007) includes three equations (hence, including products, four species) and five steps:

$$\frac{d\lambda_1}{dt} = -k_1\rho\lambda_1 - k_2\frac{\rho\lambda_1\lambda_2}{W_2} - k_3\frac{\rho^2\lambda_1\lambda_2}{W_2} \tag{1}$$

$$\frac{d\lambda_2}{dt} = k_1\frac{W_2\rho\lambda_1}{W_1} + k_2\frac{\rho\lambda_1\lambda_2}{W_1} - k_3\frac{\rho^2\lambda_1\lambda_2}{W_1} + 2k_4\frac{W_2\rho\lambda_3}{W_3} - 2k_5\frac{\rho^2\lambda_2^2}{W_2} \tag{2}$$

$$\frac{d\lambda_3}{dt} = k_3\frac{W_3\rho^2\lambda_1\lambda_2}{W_1W_2} - k_4\rho\lambda_3 \tag{3}$$

in which λ_1 corresponds to the reactant, λ_2 to a chain-branching radical, and λ_3 provides for a parallel reaction path. The rates are mostly Arrhenius, except for rates 3 and 5, which have zero activation energy:

$$k_i = A_i \exp\frac{-E_i}{RT}, \quad \text{except} \quad k_3 = A_3/T.\ \ k_5 = A_5/T \tag{4}$$

Weights were $W_1 = 0.002$ kg/mol, $W_2 = 0.017$ kg/mol and $W_3 = 0.033$ kg/mol. Values of the various A_i and E_i are taken from Liang *et al.* (2007), while the weights are as mentioned:

Apart from the weights, the scheme above is the original scheme from Liang *et al.* (2007), with quadratic termination. For linear termination the last term in the equation for λ_2 is replaced by $2k_5\rho\lambda_2/W_2$. Different values of k_5 are required, as discussed below.

The tube length is 1.00 m as in the experiments. Initial pressure and temperature are ambient. As to the mixture, it is characterized by $\gamma = 1.33$ and a speed of sound of 535.3 m/s. Heat release is

***Table 1**: Kinetic data*

Data	Rate 1	Rate 2	Rate 3	Rate 4	Rate 5
A_i	1.37×10^{9}m^3/kg/s	1.32×10^{8}m^3/mol/s	7.00×10^{5}m^3/kg/s	3.23×10^{9}m^3/kg/s	1.37×10^{9}m^6/mol/kg/s
E_i/R	24231. K	8383. K	0.	22980. K	0.

associated with products only, with value of $25.032/RT_0$, T_0 being the initial ambient temperature of 300 K.

A three step scheme is obtained using the same code by setting k_3 and k_4 to zero. If additionally setting k_2 to zero and for a very high k_5, a single step Arrhenius model is also obtained.

All results were obtained for a spatial mesh size of 2.00 μm.

3 Numerical results

3.1 *Cases*

In addition to the activation energies and A_2, with values as per Table 1 in all cases except (h) in which A_2 was set to zero, the data for the cases that were considered are shown in Table 2:

***Table 2**: Cases simulated*

Case	A_1 (m^3/kg/s)	A_3 (m^{6}K/mol/kg/s)	A_4 (m^3/kg/s)	A_5	Termination
(a)	1.37×10^{9}	7.00×10^{5}	3.23×10^{9}	1.37×10^{9} m^6/mol/kg/s	Quadratic
(b)	1.37×10^{9}	0.00	0.00	1.37×10^{9} m^6/mol/kg/s	Quadratic
(c)	1.37×10^{9}	7.00×10^{5}	3.23×10^{9}	1.00×10^{9} m^3/mol/kg^2/s	Linear
(d)	1.37×10^{9}	7.00×10^{4}	3.23×10^{9}	1.00×10^{9} m^3/mol/kg^2/s	Linear
(e)	1.37×10^{9}	7.00×10^{5}	3.23×10^{8}	1.00×10^{9} m^3/mol/kg^2/s	Linear
(f)	1.37×10^{9}	7.00×10^{4}	3.23×10^{8}	1.00×10^{9} m^3/mol/kg^2/s	Linear
(g)	1.37×10^{9}	0.00	0.00	1.00×10^{9} m^3/mol/kg^2/s	Linear
(h)	1.37×10^{16}	0.00	0.00	Large	Linear

Case (a) corresponds to the rates as per Liang *et al.* (2007), while case (b) refers to a three step scheme, still with quadratic termination, with same initiation, branching and termination, but setting the second chemical path to zero.

Cases (c) to (g) consider a linear termination. For case (c), all rates except termination are the same in in case (a), and the termination rate used was the value that led to transition at a position closest to the experimental results. That same termination rate was used in cases (c), (d), (e), (f) and (g). In the latter, rates A_3 and A_4 were set to zero, thus yielding a three step scheme. In case (d), a lower A_3 was used, in case (e), a lower A_4, and in case (f) both were lower.

The last case, (h), corresponds to a single step Arrhenius model. We had to increase A_1 by a factor 10^7 to obtain a transition within the range of the experimental data that we used for the front position vs. time (Melguizo-Gavilanes *et al.*, 2020).

3.2 *Quadratic termination*

For the five step scheme with termination proportional to λ_2^2, namely cases (a) and (b), DDT was found to occur somewhat earlier than in the experiments, approximately for at a length of 0.21 m. It is possible however that for W_i values matching Liang *et al.* (2007), results closer to the experiments (Melguizo-Gavilanes *et al.*, 2020) might have been obtained.

Results for case (a), in Fig. 1, show the evolution starting at transition and over a relatively long subsequent period, i.e. showing a sequence of profiles at times separated by relatively large intervals.

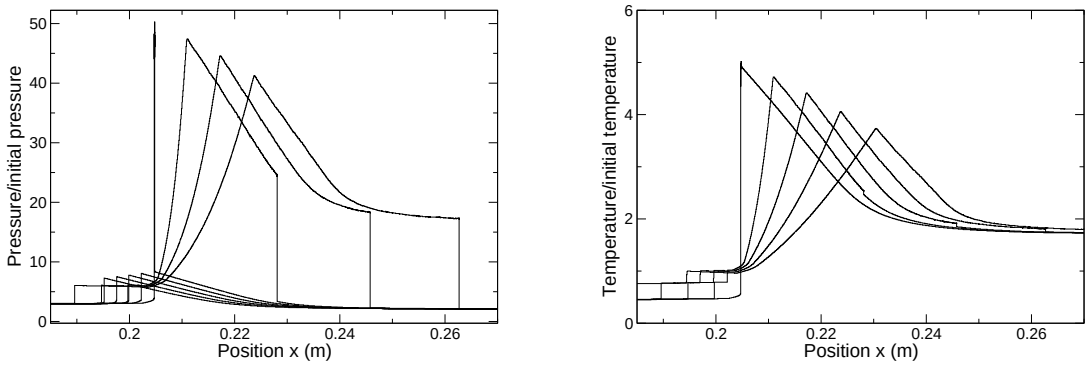

***Fig. 1**: Case (a) - Left: pressure after transition. Right: temperature at same times*

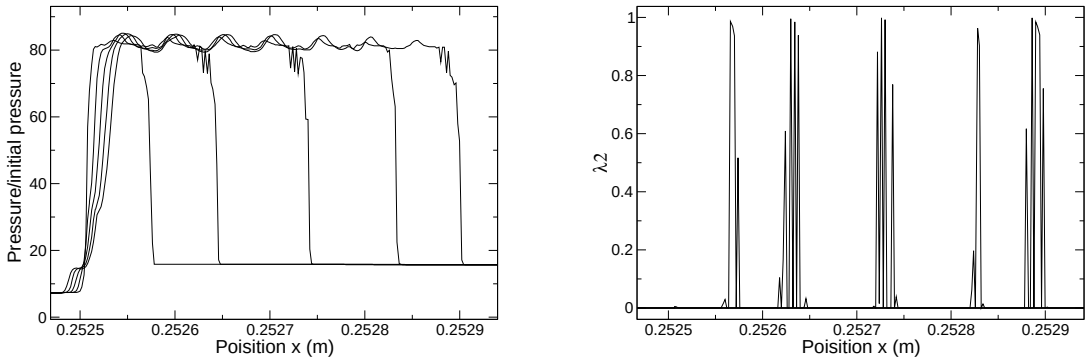

***Fig. 2**: Case (c) - Left: pressure shortly after transition. Right: λ_2 at same times.*

Still for quadratic termination, in case (b), transition occurs much earlier. Thus the second chemical path offers significant competition to the chain branching mechanism under rates k_1 and k_2. Figure 2 shows the evolution of pressure and of λ_2, starting with the transition and over narrow subsequent time intervals. The pressure graph shows oscillations happening, driven by oscillations in the production of λ_2 on the right side of the pressure peak, where temperature also suddenly increases, leading to significant reaction. Even with a resolution of 2 μm, the oscillations in λ_2 are not well-resolved, but there should be a window at that position where the reaction becomes oscillatory. In effect, that resolution is not really adequate to resolve these details is consistent with a very stiff initiation rate, with a dimensionless activation energy of 80.44. The oscillations occur over too small a width to show in Fig. 1. Oscillations were also observed in the experiments used for flame acceleration data (Melguizo-Gavilanes *et al.*, 2020); different tentative explanations have been suggested. Current results point to kinetics and oscillatory combustion also being a possible explanation. The evolution past the transition is very similar for case (a).

3.3 *Linear termination*

Figure 3 shows the location of the pressure peak for all cases. From left to right, it shows cases (b), (a), (h), (g), (d) and (f) which on this scale are indistinguishable, and likewise, (c) and (e). First, it shows, as mentioned above, that in the cases for quadratic termination, the rates used lead to a somewhat early explosion in comparison with the experimental results. This obviously does not happen in the linear cases, where rate k_5 was calibrated based upon the experiments. /newpage Second, for linear termination, zeroing the competing second chemical path has much less impact than for quadratic termination. In the latter case, as mentioned above, zeroing the second path, in case (b), leads to

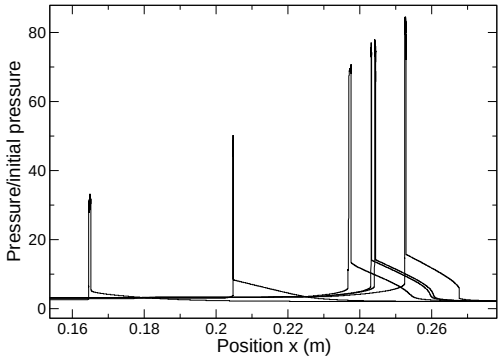

***Fig. 3**: Transition: From left to right, cases (b), (a), (h), (g), (d) and (f), (c) and (e) (indistinguishable).*

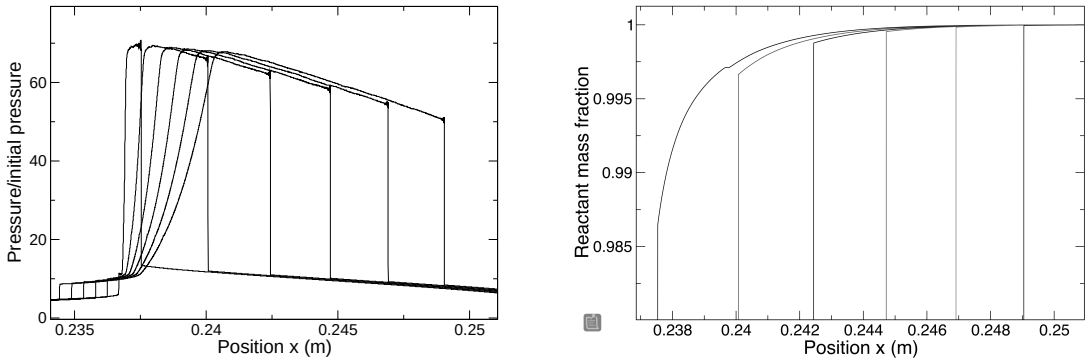

***Fig. 4**: Single step - case (h): Left, pressure shortly after transition. Right, λ_1 at same times.*

a significantly earlier explosion, which while very unrealistic compared with the experiments, was precisely the point of adding a second path. However there no longer is such a dramatic difference when comparing cases (c) and (g). With linear termination, in contrast with the case above, removing the second chemical path by zeroing rates k_3 and k_4 in case (g), results in a difference that is much less dramatic. If instead of case (c), using a somewhat different case as the reference, with somewhat lower termination rate but strengthening the competing path by increasing k_3, results might have been more similar to cases (a) and (b). However here, the choice was made to use rates in case (c) as close as possible to case (a).

That cases (d) and (f) are nearly identical points to rate k_4 being more or less saturated, effectively removing very quickly species 3 produced by rate k_3. Results in cases (c) and (e) are nearly identical for the same reason.

3.4 *Single step*

For single step kinetics, Fig. 4 shows the single step results, for the same activation energy as in all other cases. However the rate multiplier had to be increased considerably, by a factor 10^7, for the explosion to occur within the window of the experimental data (Melguizo-Gavilanes *et al.*, 2020). While there are still some oscillations on the front end of the high pressure zone, these now disappear rapidly and they look like a dispersive issue. As the front sharpens, the jump in the mass fraction becomes sharper, but it is always smooth, in contrast with the multistep cases.

4 Eigenvalues of the Jacobian of the kinetic matrix

In this section we analyze the relationship between the eigenvalues of the Jacobian of the kinetics matrix, and the explosion. It might be expected that at low temperature the eigenvalues might all be negative, but that as temperature increases due to flame acceleration, eventually one or more eigenvalue should become positive and, for a sharp transition, become large. This motivated the current analysis. For a scheme with three species hence three equations, the characteristic equation will be a cubic, while for a two equation scheme such as the three step chain branching one, it is a quadratic. Either way, one might expect that one of the eigenvalues goes through zero when going from negative to positive. However for the schemes under consideration, that is never the case, as shown below.

For the scheme with linear termination, the rate equations are:

$$\frac{d\lambda_1}{dt} = -\frac{r_1}{W_2}\lambda_1 - \frac{r_2\lambda_1\lambda_2}{W_2} - \frac{r_3}{W_2}\lambda_1\lambda_2 \tag{5}$$

$$\frac{d\lambda_2}{dt} = \frac{r_1}{W_1}\lambda_1 + \frac{r_2\lambda_1\lambda_2}{W_1} - \frac{r_3}{W_1}\lambda_1\lambda_2 + 2r_4\lambda_3 - 2r_5\lambda_2 \tag{6}$$

$$\frac{d\lambda_3}{dt} = r_3\frac{W_3}{W_1W_2}\lambda_1\lambda_2 - \frac{r_4W_3}{W_2}\lambda_3 \tag{7}$$

Using the notation:

$$r_1 = \rho W_2 A_1 \exp\frac{-E_1}{T},\ \ r_2 = \rho A_2 \exp\frac{-E_2}{T},\ \ r_3 = \frac{\rho^2 A_3}{T},\ \ r_4 = \frac{\rho A_4 W_2}{W_3}\exp\frac{-E_4}{T},\ \ r_5 = \frac{\rho^2 A_5}{pW_2} \tag{8}$$

The Jacobian then is

$$J = \begin{vmatrix} [-r_1-(r_2+r_3)\lambda_2]/W_2 & -(r_2+r_3)\lambda_1/W_2 & 0 \\ [r_1+(r_2-r_3)\lambda_2]/W_1 & (r_2-r_3)\lambda_1/W_1 - 2r_5 & 2r_4 \\ r_3W_3\lambda_2/W_1W_2 & r_3W_3\lambda_1/W_1W_2 & -r_4W_3/W_2 \end{vmatrix} \tag{9}$$

The characteristic equation being then the cubic:

$$\sigma^3 + a\sigma^2 + b\sigma + c = 0 \tag{10}$$

In which,

$$a = \frac{r_1+(r_2+r_3)\lambda_2}{W_2} - \frac{(r_2-r_3)\lambda_1}{W_1} + 2r_5 + \frac{r_4W_3}{W_2} \tag{11}$$

$$b = \frac{\{2[r_1+(r_2+r_3)\lambda_2+r_4W_3]r_5W_2 + [r_1+(r_2+r_3)\lambda_2]r_4W_3\}W_1 - [(r_2+r_3)r_4W_3 - 2r_1r_3]\lambda_1W_2}{W_1W_2^2} \tag{12}$$

$$c = \frac{2[r_1+(r_2+r_3)\lambda_2]r_4r_5W_3}{W_2^2} \tag{13}$$

Here, $-a$ is the sum of the roots while $-c$ is their product:

$$a = -\sigma_1 - \sigma_2 - \sigma_3, \quad c = -\sigma_1\sigma_2\sigma_3 \tag{14}$$

Crucially, then, given that the rates r_i are all positive-definite, the product of the roots is unconditionally negative. Thus either all three eigenvalues are negative, or one is negative and the other two, positive, or one root is negative and the other two are complex conjugate. Furthermore, none of the eigenvalues can ever be zero since their product cannot be zero. Thus transition from all eigenvalues being negative to two of them becoming positive cannot occur by passing through zero values. Instead, the only possible transition mechanism entails there being a complex range, in which the real part goes from negative to positive. The condition at which transition occurs corresponds to one root

σ_1 being negative and the other two having zero growth rate, i.e. being purely imaginary: $\sigma_{2,3} = \pm i\hat{\sigma}$. The characteristic equation is then:

$$(\sigma - \sigma_1)(\sigma^2 + \hat{\sigma}^2) = 0 \tag{15}$$

$$\sigma^3 - \sigma_1\sigma^2 + \hat{\sigma}^2\sigma - \sigma_1\hat{\sigma}^2 = 0 \tag{16}$$

So, then $\sigma_1 = -a$, $\hat{\sigma}^2 = b$ and $\sigma_1\hat{\sigma}^2 = -c$. Thus the condition for transition is $ab = c$ and

$$\hat{\sigma}^2 = b = \frac{c}{a} \tag{17}$$

Initially, $\lambda_1 = 1$ and $\lambda_2 = 0$. Then, the coefficients are

$$a = \frac{r_1}{W_2} - \frac{(r_2 - r_3)}{W_1} + 2r_5 + \frac{r_4 W_3}{W_2} \tag{18}$$

$$b = \frac{\{2[r_1 + r_4 W_3]r_5 W_2 + r_1 r_4 W_3\}W_1 - [(r_2 + r_3)r_4 W_3 - 2r_1 r_3]W_2}{W_1 W_2^2} \tag{19}$$

$$c = \frac{2r_1 r_4 r_5 W_3}{W_2^2} \tag{20}$$

For these values, all three eigenvalues are real and negative.

The argument is simpler for the three step scheme. Then r_3 and r_4 are zero so that the scheme is reduced to the first two equations, hence a quadratic characteristic equation. In the above, $c = 0$ so

$$\sigma^2 + a\sigma + b = 0 \tag{21}$$

With

$$a = \frac{W_1 r_1 + r_2(W_1\lambda_2 - W_2\lambda_1) + 2r_5 W_1 W_2}{W_1 W_2} \tag{22}$$

$$b = \frac{2(r_1 + r_2\lambda_2)r_5}{W_2} \tag{23}$$

Since b is positive, both roots have the same sign, hence the sign of $-a$, and they are never zero. However if they are complex, then their real part equals $a/2$. Thus here again transition occurs in a range where the eigenvalues are complex, i.e. oscillatory combustion, for $a = 0$. They are complex if

$$[W_1 r_1 + r_2(W_1\lambda_2 - W_2\lambda_1) + 2r_5 W_1 W_2]^2 - 8W_1^2 W_2(r_1 + r_2\lambda_2)r_5 < 0 \tag{24}$$

Thus transition occurs when

$$\lambda_1 = \frac{W_1}{W_2}\frac{r_1 + r_2\lambda_2 + 2r_5 W_2}{r_2} \tag{25}$$

To summarize, according to the current theory, for both the three and five step models, transition occurs with two negative eigenvalues becoming complex conjugate, initially still with negative but increasing real part, when that real part becomes zero. The real part subsequently further increases and eventually the pair turns back into being real, but now positive. This is known as a Hopf bifurcation.

However, for the current data, presumably because of the stiffness of initiation, it appears that that process occurs over a very narrow interval, as an evaluation of the eigenvalues shows. First, Table 3 shows the coefficients a, b and c for case (c) immediately before the explosion and immediately behind the front, scaled respectively by the speed of sound divided by the tube length, the square and finally the cube of speed of sound over length:

In most of the range of interest, $|a| \gg |b|^{1/2}$ and $|c|^{1/3}$, which implies that one eigenvalue is close to $-a$ and the other two are small. While an exact solution exists for the cubic equation, in that situation, the exact approach only yields the smaller ones in absolute value with an uncertainty of the order of the

***Table 3**: Coefficients a, b and c immediately before the explosion (dimensionless) - Case (c)*

Location x (m)	a	b	c
0.252500	-3.527 × 10^6	1.069 × 10^{10}	1.360 × 10^6
0.252502	-3.867 × 10^6	3.796 × 10^{10}	4.831 × 10^6
0.252504	-3.384 × 10^6	3.100 × 10^{10}	3.945 × 10^6
0.252506	-1.985 × 10^6	1.233 × 10^{10}	1.568 × 10^6
0.252508	8.719 × 10^4	2.707 × 10^9	3.444 × 10^6
0.252510	2.339 × 10^6	8.480 × 10^8	1.079 × 10^5
0.252512	4.512 × 10^6	4.676 × 10^8	5.951 × 10^4
0.252514	6.708 × 10^6	3.415 × 10^8	4.347 × 10^4
0.252516	8.935 × 10^6	2.782 × 10^8	3.540 × 10^4
0.252518	1.120 × 10^7	2.392 × 10^8	3.044 × 10^4
0.252520	1.348 × 10^7	2.129 × 10^8	2,710 × 10^4

numerical uncertainty for the larger one (in absolute value). However an approximate method taking these magnitudes into account will yield a reliable estimate, which, when valid, was used to evaluate the data in Table 4:

$$\sigma_{2,3} = \frac{c - ab \pm \sqrt{a^2b^2 - 2abc + c^2 - 4a^3c}}{2a^2} \tag{26}$$

Table 4 shows the eigenvalues, scaled by the speed of sound divided by the length, immediately before explosion and immediately past the front, based upon the coefficients in Table 3. Very near the transition, a, as expected goes through zero and becomes negative. Thus there is a range for which the approximate solution is not applicable. For these cases, the eigenvalues were evaluated using a symbolic math package. (The package yields the same values as the approximate solution in its range of validity.)

***Table 4**: Eigenvalues of the Jacobian immediately before explosion (dimensionless) - Case (c)*

Location x (m)	σ_1	σ_2	σ_3
0.252500	-1.2728 × 10^{-4}	3032.	3.524 × 10^6
0.252502	-1.2728 × 10^{-4}	9841.	3.857 × 10^6
0.252504	-1.2727 × 10^{-4}	9184.	3.375 × 10^6
0.252506	-1.2722 × 10^{-4}	6228.	1.979 × 10^6
0.252508	-1.2718 × 10^{-4}	-43595.+28409.i	-43595.-28409.i
0.252510	-1.2721 × 10^{-4}	-362.5	-2.339 × 10^6
0.252512	-1.2725 × 10^{-4}	-103.7	-4.512 × 10^6
0.252514	-1.2727 × 10^{-4}	-50.92	-6.708 × 10^6
0.252516	-1.2728 × 10^{-4}	-31.13	-8.935 × 10^6
0.252518	-1.2728 × 10^{-4}	-21.37	-11.19 × 10^6
0.252520	-1.2726 × 10^{-4}	-15.79	-13.48 × 10^6

Table 4 shows three negative real eigenvalues for $x \geq 0.252510$ m, and two real positive ones for $x \leq 0.252506$ m. Only for $x = 0.252508$ m does the table show a pair of complex conjugate eigenvalues. In view of the theory, it has to be the case that the entire bifurcation occurs in the narrow interval between $0.252506 < x < 0.252508$ m. Still, these results do confirm the existence of a zone where the eigenvalues are complex, as predicted.

We conclude that the explosion takes place very close to where combustion is oscillatory, which is consistent with the oscillations in the numerical results, above.

For the scheme with quadratic termination (Liang *et al.*, 2007), however, one term in the Jacobian differs and now r_5 is replaced by $2r_5\lambda_2$. As a result, the coefficient a in the characteristic equation becomes

$$a = \frac{r_1 + (r_2 + r_3)\lambda_2}{W_2} - \frac{(r_2 - r_3)\lambda_1}{W_1} + 4r_5\lambda_2 + \frac{r_4 W_3}{W_2} \tag{27}$$

Then again, initially and in most of the unburnt region, λ_2 is quite small while for that case, r_5 is very large. Small numerically induced inaccuracies in λ_2 then can lead to large oscillations in term $4r_5\lambda_2$, sufficient to result in a jumping spuriously from positive to negative values in the region of interest, ahead of the front. That makes it difficult to analyze the eigenvalues for that case, which contributed to our choice of focusing on linear termination instead. Still, overall, the behavior is similar to the linear case.

Conclusions

One-dimensional numerical simulations of transition to detonation were performed, using experimental results (Melguizo-Gavilanes *et al.*, 2020) for flame acceleration, for different kinetic models, with up to five steps and three species, assuming a thin flame model dealt with by a subgrid algorithm based upon the Rankine-Hugoniot relations. As the flame accelerates, pressure and temperature ahead of the flame front increase, up to values that trigger a sudden transition to detonation. Two different termination mechanisms were included, respectively quadratic and linear. Rates were taken from the literature (Liang *et al.*, 2007), but with slightly different molecular masses.

Results were reasonably similar with experiments, although for the rates used three step kinetic models led to an earlier transition in the case of quadratic termination.

The five step schemes feature two competing chemical paths. In the case with linear termination however, it appears the second path (absent from three step schemes) is not strong enough to make a significant difference. It might be worth trying different schemes with stronger alternate path but also with stronger termination, so as to result in transition near the same point as in the experiments (Melguizo-Gavilanes *et al.*, 2020).

We also compared how the eigenvalues of the Jacobian of the kinetic matrix evolve as the solution approaches the transition point. Because the independent term in the characteristic equation is positive-definite, none of the eigenvalues can ever be zero. Thus a switch between all eigenvalues being negative, as is the case initially, to in the current case two of them becoming positive can only happen as a Hopf bifurcation. Transition then occurs in a range where a pair of eigenvalues are complex conjugate, with their real part going from negative to zero to finally positive.

However, because the independent term in the characteristic equation is so small in the cases that were studied, the window over which two eigenvalues are complex is so narrow that even with the 2 μm resolution used, complex eigenvalues were only detected at one grid point so that the entire zone where they are complex and transition occurs is less than two mesh sizes in space. Increasing the rate multiplier for initiation, rate r_1 and also in rate r_4, both of which are very small, appears to lead to results similar to the current ones, but with a wider zone where there are complex eigenvalues. An even finer resolution might of course also yield more interesting details.

References

Bauwens, L., Bauwens, C.R.L, & Wierzba, I. 2009. Oscillating flames: multiple-scale analysis. *Proc. R. Soc. Lond. A*, **465**, 2089–2110.

Bykov, V., Koksharov, A., Kuznetsov, M., & Zhukov, V.P. 2022. Hydrogen-oxygen flame acceleration in narrow open ended channels. *Comb. Flame*, **238**, 111913.

Gamezo, V.N., Ogawa, T., & E.S., Oran. 2007. Numerical simulations of flame propagation and DDT in obstructed channels filled with hydrogen–air mixture. *Proc. Comb. Inst.*, **31**, 2463–2471.

Kapila, A.S. 1978. Homogeneous branched-chain exploion: Initition to completion. *J. Engineering Math*, **12**, 221–235.

Kuznetsov, M., Alekseev, V., Matsukov, I, & Dorofeev, S. 2005. DDT in a smooth tube filled with a hydrogen–oxygen mixture. *Shock waves*, **14**, 205–215.

Liang, Z., & Bauwens, L. 2005. Detonation structure with pressure-dependent chain-branching kinetics. *Proc. Comb. Inst.*, **30**, 1879–1887.

Liang, Z., Browne, S., Deiterding, R., & J.E., Shepherd. 2007. Detonation Front Structure and the Competition for Radicals. *Proc. Comb. Inst.*, **31**, 2445–2453.

Melguizo-Gavilanes, J., & Bauwens, L. 2022. An experimentally informed 1-D DDT model for smooth narrow channels. *28th International Colloquium on the Dynamics of Explosions and Reactive Systems*.

Melguizo-Gavilanes, J., Ballossier, Y, & Faria, L. 2020. Experimental and theoretical observations on DDT in smooth narrow channels. *Proc. Comb. Inst.*, **38**.

Taileb, S., Melguizo-Gavilanes, J., & Chinnayya, A. 2020. Influence of the chemical modeling on the quenching limits of gaseous detonation waves confined by an inert layer. *Comb. Flame*, **218**, 247–259.

Taylor, B.D., Kessler, D.A., Gamezo, V.N., & Oran, E.S. 2013. Numerical Simulations of Hydrogen Detonations with Detailed Chemical Kinetic Mechanisms. *Proc. Comb. Inst.*, **34**, 2009–2016.

Test set-up for reproducible shock wave generation

M. Gerbeit [a], H. Seeber [b], D. Grasse [a], M. Donner [a], S. Grobert [c], D. Krentel [a]

[a] Bundesanstalt für Materialforschung und -prüfung (BAM), Berlin, Germany.

[b] Helmut Schmidt University, Hamburg, Germany.

[c] Planning Office of the German Armed Forces, Berlin, Germany.

E-mail: marco.gerbeit@bam.de

Abstract

In industrial applications, the effects of explosions must be considered as important part of safety assessments. This is particularly crucial in applications involving explosives or pressurized containers. The evaluation of the effects of shock waves on the environment becomes essential in such scenarios and requires comprehensive experimental test series.
This article therefore presents a test bench that can generate and record reproducible, adjustable shock waves with short set-up times. The presented data proves the quality and validity of this set-up to generate case relevant data, like overpressure in comparison to explosives and shock tubes, with load cases of high relevance.
The presented free-field tests are carried out at BAM's Test Site Technical Safety (TTS) with a gas-operated shock wave generator. This shock wave generator consists of a pressure vessel (autoclave) that is operated with a detonable gas mixture or compressed air. The pressure is released through an orifice by the instantaneous bursting of a diaphragm.
The aim is to develop further the novel test bench that generates shock waves on models in a generic scenario and offers several advantages to create a valid database for the effects of shock waves.
In contrast to classic shock tubes, this test bench offers the advantage of realistic hemispherical shock wave propagation and scalability, both for the investigated model size and for the generation of load cases, so that different model variables can be investigated under different boundary conditions (mainly overpressure); at the same time, typical interference of a shock tube experiment due to reflections, blockage effects and the following fluid flow can be minimized. These negative influences are not realistic compared to the ideal event of a detonation.

Keywords: *shock, blast, autoclave, explosions, overpressure*

Introduction

In industrial applications, the effects of explosions must be considered as important part of safety assessments. This is particularly crucial in applications involving explosives or pressurized containers. The evaluation of the effects of shock waves on the environment becomes essential in such scenarios and requires comprehensive experimental test series to generate a valid data base.
For this scenario, common set-ups are shock tubes or the use of explosives, but both have some disadvantages.
A shock tube is a test bench for generating blast. It consists of a high pressure chamber and a low pressure chamber. They are separated by a diaphragm. The sudden failure of the diaphragm leads to a shock which is moving into the test section. The subject, which needs to be analyzed, can be placed there. Placing a subject into a shock tube can lead to a fluid flow blockage caused by the object

(Needham, Ritzel et al. 2015). This reduces the effective cross section of the flowing field of the shock tube.
The SimLab shock Tube Facility (see Aune et. al. (2016)) avoids the problem in the test section with a large tank with a 5 times larger inner diameter than the driver section. Another problem is the reflection in the shock tube caused by the repeating shock reflections with the walls along the tube (Mediavilla et al., 2011). The following fluid is also deviating from the realistic load case of an explosion.

Another way of blast testing is by using explosives. Testing with explosives requires comprehensive safety regulations, large turn-around time intervals and can lead to variation due to inaccurate placement of the explosives.
All these decisive disadvantages are minimized in this experimental setup aiming at generating a reproducible shock wave under quasi-free-field conditions.

This test rig has already been presented in the article (see Seeber et. al. (2023)). For this purpose, in this article the optimized test bench will be presented with a focus on the demonstration of the better reproducibility.

1. Experiments

The presented free-field tests are carried out at BAM's Test Site Technical Safety with a gas-operated shock wave generator (SWG). This shock wave generator consists of a 65 litre cylindrical autoclave with a pressure resistance of 400 bar.
An explosive gas mixture is filled into the autoclave. First, the gas inlet pipe, buffer tank and autoclave are evacuated. The desired gas quantity and concentration is then set in the gas mixing system and, once this has been reached, transferred to a previously evacuated buffer tank. The gas is then filled into the empty autoclave. The outlet opening, which is sealed with a bursting disc made of 0.2mm aluminum, is located at a height of 1.35 - meters in the center of the SWG. The outlet has a diameter of 132mm. An ignition device is used to trigger the ignition and start the measuring program. The gas mixture is ignited by an electric ignition source with sufficient strength, in this case an exploding wire.
The bursting disc then fails as one piece. There are no fragments flying around. Afterwards the shock propagates hemispherical in the free field. The models, sensors etc. can be placed in the open field (measuring section) depending on the application. After detonation, the whole system is flushed with Nitrogen to remove the reaction gases and to reach a defined safe state.

Kistler Pencil Probes (Kistler 6233A0025) are used to measure the incident pressure of the propagating shock. The typical sensor position is at a distance of 1 and 1.5 meters from the outlet and at an angle of 45° and 35° from the main flow direction. This has the advantage that the sensors are not exposed to the flame impulse and avoid the subsequent fluid flow. This arrangement of the sensors is possible due to the hemispherical propagation of the shock. The pressure samples are recorded at a sampling rate of 2 MHz with a TraNET-EPC-Data-Acquisition-Instrument. A pressure sensor, a Kistler 601H (PA1) and a thermocouple are installed inside the autoclave. The turn-around time between two tests is less than 30 min.

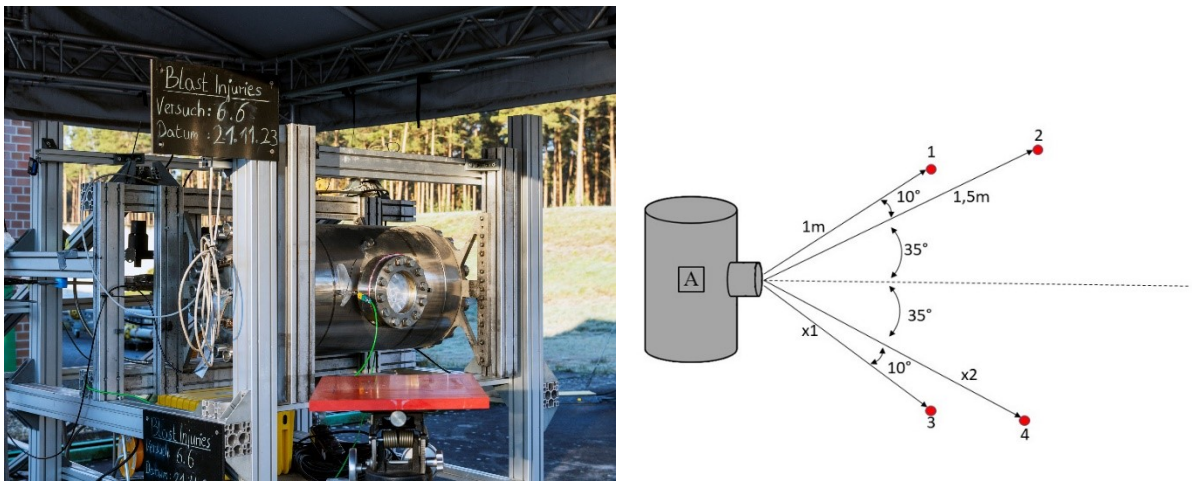

Figure 1:Test bench (left) and the corresponding schematic top view of the test bench (right); A: shock wave generator; 1-4: pencil probes

The following sections deal with the initial conditions. Two parameters are presented that have an influence on the test.

Firstly, the used gas is presented. Afterwards the ignition source used in the experiments is introduced.

1.1. Gas:

The aim of the test bench is to generate a shock wave. This requires a supersonic reaction front that causes a shock. Therefore, the autoclave is operated with acetylene and oxygen. The two gases are mixed stoichiometrically (36.5 % C_2H_2 and 62.5 % O_2) using a gas mixing system. The tolerance is ± 0.2 % for the mixture composition. The mixed gas is filled into the evacuated autoclave to atmospheric pressure.

Acetylene is a gas in the group of alkynes. It is characterised by its high carbon content and therefore has a high calorific value. Next to that, the required ignition energy is low, which helps to initiate the combustion. This is the advantage using a high energetic gas like Acetylene. A disadvantage of Acetylene is the intensive illumination of the flame and the strong sooting. This can pose visibility challenges in certain applications.

1.2. Ignition Source

Compared to the previous design (Seeber et al.(2023)) the igniter has been optimized. The two ignition methods are compared in the following.

To ignite the gas cloud and to start the exothermic reaction, an ignition source with sufficient strength to establish a stable detonation is required. Table 1 describes possible ignition sources. In this case, the common way is to use an exploding wire. The exploding wire (e.w.) is described in the DIN 1839 and has been approved to be suitable for gas testing (Filip et al.(1982)). The exploding wire consist of a thin wire (0.05 mm to 0.2 mm), e.g. nickelin, which is attached to two parallel electrodes. In this case, a nickelin wire with a thickness of 0.1 mm is soldered to the electrodes. A voltage is applied to the wire by means of an igniter, causing it to vaporize. Then an arc burns between the two electrodes. With this setup, high ignition energy can be achieved.

Table 1: Overview of different ignition source (Spitzer, Askar et al. (2021)

Ignition Source	Energy range [J]	Adjustable Energy	Used/Found in	Affecting chemical reaction
Exploding wire	Low to high, 2-5.000	Yes	EN 1839 B, ASTM E918, EN ISO 10156	No
Chemical ignitor	Moderate to high 100-10.000	No, Stepwise	EN 14034 series	Yes
Induction spark	Low, <10	Yes	EN 1839, ASTM E681	No
Surface-gap-spark	Low, 10-40	Yes	ASTM (2079)	No

As a power source for melting the wire, an ignitor HZG-1839 (half-wave ignition device) with a set ignition duration of 8.5 ms is used. A caliometric measurement of the ignitor showed an ignition energy of 38 J with this setup.

Another way is the use of an electric ignitor. The electric ignitor EMP-U-EPX2-SO is a pyrotechnic product with fusehead EPX2-S, which will conducted with an ignition device. This fusehead consists of a small amount of explosive substance (0.04 g).
One disadvantage is the variation of the ignition position which depends on the length of the wire and the twisting. Also the burn-off behavior is difficult to reproduce. Accordingly, an exploding wire is used as the ignition source.

Figure 2: Ignition of an EMP-U-EPX2-SO in Methane (left); Ignition of a exploding wire in air (right)

The ignition pattern of the two detonators also differs. This can be clearly seen in Figure 2. The pyrotechnic detonator explodes. This produces several strips of flame that are distributed randomly. This makes it difficult to reproduce the ignition. In contrast to the igniter head, the exploding wire produces an arc. The same combustion pattern is generated at the same point with each pass.

The ignitor is integrated into the vessel on the opposite and at the height of the outlet. This offers the advantage that the ignition position is the same in every pass of the test campaign.

2. Results and discussion

The results of two series of tests with different ignition sources are compared below. Test series V2 with the fusehead (Seeber et al.(2023)) and the optimized test bench with the exploding wire V6.

The aim of the experiment is to present a test bench, which generates a shock with a good reproducibility. The first point is the ignition of the denotative gas mixture in the SWG. As soon as the gas mixture is ignited, the exothermic reaction begins. A supersonic detonation front is formed. During the process, the pressure inside the autoclave rises sharply. This can be seen in the following illustration. After ignition, the pressure rises after 0.85 ms and reaches its maximum at around 10500 kPa. These high internal pressures of the autoclave may indicate unstable detonations. They can also be amplified by pressure pilling on the built-in pressure sensor if the sensor is not installed flush (Schildberg 2016). The pressure then drops because of the failure of the rupture disc, thus the compressed gas expands through the orifice to the outside. The pressure values in the autoclave fluctuate in the aftermath. Peaks are repeatedly formed in between. These can be attributed to reflections inside the SWG. The pressure converges to the ambient pressure.

The following figure shows pressures in the autoclave (PA1) from tests 1-3 within test campaign V6. These curves look almost identical and are difficult to distinguish, which is a sign of reproducibility throughout the tests. The time at which the first shock reaches the sensor and the maximum pressure varies.

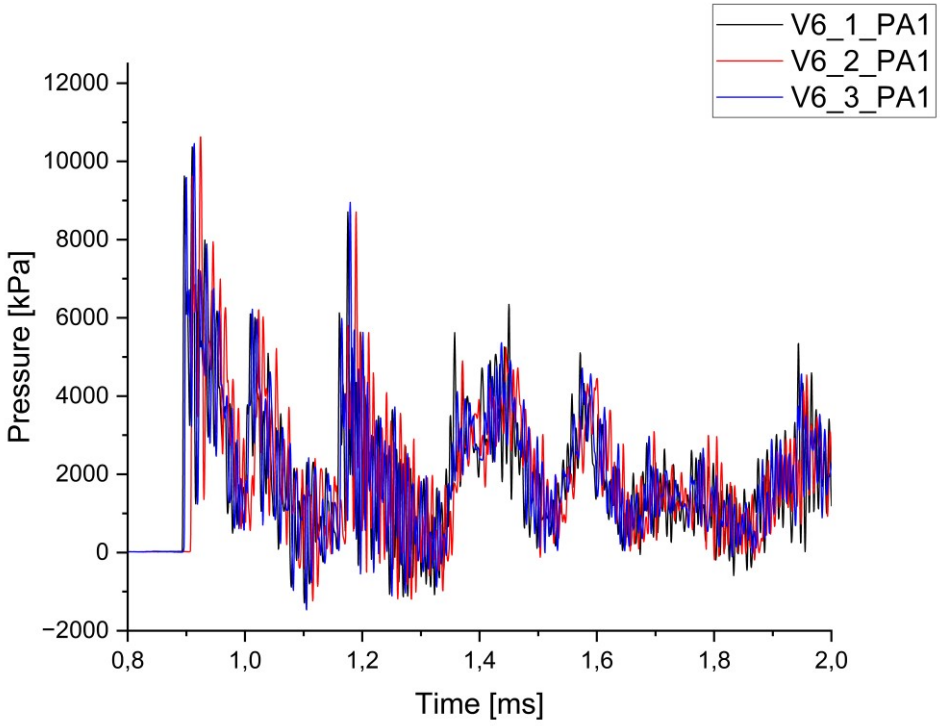

Fig. 3. *Pressure inside the SWG over the time for test run 1-3 with an exploding wire*

The following Figure 4 also shows the pressure inside the autoclave over time. In this test series the electric ignitor with a fusehead is used (V2). Compared to the curves in Figure 3, these are easy to distinguish. The significant time delay in the arrival of the blast at the sensor is striking. The time difference here is approx. 0.47 ms. The peak pressure and the subsequent fluctuation are almost identical. This can be seen in the Table 2.

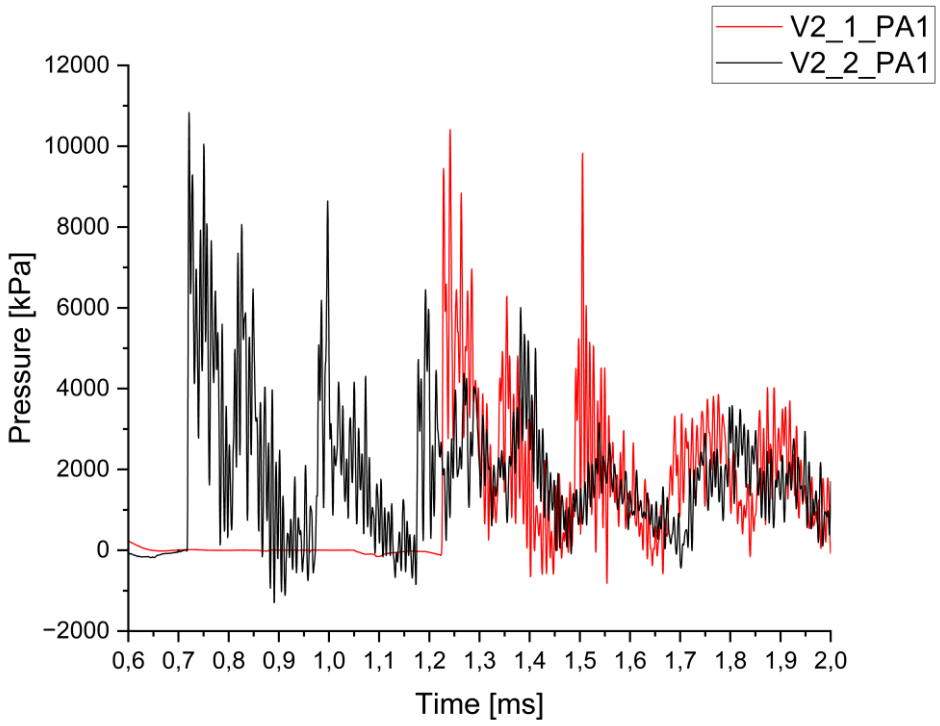

Figure 4: Pressure inside the SWG over the time with an fusehead

These pressure values are a good measure of the quality of the detonation process. If there were differences in the curves, this would be an indication of a deviation in the gas mixture or the ignition settings. These errors would propagate, as the detonation in the autoclave is the initial event in the process chain.

In order to demonstrate the improved reproducibility of the pressures generated with the electric wire (e.w.), the following table shows some of the measured values to compare the ignition source. For this purpose, the first maximum is considered, the arrival time and the standard deviation of the difference between the pressure curves $\sigma\Delta p$ are determined. The first test (V2_1 and V6_1) are used as reference values.

Table 2:Overview of the peak pressure, time of arrival and $\sigma\Delta p$ in dependence of the ignition source

	V2_1	V2_2	V2_3	V6_1	V6_2	V6_3
Igniton Source	Fusehead	Fusehead	Fusehead	e.w.	e.w.	e.w.
First peak pressure [kPa]	10830	9450	15377	9627	9620	9592
Time of arrival [ms]	0.717	1.125	3.13	0.893	0.907	0.896
$\sigma\Delta p$ [kPa]	Reference	120	526	Reference	97.8	97.2

The smaller standard deviation in terms of pressure can be clearly seen in test series V6. The arrival times also do not fluctuate as much compared to test series V2.

Shock

The ideal pressure curve according to Friedlander comprises a very steep pressure increase. After reaching the peak overpressure, the pressure decreases exponentially into a negative pressure phase. Eventually, the pressure oscillates around ambient pressure (Sochet et al. 2018). This is shown in the following Figure 5.

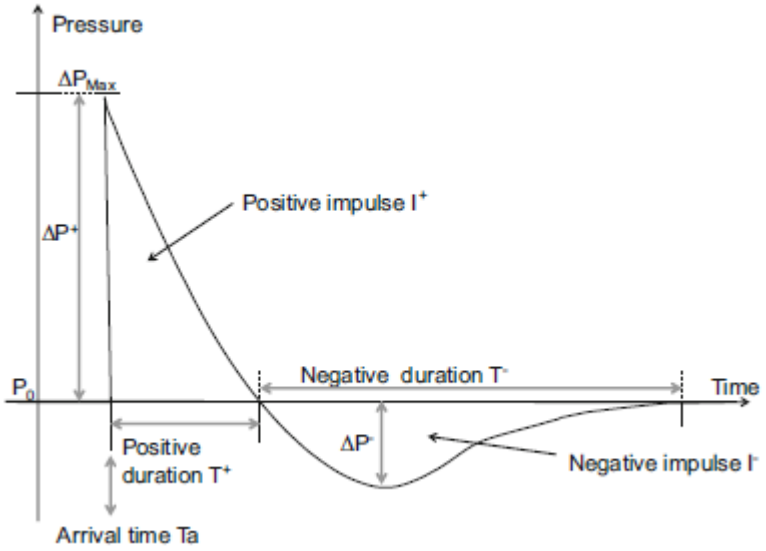

Figure 5: Ideal Friedlander waveform (Sochet et al. 2018)

The peak overpressure, the positive momentum and the positive phase duration are often used as a measure for characterisation of the shock wave. The positive phase duration is the time span with an overpressure load. The positive phase duration is difficult to determine as the pressure values are characterised by releases and fluctuations. The calculation of the positive momentum is also affected. The peak overpressure is therefore used to assess the reproducibility of the test rig.

In this test campaign, two pencil probes are used. Both stand on the same side of the outlet in 1 and 1.5 m distance.

Figure 6 shows the recorded pressures of the pencil probes of the test V6. The maximum overpressures are nearly the same. The curve also looks almost identical. The second peak of the pressure values of the 1 m sensors is remarkable. This is significantly larger in the first run. The cause must be determined in further investigations. In contrast to the ideal pressure curve in Friedlander's free field, several peaks can be recognized when the curve drops. These can be attributed to a complex reflection configuration. There is also a difference (approx. 0.2 ms) between the tests in the arrival time of the shocks. The set-up and procedure did not change between the individual tests.

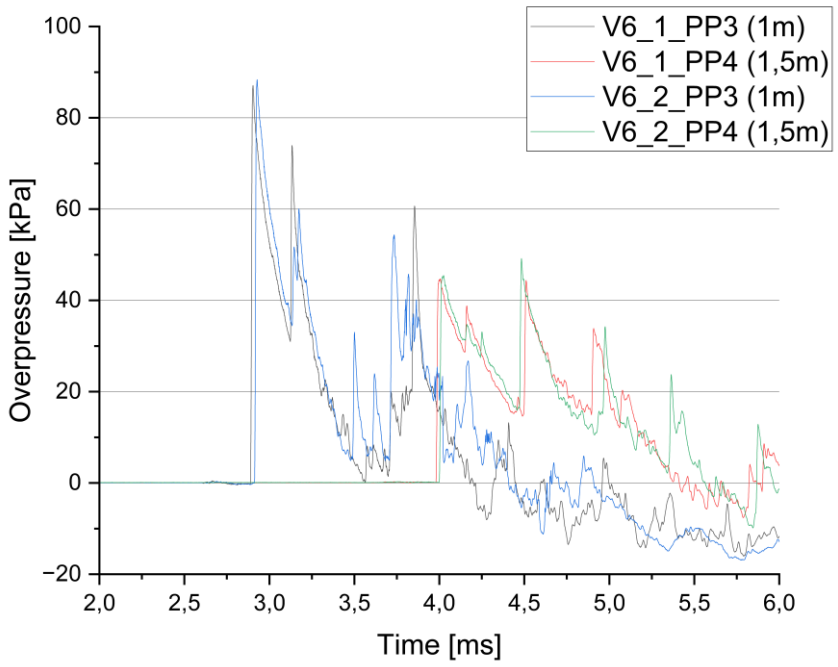

Figure 6: Overpressure measured in 1 and 1,5m distance at the test 1-3

Further test results are summarized in Table 3. In addition to the overpressure, the time of arrival of the pressure wave also fluctuates. The arrival time is the time at which the shock reaches the sensor and causes the pressure to rise. As well the difference between the arrival time from pencil probe 3 (PP3) and pencil probe 4 (PP4) is fluctuating between 1.086 - 1.107 ms. This small deviation is evidence of good repeatability of the tests. This time difference is not depending on the start of the detonation process. It is only depending on the propagation speed of the blast.

Table 3:Overview of Overpressure & Arrival time from trial 1 - 5

Trial	PP3 (1m)		PP4 (1,5m)	
	Peak Overpressure [kPa]	Arrival time [ms]	Peak Overpressure [kPa]	Arrival time [ms]
V6_1	87.08	2.889	44.73	3.98
V6_2	88.35	2.913	45.22	3.999
V6_3	84.19	2.908	44.64	3.995
V6_4	88.44	2.926	46.49	4.033
V6_5	85.87	2.887	46.28	3.992

The Figure 7 shows the measured pressure from the pencil probes in the test campaign V6 and V2.

The average overpressure is 88.1 kPa at 1 m distance in the V6 test. The standard deviation σ, which is a good tool for the reproducibility of the test bench, is 2.8 kPa. In comparison σ is 10.1 kPa for the test involving the ignitor with the fusehead.

In 1.5 m distance to the outlet the average peak overpressure is 46.5 kPa and the standard deviation is 1.3 kPa. The standard deviation from test series V2 is also higher for the distance than for test series

V6. 10 measurements are considered for the analyses, which is not reliable statistical statement, only a qualitative value.

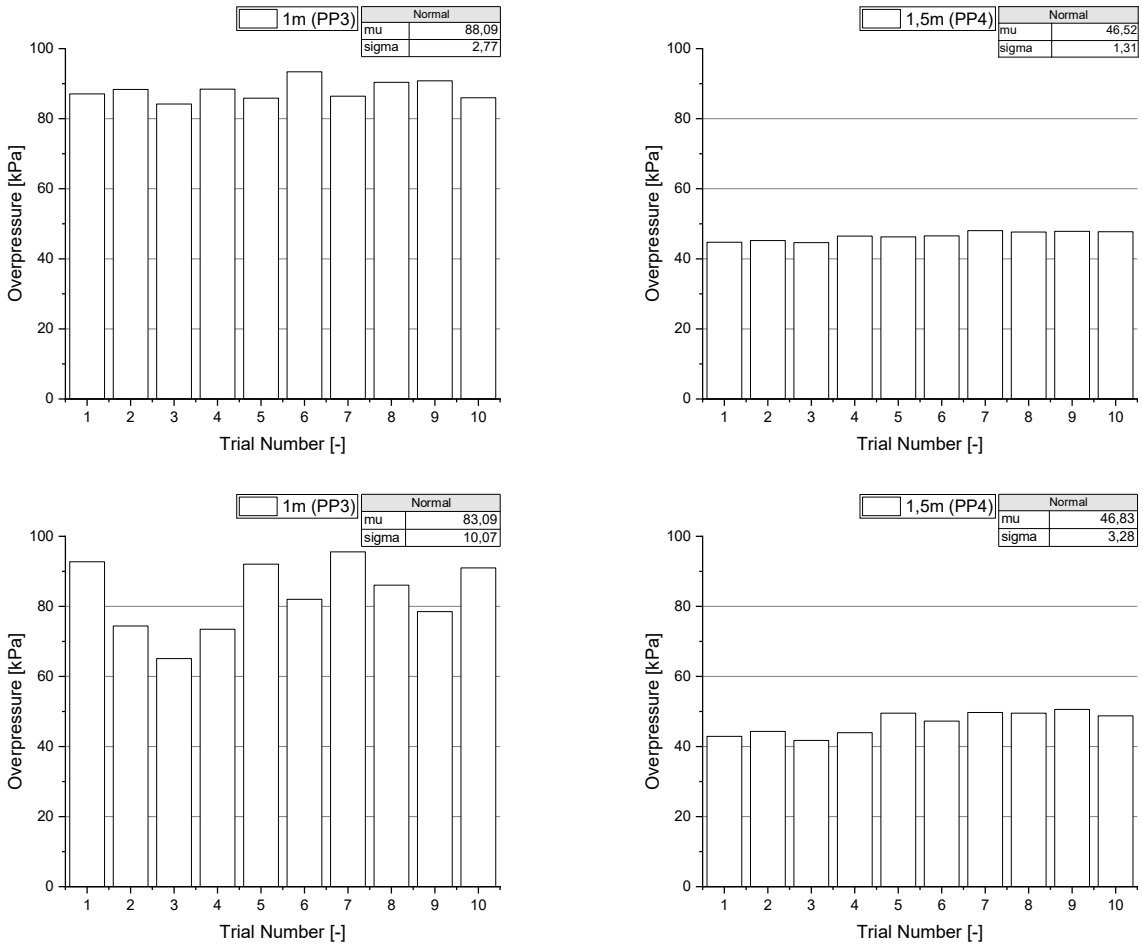

Figure 7: Comparison of the peak overpressure between 1 (left) and 1.5 m (right); test series V6 (top) and test series V2 (bottom)

3. Conclusions

In summary, this paper should demonstrate that the presented test setup is suitable for generating a shock. This should be reproducible in a short time to generate a valid and comprehensive database for the subject to be investigated.

Two different ignition sources for the generation of shock waves were presented. One is the electric igniter with a fusehead and the other is the exploding wire. For this purpose, test series were compared with the respective detonators. The exploding wire showed the better reproducibility with regard to pressure inside the autoclave and the generated shocks. Therefore, the exploding wire will be used for further tests in the future.

The presented test set-up delivered the expected results at short intervals (less than 30 min turn-around time). The peak overpressures could be reproduced well. The standard deviation in the test series with the exploding wire was 2.8 kPa in comparison to the 10.1 kPa with the fusehead at 1 meter.

Despite the good results with regard to the overpressures, there is potential for improvement that was identified. On the one hand, the aim is to further improve reproducibility and to clarify some phenomena, such as the different arrival times of the shock waves. The reflections that occur during the event need to be identified and reduced, so that the resulting curve is closer to the ideal Friedlander

curve. This would also allow better qualitative statements to be made with regard to the generated positive momentum, which was not presented in this paper.

References

Needham, C. E., et al. (2015). "Blast Testing Issues and TBI: Experimental Models That Lead to Wrong Conclusions." Frontiers in Neurology 6.

Aune V, Fagerholt E, Langseth M, Børvik T. A shock tube facility to generate blast loading on structures. International Journal of Protective Structures. 2016;7(3):340-366. doi:10.1177/2041419616666236

Mediavilla, V.R., Philippens M., Meijer S.R., van den Berg A.C., Sibma P.C., van Bree J.L.M.J, de Vries D.V.W.M. (2011). Physics of IED Blast Shock Tube Simulations for mTBI Research. Frontiers in Neurology.

Seeber, H., Krentel, D., Grasse, D. Gerbeit, M. Grobert, S. Hauer, T. (2023) "Experimental Setup for the Reproducible Generation of Pressure Waves in Free Field Conditions." International Symposium on Military Aspects of Blast and Shock 26

Filip, A., 1982. Elektrische Funken und explodierende Drähte als Zündquellen brennbarer Methan-Luftgemische, vol. 208. EMPA Bericht Nr, Dübendorf, Switzerland. https://doi.org/10.3929/ethz-a-000243429.

Schildberg, H. (2016). "Gas-Phase Detonations in Pipes: the 8 Possible Different Pressure Scenarios and their Static Equivalent Pressures Determined by the Pipe Wall Deformation Method (part 1)." Chemical Engineering Transactions 48: 241-246.

Spitzer, S., et al. (2021). "Comparative study on standardized ignition sources used for explosion testing." Journal of Loss Prevention in the Process Industries 71: 104516.

Sochet, I. (2018). Blast Effects: Physical Properties of Shock Waves, Springer Cham.

Explosion Suppression with Water Curtains Between Congested Regions

Daniel Allason [a], D. Michael Johnson [a], Andrzej Peka ski[b], Antoine Dutertre[c], Duncan Mansfield[d]

[a] DNV Spadeadam Research & Testing, Cumbria, UK

[b] Shell Research Limited, UK

[c] TotalEnergies SE, France

[d] Woodside Energy, Australia

E-mail: daniel.allason@dnv.com

Abstract

Vapour cloud explosions (VCEs) are rare events but can lead to severe consequences in terms of harm to people and damage to onshore and offshore facilities. Research conducted in the latter part of the 20th century demonstrated the key role of congestion, such as process pipework, within the flammable cloud in accelerating the flame to high speeds. In recent years it has also become accepted that at least some major VCEs have involved flame acceleration to the point where deflagration to detonation transition (DDT) occurred (Chamberlain et al, 2019). Limiting the size of congested regions can potentially reduce the chance of DDT, however in addition the regions need to be adequately separated to avoid a fast flame from one region entering a second. Previous research into explosion safety gaps at large scale has shown that the introduction of gaps between regions can significantly reduce the magnitude of an explosion (Skjold, 2016).

However, on facilities where space is at a premium, the provision of sufficient gaps may be impossible or incur high costs. The DOWSES (Development Of Water Spray Explosion Suppression) experimental research programme studied the effect of water curtains installed in the gap between congested regions. To establish the benefit provided by the water curtains, baseline explosion experiments without water sprays were performed, one of which resulted in DDT in the second congested region (Allason et al,2019), one giving a high-pressure deflagration and one with low interaction between the congested regions.

This paper extends the reporting of results to include the experiments with water spray mitigation, not available at the time of the last publication. The experiments involved variation in water spray configuration, the type of congested region and the spacing between the congested regions. In addition, an experiment was conducted with a particulate added to the water. Detailed results from the experiments are presented: ***in every instance where water was introduced into the vapour cloud, the baseline explosion was significantly mitigated***. In the configuration where DDT had occurred in the baseline experiment, the water sprays prevented DDT.

Keywords: *vapour cloud explosions, mitigation, water sprays, experiments, detonation, DDT*

Introduction

This paper details observations from large-scale experiments performed during the Joint Industry Project: Development Of Water Spray Explosion Suppression (DOWSES) experimental campaign carried out at DNV Spadeadam Testing and Research Centre in Cumbria, UK.

Building on the research carried out at Spadeadam in the 1990s (SCI, 1998, Al Hassan, 1998 and Catlin, 1993), gained through a series of large scale experimental programmes conducted in the wake of the Piper Alpha disaster, DOWSES was designed to take the outline knowledge developed in this

period and apply it to the more modern problem of highly congested process facilities prevalent in floating oil and gas production facilities.

The work conducted by British Gas in the 1990s concluded that significant mitigation of explosions can be attained through the introduction of water sprays / curtains within congested regions. The interaction of the flow ahead of the flame with the water droplets is critical in providing breakup of the droplets and subsequent mitigation through evaporation of the resulting small droplets in the combustion zone of the explosion event (Catlin, 1993). Industry funded work (Thomas, 2000) provided a summary of droplet-flow-flame interactions and conducted some fundamental experiments concerned with interaction of droplets and accelerating flows.

The experiments in DOWSES involved the ignition of a vapour cloud enveloping two separate congested regions (a donor and acceptor region) where a water curtain was installed within the gap between them to assess mitigation potential.

Four baseline experiments were performed without a water curtain to provide a comparison with the corresponding water-mitigated event. The mitigation effects of water curtains were investigated through the variation of the following parameters:

- Curtain position (near DONOR, near ACCEPTOR or central within the gap)
- Nozzle type (full cone, flat fan)
- Water quantity
- Nozzle orientation (downwards/upwards)

In Allason (2019), the results of one of the baseline experiments was detailed along with some discussion on the types of water droplet which might prove suitable for mitigating the baseline event. That publication gave the experimental arrangement in detail which is not repeated here. The remainder of this paper summarises the results obtained from the water curtain experiments and the relative effectiveness of the different arrangements in mitigating the baseline experiments.

1 Experiments

1.1 Experimental Arrangement

1.1.1 Test Facility

In order to carry out the experimental programme, a test facility was adapted for this project at Spadeadam. An illustration of the test configuration is shown in Figure 1. The facility consisted of the following components:

- 3 m high steel angle frame covering an area 26 m long by 6 m wide.
- Congested pipework regions
- Gas injection and recirculation system
- Gas sampling system

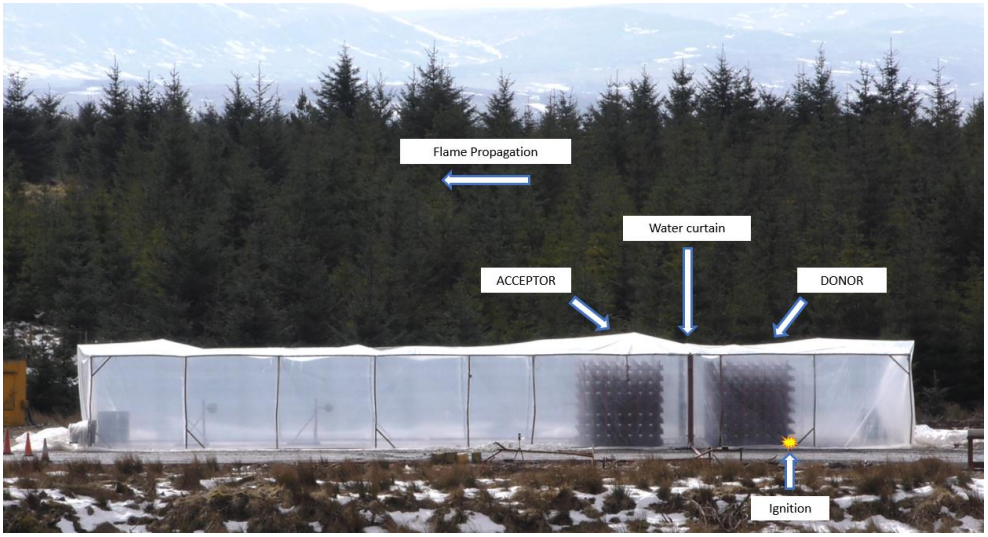

Figure 1: Experimental configuration.

The congested regions used for this study were originally constructed for a programme of experiments conducted by Shell Research. Congestion type Rig9 is formed by half of congestion type Rig7. Figure 2 and Figure 3 show the test arrangement using different congested regions. Table 1 summarises the specifications for these regions.

Table 1: Specifications of congested regions

Congestion Type (Rig)	**Pipe Diameter (mm)**	**Number of pipes (L x W x H)**	**Distance between centerlines (pitch) (mm)**	**Approx. Volume Blockage (%)**
Rig7	76.1	16 x 16 x 8	342	12
Rig9	76.1	8 x 16 x 8	342	12

For each experiment, the congested regions under test were separated by a distance defined in numbers of pitches of the congested pipework to form the gap. The definition is made such that a separation distance of SD0 is defined as when the rigs are separated by a single pitch (i.e. essentially one continuous congested region).

Figure 2: Congestion type Rig 9 (separation distance SD4)

Figure 3: Congestion type Rig 7 (separation distance SD2).

The experimental facility was instrumented for gas concentration measurements, dynamic pressure measurement, flame arrival times and high-speed videography. Principally in this paper, comparisons are made between the peak dynamic overpressure recorded at the array of dynamic pressure sensors deployed underneath the acceptor or within the vapour cloud ('Internal Sensors', Figure 4). Reference is also made to peak overpressure measurements at sensors deployed outside of the vapour cloud ('External Sensors', Figure 5).

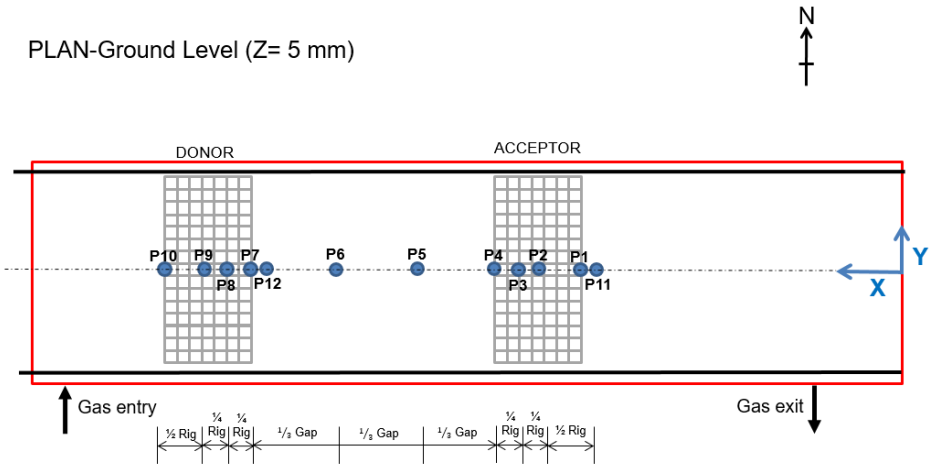

Figure 4: Location of internal pressure transducers.

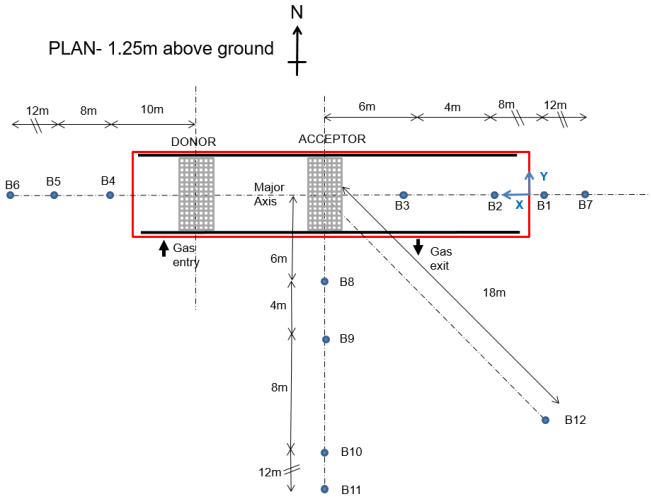

Figure 5: Location of external pressure transducers.

Further details of the experimental arrangement are provided in Allason, 2019.

1.1.2 Water curtain arrangement

Several water curtain arrangements were tested to determine a configuration with the optimal level of explosion mitigation. The experimental programme included experiments where the position of the water curtain within the gap (central, near donor or near acceptor); nozzle type (full cone/flat fan); nozzle direction (downwards/upwards) and water line pressure (i.e. water quantity) were assessed. In addition, double curtain and general area deluge configurations were used to compare with the single

curtain arrangements. Two experiments were performed using a high-pressure water mist delivery system and 40 nozzles over the acceptor region.

Figure 6 shows example photographs of the different types of water delivery arrangements installed in the facility. A remotely operated high-capacity water pump was used to provide water to the arrangements at a pre-set pressure (up to 7 barg).

Figure 6: Example of water curtain arrangements. (a) Single curtain (in middle of gap), (b) upwards curtain, (c) double curtain, (d) general area deluge

1.1.3 Nozzles and Spray Characterisation

Two types of nozzles were used in the single and double curtain arrangements throughout the experimental program. Tyco HV-17 and Bette NF-120 were full cone nozzles and flat fan type nozzles respectively and were selected to have a similar k-factor between 25-30 L/min (i.e. flow rate through the nozzle at 1 barg). Figure 7 shows some details from the data sheets for each nozzle. In single curtain arrangements 11 nozzles were equally spaced (500 mm separation) along the curtain frame. The pressure in the supply pipe to the water curtain was measured at the point of experiment initiation and a flow rate calculated using the measured pressure, the number of nozzles and the manufacturer supplied k-factor for the nozzles in use. The nominal 1 barg experiments gave total calculated water flow rates out of the curtain of between 295 and 329 litres per minute. The 3 barg experiments were conducted with calculated total flows of 464 and 457 litres per minute for the flat and full nozzle types respectively.

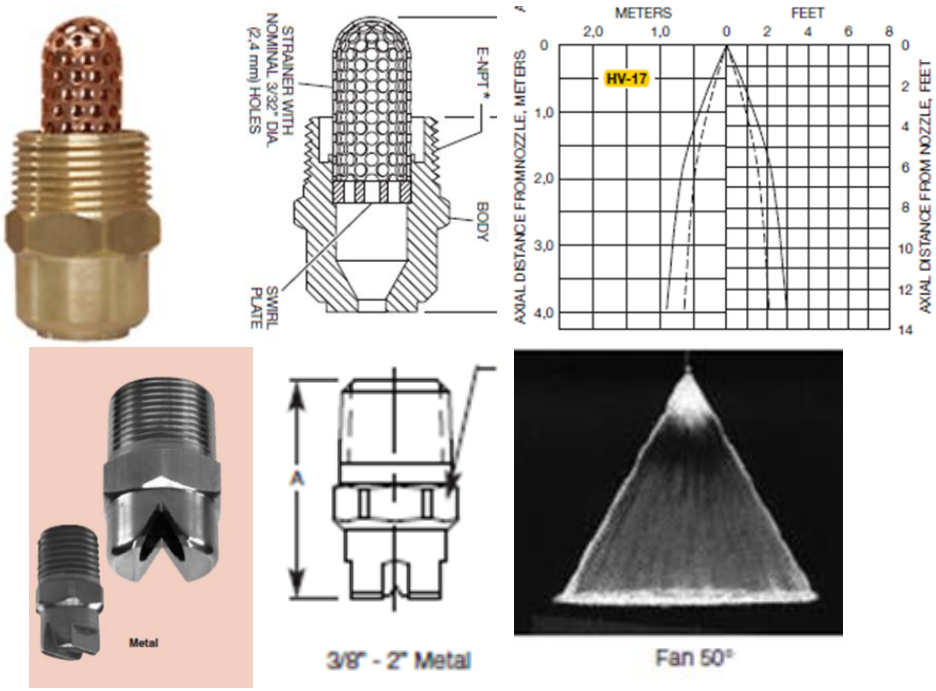

Figure 7: HV17 Full Cone nozzle (top) and NF120 Flat Fan nozzle (bottom)

A set of trials on the different spray nozzles used in the curtain experiments was conducted. These trials involved the filming of the sprays at different water supply pressure and the subsequent analysis of the video footage to determine the droplet size distribution within the spray. Each frame of a back-lit, high-speed video of the spray was first converted to a binary image and then analysed using morphological tools in MATLAB to produce a histogram of droplet sizes (equivalent radius). Analysis of multiple frames meant that tens of thousands of droplets could be measured and included in the histogram for each nozzle / pressure combination.

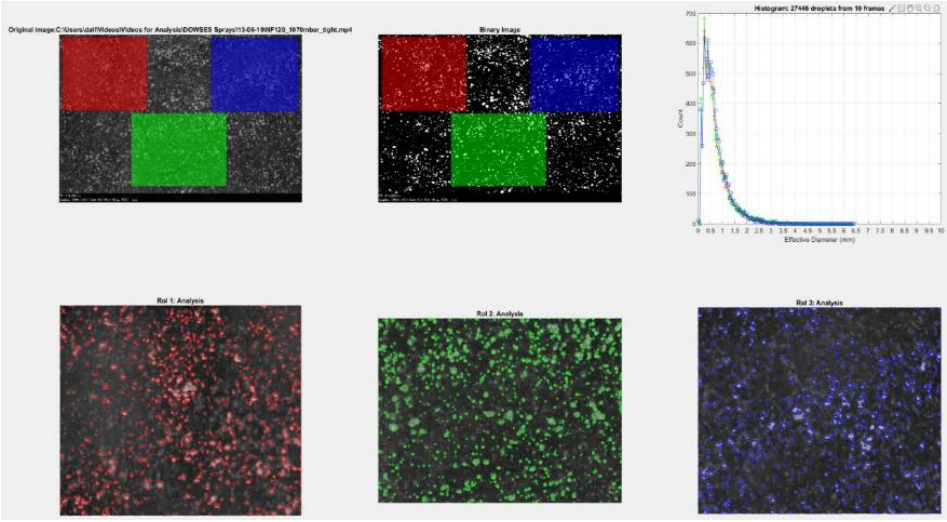

Figure 8: Example spray analysis showing original image, binary image, regions of interest, identified droplets and histogram of measured droplet diameters.

Four analyses were conducted: at nominal feed pressures of 1 bar and 2.5 bar with each of the NF120 and HV17 nozzles. The droplet size distribution by percentage of volume contributed for each nozzle / feed pressure combination is shown in Figure 9. This information can be used with knowledge of the flow rate through the nozzle to represent the make-up of the resulting spray in terms of droplet size.

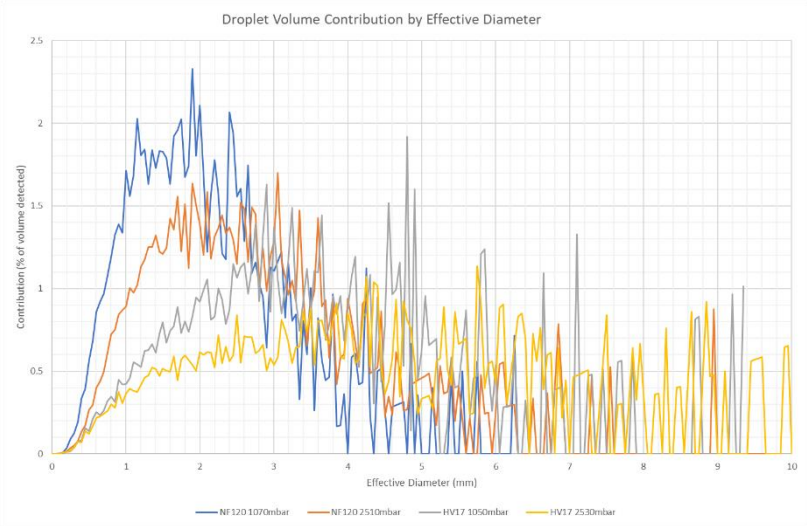

Figure 9: Normalised Droplet Distribution by Volume

It can be seen from this analysis that:

- For both nozzle types, the effect of increasing the pressure (and flow) is to marginally change the droplet size distribution (in volumetric terms) towards larger droplets.
- The HV17 nozzle has more of its volume flow being distributed as larger droplets than the NF120 at both of the feed pressures analysed.
- The most volume contribution was from droplets greater than 1 mm in diameter for all nozzle / feed pressure combinations.

1.2 Experimental Programme

Using the experimental facility and equipment described above, a set of 25 large scale explosion experiments were performed as detailed in Table 2, below. The table details the experiment ID, congestion type, curtain and nozzle arrangements and gives the prime objective of each experiment.

Table 2: Experimental Programme

Experiment ID	Congestion Type	Fuel	Unmitigated Interaction Level	Curtain Arrangement	Nozzle Arrangement	OBJECTIVE
DR9P1 SD4R	Rig9	Propane	DDT	No curtain	-	Baseline experiment
DR9P1 SD4RR	Rig9	Propane	DDT	No curtain	-	Baseline experiment with curtain frame in place
DR9P1 SD4 11HV17_1bar	Rig9	Propane	DDT	Single, central	Full cone, downwards	Find optimal curtain **location** in high interaction
DR9P1 SD4D 11HV17_1bar	Rig9	Propane	DDT	Single, Donor exit	Full cone, downwards	Find optimal curtain **location** in high interaction
DR9P1 SD4A 11HV17_1bar	Rig9	Propane	DDT	Single, Acceptor entry	Full cone, downwards	Find optimal curtain **location** in high interaction
DR9P1 SD4A 11NF120_1bar	Rig9	Propane	DDT	Single, Acceptor entry	Fan, downwards	Find optimal curtain **arrangement** in high interaction
DR9P1 SD4A 11NF120_3bar	Rig9	Propane	DDT	Single, Acceptor entry	Optimal from 1-4 but different water qty	Find optimal curtain **arrangement** in high interaction
DR9P1 SD4A 11NF120_3barUp	Rig9	Propane	DDT	Single, Acceptor entry	Fan, upwards	Find optimal curtain **arrangement** in high interaction
DR9P1 SD4A 11HV17_3barUp	Rig9	Propane	DDT	Single, Acceptor entry	Full cone, upwards	Find optimal curtain **arrangement** in high interaction
DR9P1 SD4A 11HV17_3bar	Rig9	Propane	DDT	Single, Acceptor entry	Full cone, downwards increased water qty	Check sensitivity to water quantity
DR9P1 SD4 GAD	Rig9	Propane	DDT	General Area Deluge on Acceptor	4 x MV57-140, downwards into acceptor	Comparison with General Area Deluge
DR9P1 SD4AR 11HV17_1bar	Rig9	Propane	DDT	Single, Acceptor entry	Full cone, downwards	Gain repeatability data
DR9P1 SD4 DC	Rig9	Propane	DDT	Donor exit and Acceptor entry	Full cone, downwards	Check double curtain effects
DR9P1 SD4DR 11HV17_1bar	Rig9	Propane	DDT	Single, Donor exit	Full cone, downwards	Gain repeatability data
DR9P1 SD4R 11HV17_1bar	Rig9	Propane	DDT	Single, central	Full cone, downwards	Gain repeatability data
DR9P1 SD4RR 11HV17_1bar	Rig9	Propane	DDT	Single, central	Full cone, downwards	Gain repeatability data
DR9P1 SD6A 11HV17_3bar	Rig9	Propane	Low	Single, Acceptor entry	Full cone, downwards	Effect of optimal arrangement on low interaction case
DR9M1 SD4	Rig9	Methane	High	No curtain	-	Baseline Methane Rig9 case
DR9M1 SD4A 11HV17_3bar	Rig9	Methane	High	Single, Acceptor entry	Full cone, downwards	Effect of fuel type on optimal arrangement
DR9P1 SD4 PI1	Rig9	Propane	DDT	High pressure and misting nozzle system with particulate injection (200g/L)	Misting Nozzles	Assess effect of high pressure system and misting nozzles (with particulates)
DR9P1 SD4 PI2	Rig9	Propane	DDT	High pressure and misting nozzle system with water only	Misting Nozzles	Assess effect of high pressure system and misting nozzles
DR7M1 SD2	Rig7	Methane	High	No curtain	-	Baseline experiment
DR7M1 SD2A 11HV17_3bar	Rig7	Methane	High	Single, Acceptor entry	Full cone, downwards	Effect of congestion type on optimal arrangement
DR7M1 SD2A 11NF120_3bar	Rig7	Methane	High	Single, Acceptor entry	Fan, downwards	Check optimal arrangement still optimal
DR7M1 SD2AR 11HV17_3bar	Rig7	Methane	High	Single, Acceptor entry	Full cone, downwards	Gain repeatability data

2 Results and discussion

Throughout this section observations are made of the 'peak pressure' recorded at various locations in the experimental facility. The peak pressure is reported after the high sample frequency recording has been subjected to a 0.1 ms rolling average smoothing to remove high frequency noise events and noise considered of low consequence in the scope of the explosion event.

For clarity, the peak pressure underneath the donor is taken as the highest pressure generated by the donor event, all other peak references are for the maximum recording at a location generated by the acceptor explosion event, the event with which the experimental programme is intended to mitigate. This means that, when mitigated, the value reported for peak pressure underneath the acceptor or in the field downstream of the acceptor may not be the peak value throughout the whole experiment at that location but is the maximum identified for the acceptor event in isolation.

Using these peak values, it is possible to qualitatively assess the change in severity of the donor and acceptor events in each experiment versus its corresponding baseline and other similar experiments.

2.1 Baseline experiments

Baseline experiments, where no water curtain was present, were conducted to assess and quantify the level of mitigation achieved in experiments with water curtains.

Baseline experiments were conducted with the following congestion, separation distance and fuel configurations:

1. Rig9, SD4 and propane (high interaction, resulted in severe DDT event), 2 experiments (DR9P1 SD4R and DR9P1 SD4RR)
2. Rig9, SD4 and methane (high interaction), 1 experiment (DR9M1 SD4)
3. Rig7, SD2 and methane (high interaction), 1 experiment (DR7M1 SD2)

The evolution of peak pressure in each baseline experiment can be visualised by plotting the peak value recorded against the location of the measurement. The plot in Figure 10 shows this evolution along the major axis of the experimental rig for each of the 4 baseline experiments. Both of the Rig9, propane experiments resulted in DDT and this is illustrated by the sustained high pressure recorded within the remainder of the vapour cloud after the congested region has ended. All other baseline experiments with no DDT gave a decaying pressure beyond the end of the congestion. The Rig7, methane experiment showed a similar peak overpressure at the exit of the acceptor but with a different rate of increase through a longer region of congestion. The Rig9 methane case showed a similar profile to the Rig7 methane case but with a lower peak pressure, as would be expected.

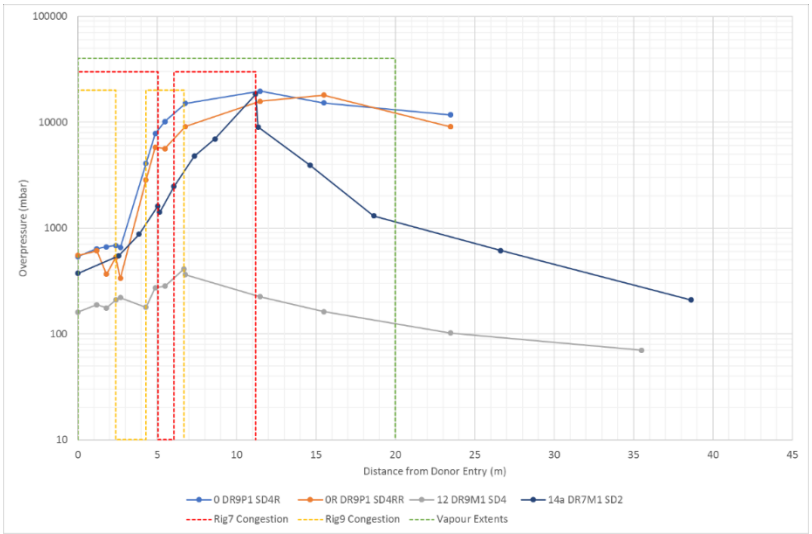

Figure 10: Evolution of peak pressure travelling east from ignition location in baseline experiments.

2.2 Water curtain location

Three locations for the water curtain frame within the gap were considered: central, near the donor and near the acceptor. These experiments were conducted with the same nozzle type (full cone nozzles), and water quantity (nominally 1 barg). These experiments were also chosen for repeatability studies, therefore, two like experiments were performed with the water curtain located both near the donor and near the acceptor, whereas three experiments were conducted in the central location. The development of peak pressure throughout the test rig is shown in Figure 11 for each of the experiments where water curtain location was the only variable to be altered. Experiments with the same water curtain location are shown as the same colour. One of the experiments conducted for a central water curtain shows as an anomaly and this is thought to be because the water pressure achieved was nominally 20% lower than in the other experiments and it is thought that the curtain was not fully developed at the time of firing. Despite best efforts to achieve equal water line pressures in every experiment, a certain degree of variability is to be expected. This resulted in lower water quantity and markedly higher explosion overpressures which were not comparable to the subsequent repeated experiments although still showed some mitigation of the baseline event. Figure 11 appears to show a clear trend for greater mitigation of the explosion as the curtain moves closer to the acceptor region. This could be attributed to a number of factors and is likely associated with the potential for a greater volume of water to be displaced into the acceptor.

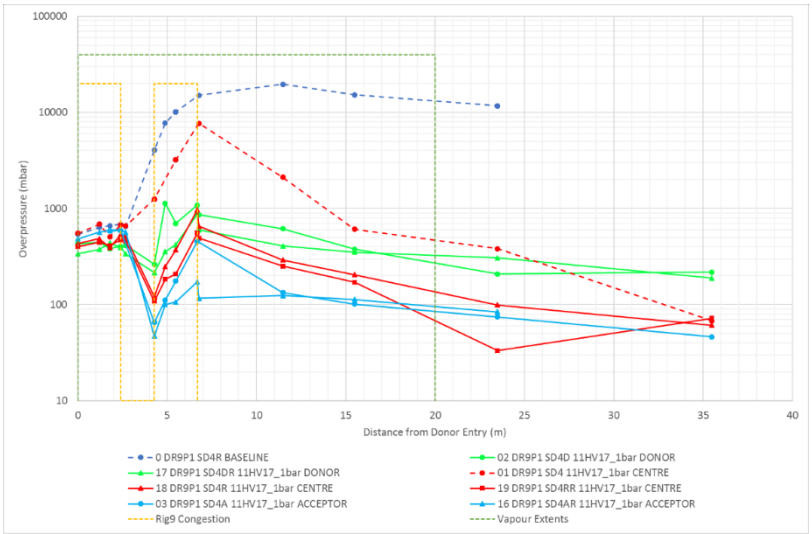

Figure 11: Peak pressure recorded on the major axis of the test rig in experiments with different curtain positions.

2.3 Effect of nozzle type

Figure 12 and Figure 13 below show the effect of nozzle type on the overpressure recorded at various locations internal and external to the vapour cloud. The experiments were conducted with a nominal water line pressure of 1 barg and 3 barg respectively. The nominal 1 barg experiments with the full cone nozzles gave total calculated water flow rates out of the curtain of between 295 and 329 litres per minute. The flat fan nozzle gave a lower total flow by about 6-10% compared to the two full cone nozzle experiments against which it is compared. The 3 barg experiments were conducted with calculated total flows of 464 and 457 litres per minute for the flat and full nozzle types respectively. At both 1 barg and 3 barg nominal curtain supply pressure, the full cone nozzles provided better mitigation of the baseline event than flat fan nozzles although both types stopped DDT from occurring.

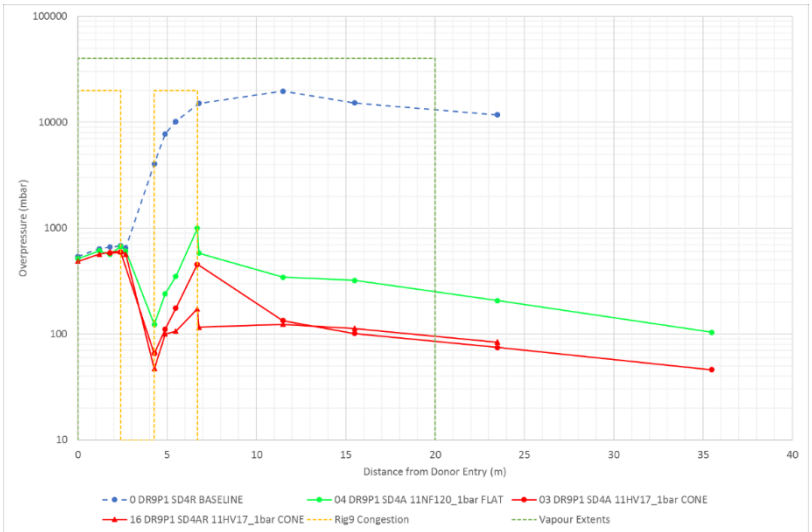

Figure 12: Effect of nozzle type (at 1 barg water line pressure) on explosion overpressure.

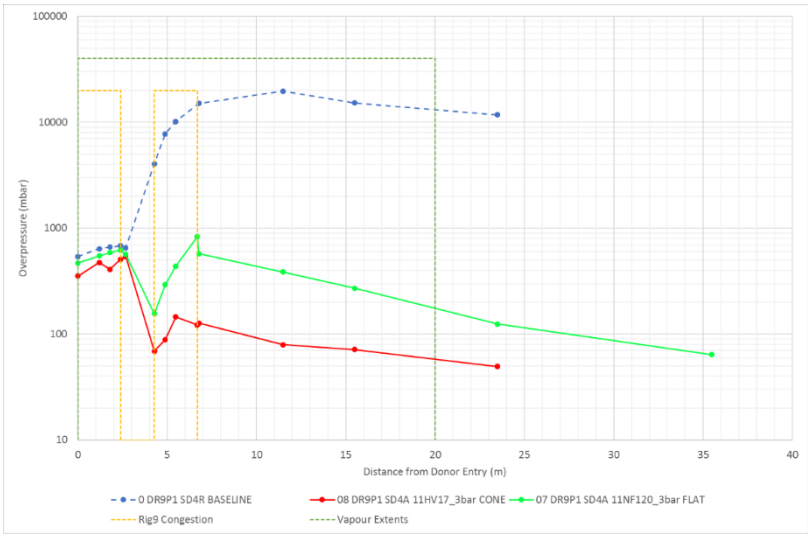

Figure 13: Effect of nozzle type (at 3 barg water line pressure) on explosion overpressure at various locations.

2.4 Water quantity and nozzle orientation

The potential for improved explosion mitigation due to water quantity increase was studied both by increasing the water line pressure and by changing the orientation of the curtain from a downwards to upwards configuration. With the flow rate of water through each nozzle being proportional to the square root of the pressure, a trebling of the pressure will only result in an increased flow of a factor of approx. 1.7 and would also give a higher initial velocity of droplet, potentially meaning that, in actuality, there may be a reduction in the number of water droplets suspended in the path of the flame. As such, it would be expected that the inversion of the nozzle from downwards facing and mounted at the top of the test rig to upwards facing and mounted at the bottom of the test rig would yield a greater quantity of droplets suspended in the path of the flame than by merely increasing the water pressure.

Figure 14 and Figure 15 show comparisons of the experiments where the pressure in the curtain was varied for the cone and flat fan nozzles respectively. For the cone experiments, very marginal increase in mitigation of the acceptor event is seen although it is also noted that the donor event appears noticeably less severe. When the pressure is increased in the flat fan nozzle configuration, no discernible increase in mitigation is observed within the congested region while a small drop in far field peak pressures is observed. Again, the donor event is marginally weaker in the increased pressure case.

Figure 14: Effect of water quantity by pressure variation with full cone nozzles.

To provide cover up to the full height of the test rig, it was ascertained that a minimum pressure of 3 barg was required at the nozzle for both types of nozzle. The upwards curtain experiments were therefore conducted at this supply pressure and they are compared in Figure 16 and Figure 17 against the corresponding 3 barg downwards experiments. For the cone nozzles, the upwards orientation appears to have had little effect. The flat fan nozzle arrangement shows a reduction in peak pressure in both the donor and acceptor.

The physical size of the gap in these experiments (~1.7m) was such that it was impossible to stop the curtain interacting with the donor region. When the pressure or orientation is changed, it makes for an increased likelihood that the donor event will be partially reduced in severity. Given that this severity is a governing factor in how effective a particular curtain arrangement can be in mitigating the acceptor explosion, it is likely that this water-donor interaction is having a significant effect on the mitigation capacity of the curtain on the acceptor. The flow rate quoted for the upwards curtains has been doubled from the calculated outflow in an attempt to represent the amount of water suspended in the rig.

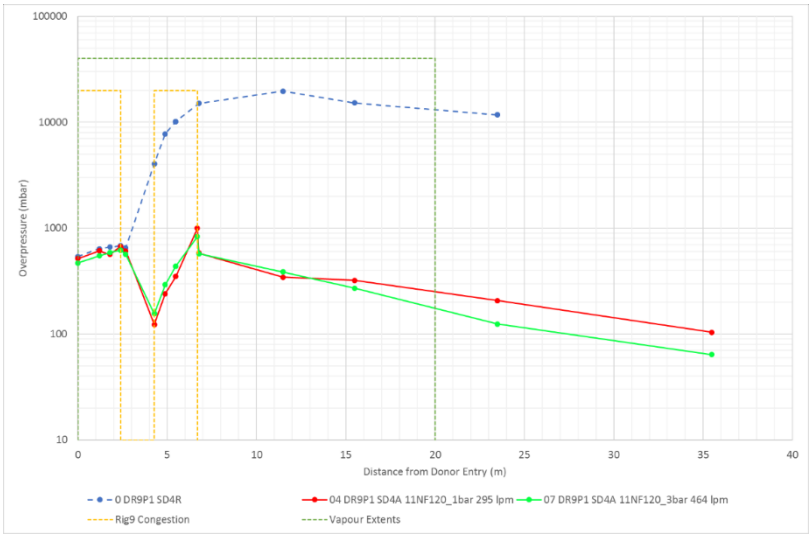

Figure 15: Effect of water quantity by pressure variation with flat fan nozzles.

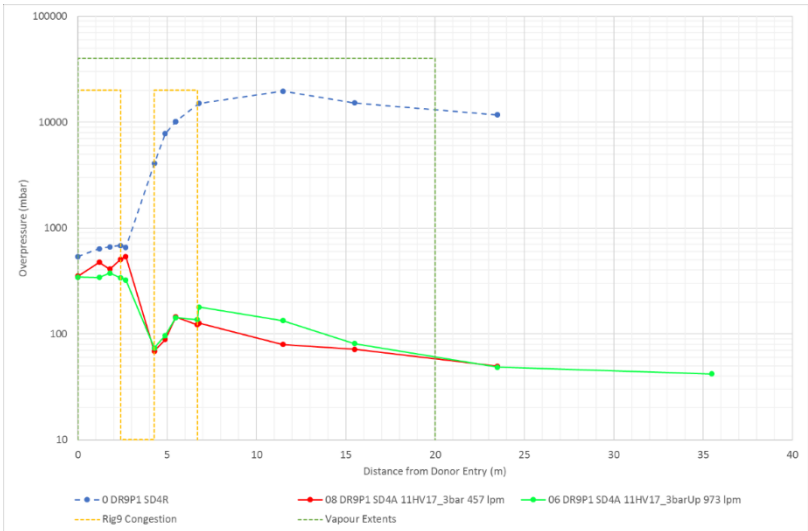

Figure 16: Effect of water quantity by nozzle orientation with full cone nozzles.

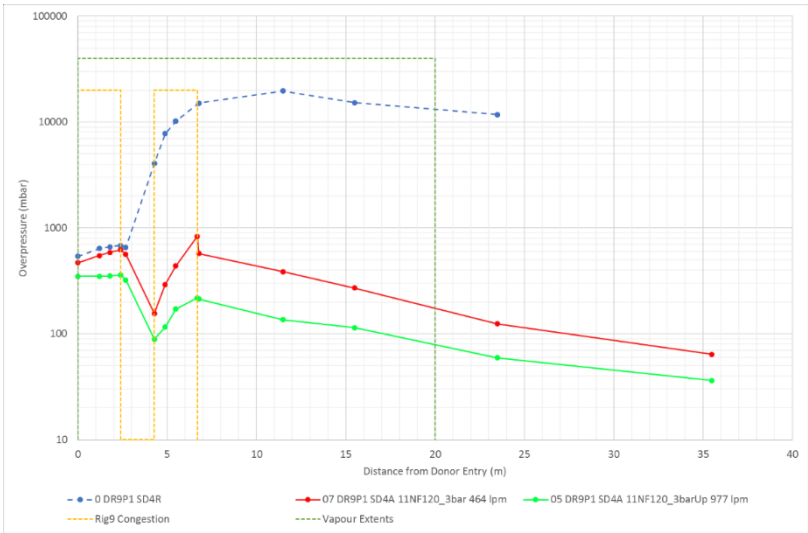

Figure 17: Effect of water quantity by nozzle orientation with flat fan nozzles.

2.5 Comparison of single, double curtains and general area deluge

A double curtain containing 2 rows of 11 HV17 cone nozzles was used in one experiment to investigate the effects of the thickness of the curtain on the mitigation effects.

A General Area Deluge (GA) system was installed to provide some information on the performance of the curtain in comparison to a system representative of that which might already be installed on some facilities. The GA system was installed with a set of 4 MV57-140 type nozzles (see Figure 18) set to give maximum coverage of the Rig9 type acceptor region. These nozzles have a much high k-factor than the other nozzles in the programme meaning that for the same pressure, they give a larger volume of water flow.

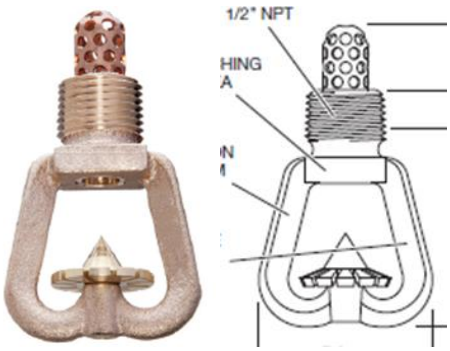

Figure 18: General area deluge nozzle detail (MV57-140)

Figure 19 shows the results for the double curtain and general area arrangement compared to both the 1 barg and 3 barg single curtain experiments. Away from the congested regions, it is observed that both the DC and GA arrangements show a reduction in measured peak overpressure when compared to the 1 barg single curtain for very similar donor events. The peak pressure recorded at these locations are similar to that of the 3 barg single curtain arrangement, although the slightly lower donor pressure event should be taken into account here (see Section 2.4).

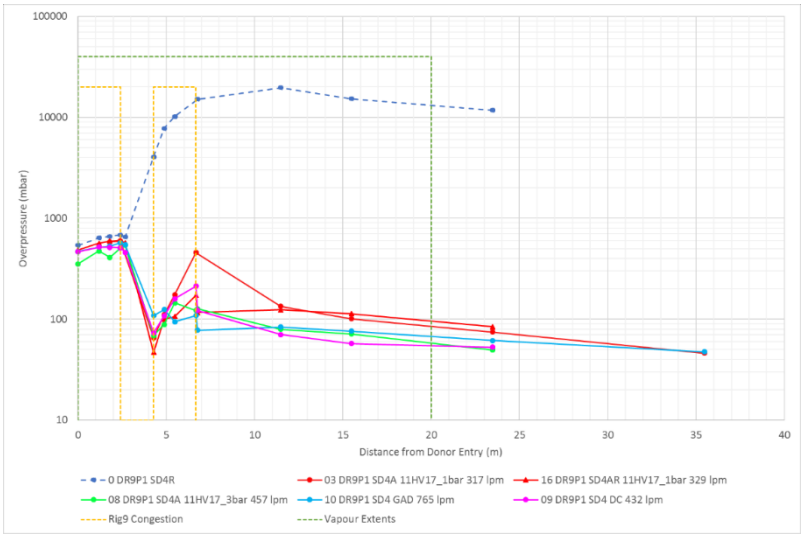

Figure 19: Comparison of double curtain (DC) and General Area deluge (GA) against the 1bar and 3bar experiments.

2.6 Performance of High-Pressure Misting System

Two experiments were performed with a high-pressure misting system provided by Desautel. The high-pressure misting nozzles produced a very fine water mist throughout the acceptor and were actuated remotely prior to ignition of the experiment. One experiment was conducted with only water injection and the second experiment included 200 g/l of particulate matter. Both mist experiments produced good mitigation of the acceptor event but with some unintended mitigation of the donor event. The experiment with particulate mixed into the water showed better mitigation than the water-alone experiment. Figure 20 shows the measurements from both of the mist system experiments compared to that of the DR9P1 SD4 baseline along with the 3 bar, full cone curtain experiment for comparison.

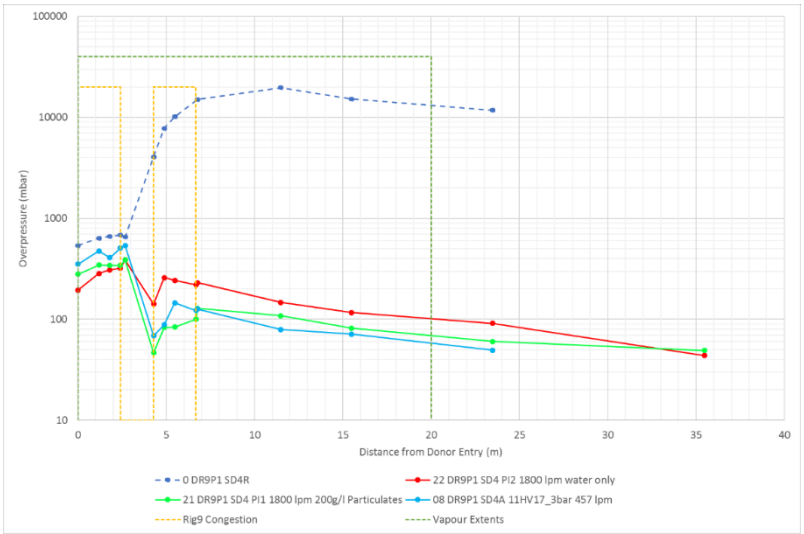

Figure 20: Comparison of particulate injection system experiments to baseline and 3 bar full cone curtain experiment.

2.7 Performance with different congestion (severe donor and acceptor events)

A total of 4 experiments were conducted with the Rig7 type congested regions and methane as the fuel. The purpose of this was to investigate the effectiveness of the curtains (both the fan and cone type nozzles, operated at nominally 3 barg) when set up to protect against a more severe donor event coupled to a larger acceptor region. The baseline experiment (14a DR7M1 SD2) gave a peak donor pressure of approximately 1.5 bar which led into a peak acceptor pressure of >18 bar. No DDT occurred meaning that the peak pressure levels recorded after the flame exited the acceptor immediately decayed with distance from the acceptor. Figure 21 shows the performance of the fan and cone nozzle curtains against the baseline experiment. Very little difference between the different curtain types is observed and the two cone nozzle experiments were noted to be relatively consistent with each other.

In all experiments with the water curtain active, the flame was not observed to show any appreciable acceleration in the acceptor.

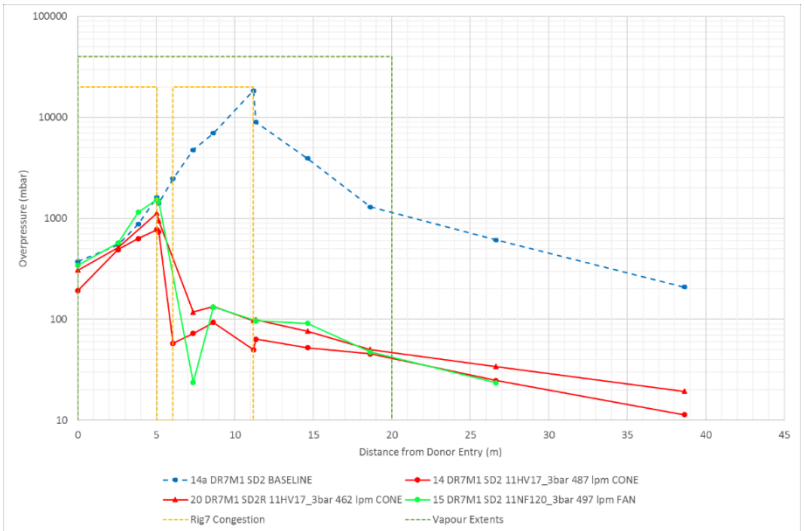

Figure 21: Performance of different nozzle types in Rig7 Congestion configuration.

2.8 Repeatability studies

2.8.1 Repeatability of the donor event

Figure 22 shows the peak pressure measurement from the donor event at the locations underneath the donor and also the free-field pressure transducers centred on the donor (to the west, away from the direction of flame propagation). The measurements are compared to the same measurements taken in the corresponding baseline experiments in which the curtain was not present. It is apparent here that the clear majority of measurements of donor peak pressure are lower than that of the original baseline experiment. Some of this can be accounted for in the small variations in fuel : air ratio between experiments but the negative bias is most likely because of the presence of the water curtain and the potential for partial wetting of the donor prior to flame arrival.

2.8.2 Repeatability of experiments

For all experiments where a repeat experiment is available, the peak pressure values recorded are compared to that of the like experiment in Figure 23. As identified earlier, the DR9P1 SD4 11HV17_1bar experiment shows as an anomalous result when compared to DR9P1 SD4R 11HV17_1bar. This is confirmed at the much greater correlation between DR9P1 SD4RR 11HV17_1bar and DR9P1 SD4RR. Excepting a few outlying measurements, the repeatability on a measurement-by-measurement basis appears to be within the +/- 50% margins. This is consistent with similar experimental programmes where no water curtains were present leading to the assertion that the introduction of the water curtain does not significantly increase the variability in the experiments.

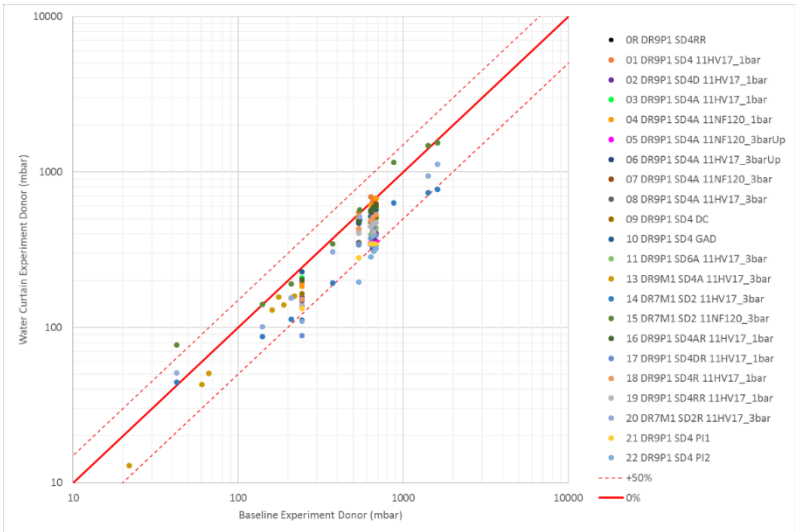

Figure 22: Peak pressure measurements from the donor event compared to the corresponding Baseline (no curtain) donor event measurements.

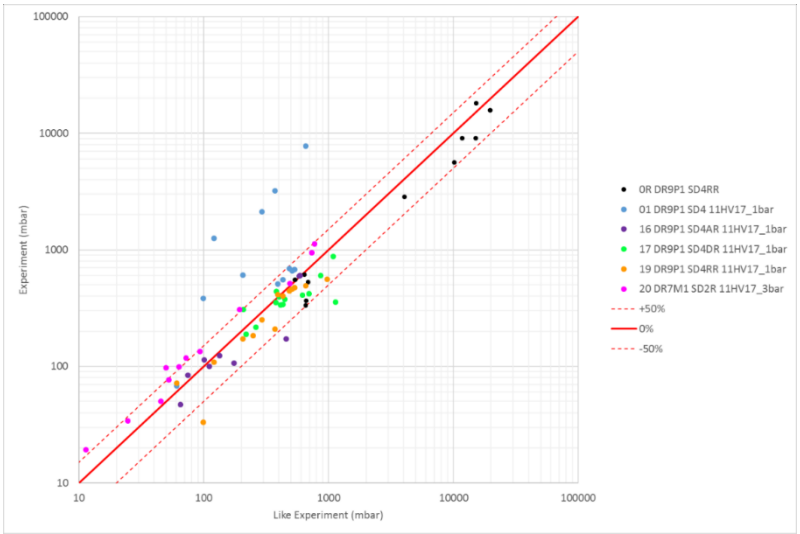

Figure 23: Peak pressure measurements compared with measurements from 'like' experiments.

3 Conclusions

In every instance where water was introduced into the vapour cloud prior to ignition, the baseline explosion was significantly mitigated. The programme of experiments was designed to enable comparison of the mitigation offer by changing each of the variables associated with a water curtain / congestion / fuel arrangement. It has been possible to compare the results and identify optimum conditions for the application of water curtain suppression in these types of events. The relative practicalities of the different arrangements have not been explored.

Acknowledgements

The DOWSES project was funded by a Joint Industry Project (JIP) arrangement with both financial and technical contributions from Shell Research Limited, TotalEnergies SE. This paper is produced with the kind permission of the JIP partners.

References

Chamberlain, G., Oran, E., Pekalski, A., Detonations in industrial vapour cloud explosions. *Journal of Loss Prevention in the Process Industries, Volume 62, November 2019.*

Skjold, T., Gexcon R&D, 2016 https://www3.gexcon.com/files/FLUGmeetings/201605_Bergen/20160531_02_Skjold_RnD.pdf

Allason, D. Huéscar Medina, C., Johnson, D.M., Pekalski, A., Dutertre, A. & Mansfield, D., Explosion safety gap reduction with water curtain. *Journal of Loss Prevention in the Process Industries, Volume 61, September 2019, Pages 66-81.*

The Steel Construction Institute (SCI) (1998). *Blast and Fire Engineering for Topside Structures, Phase 2*, Final Summary Report. SCI Publication Number 253, ISBN 1 85942 078 8, 1998

Al-Hassan T. and Johnson D.M. (1998). *Gas Explosions in Large Scale Offshore Module Geometries: Overpressures, Mitigation and Repeatability*, OMAE 98, Lisbon.

Catlin C.A., Gregory C.A.J., Johnson D.M., and Walker D.G. (1993). *Explosion Mitigation in Offshore Modules by General Area Deluge*, Trans IChemE, Vol 71, Part B.

Thomas, G.O. (2000). *On the conditions required for explosion mitigation by water sprays.* Trans IChemE, Vol 78, Part B, September 2000

Investigations on different distribution systems for dusts inside the 20L-sphere

Bretislav Janovsky [a], Adrián Pandal [b], Manuel Velasco Rodríguez [b], Martin Schmidt [c], Enrico Danzi [d], Olivier Dufaud [e] and Stefan H. Spitzer [c,g]

[a] University of Pardubice, Pardubice, Czech Republic
[b] University of Oviedo, Gijón, Spain
[c] Bundesanstalt fuer Materialforschung und –pruefung, Berlin, Germany
[d] Politecnico di Torino, Torino, Italy
[e] University of Lorraine, Nancy, France
[f] Physikalisch-Technische Bundesanstalt (PTB), Braunschweig, Germany
[g]EIfI-Tech, Schwäbisch-Gmünd, Germany

E-mail: bretislav.janovsky@upce.cz; s.spitzer@eifi-tech.eu

Abstract

The determination of several safety characteristics for dusts requires the resuspension in air. This is normally conducted using two vessels, one with an overpressure holding the dust and dispersing it into the second one, where the explosion takes place, through a nozzle. This procedure has the disadvantage, that some dusts cannot be conveyed through the nozzle properly. Another disadvantage is, that the pressure balancing between the two vessels depends on the dust loading and especially for heavy dusts and high loadings the initial pressure inside the explosion vessel might be reduced.

One very recent example testing nitrocellulose raised the question, whether some dusts pose a risk being distributed and pressed through a nozzle for the testing device and, in worst case, for the operator.

Many researchers developed alternative types of nozzles but most of the publications were designed for one type of dust and in none the CAD-files are provided for reproducing the nozzle.

This article investigates four types of nozzles, the two standard ones that are widely used already, a novel type, that got introduced into the international standard in 2016 but is still seldomly used and one that was constructed to overcome some of the observed disadvantages. The injection curves are compared with and without dust loadings as well as the explosion characteristics. Probably due to smaller free cross-section of mushroom-cup and mushroom nozzles, duration of the dispersion is longer. The other dispersion characteristics are similar. The explosion overpressure was almost unaffected by a change of the nozzle. Minor differences in the rate of pressure rise (dp/dt) and the corresponding K_{St} values were observed but these were below the usual scattering of dust explosions. Eventually, a suggestion is given for different types of dusts.

Keywords: *Safety characteristics, Turbulence, Dust Explosions, Nozzles, Distribution*

Introduction

Dust explosions occur when a fine dust or powder is suspended in the air and comes into contact with an ignition source. These explosions can have devastating consequences and pose a significant risk in various industries, particularly those involving the handling and processing of combustible materials. As a recent example, in 2020 a total of 60 dust explosions were reported worldwide (Cloney, 2020). Therefore, a precise dust explosion risk assessment is an invaluable tool to determine the likelihood of a dust cloud explosion and to develop effective risk reduction and explosion prevention & protection measures. In this regard, standard regulations such as the ASTM E1226 (ASTM International, 2019), ISO 6184 (ISO 6184-1: 1985), or EN 14034 series (CEN, 2011), provide

procedures for performing standard test methods for characterizing first, if a dust cloud can explode and, in that case, the potential explosion hazard by the determination of the dust explosibility parameters. These parameters are the maximum explosion pressure, p_{max}; the maximum rate of pressure rise, $(dp/dt)_{max}$; and the explosibility index, K_{St} (see Equation 1), for which the considered volume of the test vessel, V, is used:

$$K_{St} = \left(\frac{dp}{dt}\right)_{max} V^{1/3} \quad (1)$$

Those fundamental studies are conducted in laboratory scales inside confined test chambers. In the beginning, the 1 m³ pressure-resistant vessel conceived at the Bergbau-Versuchsstrecke (BVS) in Germany (Bartknecht, 1966) was used as the standard instrument. However, its size requires a great amount of dust as well as a special facility. Consequently, since 1988 the 20 L spherical vessel proposed by Siwek (1977), the so called "20L-sphere", became the preferred experimental apparatus for determining explosion parameters (Islas et al., 2022). The tests are done by the dispersion of a certain mass of dust particles into the test vessel with a blast of air driven by an overpressure of usually 20 barg through a nozzle. The objective is to form a uniform and turbulent dust cloud, which after a specific time (ignition delay time) is ignited with the aid of an ignition source, for dusts typically two pyrotechnical igniters with an overall energy of 2 kJ or 10 kJ, and eventually, the pressure evolution can be recorded and evaluated.

The utilized nozzle has a remarkable impact in the dust cloud formation. The first apparatuses incorporate a perforated tube in a semi-circle shape (Siwek, 1977), the so-called "annular nozzle". Later a "rebound nozzle" was invented as an alternative and nowadays it is the preferred type in most standards (EN 14034 series, ISO/IEC 80079-20-2). The reason, why there is still research on different shapes of nozzles is the fact, that it is extremely difficult to produce a perfectly uniform dust cloud (Du et al., 2015). Several studies have been done to gain a thorough understanding of the performance of these two different nozzles. The integrity of dust particles in standard explosion tests was evaluated by Sanchirico et al. (2015), concluding that dispersion through the rebound nozzle generates a more significant change in particle size. However, the particle size reduction in the 20L-sphere was attributed to the unique design of its outlet (dispersion) valve and its shearing action on the dust particles as they flow through (Kalejaiye et al., 2010). In the same line, Bagaria et al. (2016, 2019) stated that the 1-m^3 apparatus (annular nozzle) leads to less particle size reduction compared to the 20L-sphere (rebound nozzle) due to the reduced force generated during the dispersion process (smooth outlet ball valve, no sharp turns, less turbulent kinetic energy) and the lower impact force with vessel walls as a result of the larger volume.

Although Eckhoff (2003) and Siwek (1988) stated that the uniformity of the dispersion is similar for both nozzles, despite the differences in their geometry, some recent investigations provide opposite insights. According to Di Sarli et al. (2015), the perforated annular nozzle generates a quite uniform dust cloud, albeit a significant fraction of solid particles is trapped inside the nozzle. In contrast, the rebound nozzle has shown a predominant tendency of the dust cloud towards the wall region (Di Benedetto et al., 2013, Vizcaya et al., 2018, Portarapillo et al., 2020, Islas et al., 2022b), which affects the ignition and flame propagation due to a low dust concentration near the igniters (Di Sarli et al., 2014).

Additionally, the peculiar behavior of so-called "non-traditional dusts", in terms of dispersibility in air, poses a critical challenge when they need to be tested inside standard dust testing equipment (such as the 20L-sphere). This is likely due to their "flocky" nature and aggregation tendency, while the nozzle injection system could also play a relevant role. The issue was identified by Iarossi et al. (2013) and recently in the work of Portarapillo et al., (2022). Those researchers worked with nylon 6-6 dust, which is relatively lighter with respect to other non-traditional dusts investigated: this implies higher volumes of samples to be injected in the 20L-sphere, enhancing the dispersion challenge. The authors opted to insert 50% of the mass of the sample directly in the vessel (above and all around the rebound

nozzle), while the remaining is injected via the normal pressurized dust container. An alternative nozzle design may solve this issue efficiently.

The aforementioned reasons have motivated researchers to investigate new dispersion nozzle types over the last decades. The decay of turbulence was measured and compared for the rebound nozzle, the perforated annular nozzle, and a novel type (the so-called "Dahoe-nozzle") by Dahoe et al. (2001) using Laser-doppler anemometry. Huéscar-Medina et al. (2015a) used a perforated spherical nozzle for the dispersion of fibrous biomass inside the standard 1-m^3 apparatus due to the standard annular nozzle did not allow fibrous biomass milled to <63 µm to pass and compressed it as a pellet inside the nozzle (Huéscar-Medina et al., 2015b). Dispersion tests and CFD simulations were performed to compare the rebound nozzle and a novel type, the "symmetric nozzle" (Murillo et al., 2018) similar to the mushroom-cup, with the aim of enhancing the homogeneity of dust clouds in a 20L-sphere. Serrano et al. (2020) continued the investigation of the "symmetric nozzle", and evaluated seven different types of nozzles in comparison with the standard rebound nozzle by means of CFD simulations. Later, they investigated the explosion characteristics of the symmetric nozzle, the most promising one from their previous CFD work ("N6" nozzle), and the rebound nozzle, as a reference (Serrano et al., 2021). In summary, the need for an alternative injection nozzle has been pointed out by several researchers (Huéscar-Medina et al., 2015a and 2015b; Marmo et al. 2019; Portarapillo et al., 2022; Islas et al., 2022) while the one stated in the standards is not the perfect solution for all dusts.

In the present work, a systematic comparison of the injection process and the determination of dust explosion parameters is performed for the three established nozzle types, i.e., the annular nozzle, the rebound nozzle, and the mushroom-cup nozzle, which were not investigated so far. Additionally, a new designed proposal is presented and evaluated with the aim of improving the accuracy of dust explosion measurements in the 20L-sphere, providing a better uniformity of dispersion and being able to accurately introduce the right amount of dust.

1. Methods and Materials

Four different types of nozzles were used for the comparison tests. A three-step test procedure was conducted over all four types to compare not only the injection process without dusts but also with high dust loadings and the determined safety characteristics.

1.1. Nozzle types

Two types of nozzles have been used over decades for the determination of safety characteristics of dusts, the perforated annular nozzle, and the rebound nozzle.

The perforated annular nozzle was adapted from the former standard 1-m^3 apparatus used for explosion testing. When the miniaturization was developed by Siwek in 1977 it was actually an up-scaling from a 5L- and a 10L-sphere that were used before but led to big differences regarding the obtained values for p_{max} and $(dp/dt)_{max}$ (Siwek, 1977). Siwek investigated four different shapes until he came up with the now known solution he called "RD Y" ("Ringdüse" is the German word for ring nozzle and Y because the connection on the bottom has a Y-shape, see Figure 1). However, later it was also called "perforated annular nozzle" (ASTM_E_1226), "perforated semicircular spray pipe" (EN14034), "perforated dispersion ring" (Dahoe et al., 2001), and "perforated ring" (Sanchirico et al., 2015). From here on we use the term "perforated annular nozzle".

The rebound nozzle was introduced into most of the dust standards and replaced the perforated annular nozzle in most facilities (ISO 80079, EN14034). It has the benefits, that no dust is held back inside what might happen in the perforated annular nozzle and that the cleaning and replacement is easier. Consisting mainly of a thread and two metal plates it is also easier to build (see Figure 2).

With both above-described nozzles the dust must be placed inside the dust container and especially for flocky dust it is almost impossible to distribute them. In case of sensitive dust such as pyrotechnic

mixtures, metals, etc., ignition may occur already during fast flow of the dust through the outlet (dispersion) valve and further in its pathway and potentially cause its damage.

Fig. 1. *Picture of the perforated annular nozzle that was used*

Fig. 2. *Picture of the used rebound nozzle*

A third type, the so-called mushroom-cup nozzle, has been introduced into the ISO/IEC 80079-20-2 with which it is possible to place the dust directly inside the 20L-sphere (ISO 80079-2) in the cup. In the standard it is called "dispersion cup" which might be confused with another type of dispersion cup mentioned in EN14034 for 1-m^3 apparatus, so we use the term mushroom-cup.

However, the standard did not provide a proper technical drawing (only two dimensions are given) or other details to reproduce the nozzle (see Figure 3 and Figure 4)[1].

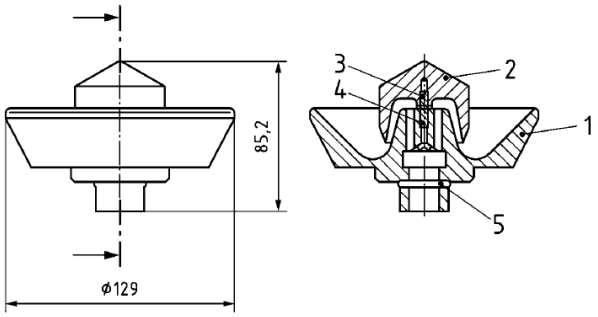

Fig. 3. *Technical drawing of the mushroom-cup nozzle; 1 cup; 2 cap (or mushroom); 3 grub screw; 4 hexagon socket; 5 O-ring seal; taken from ISO 80079-2*

[1] We got technical details from an existing one and from one of the inventors of it.

A comparison with the old two types and the mushroom-cup has also not been published yet. After first tests, it was observed that dust might fall below the cup causing the measured explosion pressure lower, maximum explosion pressure occurs at higher concentration and the cleaning is more difficult.

Fig. 4. *Picture of the mushroom-cup nozzle that was used*

A fourth type was invented, simply leaving the cup away, the mushroom nozzle or Janovsky-nozzle (see Figure 5).

Fig. 5. *Picture of the Janovsky nozzle that was used*

1.2. Injection process – no dust, no ignition

In the firsts step the injection pressure curves of all four nozzles were investigated and compared. The pressure inside the test vessel before injection was kept constant at 400 mbar abs ± 5 mbar. The injection pressure was varied between 19 barg and 24 barg in steps of one bar and additionally 21.3 barg. Differences in the pre-ignition pressure rise (PIPR = pressure rise from the evacuated test vessel up to the initial pressure before activation of the ignition source) were compared against each other by counting the time from the first detected pressure increase until the highest recorded pressure. This way, a potential difference in the initial pressure (pressure in the explosion vessel at the moment of ignition) that might influence the later determined explosion characteristics could be excluded (Spitzer et al., 2022).

1.3. Distribution tests – with dust, no ignition

In the second step a high loading of lycopodium (15 g) was injected without ignition source. The perforated annular nozzle and the rebound nozzle were used in the standard way with the dust placed inside the dust container. The mushroom-cup and the Janovsky-nozzle were used placing the dust inside the 20L-sphere. The initial pressure before injection was kept constant at 400 mbar abs ± 5 mbar. The injection pressure was varied with 21 barg, 22 barg and 23 barg. This way, the slowing down of the dust was investigated and the differences of the pre-ignition pressure rise, and the injection process were compared again. The rebound nozzle was also tested with a loading of 30 g inside the dust container and the Janovsky nozzle with a loading of 30 g inside the sphere and then with 15 g inside the dust container to investigate the role of friction on the injection process further.

1.4. Explosion tests – with dust, with ignition

The third step consisted of standard explosion tests according to the EN 14034 series. The pressure before injection was kept constant with 400 mbar abs ± 5 mbar, and the injection pressure was again varied from 21 barg over 22 barg to 23 barg. These rather high values (21 barg is the upper limit that is allowed according to the standards) were chosen to ensure an initial pressure of at least one bar. This way, the influence of the different nozzles and their distribution behavior on the safety characteristics were eventually determined. The ignition delay time was kept constant for all tests with 60 ms.

1.5. Dust sample

The dust sample, that was used for this investigation, was lycopodium with low volatile content. A particle size distribution measurement was also conducted (Mastersizer3000, Malvern Panalytical GmbH, Kassel, Germany). The percentiles were 25.6 µm (d10), 30.6 µm (d50) and 36.6 µm (d90) for three measurements in a row (see Figure 6). The measurement was repeated but the numbers did not change significantly (25.3 µm (d10), 30.6 µm (d50) and 36.9 µm (d90)).

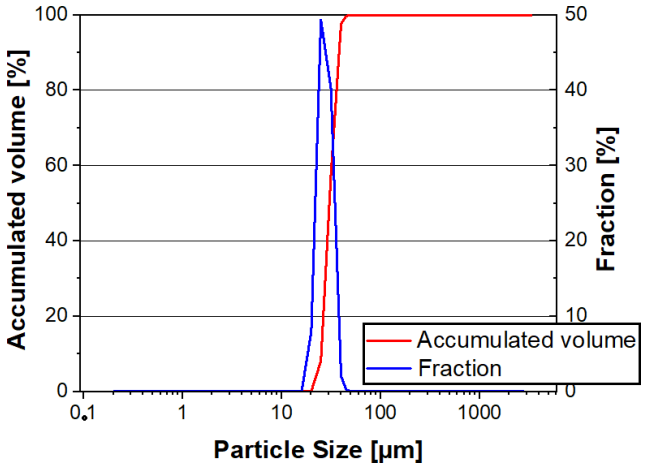

Fig. 6. *Particle sizes of the tested lycopodium*

The moisture content was determined twice using a Sartorius MA35. The determined moisture content was 3.4 weight-% and 3.8 weight-% what seems to be a matter of scattering.

2. Results and discussion

2.1. Results for the injection process with no dust

The first comparison of the four nozzles showed a prolonged injection behavior for the Mushroom-cup and the Janovsky nozzle (see Figure 7).

The reason for this might be the reduced free cross-section area in these nozzles. The rebound and the perforated annular nozzle have a free cross-section area of 363 mm², the mushroom-cup has four long holes with an overall free cross section area of 172 mm² and the Janovsky nozzle has eight holes with an overall free cross-section area of 157 mm² (19.6 mm² each).

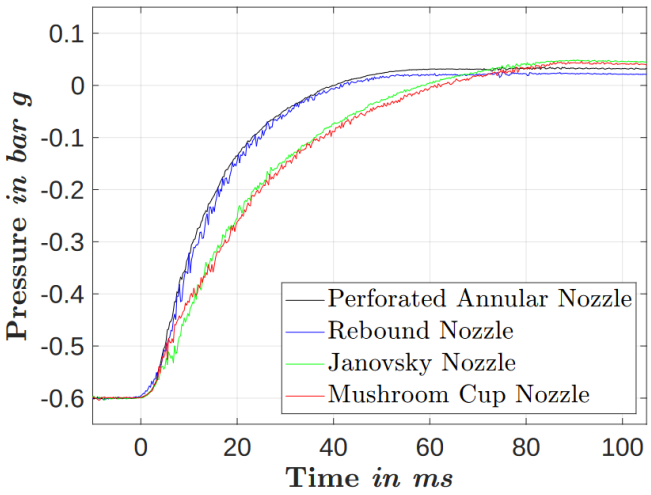

Fig. 7. *Injection process of the four different nozzles with 21 barg in the dust chamber, each line is an average of three tests*

The time from the first detection of a pressure rise until the maximum pressure (98 % of the maximum value because of the scattering of the signal) with different injection pressures is displayed in Figure 8. While the perforated annular and the rebound nozzles have an injection time of about 55 ± 10 ms, the other two have the injection time of 80 ± 10 ms.

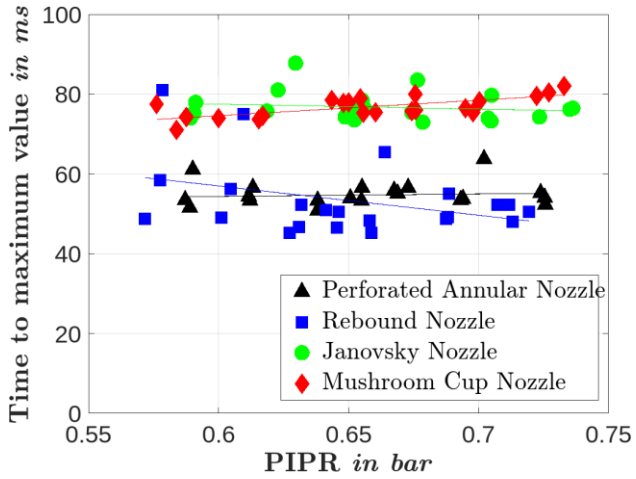

Fig. 8. *Evaluation of the time taken by each nozzle to reach a 98% of the maximum pressure value*

Because the PIPR of at least 0.64 bar is needed, the pressure range was narrowed from 21 barg to 23 barg for the other two test series.

2.2. Results for the injection process with dust

The injection process with the dust showed the same differences for 15 g of dust with all four types of nozzles. The dust sample decreased the PIPR between 42 mbar to 57 mbar. The perforated annular

nozzle showed higher decrease with 51 mbar in average, the other three nozzles 46 mbar to 47 mbar on average (see Figure 9 and Table 1).

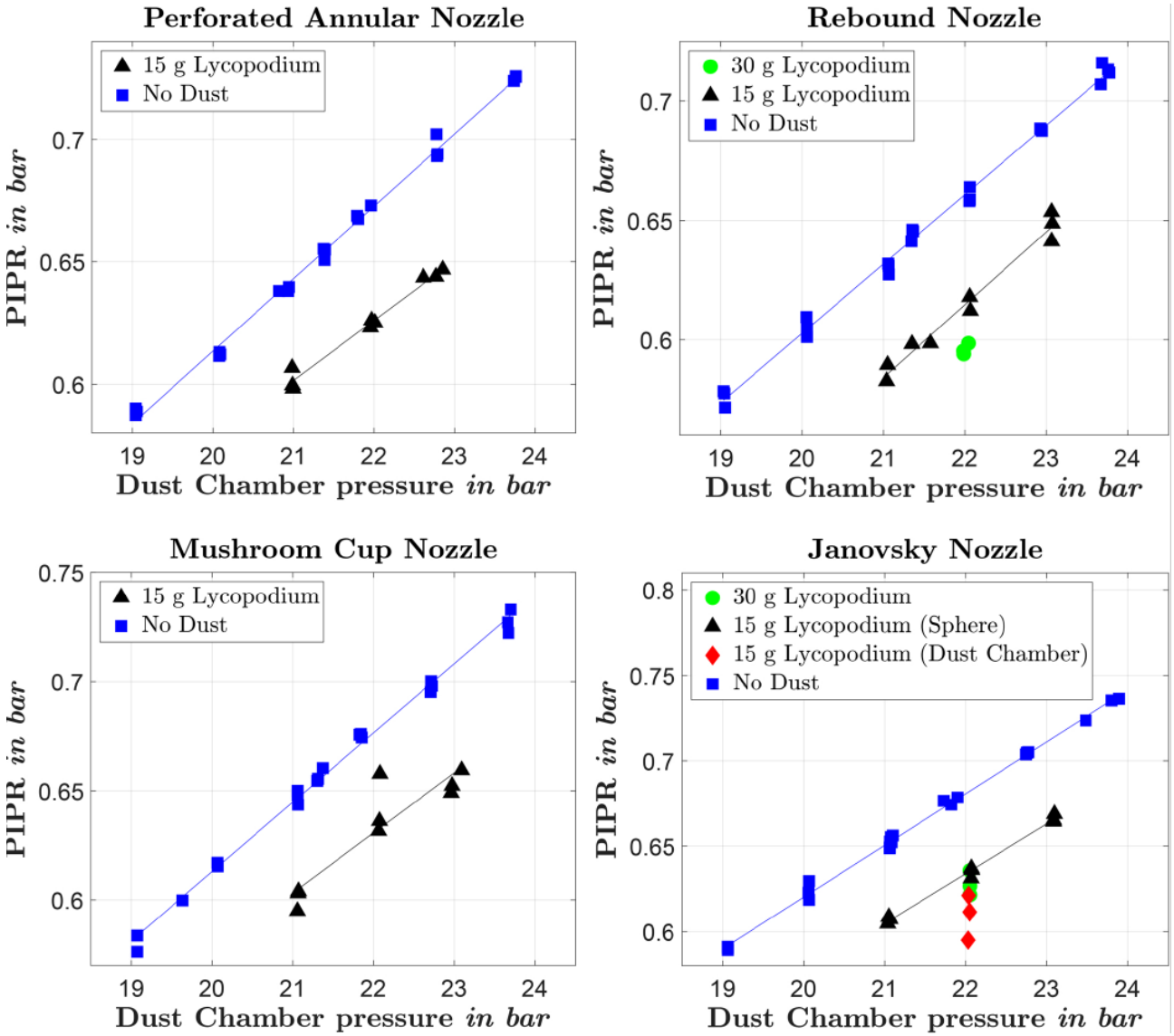

Fig. 9. *Comparison on the PIPR between tests with Lycopodium and tests without dust*

The role of friction can be clearly seen by increasing the dust loading further. While the decrease in the PIPR was higher for the rebound nozzle it stayed the same for the Janovsky nozzle since the dust is not conveyed but simply dispersed. Also comparing the points from the Janovsky nozzle between injection from the dust chamber and dispersing it inside the sphere with the same amount shows the friction of the dust. The explanation, why all four types of nozzles showed a decrease in the PIPR, might be the heat that is produced by the injection process (compression of the air in the chamber) and that this can be absorbed by the dispersed dust. It would explain why all four types showed a comparable reduction in the PIPR for the same amount of dust.

***Table 1**. Quantification of the differences in PIPR between tests with 15 g of Lycopodium and tests without dust*

Nozzle type	No dust			15 g of Lycopodium			Difference		
	21 (barg)	22 (barg)	23 (barg)	21 (barg)	22 (barg)	23 (barg)	21 (barg)	22 (barg)	23 (barg)
Perforated Annular	0,650	0,673	0,702	0,602	0,626	0,646	0,049	0,047	0,057
Rebound	0,632	0,661	0,690	0,584	0,615	0,645	0,048	0,046	0,045
Janovsky	0,650	0,681	0,711	0,605	0,634	0,663	0,046	0,047	0,048
Mushroom Cup	0,645	0,976	0,708	0,603	0,631	0,658	0,042	0,046	0,050

The dust releasing from the nozzle prolonged the injection process in both the perforated annular nozzle and the Rebound nozzle (see Figure 10). But the longer injection process is the most evident in case of perforated annular nozzle.

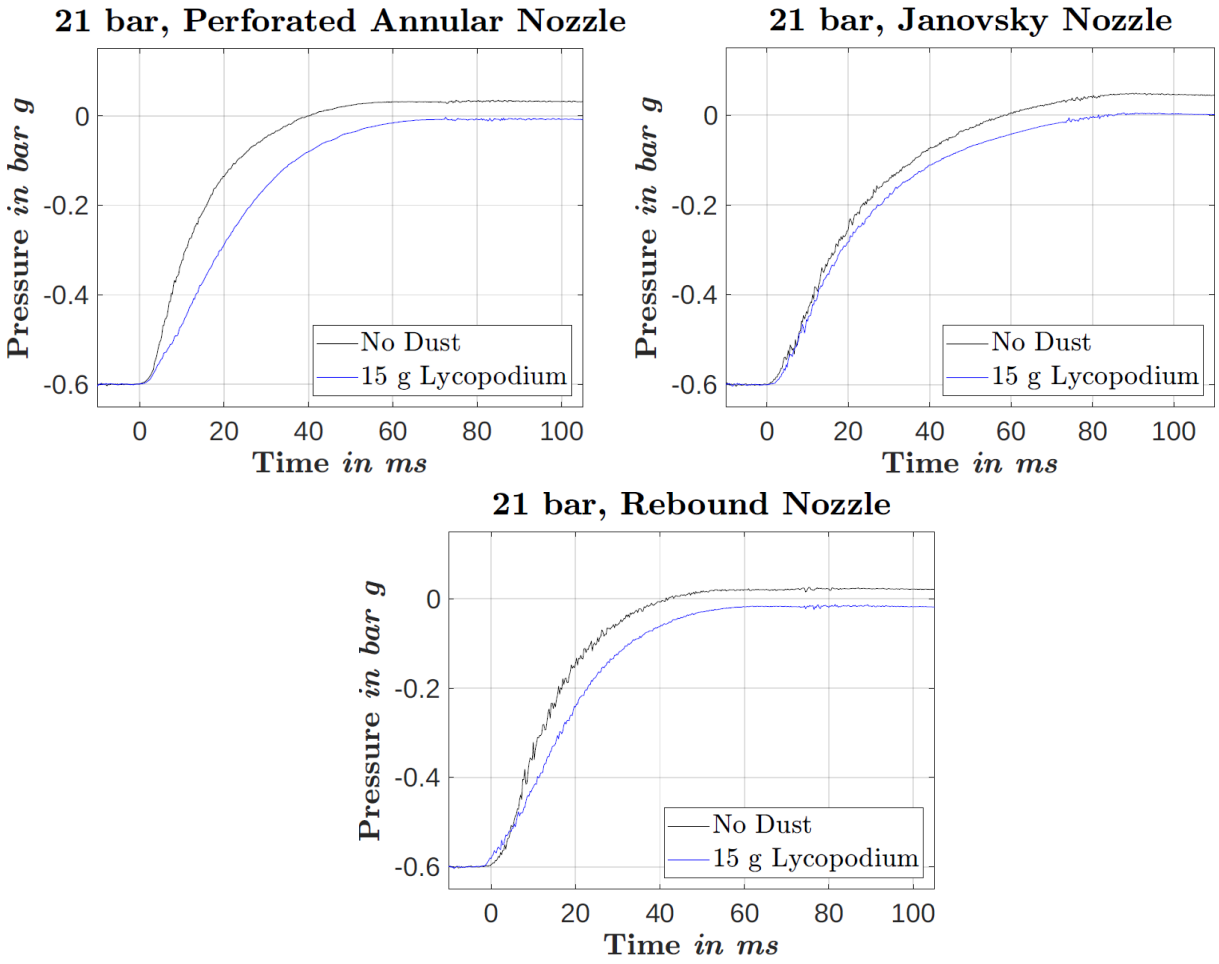

***Fig. 10.** Injection curves for three types of nozzles*

2.3. Comparison of the safety characteristics

The p_{ex} and (dp/dt) values for the four different types of nozzles and 15 g of Lycopodium are shown in Figure 11 and 12.

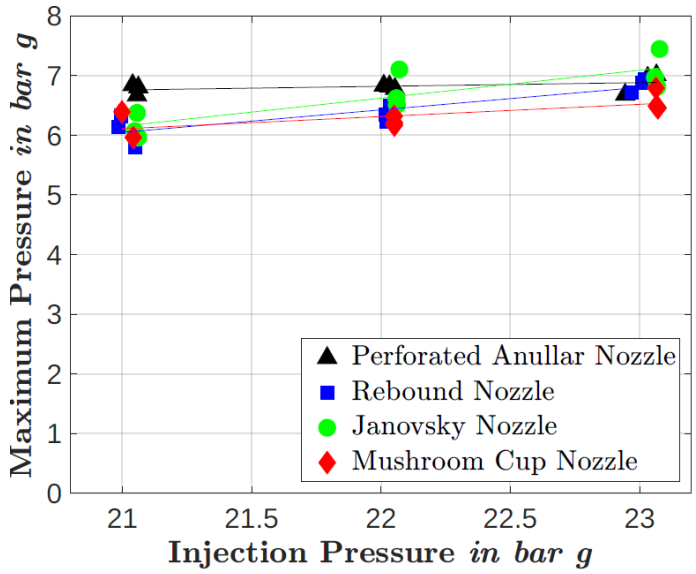

Fig. 11. *Maximum pressures achieved on the explosion tests for all nozzles against the dust chamber initial pressure, 15 g of Lycopodium (750 g/m³)*

The maximum explosion pressure for given dust concentration did not vary significantly between the four different nozzles. While the mushroom cup nozzle gave the lowest average value with 6.3 barg for an injection pressure of 22 barg, the perforated annular nozzle resulted in the highest average value with 6.8 barg. The rebound and the Janovsky nozzles were in between with 6.4 barg and 6.7 barg respectively. With that, the determined values fall within less than 10 % deviation which can be considered as reasonable for that safety characteristic. According to the European and the American standard a deviation of less than 10 % is allowed (EN14034-1, ASTM E 1226).

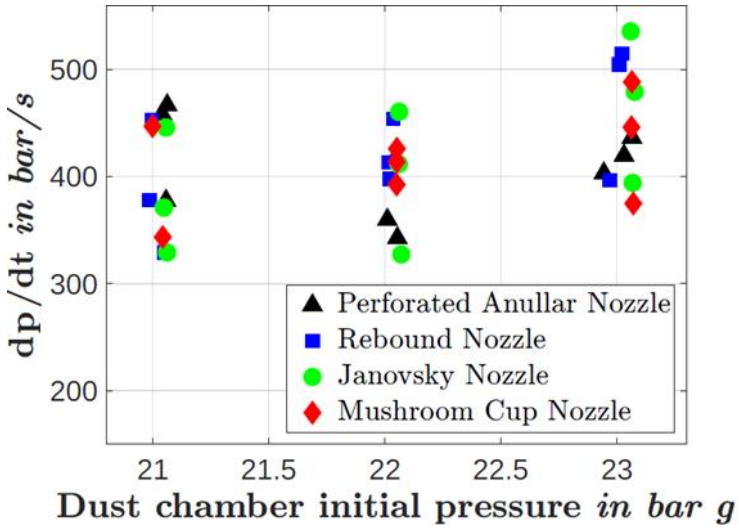

Fig. 12. *dp/dt values achieved on the explosion tests for all nozzles against the dust chamber initial pressure, 15 g of Lycopodium (750 g/m³)*

For (dp/dt), the scattering is a bit higher, but the average values are also quite close together. Here, the perforated annular nozzle gave the lowest average value with 374 bar/s and the rebound nozzle the highest value with 421 bar/s. The mushroom cup and the Janovsky nozzle were in between with 416 bar/s and 386 bar/s respectively. According to the American and the European standard, for these K_{st} values (between 100 and 200 bar*m/s ≈ 370 bar/s to 740 bar/s) a deviation of up to 12 % is allowed

from one laboratory to another or within the same laboratory at different times (EN14034-2, ASTM E 1226). So, all four types would fall within that requirement with the overall average of 399 bar/s with an injection pressure of 22 barg. With the higher injection pressures, it might also be the case, that the particles are more prone to breakage and with that lead to higher values. However, this was not tested.

3. Conclusions

Four different types of nozzles for the injection of dust in the 20L-sphere were investigated. It was shown that the injection process is prolonged for the nozzles that allow a placement of the dust directly in the 20L-sphere. However, the determined safety characteristics for lycopodium were close to each other. The explosion overpressure was almost unaffected by a change of the nozzle. Minor differences in the rate of pressure rise (dp/dt) and the corresponding K_{St} values were observed but these were below the usual scattering of dust explosions. However, more dusts at more concentrations should be tested to confirm suitability of newly proposed nozzle for tests in 20L-sphere.

The chosen dust, lycopodium, was on purpose a kind, that allows the injection from the dust container. With the new types of nozzles, it is possible to place flocky or coarse dusts or sensitive dusts, which can be ignited by the friction inside the injection system, directly into the 20L-sphere. With these investigations the safety characteristics can be linked to the existing database and the existing safety measures, that follow the usual investigations on the safety characteristics.

Acknowledgements

The authors gratefully acknowledge the manufacture of the new dispersion nozzles from OZM Research Ltd.

References

ASTM International, 2019. ASTM E1226-19, Standard Test Method for Explosibility of Dust Clouds. ASTM International, West Conshohocken, PA www.astm.org

Bagaria, P., Zhang, J., Yang, E., Dastidar, A., Mashuga, C., 2016. Effect of dust dispersion on particle integrity and explosion hazards. *Journal of Loss Prevention in the Process Industries*, 44, 424–432, https://doi.org/10.1016/j.jlp.2016.11.001

Bagaria, P., Li, Q., Dastidar, A., Mashuga, C., 2019. Classification of particle breakage due to dust dispersion. *Powder Technology* 342, 204-213, https://doi.org/10.1016/j.powtec.2018.09.089

Bartknecht, W., 1966. Gasexplosion in Rohrstrecken. Bergfreiheit, Zeitschrift fiir den Deutschen Bergbau, 5.

CEN, the European Committee for Standardization EN. 14034-1 (2011) - Determination of explosion characteristics of dust clouds – Part 1: Determination of the maximum explosion pressure p_{max} of dust clouds

CEN, the European Committee for Standardization EN. 14034-2 (2011) - Determination of explosion characteristics of dust clouds – Part 2: Determination of the maximum rate of explosion pressure rise $(dp/dt)_{max}$ of dust clouds

CEN, the European Committee for Standardization. EN 14034-3 (2011) - Determination of explosion characteristics of dust clouds – Part 3: Determination of the lower explosion limit LEL of dust clouds

Cloney, C., 2020. Combustible Dust Incident Report. https://dustsafetyscience.com/2020-report-summary/

Dahoe, A., E., Cant, R., S., Scarlett, B., 2001. On the Decay of Turbulence in the 20-Liter Explosion Sphere. *Flow, Turbulence and Combustion* 67, 159–184, https://doi.org/10.1023/A:1015099110942

Di Benedetto, A., Russo, P., Sanchirico, R., Di Sarli, V., 2013. CFD simulations of turbulent fluid flow and dust dispersion in the 20 liter explosion vessel. *AICHE J.* 59 (7), 2485–2496, https://doi.org/10.1002/aic.14029

Di Sarli, V., R. Sanchirico, P. Russo, A. Di Benedetto, A., 2015. CFD modeling and simulation of turbulent fluid flow and dust dispersion in the 20-L explosion vessel equipped with the perforated annular nozzle. *Journal of Loss Prevention in the Process Industries*, 38, 204–213, https://doi.org/10.1016/j.jlp.2015.09.015

Di Sarli, V., Russo, P., Sanchirico, R., Di Benedetto, A., 2014. CFD simulations of dust dispersion in the 20 L vessel: effect of nominal dust concentration. *Journal of Loss Prevention in the Process Industries*, 27, 8–12, https://doi.org/10.1016/j.jlp.2013.10.015

Du, B., Huang, W., Liu, L., Zhang, T., Li, H., Ren, Y., Wang, H., 2015. Visualization and analysis of dispersion process of combustible dust in a transparent Siwek 20-L chamber. *Journal of Loss Prevention in the Process Industries*, 33, 213–221, https://doi.org/10.1016/j.jlp.2014.12.017

Eckhoff, R., K., 2003. *Dust Explosions in the Process Industries: Identification, Assessment and Control of Dust Hazards*. Elsevier, https://doi.org/10.1016/B978-0-7506-7602-1.X5000-8

Huéscar Medina, C., Sattar, H., Phylaktou, H., N., Andrews, G., E., Gibbs, B., M., 2015. Explosion reactivity characterization of pulverized torrefied spruce wood. *Journal of Loss Prevention in the Process Industries*, 36, 287-295, https://doi.org/10.1016/j.jlp.2014.12.009

Huéscar Medina, C., MacCoitir, B., Sattar, H., Slatter, D., J., F., Phylaktou, H., N., Andrews, G., E., Gibbs, B., M., 2015b. Comparison of the explosion characteristics and flame speeds of pulverized coals and biomass in the ISO standard 1m^3 dust explosion equipment. *Fuel*, 151, 91-101, https://doi.org/10.1016/j.fuel.2015.01.009

Iarossi, I., Amyotte, P., R., Khan, F., I., Marmo, L., Dastidar, A., G., Eckhoff, R., K., 2013. Explosibility of polyamide and polyester fibers. *Journal of Loss Prevention in the Process Industries*, 26 (6), 1627-1633, https://doi.org/10.1016/j.jlp.2013.07.015

Islas, A., Rodríguez-Fernández, A., Betegón, C., Martínez-Pañeda, E., Pandal, A., 2022. CFD simulations of turbulent dust dispersion in the 20 L vessel using OpenFOAM. *Powder Technology*, 397, 117033, https://doi.org/10.1016/j.powtec.2021.117033

Islas, A., Rodríguez Fernández, A., Betegón, C., Martínez-Pañeda, E., Pandal, A., 2022b. Computational assessment of biomass dust explosions in the 20L sphere. *Process Safety and Environmental Protection*, 165, 791-814, https://doi.org/10.1016/j.psep.2022.07.029

ISO 6184-1: 1985. Explosion protection systems—part 1: Determination of explosion indices of combustible dusts in air. https://www.iso.org/standard/12438.html.

ISO 80079-20-2 (2016) - Explosive atmospheres – Part 20-2: Material characteristics – Combustible dusts test methods.

Kalejaiye, O., Amyotte, P., R., Pegg, M., J., Cashdollar, K., L., 2010. Effectiveness of dust dispersion in the 20-L Siwek chamber. *Journal of Loss Prevention in the Process Industries*, 23 (1), 46–59, https://doi.org/10.1016/j.jlp.2009.05.008

Marmo, L., Ferri, A., Danzi, E., 2019. Dust explosion hazard in the textile industry. *Journal of Loss Prevention in the Process Industries*, 62, 103935, https://doi.org/10.1016/j.jlp.2019.103935

Murillo, C., Amín, M., Bardin-Monnier, N., Muñoz, F., Pinilla, A., Ratkovich, N., Torrado, D., Vizcaya, D., Dufaud, O., 2018. Proposal of a new injection nozzle to improve the experimental

reproducibility of dust explosion tests. *Powder Technology*, 328, 54-74, https://doi.org/10.1016/j.powtec.2017.12.096.

Portarapillo, M., Di Sarli, V., Sanchirico, R., Di Benedetto, A., 2020. CFD Simulation of the Dispersion of Binary Dust Mixtures in the 20 L Vessel. *Journal of Loss Prevention in the Process Industries*, 67, 104231, https://doi.org/10.1016/j.jlp.2020.104231

Portarapillo, M., Danzi, E., Guida, G., Luciani, G., Marmo, L., Sanchirico, R., Di Benedetto, A., 2022. On the flammable behavior of non-traditional dusts: Dimensionless numbers evaluation for nylon 6,6 short fibers. *Journal of Loss Prevention in the Process Industries*, 78, 104815, https://doi.org/10.1016/j.jlp.2022.104815

Sanchirico, R., Di Sarli, V., Russo, P., Di Benedetto, A., 2015. Effect of the nozzle type on the integrity of dust particles in standard explosion tests. *Powder Technol.* 279, 203–208, https://doi.org/10.1016/j.powtec.2015.04.003

Serrano, J., Pico, P., Amín, M., Pinilla, A., Torrado, D., Murillo, C., Bardin-Monnier, N., Ratkovich, N., Muñoz, F., Dufaud, O., 2020. Experimental and CFD-DEM study of the dispersion and combustion of wheat starch and carbon-black particles during the standard 20L sphere test. *Journal of Loss Prevention in the Process Industries*, 63, 103995, https://doi.org/10.1016/j.jlp.2019.103995

Serrano, J., Ratkovich, N., Muñoz, F., Dufaud, O., 2021. Explosion severity behavior of micro/nano-sized aluminum dust in the 20L sphere: Influence of the particle size distribution (PSD) and nozzle geometry. *Process Safety and Environmental Protection*, 152, 1-13, https://doi.org/10.1016/j.psep.2021.05.023

Siwek, R., 1977. 20-l laborapparatur für die bestimmung der explosionskenngrößen brennbarer stäube. Diploma Thesis, Technikum Winterthur Ingenieurschule.

Siwek, R., 1988. Reliable determination of the safety characteristics in 20-l apparatus. In Proceedings of the Flammable Dust Explosion Conference, Missouri St. Louis, (pp. 529-573).

Spitzer, S., H., Askar, E., Benke, A., Janovsky, B., Krause, U., Krietsch, A., (2022). Influence of pre-ignition pressure rise on safety characteristics of dusts and hybrid mixtures. *Fuel*, 311, 122495.

Vizcaya, D., Pinilla, A., Amn, M., Ratkovich, N., Munoz, F., Murillo, C., Bardin-Monnier, N., Dufaud, O., 2018. CFD as an approach to understand flammable dust 20 L standard test: effect of the ignition time on the fluid flow. *AICHE J.* 64 (1), 42–54, https://doi.org/10.1002/aic.15883

Polymer dust explosion part I: literature review and case studies

Luca Marmo[a] Enrico Danzi [a], Almerinda Di Benedetto[b] & Maria Portarapillo[b]

[a] Dipartimento di Scienza Applicata e Tecnologia-Politecnico di Torino, C.so Duca degli Abruzzi 21, 10129, Torino, Italy

[b] Department of Chemical, Materials and Production Engineering, University of Naples Federico II, P.le V. Tecchio 80,
80125, Naples, Italy

e-mail: enrico.danzi@polito.it

The plastic industry, a global behemoth employing over 1.5 million people in Europe alone (Geyer et al., 2017), confronts a formidable challenge. Virtually all plastic is combustible, and the generation of fines during processing poses a potential explosion hazard. These fines can be present in the raw material feed or generated during mechanical operations in manufacturing or recycling activities. The flammability characteristics of these materials, primarily due to their hydrocarbon nature, are well-known, but other properties such as morphology and particle size distribution also wield significant influence.

The literature is replete with studies on polymer dust in its 'pure' form, delving into dust explosion fundamentals or gauging the efficacy of inerting powders. However, a conspicuous void exists in research on dust polymer mixtures, despite their frequent occurrence in industries. This research gap is particularly significant given the substantial amount of plastic-based material being processed in recycling plants (Hopewell et al., 2009), and the adoption of sustainable techniques for energy generation through plastic waste and biomass co-pyrolysis (Yuan et al., 2023). Implications of mixtures in terms of dust explosion severity are noticeable from the literature and need to be investigated further; polymer-based mixtures are examined in Danzi et al. (2024), the second part of this work, as well as particle size and morphology effect.

This paper is structured to provide a comprehensive overview of polymer dust explosion cases and accident dynamics. It begins by reviewing statistical data about polymer dust explosions at the global level, aiming to draw an overview of the materials involved, explosion severity in terms of consequences, and operation involved. It then provides conclusions about the correlations between the case occurrence and the amount of plastic generated and disposed of at the global level during the years. Lastly, it presents an examination of dust explosion case studies in the history of plastic industry accidents, discussing critical lessons regarding dust explosion hazards.

Keywords: dust explosion review, polymers, case studies

Introduction

Plastic is a general term for a broad class of polymeric materials mainly derived from oil. Two main categories of plastics exist: thermoplastics and thermosets. Thermoplastics are polymers that can be melted when heated and hardened when cooled. The melting and hardening cycle can generally be repeated. Thermosets are polymers that undergo a chemical change when heated. In general, heating promotes chemical reactions that form “bonds” such that a three-dimensional network is created. The process is irreversible, so these plastics cannot be re-melted and reformed after heating and forming.

Table 1 lists the most common thermosets and thermoplastic polymers.

Table 1: Thermoset and thermoplastic polymers

Thermoplastics	Thermosets
Polyethylene (PE) Polyamides (PA) Polypropylene (PP) Polycarbonate (PC) ABS SAN PEEK POM Expanded polystyrene (EPS) Polyarylsulfone (PSU) Polystyrene (PS) Thermoplastic elastomers (TPE) Polyethylene Terephthalate (PET) Polymethyl methacrylate (PMMA) Polyvinyl chloride (PVC) Fluoropolymers	Phenol - formaldehyde Epoxy resins Vinyl ester Silicone Melamine resin Unsaturated polyester Phenolic resins Etc. Polyurethane (PUR) Urea-formaldehyde Acrylic resins

Plastic production worldwide has been continuously growing since the ’50. The production amounted to 380 million tons in 2015 (Geyer et al., 2017). Plastic may be further divided into fiber and non-fiber plastics. The total production of non-fiber plastics is divided as follows (mass ratio): PE (36%), PP (21%), and PVC (12%) followed by PET, PUR, and PS (<10% each). Polyesters instead account for 70% of all PP&A (polyester, polyamide, and acrylic) fiber production. Thus, these seven materials account for 92% of all plastics ever produced (Geyer et al., 2017)

Non-fiber plastics have been extensively used for packaging, up to 42% of the total ever made (

Fig. **1**). PE, PP, and PET are the most used. The building and construction sector is the next largest consumer. Its use of non-fiber plastics accounts for 19% of the total. The most used plastic in construction is PVC, which is used 69% of all PVC made (Geyer et al., 2017).

The recent trend in the production of plastics is represented in Fig. 2.

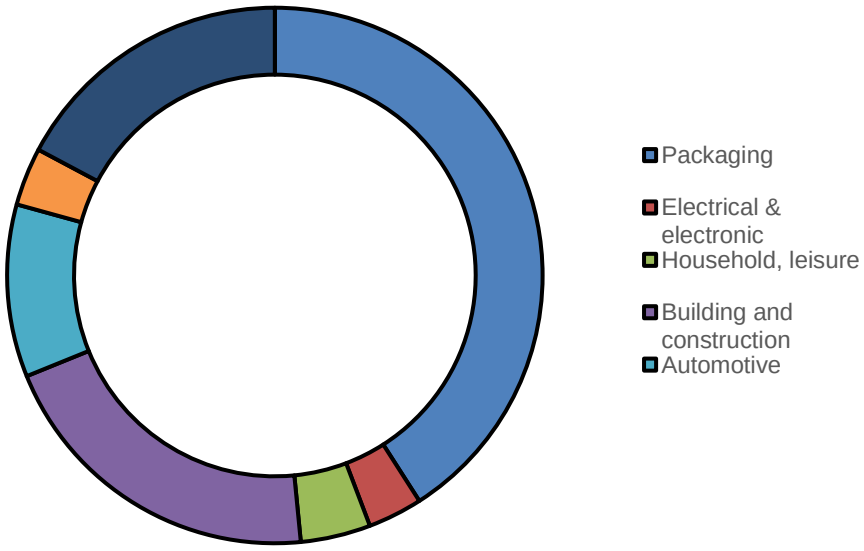

Fig. 1: *Europe consumption per sector, 2017 (from Plastics – the Facts 2018 An analysis of European plastics production, demand, and waste data, PlasticsEurope, Association of plastics manufacturers, 2018)*

Thermoplastics have been extensively produced and used, both in the past and today, and their use is encouraged because they are relatively more sustainable than non-recyclable materials, such as resins and thermosets. This is reflected in the amount of plastic waste produced, as the largest quantities come from PP, HDPE, and LDPE, respectively 18%, 14%, and 13%. Packaging is the leading sector if the quantity of waste is considered, accounting for almost half of all industrial sectors (OECD, 2022).

Table 2: Plastic demand by converters in Europe, 2017, by polymer.

Plastic	% Wt. transformed	Sectors
PP	19.3	Food packaging, sweet and snack wrappers, hinged caps, microwave containers, pipes, automotive parts, paper money, etc.
PE-LD, PE-LLD	17.5	Reusable bags, trays and containers, agricultural film (PE-LD), food packaging film (PE-LLD), etc.
PE-HD-PE-MD	12.3	Toys (PE-HD, PE-MD), milk bottles, shampoo bottles, pipes, houseware (PE-HD), etc.
PUR	7.7	Building insulation, pillows and mattresses, insulating foams for fridges, etc.
PVC	10.2	Window frames, profiles, floor and wall covering, pipes, cable insulation, garden hoses, inflatable pools, etc.
PS, EPS	6.6	Eyeglasses frames, plastic cups, egg trays (PS), packaging, building insulation (EPS), etc.
PET	7.4	Bottles for water, soft drinks, juices, cleaners
Others	19	Hub caps (ABS); optical fibers (PBT); eyeglasses lenses, roofing sheets (PC); touch screens (PMMA); cable coating in telecommunications (PTFE); and many others in aerospace, medical implants, surgical devices, membranes, valves & seals, protective coatings, etc.

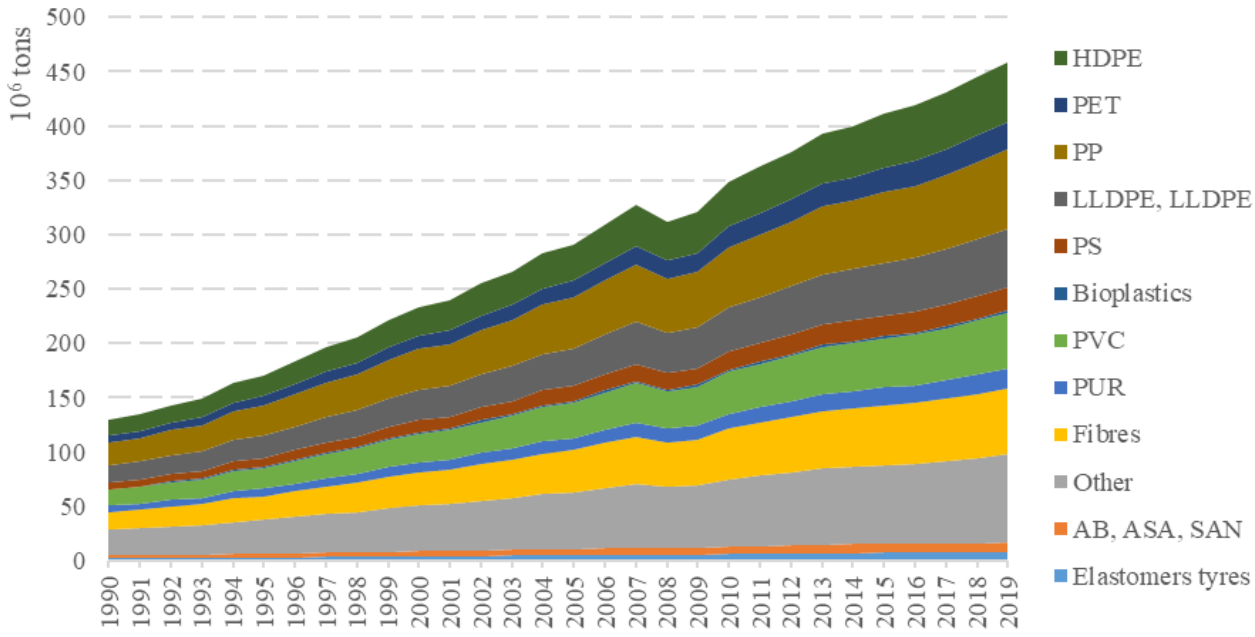

***Fig. 2**: Plastics production (1990-2019) by polymer type (OECD, 2022)*

1 Flammability of polymers

Polymeric materials are composed of macro chains of carbon and hydrogen (mostly) and other functional groups. Most polymers are combustible and could give rise to fire and explosion (in gas and solid phases). Hazard profiles could be ascribed to the thermo-chemical characteristics of polymers, depending on their chemical nature, such as the heat release potential measured through the heat of combustion. These parameters identified the potential fire hazards of such material (Fig. 3).

Almost 95% of polymers in use (commodity polymers) persist in burning after a brief exposure to a small flame, i.e., demonstrate a self-sustained burning behavior. These materials have high heat release capacity and are generally the least expensive on the market (see Lyon and Janssen, 2005).

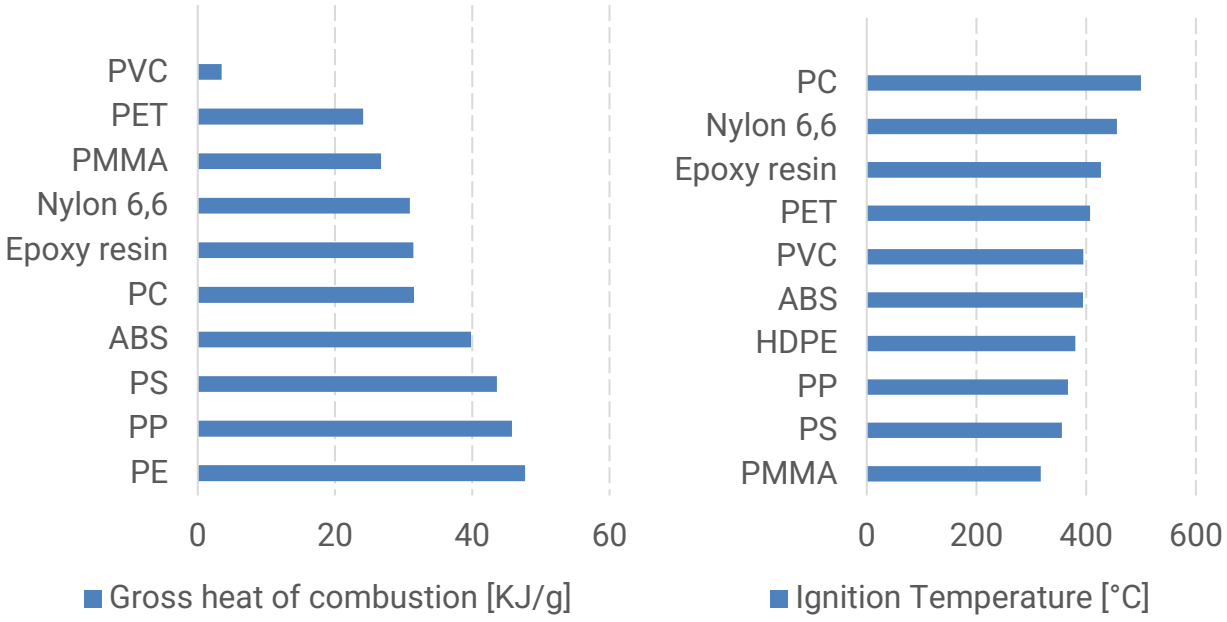

***Fig. 3**: Heat of combustion (left) and ignition temperature (right) of commonly used polymers, from Lyon and Janssens (2005).*

Parameters such as the ignition temperature or the heat release rate depend on the polymer's chemical nature and the ignition condition (external heat source, ventilation rate, etc.).

While reduced in powdered form, polymer materials behave differently, depending not only on their chemical matrix but also on other parameters (particle size, morphology, moisture) that define the dust cloud's sensitivity to ignition and explosion likelihood, as it is strictly dependent on the powder dispersibility in the air. The dispersibility of dust is often affected by the surface state of the particles, which can change their ability to cohesion.

2 Dust explosions in the polymer industry

The history of the plastic industry is dotted with accidents caused by the explosion of polymer powders or hybrid atmospheres. The scientific literature allows us to trace the history and draw useful considerations.

2.1 Data collection and availability

The availability of data concerning dust explosion cases in the polymer industry is based on the dataset collected by international associations (such as NFPA and CSB) and scientific literature

studies in the field. Data from NFPA, related to old cases, referring to Jacobson et al. (1962), until the 1960s, are not included here. The U.S. Chemical Safety Board (2006 and 2017) collected more recent cases, which spanned a period from 1980 to 2016; all information is although U.S.-based. Cases for this work were selected according to the material involved, i.e., polymer-based, identified in the dataset as "Rubber and Plastic products." Global-wide datasets are present in the Combustible Dust Incident Report released yearly by DustEx Research Ltd. website, Cloney (2018 to 2023); cases are also selected from here according to "fuel", namely "Plastic." Most recent data came from this reference and from the literature studies examined here, retrieved from the Scopus database by the academic publisher Elsevier, see Yuan et al., (2015). Key terms to identify polymer-related cases were "plastic," "polymer," "resin," "rubber," etc. Yan and Yu's (2012) incident data collection are strictly related to PRC geographical-based events.

2.2 Statistics of dust explosion cases

The first scientific study about dust explosions involving plastics was published in the 1940s, thanks to the efforts of the Bureau of Mines in the US (Hartmann & Nagy, 1944).

Concerning other powdered materials, such as flour or coal (the first flour dust witnessed episode dates to 1875), fires and explosions correlated to plastic dust have become relevant and reported only with the increasing demand and production of petrochemical-based materials.

The first registered dust explosion involving a plastic material was a phenolic resin dust explosion in the US in 1952, which caused five deaths and 21 injuries. Jacobson et al. (1962) commented that an NFPA report dated 1957 indicated that polymer dust explosions accounted for about 20% (excluding coal mining cases) of the total number since 1910.

More statistics collected by Eckhoff in his book (2003) reported a share of 5.4% for "Plastics" and 6.5% of total fatalities in the period (1900-1956). More recent data from Europe (Germany) collected by Beck and Jeske (1982) gave higher figures: 12.9% and 17.5%, respectively, for several episodes and fatalities of "plastics" dust. These data cover the decades from 1965 to 1980; at that time, the rising trend of accidental episodes likely resulted from the increasing demand for plastic.

CSB's (2006) US-based data collection gave the best overview of the severity of polymer dust explosion cases. As shown in Fig. 4, these materials are responsible for many injuries and fatalities. However, episodes involving the "food" and "wood" industries and plants have higher numbers in terms of cases (both about 24% versus 14%). Fig. 5 and Fig. 6 present more recent data, integrating different references to outline the trend from 1980 to the present.

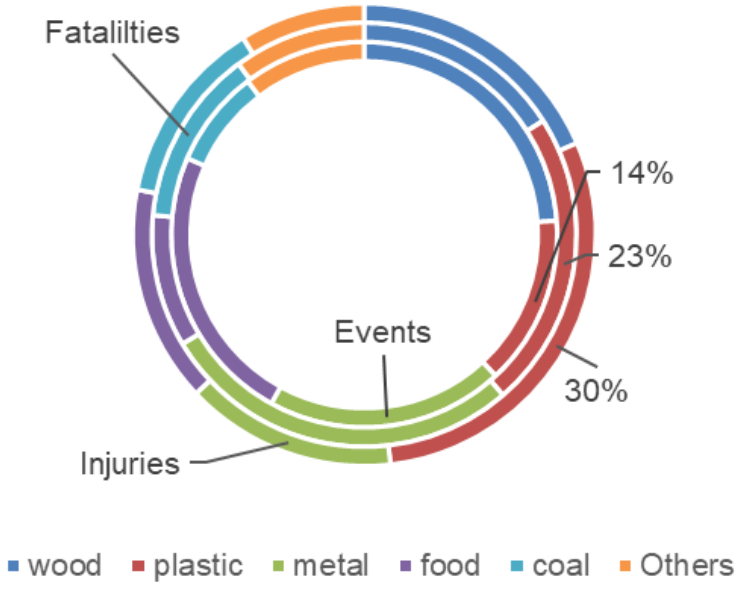

***Fig. 4**: Statistical data retrieved from CSB report (1980-2005 dust explosion events), Report 2010).*

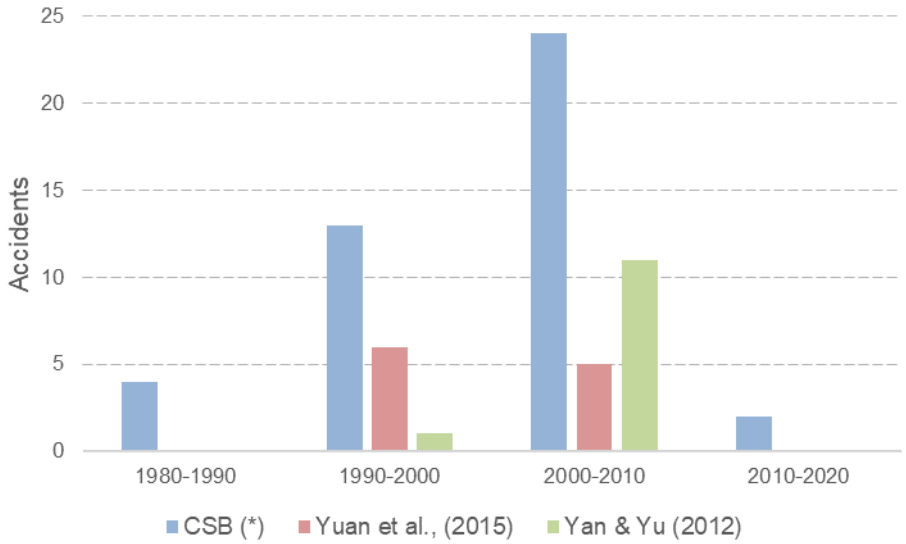

***Fig. 5**: Accidents involving "plastic and rubber" dust explosions, data retrieved from CSB (2008 and 2017, Yuan et al. (2015), and Yan & Yu (2012).*

The number of accidents increased from 1980 to 2010, but then the trend reversed (at least in the US). The increasing trend seems to be directly related to plastic demand growth. The decay after 2010 could instead be a consequence of the adoption of specific safety regulations (e.g., NFPA 654), also in response to the occurrence of serious cases such as those described below.

Different episodes, described below and listed in Table 3, involved recycling plants or operations that involved the abatement and collection of polymer waste dust from manufacturing lines. The decrease in reported accidents may be associated with increased awareness of potential hazards in recycling facilities or stricter regulations.

Recent reliable statistics came from the annual report by Cloney C. (2023), where data reporting identified different episodes in the last year: fire and explosion in a storage silo of a recycling plant where PS and PP in granular form were stored, a fire in a storage silo of a plastic waste treatment

plant, a fire and deflagration in a silo of a plastic recycling plant, a fire and explosion in a PP granules silo, a fire in a resin and rosin manufacturing site, and a fire in a dust collector in a plastic production site.

The data collected and the information obtained from the references in Table 3 allows us to classify the type of polymer involved in recent explosion cases: the highest percentage is represented by polyolefins (PE, followed by PP), while the third material involved is rubber. The rubber industry is recognized as having a high risk of dust explosion due to the nature of the materials involved (rubber compounds and additives), the presence of activities hindering the generation of fine particles (such as during milling, grinding, or transporting operations), and specific equipment that could allow dust build-up, confinement, and ignition, such as in mixers and extruders (Cloney & Barrett, 2024).

This trend is somehow also reflected in the corresponding amount of plastic waste produced globally (as in Fig. 6) where the higher percentages are associated with almost the same polymers.

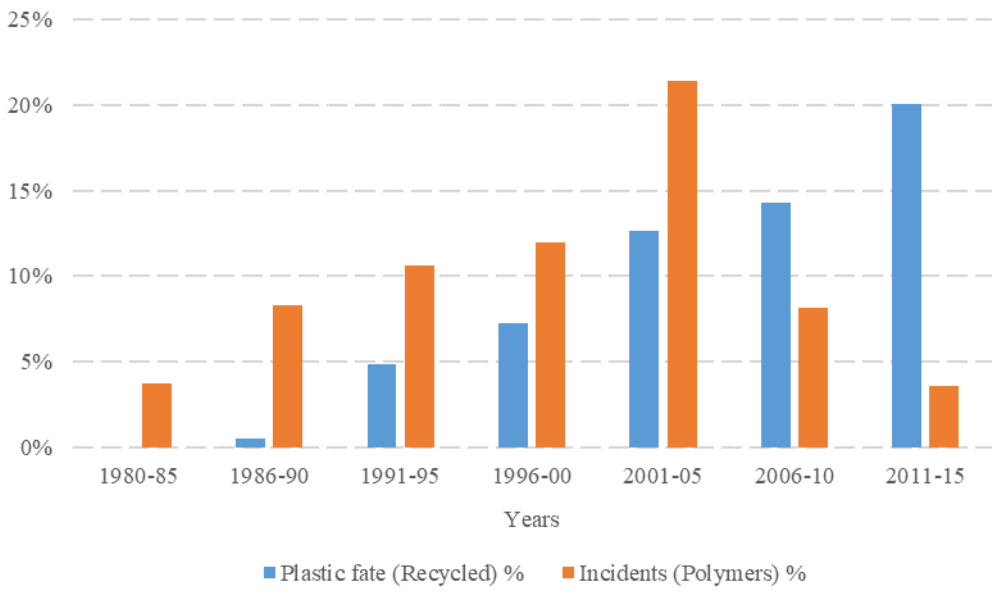

***Fig. 6**: Comparisons of percentage values associated with recycling global rate of plastics and occurrence of dust explosions in the plastic industry. Data was retrieved from CSB (2008), Yuan et al. (2015), Yan & Yu (2012), and Ritchie and Roser (2018).*

It is worth noting that data referring to the PRC in the period from 1986 to 2011 (Fig. 6), collected in the work of Yan and Yu (2012), included 11 dust explosions involving plastics (i.e., PE powder and rubber), representing 14% of the total cases. Cases of plastic dust explosions in the PRC showed a rapid increase from the 1990s to 2010. More recent data are unavailable; therefore, whether the current trend is increasing or decreasing is unknown. The 2010 figure may be a consequence of the fact that the PRC was the largest importer of plastic waste until 2017 and one of the largest recyclers in the world, second only to India (UN, 2023).

Statistics are also present for South Korea: the work from Pak et al. (2019) and Devine et al. (2023) identified data related to plastic dust explosions, with 19% of episodes accounting for about half of injuries and fatalities. This figure is relevant, as the value is relatively high compared to cases associated with metal dust.

Table 3: Relevant recent dust explosion cases involving plastic-based dust.

Date	Case	Location	Dust	I/F	Ref
1994	Kanaya Shoe Factory	JAP	Rubber waste	22/5	G. Vijayaraghavan, (2004)

1995	Malden Mills	US	Nylon flock	27/0	Frank, W. L. (2004)
1997	Hunstman Polypropylene Corporation	US	PP	0/1	OSHA (1997)
1999	Jahn Foundry	US	Phenolic resin	9/3	Myers, T., & Ibarreta, A. (2009)
2001	Finelvo	IT	Nylon flock	3/0	Marmo et al. (2018)
2002	Rouse Polymerics International, Inc	US	Rubber	6/5	McKee, J. D. (2016)
2002	Liaoyang Petrochemical Company	PRC	PE	19/8	Gan et al. (2018)
2003	West Pharmaceutical Services	US	PE	38/6	CSB, (2004)
2003	CTA Acoustics	US	Phenolic resin	37/7	CSB, (2005)
2011	Polymer Partners, LLC	US	Carbon black resin	3/1	McKee, J. D. (2016)
2013	Yeosu Industrial Complex	SKOR	HDPE	11/6	Pak et al., (2019)
2017	Yeosu Industrial Complex	SKOR	PP	-/-	Pak et al. (2019)
2017	Arakawa Chemical Industries Ltd	JAP	Resin	11/1	Cloney, C. (2018)

2.3 Plastic industry potential dust explosion hazards: process and equipment

The risk of dust explosion in the polymer manufacturing industry is present throughout the production chain, from the raw material collection, handling, and storage to the finishing operations on polymer molds. The transformation of raw polymers into finished goods implies several process operations. The raw polymer must be added by some additives that confer the required properties.

Additives could drastically modify the process blend flammability, such as in the formulation of adhesives, where highly flammable solvents are used (e.g., a mixture of acetone, hexane, and toluene), or by adding functional elements intrinsically hazardous (aziridine, highly unstable as a tackifier agent in other polymer-based adhesives). See also Groh et al. (2019).

In the case of Polyethylene, the catalyst, solvent, and ethylene monomer are mixed and reacted in a polymerization reactor; the product is a polymer slurry that needs to be filtered, dried, and extruded to be converted into a powder. These stages involved dust generation if any equipment accidentally leaks into the ambiance. Finally, the polymer powder must undergo a thermal process in a mold to obtain the shape of the final products. The last stage consists of finishing the solid products. Operations involving mechanical actions, such as grinding, refining, or cutting, are typical. These operations generate a relatively high amount of material in the form of scraps and dust.

Plastic waste recycling is the ultimate step in the polymer manufacturing chain. This last stage has become more relevant as recycling operations have risen consistently in previous decades (Danzi et al., 2022).

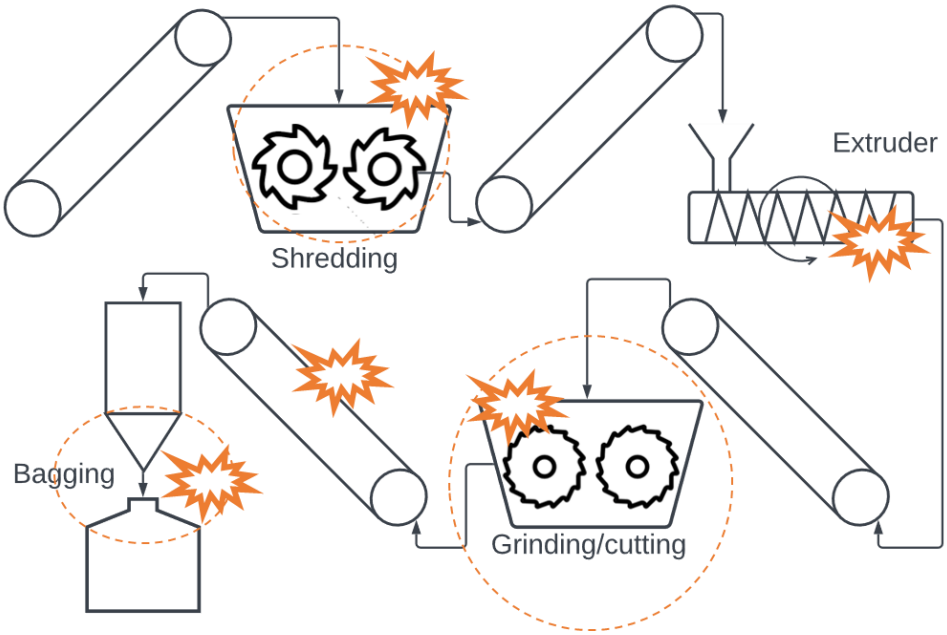

***Fig. 7**: Mechanical recycling of polymers: operations affected by dust explosion hazards.*

Potential dust cloud release and multiple ignition sources could be identified in polymer process plants and recycling facilities (Fig. 7), where mechanical operations to reduce the waste flow particle size are the most often adopted equipment. Handling and conveying of powdered material could imply fine generations due to abrasion with transportation equipment while bagging from storage silo operation is likely the most common source of dust release in ambiance if not performed accurately. Dust cloud release points and potential ignition sources are displayed respectively with dashed circles and "stars" in Fig. 7.

3 Relevant case studies

3.1 CTA Acoustics, Inc. dust explosion, 2003, KY, USA

The CSB investigation report covered the CTA Acoustics explosion (Kentucky, U.S.), CSB (2005). The main conclusions are reported here. The event occurred in the production area where acoustic insulation components for the automotive sector were manufactured.

The key findings for the case are:

- Inadequate ventilation and dust abatement system, and periodic maintenance is delayed.
- Absence of an adequate dust hazard assessment in the plant/poor communication with workers
- Combination of plant shutdown and restart with machines temporarily out of service.
- Presence of combustible dust (phenolic resin)
- Absence of fire resistance walls or barriers against fire propagation.

The concurrence of the causes illustrated above led to the likely events chain depicted in Fig. 8.

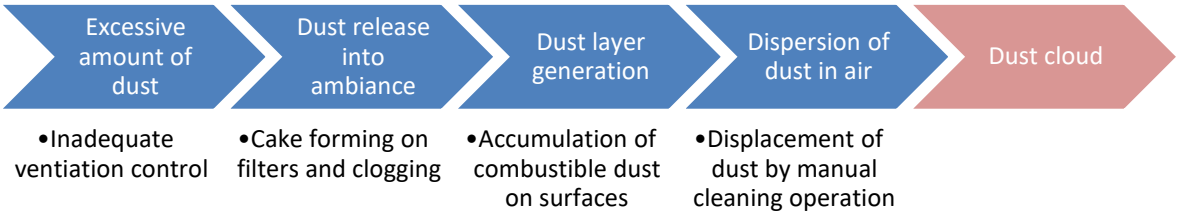

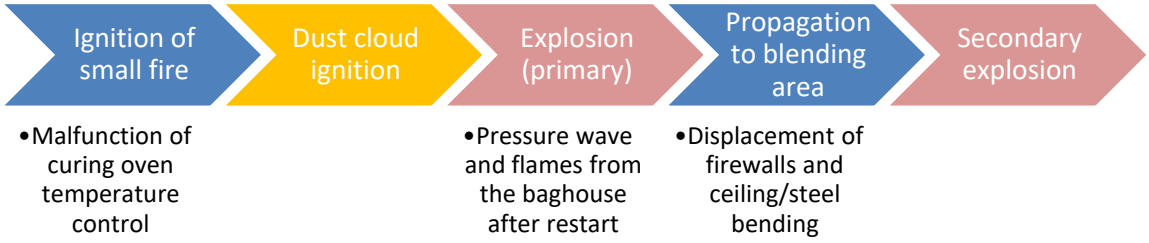

Fig. 8: *Key events sequence for CTA Acoustics explosion.*

Phenolic resin dust was known to be combustible only one year ago when an explosion caused three deaths and injured nine at the Jahn Foundry plant (US), a casting facility where phenol resin was used as a binder for sand molds (Myers & Ibarreta, 2009).

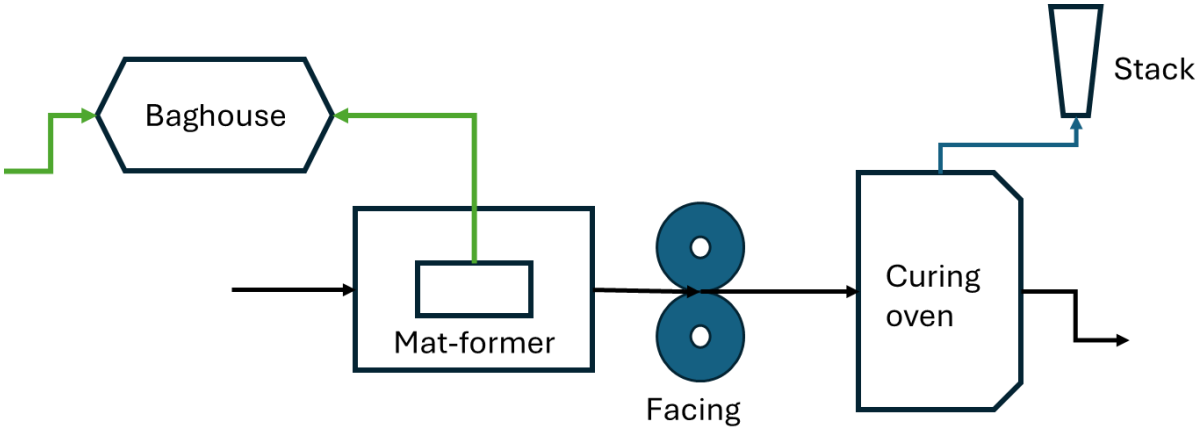

Fig. 9*: Schematic of process operations at CTA Acoustics plant: The green line is the dust abatement conveyor, the black line is the process flow, and the blue line is the gas waste to stack flow.*

3.2 Rouse Polymerics dust explosion, 2002, MI, USA

The facility was a recycling plastic site that processed fine rubber dust, where a bagging bin exploded during the daily shift, leaving five dead and more than seven injured operators (OSHA, 2002).

The conditions for this accident to occur could be listed as follows:

- The presence of a hot working operation, which may generate hot embers.
- Inadequate dust housekeeping in the ambiance.
- Piling up of dust layers on horizontal surfaces.
- Non-tight baghouse equipment.
- Failure of explosion containment.

Rubber dust that had previously been expelled from the gas-heated dryer system's exhaust stack had piled up on the bin top surface, and hot particles had escaped from the dryer.

Due to the negative pressure created inside the top of the bagging bin by the bag house blower-vacuum system, the hot smoldering embers were sucked into the bagging bin, causing violent dust deflagration.

Due to the explosion, the screw conveyor and the bagging bin itself suffered mechanical failure, allowing pressure waves and hot gases to be released and hit fugitive dust layers; this caused dust uplifting and flash fire in the surrounding production area.

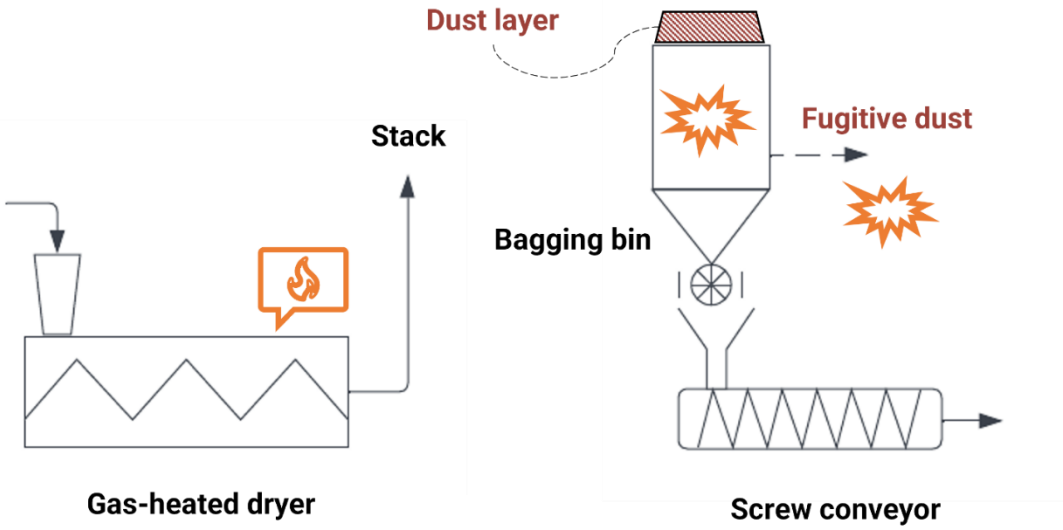

***Fig. 10**: Schematics of the key events that occurred in the Rouse Polymerics accident.*

3.3 West Pharmaceutical, Kinston, 2003, NC, USA

The facility manufactured different rubber components, and its operations included rubber molding, compounding, and extrusion. Mixers and mills were present to reduce rubber particle size. The material that fueled the event was PE dust (adopted as an anti-tacking agent for the rubber compound), which accumulated over the years on the suspended ceiling of the factory, carried by the ventilation system currents.

As in other relevant explosions, the actual trigger of the dust dispersion and ignition was not determined due to the high level of damage found in the aftermath. Investigators identified likely causes, among others, the overheating of a batch of rubber and subsequent ignition of vapors, an overheating due to electrical components (or an electrical spark) of the dust layer accumulation, or the ignition of dust cloud by the presence of an electric motor. The explosion center was estimated to be in the compounding area, close to a mill. As the blast thermal effects reached the warehouse, where rubber and other raw materials were stored, the event accelerated, and the entire building was engulfed in flames; the heat of the fire eventually caused the structure to collapse, leaving six dead and 38 injured workers, (CSB report 2004).

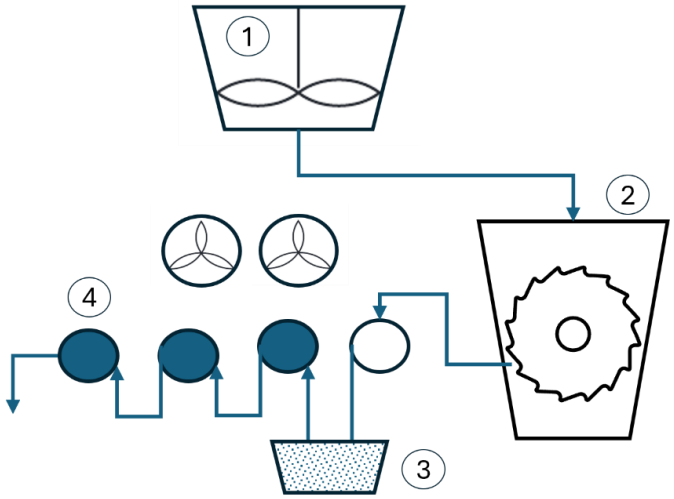

***Fig. 11**: Rubber compounding schematics: The blend is realized in the mixer (1), the rubber is milled into strips (2), these are dripped into an anti-tack PE powder slurry (3), and then air-cooled on rollers (4).*

4 Conclusions

Dust explosions have had a substantial impact on the plastics industry, and the percentage breakdown in terms of human consequences (accidents and deaths) is greater than in other sectors, although the number of cases is lower. The plastic industry presents peculiar features that make it exposed to dust explosion risk: almost every polymer, in powdered form, is flammable and could be easily lifted in clouds due to its low density; the types of equipment generate ideal conditions for an explosion (confinement, particle reduction, mechanical and thermal operations); mixing of material is carried and determines complex synergic scenario discovered by Centrella et al., 2020, and hybrid atmospheres.

Through data collection and analysis, this work demonstrated that low-chain polymers (PE, PP) are the most prevalent waste material in the industry. This is reflected in the high number of accident cases associated with them. Fiber material in the rubber and nylon sectors appeared involved in several episodes, such as the recent case studies reported here.

The recycling sector deserves attention. The increase in accidental rates seemed to be correlated to the increase in plastic waste and recycling rates. This sector is not conceived as high-tech, which could lead to poor or inadequate risk analysis. Some correspondence could be traced by observing the data reported between the plastic waste produced, according to polymer type, and the involvement of polymers in the accidental episodes. This supports the required enhancement in focusing the attention on waste and recycling processes in terms of dust risk assessment, as well as the need for a more industry-based dust explosion study on plastic mixtures and waste, representative of the actual industrial materials. The explosibility parameters of this kind of dust are analyzed in detail in the following experimental part of this work by Danzi et al. (2024).

References

Beck, H., and A. Jeske. (1982) “Dokumentation Staubexplosionen. Analyse und Einzelfalldarstellung.” Report No. 4/82. St. Augustin, Federal Republic of Germany: Berufsgenossenschaftliches Institut fur Arbeitssicherheit.

Centrella L., Portarapillo M., Luciani G., Sanchirico R., Di Benedetto A. (2020) Synergistic behavior of flammable dust mixtures: A novel classification, Journal of Hazardous Materials, 397, 122784

Chris Cloney and Jon Barrett (2024). Combustible Dust Explosion Hazards in the Rubber Industry. Retrieved Apr 5, 2024 from https://dustsafetyscience.com/combustible-dust-rubber-industry/

Cloney, C. (2018) “2017 Combustible Dust Incident Report – Version #1”. Retrieved from http://www.myDustExplosionResearch.com/2017-Report

CSB (2004). Investigation report dust explosion. West Pharmaceutical Services, Inc. Kinston, North Carolina - January 29, 2003. REPORT NO. 2003-07-I-NC.

CSB (2005) Investigation report combustible dust fire and explosions. CTA Acoustics, Inc. Corbin, Kentucky February 20, 2003, REPORT NO. 2003-09-I-KY

CSB (2006) Investigation report. combustible dust hazard study. Report NO. 2006-H-1.

CSB (2017). Dust incidents 2006-2017. U.S. Chemical Safety Board. Available on https://www.csb.gov/assets/1/6/csb_dust_incidents.pdf. Last accessed 20 Apr 2024.

Danzi E., Marmo L., Portarapillo, M., Sanchirico, R. & Di Benedetto, L. (2022). Waste and Recycling of plastics: dust explosion risk evaluation. Proceedings of 14th International Symposium on Hazards, Prevention, and Mitigation of Industrial Explosions Braunschweig, GERMANY – July 11-15, 2022

Danzi, E., Portarapillo M., Marmo, L. & Di Benedetto, A. (2024). Polymer dust explosion part II: Experimental tests. To be presented at 15th International Symposium on Hazards, Prevention, and Mitigation of Industrial Explosions. Naples, ITALY – June 10-14, 2024

Devine, C., Flores, N., & Walls, R. (2023). Literature review and hazard identification relating to fire safety in commercial plastic recycling facilities. Journal of Fire Sciences, 41(6), 269–287. https://doi.org/10.1177/07349041231199894

Echkoff, R. K. (2003). Dust Explosions in the Process Industries (3rd edition). Gulf Professional Publishing.

Frank, W.L., (2004). Dust explosion prevention and the critical importance of housekeeping. Process Saf. Prog. Journal 175–184.

Geyer, R., Jambeck, J. R., & Law, K. L. (2017). Production, use, and fate of all plastics ever made. http://advances.sciencemag.org/

Groh, K. J., Backhaus, T., Carney-Almroth, B., Geueke, B., Inostroza, P. A., Lennquist, A., … Muncke, J. (2019). Overview of known plastic packaging-associated chemicals and their hazards. Science of the Total Environment, 651, 3253–3268.

Hartmann, I. & Nagy, J. (1944). Infiammability and Explosibility of Powders used in the Plastic industry. Bureau of Mines, Rept. of investigation 3751.

Hopewell, J., Dvorak, R., & Kosior, E. (2009). Plastics recycling: Challenges and opportunities. Philosophical Transactions of the Royal Society B: Biological Sciences, 364(1526), 2115–2126. https://doi.org/10.1098/rstb.2008.0311

https://dustsafetyscience.com/ 2024 DustEx Research Ltd. Last accessed Apr 02 2024.

Jacobson, M., Nagy, J. & Cooper, A. R. (1962). Explosibility of dusts used in the plastics industry. U.S. Dept. of Interior, Bureau of Mines.

Lyon, R. E. and Janssens, M. L. (2005). Polymer Flammability. Report n° DOT/FAA/AR-05/14. U.S. Department of Transportation Federal Aviation Administration Office of Aviation Research Washington, DC 20591

McKee, J. D., "Comparative Case Study Analysis of Combustible Dust Explosions: Determining the Need for an OSHA Combustible Dust Standard" (2016). Online Theses and Dissertations. 400. https://encompass.eku.edu/etd/400

Myers, T., & Ibarreta, A. (2009). Investigation of the Jahn Foundry and CTA Acoustics dust explosions: similarities and differences. Journal of Loss Prevention in the Process Industries, 22(6), 740–745. https://doi.org/10.1016/j.jlp.2009.08.016

NFPA 654®, Standard for the Prevention of Fire and Dust Explosions from the Manufacturing, Processing, and Handling of Combustible Particulate Solids (Quincy: National Fire Protection Association, 2020)

OECD (2022), a – processed by Our World in Data. OECD, “Global Plastics Outlook - Plastics use by polymer” [original data].

OECD (2022), b – processed by Our World in Data. OECD, “Global Plastics Outlook - Plastics waste in 2019 by region, polymer and application” [original data].

OSHA (1997). Accident Summary Nr: 201770286 -- Report ID: 0213900 https://www.osha.gov/ords/imis/accidentsearch.accident_detail?id=201770286 Last accessed 10 Apr 2024.

OSHA (2022). Accident Summary Nr: 201361813 https://www.osha.gov/ords/imis/accidentsearch.accident_detail?id=201361813. Last accessed 15 March 2024.

Pak, S., Jung, S., Roh, C., & Kang, C. (2019). Case studies for dangerous dust explosions in South Korea during recent years. Sustainability (Switzerland), 11(18). https://doi.org/10.3390/su11184888

Ritchie H. and Roser M. (2018). “Plastic Pollution”. Published online at OurWorldInData.org. Retrieved from: ‘https://ourworldindata.org/plastic-pollution’ [Online Resource]

United Nations Comtrade Database (2023) – with minor processing by Our World in Data. “Share of global plastic waste imports” [dataset]. United Nations Comtrade Database, “Comtrade Database” [original data]. Retrieved April 16, 2024 from https://ourworldindata.org/grapher/share-plastic-waste-imports

Vijayaraghavan, G., Engineering, C., & College, A. E. (2011). Research Article EMERGING EMERGENCY DUE TO DUST EXPLOSIONS IN PROCESS INDUSTRY Address for Correspondence. Journal of Engineering Research and Studies, II(Iv).

Yang D, Zheng Y, Peng K, Pan L, Zheng J, Xie B, Wang B. Characteristics and Statistical Analysis of Large and above Hazardous Chemical Accidents in China from 2000 to 2020. Int J Environ Res Public Health. 19(23):15603.

Yuan, Q., Zhang, J., Amyotte, P., Zhang, H., Bu, Y., Li, C., Liu, Z., Chen, H., Li, G., & Yuan, C. (2023). Investigation of dust ignition sensitivity and co-pyrolysis properties of biomass and plastic waste during resource utilization. 2023, 950–4230. https://doi.org/10.1016/j.jlp.2023.105187

Metal Oxide Reducing Environment (MORE) Explosions: Initial Assessment

Andrew J. Furlong [a,b], Nicole K. Bond [a], Benjamin C. Strange [b], Robin W. Hughes [a] & Michael J. Pegg [b]

[a] Natural Resources Canada, CanmetENERGY Ottawa, Ottawa, ON, Canada
[b] Dalhousie University, Department of Process Engineering and Applied Science, Halifax, NS, Canada

E-mail: afurlong@dal.ca

Abstract

It has recently been proposed that select metal oxides under a reducing gas have the potential to react in an explosive fashion, in what is termed a metal oxide reducing environment (MORE) explosion. The primary materials for which this has been proposed are copper and manganese oxides, which are extensively used in chemical looping combustion (CLC) processes which can produce significant quantities of fine particles. Under the CLC process, fuels such as methane diffuse into metal oxides and exo- or endothermically reduce the materials, producing combustion products and reduced or partially reduced metals. In copper and manganese oxides this reaction is exothermic. Chemical looping oxygen uncoupling (CLOU) is another chemical looping mechanism where oxygen diffuses out of the metal oxide and then reacts with the gaseous fuels. This CLOU mechanism is not rate-limited by particle size. Analysis shows that the copper (II) oxide-methane system has the thermodynamic potential to react explosively at any operating temperature, with kinetic analysis showing the CLC and CLOU mechanisms are the rate limiting step rather than gas-phase combustion. Propagation is much slower than for standard gas or dust explosions. However, the reaction stoichiometry gives a minimum overpressure ratio of $n + m$ for a hydrocarbon C_nH_{2m} with temperature effects as a secondary multiplier, making overpressure possible in isothermal systems. These results indicate that the metal oxide/reducing gas mixtures require proper design consideration for safe venting, to mitigate potential explosions. Experiments are being completed in a 350 cm^3 pressure vessel with sample heating by a heated grid, however experiments are not yet completed. The heated grid system is noted to have potential for elevated-temperature testing of traditional dust explosions, which has previously been challenging but is necessary to evaluate parameters for operating such processes.

Keywords: *dust explosion, chemical looping combustion (CLC), chemical looping oxygen uncoupling (CLOU), oxygen carrier (OC), heated grid reactor*

1. Introduction

Chemical looping combustion (CLC) is a novel combustion mechanism in which the oxidizer and fuel are separated by using an oxygen carrier (OC) which is typically a transition metal. The overall reaction (1) is divided into reaction (2) for oxidation and reaction (3) for reduction:

$$C_nH_{2m}O_p + (n + m/2 - p/2)O_2 \rightleftharpoons nCO_2 + mH_2O, \qquad \Delta H_c = \Delta H_r + \Delta H_o \quad (1)$$

$$(2n + m - p)Me_xO_{y-1} + (n + m/2 - p/2)O_2 \rightleftharpoons (2n + m - p)Me_xO_y, \qquad \Delta H_o \quad (2)$$

$$(2n + m - p)Me_xO_y + C_nH_{2m}O_p \rightleftharpoons (2n + m - p)Me_xO_{y-1} + nCO_2 + mH_2O, \qquad \Delta H_r \quad (3)$$

This process is traditionally operated through interconnected fluidized beds, shown in Figure 1, which can result in a high level of attrition or degradation of the OC materials due to chemical, thermal, and

mechanical stresses (Galinsky et al., 2018). Particles with diameters less than 45 μm have been shown to have a high rate of elutriation shortly after initial startup (Lyngfelt and Thunman, 2005), and these particles may be retained in ducting, windboxes, and filters, where they may be disturbed by transients in operation such as startup, shutdown, and process upsets. The materials used as OCs in their reduced form have previously been examined for explosibility and have been classified as non-explosible or marginally explosible under standard test conditions (Jacobson et al., 1964; Cashdollar, 1994). Despite this, these metal dusts have reported ignition temperatures, with cloud ignition temperatures from 320 to 900 °C for the elemental form of oxygen carriers including iron, copper, cobalt, and manganese (Jacobson et al., 1964). This indicates that the activation energy makes the oxidation reaction infeasible at low temperatures, but increasing initial temperatures will overcome this barrier and make the reaction self-sustaining. Chemical looping processes use intensified environments with temperatures of up to 1 050 °C and elevated pressures of up to 22.4 bar(a) (Symonds et al., 2019) to reduce kinetic limits for reduction and oxidation, which are far beyond standard test conditions in ASTM E1226-19 (ASTM, 2019) and the ambient temperatures of ISO 6184-1 (International Organization for Standardization, 1985) for dust explosions, and may supply this initial source of energy to initiate combustion. Previous works (Cashdollar and Chatrathi, 1993; Going et al., 2000) have demonstrated that over-driving explosions by excess initial energy leads to an increased likelihood of occurrence, further supporting this hypothesis. Given the degradation of OCs from stresses, with mixing provided by process upsets and energy by process conditions, there is the potential for a dust explosion involving a metal dust, or partially oxidized metal dust, and air in chemical looping processes. However, explosion testing at CLC operating temperatures and pressures is challenging due to material limitations. In the standard 20 L chamber, initial temperatures are limited to 60 °C (TÜV SÜD Schweiz AG and Cesana AG, 2016), while the 1 m^3 chamber is limited to an initial temperature of 200 °C (OZM Research s.r.o., 2020).

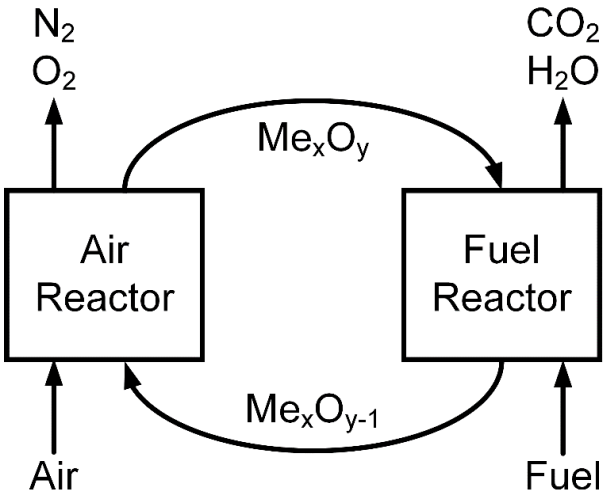

***Fig. 1**. Generalized process diagram for interconnected fluidized bed chemical looping combustion.*

Beyond traditional dust explosions, it has recently been noted that the oxidized form of the OC may also be explosible by acting as the oxygen supply to an explosion with a reducing gas (Furlong et al., 2024). This differs from a hybrid mixture explosion as the dust is not combustible and there is not necessarily oxygen initially present in the gas phase. However, because the dust is not undergoing oxidation it is also not a dust explosion. This has been termed a metal oxide reducing environment (MORE) explosion. This case has primarily been proposed for chemical looping processes because the heat of reaction for the reduction of most metal oxides used as OCs is negative (exothermic) under hydrogen and carbon monoxide (Adanez et al., 2012). Manganese (II) oxide, copper (I) oxide and copper (II) oxide, and cobalt (II, III) oxide are also all exothermically reduced by methane, counter to the standard case where reduction is endothermic, as is seen in OCs such as nickel and iron. Manganese and copper oxides are also used in chemical looping oxygen uncoupling (CLOU), in

which oxygen is released by the OC due to high temperatures based on thermodynamic equilibrium (Whitty et al., 2018). In this case, the presence of gaseous oxygen leads to higher reaction rates with fuels than would be expected by the solid-phase CLC mechanism, promoting explosions if they should occur. Beyond chemical looping this mechanism may apply to other processes containing high-temperature metal oxides and reducing gases, such as the reduction of ores to produce metals.

In this work a recently identified explosion mechanism, the MORE explosion, is examined through thermodynamics, kinetics, and experiments. The thermodynamic approach was used to examine if copper (II) oxide-methane explosions are possible, and to identify the contributing factors to the overpressure in an adiabatic case. The kinetic investigation was used to provide an initial assessment of potential reaction and propagation mechanisms and evaluate the MORE explosion severity against an oxy-methane equivalent, and to assess the validity of the adiabatic model. An experimental apparatus using a heated grid is presented and discussed for its potential to investigate explosion severity parameters at elevated temperatures representative of operating processes, including the proposed explosion mechanism.

2. Modeling and Experiments

2.1. Thermodynamic model

The thermodynamic modelling methodology has previously been described (Furlong et al., 2024), with modelling completed using FactSage 8.2 (Bale et al., 2009) at equilibrium conditions with the FactPS (pure species) and FToxid (oxides for slags, gases, ceramics, and refractories) databases, considering gas, liquid, and solid phases. A modification from the previous methodology was made in considering the formation of no hydrocarbons beyond methane. A similar approach has previously been used for metal dusts and has found reasonable agreement with experiments given the adiabatic assumption (Dastidar and Amyotte, 2004).

2.2. Kinetics

The kinetics for the gas-phase combustion of methane are well-established for computational purposes (Zettervall et al., 2021), and a simplified kinetic expression based on the concentrations of oxidizer and fuel, in addition to temperature, is given in Arrhenius form by Westbrook and Dryer (1981). This is applied at a pressure of one atmosphere with a stoichiometric mixture of oxygen and methane to represent the potential conditions in a CLC reactor. The solid-phase reactions have been examined in detail in several works using thermogravimetric analysis (TGA). In this work, kinetic data for the CLOU mechanism is based on the work of Hu et al. (2016) for copper (II) oxide using the instantaneous rate of reaction at the surface for zero initial conversion with a concentration of 7 100 g m^{-3} to examine a worst-case scenario for a stoichiometric mixture at a moderate temperature of 300 °C. Equilibrium oxygen pressures were evaluated at different temperatures by extrapolating from the work of Whitty et al. (2018) and the assumption that the bulk phase is depleted of oxygen. The CLC mechanism is evaluated using the kinetic terms established by Monazam et al. (2012) at a peak reaction rate, which occurs at approximately 35% conversion. In all cases the kinetic models are extended beyond the temperatures for which they were originally developed due to the limited availability of kinetic studies. It should also be noted that Hu et al. (2016) considered the effects of particle size on CLOU with copper (II) oxide and found that internal mass transfer limits are not significant, making the reaction rate independent of particle size.

2.3. Experimental

2.3.1 Apparatus and procedure

Preliminary experiments were conducted in a 350 cm^3 cylindrical vessel (70 mm internal diameter, 91 mm length), with supporting systems shown in Figure 2. The system is electrically pre-heated using a 304 stainless steel mesh and a (0-30) A/(0-30) V bench power supply in a system typically referred to as a heated grid microreactor (Zeng et al., 2008). Heated grid reactors allow for heating at

initial rates of up to 5 000 K s^{-1} due to their low masses relative to the heat input (Gibbins et al., 1989), which is applied here to heat the samples to a target temperature without heating the pressure vessel and reducing its structural integrity. Equation (4) describes the energy balance which is used to evaluate the transient temperature profile of the sample and the final temperature before gas addition, under the assumptions no oxygen uncoupling occurs, that the system is under total vacuum, that the emissivity of the oxide sample and the oxidized mesh are both unity, and that the temperature of the pressure vessel is constant at that of the surroundings on a short time:

$$\frac{dT}{dt} = \frac{\dot{Q}_{elec} - 2\sigma LW\left[T^4 - (293\ \mathrm{K})^4\right]}{m_{sample}c_{p,sample} + m_{mesh}c_{p,mesh}} \quad (4)$$

where $\dot{Q}_{elec}$ is the electrical energy input to the grid [W], σ is the Stefan-Boltzmann constant [W m^{-2} K^{-4}], L and W are the length and width of the mesh [m], T is the temperature [K] at time t [s], m is the mass of the sample or mesh [kg], and c_p is the specific heat capacity of the metal and mesh at their current temperature [J kg^{-1} K^{-1}].

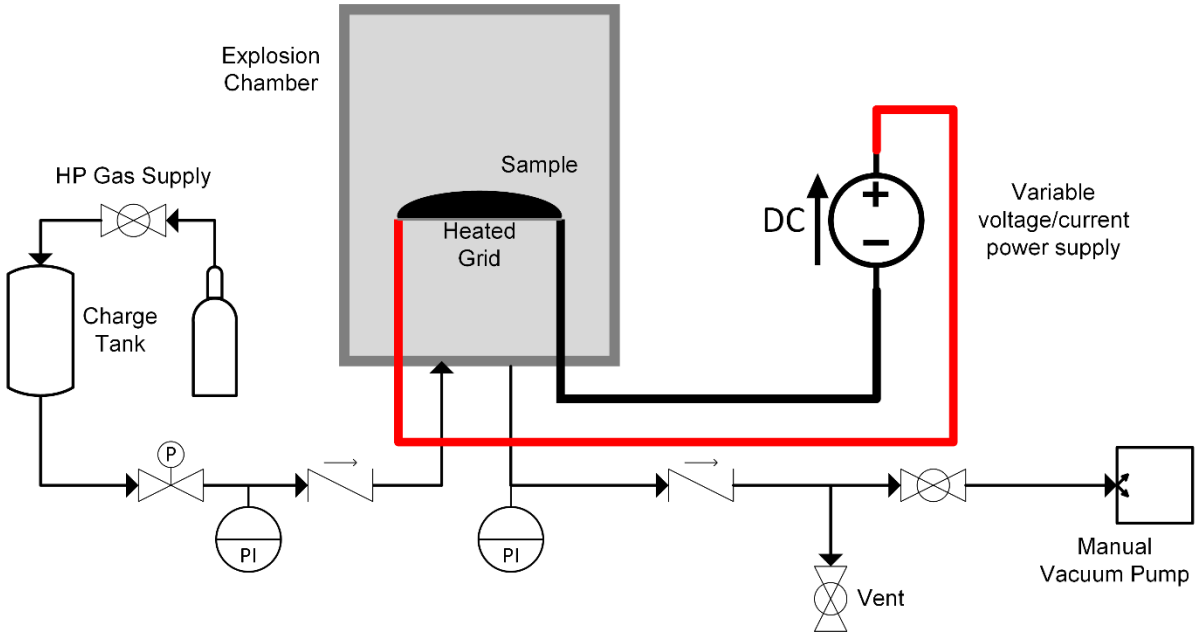

Fig. 2. *Experimental apparatus process overview showing the mechanisms for gas addition and sample dispersion, electrical sample heating, overpressure monitoring, and vacuum production.*

The apparatus uses a 50 cm^3 charge tank initially filled with methane at low-moderate pressures (1-10 bar), to provide a high-velocity gas stream to the explosion chamber, initially under vacuum, to disperse the dust and mix the reactants. This gas stream is controlled by a fast-acting electro-pneumatic ball valve. Backflow is prevented by a check valve installed in the explosion chamber inlet. Gas pressures are monitored to confirm the initial charging pressure in the explosion chamber.

The outlet line from the explosion chamber is connected directly to a pressure transducer to monitor overpressure development. The outlet is also connected to an additional check valve to prevent air ingress during vacuum development and venting. Vacuum pressures are developed by a manually operated vacuum pump because of the small size of the vessel, and the vacuum pump is protected from overpressure by a ball valve. An additional ball valve is installed on the vent line to maintain a closed system during tests. Pressure relief is included on the outlet line with a set point of 25 bar.

2.3.2 Material synthesis

The copper (II) oxide used was synthesized by dissolution of 99.9 wt.% copper using concentrated nitric acid, followed by dilution with DI water and the addition of 6 M sodium hydroxide to form copper hydroxide. The copper hydroxide solution was then heated below boiling to form a precipitate

of copper (II) oxide. The precipitate was vacuum filtered to dry. Dried samples were crushed with a pestle to form a fine powder; however, particle size distributions were not obtained due to the small quantities of copper (II) oxide produced.

3. Results and discussion

3.1. Thermodynamic model results

Examining the effects of initial temperature for the proposed system in Figure 3 shows that at any reasonable initial temperature there is the thermodynamic potential for the reaction to proceed; however, this reaction may take an infinitely long time to occur. The overpressure in this case is strongest near a stoichiometric mixture of copper (II) oxide and methane for total conversion to elemental copper, carbon dioxide, and water vapour. At high equivalence ratios ($\Phi > 1$) the overpressure is decreased with excess reducing gas, leading to a low ratio of products to reactants. At low equivalence ratios ($\Phi < 1$) the excess solids act as a heat sink and reduce temperatures, despite total conversion of the reducing gas. As previously identified, increasing temperatures leads to decreased overpressures with a reduced ratio of final to initial temperature, T_f/T_0 (Furlong et al., 2024). There are some plateaus seen in the overpressure in Figure 3. This is due to the formation of a liquid phase containing elemental copper and/or copper (I) oxide at high final temperatures leading to constant temperature ratios, and with total conversion of methane due to the lean conditions the gas quantity is also held constant.

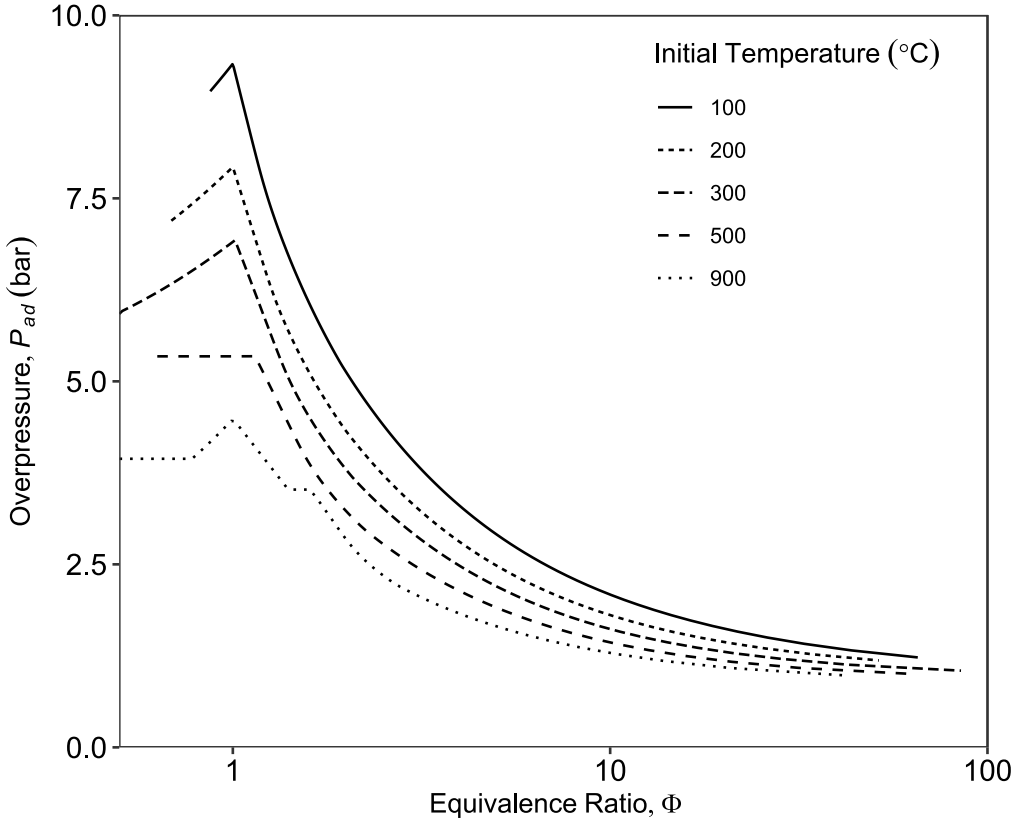

Fig. 3. *Effect of initial temperature and equivalence ratio (stoichiometric ratio of gas-solid) on overpressures in the copper (II) oxide-methane system.*

A key limitation of thermodynamic studies for explosion modelling is in the assumption that systems are adiabatic, however this assumption is not valid in the case that the reaction proceeds more slowly, as is later discussed. In the case of an infinitely slow reaction the isothermal assumption is more appropriate. For traditional gaseous explosions and dust explosions, the isothermal case produces a small overpressure due to the ratio of products to reactants being low with high amounts of gaseous

oxidizer required. The nitrogen in air can also act as a diluent which further limits the product to reactant ratio for such systems. For the proposed MORE explosion, where the phases are reversed from standard dust explosions, the ratio of products to reactants in the gas phase is $n + m$ for the general hydrocarbon C_nH_{2m}. In Figure 4, the ratio of the quantity of products to reactants in the gas phase is shown alongside the ratio of temperatures in the adiabatic case, demonstrating that the temperature effects in a MORE explosion are secondary to the gas production effects, and that an overpressure exists regardless of whether the system is assumed adiabatic or isothermal.

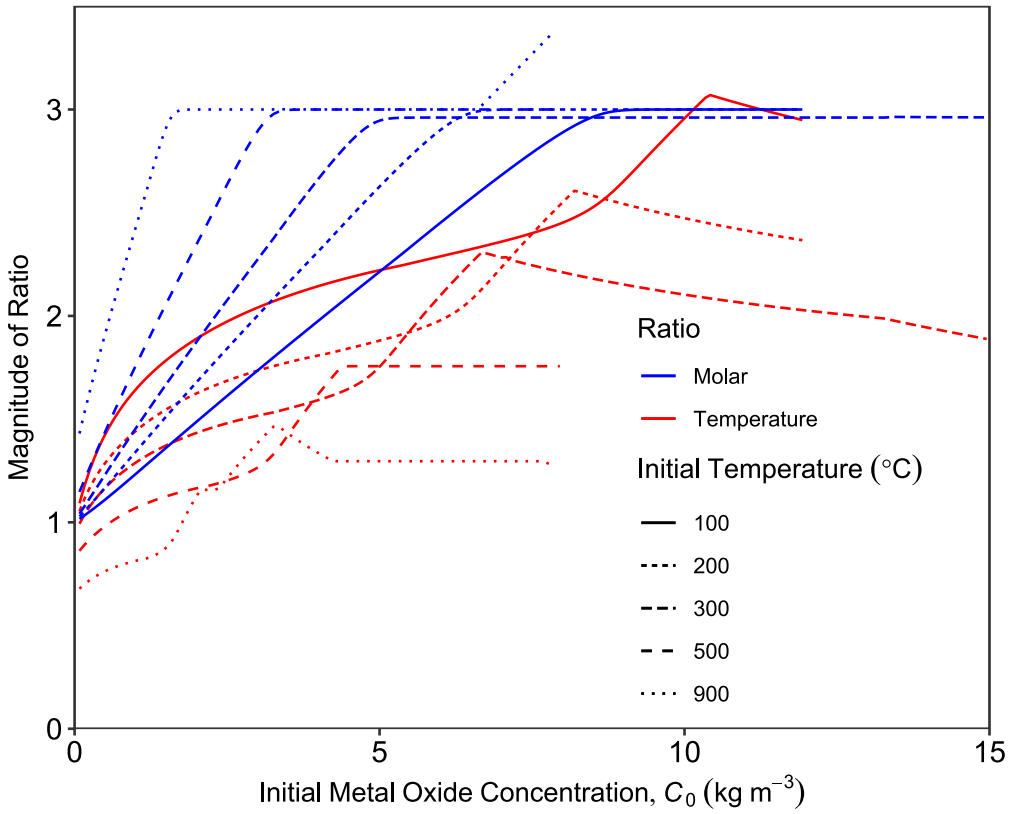

Fig. 4. *Temperature and molar ratios for the final and initial states in the copper (II) oxide-methane system showing the driving force is primarily from increasing gas quantity, with a larger relative contribution as temperatures increase.*

Using the results shown in Figures 3 and 4, it can be determined that for lean mixtures an overpressure will occur with a minimum pressure rise of $n + m$ for C_nH_{2m}. As temperatures increase and the system acts closer to adiabatic than isothermal an additional scaling factor of T_f/T_0 will apply, however as temperatures further increase this scaling factor will be reduced and potentially affected by phase changes. For rich mixtures with low solids concentrations, the overpressure is limited both in the increase in gas quantity and temperature with low gas conversions.

3.2. Proposed mechanism

3.2.1 Rate-limiting reaction

The reaction rates for the oxy-methane reaction and the two chemical looping reactions (CLOU and CLC) are shown in Figure 5. These reactions show that the rate-limiting step for the proposed MORE explosions is the oxygen uncoupling mechanism rather than gaseous combustion, and thus the kinetics should be evaluated on the uncoupling mechanism to evaluate severity. The reaction rates for the gaseous combustion of a stoichiometric oxy-methane mixture are orders of magnitude higher than for oxygen uncoupling, indicating that the partial pressure of oxygen is minimal due to constraints in kinetics of oxygen production for oxygen uncoupling. Under this case, the reactions

may be represented pictorially, as in Figure 6, where solid-phase combustion is occurring concurrently with oxygen uncoupling which leads to additional gas-phase combustion near the surface of the OC particle. The supply of heat from the combustion reactions powers the endothermic oxygen uncoupling reaction, however the overall mechanism is exothermic leading to accelerated reaction rates through time.

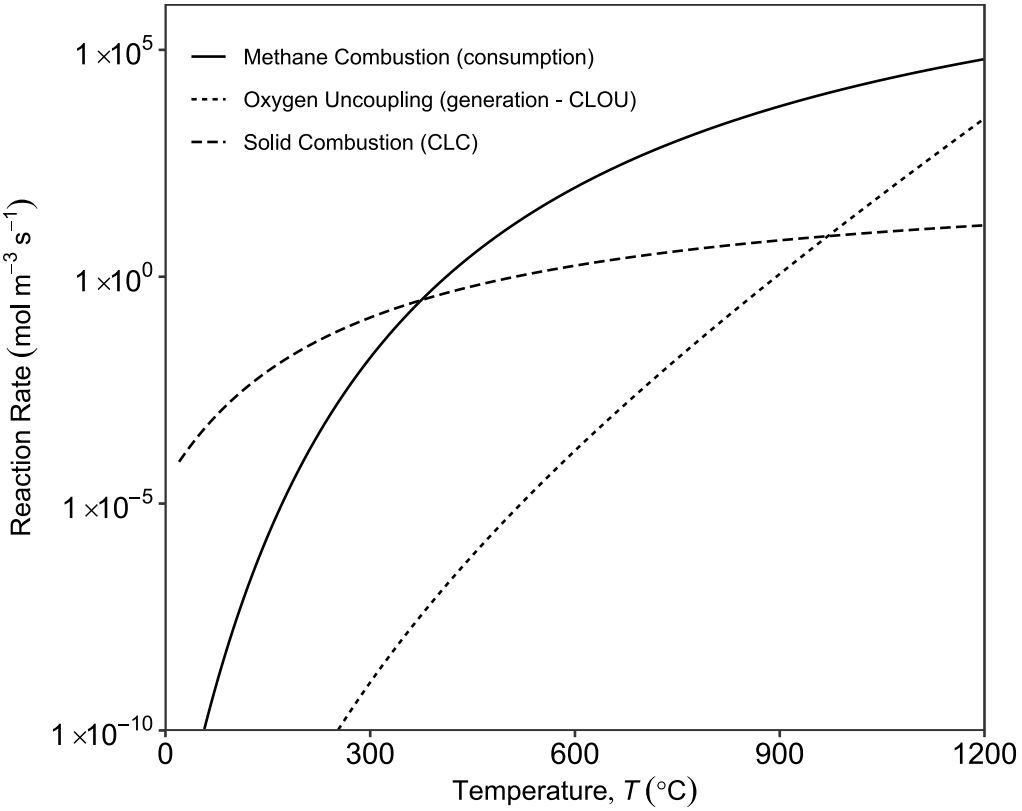

Fig. 5. *Reaction rates for the gas-phase combustion of a stoichiometric methane-oxygen mixture (gaseous oxygen consumption), CLOU mechanism (gaseous oxygen production), and the heterogeneous CLC mechanism (gaseous methane and solid oxygen carrier) at their maximum rates.*

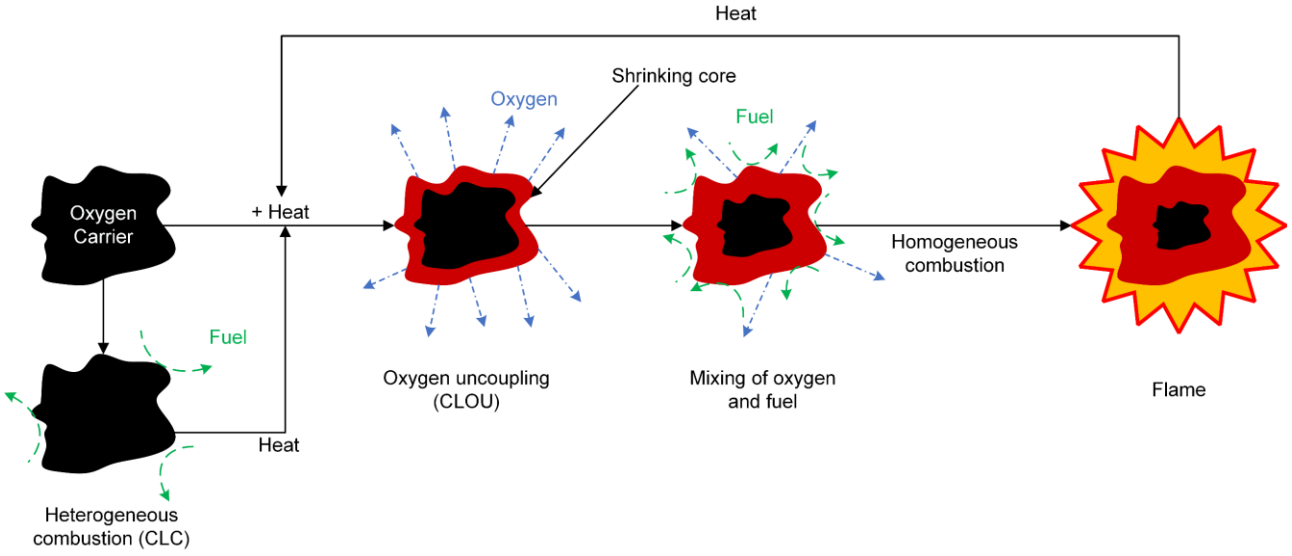

Fig. 6. *Proposed global kinetic mechanism for MORE explosions showing the concurrent homogeneous and heterogeneous reaction paths with the release and consumption of heat.*

3.2.2 Propagation

The deflagration index (a measure of explosion severity), in an analytical approach taken by Dahoe et al. (1996), has a linear relationship to the burning velocity of a mixture. The burning velocity of a mixture is proportional to the square-root of the reaction rate (Williams, 2003), which from Figure 5 implies that the deflagration index will be significantly reduced with low oxygen uncoupling rates relative to gaseous combustion. Based on the reaction rate, the deflagration index in the proposed MORE explosions will be 0.3-2.2% of their oxy-methane counterparts on an operating range of 700-950 °C. However, the relationship between relative rate and temperature is non-linear. As temperatures approach 1 200 °C, the propagation rate under this assumption reaches 22.2% of the oxy-methane equivalent, showing increasing severity with operating temperatures. Although the rate of reaction is lower, at elevated temperatures the overpressure for the MORE explosion will be higher than for their gas explosion counterparts due to the multiple overpressure generating factors discussed in section 2.1. On this basis, the deflagration index for the MORE explosions is expected to be lower than for gas explosions but may still be comparable between the two scenarios, with a residual elevated pressure following a MORE explosion as heat is lost to the surroundings. Equipment in this case should be designed with more consideration given to the overpressure of the system than the rate of pressure rise, with adequate venting for the produced gases.

3.3. Experimental results

At present, preliminary trials have not resulted in an explosion, due to two primary reasons. The first challenge is in the kinetic limits in the system as previously described, which may require a modified means of gas addition to maintain mixing while sustaining the reaction. The second reason is the complications associated with the development of a high-temperature bench-scale apparatus using relatively high electric currents. Experiments have been successful in heating the mesh grid used to temperatures ranging from dull red glows (~600 °C or higher) to yellow (~1 100 °C) or white-yellow (~1 300 °C) near the melting point of steel (Chapman, 2011), as seen in Figure 7, and ensuring melting does not occur has proven challenging. Melting is particularly difficult to manage with flaws in the grid material, as seen at the top of Figure 7, leading to increased local heating, and any defects which melt result in total failure with reduced cross-sectional areas and increased resistance. Future work will involve more direct measures of the temperature of the grid to evaluate the suitability of Equation (4), however the glow temperatures of the steel mesh serve as reasonable estimate of temperature when paired with established reference material.

With a heat input of 300 W in the grid, the maximum temperatures are obtained in approximately two seconds, agreeing with the energy balance in Equation (4). In the case shown here under air, environmental heat losses are higher than under vacuum operation and the system temperatures are theoretically limited, however these losses can be balanced by additional energy input. Additionally, Figure 7 shows the non-uniformity of the mesh temperatures, with the areas furthest from the sample having the highest temperatures and appearing more white-yellow, while areas with high sample densities are more red-black (~800 °C). In the sample, this is reflected with lone particles having a red glow like the surrounding grid while clusters appear more like copper (II) oxide under standard conditions. This shows the need for dispersion of a sample into a monolayer on the mesh to apply the analytical expression to estimate the temperatures of three-dimensional samples on the grid and indicates that the bench-scale apparatus may only be suitable for low concentrations of dust.

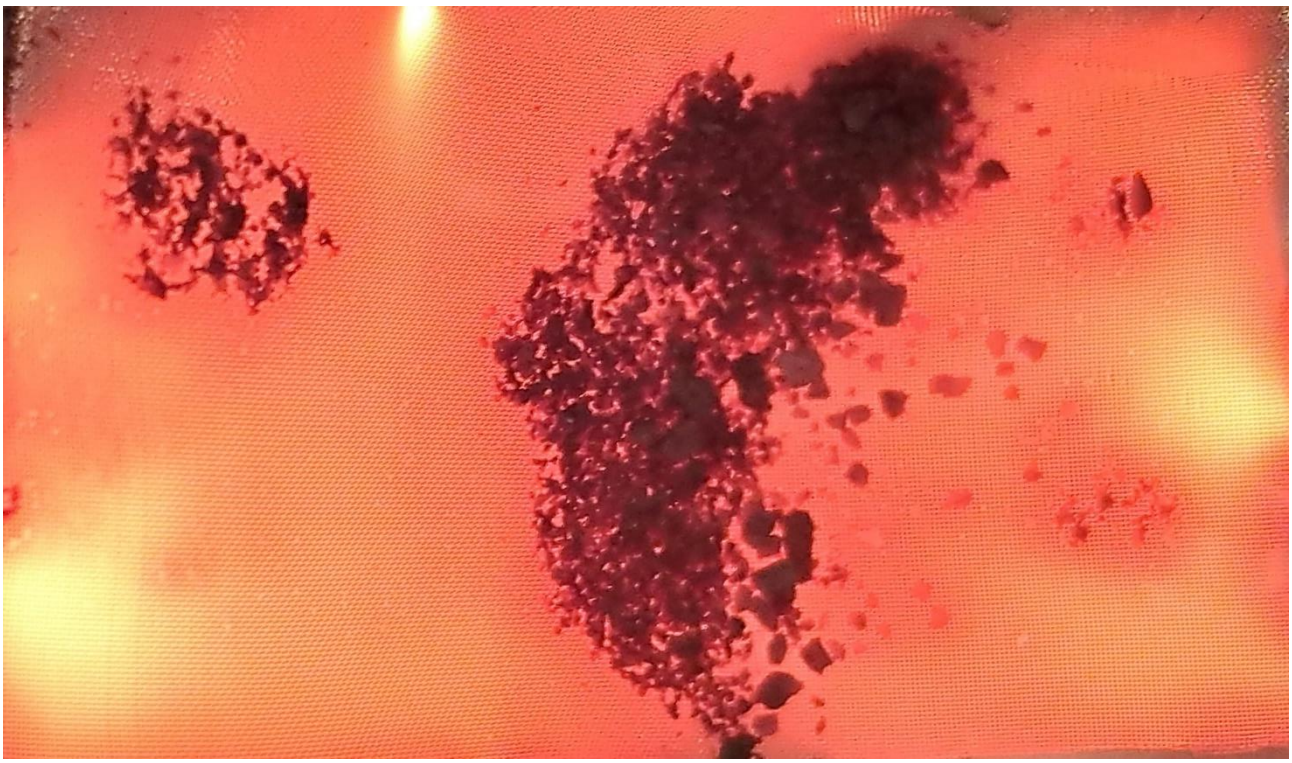

Fig. 7. *Heated wire grid with copper (II) oxide sample at varying densities under ambient air with electrical energy input of approximately 300 W.*

3.4. Higher-temperature dust explosion research potential

Because of the limitations of traditional dust explosion testing equipment, testing at elevated temperatures has been a historic challenge. In his PhD thesis, Dahoe (2000) reported on dust explosions using sawdust at initial temperatures of 20 and 170 °C in a modified 20 L sphere, identifying reduced severity parameters at elevated temperatures. Dahoe's work noted several challenges in the experimental approach, including in the dispersion of the dust, resulting in the dust being placed in the test chamber rather than a charge vessel, as has been done in this work. Temperatures beyond the 170 °C mark previously used by Dahoe (2000) are challenging with conventional operations and equipment due to the weakening of steels with increasing temperatures and the overpressures generated, however the approach presented here, in which a heated grid is used for focused heating of a sample with minimal heating of the vessel, allows for exceptionally high initial temperatures.

Testing the explosibility parameters of dusts at elevated temperatures is needed for any systems where dusts are processed beyond standard atmospheric conditions, however standard method ASTM E1226-19 (ASTM, 2019) notes that the test method is limited in that it can not assess the ignition of bulk dusts in heated environments. Reviewing a set of reports compiled by Eckhoff (2003) shows several instances in which elevated temperatures have played a role in a dust explosion, either from external heating of dusts or from smouldering combustion in storage, both of which would modify parameters such as the minimum explosible concentration and minimum ignition energy compiled for the dust. Other equipment where elevated temperature testing may be important includes spray dryers operating at high temperatures, gas-solid separators such as cyclones, and specific applications such as polymer production where hot particulates may be present prior to cooling.

Although the extension to ASTM E1226 is possible, it is also important to note that any results or data are not directly comparable. In standard methods, an ignitor is used with a fixed energy delivery, while the heated grid system is a continual input of energy intended to reach a specific temperature. This constitutes a significant modification to the method. Because the heated grid also lacks an ignitor, there is also not a set ignition delay time, which has been studied and shown to have an effect

on the turbulence and therefore severity parameters in an explosion (Amyotte et al., 1988; Mercer et al., 2001). Additionally, the gas-solid mixing in the heated grid system will not be as thorough as in other chambers as there are not turbulence-inducing nozzles. Finally, development of this system at larger scales beyond 350 cm^3 is essential for proper evaluation of severity, as the heat losses are not representative of real systems. Cooling effects have been noted in the 20 L sphere when compared to the 1 m^3 chamber, and the difference between the 350 cm^3 vessel and 20 L vessel represents a comparable scale-down which will impact the results. Future tests will demonstrate if the 350 cm^3 chamber is viable for conventional dust explosion testing at elevated temperatures.

4. Conclusions

The metal oxide reducing environment explosion is a thermodynamically possible incident at any temperature due to the exothermic reduction reaction of some metal oxides by fuels. The metal oxide/fuel pairs for which this is most severe are copper and manganese oxides with alkanes, with overpressures driven primarily by gas production and secondarily by rising temperatures. The gas production effects in the MORE explosion are more severe than in gas or dust explosions. Pending experimental results, isothermal operation may better describe the system's behaviour than adiabatic operation, making the effect of temperature null on overpressure development. The proposed reaction mechanism for the MORE explosion is a combination of an initial heterogeneous combustion reaction where the fuel diffuses into the solid and reacts, with a secondary homogeneous combustion reaction driven by the uncoupling of oxygen from the solid matrix at elevated temperatures. Present experimental work has not demonstrated a MORE explosion at the bench scale, owing to difficulties in the small scale of the apparatus and the high temperatures required, however additional work is ongoing to experimentally evaluate the proposed mechanism. The system developed for testing of MORE explosions by application of a heated grid may be a valuable tool in the study of dust explosions at high temperatures, which are more representative of some operating environments than standard test conditions.

Acknowledgements

The authors gratefully acknowledge the support of the Government of Canada's Program of Energy Research and Development, the Natural Sciences and Engineering Research Council of Canada (NSERC) [Discovery grant no. RGPIN/05156–2017 (Pegg); Postgraduate Scholarship – Doctoral (Furlong)] and the Nova Scotia Department of Natural Resources and Renewables through the Clean Economy Grant Program.

References

Adanez, J., Abad, A., Garcia-Labiano, F., Gayan, P., De Diego, L.F., 2012. Progress in chemical-looping combustion and reforming technologies. Prog. Energy Combust. Sci. 38, 215–282. https://doi.org/10.1016/j.pecs.2011.09.001

Amyotte, P.R., Chippett, S., Pegg, M.J., 1988. Effects of turbulence on dust explosions. Prog. Energy Combust. Sci. 14, 293–310. https://doi.org/10.1016/0360-1285(88)90016-0

ASTM, 2019. E1226-19 Standard Test Method for Explosibility of Dust Clouds (Standard). ASTM International.

Bale, C.W., Bélisle, E., Chartrand, P., Decterov, S.A., Eriksson, G., Hack, K., Jung, I.-H., Kang, Y.-B., Melançon, J., Pelton, A.D., Robelin, C., Petersen, S., 2009. FactSage thermochemical software and databases — recent developments. Calphad 33, 295–311. https://doi.org/10.1016/j.calphad.2008.09.009

Cashdollar, K.L., 1994. Flammability of metals and other elemental dust clouds. Proc. Saf. Prog. 13, 139–145. https://doi.org/10.1002/prs.680130306

Cashdollar, K.L., Chatrathi, K., 1993. Minimum Explosible Dust Concentrations Measured in 20-L and 1-M^3 Chambers. Combust. Sci Techol. 87, 157–171. https://doi.org/10.1080/00102209208947213

Chapman, W.A.J., 2011. Workshop Technology. Pt. 1: An introductory course: SI units, 5th ed. Arnold, London.

Dahoe, A.E., 2000. Dust Explosions: a Study of Flame Propogation (PhD Thesis). TU Delft, Delft, NL.

Dahoe, A.E., Zevenbergen, J.F., Lemkowitz, S.M., Scarlett, B., 1996. Dust explosions in spherical vessels: The role of flame thickness in the validity of the 'cube-root law.' J. Loss Prev. Process Ind. 9, 33–44. https://doi.org/10.1016/0950-4230(95)00054-2

Dastidar, A.G., Amyotte, P.R., 2004. Using Calculated Adiabatic Flame Temperatures to Determine Dust Explosion Inerting Requirements. Proc. Saf. Environ. Prot. 82, 142–155. https://doi.org/10.1205/095758204322972780

Eckhoff, R.K., 2003. Case Histories, in: Dust Explosions in the Process Industries. Elsevier, pp. 157–198. https://doi.org/10.1016/B978-075067602-1/50003-2

Furlong, A.J., Bond, N.K., Pegg, M.J., Hughes, R.W., 2024. Evaluation of dust and gas explosion potential in chemical looping processes. J. Loss Prev. Process Ind. 89, 105277. https://doi.org/10.1016/j.jlp.2024.105277

Galinsky, N., Bayham, S., Monazam, E., Breault, R.W., 2018. Oxygen Carrier Structure and Attrition, in: Breault, R.W. (Ed.), Handbook of Chemical Looping Technology. Wiley-VCH Verlag GmbH & Co. KGaA, Weinheim, Germany, pp. 263–301. https://doi.org/10.1002/9783527809332.ch9

Gibbins, J.R., King, R.A.V., Wood, R.J., Kandiyoti, R., 1989. Variable-heating-rate wire-mesh pyrolysis apparatus. Rev. Sci. Instrum. 60, 1129–1139. https://doi.org/10.1063/1.1140327

Going, J.E., Chatrathi, K., Cashdollar, K.L., 2000. Flammability limit measurements for dusts in 20-L and 1-m^3 vessels. J. Loss Prev. Process Ind. 13, 209–219. https://doi.org/10.1016/S0950-4230(99)00043-1

Hu, W., Donat, F., Scott, S.A., Dennis, J.S., 2016. Kinetics of oxygen uncoupling of a copper based oxygen carrier. Appl. Energy 161, 92–100. https://doi.org/10.1016/j.apenergy.2015.10.006

International Organization for Standardization, 1985. Explosion protection systems - Part 1: Determination of explosion indices of combustible dusts in air (No. 6184– 1:1985).

Jacobson, M., Cooper, A.R., Nagy, J., 1964. Explosibility of Metal Powders (No. 6516). U.S. Bureau of Mines, Washington, D.C.

Lyngfelt, A., Thunman, H., 2005. Construction and 100 h of Operational Experience of A 10-kW Chemical-Looping Combustor, in: Carbon Dioxide Capture for Storage in Deep Geologic Formations. pp. 625–645.

Mercer, D.B., Amyotte, P.R., Dupuis, D.J., Pegg, M.J., Dahoe, A., De Heij, W.B.C., Zevenbergen, J.F., Scarlett, B., 2001. The influence of injector design on the decay of pre-ignition turbulence in a spherical explosion chamber. J. Loss Prev. Process Ind. 14, 269–282. https://doi.org/10.1016/S0950-4230(00)00051-6

Monazam, E.R., Siriwardane, R., Breault, R.W., Tian, H., Shadle, L.J., Richards, G., Carpenter, S., 2012. Kinetics of the Reduction of CuO/Bentonite by Methane (CH_4) during Chemical Looping Combustion. Energy Fuels 26, 2779–2785. https://doi.org/10.1021/ef300072d

OZM Research s.r.o., 2020. CA 20L/CA 1M3 Explosion Chambers for Gases and Dusts.

Symonds, R.T., Sun, Z., Ashrafi, O., Navarri, P., Lu, D.Y., Hughes, R.W., 2019. Ilmenite ore as an oxygen carrier for pressurized chemical looping reforming: Characterization and process simulation. Int. J. Greenh. Gas Control 81, 240–258. https://doi.org/10.1016/j.ijggc.2018.12.006

TÜV SÜD Schweiz AG, Cesana AG, 2016. Annex to 20-l-Apparatus.

Westbrook, C.K., Dryer, F.L., 1981. Simplified Reaction Mechanisms for the Oxidation of Hydrocarbon Fuels in Flames. Combust. Sci Techol. 27, 31–43. https://doi.org/10.1080/00102208108946970

Whitty, K.J., Lighty, J.S., Mattisson, T., 2018. Chemical Looping with Oxygen Uncoupling (CLOU) Processes, in: Breault, R.W. (Ed.), Handbook of Chemical Looping Technology. Wiley-VCH Verlag GmbH & Co. KGaA, Weinheim, Germany, pp. 93–122. https://doi.org/10.1002/9783527809332.ch4

Williams, F.A., 2003. Combustion, in: Encyclopedia of Physical Science and Technology. Elsevier, pp. 315–338. https://doi.org/10.1016/B0-12-227410-5/00123-X

Zeng, C., Chen, L., Liu, G., Li, W., Huang, B., Zhu, H., Zhang, B., Zamansky, V., 2008. Advances in the development of wire mesh reactor for coal gasification studies. Rev. Sci. Instrum. 79, 084102. https://doi.org/10.1063/1.2968714

Zettervall, N., Fureby, C., Nilsson, E.J.K., 2021. Evaluation of Chemical Kinetic Mechanisms for Methane Combustion: A Review from a CFD Perspective. Fuels 2, 210–240. https://doi.org/10.3390/fuels2020013

Influence of electrode distance on the ignition and combustion properties of ammonia/hydrogen/air mixtures

Jessica Dymke [a], Wangchen Liu [a], Jacqueline Höltkemeier-Horstmann [a], Detlev Markus [a], Stefan Essmann [a]

[a] Physikalisch-Technische Bundesanstalt (PTB), Bundesallee 100, 38116 Braunschweig, Germany

E-mail: *jessica.dymke@ptb.de*

Abstract

Ammonia contains no carbon atoms and can therefore contribute to the decarbonisation of technical combustion processes. However, the ignition and combustion properties of ammonia/air mixtures do not meet the requirements for many technical applications. For instance, the self-sustaining flame propagation requires high discharge energies, and the laminar burning velocities are low compared to other fuels. These characteristics can be adjusted by adding more reactive gases, such as hydrogen. The ignition energy is a measure of the ignitability of explosive mixtures and depends, among many other parameters, strongly on the electrode distance. In this work, the influence of electrode distances of 3 mm, 2 mm, and 1 mm on the necessary capacitive discharge energy for ignition is investigated experimentally for different shares of hydrogen in the fuel gas mixture at constant equivalence ratio φ = 0.9. Additionally, the dependency of the maximum pressure as well as rate of pressure rise regarding the mixture composition is shown. Schlieren imaging is applied to study the development of the hot gas kernel in the early stage of flame propagation.

Keywords: *ammonia, hydrogen, spark ignition, electrode distance, ignition energy, explosion protection*

Introduction

Ammonia is a candidate green energy carrier for the carbon-free energy system of the future. The main advantages of ammonia are firstly, its lack of carbon atoms which enables carbon dioxide free energy transformation processes; secondly, its high energy density and it is easy to liquify, which makes it very efficient in storing and transporting energy; thirdly, it has been used for many decades as a commodity chemical and fertilizer, hence, a worldwide infrastructure is already in place. Ammonia can be used efficiently for power, heat and mobility. However, it is a toxic substance. In combustion processes, nitric oxide emissions, ammonia slip, as well as nitrous oxide emissions can have a serious impact on health and environment (Valera-Medina et al. 2021). Further, under atmospheric conditions, the laminar burning velocity of ammonia is low at < 10 cm/s (Lhuillier et al., 2020; Li et al., 2021) and it is not easily ignitable (Krämer, 1985). These challenges in ignition characteristics and burning properties limit the widespread use of ammonia as a fuel. A promising approach to overcome these issues lies in mixing ammonia with hydrogen, either by cracking the ammonia molecule or by using hydrogen from an external source (Valera-Medina et al., 2021). Hydrogen has a much higher laminar burning velocity (> 200 cm/s) (Warnatz, 1992) and its minimum ignition energy (MIE) is more than 1000 times less than that of ammonia (0.017 mJ for hydrogen and 14 mJ for ammonia) (Krämer, 1985; Wähner et al., 2013). Previous work has dealt with the ignition characteristics of such mixtures (Essmann et al., 2024). It was found that for each 10 vol.-%-point increase of the hydrogen content in the fuel, the energy required for ignition is reduced roughly by an

order of magnitude. However, these results were limited to a hydrogen content of up to 20 vol.-% in the fuel. Further, the electrode distance was held constant at 4 mm.

In this study, the scope is extended by investigating fuel mixtures with up to 45 vol.-% hydrogen. Further, the effect of electrode distance on the required ignition energy and the pressure evolution is investigated. Moreover, high-speed schlieren imaging is employed to qualitatively study the flow characteristics during the ignition and flame kernel formation phase. Lastly, the schlieren images are analysed regarding flame kernel propagation speeds.

1. Experimental parameters

This section illustrates the choice of the electrode configurations and the mixture compositions to be investigated.

1.1. Electrodes

The electrode geometry as well as the distance between the electrodes are parameters to be optimised in the context of determining the MIE (Wähner et al., 2013; Bane et al., 2015). The MIE of hydrogen was determined using spherical electrodes with an electrode distance of 0.5 mm (Wähner et al., 2013). In contrast to hydrogen, data concerning experimental investigations of ammonia are rather rare to find at present. The lowest ignition energy documented to date is 8 mJ (Verkamp et al., 1967). Nevertheless, the measurement conditions of Krämer (1985) are well documented and therefore, the experimental parameters of this work build upon his findings. Krämer (1985) found a MIE of 14 mJ using 5 mm stainless steel ball electrodes spaced 15 mm apart. The latest work by Lesmana et al. (2022) found 18 mJ using wire electrodes. A more detailed literature review is found in Essmann et al. (2024).

In this work, three cases are investigated, which differ in the ratio of the electrode diameter D and electrode distance d. The electrode diameter is kept constant at D = 2 mm (spherical tip geometry) while d is varied to be 1 mm, 2 mm, or 3 mm. Hence, the ratio D/d can be smaller, greater than, or equal to unity. Tungsten was chosen as the material due to its beneficial durability compared to stainless steel.

1.2. Mixture composition

For the combustion of ammonia/hydrogen mixtures, even small quantities of hydrogen significantly increase the laminar burning velocity (Lhuillier et al., 2020; Li et al., 2021) and reduce the required ignition energy (Fernández-Tarrazo et al., 2023; Essmann et al., 2024). In this work, the hydrogen content in the fuel, α_{H_2}, is varied from 0.05 to 0.45 according to the global reaction equation by Yu et al. (2023),

$$\alpha_{H_2} H_2 + \left(1 - \alpha_{H_2}\right) NH_3 + \frac{3-\alpha_{H_2}}{4}\left(O_2 + 3.76\ N_2\right) \rightarrow \frac{\alpha_{H_2}+2}{3}\ H_2O + \left(3.32 - 1.44\alpha_{H_2}\right) N_2. \quad (1)$$

This range of α_{H_2} is relevant for practical applications in heating, power and mobility applications (Valera-Medina et al., 2021). Additionally, α_{H_2} = 1.0 is investigated. According to the most ignitable mixture of ammonia in air (Krämer, 1985) an equivalence ratio φ = 0.9 was kept constant for all mixtures. Table 1 characterizes the gas mixtures based on the mole fraction.

***Table 1**. Mole fraction of NH_3 and H_2 in investigated mixtures, φ = 0.9±0.2 %. Note: This is the relative standard uncertainty.*

α_{H_2}	Mole fraction	
	NH_3	H_2
0.049	0.194	0.010
0.099	0.186	0.020
0.150	0.178	0.031
0.200	0.170	0.042
0.250	0.161	0.054
0.300	0.153	0.065
0.349	0.144	0.077
0.400	0.135	0.090
0.450	0.126	0.103
1.000	0.000	0.274

2. Experimental setup

The experimental setup includes a system for gas mixture preparation, an electrical system for ignition investigations and a schlieren setup for visualising the development of the hot gas kernel in the early stage after successful ignition. In general, the setup was very similar to the one used by Essmann et al. (2024).

2.1. Mixture preparation system

The explosive gas mixtures are prepared in a premixing chamber (volume 3.8 L). Spiral pipes of 6 m length are installed in front of this chamber to allow for equilibration of the temperature of each component to the ambient temperature. A cartridge with silica gel is installed to dry the air to ensure that no residual moisture is present. As the mixtures are prepared using the method of partial pressures, a static pressure sensor (Kistler 4043A2, maximum pressure 2 bar) connected to the premixing chamber and an amplifier (Kistler 4603) are utilised. To monitor that the temperature differences between the individual components are negligible, the temperature of each incoming gas is measured using a type K thermocouple. A vacuum pump enables evacuation of the entire system, but also of individual system sections. The mixture to be ignited can be transferred directly from the premixing chamber to the ignition vessel to carry out the ignition tests.

2.2. Ignition system

The discharges are generated using the electrical setup shown in Fig. 1. It consists of a high-voltage source (FuG HCN40M-40000), a variable charging resistor and a low-inductive capacitor bank. The capacitance is measured using an LCR-meter (Agilent U1733C). The high-voltage divider (Spellman HVD-100, 10000:1) and a digital multimeter (Agilent 34410A) allow to measure the voltage. A current transformer (Magnelab CT-C1.0-B) is attached to the lower electrode to record the current signal via an oscilloscope (Yokogawa DL6154).

In this work, the discharge energy W is estimated according to

$$W = \frac{1}{2} C V^2, \tag{2}$$

where the capacitance C includes both the capacitor and the stray capacitances, and V is the breakdown voltage. Note, that a residual charge remains in the capacitor after discharge, which is not considered in this equation. These ohmic losses become more distinct for higher discharge energies

(Hattwig & Steen, 2004). Consequently, the energies stated in this work represent an upper limit. The charging resistor allows for the spark frequency to be adjusted according to

$$\tau = RC, \tag{3}$$

and is exchanged with respect to the capacitance to be charged. To increase the probability of the occurrence of free electrons in the electrode gap for the gas breakdown, a UV LED (Thorlabs LED250J) is focused on this gap. The energy of its emitted peak wavelength is sufficient to release electrons from the electrodes using the photoelectric effect.

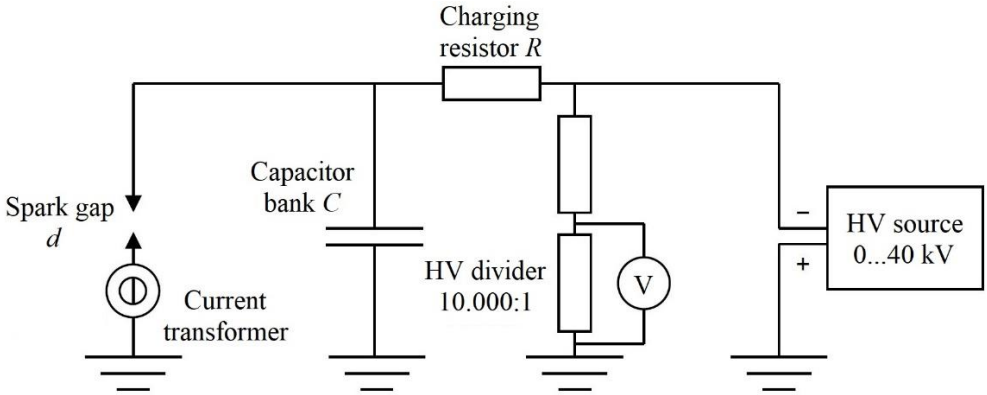

Fig. 1. *Electrical setup.*

2.3. Ignition vessel

A spherical vessel of 0.5 L volume (inner diameter 100 mm) was employed to study the ignition process. It was optically accessible via quartz windows with 15 mm clear diameter. From the top and bottom, the electrodes were fed into the vessel. The electrode gap was set by adjusting the top electrode using a micrometer screw.

2.4. Schlieren imaging and analysis

A schlieren setup consisting of a red LED (MTPS8065PT), two field lenses (focal lengths 162 mm and 500 mm) and a high-speed camera at 30 kHz (Photron SA5 colour) was used to visualise the evolution of the hot gas kernel. A horizontal and a vertical knife edge served as the schlieren stop. The image analysis followed an approach similar to the one in Essmann et al. (2024). In this work, however, the radius of the hot gas kernel was determined starting from the electrode axis towards the right side of the image. This change was made due to the higher contrast on this side.

2.5. Pressure measurement

The explosion pressure was recorded using a piezoresistive pressure sensor (Kistler 4011A, maximum pressure 20 bar), a corresponding amplifier (Kistler 4624A) and an oscilloscope (Yokogawa DLM2054). Due to the spherical geometry, no high frequency components of the pressure are expected. A 5 kHz low-pass filter on the amplifier was employed to avoid aliasing.

3. Measurement procedure

The measurement procedure can be divided into two steps. First, a mixture is prepared. Subsequently, ignition tests are carried out and schlieren images are recorded simultaneously. In this chapter, these steps are described in more detail.

3.1. Mixture preparation

All gas-carrying system parts, the gas lines and the premixing chamber are flushed with air, which is passed through a cartridge with silica gel for additional drying and then evacuated. During evacuation, the pressure is always kept below the vapour pressure of water to ensure removal of residual moisture from the system. After flushing again with dry air to create a defined system state, the premixing chamber as well as the tubes upstream are evacuated a second time. The premixing chamber is cut-off with a valve and then, the tubes flushed with dry air with overpressure. The gas mixtures are prepared using the method of partial pressures. As the first component, air is filled into the premixing chamber according to the desired filling pressure using a dosing valve. Once the desired filling pressure is reached, the premixing chamber is shut off again and the upstream lines are evacuated once more. To prevent undesired dilution of the hydrogen to be filled in with residual air, an overpressure is first built up in the gas lines in front of the premixing chamber and the tubes are then purged with overpressure. Again, overpressure is built up inside the system right in front of the premixing chamber and hydrogen is filled in. The temperature of the incoming component is measured via a thermocouple. After flushing the lines with air and evacuating one more time, ammonia is added as the last component in same procedure described for hydrogen. To support the homogeneity of the mixture, the gases are added at a slightly increased flow rate at the beginning of the dosing step. This is reduced for the rest of the dosing process to counteract undesirable effects, for instance change in gas temperature due to expansion from the tubes into the premixing chamber.

3.2. Ignition tests and schlieren imaging

Firstly, the desired electrode gap is set. To be able to adjust the capacitance as variable as possible, the capacitors were used individually as well as connected in parallel. The lowest capacitance to be achieved resulted from the measurement setup itself without any additional capacitor. According to formula (3), the charging resistor is changed to set τ for single sparks to occur when the voltage is subsequently increased. On the one hand, a low τ is desired to have more manageable charging times and therefore to determine the breakdown voltage as accurately as possible; on the other hand, high τ is desired to ensure that no compound effects occur caused by several sparks in a short time interval. The capacitance is measured five times using the LCR meter and the average value is used to estimate the discharge energy. To transfer the mixture from the premixing chamber to the ignition vessel, the connecting gas lines and the ignition vessel are first evacuated. The gas mixture is then filled in to a final pressure of (1.02±0.21) bar using a dosing valve. The UV LED and the LED for schlieren imaging are switched on. The voltage is now slowly increased until a spark occurs between the electrodes. This value is used to estimate the discharge energy. The applied voltage is immediately reduced again. The mixture is renewed after each ignition or at the latest after five sparks without ignition. By displaying the current signal on one of the oscilloscopes, every spark without ignition is also detected. If ignition is successful, the increasing pressure signal overcomes a trigger threshold used for starting the high-speed-camera and the recording is started automatically.

4. Results and discussion

Firstly, the results for the ignition energy are presented. In the following subchapter, pressure traces are shown, from which the maximum pressures and the rates of pressure rise are derived. These results are supplemented by schlieren imaging in the final subsection. The stated uncertainty values refer to standard uncertainties.

4.1. Ignition energy

Fig. 2 shows the discharge energy *W* required for ignition as a function of electrode distance *d*, varied by 1 mm, 2 mm, and 3 mm, and amount of hydrogen α_{H_2}. The solid squares mark the lowest values that were sufficient to ignite the mixture. In this work, measurements in which at least one of five sparks led to successful ignition are categorised as "ignition". The empty symbols indicate the highest values without ignition in five sparks respectively.

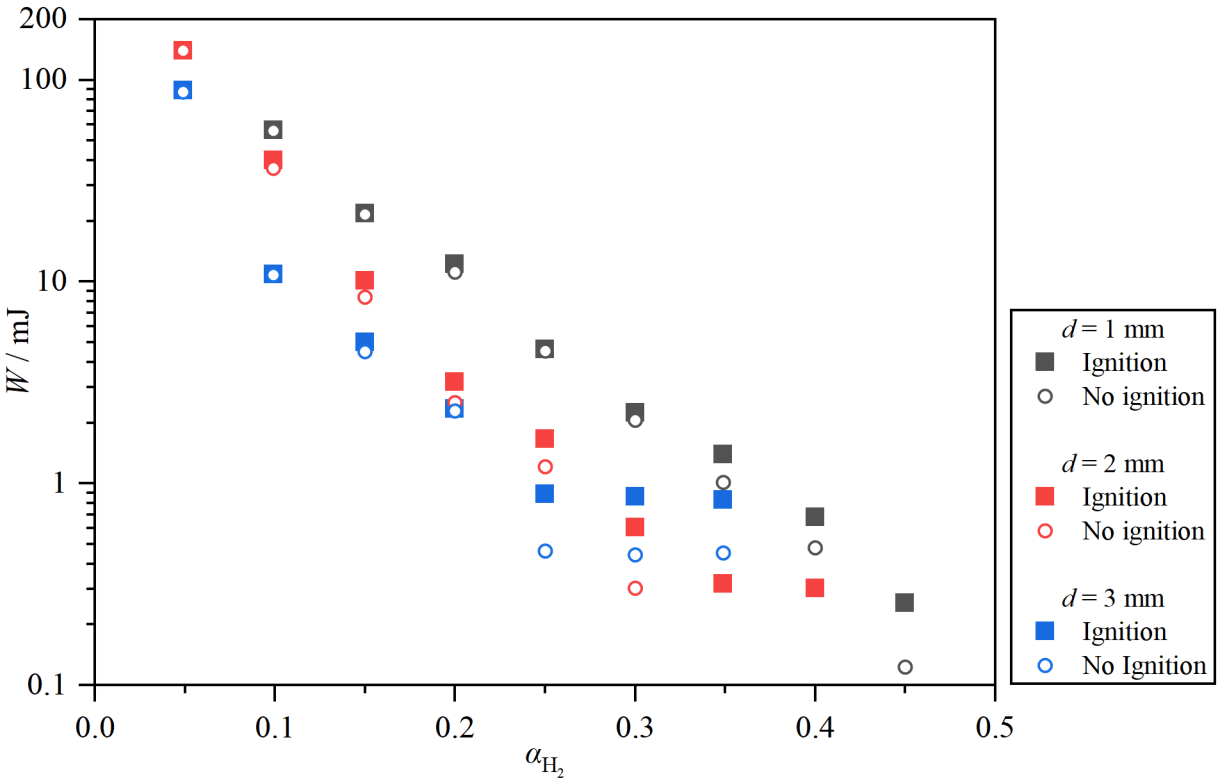

Fig. 2. *Ignition with lowest discharge energy (solid squares) and no ignition with highest discharge energy (empty circles) as a function of the electrode distance d and α_{H_2}. Note: There are no error bars shown in this plot due to their small magnitude (maximum absolute standard uncertainty: $\Delta\alpha_{H_2}$ = ±0.005, ΔW = ±0.07 mJ).*

Even small amounts of hydrogen in the fuel gas mixture result in a significant decrease in the energy required for ignition. An increase in α_{H_2} by 0.1 causes a reduction of *W* by about a factor of ten or less depending on *d*. This is consistent with the findings of Essmann et al. (2024). The ignition energies decrease with increasing electrode distance *d* for mixtures up to α_{H_2} = 0.250. At $\alpha_{H_2} \geq 0.300$ a deviation in this trend can be seen. The discharge energies for ignition of these mixtures are lower for the tests with *d* = 2 mm compared to *d* = 3 mm. It is to be assumed that a limiting case of the optimum electrode spacing for these mixtures has been encountered here. Note that for α_{H_2} = 0.349 and α_{H_2} = 0.400 with *d* = 2 mm no data for “no ignition” is shown. The smallest capacity possible was already used in this case and the resulting discharge energies are still sufficient to ignite these mixtures.

It should be noted that the results presented are no minimum ignition energies. For determining MIE, various parameters must be optimised and the requirements of the corresponding standard (E27 Committee) must be met. This optimisation processes were not carried out in this work. However, the data show the influence of *d* and α_{H_2}.

The degree of discharge of the capacitors was not quantified and therefore not included in the calculation of the measurement uncertainty. The influences considered are so small that the error bars for discharge energy are not plotted in this figure.

4.2. Explosion pressure traces

In Fig. 3 pressure as a function of time is shown using a constant electrode distance of d = 2 mm for different α_{H_2}. The raw data was smoothed with a 3rd order Savitzky-Golay filter with 1000 points. The post-processed datasets were shifted to t = 0 ms. The laminar burning velocity and the pressure increase after ignition depend strongly on the amount of hydrogen in the fuel mixture. It is visible in Fig. 3 that with increasing α_{H_2} the burning velocity is increased leading to a faster pressure rise.

4.3. Maximum pressure and rate of pressure rise

The maximum pressure p_{max} was obtained from the shifted fits. The rate of pressure rise dp/dt was determined for the range 10 % to 90 % of this value. The results are shown in Fig. 4 (a). Note the axis interruptions for the mixtures and pressure rise rates. With an increase in α_{H_2} from only 0.049 to 0.099, p_{max} increases from (4.35±0.23) bar to (5.22±0.24) bar and dp/dt from (30±2) bar/s to (43±2) bar/s. For the mixture of pure hydrogen in air, however, p_{max} is (7.48±0.26) bar and dp/dt (2370±80) bar/s. The p_{max} are lower than literature values – maximum explosion pressures for NH_3: 6.9 bar, for H_2: 8.3 bar (PTB & BAM, 2023). As the ignition vessel had a volume of only 0.5 L in this work, cooling by the vessel walls reduces the maximum pressure of all ammonia containing mixtures (Hattwig and Steen 2004). Fig. 4 (b) shows the maximum pressure and the rate of pressure rise for the three electrode distances examined for constant α_{H_2} = 0.150. The results are nearly identical, even though the minimum energy necessary for ignition varies by a factor of four. This points out that the results shown in Fig. 3 and Fig. 4 do not depend on the ignition process but only on the amount of hydrogen in the fuel mixture.

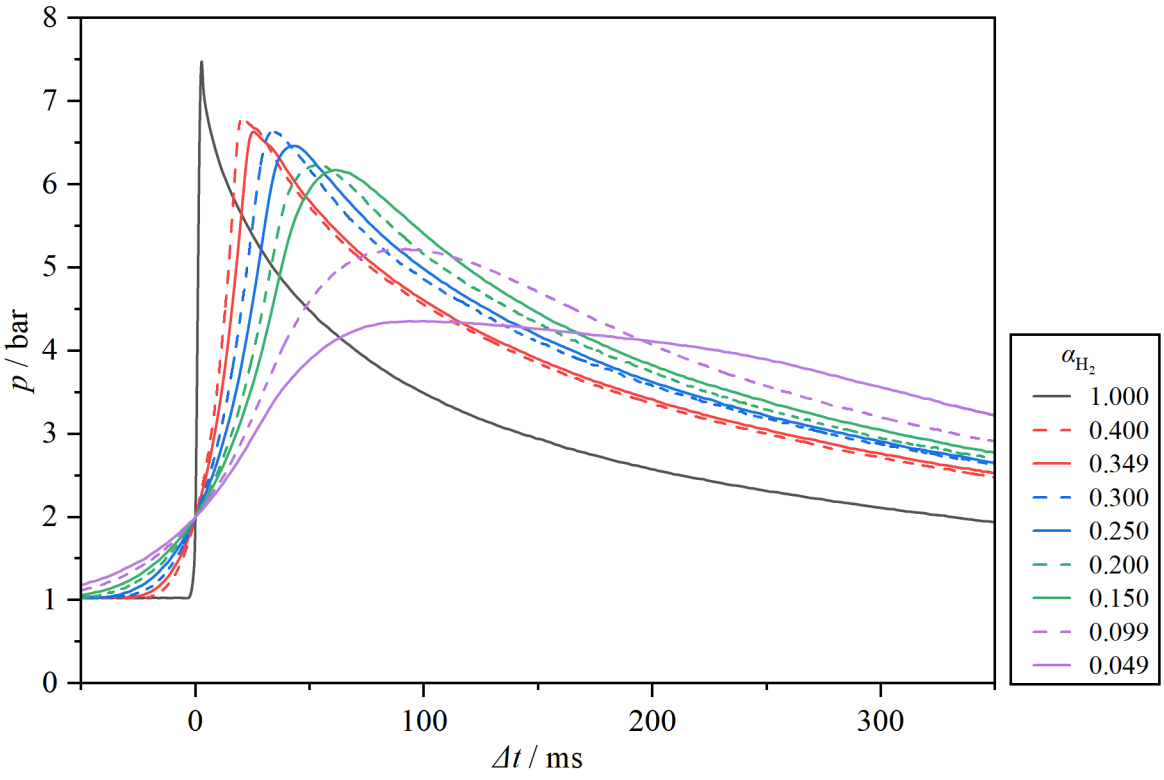

Fig. 3. *Explosion pressure traces for varying α_{H_2}. The data shown originates from measurements with the lowest discharge energy for ignition at constant d = 2 mm.*

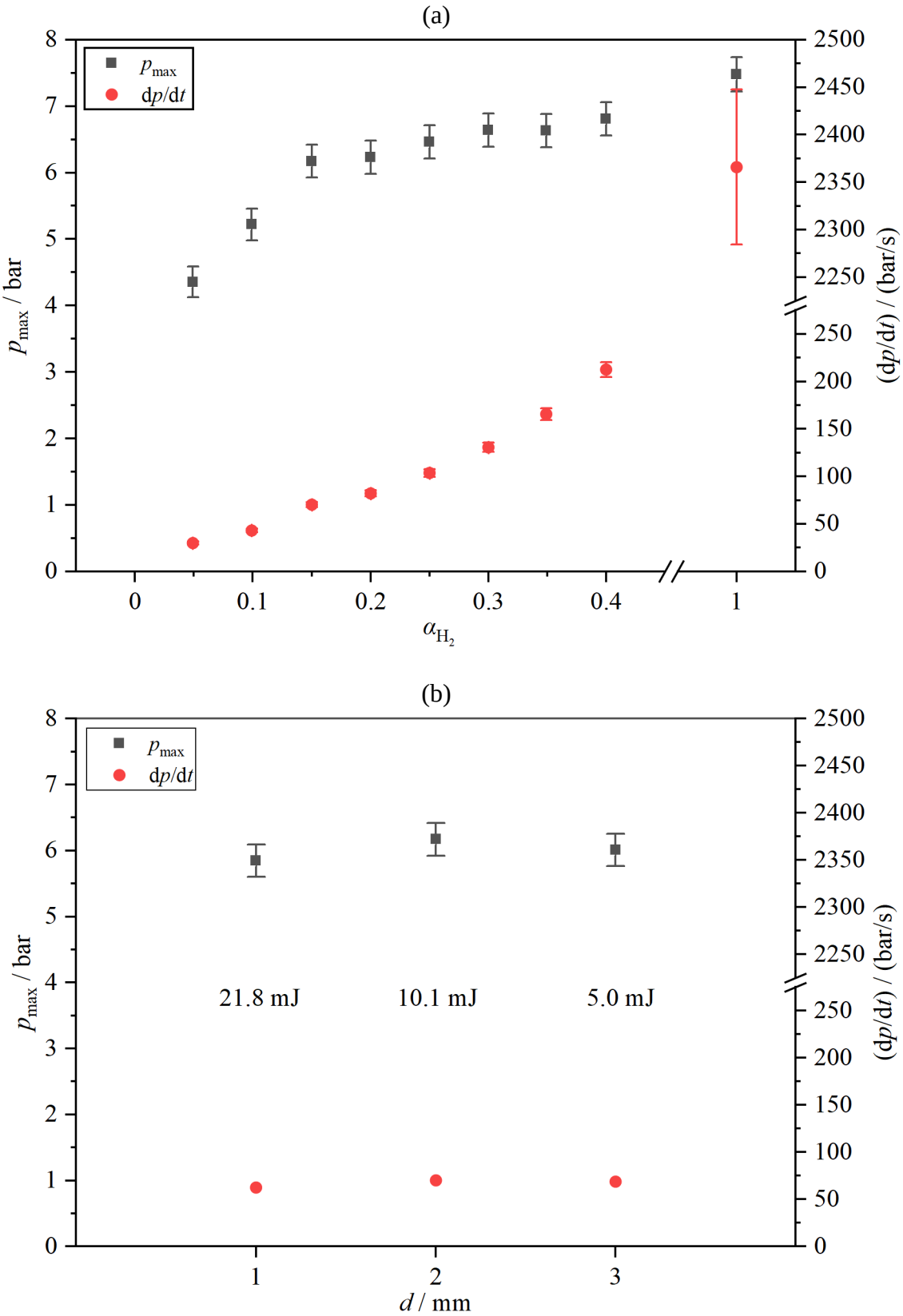

Fig. 4. *Maximum pressure and rate of pressure rise. (a): For varying α_{H_2}. The data shown originates from measurements with the lowest discharge energy for ignition at a constant electrode gap of 2 mm. (b): Varying d at constant α_{H_2} = 0.150, Note: There are no error bars shown for α_{H_2}, d and dp/dt (in (b)) due to their magnitude (maximum absolute standard uncertainty: $\Delta\alpha_{H_2}$ = ±0.005, Δd = ±3 µm, $\Delta dp/dt(b)$ = ±3 bar/s).*

4.4. Flame kernel development

In Table 2 schlieren images show the temporal development of the hot gas kernel after the spark at t_0 leading to ignition for d = 2 mm and the lowest W for ignition for each gas mixture. Note, that the recording time of the schlieren image showing the spark (t_0) is defined as 0 µs. The first two rows show the early phase up to t_0 + 1500 µs for α_{H_2} = 0.049 and 0.099. The high spark energy leads to initial discharge radii of several mm (Essmann et al., 2024) and the discharge induced flows cause rapid expansion of the hot gas kernel. For these two hydrogen fractions of the fuel mixture, flame propagation cannot yet be distinguished from the spark-induced hot gas kernel at these early times. The next four rows show schlieren images for α_{H_2} = 0.150 up to α_{H_2} = 0.300 and a time range of t_0 + 4000 µs. The ignition energy decreases with increasing α_{H_2}. The influence of the spark-induced flow is therefore weakened. At the same time, the burning velocity increases with increasing α_{H_2}, so that for $\alpha_{H_2} \geq 0.200$ a spherical flame spread can be observed. Therefore, for α_{H_2} = 0.349 and α_{H_2} = 0.400, the maximum time is reduced to t_0 + 2500 µs. Having an ignition energy of only W = 0.3 mJ, first a torus-shaped and then a spherical flame propagation can be observed. For α_{H_2} = 1.000, the maximum radius limited by the optical windows after about t_0 + 500 µs is reached due to the dominance of combustion. A comparable radius after similar timespan can be found for α_{H_2} = 0.049 because of the dominance of induced flow due to high ignition discharge.

Table 3 shows schlieren images of the temporal development of the hot gas kernel after ignition for varying d and W at constant α_{H_2} = 0.150 up to t_0 + 4000 µs. As the electrode distance d becomes smaller, the minimum energy required for ignition increases from 5.0 mJ to 21.8 mJ. At these high energies, intense flow processes due to the spark-induced vortices can be seen in all cases.

Fig. 5 shows the temporal development of the hot gas kernel for d = 2 mm and the derived propagation velocity, respectively. In Fig. 5 (a) the influence of the spark energy on the early phase is clearly visible for α_{H_2} = 0.049 up to α_{H_2} = 0.300. In case of α_{H_2} = 0.049, an energy of W = 139.4 mJ is necessary for ignition. This results in a very fast expansion of the hot gas kernel to a radius over 3.0 mm in the first 300 µs. The subsequent transition cannot be seen here due to the limited window size. If the energy is reduced with increasing α_{H_2}, this spark-induced expansion is reduced to approx. 1.3 mm at α_{H_2} = 0.250 and W = 1.7 mJ. α_{H_2} = 0.300 is a special case. After the rapid expansion at the beginning, the mixture does not appear to have ignited, only to show a self-sustaining flame propagation after 1.5 ms. This interaction between physical and chemical processes has already been observed for ethylene by Essmann et al. (2017). For $\alpha_{H_2} \geq 0.150$ it can also be seen how the gradient increases with increasing α_{H_2}, as the flame speed increases with increasing hydrogen content. The influence of the ignition energy on the early phase of the expansion becomes clear when looking at Fig. 5 (b). Here the time derivative of the radii of the hot gas kernels is plotted as a function of the radius itself. The higher the energy, the greater the initial value of the radius at which a derivative was possible and the greater the change in expansion over time. As the expansion progresses outwards, the influence of the sparks on the expansion decreases and the speed takes on a constant value dominated by the laminar burning velocity of the mixture. The higher α_{H_2}, the higher the speed of expansion. The expansion for the larger hydrogen fractions is shown in Fig. 5 (c) for α_{H_2} = 0.300 to α_{H_2} = 1.000. In contrast to Fig. 5 (a), the formation of only small hot gas kernels in the initial phase can be seen due to the low discharge energies. After ignition, the flames spread much faster for the mixtures in Fig. 5 (c).

***Table 2**. Schlieren images: Temporal development of the hot gas kernel after ignition at early stage. The shown datasets belong to d = 2 mm and lowest W for ignition. Note: t_0 refers to the image showing the ignition spark. The recording time assigned to this image was defined as 0 µs. Therefore, the given t has an uncertainty of 33.3 µs at maximum (1/framerate). Optical windows: 15 mm clear diameter.*

α_{H_2}	W / mJ	t_0 + 100 µs	t_0 + 200 µs	t_0 + 300 µs	t_0 + 500 µs	t_0 + 1000 µs	t_0 + 1500 µs
0.049	139.4	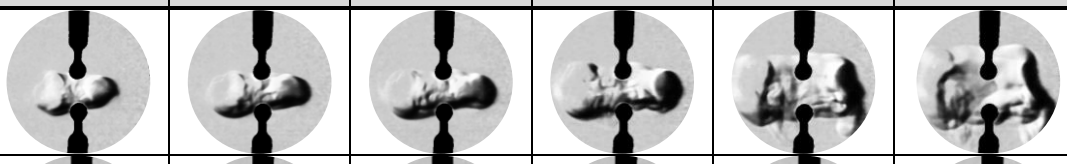					
0.099	40.0						

α_{H_2}	W / mJ	t_0 + 100 µs	t_0 + 500 µs	t_0 + 1000 µs	t_0 + 2000 µs	t_0 + 3000 µs	t_0 + 4000 µs
0.150	10.1	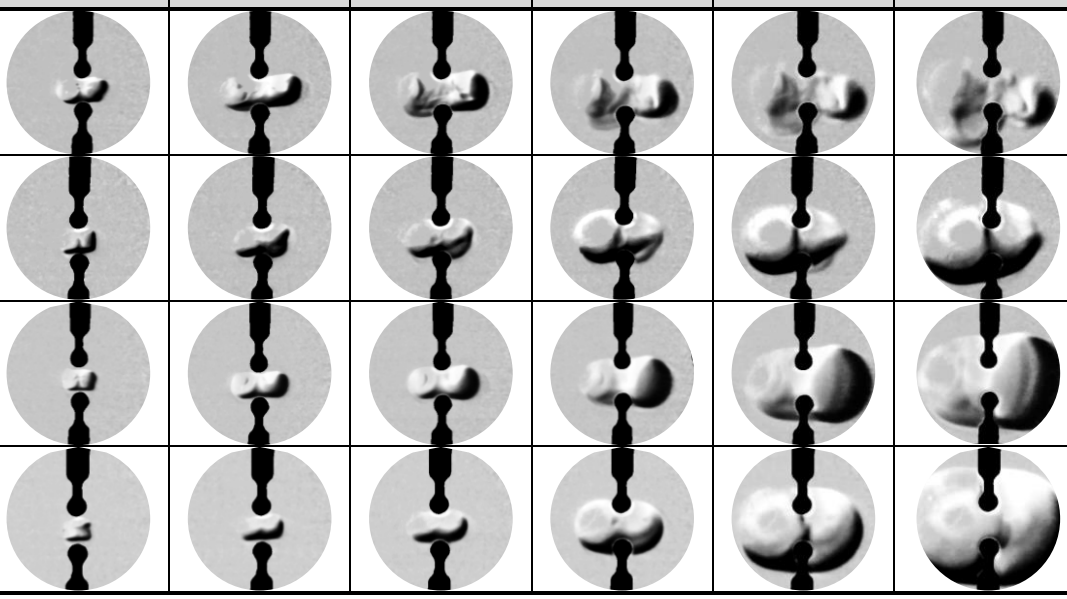					
0.200	3.2						
0.250	1.7						
0.300	0.6						

α_{H_2}	W / mJ	t_0 + 100 µs	t_0 + 500 µs	t_0 + 1000 µs	t_0 + 1500 µs	t_0 + 2000 µs	t_0 + 2500 µs
0.349	0.3	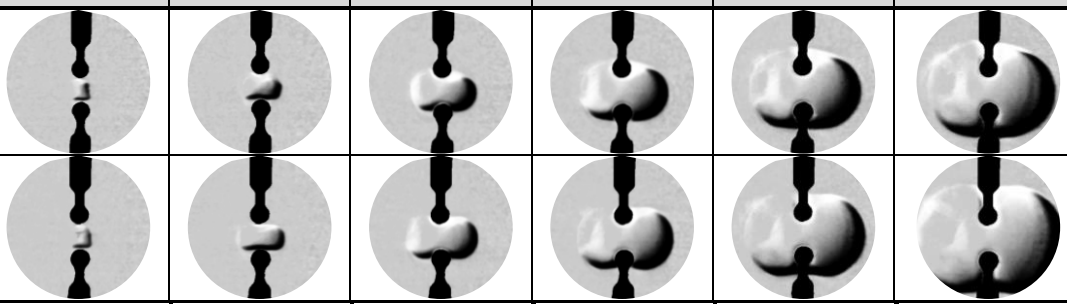					
0.400	0.3						

α_{H_2}	W / mJ	t_0 + 100 µs	t_0 + 200 µs	t_0 + 300 µs	t_0 + 500 µs	t_0 + 1000 µs	t_0 + 4000 µs
1.000	0.3	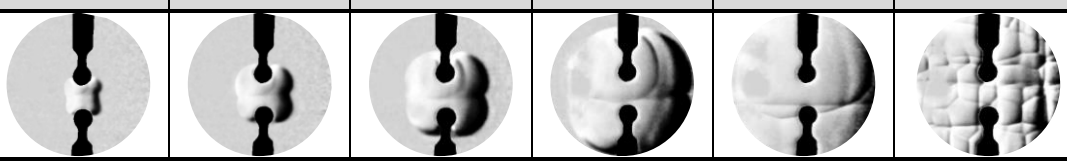					

***Table 3**. Schlieren images: Temporal development of the hot gas kernel after ignition at early stage for varying d and W at constant α_{H_2} = 0.150. Note: t_0 refers to the image showing the ignition spark. The recording time assigned to this image was defined as 0 µs. Therefore, the given t has an uncertainty of 33.3 µs at maximum (1/framerate). Optical windows: 15 mm clear diameter.*

d / mm	**W / mJ**	**t_0 + 100 µs**	**t_0 + 500 µs**	**t_0 + 1000 µs**	**t_0 + 2000 µs**	**t_0 + 3000 µs**	**t_0 + 4000 µs**
3.00	**5.0**	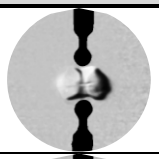	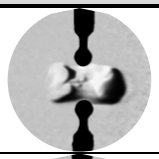	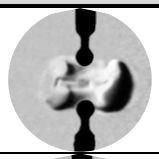	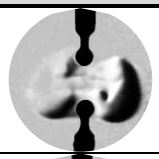	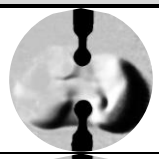	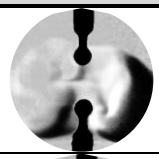
2.00	**10.1**	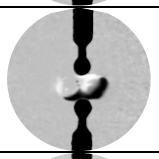	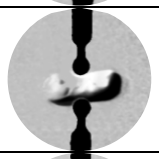	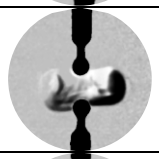	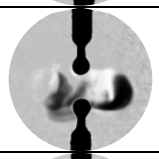	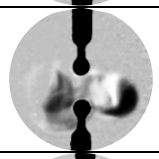	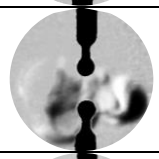
1.00	**21.8**	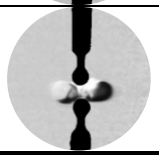	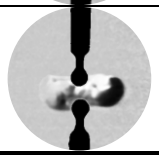	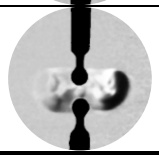	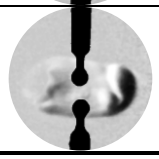	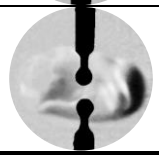	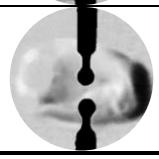

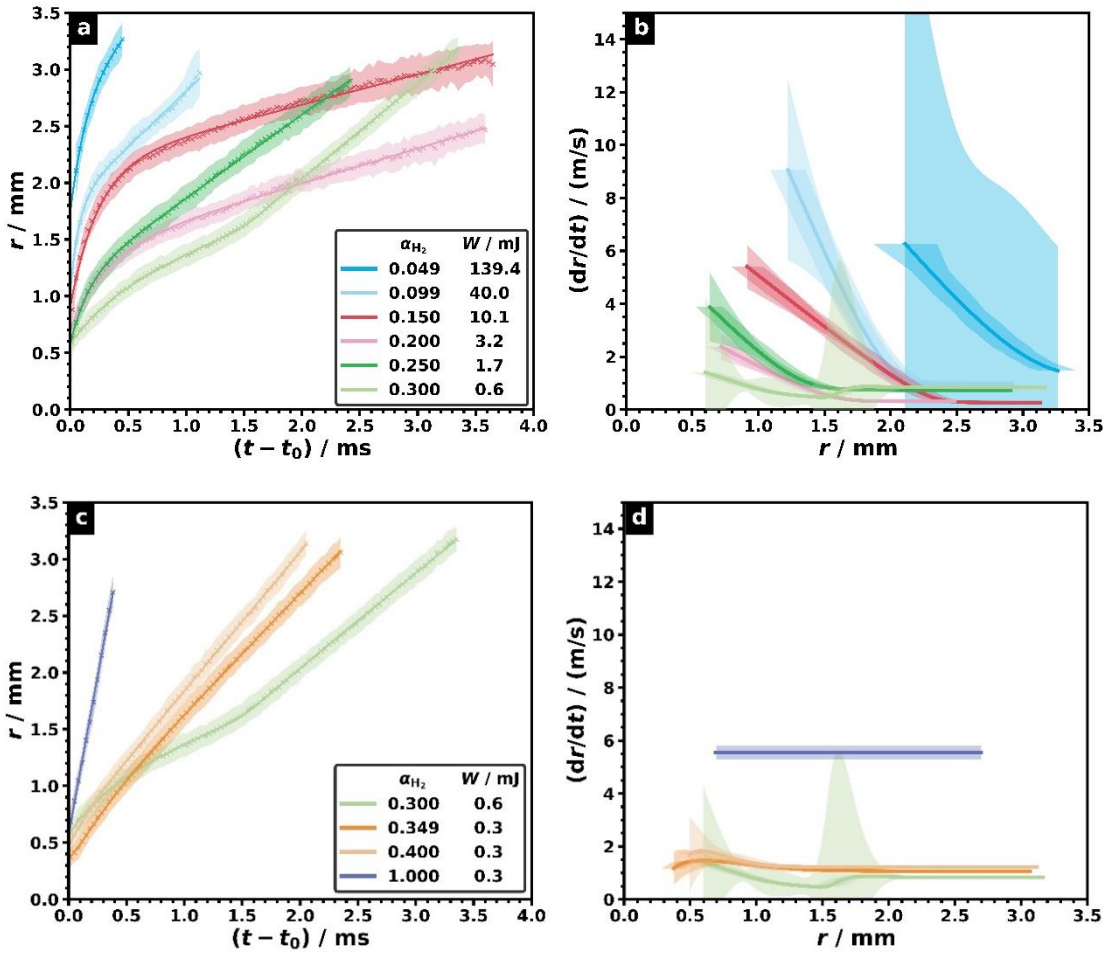

***Fig. 5.** Temporal development of the hot gas kernel for varying α_{H_2} and W at constant d = 2 mm. (a) & (c): Kernel radii. (b) & (d): Temporal change in radius with growing radius. Note: The data shown originates from measurements with the lowest discharge energy for ignition. Since W = 0.3 is the lowest discharge energy possible for given d and C, W is constant for $\alpha_{H_2} \geq 0.349$. The standard uncertainty for the data referring to α_{H_2} = 0.049 is noticeably high. The main reason is the short time until the maximum visible radius limited by the clear diameter of the windows is reached by the hot gas kernel. Therefore, there were less images for analysation compared to other datasets.*

5. Conclusions

In this work, fuel gas mixtures with varying proportions of hydrogen and ammonia were studied regarding their ignition characteristics and combustion properties. Individual parameters, such as the electrode distance investigated here, have a strong effect on the ignition energy. However, the sensitivity of the investigated variables, such as the ignition energy, the maximum pressure, and the rate of pressure rise, not only show possibilities for adapting the fuel mixture for different areas of application. The need for further research in this area also becomes clear in the context of safe use. The schlieren images show that high ignition energies and the resulting flow patterns influence the early phase of the development of the hot gas kernel. On the microsecond scale after ignition by high energy discharges, this physical process can dominate the chemical process. Further research on cases without ignition can contribute to characterize the influence of the flow patterns in greater detail.

Acknowledgements

This research did not receive any specific grant from funding agencies in the public, commercial, or not-for-profit sectors.

References

Bane, S.P., J.L. Ziegler, J.E. Shepherd, 2015. Investigation of the effect of electrode geometry on spark ignition. Combustion and Flame 162 (2), 462–469, DOI: 10.1016/j.combustflame.2014.07.017.

E27 Committee, 2021. ASTM E582-21: Test Method for Minimum Ignition Energy and Quenching Distance in Gaseous Mixtures (ASTM E582-21). West Conshohocken, PA, ASTM International, DOI: 10.1520/E0582-21.

Essmann, S., J. Dymke, J. Höltkemeier-Horstmann, D. Möckel, C. Schierding, M. Hilbert, C. Yu, U. Maas, D. Markus, 2024. Ignition characteristics of hydrogen-enriched ammonia/air mixtures. Applications in Energy and Combustion Science 17, 100254, DOI: 10.1016/j.jaecs.2024.100254.

Essmann, S., D. Markus, U. Maas, 2017. Investigation of the Flame Kernel Propagation after Ignition by a Low Energy Electrical Discharge. 26th International Colloquium on the Dynamics of Explosions and Reactive Systems (ICDERS), 2017-07-30/2017-08-04, Boston, Paper 1006.

Fernández-Tarrazo, E., R. Gómez-Miguel, M. Sánchez-Sanz, 2023. Minimum ignition energy of hydrogen–ammonia blends in air. Fuel 337, 127128, DOI: 10.1016/j.fuel.2022.127128.

Hattwig, M., H. Steen, 2004. Handbook of explosion prevention and protection. Weinheim, Wiley-VCH, ISBN: 978-1-28123-928-0.

Krämer, H., 1985. Minimum ignition energy of ammonia/air atmosphere. GD 85: Proceedings of the Eighth International Conference on Gas Discharges & their Applications, Leeds, Univ. Press, S. 504–506.

Lesmana, H., M. Zhu, Z. Zhang, J. Gao, J. Wu, D. Zhang, 2022. An experimental investigation into the effect of spark gap and duration on minimum ignition energy of partially dissociated NH_3 in air. Combustion and Flame 241, 112053, DOI: 10.1016/j.combustflame.2022.112053.

Lhuillier, C., P. Brequigny, N. Lamoureux, F. Contino, C. Mounaïm-Rousselle, 2020. Experimental investigation on laminar burning velocities of ammonia/hydrogen/air mixtures at elevated temperatures. Fuel 263, 116653, DOI: 10.1016/j.fuel.2019.116653.

Li, J., S. Lai, D. Chen, R. Wu, N. Kobayashi, L. Deng, H. Huang, 2021. A Review on Combustion Characteristics of Ammonia as a Carbon-Free Fuel. Frontiers in Energy Research 9, 760356, DOI: 10.3389/fenrg.2021.760356.

PTB, BAM, 2023. Chemsafe: Database for safety characteristics in explosion protection, URL: www.chemsafe.ptb.de.

Valera-Medina, A., F. Amer-Hatem, A.K. Azad, I.C. Dedoussi, M. de Joannon, R.X. Fernandes, P. Glarborg, H. Hashemi, X. He, S. Mashruk, J. McGowan, C. Mounaim-Rouselle, A. Ortiz-Prado, A. Ortiz-Valera, I. Rossetti, B. Shu, M. Yehia, H. Xiao, M. Costa, 2021. Review on Ammonia as a Potential Fuel: From Synthesis to Economics. Energy & Fuels 35 (9), 6964–7029, DOI: 10.1021/acs.energyfuels.0c03685.

Verkamp, F.J., M.C. Hardin, J.R. Williams, 1967. Ammonia combustion properties and performance in gas-turbine burners 11 (1), 985–992, DOI: 10.1016/S0082-0784(67)80225-X.

Wähner, A., G. Gramse, T. Langer, M. Beyer, 2013. Determination of the minimum ignition energy on the basis of a statistical approach. Journal of Loss Prevention in the Process Industries 26 (6), 1655–1660, DOI: 10.1016/j.jlp.2013.06.002.

Warnatz, J., 1992. Resolution of gas phase and surface combustion chemistry into elementary reactions. Symposium (International) on Combustion 24 (1), 553–579, DOI: 10.1016/S0082-0784(06)80070-6.

Yu, C., S. Eckart, S. Essmann, D. Markus, A. Valera-Medina, R. Schießl, B. Shu, H. Krause, U. Maas, 2023. Investigation of spark ignition processes of laminar strained premixed stoichiometric NH_3-H_2-air flames. Journal of Loss Prevention in the Process Industries 83, 105043, DOI: 10.1016/j.jlp.2023.105043.

Study on hydrogen-ammonia explosion in a horizontal closed obstructed duct

Bo Liang [a], Wei Gao [a] & Yanchao Li [a]

[a] First affiliation (State Key Laboratory of Fine Chemicals, Department of Chemical Machinery and Safety Engineering, Dalian University of Technology, Dalian 116024, China)

E-mail: liang_bo0909@163.com, gaoweidlut@dlut.edu.cn, lyc092451@dlut.edu.cn

Abstract

Hydrogen-ammonia mixture, as an emerging energy source, holds potential for industrial applications. To investigate the explosion hazards of hydrogen-ammonia mixture, the flame evolution and pressure dynamics affected by turbulent acceleration are systematically studied in a horizontal closed obstructed duct under the lean side and rich side, and different ammonia ratio. The results indicate that the turbulent effects triggered by obstacles accelerate flame propagation. Compared to the lean side, the flame surface on the rich side is smoother, the turbulence intensity of the main flame vortex is greater, and the flame tilting is weaker in the later stage. As the ammonia ratio increases, the turbulent acceleration effect of the flame gradually diminishes and the flame tip speed continues to decrease. Concerning pressure dynamics, when the ammonia ratio is below Ω=20%, the explosion overpressure curve shows significant fluctuation, while with an increase in ammonia ratio, the fluctuation gradually decreases until disappears, indicating a reduction in the strength of the reflected pressure wave. Simultaneously, the maximum explosion overpressure decreases with increasing ammonia ratio.

Keywords: *ammonia addition, flame evolution, explosion overpressure, turbulent acceleration*

Introduction

The deteriorating global environment and the crisis of traditional fossil fuels are driving the development of new energy sources. Hydrogen, recognized as the cleanest fuel, with its high calorific value, faces challenges such as excessively fast combustion rates and a wide range of explosion limits, which hinder its further industrial development (Barış et al., 2023, Teoh et al., 2023). Ammonia, on the other hand, is a carbon-free fuel with a slow-burning rate. Mixing it with hydrogen can create a hydrogen-ammonia blend fuel that combines high combustion efficiency with enhanced safety. Pessina et al. (2022) provided a generalized formula based on the chemical kinetics data of hydrogen-ammonia mixture, which correlates the laminar burning velocity of hydrogen-ammonia flames under high temperature (720K to 1200K) and high pressure (40bar to 130bar) conditions. This formula plays a crucial role in flamelet combustion models (Pessina et al., 2022). Chen et al. (2023) pointed out that with an increase in hydrogen ratio, the laminar burning velocity of the hydrogen-ammonia mixture monotonically increased. Additionally, compared to the effects of hydrogen ratio and equivalence ratio, the initial pressure has the smallest impact on the laminar burning velocity (Chen et al., 2023). Lhuillier et al. (2020) explored the influence of high temperature (298K to 473K) on laminar burning velocity. The results indicated that with an increase in temperature, the laminar burning velocity increased. Moreover, the effects of the equivalence ratio and hydrogen fraction on the laminar burning velocity remain unchanged (Lhuillier et al., 2020). Ichikawa et al. (2015) found that at a low hydrogen ratio, as the initial pressure increased from 0.1MPa to 0.3MPa, the Markstein length of the hydrogen-ammonia mixture decreased significantly. However, as the initial pressure continued to increase to 0.5MPa, the change in the Markstein length was relatively small. At a high hydrogen ratio, the

influence of the initial pressure on the Markstein length is consistently minor (Ichikawa et al., 2015). Li et al. (2022) pointed out that when the hydrogen ratio is less than 80%, the laminar burning velocity decreases with increasing initial pressure. When the hydrogen ratio is 90%, the effect of initial pressure on the laminar burning velocity is weak. However, for a hydrogen ratio of 100%, increasing the initial pressure increases the laminar burning velocity (Li et al., 2022). Jin et al. (2022) pointed out that at a high hydrogen ratio, the effects of pressure and temperature on laminar burning velocity are more significant. The equivalence ratio corresponding to the maximum laminar burning velocity depends only on the fuel composition and is independent of initial pressure and initial temperature (Jin et al., 2022). Zheng et al. (2022) considered the influence of radiation reabsorption on the laminar flame speed of hydrogen-ammonia mixture at high pressure and different equivalence ratio, and established the Statistical Narrow-Band model parameters for ammonia. The results showed that radiation reabsorption exhibited non-monotonic behavior within the equivalence ratio range of Φ=0.65 to Φ=1.6, with a maximum enhancement effect on flame speed of up to 15.6% (Zheng et al., 2022). Li et al. (2021) obtained characteristic data of hydrogen-ammonia-air cloud explosion through experiment. The results showed that with the increase in hydrogen ratio, both the average flame propagation velocity and the maximum explosion pressure decreased, while with increasing equivalence ratio, they initially increased and then decreased (Li et al., 2021). Cheng et al. (2024) studied the explosion characteristics of hydrogen-ammonia mixtures in a 20L spherical chamber. The results showed that with the increase of initial pressure, both the maximum explosion pressure and the maximum pressure rise rate increased linearly. With increasing equivalence ratio, the explosion time initially decreased and then increased. As the hydrogen ratio increased, the maximum explosion pressure and explosion time tended to reach a constant value, while the maximum pressure rise rate continued to increase (Cheng et al., 2014). Liang et al. (2023) investigated the flame propagation characteristics of hydrogen-ammonia mixtures in a horizontal closed duct. The results indicated that with an increase in the ammonia ratio, the distorted tulip flame gradually disappeared, and the flame tip speed decreased while the speed fluctuation weakened gradually (Liang et al., 2023). Sun et al. (2024) conducted a study on flame propagation of hydrogen-ammonia mixture in a closed duct at high temperature. The results showed that with the increase in initial temperature, the early flame propagation speed increased, and the peak concentrations of NH2 and H radicals increased, while Darrieus-Landau instability decreased (Sun et al., 2024).

Currently, research on hydrogen-ammonia flame mainly focuses on laminar flame propagation, with only a few studies investigating the flame propagation and release of hydrogen-ammonia mixtures in pipelines. This study investigated the influence of different ammonia ratio on hydrogen-ammonia flame explosion under lean and rich sides. The flame evolution of hydrogen-ammonia mixture, flame tip speed, and explosion overpressure dynamic is obtained. These findings provide fundamental data support for the safe industrial application of hydrogen-ammonia fuels.

1. Experiments

Fig.1 shows the experimental platform of hydrogen-ammonia-air combustion in a horizontal rectangular closed duct. A horizontal closed duct with dimensions of 323mm×50mm×50mm serves as the combustion chamber, with quartz glasses of dimensions 260mm×50mm installed on both sides of the duct. Aluminum plate obstacles with dimensions of 50mm in width, 25mm in height, and 10mm in thickness are installed at locations 50mm away from the ignition electrode, respectively. The Schlieren system, high-speed camera (FASTCAM SA-Z), pressure sensor (PCB 113B24), data acquisition recorder (Yokogawa DL950), high-voltage igniter, and timing controller collaborate to capture high-resolution images of flame evolution and comprehensive pressure dynamics data. The detailed parameters of the experimental setup have been introduced in our previous work (Liang et al. 2023, Liang et al, 2023). Ammonia of 99.999% purity, hydrogen of 99.999% purity, and dry air are used in the experiment. Before commencing the experiment, it is necessary to ensure the

cleanliness of the visualization windows, complete the installation of obstacles, and verify the airtightness of the duct. After evacuating the closed duct, ammonia, hydrogen, and air are sequentially introduced, followed by a 5-minute period of standing to ensure a homogeneous gas mixture. The initial condition of this experiment is at room temperature (300K) and normal pressure (1atm).

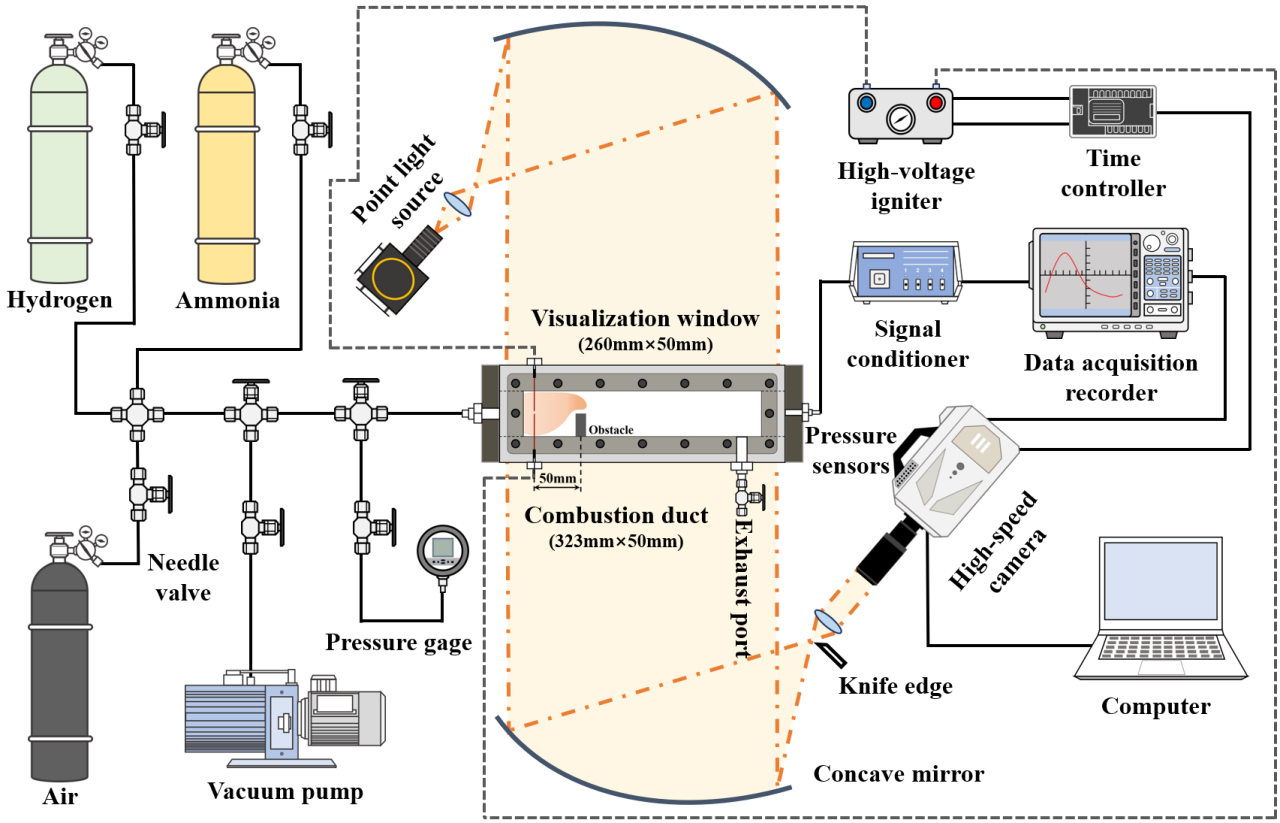

Fig.1 Experimental platform of hydrogen-ammonia-air combustion in a horizontal rectangular closed duct

2. Results and discussion

2.1. Flame evolution and flame tip speed

Fig.2 shows the effect of ammonia ratio on flame evolution on lean side. Following the discharge of the ignition electrode, the flame begins to develop in a spherical shape. Blocked by the obstacle, the speed of the lower part of the flame decreases, while the speed of the upper part increases. The flame morphology is compressed into a finger-shaped flame with an elevated upper part. As the flame crosses the obstacle, the lower surface of the flame front is nearly parallel to the upper surface of the obstacle, and the flame surface is smooth. At this point, there is no contact between the flame and the obstacle. Subsequently, to the right of the obstacle, disturbances occur between the unburned gas and the flame front, initiating a clockwise rotation of the flame front. Simultaneously, the wrinkle structure begins to form on the flame surface, and a small recirculation vortex is formed above the obstacle, resulting in some flame backflow. Then, the flame in the vortex region comes into contact with the obstacle, causing the vortex to gradually dissipate. During this process, the flame propagates in a finger-shaped and is further accelerated. Due to the contact with the duct wall by the flame skirt, the flame begins to decelerate and gradually transforms into a plane flame. Furthermore, the flame surface begins to reverse, forming a tulip flame, which is a hydrodynamic phenomenon (Ponizy et al., 2014). It is worth noting that, at all ammonia ratio, the flame in the later stage exhibits an inclined flame front with a fast upper flame tongue and a slow lower flame tongue. This is primarily attributed to the combined effects of the obstacle-induced jet and buoyancy instability. At a low ammonia ratio,

the buoyancy instability is weak, but the jet effect induced by the obstacle is strong, resulting in a tulip flame with a greater acceleration in the upper tongue compared to the lower tongue. Conversely, at a high ammonia ratio, the jet effect weakens, while buoyancy instability strengthens, causing the flame to upwell and subsequently increasing the upper tongue speed. When the ammonia ratio is less than Ω=30%, the cusp of the tulip flame is not pronounced, and the flame surface is filled with wrinkled structure. This is mainly caused by the destabilizing effect of thermal diffusion instability on the flame surface. When the ammonia ratio is Ω=40% and Ω=60%, the cusp of the tulip flame is significant, the tilt of the flame increases, and the wrinkled structure on the flame surface decreases. When the ammonia ratio is Ω=80%, the flame rises and fails to form a tulip flame. Instead, an inclined plane flame is formed, and the inclined angle increases as the flame develops. For flame acceleration, as the ammonia ratio increases from Ω=10% to Ω=80%, the time needed for the flame to propagate to the same location gradually increases. The wrinkled structure of the main flame vortex reduces, and the small recirculation vortex above the obstacle weakens. As the equivalence ratio increases from Φ=0.8 to Φ=1.4, the time required for the flame to propagate to the same position declines first and then rises. The size of the main flame vortex slightly decreases, and the density of the wrinkled structure decreases.

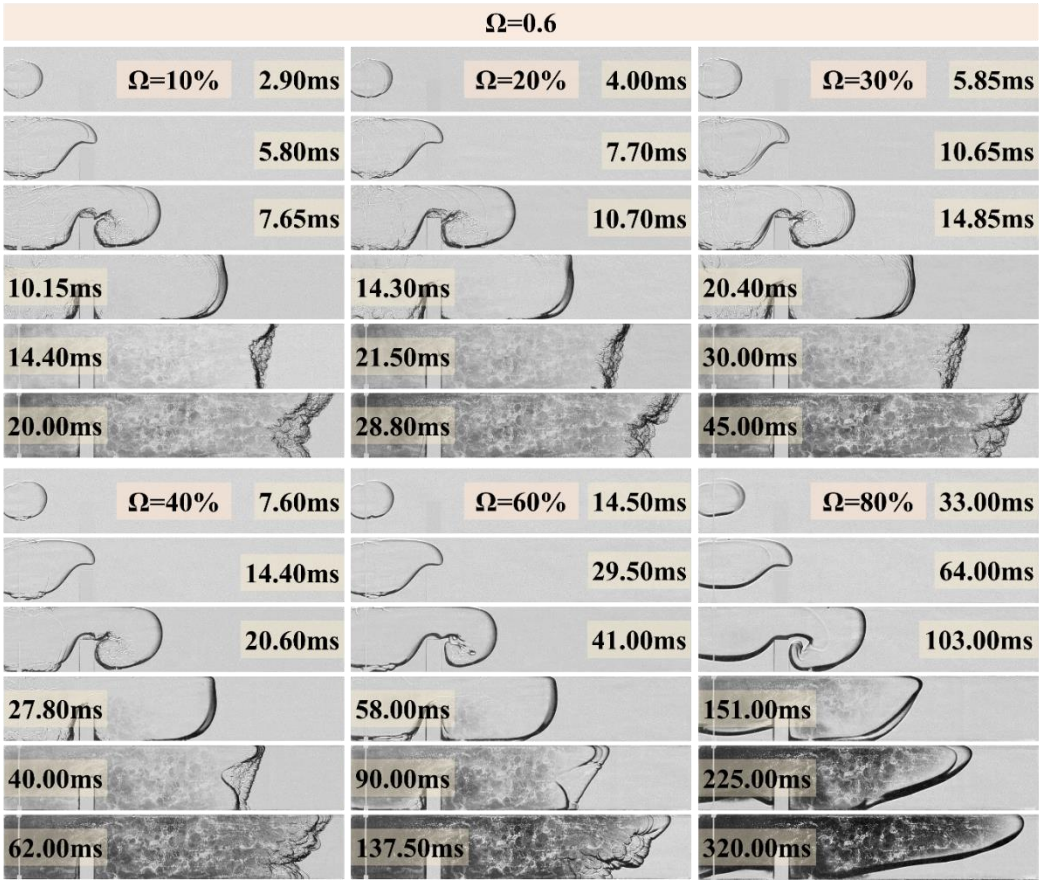

Fig. 2 *Effect of ammonia ratio on flame evolution on lean side (Φ=0.6)*

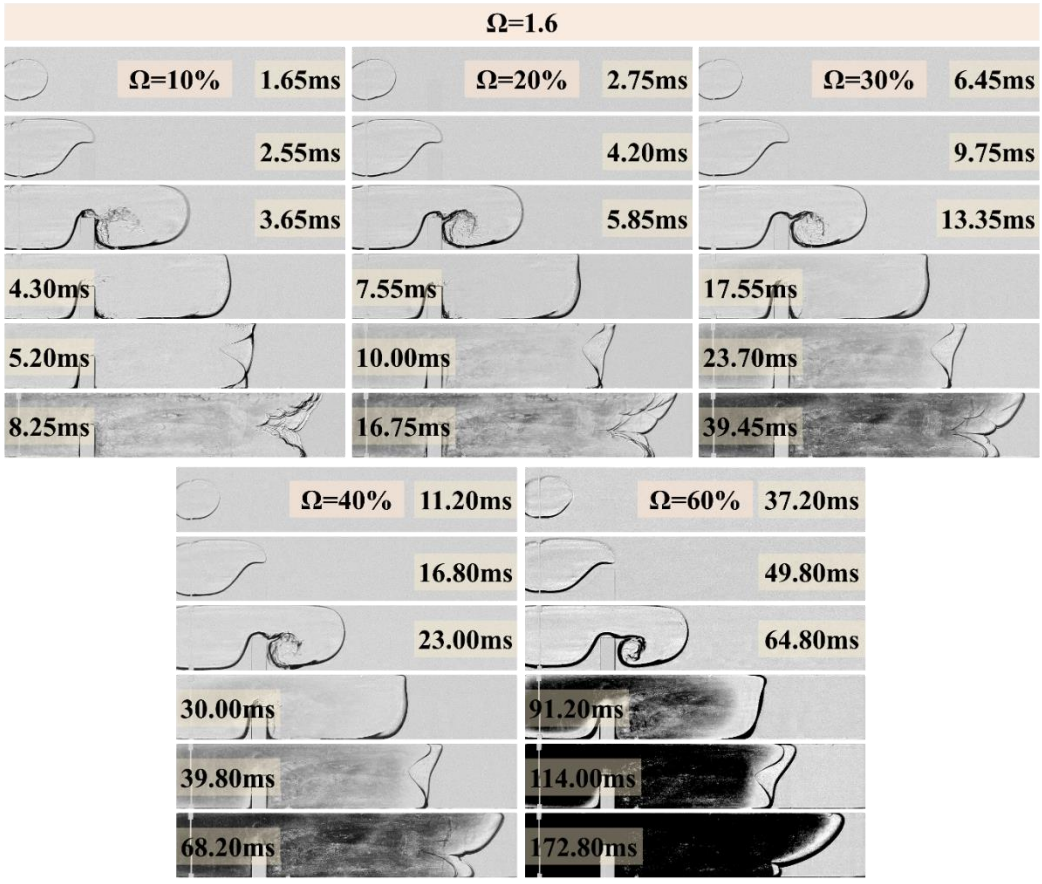

Fig. 3 *Effect of ammonia ratio on flame evolution on rich side (Φ=1.6)*

Fig.3 shows the effect of ammonia ratio on flame evolution on rich side. Before the flame crosses the obstacle, the flame evolution is similar to that on the lean side. After the flame crosses the obstacle, compared to the lean side, the main flame vortex on the rich side shows an increased wrinkled structure, indicating an increase in turbulence intensity. Additionally, the cusp of the tulip flame becomes more pronounced, and the flame surface appears smoother, with little wrinkled structure. In the later stage, the tilt of the flame is weaker, indicating a weakening effect of buoyancy instability. When the ammonia ratio is Ω=10%, a distorted tulip flame is observed at the later flame stage. The formation mechanism is mainly associated with Rayleigh-Taylor instability (Xiao et al., 2015, Xiao et al., 2013), and a detailed analysis can be found in our previous work (Liang et al., 2023). When the ammonia ratio is greater than Ω=20%, the tulip flame surface no longer exhibits a distorted cusp. For flame acceleration, as the ammonia ratio increases from Ω=10% to Ω=80%, the splitting degree of wrinkled structure on the main flame vortex weakens.

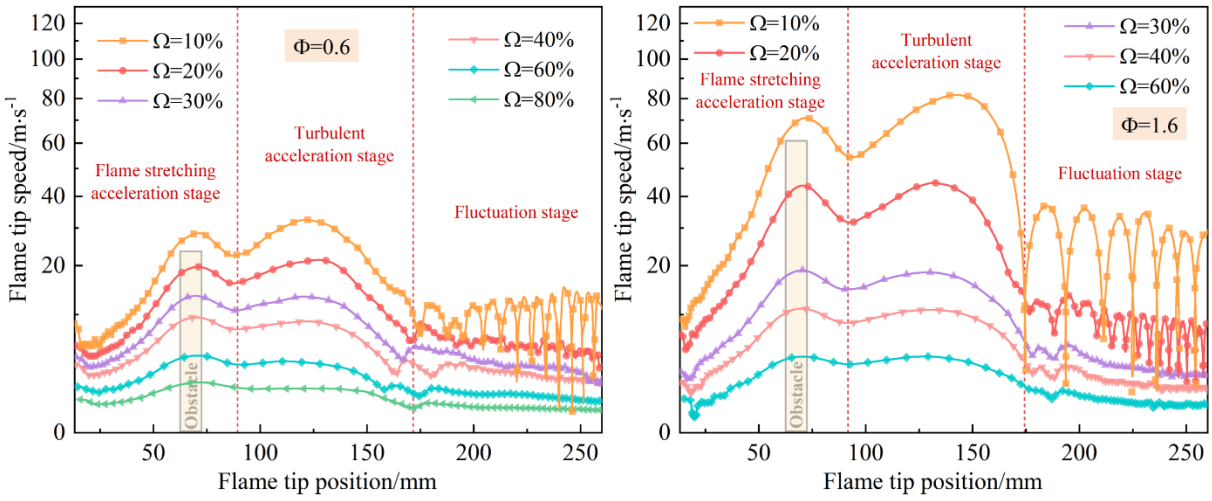

Fig. 4 *Effect of ammonia ratio on flame tip speed on lean and rich sides (Φ=0.6 and 1.6)*

Fig.4 shows the effect of ammonia ratio on flame tip speed on lean and rich sides. The flame tip position is used as the reference for measuring the flame tip speed. Influenced by the ignition energy, the initial flame tip speed is relatively significant. As the flame radius increases, the effect of ignition energy diminishes, causing the flame tip speed to decrease to a stable value before gradually increasing. As the spherical flame is stretched and deformed by the obstacle, the flame surface area gradually increases, leading to a rapid increase in flame tip speed. When crossing the obstacle, the flame tip undergoes maximum stretching, and the flame tip speed also reaches its peak. Subsequently, during the formation of the first main flame vortex, the flame tip is hindered by the expansion of unburned gas (Johansen et al., 2013), leading to a gradual decrease in flame tip speed. However, when the main flame vortex is fully formed, the turbulence within the vortex region will further accelerate the combustion rate, leading to a second rise in flame tip speed. As the flame evolves, the flame tip transitions from a finger-shaped flame to a tulip flame, with the flame skirt beginning to make contact with the duct wall. Before the flame skirt touching the duct wall, the flame speed reaches its second peak. Subsequently, due to the reduction in flame surface area, the flame tip speed gradually decreases. During the tulip flame stage, significant fluctuation in flame tip speed occurs due to the interaction between the reflected pressure wave and the flame front (Salamandra et al., 1958, Xiao et al., 2013, Xiao et al., 2012). However, as the ammonia ratio increases, the fluctuation magnitude decreases. The critical ammonia ratio for speed fluctuation is Ω=20% for both the lean side and the rich side. Additionally, at a low ammonia ratio, the second peak of flame tip speed is slightly higher than the first peak, whereas as the ammonia ratio surpasses Ω=40%, the second peak begins to fall below the first. This indicates a weakening of the turbulent acceleration with increasing ammonia ratio. As the ammonia ratio increases from Ω=10% to Ω=80%, for the lean side of Φ=0.6, the maximum flame tip speed decreases from 32.45m/s to 1.80m/s, a decreasing by 94.45%; for the rich side of Φ=1.6, the maximum flame tip speed decreases from 81.78m/s to 4.14m/s, a decreasing by 94.93%. Overall, the flame tip speed experiences two stages of increase, with two peaks observed. These peaks correspond to the flame stretching acceleration and the turbulence acceleration, respectively. In the later stages, the flame tip speed continues to fluctuate around a lower average value. The flame tip speed on the lean side and the rich side, except for the maximum value and fluctuation amplitude, do not show significant differences in trend and characteristics.

2.2. *Flame evolution and flame tip speed*

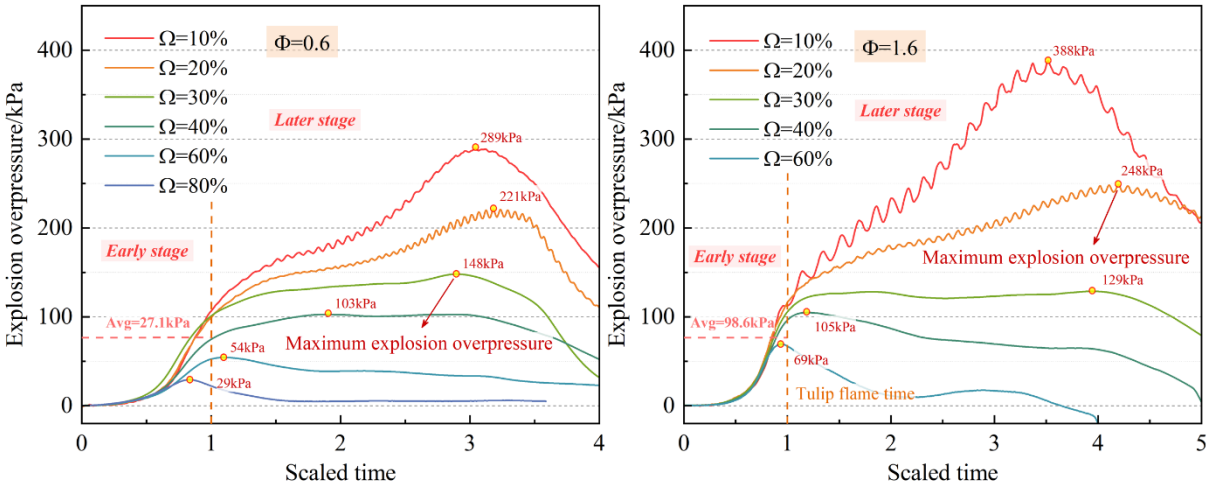

Fig.5 *Effect of ammonia ratio on explosion overpressure on lean and rich sides (Φ=0.6 and 1.6)*

Fig.5 shows the effect of ammonia ratio on explosion overpressure on lean and rich sides. To uniformly characterize the features of the explosion overpressure curve, the scaled time is used as the abscissa. Since the time of the inclined plane flame precisely marks the boundary between the turbulent acceleration stage and the fluctuation stage of the flame tip speed, the scaled time is defined

as follows: $t_s=t/t_{ip}$, which equals the physical time divided by the time of the inclined plane flame. When the scaled time equals unity, it indicates the moment when the inclined plane flame forms, which has been marked with a vertical orange dashed line on the overpressure curve graph, with the average value of the corresponding explosion overpressure depicted by a horizontal dashed line. It is interesting to note that the orange dashed line neatly divides the explosion overpressure curve into two stages: the first stage, characterized by a large rise rate and a smooth curve, and the second stage, characterized by a small decline rate and a significant fluctuation. Additionally, in the second stage, significant fluctuation is observed only in cases where the ammonia ratio is relatively low. As the ammonia ratio increases, the fluctuations gradually weaken and eventually disappear, indicating a reduction in the strength of the reflected pressure wave. Combining with Fig.2 and Fig.3, it can be inferred that the weakening interaction between the reflected pressure wave and the flame front is the direct reason for the disappearance of the distorted tulip flame as the ammonia ratio increases. The critical ammonia ratio for overpressure fluctuation is Ω=20% for both the lean side and the rich side. When the ammonia ratio exceeds Ω=60%, the second stage of the explosion overpressure curve transitions into a downward trend instead of an upward trend. As the ammonia ratio increases from Ω=10% to Ω=80%, for the lean side of Φ=0.6, the maximum explosion overpressure decreases from 289kPa to 29kPa, a decreasing by 89%; for the rich side of Φ=0.6, the maximum explosion overpressure decreases from 388kPa to 69kPa, a decreasing by 82%. Additionally, the time to reach maximum explosion overpressure first increases and then decreases. For the lean side of Φ=0.6, the maximum and minimum value of the scaled time are 3.18 and 0.82, respectively. For the rich side of Φ=1.6, the maximum and minimum value of the scaled time are 4.19 and 0.94, respectively.

3. Conclusions

This study primarily investigates the effects of ammonia ratio on the accelerated propagation of hydrogen-ammonia flames inside the obstructed duct under the lean and rich sides. The main conclusions are as follows:

(1) The flame front is stretched and the turbulent flame vortex is formed due to the effect of the obstacles. As the ammonia ratio increases, the wrinkled structure within the main flame vortex diminishes, leading to a reduction in turbulence. Compared to the lean side, the flame surface on the rich side is smoother, the turbulence intensity of the main flame vortex is greater, and the flame tilting is weaker in the later stage.

(2) The trends and characteristics of the flame tip speed on the lean side and the rich side are similar. As the ammonia increases from Ω=10% to Ω=80%, the maximum flame tip speed gradually decreases and the fluctuation magnitude diminishes. Flame stretching can rapidly increase the flame tip speed by altering the flame morphology, while turbulent acceleration increases the burning rate by enhancing the turbulent intensity of the main flame vortex, thereby accelerating flame propagation.

(3) As the ammonia ratio increases from Ω=10% to Ω=80%, the maximum explosion overpressure decreases, the time to reach maximum explosion overpressure first increases and then decreases, and the fluctuation gradually weakens and eventually disappears, indicating a reduction in the strength of the reflected pressure wave.

Acknowledgements

The authors gratefully acknowledge the financial contribution from Natural Science Foundation of China (No. 52004050, 52274178 and U22A20168), National Key R&D Program of China (No. 2022YFC3080700 and 2021YFB4000902) and the Fundamental Research Funds for the Central Universities (No. DUT22RC(3)021).

References

- **Bibliography:**

Yu, X., Yu, J., Zhang, X., Lv, X., Cao, Q., Hou, Y., Yan, X., 2018. Flame Propagation Behaviors during Hydrogen/Aluminum Dust Hybrid Explosions Article. Powder Technol. 1, 1–8.

Barış, O., Güler, İ., Yaşgül, A., 2023. The effect of different charging concepts on hydrogen fuelled internal combustion engines. Fuel. 343, 127983.

Teoh, Y., How, H., Le, T., Nguyen, H., Loo, D,. Rashid, T., Sher, F., 2023. A review on production and implementation of hydrogen as a green fuel in internal combustion engines. Fuel. 333, Part 2, 126525.

Pessina, V., Berni, F., Fontanesi, S., Stagni, A., Mehl, M., 2022. Laminar flame speed correlations of ammonia/hydrogen mixtures at high pressure and temperature for combustion modeling applications. Int J Hydrogen Energ. 47, 61, 25780-25794.

Chen, X., Liu, Q., Zhao, W., Li, R., Zhang, Q., Mou, Z., 2023. Experimental and chemical kinetic study on the flame propagation characteristics of ammonia/hydrogen/air mixtures. Fuel. 334, Part 1, 126509.

Lhuillier, C., Brequigny, P., Lamoureux, N., Contino, F., Mounaïm-Rousselle, C., 2020. Experimental investigation on laminar burning velocities of ammonia/hydrogen/air mixtures at elevated temperatures. Fuel. 263, 116653.

Ichikawa, A., Hayakawa, A., Kitagawa, Y., Somarathne, K., Kudo, T., Kobayashi, H., 2015. Laminar burning velocity and Markstein length of ammonia/hydrogen/air premixed flames at elevated pressures. Int J Hydrogen Energ. 40, 30, 9570-9578.

Li, H., Xiao, X., Sun, J., 2022. Laminar burning velocity, Markstein length, and cellular instability of spherically propagating NH3/H2/Air premixed flames at moderate pressures. Combust Flame. 241, 112079.

Jin, B., Deng, Y., Li, G., Li, H., 2022. Experimental and numerical study of the laminar burning velocity of NH3/H2/air premixed flames at elevated pressure and temperature. Int J Hydrogen Energ. 47, 85, 36046-36057.

Zheng, S., Liu, H., Sui, R., Zhou, B., Lu, Q., 2022. Effects of radiation reabsorption on laminar NH3/H2/air flames. Combust Flame. 235, 111699.

Li, Y., Bi, M., Zhou, Y., Zhang, Z., Zhang, Z., Zhang, C., Gao, W., 2021. Characteristics of hydrogen-ammonia-air cloud explosion. Process Saf Environ. 148, 1207-1216.

Cheng,J., Zhang, B., 2024. Experimental study on the explosion characteristics of ammonia-hydrogen-air mixtures. Fuel. 363, 131046.

Liang, B., Yang, M., Gao, W., Jiang, Y., Li, Y., 2023. Study on premixed hydrogen-ammonia-air flame evolution in a horizontal rectangular duct. Fuel. 354. 129427.

Sun, G., Deng, H., Xu, Z., Yan, M., Wei, S., Li, N., Wen, X., Wang, F., Chen, G., 2024. Experimental and simulation study of NH3–H2-Air flame dynamics at elevated temperature in a closed duct. Int J Hydrogen Energ. 50, Part B, 48-61.

Liang, B., Huang, L., Gao, W., Jiang, J., Jiang, J., Li, Y., 2023. Flame evolution and pressure dynamics of methane-hydrogen-air explosion in a horizontal rectangular duct. Fuel. 357, Part C, 129962.

Ponizy, B., Claverie, A. Veyssière, B., 2014. Tulip flame - the mechanism of flame front inversion. Combust and Flame. 161, 12, 3051-3062.

Xiao, H., Houim, R., Oran, E., 2015. Formation and evolution of distorted tulip flames. Combust Flame. 162, 11, 4084-4101.

Xiao, H., An, W., Duan, Q., Sun, J., 2013. Dynamics of premixed hydrogen/air flame in a closed combustion vessel. Int J Hydrogen Energ. 38, 29, 12856-12864.

Johansen, C., Ciccarelli, G., 2013. Modeling the initial flame acceleration in an obstructed channel using large eddy simulation. J Loss Prevent Proc. 26, 4, 571-585.

Salamandra, G., Bazhenova, T., Naboko, I., 1958. Formation of detonation wave during combustion of gas in combustion tube. Symposium (International) on Combustion. 7, 1, 851-855.

Xiao, H., Makarov, D., Sun, J., Molkov, V., 2012. Experimental and numerical investigation of premixed flame propagation with distorted tulip shape in a closed duct. Combust and Flame. 159, 4, 1523-1538.

Removed ARTICLE

Removed ARTICLE

Removed ARTICLE

Removed ARTICLE

Removed ARTICLE

Removed ARTICLE

Removed ARTICLE

Removed ARTICLE

Removed ARTICLE

Removed ARTICLE

Removed ARTICLE

Removed ARTICLE

Linear contractions effect on the propagation of hydrogen and methane flames in large scale pipeline

Alexandre Auvray [a,b,c], Jerome Daubech [c], Christophe Proust [b,c] & Pierre Montagne [a]

[a] General Electric Gas Power, Belfort, France
[b] Université de Technologie de Compiègne, Compiègne, France
[c] INERIS, Verneuil-en-Halatte, France

E-mail: *alexandre.auvray@ge.com*

Abstract

The motivation of gas industries to switch from fossil fuels to hydrogen raise questions related to the safety of operations. One of the scenario of interest is related to a flame propagation in a long pipe. While most of flame propagation analysis in pipes are carried in straight configuration with different sizes, the very few studies on the influence of single elements are carried at small scale.

In order to develop the knowledge on the piping geometrical effect on flame acceleration, experiments were performed in a 250mm diameter and 24m long straight pipe, closed at ignition and open to the atmosphere at the other end. The single elements tested here are two soft and sharp section changes. All single elements are located 16m from ignition in order to get a well-developed flame front when reaching the single element. Two flammable mixtures were tested that are stoichiometric methane-air and lean hydrogen-air, meaning two slow and fast nominal flame velocities.

It appears that the contraction promotes flame acceleration for both mixtures, but in a more important manner in the case of hydrogen flame compared to methane. The assumption of flame surface extension due to radial velocity gradient is put forward to explain this acceleration.

Keywords: *flame, pipe, hydrogen, methane, contraction, convergent, reduction*

Introduction

The environment of process industry usually shows several process units (tanks, reactors…) to carry basic process operations, and pipe network to connect all these units. These pipes allow the transport of fluids in the process, including flammable gases such as hydrocarbons, hydrogen etc… With the growing interest for hydrogen use in the industry, gas manufacturers have to certify the safe operations of the plant. Some scenario of fuel-oxidizer mixing in the pipe network where identified, and thus, need to be treated in a safety aspect. When compared to the methane, the specific combustion properties of hydrogen in addition to the lack of experience in the industry, leads to the need of phenomenological understanding of flame propagation in pipes in case of hazardous ignition of such cloud. It is known that flame is prone to accelerate in pipes (Ciccarelli 2008), and because a criterion of deflagration to detonation transition (DDT) is the flame velocity, understanding the mechanism of flame acceleration is a strong necessity. Most of experimental results available in the literature treats the simple configuration of a straight pipe, while pipe network may show a complex structure in real environment due to the presence of bends, tee bifurcations, section changes, etc.. It is thus of interest to understand the influence of these single elements on the flame propagation. The bend and tee bifurcation configuration are somehow largely treated in the literature (Blanchard & al. 2010, Thomas et al. 2010, Zhu et al. 2017). By contrast, very few studies concern the section change, whereas it is hugely present on pipelines.

Wang et al. (2020) studied the influence of an abrupt variation in pipe cross section using 3 square cross section size of 70*70mm, 100*100mm and 140*140mm for a total length of 1m closed pipe.

He observed that in both convergent and divergent configuration, the greater the section ratio, the higher the overpressure, but does not lead to any conclusion on the flame velocity. He further studied the influence of section change location from the ignition (Wang et al., 2021). He concluded that if the pipe expansion is sufficiently far from the ignition to allow a tulip flame to appear in the early stages of development, that leads to a slower flame propagation and a lower pressure peak generated.

The development of new technics for shock tube experiments came with the development of forward and backward detonation driver. Hongru (1999) summarizes the different steps of the development, and highlighted the situation where a detonation from driver section enters a reduction. This results in two shock waves, one transmitted forward to the short pipe diameter (driven section), and the other one reflected back (driver section). The latter further enable to weaken the rarefaction waves behind the detonation, and thus weaken the attenuation of the transmitted shock wave.

A numerical analysis was also performed by Song et al. (2021) on two sections of 150 and 100mm diameters, both 3m long to assess the convergence angle, with rich hydrogen-air mixtures. These simulations were performed with FLACS but considering cells size below 1mm. He observed a second tulip flame formation at the contraction, which is assumed to come from the reflection of the shock wave just ahead the flame. This implies a baroclinic torque responsible of the tulip formation. In addition, no effect of contraction angle where noticeable on the flame propagation.

The present study aims at examining the effect of linear contraction on well-developed flame to complete the knowledge available in the literature. The experiments are performed in large scale straight pipe representative of industrial geometry. The choice of stoichiometric methane-air and hydrogen-air as flammable mixtures enables to investigate the flame response to contraction with its velocity.

1. Experimental set-up

The test rig used in this study was previously introduced by Daubech et al. (2019). It is a modular 24m long PMMA pipe made of 12 sections of 2m long, stacked with each other (Fig. 1.). Two pipe diameters of 150mm or 250mm were used to assess the scale effect. The influence of single element is limited to the study of a soft 250mm to 150mm section change with 3° angle, and a sharp 250mm to 150mm section change with 10° angle. All pipe configurations with associated pressure probes locations from ignition are displayed on Figure 2. In all tests, the pipe is closed at one end and open to the atmosphere at the other end.

Fig. 1. *Experimental setup*

A flammable mixture, either made of methane-air or hydrogen-air blend, is prepared in a $2m^3$ spherical vessel with concentration control using partial pressure method. Then, the flammable mixture is injected at the closed end, and the pipe is swept all along with a quantity of about 5 time its volume. During this operation, the open end is covered with a thin plastic sheet drilled with a small hole at the center, allowing the gas flow. This hole reduces the plastic sheet resistance, and the reflexion of the initial pressure wave after ignition is neglected. The ignition is carried by a 100mJ

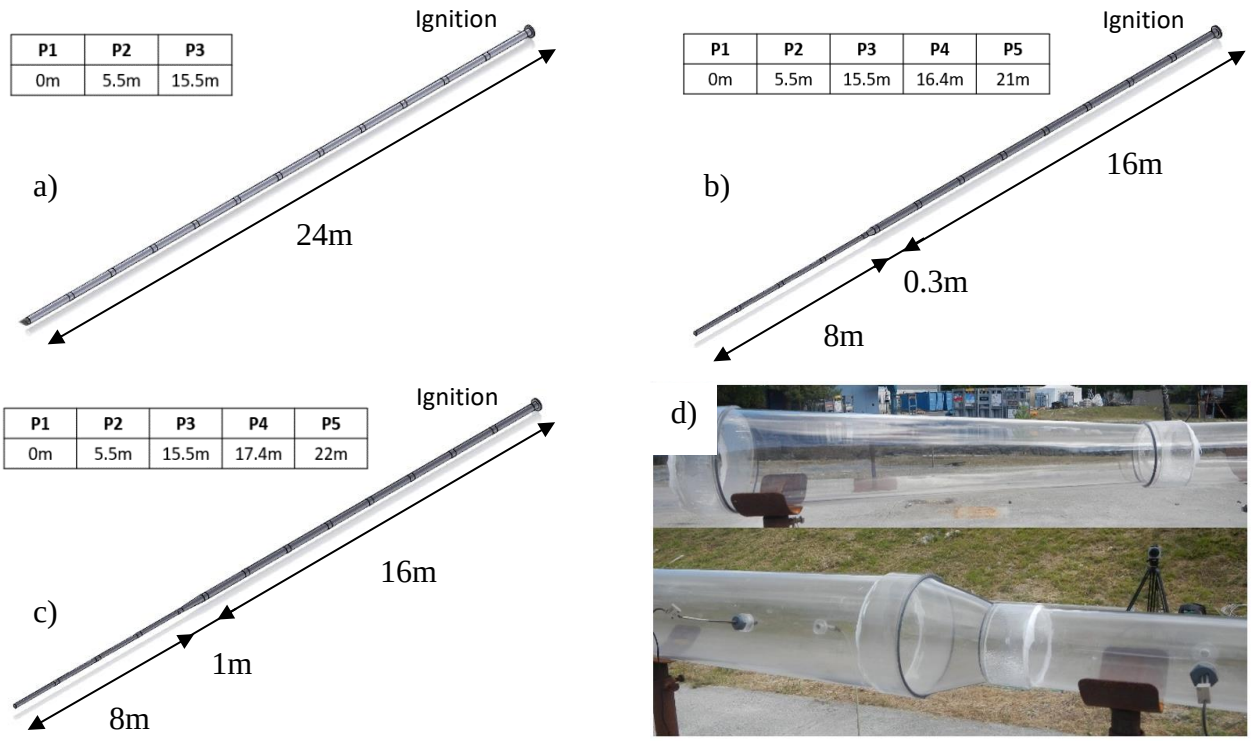

Fig. 2. *Pipe configurations and sensors location from ignition. a) straight pipe ; b) sharp contraction ; c) soft contraction. d) Pictures of short (above) and sharp (below) contractions*

electrical spark, located at the center of the closed end. A time delay of few seconds is considered before ignition, in order to ensure that no turbulence remains in the gas.

The metrology includes piezoresistives pressure sensors (Kistler; Range: 0-10 bar), all connected to an acquisition system with limited recording frequency of 10kHz. Also, since the pipe wall is transparent, a Photron fast-camera is used to record the flame development at 2000 frame/s. For the hydrogen-air tests, the flammable cloud is hazed with ammonium chloride in the pipe in order to observe the flame.

All test were double, but the visual field of the camera was either large or focus on the contraction. It must be noted that no wide-angle lens was used for both cases.

The post process of the video was carried with a specific software developed at the INERIS. This enables to do operations on the multiple images for the analysis. The image post treatment was used here for the flame position in time extraction. To do that a first image difference with the image at t=0s was processed. This enabled to highlight movements registered during the phenomenon (pressure waves, shock waves, and flame) with a difference of color (white is detected movement and black is immobile zones). Then, a line extraction along the pipe axis gives a time-position diagram. From this image, a color value threshold on pixel enable to detect the flame front, and the value are extracted in a csv file for the flame position treatment.

An example of image treatment procedure is illustrated in Figure 3.

2. Experimental results and discussion

2.1 Straight configuration - typical test

The pressure signals and flame trajectory for the 250mm diameter straight pipe is plotted on Figure 4. for both methane and hydrogen cases. The characteristic first pressure peak P_1 clearly appears in these two cases, and is related to the extinction of the flame skirt at the wall (Clanet & Searby, 1989).

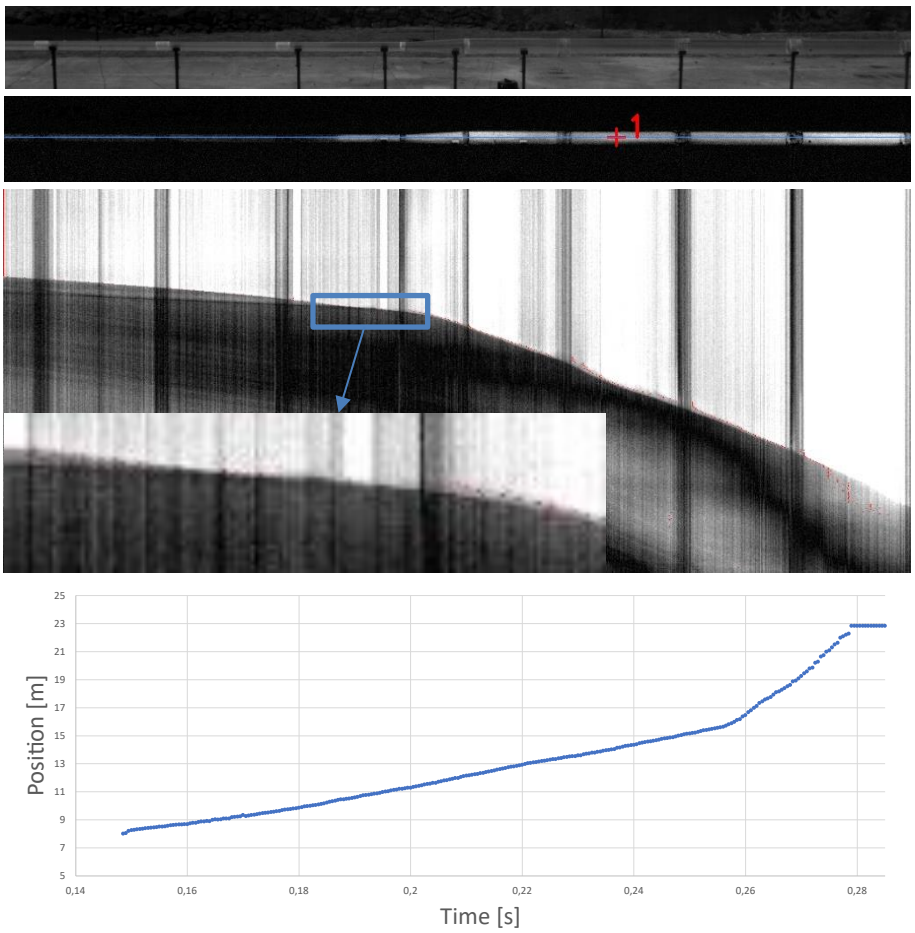

Fig. 3. *Image treatment procedure. a) Original image ; b) Difference with image 0, and line extraction ; c) Result of line extraction, and flame front position estimation (red points); d) Resulting flame front position curve*

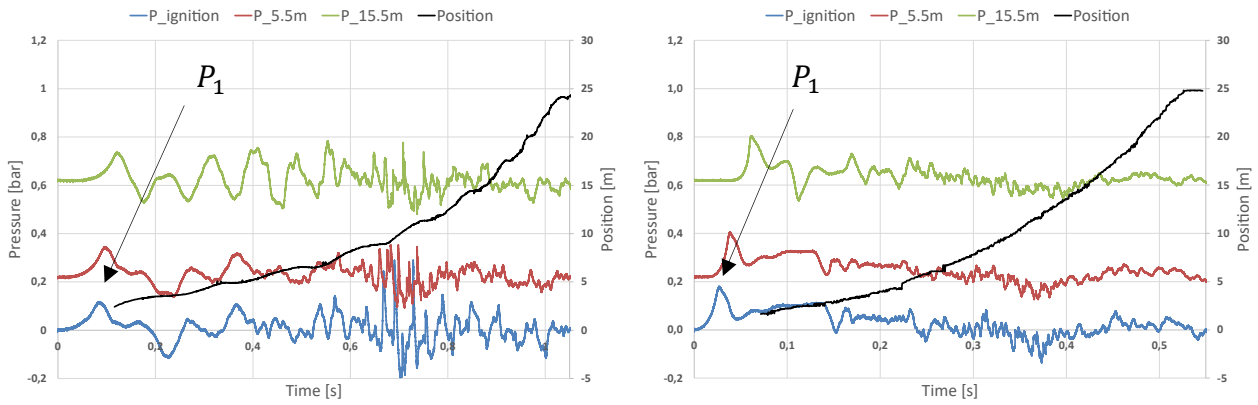

Fig. 4. *Pressure signal and flame position in 250mm straight pipe. a) methane-air (EQR = 1) ; b) hydrogen-air (EQR=0.6)*

It is also obvious that the pressure peak of the hydrogen case is steeper and occurs earlier compared to the methane's (0.03s for hydrogen, and 0.085s for the methane's). This is attributed to the lower reactivity of the methane. This slowness of the methane's flame further results in flame oscillations at 6.7Hz, due to a coupling with the pipe acoustic (pipe natural frequency estimated at 7.3Hz), as noted in short pipes experiments (Genoche, 1950 ; Kerampran, 2000).

It must be noted that the present configuration of smooth pipe does not generate too much turbulence during the flame propagation (Daubech et al., 2019), and the flame acceleration by turbulence is thus

limited (Dorofeev, 2011). As a result, the flame velocities remain below 100m/s during the propagation, and no transition to fast flame propagation were observed in this geometry.

2.2 Effect of section contraction

A comparison between the flame position curves of 250mm diameter straight pipe, 150mm straight pipe, soft contraction, and sharp contraction configurations is plotted on Figure 5. for both hydrogen and methane cases. First of all, one can observe that the flame reaches the pipe end earlier in the 150mm diameter compared to the 250mm diameter. To go further, the velocities of hydrogen-air flame in 150mm diameter goes from 160m/s à 10m to 350m/s at the pipe end, while the velocity increases from 60 to 120m/s at the same distance in the 250mm pipe.

A second observation concerns the effect of contraction. A slope rupture is noticed in both hydrogen-air and methane-air tests with contraction at approximately 16m from ignition, which is the location of the soft and sharp contraction. This is compared to the smoother curves of straight configurations (150 and 250mm diameters). In addition, whereas the first 16m of the pipes are 250mm diameter in tests with contraction, the flame reaches the contraction position (16m) earlier compared to the 250mm straight tests. That suggests an effect of the single element before the flame reaching.

The pressure measurement and flame position record of the hydrogen-air test in soft contraction configuration is plotted on Figure 6. The first moment of the flame development shows the same pressure trend when compared to the 250mm straight pipe configuration, except an additional pressure peak P_2 visible on the P_ignition and P_5.5m curves, respectively at 0.097s and 0.086s which seems to inversely to the global flow. With the assumption that the flame front is 5m from the ignition when it would meet this back flow (trustworthy regarding the prolongation of the flame position), one may obtain the time for the initial pressure peak P_1 to reach the contraction, and travel back to the ignition end as:

$$t_{P_1} = \frac{L_u}{c_u} + \frac{L_b}{c_b} = \frac{16 + 11}{380} + \frac{5}{860} = 0.077s$$

Where L_x and c_x refer to distance and sound speed, and index u, b refer to unburnt and burnt medium. The values of sound speed were calculated with Cantera for lean hydrogen-air mixture (EQR=0.6).

Adding the time of first pressure peak P_1 occurrence at the ignition end $0.022s$, the estimated time for this latter to reach the end after the reflection is $0.099s$, close to the 0.097s observed on the Figure 6. Thus, the peak P_2 is assumed to be due to the partial pressure wave reflection on the conical wall of the reduction, travelling back to the ignition side. This pressure wave is the only information of the presence of the convergent the flame can see, and might explain the difference of flame propagation in the 16 first meters between straight and convergent configurations. The early effect of the contraction was also observed in the CFD study of Song et al. (2021), where the reflected pressure wave causes a flame shape change from finger to tulip when they meet. He's analysis is that the contraction promotes an early structure of the flame front, and results in a faster flame propagation. This might explain the global faster flame in the first 16m with the presence of the contraction observed here.

The Figure 6 also shows a flame position curve's slope change when reaching the reduction at 0.253s, and a pressure peak P_3 is noticeable 10ms later on the P_17.4m curve. This time matches with the flame passing the convergent. Looking closer on the flame position record of the hydrogen test 4 with the soft reduction on Figures 7.a and 7.b, it appears that this latter may be divided in different stages. First, the flame enters the convergent with a quite constant velocity of 81m/s (stage 1) at $t_{in} = 0.253s$, and is gradually accelerated in the convergent (stage 2). The flame exits the contraction at $t_{out} = 0.261s$, and the velocity of 328m/s is kept constant for the 0.4m downstream the contraction (stage 3). Afterwards, the flame decelerates down to 240m/s and a shock with a velocity of 670m/s is emitted ahead (stage 4), which is probably responsible of the pressure peak P_4 mentioned above. The

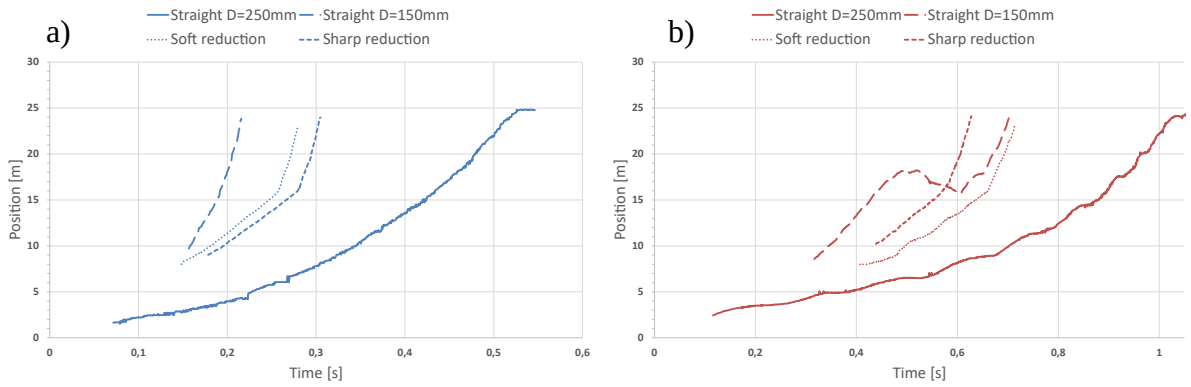

Fig. 5. *Flames positions versus time for the four tested configurations. a) lean hydrogen-air (EQR=0.6) ; b) stoichiometric methane-air*

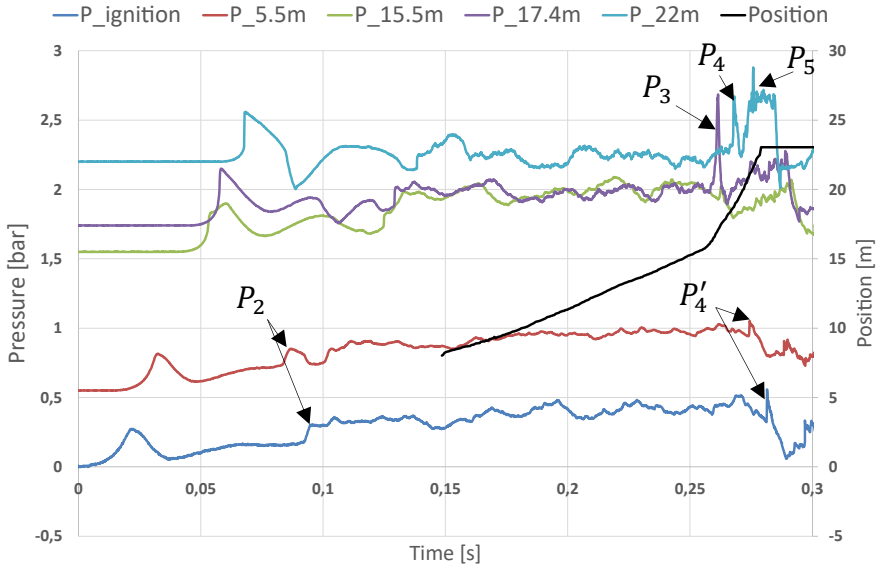

Fig. 6. *Test 3: Pressure and flame position vs time. Lean hydrogen-air (EQR=0.6) and soft reduction configuration*

flame finally gradually accelerates behind the shock and the final recorded flame velocity is about 400m/s (stage 5).

During the passage through the convergent, the flame velocity increases from 80 m/s to more than 300 m/s (Fig. 7.b) meaning about 200 m/s increase which seems in line with the amplitude of P_3 (about 1 bar). After this acceleration, the flame velocity drops to 250 m/s before accelerating again gradually. This deceleration marks the end of the adaptation of the flow and the flame to the second part of the pipe with a smaller cross section. Note that the flame velocity in this second part is similar (about 1 bar). After this acceleration, the flame velocity drops to 250 m/s before accelerating again gradually. This deceleration marks the end of the adaptation of the flow and the flame to the second part of the pipe with a smaller cross section. Note that the flame velocity in this second part is similar to that in the 150 mm straight pipe at the same distance from the ignition point. P_3 is detected later on P_22m as P_4. On the transducers upstream P_3 is visible (P_4') but strongly attenuated due to the change in the cross section. Note a sort of pressure plateau is visible on P_22m starting at P_5, about 0.27 s from the ignition. On Figure 7.b, it can be observed that the flame velocity seems to reach also a plateau at about 400 m/s from time 0.27s to 0.28 s. The pressure level is in line with this velocity.

The Table 1 summarizes the different features of the tests performed with sharp and soft convergent. First of all, the missing pressure value P_3 in methane-air test in soft convergent might be due to the slowness of the flame. The ratio of output over entry velocities are contained in the interval of 2.5

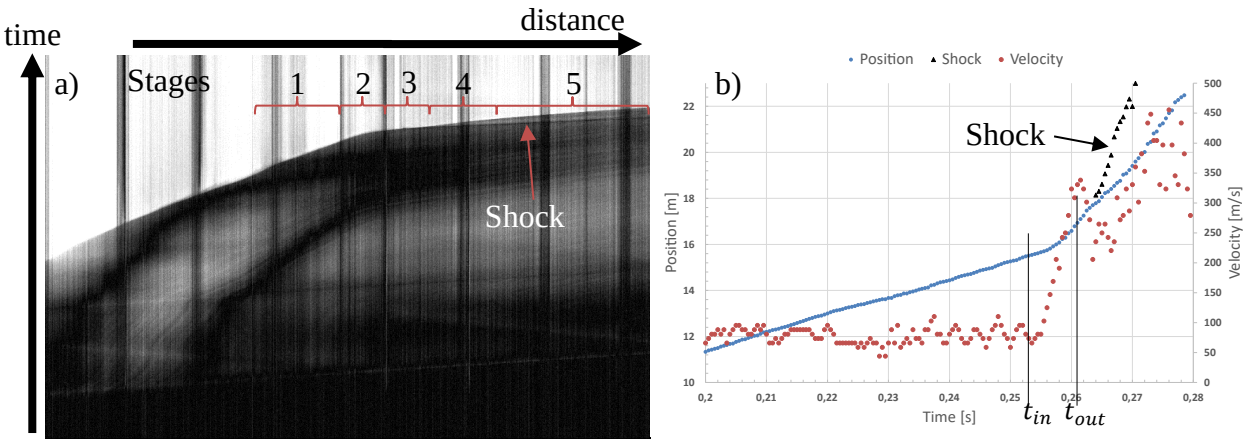

Fig. 7. *Test 3: Lean hydrogen-air (EQR=0.6) and 250mm to 150mm diameter soft reduction configuration. a) Time-distance diagram of the flame. b) Position and velocity versus time*

and 5.5 for all tests, and do not seem to be affected by the fuel or by the angle of convergence. This independency of convergence angle supports the observations made by Song et al. (2021) with angles from 15 to 90°. Considering the surface ratio of 250mm over 150mm diameter equal to 2.8, the slow flames (all methane cases and the hydrogen case 4) have velocities ratio which let suggest a simple flow described with Bernoulli's equation ($\frac{u_2}{u_1} = \frac{A_1}{A_2}$).

On the other side, the three hydrogen tests 3, 7, and 8 with high entry velocity gave rise to shock emergence at the reduction exit, and leads to higher velocities ratio of the order of 4-5.5 between the entry and the exit of the contraction.

The images taken from the previously analysed hydrogen-air test 3 in soft configuration are presented in Figure 8. The flame surface seems to follow the flow, and is sucked ahead, as observed in vented experiments in large volume (Duclos, 2019).

Table 1. *Characteristics related to the flame passing through the reduction for all tests*

Test	Fuel	Reduction	P_1 (mbar)	V_1 (m/s)	t_{in} (s)	t_{out} (s)	P_3 (mbar)	V_2 (m/s	V_2/V_1
1	CH4	Soft	78	21	0,775	0,805	-	54	2.57
2	CH4	Soft	92	39	0,650	0,670	224	126	3,23
3	H2	Soft	270	81	0,253	0,261	940	328	4,04
4	H2	Soft	210	23	0,290	0,312	660	71	3,13
5	CH4	Sharp	109	44	0,582	0,585	416	136	3,09
6	CH4	Sharp	111	43	0,571	0,576	303	133	3,09
7	H2	Sharp	220	72	0,280	0,282	897	310	4,31
8	H2	Sharp	230	71	0,265	0,267	1130	392	5,44

The computations of steady flow in 2D cylindrical coordinates geometry performed by Satish et al. (2013) and Nosrathi et al. (2017) show the iso-pressure and iso-velocity profiles in the pipe contraction as represented on Figure 9. In the present tests, pressure levels upstream and downstream the reduction are quite stabilized before the flame passing (see Figure 6.). The assumption of steady flow is suited for the present situation. Thus, keeping in mind these profiles, one may understand that the flame tip is accelerated earlier compared to wall region. This radial gradient of velocity results in a flame surface extension that may recall the flame stretch often used in laminar flame velocities measurements (Gu et al., 2000 ; Goulier et al., 2017), defined as $\alpha = \frac{1}{A}\frac{dA}{dt}$, where A is the flame surface. This flame stretch promotes the flame acceleration of lean hydrogen-air and stoichiometric methane-air.

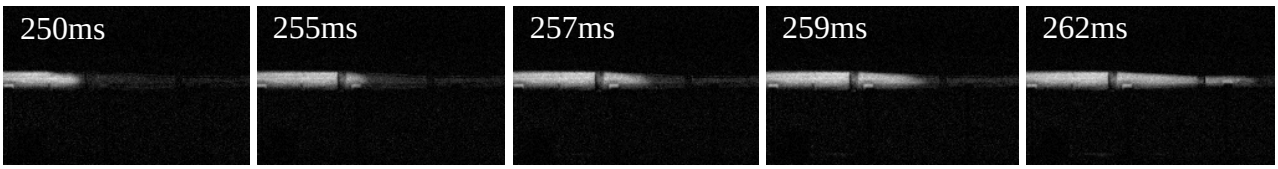

Fig. 8. *Extraction of flame propagation. Test 3: hydrogen-air (EQR=0.6) in soft convergent*

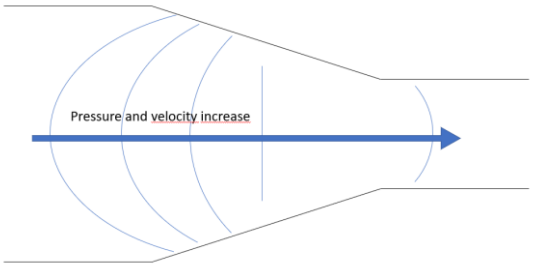

Fig. 9. *Characteristic iso-pressure and iso-velocity profiles in a contraction at steady state*

The above-mentioned mechanism of flame acceleration must not be opposed to the tulip shape occurrence in the contraction due to the baroclinic effect identified by Song et al. (2021). Indeed, in he's configuration, the flame reaches the contraction located at 3m from ignition at 4ms, and the flow is not well established, while the distance and long time implied here enable the flow to settle across the convergent.

3. Conclusion

The topic of ignition of flammable cloud and the resulting flame propagation in pipelines is of great importance for the safety assessment coming with the hydrogen use in gas industries. The present study focused on the effect of a pipe diameter reduction on the propagation of a well developed flame. This was assessed experimentally with two hydrogen-air and methane-air mixtures, and two convergence angles of 3 and 9°. These large scales experiments were compared to the straight pipe configuration that is commonly studied in the literature.

It appears that the pipe reduction increases the flame velocity when it passes through with a gradual acceleration. The output over entry velocities ratio is about 3 for slow flames (especially methane) to 4-5.5 for faster flames, and this flow acceleration generate a pressure peak at the contraction exit. The track of flow convergence on the flame stretch is mentioned as a potential explanation of the flame acceleration, and should be further looked into. This could be achieved with a CFD simulation. Neither the effect of the convergence angle, nor the fuel composition were noted on the flame response to this single element, but these parameters should be further examined. Contraction with angle about 15 and 25° would be of interest to get closer from the industrial geometries.

Acknowledgment

The authors would like to thank the INERIS laboratory for sharing the experimental results presented here, taken from the EXPRO research program.

This work was carried out as part of a PhD thesis, undertaken with CIFRE convention and supported by General Electric Vernova, GRTGaz, McPhy, INERIS and Université de Technologie de Compiègne.

Financé par GOUVERNEMENT Liberté Égalité Fraternité FRANCE RELANCE Financé par l'Union européenne NextGenerationEU

References

Blanchard, R., Arndt, D., Grätz, R., Poli, M., & Scheider, S. (2010). Explosions in closed pipes containing baffles and 90 degree bends. *Journal of Loss Prevention in the Process Industries*, 23(2), 253-259.

Ciccarelli, G., & Dorofeev, S. (2008). Flame acceleration and transition to detonation in ducts. *Progress in energy and combustion science*, *34*(4), 499-550.

Clanet, C., & Searby, G. (1996). On the "tulip flame" phenomenon. *Combustion and flame*, 105(1-2), 225-238.

Daubech, J., Leprette, E., Proust, C., & Lecocq, G. (2019). Further insight into the gas flame acceleration mechanisms in pipes. Part I: experimental work. *Journal of Loss Prevention in the Process Industries*, *62*, 103930.

Dorofeev, S. B. (2011). Flame acceleration and explosion safety applications. *Proceedings of the Combustion Institute*, 33(2), 2161-2175.

Duclos, A. (2019). Development of phenomenological and risk assessment models of explosion for the emerging hydrogen-energy industry (Doctoral dissertation, Compiègne).

Guenoche, H., & Markstein, G. H. (1964). Nonsteady flame propagation. Pergamon Press, New York, 107.

Goulier, J., Comandini, A., Halter, F., & Chaumeix, N. (2017). Experimental study on turbulent expanding flames of lean hydrogen/air mixtures. *Proceedings of the Combustion Institute*, 36(2), 2823-2832.

Gu, X. J., Haq, M. Z., Lawes, M., & Woolley, R. (2000). Laminar burning velocity and Markstein lengths of methane–air mixtures. *Combustion and flame*, 121(1-2), 41-58.

Hongru, Y. (1999). Oxyhydrogen combustion and detonation driven shock tube. *Acta Mechanica Sinica*, 15(2), 97-107.

Kerampran, S. (2000). Etude des mécanismes d'accélération des flammes se propageant depuis l'extrémité fermée vers l'extrémité ouverte de tubes horizontaux de longueur variable (Doctoral dissertation, Poitiers).

Nosrati, K., Tahershamsi, A., & Taheri, S. H. S. (2017). Numerical analysis of energy loss coefficient in pipe contraction using ansys cfx software. *Civil Engineering Journal*, 3(4), 288-300.

Satish, G., Kumar, K. A., Prasad, V. V., & Pasha, S. M. (2013). Comparison of flow analysis of a sudden and gradual change of pipe diameter using fluent software. *IJRET*, 2, 41-5.

Song, Y., Zhang, Y., Chen, Y., Liu, X., Fu, M., & Li, Y. (2021). Numerical investigation of effects on premixed hydrogen/air flame propagation in pipes with different contraction or expansion angles. *Journal of Loss Prevention in the Process Industries*, 70, 104201.

Thomas, G., Oakley, G., & Bambrey, R. (2010). An experimental study of flame acceleration and deflagration to detonation transition in representative process piping. *Process Safety and Environmental Protection*, 88(2), 75-90.

Wang, J., Wu, Y., Zheng, L., Yu, M., Pan, R., & Shan, W. (2020). Study on the propagation characteristics of hydrogen/methane/air premixed flames in variable cross-section ducts. *Process Safety and Environmental Protection*, 135, 135-143.

Wang, J., Fan, Z., Wu, Y., Zheng, L., Pan, R., & Wang, Y. (2021). Effect of abrupt changes in the cross-sectional area of a pipe on flame propagation characteristics of CH4/air mixtures. *ACS omega*, 6(23), 15126-15135.

Zhu, C. J., Gao, Z. S., Lu, X. M., Lin, B. Q., Guo, C., & Sun, Y. M. (2017). Experimental study on the effect of bifurcations on the flame speed of premixed methane/air explosions in ducts. *Journal of Loss Prevention in the Process Industries*, 49, 545-550.

Influence of Flame Instabilities and Hydrodynamic Coupling on Flame Acceleration in Methane-Hydrogen Fuel Blends

Kevin Cheevers[a], Hongxia Yang[a], Samira Kia[a], C. Regis L. Bauwens[b] & Matei Radulescu[a]

[a] University of Ottawa, Ottawa, Canada
[b] FM Global, Norwood, United States of America

E-mail: *Kevin.Cheevers@uottawa.ca*

Abstract

Hydrogen – natural gas blends are of interest due to their potential for decreasing the carbon footprint of pure natural gas. Nevertheless, the main constituents of natural gas, hydrogen and methane, have very different flame properties. The present study addresses the potential of flame acceleration in different stoichiometric blends of methane and hydrogen in atmospheric pressure experiments conducted in a shock tube in which a single bluff body obstacle is placed. The measured evolution of the flame speed and the pressure evolution along the walls highlights the higher reactivity of hydrogen-air flames when compared with flames propagating in methane-air or equimolar hydrogen-methane-air fuel blends. Following the normalization of the measured flame speed, vortex diameter, and overpressure, a unified description of the flame acceleration is presented, with differences between mixtures being attributed to the different response of the flame to the hydrodynamic coupling and flow-flame instabilities. Hydrogen, with its characteristic thin flame structure, is less affected by the turbulent features formed downstream from obstacles than mixtures containing methane, which exhibit much larger increases in flame surface area due to their longer flame times. However, a stoichiometric equimolar blend of hydrogen and methane exhibits larger flame surface area enhancement than predicted by experiments conducted in either constituent fuel, which is attributed to the combined effects of a larger turbulence intensity present in the flame-driven flow when compared to hydrogen-air flames and a sufficiently short flame time which reduces the amount of localized quenching induced by turbulence when compared with methane-air flames.

Keywords: flame instabilities, transport phenomena, natural gas, hydrogen, quenching

Introduction

The recent introduction of fuel blends of hydrogen and natural gas into the energy sector in an effort to decrease its carbon footprint has opened up new questions about the behaviour of these blends following an accidental ignition. In the process industries, the propensity of flame acceleration remains the main concern, which is augmented in the presence of congestion within the flow field. Whereas methane, the prime constituent of natural gas, is a fairly unreactive fuel as characterized by its low burning velocity and long flame time, hydrogen is much more reactive. The flame acceleration of pure fuels has previously been characterized by many studies (Ciccarelli and Dorofeev, 2008), however the behaviour of fuel blends remains unclear.

The dynamics of flame propagation are intricately linked to the dynamics of the flow field through a strong coupling between increases in the flame surface area, increases in the rate of consumption of fresh gases, and the strength of the flow induced by the volumetric expansion of gases across the flame (Lee and Moen, 1980). This is further complicated by the presence of obstacles in the flow field, which can generate turbulence as a result of the high Reynolds number typically associated with these flows. The flame surface is deformed from the interaction between flow dynamics and the flame surface, such as Darrieus-Landau instabilities associated with the gas expansion across the flame, Rayleigh-Taylor instabilities resulting from the misalignment of the flow pressure gradient and the density gradient across the flame, Kelvin-Helmholtz instabilities resulting from velocity shear

across slip-lines separating fluids with different densities, the entrainment of the flame surface through turbulent flow fields such as turbulent boundary layers and turbulence found downstream from bluff body obstacles. These dynamic phenomena each have an associated timescale which can be used to describe their interaction with the flame: those whose timescale is much longer than the flame time will be unable to meaningfully change the flame surface, whereas those whose timescales are comparable to or smaller than the flame time will affect the structure and properties of the flame.

The present study addresses the potential of flame acceleration in methane-hydrogen fuel blends. We study this experimentally using a thin rectangular cross-sectioned shock tube in which a cellular flame is ignited near a closed end using a long wire ignition technique. A single rectangular obstacle is placed ahead of the flame, and the far end of the tube is opened to the ambient environment such that the flame propagation is not restricted by a closed wall. The evolution of the flame as it passes over the obstacle is visualized using both schlieren photography to capture the details of the flow field and shadowgraphy to visualize the flame propagation over longer distances. The coupling between the flame-induced flow and the flame surface is quantified through measurements of experimental photographs and of the pressure evolution measured along the top and bottom walls of the shock tube at fixed intervals. A dimensional analysis is done to identify the scales of interest which allows the reduction of the measured flame dynamics to be unified under common flame acceleration and pressure evolution curves. Differences between mixtures are associated with the response of the flame to the hydrodynamic coupling.

1. Experimental method

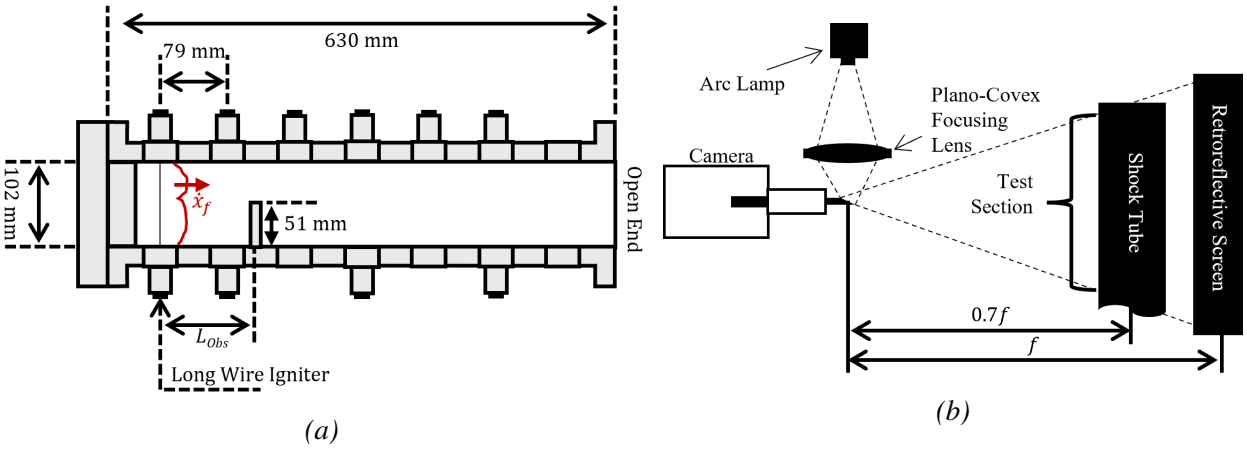

***Fig. 1**. Diagrams of the experimental setup. a) Shock tube configuration. The width of the shock tube is 19 mm. b) Implementation of the Shadowgraph using a retroreflective screen.*

***Table 1**. Mixture composition and flame properties ($P_{atm} = 101.2$ kPa, $T = 295$ K)*

Property	**$2H_2 + O_2 + 3.76N_2$**	**$CH_4 + H_2 + 2.5O_2 + 9.4N_2$**	**$CH_4 + 2O_2 + 7.52N_2$**
Expansion ratio $\sigma = \frac{\rho_u}{\rho_b}$	6.93	7.44	7.61
Laminar flame speed S_L [m/s]	2.21	0.55	0.34
Flame thickness δ_l [mm]	0.34	0.36	0.48
Flame time δ_l / S_L [ms]	0.146	0.686	1.44
Unburnt gas density [kg/m^3]	0.86	1.07	1.14

The experiments were conducted using a thin 19 mm shock tube with a height of 102 mm and a length of 630 mm, as illustrated in Figure 1 a). A tungsten wire igniter was installed near the closed end of the shock tube, and a rectangular obstacle measuring 50.8 mm $\times$ 9.5 mm $\times$ 19 mm was placed at a distance of $L_{obs} = 159$ mm from the ignition wire. The gas was prepared using the method of

partial pressures, after vacuuming a mixing tank to a pressure of 40 Pa. Prior to each experiment, an aluminium plate was placed on the open end of the shock tube to allow the evacuation of the contents to a pressure of no more than 425 Pa prior to being filled to atmospheric pressure with a pre-mixed reactive mixture, whose properties are detailed in Table 1. The flame properties were calculated using free flame calculations implemented in Cantera (Goodwin et al., 2017), using the San Diego detailed reaction mechanism (Williams, 2014). Once filled, the solid aluminium plate initially installed for the vacuuming and filling processes on the end of the shock tube opposite from the ignition wire is removed to open the tube to the ambient environment. The flame is subsequently ignited. The evolution of the flow field was visualized using shadowgraphy and z-type schlieren. Shadowgraphy allows a field of view encompassing the entire shock tube, and is implemented using a retroreflective screen as illustrated in Figure 1 b). Schlieren photography is more sensitive to density fluctuations, but has a field of view which is limited by the 315 mm diameter of the parabolic mirrors used. A 1000 W Arc Lamp was used to produce the light in both visualization methods, and a Phantom v1210 high speed camera recorded the experiments. The frame rate at which the camera recorded the experiments ranged between 21000 fps to 42000 fps, and was inversely proportional to the spatial resolution of the images taken.

2. Results and discussion

Select frames summarizing the evolution of the flames as they propagate through the channel can be seen in Figure 2. A cellular flame is ignited by the tungsten wire installed near the end of the channel. Following the ignition of the flame, it propagates away from the closed end of the tube while also driving a flow ahead of itself due to the volumetric expansion of gases as a result of the combustion process. This flow is accelerated in the vicinity of the obstacle to reach a maximum speed at the vena contracta, before decelerating after the obstacle due to the enlarging cross-section. This velocity gradient of the flow as it passes through the varying cross-section is accompanied by a pressure gradient. As the flame approaches the obstacle, it accelerates with the background flow but is also deformed through the Rayleigh-Taylor mechanism stemming from the misalignment of the pressure gradient in the flow and the density gradient across the flame. This results in cells with larger amplitudes near the top of the channel than near the bottom as the flame passes over the obstacle. Similarly, once past the obstacle, the flame is subjected to a pressure gradient in the opposite direction resulting from the deceleration of the flow and deforms further through the same mechanism all while decelerating due to the diverging flow. Shortly thereafter, the flame is entrained by an irrotational vortex which is the result of the flow driven over the obstacle since the ignition of the flame. The growth of this vortex can clearly be seen in Figure 2 a) due to the higher flow speed of the gases across the obstacle, although a similar vortex is clearly present behind the obstacle in each mixture as the flame is entrained by this feature in every case. As a result of this flame entrainment, the flame surface area grows drastically, increasing the consumption rate of the fresh gases, which in turn forces a stronger flow towards the open end of the tube. As the flame exits the shock tube, it is entrained into a toroidal vortex formed by the abrupt change area, again increasing the burning rate of the flame.

Figure 3 shows the growth of the vortex for both the hydrogen and the equimolar blend, recorded using schlieren photography to better capture the small density gradients present in the fresh gases. The limiting streamline upstream of the obstacle is clearly visible in the hydrogen-air experiment, in addition to the growth of the vortex and the formation of Kelvin-Helmholtz instabilities along the vortex's uppermost shear layer as the vortex interacts with the flame. As the flame speed is reduced, the density gradients in the fresh gases decrease, resulting in these features becoming progressively less clear. As such, only the vortex remains visible in Figure 3 b). As the flame speed is further decreased in the methane-air mixture, the vortex was not clearly visible in the schlieren images and thus was not included.

Figure 4 shows the evolution of the flame tip velocity as a function of time, measured as the forward-most flame surface location along the horizontal axis in the experimental photographs. Each curve has been adjusted in time such that the flame tip crosses the leading edge of the obstacle at a time of t=0 s. One can see that the hydrogen flame propagates much faster than the methane flame, whereas

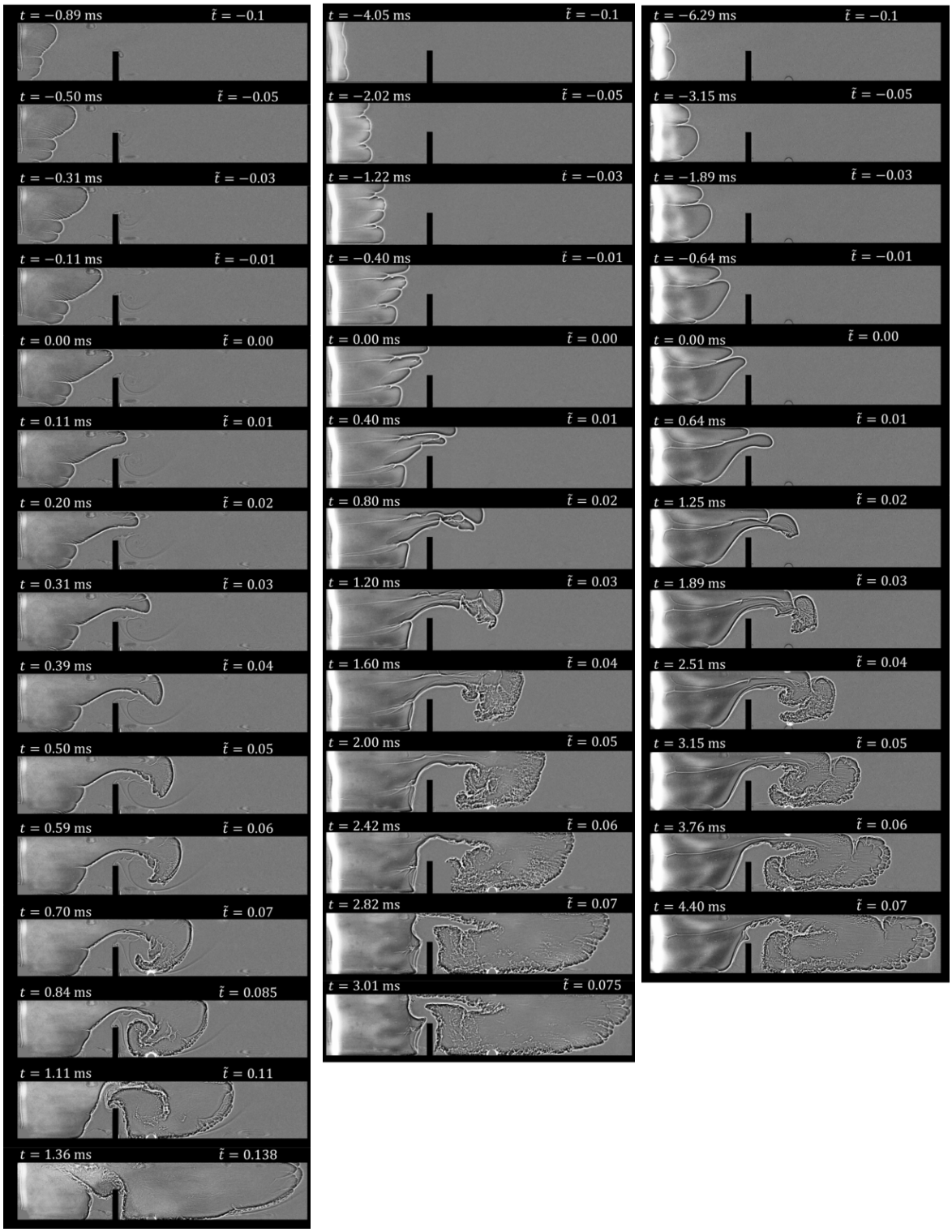

(a) H_2-Air *(b) Equimolar CH_4-H_2-Air* *(c) CH_4-Air*

***Fig. 2**. Evolution of the flame, visualized using shadowgraphy. Times are shown above each frame.*

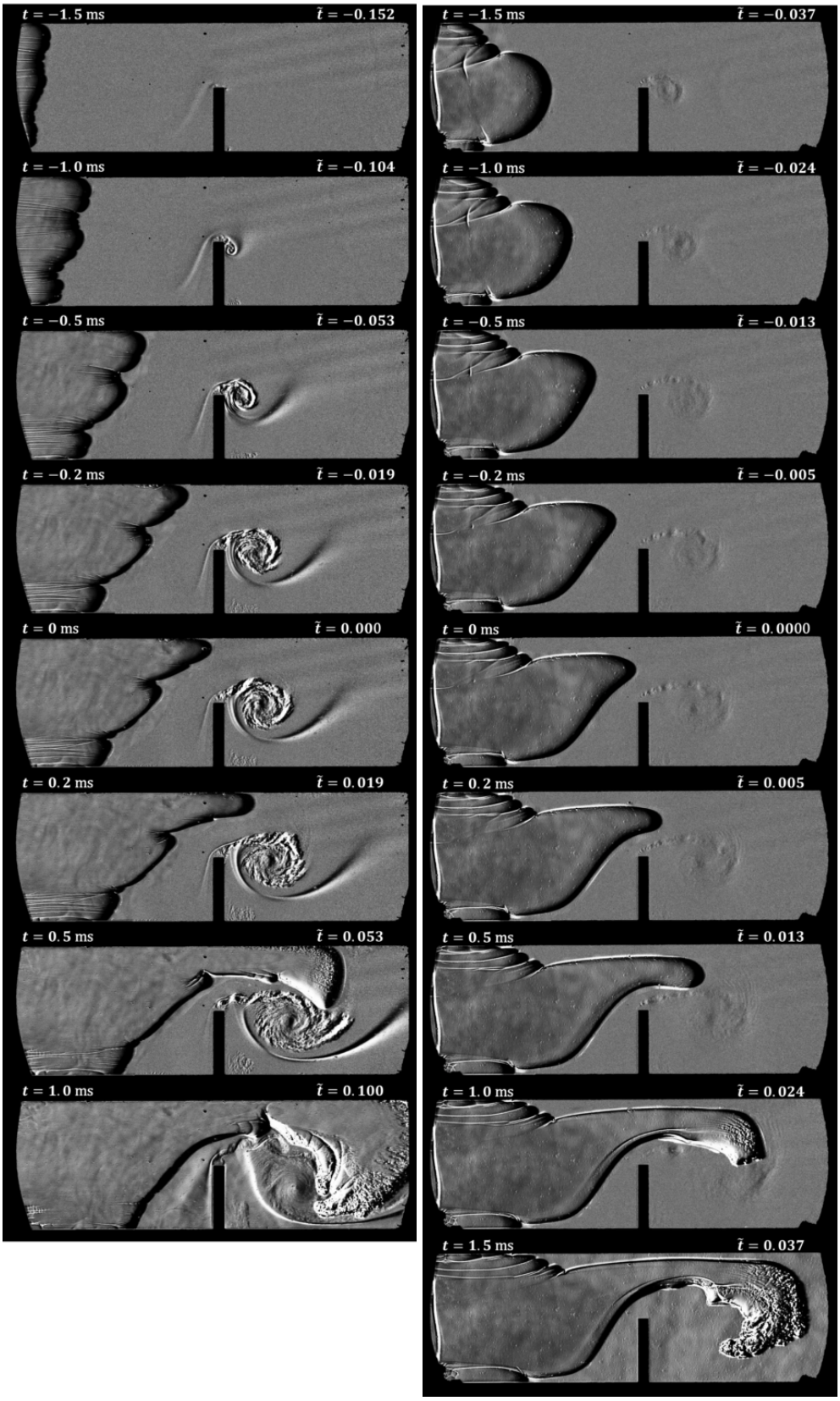

(a) H_2-Air *(b) Equimolar CH_4-H_2-Air*

***Fig. 3**. Evolution of the flame, visualized using Schlieren. The contrasts of the flame and the vortex are enhanced separately to better show the evolution of the vortex. Times are shown above each frame.*

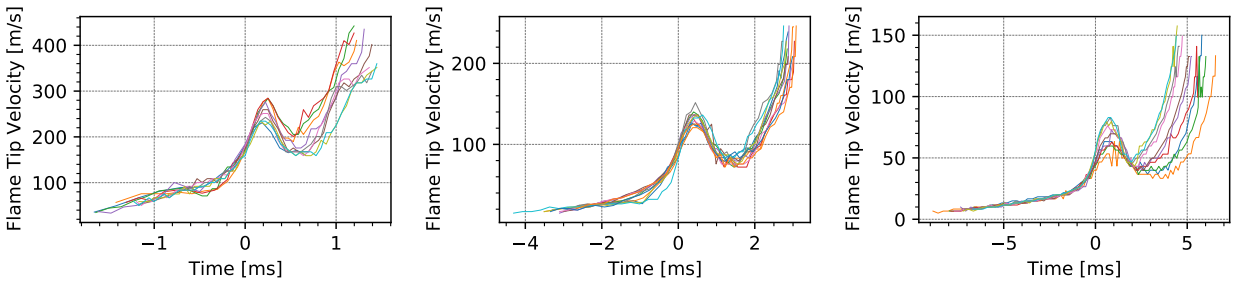

(a) H_2-Air *(b) Equimolar CH_4-H_2-Air* *(c) CH_4-Air*

***Fig. 4**. Evolution of the flame tip velocity in time, for experiments in each mixture. Time $t = 0$ is taken as the time at which the flame tip passes over the leading edge of the obstacle.*

the flame in the equimolar blend propagates at a speed in-between the two extremes throughout the experiment. Similarly, the duration of the experiment is inversely proportional to the propagation speed of the flame. The flame tip velocity evolves in a similar manner in each mixture, with the initial gradual increase in velocity for negative times associated with the initial growth of cellular structures along the flame surface from a relatively flat ignition kernel. Shortly before a time of zero, a much sharper increase in the flame tip velocity is the result of the acceleration of the flame with the background flow along with the deformation of the flame in the vicinity of the obstacle from the Rayleigh-Taylor mechanism. This deformation is caused by the negative pressure gradient in the flow resulting from the acceleration of the flow through the vena contracta, and the misalignment of this pressure gradient and the density gradient across the flame surface. After having passed the vena contracta, the flow speed decreases due to the deceleration of the flow resulting from the sudden enlargement in the cross-sectional area. This decrease in flow speed is accompanied with by a positive pressure gradient, further deforming the flame through the Rayleigh-Taylor mechanism. This decrease in flame speed continues until a minima is reached, at which point the reactive coupling between the increase in flame surface area resulting from the vortex entrainment and the flow speed induced ahead of the flame by the rapid expansion of the burnt gases results in a strong acceleration of the flow which continues until the flame exits the field of view.

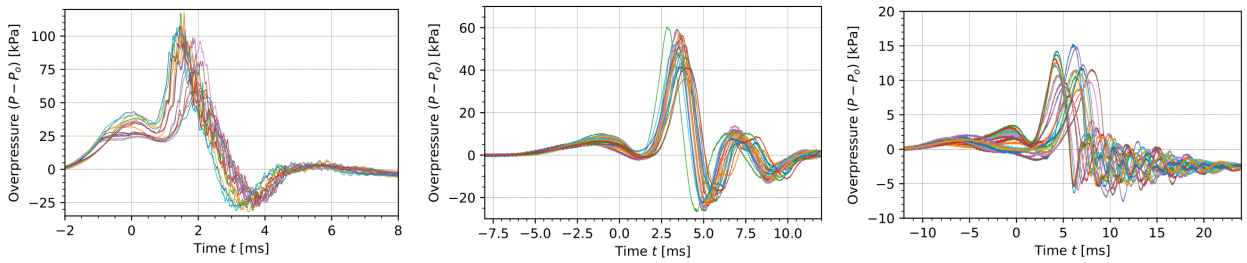

(a) H_2-Air *(b) Equimolar CH_4-H_2-Air* *(c) CH_4-Air*

***Fig. 5**. Evolution of the pressure as a function of time, for experiments in each mixture, measured near the ignition plane. Time $t = 0$ is taken as the time at which the flame tip passes over the leading edge of the obstacle.*

This evolution of the flame surface is also apparent when considering the pressure evolution measured near the ignition plane, plotted against time in Figure 5. Again, distinct pressure peaks are associated with the flame surface area growth which are apparent in the velocity plots. As for the flame tip velocity, the hydrogen flame builds up the highest overpressure whereas the methane flame builds up the weakest overpressure, and the equimolar blend reaches a peak overpressure in-between the two extremes. The duration of the pressure event is much shorter in hydrogen than in methane, with the blend evolving over an intermediate timescale. Following the maximum pressure peak resulting from the vortex entrainment downstream from the obstacle, a smaller pressure peak located around 5 ms

- 8 ms is associated with the sudden combustion of the gases exiting the shock tube when the flame is entrained by the toroidal vortex. This results in the re-compression of the product gases as flow re-enters the shock tube due to the sudden pressure increase at the exit. This peak is much more pronounced in the blend than the other two mixtures. The low scatter in the measurements of velocity and pressure is representative of the repeatability of the experiments.

2.1. Experimental Scaling

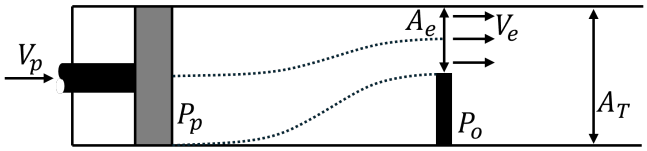

Fig. 6*. Sketch of a problem in which a piston propagating at a speed V_p drives a flow over an obstacle. The piston is a representation of the volumetric expansion of burnt gases across a flame which drives a flow ahead of the flame.*

To better compare the propagating flames, the measurements of pressure and velocity taken from experiments can be expressed non-dimensionally to remove the dependence on each mixture's chemistry. These differences are exemplified by the vastly different flame times and burning velocities included in Table 1, which vary by an order of magnitude. Normalizing for these differences will allow a better comparison effect of the flow and flame instabilities on its surface area, which are an indication of the flame's capacity to get enhanced

One can model the flow dynamics upstream of the flame as a problem in which a piston propagates at a velocity V_p into the unburnt gas, as illustrated in Figure 6. The conservation of mass applied between the piston face and the exit plane gives

$$\rho_p A_T V_p = \rho_e A_e V_e, \tag{1}$$

in which A_T is the cross-sectional area of the tube, A_e the cross-sectional area of the exit, ρ the density, and V the flow speed at the piston face denoted by subscript p and at the exit plane denoted by subscript e. From laminar flame theory, the velocity of the piston is that of the flow driven ahead of the flame, be it $V_p = (\sigma - 1)S_L$, in which $\sigma = \rho_u/\rho_b$ is the expansion ratio across the flame, and S_L the laminar flame speed. As such, the velocity of the flow at the exit in the incompressible limit is

$$V_e = \frac{A_T}{A_e} V_p = \frac{A_T}{A_e}(\sigma - 1)S_L. \tag{2}$$

An appropriate dynamic time representative of the phenomena is the time taken for a laminar flame to propagate the distance separating the ignition plane from the obstacle,

$$t_{dyn} = \frac{L_{obs}}{\sigma S_L}, \tag{3}$$

in which

$$S_F = \sigma S_L \tag{4}$$

is the flame propagation speed in a lab frame of reference of a planar laminar flame whose surface area is equal to the cross-sectional area of the shock tube. The pressure evolution along a streamline connecting the piston face and the exit plane can be given by Bernoulli's equation,

$$P_p + \frac{1}{2}\rho_p V_p^2 = P_e + \frac{1}{2}\rho_e V_e^2, \tag{5}$$

in which the pressure at the piston face and exit plane are P_p and P_e. In the limit of incompressible

flow, the pressure scales as

$$P_p - P_o = \frac{1}{2}\rho_o \left[\left(\frac{A_T}{A_e} \right)^2 - 1 \right] V_p^2 = \frac{1}{2}\rho_o \left[\left(\frac{A_T}{A_e} \right)^2 - 1 \right] (\sigma - 1)^2 S_L^2. \tag{6}$$

Figure 7 shows the flame tip velocity non-dimensionalized by the laminar flame propagation velocity (4) against a time non-dimensionalized by the dynamic time (3). It is worth noting that time $t/t_{dyn} = 0$ remains the time at which the flame tip crosses the leading edge of the obstacle. The early growth of the flame is seen to be well-recovered by this non-dimensionalization of the flame tip velocity due to the limited surface area of the flame prior to its interaction with the obstacle. An interesting property which becomes evident when correcting for the different laminar flame speeds is the additional wrinkling seen in methane-air and equimolar blend flames when compared to hydrogen flames in the vicinity of the obstacle induced by the Rayleigh-Taylor instability and following the flame's entrainment by the vortex at later times. This larger flame surface area is evident in Figure 2 when comparing flames at similar non-dimensional times. The flame velocities measured in the equimolar blend are comparable with the higher end of the methane-air experiments rather than lying in-between the two extreme mixtures.

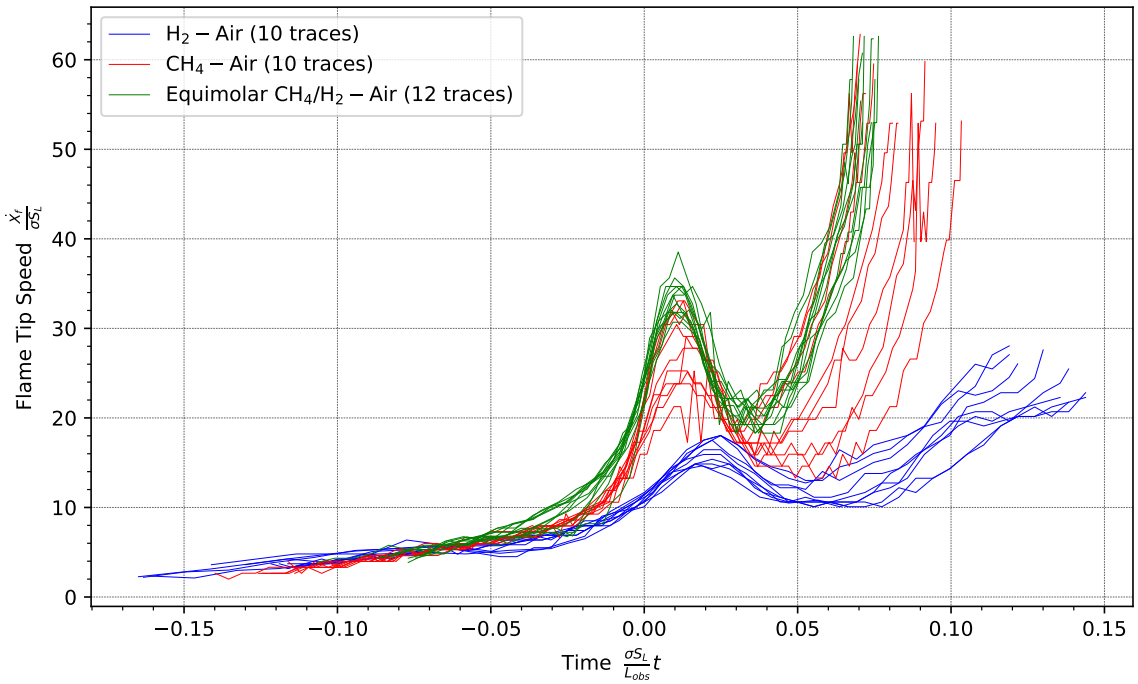

Fig. 7. *Scaled flame tip velocity as a function of time*

An important feature in these experiments is the formation and growth of the vortex, which is the main source of turbulence in the experiment, and governs the flame amplification following the obstacle. Unintuitively, the size of the vortex at the time of the passage of the flame is similar for each mixture, which can be deduced by comparing the vortices as the flame passes over the obstacle in Figure 3 or the size of the feature entraining the flame in Figure 2. This is also clearly recovered when measuring the vortex from the experimental photographs, as plotted in Figure 8, which shows the width of the vortex D_v normalized by (2) and (3),

$$\tilde{D_v} = D_v \frac{1}{\frac{A_t}{A_e}(\sigma - 1) S_L} \frac{\sigma S_L}{L_{obs}} = \frac{A_e}{A_t} \frac{D_v}{L_{obs}} \frac{\sigma}{\sigma - 1}, \tag{7}$$

against the dynamic time. One sees from this choice of non-dimensional parameters that the growth rate of the vortex is proportional to the laminar flame speed, appearing in the normalization of the

dynamic time rather than the vortex diameter. However, the amount of time the vortex is allowed to grow prior to its interaction with the flame is dictated by the time taken by the flame to reach the obstacle, be it the dynamic time, which is inversely proportional to the burning velocity. This results in a vortex which grows faster in the hydrogen-air mixture albeit for proportionally shorter times, and at a slower rate in the other mixtures over proportionally longer times. The result is a vortex that entrains the flame which is of a similar size regardless of the flame properties for a given obstacle distance. This is evident in Figure 8, as the y-axis intercepts at $t = 0$ all lie within a similar range. The larger scatter of the methane flame is a result of the decreased clarity of the vortex in the Schlieren photographs.

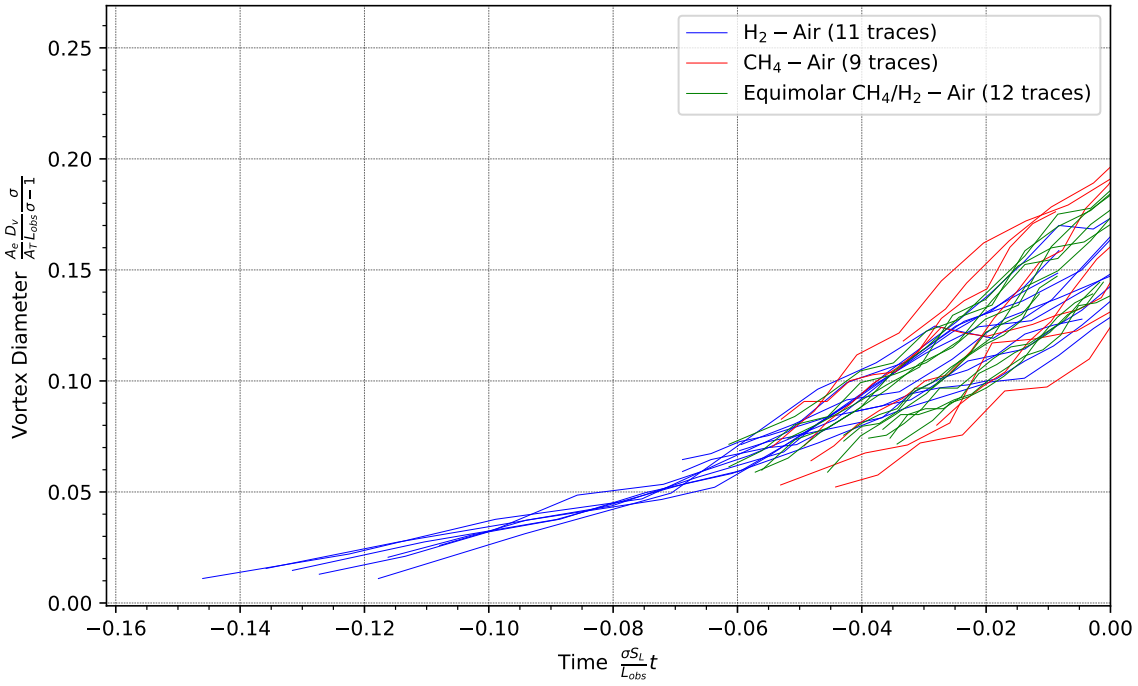

***Fig. 8**. Scaled vortex width as a function of time*

Similarly, one can normalize the pressure evolution using the relation in (6), as shown in Figure 9. When scaled in this manner, one can deduce that the higher pressures seen in hydrogen-air flames, typified by those shown in Figure 5 a), are a result of its significantly faster burning velocity when compared to slower methane flames. However, the normalized pressure of these methane-air flames end up being much higher than those of hydrogen-air flames as a result of their more effective flame wrinkling, which was also apparent when normalizing the flame propagation velocity in Figure 7. Intriguingly, the maximum normalized pressure in the equimolar blend flame does not lie between the pressures of the two extreme mixtures, but is amplified to nearly twice the amplitude of the maximum pressure in the methane-air mixture. This is indicative of a more effective amplification of the flame surface area in the fuel blend than the flame amplification process in either constituent mixture.

2.2. Flame surface area amplification in hydrogen-air mixtures

When scaling the flame propagation velocity and pressures, the smaller flame surface area enhancement of hydrogen flame when compared to the methane and equimolar hydrogen-methane flames becomes apparent. Hydrogen-air, whose flame time is much smaller than the other mixtures as seen in Table 1, is able to consume flame folds more rapidly. This leads to lower surface areas because smaller folds are consumed quicker than they can be produced. The increase in surface area is thus mainly due to the deformation of the larger scales of the flame surface. In the other mixtures, an efficient folding of flame surface at small scales also contributes to their larger surface areas, as the consumption of these folds is unable to keep pace with their growth. This is visible in figure 2 when

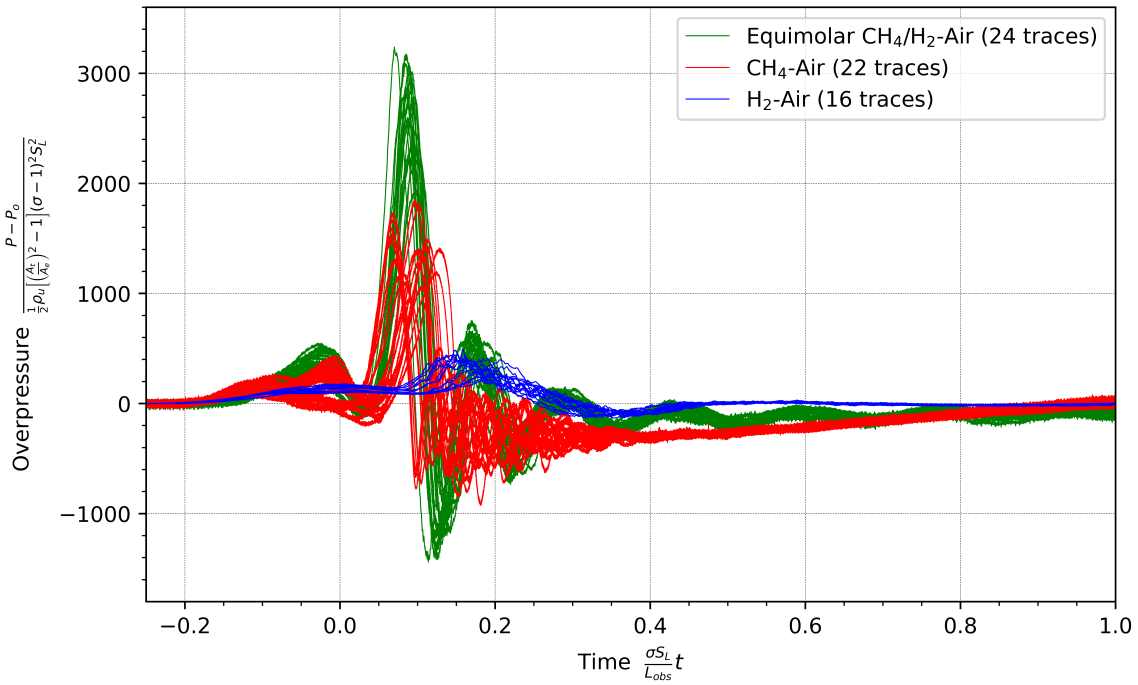

Fig. 9*. Scaled Pressure as a function of time, taken near the ignition plane*

considering differences in surface areas between the three flames at a given scaled time. Alternatively, one can compare the last frames of each image sequence to recognize that by the time it reaches the end of the field of view, the hydrogen flame has more effectively consumed the smaller features on the flames surface. However, the hydrogen flame retains the same macroscopic shape of the flame front which is shared amongst all three mixtures, simply lacking the smaller scale corrugation of the flame front seen in the other two mixtures. This results in both the slower acceleration of the flame and the lower pressures generated once normalizing the differences in flame chemistry.

An explanation for this smaller surface area is evident by comparing the flame time with the flame-generated flow time. Taking the flame Damköhler number as

$$Da = \frac{t_v}{t_f} = \frac{\frac{H_{obs}}{V_e}}{\frac{L_f}{S_L}}, \tag{8}$$

in which t_f is the flame time and t_v is the flow time taken for a vortex whose outer diameter is the size of the obstacle height H_{obs} and rotates with a tangential speed equal to the flow speed passing through the vena contracta, V_e. A representative measure of V_e is obtained by measuring the peak flame tip velocity from Figure 4. The speed calculated using (2) considers a laminar flame, which does account for the significant deformation through flame wrinkling during the initial propagation stage and the Rayleigh-Taylor mechanism leading up to the obstacle. The Damköhler number of the hydrogen flame is greater than unity whereas the other mixtures have sub-unity Damköhler numbers. In the context of turbulent combustion, this would result in different combustion regimes, and would in turn lead to smaller increases of $S_T/S_L \propto A_T/A_L$ in the hydrogen flame than the other two flames.

2.3. Flame surface amplification in the equimolar blend flame

Although the limitation of surface area growth resulting from the rapid consumption of small-scale flame folds can reasonably explain the differences between the flame propagation in the hydrogen-air mixture and the other two mixtures, this timescale argument is unable to explain the greater pressures and speeds measured in the equimolar blend-air experiments when compared to the methane-air experiments. Removing the dependence of the measured pressures on the flame chemistry, as done in

Figure 9, the equimolar flame is still shown to generate greater surface areas than the methane flame. The Damköhler number of the methane-air flame and the equimolar blend are comparable, as is the intensity of the turbulence in the flow driven by the flame measured at the integral scale.

A simple explanation for the smaller surface area of the methane-air flame relative to the equimolar blend-air flame can be inferred from previous works studying the response of methane-air and hydrogen-air flames to turbulence. When exposed to a turbulent field, the burning velocity of methane-air flames is shown to increase with increasing turbulence intensities until a maximum is reached, following which the burning velocity decreases with a further increase of the turbulence intensity (Shy et al., 2000). In contrast, hydrogen-air flames do not manifest this inflection of the burning velocity increase. Rather, the burning velocity monotonically increases over a similar range of turbulence intensities (Kitagawa et al., 2008). This is also seen in the relationship between the burning velocity and turbulence intensity in Abdel-Gayed et al. (1987), which separates conditions where the turbulent burning velocity monotonically increases with increasing turbulence intensities and those which exhibit an inflection point. One can thus deduce that despite the methane-air and equimolar blend-air flame sharing similar turbulence intensities at the integral scale, the presence of hydrogen in the latter shifts the inflection point towards higher turbulence intensities. This, in turn, results in a more efficient amplification of the flame surface area due to smaller amounts of local quenching of the flame surface. In the framework of the thermal quenching of mixed pockets model proposed by Dorofeev (2007), the range of scales which are quenched by turbulence is smaller in the blend than in the methane mixture due to the change in mixture properties, resulting in a more efficient turbulence-induced enhancement of the flame surface area.

***Table 2**. Measure of the turbulence parameters*

Property	**$2H_2 + O_2 + 3.76N_2$**	**$CH_4 + H_2 + 2.5O_2 + 9.4N_2$**	**$CH_4 + 2O_2 + 7.52N_2$**
Flow Speed V_e [m/s]	275	140	80
Vortex Time t_v [ms]	0.19	0.36	0.64
Damköhler Number	1.3	0.5	0.4
Turbulence Intensity V_e/S_L	120	260	240

3. Conclusions

A simple experiment was presented which allows the characterization of differences between flames propagating through stoichiometric mixtures of hydrogen, methane, and an equimolar hydrogen-methane blend. The initial growth and propagation of the flame is well captured by a simple control volume model. When faced with a bluff body obstacle, the flow generated by the flame results in the formation of a vortex downstream, which is shown to scale with the speed of the flow driven by the flame. This flow scales with the laminar burning velocity, whereas the time elapsed between the vortex growth and the flame entrainment into the vortex is inversely proportional to the burning velocity. As a result, vortices of comparable sizes entrain the flame for a given distance separating the ignition plane and the obstacle.

When normalized by the model predictions, differences in the response of the flame to pressure gradients and turbulence becomes apparent. That hydrogen-air flames propagate faster than methane-air flames is simply due to their higher burning velocity. After correcting for differences in chemistry, the greater effectiveness of the flame surface area enhancement during the propagation of methane flames becomes apparent, which is also clearly visible in experimental photographs. An equimolar blend of hydrogen and methane is seen to follow the more effective flame folding pathway found in methane-air flames rather than the less effective pathway of hydrogen-air flames.

When correcting for the different burning rates, the effect of this different surface area enhancement on the normalized pressure generated by the flame becomes even more pronounced, leading to an interesting case where the equimolar methane-hydrogen blend generates greater pressures than either pure fuel. At one extreme, methane-air flames, with their very long flame times, are strongly affected

by the turbulence in the flow as growth rate of the surface area is faster than the consumption rate of the flame folds. However, the flame is subjected to a sufficiently strong turbulence intensity to locally quench the smallest features of the flame. This results in a diminishment of the reactive surface area of the flame, despite its overall enhancement by turbulence. At the other extreme, the small flame time associated with hydrogen flames results in the consumption of small-scale flame features at a faster rate than they can form, limiting the overall surface area. However, the flame surface area is not locally quenched by the turbulence in the flame-driven flow, resulting in a more efficient enhancement of the surface area by smaller amounts of turbulence. Between these two extremes lies the equimolar methane-hydrogen fuel blend, which generates similar turbulence intensities as the methane-air flame, however the turbulence in the flow is less capable of locally quenching the flame in similar manner as the hydrogen-air flame. The flame propagating in the blend thus takes the best features of the turbulent enhancement from both its constituent fuels, resulting in a greater overall surface area enhancement than either of its constituent fuels.

Acknowledgements
The authors gratefully acknowledge the financial support from FM Global.

References

Abdel-Gayed, R., Bradley, D., Lawes, M. (1987). *Turbulent burning velocities: a general correlation in terms of straining rates*. Proceedings of the Royal Society of London. A. Mathematical and Physical Sciences, 414(1847):389–413.

Ciccarelli, G., Dorofeev, S. (2008). *Flame acceleration and transition to detonation in ducts*. Progress in Energy and Combustion Science, 34(4):499–550. ISSN 0360-1285.

Dorofeev, S. (2007). *Thermal quenching and re-ignition of mixed pockets of reactants and products in gas explosions*. Proceedings of the Combustion Institute, 31(2):2371–2379.

Goodwin, D. G., Moffat, H. K., Speth, R. L. (2017). *Cantera: An object-oriented software toolkit for chemical kinetics, thermodynamics, and transport processes*. Version 2.3.0.

Kitagawa, T., Nakahara, T., Maruyama, K., Kado, K., Hayakawa, A., Kobayashi, S. (2008). *Turbulent burning velocity of hydrogen–air premixed propagating flames at elevated pressures*. International Journal of Hydrogen Energy, 33(20):5842–5849. ISSN 0360-3199.

Lee, J., Moen, I. (1980). *The mechans of transition from deflagration to detonation in vapor cloud explosions*. Progress in Energy and Combustion Science, 6(4):359–389. ISSN 0360-1285.

Shy, S. S., Lin, W. J., Wei, J. C. (2000). *An experimental correlation of turbulent burning velocities for premixed turbulent methane-air combustion*. Proceedings: Mathematical, Physical and Engineering Sciences, 456(2000):1997–2019.

Williams, F. A. (2014). *Chemical mechanism*.

Stability of non-premixed methane flames: dependence on storage pressure and leak diameter

Mina Kazemi, Sile Brennan & Vladimir Molkov

Hydrogen Safety Engineering and Research Centre (HySAFER) Centre, Ulster University, Newtownabbey BT37 0QB, UK

E-mail: kazemi-m1@uklster.ac.uk

Abstract

Understanding the behavior of subsonic, sonic, and supersonic methane jet flames is crucial for safety engineering, especially in the gas industry. Knowledge and assessment of jet flame dynamics, particularly regarding stability and blow-out in various incident scenarios, can equip engineers with engineering solutions on prevention and mitigation. A Computational Fluid Dynamics model was developed and applied to reproduce the experimentally determined critical diameter and flame stability limits for methane non-premixed flames. The critical diameter denotes the minimum nozzle diameter size at which a flame remains stable at all driving pressures. Sustained flames exist for diameters equal to or larger than the critical diameter while diameters less than critical exhibit two pressure limits for sustained flames. At lower pressures, the flame is initially attached, but as pressure increases, it becomes lifted, leading to blow-out. Then, with significant increase of the storage pressure above the upper pressure limit, the sustained flame restabilizes. The blow-out zone spans the pressure range between the lower and upper pressure limits, shaping the stability curve of the flame. Blow-out and stable flame behavior in the region of the key points defining a flame stability curve are simulated here and compared to experiments, specifically the critical diameter and the two limits (points to the furthest left side of the curve). The realizable k-ε turbulence model, along with the Eddy Dissipation Concept for combustion and Discrete Ordinates model for radiation were employed. The critical diameter was predicted as 42 mm which aligns with that measured experimentally by McCaffrey and Evans (1988). The limits of the stability curve are predicted here numerically for the first time. The numerically predicted stability curve is in close agreement with the experimental study (McCaffrey and Evans, 1988). The validated model is shown to accurately predict methane flame behavior.

Keywords: *methane, flame stability, blow-out, lift-off, critical diameter*

Introduction

Understanding and evaluation of flame behavior, particularly concerning the stability of sustained flames or the potential for flame blow-out in different operating conditions can be applied by engineers, to reduce the risk of substantial industrial catastrophes (Zhu et al., 2017). For example, A genuine concern for the blow-out phenomenon can arise during flaring activities (Palacios and Bradley, 2017).

To explain flame stability and the blow-out mechanism several models were proposed which were reviewed in the previous work of the authors (Kazemi et al., 2024). According to the premixed flame propagation model proposed by Vanquickenborne and Van Tiggelen (1965), blow-out occurs when the flow velocity surpasses the turbulent burning velocity. In this model, the stabilization point of the flame base is defined as the distance from the burner exit where the turbulent burning velocity equals the mean gas velocity. For subsonic flows, as the flow velocity increases with driving pressure, the flame lifts from the burner, leading to blow-out with further pressure or velocity increments. However, at higher pressures with sonic and supersonic velocities, the flame can be restabilized, as

demonstrated by Annushkin and Sverdlov (1978). The stability limits of a flame, depicted based on nozzle diameter versus release pressure (or velocity), form a C-shaped curve with the critical diameter as the vertex. Flames from flows released at any pressure will be stable at diameters equal to or greater than the critical diameter. If gaseous fuel is released through diameters less than the critical diameter, a flame cannot be sustained within a specific pressure range.

Several experimental studies have investigated flame stability for different fuels and nozzle geometries. In 1978, Annushkin and Sverdlov (1987) determined the stable flame region for hydrogen, methane, and propane and estimated the critical diameter for methane from a convergent nozzle as approximately 24 mm. A semi-empirical model was proposed to calculate lift-off and blow-out velocity for propane, methane, and hydrogen non-premixed flames. In 1981, Kalghatgi (1981) developed a correlation for the blow-out velocity of subsonic jet flames, including methane, as a linear function of burner exit diameter. The results were extrapolated for scenarios where the flow at the burner exit is choked, and a critical diameter of 41.4 mm was estimated for methane jet flame. In 1988, Birch et al. (1988) experimentally investigated natural gas flame stability vented vertically and estimated a critical diameter between 30 mm to 35 mm for a natural gas jet fire. In 1988, McCaffrey and Evans (1988) presented a stability map for methane jet flames vented vertically which was considered the basis for the numerical study presented here. They proposed a critical diameter of approximately 42 mm. In 2007, Lowesmith et al. (2007) reviewed hazards posed by offshore natural gas fires and estimated a critical diameter of 45 mm for a horizontally vented release, comparing it to Birch et al.'s (1988) vertical jet fire study.

While some experiments have been conducted to comprehend the stability region of methane flames, no numerical studies have been done to create a predictive model for this matter which can be appliable to gaseous blends later. Recently, the authors (Kazemi et al., 2024) numerically investigated the critical diameter and flame stability of hydrogen. In their work a modelling approach was developed and applied to accurately reproduce the experimentally determined hydrogen flame stability curve. There is a trade-off between full resolution of the flame and computational expense. The previous work by Kazemi et al. (2024) present an engineering tool which is capable of accurately predicting flame behaviour of hydrogen with reasonable computational expense, whilst still accounting for the shock structure in under-expanded jets. The authors (Kazemi et al., 2024) highlight the importance of resolving concentration profile in the region of the maximum stoichiometric waistline point, where the flame base would be anchored.

A validated model for methane not only offers valuable insights into flame behaviour, but also make the research applicable when the size of methane flame is of the order of tens of meters. This study aimed to validate a numerical model which is able to reproduce methane flame stability limits, critical diameter and flame characteristics accurately and efficiently.

1. Problem description

The experimental study that conducted by McCaffrey and Evans in 1988 is the basis of this numerical analysis. The experimental facility details were explained in the (McCaffrey and Evans, 1988). In fact, methane was released vertically through an orifice with diameter ranged from 1 mm to 102 mm. The experimental results were reported based on effective parameters which refers to the theoretical concept of isentropic expansion of the fuel. In other words, as methane was released from a high-pressure storage, it expanded to atmospheric pressure outside the orifice. Therefore, with assumption of isentropic expansion, the actual orifice was replaced theoretically with a notional nozzle to simplify the expansion process. The following equations were applied to calculate the effective velocity by McCaffrey and Evans (1988):

$$M_e = \sqrt{\frac{2}{\gamma-1}\left[\left(\frac{P_0}{P_\infty}\right)^{\frac{\gamma-1}{\gamma}} - 1\right]}, \quad (1)$$

$$U_e = M_e \sqrt{\frac{\gamma \bar{R} T_0}{\left(1+\frac{(\gamma-1)}{2}{M_e}^2\right)}}, \quad (2)$$

where P_0 and P_∞ are the stagnation pressure upstream of the orifice and the ambient pressure, respectively. γ is the ratio of specific heats which is assumed as 1.3 for methane (McCaffrey and Evans, 1988), and the methane gas constant, $\bar{R}$, is equal to 518.3 J/kg/K. The upstream stagnation temperature, T_0, is taken as 300 K in this study.

Above equations are obtained using the approach of the notional nozzle (Molkov, 2012) based on the conservation of mass and energy, assumption of an isentropic expansion, uniform flow velocity through such notional nozzle and ideal gas behaviour. As the theoretical parameters (e.g. effective velocity) cannot be implemented as the boundary conditions in numerical approach, the aforementioned equations were employed here to obtain release pressure based on effective velocities reported in the original experimental study (McCaffrey and Evans, 1988). For example, effective velocity was reported approximately 545 m/s for a release through an orifice diameter of 45 mm. Employing equations 1 and 2, the release pressure was calculated as approximately 0.2 MPa. The same procedure was used to convert effective velocities to release pressures (gauge) for all data reported by McCaffrey and Evans (1988). The stability region for methane flames based on release pressure (gauge) and orifice diameter is demonstrated in Figure 2.

2. Numerical approaches

For all, simulations, ANSYS Fluent version 23.1 was employed as the numerical tool to solve the governing equations. The computational approach involved a pressure-based solver, and the ideal gas law was applied to address compressibility. A coupled solver was utilized for pressure-velocity coupling. The discretisation of density, momentum, energy, and species transport equations employed a second-order upwind scheme. Temporal discretisation was achieved through a first-order implicit scheme. Pressure values at cell faces were interpolated using a second-order scheme. The gravitational body force was considered in the conservation of momentum. The turbulent kinetic energy (k) and dissipation rate equations (ε) were solved using the realizable k-ε turbulence model (Shih et al., 1995). This model, known for its superior performance in predicting the spreading rate of axisymmetric jets (ANSYS Fluent Theory Guide, 2023) compared to other k-ε turbulence models, was applied.

The eddy dissipation concept (EDC) approach was utilised to model combustion, incorporating the treatment of chemical reactions within turbulent flow (Magnussen, 1981). A chemical reaction involving five species was applied to represent the combustion of methane with air, resulting in carbon dioxide and water as the sole products of the combustion process.

The inclusion of radiative heat transfer from the flame within the fluid phase was achieved through the implementation of the Discrete Ordinates (DO) Radiation Model. While this model incurs a higher computational cost compared to P-1 and Rosseland models, it is effective across a full range of optical thicknesses (ANSYS Fluent Theory Guide, 2023). This model accommodates both scattering and

emitting (Murthy and Mathur, 1998). It solves the transport equation for radiation intensity in each direction over a limited number of discrete solid angles.

Full details on the governing equations, combustion model and turbulence model can be found in the author's previous study (Kazemi et al., 2024).

1.1. Computational domain and mesh

The simulations of the methane flame stability relied on the geometric details obtained from the experimental investigation conducted by McCaffrey and Evans (1988), forming the foundation for the presented numerical study. The schematic of the experimental setup can be referenced in (McCaffrey, 1989). The simulated 3D geometry involved the passage of methane through a 2 m horizontal pipe with a diameter of 102 mm, followed by a bend leading to a 2 m vertical pipe with the same diameter. The methane was eventually released into the atmosphere through a sharp-edged orifice. Orifice diameters ranging from 10 to 51 mm were considered in predicting the methane flame stability map.

The simulation 3D domain was represented by a cylinder with a diameter of 100 m and a length of 200 m. This domain's size ensured that the positions of the outer boundaries had no impact on the flame. The intention was to simulate methane flames up to 20 m in length. In order to assess grid independence, three hexahedral grids were employed: "coarse," "medium," and "fine," comprising approximately 80k, 400k, and 1M control volumes (CVs), respectively. The orifice was resolved by 8, 16, and 22 CVs along the diameter, with a relatively course grid towards the boundaries of the domain. The information regarding the grid is presented in Table 1. A growth rate of 1.1 was taken both along the axis and in the radial direction. For illustration, the computational domain and a cropped cross-section near the orifice area are depicted in Figure 1a and Figure 1b, respectively, for a medium grid with an orifice diameter of 45 mm. This approach was consistently applied across all scenarios, with the grid scaled as required. The purpose of this study is to validate an engineering tool which can predict flame stability. The cold flow velocity and concentration along the axis, were previously identified as the effective parameters in flame stability behavior (Kazemi et al., 2024). Thus, these parameterswere monitored using three different grids. The results for both parameters on the medium and fine grids overlapped, confirming that grid convergence was achieved. Therefore, the medium grid was utilized in this study.

***Table 1**. Flame behavior for simulated releases through 15 mm and 30 mm diameter nozzles.*

Mesh size	Total number of cells	Number of cells along the orifice diameter
Coarse	80k	8
Medium	400k	16
Fine	1M	22

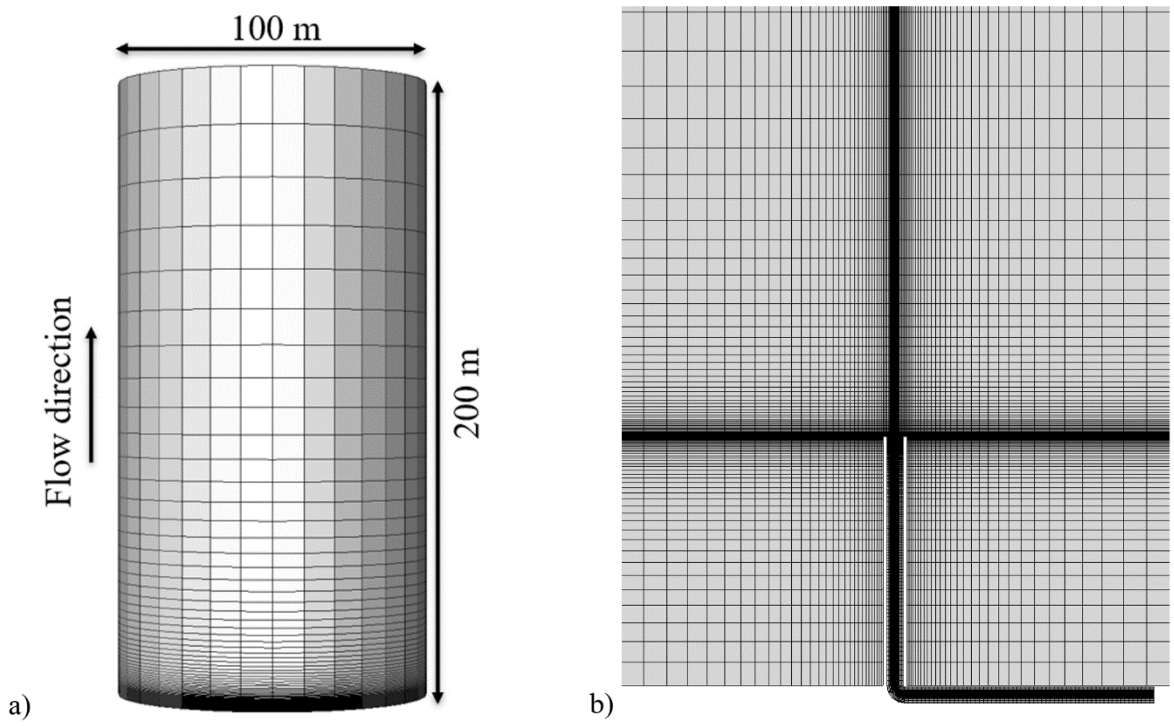

Fig. 1. *a) 3D computational domain; b) 2D centreline cropped cross section.*

The boundary condition for the methane inlet was set as a pressure inlet, positioned 2 m vertically and 2 m horizontally downstream of the orifice exit (refer to Figure 1b). This location corresponds to where the experimental mass flow rate was measured, crucial for calculating the methane pressure. At the methane inlet, conditions were defined with a methane temperature and mass fraction of 300 K and 1, respectively. The outer boundaries of the computational domain were assigned pressure inlet and outlet boundaries. Inlet values for temperature, gauge pressure, and oxygen mass fraction were specified as 300 K, 0.1 MPa, and 0.23, respectively. The nitrogen mass fraction was set at 0.77 in Fluent. All solid wall boundaries adhered to a no-slip condition.

For computational efficiency, the initial simulation focused on a steady-state solution for the unignited release. Once the unignited jet was established, the transient solution, combustion, and radiation models were activated. The turbulence model and constants remained consistent between steady-state and unsteady solutions.

To initiate ignition of the methane-air mixture, a static temperature of 2200 K was applied within a cubed region with dimensions in the range of x: 1 to 2 m, y: -0.2 to 0.2 m, and z: -0.2 to 0.2 m for 4 ms. The ignition source was activated until the generation of carbon dioxide and water appeared in the domain, confirming that combustion was occurring. Subsequently, it was deactivated, allowing the flame to propagate and form. The impact of ignition position was previously investigated by the authors, and it was found where it is positioned upstream of the maximum stoichiometric waistline position then it does not impact flame stability, when downstream flames which may otherwise be stable can blowout. It should be noted that the lift-off height for the flames considered is for example of the order of 2mm in the scenario of a release through43 mm nozzle diameter at 0.2 MPa. Thus, the ignition source was positioned upstream of the maximum stoichiometric waistline point, where the flame base would be anchored (Wu et al., 2006, Yamamoto et al., 2017). The maximum waistline of

the stoichiometric methane concentration is approximately 9.5% by volume in air which is calculated as following:

The stoichiometric combustion of methane-air considering air as a simple mixture of oxygen and nitrogen is:

$$CH_4 + 2O_2 + 7.52N_2 \rightarrow CO_2 + 2H_2O + 7.52N_2$$

The stochiometric concentration of methane in air (assuming 21% of oxygen and 79% of nitrogen) is 9.5% by volume (1/ (1+2+7.52) = 0.095) with air content of 90.5%.

3. Results and discussion

In order to reproduce the methane flame stability curve numerically, the first step was to reproduce critical diameter that is the minimum diameter size through which flame would be stable regardless of release pressure. Then, several scenarios were simulated in order to reproduce methane flame stability upper and lower curves.

2.1. Methane critical diameter

To obtained methane critical diameter, 7 scenarios were simulated all at pressure 0.2 MPa, with different orifice diameter of 40, 41, 41.5, 42, 42.5, 43, and 45 mm. The minimum diameter that resulted in a sustained flame is introduced as the critical diameter. As shown in Figure 2, a sustained flame depicted for a release through 43 mm orifice diameter at 0.2 MPa. The same behaviour was observed for releases through 42.5- and 45-mm orifice diameters. For the release through 42 mm orifice diameter at 0.2 MPa flame instability was captured in initial stages, but ultimately it became stabilised and resulted in a sustained flame. On the other hand, for the releases through 40, 41, 41.5 mm flame blow-out was observed. Figure 2 also shows the flame blow-out through 41 mm orifice diameter at 0.2 MPa. Therefore, 42 mm diameter is introduced as the methane critical diameter here which is in lines with what predicted in the McCaffrey and Evans (1988) experimental work.

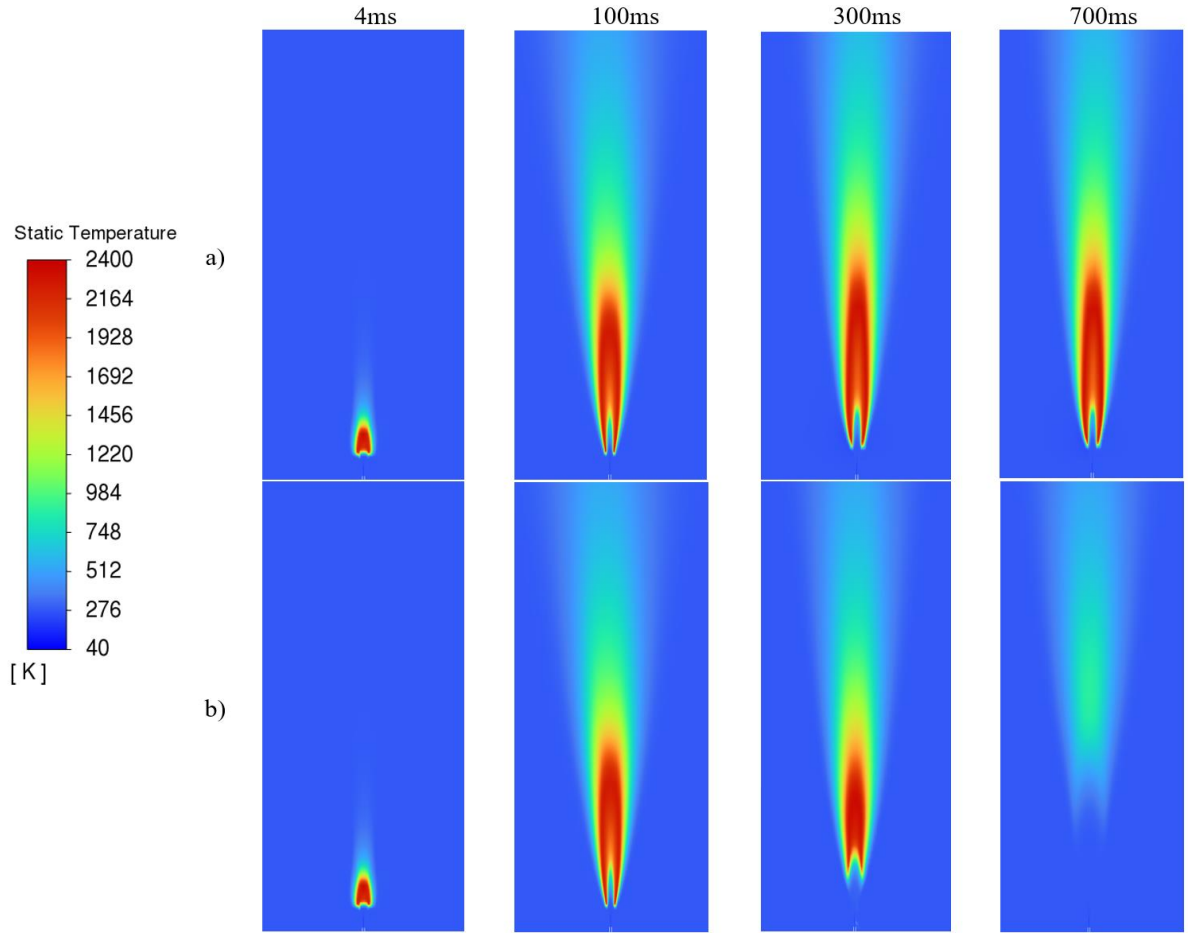

Fig. 2. *Sustained flame (a) versus blow-out (b) for 0.2 MPa driving pressure: a) Temperature (43 mm orifice); b) Temperature (41 mm orifice); Note: a cropped computational domain is shown.*

2.2. Methane flame stability

In this stage two orifice diameters were selected 15- and 30-mm. For the lower limit 15- and 30-mm orifice diameters, a release pressure starting from 0.01 MPa was increased in steps of 0.05 MPa until flame blow-out occurred. For the upper limit, for 15- and 30-mm orifice diameters, the release pressure was increased from 16 MPa and 1 MPa, respectively, in steps of 1 MPa until a sustained flame was observed. Table 1 represents all scenarios that resulted in determining the blow-out limits. Moreover, Figure 3 shows all simulated scenarios on a graph that compares simulation results with the experimental data. It should be noted, the lower curve in Figure 3 has been fitted to the blow-out data gained in the experiments, and the upper curve is McCaffrey's extrapolation (McCaffrey and Evans, 1988). As the approach for extrapolation was not explained clearly in their work, the upper curve was digitized. The experimental data for the lower curve and obtained data from digitizing for the upper curve were converted to release pressure using Eq. (1) and Eq. (2). Therefore, Figure 3 illustrates the stability of the methane flame with respect to variations in diameter and release pressure (gauge), enabling comparison with the stability graph for hydrogen flame in our previous work (Kazemi et al., 2024).

***Table 21**. Flame behavior for simulated releases through 15 mm and 30 mm diameter nozzles.*

Orifice diameter (mm)	Release pressure (MPa)	Simulated flame status
15	0.01	Sustained flame
15	0.05	Blow-out
15	20	Sustained flame
15	19	Blow-out
30	4	Sustained flame
30	3	Blow-out
30	0.05	Sustained flame
30	0.1	Blow-out

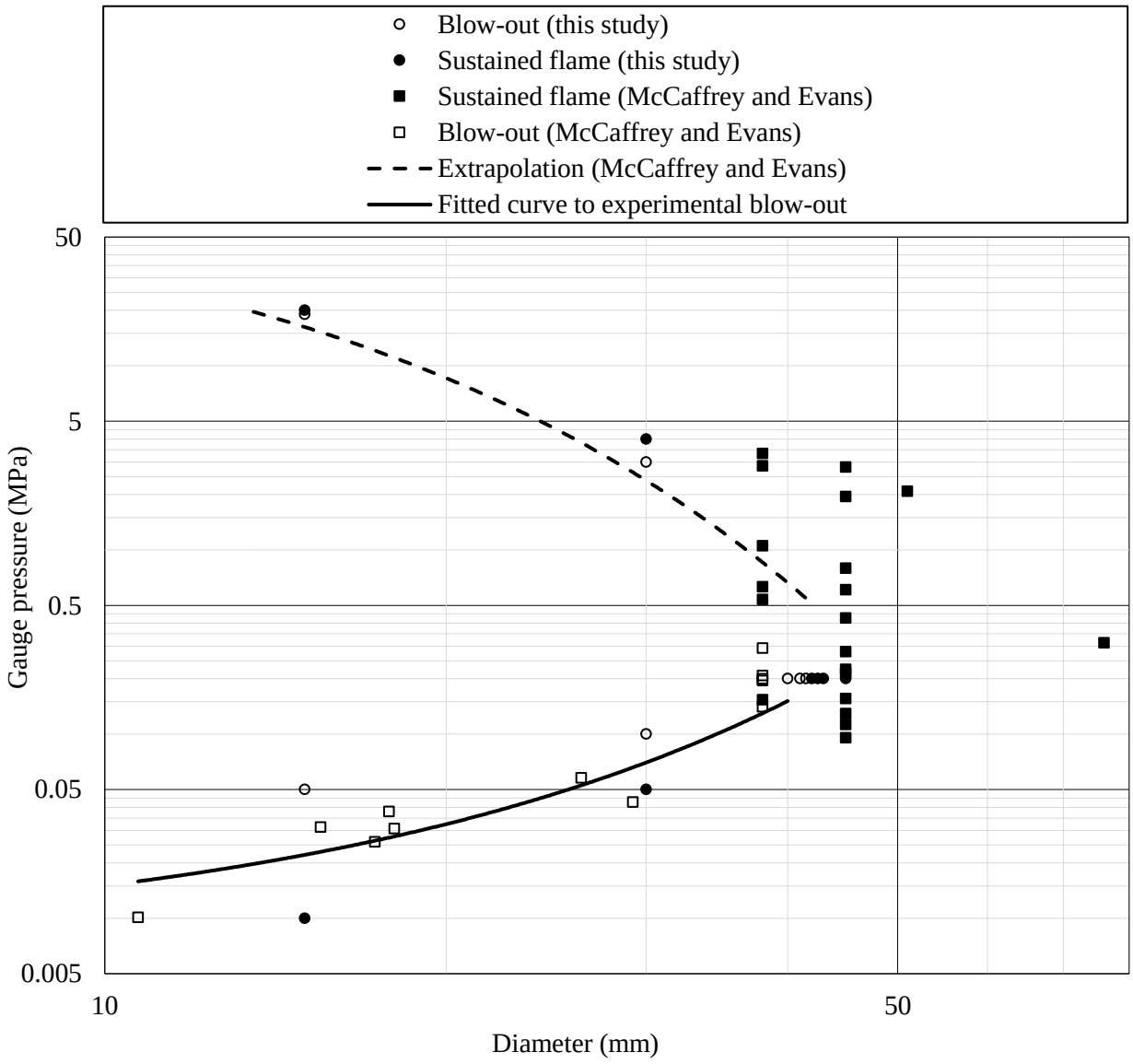

***Fig.3.** Methane flame stability limits (simulation results versus experiments)*

4. Conclusions

This work demonstrates originality through the numerical prediction of methane flame stability limits, based on validating the model for the methane critical diameter. The validated modelling method was successfully able to predict blow-out and sustained methane flames. A critical diameter of 42 mm predicted using CFD, aligns with experimental findings for vertical releases. Flame stability curve have been predicted for the first time using CFD and are in a close agreement with experiments.

The significance of this study lies in its ability to assist fire safety engineers in predicting methane flame behaviour under various operating conditions. Knowing the diameters and pressures at which blow-out or sustained flames are likely to occur informs design choices and emergency response strategies. The validated engineering model offers a means to predict critical diameter and flame stability limits of hydrogen-methane blends.

The rigor of this work is highlighted by the validation of a CFD model, given the scarcity of experimental data in this field. The model accurately predicted a 42 mm critical diameter for methane and was able to reproduce the methane flame stability limits, consistent with experimental results.

Acknowledgements

The authors are grateful to the Engineering and Physical Sciences Research Council (EPSRC) of the UK for support through the EPSRC Centre for Doctoral Training in Sustainable Hydrogen "SusHy" (Grant EP/S023909/1) and Tier 2 High-Performance Computing resources provided by the Northern Ireland High-Performance Computing (NI-HPC) facility (grant EP/T022175/1, https://www.ni-hpc.ac.uk/Kelvin2). This work is also supported by the Centre for Advanced Sustainable Energy (CASE) funded through the Department for the Economy Northern Ireland's Green Innovation Challenge Fund and aims to transform the sustainable energy sector through business research.

References

Annushkin, Y.M. and Sverdlov, E.D., 1978. Stability of submerged diffusion flames in subsonic and underexpanded supersonic gas-fuel streams. *Combustion, Explosion and Shock Waves*, *14*, pp.597-605.

ANSYS Fluent, 2023. ANSYS Fluent Theory Guide, ANSYS. *Inc., Release, 23.1*.

Birch, A.D., Brown, D.R., Cook, D.K. and Hargrave, G.K., 1988. Flame stability in underexpanded natural gas jets. *Combustion science and technology*, *58*(4-6), pp.267-280.

Lowesmith, B.J., Hankinson, G., Acton, M.R. and Chamberlain, G., 2007. An overview of the nature of hydrocarbon jet fire hazards in the oil and gas industry and a simplified approach to assessing the hazards. *Process safety and environmental protection*, *85*(3), pp.207-220.

Magnussen, B., 1981, January. On the structure of turbulence and a generalized eddy dissipation concept for chemical reaction in turbulent flow. In *19th aerospace sciences meeting* (p. 42).

McCaffrey, B.J., 1989. Momentum diffusion flame characteristics and the effects of water spray. *Combustion science and technology*, *63*(4-6), pp.315-335.

McCaffrey, B.J. and Evans, D.D., 1988, January. Very large methane jet diffusion flames. In *Symposium (International) on Combustion* (Vol. 21, No. 1, pp. 25-31). Elsevier.

Murthy, J.Y. and Mathur, S.R., 1998. Finite volume method for radiative heat transfer using unstructured meshes. *Journal of thermophysics and heat transfer*, *12*(3), pp.313-321.

Kalghatgi, G.T., 1981. Blow-out stability of gaseous jet diffusion flames. Part I: in still air. *Combustion Science and Technology*, *26*(5-6), pp.233-239.

Kazemi, M., Brennan, S., Molkov, V., 2024. Numerical simulations of the critical diameter and flame stability for hydrogen flames. *International Journal of Hydrogen Energy*. 59, pp.591-603.

Palacios, A. and Bradley, D., 2017. Generalised correlations of blow-off and flame quenching for sub-sonic and choked jet flames. *Combustion and Flame*, *185*, pp.309-318.

Shih, T.H., Liou, W.W., Shabbir, A., Yang, Z. and Zhu, J., 1995. A new k-ϵ eddy viscosity model for high reynolds number turbulent flows. *Computers & fluids*, *24*(3), pp.227-238.

Vanquickenborne, L. and Van Tiggelen, A., 1966. The stabilization mechanism of lifted diffusion flames. *Combustion and Flame*, *10*(1), pp.59-69.

Wu, C.Y., Chao, Y.C., Cheng, T.S., Li, Y.H., Lee, K.Y. and Yuan, T., 2006. The blowout mechanism of turbulent jet diffusion flames. *Combustion and Flame*, *145*(3), pp.481-494.

Yamamoto, S., Sakatsume, R. and Takeno, K., 2018. Blow-off process of highly under-expanded hydrogen non-premixed jet flame. *International Journal of Hydrogen Energy*, *43*(10), pp.5199-5205.

Zhu, C., Zhu, J., Wang, L. and Mannan, M.S., 2017. Lessons learned from analyzing a VCE accident at a chemical plant. *Journal of Loss Prevention in the Process Industries*, *50*, pp.397-402.

Mitigation of confined gas explosions using ventilation grilles and access doors

Jérôme Daubech [a] & Emmanuel Leprette [a]

[a] Institut National de l'Environnement Industriel et des Risques, (INERIS, Verneuil-en-Halatte, France)

E-mail: jerome.daubech@ineris.fr

Abstract

Developing new energies leads to installing energy production and storage systems (batteries, fuel cells, electrolysers, etc.) in containers. It is important to note that some systems have the potential to release and accumulate flammable gases, which can create a risk of a confined explosion. To address this risk, a specific research program is focused on studying the explosion protection of containerised applications using safety vents. The program aims to optimise the explosion discharge surfaces based on the specific scenario for the formation of an explosive atmosphere.

In practice, the safety studies carried out on this type of equipment show that few applications have specific vent panels to discharge the explosion overpressure outside to maintain the internal pressure at a level compatible with the mechanical strength of the container. However, in most cases, these containers are modified to accommodate fireproof access doors and ventilation grilles to ensure natural and forced air intake.

This paper aims to present the experimental study of the ability of ventilation grilles and access doors to act as explosion vent surfaces.

Two types of equipment were tested:

- Square ventilation grilles measuring 0.8 x 0.8 m^2;
- fireproof doors (2 m high and 0.83 m wide).

All the equipment was tested at explosion overpressures of 100 and 200 mbar.

Keywords: *gas explosion, protection, ventilation grille, fireproof door*

Introduction

Developing new energies leads to the implementation of energy production and storage systems such as batteries, fuel cells, electrolysers, and other methanation processes.

These systems are designed to be modular in both use and installation. This is one of the reasons why they are generally installed in ISO containers, making them easy to transport and deploy. However, when processes using flammable gases such as hydrogen or methane are installed in containers, a potentially dangerous flammable cloud is formed in the event of a leak, and there is a risk of explosion in the event of ignition.

In general, these installations should be protected using:

- detection and ventilation systems to limit the quantity of flammable gas in the container and to maintain the concentration of the flammable cloud at levels close to the lower explosive limit,
- ATEX-certified equipment to limit the risk of ignition.

These strategies are appropriate for limiting the risk of explosion for routine leaks on the installation. However, these two device types would have only a limited effect in the event of significant leaks. In such cases, fragile walls (vent panels) are required to evacuate the excess hot burnt gases produced by the flame to maintain the pressure in the container at a level compatible with its mechanical strength. Recent work by Lecocq et al. (2024) shows that the mechanical strength of the container is around 500 mbar at 1 bar and that the strength of the doors is around 450 mbar.

A specific research programme (Skjold, 2019) has been conducted to study the explosion protection of containerised hydrogen applications using safety vents to address this risk. The programme aimed to optimise the explosion discharge surfaces according to the specific scenario for forming an explosive atmosphere. The vents used were certified vents with an opening pressure of 100 mbar. The discharge areas studied ranged from 2 to 8 m^2. Numerous experimental configurations were investigated for different ignition source positions (homogeneous and stratified mixtures, at rest, turbulent, with and without obstacles). This research project has highlighted the effectiveness and the need for this type of protection to maintain the mechanical integrity of installations. There are several models for dimensioning these vent surfaces, such as the standards (EN 14994, NFPA68) or specific models such as those of Molkov et al. (2015), Bauwens et al. (2011), Sinha et al. (2019) or Shen et al. (2022).

In practice, however, safety studies on this type of equipment show that few applications have certified vent panels specifically dedicated to explosion protection. Instead, in most cases, these containers are modified to accommodate firewall-type access doors and ventilation grilles to ensure natural and forced air entry.

This work aims to investigate experimentally the overpressure relief capability of ventilation grilles and access doors to act as explosion vent surfaces.

There is little work on studying the capacity for explosion overpressure relief by devices not explicitly dedicated to this purpose. Among these studies, we can cite the work of Chmielewski et al. (2021). The authors analysed several accidents in apartment blocks and highlighted the capacity of doors, windows and roof elements to discharge explosion overpressure. The work also highlights the importance of the resistance of the materials and construction solutions used in the building. The work clearly shows that the more resistant the construction element, the greater the damage.

In this presented experimental works, two types of equipment were tested:

- Square ventilation grilles measuring 0.8 x 0.8 m^2;
- 2 m high and 0.83 m wide external and 120 min fire doors.

All the equipment was tested at explosion overpressures of 100 and 200 mbar. These overpressure levels are lower than the mechanical explosion resistance overpressure of the containers (Lecocq et al., 2024).

The tests were carried out in a 37 m^3 explosion chamber at Ineris and compared to reference tests with a identical explosion discharge surface just covered by a plastic sheet.

1. Presentation of the equipment tested and the experimental setup

This chapter presents :

- the main characteristics of the equipment tested (dimensions, mass, construction) ;
- the main characteristics of the experimental setup

1.1. Tested devices

Figure 1 shows a picture of the 0.8 x 0.8 m^2 grille. The total mass of the grille is 12.7 kg. It is made up of 10 fixed fins that are held in place on a metal frame by slots provided for this purpose. The 10 fins provide 9 air circulation spaces, each 0.76 m long and 0.065 m wide. The cross-section of a fin has the same dimensions as the airflow space. The mass of a fin is 0.85 kg. The thickness of the fin is 1.5 mm. The fins are spot-welded to a 1 mm thick metal mesh. The mesh size is 0.0013 m. The mass of the mesh is 450 g.

Fig 1. *0.8 x 0.8 m^2 grille*

Two 2h fire doors were explosion tested (Figure 2). The opening surface of the doors is 2 m high and 0.83 cm wide. The door leaf is mounted on a frame by 3 hinges. The door is held in the closed position by a closing bolt and a locking bolt. The fire door leaf weighs 52.8 kg.

Fig 2. *Fire doors*

1.2. Experimental set-up

The experimental set-up consists of a 37.5 m^3 explosion chamber (length: 6 m, width: 2.5 m, height: 2.5 m) designed and built at Ineris (Figure 3). Its estimated mechanical strength is in the order of 2 bar. This explosion chamber is fitted with a transparent face, enabling visualising internal phenomena.

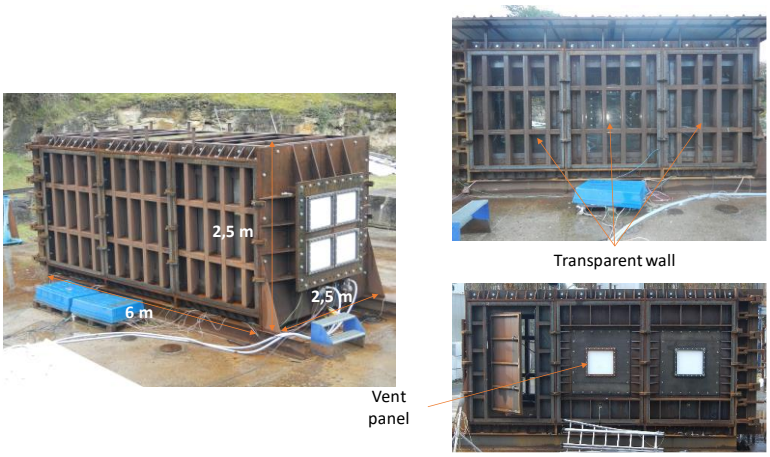

Fig 3. *37.5 m^3 explosion chamber*

Gas is injected into the explosion chamber from the 5 m^3 tank. The gas injection pressure is around 5 bar. The gas is injected through a circular orifice 20 mm in diameter. The leak rate is around 25 g/s. Three gas analysers are located in the explosion chamber to monitor the homogeneity of the flammable mixture.

The instrumentation (Figure 4) consists of :

- 2 internal pressure sensors (Kistler 0-2 bar piezoresistive sensor) ;
- 1 external pressure sensor embedded in lenticular support placed in front of the elements tested (Kistler 0-2 bar piezoresistive sensor);
- 1 high-speed camera (Phantom MIRO) to visualise the explosion and the opening of grilles and doors.

A 60 J pyrotechnic bead is used for ignition.

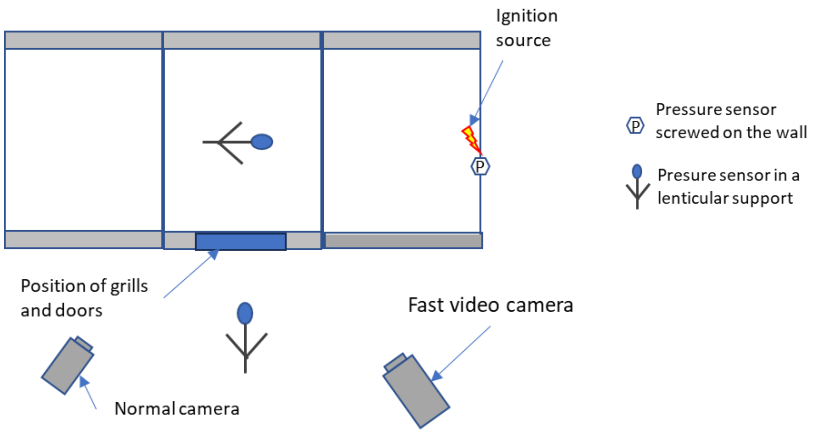

Fig 4. *Instrumentation - Top view*

Overpressure was created by the explosion of a hydrogen-air cloud obstructed by 2 metal modules (H: 1.5 m, L: 1.5 m, W: 1 m) accommodating 18 tubes 1 m long and 10 cm in diameter (Figure 5).

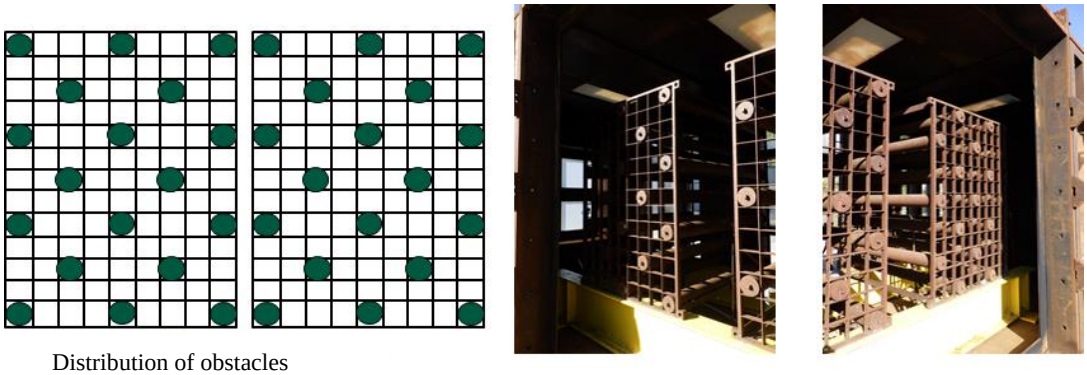

Distribution of obstacles

Installation of obstacles in explosion chamber

Fig 5. *Internal obstruction*

2. Test results

Two experimental reference configurations were carried out for each element tested, leaving the space in which the element under test was housed free. A plastic sheet stapled to wooden battens obstructed this free space to keep the gas injected before ignition. The overpressure loads created are of the order of 100 and 200 mbar, typical overpressure levels for safety vents used in industry. Once these experimental reference conditions had been obtained, they were reproduced for each element tested.

2.1. 0.8 m x 0.8 m^2 ventilation grille

For a surface area of 0.8 x 0.8 m^2 covered with a plastic sheet, an overpressure of 100 mbar is obtained for a flammable hydrogen-air cloud at 11.5%. An overpressure of 200 mbar is obtained for a flammable hydrogen-air cloud at 12.5%. Since the ventilation grille can be considered open to the injection of hydrogen, a plastic sheet stapled to the wooden battens covers the grille to keep the injected gas in the explosion chamber (Figure 6).

Fig 6. *Plastic sheet covering the grille*

Figure 7 shows the reference signals obtained with a plastic sheet and the overpressure signals obtained with the ventilation grille at the two reference levels, 100 and 200 mbar.

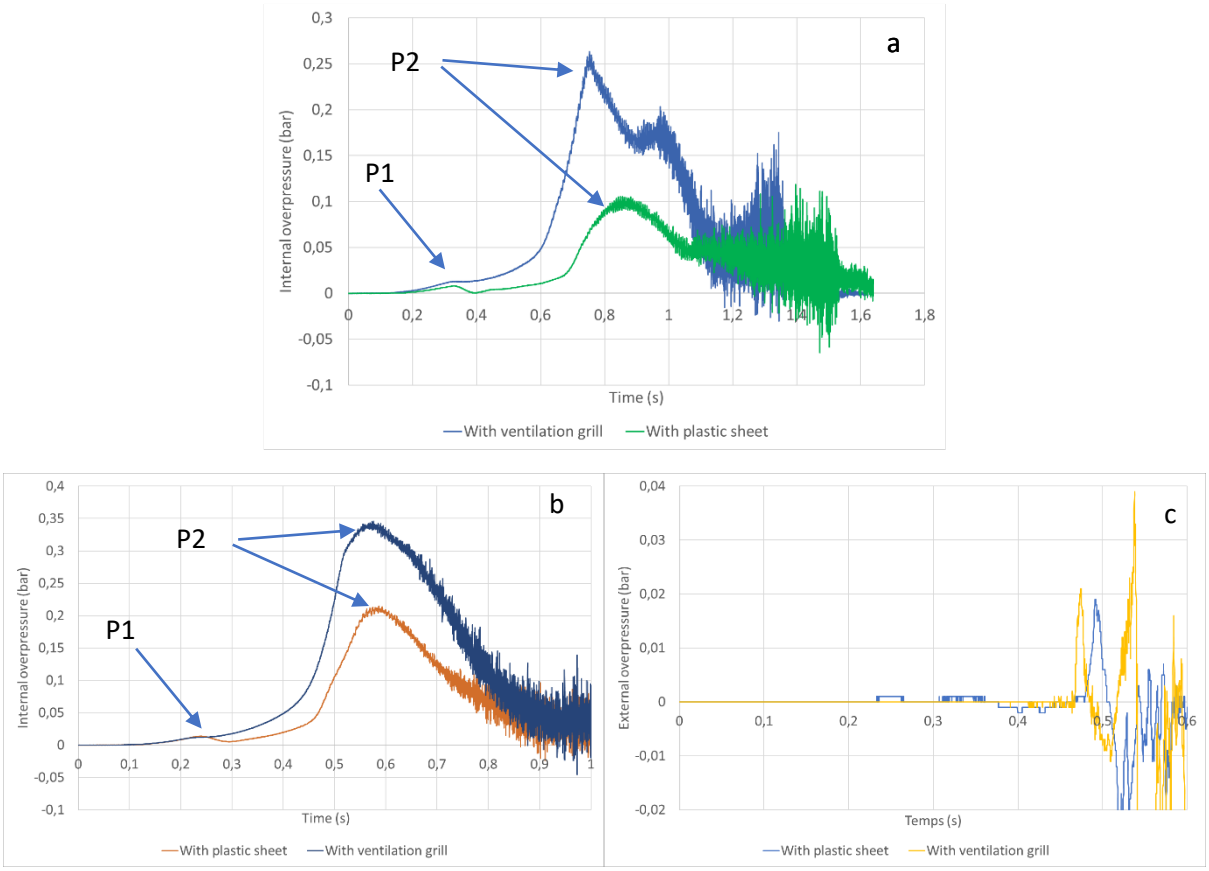

Fig 7. *Comparison of reference signals obtained with a plastic sheet and overpressure signals obtained with the ventilation grille - a - internal overpressure (100 mbar references), b - internal overpressure (200 mbar references), c - external overpressure (200 mbar references)*

Firstly, it can be seen that the internal overpressure signals include 2 overpressure peaks. The first peak, indicated by P1 on the graph in Figure 7, corresponds to the tearing of the plastic sheet at a pressure of around 10 mbar. The second peak, P2, corresponds to the maximum explosion overpressure in the 37 m^3 chamber. Figure 7.a is of the order of 100 mbar for the reference configuration and 250 mbar for the configuration with the grille. In Figure 7.b, it is of the order of 200 mbar for the reference configuration and 350 mbar for the configuration with the grille. Therefore, the presence of the grille leads to a pressure increase of 150 mbar under the same conditions of concentration and ignition.

Figure 8 shows a sequence of images obtained by fast video of the grille opening. After the plastic sheet has been torn off, plastic deformation of the grille fins can be seen before they leave the grille and are projected. The maximum projection distance is around fifty metres.

Analysis of the internal pressure signal and the fast video shows that:

- for the 100 bar test, the grille opened at 740 ms, corresponding to an overpressure of around 245 mbar,
- for the 200 mbar test, the grille opens at 515 ms, corresponding to an overpressure of around 270 mbar.

No comparison of external overpressures is given for the test at the reference pressure of 100 mbar because the external pressure sensor had not been installed for this experimental configuration.

Fig 8. *Sequence of images obtained by fast video of the grille opening for the 100 mbar test*

For the 200 mbar test (Figure 7.c), it can be seen that the external pressure levels for the configuration without a grille and with a grille are of the same order of magnitude, around 20 mbar at 2 m from the explosion discharge surface. However, a second overpressure peak can be seen in the configuration with a grille, which is not present without a grille (blue curve). Analysis of the fast video shows that this peak is linked to the opening and projection of the grille fins. The presence of these two peaks can be interpreted by the fact that after the plastic sheet is torn off, the flammable mixture is expelled

through the air circulation spaces in the grille. When the flame reaches the grille, it ignites this external cloud, causing a secondary explosion. Then, as the pressure continues to rise in the explosion chamber, the fins deform and (Figure 8) completely obstruct the surface, preventing the release of the explosion overpressure. The fins are then thrown open, opening up a large part of the surface. This sudden opening causes the second pressure peak, as shown in the yellow curve in the graph in Figure 7.c.

Figure 9 shows images of the deformation of the grille frame holding the fins and the deformation and projection of the fins.

Fig 9. *Images of the deformation of the grille frame holding the blades, the deformation and projection of the blades - Grille 0.8 x 0.8 m^2 at 100 mbar*

2.2. Fire doors

The 2h fire doors (Figure 2) were tested at an overpressure of around 100 mbar and 230 mbar. As with the ventilation grille tests, the reference configurations were created by covering the free space of the door with a sheet of plastic stapled to wooden battens. This allows the flammable mixture to be contained in the explosion chamber as it is injected before ignition. The reference overpressure of 100 mbar is obtained for a 14% hydrogen-air flammable cloud. The reference overpressure of 230 mbar is obtained for a 16% hydrogen-air flammable cloud.

It was found that the door opened without detaching or projecting for all the doors tested and for all the overpressure stresses. An illustration of the door opening dynamics is shown in Figure 10 for the 2h fire door at an overpressure of 230 mbar.

Fig 10. *Illustration of door opening dynamics for 230 mbar overpressure*

Figure 11 compares internal and external overpressures for the reference configuration at 100 mbar for a locked fire door and at 230 mbar for a door held in the closed position solely by its closing bolt.

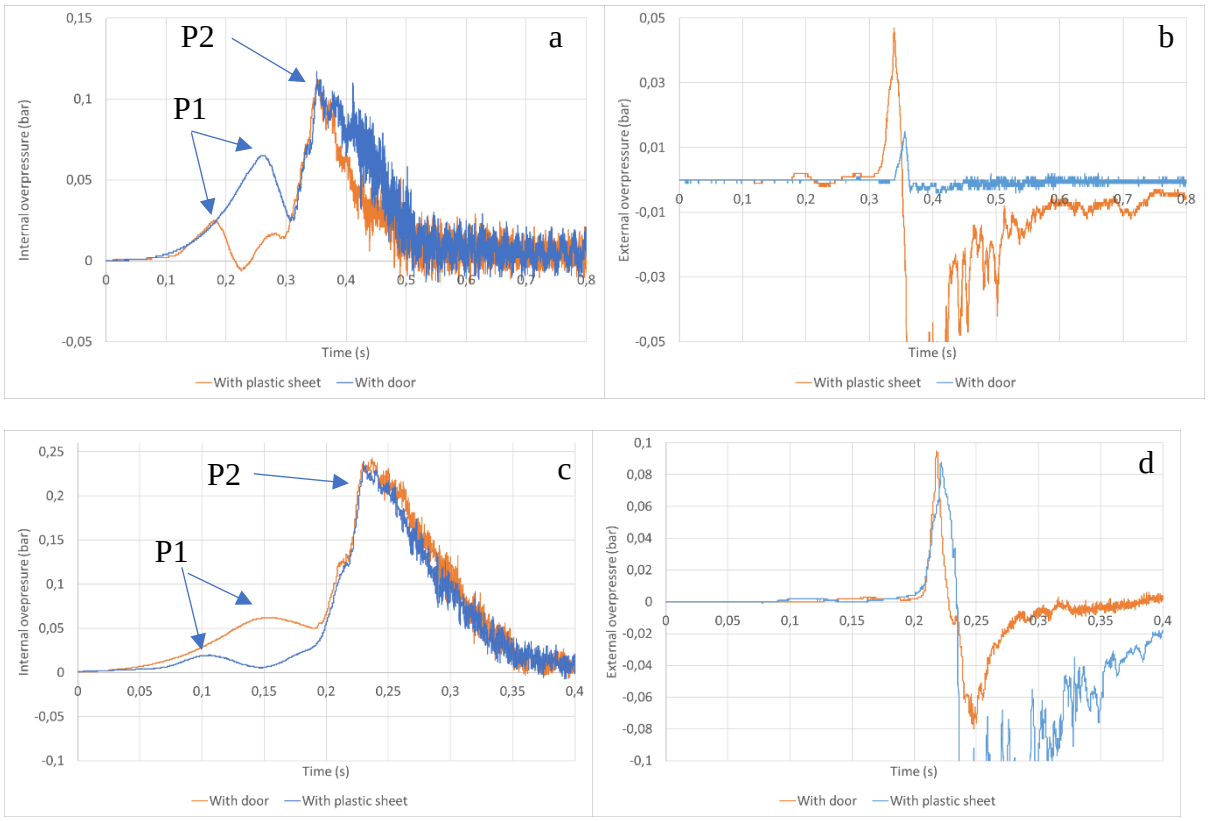

Fig 11. *Comparison of internal and external explosion overpressures for the reference configuration at 100 mbar for a locked fire door (a and b) and at 230 mbar for a door held in the closed position solely by its closing bolt (c and d).*

About the internal overpressure, it can be seen that the plastic sheet for the reference configurations opens at an overpressure of around 25 mbar. For the tests with the fire doors, it was found that they opened at an overpressure of around 60 mbar, resulting in a discharge of the explosion (drop in overpressure after peak P1). This also reflects that locking the door does not alter its opening pressure. As the combustion of the flammable cloud is incomplete, the explosion chamber is repressurised. The final overpressure loads and pressure rise dynamics are identical for the two overpressure loads, reaching the P2 peak at 100 bar and 230 mbar, the reference overpressure levels. The tests show that the doors open early enough to release the explosion overpressure and limit the overpressure to levels comparable to the reference load.

A secondary explosion was observed in each test. For the 100 mbar test, the maximum overpressure obtained with the plastic sheet is 45 mbar, whereas only 12 mbar with the door. The presence of the doors seems to have a favourable effect on the secondary explosion overpressures. This could be explained by the fact that, as the doors open more slowly than the plastic sheeting, the flammable outer cloud formed is not a fully developed vortex but a more spread-out cloud of different sizes, significantly modifying the effects of the secondary explosion.

On the other hand, for the 230 mbar test, the external overpressure effects of the secondary explosion are identical, with an identical pressure rise rate. This shows that the combustion dynamics are similar from one test to the next. It appears that the dynamics of the formation of the external cloud, which determines the effects of the explosion, are similar when the plastic sheet and the door are opened.

This experimental configuration was the first to be tested. A plastic sheet was placed upstream of the door inside the explosion chamber. When the door opened under the effect of the internal pressure, the presence of the sheet significantly modified the flow of gases through the progressive opening of the door (Figure 12).

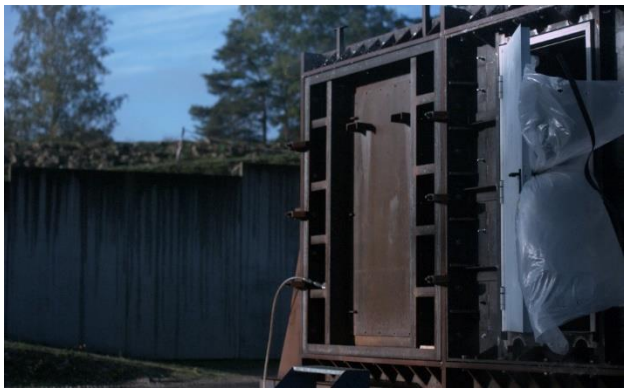

Fig 12. *Opening the door with a plastic sheet inside the explosion chamber*

Analysis of the mechanical deformations of the door for all the tests shows that the closing and locking bolts condition the opening overpressure. When the internal pressure mechanically stresses the door, the door leaf and frame deform, allowing the latch bolts to move out of their housings. Figure 13 shows the characteristic deformation of the closing and locking bolts after a test.

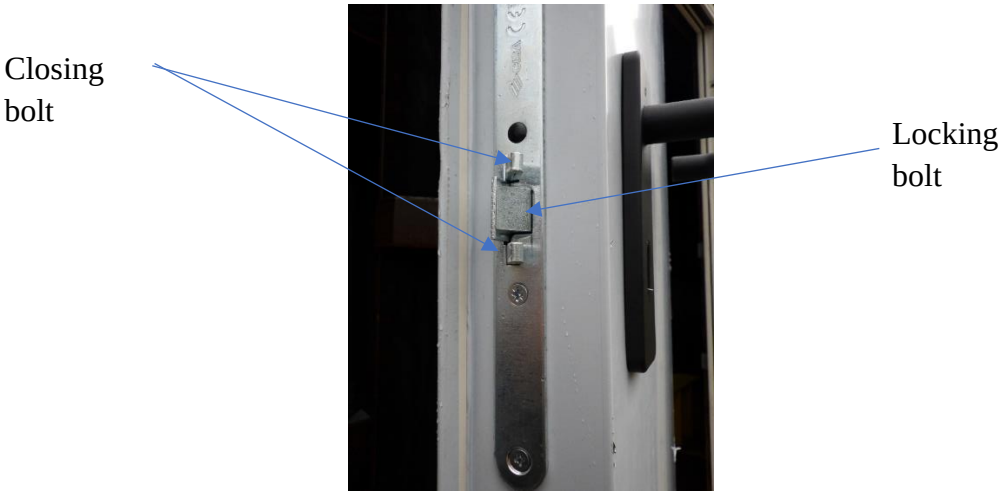

Fig 13. *Characteristic deformation of the closing and locking bolts after a test*

3. Conclusions

Safety studies carried out on containerised energy installations show that they rarely have blow-out walls designed to relieve excess pressure in the event of an internal explosion of a flammable cloud. However, these applications are equipped with ventilation grilles and access doors.

This work experimentally studied the ability of ventilation grilles and access doors to act as explosion-relief surfaces. To this end, a specific experimental campaign was set up in the 37 m^3 explosion chamber at Ineris to test ventilation grilles and 2-hour fire doors at 100 and 200 mbar overpressure stresses.

The tests showed that the ventilation grilles discharged the explosion in two stages. Given that they have a passage cross-section in the first stage, the grilles allow the flammable mixture to pass through,

which is expelled from the explosion chamber by increased internal pressure. The expelled cloud ignites when the flame reaches the grille, creating a secondary explosion. Next, the fins deform and significantly reduce the cross-sectional area, preventing the gases from being expelled to the outside. At this point, the grille can be seen as a closed surface until the opening pressure of the fins is reached. The pressure increase between the reference configuration without a grille and the configuration with a grille is of the order of 150 mbar. The cross-analysis of the internal pressure and the fast video shows that the opening overpressure of the grilles tested is of the order of 250 to 280 mbar. The fins are projected to be around 50 m. This opening causes a pressure wave to be emitted to the outside with greater intensity than the secondary explosion.

The fire doors tested were found to have an opening pressure of around 60 mbar. The opening pressure seems to be determined by the closing system. Under the test conditions proposed in this study, the doors appear as effective as a plastic sheet in relieving explosion overpressure. The tests seem to show a beneficial effect of the presence of the door on the overpressure effects induced by the secondary explosion. This is because the progressive opening of the door modifies how the gas is expelled outside the explosion chamber, compared with the tearing away of the plastic sheeting, which allows a fully developed vortex to form.

References

Lecocq, G., Amazou, S., Leprette, E., Le-Roux, B., Charrondière, S., Mathieu, L., 2024. Study of the behaviuor of walls and doors of 20 fet ISO containers through real-scale explosion test, Internation Symposium on Hasards, Prevention and Mitigation of Industrial Explosions, Naples, ITALY – June 10-14, 2024

Skjold, T., Hisken, H., Lakshmipathy, S., Atanga, G., Bernard, L., van Wingerden, M., Olsen, K.L., Holme, M.N., Turøy, N.M. Mykleby, M., van Wingerden, K., 2019. Vented hydrogen deflagrations in containers: Effect of congestion for homogeneous and inhomogeneous mixtures. International Journal of Hydrogen Energy, 44(17): 8819-8832.

EN 14994, 2007, Systèmes de protection par évent contre les explosions de gaz, European Standards

NFPA 68, 2018, Venting of deflagrations, USA Standards

Molkov, V., Bragin, M., 2015. Hydrogen-air deflagrations: Vent sizing correlation for low-strength equipment and buildings, Int J Hydrogen Energy, 40, pp. 1256-1266

Bauwens, C.R., Chaffee, J. and Dorofeev, S.B, 2011. Vented explosion overpressures from combustion of hydrogen and hydrocarbon mixtures, Int J Hydrogen Energy, 36, pp. 2329–2336

Sinha A., Madhav Rao V.C., Wen J.X., 2019, Performance evaluation of empirical models for vented lean hydrogen explosions, International Journal of Hydrogen Energy, vol 44, pp 8711-8726

Shen, A., Miller, D., 2022, Ventdef: A new engineering model for vented gas deflagration based on NFPA 68 (2018), Process safety Pregress vol 41, pp 738-750

Chmielewski, R., Bąk, A., 2021, Analysis of the safety of residential buildings under gas explosion loads, Journal of Building Engineering, Volume 43, 102815

A role of dust properties in turbulence generation by dust dispersion in the standard 1 m^3 vessel

Wojciech Adamus [a] & Zdzisław Dyduch [a]

[a] Experimental Mine "Barbara"
of Central Mining Institute – National Research Institute, Mikołów, Poland

E-mail: wadamus@gig.eu

Abstract

The standard 1 m^3 vessel is an apparatus recommended for assessing dust explosion indices by ISO, European and American standards. However, the definition of the vessel construction provided in the Standards leaves some room for design variation. This variability may lead to significantly different results obtained in vessels constructed in different laboratories, even when all meet the requirements of the standards. One of the key parameters that should be controlled in the tests is turbulence. Several authors reported measurements of turbulence in the 1 m^3 vessel. However, all of those results were obtained for pure air dispersed by the dust dispersion system. This work is a continuation of the previous research (Dyduch, 2024), and presents measurements of turbulence generated by dust-air dispersion in the 1 m^3 explosion vessel. Tests for several nominal dust concentrations of three additional dusts – *Barbara Coal d100*, *Wood Dust* and *Aluminium Dust* – were performed to supplement results obtained previously. For the turbulence measurement, the Bi-Directional Velocity Probe developed by McCaffrey and Heskestad (McCaffrey B.J., 1976) was used. The construction of the probe was modified to improve its performance in dusty conditions. The root-mean-square of instantaneous velocity u'_{rms} was calculated to characterized turbulence intensity. The results, together with those obtained previously, were analysed in search of dust properties that significantly influence turbulence generated by dust-air dispersion process.

Keywords: *dust explosion, test methods, turbulence measurement, Bi-Directional Velocity Probe*

Introduction

Maximum explosion pressure p_{max} and *maximum rate of pressure rise* $(dp/dt)_{max}$ are the most important explosion severity parameters used in safety processes during the assessment of dust explosion hazards. They are mainly used to properly design dust handling devices and apply explosion protection methods to ensure the safety of workers and property. Because the values of explosion parameters depend not only on the properties of the dust material tested but also on the method used for their assessment, standard methodology was developed to ensure repeatable assessment (ISO6184/1, 1985; EN14034+A1, 2011; ASTM-E-1226, 2012). In these procedures, a dust/air mixture is formed and ignited in a closed explosion vessel, and the pressure induced by combustion is recorded. As fast inflow is used to disperse dust, the dust/air forms turbulent flow inside the vessel. In the context of combustion, the most important property of the flow is the forced mixing of hot products and fresh fuel. As pointed out by (Shelkin, 1943), for turbulent mixtures of high intensity, the rate of combustion is controlled by the flow intensity. During the dust testing, turbulence is controlled by setting an appropriate delay between dispersion and ignition called *ignition delay time* (t_v). As different technical solutions can be used in the design of the dispersion system in the 1 m^3 explosion vessel turbulence at the moment of ignition is specific for each system and determines conditions at that moment. An actual performance of particular explosion vessel can be verified by tests of dusts of well determined explosive properties. The most widely used are *Niacin*, *Lycopodium* and *Cornstarch* dusts. The dominant effect of initial turbulence on dust

explosion was identified by (Zhen&Leuckel, 1994). In their tests the measurements were performed in a 1 m^3 vessel equipped with two pneumatic dispersion systems and hemispherical dispersion nozzle used as a dispersion nozzle. Dust containers of 5.4 L were pressurized to 15 bar. The maximum rate of pressure rise for *Cornstarch* was measured for different ignition delay times. The corresponding turbulence intensity, characterized by root-mean-square velocity (u_{rms}), ranged from 11.4 to 0.2 m/s. The maximum and minimum values of $(dp/dt)_{max}$ were over 250 bar/s for the shortest ignition delay time and below 80 bar/s for the longest. Extensive measurements in their 1 m^3 vessel equipped with one semi-circular perforated tube connected to a 5 L dust container were reported by (Proust, Accorsi and Dupont, 2007). The ignition delay time was set to 600 ms and the ignition took place when the turbulence level (u_{rms}) was 2 m/s. (Addo *et al.*, 2019) reported tests in a 1 m^3 explosion vessel for *Niacin*, *Lycopodium* and *Polyethylene.* Measurements were performed with various ignition delay times. The measured values of $(dp/dt)_{max}$ agreed with the literature data for ignition delay time set to 550 ms and 600 ms for *Niacin* and *Lycopodium*, respectively. (Hauert and Vogl, 1995) reported measurements of horizontal and vertical components of the velocity after 600 ms and obtained the values of 1.2 m/s and 5.36 m/s, respectively. (Z. Dyduch, Toman and Adamus, 2016) showed that at the time of ignition and combustion, the turbulence in the vessel is isotropic and homogeneous, with values of the u_{rms} in the range from 0.5 m/s to 1 m/s. (Tamanini, 1998) investigated the influence of dust on dispersion. Based on experiments with coal and cornstarch, he concluded that dust loadings caused a delay in flow development and a change in turbulence intensity at the combustion phase of the tests. The dominant role of the dispersion system and dust particle sizes on flow characteristics after dispersion was captured by CFD simulations (Islas *et al.*, 2023). Their CFD model predicts an increase in turbulence intensities with an increase in dust load. The pre-ignition state of the dust/air mixture in a 1 m^3 explosion vessel were reported by (Portarapillo *et al.*, 2022). Good agreement of CFD calculated turbulence intensities and experimental results was observed for times greater than 300 ms after dispersion.

This work is a continuation of previous research (Dyduch, 2024) with the aim of characterizing the performance of the dispersion process of the 1 m^3 explosion vessel. The initial conditions are described by measurements of instantaneous velocity generated during dispersion and the pressure before ignition. Measurements were performed for dusts with different particle size distributions, specific surfaces, and various bulk densities.

1. Experimental set-up

In this work, the same experimental setup was utilized as in previous tests (Dyduch, 2024). Setup details can be found there. Figure 1 presents a schematic diagram of the setup and a photo of the dispersion system. As previously, in all tests, two dispersion units with rebound nozzles were employed. The required amount of dust was equally divided between two dust containers. Before dispersion, the dust containers were pressurized up to 20 bar gauge pressure with air. Measurements of turbulence (instantaneous velocity u) in the vessel were conducted using the Bi-Directional Velocity Probe (*BDVP*). The SIRIUS HS manufactured by DEWESoft (Slovenia) was utilized as a signal amplifier and acquisition system. Data from the differential pressure transducer were collected at a rate of 20 kHz.

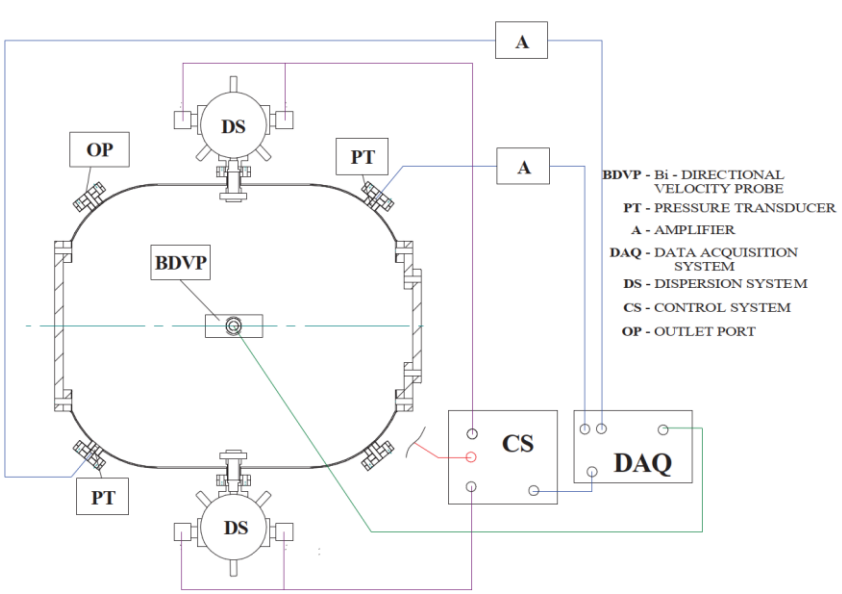

(a) Schematic diagram of experimental set-up (BDVP's sensing head not to scale) *(b) Dispersion system*

Fig. 1. *Set-up of the 1 m^3 vessel*

1.1. Bi-Directional Velocity Probe (BDVP)

For the measurements of instantaneous flow velocity, the BDVP described in detail in previous papers (Z. Dyduch, Toman and Adamus, 2016; Dyduch, 2024) was used. Unlike the original probe and types analyzed in detail by (Proust and Jamois, 2021), the differential pressure transducer was located directly inside the sensing head and used to divide the head into two zones. The size of the head was 20 mm in diameter with a length of 40 mm.

1.2. Dust properties

Tests were performed for *Aluminium powder*, W*ax dust*, hard coal *Barbara d98 dust* and *Wood dust*. The properties of dusts – particle size distribution with median (d50), bulk density and specific surface area – are summarized in Table 1. SEM analysis (Fig. 2) was used to examine the shape of the particles. *Cornstarch* and *Barbara d38* previously tested (Dyduch, 2024), are also included. The dusts were selected to cover a certain range of bulk densities and particle sizes, with the latter assessed in several ways.

Table 1*. Properties of dusts used in the experiments*

Dust	Bulk density, kg/m^3	Specific surface, m^2/g	M10, µm	M50, µm	M90, µm	D[4,3], µm	D[3,2], µm
Aluminum Al 7345	193	3.97	9.6	33	74	46.7	10.0
Barbara d38	734	2.00	31.2	96	176	100.5	43.9
Barbara d98	480	4.37	3.7	16	36	18.3	7.4
Cornstarch	328	0.52	8.6	15	29	17.3	1.8
Wax	240	2.30	1.8	8	15	8.3	2.8
Wood dust	212	1.80	37.3	270	447	245.6	44.4

Aluminium powder was in a form of fine flakes with rough surface. This form results in a very small bulk density and a large specific surface area. *Barbara d98* and *Barbara d38* dusts are samples of the same hard coal but with different granulation. These dusts have the largest bulk densities. *Wax*

consists of fine, irregular particles with a large specific surface. *Wood dust* particles are mostly elongated and of different sizes. Granulation assessment of such dust by optical methods usually lead to uncertain results. *Cornstarch* is dust of regular particles with smooth surfaces. The specific surface area of this dust is the smallest among the dusts tested.

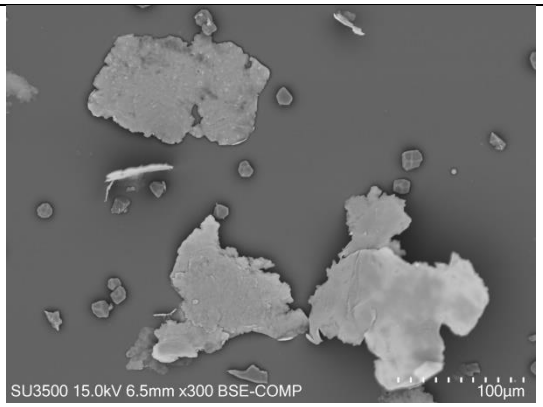

Aluminum Al 7345

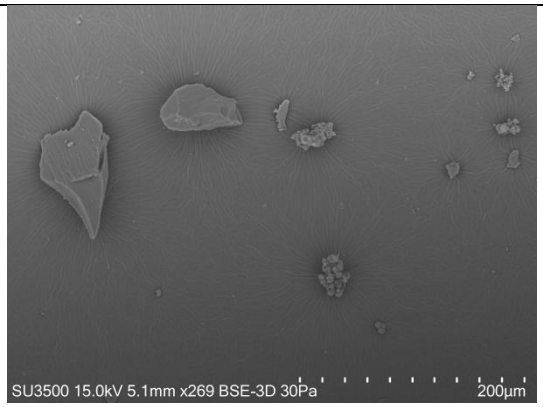

Barbara d38

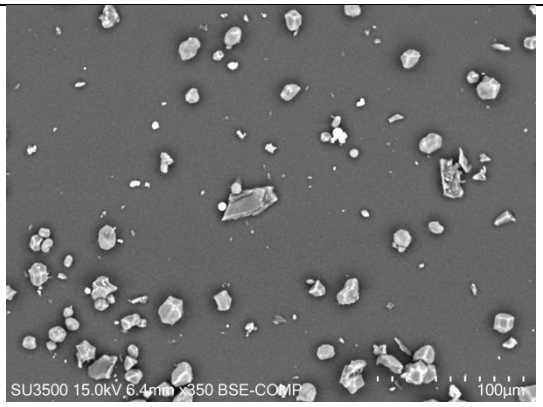

Barbara d98

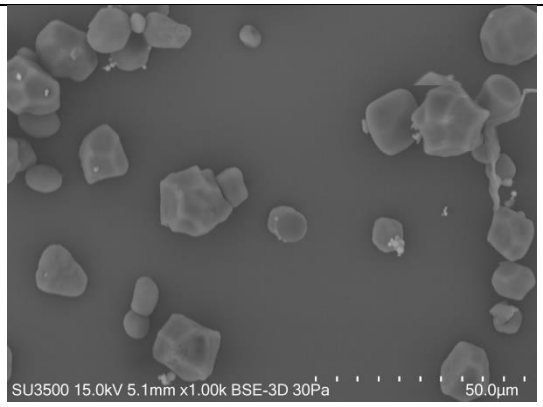

Cornstarch

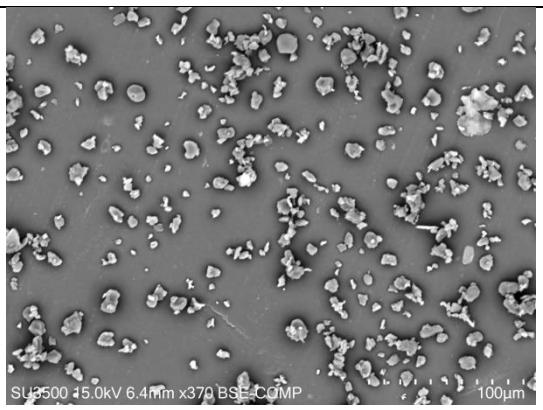

Wax

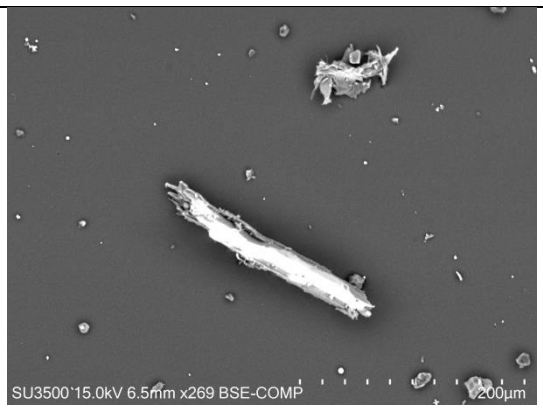

Wood dust

***Fig. 2.** SEM photos of the dusts*

2. Results and discussion

To assess the influence of dust presence in the dispersed medium, measurements of flow generated by the dispersion of the dusts were performed for five dust concentrations ranging from 125 to 1000 g/m^3. For each concentration of a given dust, the measurements were repeated at least five

times. Additionally, for reference, eight measurements of air-only flow intensity were carried out. From the measurements, instantaneous flow velocity *u'* and root-mean-square of the velocity u'_{rms} were calculated using the same method as described in (Z. Dyduch, Toman and Adamus, 2016). Below, the results of all those measurements are presented in various forms.

2.1. Turbulence generated by dispersion of dust/air mixture

The calculated average values of u'_{rms} are presented in Fig. 3. As shown in previous work (Dyduch, 2024), flow formation during dust dispersion is delayed. The delay increases with dust loading, causing a shift of the maximum of the flow intensity. The delay is similar for all dusts tested. The larger the dust concentration, the longer the delay. The maximum values of u'_{rms} are slightly larger than 10 m/s and are reached between 0.3 s and 0.4 s from the start of the dispersion. The influence of dust load is most pronounce in case of *Barbara d98*. The effect is smallest for *Wax*.

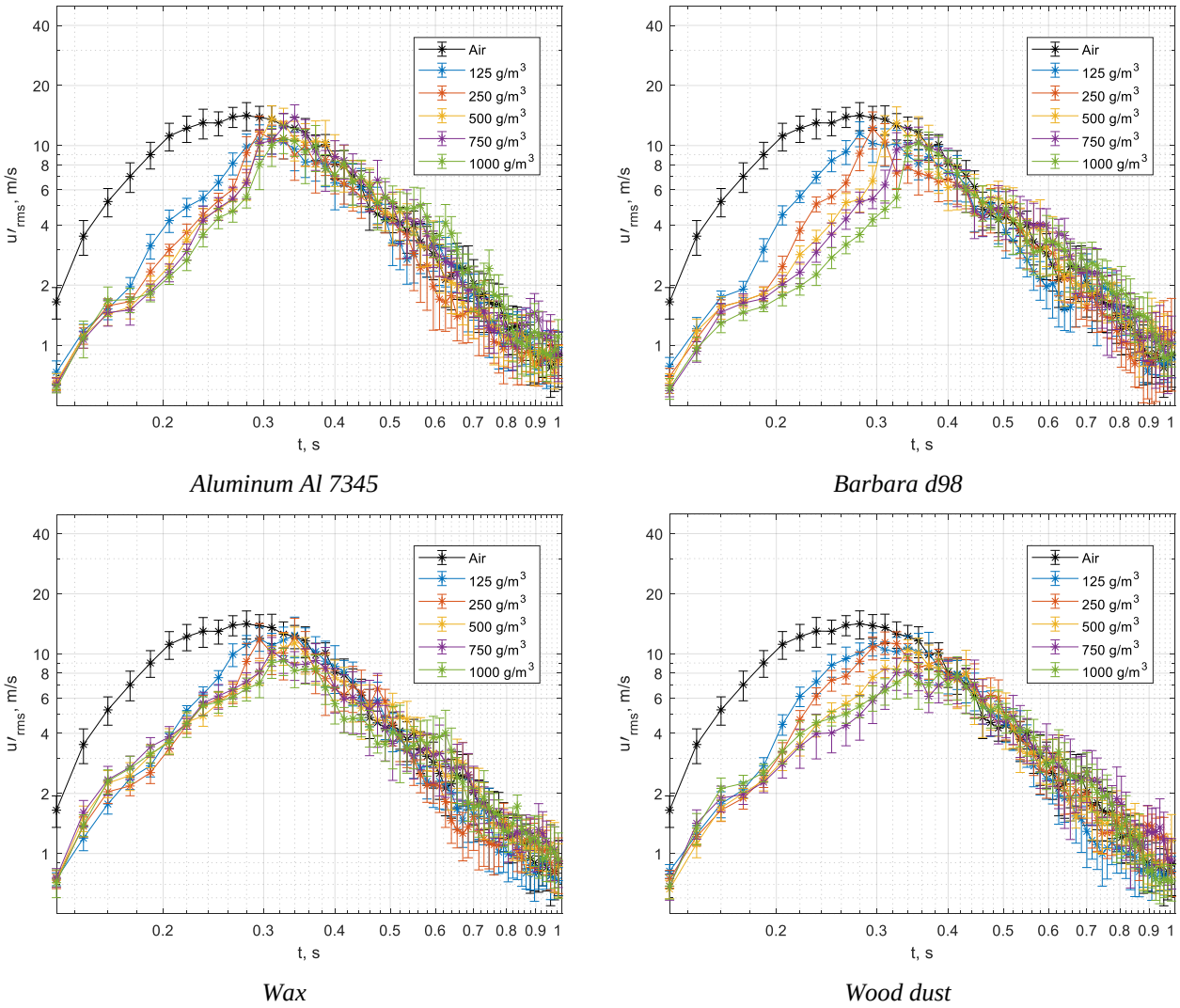

Fig. 3. *Root-mean-square of fluctuation velocity in dust/air*

Beyond maximum turbulence decay, quantify by u'_{rms}, is similar for all dust concentrations, and a reasonable analysis is practically impossible. Therefore, to examine the period of dust explosion in standard test conditions, relative differences of u'_{rms} obtained in tests with dust and pure air were analysed.

2.2. Deviation from air-only dispersion

In Fig. 4, differences between dust and air-only dispersion normalized with u'_{rms} of air are presented. Also included are results for *Barbara d38* and *Cornstarch* obtained in previous work. The differences indicate that in the case of small dust concentrations, its influence is insignificant. The outflow of the dust/air mixture from dust containers is not disturbed by small dust loads.

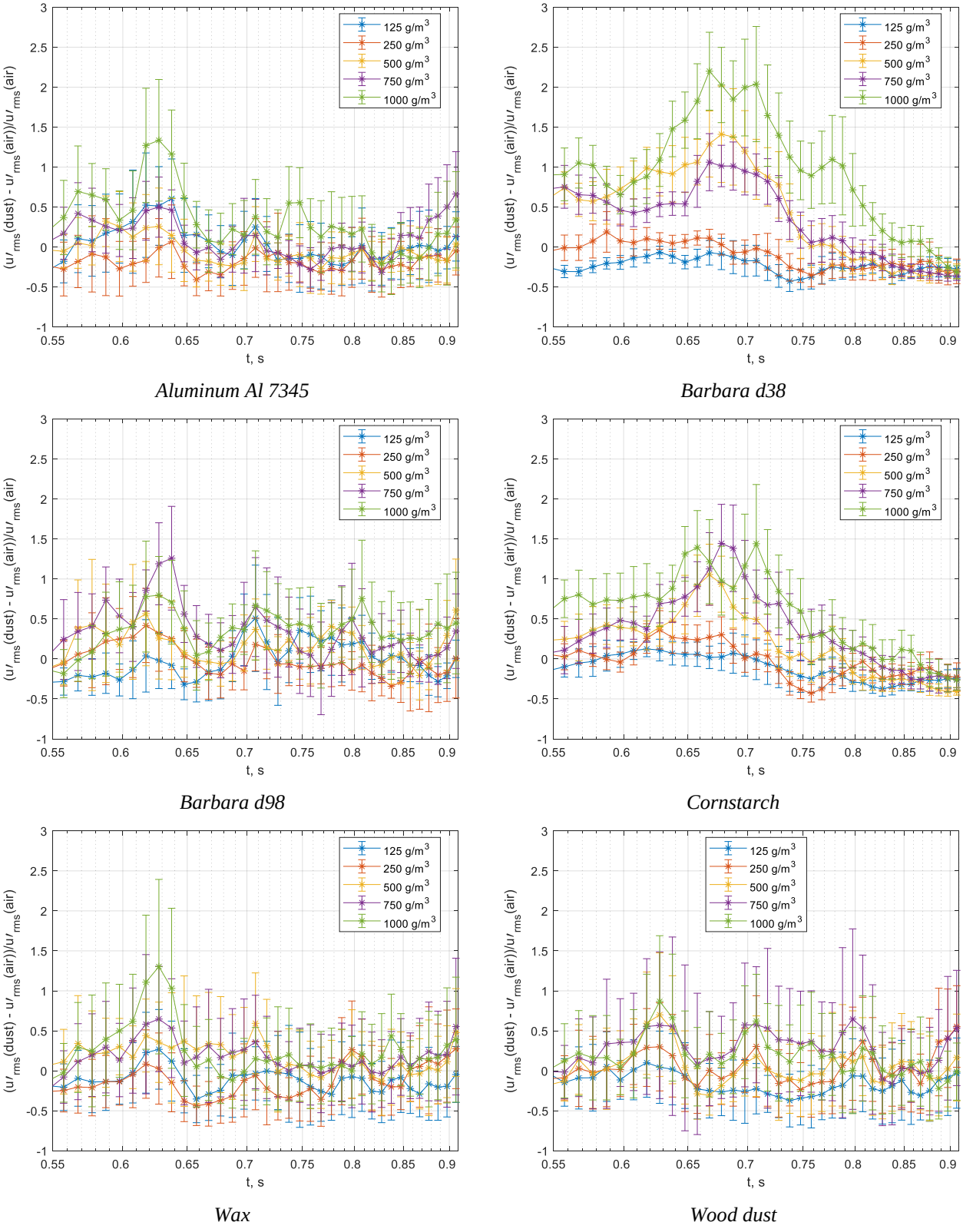

Fig. 4. *Relative differences of u'_{rms} values measured in experiments with and without dust*

However, for larger dust loads, the turbulence intensity is greater than for air-only dispersion. At their maximum values, the differences are close to 1.5 for most dusts and even over 2 in the case of *Barbara d38*. Interestingly, only for *Wood dust* does it not reach 1.

. It seems interesting to directly compare *Barbara d38* and *Barbara d98* as these are dusts of the same material that differ only in their fineness. Such a comparison is presented Fig. 5. Differences that may be significant are only in the period 0.6-0.7 ms and in case of largest dust concentration tested. After 0.7 s, turbulence inside the explosion vessel is practically the same rate.

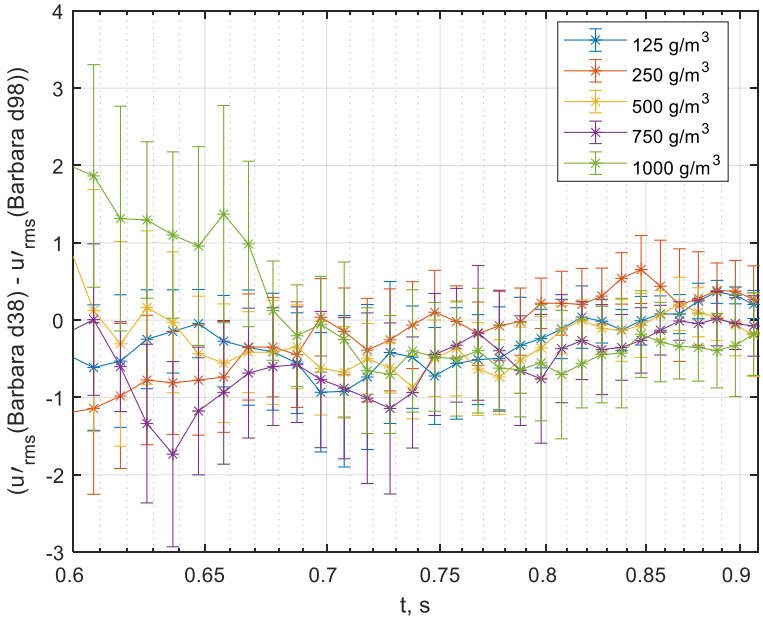

Fig. 5. *Comparison of Barbara dusts*

2.2.1. Integral measures

To enable a direct comparison of results for all dusts tested a simple parameters were introduced that defines a deviation of turbulence from air-only dispersion.

$$\Delta(dust) = \frac{1}{t_e - t_s}\int_{t_s}^{t_e} \frac{u'_{rms}(dust) - u'_{rms}(air)}{u'_{rms}(air)}\,dt$$

$$\Delta_{abs}(dust) = \frac{1}{t_e - t_s}\int_{t_s}^{t_e} \frac{|u'_{rms}(dust) - u'_{rms}(air)|}{u'_{rms}(air)}\,dt$$

The parameters are the average relative difference (Δ) and its absolute value (Δ_{abs}) of u'_{rms} in the period of dust explosion in standard test conditions: t_s = 600 ms, t_e = 900 ms. The values of these parameters as a function of dust concentration are presented in Fig. 6. Both sets of plots are similar and confirm the rising tendency of the difference with increasing dust concentration. For small concentrations, the differences Δ are insignificant. Their absolute values are at the level of 20% of air u'_{rms}. For large concentrations, the values of are in the range 20%-30%, and in case of *Barbara d98*, it exceeds 40%.

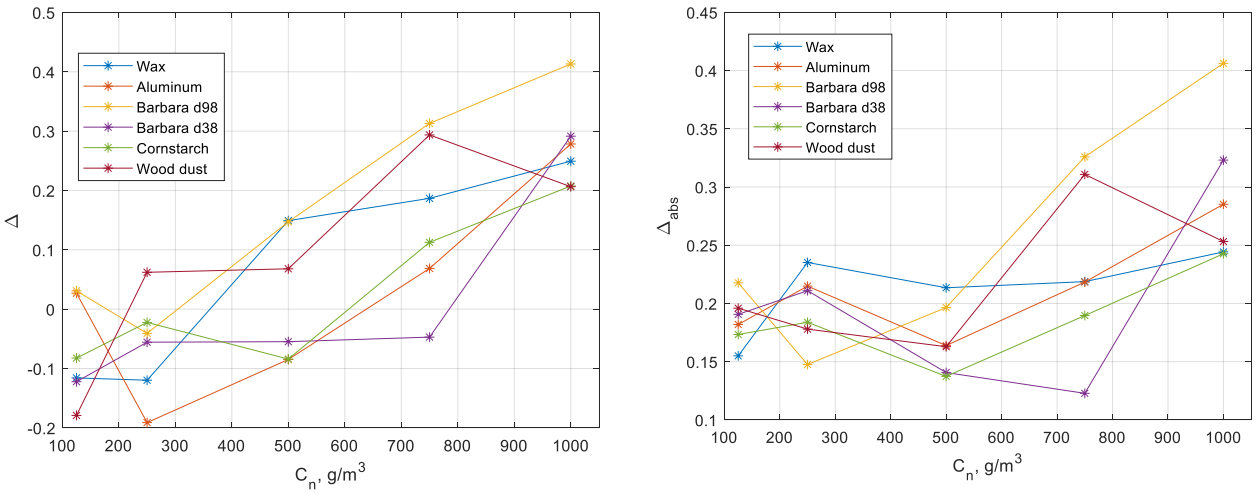

Average differences Δ *Absolute differences Δ_{abs}*

Fig. 6. *Average relative differences and absolute average difference of u'$_{rms}$ values*

2.3. Influence of dust properties

The average relative difference *Δ* can be used to check if turbulence modification by dust presence is connected with particular dust properties listed in Table 1. Results in Fig. 6 indicate that an apparent relationship could not be expected.

2.3.1. Bulk density

It could be expected that bulk density, as a factor that influences the inertia of the dust load in the dust container, may change the delay of an outflow from the container. However, no such dependence can be inferred from the plots presented in Fig. 7.

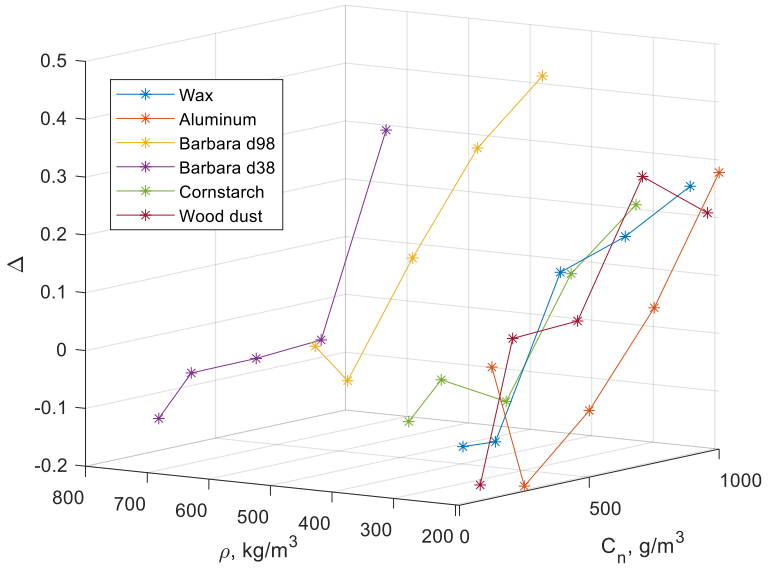

Fig. 7. *Influence of bulk density on u'$_{rms}$ on average relative differences*

2.3.2. Specific surface

Specific surface is determined by both particle sizes and the roughness of their surface. The dependence on that parameter is presented in plots in Fig. 8.

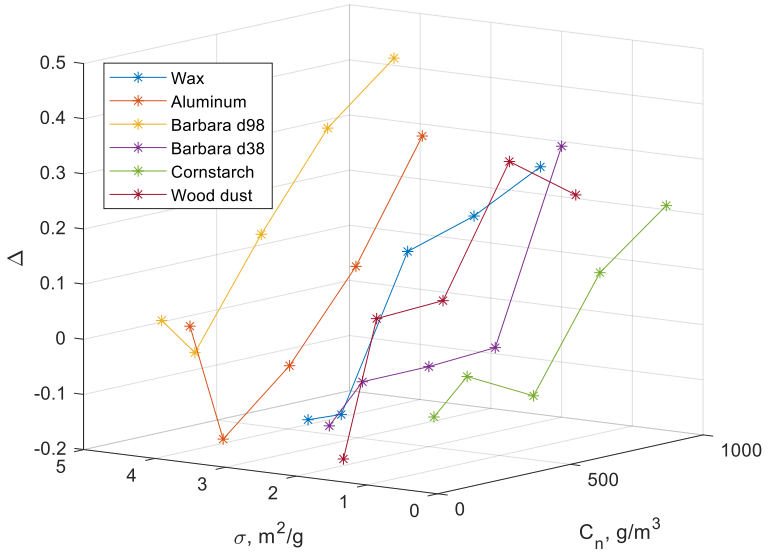

Fig. 8. *Influence of specific surface on u'$_{rms}$ on average relative differences*

For the largest dust concentration, there appears to be a weak relationship between Δ and σ. A comparison with the results in Fig. 9 might lead to a suggestion that the roughness of particle surfaces might play a certain role in flow modification. Whether roughness of particle surfaces influences fluid flow or if it's an actual effect should be further investigated.

2.3.3. Granulation

The parameter D[4,3] mathematically defines the sphere of the particle's equivalent volume. Plots in Fig. 9 present the dependence of Δ on that parameter.

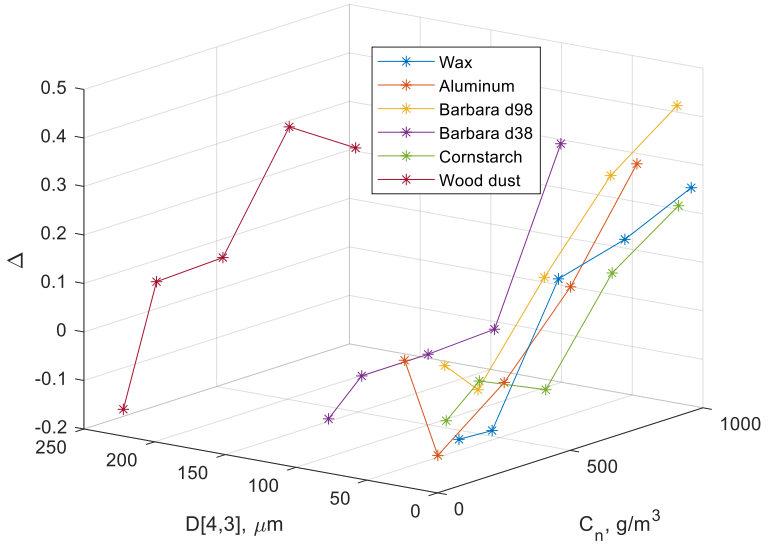

Fig. 9. *Influence of Weighted Average of the Volume Distribution on u'$_{rms}$ on average relative differences*

Again, no apparent dependence of Δ on D[4,3] can be found, even for largest dust concentrations tested.

3. Conclusions

Measurements of instantaneous flow velocity in the standard 1 m³ vessel were carried out to assess the influence of dust on turbulence generated during dispersion in the standard test of dust explosion parameters. The measurements were performed for four dusts with different particle size distributions, specific surface areas, and various bulk densities. To obtain reference values, the same measurements were also performed for air-only dispersion.

The results confirm the previously identified influence of the amount of dust load on the size of turbulence modification. No apparent dependence of the modification on the checked physical parameters of the dusts was found. The results allow for a slight suggestion that particle roughness may cause a difference, but no explanation for that has been found yet. Further investigation is required in this regard.

The dusts used in the tests differ in practically all parameters considered. As a result, capturing properties that significantly impact turbulence is difficult. An exception is the comparison between *Barbara d38* and *Barbara d98* coal dusts, but even in this case, no significant differences can be identified. Keeping most parameters as similar as possible while only changing one or a few of them may allow for a clearer picture to be obtained. Further research will proceed in this direction.

As the turbulence modification increases with a dust load, it is possible that tests with larger dust concentrations would show more apparent dependencies.

Acknowledgements

The work was conducted as part of statutory research at the Central Mining Institute – National Research Institute in Katowice (No. 11121021220), financed by the Ministry of Science and Higher Education, Poland.

References

Addo, A. *et al.* (2019) 'Niacin, lycopodium and polyethylene powder explosibility in 20-L and 1-m3 test chambers', *Journal of Loss Prevention in the Process Industries*, 62(May), p. 103937. Available at: https://doi.org/10.1016/j.jlp.2019.103937.

ASTM-E-1226 (2012) 'Standard Test Method for Explosibility of Dust Clouds', *American Standard* [Preprint].

Dyduch, Z. (2024) 'Turbulence generated by dust dispersion in the standard 1 m3 vessel', *Journal of Loss Prevention in the Process Industries*, 89(January), pp. 1–7. Available at: https://doi.org/10.1016/j.jlp.2024.105288.

Dyduch, Z., Toman, A. and Adamus, W. (2016) 'Measurements of turbulence intensity in the standard 1 m3 vessel', *Journal of Loss Prevention in the Process Industries*, 40, pp. 180–187. Available at: https://doi.org/10.1016/j.jlp.2015.12.019.

EN14034+A1 (2011) 'Determination of explosion characteristics of dust clouds', *European Standard* [Preprint].

Hauert, F. and Vogl, A. (1995) 'Measurement of Dust Cloud Characteristics in Industrial Plants, Final Technical Report: Protecting People, Equipment, Buildings and Environment Against Dust Explosion-CREDIT Project', (January).

Islas, A. *et al.* (2023) 'Biomass dust explosions: CFD simulations and venting experiments in a 1 m$ ^3 $ silo', *Process Safety and Environmental Protection*, 176, pp. 1048–1062.

ISO6184/1 (1985) 'Explosion protection systems – Part 1: Determination of explosion indices of combustible dusts in air', *ISO Standard* [Preprint].

McCaffrey B.J., H.G. (1976) 'A robust bidirectional low-velocity probe for flame and fire application', *Combustion and Flame*, 26, pp. 1125–1127.

Portarapillo, M. *et al.* (2022) 'CFD simulation of turbulent fluid flow and dust dispersion in the 1 m$ ^3 $ explosion vessel equipped with the rebound nozzle', *Journal of Loss Prevention in the Process Industries*, 76, p. 104755.

Proust, C., Accorsi, A. and Dupont, L. (2007) 'Measuring the violence of dust explosions with the

"20 l sphere" and with the standard "ISO 1 m3 vessel". Systematic comparison and analysis of the discrepancies', *Journal of Loss Prevention in the Process Industries*, 20(4–6), pp. 599–606. Available at: https://doi.org/10.1016/j.jlp.2007.04.032.

Proust, C. and Jamois, D. (2021) 'Measuring the flow and the turbulence in a harsh environment using a modified Mc Caffrey gauge', *Flow Measurement and Instrumentation*, 80, p. 101993.

Shelkin, K.I. (1943) 'On combustion in a turbulent flow', *Journal of Technical Physics*, 13(9–10), pp. 520–530.

Tamanini, F. (1998) 'The role of turbulence in dust explosions', *Journal of Loss Prevention in the Process Industries*, 11(1), pp. 1–10. Available at: https://doi.org/10.1016/S0950-4230(97)00026-0.

Zhen&Leuckel (1994) 'Zhen&Leuckel.pdf', *Journal of Loss Prevention in the Process Industries*, 10(5–6), pp. 317–324.

Experimental Determination of the Minimum Ignition Energy for Aerosols of Combustible Liquids

Adrian Toman[a], Wojciech Adamus[a]

[a]Central Mining Institute (Katowice, Poland)

E-mail: a.toman@gig.eu

Abstract

The analysis of accident incidents at workplaces has forced many experimenters to pay more attention to the hazards associated with aerosols of combustible liquids. Aerosols of these liquids are increasingly utilized and commonly encountered in various production processes. While the threat of aerosol explosions has long been recognized, precise guidelines and preventive measures have not been thoroughly defined. Preventing aerosol explosions and implementing effective countermeasures requires specific information about their flammable and explosive properties. Thus far, experimentation remains the optimal method for obtaining such information.

Knowledge of the minimum ignition energy of aerosols of combustible liquids, as a fundamental ignition parameter, appears crucial for ensuring safe practices in locations where such aerosols may be present. Unlike dust and gases, there is no established guidelines or well-defined research apparatus for aerosols. To address this gap, we designed and built a prototype device for investigating the minimum ignition energy of aerosols of combustible liquids .

The device consists of a spherical container with a 5-L capacity, equipped with an aerosol-generating system and either a spark inductive or capacitive ignition source.

This article presents the results of experiments conducted with isopropanol, ethanol, diethylether 99,5%, providing valuable insights into the minimum ignition energy of these aerosols.

Keywords: *hazards, aerosol, spray, spark ignition, explosion, flame propagation*

Introduction

The development of industry, technology and materials engineering constantly forces us to adapt the installations to ensure safe working conditions. As a result, there is a continuous increase in demand for research on the behavior of flammable mixtures under various conditions. Numerous studies are conducted on the ignition susceptibility of materials such as dust, gas, liquid vapors, and aerosols of flammable liquid. Various ignition sources are used to determine the flammability and explosive parameters of these media in laboratory tests. Typically, these are sources that occur on a daily basis in industrial installations. The type and energy of the ignition source affect the initiation of ignition/explosion and the subsequent flame propagation. One such source could be a static electricity. For dust and gases, the test of ignition from a spark ignition source is conducted using specialized equipment to determine the minimum ignition energy, as detailed in European and American standards according to established procedures. As static electricity is common in both industry and daily life most of its effects often go unnoticed. However, in the event of contact with a flammable substance, it can be an effective ignition source. One of the key parameters of flammability when assessing explosion risk is the minimum ignition energy MIE. Experimental studies for determining the MIE for dust or gas vary significantly. In the case of gases, ignition of the mixture occurs in a quiescent state (Uchman W.,Werle S. 2018). In the case of dust, there are many variable factors, and proper synchronization of dust cloud formation and ignition is of great importance. Synchronization between the generation of the transient dust cloud and sparking is

essential when studying the MIE of dust clouds (Randeberg E., et al 2007). The minimum ignition energy is therefore measured at various dust concentrations, looking for the optimal concentration and the lowest possible level of turbulence. It is reduced by prolonging the ignition delay time, according to the standard (EN 13821:2003, EN ISO/IEC 80079-20-2:2016). Unfortunately, there is no standard equipment and procedure for determining MIE for flammable liquid aerosols as there is for dust and gases. Due to the action of gravitational forces on the particles of a liquid aerosol suspended in the air, aerosols in this case seem to be closer to dust than to gases. For gaseous mixtures depend, minimum ignition energies depend on the composition and thermodynamic states of the mixtures (Oancea D., et al. 2003,), as well as the applied ignition source (Uchman W. 2018). For dust and aerosols of flammable liquid, another very significant factor affecting flammability is particle size. In the case of dust, the size reduction can be determined before the test for each sample, but for aerosols, the particle size is strictly dependent on the method of dispersion. This mainly depends on the applied aerosol generation technology and test conditions. Experimenters studying aerosol for the same liquid may obtain different results. The number of conducted studies for aerosols is incomparably smaller compared to dust or gases. The reason for this is the immense complexity of conducting the experiment, involving various configurations sophisticated enough to account for different factors in aerosol testing (Ballal, 1981, Shuai Yuan et al 2021). The MIE results obtained so far for aerosols of flammable liquid are limited to a small number of experiments, additionally conducted by different methods and apparatus. This work updates the number of the MIE studies conducted on the apparatus (Toman A., Adamus W. 2023) according to the specified procedure for isopropanol, ethanol 99%, diethyl ether 99.5% aerosols, taking into account particle size and the applied ignition sources.

1 Spark ignition sources

In industrial production processes, the static electricity can easily occur during material transport, operation of mechanical devices, or even human movement. In reality, static electricity is difficult to completely eliminate, which can result in accidental ignition and explosion of hazardous substances (Eckhoff, 2002; Eckhoff et al., 2010). Electrostatic discharge occurs as:

- Corona discharge,
- Spark discharge,
- Brush discharge,
- Propagating brush discharge,
- Cone discharge.

It is important to understand the characteristics of these discharges. The threat of fire or explosion arises when the energy of electrostatic discharge reaches a value comparable to the minimum ignition energy of the medium present. This value characterizes the ignitability of the material. It is the smallest energy value of electrostatic discharge capable of igniting a given flammable substance or initiating an explosion of a mixture formed by this substance with air or oxygen. Such a substance can be a solid material, especially in the form of dust, liquid, or gas. Generally, gas or vapor mixtures have lower ignition energies than clouds of dust or liquids alone.

In the test apparatus used, an ignition system with or without inductance is used as the ignition source, the so-called capacitive. While both capacitance and inductance, are present in the ignition system, the nature of the electric spark (capacitive or inductive) has a significant impact on the ignition phenomenon, in particular in terms of power and energy in the individual phases of the electric discharge. The duration of each phase and the amount of released energy can vary depending on the design of the ignition system (Sulaiman, 2011). The type of ignition system also determines the dominant phase of the discharge, as energy stored in the capacitance is released

during breakdown and arcing phases, while the glow phase is powered by energy stored in the inductance. As mentioned by Randeberg (2006), when testing dust for the low ignition energies, most methods of generating sparks fail on one or more of the following points:

- Precise synchronisation between dust dispersion and spark onset must be available.
- The energy losses must be insignificant or taken into account when calculating the spark energy.
- The sparks produced should be as similar as possible to purely capacitive electrostatic discharges.

Based on the above suggestions, a spark ignition source meeting these requirements was used to determine the minimum ignition energy of aerosols of flammable liquids.

2 Methods and Materials

2.1 Experimental apparatus

The experiments were conducted in the Adolf Küchner test chamber with a volume of 5-L, originally intended for the study of dusts explosivity. The adaptation of the equipment for aerosol testing and the research procedure is described in more detail in (Toman A., Adamus W. 2023). The aerosol is introduced into the internal space through an adapter at the bottom of the chamber using a pump injection system. The injection system used allows for the generation of aerosol droplets in the range of 10-50 μm. Precise control of the aerosol dosed into the chamber is ensured by a precise injection control system. With this aerosol generation method, the increase in pressure in inside the 5-L test chamber is solely caused by the volume of aerosol introduced into the chamber. The theoretical maximum increase in pressure at the highest concentration of isopropanol is about 0.1% of the initial pressure. The spark ignition source was mounted in the geometric center of the chamber with electrodes made of stainless steel with a diameter of 2 mm and a spacing between them of 3.3 mm, with sharpened tips. In the initial tests, a spark generator with variable energy with inductance was used. In further tests, four capacitive ignition sources with no inductance were built, for each energy level: 1, 3, 10, and 30 mJ. The constructed system for one of the selected energies was mounted directly onto the electrode rods. This was aimed at minimizing the parasitic capacitance, particularly significant for energies below 30mJ. A regulated high-voltage power supply up to 11 kV was used to power the ignition source, allowing for precise energy adjustment with a tolerance of ± 5%. The spark energy value was calculated according to the formula:

$$W = ½ Cu * U^2 \quad (1)$$

where: W is the stored energy in (J), Cu - capacitance of the capacitor in (pF), U - voltage of the charged capacitor in (V).

The parasitic capacitance and its influence on the spark energy were taken into account in every configuration of the system. The electrode rods had a particularly significant impact on this capacitance. With each change of the ignition head, the parasitic capacitance was measured to adjust the voltage supply (HV). The effective capacitance (Cu) for low energies is only slightly

larger, so omitting the parasitic capacitance could lead to a significant error in the result. Voltage corrections were made based on calculations.

$$Up = \frac{\sqrt{2W}}{\mathrm{Cu} + \mathrm{Cp}} \tag{2}$$

$$Uu = \frac{\mathrm{Up} * (\mathrm{Cu} + \mathrm{Cp})}{\mathrm{Cu}} \tag{3}$$

where:

Uu – charging voltage of the Cu capacitor [V]
Up – discharge voltage (spark jump voltage) [V]
Cu - working capacity [F]
Cp – parasitic capacitance [F]
W - Spark discharge energy [J]

A series of tests was conducted to determine the residual energy after the spark discharge. The results of these tests showed that for the most unfavorable case, the error amounted to 3% of the total spark energy, and therefore they were disregarded.

The spark discharge detection system was applied in the setup for spark initiation control. In MIE studies, this is crucial to confirm the ignition of the mixture and that the absence of a spark may indicate a failure to ignite the mixture. Two piezoelectric pressure sensors were used to track pressure changes in the test chamber during the explosion.

The experiments were conducted at temperatures between 21-22°C. To control the explosion chamber temperature the test chamber was equipped with a water jacket, which, along with the cooling system and temperature measurement unit, responsible for stabilizing the internal temperature. Control and maintenance of a constant temperature in aerosol studies is crucial, as even slight deviations in temperature conditions can significantly affect the final result.

A schematic diagram of the setup using an inductive ignition source is presented in Fig. 1a. A schematic diagram of the setup with a capacitive ignition source and discharge control is shown in Fig. 1b.

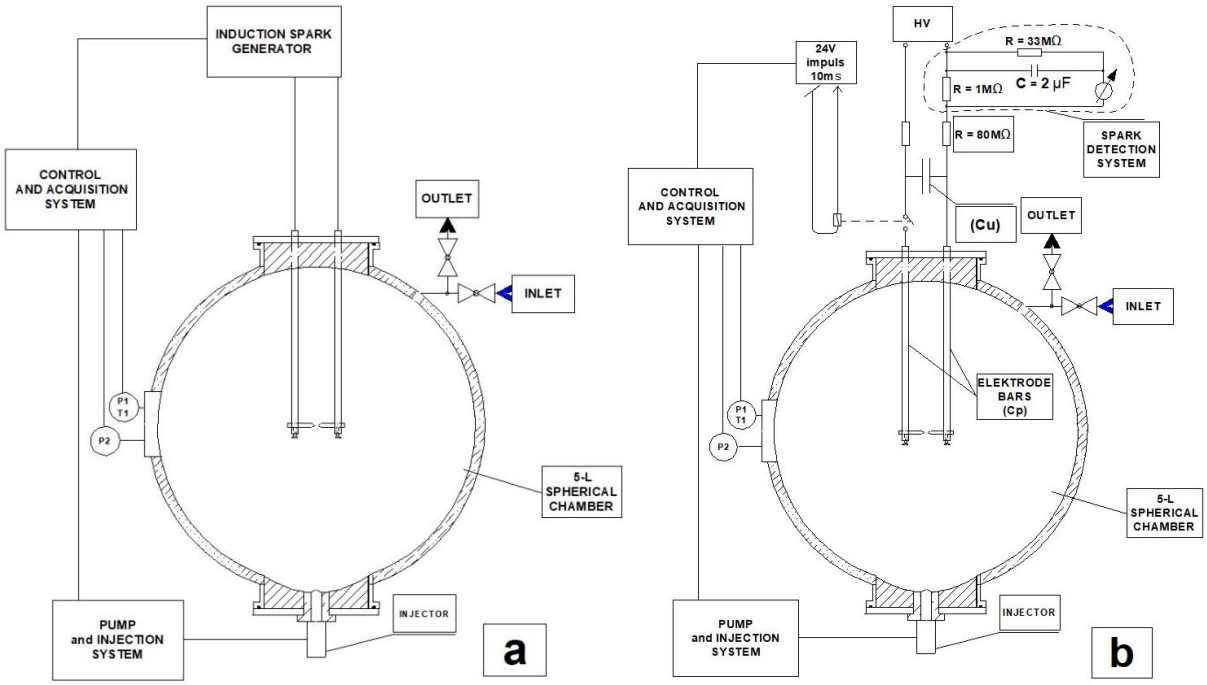

Fig. 1: *Sketch of a test stand with an inductive (a) and capacitive (b) ignition source*

2.2 Test procedure

The lack of guidelines for studying the minimum ignition energy of flammable liquid aerosols forces experimenters to search for suitable conditions according to their own needs and the specifics of the equipment used. Previous studies (Toman A., Adamus W. 2023) on determining explosivity parameters of aerosols established initial conditions before ignition. The same aerosol generation technique was also used in this study. Sequential injection of ten individual sprays was applied. The duration of such a sequence is 130 ms. Depending on the liquid density, the maximum concentration for this sequence in the case of isopropanol is 320 g/m^3. Achieving as low turbulence as possible was realized by appropriately delaying the ignition. In this study, following the procedure outlined in (EN-13821:2003, EN-80079-20-2) standards for dusts, tests were conducted for various ignition delays at different concentrations. According the recommendations of the standards, the tests were performed under the lowest possible turbulence conditions. However, considering the fact that we are investigating a different medium than dust, the ignition tests were also conducted immediately after the end of injection, without any delay. The measurement sequence is presented in Figure 2.

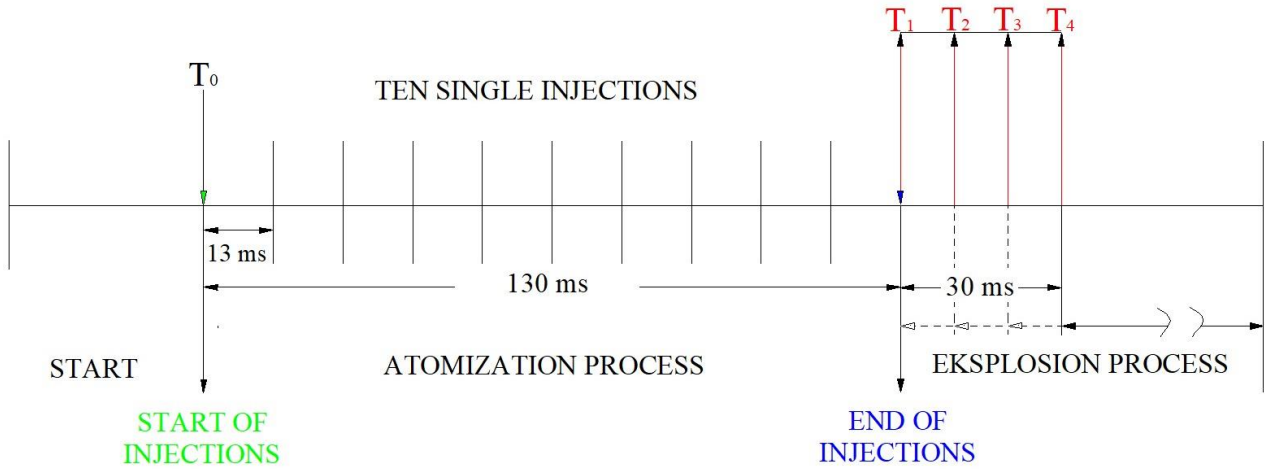

***Fig. 2**: Injection and ignition time diagram.*

The tests were conducted for various concentrations depending on the liquid being studied, ranging from 25 g/m^3 to 320 g/m^3. Before proceeding with the main experiments for each liquid under investigation, the an analysis of the aerosol droplet size distribution generated by the pump injection system was carried out. These studies were conducted using a laser diffraction particle analyzer, the Malvern Panalytical Spreytec. A technical limitation in measuring particle sizes within the 5-L test chamber necessitated the use of a different spherical Plexiglas sphere of the same volume. To avoid signal disturbance, measurement apertures with a diameter of approximately 4 cm were made on opposite walls of the sphere (Figure 3).

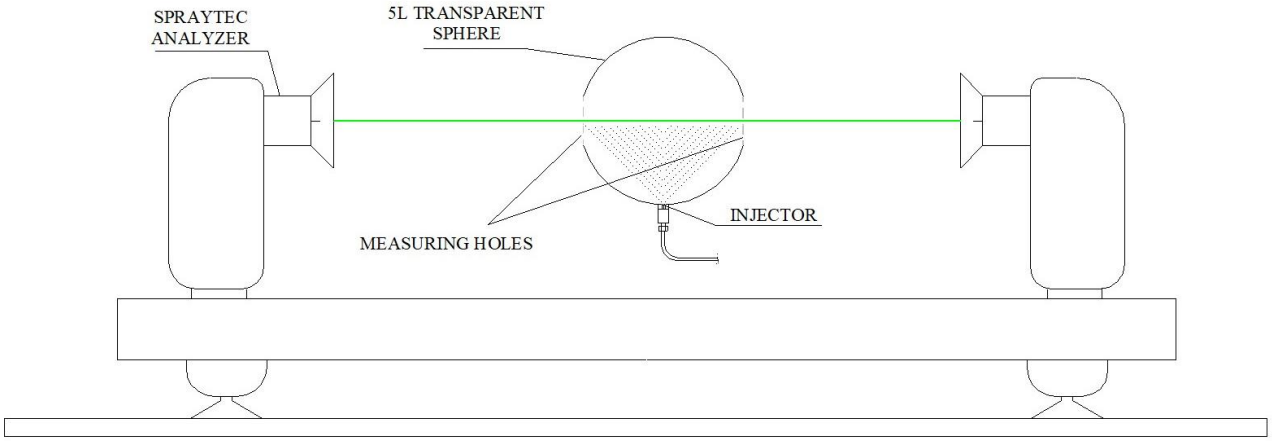

***Fig. 3.** Measurement of the aerosol particles size in the 5-L sphere with holes cut out.*

As in the case of dust or gases, a crucial aspect of MIE studies is, of course, the ignition criterion. In the conducted research, the ignition criterion was defined as a pressure increase of 0.5 bar relative to the initial pressure.

2.3 Properties of selected liquids

The generation of aerosol droplets depends not only on the system used but also on the properties of the liquid. Factors such as density, surface tension, and viscosity influence the aerosol generation process. In aerosol studies, the boiling temperature is also significant as it provides information about the evaporation rate at room temperature. Table 1 presents the essential properties of the three liquids under investigation.

Table 1. *Physical properties of different liquids*

	DIETHYL Ether 99,5%	Isopropanol	Ethanol 99%
Density (g/cm^3)	0.71	0.78	0.801
Viscosity (cSt)	0.331 mm^2/s in +20°C	2.43 (ASTM D-4052)	1.36 mm^2/s in +20°C
Surface tension (kg.s^{-2})	0.017	0,022	0.022
Flammability limits (%Vol.)	1.7–39%	2 – 12%	3.3 - 19
Flash point (°C)	- 40	11.7	12
Boiling point (°C)	35.58	85.5	78
Vapor pressure (hPa) in 20°C	589,6	43	60

3 Results and Discussion

3.1 Droplet size distribution

Taking into account the dynamic changes in the aerosol particle size distribution during dispersion in the test chamber, it was decided to refrain from providing a single-value parameter for the Sauter mean diameter for the liquids under investigation. Instead, Sauter mean diameter over a period of 200 ms from the start of injection was used. The tests were conducted for various concentrations of the liquids under consideration.

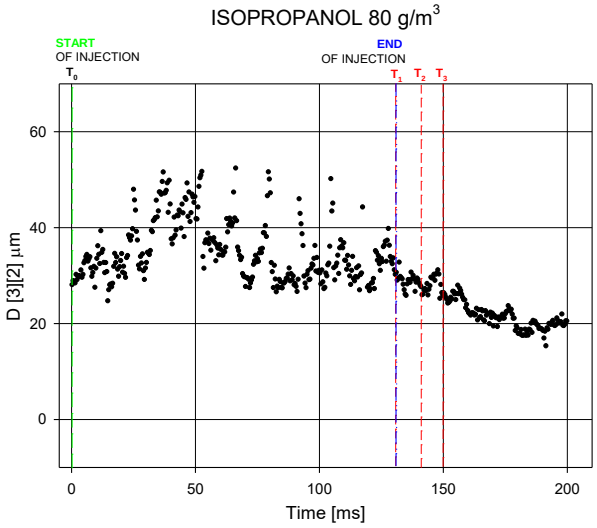

Fig. 4. *Particle size distribution of isopropanol aerosol over time for the Sauter mean diameter D [3] [2] for 80 g/m^3*

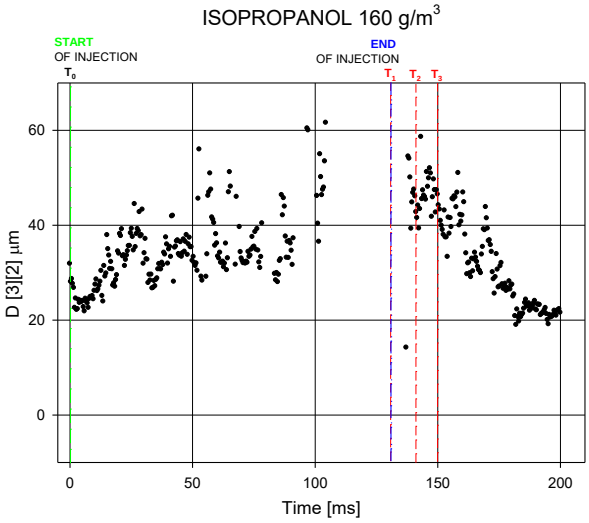

Fig. 5. *Particle size distribution of isopropanol aerosol over time for the Sauter mean diameter D [3] [2] for 160 g/m^3*

On figures 4-9, the beginning of the atomization process is marked by a green line, and its end by a blue line. We observe the evolution of the Sauter mean diameter of isopropanol over time for a concentration of 80 g/m^3 (Fig. 4) during the atomization process, where fluctuations in droplet size ranging from approximately 30-50 µm are evident. These changes may result from the sequential delivery of the aerosol. A temporary increase in droplet size is noticeable with each individual injection. This may be due to the agglomeration of aerosol particles during successive injections. In the graph for 160 g/m^3 (Fig. 5), we observe similar behavior, but for higher concentrations in the time range from approximately 100 ms to around 135 ms, the detectors of the

Spraytec analyzer temporarily lose signal. Local higher transient concentrations of dispersed aerosol hinders the flow of the laser beam to the detectors. In both cases, after the atomization process, stabilization occurs, and the particle diameter gradually decreases. The decreasing particle size may indicate the evaporation of dispersed isopropanol droplets.

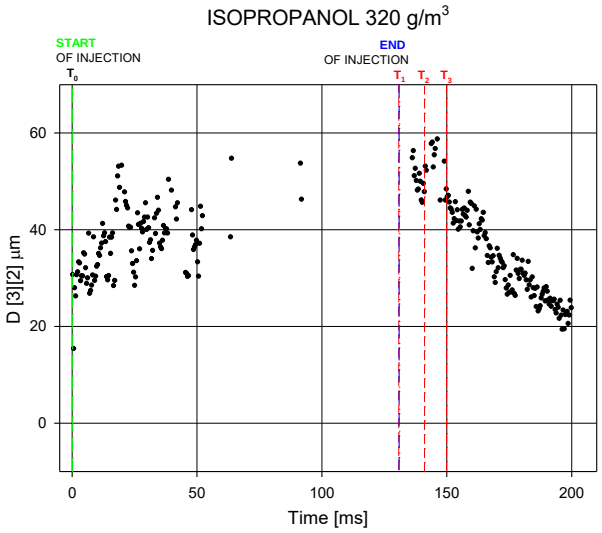

Fig. 6. *Particle size distribution of isopropanol aerosol over time for the Sauter mean diameter D [3] [2]*

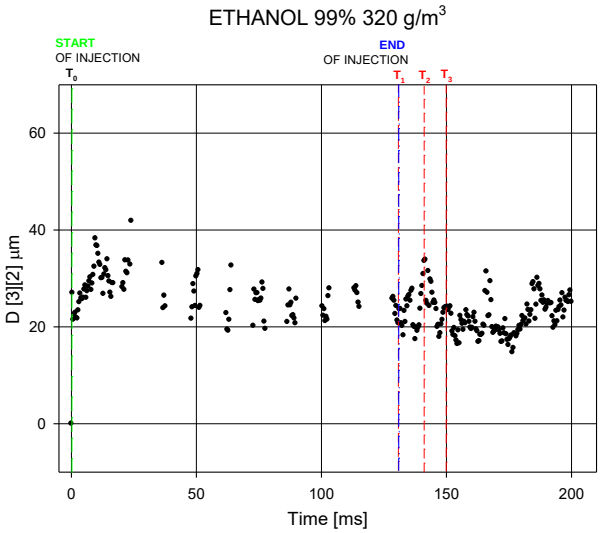

Fig. 7.*: Particle size distribution of ethanol 99% aerosol over time for the Sauter mean diameter D [3] [2]*

The dispersion process of isopropanol for a concentration of 320 g/m^3 (Fig. 6) looks very similar to that for a concentration of 160 g/m^3 (Fig. 5). However, a higher concentration disturbs the measurement is much earlier, caused by the local high concentration of aerosol in the laser path. Already after about 50 ms, the laser analyzer loses signal on the detectors, and returns similarly to the previous concentration around 135 ms. For ethanol (Fig. 7), the fragmentation course for the same tested concentration as for isopropanol looks completely different. The size of aerosol droplets to remain at a similar level throughout the entire atomization process. Nevertheless, noticeable gaps in the measurement occur at the locations of maximum aerosol injection intensity. Similar to isopropanol, these are momentary hindrances in the passage of the laser beam through the dense aerosol cloud. However, attention should be paid to the stable distribution of aerosol particles at the level of 20-30 µm throughout the measurement.

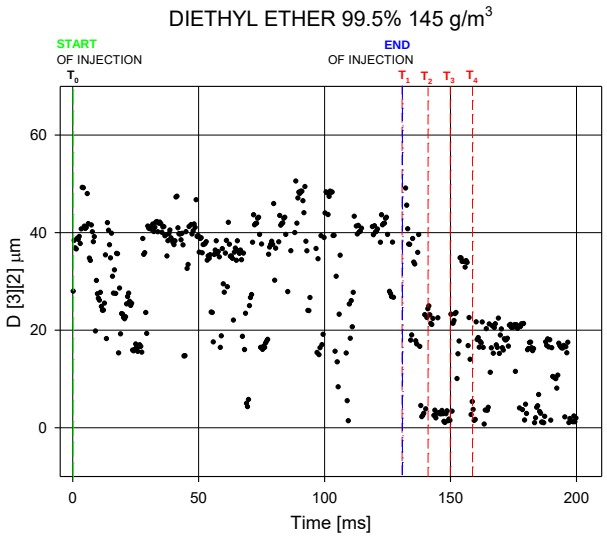

Fig. 8. *Particle size distribution of diethyl ether 99,5% aerosol over time for the Sauter mean diameter D [3] [2] for 145 g/m^3*

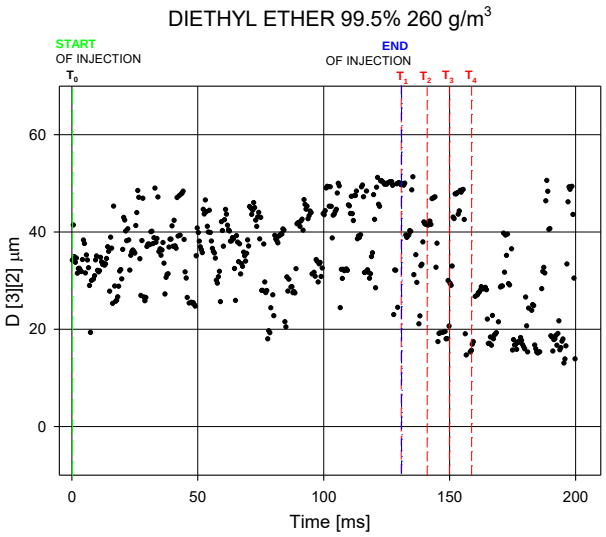

Fig. 9. *Particle size distribution of diethyl ether 99,5% aerosol over time for the Sauter mean diameter D [3] [2] for 260 g/m^3*

The characterization of the Sauter mean diameter for diethyl ether significantly differs from those for isopropanol and ethanol. A notable spread of measurement points is observed, especially for a concentration of 145 g/m^3 (Fig. 8). In the atomization zone, we observe a similar particle size measurement profile throughout the entire area, but an immediate change occurs after its completion. In the time interval from T_1 to T_2, we observe smaller differences compared to the atomization zone, unlike the interval from T_2 to T_4, where most aerosol droplets have a size below 20 µm. Significant differences in the properties of diethyl ether compared to isopropanol and ethanol are important in this case. The nearly tenfold higher vapor pressure of diethyl ether, at 589.6 hPa, and significantly lower boiling temperature (35.58°C) contribute to faster evaporation of dispersed aerosol droplets of this liquid. The faster evaporation of diethyl ether during particle size measurement may also be due to the presence of measurement openings in the sphere walls. The obtained result, conducted under these conditions, may differ from a result obtained under actual conditions, i.e., in a completely enclosed space. Much smaller differences can be observed in the case of higher concentrations, i.e., 260 g/m^3 (Fig. 9). We notice a smaller spread of measurement points and smaller changes in the T_1–T_4 ignition zone. The droplet size is mainly in the range of 20 µm – 50 µm.

As can be observed for the considered liquids, using the same aerosol dispersing device can yield different atomization effects. This is highlighted by Yuan S. et al. (2021), who mention that variability in droplet breakup and agglomeration, surface wetting, and evaporation pose challenges in conducting standardized aerosol experiments.

3.2 The minimum ignition energy for aerosols flammable liquids

The minimum ignition energy was determined for aerosols of isopropanol, 99% ethanol, and 99.5% diethyl ether. In the initial tests for isopropanol, an inductive ignition source with adjustable energy from 1.2 mJ to 7 J was used. These studies were conducted for two ignition delay times: T_1 at the end of the last injection and T_2 at 10 ms after the atomization process ended. Tests were carried out for various concentrations. If there was a lack of ignition for the tested concentration, this result

was confirmed three times. The results for isopropanol with the inductive ignition source are presented in Figure 10.

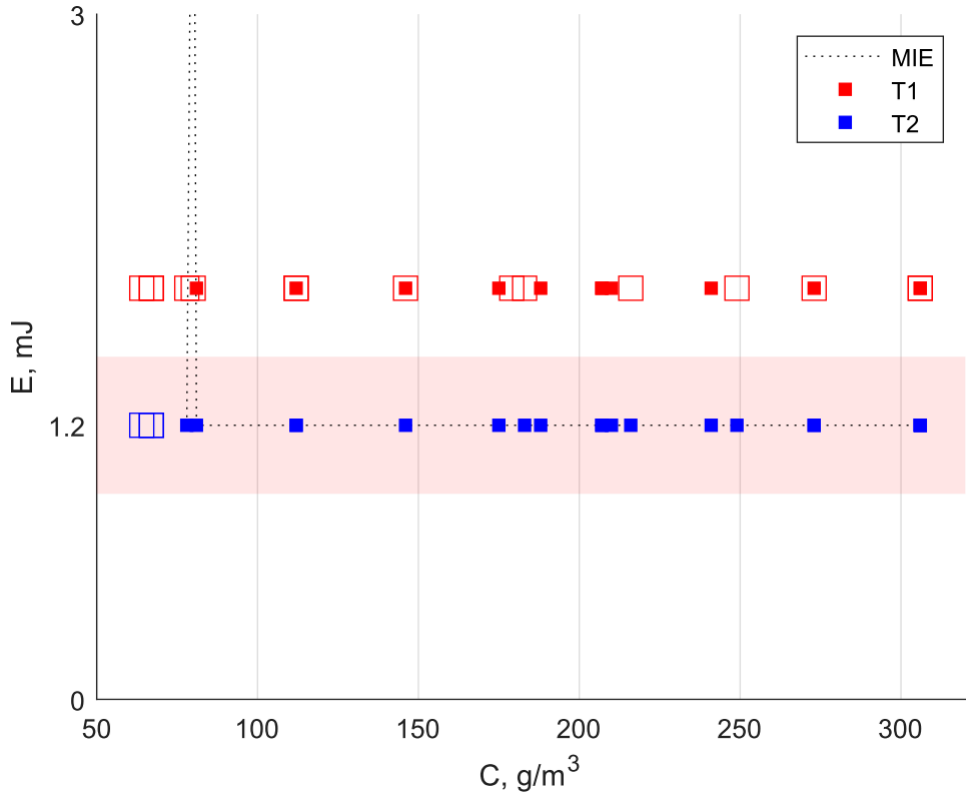

Fig. 10. *MIE for isopropanol with inductance*

For the lowest possible energy setting of 1.2 mJ, ignition for isopropanol was achieved for both delay times. Almost throughout the entire range of tested concentrations, a pressure increase higher than the accepted criterion was recorded. Only for the concentration of 70 g/m^3, the result was negative in both cases. A similar test was also conducted for ethanol but in a narrower concentration range. Ignition was achieved in every case.

Due to the inability to lower the spark energy in the used generator and its inductive nature, capacitive ignition source was employed in further studies. Capacitive ignition source for assessing fuel hazards was also used by (S.P.M. Bane et al., 2011). Capacitive spark discharges were also used for determining MIE (Babrauskas, 2003; Magison, 1990). As described by (LiuJia 2020), discharge efficiency is strongly related to the circuit generating the spark, especially the spark resistance to circuit resistance ratio. Taking this relationship and the experiences of other experimenters into account, the parasitic capacitance of the system was minimized in the newly applied ignition source. Studies with this ignition source were conducted for all three considered liquids. The obtained results are presented in Figures 11-13.

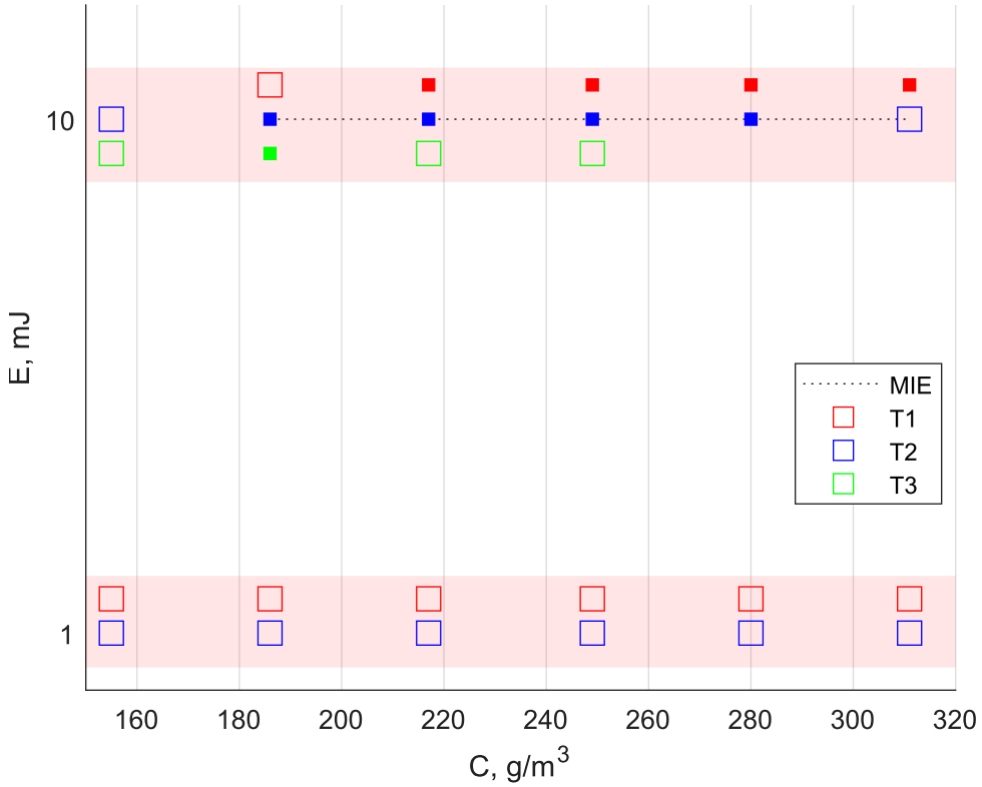

Fig. 11. *MIE for isopropanol no inductance*

The change of ignition source revealed significant differences compared to the previously obtained results. The inductive spark in the applied apparatus and conditions ignited the isopropanol aerosol more effectively than the capacitive ignition source. Ignition was registered for the ignition source energy of 10 mJ and concentrations from 185 g/m^3 for times T_2 and T_3. For T_3 (20 ms after the last injection), ignition was achieved only for concentration equal to 185 g/m^3. For T_2, ignition was recorded up to a concentration of 280 g/m^3. For T_1, ignition was observed from a concentration of 218 g/m^3 up to the maximum investigated concentration of 316 g/m^3. For an energy of 1 mJ, ignition was not achieved at any of the tested concentrations.

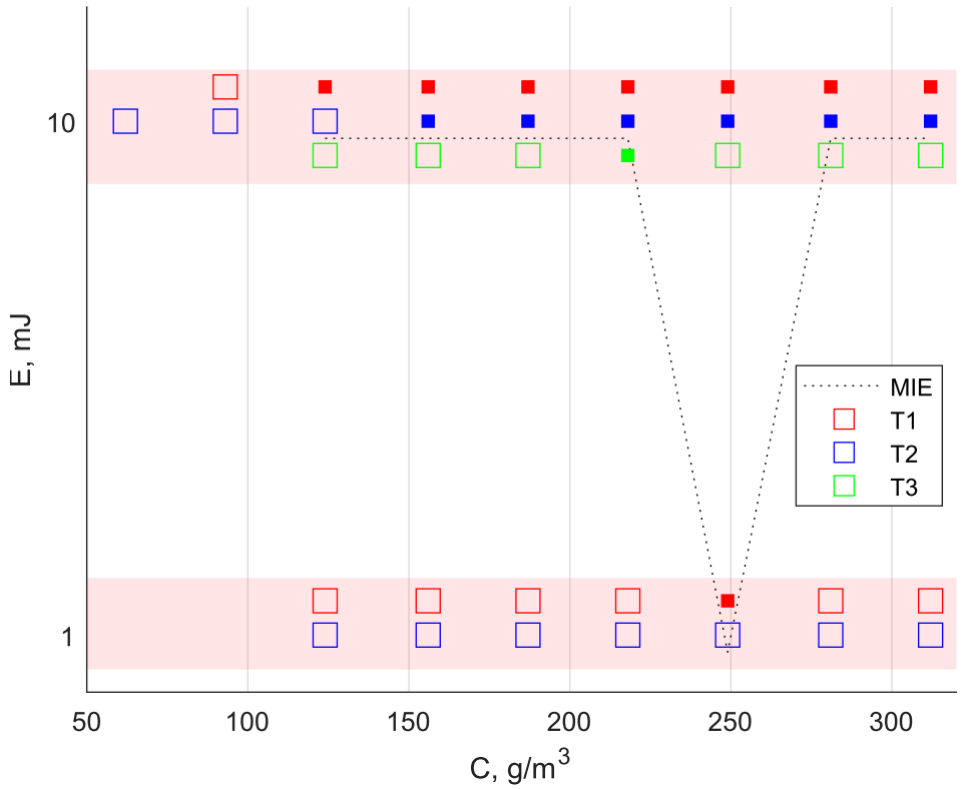

Fig. 12. *MIE for ethanol no inductance*

The conducted Minimum Ignition Energy (MIE) tests for ethanol aerosol also showed differences when using a different ignition source. This is confirmed by Eckhoff (2019), stating that there are significant differences in MIE with or without inductivity. Various triggering types may lead to different MIE results, even if the released energy is nearly the same (Wang et al., 2022). For a capacitive spark with an energy of 1 mJ, ignition was achieved only in one case at a concentration of 250 g/m^3 at time T_1. For 10 mJ at the same ignition time, the lowest concentration at which ignition was observed was 125 g/m^3. For time T_2, this concentration was 150 g/m^3. Each subsequent increase in concentration for T_1 and T_2 led to ignition, up to the maximum tested concentration of 310 g/m^3. Only one concentration of 220 g/m^3 ignited for time T_3. For both ethanol and isopropanol, favorable ignition conditions were observed in the T_1 and T_2 intervals.

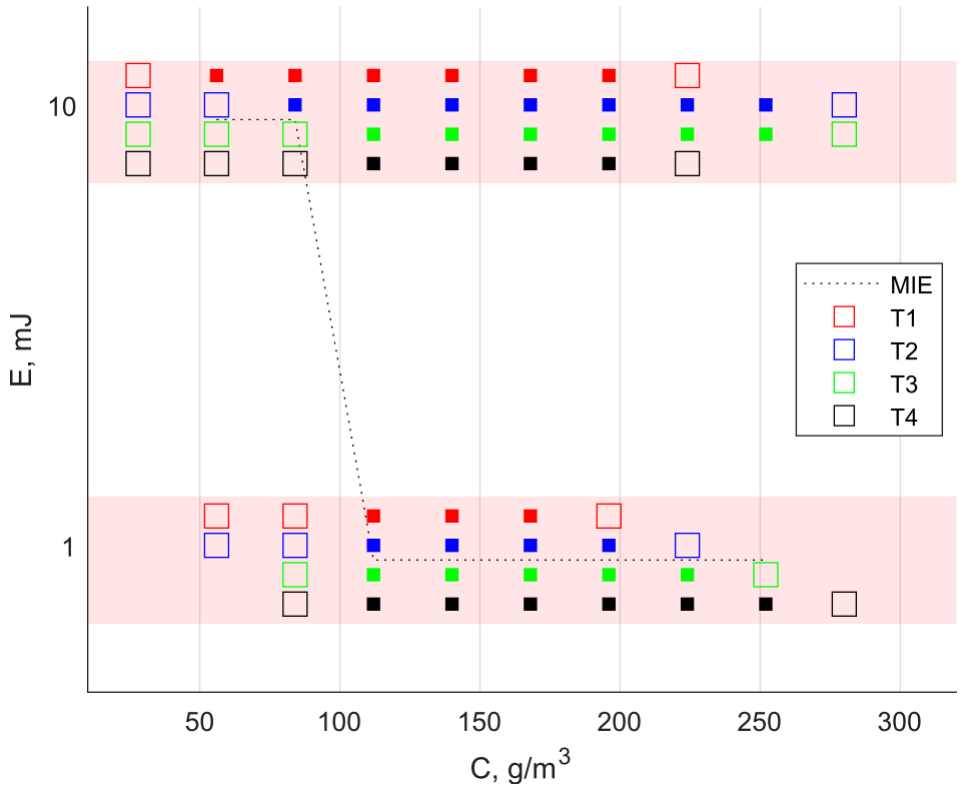

Fig. 13. *MIE for diethyl ether 99,5% no inductance*

The Minimum Ignition Energy (MIE) tests for diethyl ether were conducted only with a capacitive ignition source. For all tested ignition times $T_{1,2,3,4}$, ignition was observed from a concentrations of 112 g/m^3 with the lowest applied energy of 1 mJ. Unlike ethanol and isopropanol aerosols, dimethyl ether exhibited effective ignition at an energy of 1 mJ for all ignition delay times. The longer the time from the atomization process, the wider the concentration range that underwent ignition. The highest concentration that ignited was 253 g/m^3 for the longest tested time T4, which was 30 ms after the last injection.

3.3 Explosion characteristics of the diethyl ether

In most experiments with liquid fuel aerosols, the relationship between droplet size and flammable area is studied. If the aerosol droplet size is smaller than 10 µm, its lower flammable limit (LFL) is similar to the LFL of the corresponding vapor according to Burgoyne (1954), Faeth (1968). It has also been observed that as the droplet size increases, the LFL decreases according to Burgoyne (1963), Burgoyne (1954), Cook (1977), Danis (1988), Gam et al. (2012). In the conducted MIE tests for diethyl ether at various ignition delay times, the droplet size in the investigated time range can vary significantly. The pressure and pressure rise rate profiles for all tested times are presented in Figures 14 and 15.

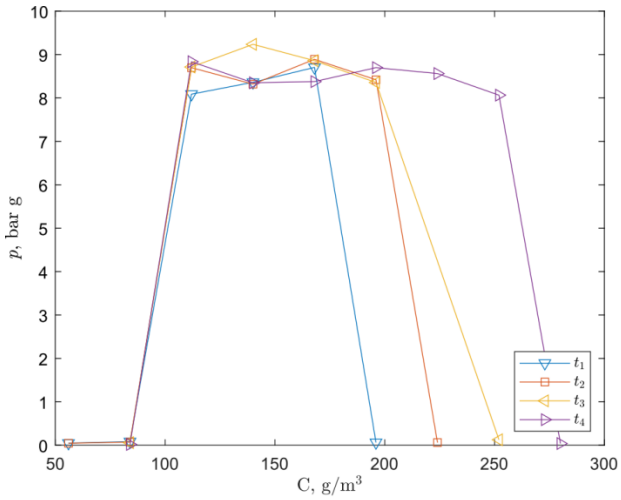

Fig. 14. *p_{max} for diethyl ether 99,5% at 21℃ for different ignition times*

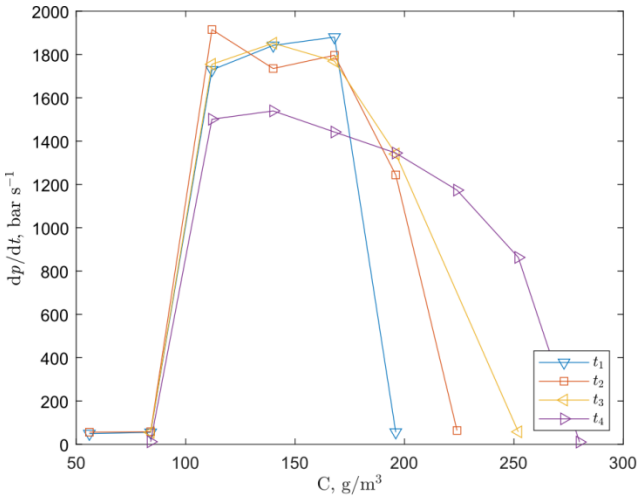

Fig. 15. *dp/dt_{max} for diethyl ether 99,5% at 21℃ for different ignition times*

As reported by Liu et al. (2020), the stoichiometric concentration of 99.5% diethyl ether is ~250 g/m^3. In actual chemical reactions, the volumetric ratio at which the peak pressure of the flammable mixture of vapor-air reaches its maximum value is always slightly higher than the stoichiometric state. Therefore, the experimental volumetric ratio of dimethyl ether/air mixtures is approximately ~3.7% (V/V), meaning the experimental concentration is ~275 g/m^3. Hence, the equivalence ratio is approximately ~1.1. (Liu et al., 2020)

In our case, for the dimethyl ether aerosol, the maximum explosion pressure p_{max} (Fig. 14) is obtained for a concentration of 150 g/m^3 at the ignition time T_3, 20 ms after the atomization process. For all four ignition delay times, the first pressure increase is observed at a concentration of 112 g/m^3. At this concentration, the lowest pressure was recorded for time T_1. For times $T_{2.3.4}$ we obtain a similar pressure values at subsequent concentrations for ignition, except for p_{max} as mentioned earlier. The highest concentration where a pressure increase was recorded was for time T_4. The maximum pressure rise rate dp/dt_{max} (Fig. 15) is obtained for a concentration of 112 g/m3 at time T_2. The level of dp/dt_{max} for times $T_{1.2.3}$ is very similar, around 1800 bar $^{s-1}$. A significant decrease in dp/dt_{max} is noticeable for time T_4, which gradually decreases from a concentration of 150 g/m^3.

4 Conclusions

The minimum ignition energy is a significant parameter in assessing explosion risk. The article presents experimental investigations of MIE for aerosols of isopropanol, 99% ethanol, and 99.5% diethyl ether. The studies were conducted under various turbulence conditions by varying the ignition delay time. In the initial tests for isopropanol and ethanol, an inductive spark generator was used. In subsequent tests, a capacitive ignition source without inductance was employed for all the considered liquids. When using the inductive ignition source for the aerosols of isopropanol and ethanol, the lowest applied spark energy was 1.2 mJ which ignited both aerosol/air mixtures. The use of the capacitive ignition source showed significant differences in the obtained MIE values for both liquids.

For diethyl ether, the lowest applied capacitive spark energy of 1 mJ ignited the aerosol of the flammable liquid for all the applied ignition delay times from a concentration of 112 g/m^3 to

253 g/m^3 for the longest ignition delay time. As indicated by the results obtained from the MIE determinations, the obtained results should be analyzed using statistical methods, as it is not a one-time threshold value, particularly noticeable when using an inductive ignition source. The explosiveness characteristics were determined for the lowest applied energy of 1 mJ at various turbulence levels. Maximum explosion pressure as well as rate of pressure rise of dimethyl ether aerosol strongly depend on the ignition delay time.

Acknowledgements

The work was conducted as part of statutory research at the Central Mining Institute in Katowice (No. 11322013220), financed by the Ministry of Science and Higher Education, Poland.

References

Uchman W., Werle S., (2018) The ignition phenomenon of gases—part I: the experimental analysis—a review Journal of Power Technologies 98 (2) 171-182

Randeberg E., Eckhoff Rolf K., (2007) Measurement of minimum ignition energies of dust clouds in the <1 mJ region,, Journal of Hazardous Materials 140 (2007) 237-244 ?

Norma Europejska EN 13821:2003, Potentially explosive atmospheres - Explosion prevention and protection - Determination of minimum ignition energy of dust/air mixtures

EN-ISO/IEC-80079-20-2:2016 Explosive atmospheres Part 20-2: Material characteristics Combustible dusts test methods

Oancea D., Razus Domnina, Munteanu V., Cojocea Irina (2003) High voltage and break spark ignition of propylene/air mixtures at various initial pressures Loss Prevention in the Process Industries, 16 5 353-361

Ballal, D.R. & Lefebvre, A.H. (1981). A general model of spark ignition for gaseous and liquid fuel-air mixtures. Symposium (International) on Combustion, Eighteenth Symposium on Combustion 18, 1737–1746.

Shuai Yuan, Chenxi Ji, Haitian Han, Yue Sun, Chad V. Mashuga (2021) A review of aerosol flammability and explosion related incidents, standards, studies, and risk analysis Process Safety and Environmental Protection Volume 146, February 2021, Pages 499-514

Adrian Toman, Wojciech Adamus, Explosive properties of selected aerosols determined in a spherical 5-L test chamber, *Journal of Loss Prevention in the Process Industries*, Pages 104992, Serial number: PR-386698-F69A493CCE74

Eckhoff, R.K, (2002) Minimum ignition energy (MIE) — a basic ignition sensitivity parameter in design of intrinsically safe electrical apparatus for explosive dust clouds Journal of Loss Prevention in the Process Industries 15 305–310

Eckhoff, R.K, M. Ngo, W. Olsen, (2010) On the minimum ignition energy (MIE) for propane/air Journal of Hazardous Materials Volume 175, Issues 1–3, 15 March 2010, Pages 293-297

Sulaiman S.A., Development of a spark electrode ignition system for an explosion vessel, World Academy of Science, Engineering and Technology, International Journal of Mechanical, Mechatronic and Manufacturing Engineering 5 (12) (2011) 2710-2715

Randeberg E., Olsen W., Eckhoff Rolf K., A new method for generation of synchronised capacitive sparks of low energy Journal of Electrostatics 64 (2006) 263–272

Bane S.P.M. , Shepherd J.E., Kwon E., Day A.C. (2011) Statistical analysis of electrostatic spark ignition of lean H2/O2/Ar mixtures International Journal of Hydrogen Energy, Pages 2344-2350

Liu Jia, Mingshu Bi, Haipeng Jiang, (2020) Evaluation of spark discharge, J. Electrost. 107 103500.

Eckhoff, R.K, (2019) Measurement of minimum ignition energies (MIEs) of dust clouds – history, present, future, J. Loss Prev. Process. Ind. 61 147–159.

Wang Zhiyu, Haoran Sheng, Suijun Yang, Shuliang Ye (2022) Reconsideration of energy measurement of spark discharge using different triggering methods and inductance loads Journal of Electrostatics 117 103724

Burgyone J.H., Cohen L., (1954)The effect of drop size on flame propagation in liquid aerosols. Proc. R. Soc. London. Ser. A. Math. Phys. Sci.. 225, 375-39210.1098/rspa.1954.0210

Faeth G.M., Olson D.R., (1968) The ignition of hydrocarbon fuel droplets in air. SAE Trans. 1793-1802

Burgyone J.H., (1963) The flammability of mists and sprays. Second Symp. Chem. Process hazards., 1-5

Cook S.J., Cullis C.F., Good A.J., (1977) The measurement of the flammability limits of mists. Combust. Flame., 10.1016/0010-2180(77)90079-7

Danis A.M., Namer I., Cernansky N.P., (1988) Droplet size and equivalence ratio effects on spark ignition of monodisperse N-heptane and methanol sprays.Combust. Flame. 10.1016/0010-2180(88)90074-0

Liu Xueling, Wang Yue, Zhang Qi (2016) A study of the explosion parameters of vapor–liquid two-phase JP-10/air mixtures Fuel 165 279-288

Emmanuel Kwasi Addai, Martin Clouthier, Paul Amyotte, Muddasar Safdar, Ulrich Krause (2019) Experimental investigation of limiting oxygen concentration of hybrid mixtures Journal of Loss Prevention in the Process Industries, 57: 120-130

Stephanie El –Zahlanieha, Augustin Charveta, Alexis Vignesb, Benoit Tribouilloyb & Olivier Dufauda (2020) Hydrocarbon aerosol explosion: towards hazardous area classification Proceedings of the 13th ISHPMIE DOI: 10.7795/810.20200724

S.D. Wehe& N. Ashgriz (1992) Ignition probability and Absolute minimum Ignition Energy in Fuel Sprays Combustion Science and Technology Volume 86, – Issue 1-6

Sally P. M. Bane 2010 Spark Ignition: Experimental and Numerical Investigation With Application to Aviation Safety

Xiaolin Li, Mingshu Bi, Zongling Zhang, Kai Zhang, Sheng Shang, Wei Gao (2023) Experimental study on electrostatic spark discharge under different electrode parameters, pressure and gas componentJournal of Loss Prevention in the Process Industries82 105001

Bradley D., Lawes, M., Liao, S. &Saat, A. (2014). Laminar mass burning and entrainment velocities and flame instabilities of i-octane, ethanol and hydrous ethanol/air aerosols. Combustion and Flame, 161: 1620–1632.

Wang He, Feng Wu, Xuhai Pan. Min Hua, Hao Yu, Xiaowei Zanga, Juncheng Jiang (2023) Spray and explosion characteristics of methanol and methanol-benzene blends near azeotrope formation: Effects of temperature, concentration, and benzene contentJournal of Loss Prevention in the Process Industries 83 (2023) 105079

Applicability of NFPA 68 for ESS Enclosures

Stefan Kraft [a] & Anil Kapahi [a]

[a] Jensen Hughes (Blacksburg, VA, USA)

E-mail: skraft@jensenhughes.com

Abstract

Large scale energy storage systems (ESS) used in grid-scale applications predominately use lithium-ion batteries which release flammable gas during thermal runaway. The battery systems are typically stored in small modular enclosures or ISO style shipping containers. The flammable gas released in the enclosure presents an explosion hazard. One method of mitigation prescribed by NFPA 855 is deflagration venting according to NFPA 68. Generally, ESS enclosures are tightly packed to optimize space usage for cooling efficiency, compact footprint, and storage capacity. The release of flammable gas during thermal runaway in this confined environment with congestion created by the obstructions within the enclosure poses a challenging explosion control design problem. This results in difficulties to achieve a practical deflagration vent design for ESS geometries. This work presents a deflagration vent sizing analysis using two ESS enclosure geometries and a range of representative flammable gas properties and volume scenarios. Laminar burning velocity of the gas was found to be the most important parameter determining the feasibility of deflagration vents as an explosion control solution. Cells using lithium iron phosphate (LFP) cathodes typically have higher burning velocity due to greater hydrogen concentration in the thermal runaway gas mixture. High laminar burning velocity gas mixtures, such as those containing more than approximately 30% hydrogen and low concentrations of carbon dioxide, were found to generally lead to non-feasible deflagration vent designs. Battery gas mixtures with low hydrogen and higher carbon dioxide concentrations yielded feasible deflagration vent designs for the designs considered in the study. Scenarios involving partial volume deflagration and varied obstruction area were also evaluated, and these parameters must be critically examined during design of deflagration vents to ensure conservative results when using this methodology.

Keywords: *li-ion, energy storage systems, NFPA 68, deflagration venting, gas explosions*

Introduction

Energy storage systems (ESS) for grid scale applications using lithium-ion battery technology pose an explosion hazard due to release of flammable gas from cells in failure conditions. U.S. fire codes, including NFPA 855 “Standard for the Installation of Stationary Energy Storage Systems” (NFPA, 2023b), require explosion protection using either NFPA 68 or NFPA 69 to mitigate this hazard. NFPA 68 “Standard on Explosion Protection by Deflagration Venting” (NFPA, 2023a) governs the design, installation, and use of vent panels to safely relieve pressure in an enclosure caused by a deflagration of flammable gas or combustible dust. NFPA 69, “Standard on Explosion Prevention Systems”, permits multiple methods for preventing explosions. In this work, the explosion control by deflagration venting was evaluated using NFPA 68 to determine the feasibility of this type of mitigation for lithium-ion battery gas deflagrations.

Lithium-ion battery cells contain a flammable liquid electrolyte which can react with other cell components if the battery experiences abuse. The uncontrolled exothermic chemical reaction of the internal materials is termed thermal runaway, and this reaction produces flammable gas (Roth & Orendorff, 2012). The high pressure and temperature which accompanies thermal runaway causes the cell to burst and release the produced gas. Propagating thermal runaway in cell packs or modules due to the heating of adjacent cells from an initiating cell can cause a significant explosion hazard because each cell undergoing thermal runaway releases gas. The explosion hazard is exacerbated in the case of confined enclosures which are typical for lithium-ion based ESS. This is because the resulting gas-air vapor cloud can correspond to well mixed stoichiometric concentrations for relatively low gas volumes as compared to other industrial environments.

As lithium-ion battery manufacturing technology improves, larger size cells with higher energy density are being used in ESS. Higher energy density and capacity typically lead to more flammable gas release during a thermal runaway. A successful design of explosion control measures such as deflagration vents can be a challenge due to competing constraints and economic factors for the energy storage industry. In this work, NFPA 68 is used to size deflagration vents for ESS containers to evaluate the feasibility of the method for lithium-ion battery offgas. This paper describes an evaluation of representative ESS geometry and explosion parameters to determine configurations which can be protected from overpressures by deflagration venting. In addition, areas of future research have been identified to assess if the physics modeled by NFPA 68 is appropriate for the specific geometric features of ESS containers.

1. Modeling Approach

A standardized approach using Chapters 6 and 7 of NFPA 68 was used to evaluate the required deflagration vent size for representative ESS enclosures. A number of parameters are required to model the deflagration pressure and vent size relationship, and in general, for this analysis conservative decisions were made and are discussed in the following sections.

1.1. Overview of key parameters

The geometry and enclosure strength of the container are used to determine the physical flow area characteristics and the reduced pressure (P_{red}). The effective volume of the enclosure and the longest distance a flame can travel are geometric parameters which are used to calculate the length to diameter ratio (L/D.) Although there are provisions in the standard (Chapter 6.4) to adjust L/D based on the position of multiple vents, this option was not used to ensure a conservative result because the ESS containers considered are highly congested and have narrow aisles. For this analysis L was taken as the length of the container. The equation for calculating vent area for low strength enclosures was used. P_{red} was assumed to be 0.2 bar-g, which is similar to the pressures experienced in 20-ft ISO containers during partial volume hydrogen deflagration and which did not experience catastrophic failure (Skjold et al., 2019).

Turbulence due to flow passing over obstructions increases the pressure caused by a deflagration. Estimation of the obstruction area is required to calculate the effect which can be challenging depending on the intricate geometric features. Accounting for the effects of turbulence (applicable for configurations which have an area of obstructions greater than 20% of the enclosure's internal surface area) can make a significant impact on the required vent area. Note that the standard accounts

for turbulence from two factors, that of the flow geometry of the enclosure and the vent(s), and that from the obstructions in the flow path. The standard does not provide a methodology to address turbulence present due to other velocity gradients in the enclosure (e.g. HVAC ventilation or jet of flammable gas released from failed battery cell) and for this study the flammable gas-air deflagration was assumed to occur in a still environment.

The thermal runaway propensity of lithium ion batteries and subsequent flammable gas release is typically characterized by UL 9540A (ANSI/CAN/UL, 2019) for battery systems installed in the United States. Design of explosion mitigation systems for ESS typically involves analysis of this data. In certain instances, scenarios based on the test data result in a flammable-air vapor cloud with a lower volume than the free air volume of the enclosure. For these scenarios, the partial volume calculation method may be used to calculate a required vent area which is smaller than that which results from the full-volume/stoichiometric method which is the default presented in the standard. In this work, scenarios were evaluated to demonstrate how feasibility of deflagration venting was affected by the vapor cloud volumes of different cell-to-cell propagation in the module.

The panel mass/inertia can also affect the required vent area. For the purpose of this analysis, the vent panel weight was assumed to be below the threshold to require a deflagration area adjustment. For some configurations, particularly with hinged or heavier metal vent panels and containers which have small volume, an adjustment may need to be applied to the initial vent area calculated via NFPA 68.

1.2. ESS Enclosure Geometry

ESS enclosures for grid scale applications, termed "containerized ESS", are commonly made of steel cabinets or ISO-style shipping containers. Their size generally ranges from small modular type containers (largest dimension of 6 to 12 ft) to 53 ft long enclosures (ISO style containers.) Battery racks, inverters, and power control systems are installed in the containers and shipped to the site of installation. The containers are typically tightly packed to store the maximum amount of energy in the available space. This results in a low free-air volume for the enclosure.

Two container types and sizes were considered for this study, a small container and a 20-ft ISO style container. Table 1 contains the dimensions and other geometric parameters which are based on industry experience. Battery racks, power control, and electronic equipment occupy significant volume, usually about 45-65% of the container. HVAC or liquid cooling systems are also required for thermal management and/or humidity control, but these units are often mounted to the wall or roof of the container, and do not take up significant interior space. Additional parameters for the two concept geometries are shown in Table 2 for comparison. The geometry was adapted from CAD files downloaded from the Trace Parts website and modified for this work (TraceParts S.A.S., 2022).

Table 1. Containerized ESS concept geometries for deflagration vent sizing study.

Container Type/Size	Volumetric Congestion (%)	Deflagration Panel Area (m^2)	Practical Maximum Vent Area (m^2)	Container Length (m)	Container Depth (m)	Container Height (m)
Small	59	2.0	4.6	3.33	1.83	2.39
20-ft ISO	50	8.0	11.0	5.87	2.35	2.39

Table 2. Geometric parameter comparison for ESS.

Container Type/Size	A_s (m^2)	Area of Obstruction (m^2)	A_{obs}/A_s (-)	V_{eff} (m^3)
Small	36.9	5	0.136	5.93
20-ft ISO	66.9	15	0.224	16.57

The small container is shown in Fig. 1 (a), with 2 m^2 of deflagration vents. Small containers are sometimes designed to have inverters and switchgears in separate containers, which can optimize space for energy storage. For the concept developed for this analysis, the equipment was assumed to take up space in the racks. Fig. 1 (b) shows a section view of the interior, with the racks occupying 59% of the space. The volume occupied by the battery racks is not expected to participate in the deflagration, thus, the free air volume of the container was calculated based on the interior dimensions less the volume of the battery racks treated as a solid.

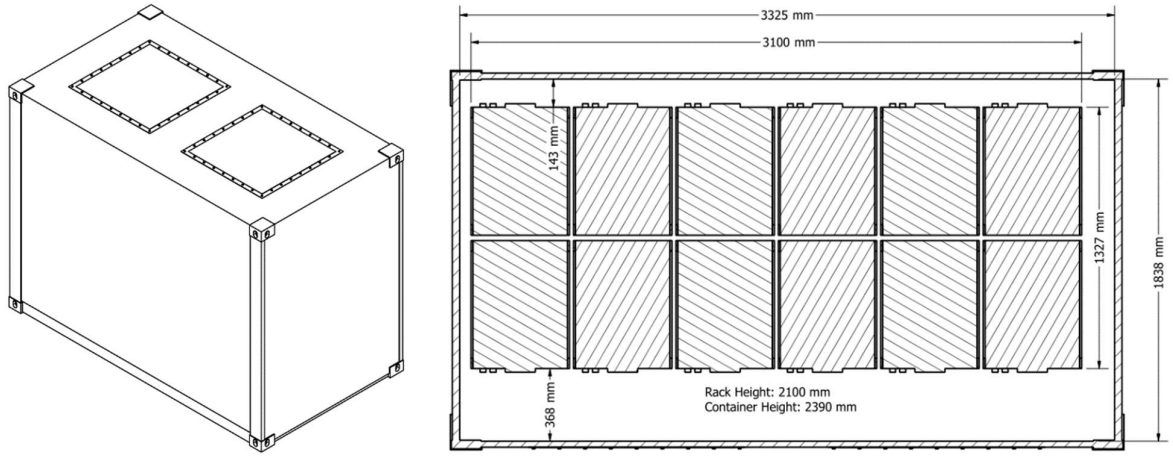

(a) (b)

Fig. 1. Small container ESS with two 1 m^2 deflagration vent panels installed. (a) CAD geometry/illustration of front of container. (b) Section view showing interior dimensions of container and battery racks.

Panels of 1 m^2 area were used in the concept designs as the size of a single deflagration vent. Typically these are installed to the ceiling of ESS containers. Various design considerations reduce the practical available vent area to some fraction of the ceiling. For the purposes of this study, a conceptual maximum for the containers was estimated based on generic panel size requirements. Design constraints which reduce the available area include structural integrity needs of the container, ceiling mounted equipment such as HVAC, and internal hardware such as electrical cables. For the small container the conceptual maximum area (for ceiling mounted vent panels) was 4.6 m^2.

Fig. 2 shows a 20-ft ISO shipping container which is a mid-size ESS. This container has 22 battery/equipment racks with the same number of modules as the small modular container, but with a longer module. The volumetric congestion was calculated as 50%. Eight 1 m^2 vent panels installed on the ceiling yielded a total design vent area of 8 m^2. The conceptual maximum area for the ceiling was assessed to be 11.0 m^2.

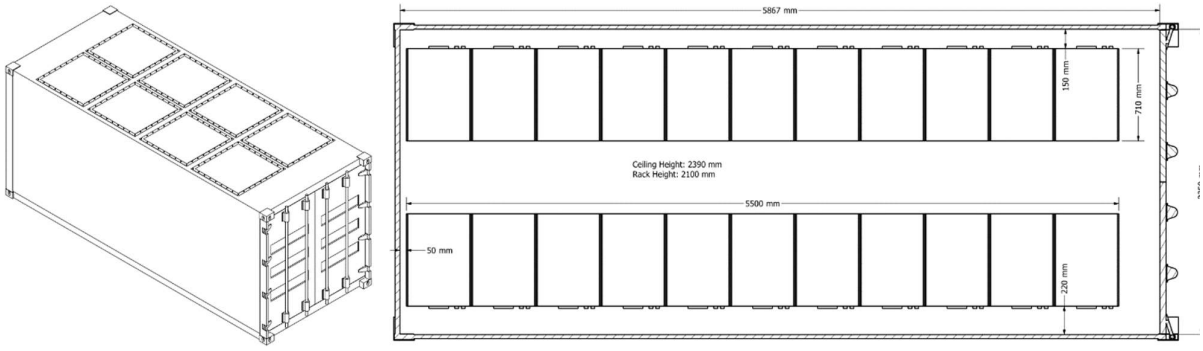

(a) (b)

Fig. 2. 20-ft ISO ESS container with eight 1 m^2 deflagration vent panels installed. (a) CAD geometry/illustration of front of container. (b) Section view showing interior dimensions of container and battery racks.

A consequence of obstructions such as pipes, conduits, and exposed structural supports in the container is to cause flow disturbance, which results in increased turbulence. The surface area of obstruction, calculated to adjust NFPA 68 flame enhancement factor, is composed of the surface area of pipe, conduits, structural columns, and other equipment in the flow path that have a characteristic dimension between 1.27 cm (0.5 inches) and 50.8 cm (20 inches.) For ESS containers, this area of obstructions can be difficult to estimate. For example, for open rack designs, air flows between the modules or around the electrical cabling connecting the modules and the battery management system (BMS.) However, the distance between modules stacked in the rack is typically small, and thus the battery racks can be assumed to act as a solid obstruction. It is assumed that the deflagration will not propagate through this free air in the container. For the rack design modeled for this work, the separation between modules is 19.6 mm (0.77 inches.) This is a relatively small dimension compared to the module height of 110 mm (4.33 inches) and the rack height of 2100 mm (82.7 inches.) The surface area of conduit, sprinkler piping, cable trays, and structural framing is usually straightforward to estimate if CAD geometry is available with all equipment.

A typical range of values for ESS enclosures for surface area of obstruction is 10-40% of the total surface area. Baird estimated that for ISO containers the percentage of total surface area was 13.4% (Baird, 2019). The area of obstructions for the small container was estimated to be 5 m^2, or 13.6% of the total surface area of the enclosure. For an enclosure that has an area of obstructions less than 20% of the surface area, no adjustment is made to the turbulent flame enhancement factor. For the 20-ft ISO concept design, area of obstructions was assumed to be 15 m^2, which is 22.4% of the surface area of the container. These values are in the range of typical ESS enclosures. To assess the sensitivity of the result with respect to significant increases of obstruction area (e.g. taking into account battery racks or presence of liquid cooling piping), the vent area calculation was also performed with doubled obstruction area.

2. Flammable Gas Mixture

2.1. Li-ion Gas Composition

Lithium-ion battery failures release flammable gas during thermal runaway. The gas is typically composed of hydrogen (H_2), hydrocarbons (abbreviated THC for total hydrocarbons), carbon monoxide (CO), and carbon dioxide (CO_2.) H_2, THC, and CO are flammable, and CO_2 is an inert

dilutant. When a battery cell undergoes thermal runaway, a mixture of the gases is released, the proportion of which depends on the characteristics of the cell and its failure mode (e.g. chemistry and material composition, abuse method, and state of charge.) The type and relative fraction of flammable gases emitted from the battery cell has been studied extensively in the literature. The relative proportion of the gases can vary widely, as shown in Fig. 3. For the experimental data, the hydrogen volume fraction varied from 6% to 54% (Archibald, 2021; Robles & Jeevarajan, 2020; Yang et al., 2022). Hydrogen is the most volatile flammable gas in the mixture based on its burning velocity of 286 cm/s (NFPA, 2023a).

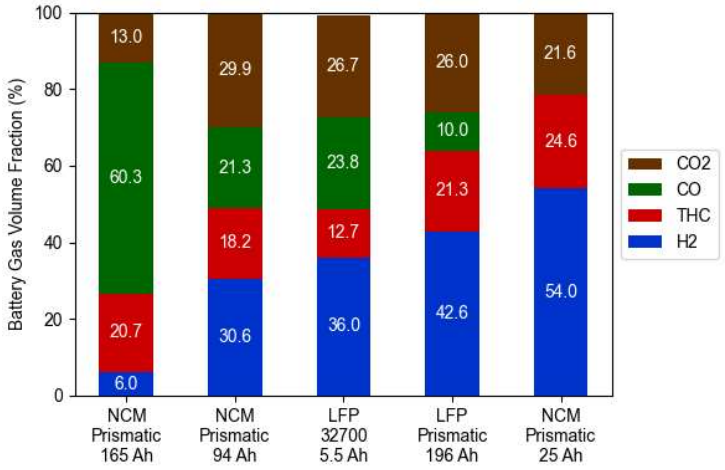

Fig. 3. Selected battery gas volume fraction for lithium ion battery cell thermal runaway experiments (Archibald, 2021; Robles & Jeevarajan, 2020; Yang et al., 2022).

2.2. Li-ion Gas Data

High volume fractions of H_2 in the battery gas mixture typically cause more hazardous flammability properties. Battery gas volume and composition was assessed based on the available data in the literature for thermal runaway experiments of lithium-ion batteries to evaluate the typical range of the flammable components of the offgas, particularly H_2 and THC. Fig. 4 presents the collected data in statistical plots, comparing LFP, NMC, and LCO cell chemistries (Archibald, 2021; Barowy et al., 2022; Barowy & Klieger, 2021; Bordes et al., 2022; Essl, Golubkov, & Fuchs, 2020; Essl, Golubkov, Gasser, et al., 2020; Fernandes et al., 2018; Golubkov et al., 2014; Kennedy et al., 2021; Robles & Jeevarajan, 2020; Shen et al., 2023; Shi et al., 2024; Walker, 2020; Y. Wang et al., 2023; Yang et al., 2022; Yuan et al., 2020; Zhang et al., 2019). H_2 concentration generally averages between 20% and 40% for all cell chemistries, with some LFP cells reaching over 50%. THC is a mixture of methane, ethylene, propylene, propane, and other hydrocarbons, and typically is between 10 and 25% of the battery gas mixture. The composition of flammable gas observed from the literature review of lithium-ion batteries is consistent with the authors' experience in evaluating thermal runaway data for cells used in the ESS industry. However, large format LFP cells (greater than 200 Ah) typically have greater proportions of H_2 of between 45% and 60%, and smaller volume fractions of CO (5-20%.)

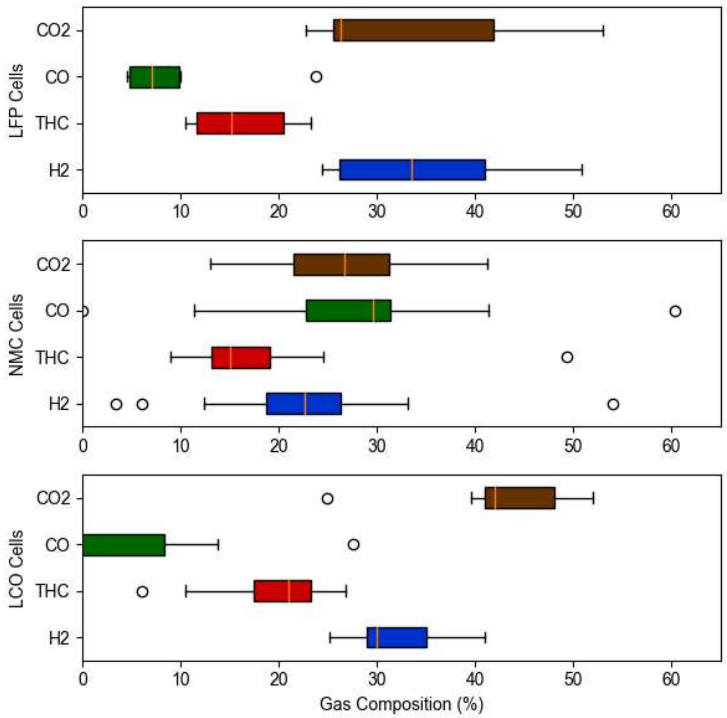

Fig. 4. Composition of lithium-ion battery cell flammable gas release by volume, from literature review. References for data provided in text.

The flammability properties of the gas required for sizing deflagration vents include laminar burning velocity (LBV / S_u) and the maximum explosion pressure (P_{max}.) UL 9540A prescribes standard test methods to determine these properties for gases. Table 3 presents battery gas compositions with experimental data for P_{max} and S_u were obtained from Henriksen et al. (2021) and Wang et al. (2022). Three compositions were used for the primary modelling evaluation. The battery gas composition data and explosion properties represent a range of values observed in lithium iron phosphate (LFP) cathode cells and other cells used in grid-scale ESS. The most common cell chemistry for grid-scale ESS is LFP (Rho Motion, 2023), and these often are large format (200+ Ah) and have high concentrations of H_2 in the thermal runaway offgas (Kapahi et al., 2023). The Low LBV LFP gas shown in the table has 34.9% H_2, which is representative of many cell types as shown in Fig. 4, but has a relatively low burning velocity relative to most LFP cells used in grid-scale ESS. Henriksen denoted this composition as "Generic Li-ion." The 23 Ah LFP cell tested by Wang (Med. LBV LFP in the table) also had lower H_2 volume fraction than is often observed in many large format LFP cells used in ESS. However, the burning velocity of 80 cm/s is representative of many cells in use. The High LBV Li-ion gas has 42.8% H_2 and a burning velocity of 105.5 cm/s. The S_u for this composition is on the higher end of the range for most lithium-ion cells' offgas and was based on the more flammable concentrations developed from LFP and nickel cobalt aluminium (NCA) cells. This gas composition and the explosion properties are also representative of many cells used in grid-scale ESS.

Table 3. Representative Battery Gases (Henriksen et al., 2021; H. Wang et al., 2022).

Gas	H_2 (%)	CO (%)	CO_2 (%)	CH_4 (%)	C_2H_4 (%)	C_2H_6 (%)	C_3H_8 + Other (%)	S_u (cm/s)	P_{max} (bar-g)
Low LBV LFP	34.9	25.0	20.1	15.0	5.0	0.0	0.0	47.9	7.5
Med. LBV LFP	36.2	7.4	25.2	6.4	15.2	2.4	7.2	80.0	6.5
High LBV Li-ion	42.8	37.1	10.0	7.1	3.0	0.0	0.0	105.5	7.8

The calculated vent area is directly correlated to S_u. To evaluate this sensitivity of the vent area with this parameter, and that of H_2 volume fraction in the mixture, S_u was modeled using Cantera for mixtures containing 0% to 70% H_2. Cantera is a chemical equilibrium code which calculates combustion products and thermodynamic properties of chemically reacting flows (Goodwin et al., 2023). It includes a set of models for premixed flames. For the calculation of S_u a 1-D freely propagating premixed flame was modeled at initially ambient conditions, using the same method in Python as provided by Ogunfuye (2023). The GRI-Mech 3.0 reaction mechanism was used, as it was the default. The portion of the mixture not H_2 was evenly divided into CH_4, CO, and CO_2. The results are shown in Fig. 5.

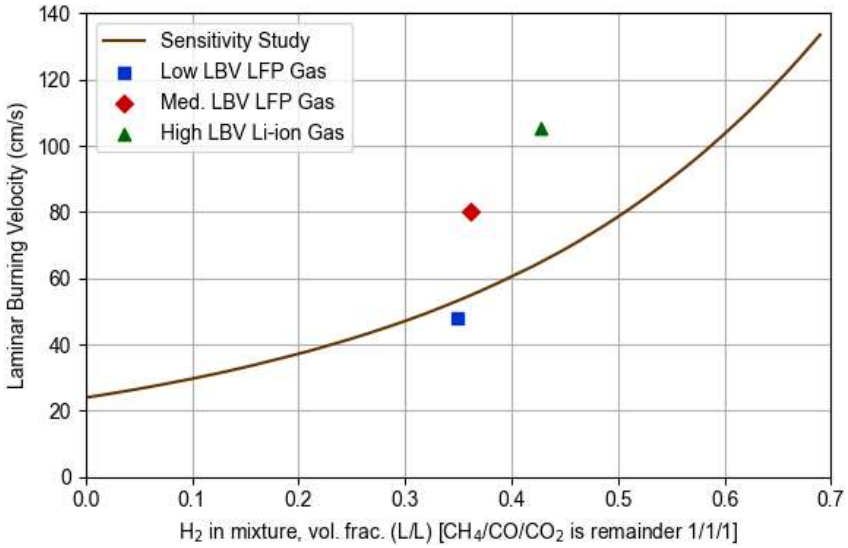

Fig. 5. Burning velocity calculated using Cantera for mixtures representative of battery gas, changing the relative fraction of hydrogen gas.

2.3. Gas Mixture Properties

The unburned and burned gas mixture properties are required to calculate vent area. Table 4 contains the values for each of the gas mixtures which were taken at the stoichiometric concentration, including the unburned mixture density (ρ_u), viscosity (μ_u), sonic flow mass flux (G_u), speed of sound (a_u), and the combustion products specific heat ratio (γ_b.) The gas properties were assessed at ambient conditions based on the assumption that the gas cools rapidly upon being released. The stoichiometric volume fraction was calculated by balancing the chemical equation for the battery gas. Mole averaging was used to calculate the density using properties from DIPPR (BYU DIPPR, 2023). The dynamic viscosity was calculated using the method of Herning and Zipperer (Davidson, 1993). The sonic flow mass flux, which is the maximum mass flow per unit area due to compressibility of the unburned fuel-air mixture, was calculated according to compressible flow principles (NASA Glenn Research Center, 2021). The specific heat ratio was calculated using the specific heat of the products (CO_2, H_2O, and N_2) at 1000 K from properties obtained from the NIST database (Linstrom, 1997).

Table 4. Battery Gas Fuel-Air Mixture Properties (BYU DIPPR, 2023; Linstrom, 1997).

Gas	x_{st} (L/L)	ρ_u, NTP (g/L)	μ_u (kg/m^{2}s)	a_u (m/s)	G_u (kg/m^2-s)	γ_b (-)
Low LBV LFP	0.219	1.12	1.76E-05	357	228.2	1.28
Med. LBV LFP	0.145	1.17	1.76E-05	349	232.1	1.28
High LBV Li-ion	0.250	1.08	1.77E-05	364	224.5	1.28

2.4. Gas Release Volume

The volume of gas released during thermal runaway varies based on a number of factors such as cell chemistry, method of abuse, and state of charge. In general, the volume of flammable gas release is correlated with the nominal energy capacity of the cell. Rappsilber (2023) reported an overall maximum of 0.75 L/Wh for multiple chemistries (LFP, NMC, NCA, LCO, and LMO) and form factors (cylindrical, pouch, and prismatic.) The concept lithium-ion based battery system had modules with 42 Ah / 134 Wh LFP cells, such that the gas release was 100 L per cell. An adverse event in the system which leads to thermal runaway in a cell causes release of flammable gas. Thermal runaway may be limited to one cell, or it may propagate to other cells in the module or unit. Test data (usually from UL 9540A) can be used to justify the expected number of cells which undergo thermal runaway. In this work, partial volume deflagration calculations were performed for one (100 L), five (500 L), and fifteen (1500 L) cells. For the small container, the stoichiometric concentration (which is assumed for the full-volume scenario) corresponded to a flammable gas volume of 1298 L, 859 L, and 1481 L for the Low LBV LFP, Med. LBV LFP, and High LBV Li-ion gases, respectively. The 1500 L volume was not used to calculate deflagration area for the small container. The stoichiometric volumes for the 20-ft ISO container were 3628 L, 2402 L, and 4143 L, respectively. The vapor cloud for the partial volume scenarios considered in the analysis are shown in Table 5. Note that the vapor cloud volumes for Med. LBV LFP gas are significantly greater than for the Low LBV LFP and High LBV Li-ion gases due to the much lower stoichiometric volume fraction.

Table 5. Battery Gas Stoichiometric Vapor Cloud Volume.

Gas	x_{st} (L/L)	$V_{100\ L}$ (m^3)	$V_{500\ L}$ (m^3)	$V_{1500\ L}$ (m^3)	$V_{eff,\ Small}$ (m^3)	$V_{eff,\ 20\text{-}ft\ ISO}$ (m^3)
Low LBV LFP	0.219	0.46	2.28	6.85	5.93	16.57
Med. LBV LFP	0.145	0.69	3.46	10.38		
High LBV Li-ion	0.250	0.40	2.00	6.01		

3. Results and Discussion

3.1. Required Deflagration Area

Deflagration vent area requirements for the small container and the 20-ft ISO container are shown in Fig. 6 and Fig. 7, respectively. For both containers and all Low LBV LFP gas release scenarios (partial and full volume), the vent area for the design satisfied the required area. Conversely, no scenario with High LBV Li-ion gas yielded vent area lower than the available 2 m^2 in the small container. The Med. LBV LFP gas scenarios failed to yield feasible deflagration vent area except for the 100 L release. Note, however, that based on the test method specified by UL 9540A for module thermal runaway initiation, multiple cells are required to undergo thermal runaway, and thus typically limiting the release to 100 L is not justifiable.

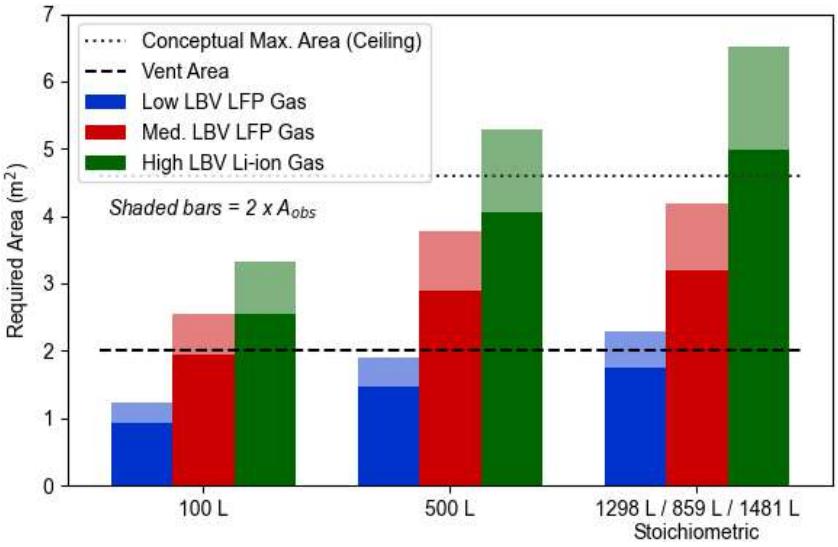

Fig. 6. Required area for small container.

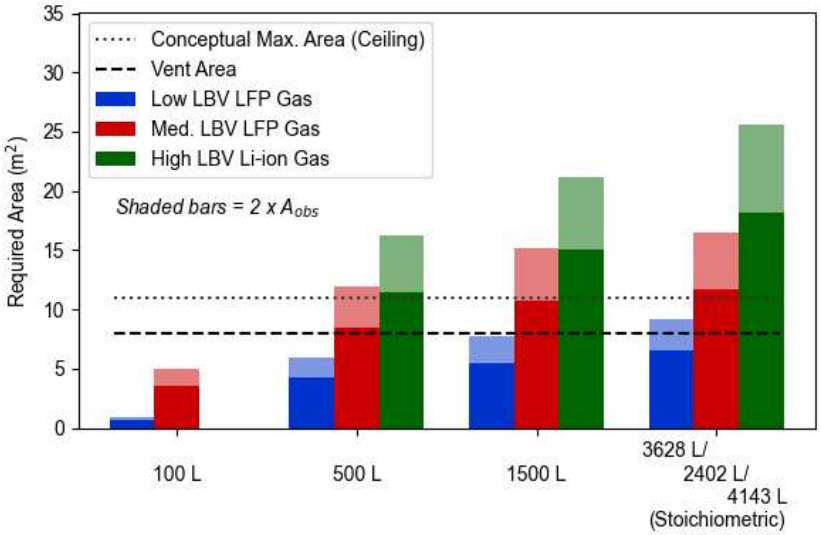

Fig. 7. Required area for 20-ft ISO container.

For the 20-ft ISO container, all partial volume 100 L gas scenarios yielded a required vent area lower than the design vent area. Note that the Low LBV LFP and Med. LBV LFP gases had higher required area for the 100 L partial volume scenario than the High LBV Li-ion gas, and this is due to the smaller stoichiometric volume fraction (21.9% and 14.5%, respectively, versus 25.0%.) For the High LBV Li-ion gas with 100 L volume, the equation for partial volume vent area becomes undefined due to the higher stoichiometric ratio, and thus for this analysis was assumed to be 0 m^2. The results for the 100 L gas release scenario show that if gas release is limited, deflagration venting is a feasible explosion control solution.

For both containers, a conceptual maximum deflagration vent area for the ceiling was estimated to provide an upper bound of what may be possible for these style containers. This vent panel area would require essentially the entire ceiling and thus does not take into account design constraints. For the small container, increasing the vent area to the conceptual maximum resulted in a feasible design for the Med. LBV LFP gas but not for all scenarios with the 20-ft ISO container.

Doubling the area of obstruction resulted in the Low LBV LFP gas failing requirements for the full volume scenario for the 20-ft container. The 100% increase in obstruction area resulted in a 30% and 41% increase in vent area requirements for the small and 20-ft ISO containers, respectively.

The high and low LBV gas mixtures had similar properties as shown in Table 3 and Table 4 (except for S_u.) Thus, although there is some effect of the gas properties based on the relative composition, the most significant factor in determining the feasibility of a deflagration vent design is S_u.

3.2. Deflagration Area Sensitivity

A sensitivity analysis was performed for two containers with battery gas compositions containing a concentration range of H_2 from 0% to about 70%. S_u calculated by Cantera is shown in Fig. 5 along with the value for the Low LBV LFP, Med. LBV LFP, and High LBV Li-ion gases. Results of the sensitivity study for the small container and 20-ft ISO container are shown in Fig. 8 and Fig. 9, respectively. The full-volume scenario was used for the calculation. In general, deflagration vents as an explosion control solution were found to be feasible for H_2 volume fractions of less than 28% and 31% for the small and 20-ft ISO containers, respectively. The Low LBV LFP gas has a hydrogen concentration of 34.9%; the Cantera result was found to be conservative for this gas compared to the S_u data provided by Henriksen. The validation of the chemical kinetic modeling is outside the scope of this work. The trend of the amount of H_2 in the mixture which yields a feasible result is generally consistent for both enclosures. The actual gas compositions used in the main study do not lie on the H_2 sensitivity line due to variation in CO, CO_2, and THC, as the actual gases have varying compositions which are not represented by the sensitivity model. Most cells used in the ESS are LFP, which typically have H_2 concentrations of greater than 30%, and thus using the prescriptive methodology as described in this work will not yield a practical design area for a significant portion of ESS container designs.

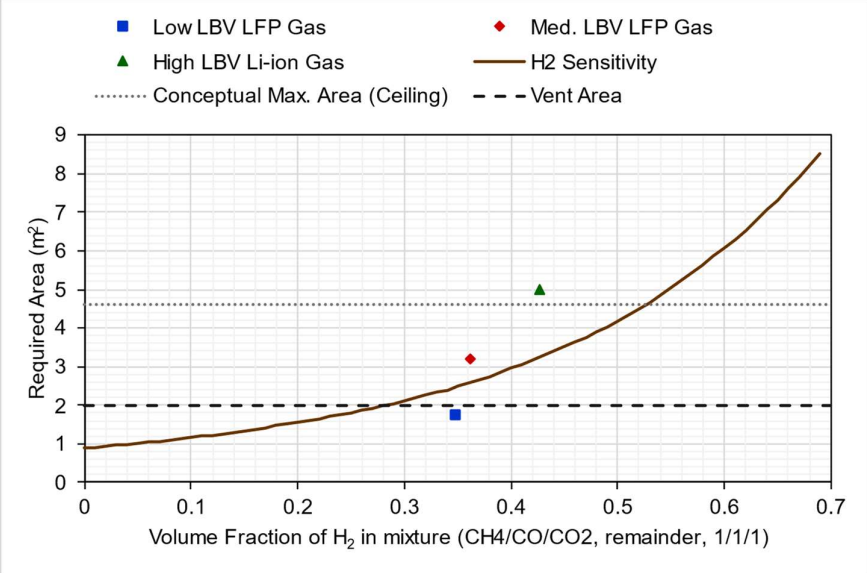

Fig. 8. Required deflagration area for stoichiometric gas release in the small container, with hydrogen concentration varied in the battery gas mixture.

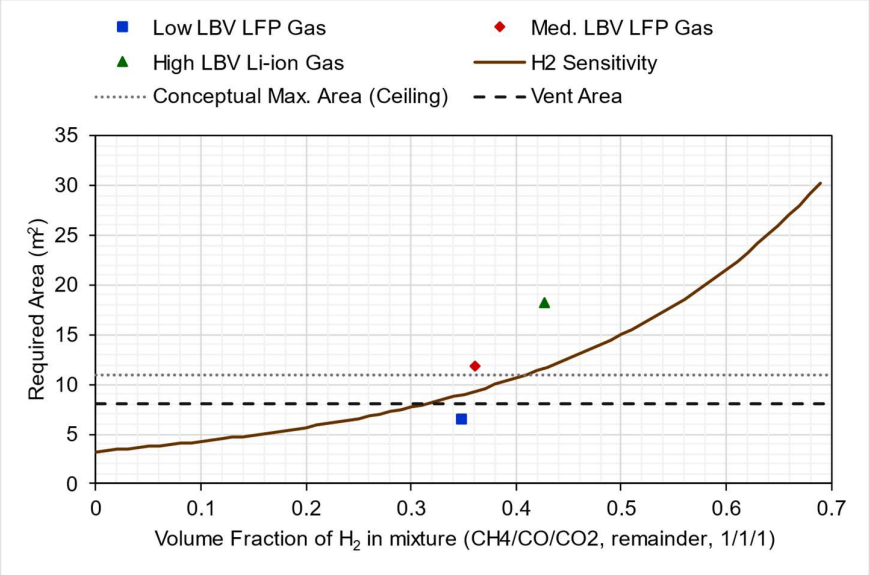

Fig. 9. *Required deflagration area for stoichiometric gas release in 20-ft ISO container, with different hydrogen content in battery gas mixture.*

3.3. Considerations for ESS Deflagration Vent Design and Future Research

Energy Storage System (ESS) enclosures are tightly packed for economic reasons. The amount of area available for deflagration vent panels is typically small. The results demonstrate the challenges for designing deflagration vents for enclosures housing lithium-ion batteries. The geometric characteristics of large scale ESS will likely not change significantly. Thus, to achieve a practical solution, the flammable gas release hazard must be addressed: lower volume of gas (partial volume scenario) and lower S_u of the flammable gas (less H_2 or more CO_2.)

The results demonstrate that a feasible deflagration vent design is challenging with a flammable gas that has a high S_u. The High LBV Li-ion gas has S_u of over 100 cm/s due to high proportion of H_2 and low proportion of CO_2. Although cells from each manufacturer are distinct and can give different results for thermal runaway gas composition, LFP type batteries generally have higher levels of H_2 and thus higher S_u. Thus, although LFP cells may be perceived as being safer due to certain characteristics of the thermal runaway of this chemistry, the flammability properties often lead to non-feasible deflagration vent designs.

Partial volume deflagration calculations can be an important tool in designing deflagration vents using the prescriptive methodology in NFPA 68. However, the justification of the total volume release of flammable gas is based on an engineering assessment of the UL 9540A data. Review and critical analysis of the specific test reports to assess the propensity for thermal runaway propagation is important to ensure sufficiently conservative assumptions are made, as in UL 9540A only one test at the module and unit level are performed. In addition, for each subject cell, only one gas volume and composition test is performed in the pressure vessel to establish properties such as maximum explosion pressure and burning velocity. Thus, it is important for practitioners to compare with experimental and modeling data in the literature to account for the uncertainty in the testing.

In the container designs for this study, obstruction area was assumed to be low, and *L/D* was taken for overall container geometry (less battery rack volume.) This method was consistent with the available literature and the authors' industry experience in prescriptive NFPA 68 analyses. However, it is an important consideration that the data used to develop NFPA 68 did not include enclosures with battery racks. Specific geometric features of battery racks and electrical equipment, and the highly congested nature of the containers, may affect the deflagration propagation and resulting pressures in ways which NFPA 68 does not take into account. In addition, the battery gas is typically released as a hot jet and can be present initially at a high local concentration which may affect the flame propagation characteristics. These topics warrant further study to determine if the current guidance in NFPA 68 is sufficient to protect ESS containers or if conservatism can be reduced for some geometric configurations.

4. Conclusions

In this work the required vent area was calculated according to the prescriptive NFPA 68 method for representative ESS enclosure designs. S_u was found to be the most important parameter in determining feasibility of deflagration vents for battery containers. A chemical kinetics code was used to evaluate S_u for a range of H_2 volume fractions, and this data was used to evaluate vent area requirements. In general, H_2 concentrations greater than about 30% yielded non-feasible deflagration vent designs for stoichiometric concentrations. The Med. LBV LFP and High LBV Li-ion gases, which are similar to many LFP cells' composition and S_u, was found to cause non-feasible deflagration vent designs for most gas release scenarios. The Low LBV LFP gas, which has a low S_u relative to most LFP cells, was found to yield feasible designs. Partial volume calculations were found to result in viable deflagration vent designs for even the higher S_u battery gas compositions when the release volume was 100 L to 500 L. However, care must be taken when using the partial volume method as it requires justification based on an assessment of a usually limited set of experimental data. The results of this study demonstrate that deflagration venting is a viable explosion control solution for ESS containers for only a small portion of scenarios. Further study using computational modeling and experiments is needed to evaluate whether the NFPA 68 prescriptive method is overly conservative, and if specific changes can be made to improve feasibility.

References

ANSI/CAN/UL. (2019). *UL 9540A: Standard for Test Method for Evaluating Thermal Runaway Fire Propagation in Battery Energy Storage Systems* (4th ed.). Underwriters Laboratories Inc.

Archibald, E. J. (2021). *Fire & explosion hazards due to thermal runaway propagation in lithium-ion battery systems*. The University of Texas at Austin.

Baird, A. R. (2019). *A Framework for Characterizing the Safety of Li-BESS using Performance Based Code Analysis and Testing*. University of Texas at Austin.

Barowy, A., & Klieger, A. (2021). *UL 9540A Installation Level Tests with Outdoor Lithium-ion Energy Storage System Mockups* (p. 245) [FIRE RESEARCH AND DEVELOPMENT TECHNICAL REPORT]. Underwriters Laboratories.

Barowy, A., Schraiber, A., & Zalosh, R. (2022). Explosion protection for prompt and delayed deflagrations in containerized lithium-ion battery energy storage systems. *Journal of Loss Prevention in the Process Industries*, *80*, 104893. https://doi.org/10.1016/j.jlp.2022.104893

Bordes, A., Marlair, G., Zantman, A., Herreyre, S., Papin, A., Desprez, P., & Lecocq, A. (2022). New insight on the risk profile pertaining to lithium-ion batteries under thermal runaway as affected by system modularity and subsequent oxidation regime. *Journal of Energy Storage*, *52*, 104790. https://doi.org/10.1016/j.est.2022.104790

BYU DIPPR. (2023). *DIADEM ELITE: The DIPPR Information and Data Evaluation Manager for the Design Institute for Physical Properties* (1.9.0 DIPPR801_Sponsor_May2023) [Computer software].

Davidson, T. A. (1993). *A Simple and Accurate Method for Calculating Viscosity of Gaseous Mixtures* (RI 9456). United States Department of the Interior.

Essl, C., Golubkov, A. W., & Fuchs, A. (2020). Comparing Different Thermal Runaway Triggers for Two Automotive Lithium-Ion Battery Cell Types. *Journal of The Electrochemical Society*, *167*(13), 130542. https://doi.org/10.1149/1945-7111/abbe5a

Essl, C., Golubkov, A. W., Gasser, E., Nachtnebel, M., Zankel, A., Ewert, E., & Fuchs, A. (2020). Comprehensive Hazard Analysis of Failing Automotive Lithium-Ion Batteries in Overtemperature Experiments. *Batteries*, *6*(2), 30. https://doi.org/10.3390/batteries6020030

Fernandes, Y., Bry, A., & de Persis, S. (2018). Identification and quantification of gases emitted during abuse tests by overcharge of a commercial Li-ion battery. *Journal of Power Sources*, *389*, 106–119. https://doi.org/10.1016/j.jpowsour.2018.03.034

Golubkov, A. W., Fuchs, D., Wagner, J., Wiltsche, H., Stangl, C., Fauler, G., Voitic, G., Thaler, A., & Hacker, V. (2014). Thermal-runaway experiments on consumer Li-ion batteries with

metal-oxide and olivin-type cathodes. *RSC Adv.*, *4*(7), 3633–3642. https://doi.org/10.1039/C3RA45748F

Goodwin, D. G., Moffat, H. K., Schoegl, I., Speth, R. L., & Weber, B. W. (2023). *Cantera: An Object-oriented Software Toolkit for Chemical Kinetics, Thermodynamics, and Transport Processes* (3.0.0) [Computer software]. [object Object]. https://doi.org/10.5281/ZENODO.8137090

Henriksen, M., Vaagsaether, K., Lundberg, J., Forseth, S., & Bjerketvedt, D. (2021). Laminar burning velocity of gases vented from failed Li-ion batteries. *Journal of Power Sources*, *506*, 230141. https://doi.org/10.1016/j.jpowsour.2021.230141

Kapahi, A., Alvarez-Rodriguez, A., Lakshmipathy, S., Kraft, S., Conzen, J., Pivarunas, A., Hardy, R., & Hayes, P. (2023). Performance-based assessment of an explosion prevention system for lithium-ion based energy storage system. *Journal of Loss Prevention in the Process Industries*, *82*, 104998. https://doi.org/10.1016/j.jlp.2023.104998

Kennedy, R. W., Marr, K. C., & Ezekoye, O. A. (2021). Gas release rates and properties from Lithium Cobalt Oxide lithium ion battery arrays. *Journal of Power Sources*, *487*, 229388. https://doi.org/10.1016/j.jpowsour.2020.229388

Linstrom, P. (1997). *NIST Chemistry WebBook, NIST Standard Reference Database 69* [dataset]. National Institute of Standards and Technology. https://doi.org/10.18434/T4D303

NASA Glenn Research Center. (2021, May 13). *Mass Flow Choking*. National Aeronautics and Space Administration. https://www.grc.nasa.gov/www/k-12/airplane/mflchk.html

NFPA. (2023a). *NFPA 68: Standard on Explosion Protection by Deflagration Venting 2023 ed.* (2023 Edition). NFPA.

NFPA. (2023b). *NFPA 855 Standard for the Installation of Stationary Energy Storage Systems*. National Fire Protection Association.

Ogunfuye, S. A. (2023). *Lithium-ion Battery Safety Analysis with Physical Sub-models* [PhD, West Virginia University Libraries]. https://doi.org/10.33915/etd.11875

Rappsilber, T., Yusfi, N., Krüger, S., Hahn, S.-K., Fellinger, T.-P., Krug von Nidda, J., & Tschirschwitz, R. (2023). Meta-analysis of heat release and smoke gas emission during thermal runaway of lithium-ion batteries. *Journal of Energy Storage*, *60*, 106579. https://doi.org/10.1016/j.est.2022.106579

Rho Motion. (2023). *Market and Technology Assessment of Grid-Scale Energy Storage required to Deliver Net Zero and the Implications for Battery Research in the UK*.

Robles, D. J., & Jeevarajan, J. (2020, November 17). *Fire and Gas Characterization Studies for Lithium-ion Cells and Batteries*. 2020 NASA Aerospace Battery Workshop.

Roth, E. P., & Orendorff, C. J. (2012). How Electrolytes Influence Battery Safety. *The Electrochemical Society Interface*, 6.

Shen, H., Wang, H., Li, M., Li, C., Zhang, Y., Li, Y., Yang, X., Feng, X., & Ouyang, M. (2023). Thermal Runaway Characteristics and Gas Composition Analysis of Lithium-Ion Batteries with Different LFP and NCM Cathode Materials under Inert Atmosphere. *Electronics*, *12*(7), 1603. https://doi.org/10.3390/electronics12071603

Shi, C., Wang, H., Shen, H., Wang, J., Li, C., Li, Y., Xu, W., & Li, M. (2024). Thermal Runaway Characteristics and Gas Analysis of LiNi0.9Co0.05Mn0.05O2 Batteries. *Batteries*, *10*(3), 84. https://doi.org/10.3390/batteries10030084

Skjold, T., Hisken, H., Lakshmipathy, S., Atanga, G., Bernard, L., van Wingerden, M., Olsen, K. L., Holme, M. N., Turøy, N. M., Mykleby, M., & van Wingerden, K. (2019). Vented hydrogen deflagrations in containers: Effect of congestion for homogeneous and inhomogeneous mixtures. *International Journal of Hydrogen Energy*, *44*(17), 8819–8832. https://doi.org/10.1016/j.ijhydene.2018.10.010

TraceParts S.A.S. (2022). *Trace Parts CAD file "Container 20ft"* [dataset].

Walker, W. Q. (2020, November 18). *Characterization of the GS Yuasa 134 Ah cell thermal runaway events with large format fractional thermal runaway calorimetry (L-FTRC)*. NASA Aerospace Battery Workshop.

Wang, H., Xu, H., Zhang, Z., Wang, Q., Jin, C., Wu, C., Xu, C., Hao, J., Sun, L., Du, Z., Li, Y., Sun, J., & Feng, X. (2022). Fire and explosion characteristics of vent gas from lithium-ion batteries after thermal runaway: A comparative study. *eTransportation*, *13*, 100190. https://doi.org/10.1016/j.etran.2022.100190

Wang, Y., Song, Z., Wang, H., Li, H., Zhang, Y., Li, C., Zhang, X., Feng, X., Lu, L., & Ouyang, M. (2023). Experimental research on flammability characteristics and ignition conditions of hybrid mixture emissions venting from a large format thermal failure lithium-ion battery. *Journal of Energy Storage*, *59*, 106466. https://doi.org/10.1016/j.est.2022.106466

Yang, X., Wang, H., Li, M., Li, Y., Li, C., Zhang, Y., Chen, S., Shen, H., Qian, F., Feng, X., & Ouyang, M. (2022). Experimental Study on Thermal Runaway Behavior of Lithium-Ion Battery and Analysis of Combustible Limit of Gas Production. *Batteries*, *8*(11), 250. https://doi.org/10.3390/batteries8110250

Yuan, L., Dubaniewicz, T., Zlochower, I., Thomas, R., & Rayyan, N. (2020). Experimental study on thermal runaway and vented gases of lithium-ion cells. *Process Safety and Environmental Protection*, *144*, 186–192. https://doi.org/10.1016/j.psep.2020.07.028

Zhang, Y., Wang, H., Li, W., & Li, C. (2019). Quantitative identification of emissions from abused prismatic Ni-rich lithium-ion batteries. *eTransportation*, *2*, 100031. https://doi.org/10.1016/j.etran.2019.100031

Vented confined explosions of lean hydrogen/methane/air mixture.

Eugenio Quartieri [a], Elena De Leo [a], Stefano Minotti [a], Stefano Rossin [a], Postacchini Alessio [a] & Dominik Becker [b], Roland Bunse [b]

[a] Baker Hughes (Engineering, Florence, Italy)
[b] REMBE® (Research + Technology Center GmbH, Brilon, Germany, REMBE® RTC)

e-mail: eugenio.quartieri@bakerhughes.com

Abstract

The use of pure hydrogen or blends with natural gas as fuel for gas turbines raises concerns about potential leakages into confined space since are installed inside an acoustic enclosure where the fuel gas supply system is also placed. Package design is done to reduce the likelihood of leakage occurrence and to prevent any ignition, nevertheless it is not possible to exclude that a gas cloud could be ignited leading to a potential explosion inside the gas turbine enclosure. The available standard for the safety of gas turbine enclosure (ISO 21789:2022), which is based on methane fuels, recognizes that if a hazardous condition is present inside the enclosure, explosion prevention and protection measures shall be implemented like pressure resistant design and or explosion relief panel. Moreover, other American and Europe standards like NFPA68 and/or EN14994 provide criteria, formula, and numerical values to be used as deflagration index (named K_G) for the design in case of an explosion of stoichiometric gas cloud of different fuel, but for lean gas cloud explosion the above standards do not provide any K_G values.

It is therefore important to review the applicability of current safety standards for these new fuels, as the pressure resulting from a hydrogen explosion is expected to be significantly higher than that from a methane explosion. This paper describes the tests executed at REMBE® RTC facility on an empty vessel filled with different blends of methane and hydrogen with and without explosion relief panel. The purpose of these tests is to verify the effectiveness of explosion relief panel in a lean gas cloud explosion to reduce the internal pressure inside the protected vessel and to verify the external pressure and temperature behaviour due to relief panel opening. The experimental test for hydrogen and hydrogen/methane fuel mixtures are also replicated using the explosion modelling tool FLACS CFD. The comparison between test campaign and numerical results is used to verify the prediction of confined vented simulations used to support the design of gas turbine package.

Keywords: *hydrogen, explosions, prevention, mitigation, relief panel*

Introduction

Land-based gas turbines are very often installed inside an acoustic enclosure to isolate it from surrounding environment and reduce the noise emissions. Creating an enclosed space around such hot engine requires to provide forced ventilation flow to cool down the turbine itself and all the instruments, equipment and items installed inside the hood [1,2]. Moreover, several auxiliary systems, which are essential for proper gas turbine operation, are located inside the enclosure. One of them is the fuel gas system, which is usually composed of a fuel gas valves skid and a piping line manifold, placed below and around the engine, respectively. Many connections, both flanged and threated, are presents along this system and all of them theoretically represent a potential source of fuel gas leakage [3,4]. The dispersion of a flammable gas inside a confined space with contemporary presence of hot surfaces, gas turbine skin and some piping, generates concerns about the potential explosion hazard [5]. Such scenario requires mitigation measures and recognized design guidelines to be implemented

for each gas turbine package during the design execution [6,7]. For this reason, the forced ventilation system of enclosure is provided not only for cooling, but also as mitigation diluting any accidental leak. It is recognized that ventilation is crucial for safety against explosion hazards if properly designed, since limits the extent of the flammable cloud and the consequences of its unexpected ignition [8].

In the frame of CO_2 footprint reduction towards energy transition, new gas turbines capable of burning pure hydrogen and blends with natural gas have been designed. The benefit in terms of impact on the CO_2 emissions is known, but the main challenge in the design is related to hydrogen criticalities such as lower ignition energy, greater Lower Heating Value (LHV), larger flammability range if compared with conventional natural gas. These aspects need to be evaluated in the design phase [9, 10] to guarantee the maximum level of safety. Package design is done to reduce the likelihood of leakage occurrence and prevent any ignition, nevertheless it is not possible to exclude that a gas cloud could be ignited. In case fuel is hydrogen and/or hydrogen blend, the consequence may lead to a potential explosion inside the gas turbine enclosure, which could create a pressure significantly higher than methane explosion [11]. The available standard for the safety of gas turbine enclosure is ISO 21789 [12], which is based on methane applications and recognizes that if a hazardous condition is present inside the enclosure, explosion prevention and protection measures shall be implemented such as pressure resistant design and/or explosion relief panel. Moreover, other American and Europe standards like NFPA68 [13] and/or EN14994 [14] provide criteria, formula, and numerical values to be used as deflagration index (named K_G) for the design in case of an explosion of stoichiometric gas cloud of different fuels, but for lean gas cloud explosion of pure hydrogen or its blends the above standards do not provide any K_G values. Therefore, it is important to review the applicability of current safety standards because they address stoichiometric methane mixture, while in the current H_2 packages it is more likely to have in case of leak lean gas cloud.

This work, done in collaboration with REMBE® RTC, shows the execution of confined vented explosions of lean mixtures for pure methane, pure hydrogen and one blend (85% H_2 and 15% CH_4). The effect of different relief panels is evaluated and numerical simulations to predict their behavior are executed with FLACS. The experimental campaign is carried out with different mixture at similar laminar flammable speed and a comparison between explosion tests and numerical results is reported. The aim of this activity is to provide data useful to support the design of gas turbine package.

1.Experiments

1.1. REMBE® RTC experimental facility

The experimental campaign was carried out at REMBE® RTC facility in Brilon. Different tests were executed to assess the behavior of relief panels without and with flame arrester evaluating the pressure trend and temperature.

The experiments were performed in a 10.8 m³ test vessel equipped with a 920 mm × 920 mm (A = 0.85m²) pressure relief opening. The first set of experiments was done using a relief device composed of two layers of aluminum foil, since it is not an invasive solution to understand the gas explosion magnitude. Then, the second set of tests was conducted using a commercial pressure relief panel equipped with a flame arrester, named Q filter, which is designed by REMBE® GmbH Safety + Control to limit the flame propagation outside the enclosed space. The fuel mixtures were prepared injecting a controlled amount of gas inside a smaller auxiliary vessel of 0.250 m^3 monitoring the pressure. Once reached the desired mass of gas, it was transferred into the bigger test vessel (10.8 m^3) ad mixed with the right amount of air before to be ignited. The resulting explosive mixture was ignited with a punctual energy of 100 J with a pyrotechnical igniter placed in the middle of the vessel on the cylinder axis. Two fast pressure transmitters (P_1 and P_2) were placed inside the vessel on the symmetrical axis at the same distance from the igniter for measuring pressure trends (Figure 1). The

pressure sensors model is Wika S 20 with a measuring range of 2kHz, an accuracy of +/-0.5% and a sampling frequency of 1kHz. Moreover, three thermocouples were placed outside the vessel to evaluate the temperature after the propagation of the explosion outside. The used thermocouples are type K with 0,22 mm^2 wire cross section, in order to reduce as much as possible the response time. Two of them (T1 and T2) were placed along the direction of venting gases 3 m away from the relief opening and the last one (T3) farer at 4.5 m. The experimental set up can be seen in Figure 1.

Fig. 1. Experimental set up

The experiments were carried out with the described set-up according to DIN 17025:2018 [15], using three different gases, 100% H_2, 100% CH_4 and blend 85% H_2-15% CH_4, at different volume concentration (6% and 10% vol) and repeated for both relief devices.

The set of experiments discussed in this work is summarized in Table 1. The gas concentration was based on its composition in order to have comparable laminar flame speed. All the mixtures in Table 1 have similar laminar flame speed (S_L) value around to 12 cm/s, but different flammable mass. The S_L curves of the gases are shown in Figure 2 [16], where Donohoe et al. show their correlation with the equivalent ratio (φ) for pure methane, pure hydrogen and several blends. Three points are added to indicate test conditions of this work. The S_L value is estimated calculating the equivalent ratio (φ) of the mixture according to equation (1):

$$\varphi = \frac{{}^{m_{fuel}}/_{m_{ox}}}{({}^{m_{fuel}}/_{m_{ox}})_{stoich}} \quad (1)$$

Table 1. Set of experiments conducted in REMBE® RTC facility.

Test	Mixture Composition %	Relief device	Vol gas/air %	φ	Flammable Mass (kg)
1	100% CH4	Aluminum Foils	6%	0.636	0.463
2	100% CH4	Relief Panel with Q filter	6%	0.636	0.463
3	100% H2	Aluminum Foils	10%	0.253	0.097
4	100% H2	Relief Panel with Q filter	10%	0.253	0.097
5	85% H2 – 15% CH4	Aluminum Foils	10%	0.390	0.198 (0.082kg H_2+0.116kg CH_4)
6	85% H2 – 15% CH4	Relief Panel with Q filter	10%	0.390	0.198 (0.082kg H_2+0.116kg CH_4)

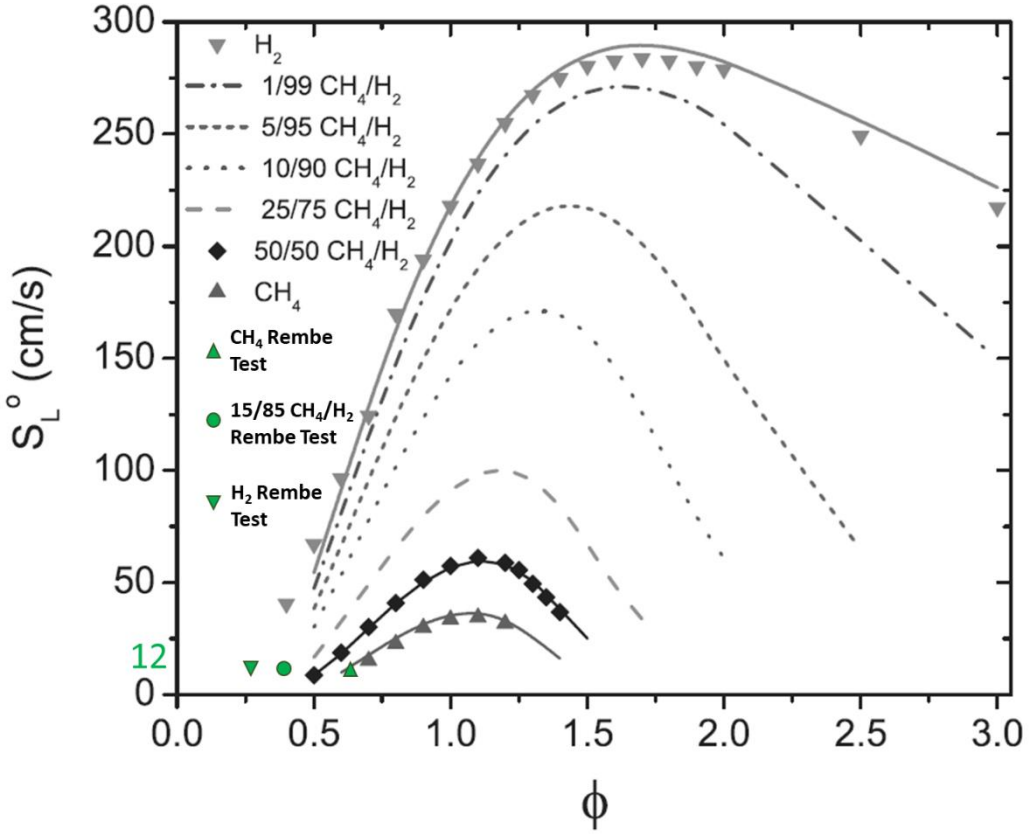

Fig. 2. *Laminar Flame Speed curves [11] and estimated points for REMBE® tests*

1.2. Tests Results

Figures 3, 4 and 5 show the pressure trends obtained during the tests for methane, hydrogen and their blend. To facilitate the picture analysis, only signal filtered with moving average of pressure transmitter P1 is represented with a thick line; while on the background dotted lines represent the unfiltered measure [17]. This choice to show only one measurement is dictated by the fact that P1 and P2 signals are very similar mainly their moving average. As a reference, the difference between P1 and P2 is shown in Figure 6 and 7 only for 100% H_2 tests, all other cases have similar behaviour and are not shown for brevity.

Figure 3 shows the comparison of the two experiments performed on the lean mixture (6% vol) of air/100% CH_4. Test 1 is executed with aluminium foils venting device and Test 2 with relief panel and flame arrester. The two tests produce similar results, since the reached maximum peak and the slope of pressure increase are quite the same. The main difference is visible after pressure peak is reached. Test 2 shows a slower decreasing than Test 1, mainly due to the back pressure generated by the presence of the flame arrester. The interaction between the flame front and the obstacle does not produce effects in terms of peak pressure and time duration of the impulsive pressure increase.

Figure 4 shows tests made with a lean mixture (10% vol) of air/100% H_2 executed with the same set-up conditions but different relief device, aluminium foils (Test 3) and the relief panel (Test 4). The major effect generated by the relief panel with the flame arrester is a higher peak. In both cases the relief device opening pressure is 0.1 barg and in Test 3 (aluminium foils) after 0.02 s the peak is reached, while in Test 4 (panel + flame arrester) after the opening there is a slight change of slope. The peak pressure reached in Test 4 is more than double respect to Test 3 due to the back pressure created by flame arrester, which represents an obstacle and it is very likely that its wrinkled structure enhances the hydrogen flame speed more than methane [18].

Figure 5 shows the tests carried out with the blend 85% H_2 and 15% CH_4 (Test 5 and Test 6). Differently from the tests with the pure methane, these are significantly affected by the different relief

device, as it occurs for pure hydrogen. The peak pressure recorded in Test 6 is the highest between all tests previously described, although the peak pressure obtained with the aluminium foils (Test 5) has the same value obtained with pure methane and hydrogen. The causes of this behaviour could be associated at different causes: the not perfectly uniform concentration inside the vessel, the high content of hydrogen (85%), which interacts with the flame arrester [19] and finally the flammable mass present inside the vessel, which is higher than Test 4. Table 1 shows the flammable mass for each test.

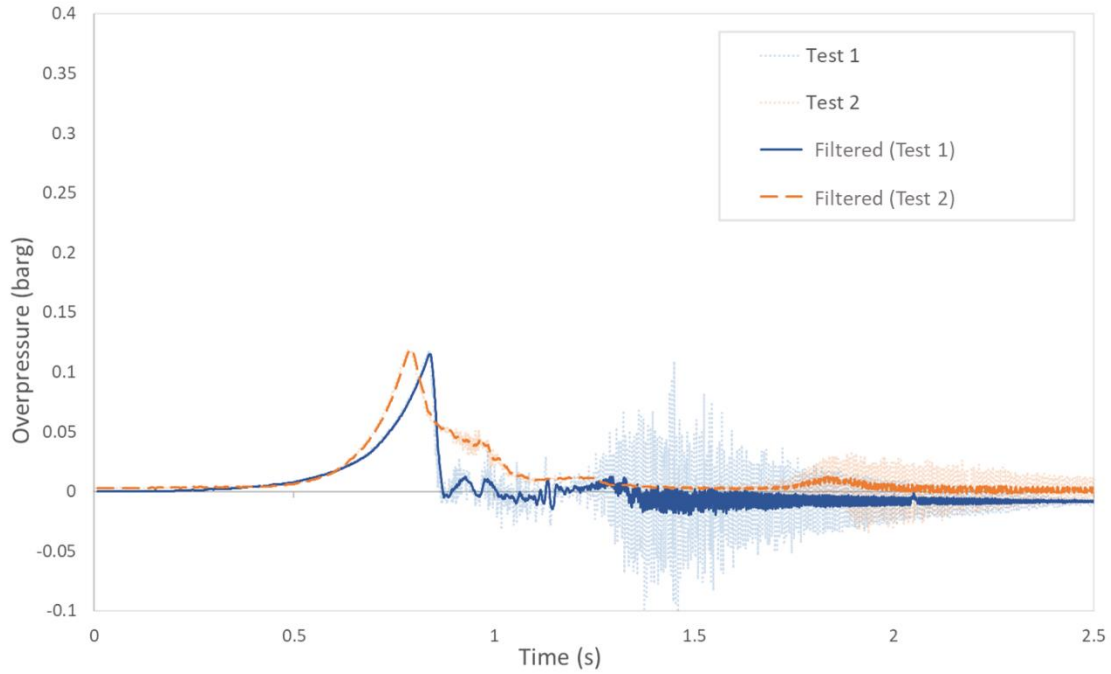

Fig. 3. *Tests with 100%CH_4 at 6% vol with aluminum foil (Test 1) and with relief panel and flame arrester (Test 2).*

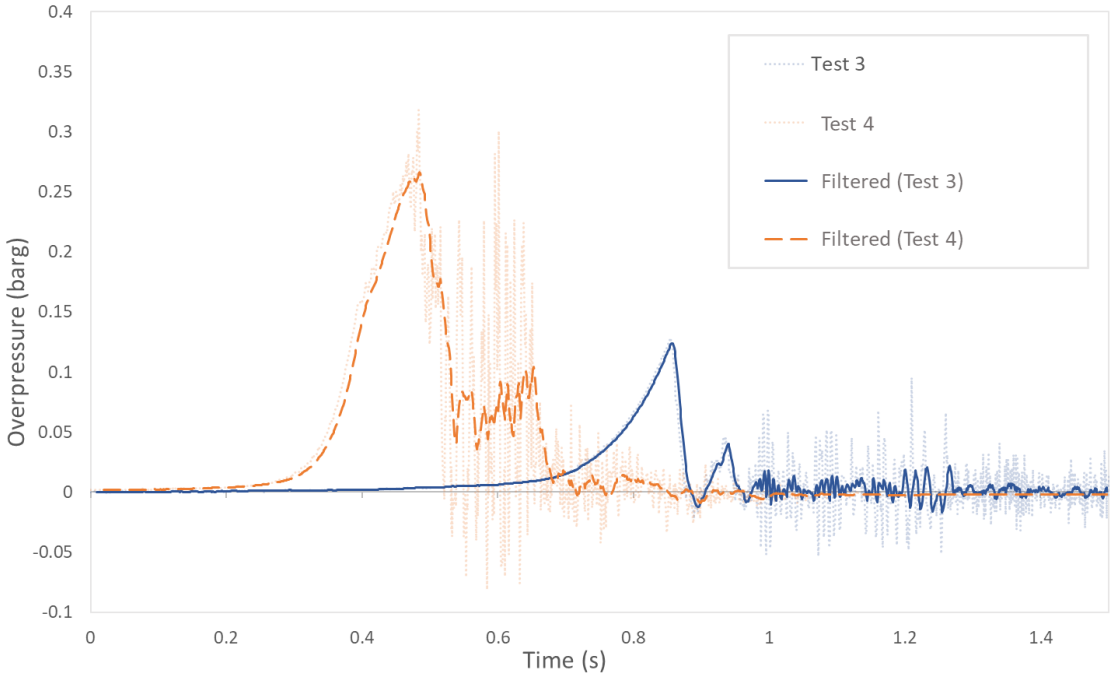

Fig. 4. *Tests with 100% H2 at 10% vol with aluminum foil (Test 3) and with relief panel and flame arrester (Test 4).*

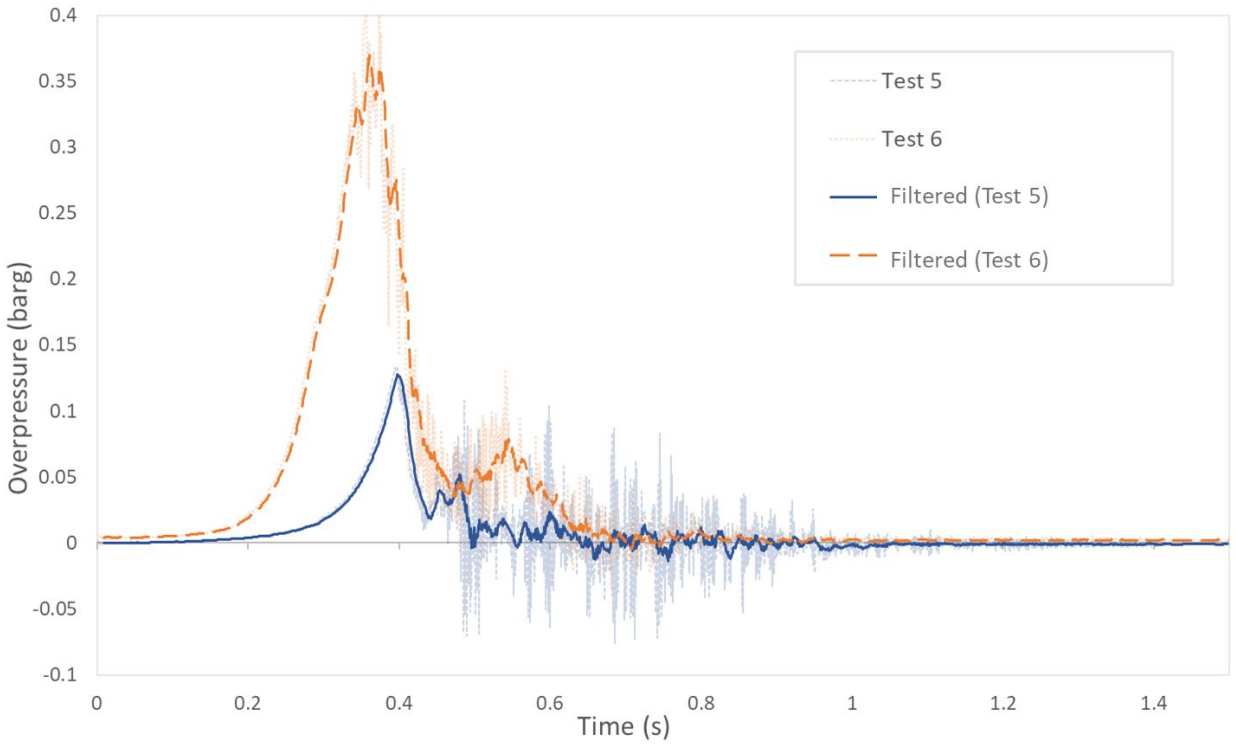

Fig. 5. *Tests with 85% H_2 – 15%CH_4 at 10% vol with aluminum foil (Test 5) and with relief panel and flame arrester (Test 6).*

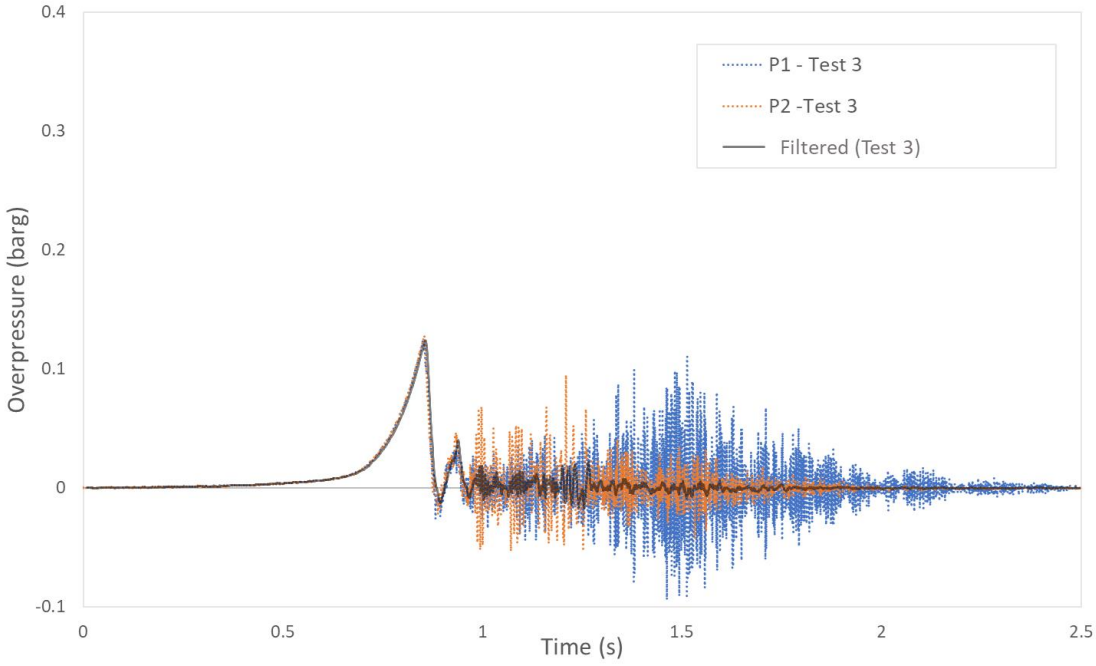

Fig. 6. *P1 and P2 in Test 3 (100% H_2 with aluminum foil)*

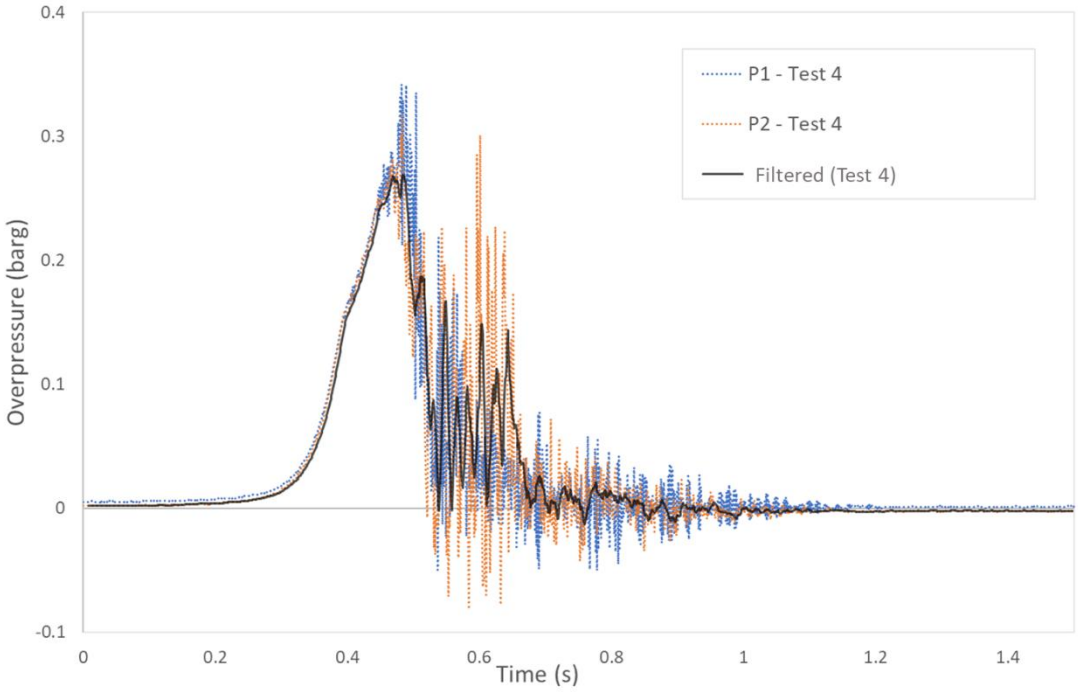

Fig. 7. *P1 and P2 in Test 4 (100% H_2 with relief panel and flame arrester)*

In summary, the overpressure generated in cases with the aluminium foils and without flame arrester reaches similar peaks for each mixture, since it is likely that there is not significant interference with the combustion process, which is dominated by laminar flame speed value. On the other hand, the interaction of the flame front with the Q filter generates different effects depending on the mixture composition. Notably, the flame arrester effectively reduces the flame length compared to free vented tests with aluminum foils, mitigating impact on the surrounding. Temperature measurements and indicators showed significantly lower values than the expected from a free flame, indicating the Q-Filter's potentiality to enhance safety measures. Table 2 shows the peak temperature value at 3 m from the venting panel and the corresponding adiabatic flame temperature. Comparing the two values, the beneficial effect of flame arrester is remarkable with all mixture compositions, obtaining a temperature reduction of 80-90%.

Table 2*. Temperature peak at 3 m from the relief panel*

Test	Mixture Composition %	Max Temperature at 3m [°C]	Adiabatic Flame Temperature [°C]
2	100% CH_4	32	1750
4	100% H_2	117	1000
6	85% H_2 – 15% CH_4	150	1100

2 Numerical simulations

2.1 FLACS CFD analysis: modelling and set up.

A series of CFD simulations is carried out to replicate the tests described above using FLACS – CFD 22. 2 by Gexcon. The turbulence model is based on Reynolds-Averaged Navier-Stokes (RANS) equations, in this specific case *k-ε* model, coupled with sub-grid models to account for the influence of objects that cannot be resolved on the computational grid [20]. FLACS models physical object through the porosity distributed resistance (PDR) approach.

Combustion and spatial distribution of the reaction rate across the flame zone is predicted by a flame model, which depends on the diffusion coefficient D and the reaction rate R_F, as shown in fuel mass fraction equation (2). The reaction rate term (R_F) is also function of the burning velocity [21].

$$\frac{\partial(\beta_v \rho Y_{fuel})}{\partial t} + \frac{\partial(\beta_j \rho u_j Y_{fuel})}{\partial x_j} = \frac{\partial(\beta_j \rho D \frac{\partial Y_{fuel}}{\partial x_j})}{\partial x_j} + R_F \qquad (2)$$

$$c = 1 - \frac{Y_{fuel}}{Y_{fuel,0}} \qquad (3)$$

$$R_F = C_{\beta R_F} \frac{S}{\Delta} \rho \min[c, 9(1-c)] \qquad (4)$$

where, $C_{\beta RF}$ is a model constant, s is the burning velocity, Δ is the control volume length in the direction of flame propagation and $Y_{fuel,0}$ is the initial fuel mass fraction. For all gases, laminar burning velocity (S) is used for equation (4), with only exception for hydrogen since FLACS applies a correction factor on the Lewis number ($S_{L,Le}$). To model the regime of cellular flame propagation the quasi-laminar burning velocity (S_{QL}) concept is used and it is modelled as shown in (5):

$$S_{QL} = S_{L,Le}(1 + C_{QL} r_F^a) \qquad (5)$$

where C_{QL} is a mixture-dependent model constant, r_F is the flame radius and a is a model constant [22].

FLACS computational domain (Figure 8) is derived from test vessel drawing and two monitoring points are placed in P1 and P2 position as it is in the real test rig. Finally, the ignition point is located as per experimental test.

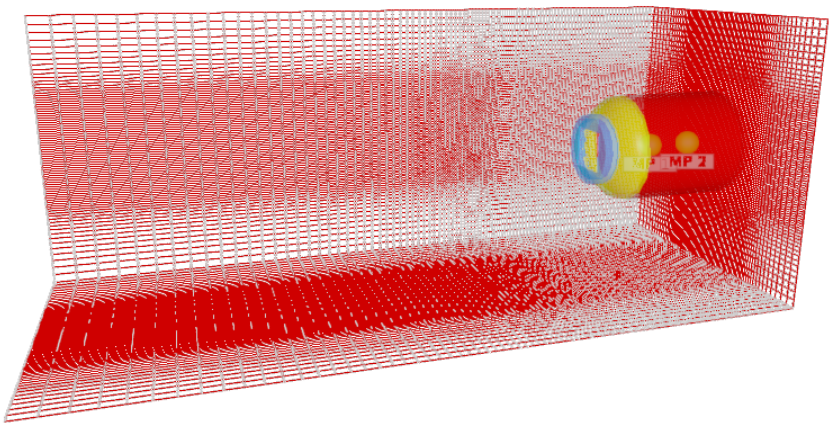

Fig. 8. *FLACS computational domain*

The mesh implemented in FLACS is a cartesian grid, a structured not-body fitted type of grid [19]. A fine grid is generated in the zone contained within the vessel and some meter outside along the vessel axis, where the explosion is expected to propagate. The mesh has a total amount of about 3M of elements and a cell size of 5 mm.

For the first set of simulations to reproduce the aluminium foils, the relief device is modelled as a massless foil. On the other hand, for the second set, relief panel is modelled considering it hinged on the lower side and with a weight of 5 kg/m^2 and the Q filter is modelled as a porous media placed on the inner side of the panel. Its thickness is 0.1 m as the real flame arrester, in order to accurately reproduce the interaction with the flame front. For each gas composition, four different simulations are carried out using different porosity values increasing progressively the blocking values: 0.5, 0.25, 0.2, 0.18. The sensitivity study is done to identify the level of porosity reproducing the experimental phenomenon. As initial condition, an uniform distribution of gas is imposed calculating the proper equivalent ration knowing pressure and temperature of the gas inside the vessel during the test. This simplified modelling without simulating the filling of the vessel introduces some differences with the executed tests, since in the reality the mixture was not perfectly uniform and quiescent inside the vessel.

2.2 FLACS CFD results

Figure 9 shows the results obtained for the first set of simulations with the aluminium foils as relief device. For all the tests, there is a good agreement between the numerical calculation and experimental data, since pressure peaks and increase rates versus time are similar. As it was expected, an evident difference is the absence in FLACS results of the acoustic oscillations of the un-filtered pressure trends [23]. As mentioned in tests results, the pressure trend development and the maximum reached is quite the same in all tests with the aluminium foil even if the mixture are characterized by different equivalent ratio. The main factors characterizing this behaviour are the relief device opening and the absence of elements able to enhance the flame front, for this reason the pressure trend is not significantly dependent on the gas type. After the opening, the combustion propagation outside the vessel creates differences visible in the remaining part of the pressure trends.

Figure 10 shows the results obtained imposing different porous medias for modelling the flame arrester. As it is evident, the best matching is obtained with the 100% methane mixture with porosity value of both 0.2 and 0.25. In all four the simulations made with 100% CH_4, the flame arrester seems to not significantly affect the pressure of the first peak inside the vessel. The highest misalignment with experiments is obtained using porosity at 0.18, due to the back pressure that is produced inside the vessel. As in the test, also FLACS results show a lower pressure decreasing in the second part (after the peak) of the trend realistically generated by the flame arrester, which represents an obstacle. Pressure increase and decrease create a sort of triangle, which has a larger base in the CFD trend due to the higher time needed for reaching the peak, but in a general overview the results are in good agreement. Pressure results for 85% hydrogen and 15% methane are shown in figure 8. Differently from the pure methane case, imposing the same values of porosity, the interaction with the flame arrester generates higher peak than the tested one. The best alignment of the maximum peak is obtained with a porosity value of 0.2, even if in all simulations the pressure trend development in time is not fully captured. The pressure peak is delayed in comparison to the real test. Similarly, the same kind of simulations are performed using pure hydrogen. In terms of maximum reached peak, the best results are obtained with a porosity value of 0.18, differently from the previous simulations. In the hydrogen simulations the effect of back pressure generates by the porous media is less effective producing lower peak than the tested one. In all the four simulations the time interval of the impulsive phenomenon is overestimated in comparison to the test.

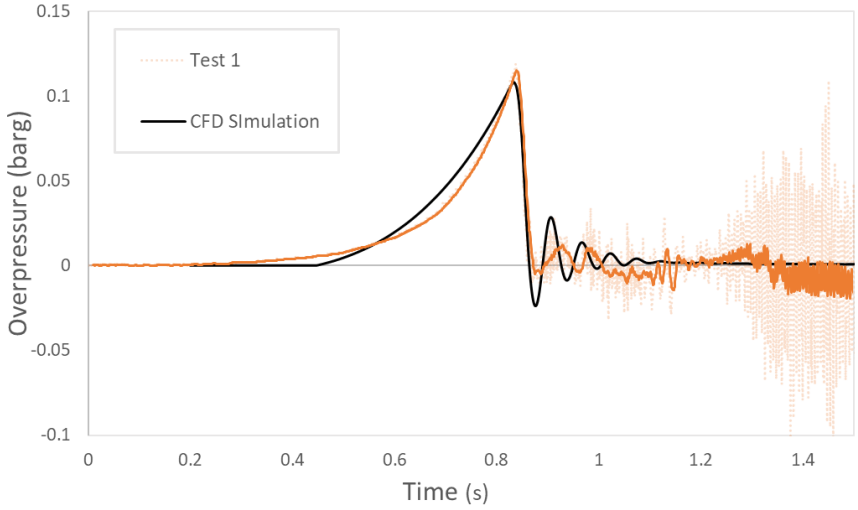

a)

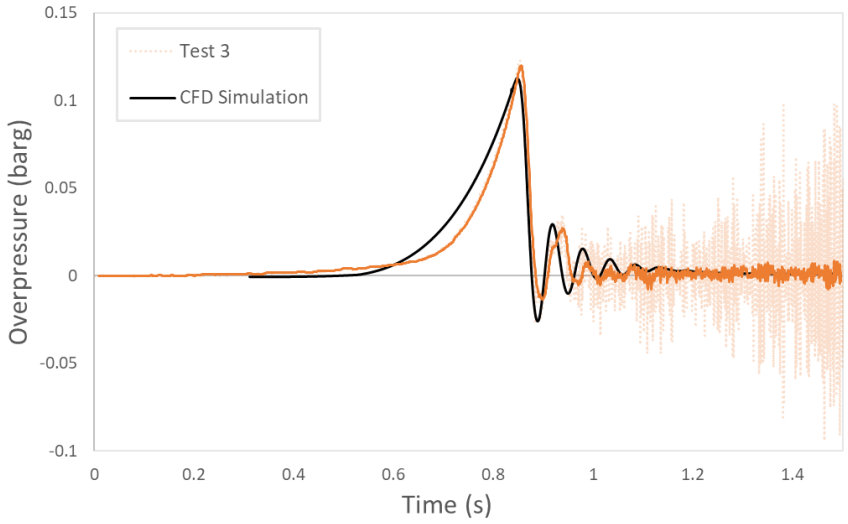

b)

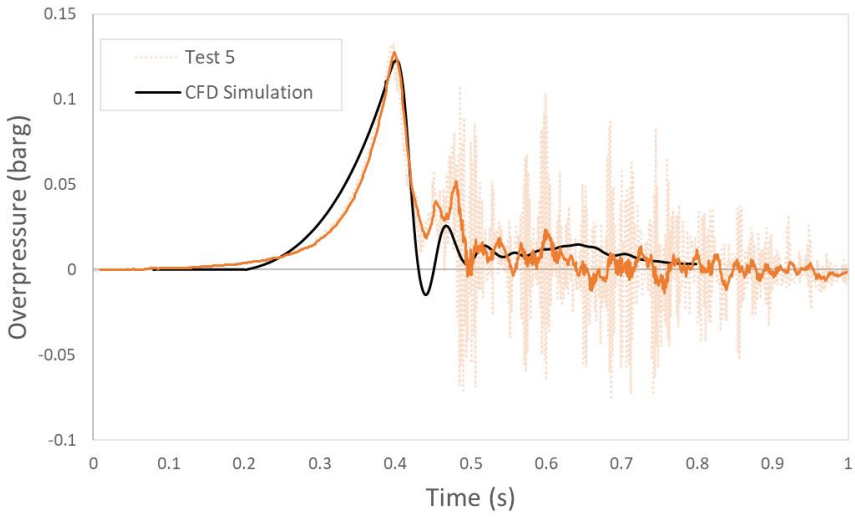

c)

Fig.9. *Experimental results versus CFD simulation: a) Test 1 - 100% CH_4; b) Test 3 -100% H_2; c) Test 5 - 85%H_2-15%CH_4*

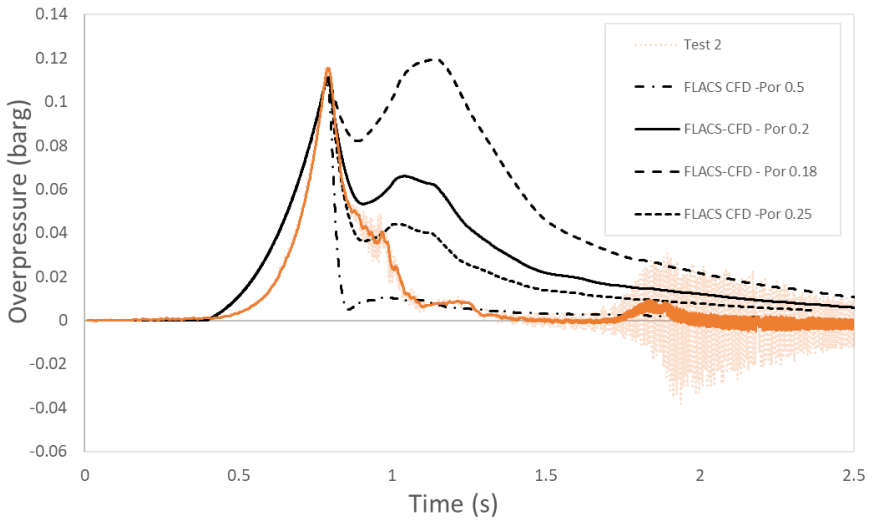

a)

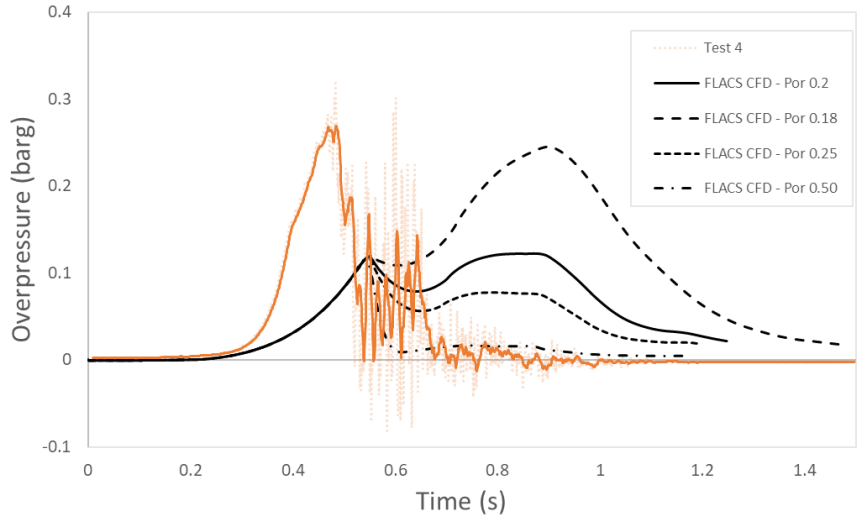

b)

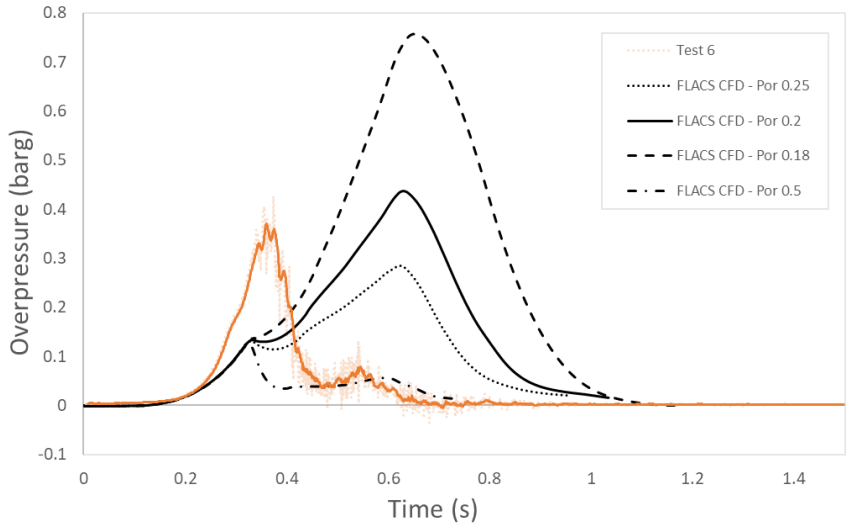

c)

Fig.10. *Experimental results versus CFD simulation: a) Tests 2 - 100% CH_4; b) Tests 4 - $CH_4$100% H_2; c) Tests 6 - 85%H_2-15%.*

3 Conclusions

This work is mainly focused on the consequences of a lean gas mixture ignition with pure hydrogen, pure methane and their blend (85% H_2 and 15% CH_4), since it is representative of real conditions that could occur inside a gas turbine enclosure in case of an accidental fuel gas leak.

Experimental ignition tests inside a 10.8 m^3 vessel with relief device were conducted at REMBE® RTC facility to demonstrate the capability of the relief panel equipped with a flame arrester to limit the effects of explosion propagation outside the vessel. FLACS was used to simulate the performed tests and to validate the relief panel modelling for their use on gas turbine packages.

The solution with compact flame arrester, named Q-Filter by Rembe®, demonstrated that pressure peak inside the vessel obtained after the ignition is higher than the aluminum foils device. This effect is due to the interaction of the flame front with the obstacle represented by the flame arrester. On the other hand, the benefit is present externally to the vessel where the exhaust gas temperature is reduced respect to requirements given by international standards.

This study showed that without flame arrester the pressure peak inside the enclosed space is lower than the case the Q filter. On the other hand, without flame arrester the propagation outside the vessel is more severe in terms of temperature and pressure. According to this finding, whenever a gas turbine enclosure needs a relief device, the choice to install a flame arrester is dependent on-site requirements.

References

- **Bibliography:**

[1] Ponnuraj, B., Sultanian, B., K., Novori, A., and Pecchi, P., 3D CFD Analysis of an Industrial Gas Turbine Compartment Ventilation System, ASME paper IMECE2003-41672, 2003 International Mechanical Engineering Congress and Exposition, Washington, DC, USA, November 15–21, 2003.

[2] Lucherini, G., Minotti, S., Ragni, G. and Bologna, F., Experimental and numerical investigation on GT package scale model, ASME paper GT2018-75694, Turbo Expo 2018, Oslo, Norway, 2018.

[3] Lucherini, G., Minotti, S. and Michelassi, V., The Impact of Model Assumptions on the CFD Assisted Design of Gas Turbine Packages, ASME paper GT2019-90781, Turbo Expo 2019, Phoenix, Arizona, USA, 2019.

[4] De Leo, E., Lucherini, G., Minotti, S. and Quartieri, E., GT Enclosure Dispersion Analysis with Different CFD Tools, International Conference on Hydrogen Safety (ICHS), Quebec City, Canada, 2023.

[5] Minotti, S., Nenciolini, A., Quartieri, E., Rossin, S., Sorgonà, F., Brekke, O., Holen, J.K., Bente, J., Gas leak ignition study for 100% H2 gas turbine package, ASME paper GT2023-106313, Turbo Expo 2023, Boston, Massachusetts, 2023.

[6] Santon, R.C., Explosion hazard at gas turbine driven powerplants, ASME Paper no.98-GT-215, 1998.

[7] Santon, R.C., Kidger, J.W., and Lea, C.J., 2002, Safety developments in gas turbine power applications, ASME Paper no. GT-2002-30469.

[8] Santon, R.C., Ivings, M.J., and Pritchard, D.K., A new gas turbine enclosure ventilation design criterion, ASME Paper no. GT-2005-68725, 2005.

[9] Samdal, U.N., Grainger, D., Hamborg, E.S., Nilsen, S.H., Sommersel, O.K, Hydrogen Safety Strategies and Risk Management in Equinor, International Conference on Hydrogen Safety (ICHS), Edinburgh, Scotland (Virtual), 2021.

[10] Baldini, M., Cinelli, R., Minotti, S., Pampaloni, G., Quartieri, E., Rossin, S., Moving Gas Turbine package from Conventional Gas to Hydrogen Blend, International Conference on Hydrogen Safety (ICHS), Edinburgh, Scotland (Virtual), 2021.

[11] Miles, D., Vye, T., Wimshurst, A., Assessment of Enclosure Ventilation Safety for Hydrogen Fuelled Gas Turbines 2021.

[12] BS EN ISO 21789:2022, Gas turbine application – Safety.

[13] NFPA68:2023, Standard on Explosion Protection by Deflagration Venting.

[14] EN14994:2007, Gas explosion venting protective systems.

[15] DIN EN ISO/IEC 17025:2018-03, General requirements for the competence of testing and calibration laboratories.

[16] Donohoe, N., Heufer, A., Metcalfe, W. K., Curran, H. J., Davis, M. L., Mathieu, O., ... & Güthe, F., Ignition delay times, laminar flame speeds, and mechanism validation for natural gas/hydrogen blends at elevated pressures. Combustion and Flame,161(6), 1432-1443, 2014.

[17] Kuznetsov, M., Friedrich, A., Stern, G., Kotchourko, N., Jallais, S., L'Hostis, B., Medium-scale experiments on vented hydrogen deflagration, Journal of Loss Prevention in the Process Industries 36, 416 – 428, 2015.

[18] Li, X., Dong, J., Jin, K., Duan, Q., Sun, J., Li, M., & Xiao, H. Flame acceleration and deflagration-to-detonation transition in a channel with continuous triangular obstacles: Effect of equivalence ratio. Process Safety and Environmental Protection, 167, 576-591, 2022.

[19] Cai, C., Dong, J., Zhao, M., Liu, L., Li, M., and Xiao, H., Flame acceleration in stoichiometric methane/hydrogen/air mixtures in an obstructed channel: effect of hydrogen blend ratio, International Conference on Hydrogen Safety (ICHS), Quebec City, Canada, 2023.

[20] FLACS-CFD v22.2 User's Manual, Copyright ©Gexcon AS, 2023.

[21] Lucas, M., Hiskena, H. Skjold, T., Arntzen, B. J., CFD Analysis of Explosions with Hydrogen-Methane-Air Mixtures in Congested Geometries, Chemical Engineering Transactions, 2022.

[22] Lucas M., Salaün N., Atanga G., Wilkins B., Martin-Barbaz S. Experiments and simulations of large scale hydrogen-nitrogen-air gas explosions for nuclear and hydrogen safety applications, International Conference on Hydrogen Safety (ICHS), Quebec City, Canada, 2023.

[23] Vyazmina, E., & Jallais, S. Validation and recommendations for FLACS CFD and engineering approaches to model hydrogen vented explosions: Effects of concentration, obstruction vent area and ignition position. International journal of hydrogen energy, 41(33), 15101-15109, 2016.

Experimental investigation of the effect of dry water and solid chemical inhibitors on premixed hydrogen-air combustion

Matthijs van Wingerden, Vegard Kallestad Stople, Erikas Stankejevas & Trygve Skjold

University of Bergen, Department of Physics and Technology, Bergen, Norway

E-mail: mattheus.van.wingerden@uib.no

Abstract

Solid chemical inhibitors, such as sodium bicarbonate and potassium carbonate, are widely used as fire suppressants in industry. In recent years, systems have been developed for using inhibitors as a safety measure for vapour cloud explosions. The aim of the joint industry project (JIP) *'Risk-reduction for hydrogen installations by partial suppression of explosions'* (HyRISE) is to develop fundamental knowledge that can support practical solutions for mitigating hydrogen explosions in congested and confined environments by means of active systems for chemical inhibition. The project addresses critical hazards related to the safe implementation of hydrogen as an energy carrier in society. However, chemical inhibition of hydrogen-air mixtures is not straightforward. Compared to hydrocarbons, hydrogen flames have several unfavourable properties: higher burning velocity, smaller flame thickness, and less radiation. This implies that the solid inhibitor particles may not achieve sufficiently high temperatures to decompose or sublimate in the flame zone. The paper presents results from an experimental investigation with various inhibitors, including solid powders and 'dry water', in a constant volume explosion vessel. It was found that dry water with 85% water content yielded the best inhibition effect. Additives in the form of potassium carbonate did not increase the effectiveness of the dry water.

Keywords: *inhibition, hydrogen-air explosions, mitigation, industrial explosions, dry water*

Introduction

Inhibitors have been widely used for fire and explosion protection. Halons were widely used in the past, but due to their impact on the environment, they are now replaced by solid inhibitors such as sodium and potassium bicarbonate in applications such as powder extinguishers and suppression systems. In recent years, a system has been developed for dispersing solid inhibitors in process facilities upon detection of flammable gas (van Wingerden & Hoorelbeke, 2011). This can have a significant mitigating effect on explosions. The main advantages of solid inhibitors, relative to gases or liquids, relate to throwing distance and mixing, and liquid droplets are also more likely to agglomerate or stick to solid surfaces.

As the industry is moving towards increased use of hydrogen as energy carrier or reducing agent, there is a need for systems that effectively can mitigate hydrogen explosions. However, published studies on the effect of inhibitors on hydrogen-air explosions are scarce (van Wingerden et al., 2023), and only a few inhibitors have proved effective (e.g. halons and iron pentacarbonyl). Experiments with solid inhibitors, such as sodium carbonate and potassium bicarbonate, have not demonstrated a significant effect (Nan et al., 2024). Whereas potassium carbonate (K_2CO_3) is a very effective inhibitor for hydrocarbons, this has not been demonstrated experimentally for hydrogen. However, from a chemical perspective, the addition of K_2CO_3 should result in the following terminating reaction becoming among the most sensitive (i.e. the terminating reaction that is most likely to occur) (Roosendans 2018):

$$K + OH + M \rightarrow KOH + M$$

This should in principle yield a significate decrease in the combustion reactivity. It is therefore likely that the limited effect observed is caused by insufficient or too slow heating of the particles to deliver active radicals in the flame zone (Dounia et. al. 2022).

Dry water is a powder consisting of water and hydrophobic fumed silica (Bomhard, 2011). When the water is stirred into fine droplets, the silica encapsulates the water droplets, forming a white powder. Dry water has been proven very effective as a cooling agent. Recent experiments with methane have shown an amplified effect of inhibitors with addition of dry water (Liu et al., 2024; Wang et al., 2023).

Experiments performed by Battersby et al. (2013) showed a positive cooling effect from water mists. The same experiments have shown that water droplets with additives can be used to deliver inhibitors into hydrogen flames. If dry water behaves similarly to water droplets it could be possible to reproduce this behaviour with dry water.

This paper summarises the results from an experimental investigation of the effect of dry water on hydrogen-air explosions.

1. Materials and methods

1.1. Dry water

The dry water was prepared using hydrophobic fumed silica (SiO_2) and distilled water stirred in a mixer at around 30 000 rpm for 30 seconds. Hydrophobic fumed silica is nanosized silica particles treated with HMDS (hexamethyldisilazane) to yield hydrophobic properties. The compositions are given as wt.% water, i.e. a 90% sample was prepared from 10 g SiO_2 and 90 g of water. A previous study concluded that a ratio of 1:10 (~91%) of respectively SiO_2 and water was found to yield the optimal form of dry water in terms of no access SiO_2 or water being observed through microscopy after the mixing process (Liu et al., 2024). In this work, ratios of 80%, 85%, 90% and 95% were tested.

1.2. Dry water and potassium carbonate

In this work, two different approaches were used for adding K_2CO_3 to the dry water. One was a 50/50 % mixture of the dry powders, with 90% water, referred to as “mixed”. The other was dry water made from SiO_2 and 0.2 M K_2CO_3 solution (90%), referred to as “modified”.

1.3. Experiments

The tests were performed in a 20-litre vessel of the USBM (United States Bureau of Mines) type, commonly used for testing explosion properties for dusts (Skjold, 2003). The tests were performed according to the method for hybrid mixtures described in the KSEP manual (Cesana & Siwek, 2012). Hydrogen was added to the main vessel by partial pressure. The vacuum pump used was unable to reduce the pressure in the vessel below -0.87 barg. In addition, an initial pressure of -0.60 barg is needed in the vessel to yield atmospheric pressure at the time of ignition, due to the addition of air from the dispersion chamber. This gave a limitation of testing hydrogen concentrations higher than 28 vol.%. All tests in the current work were therefore tested at 28 vol.% hydrogen in air. All tests were ignited with a spark generator providing a single spark with energies of around 6 J. Each test was repeated 3 times.

2. Results and discussion

2.1. The influence of dry water on hydrogen-air explosions

Tests were performed under standard conditions with 80, 85, 90 and 95% dry water. Figure 1 shows the maximum pressure P_m and Figure 2 shows the maximum rate of pressure rise $(dp/dt)_m$ for increasing concentrations of dry water. Overall, a slight decrease in pressure is observed as dry water is added to the hydrogen-air mixture. The $(dp/dt)_m$ is influenced more severely and in some cases values of half the initial values are obtained. This indicates that the dry water has a good cooling effect on the hydrogen-air flames.

The effectiveness is however highly dependent on the ratio of water to SiO_2 in the dry water powder. Powders with water content of 85% seems to perform the best, while powders with more or less water content perform slightly worse. As observed in the work by Liu et al. (2024), dry water with high water content can contain excess water which is not encapsulated by the SiO_2. This can result in agglomeration of the powders making them harder to disperse. In addition, these powders might be less resistant to the relatively harsh dispersion through the rebound nozzle of the system, causing the particles to break up during the dispersion. While Lie et al. concluded that water contents of around 90% were the optimal conditions for dry water, slight differences in the preparation of dry water (rotor blades, rotation speeds) could generate slightly different droplet sizes and requiring additional SiO_2 to fully encapsulate them. Dry water with lower water content contains excess SiO_2 which contributes less to the cooling effect of the combustion process.

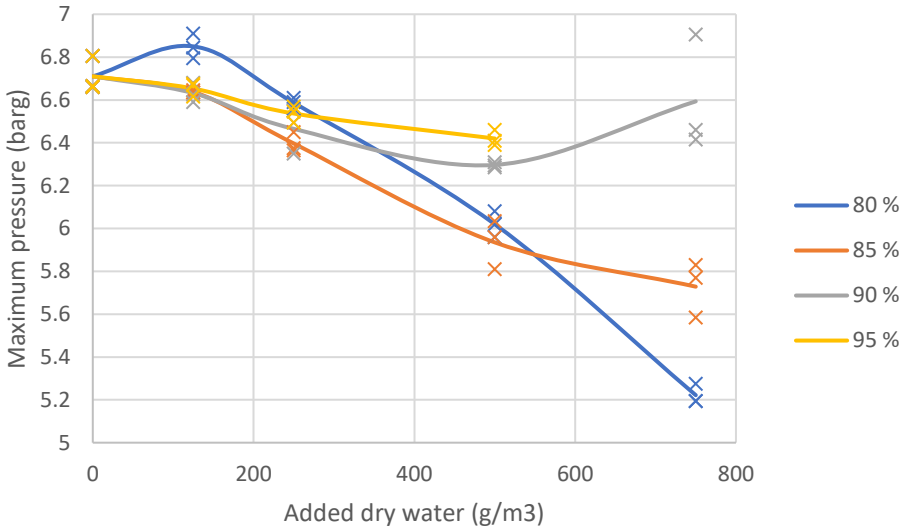

Figure 1. Maximum pressure obtained for dry water with various water content added to hydrogen-air mixtures with ignition delay of 60 ms.

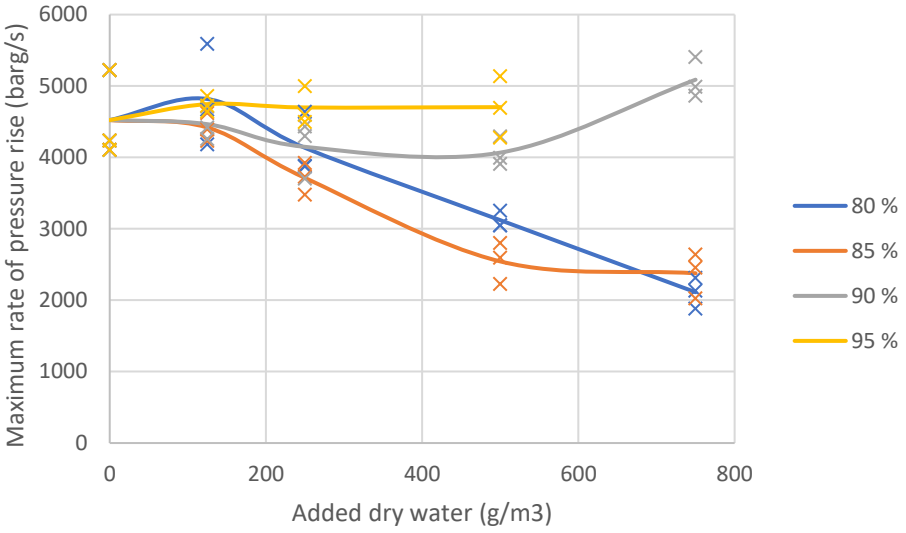

Figure 2. Maximum rate of pressure rise $(dp/dt)_m$ obtained for dry water with various water content added to hydrogen-air mixtures with ignition delay of 60 ms.

At very high amounts of added dry water, these trends seem to shift with the dry water of 80% outperforming the dry water with 85% water content. Also, both the maximum pressure and $(dp/dt)_m$ seems to increase in the case of the dry water powder with 90% water content. The reason for this shift is somewhat unclear but is most likely caused by limitations of the test equipment. The vast amounts of powder that needs to go through the nozzle can prolong the injection time and yield higher initial turbulence at ignition time, see Figure 3. Turbulence levels in the vessel will also decrease faster when there is no powder dispersed in the vessel. Increased turbulence levels from the addition of dust are also the contributors to the slight increase in P_m and $(dp/dt)_m$ we see at low dust concentrations.

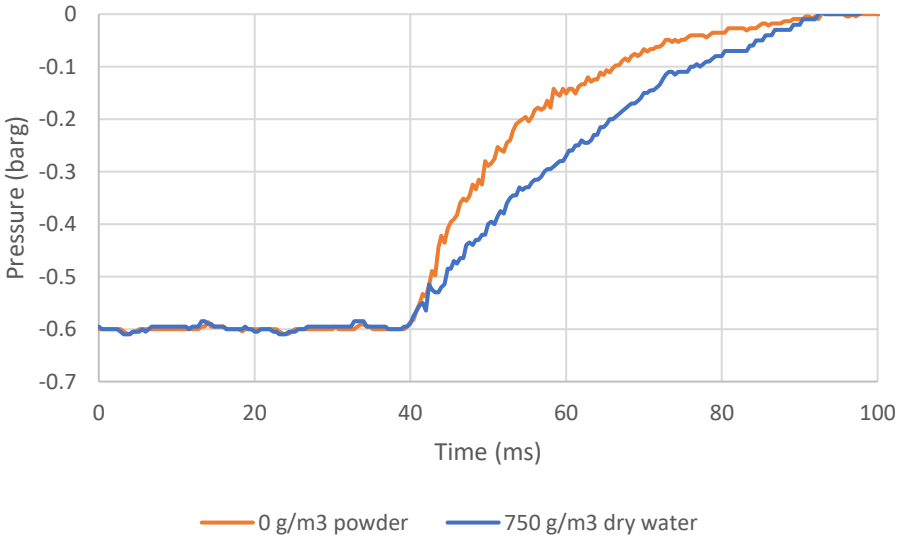

Figure 3. Dispersion phase of a test performed with no dry water and a test performed with 750 g/m3 dry water.

To avoid slight variations in the dispersion profiles to influence the results and the get turbulence levels more closely to realistic events, a series of tests were conducted increasing the delay time between dispersion and ignition from 60 to 120 ms. Figure 4 and Figure 5 show the maximum pressure and $(dp/dt)_m$, respectively, for the tests performed with a delay time of 120 ms for dry water with 85 and 90% water content.

In these tests we see no significant difference between the two types of dry water powder. The overall effect of the dry water is also not as severe as for the case with 60 ms delay. The pressure drops from its initial 6.8 barg to 6.5 barg, while the $(dp/dt)_m$ drops from 2800 to 2500 bar/s. The lack of cooling suggests that a lot of the powder might have settled during this timeframe. This is however unlikely given the small particle size of the dry powder. The structure of the dry water could have been broken up during the dispersion process, causing agglomeration of water droplets and the possibility of the water getting stuck on the walls of the vessel. Tests in the current set-up might therefore not be optimal for testing dry water. Another type of set-up that handles the dry water powder gentler might be required to investigate the full effect of this powder.

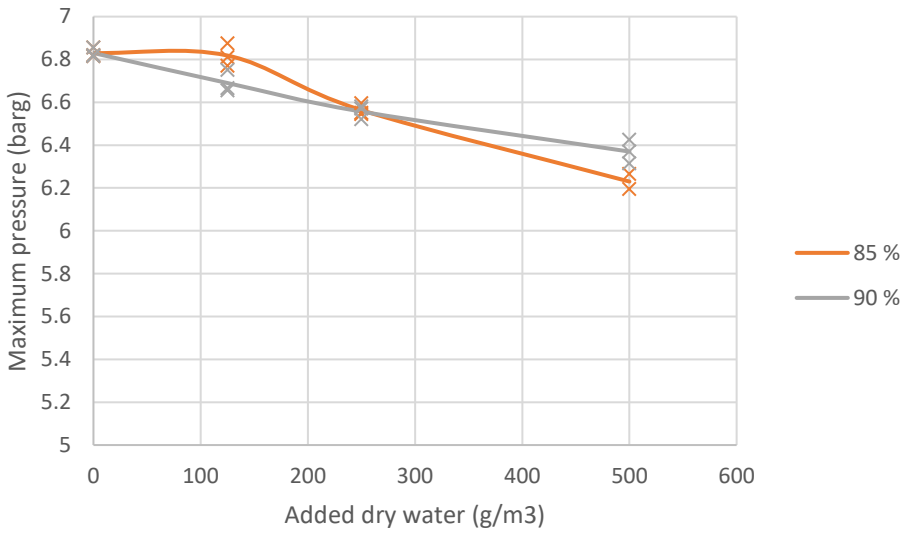

Figure 4. Maximum pressures obtained for dry water with various water content added to hydrogen-air mixtures with ignition delay of 120 ms.

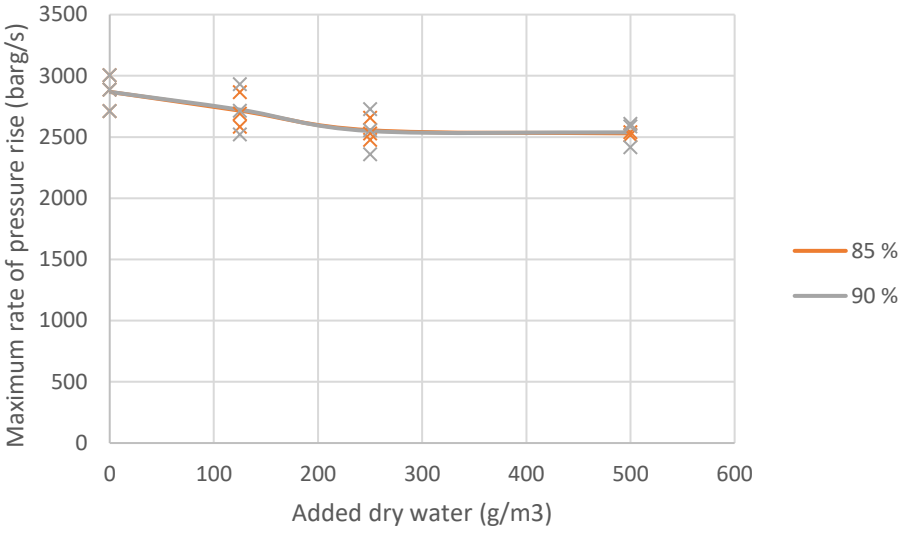

Figure 5. Maximum rate of pressure rise (dp/dt) obtained for dry water added to hydrogen-air with various water content mixtures with ignition delay of 120 ms.

2.2. The influence of modified dry water on hydrogen-air explosions

Tests were performed with potassium carbonate powder mixed with dry water powder and potassium carbonate solved in the water which the dry water powder was made from. Results for both tests compared to the dry water only case are shown in Figure 6 and Figure 7.

For the test with mixed dry water powder and potassium carbonate powder, the idea was to see whether the cooling effect of the dry water powder could slow down the flame enough for the potassium carbonate to have time to react to with the flame. The cooling effect of the dry water powder was however limited and no significant inhibition effect was observed from these tests.

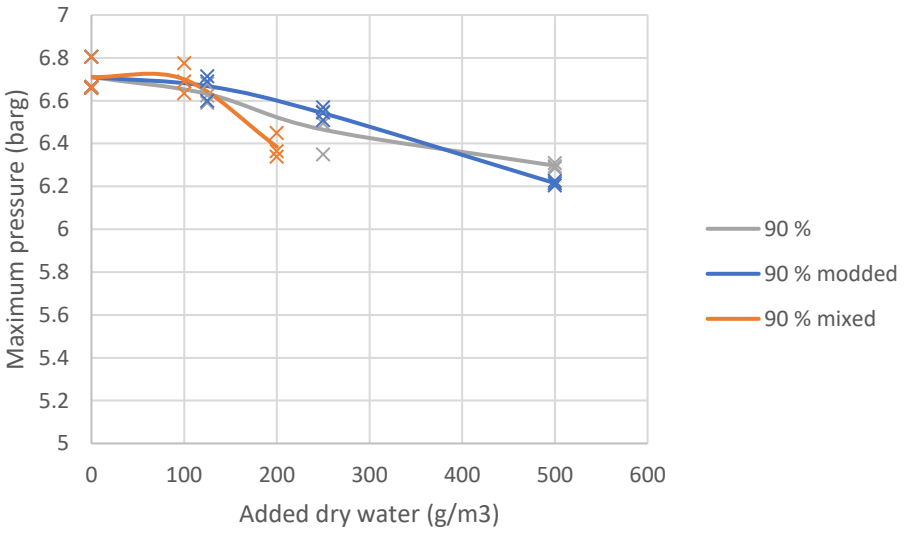

Figure 6. Maximum pressures obtained for dry water added to hydrogen-air mixtures with ignition delay of 60 ms.

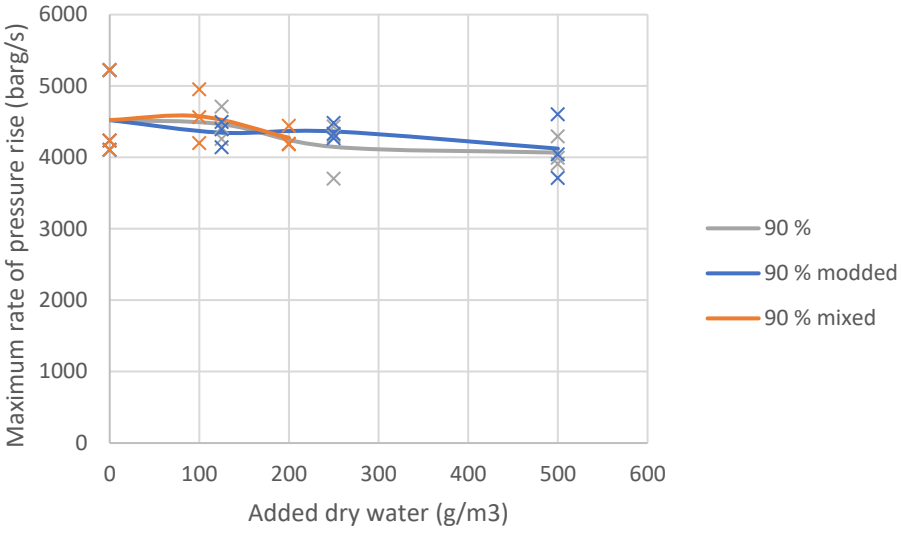

Figure 7. Maximum rate of pressure rise (dp/dt) obtained for dry water added to hydrogen-air mixtures with ignition delay of 60 ms.

For the modified dry water powder the aim was to see whether the powder could deliver potassium carbonate to the flame. The water needs to evaporate, leaving very small particles of K_2CO_3 which are easier to decompose for a flame than particles with sizes of 10 µm. When using a water mist Battersby et al. (2013) found that there was a certain threshold of water required for the inhibitor to be effective. While there was no difference between water and a NaOH/water solution, at concentrations of around 180 g/m^3 the inhibitor seemed to affect the flame. In the current tests no effect of the inhibitor was observed even with concentrations up to 500 g/m^3. As the droplets in the dry water powders are smaller than what you typically could get in a water spray, one would expect to see an effect of the inhibitor. It is possible that the main factor is the usage of K_2CO_3 instead of NaOH or possibly not much dry water powder is present in the current set-up due to the particles not surviving the dispersion process.

3. Conclusions

Tests investigating the effect of dry water powder have been conducted in a 20-litre vessel. The tests showed that dry water powder has potential as a cooling agent for hydrogen-air explosions. Dry powder with a water content of 85% water content had the best overall effect.

Adding potassium carbonate in addition to dry water or as part of the dry water (i.e. dry water prepared from a 1 M aqueous solution of potassium bicarbonate) did not yield any additional inhibiting effect. This indicates that the dry water powder was not able to reduce the flame velocity of hydrogen-air enough for the potassium carbonate to influence the combustion process.

The 20-litre vessel method used in the current work might not be the best for testing dry water. The main concern being the dispersion process breaking up the dry water particles. In addition, at standard test conditions (ignition delay time of 60ms) the turbulence level in the vessel is very high at the time of ignition. Burner type set-ups might be more suitable for testing the influence of dry water.

Acknowledgements

The authors gratefully acknowledge the support for the joint industry project (JIP) *"Risk-reduction for Hydrogen Installations by partial Suppression of Explosions"* (HyRISE) from Total E&P Norge AS, Shell Research Ltd., and University of Bergen (UiB).

References

Battersby, P., Holborn, P.G., Ingram, J.M., Averill, A.F. & Nolan, P.F., (2013), *The mitigation of hydrogen explosions using water fog, nitrogen dilution and chemical additives*, Hydrogen Tools.

Bomhard, J. (2011). *Dry Water.* Master Thesis, Luleå University of Technology

Cesana, C. & Siwek, R. (2012) *Manual KSEP 7.0* https://www.cesana-ag.ch/download/B000_071.pdf

Dounia O., Jaravel, T. & Vermorel, O. (2022), *On the controlling parameters of the thermal decomposition of inhibiting particles: A theoretical and numerical study*, Combustion and Flame, 240: 111991. DOI: https://doi.org/10.1016/j.combustflame.2022.111991.

Liu, L., Luo, Z., Wang, T,. Yang, X., Su, B, & Su, Y. (2024) *Inhibitory effects of water mist containing alkali metal salts on hydrogen–natural gas diffusion flames*, International Journal of Hydrogen Energy, 51 D: 754-764. DOI: https://doi.org/10.1016/j.ijhydene.2023.03.457

Nan, F., Luo, Z., Cheng, F., Xiao, Y., Li, R., Su, B. & Wang, T. (2024) *Research progress and development trends of hydrogen explosion suppression materials and mechanisms*, Process Safety and Environmental Protection, 184: 1318-1331. DOI: https://doi.org/10.1016/j.psep.2024.02.062.

Roosendans, D., (2018) *Mitigation of Vapor Cloud Explosions by Chemical Inhibition using Alkali Metal Compounds*., Vrije Universiteit Brussel.

Skjold, T. (2003). *Selected aspect of turbulence and combustion in 20-litre explosion vessels.* Master's thesis, University of Bergen.

van Wingerden, K. & Hoorelbeke, P. (2011). *On the potential of mitigating vapour cloud explosions using flame inhibitors*. Proceedings 11 AIChE - 2011 AIChE Spring Meeting and Seventh Global Congress on Process Safety.

van Wingerden, M., Skjold, T., Roosendans, D., Dutertre, A. & Pekalski, A. (2023). *Chemical inhibition of hydrogen-air explosions: Literature review, simulations and experiments*. Process Safety and Environmental Protection, 176: 1120-1129. DOI: https://doi.org/10.1016/j.psep.2023.03.042.

Wang, Q., Jiang, X., Deng, J., Luo, Z., Wang, Q., Shen, Z., Shu, C., Peng, B. & Yu, C. (2023) *Analysis of the effectiveness of Mg(OH)2/NH4H2PO4 composite dry powder in suppressing methane explosion*, Powder Technology, 417 DOI: https://doi.org/10.1016/j.powtec.2023.118255.

Undiscovering turbulence of dust particles in the Hartmann tube through the Image-Subtraction Method

Luca Marmo [a], Olivier Dufaud [b], Fausto Franchini[c] & Enrico Danzi [a]

[a] Dipartimento di Scienza Applicata e Tecnologia-Politecnico di Torino, C.so Duca degli Abruzzi 21, 10129, Torino, Italy

[b] Université de Lorraine, CNRS, LRGP, F-54000 Nancy, France

[c] Department of Energy (DENERG), Politecnico di Torino, Viale T. Michel 5, 15121 Alessandria, Italy

E-mail: luca.marmo@polito.it

Abstract

The present work aims to investigate the dynamics of dust clouds in space and time when dispersed inside the modified Hartmann tube commonly used for explosibility screening and Minimum Ignition Energy (MIE) measurement. In particular, this study focuses on the fluid dynamics of the dust cloud in the space between the electrodes where the ignition occurs since fundamental properties of the dust motion, such as the cloud turbulence (intensity and variation), are known to significantly affect both the ignition sensitivity and explosion severity. An imaging re-elaboration method based on an algorithm (Image-Subtraction Method, ISM) is presented and adopted in the basics of the present research. To clarify the cloud dynamics, a novel approach is proposed here, using LabVIEW® specific algorithms, namely Particle Analysis and optical flow detection methods, such as the Lukas-Kanade method, which allows the tracking of the motion and the velocity vectors of dust clusters identified in the cloud flow. Concurrently, it is then possible to measure the intensity of concentration changes between the electrodes (luminance change of the video frames in time and space) and cloud velocity, which likely represents the flow's turbulence. Different types of dust (iron, starch, silica) were used at different dispersion conditions (dispersion pressure and dust amount). The cloud motion was recorded, and videos were analyzed through LabVIEW® to explore the parameters affecting dust turbulence (powder specific gravity, particle size distribution, and air blast intensity). The outcomes of this work will help characterize the flow of a dust cloud inside a tube prior to its ignition and better define the optimal testing conditions for MIE determination.

Keywords: *dust explosion, minimum ignition energy, image processing, instantaneous kinetic energy*

Introduction

Because of its stochastic nature, the dispersion of a powder is a critical step in determining its ignition sensitivity or explosion severity. While international standards aim to limit data scattering by controlling operating conditions, their application cannot obviously lead to the same state of powder dispersion (local concentration, turbulence, etc.) when the powder characteristics differ. Particularly regarding the procedure for determining the minimum ignition energy (MIE), the dust cloud dynamics has been relatively seldom investigated in the dust explosion literature (Amyotte and Pegg, 1989). This work follows previous papers (Danzi et al., 2021; 2023), whose common goal was to identify a suitable method for studying the fluid dynamics of a dust cloud within standard ignition test equipment such as the modified Hartmann tube (EN ISO/IEC 80079-20-2, 2016) and describe the dust concentration distribution and turbulent cloud structure. This characterization is crucial for ignition test reliability (Amyotte et al., 1988; Cuervo, 2015), as "optimal conditions" need to be reproduced inside standard equipment to accurately detect the MIE. In the framework of an explosion risk assessment, the adjective "optimal" can refer to the actual conditions of a potential explosion

event in work ambiances (i.e. the “most likely case”), or to conditions leading to lowest MIE (i.e. namely the “worst conditions possible”).
Several factors are in play as concerns the ignition likelihood of a combustible dust cloud, especially:

1. The dust cloud concentration distribution,
2. The cloud turbulence at ignition,
3. The ignition energy.

The optimal conditions for an explosion ignition are met for an almost stoichiometric dust cloud concentration and the lowest turbulence intensity at the ignition location. MIE measurement should be carried out when the cloud is at such conditions. Due to the transient behavior of the dust cloud in the modified Hartmann tube, it is essential to study aerodynamics at the ignition location to ensure optimal conditions are realized at ignition. Eventually, ignition delay time (also called tv) may be adjusted to meet such requirements. In this light, it is necessary to provide detailed information on the dust cloud turbulence and concentration distribution in the test chamber. Since conventional MIE setups do not allow in-situ measurements, and their viewing area is limited, a reliable method to measure the latter two parameters is essential.

The investigation performed in this work is focused on the “early dispersion” stage, i.e., it is centered on the dust cloud dynamics before ignition. The standard procedures for MIE measurement (ASTM, 2019; EN ISO/IEC 80079-20-2, 2016) imply the ignition source is triggered at a delay from the air blast valve opening, which may be customized (usually 60, 120, or 180 ms after the dispersion). For this reason, this work investigates the dust cloud concentration distribution and the turbulence intensity, i.e., the intrinsic dust cloud dynamics in the modified Hartman tube, without considering the ignition interference.

Recent authors, such as Danzi et al. (2023), Pan et al. (2022), and Puttinger et al. (2023), have demonstrated the transient behavior of the cloud structure during the earliest dispersion stage. The cloud structure is influenced by dust concentration, characteristics (i.e. nature, shape, particle size distribution - PSD), and blast pressure, affecting the cloud’s turbulence. As a consequence, these variables affect the ignition effectiveness. This paper focuses on the impact of some of these variables on the dust cloud turbulence described by the turbulence intensity and kinetic energy at the ignition location and during cloud dispersion.

1. Experiments

High-speed videos (2000 acquisition fps) of a dust cloud dispersion in a cylindrical modified Hartmann tube were acquired under various experimental conditions. Different powders were used to study the effect of the PSD and density on the cloud behavior: iron powder, maize starch, and silica, although the latter powder is not flammable. Silica and iron powders were available in two different PSD (say coarse and fine). Powder characteristics are listed in **Table 1**.

1.1. Optical setup configuration

This work adopted the same video acquisition method and data post-treatment technique used by Danzi et al. (2023). The authors reported to this latter for detailed information about the experimental setup, which is shown in Fig. 2. Dust dispersion tests were carried out in a modified Hartmann tube. The vessel consists of a 1.2L cylindrical glass tube (68 mm internal diameter and 300 mm height) closed at its lower part by a dispersion cup equipped with a mushroom-shaped nozzle. The powder is placed in the cup and is then dispersed by an air blast at different pressures. Two electrodes were placed at 100 mm from the bottom of the tube to reproduce the MIE measurement test environment accurately (EN ISO/IEC 80079-20-2, 2016).

This paper presents further elaborations on the high-speed videos presented by Danzi et al. (2023). The dispersion tests adopted here are #1 to #16, as summarized in Table 1.

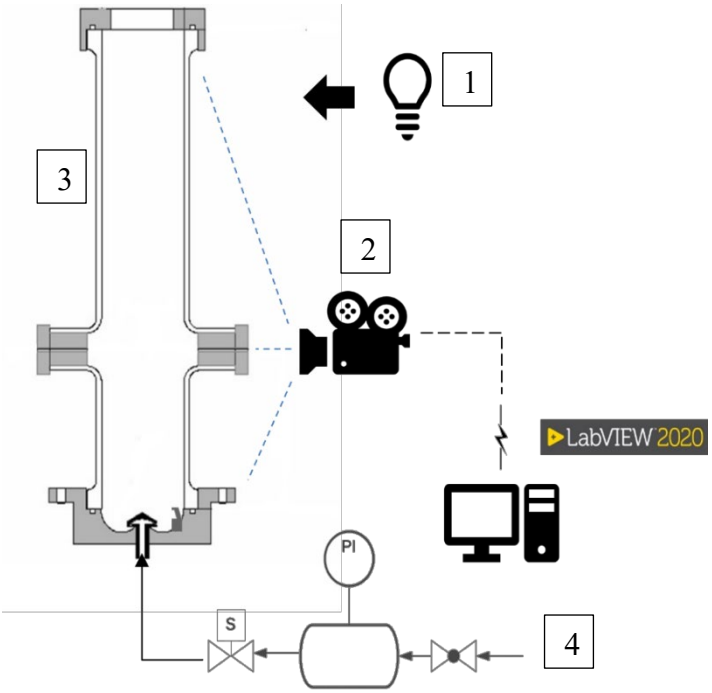

Fig. 1. *Scheme of the experimental setup, where 1 stands for the illumination setup, 2 is the high-speed camera, 3 is a modified Hartman tube, and 4 is the air pulse system.*

Table 1. *Dispersion tests*

Test	Dust	Mass dispersed [g/m^3]	P [bar]	PSD [µm]				Density (particle) [g/cm^3]
				d_{10}	d_{50}	d_{90}		
1	Maize starch	300	3.5	12.9	28.1	58.2		0.54
2	Maize starch	300	7	12.9	28.1	58.2		0.54
3	Maize starch	600	3.5	12.9	28.1	58.2		0.54
4	Maize starch	600	7	12.9	28.1	58.2		0.54
5	Iron	600	3.5	22.1	39.2	65.3	Coarse	7.8
6	Iron	600	7	22.1	39.2	65.3	Coarse	7.8
7	Iron	600	3.5	0.8	1.9	4.3	Fine	7.8
8	Iron	600	7	0.8	1.9	4.3	Fine	7.8
9	Silica	300	3.5	62.2	72.8	84.8	Coarse	2.19
10	Silica	300	3.5	32.5	41.4	51.9	Fine	2.19
11	Silica	300	7	62.2	72.8	84.8	Coarse	2.19
12	Silica	300	7	32.5	41.4	51.9	Fine	2.19

Operating conditions for the dispersion tests are set to investigate their effect on the dust cloud dynamics, both at the conditions likely suggested for MIE measurement, with some changes to detect possible improvements:

- Air pulse pressure (3.5 and 7 bar$_g$),
- Mass dispersed (300 and 600 g/m^3),
- Dust PSD (fine and coarse, depending on the sample use - Table 1),
- Dust nature.

A high-speed video camera (MotionBlitz EoSens mini2) was used to record dust cloud dispersion at 2000 fps. A black screen was placed behind the Hartmann tube to limit light reflections, while a halogen lamp provided a light source to limit light intensity oscillations.

1.2. Video elaboration – Image Subtraction Method (ISM)

ISM is adopted to elaborate the video frames (Danzi et al., 2021 & 2023); the information collected from the post-treatment data allowed us to estimate the dust cloud motion and dust concentration gradients in time and space.

The method consists of three steps: video filtering, detection of light brightness induced by the dust in each row of the video frames, and finalization of brightness data outcomes. "InitialDifference" is adopted in this work among the other filtering algorithms as it allows the cancellation of the background without losing information on the dust clusters' movement and distribution (Danzi et al., 2023). Fig. 1 presents an example of the original and elaborated videos.

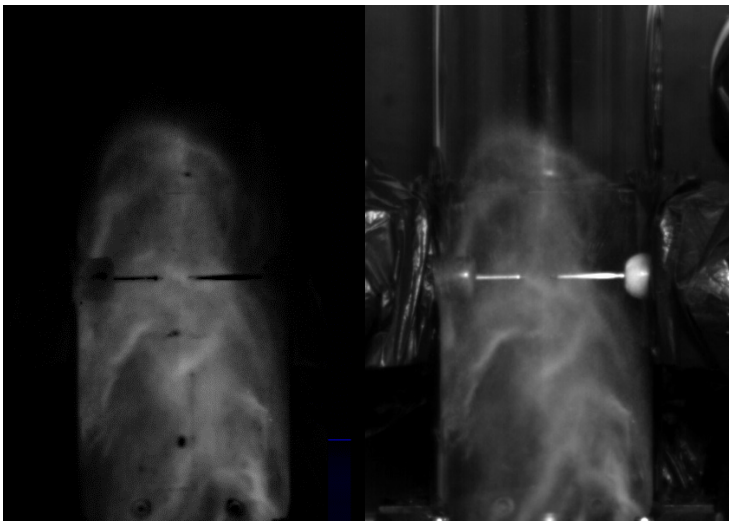

Fig. 2. *Test# 10 performed on silica: InitialDifference, 80 msec (left), original video (right).*

1.3. Video elaboration – Particles' optical flow

Optical flow is defined as the distribution of apparent velocities of a bright pattern moving in an image. It relies on the relative motion of objects and an observer. In our case, the apparent velocities are those related to a particle cluster in the dispersion tube. The velocity field was calculated using the Horn and Schunck method (Horn and Schunck, 1981). It is an iterative implementation of an algorithm that assumes smoothness in the dust flow (represented by its global energy E) over the whole image, i.e., it minimizes distortions in flow and favors solutions that show an increased smoothness.

$$E = \iint \left[\left(I_x u + I_y v + I_t \right)^2 + \alpha^2 \cdot \left(\|\nabla u\|^2 + \|\nabla v\|^2 \right) \right] dxdy \qquad (1)$$

where I_x, I_y and I_t are the image intensity derivatives and α is a constant. An alternative to the Horn and Schunck method is the Lucas-Kanade method, which was not adopted since it requires small motions per frame for best results, even less than one pixel per frame. The first attempts resulted in a very noisy speed field detection, almost unusable with the available video data.

The algorithm (Eq. 1) is implemented in LabVIEW®, whose development environment natively includes complete optical flow function libraries within the IMAQ package (Image Acquisition). The analyzed image area is located in the space surrounding the electrodes, its center corresponding to the middle point between them. The analyzed area was 90 by 90 pixels wide, and the horizontal and vertical velocity components were calculated at each pixel in that area. The final traces representing the velocity evolution over time consist of the single center pixel only, which, again, is located

between the electrodes. The Horn and Schunck method is of the iterative type, and several convergence and stopping parameters can be set in the adopted function. The *"smoothness"* parameter was particularly useful in compensating for excessive noisiness in the calculation results, and it was set to a value of 10 pixels, empirically stated as the lowest value, giving optimal convergence results, meaning that a further increase of the parameter's value did not bring advantages in the convergence.

2. Results and discussion

The image processing developed here allows to extract a wide range of information useful to define the cloud dynamics. This paper will focus particularly on the motion field of the cloud in the area between the electrodes.

2.1. Cloud dynamics

Fig. 3 and **Fig. 4** clearly illustrate how the standard procedure (ASTM E2019-03, 2019, EN ISO/IEC 80079-20-2, 2016) may be further optimized, as dust cloud ignition "optimal" conditions may vary according to different parameters. Since light intensity is directly correlated to the dust cloud concentration, it can be seen from Fig. 1 that dust concentration is not steady after 60 ms from the air blast. Maximum dust concentration peaks repeatedly from the early dispersion phase up to about 170ms, finally stabilizing from 200 ms on when a "steady" state is reached.

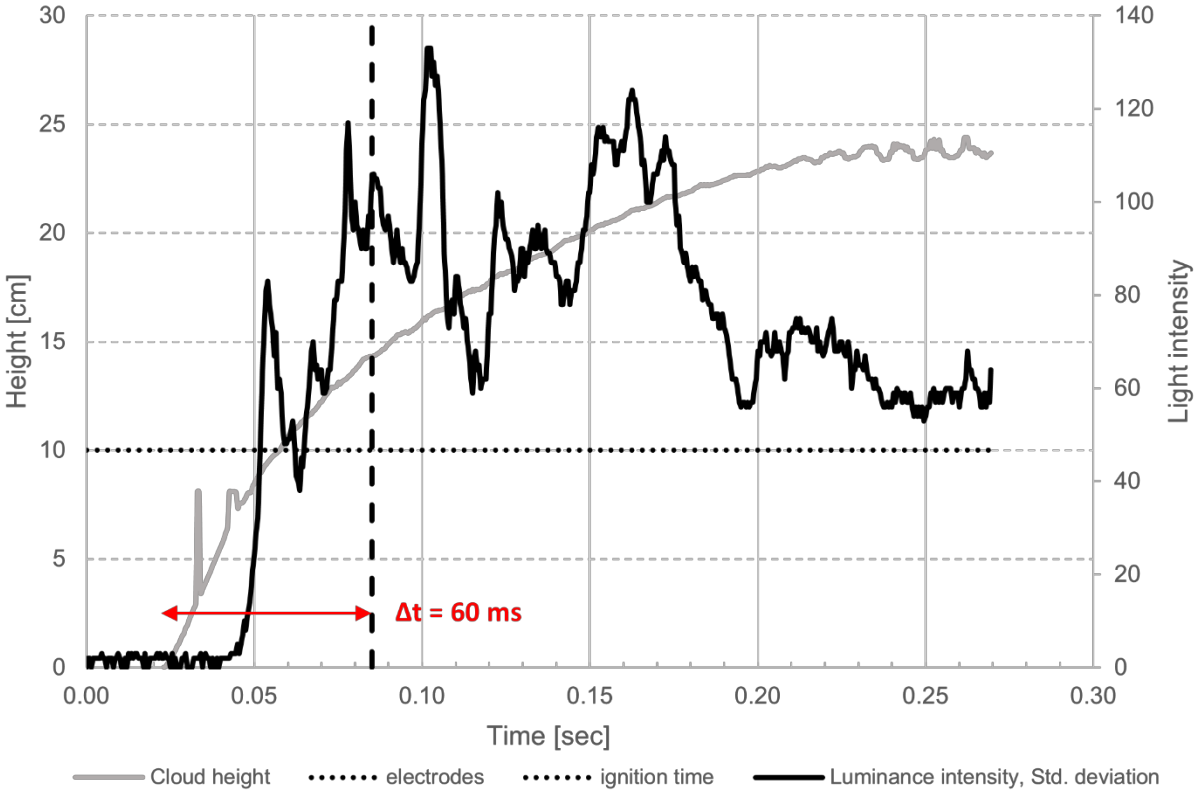

Fig. 3. *Test #10 (silica), evolution of the light intensity of the dust cloud dispersion and dust cloud rise estimate, based on the algorithm developed by Danzi et al. (2023).*

Dust concentration and turbulence intensity are relevant parameters on ignition likelihood. If cloud lift only is considered (**Fig. *5***), it is worth noting that, at the ignition time, the cloud front has already risen above the electrodes, but no other information is displayed about the dust cloud distribution and turbulence at that time. Only average and maximum intensity values could be estimated and reported to indicate the variation of this parameter at ignition time.

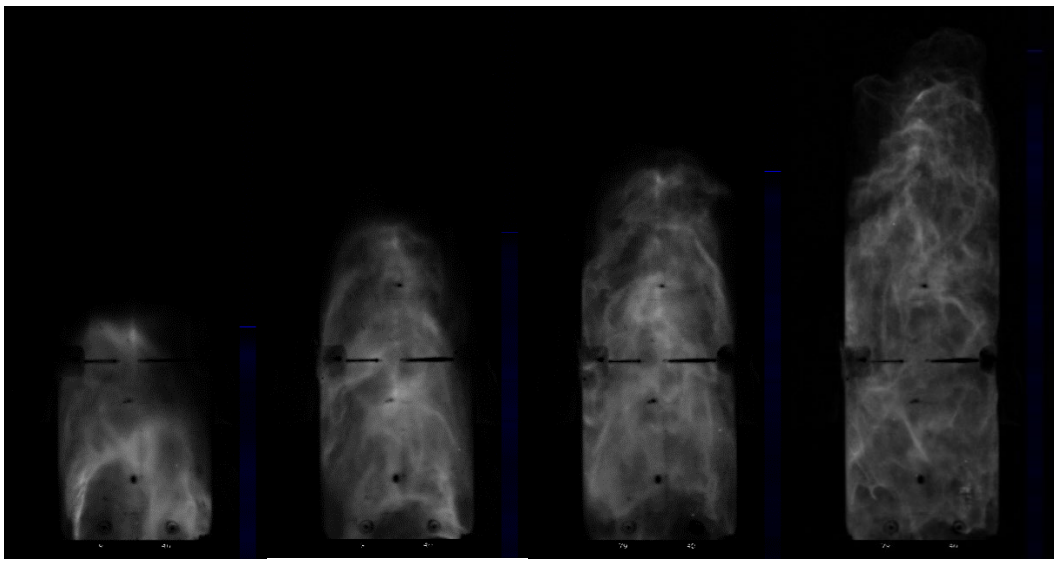

Fig. 4. *Test #10 (silica) shows the evolution of the dust cloud in the tube at 60, 90, 150, and 210 msec after the sample's dispersion.*

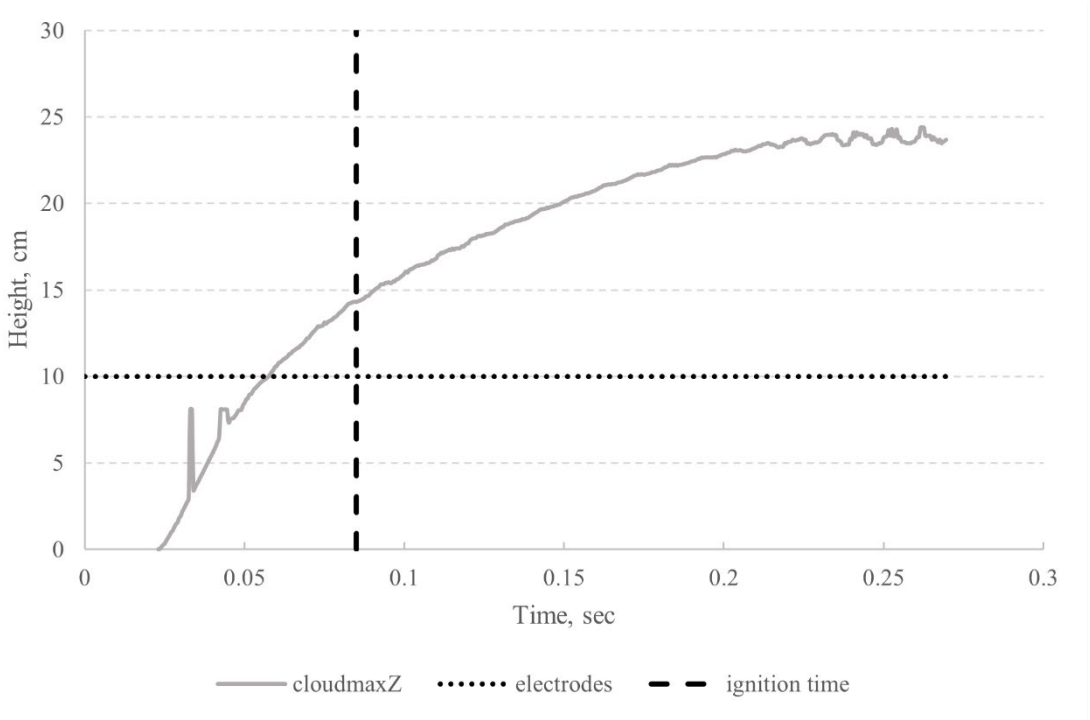

Fig. 5. *Test #10 (silica): dust cloud rise vs time, compared with electrode location and ignition time (60 ms after triggering dispersion).*

2.2. Velocity of particles and flow dynamics

Instantaneous dust cluster velocity is estimated through the algorithm presented in section 1.3. **Fig. 6** shows the vertical v(t) and horizontal velocity u(t) components in the area between the two electrodes. As expected, the horizontal component has significant turbulent oscillations around an average value of almost zero in any time interval. The vertical velocity component has much more marked oscillations than the horizontal component, around average values that are positive in the first phase and become negative in the second phase of dispersion. This trend is consistent with the dynamics of the cloud, which has a first ascending phase followed by a phase during which the particles move substantially in free fall.

The comparison between the different tests presented in **Fig. 6** allows some interesting considerations. Obviously, as the dispersion pressure increases, the velocity value and the root mean square u'

increase. This effect testifies to the increased turbulence that occurs during high-pressure dispersions. However, high-pressure blasts cause dust dispersion to occur faster and speed fluctuations to decay faster (compare tests #1 and 2, 3 and #4, 9 and 11, 10 and 12). Further discussion will follow in the next paragraph. It is very interesting to compare tests carried out at the same pressure using powder of different sizes. In this case, the smaller the size of the dust, the wider the initial speed fluctuations (compare tests # 9 and 10, 11 and 12). In the case of fine dust, speed fluctuations decay faster than with coarse dust. Experiments with iron powders produced low-contrast films because of the powder's color. For this reason, the information obtained by processing the videos is more difficult to analyze.

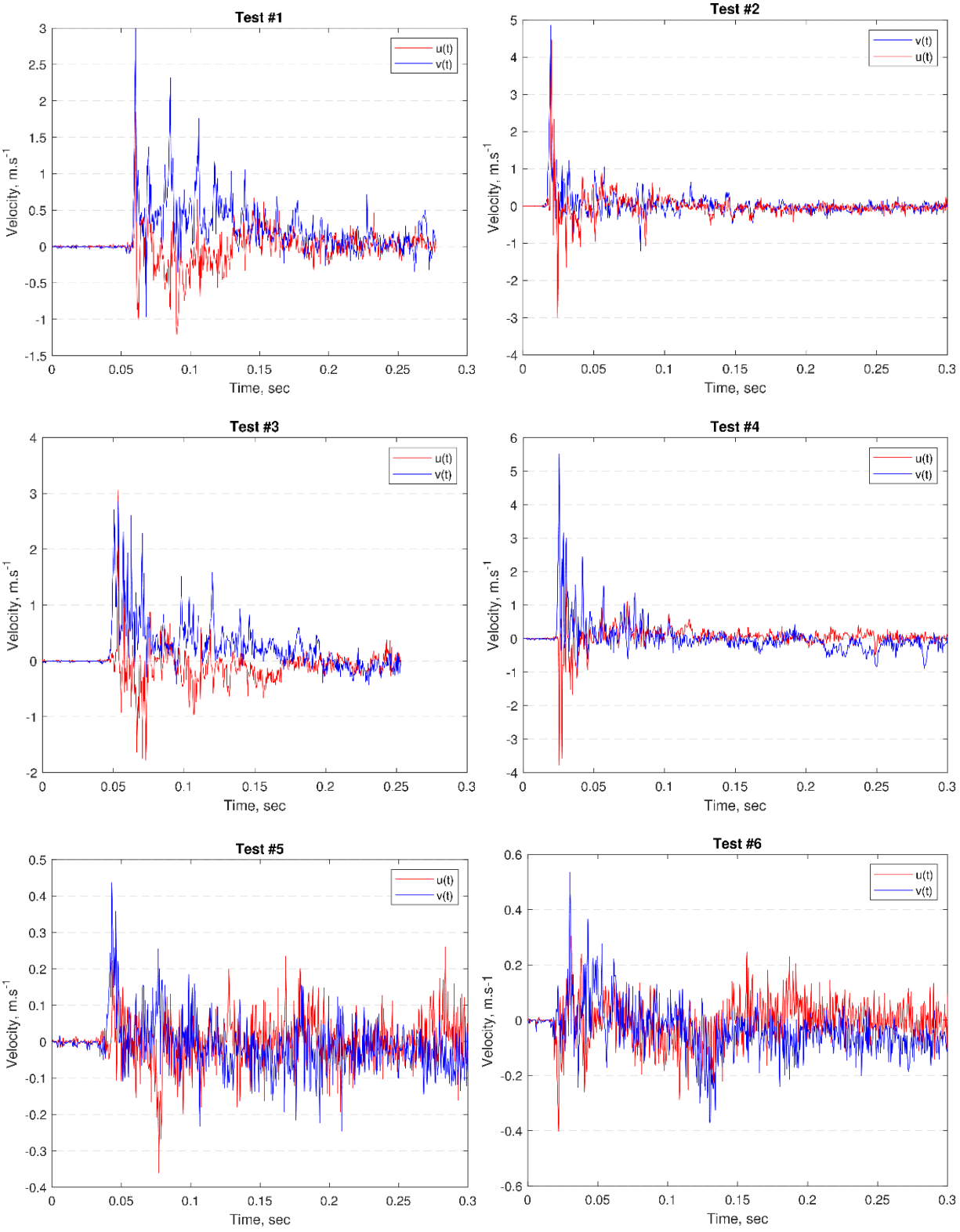

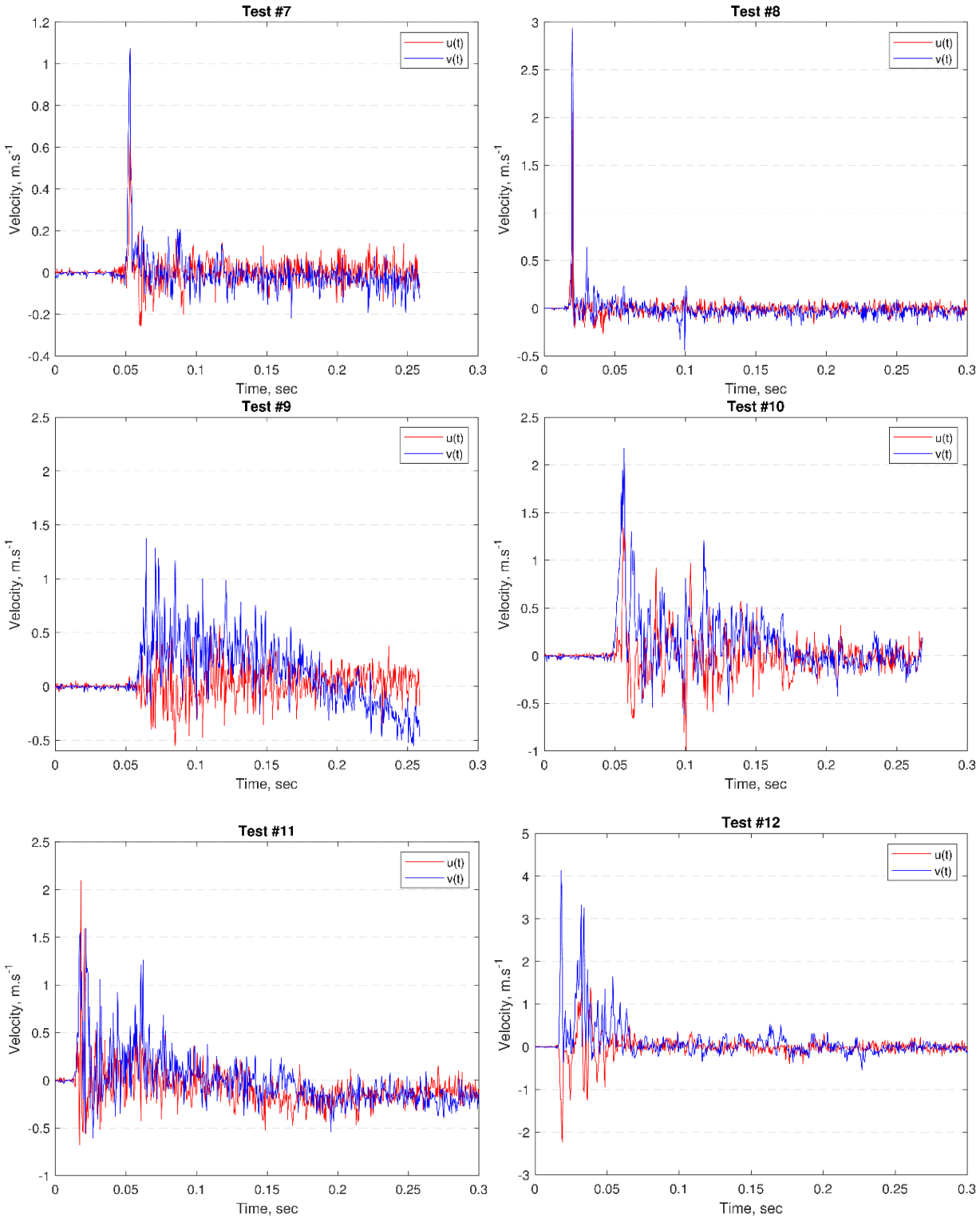

Fig. 6. *Velocity components for different dispersion tests.*

2.3. Instantaneous kinetic energy

The speed fluctuations shown in **Fig. 7** characterized the cloud's turbulence. As is known, the speed fluctuations are used in a stationary motion field to characterize the turbulence intensity according to the following equation:

$$I = {u'}/{\overline{U}} \qquad (2)$$

where u' is the root mean square (or Standard deviation) of the velocity fluctuations at a particular location during a specified time duration, while $\overline{U}$ is the average velocity in the same location calculated over the same time interval.

In the case of dust dispersion in the modified Hartmann tube, the cloud motion is strongly non-stationary, which makes the estimate of $\overline{U}$ unreliable. Moreover, let's consider the whole temporal extension of the phenomenon, from the dispersion to the sedimentation of the cloud. In this case, we can assume that $\overline{U}$ is equal to zero. Therefore, the turbulence intensity cannot be estimated appropriately in our case, but u' can still be determined.

On the contrary, it is possible to estimate the instantaneous turbulent kinetic energy (IKE) using the equation shown below, where only the two components of the velocity vector appear that the experimentation allows to determine (horizontal and vertical)

$$IKE = \frac{1}{2} \cdot \left(\sigma_x^2 + \sigma_y^2\right) = \frac{1}{2} \cdot \left(\overline{u'^2} + \overline{v'^2}\right) \quad (3)$$

where σ is the standard deviation along the different spatial coordinates, and each turbulent velocity component (u', v') is the difference between the instantaneous and the average velocity:

$$u' = u - \bar{u} \quad (4)$$

Fig. 7 shows the time course of *IKE* in the various tests. The *IKE* is calculated at a point on the diameter of the modified Hartmann tube, at the height of the electrodes, so that it represents turbulence at the point where the electric arc is generated.

The IKE trend is very interesting. As expected, there is a clear maximum when the cloud reaches the point of interest. Then, the *IKE* decreases to almost negligible values. It is especially interesting to compare *IKE* values calculated in different test conditions.

2.3.1. The effect of the blast pressure

By comparing tests at different pressures, it is evident that the dispersion pressure generates turbulence (compare tests #1 and 2, #3 and 4, #9 and 11, #10 and 12). Therefore, high-pressure tests have higher *IKE* at the early phase of dispersion. *IKE* maximum more than doubles passing from 3.5 bar to 7 bar shot pressure. With reference to the same tests, the *IKE* decays more quickly when the jet is carried out at high pressure. These results are consistent with the maximum values of turbulent kinetic energy determined by Murillo (2016) on wheat starch, although the decay observed here is faster. At typical MIE determination time (90-180 ms delay time), *IKE* has significantly decayed in all runs at 3.5 and 7 bar. As *IKE* decays quickly at higher pressure blasts, after 60 ms, runs performed at 7 bar apparently exhibit a lower *IKE* than runs at 3.5 bar.

2.3.2. The effect of dust properties

Dust PSD greatly affects the *IKE*. Comparing tests conducted with "*fine*" and "*coarse*" dust (#9 and 10, 11 and 12), it is clear that tests carried out with *"fine"* dust show *IKE* much greater than tests carried out with "coarse" dust. Also, the decay of *IKE* is slower in the case of "*fine"* dust. As a result, after 60 ms (but also after 180 ms) from the jet, the *IKE* value is much higher in the case of "*fine"* dust. This may be because smaller particles have less inertia and, therefore, smaller characteristic time and low Stokes number. Therefore, smaller particles can better follow turbulent gas fluctuations than larger ones, meaning they perceive the lower-scale turbulence of the gas phase and follow fluid streamlines. The same phenomenon is observed in tests carried out with at low or high pressure (3.5 or 7 bar) jet pressure. Using small PSD powder, the *IKE* is much larger and decays much more slowly. The effect of density is also noticeable: as particle density increases, IKE tends to decrease.

2.4. Optimal conditions for MIE measurement

In principle, as previously noted, the optimal conditions for measuring the MIE include homogeneous concentration and turbulence as low as possible. Due to the transient nature of the cloud in the modified Hartmann tube, these conditions are only met over a limited period of time.

During the initial phase, the cloud is very heterogeneous, with high turbulence. In the final stages, the cloud has very low turbulence because, basically, the particles fall in free fall. The concentration decreases, and the cloud becomes heterogeneous again. There is an intermediate phase during which turbulence (*IKE*) is significantly reduced, and the cloud is practically homogeneous. This is the optimal phase for measuring the MIE. However, the start and end times of this phase are influenced by numerous operational variables. Some of them are already defined by current standards (blast pressure); others, such as PSD, are not controllable a priori. Since the decay rate of the *IKE* depends on the particle's properties, it is likely that the optimal delay time for the measurement of MIE should be adjusted according to their PSD, particle shape, and density.

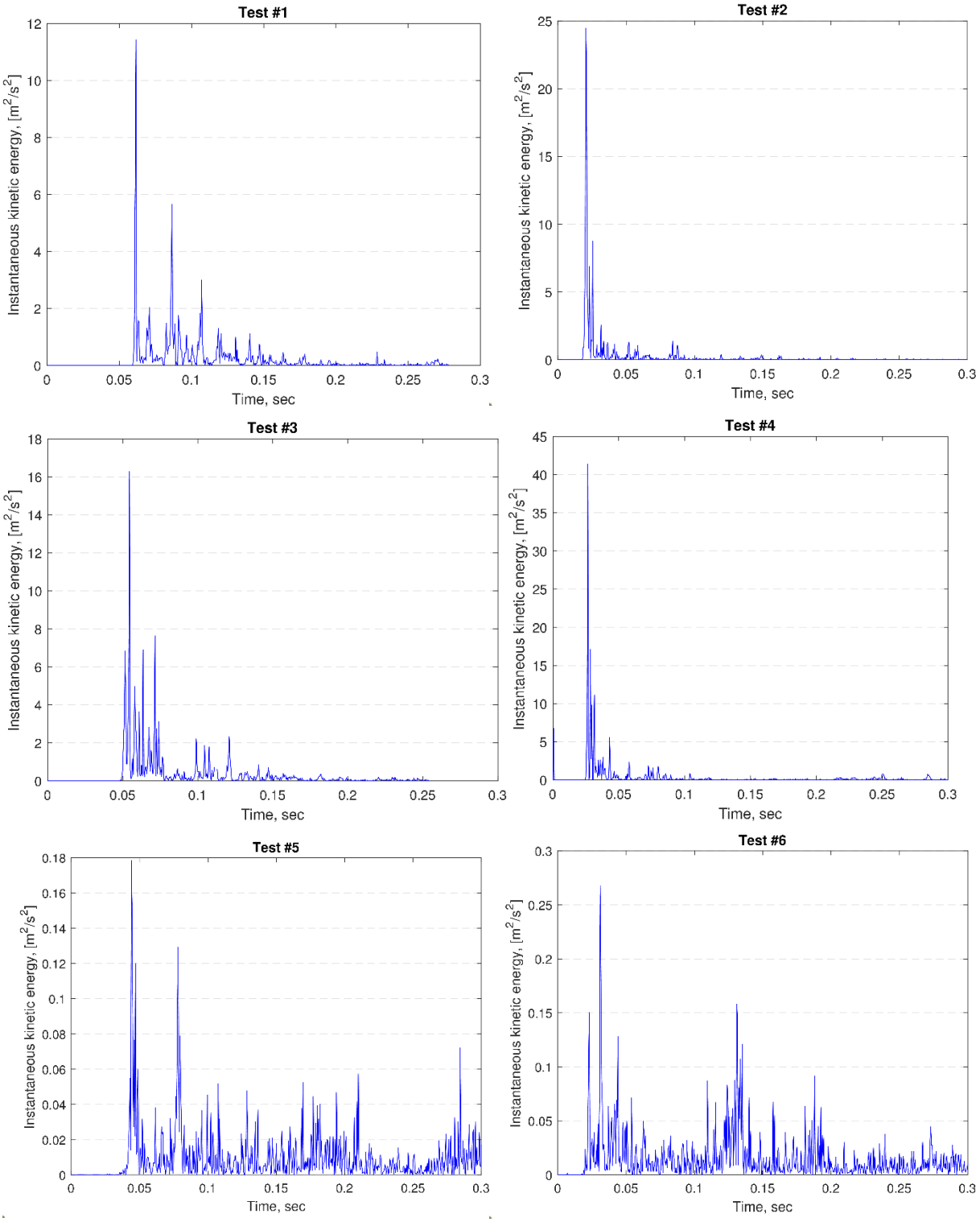

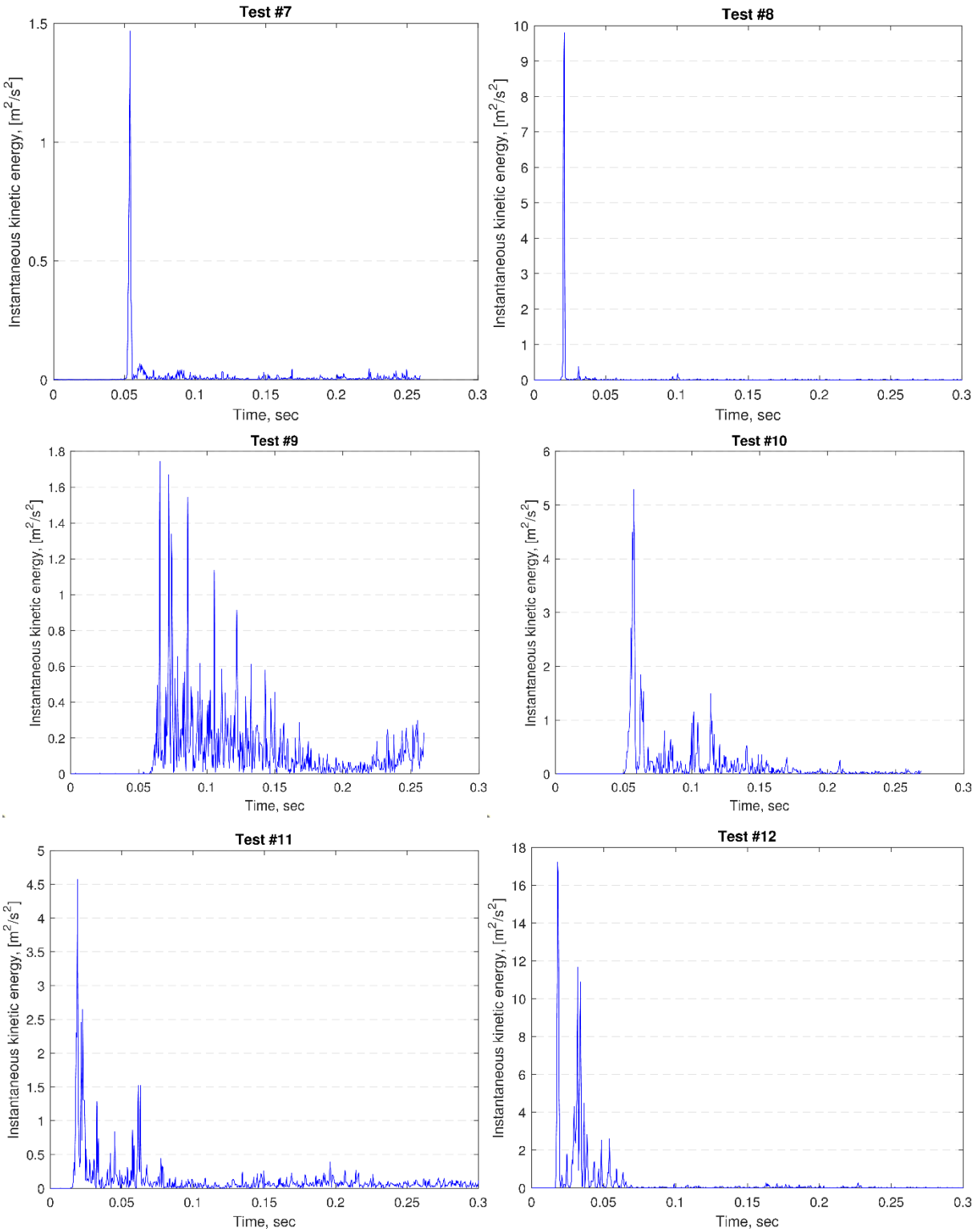

Fig. 7. *Turbulent kinetic energy (IKE) calculated at different dispersion conditions.*

3. Conclusions

This work presented a post-treatment method for high-speed films of Hartmann tube dust clouds. The developed algorithm extracts information about the local components of the instantaneous dust velocity, from which turbulent speed fluctuations and turbulent kinetic energy (IKE) can be traced. This method offers an accessible alternative to optical methods such as particle image velocimetry (PIV) without achieving the same definition but with a lower cost.

A comparison of tests carried out at different blast pressures, concentrations, and types of solid showed the effects of the main variables on cloud dynamics. The blast pressure increases the initial turbulence, but it decays faster than at low blast pressures. Fine dust leads to more turbulence, which decays more slowly.

These preliminary indications require cross-confirmation by comparison with other methods of measuring cloud turbulence. In any case, these results provide useful indications to optimize the measurement procedure of the MIE. This work/These results confirm/s that it is imperative to vary ignition delay times over wide turbulence ranges during MIE tests to increase the chances of testing the dust under "optimal" conditions.

References

Amyotte P.R., Pegg M.J., 1989. Lycopodium dust explosions in a Hartmann bomb: effects of turbulence, Journal of Loss Prevention in the Process Industries, 2 (2), 87-94, https://doi.org/10.1016/0950-4230(89)80004-X.

Amyotte P.R., Chippett, S., Pegg, M.J., 1988. Effects of turbulence on dust explosions, Progress in Energy and Combustion Science, 14 (4), 293-310, https://doi.org/10.1016/0360-1285(88)90016-0.

ASTM E2019-03 (2019), Standard test method for Minimum Ignition Energy of a dust cloud in air

Cuervo, N., 2015. Influences of turbulence and combustion regimes on explosions of gas- dust hybrid mixture. PhD Thesis (in English). University of Lorraine, Nancy, France.

Danzi, E., Franchini, F., Dufaud, O., Pietraccini, M., & Marmo, L. (2021). Investigation of the Fluid Dynamic of the Modified Hartmann Tube Equipment by High-speed Video Processing. Chemical Engineering Transactions, 86, 367–372. https://doi.org/10.3303/CET2186062

Danzi, E., Dufaud, O., Franchini, F., Pietraccini, M., & Marmo, L. (2023). Study of dust cloud behaviour in the modified Hartmann tube using the image subtraction method (ISM). Journal of Loss Prevention in the Process Industries, 82, 104997. https://doi.org/10.1016/j.jlp.2023.104997

EN ISO/IEC 80079-20-2:2016 - Explosive atmospheres - Part 20-2: Material characteristics - Combustible dusts test methods (ISO/IEC 80079-20-2:2016)

Horn, B.K.P., Schunck, B.G., 1981. Determining optical flow, Artificial Intelligence, 17, 185–203.

Murillo, C., 2016. Experimental and numerical approaches to particles dispersion in a turbulent flow: Application to dust explosions. PhD Thesis (in English). University of Lorraine, Nancy, France.

Pan, Y., Spijker, C., & Raupenstrauch, H. (2022). CFD modeling of particle dispersion behavior in the MIKE 3 apparatus. Alexandria Engineering Journal, 61(12), 9305–9313. https://doi.org/10.1016/j.aej.2022.03.039

Puttinger, S., Spijker, C., Schneiderbauer, S., Pirker, S., Meyer, G., Buchner, C., & Kerbl, A. (2023). Journal of Loss Prevention in the Process Industries 83 (2023) 105042 Available online. 950–4230. https://doi.org/10.1016/j.jlp.2023.105042

Improving turbulence combustion modelling in FLACS-DustEx

Maryam Ghaffari [a,b], Kees Van Wingerden[c] & Bjørn J. Arntzen [a,b]

[a] Gexcon As, Bergen, Norway
[b] University of Bergen, Norway
[c] Vysus Group, Bergen, Norway

E-mail: maryam.ghaffari@gexcon.com

Abstract

The turbulence term associated with shear generation is specifically designed for incompressible flows and requires cautious consideration when implemented in reactive compressible CFD codes such as FLACS-CFD. In our study, we will remove the inclusion of the shear turbulence generation within grid cells located in the reaction zone for cells smaller than 20 cm. The efficacy of the updated FLACS-DustEx model was evaluated through simulations of two sets of large-scale explosion experiments featuring varying geometries, as well as experiments conducted in 1 m^3 spherical bombs. These simulations, performed across a range of grid resolutions, serve a twofold purpose: to validate the reliability of the enhanced FLACS-DustEx model and to mitigate grid sensitivity issues. This systematic testing approach ensures that the refined combustion model can confidently handle diverse scenarios and yield dependable predictions under a variety of conditions.

Keywords: *Combustion improvement, FLACS-DustEx*

1. Introduction

Turbulent combustion is dictated by the intricate interplay of convective and diffusive transport mechanisms alongside chemical reactions and heat release. Chemical reactions exhibit significant nonlinearity concerning temperature and species concentrations, making their rates highly reliant on transport fluxes that govern these variables. Additionally, the rates and intensities of heat release, stemming from the chemical oxidation of real-world fuels, are sufficiently substantial to impact flow dynamics and, consequently, transport phenomena.

The k-ε model is widely employed to represent the multifaceted dynamics of convection, diffusion, turbulence production, and dissipation, collectively known as FLACS-CFD. However, its efficacy diminishes when tasked with modeling chemical reactive flows characterized by substantial normal stresses arising from the volume expansion induced by heat release in flames. Designed primarily for steady flows, the k-ε model confronts significant hurdles when applied to transient flow scenarios, as outlined in subsequent sections. Moreover, its demand for finer grid resolutions to capture complex geometries imposes practical constraints, particularly evident in applications like FLACS-CFD, where coarse grid resolutions are necessitated, such as in gas explosion simulations (Arntzen, 1998).

In response to these challenges, we are devising strategies to refine turbulence modeling for enhanced applicability in such contexts. A focal point of improvement entails modifying the turbulence generation term to mitigate the unrealistic effects stemming from volume expansion. This refinement holds promise not only in improving the model's performance in simulating highly transient chemical reactive flows with coarse grid resolutions but also in advancing our comprehension of turbulent flows within intricate, reactive environments. Ultimately, such enhancements are kept to propel the

development of more robust modeling techniques in fluid dynamics, fostering greater accuracy and insight across diverse applications.

To validate the efficacy of this proposed enhancements, rigorous testing protocols have been outlined. The new models will undergo scrutiny through the simulation of two series of large-scale explosion experiments with different geometries, alongside experiments conducted in 20-liter and 1 m^3 spherical bombs. Conducted across various grid resolutions, these simulations serve a dual purpose: validating the reliability of the upgraded FLACS-DustEx model and minimizing grid sensitivity. This systematic testing approach ensures that the enhanced combustion model can effectively handle diverse scenarios and deliver reliable predictions under various conditions.

2. Turbulent shear flows (Shear turbulence)

Turbulence, particularly in its natural manifestations or those of engineering significance, is characterized by spatial non-uniformity. It typically emerges in response to the instability of externally-driven circulations with a "mean" shear component. (In the realm of 2D flows, this instability is termed barotropic instability.) Initially, turbulence tends to manifest at a specific scale, but subsequent secondary instabilities and nonlinear interactions trigger motions at various scales, broadening the spectrum in line with previously discussed pathways.

Among the array of flow instabilities, shear stands out as fundamental. Beyond mean shear instability's role in generating turbulence, transient shear plays a crucial part in both the cascade and eventual dissipation of turbulent energy. Shear is intrinsic to convective, stratified, boundary-layer, and geostrophic flows.

In contrast to homogeneous turbulence, shear turbulence exhibits anisotropy due to the favored direction of the mean flow and often displays spatial non-uniformity. Consequently, it involves interactions between turbulent eddies and the mean flow, a phenomenon not addressed in discussions of homogeneous turbulence where the presence of a mean flow is assumed absent. However, according to the hypothesis of Kolmogorov universality, at sufficiently small scales and high Reynolds numbers, shear turbulence converges towards the behavior of 3D homogeneous turbulence.

The dynamics of this issue offer valuable insights. To illustrate, we narrow our focus to what are commonly termed unbounded or free shear flows. A pertinent example for mathematical analysis is a triply periodic domain subject to a constant pressure gradient, often referred to as the uniform or homogeneous shear scenario. Conversely, examples of inhomogeneous flows encompass jet streams, channel flows, and pipe flows with free slip boundaries, where fluctuations in quantities become negligible. These types of flows are often denoted as free-shear layers. To ensure physical feasibility, it is essential that the velocity gradient tensor, represented by S, possesses compact support in the z-direction while remaining unbounded in the x-direction.

1.1. k-ε turbulence models as used in FLACS

The *k*-ε model as in FLACS includes the equation for turbulent kinetic energy:

$$\frac{\partial}{\partial t}(\rho k) + \frac{\partial}{\partial x_i}(\rho k U_i) = \frac{\partial}{\partial x_i}\left(\frac{\mu_{eff}}{\sigma_i}\frac{\partial k}{\partial x_i}\right) + P_k - \rho\varepsilon \qquad 1$$

and the equation for dissipation of turbulent kinetic energy:

$$\frac{\partial}{\partial t}(\rho \varepsilon) + \frac{\partial}{\partial x_i}(\rho \varepsilon U_i) = \frac{\partial}{\partial x_i}\left(\frac{\mu_{eff}}{\sigma_\varepsilon}\frac{\partial \varepsilon}{\partial x_i}\right) + \frac{\varepsilon}{k}P_k - C_{2\varepsilon}\rho\frac{\varepsilon\varepsilon}{k}$$

Please note that the turbulent production term P_k consist of several teams, both shear generated, buoyancy generated and subgrid generated production, it is only the shear generated term which is problematic.

1.2. Deficiencies of the k- ε model

The k-ε model is not designed to address the complexities of chemical reactive flows, particularly those characterized by significant normal stresses resulting from volume expansion due to heat release within flames. Developed primarily for steady flows, the model encounters challenges when confronted with transient flow scenarios, as elaborated in the subsequent subsection. Consequently, the k-ε model presents limitations when applied within gas explosion simulations like FLACS-CFD, which aim to simulate highly transient chemical reactive flows while resolving the geometry on a coarse grid.

The reason for this unphysical turbulence generation for small grid cells is as follows:

The production term for turbulent kinetic energy is proportional to the turbulent viscosity and the square of the mean rate of strain tensor. The strain tensor is represented by velocity gradients. In the FLACS code the flame is represented by a flame zone with thickness around 3 grid cells. The velocity gradient for normal stress created due to expansion of flame will therefore be proportional to the flame velocity divided with the grid cell size. Reducing the grid cell size from 10 cm to 1 cm will therefor result in a 10 times larger gradient and 100 times larger turbulence production. This unphysical turbulence development from this generation can be seen in the Figures 1 (top) from the 1 m3 spherical bomb, with an initial turbulence intensity of 0.1 and initial velocity of 2.0 m/s.

In addition to, the high reaction rate for the fine grid is due to the burning rate increasing with the turbulence level, (which is far too high). The solution to this problem is to set the shear generated turbulence production to zero in the reaction zone (where RFU>0). The turbulence development in the bomb with this modification is shown in Figure 1, which depicts the turbulence decay with time at the same rate, independent of grid cell size.

3. Results and discussion

We have deliberately omitted the shear generated turbulence term to remove the unphysical generation of turbulence due to expansion. When shear generated turbulence is removed, dP/dt (pressure rise rate) is nearly grid-independent as shown in the figure 1 in the left. Pressure rise rate could be considered as a representative rate of reaction in dust explosions (Skjold, 2014)

In figure 1, TURBU (the parameter for turbulent velocity) and dP/dt (pressure rise rate) were plotted for standard FLACS-DustEx v. 22.2 in the right figures, and in the left figures they were plotted without shear generated turbulence.

The grid resolution are 14, 10, 7, 5, 2 and 1 cm (corresponding to job no. 000750, 000751, 000752, 000753, 000754 and 000755). As can be seen from the lower right figure dP/dt increase with the inverse of cell size. As it can be seen, this increase in reaction rate is much higher for finer grid. The reason for this is unphysical generated turbulence. It is interesting that unphysical turbulence is generated even for grid cell size of 15 cm.

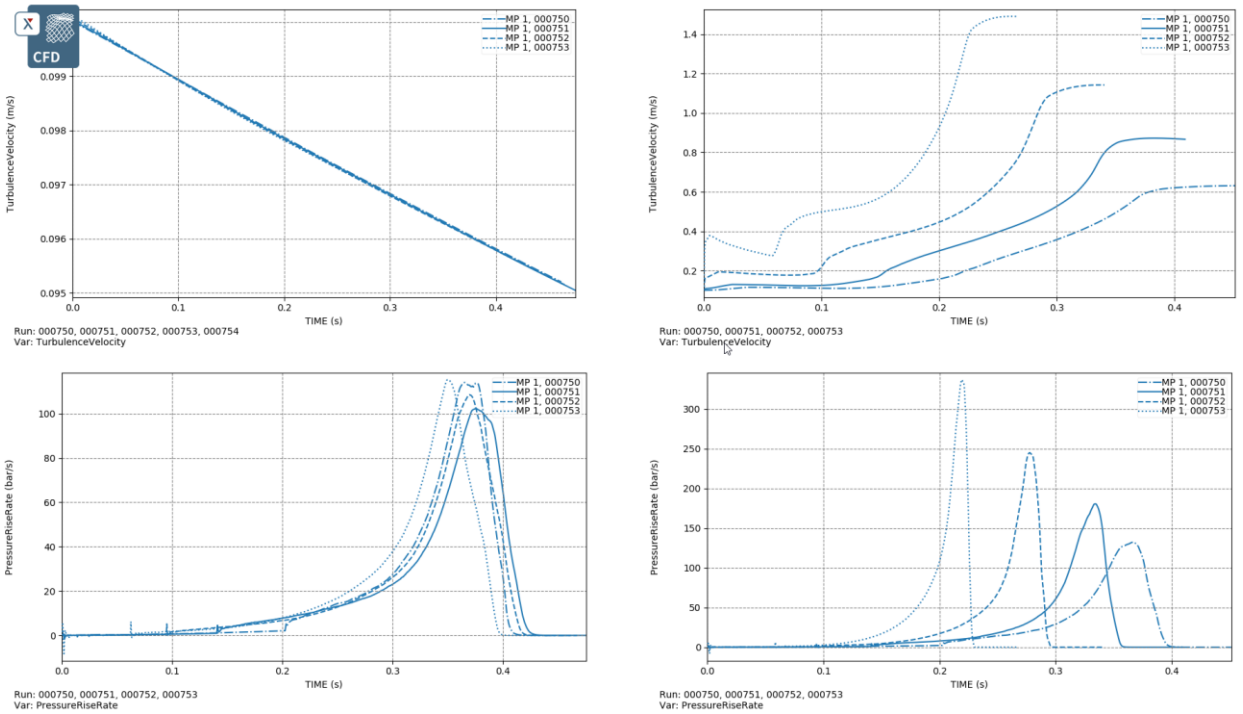

Fig. 1a. *The Results of 1 m^3, turbulent velocity and pressure rise rate with FLACS-DustEx before (two graphs on the right) and after (two graphs on the right) removing the shear turbulence (all the simulations were run with default turbulent parameters in the solver)*

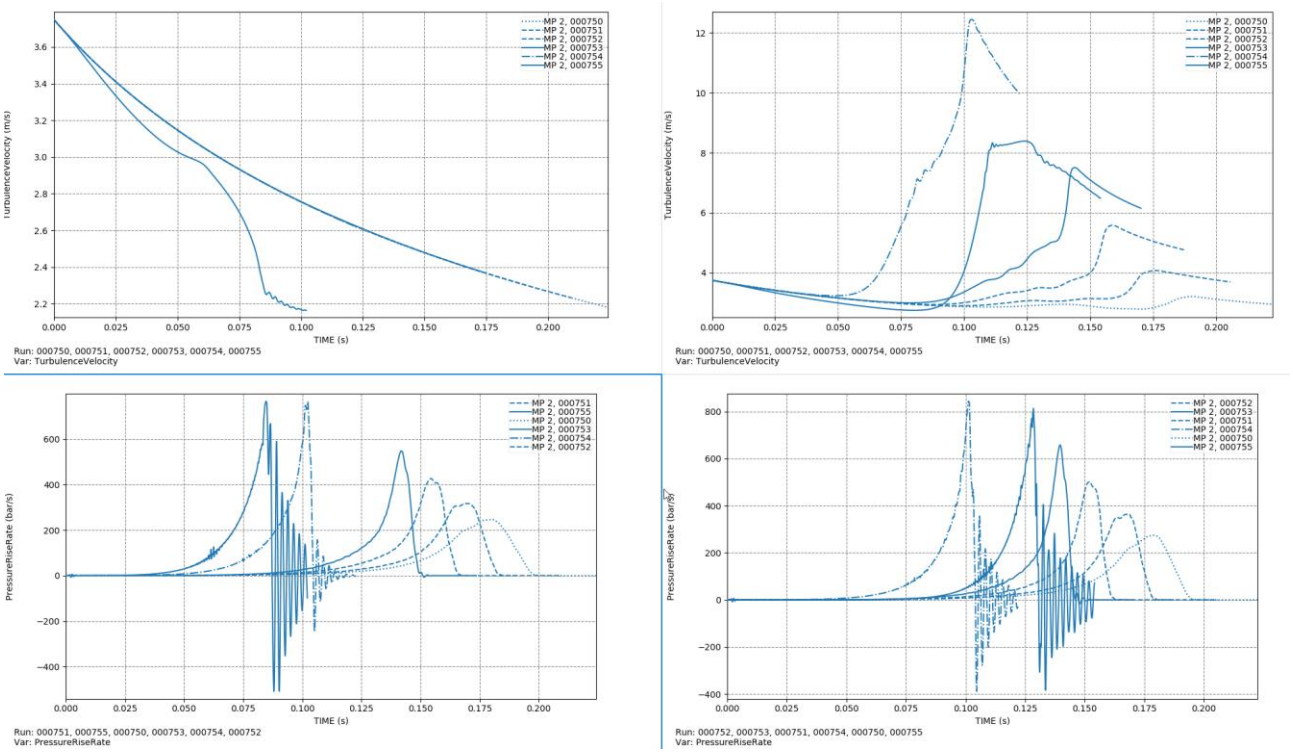

Fig. 2b. *The Results of 1 m^3, turbulent velocity and pressure rise rate with FLACS-DustEx before (two graphs on the right) and after (two graphs on the right) removing the shear turbulence (theses simulation results obtained by rerunning the simulations after adding the correct initial turbulence parameters)*

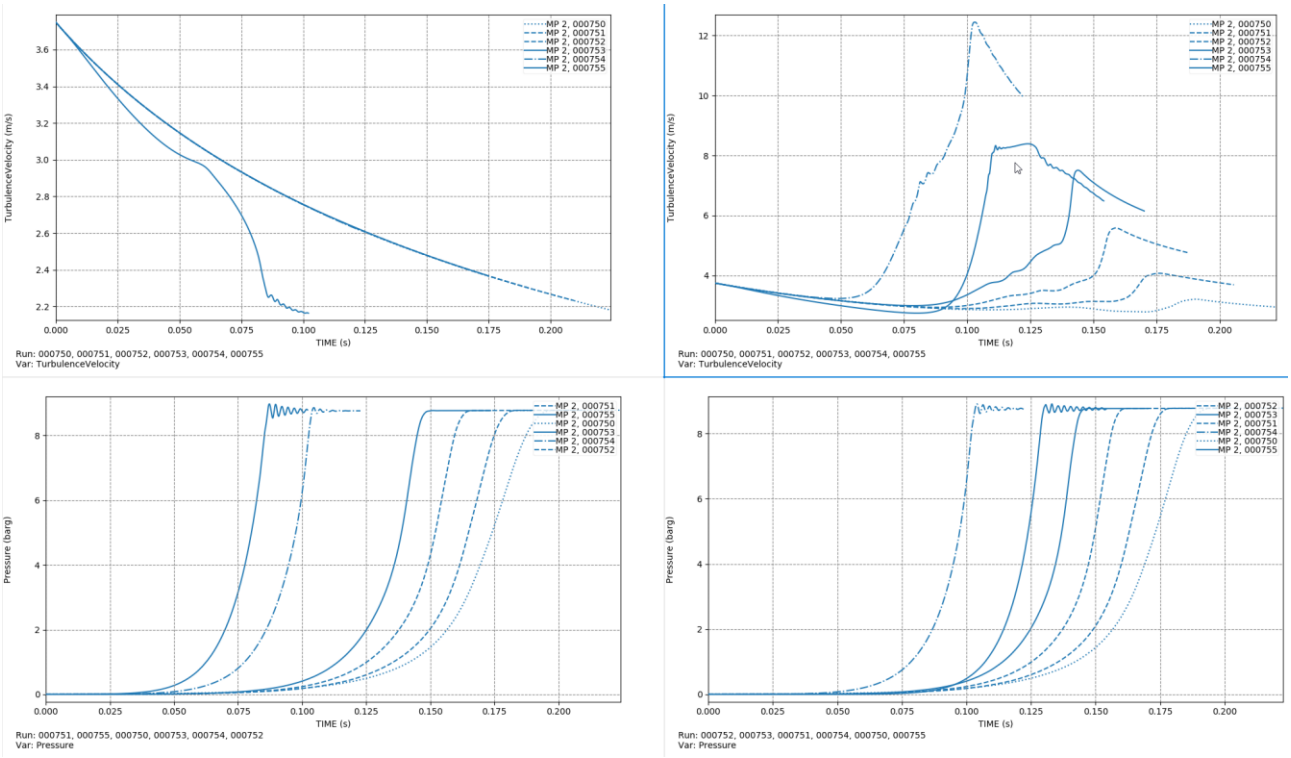

Fig. 3c. *The Results of 1 m^3, turbulent velocity and pressure rise rate with FLACS-DustEx before (two graphs on the right) and after (two graphs on the right) removing the shear turbulence (theses simulation results obtained by rerunning the simulations after adding the correct initial turbulence parameters)*

In this figure, in 1a all the simulations were run with default turbulent parameters in the solver. In 1b and 1c are similar figures where theses simulation results obtained by rerunning the simulations after adding the correct initial turbulence parameters. In figure 1b pressure rate rise-time curve was plotted while in 1c pressure-time curve were plotted in addition to turbulent velocity.

By removing this unphysical turbulence the pressure rise are more independent of grid size. However, when the initial turbulent parameters (initial turbulent velocity and turbulent length scale and turbulent velocity fluctuations) are set realistically, the results of the simulation using removing shear generated turbulence seems not to have influence on pressure or pressure rise any more.

3.1. 236 m^3 Silo

We investigate the effect of changes to shear generated turbulence on large-scale maize starch explosion experiments in a vented 236-m^3 silo. The silo dimensions were 22 meters in height and 3.7 meters in diameter. Two distinct vent areas were employed, measuring 3.4 and 5.7 square meters respectively. Dispersed clouds were ignited at different elevations above the silo's base. The ignition was initiated by 50 grams of desiccated nitrocellulose powder (equivalent to 200 kJ of energy) contained within a plastic bag, activated by a fuse head. The average dust concentration within the silo was estimated through measurements conducted with dust concentration probes, supplemented by the weighing of dust collected from the silo's bottom. (Eckhoff et al., (1985, 1987), Skjold(2006)).

In this study we limited the simulations to vent area of 3.4 m^2 and ignition close to the silo bottom.

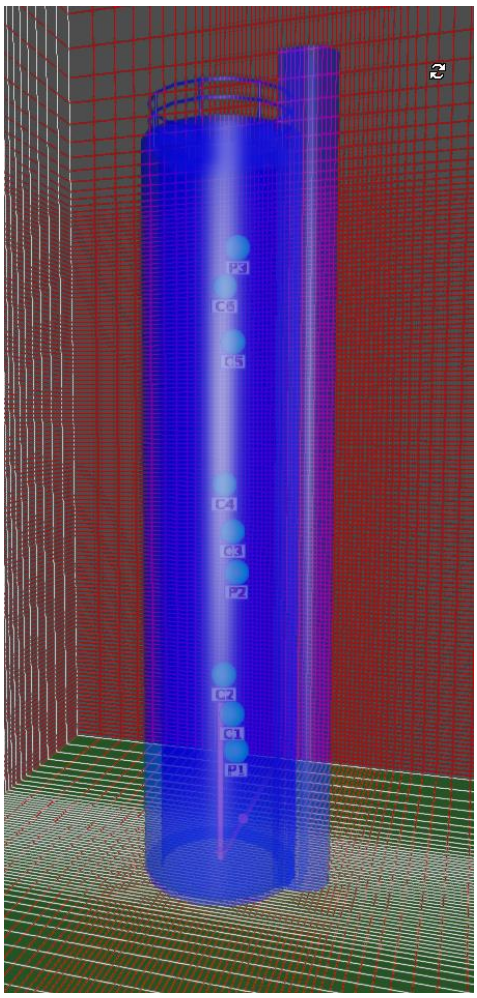

Fig. 2. 236 m3 Silo, the location of monitor points are marked

In figure 3, turbulent velocity-time and pressure -time curve are plotted for monitor point C5 simulated with FLACS-DustEx v22.2 (003000: 0.176 m grid, 003001 0.15 m grid, 003002 0.1 m grid, 003003 0.05 m grid, 003004 0.04 m grid and 003005 0.3 m grid) on the right and in the left side after changes by removing the shear turbulence.

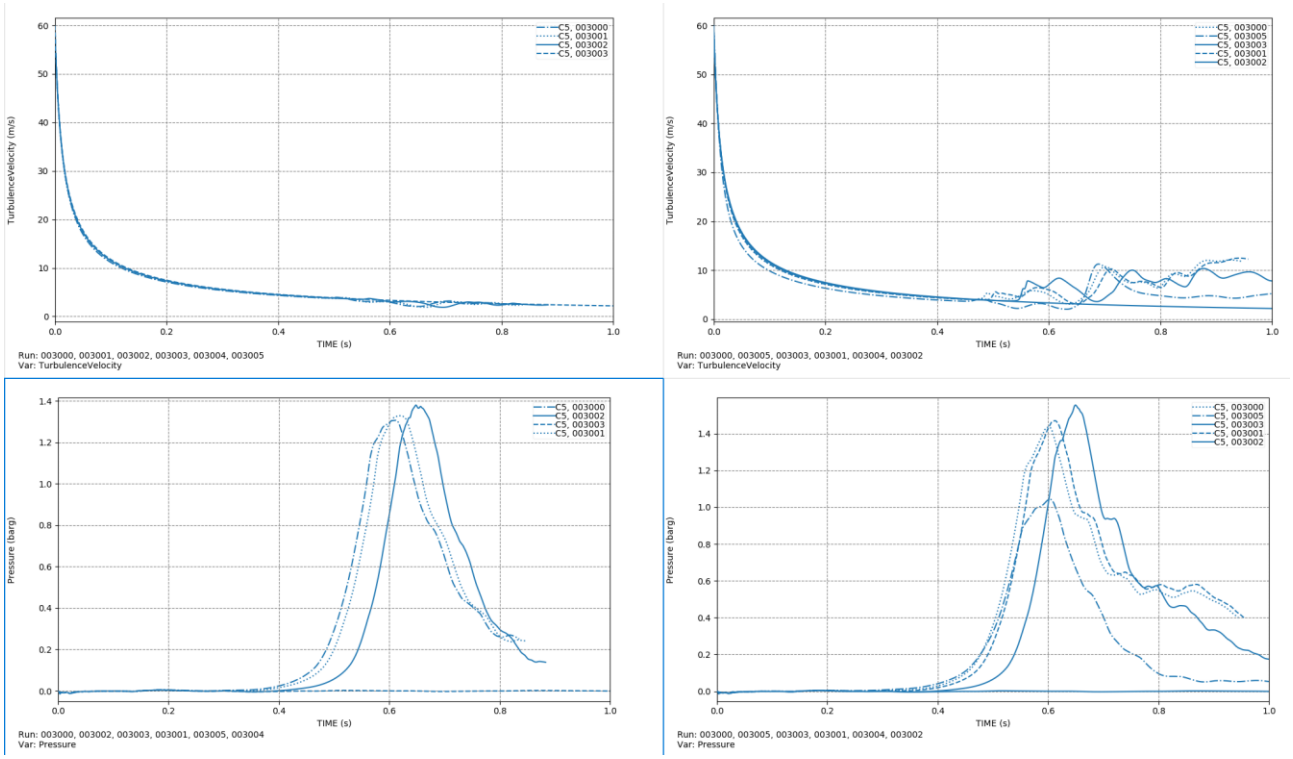

Fig. 3. *Turbulent velocity-time and pressure -time curve for monitor point C5 simulated with FLACS-DustEx v22.2 (003000: 0.176 m grid, 003001 0.15 m grid, 003002 0.1 m grid, 003003 0.05 m grid, 003004 0.04 m grid and 003005 0.3 m grid) on the right and in the left side after changes by removing the shear turbulence.*

Comparing the two version of solver results show that removing the shear generated turbulence does not influence the results in the large geometries. This is expected as described before, this unphysical effect of shear generated turbulence will influence the subgrid scales.

3.2.FM Global 64 m^3

We investigate further the effect of changes to shear generated turbulence on another large-scale dust explosion experiments in a vented 64-m^3 vessel reported by Tamanini (1990) and Tamanini & Chaffee (1989). The experiments were conducted in an empty 64 m^3 chamber with dimensions 4.6m x 4.6m x3m with an open 2.4 × 2.4 m vent door in one wall. In our CFD simulations with FLACS-DustEx we used the tests with maize starch, nominal dust concentration 250 g/m^3, vent ratio Av/V v2/3 = 0.35, ignition by a 5 kJ chemical igniter in the centre of the enclosure, and ignition delays in the range 0.5–1.1 s (Skjold et al., 2008).

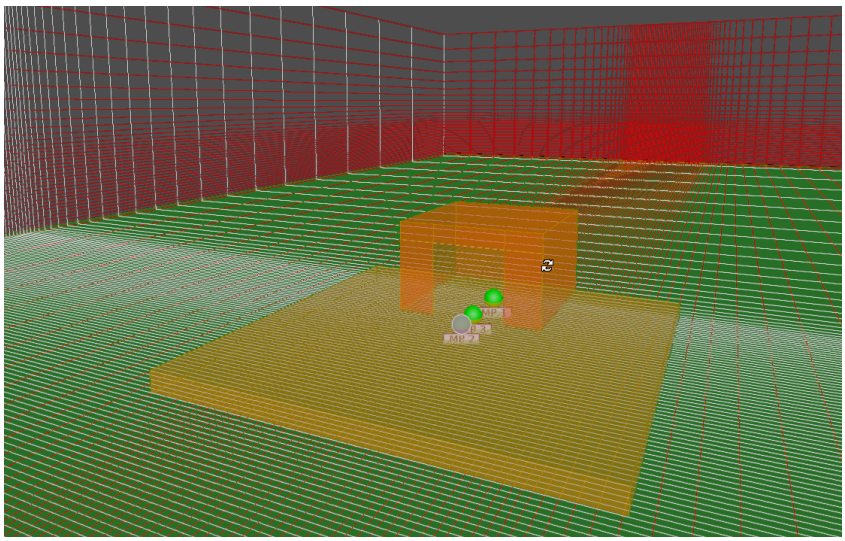

Fig. 4. the implemented geometry and computational grid used in the simulations of FM Global 64 m^3

Figure 4 illustrates the implemented geometry and computational grid used in the simulations. The grid inside the enclosure consisted of 0.1 m cubical grid cells for the dispersion simulation (cell size dictated by the maximum pseudo diameter of the transient release), and 0.1 or 0.2 m cubical grid cells for the explosion simulations (to illustrate the effect of grid resolution on the simulation results).

Simulation results of 64 m^3 for grid sizes 10, 15 and 20 cm are shown in figure 5.

Pressure-time curve for monitor point one for job. numbers 022001 20cm grid, 022002 15cm grid 022003 10cm grid simulated with FLACS-CFD v22.2 (on the left) and after changes by removing the shear turbulence (on the left) are shown in this figure.

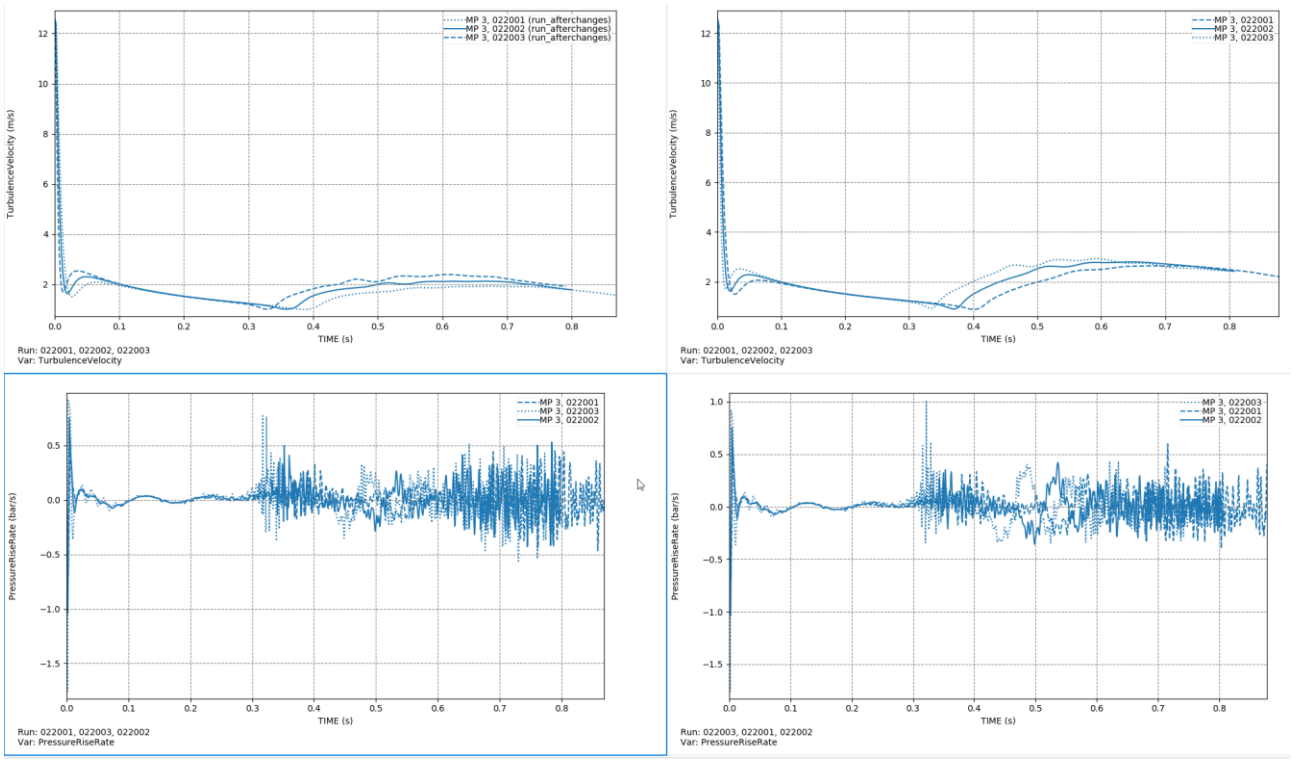

***Fig.5**. Turbulent velocity-time and pressure rise rate-time curve for monitor point three(3) simulated with FLACS-DustEx v22.2 (022001 20cm grid, 022002 15cm grid 022003 10cm grid) on the right and in the left side after changes by removing the shear turbulence.*

Comparing the two results show that removing the shear generated turbulence does not influence the results in the large geometries. This is expected as described before, this unphysical effect of shear generated turbulence will influence the subgrid scales.

4. Conclusions

In conclusion, our study intentionally excluded the consideration of shear turbulence generation within grid cells situated in the reaction zone for cells smaller than 20 cm. The effectiveness of the refined FLACS-DustEx model was assessed through simulations encompassing two series of large-scale explosion experiments characterized by diverse geometries, alongside experiments conducted within 1 m³ spherical bombs. These simulations, conducted across various grid resolutions, fulfill a dual objective: validating the enhanced FLACS-DustEx model's dependability and addressing grid sensitivity concerns effectively.

References

Arntzen, B.J. (1998). Modelling of turbulence and combustion for simulation of gas explosions in complex geometries. Dr. Ing. Thesis, NTNU, Trondheim.

Eckhoff, R.K. (2003). Dust explosions in the process industries. Third edition. Gulf Professional Publishing, Amsterdam.

Eckhoff, R. K., Fuhre, K., & Pedersen, G. H. (1985). Vented maize starch explosions in a 236 m, 843307-2. Bergen, Norway: Christian Michelsen Institute (CMI No. 843307-2).

Eckhoff, R. K., Fuhre, K., & Pedersen, G. H. (1987). Dust explosion experiments in a vented 236 m3 silo cell. Journal of Occupational Accidents, 9, 161–175.

Skjold, T., Arntzen, B., Hansen, O. R., Storvik, I.E. and Eckhoff, R. K. (2006). Simulation of dust explosions in complex geometries with experimental input from standardized tests, Journal of Loss Prevention in the Process Industries 19 (2006) 210–217

Skjold, T., van Wingerden, K., Hansen, O. R. and Eckhoff, R. K. (2008). Modeling of vented dust explosions- empirical foundation and prospects for future validation of CFD codes, SYMPOSIUM SERIES NO. 154, IChemE 2008

Skjold, T., (2014). Flame Propagation in Dust Clouds – Numerical Simulation and Experimental Investigation. PhD. dissertation, University of Bergen (UiB).

Tamanini, F., 1990, Turbulence effects on dust explosion venting, Plant/Operations Progress, 9: 52–60

Effect of Nickel and Silver Coating on Surface Functionalized Alumina Ceramic Foam as Explosion-Suppressing Material

Nur Faazila Hamzah[a], Rafiziana Md. Kasmani[a,*], and Sheela Chandren[b]

[a]*Faculty of Chemical and Energy Engineering, Universiti Teknologi Malaysia, Johor Bahru 81310, Johor, Malaysia.*

[b]*Faculty of Science, Universiti Teknologi Malaysia, Johor Bahru 81310, Johor, Malaysia*

E-mail: *rafiziana@utm.my*

Abstract

In the energy security field, porous materials play a crucial role as effective explosive attenuators, capable of extinguishing flames and dispersing energy waves generated by explosions. Ceramic foam, known for its substantial porosity and resistance to high temperatures and shocks, emerges as a promising medium for this purpose. This study delves into the potential of ceramic foam to suppress free radicals produced during gas combustion through collisions within its structure, thereby restraining reactive heat release and quenching flame propagation. While ceramic foams effectively attenuate shock waves, their brittleness limits their applications. To overcome this drawback, the study proposes surface coating with metallic materials, specifically nickel and silver nanoparticles (NPs) on alumina foams, to enhance desired characteristics such as anti-fouling, self-cleaning, high thermal ability, and wear resistance. Previous research has highlighted the varied performances of porous materials composed of metal and ceramic as flame-suppression elements in mitigating explosions. The metal-coated ceramic foams undergo comprehensive analysis, including examination of physical properties, elemental composition, crystallinity, phase identification, morphology, and compressive strength. Explosion tests using aluminium powder at various concentrations are conducted in a 1.2-L Hartmann vessel to evaluate the ability of the metal-coated ceramic foam to quench flames. Results show a significant reduction, up to 20%, in maximal explosion overpressure (P_{max}), with Ag-coated ceramic foam demonstrating ~15.4% reduction compared to Ni-coated ceramic foam (P_{max}: 0.1729 bar) and ceramic foam (P_{max}: 0.1862 bar). The pressure dynamics evolution is closely linked to the interaction of flame with the coated foam struts, dependent on how free radicals attach to Ni or Ag elements during combustion. Overall, Ag-coated ceramic foam exhibits the most effective suppression of flame propagation and pressure buildup. The study's findings hold great significance for guiding the safety design of spherical suppression materials in engineering applications, offering valuable insights for process safety researchers and engineers.

Keywords: ceramic foam; metal coating; dust explosion; flame quenching; overpressure

Introduction

Improving the safety of processes related to dust requires the development of inhibition technologies designed to prevent the spread or escalation of explosions. One particularly promising and environmentally friendly approach to suppress explosions feasibly involves advancing technology, by adopting porous materials. Yet, the effectiveness of this method depends largely on the characteristics of the substances used for explosion suppression and their uniform distribution in areas

prone to explosions. Ceramic foam, characterized by its high porosity and extensive specific surface area, possesses an interconnected micro-network structure that has been discovered could extinguish gas explosion flames and alleviate shock wave overpressure (Nie et al, 2011). While ceramic foam has been proven effective in preventing fires and suppressing gas explosions, its application in dust explosions has been limited. Duan et al. (2021) observed that foam ceramics significantly disrupt the free radicals generated by chemical reactions during methane explosions. The free radicals repeatedly collide with the foam ceramic during the propagation process, leading to substantial destruction of the free radicals through chemical conversion and the cooling process of combustion products in the porous material. This, in turn, reduces the release of heat from chemical reactions, renders the reaction unsustainable, and suppresses both the explosion flame and overpressure (Dong et. al, 2011; Korzhavin, et al, 1982).

The study of porous materials is not limited to foam ceramics, both the wire mesh and the foam ceramic have a certain effect of attenuating the explosion shock wave. The explosion suppression effect of the porous material is achieved by its unique structural characteristics, destroying and interfering with the coupling effect of the explosion overpressure and the explosion flame and interfering with the mutual promotion between the flame and the shock wave to achieve the effect of suppressing the explosion.

Additionally, ceramic foams are recognized for their inherent brittleness, making them less suitable as materials for suppressing explosions, particularly in harsh environments characterized by elevated temperatures and pressures. To address this limitation and enhance the mechanical strength of ceramic foam, this study introduces the coating of metal nanoparticles onto ceramic foam to engineeredly, change its surface functionality by modifying the physicochemical properties of the foam, thereby strengthening its structural integrity and durability. Our previous work done by Mokhtar et al. (2019) concluded that nanosilver particles have a suppressive effect in reducing overpressure during aluminum-dust explosions, making them a promising candidate with high thermal and mechanical properties as a metal suppressant. In this work, non-precious metals of silver and nickel were chosen as the coating powder due to their favorable electrical conduction and thermal abilities. Given the robust nature of ceramic foam to withstand high temperatures and challenging environments, the hypothesis is that modifying the ceramic foam with a metal coating could reinforce its mechanical properties, enabling it to withstand mechanical impact and higher mechanical loading. As both ceramic (non-metallic) and metallic nanopowder coatings hold significant importance, exploring the synergistic effect of metal deposition on ceramic foam is interesting, anticipating benefits such as higher porosity, improved mechanical stability, increased heat resistance, and enhanced adhesion to the ceramic support. This, in turn, minimizes blockages in smaller microchannels. The objective of this study was to investigate the inhibitory effect of nickel and silver metal on aluminum dust explosions. The synergistic impact of metal inhibition on coated metal-ceramic foam for explosion parameters (P_{max} and dP/dt_{max}) and quenching behavior during aluminum powder vented explosions was quantitatively examined using a designed aluminum dust explosion experimental system in a 1.2-L vertical vessel at various concentrations. This research not only demonstrates the significant inhibitory effect of metal nanoparticles in suppressing explosions but also contributes to enhancing the intrinsic safety of the metal-processing industry and reducing the risks associated with dust explosions.

1. Experimental

1.1 Materials and Chemicals

The main porous element used in this study is white alumina porous ceramic foam was purchased from Pingxiang Bestn Chemical packing) with a thickness of 25 mm, a diameter of 70 mm and a pore size of 60 pores per inch (ppi). Nickel (Ni), silver (Ag) and aluminium (Al) powder with a particle size of 70 nm and 99.8% purity, were purchased from Hongwu International Group Ltd., China. All

materials and reagents used in this work were of analytical grade as tabulated in Table 1. The aqueous solution used was distilled water.

Table 1. List of materials and chemicals reagents.

Materials/Chemical reagents	Molecular formula
Acetone	CH_3COCH_3
Ethanol	C_2H_5OH
Polyvinylpyrrolidone (PVP10)	$(C_6H_9NO)_n$
Absolute ethanol	C_2H_6O
3-Aminopropyltrimethoxy silane	$C_6H_{17}NO_3Si$

1.2 Sample Pre-treatment and Modification by Silanization Agents

The procedures for sample pre-treatment and surface modification by silanization agent of 3-aminopropyltrimethoxy silane (APTMS) can be found elsewhere (Hamzah et. al, 2023).

1.3 Dispersion of Nickel and Silver Nanoparticles

In this study, no synthesis has been done to obtain Ni and Ag NPs as it was readily purchased in the form of metallic nanopowder with a specific size of 70 nm and the size has been controlled by dispersing Ni and Ag powder respectively through ultrasonic dispersion in a solvent containing a surface stabilizer before the coating process was done onto the ceramic substrates. 10 g of nanopowder was dispersed in 250 mL absolute ethanol. The resulting solution was stirred gently. The particle size was observed. If it agglomerates, 1 – 2% PVP (MW 10,000) was added dropwise. The desired particle size of the Ni and Ag coated on ceramic foam is expected to be maintained at 70 nm.

1.4 Coating Technique Used

The coating method used in this study was dip-coating. This method can be done manually without the use of a dipping device. It involves a four-step process: (1) immersion, (2) deposition, (3) removal, and (4) evaporation (Neacşu et. al, 2016). Since this method was done manually, parameters such as the immersion time, number of coating layers, and withdrawal speed are difficult to control. However, errors are minimized by maintaining the immersion time at 30 min per layer, standardizing the number of coating layers to 4, and employing moderate removal speed. The APTMS-modified foams were coated with the respective nickel and silver solution by completely immersing each in solution each layer for 20 min. The steps were repeated four times to ensure uniform coating. The coated foams were further heat-treated at 80 °C (Hamzah et. al, 2023).

1.5 Characterization Methods and Instruments

Preliminary characterizations and instrumentations used for the pre-explosion samples were explained in detail based on previous research (Hamzah et. al, 2023). The additional characterizations i.e., thermogravimetric (TGA) analysis and compressive test were further discussed in this study. The crystallinity and phase content of the prepared coating films were determined by X-ray diffraction (XRD), morphological studies of metal NPs were carried out by Field Emission Scanning Electron Microscopy (FESEM), thermal analysis was performed by Thermogravimetric Analyzer (TGA) at a rate of 30 °C/min from 30 °C to 1000 °C under purified air and compressive mechanical testing was carried out by using the universal testing machine (Instron 5982) with a crosshead of 0.5 mm/min. The post-explosion samples were analyzed for their morphologies, crystallinity, phase content, and elemental composition to determine the amounts of metal oxide produced after the powder explosion test. This was used for comparison purposes with the pre-explosion samples.

1.6 Dust Explosion Set-up

Detailed set-up for the Al explosion test is shown in Fig. 1. The installation of nickel- and silver-coated foam in a vented explosion has been adopted for the quantification of the synergetic effect of metal inhibition on coated metal-ceramic foam for explosion parameters and quenching behavior on aluminium powder explosion and compared to that of the non-coated foams. As such, the double suppression system was adopted in this work, for which filter paper was used as a vent cover together with the ceramic foam to evaluate the effectiveness of flame quenching of metal dust explosion.

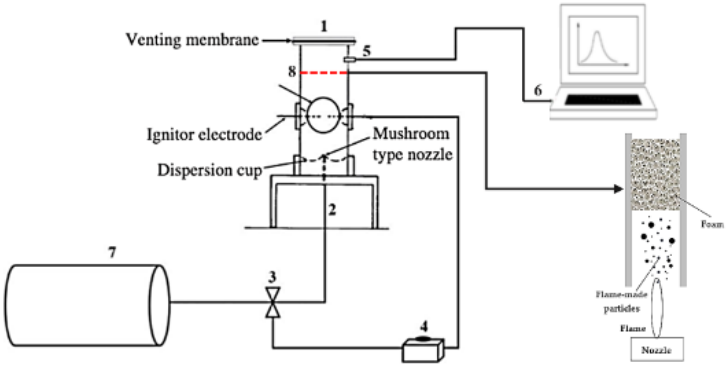

Fig. 1. Experimental apparatus: 1. Venting device, 2. Gas nozzle, 3. Solenoid valve, 4. Time controller, 5. Pressure transducer/sensor, 6. Data acquisition system, 7. Air compressor, and 8. Ceramic foam.

Concentrations of aluminium powder are between 300 – 1200 g/m^3, following ASTM E1226 (Standard Test Method for Explosibility of Dust Clouds). The metal-coated ceramic foam was placed in the vessel chamber slightly below the pressure sensor, whilst filter paper was mounted on the top of the vessel as venting membrane. The metal powder was placed in the dispersion cup and the test vessel was tightened up. The sample was dispersed by compressed air at a pressure of 6 bar. After the dispersion, the sample was ignited by a centrally mounted igniter, following a 60-ms time delay. The software was operated and the igniter capacitor (10 J) was switched on continuously. The explosion pressure evolutions were measured by a piezoelectric pressure transducer (Keller Series 11, with accuracy ± 0.001 s). The data yield of the experiment was recorded by a data acquisition system from National Instruments with a sampling rate of 100 MHz. Each test was performed in at least three replications for accuracy and reproducibility. The resulting data yielded maximum explosion pressure (P_{max}) from the pressure–time profiles. Further, the maximum rate of pressure rise (dP/dt_{max}) was calculated based on the tangent of the pressure–time profiles (Mokhtar et.al, 2021). The current findings were then compared to that of the P_{max} and dP/dt_{max} of the non-coated foams.

2. Results and Discussion

2.1 Thermal Analysis by TGA

Thermogravimetric Analysis (TGA) was performed to investigate the thermal behaviour of the ceramic foam together with Ni and Ag NPs coated on it. The TG/DTG analysis carried out under air atmosphere was plotted in Fig. 2, showing the percentage weight loss of samples which is represented by TG% as a function of heating temperature. From Fig. 2(a), the TG curve for Ni-coated ceramic foam showed a small weight loss of about ~0.2% from 23.1 to 291.2 °C due to the removal of volatiles, and then a rapid and large weight gain from 291.3 to 982 °C due to the oxidation of nickel as the analysis was carried out in purified air. In the presence of air, the oxidation of nickel is more pronounced because nickel is easily oxidized as shown in the XRD as well as FESEM from the previous study (Hamzah et. al, 2023). Due to this, the TG curve for Ni-coated ceramic foam in Fig. 2(a) differs from Fig. 2(b). It is also noted that Ag-coated ceramic foam is thermally stable and less prone to oxidation as compared to Ni-coated ceramic foam. It can be susceptible that silver deposition on the ceramic foam could reinforce the physicochemical compatibility between metallic silver and non-metallic ceramic foam, leading to the easy attachment of free radicals of •OH and •H with silver during combustion. The DTG curve of Ni-coated ceramic foam gave two peaks showing deviation

below zero at temperatures 381 °C and 855 °C (indicating weight gain by oxidation of nickel). Based on these two figures, the peculiar weight gain for Ni-coated ceramic foam occurred above 350 °C, and this is due to the formation of respective metal oxides of alumina and nickel (Awad et.al, 1991).

Observation on TG curves of Ag-coated ceramic foam shows a constant weight above 600 °C as illustrated in Fig. 2(b). It showed an almost similar trend as typical ceramic foam that can be found elsewhere; however, the weight loss was still experienced up until 1000 °C, suggesting that Ag-coated ceramic foam can sustain combustion at higher temperatures > 1000 °C due to a very low oxidation rate of silver. It is observed from the TG curve for Ag-coated ceramic foam showed a very small weight loss of about 1% occurred in temperatures up to 400 °C. DG plot displays an exothermic peak between 300°C and 400°C which is mainly attributed to the crystallization of Ag NPs (Khan et.al, 2011). This indicates that more attachment of silver onto ceramic struts is favorable for flame flame-quenching mechanism. DG profiles show that complete thermal decomposition and crystallization of the sample occur simultaneously. This suggests that the silver nanoparticles (NPs) on the ceramic foam are less prone to oxidation. Fergus et al. (1998) also presented a similar finding in the case of the TGA on the silver powder.

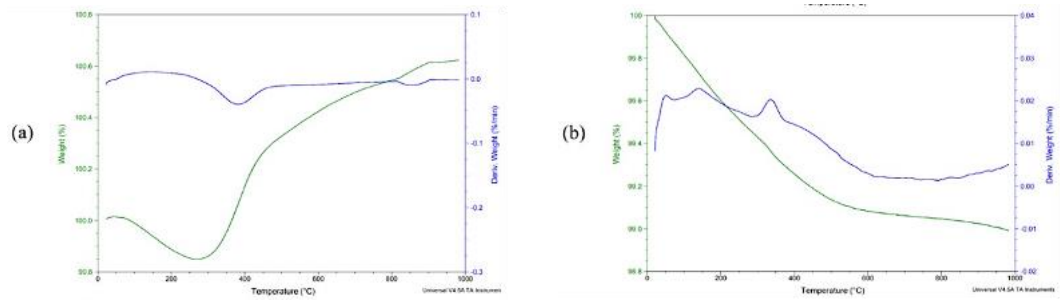

Fig. 2. TG/DTG spectrum for (a) Ni-coated ceramic foam and (b) Ag-coated ceramic foam operated at the temperature range of 30 – 1000 °C and at a heating rate of 10 °C/min under purified air.

2.2 Compressive Strength by Universal Testing Machine (UTM)

In this study, the compressive strength outcomes of non-coated ceramic foam denoted by P1, nickel-coated ceramic foam as N1, and silver-coated ceramic foam denoted by S1 were characterized by an initial linear phase followed by a long distance of plateaus due to the progressive collapse of the structure. Consequently, it confirms that it is possible to enhance the strength of the ceramic foams by the addition of metal nanoparticles through coating. Fig. 3 shows the typical load versus extension curves, where all the samples showed a linear part followed by an abrupt drop when the load is applied, indicating a brittle failure. In the initial stage, the load increases linearly. This corresponds to the linear elastic behaviour for the typical fracture of brittle foams.

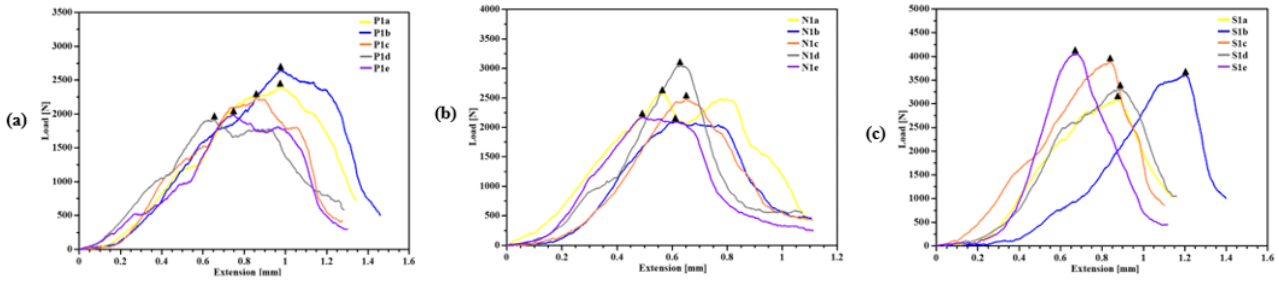

Fig. 3. Graph of load vs. extension for ceramic foam (P), Ni-coated ceramic foam (N), and Ag-coated ceramic foam (S) at crosshead of 0.5 mm/min.

The compressive strength was also determined from the point in the chart recorder where the load reached its maximum indicated by the (▲) symbol. At the crushing point, the propagation of macroscopic cracks has resulted in a load drop. Additional deformation of the foam occurs as the sample becomes progressively damaged (layer by layer) from either the top or the bottom owing to

breakage of struts. It was observed that struts were failing before attaining the maximum stress and that the failure of these struts was accompanied by slight drops in the load/extension curve.

As seen from Fig. 3(c), it was found that the Ag-coated ceramic foam showed the highest load applied with an average of 3588.56 N at 0.90 mm compression extension, followed by Ni-coated ceramic foam with a maximum load of 2475.93 N at 0.59 mm extension (see Fig. 3(b)). The results obtained show a significant increase in the required load percentage before foam fails, whereas non-coated ceramic foam in Fig. 3(a) attained the foam's shape up to 0.84 mm extension with 2237.50 N of loads. The percentage increases for maximum load for both nickel- and silver-coated ceramic foam as compared to the non-coated ceramic foam was about 10.7% and 60.4% respectively. It can be deduced that P1, N1, and S1 showed similar failure mechanisms irrespective of the surface modification with metal nanoparticles.

From the result obtained, it was found that sample S1 had the highest average compression strength value of 0.93 MPa with the shortest deformation of plateau due to the small and uniform pores of the samples. Meanwhile, sample N1 has a moderate compressive strength value of 0.64 MPa but greater plateau deformation. P1 showed the lowest compression strength of 0.58 MPa due to the presence of a large pore diameter. As explained by Yu et al. (2007), the larger diameter of the cell size will produce inhomogeneity of density and the stress drop ratio will develop into larger. The smaller the diameter of the pores, the higher the compressive strength of the ceramic foams. This could be due to the densification between the metal nanoparticles of nickel and silver deposited on the porous structure of the non-coated ceramic foam.

2.3 Morphological Analysis by FESEM

The results of the FESEM analysis before and after the explosion for the non-coated ceramic foam at different magnifications of 35×, 10,000×, and 50,000× can be found from the previous research (Hamzah et. al, 2023) while the FESEM analysis for nickel-coated ceramic foams are presented in Fig. 4. The results showed that the aluminium powder and nickel nanoparticles have a spherical shape and are clusters of agglomerates, which is typical for nanoparticle powders deposited on the strut wall of the porous ceramic surface as compared to the Ni-coated ceramic foam before the explosion. From the images, it clearly can be seen that both aluminium and nickel are present after the explosion and cause high agglomerations as compared to the explosion of the ceramic foam from the previous study (Hamzah et. al, 2023). Due to the agglomeration effect between both aluminium and nickel nanoparticles after the explosion, they tended to produce bigger particle sizes especially when the aluminium particles come into contact with each other of similar spherical shapes. Thus, making it easier for agglomerations to take place. As a result of post-explosion, the particle size ranges from 70–191 nm.

The results of the FESEM analysis before and after the explosion for the Ag-coated ceramic foam at different magnifications of 35×, 10,000×, and 50,000× are presented in Fig. 5. Ag NPs are mostly irregular and agglomerated with one another prior to the explosion test as depicted in Fig. 5(a). The agglomeration effect of aluminium and silver powder is more pronounced after explosion compared to that of the aluminium and nickel powder, implying that the degree of oxidation for larger particle size (due to agglomeration) was significantly lower, leading to lower mass burning rate and hence justifying the lower P_{max} shown in Fig. 7(c). It can be seen that different metals displayed varying morphological structures. The mechanism involved was the intraparticle agglomeration of both aluminium and silver nanoparticles at 70 nm.

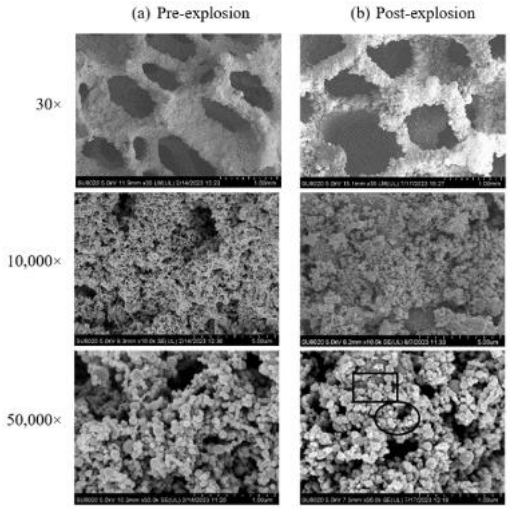

Fig. 4. FESEM micrographs of Ni NPs (in rectangle) on ceramic foams, (a) before and (b) after Al nanodust (in circle) dust explosion at different magnifications corresponding to Fig. 7(b).

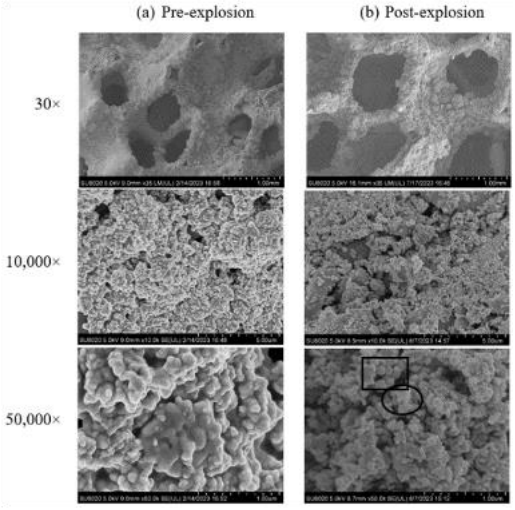

Fig. 5. FESEM micrographs of Ag NPs (in rectangle) on ceramic foams, (a) before and (b) after Al nanodust (in circle) explosion at different magnifications corresponding to Fig. 7(c).

From the picture, it is quite difficult to differentiate both nanoparticles at a glance. However, based on a previous study by Mokhtar et al. (2019), they found that both metals tend to agglomerate with each other, causing larger effective particle sizes. From the current study, the size of the nanoparticles after the explosion ranges from 81 – 205 nm. The findings revealed that the silver NPs coated on ceramic foams are non-uniform with obvious agglomerations of metallic-silica present on the strut structure. The morphological structures of aluminium powder are consistent with the literature which reported that the aluminium morphology is formed as a result of the condensation of gas-phase reaction (Bouillard et.al, 2010; Sun et.al, 2011).

2.4 Crystallinity Study by XRD

The preliminary characterization to determine the crystallinity of the APTMS-modified sprayed samples of nickel-ceramic foam was determined by XRD based on the previous work (Neacşu et.al, 2016). The XRD patterns of S1 in Fig. 6 indicated that the structure of Ag NPs is face-centered cubic (FCC). In addition, all the Ag NPs had a similar diffraction profile, and XRD peaks at $2\theta = 38.1°$, 44.3°, 64.4°, and 77.4° could be attributed to the (111), (200), (220) and (311) crystallographic planes of the face-centered cubic silver crystals, respectively. The XRD pattern thus clearly illustrated that the Ag NPs (S1) formed in this study were crystalline in nature. The main crystalline phase was

alumina with a trace of Ag NPs as impurities were found in the XRD patterns. As can be seen, the diffraction peaks for Ag-coated ceramic foam before and after the explosion showed almost similar positions. This could be attributed to the low degree of oxidation shown by silver NPs resulting in the crystal structure being maintained as FCC. The findings are coherent with the TGA for silver in Fig. 2(b). Since the FCC crystal structure of silver is characterized by closely packed atoms in a three-dimensional arrangement, it results in a relatively lower surface area per unit volume compared to other crystal structures, such as irregular or amorphous ones.

In an explosion, where combustion occurs on the particles' surface, having a lower surface area can lead to a decreased rate of combustion. This could be due to fewer exposed sites for chemical reactions to take place, slowing down the overall burning process. In addition, the FCC structure of silver NPs can offer an increase in chemical stability as compared to other structures. This condition could reduce the reactivity of the material and inhibit rapid combustion reactions. Further, the crystal structure of silver also provides specific adsorption sites on the coated ceramic foam surface. In contrast to nickel NPs coated on ceramic foam, the FCC structure of pure nickel experiences rapid oxidation after the explosion as shown by the changes in the intensity of the diffraction peaks resulting in the FCC of nickel oxide (NiO). This is evident that nickel easily oxidized upon the explosion as compared to silver NPs coated on ceramic foam.

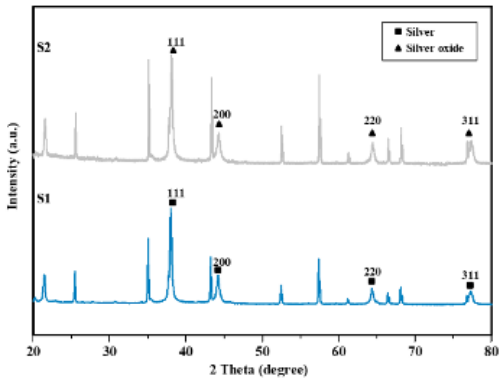

Fig. 6. XRD patterns for pre-explosion (S1) and post-explosion (S2) of silver-coated ceramic foams.

2.5 Explosion Characteristics of Nano-Aluminium Powder with Ceramic

The explosion characteristics of aluminium dust are the basis of the inhibiting effect analysis. It was found that the P_{max} for both metal-coated ceramic foams are lower compared to non-coated ceramic foam at a similar powder concentration (see Fig. 7(a)). At 500 g/m^3 powder concentration, the P_{max} value obtained with the presence of ceramic foam was 0.186 bar which is 8.4% lower than that of overpressure with venting only, indicating that the combination of ceramic foam as barrier and venting as mitigation measures in aluminium powder explosion, P_{max} is reduced; suggesting a dual suppression mechanism. It should be noted that there are multiple peaks of overpressure observed during aluminium powder explosion using ceramic foam, suggesting that due to numerous collisions with the walls in foam ceramics, the free radicals -generated in the chemical reactions of metal combustion and responsible for flame propagation, experienced the flame quenching when passing the struts and re-ignition during flame propagation until the reactive heat release be restrained, thus making the chemical reactions non-self-sustained. As a result, flame propagation is quenched and lowers the P_{max}.

Based on Fig. 7(b) and (c), the pressure–time profile of metal-coated ceramic foam shows similar metal explosion development as ceramic foam, only the combustion time is shortened at lower P_{max}. It can be susceptible that the chemical interaction between Ni-Al and Ag-Al causes a remarkable reduction in surface area for the oxidation reaction, shortens the combustion time for flame to propagate and hence, lowers the burning rate (Gao et.al, 2017). It is obvious at 500 g/m^3 powder concentration that the P_{max} value attained for Ni-coated ceramic foam was 0.028 bar and 0.032 bar

for Ag-coated ceramic foam. The results demonstrate that both nickel- and silver-coated ceramic foams attenuate the maximal explosion pressure drastically, by up to 20%. It can be said that the flame wave was trapped in porous media and contacted the wall for a long time, which contributed to the sharp decrease in the number of free radicals (such as •H and •OH) involved in the combustion that has been attached to the metal NPs coated on the ceramic foam due to the collision making the combustion not sustained and further quenched into struts of ceramic foam. Due to a lack of energy supply, the pressure wave is decayed, until it disappears, and then the destructive effects of the blast wave are reduced effectively. In other words, the unique structure of foam ceramics interferes with the coupling of flame and shock wave effects (Zhang et.al, 2012).
Based on the physicochemical characteristic and explosion test, ceramic foam with silver coating performs better with the increase in density due to the presence of the silver NPs deposited on the foam surface enhancing the overall strength of the foam.

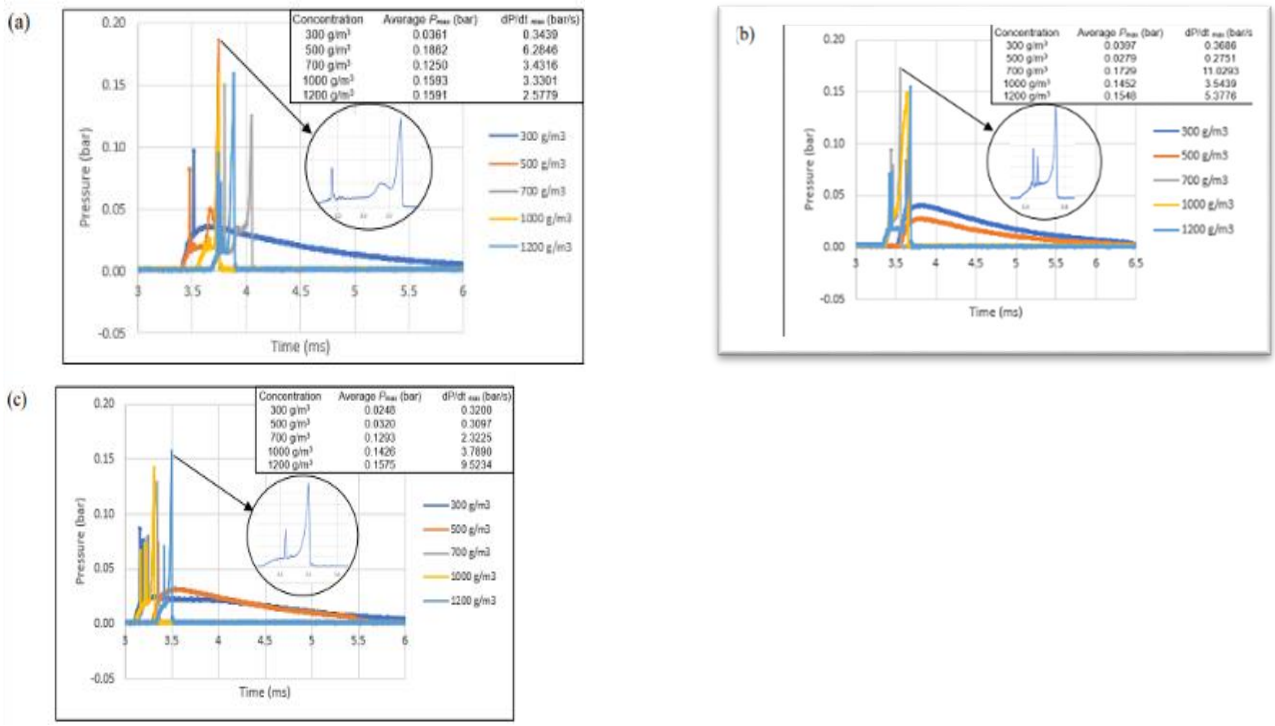

Fig. 7. Pressure–time profile of Al dust explosion at various concentrations with (a) non-coated ceramic foams, (b) Ni-coated ceramic foams, and (c) Ag-coated ceramic foams.

2.7 Suppression Mechanism of Silver-Coated Ceramic

In contrast to the ceramic foam and nickel-coated ceramic foam from the previous study [7], it has been observed that Ag-coated ceramic foam exhibits a superior inhibitory effect on reducing overpressure. This enhanced performance can be attributed to the larger surface area provided by the metallic coating compared to the non-coated foams, thus creating more sites for reactions to occur. Consequently, this leads to the extinguishing of the flame within a specified time frame. As the flame enters the narrow channel, its temperature drops due to the cooling effect of the channel walls, resulting in flame extinction, a phenomenon known as the "cold wall effect". Additionally, the tiny channels within ceramic foam absorb the free radicals generated during the combustion of aluminium powder, subsequently weakening the combustion reaction, referred to as the "wall effect" (Iida et.al, 1985; Radulescu and Lee, 2002).

This deposition creates a noticeable contrast in color between the aluminium dust and the silver nanopowders. The residual yellow hue in Fig. 9 was a consequence of the oxidation of aluminium powder in response to the clustered silver NPs on the bottom surface of the foam. The flame that traverses the foam undergoes a notable decrease, leading to the manifestation of irregularities in the flame on the upper surface of the ceramic foam. During the explosion, the deposited Ag NPs on the lower part of the ceramic foam come into contact with a substantial quantity of dispersed aluminium

dust spread across the foam. This progression happens from the lower to the upper surface of the foam until the advancement of the flame is stopped. The ceramic foam's porous structure obstructs unburned and burning powder particles, disrupting the fuel supply and thus interrupting the reaction. In order to understand the mechanism better, the overall chemical reactions for the Al powder explosion with Ag-coated ceramic foam were expressed as well in Fig. 9.

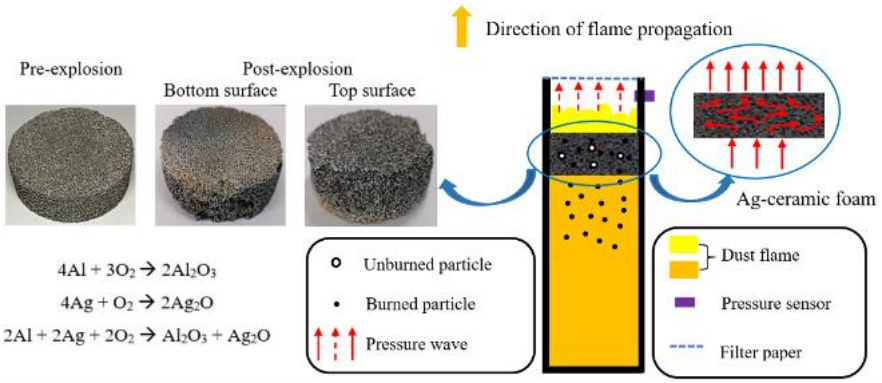

Fig. 9. Flame propagation mechanism in (a) non-coated foam, and (b) silver-ceramic foam.

Based on the TGA results in sub-section 3.1, since Ag is thermally stable above 600 °C when it is synergised functionally with the ceramic substrates, all the available radicals can be easily attached causing the flame to be unable to reach up to the top surface of the ceramic foam because of the unburned aluminium powder are trapped, supporting higher flame to quench at the porous structure of Ag-coated ceramic foam. It is worth noting that, metal-coated ceramic foam blocks unburned and burning powder particles, causing the reaction to lose its supply of fuel, thereby interrupting the process. The amount of •O and •OH radicals affect overall combustion, leading to lower P_{max}.

3. Conclusions

In this study, the explosion characteristics of aluminium dust explosion, which was suppressed by Ag-coated ceramic foam were experimentally investigated. The main conclusions are as follows:

1) From the pre-explosion and post-explosion analysis, Ag-coated ceramic foam outperformed Ni-coated ceramic foam and non-coated foam in terms of its mechanical strength, thermal stability, and robustness in lowering the explosion overpressure during the aluminium powder explosion.

2) From the TGA analysis, it was found that the Ag-coated ceramic foam is less prone to oxidation as no obvious weight gain was observed on the TG curve as compared to Ni-coated ceramic foam. Thus, it can be depicted that Ag-coated ceramic foam can sustain combustion of more than 1000 °C in aggressive environments due to a very low oxidation rate of silver as compared to nickel.

3) From the compression test, the percentage increase of maximum load for both Ni-coated ceramic foam and Ag-coated ceramic foam from as-received ceramic foam was about 10.7% and 60.4% respectively. The results indicate that Ag-coated ceramic foam has a better compressive strength of 0.93 MPa as compared to 0.64 MPa by Ni-coated ceramic foam and 0.58 MPa by non-coated ceramic foam.

4) From the Al explosion test, Ag-coated ceramic foam gives a significant reduction in P_{max} of about 15.4%, while Ni-coated ceramic foam experienced a reduction of about 7.1% when both are compared to that of the P_{max} of the non-coated ceramic foam, thus giving better quenching effect and can be considered as a good candidate for suppressing material for dual suppression mechanism.

5) From the Al explosion test, Ag-coated ceramic foam gives a significant reduction in P_{max} of about 15.4%, while Ni-coated ceramic foam experienced a reduction of about 7.1% when both are compared to that of the P_{max} of the non-coated ceramic foam. This is due to the condition that Ag takes at extremely high temperatures i.e., > 1000 °C to oxidize, and easily bonding of the silver metals to the free radicals such as •OH, •O, and •H during combustion, giving better quenching effect of Ag-

coated ceramic foam and this combination can be considered as a good candidate for suppressing material for dual suppression mechanism.

Declaration of competing interest

The authors declare that they have no known competing financial interests or personal relationships that could have appeared to influence the work reported in this paper.

Acknowledgements

The authors would like to express their appreciation for the funding assistance of the sponsors – Ministry of Higher Education Malaysia (MOHE) under the Fundamental Research Grant Scheme (FRGS) (FRGS/1/2020/STG07/UTM/02/6), and Universiti Teknologi Malaysia under a Collaborative Research Grant (Q.J130000.2451.08G95).

References

Awad, A., Salam, M. A., and Abdullah, B., 1991. Thermocatalytic decomposition of methane/methanol mixture for hydrogen production: Effect of nickel loadings on alumina support, AIP Conference Proceedings, 020030.

Bouillard, J., A. Vignes, O. Dufaud, L. Perrin, D. Thomas, 2010. Ignition and explosion risks of nanopowders, Journal of Hazardous Materials 181(1–3), 873-880.

Dong, Z., B. Nie, W. Chao, Z. Fei, J. Guo, X. Liu, L. Qian, H. Li, and Z. Chen, 2011. Preliminary Research on Porous Foam Ceramics Against Gas Explosions In Goaf, Procedia Engineering 26, 1330-1336.

Duan, Y., Wang, S., Yang, Y., Li, Y., and Zheng, K., 2021. Experimental study on methane explosion characteristics with different types of porous media. J. Loss Prev. Process. Ind., 69, 104370.

Fergus, J. W., Mallipedi, C. V. S., and Edwards, D. L., 1998. Silver/silver-oxide composite coating for intrinsically adaptive thermal regulation, Compos. Part B Eng. 29, 51–56.

Gao, W., X. Zhang, D. Zhang, Q. Peng, Q. Zhang, R, Dobashi, 2017. Flame propagation behaviours in nano-metal dust explosions, Powder Technology 321, 154-162.

Hamzah, N. F., Kasmani, R. M., Chandren, S., Ibrahim, N., and Jalil, A. A., 2023. Effect of metal coating on physicochemical properties of ceramic foam for flame suppression application. Ceramics International 49(22)(B), 36646-36658.

Iida, N., Kawaguchi, O., Sato, G.T., 1985. Premixed flame propagating into a narrow channel at a high speed, part 1: flame behaviors in the channel, Combust. Flame 60, 245–255.

Khan, M. A. M., Kumar, S., Ahamed, M., Alrokayan, S. A., and Alsalhi, M. S., 2011. Structural and thermal studies of silver nanoparticles and electrical transport study of their thin films, Nanoscale research letters 6(1), 434.

Korzhavin, A. A., V. A. Bunev, R. K. Abdullin, and V. S. Babkin, 1982. Flame zone in gas combustion in an inert porous medium, Combust. Explos. Shock Waves 18. 628–631.

Mokhtar, K.M., R.M. Kasmani, C.R.C. Hassan, M.D. Hamid, M.I.M. Nor, N. Ibrahim, 2019. Study of the Explosibility Characteristics of Aluminium-Silver Metal Mixtures, Combustion Science and Technology 192(5), 885–901.

Mokhtar, K.M.,R.M. Kasmani, C.R.C. Hassan, M.D. Hamid, M.I.M. Nor, M.U.M. Junaidi, N. Ibrahim, 2021. Nanometal Dust Explosion in Confined Vessel: Combustion and Kinetic Analysis, ACS omega 6(28), 17831–17838.

Neacşu, I.A, Nicoară, A.I., Vasile, O.R., and Vasile, B.S., 2016. Chapter 9 - Inorganic micro- and nanostructured implants for tissue engineering, Editor(s): Alexandru Mihai Grumezescu, Nanobiomaterials in Hard Tissue Engineering, William Andrew Publishing, 271–295.

Nie, B., X. He, R. Zhang, W. Chen, J. Zhang, 2011. The roles of foam ceramics in suppression of gas explosion overpressure and quenching of flame propagation, Journal of Hazardous Materials 192(2), 741-747.

Radulescu, M.I., Lee, J.H.S., 2002. The failure mechanism of gaseous detonations: experiments in porous wall tubes, Combust. Flame 131, 29–46.

Sun, J., R. Dobashi, T. Hirano, 2006. Structure of flames propagating through aluminum particles cloud and combustion process of particles, Journal of Loss Prevention in the Process Industries 19(6), 769-773.
Yu, H., Guo, Z., Li, B., Yao, G., Luo, H., and Liu, Y., 2007. Research into the effect of cell diameter of aluminum foam on its compressive and energy absorption properties, Materials Science and Engineering: A. 454–455.
Zhang, J., Wang, H., and Yuan W., 2012. Effects of multi-layer metal wire mesh on the propagation of premixed flammable gas explosion in pipes, Journal of Hunan University of Science and Technology (Natural Science Edition) 27(2), 18–21.

Prediction of self-heating for direct reduced iron due to reoxidation

Christoph Spijker [a], Michael Hohenberger [a], Richard Schanner [b] & Peter Gluschitz [b]

[a] Montanuniversitaet Leoben, Chair of Thermal Processing Technology, Leoben, Austria
[b] INNOFREIGHT Solutions GmbH, Bruck an der Mur, Austria
E-mail: christoph.spijker@unileoben.ac.at

Abstract

The steel production using direct reduced iron (DRI), in an electric arc furnace has a lower carbon footprint in comparison to the blast furnace route (Bhaskar, 2019). When the iron ore is reduced by hydrogen, called H-DRI it presents one of the routes for green steel. The direct reduced iron ore, based on the initial ore type, the reduction process and the form, density and size of the pellets has a tendency for reoxidation. This exothermic reaction could lead to a thermal runaway in storage or transport. The reoxidation kinetics was investigated by an isothermal differential loop reactor at different temperatures. The reoxidation could be separated in three by transport effects dominated segments. A correlation for the reoxidation rate as function of the temperature and the relationship between the mass fractions of oxygen and oxidized iron could be found. This reaction kinetic was implemented as surface reactions into a coupled Computational Fluid Dynamics (CFD)-Discrete Element Method (DEM) model, based on OpenFOAM 6 (OpenFOAM, 2018). The model considers the heat transport by particle-particle conduction, and convection. Based on this model, 7 different scenarios for a rail transport container were investigated. For dry air with the determined reaction rates, the H-DRI has a tendency for self-heating but reaches a stable temperature and no thermal runaway could be observed. Under the assumption that the reaction has an unlimited supply of water vapor, a thermal run away could be observed in every case, expect for a totally sealed container.

Keywords: *DRI, reoxidation, railway safety, self-heating, thermal runaway, particle modelling, CFD-DEM*

Introduction

Direct reduced iron (DRI) basically represents iron ore, that is reduced below the melting point of the material. The most common method is the reduction in gas fired shaft furnaces-based process namely MIDREX and HYL-ENERGIRON. These two processes accounting for 90 % of the worldwide production of DRI (Cavaliere, 2019). DRI is mostly used in an electric arc furnace for steel production. This route of steel production has a lower carbon footprint in comparison to the blast furnace route (Bhaskar, 2019). Reducing the iron ore with hydrogen to H-DRI instead of using natural gas, is one of the future routes for green steel. DRI has a tendency to reoxidize, strongly based on the particle size, ore type, porosity, reduction process and if it was hot-briquetted. Therefore, DRI is classified in three categories for maritime transport by the standards (International Maritime Organization, 2009). DRI type A is hot bracketed after the reduction process, also called hot bricked iron (BHI) or hot moulded briquettes (HMB). This is the is the less reactive, high-density variety. DRI type B is highly reactive, low density mostly in the form of spherical pellets and type C are fines with average particle size smaller than 6,35 mm, that only be carried under an inert gas atmosphere (International Maritime Organization, 2009). The standard also differentiates between hot and cold transport by a temperature of 60 °C. For the land transport of DRI currently no applicable standards for self-heating exists. This effect is based on the exothermic reoxidation with oxygen (Eq. 1) or oxygen and water vapor (Eq. 2).

$$Fe + \frac{1}{2}O_2 \rightarrow FeO \quad (1)$$

$$Fe + \frac{1}{2}O_2 + H_2O \rightarrow Fe(OH)_2 \quad (2)$$

In the worst case the reoxidation could lead to a thermal run-away during transport and storage. In 2003 bulk carrier Adamandas, transporting 21 000 t of DRI, encounter the issue of reoxidation and the DRI reached temperatures over 300 °C and had to be sunk. (Cedre, 2007). For transporting the DRI in continental Europe, rail transport is an efficient and environmentally friendly method. To safely transport the DRI the INNOFREIGHT Solutions GmbH has developed a patented rail transport container (Schanner, 2023) for the cold transport of H-DRI type B. Based on this design the self-heating process was investigated for seven different scenarios. First the reaction kinetics were obtained in a differential loop reactor These reaction kinetics were used in a Computational Fluid Dynamics (CFD)-Discrete Element Method (DEM) model for the investigations.

1. Experimental determination of the reaction kinetics

To experimentally measure the kinetics of the reoxidation behaviour of hydrogen-reduced iron pellets (H-DRI) different methods are possible, e.g. gravimetric, optical and chemical analysis (Szekely 1976). Gravimetric pre-experiments for the duration of 420 hours at room temperature showed, that if parts of the DRI pellets are not in direct contact with water, there is no measurable weight change. Therefore, a different method was applied for dry reoxidation at low temperatures. In a loop reactor system the oxygen consumption of the iron pellets were measured in the gas stream.

1.1. Materials

Industrial hematite pellets were reduced with hydrogen in a laboratory furnace at 800 °C to 900 °C until a metallization degree of at least 92% was reached. The chemical composition before and after the reduction process is given in Table 1. There Fe_{tot} is the total iron content and Fe_{met} is the metallic iron content. The ratio between these parameters is the metallization degree MD, as can be seen in Eq. 3. The pellet sizes reached from a diameter of 12.2 to 17.3 mm. The used pellets had no visual openings or cracks.

***Table 1**. Chemical composition of the hematite pellet and hydrogen reduced pellet (wt%)*

	Fe_{tot}	Fe_{met}	Fe^{2+}	Fe^{3+}	Fe_2O_3	MD
Raw hematite pellet	68.6	-	1.12	67.5	96.4	-
Hydrogen reduced pellet	92.2	87.7	4.14	0.33	-	95.2

$$MD = \frac{Fe_{met}}{Fe_{tot}} \cdot 100\% \quad (3)$$

1.2. Experimental procedures

In the laboratory unit the samples, which consist of four crack free H-DRI pellets, that are cooled and stored under inert gas after reduction. These pellets are kept in an electrical heated pipe reactor (Fig. 1) to measure the temperature dependence of the reaction kinetics, for each experiment the sample temperature is held constant. The heating up is done under 100% nitrogen atmosphere. After the temperature is constant the system is filled with laboratory air (80 vol.-% N_2, 20 vol.-% O_2) and through solenoid valves the gas flow is switched to loop mode. The gas is then pumped at 5 l/min at

an overpressure of around 500 mbar over the sample at the defined temperature. Afterwards the gas is cooled to room temperature and filtered to be analysed in the gas analyser (ABB caldos, continuous thermal conductive measuring system of oxygen). Because of the gas cooler, the gas atmosphere was not completely humidity free, a maximum of 5.6 g H_2O/m^3 was measured. The overall volume of the system was 1.21 litres. Measurements were done up to 167 hours.

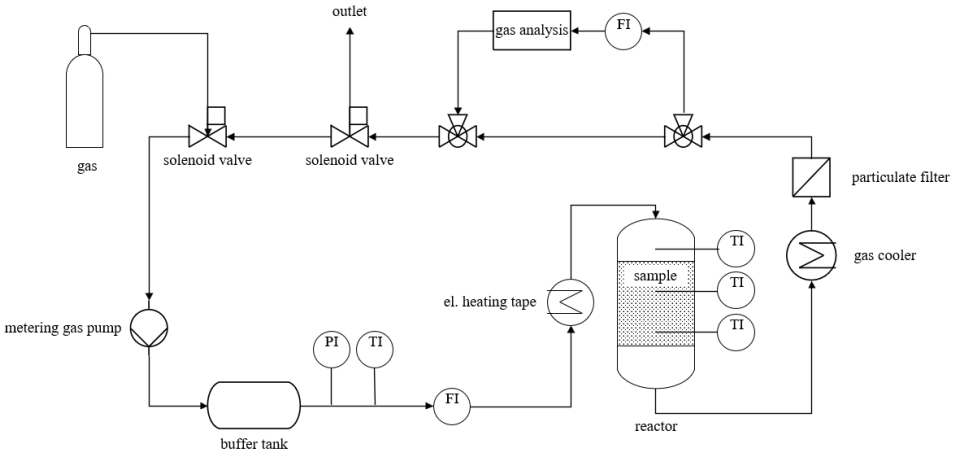

Fig. 1. *Experimental laboratory setup (Hohenberger 2024)*

2. Numerical Approach

The numerical model is separated into two parts. First a randomized packed ped is created by filling the rail transport box, using a DEM model. Since the particles represent a fixed bed, the particle positions could be fixed and the reactive CFD-DEM model applied.

2.1. Modelling of the filling process

To model the filling process the unmodified uncoupledKinematicParcelFoam solver in OpenFOAM 6 (OpenFOAM, 2018) was used. For the particle forces the Pair Spring Slider Dashpot approach by Cundall and Strack (Cundall, 1979) was chosen. To characterize the direct reduced iron pellets, a sample of 100 pellets was measured for the diameter and the mass, leading to an average density of 3 580 kg/m^3. The particle diameter reaches from 7.3 mm to 17.0 mm with a d_{50} of 12.2 mm. This size distribution was implemented in the model by a Rosin-Rammler-Sperling-Bennett-distribution (Rosin, 1933) with a spread parameter of 9.8 and a d_{63} of 12.7 mm. The rebound energy factor for the particle wall collisions was measured on a steel plate for 25 particles of different diameters with an average of 0.13. The rebound energy factor for the particle-particle collision was set to 0.52, the Younge module $2{,}4 \cdot 10^7$ Pa and the Poisson's ratio 0.25 based on literature (Fernando, 2018). To fill the rail transport box, the particles where randomly injected at the top opening (Fig. 2a) with a downward velocity of 0.1 m/s. The rail transport box was filled with 4 578 816 particles (Fig. 2b), representing a mass of 36 161 kg.

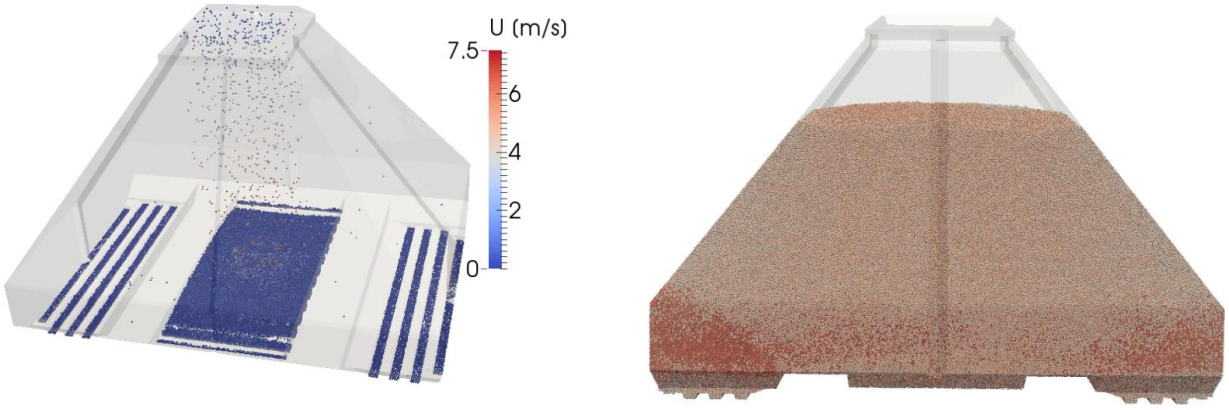

a.) b.)

Fig. 2. *Filling of the rail transport box. The particles are injected at the top opening, with a downwards velocity of 0.1 m/s (a.)). b.) shows the final state of the filling process with 4 578 816 particles and a mass of 36 161 kg.*

2.2. Reactive model

The reactive model is based on the shaft furnace model by Spijker & Pollhammer (Spijker, 2023), excluding the radiative heat transfer due to the low temperatures. Since the particles in rail transport container represent a fixed bed, the particle positions were fixed to increase in numerical efficiency.

2.2.1. Modelling the discrete phase

2.2.1.1. Reaction model

The reaction model is based on the look up-table (Fig. 7) from the experimental results. Based on a 2D linear interpolation the specific reaction rate rr_s for oxygen is determined from the temperature and the relationship between the mass fractions of oxygen in the gas phase and oxidized iron in the particle. From the specific reaction rate rr_s the reaction rates for oxygen rr is calculated, based on the particle surface (Eq. 4). Here d_p represents the particle diameter. The experiments were preformed to with crack free particles. Since DRI particles could crack during production and handling the dimensionless multiplicator F is used to increase the reactive surface. Based on this reaction rate, the change of particle mass m_p (Eq. 5) and mass fractions $Y_{Fe,p}$ and $Y_{FeO,p}$ (Eq. 6,7) can be computed, where *M* represents the molar mass. The volume of the particle stays constant during the reaction and the density increases.

$$rr = rr_s \, {d_p}^2 \pi * F \tag{4}$$

$$\frac{\partial m_p}{\partial t} = rr \tag{5}$$

$$\frac{\partial Y_{FeO,p}}{\partial t} m_p = rr \frac{M_{FeO}}{M_O} \tag{6}$$

$$\frac{\partial Y_{Fe,p}}{\partial t} m_p = -rr \frac{M_{Fe}}{M_O} \tag{7}$$

2.2.1.2. Energy and heat transfer

The Biot numbers observed for the particles during the self-heating process are lower than 0.011, so the temperature gradient inside the particle could be neglected. The energy equation (Eq. 8) could be formulated by the particle mass m_p and the heat capacity $c_{p,p}$ as function of the on the particle temperature T_p. Here $S_{r,p}$ is the source term for the heat of reaction, due to reoxidation, $S_{kond,pp}$ the heat transferred by particle-particle heat conduction and $S_{kond,pw}$ the conducted heat between the particles and the walls. The heat transfer between the particles and the gas phase $S_{konv,p}$ is modelled by the approach of Gunn (Gunn, 1978).

$$\frac{\partial T_p}{\partial t} m_p c_{p,p}(T_p) = S_{r,p} + S_{kond,pp} + S_{kond,pw} + S_{konv,p} \quad (8)$$

To model the conductive heat transfer between the contacting particles and particles contacting the walls, the approach of Zhang et al. (Zhang, 2007) was used. Based on the particle forces the area of the overlap A_{pp} between particles and A_{pw} contact area with the wall are computed. Since the particle positions are fixed, the computation of the contact areas is only necessary at the start of the simulation. With these areas the heat flux can be calculated using the thermal resistance R_{th}, the temperature of the particles $T_{p,i}, T_{p,j}$ and the temperature of the wall T_w.

$$S_{kond,pp,i} = -\frac{A_{pp}}{R_{th}}\left(T_{p,i} - T_{p,j}\right) \quad (9)$$

$$S_{kond,pw,i} = -\frac{A_{pw}}{R_{th}}\left(T_{p,i} - T_w\right) \quad (10)$$

The heat source of the reaction $S_{r,p}$ in modelled by the reaction rate, standard enthalpy of reaction h_r^0, heat capacities $c_{p,Feo}, c_{p,Fe}, c_{p,O2}$, particle temperature T_p and the standard temperature T_0.

$$S_{r,p} = rr\left(\int_{T_0}^{T_p} c_{p,Feo} - c_{p,Fe} - c_{p,O2} dT + h_r^0\right) \quad (11)$$

2.2.2. Modelling the gas phase

2.2.2.1. Flow

The rail transport box is only filled partially with particles. Therefore, the momentum equation (Eq. 12) must differentiate between the packed bed and the free fluid flow. If the volume fraction ε is smaller than 0.9 the viscos term S_μ is modelled for a packed bed, using the Ergun equation (Eq. 13). Otherwise, the viscos term for a laminar flow is used (Eq. 14). Here $\vec{u}$ is the velocity vector of the gas phase, ε the gas phase volume fraction, ρ presents the density, modelled by the ideal gas equation, under consideration of the chemical composition. The pressure is represented by p and dynamic viscosity by η. Since the particle in a cell have different diameters, the Sauter mean diameter $\overline{d_p}$ for the particles of each cell are calculated. To solve this momentum equation in conjunction with the continuity the PIMPLE algorithm (OpenFOAM, 2018) is used.

$$\frac{\partial(\rho\varepsilon\vec{u})}{\partial t} + \vec{u}\nabla(\rho\varepsilon\vec{u}) + S_\mu = -\nabla(p\varepsilon) + \rho\varepsilon g \quad (12)$$

$$S_\mu = \left[150\frac{(1-\varepsilon)^2}{\varepsilon^3}\frac{\eta\vec{u}}{{d_p}^2} + 1.75\frac{(1-\varepsilon)}{\varepsilon^3}\frac{\eta\vec{u}|\vec{u}|}{\overline{d_p}}\right]\frac{1}{\varepsilon(1-\varepsilon)} \quad (13)$$

$$S_{\mu} = \eta\nabla^2(\varepsilon\vec{u}) + \frac{1}{3}\eta\nabla \quad (\nabla\varepsilon\vec{u}) \tag{14}$$

2.2.2.1. Species

The species equation (Eq. 15) considers convective and diffusive transport of the oxygen mass fraction, represented by Y_i under consideration of the gas phase volume fraction ε. The diffusivity is calculated by the viscosity η and the Schmidt number Sc. The source term for the heterogeneous reaction $S_{p,Yi}$ is modelled by the negative sum of the particle reaction rates in a cell.

$$\frac{\partial(\rho\varepsilon Y_i)}{\partial t} + \vec{u}\nabla(\rho\varepsilon Y_i) - \nabla\left(\frac{\eta}{Sc}\varepsilon\nabla Y_i\right) = S_{p,Yi} \tag{15}$$

2.2.2.1. Energy

The energy equation (Eq. 16) is formulated for the enthalpy h. To compute the temperature from the enthalpy the temperature dependent heat capacity formulation using the JANAF (NIST, 1998) polynomial formulation is used. The thermal conductivity is determined by the temperature dependent viscosity η and the Prantl number Pt. The heat transfer between the phases is calculated on the particle side by the model of Gunn (Gunn, 1978). The negative sum of the heat flux of the particles in a cell is represented by the source term $S_{konv,g}$.

$$\frac{\partial(\rho\varepsilon h)}{\partial t} + \vec{u}\nabla(\rho\varepsilon h) - \nabla\left(\frac{\eta}{Pt}\varepsilon\nabla h\right) = S_{konv,g} \tag{16}$$

2.2.3. Evaluation of the reactive model

The model for the flow and particle-particle heat conduction where already evaluated by Pollhammer (Pollhammer, 2019). To evaluate the reactive model, a simple geometry with the volume of the circular loop reactor (Fig. 3) was created. Four particles, with identical diameter to the measurements are inserted in this volume. Because the differential loop reactor operates isothermal, with a certain flow, a cell zone with fixed temperature and velocity was created. This cell zone is marked in Fig. 3 with the green box. In the initial state the reactor is filled with 20 vol.-% oxygen at atmospheric pressure and the particles consist of pure iron.

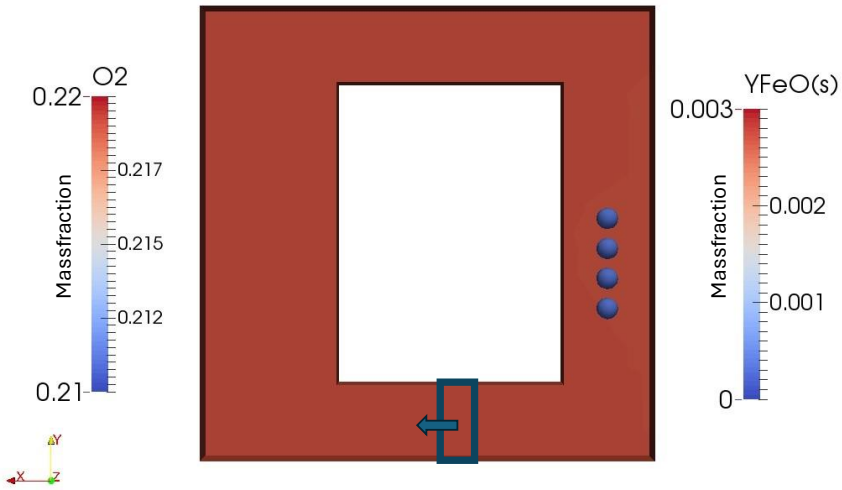

Fig. 3. *Geometry and initial state of the evaluation for the reactive model. The particles are containing no oxides and the gas has an oxygen concentration of 20 vol.-%. The box represents the zone, where velocity and temperature are fixed, to achieve similar conditions to the differential loop reactor.*

To evaluate the model, the experiments at 60 °C and 85 °C were modelled for $1{,}6 \cdot 10^5$ seconds and the oxygen concentration over time was compared to the experiment. Fig. 4 shows the comparison for a temperature of 60 °C. The model has a slightly higher reaction rate than shown in the experiment. The same behaviour could be observed at 85 °C.

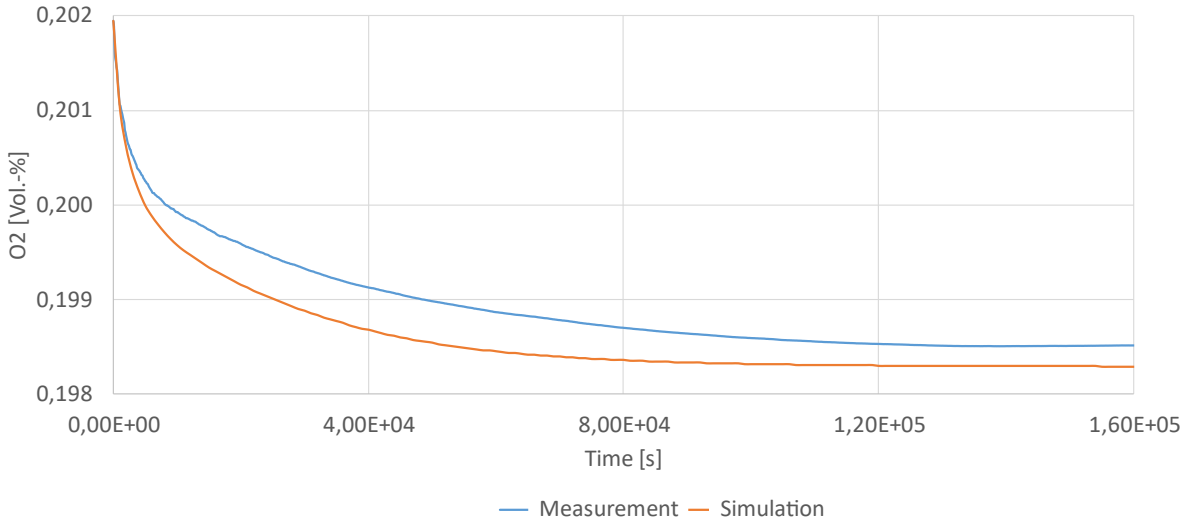

Fig. 4. *Comparison for the oxygen concentration as function of time between the model and the experiment at 60 °C the model sightly overpredicts the oxygen consumption.*

3. Case studies

Based on the development model, 7 cases studies where preformed, to characterize the behaviour of direct reduced iron in the rail transport container. The case 0 represents the patented rail transport container. The other cases differ in the openings of the rail transport container, to study the oxygen delivery by natural convection. The oxidation from iron to wuestite (FeO) has a standard enthalpy of reaction of 3 786 kJ/kg oxygen, representing the main reaction. In conjunction with moister in the air ferrous hydroxide could be formed. Here the standard enthalpy of reaction is 7 920 kJ/kg oxygen. To investigate the effect of higher reaction enthalpies, the value was doubled to 7 572 kJ/kg. Since DRI pellets could have cracks from production or handling, The reactive surface was increased by setting the dimensionless multiplicator *F* for certain cases to 2.

Table 2*. List of computed cases*

Case number	**Top opening**	**Bottom opening**	**Enthalpy of reaction (h_r^0)**	**Dimensionless multiplicator** (*F*)
0	None	None	7 572 kJ/kg	2
1	Large	None	3 786 kJ/kg	1
2	Large	Center	3 786 kJ/kg	1
3	Small	None	3 786 kJ/kg	1
4	Large	None	7 572 kJ/kg	2
5	Small	Side limited	7 572 kJ/kg	1
6	Small	Side limited	7 572 kJ/kg	2

3.1. Geometries

The oxygen, necessary for the reoxidation is transported in the container by natural convection. To study this process two different top and bottom openings are included in the geometry. The large top opening (Fig. 5 a.)) represents the rail transport container without a lid and the small with a partially closed lid (Fig. 5 b.)). Rail transport containers could also have gravity unloading ports in the bottom, to represent these, a middle (Fig. 5 c.)) and a side opening (Fig. 5 d.)) where included.

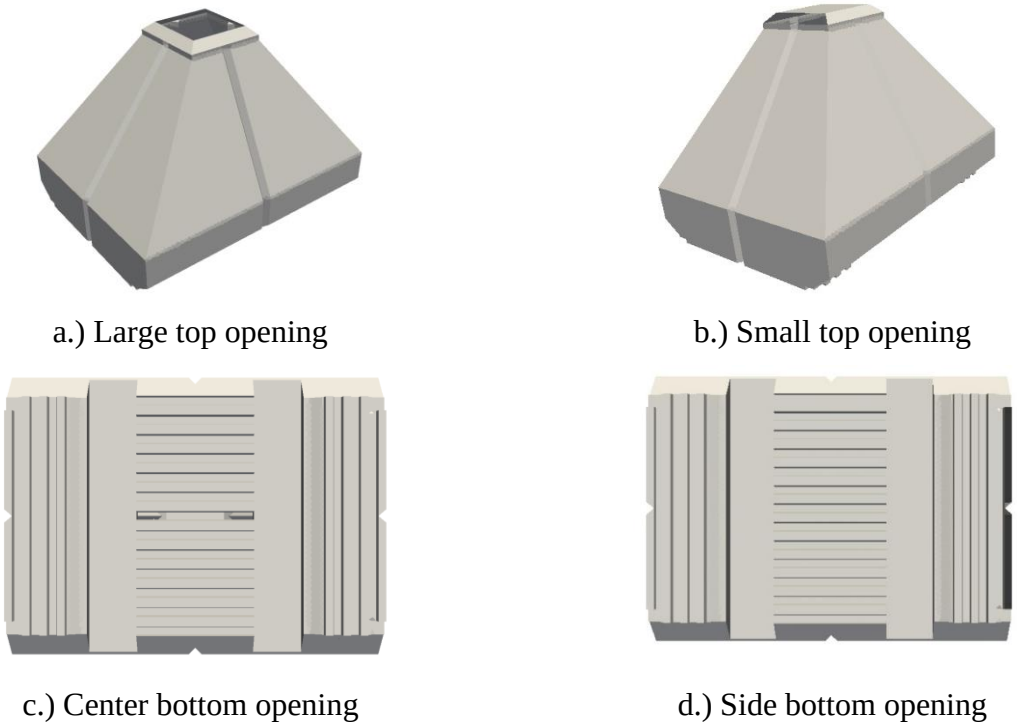

a.) Large top opening b.) Small top opening

c.) Center bottom opening d.) Side bottom opening

Fig. 5. *Openings for the surrounding atmosphere for natural convection. The large top opening a.) represents the rail transport container without a lid, b.) the small top opening a not fully closed lid. The openings in the bottom (c.), d.)) where introduced to study the effect of a bottom outlet for granular material.*

3.2. Initial- and boundary conditions

All cases are based on the same initial conditions. At the start of the simulation the particles consist of pure iron and have a uniform temperature of 60 °C. This represents the highest temperature where the cold transport of DRI is allowed. The gas phase is also initialized with 60 °C, 23 m.-% (21 vol.-%) oxygen and no flow velocity. The pressure was initialized with a height based linear profile form 100 031 Pa at the bottom to 100 000 Pa for modelling the natural convection. The assumption was made that the air, surrounding the container, has a constant temperature of 30 °C. Therefore, the temperature of the openings was set to 30 °C and 23 m.-% (21 vol.-%) oxygen. To model the natural convection the height based pressure profile was applied. The heat flux of the walls is modelled by the thermal resistance of the steel from the rail transport container in combination with a heat transfer coefficient. This heat transfer coefficient representing the cooling by natural convection outside with an ambient air temperature of 30 °C.

4. Results

4.1. Experimental results

For isothermal measurements at 60, 110 and 160 °C the oxygen consumption is shown in Fig. 6. The temperature dependence of the oxygen consumption can clearly be seen. The experiments were stopped after a maximum was visible, which was at 1.51, 3.63 and 9.15 g O_2/kg DRI for respectively 60, 110 and 160°C.

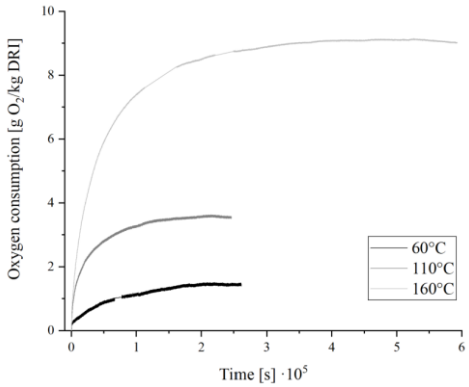

Fig. 6. *Isothermal oxygen consumption of five H-DRI pellets (Hohenberger 2024)*

According to Landolt (Landolt, 2007) low temperature oxidation kinetics will have a logarithmic trend if the film growth is limited by exchange of ions because of electron tunnelling. Oxygen ions are diffusing through the oxide layer, where a typical film thickness is around 2-3 nm. A linear film growth is detected if the oxide layer is porous and not uniformly distributed. At higher temperatures a parabolic trend displays that the limiting process is the ion diffusion of the iron cations through the oxide layer. The measured oxygen consumption from Fig. 1 cannot be described by a mathematical function overall. However, if the data is divided into time intervals a good mathematical description is possible, as can be seen in Table 1. There 3-4 stages can be identified, which can also be found in the Literature (El-Geassy, 1994). At higher temperature the time period of the stages become smaller.

Table 3*. Rate laws for the oxygen consumption of dry reoxidation of H-DRI pellets (Hohenberger 2024)*

60°C	**Time interval [h]**	**Rate law**	**R^2**
1. Stage	0.00 – 1.70	Logarithmic	0.842
2. Stage	1.70 – 6.78	Linear	0.913
3. Stage	6.78 – 49.4	Logarithmic	0.983
110°C			
1. Stage	0.00 – 1.66	Parabolic	0.991
2. Stage	1.66 – 3.35	Linear	0.965
3. Stage	3.35 – 34.1	Logarithmic	0.996
160°C			
1. Stage	0.00 – 0.778	Parabolic	0.997
2. Stage	0.778 – 1.97	Linear	0.995
3. Stage	1.97 – 11.3	Logarithmic	0.999
4. Stage	11.3 – 164	Logarithmic	0.998

As input data for the simulation experiments were done additionally at lower temperatures, namely 60, 85 and 110 °C. As the there was no overall mathematical function a 3D-look up table was used, to compute specific reaction rate rr_s , as a function of the temperature and the wuestite (FeO) - oxygen relation. In Fig. 7 the data of the table is presented by a surface grid. The blue points represent the measurements at 110 °C, the yellow 85 °C and the orange 60 °C. Additionally, a curve at 0 °C (purple points) representing a reaction rate of 0 was introduced to create the table.

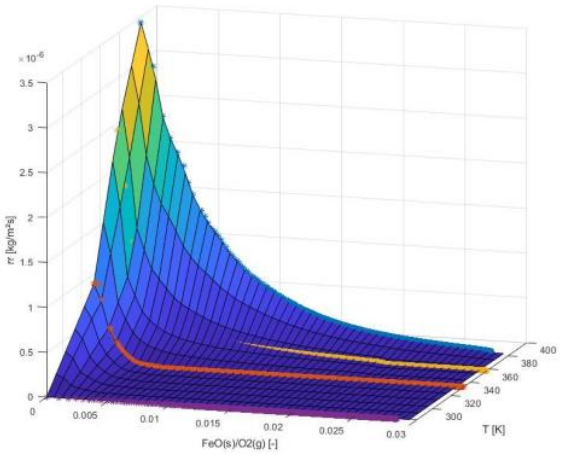

Fig. 7. *Look-up table to calculate the specific reaction rate rr_s as function of temperature and the wuestite - oxygen relation for the numerical model. The experimental data is shown by the blue crosses for 110 °C, the yellow crosses for 85 °C, the orange crosses for 60 °C and the purple crosses represents 20 °C, where no reaction could be observed.*

4.2. Case 0

This case represents the patented rail transport container, totally sealed under worst case assumptions. The dimensionless multiplicator F was set to 2, to represent particles with doubled reactive surface due to cracks and doubled enthalpy of reaction, assuming the iron hydroxide reaction with an unlimited supply on water vapor. The oxygen is consumed, down to a level, where the reaction rates are so low, that the heating by reoxidation is insignificant. During the consumption of the oxygen the temperature rises 3 K. Then the container cools slowly by the heat loss of the walls. In all cases, the temperature difference between the gas and particle phase is minimal.

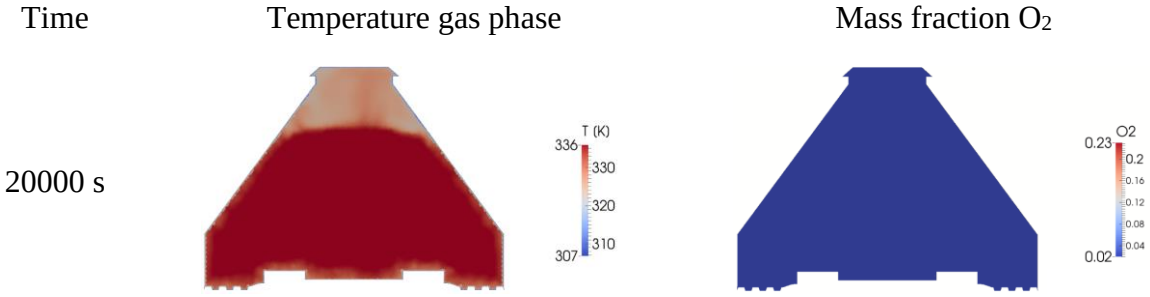

Fig. 8. *Temperature and oxygen mass fraction at different times for the case 0.*

4.3. Case 1

This case represents the rail transport container with an open lid. Due to the difference between the temperature at the opening and the initial particles particle temperature a natural convection patter evolves. The particles consume the oxygen, and the natural convection introduces oxygen into the

packed bed. When the mass fraction of wuestite (FeO) in the particles increase, the reaction rate decreases and more oxygen in available in the packed bed (Fig. 9). Due to the slowed reaction and the cooling by convention, the particles reach a stable temperature after 18 200 s. The reoxidation of the particles around the center is higher due to more available oxygen (Fig. 10). It can also be observed that the particles near the walls are cooler and get less oxidized.

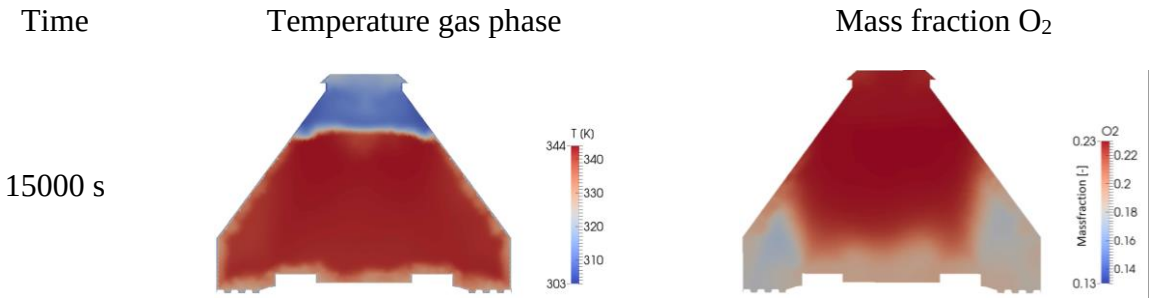

Fig. 9. *Temperature and oxygen mass fraction at different times for the case 1.*

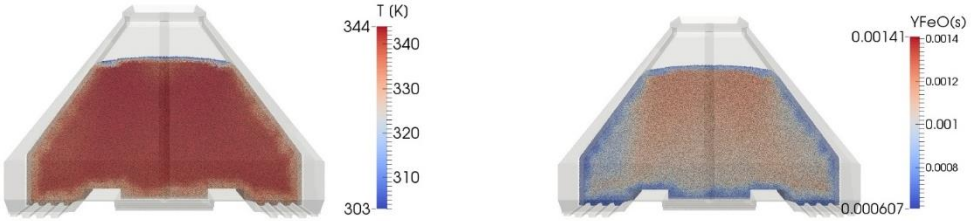

a.) Temperatures of the particles

b.) Mass fraction FeO of the particles

Fig. 10. *Temperature (a.)) and wuestite mass fraction (b.)) of the particles at 18 200 seconds for the case 1.*

4.4. Case 2

In this case the influence of an opening in the bottom in conjunction with an open lid is studied. Due to natural convection, a straight flow pattern from the bottom to the top evolves. This pattern is cooling the particles near the bottom opening and the oxygen is distributed evenly. Due the high flowrate the particles are cooled and no significant heat up can be noticed, decides the oxidation of the particles. The system reaches a stable maximum temperature after 2 000 seconds. The highest particle oxidation and particle temperatures occur near the bottom, between the wall and the opening (Fig. 12). Directly at the opening, the particles oxidize less, due to the lower temperatures.

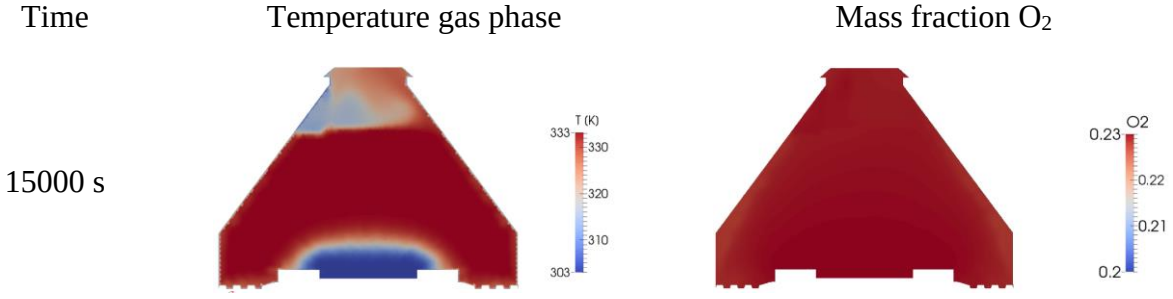

Fig. 11. *Temperature and oxygen mass fraction at different times for the case 2.*

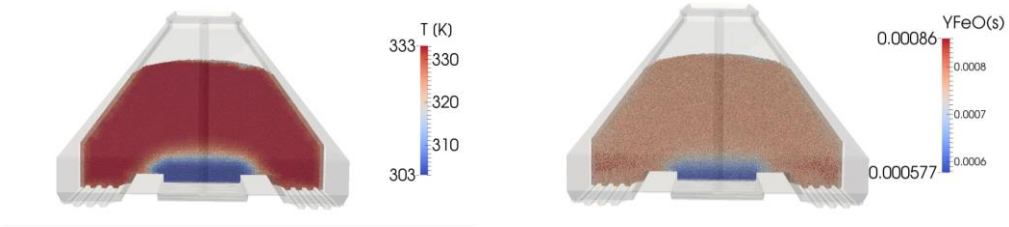

a.) Temperatures of the particles

b.) Mass fraction FeO of the particles

Fig. 12. *Temperature (a.)) and wuestite mass fraction (b.)) of the particles at 15 000 seconds for the case 2.*

4.5. Case 3

This case studies the behavior of the rail transport container, when there is a small gap in the lid. Even with the small gap, a flow by natural convection evolves. The cooler air enters at the sides of the gap and flows down near the wall. The warmer air leaves the container in the middle of the gap. This is a highly transient process. The oxygen concentration is one sided increased (Fig. 13) and leading to higher oxidation and heat up near the middle. The air entering the container has a cooling effect. Due to lower oxygen concentrations the oxidation process is slower, but reaches a maximum particle temperature of 342 K. Case 1 with the fully open lid, reaches 344 K.

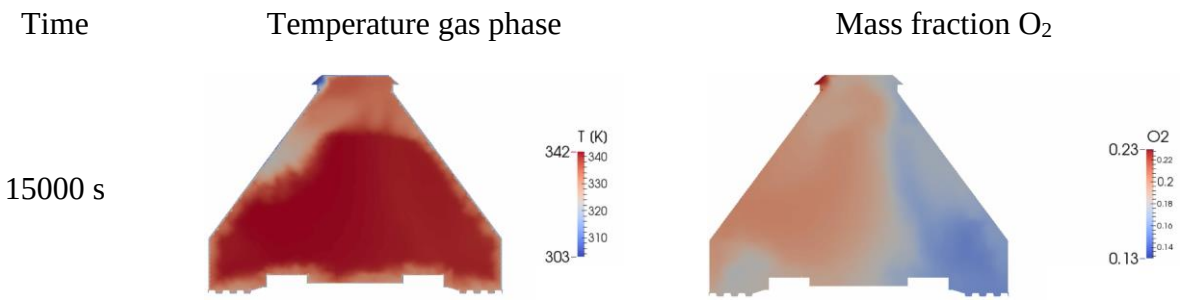

Fig. 13. *Temperature and oxygen mass fraction at different times for the case 3.*

4.6. Case 4

The case 4 presents the setup of case 1 with a dimensionless multiplicator (*F*) of 2, doubling the reaction rate and the doubled enthalpy of reaction. In the beginning, the oxygen is consumed, locally down to 15 m.-% and the particles heat up, increasing the natural convection. At 5 000 seconds large parts of the rail transport have oxygen levels over 22 m.-% and the particle heated uniformly to 355 K (Fig. 14). This increases the natural convection effect, where the flow rises in the center and goes down near the wall, cooling the particles. At 10 600 seconds, 110 °C are reached and the reaction rate is limited due to the model approach by the look-up table. The temperature is still increasing, this case shows the first thermal runaway.

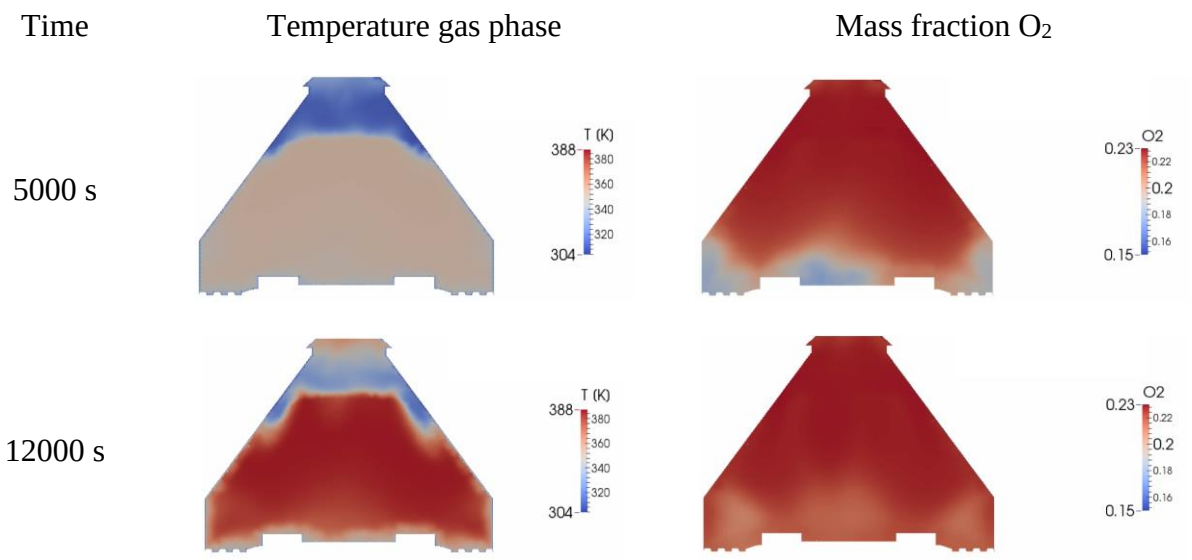

Fig. 14. *Temperature and oxygen mass fraction at different times for the case 4.*

4.7. Case 5

In this case the influence of small openings at the button and top a with dimensionless multiplicator F of 2, doubling the reactive surface and the doubled enthalpy of reaction are investigated. The evolving flow pattern consists of cooler air enters at the sides of the gap and flows down near the wall and an uprising flow from the bottom gap along the opposite wall. Due to the high reaction rates and small openings, the oxygen level in the container drops lowering the reaction rate. Two hot spots form, one near the bottom opening and one in the recirculation zone. The maximum temperature in these regions is constantly increasing, showing a thermal runaway behavior. Due to the limitation in oxygen, the temperature rise is slower than in case 4.

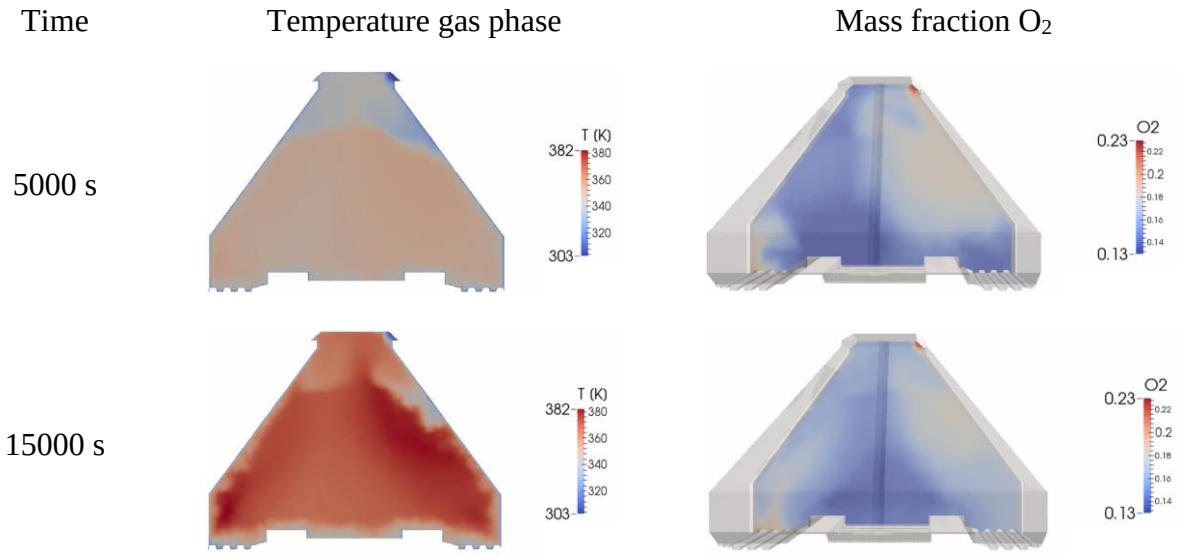

Fig. 15. *Temperature and oxygen mass fraction at different times for the case 5.*

4.8. Case 6

This case is like the case 5, but the dimensionless multiplicator F of 1 is used, representing the particles without cracks. The evolving flow pattern is similar to case 5, cooler air enters at the sides of the gap and flows down near the wall and an uprising flow from the bottom gap along the opposite wall. Also, the hot spots develop in the same regions, but to the lower reaction rates slower.

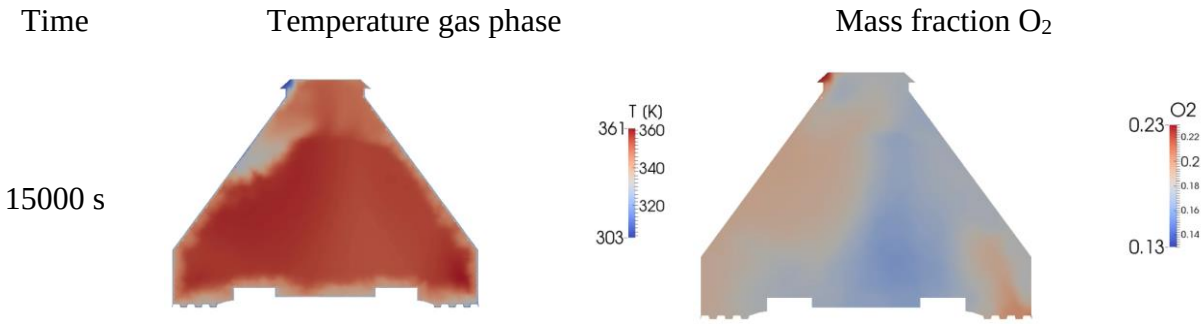

Fig. 16. *Temperature and oxygen mass fraction at different times for the case 6.*

5. Discussion

Fig. 17 shows the development of the maximum temperature as function of time for the different cases. In the cases 4-6, where the transport container has openings and the iron hydroxide reaction is assumed, a thermal run away can be observed. Case 0, the fully sealed container, shows under the same conditions just a heat up of 3 K due to oxygen starvation. Case 5 differs from case 6 by a doubled reactive surface due to cracks. Here it can be observed that the double surface are increases the speed of heat up, more than twice. This is based on the stronger convection. The position and size of the hot spots depends on the openings, due to the flow pattern. The container with the open lid (case 4) shows the hot spot in the upper centre and has the fastest heat-up. The geometry with the side openings at the top and bottom (case 5 and 6) shows two hot spots based on the available oxygen. The restriction in oxygen concentration leads also to a slower heat up. Also, Cases 1-3 with the heat of reaction for wuestite, show different heating behaviours, based on the openings in the container. In these cases, a heat-up of the DRI particles up to 11 K could be observed. The cooling by natural convection due to an opening in the bottom, could lower the maximum temperature in case 2, but is based on ambient and particle temperature.

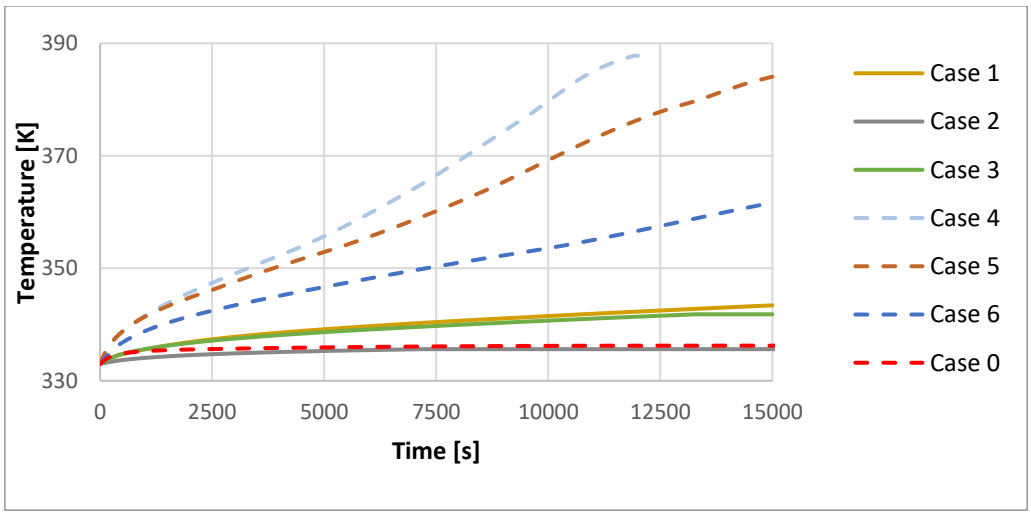

Fig. 17. *Comparison of the maximal particle temperatures over time. The cases with the dotted line, represents the increased heat of reaction.*

6. Conclusions and outlook

The combined approach of reaction kinetic measurements in the differential loop reactor and applying them to a reactive packed bed model for modelling self-heating an established method (Wallner 2003, Kern 2013). The novelty of the present approach is to use an CFD-DEM model, instead of a Eulerian CFD approach. This model has the advantage of better implemented physics. The heat conductivity is based on the actual particle forces and the flow resistance is modelled, based on the local particle packing. In the presented work, the reaction kinetics for the iron hydroxide reactions couldn't be determined in the laboratory tests. Therefore, the heat of reaction was increased to model the hydroxide reactions where an unlimited supply on water vapor assumed. DRI particles could crack during manufacturing and handling, to approximate this effect, the reactive surface was increased. Both changes were applied to create a worst case scenario. The cases how consider the oxidation from iron to wuestite (FeO), show a self-heating behaviour, but no thermal run away. The cases with the assumed iron hydroxide formation showed a thermal run-away behaviour, except the fully sealed rail transport container. Smaller openings in the container can introduce enough oxygen for the oxidation by iron hydroxide reaction. The presented studies don't consider the pressure difference on an opening for variation speeds of the rail transport container during transport. This could lead to an increased oxygen concentration inside the container. Also, different ambient and particle temperatures lead to convective flows and oxygen concentrations in the container, so a gravity unloading port could become problematic, when not sealed tightly. This leads to the conclusion that the container for the transport of DRI should be as tightly sealed as possible, to supress the reoxidation doe to oxygen starvation. Other methods like cooling by natural convection, are based on parameters that can't be influenced and vary strongly on rail transport.

The presented work investigated the self-heating behaviour only on one type of H-DRI. The tendency for reoxidation could differ between ore types and manufacturing methods and ores. Also, lager geometries have a higher tendency for self-heating. In the future measurements of different types of DRI, including the hydroxide reactions in the differential loop reactor are planned, to create a kinetics database for modelling the self-heating of storage facilities and transport methods.

Acknowledgements

FFG funding and services enable this innovative project with partners between science and industry. FFG funding programs are financed by the Republic of Austria - specifically the Federal Ministry for Climate Protection, Environment, Energy, Mobility, Innovation and Technology (BMK) and the Federal Ministry of Labor and Economic Affairs (BMAW) - but also by participating federal states as well as companies and research organizations. www.ffg.at

References

Bhaskar, A., Assadi, M. & Somehsaraei, H. (2019). Lowering the carbon footprint of steel production using hydrogen direct reduction of iron ore and molten metal methane pyrolysis. Preprints 2019, doi: 2019100107.

Cavaliere P. (2019), Clean Ironmaking and Steelmaking Processes, Springer Nature Switzerland AG, https://doi.org/10.1007/978-3-030-21209-4_8

Cedre, (2007), ULR: https://wwz.cedre.fr/en/Resources/Spills/Spills/Adamandas, referenced 25.11.2023

Chase M. W., Jr. (1998) NIST-JANAF Thermochemical Tables. Washington, DC : New York ,American Chemical Society, American Institute of Physics for the National Institute of Standards and Technology

Cundall P. A., Strack O. D. L. (1979), A discrete numerical model for granular assemblies, Geotechnique 29 , 47–65.

El-Geassy, A. A., El-Kashif, F.O., Nasr, M.I., Omar, A.A., (1994). Kinetics and Mechanisms of Re-oxidation of Freshly Reduced Iron Compacts. ISIJ International, Vol. 34, No.7, pp. 541-547.

Fernando O. Boechat et. al. (2018), Simulation of Mechanical Degradation of Iron Ore Pellets in a Direct Reduction Furnace, KONA Powder and Particle Journal 35

Gunn, D. J., (1978) Transfer of heat or mass to particles in fixed and fluidised beds. International Journal of Heat and Mass Transfer, 21(4):467–476, 1978. ISSN 00179310. doi: 10.1016/0017-9310(78)90080-7

Hohenberger, M., (2024). Working Title: Experimental investigarion of the reaction kinetics of hydrogen-reduced iron pellets as a basis for fire and explosion safety measures. PhD-Thesis, Montanuniversität Leoben, Leoben.´

International Maritime Organization (2009), International Maritime Solid Bulk Cargoes (IMSBC) Code

Landolt, D., (2007). Corrosion and Surface Chemistry of Metals. First Edition, EPFL Press, Lausanne, ISBN: 978-2-940222-11-7.

OpenFOAM Foundation, (2018), URL: https://openfoam.org/version/6/, referenced 13.06.2019

Pollhammer W. R. (2019), A CFD-DEM model for nitrogen oxide prediction in shaft furnaces using OpenFOAM, Ph.D. Thesis, Montanuniversitaet Leoben

Rosin, P. and Rammler, E. (1933) The Laws Governing the Fineness of powdered coal. Journal of the Institute of Fuel 7, 29-36.

Schanner, R., (2023), Österreichische Patentanmeldung, patent AT 52868

Spijker, C., Pollhammer, W. and Raupenstrauch, H. (2023), CFD-DEM Modeling of Shaft Furnaces Using the Volume Fraction Smoother Approach. Chem. Eng. Technol., 46: 1333-1339. https://doi.org/10.1002/ceat.202200617

Szekely, J., Evans, J.W., Sohn, H.Y., 1976. Gas-Solid Reactions. Academic Press, New York, ISBN: 0-12-680850-3.

Zhang X., Cong P., Fujiwara S., Fujii M. (2007), Analysis of heattransfer between two particles for DEM simulations, presented at the12th International Conference on Fluidization,Vancouver

Enhancing safety in the storage of hazardous molecules: the case of hydroxylamine

Giuseppe Andriani [a], Paolo Mocellin [a], Gianmaria Pio [b], Chiara Vianello [a] & Ernesto Salzano [b,*]

[a] Università degli Studi di Padova. Dipartimento di Ingegneria Industriale. Padova, Italia.
[b] Università di Bologna. Dipartimento di Ingegneria Civile, Chimica, Ambientale e dei Materiali. Bologna, Italia.

E-mail: ernesto.salzano@unibo.it

Abstract

When handled in large quantities, like in storage vessels, species prone to thermal decomposition can lead to severe accidents triggered by runaway reactions. Hence, developing an inherently safe design strategy for storage equipment can enhance the reliability of a chemical plant, avoiding the establishment of undesired scenarios. The Frank-Kamenetskii theory (FKT) of self-heating provides practical tools for implementing a design procedure to consider phenomena potentially leading to uncontrolled chemical reactions. The present work proposes a procedure based on the FKT for an intrinsically safe storage vessel design. An expanded version of the FKT involving the parametric sensitivity analysis has been formulated to enhance the reliability of the method. Besides, to understand the self-heating phenomena, a stability diagram was produced relating the main design parameter (i.e., the critical value of the Frank-Kamenetskii number) and the dimensionless activation energy (γ). In addition, the adopted design strategy integrates a procedure for the design of relief systems, to reduce the risk of equipment explosion due to the onset of runaway scenarios. To elucidate the applicability of the procedure, the developed design strategy of storage equipment and relief systems was tested for the case of: (I) an aqueous solution containing 50 %w hydroxylamine (HA) and (II) a 50 %w HA aqueous solution added with 1 %w of an HA-derived salt, the hydroxylamine hydrochloride. Results show that, for large γ values, the traditional formulation of the FKT and the developed expanded theory practically allow the design of vessels with the same characteristic dimension. On the contrary, for a finite value of γ (i.e., $\gamma \leq 100$), the proposed refined version of the FKT allows the design of less conservative storage equipment. Regarding the relief systems, coupling the DIERS and standard procedures provides a more versatile and consistent protocol. Eventually, for large storage vessels, the possibility of adding relief systems to the equipment can not be taken as an option due to the too-large venting area required in the case of runaway reactions. In this case, an intrinsically safe vessel is the only practicable solution to avoid the occurrence of devastating incidents.

Keywords: *Storage vessels; Process safety; Stability diagrams; Thermal decompositions; Runaway reactions.*

Nomenclature

Symbols

A_{gas}	Gas orifice area determined with DIERS method	$\dot{P}_{peak}$	Temporal pressure rate at peak conditions
A_{vap}	Vapour orifice area determined with DIERS method	P_{onset}	Onset pressure
A_{tot}^{DIERS}	Total orifice area determined with DIERS method	P_{relief}	Relief pressure
A_{tot}^{std}	Total orifice area determined with standard method	PM	Molecular weight of mixture
ARSST™	Advanced reactive system screening tool	PM_{gas}	Molecular weight of gas
Bi	Biot number	PM_{vap}	Molecular weight of vapour
C	Fluid flow coefficient	PM_w	Molecular weight of water
C_{A0}	Initial molar concentration of the main reactant A	QRA	Quantitative risk assessment
$\tilde{C}_p$	Heat capacity per unit moles of the liquid mixture	R_g	Universal gas constant

$\hat{C}_p$	Heat capacity per unit mass of the liquid mixture	$\mathcal{R}\|_{T_w,C_{A0}}$	Reaction rate at wall temperature and initial main reactant concentration
$\tilde{C}_{p,w}$	Heat capacity per unit moles of water	r_w	System radius
D	System diameter	$S(\Theta;\delta)$	Normalized sensitivity of Θ to the respect of δ
d	Diameters ratio	$\mathcal{T}$	Dimensionless time
D_{valve}	Valve diameter under the assumption of circular orifice	T_{center}	Temperature in the centre of the system
DIERS	Design Institute for Emergency Relief Systems	T_{max}	Maximum system's temperature
E_a	Apparent activation energy	T_{onset}	Onset temperature
FKT	Frank-Kamenetskii theory of self-hating	$\dot{T}_{onset}$	Temporal temperature rate at onset conditions
H	System height	T_{relief}	Relief temperature
H/D	Aspect ratio	$\dot{T}_{relief}$	Temporal temperature rate at relief conditions
HA	Hydroxylamine	T_w	Wall temperature
K_b	Backpressure coefficient	t_{cond}	Characteristic time for heat conduction
K_c	Combination factor coefficient	TRA	Thermal risk assessment
K_d	Discharge coefficient	TS^U	Thermal screening unit
$k_{k\infty}$	Apparent Arrhenius pre-exponential factor	V	System volume
k_T	Thermal conductivity of the liquid mixture	V_{gas}^{test}	Gas volume in the test apparatus
$k_{T,w}$	Thermal conductivity of water	VMWT	Varma, Morbidelli and Wu theory
m_{tot}	Initial reactive mass in the test apparatus	VSP2™	Vent size package 2
n	Apparent reaction order	$\dot{W}_{gas}$	Gas required relief mass flow rate

Greek symbols

α_0	Void fraction	$\hat{\lambda}$	Heat of vaporization of the mixture per unit mass
γ	Dimensionless activation energy	ρ	Liquid mixture density
$\Delta\tilde{H}_r$	Molar enthalpy of reaction	ρ_{gas}	Gas density measured at relief conditions
δ	Frank-Kamenetskii number	ρ_w	Water density
δ_{crit}	Critical Frank-Kamenetskii number	χ	Main reactant conversion
Θ	Dimensionless temperature	Ω	Dimensionless radial coordinate
Θ_{max}	Maximum value of the dimensionless temperature		

Introduction

Exothermic thermal decomposition reactions can induce severe concerns because of the potential occurrence of runaway reactions. Hence, the understanding of the decomposition reaction dynamic is paramount (Deng et al., 2016). To this scope, either experimental or numerical approaches can be adopted. Typically, the experimental studies are based on calorimetric analysis (Pio et al., 2021), aiming at the quantification of apparent reaction kinetic, thermodynamic properties, onset, and peak features (Vianello et al., 2018). The acquired data are commonly used for a quantitative risk assessment (QRA) (Juncheng et al., 2020), a thermal

risk assessment (TRA) (Wang et al., 2009), reactor design and control (Varma et al., 1999) (Strozzi et al., 1999) or for process development (Ozawa, 2000). However, unexpected hazardous scenarios could also arise during storage due to self-heating features (Guo et al., 2013) (Shanley, 1953). Hence, the ideal perspective is to design storage vessels following the inherent safety paradigm (Kletz and Amyotte, 2010) considering the self-heating phenomenon and avoiding accidental runaway of the stored mass.
From a numerical perspective, the Frank-Kamenetskii theory of self-heating (FKT) is usually employed to investigate the behaviour of spontaneous self-heating phenomena potentially leading to hazardous scenarios (Frank-Kamenetskii, 1955). The FKT, a complementary envision of the Semenov theory of thermal explosion, is based on the hypothesis of a quiescent fluid contained in a system with a negligible wall thermal resistance, a $Bi \to \infty$ (Boddington et al., 1983), a $\chi \to 0$ and almost infinite dimensionless activation energy, defined as $\gamma = E_a/R_g T_w$.
The FKT allows the design of a storage system suitable to avoid ignition or explosion (Babrauskas, 2003). For liquids, the assumption of a stored quiescent fluid is legitimate since, even if temperature gradients can induce natural convection, the average fluid velocity is practically equal to zero (Campbell, 2015). In addition, the vessel will be conservatively designed because natural convection, even if almost absent, will help to dissipate heat (Novozhilov, 2017) (Lazarovici et al., 2005).
Considering a conductive static fluid, assuming that a $Bi \to \infty$ can be easily verified without compromising the modelling outcomes. Moreover, the hypothesis of $\chi \to 0$ is totally realistic because the storage vessel must be designed to avoid the material stored undergoing a fully developed decomposition reaction, accepting only a negligible consumption due to collateral effect. Whereas the assumption that $\gamma \to \infty$ could lead to misleading conclusions because it could be verified only for $E_a \to \infty$ or $T_w \to 0$. The former statement can be related to unphysical scenarios, whereas the latter is to temperatures not reachable in the standard industrial practice during conventional storage. For these reasons, it could be better to investigate the dependence of the modelling outcomes on the values of γ, to avoid misleading conclusions.
To overcome the possible limitations to the applicability of the FKT, it is recommended to expand the theory considering the effect of γ on the primary variable involved in the storage vessel design: the critical value of the Frank-Kamenetskii number (δ_{crit}). Considering that the δ_{crit} is a a meta-stable value, above which a steady-state solution for a particular system becomes impossible to reach due to runaway phenomena, the idea is to retrieve the δ_{crit} for a series of γ values, performing a sensitivity analysis (Andriani et al., 2024a). In this sense, the sensitivity analysis can be seen as applying the bifurcation theory to the chemical reactive system (Lengyel and West, 2018). More specifically, the δ_{crit} value can be defined as a system meta-stable parameter above which the system behaviour deviates from stable to unstable. A $\delta - \gamma$ stability diagram will report the functional dependence of δ_{crit} to the respect of γ with a safe to runaway transition curve. Under the limit curve, it is possible to retrieve the combination of parameters that allows the storage of the material in a stable way, and above the curve will be reported the enable of parameters' combination able to trigger a runaway scenario. Eventually, the $\delta - \gamma$ stability diagram can be used to assess, for a particular value of γ, the δ_{crit} number to involve a more refined storage vessel design.
Even if inherent safety is fundamental for a correct design, passive and active protective items can be added to the equipment to keep hazards under control (Kletz, 2003). More specifically, relief devices can help avoid explosions and reduce potential losses related to runaway reactions (Singh, 1994). Moreover, because reactors and storage vessels are the equipment usually involved in accidents (Ho et al., 1998), proper-sized relief systems are strongly recommended.
In the light of these considerations, the present work proposes a reproducible methodology for the intrinsically safe design of storage vessels containing thermally unstable components. Stability diagrams will be produced and adopted as a support for the design procedure. To test the reliability of the proposed strategy, the procedure will be applied to the case of a 50 %w aqueous solution of hydroxylamine (HA) and 50 %w HA containing an additional 1 %w of hydroxylamine hydrochloride (HH), experimentally investigated in previous studies (Andriani et al., 2024b).Through the comparison with an HA aqueous solution added with HA-derived salt, it will be possible to quantify the effect of salt addition on the thermal stability of HA.

1. Materials and methods

For clarity, Figure 1 reports the logical workflow of the proposed methodology. The following sections will elucidate each step presented in Figure 1. More specifically, in Section 2.1. the list of data needed for further implementation of the proposed sizing method of storage vessels and relief systems, handling liquid materials prone to decomposition reactions, is reported. Then, in Section 2.2. the methodology aimed at storage vessel sizing is illustrated, involving the original FKT or information retrieved from the $\delta - \gamma$ stability diagram, obtained improving the FKT and compiling it with the sensitivity analysis. In Section 2.3. the procedure for the sizing of the relief system is elucidated. Eventually, in Section 2.4., the data required to apply the proposed procedure to the case study of the two mentioned hydroxylamine aqueous solutions will be provided.

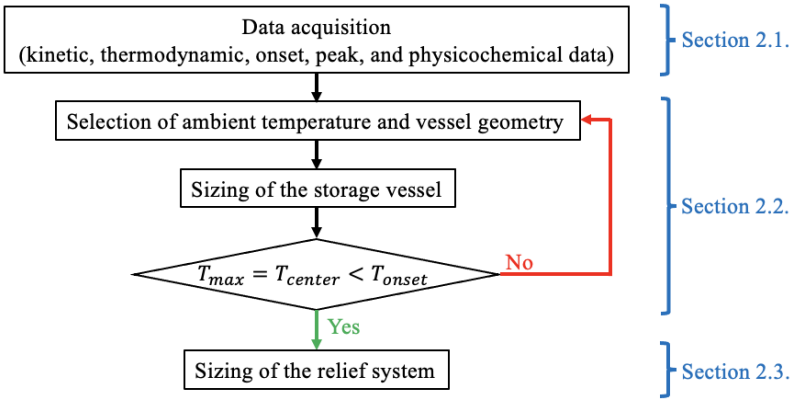

Figure 1. *Logical workflow of the methodology proposed in this work.*

1.1. Data acquisition

As reported in Figure 1, the first step of the proposed method is to acquire the numerical values of the main constitutive variables. The set of the input data is composed of kinetic (E_a, $k_{k\infty}$, n, C_{A0}), thermodynamic ($\Delta\tilde{H}_r$), onset (T_{onset}, $\dot{T}_{onset}$), peak ($\dot{P}_{peak}$) and physicochemical ($\tilde{C}_p$, k_T) information. The mentioned quantities can be determined experimentally via the literature's correlation. For clarity, the meaning of the involved symbols can be retrieved in the Nomenclature Section.

1.2. Sizing of the storage vessel

The governing equation adopted to size the storage vessel is reported in Eq. 1 (Restuccia et al., 2017) based on the definition of the Frank-Kamenetskii number. The ambient temperature was assumed to be equal to T_w, due to the assumption of a negligible thermal resistance of the wall. Three different ambient temperatures will be considered (i.e., 5 °C, 20 °C and 35 °C). The system geometry is considered as a vertically oriented cylindrical storage vessel, thus, a $\delta_{crit} = 2.00$ was assumed, in line with the original FKT (Balakrishnan and Wake, 1996), invariant with γ. The maximum reached temperature in the bulk of the storage vessel will be verified, ensuring that it will be lower than the T_{onset} to avoid any decomposition feature. This verification step can be performed using Eq. 2(Chambré, 1952). This relationship has been adopted starting from the definition of the dimensionless temperature adopted in the FKT (Eq.4), and the maximum dimensionless temperature value reached for $\delta = \delta_{crit}$ (i.e., $\Theta_{max} = \ln 4$).

$$r_{w,crit} = \sqrt{\frac{\delta_{crit}\, k_T\, R_g\, T_w^2}{(-\Delta\tilde{H}_r)\, \mathcal{R}|_{T_w, C_{A0}}\, E_a}} = \sqrt{\frac{\delta_{crit}\, k_T\, R_g\, T_w^2}{(-\Delta\tilde{H}_r)\, k_{k\infty} \exp\left(-\frac{E_a}{R_g T_w}\right) C_{A0}^n\, E_a}} \tag{1}$$

$$T_{center} = T_w + \frac{R_g\, T_w^2}{E_a} \ln 4 < T_{onset} \tag{2}$$

Then, V can be calculated by keeping constant H/D. However, this value significantly depends on the nature of the seismic zone where the tank is placed (Myers, 1997), ranging from 0.5 to 2.4. Moreover, a unique value of α_0 can not be retrieved in the literature (Geyer and Wisuri, 2000) because it could vary depending on the application. Thus, the effect of these two degrees of freedom variation has been considered and discussed.

To retrieve the dependence of δ_{crit} on γ, the dimensionless transient heat balance equation for a conductive quiescent fluid, under the assumption of negligible conversion must be considered. Then, performing a sensitivity analysis, the δ_{crit} related to a specific γ, will be found as the characteristic value that maximises the normalised sensitivity $S(\Theta; \delta)$ in the centre of the system (i.e., $\Omega = 0$) at steady-state (i.e., $\mathcal{T} \to \infty$). The sensitivity analysis results can be reported in a $\delta - \gamma$ stability diagram, highlighting δ_{crit} functional dependence to respect γ with a safe to runaway transition curve. For each $\delta > \delta_{crit}$ the system exhibits an unstable behaviour due to the onset of a runaway condition triggered by an uncontrollable self-heating phenomenon that makes a steady state unreachable. For $\delta < \delta_{crit}$ the system can operate safely, reaching a stable, steady state. Moreover, to be able also to ensure that $T_{center} < T_{onset}$, the Θ_{max} value will be reported for each δ_{crit} value. Table 1 reports the various equilibrium characteristics, operational regimes and temperature check needs for different δ values. It is better to underline that the obtained parameters map will have a general meaning applicable to every kind of reactive system for which a storage vessel is intended to be designed.

Table 1. *Equilibrium characteristics, operational regime and requirement for temperature check as a function of different Frank-Kamenetskii number values.*

	Thermal equilibrium	Regime	Check on T_{center}
$\delta < \delta_{crit}$	Stable	Safe	Not required
$\delta = \delta_{crit}$	Metastable	Transitional	Not required
$\delta > \delta_{crit}$	Unstable	Runaway	Required

1.2.1. Constitutive model

In Eq. 3, the transient heat balance equation involved in determining the $\delta - \gamma$ stability diagram, written considering a quiescent conductive fluid and a negligible conversion of the reactant subjected to a decomposition reaction. The mentioned equation presents various dimensionless parameters, including Θ, γ, $\mathcal{T}$, δ and Ω. Due to the idealised cylindrical symmetry of the system, the spatial dependency of Θ can be considered mono-dimensional, dependent only on Ω itself. The meanings of all the above-mentioned dimensionless parameters are reported in Eqs. from 4 to 7. In addition, $\mathcal{T}$ depends on t_{cond}, defined as the ratio between the square radius of the system r_w^2 and the heat diffusivity $\alpha = k_T/\rho\hat{C}_p$, as also reported in Eq. 8. Concerning the sensitivity equation involved, it is reported in Eq. 9. The expression of the sensitivity of Θ to the respect of δ is reported in Eq. 10 whereas the expression of $S(\Theta;\delta)$ is reported in Eq. 11.

$$\frac{\partial\Theta}{\partial\mathcal{T}} = \frac{\partial^2\Theta}{\partial\Omega^2} + \frac{1}{\Omega}\frac{\partial\Theta}{\partial\Omega} + \delta\exp\left(\frac{\Theta}{1+\Theta/\gamma}\right) \tag{3}$$

$$\Theta = \gamma\frac{T-T_w}{T_w} \tag{4}$$

$$\gamma = \frac{E_a}{R_g T_w} \tag{5}$$

$$\delta = \frac{\gamma\,\tilde{Q}_r\,\mathcal{R}|_{T_w,c_{A0}}\,r_w^2}{k_T\,T_w} \tag{6}$$

$$\mathcal{T} = \frac{t}{t_{cond}} \tag{7}$$

$$t_{cond} = \frac{r_w^2}{\alpha} \tag{8}$$

$$\frac{\partial s(\Theta;\delta)}{\partial\mathcal{T}} = \frac{1}{\Omega}\frac{\partial}{\partial\Omega}\left[\Omega\frac{\partial s(\Theta;\delta)}{\partial\Omega}\right] + \exp\left(\frac{\Theta}{1+\Theta/\gamma}\right)\left[1 + \frac{\delta s(\Theta;\delta)}{(1+\Theta/\gamma)^2}\right] \tag{9}$$

$$s(\Theta;\delta) = \frac{\partial\Theta}{\partial\delta} \tag{10}$$

$$S(\Theta;\delta) = \frac{\delta}{\Theta}\frac{\partial\Theta}{\partial\delta} \tag{11}$$

1.3. Sizing of the relief system

The first step of the relief device sizing procedure concerns the orifice and the determination of the flow rate of the discharged stream. For the case of runaway gasses and vapour venting, it is recommended to follow the technique developed by the Design Institute for Emergency Relief Systems (DIERS) (Green and Southard, 2019). The research effort of the DIERS under the auspices of AIChE has led to an increased understanding of the venting technology, with significant emphasis on the application to the runaway reaction category (Fisher et al., 1992). Applying the DIERS procedure for relief system design in the presence of a runaway reaction is also strongly recommended by API 521 (ANSI/API, 2007) and API 2000 (API, 1998). The design relationships are reported in Eqs. 12 and 13. It is better to underline that in the present work, the information for implementing the method equations was retrieved from a TS^U calorimeter instead of an ARSST™ coupled with a VSP2™. Moreover, to avoid inaccuracies and ensure data accuracy, the correction on the effect of cell instrument thermal inertia and heating rate of the oven was included.

$$\dot{W}_{tot} = \dot{W}_{vap} + \dot{W}_{gas} = \frac{V(1-\alpha_0)\rho\hat{C}_p\dot{T}_{relief}}{\hat{\lambda}} + \frac{V(1-\alpha_0)\rho V_{gas}^{test}\dot{P}_{peak}\rho_{gas}}{m_{tot}P_{relief}} \tag{12}$$

$$A_{tot}^{DIERS} = A_{vap} + A_{gas} = \frac{V(1-\alpha_0)\rho\hat{C}_p\dot{T}_{relief}}{0.61K_d\lambda P_{relief}}\left(\frac{R_g T_{relief}}{PM_{vap}}\right)^{0.5} + \frac{V(1-\alpha_0)\rho V_{gas}^{test}\dot{P}_{peak}}{0.61K_d m_{tot}P_{relief}}\left(\frac{PM_{gas}}{R_g T_{relief}}\right)^{0.5} \tag{13}$$

In Eqs. 12 and 13, a two-phase vapour and gas flow have been assumed (i.e., a hybrid venting system). The vapour phase is formed due to the tempering of the reaction employing the vaporisation of the liquid phase, and the gaseous phase is a consequence of the decomposition of the unstable materials. To test the reliability of the proposed sizing procedure, it will be compared to standard safety relief valve (SRV) design methods

(Emerson, 2012) (Hellemans, 2009). To apply these more traditional algorithms, $\dot{W}_{tot}$ must be known in advance, and a specific correlation for runaway reactions is absent. The strength of the methodology is to consider more valve functionalities details with two adding coefficients apart from the K_d: the backpressure correction factor for gasses and the K_c combination factor for installations with a ruptured disc upstream of the valve. The design equation is reported in Eq. 14 where a churn turbulent flow has been assumed with an associated coefficient $C = 3.5\ 10^{-3}$. Eventually, all the quantities reported above must be expressed in SI units, and relief conditions are assumed to be equal to the onset one.

$$A_{tot}^{std} = \frac{3600\, W_{tot}}{2.39\ 10^{-5} P_{relief} K_d K_b K_c} \sqrt{\frac{T_{relief} Z}{PM}} \tag{14}$$

1.4. Case study

The acquisition of the main physico-chemical data represents the primary input of the procedure reported schematically in Figure 1. Regarding the kinetic (E_a, $k_{k\infty}$, n, C_{A0}), thermodynamic ($\Delta\tilde{H}_r$), onset (T_{onset}, $\dot{T}_{onset}$) and peak ($\dot{P}_{peak}$) data for 50 %w aqueous solution of HA and 50 %w of HA added with 1 %w of HH, they were retrieved in the work of Andriani et al. (2024) (Andriani et al., 2024b). The dataset has been corrected taking into account the thermal inertia of the instrument cell and the effect of the oven heating rate. Their numerical values are reported in Table 2. The remaining physical properties can be calculated via correlations. The $\tilde{C}_p$ has been determined following the methodology reported in the literature (Andriani et al., 2024b), whereas for k_T, the Predvoditelev correlation (Ozbek and Phillips, 1980) has been adopted (Eq. 15).

$$k_T = k_{T,w} \frac{\tilde{C}_p}{\tilde{C}_{p,w}} \left(\frac{\rho}{\rho_w}\right)^{4/3} \left(\frac{PM_w}{PM}\right)^{1/3} \tag{15}$$

Table 2. *Variables required for method implementation.*

	E_a kJ mol^{-1}	$k_{k\infty}$ s^{-1}	n -	C_{A0} kmol m^{-3}	$\Delta\tilde{H}_r$ kJ mol	T_{onset} K	$\dot{P}_{peak}$ Pa s^{-1}	$\dot{T}_{onset}$ K s^{-1}
50 %wHA	103	$9.33{\cdot}10^{9}$	1	16.56	-79.8	393.15	$6.85{\cdot}10^{4}$	$6.26{\cdot}10^{-3}$
50 %wHA+1 %wHH	117	$6.51{\cdot}10^{10}$	1	17.82	-78.1	392.15	$6.85{\cdot}10^{4}$	$6.90{\cdot}10^{-3}$

2. Results and discussions

This section first illustrates the $\delta - \gamma$ stability diagram (Section 3.1.). Then, Section 3.2. presents and critically discusses the outcomes of the sizing of the storage vessels. Eventually, in Section 3.3. will be elucidated and commented on the results obtained from the implementation of the sizing of the relief systems, reported in Section 2.3.

2.1. $\delta - \gamma$ stability diagram

The $\delta - \gamma$ stability diagram has been determined following the procedure reported in Section 2.2. The obtained parameters map has a total generic meaning that can be applied to the design of every cylindrical storage vessel that handles a liquid prone to a decomposition reaction, which can trigger a self-heating phenomenon, potentially leading to runaway conditions. Before seeing in detail how to apply the retrieved information for an intrinsic design of storage vessels, in Figure 2 the parameter map mentioned above has been reported.
As can be noticed from Figure 2, the δ_{crit} value depends on the specific value of γ. An interesting feature of the trend is that increasing the value of γ, the δ_{crit} approaches asymptotically the value predicted by Frank-Kamenetskii under the approximation of $\gamma \to \infty$ (i.e., $\delta_{crit} = 2$). This agreement between the results obtained by the original version of the FKT and those retrieved in the present work using an expanded FKT coupled with the VMWT can be seen as a first validation of the recovered modelling outcomes. From a practical perspective, knowing the exact value of γ in advance can help design a storage vessel more reliably, considering a less approximated δ_{crit} value. Indeed, for low γ values, the actual δ_{crit} value deviates significantly from the asymptotic one.

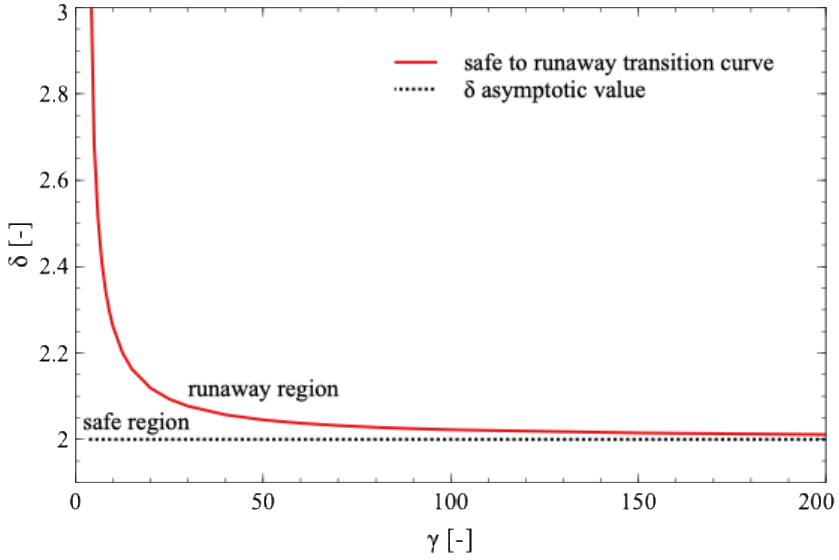

Figure 2. *$\delta - \gamma$ stability diagram. The red curve represents the safe-to-runaway transition boundaries, whereas the safe and runaway regions are under and above the red curve, respectively. In addition, the dotted style reports the asymptotic value of the Frank-Kamenetskii number, determined with the original version of the self-heating theory.*

To understand deeply the behaviour of a system modelled with the proposed expanded version of the FKT, it has also reported how the Θ_{max} will vary with γ for $\delta = \delta_{crit}$ and for $\delta = 2$. The reason behind the analysis of the trend of Θ_{max} for a $\delta = \delta_{crit}$ obtainable with the present expanded FKT and with its original formulation is to emphasise the consequences of a selection of a different δ_{crit} value during the design phase. The Θ_{max} can retrieve the T_{max} value usable for verification of the onset temperature, as reported in Section 2.2. Ensuring that $T_{max} < T_{onset}$ is possible to state that the system has been designed to avoid, as much as possible, the onset of runaway conditions triggered by the thermal decomposition of the stored material.
Looking at the trend reported in Figure 3, it is possible to notice an excellent agreement between the outcomes obtained by the expanded version of the KFT proposed in this work and its original version. Indeed, as γ approaches larger values, the Θ_{max} values determined both for $\delta = \delta_{crit}$ and $\delta = 2$ asymptotically tend to the one predicted by the original FKT (i.e., $\Theta_{max} = \ln 4$). Moreover, designing a storage vessel imposing a constant $\delta_{crit} = 2$ independently on the value of γ will produce a more conservative system the lower is the γ value. The difference between the δ_{crit} values obtainable with the expanded and the original FKT will increase for lower γ. Thus, the difference between the Θ_{max} values obtainable for $\delta = \delta_{crit}$ and $\delta = 2$ will follow the same trend, increasing as γ decreases. This is a consequence of the fact that, as the distance between δ_{crit} and the constant value of 2 imposed by the FKT decreases, the more stable the system becomes and the lower the magnitude of the self-heating phenomenon. Consequently, the reachable Θ_{max} will decrease. This means that using a refined value of δ_{crit}, it is possible to design a less conservative system compared to the one dimensioned imposing the constant value of δ_{crit} predicted with the original FKT. This less conservative system can be ideated with a larger value of vessel critical diameter according to Eq. 2, always avoiding the onset of runaway conditions. A vessel with a larger critical diameter can handle a larger amount of reactive chemicals safely for a constant value of considered aspect ratio. However, for vessels designed with the refined δ_{crit} value, the need for a check on the T_{center} will be more stringent because the extent of the self-heating phenomenon will increase, as evidenced by the trend reported in Figure 3. Using a refined value of δ_{crit} implies checking the $T_{max} < T_{onset}$ with the appropriate value of Θ_{max} to avoid incurring a potential runaway phenomenon. If the condition of $T_{max} < T_{onset}$ can not be met, the δ value adopted must be decreased for a specific γ to make the storage safe and reliable. Nevertheless, a practical application of the $\delta - \gamma$ stability diagram and the $\Theta_{max} - \delta$ diagram will be presented in Section 3.2.

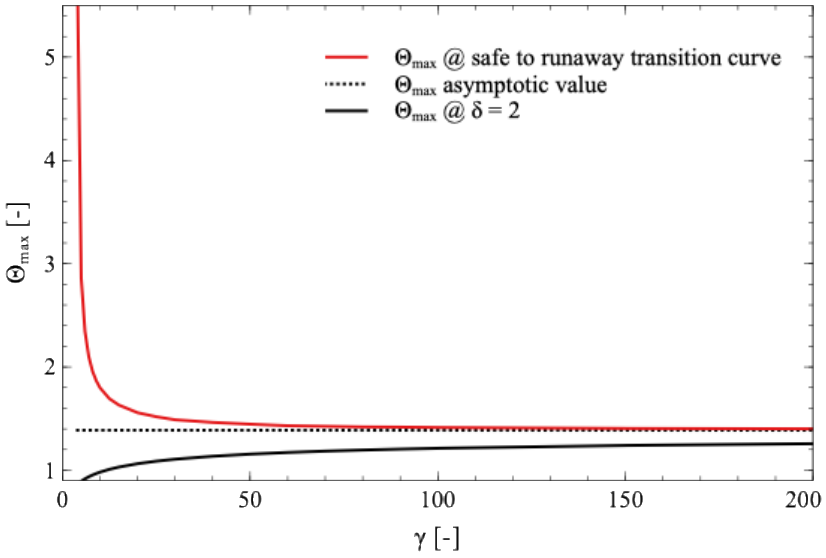

Figure 3. *Trend of the* Θ_{max} *as a function of* γ*. Red curve: trend of* Θ_{max} *determined for* δ *related to the safe-to-runaway transition boundary. Black curve: trend of* Θ_{max} *determined for* $\delta = 2$*. The dotted style reports the asymptotic value of* Θ_{max} *determined with the original FKT.*

2.2. Sizing of the storage vessel

According to Section 2.2, three different values of atmospheric temperature have been considered (i.e., 5°C, 20°C and 35°C). For clarity, the atmospheric, external, and internal vessel wall temperatures can be considered the same input values because of the assumptions that $Bi \to \infty$ and negligible thermal resistance of the equipment wall. Thus, any change in the atmospheric temperature will result in the same variations in the external and internal temperature walls. Using the information outlined in Section 2.1., the related $r_{w,crit}$ for intrinsic safe storage in cylindrical vessel have been calculated and are reported in Table 3. For comparison, the δ_{crit} and Θ_{max} values have been retrieved from the original and expanded FKT.

Table 3. *Output of the storage vessel design method using both the original and the expanded FKT, for the case of an aqueous solutions on 50 %$_w$ of HA and for the case of 50 %$_w$ aqueous solution of HA added with 1 %$_w$ of HH, respectively.*

50 %$_w$HA									
Input	Original FKT			Expanded FKT					
T_w	$r_{w,crit}$	T_{center}	γ	δ_{crit}	$\Theta_{max}\|_{\delta_{cr}}$	$\Theta_{max}\|_{\delta=2}$	$r_{w,crit}$	$T_{center}\|_{\delta_{crit}}$	$T_{center}\|_{\delta=2}$
[K]	[m]	[K]	[-]	[-]	[-]	[-]	[m]	[K]	[K]
278.15	2.93	286.8	44.50	2.045	1.454	1.147	3.20	287.2	285.3
293.15	1.03	302.8	42.23	2.054	1.462	1.140	1.08	303.3	301.1
308.15	0.40	318.8	40.17	2.057	1.462	1.135	0.41	319.4	316.9
50 %$_w$HA+1 %$_w$HH									
Input	Original FKT			Expanded FKT					
T_w	$r_{w,crit}$	T_{center}	γ	δ_{crit}	$\Theta_{max}\|_{\delta_{cr}}$	$\Theta_{max}\|_{\delta=2}$	$r_{w,crit}$	$T_{center}\|_{\delta_{crit}}$	$T_{center}\|_{\delta=2}$
[K]	[m]	[K]	[-]	[-]	[-]	[-]	[m]	[K]	[K]
278.15	22.65	285.8	50.72	2.044	1.446	1.157	24.65	286.1	284.5
293.15	6.79	301.6	48.12	2.047	1.449	1.152	7.10	302.0	300.2
308.15	2.29	317.5	45.78	2.049	1.452	1.147	2.32	317.9	315.9

As can be noticed from Table 3, the external temperature strongly affects the critical radius of the system because the characteristic size of the vessel decreases significantly as the value of the input parameter increases. This observation is valid for the outcomes derived from the FKT in its original and expanded version. Thus, to protect a hypothetical plant most reliably, retrieving temperature temporal distribution data and taking the maximum recorded value as a representative design value is crucial. Hence, further considerations relating to the relief system sizing (Section 3.3.) will be addressed only concerning a storage vessel designed for the higher temperature (i.e., 35°C). Also, considering an average temperature between a reference value for a hypothetical winter and summer season (i.e., 5°C and 35°C) could lead to misleading conclusions. Eventually, all the systems reach a bulk temperature far below the onset, regardless of the modelling theory used for the calculations. This remark can confirm the robustness of the adopted procedure because, according to both versions of the FKT, the temperature in the centre of the tank at steady state is the maximum temperature the

system can reach. Thus, having a maximum system temperature far below the onset is a way to guarantee that any runaway conditions induced by self-heating phenomena linked to a thermal decomposition reaction of the stored material have been avoided. In addition, considering the intrinsic conservatism of the FKT, neglecting any heat dissipation due to natural convection or any primary reactant consumption, the bulk steady-state temperature will also be lower than the determined one, enhancing safety.
Comparing the results obtained with the original and expanded FKT, the first remarkable result regards the δ_{crit} values. In the considered γ interval, ranging approximatively from 40 to 51, the δ_{crit} differs by approximately 2.5 % compared to the characteristic value of 2.00 predicted by the original FKT for cylindrical geometry. The design outcomes would have been significantly different for $\gamma < 10$, where the difference between the predicted δ_{crit} will be approximately equal to or greater than 15 %. However, for the considered γ interval, the storage vessels can be designed with both theories without deteriorating the quality of the results. Moreover, sizing the storage equipment imposing $\delta_{crit} = 2$ independently from the γ value will conduce to a system having an even lower T_{center} value than the one predicted with the original FKT, enhancing the safety and reliability of the equipment by increasing the distance from the maximum reachable temperature and the onset ones. If, instead, the storage vessel had been designed considering the more refined value of δ_{crit} predicted with the expanded FKT, the maximum allowable system size would be slightly higher than the one predicted with the original FKT, with a difference in the T_{center} practically negligible.
An interesting conclusion that can be derived from the analysis of the results regards the different stability of the two mixtures considered. Indeed, the solution containing 50 %w HA and 1 %w HH is considerably more stable than the 50 %w HA one. This statement can be legitimate by looking at the $r_{w,crit}$ obtained with both the formulations for the exact value of T_w and characteristic considered geometry. The critical vessel characteristic size is almost seven times higher for the solution containing the HA-derived salt than the one holding only the HA. This discrepancy can be further supported by considering the physicochemical properties of both materials. Adding only 1 %w of HH has the effect of increasing the E_a and decreasing the $\Delta\widetilde{H}_r$. The former feature tends to reduce the likelihood of the decomposition reaction because of the highest energy barrier that has to be overcome before inducing thermal degradation. The latter characteristic mitigates the severity of the thermal decomposition phenomenon, reducing the self-heating of the system. Thus, with an aqueous solution of 50 %w HA added with 1 %w HH, it is possible to design storage vessels with higher capacity without triggering any self-heating phenomenon potentially responsible for a runaway reaction.

2.3. Sizing of the relief system

Regarding the relief device sizing, a value of $K_d = 0.975$, typical for gas and vapours venting (Crowl and Tipler, 2013) has been adopted, also assuming a negligible effect of the back pressure (i.e., $K_b = 1$) and the absence of any rupture disk placed before the relief valve (i.e., $K_c = 1$). The corrective factor for backpressure K_b has been assumed according to a conventional relief valve design (Crowl and Tipler, 2013). For other pressure relief systems to be considered, the backpressure and the corresponding K_b value must be quantified (Liptak, 2003). In addition, any rupture disk has been considered to be placed upstream of the relief valve because it has been assumed that the stored fluids are not fouling, and there is no need to put a seal between the equipment and the relief valve (Hellemans, 2009). Moreover, during the experimental campaign, a $V_{gas,test} = 8.9 \cdot 10^{-6} m^3$ has been adopted together with an $m_{tot} = 1.2\ 10^{-3} kg$. Eventually, the relief pressure has been taken $P_{relief} = 1.25\ P_{op}$ (Ennis, 2006) assuming an atmospheric storage tank having $P_{op} = P_{atm}$, $\dot{T}_{relief} = \dot{T}_{onset}$ to be conservative regarding the temperature increase rate at relief conditions and $T_{relief} = T_{center}$ considering that when the system deviates from standard operating conditions, the temperature in the centre will be the most representative in case of the onset of runaway conditions. Figure 5 shows the outcome of the relief system sizing DIERS and standard procedures for a storage vessel designed involving the original FKT and $T_w = 308.15\ K$. Whereas, in Figure 4, the expanded version of the FKT has been implemented, considering $T_{relief} = T_{center}|_{\delta_{crit}}$ and $T_w = 308.15\ K$. The results are presented reporting the diameter ratio $d = D_{valve}/D$ as a function of the aspect ratio H/D for various void fraction values, ranging from 0.1 to 0.4. Eventually, the behaviour of the considered HA aqueous solutions (i.e., HA 50 %w and HA 50 %w + HH 1 %w) was evaluated.

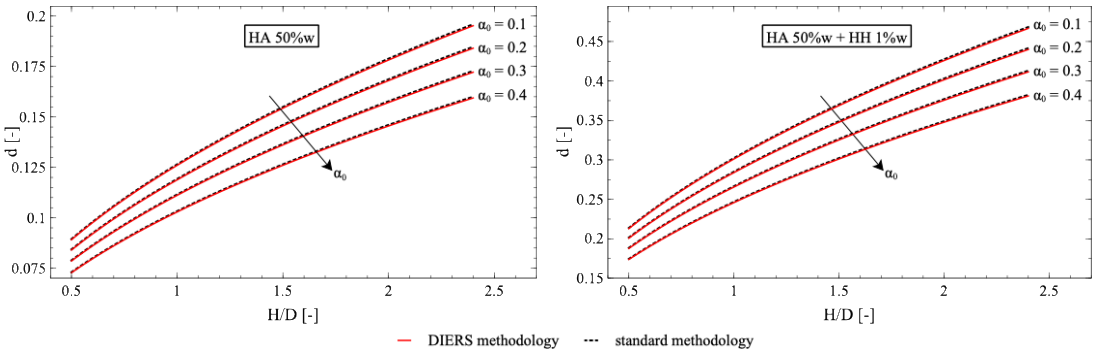

Figure 4. *Relief devices sizing outcomes using the expanded FKT for various values of the filling ratio.*

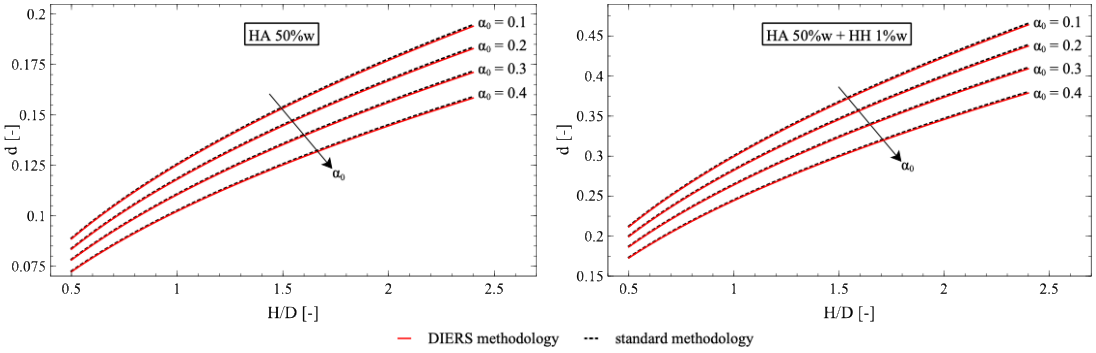

Figure 5. *Relief devices sizing outcomes using the original FKT for various values of the filling ratio.*

Figure 4 and Figure 5 show an agreement between the two adopted methodologies (i.e., DIERS and standard) for both the considered HA aqueous solutions and FKT's versions, even if the standard method is slightly more conservative than the DIERS one in all the cases. Furthermore, if the effect of backpressure and the presence of relief devices in series want to be considered, these results in K_b and K_c coefficients are lower than 1. Thus, the deviation between the two sizing strategies will further increase. For these reasons, the standard algorithm must be preferred regarding the relief device sizing, coupled with DIERS for determining $\dot{W}_{tot}$. Moving to the analysis of the dependence of d to the respect of H/D, the connection between the vessel geometry and the relief device size is evident. For a fixed value of D, higher H/D mean higher V, hence a higher amount of stored mass. The greater the quantity of the mixture contained in the vessel, the larger the quantity of material that can undergo thermal degradation. Therefore, a larger relief device is needed to vent all the gases and vapours generated during a runaway reaction. Higher H/D ratios could be advantageous in vertical storage tanks in better use of the storage vessel footprint. By preserving D constant and increasing H, it is possible to increase V available for storage, holding the base area constant, which can primarily impact the plant layout. Also, from the filling ratio point of view, the higher liquid level handled by the equipment must be considered during the relief device sizing to avoid underestimating the required orifice. It is worth noting that the literature does not provide a reference value to assess the maximum safe tank filling ratio. Considering the central norms that discuss the maximum storage tank liquid level, the API 2350 (ANSI/API, 2020) defines the various liquid heights that must be considered for safe liquid storage (i.e., critical high level, automatic overfill prevention system level, high-high level, high-level, maximum working level and minimum working level) and the way to determine their values for each specific case, together with some practical calculation examples. Meanwhile, in the AS 1940:2017 (AS, 2017), the various liquid heights are defined similarly to the API 2350. Moreover, the maximum working level must not exceed 95 % of the chosen critical high level. Thus, the critical high level, defined as the highest liquid level in the tank without detrimental impacts, must be critically selected by the designer, and a general rule of thumb for its quantification can not be retrieved. As can be noted from both **Errore. L'origine riferimento non è stata trovata.** and **Errore. L'origine riferimento non è stata trovata.**, the lower α_0 (i.e., the higher the liquid level), the higher is d for a fixed value of H/D. Consequently, both the aspect and the filling ratio must be reasonably assessed during the design phase to meet productive and operative constraints reliably. A filling ratio corresponding to the critical high liquid level must be chosen to avoid undersizing the relief systems. Eventually, both **Errore. L'origine riferimento non è stata trovata.** and **Errore. L'origine riferimento non è stata trovata.** exhibit the same trend of d versus H/D for the same HA aqueous solution (i.e., 50 %w HA or 50 %w HA added with 1 %w HH) independently from the considered version FKT. This is a consequence that both versions predict almost the same value of $r_{w,crit}$ and T_{center} for the considered γ value.

Another interesting conclusion that can be drawn from both **Errore. L'origine riferimento non è stata trovata.** and **Errore. L'origine riferimento non è stata trovata.** is the effect of a more significant storage vessel on the relief system. Considering Eqs. from 12 to 14, the linear relationship between V and the $\dot{W}_{tot}$ and the orifice area is evident. This means that, even if the mixture containing 1 %w HH is intrinsically more stable and permitted to be handled safely in more prominent equipment, there is a significant drawback related to higher storage volumes. Indeed, the greater the V, the greater the amount of the material stored, and the more considerable the amount of mixture that can undergo a decomposition reaction. Thus, this means that the corresponding flow rate of decomposition products to the vent will increase accordingly, resulting in a more prominent overpressure relief system. Indeed, this conclusion can be legitimate considering that the greater the material amount, the greater the vapours and gasses produced with a decomposition reaction. However, looking more critically at the obtained values of d, especially for the 50 %w HA added with 1 %w HH aqueous solution, or for higher H/D values for the 50 %w HA ones, something peculiar can be noticed that is always related to larger V. Indeed, the relief systems have an oversized orifice area that couldn't be practically realisable for mechanical reasons of equipment integrity. This eventuality is also considered by (Lees, 2012), who clearly states that sometimes the vent area is so large that it can not fit on some vessels, mainly when chemical reactions occur inside the system. When this eventuality arises, pressure relief systems are not a practical option. This further strengthens the need for an intrinsically safe design of processes and equipment to enhance the reliability of an industrial plant and the higher hazards related to a large storage vessel, often desired to improve the efficiency in the use of the available space in the plant.

4. Conclusions

Storage vessels are one of the industrial equipment in which a more significant amount of materials is usually present. Thus, the safety of the stored materials must be considered during the design of this kind of system, especially when thermally unstable molecules are taken into consideration. Under these perspectives, a methodology that can assess an intrinsically safe system size able to prevent runaway conditions triggered by exothermic decomposition mechanisms has been presented in this work. A stability diagram was produced and involved selecting the main design variable to consider both to saturate the system degrees of freedom and to test the consistency of the numerical outcomes. Then, to enhance the safety of a plant, active protection measures like relief systems can be considered to vent gaseous and vapour decomposition products.

The proposed methodology has been tested by applying it to two inherent unstable mixtures (i.e., aqueous solutions of 50 %w HA and 50 %w HA added with 1 %w HH). From a preliminary screening, the solution containing 50 %w HA and 1 %w HH has shown a lower tendency to thermal degradation to the respect of the solution containing only 50 %w HA. Because of the higher stability of the 50 %w HA + 1 %w HH aqueous mixture, results have shown the possibility of designing a storage vessel with a higher characteristic dimension (i.e., the vessel radius) if compared to the 50 %w HA one, always avoiding runaway phenomena induced by self-heating features. Thus, adding only 1 %w of HH to a 50 %w HA aqueous solution can not only enhance the reliability of a chemical plant, reducing the probability and severity of potential decomposition reactions, but also allow the involvement of larger storage vessels without any detrimental effects on the process safety. The presented procedure offers the possibility of involving a $\delta - \gamma$ stability diagram coupled with $\Theta_{max} - \gamma$ map as a versatile tool for designing any cylindrical storage vessel handling hazardous materials prone to thermal degradation. Eventually, the design of relief systems must be approached critically and carefully when runaway conditions are triggered in industrial systems. By doing so, it is possible to understand the centrality of an intrinsically safe design of storage equipment and to realise that sometimes active protection measures could not be an option when large quantities of chemicals and devastating side phenomena are involved.

References

Andriani, G., De Liso, B.A., Pio, G., Salzano, E., 2024a. Design of sustainable reactor based on key performance indicators. Chem Eng Sci 285, 119591.

Andriani, G., Pio, G., Vianello, C., Mocellin, P., Salzano, E., 2024b. Safety parameters and stability diagram of hydroxylamine hydrochloride and sulphate. Chemical Engineering Journal 148894.

Arvind Varma, Massimo Morbidelli, Hua Wu, 1999. Parametric Sensitivity in Chemical Systems, First Edition. ed. Cambridge University Press.

Babrauskas, V., 2003. Ignition Handbook: Principles and Applications to Fire Safety Engineering, Fire Investigation, Risk Management and Forensic Science.

Balakrishnan, E., Wake, G.C., 1996. Critical Values for Some Non-Class A Geometries in Thermal Ignition Theory. Mathl. Comput. Modelling 24.

Boddington, T., Feng, C.-G., Gray, P., 1983. Thermal Explosions, Criticality and the Disappearance of Criticality in Systems with Distributed Temperatures. I. Arbitrary Biot Number and General Reaction-Rate Laws. Source: Proceedings of the Royal Society of London. Series A, Mathematical and Physical Sciences 390, 247–264.

Campbell, A.N., 2015. The effect of external heat transfer on thermal explosion in a spherical vessel with natural convection. Physical Chemistry Chemical Physics 17, 16894–16906.
Chambré, P.L., 1952. On the solution of the poisson-boltzmann equation with application to the theory of thermal explosions. J Chem Phys 20, 1795–1797.
Crowl, D.A., Tipler, S.A., 2013. Sizing pressure-relief devices. Chem Eng Prog 109, 68–76.
Deng, J., Zhao, J., Zhang, Y., Huang, A., Liu, X., Zhai, X., Wang, C., 2016. Thermal analysis of spontaneous combustion behavior of partially oxidized coal. Process Safety and Environmental Protection.
Ennis, T., 2006. Pressure relief considerations for low-pressure (atmospheric) storage tanks. IChemE Symposium Series 1–13.
Fisher, H.G., Forrest, H.S., Grossel, S.S., Huff, J.E., Muller, A.R., Noronha, J.A., Shaw, D.A., Tilley, B.J., 1992. Emergency relief system design using DIERS technology: the design institute for emergency relief systems (DIERS) project manual, 1st ed. American Institute of Chemical Engineers.
Frank-Kamenetskii, D.A., 1955. Diffusion and Heat Exchange in Chemical Kinetic.
Geyer, W.B., Wisuri, J., 2000. Handbook of storage tank systemns: codes, regulations, and designs, 1st ed. Marcel Dekker.
Green, D.W., Southard, M.Z., 2019. Perry's Chemical Engineers' Handbook, 9th ed. McGraw-Hill Education.
Guo, W., Lim, C.J., Bi, X., Sokhansanj, S., Melin, S., 2013. Determination of effective thermal conductivity and specific heat capacity of wood pellets, in: Fuel. pp. 347–355.
Hellemans, M., 2009. The Safety Relief Valve Handbook: Design and Use of Process Safety Valves to ASME and International Codes and Standards, 1st ed. Elsevier.
Ho, T.C., Duh, Y.S., Chen, J.R., 1998. Case Studies of Incidents in Runaway Reactions and Emergency Relief. Process Safety Progress 17, 259–262.
Juncheng, J., Dan, W., Lei, N., Gang, F., Yong, P., 2020. Inherent thermal runaway hazard evaluation method of chemical process based on fire and explosion index. J Loss Prev Process Ind 64.
Kletz, T., Amyotte, P., 2010. Process Plants: A Handbook for Inherently Safer Design, 2nd ed. CRC Press - Taylor & Francis Group.
Kletz, T.A., 2003. Inherently safer design - its scope and future. Process Saf Environ Prot 81, 401–405.
Lazarovici, A., Volpert, V., Merkin, J.H., 2005. Steady states, oscillations and heat explosion in a combustion problem with convection. European Journal of Mechanics, B/Fluids 24, 189–203.
Lees, F., 2012. Lees' Loss Prevention in the Process Industries: Hazard Identification, Assessment and Control, 4th ed. Butterworth-Heinemann.
Lengyel, I., West, D.H., 2018. Numerical bifurcation analysis of large-scale detailed kinetics mechanisms. Curr Opin Chem Eng 21, 41–47.
Liptak, B.G., 2003. Instrument Engineers' Handbook - Volume 1: Process Measurement and Analysis, 4th ed. CRC Press.
Myers, P.E., 1997. Aboveground storage tanks, 1st ed. McGraw-Hill.
Novozhilov, V., 2017. Effects of initial and boundary conditions on thermal explosion development, in: AIP Conference Proceedings. American Institute of Physics Inc.
ANSI/API, 2020. Overfill Prevention for Storage Tanks in Petroleum Facilities: ANSI/API Standard 2350, 5th ed. ANSI/API.
Ozawa, T., 2000. Thermal analysis — review and prospect. Thermochim Acta 355, 35–42.
Ozbek, H., Phillips, S.L., 1980. Thermal conductivity of aqueous sodium chloride solutions from 20°C to 330°C. J Chem Eng Data 25, 263–267.
Pio, G., Mocellin, P., Vianello, C., Salzano, E., 2021. A detailed kinetic model for the thermal decomposition of hydroxylamine. J Hazard Mater 416.
Emerson, 2012. Pressure relief valve engineering handbook, 1st ed. Emerson.
ANSI/API, 2007. Pressure-relieving and depressuring systems: ANSI/API 521, 5th ed. ANSI/API.
Restuccia, F., Ptak, N., Rein, G., 2017. Self-heating behavior and ignition of shale rock. Combust Flame 176, 213–219.
Shanley, E.S., 1953. Self-Healing of Hydrogen Peroxide Storage Vessels. Ind Eng Chem 45, 1520–1524.
Singh, J., 1994. Vent sizing for gas-generating runaway reactions. J Loss Prev Process Ind 7, 481–491.
Strozzi, F., Zaldıvar´, J.M.Z., Kronberg, A.E., Westerterp, K.R., 1999. On-line runaway detection in batch reactors using chaos theory techniques. AIChE Journal 45, 2429–2443.
AS, 2017. The storage and handling of flammable and combustible liquids: AS 1940, 7th ed. Standards Australia.
API, 1998. Venting atmospheric and low-pressure storage tanks: API 2000, 5th ed. API.
Vianello, C., Salzano, E., Maschio, G., 2018. Thermal behaviour of Peracetic Acid for the epoxydation of vegetable oils in the presence of catalyst. Process Safety and Environmental Protection 116, 718–726.
Wang, Q., Rogers, W.J., Mannan, M.S., 2009. Thermal risk assessment and rankings for reaction hazards in process safety. J Therm Anal Calorim 98, 225–233.

Investigation of an Organic Peroxide Explosion Incident

Yi-Peng Huang [a], Ho-Jan Chang [a], Li-Yu Yeh [a], Hsiang-Ching Peng [a], Po-Hsun Huang [a], Hsiao-Yun Tsai [a,b] & Jenq-Renn Chen [a,b]

[a] Department of Safety, Health and Environmental Engineering, National Kaohsiung University of Science and Technology (NKUST), Kaohsiung, Taiwan
[b] Southern Center of Emergency Response of Toxic Chemical Substance (SERT), National Kaohsiung University of Science and Technology (NKUST), Kaohsiung, Taiwan

E-mail: jrc@nkust.edu.tw

Abstract

A detailed investigation was performed for a fatal explosion involving a solid organic peroxide in a warehouse. The organic peroxide is a white powder containing approximately 40% of 1,1-Di(tert-butylperoxy) cyclohexane (DTBCH), 40% of silicon dioxide, and balanced isoparaffin. It is classified as type D solid peroxide according to UN Recommendations on the Transport of Dangerous Goods. Maximum storage temperature is 30°C according to the manufacturer. The warehouse was however not temperature controlled. Extensive thermal and explosive testing were performed, including DSC, ARC, GC-MS, FTIR-ATR, dust MIE, and bomb calorimeter. DSC and ARC tests showed only medium thermal hazards with average decomposition energy of 985 J/g. Dust MIE confirmed that the peroxide powder has high sensitivity to ignition. It is concluded that the thermal runaway of the peroxide under poor storage condition leading to decomposition and generation of long-chain alkanes gases with AIT as low as 205°C. The gas generation also dispersed the peroxide powder into air. Ignition was most likely initiated by autoignition of the long-chain alkanes. The visible flame subsequently ignited the erupted and dispersed peroxide leading to a severe dust explosion. Special cares should be taken regarding the safe storage of solid form organic peroxides to prevent the direct dust explosion from thermal runaway.

Keywords: *organic peroxide, thermal runaway, decomposition, dust explosion.*

Introduction

Organic peroxides are well known for their potential explosive hazards. Classification, transportation and storage of organic peroxides are regulated by United Nations Recommendations on the Transport of Dangerous Goods (UN DG, 2006). The hazards of organic peroxides are classified into Type A to G, with descending hazards. Factory Mutual Global (2020) further classified the hazards of organic peroxides into types: explosion hazard (EH), deflagration hazard (DH), severe fire hazard (SFH), fire hazard (FH), and low hazard (LH). Numerous incidents were reported and most incidents involving Type C and above organic peroxides with high assay and active oxygen contents. There were few destructive incidents involving Type D and lower hazards peroxides during storage. This is consistent with the fact that lower hazards organic peroxides generally have lower thermal hazards. Decomposition with fuming and fire, instead of explosion, were the common hazards for Type D and lower hazards peroxides.

On September 22, 2023, a deadly explosion occurred in a production plant that manufacturing golf balls in southern Taiwan. The incident was first reported as unknown smoke coming out from the warehouse storing raw materials and organic peroxides used for cross-linking in resin polymerization for the core of golf balls. The smoke was identified to come out from one of three pallets of a solid organic peroxide each stacked with 50 paper boxes and 20 kg in each box. The smoke than triggered fire sensor and evacuation was ordered. Fire department was notified and arrived the site shortly.

Before the fire department entering the warehouse, explosion occurred which resulted in 10 fatalities including 4 firemen, more than 100 injuries, and very extensive damage to the production building. The organic peroxide is a white powder containing approximately 40% of 1,1-Di(tert-butylperoxy) cyclohexane (DTBCH), 40% of silicon dioxide, and balanced isoparaffin. It is classified as type D solid peroxide according to UN Recommendations on the Transport of Dangerous Goods (UN DG, 2019). Maximum storage temperature and self-accelerating decomposition temperature (SADT) are 30°C and 60°C, respectively, according to the manufacturer. The warehouse was however not temperature controlled. Clearly, a thermal runaway occurred in the boxed peroxide. Detailed investigation of the explosion site and a series of testing and analyses were performed based on similar batches of sample from the peroxide manufacturer to find out the cause of the explosion.

1. The site investigation before and after explosion

1.1. The warehouse

The incident site has been manufacturing golf ball for more than a decade. Different organic peroxides were used as cross-linking agent for polymerization of the core of golf balls. The organic peroxides are treated as raw materials, rather than hazardous materials, and stored with other raw materials. There were four different organic peroxides which are summarized in Table 1. Only one of them, 1,1-Di(tert-butylperoxy) cyclohexane or commercial name of C40-P, was Type D and the remaining three peroxides were Type F. According to the Safety Control Regulation of Hazardous Substance (Ministry of Interior, 2021), only Type D organic peroxide is regulated and the controlled quantity is 100 kg. The warehouse had a storage amount of 30 times of controlled quantities in which the regulation requires the warehouse shall be an independent dedicated building, plus the width of reserved space shall be at least 3 m and above. The site has never declared the regulated peroxide. Furthermore, the warehouse was located *inside* the manufacturing building for easy assessing. There was no air conditioning and no fire sprinkler in the storage room. There was also no separate compartment wall inside the room. All stock piled next to each other. All the other materials stored in the storage room were non-hazardous materials as shown in Figure 1.

***Table 1**. List of organic peroxides in the warehouse*

Commercial name	Peroxide Name	CAS No.	Conc. (%)	Classification	State	Max. storage temp. (°C)	SADT (°C)	Amount (kg)
C40-P	1,1-Di(tert-butylperoxy) cyclohexane	3006-86-8	40%	D	Solid	30	60	3,000
TR29B-40	1,1-Bis(t-butyl peroxy)-3,3,5-trimethyl cyclohexane	6731-36-8	40%	F	Solid	30	60	3,200
29-50D	1,1-Bis(t-butyl peroxy)-3,3,5-trimethyl cyclohexane	6731-36-8	50%	F	Solid	30	55	6,300
BC-FF	Dicumyl Peroxide	80-43-3	99%	F	Solid	30	75	625

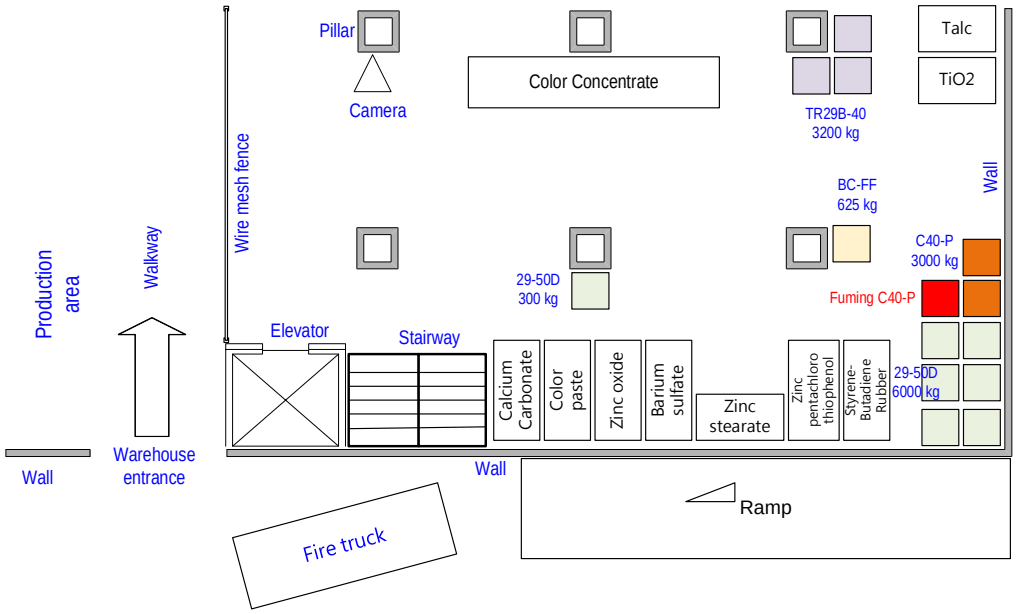

Fig. 1. *Layout of the warehouse before the explosion*

1.2. The initial events

The incident was first reported as unknown smoke in the warehouse area near 17:00 September 22 2023. Later operators noticed that the smoke was coming out from the warehouse in one of the C40-P pellets as shown in Figure 2. Left photo in Figure 2 was taken on September 8 2023 showed the two pellets of C40-P that were shipped to the site on August 14 2023. The red circle was the location when the 3rd pellet of C40-P moved in on that day. Right photo showed the fuming and partially melted PE films of the front C40-P pellet on 17:06. Figure 3 contains video clips from surveillance video camera where the peroxides were stored on the far-left side of camera. On 17:12:30, smoke spread to reach the camera view. Between 17:13 and 17:15, staffs tried to determine the cause and control the smoke but failed. By 17:30, the video clips shown heavy smoke with almost zero visibility. The smoke triggered the fire alarm around 17:20. On 17:31, County Fire Department was notified. On 17:41, first team of Fire Department arrived. On 17:57, firefighters reported that a chemical leaks and ready to enter site for inspection. On 18:01, a strong explosion occurred.

Fig. 2. *The organic peroxides storage. Left photo showed the two pellets of C40-P on two weeks before the explosion. Right photo showed the fuming and partially melted PE films of the same pellet on 17:06 of the day of explosion. (Photos curtesy of Pingtung County Fire Department)*

Fig. 3. *Video clips near the outside of the warehouse. The peroxides storage was at the far-left side of the video camera. (Video curtesy of Pingtung County Fire Department)*

1.3. The explosion

Figure 4 shows the clips from the side-mount video camera on the fire truck of Fire Department. Each frame is differed by around 0.33 s. Firefighters were about to enter the building but smoke erupted and engulfed them. Figure 5 shows the clips from the video camera on the fire truck of Fire Department. Each frame is differed by around 0.27 s. The video showed a strong, visible flame, followed by partial clasping of the building. The first explosion was the strongest, followed by fire spread throughout the plant with numerous smaller-scale explosions.

Fig. 4. *The clips from the side-mount video camera on the fire truck of Fire Department. Each frame is differed by around 0.33 s. (Video curtesy of Pingtung County Fire Department)*

Fig. 5. *The clips from the top-mounted video camera on the fire truck of Fire Department. Each frame is differed by around 0.27 s. (Video curtesy of Pingtung County Fire Department)*

1.4. The damage

Fig. 6. shows the aerial view of the explosion with fire remaining on rear part of the plant. The arrow indicates the location of the peroxides storage while the circle marks the same fire truck that fitted with video cameras as in Figures 4 and 5. One notable damage is that the roof near the warehouse entrance and the fire truck was blown apart. Also blown apart were the four brick walls on the far end of the peroxide storage as shown in Figure 7. The longest distance between the peroxide storage and the blown-out brick wall is approximately 60 m. Figure 8 shows the damage of warehouse interior and partially ruptured reinforced concrete floor on the second floor. Higher floors and roof on top of the peroxide storage remained intact. One possible reason that the damage to higher floor and roof near the entrance is that there were one elevator and one stairway located next to the entrance as shown in the layout of Fig. 1 which could provide vertical channels for the explosion shock wave to penetrate the floors and thus damaged the roof.

The explosion damage is considered excessive with multiple wall and floor damaged. The brick wall at 60 m from the peroxide storage was complete fragmented but the wall at further downstream is intact. According to Clancy (1972), the overpressure for 50% of destruction of brickwork of houses is estimated to be 17.2 kPa. Thus, it is reasonable to estimate the overpressure at 60 m from the storage is at least 17.2 kPa. Assuming an explosion efficiency of 0.1 based on the TNT equivalency model, the TNT equivalent mass of the explosion is estimated to be 154 kg. Certainly, this TNT equivalency is an approximation but the fuel that contribute to the explosion should had higher or at least equivalent explosion energy.

Fig. 6. *Aerial view of the explosion with fire remaining on most part of the plant. Yellow arrow indicates the location of the peroxide's storage, pink arrow is the entrance of warehouse and circle indicates the fire truck that took video in Figure 3*

Fig. 7. *Damage of the plant exterior. The 4 red arrows indicate the brick walls that were blown away. The red circle is a fragment of brick wall. Pink arrow indicates the entrance of warehouse*

Fig. 8. *Damage of warehouse interior (left) and ruptured floor on second floor (right)*

2. Thermal and flammability analyses

As a potential thermal runaway in one of the C40-P peroxide pellet, extensive testing were done to confirm the thermal and flammability properties.

2.1. The C40-P sample

The C40-P peroxide was a blend of a silicon dioxide powder and a liquid form peroxide containing 79% of 1,1-Di(tert-butylperoxy) cyclohexane (DTBCH) balanced with isoparaffin. Final assay is 40% DTBCH and the appearance is fine white powder. The 79% DTBCH was from a Japanese source and shipped into the manufacturer on April 7 2023. The manufacturer shipped it to processing plant on April 15. When blending processing was completed on May 18, the powder peroxide was packed in a PE bag, boxed for every 20 kg, and packed and wrapped by PE film and placed on a pellet for every 50 boxes. Two pellets of the incident batches were shipped to the incident warehouse on August 14. Another pellet with newer processing batch was shipped into the warehouse on September 9. It should

be note that there was no temperature control after the processing. Three samples were acquired from the manufacturer for three batches processed in January, May, and July 2023. Thus, the samples taken represent not only the same batch but also older and newer batches of peroxide.

2.2. Differential scanning calorimetry

Preliminary thermal analysis of the C40-P sample was done by Differential Scanning Calorimetry (DSC). The DSC used was Mettler HP-2 DSC with 30 μL HP reusable gold-plated crucible which has pressure resistance up to 15 MPa. The crucible was cleaned after each use. Single used 25 μL HP crucibles were also used and results are similar to the reusable ones. Sample mass was limited to 2~3 mg and dynamic heating rate was fixed at 4°C/min. Temperature scanning range was 30~250°C. Calibration was done with Indium metal for the melting point and heat of fusion to less than 1% deviation from literature data. Figure 9 shows a typical result of DSC curve for July batch sample. The onset of exothermic decomposition (T_{onset}) is 120.13°C while the heat of decomposition (ΔH_d) is 1180.62 J/g. Three more repeats gave some scattered data ranging from 794 to 1180 J/g with average value of 1062.3±181.6 J/g. The data scattering raised the issue of homogeneity of the sample. Standard ASTM sieves with different mesh sizes of 35, 40, 50, 80, and 200 were used to screening the powder. The results are shown in Figure 10 and Table 2. Clearly, the peroxide is mainly fine powder with diameter less than 0.177 mm. In Table 2, DSC results for different batches show that scattering of the heat of decomposition data occurred for all particle size range. Nevertheless, the scattered data showed a maximum of 1287.1 J/g which is only 30% higher than the overall average of 985 J/g.

The C40-P manufacturer did not provide relevant data. However, one manufacturer, NOF Co. (2024), gives ΔH_d of 754 J/g and T_{onset} of 132°C for their Perhexa C-40 product which contains 40% of DTBCH in powder form. Thus, it has a lower ΔH_d and a higher T_{onset} in comparison with that of C40-P. NOF Co. (2024) also gives ΔH_d of 1370 J/g and T_{onset} of 134°C for their Perhexa C-70 product which contains 70% of DTBCH in liquid form. There are also several studies on liquid form DTBCH. For example, Lin et al. (2012) studied the 70% DTBCH by DSC giving ΔH_d of 1354 J/g and T_{onset} of 121.66°C. This is about 30% higher than the average value of C40-P. Thus, the current DSC studies do not find abnormally high heat of decomposition or low decomposition temperature for the C40-P samples. DSC data are however scattered but the peak heat of decomposition remains smaller than those of 70% sample given in the literature or manufacturer data.

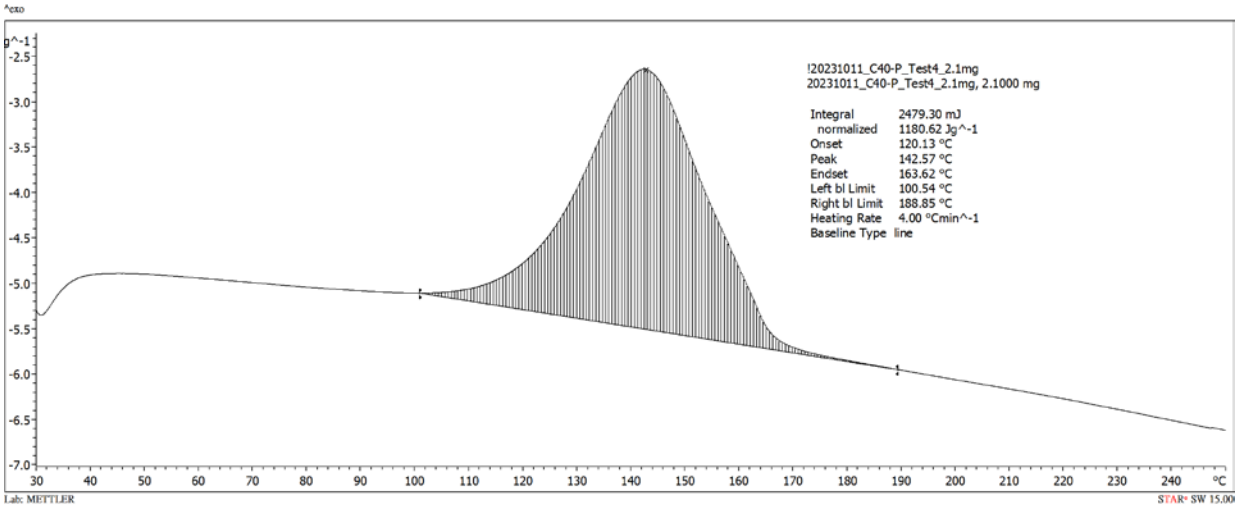

Fig. 9. *A typical result of DSC curve of C40-P July batch sample*

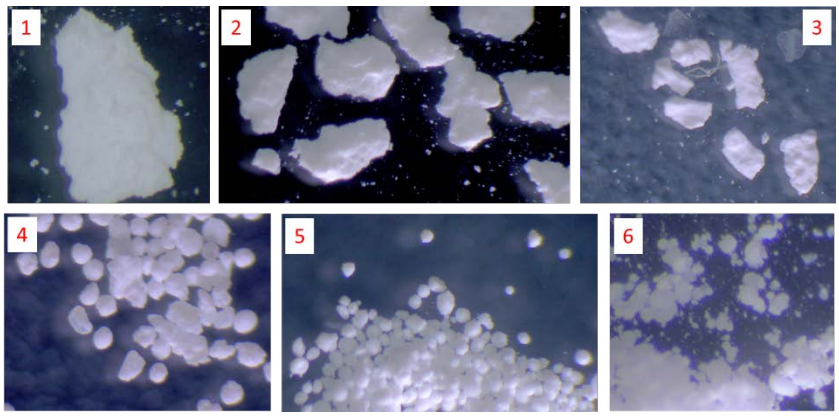

Fig. 10. *Microscopic photos of screened sample for the July batch. Number refers to the sample group*

Table 2*. Screened sample weight and respective DSC results for different batches*

Screened Sample	ASTM Mesh No.	Particle size range (mm)	January batch			May batch				July batch test 1		July batch test 2	
			Wt fraction (%)	ΔH_d (J/g)	T_{onset} (°C)	Wt fraction (%)	ΔH_d (J/g)	T_{onset} (°C)	Wt fraction (%)	ΔH_d (J/g)	T_{onset} (°C)	ΔH_d (J/g)	T_{onset} (°C)
1	>35	> 0.5	0.40%	1287.1	120.26	0.37%	873.8	119.60	0.76%	1015.80	121.78	692.57	121.21
2	35~40	0.5~0.42	0.11%	966.8	117.71	0.09%	1022.1	122.28	0.65%	972.23	119.18	824.36	119.87
3	40~50	0.42~0.297	0.14%	987.8	118.77	0.12%	1006.2	119.26	0.55%	1127.55	122.72	929.48	119.42
4	50~80	0.297~0.177	1.30%	968.6	118.82	1.28%	1268.6	120.25	2.78%	1077.86	122.22	656.94	119.87
5	80~200	0.177~0.074	66.02%	726.0	118.98	51.99%	1165.4	119.79	58.74%	862.06	122.28	1086.03	120.87
6	<200	<0.074	32.03%	1005.6	119.54	46.14%	1206.3	120.19	36.51%	1005.48	122.44	909.71	119.40
		Average		**990.3**	**119.01**		**1090.4**	**120.23**		**1010.2**	**121.77**	**849.9**	**120.11**
		Standard deviation		178.4	0.85		147.9	1.07		91.4	1.31	169.2	0.76

2.3.Accelerating rate calorimetry

The thermal runaway behaviour of C40-P sample was studied by the accelerating rate calorimeter (ARC) using Phi-Tec from HEL. Chen et al. (2023) have performed ARC tests for 80% DTBCH and the current studies aimed to follow their test condition so that the results can be compared and assessed for relative hazards. A spherical stainless-steel test can, ARC-FS-2-TW25 from Fauske, with a volume of 9 ml was used. Amount of sample is 0.7 g. The results are shown in Figure 11.

In comparison with the results of ARC tests done by Chen et al. (2023), it is clear that thermal runaway of C40-P sample is less energetic as those of 80% DTBCH which is as expected. Notably peak pressure of 3.78 bar is far less than the 13.75 bar of 80% DTBCH while peak temperature of 177.1°C is comparable to the 176.7°C of 80% DTBCH. The peak pressure represents the gas generation from decomposition of the O-O bonds and thus should be proportional to the concentration of peroxide. On the hand, C40-P is a powder form in silicon dioxide substrate which suffers the drawback of low thermal conductivity and low heat capacity, and thus higher temperature rise. Nevertheless, the ARC and DSC results seem unable to support an explosion from direct runaway reaction for a scale of damage described in Section 1. Additional tests were carried out for alternative causes such as metal contamination and dust explosion.

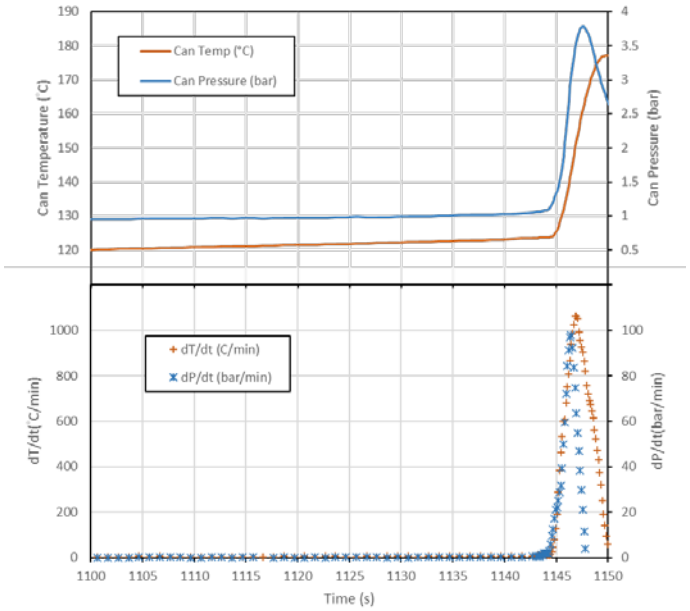

Fig. 11. *Results of ARC tests*

2.4. EDX, ATR- FTIR and GC-MS Analysis

To confirm that the C40-P sample do contain the correct assay as claimed by the manufacturer and without contamination, SEM-EDX was used for elemental analysis. The results found only oxygen and silicon with the atomic ratios roughly match silicon dioxide. There is no metal contaminant found. The samples were then analysed with ATR- FTIR. Spectra for the samples from the three batches are identical. Figure 12 shows the spectra for May batch sample. Also included are the spectra for the residue from the bomb calorimetry test in which the sample was burnt with pure oxygen to measure the heat of combustion. Clearly, the spectra for the sample after bomb test matches the major peak of C40-P which, as expected, can be attributed to silicon dioxide. Additional functional group identified is dodecane for the bands near 2800-3000 cm^{-1}. This is consistent with the fact that C40-P contains isoparaffin which are typically branched paraffin with 12-14 carbon chain. For confirmation, the vapor space of the sample was analysed by Inficon HAPSITE portable GC-MS. The result is shown in Figure 13 which contains a broad group of dodecane and higher alkanes. Also noted is the presence of acetone and cyclohexane which are known decomposition of DTBCH according to Chen et al. (2023). In summary, all assay analysis confirmed the C40-P roughly matched the claimed content of silicon dioxide and isoparaffin. There is not metal or other contamination found.

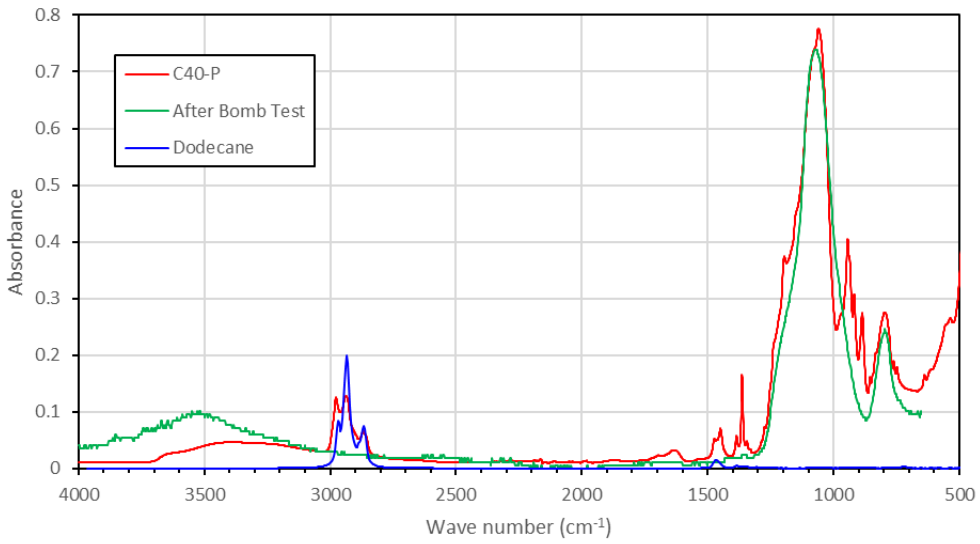

Fig. 12. *IR Spectra of C40-P*

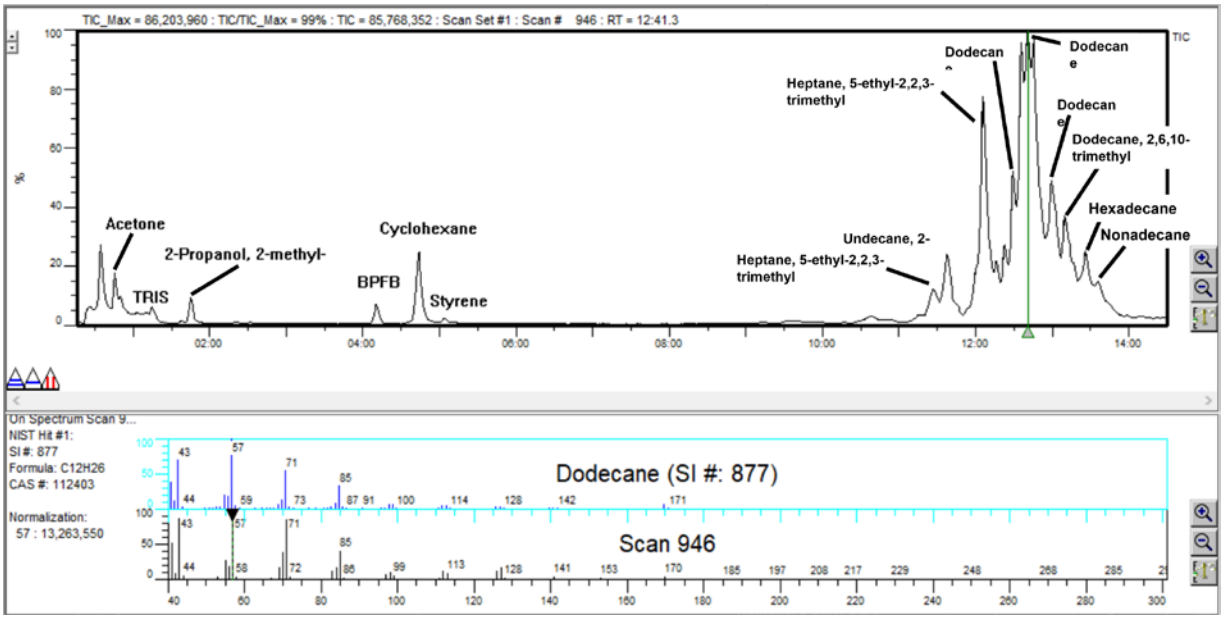

Fig. 13. *Headspace analysis of C40-P sample with GC-MS.*

2.5. Dust MIE

According to UN DG, the hazard classification is different for solid and liquid DTBCH. For example, solid form of DTBCH with concentration less than 42% and inert solid greater than 45% is classified as Type D while liquid form of the same concentration DTBCH is classified as Type F (UN DG, 2006). The difference mainly lies in the fact solid form peroxide has poor thermal conductivity and forms hot spot while liquid form peroxide simply flowed and spread out when the container was failed during thermal runaway.

An additional risk associate with solid organic peroxides is their potential dust explosion risk. For example, Lu et al. (2009) measured the dust minimum ignition energy (MIE) for 98% crystalline benzoyl peroxide (BPO) to be less than 1 mJ. Lu et al. (2010) measured 98% crystalline dicumyl peroxide (DCP) dust MIE to be less than 3 mJ. All these results suggest that powder form organic peroxides may possess high risks of dust explosion, even through that BPO and DCP are both classified as Type F organic peroxide. Thus, dust MIE measurement was done for the C40-P sample.

An MIE Apparatus from Chilworth Technology UK was used which met IEC1241-2-3 and BS5958 standard. Sample from the July batch with an initial sample mass of 0.5 g was used. First test with 100 mJ ignition energy gave a loud pop sound and a very strong flame propagating upwards and downwards in the Hartmann tube as shown in Figure 14. Subsequent ignitions with lower energies of 25 and 10 mJ produced similar, strong flames. The MIE was concluded to be less than 10 mJ, the lowest possible value that the apparatus can performed. Thus, the C40-P dust has a high sensitivty to ignition and dust explosion is a possible scenario for the incident.

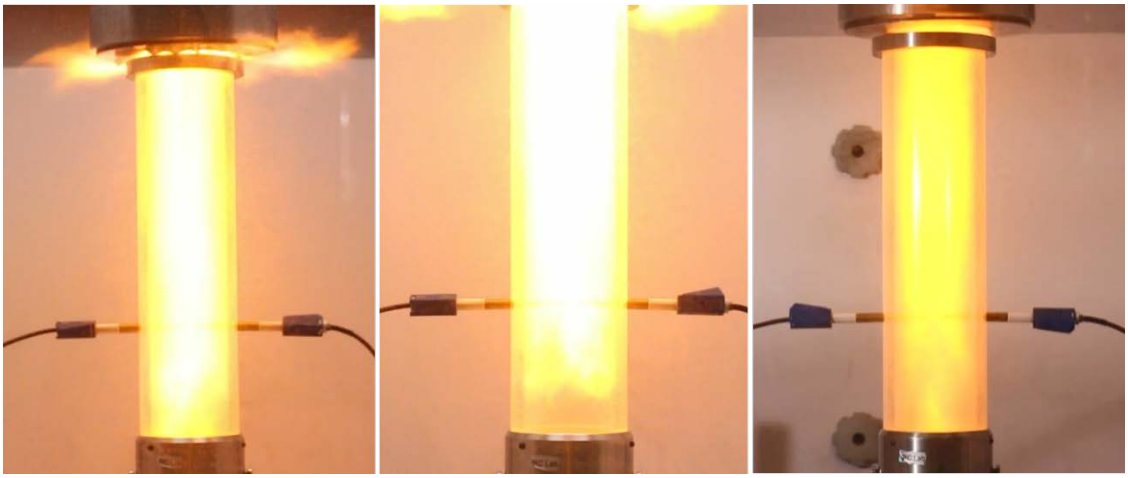

Fig. 14. *Flame from the MIE tests. From left to right: 10 mJ, 25 mJ and 100 mJ ignition energies.*

2.6. Bomb calorimetry

Althogh the DSC and ARC studies showed relatively low energy release towards thermal runaway, the energy is only from thermal decomposition of O-O bonds. To assess the potential of dust explosion, the energy from combustion of the dust was measured with a Parr 6200 Oxygen Bomb Calorimeter. The Bomb Calorimeter uses pure oxygen to ensure a complete combustion of the sample and is a standard method for characterizing the calorific values of foods and fuels. Calibratrion was done with benzoic acid and the measured heat of combustion was within 3.6% from the literature data.

Samples from three batches were measured and the combustion energies are roughly the same with an average value of 14,158 ± 417 J/g. This is about 14 times higher than the decomposition energy measured from DSC. Assuming an explosion efficiency of 0.1, one pellet of 1000 kg of C40-P undergoes dust explosion will have a TNT equivlancy of 302 kg which is above the estimated TNT equivalency of 154 kg from the actual damage. Thus, the current incident is more likely a dust explosion rather than just a thermal exploion.

2.7. Discussion

Although Lu et al. (2009, 2010) highlighted the risk of dust explosion, both studies did not mention the potential of a thermal runaway leading to a dust explosion. The ARC results in Section 2.3 highlightes only limited temperature rise. The maximum temperature for adiabatic runaway of 80% DTBCH is estimated to be 537°C after considering thermal inertia factor (Chen et al., 2023). Heat capacity of C40-P is calculated to be 1.42 J/g based on average of those of silicon dioxide and 80% DTBCH. The maximum temperature for adiabatic runaway of C40-P is estimated to be 466°C. Although it is possible to ignite the dust through direct heating, the minimum autoignition temperature (MAIT) of dust is generally higher than 500°C (Eckhoff, 2003). The MAIT for C40-P remains to be determined but it is expected to be higher than AIT of the decomposition gases.

Chen et al. (2024) studied the decomposition products of 80% DTBCH. The main pyrolysis products, in the order of GC-MS peak intensity, were isobutene, acetone, cyclopropane, 2, 2-dimethyl heptane and n-undecane. The AITs of the pyrolysis products are 435, 700, 498, 205, and 240. Furthermore, the main component in isoparaffin of C40-P is dodecane which also has a relatively low AIT of 205°C. The maximum temperature for adiabatic runaway of C40-P is expected to be higher than the AIT for all these products except for acetone and cyclopropane. Thus, explosion is likely to be caused by ignition of the decomposition gases, followed by dust ignition of the visible flame to produce the dust explosion. The following sequences are proposed and summarized in Figure 15:

- Poor packaging giving poor heat dissipation
- No temperature control in warehouse

- C40-P slowly decomposed and heat accumulated
- Temperature rise to above SADT
- Gas generation and temperature rise accelerated
- Dust dispersed by gas generation
- When temperature rise above the AIT, the gases were ignited giving visible flame
- Dust ignited by the visible flame giving dust explosion

Thus, thermal runaway of the solid form organic peroxide does not only lead to decomposition and gas generation, but also a possible autoignition of the gas generated and eventually a severe dust explosion. Special cares should be taken regarding the safe storage of solid form organic peroxide to prevent the direct dust explosion from thermal runaway.

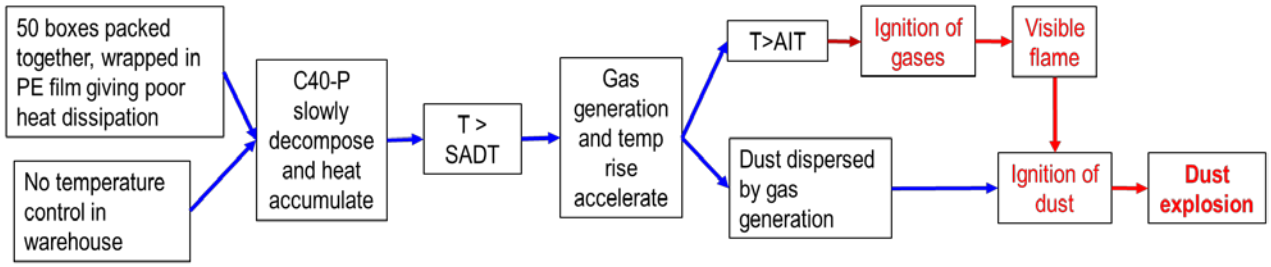

Fig. 15. *Sequence of organic peroxide dust explosion*

3. Conclusions

Detailed investigation of a fatal organic peroxide explosion incident was done. The explosion was estimated to have TNT equivalency of 153 kg from thermal runaway of a pellet of 1000 kg solid form of 40% DTBCH. Although thermal analysis by DSC and ARC did show thermal decomposition at temperature above 120°C, the exothermic enthalpy and adiabatic temperature rise were relatively low to cause the explosion with TNT equivalency of 153 kg. Further analysis of volatile emission and decomposition products revealed long-chain aliphatic compounds which have relatively low AIT. Dust MIE of the peroxide powder showed extreme sensitivity towards ignition. Bomb calorimetry confirmed the enthalpy of dust combustion. It is concluded that the thermal runaway of the peroxide under poor storage condition leading to emission of volatile organic compounds (VOCs) with AIT as low as 205°C. The decomposition generated significant gas that also disperse the peroxide powder in air. Ignition is most likely initiated by autoignition of the decomposition gases and subsequently the erupted and dispersed peroxide that led to a severe dust explosion. It should be note that most studies on organic peroxides place emphasis mainly on the thermal runaway hazards and there is no report of direct dust explosion from thermal runaway of solid form organic peroxide. The results highlight the risk of dust explosion of organic peroxide in solid powder form.

Acknowledgements

The authors gratefully acknowledge the assistance from Pingtung County Fire Department for the incident investigation.

References

Chen, N., Yao, H., Liu, X., Jiang, J., Ni, L., 2023. Investigation of the thermal hazard and decomposition mechanism of 1,1-di (tert-butylperoxy) cyclohexane by experiment and DFT simulation, Process Safety and Environmental Protection 177, 1116–1128.

Clancey, V. J., 1972. Diagnostic Features of Explosion Damage, Sixth International Meetings of Forensic Sciences, Edinburg, Uk.

Crowl, D. A., J. F. Louvar, 2013. Chemical Process Safety Fundamentals and Application, 3rd ed., Prentical-Hall.

Eckhoff, R., 2003. Dust Explosions in the Process Industries, 3rd Edition, Gulf Professional Publishing.

Factory Mutual Global, 2020. Organic Peroxides and Oxidizing Materials, FM Global Property Loss Prevention Data Sheets 7-80.

Lin, Y.F., Lin, C.P., Chen, L.Y., Su, T.S., Tseng, J.M., 2012. Effect of different concentrations of acetone for the decomposition reactions of peroxyketal peroxides. Thermochim. Acta. 527, 27-32.

Lu, K. T., Chen, T. C., & Hu, K. H., 2009. Investigation of the decomposition reaction and dust explosion characteristics of crystalline benzoyl peroxides. Journal of hazardous materials, 161, 246-256.

Lu, K. T., Chu, Y. C., Chen, T. C., & Hu, K. H., 2010. Investigation of the decomposition reaction and dust explosion characteristics of crystalline dicumyl peroxide. Process Safety and Environmental Protection, 88, 356-365.

Ministry of the Interior, Taiwan, 2021. Establishment Standard and Safety Control Regulation for Manufacturing, Storing, Processing Public Hazardous Substances and Flammable Pressurized Gases Places, Nov. 10.

NOF Co., 2024. PERHEXA® C: 1,1-Di(t-butylperoxy)cyclohexane, https://www.nof.co.jp/files/product/catalog/kobetsu/PERHEXA%20C.pdf, accessed March 1.

United Nations, 2019. Recommendations on the Transport of Dangerous Goods, Model Regulations, Volume I, 21st Rev. Ed.

Experimental Research Of A Tank For A Cryogenic Fluid With A Wall Rupture In A Fire Scenario

R. Eberwein [a], A. Hajhariri [a], D. Camplese [b], G.E. Scarponi [b], V. Cozzani [b], & F. Otremba [a]

[a] Bundesanstalt für Materialforschung und -prüfung (BAM), Berlin, Germany
[b] Alma Mater Studiorum - Università di Bologna, Bologna, Italy

E-mail: *robert.eberwein@bam.de*

Abstract

In the course of decarbonizing the energy industry, cryogenic energy carriers as liquefied hydrogen (LH2) and liquefied natural gas (LNG) are seen as having great potential. In technical applications, the challenge is to keep these energy carriers cold for a long time. This is achieved in the road transport sector and also stationary applications by thermal super insulations (TSI) which based on double-walled tanks with vacuum and multilayer insulation (MLI) in the interspace. This study focuses on the behaviour of widely used combustible MLI in a fire scenario, at vacuum and atmospheric pressure conditions. The former corresponds to the typical design condition and the latter to the condition after an outer hull rapture of a tank. Furthermore, two fire scenarios were taken into account: a standard-oriented approach and a hydrocarbon fire-oriented approach. For the study, a test rig was applied that allows testing of TSI at industrial conditions and subsequent analysis of TSI samples. The test rig allows thermal loading and performance analysis of TSI samples at the same time. Comparing the tests, the samples degraded differently. However, no sudden failure of the entire MLI was observed in any test. These results are relevant for the evaluation of incidents with tanks for the storage of cryogenic fluids and can thus contribute to the improvement of TSI and the development of emergency measures for the protection of persons and infrastructures.

Keywords: Liquefied hydrogen, Liquefied natural gas, cryogenic storage tank, Fire, thermal insulation, Multi-Layer Insulation

1. Introduction

Cryogenic energy carriers such as liquefied hydrogen (LH2) and liquefied natural gas (LNG) are establishing themselves more and more. One aspect therefore is their volumetric energy density, which is significantly higher compared to their gaseous representatives stored at ambient conditions. The storage at cryogenic conditions for prolonged time requires pressure tanks with thermal super insulation (TSI) that hinders the heat flow from the environment into the tank at design conditions (Lisowski and Lisowski, 2018).

However, pressure tanks can fail, and can cause large losses on infrastructures and persons. A typically assumed worst case in this concern is a BLEVE where a tank failed because of a fire. Such real scenarios were investigated by Planas et al. (2004, 2015), and Vollmacher (2018) for instance. By tests, Pehr (1996) observed the behavior of LH2 tanks for the scenarios crash, vacuum fracture, and a full engulfing fire, for a tank from the passenger car segment of BMW. Kamperveen et al. (2016) studied the effects of a fully engulfed fire on a vacuum/perlites, and a rock wool insulated tank designed for LNG. Similarly, three tanks for LH2 were tested in the SH_2IFT Project (van Wingerden, 2022, Kluge, 2024): two tanks equipped with vacuum/perlites TSI and one equipped with a vacuum/MLI TSI. Furthermore, some studies are dealing with the behavior of insulation material under heat exposure, representing a fire. Here, Camplese et al. (2023, 2024) investigated the effect of heat on parts of MLI under atmospheric and vacuum conditions. Eberwein et al. (2023) presented a methodology for the fire orientated thermal exposure of TSI samples at industrial conditions, which

was applied to polyester-based MLI. Additionally, Eberwein et al. (2024) applied this method to different types of TSIs typically applied in the industry.

The present study focuses on the experimental investigation of TSI in a combined incident scenario, which regards an outer hull rupture and an external heat source. Two approaches are considered for thermal loading, one that is orientated on tests for the approval of vehicle tanks for LH2 and LNG and one that aims at analyzing the TSI behavior under exposure to a hydrocarbon fire. For the observation, a High-Temperature Thermal Vacuum Chamber (HTTVC) was used as presented in detail in Eberwein et al. (2023), that enables thermal loading of TSI under vacuum conditions and simultaneous measurement of heat flow through the TSI system.

The results are relevant for the evaluation of accident scenarios involving full-scale cryogenic tanks. They can thus contribute to the improvement of TSI, the development of safer tank designs, as well as the development and definition of emergency measures for the protection of persons and infrastructures.

2. Tank design and material

Land transport comes typically with limited volumetric space and the aim to maximize the payload. These requirements can be met from tanks with a double-walled design which is shown in Fig. 1.

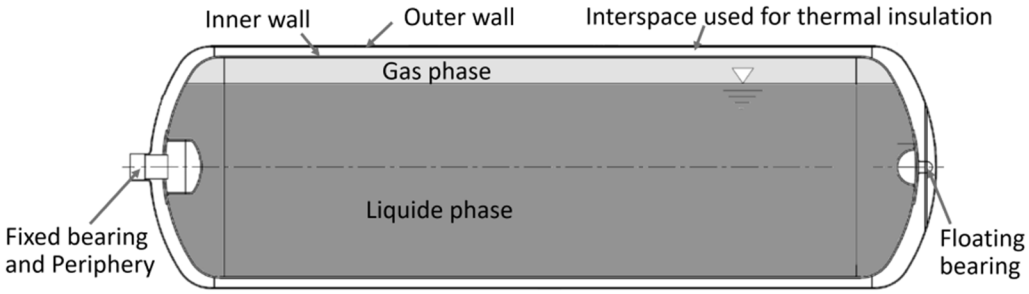

Fig. 1 Scheme of a tank typically used for cryogenic fluids in the land transport

This construction is based on an outer tank in which an inner tank is held by a floating and a fixed bearing. The inner tank contains the cryogenic fluid. The fixed bearing serves as the tank periphery for the inner tank, by which the cryogenic fluid is loaded and unloaded.

The outer and inner wall form a double-wall with interspace, that is used to generate a super insulation for the stored cryogenic fluid through vacuum and an additional filling material. The fill material can be structured into the types of foams, bulk-fill, and layered. For instance, Lisowski & Lisowski (2018) presented that layered systems with vacuum such as multilayer insulations (MLI) have shown better performances in terms of space, and thermal insulation compared to TSI's with other fill-materials. Layered fill materials based on reflective foils alternated with spacer foils. This structure hinders heat transfer by conduction as well as radiation. Furthermore, the vacuum hinders heat transfer by convection. Layered systems are subdivided into combustible and non-combustible. Combustible systems are often based on aluminium-coated polyester or Mylar® foils and polyester fleece spacers which have several advantages compared to non-combustible systems that often based on aluminium foils and glass-based spacers. Exemplary advantages are better thermal insulation performance and better integrability (Duval, 2019), which increases the overall system performance and its availability.

According to the technical regulations ECE R110 and GTR13, which apply to vehicle fuel tanks, both MLI classes can be used for TSIs. The transportation of dangerous goods, which also includes LH2 and LNG, is regulated by the ADR. This permits the use of both classes of MLI for LNG storages, and with exceptions for LH2 storages.

In this study, MLI based on 10 layers of polyester foil, 12 µm thick, double-sided aluminized with 400Å, perforated with an open area of 0.075 % and interleaved with 9 layers of polyester-fleece material was used, which has an overall nominal area-specific weight of 0.308 kg/m², and which is classified as combustible.

3. Experimental setup

The experimental setup's fundament is the High-Temperature Thermal Vacuum Chamber (HTTVC) where diverse TSI systems can be tested in vacuum conditions. The application of the HTTVC is supported by a heating and cooling system, a vacuum pump, a data acquisition system, and a water supply system that is used to estimate the heat flow through the TSI for instance. The overall test setup and the electrical heating system is shown in Fig. 2.

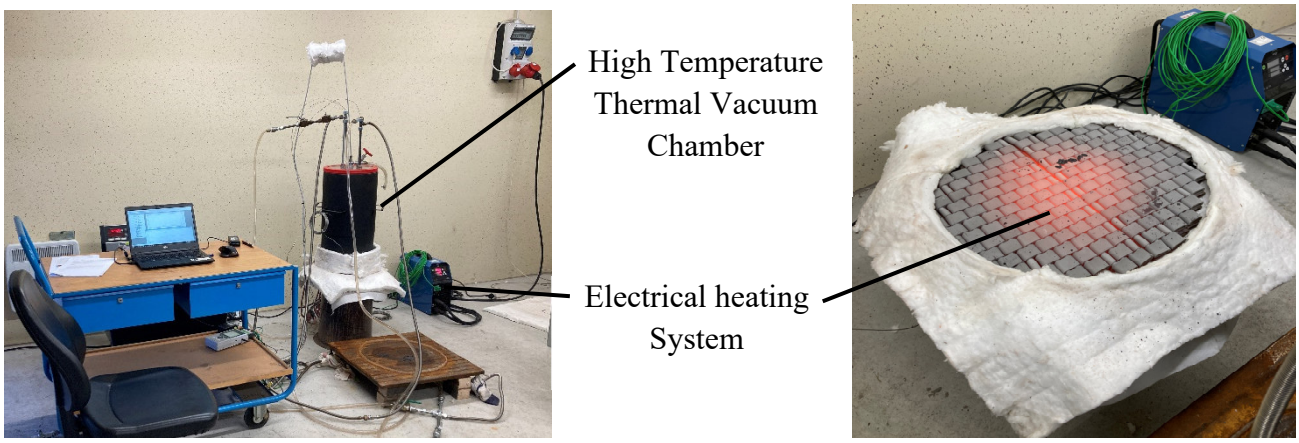

Fig. 2 The test setup with the High Temperature Thermal Vacuum Chamber and the electrical heating system

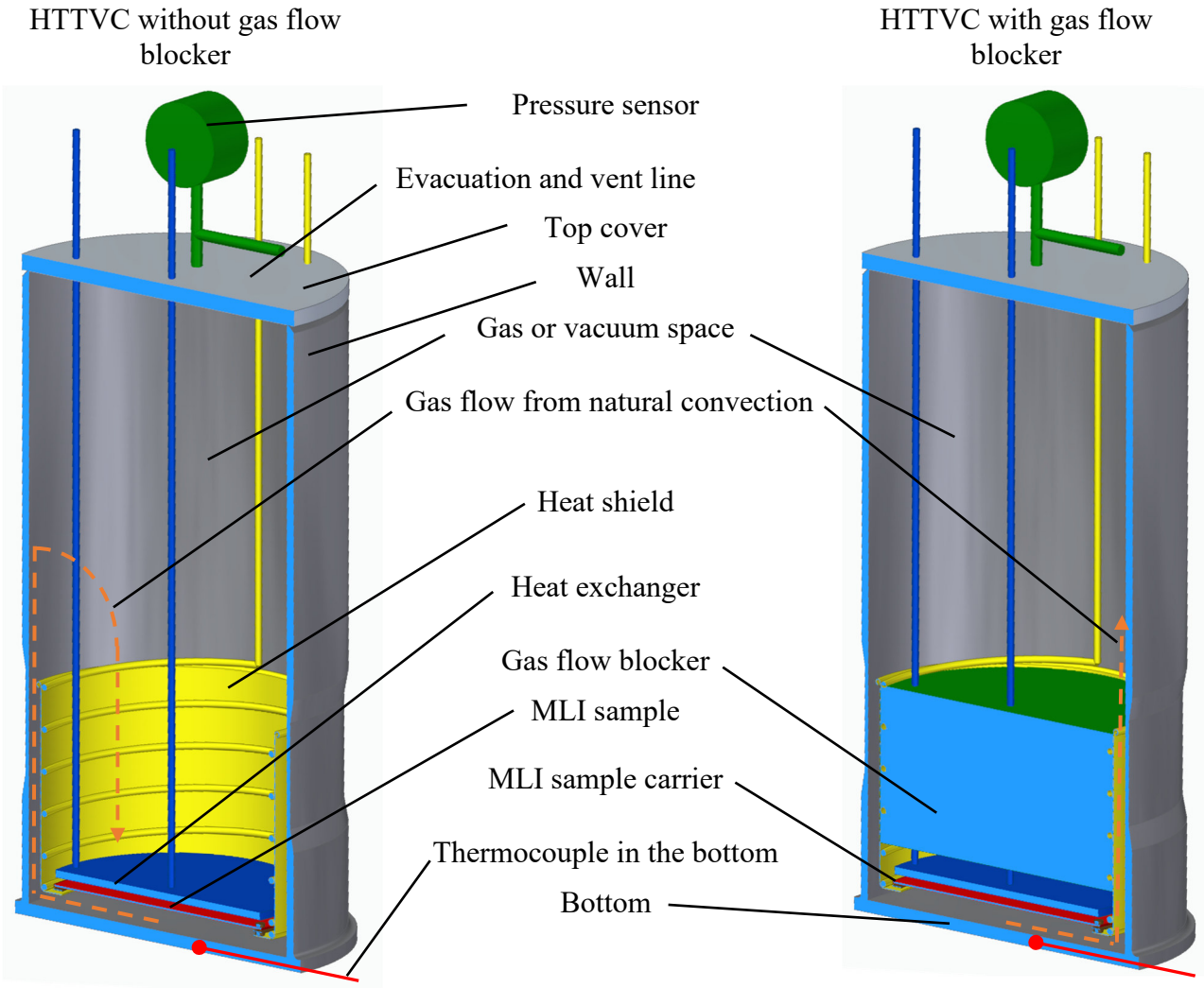

Fig. 3 HTTVC in a sectional view: without gas flow blocker (left), with 'gas flow blocker' (right)

The HTTVC, shown in Fig. 3 in a sectional view, has a length of 600 mm and an outer diameter of 320 mm. The bottom and the heat exchanger in the HTTVC represent two walls in parallel with a space of up to 300 mm in between where different TSIs can be placed. This structure represents a typical design of a TSI.

The TSIs components bottom, the MLI, and the heat exchanger applied in this study shows Fig. 4 exemplary for the experiment campaign 1-3 before the test, which are representatives for all tests of this study. Within this study, two configurations of the HTTVC were applied. Fig. 3 on the left side shows the HTTVC without a gas flow blocker as it was also presented in the studies of Eberwein et al. (2023, 2024). Additionally, Fig. 3 shows the HTTVC with a gas flow blocker (right) made from 150 mm thick Promaglaf®, which was mounted in the heat shield. The gas flow blocker aimed to block a gas flow founded on natural convection through the center of the heat shield in case there is gas (no vacuum) in the HTTVC as it is schematically shown in Fig. 3 for both HTTVC configurations.

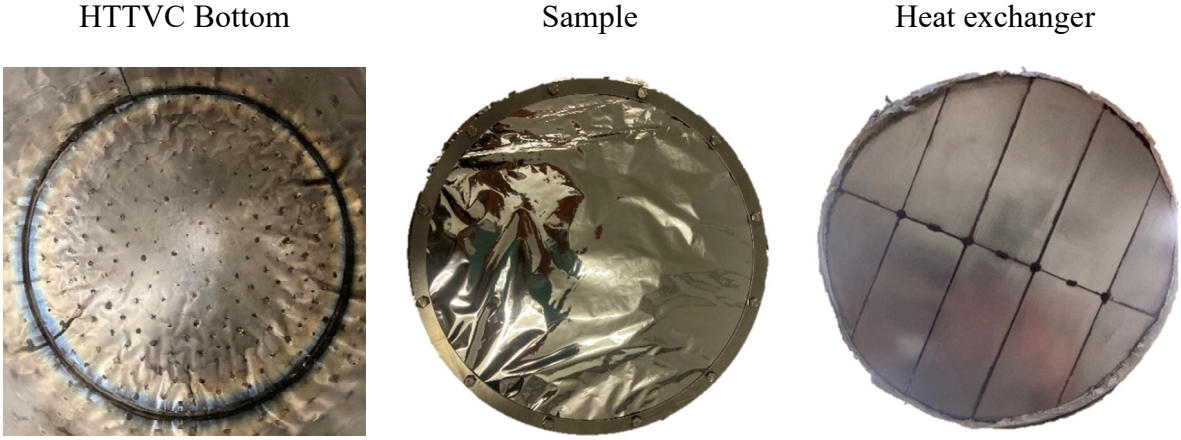

Fig. 4 The components of the double-wall in the HTTVC before experimental Campaign 1-3

For each experiment, the bottom of the HTTVC serves as the radiative heat source for the thermal loading of MLI samples. The bottom is electrically heated by an inverter heat treatment unit and 4 resistant heating mats, that enable the generation of heat flows up to 100 kW/m². This approach allows the reproducible simulation of various fire conditions, e.g. ISO 834 (ISO Curve), EN 1991-1-2 (Hydrocarbon Curve), RABT (ZTV Curve), or ISO 21843. In the tests, the side walls of the HTTVC are also heated. In order to thermally load an MLI sample solely from the bottom of the HTTVC, the chamber is equipped with a heat shield that has a circular opening with a diameter of 230 mm, which is aligned with the bottom of the HTTVC. The heat exchanger represents the cold inner wall of a double-walled tank. Therefore, it is water-supported. Based on the measured mass flow of water ($\dot{m}_f$), its measured inlet (T_{fi}) and outlet (T_{fo}) temperature, and the waters heat capacity (c_f) which was assumed with 4190 J/kg/k, the heat flow transported by the fluid ($\dot{Q}_f$) can be calculated by equation 1, which represents also the heat flow transported by the double wall.

$$\dot{Q}_f = \left(T_{fi} - T_{fo}\right) c_f \, \dot{m}_f \qquad (1)$$

For measuring temperatures type K thermocouples were used at: a heating wire of the heating mat; between the heating mat layers; in the bottom of the HTTVC; at the inlet and outlet of the heat exchanger; at the outlet temperature of the heat shield; and in the environment for measuring the room temperature. The absolute pressure was measured with a piezo-Pirani sensor type VSR53MV from Thyracont Vacuum Instruments GmbH. For data logging and synchronization of the sensors, an Ahlborn ALMEMO® 2890-9 was applied.

Additional details on the HTTVC setup can be found in Eberwein et al., 2023 and 2024.

4. Test program

Two test campaigns were carried out with different thermal loading procedures but the same loading duration of 70 minutes and regarding combustible MLI as fill-material.

The first campaign was oriented on design fires defined in the standards GTR 13 and ECE R110 and which are applicable for approval tests on LNG and LH2 tanks. These standards require a minimum temperature of 590°C measured in the fire close to the outer tank wall. In the campaign, the heating mats were heated to a temperature of 600°C before a test with the HTTVC. Afterward, the HTTVC was placed on the heating mats for 70 minutes. During the test period, the temperature of the heating mats was controlled to a target value of 600°C. After the thermal loading, the HTTVC was removed from the heating mats and cooled to ambient temperature. Finally, the sample was removed from the HTTVC. Campaign 1 contained 6 experiments with and without combustible MLI, with vacuum, nitrogen or air in the HTTVC and the 2 configurations of the HTTVC as shown in Figure 2.

In the second experimental campaign, the temperature for thermal loading the double-wall was with 800°C orientated to the temperature measured on average on a tank for a cryogenic fluid in a fully engulfing hydrocarbon fire observed from Kamperveen et al. (2016). The heating procedure was divided into three periods, the heating period with a gradient of approximately 20 K/minute, the constant bottom-temperature period with a temperature of about 800°C maintained about 30 minutes, and the cool-down period within about 40 minutes. Campaign 2 comprised 4 experiments with and without combustible MLI, with vacuum or air in the HTTVC and the 2 configurations of the HTTVC as shown in Fig. 3.

All experiments with its details are summarized in Table 1.

Table 1 Overview of the experiments of the two test campaigns on combustible MLI

Experiment	Fill-material	Fill-material environment	Gas flow blocker	Fire simulation
Campaign 1-1	-	vacuum	No	Heating mat 600°C
Campaign 1-2	-	Air	No	Heating mat 600°C
Campaign 1-3	MLI	Vacuum	No	Heating mat 600°C
Campaign 1-4	MLI	Nitrogen	No	Heating mat 600°C
Campaign 1-5	MLI	Air	No	Heating mat 600°C
Campaign 1-6	MLI	Air	Yes	Heating mat 600°C
Campaign 2-1	-	vacuum	No	Bottom HTTVC 800°C
Campaign 2-2	MLI	vacuum	No	Bottom HTTVC 800°C
Campaign 2-3	MLI	Air	No	Bottom HTTVC 800°C
Campaign 2-4	MLI	Air	Yes	Bottom HTTVC 800°C

5. Results and Discussion

In this section, the results of the two experimental campaigns are presented. For any experiment, the course of temperature in the bottom of the HTTVC, and the calculated heat flow by the double wall observed in the experiment are presented in Fig. 5 and Fig. 8 by time. The calculation of the heat flow is based on a water-supported heat exchanger, which stays in visual contact with the bottom of the HTTVC by the circular opening, with a diameter of 230 mm, of the heat shield presented in Fig. 3 and Fig. 4. The TSIs components presented in Fig. 4 before a test are presented in Fig. 6 and Fig. 7 after the thermal loading procedure.

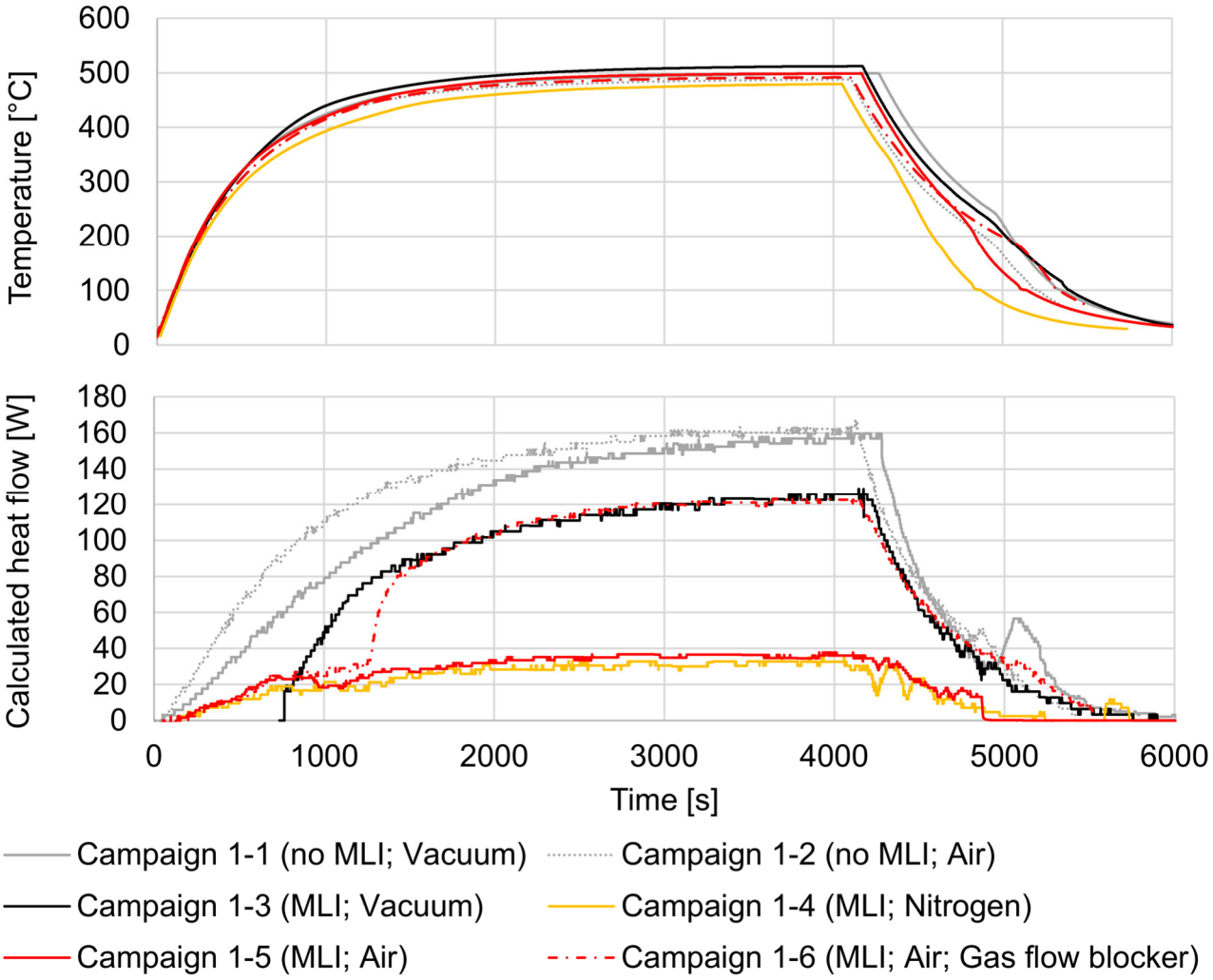

Fig. 5 Temperature and calculated heat flow over time for the experimental campaign 1

A flaming combustion of the combustible MLI was observed in none of the experiments. On the contrary, even after the experiment with air in the double wall, some layers of the MLI were fully intact. The reason for this is assumed to be the interaction of convection, heat conduction, and heat radiation. The fire heated outer wall heats the gases close to it, which reduces their density and thus the heat transport capacity by convection and heat conduction. Nevertheless, the transport capacity for heat by radiation is similar to the scenario with vacuum, due to its dependence on the 4th power of temperature (Christiansen, 1883). The damage potential of the MLI is therefore assumed to be similarly high for the scenario with vacuum and degraded vacuum.

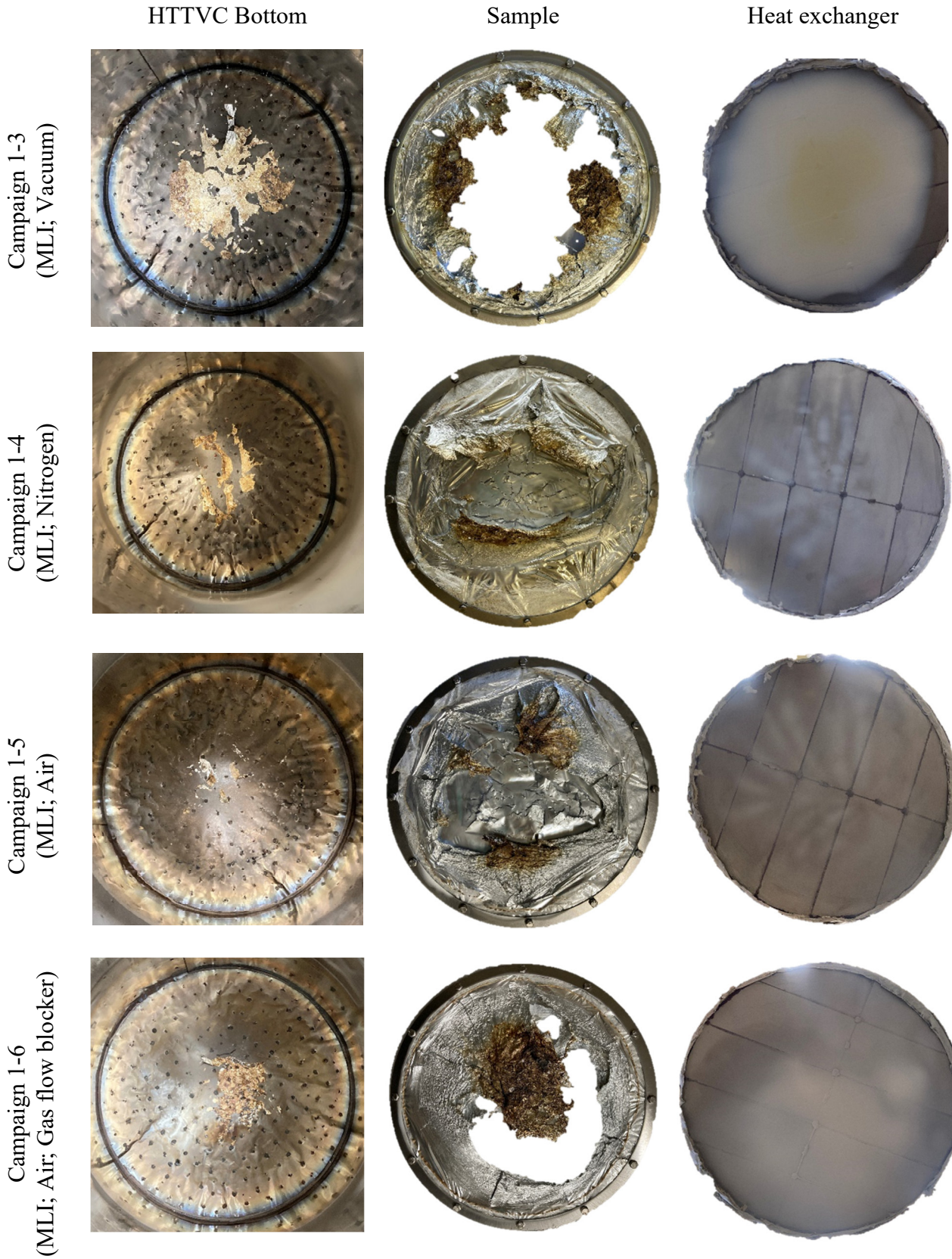

Fig. 6 The components of the double-wall in the HTTVC after thermal loading of experimental campaign 1

In contrast to the outer wall heated by the fire, the inner wall is constantly cooled by the stored, cryogenic fluid and thus also the gases which are in contact with this wall. As the temperature of the gases decreases, their density increases, and with it the potential of the gases to transport heat by conduction and convection. Furthermore, near the cold inner wall the heat transport capacity by

radiation is very low, as it depends on the fourth power of the temperature. The latter applies equally to the nominal operation of the tank and to the hazardous incident investigated in this study. A degradation of the vacuum leads to a reduction in the insulation performance and thus promotes the cooling of the layers of the MLI close to the inner wall, whereby their damage by pyrolysis starts at a later time of this experiment and at higher temperatures of the bottom. In consequence, a lower damage of the MLI in the experiments with degraded vacuum compared to the experiments of the same campaign with vacuum was observed. In the fire scenario, each fully or partially preserved layer protects the inner tank from thermal radiation emanating from the fire-exposed outer tank, as described in Eberwein et al 2023 using experimental data.

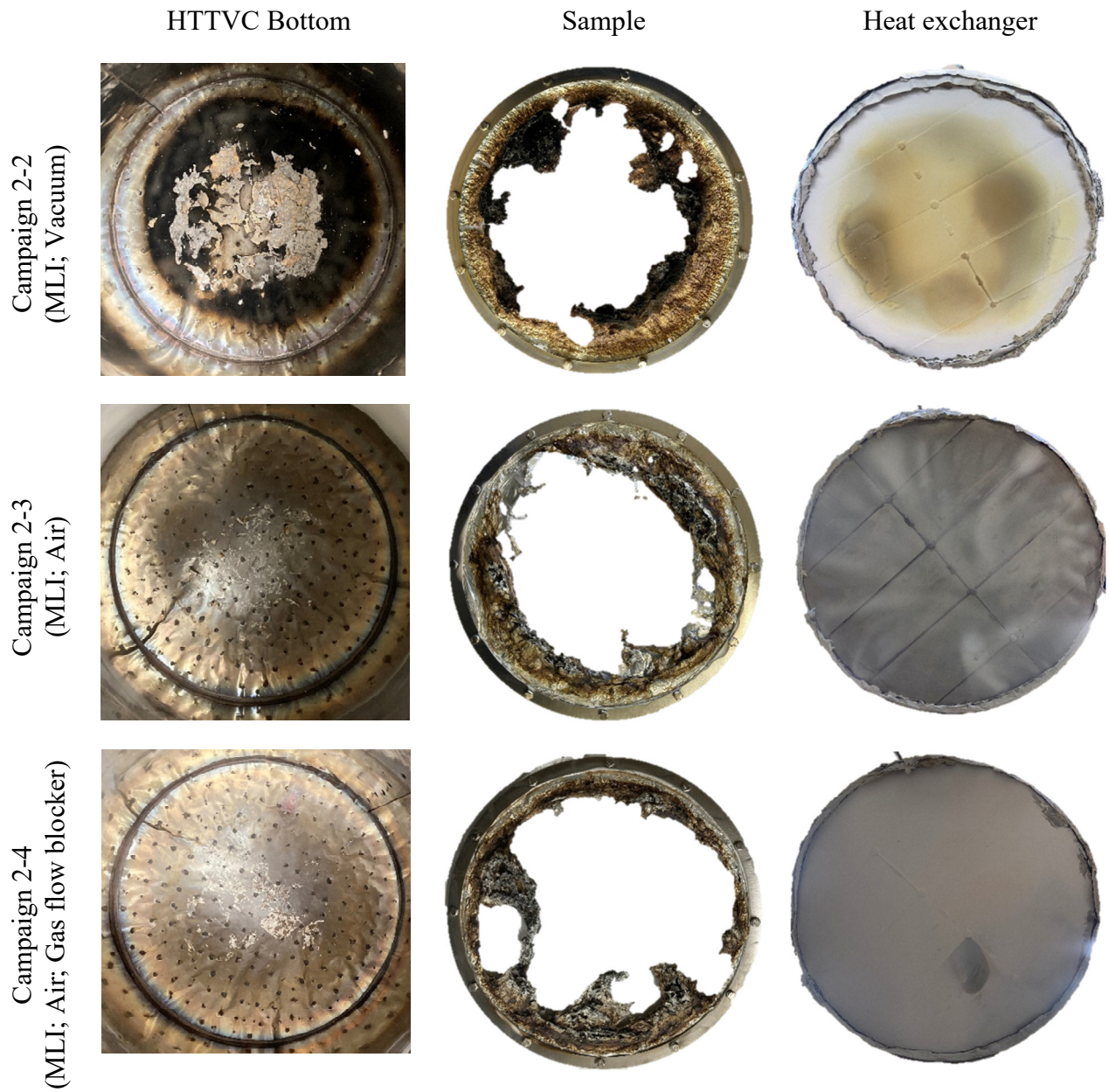

Fig. 7 The components of the double-wall in the HTTVC after thermal loading of experimental campaign 2

Furthermore, in the experiments with air or nitrogen in the double wall and without gas flow blocker in the HTTVC, a significantly lower accumulation of pyrolysis products of the MLI at the heat exchanger was observed. As a result, there was no extreme change in the emissivity factor at the heat exchanger in these experiments, as observed in Eberwein et al. 2023, and which represents the inner wall of an industrial tank. The reason for this is assumed to be the partially intact layer of MLI near the inner wall and its delayed degradation over time. This layer, which remains intact for a long time,

prevents the pyrolysis products of the outer MLI layers from reaching the heat exchanger and accumulating there. This would also be conducive to the conversion of the MLI pyrolysis products in a further pyrolysis stage, e.g. on the outer wall of a tank heated by the fire.

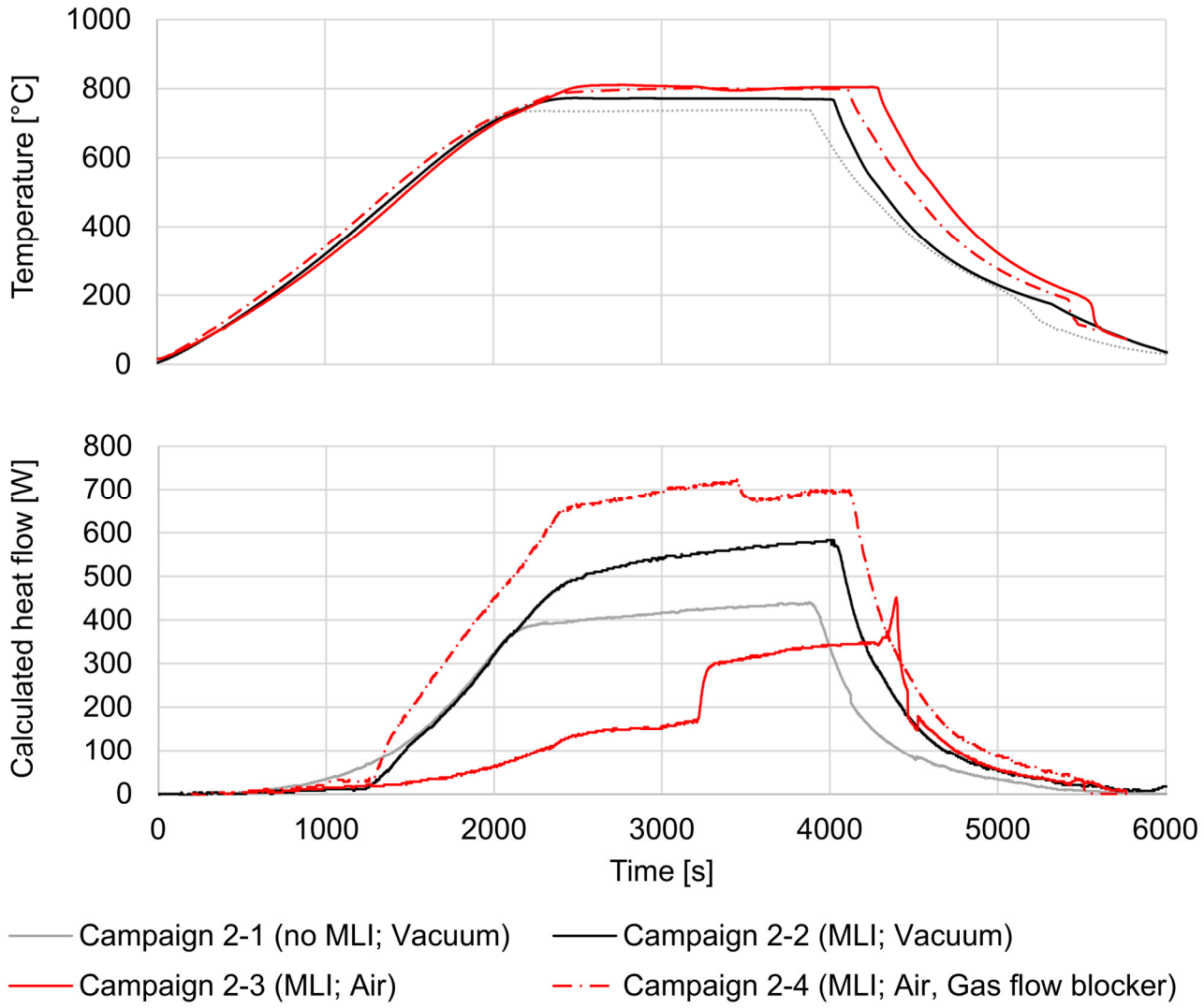

Fig. 8 Temperature and calculated heat flow over time for the experimental campaign 2

In addition to the changes at the heat exchanger, the observations away from the simulated double wall in the HTTVC without vacuum should also be noted. During these experiments, white powder accumulation was observed on the outer wall of the heat shield and a white opacity of the gas in the upper area of the HTTVC through its viewing window. The latter two effects were not observed in any experiment with vacuum, which indicates an altered circulation of gases and pyrolysis products within the HTTVC. In the experiments Campaign 1-4 and Campaign 1-5, which were conducted without gas flow blockers, there was also the previously mentioned lower damage to the MLI layer close to the cold wall and a significantly lower calculated heat flow compared to the other experiments in this test campaign. The reason for this is assumed to be the gas circulation in the HTTVC, which could have ensured that the heat exchanger and therefore also the inner MLI layer is exposed to a cold gas flow, which additionally cools the MLI layer near the heat exchanger in particular. This flow is driven by the natural convection of gases. The gas phase at the heated bottom and near the lower wall is heated and receives buoyancy. Afterward, this up-moving gas phase is cooled at the upper wall area, the outer cold heat shield, the cold cover of the HTTVC, and the cooled inner wall of the heat shield, so that a gravity-induced circulation occurs. This could also be performed in a real incident and thus protect individual layers of an MLI. This potentially cooling gas flow was reduced

in the tests with the gas flow blocker component. As a result, significantly greater damage occurred in both tests with the gas flow blocker and greater heat flows were observed.

In the experiments of Campaign 1, the measured temperatures of 500°C in the bottom of the HTTVC were significantly lower than the boundary conditions specified by the heating mats. This is typical for such scenarios and was also observed in the experiments by Kamperveen et al. (2016). Polyester-based MLI is damaged above temperatures of approx. 400°C (Bautista et al. 2018). In Eberwein et al. 2023, damage was not even observed until the bottom reached a temperature of 470°C. This means that during acceptance tests for tanks by ECE R 110 or GTR 13, the temperature threshold at which combustible MLI is damaged could be exceeded only marginally, and due to the geometry of the tank, only locally and not above the entire double wall. This can also be observed in campaign 2, in which a wall temperature of 800°C was used, which is to be expected in a hydrocarbon fire and led to severe damage to the MLI in all experiments of campaign 2. At the same time, a seven times higher heat flow was observed on average of all experiments with combustible MLI of campaign 2 compared to campaign 1.

6. Conclusions

In this study, the effect of a fire to a thermal super insulation (TSI) usually applied on tanks for the storage of cryogenic fluids such as liquefied hydrogen (LH2) or liquefied natural gas (LNG) was observed. The tested material was a combustible Multi-Layer Insulation (MLI), which was loaded by temperatures up to 800°C in a high temperature thermal vacuum chamber (HTTVC) at vacuum conditions and in a gas environment, which represents an outer hull rupture of a double-walled tank. For thermal loading 2 procedures were applied, one which is typically used for the acceptance of tanks, and one which is representative of a full engulfing hydrocarbon fire.

The experimental results present that the course of a tank in a scenario can be changed means by a strong or full degradation of the vacuum in the double wall and by the maximum temperature of the outer wall attained in a fire scenario.

The gas contamination of the double wall changes strongly the accumulation of the MLIs pyrolysis products at the cold inner wall of a cryogenic tank and also its overall distribution within the double wall, which is of great importance for the magnitude of the heat flow during and after the fire event.

Furthermore, in the presence of air and combustible MLI, there was no flaming combustion observed in any of the tests while thermal loading, which could result in a sudden failure of the entire thermal insulation.

Acknowledgements

This work was undertaken as part of the research project ‘Research of the influence of fires to tanks for cryogenic fluids’ (FETLHy), where the authors wish to acknowledge the financial support of the research from the German Federal Ministry for Economic Affairs and Climate. Furthermore, this work is part of the project ‘Novel Insulation Concepts for the Storage of Liquefied Hydrogen’ (NICOLHy) funded by the European Union and Clean Hydrogen Partnership by the Grand (Grant No. 101137629), which the authors would also like to thank for their financial support. Views and opinions expressed are however those of the author(s) only and do not necessarily reflect those of the European Union or Clean Hydrogen JU. Neither the European Union nor the granting authority can be held responsible for them.

References

Bautista, Y., Gozalbo, A., Mestre, S., Sanz, V., 2018, Thermal degradation mechanism of a thermostable polyester stabilized with an open-cage oligomeric silsesquioxane. Materials, 11, 22, pp. 1-13, https://doi.org/10.3390/ma11010022

Camplese, D., Chianese, C., Scarponi, G. E., Eberwein, R., Otremba, F., Cozzani, V., 2023, Analysis of high temperature degradation of multi-layer insulation (MLI) systems for liquid hydrogen storage tanks, CEt Vol. 99, pp. 415-420, https://doi.org/10.3303/CET2399070

Camplese, D., et al., Multilayer Insulation in Cryogenic Tanks undergoing External Fire Scenarios, 2024, PROCESS SAF ENVIRON 186, pp. 1169 -182, https://doi.org/10.1016/j.psep.2024.04.061

Christiansen, C., 1883, Absolute Determination of the Heat Emission and Absorption Capacity, Ann. Phys. Wied., Vol.19

Duval, S., 2019, Cryogenic Storages and distribution Lines, EASISchool

Eberwein, R, Hajhariri, A., Camplese, D., Scarponi, G. E., Cozzani, V., Otremba, F., 2023, Insulation Materials Used In Tanks For The Storage Of Cryogenic Fluids In Fire Scenarios, Proc. PVP 2023, pp. 1-8, https://doi.org/10.1115/PVP2023-105201

Eberwein, R. et al., 2024, Experimental Investigation on the Behavior of Thermal Super Insulation Materials for Cryogenic Storage Tanks in Fire Incidents, PROCESS SAF ENVIRON, https://doi.org/10.1016/j.psep.2024.04.131

Kamperveen, J. P., Spruijt, M. P. N., Reinders, J. E. A., 2016, Heat load resistance of cryogenic storage tanks – Results of LNG Safety Program, TNO Report

Kluge, M., Habib, A. K., van Wingerden, K., 2024, Unterfeuerung von Flüssigwassersttofftanks - Topologie eines kritischen Behälterversagens, Proceedings Magdeburg-Köthener Brandschutz- und Sicherheitstagung 2024, Magdeburg

Lisowski, E., Lisowski, F., 2018, Influence of vacuum level on insulation thermal performance for LNG cryogenic road tankers, ICCHMT 2018, MATEC Web Conf. Volume 240, pp. 1-4, https://doi.org/10.1051/matecconf/201824001019

Pehr, K., 1996, Experimental examinations on the worst-case behaviour of LH2/LNG tanks for passenger cars. Proc. 11th World Hydrogen Energy Conference, pp. Stuttgart

Planas, E., Gasulla, N., Ventosa, A., Casal, J., 2004, Explosion of a road tanker containing liquified natural gas, JLP 17, pp. 315-312, https://doi.org/10.1016/j.jlp.2004.05.005

Planas, E., Pastor, E., Casal, J., Bonilla, J. M., 2015, Analysis of the boiling liquid expanding vapor explosion (BLEVE) of a liquefied natural gas road tanker: The Zarzalico accident; JLP 34, pp. 127-138, https://doi.org/10.1016/j.jlp.2015.01.026

van Wingerden, K., Kluge, M., Habib, A. K., Ustolin, F., Paltrinieri, N., 2022, Medium-scale tests to investigate the possibility and effects of BLEVEs of storage vessels containing liquified hydrogen, 17th EFCE, Prague, pp.1-6, https://doi.org/10.3303/CET2290092

Vollmacher, K., 2018, Accident involving LNG Truck, CTIF Commission for Extrication & New Technology, 2018

ADR, 2023 - Agreement concerning the International Carriage of Dangerous Goods by Road, United Nations, New York

EN 1991-1-2, 2021, Eurocode 1: Actions on structures - Part 1-2: General actions - Actions on structures exposed to fire

ISO 834-1, 1999, Fire-resistance tests - Elements of building construction - Part 1: General requirements

ISO 21843, 2023, Determination of the resistance to hydrocarbon pool fires of fire protection materials and systems for pressure vessels

RABT, 2006, Richtlinien für die Ausstattung und den Betrieb von Straßentunneln. Forschungsgesellschaft für Straßen- und Verkehrswesen

UN ECE R-110, 2018, Rev. 4

Simulation of Joule-Thomson effect at PCV in a hydrogen refuelling station using dynamic mesh

Hazhir Ebne-Abbasi [a*], Dmitriy Makarov [a] & Vladimir Molkov [a]

[a] Hydrogen Safety Engineering and Research Centre (HySAFER), Ulster University
Newtownabbey, BT37 0QB, Northern Ireland, UK

[*] E-mail: ebne_abbasi-h@ulster.ac.uk

Abstract

The study focuses on the significance of Pressure Control Valves (PCV) in hydrogen refuelling and the associated Joule-Thomson (JT) effect, wherein the negative JT coefficient leads to a temperature increase at the PCV during refuelling. A three-dimensional Computational Fluid Dynamics (CFD) model of a hydrogen refuelling station (HRS) is developed and validated, incorporating various components such as high-pressure tanks, pipes, valves, heat exchangers (HE), hoses, breakaway, nozzle, and onboard hydrogen storage tanks. The dynamic mesh technique is employed to model the dynamics of the PCV to analyse the JT effect. The CFD model effectively replicates heat and mass transfer within the NREL refuelling station. Utilizing the National Institute of Standards and Technology (NIST) real gas equation of state, the model compares hydrogen behaviour with an imaginary scenario using methane and air for refuelling, highlighting a significant temperature increase for hydrogen due to the negative JT coefficient. The study underscores the importance of considering the JT effect in designing HRS equipment and optimizing refuelling protocols.

Keywords: *hydrogen, refuelling, Joule-Thomson effect, Hydrogen safety, CFD*

Introduction

High-pressure gaseous hydrogen storage is widely used due to the cost-effectiveness and maturity of the technology (Zheng *et al.*, 2012; Kim, Shin and Kim, 2019). Pressure control valves (PCVs) are crucial in hydrogen refuelling stations (HRS), ensuring safe refuelling (Apostolou and Xydis, 2019). The PCV consist of three general sections: a pressure-reducing or limiting element, often in the form of a spring-loaded spool; a sensing element, in the form of a diaphragm or piston; and a reference force element, typically a spring to reduce pressure from high-pressure tanks during refuelling (Beswick Engineering, 2023). The JT effect (Joule and Thomson, 1852), negative for hydrogen, increases temperature during throttling and expansion in PCV, especially during the initial refuelling stages when the pressure difference is large (Genovese *et al.*, 2023). Numerical studies reveal the importance of temperature change in PCV on temperature at HRS outlet (Rothuizen, Elmegaard and Rokni, 2020). Uncertainty in temperature prediction after the PCV can affect HRS efficiency and safety (United Nations Economic Commission for Europe, 2023). The JT effect's downsides and its role in pre-cooling systems have been studied in studies done by Johnson et al. (2015) and Wang et al., 2023). Regulations limit hydrogen tank temperatures to 85°C (United Nations Economic Commission for Europe (2023). CFD models, required for the design of safe and efficient HRSs or improvement of fuelling protocols, must consider the JT effect to ensure temperature and pressure compliance with the current standards and regulations (Chen *et al.*, 2019).

CFD modelling can provide results with higher accuracy compared to lumped-parameter thermodynamic or zero-dimensional models, though at the expense of significantly larger computational resources. Using dynamic mesh techniques enables detailed modelling of moving valve details behaviour and associated physics from first principles. Turesson (2011) performed a comparison between a 1D hydraulic and a 3D quasi-stationary CFD analysis to model a check valve's dynamic behaviour. In the quasi-stationary CFD model, a dynamic mesh technique was used to model the changing valve geometry. The numerical mesh updates were performed during the simulations to reflect the valve dynamic behaviour. The results showed that the 1D analysis under-predicts the results and the full 3D dynamic mesh technique is needed to simulate the valve's transient characteristics. Hence, CFD models, where possible - using dynamic mesh, are capable of providing more accurate and physically grounded results compared to analytical models based on a number of simplifications.

In this study, a CFD model of refuelling through the entire equipment of HRS is developed and validated against NREL tests. The HRS includes a high-pressure tank, various types of pipes with bends, valves, HE, hose, breakaway, nozzle and three onboard hydrogen storage tanks. To quantify the JT effect at PCV, the dynamic mesh technique that allows to simulation of the PCV spool movement and thus to control the mass flow rate is applied.

1. Experiments

The experiment used in this study for the CFD model validation was performed at the Hydrogen Infrastructure Research Facility of NREL by Kuroki et al. (2021). Figure 1 presents the piping and instrumentation diagram (PID) of the fuelling line components. The temperature was measured in several locations: in each of two HP tanks (TE1, located 1.52 m from the tank wall directly opposite the inlet), before and after the PCV (TE2 and TE3), after the HE (TE4), and in the centre of two of the onboard tanks (TE5 and TE6) with an accuracy of ±1.5 K. The pressure was also measured at the exit of the HP tanks (PT1), before valve 4 (PT2) and at one of the onboard tanks with an accuracy of ±1.0 MPa (Kuroki et al., 2021). The hydrogen flows from one of two 300-litre HP tanks, through almost 62 meters of pipe with 24 bends (90-degree), PCV, mass flow rate meter (MFM), HE, breakaway, hose, nozzle and 5 other valves to the three 36-litre onboard storage tanks. The length-to-diameter (L/D) ratio of the onboard tanks is reported as 3.4 and is unknown for HP tanks. The dimensions, materials and thermal properties for each piping section are available in the appendix section of the experimental paper (Kuroki et al., 2021).

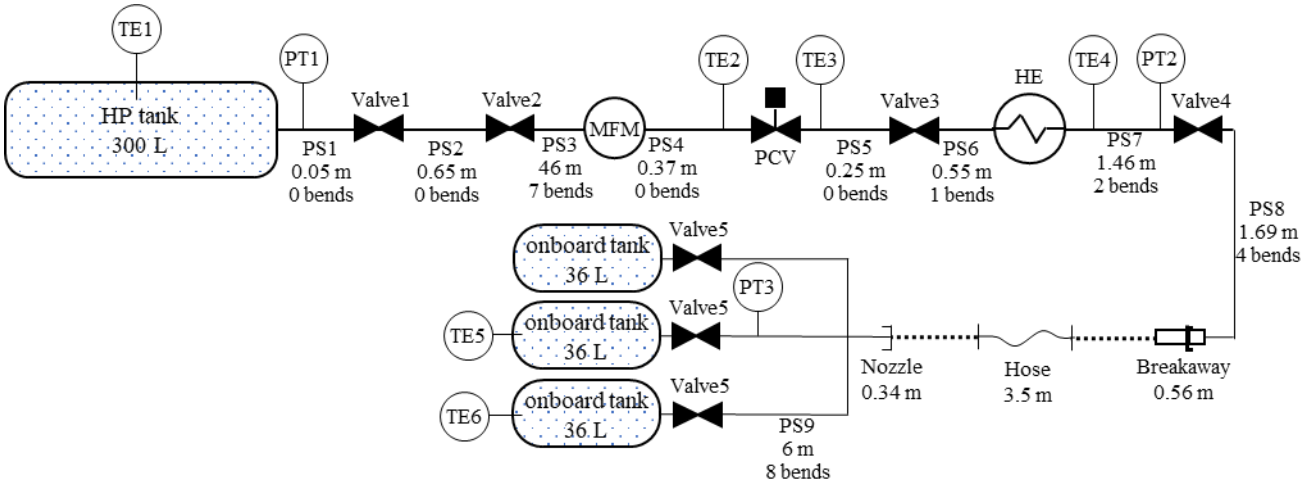

Fig. 1. *PID of the NREL experimental facility.*

Two tests were carried out by the experimentalists (Kuroki et al., 2021). Test No.1 was performed with one startup leak check, but without any leak checks during the main fuelling stage, under the ambient temperature of 23°C and average pressure ramp rate (APRR) of 19.8 MPa/min. This test is selected for the validation of the described CFD model simulations below.

2. CFD model

2.1.Calculation domain and numerical mesh

The numerical grid and PCV dynamic mesh details are crucial for simulating the pressure control valve's behaviour accurately. In this study, the numerical mesh employed tetrahedral control volumes (CVs) for the PCV and hexahedral CVs for the rest of the domain. The transition between tetrahedral and hexahedral mesh was facilitated using pyramid CVs. The computational domain, excluding the PCV, comprised 207,252 CVs with a minimum orthogonal quality of 0.7. The details for hexahedral mesh are presented in the authors' previous paper (Molkov, Ebne-Abbasi and Makarov, 2023).

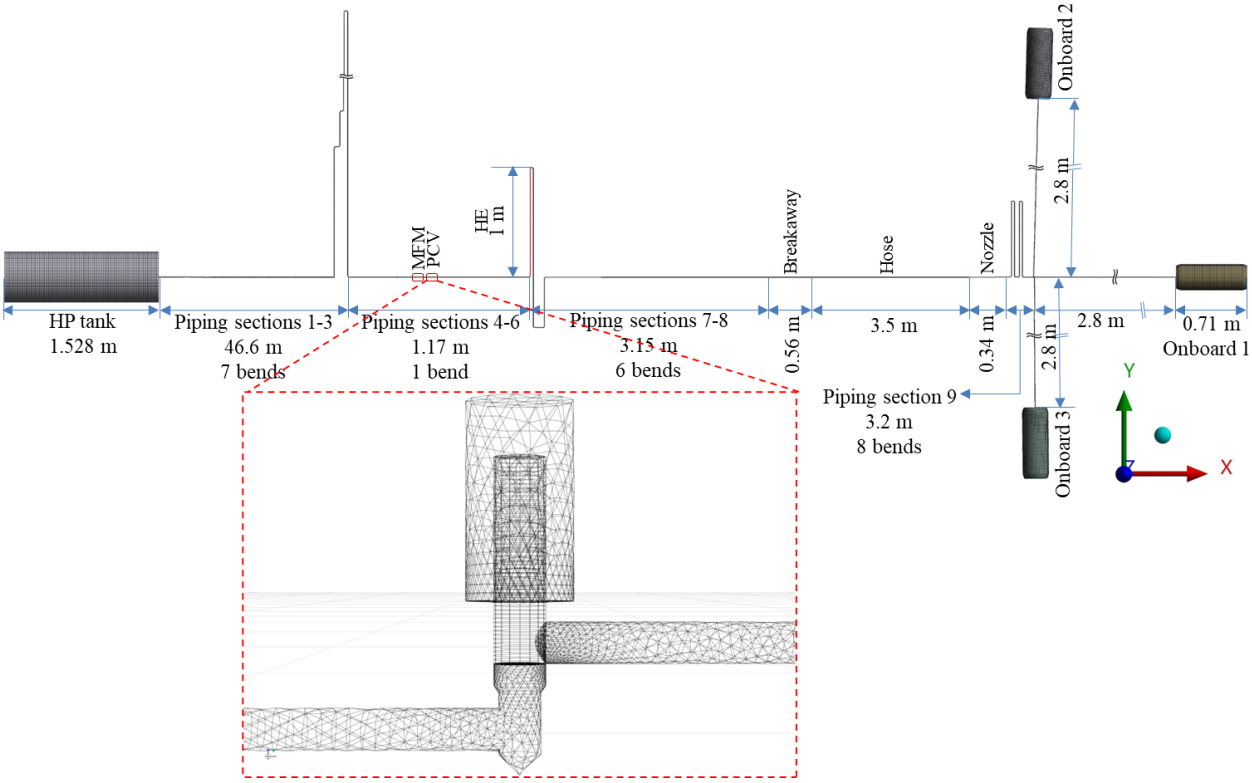

Fig. 2. *Top view of the computational domain representing the HRS facility at NREL.*

The dynamic mesh technique was utilized to simulate the movement of the PCV spool and subsequent alterations in the fluid domain mesh over time. Movement of the spool, considered a non-deformable solid body, regulated the valve's opening and closure to achieve the required pressure ramp in onboard storage. Local re-meshing (Weatherill, 1992) and spring-based smoothing (Batina, 1990) techniques were systematically applied to accommodate grid deformation.

During spool movement, the mesh is updated with minimum and maximum CV volumes between 10^{-4} mm^3 and 3×10^{-3} mm^3. The PCV is meshed using 37,205 CVs (while it is closed) which could increase to 49,324 CVs when it is 100% open while having a minimum orthogonal quality of 0.8. Figure 3 illustrates the mesh in the PCV cross-section.

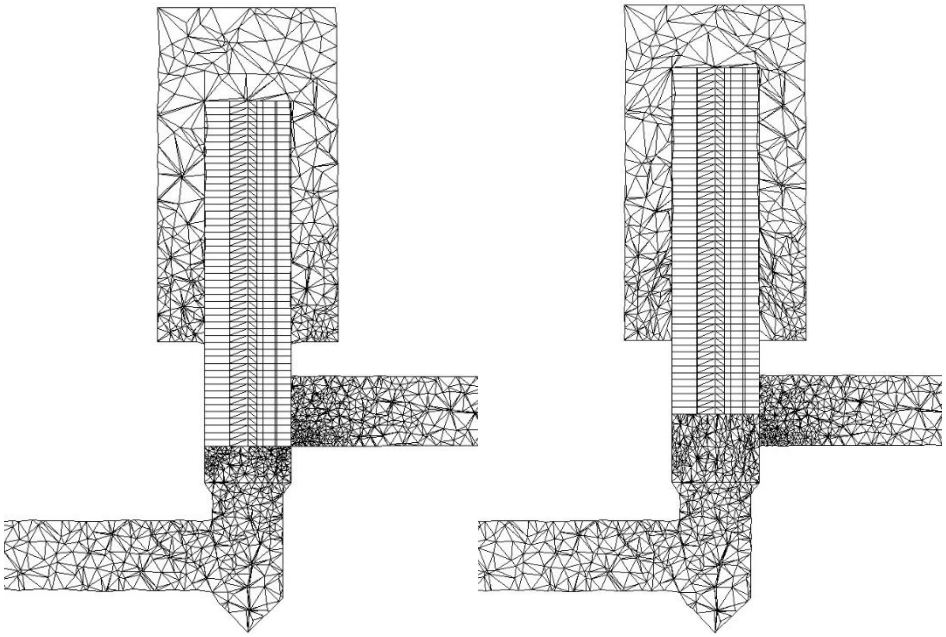

Fig. 3. *The PCV boundary mesh in the fully closed (left) and 50% open (right) states.*

The spool's motion is controlled by a user-defined function (UDF) based on the required mass flow rate or pressure profile, such as APRR. In the current simulation, the UDF code governs the spool movement to achieve the prescribed APRR, using pressure readings from downstream transducers.

In summary, the numerical grid and dynamic mesh techniques, along with precise control mechanisms, are all equally important to accurately simulate the behaviour of the pressure control valve in hydrogen refuelling systems.

2.2.Initial and boundary condition

The parameters for temperature and pressure across all components, including fluids and adjacent walls, match those specified in the experimental paper (Kuroki *et al.*, 2021). The initial pressure in the high-pressure storage tank and down to PCV was 88.0 MPa and from PCV to onboard storage – 6.0 MPa. The initial temperature of high-pressure storage and hydrogen within it was 17.5°C and the initial temperature in the rest of the PID components was 23°C. At the start of fuelling, the PCV is presumed to be fully closed, while all other valves are assumed to be fully open. Walls are designated as non-slip impermeable surfaces. ANSYS Fluent was used as a CFD engine and its "**shell conduction**" feature was employed to compute heat transfer through tank, pipe and other component solid walls. This method calculates conjugate heat transfer across walls in both perpendicular and parallel orientations to the wall surface. Material properties such as density, specific heat, thermal conductivity, and wall thickness for each PID component are specified to generate layers of cells on the wall surface, simulating 3D heat conduction (Ansys Inc, 2023). This modelling approach accounts for prescribed wall thicknesses, relevant thermal properties of materials, and convective heat transfer on the external wall surface. The heat transfer coefficient between the outer pipe surface and the ambient atmosphere is set as 7 W/m^2/K following the conclusions of Simonovski *et al.*, 2015. Since the thermal mass of valves is not provided in the experiment, it is assumed that valves share the same external diameters and materials as their upstream pipes (Ebne-Abbasi, Makarov and Molkov, 2023).

In the case of the HE, specific parameters are absent from the experimental paper (Kuroki *et al.*, 2021). HE modelling adopted the same approach as in the study (Molkov, Ebne-Abbasi and Makarov, 2023) and (Ebne-Abbasi, Makarov and Molkov, 2023): the HE was represented in the calculation domain as a pipe with a length of 1 meter with the equivalent pipe diameter found using HE flow coefficient in the experimental reference (Kuroki *et al.*, 2021). The HE outflow temperature was controlled using a technique implemented as another in-house Fluent UDF subroutine to make sure it follows the experimentally measured temperature dynamics in location TE4, see Figure 1.

3. Results and discussion

Figure 4 (left) presents the comparison of experimental and simulated pressure at sensor PT2. The UDF to control spool motion successfully replicates the pressure within a 3% deviation from the experimental value and less than 1% error compared to the UDF input. Notably, the simulated pressure transient exhibits a smoother profile compared to the experimental data, likely attributable to the non-inertial behaviour of the numerical PCV's spool in the simulations.

Figure 4 (right) illustrates the comparison of experimental and simulated temperatures at sensor TE4, positioned just after the HE exit. The simulated HE outflow temperature closely aligns with the experimental data, with a maximum deviation of 3.5% compared to the experiment and less than 1% deviation compared to the UDF input correlation.

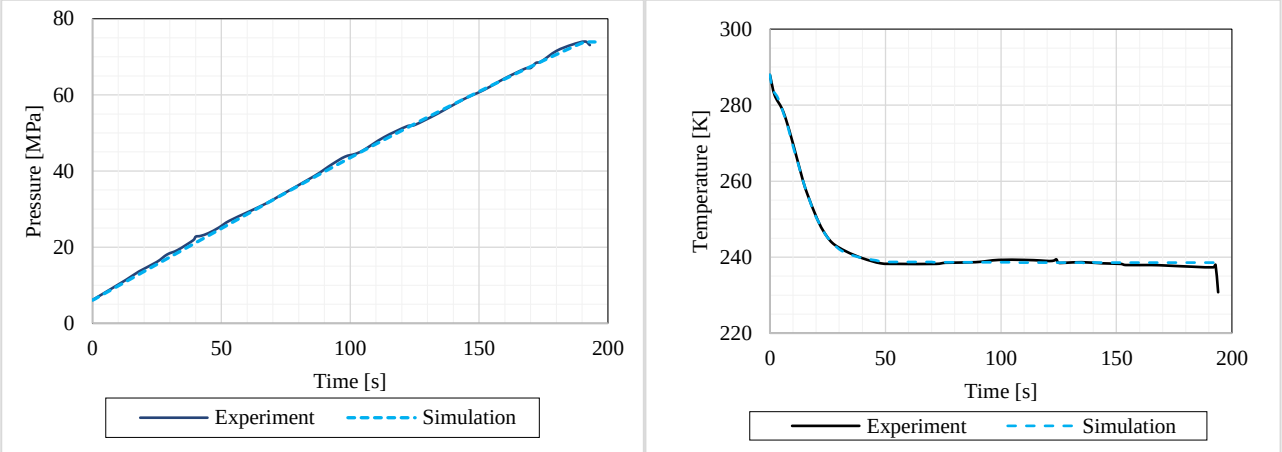

Fig. 4. *Pressure in PT2 located 2.5 m after the PCV (left); hydrogen temperature at the HE exit (right).*

The authors conclude that the procedures for controlling the PCV spool motion and the HE temperature are sufficiently accurate for the automatic simulation of the PCV and the HE functions. This ensures that the APRR and temperature align with the data recorded in the experiment, as presented in this paper, or as prescribed by a fuelling protocol for arbitrary HRS conditions.

3.1. The PCV spool displacement and mass flow rate

The accurate achievement of the pressure ramp rate in onboard storage relies heavily on attaining the correct mass flow rate, which must account for continuous changes in temperature and pressure across the entire array of HRS components. Figure 5 juxtaposes experimentally measured and simulated

mass flow rates alongside the PCV spool displacement. The visual contrast observed between the measured (oscillating) and simulated (smooth) mass flow rates can be attributed to several factors. Firstly, the experimental mass flow rate was derived from HP tank weight measurements, potentially introducing oscillations due to recoil force. Secondly, differences in the inertia of the actual PCV spool movement mechanism compared to the non-inertial "numerical spool" utilized in the simulations may contribute to this variance. These distinctions may account for the discrepancy between the oscillatory nature of the experimental mass flow rate and the smoother (non-inertial) simulated mass flow rate.

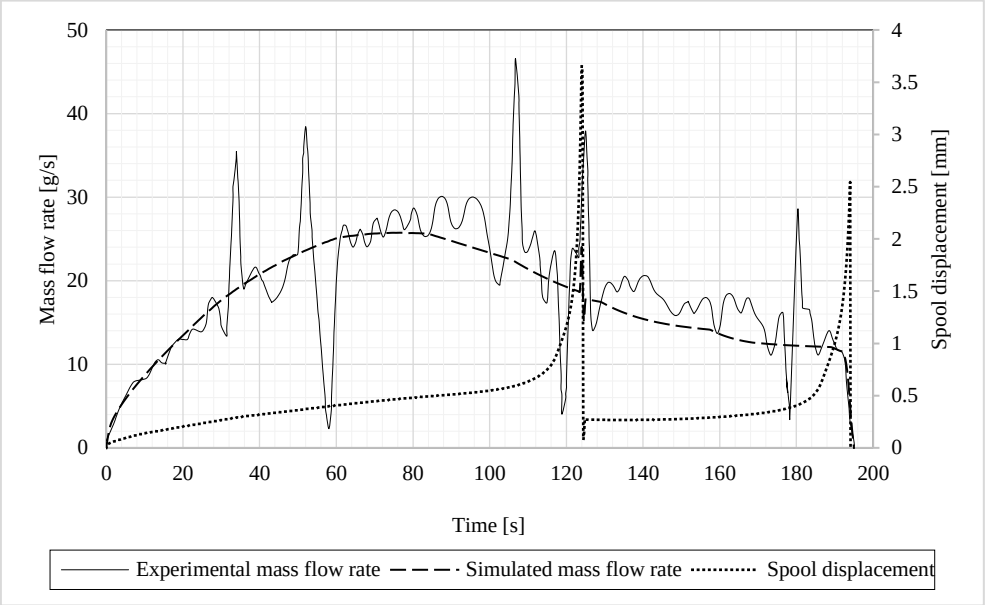

Fig. 5. *Experimentally measured and simulated mass flow rate along with the PCV spool displacement.*

In Figure 5, a sudden drop in spool displacement at t=124 s is explained by the replacement of the depleted HP tank with a second tank at a higher pressure of 88.0 MPa. This abrupt pressure increase upstream of the PCV requires maintaining pressure at PT2, causing the spool displacement to decrease to 0.28 mm. Subsequently (t=124-195 s), refuelling from the second HP tank mirrors the behaviour observed with the first tank (t=0-124 s). The PCV spool velocity increases gradually to counteract decreasing tank pressure and ensure simulated pressure dynamics at PT2 align with the prescribed APRR. At t=195 s, refuelling concludes, and the spool displacement returns to zero, indicating PCV closure.

The experiments (PRHYDE - Deliverable 6.7, 2022) demonstrated that the flow coefficient directly impacts the pressure drop, which in turn influences the temperature in the compressed hydrogen storage system (CHSS). The larger the pressure drop is, the stronger is expected to be the Joule-Thomson heating. **Errore. L'origine riferimento non è stata trovata.**6 illustrates both the experimental (solid black lines) and the simulated (red dashed lines) temperatures at the inlet and outlet of the PCV where TE2 and TE3 sensors are positioned.

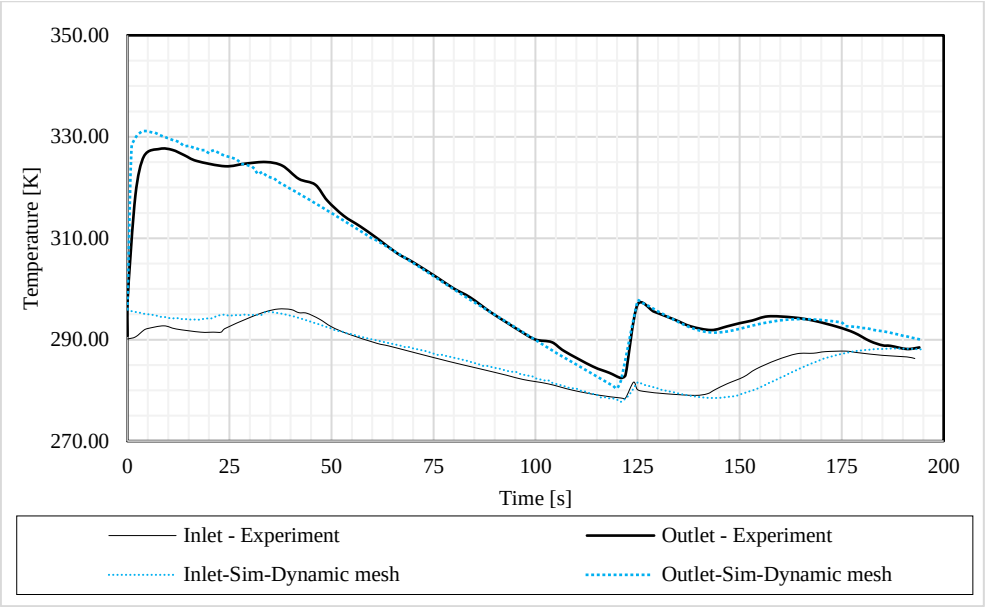

Fig. 6. *Experimental and simulated temperature dynamics at the inlet (TE2) and outlet (TE3) of the PCV.*

At the onset of refuelling, the PCV experiences the highest pressure difference, resulting in a significant temperature increase of 40 K due to the JT effect during throttling. As refuelling progresses, the pressure drop across the PCV gradually diminishes due to the depletion of the HP tank. By t=124 s, before the HP tank replacement, the temperature rise reduces to 5 K in the test and 3.5 K in the simulations.

The replacement of the HP tank induces a pressure surge upstream of the PCV, elevating the pressure difference across the PCV. This surge is accompanied by a notable temperature increase due to the JT effect: from 3.5 K before the tank switching to 15.5 K during refuelling from the fully charged second tank. At the refuelling's end, the temperature rise reduces to about 2 K due to the JT effect and associated heat transfer.

Figure 6 demonstrates that simulated temperature dynamics closely mirror experimental transients, with the model accurately simulating pressure gradients and temperature increases in the fuelling line due to the JT effect.

Figure 7 (left) depicts the temperature contour in the PCV cross-section at 6 s, during which the temperature remains high after the PCV without significant fluctuations. Notably, the temperature at the downstream sensor location TE3 increases. However, closer to the gap between the PCV body and the spool, the temperature notably decreases from 296 K before the PCV to 196 K in the "blue colour" zone. This observation can be understood by examining the velocity contour (Fig. 7, right).

Figure 7 (right) illustrates the velocity distributions within the PCV cross-section. The velocity contour, as depicted in Figure 7 (right), shows that hydrogen flow near the opening can achieve velocity up to 1956 m/s, i.e. hydrogen supersonic flow, given the speed of sound in hydrogen at 196 K is 1068 m/s. Comparison between the velocity contour (Figure 7, right) and the temperature contour (Figure 7, left) reveals that gas temperature decreases in high-velocity areas following the total energy equation:

$$E = u + \frac{|v|^2}{2} = h + \frac{|v|^2}{2} - \frac{p}{\rho}, \quad (1)$$

where E is total energy, u is internal energy, v is velocity, h is enthalpy, p is pressure and ρ is density.

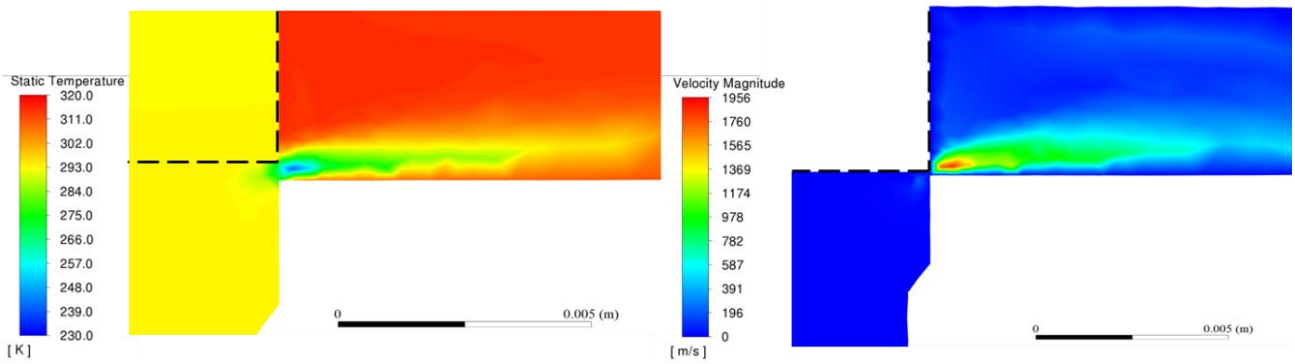

Fig. 7. *Distribution of temperature (left) and velocity (right) in the PCV cross-section at t=6 s.*

According to the above total energy conservation equation, in the absence of friction or heat losses, the expanding gas's internal energy is converted to kinetic energy, resulting in a decrease in temperature, particularly noticeable in areas of high velocity near the PCV opening where rapid expansion occurs. Conversely, as hydrogen moves away from the PCV spool, it slows down, converting kinetic energy back to internal energy, leading to a temperature increase as observed in Figure 7 (left). This dynamic creates a balance between adiabatic expansion, which tends to reduce temperature due to the conversion of internal and kinetic energies during acceleration, and the Joule-Thomson effect, which tends to raise temperature. This interaction underscores the intricate relationship between fluid dynamics and thermodynamics governing gas flow within the PCV.

Figure 8 juxtaposes the enthalpy h (right) with the total enthalpy, $H = h + \frac{|v|^2}{2}$ (left). Enthalpy decreases where kinetic energy increases (indicated by blue-coloured areas) and rises again when flow decelerates. Analysis indicates that total enthalpy upstream and downstream of the PCV (evaluated at TE2 and TE3 locations) only differs by -0.5% (Figure 8, left), a discrepancy explained by the energy conservation equation (Landau and Lifshitz, 1987):

$$\frac{\partial}{\partial t}\left(\frac{1}{2}\rho v^2 + \rho u\right) = -div\left[\rho \mathbf{v}\left(\frac{1}{2}v^2 + h\right) - \mathbf{v}\cdot\boldsymbol{\sigma} - \kappa\,\mathbf{grad}\,T\right], \quad (2)$$

where u is internal energy, $\mathbf{v}$ is velocity vector, v is velocity magnitude, $\boldsymbol{\sigma}$ is the stress tensor term, κ is thermal conductivity and T is temperature. Under assumptions of steady-state flow, adiabatic boundaries, no work performed on the system, no friction, and negligible heat transfer within the fluid, the equation $div\left[\rho \mathrm{v}\left(\frac{1}{2}v^2 + h\right)\right] = 0$ holds. This implies that the enthalpy inflow upstream of the PCV and the enthalpy outflow downstream of the PCV should be equal.

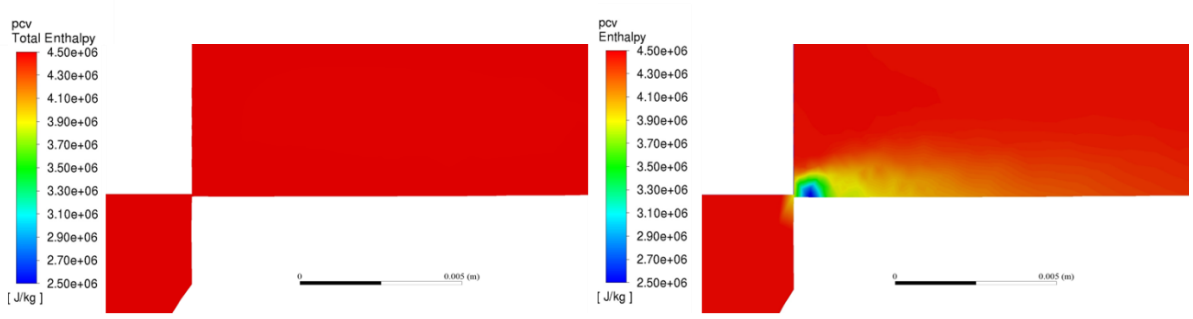

Fig. 8. *Distribution of total enthalpy H (left) and enthalpy h (right) in the PCV cross-section at t=6 s.*

To assess the impact of wall friction and heat transfer on the system's energy change, two additional simulations were conducted: one with adiabatic wall boundaries to eliminate heat transfer and the other with both slip conditions (to eliminate friction) and heat transfer coefficient set to zero (to eliminate heat transfer). Table 1 presents the comparison of total enthalpy at the inlet (TE2 location) and outlet (TE3 location) of the PCV for these scenarios.

In the scenario devoid of both heat transfer and friction, the total enthalpy change is minimal and equal only -0.033%. This difference is primarily attributed to internal friction in the gas. For the scenario with non-slip walls, the difference is slightly higher at -0.038%, indicating that wall friction has a negligible impact on energy flux.

Conversely, the inclusion of heat transfer in the simulation results in a total enthalpy change of - 0.525%, which appears substantial compared to the two previous figures. This finding suggests that heat transfer is the primary factor contributing to the loss of energy flux in the PCV.

Table 1. *Comparison of total enthalpy at t=6 seconds at the inlet and outlet of PCV (TE2 and TE3 location).*

Case	Total Enthalpy at the inlet (TE2) [J/kg]	Total Enthalpy at the outlet (TE3) [J/Kg]	Difference (%)	Temperature at TE3 [K]
Ideal case, isenthalpic expansion (using NIST data)	4,473,342	4,473,342	0%	330.5
Slip wall conditions, no heat transfer	4,473,342	4,471,888	-0.033%	330.9
Non-slip conditions, no heat transfer	4,473,342	4,471,654	-0.038%	331.1
Non-slip conditions, with heat transfer	4,473,342	4,449,820	-0.525%	329.5

Comparing the temperature at TE3 location, it's observed that scenarios with no heat transfer show higher temperatures, even surpassing the NIST isenthalpic expansion condition where temperature peaks at 330.5 K. This difference could stem from variations in temperature measurement at TE3 compared to mass-averaged cross-section temperatures, or from losses incurred due to wall and viscous friction. These losses cause the system's kinetic energy to convert into thermal energy due to encountered resistance.

As expected, the scenario with heat transfer exhibits the lowest temperature at the PCV outlet (TE3 location) due to convective heat exchange with the ambient environment. This comparison underscores the intricate interplay between kinetic energy, friction, viscous losses, and enthalpy within the PCV assembly, collectively influencing the thermodynamic parameters of the refuelling system.

3.2. Impact of the JT coefficient: "numerical refuelling" with methane and air

In order to evaluate the impact of the JT coefficient value, we utilized a sophisticated CFD model with comprehensive PCV resolution and dynamic mesh. We simulated the theoretical "refuelling" of methane and subsequently air, both of which possess positive JT coefficients, unlike hydrogen. These simulations were conducted using the same equipment setup as for hydrogen refuelling in an HRS, enabling a comparative analysis. Figure 9 illustrates that although the inlet temperature remains constant across all simulations the PCV outlet temperature rises for hydrogen, whereas it decreases for air and methane.

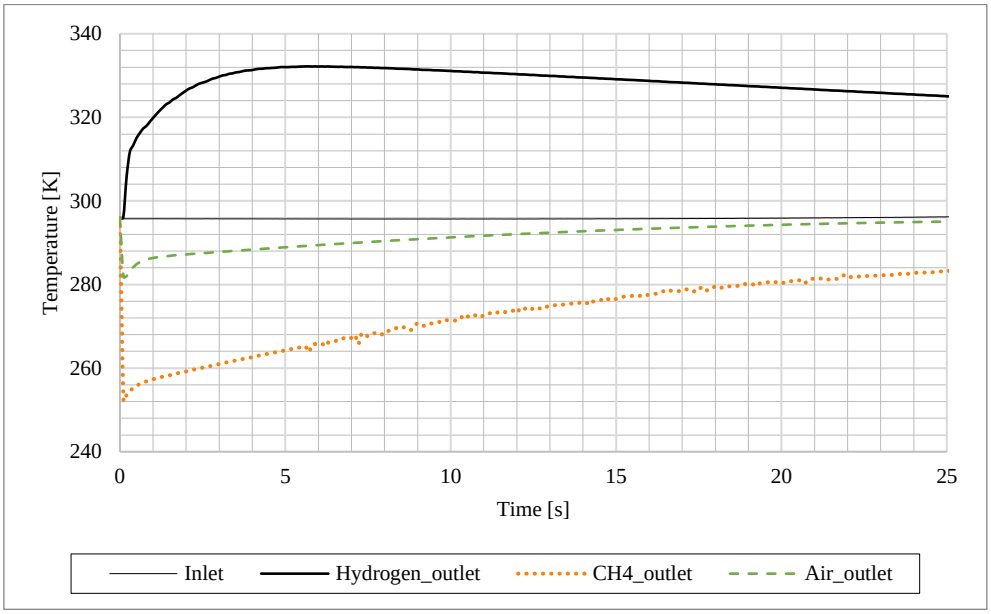

Fig. 9. *The joint effect of the heat transfer and the JT phenomenon on the PCV outlet temperature for the same HRS and initial conditions for three gases: hydrogen, air, and methane.*

Figure 10 displays a comparison of temperatures at the PCV inlet and outlet, derived from CFD simulations, focusing on hydrogen, air, and methane during the initial 25-second phase of the gas transfer process. At t=1 s, with the inlet PCV temperature set at 296 K, the PCV outlet temperatures drop to 282 K for air (a reduction of -14 K in Figure 10, left). This is consistent with an isenthalpic expansion using the NIST database resulting in 281.6 K (Lemmon *et al.*, 2018). Similarly, for methane, the outlet temperature decreases to 251 K (Figure 10, centre), marking a -45 K reduction. This is in line with an isenthalpic expansion value of 247.2 K using the NIST database. Due to its negative JT coefficient, hydrogen, however, exhibits a different trend. The PCV outlet temperature for hydrogen rises to 321 K (+25 K) at t=1 s and further increases to 329.5 K at t=6 s (Figure 10, right), which is also in line with an isenthalpic expansion using the NIST database showing 330.5 K.

The CFD model-derived outlet temperature values surpass the NIST values for air and methane while remaining below the NIST values for hydrogen. This aligns with the fundamental physics of the process, suggesting that heat transfer in the CFD simulations occurs from HRS equipment to gas (air and methane) and conversely from gas to equipment for hydrogen. It's noteworthy that over time, cooled gases after the PCV (air and methane) gradually warm up after the initial decline, whereas heated gas (hydrogen) experiences a slow temperature decrease.

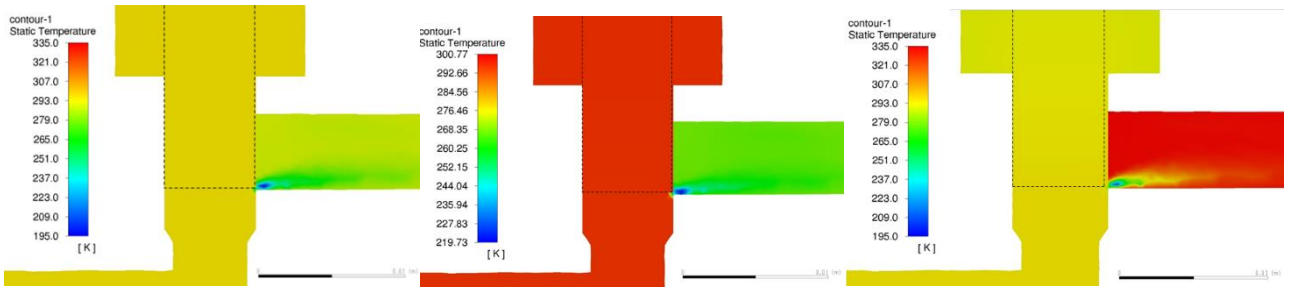

Fig. 10. Temperature field in PCV cross-section, t=6 s: air (left), methane (centre), and hydrogen (right).

Table 2 summarizes the temperature change across the PCV for Hydrogen, air and methane and compares that to the values calculated by assuming isenthalpic expansion using the NIST database.

Table 2. *Comparison of total enthalpy at t=6 seconds at the inlet and outlet of PCV (TE2 and TE3 location).*

	T_{inlet}	$T_{outlet\ CFD}$	ΔT_{CFD}	$T_{outlet\ NIST}$	$\Delta T_{CFD} - \Delta T_{NIST}$
Hydrogen	296 K	329.5 K	+25 K	330.5 K	-1 K
Air	296 K	282 K	-14 K	281.6 K	+0.4 K
CH4	296 K	251 K	-45 K	247.2 K	+3.8 K

The above sensitivity analysis shows that the hydrogen temperature rise at the PCV outlet is indeed due to the JT effect and highlights the complex character of heat and mass transfer for gases having variable JT coefficients.

3.3. Temperature and pressure at onboard tanks

Figure 11 presents a comparison between experimental and simulated pressures (left) and temperatures (right) within the onboard tanks. Throughout the fuelling process, the CFD model accurately reflects the temperature trends within the tanks, maintaining a deviation of less than 5 K, with final temperatures showing only a 3 K deviation. This level of accuracy closely mirrors the experimental temperature fluctuations observed in onboard Tank 2 during refuelling. Additionally, the simulated pressure demonstrates a deviation of less than 0.95 MPa, equivalent to ±1.5% across the entire refuelling duration. Importantly, this deviation falls within the pressure transducer's accuracy of ±1.0 MPa.

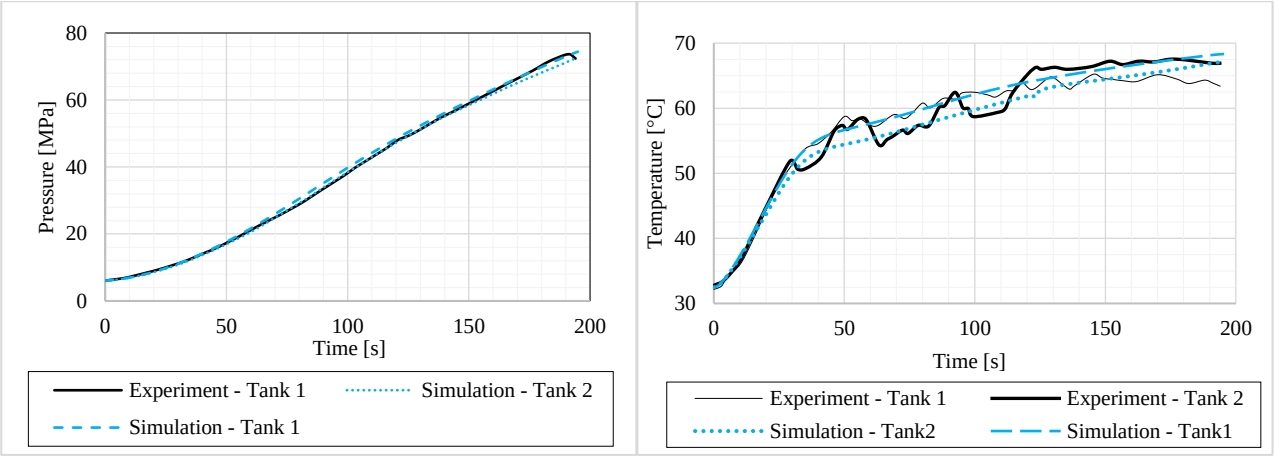

Fig. 11. *Experimental and simulated pressures (left) and temperatures (right) in two of three onboard tanks.*

4. Conclusions

The *originality* of this work is in the development of the CFD model with an explicit numerical resolution of the PCV with spool displacement to regulate the required pressure ramp after the PCV in a hydrogen refuelling station. The PCV geometry was modelled based on a real valve design and discretised using dynamic mesh, ensuring practical relevance. The PCV spool motion was controlled by an in-house developed algorithm grounded in the sampling of numerical pressure deviation from the experimental pressure, as defined by the prescribed APRR for NREL Test No.1. The results revealed that during the throttling process, the total enthalpy change of gas is negligible. Consequently, for future engineering applications such as valve and/or PCV performance analysis, designing HRS components, and developing numerical models, the assumption of an isenthalpic process for high-pressure hydrogen flow in valves remains valid.

The *significance* of this study lies in developing and validating a CFD model, which serves as a contemporary engineering tool for the design of HRS equipment and fuelling protocols. This model incorporates the Joule-Thomson effect and considers heat and mass transfer at the PCV, impacting pressure and temperature dynamics at various locations of HRS.

The *rigour* of this work is in the validation of the model against the available hydrogen refuelling data generated at NREL.

Acknowledgements

This research has received funding from the Engineering and Physical Sciences Research Council (EPSRC) of the UK through: the Centre for Doctoral Training in Sustainable Hydrogen (“SusHy”), Grant number EP/S023909/1; UK National Clean Maritime Research Hub (UK-MaRes Hub), Grant number EP/Y024605/1; Tier 2 Northern Ireland High-Performance Computing facility (NI-HPC “Kelvin-2”), Grant number EP/T022175/1. Funding was also received from Fuel Cells and Hydrogen 2 Joint Undertaking (now Clean Hydrogen Partnership) under the European Union’s Horizon 2020 research and innovation programme through the SH2APED project under Grant Agreement No.101007182. This work was undertaken as part of the DelHyVEHR project No. 101137743

supported by the Clean Hydrogen Partnership and its members where Ulster University is supported by UKRI grant No.10110515. Views and opinions expressed are however those of the author(s) only and do not necessarily reflect those of the European Union or the Clean Hydrogen Partnership. Neither the European Union nor the Clean Hydrogen Partnership can be held responsible for them.

References

Ansys Inc (2023) *Ansys® Fluent 2023 R1 User Manual*. Available at: https://ansyshelp.ansys.com/account/secured?returnurl=/Views/Secured/corp/v202/en/ (Accessed: 4 February 2023).

Apostolou, D. and Xydis, G. (2019) 'A literature review on hydrogen refuelling stations and infrastructure. Current status and future prospects', *Renewable and Sustainable Energy Reviews*, 113, p. 109292. Available at: https://doi.org/10.1016/j.rser.2019.109292.

Batina, J.T. (1990) 'Unsteady Euler airfoil solutions using unstructured dynamic meshes', *AIAA Journal*, 28(8), pp. 1381–1388. Available at: https://doi.org/10.2514/3.25229.

Beswick Engineering (2023) *The basics of pressure regulators*. Available at: https://www.beswick.com/resources/the-basics-of-pressure-regulators/ (Accessed: 5 September 2023).

Chen, J. *et al.* (2019) 'Modeling a hydrogen pressure regulator in a fuel cell system with Joule–Thomson effect', *International Journal of Hydrogen Energy*, 44(2), pp. 1272–1287. Available at: https://doi.org/10.1016/j.ijhydene.2018.11.020.

Ebne-Abbasi, H., Makarov, D. and Molkov, V. (2023) 'CFD model of refuelling through the entire equipment of a hydrogen refuelling station', *International Journal of Hydrogen Energy*, 53(May 2023), pp. 200–207. Available at: https://doi.org/10.1016/j.ijhydene.2023.12.056.

Genovese, M. *et al.* (2023) 'Hydrogen refueling process: theory, modeling, and in-force applications', *Energies*, 16(6), p. 2890. Available at: https://doi.org/10.3390/en16062890.

Johnson, T. *et al.* (2015) 'Thermal model development and validation for rapid filling of high pressure hydrogen tanks', *International Journal of Hydrogen Energy*, 40(31), pp. 9803–9814. Available at: https://doi.org/10.1016/j.ijhydene.2015.05.157.

Joule, J.P. and Thomson, W. (1852) 'LXXVI. On the thermal effects experienced by air in rushing through small apertures', *The London, Edinburgh, and Dublin Philosophical Magazine and Journal of Science*, 4(28), pp. 481–492. Available at: https://doi.org/10.1080/14786445208647169.

Kim, Y., Shin, D. and Kim, C. (2019) 'On-board cold thermal energy storage system for hydrogen fueling process', *Energies*, 12(3), p. 561. Available at: https://doi.org/10.3390/en12030561.

Kuroki, T. *et al.* (2021) 'Thermodynamic modeling of hydrogen fueling process from high-pressure storage tank to vehicle tank', *International Journal of Hydrogen Energy*, 46(42), pp. 22004–22017. Available at: https://doi.org/10.1016/j.ijhydene.2021.04.037.

Landau, L.D. and Lifshitz, E.M. (1987) *Fluid Mechanics*. 2nd edn, *Developments in Geotechnical Engineering*. 2nd edn. Pergamon Press. Available at: https://doi.org/10.1016/B978-0-444-98761-7.50001-7.

Lemmon, E.W. *et al.* (2018) 'NIST standard reference database 23: reference fluid thermodynamic and transport properties-REFPROP, version 10.0, national institute of standards and technology, standard reference data program, Gaithersburg'. Available at: https://doi.org/10.18434/T4/1502528.

Molkov, V., Ebne-Abbasi, H. and Makarov, D. (2023) 'CFD model of refuelling through the entire HRS equipment: the start-up phase simulations', *Hydrogen*, 4(3), pp. 585–598. Available at:

https://doi.org/10.3390/hydrogen4030038.

PRHYDE - Deliverable 6.7 (2022) *Results as Input for Standardisation.* Available at: https://lbst.de/wp-content/uploads/2022/12/PRHYDE_Deliverable_D6-7_Results_as_Input_for_Standardisation_V1_final_Dec_2022.pdf (Accessed: 1 July 2023).

Rothuizen, E., Elmegaard, B. and Rokni, M. (2020) 'Dynamic simulation of the effect of vehicle-side pressure loss of hydrogen fueling process', *International Journal of Hydrogen Energy*, 45(15), pp. 9025–9038. Available at: https://doi.org/10.1016/j.ijhydene.2020.01.071.

Simonovski, I. *et al.* (2015) 'Thermal simulations of a hydrogen storage tank during fast filling', *International Journal of Hydrogen Energy*, 40(36), pp. 12560–12571. Available at: https://doi.org/10.1016/j.ijhydene.2015.06.114.

Turesson, M. (2011) *Dynamic simulation of check valve using CFD and evaluation of check valve model in RELAP5*. Chalmers University of Technology, Sweden.

United Nations Economic Commission for Europe (2023) *Addendum 13: UN Global Technical Regulation No. 13 (Hydrogen and fuel cell vehicles), Amendment 1, Global Registry Geneva Switzerland*. Available at: https://unece.org/sites/default/files/2023-07/ECE-TRANS-180-Add.13-Amend1e.pdf (Accessed: 4 January 2024).

Wang, X. *et al.* (2023) 'Review of researches on important components of hydrogen supply systems and rapid hydrogen refueling processes', *International Journal of Hydrogen Energy*, 48(5), pp. 1904–1929. Available at: https://doi.org/10.1016/j.ijhydene.2022.09.303.

Weatherill, N.P. (1992) 'Delaunay triangulation in computational fluid dynamics', *Computers and Mathematics with Applications*, 24(5–6), pp. 129–150. Available at: https://doi.org/10.1016/0898-1221(92)90045-J.

Zheng, J. *et al.* (2012) 'Development of high pressure gaseous hydrogen storage technologies', *International Journal of Hydrogen Energy*, 37(1), pp. 1048–1057. Available at: https://doi.org/10.1016/j.ijhydene.2011.02.125.

Large-Eddy Simulation of pressurized hydrogen releases: dispersion and fire stabilization mechanisms

Félicia Garnier [a], Thomas Jaravel [a], Quentin Douasbin [a] & Thierry Poinsot [a,b]

[a] CERFACS (Toulouse, France)
[b] IMFT (Université de Toulouse, CNRS, Toulouse, France)

E-mail: garnier@cerfacs.fr

Abstract

Stabilized jet flames subsequent to a leak of pressurized hydrogen take part in various safety scenarios. The mechanisms stabilizing such flames are not fully understood and high-fidelity numerical simulation of these configurations remains a challenge. This study reports one of the first attempts to capture a hydrogen under-expanded jet flame in ambient conditions with high-fidelity computational tools. A Large-Eddy Simulation (LES) of a sonic under-expanded hydrogen jet is performed in non-reacting and reacting conditions. The simulated configuration is at ambient temperature with a Nozzle Pressure Ratio (NPR) of 10. The accurate capture of the dispersion of the inert jet is emphasized, as the ignited jet is controlled by the mixing rates. Both the near field under-expanded shock train structures and the subsonic far field dispersion quantities exhibit fair agreement with the available mean and RMS experimental measurements of the inert jet. The location of the various shock waves and their reflections show a good agreement with the experimental Schlieren dataset. In the subsonic self-similar region of the jet, the validation of aerodynamics and mixing rate confirms the ability of the LES modeling to accurately predict hydrogen dispersion in quiescent air. The jet is then ignited to evaluate the ability of the numerical model to predict the lifted flame. The predicted lift-off height is in agreement with experimental correlations from the literature and the resulting structure of the flame is in accordance with previous studies of lifted hydrogen flames.

Keywords: *hydrogen safety, Large-Eddy Simulation, under-expanded jet flames*

Introduction

The use of hydrogen at the industrial scale requires cryogenic or pressurized storage. For a Nozzle Pressure Ratio (NPR) higher than a critical value ($NPR_c \simeq 2$), an accidental continuous leak through a small aperture generates an established under-expanded jet of hydrogen into air. In case of ignition, a jet flame may stabilize at a significant distance downstream from the leak. The stabilization mechanisms of such flames, and their resulting lift-off distance, are not fully understood and this topic remains an active field of research. A misprediction of the lift-off height affects the flame characteristics, thermal loads, and subsequent determination of adequate safety metrics. Stabilization mechanisms of subsonic turbulent non-premixed jet flames have been extensively studied, both experimentally, as reviewed by Lyons (2007), and numerically (Mortada et al. 2019; Karami et al. 2015; Ferraris et al. 2007; Kim et al. 2005; Devaud et al. 2003; Mizobuchi et al. 2002). A turbulent hydrogen lifted jet flame was computed by Direct Numerical Simulation (DNS) by Mizobuchi et al. (Mizobuchi et al. 2002; Mizobuchi et al. 2005; Ruan et al. 2012). Their study revealed an edge flame structure stabilizing the flame base. Focusing on supersonic under-expanded jets, free hydrogen under-expanded jet flames were vastly studied mainly through experimental works investigating global safety metrics (Yu et al. 2022; Hecht et al. 2021; Panda et al. 2017; Veser et al. 2011; Mogi and Horiguchi 2009; Schefer et al. 2007; Swain et al. 2007), stability limits (Takeno et al. 2020; Yamamoto et al. 2018; Mogi and Horiguchi 2009; Devaud et al. 2002), or spontaneous ignition in the release pipe (Jiang et al. 2023; Kim et al. 2013; Lee et al. 2011; Mogi, Wada, et al. 2009; Mogi et al.

2008). Predicting these ignition events with Large-Eddy Simulation (LES) is challenging, as combustion models strongly impact their accurate capture. High-fidelity numerical studies are sparse and they are usually restricted to a near field investigation of the transient ignition phase (Jiang et al. 2023; Wen et al. 2009; Xu et al. 2009). The few LES of sustained lifted hydrogen under-expanded flames include the works of Ren et al. (2022) and Brennan et al. (2009), in which no in-depth analysis of the stabilization mechanism was performed.

This paper aims to investigate the ability of LES to predict dispersion and flame lift-off mechanism in under-expanded jets in ambient conditions. Since non-premixed jet flames are directly controlled by mixing rates, their accurate prediction is a necessary condition to capture the flame stabilization process. As such, in this study, particular attention is paid to the predictive accuracy of the LES modeling of the dispersion of an inert hydrogen jet in ambient air. In a first step, the near field compressible structures are assessed by comparison against Schlieren measurements. Then, a validation of the hydrogen dispersion in the far field is performed by comparing LES results to mean and RMS fields of velocity and hydrogen mass fraction provided by the experiments. Finally, the jet is ignited, which leads to a lifted jet flame stabilized at a given axial location. The flame lift-off is subsequently analyzed in light of previous experimental findings.

1. Configuration

1.1. Flow parameters and diagnostics

The LES of the Sandia non-reacting under-expanded hydrogen jet is performed (Ruggles et al. 2012; Li et al. 2021). Pressurized, ambient temperature hydrogen accelerates through a smoothly contracting nozzle (ASME MFC-3M-2004) of diameter D = 1.5 mm, located in the center of a planar surface. With NPR = 10, the flow is choked when it reaches the nozzle outlet and expands into initially quiescent air at atmospheric conditions (Table 1). Schlieren photographs are available to characterize the compressible structures in the near field (Ruggles et al. 2012). In the far field, the jet has returned to a subsonic jet structure with self-similar characteristics. In this region, mean and RMS velocity (Li et al. 2021) and hydrogen concentration (Ruggles et al. 2012) measurements are available.

Table 1. *Total temperature and total pressure in air (∞) and hydrogen (H_2) tanks.*

T_∞	P_∞	T_{H_2}	P_{H_2}
296 K	98,370 Pa	295.4 K	983,200 Pa

1.2. Numerical set-up

The LES is performed with the AVBP solver developed at CERFACS (Schonfeld et al. 1999). Modeling of supersonic reacting jets by the AVBP code was previously assessed through the LES of a lifted hydrogen-air diffusion flame stabilized by autoignition processes (Boivin et al. 2012; Dauptain et al. 2005). The compressible Navier-Stokes equations are solved in time explicitly. Advection terms are discretized according to a two-step Taylor-Galerkin centered scheme of order 3 in space and time (TTG4A) (Selmin 1987). The SIGMA model accounts for subgrid scale turbulence (Nicoud et al. 2011). The shocks are captured with Localized Artificial Diffusivity based on a pressure sensor to detect shocks (Schmitt 2020). As the studied regimes of the jet are momentum-dominated, buoyancy effects are neglected. In the targeted pressure and temperature range, non-ideal gas effects are negligible (Rahantamialisoa et al. 2022), such that the ideal gas equation of state is used in this work. The dynamic viscosity follows a simplified Wilke law for a binary mixture of H_2 and air, with their dynamic viscosity varying with temperature as a power law. Finally, the molecular transport assumes a constant but not unity Lewis number for each species and constant Prandtl number is assumed for the mixture.

The jet is discretized with a three-dimensional, fully unstructured grid of 124×10^6 tetrahedra (Fig. 1). Two hemispheric tanks of radius 667D are filled respectively with H_2 and air at the conditions displayed in Table 1. A target cell size of D/25 = 60 μm is imposed in the contracting nozzle and the compressible potential core region, as previous studies in the literature have shown that this level of resolution is suitable to capture the main compressible structures on similar jets (Dauptain et al. 2010; Liu et al. 2009). Further downstream, the grid is stretched: between 17D and 83D, the target cell size is D/5 = 300 μm and between 88D and 160D, the cell size is equal to 700 μm. Stretching is lower than 5% in the region of the jet and it is set to 20% in the rest of the domain. The grid resolution quality is assessed *a posteriori* through the quality index LES_IQ_v, proposed by Celik et al. (2005):

$$LES\_IQ_v = (1 + \alpha_v((\nu_{SGS} + \nu_{lam}) \,/\, \nu_{lam}\,)^n)^{-1}, \tag{1}$$

where $\alpha_v = 0.05$, $n = 0.53$ and ν_{SGS} and ν_{lam} are the turbulent and molecular viscosities respectively. The quality index is close to 80% in the turbulent regions of the jet, thus indicating sufficient levels of resolved turbulence. Moreover, a grid convergence study is performed in the near field, showing that the jet major compressible and turbulent characteristics can be retrieved by the present grid (not shown here). The ability of the near field discretization to capture the jet features accurately is further discussed in Section 2.1.

To prevent thermo-acoustic instabilities, the far field boundary opposite the jet flow is defined as an air inlet with zero velocity. The Navier-Stokes Characteristic Boundary Conditions (NSCBC, Poinsot et al. 1992) are used to minimize the reflection coefficient of the inlet boundary. All other boundaries of the domain are adiabatic walls. The nozzle boundary layer is not resolved: an adiabatic slip condition is imposed on all walls, as previously published literature extensively validated this simplified approach for the LES of under-expanded jets (Vuorinen et al. 2013; Dauptain et al. 2010; Liu et al. 2009).

The pressure in the H_2 tank is estimated to decrease by 0.1% in a time $\Delta t = \Delta m/\dot{m} = 1.69$ s, where Δm is the discharged H_2 mass and $\dot{m} = 10^{-3}$ kg/s is the empirical mass flow rate (Ruggles et al. 2012). Based on the velocity measurements at various axial locations (Li et al. 2021), the jet convective time between the nozzle and 160D is estimated to be $t_c = 3.05 \times 10^{-3}$ s. The LES results are averaged after a transient time of $3t_c$, over a duration of $3t_c$, ensuring that the simulation reaches steady-state without any discharge or initial transient effects.

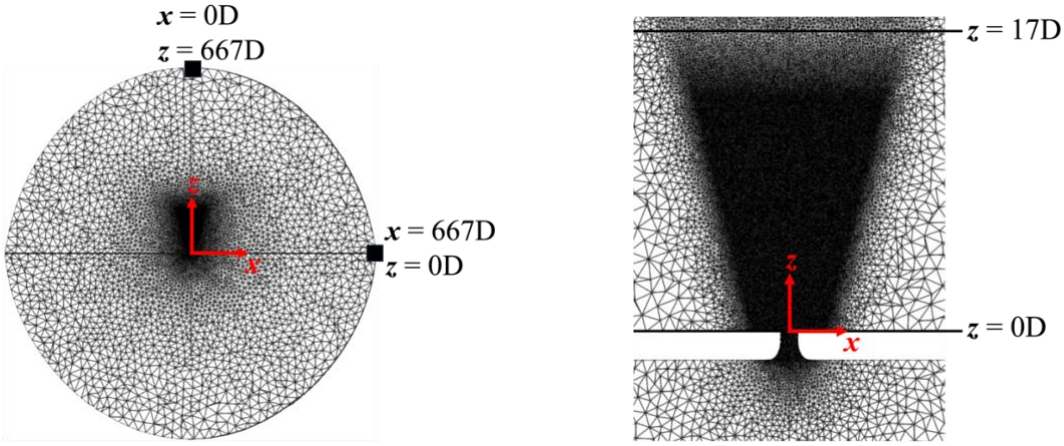

(a) Full computational domain *(b) Nozzle and potential core region*

Fig. 1. *Mid-plane view of the computational grid.*

2. Results and discussion

2.1. Validation of near field compressible structures

By definition, the under-expanded jet undergoes an expansion at the nozzle exit. The deviation of the expansion process from an isentropic expansion is quantified by the discharge coefficient, defined as $C_D = \dot{m}_{real}/\dot{m}_{isentropic}$, where $\dot{m}$ is a mass flow rate. As such, the discharge coefficient represents how much the effective mass flow rate ($\dot{m}_{real}$) decreases by non-isentropic effects. In the LES, the numerical discharge coefficient is almost one ($C_D = 0.998$), which is expected, since the boundary layer effects in the nozzle are not taken into account. Ruggles et al. (2012) reported a slightly lower discharge coefficient of 0.979, showing that the nozzle is almost ideal. Despite this 2% discrepancy on the mass flow rate, the LES jet's main shock structures display a fair agreement with the experimental Schlieren images (Fig. 2). Following the terminology of Franquet et al. (2015), they are organized according to a highly under-expanded jet structure, with a repetitive pattern of shock cells following an initial barrel-shaped structure. At the nozzle exit, an expansion fan forms and gets reflected into the barrel shock (marker A), or intercepting shock, leading to a Mach disk (marker B) and a reflected shock (marker C). This pattern repeats several times until the outer mixing layer reaches the jet axis and leads to the jet's potential core breakup, which occurs around 13D above the nozzle (Fig. 3). The intercepting shock, the Mach disk and the first reflected shock display a good accordance with the available experimental data (Fig. 2a). The Mach disk is located at a distance L_{MD} = 3.16 mm from the nozzle exit with a diameter of 1.22 mm. Ruggles et al. (2012) measured a Mach disk height of 3.05 mm with a diameter of 1.30 mm, implying numerical relative errors of 3.6% and 6%, respectively. The reflected shock angle is found to be equal to 30.1°. Behind the Mach disk, the flow is subsonic (Fig. 3a). By a converging nozzle effect induced by the surrounding triple point shear layer (markers D and E), the flow accelerates and reaches supersonic velocities again. A normal shock stabilizes at this location (marker F on Fig. 2b), which is found to be 3.8D = 5.75 mm above the nozzle exit, showing a fair agreement with the experimental data, which report a height of 6 mm. Just upstream of the Mach disk, the temperature drops to 60 K (Fig. 3a) and the pressure reaches 7100 Pa. Because of the locally low temperatures, the Mach number increases up to M = 4 in the first barrel-shaped cell. Such cryogenic temperatures were also found in other studies accounting for real gas effects (Bonelli et al. 2013; Khaksarfard et al. 2010). Moreover, at these temperature and pressure conditions, hydrogen density is still well-predicted by the ideal gas equation of state.

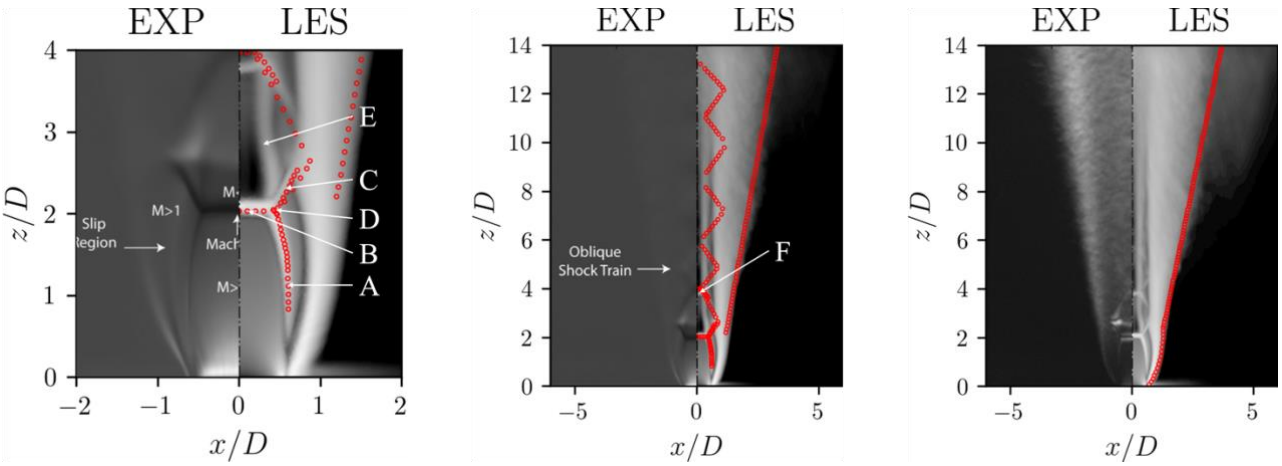

(a) Mean Schlieren in the region of the first shock cells ($z/D = 0 - 4$)

(b) Mean Schlieren in the near field ($z/D = 0 - 14$)

(c) RMS Schlieren in the near field ($z/D = 0 - 14$)

Fig. 2. *Comparison of mid-plane numerical Schlieren with line of sight Schlieren photographs from Ruggles et al. (2012) in the near field of the jet. Extracted experimental data is shown with ◦ symbols.*

Figure 2b shows that the compressible structures following the first two normal shocks are slightly mispredicted. It could be linked to the grid resolution as well as the use of a slip condition at the nozzle wall. Indeed, the discrepancy was reduced by increasing the grid resolution and by resolving the nozzle boundary layer with a no slip wall boundary condition: they were found to have a significant impact on the destabilization of the mixing layer, which interacts with the various shocks and wave reflections in the shock train (not shown here). However, such levels of resolution are impractical for far field computations, which are the objective of the present study.

The unsteadiness of the compressible structures is assessed through RMS Schlieren (Fig. 2c). The agreement with the experimental photograph is fair. In particular, the outer mixing layer width is well-retrieved. Avduevskii et al. (1971) defined an initial Reynolds number $Re_i = U_e L_{MD}/\nu_\infty$, where $U_e = 1231$ m/s is the mean velocity at the nozzle exit and ν_∞ is the ambient air kinematic viscosity, to predict the location of the destabilization of the mixing layer. Here, the initial Reynolds number $Re_i = 2.2 \times 10^5$ should yield a turbulent shear layer directly at the nozzle exit since it is higher than 10^4 (Avduevskii et al. 1971; Franquet et al. 2015). In their LES of the Sandia under-expanded hydrogen jet, Hamzehloo et al. (2014) observed mixing upstream of the Mach disk. In the present LES, Taylor-Goertler vortices around the intercepting shock destabilize the outer mixing layer, which seems to transition to turbulence approximately at the second normal shock height (Fig. 3b, 3c).

Overall, even though some discrepancies exist in the jet potential core structure, the jet width seems to be captured fairly accurately. As it controls the transition to the subsonic mixing region, the near field modeling is considered acceptable to go further in the investigation of the far field and the lifted flame in reactive conditions.

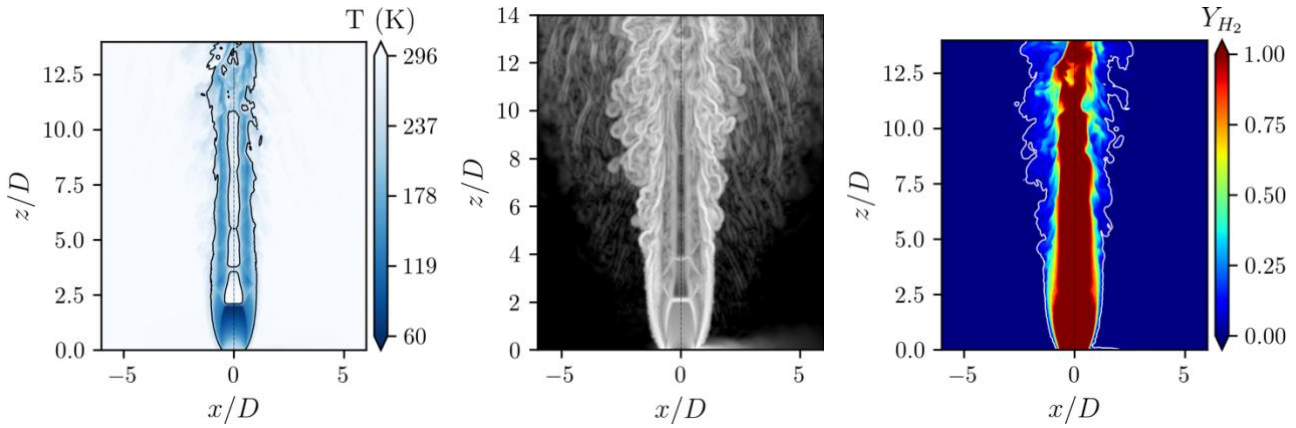

(a) Temperature and sonic line (black) *(b) Numerical Schlieren* *(c) H_2 mass fraction and stoichiometric line (white)*

Fig. 3. *Instantaneous mid-plane fields in the near field of the inert jet.*

2.2. Validation of hydrogen dispersion in the far field

In the far field, delimited by the region 53D to 160D where velocity and hydrogen concentration were measured, the jet has lost enough momentum and falls back to a subsonic regime. Its main characteristics are self-similar, and the pressure and temperature have reached those of the ambient air. Ruggles et al. (2012) indicate that the mean centerline temperature is within 1 K of the ambient temperature 53D above the nozzle exit. In the LES, ambient temperature is reached downstream of the 160D limit, indicating an overestimate of the jet transition region's length. However, 53D above the nozzle, the centerline mean temperature is 289 K, hence within 2% of that of the ambient air.

The far field jet dynamics are assessed using the velocity measurements conducted by Li et al. (2021). Overall, the LES results display a good agreement with the experimental data (Fig. 4, 5). At the most upstream section, the velocity magnitude is overpredicted near the jet centerline. The underprediction

of momentum dissipation also yields a slight underestimation of the jet width. Further downstream ($z \geq 133D$), momentum significantly decreases and matches the experimental data.

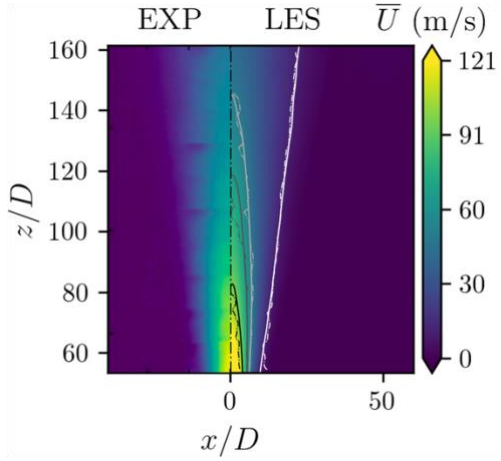

Fig. 4. *Comparison of mean velocity magnitude from the experimental data (Li et al. 2021) with LES results, superimposed with mean velocity isolines (from black to white: 95, 65, 50, 10 m/s). Continuous lines represent LES isolines. Dash-dotted lines represent experimental data.*

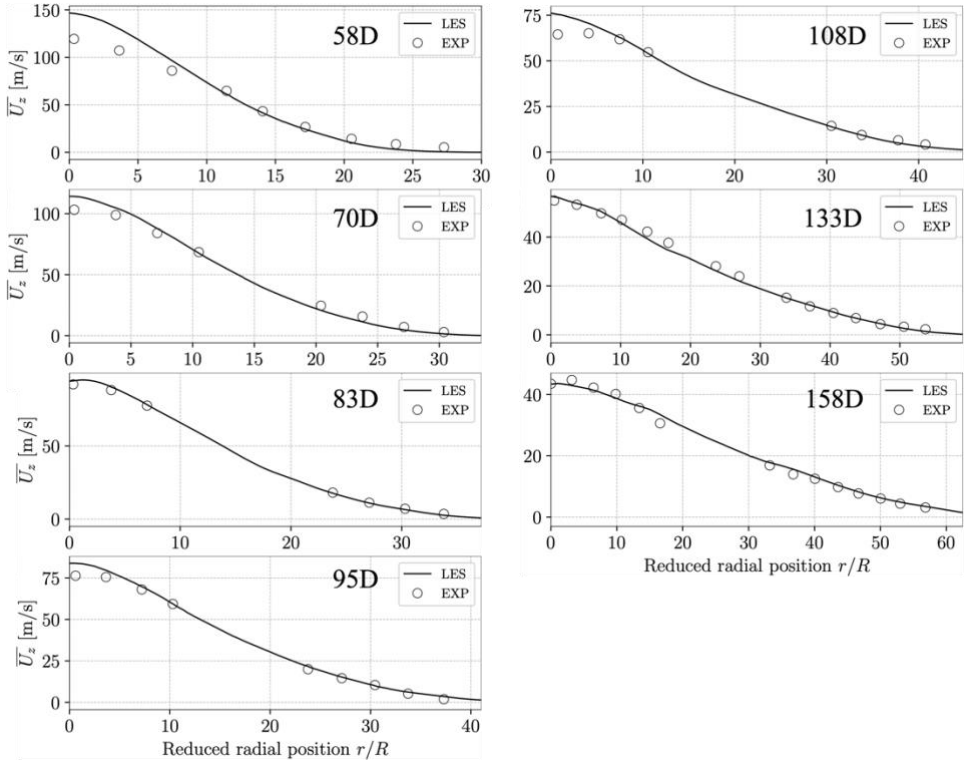

Fig. 5. *Radial profiles of mean axial velocity at different axial locations.*

The jet mixing rate is correctly captured by the LES (Fig. 6). The mean and RMS hydrogen mass fraction fairly agree with the measurements. The rate of decay of centerline hydrogen mass fraction is well-retrieved, as well as its fluctuations (Fig. 7). The jet half width, where half the centerline mixture fraction is reached, is also accurately captured (Fig. 8).

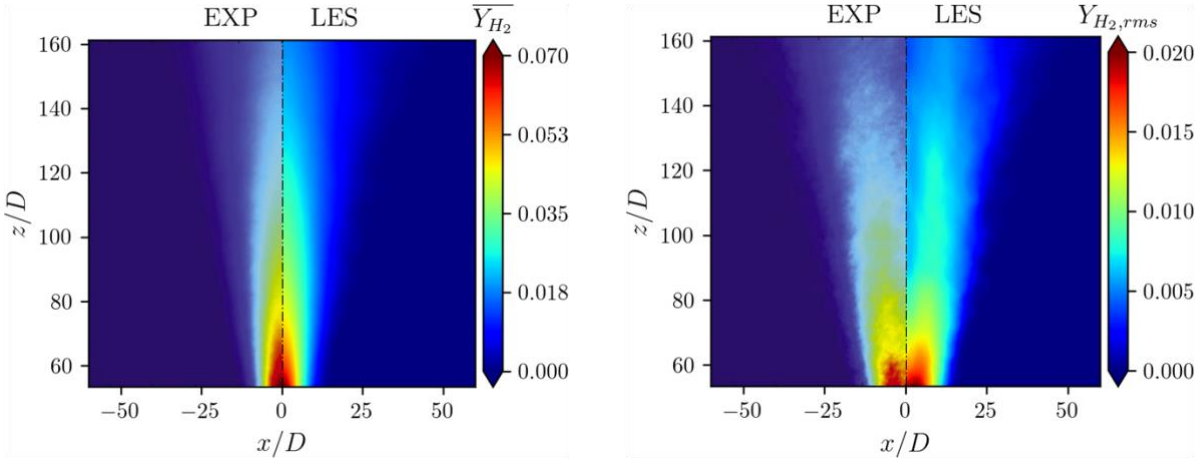

(a) Mean *(b) RMS*

Fig. 6. *LES results and experimental data (Ruggles et al. 2012) of mean and RMS H_2 mass fraction.*

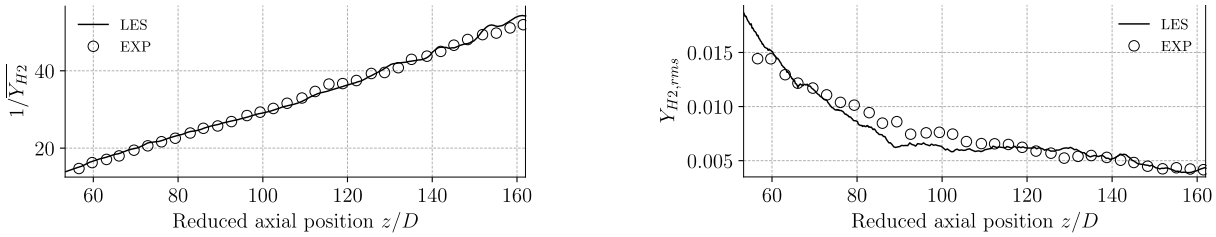

(a) Inverse of mean H_2 mass fraction *(b) RMS H_2 mass fraction*

Fig. 7. *Centerline mean and RMS H_2 mass fraction versus axial distance from the nozzle exit.*

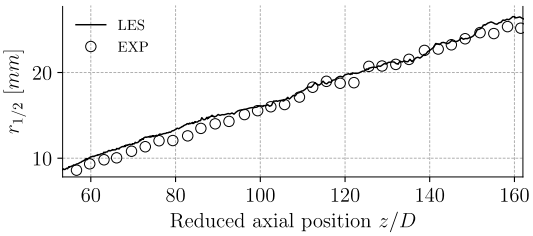

Fig. 8. *Jet half-width versus axial distance from the nozzle exit.*

The mean flammability limits in the jet are shown in Fig. 9 along with the stoichiometric line. The Upper Flammability Limit (UFL) contour tip reaches 35D = 51.9 mm and its maximum radius is 2.5 mm, located 22D = 33.55 mm above the nozzle. As the Lower Flammability Limit (LFL) contour tip is located outside the grid well-refined region, it is extrapolated from the rate of decay of the mean hydrogen mass fraction displayed in Fig. 7a. The LFL contour is estimated to cross the jet axis at $z = 1040D = 1.56$ m above the nozzle. The flammability limits of hydrogen lead to a large flammable region so that the presence of an ignition source in most of the jet would ignite it. Experimental studies of high-speed hydrogen jet flames report that the flame tip coincides with a hydrogen mole fraction of 11% (Molkov et al. 2013). In the present case, the 11% limit extrapolated from the hydrogen decay rate is found to be $L/D = 360$. One may note that this value is of the same order as the value estimated by the correlation for flame length proposed by Bradley et al. (2016), which yields $L/D = 42U^{*0.4} = 454$. The stoichiometric line reaches the centerline at a height L_{st} = 118D = 177.35 mm above the nozzle. The stoichiometric contour reaches its maximum radius at a height of 67D = 100.22 mm with a radius of 7D = 10.76 mm.

The assessment of the far field LES results demonstrates that they are adequate to potentially feed lower fidelity models or LES relying on a notional nozzle approach. This could be an advantage when

studying configurations that are outside the scope of notional nozzle models such as jets exposed to some degree of confinement, jets in cross-flow, or exiting from high aspect ratio nozzles.

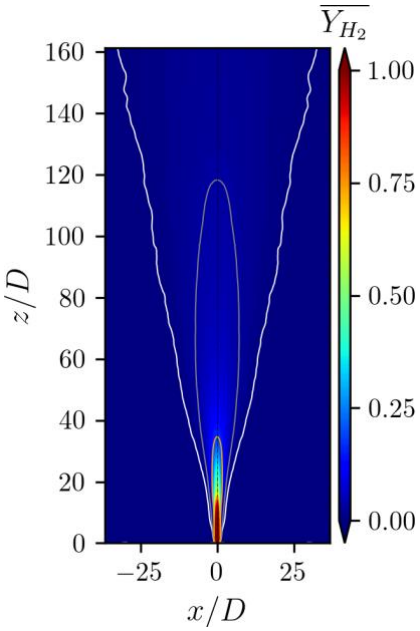

Fig. 9. *Mean H_2 mass fraction in the inert jet, superimposed with LFL (white), stoichiometric (gray), and UFL (orange) isolines.*

2.3. Lifted flame stabilization

In this section, the hydrogen jet is ignited and an established lifted flame forms in the far field region of the jet. The present study focuses on the established jet fire and does not address its ignition dynamics. For the reactive case, hydrogen-air chemistry is modeled by the detailed San Diego mechanism for hydrogen composed of 9 species and 21 reactions (Saxena et al. 2006). The Thickened Flame model (Colin et al. 2011) is used to handle premixed fronts using dynamic thickening combined with the Takeno flame index (Yamashita et al. 1996) to identify premixed flame fronts.

After ignition, the established flame stabilizes 52D = 78 mm above the nozzle. This lift-off height is in accordance with the correlation developed by Bradley et al. (2019), which yields a lift-off height H = 53D where

$$\frac{H}{D} = (-0.0002U^{*2} + 0.19U^{*} - 3.3)/f\,, \tag{2}$$

with $f = 0.756$ the ratio of hydrogen to air mole fractions at an equivalence ratio $\phi = 1.8$ and

$$U^{*} = \frac{u}{s_L}\left(\frac{\nu}{Ds_L}\right)^{0.4}\frac{P_{H_2}}{P_\infty} = 385\,. \tag{3}$$

In the present case, u = 940 m/s is the sonic velocity after isentropic expansion, $s_L = 3.07$ m/s is the maximum laminar flame speed and ν is the hydrogen-air viscosity at $\phi = 1.8$ under ambient conditions. In the LES, the flame stabilizes in a region where fuel and oxidizer are well mixed and the lift-off plane is located downstream of the UFL contour tip. The flammability of the jet core is expected to have a significant impact on the flame stabilization mechanism. The lift-off height is unperturbed by the local turbulent fluctuations and remains constant in time. This observation is consistent with the findings of Upatnieks et al. (2004), who reported that only large eddies, of diameter larger than the jet radius at the lift-off location, could disturb the lift-off height, up to a factor of 5%.

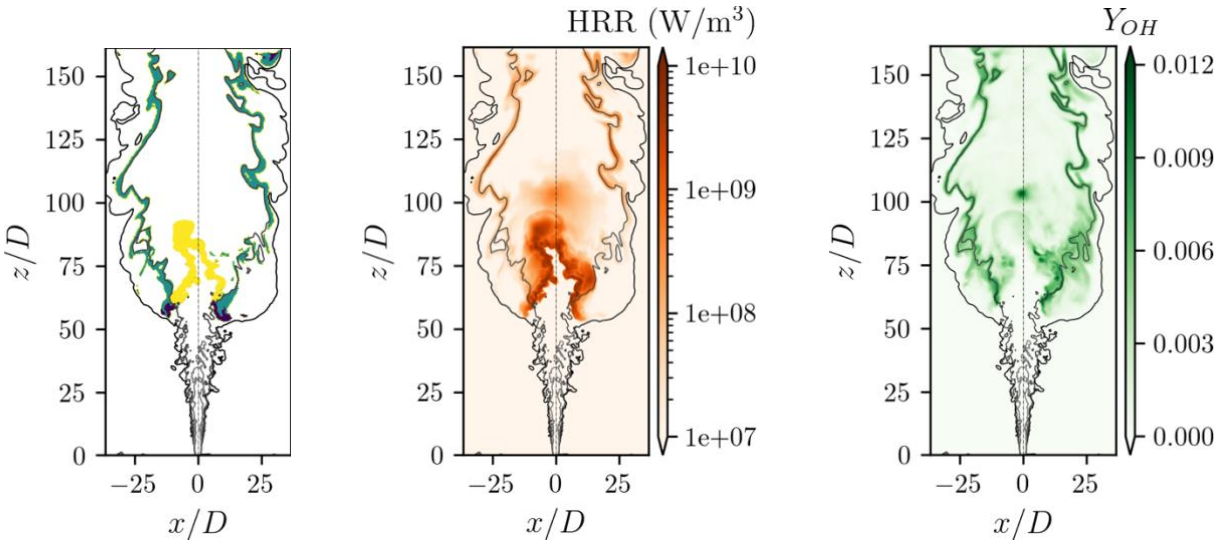

(a) Flame index η *(b) Heat release rate* *(c) Hydroxyl mass fraction*

Fig. 10. *Instantaneous mid-plane fields of the reacting jet, superimposed with LFL (black), UFL (light gray) and stoichiometric (medium gray) isolines. The flame index is defined by* $\eta = (\xi - \xi_{st})/|\xi - \xi_{st}| \times \frac{1}{2}(1 + G_{FO}/|G_{FO}|)$ *(Lock et al. 2005) with the following coloring: deep blue is lean premixed, yellow is rich premixed, and green is non-premixed.*

The envelope of the flame is a diffusion front burning on the stoichiometric line $\xi_{st} = 0.028$ (Fig. 10). A rich premixed branch, curved by the high momentum of the jet, stabilizes in the jet's core, which was also captured in the DNS of a high speed hydrogen lifted flame by Mizobuchi et al. (2002). The rich premixed fronts extend towards the outer boundary of the jet and meet the flame's diffusion envelope on the stoichiometric line (Fig. 11). The rich premixed fronts burn at a maximum equivalence ratio of 2.6 and the lean premixed branch extends down to the LFL, burning at a minimal equivalence ratio of 0.1. In consequence, the flame base is formed by 3 branches, burning in different combustion regimes, with lean premixed fronts forming the flame leading edges. The determination of the precise mechanism controlling the flame tip stabilization is left for future work.

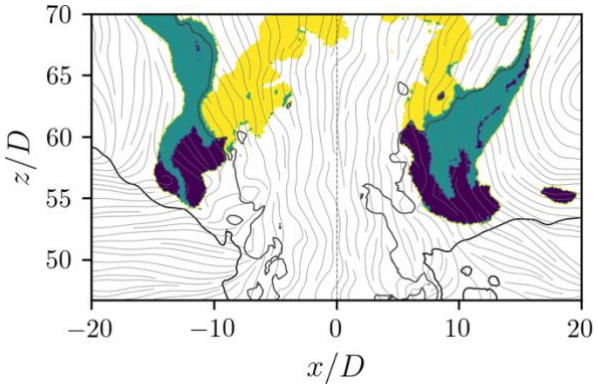

Fig. 11. *Mid-plane instantaneous flame index η (Lock et al. 2005) at the flame base, superimposed with streamlines, LFL (black) and stoichiometric (medium gray) isolines. Deep blue is lean premixed, yellow is rich premixed, and green is non-premixed.*

3. Conclusions

The LES of a hydrogen under-expanded jet in ambient air is performed in non-reacting and reacting conditions. Results are validated against non-reacting experimental measurements in the near and far fields. The shock train and the initial shear layer spreading rate are accurately captured. However, the destabilization of the mixing layer is not fully resolved on the grid, which affects the capture of some shock train structures. The near field discrepancies do not seem to affect the far field to a significant

extent, as both velocity and mixing rate are well-retrieved in this region. In the far field, the self-similar dynamics of the jet and the hydrogen rate of decay are accurately captured. It is found that hydrogen mass fraction decays rapidly on the jet axis, making the central part of the jet flammable at the observed lift-off height of the reacting jet. The lift-off distance captured by the LES is consistent with the correlation proposed by Bradley et al. (2019) and the global structure of the flame is in accordance with previous studies of lifted hydrogen flames. The flame base is composed of an inner rich front, an outer lean front, and a non-premixed envelope.

Immediate perspectives include the investigation in further detail of the stabilization mechanism of the under-expanded jet flame. In particular, the role of the edge flame and turbulent premixed flame concepts will be evaluated. In a subsequent step, the effect of injector geometry on flame stabilization should be considered, using high aspect ratio nozzles. LES has been validated in this canonical setup, and should be able to tackle more realistic scenarios such as the presence of a strong cross-flow and confinement effects, which could alter significantly the flame stabilization and thermal loads.

Acknowledgements

This work was performed using HPC resources from GENCI-IDRIS and GENCI-TGCC (Grants 2023-A0132B10157 and 2024-A0152B10157). Funding from Airbus, DGAC and the European Union within the project NextGenerationEU is gratefully acknowledged. No content in the paper is subject to any Export Control regulation neither of the United States of America nor the European Union. In addition, this paper does not contain any U.S. origin ITAR or EAR content.

References

ASME MFC-3M-2004, 2004. Measurement of fluid flow in pipes using orifice, nozzle, and venturi. Tech. rep.

Avduevskii, V.S., Ivanov, A.V., Karpman, I.M., Traskovskii, V.D., Yudelovich, M.Y., 1971. “Effect of Viscosity on the Flow in the Initial Part of a Highly Underexpanded Jet.” In: Soviet Physics Doklady. Vol. 16, p. 186.

Boivin, P., Dauptain, A., Jiménez, C., Cuenot, B., 2012. “Simulation of a supersonic hydrogen-air autoignition-stabilized flame using reduced chemistry”. In: Combust. Flame 159.4, pp. 1779–1790.

Bonelli, F., Viggiano, A., Magi, V., 2013. “A numerical analysis of hydrogen underexpanded jets under real gas assumption”. In: J. Fluids Eng. Trans. ASME 135.12, pp. 1–11.

Bradley, D., Gaskell, P.H., Gu, X., Palacios, A., 2016. “Jet flame heights, lift-off distances, and mean flame surface density for extensive ranges of fuels and flow rates”. In: Combust. Flame 164, pp. 400–409.

Bradley, D., Casal, J., Palacios, A., 2019. “Prediction of lift-off distance in choked and subsonic hydrogen jet fires”. In: Catal. Today 329, pp. 221–224.

Brennan, S.L., Makarov, D. V., Molkov, V., 2009. “LES of high pressure hydrogen jet fire”. In: J. Loss Prev. Process Ind. 22.3, pp. 353–359.

Celik, I.B., Cehreli, Z.N., Yavuz, I., 2005. “Index of resolution quality for large eddy simulations”. In: ASME Trans. 127.5, pp 949–958.

Colin, O., Ducros, F., Veynante, D., 2011. “A thickened flame model for large eddy simulations of turbulent premixed combustion”. In: Combust. Flame 158.11, pp. 2199–2213.

Dauptain, A., Cuenot, B., Poinsot, T.J., 2005. “Large eddy simulation of a supersonic hydrogen-air diffusion flame”. In: Complex Eff. Large Eddy Simul. 71, pp. 9–20.

Dauptain, A., Cuenot, B., Gicquel, L.Y.M., 2010. “Large eddy simulation of stable supersonic jet impinging on flat plate”. In: AIAA J. 48.10, pp. 2325–2338.

Devaud, C.B., Kelman, J.B., Moss, J.B., Stewart, C.D., 2002. “Stability of underexpanded supersonic jet flames burning H2-CO mixtures”. In: Shock Waves 12, pp. 241–249.

Devaud, C.B., Bray, K.N.C., 2003. “Assessment of the applicability of conditional moment closure to a lifted turbulent flame: First order model”. In: Combust. Flame 132.1-2, pp. 102–114.
Ferraris, S.A., Wen, J.X., 2007. “Large eddy simulation of a lifted turbulent jet flame”. In: Combust. Flame 150.4, pp. 320–339.
Franquet, E., Perrier, V., Gibout, S., Bruel, P., 2015. “Free underexpanded jets in a quiescent medium: A review”. In: Prog. Aerosp. Sci. 77, pp. 25–53.
Hamzehloo, A., Aleiferis, P.G., 2014. “Large eddy simulation of highly turbulent under-expanded hydrogen and methane jets for gaseous-fuelled internal combustion engines”. In: Int. J. Hydrogen Energy 39.36, pp. 21275–21296.
Hecht, E.S., Chowdhury, B.R., 2021. “Characteristic of cryogenic hydrogen flames from high-aspect ratio nozzles”. In: Int. J. Hydrogen Energy 46.23, pp. 12320–12328.
Jiang, Y., Pan, X., Cai, Q., Klymenko, O.V., Wang, Z., Hua, M., Wang, Q., Jiang, J., 2023. “Physics of flame evolution following spontaneously combusting hydrogen emerging from a tube into the unconfined space”. In: Combust. Flame 251.
Karami, S., Hawkes, E.R., Talei, M., Chen, J.H., 2015. “Mechanisms of flame stabilisation at low lifted height in a turbulent lifted slot-jet flame”. In: J. Fluid Mech. 777, pp. 633–689.
Khaksarfard, R., Kameshki, M.R., Paraschivoiu, M., 2010. “Numerical simulation of high pressure release and dispersion of hydrogen into air with real gas model”. In: Shock Waves 20.3, pp. 205–216.
Kim, I.S., Mastorakos, E., 2005. “Simulations of turbulent lifted jet flames with two-dimensional conditional moment closure”. In: Proc. Combust. Inst. 30.1, pp. 911–918.
Kim, Y.R., Lee, H.J., Kim, S., Jeung, I.S., 2013. “A flow visualization study on self-ignition of high pressure hydrogen gas released into a tube”. In: Proc. Combust. Inst. 34.2, pp. 2057– 2064.
Lee, H.J., Kim, Y.R., Kim, S.H., Jeung, I.S., 2011. “Experimental investigation on the self-ignition of pressurized hydrogen released by the failure of a rupture disk through tubes”. In: Proc. Combust. Inst. 33.2, pp. 2351–2358.
Li, X., Chowdhury, B.R., He, Q., Christopher, D.M., Hecht, E.S., 2021. “Validation of two-layer model for underexpanded hydrogen jets”. In: Int. J. Hydrogen Energy 46.23, pp. 12545–12554.
Liu, J., Kailasanath, K., Ramamurti, R., Munday, D., Gutmark, E., Lohner, R., 2009. “Large-eddy simulations of a supersonic jet and its near-field acoustic properties”. In: AIAA J. 47.8, pp. 1849–1864.
Lock, A.J., Briones, A.M., Qin, X., Aggarwal, S.K., Puri, I.K., Hegde, U., 2005. “Liftoff characteristics of partially premixed flames under normal and microgravity conditions”. In: Combust. Flame 143.3, pp. 159–173.
Lyons, K.M., 2007. “Toward an understanding of the stabilization mechanisms of lifted turbulent jet flames: experiments”. In: Progr. Energ. Combust. Sci. 33.2, pp. 211–231.
Mizobuchi, Y., Tachibana, S., Shinio, J., Ogawa, S., Takeno, T., 2002. “A numerical analysis of the structure of a turbulent hydrogen jet lifted flame”. In: Proc. Combust. Inst. 29.2, pp. 2009–2015.
Mizobuchi, Y., Shinjo, J., Ogawa, S., Takeno, T., 2005. “A numerical study on the formation of diffusion flame islands in a turbulent hydrogen jet lifted flame”. In: Proc. Combust. Inst. 30.1, pp. 611–619.
Mogi, T., Kim, D., Shiina, H., Horiguchi, S., 2008. “Self-ignition and explosion during discharge of high-pressure hydrogen”. In: J. Loss Prev. Process Ind. 21.2, pp. 199–204.
Mogi, T., Horiguchi, S., 2009. “Experimental study on the hazards of high-pressure hydrogen jet diffusion flames”. In: J. Loss Prev. Process Ind. 22.1, pp. 45–51.
Mogi, T., Wada, Y., Ogata, Y., Koichi Hayashi, A., 2009. “Self-ignition and flame propagation of high-pressure hydrogen jet during sudden discharge from a pipe”. In: Int. J. Hydrogen Energy 34.14, pp. 5810–5816.
Molkov, V., Saffers, J.B., 2013. “Hydrogen jet flames”. In: Int. J. Hydrogen Energy 38.19, pp. 8141–8158.
Mortada, M., Devaud, C., 2019. “Large Eddy Simulation of lifted turbulent flame in cold air using Doubly Conditional Source-term Estimation”. In: Combust. Flame 208, pp. 420–435.

Nicoud, F., Toda, H.B., Cabrit, O., Bose, S., Lee, J., 2011. “Using singular values to build a subgrid-scale model for large eddy simulations”. In: Phys. Fluids 23.8.
Panda, P.P., Hecht, E.S., 2017. “Ignition and flame characteristics of cryogenic hydrogen releases”. In: Int. J. Hydrogen Energy 42.1, pp. 775–785.
Poinsot, T.J., Lele, S.K., 1992. “Boundary conditions for direct simulations of compressible viscous flows”. In: J. Comput. Phys. 101.1, pp. 104–129.
Rahantamialisoa, F.N.Z., Zembi, J., Miliozzi, A., Sahranavardfard, N., Battistoni, M., 2022. “CFD simulations of under-expanded hydrogen jets under high-pressure injection conditions”. In: J. Phys. Conf. Ser. 2385.
Ren, Z., Giannissi, S., Venetsanos, A. G., Friedrich, A., Kuznetsov, M., Jordan, T., Wen, J.X., 2022. “The evolution and structure of ignited high-pressure cryogenic hydrogen jets”. In: Int. J. Hydrogen Energy 47.67, pp. 29184–29194.
Ruan, S., Swaminathan, N., Bray, K.N.C., Mizobuchi, Y., Takeno, T., 2012. “Scalar and its dissipation in the near field of turbulent lifted jet flame”. In: Combust. Flame 159.2, pp. 591–608.
Ruggles, A.J., Ekoto, I.W., 2012. “Ignitability and mixing of underexpanded hydrogen jets”. In: Int. J. Hydrogen Energy 37.22, pp. 17549–17560.
Saxena, P., Williams, F.A., 2006. “Testing a small detailed chemical-kinetic mechanism for the combustion of hydrogen and carbon monoxide”. In: Combust. Flame 145.1-2, pp. 316– 323.
Schefer, R.W., Houf, W.G., Williams, T.C., Bourne, B., Colton, J., 2007. “Characterization of high-pressure, underexpanded hydrogen-jet flames”. In: Int. J. Hydrogen Energy 32.12, pp. 2081–2093.
Schmitt, T., 2020. “Large-eddy simulations of the mascotte test cases operating at supercritical pressure”. In: Flow, Turbulence and Combustion 105.1, pp. 159–189.
Schonfeld, T., Rudgyard, M., 1999. “Steady and unsteady flow simulations using the hybrid flow solver AVBP”. In: AIAA journal 37.11, pp. 1378–1385.
Selmin, V., 1987. Third-order finite element schemes for the solution of hyperbolic problems. Tech. rep. INRIA.
Swain, M.R., Filoso, P.A., Swain, M.N., 2007. “An experimental investigation into the ignition of leaking hydrogen”. In: Int. J. Hydrogen Energy 32.2, pp. 287–295.
Takeno, K., Yamamoto, S., Sakatsume, R., Hirakawa, S., Takeda, H., Shentsov, V., Makarov, D., Molkov, V., 2020. “Effect of shock structure on stabilization and blow-off of hydrogen jet flames”. In: Int. J. Hydrogen Energy 45.16, pp. 10145–10154.
Upatnieks, A., Driscoll, J.F., Rasmussen, C.C., Ceccio, S.L., 2004. “Liftoff of turbulent jet flames - Assessment of edge flame and other concepts using cinema-PIV”. In: Combust. Flame 138.3, pp. 259–272.
Veser, A., Kuznetsov, M., Fast, G., Friedrich, A., Kotchourko, N., Stern, G., Schwall, M., Breitung, W., 2011. “The structure and flame propagation regimes in turbulent hydrogen jets”. In: Int. J. Hydrogen Energy 36.3, pp. 2351–2359.
Vuorinen, V., Yu, J., Tirunagari, S., 2013. “Large-eddy simulation of highly underexpanded transient gas jets”. In: Phys. Fluids 25.
Wen, J.X., Xu, B.P., Tam, V.H.Y., 2009. “Numerical study on spontaneous ignition of pressurized hydrogen release through a length of tube”. In: Combust. Flame 156.11, pp. 2173– 2189.
Xu, B.P., Wen, J.X., Dembele, S., Tam, V.H.Y., Hawksworth, S.J., 2009. “The effect of pressure boundary rupture rate on spontaneous ignition of pressurized hydrogen release”. In: J. Loss Prev. Process Ind. 22.3, pp. 279–287.
Yamamoto, S., Sakatsume, R., Takeno, K. 2018. “Blow-off process of highly under-expanded hydrogen non-premixed jet flame”. In: Int. J. Hydrogen Energy 43.10, pp. 5199–5205.
Yamashita, H., Shimada, M., Takeno, T., 1996. “A numerical study on flame stability at the transition point of jet diffusion flames”. In: Symp. Combust. 26.1, pp. 27–34.
Yu, X., Wu, Y., Zhao, Y., Wang, C., 2022. “Flame characteristics of under-expanded, cryogenic hydrogen jet fire”. In: Combust. Flame 244.

Study the Impact of Spacer at Thermal Degradation Process of MLI-based Insulation in Fire Condition

A. Hajhariri [a, *], R. Eberwein [a], L.P. Perrone[b], V. Cozzani[b], F. Otremba[a], H. Seidlitz[c]

[a] Bundesanstalt für Materialforschung und -prüfung (BAM), Berlin, Germany

[b] Alma Mater Studiorum - Università di Bologna, Bologna, Italy

[c] Brandenburgische Technische Universität, Cottbus, Germany

* E-mail contact: Aliasghar.hajhariri@bam.de

Abstract

To reduce carbon dioxide emissions, energy carries such as hydrogen consider to be a solution. Consumption of hydrogen as a fuel meets several restrictions such as its low volumetric energy density in gas phase. To tackle this problem, storage as well as transportation in liquid phase is recommended. To be able to handle this component in liquid phase, an efficient thermal insulation e.g., MLI insulation is required. Some studies have been revealed vulnerability of this type of insulation against high heat flux, for instance a fire accident. Some investigations have been depicted the importance of consideration of the MLI thermal degradation in terms of its reflective layer. However, limited number of studies have been focused on the thermal degradation of spacer material and its effect on the overall heat flux.

In this study, through systematic experimental measurements, the effect of thermal loads on glass fleece, glass paper as well as polyester spacers are investigated. The results are reported in various temperature and heat flux profiles. Interpreting the temperature profiles revealed as the number of spacers in the medium increases, the peak temperature detectable by the temperature sensor on the measurement plate decreases. Moreover, the contribution of each individual spacer in all cases regarding the experimental temperature range is assessed to be around 8%. This value may increase to around 50% for glass paper and polyester spacers, and to around 25% for glass fleece spacers as the number of spacer layers increases up to six layers.

To utilize the outcomes of the experiment later and integrate the results into numerical and CFD simulations, a model is proposed for the mentioned experimental temperature range up to 300°C to predict a heat flux attenuation factor. The model proposes a fitting factor that can reproduce the least square fitted line to the experimental data.

Keywords: *Multi-Layer Insulation, Cryogenic, Liquid Hydrogen, Heat transfer*

Nomenclator

A	*Area [m2]*	L	*Total thickness of spacers layers [m]*
C	*Thermal capacity per unit area [J/ (K m^2)]*	M	*Air molar mas [kg/mol]*
cp	*Specific heat at constant pressure [(J kg)/K]*	n	*Effective refractive index [-]*
d	*Fiber diameter [m]*	Pr	*Residual pressure [Pa]*
Dx	*Spacer thickness [m]*	q	*Heat flux [w/m^2]*
e	*Effective extinction factor [kg/m^2]*	R	*Universal Gas constant [J/mol K]*
f	*Relative density of spacer material [-]*	α	*Fitting parameter [-]*

h_{diss}	*Energy dissipation factor*	δ	*Measurement plate Thickness [m]*
k_g	*Gas conduction constant in continuum regime [w/ (m K)]*	ε	*Emissivity [-]*
ζ	*Molecular degree of freedom*		***subscripts***
θ	*Accommodation coefficient [-]*	exp	*Experimental*
ρ	*Density [kg/m^3]*	$g.con$	*Gas conduction*
σ	*Stefan Boltzmann coefficient [W/m^{2}K^4]*	MP	*Measurement plate*
φ	*Attenuation factor [-]*	P	*Pressure*
		Rad	*Radiation*
		RS	*Radiative Source*
		th	*Theoretical*

1. Introduction

Now a days, transitioning towards achieving zero CO_2 emissions has become a global concern, necessitating rigorous efforts across various industrial sectors (Preuster et al., 2017; Speirs et al., 2019). In this attempt, hydrogen is identified as a promising alternative to fossil fuels. Notably, its liquid form (LH2) is favored for energy storage, offering a higher energy density per unit volume than its gaseous counterpart, even under high-pressure conditions (Kunze & Kircher, 2012). However, the transition to liquid hydrogen requires significant energy for liquefaction and demands secure and cost-effective storage solutions.

Double-walled storage tanks, featuring high vacuum levels of insulation part, are commonly used in small to medium scale applications. To further improve insulation efficiency, the industry standard now includes the use of multi-layer insulation (MLI) systems in conjunction with high vacuum. Referring to the study of Fesmire (2015), high vacuum considers pressure from 1.33×10^{-4} to 0.133 Pa, and moderate vacuum from 0.133 to 1333 Pa. An MLI insulation system consists of reflective layers interlevel with low conductive spacer materials. Reflective layers are aimed to block the radiation mood of energy transportation whereas spacers are required to reduce the conduction heat transfer between reflective layers by providing sufficient space that prevent any direct contact between reflective layers. These systems are compact and provide superior insulation efficiency (Sutheesh & Chollackal, 2018). Although primarily designed for cryogenic applications, MLI systems are susceptible to damage from high heat flux events, such as those experienced during fire accidents. The material composition of MLI become important in its degradation. The MLI degradation can significantly increase heat leakage toward the stored cryogenic fluids, causing rapid vaporization and leading to Boiling Liquid Expanding Vapor Explosion (BLEVE). This not only risks the integrity of the storage tanks but also poses significant safety hazards. The degradation affects both the reflective layers and the spacers within the MLI system.

Primarily, the MLI insulation has been extensively studied by researchers such as McIntosh (1994) and Lisowski & Lisowski (2019). However, these studies did not account for any thermal deterioration effects on the performance of the insulation system. Wingarden et al. (2022) conducted a study that highlighted the short time to failure of medium-scale liquid hydrogen (LH2) tanks equipped with MLI insulation. Additionally, research by Eberwein et al. (2023) and Complese et al. (2023, 2024) has shown the vulnerability of polyester based MLI and its spacers to high temperatures, such as those experienced in fire accident scenario. Eberwein et al. (2024) further revealed that in the case of non-combustible MLI, spacers within the insulation system remain intact even after the deterioration of reflective layers. Therefore, their investigations reported considerable heat flux difference in case of different spacers.

This observation underscores the importance of investigating the impact of spacer on the overall performance of the insulation system. To date, only a limited number of studies, including those by DeWitt (1968), Daryabeigi et al. (2007, 2011), and Johnson et al. (2014), have examined heat transfer

through spacer materials under conditions of high temperature and pressure. These studies typically employ a two-flux heat transfer model to explore the effects of extreme boundary conditions on heat transfer, both in steady-state and transient scenarios. However, research into the thermal degradation impacts on insulation systems remains rare, primarily due to technical complexities and the need for extensive data.

To enhance the safety margins of insulation designs and extend the time to failure of tanks, it is imperative to conduct comprehensive studies on the behavior of spacers under various conditions. This study assesses the influence of spacers on the overall heat transfer from the radiative source toward the measurement plate. Based on experimental observations, a straightforward model has been developed to quantify the effect of the number of spacer layers on heat resistance applied on direct radiative heat flux. This model aims to provide insights into optimizing MLI systems for enhanced thermal performance and safety in cryogenic storage applications.

2. Experiments

In this study, the specimens utilized are polyester, glass fleece, and glass paper spacers which are commonly applied in either combustible or non-combustible MLI insulations, as detailed in Table 1.

***Table 1**. Spacer samples specifications*

Property	**Symbol**	**Unit**	**Spacer**		
Material	-	-	Glass fleece	Glass paper	Polyester
Thickness	Dx	m	6.27×10^{-4}	-	2.88×10^{-4}
Fiber Diameter	d	m	1.6×10^{-5}	-	-
Density	ρ	kg/m^3	2500*	2500*	1180-2200
Thermal Conductivity	k	W/ (m K)	0.8*	0.8*	0.195
Specific heat capacity	c	J/ (kg K)	-	-	1100
Relative density	f	-	0.0176	0.011	0.0358

A superscript (*) denotes the base material from which the spacer is fabricated.

To prevent bending of spacer at the center and holding the spacer as flat as possible, all samples are supported with a steel ring, as depicted in Fig. 1. The experimental setup shown in Fig. 1 involves subjecting the sample to thermal loads within a Low Temperature Thermal Vacuum Chamber (LTTVC). This chamber is equipped with a gas-tight lid, to which temperature and pressure sensors, as well as a vacuum pump, are connected. The LTTVC is engineered to maintain a moderate vacuum condition of around 1.2 mbar to simulate the degraded vacuum and creating an appropriate test environment. Since for analysing fire scenarios, all insulating materials cause a degradation of the vacuum (Eberwein et al., 2024). Thermal loading is achieved through an electrical heating system on which the chamber is placed. The bottom of the chamber is equipped with a thermocouple to report the time dependent temperature of the bottom part which from now on is termed the ‘Radiative Source (RS)’.

A vertical rod supports an insulation screen that is positioned parallel to the radiative source (heating system in Fig. 1) and is adjustable in height. Heat flux measurements are facilitated by a 0.05 mm thin rectangular steel plate 50 to 80 mm2 designated as the Measurement Plate (MP), which is mounted on the screen. A thermocouple is attached to its surface via spot welding to monitor temperature changes.

Fig. 1. *LTTVC, spacer, and measurement plate*

To ensure precise boundary conditions for the experimental setup, both the RS and one side of the MP (faced down toward the RS) are coated with high emissivity paint to bring the surface emissivity of 0.82 in applied temperature range of the LTTVC. Insulation screen is aimed to minimize heat loss of the non coated side of the MP, by using 10 layers of non-combustible MLI. Furthermore, the chamber's inner sidewall was insulated with 20 mm thick PROMAGLAF®. This insulation reduces thermal dissipation by radial radiation and build the support of the sample holder, which can be adjusted at a desirable height relative to the RS.

3. Method

The investigation is focused on the various types of spacers used in both combustible and non-combustible sets of MLI insulation. Therefore, polyester type spacer is used in case of combustible MLI materials whereas glass fleece and glass paper spacers are chosen in case of non-combustible MLI materials. Previous experimental investigations conducted by Eberwein et al. (2024) have shown, in terms of non-combustible MLI insulation, its spacers can withstand fire conditions even after the degradation of their underlaying reflective layer. As a result, during the MLI degradation process and reflective layer deterioration, the spacers may directly be exposed to radiation from the radiative source.

To assess the contribution of a single spacer to the overall heat transfer, calibration of LTTVC system is initially required. The experimental setup facilitates the indirect determination of the heat stored in the measuring plate at any moment, referred to as the 'Experimental heat flux (q_{exp})' which can be seen in Eq. 1. This determination is based on the measurement plate's temperature and its thermal capacity per unit area C (Eq. 2). In LTTVC, a part of energy is considered to be dissipated through the lateral wall as it is connected to the RS. Hence, the calibration test only considers the radiative heat transfer from the radiative source as well as gas conduction heat transfer and excludes the dissipated portion of energy flow that happens through the wall. Since the area of the MP is relatively small in comparison to the radiative source, some heat is also expected to be dissipated through the background screen behind the measuring plate which is accounted in the calibration test as well.

As mentioned above, within a moderate vacuum environment of approximately 1.2 mbar, the dominant heat transfer modes are assumed to be radiation and gas conduction (Daryabeiygi, 2011). Hence, by comparing the theoretical heat transfer (q_{th}) from Eq. 3 with the experimental data, it is possible to calculate an overall dissipation heat transfer coefficient (h_{diss}), which reflects all possible dissipation of heat in calibration experiments. This coefficient is obtained using the least squares method to analyse the discrepancy between theoretical and calibration experiment in Eq. 4. Roles of

radiation q_{rad}, and gas conduction $q_{g,cond}$ in the system's heat transfer are outlined in Eq. 5 and Eq. 6, respectively.

***Table 2**. Equations used in the analysis.*

$$q_{exp} = C\,\frac{dT}{dt} \tag{1}$$

$$C = \frac{\delta\, A\, \rho\, C_p}{A} \tag{2}$$

$$q_{th} = q_{rad} + q_{g,cond} \tag{3}$$

$$\Delta q = q_{th} - q_{exp} - (h_{\mathrm{diss}} * \Delta T) \tag{4}$$

$$q_{rad} = \frac{\sigma}{\left(\frac{1}{\varepsilon_{RS}} + \frac{1}{\varepsilon_P} - 1\right)} (T_{RS}^4 - T_P^4) \tag{5}$$

$$q_{g,cond} = \frac{1}{\left(\frac{D_x}{k_g} + \frac{2-\theta}{\theta} \cdot \frac{\sqrt{\frac{\pi M T_M}{2R}}}{\left(1 + \frac{\zeta}{4}\right) P_r}\right)} (T_{RS} - T_P) \tag{6}$$

$$\varphi = \frac{\Delta q + q_{exp} - q_{g,cond} + (h_{\mathrm{diss}} * \Delta T)}{q_{rad}} \tag{7}$$

The reduction in heat transfer by imposing each spacer is primarily due to two mechanisms: the attenuation of incident radiation, known as radiation resistance, and the reduction of gas conduction heat transfer. Comparing the experimental heat transfer in the presence of a spacer with that of the calibration test enables the determination of an attenuation factor (φ), that accounts for any means of heat flow attenuation. In this study, it is suggested that the spacer's contribution to conduction heat resistance is negligible compared to radiation resistance. Eq. 7 is used to calculate the attenuation factor that directly applied on radiation heat transfer. Sequentially, the effective portion of heat that meets MP is assumed to equal to 1-φ of the total radiation heat transfer. It is important to note that φ varies with the number of layers and the medium's temperature.

4. Results and discussion

Fig. 2 to Fig. 5 display the temperature profiles of the RS with solid lines, and the temperature of the MP with dashed lines, to offer insight into temperature variations of glass fleece spacer across four experiments. Each figure includes three trials under the same experimental conditions, with the calibration test being the only scenario without a spacer. The analysis begins when the MP's temperature reaches 25°C. The temperature increasement trend of the other specimens is also the same trend as in glass fleece spacer specimen.

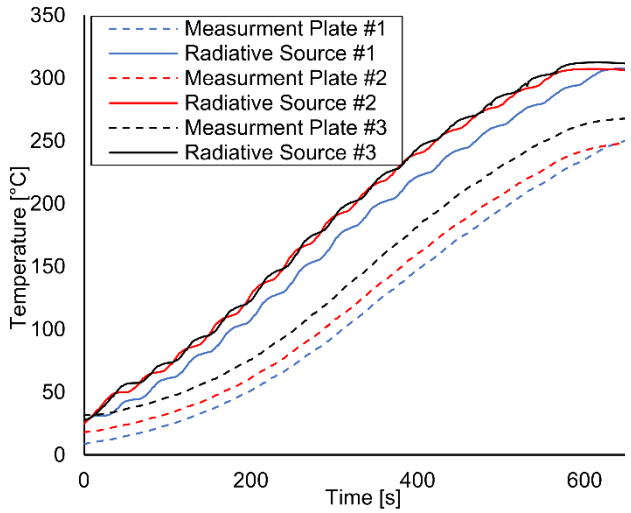

Fig. 2. *RS temperature vs MP temperature in the calibration experiment*

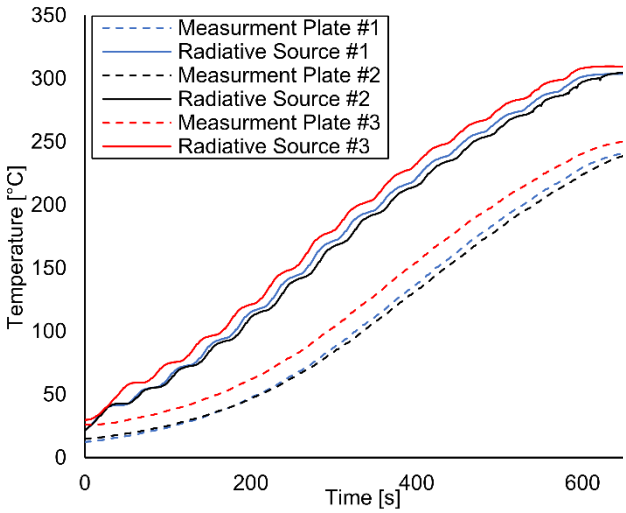

Fig. 3. *RS temperature vs MP temperature for experiment with one glass fleece spacer layer*

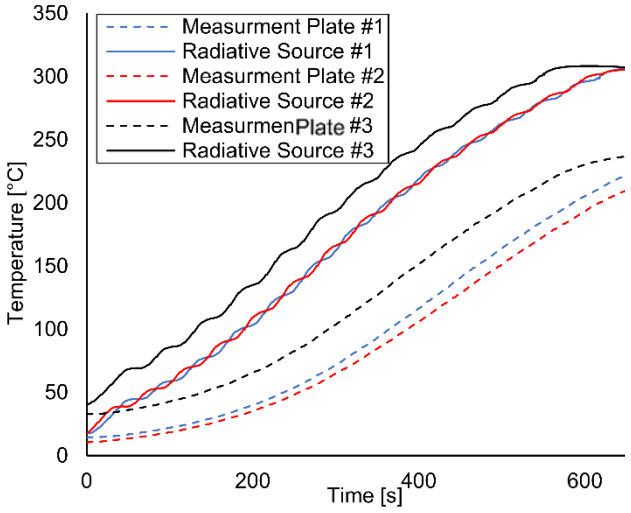

Fig. 4. *RS temperature profile vs MP temperature profile for experiment with 3 glass fleece spacer layers*

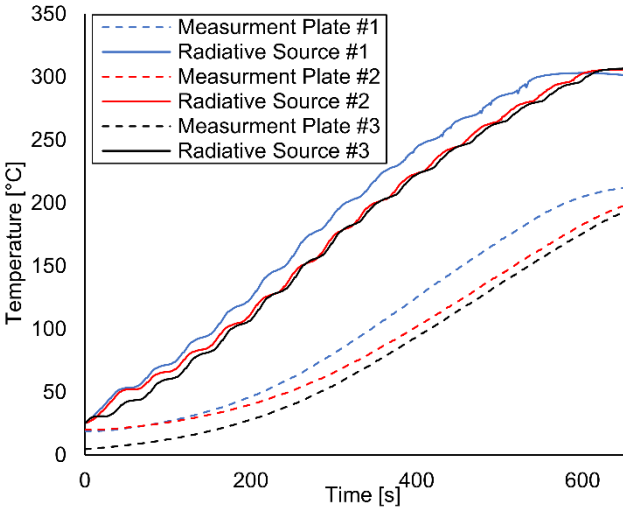

Fig. 5. *RS temperature profile vs MP temperature profile for experiment with 6 glass fleece spacer layers*

Due to the RS's higher heat capacity, its temperature profile initially rises gradually, in contrast to the MP's temperature profile, which increases more steeply. However, after 200 seconds of the experiments, both the RS and MP profiles exhibit comparable temperature increase trend across all experiments. Notably, the MP's temperature profile in the calibration experiment shows the highest temperature peak, closely mirroring the RS's profile. Introducing spacer layers leads to a gradual reduction in the slope of the MP's temperature profile. A comparison of the MP's maximum temperatures across different experimental scenarios indicates that adding spacer layers reduces the MP's peak temperature.

It's important to note that one potential reason for observing minor differences in temperature profiles across different trials in an experiment could be due to variations in the orientation of the fibres within the glass fleece material. Additionally, the way that the spacer layers are stacked on top of each other

might not be consistent, leading to changes in the fibre geometry from one sample to another. This could result in slight variations in temperature profiles. Building on the research of Caps et al. (1996), the radiative conduction coefficient is related to the radiation incident that directly connected to the design of fibres in spacers as mentioned above, see Eq. 8.

$$k_{rad} = \frac{16}{3}\frac{n^2 \sigma T^3}{e f} \qquad (8)$$

Where e refers to the effective extinction factor [kg/m^2], f represents the relative density of a spacer [kg/m^3], T is the spacer temperature [K], n is the effective refractive index of the insulation medium and σ is the Stefan Boltzmann coefficient 5.67×10^{-8} [W/m^{2}K^4]. Both refractive index and extinction coefficient are depending on the incident radiation wavelength and the temperature of the medium. In line with the outcome of the experimental evidence, the radiative coefficient of the spacer material depends on the relative density which in turn can be shown by the number of layers.

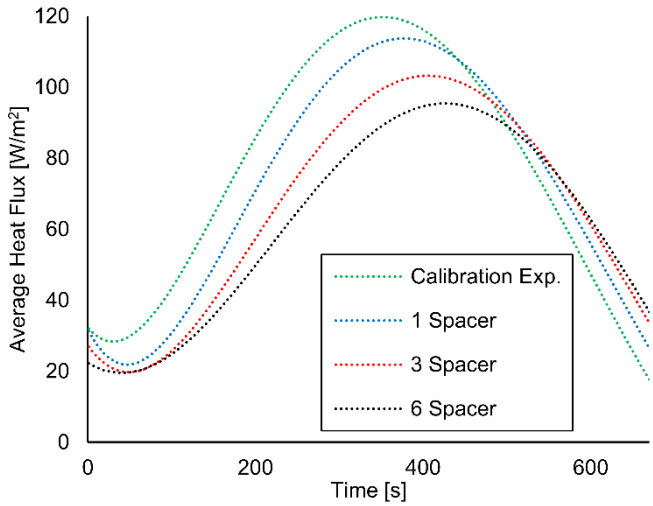

Fig. 6. *Average heat transfer shown with polynomial fitted line for experimental cases for glass fleece.*

Consistent with these observations, Fig. 6 illustrates the time dependent average experimental heat flux through glass fleece spacer for various trials over the experimental duration. An initial drop in heat flux is observed due to a delay in the temperature increasement of the RS. However, as the RS approaches its maximum heat capacity, the temperature rise becomes dominant, resulting in a linear increase in experimental heat flux. When the RS temperature approaches the MP's temperature profile, consequently, the temperature difference across the MP decreases, leading to a reduction in absorbed heat over time. Analysis of the average heat flux absorbed by the MP indicates that increasing the number of spacer layers reduces overall heat flux. Moreover, comparing the slope of the heat fluxes between 200 s and 400 s reveals that the effect of adding spacer layers on the attenuation factor is not linear.

The attenuation factor, indicative of the portion of heat flux mitigated by additional radiative thermal resistance, is calculated by analysing two distinct experimental time frames separately. Despite varying trends in heat flux between 0 to 300 s and 300 s to 400 s, the experimental attenuation factor shows up to 20% variation in the results for the case of glass fleece and 10% in the results of glass paper as well as polyester spacers between two different time frames.

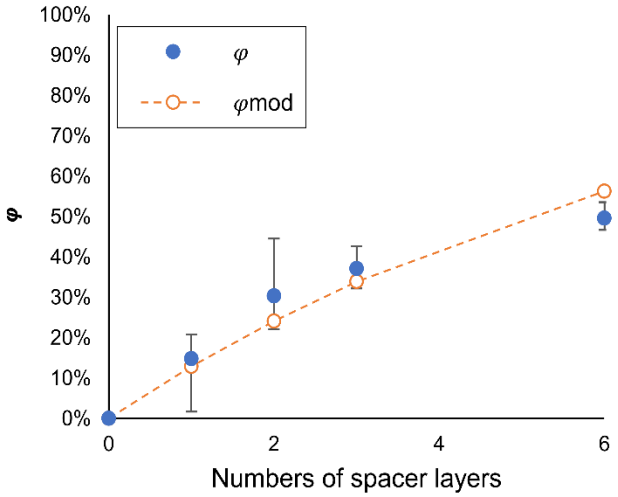

Fig. 7. *Attenuation factor vs the number of spacer layers of glass fleece for time frame of 0 to 300s*

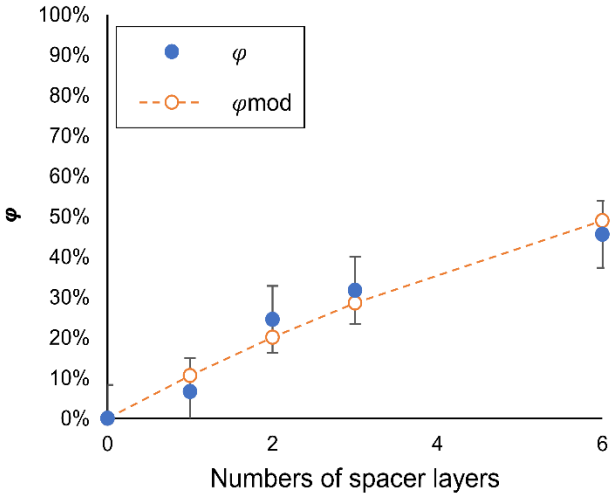

Fig. 8. *Attenuation factor vs the number of spacer layers of glass fleece for time frame of 300s to 400s*

Fig. 7 and Fig. 8 detail the attenuation factor attributed to the number of spacer layers. In calibration experiments, where no sample is present, the attenuation factor φ is zero. As the number of layers increases, the resistance grows. The error bars indicate the variability in additional heat resistance across different trials, with resistance contributions reaching approximately 50% in scenarios with the maximum number of spacer layers. This finding aligns with the earlier analysis of the average heat flux slope.

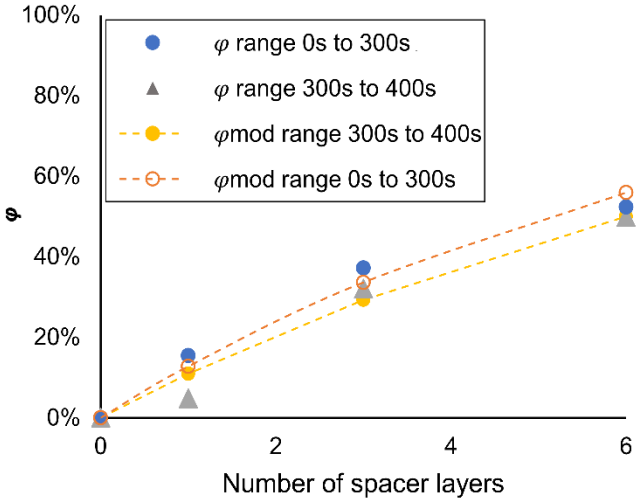

Fig. 9. *Comparison of different time frame for glass paper spacer and its impact on attenuation factor*

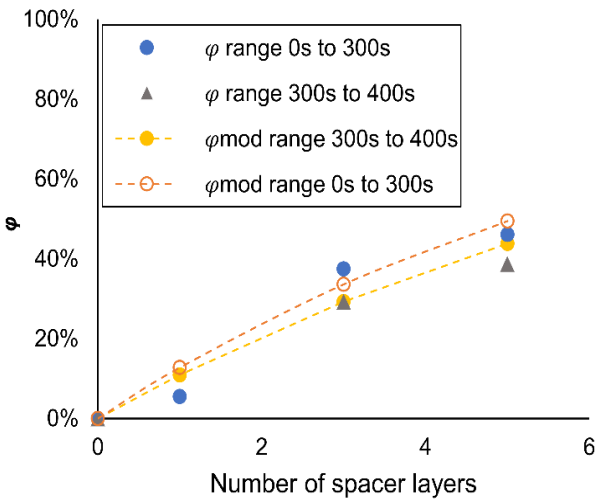

Fig. 10. *Comparison of different time frame for polyester spacer and its impact on attenuation factor*

Similarly, Fig. 9 and Fig. 10 are illustrated the impact of glass paper and polyester spacer on the overall heat transfer in two different time frames of experiments, respectively. There is slightly variation with respect to the time frame in both cases that are not exceeding 10% regarding the maximum predicted value. As the range of the time of analysis increases, the measured heat resistance is being slightly higher than when the time frame is being smaller. However, in the case of polyester spacer it can be seen that even 5 layers of those spacers can bring the same resistance as the glass paper imposes in the system.

Interpreting the results for all spacer materials has led to the development of an empirical correlation that can predict the amount of additional heat resistance in terms of the number of layers, which also depends on the temperature range. The experimental results suggest that the attenuation factor, represented by the φ value, is not a linear function of the number of spacer layers but instead follows an exponential trend. Consequently, an exponential model (Eq. 9) is proposed, fitted to the data using the least squares method.

$$\varphi mod = e^{-\alpha\Gamma} \qquad (9)$$

This model, which predicts the attenuation of radiative heat transfer based on the number of layers (Γ), incorporates a fitting parameter α to minimize the difference between the model and the experimental least square attenuation factors that you can find the fitted value in Table 2.

Table 3. *α value for all spacer materials in the specific time frame*

Spacer material	**Time range**	**α**
Glass fleece	300s to 400s	0.1121
Glass paper	300s to 400s	0.1154
Polyester	300s to 400s	0.092

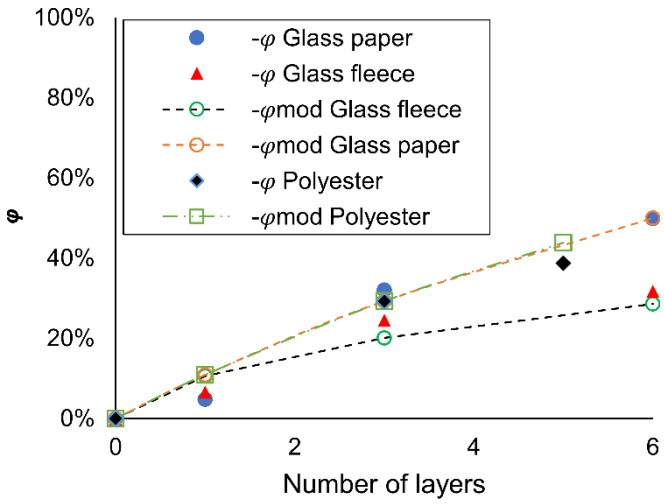

Fig. *11 Comparison of polyester, glass fleece and glass paper spacers*

In summary, Fig. 7 to Fig. 11 present for all tested samples, that with the increasing number of spacers the heat resistance increases which also results in an increasing attenuation factor. Furthermore, from all samples glass paper spacers have the lowest attenuation factor. This result aligns with the findings of Eberwein et al. (2023), where lower damage in the test regarding MLI with glass paper was observed compared to the test regarding MLI with glass fleece. As previously mentioned, the relative density of the material, the geometry of fibers in these spacers, and optical properties may play a crucial role in reducing radiative heat transfer from the RS. Note that for higher temperature beyond the pyrolysis temperature of polyester it is expected that the polyester spacer cannot withstand for all the duration and become completely deteriorate similar to the results of Eberwein et al., as mentioned before.

It is worth noting that in real conditions, there is an optimum ratio of spacer thickness (in term of number of spacer) to insulation thickness. However, using a spacer with higher density may increase the attenuation of radiation; it may also increase solid and gas conduction within the spacer material and lead to an increase in the overall heat transfer coefficient.

5. Conclusions

This study focuses on analyzing spacer materials used in MLI insulation systems either combustible or non-combustible, particularly their impact on radiation transmission from a heat source through the spacer after thermal deterioration. Utilizing systematic experimental methodologies, the behavior of glass fleece, glass paper and polyester spacers under thermal loads are explored. The experiments, conducted in a LTTVC simulating a moderately degraded vacuum condition, assess heat transfer mechanisms, including radiation and gas conduction, and evaluate the spacers' effectiveness in attenuating heat flow.

Comparative analysis of temperature profiles and heat flux measurements across various experimental setups for different types of spacers reveals that spacers not only modify the thermal gradient within the system but also may lower the peak temperature on the Measurement Plate (MP). Variations in temperature profile observed in each test trial of an experiment may occurred due to the orientation and geometry of the fibers; however, multiple trials indicate that this deviation does not exceed a 20% variance from the average value in case of glass fleece or polyester spacers. Furthermore, experiments with glass paper also shown even smaller deviation in their temperature profile.

Importantly, comparing the effect of radiation versus gas conduction point to the fact that the reduction in heat transfer in case of MLI layer thermal deterioration is primarily due to the attenuation of incident radiation, with a secondary effect from diminished gas conduction heat transfer. This attenuation, however, does not scale linearly with the number of spacer layers but instead follows an exponential trend.

The result of attenuation factor shows that introducing even a single spacer layer to the direct radiation can reduce thermal radiation transmission toward the MP by less than 8% for both glass paper and polyester spacer whereas glass fleece shows slightly lower value. Moreover, this attenuation for both glass paper and polyester spacer as well as glass paper spacers are potentially increasing to around 50% and 25%, respectively, as the number of layers increases up to six. Based on this research, radiation heat flux especially at higher temperature may decrease using thicker spacers (more spacer layers) in order to increase the safety margins. Nevertheless, increasing the spacer material in the insulation system may negatively impact the vacuum pressure by introducing more pyrolyzed material in the mentioned space during MLI thermal deterioration.

This research underscores the importance of considering the properties and configuration of spacer materials in design and optimization of insulation for cryogenic conditions and high-heat-flux environments. The empirical modeling approach based on the material and number of spacer layers represents a significant understanding in the thermal dynamics within MLI systems. Moreover, it can

cover the way for prediction of durability of an insulation system under high thermal loads. Supported by experimental data, this model highlights the crucial role of spacers in enhancing the insulation efficiency of MLI systems against direct radiative heat transfer. However, the thermal behavior of different spacer materials within insulation systems needs more investigation on inception of spacer and reflective material in degradation mechanism.

Acknowledgements

This work was undertaken as part of the research project 'Research of the influence of fires to tanks for cryogenic fluids' (FETLHy), where the authors wish to acknowledge the financial support of the research from the German Federal Ministry for Economic Affairs and Climate.

6. References

Camplese, D., Chianese, C., Scarponi, G. E., Otremba, F., & Cozzani, V. (2023). Analysis of high temperature degradation of multi-layer insulation (MLI) systems for liquid hydrogen storage tanks. *Chemical Engineering Transactions 99*, 415-420.

Camplese, D., Scarponi, G. E., Chianese, C., Hajhariri, A., Eberwein, R., Otremba, F., & Cozzani, V. (2024). Modeling the performance of Multilayer Insulation in Cryogenic Tanks undergoing external Fire Scenarios. *Process Safety and Environmental Protection, 186*, 1169-1182. doi:https://doi.org/10.1016/j.psep.2024.04.061

Caps, R., Hetfleisch, J., Rettelbach, T., & Fricke. (1996). Thermal Conductivity of Spun Glass Fibers as Filler Material for Vacuum Insulations. In *Thermal conductivity 23.*

Daryabeigi, K., George , R., & Cunnington. (2011). Combined heat transfer in high-porosity high-temperature fibrous insulation: Theory and experimental validation. *Journal of thermophysics and heat transfer*, 536-546.

Daryabeigi, K., Miller, S. D., & Cunnington, G. R. (2007). Heat transfer in high temperature multilayer insulation. *5th European Workshop on Thermal Protection Systems and Hot Structures.*

DeWitt, W. D., Gibbon, R. L., & Reid, R. L. (1968). Multi-foil Type Thermal Insulation. *Intersociety Energy Conversion Engineering Conference Record Institute of Electrical and Electronics Engineers*, (pp. 263-271). New York.

Eberwein, R., Hajhariri, A., Camplese, D., Scarponi, G. E., Cozzani, V., & Otremba, F. (2023). A comparative study on insulation materials in tanks for the storage of cryogenic fluids in fire incidents. *Proceedings ASME International Mechanical Engineering Congress and Exposition 2023*, (pp. 1-7).

Eberwein, R., Hajhariri, A., Camplese, D., Scarponi, G. E., Cozzani, V., & Otremba, F. (2024). Experimental Investigation on the Behavior of Thermal Super Insulation Materials for Cryogenic Storage Tanks in Fire Incidents. *Process Safety and Environmental*. doi:https://doi.org/10.1016/j.psep.2024.04.131

Fesmire, J. E. (2015). Standardization in Cryogenic Insulation Systems Testing and Performance Data. *Physics procedia. 67*, (pp. 1089-1097).

Johnson, W. L., Kelly, A. O., Heckle, K. W., Jumpe, K. M., & Fesmire, J. E. (2014). Calorimeter testing of thermal degradation of multilayer insulation due to the presence of penetrations. *AIP Conference Proceedings. Vol. 1573.* American Institute of Physics.

Kunze, K., & Kircher, O. (2012). Cryo-compressed hydrogen storage cryogenic cluster day. Oxford.

Lisowski, E., & Lisowski, F. (2019). Study on thermal insulation of liquefied natural gas cryogenic road tanker. *Thermal Science, 23*, 1381-1391.

McIntosh, G. E. (1994). Layer by Layer MLI Calculation Using a Separated Mode Equation. *Kittel, P. (eds) Advances in Cryogenic Engineering. Advances in Cryogenic Engineering, 39*. doi:https://doi.org/10.1007/978-1-4615-2522-6_206

Preuster, P., Alekseev, A., & Wasserscheid, P. (2017). Hydrogen Storage Technologies for Future Energy Systems. *Chem. Biomol. Eng. 8*, 445–471. doi:https://doi.org/10.1146/annurev-chembioeng-060816-101334

Speirs, J., Balcombe, P., Blomerus, P., & Stettler. (2019). Can natural gas reduce emissions from transport. *Heavy Good Veh. Shipp.*

Sutheesh, P., & Chollackal, A. (2018). Thermal performance of multilayer insulation: A review. *IOP Conf. Ser. Mater. Sci. Eng. 396.* doi:https://doi.org/10.1088/1757-899X/396/1/012061

van Wingerden, K., Kluge, M., Habib, A. K., Ustoli, F., & Paltrinieri, N. (2022). Medium-scale tests to investigate the possibility and effects of BLEVEs of storage vessels containing liquified hydrogen. *Chemical Engineering Transactions, 90*, 547-552.

Detonation initiation by fast-flame reflection from an obstacle

Madeleine Moran, Gaby Ciccarelli

Queen's University, Kingston, Canada

E-mail: gaby.ciccarelli@queensu.ca

Abstract

Experiments were performed in a 12.7 cm by 7.6 cm rectangular channel to study the interaction of a fast-flame with an obstacle mounted on the channel bottom wall after a back-facing step. A fast-flame was generated upstream of the back-facing step by passing a CJ detonation wave through a perforated plate and then the diffracting shock-flame complex interacted with the obstacle. Two obstacle heights (2.54 cm, 3.81 cm) and standoff distances from the back-facing step (6.35 cm, 11.43 cm) were investigated. The test mixture was stoichiometric hydrogen-oxygen and nitrogen-diluted stoichiometric ethylene-oxygen. The fast-flame velocity was varied via the initial pressure in the range of 15 and 24 kPa. High-speed side-view schlieren, chemiluminescence visualization, and soot foils were used to study the interaction. For all obstacle configurations, two detonation initiation modes were observed: one directly due to shock reflection from the obstacle face (strong ignition) and the other due to the interaction of the obstacle-reflected shock with the trailing flame. For the shorter obstacle standoff position, shock focusing resulted in strong detonation initiation at the bottom internal corner of the obstacle. For the larger obstacle standoff position, strong detonation initiation occurred following normal reflection of a Mach stem shock with the obstacle face. Because the Mach stem height was smaller than the obstacle height, the reflection of the incident shock with the obstacle top external corner produced a shock traveling down the obstacle face that affected the critical condition for strong detonation initiation compared to that reported in other studies for a planar shock.

Keywords: *detonation, shock, shock reflection, DDT*

Introduction

Explosions occur in industries that process, store, and transport flammable gas. The increased interest in the use of hydrogen, and hydrogen-enriched fuels for transportation and power generation has brought this concern to the forefront (Midilli et al. 2005). The worst-case explosion scenario involves the ignition of a flame via a weak energy source, and its subsequent acceleration and transition to detonation. For deflagration-to-detonation transition (DDT) to occur the flame accelerates to a velocity of roughly the speed of sound of the combustion products. At this velocity a shock wave precedes the turbulent flame, and the shock-flame complex is referred to as a fast-flame. This magnitude of flame acceleration is possible if the flame is laterally confined and the flow path contains obstructions that can distort the flame and generate turbulence ahead of the flame (Ciccarelli and Dorofeev, 2008). This phenomenon is typically studied in a cylindrical tube equipped with orifice plates (Cross and Ciccarelli, 2015). Hashemi Mehr and Ciccarelli (2023) showed that in this geometry the transition to detonation is driven by shock reflection from the orifice plate face. If the orifice plate diameter, d, is equal to or smaller than 13 detonation cells, i.e., $d<13\lambda$, the detonation wave fails due to diffraction as it passes through the orifice. The shock, trailed by the decoupled reaction zone (i.e., turbulent flame), subsequently interacts with the next orifice plate potentially leading to detonation re-initiation. Shock interaction with an obstacle is thus an important phenomenon both in terms of DDT as well as detonation propagation in an obstructed channel.

Voevodsky and Soloukhin (1965) used streak schlieren photography to study detonation initiation at a wall following normal shock reflection using in a stoichiometric hydrogen-oxygen mixture. They reported two types of detonation initiation modes. Strong ignition was found for high-reflected shock

temperatures where a detonation initiated from a single ignition site, and mild ignition occurred at lower temperatures at multiple flame ignition sites that merge and transition to detonation some distance from the end wall. Meyer and Oppenheim (1971) used full channel-height high-speed schlieren visualization to study strong and weak detonation initiation in great detail. Theys showed that for the highest reflected shock temperatures ignition was homogeneous across the end wall producing a planar detonation that overtakes the reflected shock wave. For lower temperatures, weak detonation initiation involved a loci of ignition sites at the end wall (referred to as mild ignition in (Voevodsky and Soloukhin, 1965)) that resulted in an accelerating flame that transitioned to detonation. They observed that weak detonation initiation typically occurred where multiple flame fronts converged and hypothesized that initiation was driven by converging compression waves ahead of the flame (Meyer and Oppenheim, 1971). They proposed a criterion for the transition from strong to weak detonation initiation based solely on chemical kinetics. For a planar incident shock interaction with an obstacle, Thomas et al. (2002) showed that expansion of the doubly shocked gas next to the obstacle increases the minimum (or critical) incident shock Mach number required for strong detonation initiation compared to a wall reflection. They proposed a detonation initiation limit that took into account the ratio of the chemical reaction time-scale at the reflected shock temperature and pressure and the time for an acoustic wave to transit across the obstacle face. Thomas et al. only reported strong ignition. Recently, Yousefi Asli Mozhdehe et al. (2024) performed similar shock tube experiments and reported a new type of weak detonation initiation mechanism linked to the reflected shock bifurcation stagnation bubble.

For DDT in an obstacle-laden channel, the shock wave preceding the turbulent flame approaches the obstacle obliquely. Gelfand et al. (2000) performed experiments in a shock tube with a symmetric 90^o wedge reflector (90^o re-entrant corner). They showed that shock focussing greatly enhances the initiation process due to the higher pressure and temperature generated in the wedge. Direct detonation initiation (strong ignition) occurred at the wedge apex, but mild ignition could also lead to detonation initiation outside the wedge, i.e., weak detonation initiation (Meyer and Oppenheim, 1971). Chan et al. (1995) studied the detonation initiation process when a Mach stem forms before a 2.54 cm obstacle. They showed that for stoichiometric hydrogen-oxygen the critical Mach number of the Mach stem ranged from 2.5-2.8. They also studied the initiation process when a steady-state Mach stem collides with an obstacle mounted onto a variable angle ramp. They found that detonation occurs if the post reflected shock temperature exceeded 1150 K. They did not report weak detonation initiation, as in (Gelfand et al., 2000). Recently, Rudy et al. (2023) investigated detonation initiation in a 90^o wedge reflector, where the shock was generated ahead of a flame. Experiments were performed with hydrogen-air at 1 atm with pressure transducers and ionization probes but no visualization. Based on the ignition delay time obtained from the pressure measured at the apex of the wedge, strong and weak detonation initiation was reported.

The objective of this study is to investigate the interaction of a fast-flame that diffracts at a backward facing step and then interacts with an obstacle. This simulates an obstacle laden channel experiment but removes the variability of the orientation and the strength of the shock-flame before the diffraction on the downstream-side of each obstacle. The distance from the back-facing step to the obstacle was varied and the effect of the trailing flame in promoting or mitigating detonation initiation was sought.

1. Experimental details

A test channel composed of four sections arranged in series was used to investigate the interaction of a fast-flame with an obstacle after it diffracts over a back-facing step, see Fig. 1. The first section, consisting of a 1.22 m long, 7.6 cm inner-diameter round tube with repeating 50% blockage ratio orifice plates spaced at 7.6 cm, was used to generate a detonation wave. A spark plug mounted on the endplate was used for ignition of the mixture at different sub-atmospheric initial pressures. The detonation exiting the round tube section stabilized in an obstacle-free 61 cm long, 7.6 cm square

cross-section. The third section was also 61 cm long, and 7.6 cm square cross-section and housed a perforated plate 15 cm downstream from the beginning of the section. The perforated plate, consisted of thirty-six uniformly distributed 6.4 mm diameter holes, quenched the detonation producing a fast-flame. Note that a fast-flame is velocity based and can be produced at any scale.

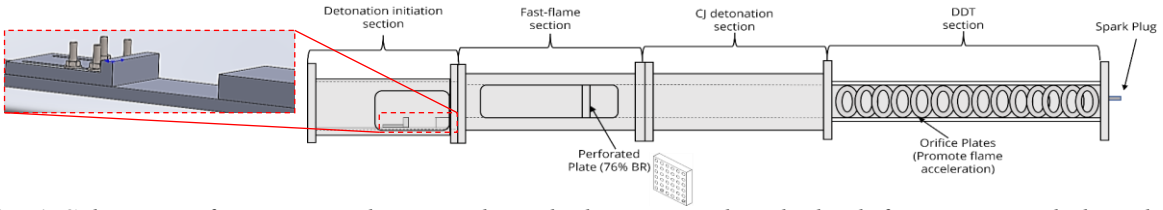

Fig. 1. *Schematic of experimental set-up where the last section has the back-facing step and obstacle. An isometric view of the experimental configuration is also provided.*

The final 12.7 cm by 7.6 cm rectangular test section had a 2.54 cm back-facing step followed by a 12.7 cm thick fence-type obstacle that spanned across the channel width where detonation initiation occurs. Obstacle heights of 2.54 cm and 3.8 cm were used in experiments. The obstacle stand-off position from the back-facing step was set to 6.35 cm and 11.4 cm. Tests with the 3.81 cm tall obstacle were only performed at the further stand-off position. This section was equipped with two acrylic-windows on either side through which schlieren video was recorded. The schlieren system included a 25.4 cm diameter parabolic mirror and either a Shimadzu HPV-X2 or Photron SAZ camera to capture the diffraction of the fast-flame and subsequent interaction with the obstacle. Soot coated 0.5 mm aluminium foils were used on the floor and rear window of this section to record the detonation initiation cell structure evolution. Regular photography at a 45-degree angle to the channel axis captured the flame chemiluminescence as it enters the section and diffracts over the back-facing step, providing insight on the consistency of its shape. The shock velocity was measured by dividing the distance travelled in three consecutive schlieren video frames by the elapsed time before shock collision with the obstacle, the spatial resolution resulted in a 3% uncertainty in the measurement. The test mixtures for this study were $2H_2 + O_2$ and $C_2H_4 + 3O_2 + 3N_2$. The hydrogen mixture was selected to compare to Mach stem reflection studies reported in (Chan, 1995) and the ethylene mixture was selected to compare with the wall and obstacle reflection studies in (Yousefi Asli Mozhdehe et al., 2024). The incident shock velocity just before the back-facing step was varied via the initial pressure between 15 kPa and 24 kPa.

2. Results and discussion

2.1. Obstacle stand-off position of 6.35 cm downstream from the back-facing step

Experiments were only performed with the 2.54 cm obstacle at the 6.35 cm standoff position. The schlieren video and soot foils captured for both mixtures were similar; select schlieren images showing strong detonation initiation for $2H_2 + O_2$ at an initial pressure of 20 kPa are provided in Fig. 2a). Images 1 and 2 show the shock-flame complex as it diffracts over the back-facing step. The Mach number of the incident shock (I) as it diffracts is 2.3 (measurement location corresponds to the red arrow in image 3). The flame (F) that trails the shock wave is highly turbulent and non-planar as it is more advanced at the bottom and the top of the channel. Direct photography of the chemiluminescence from a 45-degree angle to the channel axis confirmed that the flame consistently takes this profile as it propagates into the test section. The top half of the shock remains largely planar, and diffraction makes the bottom half curved, reflecting obliquely off the bottom wall in image 3, and off the obstacle in image 4. Image 6 captures the instance when the incident shock reaches the vertex of the obstacle-floor internal corner. A bright spot (see arrow) appears in the corner indicative of strong detonation initiation. Significant luminescence appears due to the high temperature and pressure behind the detonation front. Importantly, initiation occurs before the reflected shock interacts

with the trailing flame. Image 7 shows the interaction of the detonation front with the flame and image 8 shows the evolution of the curved detonation front.

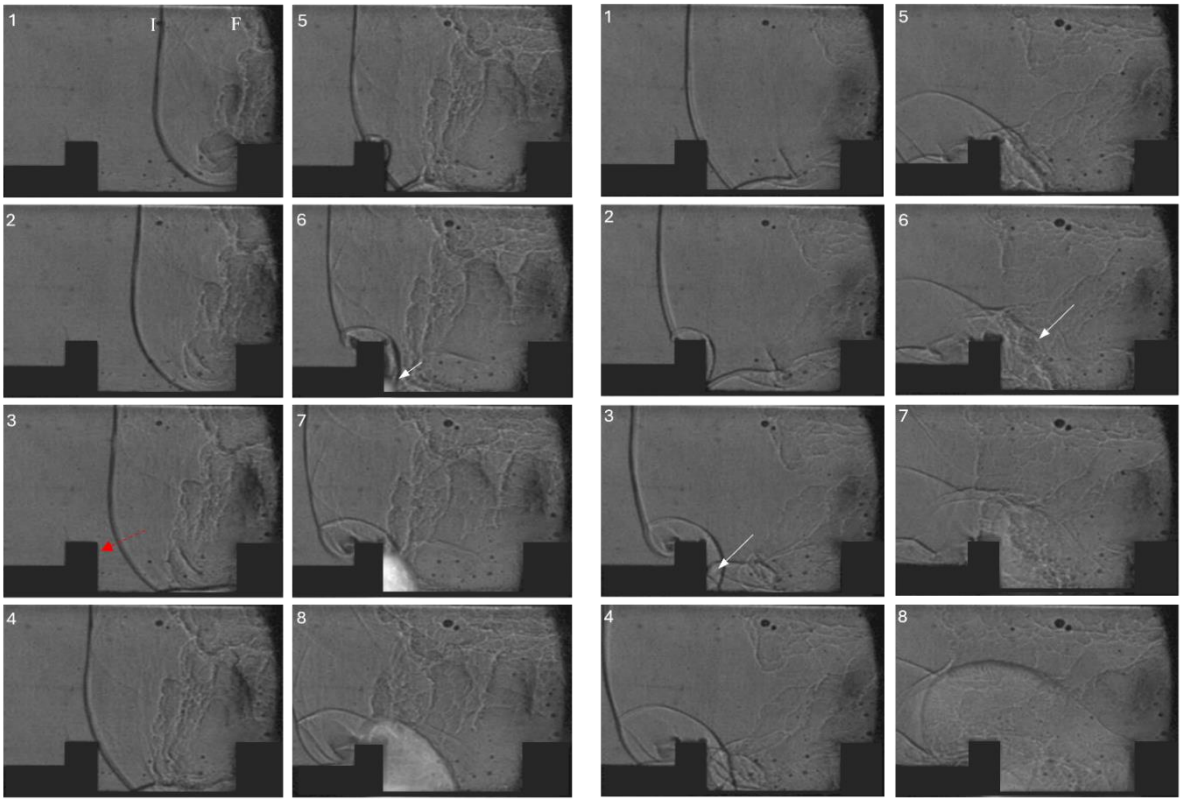

Fig. 2. *Fast flame interaction with a 2.54 cm height obstacle with 6.35 off-set in $2H_2+O_2$: a) Strong detonation initiation for $P_i = 20\ kPa$, $M_s = 2.25$, 7 μs between frames, b) Detonation initiation via shock-flame interaction for $P_i = 18\ kPa$, $M_s = 1.95$, 10 μs between frames.*

The soot foil provided in Fig. 3a) shows the development of the cell structure for strong detonation initiation obtained for $2H_2 + O_2$ at an initial pressure of 21 kPa. The right-most edge of the foil corresponds to the downstream face of the back-facing step, and the left-most edge of the floor foil corresponds to the obstacle face. The 'step' cutout in the rear-window foil accommodates the obstacle. The floor foil shows that the onset of detonation is relatively uniform across the width of the obstacle. A white horizontal line (see arrow) on the foil appears due to the collision of two local detonation waves, which merge to form a singular detonation. Very fine cells, characteristic of an overdriven detonation, are imprinted on the foil immediately upon initiation, which grow as the detonation propagates away from the obstacle. After the detonation encounters the flame the cell structure is no longer visible on the floor foil. The measured cell size just before this interaction is 1.4 mm, slightly smaller than the CJ cell size calculated for the post-incident shock conditions (P_R = 171 kPa, T_R = 667 K. The location of the obstacle-reflected shock when it is overtaken by the detonation is imprinted on the rear-window foil (see arc highlighted by the arrow). The detonation overtakes the reflected shock over a short period of time, but due to the low velocity of the reflected shock relative to the detonation wave, the imprint on the foil gives the impression that it is overtaken at a single instance. The cell structure inside the arc is suppressed due to the detonation overdrive corresponding to the post-reflected shock conditions of 777 kPa and 1093 K. The cells outside the arc near the top of the obstacle grow in size with vertical distance indicating a decrease in strength of the detonation as it diffracts over the obstacle. The axial location of the detonation front when it reaches the flame corresponds to the white dotted line on the rear window foil. The dotted line leans forward partly because of the flame shape and the fact that the flame propagates forward as the detonation propagates vertically. The soot to the right of the white dotted line has been scrubbed out by the flame. Cells are imprinted on the foil far downstream from the interaction of the detonation with the flame, indicating that the detonation is sustained although the cell size has not yet stabilized.

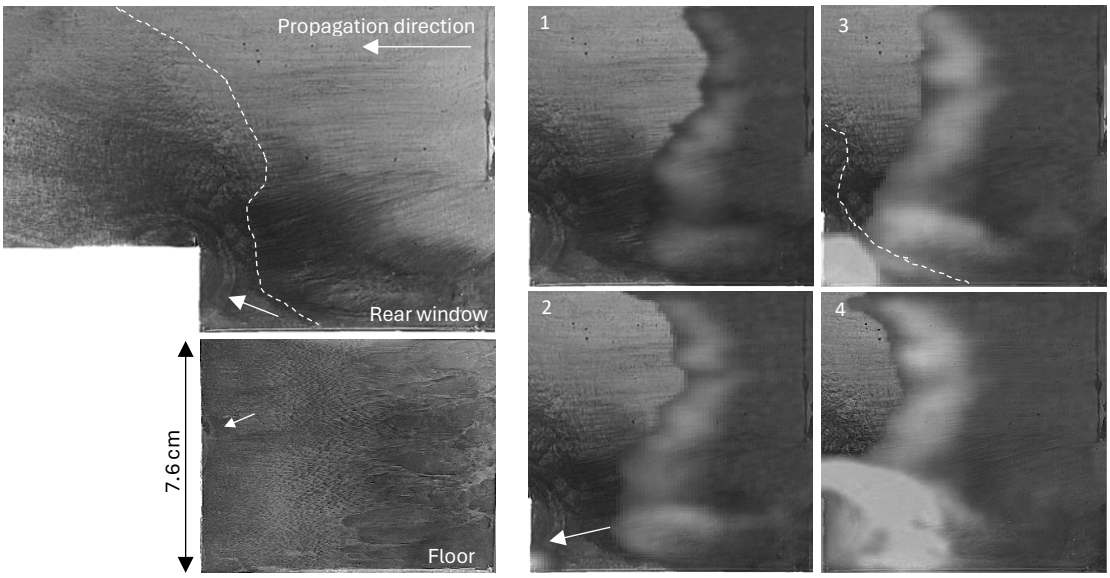

Fig. 3. *a) Soot foil for strong detonation initiation of* $2H_2 + O_2$ *(*P_i *= 21 kPa). Post-incident shock CJ cell size =1.85 mm. b) Recorded luminescence overlaid on rear-window foil in a). Right- and left- edges of the foil correspond to the back-facing step and obstacle respectively. Video was captured using a 430 nm narrowband filter. 7μs between frames.*

Fig. **3**b) shows the soot foil from Fig. 3a) overlayed with light emission recorded by direct photography. Only the parts of the video frame displaying light emissions are provided so that the rest of the foil was not obscured. The passage of the incident shock lofts some of the fine soot particles off the foil surface. The lofted soot particles are heated by the combustion products yielding intense incandescence that dominates the chemiluminescence from the gas. In image 1 the leading edge of the illuminated area corresponds to the flame, a similar profile to that observed in the schlieren image 3 in Fig. 2a). The strong detonation initiation event is seen in image 2, where a bright incandescence appears in the corner between the obstacle face and channel floor (see white arrow). As observed in Fig. 2a) this event occurs before any interaction between the reflected shock and the flame. Image 3 depicts when the detonation front encounters the flame which aligns perfectly with the imprint on the soot foil (white dotted line in Fig. 3a). After the detonation encounters the flame, a shock wave continues to propagate in the products increasing the intensity of the light illuminated from the hot particles and gas behind the flame, see image 4.

Side-view schlieren video showed that strong detonation initiation always occurs in the corner between the obstacle face and channel floor. Top-view schlieren was used to visualize the uniformity of detonation initiation across the channel width. Fig. **4** shows select images from a test for $2H_2 + O_2$ initially at 24 kPa. This initial pressure was selected because of the repeatability of strong detonation initiation. The downstream edge of the back facing step and the obstacle are seen on the right-hand and left-hand side of each image respectively. Image 1 shows the decoupled incident shock and flame as they diffract over the back-facing step. The shock front has a finite thickness due to shock curvature. This image also shows that the shock is not perfectly planar with respect to the width of the channel, i.e., it is further downstream at the bottom of the image. The interaction of the incident shock and the channel floor is assumed to correspond to the smooth red dotted line in image 2. This assumption is supported by the location of regular reflection observed in side-view schlieren at the same initial pressure. The interaction of the flame with the channel floor corresponds to the turbulent region upstream from the red dotted line. Image 2 corresponds to the time of collision of the incident shock with the obstacle. The bottom half of the reflected shock can be seen in image 3 and the entire reflected shock can be seen in image 4. Detonation initiation occurs in the 7μs between images 4 and 5. In image 5 the detonation overtakes the reflected shock. The bright spot in image 5 (red arrow), could be the result of the collision of the two detonation waves initiated on either side of the obstacle. Image 6 shows evidence that detonation initiation took place at two locations resulting in two

interacting detonation fronts that propagate along the bottom wall, just below the flame surface. Based on the cell structure recorded on the foil in Fig. 3a), the detonation fronts in image 6 of Fig. 4 are close to reaching the flame on the bottom wall.

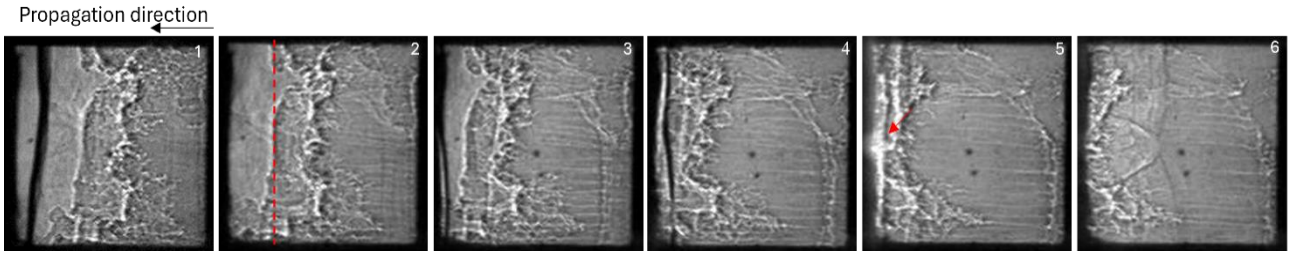

Fig. 4. *'Top view' schlieren photography for strong detonation initiation of* $2H_2 + O_2$ *(*$P_i = 24\ kPa$*). 7 μs between frames.*

Select side-view schlieren images showing detonation initiation via shock-flame interaction of $2H_2 + O_2$ at a lower initial pressure of 18 kPa are provided in Fig. 2b). The shock structure in the first few images looks like that observed at the higher initial pressure; however, the shock in this test is weaker, the Mach number of the incident shock (in the normal propagation direction at the obstacle height) was calculated to be 1.95. The gap between the shock and flame is also more significant. The incident shock interacts obliquely with the obstacle in image 1. The incident shock reaches the bottom of the obstacle in image 2 and diffracts around the downstream external corner of the obstacle in image 3. The reflected shocks from the obstacle and the bottom wall cross each other in image 3. This results in a very high temperature and pressure region between the reflected shocks (see arrow) but does not result in ignition. Image 4 shows the earliest instance of interaction between the obstacle-reflected shock and the bottom part of the flame. The reflected shock interacts with more of the flame in image 5, and in images 6 and 7 there are indications of detonation initiation (see arrow). Detonation initiation due to the interaction of the obstacle-reflected shock and the flame is different from the weak detonation initiation mode observed in (Voevodsky and Soloukhin, 1965; Meyer and Oppenheim, 1971) that occurs due to flame ignition at the obstacle face followed by DDT; rather, it is a result of Richtmyer-Meshkov interface instability that perturbs the flame surface that results in rapid mixing of unburned mixture with hot products leading to detonation initiation (Scarinci et al., 1993). The expanding detonation front is clearly seen in image 8.

2.2. Obstacle stand-off position of 11.43 cm downstream from back facing step

This section discusses the results from experiments performed with 2.54 cm and 3.81 cm obstacles at a stand-off position of 11.43 cm downstream from the back-facing step. The schlieren photography and soot foils for both mixtures, regardless of obstacle height, were similar so only the results for $2H_2 + O_2$ will be described.

2.2.1. Detonation initiation mechanism

Schlieren video images showing strong detonation initiation at an initial pressure of 20 kPa (obstacle height of 2.54 cm) are provided in Fig. 5a). The shock-flame complex that diffracts over the back-facing step looks identical to that exhibited in Fig. 2, where the trailing flame front is turbulent and non-planar. For an obstacle stand-off distance of 11.43 cm the incident shock (I) reflection off the channel floor develops a transverse-reflected shock (T) and Mach stem perpendicular to the bottom wall; also evident in images 1 and 2 is the shear layer coming off the triple point that curls at the floor in image 2. The Mach stem grows in height as it propagates; upon collision with the obstacle, it is ~ 1.25 cm tall (roughly half the obstacle height). The Mach number of the Mach stem was calculated to be 2.7 for this test. The transverse-reflected wave bends up as it travels faster through the combustion products. Between images 2 and 3, the Mach stem reflects normally from the obstacle face and detonation initiation occurs at the bottom half of the obstacle face, i.e., below the triple point collision point. Detonation initiation occurs before the obstacle-reflected shock interacts with the flame, the detonation front is clearly visible in Image 4. The detonation front diffracts around the

external corner of the obstacle (see arrow in image 5); the other part of the detonation front that encounters the flame continues as a shock wave (see arrow in image 6).

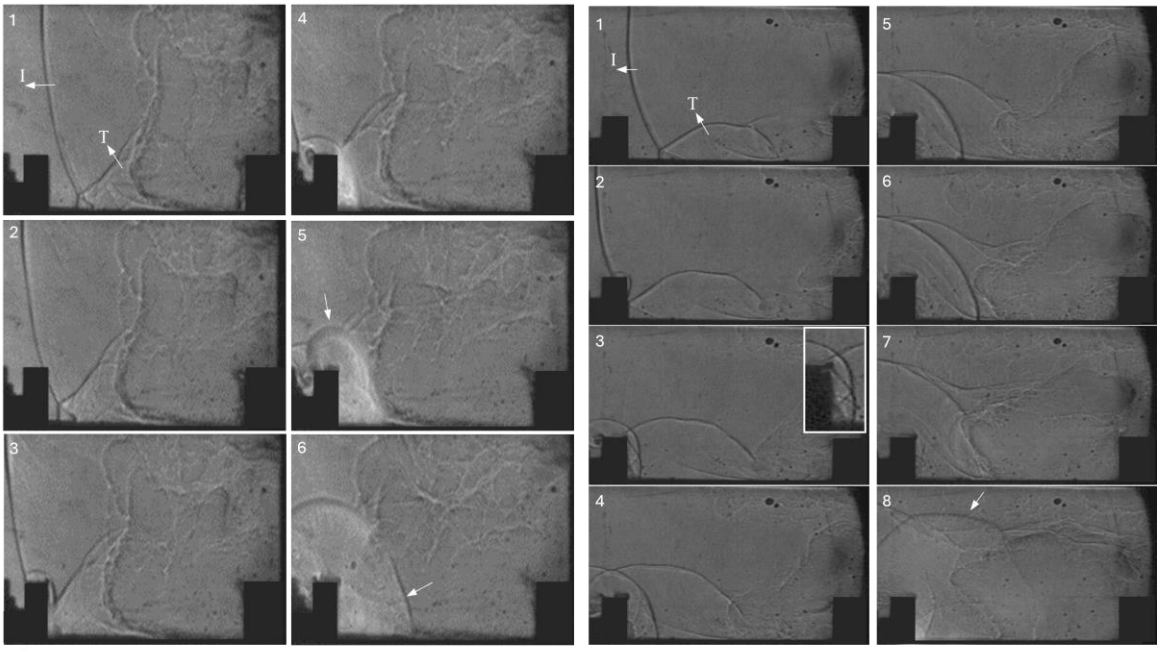

Fig. 5. *a) Strong detonation initiation of $2H_2 + O_2$ ($P_i = 20\ kPa$, 2.54 cm obstacle), M_s=2.7. 7 μs between frames. b) Detonation initiation via shock-flame interaction of $2H_2 + O_2$ ($P_i = 17\ kPa$, 2.54 cm obstacle), M_s = 2.4. 15 μs between frames. A zoomed-in view of the obstacle face interaction is provided in image 3.*

The soot foil imprint obtained for a $2H_2 + O_2$ test at an initial pressure 17 kPa (obstacle height of 3.81 cm) is provided in Fig. 6. The floor foil shows that detonation initiation occurs relatively uniformly across the face of the obstacle. The red dotted line on both foils represents where the detonation overtakes the obstacle-reflected shock, and where cell structure appears; there are no discernible detonation cells between the obstacle and the red dotted line. This is because the detonation is severely overdriven because it propagates into the gas at the reflected shock state of 135 kPa and 658 K, compared to the post incident shock state of 605 kPa and 1075 K after the red dotted line. The size of the detonation cells grow as the detonation propagates upstream from the red dotted line. The measured cell size when the detonation front reaches the flame (see arrow location) is roughly 2.2 mm. The calculated detonation cell size for the post incident shock state is 2.75 mm using the Ng et al. (Ng, Ju, and Lee, 2007) correlation and SD Toolbox (Shepherd, 2021). On the rear window foil cell structure disappears where the detonation reaches the flame (denoted by the white dotted line). This suggests that the flame profile was relatively planar for this test. The detonation cell size increases around the top of the obstacle as it decreases in strength due to diffraction. The cell size stabilizes to the CJ cell size downstream from the detonation-flame interaction line, indicating that the detonation is sustained.

Select schlieren video images showing detonation initiation via shock-flame interaction at a lower initial pressure of 17 kPa (obstacle height of 2.54 cm) are provided in Fig. 5b). The flame front is more separated from the incident shock compared to the strong initiation test shown in Fig. 5a). In image 2 the Mach stem collides with the obstacle face, coincidently the incident shock interaction with the top external corner of the obstacle produces a curved reflected shock. The Mach number of the Mach stem was measured from consecutive video frames to be 2.4, compared to 2.7 for the test in Fig. 5a). For this test the Mach stem reflection results in flame ignition at the internal corner vertex; because there is no detonation initiation, more details of the incident shock reflection off the obstacle are observed. Specifically in image 3 the reflected shock formed at the obstacle external corner propagates down the obstacle face while the transverse-reflected shock travels up (see zoom-in image inset). This obstacle external corner reflection produces high pressure that mitigates the expansion

that occurs down the face of the obstacle following normal shock reflection (Thomas et al., 2002; Yousefi Asli Mozhdehe et al., 2024).

Because of the large gap between the incident shock and flame, the transverse-reflected shock interacts with the flame much further back, see image 3. Images 4 and 5 show the propagation of the obstacle-reflected shock as it approaches the flame. Detonation is initiated when the obstacle-reflected shock interacts with the flame, between images 6 and 7. Note, the transverse-reflected shock had previously (uneventfully) traversed this part of the flame in images 4 and 5. In image 8 a curved detonation (see arrow) is clearly observed that can be tracked back to a bright spot (see arrow) that is surrounded by what could be interpreted as a detonation kernel originating at a point on the flame surface. Since the detonation kernel size is much smaller than the channel width, the unaffected part of the flame is observed in the image 7 since schlieren integrates cross the channel width.

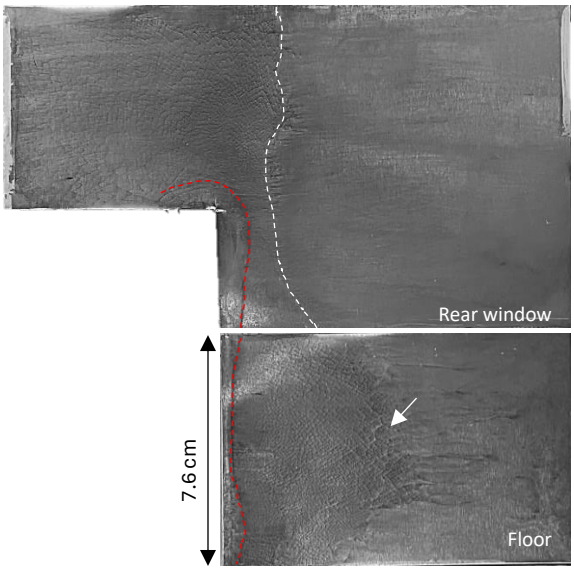

Fig. 6. *Soot foils for strong detonation initiation of* $2H_2 + O_2$ *(*P_i *= 17 kPa, 3.81 cm tall obstacle).*

2.3. Detonation initiation transition data

2.3.1. Critical incident shock Mach number for the shorter obstacle stand-off distance

Detonation initiation data for $2H_2 + O_2$ and $C_2H_4 + 3O_2 + 3N_2$ at an obstacle stand-off distance of 6.35 cm are summarized in Fig. 7. The shock velocity, measured from schlieren video, was taken before reflecting off the obstacle external corner. There was significant variability in the incident shock strength for a given initial pressure. For example, for the four $C_2H_4 + 3O_2 + 3N_2$ tests performed at an initial pressure of 20 kPa, three different Mach numbers were obtained. The variability can be attributed to the uncertainty in Mach number calculation, but more importantly the

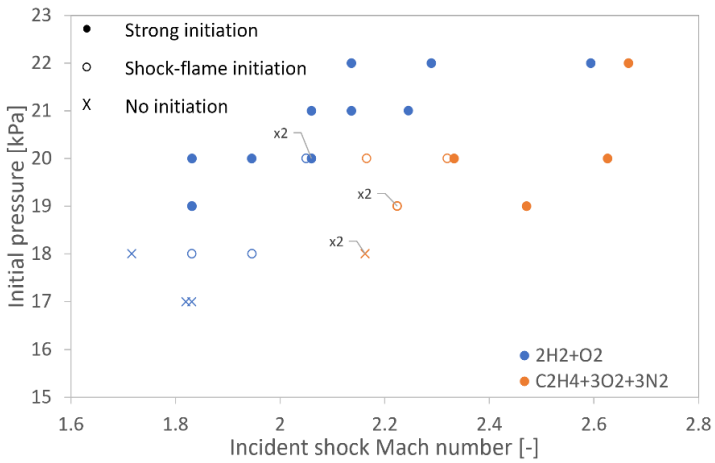

Fig. 7. *Summary of initiation behaviour for* $2H_2 + O_2$ *and* $C_2H_4 + 3O_2 + 3N_2$ *at an obstacle stand-off position of 6.35 cm.*

irreproducibility of the fast-flame generation using the perforated plate. The critical incident shock Mach number range for the transition between detonation initiation modes for $2H_2 + O_2$ and $C_2H_4 + 3O_2 + 3N_2$ are (1.8 - 2.1) and (2.2 - 2.3) respectively. Regardless of mixture, strong detonation initiation was observed for all tests performed at an initial pressure of 21 kPa or greater. The critical Mach number for strong detonation initiation is greater for $C_2H_4 + 3O_2 + 3N_2$ compared to $2H_2 + O_2$ which is expected because of the lower reactivity of the nitrogen-diluted ethylene mixture.

2.3.2. Detonation initiation criterion for the larger obstacle stand-off distance

At an obstacle stand-off position of 11.43 cm from the back-facing step, strong detonation initiation resulted from the normal reflection of the Mach stem from the obstacle face. The normal reflected shock state was calculated using SD Toolbox (Shepherd, 2021) with the 'Sandiego' mechanism.

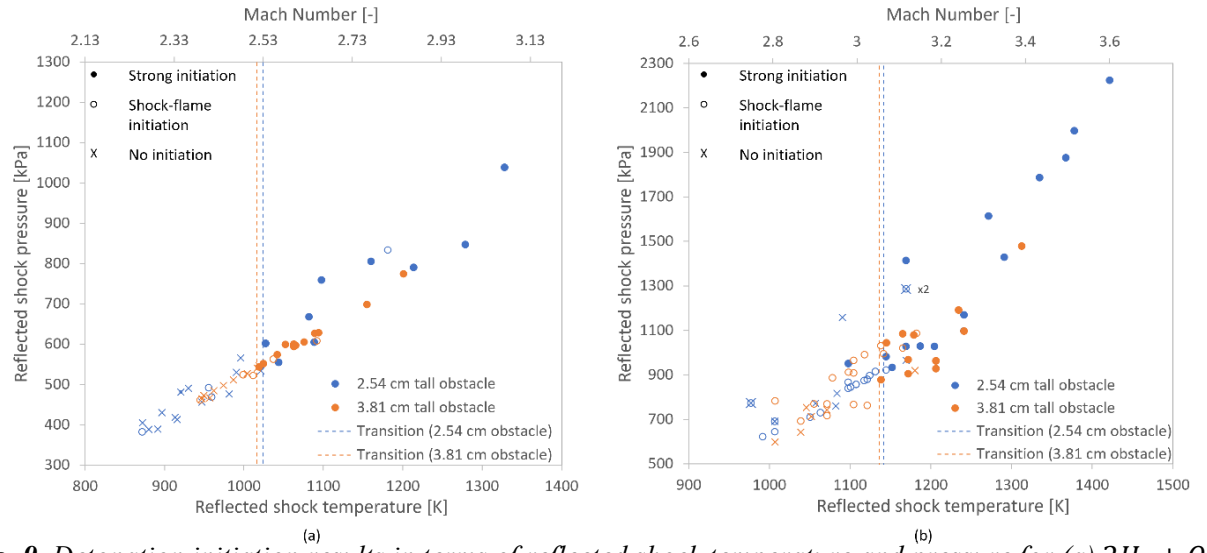

Fig. 9. *Detonation initiation results in terms of reflected shock temperature and pressure for (a) $2H_2 + O_2$ and (b) $C_2H_4 + 3O_2 + 3N_2$. Vertical dotted lines correspond to the critical temperature for transition between initiation modes.*

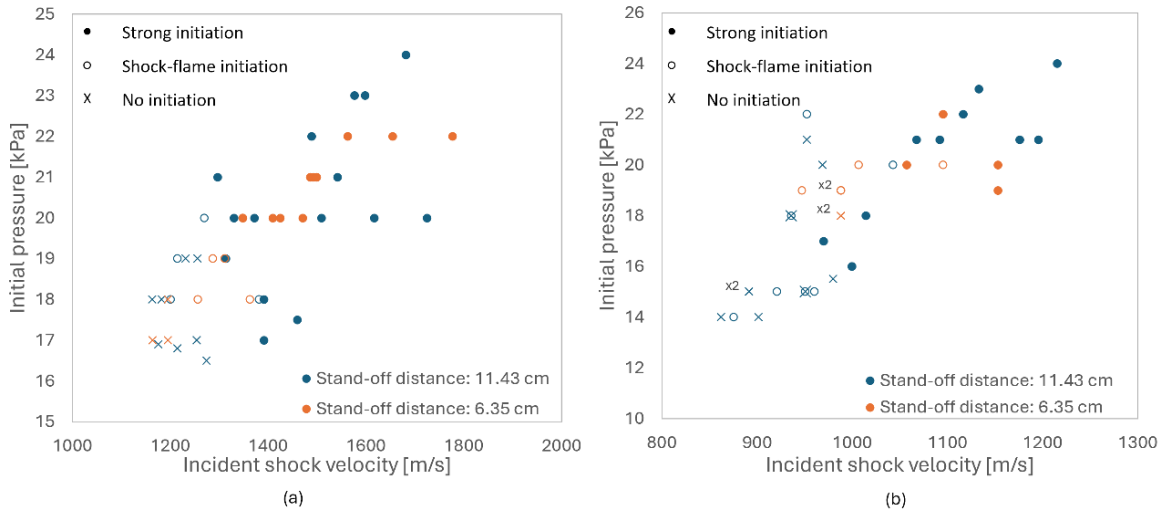

Fig. 8. *Detonation initiation results for the 2.54 cm obstacle in terms of incident shock velocity and initial pressure for (a) $2H_2 + O_2$ and (b) $C_2H_4 + 3O_2 + 3N_2$.*

The detonation initiation data for both mixtures with respect to calculated reflected shock temperature and pressure (Mach stem Mach number provided on upper x-axis) are provided in Fig. 8. The filled in symbols represent strong detonation initiation, open circles represent shock-flame interaction driven initiation, and X's are no detonation initiation. The vertical dotted lines correspond to the weakest (or critical) shock strength that produced strong initiation for each obstacle height. Note there are some random tests that produced shock-flame interaction driven detonation initiation for shock

Mach numbers larger than the critical value. The difference in critical strong detonation initiation for the two obstacle height is negligible. The critical shock Mach number for $2H_2 + O_2$ and $C_2H_4 + 3O_2 + 3N_2$ are 2.5 and 3.1 respectively, and the critical reflected shock temperature are roughly 1020 K and 1140 K, respectively. The larger critical Mach number for the nitrogen-diluted stoichiometric ethylene-oxygen mixture is expected as it is less reactive than the hydrogen-oxygen mixture.

The detonation initiation data for the two standoff distances can also be plotted together in terms of the incident shock velocity measured before the back-facing step, see Fig. 9. For $2H_2 + O_2$, strong detonation initiation was observed for incident shock velocities greater than roughly 1300 m/s (within the ±20 m/s uncertainty) measured before the step for both obstacle standoff distances, indicating that the nature of the shock focusing (i.e., Mach stem or not) is not important. For $C_2H_4 + 3O_2 + 3N_2$, the minimum velocity range was 1000-1050 m/s for the longer standoff, and 970-975 m/s for the shorter standoff, considering the ±15 m/s measurement uncertainty these are also similar. The minimum step incident shock Mach number for hydrogen is roughly 2.4, and for ethylene it is 2.8.

2.3.3. Mach stem detonation initiation comparison with other studies

The hydrogen-oxygen critical strong initiation condition for a 2.54 cm obstacle from this experiment (see Fig. 8a)) is compared to results obtained by Chan (1995) in Fig. 10. The Chan 15° wedge-baffle experiments were performed with the same mixture and obstacle height. Chan found that the strong initiation critical condition corresponded to a reflected shock temperature of 1150K, and the critical reflected temperature increased with decreasing obstacle height. For the current experiment, the critical Mach number for detonation initiation ranged from ~2.45-2.55 (blue shaded region in Fig. 10) corresponding to a reflected temperature of just over 1000K. This implies that a weaker Mach stem is required in the present experiment than that found in (Chan, 1995). A significant between experiments is that in the present experiment the triple-point contacts the obstacle at roughly mid-height, whereas in (Chan, 1995) the Mach stem height at the time of collision was larger than the obstacle height. As a result, in the Chan experiment there is an expansion fan that travels down the face of the obstacle, cooling the gas, whereas in the present experiment a shock traverses the obstacle face (see inset of image 3 of Fig. 5b) increasing the temperature. This also explains why Chan observed an effect of the obstacle height that was not observed in the present experiments.

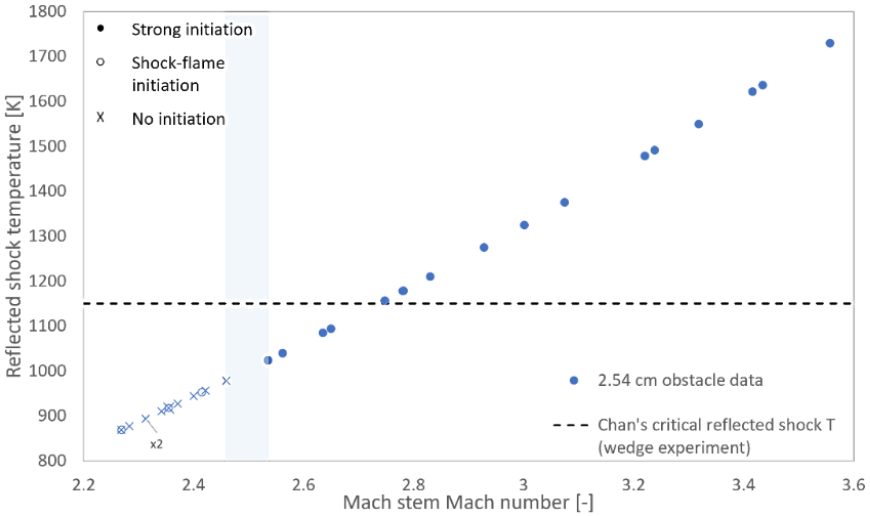

Fig. 10. *Detonation initiation data for $2H_2 + O_2$ in terms of the calculated reflected shock temperature versus the Mach stem Mach number for tests with 2.54 cm obstacle. Strong to no initiation transition highlighted by blue band, also shown is the critical Mach stem reflected temperature of 1150K (Chan, 1995).*

Fig. **11** shows the $C_2H_4 + 3O_2 + 3N_2$ detonation initiation data for the two obstacle heights in terms of the calculated induction time versus the reflected shock temperature. The transition from strong initiation to no initiation for the 2.54 cm and 3.81 cm obstacles corresponds to the blue and orange bands on each plot respectively. The red vertical bands denote the transition between strong and weak detonation initiation reported in (Yousefi Asli Mozhdehe et al., 2024) for the reflection of a planar shock from an obstacle. The black horizontal dotted line corresponds to the Thomas et al. criterion

where the calculated reaction induction time equals the transit time for an expansion wave to travel the height of the obstacle at the reflected shock temperature. As per Fig. 11a), the critical reflected shock temperature for strong detonation initiation for the 2.54 cm obstacle falls in the range 1140 K - 1169 K. This is lower than the critical temperature range for the planar normal-shock reflection reported in (Yousefi Asli Mozhdehe et al., 2024) of 1223 K - 1251 K. From Fig. 11b), the critical temperature range for strong detonation initiation for the 3.81 cm obstacle was found to be 1139 K - 1166 K. Much like the case of the 2.54 cm obstacle, this range is lower than the 1190 K - 1250 K range reported in (Yousefi Asli Mozhdehe et al., 2024). Further, in the current experiment strong detonation initiation was realized even when the induction time was longer than the acoustic transit time across the obstacle height. As explained above, when the incident shock reflects off the obstacle external corner it not only mitigates the generation of an expansion wave, that cools the gas at the obstacle face limiting strong initiation, but also a shock travels down the obstacle face increasing the temperature above the Mach stem reflected temperature. As a result, strong detonation initiation in the present experiment is possible at a lower reflected shock temperature and longer ignition time calculated based on the measured Mach stem Mach number. The strong initiation criterion proposed by Thomas et al. (2002) is non-dimensional and is thus applicable at any scale. So the mitigation of the expansion fan by the reflected shock at the obstacle external corner resulting in strong initiation when the ignition time is longer than the acoustic transit time across the obstacle height is an expected result if the current study was performed at a larger scale.

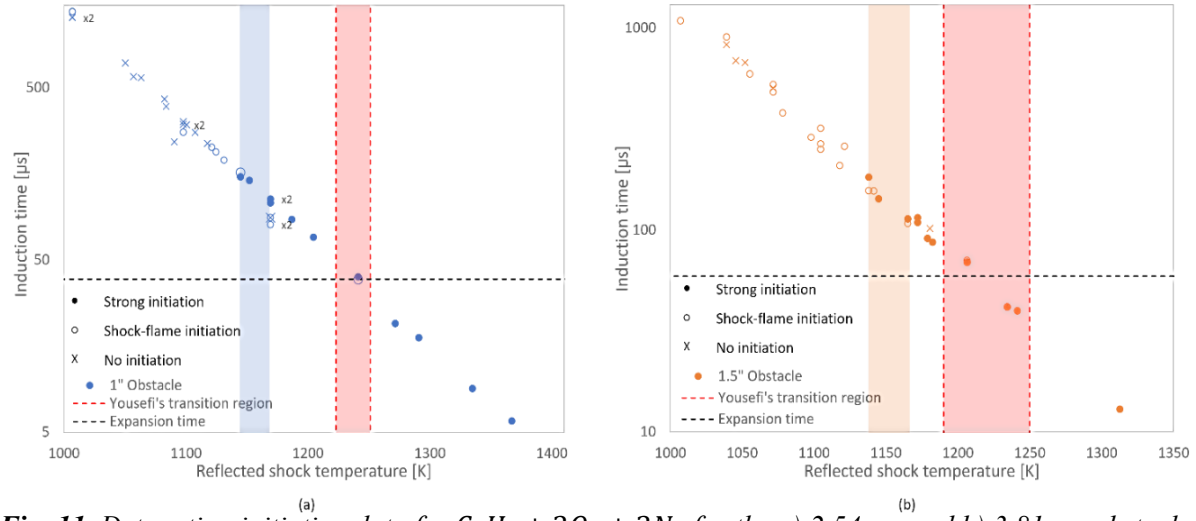

Fig. 11. *Detonation initiation data for $C_2H_4 + 3O_2 + 3N_2$ for the a) 2.54 cm and b) 3.81 cm obstacles plotted in terms of the calculated induction time versus the reflected shock temperature. The transition range from strong to weak initiation is highlighted in blue and orange, and in red for normal planar shock reflection (Yousefi Asli Mozhdehe et al., 2024).*

3. Conclusion

We studied detonation initiation via the interaction of a diffracting shock-flame complex with an obstacle. Strong detonation initiation was observed for the highest incident shock Mach numbers. For the longer obstacle standoff distance, detonation initiation resulted from Mach stem reflection off the obstacle face. For the shorter obstacle standoff distance, a Mach stem did not form; symmetric shock focusing resulted in detonation initiation at the internal corner at the bottom of the obstacle face, uniformly across the width of the obstacle. At both obstacle standoff positions, weak detonation initiation occurred due to the interaction of the obstacle-reflected shock and the trailing flame, driven by Richtmyer-Meshkov interface instability.

A comparison of the measured strong ignition critical condition for the large standoff distance (where a Mach stem forms) with previous studies (Chan, 1995; Yousefi Asli Mozhdehe et al., 2024) showed that the reflected shock formed at the obstacle external corner that propagates down the obstacle face has an impact on detonation initiation. The obstacle external corner reflection produces high pressure at the top of the obstacle that mitigates the expansion that occurs for a planar shock reflection (Yousefi

Asli Mozhdehe et al., 2024), and for Mach stem reflection when the triple-point height is greater than the obstacle height (Chan, 1995).

The study shows that for oblique shock reflection, in the diffraction geometry tested, shock focusing plays an important role in detonation initiation. For the large obstacle standoff position, this focusing is manifested as a Mach stem that reflects normally off the obstacle producing a high temperature region that extends up to the triple-point collision. This is amplified if the Mach stem is shorter than the obstacle height as in the present experiment. For the shorter obstacle standoff position, the focusing is more symmetric, where regular reflection off both the floor and obstacle surfaces produces a hot spot at the vertex of the internal corner. Based on the critical incident shock velocity measured before the back-facing step, the exact nature of the shock focusing is not important.

Acknowledgements

Funding for the project was from Natural Sciences and Engineering Research Council of Canada. The authors thank Jason Loiseau and Shem Lau-Chapdelaine for the use of the Shimadzu camera.

References

Chan, C. K. 1995. "Collision of a Shock Wave with Obstacles in a Combustible Mixture." *Combustion and Flame* 100(1):341–48. doi: 10.1016/0010-2180(94)00139-J.

Ciccarelli, G., and S. Dorofeev. 2008. "Flame Acceleration and Transition to Detonation in Ducts." *Progress in Energy and Combustion Science* 34(4):499–550. doi: 10.1016/j.pecs.2007.11.002.

Cross, M., and G. Ciccarelli. 2015. "DDT and Detonation Propagation Limits in an Obstacle Filled Tube." *Journal of Loss Prevention in the Process Industries* 36:380–86. doi: 10.1016/j.jlp.2014.11.020.

Gelfand, B. E., S. V. Khomik, A. M. Bartenev, S. P. Medvedev, H. Grönig, and H. Olivier. 2000. "Detonation and Deflagration Initiation at the Focusing of Shock Waves in Combustible Gaseous Mixture." *Shock Waves* 10(3):197–204. doi: 10.1007/s001930050007.

Hashemi-Mehr, S., and G. Ciccarelli. 2023. "DDT Run-up Distance in an Obstructed Tube." *Combustion and Flame* 255:112906. doi: 10.1016/j.combustflame.2023.112906.

Meyer, J. W., and A. K. Oppenheim. 1971. "On the Shock-Induced Ignition of Explosive Gases." *Symposium (International) on Combustion* 13(1):1153–64. doi: 10.1016/S0082-0784(71)80112-1.

Midilli, A., M. Ay, I. Dincer, and M. A. Rosen. 2005. "On Hydrogen and Hydrogen Energy Strategies: I: Current Status and Needs." *Renewable and Sustainable Energy Reviews* 9(3):255–71. doi: 10.1016/j.rser.2004.05.003.

Ng, H. D, Y. Ju, and J. H. S. Lee. 2007. "Assessment of Detonation Hazards in High-Pressure Hydrogen Storage from Chemical Sensitivity Analysis." *International Journal of Hydrogen Energy* 32(1):93–99. doi: 10.1016/j.ijhydene.2006.03.012.

Rudy, W. 2023. "Transition to Detonation in a Hydrogen-Air Mixtures Due to Shock Wave Focusing in the 90 - Deg Corner." *International Journal of Hydrogen Energy* 48(33):12523–33. doi: 10.1016/j.ijhydene.2022.12.240.

Scarinci, T., J. H. Lee, G. Thomas, R. Bambrey, and D. H. Edwards. 1993. "Amplification of a Pressure Wave by Its Passage through a Flame Front." *Prog. Astronaut. Aeronaut.* 152:3–24.

Shepherd, J. 2021. "Explosion Dynamics Laboratory." Retrieved February 13, 2024 (https://shepherd.caltech.edu/EDL/PublicResources/sdt/).

Thomas, G. O., S. M. Ward, R. Ll. Williams, and R. J. Bambrey. 2002. "On Critical Conditions for Detonation Initiation by Shock Reflection from Obstacles." *Shock Waves* 12(2):111–19. doi: 10.1007/s00193-002-0148-z.

Voevodsky, V. V., and R. I. Soloukhin. 1965. "On the Mechanism and Explosion Limits of Hydrogen-Oxygen Chain Self-Ignition in Shock Waves." *Symposium (International) on Combustion* 10(1):279–83. doi: 10.1016/S0082-0784(65)80173-4.

Yousefi Asli Mozhdehe, S. Lau-Chapdelaine, G. Ciccarelli. 2024. "Novel weak detonation initiation from normal shock reflection in square cross-section shock." Combustion and Flame in press.

Investigation of iso-propyl nitrate as a detonation improver

A.Mousse-Rayaleh [a], M.Burnett [b], S. Abid [a] , S. de Persis [a], A. Comandini [a] , M. Wooldridge[b] N. Chaumeix[a]

[a] ICARE, CNRS-INSIS, 1C Avenue de la Recherche Scientifique, 45071 Orléans Cedex 2, France
[b] Department of Mechanical Engineering, University of Michigan, Ann Arbor, MI 48109, USA

E-mail: ayan.mousse-rayaleh@cnrs-orleans.fr

Abstract

This study aims at studying the sensitizing effect achieved by the addition of IPN (iso-propyl nitrate) on propane in the presence of oxygen and the dilution with nitrogen in the framework of Pulsed Detonation Engine (PDE) applications. It consists of studying the shock-to detonation-transition (SDT) process in a 78 mm diameter tube in order to reduce the distance and transition time. The shock to detonation transition is monitored via 22 fast shock and pressure transducers. The stoichiometric C_3H_8/O_2 and $C_3H_8/O_2/N_2$ were studied at 2 different initial pressure, 6.7 kPa and 13.3 kPa. The addition of IPN proved to be very efficient in increasing the sensitivity of propane mixtures. Detonation cell size were measured for non-diluted mixture.

Keywords: *PDE, detonation, Propane, IPN*

Introduction

Scientific studies of detonation phenomena date back to the end of the 19th century and persist as an active field of investigation (Glassman, 2015). An abundant literature has developed during this period, particularly on hydrocarbons containing less than five carbon atoms. The aim of this work is to experimentally and numerically study the feasibility and interest of a detonation wave propulsion mode in the context of space applications. The developments of Pulsed Detonation Engines (PDE), Rotary Detonation Wave Engines (RDWE) or Oblique Detonation Wave Engines (ODWE) lead to increased demand for detailed characteristics of fuel combustion. The detonation properties of propane are close to those of heavy hydrocarbons such as JP-10 and Kerosene which are suitable fuels for use in pulsed detonation engines (Penyazkov et al. 2005). For this reason, a complete study (detonation properties, laminar flame behavior, etc.) based on propane is of fundamental interest for safety reasons and also for applications, such as automotive industries and detonation engines. The work presented below has specifically focused on the detonation of propane (C_3H_8) under stoichiometric conditions using both pure oxygen and oxygen + nitrogen dilution rates up to 1.5 and the impact that an addition of 10% concentration of IPN as a promoter (Iso-propyl nitrate: $C_3H_7NO_3$) has on the sensitivity of these mixtures to detonation.

Numerous studies have been carried out on the detonation of propane, but never with the addition of promoters. The literature data includes studies on the delay of the transition to detonation for propane-oxygen mixture diluted with nitrogen and argon in a 76 mm shock tube (Brown et Thomas 1999). Penyazkov also conducted experiments in a 50 mm shock tube to determine the self-ignition delay behind reflected shock of propane in air at different riches (Penyazkov et al. 2005). Frolov et al. studied the influence of propane as an additive on the characteristics of the hydrogen-air mixture

(Frolov et al. 2020). Finally, Silvestrini et al. studied the propane flame acceleration in the presence of obstacles (Silvestrini et al. 2008).

Unlike propane, only two studies of the detonation properties of IPN have been carried but in a two-phase medium (Liu et al. 2011; Zhang et al. 2001). The study of IPN as a promoter fuel on propane is thus of interest.

Detonation sensitivity can be measured in several different ways, the most common of which is the size of the detonation cell. In addition, the pressure and temperature behind an incident shock wave required to cause a combustion reaction leading to detonation can be determined by measuring the velocity of the initial impulse shock wave before the transition to detonation. Changing these parameters can also indicate whether the initiation energy required for detonation increases or decreases with the addition of a promoter such as IPN.

A gas phase detonation can be initiated either directly by a strong shock wave such, often generated by powerful explosives driving the shock-to detonation-transition (SDT) mechanism, or by a weak energy source which accelerates the flame to create detonation wave via the deflagration-to detonation-transition (DDT) mechanism. In SDT experiments, initiation energy is provided by a shock wave generated by the bursting of a diaphragm separating a high-pressure region of non-reactive gas (helium in the present study) and a low-pressure region containing the mixture of interest. The high-pressure region can be increased to identify the P4 required to cause a shock to detonation, which will vary depending on the mixture conditions and fill pressure. In this work, the critical conditions for shock to detonation transition have been investigated for 2 initial pressure 6.7 and 13.3 kPa, at ambient temperature for stoichiometric mixtures in pure oxygen and for a N_2/O_2 =1.5 with and without iso-propyl nitrate (IPN).

1. Experimental methodology

1.1. Shock tube

The experimental set-up consisted of a stainless-steel shock tube shown in figure 1. It consists of a driver section (high pressure with an internal diameter of 115 mm over a length of 165 cm), a working section (low pressure with an internal diameter of 78 mm and a length of 4.3 m) and a removable intermediate volume, called a double diaphragm (internal diameter of 78 mm, length 78 mm). The two sections, low and high pressure, are separated by two polyester membranes and are designed to be quickly ruptured after sudden depressurization using a vacuum tank. This double diaphragm is initially filled with an inert gas, generally helium at half the pressure of the motor tube (P4/2). Thus, the initial pressures in the driver section and working section, P4 and P1 respectively, can be adjusted with precision without breaking the membranes in order to obtain the selected pressure behind the precursor shock wave. The working section is equipped with twenty shock detectors (SD1 to SD20) of very small sensitive area (0.5 mm^2) spaced with precise distances. Eight among the SD (SD: Shock Detector) are piezoelectric pressure (PCB), which record the pressures after the passage of the shock wave. These sensors are introduced into the tube and connected to two acquisition cards through amplifiers. A soot sheet covering a 21 cm x 27 cm area of the inner side wall of the shock tube was placed against the end flange and was placed behind SD17 of the shock tube to not disturb the recordings.

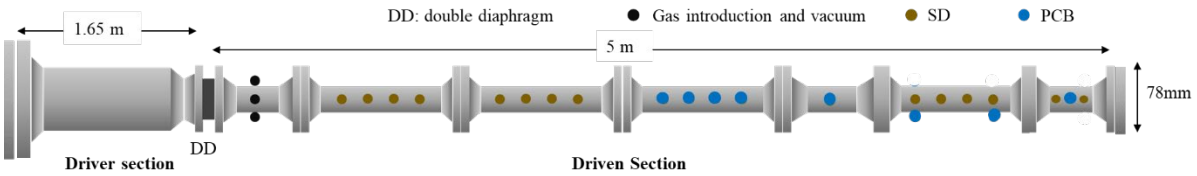

Fig. 1. *Shock tube configuration for SDT*

1.2. Experimental conditions

The experiments are carried out with mixtures of C_3H_8/O_2 with N_2 dilution rates between 0 and 1.5 at stoichiometric conditions (ER = 1), for two initial pressure conditions (P1 =6.7 and 13.3 KPa). The initial temperature (T1) is roughly 293 K at conditions both with and without the addition of 10% IPN. The mixtures were prepared and injected into the tube through two processes: using mass flowmeters or by using partial pressure method. The pressure P_4 varies from 2 to 19 bars in order to study the self-sustaining detonation. Fourteen shock detector (Chimie-Metal) and 8 pressure transducers (PCB 113B24) are mounted flush with the inner wall of the tube connected to 7 oscilloscopes for shock wave and detonation velocity measurements.

The purity of the reagents used as constituents of the reaction mixture for this study is as follows:

- Propane (Propane N25, Air-liquid, purity greater than 99.5%)
- IPN (Iso-propyl nitrate, Sigma Aldrich and matrix fine chemicals company, purity less than 98%)
- Oxygen (alpha gas 1 O_2, liquid air, purity greater than 99.995%)
- Nitrogen (alpha gas 2 N_2, liquid air, purity greater than 99.9999%)

2. Results and discussion

2.1. Methodology

The wave velocity is measured by the SDs within the tube and is marked by a very rapid rise in voltage. The very small sensitive area (rise time of 0.4 µs, 0.75 mm^2) of the SDs allows the reduction of the uncertainty associated with the wave speed measurements. However, they are very sensitive to heat transfer and as such cannot be used to measure the pressure behind the waves. Instead, pressure profiles are captured using the PCB detectors. Figure 2 illustrates an example of recording the pressure profiles measured by the piezoelectric sensors PBC10 to PCB13 on the 4-channel memory oscilloscope (Rohde & Schwarz RTB2004; 2.5 GSa/s). For each sensor, the pressure peak detected also corresponds to the passage of the incident shock wave.

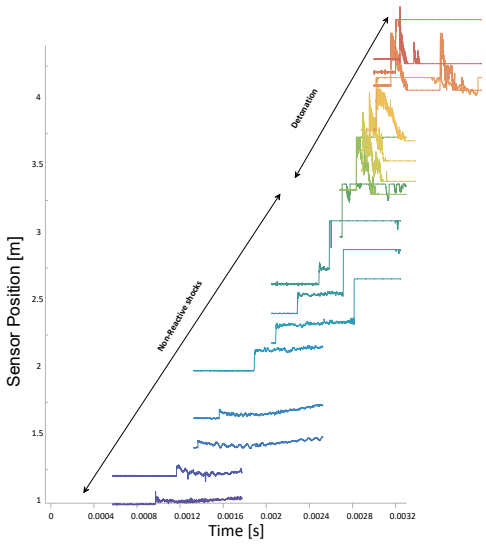

Fig. 2. *Example of the signals produced by the pressure sensors with non-reactive shocks up to 3 m followed by a transition to a detonation wave in a C3H8-O2 mixture initially at 13.3 kPa.*

The time of arrival of the shock wave or the detonation wave is determined from the instantaneous rise of the electrical signals recorded by the sensors. Knowing the positions of the sensors, a polynomial fit is used to describe the trajectory (x_{SDi} or x_{PCBi} = f (t_{SDi} or t_{PCBi})). From the trajectory fit the velocity of the waves (shock or detonation) is deduced (Speed=dx/dt) at each sensor position.

2.1. Identification of the shock to detonation transition

From the trajectory fit the velocity of the waves (shock or detonation) is deduced (Speed=dx/dt) at each sensor position. Using the classical gas dynamic equations (COSILAB software), the conditions behind the incident shock, P_2 and T_2, are calculated for each shock speed. For an explosive mixture given at an initial pressure P_1, greater than the limit pressure of detonation, a transition from a non-reactive shock wave to a detonation wave occurs when the incident shock wave exceeds a given strength. This transition can be characterized by plotting the wave speed versus the driver pressure P_4, or versus the ratio $\frac{P_2-P_1}{P_1}$ which both represents the shock wave strength.

When a selfsustained detonation is obtained, thee experimental detonation speed is compared to the Chapman-Jouguet detonation speed. This was determined using the chemical equilibrium code "Equilibrium" using the chemical kinetics software Cosilab.

The influence of the composition of the mixture on the detonation properties was investigated in terms of dilution and the impact of adding IPN. Four stoichiometric mixtures were studied: (i) C_3H_8/O_2, (ii) $\{0.1IPN\text{-}0.9C_3H_8\}/O_2$, (iii) $C_3H_8/O_2/N_2$, (iv) $\{0.1IPN\text{-}0.9C_3H_8\}/O_2/N_2$ with N_2/O_2=1.5. Two different initial pressures are investigated: 6.7 and 13.3 kPa.

The results are plotted in Figure 3 which shows the variation of the speed of the wave (V_{exp} for the experimental speed and D_{CJ} for the theoretical speed of the detonation) versus P_4 (Fig. 3 (a) and (b)) and $\frac{P_2-P_1}{P_1}$ (Fig. 3 (c) and (d)) for an initial pressure of 6.7 kPa.

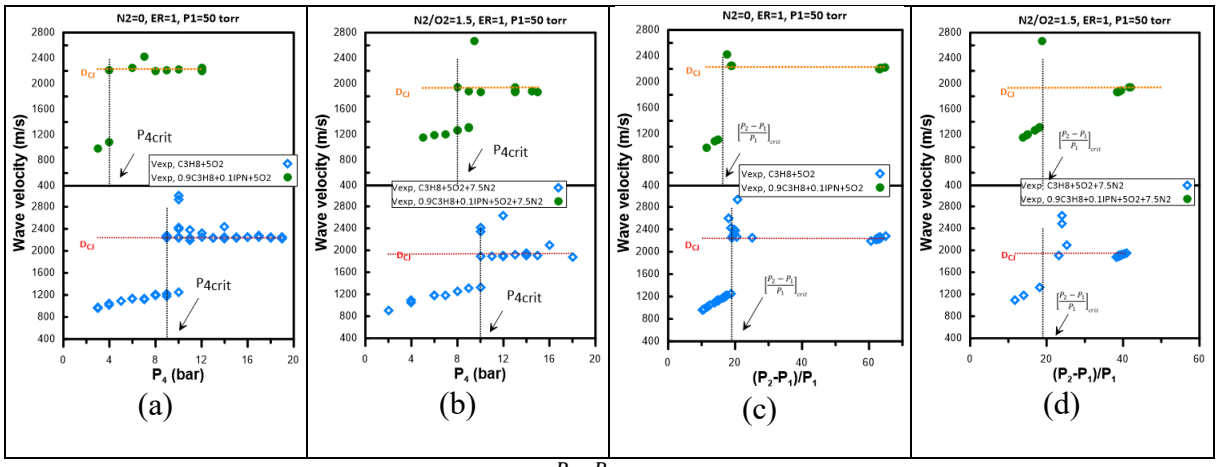

Fig. 3. *Wave speed versus P_4, (a) and (b), and $\frac{P_2-P_1}{P_1}$, (c) and (d), for P_1 = 6.7 kPa. The mixtures are (i) C_3H_8/O_2, (ii) {0.1IPN-0.9C_3H_8}/O_2, (iii) $C_3H_8/O_2/N_2$, (iv) {0.1IPN-0.9C_3H_8}/O_2/N_2 with N_2/O_2=1.5. The blue and green dots correspond to the speed (V_{exp}) of the wave (experimental data) while the the orange and red dot line show the theoretical speed of the Chapman-Jouguet detonation (D_{CJ}).*

As one can see for C_3H_8/O_2 mixtures, non-reactive shock waves are observed for P_4 below 9 bars. When the driver pressure exceeds this critical value, a detonation is formed and propagates at CJ conditions. When IPN is added to the mixture, this critical driver pressure drops to 4 bars. The addition of IPN favors the transition to detonation at lower Mach numbers. When the mixtures are diluted with N_2, the critical driver pressure is 10 bars for $C_3H_8/O_2/N_2$ and drops to 8 bars when IPN is added to the mixture. The limit between non-reactive shock waves and the transition to detonation is much clearer when the wave speeds are reported versus $\frac{P_2-P_1}{P_1}$ as it is shown in Fig. 3 (c) and (d). Indeed, one has to keep in mind, that P_4 is a good indicator of the shock strength but, close to the limit, the effect of the opening of the membrane becomes important and will be responsible for a larger discrepancy in the definition of the limit between conditions leading to pure non-reactive waves and leading to the onset of a detonation wave. The same characterization was also done at an initial pressure of 13.3 kPa. The addition of IPN reduces the P_4 required to drive the detonation under all conditions. These reductions were significant for Fuel + O_2 conditions, but less dramatic under conditions using a nitrogen dilution of 1.5. The impact of adding IPN on key parameters is summarized in Table 1, showing how $P_{4,c}$, $T_{2,c}$ and $P_{2,c}$ required for detonation with respect to and without the 10% fuel concentration of the IPN.

Table 1. *Comparison of P_4 critique shock temperatures and pressures required for stoichiometric C_3H_8/O_2 detonation with and without N_2 dilution.*

P_{ini} (kPa)	Mixture	$P_{4,c}$ (bar)	$T_{2,c}$ (K)	$P_{2,c}$ (bar)	Cell size (mm)
6.7	C_3H_8/O_2	9	806.2	1.22	11.6±3.13
	C_3H_8/O_2+IPN	4	727.6	1.02	9.29±2.31
13.3	C_3H_8/O_2	5	610.6	1.38	4.83±1.32
	C_3H_8/O_2+IPN	All Detonation			3.73±0.82
6.7	$C_3H_8/O_2/N_2$	10	972.6	1.31	
	$C_3H_8/O_2/N_2$+IPN	8	924.2	1.22	
13.3	$C_3H_8/O_2/N_2$	11	832.2	2.00	
	$C_3H_8/O_2/N_2$+IPN	8	794.5	1.88	

2.2. Cell structure: sensitivity to detonation

The three-dimensional structure of the self-sustaining detonation wave was recorded on a soot foil. Cell size λ is a measure of the sensitivity to detonation for a given mixture and allows comparison with other mixtures. Cell size measurements were taken under stable detonation conditions for all conditions studied. Unfortunately, cell size and resolution of cell size measurements under nitrogen dilution conditions were inconclusive due to their large cell size. A few cells could be measured, but not enough to draw statistically significant conclusions. Therefore, the only cell size results presented here are for the Fuel + O_2 experiments. Figure 4 shows the change in measured cell width caused by adding IPN to mixtures.

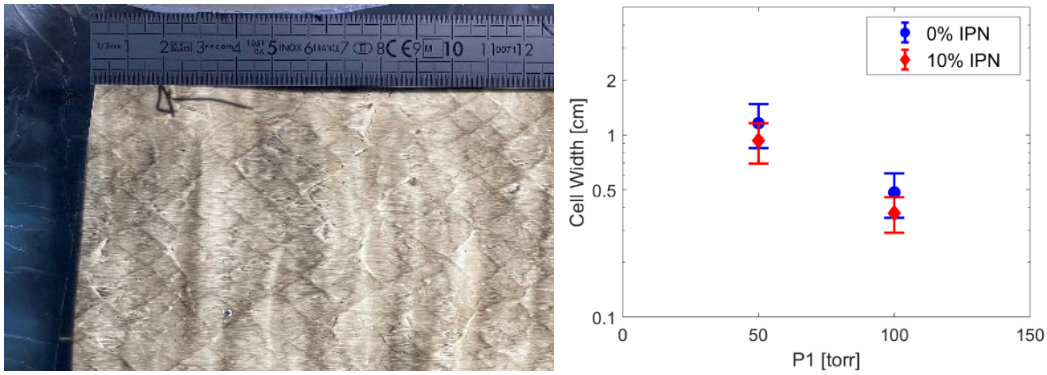

Fig. 3. *Measurements of cell width versus concentration of addition P_1 and IPN for C_3H_8.*

There is a marked decrease in the average cell width at 6.7 and 13.3 kPa and Table 1 summarizes the average cell width and standard deviation for the four Fuel + O_2 conditions. Figure 4 also shows the change in measured cell width caused by adding IPN to mixtures. In the case of pure C_3H_8/O_2 mixtures, the cell sizes are in good agreement with the literature (Knystautas, Lee, et Guirao 1982) (Kaneshige, 1999).

3. Conclusions

The results presented above indicate that IPN, even at 10% fuel concentration, increases the sensitivity of propane to detonation. Its addition resulted in a decrease in the P_4, P_2 and T_2 required to initiate detonation as well as a decrease in the average cell size observed in the detonation shock experiments.

The next steps in this work involve the kinetic analyses of the IPN role in promoting the detonation of propane, in particular in the calculations of the auto-ignition delays behind different shock conditions, the length of formation of the detonation wave and more detailed accounting. transition characteristics for each of the conditions of interest. Beyond this, DDT experiments at comparable concentrations and mixing conditions are continuing and will complement existing work to provide a more detailed view of the impact of IPN as an additive for the detonation of propane. . Ideally, cell size measurements under DDT conditions will produce more conclusive results for the N_2 dilution conditions of interest. Finally, these results will be compared to the impact of adding IPN on propene to provide a comparison on how it interacts with non-NTC (negative temperature coefficient) fuel and on weather, any significant difference can be observed.

Acknowledgements

A. Mousse-Rayaleh acknowledges the financial support from the Frecnh Ministery of Higher Education and Research (MESRI PhD grant).

References

Brown, C.J, et G.O Thomas. 1999. « Experimental Studies of Shock-Induced Ignition and Transition to Detonation in Ethylene and Propane Mixtures ». *Combustion and Flame* 117 (4): 861-70. https://doi.org/10.1016/S0010-2180(98)00133-3.

Frolov, S. M., V. A. Smetanyuk, I. O. Shamshin, A. S. Koval', F. S. Frolov, et S. A. Nabatnikov. 2020. « Cyclic Detonation of the Ternary Gas Mixture Propane–Oxygen–Steam for Producing Highly Superheated Steam ». *Doklady Physical Chemistry* 490 (2): 14-17. https://doi.org/10.1134/S0012501620020025.

Knystautas, R., J.H. Lee, et C.M. Guirao. 1982. « The Critical Tube Diameter for Detonation Failure in Hydrocarbon-Air Mixtures ». *Combustion and Flame* 48 (janvier): 63-83. https://doi.org/10.1016/0010-2180(82)90116-X.

Liu, Qingming, Chuhua Bai, Wenxi Dai, et Li Jiang. 2011. « Deflagration-to-Detonation Transition in Isopropyl Nitrate Mist/Air Mixtures ». *Combustion, Explosion, and Shock Waves* 47 (4): 448-56. https://doi.org/10.1134/S0010508211040083.

Penyazkov, O.G., K.A. Ragotner, A.J. Dean, et B. Varatharajan. 2005. « Autoignition of Propane–Air Mixtures behind Reflected Shock Waves ». *Proceedings of the Combustion Institute* 30 (2): 1941-47. https://doi.org/10.1016/j.proci.2004.08.122.

Silvestrini, M., B. Genova, G. Parisi, et F.J. Leon Trujillo. 2008. « Flame Acceleration and DDT Run-up Distance for Smooth and Obstacles Filled Tubes ». *Journal of Loss Prevention in the Process Industries* 21 (5): 555-62. https://doi.org/10.1016/j.jlp.2008.05.002.

Yu, Xiaozhe, Jianliang Yu, Xinyan Zhang, Xianshu Lv, Qi Cao, Yujie Hou, et Xingqing Yan. 2018. « Flame Propagation Behaviors during Hydrogen/Aluminum Dust Hybrid Explosions Article ». *Powder Technology* 1 (1): 1-8.

Zhang, F., R. Akbar, P.A. Thibault, et S.B. Murray. 2001. « Effects of Nitrates on Hydrocarbon-Air Flames and Detonations ». *Shock Waves* 10 (6): 457-66. https://doi.org/10.1007/PL00004054.

Glassman, I. (1996). Combustion, 3rd edition. Academic Press. San Diego. California (ISBN 0 12 285852 2).

Kaneshige, M.J. *Gaseous Detonation Initiation and Stabilization by Hypervelocity Projectiles*. PhD thesis, California Institute of Technology, 1999.

Investigation on analog system of detonation with two step chemical reaction model

Yuanxiang Sun

State Key Laboratory of Explosion Science and Technology,
Beijing Institute of Technology, Beijing, China

E-mail: sunyuanxiang002@126.com

Abstract

The analog system of detonation with loss and the chemical reaction of two step reaction model is constructed, wherein an induction zone is followed by a energy and heat release zone.Steady state of detonation wave structures are obtained by analytic method. Linear stability analysis is carry out under the condition of the ideal and non-ideal (with loss) analog system of detonation. The influence of reaction rate parameter and loss parameter on the stability is analyzed.

Keywords: *detonation, analog system, two step, chemical reaction, stability*

1. Introduction

The original Euler system which simulates behavior of detonation contains too much physical details, these will cause mathematical difficulties because of the nonlinearity of the equations. To simplify the reactive Euler equation in the theory of detonation, the analog system of detonation which contains one or more partial differential equations is obtained. The analog system of detonation as a simple model to study detonation behavior, can capture a rich set of detonation phenomenon.

The Euler system which simulates behavior of detonation contains too much physical details, these will cause mathematical difficulties because of the nonlinearity of the equations. To simplify the reactive Euler equation in the theory of detonation, the analog system of detonation which contains one or more partial differential equations is obtained. The analog system of detonation as a simple model to study detonation behavior, can capture a rich set of detonation phenomenon.

2. Analog System of Detonation

On the basis of the Fickett(1979,1985) model, consider the effect of the loss term (Faria et al 2014) and establish a new detonation simulation system as follows:

$$\frac{\partial u}{\partial t}+\frac{\partial}{\partial x}(\frac{1}{2}u^2)=q\frac{\partial \lambda}{\partial t}-\kappa\left(\frac{u}{u_{CJ}}\right)^m \tag{1}$$

Analog quantities u can represent such as speed, pressure, temperature. The reaction term is used to simulate the reaction rate in the Euler equation, where the form of the simplified combustion model is chosen. In the reaction term, q is the exothermic coefficient of the reaction, that unit of

chemical reaction to release energy, and λ is the reaction progress variable that records the completion of the reaction, $\lambda = 0$ in the case of no reaction, $\lambda = 1$ in the case of completion of the reaction.

In the loss term, κ is the loss parameter, which represents the curvature of the detonation wave front. The loss index m represents the sensitivity of the loss term to the local thermal state, and u_{CJ} is a constant based on the CJ state. The chemical reaction is a two-step induction-reaction model(Tang et al 2013) with independently controlled induction and reaction stages in the form:

$$\begin{aligned}\frac{\partial \lambda_i}{\partial t} &= -H(\lambda_i)e^{\alpha\left[(u/2u_{CJ})-1\right]} \\ \frac{\partial \lambda_r}{\partial t} &= \left[1-H(\lambda_i)\right]H(1-\lambda_r)(1-\lambda_r)^{\upsilon}\left(u/u_{CJ}\right)^n\end{aligned} \tag{2}$$

In the chemical reaction, λ_i is the process variable of the induction zone, λ_r is the process variable of the reaction zone, ν is the reaction order, $H(\ )$ is the Heaviside function, α is the reaction rate induction parameter, and the reaction rate index n is the sensitivity of the reaction rate to the local thermal state.

The detonation simulation system which takes into account the loss and the two-step reaction is obtained by integrating the specific forms of all equations:

$$\begin{aligned}\frac{\partial u}{\partial t^l}+\frac{\partial u}{\partial x^l} &= q\frac{\partial \lambda}{\partial t^l}-\kappa\left(\frac{u}{u_{CJ}}\right)^m \\ \frac{\partial \lambda_i}{\partial t^l} &= -H(\lambda_i)e^{\alpha\left[(u/2u_{CJ})-1\right]} \\ \frac{\partial \lambda_r}{\partial t^l} &= \left[1-H(\lambda_i)\right]H(1-\lambda_r)(1-\lambda_r)^{\upsilon}\left(u/u_{CJ}\right)^n\end{aligned} \tag{3}$$

The coordinate system is rewritten to follow the wave coordinate system:

$$\begin{aligned}\frac{\partial u}{\partial t}+(u-D)\frac{\partial u}{\partial x} &= q\left(\frac{\partial \lambda}{\partial t}-D\frac{\partial \lambda}{\partial x}\right)-\kappa\left(\frac{u}{u_{CJ}}\right)^m \\ -D\frac{\partial \lambda_i}{\partial x}+\frac{\partial \lambda_i}{\partial t} &= -H(\lambda_i)e^{\alpha\left[(u/2u_{CJ})-1\right]} \\ -D\frac{\partial \lambda_r}{\partial x}+\frac{\partial \lambda_r}{\partial t} &= \left[1-H(\lambda_i)\right]H(1-\lambda_r)(1-\lambda_r)^{\upsilon}\left(u/u_{CJ}\right)^n\end{aligned} \tag{4}$$

Assuming that the detonation wave is already in a stable propagation state, the partial derivative with respect to time t is zero, then the equation of the change of the u in the reaction zone and the reaction zone is deduced:

$$\begin{aligned}\frac{\partial u}{\partial x} &= \frac{-qD\dfrac{\partial \lambda}{\partial x}-\kappa\left(\dfrac{u}{u_{CJ}}\right)^m}{(u-D)} \\ \frac{\partial \lambda_i}{\partial x} &= \frac{1}{D}H(\lambda_i)e^{\alpha\left[(u/2u_{CJ})-1\right]} \\ \frac{\partial \lambda_r}{\partial x} &= -\frac{1}{D}\left[1-H(\lambda_i)\right]H(1-\lambda_r)(1-\lambda_r)^{\upsilon}\left(u/u_{CJ}\right)^n\end{aligned} \tag{5}$$

Assuming the state of the wave front is known, the initial conditions of the equation are obtained according to the Rankine-Hugoniot condition:

$$u(x=0)=2D, \lambda_i(x=0)=1, \lambda_r(x=0)=0 \tag{6}$$

The ideal state CJ speed is:

$$u_{CJ}=D_{CJ}=2q \tag{7}$$

A shock wave velocity is arbitrarily selected, and the steady-state equation is numerically integrated. If the numerator and denominator of the governing equation are not zero at the same time, the singularity of the velocity of sound occurs when u-$D \rightarrow 0$. The criterion solution requires that when the speed of sound is singular, the numerator is 0, which is the generalized CJ criterion. Steady - state detonation wave structure can be obtained.

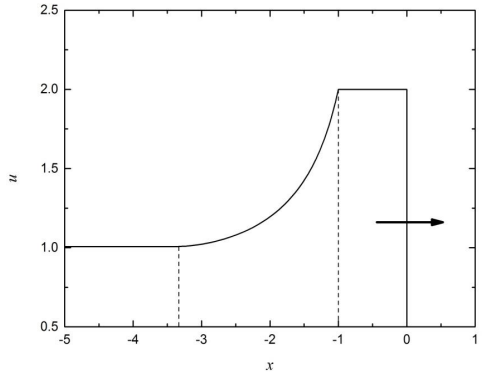

Figure 1 Steady - state detonation wave structure

3. Criticality of detonation

Based on the generalized CJ criterion, the relationship between detonation velocity and curvature is drawn. With the increase of the curvature, the steady - state detonation velocity decreases gradually. The turning point that appears on the curve corresponds to the maximum permissible curvature above which the detonation fails. Since the value of n is small, the reaction term can not compensate for the increase in curvature, so the curvature increases monotonically without turning points. As the value of n increases, the steady-state detonation curve is shifted to the left.

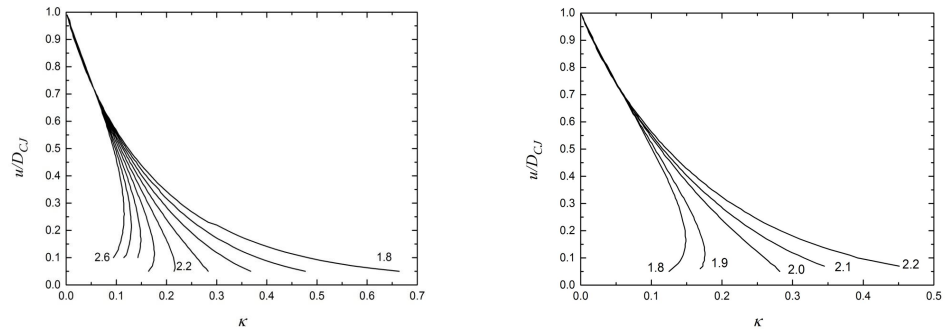

Figure 2 Detonation velocity~curvature curve with (a) different *n* (left); (b) different *m*(right)

Each different response rate index *n* corresponds to a different maximum loss coefficient κ, so a linear boundary of detonation propagation and failure can be made.

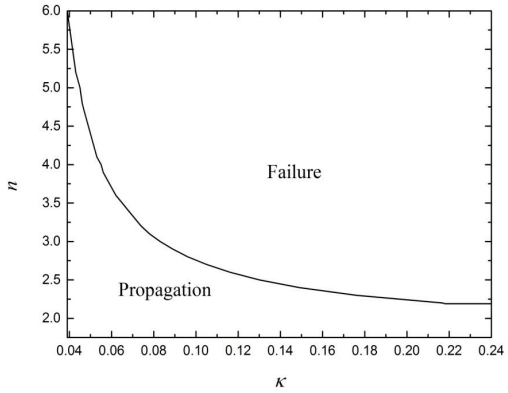

Figure 3 Linear boundary of detonation propagation and failure

The inflection point required for the relationship between *n* and *m*. Where the reaction rate of the local thermal state of the sensitivity of *n* than the loss rate of the local thermal state of the sensitive *m* degree of 0.2 and above the case will appear inflection point.

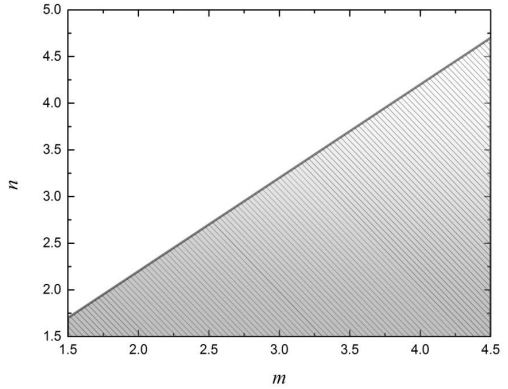

Figure 4 The diagram of *m* and *n* when the inflection point

4. Linear model analysis

The linear stability problem is observed by applying the unsteady small perturbations in the steady-state ZND solution to observe the perturbation growth or decay process.

$$D = D_0 + \varepsilon\sigma \exp(\sigma t), u = u_0 + \varepsilon u_1(x)\exp(\sigma t), \lambda = \lambda_0 + \varepsilon\lambda_1(x)\exp(\sigma t) \tag{8}$$

By introducing the disturbance into the steady-state equation， the higher order term and the steady state solution are obtained, and the binomial theorem is used：

$$\begin{aligned} &\sigma u_1 + (u_0 - D_0)u_1' + u_0' u_1 - \sigma u_0' = q\left(\sigma\lambda_1 - D_0\lambda_1' - \sigma\lambda_0'\right) - \kappa m \frac{u_1}{u_{CJ}}\left(\frac{u_0}{u_{CJ}}\right)^m \\ &\sigma\lambda_1 - D_0\lambda_1' - \sigma\lambda_0' = \frac{n u_1 (1-\lambda_0)^\nu}{u_{CJ}}\left(\frac{u_0}{u_{CJ}}\right)^{n-1} - \nu\lambda_1 (1-\lambda_0)^{\nu-1}\left(\frac{u_0}{u_{CJ}}\right)^n \end{aligned} \tag{9}$$

The initial boundary conditions of the equation variables are obtained by bringing the steady-state solution with small perturbations into the initial shock condition:

$$u_1(x=0) = 2\sigma, \lambda_1(x=0) = 0 \tag{10}$$

In order to determine the eigenvalues of the frequency eigenvalue σ, we can get the following result by suppressing the perturbation on the front-finger characteristic line of the steady-state wave,

$$\frac{u_1}{\omega_1(u_0 - D_0)i + a} + \frac{\lambda_1}{\omega_2(u_0 - D_0)i + a} = 0 \tag{11}$$

In order to determine the frequency eigenvalue σ in the stability equation, we first need to satisfy the dispersion condition. The absolute value of the dispersion relation Y (σ) is calculated by setting the frequency eigenvalues of different real and imaginary parts, and the distribution condition is satisfied only when its value is equal to zero, and then the logarithm of the absolute value is made in the complex complex plane high - line chart.

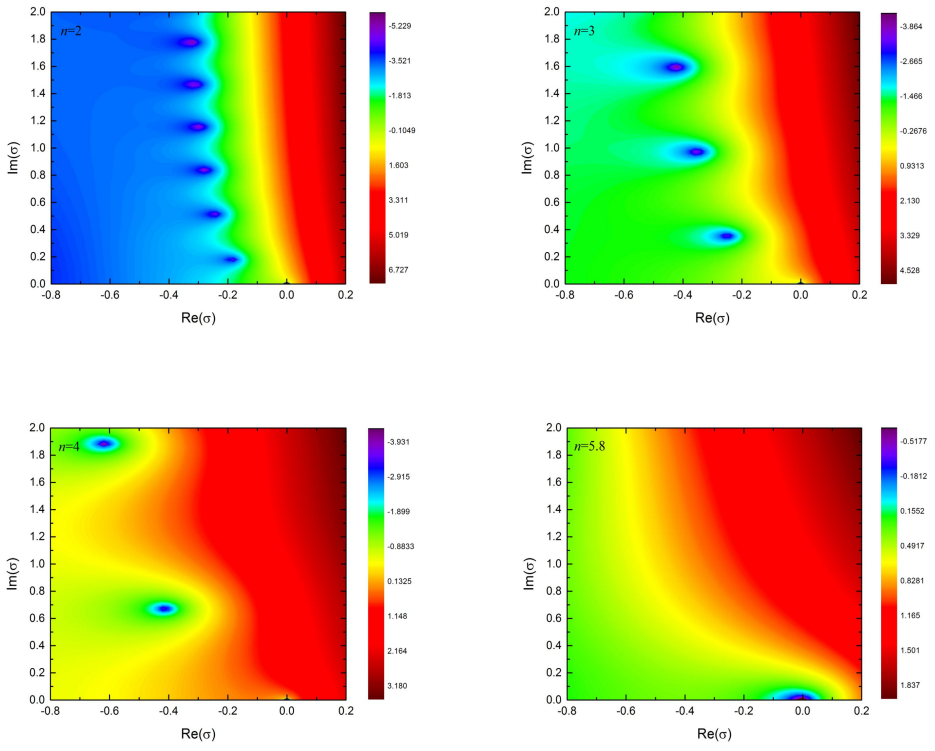

Figure 5 Stability results under ideal conditions

The local minimum value (purple point) in the contour plot represents the frequency eigenvalue satisfying the dispersion condition. If the frequency eigenvalues satisfying the condition are present only in the negative region of the real part of the eigenvalue, the perturbation of the steady- With time and gradually increase, that detonation simulation system is stable.

The region of the detonation steady-state solution will decrease gradually, but it still does not appear in the positive region of the real part of the eigenvalue. The steady-state solution of the detonation simulation system is a one-dimensional The linear perturbation is stable. When the value of the reaction rate index n is equal to or greater than 5.8, no matching frequency characteristic value can be found in the contour map of the existing area.

Under the non-ideal condition, let the loss item parameter, the loss item exponent, other parameters remain unchanged, to make the response rate index contour chart as shown.

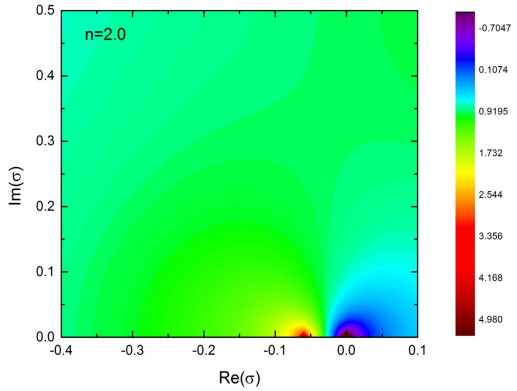

Figure 6 Stability results under non-ideal conditions

The frequency characteristic value satisfying the dispersion condition does not appear in the contour plot, and even if the value of the reaction rate index n and the loss term exponent m are changed, the dispersion condition can not be satisfied. Therefore, the steady state solution of the detonation simulation system is always unstable for one-dimensional linear perturbations due to the existence of the loss term under non-ideal conditions.

5 Conclusions

An analog system of detonation with two step chemical reaction model is is built. This simple detonation analog system with losses captures the critical behaviour of detonation propagation: If the state-dependence of the reaction rate is more sensitive than that of the rate of losses, i.e.

$m \le n - 0.2$, the system exhibits a critical point in the D-κ relation . And , linear stability analysis shows that the ideal steady state detonation is stable to small perturbations even with large n.

Acknowledgements

The authors gratefully acknowledge the financial contribution from the State Key Laboratory of Explosion Science and Technology, Beijing Institute of Technology,China and Deutscher Akademischer Austauschdienst (DAAD)

References

Fickett, W. , 1979, Detonation in miniature. American Journal of Physics, 47(12),1050-1059.

Fickett,W., 1985, Introduction to Detonation Theory.University of California Press, 133-181.

Faria, L. and Kasimov, A., 2014, Qualitative modeling of the dynamics of detonations with losses. Proceedings of the Combustion Institute, 35(2):1-23.

Tang, J, Radulescu, M.I. 2013, Dynamics of shock induced ignition in Fickett's model: Influence of χ, Proceedings of the Combustion Institute, 34(2), 2035-2041

An Arrhenius reaction rate based burning model for simulation of dust explosions

Bjørn J. Arntzen [a,b], Melodía Lucas [a,b] & Maryam Ghaffari [a,b]

[a] Gexcon, Bergen, Norway
[b] University of Bergen, Norway

E-mail: bjorn.arntzen@uib.no

Abstract

The handling of combustible dust poses inherent risks, potentially leading to dust explosions whose strength and consequences hinge on various factors. Computational Fluid Dynamics (CFD) simulations of dust explosions can effectively incorporate these factors, contributing to the design of safer processes and equipment. The FLACS DustEx CFD code has demonstrated notable efficacy in simulating explosions in organic dusts such as maize starch, even in substantial structures like a 236-m³ silo. This code, formerly known as DESC, has been utilized by multiple industries for over a decade. The accurate functioning of the DustEx code relies on the combustion properties of the dust, influenced by factors like dust concentration and particle size. These crucial properties are derived from P_{max} and $(dP/dt)_{max}$ values obtained through standardized experimental tests conducted in 20-liter and 1-m³ environments.

The enhanced combustion modeling in DustEx comprises three key components. First, the burning rate is linked to an Arrhenius reaction rate based on the product temperature. Second, the impact of particle size distribution and dust concentration on the burning rate is considered by making it a function of the total surface area of all particles. Third, a substantial database at Gexcon is leveraged to formulate the burning rate model across a spectrum of dust types, particle sizes, and dust concentrations. These models are fine-tuned through optimization using least square fitting to align with experimental data.

In contrast to previous iterations of DustEx, which necessitated experimental tests for all combinations of dust concentrations and particle size distributions for each dust sample, the new models significantly reduce the need for such extensive testing. This innovation facilitates a more streamlined process, wherein experimental testing of dusts before CFD simulations can be minimized. The efficacy of these new models has been validated through simulations of large-scale explosion experiments, as well as experiments conducted in 20-liter and 1 m³ spherical bombs. This comprehensive testing approach ensures the reliability and applicability of the improved combustion model across a range of scenarios and conditions.

Keywords: *FLACS DustEx, industrial dust explosions, Arrhenius reaction rate*

1. The FLACS DustEx CFD code

Handling combustible dust presents inherent risks, which can result in dust explosions of varying strength and severity, contingent upon numerous factors. Computational Fluid Dynamics (CFD) simulations offer an effective means to account for these factors, thereby enhancing the design of safer industrial processes and equipment. Notably, the FLACS DustEx CFD code has demonstrated significant effectiveness in modeling explosions involving organic dust types, such as maize starch, even within large-scale structures like a 236-m³ silo. FLACS DustEx is based on the gas explosion simulator FLACS and were presented early in the PhD thesis of Arntzen (1998) and by Arntzen et al. (2003). The dust explosion CFD code were originally known as DESC (Skjold et al. 2005) and has been extensively employed across multiple industries for more than two decades.

1.1. Dust explosion parameters needed for calculation of dust explosions

The accurate performance of the DustEx code hinges on the precise characterization of combustion properties inherent to the dust, which are influenced by factors including dust concentration and particle size distribution. These pivotal properties are deduced from standardized experimental tests, involving determination of p_{max} and $(dp/dt)_{max}$ values, conducted within both 20-liter and 1-m³ spherical explosion vessels as function of dust concentration, particle size distribution and dust type. Figure 1 show an example of the pressure time history of such test

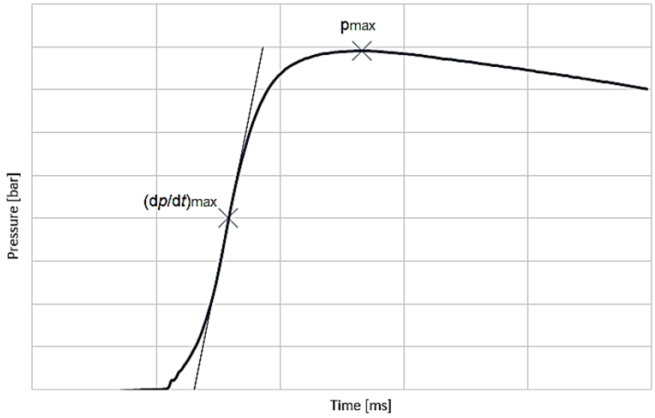

Fig. 1. *Pressure-time history for a typical explosion test, from Skavland (2018)*

1.1. The turbulent burning velocity from spherical bomb experiments

In FLACS DustEx, the turbulent burning velocity S_T as function of dust concentration is found from $(dp/dt)_{max}$ and p_{max} values by the relation presented by Skjold (2007)

$$S_T(t_{ip}) = \frac{(\frac{dp}{dt})_{max}}{3(p_f - p_i)} (\frac{3V}{4\pi})^{1/3} (\frac{p(t_{ip})}{p_i})^{-1/\gamma} \left\{1 - (\frac{p_f - p(t_{ip})}{p_f - p_i})(\frac{p(t_{ip})}{p_i})^{-1/\gamma}\right\}^{-2/3} \quad Eq\ 1$$

Where t_{ip} is the time for the maximum time dependent pressure gradient $(dp/dt)_{max}$, p_f is the maximum total pressure, p_i is the initial total pressure and γ is the compressibility factor (1.4 for air). With $p_{max}=p_f-p_i$, p_i =1 atm and $p(t_{ip})=0.6p_f$, the expression for S_T (Eq 1) can be simplified to

$$S_T \approx 0.3 \frac{(\frac{dp}{dt})_{max}}{p_{max}^{7/4}} \qquad Eq\ 2$$

The maximum $(dp/dt)_{max}$ for all dust concentrations is named K_{st} value, where V is the volume of the bomb

$$K_{st} = \left(\frac{dp}{dt}\right)_{max} V^{1/3} \qquad Eq\ 3$$

Constant volume dust explosion test should be done in as large volume as possible to minimize the effect of chemical ignitors and heat loss to the walls per volume. Two chemical ignitors with 2x10kJ will alone give a pressure rise of 1.6 barg in a 20 liter bomb, but only 0.032 barg in a 1 m^3 bomb. Explosion pressure p_{ex} obtained in the 20-litre bomb is corrected to give similar p_m as in the 1 m^3 bomb. For $p_{ex}>5.5$ the correction is done by equation 4 (Østgård 2022)

$$p_m = 0.775 p_{ex}^{1.15} \qquad Eq\ 4$$

1.2. The turbulent burning velocity model in FLACS, including DustEx

The turbulent burning velocity model in FLACS DustEx is given by equation 5.

$$S_T = 0.875 u' Ka^{-0.392} \quad Eq\ 5$$

where u' is the turbulent RMS velocity fluctuation and the Karlowitz number is given by Eq 6.

$$Ka = \tau_c \sqrt{\frac{u'^3}{\alpha l_m}} \quad Eq\ 6$$

In addition to the burning model in equation 5 is two correction models which reduces the burning rate for high Ka and secure that $S_T \xrightarrow[u'\to 0]{} S_L$ (else S_T would be 0). S_L is the laminar burning velocity.

In present version of FLACS and DustEx the chemical time scale τ_c has been modeled as function of the thermal diffusivity α and S_L,

$$\tau_c = \alpha / S_L^2 \qquad Eq\ 7$$

The model requirs that S_L as function of dust concentration, C_{dust}[g/m^3] has to be estimated through Eq 1, 5 and 6, from $(dp/dt)_{max}$, p_m and the turbulent parameters $u'$and l_m at t_{ip}. As described by Skjold et al (2005) these turbulence parameters vary with the time t_{ip} and are likely to depend also on dust type, concentration and size of experiment. A longer t_{ip} results in a lower $u'$and thereby a lower $(dp/dt)_{max}$ (named hereafter $(dp/dt)_m$).

2 Reaction rate bases on an Arrhenius based chemical time scale

The new approach is to set the inverse chemical time scale proportional to both an Arrhenius based reaction rate multiplied and the dust concentration.

$$\tau_c^{-1} = A_{dust} C_{dust} e^{-T_A/T_P} \qquad Eq\ 8$$

where T_P is the product temperature (estimated from P_{max}), T_A is the activation energy for the dust and A_{dust} is a constant specific for each dust sample.

$$\tau_c^{-1} = \sqrt{\frac{u'^3}{\alpha l_m}} \left(\frac{S_T}{0.875 u'}\right)^{2.55} \qquad Eq\ 9$$

With u'=1.6, thermal diffusivity α=2 10^{-5} and a turbulent mixing length l_m=2.7mm inserted

$$\tau_c^{-1} = \sqrt{\frac{1.6'^3}{2\ 10^{-5} 0.0027}} \left(\frac{S_T}{0.875\ 1.6}\right)^{2.55} = 3692 S_T^{2.55} \quad Eq\ 10$$

By combining equation 4 and 10 an expression for the chemical time scale is found as function of $(dp/dt)_m$ and p_m.

$$\tau_c^{-1} = 171.4 \left(\frac{\left(\frac{dp}{dt}\right)_{max}}{p_m^{7/4}}\right)^{2.55} \qquad Eq\ 11$$

If only the K_{st} value is known (and no other $(dp/dt)_{max}$ values for other dust concentrations), a typical T_A value for the dust type is used and the constant A_{dust} is calculated by combining equation 8 and 11 to get equation 12

$$A_{dust} = \frac{171.4e^{T_A/T_P}}{C_{dust}} \left(\frac{K_{st}}{p_m^{7/4}}\right)^{2.55} \quad Eq\ 12$$

If $(dp/dt)_{max}$ values are known for a range a dust concentrations, A_{dust} and T_A are chosen so

$$K_{st}(dp/dt)_m = \frac{p_{m*}^{7/4}}{7.51}\left(A_{dust}C_{dust*}e^{-T_A/T_{P*}}\right)^{0.392} \quad Eq\ 13$$

where values marked with * are values from the concentration with maximum $(dp/dt)_m$ (=K_{st}). A value for T_A can be found by e.g. a least square fit by minimizing the expression below, Eq 14.

$$\sum_{All\ dust\ concentrations}\left\{(dp/dt)_m - K_{st}\left(\frac{p_m}{p_{m*}}\right)^{7/4}\left(\frac{C_{dust}}{C_{dust*}}e^{T_A/T_{P*}-T_A/T_P}\right)^{0.392}\right\}^2 \quad Eq\ 14$$

The constant A_{dust} is found by inserting the T_A found into equation 12.

T_A could also be found from report values in the literature. Ogle(2016) reports T_A≈8000 for coal dust. Reding (2021) report in Table 2.4 in his PhD thesis E_a values of 20,4 [kJ/mole] and 60.3 for two different corn starch, 41.9 for Zinc powder and 32.4 for Iron powder. T_A values is obtained by dividing E_A with the universal gas constant R (=8.3145 J/K*mole) which results in T_A=0.1203E_A

Regarding the validity of an Arrhenius reaction rate, Bardon et al (1983) argue for coal and similar carbonaceous material: combustion of volatiles' is controlled by diffusion of oxygen for particles greater than 65um and by chemical reaction below 15 um. After all volatiles is consumed chemical reaction is most important for all particle sizes

Using an Arrhenius reaction base formulation has several advantages:
Less need to find coefficients for the turbulent or laminar burning velocity dependency with pressure, reactant temperature or oxygen concentration in air.

2.1 The effect of scale on the reaction rate

Van Wingerden (2019) reports that K_{st} values for metal dusts typically are twice as high in 1m^3 sphere as in the 20 litre sphere and argue for use a twice as high value if K_{st} is obtained in 20 litre tests for metal dusts.
In FLACS DustEx the turbulent burning velocity is proportional to $l_m^{0.196}$ as can be seen from equation 5 and 6. With l_m typical set proportional to the flame radius, the maximum turbulent burning velocity will be 50% higher in the 1m^3 sphere than in the 20 litre sphere due to a 6 times larger radius.

Our master student, Skavland (2018), performed explosion experiments with aluminum dust in both a 20- and a 500-liter vessels. As can be seen in figure 2, $(dp/dt)_{max}$ were significant higher in the smaller 20 liter vessel an not opposite which was expected. The reason for the lower $(dp/dt)_{max}$ value in the 300 vessel may be due to lower turbulence velocity fluctuation or that dusts start to settle out of the cloud before the flame arrives.

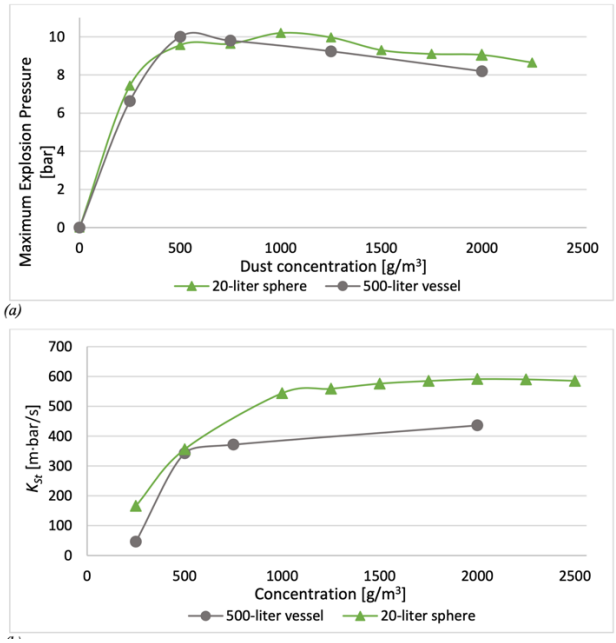

Fig. 2. Experimental test results for Aluminum dust. From Skavland

2.2 The effect of particle size on the reaction rate

Eckhoff (2003) present experiments which shows that K_{st} is inverse proportional to the average particle diameter for a range of fuels. Since the reaction rate is typical proportional to K_{st} squared, the reaction rate (=inverse chemical timescale) should have a d-squared dependence as shown in equation 17.

$$\tau_c \propto d_{3,2}^2 + d_x^2 \quad Eq\ 15$$

where $d_{3,2}$ is the volume to surface weighted diameter, also known as the Sauter diameter. d_x is a dust type dependent parameter with value around 1 µm for metal dusts like aluminium and larger for organic dusts, which secure a maximum value for the burning rate for very small dust particles.

However, when inserting the particle size dependence into equation 8, one must consider that T_P decreases with increasing particle diameter. Equation 18 will therefore have a $d_{3,2}$ dependence instead of a $d^2_{3,2}$ dependence. The reaction rate (=inverse chemical timescale) with $d_{3,2}$ dependence will there be proportional to the total surface area of all particles in the dust cloud as shown by equation 18.

$$\tau_c^{-1} = A_{dust} \frac{C_{dust}}{d_{3,2}+d_x} e^{-T_A/T_P} \qquad Eq\ 16$$

Castellanos et al. (2014) reports p_{max} and $(dp/dt)_{max}$ values for 7 different particle size distributions for a range of dust concentrations for aluminum in a 36 liter vessel. These data show the same trends, that $(dp/dt)_{max}$ decrease with particle diameter, as shown in Figure 3.

Skavland (2018) reports particle size from sieving d_{50}=56µm and $d_{3,2}$=46µm and maximum explosion pressure around 10 barg in both 20- and 200-liter vessels. Castellanos et al (2014) got 10 barg for $d_{3,2}$=d_{50}= 5µm from Mastersizer 3000 analyzer. Most likely the particle of Skavland has similar size, but since aluminum particles often are flat with very small size in on direction, measurements by sieving can typically give 10 times larger $d_{3,2}$ since spherical particles is assumed.

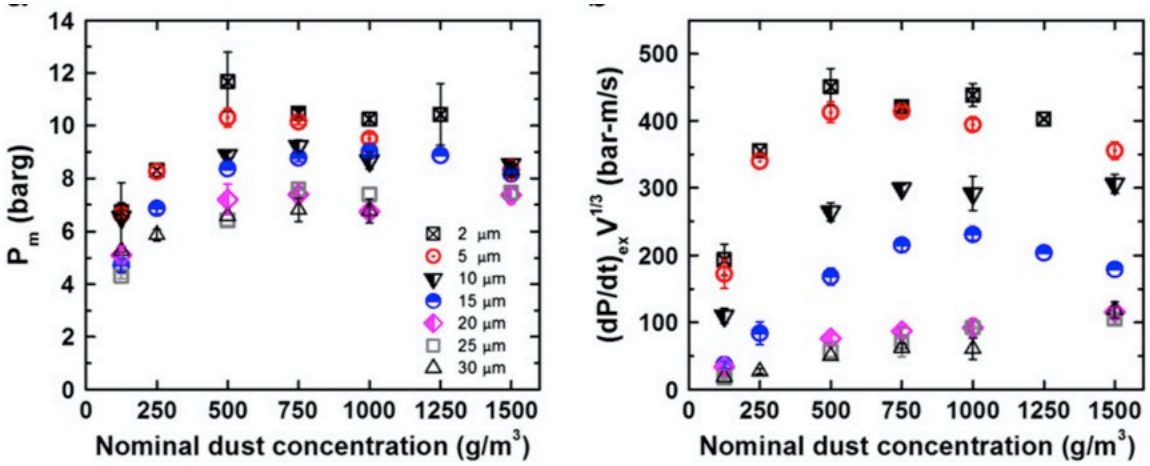

Fig. 3. Experimental results from aluminum dust with 7 different d_{50}. From Castelleano (2014)

.

3 Estimation of fraction burned *(λ)* and product temperature *(T_P)*

Fraction dust burned, λ, as function of dust concentration is needed by DustEx to perform calculations. It is calculated with basis in p_m , the ideal gas law and an Enthalpy balance as shown in Figure 19

$$h_{products} = h_{reactant} + -Q_{walls} + Q_{ignator} + p_m V \qquad Eq\ 17$$

The two last terms, heat loss to the walls and energy from ignition is negligible for the 1m^3 bomb and are adjusted for by equation 4 for 20 litre experiments. In the calculations we also assume that the volume of the dust is negligible compared to air since it is not likely to occupy more than 0.1% of the volume.

Estimation of of fraction burned, **λ,** and product temperature, T_P, have up to now been done by adjusting the fraction burned for each dust concentration with experimental p_{max} values so the enthalpy released from combustion is equal to the enthalpy needed to heat all products up to the product temperature T_P. Unburned dust is assumed not to be in gas phase but have temperature T_P. To have the product temperature is likely if the particles are small, but if they are big their temperature are more likely lower. Unburnt organic dusts may not be in gas phase, but e.g. metal dusts can obtain much higher temperatures and may be in gas phase.

The ideal gas low must also hold.

$$p_m = p_0\left(\frac{T_P}{T_0}\frac{n_{N2p}+n_{O2p}+n_{CO2}+n_{CO}+n_{H2}}{n_{N2}+n_{O2}} - 1\right) \qquad Eq\ 18$$

This model has sometimes problem finding a value for λ, typical if the heat of formation for dust are wrong. If the particles are large the heat/enthalpy loss to unburned particles will be lower than estimated, since they may have a lower temperature than T_P. If the particles are small the enthalpy loss may be higher than estimated since the unburned particles may melt and evaporate.

Figure 4 shows the burnable fuel fraction, λ, as function of dust concentration typically used in DustEx. The figure shows that λ has a maximum value of 0.7 for concentration 125g/m^3 and drops to o for concentration 65 g/m^3. This must be corrected so a decrease in dust concentration always lead to a value of λ which newer decrease. As it is now, if burned dust with concentration 125g/m^3 mixes with an equal volume with air, the concentration falls to 62g/m^3. Then all burned fuel will be converted to reactants again (since λ =0) and strange unphysical simulation results will occur.

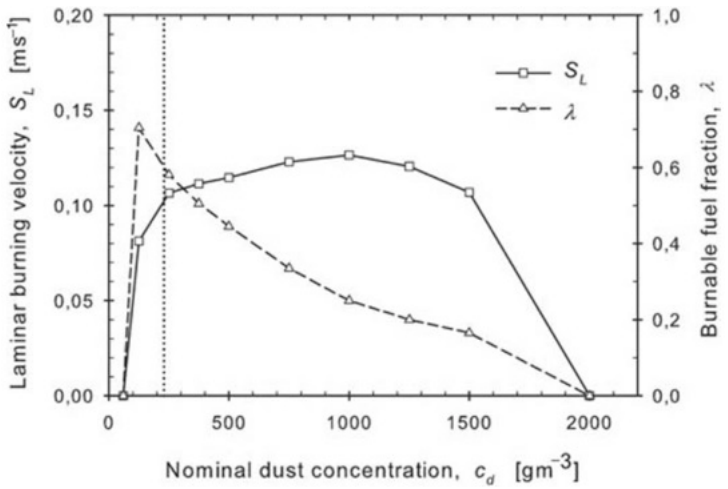

Fig. 4. *Laminar burning velocity and fraction burnable fuel to be used in DustEx. From Skjold et al. (2005)*

In the new approach it is assumed that all oxygen is consumed if it is enough burnable dust to do so and the distance between the dust particles (which is a function of $d_{3.2}^3/C_{dust}$) is small enough, Else there will be some oxygen left (typically for low dust concentrations and large particles) The value of burned dust, λ, is then known. The enthalpy released will then only depend on T_P and the enthalpy of formation for the h_{dust} which may need adjustment to give a correct p_{max}.

The heat loss to unburned reactant will be $h_{unburned} = \gamma C_{p,dust}(T_P-T_0)$ where γ=1 if the hole particle get the product temperature, else γ<1. γ can be used as an adjustment factor to get reasonable good p_{max} values for all dust concentrations.

The enthalpy in FLACS DustEx is given as a second order polynomial relationship, $h=aT+0.5bT^2-d$. At temperatures around 2000K the enthalpy can be represented by $h\approx a^*T-d$. Table 1 gives the values of a,b,d and a^* used in FLACS DustEx for the gases in the products where enthalpy is in J/mole.

A product temperature is found by solution of the second order equation. The temperature is used in the ideal gas law to find p_m. h_{dust} and x are adjusted so p_{max} fits well with experimental values.

Table 1*. Constants for the enthalpy formula for the gases in the products*

	h_{f298} [kJ/mole]	a	$b\ 10^3$	$d\ 10^{-3}$	a^* (=C_p)	M [g/mole]
N_2	0	29.0	3.304	8.68	34	28
O_2	0	30.4	3.584	9.28	38	32
CO	-110.628	29.4	3.22	119.56	36	28
CO_2	-394.108	46.64	6.908	408.32	60	44
H_2O	-241.74	32.04	9.27	252	50	18
$C_6H_{10}O_5$ products	-3432	431.4	86.0	3565.54	598	346

For the 1 m^3 sphere the following assumptions can be assumed. The number of mole air is given by

$$n_{air} = \frac{PV}{RT} = \frac{1E5\ \ 1}{8.3145\ \ 298} = 40.36\ mole \quad Eq\ 19$$

- The number of moles oxygen is: $n_{O2} = 0.2095 n_{air} = 8.455\ mole$
- The number of moles inert gas, nitrogen and argon: $n_{N2} = n_{air} - n_{O2} = 31.905\ mole$
- The number of moles dust (with V=1m^3) is $n_{dust} = C_{dust}V/M_{dust} = C_{dust}/M_{dust}$
- The number of moles product n_{prod} in gas phase will depend on the chemical composition of the dust and the fraction λ of the dust which have burned, $n_{burnt} = \lambda\ n_{dust}$

The ideal gas law gives the relation between pressures, temperatures and number of moles in the gas fraction before and after combustion

$$\frac{p_0+p_m}{p_0} = \frac{T_P}{T_0}\frac{n_P}{n_R} \quad Eq\ 20$$

For aluminium (Al) the product Al_2O_3 will be liquid (eventually solid) since the enthalpy of formation of the gas phase at the boiling temperature is positive (more energy is needed than is released in the combustion process) T_P can therefore not be higher than the boiling temperature which is 3250K at atmospheric pressure and some hundred degrees higher at 10 barg. According to Cashdollar and Zlochower (2007) the boiling temperature is 4060K at the maximal theoretical pressure ratio p_{max}/p_0=12.4. To obtain above 11 barg as shown in Figure 3, some of the unburned Al must be in gas phase when the temperature is is above the boiling temperature of Al (around 2467K) to satisfy the ideal gas law (equation 20).

Cashdollar and Zlochower (2007) gives a lot of useful information for a range of metals which will be needed in FLACS DustEx to implement these metals as reactants in the code. The chemical formula is needed for all metal oxides, as well as melting- and boiling temperatures as function of pressure and enthalpy as function of temperature for all actual phases for both the metals and their oxides. This is needed to give a good estimate on both product temperatures (T_P) and number of moles in the products, to give accurate explosion pressures. T_P will also be needs in to calculate burning velocities based on the chemical time scale as shown in equation 16.

To do simulation of e.g. corn starch dust explosion the chemical reaction balance must be set up to find the mole ratio, oxygen consumption and products from the reaction:

$C_6H_{10}O_5 + 5.75O_2 \rightarrow 5.5CO_2 + 0.5CO + 5H_2O$

The mole ratio between products and reactants in the gas phase for corn starch needed in equation 20 is: n_P/n_R=(5.5+0.5+5)/5.75/3.774+0.79056=1.113 In dustEx it is assumed that unburned dust are not in the gas phase.

The enthalpy balance gives

$$n_{burned}(h_{burned} - h_{dust}) + \gamma C_p(T_P - T_0)n_{unburnt} + n_{N2}h_{N2} = p_m 10^5 V \quad Eq\ 21$$

where enthalpies can be found from table 1.

Conclusions

Using a Arrhenius reaction based formulation based on the product temperature has several advantages. First, no need to to find coefficients for the turbulent or laminar burning velocity dependency with pressure and reactant temperature. Second, the impact of particle size distribution and dust concentration on the burning rate is included by making the reaction rate a function of the total surface area of all particles. The formulation make is possible to do DustEx explosion calculations if only the K_{st} value is known. In the earlier model $(dp/dt)_{max}$ values must be known for a range of dust concentrations to be able to perform the dust explosion simulations.

References

Arntzen, B.J.,1998 Modelling of turbulence and combustion for simulation of gas explosions in complex geometries. Dr. Ing. Thesis, NTNU, Trondheim.

Arntzen, B.J., Salvesen, H.C., Nordhaug, H.F., Storvik, I.E. and Hansen, O.R., 2003, CFD modelling of oil mist and dust explosion experiments, Proc 4th Int Seminar on Fire and Explosion

Hazards, September 8–12, 2003, Londonderry, Northern Ireland, UK, 601–608.

Bardon, M.F., Fletcher, D.E. 1983, Dust explosions, Sci. Prog Oxf 68, 459-473

Cashdollar, K.L, Zlochower, I.A., 2007, Explosion temperatures and pressures of metals and other elemental dust clouds, Journal of Loss Prevention in the Process Industrues 20 . 337-348

Eckhoff, R, 2003, Dust explosions in the process industries: identification, assessment and control of dust hazards. Elsevier,

Ogle, Russell A. 2016, Dust Explosion Dynamics. Amsterdam: Elsevier Butterworth-Heinemann. ISBN 9780128038291.

Reding, N. 2021. *Metal Dust Combustion Dynamics & Novel Concepts of Explosion Protection Application* (Doctoral dissertation). University of Kansas.

Skavland, Camilla, 2018, Pressure Development in Dust Explosions, Master thesis at University of Bergen

Skjold, T., B. J. Arntzen, O. R. Hansen, O. J. Taraldset, I. E. Storvik, and R. K. Eckhoff. 2005. Simulating Dust Explosions with the First Version of DESC. Process Safety and Environmental Protection 83 (B2): 151–160. doi:10.1205/psep.04237.

Skjold, Trygve. 2007. "Review of the DESC Project." Journal of Loss Prevention in the Process Industries 20 (4): 291–302.

van Wingerden, Kees, 2019, Application of laboratory-scale determined Kst-values of metal dust to industrial scale processes," Chemical Engineering Transactions, vol. 77, pp. 679–684

Østgård, 2022 "En eksperimentell studie av partikkelstørrelsesfordelingens innvirkning på utvalgte eksplosjonsparametere for silisiumstøv," Master thesis, University of Bergen

Direct determination of turbulent burning velocity during aluminum flame propagation: comparison to the classical open-tube method

Clément Chanut [a], Farès Saad Al Hadidi [a] , Frédéric Heymes [a] & Ernesto Salzano [b]

[a] Laboratoire des Sciences des Risques (LSR), IMT Mines Alès, Alès, France
[b] Dipartimento di Ingegneria Civile, Chimica, Ambientale e dei Materiali, Università di Bologna, Bologna, Italy

E-mail: *ernesto.salzano@unibo.it*

Abstract

Burning velocity is a key parameter of main flame propagation models. However, its experimental determination while studying propagating dust flame is still challenging. In this work, aluminum flame propagation in a vertical tube is studied. Two aluminum powders with different particle size distributions with a median diameter of 6.2 and 20.7 µm are analyzed for different equivalence ratios with air. The main objective of this work is to compare the methods commonly used in the literature to determine the burning velocity in the case of propagating flames. One of these methods is based on the estimation of the thermal expansion coefficient. This article focuses first on the estimation of this coefficient and presents the limits of considering the adiabatic flame temperature for its estimation; this coefficient is here deduced from preliminary experiments presented in this article. As detailed in the paper, these methods have some limitations and are therefore compared with an innovative method based on a local direct determination of the burning velocity. This local method is based on the measurement of the unburned flow velocity just ahead of the propagating flame front by Time-Resolved Particle Image Velocimetry (TR-PIV). The methods commonly used in the literature mainly underestimate the burning velocity when compared with the local method. The local method is then used to study the influence of the particle size distribution and the equivalence ratio on the turbulent burning velocity. Firstly, we observe that the turbulent burning velocity increases while the flame is propagating in the vertical tube. Furthermore, the turbulent burning velocity with the 6-µm powder is higher than with the 20-µm powder.

Keywords: *dust explosion, burning velocity, Particle Image Velocimetry, aluminum combustion, flame propagation*

Introduction

Metal combustion, especially aluminum dust combustion, is widely studied as it is involved in different scientific fields (process safety, aerospace propulsion, defense). Fundamental understanding of dust combustion is therefore required to prevent accidental explosions and improve the performance of propulsion systems (Han et al., 2017). However, modeling metal dust flame propagation is still challenging due to the complex processes governing this multi-phase combustion and the inherent difficulties in performing experiments on dust flame propagation (Goroshin et al., 2022). Modeling flame propagation is mandatory to predict the consequences of accidental explosions. One key parameter of these flame propagation models is the burning velocity, i.e. the consumption rate of the reactants by the flame front. Besides, modeling the flame propagation requires modeling the combustion dynamics but also the induced flow and turbulence. Thus, the evolution of the turbulent burning velocity while the flame is propagating has to be determined.

Experimental determination of this turbulent burning velocity is challenging, particularly for metallic flames. A first setup commonly used to estimate the burning velocity is the burner. In this case, the burning velocity is deduced from the visualization of the shape of the stationary flame (Goroshin et al., 1996; Julien et al., 2017). A confined explosion sphere can also be used to obtain the burning velocity in case of propagating flames. The burning velocity is deduced from pressure data (Dahoe and de Goey, 2003); as highlighted by Faghih and Chen (2016), the estimation of the burning velocity from the evolution of the pressure is based on some assumptions. Furthermore, the flame propagation process inside the explosion sphere is difficult to observe and study.

To develop and validate flame propagation models, the propagation of flames inside tubes can be studied. Andrews and Bradley (1972) proposed a method for estimating the burning velocity while studying propagating flames inside tubes, called the "tube method" in this article. This method is based on the visualization of the flame propagation, the estimation of the flame surface area and the measurement of the mean unburned flow velocity averaged over the tube cross-sectional area. Other authors adapted this method to estimate the burning velocity without measuring the unburned flow velocity (Di Benedetto et al., 2011; Khalili, 2012). This method is based on the estimation of the thermal expansion coefficient; this coefficient is defined as the ratio between the unburned mixture density and the burned mixture density. This method is called the "thermal expansion method" in this paper. The estimation of the thermal expansion coefficient is an important point, detailed in this paper. For both methods, the accurate estimation of the 3D flame surface area is tricky and can lead to errors up to 20 % (Andrews and Bradley, 1972). An innovative direct local method has been proposed in a previous paper (Chanut et al., 2022), called the "direct method" in this article. This method is based on the measurement of the unburned flow velocity just ahead of the propagating flame front by Time-Resolved Particle Image Velocimetry (TR-PIV). This method consists of a local estimation of the burning velocity at the top of the flame front, whereas the two other methods are global estimations of the burning velocity assuming a constant burning velocity over the tube cross-sectional area.

In this article, aluminum flame propagation in a vertical tube is studied. Two aluminum powders with different particle size distributions with a median diameter of 6.2 and 20.7 µm are analyzed for different equivalence ratios with air. This article focuses first on the estimation of the thermal expansion coefficient. Results from preliminary experiments are presented to estimate this coefficient; these results are compared with previous estimations proposed in the literature. Then, the turbulent burning velocity is obtained by using the three methods: "tube method", "thermal expansion method" and "direct method". Finally, the results obtained with the direct method are detailed and discussed to investigate the influences of particle size distribution and equivalence ratio.

1. Experiments

1.1. Experimental setup

The setup is a square-cross section vertical tube divided into three different sections of 700 mm height and 155 x 155 mm cross-section (**Fig. 1**). The walls are made of glass to allow the visualization of the flame propagation process. During the experiments, dust is injected in the two lower sections by discharge of pressurized vessels connected to four injection tubes located in the corners of the section. Special attention has been paid to the design of the injection tubes to obtain a homogeneous cloud, especially along the vertical axis (axis of flame propagation). Details about the design of the injection tubes and the method for characterizing the initial dust cloud can be found in (Chanut et al., 2020).

Dust concentration is determined by weighting the dust inside the injection tubes before and after each experiment. Dust is ignited by an electrical spark between two tungsten electrodes located inside the lower section of the prototype. After ignition, the flame propagates upward from the closed bottom end to the open upper end of the prototype. More details on the setup can be found in (Chanut et al., 2022).

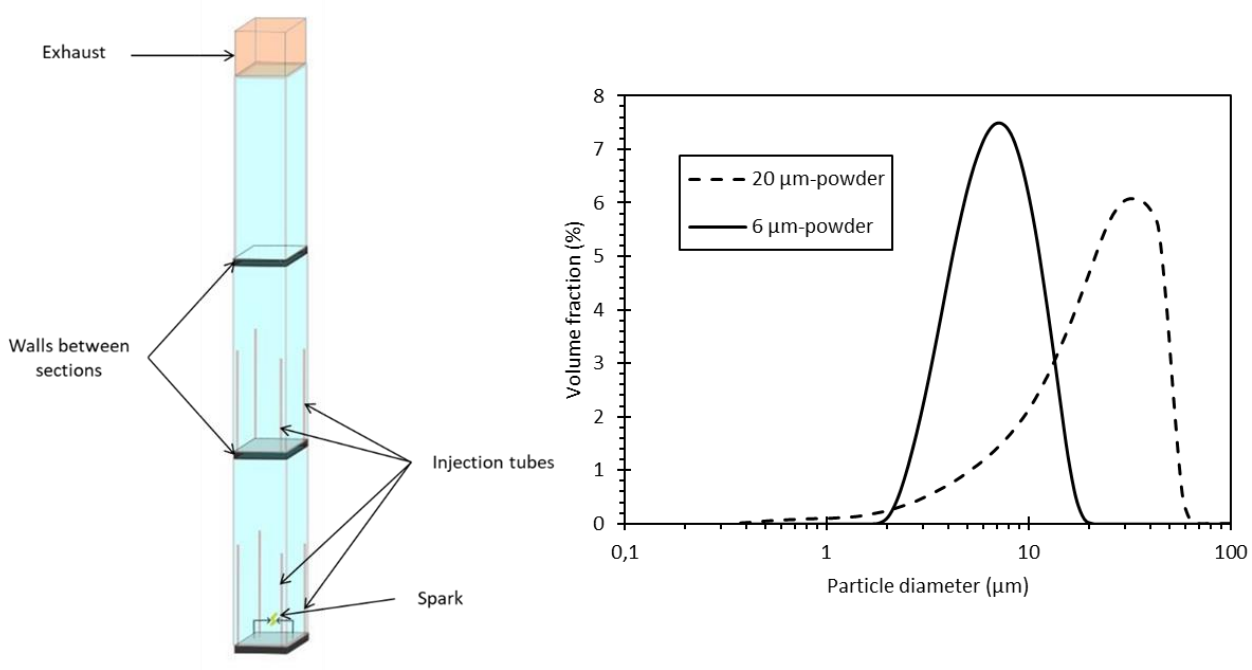

Fig. 1. *Experimental setup and particle size distributions of the powders*

In these experiments, two powders of aluminum are studied. **Fig. 1** shows the particle size distributions of the two powders. The median diameters of each powder are 20.7 µm and 6.2 µm; characteristic diameters describing these particle size distributions are detailed in Table 1. In the following, the two powders are called "20-µm powder" and "6-µm powder" respectively.

For each particle size distribution, three dust concentrations are studied. They are defined in terms of equivalence ratio, which corresponds to the ratio of the actual dust concentration and the stoichiometric concentration. The value of the stoichiometric concentration is here estimated to be about 310 $g.m^{-3}$. For the 20-µm powder, fuel-rich mixtures are studied corresponding to equivalence ratio of 1, 1.2 and 1.4. With fuel-lean mixtures, difficulties for igniting the 20-µm powder mixtures are observed. For the 6-µm powder, fuel-lean mixtures are studied corresponding to equivalence ratio of 0.8, 0.9 and 1. For each experimental configuration (defined by a particle size distribution and an equivalence ratio), two tests are carried out.

Table 1. *Characteristic diameters of the particle size distributions of the powders*

	d_{10}	$d5_0$	d_{90}
6-µm powder	3.2 µm	6.2 µm	10.8 µm
20-µm powder	5.6 µm	20.7 µm	39.8 µm

1.2. Optical setup

Two optical techniques are implemented to analyze the flame propagation process: the direct visualization technique and the PIV (Particle Image Velocimetry) technique. The direct visualization technique records the light emitted by the flame front by using a high-speed camera. The PIV measures the velocity of the flow field, seeded with the aluminum particles, by using a high-speed camera synchronized with a laser. Direct visualization technique is widely used to visualize the propagating flame. However, the flow field ahead of the flame front is rarely studied in experimental works, especially in front of dust flames, because of the difficulty to implement this technique. Nevertheless, a TR-PIV (Time-Resolved PIV) setup has been successfully implemented to study the unburned flow just ahead of the luminous flame front.

A first high-speed camera (Photron SA3) records the flame propagation process by direct visualization technique on the two lower sections of the prototype. The resolution of this camera is set at 1024 x 128 pixels with a frequency of 10,000 fps (frames per second). A second high-speed camera (Photron SA5) records the flame propagation process on the third upper section. The resolution of this camera is set at 1024 x 1024 pixels with a frequency of 7,000 fps (frames per second). Using these two cameras the flame front is detected during the propagation along all the height of the prototype.

In addition to this direct visualization technique, two zones of TR-PIV measurement have been implemented. The first zone corresponds to the middle of the second section. For this measurement, a Litron TR-PIV 30-1000 laser (30 mJ at a frequency of 1 k Hz) is synchronized with a Phantom V711 high-speed camera. The second zone corresponds to the top of the prototype. For this measurement, a Litron TR-PIV 15-1000 laser (15 mJ at a frequency of 1 k Hz) is synchronized with a Phantom V2512 high-speed camera. For each PIV measurement, the time between each double image (time between two successive velocity vectors) is 1 ms. The size of each PIV measurement zone is around 15.5 cm x 10 cm. The resolution of the images is 1280 x 800 pixels.

2. Methods: Determination of the burning velocity

The objective is to determine the turbulent burning velocity from these experimental data. Three methods are compared: the “tube method”, the “thermal expansion method” and the “direct method”. These three methods are presented on the next subsections.

2.1. “Tube Method”

In our case of a flame propagating from the open bottom end to the closed top end of a vertical tube, the "tube method" is based on the following expression (Andrews and Bradley, 1972):

$$S_u = \frac{a}{A}.(V_p - U_g)$$

where S_u is the burning velocity, V_p is the flame propagation velocity (i.e. the flame speed in the laboratory referential), U_g is the mean unburned flow velocity averaged over the tube cross-sectional area, a is the tube cross-sectional area, A is the 3D flame surface area. For our experiments, the 3D flame surface area is deduced from the images of flame propagation obtained by direct visualization of the light emitted by the flame front. 2D images are obtained; therefore, the flame shape in the perpendicular plan is approximated with ellipses as explained in details in (Chanut et al., 2020)

U_g is deduced from the PIV data. It is defined as the vertical component of the mean flow velocity averaged over the line located at the top of each PIV zone. This method is implemented only for the experiments with the 20-µm powder. With the 6-µm powder, velocity vectors on all the depth of the PIV zones are not obtained due to the quality of the TR-PIV images. Indeed, the laser light is attenuated while passing through the highly concentrated cloud of aluminum particles; thus, velocity vectors are difficult to deduc by the PIV algorithm in the highly attenuated zones.

2.2. "Thermal expansion method"

The "thermal expansion method" is adapted from the "tube method". For this method, the unburned flow velocity is not measured. This method is based on the following expression (Di Benedetto et al., 2011):

$$S_u = \frac{V_p}{\chi}.\frac{a}{A}$$

where χ is the thermal expansion coefficient defined as:

$$\chi = \frac{\rho_u}{\rho_b}$$

To implement this method the thermal expansion coefficient has to be estimated. Di Benedetto et al. (2011) studied the flame propagation of nicotinic acid dust. They calculated this thermal expansion coefficient as the ratio of the burned mixture temperature to the unburned mixture temperature. However, this equality is not exact for such solid powders devolatilizing before combustion. These authors approximated the burned mixture temperature to the adiabatic flame temperature.

Altman and Pantoya (2024) discussed the estimation of this thermal expansion coefficient for metal particles. They explained that thermal expansion coefficient is overestimated while considering adiabatic flame. Furthermore, the discrete nature of the aluminum dust flame leads to another overestimation of the thermal expansion coefficient in literature. These authors estimated the thermal expansion coefficient from previous experiments conducted by Lomba et al. (2019). They obtained a thermal expansion coefficient of about 5.5 from these experiments, much lower than the value of about 12 obtained while considering an adiabatic flame.

Preliminary experiments were conducted to estimate this thermal expansion coefficient. For this purpose, one section of the prototype has been isolated and slightly modified. With this new experimental setup, upward flame propagations from the open bottom end to the closed top end of the tube were studied. From a mass balance, the following expression is used to determine the thermal expansion coefficient:

$$\chi = \frac{\rho_u}{\rho_b} = \frac{V_p + U_g}{V_p}$$

Here, U_g is the flow velocity of burned mixture exiting the bottom of the prototype and is estimated by performing the PIV algorithm on the combustion products exiting the bottom end of the prototype. This equation is obtained by assuming a constant propagation velocity and unburned flow velocity over the cross-section of the prototype. For these experiments, with the 6-µm powder, a thermal

expansion coefficient of about 5.5 is obtained, in accordance with the value proposed by Altman and Pantoya (2024).

2.3. "Direct method"

The "direct method" is based on the measurements of the propagation velocity and of the unburned flow velocity just ahead of the propagating flame. At the top of the flame front, the vectors are colinear thus the burning velocity is defined as the difference between these two velocities. One main difficulty of this method is the accurate measurement of the unburned flow velocity just ahead of the propagating flame, especially in case of metallic dusts. Here, the TR-PIV technique is used to determine the most probable movement of particles between two images separated by a known time delay. With this technique, velocity vectors on a plane of the flow are obtained. The software Dynamic Studio (Dantec Dynamics) is used to perform the PIV analysis.

Fig. 2. *Examples of raw TR-PIV images with the 20-µm powder (delay between images: 1 ms)*

Fig. 2 shows an example of raw TR-PIV of a propagating flame of the 20-µm powder. A first step of pre-treatment is mandatory to improve the quality of the images before performing the PIV algorithm. Indeed, because of the presence of a dense dust cloud, the laser light is attenuated while passing through the prototype. Moreover, the power of each of the two laser cavities (used to obtain the pair of images analysed by the PIV algorithm) are not exactly equal. For these two reasons, a first pre-treatment step is performed to uniform the grey levels of the images.

An adaptative PIV algorithm is used to modify the size and shape of the interrogation areas depending on the velocity and concentration gradients. The quality of the images obtained with the powder 20 µm is better for performing the PIV algorithm as the laser light is less attenuated by these larger particles present inside the unburned mixture. Thus, input parameters for the PIV algorithm are slightly different for the images corresponding to this powder. For the images corresponding to the powder 20 µm, the distance between two velocity vectors is 0.5 mm while this distance is equal to 1 mm for the powder 6 µm. From these velocity vectors, the burning velocity is deduced; it is defined as the difference between the propagation velocity and the unburned flow velocity just ahead of the flame front.

3. Results and discussion

3.1. Comparison of the different methods

The "tube method" is first compared to the "thermal expansion method" for the experiments with the 20-µm powder (**Fig. 3**). On this figure and on the following figures, the dotted lines correspond to +/- 20 % of variations from the ideal curve $y = x$ (continuous line).

The “thermal expansion method” is applied considering the two values of the thermal expansion coefficient (χ) proposed previously: 12 and 5.5. The value of χ of 5.5 gives results of burning velocity closer to the “tube method”. The value of χ based on the adiabatic flame temperature is thus overestimated leading to an underestimation of the burning velocity. It is thus important to evaluate first this coefficient by studying a stabilized flame on a Bunsen burner, as proposed by Altman and Pantoya (2024), or by studying the upward flame propagation from the open bottom end to the closed top end of a vertical tube, as proposed in this paper.

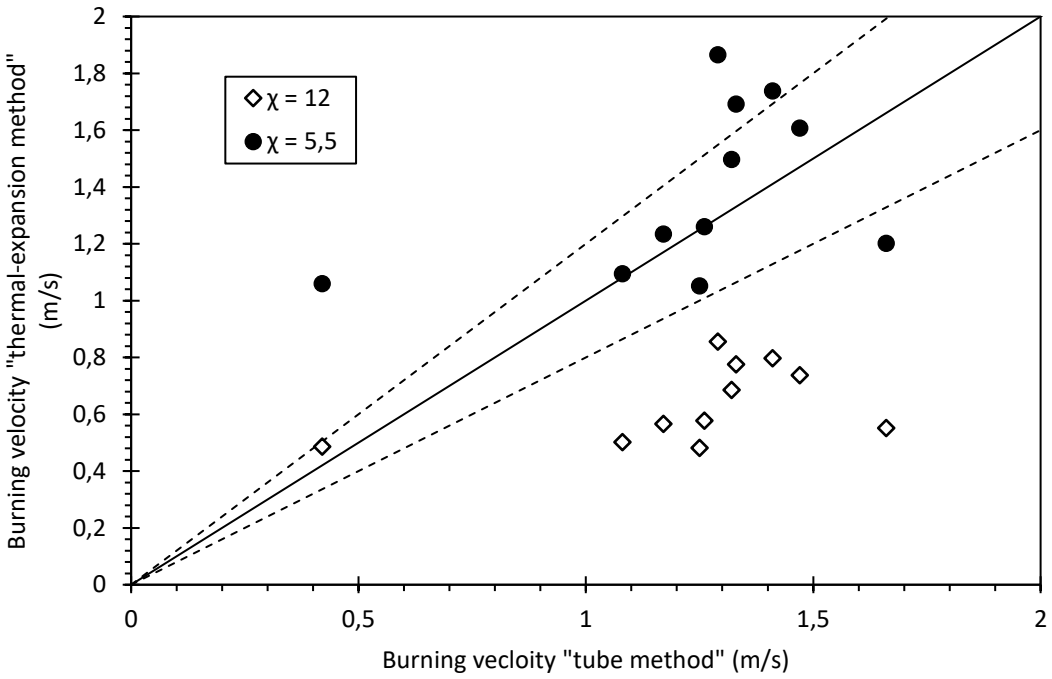

Fig. 3. *Comparison of the burning velocity calculated from the “thermal expansion method” and the “tube method”*

The “thermal expansion method” gives results in accordance with the “tube method”. Measuring the unburned flow velocity can be challenging, therefore the “thermal expansion method” can be preferred. This method is compared to the estimation of the local burning velocity with the “direct method” (**Fig. 4**). These two methods are applied on the experimental data with the two granulometric distributions. Taking the “direct method” as reference, the “thermal-expansion method” mainly underestimates the burning velocity.

With the “thermal expansion method”, a global estimation of the burning velocity over the flame surface is obtained, whereas the “direct method” is a local estimation of the burning velocity at the top of the flame front. The “thermal expansion method” assumes a constant burning velocity over the flame surface area. However, as mentioned by Andrews and Bradley (1972), this burning velocity is reduced close to the walls. Thus, the “thermal expansion method” underestimates the value of the burning velocity at the top of the flame front.

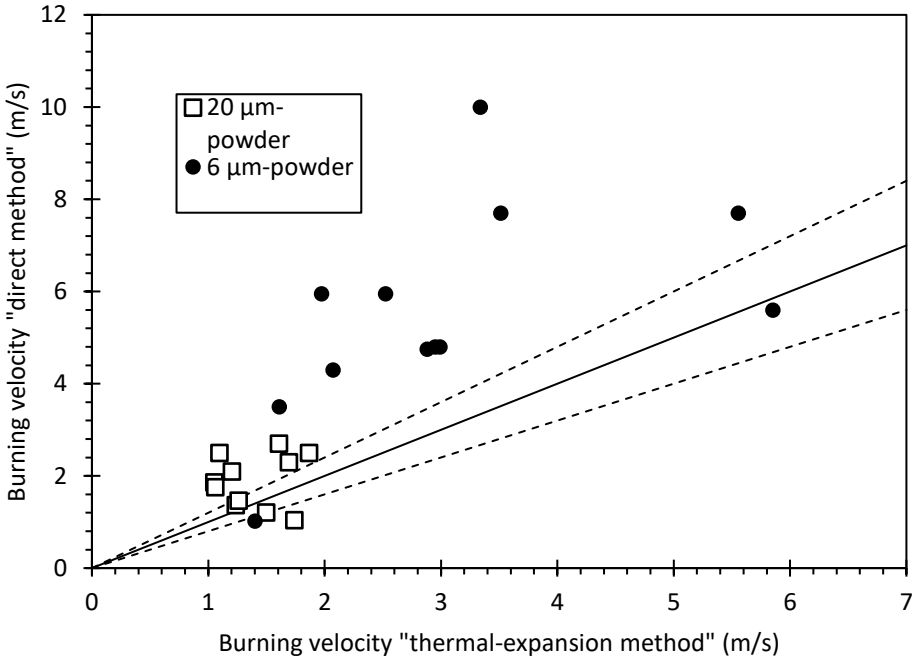

Fig. 4. *Comparison of the burning velocity calculated from the "thermal expansion method" ($\chi = 5.5$) and the "direct method"*

Moreover, the evaluation of the real 3D flame surface area is challenging. **Fig. 5** shows an example of a zoom on the flame front of an image of the propagating flame. It is difficult to define the real "reactive area" of the flame front, i.e. the flame height (H_1 or H_2 or another value). This value is important for estimating the flame front area. If we consider all the flame surface area until the flame reaches the tube walls (H_2), a high value of the flame surface area is obtained resulting in a lower value of the burning velocity.

Due to the difficulties for estimating the flame surface area and the global nature of the burning velocity calculated with the "thermal expansion method", the local "direct method" is preferred for estimating the burning velocity at the top of the flame front.

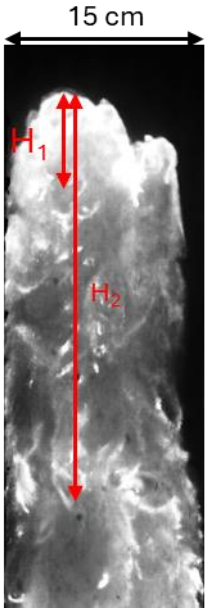

Fig. 5. *Zoom on the flame front of the aluminum propagating flame*

3.2. Analysis of the turbulent burning velocity: "direct method"

The "direct method" is used to determine the burning velocity for the different experimental configurations. First, **Fig. 6** shows the relation between the burning velocity and the propagation velocity for all the experimental configurations and for both PIV measurement zones. The black line represents the best fit of these experimental points with an affine function. An increase of the propagation velocity corresponds to an increase of the burning velocity.

Analysing separately the results of both powders, we can observe that the coefficient of the best fit for each granulometric distribution is slightly different. For the 20-µm powder, the value of the slope is 0.121 while this value is 0.156 for the 6-µm powder. This difference can be due to the difference of granulometric distribution. However, this difference could also be due to the difference of equivalence ratio for both granulometric distribution; indeed, fuel-lean mixtures of the 6-µm powder are studied while fuel-rich mixtures of the 20-µm powders are studied.

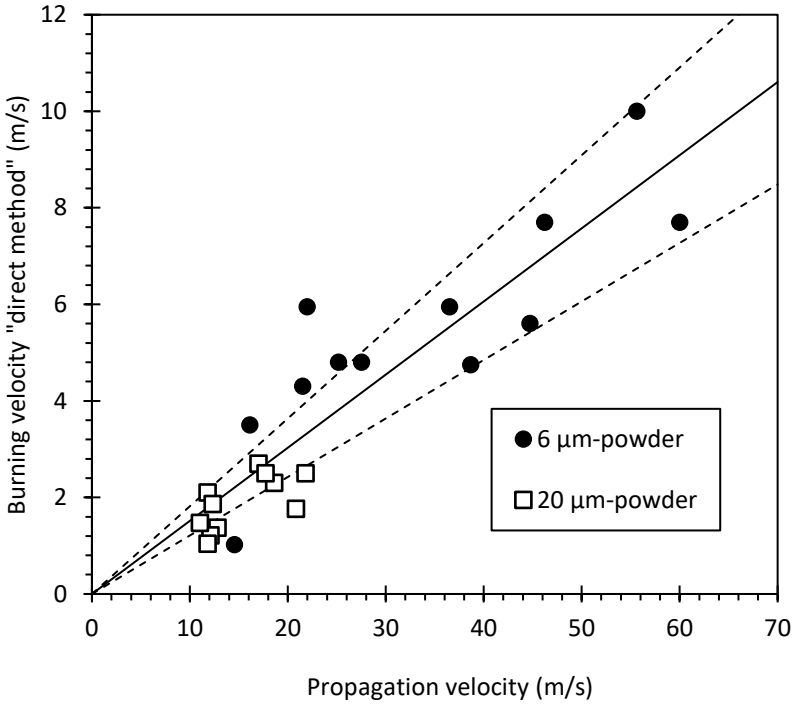

Fig. 6. *Relation between burning velocity and propagation velocity*

Fig. 7 shows the values of the turbulent burning velocity determined with the "direct method" for all the experimental configurations and for both PIV measurement zone. As expected, the burning velocity with the 6-µm powder is higher than with the 20-µm powder. This observation can be explained by an increase of the specific surface area, corresponding to an increase of the reactive surface, with finer particles. This result is in accordance with other results from the literature (Danzi et al., 2021).

Moreover, the values of burning velocity determined while the flame passes on the PIV measurement zone 2 are higher compared to the PIV measurement zone 1. The PIV zone 1 is located at the center of the second section while the PIV zone 2 is located at the top of the third section of the prototype. Thus, the burning velocity increases while the flame propagates inside the vertical tube. This increase could be due to an increase of turbulence due to the induced unburned flow ahead the flame front.

With this TR-PIV setup, measurements of the local turbulence while the flame propagates is possible as already proposed in a previous paper (Chanut et al., 2022).

Analyzing the fuel-lean mixtures of the 6-µm powder, an increase of the burning velocity with the equivalence ratio is observed; this increase can be due to an increase of the quantity ofdust participating to the combustion, increasing the global reactivity of the mixture. On the contrary, a quite constant behavior of the burning velocity with the equivalence ratio is obtained while analysing the fuel-rich mixtures of the 20-µm powder; in this case, additional powder does not increase the global reactivity of the mixture and can absorb some part of the energy of the combustion.

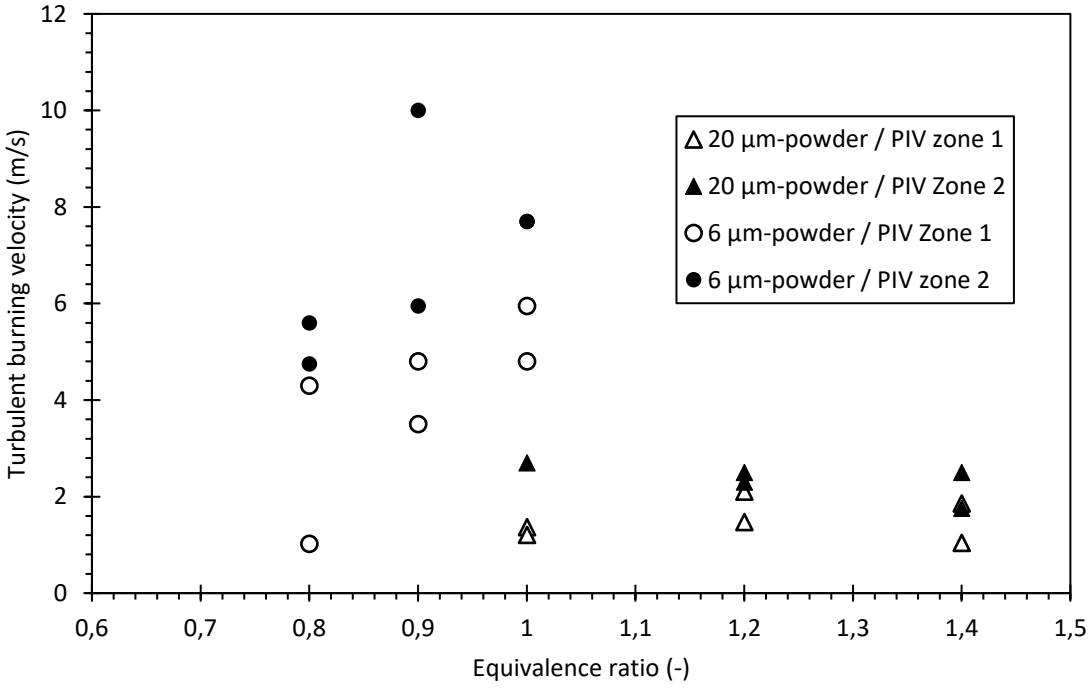

Fig. 7. *Turbulent burning velocity as a function of the equivalence ratio for both granulometric distribution*

4. Conclusions

Aluminum flames propagating in a vertical tube have been studied. The main objective of the present study was to study the turbulent burning velocity of these propagating flames. Indeed, the burning velocity is an important input parameter of numerical models used for predicting the consequences of accidental explosions. For this purpose, a novelly developed method has been implemented to determine this burning velocity: the “direct method”.

Two other methods usually used in the literature have also been implemented: the “global method” and the “thermal expansion method”. One method is based on the thermal expansion coefficient. This paper discusses the determination of this coefficient and its influence on the burning velocity results. An experimental method for estimating this coefficient was proposed; this method is based on the observation of the propagation of the flame in an open tube. The results from this method are equal to the results obtained in the literature while studying stabilized flames. The comparison of the results obtained with the “thermal expansion method” and the “global method” confirms the importance of using the value of the thermal expansion coefficient proposed in this paper. The method generally used in the literature for determining this coefficient is based on the hypothesis of a uniform flame

front with a temperature equal to the adiabatic flame temperature. This method leads to an overestimation of the thermal expansion coefficient and an underestimation of the burning velocity.

The innovative “direct method” is promising to determine the local burning velocity of propagating dust flames. Indeed, the two other methods used in the literature are based on the hypothesis of a constant burning velocity over the flame surface, while this velocity is lower close to the walls (Andrews and Bradley, 1972). Moreover, the 3D flame surface area has to be evaluated to implement these methods. Due to the complex geometry of the flame front and the difficult definition of the burning zones, this estimation is challenging.

The “direct method” is here based on a TR-PIV (Time-Resolved Particle Image Velocimetry) setup. With this setup, the evolution of the local unburned flow velocity and of the local turbulence can be obtained. These values are mandatory for accurately validate future numerical simulations of propagating flames. Moreover, the local turbulence just ahead the flame front can be deduced from these TR-PIV data. Therefore, the relation between turbulence and burning velocity can be determined. This relation is an important input parameter of numerical models of flame propagation.

Acknowledgements

The authors are grateful to IRSN (Institut de Radioprotection et de Sûreté Nucléaire) for scientific and financial support to this project.

References

Altman, I., Pantoya, M.L., 2024. Energy balance and global characteristics of metal dust flames. Combust. Flame 261, 113310. https://doi.org/10.1016/j.combustflame.2024.113310

Andrews, G.E., Bradley, D., 1972. Determination of burning velocities: A critical review. Combust. Flame 18, 133–153. https://doi.org/10.1016/S0010-2180(72)80234-7

Chanut, C., Al Hadidi, F.S., Heymes, F., Lopez, C., 2022. Simultaneous Measurement of Burning Velocity and Turbulence Intensity Ahead of the Flame Front during Aluminium Flame Propagation. Chem. Eng. Trans. 90, 391–396. https://doi.org/10.3303/CET2290066

Chanut, C., Heymes, F., Lauret, P., Essaidi, Z., Slangen, P., 2020. Visualization of aluminum dust flame propagation in a square-section tube: comparison of schlieren, shadowgraphy and direct visualization techniques. J. Vis. 23, 885–894. https://doi.org/10.1007/s12650-020-00676-5

Dahoe, A.E., de Goey, L.P.H., 2003. On the determination of the laminar burning velocity from closed vessel gas explosions. J. Loss Prev. Process Ind. 16, 457–478. https://doi.org/10.1016/S0950-4230(03)00073-1

Danzi, E., Pio, G., Marmo, L., Salzano, E., 2021. The explosion of non-nano iron dust suspension in the 20-l spherical bomb. J. Loss Prev. Process Ind. 71, 104447. https://doi.org/10.1016/j.jlp.2021.104447

Di Benedetto, A., Garcia-Agreda, A., Dufaud, O., Khalili, I., Sanchirico, R., Cuervo, N., Perrin, L., Russo, P., 2011. Flame propagation of dust and gas-air mixtures in a tube 11–13.

Faghih, M., Chen, Z., 2016. The constant-volume propagating spherical flame method for laminar flame speed measurement. Sci. Bull. 61, 1296–1310. https://doi.org/10.1007/s11434-016-1143-6

Goroshin, S., Fomenko, I., Lee, J.H.S., 1996. Burning velocities in fuel-rich aluminum dust clouds. Symp. Combust. 26, 1961–1967. https://doi.org/10.1016/S0082-0784(96)80019-1

Goroshin, S., Pale, J., Bergthorson, J.M., 2022. Some fundamental aspects of laminar flames in nonvolatile solid fuel suspensions. Prog. Energy Combust. Sci. 91. https://doi.org/10.1016/j.pecs.2022.100994

Han, D.H., Shin, J.S., Sung, H.G., 2017. A detailed flame structure and burning velocity analysis of aluminum dust cloud combustion using the Eulerian-Lagrangian method. Proc. Combust. Inst. 36, 2299–2307. https://doi.org/10.1016/j.proci.2016.06.189

Julien, P., Whiteley, S., Soo, M., Goroshin, S., Frost, D.L., Bergthorson, J.M., 2017. Flame speed measurements in aluminum suspensions using a counterflow burner. Proc. Combust. Inst. 36, 2291–2298. https://doi.org/10.1016/j.proci.2016.06.150

Khalili, I., 2012. Sensibilité, sévérité et spécificités des explosions de mélanges hybrides gaz/vapeurs/poussières.

Lomba, R., Laboureur, P., Dumand, C., Chauveau, C., Halter, F., 2019. Determination of aluminum-air burning velocities using PIV and Laser sheet tomography. Proc. Combust. Inst. 37, 3143–3150. https://doi.org/10.1016/j.proci.2018.07.013

Study of the behaviour of walls and doors of 20 ft ISO containers through real-scale explosion tests

Guillaume Lecocq[a], Seyth Amouzou[a], Emmanuel Leprette[a], Benjamin Le Roux[a], Stéphane Charrondière[a] & Laurent Mathieu[a]

[a] INERIS, Verneuil-en-Halatte, France

E-mail: guillaume.lecocq@ineris.fr

Abstract

ISO containers are increasingly used to house processes involving a potential explosion risk such as Battery Energy Storage Systems or hydrogen-based systems. For both examples, explosions may be powerful because of the potentially large obstruction in the container promoting flame acceleration and/or the high dynamics of the hydrogen flames.

An important part of the modelling strategy for predicting residual pressure effects of an explosion in an ISO container is the knowledge of the mechanical behaviour of the structure initially confining the flammable cloud.

In order to improve knowledge regarding the mechanical behaviour of the container and get a database suitable for validation purposes of the modelling tool, hydrogen explosions tests in 20-foot ISO containers were performed at INERIS testing facilities. The goal was to generate distinctive pressure signals and to collect comprehensive measurements related to the mechanical behaviour of the doors and walls.

The paper details the experimental set-up, the metrology dedicated to mechanical measurements and the main results. First conclusions of the experimental campaign are also supplied.

Thus, the comparative analyses of dynamic explosion load tests (20%, 22%) highlight the significant differences in the intensity of the stress imposed on the structure of the container. The 20% test presents less severe conditions with reduced deformations and recorded stresses compared to the 22% test. These results underline the importance of considering the variable nature of dynamic loads when evaluating container resistance and offer valuable insights for improving the design of protective barriers (like explosion vent panels for example) in similar conditions.

Keywords: *container, explosion, hydrogen, walls, doors*

Introduction

ISO containers are used to house processes or parts thereof which may accidentally produce flammable gases in quantities sufficient to fill the entire free volume or a large part of it with a flammable cloud. Indeed, Batteries arranged as racks can be placed in ISO containers. In the case of thermal runaway, a flammable mixture of gases can be released at one or several battery vents and mixed with air. If the obtained flammable mixture is ignited, a flame will propagate in a medium obstructed by the racks. Electrolyzers or hydrogen compressors can also be placed in ISO containers. Such systems could undergo high pressure hydrogen leaks. The potential flame would propagate in a medium occupied with reservoirs and complex pipework. For battery and hydrogen applications, the explosion may be violent because of obstruction, obstacles, and the initial turbulence of the flammable cloud before ignition. An important parameter limiting the internal pressure of a confined explosion is the mechanical resistance of the confinement walls. They are basically the double door

and the container walls, and sometimes an additional access door, ventilation grid and explosion vent panels.

A previous experimental work was dedicated to the study of the response of metal plates to pressure signals generated by deflagrations (Pini et al., 2019) in an about 1 m^3 enclosure. The maximum displacement, measured with a Laser, was then compared to the peak pressure.

Explosions tests were in ISO containers also documented by Sommersel et al. (2017), Skjold et al. (2019) and Hao et al. (2021). Sommersel et al. carried out 39 tests in total in 2005 in a 20-foot container. The flammable mixture was made with the injection of hydrogen. The door was open. For the 37 first tests, the container was empty. The peak pressure was then limited to a few dozens of mbar. For the two last tests, euro pallets were placed in the container to promote flame acceleration. The strongest explosion was characterized by an unmeasured pressure peak but estimated at around 1 bar. The welded seams along a wall and the roof were ruptured. Skjold et al. report results of more than 60 explosion tests. They were carried out during the HySea project that aimed at gaining knowledge on vented deflagrations in containers and enclosures for hydrogen energy applications. The parameters of the campaign include notably: the position of the double door before ignition, the ignition source location, the value of the mean hydrogen mole fraction in the flammable mixture, the vent surface area … Concerning measurements, the focus was put of the pressure field characterization with the use of eight pressure sensors. The structural response of the container was obtained with two Lasers for measuring the displacement of the points at the centre of the large walls. A more recent work was proposed by Hao et al. with 48 explosion tests in a 40-foot container. This specific container with substantial horizontal and vertical stiffeners was designed for the hydrogen explosion venting experiments. A series of experiments including roof vented and end-vented explosions were conducted to investigate the effects of the hydrogen concentration, ignition position, and obstacles on the structural dynamic responses. Pressure probes, eddy current displacement sensors and piezoelectric acceleration sensors were used. Nevertheless, the maximum internal pressure was limited to a few dozens of mbar.

The current paper presents the first results of an experimental campaign designed to produce a validation database for a finite element modelling tool for predicting the global response of a 20-foot ISO container to an internal explosion.

Second-hand 20-foot ISO containers were used in the campaign. The pressure signals were generated, as in the previous works, with the internal explosion of hydrogen-air mixtures. The pressure fields inside and outside the container were measured.

The tests presented were extensively instrumented concerning the deformation of a sidewall and the doors with a Laser, accelerometers, strain gauges and several high-speed cameras. The large instrumentation of the door is particularly original compared to the explosion tests in the literature.

The experimental set-up, metrology and main results concerning the generated pressure fields and container deformations are detailed in what follows.

1. Strategy, experimental set-up, and tests carried-out

Three second-hand 20 ft ISO containers were bought for the tests. Fig. 1 shows one of them. Zones with plastic deformation are visible on the large wall, probably due to shocks received during the life of the container. Each door is closed with two turning bars (Fig. 1). When the bars are rotated, their lower and upper extremities are locked or unlocked to the container hooking system.

Fig. 1. *Left: general view of the container N°1. Right: detailed view of the upper part of the closing system of the doors.*

The experimental campaign aims to study in detail the temporal response of container walls and doors to pressure signals.

Explosion computations are performed with the open-source CFD code OpenFoam (Weller et al., 1998) to determine conditions leading to this maximum overpressure, assuming that the double door remained closed during the explosion. A peak of 800 mbar was calculated with an ignition point close to the ground center, a 1 m² opening located at the center of the roof, and a hydrogen-air mixture at rest with a hydrogen mole fraction of 22 %.

A preliminary explosion test (Test 1) with a targeted hydrogen volume fraction of 14 % was performed in Container 1. Test 3 is then performed in Container 1 with a hydrogen mole fraction of 20 %. Test 4 is performed in Container 2 with a hydrogen mole fraction of 22 %.

To prepare the chosen flammable mixture in the container, a 50 L bottle of high-pressure hydrogen is discharged in the container through two nozzles, directed towards the ground, 50 cm away from this latter. The nozzles diameter is 2 mm. The bottle pressure is adjusted to inject the required amount of hydrogen. The mixture homogeneity and the hydrogen content are checked with a Servomex oxygen analyser and three probes positioned across the container.

The 1m² square hole in the container roof is closed with a plastic sheet held in place with four sand-filled plastic tubes. The weight of each tube is about 5 kg (Fig. 2).

Fig. 2. *Inner and outer views of the vent on the container roof.*

The ignition device is a 60 J pyrotechnic match located 50 cm below the roof opening. This location was chosen to limit explosion effects outside the container.

Two columns, each made up of four 1 t concrete blocks, are placed just behind the wall opposite of the double door to limit the movement of the container when this latter opens. Six braided steel cables

were used to wrap the side walls and the roof of the container and retain the doors (Figure 1). This setup prevents the projection of wall elements or doors. The cables are sufficiently loose to permit free deformation of the walls.

Six piezoresistive Kistler pressures sensors are used (Fig. 3). Three of them are placed inside the container, on the symmetry plane of this latter. One probe is located near the doors, 1 m above the ground, two probes next to the wall opposite the doors, one on the ground, the other 1 m above. A probe is located 1.5 m above the roof vent. Two probes are placed 1 m above the ground in front the container doors: 2 m and 5 m away for Container 1 and 5 m and 7.8 m away for Container 2.

a)  b) 

c) 

Fig. 3. *a) Global view of the pressure probes inside the container. b) Detailed view of the two pressure probes close to the wall opposite to the door. c) View of the three external pressure probes.*

Four accelerometers have been strategically placed on a large wall, a door, and its hooking system to measure local stresses. In addition, around twenty Kyowa strain gauges are distributed across the same components. An Optimess MLC Laser is also employed to measure the distance between its emission point and the middle of the sidewall. The locations of some of the measurement points are shown in Figure 4.

Between 2 and 4 high-speed cameras were used for each test. They framed a sidewall and parts of the double door. 3 high-definition cameras also filmed the experiment, two on the ground oriented on each side of the container and the last one was mounted on a flying drone.

Fig. 4. *Locations of some strain gauges (green), accelerometers (yellow) and the point aimed by the Laser (red) on the lateral wall and the door.*

2. Results obtained with container N°1

2.1 Test 1: preliminary test with a hydrogen volume fraction of 14 %

Test 1 is performed with an ignition device located 50 cm below the vent. The pressures measured in the container and in front of the roof vent are shown in Figure 5. A first peak at 1 mbar can be seen. It corresponds to early venting of the burned gases. It is followed by a pressure rise and a plateau whose mean value is about 20 mbar. The end of the explosion leads to a pressure peak of 100 mbar (after filtering the raw signal). The pressure peak at the vent is negligible. A peak displacement about 70 mm is measured by the laser in the middle of the sidewall, with the residual displacement being approximately of 10 mm. Additionally, the container roof appears slightly deformed, and the double door was kept closed.

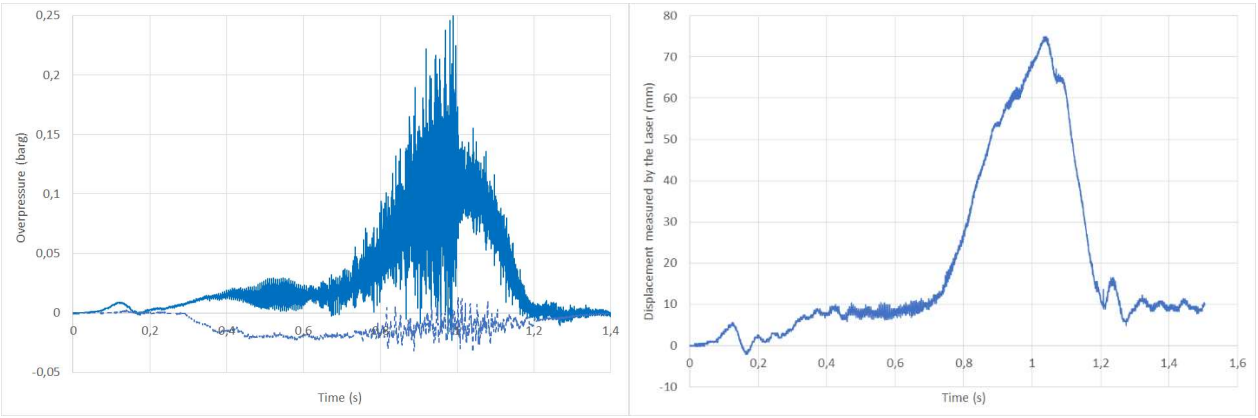

Fig. 5. *Left: internal pressure (line) and pressure in front of the vent (dash-line) for Test 1. Right: displacement measured by the Laser for Test 1.*

2.2 Test 3: nominal test with a hydrogen volume fraction of 20 %

The Container 1 is reused for the nominal test with a hydrogen volume fraction of 20 %.

The internal pressure signal in Figure 6 shows a first pressure peak, about 70 mbar (t~70 ms) related to a venting at the roof. At the vent, the pressure remains moderate (Δp~26 mbar). Then the internal pressure keeps on increasing until a peak about 500 mbar (t~180 ms) is reached. A gap starts to appear between the two doors at t~160 ms (Δp~400 mbar). The internal upper hooking point of the right door is sufficiently deformed and does not hold in place anymore at t~170 ms. At this instant, the

overpressure is about 475 mbar and the pressure impulse about 21 bar.ms. The other upper hooking point of the right door is no more held at t~175 ms (Δp~510 mbar). The other door is fully unlocked in the upper part between t~178 ms and t~182 ms (Δp~535 mbar). The lower part of the double door is free at t~200 ms. A 90° opening angle is observed for the left door at t=228 ms and at t~218 ms for the other one. The external explosion at the door leads to pressure peaks about 450 mbar and 270 mbar 2 m and 5 m from this latter.

The Figure 7 shows some key instants of the explosion sequence. The overall deformation of the container during the pressure rise can be seen. When the door opened, the container moved 30 cm away from the two concrete columns.

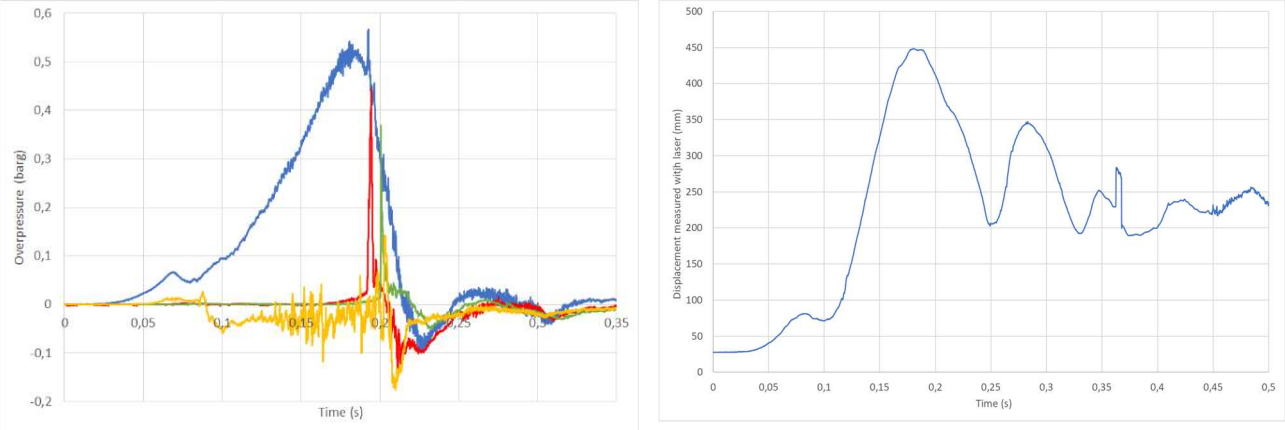

Fig. 6. *Left: pressure signal inside the container (blue), 1.5 m from the vent at the roof (orange), 2 m (red) and 5 m (green) from the double door. Case of Test 3. Right: displacement measured by the Laser for Tests 3 (blue) and 4 (red).*

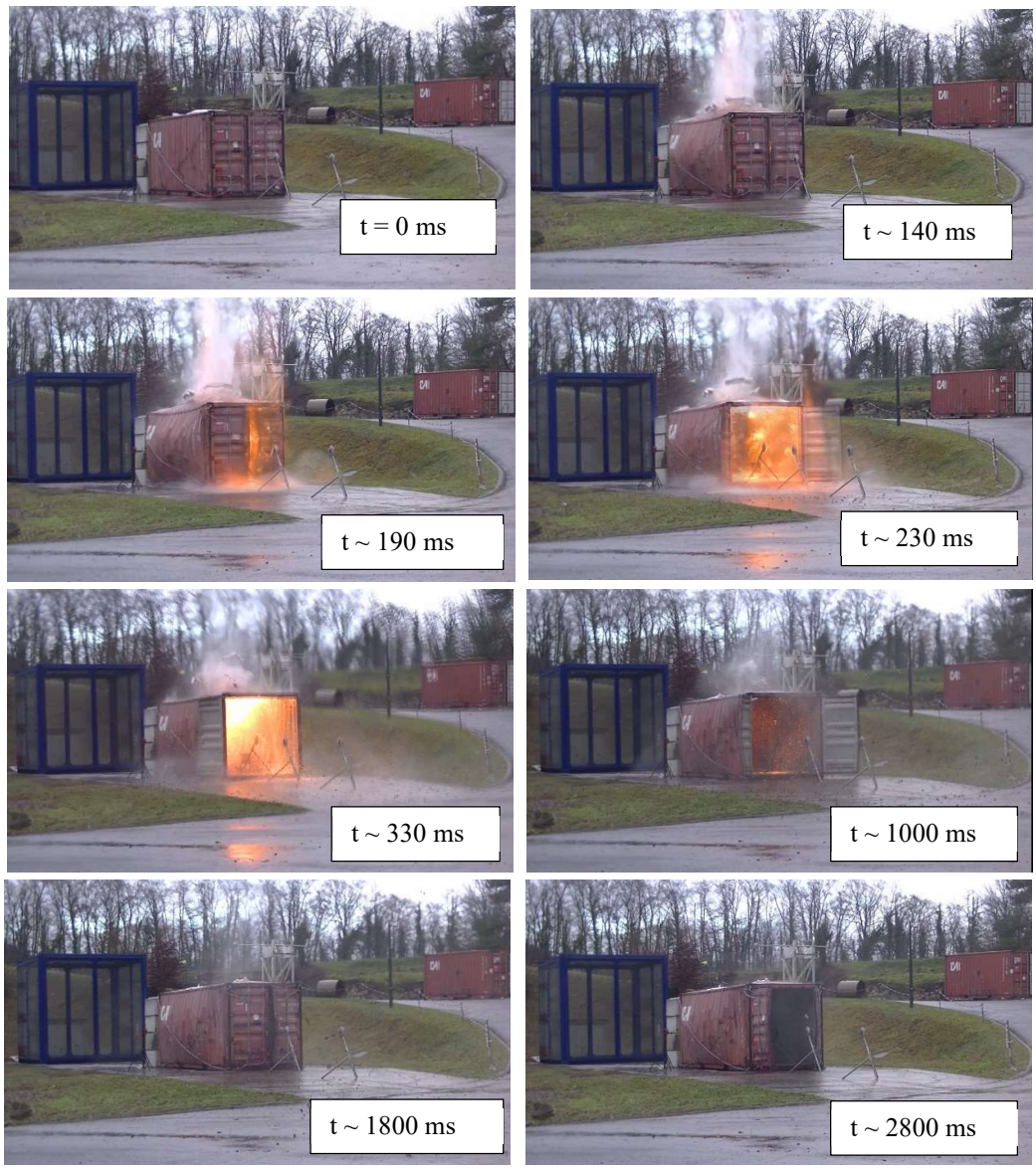

Fig. 7. *Temporal evolution of the explosion from the left side of the container for Test 3.*

The Laser (Figure 6) measured a peak displacement of approximately 500 mm in the middle of the sidewall and a residual displacement of approximately 250 mm.

Figure 8 shows some temporal signals of elongation rate obtained on the wall and the door of the container.

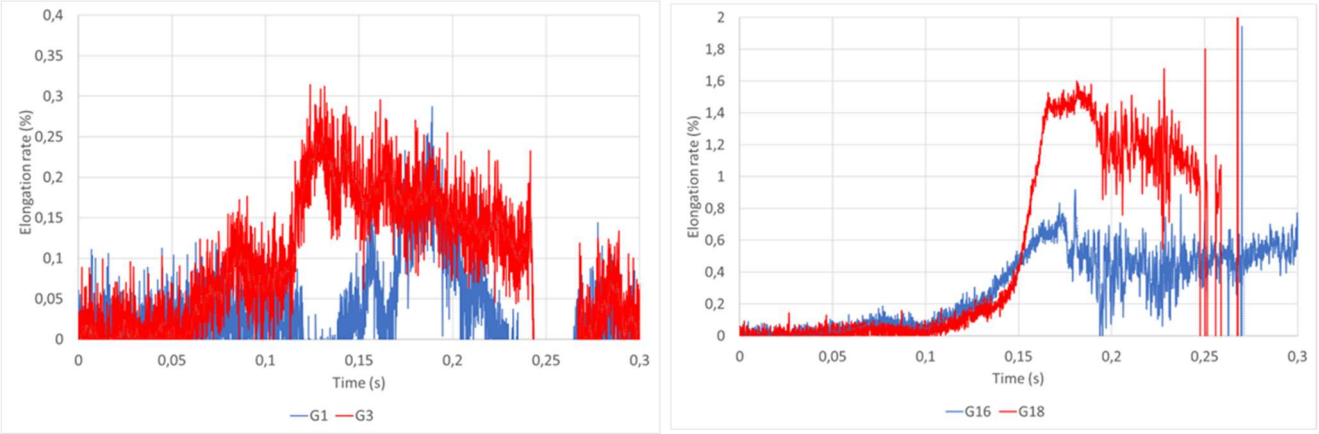

Fig. 8. *Temporal signals of elongation rates for strain gauges representative of the behaviour of the wall (left) and the door (right). Case of Test 3.*

Strain measurements at mid-height of the sidewall (G3) show values of around 0.25%. Although some plastic deformation was observed, the strain values remain significantly lower than the minimum admissible deformation of 20% for the steel studied, type S355.

Regarding the door, the maximum elongation rates on the closing bars (G16 and G18) are approximately equal to 1.6% during the pressure rise, just before the door opens. These values suggest more substantial strain compared to the wall measurements.

Figure 9 presents the temporal evolution of the stress calculated from the acceleration measurement at location 1 on the door (Figure 2). The stress is higher at location 1 than at location 2.

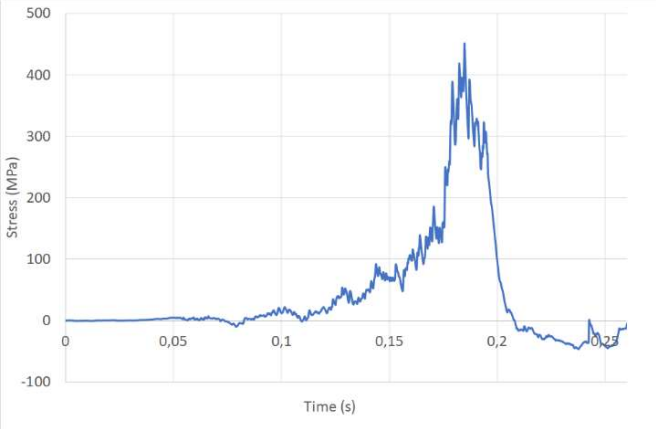

Fig. 9. *Temporal signals of stress at location 1. Case of Test 3.*

The maximum stress value at mid-height of the door is of the order of 410 MPa, falling within the plasticization range of the S355 material (Forni et al., 2016). This confirms the permanent deformations observed.

3. Results obtained with container N°2

For this test, the mean hydrogen volume fraction before ignition is 22 %. Figure 10 shows the pressure signals. The internal pressure signal is qualitatively similar to that of Test 3. However, in this case, the peak pressure when the flame reaches the vent is about 120 mbar and the overall peak pressure is 750 mbar.

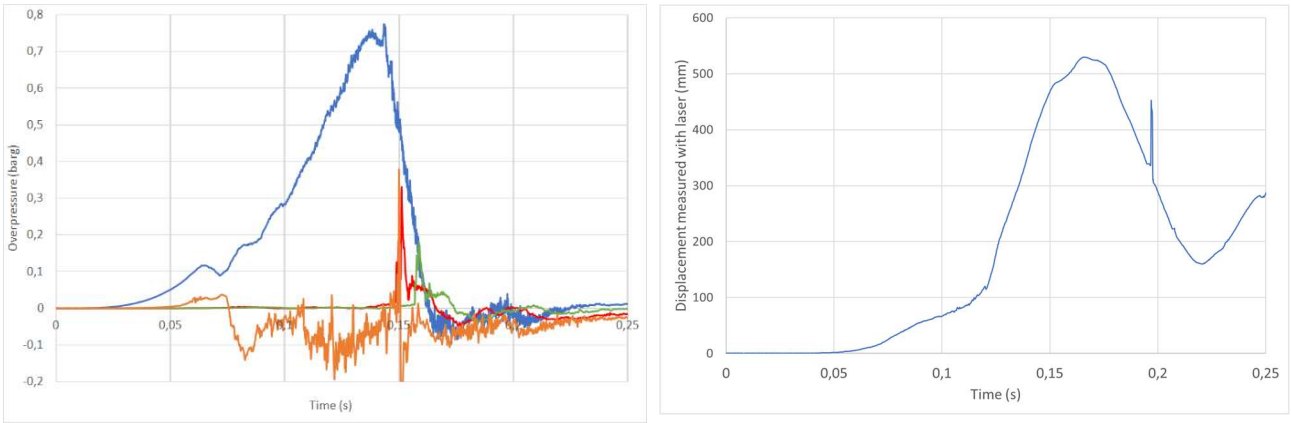

Fig. 10. *Pressure signals inside the container (blue), 1.5 m from the vent at the roof (orange), 5 m (red) and 7,8 m (green) from the double door.*

Figure 11 exhibits the qualitative response of the container to the explosion. Significant wall deformation is visible before the door opens. At t~115 ms (time at which Δp~470 mbar), a gap between the two doors is created and its width increases with time. At t~130 ms (Δp~670 mbar), the left door is sufficiently deformed to unlock the upper hooking system. The lower hooking system of

this door is open at t~140 ms (Δp~750 mbar). The opening angle for the left (resp. right) door is 90° at t~160 ms (resp. t~175 ms). Three of the four hinges of the left door are ripped off between t~150 ms and t~215 ms. Additionally, the junction between the left wall and the roof starts to tear at t~140 ms and is completely open at t~160 ms. The surface area left for gas exhaust in this location changes over time and depends on the deformation of the roof. The peak pressure inside the container is reached at t~140 ms when the discharge effects start to compensate for the volume production of burned gases. During the explosion, the container moves 60 cm away from the concrete columns.

In front of the roof vent, the peak pressure during the first venting is 30 mbar. After the door opens, a peak pressure of 330 mbar is reached 5 m away from these latter. 7.8 m away, the peak pressure is 180 mbar.

When the upper hooking system of the left door is unlocked, a pressure impulse about 22 bar.ms is reached. This value is close to the pressure impulse reached when the first hooking system was open in Test 3, while in this case, the pressure reached was way lower than in Test 4.

A wall rupture is also observed for a peak pressure of 750 mbar. This is consistent with previous experiments (Skjold, 2019) for which wall rupture was noticed for peak explosion pressures of approximately 575 mbar.

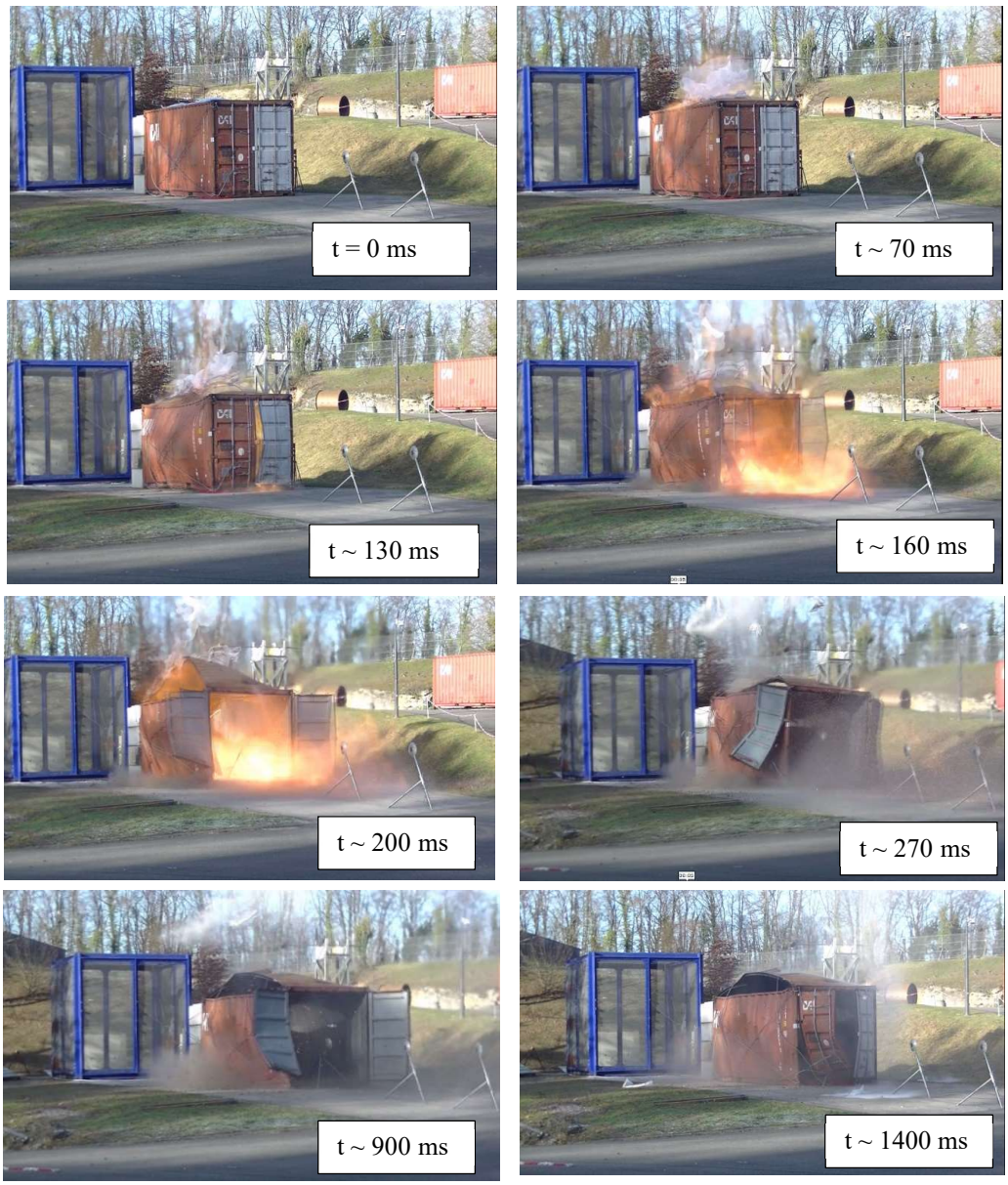

Fig. 11. *Temporal evolution of the explosion from the left side of the container for Test 4.*

According to the Laser (Figure 10), the peak displacement at the middle of the side wall is about 530 mm.

Figure 12 shows some temporal signals of elongation rate obtained on the door of the container.

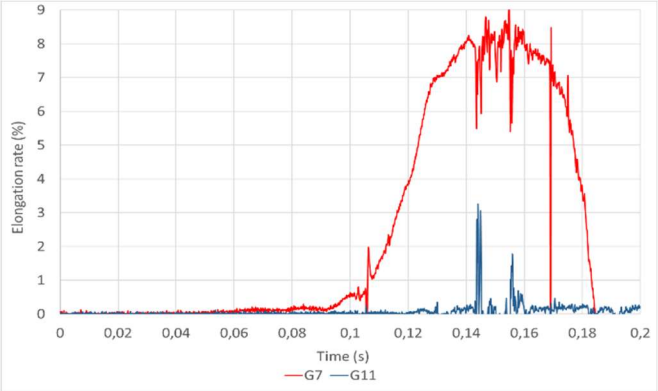

Fig. 12. *Temporal signals of elongation rates for strain gauges representative of the behaviour of the door. Case of Test 4.*

The measurements align with the deformations and damages observed on the doors and walls. Notably, Test 4 exhibits greater damage than Test 3, which can be attributed to the intensity of pressure signals felt by the doors or walls. The elongation gauges manifest these significant deformations by higher measured values. For example, the maximum elongation rate at one of the door hinges (Gauge 7) is around 8.5%.

The Figure 13 presents the time evolution of stress calculated from the acceleration measurement at location 2 on the door. In this Test, the stress is higher at location 2 than at location 1.

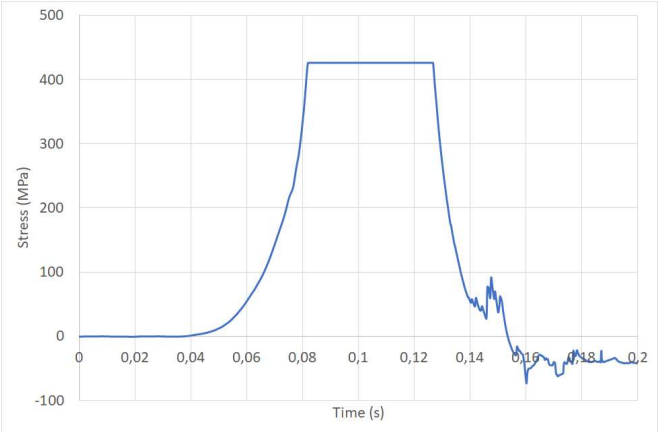

Fig. 13. *Temporal signals of stress at location 2. Case of Test 4.*

Stress levels observed on the door are significantly pronounced before the door openings. The recorded stress exceeds 430 MPa, which can be attributed to the limitations of the accelerometer factors at this magnitude. This elevated value indicates the permanent deformation of the door (Forni et al., 2016).

4. Conclusions

Some results of an experimental campaign aimed at better characterizing the response of the walls and doors of a 20-foot ISO container to an explosion have been presented in this article. A large database consisting of similar tests has already been generated by Skjold et al. (2019). In the current

work, extensive instrumentation has been used to measure the behavior of walls and doors, with numerous strain gauges, accelerometers, and high-speed cameras.

Preliminary explosion tests with a hydrogen mole fraction of 14% led to moderate container deformation and no door opening. Nominal tests with a hydrogen mole fraction of approximately 20% showed significant qualitative effects with opening the door and moving the container back. No wall rupture was observed at a mole fraction of 20%, but this was no longer the case when it increased to 22%.

The comparative analysis of the two tests (20% and 22%) reveals a significant difference in the intensity of the dynamic loads imposed on the container. The first test is clearly characterized by less severe conditions than the second test, both in terms of deformations and recorded stresses. Elongation rates, maximum stress values, and critical moments of plasticization all suggest that the first test imposes less violent loads on the container structure.

This study underlines the importance of considering the variable nature of dynamic loads and pressure impulses when evaluating container structural performance. It also provides valuable insights for improving the design of protective barriers (like explosion vent panels for example) under similar conditions.

The data generated during the experimental campaign will be thoroughly post-processed in future work, enabling to better understand the container response to explosion and will be used as reference data for improving a finite element model of an ISO container.

References

Pini T, Grosund-Hansen A., Schiavetti M. and Carcassi M. (2019) Small scale experiments and Fe model validation of structural response during hydrogen vented deflagration. International Journal of Hydrogen Energy 44(17), pp. 9063-9070

Sommersel O.K., Vaagsaether K. and Bjerketvedt D. (2017) Hydrogen explosions in 20' ISO container. International Journal of Hydrogen Energy 42, pp. 7740-7748

Skjold T., Hisken H., Lakshmipathy S., Atanga G., Bernard L., van Wingerden M., Olsen K.L., Holme M.N., Turoy N.M., Mykelby M. and van Wingerden K. (2019) Vented hydrogen deflagrations in containers: Effect of congestion for homogenous and inhomogeneous mixtures. International Journal of Hydrogen Energy 44, pp. 8819-8832

Hao T.-T., Wang C.-J., Yan W.-J., Ren W.-X. and Yuen K.-V. (2021) Experimental investigation of the dynamic responses of vented hydrogen explosion in a 40-foot container. International Journal of Hydrogen Energy 46, pp. 19229-19243

Livermore software technology corporation (LSTC)

(https://www.ansys.com/products/structures/ansys-ls-dyna)

Weller, H.G, Tabor, G. (1998). A tensorial approach to computational continuum mechanics using object-oriented techniques. *Computational Physics*, 12: 620-631.

Forni D., Chiaia B., Cadoni E. (2016). Strain rate behaviour in tension of S355 steel: Base for progressive collapse analysis. *Engineering Structures*, 119:164-173

Visualization of Hydrogen Flames in the UV Region by ZnO-based Camera

Nan Sun[1], Xu Han[1], Junxiu Piao[1], Chengming Jiang[1,*], Sheng Bi[1,*]

1 Key Laboratory for Precision and Non-traditional Machining Technology of the Ministry of Education, Dalian University of Technology, Dalian, 116024, China

Corresponding Authors:

*E-mail: bish@dlut.edu.cn,

jiangcm@dlut.edu.cn;

Abstract

Since the hydrogen flame only radiates in the UV and IR spectrum, it cannot be seen. The emission of the hydrogen flame can be observed by our prepared ZnO-based camera, and the peak of the corresponding OH emission is between the spectral range of our prepared ZnO-based image sensor, and the background is imaged in the visible range using a silicon-based camera, which cannot observe the presence of the hydrogen flame. The flame images were extracted using the differences in image intensities in different bands. The differential pictures were subjected to (1) threshold intensity level digitization and (2) Gaussian blurring in order to suppress pseudo-speckles brought on by the grainy appearance of the images produced by the image intensifier. Imaging in the visible wavelength range can be removed using this technique. The flame zone can operate up to 20 meters in the open during daylight hours. We anticipate that our findings will shed light on and offer guidance for the development of highly sensitive hydrogen flame detection methods.

Introduction

In reaction to the depletion of fossil fuels and tightening regulations on CO_2 emissions, hydrogen energy is being introduced more and more. For widespread usage of fuel cell vehicles, which are among the hydrogen energy sources that are closest to commercialization, it is necessary to construct hydrogen refueling stations. Detecting hydrogen flames is crucial for safety precautions at hydrogen refueling stations since hydrogen is explosive and combustible.

Flame detectors currently in use that operate in the UV region can detect UV radiation over a wide-spectrum range and include mainly UV photomultipliers, imaging-type UV transistors, UV intensifiers, and silicon-based UV detectors.[1-3] Among them, photomultiplier tubes and silicon-based UV photodiodes are commonly used. Photomultiplier tube has the advantages of high sensitivity and insensitivity to photons larger than the cutoff wavelength, but it is easy to damage and needs to work under high voltage, which makes the system bulky and costly. Silicon-based UV phototube can avoid the above shortcomings, but it has low quantum efficiency, been sensitive to infrared-visible spectral range photons, and has a serious radiation aging effect.[4-6] To exclude visible-IR light interference it is necessary to include expensive and troublesome filters. Flame detectors that operate in the ultraviolet (UV) portion of the electromagnetic spectrum are prone to false alarms brought on by transient

UV radiation, such as sunlight reflections and arc welding.[7,8] Additionally, since these flame detectors can only detect the presence of hydrogen flames by radiation and cannot see hydrogen flames, manual identification of flame zones is required.

The wide band width (2.5 to 6.2 eV) of third-generation broadband semiconductors makes it possible to detect hydrogen flames in the ultraviolet region.[9-14] Among them, zinc oxide (ZnO) is a broadband direct bandgap semiconductor with high UV response because of its similar lattice structure and optical properties to GaN.[15,16] Simultaneously, because of the advantages of high melting point, low epitaxial growth temperature, low cost, non-toxic material, easy etching, and convenient process handling, ZnO shows a greater development potential than GaN. Therefore, ZnO UV detectors have a very promising future.[17-19]

This research aims to visualize hydrogen flames by using Zno-based camera to obtain images of hydrogen combustion flames that can be observed in the wide spectral response range of the ultraviolet with conventional visible silicon-based cameras to extract flame regions from images that cannot be observed in the same scene. Since the hydrogen refueling station is located outdoors, it is expected that sunlight and its reflection will cause problems for the extraction of flame regions. By extracting flame images in the difference of image intensities at different wavelengths in the same scene, the pseudo-speckles caused by the grainy

appearance of the images obtained by the image intensifier are suppressed by using digitization of threshold intensity levels and Gaussian blur applied to the differential images. This method eliminates the effect of false alarms such as reflected sunlight. The method is also used to image hydrogen flames in different wavelength ranges. Under outdoor daylight conditions, the flame region can be operated at a distance of up to 20 m.

According to Fig. 1, the $A^2\Sigma - X^2\pi$ electron leap of the hydroxyl radical (OH) is what causes the emission of the hydrogen flame in the UV region, with emission maxima between 306.5 nm and 309 nm. Numerous rotating lines make up the sharp peaks at 306.5 and 309 nanometers, however, they are not resolved in Figure 1.[20] The dashed line in Figure 1 illustrates the UV-Vis absorption spectra of ZnO. The ZnO films exhibit significant UV absorption from 300 to 380 nm and weak visible absorption from 400 to 800 nm (not fully shown in Figure 1). The absorption edge of ZnO is visible in the figure at a wavelength of 375 nm, which corresponds to the material's prohibited bandwidth. It can also be seen that the absorption edge of ZnO in the absorption spectrum is steep, which indicates that the prepared ZnO has a good UV response. All emission spectra were obtained by an Ocean Optics QE65PRO spectrometer.

Experimental Instrument

The experimental instrument that can image the hydrogen flame was

constructed and the schematic diagram of the instrument is illustrated in Figure 2. The ultraviolet radiation from the hydrogen flame is cellularized by the ultraviolet camera lens (Nikon 105mm/F4.0) and divided into two paths by the beam splitter. Path one leads to a channel incorporating a 400 nm filter, an interference filter, an image intensifier (Hamamatsu C9016), a relay lens (Hamamatsu A2098), and a silicon-based camera. Path two leads to a channel consisting of a ZnO-based camera. These components are installed on optical rails that are fixed on an aluminum optical stage that is 800 mm long and 500 mm wide to make beam alignment and position modification easier.

The UV light that is passing through the interference filter is amplified by the image intensifier and changed to visible light, which is captured on the silicon-based camera. A video capture device is used to store these images on a personal computer. The silicon-based camera's video output is employed to modify the image intensifier's gain when it is operating in continuous mode. The silicon-based camera and ZnO-based cameras have a shutter speed of 1/60 second and operate at a video rate of 30 frames per second (interlaced). Grayscale 800 x 600 pixels, 8-bit (256 colors) image obtained.

Result and Discussion

1. UV-filtered visualization of hydrogen flames

A UV filter (400 nm) was employed in channel 1 to acquire the background image at the specified wavelength. In channel 2, a ZnO-based camera was employed to capture the background image based on the UV-Vis absorption properties of ZnO. A hydrogen burner was located at a distance of 5 m from the instrument and images were obtained at both wavelengths. About 15 liter/min of hydrogen gas flowed through the system.

A section of 400 x 400 pixels was isolated from each image for the experimental results, which are displayed in Figure 3. Images at 309 nm and 400 nm are shown in Figures 3a and 3b, respectively. Figure 3(c) displays the outcomes of pixel-level differentiation of Figures 3a and 3b. In Figure 3c (brightness 128/255), pixels having the same brightness as those in Figures 3a and 3b are depicted in gray. Figure 3a shows the building's reflection on both sides of the flame (the reflection on the right side is more pronounced), whereas Figure 3c shows the reflection fading and being nearly black. The results of binary digitizing Figure 3c at a 75% threshold level (luminance 191/255) are shown in Figure 3d. The reflections of the building have been eliminated, but some false pixels appear. These outcomes are a result of the image's graininess, which was caused by the image intensifier.

To get rid of the fake speckles that grainy photos cause, employ spatial averaging. Since the luminance of the surrounding pixels in the flame zone

is identical, averaging has no effect on it. Conversely, in the case of pseudo speckle, the luminance is greatly lowered after averaging because the neighboring pixels have lower luminance. Pseudo dots can thus be eliminated after spatial averaging by utilizing binary digitization with the appropriate threshold level.

Gaussian blur is a typical technique for spatial averaging, as stated by

$$I(i,j) = \sum_{k,l} I(k,l) C \exp\left[-\frac{(i-k)^2 + (j-l)^2}{\sigma^2}\right]$$

The brightness of pixel (i,j) is weighted using a Gaussian function to create a spatial average over its nearby pixels. The complete width at the $1/e^2$ points, $d=2\sigma$, provides the blur's level. The constant C is chosen to preserve the overall brightness (the sum of all pixels).

The use of Gaussian blur eliminates the effect of pseudo-spotting, which is a state of 255 brightness at one pixel and 0 brightness at surrounding pixels when the total brightness is constant and can be reduced by Gaussian blurring. This helps to use threshold levels for subsequent deletion by binary digitization. Figure 4a demonstrates the outcomes of applying the 5-degree Gaussian blur to the pixel-level differential image of the hydrogen flame from Figure 3d. There is no significant change in the flame region, but the luminance of the pseudo-light spot is significantly reduced. The results of applying binary digitization to Figure 4a with a threshold level of 50% (luminance 128/255) are displayed in Figure 4b,

where the flame zone is effectively retrieved and the pseudo-spots are eliminated.

Gaussian blur causes a reduction in the area of the flame region, as the brightness of the disconnected pixels is significantly reduced and is eliminated during the digitization process. Several flame images were captured using pixel level difference splitting. The results of the Gaussian blur and the binarization with a threshold of 50% are shown in Figure 5 to have an assessment of the error concerning this operation. By acquiring images under different wind conditions to verify the universality of our adopted method, it is observed that the direction and size of the flames in each image are different.

The quantity of pixels in the differential image for each image in Figure 5 that are brighter than 75% of the threshold is added together and split into the number of pixels that belong to the flame area (F) and the pseudopoints (S). Similar to this, the total of all the bright pixels in the processed image is considered when determining which pixels belong to the flame region (F'). There are no pseudopoint-belonging pixels in the processed image (S'=0) because all pseudopoints were eliminated. Table 1 provides a summary of the results. F=F' should be optimal, however, some variations are owing to the granular exteriors of the flame in some images.

For instance, in the six images in Figure 5, the average relative difference in pixel count caused by the utilization of Gaussian blurring is

0.72%. The inaccuracy is significantly less than 1% in images C through F, where the flame boundary is clearly defined. Since the bright pixels in image A's upper portion of the windy flame are disconnected due to granularity, the Gaussian blur causes an area reduction of 1.42%. The reduction in area is allowed even if some of the flames appear to be spread because the 1% inaccuracy is acceptable when setting off an alert in accordance with the region of the flame.

2. Simplified hydrogen flame imaging apparatus

UV filters can be applied to view hydrogen flames, as demonstrated by the obtained results in the preceding section. Nevertheless, the inclusion of image intensifiers and relay lenses increases the manufacturing cost. The material cost of the detection instrument could be decreased if it is possible to filter the image created from visible light using simply the filter and yet acquire the hydrogen flame's emission position. It is vital to determine whether the previous pixel linear difference imaging approach is still effective for recovering the flame zone without including the higher transmission of certain background light due to the structure's simplicity. Figure 6 displays the results of hydrogen flame imaging tests employing a 400 nm filter in channel 1 and a ZnO-based camera in channel 2. Figures 6a and 6b show the images at 309 and 400 nm, respectively. The outcomes of the pixelwise difference of Figures 6a and 6b are displayed in Figure 6c.

Figure 6d exhibits the outcomes of manipulating a Gaussian blur and a 50% threshold level for binary digitization. The increase of the partially visible background can be observed in Figure 6b (compared to Figure 3b), of which the hydrogen flame range has been successfully extracted in Figure 6d, leaving no background or false spots. The reduplicate experimentations produced analogous findings, manifesting that the designed modified structure to inspect the hydrogen flame is still valid, and the simplified structure is shown in Figure 7.

3. Visualization of a distant hydrogen flame

Additional tests were conducted to check the capabilities of the device to detect hydrogen flames at wider distances. Using the condensed structure of previous section, the hydrogen burner was placed 20 meters away from the equipment and photographed. The outcomes are illustrated in Figure 8. Here, Figure 8a shows the image at 309 nm and Figure 8b presents the background image at 400 nm. Figure 8c illustrates the pixel difference between Figures 8a and 8b, and Figure 8d demonstrates the consequences of employing both Gaussian blur and binary digitization employing threshold levels. The flame area extracted in Figure 8d is smaller than in Figure 8a, but a bright image of the flame can still be extracted, suggesting that the simplified device for the capture of hydrogen flame is still feasible. A lens with a higher magnification can be employed

to enhance this but at the expense of a limited field of view. Using a zoom lens to change the magnification when flames are detected is useful in practical applications when a vast area needs to be observed.

Summary

It is possible to see hydrogen fires by using UV emission. The experimental results demonstrate that the hydrogen flame can be detected at a distance of 20 m in daylight using our prepared ZnO-based camera. The background light can be reduced using a UV filter, and pseudo-spots caused by image granularity can be removed using a combination of threshold-level binarization and Gaussian blurring.

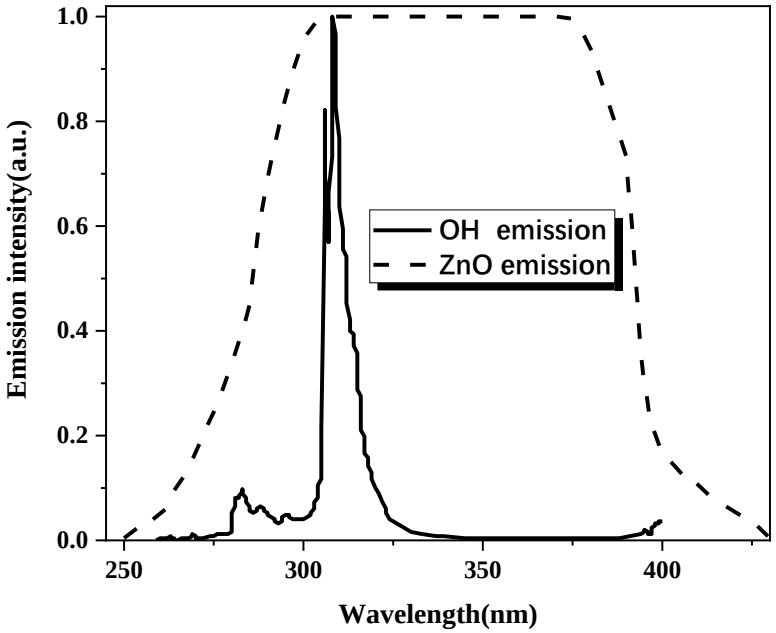

Figure 1. Emission spectrum of hydrogen flame (solid line) and UV-Vis absorption spectrum of zinc oxide (dashed line)

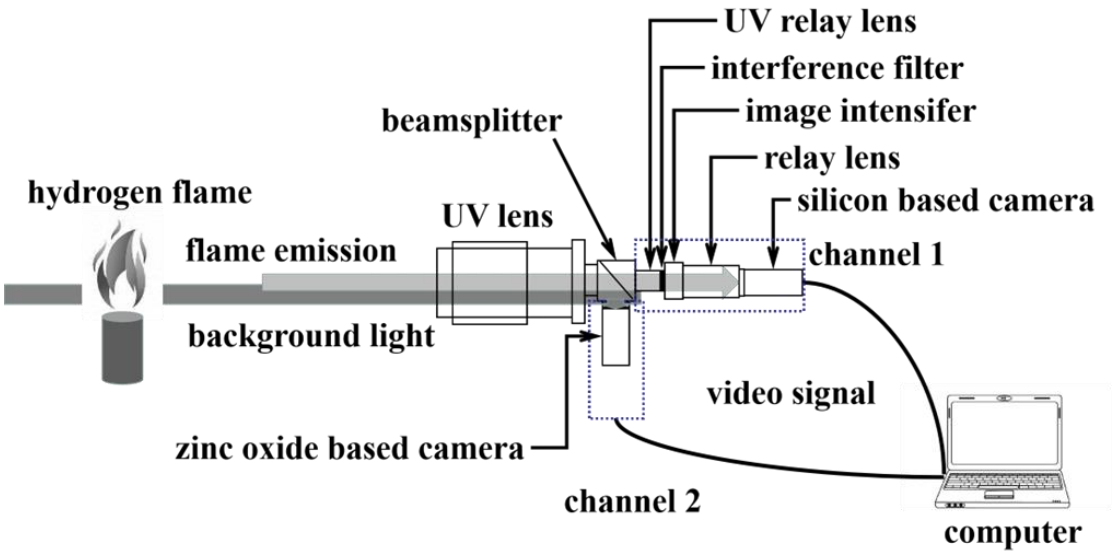

Figure 2. Schematic diagram of hydrogen flame imaging instrument

Figure 3. Results of photographing a hydrogen flame include (a) an image at 309 nm, (b) an image at 400 nm, (c) pixelwise differential of (a) and (b), and (d) the outcome of binary digitizing (c) with a threshold level of 75%

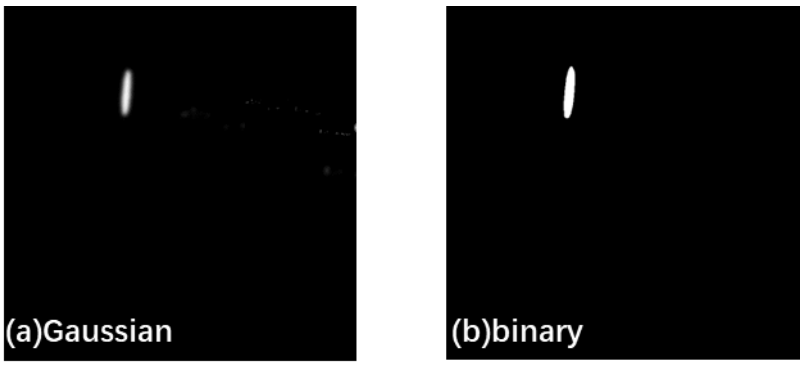

Figure 4. Result of application of Gaussian blur to the pixelwise differential image of hydrogen flame: (a) Gaussian blur applied, (b) binary digitization of (a)

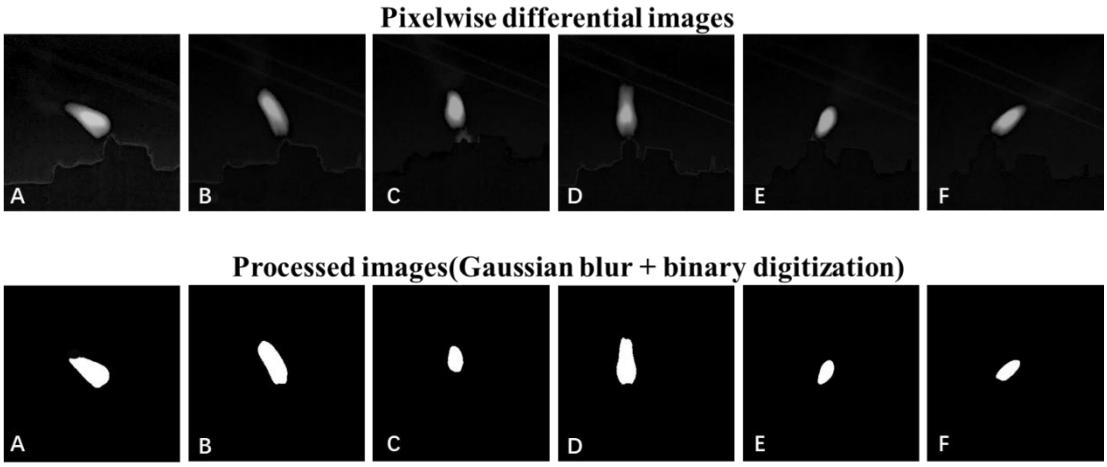

Figure 5. Hydrogen flame images taken under different wind conditions

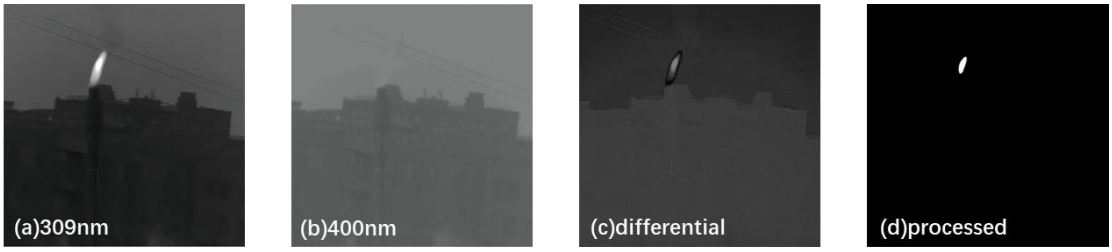

Figure 6. Experimental results of the simplified instrument: (a) image at 309 nm, (b) image at 400 nm, (c) pixelwise differential of (a) and (b), (d) processed image after applying Gaussian blur and binary digitization to (c)

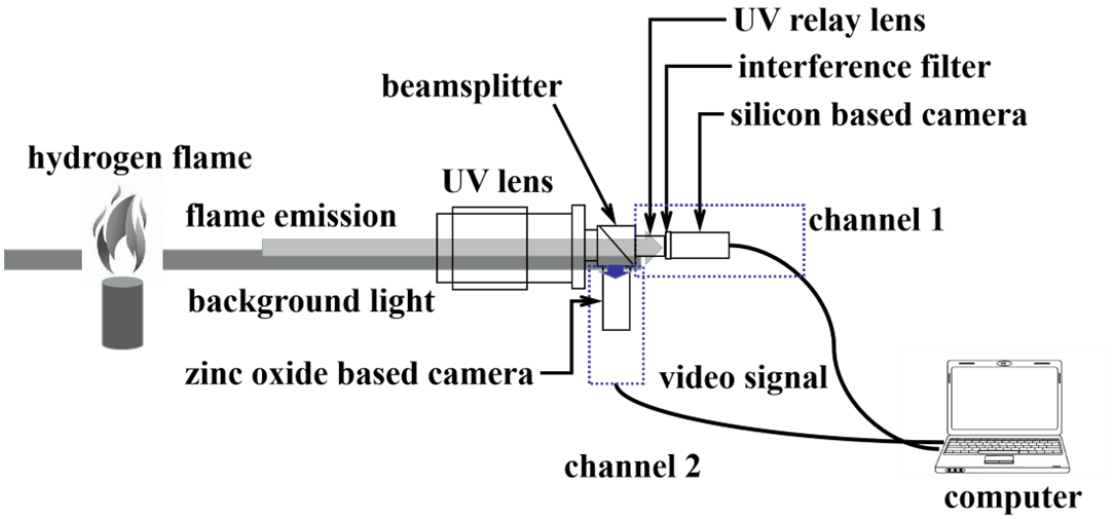

Figure 7. Schematic diagram of the simplified hydrogen flame imaging instrument

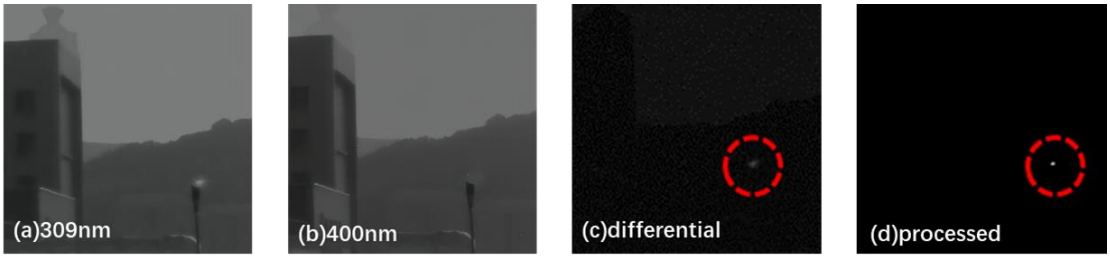

Figure 8. Experimental result with hydrogen flame at 20 m distance: (a) image at 309 nm, (b) image at 400 nm, (c) pixelwise differential of (a) and (b), (d) processed image after applying Gaussian blur and binary digitization to (c)

Table 1. Number of pixels in flame region in differential image and processed image

Image	Differential image		Processed image		Difference	
	pixels in flame region (F)	pixels in spurious spots (S)	pixels in flame region (F')	pixels in spurious spots (S')	F-F'	F-F'/F
A	1825	27	1799	0	26	1.42%
B	1908	31	1894	0	18	0.94%
C	1479	54	1474	0	5	0.34%
D	1484	23	1477	0	7	0.47%
E	1191	19	1184	0	7	0.59%
F	1392	11	1384	0	8	0.57%
Mean	1766	28	1535	0	7	0.72%

Reference

[1] Lei K, Yan G. Research on the Application of UV Image Intensifier in Security Detection of Power Equipment. Infrared Technology. 2016, 37(11): 986-990.

[2] L. C. Passos M, M. F. S. Saraiva M L. Detection in UV-visible spectrophotometry: Detectors, detection systems, and detection strategies. Measurement. 2019, 135: 896-904.

[3] Okino T, Yamahira S, Yamada S, et al. A Real-Time Ultraviolet Radiation Imaging System Using an Organic Photoconductive Image Sensor. Sensors. 2018, 18(1): 314.

[4] Bai Y, Bajaj J, Beletic J W, et al. Teledyne Imaging Sensors: Silicon CMOS imaging technologies for x-ray, UV, visible, and near infrared. Bellingham, Wash: SPIE, 2008.

[5] Wilkinson E, Vincent M, Kofoed C, Andrews J, Brownsberger J, Siegmund O. Southwest Research Institute Intensified Detector Development Capa bility. Proceedings of SPIE. 2012, 84432K.

[6] Fukuchi T, Ninomiya H. Visualization of hydrogen flame by differential imaging in the ultraviolet region. Proceedings of the SPIE - The International Society for Optical Engineering. 2005, 1: 58800L-1-8.

[7] Shen Z, Wang J, Wei G. An Improved Partial Discharge Detection

System Based on UV Pulses Detection. Sensors. 2020, 20(17): 4767.

[8] Tian J, He Y, Li J, et al. Fast, Real-Time, In Situ Monitoring of Solar Ultraviolet Radiation Using Sunlight-Driven Photoresponsive Liquid Crystals. Advanced Optical Materials. 2018, 6(6): 1701337.

[9] Chen Y, Zheng C, Chen Y. High-Performance AlGaN-Based Solar-Blind UV Photodetectors for Sensing Applications. physica status solidi (a). 2021, 218(18): 2100207.

[10] Manjunath G, Pujari S, Patil D R, et al. A scalable screen-printed high performance ZnO-UV and Gas Sensor: Effect of solution combustion. Materials Science in Semiconductor Processing. 2020, 107: 104828.

[11] Su L, Zhou D, Lu H, et al. Recent progress of SiC UV single photon counting avalanche photodiodes. Journal of semiconductors. 2019, 40(12): 121802.

[12] Tsai Y, Wang D, Lin Y, et al. UV Light and H_2 Gas Dual Sensing Properties of ZnO/InGaZnO Match-Head Nanorods. IEEE Electron Device Letters. 2022, 43(4): 607-610.

[13] Reddeppa M, Nam D, Bak N, et al. Proliferation of the Light and Gas Interaction with GaN Nanorods Grown on a V-Grooved Si(111) Substrate for UV Photodetector and NO2 Gas Sensor Applications. ACS Applied Materials & Interfaces. 2021, 13(25): 30146-30154.

[14] Sood A K, Zeller J W, Ghuman P, et al. GaN/AlGaN avalanche

photodiode detectors for high performance ultraviolet sensing applications[C]. SPIE, 2019.

[15] Sang L, Liao M, Sumiya M. A Comprehensive Review of Semiconductor Ultraviolet Photodetectors: From Thin Film to One-Dimensional Nanostructures. Sensors. 2013, 13(8): 10482-10518.

[16] Shetti N P, Bukkitgar S D, Reddy K R, et al. ZnO-based nanostructured electrodes for electrochemical sensors and biosensors in biomedical applications. Biosensors and Bioelectronics. 2019, 141: 111417.

[17] Kathiravan D, Huang B. Concurrent enhancement in the H2 and UV sensing properties of ZnO nanostructures through discontinuous lattice coating of La3+via partial p–n junction formation. Journal of Materials Chemistry C. 2018, 6(9): 2387-2395.

[18] Ren Q, Cao Y, Arulraj D, et al. Review-Resistive-Type Hydrogen Sensors Based on Zinc Oxide Nanostructures. Journal of the Electrochemical Society. 2020, 167(6): 67528.

[19] Pan Z, Zhao X, Peng W, et al. A ZnO-Based Programmable UV Detection Integrated Circuit Unit. IEEE sensors journal. 2016, 16(22): 7919-7923.

[20] Izarra C D. UV OH spectrum used as a molecular pyrometer. Journal of physics. D, Applied physics. 2000, 33(14): 1697-1704.

The Effect of Fuel Concentration on Intrinsic Flame Instabilities and Flame Acceleration in Lean H_2-CO-Air Mixtures

Kajetan Planötscher [a], Agnes Jocher [a]

[a] Technical University of Munich, TUM School of Engineering and Design, Department of Aerospace and Geodesy, Boltzmannstraße 15, D-85748 Garching, Germany

E-mail: kajetan.planoetscher@tum.de

Abstract

In large scale accident scenarios of nuclear power plants core meltdown and molten-core-concrete-interaction can occur. Large amounts of syngas mainly consisting of hydrogen (H_2) and carbon monoxide (CO) might be formed and mixed with the surrounding air, developing a potentially explosive mixture. The ignition of the flammable mixture might lead to flame acceleration and in worst cases to the destruction of the reactor building, causing the detachment of radioactive substances to the environment. To prevent future accidents, the understanding of flame accelerating conditions of syngas-air mixtures, in specific the understanding of the flame topology, must be improved. To the authors' knowledge, insufficient data on flame topology investigating ignition and early stages of flame propagation in lean H_2-CO-air mixtures is available. Therefore, in this study experiments are carried out to analyze the ignition and slow deflagration of a 50/50 H_2/CO fuel mixture with fuel-to-air concentrations between 13.0 vol.-% - 29.5 vol.-%. A model calculating the flame acceleration in early stages of flame propagation is suggested. The GraVent explosion channel located at Technical University of Munich is used for the experiments in this study in its configuration of 1300 mm in length and a rectangular cross section of 300 x 60 mm. OH-PLIF measurements are used to determine flame front speed, flame acceleration and flame front length. Wrinkling factors are determined by the division of the wrinkled flame front length caused by intrinsic flame front instabilities and the smooth flame front length to quantify the influence of intrinsic flame front instabilities on early stages of flame acceleration. The optical experimental data contains the ignition of the gas mixtures as well as early stages of flame propagation. In conclusion, the results gathered in this study provide information on the topology of H_2-CO-air flames under lean conditions enhancing the understanding of syngas flame acceleration and extending experimental data provided in former studies with relevance to large scale accident scenarios of nuclear power plants.

Keywords: *H_2-CO-air, flame topology, lean combustion, intrinsic flame instabilities, flame acceleration*

1. Introduction

The syngas mixture of H_2 and CO plays an important role in large scale accident scenarios of nuclear power plants. It might be produced during the ex-vessel phase through the interaction of molten fuel rod materials with the surrounding water and concrete (Kumar et al. 2000; Kusharin et al. 1998). For example, studies reconstructed the Fukushima Daiichi accident and were able to trace back the destruction of the nuclear power plant to syngas explosions (Gauntt et al. 2012). After the power plant's energy supply collapsed, cooling water could not be pumped through the reactor pressure vessel (RPV) anymore. In the following, the cooling water's temperature increased until the point at which the zirconium of coating the fuel rods oxidized with oxygen (O_2) bound in the water, producing

large amounts of H_2. Furthermore, core meltdown and the failure of the RPV occurred because of continuously rising temperatures. Consequently, the molten core material as well as the H_2 were able to exit the RPV, entering the containment of the reactor building. Here, the molten core material interacted with the concrete of the containment in a molten-core-concrete-interaction, producing CO in addition to the H_2 produced in the RPV. Eventually, a malfunction of pressure valves installed in the containment released the H_2-CO mixture into the reactor building. H_2 and CO mixed with the air the reactor building was filled with, creating a potentially flammable mixture. Finally, contact with an ignition source led to an explosion destroying the reactor building which caused the detachment of nuclear substances to the environment.

To prevent future accidents, the flame acceleration (FA) of H_2-CO combustion was the subject of investigation of various studies in the past. Veser et al. investigated H_2-air combustion with varying H_2-CO fuel mixtures with fuel-to-air concentrations between 11 – 15 vol.-% in an obstructed, rectangular channel (Veser et al. 2001). They showed that the addition of CO to an H_2-air mixture shifts the minimum fuel concentration for reaching fast deflagration and potentially deflagration-to-detonation transition (DDT) to higher fuel concentrations in air. Moreover, the influence of CO onto the flame speed can't be neglected for fuel-to-air concentrations below 13 vol.-%. Heilbronn et al. extended the findings of Veser et al. using the fully modular GraVent test rig (GraVent) at Technical University of Munich (Heilbronn et al. 2021a, 2021b). Heilbronn et al. used the GraVent in its 6 m long, closed and obstructed configuration. The investigated fuel mixtures consisted of 100/0, 75/25, 50/50 H_2/CO and were mixed with air at ambient pressure with fuel-to-air concentrations between 15 – 40 vol.-%. Heilbronn could confirm Veser's et al. findings that the addition of CO to the fuel shifts the FA and detonation limits to higher fuel-to-air concentrations. Moreover, Heilbronn showed that pure H_2-air mixtures at fuel-to-air concentrations above 30 vol.-% did not reach DDT in contrast to the H_2-CO-air mixtures investigated. Because of that, Heilbronn concludes that H_2-air mixtures can't be used as a conservative model for the simulation of H_2-CO-air mixtures at the same fuel-to-air concentration.

Even though studies are available for FA and DDT of H_2-CO-air mixtures, few data has been gathered on the early stages of FA. In the initial phases of FA within an unobstructed channel, intrinsic flame instabilities play a crucial role (G. Ciccarelli and S. Dorofeev 2008). The Landau-Darrieus (LD) instability is a key factor contributing to the wrinkling of the flame front, leading to an augmentation in flame front curvature and, consequently, an increase in the flame surface area (Darrieus 1938; Landau 1988). This increased surface area results in a rise of the volumetric burning rate, causing an acceleration of the flow velocity ahead of the flame front. Concurrently, the thermal diffusive (TD) flame front instability further enlarges the flame surface area for fuel-air mixtures with Lewis numbers below unity, facilitating continuous FA. Bauwens et al. conducted a direct investigation into LD instability in spherical propane-air flames, observing a notable FA effect on the flame front (C. Regis Bauwens et al. 2015). Additionally, the LD instability induced oscillatory velocity fluctuations, resulting in small-scale disturbances of the flame front surface. These small-scale disturbances are each of the same characteristic size, turning the flame front surface into a structure composed of a large number of cells. The fluctuations were attributed to the continuous growth and breakup of cells. Following cell breakup, a new generation of cells promptly formed, contributing to a further increase in the flame surface area and, consequently, promoting FA. Katzy et al. investigated the influence of LD and TD instabilities onto FA of H_2 -air mixtures in the unobstructed GraVent by recording simultaneous OH-PLIF and shadowgraphy images (Katzy et al. 2017). The FA was divided into

different stages of FA, namely the development regime A, the flattening regime B and the propagation regime C. Katzy et al. determined the wrinkling factors of mixtures with different reactivities and developed a model predicting the effective burning velocity of the mixtures. The model was tested simulating the flame propagation inside the GraVent with URANS simulations. The simulated flames showed improved results when compared to results gathered without modelling the effective burning velocity of the mixtures. However, strong deviations to experimental data were still apparent. To close the gap between experiment and simulation, Katzy expanded the model to take several other factors, such as pressure influence, flame stretch, etc., into account (Katzy 2021). After the expansion of the model, the URANS simulations were able to reproduce experimental results accurately as well as computation time efficiently. To expand the physical understanding and model towards H_2-CO-air mixtures, experimental data on H_2-CO-air combustion must be gathered. In this work, the GraVent is used to record OH-PLIF images of the early stages of FA of H_2-CO air mixtures. In the following, the experimental setup is described, followed by the data evaluation procedure. Then, the results are presented, discussed and conclusions are drawn.

2. Experimental setup

2.1. Geometry and measurement equipment

The spark plug ignited GraVent with a rectangular cross-section of 300 mm x 60 mm (width x height) of the Technical University of Munich is used for the experiments (Fig. 1). The configuration consists of one segment with optical access enabling investigations on the ignition as well as early flame propagation and one segment without optical access resulting in a total explosion channel length of 1.3 m. Both segments are equipped with one Kistler 601 A pressure transducer each, operating at a frequency of 225 kHz to measure the dynamic pressure. The channel is unobstructed in both segments. The optical segment (OS) is placed first. In addition, the spark plug is in the field of view (FOV) of the OS. This way, ignition could be observed by optical measurement techniques. For gathering data of the flame front morphology, an OH-PLIF system is used (Fig.1). A Sirah Credo Dye laser system is used to excite the hydroxyl (OH) radicals in the reaction zone. The Photron SA-X2 camera operating at 20 kHz is used to record flame propagation. The intensity of the images is

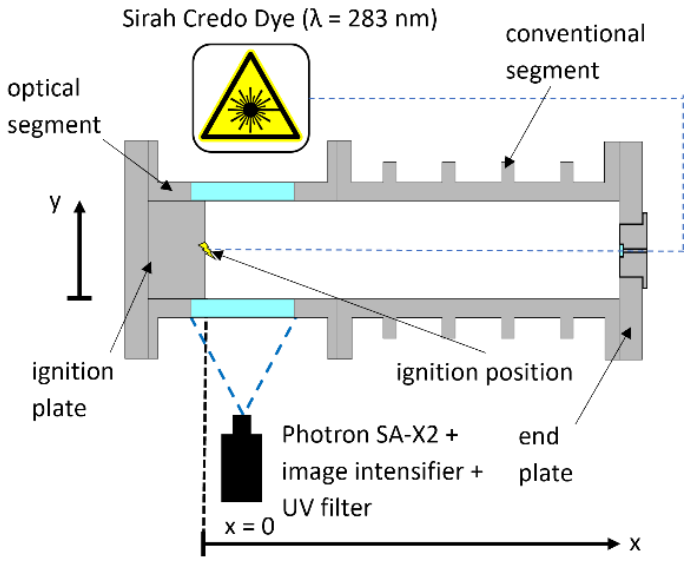

Fig. 1. *Schematic of the OH-PLIF setup.*

increased by a Hamamatsu C10880-03F image intensifier. To filter the light reaching the image intensifier, a Brightline HC 320/40 UV filter is mounted onto the lens of the image intensifier.

2.2. Experimental procedure

Previous to the experiments, the fuel consisting of H_2 and CO is produced using the method of partial pressures in a separate fuel mixing unit. This way, the fuel mixture can be considered homogeneous by the time of injection. The quality of the fuel mixture was evaluated by gas chromatography, yielding in an accuracy of 1 % (Heilbronn et al. 2021a). At the beginning of each experiment, the GraVent is filled with air at ambient pressure and temperature. In the first step, air is partially removed out of the GraVent, creating a negative pressure compared to the atmospheric pressure. A first pressure measurement is taken, which is used in a later step for the calculation of the fuel concentration in air. The pressure equalization between the GraVent's inside and its surroundings due to leakage is quantified to a maximum 20 % per minute. After that, fuel is injected at 800 kPa into the explosion channel through five fuel injection units located in the ceiling of the GraVent. Homogeneous fuel distribution during the injection is ensured by nine fuel injection holes distributed uniformly over the explosion channel ceiling per fuel injection unit, yielding in 45 injection holes in total. Deflection plates promoting the diffusion of the fuel in the air inside of the GraVent are mounted in sequence of the injection holes (Fig. 2) and result in a blockage ratio of the explosion channel of 2 %. After the fuel injection, the diffusion time t_d between the end of injection and ignition is awaited to enable diffusion driven mixing of fuel and air. Heilbronn et al. investigated the fuel diffusion into air, finding that $t_d = 60\ s$ is sufficient for the assumption of a homogeneous fuel distribution in vertical and horizontal direction (Heilbronn et al. 2021a). For t_d < 60 s, fuel density gradients are present in z-direction. The shorter t_d, the greater the fuel density gradient in z-direction will be. After t_d has passed, another pressure measurement is taken and used to determine the fuel concentration in air before the fuel-air mixture is ignited. The ignition leads to flame propagation from the ignition plate to the endplate. After each experiment, the GraVent is flushed with pressurized air for four minutes to remove combustion products as well as possible fuel remnants, restoring the initial boundary conditions of the experiment.

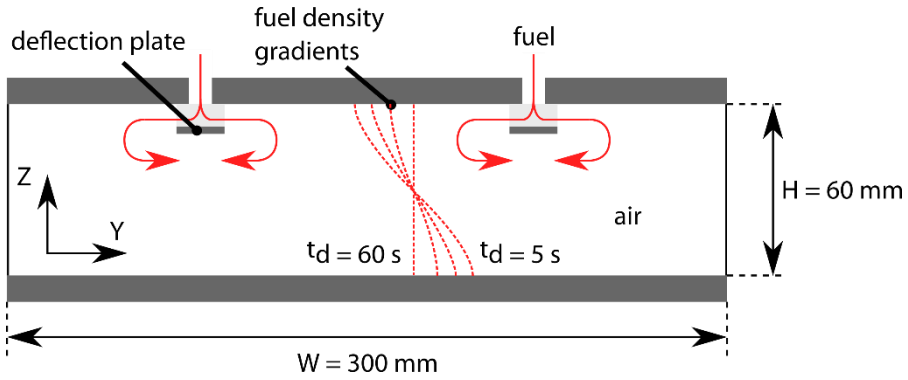

Fig. 2. *Fuel injection and diffusion into the GraVent (red solid lines). The fuel density gradients 5 to 60 s after the fuel injection are represented by red dashed lines.*

The synchronization scheme of the OH-PLIF setup is described in Fig. 3. A single pulse from the computer controlling the GraVent triggers to the Photron SA-X2 high speed camera is sent to start the recording. After that, triggers with a frequency of 20 kHz and 3 µs delay are sent from the Photron SA-X2 to the laser system and the image intensifier. The delay ensures that the laser sheet as well as the image intensifier are triggered during the 50 µs exposure time of the camera. The 8 ns laser pulse is fitted centrally into the 30 ns exposure window of the image intensifier to ensure capturing the entire pulse energy of the laser system in the images. Using the OH-PLIF setup described previously, flame front lengths, flame front wrinkling factors as well as flame front propagation speeds are

determined. The experiments are carried out at least three times for each fuel-to-air ratio investigated. Hereby, only 10 cm of the FOV of the high-speed camera are used for post processing to avoid lens distortion effects on the edges of the images. However, to enlarge the FOV being valid for post processing, the camera recorded images with its center focused at 6 cm distance from the ignition and

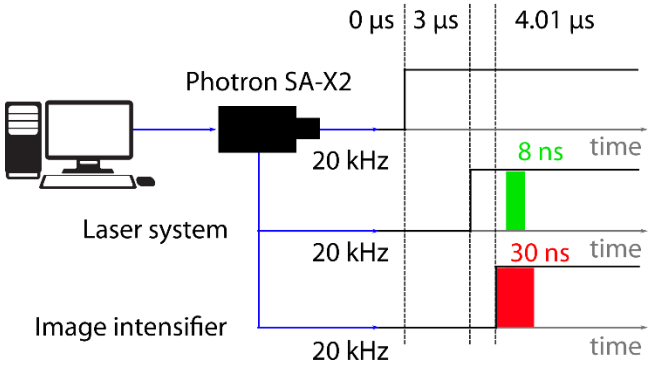

***Fig. 3**. Synchronization scheme of the OH-PLIF system. Black, squared lines indicate trigger signals, coloured areas mark the arrival of the laser beam in the combustion chamber and the exposure time of the image intensifier, respectively.*

is later moved to a new focus point at 14 cm distance to the ignition. For both focus points, at least 3 valid experiments are carried out. The data recorded at the two different focus points is put together in post processing, enabling data analysis between 0 – 18 cm distance of the ignition.

3. Data evaluation

As the description of the experimental setup is concluded, the following section explains the data evaluation. Hereby, the post processing routines for determining the fuel concentration, the flame front in the OH-PLIF images and the calculation of the flame front speeds are described in detail.

The fuel concentration x_{fuel} is determined using

$$x_{fuel} = \frac{p_{pre} - p_{after}}{p_{atm}} \tag{1}$$

where p_{pre} is the pressure measured just before fuel injection, p_{after} is the pressure after injection and before ignition and p_{atm} is the atmospheric pressure. The error in the calculated fuel concentration due to leakage is determined to a maximum of 0.03 %.

In the following, the postprocessing routine for the OH-PLIF images, originally developed for H_2-air flames by Katzy et al. (Katzy et al. 2017) and further developed in this work, is described and visually presented in Fig. 4. In the first step, the raw 8-bit OH-PLIF image is imported. Inhomogeneities of the laser light sheet distribution may be apparent, making a vertical laser light sheet correction necessary (Fig. 4 a). Hereby, the mean intensity of each row of the raw image is determined. Second, the inverse of the mean intensity of every row is multiplied once more onto the corresponding row, yielding in a homogeneous light intensity distribution over the channel height. Moving on to image 4 b), the images are binarized to enable the use of binary edge detection algorithms. To this purpose, a limit pixel value is chosen. Pixels with smaller values than the limit pixel value are set to zero, whereas pixels with values greater than the limit pixel value are set to 255. This may lead to the formation of white, high intensity islands without a direct connection to the flame front, so called white islands. Some of the white islands may belong to the flame front and thus contain information about the flame front structure, while others don't contribute to the flame front. The white islands

belonging to the flame front are now identified. In Fig. 4 c), the white islands contributing to the flame front are connected to the flame front at the location of their smallest distance. The rest of the white islands is deleted. Now, the wrinkled flame front surface A_{eff} is determined using the MATLAB function *bwboundaries*. However, for the calculation of the wrinkling factor Ξ, the determination of the smooth flame front surface A_{smooth} is necessary. A_{smooth} models the flame front surface calculated in state-of-the-art URANS simulations and is interpolated by a cubic spline function through A_{eff} (Fig, 4 d). Finally, A_{eff} and A_{smooth} are plotted into the corrected image

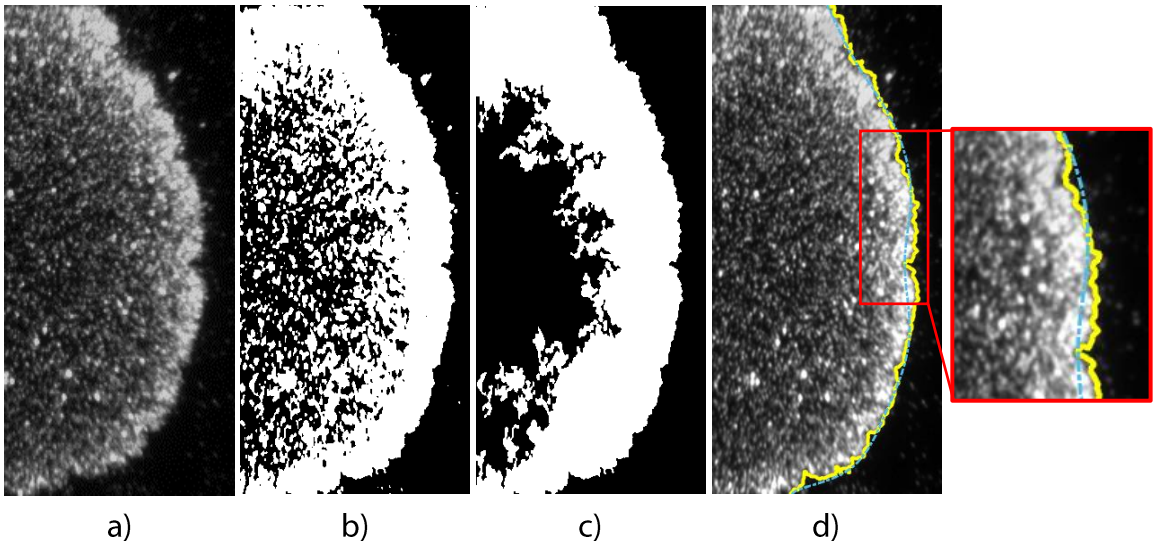

Fig. 4. *Post processing routine of the OH-PLIF images. The wrinkled flame front is marked by the yellow line, the smoothed flame front is represented by the dashed blue line.*

depicted in Fig. 4 a) and the analysis results are stored for further post processing.

After completing the analysis of the OH-PLIF images, the flame front propagation speed v_{FF} is determined. v_{FF} is calculated as follows:

$$v_{FF} = \frac{x_{FF,n+1} - x_{FF,n}}{t_{n+1} - t_n} \tag{2}$$

x_{FF} is the flame front position, while t depicts the point in time at which the image is taken. x_{FF} is determined by the flame front position with the largest distance to the ignition. This way, flame front speed measurements could be taken at 20 kHz, the same frequency the camera is operating with. To obtain x_{FF}, images of a checkered target are recorded. The target images are used to determine the conversion factor between pixels and millimeters $c_{mm,pix}$. x_{FF} was then calculated by the multiplication of the flame front pixel position $x_{FF,pix}$ with $c_{mm,pix}$.

$$x_{FF} = x_{FF,pix} \cdot c_{mm,pix} \tag{3}$$

In the last step, the wrinkling factor Ξ is determined by equation (4). Ξ is calculated by the quotient of A_{eff} and A_{smooth} extracted from Fig. 4 d).

$$\Xi = \frac{A_{eff}}{A_{smooth}} \tag{4}$$

As soon as the image processing is done, flame front lengths, wrinkling factors, flame front positions and the corresponding time markers are stored in text files for subsequent analysis.

4. Results and discussion

4.1. Evaluation of the data quality

In this study, flame front propagation speed v_{FF}, the FA a_{FF} and the wrinkling factors of 50/50 H_2/CO fuels in air are analyzed at varying fuel-to-air concentrations. First, the data quality is analyzed determining the standard deviation σ of the slope a_{FF} of v_{FF} in the v-x-plane. In addition, the so called relative standard deviation σ_{rel} of a_{FF} is calculated dividing σ by the mean slope a_{mean} of v_{FF} over all experiments investigated for calculating σ.

$$\sigma_{rel} = \frac{\sigma}{a_{mean}} \tag{5}$$

σ and σ_{rel} of a_{FF} are depicted in Tab.1. Hereby, σ and σ_{rel} of a_{FF} are given in the v-x-plane, leading to [1/s] as acceleration unit. For x_{Fuel} = 15.0 vol.-%, 17. 5 vol.-%, 25 vol.-% and 29.5 vol.-%, σ_{rel} is comparatively small and is in the cases with fuel concentrations equal or greater than 15.0 vol.-% smaller than 5 %. The measurement series with σ_{rel} > 5 % are found for x_{Fuel} = 13.0 vol.-%. This can be explained by intrinsic combustion instabilities. The leaner the H_2-CO-air mixture gets, the lower its Lewis number will become and the more prone it will be to the influence of LD and TD instability (G. Ciccarelli and S. Dorofeev 2008; Yang et al. 2020). Because of that, a more irregular and wrinkled flame front develops. This finally yields in a higher mean variation compared to H_2-CO-air mixtures with higher Lewis numbers.

Tab. 1: *(Relative) Standard deviations of a_{FF}.*

Fuel-to-air Concentration [vol.-%]	**13.0**	**15.0**	**17.5**	**25.0**	**29.5**
σ [1/s]	1.95	1.16	0.90	3.15	1.53
σ_{rel} [%]	6.15	2.20	1.27	3.33	1.64
Number of Experiments	3	3	9	3	3

4.2. The effect of fuel concentration on the flame front morphology

The influence of the intrinsic flame front instabilities occurring is displayed in Fig. 5. The figure shows flame fronts with different fuel-to-air concentrations during their propagation through the OS of the GraVent. The upper image shows flame fronts with 13.0 vol.-% concentration, the middle image contains flame fronts with 17.5 vol.-% fuel in air and the lower image depicts a flame front with stoichiometric concentration at 29.5 vol.-%. The stoichiometric flame front shows a regular bow-like shape throughout the entire FOV. Small-scale wrinkles occur on the surface, but the overall morphology of the flame front keeps its bow-like shape, nevertheless. At 17.5 vol.-%, the flame front is still of a bow-like shape. However, two differences can be spotted compared to the stoichiometric mixture: Slightly more flame front instabilities disturb the flame front and a tendency of a shift of the flame front in positive z-direction is apparent from 6 cm distance to the ignition source on. The flame front in the leanest case starts with the bow-like shape as well. However, first macroscopic morphology changes are spotted when the flame tip reaches 4 cm distance from the ignition source. The further the lean flame propagates in the OS, the more irregular the overall flame front shape becomes. Several large-scale wrinkles already develop between 6 – 8 cm distance from the ignition. Also, the flame front drifts to GraVent's ceiling potentially due to buoyancy. This effect is not present in the data shown of the flame front with 29.5 vol.-%, because the stoichiometric flame propagates significantly faster than the lean flame front and already has left the FOV when the buoyancy effect could manifest.

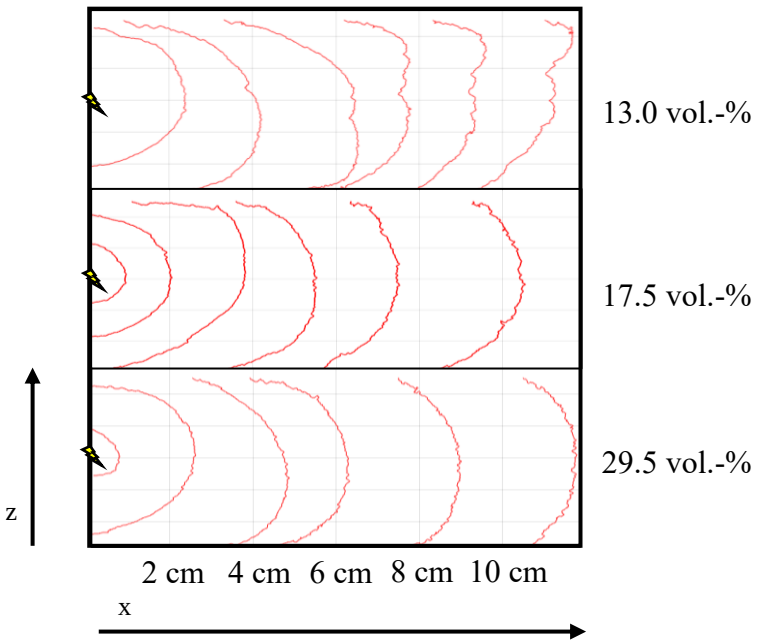

Fig. 5. *Morphological comparison of flame fronts with different fuel-to-air concentrations at different positions. Flashes mark the point of ignition.*

4.3. Influence of fuel composition and concentration onto flame front speed and FA

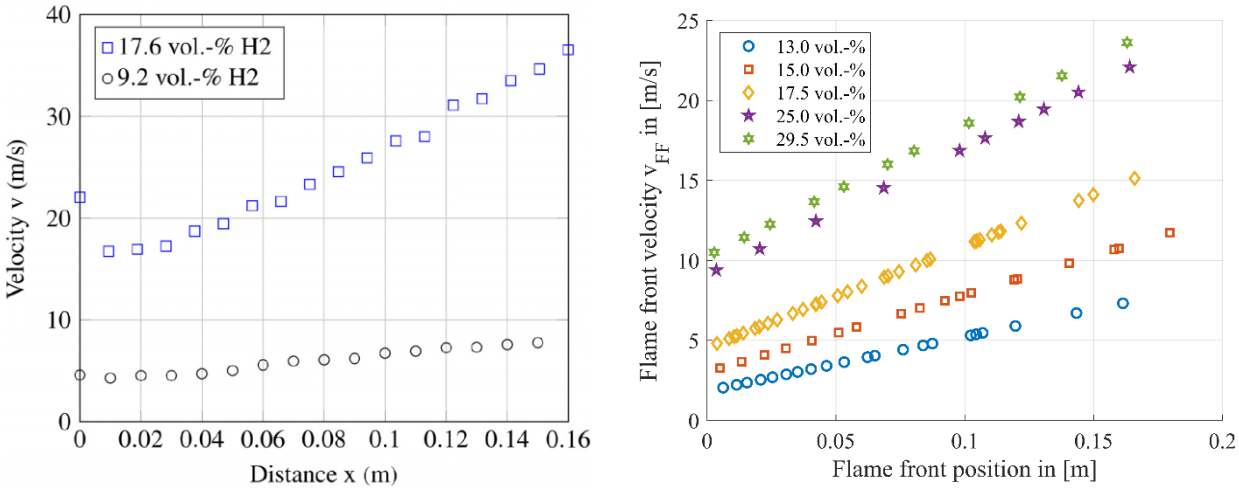

a) Flame front velocities of H_2-air mixtures measured by Katzy (Katzy et al. 2017).

b) Flame front velocities of H_2-CO-air mixtures measured in this study.

Fig. 6: *Flame front velocities with respect to the flame front's distance to the ignition source.*

After discussing the effect of fuel concentration on the flame front morphology in the previous subchapter, flame front propagation speeds of 50/50 H_2/CO fuel mixtures with 13.0 – 29.5 vol.-% are investigated in the following. The flame front speeds of H_2-air mixtures with 9.2 vol.-% and 17.6 vol.-%, respectively, measured by Katzy (Katzy et al. 2017) are depicted in Fig. 6 a), while the flame front speeds of the 50/50 H_2/CO fuel mixtures at fuel-to-air concentrations between 13.0 vol.-% and 29.5 vol.-% measured in this study are plotted in Fig. 6 b). Both graphs show a linear rise in flame front velocity in combination with an increased amount of fuel concentration. Hereby, the flame front speeds with pure H_2 as fuel reach significantly higher propagation speeds than the 50/50 H_2/CO fuel mixtures investigated in this study. The maximum flame front velocities of 50/50 H_2/CO mixtures

measured are in a range between 7.5 – 25 m/s, dependent on the fuel concentration. The pure H_2 fuel however reaches a maximum speed of 37 m/s at 16 cm distance to the ignition source. Compared to the maximum flame front speed of the stoichiometric 50/50 H_2/CO mixture, the H_2 fuel with 17.5 vol.-% is still approximately 54 % faster.

Regardless of fuel mixture and concentration, all velocity graphs show linear behaviour in early stages of FA. Comparing the flame front speeds of the fuel concentrations investigated in Fig. 6 b), it can be seen that an increase of the fuel concentration increases the FA in the v-x-plane of the mixtures as well as maximum flame front speeds at the end of the FOV. However, pure H_2-air flames accelerate significantly faster than H_2-CO-air flames with the same fuel concentration. The FA of the 9.2 vol.-% H_2-air mixture $a_{H2,9.2\,\%} = 27\frac{1}{s}$ measured by Katzy shows only a slightly slower FA compared to the FA of the 50/50 H_2/CO fuel mixture with 15 vol.-% fuel concentration in air $a_{H2/CO,17.6\,\%} = 33\frac{1}{s}$. The difference becomes even larger comparing the 17.6 vol.-% H_2-air mixture to the H_2-CO-air mixtures measured in this study. The flame front speed of 17.6 vol.-% H_2 in air exceeds even the flame front speed of the stoichiometric H_2-CO-air mixture at all times. The FA of 17.6 vol.-% H_2 in air is quantified to be approximately $a_{H2,17.6\,\%} = 154\ \frac{1}{s}$. The FA of the H_2-CO-air mixture with 17.5 vol.-% however is measured to be $a_{H2/CO,17.5\,\%} = 67\frac{1}{s}$, which is less than 50 % of the FA of pure H_2-fuel at a comparable fuel-to-air concentration. Next to the strong dependency of FA on the fuel composition, the dependency of FA on the fuel-air concentration was examined. Fig. 7 shows the fuel-to-air concentration on the x-axis and the FA on the y-axis. As the flame front velocities increase constantly in time, the FA is assumed to be constant within the FOV. Combining the flame front acceleration for various fuel concentrations in Fig. 7, a clear quadratic concentration dependency on the FA is observed. An increase of the fuel content yields in an increase of FA until 25 vol.-% fuel concentration, reaching $a_{FF,25.0\%} = 96.10\frac{1}{s}$. This is in accordance with Heilbronn's et al. paper (Heilbronn et al. 2021b), showing that different H_2-CO-air mixtures reach their maximum terminal velocities at 25.0 vol.-% fuel concentration in the least obstructed GraVent configuration investigated in their paper. Therefore, the maximum FA at 25.0 vol.-% fuel concentration seems reasonable and a

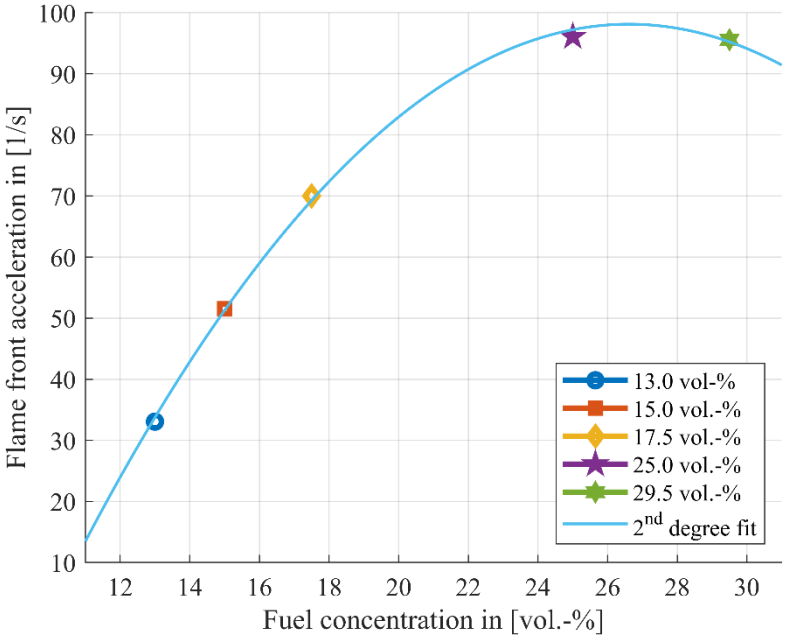

Fig. 7. *Influence of fuel concentration on FA.*

subsequent decrease of FA for fuel concentrations above 29.5 vol.-% is expected. The FA development of H_2-CO-air mixtures with fuel concentrations between 13.0 – 29.5 vol.-% in up to 18 cm distance from the ignition source is eventually modelled by the polynomial fit of 2nd degree in equation (6).

$$a_{50/50\ H2/CO} = -0.3474\frac{1}{s}\cdot x_{fuel}^2 + 18.49\frac{1}{s}\cdot x_{fuel} - 147.9\frac{1}{s} \quad (6)$$

In conclusion, the addition of CO to H_2 yields in a strong inhibition of the combustion process, resulting in a significantly slower FA of H_2-CO fuels compared to pure H_2 fuels with concentrations from lean to stoichiometric mixtures. The new data gathered complements existing FA studies for lean H_2-CO-air mixtures, investigating the early stages of FA by providing optical data of the reaction zone by OH-PLIF images and by providing flame front speeds measured with a high resolution. In addition, equation (6) proposed in this paper allows the determination of the investigated mixtures' FA in a distance up to 18 cm from the ignition source.

4.4. Influence of fuel concentration onto the wrinkling factor Ξ

After the analysis of the flame front speeds and the FA, the flame front wrinkling factor Ξ is determined from the OH-PLIF images. Ξ is determined in this study, because it describes the flame front enlargement due to intrinsic flame instabilities and thus affects the burning velocity of the H_2-CO-air mixture strongly. Fig. 8 shows the development of the wrinkling factor of 50/50 H_2/CO fuel mixtures with different fuel-to-air concentrations between 0 cm and 18 cm distance from the ignition. All graphs are plotted using a polynomial fit of 3rd degree throughout all data points captured for Ξ in each experiment. A 3rd degree polynomial fit is chosen, because FA regimes similar to the regimes defined by Katzy (Katzy et al. 2017) were expected. However, only the first out of the three FA regimes could be spotted observing the results of this study due to limited optical access downstream.

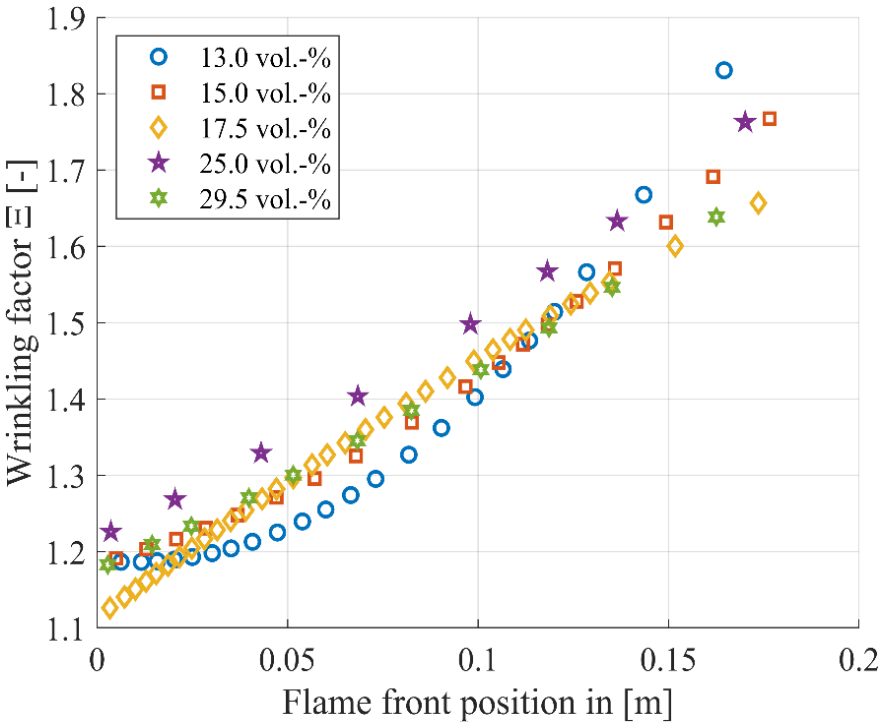

Fig. 8. *Wrinkling factors of the 50/50 H_2/CO fuel mixture at varying fuel concentrations.*

Gas mixtures with fuel contents of 17.5 vol.-% and higher show a linear behavior in the entire FOV. The leaner the mixture becomes, the stronger the graphs deviate from the linear shape. Ξ of 13.0 and 15.0 vol.-%, respectively, increase initially slower than the rest of the gas mixture until a turning point. At 6 cm and 8 cm distance from the ignition, respectively, the Ξ of 13.0 and 15.0 vol.-%, respectively, begins to increase faster than in the rest of the gas mixtures. At the end of the FOV, both mixtures reach higher Ξs than every other mixture. The highest Ξ is observed for 13.0 vol.-% in air. The other mixtures however are hardly distinguishable, because their Ξs are very similar to each other throughout the FOV. One exception is the 25.0 vol.-% mixture, which depicts a slightly higher Ξ than the rest of the gas mixtures with fuel concentrations of 17.5 vol.-% and above. Without taking flame front instabilities into account, 29.5 vol.-% should be the hottest and fastest flame measured. The high Ξ for 25.0 vol.-% in combination with the greatest FA of all gas mixtures measured indicates that there is a trade-off concerning FA between fuel concentration and flame front enlargement due to flame front instabilities. This trade off may lead to the increased FA of 25.0 vol.-%, potentially yielding in a higher explosion hazard compared to the stoichiometric mixture. Reading through section 4.3, it is clear that the addition of CO to H_2 inhibits the combustion strongly and also affects the development of Ξ. Since the combustion process is inhibited strongly by the addition of CO compared to pure H_2-air flames, the fact that the different FA regimes can't be spotted observing Ξ might indicate that the flames in the FOV are still in the development regime. The fact that all Ξs are rising in the entire FOV supports this, because the flame surface area can't increase indefinitely and thus needs to reach at least the flattening regime. In this case, the transition to the flattening regime, and maybe the propagation regime, would appear at later stages of FA. To answer this question about the further development of the flame front surface, further experiments with a larger FOV and varying H_2 contents are needed.

5. Conclusion and outlook

In the present study, OH-PLIF measurements were conducted to investigate early stages of flame propagation of 50/50 H_2/CO fuel mixtures with fuel concentrations between 13.0 – 29.5 vol.-% in air. The influence of the fuel concentration on the flame front morphology was discussed, finding that leaner fuel-air-mixtures are more prone to flame front instabilities. Apart from that, the effect of fuel composition and concentrations on flame front velocity and FA in early stages of FA was quantified. The addition of CO to H_2 as fuel lead to a strongly inhibiting effect, resulting in lower flame front velocities and slower FA. Analyzing the fuel concentrations investigated in this study, it was found that increased fuel concentrations yielded in higher flame front velocities for all concentrations and in increased FA up to 25.0 vol.-% fuel concentration in air. A model calculating the FA of 50/50 H_2/CO mixtures with 13.0 – 29.5 vol.-% in air in the first stages of FA was proposed. Finally, Ξ was determined for H_2-CO-air mixtures using OH-PLIF. A significant effect of fuel concentration on the development of Ξ could not be identified for mixtures of 17.5 vol.-% and above. An influence on lower concentrations was visible, as the Ξ curve was not linear for very lean mixtures. The three FA regimes for the flame front surface area found in previous studies could not be observed due to a limited optical observation window.

To deepen the knowledge about flame surface evolution and flame front instabilities in early stages of flame propagation of H_2-CO-air mixtures, additional studies have to be carried out. The constant rise of Ξ throughout the entire FOV suggests that the flame is still in its development regime and will eventually settle in the flattening regime. To investigate whether the propagation regime establishes

as well, further experiments with a wider FOV should be carried out. This way, the direct observation of the development of the flattening and the propagation regime might be possible. In addition, experiments with higher H_2 contents should be conducted. The additional H_2 in the fuel will increase the mixture's reactivity at the same fuel-to-air concentration compared to the fuel mixture investigated in this study. Consequently, the combustion process will speed up and the development of the different FA regimes observed for H_2-air flames should take place within the FOV for H_2-CO-air flames as well. If the flattening and the propagation regime can be observed for H_2/CO fuels with increased H_2 concentrations, another indication for the existence of these two regimes for 50/50 H_2/CO mixtures is found.

6. References

C. Regis Bauwens, Jeffrey M. Bergthorson & Sergey B. Dorofeev. 2015. Experimental study of spherical-flame acceleration mechanisms in large-scale propane-air flames. *Proceedings of the Combustion Institute* 35(2). 2059–2066. https://www.sciencedirect.com/science/article/pii/S1540748914002764.

Darrieus, G. 1938. Propagation d'un front de flamme La Technique Moderne (Paris) and in 1945 at Congrès de Mécanique Appliquée. *Unpublished work*.

G. Ciccarelli & S. Dorofeev. 2008. Flame acceleration and transition to detonation in ducts. *Progress in Energy and Combustion Science* 34(4). 499–550. https://www.sciencedirect.com/science/article/pii/S0360128507000639.

Gauntt, Randall O., Donald A. Kalinich, Jeffrey N. Cardoni, Jesse Phillips, Andrew Scott Goldmann, Susan Y. Pickering, Matthew Francis, Kevin Robb, Larry J. Ott, Dean Wang & others. 2012. Fukushima Daiichi accident study: status as of April 2012: Sandia National Laboratories (SNL), Albuquerque, NM, and Livermore, CA

Heilbronn, Daniel, Christoph Barfuss & Thomas Sattelmayer. 2021a. Deflagration-to-detonation transition in H2-CO-Air mixtures in a partially obstructed channel. *International Journal of Hydrogen Energy* 46(23). 12372–12383.

Heilbronn, Daniel, Christoph Barfuss & Thomas Sattelmayer. 2021b. Influence of geometry on flame acceleration and DDT in H_2-CO-air mixtures in a partially obstructed channel. *Journal of Loss Prevention in the Process Industries* 71. 104493.

Katzy, Peter. 2021. Combustion Model for the Computation of Flame Propagation in Lean Hydrogen-Air Mixtures at Low Turbulence, Technische Universität München.

Katzy, Peter, Josef Hasslberger, Lorenz R. Boeck & Thomas Sattelmayer. 2017. The effect of intrinsic instabilities on effective flame speeds in under-resolved simulations of lean hydrogen-air flames. *Journal of Nuclear Engineering and Radiation Science* 3(4). 41015.

Kumar, R. K., G. W. Koroll, M. Heitsch & E. Studer. 2000. Carbon monoxide-hydrogen combustion characteristics in severe accident containment conditions. *Organisation for Economic Co-operation and Development, Paris, France, Report No. NEA/CSNI*.

Kusharin, A. Yu, G. L. Agafonov, O. E. Popov & B. E. Gelfand. 1998. Detonability of H_2/CO/CO_2/Air Mixtures. *Combustion science and technology* 135(1-6). 85–98.

Landau, L. 1988. On the theory of slow combustion. In *Dynamics of curved fronts*, 403–411: Elsevier.

Veser, A., G. Stern, J. Grune, W. Breitung & B. Burgeth. 2001. CO-H2-air combustion tests in the FZK-7m-tube. *Programm Nukleare Sicherheitsforschung, Jahresbericht*.

Yang, Xufeng, Minggao Yu, Kai Zheng, Pengpeng Luan & Shixin Han. 2020. On the propagation dynamics of lean H2/CO/air premixed flame. *International Journal of Hydrogen Energy* 45(11). 7210–7222.

Experimental Investigation of Direct Reduced Iron Dust Explosion Characteristics in the 20 L Sphere

Aleksandra Semenova[a], Theresa Angerler[a], Michael Hohenberger[a] & Harald Raupenstrauch[a]

[a] Montanuniversitat Leoben, Chair of Thermal Processing Technology, Leoben, Austria

E-mail: *aleksandra.semenova@unileoben.ac.at*

Abstract

With the European iron and steel industry considering a shift towards environmentally sustainable processes, such as direct reduction leading to electric arc furnaces, the transportation and handling of Direct Reduced Iron (DRI) becomes crucial. However, the potential for finely dispersed iron dust to generate explosions poses a significant safety concern. This study investigated the explosion characteristics of DRI (D) dust, along with the effects of storage conditions and the presence of hydrogen in the atmosphere, utilizing a 20 L explosion chamber. Key findings include: Analysis of DRI D dust explosion characteristics, significance of storage conditions on maximum pressure and rate of pressure rise, observation of explosion behavior of hybrid mixtures.

Keywords: *hazards, industrial explosions, dust explosions, iron, humidity*

1. Introduction

The European iron and steel industry is considering a shift from blast furnace to direct reduction process, aiming for a more environmentally sustainable approach (Dutta & Sah, 2016). This factor underscores the necessity of investigating the transportation of DRI products. Direct Reduced Iron (DRI) is classified into three types under the IMSBC Code: DRI (A) Hot Briquetted Iron (HBI), DRI (B) in lumps and pellets, and DRI (C), comprising by-product fines from manufacturing and handling processes of DRI (A) and/or DRI (B) (*Cargo Handbook*, n.d.).

The main sources of DRI fines are twofold:

Generation during Direct Reduction Process Handling: During the handling of DRI (B) and its transformation into DRI (A), fines are inevitably produced due to abrasion. Users of both DRI types require minimal fines content to avoid drawbacks in the EAF process. To meet this demand, DRI (A) and (B) undergo screening before shipment, generating Metallised DRI fines. Additionally, the cooling process of DRI (A) in a quench tank also produces fines, known as "quench tank fines," which are included with the Metallised DRI fines (International Iron Metallics Assosiation, 2020).

Generation in Gas-Based Shaft Direct Reduction Furnaces: In these furnaces, iron ore fines reduce the permeability of the iron ore burden, affecting the reduction process. Screening removes fines before charging into the furnace (Umadevi et al., 2022).

The current classification under the IMSBC Code as DRI (C) poses challenges due to impractical moisture content restrictions and the requirement for inert gas, which is more suited for a different classification. As a result, there are discussions underway at the IMO to introduce a new classification, DRI (D), which would likely address these discrepancies and improve the regulations governing the transport of DRI Fines. DRI (D) defined as a by-product with moisture content of at least 2% and

particles with an average size less than 6.35 mm, aged for at least 30 days prior to loading. DRI (D) poses hazards such as risk of overheating, fire and explosion during transport due to the fact that this cargo reacts with air, fresh water and seawater to produce hydrogen and heat (International Iron Metallics Assosiation, 2020).

Understanding the explosion characteristics of DRI (D) is crucial for industrial safety (Danzi & Marmo, 2019a). Past research indicates a correlation between iron dust explosion behavior and explosion risks, influenced by various factors such as particle size, concentration, and turbulence conditions (Chanut & Heymes, 2022; Clouthier et al., 2019a; Danzi et al., 2021a; Guo, Ren, Huang, et al., 2022; Meng et al., 2023). However, research often overlooks diverse storage conditions, especially for DRI (D), necessitating further investigation.

The capacity of DRI (D) to generate hydrogen underscores the importance of comprehending DRI (D) explosion characteristics in hydrogen-containing environments. Addressing this gap in research is essential for enhancing safety measures and mitigating explosion risks in industrial settings where iron dust is prevalent.

2. DRI (D) dust samples characteristics

The HBI material used in this study industrial is a by-product from the HBI Plant in Corpus Christi. To investigate the explosion characteristics and to obtain DRI (direct reduced iron) grade D, the input material was ground under nitrogen atmosphere to a particle size of less than 500 µm. Grain size analysis of this ground dust was conducted according to ÖNORM EN 15415-1 standards. Detailed results of the particle size distribution can be found in Table 1 and Fig. 1. The median value (d_{50}) of the particle size distribution was determined to be 53.7 µm.Upon receiving and grinding the sample, the water content was determined at 105°C under vacuum until a constant mass was achieved, following DIN EN ISO 18134-1 standards. The sample exhibited a water content of 3.90%.

Table 1. *Particle size distribution of DRI sample*

Mesh size [µm]	Residue [Ma.-%]	Passage [Ma.-%]
500	0,0	100,0
250	2,5	97,5
125	20,2	79,8
71	37,2	62,8
63	42,8	57,2
32	68,0	32,0
20	84,8	15,2
0	100,0	0,0

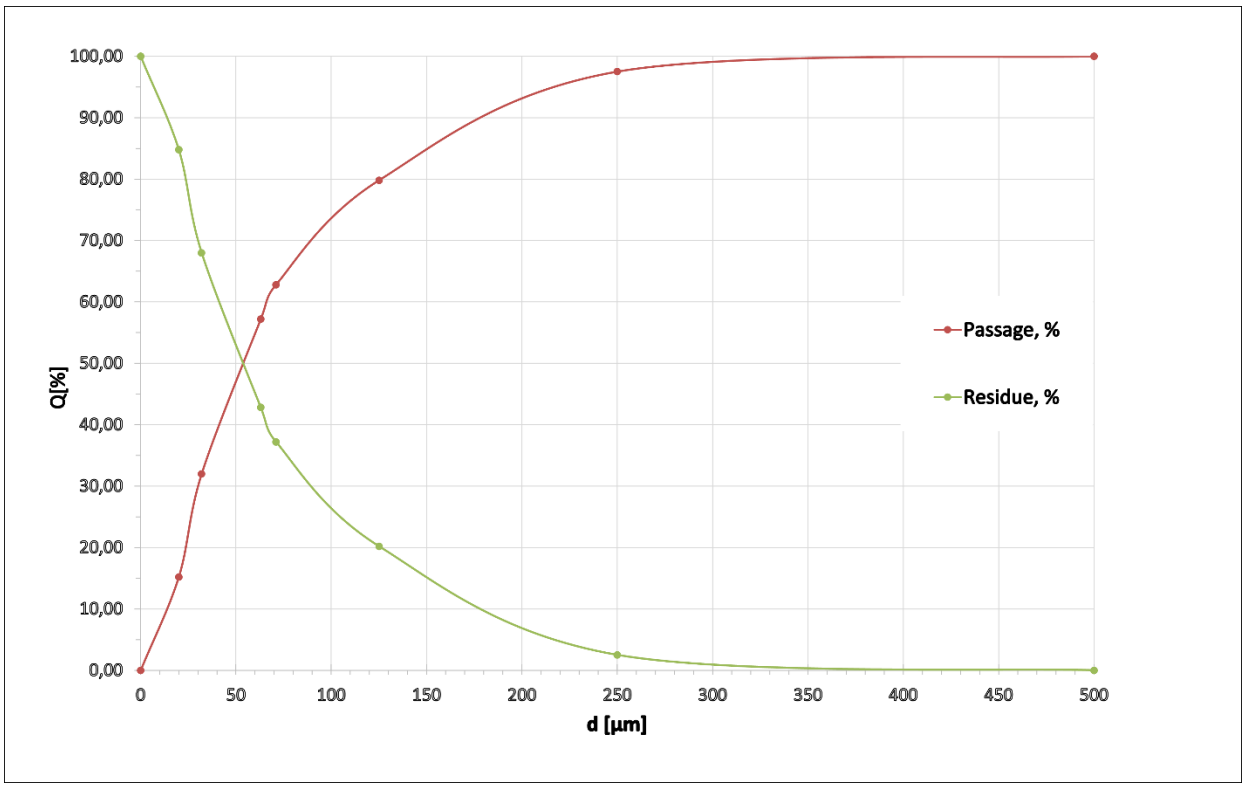

Fig. 1. *Particle size distribution of DRI (D) dust*

Given the properties of the material and the manner in which the dust was generated, it can be classified as DRI (D). Further, we will refer to it as DRI (D) dust.

3. The sample preparation

3.1 Storing DRI dust under different storage conditions

During the transportation of DRI (D), changes in the storage conditions of the dust may occur. According to the "Guide for Handling, Storage and Shipping of Direct Reduced Iron By-Product Fines (DRI D)" from October 2020 (International Iron Metallics Assosiation, 2020), these alterations may involve:

Temporary Temperature Increase: DRI (D) might undergo a transient temperature rise of approximately 30°C (86°F) above ambient temperature post-bulk handling, like loading onto a ship. This increase results from the brief exposure of all material surfaces to air, although the material typically reverts to ambient temperature levels over time.

Moisture Content Concerns: DRI (D) could liquefy if transported with a moisture content surpassing its Transportable Moisture Limit (TML), typically ranging from 9-12%.

DRI (D) can be stored in diverse locations or containers, including stockyards/warehouses (covered or uncovered) and silos, hoppers, or other confined spaces. Hence, it's vital to evaluate the potential impact of various storage conditions on the material's properties and transportation safety.

The present study aimed to simulate real-world conditions encountered by DRI (D) during handling, transportation, and storage, particularly focusing on short-term reoxidation conditions (1 week). The objective was to assess the alteration in the behaviour of DRI (D) regarding explosion characteristics. Five distinct climatic boxes were employed to evaluate the behaviour of DRI (D) dust samples under simulated conditions.

In Box 1, DRI dust samples' explosion parameters were examined after storing as delivered in sealed barrels to prevent oxidation. In Box 2, the procedure entailed filling the sample with water once and allowing the water to evaporate under normal conditions. Following this, the sample was exposed to ambient lab air for one week. Samples in Box 3 were stored at 60 degrees Celsius and 80% humidity in a climate closet. Continuous immersion of samples in deionized water was conducted in Box 4. In Box 5, samples were immersed in saltwater (35 grams of salt per 1 liter of water) for one week.

Boxes 1, 2, 4 and 5 were maintained at room temperature, ranging from 22-25°C. These boxes are sealable and constructed from transparent plastic. Upon completion of the storage process, the drying procedure was carried out using nitrogen at 105 degrees Celsius in an oven, followed by the assessment of explosion parameters.

3.2 Explosion severity

The parameters of explosion severity, including P_{max} (maximum pressure) and $(dP/dt)_{max}$ (maximum rate of pressure rise), were determined using a 20 L apparatus depicted in Figure 2, following the guidelines outlined in ISO 6184-1/2 .

The test chamber comprises a stainless-steel hollow sphere with a capacity of 20 liters. It features a water jacket designed to dissipate heat from explosions or maintain controlled temperatures during tests. Dust is introduced into the sphere from a pressurized storage chamber via an outlet valve and a nozzle. The outlet valve is operated pneumatically using an auxiliary piston, while compressed air valves are electrically activated. The ignition source is centrally positioned within the sphere. Two "Kistler" piezoelectric pressure sensors are mounted on the measuring flange (Cesana & Siwek, n.d.). Two pyrotechnic igniters, each with a power of 5 kJ, were utilized as ignition sources. The ignition delay, indicating the time between dust dispersion onset and ignition activation in the dust/air mixture, was standardized at 60 ms for consistent dust testing procedures. This consistency ensures that the level of turbulence remains consistent across all experiments.

Modifications were implemented on the sphere to assess the explosibility of dust in the atmosphere containing hydrogen. In order to obtain a comparable result, the procedure was conducted according to (Spitzer et al., 2023). Two pre-test procedures are required to check leakage rate and deviation and scattering of gas amount (Spitzer, 2021). The flowchart of the modified 20L apparatus is illustrated in Figure 2. In the main experiment, the explosion characteristics of the hybrid mixture of hydrogen and DRI (D) dust are determined. At each test, two chemical igniters with an ignition energy of 1 kJ were used as the ignition source. After that, the desired amount of dust is weighed and poured into the dust container. The 20-liter apparatus is then evacuated to a certain pressure by means of a vacuum pump and then filled up to 400 mbar with the calculated pressure quantity of hydrogen. The concentrations are entered in the program and the ignition is carried out. After each attempt, the 20 L must be thoroughly cleaned.

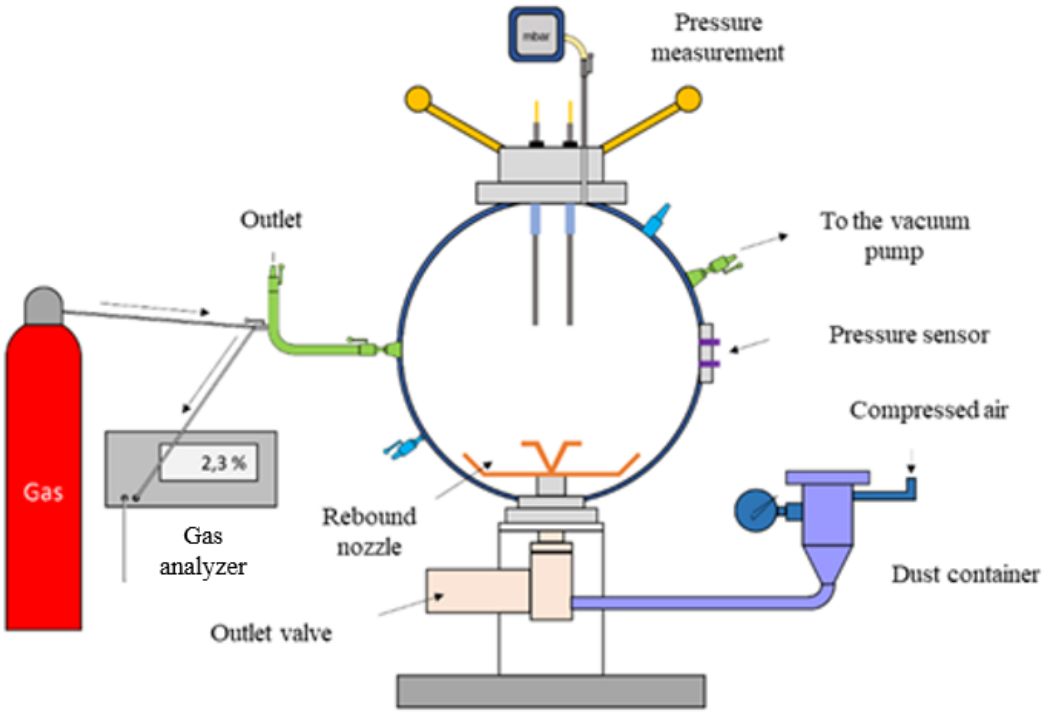

Fig. 2. *20L-sphere setup for hybrid dust gas mixtures with additional absolute pressure and gas analyser.*

During test, the explosion pressure is recorded as a function of time using piezoelectric pressure sensors (Figure 4). Explosion overpressure P_{ex} shows the difference between the pressure at ignition time and the pressure at the culmination point at nominal fuel concentration. The maximum slope of a tangent through the point of inflexion in the rising portion of the pressure vs. time curve is a rate of pressure rise with time $(dP/dt)_{ex}$ at nominal fuel concentration. Maximum value of P_{max} and Maximum value of $(dP/dt)_{max}$ determined by tests over a wide range of fuel concentrations.

3.3 Mechanisms of iron dusts explosion

Iron combustion is a nonvolatile process, meaning it occurs through a heterogeneous reaction rather than evaporation. When iron combusts in air, it doesn't produce a gas-phase diffusion flame typical of volatile substances. Instead, the iron particle itself emits light as it undergoes combustion. This process is governed by the reaction between iron and oxygen, which takes place at the interface between the iron surface and the surrounding air (Bidabadi & Mafi, 2013).

The adiabatic flame temperature, representing the maximum temperature achieved during combustion without heat loss, for iron combustion in air is approximately 2285 K. However, it's important to note that despite the high temperature, iron does not reach its boiling point of 3023 K during combustion. This is because the reaction primarily occurs on the surface of the iron particles rather than throughout the entire particle (Sun et al., 1990).

During combustion, a layer of iron oxide product accumulates on the surface of the iron particle as the reaction progresses. This reaction at the air-iron oxide interface is considered the rate-controlling step, meaning it determines the overall rate of combustion (Ogle, 2016).

In summary, iron combustion relies on a heterogeneous reaction between iron and oxygen, resulting in the emission of light from the iron particle as it undergoes combustion. The accumulation of iron oxide product on the particle's surface further characterizes this process.

4. Results and discussion

4.1 Influence of different storage facilities on DRI dust explosion characteristics

The DRI (D) dust obtained without specific storage conditions (box 1) showed the highest explosion pressure at a concentration of 3750 g/m^3. The evaluation of the measured data depicted in Figure 3 and agrees with a typical dust-type pressure history for metallic powder (Danzi et al., 2021). It implies that the progression of dust explosion pressure can be segmented into three phases. The initial phase involves the injection of dust from t_1 to t_2, with t_{ig} denoting the ignition delay time. The subsequent phase pertains to the expansion of dust explosion from t_1 to t_2, where t_c represents the combustion duration time. Following t_3, the explosion ceases, and the pressure begins to decrease due to heat dissipation towards the walls of the 20-L chamber. An initial rapid pressure increases attributable to a combustion regime for Direct Reduced Iron (D) dust with optimal oxygen availability. Non-adiabatic effects become evident post maximum pressure, as gradual reduction occurs due to heat losses. The results indicate a value of $(dP/dt)_{max}$ = 130 bar/s and the value of P_{ex} = 4.5 bar. Obtained value is similar to other experimental values retrieved from the literature (Clouthier et al., 2019b; Danzi et al., 2021b; Danzi & Marmo, 2019b).

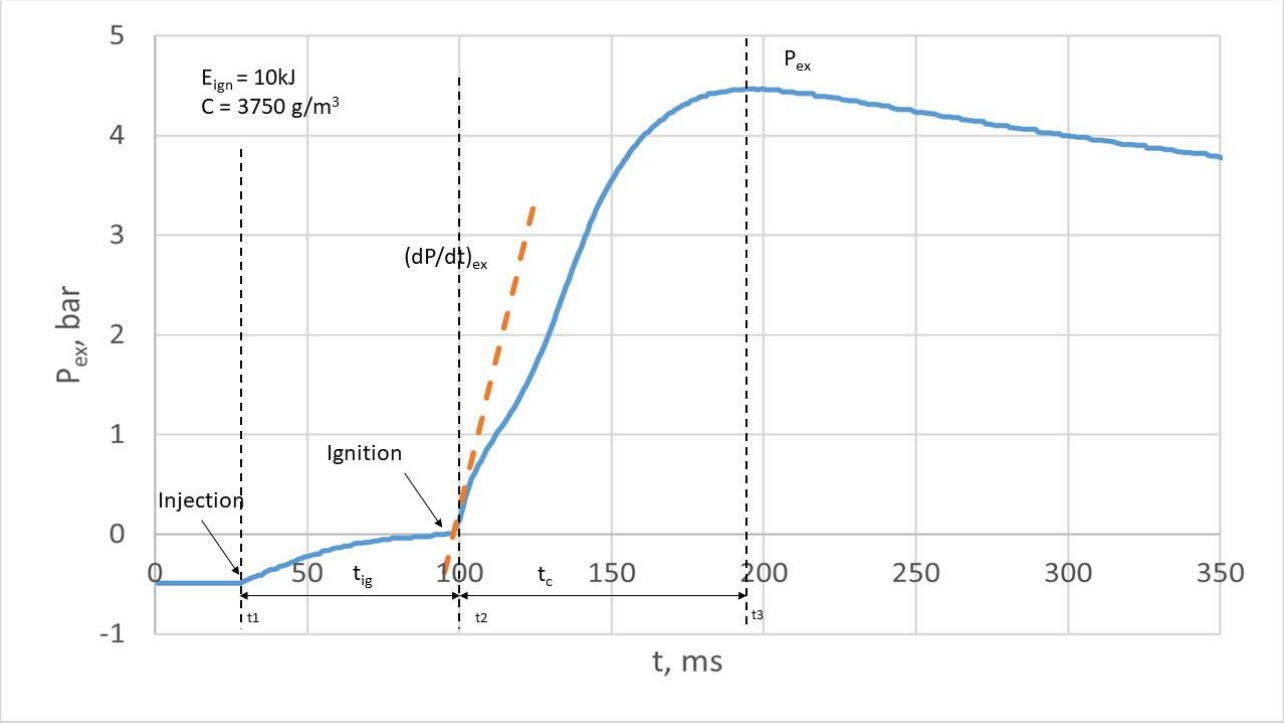

Fig. 3. *Explosion process curve of DRI (D) dust in the standardized 20-L spherical chamber*

Given the potential storage locations including stockyards, warehouses, silos, and confined spaces, it's vital to evaluate the impact of different storage conditions on the material's properties and transportation safety. In order to identify explosion parameters during shipping, handling and storage of Direct Reduced Iron Fines, samples were stored in controlled environment. Table 2 represent the maximum pressure P_{max} of the samples after different storage conditions, as well as the percentage

decrease in maximal pressure after the storage procedure. To better quantitatively analyze the inhibition effect of iron oxides, a weakening efficiency (WE) is defined as

$$WE = \frac{P_{max(box\_1)} - P_{max(box\_n)}}{P_{max(box\_1)}} \cdot 100\%$$

where $P_{max(box\_1)}$ is the explosion pressure before storage, and $P_{max(box\_n)}$ is the explosion pressure after storage.

***Table 2**. Explosion parameters of the samples*

Storage conditions	P_{max}, bar	Weakening efficiency (WE), %
Box 1	4,5	-
Box 2	4,3	4
Box 3	4,2	7
Box 4	3,8	16
Box 5	3,2	29

The storage conditions have a decreasing effect on the maximum pressure as soon as was faced water influence. While the effects in Box 2 and 3 may be deemed insignificant (up to 7%), the constant presence of water and saltwater in Box 4 and 5 does indeed exert a more substantial influence (up to 29%). Figure 4 represent the evaluation of the rate of pressure rise of samples during the explosion at 3000 g/m^3.

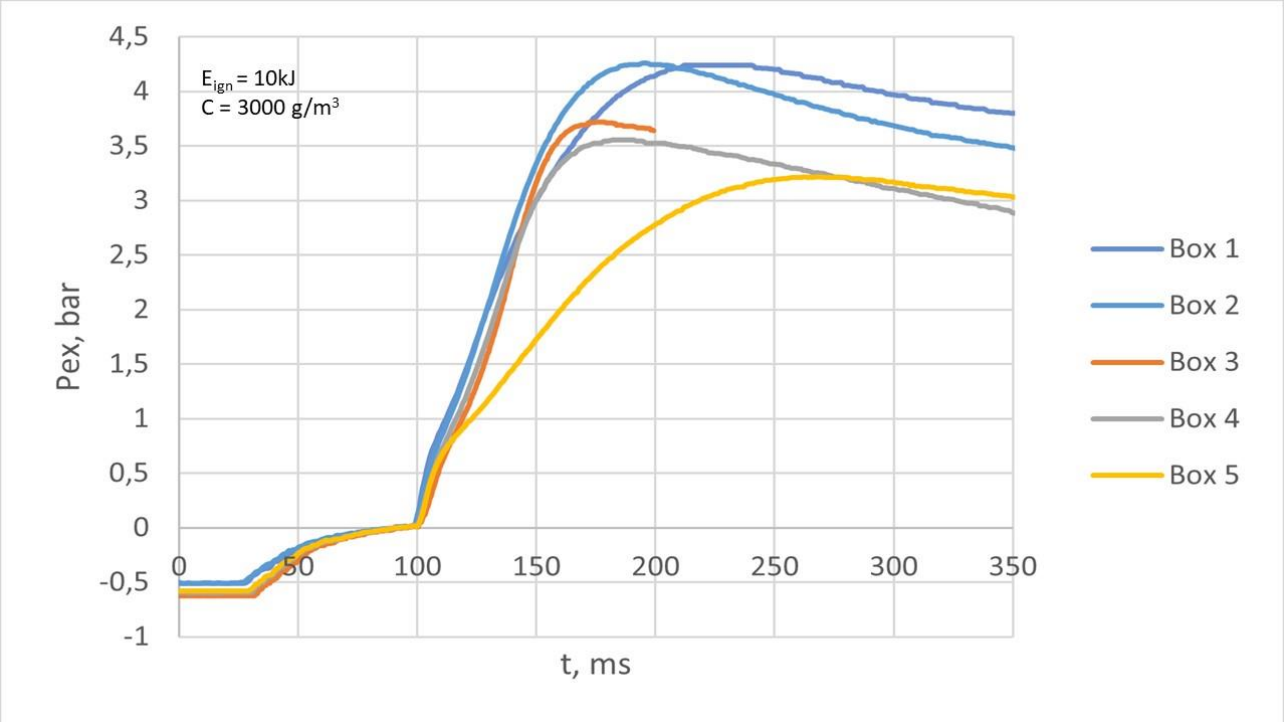

***Fig.4.** Explosion process curve of DRI (D) dust in the standardized 20-L apparatus after different storage conditionals*

Figure 5 shows steady reduction of P_{ex} from Box 1 to Box 5. The reduction in explosion violence can be attributed directly by oxidation of DRI (D) dust during storage (Daghagheleh et al., 2023). Iron oxides, such as Fe_2O_3 and Fe_3O_4, exhibit inhibitory effects, which can lessen the severity of iron dust

explosions and dampen the combustion process (Guo, Ren, Wei, et al., 2022). Notably, the mechanism of explosion after storage remains the same as it was described above. From Figure 5, it follows that storage in Box 5 leads to the fact, that combustion duration lasts longer (t_c). As a result of oxidation, the oxide covers the surface of iron dust, increasing the resistance of oxygen diffusion to the DRI (D) dust, slowing down the combustion process and prolonging the combustion duration. The longer period of storage can cause a more significant influence on burning velocity of particles. Further research into the oxidation of DRI (D) dust during storage is necessary to comprehend particle behavior during explosions for the purpose of implementing protective measures.

4.2 Explosion characteristics of DRI D dust in hydrogen/air mixed gas environment

According to "A Guide to Handling, Storage & Shipping", the main risk linked with DRI (D) is the potential buildup of hydrogen in confined areas, like ship holds and nearby spaces, due to the material's generation and emission of hydrogen. The constant evolution of hydrogen in DRI (D) occurs due to its moisture content, which initiates the aqueous corrosion of iron (International Iron Metallics Assosiation, 2020).

Such a hybrid mixture of combustible dusts and flammable gases may pose a higher explosion risk since the hybrid explosions can still be initiated even though both the gas and the dust concentration are lower than their lower explosion limit (LEL) values (Wu et al., 2023). Many investigations have been performed focusing on explosion behavior of the hybrid mixtures (Addai et al., 2015; Amyotte et al., 2010; Russo et al., 2012). Knowledge of the explosibility of the hybrid mixtures is therefore vitally important when conducting safety reviews for process hazards (Ji et al., 2022). Unique explosion protection measures might need to be established for hybrid mixture with DRI (D) dust, differing from those typically designed for-phase mixtures.

For that reasons DRI (D) dust (Box 1) at the concentration of 3000 g/m^3 were used to test the dust explosion in three different volume rations of hydrogen/air gas environments (1, 4 and 10 % of H_2). To monitor the behavioral shifts occurring with the hybrid mixture, all tests were conducted using 2kj ignitors. The test results are presented in Table 3 and Figure 5.

Table 3. *Obtained explosion parameters of the samples*

Presence of hydrogen in a hybrid mixture, %	DRI (D) dust concentration, g/m^3	P_{ex}, bar	$(dP/dt)_{ex}$, bar/s
0	3000	4,2	130
1	0	0,3	0
4	0	0,3	0
10	0	2,6	257
1	3000	4,1	70
4	3000	4,3	175
10	3000	4,6	575

Table 3 reveals that hybrid mixtures yield more intense explosions in comparison to scenarios involving only dust or hydrogen. While the dust explosion resulted in a P_{ex} value of 4,2 bar, the addition of 10% hydrogen led to an increase of up to 4,6 bar. Similarly, the rate of pressure rise over time exhibited a similar trend. Despite the lower explosive limit (LEL) of hydrogen being 4%, we did not observe an explosion at hydrogen concentrations of 1% and 4%. Hydrogen explosions only

occurred at a 10% concentration, unlike hybrid mixtures where, as anticipated, explosions transpired at a 1% concentration. Comparative analysis of the explosion process showed in Fig. 6.

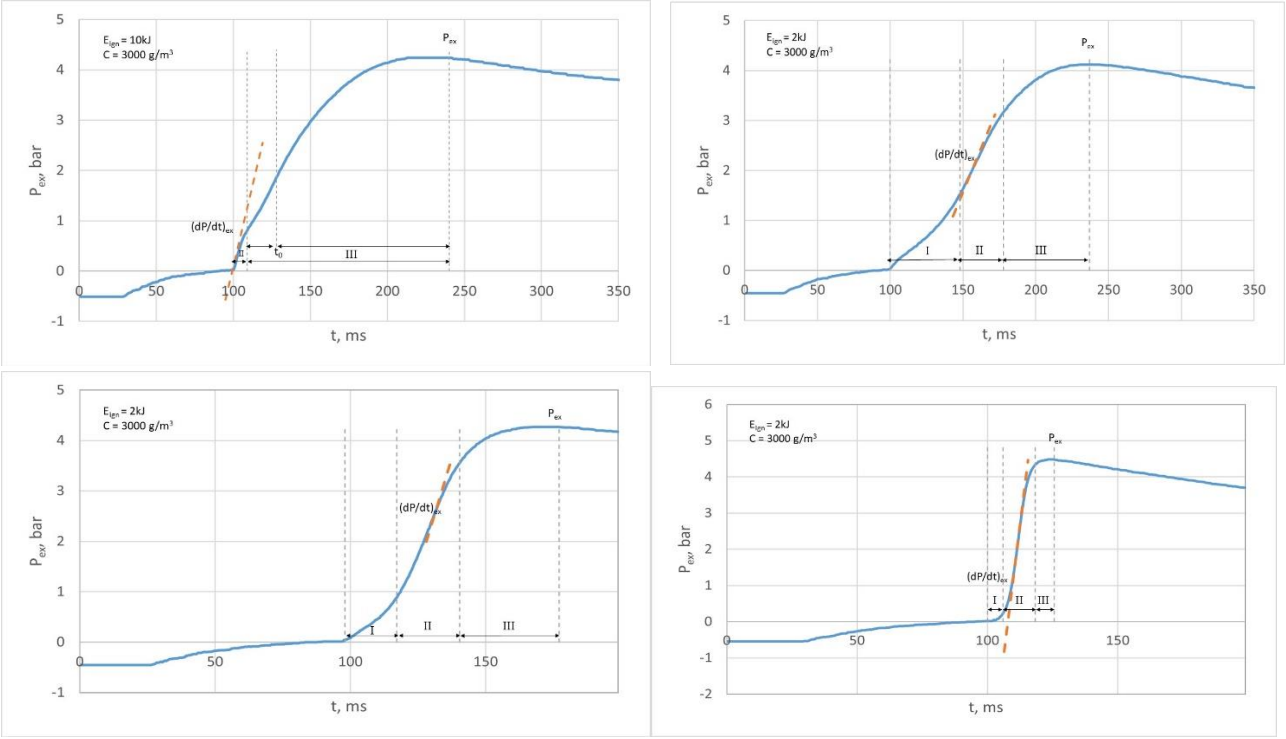

Fig. 5. *Different hybrid explosion process curves: (a) DRI (D) dust; (b) DRI (D) dust and 1% H_2; (c) DRI (D) dust and 4% H_2; (d) DRI (D) dust and 10% H_2;*

According to (Guo, et al., 2022), the typical explosion curve can be divided into three stages. Period I is characterized as the induction period, denoting the formation of the front of the dust flame and the self-acceleration process of flame propagation. Period II delineates the self-sustaining propagation of the flame, illustrating the stable and efficient propagation of flame waves following self-acceleration. Period III denotes the non-adiabatic phase, signifying the deceleration of the curve's upward trend. The flame front reaches the wall of the explosion sphere, and the subsequent combustion reaction zone continues to propagate towards the wall until the culmination of the entire combustion process, where the explosion pressure peaks before gradually dissipating due to heat loss(Kuai et al., 2013).

However, the explosion process of iron dust differs significantly from that of other dusts. Firstly, according to (Guo, Ren, Wei, et al., 2022) there is no observed self-accelerating process (period I) during the explosion, and the rate of explosion pressure rise reaches its maximum almost immediately after ignition. This statement agrees with result on Fig. 3, 4 and 5 *a*. However, in a hybrid mixture with hydrogen, the reaction mechanism changes: Period I is illustrated in Fig.5 *b,c,d.*

Also, on iron dust explosion there are two pressure accelerations: the iron dust has a turning time point t_0 in the period III. The pressure rise rate slows down before t_0, and then accelerates for the second time. (Guo, Ren, Wei, et al., 2022). The same behavior demonstrates DRI (D) dust (Fig. 5a). But in hybrid mixture (Fig. 5 bcd) the pressure rise rate begins to decrease after the end of the period II. Furthermore, the combustion time shortens with the presence of hydrogen.

Further studies are necessary to fully understand the unique explosion characteristics of DRI (D) dust. By gaining a comprehensive understanding of these factors, researchers can develop effective mitigation strategies to prevent or control explosions in industrial settings, ensuring the safety of workers and the public.

5. Conclusions

In order to prevent damages to health, environment and productivity, adequate prevention and protection means should be specify regarding DRI (D) transportation. With inherent hazards of explosions during transport of DRI (D), comprehending the explosion characteristics of DRI is paramount for industrial safety. The explosion characteristics of DRI (D) dust, the storage effect and presence hydrogen in atmosphere were studied by using a 20 L explosion chamber. The following results were obtained:

1. The explosion characteristics of DRI D dust have been determined. The data reveals, that the maximum pressure recorded (P_{max}) is 4.5 bar, the maximum rase of pressure raise is 130 bar/s ($(dP/dt)_{max}$).

2. The created storage conditions diminish the maximum explosion pressure when compared to the value of the sample in Box 1. While the effects in Box 2 and 3 may be deemed insignificant (up to 7%), the constant presence of water and saltwater in Box 4 and 5 does indeed exert a more substantial influence (up to 29%), which can be attributed directly by oxidation of DRI (D) dust during storage.

3. Hybrid mixtures lead to more intense explosions compared to scenarios involving only dust or hydrogen. The presence of hydrogen also prompts a noted alteration in the explosion mechanism: in hybrid mixture was recorded the presence of induction period, the self-sustaining propagation of the flame and the non-adiabatic phase, while the DRI (D) explosion curve demonstrates only the last two steps. DRI (D) dust demonstrated two pressure accelerations, meanwhile hybrid mixture has the pressure rise rate begins to decrease after the end of the reaching maximum.

Further research into explosion behavior of DRI (D) is imperative to understand particle behavior during explosions, with the aim of implementing more effective protective measures.

Acknowledgments

The authors would like to thank the Austrian Research Promoting Agency (FFG) and Innofreight Solutions GmbH. FFG funding and services enable this innovative project with partners between science and industry. FFG funding programs are financed by the Republic of Austria - specifically the Federal Ministry for Climate Protection, Environment, Energy, Mobility, Innovation and Technology (BMK) and the Federal Ministry of Labor and Economic Affairs (BMAW) - but also by participating federal states as well as companies and research organizations. www.ffg.at.

References

Addai, E. K., Gabel, D., & Krause, U. (2015). Explosion characteristics of three component hybrid mixtures. *Process Safety and Environmental Protection*, *98*, 72–81. https://doi.org/10.1016/j.psep.2015.06.013

Amyotte, P., Lindsay, M., Domaratzki, R., Marchand, N., Di Benedetto, A., & Russo, P. (2010). Prevention and mitigation of dust and hybrid mixture explosions. *Process Safety Progress*, *29*(1), 17–21. https://doi.org/10.1002/PRS.10333

Bidabadi, M., & Mafi, M. (2013). Time variation of combustion temperature and burning time of a single iron particle. *International Journal of Thermal Sciences*, *65*, 136–147. https://doi.org/10.1016/J.IJTHERMALSCI.2012.10.019

Cargo Handbook. (n.d.). Retrieved March 18, 2024, from https://www.cargohandbook.com/Direct_Reduced_Iron_(DRI)

Cesana, C., & Siwek, R. (n.d.). *KSEP - Manual*. Retrieved March 10, 2024, from www.cesana-ag.ch

Chanut, C., & Heymes, F. (2022). Determination of iron burning velocity using the 20-L sphere. *Chemical Engineering Transactions*, *91*, 169–174. https://doi.org/10.3303/CET2291029

Clouthier, M. P., Taveau, J. R., Dastidar, A. G., Morrison, L. S., Zalosh, R. G., Ripley, R. C., Khan, F. I., & Amyotte, P. R. (2019a). Iron and aluminum powder explosibility in 20-L and 1-m3 chambers. *Journal of Loss Prevention in the Process Industries*, *62*. https://doi.org/10.1016/j.jlp.2019.103927

Clouthier, M. P., Taveau, J. R., Dastidar, A. G., Morrison, L. S., Zalosh, R. G., Ripley, R. C., Khan, F. I., & Amyotte, P. R. (2019b). Iron and aluminum powder explosibility in 20-L and 1-m3 chambers. *Journal of Loss Prevention in the Process Industries*, *62*, 103927. https://doi.org/10.1016/J.JLP.2019.103927

Daghagheleh, O., Schenk, J., Zheng, H., Taferner, B., Forstner, A., & Rosenfellner, G. (2023). Long-Term Reoxidation of Hot Briquetted Iron in Various Prepared Climatic Conditions. *Steel Research International*, *94*(1). https://doi.org/10.1002/srin.202200535

Danzi, E., & Marmo, L. (2019a). Dust explosion risk in metal workings. *Journal of Loss Prevention in the Process Industries*, *61*, 195–205. https://doi.org/10.1016/J.JLP.2019.06.005

Danzi, E., & Marmo, L. (2019b). Dust explosion risk in metal workings. *Journal of Loss Prevention in the Process Industries*, *61*, 195–205. https://doi.org/10.1016/J.JLP.2019.06.005

Danzi, E., Pio, G., Marmo, L., & Salzano, E. (2021a). The explosion of non-nano iron dust suspension in the 20-l spherical bomb. *Journal of Loss Prevention in the Process Industries*, *71*. https://doi.org/10.1016/j.jlp.2021.104447

Danzi, E., Pio, G., Marmo, L., & Salzano, E. (2021b). The explosion of non-nano iron dust suspension in the 20-l spherical bomb. *Journal of Loss Prevention in the Process Industries*, *71*, 104447. https://doi.org/10.1016/J.JLP.2021.104447

Dutta, S. K., & Sah, R. (2016). Direct Reduced Iron: Production. In *Encyclopedia of Iron, Steel, and Their Alloys* (pp. 1082–1108). CRC Press. https://doi.org/10.1081/e-eisa-120050996

Guo, Y., Ren, K., Huang, W., & Wu, D. (2022). An alternative explosion criterion of combustible dusts based on combustion duration time: Applications for minimum explosion concentration

and limiting oxygen concentration. *Powder Technology*, *409*, 117851. https://doi.org/10.1016/J.POWTEC.2022.117851

Guo, Y., Ren, K., Wei, A., Tao, C., Huang, W., Zhao, P., & Wu, D. (2022). Iron dust explosion characteristics with small amount of nano-sized Fe2O3 and Fe3O4 particles. *Fuel*, *324*, 124786. https://doi.org/10.1016/J.FUEL.2022.124786

International Iron Metallics Assosiation. (2020). *Direct Reduced Iron By-Product Fines (DRI D): A Guide to Handling, Storage & Shipping*.

Ji, W.-T., Gan, X.-Y., Li, L., Li, Z., Wen, X.-P., & Wang, Y. (2022). *Prediction of the explosion severity of hybrid mixtures*. https://doi.org/10.1016/j.powtec.2022.117273

Kuai, N., Huang, W., Du, B., Yuan, J., Li, Z., Gan, Y., & Tan, J. (2013). Experiment-based investigations on the effect of ignition energy on dust explosion behaviors. *Journal of Loss Prevention in the Process Industries*, *26*(4), 869–877. https://doi.org/10.1016/j.jlp.2013.03.005

Meng, X., Wang, Z., Zhang, Y., Xiao, Q., & Yang, P. (2023). Experimental study of explosion overpressure and flame propagation of micro-sized and nanosized iron powder. *Process Safety Progress*, *42*(1), 116–125. https://doi.org/10.1002/prs.12413

Ogle, R. A. (2016). Dust Explosion Dynamics. *Dust Explosion Dynamics*, 1–639. https://doi.org/10.1016/c2014-0-03833-6

Russo, P., Di Benedetto, A., & Sanchirico, R. (2012). Theoretical evaluation of the explosion regimes of hybrid mixtures. *Chemical Engineering Transactions*, *26*, 51–56. https://doi.org/10.3303/CET1226009

Spitzer, S. H. (2021). *Operating Procedure-Round Robin Instructions for HYBRID 1 Operating Procedure for a Round Robin Test on Hybrid Dust/Gas-Mixtures in the 20L-sphere*.

Spitzer, S. H., Askar, E., Benke, A., Cloney, C., D'Hyon, S., Dufaud, O., Dyduch, Z., Gabel, D., Geoerg, P., Heilmann, V., Jankuj, V., Jian, W., Krause, U., Krietsch, A., Mynarz, M., Norman, F., Skrinsky, J., Taveau, J., Vignes, A., … Zhong, S. (2023). 1st international round robin test on safety characteristics of hybrid mixtures. *Journal of Loss Prevention in the Process Industries*, *81*, 104947. https://doi.org/10.1016/J.JLP.2022.104947

Sun, J. H., Dobashi, R., & Hirano, T. (1990). Combustion Behavior of Iron Particles Suspended in Air. *COMBUSTION SCIENCE AND TECHNOLOGY*, *150*(1–6), 99–114. https://doi.org/10.1080/00102200008952119

Umadevi, T., Sridhara, K. S., Raju, M., Karthik, P., Sah, R., Basavaraja, M., & Desai, S. (2022). Development of process for reduction in fines generation at direct reduced iron plant by coating of magnetite iron ore fines on hematite iron ore pellets. *Metallurgical Research & Technology*, *119*(6), 604. https://doi.org/10.1051/METAL/2022088

Wu, D., Zhao, P., Spitzer, S. H., Krietsch, A., Amyotte, P., & Krause, U. (2023). A review on hybrid mixture explosions: Safety parameters, explosion regimes and criteria, flame characteristics. In *Journal of Loss Prevention in the Process Industries* (Vol. 82). Elsevier Ltd. https://doi.org/10.1016/j.jlp.2022.104969

Analysing the Impact of Solid Contaminants on Grease Viscosity and the theoretical Temperature Performance of Rolling Bearings

Leo Siegle [a], André Hilliger [a], Sabrina Herbst [a]& Frank Engelmann [a]

[a] Ernst-Abbe-University of Applied Sciences, Jena, Germany

E-mail: *leo.siegle@eah-jena-de*

Abstract

This study systematically investigates the increase in grease viscosity due to solid contamination with common industrial particles and the effects on the theoretical bearing operating temperature before plastic damage occurs. Since around 30 % of explosions in the industry are caused by non-electrical equipment, understanding the development of the ignition potential of rolling bearings at elevated temperatures due to lubricant contamination is of great importance for safety in explosion protection. Empirical data from various test series are analysed using ANOVA and regression analysis. The work results show a statistically significant correlation between contamination concentration and viscosity increase. It is, therefore, scientifically proven that an increase in contamination increases the viscosity of the lubricating grease by a factor of 2.199. The resulting theoretical temperature increase of the bearings analysed with contaminated lubricants amounts to a maximum of 2.42 Kelvin, compared to the calculation with viscosity values of clean lubricants. However, further practical investigations on a bearing test rig are necessary to determine whether the theoretical findings can be validated and further unexplored rheological and tribological factors investigated.

Keywords: *rolling bearings, viscosity, lubricant contamination, operating temperature*

Introduction

Around 30 per cent of internal explosions and deflagrations are caused by non-electrical equipment (Bartknecht & Zwahlen, 2013). In addition to machine elements such as seals, axles and shafts, potential ignition sources such as hot surfaces can also occur on rolling bearings. Even in regular operation, heating must be expected when using rolling bearings. This is caused by the heat loss from friction between moving bearing components. According to the current state of the art, this heating can be predicted by calculation (SKF Group, 2014).

Using the extended rating life calculation, the rating life of a rolling bearing can be statistically predicted by the standard, considering various influencing factors such as bearing load, speed, or lubricant contamination (SKF Group, 2014). Using multiple approaches according to Palmgren, Stribeck, or SKF, the operating temperature, which is essential for explosion protection, can also be determined via the bearing's power loss.

However, a deviation from the ideal operating conditions aimed for by the manufacturer can lead to premature bearing failure and the calculated operating temperature being exceeded. The most common causes of bearing failure are contaminations in the lubricant, aged lubricant or unsuitable lubricant (Schaeffler Technologies AG & Co. KG, 2013) (Fig. 1.).

According to the current state of the art, the lubricant's condition can be considered in the extended rating life calculation. Still, changes in the lubricant's condition cannot be included in determining the operating temperature.

In practice, contaminations in the bearing influence temperature development even before mechanical damage occurs. This was confirmed in discussions with managers from the SKF Group (personal communication, January 11, 2024), LUBRICANT CONSULT GmbH (personal communication, January 18, 2023) as well as Josef Blässinger GmbH + Co. KG (personal communication, December 12, 2023). Theoretically, viscosity is an influencing factor of the calculated operating temperature. Current literature does not indicate the influence of contamination on the viscosity of conventional rolling bearing greases. Taking into account the temperature classes that are important for explosion protection and the required safety distance of the maximum surface temperature, an increase in the rolling bearing temperature of just 5 Kelvin (temperature classes T6 to T3) can lead to an ignition source becoming effective (IEC 60079-0).

To close this gap, this work uses various test series to analyse the effects of lubricant contamination from dust frequently encountered in explosion protection on the viscosity of rolling bearing greases and the theoretical impact on the calculated operating temperature.

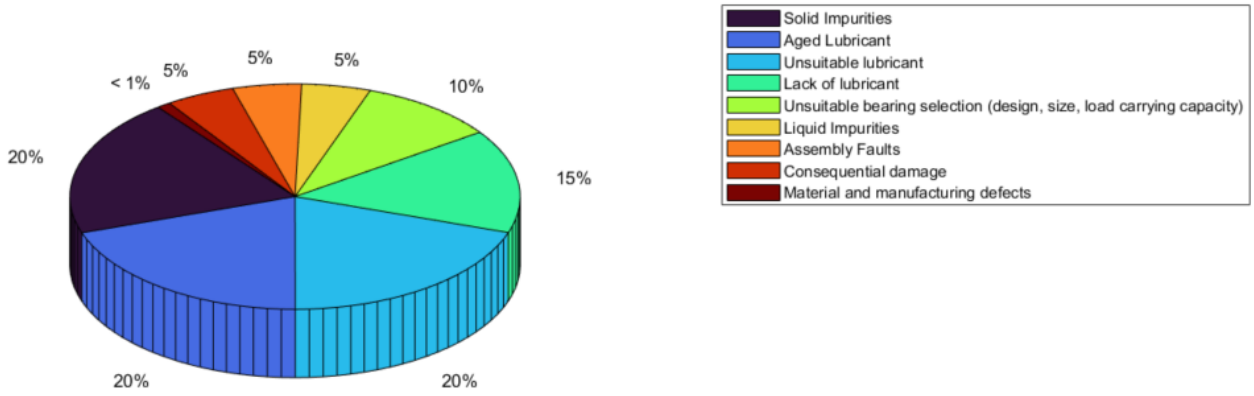

Fig. 1. *Causes of failure for rolling bearings after (Schaeffler Technologies AG & Co. KG, 2013)*

1. Theoretical Foundations

The friction of the bearing components is the leading cause of the increase in bearing temperature. Due to the rotation of the rolling elements around their axis (spin) and the shaft axis, friction occurs between the contact points of the rolling elements and the surrounding bearing components. (Baalmann, 1994)

The frictional torque that occurs is made up of rolling, sliding and lubricant friction. Rolling friction is caused by micro-sliding processes between the rolling elements and the raceway. The raceway and balls have different curvature radii, resulting in different strains on the contact surfaces. Micro-sliding movements occur if the resulting forces are more significant than the transmissible frictional forces. As a result, the balls cannot roll evenly. Consequently, the rolling elements lag behind the raceway. Sliding friction involves macro sliding processes on the surfaces of the rolling bearing components. Instead of rolling, the rolling elements slide on the raceway and cage. The lubricant also generates friction. When the rolling elements roll, part of the lubricant is rolled over while the other part is pushed along as an advance. (Baalmann, 1994)

There are several methods for calculating the bearing frictional torque. These include Stribeck (1901) and Palmegren (1957). In practice, this method has been adopted and extended by the bearing manufacturers Schaeffler (2008) and SKF (2014).

The calculation basis further developed by Schaeffler (2008) based on the Palmgren (1957) approach does not take into account the lubricant-dependent frictional torque, which according to Baalmann (1994) has a significant influence on the total frictional torque. A comparison of the various methods

for calculating the frictional torques shows that the method according to SKF provides the highest frictional torques (Wang, 2015).

The total frictional torque, according to SKF (2014), is to be used in this analysis. With the SKF (2014) method, it is thus possible to consider rolling and sliding friction processes separately to determine all friction components in the rolling contact more precisely. With the SKF method, the total frictional torque is determined depending on the cause using equation (1).

$$M_R = M_{rr} + M_{sl} + M_{seal} + M_{drag} \quad (1)$$

M_R	[Nmm]	Total frictional torque
Mrr	[Nmm]	Rolling frictional torque
Msl	[Nmm]	Sliding friction torque
$Mseal$	[Nmm]	Frictional torque of contact seals
$Mdrag$	[Nmm]	Frictional torque due to flow, splash or spray losses

The rolling frictional torque, the sliding frictional torque and the frictional torque are directly influenced by the viscosity of the rolling bearing lubricant due to flow, splash or spray losses.

It should be noted that the frictional torque generated by flow, splash and spray losses relates to an oil bath or oil injection lubrication. The oil resists the rolling elements during movement. This results in a frictional torque dependent on the flow loss. The investigations consider permanently grease-lubricated bearings. In this case, no splash losses occur as the lubrication by the grease is permanent, and the rolling elements are not regularly immersed in the lubricant. Therefore, the frictional torque caused by flow, splash and spray losses can be set to zero Nmm.

The lubricant's viscosity does not influence the frictional torque of the contact seals. To simplify matters, non-contact seals are assumed in this analysis, resulting in a frictional torque of zero Nmm.

The friction-reducing properties of the lubricant film thickness factor and the lubricant displacement factor are considered when calculating the rolling friction torque. Not all of the lubricant is used to build up the lubricating film. Only part of it is rolled over by the rolling elements, while the other part is displaced outwards. When the lubricant is rolled over, part of it is pushed in front of the rolling elements. This creates what is known as a pre-run. This advance causes the lubricant to be subjected to thrust, which generates heat. The viscosity, lubricant film thickness, and, therefore, the rolling friction torque decrease due to the heating. The lubricant displacement factor considers how much the rolling process displaces the lubricant. At high speeds, the displaced lubricant can't flow back into the centre of the contact zone. This reduces the lubricant film thickness and, thus, the rolling friction torque.

Friction is also generated by the rolling elements sliding on the raceway. This depends on the shape of the contact surfaces. Ball bearings have a curved shape. External loads can compress or stretch the contact surface, resulting in slippage. The dynamic frictional torque depends on the lubricating film's thickness, the rolling elements' surface quality, and the raceway.

The SKF approach determines the expected rolling bearing temperature (SKF Group, 2014). By selecting the total frictional torque, the power loss of the bearing can be calculated. When the rolling bearing starts operating, friction causes a rise in temperature in the bearing. The heat is dissipated from the bearing. A constant temperature is achieved when there is a balance between the amount of heat produced in the bearing and the amount of heat that can be dissipated. The heat generated in the operating rolling bearing is due to the bearing power loss. This depends on the total frictional torque and the speed, which are determined using equation (2).

$$N_R = 1{,}05 * 10^{-4} * M_R * n \quad (2)$$

N_R	[W]	Bearing power dissipation
n	[min^{-1}]	Speed

The heat dissipated by the rolling bearing can be described using the cooling factor. This depends on the heat-dissipating surface of the bearing and the heat transfer coefficient.

Half of the bearing power loss is assumed to be transferred to the inner and outer rings (Schleich, 2013). The heat dissipation of the inner and outer ring is determined via the heat-dissipating surface by DIN ISO 15312 (equation (3)).

$$A = \pi * B * (D + d) \quad (3)$$

A	[mm2]	Heat dissipating surface
B	[mm]	Bearing width
D	[mm]	Bearing outside diameter
d	[mm]	Bearing inner diameter

According to DIN ISO 732, a heat transfer coefficient of 0.0003 W/mm²K can be assumed for all bearings where $A \leq$ 50,000 mm².

This allows the cooling factor W_s be determined as seen in equation (4).

$$W_s = A * \alpha \quad (4)$$

W_s	[W/K]	Cooling factor
α	[$\text{W/m}^2\text{K}$]	Heat transfer coefficient

Using the bearing power loss and cooling factor, the increase in bearing temperature compared to the ambient temperature can be approximated from SKF (2014) (equation (5)).

$$\Delta T = \frac{N_R}{W_s} \quad (5)$$

ΔT	[K]	Temperature difference between bearing and environment

2. Experiments

The tests to determine the change in viscosity were carried out by DIN 51810-1 *„Testing of lubricants – Testing rheological properties of lubricating greases – Part 1: Determination of shear viscosity by rotational viscosimeter and the system of cone/plate“* (DIN 51810-1).

DIN 51810-1 specifies a method for determining the shear viscosity of lubricating greases of NLGI classes 000 to 2 at a constant shear rate after defined pre-shearing with the cone/plate measuring system.

The shear viscosity η of a lubricating grease is determined at a constant temperature by measuring the torque M as a function of the speed n using a cone/plate measuring system. The shear stress τ and the shear rate $\dot{\gamma}$ are determined from the torque M and the speed n. This results in the relationship (equation 6):

$$\tau = \eta * \dot{\gamma} \qquad (6)$$

τ	[Pa]	Shear stress
η	[Pas]	Shear viscosity (apparent dynamic viscosity)
$\dot{\gamma}$	[s^{-1}]	Shear rate

A typical rolling bearing grease LGMT 2 from SKF with a dust-like additive (hereinafter called "dust") is tested.

Wheat flour type 405 from Roland Mills West GmbH was selected as the test dust. This dust is expected primarily in mills and the food industry during the further processing of flour into foodstuffs. The particle size distribution is shown in figure 2. This shows the cumulative percentage distribution curve against the particle sizes in micrometres (µm). The 50th percentile is 62.2 µm. (Stahmer, 2019)

According to the manufacturer, the density of the dust is approx. 550 - 600 kg/m³. (Roland Mills West GmbH, 2022)

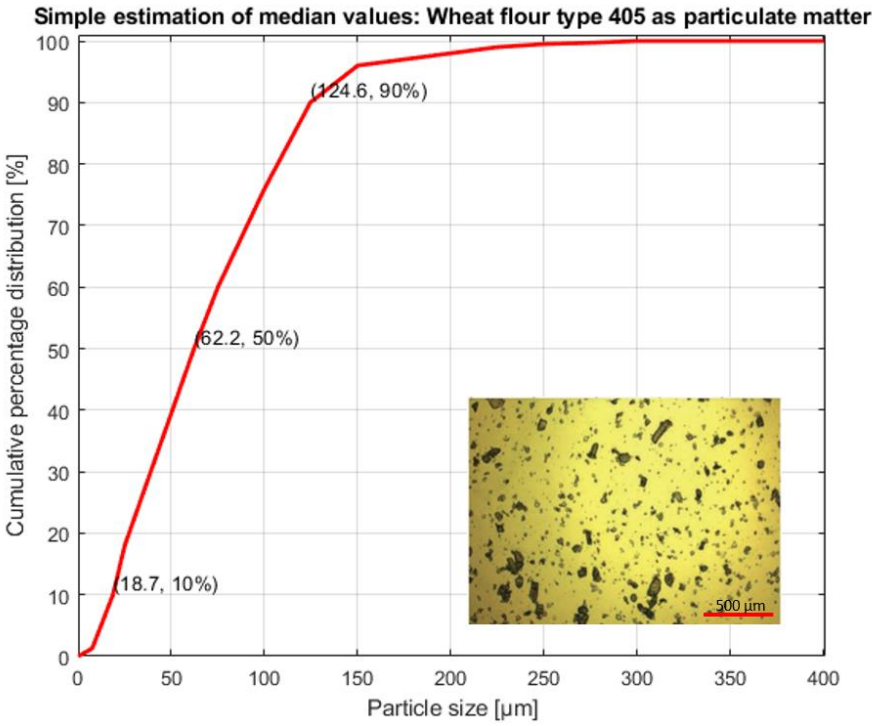

Fig. 2. *Percentage sum frequency of particle size as a function of particle size including the 10th, 50th and 90th percentile targets of the distribution of a wheat flour type 405. Taken from Stahmer (2019)*

The test is carried out on a HAKE RheoStress 600, and a Thermo UTCE/C is used for temperature control.

Contrary to the standard, a cone diameter of 35 mm is used with an opening angle between the cone and plate of 1.0°. The standard specifies a cone diameter of 25 mm with the same opening angle.

The test is carried out at 70°C±0.1K. This temperature is a typical bearing operating temperature and is assumed by SKF (2012), among others, as the reference temperature for rolling bearings when calculating the reference speed.

The measuring programme is the same as in the standard (Fig. 3, shear rate $\dot{\gamma}$). Only the change between the shear rates is adapted to the rheometer. Unlike described in the standard, this takes place

between the periods t_1 and t_2 throughout the one second. As this is an NLGI class 2 grease, the shear rate $\dot{\gamma}$ is set to 500 s-1 during the period t_1. (DIN 51810-1)

The experimental design provides for a variance in the amount of dust with otherwise identical experimental conditions. The selected amount of dust aims to maximise the change in viscosity. For this reason, the "contamination" factor levels are set to 25 vol. % dust or 35 vol. % dust. This contrasts with a sample without contamination (0 vol. % dust). The selected amount of contamination is random. The aim is to achieve the greatest possible effect on the viscosity change. Preliminary tests have shown that larger quantities of impurities can only be insufficiently absorbed by the lubricant.

The standard specifies a repeatability r for lubricating greases of NLGI class 2 of 8% relative to the mean value of the results. To achieve comparability of the results, five tests are carried out for each stage. This results in the following test plan (Tab. 1.).

Tab. 1. *Test Plan*

Test series	Contamination	Number of experiments n
1.1-n	0 Vol. % Dust	5
1.2-n	25 Vol. % Dust	5
1.3-n	35 Vol. % Dust	5

The individual test results show a similar progression of shear viscosity η versus time. The tests are analysed using the viscosity of section t5 (Fig. 3).

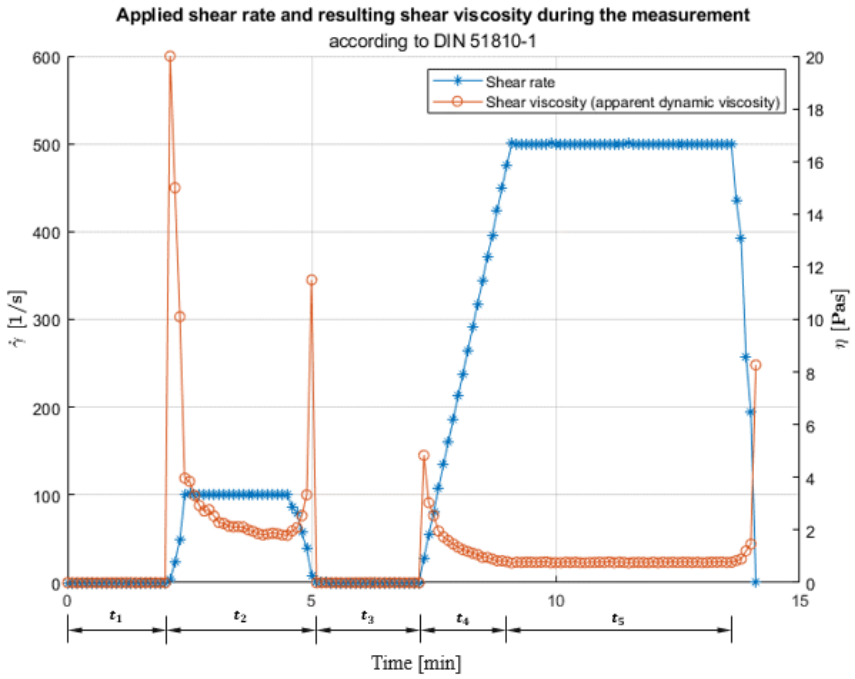

Fig. 3. *Applied shear rate (orange curve) and resulting shear viscosity (blue curve) during the measurement according to DIN 51810-1 for sample 1.3 at 70°C*

A single-factor ANOVA (Analysis of Variance) is used to analyse the data. Statistically significant results are then analysed using Tukey's HSD post-hoc test. Statistically substantial is assumed to be $p < 0.05$.

Regression analysis and the analysis of the correlation coefficient are carried out to make a statement about a linear relationship between the results.

To be able to make a statement about the extent to which the change in viscosity negatively influences the temperature development of the rolling bearings, control calculations are carried out. The bearing friction torques and the resulting rolling bearing temperatures of three deep groove ball bearings of different sizes (6004-2Z, 6005-2Z and 6006-2Z) are analysed.

Table 2 lists the parameters assumed in the bearing calculation. For the radial load, a high load of P/C of 0.1 was selected.

Tab. 2. *Selection of bearing parameters*

Speed **n** [rpm]	3 x 10^3
Radial force $\mathbf{F_r}$ [N]	C/P = 0.1 with F_a = 0
Axial force $\mathbf{F_a}$ [N]	0
Viscosity of the lubricant [mm²/s]	20.5

C	[kN]	Dynamic load rating
P	[kN]	Equivalent dynamic bearing load

A viscosity factor is introduced to calculate the bearing friction torques and the resulting rolling bearing temperature. The viscosity factor is calculated according to equation 7. It describes the ratio of the mean value of the test series 2.1-5 and 3.1-5 to the test series 1.1-5. For the calculation, the viscosity factor is multiplied by the kinematic viscosity specified by the manufacturer.

$$Viscosity\ factor = \frac{Mean\ value\ of\ the\ measurement\ series\ x.1-n}{Mean\ value\ of\ the\ measurement\ series\ 1.1-n} \qquad (7)$$

The conversion of the dynamic viscosity into the kinematic viscosity using the mathematical relationship according to equation 8 with a density of the lubricant of 1 g/cm^3.

$$\nu = \frac{\eta}{\rho} \qquad (8)$$

ν	[mm^2/s]	Shear stress
ρ	[g/cm^3]	Density of the lubricant

All statistical and mathematical analyses are done using the MATLAB R2021b program.

During test preparation, the samples are enriched with dust and mixed according to the test plan (Tab. 1). After mixing the samples with the dust, they show apparent inclusions of air under the microscope (Fig. 7). To obtain valid results, the samples are deaerated. To do this, the fat is exposed to a vacuum of -1 bar while the temperature is increased by 50 Kelvin. This leads to a significant reduction in air inclusions (Fig. 5. and Fig. 6.). Fig. 4. shows the sample without contamination.

The contaminations of the samples "75 vol. % LGMT 2 + 25 vol. % dust" and "65 vol. % LGMT 2 + 35 vol. % dust" can be recognised by a uniform distribution of darkened areas in the samples (comparison Fig. 5. and Fig. 6.). Some particles of the dust have a coarser structure and stand out clearly from the rest of the sample (Fig. 9. areas a-c). Figure 8 shows the lubricant without contamination and deaerated.

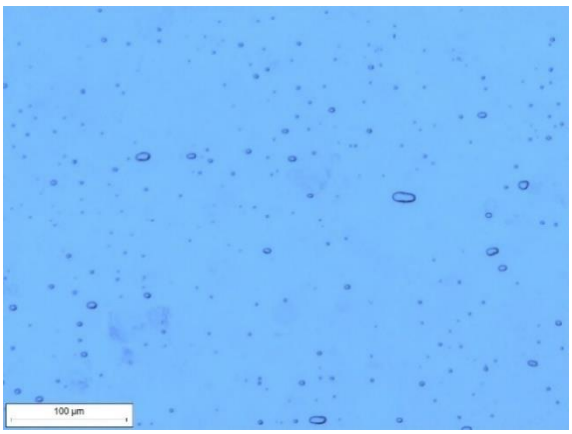

***Fig. 4**. 100 Vol. % LGMT 2 + 0 Vol. % Dust*

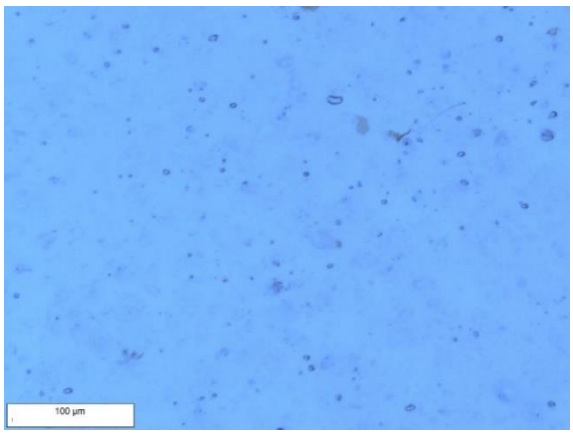

***Fig. 5**. 75 Vol. % LGMT 2 + 25 Vol. % Dust*

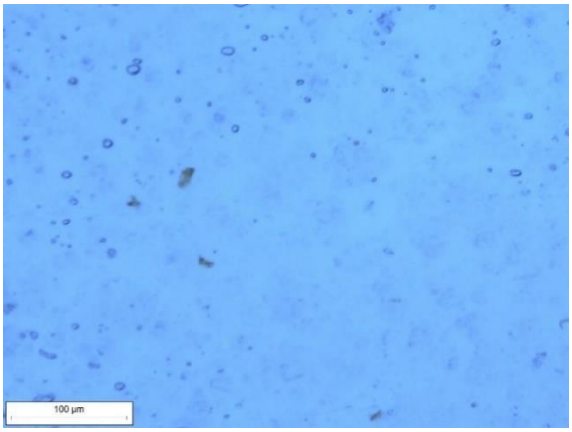

***Fig. 6.** 65 Vol. % LGMT 2 + 35 Vol. % Dust*

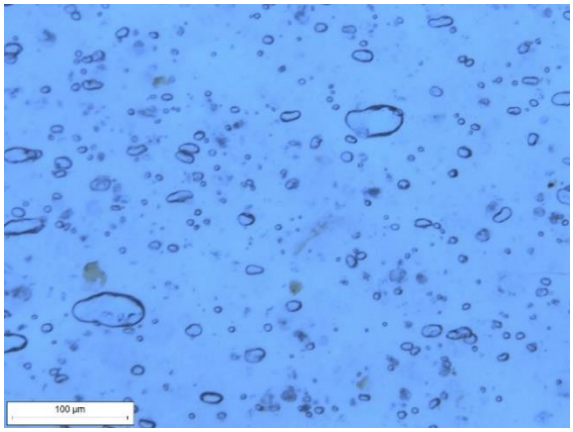

***Fig. 7**. 75 Vol. % LGMT 2 + 25 Vol. % Dust without venting*

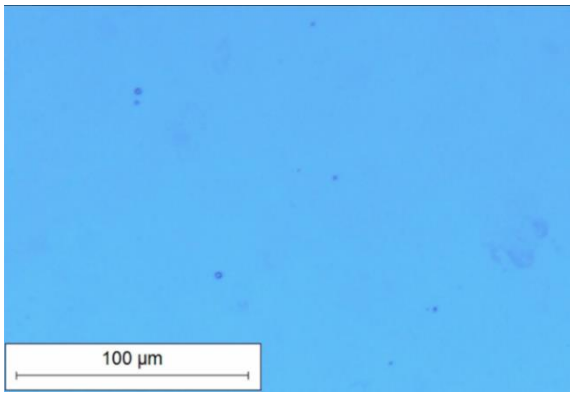

***Fig. 8.** Magnification 100 Vol. % LGMT 2 + 0 Vol. % Dust*

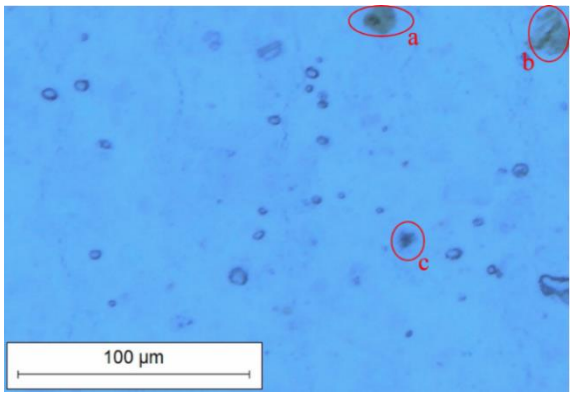

***Fig. 9.** Magnification 75 Vol. % LGMT 2 + 25 Vol. % Dust*

3. Results and Discussion

The investigations should provide information on whether and to what extent contaminations in lubricants lead to an increase in their viscosity. Furthermore, the effect on the theoretical rolling bearing temperature will be analysed based on the determined viscosities. The evaluation is based on the test series of the lubricant LGMT 2 without contamination (1.1-5), 25 % contamination by volume (2.1-5) and 35 % contamination by volume (3.1-5) carried out using a rheometer.

Figure 10 shows the averaged results (arithmetic mean) of the test series 1.1-n (blue), 2.1-n (red) and 3.1-n (green) of the period t_5 of the measuring procedure according to figure 3, with n=5 with their standard deviation. It can be seen that the viscosity η of test series 2.1-5 and 3.1-5 differs significantly from the viscosity η of test series 1.1-5. The viscosity η test series 1.1-5 and 2.1-5 remain constant over the observed measurement cycle of 5 minutes (t_5). The course of test series 3.1-5 is striking after approx. one hundred twenty seconds; the viscosity begins to fall and is reduced by 0.1 Pas over 180 seconds. The high viscosity of the lubricant sample may reduce the backflow into the contact zone of the disc/cone system. As a result, the gap is emptied, and the viscosity in the lubricant appears to drop.

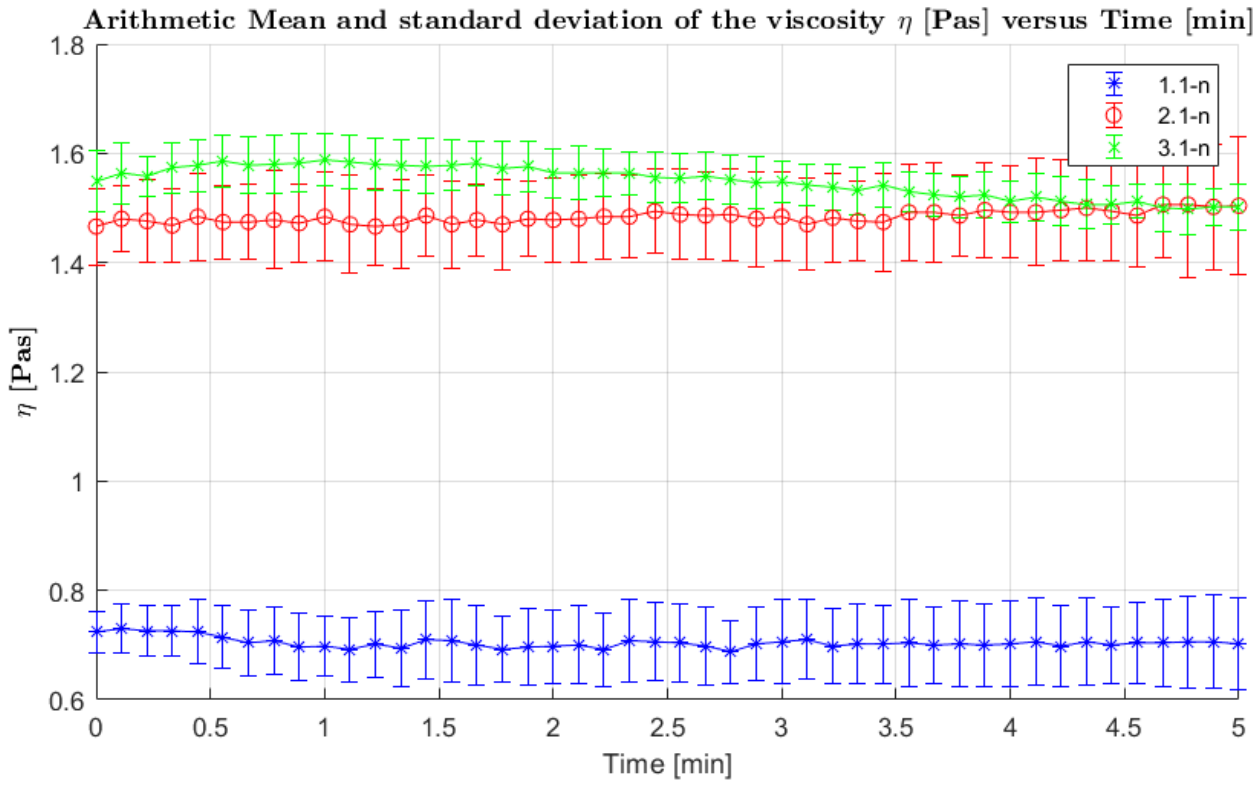

Fig. 10. *Arithmetic mean and standard deviation of the viscosity η in Pas versus time in minutes, for experiments 1.1-n, 2.1-n and 3.1-n, with n = 5, at a test temperature of 70°C*

The result of the ANOVA confirms the assumption of a significant difference between the mean values of the test series 1.1-5 and 2.1-5, as well as 3.1-5 (Fig. 11). The boxes represent the interquartile range (IQR), which covers the range from the lower (25%) to the upper quartile (75%) and thus contains the middle 50% of the data. The lines within the boxes represent the median. The "whiskers" extend from the box to the smallest or largest values of the 1.5*quartiles. Points outside the whiskers are considered outliers and are shown with a "+" sign. The result of calculating the F-value (12453.18) is very high, and the p-value is close to zero ($p < 0.001$). The group variation can be estimated as relatively low (sum of squares (SS) value of 2.802). The total sum of squares measures the total variability in the data relative to the overall mean. The Tukey's HSD test confirms the significant differences between the groups.

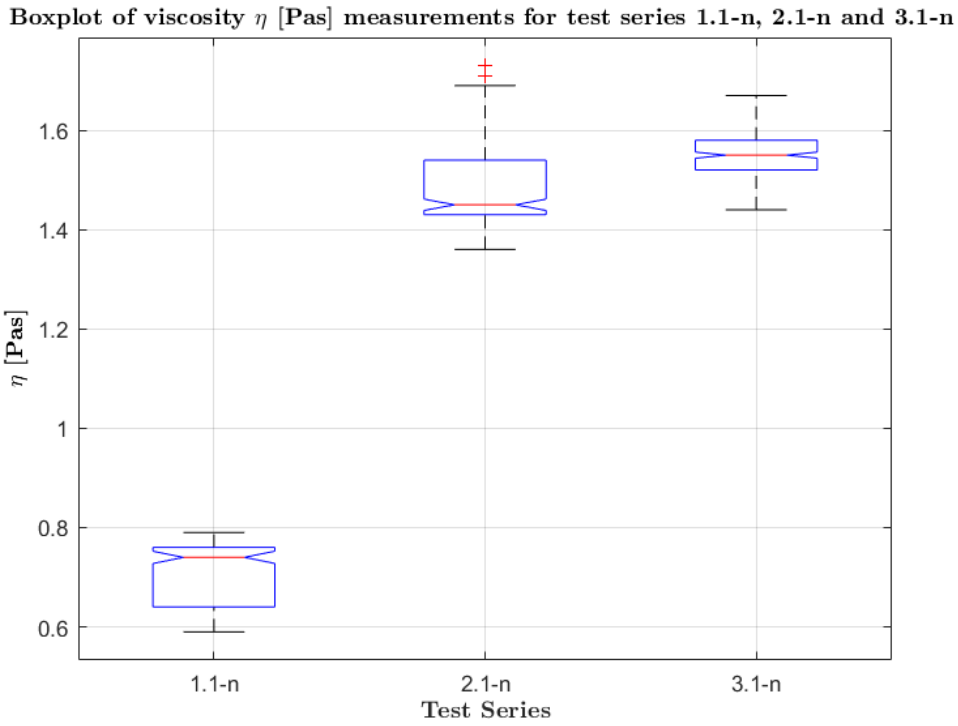

Fig. 11. *Boxplot of the viscosity η in Pas measurements, for experiments 1.1-n, 2.1-n and 3.1-n, with n = 5, at a test temperature of 70°C*

The regression analysis (Figure 12) results in a correlation coefficient (r) of 0.9779 with a coefficient of determination (r_2) of 0.9562 and a p-value of 0.1342. The high correlation coefficient of around 0.978 indicates a solid linear relationship. However, due to the low P-value and the small amount of data, the result cannot be considered statistically significant.

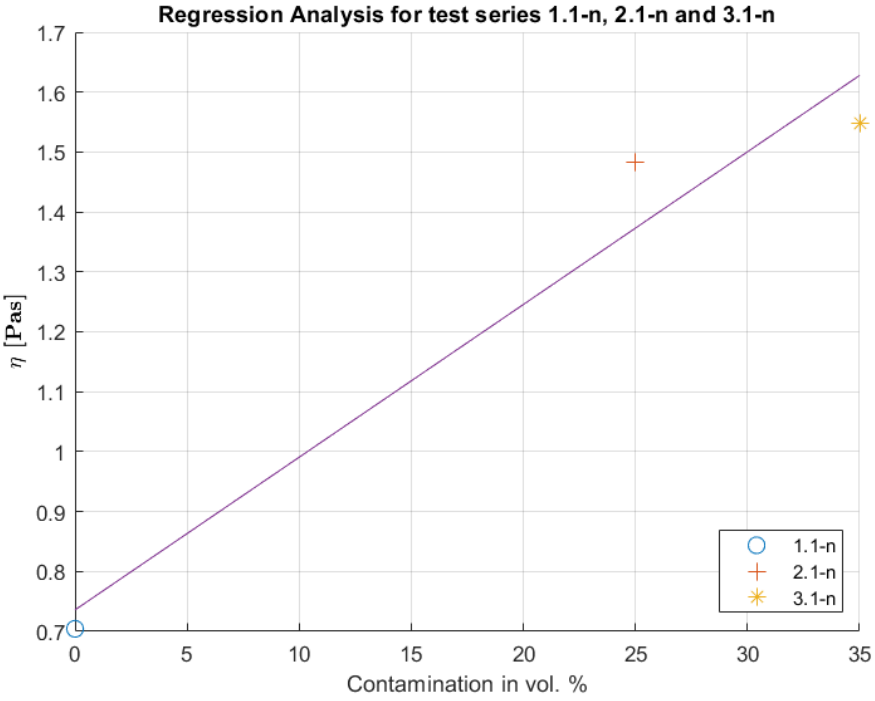

Fig. 12. *Regression analysis of the experiments 1.1-n, 2.1-n and 3.1-n, as a function of viscosity η versus contamination content in vol. %, at n=5 and a test temperature of 70°C*

Table 3 shows the bearing operating temperature ΔT increase compared to the ambient temperature, considering the viscosity factor from experiments 1.1-5, 2.1-5 and 3.1-5. In addition, the temperature difference ΔT_1 and ΔT_2 can be taken from the table. This describes the relative increase in temperature compared to the tests with the normal viscosity, taking into account the viscosity $factor_1$ and viscosity $factor_2$.

Furthermore, Table 3 shows that the friction torque and power loss increase with increasing viscosity, leading to an increased operating temperature. The temperature increases are bearing-specific and range from an increase in temperature of 1.64 Kelvin to a rise of 2.42 Kelvin. Therefore, the results of the theoretical analysis are below the safety margins of 5 Kelvin for temperature classes T6-T3, which are essential for explosion protection. Based on this theoretical consideration, the temperature increase is not initially critical for explosion protection. However, it should be noted that, in reality, further rheological and tribological effects can lead to a further increase in temperature. The rolling bearings used in this analysis and the selected load parameters only describe a specific application of a small selection of bearings. An increase in viscosity on bearings of a different design and size will likely result in a comparatively higher power loss. However, more oversized bearings have a more extensive heat-dissipating reference surface, which does not necessarily lead to a higher temperature difference.

Tab. 3. *Results of the theoretical calculation of the rolling bearing frictional torques and the rolling bearing operating temperature with the manufacturer's lubricant viscosity compared to the experimentally determined viscosity*

Rolling bearing	**6004-2Z**	**6005-2Z**	**6006-2Z**
Heat dissipating reference surface A [mm²]	2,337.34	2,714.34	3,471.46
Heat transfer coefficient α [W/mm²K]	0.0003	0.0003	0.0003
Calculation of the total frictional torque and the temperature increase with the normal viscosity according to the manufacturer			
Total frictional torque M_R [Nmm]	16.94	24.46	33.53
Power loss N_R [W] nach SKF	5.32	7.69	10.53
Increase in bearing operating temperature ΔT according to SKF, DIN 732 und 15312 [K]	6.90	8.58	9.19
Calculation of the total frictional torque and the temperature increase with the viscosity factor from tests 2.1-5 (viscosity $factor_1$ = 2.10625)			
Total frictional torque M_R [Nmm]	20.97	30.30	41.86
Power loss N_R [W] nach SKF	6.59	9.52	13.15
Increase in bearing operating temperature ΔT according to SKF, DIN 732 und 15312 [K]	8.54	10.63	11.48
Temperature difference ΔT_1 compared to bearing operating temperature with normal viscosity	1.64	2.05	2.28
Calculation of the total frictional torque and the temperature increase with the viscosity factor from tests 3.1-5 (viscosity $factor_2$ = 2.199345)			
Total frictional torque M_R [Nmm]	21.24	30.66	42.35
Power loss N_R [W] nach SKF	6.67	9.63	13.30
Increase in bearing operating temperature ΔT according to SKF, DIN 732 und 15312 [K]	8.65	10.75	11.61
Temperature difference ΔT_2 compared to bearing operating temperature with normal viscosity	1.75	2.17	2.42

4. Conclusion and forecast

The detailed analysis and statistical evaluation of the series of measurements in this study convincingly confirm the hypothesis that contaminations in lubricants cause a significant increase in viscosity.

Several tests were conducted to verify this hypothesis by measuring the viscosity on a rheometer. The addition of defined dust particles artificially contaminated the samples used. Different concentrations of contaminants are investigated to analyse the influence of the amount of contaminations. It can be said that, with a high level of statistical evidence, the lubricant's viscosity increases with increasing contamination. Investigations into the linearity of the viscosity change as a function of the contamination of impurities could be proven. However, the statistical significance is not given due to the small number of tests in this case.

The analysis of the calculation of power loss and bearing temperature increase of different bearing sizes of the same type with changed viscosity values results in a maximum change in the total frictional torque of 42.35 Nmm and a resulting temperature increase of 2.24 Kelvin.

It should be noted here that the results relate only to the rolling bearings considered in the work. Other bearings can reach different, sometimes higher temperatures due to different bearing geometry, such as their size, the shape of the rolling element, the number of rows, etc.

Furthermore, these changes are based solely on the theoretical assumption that the change in viscosity has a sole influence on the temperature development. This study did not consider other rheological and tribological effects within the bearing. The actual impact of the contamination must be analysed in further investigations on a rolling bearing test rig. It can be assumed that other effects not analysed in this study further increase the temperature in the rolling bearing during operation with contaminated lubricants.

To gain more detailed insights into the effect of contaminations on the development of the rolling bearing friction torque and the resulting increase in operating temperature, further tests are necessary. One approach for future investigations is to analyse the influence of particle size and hardness on viscosity and the combination of the contaminations with other lubricating greases. In addition to tests using a rheometer, investigations on a rolling bearing test rig will be of great interest in the future. These investigations could provide information on whether and, if so, which other influences affect the frictional torques before plastic damage to the bearing occurs.

References

Bartknecht, W., & Zwahlen, G. (2013). *Explosionsschutz: Grundlagen und Anwendung.* Springer Berln Heidelberg, Berlin.

DIN 732 (2010-05). *Rolling bearings - Thermally safe operating speed - Calculation and correction values.* Beuth Verlag GmbH, Berlin.

DIN 51810-1 (2017-04). *Testing of lubricants - Testing rheological properties of lubricating greases - Part 1: Determination of shear viscosity by rotational viscosimeter and the system of cone/plate*. Beuth Verlag GmbH, Berlin.

IEC 60079-0 (2017, December 13). *Explosive atmospheres - Part 0: Equipment - General requirements*. Beuth Verlag GmbH, Berlin.

DIN ISO 15312 (2019-04). *Rolling bearings - Thermal speed rating - Calculation.* Beuth Verlag GmbH, Berlin.

Baalmann, K. (1994). *Verfahren zur Bestimmung der stationären Betriebstemperatur von Wälzlagerungen.* Doctoral Thesis. Leibniz Universität Hannover , Hannover.

Palmgren, A. (1957). *Neue Untersuchungen über Energieverluste in Wälzlagern.* SKF Kugellagerfabriken, Schweinfurt.

Roland Mills West GmbH (2022). *Produktinformationsblatt Getreidemahlprodukte.* Datasheet. Roland Mills West GmbH, Recklinghausen.

Schaeffler Gruppe Industrie (2008). *Wälzlager.* Schaeffler Gruppe, Herzogenaurach.

Schaeffler Technologies AG & Co. KG (2013). *Wälzlagerschäden.* Schaeffler Technologies AG & Co. KG, Herzogenaurach.

Schleich, T. J. (2013). *Temperatur- und Verlustleistungsverhalten von Wälzlagern in Getrieben*. Doctoral Thesis. Dr. Hut, München.

SKF Group (2014). *Wälzlager* (PUB BU/P1 10000/2 DE). SKF Group, Schweinfurt.

SKF Gruppe (2012). *SKF Service-Handbuch* (No. PUB SR/P7 10001/1 DE). SKF Group, Schweinfurt..

Stahmer, K.-W. (2019). *Datenbank GESTIS-STAUB-Ex - Ermittlung von Kenngrößen explosionsfähiger Stäube durch Recherche.* Technische Sicherheit, *9*(04). VDI Fachmedien, Düsseldorf.

Stribeck, R. (1901). *Kugellager für beliebige Belastungen:* Springer Berlin, Berlin.

Wang, D. (2015). *Berechnung der Wälzlagerreibung aufgrund weiterentwickelter rheologischer Fluidmodelle.* Doctoral Thesis. Leibniz Universität Hannover, Hannover.

Fire and Explosion risks of Maltodextrin

Jef Snoeys [a], Gerard Van Laar [b], René Dworschak [b]

[a] INBUREX Consulting Corp. (Fl, USA)

[c] INBUREX Consulting GmbH (Hamm, Germany)

E-mail: *jef.snoeys@inburex.com*

Abstract

This work provides a concise overview of the fire and explosion risks associated with maltodextrin, a widely used carbohydrate polymer in the food and pharmaceutical industries. Maltodextrin's unique functional properties, including its hygroscopic nature and fine powder form, present challenges in handling and storage, contributing to potential fire and explosion hazards.

This work summarizes the intrinsic properties of maltodextrin, identifies key factors influencing its combustibility, resistivity, ignition properties and outlines preventive and protective measures to mitigate the fire and explosion risks of maltodextrin. Special attention is given to the unique nature of ignition by propagating brush discharges and how process parameters like pressure, temperature and humidity impact the risk potential of electrical ignition sources.

Three case studies of incidents with maltodextrin are reported which collectively underscore the multifaceted nature of fire and explosion risks associated with maltodextrin. From inadequate dust control to electrostatic discharge and agglomeration-induced hazards, each case emphasizes the necessity of a holistic approach to industrial safety.

Understanding and addressing these concerns are vital for ensuring industrial safety in the production and processing of maltodextrin. Ongoing research and collaborative efforts are essential for refining safety protocols and minimizing the impact of potential incidents.

Keywords: *hazards, prevention, mitigation, industrial explosions, propagation brush discharge, maltodextrin*

1. Introduction

Maltodextrin is a white powder that is relatively tasteless and dissolves in water.

Maltodextrins are used as fillers, carriers for flavours, to coat pills and tablets in the manufacturing of prescription drugs and dietary supplement products.

It is also used as a horticultural insecticide both in the field and in greenhouses.

Maltodextrin is a polysaccharide obtained by partial hydrolysis of starch. The most commonly used sources of starch are corn, potatoes and rice. The specific manufacturing method and starch source used may influence the physicochemical properties of the resulting maltodextrin.

Maltodextrin consists of D-glucose units connected primarily by α-1,4-glycosidic bonds. The length of the glucose chains in maltodextrin varies, resulting in a mixture of oligo- and polysaccharides. The structure of maltodextrin is largely determined by the degree of hydrolysis, which is quantified by the dextrose equivalent value (DE value).

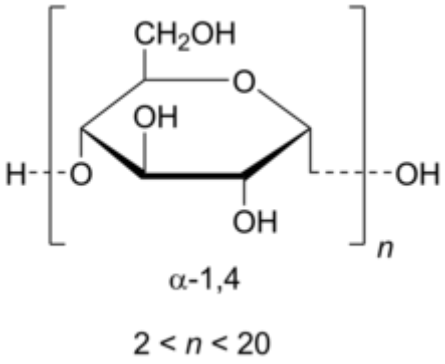

Figure 1. Chemical structure of Maltodextrin – typical

The physical and chemical properties of maltodextrin vary depending on the DE value. Properties such as solubility, sweetness, viscosity and hygroscopicity are directly dependent on the DE value.

Table 1. Maltodextrin DE and composition

DE—Dextrose Equivalent	Glucose	Maltose	Higher Saccharides	Sweetness (Sucrose=100)
10	0.7	2.8	96.5	2
15	1.3	4.7	94	3.3
18	1.6	5.7	92.7	4

Data: ADM Food Ingredient Catalogue 2015/2016 and others.

The particle size range of Maltodextrin can be quite different, depending on the source and manufacturing method. Attention must be paid to mixtures of Maltodextrin and oils or flavours because the explosion safety characteristics can be substantially altered resulting in a higher risk potential.

2. Explosion Case studies

Maltodextrin in fine powder form presents challenges in safe handling and storage, contributing to potential fire and explosion hazards, as illustrated in the following case studies.

A dust explosion incident occurred in 2005 in an outside silo during unloading Maltodextrin from a road tanker via a rubber hose. The aluminum silo was properly explosion vented. However, a fire broke out after the incident inside the silo causing the silo wall to melt, only the insulation on the outside of silo prevented a total collapse. Nobody got hurt at the incident.

The MIE of the Maltodextrin involved was in between 100 and 300 mJ. The conveying air from the road tanker compressor was about 50°C which resulted in a lower MIE of approximately 30 mJ, see further.

The investigation showed that the most likely ignition source was a propagating brush discharge due to the rubber transport hose that was not internally conductive enough: the internal of the hose showed typical damage and punctures caused by propagating brush discharges, see the figure below.

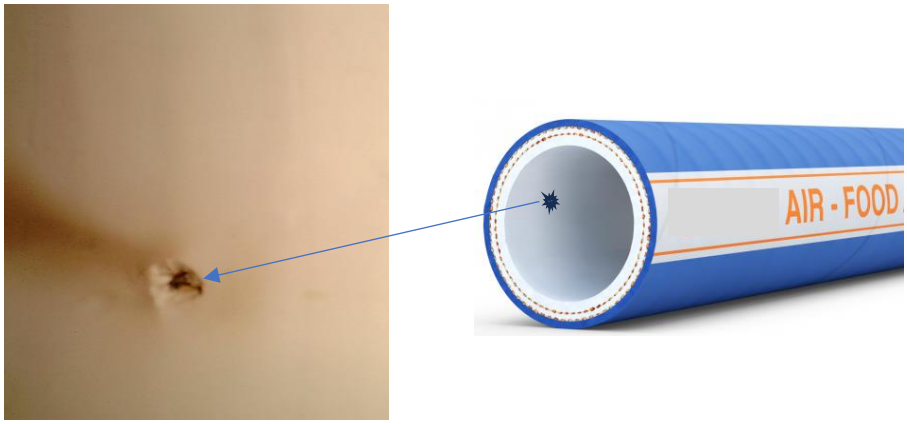

Figure 2. Typical damage of the rubber liner, caused by propagating bush discharges triggered by pneumatic transport of Maltodextrin through a not sufficiently conductive hose. From Van Laar G.

The silo was declared a total loss and was not rebuilt. Today, the process receives Maltodextrin from big bags without using any hoses.

In 2003, an explosion in an inside located Maltodextrin silo destroyed the roof of the building. One person just leaving the building, on the ground floor, was blown out of the exit and was serious injured.

The explosion incident occurred during pneumatic loading the silo from a big bag unloading station.

The MIE of the Maltodextrin involved was in between 300 and 1000 mJ. Because the conveying air was cooled, the MIE was not affected.

The investigation showed that the most likely ignition source was a propagating brush discharge: either due to a rubber transport hose that was not internally conductive enough or to the isolating epoxy coating in the silo.

The rubber hose was replaced by a metal hose, but the epoxy inner coating from the silo was not removed. The exploded silo was repaired and fitted with explosion vents and vent duct to the outside. Later, in 2014 and in 2017, two more explosion incidents occurred that were attributed to the replacement of the metal hose, which was heavy to handle, by an unsuited rubber hose and /or

the silo inner lining. It was decided to stop using the silo and to feed the process directly from the big bag unloading station, not using rubber hoses anymore.

In 2021, a dust explosion occurred in a food factory (2023, VDI). During manual filling of a weighing/mixing hopper, an electrostatic discharge occurred at the mouth of the filling opening. A dust explosion developed within the hopper and a large explosion fireball was vented though the filling opening into the manned room. Miraculously, the operated suffered only minor burns and the installation could be repaired after the explosion. It was found that a broken grounding lug resulted in an electric charge difference between the hopper and the operator, creating an electrostatic difference during filling when the operator approached, perhaps touched the hopper.

The incidents show that Maltodextrin can be very easily statically charged and poses a real dust explosion hazard, sometimes not deliberately forgotten. At some of the plants, other products such as Sugar, Maize starch and Dextrose were handled in the same way but without creating explosions.

3. Explosion Safety parameters

The safety parameters of dry maltodextrin in dust form, including ignition temperature, minimum ignition energy as well as maximum explosion pressure and rate of pressure rise, are influenced by a variety of factors. Two of the most important factors are the physical properties of the substance, such as the particle size or fineness of the dust, and the chemical composition or structure of the material.

It is not uncommon that the Material safety datasheet as supplied by the manufacturer or supplier of the Maltodextrin does not specify the explosion safety-related parameters. For example, the safety data sheet of STAR DRI 18 from Tate&Lyle does mention that combustible dust concentrations in air may be formed and dust explosions may happen. The safety sheet further recommends that all dust control equipment and material transport systems involved should be engineered to prevent conditions contributing to dust explosions. No values however are given for the explosion vehemence, explosion pressure, concentration limits or ignition properties.

Whereas the North American standard NFPA 654 requires that test data for specific dust and diluent combinations shall be provided and shall be acceptable to the AHJ, there is no such requirement specified in the ATEX directives. More than often, the explosion safety engineer will consult a published database such as GESTIS-DUST-EX , or the printed BIA-Report 13/97 combustion and explosion characteristics database. A search in the GESTIS database for maltodextrin gives 54 hits. Two groups can be identified: Maltodextrin and mixtures of maltodextrin and flavours/aromas. The latter products are formed by mixing and/or spray drying techniques and exhibit lower ignition energies, MIE in mJ, and higher explosion vehemence values, K_{St} in bar.m.s^{-1},) than the ‘pure’ Maltodextrin product. The GESTIS database shows 21 hits for ‘pure’ Maltodextrin product.

The K_{St}/P_{max} ranges from 68/7.3 to 147/8.3, and the MIE between 5 mJ and >1000 mJ, depending on the material number in GESTIS and the particle size distribution.

A search in the BIA-Report for Maltodextrin gives 16 hits. Note that mixtures of maltodextrin with oils or flavour extracts are not mentioned in the BIA-Report. The Maltodextrin K_{St}/P_{max} ranges from 68/7.3 to 120/8.6, and the MIE between 5 mJ and >1000 mJ, depending on the material number in the database and the particle size distribution.

The product involved in the 2003 explosion, and the subsequent incidents in 2014 and 2017, see above case study section, was tested respectively in 2015 and 2017 with following results: K_{st} 165 bar.m. $.s^{-1}$, Pmax 8.3 bar. Also ignition properties were measured: MIE with induction: 10-30 mJ; MIE without induction: 300-1000 mJ and volume resistivity: 4,12 . 10^{13} Ωm for a moisture content of 2,5%.

4. Influence of the DE value and particle size on safety-related parameters

As shown in the previous section, the explosion safety parameters of dry maltodextrin in dust form, including ignition temperature, minimum ignition energy as well as maximum explosion pressure and rate of pressure rise, exhibit a wide range, influenced by a variety of factors. Two of the most important factors are the physical properties of the substance, such as the particle size or fineness of the dust, and the chemical composition or structure of the material.

• DE value and chemical structure: A higher DE value in maltodextrin indicates shorter glucose chains, which means a changed chemical composition. This altered chemical composition can theoretically affect the combustion properties of maltodextrin, as smaller molecules tend to react or burn more easily than larger molecules. However, the direct influence of the DE value on safety-related parameters such as ignition temperature, ignition energy and explosion pressure is less clear and probably less significant than the influence of physical properties such as particle size.

• Particle size (fineness of the dust): Particle size is a decisive factor for the safety properties of powdery substances. Finer particles have a greater surface area relative to their volume, resulting in greater reactivity with oxygen and therefore greater flammability and explosiveness. Fine dust can ignite more easily and cause more violent explosions than coarse dust.

In an attempt to develop classes of explosivity within the family of Maltodextrins, powders with different DE numbers were purchased from the market, see table 1.

Table 2. Maltodextrin DE and composition

Supply	Sample	Moisture [wt-.%]	d50 (µm)	DE-value
Nestle	Maltodextrin 11# DE Halai	3.5	198.8	11
Nestle	Maltodextrin 11# DE Halai (milled and sieved)	3.5	62.5	11
Inburex	Maltodextrin DE6	3.38	62.5	6
Inburex	Maltodextrin DE12	4.33	200	12
Inburex	Maltodextrin DE12 (milled and sieved)	4.33	55.6	12
Inburex	Maltodextrin DE19	4.38	107	19

In the EEA, combustible dust testing is typically performed according to standard procedures as described in European standards (EN ISO/IEC 80079-20-2, 2016; EN 14034-3, 2011). Next to these ignition tests, the explosion severity is determined by recording the maximum explosion pressure (P_{max}) and the dust vehemence parameter K_{St}, which is derived from the maximum rate of explosion pressure rate $(dP/dt)_{max}$ (EN 14034-1, 2011; EN 14034-2, 2011). Sample preparation by particle size reduction and/or drying is recommended but left to the discretion of the explosion protection engineer or consultant. ASTM E1226-19 (2020) is similar in set up and methodology, but this standard requires that particle size be reduced to 95% < 75 µm and dried to moisture content < 5%. This is the preferred preparation method for obtaining conservative results and determining worst case scenario. Note that the moisture content of all tested samples was < 5%, as indicated in the table above. In table 3, the results are given of the 20 L explosibility and MIKE-3 ignitability testing of selected samples.

Table 3. Maltodextrin explosibility and ignitability testing of selected samples

Sample	P_{max} (bar)	K_{St} (bar.m.s^{-1})	P_{max} * K_{St}	MIE (mJ)
Maltodextrin 11# DE Halai	7.9	37	292.3	>1000
Maltodextrin 11# DE Halai (milled and sieved)	8.2	90	738	300<MIE<1000
Maltodextrin DE6	8.7	123	1070.1	>1000
Maltodextrin DE12	8	60	480	>1000
Maltodextrin DE12 (milled and sieved)	8.3	145	1203.5	30<MIE<100
Maltodextrin DE19	7.3	75	547.5	>1000

In Figure 3, the product of K_{St} and P_{max} is plotted as a function of d50.

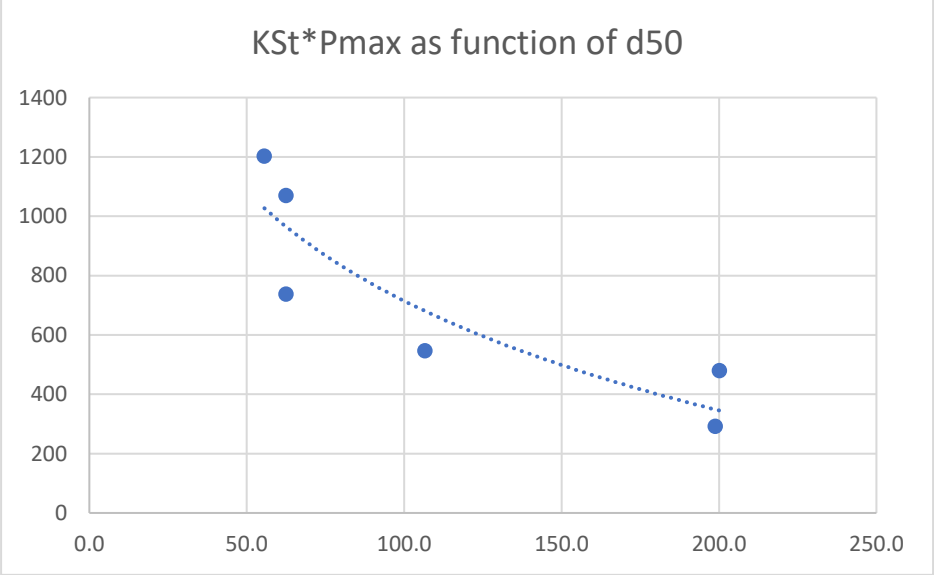

Figure 3. KSt * Pmax plotted as function of d50

As can be seen in table 3 and figure 3, the explosivity increases with the fineness of the sample, expressed by the d50 number. When the DE12 sample was milled and sieved from d50 200 µm to 55.6 µm (factor of four), the K_{St} rose from 60 bar.m.s^{-1} to 145 bar.m.s^{-1}. The maximum explosion pressure P_{max} only marginally increased from 8 to 8.3 bar. The same was observed for sample 11: when the d50 was decreased by a factor of four, the K_{St} rose by a factor of three, approximately.

When comparing samples DE6 and DE12, the explosibility expressed as KSt or K_{St}*P_{max} , was nearly the same when the d50 of the DE12 sample was decreased from 200 µm to 55.6 µm, approaching the d50 52.5 µm value of the DE6 sample.

Although the length of the glucose chains (DE value) could theoretically influence the reactivity of maltodextrin, the particle size or fineness of the dust is probably the dominant factor determining the ignition temperature, minimum ignition energy, as well as the maximum explosion pressure and pressure rise rate. While chemical composition can also play a role, the physical nature, particularly particle size, is more important when assessing the safety risks of maltodextrin dust.

5. Minimum Ignition Energy of Maltodextrin and ignition hazards

As can be seen in table 3, the minimum ignition energy of samples 11#DE and DE12 decreased when the sample was milled and sieved. However, the minimum ignition energy of sample DE6 with a similar fineness as the milled and sieved 11#DE and DE12 was higher than the latter samples. This effect can be attributed to the morphology differences between the sample: sample DE6 seemed more uniform in shape, mono spherical even, the milled and sieved samples appeared less uniform and greasy. This is in line with observations as described by Pranav et al (2019). They found that irregular shaped dusts had lower MIE compared to spherical shaped dust. They attributed this effect to the higher specific surface area of irregular shaped dust, which affects the dust cloud dynamics (turbulence, cloud concentration) and leads to lower resistance to thermal conduction.

As mentioned earlier, mixtures of maltodextrin and flavours/aromas exhibit very low ignition energies. The MIE can be less than 10 mJ, making such maltodextrins easily ignitable by electrostatic discharges with energies of 10 mJ or more. Movement of the powder can generate static charge, but a discharge from the powder itself would not be expected to ignite a dust cloud. However, movement of the powder can also lead to charge accumulation on ungrounded (metal) equipment, and (spark) discharges from such equipment can easily ignite a dust cloud with this level of sensitivity.

Pneumatic transportation of explosive dusts through plastic ducts, hoses, in coated metal ducts and internally coated silos, but also at fast emptying of non-conductive big bags, can lead to so-called propagating brush discharges. Ptak S. et al. (2020) showed that this kind of discharge can liberate up to 2 J, which is much higher than the MIE of some Maltodextrin products. If silo walls are coated with insulating materials or the walls themselves are made of insulating material, such discharges may be triggered at tangential inlets or during a collapse of a product bridge in the silo.

In addition, when operators become electrostatically charged, they can create sparks that are incendive for sensitive powders like maltodextrin, as illustrated in case study 3 above. Such spark discharges originate between charged conductors with different voltage and may ignite the dust in air cloud when the sparked energy is larger than MIE. In practice, an operator is capable of discharging 15 mJ of spark energy, a 200 L drum 40 mJ and a road tanker 100 mJ.

As described by Eckhoff in his book Explosions in the Process Industries (2006), the initial temperature has a strong influence on the minimum ignition energy of dusts. Glarner (1984)

showed that regression of the MIE as a function of initial temperature of the dust cloud could be determined starting from the MIE at ambient temperature.

In figure 4 below, this regression is plotted for 2 fictive Maltodextrin samples A and B for which the MIE determined at ambient temperatures was 100 and 300 mJ, respectively.

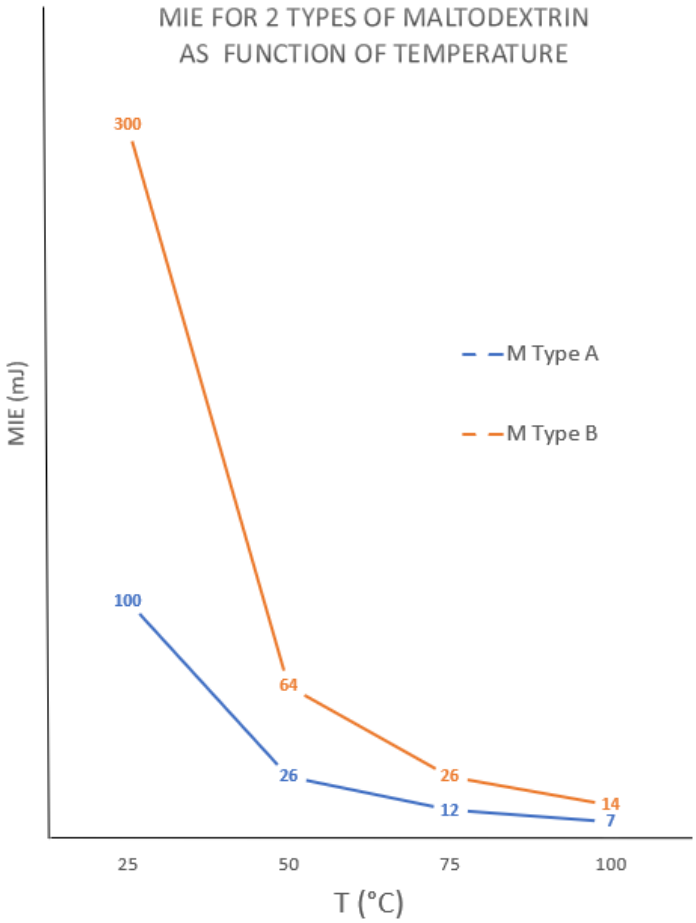

Figure 4. MIE as function of temperature for 2 Maltodextrin products - typical

For the 2005 silo incident as described above, the MIE of the Maltodextrin involved was in between 100 and 300 mJ. The conveying air from the road tanker compressor was about 50°C which lowered the MIE to approximately 30 mJ. Note that this example illustrates the need to evaluate the influence of process temperature on ignition properties of dust processed in the industries, especially in combination with a high resistivity of the powder. The resistivity is not a pure characteristic, but it indicates whether the product can be charged and if it can remain charged. The reported value of 4,12 . 10^{13} Ωm in the case study means the product is insulating so that it can be charged easily and will retain its charge for a long time, increasing the risk of a dust explosion ignited by electrostatic discharges.

As described by Eckhoff in his book Explosions in the Process Industries (2006), the moisture content also has a strong influence on the minimum ignition energy of dusts. Van Laar and Zeeuwen (1985) showed that regression of the MIE as a function of moisture is quite significant. If safety measures against electric sparks ignition are based on MIE data for a finite dust moisture content, it is essential that this moisture content will not become subsided in practice, for example

in drying processes. The presented data by van Laar shows that for starches, the source material of Maltodextrin, the MIE may drop by 50% and more when the moisture decrease from 5% wt. to 1% wt..

6. Summary and conclusions

Maltodextrin in fine powder form presents challenges in safe handling and storage, contributing to potential fire and explosion hazards, as illustrated in the three cases studies.

Maltodextrin can be regarded as a common denominator for a wide family of products that share the same chemical building blocks yet exhibit very difference fire and explosion characteristics.

The most commonly used sources of starch are corn, potatoes and rice. The specific manufacturing method and starch source influences the physicochemical properties of the resulting maltodextrin.

In an attempt to develop classes of explosivity within the family of Maltodextrins, powders with different DE numbers were purchased from the market and subjected to explosion tests to determine selected explosion characteristics.

Although the length of the glucose chains (DE value) could theoretically influence the reactivity of maltodextrin, the particle size or fineness of the dust is the dominant factor determining the ignition temperature, minimum ignition energy, as well as the maximum explosion pressure and pressure rise rate. While chemical composition can also play a role, the physical nature, particularly particle size, and process conditions, especially temperature, are more important when assessing the fire and explosion safety risks of maltodextrin dust as processed in the industry.

Because of its typical high resistivity, in combination with a medium to high ignition sensitivity, the ignition risk of maltodextrin shall be determined by testing, and taking all relevant process conditions into account, including but not limited to particle size distribution, process temperature and moisture. Because rubbing and/or segregation must be considered in transportation systems, it is advised to mill, sieve, dry, if necessary, before testing.

As pointed out in the presented case studies, explosions of Maltodextrin typically result from electrostatic hazards. Explosion prevention measures must be implemented as the first line of defence: use of suitable electrical equipment, grounding and bonding of all conductors whereby the resistance to earth should be regularly checked and be less than 1 MΩ, the wetted section of flexibles shall be conductive with a surface resistance of 10^8 Ω or less in combination with bonding the imbedded metal spiral(s) on both ends of the duct, and filter media shall be anti-static and supporting cages bonded.

References

IFA (2022) GESTIS-DUST-EX online database, https://staubex.ifa.dguv.de/

BIA (1997), Report Combustion and explosion characteristics of dusts 13/97, HVBG, ISBN 3-88383-496-6

Marchal M. et al. (1999), Towards a rational design of commercial maltodextrins, Trends in Food Science & Technology, Volume 10, Issue 11, November 1999, Pages 345-355

Marcus J.B. et al. (2019), Aging, Nutrition and Taste, Elsevier, ISBN: 9780128135273

EN ISO/IEC 80079-20-2, 2016. Explosive atmospheres – Part 20-2: Material characteristics – Combustible dusts test methods. International Organization for Standardization, Geneva.

ASTM E1226-19, 2020, Standard Test Method for Explosibility of Dust Clouds, American Society for Testing and Materials

EN 14034-1, 2011. Determination of explosion characteristics of dust clouds – Part 1: Determination of the maximum explosion pressure pmax of dust clouds. European Committee for Standardization, Brussels.

EN 14034-2, 2011. Determination of explosion characteristics of dust clouds – Part 2: Determination of the maximum rate of explosion pressure rise (dp/dt)max of dust clouds. European Committee for Standardization, Brussels, 2011. EN 14034-3, 2011.

Bagaria P. et al. (2019), Effect of particle morphology on dust minimum ignition energy, powder technology, Elsevier

Kwasi Addai E. et al. (2016), Ignition energy of hybrid mixtures of combustible dusts and gases, Process Safety and Environmental Protection, Elsevier

Eckhoff R.K. (2006), Dust Explosions in the Process Industries, Elsevier Butterworth-Heinemann

Glarner, Th. (1984), MIE – Einfluss der Temperatur, VDI Berichte 494, VDI-Verlag GmbH, Düsseldorf

Laar van G., and Zeeuwen J.P. (1985) On the MinimumIgnition Energy of Dust-Air Mixtures, Archivum Combustionis 5 pp. 145-159

Ptak S. et al. (2020). Estimation of the energy released during propagating brush discharge. Journal of Electrostatics, Volume 103, 2020, 103416, ISSN 0304-3886.

Pavey, I. (2009). Propagating brush discharges in flexible hoses. Journal of Electrostatics 67(2):251-255

Van Laar, G. (2003), Dust Explosion Risk Assessment of powder installation. ISMA, Report VBI03/0 (internal, unpublished)

Van Laar, G. (2005), Possible cause of explosion in maltodextrin silo. ISMA, Report VBI05/0047 (internal, unpublished)

VDI, (2023), from a case study presented at the VDI-Fachtagung Sichere Handhabung brennbarer Stäube 2023 in Nuremberg, Germany.

Effects of particle size homogeneity on dust ignitability and explosibility

Alberto Tascón [a,b], Blanca Castells [c,d], Ljiljana Medic [c,d], Francisco J. Castillo-Ruiz [a], Julia Arbizu-Milagro [a]

[a] Department of Agriculture and Food Science, Universidad de La Rioja, Logroño, Spain
[b] CIVA Research Center, Universidad de La Rioja, Logroño, Spain
[c] Department of Energy and Fuels, Universidad Politécnica de Madrid, Madrid, Spain
[d] Laboratorio Oficial J.M. Madariaga (LOM), Madrid, Spain

E-mail: alberto.tascon@unirioja.es

Abstract

The aim of this study was to analyse the influence of the sample origin and preparation on the ignition sensitivity and explosibility severity of combustible dusts, with a particular emphasis on the effects of the particle size distribution. Several dust samples were prepared by milling and sieving pine wood pellets. Some samples were homogeneous in size, while others were polydispersed. All samples were tested to determine their ignitability and explosibility properties following standardised procedures. The results indicated that neither D_{50} nor $D_{3,2}$ nor SSA correlated with the minimum ignition energy. In contrast, D_{10} showed a stronger link with the experimental results and it smoothed the differences between the homogeneous and polydispersed samples. The same trends were obtained for the minimum explosible concentration. In fact, samples with almost the same $D_{3,2}$ and SSA values behaved very differently in these two ignition tests; this dissimilar behaviour could be explained by the degree of homogeneity of the samples, which was also related to their skewness and span values. Therefore, the quantity of fine particles in the samples had a strong impact on these two ignition sensitivity parameters. On the other hand, the minimum ignition temperature of a layer hardly showed any variation with particle size, while the ignition temperature of a cloud and the explosion severity showed a good correlation with D_{50}. These results have implications for the risk management of real industrial facilities. The homogeneity of the samples tested in laboratory, which is determined by the sampling and/or prior preparation process, affects the dust ignitability and is therefore relevant to the design of dust explosion mitigation measures.

Keywords: *wood, biomass, particle size, sample preparation, polydispersity, dust explosions*

1. Introduction

Biomass materials are combustible (Mularski and Li, 2023) and their handling and processing generate dust particles that can form layers, deposits and dust clouds (Esteban and Carrasco, 2006; Varela et al., 2024), which pose a fire and explosion hazard in industrial facilities (García-Torrent et al., 2016). Since biomass plays a major role in the renewable energy portfolio of many countries around the world, the safe design and management of facilities dealing with these materials is an important topic.

Combustible dusts are characterised by means of a series of experimental techniques, including the cloud minimum ignition temperature (MIT_c), the layer minimum ignition temperature (MIT_l), the minimum ignition energy (MIE) and the lower explosion limit (LEL). These tests are usually performed following standardised procedures, for example those in the corresponding European standards (EN ISO/IEC 80079-20-2, 2016; EN 14034-3, 2011). Apart from these ignitability tests, explosion severity can also be assessed by measuring the maximum explosion pressure (p_{max}) and the

dust parameter K_{St}, which is derived from the maximum rate of explosion pressure rate $(dp/dt)_{max}$ (EN 14034-1, 2011; EN 14034-2, 2011).

A recent review by Castells et al. (2023) has highlighted the significant uncertainties in the properties of biomass dusts. They analysed 89 samples reported in the scientific literature during the last 25 years, and detected a great variability of materials and particle sizes, along with a poor identification of the origins of the samples. In addition, they remarked the necessity of rigorous preparation and characterisation of biomass samples prior to the tests. In this sense, there is a vagueness in international standards about the particle size of the dust samples to be tested, its determination and its reporting. Combustible dust standards do not offer precise rules for sample selection and preparation, but the more dangerous nature of fine dust is indicated by EN ISO/IEC 80079-20-2 (2016): *"where finer fractions are present in a facility it is appropriate to take fractions of less than 63 μm to give the most easily ignitable mixtures"*; similar recommendation can be found in the American ASTM standards, but for 75 μm. In the particular case of fibrous dusts –woody biomass is mostly composed of elongated fibres– the uncertainties increase even further since laser diffraction and sieving, which are the two most common methods for particle size determination, are only precise for round particles (Castells et al., 2023).

It is well-known that the particle size influences the ignition and explosion behaviour of dust samples (Cashdollar, 2000; Mishra and Azam, 2018); this is also true in the case of biomasses (Castells et al., 2023). Furthermore, Di Benedetto et al. (2010) developed a model for dust explosions based on dimensionless numbers that also considered the particle size, which was later applied to fibrous particles as well (Russo et al., 2013); they pointed out that the particle size determines the controlling combustion regime. Also, Fumagalli et al. (2018) developed a mathematical model for predicting the K_{St} reduction with the particle size increase for organic dusts. On the other hand, Eckhoff (2009) remarked the major role that powder science and technology play in dust explosions. Castellanos et al. (2014) pointed out the importance of polydispersity, while Tascón (2018) suggested that the skewness of the particle size distribution curve could play a role in the explosion behaviour of dust samples. In addition, Santandrea et al. (2019) also remarked the necessity for choosing the right particle size metrics.

However, as mentioned above, little attention is paid to how we measure and report the particle size of dust samples. The aim of this work was to study the effects of particle size on the dust ignitability and explosibility considering how samples are prepared and reported.

2. Material and methods

Several dust samples were prepared by milling and sieving commercially available pine wood pellets. Two different types of samples were obtained: samples consisting of the fraction retained between two sieves, and samples with particles that passed through a specific sieve size. The former samples were expected to be more homogeneous, while the latter were thought to have a wider distribution of particles with higher fractions of material in the fine and coarse parts of the PSD (particle size distribution) curve. All samples were tested to determine their ignition sensitivity and explosion severity following standardised procedures.

2.1. Preparation of dust samples

Pine wood pellets of quality class A-1 were used in this study. Several samples were obtained by milling and sieving the pellets. A hammer mill with 1.8 kW (GME-1100C by Garhé, Amorebieta, Spain) and circular 400, 250, and 80 μm sieves and a sieving shaker (Controls, Milan, Italy) were used.

Two different types of samples were obtained: homogeneous samples (H samples) and polydispersed or heterogeneous (P samples). The H-samples consisted on a fraction retained between two sieves and were produced by dividing a quantity of material in several different size fractions, while the P-

samples were formed by the particles that just passed through a specific sieve size. Therefore, a part of the milled sample was divided in three size ranges to generate H-samples: 400-250 µm, 250-80 µm and <80 µm. Another part of the milled material was sieved to produce two different polydispersed samples: <400 µm and <250 µm. Actually, the < 80 µm sample participates in both procedures but it was initially classified as homogeneous. The whole set of samples is presented in Table 1.

The homogeneous samples could be similar to the dust deposits created by segregation processes that occur in industrial facilities. In some cases, this particle size segregation can be desired and forms part of the material processing, but in other cases is an undesirable phenomenon. On the contrary, the heterogenous samples resembled the dust created by abrasion and crushing of the larger material particles during handling or storing in silos. These considerations have implications for real industrial processes. Therefore, the H400-250, H250-80 and H<80 samples represent the result of a segregation process, while the P<400 and P<250 samples –and the H<80 sample as well– represent different degrees of attrition of the pellets (see Table 1).

The particle size distribution of the samples was determined using a Malvern Mastersizer 2000 laser diffraction apparatus. Also, moisture contents were obtained in a halogen analyser (HB43 Mettler Toledo).

2.2. Characterisation of the samples

Samples were tested to characterise their ignitability and explosibility properties following standardised procedures. The minimum ignition temperature was obtained in the hot plate apparatus for layers and in the Godbert-Greenwald furnace for clouds (EN ISO/IEC 80079–20-2, 2016). The 20-L sphere was used to determine the LEL value (EN 14034-3, 2011), the maximum explosion pressure (EN 14034-1, 2011) and the dust parameter K_{St} (EN 14034-2, 2011). Finally, the minimum ignition energy was measured in the MIKE 3 device (EN ISO/IEC 80079–20-2, 2016). All determinations were carried out for every sample with the exception of the explosion severity of H<400.

The following higher values were established for the experimental procedures: 400 ºC in the MIT_l tests, 800 ºC in MIT_c, 1000 mJ in MIE and 1000 g/m^3 in LEL. Therefore, if the ignition (or explosion, in case of LEL) was not recorded applying lower values than these maximum ones, the test was stopped and no experimental MIT, MIE or LEL value was defined.

On the other hand, the explosion pressure and the rate of explosion pressure rise were calculated as the average of three repetitions. According to the standard, it is necessary to find the concentration (c_{max}) at which the maximum explosion pressure (and the maximum explosion rate) is recorded, and then repeat the test twice at $c_{max} \pm 250$ g/m^3. The 20-L sphere was equipped with two pressure sensors and for each test the pressure-time curves were obtained by both sensors; the results reported were calculated as the average of the data recorded by these two sensors.

The results were analysed and compared with the particle size properties of the samples. A comparison between the behaviour of the homogeneous samples and polydisperse samples was also carried out. Different size parameters were considered to explore their relation with the flammability and explosibility behaviours.

3. Results and discussion

3.1. Particle size of the samples

The particle size characteristics of the samples prior to the combustion tests are shown in Table 1. All particle size parameters except the skewness (S_k) were obtained from the laser diffraction measurements. The modified graphic Folk & Ward method proposed by Blott and Pye (2001) was used to calculated S_k (Tascón, 2018). The span –also called polydispersity index– was calculated as $(D_{90} - D_{10})/D_{50}$ (Castellanos et al., 2014); D_{xx} represents the particle size value for which xx% of the

particles are smaller on a volume or mass basis. In addition, SSA represents the specific surface area (m^2/g) of the sample and $D_{3,2}$ is the Sauter diameter or volume/surface diameter; actually, SSA and $D_{3,2}$ are related to each other since both of them are based on data obtained by laser diffraction assuming spherical particles ($D_{3,2}$ = 6/SSA).

As can be seen in Table 1, the samples included particles that were coarser that the corresponding sieve size. For example, the H<80 sample had a D_{90} of 169.8 µm, which doubled the theoretically maximum size of the particles after being sieved with the 80 µm sieve. This was detected in every fraction in Table 1. Notably, the H-sample of 400-250 µm gave D_{50} = 440.7 µm, i.e. the median diameter was higher than the top sieve size. Analogously, fine particles were also present in the coarser samples. For example, the D_{10} value of H400-250 was smaller than the 250 µm sieve. This behaviour was also reported by Saeed et al. (2018), which remarked that sieving does not eliminate fines or coarse particles, but it simply reduces the proportion in the final sieved sample.

***Table 1**. Particle size and moisture of samples*

Sample	D_{10} (µm)	D_{50} (µm)	D_{90} (µm)	$D_{3,2}$ (µm)	SSA (m^2/g)	S_k	Span
P<400	80.9	315.3	683.9	158.1	0.0380	-0.264	1.912
P<250	38.8	169.6	406.2	80.8	0.0742	-0.291	2.166
H<80	17.8	67.7	169.8	31.4	0.1910	-0.197	2.245
H250-80	99.3	227.1	465.6	151.5	0.0396	-0.061	1.613
H400-250	233.6	440.7	794.8	361.0	0.0166	-0.047	1.273

It is clear that sieving introduced a great uncertainty in the real particle size of the fractions due to its incapability to deal with fibrous materials. As Gil et al. (2014) pointed out, the dimension that is actually measured by sieving is the width. On the other hand, laser diffraction also added a further uncertainty: deviation from the spherical shape introduces some degree of error (Jillavenkatesa et al., 2001). Despite of these known limitations, sieving and laser diffraction are by large the most used methods in laboratories all around the world (Castells et al., 2023) and have also been applied in this study.

All the five samples gave negative value of S_k, which means that the distributions were skewed to the left; the PSDs were largely unimodal and presented a tail in the fine part of the curve. Skewness was higher in absolute value for the polydispersed samples since these samples presented a wider range of sizes. On the other hand, the homogeneous samples presented PSD curves that were more similar to normal distributions, as the lower S_k values indicated (a perfectly symmetrical curve has S_k = 0.00). Considering the absolute mathematical limits of skewness (−1.00 and +1.00), it can be noticed that the skewness values were always lower than 30%. Therefore, the P-samples were slightly asymmetrical or fine skewed, while the H-samples were nearly symmetrical.

As expected, the polydispersity index was high in the P-samples. However, the differences in the span values were lower than what could be expected and, quite surprisingly, we found that the highest span corresponded to the H<80 sample, which was followed by the P-samples, while the lowest spans were obtained for the other two H-samples. Therefore, just dividing a biomass material into several fractions by sieving could be insufficient to obtain homogeneous samples with low relative span. The notation H<80 is maintained throughout the manuscript to avoid confusion, though is not clear if this sample could be considered as homogeneous. In fact, the H<80 was homogeneous from the point of view of its preparation (three fractions obtained from the same sample amount) but heterogeneous if the polydispersity index or the skewness values were considered.

The moisture content of the five samples varied between 6.8% and 8.1% (average value of 7.6% and standard deviation of 0.51). The samples were not dried. Although the moisture content could have

some influence in the results, it was thought not to be relevant. In this respect, Pietraccini et al. (2021) reported a 20% reduction in p_{max} when there was a 5% wt. difference in the moisture content. In the present study the differences between samples were far smaller than that value.

3.2. Ignition sensitivity properties

Figure 1 shows the significant differences detected between the MIE values for both type of samples. The P<400 sample ignited at 660 mJ, while the H250-80 sample, which had a lower D_{50}, did not ignite at all. The highest energy applied in these tests was 1000 mJ and the maximum concentration used was 1000 g/m^3; H250-80 and H400-250 samples could therefore be ignited at energies > 1000 mJ but this was not verified (they are pictured in the graph as 1000 mJ points). Apart from the <80 sample, it is clear that the P-samples ignited much easier than the H-samples. Thus, the D_{50} value by itself did not properly reflect the ignition behaviour of these samples in the MIKE 3 apparatus.

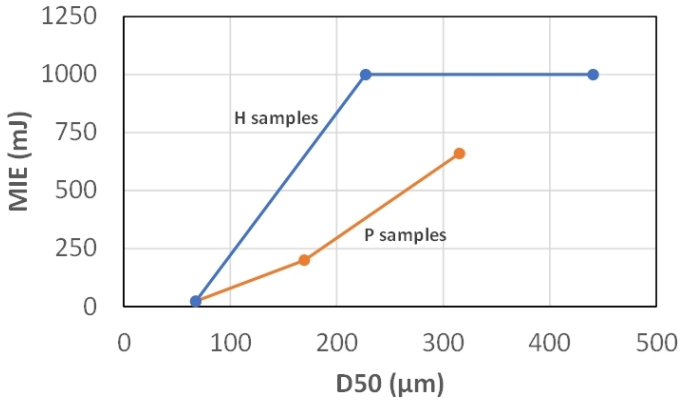

Fig. 1. *MIE results for homogeneous (H) and polydispersed (P) samples*

Again, significant differences were obtained in the LEL experiments between homogeneous and polydispersed samples. Figure 2 shows the behaviour of both types of samples. While the P<400 (D_{50} = 315.3 µm) gave a LEL of 125 g/m^3, the H250-80 (D_{50} = 227.1 µm) reached 250 g/m^3. Therefore, the D_{50} values did not correlate properly with LEL. It has to be noted that no explosion was recorded for the H400-250 sample during the tests when applying the maximum concentration defined in the methodology section (1000 g/m^3); this maximum limit was used to include it in the graph, tough a higher value could produce an explosion. It is remarkable the great range existing between the finest sample (just 30 g/m^3) and the coarsest sample that ignited (250 g/m^3).

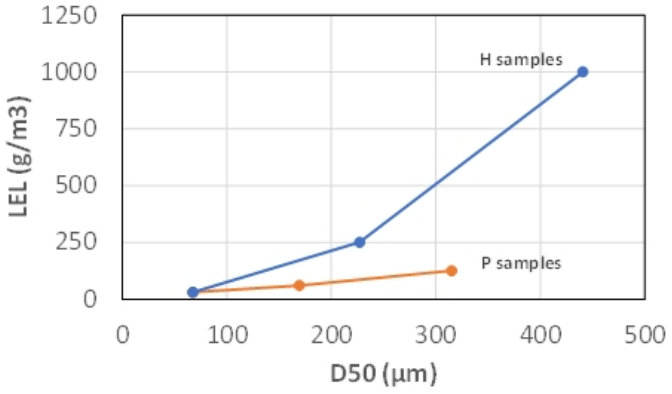

Fig. 2. *LEL results for homogeneous (H) samples and polydispersed (P) samples*

To find a more appropriate metric, the MIE and LEL results were compared with other several particle size parameters ($D_{3,2}$, SSA and D_{10}). Figure 3 illustrates this comparison. As can be seen, neither $D_{3,2}$ nor SSA improved the correlation. On the contrary, D_{10} showed a stronger link with both MIE and LEL, and smoothed the differences between the H-samples and P-samples.

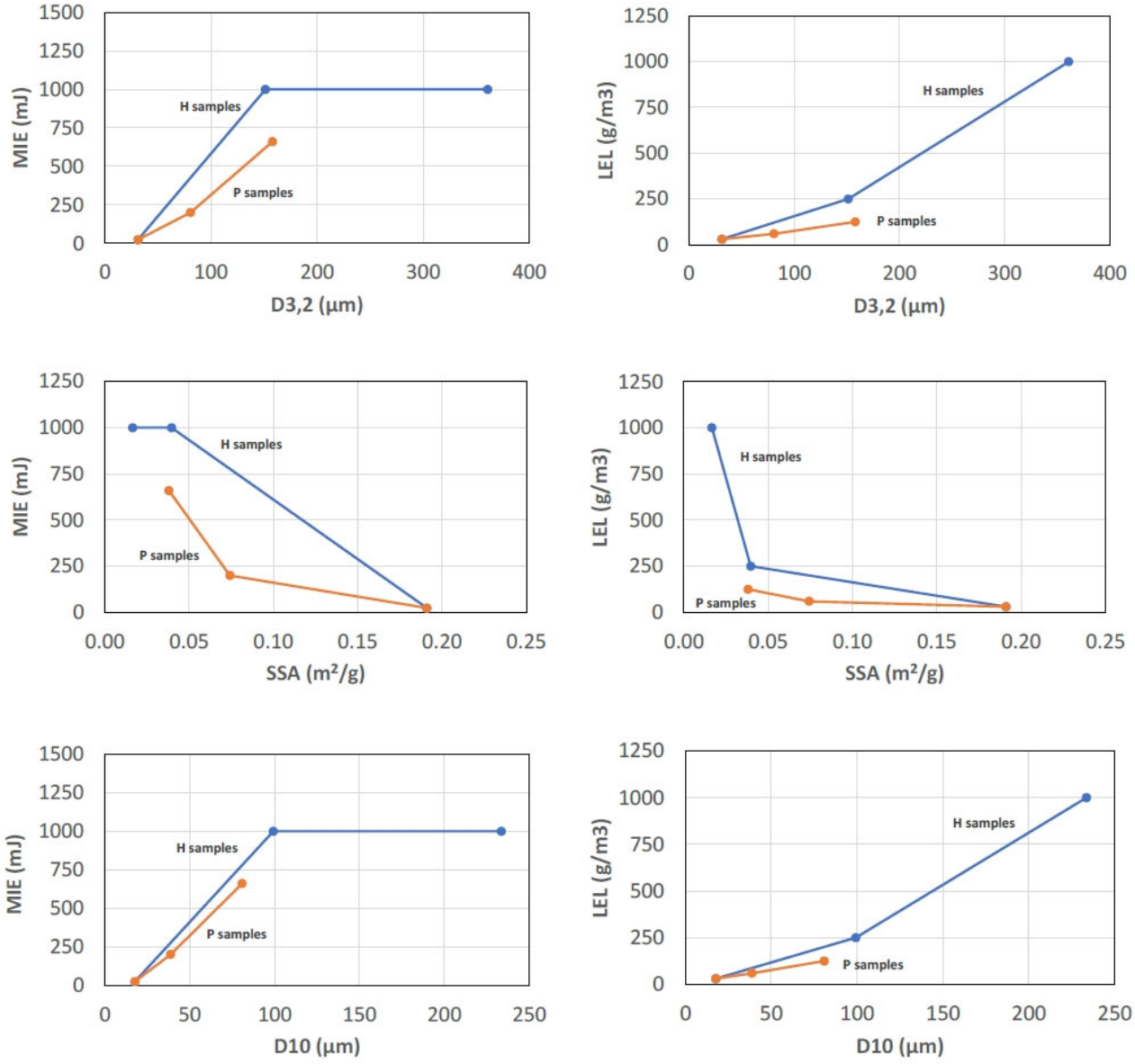

Fig. 3. *Variation of MIE (left) and LEL (right) with particle size*

The reason for the above MIE and LEL results in Figures 1 and 2 was the differences in the PSDs. As shown in Figure 4, the P-samples had a significantly greater quantity of < 63 µm particles than the H250-80 and H400-250 samples. This aspect was not reflected properly by the D_{50} values.

Thus, it is clear that the fine particles that were present in the samples exhibited a strong impact on the ignition sensitivity. This behaviour agreed with the MIE results reported by Santandrea et al. (2019) and the LEL results presented by Pietraccini et al. (2021). In fact, the fundamental role that the fine particles played can be demonstrated by considering the quantity of fine particles in the LEL results. Table 2 shows the results of multiplying the LEL concentration by the percentage of fine particles in the dust according to the laser diffraction tests. As can be seen, the differences between the four samples that could be ignited are now smoothed. This means that there could exist a minimum

quantity of fine particles required to produce the ignition, which led to very different minimum explosible concentrations (LEL) due to the dissimilar particle size distributions. However, the H400-250 sample presented similar quantities for the maximum concentration tested (1000 g/m^3): 10.1 g/m^3 of particles <63 µm and 29.0 g/m^3 of particles <100 µm. Therefore, it seems that other aspects, apart from the quantity of fine particles, determine the ignitability of the sample. In this particular case, the heat-sink effect of larger particles and the excess of fuel could play a role.

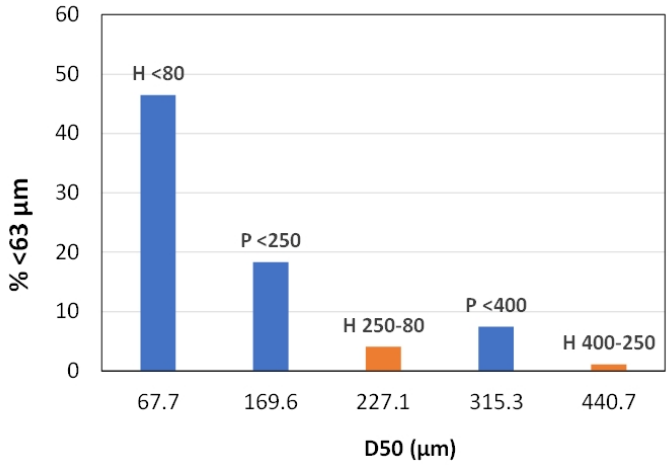

Fig. 4. *Fine particles (< 63 µm) in the five biomass samples expressed in % volume*

Table 2*. Fine particles in the LEL experiments*

Sample	LEL (g/m^3)	% <63 µm	<63 µm in LEL (g/m^3)	% <100 µm	<100 µm in LEL (g/m^3)
P<400	125	7.45	9.3	13.40	16.8
P<250	60	18.30	11.0	31.47	18.9
H<80	30	46.52	14.0	72.00	21.6
H250-80	250	4.05	10.1	11.61	29.0

It is therefore clear that D_{10} could be a proper metric for dust samples when MIE and LEL properties were important since it provided a better correlation with the flammability properties irrespective of the span or homogeneity of the sample. It is remarkable that neither $D_{3,2}$ nor SSA correlated properly with the MIE and LEL values. As can be seen, the P<400 and H250-80 samples presented an almost identical particle size according to the $D_{3,2}$ and SSA values but they behaved notably different when tested to determine their minimum ignition energy and lower explosion limit. On the other hand, skewness (see Table 1) reflected the higher quantity of < 63 µm particles in the P<400 sample in comparison with that in the H250-80, which explained their dissimilar behaviour. Therefore, differences in skewness between samples with the same particle size could call the attention of practitioners to the fact that the samples are not equal, as Tascón (2018) already suggested.

The particle size also influenced the MIT_c (see Figure 5). The ignition temperature of the dust cloud became higher when D_{50} increased. On the contrary, MIT_l hardly showed any variation with particle size: all samples presented the same ignition temperature in layer (340 ºC) excepting the finest sample (H<80), which ignited at 330 ºC. This behaviour in layer form agrees with the self-heating results in basket for wheat straw pellets reported by Restuccia et al. (2019), which pointed out that the critical oven temperature for self-heating ignition marginally decreases with particle size, i.e. particle size does not have a significant effect on the self-heating behaviour.

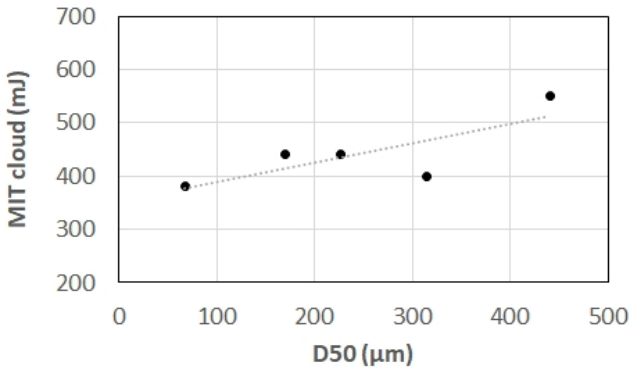

Fig. 5. *Correlation of MIT_c with D_{50}*

3.3.Explosion severity properties

Figure 6 illustrates the influence of D_{50} on the p_{max} and K_{St} results. Trend lines and R^2 values are also provided. As can be seen, the correlation is very clear in both graphs. In the case of p_{max} a polynomial equation was used for the trend line, while an exponential one was selected for K_{St}; mixture reactivity for aluminium also follows a d^{-n}-law, with d being D_{50} (Huang et al., 2009; Tascón, 2018). The greater the particle size, the lower the explosion severity. In this case the degree of homogeneity (or polydispersity) of the samples did not affect the correlation between particle size and explosion severity. Furthermore, the other size parameters ($D_{3,2}$, SSA and D_{10}) were also examined, though are not shown here. They presented similar good correlations with p_{max} and K_{St}. According to Figure 6, the maximum pressure was reduced by ~27% –and the K_{St} was reduced by ~44%– when the particle size increased. However, p_{max} varied very little for the three finest samples. The most significant reduction in p_{max} occurred when D_{50} increased above 227.1 µm, while the greater increment in K_{St} was obtained for D_{50} lower than 227.1 µm.

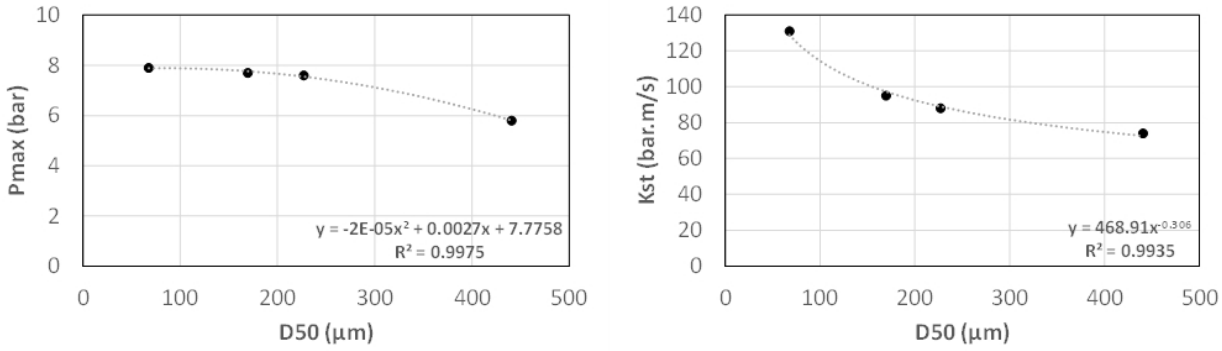

Fig. 6. *Variation of explosion severity with D_{50}*

It is important to note that the dust concentrations (c_{max}) that gave the maximum pressure and the maximum pressure rate differed greatly between samples. Higher concentrations were registered for the coarse samples. While 500 g/m^3 produced the p_{max} in the P<250 and H<80 samples, 1750 g/m^3 was necessary in the case of H450-250 and H250-80. A similar behaviour was detected for $(dp/dt)_{max}$ (750 g/m^3 for P<250 and 1000 g/m^3 for H<80, while 1500 g/m^3 for H450-250 and H250-80). A possible reason for these richer mixtures in the case of coarse dust was given by Saeed et al. (2018) following the turbulent combustion model previously proposed by the same research group (Saeed et al., 2017): sufficient fines are required –involving higher dust concentrations in the case of coarse

samples– since the fines follow the gas flow in the explosion vessel but the coarse particles lag behind due to drag effects; the larger particles are pyrolysed by the hot products of combustion of the fines, while the flame propagates ahead in the fine particles.

4. Conclusions

Homogeneous and polydispersed samples of commercial pine wood pellets were prepared by milling and sieving. Significant differences were detected between both types of samples in relation to their MIE and LEL properties. The much higher content of small particles in the polydispersed samples could explain their dissimilar behaviour. Neither D_{50} nor $D_{3,2}$ nor SSA correlated well with the MIE and LEL values considering the whole set of samples. Actually, it was demonstrated that samples with almost the same $D_{3,2}$ and SSA behaved very differently in these two ignition tests (MIE and LEL). On the contrary, D_{10} showed a much better correlation, indicating the importance of the smaller fraction of the particle size distribution.

However, no differences were detected in explosion severity behaviour between homogeneous and polydispersed samples. Both p_{max} and K_{St} correlated well with D_{50} (also with $D_{3,2}$, D_{10} and SSA). On the other hand, MIT_c showed a linear increment D_{50}, while MIT_l hardly presented any change with particle size.

In general, a decrease in particle size enhanced the ignition of the material and increased its explosion severity but the metric chosen to report the particle size could reveal or hide this behaviour. The present study supports the idea that considering just one single metric is misleading and can lead to crucial mistakes when evaluating combustible dust risks. Therefore, sampling and reporting the particle size are not trivial issues. Care has to be taken when assessing a real industrial facility to avoid producing a false sense of security. Moreover, the design of the corresponding mitigation measures depends on the properties of the dust, including its particle size. Further research seems necessary to understand the role played by the whole particle size distribution and the proper way of preparing samples and reporting their particle size.

Acknowledgements

The authors gratefully acknowledge the financial contribution from the Autonomous Community of La Rioja (Gobierno de La Rioja) through grant No. PID2019-106560RA-I00.

References

Blott, S.J., Pye, K., 2001. GRADISTAT: a grain size distribution and statistics package for the analysis of unconsolidated sediments. Earth Surf. Process. Landf. 26, 1237–1248.

Cashdollar, K.L., 2000. Overview of dust explosibility characteristics. J. Loss Prev. Process Ind. 13, 183–199.

Castellanos, D., Carreto-Vazquez, V.H., Mashuga, C.V., Trottier, R., Mejia, A.F., Mannan, M.S., 2014. The effect of particle size polydispersity on the explosibility characteristics of aluminium dust. Powder Technol. 254, 331–337.

Castells, B., Tascón, A., Amez, I., Fernandez-Anez, N., 2023. Influence of particle size on the flammability and explosibility of biomass dusts: Is a new approach needed?. Fire Technol. 59, 2989–3025.

Di Benedetto, A., Russo, P., Amyotte, P., Marchand, N., 2010. Modelling the effect of particle size on dust explosions. Chem. Eng. Sci. 65, 772–779.

Eckhoff, R.K., 2009. Understanding dust explosions. The role of powder science and technology. J. Loss Prev. Process Ind. 22, 105–116.

Fumagalli, A., Derudi, M., Rota, R., Snoeys, J., Copelli, S., 2018. A kinetic free mathematical model for the prediction of the K_{St} reduction with the particle size increase. J. Loss Prev. Process Ind. 52, 93–98.

Gil, M., Teruel, E., Arauzo, I., 2014. Analysis of standard sieving method for milled biomass through image processing. Effects of particle shape and size for poplar and corn Stover. Fuel 116, 328–340.

EN ISO/IEC 80079-20-2, 2016. Explosive atmospheres – Part 20-2: Material characteristics – Combustible dusts test methods. International Organization for Standardization, Geneva.

EN 14034-1, 2011. Determination of explosion characteristics of dust clouds – Part 1: Determination of the maximum explosion pressure p_{max} of dust clouds. European Committee for Standardization, Brussels.

EN 14034-2, 2011. Determination of explosion characteristics of dust clouds – Part 2: Determination of the maximum rate of explosion pressure rise $(dp/dt)_{max}$ of dust clouds. European Committee for Standardization, Brussels, 2011.

EN 14034-3, 2011. Determination of explosion characteristics of dust clouds – Part 3: Determination of the lower explosion limit LEL of dust clouds. European Committee for Standardization, Brussels.

Esteban, L.S., Carrasco, J.E., 2006. Evaluation of different strategies for pulverization of forest biomasses. Powder Technol. 166, 139–151.

García Torrent, J., Ramírez-Gómez, Á., Fernandez-Anez, N., Medic Pejic, L., Tascón, A., 2016. Influence of the composition of solid biomass in the flammability and susceptibility to spontaneous combustion. Fuel 184, 503–511.

Huang, Y., Risha, G.A., Yang, V., Yetter, R.A., 2009. Effect of particle size on combustion of aluminum particle dust in air. Combust. Flame 156, 5–13.

Jillavenkatesa, A., Dapkunas, S.J., Lum, L.S.H., 2001. Particle Size Characterization, NIST Recommended Practice Guide, Special Publication 960-1. National Institute of Standards and Technology, US Department of Commerce, Gaithersburg, MD, USA.

Mishra, D.P., Azam, S., 2018. Experimental investigation on effects of particle size, dust concentration and dust-dispersion-air pressure on minimum ignition temperature and combustion process of coal dust clouds in a G-G furnace. Fuel 227, 424–433.

Mularski, J., Li, J., 2023. A review on biomass ignition: Fundamental characteristics, measurements, and predictions. Fuel 340, 127526.

Pietraccini, M., Danzi, E., Marmo, L., Addo, A., Amyotte, P., 2021. Effect of particle size distribution, drying and milling technique on explosibility behavior of olive pomace waste. J. Loss Prev. Process Ind. 71, 104423.

Restuccia, F., Fernandez-Anez, N., Rein, G., 2019. Experimental measurement of particle size effects on the self-heating ignition of biomass piles: Homogeneous samples of dust and pellets. Fuel 256, 115838.

Russo, P., Amyotte, P.R., Khan, F.I., Benedetto, A.D., 2013. Modelling of the effect of size on flocculent dust explosions. J. Loss Prev. Process Ind. 26, 1634–1638.

Saeed, M.A., Andrews, G.E., Phylaktou, H.N., Gibbs, B.M., 2018. Burning properties and flame propagation of varying size pulverised rice husks. Proceedings of the 12th International Symposium on Hazards, Prevention and Mitigation of Industrial Explosions, Kansas City, MO, USA.

Saeed, M.A., Andrews, G.E., Phylaktou, H.N., Gibbs, B.M., 2017. Flame speed and K_{st} reactivity data for pulverised corn cobs and peanut shells. J. Loss Prev. Process Ind. 49, 880–887.

Santandrea, A., Bonamis, F., Pacault, S., Vignes, A., Perrin, L., Dufaud, O., 2019. Influence of the particle size distribution on dust explosion: How to choose the right metrics?. Chem. Eng. Trans. 77, 667–672.

Tascón, A., 2018. Influence of particle size distribution skewness on dust explosibility. Powder Technol. 338, 438–445.

Varela, A., Castillo-Ruiz, F.J., Arbizu-Milagro, J., Tascón, A., 2023. The influence of moisture on the sieving performance of lignocellulosic biomass. Biofuels Bioprod. Bioref. 17, 1708–1723.

Review and evaluation of engineering models for simulating small hydrogen releases in large enclosures

Andrine Hildershavn [a], Trygve Skjold [a] & Helene Hisken [a,b]

[a] University of Bergen, Bergen, Norway

[b] Sweco Norway AS, Bergen, Norway

E-mail: andrine.hildershavn@student.uib.no

Abstract

This paper reviews and evaluates engineering models for simulating loss of containment scenarios involving small releases of hydrogen in large enclosures. Several models were considered in the initial screening, but only three were selected for further analysis based on specific criteria: the multi-zone model MZgas and the computational fluid dynamics (CFD) tools FLACS and KFX. Only results obtained with MZgas and FLACS are included in the paper, since the simulations with KFX could not be completed in time. The efficiency and accuracy of the models are assessed through analysis of two experiments described in literature. Although both models reproduce the overall trends observed in the experiments, there are significant deviations between model predictions and experimental results for both models. The discussion elaborates on the accuracy of the model predictions, as well as practical aspects such as simulation time and post-processing of results.

Keywords: *hydrogen, loss of containment, confined spaces, accumulation, stratification, CFD*

Introduction

The use of hydrogen as a carbon-free energy carrier can enable a transition towards increasing use of renewable energy sources, such as solar and wind. However, hydrogen is highly flammable, has exceptionally low minimum ignition energy, and a propensity for deflagration-to-detonation-transition (DDT). Releases of hydrogen inside confined systems may result in stratified mixtures (Swain et al., 2003), and for a given mass of released hydrogen, rapid combustion of the reactive parts of a fuel-air cloud may produce significantly higher overpressures than flame propagation through a lean and less reactive homogeneous mixture that occupies the entire enclosure (Makarov et al., 2018).

The aim of the present study is to review and evaluate engineering models suitable for simulating scenarios involving small releases of hydrogen in relatively large enclosures, such as ships, domestic houses, laboratories, containers, and nuclear facilities. Detailed numerical modelling of hydrogen releases from high-pressure sources through small openings is inherently time-consuming, and it is crucial to use models that can reproduce the phenomena involved in sufficient detail to support risk assessments and safety engineering. Hence, the approach adopted for the present study entailed an initial review of available engineering models, followed by a critical evaluation of the performance of selected models with respect to accessibility, accuracy, simulation time, and user-friendliness. The models selected for detailed analysis included the open-source multi-zone model MZgas (Runefors & Johansson, 2023) and the commercial computational fluid dynamics (CFD) tool FLACS. The model predictions were validated against experimental results described in literature.

The first section presents the two experiments selected for model validation. The second section outlines the process of selecting simulation models, including an overview of the various models considered during the initial screening. The third section compares results from simulations and experiments. Finally, the fourth section summarizes the conclusions from the study and suggestions for further work.

1. Experiments

To effectively achieve the aim of the study, i.e. to evaluate the predictive capabilities of models for simulating small leaks within relatively large enclosures, it was essential to identify validation cases that could be defined and simulated within reasonable time, with the available computational resources. Consequently, the following criteria were defined for prioritising validation experiments:

- The experiment should involve small releases.
- The duration of the leaks should be less than 1000 seconds.
- The experiment should not have forced ventilation.
- The experiment should have limited or no natural ventilation.
- The dimensions of the enclosures should be comparable to laboratories or containers, and not exceeding the size of a small house.
- The scenarios should be easy to define based on the available information.

1.1 Experiment 1

The first validation case is based on one of the experimental configurations in model of a garage described by Gupta *et al.* (2009). Figure 1 shows the enclosure, dimensions 5.76 m x 2.96 m x 2.45 m (total volume 42 m^3). The leak was positioned in the centre of the enclosure, 0.22 m above ground level. Table 1 summarises relevant parameters from the scenario selected for model validation. It is worth noting that helium was used in the experiments, due to safety reasons.

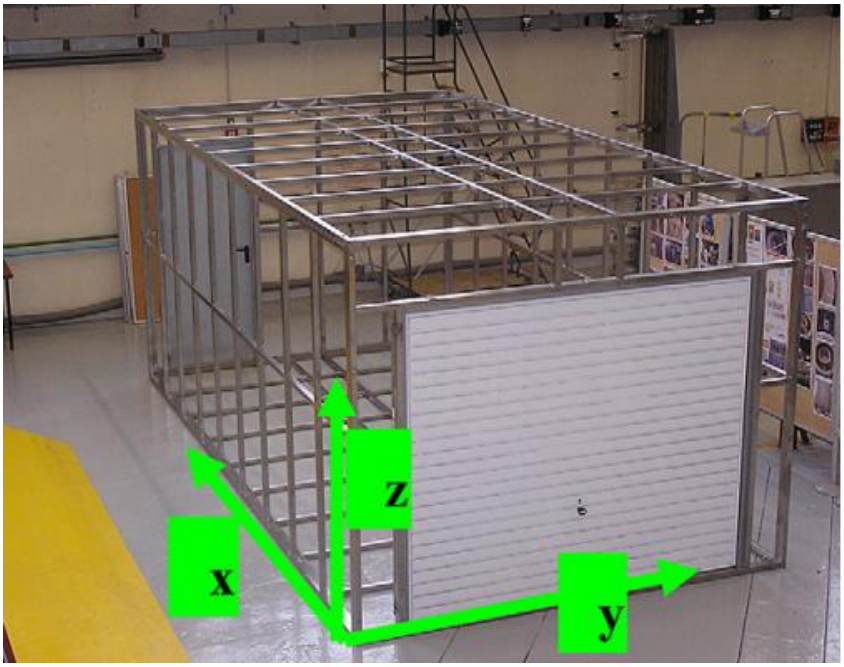

Figure 1: Experimental setup of the first validation scenario (Gupta et al., 2009).

Table 1: Experimental parameters for hydrogen release scenario adapted from Gupta et al. (2009).

Mass Flow Rate (kg/s)	0.00199
Volumetric Flow Rate (L/min)	668
Exit diameter (m)	0.0207
Exit Velocity (m/s)	35.5
Release direction	+Z
Release duration (s)	500
Enclosure Temperature (°C)	20

1.1 Experiment 2

The second validation scenario is one of the experiments conducted by Pitts *et al.* (2012) in a model of a residential garage. Figure 2 shows the garage, with dimensions 6.10 m x 6.10 m x 3.05 m (total volume 113 m^3). The hydrogen was released from a square box with an open top. The leak was placed in the middle of the enclosure, 0.15 m above ground. Table 2 summarises relevant parameters from the scenario selected for model validation.

Figure 2: Experimental setup of the second validation experiment (Pitts et al., 2012).

Table 2: Experimental parameters for hydrogen release scenario adapted from Pitts et al. (2012).

Mass Flow Rate (g/min)	83.3
Volumetric Flow Rate (L/min)	956
Source area (cm^2)	30.5
Exit Velocity (m/s)	5.5
Release direction	+Z
Release duration (s)	506
Enclosure Temperature (°C)	20

2. Simulation models

The models evaluated in the initial screening were the commercial consequence software products KFX, FLACS, FRED and EFFECTS, and the freely available tools HyRAM and MZgas. Each model should fulfil specific criteria for simulation suitability, including flexibility in geometry modification, and applicability to simulating small release scenarios within enclosures. Table 3 summarises the results from the initial screening.

Table 3: Summary of the evaluated models against the specific criteria.

Model	Geometry modification	Applicability to small release scenarios	Free or commercial	Included in the present study?
KFX	Excellent	Excellent	Available at Cost	No (ongoing analysis)
FLACS	Excellent	Excellent	Available at Cost	Yes
FRED	Limited	Limited	Available at Cost	No
EFFECTS	Limited	Limited	Available at Cost	No
HyRAM	Limited	Good	Free	No
MZgas	Good	Excellent	Free	Yes

Half of the models were ultimately discarded. EFFECTS and FRED are not suitable for simulating releases inside enclosures, and HyRAM has limited options for modifying the enclosure geometry. Among the chosen models, MZgas was selected for its user-friendly interface and availability as an open-source tool. FLACS and KFX are both commercially available CFD tools commonly used for dispersion and accumulation scenarios. FLACS and KFX were both selected based on their fulfilment of all the specified criteria. Unfortunately, the KFX simulations could not be completed in time to be included in this version of the paper.

2.1 MZgas

The multi-zone model MZgas is an open-source model for simulating accumulation and ventilation of hydrogen in enclosures (Runefors & Johansson, 2023).

2.1.1 Model description

The model is based on the multi-zone concept, where the enclosure is divided into multiple regions (horizontal) and layers (vertical) that represent computational zones. Maintaining uniform species concentrations in each computational zone ensures mass conservation. Density disparities arise due to variations in concentration between zones, leading to pressure differentials. The pressure gradients drive the flow between the cells, adhering to the Bernoulli equation (Johansson & Runefors, 2023).

2.1.2 Setup and post-processing

The input file comprises a script consisting of seven lines of text. This script serves as a tool for altering various parameters governing the simulation, including the size and mesh configuration of the domain, simulation duration, ambient temperature, leak properties, gas properties, and ventilation parameters. The mesh structure created consists of uniformly structured quadrilaterals. Upon completion of the simulation, two distinct text files are automatically generated. The first file contains concentration data encompassing all zones at each timestep, while the second file contains the maximum concentration values at each timestep throughout the simulation duration.

After running the simulations, the concentration data obtained from the simulations were processed using custom Python scripts build from scratch. The concentrations were adjusted based on the mesh resolution and enclosure dimensions to calculate the volume fraction of hydrogen in each cell. The processed data was then organized into a dictionary, where concentrations were stored for each layer and timestep. Using the dictionary, plots for volume fraction against elevation for different timesteps and simulation were created.

For simulating Experiment 1, a box with dimensions of 6 m x 3 m x 2.5 m and a mesh resolution of 6 x 3 x 12 was specified in the input script. For the subsequent Experiment 2, a box with dimensions of 6 m x 6 m x 3 m and a mesh resolution of 6 x 6 x 15 was employed. Leak properties were set to represent those in the specific experiment. Hydrogen was used as the gas for both experiments.

2.2 FLACS

2.2.1 Model description

FLACS™ is a CFD-based engineering tool developed by Gexcon, and is primarily used for consequence modelling related to safety and security in industry. FLACS solves transport equations for mass, momentum, enthalpy, turbulent kinetic energy, rate of dissipation of turbulent kinetic energy, mass fraction of fuel, and mixture fraction on a structured Cartesian grid. FLACS uses the porosity/distributed resistance (PDR) concept to represent the geometry, and turbulence is modelled with the standard k-ε model. The PDR approach allows for the representation of complex geometries on relatively coarse computational meshes, where large objects and walls are represented on-grid, while smaller objects are represented sub-grid (Gexcon, 2023).

Users set up the simulations in the pre-processor CASD, start and monitor simulations in the Run Manager, and visualise results in the post-processor Flowvis.

2.2.2 Simulation setup

Figure 3 shows the setup for Experiment 1 in FLACS, with a vertical hydrogen leak in the middle of the enclosure, monitor points at heights 0.3 - 2.5 m, and grid cells of size 0.5 m with local refinement to resolve the release.

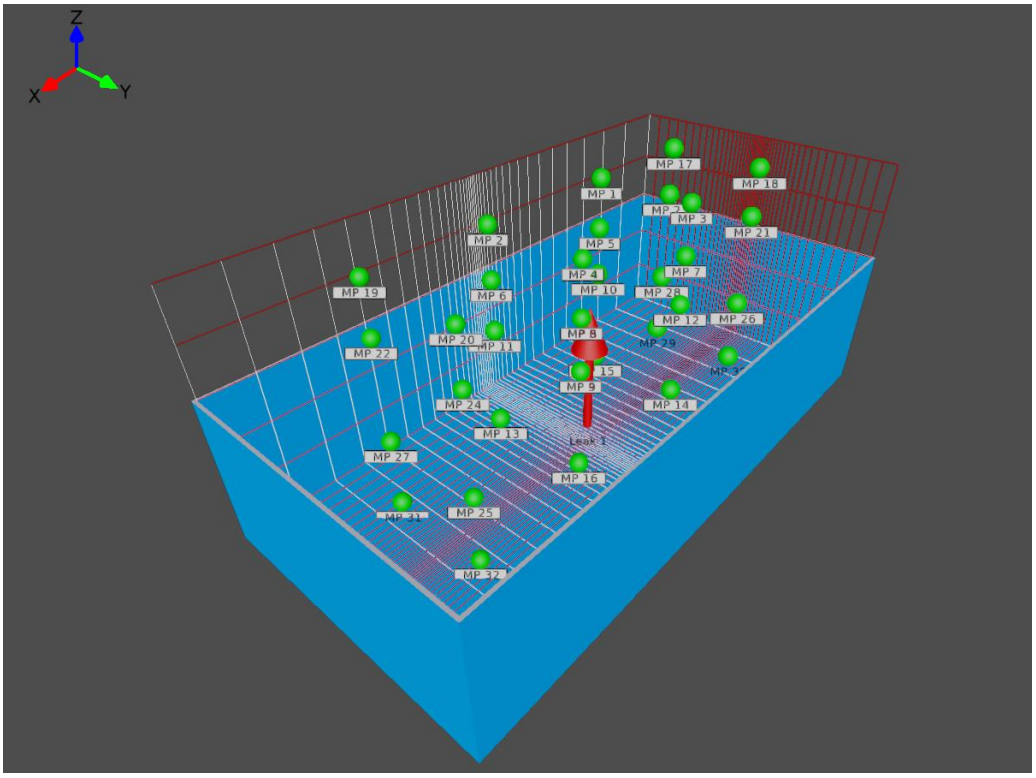

Figure 3: Setup for Experiment 1 in FLACS, illustrating the computational grid and monitor points.

Figure 4 shows the setup for Experiment 2 in FLACS, with a vertical hydrogen leak in the middle of the enclosure, monitor points at heights 0.5 - 3.0 m, and grid cells of size 0.5 m with local refinement to resolve the release.

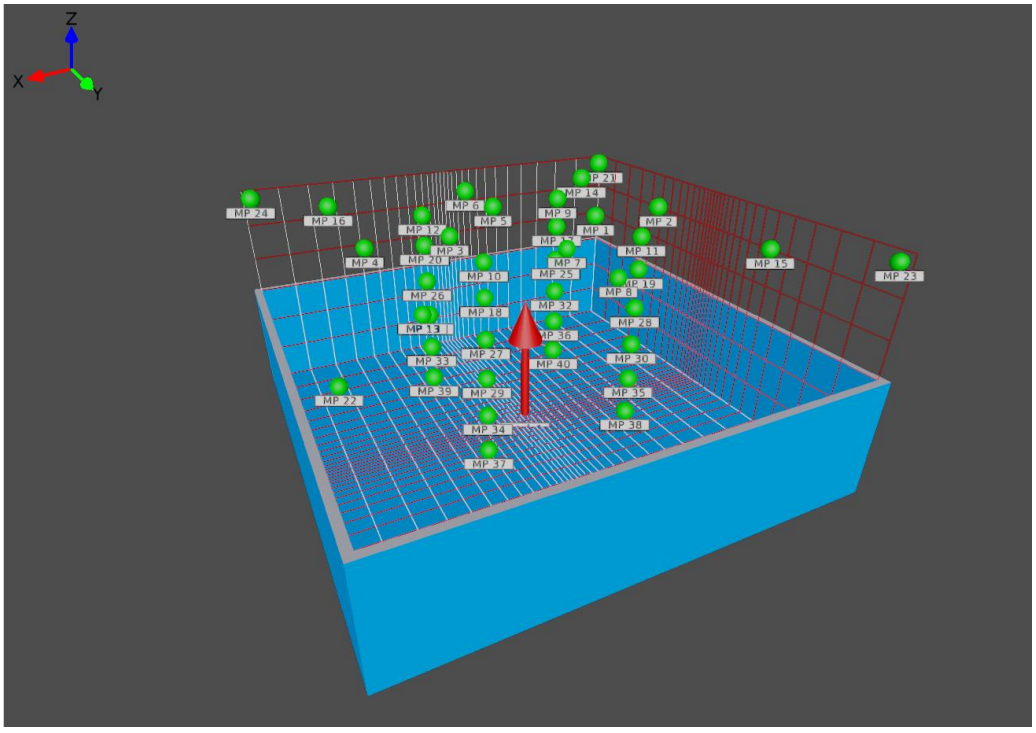

Figure 4: Setup for Experiment 2 in FLACS, illustrating the computational grid and monitor points.

3. Results and discussion

MZgas was used on a computer with an 11th Gen Intel(R) Core(TM) i5-11300H processor and 16 GB RAM. The simulation time varied from less than a minute to 45 minutes for Experiment 1, depending on the mesh resolution. The simulation time for Experiment 2 was 10 minutes. MZgas was straight forward to use, with clear instructions provided in the user guide. All post processing were done with custom python scripts made from scratch.

The stationary computers available at the University of Bergen are not suited these specific CFD simulations. The computers used had and Intel(R) Core(TM) i5-6500 CPU processor and 16 GB RAM. The FLACS simulations took 0.5-7 days, depending on grid resolution. FLACS was fairly easy to use, although finding information in the long and comprehensive user manual proved difficult at times. There were also issues in the post processing of the data. It could take up to ten minutes to load the data for a scalar plot in Flowvis, but this was due to the computers and not the program itself.

3.1 Experiment 1

The dimensions of the enclosure used by Gupta et al. (2009) was rounded to 6.0 m x 3.0 m x 2.5 m in the simulation geometry. To assess the sensitivity of the selected mesh configuration in MZgas, a grid sensitivity analysis was conducted. The mesh specifications utilised by the developers in Runefors & Johansson (2023) served as the reference, employing a 3 x 3 x 10 mesh within a 2.6 m x 2.6 m x 2.45 m enclosure. Subsequently, a mesh configuration of 6 x 3 x 10 was adopted as the initial setup for the 6 m x 3 m x 2.5 m enclosure. The objective was to systematically evaluate whether increasing the mesh resolution along the z-axis or in the x and y directions gave better results. Some of the validation simulations from Runefors & Johansson (2023) have been replicated, to ensure that the program had been used as the developers envisioned.

Table 4 summarises the mesh resolution and simulation times for MZgas. Test 1 involved the initial configuration of the 6 x 3 x 10 mesh. Tests 2 and 3 focused on increasing mesh resolution along the z-axis, while tests 4 and 5 explored enhancements in the x and y directions.

Table 4: Overview of mesh configurations and simulation times with MZgas for Experiment 1.

	Test 1	**Test 2**	**Test 3**	**Test 4**	**Test 5**
Mesh	6 x 3 x 10	6 x 3 x 12	6 x 3 x 18	12 x 6 x 9	12 x 6 x 12
Total cells	162	216	324	648	864
Time (min)	4	6	11	27	40

Figure 5 shows the volume fraction of fuel as function of elevation at various times. Notably, Test 2 (orange) exhibited the highest volume fraction across all timesteps, while Test 5 (purple) demonstrated the second-highest volume fraction at 250 and 500 seconds, albeit registering as the second lowest at 10 seconds. Both Test 1 (blue) and Test 4 (red) exhibited sparse data representation at lower elevations, due to their relatively low mesh density in the z-direction. The most evident disparities between mesh configurations were observed at lower elevations during later timesteps, indicating that a higher mesh resolution along the z-axis generally provides more accurate information at lower elevations.

The disparity between the highest and lowest volume fraction values at 2.5 meters remained consistent across all timesteps, with differences remaining below 0.01 for 10, 250, and 1000 seconds, but exceeding 0.01 at 500 seconds. Increasing mesh resolution in the x and y directions gives a greater total number of mesh cells compared to solely augmenting the z-direction. Consequently, simulation times substantially increased for Test 4 and Test 5 compared to other mesh configurations.

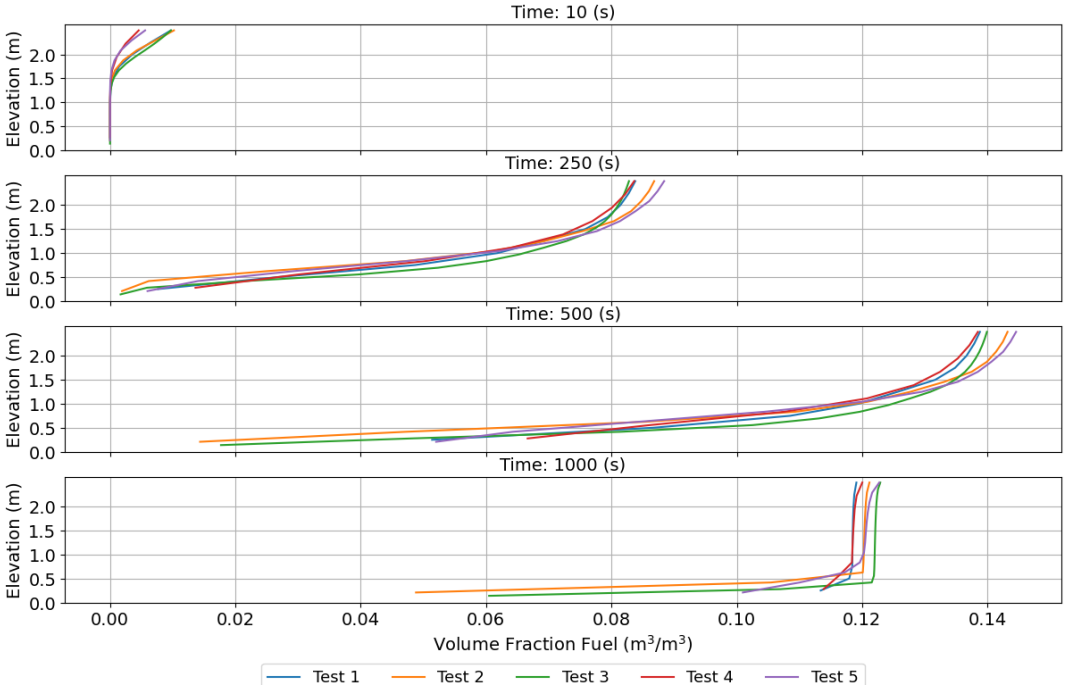

Figure 5: Volume fraction of hydrogen distribution along elevation. Test 1 shown as the blue graph, Test 2 as the orange graph, Test 3 as the green graph, Test 4 as the red graph, Test 5 as the purple graph.

All the mesh configurations give lower volume fractions than the test conducted by Gupta et al. (2009), shown Figure 6a. Considering the marginal disparity in concentration outcomes across the mesh resolutions, a sensible choice might be a configuration of L m x W m x 4H or L m x W m x 5H.

Figure 6c shows that MZgas gives a consistent upward trend, mostly mirroring the increase observed in Figure 6a. Helium volume fractions of 0.20-0.225 were recorded at elevations of 1.9 – 2.37 m in the validation experiment (Figure 6a). A maximum hydrogen volume fraction of 0.15 was calculated at 2.50 m in MZgas, around 46% less than the experimental value. The simulation shows that after the leak stopped at 500 seconds, the volume fractions from 1.00 m and above were gradually reduced, whilst the volume fraction at lower elevations increased. This behaviour differs from that observed in the validation experiment, where most of the volume fractions remained constant. The final simulated volume fractions from 0.5m and above were all slightly higher than 0.125, this is 37.5-40.5% less than the experimental values.

The plot from the FLACS simulation (Figure 6b) shows a similar increase of the volume fraction of hydrogen as the experimental volume fractions of helium in Figure 6a. At the monitor positioned at 2.5 m, the highest calculated volume fraction was 0.26. This value decreased to 0.16 at 0.5 meters and further to 0.15 at 0.3 meters. The simulated volume fractions closely resemble the experimental values after the leak period (after 500s), exhibiting predominantly constant volume fractions, except for those at 1.5 m, which decrease. FLACS calculates a slight increase in the volume fractions at 0.5 m after 500s, which is consistent with the experimental values. The highest simulated volume fractions in FLACS are 15-33% higher than the experimental values, except for the value at 0.3m. FLACS predicted a value three times higher than the experimental value at 0.3 m.

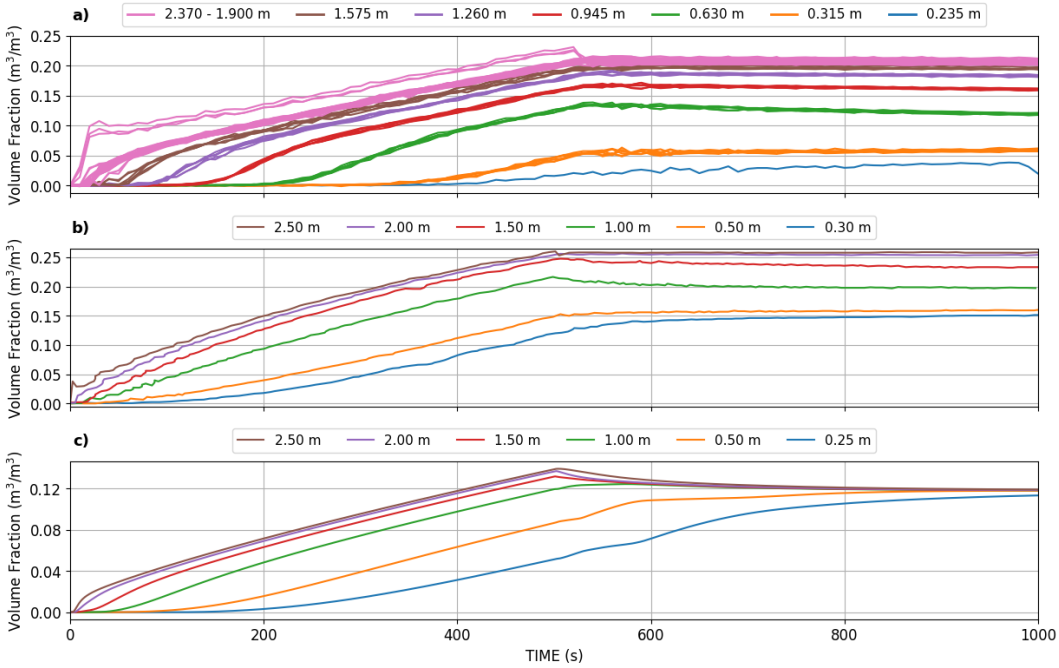

Figure 6: Hydrogen volume fraction development with time for Experiment 1. Graph a) displaying experimental values, adapted from Gupta et al. (2009). Graph b) displaying the simulation results from FLACS. Graph c) displaying simulation values from MZgas.

3.2 Experiment 2

The enclosure was modelled with dimensions rounded to 6.0 m x 6.0 m x 3.0 m. Table 5 summarises the effect of varying the grid resolution in FLACS. This analysis was only done for Experiment 2, since the larger leak area allowed for shorter simulation times. The refined grid was chosen based on the established grid guidelines and were not changed for the different tests due to time and computational resource constraints. The main grid was changed for the different tests. Grid information and simulation time for each test is shown in Table 5.

Table 5: Overview of grid configurations for the three tests.

	Test 1	**Test 2**	**Test 3**
Size main grid-cells (m)	0.5	0.25	0.125
Size refined grid-cells (m)	0.065	0.065	0.065
Refined grid region (m x m)	2 x 2	0.75 x 0.75	0.375 x 0.375
Simulation time (days)	0.5	1.5	3.5

Figure 7 summarises the development of the hydrogen volume fraction over time. Test 1(blue) gave higher values compared to the finer grids employed in Test 2 (green) and Test 3 (red). Across all tests, the maximum volume fraction recorded at the end of the simulation was between 0.12 and 0.13. As the grid resolution increased, the calculated minimum values at the simulation end decreased. The lowest predicted value at the end of the simulation for the experiment conducted by Pitts et al. (2012) was 0.03, which is significantly higher than all the tests. The simulation time increased with finer grid resolutions. Considering these observations, the decision was made to proceed with the coarsest grid for subsequent analyses.

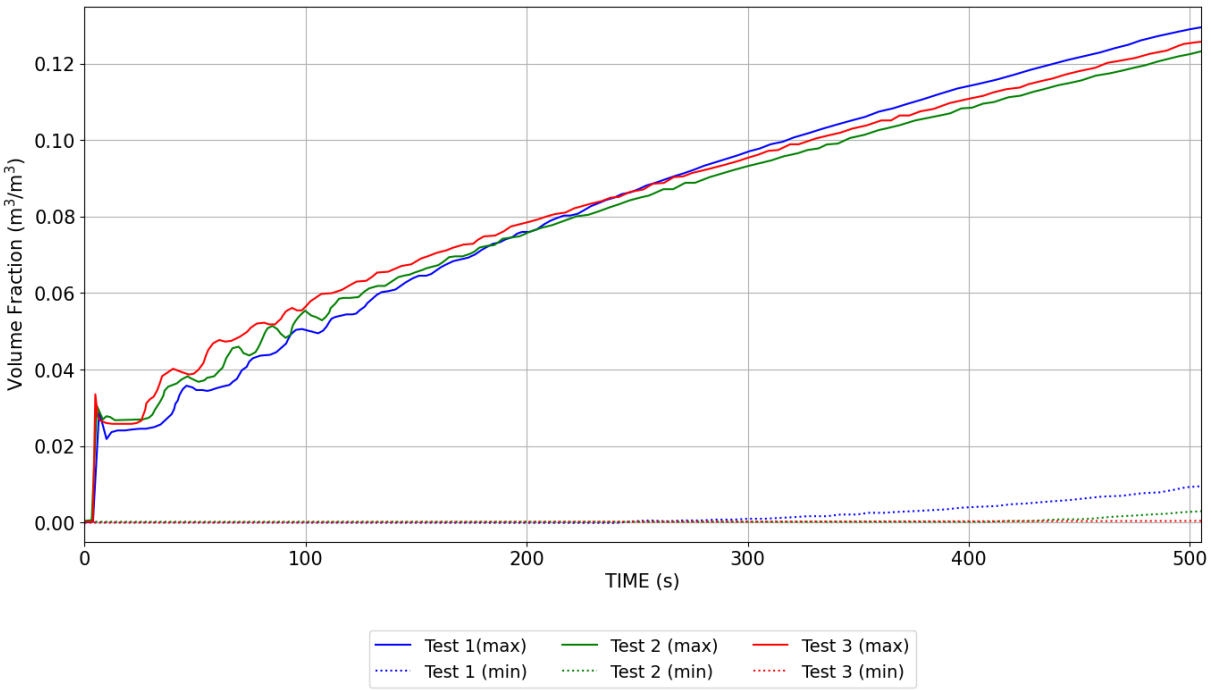

Figure 7: Development of hydrogen volume fraction with time for Test 1, Test 2, and Test 3.

Figure 8 shows the development of hydrogen volume fraction over time at different elevation. The maximum value measured in the experiment was 0.092 at 506 seconds (Figure 8a). All volume fractions increased gradually through the leak period. MZgas (Figure 8c) predicts a maximum volume fraction of 0.068 at 506 seconds (i.e. 26 % underprediction), while the highest volume fraction predicted by FLACS (Figure 8b) was 0.13 at 3 m (i.e. 41% overprediction).

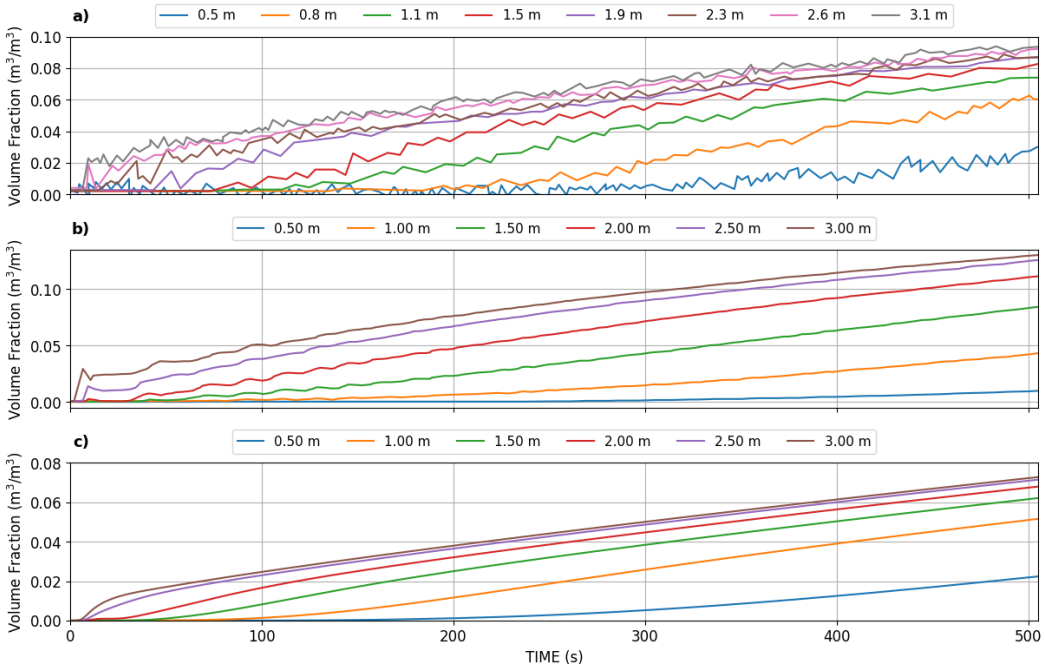

Figure 8: Development of hydrogen volume fraction with time for Experiment 2. Graph a) displaying experimental values, replicated from Pitts et al. (2012). Graph b) displaying the simulation results from FLACS. Graph c) displaying simulation values from MZgas.

4. Conclusions and suggestions for further work

This study presents an evaluation of the accuracy and efficiency of two engineering models used for simulating small hydrogen releases in large enclosures: MZgas and FLACS-CFD. Both models predict the overall trend observed in experiments, but MZgas tends to underpredict the measured volume fractions, while FLACS overpredict concentrations at high elevations for some scenarios.

The simulation time varies significantly between the two models. For the scenarios investigated in this work, a CFD simulation with FLACS could take from a day to over a week depending on grid resolution and the duration of the leak, whereas a typical simulation with MZgas took 5-10 minutes.

MZgas proved to be remarkably accessible, offering straightforward download and immediate usability. The user guide provided clear instructions on input file description, facilitating ease of use even for those with minimal prior experience. The post-processing required basic programming skills.

FLACS is a significantly more complex model system than MZgas, and dedicated training is generally required. Setting up simulations was relatively straightforward with basic training, but both simulations and post-processing requires appropriate hardware.

Further research in this area should include validation of additional models, against additional experiments. For practical applications in industry, it is of crucial importance to assess the time and resources required to provide reliable predictions with a sufficient level of accuracy to support risk assessments and safety engineering.

Acknowledgements

The authors gratefully acknowledge the support from the Research Council of Norway for the project *Safe Hydrogen Implementation: Pre-normative research for Ships* (SH2IPS) under grant agreement number 326281, and the support from the focus area *Climate and Energy Transition* at the University of Bergen.

References

Gupta, S., Brinster, J., Studer, E. & Tkatschenko, I. (2009). Hydrogen related risks within a private garage: concentration measurements in a realistic full scale experimental facility. *International Journal of Hydrogen Energy*, 34, 5902-5911.

Gexcon (2023). *FLACS-CFD v22.2 User's Manual*.

Hooker, P., Hoyes, J.R. & Hall, J. (2014). Accumulation of hydrogen released into an enclosure fitted with passive vents – Experimental results and simple models. *Hazards* 24, 12 pp.

Johansson, N. & Runefors, M. (2023). User guide MZ_gas: A multi-zone model for calculating hydrogen concentrations in an enclosure, April 2023.

Makarov, D., Hooker, P., Kuznetsov, M. & Molkov, V. (2018). Deflagrations of localised homogeneous and inhomogeneous hydrogen-air mixtures in enclosures. *International Journal of Hydrogen Energy*, 43: 9848–9869.

Pitts, W.M., Yang, J.C., Blais, M. & Joyce, A. (2012). Dispersion and burning behavior of hydrogen released in a full-scale residential garage in the presence and absence of conventional automobiles, *International Journal of Hydrogen Energy*, 37, 17457-17469.

Runefors, M. & Johansson, N. (2023). A multi-zone model for hydrogen accumulation and ventilation in enclosures. International Conference on Hydrogen Safety (ICSH), 19-21 September 2023, Québec, Canada.

Swain, M.R., Filoso, P., Grilliot, E.S. & Swain, M.N. (2003). Hydrogen leakage into simple geometric enclosures. *International Journal of Hydrogen Energy*, 28: 229-248.

Study on strength of plastic piping against detonation of hydrogen/oxygen mixture

Jin Hosoi [a], Toshio Mogi [a] & Ritsu Dobashi [a]

[a] The University of Tokyo, Tokyo, Japan

E-mail: hosoi-jin0509@g.ecc.u-tokyo.ac.jp

Abstract

Piping in facilities that handle hydrogen must be designed with appropriate strength against explosions. Particularly in photocatalytic water decomposing systems, a mixture of hydrogen and oxygen is produced at the catalyst. Assuming a transportation piping accident, detonation of a mixture of hydrogen and oxygen at an equivalent ratio of 1 was generated inside the resin piping, and the strain and destruction phenomena of the resin piping were investigated.

At the beginning of the study, it was verified that there is almost no change in detonation characteristics judging from the detonation velocity measured in pipe experiments with a radius of 12 to 44 mm. Next, the strain waveforms of resin materials with different hardness were measured, and the deformation behaviors of the different materials were analysed. To investigate the relationship between strain and pressure, the maximum pressure and impulse as indicators of the effective force exerted on pipe deformation was defined. As a result, the degree of correlation with strain was greater for maximum pressure than for impulse. Furthermore, the degree of deformation of resin materials with low hardness changes greatly for the same amount of pressure when exposed to repeated detonation pressure and heat, indicating that soft vinyl chloride is not suitable for long-term use in plants. Finally, for each pipe failure condition, observations were made using a high-speed camera and strain to discuss the dominant factors for plastic pipe failure, and it was described what has been discovered regarding safety.

Keywords: *prevention, hydrogen, detonation, strain, pipe, plastic*

1. Experiments

Building a hydrogen recycling society as a carbon-neutral approach that virtually eliminates carbon dioxide emissions has been proposed as one measure to stop global warming. It is important that hydrogen production methods are also sustainable, so green hydrogen, which does not release any carbon dioxide during the production process, could be important. Therefore, it is necessary to improve safety in the green hydrogen production process. This research will focus on ways to decompose water and produce hydrogen using sunlight and catalysts.

In the method using a photocatalyst, hydrogen and oxygen are generated together, so hydrogen and oxygen exist in the pipe at a material ratio of 2:1 from the catalyst part to the separation module that extracts hydrogen. Hydrogen has a very low minimum ignition energy and a detonation speed of about 2800 m/s, which is extremely fast compared to other gases (Shepherd, 2009). The concentration range in which it can explode is wide, and if the mixture ignites, there is a high probability that it will detonate. If a detonation occurs in this section, there is a risk of serious facility destruction and human injury.

Currently, small-scale experimental plants are considering using low-cost, flame-retardant hard vinyl chloride piping(Nishiyama, 2020). Past research uses metal or glass piping, so experiments with resin materials such as hard vinyl chloride have not been conducted much. In this research, it is verified

the detonation characteristics of the hydrogen/oxygen mixture in resin piping and its effect on pipe failure, in order to obtain the missing knowledge that would contribute to process piping design.

The effects on pipe strain and destruction when detonation occurs inside pipes have been studied using metallic materials such as carbon steel pipes. It was shown that in carbon steel pipes, the strain caused by detonation pressure does not statically follow the pressure wave, but takes a dynamic response (Nebu et al., 2013). This is because the response speed of hoop strain is slower than that of pressure increase. In this way, steel, which has ductility and malleability, undergoes dynamic deformation, but it is necessary to analyze the strain response to detonation pressure for resin materials, which have almost no such properties and are less durable. Furthermore, for any substance, even if an unbearable stress is applied, cracks do not necessarily occur immediately and lead to destruction. The time it takes for cracks to occur after stress is applied is called induction time (Honma, 2008). Since the time during which pressure is applied is also considered to be important for fracture, it is focused the time from when pressure is reached until maximum strain is reached.

This time, by checking whether the detonation waves that generate distortion have similar characteristics, it is possible to proceed with the analysis under the same conditions. The theoretical value of detonation speed is based on Chapman-Jouguet Theory (Lee, 2008)(Strehlow, 1973). The detonation velocity in a glass pipe is lower than the CJ detonation velocity when the initial pressure and pipe diameter are small, due to energy loss due to heat conduction to the pipe wall and friction (Koshi, 2011). Therefore, in this study, there is a possibility that the detonation characteristics may vary depending on the pipe diameter and material, so it is verified that the detonation characteristics do not vary significantly by focusing on whether the detonation speed is under similar conditions. Next, it is examined the strain waveforms of piping depending on the material, and gain knowledge about the materials, standards, and terminal structures that are appropriate for use in the plant. Furthermore, since statically measured physical property values cannot be applied to very short-term loading due to detonation, it is necessary to consider an index related to strain and pressure. Finally, it is analyzed that the pressure and strain waveforms and videos under conditions where the pipe is destroyed, and showed the mechanism of failure in resin piping.

2. Experiments

Piping used in plants often has a complex structure, combining straight pipes, bent pipes, and valves. First, in order to understand the effects of detonation waves on resin piping, a detonation experiment using a straight pipe with a simple structure is conducted. Conduct experiments to analyze the effects of detonation. This section defines the materials, equipment, and formulas used in the experiment.

Table 1. *Material and diameter of piping used.*

Piping Material	**ID/OD [mm]**
Soft vinyl chloride	12/18, 25/31, 38/44
Braided hose	12/18, 25/31, 38/48
Hard vinyl chloride	13/18, 25/32, 40/48, 44/48(VU)

In the experiment, piping made of three different materials was used to compare experimental results with resins of different strengths as shown in Table 1. In past research, detonation experiments have been conducted using highly durable materials such as steel (Nebu et al., 2013), and the hardness and tensile strength is a major difference in destructive analysis between steel and resin. Therefore, experiments are conducted with multiple resin materials and observed changes in the magnitude and waveform of strain due to changes in hardness. If it can be confirmed that hard vinyl chloride exhibits

strain fluctuations similar to that of steel, it is possible that conventional research into steel can be partially used for safety considerations. The diameter and thickness of the used piping are commercially available standards. Hard vinyl chloride is opaque gray, and soft vinyl chloride is transparent. Table 2 shows the tensile strength for two of the three materials used. The material for the braided hose was chosen as it has a hardness between that of hard vinyl chloride and soft vinyl chloride. Braided hose is made of a soft vinyl chloride tube wall that is reinforced with polyester threads embedded inside it. Hardness increases in the order of soft vinyl chloride, braided hose, and hard vinyl chloride. Since other materials had problems such as being expensive or lacking in commercially available types, a structurally durable braided hose is chose. Also, the thinner standard of hard vinyl chloride is called VU (OD/ID=44/48mm only), and the others are called VP.

Table 2. *Physical Properties of the Experimental Material.*

Material	Tensile Strength [MPa]	Combustion Quality (Oxygen Index)
Soft vinyl chloride	11~25	Flame Retardance (45~49)
Hard vinyl chloride	41~52	Flame Retardance (45~49)
Steel STPT410 (Reference)	410~	Incombustibility

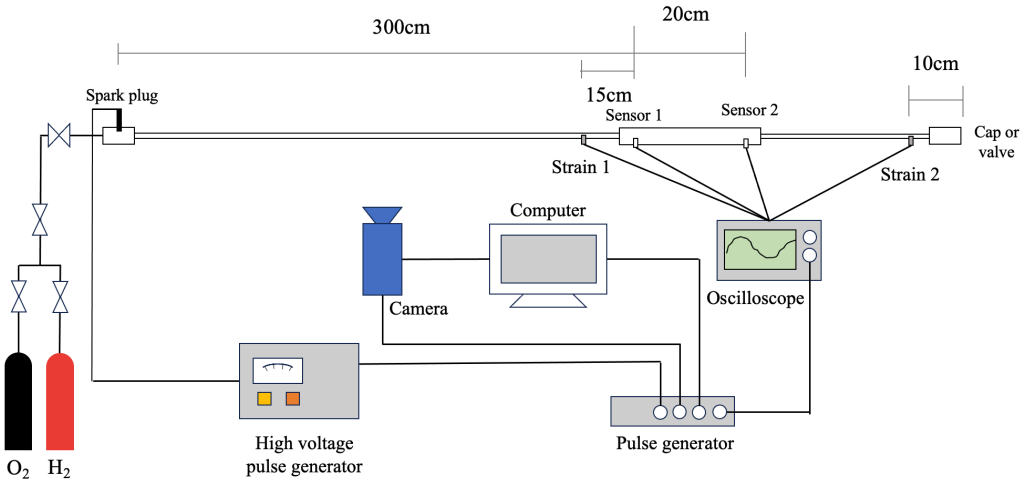

Fig. 1. *Experimental equipment diagram*

Figure 1 shows the gas introduction device used and the detonation pressure and strain observation device. Since the DDT for a hydrogen-oxygen mixture with an equivalence ratio of 1 to reach the detonation is less than 1 m (Kuznetsov, Alekseev, Matsukov & Dorofeev, 2005), the experiment was conducted by measuring at a distance of 3 m from the ignition point to generate a stable detonation. Check the pressure waveform to see whether it is actually detonating. Hydrogen and oxygen were supplied at 2 L and 1 L per minute, respectively, using a flow meter, and the mixture was filled into the pipes by mixing them before introducing them into the pipes. The experiment was conducted after introducing enough gas to replace the gas inside about 2 to 3 times. To prevent gas from leaking from the open end as much as possible, the air-fuel mixture was kept at atmospheric pressure by lightly sealing the gap with tape and releasing the gas through a small gap during filling. The piping was supported at five or more locations to reduce strain caused by its own weight other than pressure.

To measure pressure, piezoelectric pressure sensors (113B24, PCB Piezotronics) were used, and strain gauges (KFEM-5-120-C1, Kyowa Electronic Instruments) were used to measure strain, and the sensors were named as shown in Figure 1. A hard vinyl chloride fixture approximately 30 cm long is attached in the middle to install the pressure sensor, but since the inner diameters are the same, the

effect of changes on detonation characteristics is thought to be limited. A scope coder (DL950, Yokogawa Electric) was used to record the measured waveforms.

Strain is defined as ε in the following equation.

$$\varepsilon = \frac{\Delta l}{l} \tag{1}$$

The equation is for a case where a pipe of length l [m] becomes length $l + \Delta l$ [m] due to detonation. Consider strain in the circumferential direction. Since shrinkage fluctuations are small in resin piping, $m\varepsilon$, which is a unit of 1/1000 of strain, is defined and used.

Further, the detonation speed v [m/s] is calculated by the difference between the times t_1 [s] and t_2 [s] at which the detonation reaches Sensors 1 and 2.

$$v = \frac{d}{t_2 - t_1} \tag{2}$$

Here, d [m] is the difference between Sensor 1 and Sensor 2, $d = 0.2[m]$.

The circumferential stress σ_t [Pa] applied to the thin-walled cylinder due to internal pressure is

$$\sigma_t = \frac{pr}{t} \ (r \gg t) \tag{3}$$

where p [Pa] is static internal pressure, r [m] is radius, t [m] is thickness of cylinder.

3. Results and discussion

3.1. Effect of piping on detonation velocity

Figure 2 shows the relationship between pipe diameter and detonation speed for hard vinyl chloride and braided hoses. It should be noted here that the time unit of measurement is 1 μs, so multiple points may be marked at one coordinate.

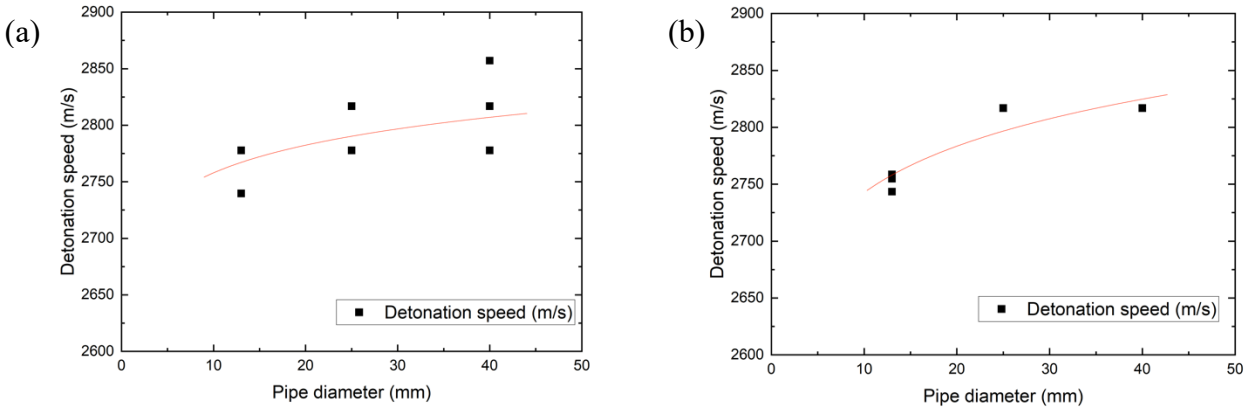

Fig. 2. *Relationship between tube diameter and detonation speed: (a)Hard vinyl chloride (open end), (b) braided hose (open end)*

First, since the hard vinyl chloride has high hardness and little deformation, the effect of the pure pipe diameter on the detonation characteristics is shown in Fig. 2(a). As the pipe diameter gradually decreases, the detonation velocity tends to decrease. However, since the max speed decrease is about 2%, it can be said to be within the margin of error. The CJ velocity of a hydrogen-oxygen mixture with an equivalence ratio of 1 is 2814 m/s (NASA, 2023). It can be seen that as the diameter of the pipe increases, friction with the pipe wall decreases, and the speed approaches the CJ velocity. It was found that when detonating at atmospheric pressure, the characteristics of the detonation pressure are

almost close to the theoretical values for pipes with a practical diameter. Experiments using hard vinyl chloride, where no further destruction occurs, indicate that the piping does not affect the detonation characteristics.

Next, the detonation speed for braided hose with low hardness and large deformation is shown in Fig. 2(b). It was expected that the energy of the detonation would decrease due to deformation of pipe and the speed would slow down, but the trend was almost the same as in Fig.2(a). From the above, in a hydrogen-oxygen mixture with an equivalence ratio of 1 under atmospheric pressure, there is a slight decrease in speed from an inner diameter of 13 mm due to friction on the pipe wall, but the speed is not affected by the material of the pipe. In the following sections, the analysis assumes that the material does not have a significant effect on the detonation characteristics.

3.2. Differences in strain due to material

When a pipe breaks, the phenomenon occurs in a very short period of time, so it is first necessary to understand the timing of maximum strain and the waveform of the strain under conditions that will not cause the pipe to break. By predicting the vicinity of the limit that does not lead to rupture, it will help in terms of safety to prevent accidents due to rupture. It is examined what kind of strain occurs in each resin material with different hardness. The waveforms of detonation pressure and circumferential strain in soft PVC and braided hoses in Fig. 3. The value measured by Sensor1 is used for pressure, and the value measured by Strain1 is used for strain in Fig. 1. The horizontal axis is the time when the spark plug starts emitting sparks, which is 0ms. Assuming that the distance between the two sensors is 150 mm and the detonation speed is the theoretical value of 2814 m/s, the measurement time difference between sensors is 0.053 ms.

(a) (b)

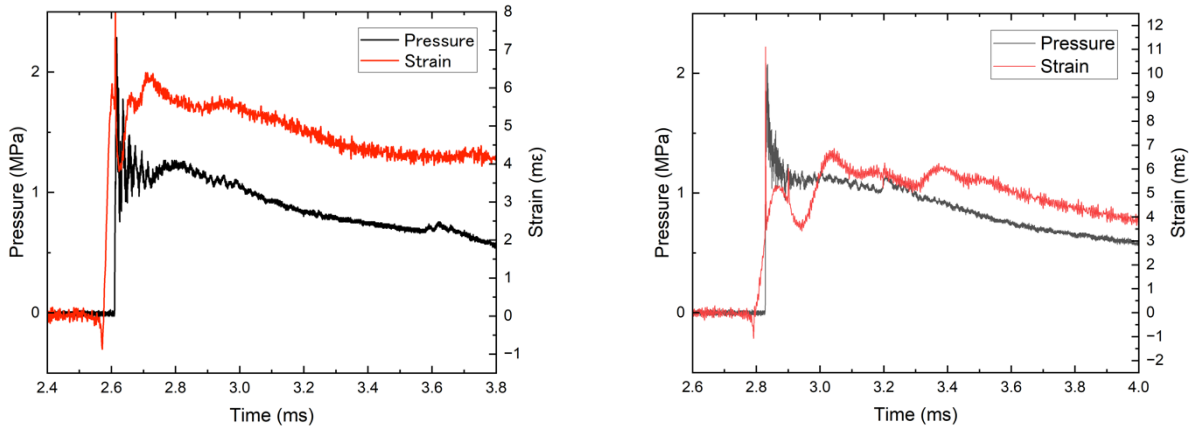

Fig. 3. *Strain and pressure waveforms: (a) Braided hose 13/18mm open end, (b) Soft vinyl chloride 25/32mm open end.*

The time from when the pressure is reached until the strain reaches its maximum value is 0.14ms for the braided hose and 0.24ms for the vinyl hose as shown in Fig. 3. It can be seen that the deformation speeds of the two materials are different. However, after the maximum strain is reached, the strain waveform follows the pressure movement. No contractional movement was observed in the circumferential strain. This is thought to be because the hardness is low and the flexibility is high, so there is not enough repulsive force to cause contraction vibration. The maximum strain is approximately 6mε for both the braided hose and soft vinyl chloride. Additionally, the maximum strain tends to occur at the second peak, and it is thought that the material is pushed back once by repulsive force before it reaches an equilibrium state.

(a) (b)

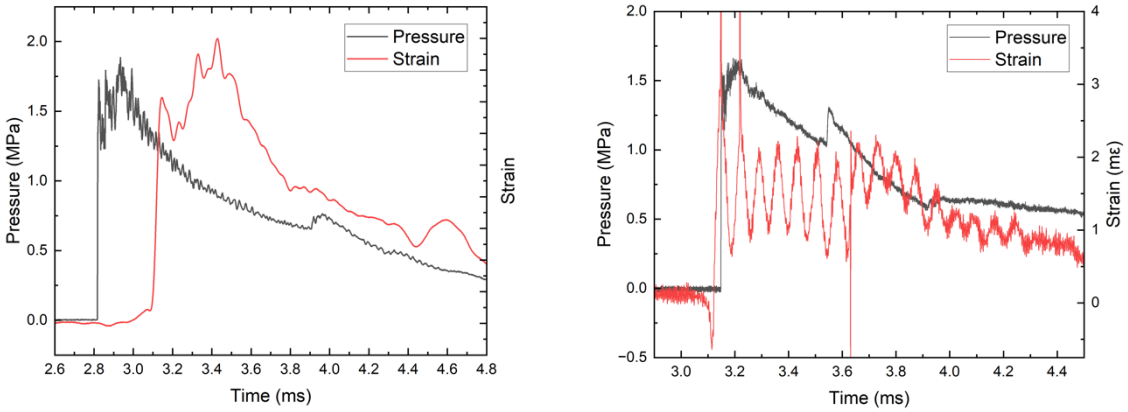

Fig.4. *Strain and pressure waveforms of hard vinyl chloride (open end): (a)25/32mm, (b)40/48mm*

Next, the waveforms of detonation pressure and circumferential strain in hard vinyl chloride is shown in Fig. 4. Only in Fig. 4(a) is the pressure measured by Sensor 2 and the strain measured by Strain 2.

The strain of the hard vinyl chloride 25/32mm was applied with a low-pass filter, and the amplifier was not calibrated, so we focused only on the waveform in Fig. 4(a). These two graphs are the results of experiments using the same material but different pipe diameters. Piping of the hard vinyl chloride 25/32mm has a waveform similar to a pressure wave, as is the case with soft materials. It takes 3.2ms for the strain to reach its maximum. The rate of increasing strain is slow, but this is also thought to reflect the gradual rise of the pressure wave around 1.5MPa.

From the strain waveform in Fig. 4(b), it can be seen that a clear radial contraction movement occurs. At the pipe of hard vinyl chloride 25/32mm, the strength is sufficient, and the deformation generates a repulsive force against the detonation pressure, so the strain follows the pressure wave. But at the pipe of 40/48mm in Fig. 4(b), the repulsive force due to deformation is close to the limit of durability. It is thought that the detonation pressure is insufficient, causing contraction vibration. Therefore, from a safety perspective, it is expected that the limit for hard vinyl chloride standards is 40/48 mm in market standard.

The frequency of the contraction vibration that occurred this time was 1.39×10^4Hz. When the detonation velocity approaches a speed called the critical velocity, the strain increases by about three times as a result of resonance to vibration (Beltman & Shepherd,2002), so it is possible that the strain will be larger than the current measurement results. However, in the case of a hydrogen-oxygen mixture with an equivalence ratio of 1, the detonation speed is much higher than the critical speed, so there is no need to take this into consideration.

3.3. Relationship between pressure and strain

Since the pressure rises very quickly and an impact is applied to the piping, it is necessary to consider impact stress, which is a stress greater than the pressure value. Considering a rod model, the impact stress can be derived to be twice the stress at static pressure (Hagiwara, miyasaka & Sekiguchi,1996). Although this is a different model from the used piping in point of $r \gg t$, it is assumed that stress greater than that under static pressure is applied in this experiment as well. Therefore, the relationship between the maximum pressure value and strain is investigated, and then compare the conventional physical property values with the pressure values measured in this experiment.

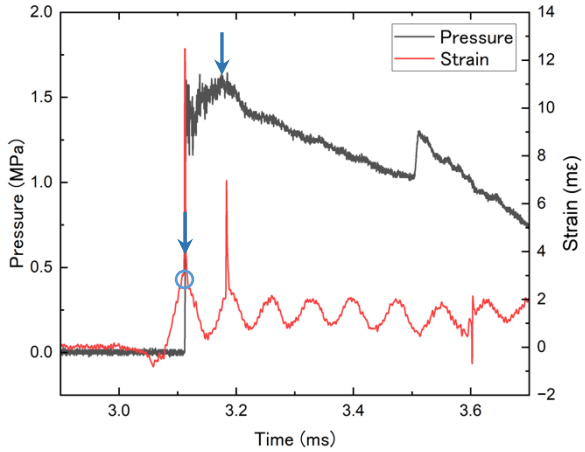

Fig. 5. *How to take the maximum pressure and maximum strain values (Hard vinyl chloride 44/48mm)*

First, specify how to take the maximum pressure and maximum strain values. The graph showing pressure and strain waveforms for 40/48 mm hard vinyl chloride is exhibited in Fig. 5, with an arrow pointing to the vicinity of the maximum value. Very fine voltage fluctuations caused by the sensor are reflected in the pressure and strain waveforms. While trying not to oversimplify the phenomenon, consider a smooth graph and take the maximum value. The maximum pressure and maximum strain were calculated by averaging the data in the range of 5 to 10 μs around the maximum value indicated by the arrow to take the middle of the amplitude. In addition, when the strain or pressure has a jump value as shown in Fig. 5, that value is removed, and the maximum value was set at a place where it becomes gentle (blue circle on the graph).

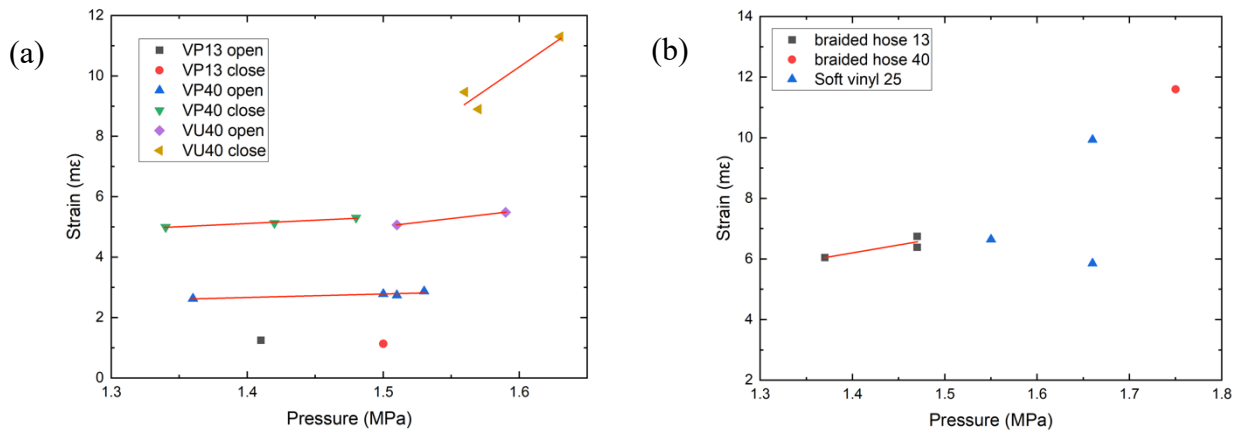

Fig. 6. *Relationship between maximum pressure and maximum strain: (a)Hard vinyl chloride, (b)Soft vinyl chloride and braided hose.*

The experimental results of strain and pressure by material is shown in Fig. 6. The maximum pressure is the value for Sensor1, and the maximum strain is the value for Strain1 or 2. In order to show the detonation characteristics, the horizontal axis shows the pressure of the first detonation reached, which does not include reflected waves in the close condition. VP indicates hard vinyl chloride with ID/OD of 13/18, 25/32, 40/48 mm, and VU is the standard name for hard vinyl chloride with ID/OD of 44/48 mm. Hereafter, they will be referred to as VP and VU with inner diameter. This is the name used to indicate the thickness of hard vinyl chloride piping in JIS standards. Since VP13mm has sufficient strength, the maximum strain remained almost unchanged even under closed-end conditions where the pressure was about doubled as much.

The maximum strain under the closed end condition at VP40mm and VU40mm is approximately twice the maximum strain under the open condition, and the strain is proportional to the maximum pressure fluctuation. Also, from Eq. (3), VP40close has twice the pressure and twice the thickness compared to VU40open, so it is thought that the stress will be about the same. In that case, the maximum strain is predicted to be about the same. In Fig. 6(a), the maximum strain of VP40mm close end and VU40mm open end is about the same, which confirms the agreement between theory and reality.

The results for a braided hose made of soft vinyl chloride, which is a soft material, are shown in Fig.6(b). The strain measured with the braided hose 13mm was higher than that of VP13mm. What is noteworthy is that the strain values for 25mm soft vinyl chloride vary widely. As the experiment was repeated, the maximum strain of soft vinyl chloride tended to decrease, which is thought to be due to changes in hardness due to heat or expansion of the pipe. Resin materials with low hardness are often susceptible to heat, and repeated detonation can cause changes in their durability. Therefore, soft vinyl chloride and braided hoses should not be used for long periods in plants.

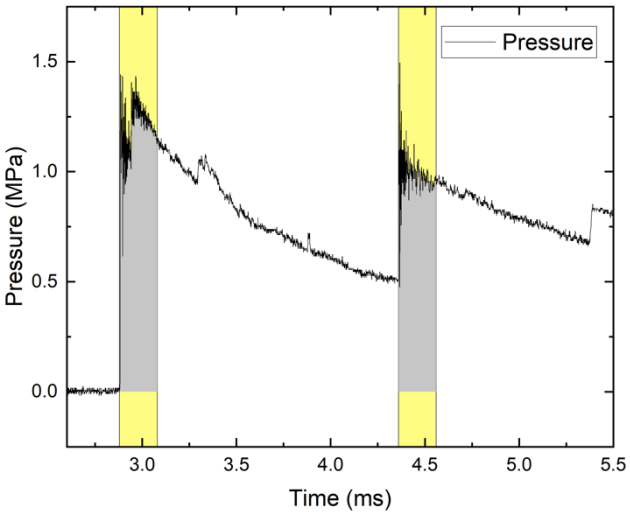

Fig. 7. *Example of impulse calculation at sensor 2 of close end condition: The gray part is integrated (Expanded time range for easier viewing)*

However, the problem is that the time history of detonation pressure, which affects strain, is not incorporated at maximum pressure. Therefore, the relationship between impulse and strain until the strain reaches its maximum value is examined. Impulse takes the time integral of pressure, so the time history of pressure can be taken into account. This time hard vinyl chloride is only considered, which is promising for use in experimental plants. The time impulse from reaching the pressure to the end of the first strain increase was calculated. The average strain rise time is used for calculating impulse in each experimental condition. In the close end condition, two pressure waves are mainly involved in deformation, so as shown in the graph shown in Fig. 7, the impulse of the pressure wave in the part that is effective for deformation is more than double near the end. For simplicity, this time I calculated the impulse at the closed end I_{en} in the same way as the impulse at the open end I_{op} based on the graph and multiplied it by 2.5 in shown Eq. (4),(5) where t_a is the time when strain starts to increase, t_b is the time when maximum strain is achieved in the first wave.

$$I_{op} = \int_{t_a}^{t_b} P dt \tag{4}$$

$$I_{en} = 2.5 \int_{t_a}^{t_b} P dt \tag{5}$$

The impulse and maximum strain are compared, and the results are shown in Fig. 8. Points of the same material with open end and closed end conditions approximately line up in a straight line. However, even though the thicknesses of VP40mm and VU40mm are different, the strain is almost the same for the same impulse. This is thought to be because the time range that determines the integration range is defined by the strain rise time measured for each experiment, but this time the average strain rise time of multiple experiments was used. In order to predict strain using impulses, the strain rise time for each experiment must be considered. The strain rise time vary widely from experiment to experiment, so impulse can lack precision as indicator.

From the above, it can be seen that the relationship between maximum strain and detonation pressure is more relevant when considering maximum pressure than impulse. The reason why there is a strong correlation between maximum pressure and strain is thought to be that an instantaneous pressure increases results in a fast expansion rate, and there are times when the expansion occurs due to inertia without being related to pressure.

Finally, the previously presented physical properties are compared with the observations. Impact strength is used as the durability value of a material against phenomena that have an impact aspect, such as detonation pressure. The impact strength of hard vinyl chloride is said to be around 22 to 1117 J/m (Osaka municipal Industrial Research Institute., & Plastics Technology Association. 2009). When converting units, J/m is same as $Pa \cdot m^2$. Therefore, the range of piping that maintains around the maximum pressure is determined from the pressure waveform, and the impact strength is calculated by multiplying pressure and lateral area. As shown in Fig. 4(b), if the time range where the detonation pressure maintains its maximum is 0.1ms, the range where high pressure is maintained is 281mm, assuming the detonation speed is the theoretical value of 2814m/s. If the maximum pressure of 1.7MPa in Fig. 4(b) is applied to that range, impact strength becomes $6.01\times 10^3\ Pa \cdot m^2$or J/m. Therefore, despite being subjected to an impact that greatly exceeded the physical property values, no damage was caused to the hard PVC 40/48 mm pipes. Therefore, when considering the durability of a material against detonation of a hydrogen-oxygen mixture with an equivalence ratio of 1, it is necessary to verify it experimentally, rather than using conventional physical property values, and to create further indicators.

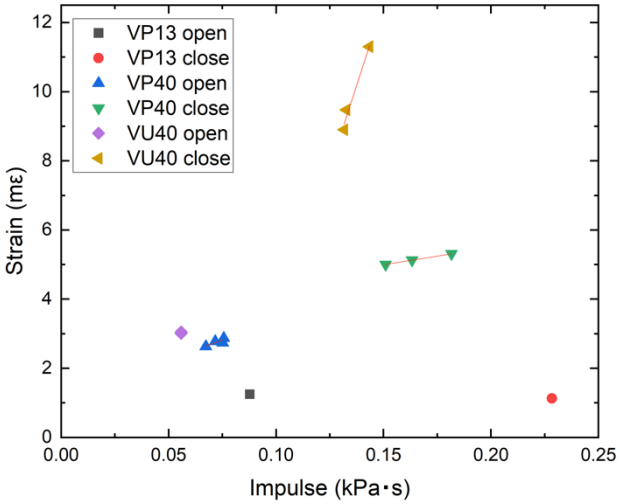

Fig. 8. *Relationship between impulse and maximum strain in Hard vinyl chloride*

3.4. Mechanism of destruction

During long-term plant operation, in order to prevent damage accidents that may result in human accidents, it is necessary to consider standards and destruction mechanisms for plastic materials that are at risk of destruction. In the experiments of this study, failure occurred under several conditions, and the conditions are shown in Table 3 by failure method. There were three types of failure: damage

and falling off near the joint, damage to the joint and piping, and damage due to expansion of the piping. All of these fractures occur at the ends or at connections with different parts.

Table 3. *Conditions under which destruction occurred and destruction form*

Destruction form	Material and ID/OD [mm]
Damage and falling off the joint	VP 40/48(close), Braided hose 38/48(close)
Damage to the joint and piping	VU 44/48 (close by thick cap)
Corruption due to expansion of the piping	Soft vinyl chloride 38/44 (open)

First, the material of all the joints used this time is hard vinyl chloride. Apply enough vinyl adhesive to connect the pipes and fittings. Breakage and falling off of the joints were observed under two conditions. Repeated detonations cause strain in the joints, and the hardened adhesive peels off, creating small gaps between the piping and the joints, through which detonation pressure leaks, causing cracks and causing the joints to rupture. Therefore, it is necessary to use a connection method that takes into account the repeated loading of strain at the connection portion between the resin pipe and the joint.

Furthermore, even if the experiment was conducted with open end, extreme deformation and piping destruction may occur when using soft resin. There is a risk of destruction at the joint between resin materials of different hardness. As shown in Fig. 9, the softer material at the joint expanded and broke because the strains generated in the two materials were different. Materials that expand greatly are not suitable for use in areas where detonation occurs, and care must be taken when joining different materials.

Fig. 9. *Destruction part near sensor 1 at soft vinyl chloride 38/44mm (open)*

It was under the experimental conditions of hard vinyl chloride 44/48 mm that the destruction of the terminal led to damage to the piping. The end was wrapped with 4 mm PVC cap that was thicker than the pipe, but the cap broke from the closed end and the damage progressed to the pipe. As shown in Fig. 10, the crack that was created when the surface of the cap was blown away grew due to the detonation wave, where the pressure was approximately doubled due to the reflected wave, and the crack propagated to the piping on the ignition side. Therefore, hard vinyl chloride 44/48mm has a high possibility of rupturing due to cracks from other parts, making it unsuitable for transporting mixtures.

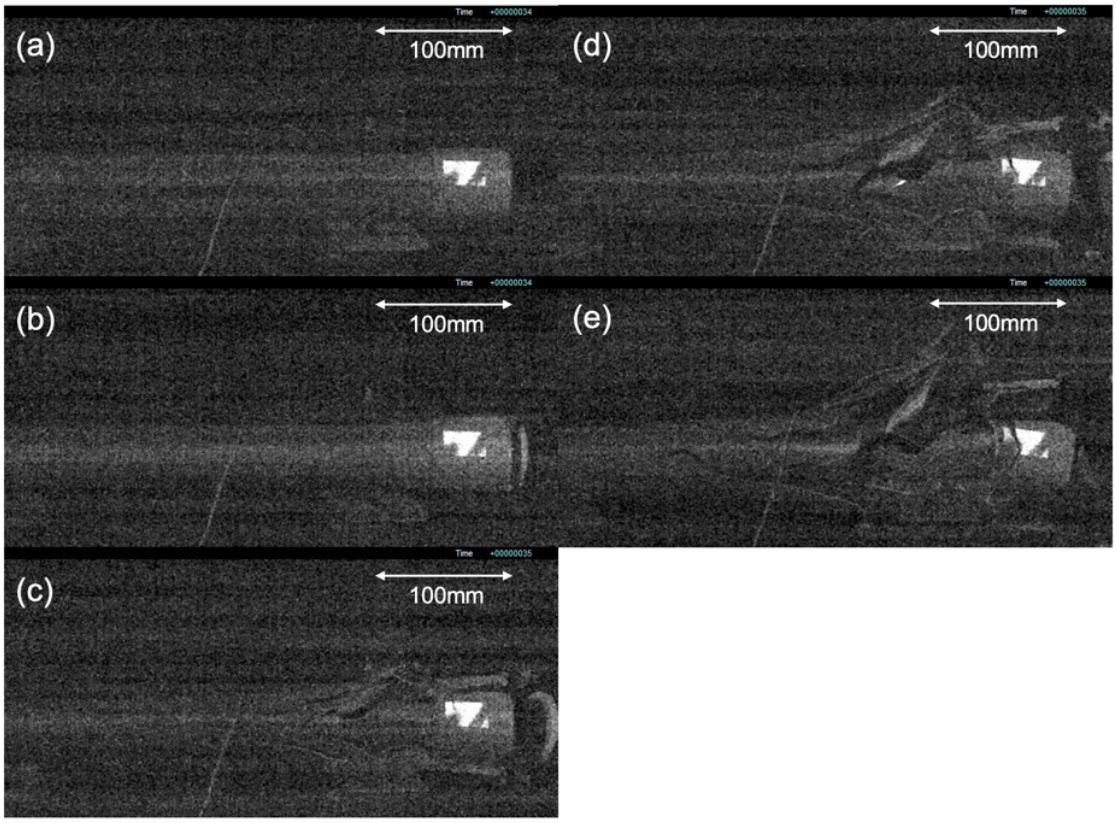

Fig. 10. *Photos showing destruction every 0.25ms of hard vinyl chloride 44/48 mm. (a)0ms, (b)0.25ms, (c)0.5ms, (d)0.75ms, (e)1ms*

From the above, it is expected that the safe transportation of a hydrogen-oxygen mixture at atmospheric pressure with an equivalence ratio of 1 using a straight pipe is limited to 40/48 mm hard vinyl chloride piping with reinforced connections.

4. Conclusions

Experimental research has shown that the detonation characteristics of a hydrogen-oxygen mixture with an equivalence ratio of 1 under atmospheric pressure are almost unchanged for resin piping with an inner diameter of 13 to 40 mm. We also showed the relationship between maximum pressure and maximum strain in piping, and between impulse and maximum strain, and showed that maximum pressure is a better indicator. Furthermore, the characteristics of strain waveforms for different resin materials with different hardness was shown. The durability of low-hardness plastics such as soft vinyl chloride changes significantly when detonation is repeated. Through three detonation experiments with soft vinyl chloride and braided hose, the variation in strain with respect to pressure is smaller than in the case of hard materials, and there is no significant correlation. Based on the conditions that led to the breakage and the footage from the high-speed camera, it was found that the standard limit for maintaining safe transportation was approximately VU44/48mm. It was shown that fractures in plastic materials occur from strain at the ends and joints of different materials. In experiments on hard vinyl chloride, the impact strength calculated from the measured values was significantly higher than the physical property values, but no breakage occurred under those conditions. Therefore, it was suggested that when evaluating the durability of materials against detonation of a hydrogen-oxygen mixture with an equivalence ratio of 1 from strain, it is necessary to create an additional index related to the maximum pressure. This time, it was found that there is a linear relationship between maximum pressure and strain, but further experiments are needed to show the pressure value at which rupture occurs from the perspective of strain.

Acknowledgements

This paper is based on results obtained from a project commissioned by the New Energy and Industrial Technology Development Organization (NEDO).

References

Shepherd, J.E. (2009). Structural Response of Piping to Internal Gas Detonation. *Journal of Pressure Vessel Technology*, *131*(3), 1-13.

Nishiyama, H., Yamada, T., Nakabayashi, M., Maehara, Y., Yamaguchi, M., Kuromiya, Y., & Nagatsuma, Y. (2020). Photocatalytic solar hydrogen production from water on a 100-m^2 scale. *Nature*, *598*(7880) 304-307.

Nebu, A., Yamada, K., Dozaki, K., Hidaka, A., Uchida, M., & Sone, T. (2013). Investigations on strength of piping for non-condensable gas combustion (Part 1: Fracture and deformation of carbon steel pipes induced by hydrogen-oxygen detonation). *Transactions of the JSME*, *79*(797), 34-48.

Honma, S. (2008). *Strength properties of plastics for designers*. (in Japanese) Tokyo, Japan: Maruzen Publishing.

Lee, J.H.S. (2008). *The Detonation Phenomenon*. Cambridge: Cambridge University Press.

Strehlow, R.A. (1973) *Basic combustion science* (Y. Mizutani, Trans.). Tokyo, Japan: Morikita Publishing.

Koshi, M. (2011). Fundamentals of hydrogen safety chemical kinetics of combustion and explosion of H_2. *Hydrogen energy system*, *36*(3), 5-13.

Kuznetsov, M., Alekseev, V., Matsukov, I., & Dorofeev, S. (2005). DDT in a smooth tube filled with a hydrogen-oxygen mixture. *Shock Waves, 14(3)*, 205-215.

National Aeronautics and Space Administration [NASA]. (1994) NASA CEA. Retrieved January 5, 2023, from https://cearun.grc.nasa.gov

Beltman, W., & Shepherd, J. (2002). Liner Elastic Response of Tubes to Internal Detonation Loading. *Journal of Sound and Vibration*, *252*(4), 617-655.

Osaka municipal Industrial Research Institute., & Plastics Technology Association. (2009) *Plastic reader*. (in Japanese) Tokyo, Japan: Plastics age.

Provisions for a safer performance of a standard tank-TPRD systems in fire conditions

Sergii Kashkarov [a], Dmitriy Makarov [a] & Vladimir Molkov [a]

[a] Hydrogen Safety Engineering and Research Centre (HySAFER), University of Ulster, Newtownabbey, BT37 0QB, Northern Ireland, UK

E-mail: s.kashkarov@ulster.ac.uk

Abstract

The performance of composite hydrogen tanks with TPRD in fire conditions was investigated. The largest studied 244 L, 70 MPa tank has a TPRD orifice diameter of 0.75 mm. The lower limit for this diameter is determined for each tank and is sufficient to prevent the tank from rupturing in the event of a fire, while also reducing the flame length and mitigating the pressure peaking phenomenon in a garage-like enclosure, to exclude its destruction. The phenomenon of Type IV tank liner melting for reduced diameter TPRD is presented and the authors evaluated its effect on hydrogen blowdown. Although it appears that this phenomenon makes the blowdown faster, more thorough experimental validation is still needed. The pressures in hydrogen storage tanks at 100% of nominal working pressure (NWP) are expected only after refuelling. Operating a vehicle between fuel stops is defined by a state of charge of less than 100%. Experimental data indicates that, depending on the fire source, Type IV tanks tested in a fire at initial pressures less than one-third of their NWP were leaking without rupturing. The polymer liner can be melted by the heat transferred through the composite overwrap, as shown in this study. Once the liner is melted, this starts the process of hydrogen microleaks through the composite wall before the resin degrades thermally to the point where the tank explodes as it can no longer bear any load exerted by compressed hydrogen. The issue of tank wall thickness non-uniformity, namely the thinner composite at the dome area, was addressed in the study too.

Keywords: *Hydrogen storage system, rupture, prevention, tank, rupture, TPRD, fire.*

Introduction

The worldwide market for high-pressure hydrogen storage tanks primarily consists of lightweight composite Type III (aluminium liner) and Type IV (polymer liner) tanks for use in road, rail, marine, aircraft, and stationary household. Hydrogen tanks come in a range of capacities. For example, a passenger car might have two tanks that hold a total of around 5 kg of hydrogen [1], buses could carry 50 kg, and trains could carry 100–200 kg. At now, the pressure for storing hydrogen on buses, trains, and other vehicles is 35 MPa, whereas for automobiles and trucks, it is 70 MPa. Up to 95 MPa could be the storage pressure [2]. The tank capacity is 7.5 L to 360 L. For instance, a ship's hydrogen storage system [3] is made up of nine cylinders, each weighing 8.5 kg at 35 MPa.

Aside from their many benefits, such strength and light weight, composite tanks' primary flaw is how they respond to fire. The UN GTR#13 [4] and the EU Regulations No.134 [5] assume that a thermally activated pressure relief device (TPRD) is installed on hydrogen onboard storage tanks to release hydrogen and exclude rupture in a fire. This prevents tank rupture in a fire and its catastrophic consequences, such as blast wave, fireball, and projectiles. Nevertheless, the requirements for a tank-TPRD system's comprehensive safety design are now unavailable since the effectiveness of the system in a fire is still not fully understood. This study fills in that information.

Dependence of hydrogen hazards on TPRD release diameter

The previous "intuitive" method, which involved fast release of hydrogen from a fire-damaged tank by utilising a relatively large TPRD diameter of 5–6 mm to stop it from rupturing, lacked scientific support and had a number of significant safety flaws. One of these is a long flame length that has a known direct relationship to the diameter of the TPRD (Molkov, 2012). For instance, the flame length from the 87.5 MPa storage tank's 6 mm diameter TPRD (which is regarded as the minimum diameter in the release path in this and other places in the study) is greater than 21 metres. It is important to note that for momentum-dominated jets, the "no-harm" danger distance is 3.5 times larger than the free flame length (Molkov, 2012). The delayed ignition of a highly turbulent hydrogen jet, which might produce pressure loads capable of gravely injuring humans, is the second disadvantage of a bigger diameter TPRD (Molkov, 2012). The third disadvantage has to do with cramped areas like tunnels, parking garages below ground, warehouses, etc. If a unignited discharge from a large diameter TPRD occurs in confined space, it may form a flammable cloud or layer beneath a ceiling that could undergo deflagration or even transit to explosion. This is the worst-case situation that needs to be avoided in order to prevent a hydrogen crisis. The pressure peaking phenomena (PPP), which is unique to hydrogen in comparison to other fuels, is an even more significant drawback of bigger diameter TPRDs (Brennan and Molkov, 2013; Hussein et al., 2018; Johnston, 2005; Makarov et al., 2018). It is well known that overpressures up to around 10 kPa can be applied to civil constructions without causing harm. If the TPRD diameter is fractions of a millimetre, the overpressure threshold of 10 kPa would not be surpassed in garages with vent areas of the order of brick size.

All four of the safety problems listed above could be resolved with TPRDs of a smaller diameter. The goal of this paper is to determine the lower limit of the TPRD diameter that is both sufficiently "large" to prevent a tank rupture in the event of a fire and sufficiently "small" to prevent large flames, hazardous pressure loads from the under-expanded jet's delayed ignition, the formation, deflagration, and eventual detonation of the flammable hydrogen-air layer in confined spaces, and the destructive PPP in enclosures similar to garages. The use of novel explosion-free in-fire TPRD-less tanks (Molkov et al., 2018) can also accomplish this goal; however, this ground-breaking safety innovation is the topic of a different paper.

Failure mechanism of a composite tank subject to fire

Understanding the fundamental physical processes involved in an engulfing fire is necessary to comprehend the thermal behaviour of a tank-TPRD system. Two events working in opposite directions affect the temperature and pressure of hydrogen within the tank. The temperature and pressure of hydrogen within the tank are lowered by the blowdown. The temperature and pressure of hydrogen are raised by the heat transfer from the fire through the tank wall. The fire's heat flux raises the temperature of the composite, and some of that heat flux is utilised to break down the wall composite's resin beginning at the exterior tank surface.

The following is the composite tank failure mechanism that our research has validated. A considerable resin mass loss because of fire energy being transmitted and partially used for decomposition establishes the resin decomposition front. Under heat flux, the composite material undergoes a variety of physical and chemical reactions, such as gasification, ignition, and glass transition. As an illustration, research (Quang Dao et al., 2013) looks at the intricate breakdown of a composite with varying fibre contents. The primary characteristic of a fire-related tank rupture is the loss of resin mass, which results in an inability to fuse fibre plies together and preserve the strength of the composite material.

The carbon fibre plies in these places become "unbound" or "loose" when the resin breaks down, making the composite non-load bearing. The standards stipulate that the minimum burst pressure of an overwrapped tank made of carbon fibre reinforced polymer (CFRP) must be 2.25 times the normal working pressure. This indicates that just 1/2.25, or 0.44 of the wall thickness, is required as the load-bearing wall thickness fraction to endure pressure equivalent to NWP. This proportion rises when the

tank's internal pressure rises, for example when the temperature of hydrogen rises. When the load-bearing wall thickness fraction moves outward and the resin decomposition front moves inward, the tank without TPRD bursts. This is an illustration of the tank failure mechanism we used in our research. The authors (Dadashzadeh et al., 2019; Molkov et al., 2021) carried out the modelling which included separate FRR evaluations for a tank without TPRD and non-adiabatic tank blowdown scenarios. Here, we examine the performance of a tank-TPRD system under circumstances when the fire and blowdown have a simultaneous impact on the system's functionality.

Previous research has shown that using hydrogen-powered cars on London roads carries an acceptable risk if the tank has a fire-resistance rating (FRR), or a time interval more than 50 minutes from the start of the fire to tank rupture (Dadashzadeh et al., 2018). This was determined in light of the fact that the TPRD is neither blocked from the fire in the accident nor activated in a localised fire. The evaluation was carried out for situations in which an onboard hydrogen storage tank was filled to its nominal working pressure (NWP) in full. When the state of charge (SoC) of the compressed hydrogen storage system (CHSS) is less than 100%, the pressure is not always at NWP. The "ratio of CHSS hydrogen density to the density at NWP rated at the standard temperature 15ºC" (SAE, n.d.; SAE J2601, 2016) is how SAE J2601 defines the SoC. Hydrogen tank is filled at NWP (SoC=100%) typically only during the initial moments following tank refuelling (Kashkarov et al., 2021).

To establish the FRR, 36 L NWP=70 MPa Type IV tanks were tested in localised and enveloping fires without TRPD at various SoC (starting pressures were 70.3, 70.6, 35.6, and 17.8 MPa) in the experimental work (Ruban et al., 2012). A 0.96 m^2 heptane pan served as the fire's source. After 6 minutes 32 seconds and 5 minutes 20 seconds, respectively, tanks filled at 70.3 MPa and 70.6 MPa, ruptured. The second tank was tested in a localised fire, while the first tank was tested in an engulfing fire (Kashkarov et al., 2021).

These tests also showed that one of the NWP=70 MPa tanks burst after 9 min 49 s, or about 1.5 times longer FRR than the first tank filled at virtually NWP, or 70.3 MPa, when it was filled at 35.6 MPa (51% NWP) and experienced the same enveloping fire. If the original composite tank failure in a fire mechanism (Kashkarov et al., 2018; Molkov et al., 2021) is used, then this can be justified. According to the mechanism, a tank ruptures when the outward "propagating" load-bearing percentage of the composite wall thickness reaches the inwardly propagating resin decomposition front. Since there is less load-bearing thickness in this test with a lower beginning pressure to endure the internal pressure without rupturing, it will take longer for the resin decomposition front to reach it. In conclusion, during the studies involving a tank filled at a lower pressure of 17.8 MPa (25% NWP), hydrogen leaking without tank rupture was detected at 11 minutes. In this instance, the non-load-bearing wall thickness fraction was sufficiently large to permit heat transfer to melt the liner, while the remaining unaltered composite wall continued to support the lower internal pressure load (Ruban et al., 2012), (Kashkarov et al., 2021).

Another experimental investigation (Blanc-Vannet et al., 2019) examines the fire testing of 36 L Type IV tanks with a NWP of 70 MPa at various beginning pressures. The initial temperatures of roughly 42ºC (315 K) were indicated by the composite in-thickness integrated thermocouples, but there were no measurements of the temperature of hydrogen gas. In this study, the fire source was simulated by a hydrogen diffusion burner with four pipes pointing in opposing directions towards tanks. The tanks were filled to 70 MPa, 52.5 MPa, 25 MPa, and 10 MPa. The first two tanks burst at 3 minutes, 58 seconds, and 5 minutes, 11 seconds, respectively, at pressures of 70 MPa and 52.5 MPa. The other two tanks, which had been filled at lower pressures – 25 MPa and 10 MPa, respectively – leaked after 6 minutes, 40 seconds and 8 minutes, 10 seconds, respectively, but did not burst. Even though the experiments used a different fire source, they still supported the findings of the earlier study (Ruban et al., 2012), which stated that lower initial pressures in the tank allowed for a larger portion of the composite wall thickness to be non-load-bearing. This allowed the fire's heat flux to thermally decompose the wall without endangering the tank's ability to support weight and allowed for a longer

period of time for heat transfer to the liner to reach a temperature high enough to melt it and cause release.

The investigation of the tank-TPRD system's performance in the engulfing fire is one of the aims of this paper. The continuous localised fire that is unaffected by TPRD will eventually cause a tank to rupture. If a fire is localised, a TPRD that is far from a fire source could fail to release gas. This study shall also look at how tank FRR is impacted by the state of charge (SoC). Additionally, the non-uniformity of tank wall thickness on FRR is addressed. The validated non-adiabatic blowdown in a fire model will be used for the investigation (Molkov et al., 2021).

To permit the parking of HPVs in restricted areas such as garages and maintenance shops without the risk of PPP destroying civil structures, this study attempts to investigate the thermal behaviour of a tank-TPRD system in a fire. The under-expanded jet theory serves as the foundation for the study model, which takes into consideration a number of variables and events that are known to have an impact on a tank-TPRD system's performance: heat transfer from the fire to the tank, convective heat transfer from the fire to the external wall surface and from the liner to hydrogen, conductive heat transfer through the load-bearing wall and the liner, thermal degradation of the composite resin, liner melting, and other factors are all included in the hydrogen tank parameters.

1. Methodology to assess fire performance of tank-TPRD system

In this study, HRR/A=1 MW/m^2 is used to be on the conservative side and account for gasoline/diesel fires. Since Type IV tanks with a NWP of 70 MPa and HDPE liners are the focus of this study, the conclusions drawn from the calculations cannot be directly extended to other types of liners or composite wall materials. The approach used here for the two 244 L and 62.4 L tanks can be used to any tank-TPRD system. For consistency, the authors assume in this study that all tanks have HDPE liners, all composite overwraps are made of the same CFRP, and all tank materials have the same thermal properties (Kashkarov et al., 2021; Molkov et al., 2021). In the numerical investigation, it is assumed that the initial tanks have a temperature of 293 K and a nominal working pressure (NWP) of 70 MPa.

1.1. Tank-TPRD system (V=244 L)

Figure 1 shows the propagation of the resin decomposition front, load-bearing wall thickness fraction (left y-axis) related to hydrogen pressure (right y-axis) and the liner melting front (blue colour steps) in the three numerical fire tests with HRR/A=1 MW/m^2 for 244 L, 70 MPa tank-TPRD system for three different TPRD diameters: 0.5 mm, 0.75 mm, 1 mm. The system with the smallest TPRD diameter of 0.5 mm ruptures at 1457 s (24 min 17 s) when the resin decomposition front meets the load-bearing wall thickness fraction “front” (just before the liner melting through the entire depth). The system does not rupture if the TPRD diameter is equal to or larger than 0.75 mm until the full liner melting, which can be considered as an “additional” channel of hydrogen release. See section 7.4 on the effect of liner melting on the blowdown dynamics.

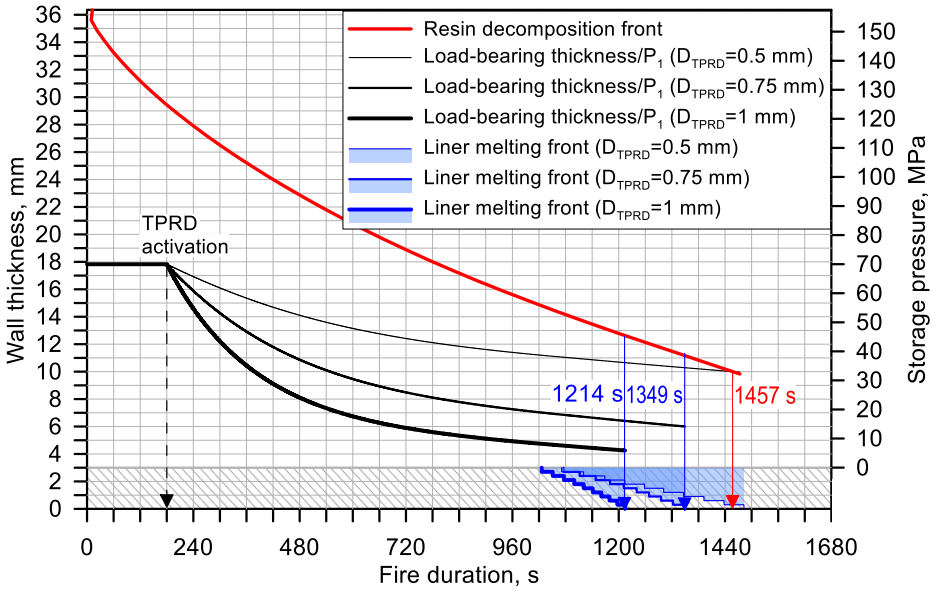

Figure 2. Performance of 244 L, 70 MPa tank-TPRD system in a fire with HRR/A=1 MW/m^2 for three different TPRD diameters: 0.5 mm, 0.75 mm, 1 mm (Molkov et al., 2021).

The study allows insights into the thermal behaviour of the tank equipped by TPRD of comparatively small diameter. The performance of the tank-TPRD system is not trivial. For 0.75 mm TPRD when the pressure (right y-axis) drops to about 14 MPa at 1349 s, the liner melts through its depth. For TPRD of 1 mm, the liner fully melts at 1214 s when the pressure drops to about 6 MPa. The melting of the liner allows hydrogen to leak through the wall in addition to the release through TPRD.

It is worth mentioning the following published experimental observations. When the initial pressure inside a Type IV tank is substantially less than NWP the tank will leak and not burst in the fire. For example, a series of fire tests were performed with 36 L tanks of NWP=70 MPa but with different initial pressure in the range of 10-70 MPa. Two tanks with initial pressure 70 MPa (100% NWP) and 52.5 MPa (75% NWP) ruptured in a fire but two other tanks with initial pressure 25 MPa (36% NWP) and 10 MPa (14% NWP) leaked in the fire tests without rupture. Indeed, when initial pressure is substantially below NWP there is substantial "load+" wall thickness to be passed through by the resin decomposition front before it reaches the "reduced" load-bearing wall thickness fraction, and thus more time is available to melt the liner before the tank burst and thus initiate hydrogen release through the wall. These experimental observations are in line with the presented simulations of the tank-TPRD system performance in the fire demonstrating melting of the liner and thus leakage through the wall before tank rupture. Results of a study of the effect of the state of charge (SoC) of a tank, i.e. reduced compared to NWP initial pressure, on the possibility of tank rupture in a fire will be described in a separate paper.

The experiments with several series of explosion free in a fire TPRD-less tank prototypes (Molkov et al., 2023a, 2023b; Monde et al., 2012) demonstrated that if hydrogen leak through the wall starts after the liner melts then no tank rupture is observed. This could be explained by the expected increase of the leaking area of the wall as the wall thickness decreases significantly while the resin decomposition front propagates inwards. This innovative TPRD-less safety technology is out of the scope of this paper. Thus, we assume further in this study that after the liner melting the tank loses its tightness to hydrogen and no rupture of a tank will happen. This statement requires more experimental validation.

Figure 3a shows the hydrogen temperature in the tank that obeys the behaviour explained in the publication (Molkov et al., 2021), i.e. temperature decreases after TPRD release start due to hydrogen expansion and then increases when the heat transfer through the tank wall takes over with some delay (about 5 min for this large volume tank).

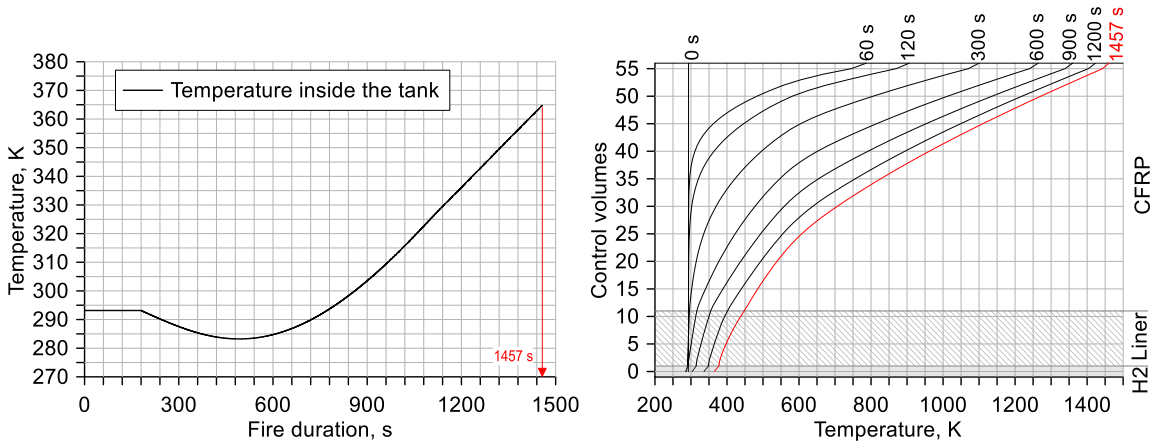

(a) (b)

Figure 3. (a) - temperature profiles in the tank wall, including the liner; (b) - hydrogen temperature dynamics in a 244 L, 70 MPa tank during blowdown through TPRD=0.5 mm and TPRD activation delay of 180 s in HRR/A=1 MW/m^2 fire (Molkov et al., 2021).

For the scenario of TPRD=0.5 mm, Figure 3b shows temperature trends through the tank wall, including the liner, for 10 instances between the fire's start and 1457 s (the tank rupture time). Because of the fire, the temperature of the tank's surface (control volume 55) rises over time. The cooling of hydrogen during expansion causes the liner's temperature to drop at the start of the operation. Within 300 seconds of the release (or 480 seconds of the fire duration), the heat flux from the fire travels through CFRP, raising its temperature and subsequently the liner temperature and beginning to heat hydrogen.

1.2. Tank-TPRD system (V=62.4 L)

Let's examine the operation of a typical onboard hydrogen storage tank-TPRD system, which consists of a 62.4 L tank with two distinct TPRD diameters (0.5 mm and 0.75 mm). In this example, there is a 3 min delay in the event of a fire with an HRR/A=1 MW/m^2, and there is no TRPD activation delay. The progression of the liner melting front, pressure, load-bearing wall thickness fraction, and resin decomposition front over time are depicted in Figure 4.

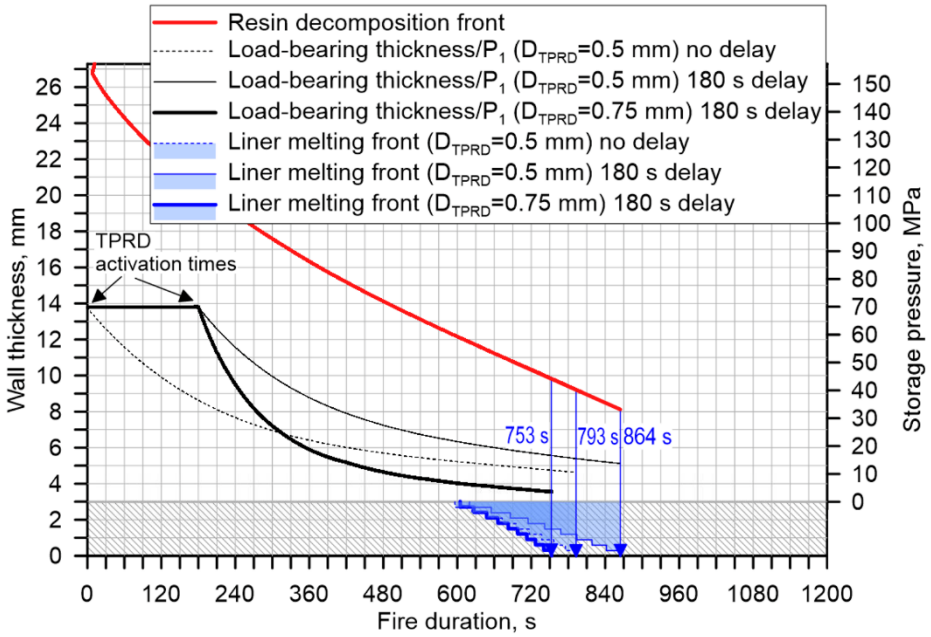

Figure 4. Performance of 62.4 L, 70 MPa tank-TPRD system in a fire with HRR/A=1 MW/m^2 for two different TPRD diameters (0.5 mm and 0.75 mm), and TPRD activation delay 0 s and 180 s (Molkov et al., 2021).

The liner melts in all scenarios modelled well before the resin decomposition front would eventually reach the decreasing load-bearing wall thickness portion. Therefore, if TPRD is started within three minutes of the fire, a 0.5 mm TPRD diameter is sufficient to exclude a 62.4 L, 70 MPa Type IV tank with an HDPE liner rupture. As far as preventing tank rupture is concerned, the scenario with TPRD=0.75 mm is safer by definition. To stop PPP from demolishing the garage, an increase in the TPRD diameter would necessitate a larger minimum vent space.

1.3. TPRD orifice diameter and the pressure peaking phenomenon

It is quite improbable that passenger automobiles will make use of 244 L onboard storage tanks. This means that for high volume tanks, like 244 L, it is not required to take the PPP into account in an enclosure (Brennan and Molkov, 2013; Hussein et al., 2018; Makarov et al., 2018). Thus, in this PPP overpressure calculations, only the tank-TPRD system is taken into consideration. Let us assume a 30 m^3 residential garage. By using the ignited release model (Makarov et al., 2018) the pressure dynamics in the enclosure can be calculated. Enclosure vents range in size from one brick (50×250 mm) to four bricks (200×250 mm). The overpressure dynamics in the garage for discharges from a 62.4 L tank for varying TPRD diameters and garage vent sizes are depicted in Figure 5.

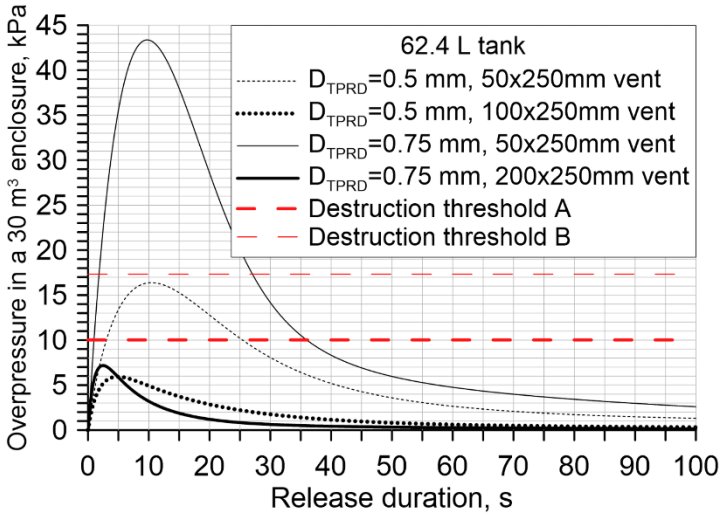

Figure 5. The PPP in 30 m3 enclosure and structural damage thresholds A (10 kPa (Molkov, 2012; Shentsov et al., 2019)) and B (17.3 kPa (Baker et al., 1983)): 62.4 L, 70 MPa tank-TPRD system (Molkov et al., 2021).

Releases from the 62.4 L tank through the 0.5 mm and 0.75 mm TPRD diameters in the garage with a single brick size (50×250 mm) (threshold A) result in overpressures greater than 10 kPa. The overpressure can be reduced to 6 kPa by increasing the vent size to two bricks (100x250 mm) with a TPRD of 0.5 mm. Only four brick vents (200x250 mm) are required with TPRD=0.75 mm in order to reduce the PPP overpressure to an acceptable 7 kPa. As expected, in poor ventilation garages, which are common in cold climates, TPRD=0.5 mm is preferable to TPRD=0.75 mm from a PPP standpoint. It is inherently safer to use TPRD diameters of 0.45–0.5 mm for blowdown in a fire to meet standards for the prevention of the PPP repercussions in a garage for hydrogen applications with onboard tanks of 70 MPa and V=62.4 L with HDPE liner. It is important to note, nevertheless, that garages with vent sizes of 50×250 mm or less, or one brick vent area, may experience unfavourable PPP effects. As such, it is advisable to have a vent area of at least two brick vent sizes, or 100×250 mm.

2. State of charge and its effect on the tank's FRR

The accurate reproduction of the result observed in fire tests using the same tanks at an initial pressure of 17.8 MPa is demonstrated by the simulated performance in the fire of the NWP=70 MPa tank, which resulted in leaking rather than rupture at 17.8 MPa (Ruban et al., 2012). The pressure is then increased in the simulation to the uppermost value that can occur before a tank bursts. It was

determined that the initial pressure of 24 MPa (SoC=42.5%) was "on the border" between rupture and leak. This value is just 4% different from the experimental value of 25 MPa (Blanc-Vannet et al., 2019), when the leak without burst was documented. The physical phenomena undergoing in the 62.4 L tank at 70 MPa (till its rupture) and 30 MPa (with rupture happening) is shown in Figure below.

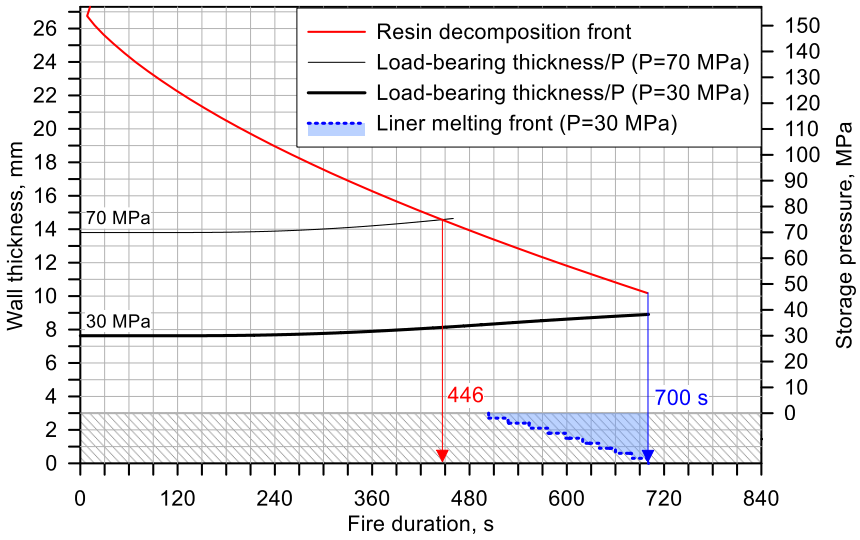

Figure 6. In a fire with HRR/A = 1 MW/m^2, the performance of tank V = 62.4 L, NWP = 70 MPa is as follows: rupture at initial pressure NWP = 70 MPa and no rupture at starting pressure 30 MPa (Kashkarov et al., 2021).

Figure 6 shows that if the hydrogen pressure inside the 62.4 L, NWP=70 MPa tank is 30 MPa (SoC=51%), the tank will not burst during the fire. This is believed to be caused by the thinner liner and thicker walls of the larger volume tank, which cause the liner to melt sooner.

3. Effect of tank wall thickness non-uniformity on the FRR

Assuming both the dome and the sidewall of the tank are subject to a fire, Figure 7 shows the performance of both these parts in a fire for 36 L, NWP=70 MPa tank causing a rupture and lowered pressure preventing rupture by causing hydrogen leak.

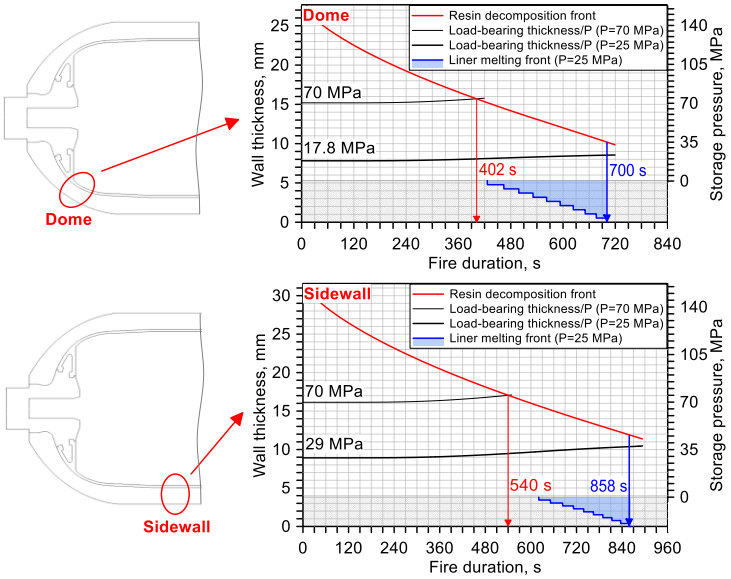

Figure 7. Performance of a Type IV tank of 36 L volume and 70 MPa nominal working pressure in a fire (HRR/A=1 MW/m^2): thinner wall thickness in the dome (top) and thicker cylindrical part (bottom) for 70 MPa and the pressure at which the liner melts and the tank does not rupture (Kashkarov et al., 2021).

In the considered example of 36 L, NWP=70 MPa tank the dome part has liner thickness 5.27 mm and CFRP thickness 22.26 mm while the sidewall has 3.81 mm and 27.75 mm for liner and CFRP respectively. The thickened liner in the dome region is probably the manufacturer's technical necessity due to the liner and boss connection.

Figure 7 demonstrates that, as expected, at NWP=70 MPa the increase of composite wall thickness by 20% from 22.26 mm (dome) to 27.75 mm (sidewall) results in an increase of FRR by 34%, i.e. from 402 s (6 min 42 s) to 540 s (9 min). The initial pressure that prevents rupture is higher for the thicker sidewall. The liner melts in the sidewall at an initial pressure of 29 MPa (SoC=50%) (Figure 7, bottom), while for the dome region it is only 17.8 MPa (SoC=32.6%) (Figure 7, top). In the engulfing fire, the tank would rupture at the dome area after 402 s while the sidewall still can bear the load. This is an apparent disadvantage in the current design of composite storage tanks that must be addressed by tank manufacturers and OEMs.

4. Conclusions

Numerical investigations indicate a possibility of liner melting during non-adiabatic blowdown of a tank through a reduced diameter of a TPRD orifice. When in a fire, the inherently safer hydrogen blowdown from the tank is facilitated by the "additional" hydrogen leakage through the composite wall following the liner melting. The previously validated model of non-adiabatic tank blowdown in fire, which includes the original composite tank failure in a fire mechanism, was utilised for this numerical analysis.

The inclusion of all significant physical phenomena affecting the complex process of heat and mass transfer during high-pressure hydrogen tank blowdown in a fire provides the foundation for the model's strength. For the examined Type IV tanks with NWP=70 MPa, a TPRD diameter of 0.75 mm for 244 L tanks and 0.5 mm for 62.4 L tanks can be used to exclude rupture. At least two bricks totalling 100×250 mm in vent area are required for releases in a garage from a passenger car (from an onboard storage tank of V=62.4 L) in order to avoid the PPP from having a destructive effect on a structure.

Using the validated model, the effect of SoC of the selected 70 MPa Type IV tanks on their FRR was investigated. The simulations accurately reproduce the experimentally observed phenomena of tanks leaking instead of rupturing in a fire at initial pressures below approximately NWP/3. The underlying physics is also examined. After investigating how tank wall non-uniformity affects the decrease of the tank FRR, it is determined that tank manufacturers need to take measures to address this problem in order to enhance the FRR and provide a greater level of life safety and property protection.

When exposed to a fire, the tanks with volumetric capacities of 62.4 L and 244 L, NWP=70 MPa and SoC=51% (30 MPa) and 54% (32 MPa), respectively, do not rupture. The chosen industrial 36-liter tank's non-uniform wall thicknesses revealed a 34% variation in FRR. Only Type IV tanks – where the liner is metallic – can be protected from a catastrophic tank rupture in a fire at a lower SoC from melted liner and hydrogen leakage. Type III tanks cannot be protected from this risk. This is the safety benefit of Type IV tanks.

Firefighters and first responders should be informed on the FRR of hydrogen storage tanks while developing their intervention tactics. To meet the demands of first responders, the appropriate regulations need to require FRR experimental measurements, i.e., carrying out fire tests without TPRD.

Acknowledgements

The authors gratefully acknowledge the financial contribution from the UK EPSRC grant "SUPERGEN Hydrogen and Fuel Cells Challenge: Safety Strategies for Onboard Hydrogen Storage Systems" (EP/K021109/1), Invest Northern Ireland (NI) grant Proof of Concept PoC 629 "Composite

tank prototype for onboard compressed hydrogen storage based on novel leak-no-burst safety technology" and PoC Plus "Optimisation of explosion free in a fire composite cylinder to industrial requirements", Invest NI Centre for Advanced Sustainable Energy (CASE) "Breakthrough safety technologies for hydrogen vessels from Northern Ireland", Innovate UK Clean Maritime Demonstration Competition "Hydrogen Fuel Cell Range Extender", Fuel Cells and Hydrogen 2 Joint Undertaking (now Clean Hydrogen Joint Undertaking) through the HyTunnel-CS "Pre-normative research for safety of hydrogen driven vehicles and transport through tunnels and similar confined spaces" and SH2APED "Storage of hydrogen: alternative pressure enclosure development" projects. The HyTunnel-CS project has received funding from the FCH2 JU under grant agreement No. 826193, and SH2APED project under grant agreement No. 101007182. This Joint Undertaking receives support from the European Union's Horizon 2020 research and innovation programme, Hydrogen Europe, and Hydrogen Europe Research.

References

Baker, W.E., Cox, P.A., Westine, P.S., Kulesz, J.J., Strehlow, R.A., 1983. Explosion hazards and evaluation. Elsevier Scientific Publishing Company.

Blanc-Vannet, P., Jallais, S., Fuster, B., Fouillen, F., Halm, D., van Eekelen, T., Welch, S., Breuer, P., Hawksworth, S., 2019. Fire tests carried out in FCH JU Firecomp project, recommendations and application to safety of gas storage systems. Int. J. Hydrog. Energy, Special issue on The 7th International Conference on Hydrogen Safety (ICHS 2017), 11-13 September 2017, Hamburg, Germany 44, 9100–9109. https://doi.org/10.1016/j.ijhydene.2018.04.070

Brennan, S., Molkov, V., 2013. Safety assessment of unignited hydrogen discharge from onboard storage in garages with low levels of natural ventilation. Int. J. Hydrog. Energy 38, 8159–8166.

Dadashzadeh, M., Kashkarov, S., Makarov, D., Molkov, V., 2018. Risk assessment methodology for onboard hydrogen storage. Int. J. Hydrog. Energy 43, 6462–6475. https://doi.org/10.1016/j.ijhydene.2018.01.195

Dadashzadeh, M., Makarov, D., Kashkarov, S., Molkov, V., 2019. Non-adiabatic under-expanded jet theory for blowdown and fire resistance rating of hydrogen tank. Presented at the International Conference on Hydrogen Safety, Adelaide, Australia.

Hussein, H.G., Brennan, S., Shentsov, V., Makarov, D., Molkov, V., 2018. Numerical validation of pressure peaking from an ignited hydrogen release in a laboratory-scale enclosure and application to a garage scenario. Int. J. Hydrog. Energy 43, 17954–17968. https://doi.org/10.1016/j.ijhydene.2018.07.154

Johnston, I.A., 2005. The Noble-Abel Equation of State: Thermodynamic Derivations for Ballistics Modelling. Report DSTO–TN–0670 (Report DSTO–TN–0670 No. Report DSTO–TN–0670), Report DSTO–TN–0670. Australian Government: Department of Defence. Defence Science and Technology Organisation.

Kashkarov, S., Makarov, D., Molkov, V., 2021. Performance of Hydrogen Storage Tanks of Type IV in a Fire: Effect of the State of Charge. Hydrogen 2, 386–398. https://doi.org/10.3390/hydrogen2040021

Kashkarov, S., Makarov, D., Molkov, V., 2018. Effect of a heat release rate on reproducibility of fire test for hydrogen storage cylinders. Int. J. Hydrog. Energy 43, 10185–10192. https://doi.org/10.1016/j.ijhydene.2018.04.047

Makarov, D., Shentsov, V., Kuznetsov, M., Molkov, V., 2018. Pressure peaking phenomenon: Model validation against unignited release and jet fire experiments. Int. J. Hydrog. Energy 43, 9454–9469. https://doi.org/10.1016/j.ijhydene.2018.03.162

Molkov, V., 2012. Fundamentals of Hydrogen Safety Engineering. bookboon.com.

Molkov, V., Dadashzadeh, M., Kashkarov, S., Makarov, D., 2021. Performance of hydrogen storage tank with TPRD in an engulfing fire. Int. J. Hydrog. Energy. https://doi.org/10.1016/j.ijhydene.2021.08.128

Molkov, V., Kashkarov, S., Makarov, D., 2023a. Breakthrough safety technology of explosion free in fire self-venting (TPRD-less) tanks: The concept and validation of the microleaks-no-burst technology for carbon-carbon and carbon-glass double-composite wall hydrogen storage systems. Int. J. Hydrog. Energy. https://doi.org/10.1016/j.ijhydene.2023.05.148

Molkov, V., Kashkarov, S., Makarov, D., 2023b. Explosion free in fire self-venting (TPRD-less) composite tanks: Performance during fire intervention. Int. J. Hydrog. Energy. https://doi.org/10.1016/j.ijhydene.2023.07.067

Molkov, V., Makarov, D., Kashkarov, S., 2018. Composite Pressure Vessel for Hydrogen Storage. European (EPO) Patent Application No. 18706224.5. International (PCT) Application No: PCT/EP2018/053384. WO 2018/149772 A1.

Monde, M., Woodfield, P., Takano, T., Kosaka, M., 2012. Estimation of temperature change in practical hydrogen pressure tanks being filled at high pressures of 35 and 70 MPa. Int. J. Hydrog. Energy, XII International Symposium on Polymer Electrolytes: New Materials for Application in Proton Exchange Membrane Fuel Cells 37, 5723–5734. https://doi.org/10.1016/j.ijhydene.2011.12.136

Quang Dao, D., Luche, J., Richard, F., Rogaume, T., Bourhy-Weber, C., Ruban, S., 2013. Determination of characteristic parameters for the thermal decomposition of epoxy resin/carbon fibre composites in cone calorimeter. International Journal of Hydrogen Energy 38, 8167–8178.

Ruban, S., Heudier, L., Jamois, D., Proust, C., Bustamante-Valencia, L., Jallais, S., Kremer-Knobloch, K., Maugy, C., Villalonga, S., 2012. Fire risk on high-pressure full composite cylinders for automotive applications. Int. J. Hydrog. Energy, International Journal of Hydrogen Energy 37, 17630–17638. https://doi.org/10.1016/j.ijhydene.2012.05.140

SAE, n.d. J2601_202005: Fueling Protocols for Light Duty Gaseous Hydrogen Surface Vehicles - SAE International [WWW Document]. URL https://www.sae.org/standards/content/j2601_202005/ (accessed 11.10.22).

SAE J2601, 2016. SURFACE VEHICLE STANDARD (No. (R) Fueling Protocols for Light Duty Gaseous Hydrogen Surface Vehicles).

Shentsov, V., Makarov, D., Molkov, V., 2019. Scientific Principles of e-Laboratory of Hydrogen Safety, in: Proc. of the Ninth International Seminar on Fire & Explosion Hazards (ISFEH9). St. Petersburg, Russia.

Hydrogen flammability and explosion concentration limits for a wide temperature range

Plaksin V.Yu. [a], Kirillov I.A. [b]

[a] KinTechLab Ltd., Moscow, Russia

[b] Servel d.o.o., Izola, Slovenia

E-mail: kirillov.igor@gmail.com

Abstract

Concentration limits of the different hydrogen-air combustion modes are of vital importance for the multiple technological and safety applications. This paper restricted to assess the rich flammability limits and both lean and rich flame acceleration limits in hydrogen-air mixtures over a wide temperature range (90 K to 858 K) at normal initial pressure. A non-empirical model is utilized to determine the fundamental concentration limits of plane deflagration flames based on two inherent characteristics of hydrogen-air mixtures: crossover temperature and adiabatic isobaric complete combustion temperature. These characteristic temperatures are considered fundamental as they are not influenced by experimental combustion characteristics, measurable in the specific test apparatuses. The proposed model provides estimates for plane deflagration concentration limits, which serve as absolute envelopes compared to earlier empirical limits of the slow flames that can lead to explosions when accelerated. The proposed "from-the-first-principles" model offers quantitative predictions that can elucidate previous experimental findings and suggest further experiments to improve our understanding and accurate quantification of the hydrogen-air concentration limits for the different combustion modes.

Keywords: *hydrogen-air, flammability, ascending and descending flames, flame acceleration, detonation, concentration limits, empirical, fundamental, "from-the-first-principles" model*

Introduction

For practical implementation of the hydrogen transport and energy infrastructures, for design, safety assessment and engineering development of the apparatuses and technical systems, consuming hydrogen, it is necessary to extend and refine the available databases on safety characteristics of the different modes of hydrogen-air combustion (drifting flame balls, slow (laminar) and fast (turbulent) deflagrations, spinning/cellular/pulsating/galloping detonative waves, ets.) under ever possible ambient conditions. In particular, the temperature dependencies of the hydrogen-air flammability and explosion concentration limits within a wide range – from cryogenic (around 90K) to the high temperatures (around 850K) – are of vital importance. Despite the multiple empirical-based studies – experimental and computational - understanding of the nature, criteria and quantitative characterization of the hydrogen combustion concentration limits are still incomplete and require further development.

The paper aims to describe a non-empirical approach to a quantitative estimation of the temperature dependencies of the concentration limits for the rich hydrogen-air flammability concentration limits and for the lean and rich flame acceleration concentration limits, applicable to a wide temperature range - from 91 K to 858 K - under normal pressure conditions.

1. Empirical-based estimates

1.1. Primary experimental data

After seminal work of Coward (1914) the flammability limits (FL) of the single fuel-air premixed gas mixtures have been measured using two empirical criteria (see details in Molnarne (2017).) – 1) pressure rise in the closed chambers (for example, in the technical standards ASTM E 918, ASTM E 2079 and EN 1839(B), and

2) visual flame spread length in the vertical or horizontal open tubes with predefined diameter and length (in the ASTM E-681, DIN 51649-1 and EN 1839 (T) standards). Both criteria have been the subject of discussion and, ultimately, an agreement within the committed research, engineering, and technical standardization communities (at the national, regional, or international level). It should be noted that the concentration limits, determined using the above-mentioned empirically based criteria, have appropriate quantitative differences and can be referred to as nominal concentration limits.

Besides the mentioned observation criteria, the numerical values of the empirical-based flammability limits substantially depend upon test apparatus design, size, material, and measurement procedure (see details in SAFEKINEX, 2003). All these factors result in a variation of the empirical-based concentration limits for flammability and explosion (see Fig. 1) in the different temperature ranges. At Fig.1 the following abbreviations for the experimental and theoretical data are used: CL – Choked Limits, FAL – Flame Acceleration Limits, FDL – Fundamental Detonation Limits, FFL – Fast Flame Limits, LFL – Lower Flammability Limits, LFDL – Lower Fundamental Deflagration flame propagation Limits, UFL – Upper Flammability Limits, UFDL – Upper Fundamental Deflagration flame propagation Limits.

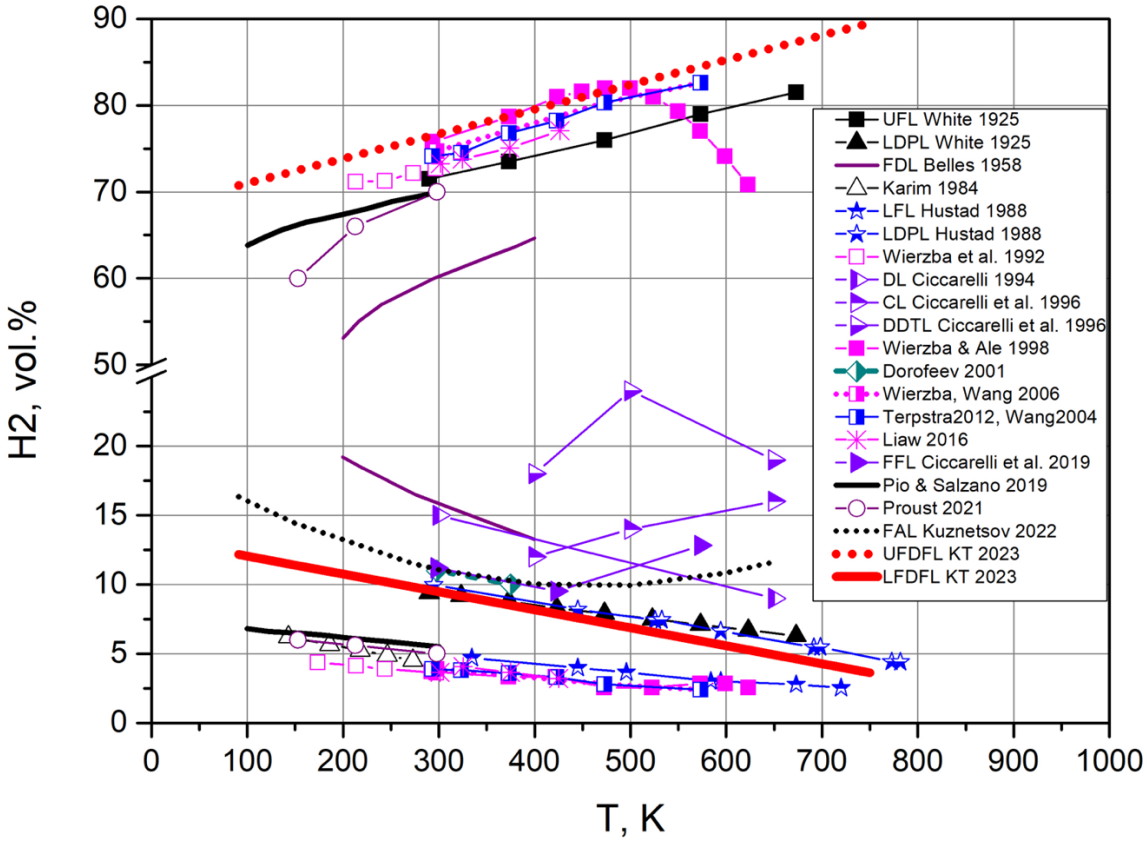

***Fig. 1**. Comparison of the temperature dependence of the empirical and fundamental concentration limits for flammability and explosive combustion phenomena in hydrogen-air-steam mixtures under normal initial pressure over a wide initial temperature range (90K – 858K). Symbols - primary experimental data; lines/curves: brown curve – fundamental detonation limits (Belles 1958), black solid curve – UFL and LFL, estimated numerically on empirical-based assumption (limiting burning velocity – Pio&Salzano 2019); black dotted curve – empirical correlation, based on critical expansion ratio assumption (Kuznetsov 2022); red solid line and red dotted line – lower and upper fundamental deflagration flame propagation limits (this work).*

To minimize the uncertainties and to reconcile the quantitative variations, associated with the differences in the empirical-based criteria, apparatuses and test procedures for the flammability limits, the systematic efforts are still ongoing in developing (Molnarne and Schroeder (2017)) the Standard Operating Procedures (SOP) or the ""standard" gas flammability vessels" (Britton (2020)) for flammability characterization under normal initial conditions (temperature and pressure).

1.2. Empirical-based correlations

1.2.1. Fitting lines

Practical needs in quantitative estimations of the flammability limits within a wide temperature range (from one side - for the elevated and high temperatures, on the other side – for the low and cryogenic temperatures) resulted in appearance of the different fitting curves, which were used to extrapolate the available primary experimental data, measured, mainly, under the normal initial conditions, into the requested temperatures range.

Coward and Jones (1952) recommended the correlation, which fitted the primary data, measured by White (1925), as most reliable (in 1952 year) for the temperature range between 300 K and 673 K. For the same temperature range, Schoreder (2005) proposed the analytical fitting lines for the primary data on UFL_U and LFL_U (for the upward propagating flames), obtained according to DIN 51649 by Gasse (1992), for temperature range between 293 K and 673 K. Kuznetsov (2013) proposed two linear approximations: for the LFL in the temperature range 130 K < T < 300 K and for the UFL in the temperature range 213 K < T < 673 K, using primary data of Karim et al. (1984) and Zabetakis (1965).

1.2.2. Rule-of-thumb and phenomenological models

For the slow flames, which have a velocity much less than the speed of sound in the unburned mixture, Zabetakis (1967) proposed a correlation for temperatures below 300 K. He used modified Burgess-Wheeler's (1911) empirical observations for the LFL (lower flammability limit) and the idea of Egerton (1953), that "the heat of combustion per mole of mixture is the most important factor" in determining the concentration limits. The Burgess-Wheeler's "rule of thumb" is aimed to evaluate a LFL for requested temperature, if the respective LFL value is known from experiment for the reference temperature. It is based on the two phenomenological assumptions: 1) energy conservation and 2) constant values of the adiabatic flame temperatures (AFT) at the flammability limits. Correlation for the UFL have been proposed by Eichert (1992) for the temperature range 150 K < T < 673 K.

Pio and Salzano (2019) estimated the UFL and LFL of hydrogen-air mixtures in temperature range 120 K < T < 300 K by using a notion "limiting value of the laminar burning velocity" and numerical simulations of a 1D plane deflagration flame model with detailed kinetic (KIBO) mechanism.

The concept of "limit burning velocity" was developed by Hertzberg in 1984 by considering the balance between the rate of thermal energy generation due to the chemical reaction in an ideal propagating flame and the rate of energy loss due to various competing processes. He assumed, that "the limit compositions, whether measured in upward, downward, or horizontal propagation, reflect the competition between two forces: the combustion force and the buoyancy force" and derived three explicit formulas for the three mentioned flame propagation directions.

Abovementioned phenomenological models are based on two specific features of combustion in the near-limit mixtures – 1) flame temperature is nearly constant, 2) ascending flame velocity depends on the Earth gravity constant and expansion ratio. These estimates will, probably, be invalid for the zero-gravity conditions, where buoyancy effects are absent and, consequently, the associated heat losses will be negligible.

Phenomenological models of the concentration limits for the slow flames are unable to answer the following research and practical questions: 1. What is a physico-chemical reason for the slow flame temperature invariance in the near-limit mixtures? 2. What are the ultimate concentration limits to which the various experimental values obtained in flammability characterization experiments using different experimental setups, testing procedures, and measurement criteria can converge? 3. Is there a fundamental limit that is independent of test equipment, procedure, or criteria? 4. What will be the hydrogen-air flammability limit in microgravity? 5. Why is there a linear dependence of flammability limits on initial temperature?

For the fast flames, whose velocity is equal or higher than the sound speed in the unburned mixtures, Dorofeev et al. (2001) analyzed the experimental data on hydrogen turbulent flame propagation in horizontal obstructed and smooth channels at normal and elevated initial temperatures (from 298 to 650 K). It was assumed "that basic flame parameters, such as mixture expansion ratio σ, Zeldovich number β and Lewis number Le, can be used to estimate a priori a potential for effective flame acceleration for a given mixture. Critical conditions for effective flame acceleration are suggested in the form of correlations of critical expansion ratio σ^* versus dimensionless effective activation energy". Uncertainties in determination of critical σ^* values have been assessed as $\pm 8\%$. It was proposed, that "…The critical values of σ can be used in practical applications as the necessary criteria for development of fast combustion regimes. One can define on their basis flame acceleration

limits (similar to flammability limits) as the critical mixture compositions for effective flame acceleration at given initial temperature and pressure".

Specific values of the concentration limits for different fast flame combustion regimes have been measured in several experimental works: by Ciccarelli et al. (1994) for Detonability Limits (DL) in dry hydrogen-air mixtures at initial temperatures 298 K, 500 K, 650 K; by Ciccarelli et al. (1996) for Choking Limits (CL) and DDT Limits (DDTL) in hydrogen-air-steam mixtures at initial temperatures 400 K, 500 K, 650 K; by Ciccarelli et al. (2018) for Fast Flame Limits (FFL) at initial temperatures 298 K, 423 K, 573 K.

Kuznetsov et al. (2022) performed more than 100 experiments with hydrogen-air mixtures at ambient pressure and at cryogenic temperatures from 90 to 130K. In this work, it was also suggested to use a fitting curve ("cut-off line") for the concentration boundary between the slow and fast deflagrations, in terms of the critical expansion ratio $\sigma^* = 2200 \cdot T^{-1.12}$ within a wide temperature range – from cryogenic 90 K to elevated temperature 650 K. This relationship was used to derive a correlation of the critical hydrogen concentration $[H_2]_{cr}$ in molar percent for fast flame propagation as a function of the initial temperature T[K]: $[H_2]_{cr} = 4.817 \times 10^{-5} \cdot T^2 - 0.441 \cdot T^{\square} + 19.96$ in the lean hydrogen-air mixtures. An analogous correlation for $[H_2]_{cr}$ in the rich mixtures at cryogenic initial temperatures was not explicitly shown.

Dorofeev et al. (1999) remarked, that "it should be noted, also, that no experimental data are available for rich hydrogen-air-steam mixtures at T_u > 383K. Additional experiments are required to evaluate the limit (correlation for σ^*) for H_2-rich mixtures at T_u> 383K". This observation is still relevant today.

2. Non-empirical estimates

In the first half of the 20th century, the combustion community generally agreed that the concentration limits for various combustion modes (known at that time, such as deflagrations and detonations) could only be estimated quantitatively through experiments. Numerous empirical observations showed that flammability limits were not absolute, but depended on factors such as the type, size, and material of the test apparatus; the strength of the ignition source; the test procedure; and the criterion used for observation. Linnett and Simpson (1957) claimed, that "…there is no experimental evidence proving that any limits that have been observed in gaseous systems are fundamental…".

2.1. Belles' model for fundamental detonation concentration limits

In contrast to the empirical approach for estimating concentration limits that dominated in the first half of the 20th century, Belles (1959) proposed a non-empirical approach based on the kinetic balance between chemical chain propagation and termination to estimate detonation concentration limits. He suggested that detonation limits in hydrogen-air and hydrogen-oxygen systems are compositions for which conditions at the von Neumann spike lie outside isothermal branching chain explosion limits. Later, Nolan (1973) used this idea to quantitatively estimate the detonation limits of hydrocarbon-oxygen mixtures.

2.2. Theoretical models for the concentration limits of gaseous combustion

The idea that the "fundamental concentration limit" is an inherent physical and chemical property of a combustible mixture, which depends on its initial chemical composition and thermodynamic state under adiabatic conditions, and is unaffected by external influences associated with or defined by a specific experimental setup, measurement procedure, or empirical observation criteria for a given combustion mode (flame ball, deflagration, detonation, etc.), has been developed in a series of theoretical and computational studies on flammability limits for gaseous mixtures.

Williams (1985) proposed that "flammability limits can be effectively controlled by chemical kinetics if there is a specific value (concentration) at which the overall rate of heat release abruptly decreases" and used the concept of "crossover temperature" T_{cross} as a quantitative indicator for characterizing abrupt changes in the kinetic behavior of gaseous mixture combustion. These kinetic changes are characterized by a loss of chemical chain reaction continuity, which subsequently results in a lack of chemical heat production. As soon as the initial mixture temperature falls below the crossover temperature, the energy balance at the reaction zone shifts towards heat loss of all kinds (convective, conductive, radiative, etc.), and flame propagation becomes impossible.

Law and Egolfopoulos (1990) showed, "that $H + O_2 = OH + O$ is the dominant branching reaction for both lean and rich mixtures, while $H + O_2 + M = HO_2 + M$ is the dominant termination reaction for lean mixtures,

that the dominant termination reaction for rich limits can be mixture specific, and that as the flammability limit is approached the maximum termination rate occurs in the same physical region as that of the maximum branching rate. This allow for the most efficient radical scavenging." They "formulated a first- principle, predictive theory for the phenomena of flammability limits based on the concept of the competition between chain branching and termination reactions". Law and Egolfopoulos (1992) calculated adiabatic and non-adiabatic fundamental limits for the rich H_2-air and rich CH_4-air mixtures, using proposed kinetic criterion ("flammability exponent").

He and Clavin (1993) estimated the lean and rich limits for the plane deflagration flames in hydrogen-oxygen mixtures, assuming, that at crossover temperature chemical chain propagation rate is equal to chain termination rate.

Ju Y. et al. (2001) differentiated the classical "flammability limits" and "combustion limits" for the specific combustion modes – "planar and curved propagating flames", "flame balls", "stretched premixed flames", "counterflow diffusion flames", "droplet flames", "lifted flames", "edge flames".

Fernandez-Galisteo (2009) computed the lean concentration limit for steady plane flame for the crossing point, where crossover temperature T_{cross} $(\emptyset_{lim})$ and adiabatic flame temperature T_b $(\emptyset_{lim})$ coincide.

Kirillov (2017) computed both the lean and rich concentration limits for propagation of the plane deflagration flames in hydrogen-air mixtures at normal pressure for temperature interval from 293K to 673K.

2.3. Kinetic-Thermodynamic (KT) Model for the fundamental concentration limits of the plane deflagration flames and the adiabatic spherical flame balls

Following the initial ideas of Belles and the proposals of other authors who have contributed to the concept of "fundamental concentration limits" for different modes of combustion and mentioned above, Plaksin and Kirillov (2023) have proposed a unified approach to non-empirically estimate concentration limits for two specific combustion modes. In particular, they focused on slow (laminar) planar deflagrations and adiabatic spherical flame balls:

Step 1: kinetic index estimation - calculate dependencies of the crossover temperature $T_{cross}(\phi)$ upon equivalence ratio ϕ (or hydrogen concentration) for the lean and rich mixtures under given initial conditions (temperature T_u and pressure p_u) by equating the rates of the leading elementary reactions for chain branching $\mathrm{H + O_2 = OH + O}$ and for chain termination $\mathrm{H + O_2 + M = HO_2 + M}$

$$k_b\left(T_{cross}^{\square}\right) = 1 \cdot k_t\left(T_{cross}^{\square}\right) \cdot c_M(\phi,\ \alpha, T_u, \varepsilon_{H_2O}^{\square}) \quad (1)$$

Kinetic parameters for the elementary reaction rates $\mathrm{k_b(T) = A \cdot T^{n}_{\square} exp(-T_a/T)}$ and $\mathrm{k_t(T) = f(k_0, k_\infty, F)}$ have been selected as: $\mathrm{A = 3.52 \cdot 10^{16}}$, n= - 0.7, $\mathrm{T_a = 8590K}$; chaperon efficiencies are - $\varepsilon_{H_2}^{\square}$ =2.5 for H2, $\varepsilon_{H_2O}^{\square}$ =12.7 for $\mathrm{H_2O}$, and 1.0 for all other species; $\mathrm{k_0 = [5.75 \cdot 10^{19},\ -1.4]}$, $\mathrm{k_\infty = [4.65 \cdot 10^{12},\ 0.44]}$, original Troe's formula.

Step 2: thermodynamic index estimation - calculate dependence of adiabatic flame temperature T_b upon equivalence ratio ϕ (or hydrogen concentration) for the given initial conditions (temperature T_u and pressure p_u);

Step 3: fundamental concentration limits estimation - define fundamental concentration limits at the intersection points, where the following kinetic-thermodynamic criterion is satisfied

$$T_b\ (\emptyset_{lim}) = T_{cross}\ (\emptyset_{lim}). \quad (2)$$

During estimation of the fundamental limits for the plane deflagrations in [14-18] the following assumptions was used:

1) flame temperature $T_b(\phi, T_u, p_u\ ) = T_{AICC}(\phi, T_u, p_u)$ (3)

where T_{AICC} – adiabatic isobaric complete combustion temperature;

2) stoichiometric mixture - border between lean and rich gas mixtures – is characterized by value $\phi_{DF} = 1$ $(29{,}6\ vol.\%H2)$. (4)

For estimation of the fundamental limits for the stationary flame balls, where spherical geometry of mass diffusion and heat transfer is essential, set of the assumptions is different from planar case of the deflagration flames:

1) flame temperature $T_b(\phi, T_u, p_u) = T_b^{FB}(\phi, T_u, p_u, \mathrm{Le}(\phi))$ (5)

where $T_b^{FB}(\phi, T_u, p_u, Le(\phi))$ - flame ball temperature, $Le(\phi)$ – effective Lewis number of hydrogen-containing mixture;

2) stoichiometric mixture - border between lean and rich gas mixtures – is characterized by value $\phi_{FB} = \frac{D_{O_2}}{D} = 0{,}2342$. (6)

where D_{O_2} - binary diffusion coefficient of oxygen, $D = 1{,}154 \cdot D_{H_2}$ – binary diffusion coefficient of hydrogen with explicit considering thermo-diffusion different (Soret effect). Physical meaning of equation (6) is - at spherical surface of stationary flame ball stoichiometry is attained (see Buckmaster et al., 1993) due to balance between two diffusion fluxes – oxygen and hydrogen. This is the case for 8,95 vol.% H_2 in the H_2-air mixtures and 18.99 vol.% H_2 in the H_2-O_2 mixtures (see Fig. 2).

At Fig. 2 the following dependencies of the fundamental concentration limits upon initial concentration of water steam are shown – red lines for the plane deflagration flames (DF), blues line – for the spherical adiabatic flame balls (or Zeldovich's FBs).

Comparison of the non-empirical estimations with the appropriate experimental data of Kumar (1985) and Cheikhravat et al. (2015) (see details in Plaksin&Kirillov 2023) results in the following conclusions: 1) lean fundamental concentration limits for the spherical adiabatic flame balls ((line ED at Fig.4)) locate below the lean empirical limits of the upward propagating flames, 2) rich fundamental concentration limits for the plane deflagration flames (line BC at Fig.4) locate above the experimental limits of downward propagating flame 3) lean fundamental concentration limits (line AC) of the plane deflagration flames is a concentration limit for the Flame-Ball-to-Deflagration-Transition (FBDT) (see details in Kirillov (2021)). In the ultra-lean hydrogen-air mixtures (shown at Fig. 2 as tetragon ACDE), where combustion is incomplete, only systems of the drifting flame balls, characterized by the intact/non-coherent reaction fronts, can exist. Propagation of the deflagration flames with continuous reactions front is impossible here.

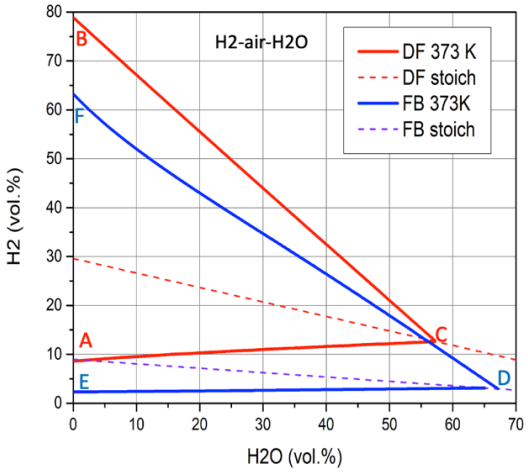

Fig. 2. *Non-empirical concentration limits for the plane deflagration flames (ABC) and the spherical adiabatic flame balls (EFD) in hydrogen-air-water steam mixtures at initial temperature 373K and pressure 1 atm.*

2.4. Temperature dependencies of the fundamental concentration limits for planar deflagration flames

In contrast to the near isobaric flame balls, which can only drift in the external force, temperature or concentration fields and cannot, in principle, to accelerate, the self-propagating deflagration flames can accelerate, - due to inherent instabilities of their reaction fronts or due to interactions with external obstacles or ambient turbulent flows, - and can result in formation of the dangerous blast waves. That is why the temperature dependencies of the different types (cellular, unwrinkled, pulsating) of the deflagration waves is, in first turn, important for safety practice. At Fig. 1 the results of the non-empirical estimations are shown by red dotted line – for upper fundamental deflagration flame limits (UFDFL) in rich mixtures, red solid line – for lower fundamental deflagration flame limits (LFDFL) in lean mixtures.

3. Discussions

3.1. Major findings

Comparison of the proposed non-empirical estimates of the fundamental concentration limits of plane deflagration flames in hydrogen-air mixtures within a wide temperature range (from 90 K to 858 K) with the empirical ones, results in the following conclusions:

1. The fundamental concentration limits for plane deflagration flames in both lean and rich hydrogen-air mixtures can be considered as the "conservative" or "absolute" envelopes for the empirical limits of slow ascending or descending flames that can be accelerated and lead to explosions. The term "envelope" refers to all empirical data and correlations related to the concentration limits of downward and upward propagating flames that can be accelerated. These limits are within the proposed non-empirical boundaries shown by the red solid and dotted lines in Fig. 1. Flames outside these computed concentration limits cannot be principally accelerated and belong to the family of drifting flame balls (Kirillov (2021)).

2. A proposed kinetic-thermodynamic model for the fundamental concentration limits of the two basic slow hydrogen- air flames - flame balls and deflagration flames - is an extension of the Belles' model, focusing on the fundamental detonation limits. Both models (Belles' and proposed in described in this paper) are based on the theoretical assumption, that the concentration limits of different combustion modes (detonation, deflagration, flame balls) depend on the ratio of two characteristic temperatures – the crossover temperature T_{cross}, which is an intrinsic (in other words - fundamental) kinetic characteristic of hydrogen-air premixed combustion and the burning temperature T_b at reaction front. For plane deflagration flames the burning temperature T_b has a purely thermodynamic nature and equals the $T_{AICC}(\phi, T_u, p_u)$ – adiabatic isobaric complete combustion temperature. In case of the spherical adiabatic flame balls the burning temperature $T_b = T_Z(\phi, T_u, p_u, Le)$ is a combination of thermodynamic, mass and energy transfer characteristics of the mixture. For the 1D detonation flames the burning temperature $T_b = T_{vN}(\phi, T_u, p_u, M)$ is the von Neumann temperature.

For a given initial pressure p_u the crossover temperature T_{cross}, defined by an implicit equation (1), is a function of the following macroscopic, measurable in experiment, initial characteristics of the hydrogen-air mixture: stoichiometry ratio ϕ and water steam content α. Non-dimensional values of the crossover temperature - $\Sigma_{cross}(\phi, T_u) = T_{cross}(\phi, T_u)/T_u$ - in the dry hydrogen-air mixtures for the different initial temperatures T_u at $p_u = 1\ atm$ are shown in Fig.3.

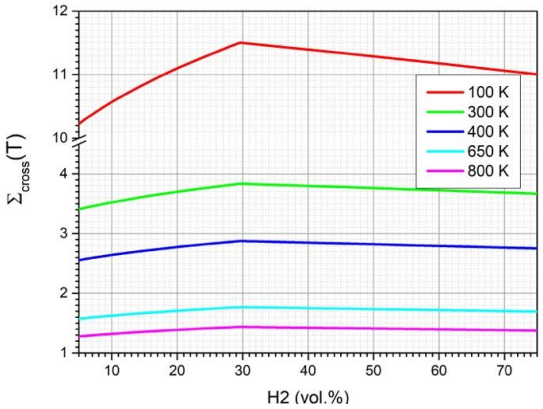

Fig. 3. *Dependence of nondimensional crossover temperature $\Sigma_{cross}(\phi, T_u)$ on initial hydrogen concentration in the dry hydrogen-air mixtures for different initial temperatures at $p_u = 1\ atm$.*

Crossover temperature is weakly depending on initial hydrogen concentration and is, practically, independent on initial mixture temperature. Even for the lowest considered initial temperature $T_u = 100\ K$, variation of the crossover temperature (see Fig.3) within the flammability limits is less than (11,5-10,2)*100%/11,5=11%. These features of the fundamental kinetic characteristic of the hydrogen-air combustion result in two consequences (see Fig.4) – 1) weak dependence (nearly invariance) of the deflagration flame burning temperature $T_b = T_{AICC}$ in the near-limits mixtures, 2) practically linear dependence of the flammability limits with variation of initial mixture temperature.

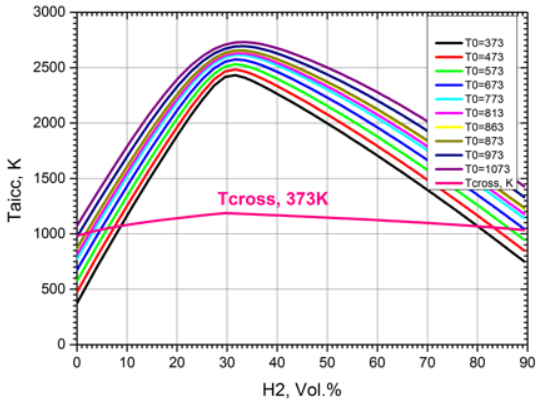

Fig. 4. *Location of the intersection points of the burning temperatures $T_{AICC}(\phi, T_u)$ and the crossover temperature $T_{cross}(\phi, T_u)$ for the plane deflagration flames.*

3. A comparison of the temperature dependence of the non-dimensional of the crossover temperature, non-empirically estimated at concentration limits - $\Sigma_{cross}^{lim}(T_u)$ - with the appropriate dependence of the critical expansion ratio $\sigma_{\square}^{*}(T_u)$, proposed by Kuznetsov et al. (2022), is shown in Fig.5.

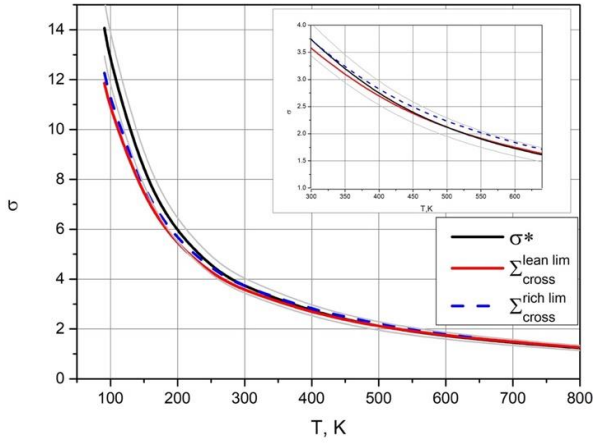

Fig. 5. *Temperature dependencies of the non-dimensional crossover temperature, estimated for the fundamental plane deflagration flame concentration limits $\Sigma_{cross}^{lim}(T_u)$ (red solid curve – lean limits ($\Sigma_{cross}^{lean\ lim}$), blue dashed line – rich limits ($\Sigma_{cross}^{rich\ lim}$)), and the critical expansion ratio $\sigma_{\square}^{*}(T_u)$ for effective flame acceleration (black solid line – formula (7) in Kuznetsov et al. (2022)), thin black lines – borders of 8% confidence interval).*

Analysis of the Fig.5 revealed a fact – both temperature dependencies of the dimensionless crossover temperature for the lean and rich fundamental plane deflagration limits are located within the confidence interval of the experimental correlation (Kuznetsov et al. (2022)) for the critical expansion ratio for the effective flame acceleration at the normal and elevated initial temperatures (between 300 K and 640 K). For the cryogenic temperatures, such as 100 K, the maximal deviation is no more than 17 %.

4. Detonation limits, as measured by Cicarelli et al. (1996), have a reasonable correlation with the fundamental detonation limits, estimated by Belles (1958), using a simplified 1D approach for detonation wave structure analysis, as proposed by Zeldovich, Neumann and Döring. However, for a more detailed reconciliation of the experimental and theoretical estimates of detonation limits it is necessary to explicitly consider the 3-dim nature of the detonation front.

5. The correlation of the critical hydrogen concentration for fast flame propagation as a function of initial temperature $[H_2]_{cr}(T_u)$, proposed by Kuznetsov et al. (2022), shows a non-monotonic behaviour during a gradual increase in initial temperature T_u. In the temperature range between 90 K and 300 K, the critical concentration of hydrogen $[H_2]_{cr}$ decreases, while in the range between 300 K and 640 K it increases. It will be important for many practical hydrogen safety applications understand the reasons for this revealed change in trends.

3.1. Future works

1. Credible experimental validation of the fundamental limits of concentration for both self-propagating deflagration flames and flame balls can be achieved under micro- and zero-gravity conditions. These flames are characterized by integral/continuous reaction fronts that generate blast waves and discrete/non-coherent reaction fronts in flame balls. Under these conditions, buoyancy effects can be neglected.

2. Non-empirical estimates have been made in assumption, that under the low temperature and cryogenic conditions an impact of the quantum tunnelling effects on the elementary reaction rates of the leading chemical chain propagation reaction is negligible. Confirmation or rejection of the proposed hypothesis requires additional experiments in explosion spheres (flammability limits) and in the vertical shock tubes (flame acceleration and DDT limits) in temperature range between 20K and 91K.

3. Validity, completeness, and accuracy of the experimental database for the effective flame acceleration limits will be higher, if the data, measured in the horizontal shock tubes, will be complemented by the experimental datasets, measured in the vertical shock tubes (see details in Bezgodov et al. (2022)).

4. This paper discusses cases of planar deflagrations and adiabatic spherical flame balls only. However, future research should also investigate experimental and theoretical concentration limits for other modes of hydrogen-air combustion that have been observed in the past. This includes, at the very least, self-quenching, self-sustaining, and self-branching flame balls, as well as cellular, unwrinkled, pulsating deflagration flames, and spinning, cellular, pulsating, and galloping detonation flames.

5. To avoid incorrect interpretation of different types of flames (e.g., slow "finger" flames with wrinkled front in lean hydrogen-air mixtures and fast "finger" flames during the transition from deflagration to detonation), it is advisable to develop a unified classification system for both slow and fast flames based not only on the physical and chemical characteristics of the reaction fronts but also on their topology, geometry, and dynamics. Based on this classification, accurate concentration limits can be determined for each type of flame.

4. Conclusions

Available experimental data on the flammability and explosion (effective flame acceleration, DDT, detonation) concentration limits for a wide initial temperature range (from 90 K to 858 K) have been compiled and analyzed in terms of their consistency, accuracy and completeness.

It was found that certain inconsistencies and contradictions in the empirical estimations of these limits could be addressed by using a non-empirical approach based on the concept “fundamental concentration limits” for the drifting flame balls and the self-propagating deflagration flames.

Unlike empirical or phenomenological models that rely on measurable combustion characteristics, the non-empirical model for planar deflagration flames is based on fundamental kinetic and thermodynamic characteristics of hydrogen-air mixtures that can be calculated “from-the-first principles”.

The fundamental concentration limits determined by our model for the planar deflagration flames in rich hydrogen-air mixtures closely align with published experimental values for rich flammability concentration limits and providing conservative envelopes for the lean and rich empirical limits of the flames that could potentially accelerate and lead to explosions.

By providing explanations for previous experimental data, this non-empirical model enables the formulation of focused experiments to further elucidate the nature and accurate quantification of the flammability and explosion limits across a wide temperature range.

Bibliography:

Belles, F.E., 1959. "Detonability and Chemical Kinetics: Prediction of Limits of Detonability of Hydrogen," 7th Symposium Int. on Combustion, P745-751, Butterworths.

Bezgodov, E.V., et al., 2022. The effect of buoyancy on flame acceleration in hydrogen-air mixtures: experiments in horizontal and vertical tubes, 28th ICDERS, Napoli, paper 194.

Britton, L.G., 2002. Two hundred years of flammable limits, *Process Safety Prog.* 21(1): 1–11.

Buckmaster J., Smooke M., Giovangigli V., 1993. Analytical and Numerical Modeling of Flame Balls in

Hydrogen-Air Mixtures, *Combustion and Flame*, 94: 113-124.

Burgess, M.J., Wheeler, R.V., 1911. The lower limit of inflammation of mixtures of paroffin hydrocarbons with air. *J. Chem. Soc.*, 99:2013–2030.

Cheikhravat H. et al., 2015. Effects of water sprays on flame propagation in hydrogen/air/steam mixtures, Proc. Comb. Institute 35, 2715-2722.

Ciccarelli, G. et al., 1994. High-Temperature Hydrogen-Air-Steam Detonation Experiments in the BNL Small-Scale Development Apparatus, NUREG/CR -6213, BNL-NUREG -52414.

Ciccarelli, G. et al., 1996. The Influence of Initial Temperature on Flame Acceleration and Deflagration-to-Detonation-Transition, 26th Symp. Int. on Combustion, 2973-2979.

Ciccarelli, G. et al., 2019. Fast-flame limit for hydrogen/methane-air mixtures, Proc. Combustion Institute, 37(3): 3661-3668.

Coward, H. F., and Brinsley F., 1914. Dilution limits of inflammability of gaseous mixtures. I. Determination of dilution limits. II. Lower limits for hydrogen, methane, and carbon monoxide in air. *J. Chem. Soc*., 105: 1859.

Coward, H.F. and Jones, G.W., 1952. Limits of flammability of gases and vapors. Bureau of Mines, US government printing office, Washington.

Dorofeev, S.B. et al., 1999. Evaluation of Limits for Effective Flame Acceleration in Hydrogen Mixtures. FZKA 6349, Forschungszentrum Karlsruhe.

Dorofeev, S.B. et al., 2001. Evaluation of limits for effective flame acceleration in hydrogen mixtures. *J. Loss. Prev.* 14:583-589.

Egerton, A.C., 1953. Limits of inflammability. Proc. Combust. Inst. 4: 4–13.

Eichert H., et al., 1992. Gefährdungspotential bei einem verstärkten Wasserstoffeinsatz. Deutsches Zentrum für Luft- und Raumfahrt (DLR), Stuttgart.

Fernandez-Galisteo, D.F., 2009. Numerical and asymptotic analyses of lean hydrogen-air deflagrations. PhD thesis. Uni. Carlos de Madrid.

Fernández-Tarrazo, E., et al., 2012. Flammability conditions for ultralean hydrogen premixed combustion based on flame-ball analyses, *Int. J. Hydrogen Energy,* 37, 2012, pp.1813–1825.

Gasse, A., 1992. Experimentelle Bestimmung and Simulation von Explosionsgrenzen, untersuch an wasserstoff Brenngasgemishen, Dissertation, Uni-GH Paderborn, Germany.

He, L., Clavin, P., 1993. Premixed Hydrogen-Oxygen Flames. Part I: Flame Structure Near the Flammability Limit, *Combustion and Flame*, 93, 391-407.

Hertzberg, M., 1984. The Theory of Flammability Limits, Flow Gradient Effect and Flame Stretch, 1st ed., University of Michigan Library.

Ju, Y., Maruta, K., Takashi, N., 2001. Combustion limits, *Appl. Mech. Reviews*, 54(3): 257-274.

Karim, G.A. et al., 1984. The Lean Flammability Limits in Air of Methane, Hydrogen and Carbon Monoxide at Low Temperatures. *Cryogenics*, 21, 1984, p. 305.

Kirillov, I.A., 2017. Non-empirical method for quantitative estimation of the concentration limits for deflagration flame propagation in hydrogen-air gaseous mixtures. Proc. XXIX Int. Scientific and practical conference dedicated to the 80th anniversary of VNIIPO, Russian Ministry of Emergency, part 2, 5-8 (in Russian).

Kirillov, I.A., 2018. Physics-based Approach for Reduction Uncertainties in Concentration Limits of "Slow-to-Fast" Flame Transition in Hydrogen-Air Gas Mixtures, Hydrogen Management in Severe Accidents, Technical Meeting EVT1701911, 25-28 September 2018, Vienna, TECDOC, IAEA, 259-277.

Kirillov, I.A. et al, 2019. Theoretical estimation of concentration limits for water steam capability to suppress flame acceleration in hydrogen-air mixtures. 27th ICDERS, paper 310.

Kirillov, I.A., 2021. On Flame Ball-to-Deflagration Transition in Hydrogen-Air Mixtures, Int. Conf. Hydrogen Safety, paper 134.

Kumar, R., 1985. Flammability limits of hydrogen-oxygen-diluent mixtures. *J. Fire Sci.*, 3:245-262.

Kuznetsov, M., et al., 2022. Flame propagation regimes and critical conditions for flame acceleration and detonation transition for hydrogen-air mixtures at cryogenic temperatures. *J. Hydrogen Energy*. 47(71):30743-30756.

Law, C.K., and Egolfopoulos, F.N., 1990. A kinetic criterion of flammability limits: the C-H-O-inert system. 23rd Symp. Int. Comb. 413-421.

Law, C.K., and Egolfopoulos, F.N., 1992. A unified chain-thermal theory of fundamental flammability limits. 24th Symp. Int. Comb. 137-141.

Linnett, J.W., and Simpson C.J.S.M., 1957. Limits of inflammability. Symp. on Comb. 6(1): 20-26.

Molnarne, M., Schroeder, V., 2017. Flammability of gases in focus of European and US standards. *J. Loss Prev.* 48: 297-304.

Nolan, M.E., 1973. A simple model for the Detonation Limits of Gas Mixtures. *Comb. Sci. Tech.* 7(2): 57-63.

Pio, G., Salzano, E., 2019. Flammability Limits of Methane (LNG) and Hydrogen (LH2) at Extreme Conditions. *Chem. Eng. Trans.*, 77: 601-606.

Plaksin, V.Yu., Kirillov, I.A., 2023. “Lean” Unified Non-Empiric Model for Fundamental Concentration Limits of Spherical Flame Balls and Plane Deflagration Flames in the Hydrogen-Containing Mixtures. 29th ICDERS, July 23-28, 2023, paper 225.

Proust, C., 2021. Summary of experiment series E4.1 results (Ignition parameters), PRESLHY project, deliverable D4.4.

SAFEKINEX, 2003. Report on the experimental factors influencing explosion indices determination, Deliverable No.2., Project SAFEKINEX: SAFe and Efficient hydrocarbon oxidation processes by KINetics and Explosion eXpertise.

Schroder, V. and Holtappels, K., 2005. Explosion characteristics of hydrogen-air and hydrogen-oxygen mixtures at elevated pressures. Int. Conf. on Energy Materials.

Terpsta, M., 2012. Flammability limits of hydrogen-diluted mixtures in air. MSc thesis, Uni. Calgary.

White, A.G., 1925. Limits for the propagation of flame in inflammable gas-air mixtures. III. The effects of temperature on the limits. *J. Chem. Soc.* 127: 672-684

Wierzba, I., et al., 1992. Effect of low temperature on the rich flammability limits in air of hydrogen and some fuel mixtures containing hydrogen. *Int. J. Hydrogen Energy,* 17(2):149-152. LFL UFL

Wirzba, I., Ale, B. B., 1998. Effects of temperature and time of exposure on the flammability limits of hydrogen-air mixtures. *Int. J. Hydrogen Energy*, 23(1): 1197-1998.

Wierzba, I., Wang, Q., 2006. The flammability limits of H2-CO-CH4 mixtures in air at elevated temperatures. *Int. J. Hydrogen Energy*, 31:485-489. LFL UFL. 20 – 300C

Williams, F.A., 1985. Combustion Theory, Second Edition, Benjamin/Cumming Publ, New York.

Zabetakis, M.G., et al., 1959. Flame temperatures of limit mixtures. 7th Symp. Int. on Combustion, The Combustion Institute, 484–487.

Zabetakis, M.G., 1965. Flammability Characteristics of Combustible Gases and Vapors, Bulletin 627, US Bureau of Mines, XMBUA

Zabetakis, M.G., 1967. Safety with cryogenic fluids. Plenum Press, New York.

Assessment of Electrostatic Ignition Hazards during Water Spray Cleaning Processes above 50 MPa

F. Baumann [a], M. Himstedt [a], D. Möckel [a] & M. Beyer [a]

[a] Physikalisch-Technische Bundesanstalt, 38116 Braunschweig, Germany

E-mail: florian.baumann@ptb.de

Abstract

Pump pressures of a few tens to several hundred MPa are used for vessel cleaning processes with water. Where an explosive atmosphere is present, the pump pressure used must be limited to 50 MPa in order to avoid electrostatic ignition hazards due to brush discharges from charged droplet clouds to earthed installed parts. Pressures above 50 MPa are not considered in electrostatic regulations such as technical specification IEC TS 60079-32-1. This pressure limit originates from the performance limits of the cleaning technologies investigated in the past. The pump pressure above which an electrostatic ignition hazard exists is, however, unknown. This limitation works to impair the effectiveness of the cleaning processes. To satisfy the technical state of the art, tests were conducted in vessels of up to 44 m³ and pump pressures of up to 250 MPa. Based on the outcome of these extensive tests and on relevant references, an assessment method is described that takes account of the space charge densities present in the vessel when water is sprayed into it. The derived flow chart enables manufacturers and operators to safely carry out assessments of cleaning processes with water up to 250 MPa in explosive atmospheres, factoring in the vessel dimensions, cleaning technology parameters, and water type. This opens new possibilities for more economical cleaning processes and better-quality cleaning results while maintaining the same level of safety.

Keywords: *electrostatic, brush discharge, hazards, high pressure, water, vessel, spraying*

1. Introduction

After use, transport vessels for chemicals - from intermediate bulk containers to ship tanks - must be thoroughly cleaned. During this process, residues in the vessel can form a potentially explosive atmosphere that can ignite under unfavourable circumstances. In 1969, there were serious explosions on three very large crude carriers during the use of powerful cleaning technologies, resulting in several injuries and deaths (Steen, 2000). The reason: electrostatic discharges caused by the spraying of water. To avoid such disasters, the thresholds and measures of the International Safety Guideline for Inland Navigation Tankers and Terminals (ISGINTT, 2010) and the International Safety Guideline for Oil Tankers and Terminals (ISGOTT, 2006) must be observed.

The cleaning technologies used in the chemical and food industries differ considerably in the pressure range - several 10 MPa to several 100 MPa (Baumann, 2023) - from those used in ship cleaning - up to 1 MPa (Bustin and Dukek, 1983) -. Therefore, the thresholds applicable in this area cannot be transferred. Based on studies from the 1970s and 1980s (Post et al., 1983), the thresholds of the international technical specification IEC TS 60079-32-1 (IEC TS 60079-32-1:2013+AMD1:2017 CSV) summarised in Fig. 1 were defined for spraying technologies and vessel dimensions. The threshold of the pump pressures is 50 MPa because of the spraying technologies were not able to achieve more at that time. Today's spraying technologies, however, work with pump pressures of up to 250 MPa. It is therefore necessary to define thresholds for this pressure range as well.

Spraying technology	Pump pressure ≤ 1.2 MPa	1.2 MPa < Pump pressure ≤ 50 MPa
Flow rate	-	5 l/s
Vessel		
Diameter	-	3 m
Volume	Very low hazard level for < 100 m³	-

Fig. 1. *IEC TS 60079-32-1 thresholds for spraying technology and vessel dimensions (Baumann, 2023)*

In cooperation with the Physikalisch-Technische Bundesanstalt (PTB), a group of companies that manufacture and operate cleaning technology have analyzed the necessary thresholds for safe use. The basis for this is the new approach to safety assessment, with which the measured values were compared.

The investigations served as the basis for a user-friendly flow chart that PTB developed in collaboration with a group of experts on electrostatics from the German Social Accident Insurance Institution for the raw materials and chemical industry (BG RCI) in 2023. The flow chart makes it possible to exceed the thresholds without the risk of electrostatic ignition due to brush discharges from charged spray clouds when spraying tap water into conductive, earthed vessels. The parameters of the spraying technologies and vessel dimensions are considered.

2. Safety assessment based on electrostatic variables

When spraying water, there is an electrostatic ignition hazard due to brush discharges that occur between the charged droplet cloud and conductive, earthed installation parts. In relation to the state of the art, dust cannot be ignited by brush discharges (IEC TS 60079-32-1:2013+AMD1:2017 CSV). The following thresholds and assessment criteria for electrostatic variables apply:

2.1 Space Potentials

Space potentials from 58 kV are considered ignitable for the representative propane/air mixture of explosion group IIA with a minimum ignition energy (MIE) of 0.24 mJ (IEC TS 60079-32-1:2013+AMD1:2017 CSV).

2.2 Electric field strength

Electric field strengths above 100 kV/m can cause brush discharges. This threshold is shown as a horizontal dashed line in Fig. 2 top. This statement also remains valid when field-distorting components are installed (TRGS 727, 2016).

Brush discharges occur when the product of the electric field strength at the vessel wall $E(R)$ and the squared vessel diameter D_R reaches or exceeds 100 kVm (Freytag, 1965). See equation 1:

$$E(R) \cdot D_R^2 < 100\ kVm \qquad 1$$

Conversion of equation 1 results in the electric field strength at the vessel wall at which no brush discharges are to be expected (equation 2).

$$E(R) < \frac{100\ kVm}{D_R^2} \qquad 2$$

This still safe electric field strength is shown as a black curve depending on the vessel diameter in Fig. 2 top. There are no brush discharges to the left of the curve, but brush discharges are to be expected to the right of the curve.

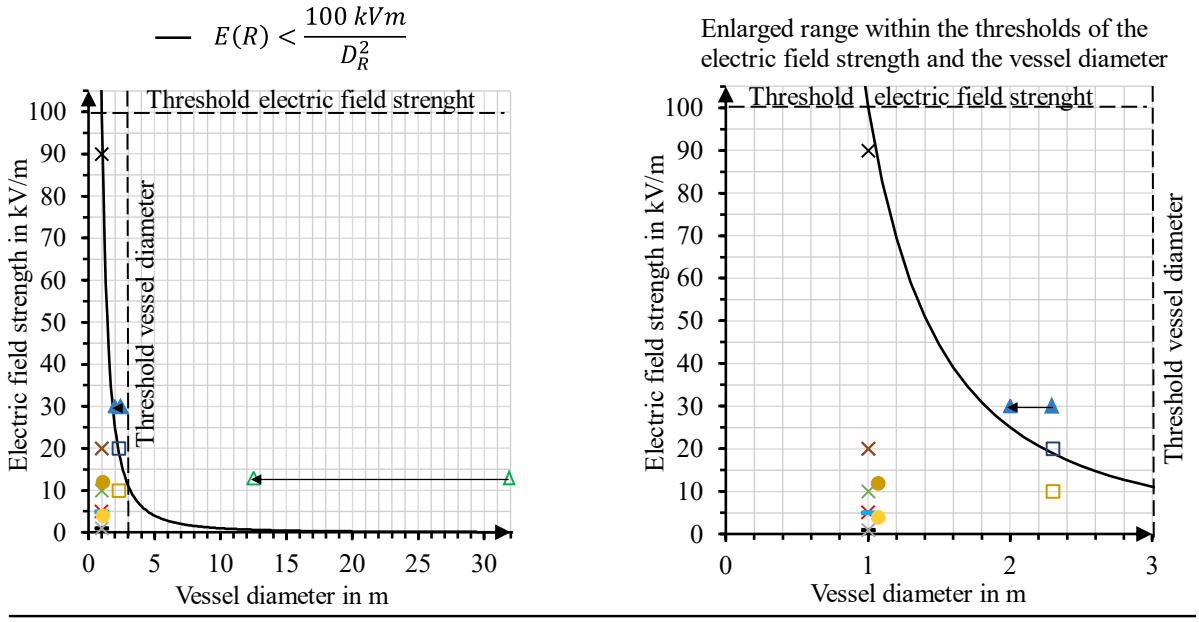

References	Liquid	Electrical conductivity in S/m	Ø Nozzle in mm	Pressure in Mpa
(Post et al., 1983)	Toluene	$5 \cdot 10^{-10}$	1.8	5
	Acetone	$5 \cdot 10^{-7}$	1.8	5
	Industrial water	$5 \cdot 10^{-2}$	1.8	5
	Xylene	$1 \cdot 10^{-9}$	1.8	5
	Deionized water	$1 \cdot 10^{-5}$	1.8	5
	Toluene + 8 % Vol. of water	$2.5 \cdot 10^{-10}$	1.8	5
	Xylene + 4.7 % of active carbon	$5 \cdot 10^{-11}$	1.8	5
	Xylene + 2.6 % of SiO_2	$3 \cdot 10^{-10}$	1.8	5
	Industrial water	$5 \cdot 10^{-2}$	1.5	10 bis 40
	Industrial water	$5 \cdot 10^{-2}$	2.5	10 bis 40
(Blum, 2015)	Tap water	$6.6 \cdot 10^{-2}$	1.05	50
	Deionized water	$9.2 \cdot 10^{-5}$	1.05	50
(Bright et al., 1975 & Hughes et al., 1973)	Tap water	$5 \cdot 10^{-2}$	Electrostatic application system	
(Van de Weerd, 1971)	Water	Not specified	Tank washing head or steam	

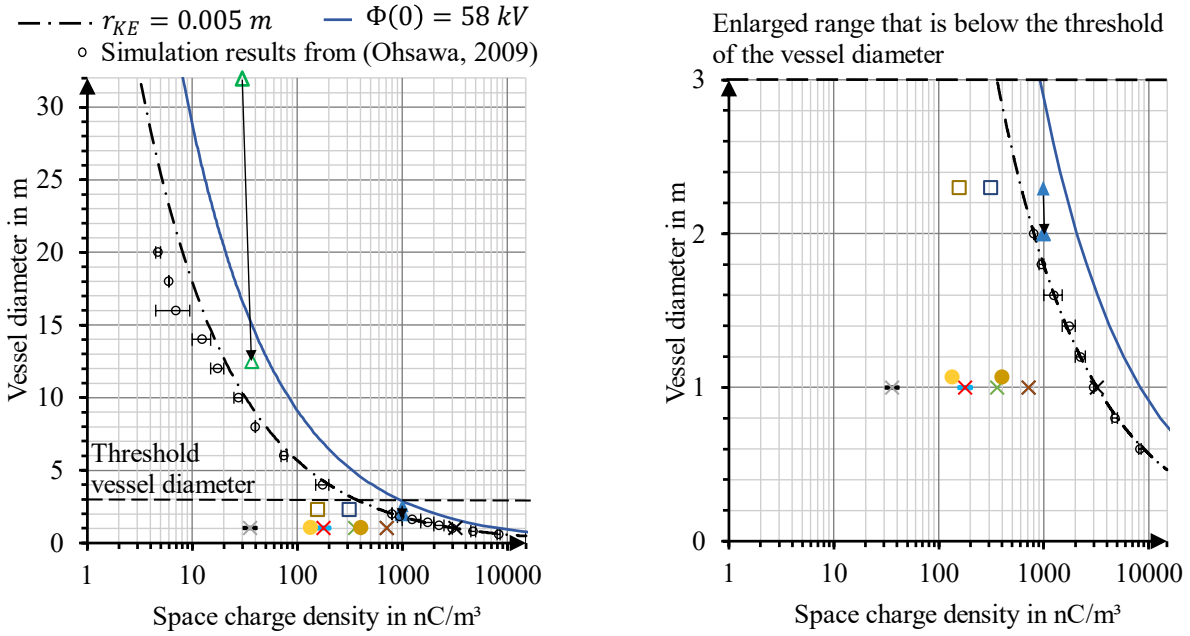

Fig. 2. *Top: Curve of the electric field strength, from which the occurrence of brush discharges is to be expected, plotted against the vessel diameter; bottom: Curves of the vessel diameter plotted against the space charge density, from which the occurrence of brush discharges is to be expected; in both cases with values from the literature (Baumann, 2023)*

2.3 Space charge density

Space charge densities ρ in cylindrical vessels with a radius R are calculated using the electric field strength $E(R)$ at the vessel wall or the space potential $\Phi(0)$ in the centre of the vessel, see equation 3 (Krämer, 1983).

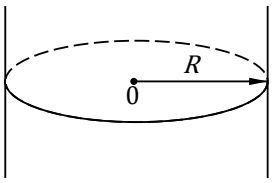

(Baumann, 2023)

$$\rho = \frac{\Phi(0) \cdot 4 \cdot \varepsilon}{R^2} = \frac{E(R) \cdot 2 \cdot \varepsilon}{R} \quad (3)$$

The permittivity ε results from the product of the permittivity number of 1.01 for fine, suspended water droplets (Baumann, 2023) and the electric field constant ε_0, see equation 4.

$$\varepsilon = \varepsilon_r \cdot \varepsilon_0 \quad (4)$$

The vessel diameter D_R can be calculated using equation 5 on the basis of the breakdown field strength E_i (Bright et al., 1975). As in (Post et al., 1983), a breakdown field strength of 3 MV/m (Lüttgens et al., 2020) is used. From this vessel diameter, the occurrence of brush discharges of the charged droplet cloud is to be expected at field-distorting built-in parts with the radius of curvature r_{KE} in the centre of the vessel (Post et al., 1983).

$$D_R = 2 \cdot R = 2 \cdot \sqrt{\frac{E_i \cdot 6 \cdot \varepsilon \cdot r_{KE}}{\rho}} \quad (5)$$

Brush discharges between the charged droplet cloud and built-in parts close to the wall are considered unlikely compared to built-in parts in the centre of the vessel (Ohsawa, 2009). For this reason, no consideration is given to built-in parts close to the wall. Based on the following considerations, curves were drawn in Fig. 2 bottom as an assessment criterion:

- Ignitable for gas and vapour/air mixtures of explosion groups IIC and IIB: At radii of curvature of more than approx. 0.005 m, mainly brush discharges occur (Hearn and Jones, 1995; TRGS 727, 2016). The probability of corona discharges occurring increases with smaller radii of curvature. Corona discharges are not considered to be ignitable for gas and vapour/air mixtures of explosion groups IIA and IIB (Lüttgens et al., 2020). Depending on a radius of curvature of 0.005 m, equation 5 can be used to determine the safe vessel diameter for gas and vapour/air mixtures of explosion group IIB via the space charge density (dashed-dotted line in Fig. 2). The black circles in Fig. 2 show the simulation results from Ohsawa (2009), which indicate the space charge density at which brush discharges can be expected at this radius of curvature.

- Ignitable for gas and vapour/air mixtures of explosion group II: Exceeding the space potential of 58 kV, which is considered ignitable for the representative propane/air mixture (MIE of 0.24 mJ) of explosion group IIA (IEC TS 60079-32-1:2013+AMD1:2017 CSV). This condition can be shown by equation 3 in Fig. 2 as a dark blue curve.

In order to check the applicability of the assessment criteria of the space potential, the electric field strength and the space charge density shown as curves in Fig. 2, a comparison is made with measured values from the literature. The smallest space-limiting dimension is to be used for the vessel diameter and requires an adjustment of the literature values, see Fig. 2 black arrows (Baumann, 2023). In addition, the threshold of the vessel diameter of 3.0 m is shown in Fig. 2 (below) as a vertical, dashed line.

- No brush discharges occurred below, on or near the electric field strength curve and the curve of the radius of curvature of 0.005 m in the literature values from Post et al. (1983). In (Blum, 2015), the safety-related statement was made that no ignitable discharges occur.

- Above the curve of the electric field strength and the curve of the radius of curvature of 0.005 m, the first brush discharges occur in the literature values from Bright et al. (1975); Hughes et al. (1973) and van de Weerd (1971), see green and blue triangle in Fig. 2. These literature values lie below the curve formed by the threshold of the space potential of 58 kV. In confirmation of this curve, the brush discharges in the ignition tests carried out by Hughes et al. (1973) and van de Weerd (1971) with a propane/air and a town gas/air mixture were not ignitable.

3. New approach to safety assessment

The threshold of the electric field strength of 100 kV/m is not used for the safety assessment, as it has been proven that brush discharges occur below this value. The electric field strength curve formed from equation 2 (black curve in Fig. 2, above) can only be used to make a statement about the occurrence of brush discharges. A more specific statement on the electrostatic ignition hazard due to brush discharges for hazardous substances of explosion group II is possible by analysing the curves of the vessel diameter plotted against the space charge density (Fig. 3). This results in threshold curves and ranges:

- Range II: Below K2. Applies as a transition range from corona to brush discharges. Discharges that occur are ignitable for hazardous substances whose MIE is smaller than that of the representative mixture of explosion group IIB (MIE 0.082 mJ).

- Threshold curve K2: From this threshold curve onwards, brush discharges are considered ignitable for the representative ethylene/air mixture (MIE 0.082 mJ) of explosion group IIB. K2 is based on investigations by Langer et al. (2011) to determine the ignitability of brush discharges against representative gas mixtures of explosion groups IIA, IIB and IIC. The brush discharges took place between the spherical electrode and charged insulating plastic surfaces. A comparability with the brush discharges of the charged droplet clouds to be regarded as insulating to earthed built-in parts is assumed. The ignition capability of the brush discharges from charged droplet clouds will be reduced due to the moving droplets, the Taylor cones - Taylor cones are droplets that form a cone with a small radius of curvature under the influence of an electric field and generate corona discharges -, and the formation of liquid bridges to a previously unknown extent. The directly proportional relationship to the potential or space potential is given in both systems, which justifies the comparability. From the investigations described in (Langer et al., 2011), a ratio of the ignition capability of brush discharges to representative gas mixtures of explosion group IIA to IIB of 2.97 can be derived. Applied to the threshold curve K3, corresponding to 58 kV, this results in the curve K2, corresponding to 19.5 kV. K2 is slightly below the curve of the radius of curvature of 0.005 m (Fig. 2), is therefore more conservative and is used for the further safety assessment. From a vessel diameter of 2 m, K2 is adapted to the more conservative simulation results from Ohsawa (2009) for the radius of curvature of 0.005 m. Curve K2, the curve of the radius of curvature of 0.005 m and the simulation results are close to each other and are confirmed by the ignition tests mentioned in chapter 2.3.

- Range III: Below K3 up to and including K2. Brush discharges occur predominantly. These are considered ignitable for hazardous substances whose MIE is equal to that of the representative mixture of explosion group IIB (0.082 mJ) or whose MIE is less than that of the representative mixture of explosion group IIA (0.24 mJ).

- Threshold curve K3: The threshold curve corresponds to the space potential of 58 kV. From this threshold curve, brush discharges for the representative propane/air mixture (MIE 0.24 mJ) of explosion group IIA are considered ignitable.
- Range IV: Above K3 is range IV, where ignitable brush discharges occur for hazardous substances of explosion group II.

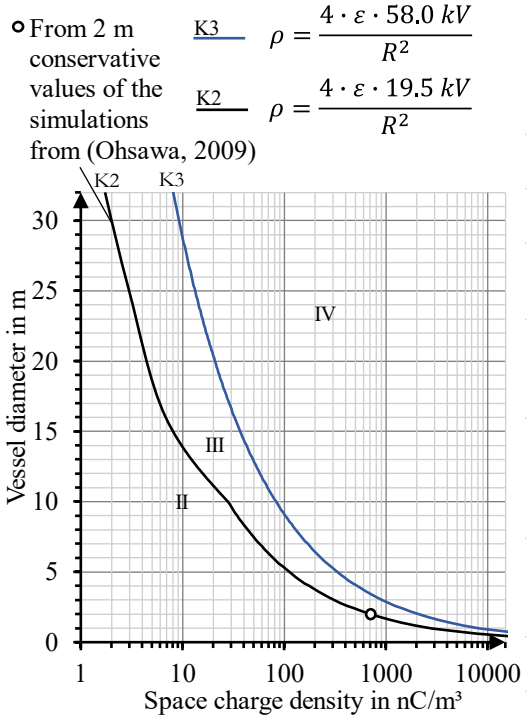

Curve or range in the diagram	Ignition capability	The highest-energy type of discharge that occurs
II < K2	Ignitable for hazardous substances whose MIE is below that of the representative mixture of explosion group IIB	Transition range from corona to brush discharges
K2	Ignitable for the representative mixture of explosion group IIB (ethene/air mixture MIE 0.082 mJ) and for hazardous substances with a lower MIE	Predominantly brush discharges
K2 ≤ III < K3	Ignitable for hazardous substances whose MIE is equal to that of the representative mixture of explosion group IIB or is below the MIE of the representative mixture of explosion group IIA	
K3	Ignitable for the representative mixture of explosion group IIA (propane/air mixture MIE 0.24 mJ) and for hazardous substances with a lower MIE	Brush discharges
K3 < IV	Ignitable for hazardous substances of explosion group II	

Fig. 3. *Threshold curves and ranges for the safety assessment of electrostatic ignition hazards due to brush discharges of the charged droplet cloud for hazardous substances of explosion group II (Baumann, 2023)*

4. Measurements

The basis of charge separation when spraying water is the formation of an electrical double layer on the droplet surface. Due to the impact on the vessel wall and the hydrodynamic instability of the jet, the outermost molecular layer of one polarity of the double layer is detached and forms the droplet cloud (Baumann, 2023; Lenard, 1892, 1915). When spraying tap water, the jet is positively charged and the droplet cloud is negatively charged (Baumann, 2023; Pierce, 1970). This charge separation effect was named after its discoverer Philipp Lenard (Lenard, 1892, 1915).

When spraying tap water, the dominant process of charge separation is the impact of the jet on the vessel wall (Baumann, 2023). The space charge density is fundamentally maximized by the parameters listed in Table 1 (Baumann et al., 2024):

Table 1. *Parameters for maximising the space charge density when spraying tap water (Baumann et al., 2024)*

Maximize the spatial charge separation between jet and droplet cloud:	Increase the generation of the droplet cloud (Lenard-Effect):	Maximize the droplet density of the droplet cloud:
▪ Spraying into the upper part of the vessel ▪ Use round jet nozzle	▪ Reduce distance between nozzle and wall ▪ Increasing the pump pressure ▪ Increase the temperature of the sprayed water	▪ Use a sufficiently large nozzle diameter and flow rate for the existing vessel volume

In the tests carried out, the nozzles had a diameter of 0.5 mm to 4.0 mm and, like the vessels, were conductive and earthed. The electrical conductivity of the tap water was (5.15 ± 3.41) - 10^{-2} S/m. The water temperature was measured at the drain using a calibrated type K thermocouple (uncertainty ±2 K). When spraying into the lower part of the vessel, the spray jet from one nozzle hit the vessel wall as directly as possible. The test set-up with the 1 m³ vessel is shown in Fig. 4. The setup is the same for the 6.2 m³ and 16.8 m³ vessel. The 44.0 m³ vessel was set up vertically. The installed agitator reduced the effective diameter from 4.10 m to 2.50 m. The 250 N threshold for the repulsive force of the hand-operated spraying technology was maintained (DGUV Regel 100-500, 2017). This threshold restricts the flow rate, nozzle diameter and pump pressure.

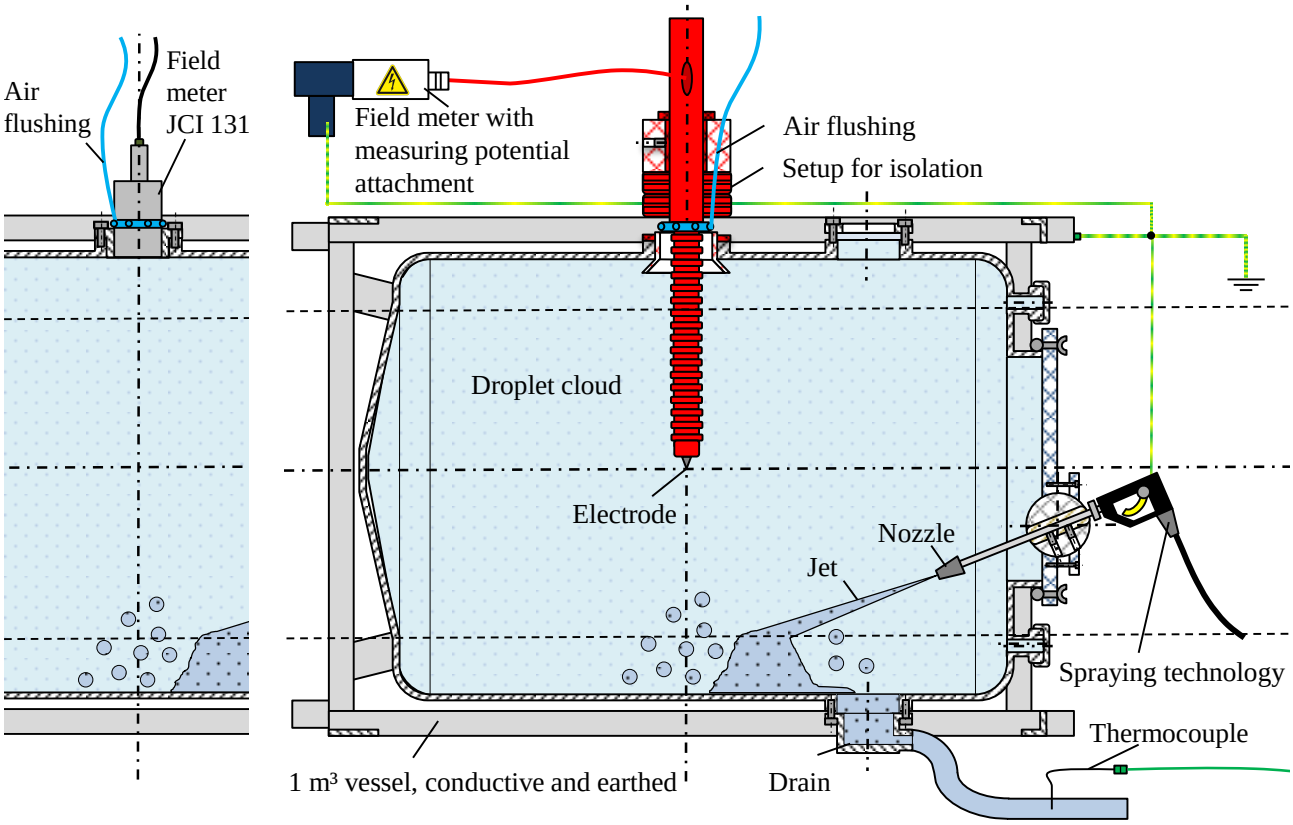

Fig. 4. *Test setup of the 1 m³ vessel with mounted air-flushed field meter JCI 131 (left) or the mounted space potential measurement technology (right) (Baumann et al., 2024)*

The air-flushed field meter JCI 131 from Chilworth Ltd. measured the electric field strength $E(R)$ (Baumann, 2023; Chilworth Technology Limited, 2006). The measuring accuracy depends on the upper end of the measuring range. It is ±1.5 % of ±2 kV/m, ±20 kV/m and ±200 kV/m (Chilworth Technology Limited, 2006). The measuring device was mounted flush in the inner shell surface halfway along the inner length of the vessel (Fig. 4, left). The space potential $\Phi(0)$ in the centre of the vessel was measured using a space potential measurement technology (Fig. 4, right) (Baumann et al., 2021; Baumann, 2023; Baumann et al., 2024). The tip electrode with a length and diameter of 10 mm was mounted insulated from earth potential. The space potential of the charged droplet cloud in the vessel was measured by contact with this electrode. The electrode was connected to a ±40 kV voltage measuring attachment of the EMF 58 field measuring device from Eltex GmbH or the EFM 235 from Kleinwächter GmbH. This measurement technology works in the same way as an electrostatic voltmeter. The space potential was therefore measured in an unencumbered manner (Baumann et al., 2021; Baumann, 2023; Baumann et al., 2024). The measurement accuracy was ±2.5 % of the full scale values of ±1 kV, ±2 kV, ±4 kV, ±8 kV, ±10 kV and ±40 kV.

Table 2 summaries the measured values of the electric field strength and the space potential in dependence on the investigated vessel dimensions. A detailed presentation of all measurement results can be found in (Baumann, 2023; Baumann et al., 2024).

Table 2. *Measured electric field strengths and space potentials in dependence on the dimensions of the conductive earthed vessels (Baumann, 2023; Baumann et al., 2024)*

Volume in m³	Diameter in m	Inner length in m	Electric field strength in kV/m	Space potential in kV
1.0	1.07	1.00	-26.5 bis -3.1	-2.29 bis 0.51
6.2	1.40	4.19	-14.1 bis -3.7	-2.94 bis 0.94
16.8	1.79	7.04	No measurement	-1.97 bis -0.14
44.0	4.10 (2.50)	4.00	-10.9 bis 0.6	No measurement
Without the spatial limitation of the vessel			-1.0 bis 1.1	-0.62 bis 0.32

5. Safety assessment of the measurements

The measured electric field strengths and space potentials are converted into space charge densities using equation 3. With the known vessel diameter and the calculated space charge densities, an entry is made in the diagram of the boundary curves K2 and K3 and their ranges, enlarged to a maximum vessel diameter of 3 m (Fig. 5, left). All space charge densities fall below K2 and are in range II. Fig. 5, right, shows the space charge densities considering the following necessary correction of the space potentials and "worst case" assumptions:

- Application of the space potential correction factor of 2 ± 0.5. The correction factor depends on the electrical conductivity of the sprayed water and was determined by comparing the measured electric field strength with the space potential (Baumann, 2023).
- Assuming a temperature of 100 °C for the sprayed water. Increase the space charge density by 1 % per 1 K (Baumann, 2023; Baumann et al., 2024).
- A factor of 2 was used for the 16.8 m³ and 44.0 m³ vessel, as the most critical nozzle diameter of 2.0 mm was not investigated (Baumann, 2023).
- Generation of maximum space charge densities through constant nozzle alignment and no built-in parts in the vessel during the tests carried out (Baumann, 2023; Baumann et al., 2024).

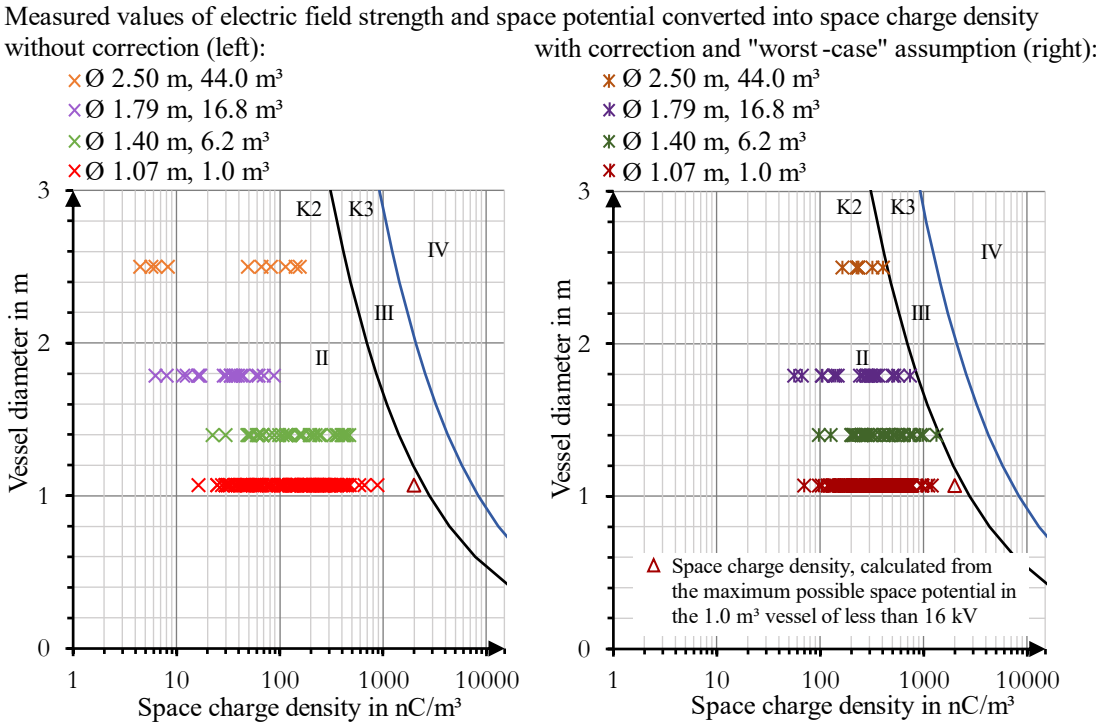

Fig. 5. *Calculated space charge densities of the measured electric field strengths and space potentials and their vessel diameters in the diagram of the boundary curves K2 and K3 and their ranges, enlarged to a maximum vessel diameter of 3 m. Left without correction, right with correction and "worst-case" assumption (Baumann, 2023)*

Depending on the vessel volume, the following safety-related statements are made:

- 1.0 m³: Even the maximum space charge density in this vessel due to the use of an electrostatic application system (Baumann et al., 2019), see red triangle in Fig. 5, did not result in K2 being exceeded.
- 6.2 m³: The use of several nozzles can lead to K2 being exceeded.
- 16.8 m³ and 44.0 m³: No tests were carried out with the most critical nozzle diameter of 2.00 mm and several nozzles. Exceeding K2 is possible.
- Without the spatial limitation of the vessel and without the jet hitting a surface, there is no electrostatic ignition hazard due to brush discharges of the droplet cloud when spraying tap water (Table 2).

6. Conclusions

The results of measurements carried out in this work were compared with the new approach to safety assessment. Based on this, a flow chart for the safety-related assessment of the electrostatic ignition hazard of brush discharges from charged droplet clouds when spraying tap water into conductive, earthed vessels was developed in collaboration with the BG RCI's electrostatics working group (Fig. 6).

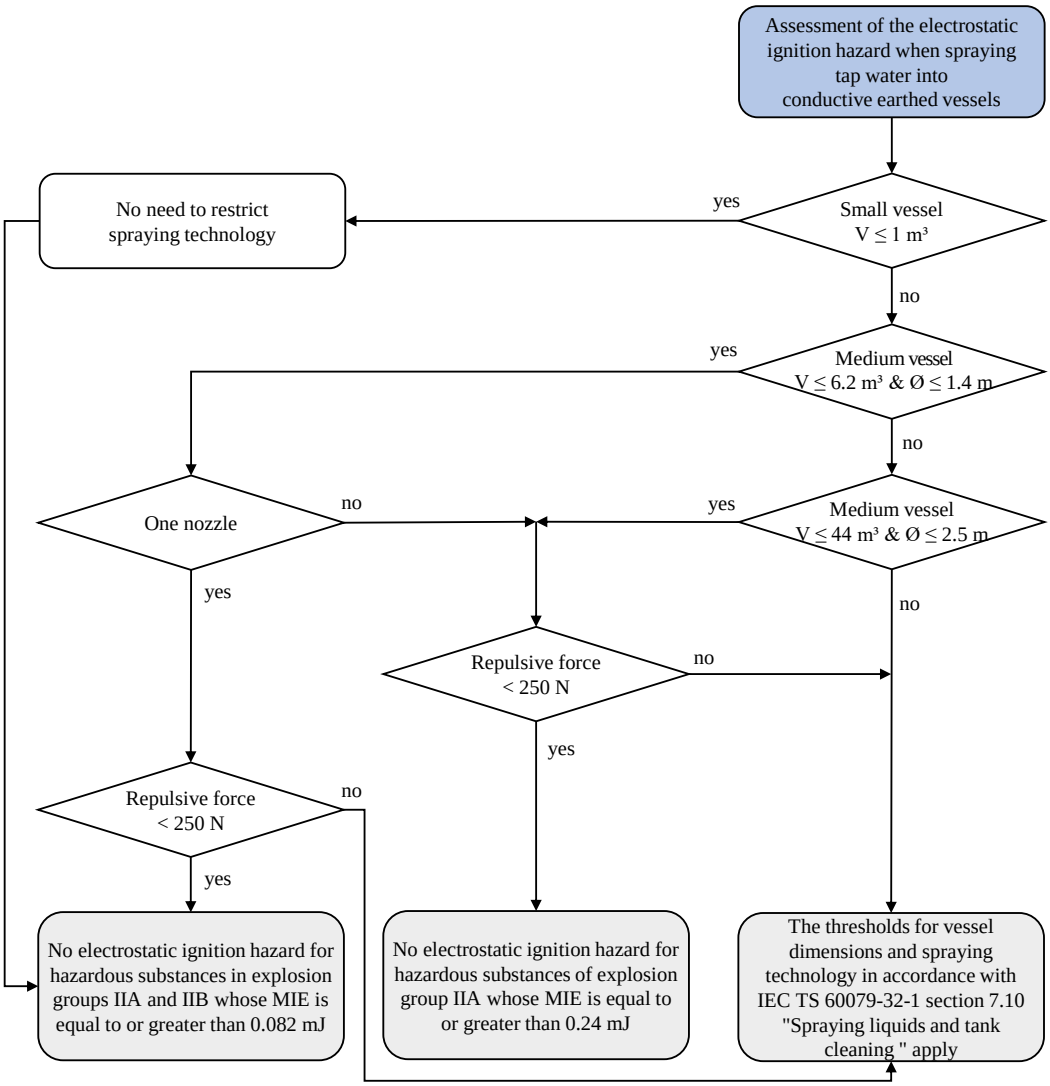

Fig. 6. *Flow chart developed with the BG RCI's electrostatics working group for the safety-related assessment of the electrostatic ignition hazard of brush discharges from charged droplet clouds when spraying tap water into conductive, earthed vessels (EXINFO, 2023)*

If falling coherent water clusters occur, IEC TS 60079-32-1 section 7.10.1 must be observed. When spraying deionized water, charge separation dominates at the conductive earthed nozzle. Electric field strengths of several 100 kV/m, potentials above 48 kV, low-energy gas discharges from the jet and a "blue glow" when hitting surfaces occur (Baumann, 2023). IEC TS 60079-32-1 section 7.10 applies.

As shown in Fig. 2 other liquids than water can generate different space charge densities. With regard to the cleaning processes, further investigations of water with added detergents/surfactants or water contaminated with various impurities (liquid or solid) are of interest.

Acknowledgements

The authors gratefully acknowledge the financial contribution from he German Social Accident Insurance (DGUV) and the five professional associations involved, BG RCI, BG ETEM, BG HM, BG Verkehr and BG HW. We extend our gratitude to the over ten industry partners who provided their spraying technology and expertise. This article was also published in German at the “Magdeburg-Köthener Brandschutz- und Sicherheitstagung” in Magdeburg in March 2024.

References

Baumann, F., 2023. Dissertation: Über elektrostatische Zündgefahren beim Versprühen von Wasser in explosionsgefährdeten Bereichen. Physikalisch-Technische Bundesanstalt.

Baumann, F., Esslinger, J., Möckel, D., Thedens, M., Losert, O., 2019. Measurement of electric fields of charged spray clouds of conductive liquids in free space and in a conductive vessel. Journal of Physics: Conference Series 1322, 012019 (p. 1–5).

Baumann, F., Himstedt, M., Möckel, D., Thedens, M., 2021. Charge-separating processes by spraying water under high pressure. Journal of Loss Prevention in the Process Industries 72, 104527 (p. 1–11).

Baumann, F., Schierding, C., Himstedt, M., Möckel, D., Beyer, M., 2024. Parameters Influencing Space Charge Density in Vessels by Spraying Water. J. Phys.: Conf. Ser. 2702 (1), 12024.

Blum, C., 2015. Forschungsbericht, Aufladung beim Versprühen von Flüssigkeiten - Voruntersuchungen zur Bestimmung relevanter Parameter. Berufsgenossenschaft Rohstoffe und chemische Industrie (BG RCI) Projekt Nr. 617.0 - FP290, 26 pp. https://www.bgrci.de/fileadmin/BGRCI/Downloads/DL_Praevention/Explosionsschutzportal/Wissen/Abschlussbericht_Verspr%C3%BChen_Endversion.pdf.

Bright, A.W., Hughes, J.F., Makin, B., 1975. Research on Electrostatic Hazards Associated with Tank Washing in Very Large Crude carriers (Supertankers) : I. Introduction and Experiment Modelling. Journal of Electrostatics 1, p. 37-46.

Bustin, W.M., Dukek, W.G., 1983. Electrostatic Hazards in the Petroleum Industry. Research Studies Press LTD., Letchworth, Engl., 84 pp.

Chilworth Technology Limited, 2006. USER MANUAL: JCI 131 / JCI 131F Adverse Conditions Electrostatic Fieldmeter.

DGUV Regel 100-500, 2017. Betreiben von Arbeitsmitteln, Kapitel 2.36 Arbeiten mit Flüssigkeitsstrahlern, Ausgabe 3/2017 ed. Deutsche Gesetzliche Unfallversicherung e.V. (DGUV), Berlin.

EXINFO, 2023. FAQ; Elektrostatik; 3 Elektrostatische Aufladungen bei Tätigkeiten mit Flüssigkeiten; 3.41 Ist das Reinigen von mit Kohlenwasserstoffen benetzten, leitfähigen geerdeten Behältern durch Wasserstrahlen mit Drücken über 500 bar ohne Zündgefahr möglich? https://www.bgrci.de/exinfode/ex-schutz-wissen/antworten-auf-haeufig-gestellte-fragen/elektrostatik#c5499. Accessed 01/2024.

Freytag, H.H., 1965. Handbuch der Raumexplosionen. Verlag Chemie, Weinheim.

Hearn, G.L., Jones, R.T., 1995. Electrostatic Hazards Associated with Water Deluge and Explosion Suppression Systems Offshore : OFFSHORE TECHNOLOGY REPORT - OTO 95 026 der Health and Safety Executive. (OTO series).

Hughes, J.F., Bright, A.W., Makin, B., Parker, I.F., 1973. A study of electrical discharges in a charged water aerosol. J. Phys. D: Appl. Phys. 6 (8), p. 966–975.
IEC TS 60079-32-1:2013+AMD1:2017 CSV. Explosive atmospheres - Part 32-1: Electrostatic hazards, guidance, Edition 1.1 2017-03 ed. VDE-Verlag, Berlin.
ISGINTT, 2010. Zentralkommission für die Rheinschifffahrt; Oil Companies International Marine Forum: Internationaler Sicherheitsleitfaden für die Binnenschifffahrt und Binnentankterminals, erste Auflage ed. Zentralkommission für die Rheinschifffahrt, Strasbourg.
ISGOTT, 2006. International Champer of Shipping; Oil Companies International Marine Forum: International safety guide for oil tankers and terminals, 5. ed. ed. Witherby's, London.
Krämer, H., 1983. Kriterien zur Beurteilung der Zündgefahren infolge elektrostatisch aufgeladener Flüssigkeiten: Übersichtsbeiträge. Chemie Ingenieur Technik 55 (6), p. 419–428.
Langer, T., Möckel, D., Beyer, M., 2011. Transferred charge of brush discharges in explosive gas atmospheres – A verification of the ignition threshold limits. Journal of Electrostatics 69 (3), p. 200–205.
Lenard, P., 1892. Ueber die Electricität der Wasserfälle. Annalen der Physik und Chemie 282 (8), p. 584–636.
Lenard, P., 1915. Über Wasserfallelektrizität und über die Oberflächenbeschaffenheit der Flüssigkeiten. Annalen der Physik und Chemie 352 (12), p. 463–524.
Lüttgens, G., Schubert, W., Lüttgens, S., Pidoll, U. von, Emde, S., 2020. Statische Elektrizität: Durchschauen - Kontrollieren - Einsetzen. Wiley-VCH, Weinheim, 470 pp.
Ohsawa, A., 2009. Prevention criteria of electrostatic ignition by a charged cloud in grounded tanks. Journal of Electrostatics 67 (2-3), p. 280-284.
Pierce, E.T., 1970. WATERFALLS, BATHROOMS AND--PERHAPS--SUPERTANKER EXPLOSIONS. SAE technical papers (700922), p. 89–96.
Post, L., Lüttgens G., Maurer, B., Glor, M., 1983. Vermeidung von Zündgefahren infolge elektrostatischer Aufladungen beim Versprühen von Flüssigkeiten unter hohem Druck. Sonderdruck aus "Die BG" Heft 7/83.
Steen, H. (Ed.), 2000. Handbuch des Explosionsschutzes. Wiley-VCH, Weinheim, 760 pp.
TRGS 727, 2016. Technische Regel für Gefahrstoffe 727: Vermeidung von Zündgefahren infolge elektrostatischer Aufladungen, Ausgabe 8/2016 ed., 159 pp.
van de Weerd, J.M., 1971. Electrostatic charge generation during the washing of tanks with water sprays-II: Measurements and interpretation. static electrification: invited and contributed papers from the Inst London [u.a] (paper 15 (II)), p. 158–177.

Unmasking hidden ignition sources: A new approach to finding extreme charge peaks in powder processing

Holger Grosshans[a,b], Wenchao Xu[a], Simon Jantač[a] & Gizem Ozler[a,b]

[a] Physikalisch-Technische Bundesanstalt (PTB), Braunschweig, Germany
[b] Otto von Guericke University of Magdeburg, Institute of Apparatus and Environmental Technology, Magdeburg, Germany

E-mail: *holger.grosshans@ptb.de*

Abstract

Powders acquire a high electrostatic charge during transport and processing. Consequently, in the aftermath of dust explosions, electrostatic discharge is often suspected to be the ignition source. However, definite proof is usually lacking since the rise of electrostatic charge cannot be seen or smelled, and the explosion destroys valuable evidence. Moreover, conventional methods to measure the bulk charge of powder flows, such as the Faraday pail, provide only the aggregate charge for the entire particle ensemble. Our simulations show that, depending on the flow conditions, contacts between particles lead to bipolar charging. Bipolar charged powder remains overall neutral; thus, a Faraday pail detects no danger, even though individual particles are highly charged. To address this gap, we have developed a measurement technology to resolve the powder charge spatially. The first measurements have revealed a critical discovery: a localized charge peak near the inner wall of the conveying duct is 85 times higher than the average charge that would be measured using the Faraday pail. This finding underscores the possibility of extremely high local charges that can serve as ignition sources, even though they remain undetected by conventional measurement systems. Our new technology offers a solution by spatially resolving the charge distribution within powder flows, unmasking hidden ignition sources, and preventing catastrophic incidents in the industry.

Keywords: *industrial explosions, powder processing, electrostatics, measurement, simulation*

1 Introduction

For many dust explosions (43% according to Zhi, 2015, Newson Gale, 2013), the ignition source remains unclear (figure 1a). When investigators fail to identify the source of an explosion, they often suspect electrostatic discharges because electrostatic discharges leave little or no traces. They cannot be smelled or felt, so they are not reported by eyewitnesses. Further, as we will elaborate in this article, conventional measurement equipment cannot detect the local rise of charge. Thus, evidence is usually lacking.

In the pursuit of finding processes or locations in industrial plants where charge separates at high rates, pneumatic conveyors are a top candidate. Pneumatic conveying, as other powder operations, induces tribocharging through frictional contact of particles with pipes and ducts (Xu and Grosshans, 2023). The conveying pipeline, bends, and other components act as charge generators, resulting in the accumulation of electrostatic charges on the conveyed powder and flown-through devices. Compared to other powder process operations, pneumatic conveying reaches several orders of magnitude higher charge levels (figure 1b).

Being the operation that generates the most charge does not mean that pneumatic conveyors are at the highest risk of experiencing an explosion. Instead, the charge generated in conveyors can cause discharges in the conveyor itself and any other downstream process. The conveying pipeline itself, along with bends and transitions, is prone to discharges, but explosions are unlikely in this location if the equipment is electrically bonded and the dust concentration is low. Even during close proximity between particles or between particles and the pipeline wall, electrostatic discharges occur due to

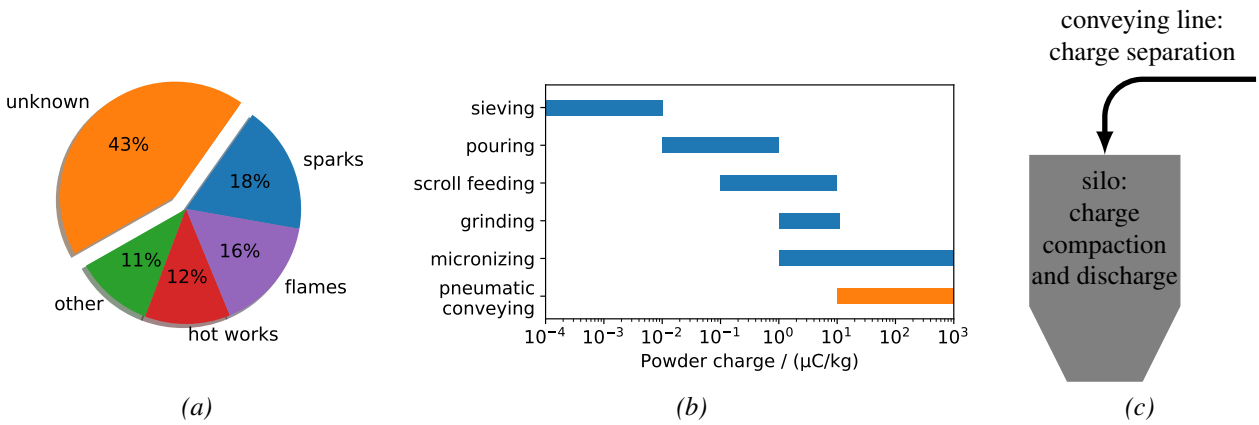

***Fig. 1**: (a) The ignition source of 43% of dust explosions around the world from 1785 to 2012 (data collected by Zhi (2015) and compiled by Newson Gale (2013)) is unknown. (b) pneumatic conveying generates high electrostatic charge, which then (c) compacts and often discharges in silos.*

differences in charge potential (Matsuyama and Yamamoto, 1995), but the energy of these discharges is small compared to the dust's Minimum Ignition Energy (MIE).

The potential dust explosion locations are downstream of pneumatic conveyors, where particles pile up or form layers, increasing the particle concentration and energy density. Especially inside silos, combustible dust clouds can form, and cone discharges can lead to dust explosions (Choi et al., 2018). Silos are filled with products by trucks, bucket elevators, or pneumatic conveyors, all of which have the likelihood of producing a dust cloud during the filling process. Particles that received a high charge in the conveying line can experience cone discharges due to charge compaction (Glor, 1984). Charge compaction describes the mechanical and electrostatic charge compression when filling a conveyed product into a silo. If the powder's surface conductivity is low, the charge dissipates slowly toward the ground, and the charge density at the silo's bed becomes much higher than in the conveying system or the charged dust cloud (Glor, 2001). In other words, pneumatic conveying generates a high powder charge, and filling a silo compacts the charge to high densities (figure 1c).

Dust explosions in silos are not uncommon. In 2022, one-quarter of all industrial dust explosions happened in silos and other storages (Cloney, 2023), and the root of these explosions often remains unclear. For example, the 2020 grain dust explosion at Tilbury docs in Essex, the largest grain terminal in the UK, destroyed several silos and produced 75-meter-high flames. The fire brigade worked at the explosion site for 20 days, repeatedly extinguishing smoldering fires from the destroyed silos. However, the source of the explosion was not found. In the same year, the explosion at Ag Partners in Royal (Iowa, USA) destroyed a silo where a mixture of corn and soybean was stored along with the adjacent installations. Again, the cause of the explosion is unknown.

While the roots for these dust explosions remain unknown, we do know that the measurement of electrostatic charge that is introduced from the conveying line to the storage has limitations. Conventional Faraday pails, or cups, can be strategically placed at selected points in the pneumatic conveying system to detect the charge buildup during various conveying stages. Faraday pails measure the charge induced on their inner surface; thus, they provide the total sum of the enclosed powder's electrostatic charge. They cannot provide any other detailed quantity. In other words, the charge read by a Faraday pail is the integral of the charge in the enclosed volume, $Q(t) = \int_{\mathcal{V}} Q(\boldsymbol{x},t)$. If part of the powder carries a positive and the other part a negative charge, the Faraday pail may return a close-to-zero reading. Similarly, if the powder's charge at one duct wall is extremely high but low within the rest of the duct's area, the Faraday pail returns a mediocre overall charge.

The guidelines (TRBS 2153 (2009), IEC 60079-32-1 (2012)) recommend measuring the electric field strength above the powder heap within the silo to assess the probability of cone discharges. However, according to Glor (2013), such measurement is too sophisticated for regular industrial practice.

We found, through simulations, that pneumatic conveying leads to highly distributed charge. That means the powder can charge bipolar despite remaining overall neutral (Jantač and Grosshans, 2024). And, charge distributes in space, meaning that some flow regions become highly charged while others remain uncharged (Grosshans and Papalexandris, 2017a). Experimental studies indicated that the spatial charge profiles generated during pneumatic conveying affect downstream processes. More specifically, depending on whether the conveying line filled a silo from a central or a tangential location, the most frequently measured cone discharge nearly tripled from 50 nC to 140 nC (Glor and Schwenzfeuer, 1997). This increase might result from a differently distributed powder charge in the silo, generated during pneumatic conveying and propagated to the silo during filling.

As discussed above, today's measurement equipment cannot detect these charge distributions. Therefore, we developed a new measurement technology that can resolve so-far hidden charge peaks. This paper reports on the simulations predicting distributed flow charge and the new measurement technology that can resolve these distributions.

2 Simulations predicting bipolar and spatially distributed charge

Our simulations found powder transported by turbulent air to charge nonuniformly. The distributed charge presented in the following cannot be detected by today's measurement equipment, which provides only the integral charge. The mathematical model and numerical methods of our simulation tool pafiX (2021) are described in detail by Grosshans (2022) and are summarized in the following.

2.1 Mathematical model and numerical methods

pafiX (2021) employs a four-way coupled Eulerian-Lagrangian approach that tracks each particle individually. The particle motion is sensitive to perturbations; therefore, turbulence is modeled by DNS. Further, the interaction between charged particles and the incident electric field is captured by advanced methods as outlined below.

The Navier-Stokes equations for constant densities and diffusivities,

$$\nabla \cdot \boldsymbol{u}_\mathrm{g} \;=\; 0\,, \tag{1a}$$

$$\frac{\partial \boldsymbol{u}_\mathrm{g}}{\partial t} + (\boldsymbol{u}_\mathrm{g} \cdot \nabla)\boldsymbol{u}_\mathrm{g} \;=\; -\frac{1}{\rho}\nabla p + \nu \nabla^2 \boldsymbol{u}_\mathrm{g} + \boldsymbol{f}_\mathrm{s} + \boldsymbol{f}_\mathrm{f}\,, \tag{1b}$$

describe the carrier gas flow. Therein, $\boldsymbol{u}_\mathrm{g}$ is the fluid velocity, ρ the density, p the dynamic pressure, and ν the kinematic viscosity. Further, $\boldsymbol{f}_\mathrm{s}$ is the source term for the momentum transfer from the particles to the gas. To simulate pneumatic conveying, we model a short section of the duct, apply periodic boundary conditions in streamwise (x) direction, and drive the flow by the pressure gradient, $\boldsymbol{f}_\mathrm{f}$. In the above equations, second-order schemes approximate the spatial and temporal derivatives.

For each particle of the mass m, we solve the acceleration, $\boldsymbol{a}$, based on Newton's second law of motion in the Lagrangian framework,

$$m\boldsymbol{a} \;=\; \boldsymbol{F}_\mathrm{d} + \boldsymbol{F}_\mathrm{c} + \boldsymbol{F}_\mathrm{e} + \boldsymbol{F}_\mathrm{g}\,. \tag{2}$$

The drag force acting on the particle, $\boldsymbol{F}_\mathrm{d}$, is computed according to the empirical correlation provided by Putnam (1961). The collisional force, $\boldsymbol{F}_\mathrm{c}$, includes particle-particle and wall-particle collisions. To detect particle-particle collisions, we implemented ray casting (Roth, 1982, Schroeder, 2001), a variant of the hard-sphere approach.

A hybrid method (Grosshans and Papalexandris, 2017b) computes the electrostatic forces, $\boldsymbol{F}_\mathrm{e}$, on a particle carrying the charge Q. This method adds the the Coulomb interactions between the particle and its neighboring particles to the far-field forces calculated with Gauss law. The last term in equation (2), $\boldsymbol{F}_\mathrm{g}$, denotes the gravitational force.

2.2 Simulation results

Figure 2 shows the spatial powder charge profiles from channel flow simulations. The gas flow's frictional Reynolds number, $Re_\tau = 360$, is at the lower end but still representative of pneumatic conveying.

Figure 2a depicts the temporal charge evolution of particles of a Stokes number of 20 ($St = \tau/\tau_f^+$, where τ is the particle's reponse time and τ_f^+ the gas flow's frictional time scale). For this simulation, the condenser model (Soo, 1971, Masuda et al., 1976, John et al., 1980) predicted the charge exchange between particles and walls and other particles.

Figure 2b displays the charge profile of three different Stokes numbers, each when the powder reaches half its saturation charge. Here, a simple, generic model computes the transfer of charge from a wall to a particle, $\Delta q_{\mathrm{pw},n}$, and between particles, $\Delta q_{\mathrm{pp},n}$,

$$\Delta q_{\mathrm{pw},n} = C_1 A_{\mathrm{pw}} \left(q_{\mathrm{eq}} - q_n\right)/A_{\mathrm{p}} \quad \text{and} \quad \Delta q_{\mathrm{pp},n} = C_2 A_{\mathrm{pp}} \left(q_m - q_n\right)/A_{\mathrm{p}}\,. \tag{3}$$

In these equations, q_n and q_m denote the charge of the particles before the contact, q_{eq} their saturation charge, A_{pw} and A_{pp} the contact areas calculated by a Hertzian model, A_{p} the particle's total surface area, and C_1 and C_2 are constants.

In these simulations, no matter which charge model and Stokes number, the charge at the walls rises quickly while the charge in the bulk of the flow remains low. In other words, the charge of the flow is spatially non-uniform regardless of the particle type or precise physical and chemical charging mechanisms.

As discussed in the introduction, a Faraday pail or induction probe cannot resolve the charge in space. Thus, these charge peaks, which may be a potential ignition source, have been hidden from measurement.

Besides missing ignition sources, measuring only the integral of the charge comes with another severe disadvantage: simulations lack validation data. Simulation codes of powder charging have evolved enormously in recent years. Now, they can resolve all turbulence scales and the dynamics of each particle. Whereas experimentally derived, time-averaged, and spatially-resolved profiles of turbulence statistics and particle concentrations are standard to validate the simulations of uncharged particles, the equivalent data for powder charging is lacking. The lack of time-averaged and spatially-resolved

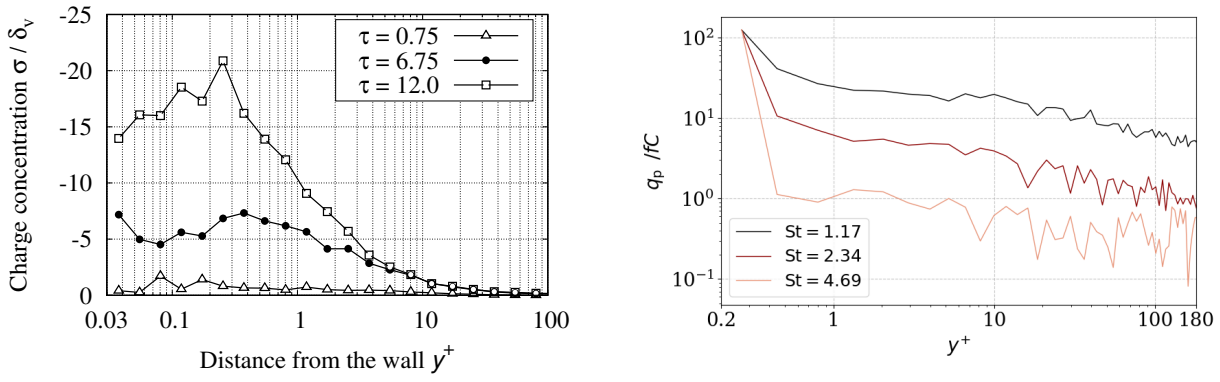

(a) St = 20 *(b) St = 1.17, 2.34, 4.69*

***Fig. 2**: Simulation of powder charge profiles during pneumatic conveying. The extremes of the profiles close to the conveying duct's walls are hidden from conventional Faraday pails that provide the integral charge ((a) reprinted with permission from Grosshans and Papalexandris, 2017a).*

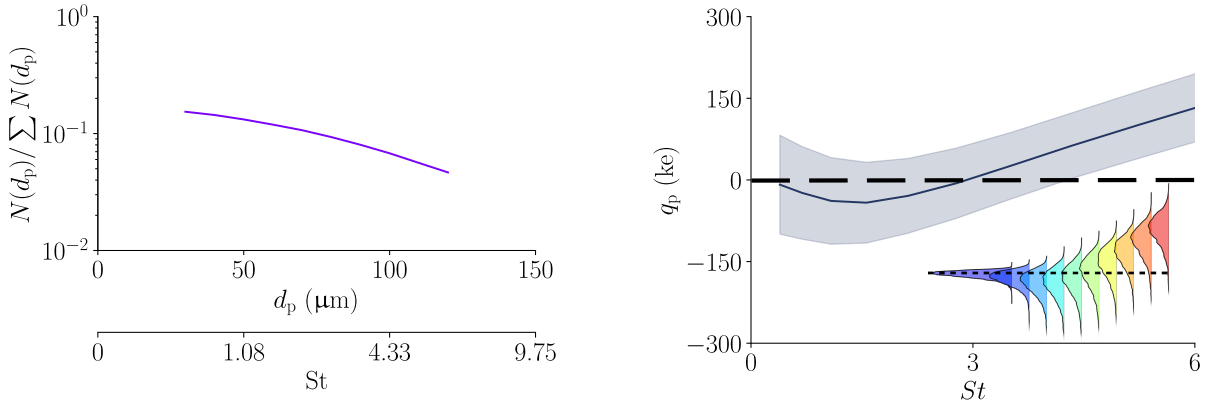

(a) *(b)*

***Fig. 3**: Simulation of bipolar powder charging during pneumatic conveying. (a) Size distribution of polydisperse powder. (b) The extremes of the particle charge distribution remain hidden from the averages provided by conventional Faraday pails (Jantač and Grosshans, 2024). The inset gives the charge distribution per particle size.*

powder charge profiles hinders the validation and further development of simulation codes for powder flow charging.

The simulation presented in figure 3 depicts bipolar powder charging. Powder charges bipolar if its size distribution is polydisperse and particles of different sizes collide (Waitukaitis et al., 2014).

We computed the collisional charge exchange by the surface-state/mosaic model in the formulation of Konopka and Kosek (2017). According to this model, the charge

$$\Delta q_{\mathrm{pp},n} = \varepsilon (c_{\mathrm{s},m} - c_{\mathrm{s},n}) A_{\mathrm{pp}} \tag{4}$$

transfers from particle m to n during collision. In the above equation, ε denotes the charge of an electron or anion with a charge number of -1, and $c_{\mathrm{s},n}$ and $c_{\mathrm{s},m}$ the density of transferrable elementary charges available on the particles' surfaces.

The simulation of the particle size distribution in figure 3a results in the charge distribution in figure 3b (Jantač and Grosshans, 2024). We found that the turbulent carrier flow has a leading influence on the shape of the resulting charge distribution. More specifically, mid-sized particles collect the most negative and large particles most positive charge.

Despite the high charge of both polarities collected by specific particle size classes, the charge of the overall powder remains neutral. That means the integral charge read by a Faraday pail would be zero. Therefore, the powder charge and the related hazard remain unnoticed.

3 Experiments resolving spatially distributed charge

3.1 Test-rig & measurement system

In response to the need for the resolved powder charge transported by a turbulent flow, we developed a new measurement technology and installed it at a laboratory-scale pneumatic conveyor (figure. 4a). The measurement system's details and accuracy are discussed by Xu et al. (2024). In the following, we describe modifications to the system and further tests.

At the top of the conveyor, the feeder supplies particles to the duct's inlet. Optionally, a narrow aluminum pipe assigns pre-charge to the particles before entering the duct. According to our previous tests, the net pre-charge is positive (Xu and Grosshans, 2023). The duct conveys the powder vertically downward, aligned with the gravitational acceleration. After the duct's outlet, a cyclone followed by a filter separates the particles from the airflow. A blower sucks the air and powder through the rig.

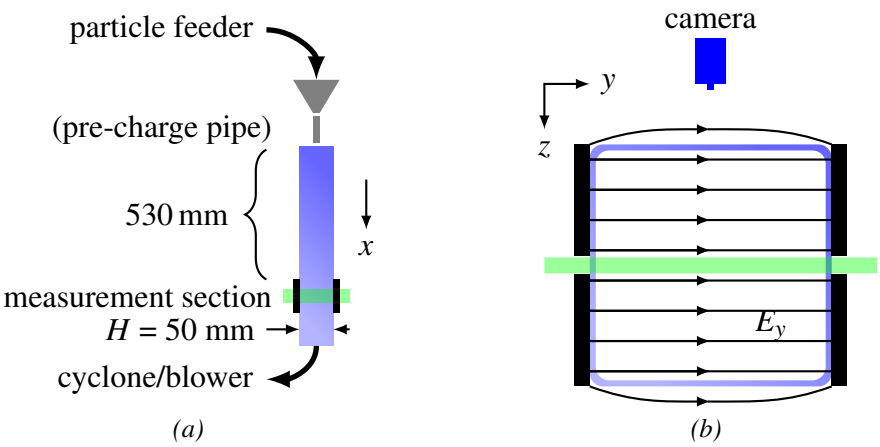

***Fig. 4**: (a) Pneumatic conveying pilot plant to test the new measurement system. (b) Components of the measurement section: electric field (E_y), laser sheet (green), and PTV camera (Xu et al., 2024).*

The duct is made of transparent PMMA, providing optical access for Particle Tracking Velocimetry (PTV) (figure 4b). The duct's length, from the inlet to the beginning of the electric field, is 530 mm. When flowing downstream, the particles reach the measurement section, where two parallel plates generate an electric field (E_y) that can be switched on or off. The plates are electrically conductive but transparent so the laser can pass through and illuminate the flow. The duct has a square cross-section. Each planar wall's inner side length is $H = 50$ mm. The laser beam points in spanwise (y) direction. In streamwise direction (x), the sheet begins 80 mm after the edge of the electric field and spans about 50 mm.

The tests were conducted at a frictional Reynolds number of 360, equal to the abovementioned simulations. The particles were monodisperse, spherical, of a size of $d = 100$ µm, and made of PMMA. Their mass flow rate was 0.2 g/s. During the tests, the relative humidity and temperature in the lab were 52.5% and 21.5 °C.

The measurement system derives the particles' charge from the force balance and their response to the electric field. In y direction, the longitudinal axis of the laser beam, the force balance of equation (2) reduces to

$$m a_y^E = F_{\mathrm{d},y} + F_{\mathrm{c},y} + F_{\mathrm{e},y}\,. \tag{5}$$

Here, the superscript E indicates the influence of the electric field. Gravitational forces vanish since the laser points horizontally.

The problem in solving equation (5) lies in the unknown terms $F_{\mathrm{c},y}$ and $F_{\mathrm{d},y}$. The collisional force is generally unknown, but it can be locally large, even in dilute flows. For particles of $St \ll \infty$, the drag force requires knowledge of the instantaneous gas velocity. However, in turbulent flows, due to the chaotic fluctuations, the instantaneous gas velocity is unknown.

We proposed a solution to this problem based on averaging,

$$\bar{Q} = \left(\bar{a}_y^E - \bar{a}_y + \frac{\bar{u}_y^E - \bar{u}_y}{\tau} \right) \frac{m}{E_y}\,. \tag{6}$$

In this equation, the collisional forces and gas velocity vanish even though being implicitly included. The operator $\bar{\phi}$ denotes the average over many particles at fixed points in space. The particle velocities and accelerations in the above equation are measured in two separate experiments; one experiment with the electric field switched off (u_y and a_y) and one experiment with the electric field switched on (u_y^E and a_y^E). For the mathematical details of deriving equation (6), we refer to the original publication (Xu et al., 2024).

3.2 *Experimental results*

Figure 5 presents the particles' measured average velocities and accelerations. Figure 6 gives the particles' derived charge, in terms of the specific charge (6a) and the electric current (6b).

All data are time-averaged and depict a slice through the duct's centreline. We succeeded resolving the flow for $7.4\,\text{mm} < y < 42.6\,\text{mm}$. Outside of this region, the particles frequently collide with the walls. Within the electric field, the wall collision frequency changes, which violates the assumptions underlying equations (6). Further, the limited camera view close to the duct's walls led to the erroneous identification of particle trajectories.

To qualitatively validate the measurement system, we conducted two experiments, one with the pre-charge pipe and one without. Without the pipe, the particles charge during feeding and flowing through the duct; they are called *flow-charged*. With the pipe, the particles receive an additional pre-charge before entering the duct; they are called *pre-charged*.

The average wall-normal velocities (figure 5a) and accelerations (figure 5b) fill the terms on the right-hand side of equation (6). Each data point averages 9000 to 80 000 measured values.

Downstream of the point-like feeding position, the particle flow widened up from the center toward the walls, as reproduced by the nearly symmetric velocity profile in figure 5a of the flow-charged particles without the electric field. The particle velocities and accelerations of the pre-charged particles responded stronger to the electric field than the flow-charged ones.

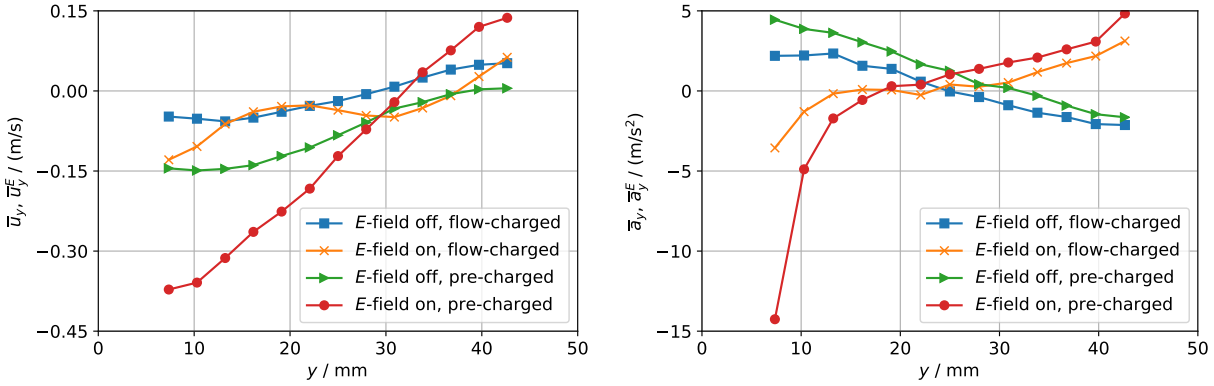

(a) *(b)*

***Fig. 5**: Measured response of the particles to the electric field; Average particle wall-normal (a) velocities and (b) accelerations.*

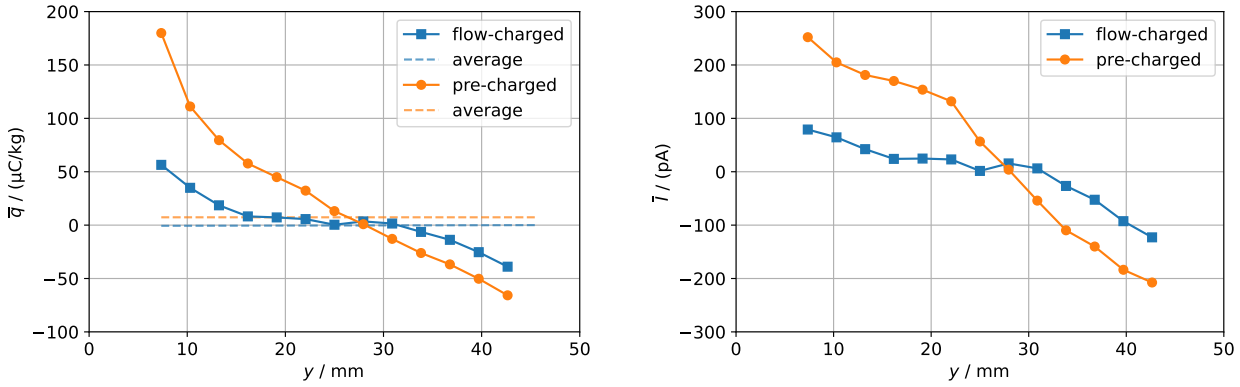

(a) *(b)*

***Fig. 6**: Bipolar powder flow resolved with the new measurement system. (a) Time-averaged specific particle charge compared to total average particle charge. (b) Time-averaged electric current.*

Based on the locally highest measured induced wall-normal acceleration, the flow-charged particles changed their location while passing the electric field in y direction on the average up to 4.9 mm and the pre-charged particles up to 5.6 mm. Thus, the measurement was invasive. Moreover, this location change propagates to an uncertainty of the charge profiles' spatial coordinate in figure 6. Reducing the downstream distance between the beginning of the electric field and the laser sheet would reduce spatial uncertainty. However, the chosen distance ensures a low signal-to-noise ratio of the measured velocity and acceleration responses and the minuscule uncertainty of the derived charge, which we prioritized over spatial accuracy.

The profiles in figure 6 of both experiments reveal a bipolar charged particle flow. For the flow-charged particles, the profile is nearly symmetric to the duct's centreline. Close to the left wall, the particles carry a positive charge, and close to the right wall, they carry a negative charge.

The measured bipolar charge emanated from same-material contacts with the feeder and the duct's walls. During feeding, the particles contacted the feeder's screw, which was already covered with other adhering particles. Since also the duct is made of PMMA, the flow-charged particles underwent only same-material contacts. Same-material contacts, lacking a net direction of charge transfer, resulted in the observed bipolar charging.

When passing the pre-charge pipe, the particles received, on average, a positive charge before entering the PMMA duct. In the duct's left half, the pre-charged profile in figure 6 qualitatively reflects the charge increase.

On the other hand, in the duct's right half, the pre-charged particles carried less average charge than the flow-charged particles. Pre-charging did not simply offset the charge profile; instead, being refined by the pipe and the assigned charge, changed the flow pattern. An electric field affects the particles, even without the external field, for example, due to charge spots on the duct. The positively charged particles moved toward the duct's left, resulting in the negative offset of the pre-charged particles' velocity profiles in figure 5a. When the positively charged particles moved to the left, but the negative ones remained, the local ($y > 30$ mm) average negative charge increased. Thus, the pre-charged profile shows the charge increase and its influence on the particle concentration and the local charge distribution.

Additionally, figure 6 displays the total average charge as a Faraday pail would detect it. That means the average of the charge profiles weighted by the local particle concentration. Pre-charging increased the average charge from -0.4 fC to 4.4 fC. However, the resolved peak of the flow-charged particles is 85 times higher than the average, and the peak of the pre-charged particles is 25 times higher than the average. Thus, a Faraday pail would dramatically underestimate the flow's charge.

4 Conclusions

Our simulations demonstrate that whichever powder type or charging mechanism, powder flows charge non-uniformly. Non-uniform charge means some flow regions or particle size classes charge stronger or with a different polarity than others. Conventional measurement equipment, such as Faraday pails and induction probes, give only the integral flow charge but fail to detect local charge peaks of both polarities. Our newly developed measurement system can resolve the powder charge in space. Thus, the new measurement system can detect local extreme charge peaks that were thus far hidden from measurements. Even though these charge peaks arise during pneumatic conveying, they might propagate to downstream processes, storages, and silos and ignite the dust. These hidden charge peaks might enlighten some of the large number of unexplained industrial dust explosions. In any case, finding these peaks demonstrates that future research in explosion protection should not only focus on mitigating known hazards but, also, on revealing the hidden ones.

Acknowledgements

This project received funding from the European Research Council (ERC) under the European Union's Horizon 2020 research and innovation programme (grant agreement No. 947606 PowFEct).

References

Choi, K. S., Endo, Y., Suzuki, T. (2018). *Experimental study on electrostatic charges and discharges inside storage silo during loading of polypropylene powders*. Powder Technol., 331:68–73.

Cloney, C. (2023). *2022 Combustible Dust Incident Report - Version #1*. Report, DustEx Research Ltd. Retrieved from http://dustsafetyscience.com/2022-Report.

Glor, M. (1984). *Conditions for the appearance of discharges during the gravitational compaction of powders*. J. Electrostat., 15:223–235.

Glor, M. (2001). *Overview of the occurrence and incendivity of cone discharges with case studies from industrial practice*. J. Loss Prev. Process Ind., 14:123–128.

Glor, M. (2013). *Modelling of electrostatic ignition hazards in industry: too complicated, not meaningful or only of academic interest?* Chem. Eng. Trans., 31:583–588.

Glor, M., Schwenzfeuer, K. (1997). *Occurrence of cone discharges in production silos*. J. Electrostat., 40&41:511–516.

Grosshans, H. (2022). *Influence of weak electrostatic charges and secondary flows on pneumatic powder transport*. Can. J. Chem. Eng., 101:2347–2360.

Grosshans, H., Papalexandris, M. V. (2017a). *Direct numerical simulation of triboelectric charging in a particle-laden turbulent channel flow*. J. Fluid Mech., 818:465–491.

Grosshans, H., Papalexandris, M. V. (2017b). *On the accuracy of the numerical computation of the electrostatic forces between charged particles*. Powder Technol., 322:185–194.

IEC 60079-32-1 (2012). *Explosive atmospheres – Part 32-1: Electrostatic hazards*. Technical specification.

Jantač, S., Grosshans, H. (2024). *Suppression and control of bipolar powder charging by turbulence*. Phys. Rev. Lett., 132:054004.

John, W., Reischl, G., Devor, W. (1980). *Charge transfer to metal surfaces from bouncing aerosol particles*. J. Aerosol Sci., 11(2):115–138.

Konopka, L., Kosek, J. (2017). *Discrete element modeling of electrostatic charging of polyethylene powder particles*. J. Electrostat., 87:150–157.

Masuda, H., Komatsu, T., Iinoya, K. (1976). *The static electrification of particles in gas-solids pipe flow*. AIChE J., 22:558–564.

Matsuyama, T., Yamamoto, H. (1995). *Charge relaxation process dominates contact charging of a particle in atmospheric conditions*. J. Phys. D: Appl. Phys., 28:2418–2423.

Newson Gale (2013). *Controlling dust explosions caused by a static ignition*. Report NG US AS05 MPII 170823 R4.

pafiX (2021). `https://gitlab1.ptb.de/asep/pafix`.

Putnam, A. (1961). *Integratable form of droplet drag coefficient*. ARS J., 31:1467–68.

Roth, S. D. (1982). *Ray casting for modeling solids*. Comput. Graphics Image Process., 18:109–144.

Schroeder, T. (2001). *Collision detection using ray casting*. Game Dev., 8:50–56.

Soo, S. L. (1971). *Dynamics of charged suspensions*. In *Topics in Current Aerosol Research*, pages 71–73. Pergamon Press.

TRBS 2153 (2009). *Avoidance of ignition sources due to static electricity*. Technical rules plant safety.

Waitukaitis, S. R., Lee, V., Pierson, J. M., Forman, S. L., Jaeger, H. M. (2014). *Size-dependent same-material tribocharging in insulating grains*. Phys. Rev. Lett., 112:218001.

Xu, W., Grosshans, H. (2023). *Experimental study of humidity influence on triboelectric charging of particle-laden duct flows*. J. Loss Prev. Process Ind., 81:104970.

Xu, W., Jantač, S., Matsuyama, T., Grosshans, H. (2024). *Spatially resolved measurement of the electrostatic charge of turbulent powder flows*. Exp. Fluids, 65:1–10.

Zhi, Y. (2015). *Dynamic Risk Analysis of Dust Explosions*. Ph.D. thesis, Memorial University of Newfoundland.

Near-field Aerial Overpressure and Impulse from Small-scale BLEVE

E.M. Laamarti [a,b], A.M.Birk [a] & F.Heymes[b]

[a] Queen's University Department of Mechanical and Materials Engineering, Kingston ON Canada K7L 3N6

[b] Laboratoire des Sciences des Risques, IMT Mines Ales, Ales, France

E-mail: frederic.heymes@mines-ales.fr

Abstract

This paper presents an investigation into one of the most damaging hazards associated with Boiling Liquid Expanding Vapor Explosion (BLEVE), specifically focusing on the near-field overpressure and impulse effects. Experiments were conducted at a small-scale to study the overpressure and impulse using aluminum tubes with a diameter of 50 mm and a length of 300 mm. The tubes were filled with pure propane liquid and vapor. The controlled variables, on this work included the failure pressure, the liquid fill level, and the weakened length along the tube top. These variables control the strength of the overpressure that is characterized by the peak overpressure amplitude, duration of this overpressure event and the resultant impulse. Notably, these experiments at a small scale included experiments with 100 % liquid fill level. This provided further confirmation that the vapor space is the main driver of the lead overpressure hazard. High speed cameras and blast gauges effectively illustrated the progressive formation of the shock wave in both temporal and spatial dimensions. Furthermore, various predictive models available in the literature are discussed in this paper and new correlations were developed to quantify the overpressure duration and impulse. The current analysis aims to predict the potential consequence of overpressure events during a BLEVE.

Keywords: *Overpressure, Shock wave, Impulse, Propane, Boiling liquid expanding vapor explosion, BLEVE , Vessel failure, Liquid full.*

Introduction

The boiling liquid expanding vapor explosion (BLEVE) constitutes a distinctive form of physical explosion involving a pressure liquefied gas (PLG). It can happen when the pressure vessel containing the PLG is severely weakened by some process such as fire heating. Not all explosions observed fall under the BLEVE classification as it requires rapid total loss of containment (i.e., full opening of the vessel) as proposed by Birk et al. (2007). The BLEVE happens during the sudden explosive release of the vapor and liquid energy upon rapid opening of the vessel. The BLEVE results in rapidly expanding vapor and flashing liquid that will generate hazards including projectiles, fireballs if the commodity is flammable, toxic, or flammable vapor clouds, ground loading, and blast overpressures. These hazards close to urban areas, can cause significant consequences in terms of material losses and human casualties.

Numerous researchers have devised models aimed at facilitating hazard mitigation and prediction. Casal and Salla, (2006); Planas-Cuchi et al. (2004) developed models based on expansion energy using flash fraction of the liquid to quantify the lead shock overpressure. Birk et al. (1996) in response to risk and prevention, developed a model to predict the fireball diameter and duration. Moreover, Baum et al. (2005) established correlations to predict the projectiles velocity and radius of action based on the isentropic expansion energy. As for the ground load, Laamarti E.M. et al. (2024) formulated correlations for estimating peak ground load variables associated with small-scale BLEVE events. The present study focuses on the near-field overpressure and impulse.

Overpressures are produced by the expanding vapor and the flashing liquid. They manifest as waves that propagate over finite distances, yet they possess sufficient strength to induce structural damage to buildings, fracture surrounding glass, and even initiate a cascading chain reaction. Birk et al. (2007) identified three overpressures from a BLEVE. The first two are produced primarily by the vapor space

release and the third by both vapor phase and flashing liquid. The first overpressure is a steep shockwave, followed by a negative phase rarefaction wave caused by the overexpansion of the vapor space. The overexpansion leads to a second weaker shock wave. The third wave is produced by the flashing liquid and is not a shock wave. The prediction of this specific hazard has been extensively explored experimentally and numerically by several authors.

The exact nature of whether the shock wave overpressure results exclusively from vapor and liquid remains a subject to controversy. Giesbrecht et al. (1981) conducted experiments involving rapid catastrophic failure of fully propylene filled glass spheres, showing the generation of an overpressure wave. However, it is not clear if this overpressure was a shock wave (supersonic). Consequently, definitive conclusions regarding the role of liquid phase in shockwave formation remain elusive.

Van der Berg et al. (2004-2005) formulated a one-dimensional expansion-controlled model assuming that flash fraction of the liquid contributes to shock formation. While this assumption leans towards a conservative approach, its accuracy remains uncertain. This perspective contrasted with Baker et al. (1983) that suggested that BLEVE shock formation is only a result of vapor expansion as the liquid flashing is too slow to produce a shock wave. Presently, advancements in data acquisition technologies are leaning toward the understanding that the primary shockwave from BLEVE, is an outcome of the vapor expansion alone, with no significant contribution from liquid phase. The liquid produces a slower and powerful contribution in the form of ground loading, projectiles, and dynamic pressure (drag) effects. Across different scales, Birk et al. (2007), Eyssette (2018) and current experiments provided experimental evidence on contributions of vapor and liquid to BLEVE hazards.

Currently, to estimate the overpressure theoretically, a predominant approach has been based on isentropic expansion energy derived from thermodynamic first principles. Researchers like Brode et al. (1959), and Prugh et al (1991) adopted this method. In contrast, some other models integrated irreversibly to account for heat losses as the one developed by Planas-Cuchi et al. (2004) and Casal et al. (2006). While both approaches yielded conclusive results when compared to experiments, these models, while informative, fail to account for the complexity of opening dynamics in real-world scenarios and do consider flash fraction of the liquid in shock formation. Nevertheless, a new approach, far from energy models, was introduced by Birk et al. (2018) with the shock start model using the 1D shock tube equation and spherical shock wave theory.

This paper presents a set of new overpressure data from 2022 experimental campaign done by Laamarti E.M. et al. (2024) complemented by data from Eyssette (2018). The collected data include a broader range of controlled variables, including failure pressure, liquid fill level and weakened length, thereby extending the scope of the existing data. Notably, analysis on unaddressed aspects of overpressure was carried out using all the experimental results from a small-scale apparatus. This study further investigates the use of Friedman-Whitham approach for spherical shock waves combined with the shock tube model. Correlations are introduced to address the interplay of dependent overpressure variables, specifically the lead overpressure peak and duration, and the resulting impulse.

1. Small scale propane BLEVE experiments

1.1. Experimental apparatus

The experiments were conducted with small-scale tubes of 300 mm length and 50 mm diameter. A total of 36 experiments were conducted in 2022. The tubes were made from aluminum type 6061 T6 annealed to T0 temper to reduce the material's yield and ultimate strength. The tubes were machined along the top to reduce the wall thickness along a defined weakened length. To reduce the effects of age hardening, the tubes were stored in a freezer at -40ºC before the testing. The tube preparation facilitated tube rupture at desired failure pressures, thereby delineating both the location and size of the burst opening. To initiate the BLEVE, the tubes were filled with propane and subjected to an external heater, along the tube bottom (Fig.1.[Left]). The heater primarily heated the liquid to produce saturated mixture of liquid and vapor. The heating caused the pressure to rise in the vessel until it

failed. Failure occurred in the weakened length when the von Mises stress reached the yield strength of the annealed aluminum. High and low speed instruments were used to capture the hazards produced by the small-scale BLEVE. This included thirteen pencil blast gages positioned at varied locations, diverse angles, and elevations [vertical, horizontal, 45º angle] around the subjected tubes. The vertical gages PCB 137B28 labelled TOP 1,2,3 and 4, are positioned respectively at 15,20,30 and 40 cm above the tube. These gages boast a range of 3.45 bar, a response time of 1 µs, a sensitivity of 14.5mV/kPa and an uncertainty of under 2%. The remaining gages, PCB 137A23, are placed at different angles and sampled at 200 kHz. They also have a range of 3.45 bar, a response time of 4 µs, a sensitivity of 14.5 mV/kPa and an uncertainty of 0.2 %.

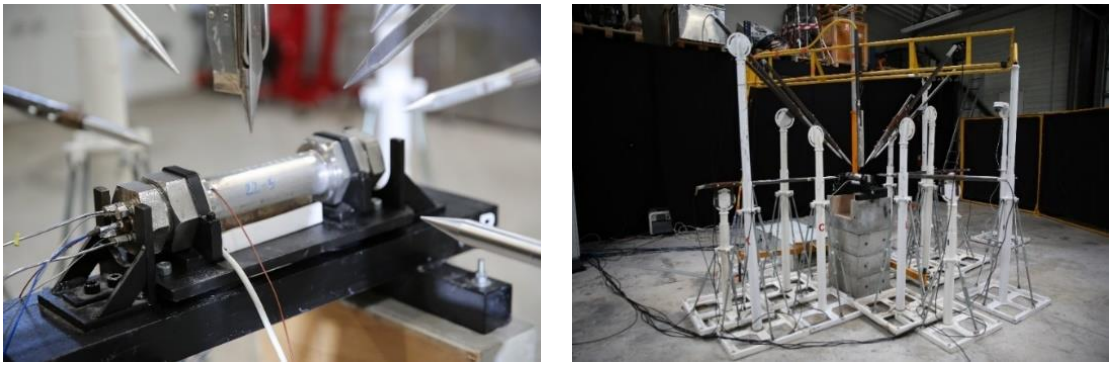

Fig. 1. *BLEVE 2022 Experimental apparatus*

Three high speed cameras were strategically positioned at the front, side, and window views to capture the details of the explosion and observe the overpressure details. Operating at a rate of approximately 24,000 fps, these cameras featured an exposure duration of 40 µs. A detailed description of the apparatus is presented in Laamarti.E.M et al. (2024).

1.2. Experimental apparatus

The small-scale BLEVE experiments carried out in 2022 [Fig.2] by Laamarti.E.M et al. (2024) for various operating conditions has been complemented by data from Eyssette (2018) [Fig.3]. The controlled variables that were selected to attain the desired burst conditions included:

- Failure pressure P_f [Barg or Bara] : g and a stand for gage and absolute pressure
- Liquid fill (volume fraction) φ [%]
- Weakened length L_c [m]

These variations in operating conditions help understand the impact of controlled variables and whether similar conditions can yield to same outcomes.

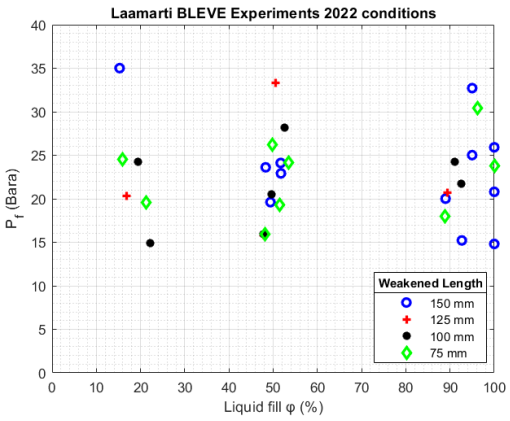

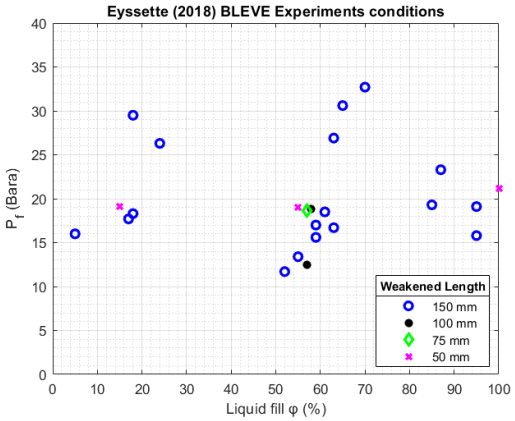

Fig. 2. *Summary Laamarti BLEVE Experiments 2022* ***Fig. 3.*** *Summary Eyssette (2018) BLEVE Experiments*

New data for 100 % liquid fill level was achieved to discern the specific contribution of liquid phase in the formation of shockwaves. The experimental variables were systematically modified in a progressive manner, thereby facilitating an investigation into the individual influence exerted by each

variable on the resultant blast wave. Among the experiments, a total of nine experiments resulted in partial opening of the vessel, thus showing the effect of opening size on the strength of the hazards produced by the BLEVE.

1.3. BLEVE Overpressures

Variations in the operating conditions generate various data on the dependant near-field overpressure variables. Conventionally, a BLEVE produces a sequence of overpressure events, consisting of an initial first lead shock overpressure from vapor phase followed by an under-pressure wave, a second wave from vapor phase and a third wave overpressure from both vapor phase and liquid flashing. Fig.4 shows a typical blast data measured at 20 m from a 2000 L propane tank. Three successive wave overpressures generated during a BLEVE are visible on the graph. The magnitude, the duration and the impulse of the lead shock overpressure will be explored in this study.

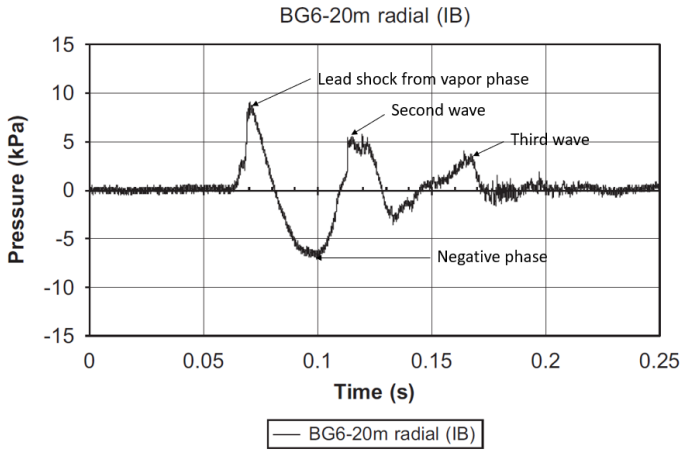

Fig. 4. *Overpressure measured at 20 m from the side of a 2000 L propane tank, Birk et al. (2007)*

The objective is to formulate a physics-based analysis of the dependant variables, specifically extracted from vertical blast gages, because they measured the strongest overpressure for the top opening failure. The variables were:

- Peak overpressure of the first wave [Bar]
- Duration of the first wave overpressure [s]
- Impulse per unit area of the first wave overpressure [Bar.s]

The lead shock decays with distance and is assumed to follow spherical shock theory. The data suggests that vessel filled to 100 % capacity with liquid generate solely an overpressure with no shockwaves. Thus, the shock tube equations and the Friedman-Whitham spherical shock theory cannot be applied.

2. Numerical Methods

2.1. Shock tube theory

During a BLEVE, the pressure vessel fails, and the vapor leaves the vessel, creating pressure on the surrounding air. This rapid pushing on the atmosphere results in a series of compression waves that pile up and forms a supersonic shock wave to meet the flow constraints (Fig.5).
Commonly referred to as a “surface of discontinuity”, the shock wave refers to a sharp pressure rise that then tails off with distance. The shock strength and shape depend on many factors, such as:

- The operating conditions: Failure pressure, weakened length, liquid fill.
- The type of opening: whether partial or full opening of the pressure vessel.
- The rate of opening due to the uneven thickness of the weakened length

The BLEVE resulting from a cylindrical vessel will generate a cylindrical shock that will transition to a spherical shock as it propagates through an unconfined environment at a transient state. The

initial overpressure can be calculated using the shock tube equation, especially if the opening of the vessel is extremely rapid. To use the normal shock tube equations and accurately determine the stagnation properties, it is essential to transition from the unsteady moving normal shock resulting from the explosion to a steady state by moving with the shock [Fig.5].

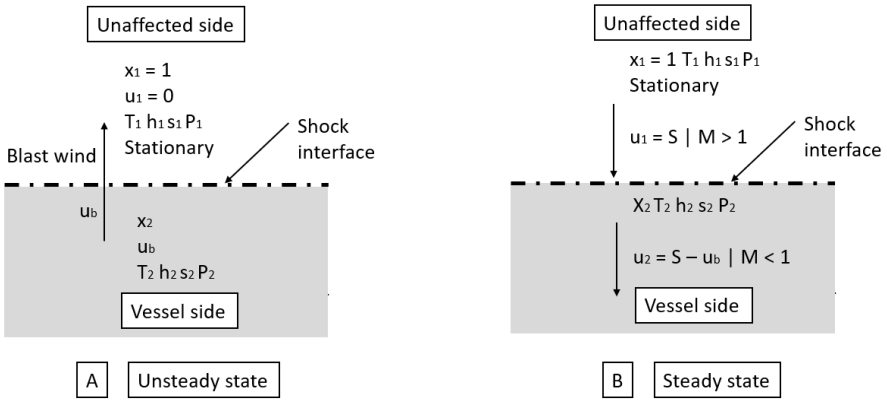

Fig. 5. *Shock wave for [A] unsteady and [B] steady cases*

The 1D normal shock tube equations developed by Rankine-Hugoniot (1870) can then be applied to address the stationary problem. These equations satisfy the continuity, momentum and energy equations which result in:

$$\frac{P_4}{P_1} = \frac{P_2}{P_1}\left[1 - \frac{(\gamma_4 - 1)\frac{a_1}{a_4}(\frac{P_2}{P_1} - 1)}{\sqrt{2\gamma_1(2\gamma_1 + (\gamma_1 + 1)(\frac{P_2}{P_1} - 1)}}\right]^{\frac{-2\gamma_4}{\gamma_4 - 1}} \quad (1)$$

The static pressures obtained by transitioning to steady state are: (White,1986):

$$\frac{P_2}{P_1} = \frac{2\gamma_1 M^2}{(\gamma_1 + 1)} - \frac{(\gamma_1 - 1)}{(\gamma_1 + 1)} \quad (2)$$

$$\Delta p_{st} = (P_2 - P_1) => overpressure \quad (3)$$

- *State 2:* Explosion side (before shock = downstream part)
- *State 1:* Unaffected side (after shock = upstream part) at ambient conditions

h_1 and h_2: Enthalpy at state 1 and 2
T_1 and T_2: Static temperature at state 1 and 2
P_1 and P_2: Static pressure at state 1 and 2
S_1 and S_2: Entropy at state 1 and 2
γ_4: Propane specific heat ratio (1.3)
u_b: Blast wind speed (speed of air behind the shock)
S: Supersonic shock speed
P_4: Static failure pressure
γ_1: Air specific heat ratio (1.4)
a_4: Speed of sound in propane
M: Mach number
a_1: Speed of sound in air

All terms are expressed in SI units : meters (m), seconds (s), pascals (Pa), Joule (J), Kelvin (K).

2.2. Friedman Whitham approach

Under the assumption of spherical expansion, the variation of shock strength with distance can be predicted using the Friedman Whitham relation (Friedman,1960) as follows:

$$\left[\frac{R}{R_0}\right]^2 = e^{(2\gamma_1 - 2)^{-\frac{1}{2}}} \sin^{-1}\left[\frac{2Y^2 - (\gamma_1 - 1)Z^2}{(\gamma_1 + 1)^2 M^2}\right] \quad (4)$$

Where

$$Y = (2\gamma_1 M^2 - \gamma_1 + 1)^{\frac{1}{2}} \quad (5)$$

$$Z = ((\gamma_1 - 1)M^2 + 2)^{\frac{1}{2}} \quad (6)$$

$$W = \frac{(Y-Z)^2}{M}\left[Y(\gamma_1-1)^{\frac{1}{2}} + Z(2\gamma_1)^{\frac{1}{2}}\right]^{\left(\frac{2\gamma_1}{\gamma_1-1}\right)^{\frac{1}{2}}} Y^{\frac{2}{\gamma_1}} \quad (7)$$

R: Radius of the hemispherical shock

R_0: Radius of the hemispherical sphere surface of the vapour phase where the shock started

$$R_0 = \left[\frac{3(1-\varphi)}{4\pi}\frac{V_{tube}}{2}\right]^{\frac{1}{3}} \quad (8)$$

V_{tube}: Volume of the tube

$$\left[\frac{\Delta p_{exp}}{\Delta p_{st}}\right] = \left[\frac{R}{R_0}\right]^n \simeq \left[\frac{\Delta p_{Fw}}{\Delta p_{st}}\right] = \left[\frac{R}{R_0}\right]^n \quad (9)$$

Δp_{Fw} : Overpressure from Friedman Whitham

Δp_{exp}: Experimental overpressure

Δp_{st} : Overpressure from shock tube equations

n: Index

2.3. Duration of lead overpressure

The duration of the lead overpressure is an important dependant variable that helps evaluate the strength of the shock. The longer the duration of lead overpressure prolongs the exposure of structures to the intense force exerted by the blast wave potentially leading to great damage. Moreover, prolonged overpressure can result in secondary effects such as structural fatigue and domino effects. The experimental value is found from the base of the triangular shaped peak overpressure. The duration of lead overpressure, being solely an outcome of the vapor phase, can be rendered non-dimensional by dividing it by the duration of vapor release.

$$t^*_{ov} = \frac{t_{ov}}{t_{vap}} \quad with \;\; t_{vap} = \frac{D}{a} \quad (10)$$

t_{ov} : Experimental duration of overpressure [s]

D : Tube diameter [m]

t^*_{ov}: Dimensionless duration of overpressure

t_{vap}: Duration of the vapor phase [s]

a : Speed of sound in vapor propane [m/s].

2.4. Impulse per unit Area

The impulse per unit area is determined by integrating the first peak overpressure over its duration. The wave form is nearly an isosceles triangle, and the integral is approximately equal to :

$$I_{ov} = \frac{\Delta p_{exp}\, t_{ov}}{2} \quad (11)$$

I_{ov} : Experimental Impulse per unit area [bar. s]

The formula corresponds to the impulse per unit area experienced by an object exposed to a blast. The condition is that the object is small enough for the impulse per unit area to remain constant across its surface.

2.5. Correlation equation

The duration and the impulse from the first overpressure have been correlated to the independent variables to formulate a predictive equation equal to:

$$t^*_{ov} = \frac{t_{ov}}{t_{vap}} \qquad \frac{t_{ov\_cor}}{t_{vap}} = \; t^*_{ov\_cor} = K_1\left(\frac{P_f}{P_{atm}}\right)^a (\varphi)^b \left(\frac{L_c}{L_v}\right)^c$$

$$t_{ov} \simeq t_{ov\_cor} = K_1\left(\frac{P_f}{P_{atm}}\right)^a (\varphi)^b \left(\frac{L_c}{L_v}\right)^c t_{vap} \quad (12)$$

t_{ov_cor}: Correlated duration of lead overpressure [s]

a, b. c, K_1, are constants

For the impulse per unit area, and the corresponding equation is :

$$I_{ov\_cor} = \frac{\Delta p_{Fw}\, t_{ov\_cor}}{2} \tag{13}$$

3. Results and discussion

3.1. Opening dynamics

The opening dynamics of the vessel are believed to strongly influence the resultant overpressure. Experiment 30 from Laamarti BLEVE experiments 2022 can be compared with Experiment 26 by Eyssette (2018) under similar initial conditions of failure pressure, liquid fill and weakened length. Fig.6 [Left] shows the lead overpressures and Fig.6 [Right] shows the tube opening. As it can be seen, the overpressure vs time is quite similar except the Eyssette (2018) data shows a rising pressure after the initial overpressure. This could be attributed to the larger size of the laboratory used in the Eyssette (2018) experimental campaign and the difference of 5-10 % liquid fill, which couldn't be precisely controlled due to leaking issues.

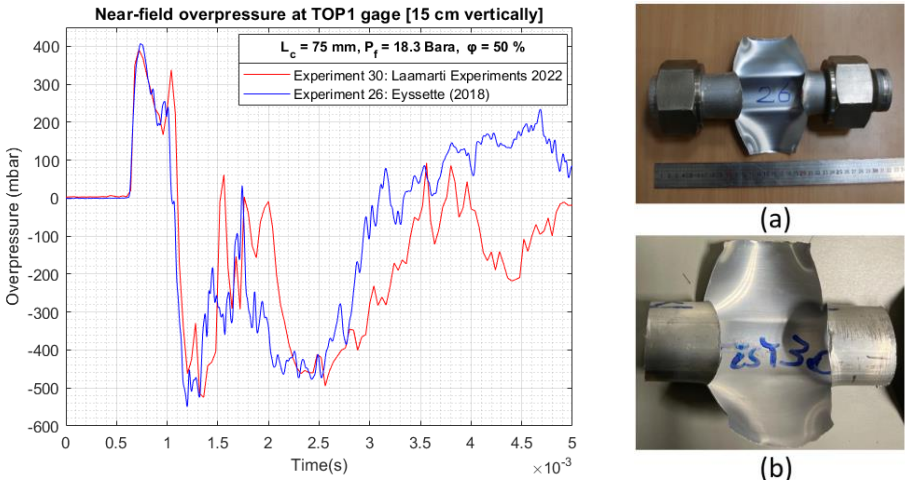

Fig. 6. *Lead overpressure TOP 1 vertical gage (15cm) [a] Eyssette (2018) [b] Laamarti Experiments 2022*

3.2. Influence of failure conditions on top vertical blast overpressure

The controlled failure conditions influence the lead overpressure strength and impulse. While prior studies on near field overpressure predominantly focused on the blast wave's peak overpressure, this investigation extends its scope to include the study of the impulse. To discern the impact of the controlled variables, experiments were selected with similar conditions and with only one parameter changing at a time (Fig.7).

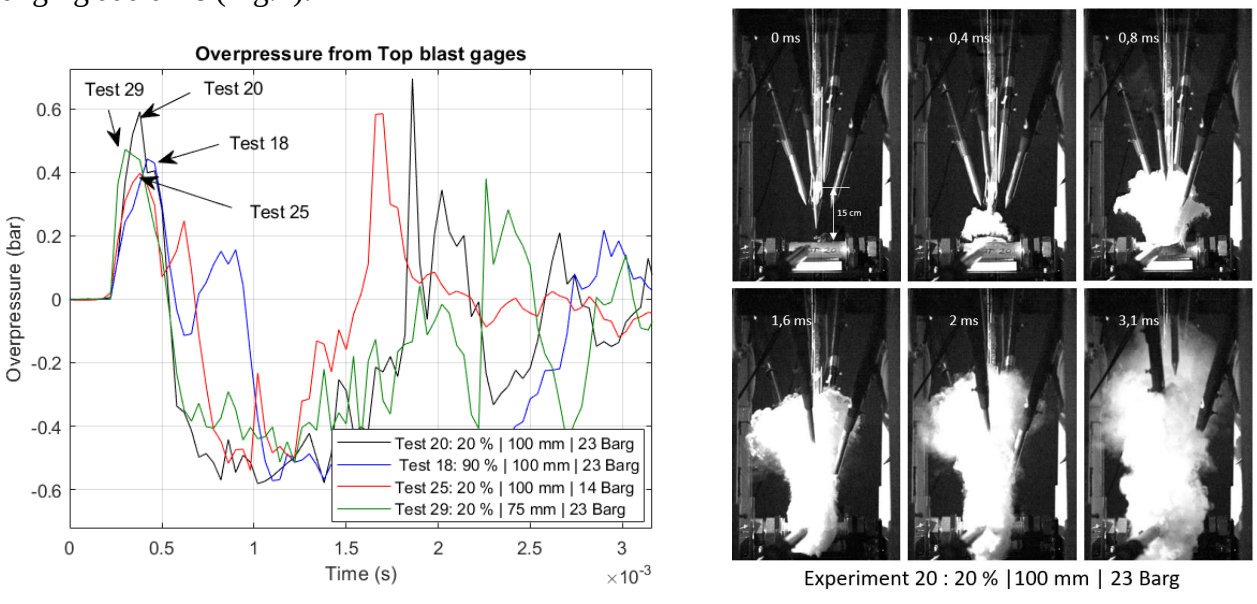

Fig. 7. *[Left]Comparative study of the first lead peak overpressure from TOP 1 blast gage [Right]High-speed camera Experiment 20; Frame 1 (time =0 ms): no failure, Frame 2 (time = 0.4 ms): Lead shock reached TOP 1 (15 cm), small white cloud (vapour) starting. Frame 3 (time = 0.8-1.2 ms): Flashing process. Horned beast expansion of contents. Frame 4-5 (time = 1.6-2 ms): Internal vessel pressure drops progressively to atmospheric pressure and the second wave reaches TOP 1 gage. Frame 6 (time = 3.1=5.2 ms): Cloud dispersion*

The sequence of events remains consistent across the experiments; however, the duration of these events varies depending on the operating conditions and the opening dynamics involved.
Using experiment 20 as a reference point, experiments 18, 25 and 29 respectively represent an increase of liquid fill, a decrease of failure pressure and a decrease of weakened length. Fig.7a shows the overpressures measured by the blast sensor TOP 1 positioned 15 cm above the top of the tube. Below are summaries of the experiments.

Experiment 20 \Experiment 18: Increase of the liquid fill level from 20 % to 90 %

- reduced maximum peak overpressure.
- increased duration of the peak wave.
- reduced impulse.
- formed two clear pressure peaks.
- negative phase amplitude is similar for both experiments.

In fact, high liquid fill level does imply lower amount of vapor phase energy and thus a more rapid decay of overpressure with distance.

Experiment 20 \ Experiment 25: Decrease of the failure pressure from 23 to 14 Barg.

- reduced maximum peak overpressure.
- increased duration of the peak wave
- reduced impulse.
- reduced the negative phase amplitude.
- ratio of failure pressures is equal to the ratio of peak overpressures (0.67)

The failure pressure describes the pressure difference between the atmospheric pressure and the tube pressure. As expected, lower failure pressure produces a weaker pressure wave.

Experiment 20 \ Experiment 29: Decrease of the weakened length from 100 to 75 mm.

- smaller opening
- reduced maximum peak overpressure.
- no change on duration of peak wave
- slightly reduced the negative phase amplitude.

The contents exiting the pressure vessel through a smaller opening area had an impact on the maximum peak overpressure, as the reduced opening of the vessel walls interfered with the formation of the shock.
Overall, it was observed that all controlled operating conditions resulted in changes to the overpressure characteristics measured at 15 cm above the tube. An important dependence was noted for failure pressure and liquid fill level, while a partial dependency was identified for weakened length. This underscores the necessity to develop correlations that link lead overpressure characteristics to the controlled variables. While the crack velocity, which describes the way the pressure vessel opens, is believed to exert a certain impact, control over this parameter has not been achieved to date.

3.3. Estimation of the lead peak overpressure

The lead peak overpressure from the vertical blast gage at 15 cm above the tube is presented in Fig. 8 and 9 for both Laamarti BLEVE 2022 campaign and Eyssette (2018) as a function of the failure pressure, liquid fill, and weakened length. The graphical representations reveal a discernible pattern: the magnitude of the experimental overpressure consistently increases with an increase in failure pressure and weakened length, while it decreases with a rise in liquid fill. This phenomenon can be attributed to the vapor phase; a larger volume of vapor phase correlates to a slower pressure decay over distance, resulting in a higher magnitude of overpressure at a specified distance. Moreover, the graph shows that at a similar failure pressure, the 100 % liquid fill cases failed partially and gave the lowest peak overpressure.

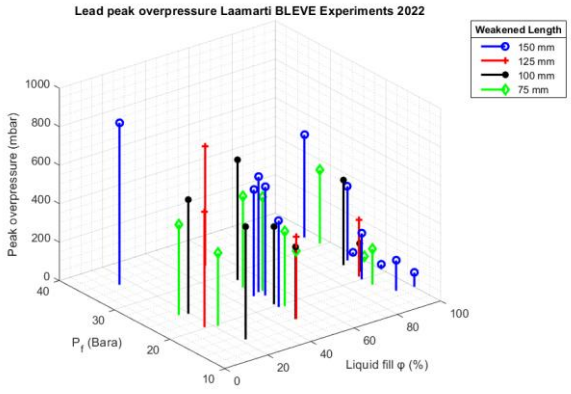

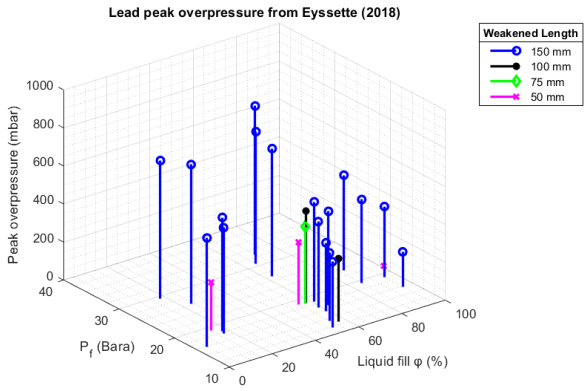

Fig. 8. *Lead peak overpressure Laamarti Experiments 2022* ***Fig. 9.*** *Lead peak overpressure Eyssette (2018)*

The experimental peak overpressures were normalized by the calculated peak overpressures from the shock tube equation under identical operating conditions. These normalized values are represented in Fig.10 with respect to dimensionless distance.

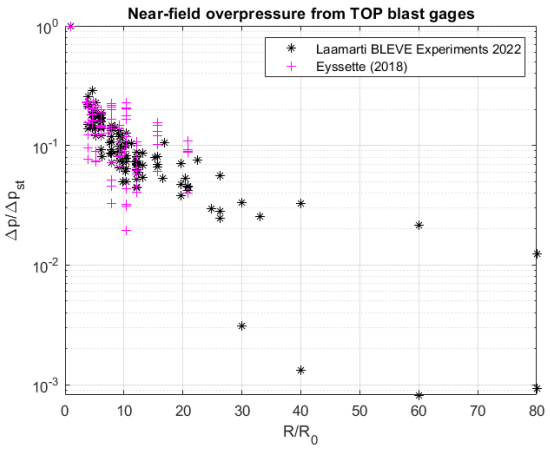

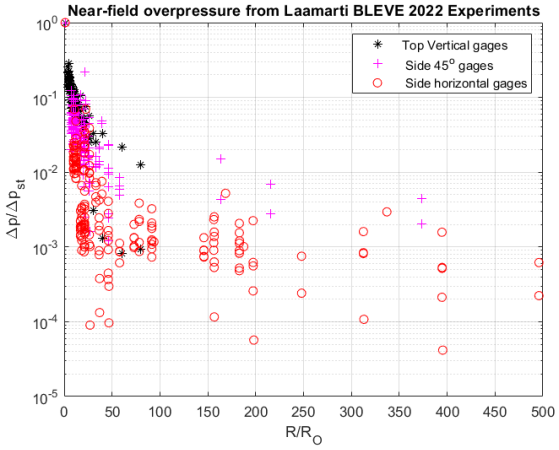

Fig. 10. *Lead peak overpressure from TOP blast gages* ***Fig. 11.*** *Lead peak overpressure from all gages*

Results from both campaign exhibit similarities, overlaying each other and revealing the general behaviour of the shock wave. As distance increases, the overpressure shows a 1/R rate of decay, indicative of the weakening shock because of energy dissipation in the surrounding atmosphere and an expanding shock surface area. Experimental findings demonstrate that the vertical overpressures are more powerful compared to those measured by the 45º angle gages and the horizontal gages, as depicted in Fig.11. This can be primarily attributed to the dynamics of opening, particularly the energy required to flatten the vessel walls.

The experimental findings presented above can then be contrasted with the prediction from the Friedman-Whitham theory for each experiment, for instance experiment 2 and 6 are illustrated in Fig. 12. The overpressures were normalized by the overpressure from the shock tube equations.

The comparison between experiments and the Friedman Whitham approach for experiment 2 indicates a good approximation of the solution with a minor discrepancy observed in the exponent value. This deviation in results can be attributed to small differences in the opening of the vessel. For lower liquid fill levels, the overpressures are faster and stronger and the Friedman-Whitham model tends to overpredict the actual experimental data. Furthermore, the shock fully forms within the 3-4 times the tube diameter range, thus it may fully form at TOP 2, 20 cm above the tube, rather than TOP 1 (15 cm). This is visible for experiment 6 where the second experimental overpressure data point at 20 cm surpasses the first one at 15 cm.

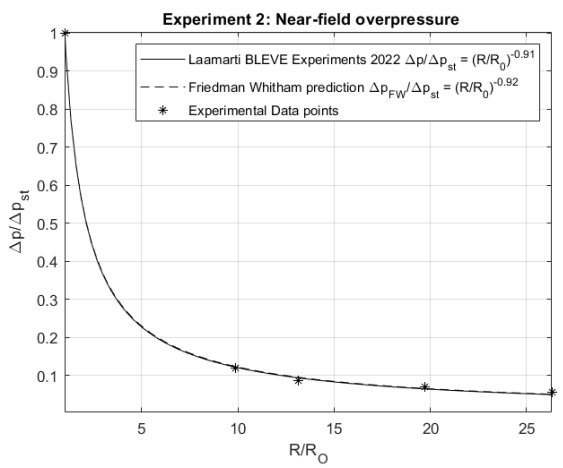

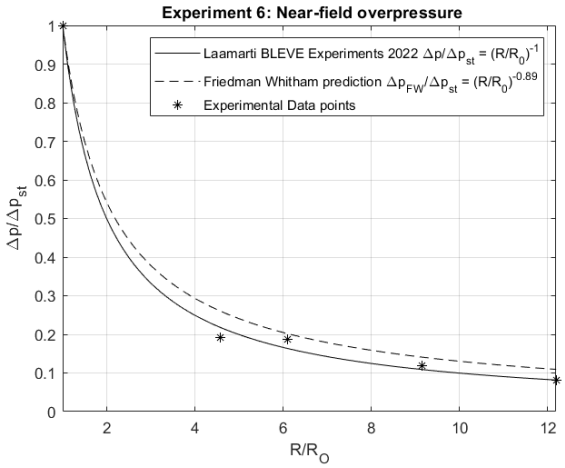

Experiment 2: 99 % | 150 mm | 24 Barg **Experiment 6:** 50 % | 150 mm | 23.1 Barg

Fig. 12. *Comparative study of the prediction of the overpressure from blast vertical top gages*

The Friedman-Whitham prediction is compared with the experimental overpressure data obtained for all experiments at various heights above the tube as illustrated in Fig.13.

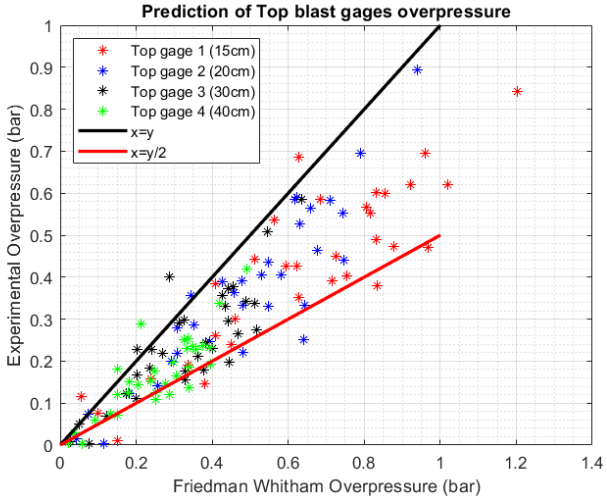

Fig. 13. *Comparative study of the prediction of the overpressure from blast TOP gages*

The graph distinctly illustrates that the Friedman-Whitham relation tends to slightly overestimate the experimental overpressure. However, it is noteworthy that dividing the Friedman-Whitham formula by approximately half underestimate the weakest overpressures.

On the overall experiments, the exponent for vertical blast gages was obtained between -0.8 and -1.02 for the Friedman-Whitham approach and between -0.87 to -1.25 for the experiments such as:

$$\left[\frac{\Delta p_{exp}}{\Delta p_{st}}\right] = \left[\frac{R}{R_0}\right]^{-0.87\ to -1.25} \simeq \left[\frac{\Delta p_{Fw}}{\Delta p_{st}}\right] = \left[\frac{R}{R_0}\right]^{-0.8\ to -1.02}$$

3.4. Estimation of the duration of lead overpressure

The power of a shock aligns with the energy of the overpressure over time – indicating that a longer duration of overpressure corresponds to a stronger shock. Thus, this investigation targets the duration of overpressure quantified by measuring the integral under the maximum peak overpressure, evenly distributed along the isosceles triangle. Fig.14 illustrates the overpressure duration under various operating conditions derived from 2022 and Eyssette (2018) experimental campaigns. In Fig.14, it is observed that the experimental duration of lead overpressure increases with higher liquid fill. Conversely, an increase in failure pressure leads to a decrease in experimental duration. The influence

of weakened length is less evident. Importantly, cases with 100 % liquid fill showed the longest duration of lead overpressure.

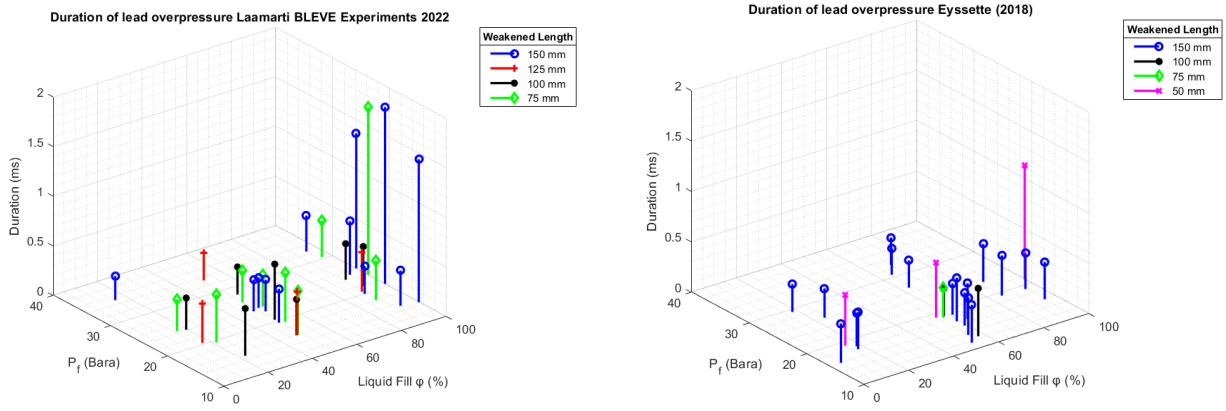

Fig. 14. *Duration of TOP 1 gage [15cm] lead overpressure from [Left] BLEVE 2022 [Right] Eyssette(2018)*

The dimensionless duration of lead overpressure [Equation 10] has been calculated for both Laamarti BLEVE 2022 experiments and Eyssette (2018). A correlation [Equation 12] with specific exponents has been numerically derived to match the dimensionless duration from 2022 experimental data based on operating conditions. Subsequently, this correlation has been then applied to Eyssette (2018) experiments, showing a very consistent fit with the results ($y = x^{0.99}$). Fig. 15 [Left] shows the dimensionless duration of overpressure with respect to the correlation for both campaigns.

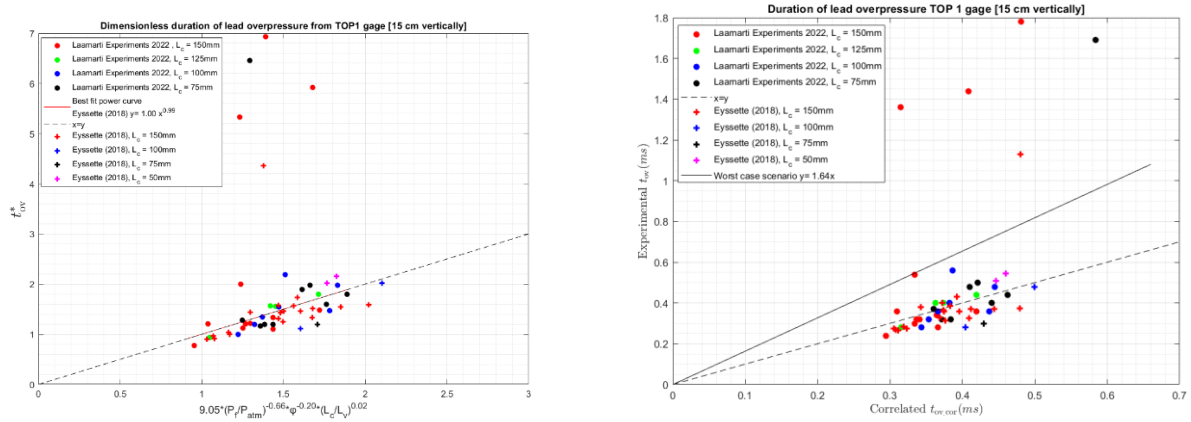

Fig. 15. [Left] *Dimensionless duration of lead overpressure at TOP 1 gage (15 cm vertically) [Right] Experimental vs correlated duration of lead overpressure from TOP 1 gage (15 cm vertically)*

The graph reveals five data points with a distinct behaviour from the rest. These points are 100 % liquid fill scenarios, and they have a prolonged duration of lead overpressure compared to other experiments because of the different opening dynamics involved. Consequently, the 100 % liquid fill cases are not included in the formulation of the duration of lead overpressure. The average duration of lead overpressure found numerically is expressed as follows:

$$t_{ov\_cor} = 9.05\left(\frac{P_f}{P_{atm}}\right)^{-0.66} (\varphi)^{-0.20} \left(\frac{L_c}{L_v}\right)^{0.02} t_{vap}$$

Fig. 15 [Right] shows the experimental vs correlated duration of lead overpressure. From the graph, the highest duration covering the upper bound of data cloud (100 % liquid fill excluded) is

$$t_{ov\_cor\_max} = k t_{ov\_cor} \qquad with\ k = 1.64$$

This correlation is applicable within 3-4 times the diameter (3-4D) range, where the maximum peak overpressure was registered, and has undergone validation exclusively at small scale (D = 50 mm L/D = 6) for both Laamarti Experiments 2022 and Eyssette (2018) data. There are not applicable for 100 % liquid fill, and they require validating at larger scale.

3.5. Estimation of the impulse per unit area

The experimental peak overpressure is shown as a function of the lead overpressure duration in Fig. 16 [Left]. The plot shows that the highest peak overpressures have shorter durations. The duration will depend on the weakened length, the failure pressure, the liquid fill, and the opening dynamics. Fig.16. [Left] shows again the five points, each with 100 % liquid fill, as observed in Fig.15. These points exhibit a combination of low overpressure magnitude and long duration, despite having similar failure pressures as the other liquid fill cases. This suggests the distinctive characteristics of BLEVEs with 100 % liquid fill. Further investigation is required for this specific BLEVE scenarios. Fig.16 [Right] shows that most of experimental results lie beneath the average predicted impulse line, aligning with the intended goal of overpredicting the results. The upper and lower bounds of the experimental impulse are determined by twice and one-fourth the average impulse.

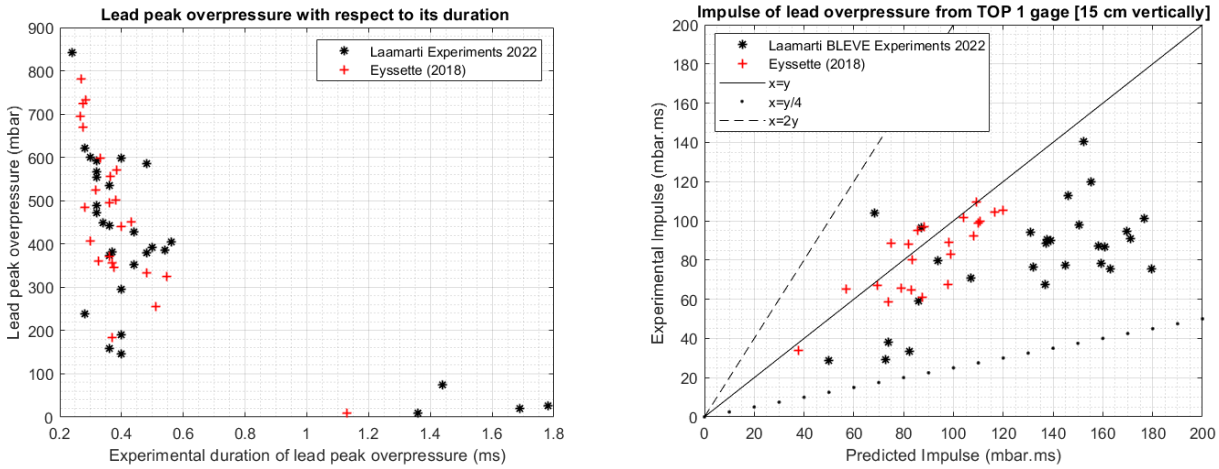

Fig. 16. [Left] Experimental Lead peak overpressure vs overpressure duration [Right] Experimental Impulse per unit area vs Correlated Impulse per unit area.

By employing Equation 13, the correlation for impulse per unit area can be written as:

$$I_{ov\_cor} = \frac{\Delta p_{Fw} 9.06 \left(\frac{P_f}{P_{atm}}\right)^{-0.66} (\varphi)^{-0.20} \left(\frac{L_c}{L_v}\right)^{0.02} t_{vap}}{2}$$

$$I_{ov\_cor} = \frac{\Delta p_{st} \left[\frac{R}{R_0}\right]^{-0.8\ to -1.02} 9.06 \left(\frac{P_f}{P_{atm}}\right)^{-0.66} (\varphi)^{-0.20} \left(\frac{L_c}{L_v}\right)^{0.02} t_{vap}}{2}$$

4. Conclusion

The investigation into near-field overpressure from small-scale propane BLEVE experiments (D = 50 mm, L = 300 mm, volume =589 cm^3) provides new insights into the calculation of impulse per unit area from the lead blast overpressure. The study focused on vertical blast gages positioned above the tube, precisely where the maximum peak overpressure is registered.

Analysis of the Laamarti BLEVE experiments 2022 and Eyssette (2018) experimental campaign revealed that experiments with high failure pressures, low liquid fill levels, and long weakened lengths produced the highest peak overpressures. Notably, experiment 16 from BLEVE experiments 2022 exhibited the greatest peak overpressure, aligning with the highest failure pressure (35 Barg), the longest weakened length (150 mm), and the lowest liquid fill level (15 %). This observation suggests that the vapor phase contributes to high overpressure magnitude and is mainly responsible for shock formation.

The duration of lead overpressure was found to increase with high liquid fill levels and low failure pressures. However, when the liquid fill level reached 100 % (compressed liquid), the duration of lead overpressure was relatively longer. Consequently, the established correlation is not applicable to scenarios involving 100 % liquid fill.

Finally, a formula for the impulse per unit area was derived based on the Friedman-Whitham approach and the developed correlation for the duration of lead overpressure. Presently, this impulse formula

is validated only at a small scale and still require validation at a larger scale. Moreover, it is important to reiterate that the correlation does not apply to liquid full fill cases where the vessel fails under hydrostatic conditions. Hence, additional investigation is necessary for scenarios involving 100 % liquid fill, as they represent a specific case of BLEVE.

Acknowledgements

The authors gratefully acknowledge the financial contribution from Queen's University, Kingston, Canada and IMT mines Ales, Ales, France.

References

Baker, W.E., Cox, P.A., Westine, P.S., Kulesz, J.J., Strehlow, R.A., 1983. Explosion hazards and evaluation. Elsevier Scientific Pub. Co. doi:10.1016/0010-2180(85)90099-9

Baum, H. and Rehm, R. (2005), Simple Model of the World Trade Center Fireball Dynamics., , Chicago, IL, [online], https ://tsapps.nist.gov/publication/getpdf.cfm?pubid = 101087

Birk, A. M. (1996). Hazards from propane BLEVEs: An update and proposal for emergency responders. Journal of Loss Prevention in the Process Industries, 9(2), 173–181.doi:10.1016/0950-4230(95)00046-1

Birk,A.M.,Vandersteen,J.D.J.,2006.On the transition from non BLEVE to BLEVE failure for a1.8 m3propane tank.ASMEJ.Press.VesselTechnol.128(4),648–655.

Birk, A.M., Davison, C., Cunningham, M., 2007. Blast overpressures from medium scale BLEVE tests. J. Loss Prev. Process Ind. 20, 194–206. doi:10.1016/j.jlp.2007.03.001

Birk, A.M., Heymes, F., Eyssette, R., Lauret, P., Aprin, L., Slangen, P., 2018. Near-field BLEVE overpressure effects: the shock start model. Process. Saf. Environ. Prot. 116, 727–736.

Birk, A.M., Eyssette, R., Heymes, F., 2020. Analysis of BLEVE overpressure using spherical shock theory. Process. Saf. Environ. Prot. 134, 108–120.

Brode, H., 1959. Blast Wave from a Spherical Charge. Phys. Fluids 2, 217–229.

Casal, J., Salla, J.M., 2006. Using liquid superheating energy for a quick estimation of overpressure in BLEVEs and similar explosions. J. Hazard. Mater. 137, 1321–1327.
Eyssette, R., 2018. Characterization and modeling of near-field BLEVE overpressure and ground loading hazards. Queen's University (Canada) / IMT Mines Ales (France).

Eyssette, R., Heymes, F., Birk, A.M. "Ground Loading from BLEVE through Small Scale Experiments: Experiments and Results." Process Safety and Environmental Protection, (2021), 148, pp. 1098-1109. doi: 10.1016/j.psep.2021.02.031. [hal-03158570]

Friedman, M P. A SIMPLIFIED DESCRIPTION OF SPHERICAL AND CYLINDRICAL BLAST WAVES. United States: N. p., 1960. Web. doi:10.2172/4115078.

Giesbrecht, H., Hess, K., Leuckel, W. Maurer, B. (1981), 'Analysis of explosion hazards on spontaneous release of inflammable gases into the atmosphere. part1/part2

Laamarti, E.M., Birk, A.M., Chanut, C., Heymes, F., 2024. Correlations to estimate the ground loading from small scale propane BLEVE experiments. Process Safety and Environmental Protection. https://doi.org/10.1016/j.psep.2024.03.006

Laboureur, D., Birk, A.M., Buchlin, J.M., Rambaud, P., Aprin, L., Heymes, F., Osmont, A., 2015. A closer look at BLEVE overpressure. Process Saf. Environ. Prot. 95, 159–171. doi:10.1016/j.psep.2015.03.004

Planas-Cuchi, E., Salla, J.M., Casal, J., 2004. Calculating overpressure from BLEVE explosions. J. Loss Prev. Process Ind. 17, 431–436. doi:10.1016/j.jlp.2004.08.002

Prugh, R.W., 1991. Quantitative Evaluation of Bleve Hazards. J. Fire Prot. Eng. 3, 9–24. doi:10.1177/104239159100300102

Rankine, W. J. M. (1870). "On the thermodynamic theory of waves of finite longitudinal disturbances". Philosophical Transactions of the Royal Society of London. 160: 277–288. doi:10.1098/rstl.1870.0015.

Van den Berg, A., Van der Voort, M., Weerheijm, J., Versloot, N., 2006. BLEVE blast by expansion-controlled evaporation. Process Saf. Prog. 25 (1), 44–51

White, F.M., 1998. Fluid Mechanics, Fourth edition. WCB McGraw-Hill, New York.

Large eddy simulations of flow electrification of liquid dielectrics

Mathieu Calero[a], Holger Grosshans[b] & Miltiadis V. Papalexandris[a]

[a] Institute of Mechanics, Materials and Civil Engineering, 1348 Louvain-la-Neuve, Belgium
[b] Physikalisch-Technische Bundesanstalt, 38116 Braunschweig, Germany

E-mail: *miltos@uclouvain.be*

Abstract

In this paper we present a computational study of electrification of liquid dielectrics in channel flow and at moderate turbulence intensities. For purposes of computational savings this study consists of large eddy simulations, according to which the large turbulent scales are directly resolved by the computational grid while the effect of the smaller unresolved scales is suitably modeled. First we examine different subgrid-scale models for the electric charge density. Their efficacy is then assessed via comparisons with results from direct numerical simulations at low turbulence intensities. According to our analysis, the most efficient model is the one based on the eddy diffusivity approach and the introduction of the turbulent electric Schmidt number. Subsequently, we present numerical results of electrification of benzene in channel flow and at different Reynolds numbers. Herein we discuss the various stages of the electrification process and the variation of the total charge and streaming current with the turbulence intensity. According to our findings, the increase of the turbulence intensity rises dramatically not only the amount of charge transported in the bulk of the fluid but also the rate at which this transport takes place. Finally, we present results for the statistics of the charge density, which provide additional insight about the distribution of the electric charges in the liquid.

Keywords: *flow electrification, turbulent flows, dielectric liquids, large eddy simulations, electrical double layer, electrohydrodynamics.*

1 Introduction

Flow electrification occurs when electric charges are transported from the interface between a solid boundary and a flowing liquid dielectric towards the bulk of the flow domain. The class of liquid dielectrics includes several hydrocarbons like benzene, toluene, heptane and others. In their pure state, liquid dielectrics are free of electric charges. However, they inevitably contain impurities. In turn, these impurities get dissolved into particles carrying electric charge, namely, anions and cations. These charged particles then participate in the formation of the Electrical Double Layer (EDL) at the interface between a solid boundary and the liquid dielectric. The first layer of the EDL is referred to as the surface charge and is on the side of the solid body.

The second layer is on the side of the liquid and is composed of ions attracted to the surface charge. It consists of two sublayers, the Stern and the diffuse layer. The Stern layer, whose thickness is of the order of the ion size, is anchored to the solid boundary and contains ions whose charge is opposite to that of the surface charge, so as to maintain an electrically neutral interface. On the other hand, the diffuse layer has a more loose structure and the concentration of ions therein decreases away from the solid surface. Typically, the thickness of the EDL is a few Debye lengths. The Debye length is the characteristic length-scale of electrostatic effects in fluids and plasmas. It is of the order of a micron and its precise value depends on the electrical properties of the medium (Atkins et al., 2018, Berg, 2010). In particular, it is proportional to the square root of the electrical resistivity of the liquid.

Liquid dielectrics have high resistivity hence Debye length. Accordingly, the thickness of their diffuse layers is comparatively higher than in other liquids. This makes it easier for electric charges to be transported away from the diffuse layer and towards the bulk of the flow domain. In other words, a thicker diffuse layer facilitates flow electrification. However, this phenomenon leads to high streaming currents, i.e. electric currents due to the convective motions (flow) of the liquid, which

constitute a major safety hazard. By now it is well documented that electric discharges caused by flow electrification of flammable dielectrics have caused many accidents in the petroleum and process industries; see for example the earlier reports of Klinkenberg (1959, 1964) and the more recent account of Ohsawa (2011). Additionally, flow electrification is often responsible for the failure of power transformers (Bourgeois et al., 2005).

Since flow electrification represents a major safety hazard, it has been the subject of concentrated research efforts in the past. Moreover, since the phenomenon involves convective transport of charges, it had been proposed early on that flow turbulence plays a significant role to it. For example, Touchard (1978) proposed a model for the charge-density profile in turbulent flows that assumed constant charge density in the bulk of the flow. However, that profile was discontinuous at the edge of the diffuse layer. This was corrected later in the model of Cabaleiro et al. (2019) who proposed a continuous profile but without properly taking into account the convective transport of ions. Very recently, Touchard (2021a) proposed to combine those two models. Comparisons of these three models with experimental results were reported by Touchard (2021b). Additional studies on the streaming current in the diffuse layer have been provided by Abedian and Sonin (1982), Domínguez and Touchard (1997), Paillat et al. (2001) and others.

The above works have provided important physical insight on the phenomenon and elucidated the role of several underpinning mechanisms. However, they all focused on the charge-density distribution in a stationary state, i.e. by assuming that the electrification process has been completed. Further, they necessarily relied on approximate expressions for the mean velocity profile in a turbulent flow. Therefore, they did not provide information about the evolution of the electrification process and, furthermore, did not quantify the role of the turbulence intensity.

In a recent paper (Calero et al., 2023), we presented a numerical study of the electrification process in turbulent channel flows at weak turbulence intensities. This study consisted of Direct Numerical Simulations (DNS), which means that the computational grid of the flow domain was sufficiently refined so as to resolve all turbulent structures and flow scales. According to our simulations, the amount of electric charge transported in the interior of the channel increases dramatically when the flow becomes turbulent. Also, the electrification rate increases with the turbulence intensity. This is due to the fact that, as the turbulence intensity increases, the thickness of the hydrodynamic boundary layer becomes comparable to that of the diffuse layer which, in turn, facilitates and enhances the convective transport of charged particles. Accordingly, electric charge is built up rapidly in the interior of the channel until it reaches a plateau, which signals the completion of the electrification process.

In the present paper, we expand upon our earlier results and study numerically the electrification process at higher turbulence intensities, i.e. at higher Reynolds numbers. The grid-resolution requirements increase tremendously as the turbulence intensity increases because of the development of ever smaller flow structures (eddies). Therefore, for purposes of computational savings, the present study is based on Large Eddy Simulations (LES) instead of DNS. According to the LES approach, the computational grid is sufficiently fine to resolve the large turbulent structures of the flow-field, which are also the ones that contain most of the turbulent kinetic energy. Whereas the effect of the smaller unresolved structures is modeled.

2 Governing equations

In the flows of interest, dynamic currents due to charge transport are very small so that electromagnetic induction is negligible. Variations of the fluid density and temperature are assumed to be negligible as well. Accordingly, the governing equations are the Navier-Stokes equations, supple-

mented by the transport equation for the electric charge and the Gauss law for the electric field (Calero et al., 2023). In the context of LES, the filtered version of these equations read,

$$\nabla \cdot \widetilde{\boldsymbol{u}} = 0, \tag{1}$$

$$\frac{\partial \widetilde{\boldsymbol{u}}}{\partial t} + (\widetilde{\boldsymbol{u}} \cdot \nabla)\,\widetilde{\boldsymbol{u}} + \frac{1}{\rho}\nabla \widetilde{p} = \nu \nabla^2 \widetilde{\boldsymbol{u}} + \frac{1}{\rho}\widetilde{\boldsymbol{F}}_{el} - \nabla \cdot \boldsymbol{\tau}, \tag{2}$$

$$\frac{\partial \widetilde{\rho}_{\mathrm{el}}}{\partial t} + \widetilde{\boldsymbol{u}} \cdot \nabla \widetilde{\rho}_{\mathrm{el}} = D \nabla^2 \widetilde{\rho}_{\mathrm{el}} - \frac{\sigma}{\epsilon}\widetilde{\rho}_{\mathrm{el}} - \nabla \cdot \boldsymbol{\zeta}, \tag{3}$$

$$\nabla^2 \widetilde{\phi} = -\frac{\widetilde{\rho}_{\mathrm{el}}}{\epsilon}. \tag{4}$$

In the above system, $\widetilde{\boldsymbol{u}} = (\widetilde{u}, \widetilde{v}, \widetilde{w})$ and $\widetilde{p}$ stand respectively for the filtered fluid velocity and dynamic pressure, while ρ and ν denote the fluid density and kinematic viscosity. Also, $\widetilde{\rho}_{\mathrm{el}}$ and $\widetilde{\phi}$ are the filtered electric-charge density and electric potential. In other words, $\widetilde{\boldsymbol{E}} = -\nabla\widetilde{\phi}$ with $\widetilde{\boldsymbol{E}}$ being the filtered electric field. Further, σ, ϵ and D are, respectively, the electric conductivity, electric permittivity and ionic diffusivity of the fluid. For the problems of interest these quantities can be assumed to be constant; see relevant discussion in Calero et al. (2023).

Assuming that the absolute values of the valences of anions and cations are equal, the electric charge density is defined by,

$$\rho_{el} = e_0 z (n_{\mathrm{P}} - n_{\mathrm{N}}), \tag{5}$$

where e_0 is the elementary charge, z the absolute ionic valence and n_{P} and n_{N} the concentrations of cations and anions, respectively. Also, the expreesion for the Debye length reads, $\lambda_{\mathrm{D}} = \sqrt{\epsilon\, D/\sigma}$ (Paillat et al., 2001).

In the momentum equation (2), the forcing term $\widetilde{\boldsymbol{F}}_{el}$ is the filtered Lorentz force, i.e. the volumetric electric force acting on the fluid. Also in (2), the residual tensor $\boldsymbol{\tau}$ represents the unclosed terms of the filtered momentum equation (2) and has to be modeled. Similarly, the residual vector $\boldsymbol{\zeta}$ represents the unclosed terms of the filtered charge-density equation and has to be modeled as well.

In the problems of interest, the relevant hydrodynamic dimensionless group is the Reynolds number. Our study is concerned with electrification in turbulent channel flows and it is therefore convenient to introduce the friction Reynolds number $Re_\tau = u_\tau h/\nu$, where h is the half-width of the channel and u_τ is the friction velocity. The latter one is defined as $u_\tau = \sqrt{\tau_{\mathrm{w}}/\rho}$ with τ_{w} being the wall shear stress. Also, the dimensionless groups related to charge transport are the electric Schmidt number, $Sc = \nu/D$, and the ratio between the hydrodynamic and electrostatic time scales $r_{\mathrm{t}} = (h/u_\tau)/(\epsilon/\sigma)$. The ratio ϵ/σ appears in the ohmic-resistance term of (3) and is commonly referred to as the charge relaxation time.

The literature on subgrid-scale modeling for the Navier Stokes equations is vast; see, for example, (Sagaut, 2005) and references therein. The most common approach is to introduce the eddy-viscosity concept according to which $\boldsymbol{\tau}$ is represented as an additional viscous stress-tensor. Then, we have,

$$\boldsymbol{\tau} - \frac{1}{3}\mathrm{tr}(\boldsymbol{\tau})\boldsymbol{I} = -2\nu_{\mathrm{t}}\widetilde{\boldsymbol{S}}, \tag{6}$$

where $\mathrm{tr}(\boldsymbol{\tau})$ is the trace of $\boldsymbol{\tau}$, $\boldsymbol{I}$ the identity tensor and $\widetilde{\boldsymbol{S}}$ the filtered strain-rate tensor, $\widetilde{\boldsymbol{S}} = 1/2\left(\nabla\widetilde{\boldsymbol{u}} + (\nabla\widetilde{\boldsymbol{u}})^{\top}\right)$. Typically, the eddy viscosity ν_{t} is assumed to scale linearly with the amplitude of the strain rate, i.e.

$$\nu_{\mathrm{t}} = (C_{\mathrm{S}}\,\Delta)^2 \sqrt{\widetilde{\boldsymbol{S}} : \widetilde{\boldsymbol{S}}}, \tag{7}$$

where the double dot denotes the double interior product between two 2nd-order tensors, C_{S} the so-called Smagorinsky coefficient and Δ the nominal filter size: $\Delta = (\Delta x\,\Delta y\,\Delta z)^{1/3}$ with Δx, Δy and Δz the dimensions of a given computational cell. This choise for the nominal filter size is the one that is most often used in practice.

In our simulations we set $C_S = 0.17$, which is the value proposed by Lilly (1992) for channel flows. To correct the behavior of the eddy viscosity in the near-wall regions, it is common to add in (7) the van Driest damping function (Pope, 2000). This approach was also adopted in our study. Accordingly, the eddy viscosity reads,

$$\nu_t = \left(0.17\Delta\left(1-e^{-y^+/25}\right)\right)^2\sqrt{\widetilde{\boldsymbol{S}}:\widetilde{\boldsymbol{S}}} \tag{8}$$

where y^+ is the distance from the wall measured in wall units, $y^+ = yRe_\tau/h$. Validation tests of the proposed LES model for the flows of interest, consisting of comparisons between LES and direct numerical simulations (DNS), can be found in Calero (2023).

With regard to the modeling of $\widetilde{\boldsymbol{F}}_{el}$, we remark that, for constant emissivity, the Lorentz force is given by $\boldsymbol{F}_{el} = \rho_{el}\boldsymbol{E}$. Earlier numerical studies (Calero et al., 2023) have shown that in the flows of interest the Lorentz force is very weak. Accordingly, it can be approximated simply by,

$$\widetilde{\boldsymbol{F}}_{el} \approx \widetilde{\rho}_{el}\widetilde{\boldsymbol{E}}\,. \tag{9}$$

Finally, the turbulent flux $\boldsymbol{\zeta}$ is approximated via the so-called gradient assumption, which is the standard approach for the modeling of turbulent fluxes in scalar transport equations. According to it,

$$\boldsymbol{\zeta} = -D_t\boldsymbol{\nabla}\widetilde{\rho}_{el}\,. \tag{10}$$

In the above equation, D_t stands for the ionic eddy diffusivity. Herein, it is estimated via the introduction of a turbulent electric Schmidt number,

$$Sc_t = \frac{\nu_t}{D_t}\,. \tag{11}$$

Since ν_t vanishes as we approach the wall, then so does D_t. The value of Sc_t is typically estimated via comparisons with DNS results. Numerical tests that we conducted in the framework of our study showed that for the flows of interest, the estimate that yielded the most accurate result is $Sc_t = 4$.

The governing system (1)-(3) is integrated numerically via the algorithm proposed by Calero et al. (2022). The hydrodynamic component, i.e. the Navier-Stokes equations, is solved via a SIMPLE-based scheme (Ferziger et al., 2019). Whereas, the discretization of the Poisson equation (4) for the electric potential leads to a linear system that is solved via Jacobi iterations. Finally, the charge-density equation is integrated numerically via an upwind method. The combined algorithm has been parallelized using the Message Passing Interface (MPI) protocol and implemented in a Cartesian mesh with a staggered-grid arrangement. Validation tests for the combined algorithm and full details for its implementation are available in (Calero et al., 2022). It is also worth adding that this algorithm is part of pafiX (2019), which is an open-source computational tool for electrohydrodynamics.

3 Numerical setup

The computational domain consists of a channel with half-width $h = 0.5$ cm. The channel is periodic in the streamwise x and spanwise z directions. The cross-stream direction is then parallel to the y axis. The midplane of the channel is located at $y = 0$. The working dielectric liquid is benzene at room temperature and its properties are listed in table 1. The electrical conductivity σ is particularly low, as is the case for several liquid hydrocarbons, and its precise value depends on the concentration of impurities. The value listed in table 1 is the one measured in the experiments of (Forster, 1962). The value of D is calculated via the Einstein-Stokes formula, $D = k_BT/(3\pi\nu\rho d)$ with d being the presumed diameter of the impurities (Ohshima and Furusawa, 1998). For the value listed in table 1, we assumed that $d = 4$ nm. The Debye length is then estimated at $\lambda_D \approx 5.73\times10^{-5}$ m.

In our study we consider flows at 4 different friction Reynolds numbers: $Re_\tau = 180$, 210, 300 and 395. The corresponding flow rates are sufficiently high for the thickness of the hydrodynamic boundary layer to be comparable to that of the diffuse layer. Accordingly, flow electrification takes places in all the cases presented herein. For $Re_\tau = 180$ and 210 the length and depth of the channel are: $L_x = 4\pi h$ and $L_z = 2\pi h$, respectively. Whereas for computational savings, in the cases of $Re_\tau = 300$

***Table 1**: Material properties of benzene at 298.23 K.*

Quantity	Source	Value
ρ	(Chemical-Book, 2022)	874 Kg/m^3
ν	(Reid et al., 1987)	6.95×10^{-7} m^2/s
ϵ	(Brown et al., 1951)	2.01×10^{-11} F/m
σ	(Forster, 1962)	1.1×10^{-12} S/m
D	(Ohshima and Furusawa, 1998)	1.8×10^{-10} m^2/s

***Table 2**: Properties of the computational meshes. L_x, L_y and L_z are the channel dimensions, and N_x, N_y and N_z are the number of grid points in the respective directions. Δx^+ and Δz^+ are the uniform cell spacings in the x and z directions. Δy^+_max is the largest grid spacing in the y direction.*

Re_τ	$L_\mathrm{x}\times L_\mathrm{y}\times L_\mathrm{z}$	$N_\mathrm{x}\times N_\mathrm{y}\times N_\mathrm{z}$	Δx^+	Δz^+	Δy^+_max
180	$4\pi h\times 2h\times 2\pi h$	$96\times65\times80$	23.56	14.14	8.71
210	$4\pi h\times 2h\times 2\pi h$	$96\times65\times80$	27.48	16.49	10.16
300	$2\pi h\times 2h\times \pi h$	$96\times65\times96$	19.63	9.81	14.49
395	$2\pi h\times 2h\times \pi h$	$128\times96\times128$	19.38	9.70	12.92

and 395 we set $L_x = 2\pi h$ and $L_z = \pi h$. In the high Re_τ cases, the extent of the channel in the periodic directions have been reduced for purposes of computational savings; nonetheless these dimensions are still sufficiently large so as to prevent spurious interactions between the resolved turbulent structures and to accurately compute the statistical properties of the flow (Lessani and Nakhaei, 2013).

Our simulations are wall-resolved LES, which means that the fluid structures in the near-wall regions, including the boundary layer, are fully resolved. To this end, the distance of the center of the first computational cell from the adjacent wall, y^+_{fp}, satisfies $y^+_{fp} < 1$. For example, for the case of $Re_\tau = 180$, $y^+_{fp} = 0.1$. The width Δy of the computational cells is then increased away from the walls and towards the midplane following a hyperbolic tangent distribution. Nonetheless, in all cases, care has been taken so that a sufficient number of computational cells is placed inside the boundary layers. On the other hand, the grid spacing in the periodic directions is uniform. The summary of the properties of the computational meshes is given in table 2.

In our simulations, the Stern layers are not resolved because their thickness is at the order of the ion size; instead, for purposes of computation of the electric charge density, they are assumed to be part of the solid wall-liquid interface. Then at the solid boundaries we prescribe the no-slip condition for the velocity and a non-zero Dirichlet condition for the electric charge density ρ_el. In other words, the electric charge density in the Stern layers is assumed to remain constant; see also the relevant discussion in Abedian and Sonin (1982). More specifically, the charge density at the walls is set to $\rho_\mathrm{el} = 10^{-4}$ C/m^3. Further, a zero-Neumann condition is applied for the electric potential at the top and bottom walls.

In terms of initial conditions, we first perform a preliminary simulation of turbulent channel flow in absence of electric charge. Once the flow becomes fully developed, we then apply the initial profile for the electric charge density and start the simulation of flow electrification. In the cross-stream y direction, the initial charge density consists of an exponentially decreasing profile, starting with the (dimensionless) value of unity at the wall and decreasing so that approximately 95% of the initial

charge is located within 3 Debye lengths. This choice has been based on Paillat et al. (2001) who suggested that 95% of the charge in the diffuse layer is located between the Stern layer and a distance of $3\lambda_D$ from the wall. In this manner, the thickness of the initial charge-density profile corresponds to the actual thickness of the diffuse layer of an EDL for the presumed λ_D. On the other hand, this profile is constant in the x and z directions. For all the simulations presented therein, we determine the time step via the Courant-Friedrichs-Lewy (CFL) condition (Ferziger et al., 2019) with the Courant number set to 0.25. These results have been non-dimensionalized by the value at the wall ρ_w. Similarly, the coordinate y has been non-dimensionalized by the channel half-width h, and the time variable t by h/u_τ.

4 LES results

In this section we present results obtained from LES for electrification of liquid benzene during channel flow. As mentioned above, we consider four different friction Reynolds numbers, $Re_\tau = 180$, 210, 300 and 395.

The evolution of the average charge density at the midplane, $\langle \rho_{el} \rangle_{xz}$, is plotted in Figure 1. In all cases, the electrification process consists of three stages, as outlined by Calero et al. (2023): the initial rapid build-up of charge (high electrification rate), a transition stage (lower electrification rate) and the statistically stationary stage which signals the completion of electrification. As expected, the electrification rate increases substantially with the turbulence intensity. For example, at $Re_\tau = 395$, the working medium (liquid benzene) attains the third stage of electrification approximately three times faster than it does at $Re_\tau = 180$. This is due to the fact that as the turbulence intensity increases, the thickness of the boundary layer decreases and, therefore, there are more turbulent structures that enter the diffuse layer and transport charges towards the bulk of the channel.

Similarly, the peak value of $\langle \rho_{el} \rangle_{xz}$ also increases with Re_τ. For instance, at $Re_\tau = 300$ the final (peak) value of $\langle \rho_{el} \rangle_{xz}$ is 12.3% higher than at $Re_\tau = 210$. However, at high Re_τ this increase becomes much less pronounced. For example, the final value of $\langle \rho_{el} \rangle_{xz}$ at $Re_\tau = 395$ is only 2.7% higher than at $Re_\tau = 300$.

It is also interesting to observe that for $Re_\tau = 180$ and 210, the average charge at the midplane $\langle \rho_{el} \rangle_{xz}$ exhibits some low-frequency and small-amplitude oscillations in the final stage of the electrification process, i.e. in the statistically stationary state. These oscillations have also been observed at lower Reynolds numbers (Calero, 2023). Their amplitude progressively decreases with Re_τ. More specifically, at $Re_\tau = 300$ these oscillations have all but disappeared. The presence of these oscillations at low Re_τ is attributed to the convective term in the charge density equation (3), i.e. to the local

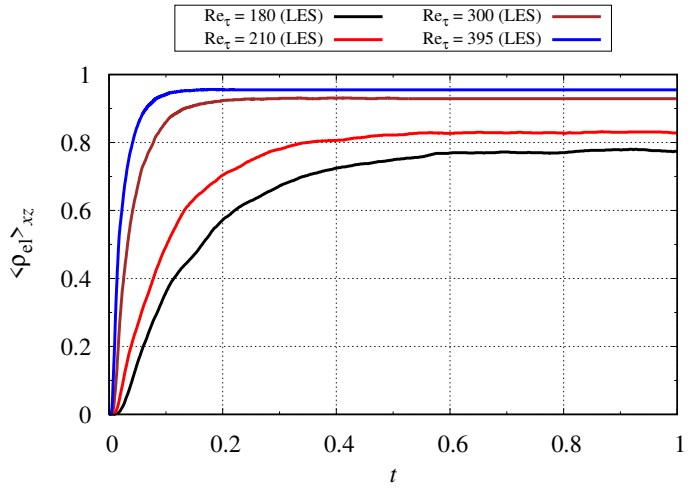

***Fig. 1**: Evolution of the area-averaged charge density $\langle \rho_{el} \rangle_{xz}$ at the midplane ($y = 0$) for the friction Reynolds numbers considered herein.*

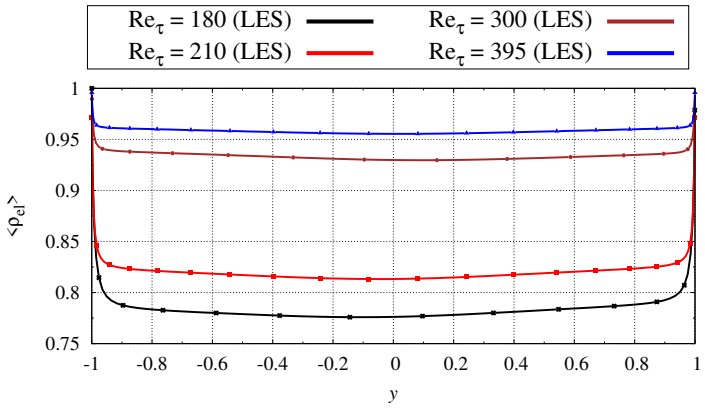

***Fig. 2**: Profiles of the mean charge density, $\langle\rho_{el}\rangle$, across the channel.*

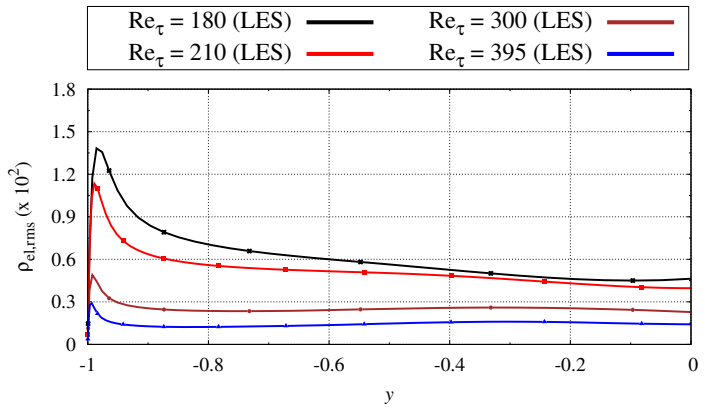

***Fig. 3**: Profiles of the charge density rms, $\rho_{el,rms}$, across the channel.*

misalignment of the velocity vector and the charge gradient. Their amplitude diminishes at high Re_τ because as the turbulence intensity increases, the mixing of electric-charge carriers becomes more efficient, thereby reducing the fluctuations of ρ_{el}.

Next, we present the predictions of our LES for the first and second-order statistics of the charge density. As before, the sampling period is 80 flow-through times. In Figure 2 we have plotted the profiles of the mean charge density, $\langle\rho_{el}\rangle$, across the channel for the four values of Re_τ considered herein. Overall, the shape of the profiles is the same as the one predicted by DNS at low turbulence intensities reported in (Calero et al., 2023). More specifically, the $\langle\rho_{el}\rangle$ profiles consist of three zones. The first one is adjacent to the wall and within both the hydrodynamic boundary layer and the diffuse layer. Inside this zone, the fluid velocity is exceedingly small and the dominant mechanism of transport of charge is the ionic diffusion. Its thickness is a couple of percentage points of the unit length (the channel half-width h). In the second zone, convective transport of charge becomes important and, therefore, the competing mechanisms therein are the convective and conductive currents. This zone terminates at a distance of 0.10 to 0.15 unit lengths from the wall. Finally, the third zone is characterized by a very slow decrease of the charge density away from the walls. From the plots of Figure 2 we can also infer that an increase of the turbulence intensity reduces the thicknesses of the first and second zones and also uniformizes the charge-density distribution away from the walls.

Finally, results for the rms of the charge density, $\rho_{el,rms}$, across the channel are provided in Figure 3. Once again, the shape of these profiles are the same as those predicted by DNS at lower turbulence intensities. In particular, the rms values exhibit a strong peak near the wall and then drop in the bulk of the channel. This peak coincides with the end of the first zone mentioned above. The location of the peak moves closer to the wall as Re_τ increases, i.e. the thickness of the first zone of the $\langle\rho_{el}\rangle$ profile

becomes smaller. Additionally, the values of $\rho_{\mathrm{el,rms}}$ across the channel decrease as Re_τ increases. This is due to the fact that mixing is enhanced as the turbulence intensity increases. The same trend is also observed in passively advected scalars in turbulent flows; for example, in free convection the rms of the (normalized) temperature decreases as the turbulence becomes more intense (Hay and Papalexandris, 2019, 2020).

It is also interesting to observe that in the bulk of the channel the predicted rms profiles are not completely flat but exhibit some very small variation. This is most likely a numerical artifact due to the subgrid-scale modeling. Nonetheless, the amplitude of this variation is very low, from which we may infer that overall the performance of the subgrid-scale model is satisfactory.

5 Conclusions

In this paper we have studied electrification of liquid dielectrics in channel flows of moderate turbulence intensities via large eddy simulations. Accordingly, we first derived the filtered version of the governing equations. The unclosed terms in the momentum equation are approximated by the eddy-viscosity model that incorporates a constant Smagorisnky coefficient and the van Driest damping function. Similarly, the unclosed term in the charge-density equation are modeled via the eddy diffusivity approach and the introduction of a the turbulent electric Schmidt number.

Our simulations predicted that the electrification rate increases monotonically with the turbulence intensity. The electrification process consists of three stages, namely, the initial build-up of charge in the channel, the transition stage, and the statistically stationary stage in which the charge in the channel remains constant. We have also confirmed that in the last stage the mean charge-density profile consists of three zones. The first one is dominated by charge diffusion of the wall and the second one by increased convective current. The third zone is characterized by a very slow decrease of the charge density away from the walls. As expected, the first zone becomes thinner as the turbulence intensity increases. At the same time, the rms value of the charge density become smaller due to enhanced turbulent mixing. In the future we plan to perform simulations at even higher Reynolds number and also extend our studies in pipe and duct flows.

Acknowledgements

The first and third authors gratefully acknowledge the financial support of the National Research Fund of Belgium (FNRS) under the FLOW-CHARGE grant.The second author gratefully acknowledges the financial support from the European Research Council (ERC) under the European Union's Horizon 2020 research and innovation programme (grant agreement No. 947606 PowFEct).

References

Abedian, B., Sonin, A. (1982). *Theory for electric charging in turbulent pipe flow*. J. Fluid Mech., 120:199–217.

Atkins, P., de Paula, J., Keeler, J. (2018). *Atkins' Physical Chemistry*. Oxford University Press, London, 11th edition.

Berg, J. (2010). *An introduction to Interfaces and Colloids*. World Publishing.

Bourgeois, A., Paillat, T., Moreau, O., Mortha, G., Touchard, G. (2005). *Flow electrification in power transformers: salt-type additive as a potential remedy?* J. Electrostat., 63(6):877–882. 10th International Conference on Electrostatics.

Brown, A. S., Levin, P., Abrahamson, E. (1951). *Dielectric Constant of Benzene at 25°c by the Wyman Method*. J. Chem. Phys., 19(10):1226–1229.

Cabaleiro, J., Paillat, T., Artana, G., Touchard, G. (2019). *Flow Electrification in Turbulent Flows of Liquids—Comparison of Two Models for One Specific Case*. IEEE Trans. Ind. Appl., 55(5):5235–5328.

Calero, M. (2023). *Flow Electrification of Dielectric Liquids: Modeling and Numerical Study*. Doctoral Dissertation, UCLouvain.

Calero, M., Grosshans, H., Papalexandris, M. (2022). *A computational framework for electrification of liquid flows*. J. Loss Prevent. Proc., 74:104637.

Calero, M., Grosshans, H., Papalexandris, M. (2023). *Electrification in turbulent channel flows of liquid dielectrics*. Phys. Fluids, 35(4):045119.

Chemical-Book (2022). `https://www.chemicalbook.com/`.

Domínguez, G., Touchard, G. (1997). *Streaming current development in a rectangular channel*. J. Electrostat., 40-41:153–159. Proceedings of the 8th International Conference on Electrostatics.

Ferziger, J. H., Perić, B., Street, R. (2019). *Computational Methods for Fluid Dynamics*. Springer, 4th edition.

Forster, E. (1962). *Electric Conduction in Liquid Hydrocarbons. I. Benzene*. J. Chem. Phys., 37(5):1021–1028.

Hay, W., Papalexandris, M. (2019). *Numerical simulations of turbulent thermal convection with a free-slip upper boundary*. Proc. Roy. Soc. A., 475:20190601.

Hay, W., Papalexandris, M. (2020). *Evaporation-driven turbulent convection in water pools*. J. Fluid Mech., 904:A14.

Klinkenberg, A. (1959). *Le Mouvement d'électricité accompagnant le Mouvement des Liquides et sa Conséquence, l'électricité dite Statique*. G. Chim., 82:149–157.

Klinkenberg, A. (1964). *Elektrische Aufladung schlecht leitender Flüssigkeiten bei turbulenter Strömung*. Chem. Ing. Tech., 36(3):283–290.

Lessani, B., Nakhaei, M. (2013). *Large-eddy simulation of particle-laden turbulent flow with heat transfer*. Int. J. Heat Mass Trans., 67:974–983.

Lilly, D. (1992). *The representation of small-scale turbulence in numerical simulation experiments*. IBM Form., 4:195–210.

Ohsawa, A. (2011). *Statistical analysis of fires and explosions attributed to static electricity over the last 50 years in japanese industry*. J. Phys. Conf. Ser., 301:1–6.

Ohshima, H., Furusawa, K., editors (1998). *Electrical Phenomena at Interfaces. Fundamentals, Measurements, and Applications*, volume 76 of *Surfactant Science*. Routledge, New York, 2nd edition.

pafiX (2019). `https://www.ptb.de/cms/asep`.

Paillat, T., Moreau, E., Touchard, G. (2001). *Space charge density at the wall in the case of heptane flowing through an insulating pipe*. J. Electrost., 53(2):171–182.

Pope, S. B. (2000). *Turbulent Flows*. Cambridge University Press, New York.

Reid, R., Prausnitz, J., Poling, B. (1987). *The properties of gases and liquids*. McGraw-Hill, New York, 4th edition.

Sagaut, P. (2005). *Large eddy simulation for incompressible flows: an introduction*. Springer Science & Business Media.

Touchard, G. (1978). *Streaming currents developed in laminar and turbulent flows through a pipe*. J. Electrostat., 5:463–476.

Touchard, G. (2021a). *Turbulent flow electrification with hydrocarbon liquids, liquid hydrogen, liquefied natural gas (LNG) and liquid nitrogen: Part I–Three different models*. Int. J. Plasma Environ. Sci., 15(2):1–32.

Touchard, G. (2021b). *Turbulent flow electrification with hydrocarbon liquids, liquid hydrogen, liquefied natural gas (LNG) and liquid nitrogen: Part II–Experiments and comparison with different models*. Int. J. Plasma Environ. Sci., 15(2):1–15.

Ignition sensitivity moderation of animal feed organic/mineral mixtures

José Serrano [a,b], Fabrice Putier [b], Laurent Perrin [a] & Olivier Dufaud [a]

[a] Université de Lorraine, CNRS, LRGP, F-54000 Nancy, France
[b] Tecaliman, 44300 Nantes, France

E-mail: olivier.dufaud@univ-lorraine.fr

Abstract

Mixing inert materials with combustible dust can reduce electrostatic ignition risks and prevent dust explosions. The admixing of solid inertants is a feasible safety strategy for premix production in the animal feed sector. The premix is a complex blend of cereals, vitamins, amino acids, and minerals to meet animal nutritional needs. However, characterizing the ignition sensitivity of industrial premixes requires time-consuming experimental analysis due to the array of the ingredients' properties (e.g., chemical nature, Particle Size Distribution – PSD, and mass fraction). Therefore, this research aims to study the influence of the chemical nature and the PSD of minerals on the Minimum Ignition Energy (MIE) of organic/mineral binary mixtures to broaden the understanding of the involved physicochemical mechanisms. DL-Methionine was mixed with three minerals ($CaCO_3$, NaCl, and $NaHCO_3$) with distinct PSD, which undergoes different physical and chemical inerting mechanisms. The ignition tests were conducted in the MIKE3 based on the standard ISO/IEC 80079-20-2. In addition, thermal analysis by Differential Scanning Calorimetry and pyrolysis gas identification using a modified Godbert-Greenwald and Micro Gas Chromatography were performed to characterize the minerals' inerting mechanism. The results showed that the PSD of the mineral is the most significant factor in the MIE moderation. However, its influence also depends on the mineral nature. For instance, the PSD of $CaCO_3$ should be low (d_{50} = 52 µm) to achieve efficient inerting. Similarly, NaCl achieved a successful ignition inerting at a low median diameter (d_{50} = 35 µm) because of the particle heating time to reach its decomposition into scavenging agents. By contrast, $NaHCO_3$ was the most effective inerting agent due to thermal and chemical effects. Its addition to methionine increased by 80% the decomposition enthalpy of the mixture and by 30% the amount of CO_2 released during the pyrolysis. These findings may be applicable for designing safer preventive measures considering inherent safety principles for animal feed premixes manufacturing.

Keywords: *ignition energy, dust mixture, prevention, animal feed, inerting, particle size.*

1. Introduction

The organic matter is combustible, and if it is in powdered form, it can lead to an explosion under certain conditions: the simultaneous presence of an oxidant and an ignition source when the dust is suspended in a cloud (Amyotte et al., 2009). An average of 29 dust explosions per year happened in the United States from 2016 to 2023, causing 185 injuries and 15 fatalities, half related to the agri-food industry (Cloney, 2023). Nevertheless, suitable dust explosion preventive measures based on the risk assessment can be applied to improve the safety level at industrial facilities. For instance, inerting systems can use solid inert materials for dust explosion prevention (Amyotte, 2006), which is associated with diminishing the ignition sensitivity (Amyotte et al., 2009) through parameters such as the Minimum Ignition Energy (MIE), which provides information about the type of electrostatic discharges that are likely to ignite a dust cloud. The admixing of inert or non-combustible (e.g., mineral) agents into combustible powder is widely used in diverse industries, such as mining,

pharmaceuticals, food, and animal feed. In the latter industry, minerals are added to mixtures of vitamins, amino acids, and cereals to constitute a complex compound feed named "premixes" to satisfy nutritional animal needs through subsequent post-treatment processes, such as pelleting. These minerals are intentionally mixed into premixes to provide nutrients, enhance flowability, and modify organoleptic product properties. Although their primary purpose is not to prevent explosion, modifications of their chemical nature and mass fraction can then be considered an application of the moderation principle of inherent safety (Amyotte et al., 2009).

The mineral products can inhibit combustible dust ignition and, subsequently, flame spread by physical or chemical inerting mechanisms. The first method comprises processes including the cooling of reacting gases through thermal decomposition, the dilution of combustibles, and the dissipation of combustion heat via the heat sink effect. On the other hand, chemical inerting is associated with the scavenging of combustion reactive radicals, termination reactions, and alteration of combustion kinetics. For instance, Lin et al. (2020) studied the inerting efficiency of four minerals ($NaHCO_3$, $Na_2C_2O_4$, $KHCO_3$, and $K_2C_2O_4$) on the MIE and Minimum Ignition Temperature (MIT) of polyethylene (PE) dust. They found that the bicarbonate group and potassium element had the best inerting performance due to its low thermal decomposition temperature. Similar research analyzed the inerting and inhibition of the explosion severity of organic/mineral mixtures (Liu et al., 2022; Serrano et al., 2023; Yang et al., 2022). In addition, various authors (Addai et al., 2016; Dufaud, Perrin, et al., 2012; Janès et al., 2014) also evaluated the MIE of mixtures of organic dust samples, such as lycopodium, niacin, cornstarch, and minerals, like MgO, $(NH_4)_2SO_4$, SiO_2, and $NaHCO_3$. They reported that the mixtures' MIE significantly increased after a certain mineral concentration threshold between 60 and 90 wt% regarding the inert agent's chemical nature.

Moreover, Zheng et al. (2021) analyzed the inerting efficiencies of other mineral compounds (hydroxides and phosphates) on the MIE of wood dust, in which the O_2 dilution by NH_3 decomposed from phosphate inert agent led to the best ignition sensitivity moderation. Furthermore, the mineral agents' inerting efficiency is also related to their PSDs, in which finer particles are more effective at explosion inerting than coarser ones because of a significant increase in the specific surface area (Amyotte, 2006). Moreover, Amez et al. (2023) illustrated this by comparing the ignition inhibition of toner, lycopodium, and Holi dust by mixing with $NaHCO_3$ at different PSD. They highlighted that the optimum mineral PSD does not need to match the organic sample's PSD because of the influence of the particle shape and agglomeration trends on the mixture dispersibility. Besides, Zhong et al. (2022) observed the most efficient inerting effect on sucrose flame propagation by adding fine $NaHCO_3$ (25 – 37 µm). Nevertheless, research on organic/inert mixtures has rarely considered amino acids as the combustible fraction (common additives into premixes) and their potential interactions with minerals allowable for animal feed. Moreover, most powder products used in the industry have PSD with a large span and coarser particle size, which diverges from the properties of the dust samples commonly used in previous research studies. Therefore, this study aims to study the influence of the mineral's chemical nature and PSD on the MIE of binary mixtures commonly used in premix manufacturing. Consequently, it will broaden the understanding of the involved physicochemical mechanisms and contribute to applying suitable preventive measures.

2. Materials and methods

The methodology followed in this study is divided into four steps: first, the selection of the combustible and mineral powders; second, the selection and characterization of the samples' PSD;

third, the MIE evaluation; and lastly, the mixture thermal analysis and pyrolysis gases identification to improve the understanding of the minerals inerting mechanisms.

2.1. Organic and mineral powder selection

The binary mixture ingredients were selected according to their physicochemical properties and relevance in the animal feed industry. For the combustible fraction, DL-methionine was chosen because it is a widely used organic additive in premix formulations, has low cohesive behavior, and is very sensitive to electrostatic ignition (IFA, 2023). On the other hand, Table 1 shows the three mineral powders chosen based on their distinctness in chemical nature and material properties, like the thermal decomposition temperature (T_{decomp}) and specific heat capacity (C_p). Thus, the inerting effect of each mineral will follow different mechanisms: heat sink by the solid heat capacity and decomposition enthalpy, O_2 dilution, and scavenging of free radicals, as reported by (Amez et al., 2023; Janès et al., 2014; Reding & Shiflett, 2019; Yang et al., 2022).

Table 1. *Mineral material properties*

Compound	Chemical formula	T_{decomp} [K]	C_p [J/mol·K] (400 K – 1000 K)
Calcium Carbonate	$CaCO_3$	923 – 1073	99 – 126
Sodium Chloride	NaCl	1080 – 1235	52 – 65
Sodium Bicarbonate	$NaHCO_3$	400 - 460	88 – N/A

2.2. Particle size characterization

The Particle Size Distribution (PSD) is one of the most influential variables on dust ignition sensitivity (Amyotte, 2006). The PSD of the dust samples was measured using Mie diffraction theory by a Mastersizer 3000 Particle Size Analyzer (Malvern Instruments), which was equipped with the Aero S dry dispersion unit (dispersion pressure: 0.3 bar). Subsequently, the mineral dust samples were sieved in three distinct ranges relevant to industrial applications (A: small – B: medium – C: coarse) to evaluate the inerting effectiveness of the mineral PSD and the mineral's chemical nature considering comparable PSD ranges. Thus, the characteristic diameters (d_{10}, d_{50}, and d_{90}) of the sieved mineral samples are shown in Fig. 1. Otherwise, the methionine sample was sieved only at the lowest range (A) to mitigate the impact of the polydispersity and high ignition sensitivity (Castellanos et al., 2020). The methionine characteristic diameters (d_{10}, d_{50}, and d_{90}) are shown in Table 2.

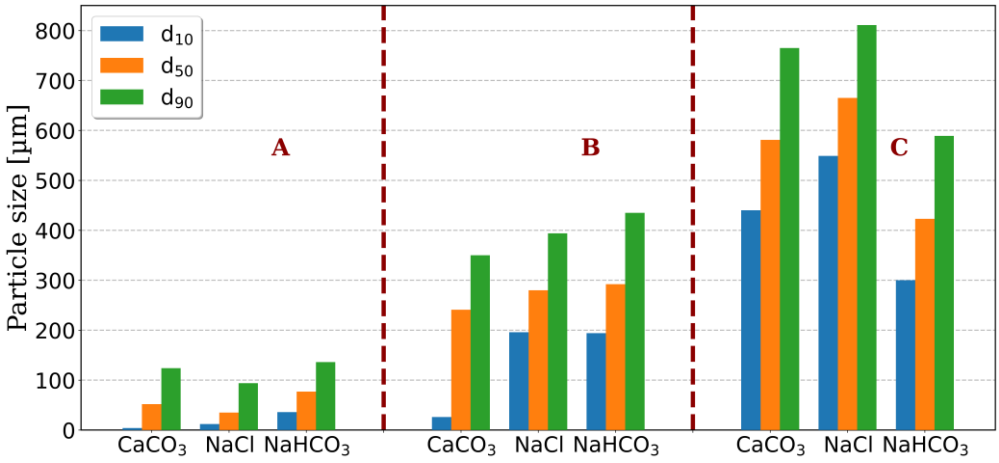

Fig. 1. *Characteristic diameters (d_{10}, d_{50}, d_{90}) of the sieved mineral dust samples at each particle size range category (A, B, C).*

***Table 2**. Methionine material properties*

Compound	Chemical formula	d_{10} [µm]	d_{50} [µm]	d_{90} [µm]
DL-Methionine	$C_5H_{11}NO_2S$	13	62	161

2.3. Ignition sensitivity

The ignition sensitivity of the binary (methionine/mineral) mixtures was studied by evaluating their Minimum Ignition Energy (MIE) ranges. The MIKE3 apparatus was used for the electrostatic ignition tests and the standard MIE determination according to ISO/IEC 80079-20-2 (2016). The experimental runs were performed with an inductance of 1 mH at two ignition delays (t_v = 120 and 150 ms) and for a maximum mixture mass of 3.6 g. The binary mixtures were blended before the MIE test using a 3D mixer (Turbula) to achieve high mixing efficiency, homogeneity, and replicability. Tests were conducted on powders stored at constant relative humidity but not dried to avoid the effects of rapid water adsorption and powder modification. Moreover, the experimental runs for each mineral chemical nature ($CaCO_3$, NaCl, $NaHCO_3$) were chosen based on a factorial experimental design (3^2). Therefore, the DoE factors and levels were the methionine mass fraction (10, 30, 50 wt%) and the mineral's particle size class (A, B, C). A similar approach was followed by (Serrano et al., 2023).

2.4. Inerting mechanism analysis

To highlight the inerting mechanism, the characterization of the thermal behavior by Differential Scanning Calorimetry (DSC) and pyrolyzed gases through the modified Godbert-Greenwald oven and Micro Gas Chromatography (µGC) were performed for the binary mixtures with class A minerals (finest PSD, thus more "reactive" class).

2.4.1. Differential Scanning Calorimetry (DSC)

The DSC analysis was performed using a Mettler Toledo DSC 1, placing 10.0 ± 0.1 mg of the sample inside a 100 µL aluminum crucible under a nitrogen atmosphere inside the furnace. Nitrogen was used to avoid exothermic effects due to oxidation reactions. The tests were performed from 298 K to 773 K under a heating rate of 10 K/min. In this case, the DSC was used to determine the onset temperature of thermal decomposition, measure the heat absorbed during the endothermic decomposition/pyrolysis, and compare the minerals' heat sink efficiency. The samples were prepared at a 1:1 mass ratio between methionine and each mineral sample with PSD class A.

2.4.2. Modified Godbert-Greenwald oven

The Godbert-Greenwald oven, conventionally used for the dust cloud Minimum Ignition Temperature (MIT_c) according to the standard ISO/IEC 80079-20-2 (2016), was modified to be used as a single plug-flow reactor to collect the post-pyrolysis gases of methionine and its mixtures with class A minerals: $CaCO_3$, NaCl, and $NaHCO_3$. For a detailed description of the experimental setup, see (Pietraccini et al., 2023). Nevertheless, the solid trap was not installed because the analysis of the tar and char generated during the pyrolysis is out of the scope of this study. In addition, an argon pulse (0.6 bar) dispersed the powder mixtures into the furnace, and then a collapsible Tedlar bag collected the pyrolysis gases at the oven outlet. Besides, the mass of the tested samples was set at 0.5 g to promote enough pyrolyzed gases in the Tedlar bag and reduce the experimental uncertainties. It is important to note that the furnace setup was flushed with argon before each experimental test to remove the residual air and moisture. Moreover, the oven temperature (923 K) was set considering the operational limitations of the setup; the methionine MIT_c, which is approximately 660 K depending on its PSD (IFA, 2023); and the dust cloud residence time in the heated chamber.

Therefore, this analysis aims to characterize the impact of the admixed minerals in methionine's pyrolyzed gas composition by their thermal contribution. Subsequently, the gas sample was analyzed using a micro gas chromatograph (SRA 3000 µGC equipped with a TCD detector, three ways), in which permanent gases (H_2, O_2, N_2, CH_4, CO, and CO_2), some light hydrocarbons (C_2H_2, C_2H_4, and C_2H_6) and some aromatics (benzene, toluene, and xylene isomers) were measured. The gas samples were injected by triplicate.

3. Results and discussion

The MIE of the binary mixtures with different combustible mass fractions was analyzed in two steps: first, comparing the effect of the mineral's chemical nature (sodium bicarbonate, calcium carbonate, and sodium chloride) at comparative PSD and, second, varying the minerals' PSD. Subsequently, the impact of the mineral fraction on the endothermic decomposition/pyrolysis enthalpy and pyrolyzed gas composition are presented using DSC and µGC techniques, respectively.

3.1. Mineral chemical nature effect

Firstly, the mineral chemical nature effect on the MIE of the methionine mixtures was analyzed considering equivalent particle size ranges for the mineral products to obtain comparative results. Fig. 2 shows the MIE of the binary mixtures at three mass fractions (10, 30, and 50 wt%) and for each mineral sample ($CaCO_3$, NaCl, $NaHCO_3$) with PSD classes B and C. The MIE of the mixtures with 50 and 70 wt% of any mineral was in the same range as the pure methionine MIE, marked as a shaded yellow area (Fig. 2), demonstrating no ignition sensitivity moderation regardless of the mineral's chemical nature. Therefore, the ignition preventive measures recommended for these mixtures are equivalent to the pure combustible product (Amyotte et al., 2009), which agrees with the trend found by other authors (Addai et al., 2016; Amez et al., 2023). Moreover, the MIE of the mixtures at 10 wt% methionine displayed a significant increase, which was more gradual for the blends with class C minerals, as shown in Fig. 2. Such evolution was expected because of the PSD effect on the particle heating time (Zheng et al., 2021). However, the mixture with 90% $NaHCO_3$ class B was the only sample with a MIE > 1000 mJ, corresponding to an almost insensitive powder to electrostatic ignition.

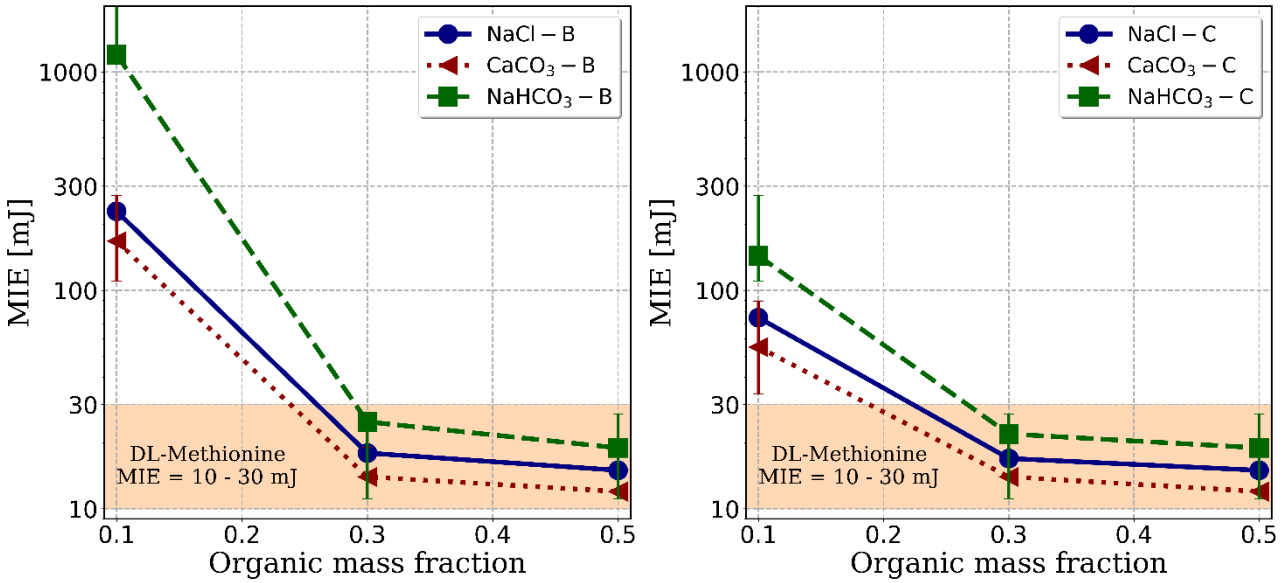

Fig. 2. *Effect of the mixed mineral (NaCl, $CaCO_3$, and $NaHCO_3$) at different particle size range classes (B and C) on the MIE of methionine mixtures. Pure methionine MIE's range is indicated in a yellow shade.*

The $CaCO_3$ and NaCl mixtures evidenced the same MIE evolution throughout the studied methionine mass fraction range (Fig. 2), regardless of the difference between their inerting mechanism. Indeed, the calcium carbonate decomposes into CO_2, diluting the oxygen concentration and modifying the local concentration in reactive species (Liu et al., 2022). On the other hand, the NaCl decomposes into Na· and Cl·, which are reactive agents that are well-known to scavenge free radicals (especially H·, OH·), leading to termination reactions, flame cooling, and potentially flame quenching (Janès et al., 2014; Yang et al., 2022). However, the inerting impact of $CaCO_3$ and NaCl over classes B and C is limited, considering the particle heating times and their thermal stability (T_{decomp} > 800 °C, Table 1) (Amez et al., 2023; Zhong et al., 2022). For instance, the particle heating of calcium carbonate is rate-limited by the heat external transfer (Biot < 0.1), in which, if for class A sample, the heating time necessary to reach the T_{decomp} can be lower than 100 ms, it is multiplied by 10 for class C. Therefore, as shown in Fig. 2, the thermal inerting mechanism predominates over the chemical ones, and the amount of CO_2, Na·, and Cl· released is not sufficient to prevent the ignition phenomenon. Nevertheless, the assortment of heat sinks and species generation by these minerals are enough to modify the ignition sensitivity of the mixtures with 10 wt% methionine. Conversely, the mixtures with 90 wt% $NaHCO_3$ were the least sensitive ones to ignition at both particle classes, as shown in Fig. 2. The $NaHCO_3$ particles undergo a combination of physical (O_2 dilution) and chemical (scavenging of free radicals) inerting mechanisms in the dust flame (Lin et al., 2020). In addition, its thermal decomposition occurs at a significantly lower temperature (Table 1), which implies a higher volume of the concerned species (CO_2, Na·, and Cl·) and more efficient ignition prevention. Moreover, the higher inerting efficiency of $NaHCO_3$ could be seen even with coarse particles with longer heating times (Class C). Hence, the decomposition at lower temperatures into reactive species ($NaHCO_3$) is a more critical parameter than the potential to generate them (NaCl) for preventing dust mixture ignition (Yang et al., 2022).

3.2. Mineral particle size effect

Subsequently, the mineral's particle size effect was evaluated more thoroughly by considering the corresponding PSD's characteristic diameters (d_{10}, due to the large specific surface area developed by small particles and d_{50}). Fig. 3 shows the MIE of the binary mixtures between each mineral sample (chemical nature and particle size class) at a mass fraction of 50 and 90 wt% with methionine. As a general result for methionine-based mixtures, the minerals' inerting efficiency was enhanced by reducing their PSD and increasing their mass fractions (Addai et al., 2016). In addition, the mixes with 50 wt% minerals and coarser particles did not modify the pure methionine MIE, as illustrated by Fig. 3. Such result should notably be analyzed, considering the influence of the mineral's particle segregation (Janès et al., 2014) and the particle heating time. Nonetheless, the PSD threshold at which 90% $NaHCO_3$ inhibits the methionine mixture ignition (d_{50} = 300 µm and d_{10} = 200 µm) is significantly higher than for the other minerals, which agrees with the results obtained by (Amez et al., 2023) with comparable PSD values. Moreover, the 50% methionine mixture can even become insensitive to electrostatic ignition with coarser particles of $NaHCO_3$ (Fig. 3b).

Furthermore, the similarities between the MIE evolution of the 90 wt% $CaCO_3$ and NaCl mixtures (Section 3.1) are reinforced due to the correspondence between the d_{50} of these minerals at each particle size class (Fig. 3a). However, the d_{10} of the $CaCO_3$ samples class A and B are significantly lower than the NaCl equivalent ones (Fig. 3b), pointing out a higher polydispersity and specific surface area. This result suggests that, for a given PSD, $CaCO_3$ particles are more efficient by the thermal sink (Castellanos et al., 2020) than the NaCl ones, leading to potentially higher released amounts of CO_2 than Na· and Cl· reactive species (Zheng et al., 2021). Nevertheless, the NaCl mixtures showed equal or lower ignition sensitivity than $CaCO_3$, implying that the scavenging of free radicals is a more efficient inerting mechanism, as reported by (Janès et al., 2014). Moreover, 50 wt% of NaCl and $NaHCO_3$ could inhibit the methionine mixture ignition if their d_{50} and d_{10} are below 35 and 10 µm, respectively, consistent with the results reported by (Zhong et al., 2022). By contrast, adding 50 wt% $CaCO_3$ with comparable d_{50} and even lower d_{10} (4 µm) is insufficient to prevent the methionine ignition. Such results should be considered for risk assessment and ATEX zoning.

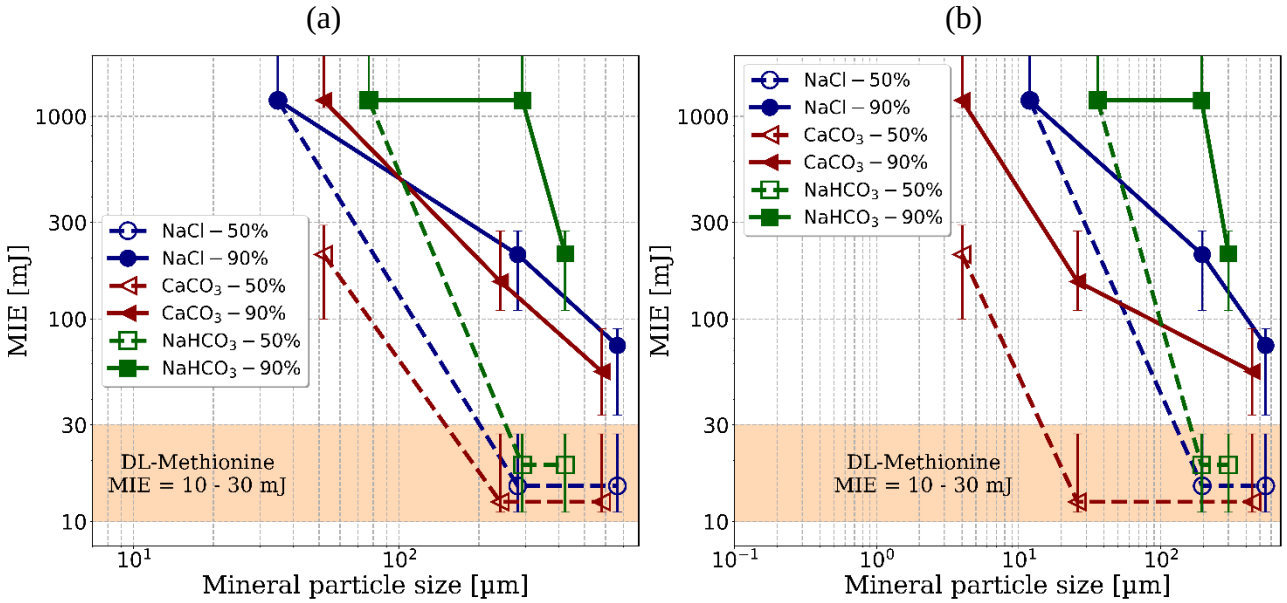

Fig. 3. *Effect of the d_{50} (a) and d_{10} (b) of the mixed mineral (NaCl, $CaCO_3$, and $NaHCO_3$) at different mass fractions on the MIE of methionine mixtures. Pure methionine MIE's range is marked in a yellow shade.*

3.3. Inerting thermal effect

As previously shown, the inerting agent's heat absorption and endothermic thermal decomposition can significantly reduce the combustible dust's MIE (Janès et al., 2014). Hence, the thermal effect of the three admixed minerals ($CaCO_3$, NaCl, and $NaHCO_3$) was characterized using DSC techniques, and the main parameters of their heat flow curve are detailed in Table 3, including the values of the pure $NaHCO_3$ and methionine (Met). A comparison, at equal mass, between pure Met and its mixtures with $CaCO_3$ and NaCl shows that no significant changes are observed in the onset temperature or the heat absorbed by the samples. This behavior is undoubtedly due to the high thermal stability of both compounds in the studied temperature range (Table 1). Nevertheless, the $CaCO_3$ sample removed slightly more heat because of its higher polydispersity and lower d_{10}, as shown in Fig. 1 (class A).

Table 3. *DSC curves parameters of the binary mixture and some pure ingredients*

Mixture	Onset temperature [K]	Peak temperature [K]	Heat absorption [J]
Met	548	550	-328[a]
$NaHCO_3$	396	428	-339[a]
Met – NaCl	539	549	-342
Met – $CaCO_3$	547	551	-356
Met – $NaHCO_3$	492	500	-593

[a] *Decomposition enthalpy of the actual mass admixed*

By contrast, adding $NaHCO_3$ increased by 80% the amount of heat required to pyrolyze the methionine present in the mixture and led to a shift in the onset and peak temperatures. Hence, this inerting agent is significantly the most efficient because of its decomposition at low temperatures (430 K). The $NaHCO_3$ particles efficiently removed heat from the Met particles and released inert gases (CO_2) that diluted the oxygen concentration even before the pyrolysis step (550 K), as indicated

by Table 3, which evidences the main difference with the other minerals inerting mechanisms. Nevertheless, it is essential to highlight that the chemical mechanisms and the high-temperature decomposition of $CaCO_3$, NaCl, and the generated Na_2CO_3 (Lin et al., 2020; Liu et al., 2022; Yang et al., 2022) were not analyzed due to operational constraints (Section 2.4.1).

3.4. Methionine pyrolysis gases and mineral effect

Evaluating the admixed minerals' effect on the methionine pyrolysis step could give more clues about the inert/combustible interactions during the ignition stage. Therefore, the pyrolyzed gases of methionine and methionine/minerals binary mixtures were analyzed using the modified Godbert-Greenwald oven (Section 2.4.2). The identified pyrolysis gases of methionine and their molar concentrations are shown in Fig. 4. They are consistent with the compounds obtained by Merritt and Robertson (1967). The traces of light hydrocarbons (C_2H_6, C_2H_2, and C_3H_8) and aromatic compounds (benzene and toluene) were disregarded. In addition, the measured oxygen concentration and the corresponding nitrogen values were neglected because they were associated with air leaks in the experimental setup. Nevertheless, the results indicate that some N_2 was generated during the methionine pyrolysis (Fig. 4), as expected considering its chemical nature (Table 2). Furthermore, the relative concentration of CH_4 and C_2H_4 regarding H_2 is significantly larger than the pyrolysis gas composition of starch and cellulose obtained by (Pietraccini et al., 2021), which is consistent with the fact that methionine is a sulfur-containing amino acid that generates hydrogen sulfide (H_2S) as one of its main compounds (Choi et al., 1995). Nevertheless, the sulfur group leads to more complex pyrolysis patterns (Fujimaki et al., 1969; Posthumus & Nibbering, 1977) that are out of the scope of the present study. For instance, the methionine pyrolysis could generate a group of amines (e.g., $C_4H_{11}NS$) and more complex compounds at significant amounts like methanethiol (CH_3SH), dimethyl sulfide ($(CH_3)_2S$) and dimethyl disulfide ($C_2H_6S_2$) (Xu et al., 2021), which were not measurable by the experimental setup used. In this perspective, the tar trap used by (Pietraccini et al., 2023) could be used in the future.

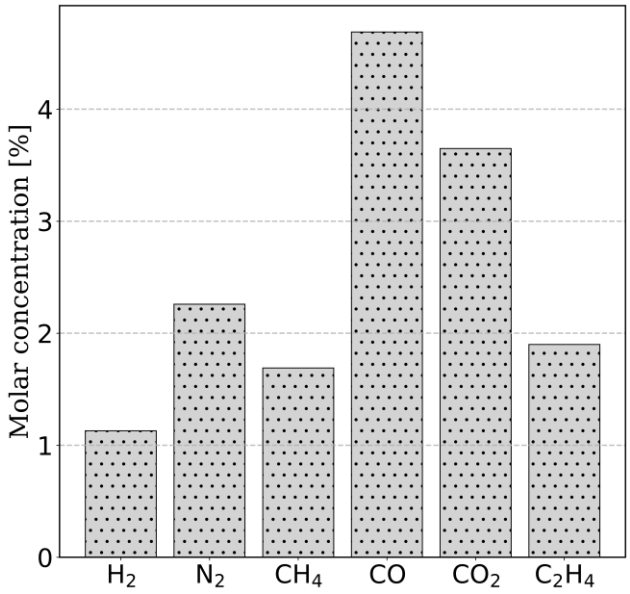

Fig. 4. *Molar concentration of gases obtained from methionine flash pyrolysis.*

Subsequently, the pyrolysis gases from mixtures of a 1:1 mass ratio between methionine and mineral ($NaHCO_3$, NaCl, and $CaCO_3$) were analyzed. However, considering the complexity of methionine's pyrolysis previously detailed, the mineral effect analysis focuses on the impacts of the heat sink and oxygen dilution (e.g., CO_2 release), not on the pyrolysis mechanism itself. Therefore, the calculated ratio between the CO/CO_2 obtained by the binary mixtures was chosen as the variable of interest, as shown in Fig. 5. The trend between NaCl and $CaCO_3$ mixtures is consistent with the shift of the C/CO_2 equilibrium towards CO when the temperature increases (Dufaud, Poupeau, et al., 2012; Pietraccini et al., 2021). The $CaCO_3$ sample removes heat more efficiently because of its PSD, as shown in Table 3, and lower T_{decomp} than NaCl (Liu et al., 2022). Nevertheless, the CO_2 generation from $CaCO_3$ is not considered because it occurs at a temperature higher than the one set for the experiment (Table 1). However, this result is invalid for the conclusion that $CaCO_3$ is a better inerting agent than NaCl. Indeed, the experimental setup did not emulate the ignition and flame kernel growth, for which the chemical inerting mechanism of NaCl is more efficient, as shown by Fig. 2. On the other hand, $NaHCO_3$ behaved as a more efficient heat sink (endothermic decomposition). It generated CO_2, reducing more than half the other compounds' CO/CO2 ratio (Fig. 5). Thus, $NaHCO_3$ is validated as the most efficient inerting agent, considering its influence since the organic pyrolysis step, where it absorbs heat and dilutes local O_2 concentration.

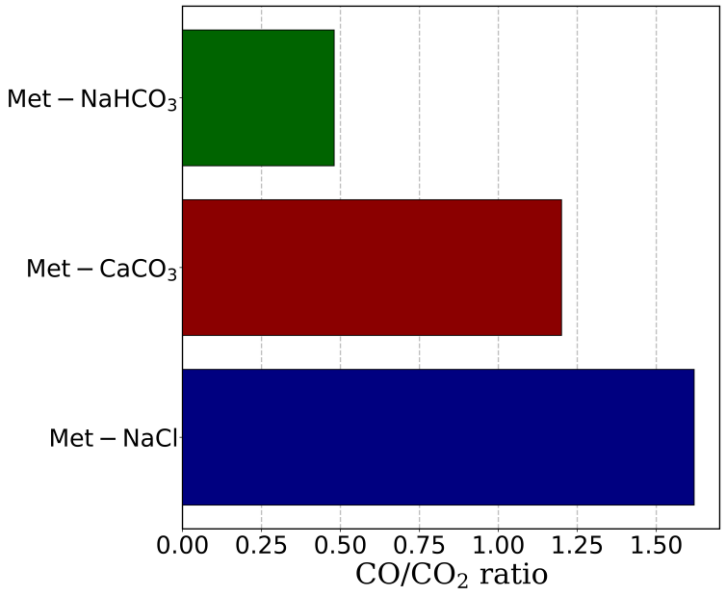

Fig. 5. *The ratio between CO and CO_2 generated by the pyrolysis of methionine (Met) and minerals mixtures.*

4. Conclusions

Admixing solid inertants is a compelling ignition prevention strategy for premix production in the animal feed sector by applying the moderation principle of inherent safety. This option is all the easier to consider as it is already part of the manufacturing process. A better understanding of the modes of action of these inert powders means that, within the limits of the industrial applications targeted, safer formulations can be chosen. Moreover, this study contributes to determining ATEX zones and implementing the associated preventive measures (e.g., earthing, choice of FIBC type - Flexible Intermediate Bulk Container).

The MIE characterization of simplified versions of premixes with different combustible fractions, PSD, and mineral chemical nature contributes to a better understanding of the ignition sensitivity of

industrial premixtures. This study determined that $NaHCO_3$ is the most efficient ignition inhibitor agent due to its physical and chemical inerting mechanisms. It endothermically decomposes at a temperature lower than the methionine pyrolysis, removes heat from the preheating flame zone, releases inert gases (CO_2) that drop down local O_2 concentration, and generates reactive species ($Na\cdot$), which hinders combustion radicals at elevated temperature. For instance, in parallel experimental tests, the mass fraction range in which $NaHCO_3$ class A prevented the methionine ignition is between 30 and 45%. However, this mineral did not inhibit the ignition when coarser particles were used, which evidences that the mineral PSD is the most significant factor for defining the inerting efficiency. Such behavior is notably due to particle segregation (e.g., caused by the differential sedimentation between finer, lighter organic particles and mineral powders) and the heating time to reach the onset decomposition temperature while the flame propagates. Hence, the suitable mineral chemical nature (oxide, carbonate, and bicarbonate) intended to moderate the ignition sensitivity of a premix should consider the proper particle size range constraints. Nevertheless, the chemical interactions between the minerals and complex organic additives (sulfur-containing) still represent an uncertainty. Further research aims to develop a simplified MIE model for organic/mineral mixtures.

Acknowledgments

The authors gratefully acknowledge the support of the Club EMIX partners.

References

Addai, E. K., Gabel, D., & Krause, U. (2016). Experimental investigations of the minimum ignition energy and the minimum ignition temperature of inert and combustible dust cloud mixtures. *Journal of Hazardous Materials*, *307*, 302–311. https://doi.org/10.1016/j.jhazmat.2016.01.018

Amez, I., Castells, B., León, D., García-Torrent, J., & Medic, L. (2023). Experimental study on inert products, moisture, and particle size effect on the minimum ignition energy of combustible dusts. *Journal of Loss Prevention in the Process Industries*, *81*, 104968. https://doi.org/10.1016/j.jlp.2022.104968

Amyotte, P. (2006). Solid inertants and their use in dust explosion prevention and mitigation. *Journal of Loss Prevention in the Process Industries*, *19*(2–3), 161–173. https://doi.org/10.1016/j.jlp.2005.05.008

Amyotte, Paul., Pegg, M. J., & Khan, F. I. (2009). Application of inherent safety principles to dust explosion prevention and mitigation. *Process Safety and Environmental Protection*, *87*(1), 35–39. https://doi.org/10.1016/j.psep.2008.06.007

Castellanos, D., Bagaria, P., & Mashuga, C. V. (2020). Effect of particle size polydispersity on dust cloud minimum ignition energy. *Powder Technology*, *367*, 782–787. https://doi.org/10.1016/j.powtec.2020.04.037

Choi, S. Y., Kim, M. G., & Inoue, H. (1995). Determination of sulfur in biologically important substances by pyrolysis-gas chromatography. *Journal of Analytical and Applied Pyrolysis*, *32*, 127–136. https://doi.org/10.1016/0165-2370(94)00833-M

Cloney, C. (2023). 2022 Combustible Dust Incident Report - Version #1. *DustEx Research Ltd.* https://dustsafetyscience.com/2022-Report

Dufaud, O., Perrin, L., Bideau, D., & Laurent, A. (2012). When solids meet solids: A glimpse into dust mixture explosions. *Journal of Loss Prevention in the Process Industries*, *25*(5), 853–861. https://doi.org/10.1016/j.jlp.2012.04.011

Dufaud, O., Poupeau, M., Khalili, I., Cuervo, N., Christodoulou, M., Olcese, R., Dufour, A., & Perrin, L. (2012). Comparing Pyrolysis Gases and Dusts Explosivities: A Clue to Understanding Hybrid Mixtures Explosions? *Industrial & Engineering Chemistry Research*, *51*(22), 7656–7662. https://doi.org/10.1021/ie201646s

Fujimaki, M., Kato, S., & Kurata, T. (1969). Pyrolysis of Sulfur-containing Amino Acids. *Agricultural and Biological Chemistry*, *33*(8), 1144–1151. https://doi.org/10.1080/00021369.1969.10859440

IFA, I. for O. S. and H. of the G. S. A. I. (2023). *GESTIS-DUST-EX: Database Combustion and explosion characteristics of dusts*.

ISO/IEC 80079-20-2. (2016). *Explosive atmospheres — Part 20-2: Material characteristics — Combustible dust test methods*. International Electrotechnical Commission.

Janès, A., Vignes, A., Dufaud, O., & Carson, D. (2014). Experimental investigation of the influence of inert solids on ignition sensitivity of organic powders. *Process Safety and Environmental Protection*, *92*(4), 311–323. https://doi.org/10.1016/j.psep.2014.04.008

Lin, C., Qi, Y., Gan, X., Feng, H., Wang, Y., Ji, W., & Wen, X. (2020). Investigation into the Suppression Effects of Inert Powders on the Minimum Ignition Temperature and the Minimum Ignition Energy of Polyethylene Dust. *Processes*, *8*(3), 294. https://doi.org/10.3390/pr8030294

Liu, J., Meng, X., Yan, K., Wang, Z., Dai, W., Wang, Z., Li, F., Yang, P., & Liu, Y. (2022). Study on the effect and mechanism of Ca(H2PO4)2 and CaCO3 powders on inhibiting the explosion of titanium powder. *Powder Technology*, *395*, 158–167. https://doi.org/10.1016/j.powtec.2021.09.067

Merritt, C., & Robertson, D. H. (1967). The Analysis of Proteins, Peptides and Amino Acids by Pyrolysis-Gas Chromatography and Mass Spectrometry. *Journal of Chromatographic Science*, *5*(2), 96–98. https://doi.org/10.1093/chromsci/5.2.96

Pietraccini, M., Badu, P., Tait, T., Glaude, P.-A., Dufour, A., & Dufaud, O. (2023). Study of flash pyrolysis and combustion of biomass powders using the Godbert-Greenwald furnace: An essential step to better understand organic dust explosions. *Process Safety and Environmental Protection*, *169*, 458–471. https://doi.org/10.1016/j.psep.2022.11.041

Pietraccini, M., Delon, E., Santandrea, A., Pacault, S., Glaude, P.-A., Dufour, A., & Dufaud, O. (2021). Determination of heterogeneous reaction mechanisms: A key milestone in dust explosion modelling. *Journal of Loss Prevention in the Process Industries*, *73*, 104589. https://doi.org/10.1016/j.jlp.2021.104589

Posthumus, M. A., & Nibbering, N. M. M. (1977). Pyrolysis mass spectrometry of methionine. *Organic Mass Spectrometry*, *12*(5), 334–337. https://doi.org/10.1002/oms.1210120516

Reding, N. S., & Shiflett, M. B. (2019). Characterization of Thermal Stability and Heat Absorption for Suppressant Agent/Combustible Dust Mixtures via Thermogravimetric Analysis/Differential Scanning Calorimetry. *Industrial & Engineering Chemistry Research*, *58*(11), 4674–4687. https://doi.org/10.1021/acs.iecr.8b06143

Serrano, J., Nowicki, A., Perrin, L., & Dufaud, O. (2023). Effect of Particle Size Distribution and Inerting Mechanism on Explosion Severity of Organic/Mineral Mixtures. *Chemical Engineering Transactions*, *104*, 55–60. https://doi.org/10.3303/CET23104010

Xu, L., Cheng, J.-H., Ma, X.-Q., Shen, J.-Y., Xu, Z.-X., & Duan, P.-G. (2021). Transformation of the Sulfur Element during Pyrolysis of Sewage Sludge at Low Temperatures. *Energy & Fuels*, *35*(1), 501–509. https://doi.org/10.1021/acs.energyfuels.0c02706

Yang, P. P., Meng, X., Zhang, Y., Liu, J. Q., Yan, K., Li, F., Wang, Z., Liu, Y., Dai, W. J., & Wang, Z. (2022). Experimental study and mechanism analysis on the suppression of flour explosion by NaCl and $NaHCO_3$. *Combustion Science and Technology*, 1–16. https://doi.org/10.1080/00102202.2022.2056412

Zheng, L., Yu, Y., Yang, J., Zhang, Q., & Jiang, J. (2021). Inhibiting effect of inhibitors on ignition sensitivity of wood dust. *Journal of Loss Prevention in the Process Industries*, *70*, 104391. https://doi.org/10.1016/j.jlp.2021.104391

Zhong, Y., Li, X., Jiang, J., Liang, S., Yang, Z., & Soar, J. (2022). Inhibition of Four Inert Powders on the Minimum Ignition Energy of Sucrose Dust. *Processes*, *10*(2), 405. https://doi.org/10.3390/pr10020405

Passive Ventilation of a Volatile Liquid Spill in an Enclosure

S. Raghuram [a], V. Raghavan [a] & Ali S. Rangwala [b]

[a] Department of Mechanical Engineering, Indian Institute of Technology Madras, Chennai 600036, India
[b] Department of Fire Protection Engineering, Worcester Polytechnic Institute, Worcester, MA 01609, USA

E-mail: rangwala@wpi.edu

Abstract

Flammable liquid spill in an enclosure poses a common explosion hazard in an industrial setting. The ensuing explosive vapor leak is analysed in an enclosure with a single opening on the wall at two different ambient temperatures, 293 K and 350 K. Ten different liquids, with wide range of flammability, used in varied applications (fuels in automobiles/aircrafts, electrolytes in batteries of e-mobility devices, solvents in chemical process industry) are chosen and their area of spread (typically less than the floor area) is calculated for a given spillage volume. Quasi-steady evaporation from the unrestrained liquid spill is modelled considering fuel properties at constant temperature and pressure. This is coupled with the passive ventilation model of a heavy vapor (which assumes a uniform mixing of fuel and air), to predict the steady state concentration within the enclosure. This forms a neutral plane which demarcates the regions of the mixture exiting and air entraining the enclosure. The assumption of equal flow rates (of the exiting mixture and the entraining air, resulting in neutral plane at the center of the opening) in the natural ventilation model is relaxed in the passive ventilation model, resulting in 25% higher values of the concentration predicted. For a given geometric parameter of the opening and spill area, the model solves for the height of the neutral plane, the mass flow rate of the mixture issuing out, the mass flow rate of entraining air, and the density of the mixture in the enclosure. The critical geometric parameter of the opening that leads to an explosive mixture is identified for each of the liquid spills. This value for n-Pentane (which poses the highest explosion hazard) is 45%, 83% of the corresponding wall value at 293 K and 350 K respectively. For a standard range of vent sizes, Class II and Class III spills are found to result in safe concentration levels at standard room temperature (293 K), with Class III B being safe even at 350 K.

Keywords: *liquid spill, enclosure, passive ventilation, geometric parameter, explosion hazard*

Introduction

Several flammable liquids are being used on a daily basis in various industrial, commercial and domestic applications and are stored in containers placed in enclosures. In the event of a spillage, the liquid would vaporize, mix with ambient air, possibly forming a flammable mixture within the enclosure. Understanding the potential hazard associated with flammable liquid spills in vented enclosures is crucial to the safe storage of these liquids. This requires prediction of evaporation rate and concentration buildup for a given opening size in the enclosure. Natural ventilation was assumed by Brown and Solvason (1962), where equal volume flow rate of exiting mixture and entraining air is considered. This assumption will not hold good for large gas buildup where the enclosure is almost completely filled by the vapor. Also ceiling and floor openings, instead of opening on the walls cannot be analyzed using this approach. A comprehensive review has been provided by Linden (1999), discussing various aspects related to natural ventilation.

Passive ventilation model was developed by Molkov et al. (2014), where the assumption of equal volume flow rate is relaxed. In this model, the location of the neutral plane (NP), which divides the

exiting mixture from the entraining air, is a function of the opening size, the gas properties and the mass flow rate. Molkov et al. (2014) have validated the model with experimental data of Cariteau and Tkatschenko (2013) for leakage of helium gas. They found that the concentration predicted using the passive ventilation model closely follows the experimental data, while the results from the natural ventilation model are unrealistic. They further derive an expression for minimum gas flow rate that would lead to 100% concentration buildup within the enclosure.

The natural and passive ventilation models discussed above have been formulated for sustained leakage of a light gas in an enclosure. In the present work, the passive ventilation model of a heavy vapor, adapted from Molkov et al. (2014) is coupled with quasi-steady evaporation model to predict concentration buildup due to a liquid spill within an enclosure with single opening. Ten different commonly used liquids spanning a wide range of flammability/combustibility are considered and their steady state concentration buildup within the enclosure is evaluated.

The paper is organized as follows. Section 1 presents the model for evaporation of liquid spill coupled with the enhanced passive ventilation model for sustained leak of heavy gas in an enclosure with single opening. This is followed by a subsection on validation of the model with experimental data from literature. In Section 2, the steady state vapor concentration buildup within the enclosure for the flammable liquids chosen in the analysis are presented and compared. The paper ends with a Section 3 on the conclusions of the study.

1. Mathematical Model

The model focuses on predicting the concentration buildup in an enclosure due to a liquid spill. The liquid spill could possibly be due to a leak in the container storing the fuel placed inside an enclosure. The size of spread of the liquid spill is first characterized. The rate of evaporation of the liquid spill is next determined assuming steady evaporation. Finally, for the calculated steady evaporation rate of the liquid spill, the concentration buildup of the fuel vapor within the enclosure for a given opening configuration is evaluated. This enables the prediction of the potential explosion hazard associated with a particular fuel due to a spillage event.

1.1. Size and spread of the liquid spill

The size and spread of the spill will depend on various external factors such as surface elevation difference, porosity of the surface, surface undulations. For a relatively flat, smooth and non-porous surface, the minimum depth of the spillage can be obtained assuming a balance between hydrostatic pressure and surface tension (Rangwala and Zalosh, 2023; Hiemenz and Rajagopalan, 2016)

$$d = \sqrt{\frac{2\sigma(1-cos\theta)}{\rho_L g}} \tag{1}$$

where d is the minimum spill depth (m), σ is the surface tension (N/m), ρ_L is the density of the liquid fuel, g is the acceleration due to gravity and θ is the contact angle. For concrete surfaces, most commonly used in an industrial setting, $\theta = 25^oC$ (Rangwala and Zalosh, 2023; Hiemenz and Rajagopalan, 2016).

1.2. Steady evaporation of the liquid spill

The properties of the liquid fuel that largely influence the evaporation rate are the boiling temperature and the volatility. Solving the coupled heat and mass transfer conservation equations at the surface of the spill, results in an expression for evaporation rate in terms of the mass flux of fuel vapor emanating from the spill surface (Rangwala and Zalosh, 2023; Kanury, 1977),

$$\dot{m}_F'' = \frac{h}{C_{p,G}} \ln(1+B_T) = \frac{\rho_G h D}{k_G} \ln(1+B_D) \tag{2}$$

where k_G is the thermal conductivity of air (W/mK), $C_{p,G}$ is the specific heat of air (J/kgK), ρ_G is the density of air (kg/m^3), D is the fuel vapor mass diffusivity in air (m^2/s). B is the Spalding number, which can be calculated using energy/species balance as

$$B_T = \frac{C_{p,F}\left(T_\infty - T_s\right)}{L} \tag{3}$$

$$B_D = \frac{Y_{F,s}}{1 - Y_{F,s}} \tag{4}$$

where $C_{p,F}$ is the specific heat of the fuel vapor (J/kgK) T_s, $Y_{F,s}$ are the temperature, mass fraction at the spill surface, T_∞ is the ambient temperature and L is the latent heat of vaporization of the fuel (J/kg). The Spalding heat transfer number, B_T is the ratio of the rate of heat transfer from the spill surface to the ambient to the rate of heat transfer from the bulk of the spill to the spill surface. Here, the sensible heat required to raise the temperature of the liquid bulk to the surface temperature is neglected due to the assumption of rapid heat transfer in the liquid phase, the latent heat required to vaporize the liquid fuel is considered. The Spalding mass transfer number, B_M is the ratio of the rate of mass transfer from the fuel surface to the ambient, to the rate of mass transfer from the fuel bulk to the fuel surface. Here, the fuel mass fraction of the liquid bulk is one, since pure liquid fuels are considered, the fuel vapor mass fraction in the ambient is assumed zero. The mass fraction at the spill surface, $Y_{F,s}$ can be obtained from the mole fraction, $X_{F,s}$, which is related to the partial vapor pressure, and can be calculated using the thermodynamic equilibrium relations like the Clausius Clapeyron equation given by

$$X_{F,s} = \exp\left\{\frac{-L\,MW_F}{R_u}\left(\frac{1}{T_s} - \frac{1}{T_b}\right)\right\}; Y_{F,s} = \frac{X_{F,s}\,MW_F}{MW_{mix}} \tag{5}$$

where MW_F is the molecular weight of the fuel (kg/kmol), T_b is the boiling temperature (K), R_u = *8314 J/kmol-K* is the universal gas constant, and the mixture molecular weight is calculated as $MW_{mix} = X_{F,s}\,MW_F + (1\text{-}X_{F,s})\,MW_{air}$. Equations 3-5 are solved iteratively to obtain the equilibrium spill surface temperature and concentration, T_s, $Y_{F,s}$. The value of surface temperature is initially taken as $T_s = T_\infty - 20$, and is changed in every iteration till the equality in Equation (2) is satisfied. Heat is convected from the spill surface to the ambient air by natural convection. The typical value of heat transfer coefficient that corresponds to heat transfer by natural convection from internal surfaces of rooms in buildings lies in the range of 1-5 W/m^{2}K (Awbi, 1998). Hence, a value of h = *5 W/m^{2}K* is chosen and used throughout the present analysis.

1.3. Concentration buildup within the enclosure

The fuel vapor generated is assumed to mix steadily with the air within the enclosure, leading to a homogeneous fuel-air mixture. The passive ventilation model of Molkov et al. (2014), which is based on this uniform and steady mixing assumption is employed to determine the mass flow rates of the exiting mixture and entraining air and thus the concentration of the mixture. The height of the neutral plane (NP) which demarcates the regions of mixture exiting and air entraining the enclosure as shown in Figure 1 is also evaluated. The mixture if heavier compared to air, exits below the NP, while a lighter mixture exits above it. This would mean, the pressure difference about the opening of the enclosure is zero only at the NP and is non-zero otherwise.

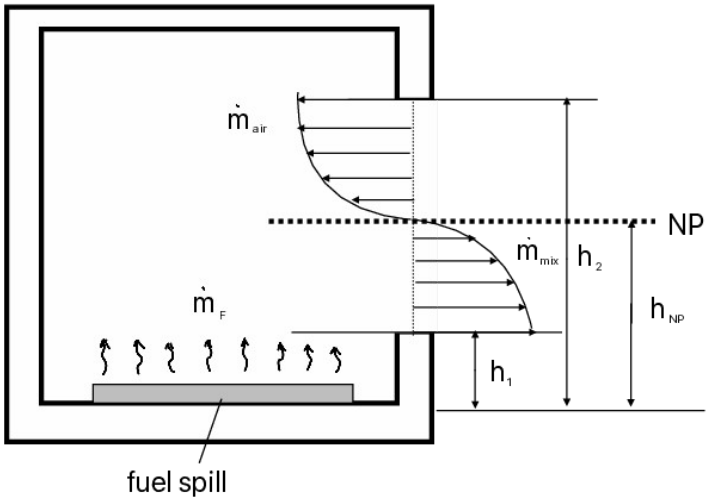

Fig. 1. *Schematic showing gaseous leak in an enclosure due to liquid spill with a single opening, considering passive ventilation. The neutral plane (NP) demarcates the region of exiting mixture from that of the entraining air. Mass flow rate of the exiting heavy mixture and entraining air are denoted as $\dot{m}_{mix}$, $\dot{m}_{air}$. The mass flow rate of evaporation of the liquid spill is denoted as $\dot{m}_F$. All heights are measured from the bottom of the enclosure. The height of the lower edge, upper edge and NP of the opening are denoted as h_1 , h_2 , h_{NP}.*

The following hydrostatic equations give the variation of the external and internal pressures.

$$p_{\text{ext}}(h)+\rho_{\text{mix}}\, g h = p_{NP}+\rho_{\text{mix}}\, g\, h_{NP} \tag{6}$$

$$p_{\text{int}}(h)+\rho_{\text{air}}\, g h = p_{NP}+\rho_{\text{air}}\, g\, h_{NP} \tag{7}$$

The pressure difference, $\Delta p\,(h) = p_{ext}(h) - p_{int}(h)$ that drives the flow across the opening is given as

$$\Delta p(h) = \Delta\rho g\left|h - h_{NP}\right| \tag{8}$$

where $\Delta\rho = |\rho_{air} - \rho_{mix}|$ is the absolute density difference. Using Bernoulli's equation, the velocity profile for the exiting mixture and entraining air is calculated from $\Delta p\ (h)$ expression.

$$U_{\text{mix}}(h) = \left\{ 2g\left|1-\frac{\rho_{\text{air}}}{\rho_{\text{mix}}}\right|\left|h-h_{NP}\right|\right\}^{1/2} \tag{9}$$

$$U_{\text{air}}(h) = -\left\{ 2g\left|1-\frac{\rho_{mix}}{\rho_{air}}\right|\left|h-h_{NP}\right|\right\}^{1/2} \tag{10}$$

The mass flow rates on either side of the NP are calculated by the integration of the respective velocity profiles.

$$\dot{m}_{\text{mix}} = \rho_{\text{mix}}\, W\left|\int_{h_{\text{NP}}}^{h_m} U_{\text{mix}}(h)\,dh\right| = \frac{2}{3} W\left(2g\,\rho_{\text{mix}}\,\Delta\rho\right)^{1/2}\left|h_m - h_{NP}\right|^{3/2} \tag{11}$$

$$\dot{m}_{\text{air}} = \rho_{\text{air}}\, W\left|\int_{h_{\text{NP}}}^{h_k} U_{\text{air}}(h)\,dh\right| = \frac{2}{3} W\left(2g\,\rho_{\text{air}}\,\Delta\rho\right)^{1/2}\left|h_k - h_{NP}\right|^{3/2} \tag{12}$$

where W is the width of the opening and k=1, m=2 for light gas; k=2, m=1 for heavy gas. Mass conservation applied to the enclosure gives

$$\dot{m}_{\text{mix}} - \dot{m}_{\text{air}} = \dot{m}_F = Y_F\,\dot{m}_{\text{mix}} = X_F\,\rho_F/\rho_{\text{mix}} = \rho_F\, Q_F \tag{13}$$

where Y_F is the mass fraction of the fuel and X_F is the volume fraction of the fuel (hereafter referred to as the steady state fuel concentration or simply concentration). Q_F is the volumetric leak flow rate of the gas. The mass flow rate of the fuel vapor leaking into the enclosure, $\dot{m}_F$ in Equation 13 is obtained from the spill evaporation mass flux, $\dot{m}_F''$ (from the evaporation model) in Equation 2, as $\dot{m}_F = \dot{m}_F'' A$, where $A_s = V_s/d$ is the spillage area, V_s is the volume of the spillage. The concentration buildup within the enclosure for a given fuel spill depends both on the evaporation characteristics and the buoyancy driven flow characteristics. The Equations 5, 6, 7, 8 can be rearranged to give

$$\frac{\rho_{\text{mix}}}{\rho_{\text{air}}} = 1 + X_F\left(\frac{\rho_F}{\rho_{\text{air}}} - 1\right), \tag{14}$$

$$Q_F = \frac{2\sqrt{2}}{3} C_D A \sqrt{g' H}\left(\frac{X_F}{Z_F}\right)^{3/2}, \tag{15}$$

$$\Delta h_{NP} = \frac{H\left(\frac{\rho_{mix}}{\rho_{air}}\right)^{1/3}}{Z_F}, \tag{16}$$

$$Z_F = \left(1 - X_F\right)^{2/3} + \left(\frac{\rho_{mix}}{\rho_{air}}\right)^{1/3} \tag{17}$$

$g' = g\left|1 - \rho_F/\rho_{air}\right|$ is the reduced gravity, g is the acceleration due to gravity, $\Delta h_{NP} = |h_{NP} - h_m|$ is the height from NP through which the mixture exits, H = h_2 - h_1 is the height of the opening and C_D is the coefficient of discharge, a multiplier that accounts for the exit losses, with typical values between 0.60 and 0.65 for small square edged openings (ASHRAE Handbook, 2001). $C_D = 0.6$ is used in the present study. The mass flow rate of the exiting mixture and that of the entraining air can be calculated as $\dot{m}_F = \rho_{mix} Q_F/X_F$ and $\dot{m}_{air} = (1+Y_F)\,\dot{m}_{mix}$. It is to be noted that this formulation assumes the mixture to be uniform throughout the enclosure and does not consider stratification.

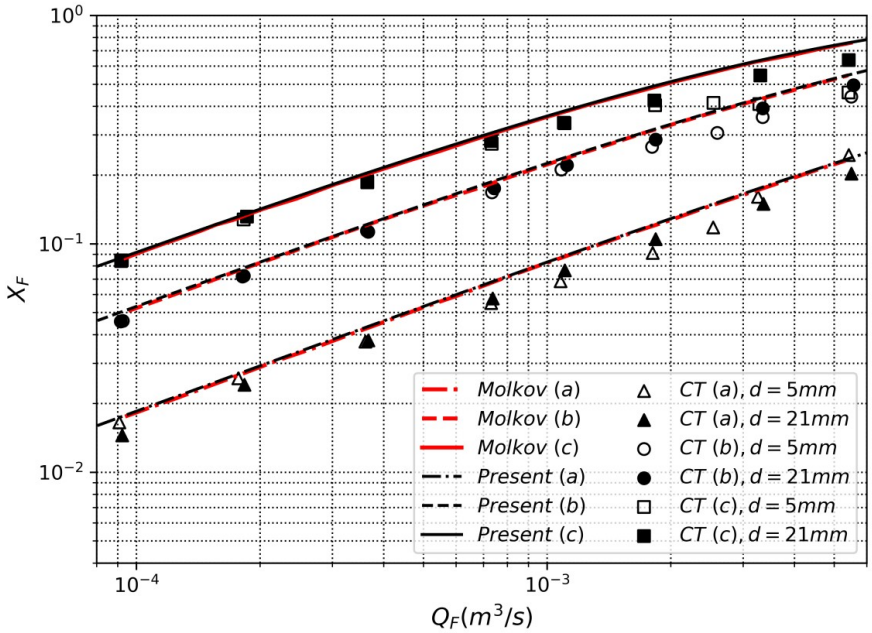

Fig. 2. *Steady state mixture concentration predicted by the passive ventilation model (shown using thin black lines for the present model, thick red lines for Molkov et al., 2014), compared with the maximum helium concentration from experiments (shown using symbols) of Cariteau and Tkatschenko (2013) plotted with leak flow rates for the various opening configurations considered.*

1.3.1. Comparison with experimental data

In order to validate the closed form solution obtained for the passive ventilation model, the results are compared with experimental data of Cariteau and Tkatschenko (2013). The leakage of helium gas ejected from a tube placed 21 cm above the floor in an enclosure with base dimensions 0.93 m x 0.93 m and height 1.26 m was studied by Cariteau and Tkatschenko (2013) for various flow rates. Three different opening configurations are considered here for validation of the model: *W x H = 90 cm x 18 cm* (Opening a), *W x H = 18 cm x 18 cm* (Opening b) and *W x H = 90 cm x 3.5 cm* (Opening c). The steady state concentration for these configurations is calculated using the model for various leak flow rates using Equation 10 and compared with experimental data of Cariteau and Tkatschenko (2013) in Figure 2. The model slightly overpredicts when compared to the experimental data possibly due to the uniform mixing assumption made.

2. Results and discussion

The purpose of this study is to evaluate the concentration buildup in an enclosure due to a volatile, flammable liquid spill. Flammability is characterized by the flash point, T_F and the boiling temperature, T_b of the liquid. NFPA 30 (Benedetti, 1998) classifies flammable/combustible fuels into three major classes with minor divisions, based on the values of T_F and T_b: flammable liquids belong in Class I, and combustible liquids in Class II (low flash point) and Class III (high flash point). Various widely used liquid fuels (employed in automobile, industrial and domestic applications) that fall under these three classes (and their divisions) are chosen for the current study. Two fuels, dimethyl carbonate and ethylene carbonate, which are used as solvents in electrolytes of lithium-ion batteries are chosen. They are of particular interest due to the increasing importance of addressing the issue of thermal runaway and the resulting explosion hazard in such batteries, which are now widely being used in e-mobility devices. These fuels (in increasing order of T_F) are listed in Table 1 along with their NFPA 30 classification and their important properties required in this study. Surrogate fuels have been used to evaluate the properties of blended fuels, Iso-octane for Gasoline (Zhen et al., 2017), n-Dodecane for Diesel Fuel (Farrell and Peters, 1986), n-Heptylcyclopentane for Kerosene (Wang, 2001), n-Hexadecane for Motor Oil (Maharjan et al., 2018).

***Table 1**. Properties of various flammable liquids considered in the present study at 293 K*

Liquid Fuels	**NFPA 30 Class**	**T_F (K)**	**T_b (K)**	**LFL (%)**	**MW (g/mol)**	**ρ_L (kg/m^3)**	**σ x 10^2 (N/m)**	**d (mm)**	**A_s (m^2)**
n-Pentane	I A	222.0	309.2	1.5	72.2	626.0	1.603	0.699	0.715
Gasoline	I B	227.5	372.4	1.4	114.2	692.0	1.963	0.712	0.703
Toluene	I B	277.0	383.8	1.3	92.1	867.0	2.854	0.793	0.631
Dimethyl Carbonate	I B	290.0	363.4	4.2	90.1	1069.4	2.880	0.717	0.697
Xylene	I C	298.0	412.3	1.0	106.2	864.0	2.885	0.799	0.626
Turpentine	I C	308.0	429.3	0.8	136.2	861.0	5.480	1.103	0.453
Diesel Fuel	II	313.0	525.6	0.6	170.3	653.0	2.584	0.762	0.656
Kerosene	III A	338.0	497.3	0.7	168.3	758.0	2.300	0.732	0.683
Ethylene Carbonate	III B	423.0	521.4	3.6	88.1	1337.4	6.639	0.974	0.513
Motor Oil	III B	473.0	634.0	1.4	295.2	905.6	2.700	0.858	0.583

Enclosure dimensions as used in the study with base dimensions 0.93 m x 0.93 m (floor area of 0.865 m^2) and height 1.26 m is considered. Using the surface tension and liquid density of the fuels, the depth of the liquid spill is calculated using Equation 1. The area of spread is calculated as the ratio of the initial volume and the depth of liquid spill. An initial spillage volume, $V_s = 0.5\ L$ ($= 5 \times 10^{-4}\ m^3$ = 13.2 % of a gallon) is chosen such that the spillage occupies about 40-80 % of the floor area and is left unrestrained. The depth of the liquid spill and the spread area, calculated for the various fuels considered are included in Table 1. While the average surface tension of the fuels considered is 0.0285 N/m, the surface tension of Turpentine is almost twice this value (liquid density not very different) and hence has the highest (lowest) depth of spillage (spread area). The lowest depth of spillage is reported for n-Pentane, due to the low surface tension value (~ 60 % of the average surface tension value).

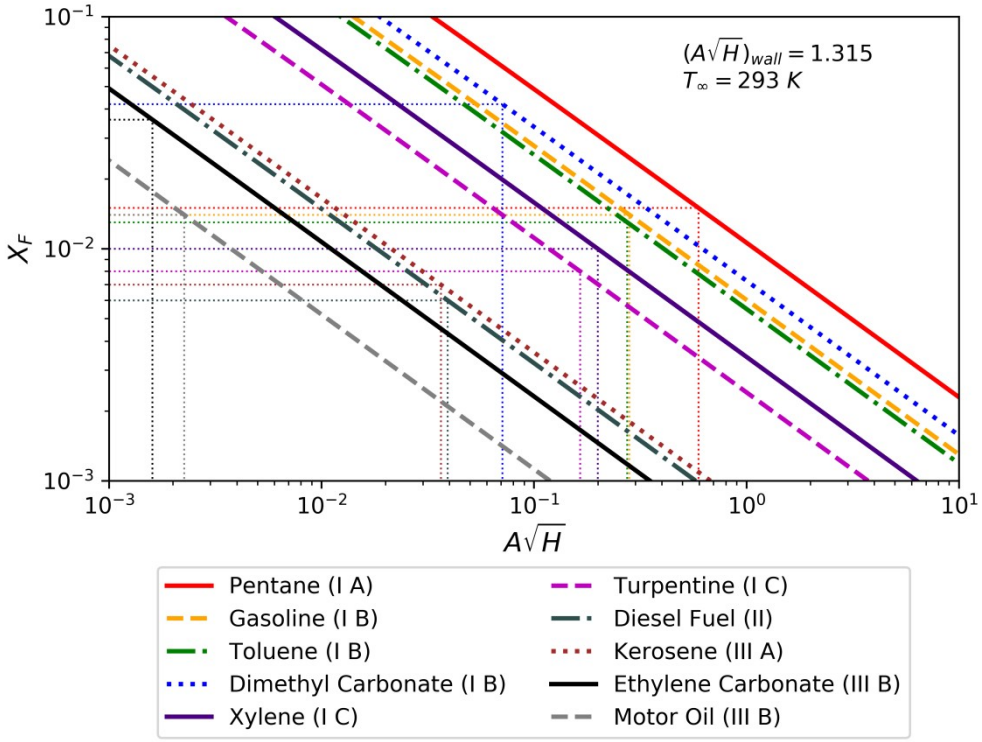

Fig. 3. *Variation of fuel concentration with the vent parameter, $A\sqrt{H}$ for the various fuels considered at T_∞ = 293 K. The horizontal lines point to the LFL value of the respective fuels. The reference value of $(A\sqrt{H})_{wall}$ is calculated using the dimensions of one of the walls of the enclosure considered.*

The evaporating mass flux of the liquid spill is next calculated for the fuels considered by solving Equations 3-5 iteratively. The mass flow rate of the vapor, $\dot{m}_F$ that corresponds to the spillage area of each fuel is calculated. Also calculated are the regression rate of the liquid spill using the liquid density and the time required for complete evaporation of the spill volume considered. These values are presented in Table 2 for $T_\infty = 293\ K$. Based on the vapor mass flow rate of each of the fuel calculated, the steady state concentration within the enclosure is determined using Equations 14-17 for two different ambient temperatures, $T_\infty = 293\ K, 350\ K$. The steady state concentration is plotted with the vent parameter for the fuels considered in Figure 3 in log-log scale.

The variation of concentration with the vent parameter is evident from Equation 15, $X_F\left(A\sqrt{H}\right)^{-2/3}$, showing an asymptotically decreasing trend, consistent with Figure 3. This is due to higher air entrainment reducing the concentration for larger opening. For a given vent parameter, the concentration varies as $X_F\left(\dot{m}_F/\rho_F\right)^{2/3}\left(g'\right)^{-1/3}$, again from Equation 15. This shows the concentration

strongly varies with the vapor flow rate and weakly with the relative density difference. This trend is evident from Figure 3, where fuels with higher $\dot{m}_F$, exhibit higher concentration buildup.

***Table 2**. Gas-phase properties, evaporation and spill regression rate of various flammable fuels considered for T_∞ = 293 K.*

Liquid Fuels	$C_{p,F}$ **(kJ/kgK)**[1]	L **(kJ/kg)**[2]	D **x 10^6 (m^2/s)**[3]	T_s **(K)**	$Y_{F,s}$	v_F **(mm/min)**	$\dot{m}_F$ **x 10^5 (kg/s)**	t_E **(mins)**
n-Pentane	1.681	373.489	8.111	261.3	0.299	0.0633	47.25	11.0
Gasoline	1.640	313.169	6.085	286.4	0.113	0.0135	11.71	52.7
Toluene	1.137	417.626	8.198	285.8	0.049	0.0066	5.987	120.7
Dimethyl Carbonate	1.114	388.092	8.446	279.7	0.091	0.0104	12.87	69.3
Xylene	1.190	406.492	6.615	290.9	0.019	0.0020	1.815	396.8
Turpentine	1.015	315.474	6.152	291.5	0.016	0.0016	1.015	709.3
Diesel Fuel	1.670	347.745	4.550	292.9	$3.38\text{x}10^{-4}$	$2.48\text{x}10^{-5}$	0.023	30676.6
Kerosene	1.438	341.598	4.991	292.9	$3.55\text{x}10^{-4}$	$2.97\text{x}10^{-5}$	0.028	24627.1
Ethylene Carbonate	1.025	722.260	8.883	292.9	$4.34\text{x}10^{-5}$	$3.96\text{x}10^{-6}$	0.005	245745.5
Motor Oil	1.255	222.048	3.878	292.9	$2.73\text{x}10^{-5}$	$2.08\text{x}10^{-6}$	0.001	413426.0

[1]Yaws (1999), [2]Yaws (2008), [3]Yaws (2014)

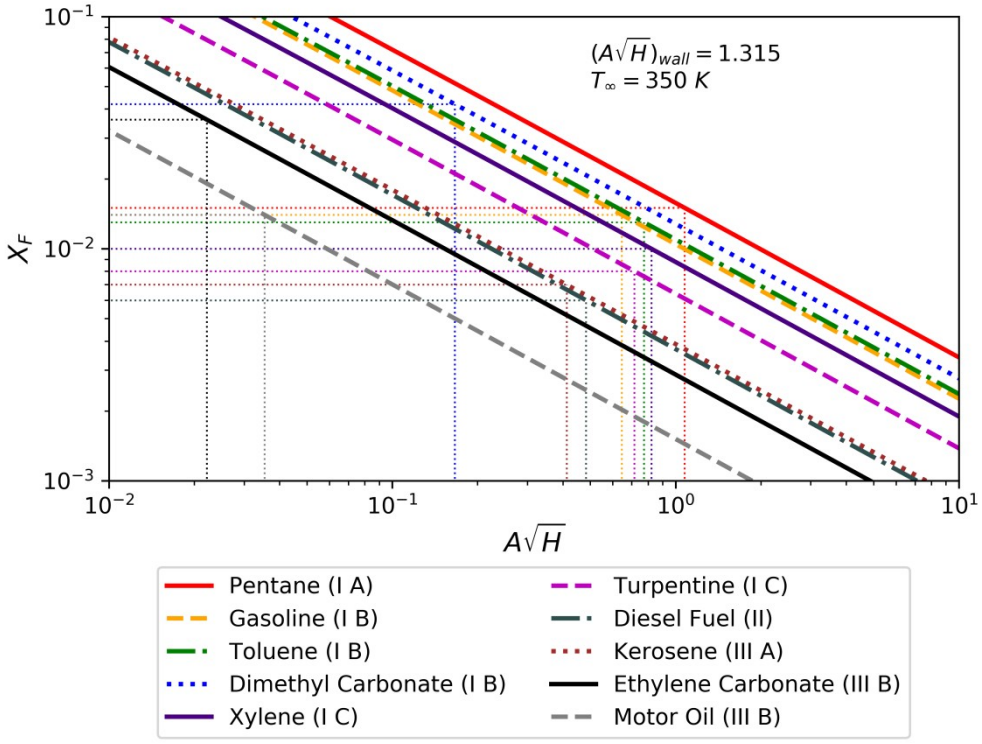

***Fig. 4.** Variation of fuel concentration with the vent parameter, $A\sqrt{H}$ for the various liquids considered at T_∞ = 350 K. The horizontal lines point to the LFL value of the respective fuels. The reference value of $\left(A\sqrt{H}\right)_{wall}$ is calculated using the dimensions of one of the walls of the enclosure considered.*

With a low LFL value, n-Pentane poses the most critical explosion hazard with the venting needed to avoid LFL, being 45 % of $\left(A\sqrt{H}\right)_{wall}$ of the enclosure. Gasoline and Toluene also pose a greater explosion hazard, compared to the other fuels. Despite the high concentration of Dimethyl Carbonate, the $A\sqrt{H}$requirement is low (lower than Xylene and Turpentine) due to the high LFL value. However, for the typical opening sizes considered by Cariteau and Tkatschenko (2013), (with vent parameter values are in the range 10^{-2} - 10^{-1}), leads to concentration buildup within the enclosure higher than the LFL value, for all the Class I liquid spills, and hence the Class II, III spills can be considered safe.

Table 3*. Gas-phase properties, evaporation and spill regression rate of various flammable fuels considered for T_∞ = 350 K.*

Liquid Fuels	$C_{p,F}$ **(kJ/kgK)**[1]	L **(kJ/kg)**[2]	D **x 10^6 (m^2/s)**[3]	T_s **(K)**	$Y_{F,s}$	v_F **(mm/min)**	$\dot{m}_F$ **x 10^5 (kg/s)**	t_E **(mins)**
n-Pentane	1.923	322.738	12.00	275.3	0.549	0.1753	130.8	4.0
Gasoline	1.921	284.332	9.077	317.4	0.433	0.0801	69.41	8.9
Toluene	1.353	385.759	11.90	314.1	0.227	0.0407	37.06	19.5
Dimethyl Carbonate	1.276	352.965	12.44	301.4	0.286	0.0450	55.96	15.9
Xylene	1.405	378.050	9.949	329.8	0.172	0.0249	22.46	32.1
Turpentine	1.360	295.191	9.058	335.2	0.172	0.0228	14.84	48.3
Diesel Fuel	1.901	326.305	6.841	348.9	0.024	0.0022	2.045	346.4
Kerosene	1.718	321.731	7.359	348.8	0.022	0.0023	2.105	324.6
Ethylene Carbonate	1.158	691.053	13.08	348.7	0.004	0.0004	0.496	2246.3
Motor Oil	1.409	213.238	5.778	349.9	0.003	0.0003	0.196	2982.7

[1] Yaws (1999), [2]Yaws (2008), [3]Yaws (2014)

The calculation is repeated for an ambient temperature of T_∞ = *350 K*. The regression rate of the liquid spill calculated using the liquid density and the time required for complete evaporation of the spill volume considered are presented in Table 3. The steady state concentration is plotted with the vent parameter for the fuels considered in Figure 4 in log-log scale. n-Pentane remains to be the most critical explosion hazard with a much higher venting (compared to the lower temperature), 83 % of of the enclosure needed to avoid LFL. The concentration trends are broadly similar to what is observed in the lower temperature case with some differences. Toluene, though having a lower evaporation rate compared to Gasoline, shows marginally higher concentration due to small value of relative density difference. Xylene and Turpentine, despite their low concentration, along with Toluene and Gasoline, pose high explosion hazard compared to the other fuels due to the low LFL values. Dimethyl Carbonate, despite the high concentration, remains to be less hazardous at 350 K, due to the high LFL value. Least concentration is observed for Ethylene Carbonate for a given vent parameter as opposed to the 298 K case and poses the least explosion hazard, with a high LFL value adding to its advantage. With $A\sqrt{H}=0.1$, considered as the upper limit of nominal venting size, we can observe that all liquid spills except Ethylene Carbonate and Motor Oil (Class III B) fuels lead to concentration build up higher than the respective LFL values. Class III B spills (unrestrained) can therefore be considered safe up to temperatures as high as 350 K.

3. Conclusions

The ensuing explosive vapor leak from a flammable liquid spill is analysed in an enclosure with a single opening on the wall at two different ambient temperatures, 293 K and 350 K. Ten different liquids, with wide range of flammability, that belong to various classes of flammable/combustible liquids according to the NFPA 30 classification, and used in varied applications (fuels in automobiles/aircrafts, electrolytes in batteries of e-mobility devices, solvents in chemical process industry) are considered. An initial spill volume of 0.5 L is chosen so that the area of spill for all the fuels considered is within 40-80 % of the floor area of the enclosure considered. Turpentine has the highest (lowest) depth of spillage (spread area) since the surface tension is almost twice the average value of the liquids considered (liquid density not very different). Quasi-steady evaporation from the liquid spill is modeled considering fuel properties at constant temperature and pressure. Thermodynamic equilibrium is assumed to prevail at the liquid-vapor interface, and the thermal and molecular diffusivity are assumed to balance each other. Passive ventilation of the heavy vapor generated is considered, extending the model of Molkov et al. (2014) for light vapor. The model assumes uniform mixing of fuel and air, leading to a steady state concentration within the enclosure. This forms a neutral plane (NP) which demarcates the regions of the mixture exiting and air entraining the enclosure. For a given vent parameter and spill area, the model solves for the height of the neutral plane, the mass flow rate of the mixture issuing out, the mass flow rate of entraining air, and the density of the mixture in the enclosure. The concentration is found to strongly vary with the vapor flow rate and weakly with the relative density difference. The critical geometric parameter of the opening that leads to an explosive mixture is identified for each of the liquid spills. This value for n-Pentane (which poses the highest explosion hazard) is 45%, 83% of the corresponding wall value at 293 K and 350 K respectively. Gasoline and Toluene also pose relatively high explosion hazard at both temperatures. Dimethyl Carbonate, despite the high concentration buildup is relatively safer due to the high LFL value. It has been observed for the unrestrained spill considered, Class II and Class III liquid spills result in safe concentration levels at the standard room temperature of 293 K, while the Class III B liquid spills result in safe concentration levels at temperatures as high as 350 K.

References

Brown, W.G., Solvason, K.R., 1962. Natural Convection Heat Transfer through Rectangular Openings in Partitions-ii. International Journal Heat and Mass Transfer, 5, 869–78.

Linden, P.F., 1999. The Fluid Mechanics of Natural Ventilation. Annual Review of Fluid Mechanics, 31, 1, 201–238.

Molkov, V., Shentsov, V., Quintiere J., 2014. Passive Ventilation of a Sustained Gaseous Release in an Enclosure with One Vent. International Journal of Hydrogen Energy, 39, 15, 8158–8168.

Cariteau, B., Tkatschenko, I., 2013. Experimental Study of the Effects of Vent Geometry on the Dispersion of a Buoyant Gas in a Small Enclosure. International Journal of Hydrogen Energy, 38, 19, 8030–8038.

Rangwala, A.S., Zalosh, R.G., 2023. Explosion Dynamics: Fundamentals and Practical Applications. John Wiley & Sons.

Hiemenz, P.C., Rajagopalan, R., 2016. Principles of Colloid and Surface Chemistry, Revised and Expanded. CRC Press.

Kanury, A.M., 1977. An Introduction to Combustion Phenomena. Gordon & Breach Science Publishers, Inc.

Awbi, H.B., 1998. Calculation of Convective Heat Transfer Coefficients of Room Surfaces

for Natural Convection. Energy and Buildings, 28, 2, 219-227.

ASHRAE Handbook, Fundamentals, 2001. Society of Heating, Refrigeration and Air-Conditioning Engineers, Atlanta, GA.

Benedetti, R.P., 1998. NFPA 30: An Update and a Look into the Future. Process Safety Progress, 17, 1, 23-31.

Zhen, X., Wang, Y., Liu, D., 2017. An Overview of the Chemical Reaction Mechanisms for Gasoline Surrogate Fuels. Applied Thermal Engineering, 124, 1257-1268.

Farrell, P.V., Peters, B.D., 1986. Droplet Vaporization in Supercritical Pressure Environments. Acta Astronautica, 13, 11-12, 673-680.

Wang, T.S., 2001. Thermophysics Characterization of Kerosene Combustion. Journal of Thermophysics and Heat Transfer, 15, 2, 140-147.

Maharjan, S., Qahtani, Y., Roberts, W., Elbaz, A., 2018. The Effect of Pressure, Temperature and Additives on Droplet Ignition of Lubricant Oil and its Surrogate. SAE Technical Paper, 2018-01-1673.

Yaws, C.L., 1999. Chemical Properties Handbook: Physical, Thermodynamic, Environmental, Transport, Safety and Health Related Properties for Organic and Inorganic Chemicals. McGraw-Hill.

Yaws, C.L., 2008. Thermophysical Properties of Chemicals and Hydrocarbons. William Andrew.

Yaws, C.L., 2014. Transport Properties of Chemicals and Hydrocarbons. William Andrew.

Ignition tests in explosive atmospheres using absorption of High-Frequency Electromagnetic radiation based on tests of small hot components

Carola Schierding [a], Frauke Gellersen [a], Michael Hau [a], Karsten Kuhlmann [a], Martin Thedens [a] & Michael Beyer [a]

[a] Physikalisch-Technische Bundesanstalt, Braunschweig, Germany

E-mail: carola.schierding@ptb.de

Abstract

Further developments in wireless communication technology (e.g. Wifi, mobile technology such as 5G) offer various advantages, including higher transmission rates and enhanced connectivity between individual devices. These and other advantages are also important in the process industries. However, using these transmission technologies in a potentially explosive atmosphere requires a safety investigation into the possible ignition hazards caused by devices with integrated high-frequency transmitters operating directly in a hazardous area. Electromagnetic radar level measuring devices are an example, which must be approved in accordance with IEC 60079-0 section 6.6.2 (radio frequency sources). Thresholds are limited to a frequency range from 9 kHz to 60 GHz. Modern devices operate at much higher frequencies, e.g. 80 GHz or more, which requires a safety investigation of the possible ignition hazards posed by the electromagnetic radiation necessary.

In this work, the possible ignition of explosive atmospheres caused as a result of hot surfaces of solids irradiated by electromagnetic radiation is investigated. In order to be able to determine if a hot surface of the solid material due to this process leads to a hazard, radiation absorbing solids are examined at a frequency of 92 GHz. Due to the small size of the application-based solids, the ignition tests are carried out in accordance with the test specifications for small hot components according to IEC 60079-0 Section 5.3.3 (small component temperature for Group I or Group II electrical equipment) and 26.5.3 (small component ignition test (Group I and Group II)). During the ignition tests, a cubical absorber is used as a measurement object, which is centred in a temperature-controlled ignition vessel by a holding device. Therefore, the measuring object is adjustable in three axes in order to position this absorber in the focus of a lens horn antenna. In this way, it is possible to irradiate the underside of the measuring cube in the test vessel in a focussed arrangement through the lens horn antenna with a high frequency of 92 GHz and a maximum output power of 3.3 W. The measurement setup for generating the radio frequency (RF) radiation consists of a signal generator with a frequency extender and an amplifier, which are connected to the lens horn antenna by waveguides. The temperature of the measurement object is measured by an integrated, highly sensitive wire thermocouple. Additionally, the temperature in the ignition vessel is measured by means of mantle thermocouples at various positions. Ignition tests are carried out with mixtures of diethyl ether-air (temperature class T4) and carbon disulphide-air (temperature class T6). Here, different percentages of the individual mixtures are used, starting with the stoichiometric concentration. Furthermore, the ignition tests are carried out depending on different output powers to a maximum of 3.3 W at 92 GHz.

The results of the ignition tests by absorption of radio frequency radiation are presented and interpreted in this work. Thus, the limit values for radio frequency power thresholds specified in IEC 60079-0 for the safe operation of wireless communication devices in potentially explosive atmospheres shall be extended in future based on these investigations.

Keywords: *ignition hazards, high frequency, explosion prevention, small hot components, wireless communication*

1. Introduction

As advancements in wireless communication technology accelerate, we face the challenge of safely integrating radio frequency transmitters into potentially explosive atmospheres. This development offers the promise of improved connectivity and higher transmission rates, resulting in a higher level of efficiency and innovation both in everyday life and in process industries. However, while these advances are promising, safety considerations must be taken into account, especially when integrating high-frequency transmitters in explosive atmospheres. Devices such as electromagnetic radar level transmitters are critical in industrial applications and are required to follow the standards according to IEC 60079-0 (2017) section 6.6.2 (radio frequency sources). Modern devices use frequencies that often exceed the standard frequency limits of 9 kHz to 60 GHz, which creates the need for increased radio frequency power thresholds specified in the standard. Addressing these challenges requires a comprehensive understanding of ignition hazards and explosion prevention. Particularly heated surfaces of solids irradiated by high-frequency electromagnetic radiation require thorough investigations. Current standards, as defined in IEC 60079-0 (2017) section 6.6.2, must therefore be extended to ensure the safety of using modern high-frequency devices. To achieve this, heating experiments using high-frequency electromagnetic radiation are combined with the "ignition tests for small hot components" in accordance with IEC 60079-0 (2017) sections 5.3.3 and 26.5.3. These tests aim to investigate the ignition hazards due to radio frequency (RF) radiation under various conditions, including different gas mixtures and output powers up to 3.3 W maximum at 92 GHz.

Measurements are carried out using mixtures of diethyl ether-air and carbon disulphide-air, based on the known low ignition temperature derived from experience and previous research. For instance, diethyl ether corresponds to temperature class T4 in the explosion protection of electrical equipment, while carbon disulphide corresponds to temperature class T6. (Setchkin, 1954), (Markworth, et al., 1985). Due to their low ignition temperatures, these mixtures are suitable for ignition tests and allow detailed investigations of the effects of radio-frequency radiation as a potential ignition source in explosive atmospheres. Through the selection of these mixtures for testing, safety considerations regarding using radio frequency devices in potentially explosive atmospheres can be evaluated and appropriate safety protection derived. By means of experiments and analytical considerations, a threshold value is determined at which the RF radiation under consideration does not pose an ignition hazard. This threshold value is intended to serve as a basis for improvements to existing standards and to facilitate the integration of wireless communication technologies into potentially hazardous environments in the future. Thus, this work contributes to the constant efforts of explosion protection and industrial safety.

2. Test setup for ignition tests based on small hot components

Here, the test setup for the ignition tests consists of three main parts: the preparation and analysis of the explosive gas-air atmosphere, the RF signal generation and the ignition vessel with the measurement object and lens horn antenna. The principal test setup is shown in Figure 1. The explosive gas-air atmosphere is prepared using the standard method consisting of a mass flow regulator, a chemical pump and an evaporator as well as gas analysis using an oximeter. The generated gas-air mixture is then heated through a pipe system and directed into a preheated ignition vessel (12 liter volume). For the ignition tests carried out here, carbon disulphide for temperature class T6 and diethyl ether for T4 are used in accordance with IEC 60079-0 (2017) section 26.5.3. The RF signal is generated through a high-power amplifier from a weather radar application (see chapter 2.1). Due to the high output power of the amplifier and the resulting self-heating of the amplifier, it is necessary to cool it down to at least 24 °C using a water-cooling system. Otherwise, the output power of the amplifier would decrease with increasing self-heating.

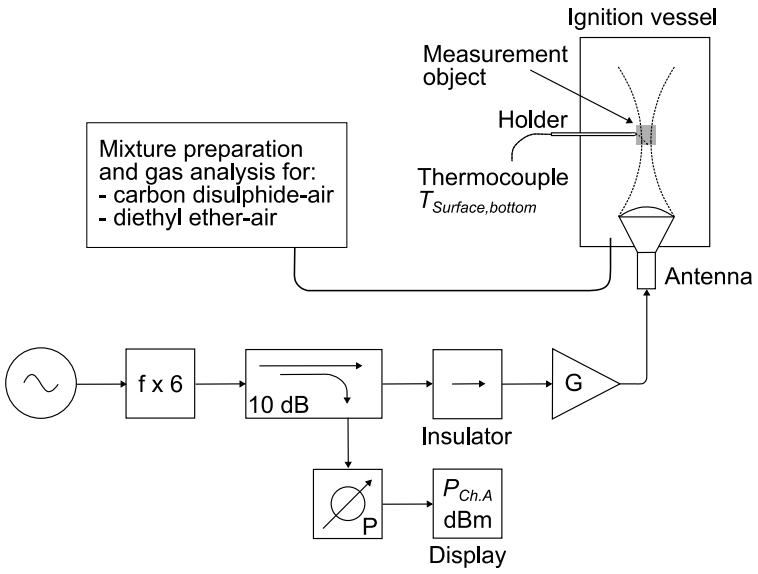

Figure 1. *Test setup for the ignition tests with RF radiation generation.*

2.1. RF signal generation

In order to generate RF radiation with a high output, the high power amplifier (HPA) (Millitech AMP-10-41300) is used here. This amplifier operates at a frequency of 92 GHz and a power amplification of 4 W maximum. To generate the output signal at 92 GHz and 4 W, first a signal is generated at 15.33 GHz using a signal generator (Rohde&Schwarz SMF100A). The frequency of the generated signal is then increased by factor 6 to 92 GHz using a signal frequency extender (VDI WR10SGX-M). The extended signal is amplified to up to 4 W using the HPA and is radiated through a connected waveguide by the focusing circular horn antenna (see Figure 1). To be able to adjust the power at the input of the amplifier to a defined value, a part of the power $P_{Ch.A}$ is coupled out before the HPA by means of a directional coupler. The output power of the RF signal generation is controlled by the output power of the signal frequency extender. For this purpose, the signal frequency extender is provided an input voltage of 0 V to 5 V. The isolator between the signal frequency extender and the HPA protects both devices from reflections in the path.

Due to the test setup for the ignition tests, the output power of the HPA cannot be measured at the same time as the ignition tests. For this reason, the power applied to the antenna was determined additionally to the adjusted input power of the HPA. The setup to measure the output power at the power amplifier is shown in Figure 2.

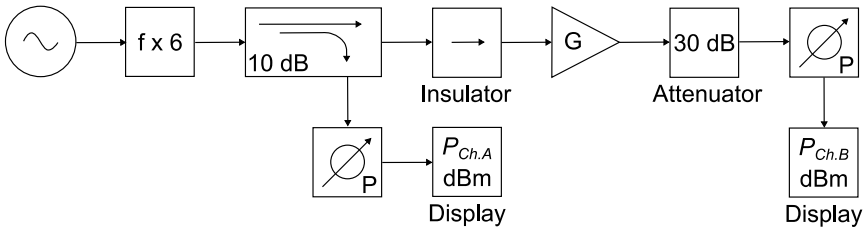

Figure 2. *Measurement setup for determining the output power of the power amplifier (HPA).*

By means of an attenuator and directional coupler, the output power $P_{Ch.B}$ is displayed. By considering the specific attenuations of the attenuator $A_{Attenuator}$ and the waveguide $A_{Waveguide}$, it is possible to

determine the power P_{out} [dBm] applied to the antenna input in dBm by using (1).

$$P_{Out}[dBm] = P_{Ch.B}[dBm] + A_{Attenuator} + A_{Waveguide} \quad (1)$$

The measured attenuation values are given in formula (2).

$$P_{Out}[dBm] = P_{Ch.B}[dBm] + 29.45 - 0.94 \quad (2)$$

The power P_{out} is converted from dBm to watts according to equation (3).

$$P_{Out}[W] = \frac{10^{P_{Out}[dBm]/10}}{1000} \quad (3)$$

An overview of the input powers at the antenna considered here as a function of the input powers $P_{Ch.A}$ adjusted at the amplifier can be seen in Table 1.

***Table 1**. Overview of the considered RF radiation power at the antenna input for the ignition tests.*

Adjusted input power of the power amplifier $P_{Ch.A}$ in dBm	Measured output power of the power amplifier $P_{Ch.B}$ in dBm	Power at the antenna input P_{out} in dBm	Power at the antenna input P_{out} in W
10.75	6.67	35.18	3.3
8.01	4.18	32.69	1.9
7.54	3.57	32.08	1.6

The maximum output power of the amplifier of 4 W is not reached. The reason for this could be the attenuation losses during RF signal generation and the self-heating of the amplifier. Thus, the maximum output power of P_{out} = 3.3 W at 92 GHz is possible for the ignition tests. The power values of P_{out} = 1.9 and P_{out} = 1.6 are derived from the possible input power adjustments of the HPA as well as the already performed heating tests (Walkemeyer, et al., 2022(a)), (Walkemeyer, et al., 2022 (b)).

2.2. Measuring object and temperature measurement

The measurement object is a material cube (PEEK ESD101) with a high absorption capacity and an edge length of 5 mm x 5 mm x 5 mm (Walkemeyer, et al., 2022(a)), (Walkemeyer, et al. 2022(b)). This measurement object size corresponds to the specifications for small components according to IEC 60079-0 (2017) section 5.3.3. During the ignition tests, the surface temperature of the measurement object is measured using a thermocouple (type K, diameter 0.003 inch, Omega Engineering Ltd.). For this purpose, the thermocouple is placed in a diagonal drill hole with a diameter of 0.4 mm in the absorber. This measurement object with thermocouple is attached to a holder made of PTFE from the side using a spring-mounted Kapton tape and then inserted into the ignition vessel through a bushing. However, this measuring object holder is constructed in a way that the measuring object can be adjusted in three axes. This allows the absorber to be positioned in the focus of the antenna. Furthermore, the thermocouple is aligned with the surface of the measurement object. Based on previous investigations (Walkemeyer, et al., 2022(a)), (Walkemeyer, et al., 2022(b)), it was determined that the thermocouple does not react with the RF radiation.

In order to read the thermocouple, an A/D converter (National Instruments (NI) TB-9212) is used, which is capable of reading up to eight thermocouples simultaneously. This module is connected through a PC interface (NI cDAQ-9174) to a computer running the LabView control software. In

addition to the surface temperature, this system also monitors the temperatures of the power amplifier, mixture, vessel and 100 mm above the measurement object.

Additionally, the holder can be rotated to determine the surface temperatures at different positions on the measurement object. This allows the surface temperature to be measured at the top $T_{Surface,top}$ or bottom $T_{Surface,bottom}$ of the measuring cube. The positioning of the thermocouple in dependence on the focus of the antenna is represented in Figure 3 a) and b).

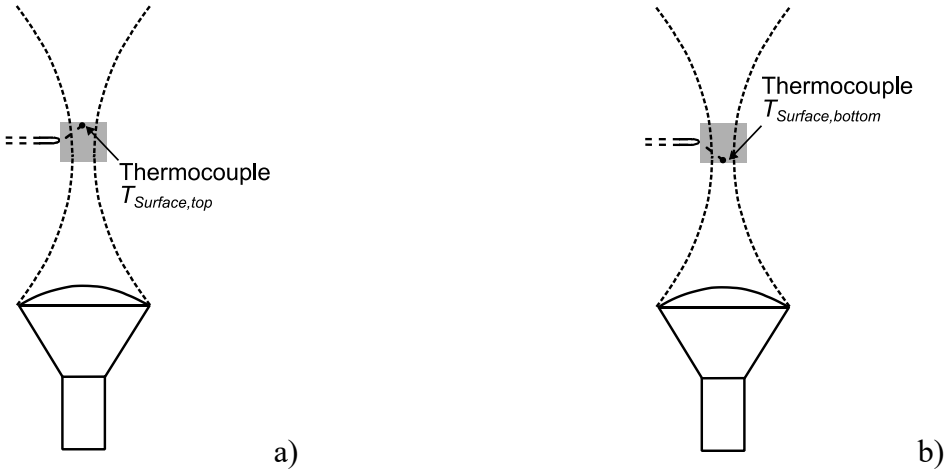

Figure 3. *a) Thermocouple position on the top side of the measurement object surface. b) Thermocouple position on the bottom side of the measurement object surface.*

For the investigation regarding the maximum surface temperatures of the measurement object depending on the two positions of the thermocouple and the RF radiation power considered here, temperature measurements were carried out in air. Therefore, the temperatures of $T_{Surface,bottom}$ and $T_{Surface,top}$ were measured at the power values of P_{out} = 3.3 W, 1.9 W and 1.6 W respectively. The results of the maximum possible temperatures due to the absorption of the RF radiation are given in Table 2.

Table 2*. Surface temperature of the measurement object depending on the thermocouple position and the RF radiation power in air.*

P_{out} in W	$T_{Surface,bottom}$ in °C	$T_{Surface,top}$ in °C
3.3	500	256
1.9	292	198
1.6	265	181

There is a significant temperature difference between the direct focused bottom side of the absorber and the opposite top side. Comparing the surface temperatures measured here on the top side of the measurement object (see Figure 3 a)) with the results of the core temperatures obtained from the heating experiments of (Walkemeyer, et al., 2022(a)), (Walkemeyer, et al., 2022(b)), these correspond with a deviation of ± 15 °C. This means that the approximate core temperature of the absorber material can be derived from the surface temperature.

3. Test procedure and measurement results

To determine the most favourable gas/air mixture for ignition depending on the power of the RF radiation, ignition tests are carried out in the stoichiometric mixture concentration range. For this purpose, investigations are conducted regarding the direct and indirect ignition characteristics with different parameters of the power and the mixture concentrations of carbon disulphide-air and diethyl ether-air. In each case, tests start with the mixture concentrations known to be most favourable for ignition and then the power of the RF radiation is adjusted to determine the power at which no ignition occurs. Afterwards, the volume percentages in the gas mixture are changed and the power of the RF radiation is varied again. For carbon disulphide-air mixture, the test starts with a volume percentage of 1.8 % according to (Setchkin, 1954) and for diethyl ether-air mixture, it starts with a volume percentage of 23 % according to (Markworth, et al., 1985). This volume percentage complies with the recommended volume percentage in the range of 22.5 % and 23.5 % according to the standard IEC 60079-0 (2017) section 26.5.3 regarding ignition tests for small hot components.

Furthermore, the surface temperatures on the bottom and top of the measurement object is measured alternately for each ignition test and parameter combination (see Figure 3 a) and b)). If an ignition occurs, the ignition temperature $T_{Ignition,bottom}$ or $T_{Ignition,top}$ is determined by the thermocouple in the measurement object.

In addition to the surface temperatures, the ignition delay time $t_{Ignition\ delay}$ is also determined for each test. Here, the ignition delay time is defined as follows. The ignition delay time begins with the heating of the absorber (starting of RF radiation) and ends at the time of ignition. This ignition delay time is used as an indicator to evaluate ignition efficiency of the respective mixture concentrations depending on the set power of the RF radiation.

As another test parameter, the cut-off temperature $T_{Surface,cut\text{-}off}$ is used. This parameter is used to protect the test setup consisting of the measurement object with thermocouple as well as the antenna. Observations indicated that the measurement object can be destroyed during the test duration until the maximum possible surface temperature of the absorber is reached at the maximum power of 3.3 W (see Table 2). Therefore, the ignition tests at the power of 3.3 W are aborted when the surface temperature on the bottom or top reaches 250 °C and no ignition occurs.

3.1 Measurement results for carbon disulphide-air mixtures

In the following, the results of the ignition tests with a carbon disulphide-air mixture are presented depending on the output power of RF radiation. For this purpose, Table 3 indicates the mixture concentrations and powers at which ignition occurred. Additionally, the defined ignition delay time is stated when ignition takes place. The ignition delay time indicated is the maximum ignition delay time $t_{Ignition\ delay,max}$ determined respectively. Table 3 shows that ignitions occurred at a power of P_{out} = 3.3 W for mixture concentrations from 1.5 % to 8 % carbon disulphide in air. At a volume percentage of 1 %, no ignitions could be achieved. Due to the observed increase in the maximum ignition delay time $t_{Ignition\ delay,max}$, from 26 s at a mixture concentration of 2 % to 40 s at 8 %, along with the resulting decrease in the ignition efficiency of the gas mixture, ignition tests were stopped at a volume percentage of 8 %. This reduction in ignition efficiency of the gas mixture corresponds to known references (Setchkin, 1954), (Markworth, et al., 1985). According to (Markworth, et al., 1985), no ignition is possible for small hot components with a volume percentage of more than 9.6 % of carbon disulphide in air.

At a reduced power of P_{out} = 1.9 W, ignitions could only be detected at mixture concentrations of 1.5 %, 1.8 % and 2.0 %. These ignitions are a so-called cold flame reaction (Markworth, et al., 1985). During this process, the heat released leads to an abrupt rise of surface temperature, which can result in a cold-flame ignition. Due to this increase of temperature, the gas mixture was ignited in a concentration range from 1.5 % to 2.0 %. Reducing the irradiated power from 3.3 W to 1.9 W into the measurement object results in the fact that ignitions above a volume percentage of 2.5 % could

no longer be detected. Also, no more cold flame reaction could be observed. Like the ignition tests at a power 3.3 W, no ignitions could be achieved at a volume percentage of 1 %. Furthermore, no ignitions were obtained in the concentration range from 1 % to 8 % carbon disulphide in air at an RF radiation power of 1.6 W.

***Table 3**. Results of the ignition tests for carbon disulphide-air mixtures.*

Vol. % carbon disulfide in air	1	1.5	1.8	2	2.5	3	3.5	5	6.5	8
P_{out} = 3.3 W	-	x	x	x	x	x	x	x	x	x
$t_{Ignition\ delay,max}$	-	47 s	40 s	26 s	29 s	32 s	27 s	26 s	35 s	40 s
P_{out} = 1.9 W	-	x	x	x	-	-	-	-	-	-
$t_{Ignition\ delay,max}$	-	287 s	257 s	204 s	-	-	-	-	-	-
P_{out} = 1.6 W	-	-	-	-	-	-	-	-	-	-

"x": Ignition; "x": cold flame ignition; "-": no ignition

A decreasing and increasing behaviour of the ignition delay time can be observed for both powers P_{out} = 3.3 W and 1.9 W. This indicates that the most favourable mixture concentration for ignition is 2 % carbon disulphide in air. Differences to the reference value of the most favourable ignition mixture concentration of 1.8 % carbon disulphide in air for small hot components (Setchkin, 1954) can be caused by different influencing parameters, for example characteristics and location of the measurement object as well as convection and flow conditions.

Figure 4 provides a further representation of the results. This figure presents the maximum ignition temperatures $T_{Ignition}$ measured at the bottom and top of the measurement object depending on mixture concentrations. Observing the ignition temperatures at a mixture concentration of 2 % in Figure 4, it can be seen that the temperatures measured on the bottom of the measurement object $T_{Ignition,bottom}$ = 337 °C are the same for the powers of 3.3 W and 1.9 W applied. Furthermore, with the power of 1.9 W, the ignition temperatures on the bottom of the measurement object are approximately the same. The same behaviour can also be observed for the surface temperatures on the top of the measurement object $T_{Ignition,top}$, here the ignition temperatures are between 207 °C and 212 °C.

In comparison, the measured ignition temperatures at a power of 3.3 W both on the bottom and on the top of the measurement object display temperature deviations. The maximum measured ignition temperature of $T_{Ignition,bottom}$ = 412 °C was determined at a volume percentage of 1.5 % and the minimum ignition temperature of $T_{Ignition,bottom}$ = 308 °C at a volume percentage of 2.5 % on the bottom of the measurement object. These deviations in temperature behaviour depending on the mixture concentration are not in accordance with the expected ignition curve. Based on ignition tests for small hot components with carbon disulphide-air mixtures, the ignition temperature $T_{Ignition}$ is expected to rise with increasing volume percentage (Setchkin, 1954), (Markworth, et al., 1985). A possible influencing factor for this deviating behaviour of the ignition temperature could be the power of the RF radiation of 3.3 W and the resulting heating of the measurement object. Because at P_{out} = 3.3 W, the absorber material of the measurement object heats up faster compared to irradiation with a power of 1.9 W. Here, the heating behaviour of the absorber depending on the power of the RF radiation is shown by considering the maximum ignition delay time (see Table 3). Additionally, there is no deviation in the ignition temperature at a reduced power of 1.9 W. That the ignition temperatures at P_{out} = 1.9 W does not indicate a noticeable increase in temperature can be attributed to the observed range between 1.5 % and 2.0 % of the mixture concentrations.

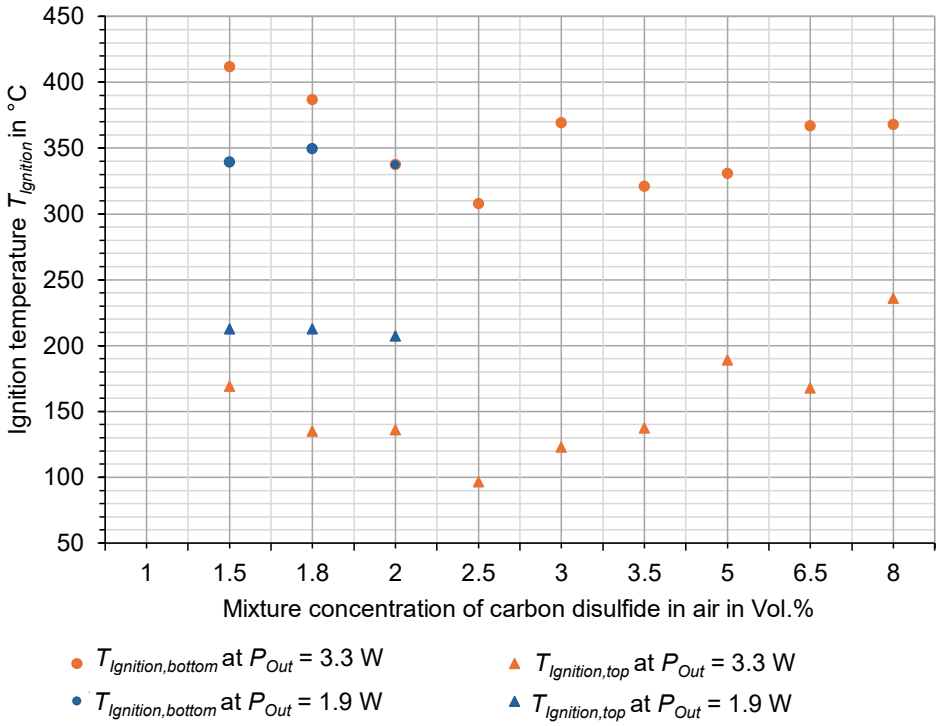

Figure 4. *Surface temperatures of the measured object at time of ignition depending the position of the thermocouple and the RF radiation power.*

Based on the investigations, it was determined that no ignitions occurred at powers of RF radiation of P_{out} = 1.6 W for carbon disulphide-air mixtures. Thus, the resulting surface temperature of the measurement object due to irradiation by high-frequency electromagnetic radiation represents no ignition source for the test parameters considered here. However, it should be considered that this is a determined limit value for the power output of the RF radiation without taking into account relevant measurement uncertainties and a suitable safety factor.

3.2 Measurement results for diethyl ether-air mixtures

The results of the ignition tests with diethyl ether-air mixture are presented in the following depending on the output power of RF radiation. Therefore, the mixture concentrations and powers at which ignition occurred are indicated in Table 4. Furthermore, the defined ignition delay time is specified when ignition takes place. The ignition delay time indicated is the maximum ignition delay time determined respectively. To protect the test setup, the cut-off temperature $T_{Surface,cut\text{-}off}$ for the power of 3.3 W is considered here in addition to the results for carbon disulphide/air mixtures.

Table 4*. Results of the ignition tests for diethyl ether-air mixtures.*

Vol. % diethyl ether in air	2.5	3.4	6	9	12	15	18	23	24	30
P_{out} = 3.3 W with $T_{Surface,cut\text{-}off}$	-	-	-	-	-	-	-	-	-	-
P_{out} = 3.3 W without $T_{Surface,cut\text{-}off}$ $t_{Ignition\ delay,max}$					x 73 s			x 52 s		
P_{out} = 1.9 W	-	-	-	-	-	-	-	-	-	-

"x": Ignition; "-": no ignition

In Table 4, it can be seen that no ignitions occur at a power of 3.3 W when the cut-off temperature is used. Based on the low ignition temperature of diethyl ether, ignitions should be achieved without restriction due to $T_{Surface,cut\text{-}off}$ = 250 °C, at least at the most favourable ignition mixture concentration of 23 % diethyl ether in air (IEC 60079-0, (2017), (Markworth, et al., 1985). This was proven by ignition tests without taking the cut-off temperature into account, at a mixture concentration of 23 % and an additional 12 %. With the recommended mixture concentration of 23 % diethyl ether in air, ignitions could be obtained at an ignition temperature of 290 °C and a maximum ignition delay time of 52 s. At a mixture concentration of 12 %, the ignition tests showed ignitions at an ignition temperature of 490 °C at $t_{Ignition\ delay,max}$ = 72 s. This increase in ignition delay time indicates the expected reduction of the ignition efficiency of the gas mixture. It should be noted that the results of the ignition tests could only be obtained by destroying the measurement object at a power of 3.3 W, without considering the cut-off temperature.

At a reduced power of 1.9 W, no ignitions could be achieved in the concentration range of 2.5 % to 30 % diethyl ether in air. Also, no cold flame reactions (Markworth, et al., 1985) could be observed. Therefore, no ignition tests were carried out using RF radiation at a power of 1.6 W.
Based on the investigations, it was determined that no ignitions occurred at powers of RF radiation of P_{out} = 1.9 W for diethyl ether-air mixtures. Thus, the resulting surface temperature of the measurement object due to irradiation by high-frequency electromagnetic radiation represents no ignition source for the test parameters considered here. However, it should be considered that this is a determined limit value for the power output of the RF radiation without taking into account relevant measurement uncertainties and a suitable safety factor.

4. Conclusions

Within the scope of this study, it could be shown that hot surfaces of solids that are irradiated with electromagnetic radiation can be an ignition source in explosive atmospheres. The measurement results indicate that the required surface temperature of the absorber at which an ignition can occur depends essentially on the following influencing parameters:

- the output power of the high-frequency electromagnetic radiation and

- the gas mixture type and concentration.

Further influencing parameters, which were not considered here, are the characteristics of the measurement object such as shape, surface area and material as well as convection and flow conditions. These influencing parameters are known from ignition tests for small hot components (Setchkin, 1954), (Markworth, et al., 1985). During the investigations, a measurement object cube with a high absorption capacity (absorber material: PEEK ESD101) was irradiated with a constant RF radiation of maximum 3.3 W at 92 GHz by a focussing lens horn antenna. A worst-case scenario was considered here due to the choice of antenna shape, the constant irradiation with an RF signal and the absorber material. As a result, limit values for the output power of the RF radiation of P_{out} = 1.9 W for diethyl ether-air mixtures and P_{out} = 1.6 W for carbon disulphide-air mixtures could be determined at which the resulting surface temperature of the measurement object represents no ignition source. However, it should be considered that these are only the limit values for the output power of the RF radiation without taking into account relevant measurement uncertainties and a suitable safety factor. Based on the results of these investigations and further considerations, the determination of a maximum RF power for the safe operation of wireless communication devices in potentially explosive atmospheres is to be revised in future.

References

IEC 60079-0: Explosive Atmospheres - Part 0: Equipment - General Requirements. 7.0. IEC - International Electrotechnical Comission, Dez. 2017.

Walkemeyer, P., M. Thedens, M. Beyer und C. Damm (2022)(a): Using RF Measurement Techniques to Evaluate Ignition Hazards due to Dielectric Heating in Explosive Atmospheres, Kleinheubacher Tagung 2022, 27-29, September, 2022, Miltenberg, Deutschland.

Walkemeyer, P., M. Thedens, M. Beyer und C. Damm (2022)(b): Investigation of ignition hazards due to the absorption of high-frequency electromagnetic radiation by solids, gases and vapours, 14th International Symposium on Hazards, Prevention and Mitigation of Industrial Explosions ; ISHPMIE, 11-15, July, 2022, Braunschweig, Germany.

Setchkin, N. P., (1954): Self-Ignition Temperatures of Combustible Liquids, Journal of Research of the National Bureau of Standards, Research Paper 2516, Vol. 53, No, 1, July 1954.

Markworth, D., Schebsdat, F., (1985): Zündverhalten kleiner heißer Bauteile in Explosionsfähiger Atmosphäre, PTB-W-25, PTB Bericht, ISSN .0341-6739, April 1985.

The effect of water on the explosion characteristics of pure and diluted light alcohols

Rafal Porowski[a], Benedetta De Liso[b], Gianmaria Pio[b], Tomasz Gorzelnik[a] & Ernesto Salzano [b,*]

[a] AGH University of Krakow, Faculty of Energy and Fuels, Krakow, Poland
[b] Dipartimento di Ingegneria Civile, Chimica, Ambientale e dei Materiali, Università di Bologna, Bologna, Italy

E-mail: ernesto.salzano@unibo.it

Abstract

Light alcohols are under investigation in recent years as alternative fuels and in the framework of hydrogen development for its production from bio-resources (Pio et al., 2021). Furthermore, the use of water-diluted alcohols is ubiquitous for the chemical, food, pharmaceutical, and polymer industry, as a solvent or reactant. Hence, detailed analysis for the safe use, for the design of prevention and mitigation measures, and for the consequence analysis are required. It is also of great importance to get more practical knowledge on fundamental explosion characteristics of common alternative fuels that can be applied in the process industries, including mixtures with hydrogen as a green energy carrier (Porowski et al, 2023). In this work we have investigated the explosion characteristics of alcohol-water-air mixtures, including explosion pressure (P_{ex}) and the maximum rate of explosion pressure rise $(dp/dt)_{max}$ in the standard 20-liter explosion sphere. Results first clarify the effect of carbon number and the chemical structure on the explosion phenomenon. Furthermore, the effect of water (total water and water vapour) has been defined on the explosion characteristics of light alcohol-air mixtures.

Keywords: *gas explosion, deflagration index, light alcohols, inerting, mitigation measures, water effects.*

Introduction

The depletion of fossil fuel reserves and the rising awareness of greenhouse gas emissions, particularly carbon dioxide, on climate change are driving the search for alternative fuels. This search is also motivated by a growing desire to mitigate the environmental impact of fuel combustion. Light alcohols such as methanol, ethanol, propanol, and butanol are emerging as promising candidates, especially when sourced from bio-based materials like sugar cane, corn, starch, waste biomass, and agricultural residues. These bio-sourced fuels are renewable and produce fewer air pollutants and carbon dioxide than fossil fuels. Additionally, they possess favorable combustion characteristics; for instance, methanol, ethanol, and propanol have high research octane numbers (RON), while the octane ratings of butanol isomers are comparable to those of conventional gasoline (Sarathy et al., 2014). Moreover, these alternative fuels can be used in conjunction with other fuels, blended, or mixed with green energy carriers such as hydrogen (Porowski et al., 2023). As noted by Kumar and Ashok (2021), light alcohols can serve as supplementary fuels when combined with substances like n-butanol, iso-butanol, and hydrogen, enhancing the combustion properties of methanol. Research also shows potential for producing hydrogen through oxidative steam reforming of ethanol (Palma et al., 2017). Beyond energy, diluted light alcohols have applications in the chemical, pharmaceutical, and food industries, where their safe usage and the understanding of their physicochemical properties are critical (Porowski et al, 2024). In terms of fire safety and assessing the combustion properties of alternative fuels, it is vital to investigate the explosion characteristics of these substances, including explosion pressure, maximum rate of explosion pressure rise, laminar burning velocity, flame stretch and curvature, ignition delay time, and mass burning rates (Cammarota et al., 2009; Giannakopoulos

et al., 2015; Wako et al., 2021). This comprehensive approach not only advances our understanding of alternative fuels but also contributes to safer and more sustainable energy practices. Laminar burning velocity (LBV) is a crucial physicochemical property that characterizes the combustible mixture of fuel and oxidizer, influenced by factors such as fuel composition, equivalence ratio (ϕ), flame stretch, and mixture dilution (De Goey et al., 2011; Egolfopoulos et al., 2014; Konnov et al., 2018). LBV measures the rate at which a flame front propagates under laminar conditions in an unburned gas mixture. Understanding LBV is essential for determining turbulent combustion, such as in engines, validating kinetic models, and ensuring the fire safety of systems utilizing various gaseous or liquid fuels, including methane, ethanol, hydrogen, or fuel blends (Cracknell et al., 2013; Konnov et al., 2018; Rallis & Garforth, 1980). Numerous studies have focused on the laminar burning velocity of combustible gases and mixtures (Gu et al., 2010; Konnov et al., 2018; Liao et al., 2007; Rallis & Garforth, 1980; Sileghem et al., 2014; Veloo et al., 2010; Y. Zhang et al., 2014). A detailed review by Konnov et al. (2018) outlined various LBV measurement techniques for different fuel and air mixtures, including the spherical flame method, stagnation flame method, heat-flux method, and burner method. It has generally been observed that the laminar burning velocity for many combustible mixtures, including light alcohols, peaks at an equivalence ratio slightly above 1.0 and decreases for both leaner and richer fuel mixtures (Chen, 2011; Dahoe & de Goey, 2003; Gu et al., 2010; Hechinger & Marquardt, 2010; Rallis & Garforth, 1980; Y. Zhang et al., 2014). Further studies have also explored other characteristics and their impacts on LBV, such as flame stretch (Marshall et al., 2011). Research by Sileghem et al. (2014) not only investigated the LBV of blends of methanol, ethanol, iso-octane, and n-heptane but also examined the temperature dependence of LBV for methanol and ethanol. In another study, Bradley et al. (2009) measured the laminar burning velocities in conjunction with other parameters like Markstein numbers and critical Peclet numbers for gas phase mixtures of ethanol and air. Additionally, the Markstein length for light alcohols was investigated in a study by Bechtold & Matalon (2001). This body of research highlights the complexity and significance of studying LBV to enhance our understanding of combustion processes, particularly for developing safer and more efficient fuel systems.

Alcohols and alcohol blends have proven to be valuable fuels for a wide range of combustion applications, particularly in modern spark ignition (SI) and compression ignition (CI) engines. Their high octane numbers and favorable emission profiles make them attractive alternatives, with no need for significant engine design modifications (Konnov et al., 2018; Sarathy et al., 2014). Bio-ethanol, as highlighted by Vancoillie et al. (2012), is a reliable alternative fuel for spark-ignition engines due to its renewable origins and lower emissions. Higher alcohols, such as those containing four or more carbon atoms, are especially suited for use in internal combustion engines because of their higher energy densities. However, their ignition delay times and octane numbers are generally lower, making them more suitable for CI engines (Sarathy et al., 2014). Recent studies, such as those by Vargün et al. (2023) and Z. Zhang et al. (2022), have suggested that injecting alcohols into commercial diesel engines can reduce NOx emissions and lower the levels of soot, hydrocarbons, and carbon monoxide. However, there are concerns about increased cancer risks and ozone-related illnesses due to higher aldehyde emissions and unburned ethanol, particularly when ethanol is used extensively as a fuel (Sarathy et al., 2014). Methanol, the simplest aliphatic alcohol with a molar mass of approximately 32.04 g/mol, consists of a methyl group and a hydroxyl group. It is used both as a fuel and a fuel additive, contributing to low NOx emissions due to its high H/C ratio, absence of C-C bonds, and high latent heat. These properties also enhance the speed of combustion (Wako et al., 2021). The laminar burning velocity (LBV) and temperature exponent (α) for methanol-air mixtures were thoroughly investigated in studies such as Katoch et al. (2016), demonstrating good consistency with existing literature, especially for slightly rich mixtures. Ethanol, the second aliphatic alcohol in the homologous series with a molar mass of about 46.07 g/mol, remains the most widely used biofuel. Derived primarily from the microbial fermentation of sugars and starches, ethanol's burning rates and its blends with fossil fuels have been extensively studied. Parag & Raghavan (2009) found that water addition to ethanol reduces its mass burning rate, whereas the burning rate increases with higher gasoline content in ethanol-gasoline mixtures. Research by Katoch et al. (2018) on the LBV of

ethanol-air flames across a temperature range confirmed these findings, noting a minimum temperature exponent value for slightly rich mixtures ($\phi = 1.1$). Propanol is available in two isomers: 1-propanol (or n-propanol) and 2-propanol (or iso-propanol), typically derived from petrochemicals, though novel biological sources are also being explored. Veloo & Egolfopoulos (2011) examined the flame speeds and extinction strain rates of propanol isomers and compared them to propane/air mixtures, revealing how the hydroxyl functional group affects flame characteristics. Beeckmann et al. (2014) conducted LBV measurements for methanol, ethanol, n-propanol, and n-butanol, finding that the LBV for n-propanol was similar to those of other alcohols at slightly rich mixtures. This consistency was further supported by Li et al. (2022), who reported peak laminar burning speeds for n-propanol at an equivalence ratio of about 1.1. This literature review clearly indicates that there is a need for experimental and numerical data on thermodynamic and reactivity properties of light alcohols. To assess their potential as energy carrier and for safety evaluations. So that mitigation strategies and technologies may be devised and implemented to cope with accidental releases of alcohol vapours. For indeed: when mixed with air, these may pose serious hazards to people, the environment and infrastructure in form of fires and explosions. Furthermore, inspection of the scientific literature revealed that there is a knowledge gap in the safety literature pertaining to the lower alcohols. For this reason the main focus of this paper is on the determination of the explosion severity parameters of alcohol – water mixtures.

1. Experiments

All experiments were carried out in a 20-liter combustion testing vessel depicted in Figure 1. This apparatus allows for the investigation of the deflagration mode of combustion, often referred to as the "explosion phenomenon," along with related explosion parameters of alcohol-air mixtures. These parameters include explosion pressure (P_{ex}), maximum rate of explosion pressure rise $(dP/dt)_{max}$, and explosion delay time (t_{del}). Here's a breakdown of these terms:

- Explosion Pressure (P_{ex}): This parameter represents the peak pressure attained during the explosion, measured above the initial atmospheric pressure. It is considered an excess pressure, additional to the baseline atmospheric pressure.
- Maximum Rate of Pressure Rise $(dP/dt)_{max}$: This measures the highest rate at which pressure increases within the vessel or engine during the combustion event. It is closely linked with the intensity of the explosion and is crucial for safety considerations and engine design.
- Explosion Delay Time (t_{del}): This is the duration between the initiation of the combustion process (such as the introduction of a spark or reaching the auto-ignition temperature) and the occurrence of the maximum explosion pressure. It indicates the reactivity of the fuel-air mixture and is influenced by factors such as the mixture's composition, temperature, pressure, and the presence of any diluents like water vapor.

These parameters are essential for understanding the combustion dynamics and safety implications of using alcohol-air mixtures in various applications. Tested mixtures are methanol, ethanol, 1-propanol and 2-propanol at equivalence ratio ranging between 0.3 and 0.7 as calculated by considering the vapour pressure at initial conditions of 323.15 K and 1 bar. Pure alcohols were initially diluted in water such that the volumetric content of the latter ranged from 0 % to 70 % vol. Also, for each alcohol-water ratio, four different volumes were injected, from 2 to 8 cm3. The dedicated injection device was applied to provide the liquid samples of light alcohols going at the bottom of the testing vessel. The heating plate was mounted and kept at temperature of 333.15 K. A magnetic mixing device was also deployed for at least 5 minutes to allow the liquid sample of light alcohols to evaporate. The heating plate’s temperature was decreased to 323.15 K and the air was slowly administered to bring the pressure in the testing vessel to the pressure of 1 bar. After

disengaging the magnetic stirrer, a time span of at least 5 minutes was permitted to elapse prior to ignition. Each sample was tested at least three times.

Fig. 1. *3D drawing (left) and the picture (right) of the 20 L combustion vessel.*

Liquid light alcohol samples were admitted into the combustion vessel mixed with air, including ϕ = 0.3–0.7 as determined at experimental conditions. Specific details on the samples, their composition and volumetric water content are given in Table 1.

Table 1. *Molecular mass (M) density (ρ), critical temperature (T_c), critical pressure (P_c), critical volume (V_c), acentric factor (ω), boiling point (T_b) and vapour pressure (P^{Sat}) of CH_3OH, C_2H_5OH, 1-C_3H_7OH, 2-C_3H_7OH, H_2O and air [1,2].*

Substance	M (kg mol^{-1})	P (†) (kg m^{-3})	T_c (⊕) (K)	P_c (⊕) (bar)	V_c (⊕) (cm^3 mol^{-1})	ω (-)	T_b (‡) (K)	P^{Sat} (*) (bar)	Fl. lim. (y) (vol%)
CH_3OH	32.04 × 10^{-3}	787.2	512.16	80.92	117.88	0.565	338.15	0.17	6–37
C_2H_5OH	46.07 × 10^{-3}	787.3	513.9	61.37	167.10	0.649	351.15	0.079	3–19
1-C_3H_7OH	60.10 × 10^{-3}	802.0	536.8	51.70	218.41	0.629	370.15	0.028	2–14
2-C_3H_7OH	60.10 × 10^{-3}	782.7	508.3	47.62	220.10	0.665	355.15	0.061	2–12
H_2O	18.015 × 10^{-3}	997.05	647.10	220.64	56.02	0.344	373.13	0.0317	
Air	28.964 × 10^{-3}	1.161	132.63	37.858	92.35				

(†) At 298.15 K and 1 bar. (‡) At 1 bar. (*) At 298.15 K. (⊕) These quantities permit the calculation of the critical density $\rho_c = MP_c/RT_c$ and the critical compressibility $Z_c = P_cV_c/RT_c$. (y) Flammability limits in air at 298.15 K and 1 bar as tabulated in (Poroewski et al, 2024). Notice that the upper flammability limit in air supersedes the vapour pressure of the pure substances at these conditions. () From Ref. (Porowski et al, 2024).

Each sample was subjected to at least three trials to ensure reliability and reproducibility of the results. The protocol for creating initially quiescent combustible mixtures within the combustion vessel was rigorously adhered to. To begin, various volumes of liquid samples were prepared and introduced into the vessel to achieve different equivalence ratios. Specifically, volumes of 4 cm³, 6 cm³, and 8 cm³ were used, corresponding to equivalence ratios (ϕ) of 0.3, 0.5, and 0.7, respectively. These setups included both alcohol-air mixtures and alcohol-water-air mixtures under the initial experimental conditions. This careful preparation of the samples was crucial for evaluating the combustion characteristics of the mixtures at different concentrations and compositions, providing comprehensive understanding of the behavior of light alcohols in combustive environments. Following the initial setup, the combustion vessel was preheated to 323.15 K and then evacuated until the internal pressure dropped below 1 millibar, creating a near-vacuum condition. To introduce the liquid samples of light alcohols for testing, a dedicated injection device was used, placing the samples at the bottom of the vessel. A heating plate was then installed and maintained at a temperature of 333.15 K to facilitate the evaporation of the alcohol samples. To ensure thorough evaporation, a magnetic mixing device was deployed and operated for at least 3 minutes. After ensuring complete evaporation, the

temperature of the heating plate was adjusted back down to 323.15 K. Subsequently, air was gradually introduced into the vessel to increase the internal pressure to 1 bar. Throughout this process, the magnetic stirrer remained active to guarantee thermal uniformity across the vessel and to aid in the thorough mixing of the combustible mixtures. This meticulous preparation was essential for creating a controlled environment for studying the combustion characteristics of light alcohols under specific thermal and pressure conditions. After the magnetic stirrer was turned off, the combustible mixtures were allowed to stabilize for at least 5 minutes before proceeding with ignition. This resting period ensured that any turbulence within the mixture had subsided, allowing for more controlled combustion conditions. Ignition was then initiated using a spark to trigger the deflagration mode of the combustion process, commonly referred to as the "explosion phenomenon." The dynamic development of pressure during the combustion was meticulously monitored using a piezoelectric pressure transducer. This device is sensitive to changes in pressure and capable of providing accurate and real-time data. The pressure signals captured by the transducer were recorded at a high sample rate of 150 kHz by a data acquisition system, ensuring detailed and precise measurements of the pressure fluctuations during the combustion events. Following each experiment, the combustion vessel underwent a thorough cleaning and was flushed with air to remove any residual gases or particulate matter. This procedure was crucial for maintaining the integrity of the vessel and ensuring consistent conditions for each trial, thereby eliminating cross-contamination between tests and ensuring the reliability of the results.

2. Results and discussion

Methanol-water mixtures were found to be combustible within a range of 0% to 60% water addition, although the 4 cm³ samples were an exception to this general finding. Figures 2-4 in the study illustrates a typical pressure profile recorded during these experiments. Generally, the pressure behaviors observed during the tests of specific samples were consistent, though there were notable variations when testing with extreme water additions and different volumes of alcohol samples. During the experiments, an explosion pressure of 6.88 bar was achieved when testing a 4 cm³ sample of pure methanol-air mixture, corresponding to an equivalence ratio (ϕ) of 0.3. This scenario also exhibited the highest rate of pressure rise, recorded at 365.29 bar/s, signaling it as the most reactive scenario among all the methanol-water mixtures tested.

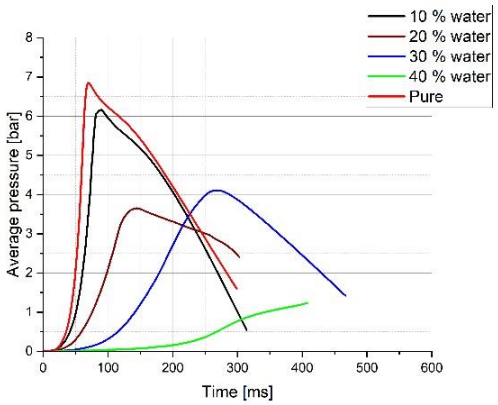

Fig. 2. *Pressure increase of 4 cm^3 of methanol and 10-40% water addition.*

The explosion delay time (t_{del}) for methanol-air mixtures with an equivalence ratio (ϕ) of 0.3 showed an increasing trend as the concentration of water in the mixture rose. However, the behavior differed with other sample volumes and equivalence ratios.

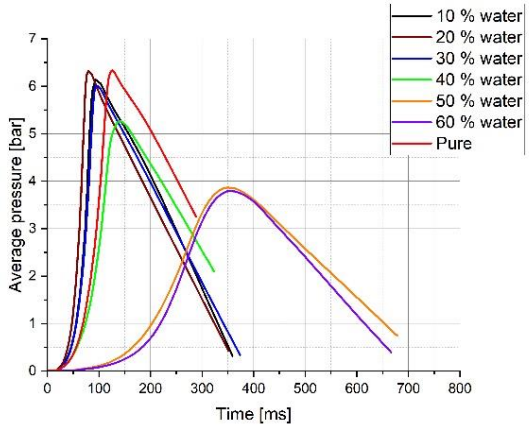

Fig. 3. *Pressure increase of 6 cm^3 of methanol and 10-60% water addition.*

Specifically, for the 6 cm³ samples at $\phi = 0.5$, the minimum t_{del} was observed with a 30% water addition. Similarly, for the 8 cm³ samples with $\phi = 0.7$, the shortest delay time occurred at a 20% water concentration, indicating an optimal level of water addition for these specific conditions that enhances the combustion characteristics.

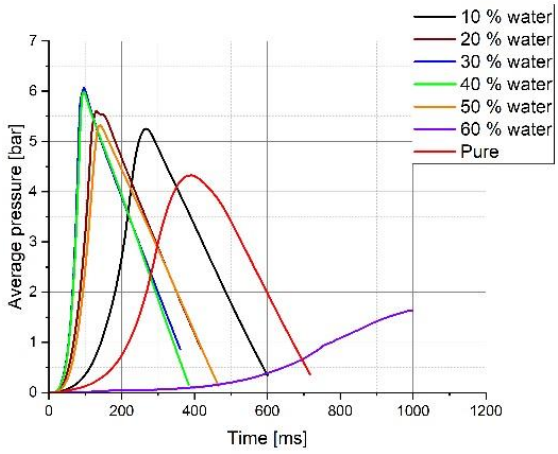

Fig. 4. *Pressure increase of 8 cm^3 of methanol and 10-40% water addition.*

Pure mixture of methanol (no water) reaches the highest peak pressure quickly, which then sharply declines. The addition of water results in a lower peak pressure, with 10% water still achieving a significant peak, but as more water is added (20% and beyond), the peak pressure is noticeably reduced. The 40% water mixture is the least reactive, barely reaching 1 bar of pressure. For the sample of 6 cm^3, the pressure peaks are higher compared to the 4 cm³ mixtures, suggesting a greater reactivity possibly due to the larger amount of methanol present. The 10%, 20%, and 30% water mixtures all reach similar peak pressures, with the 30% water mixture having a slightly delayed peak. Interestingly, the 50% and 60% water mixtures have reduced reactivity, but the decrease is not as dramatic as in the 4 cm³ mixtures, potentially due to the greater initial volume of methanol allowing for more sustained combustion. In case of 8 cm^3 for methanol, a general trend is similar to the 6 cm³ mixtures. However, the peak pressures are even higher, again likely due to the increased amount of methanol. Here, the 10% water mixture achieves the highest peak, closely followed by the pure methanol mixture. The reactivity decreases with increasing water content, yet all mixtures up to 50% water show a significant explosion pressure. The mixture with 60% water shows a very gradual increase in pressure, indicating that the high water content substantially impedes the reaction.

Ethanol-water mixtures demonstrate combustibility over a comparable range of water additions, from 0% to 60%. This suggests that both methanol and ethanol exhibit similar trends in terms of water dilution impact on combustion properties, although specific reaction dynamics such as explosion delay times and the most reactive mixture compositions may vary between the two alcohol types. This information is crucial for optimizing the use of alcohol-water mixtures in combustion processes, ensuring efficient and controlled combustion in practical applications.

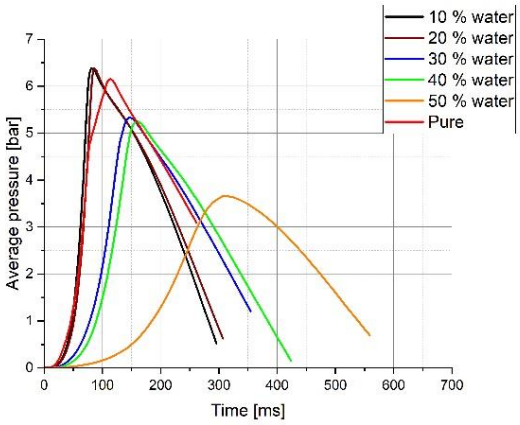

Fig. 5. *Pressure increase of 4 cm^3 of ethanol and 10-40% water addition.*

The pressure profiles observed during tests of ethanol samples were generally consistent, though exceptions were noted in scenarios involving extreme water additions and varying sample volumes. Specifically, testing 8 cm³ of pure ethanol with an equivalence ratio (ϕ) of 0.7 produced random outcomes, with only one instance qualifying as a true explosion phenomenon (characterized by an overpressure greater than 0.5 bar). As a result, reliable estimation of explosion delay time (t_{del}), explosion pressure (P_{ex}), and maximum rate of pressure rise ($(dP/dt)_{max}$) for this sample volume and composition was deemed unreliable. In contrast, more consistent and meaningful results were observed with smaller volumes. For the 4 cm³ samples of pure ethanol at $\phi = 0.3$, an explosion pressure of 6.70 bar was achieved. Additionally, a sample of the same volume but with 10% water content exhibited the highest rate of pressure rise, approximately 260.05 bar/s, indicating it was the most reactive among all tested ethanol-water mixtures. Furthermore, this specific mixture (4 cm³ of 10% water) also showed a notably reactive behavior with an explosion delay time of about 79 milliseconds. These findings highlight the influence of water content and sample volume on the reactivity and combustion characteristics of ethanol-air mixtures. They suggest that while higher volumes of ethanol can lead to unpredictable results, moderate water addition to smaller volumes can enhance reactivity, making these parameters critical for optimizing combustion processes in practical applications.

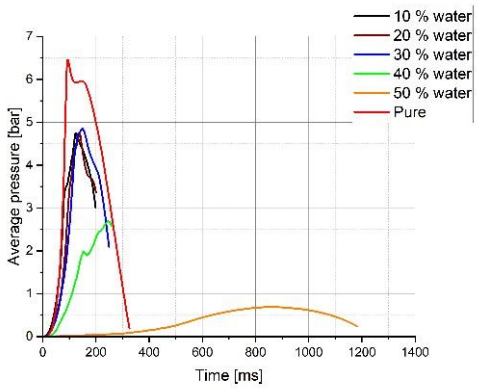

Fig. 6. *Pressure increase of 4 cm^3 of 1-propanol and 10-50% water addition.*

For the mixtures of 1-propanol with water at 4 cm^3, it can be observed that the pure mixture reaches the highest peak pressure, and it does so more rapidly than the other mixtures, suggesting it has the most reactive and energetic combustion characteristics. As the water content increases, there's a clear trend of both reduced peak pressure and a slower rise to that peak, indicating that water addition dampens the reactivity of the mixture. For example, the 10% water mixture still reaches a relatively high peak pressure, but the time to reach this peak is slightly longer compared to the pure mixture. As more water is added (20%, 30%, and so on), the peak pressures continue to decrease, and the time to reach these peaks becomes progressively longer. The mixture with 50% water content shows a very gentle pressure increase, never reaching the pressure levels of the less diluted mixtures, suggesting that it is the least reactive among those tested. This could indicate a limit to the flammability or combustibility of the mixture at this level of dilution. These pressure profiles are valuable for understanding the combustion characteristics of 1-propanol with different water concentrations, which is crucial for safety assessments, engine performance, and other applications where the fuel mixture's behavior under combustion is important.

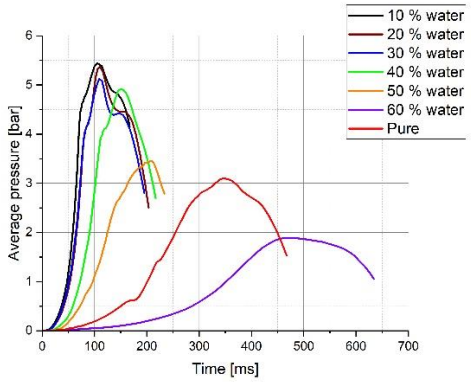

Fig. 7. *Pressure increase of 6 cm^3 of 1-propanol and 10-60% water addition.*

For the mixtures of 1-propanol with water at 6 cm^3, it can be observed that pure 1-propanol-air mixture reaches the highest peak pressure, indicating the most vigorous reaction compared to the diluted mixtures. The 10%, 20%, 30%, and 40% water content mixtures show a peak pressure that progressively decreases with increasing water content, as expected due to the dilution effect of water on combustion. Interestingly, the 50% water mixture exhibits a pressure peak that surpasses the 40% water mixture, which could indicate a specific interaction between the fuel and water at this concentration affecting combustion dynamics. The 60% water content mixture has a notably lower peak pressure, suggesting that this level of dilution significantly impedes the combustion process. Each mixture reaches its peak pressure at different times, indicating variations in the speed of the combustion process influenced by the water content. The shape of the pressure curves after the peak suggests different rates of pressure decay, which can inform the energy release rate and the stability of the combustion process. The exact reasons behind the pressure behaviors, especially the unusual trend between the 40% and 50% water addition mixtures, would require a deeper investigation into the combustion chemistry and physical phenomena occurring within the vessel.

For the mixtures of 1-propanol with water at 8 cm^3, it can be observed that pure 1-propanol mixture without water addition again shows a higher peak pressure than the diluted mixtures, which is consistent with expectations that pure fuel-air mixtures tend to be more reactive. The addition of water generally reduces the peak explosion pressure. However, each water content percentage results in a distinct curve, with some mixtures showing an increased pressure peak relative to their adjacent higher or lower water concentration mixtures. This could be due to complex interactions within the combustion chemistry at specific concentrations. As with the other graphs, as the percentage of water increases, the peak pressure generally decreases, and the time to reach peak pressure tends to be

delayed. It's notable that the curve for the mixture with 60% water addition is significantly lower than the others, indicating reduced combustibility at this concentration.

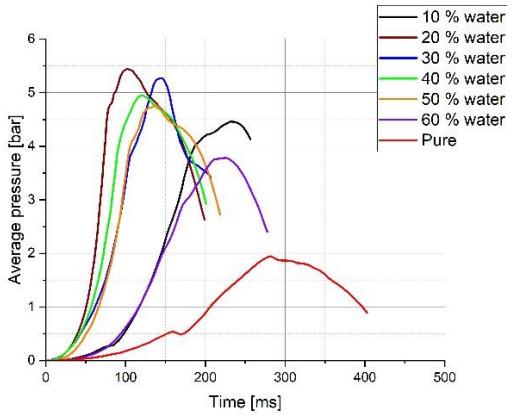

Fig. 8. *Pressure increase of 8 cm^3 of 1-propanol and 10-60% water addition.*

The variations in the profiles, particularly any anomalous trends, could be a topic of interest for further investigation. These variations might be due to the chemical properties of 1-propanol when mixed with water at different ratios, or they might result from the physical properties of the mixture as it influences the combustion process. Understanding these profiles is important for safety assessments, engine performance evaluations, and optimizing combustion conditions in practical applications.

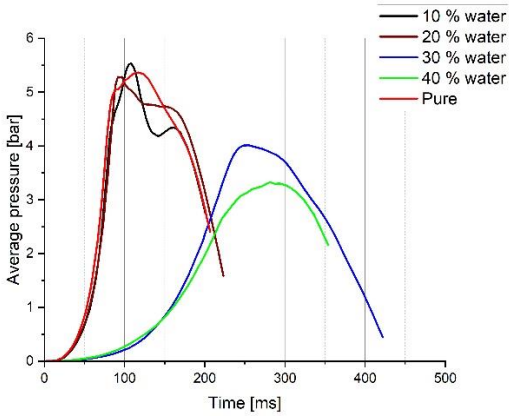

Fig. 9. *Pressure increase of 4 cm^3 of 2-propanol and 10-40% water addition.*

Mixtures of 2-propanol with water at 4 cm^3 can be concluded that pure 2-propanol mixture attains the highest peak pressure, indicating a strong reaction due to the lack of water dilution. As water content increases to 10% and 20%, there is a noticeable reduction in the peak pressure, reflecting the diluting effect of water on the flammability of the mixture. The mixture with 30% water shows a further decrease in peak pressure and also a delay in reaching this peak compared to mixtures with lower water content. Interestingly, the 40% water mixture curve appears to flatten and elongate significantly, indicating a much slower combustion process, possibly approaching the flammability limits of the mixture. The pressure increases for the 10% and 20% water mixtures occur relatively quickly after ignition, suggesting that these mixtures still retain a good level of combustibility. In contrast, the 40% water mixture shows a much more gradual increase and a lower peak, suggesting that the water content is nearing the point where combustion becomes much less vigorous or may even fail to propagate.

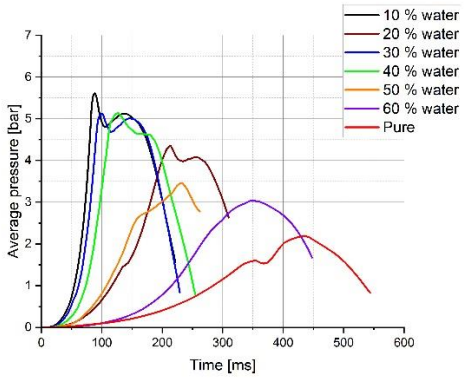

Fig. 10. *Pressure increase of 6 cm^3 of 2-propanol and 10-60% water addition.*

For the mixtures of 2-propanol with water at 6 cm^3, it can be observed that pure 2-propanol mixture exhibits the highest and most rapid pressure rise, reaching the peak pressure swiftly, which is indicative of a highly reactive mixture. As water is added (10% to 30%), there is a noticeable decrease in peak pressure, which is expected as water tends to inhibit combustion. The 40% water mixture reaches a peak pressure that's lower than the 30% mixture but seems to do so with a similar rapid pressure rise. Interestingly, the 50% water mixture shows a peak that is higher than the 40% water mixture. This could suggest an optimal water concentration for this specific mixture in terms of combustion behavior or might reflect complex chemical interactions at that particular dilution level. The mixture with 60% water has a significantly reduced peak pressure, and the pressure rise is more gradual, suggesting that the higher water content greatly dampens the combustion reaction. The fact that the 50% water mixture has a higher peak than the 40% could indicate a non-linear response to water addition, possibly due to various factors like changes in the evaporation rate, flammability limits, and the thermal properties of the mixture. Such behaviors are valuable for understanding combustion dynamics and can inform the development of fuel blends and safety protocols for handling and using 2-propanol as a fuel source.

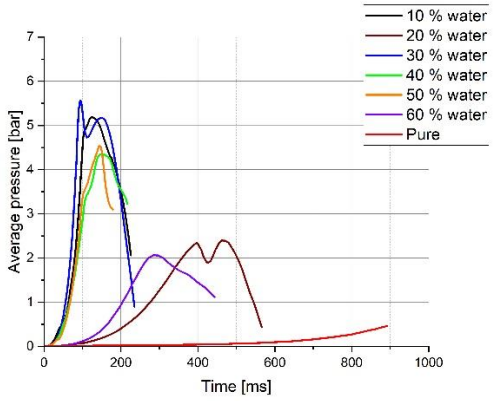

Fig. 11. *Pressure increase of 8 cm^3 of 2-propanol and 10-60% water addition.*

For the mixtures of 2-propanol with water at 8 cm^3, it can be observed that pure 2-propanol mixture exhibits the sharpest peak, suggesting that without any dilution, the mixture is highly reactive and combusts rapidly. The 10% and 20% water content mixtures still maintain a relatively high peak pressure, although there's a slight delay in reaching the peak compared to the pure mixture. This is consistent with expectations that a small amount of water doesn't severely hamper combustion but does have a noticeable effect. The pressure peaks continue to decrease with the 30%, 40%, and 50% water mixtures, and the time to peak pressure extends further, illustrating the dampening effect of

water on combustion. Interestingly, the 60% water mixture has a very low peak pressure and a very gradual rise, suggesting that the high level of water significantly impedes the combustion process, possibly approaching the flammability limit of the mixture. The gradual increase in time to reach peak pressure with increasing water content indicates that water acts as an inhibitor, prolonging the combustion process. The presence of water likely affects the vaporization of the fuel, the chemistry of the combustion process, and the overall energy release rate. These explosion pressure profiles are critical for understanding the reactivity and combustion characteristics of 2-propanol in the presence of water, which is vital for applications in fuel formulations and safety protocols.

3. Conclusions

Based on experimental results, it can be stated that while both methanol and 2-propanol exhibit reduced combustion reactivity with increasing water content, the specific relationship between water concentration and combustion behavior is complex and dependent on multiple factors including the volume of the mixture and the inherent properties of the alcohols involved. These insights are instrumental for the practical use of these substances in energy production, industrial processes, and safety engineering. Furthermore, several detailed conclusions can be drawn from these experimental results:

- Pure methanol and 2-propanol mixtures exhibit the highest reactivity, indicated by the rapid rise to peak pressure. The reactivity decreases with the addition of water across all sample volumes, but the rate of decrease is not uniform.
- Moderate amounts of water (10%-30%) in the methanol and 2-propanol mixtures do not dramatically reduce peak pressures but do impact the time to reach peak pressure. High water content (40%-60%) significantly lowers the peak pressure, indicating that water acts as an inhibitor to the combustion process.
- Larger volumes of methanol (6 cm^3 and 8 cm^3) show higher peak pressures than the smaller volume (4 cm^3), suggesting that the amount of fuel plays a significant role in the combustion dynamics. For 2-propanol, the impact of sample volume on peak pressure is less pronounced, indicating that other factors may compensate for the volume differences.
- There is a general trend where higher water content leads to both lower peak pressures and a longer time to reach these peaks, reflecting a slower and less intense combustion process. The presence of a non-linear response to water addition, particularly where certain water percentages result in higher peak pressures than adjacent concentrations, suggests complex interactions that could involve the chemistry of combustion, heat transfer, and phase changes.
- The data indicate there is a limit to the flammability of these alcohol-water-air mixtures. As the water content approaches 60%, the explosion pressures are significantly reduced, nearing the point where the mixture may not be viable for combustion.

Understanding the reactivity and the explosion pressure profiles of alcohol-water-air mixtures is crucial for their application in engines and safety protocols. These findings could guide the design of fuel blends, optimizing for desired combustion characteristics while considering the trade-offs between efficiency and safety.

Acknowledgements

This work was supported by the research project of the program “Excellence initiative – Research University” for the AGH University of Krakow in Poland.

References

Bechtold, J. K., & Matalon, M. (2001). The Dependence of the Markstein Length on Stoichiometry. Combustion and Flame, 127, 1906–1913.

Beeckmann, J., Cai, L., & Pitsch, H. (2014). Experimental investigation of the laminar burning velocities of methanol, ethanol, n-propanol, and n-butanol at high pressure. Fuel, 117(PART A), 340–350.

Black, G., Curran, H. J., Pichon, S., Simmie, J. M., & Zhukov, V. (2010). Bio-butanol: Combustion properties and detailed chemical kinetic model. Combustion and Flame, 157(2), 363–373.

Bradley, D., Lawes, M., & Mansour, M. S. (2009). Explosion bomb measurements of ethanol-air laminar gaseous flame characteristics at pressures up to 1.4 MPa. Combustion and Flame, 156(7), 1462–1470.

Broustail, G., Seers, P., Halter, F., Moréac, G., & Mounaim-Rousselle, C. (2011). Experimental determination of laminar burning velocity for butanol and ethanol iso-octane blends. In Fuel (Vol. 90, Issue 1, pp. 1–6).

Cammarota, F., Di Benedetto, A., Di Sarli, V., Salzano, E., & Russo, G. (2009). Combined effects of initial pressure and turbulence on explosions of hydrogen-enriched methane/air mixtures. Journal of Loss Prevention in the Process Industries, 22(5), 607–613.

Chen, Z. (2011). On the extraction of laminar flame speed and Markstein length from outwardly propagating spherical flames. Combustion and Flame, 158(2), 291–300.

Cracknell, R., Head, B., Remmert, S., Wu, Y., Prakash, A., & Luebbers, M. (2013). Laminar burning velocity as a fuel characteristic: Impact on vehicle performance. In Internal Combustion Engines: Performance, Fuel Economy and Emissions: IMechE, London, 27-28 November 2013 (pp. 149–156). Elsevier Ltd.

Dahoe, A. E., & de Goey, L. P. H. (2003). On the determination of the laminar burning velocity from closed vessel gas explosions. Journal of Loss Prevention in the Process Industries, 16(6), 457–478.

De Goey, L. P. H., Van Oijen, J. A., Kornilov, V. N., & Ten Thije Boonkkamp, J. H. M. (2011). Propagation, dynamics and control of laminar premixed flames. Proceedings of the Combustion Institute, 33(1), 863–886.

Dirrenberger, P., Glaude, P. A., Bounaceur, R., Le Gall, H., Da Cruz, A. P., Konnov, A. A., & Battin-Leclerc, F. (2014). Laminar burning velocity of gasolines with addition of ethanol. Fuel, 115, 162–169.

Egolfopoulos, F. N., Hansen, N., Ju, Y., Kohse-Höinghaus, K., Law, C. K., & Qi, F. (2014). Advances and challenges in laminar flame experiments and implications for combustion chemistry. In Progress in Energy and Combustion Science (Vol. 43, pp. 36–67). Elsevier Ltd.

Gainey, B., & Lawler, B. (2021). The role of alcohol biofuels in advanced combustion: An analysis. Fuel, 283.

Giannakopoulos, G. K., Matalon, M., Frouzakis, C. E., & Tomboulides, A. G. (2015). The curvature Markstein length and the definition of flame displacement speed for stationary spherical flames. Proceedings of the Combustion Institute, 35(1), 737–743.

Gu, X., Huang, Z., Wu, S., & Li, Q. (2010). Laminar burning velocities and flame instabilities of butanol isomers-air mixtures. Combustion and Flame, 157(12), 2318–2325.

Hechinger, M., & Marquardt, W. (2010). Targeted QSPR for the prediction of the laminar burning velocity of biofuels. Computers and Chemical Engineering, 34(9), 1507–1514.

Katoch, A., Asad, M., Minaev, S., & Kumar, S. (2016). Measurement of laminar burning velocities of methanol-air mixtures at elevated temperatures. Fuel, 182, 57–63.

Katoch, A., Millán-Merino, A., & Kumar, S. (2018). Measurement of laminar burning velocity of ethanol-air mixtures at elevated temperatures. Fuel, 231, 37–44.

Konnov, A. A., Mohammad, A., Kishore, V. R., Kim, N. Il, Prathap, C., & Kumar, S. (2018). A comprehensive review of measurements and data analysis of laminar burning velocities for various fuel+air mixtures. In Progress in Energy and Combustion Science (Vol. 68, pp. 197–267). Elsevier Ltd.

Kumar, T. S., & Ashok, B. (2021). Critical review on combustion phenomena of low carbon alcohols in SI engine with its challenges and future directions. In Renewable and Sustainable Energy Reviews (Vol. 152). Elsevier Ltd.

Li, Q., Cao, X., Yang, Y., Zhang, X., Yan, Z., & Huang, Z. (2022). Experimental and chemical kinetic study on the laminar flame characteristics of the blends of n-propanol and isooctane at elevated temperature and pressure. Fuel, 324.

Liang, K., & Stone, R. (2017). Laminar burning velocity measurement of hydrous methanol at elevated temperatures and pressures. Fuel, 204, 206–213. https://doi.org/10.1016/j.fuel.2017.05.060

Liao, S. Y., Jiang, D. M., Huang, Z. H., Shen, W. D., Yuan, C., & Cheng, Q. (2007). Laminar burning velocities for mixtures of methanol and air at elevated temperatures. Energy Conversion and Management, 48(3), 857–863.

Marshall, S. P., Taylor, S., Stone, C. R., Davies, T. J., & Cracknell, R. F. (2011). Laminar burning velocity measurements of liquid fuels at elevated pressures and temperatures with combustion residuals. Combustion and Flame, 158(10), 1920–1932.

Nativel, D., Pelucchi, M., Frassoldati, A., Comandini, A., Cuoci, A., Ranzi, E., Chaumeix, N., & Faravelli, T. (2016). Laminar flame speeds of pentanol isomers: An experimental and modeling study. Combustion and Flame, 166, 1–18.

Palma, V., Ruocco, C., Meloni, E., & Ricca, A. (2017). Renewable hydrogen from ethanol reforming over CeO2-SiO2 based catalysts. Catalysts, 7(8).

Parag, S., & Raghavan, V. (2009). Experimental investigation of burning rates of pure ethanol and ethanol blended fuels. Combustion and Flame, 156(5), 997–1005.

Pio G., Ruocco C., Palma V., Salzano E. (2021) Detailed kinetic mechanism for the hydrogen production via the oxidative reforming of ethanol, Chemical Engineering Science 237, 116591.

Porowski R., et al. (2023) Influence of initial temperature on laminar burning velocity in hydrogen-air mixtures as potential for green energy carrier, International Communications in Heat and Mass Transfer, 1146, 106861.

Porowski R., et al (2024) Thermodynamic Reactivity Study during Deflagration of Light Alcohol Fuel-Air Mixtures with Water, Energies 17, 1466.

Rallis, C. J., & Garforth, A. M. (1980). The determination of laminar burning velocity. Prog. Energy Combust. Sci, 6, 303–329.

Sarathy, S. M., Oßwald, P., Hansen, N., & Kohse-Höinghaus, K. (2014). Alcohol combustion chemistry. In Progress in Energy and Combustion Science (Vol. 44, pp. 40–102). Elsevier Ltd.

Sileghem, L., Alekseev, V. A., Vancoillie, J., Nilsson, E. J. K., Verhelst, S., & Konnov, A. A. (2014). Laminar burning velocities of primary reference fuels and simple alcohols. Fuel, 115, 32–40.

Vancoillie, J., Demuynck, J., Galle, J., Verhelst, S., & Van Oijen, J. A. (2012). A laminar burning velocity and flame thickness correlation for ethanol-air mixtures valid at spark-ignition engine conditions. Fuel, 102, 460–469.

Vargün, M., Özsezen, A. N., Botsalı, H., & Sayın, C. (2023). A study on the impact of fuel injection parameters and boost pressure on combustion characteristics in a diesel engine using alcohol/diesel blends. Process Safety and Environmental Protection, 177, 29–41.

Veloo, P. S., & Egolfopoulos, F. N. (2011). Studies of n-propanol, iso-propanol, and propane flames. Combustion and Flame, 158(3), 501–510.

Veloo, P. S., Wang, Y. L., Egolfopoulos, F. N., & Westbrook, C. K. (2010). A comparative experimental and computational study of methanol, ethanol, and n-butanol flames. Combustion and Flame, 157(10), 1989–2004.

Wako, F. M., Pio, G., & Salzano, E. (2021). Laminar burning velocity and ignition delay time of oxygenated biofuel. In Energies (Vol. 14, Issue 12). MDPI.

Yi, F., & Axelbaum, R. L. (2013). Stability of spray combustion for water/alcohols mixtures in oxygen-enriched air. Proceedings of the Combustion Institute, 34(1), 1697–1704.

Zhang, Y., Shen, W., Fan, M., Zhang, H., & Li, S. (2014). Laminar flame speed studies of lean premixed H2/CO/air flames. Combustion and Flame, 161(10), 2492–2495.

Zhang, Z., Tian, J., Li, J., Lv, J., Wang, S., Zhong, Y., Dong, R., Gao, S., Cao, C., & Tan, D. (2022). Investigation on combustion, performance and emission characteristics of a diesel engine fueled with diesel/alcohol/n-butanol blended fuels. Fuel, 320.

Zhu, Y., Davidson, D. F., & Hanson, R. K. (2014). 1-Butanol ignition delay times at low temperatures: An application of the constrained-reaction-volume strategy. Combustion and Flame, 161(3), 634–643.

The lower explosion limit of a hybrid dust gas mixture of hydrogen and activated carbon

Dilip Arulappan[a,c], Frederik Norman[b], Vojtech Jankuj[c] and Stefan H. Spitzer[d,]
[a]FIKE Europe, Herentals, Belgium
[b]Adinex, Herentals, Belgium
[c]Faculty of Safety Engineering VSB - TUO, Ostrava, Czech Republic
[d] Eifi-Tech, Schwäbisch-Gmünd, Germany

E-mail:dilip.arulappan@fike.com

Abstract

The lower explosion limit of hybrid mixtures has been investigated by various scientists. The conclusions about the ignition behaviour are inconsistent and leave the person in charge of safety measures behind with no clue, how to estimate the danger that might arise from the used materials.

In the first part, this article summarizes and discusses the literature that has been published so far about the lower explosion limit of hybrid mixtures. In the second part new data about a simple hybrid system consisting of only two different atoms, Carbon and Hydrogen, is presented. Numerous scholars have released findings while attempting to devise estimation techniques for the simultaneous combustion of solid materials and gases. The earliest method, introduced by Le Chatelier, was initially designed exclusively for gas-gas mixtures. Another method involved the utilization of the Bartknecht curve, which was specifically applied to certain hybrid mixtures; however, notable discrepancies persist. Enhancing the accuracy of a correlation for predicting the lower explosion limit (LEL) in the context of hybrid mixture explosions is imperative for future industrial design. This research paper focuses on the study of a hybrid mixture explosion in a modified 20L sphere for the material combination Hydrogen/Activated carbon. Using the determined value, a new approach is presented to increase the efficiency in determining the LEL of the hybrid mixture.

Keywords: *Dust explosion, Hybrid mixtures, Lower flammability limit, Le Chatelier Law, Bartknecht curve*

1. Introduction

Dust explosions are a common industrial occurrence which damage property and cause harm to the workforce. A hybrid mixture is a combination of a combustible dust and a flammable gas or vapour. However, combustible dust below its MEC (minimum explosible concentration) and flammable gas or vapour below its lower explosion limit cannot be ignited (Amyotte et al., 1993; Amyotte & Eckhoff, 2010; Denkevits, 2007; Dufaud et al., 2009; Eckhoff, 2005; Garcia-Agreda et al., 2011). When these two are mixed they can form an explosive atmosphere below the explosive region of each single component. The hybrid mixture (fermentation combustible gas/grain dust/air) explosion in the grain silo at Semabla Company in Blaye, France, in 1997 (Abuswer, 2012) is a good case point. These types of explosions not only occur in other industries such as food, pharmaceutical, paint, as well as chemical manufacturing (Amyotte & Eckhoff, 2010) but also industries handling hybrid conditions causing significant problems for growing renewables and other process industries. These accidents will result in loss of lives, property and reputation loss (Almerinda Di Benedetto et al., 2013).

In a process, a so-called hybrid mixture might occur containing gaseous flammable components and combustible dust. Numerous investigations have been conducted to enhance the fundamental comprehension of hybrid mixture systems. One intriguing aspect revolves around the lower explosion limit (LEL) of these hybrids. The LEL stands out as a crucial factor in hazard assessments and the formulation of mitigation strategies for processes utilizing such mixtures (Jiang et al., 2014). Le Chatelier's Law was originally developed and adopted for homogeneous gas mixtures based on the concept of a constant limit flame temperature for a given class of fuels (Glassman, 1996). If extended to hybrid mixtures, Le Chatelier's Law is a relationship between the LEL of gas and the MEC of dust, and the weighting factor for each fuel is its fractional content in the mixture as represented in a model proposed by (Glassman, 1996) taking Le Chatelier law as an origin that describes a homogenous mixture by considering a constant flame temperature.

$$LEL_{\,hybrid} = \frac{1}{\frac{X_{gas}}{LEL_{gas}} + \frac{X_{dust}}{MEC_{dust}}} \quad (1)$$

X_{gas} is the relative fuel concentration of the flammable gas,%; LEL_{gas} is the lower explosion limit of the gas, g/m³; x_{dust} is the relative fuel concentration of the combustible dust, % $x_{gas}+x_{dust}=1$; MEC is the minimum explosible concentration of the dust, g/m³.

However, some deviation from Le Chatelier's Law was found when applied to the low-volatile Pocahontas coal with methane (Cashdollar, 1996). Closer to this, another deviation was also found by (Bartknecht et al., 1981). A model proposed by Bartknecht is an empirical equation derived from a series of experimental measurements. The LEL of hybrid mixtures decreases with increasing the gas concentration by a second-order equation, named the Bartknecht curve as represented.

$$LEL_{\,hybrid} = MEC_{dust}\left[\frac{y}{LEL_{gas}} - 1\right]\text{^}2 \quad (2)$$

Cornstarch dust with hydrogen was tested by Gaug and referred to by (Cashdollar et al., 1987). It was established that more dust is required to render the system flammable, which deviates from the above equations i.e. linear relationship defined by Le Chatelier's Law or the second order curve as defined by Bartknecht. In a motive to investigate the deviations in the heat capacity and the deflagration index of the fuel (Prugh, 2008) concluded that the straight-line relationship applies to mixtures where the heat capacity of dust and gas/vapour are similar and deflagration indices are moreover equivalent. Another method was proposed by (Jiang et al., 2014) based on a correlation between the Le Chatelier Law and the Bartknecht equation.

$$LEL_{\,hybrid} = MEC_{dust}[1 - \frac{y}{LEL_{gas}}]^{(1.12\pm0.03)\frac{K_{St}}{K_G}} \quad (3)$$

In general, it's understood that hybrid mixtures have the potential to ignite when the concentration of each fuel falls below its lower explosion limit. While Le Chatelier's Law and the Bartknecht curve offer predictive tools for estimating the LEL of these mixtures, discrepancies persist, particularly in scenarios where additional dust or gas is required to induce flammability. Hence, there's a pressing need for a more precise correlation to anticipate the LEL of hybrid mixtures. So far there is no standardized test method for this case. The LEL is an often-used safety characteristic in primary explosion protection. Standardized test methods for gases and vapours (European Standard: EN 1839, American Standard: ASTM E681-09) and for dust (European Standard: EN 14034-3, American Standard: ASTM E1226) are available and widely used. This work aims to focus on the study of hybrid mixture explosion

in a modified 20L sphere for mixtures to help future research to control and or limit hybrid explosion within industries like HDPE production where dust mixes with monomer hydrocarbons e.g ethylene and Spray dryers that combine dust with drops and flammable vapours.

2. Methods and Materials

The experiments were performed in a Kühner 20L sphere with some modifications, such as the addition of a pressure sensor to measure the pressure before and after the injection of hydrogen. An additional piezoresistive sensor was added to measure the static pressure of the hybrid mixture as shown in Figure 1 (Spitzer et al., 2022). Unlike the standard pure dust testing method as per (EN 14034, 2011), for testing the hybrid materials partial pressure mixing was applied to prepare a flammable air mixture within the chamber before performing the test. To the standard 20L sphere one piezo-resistive pressure sensor was additionally installed for a resolution between (0.1mbar and -2 bar). These sensors were used for the filling process and had to be closed before initiating each ignition and for the determination of the post-injection pressure drop. As igniters two 1000J Sobbe pyrotechnical igniters, pointing in opposite directions and placed in the centre of the sphere according to the standards for the determination of explosion characteristics of dust clouds.

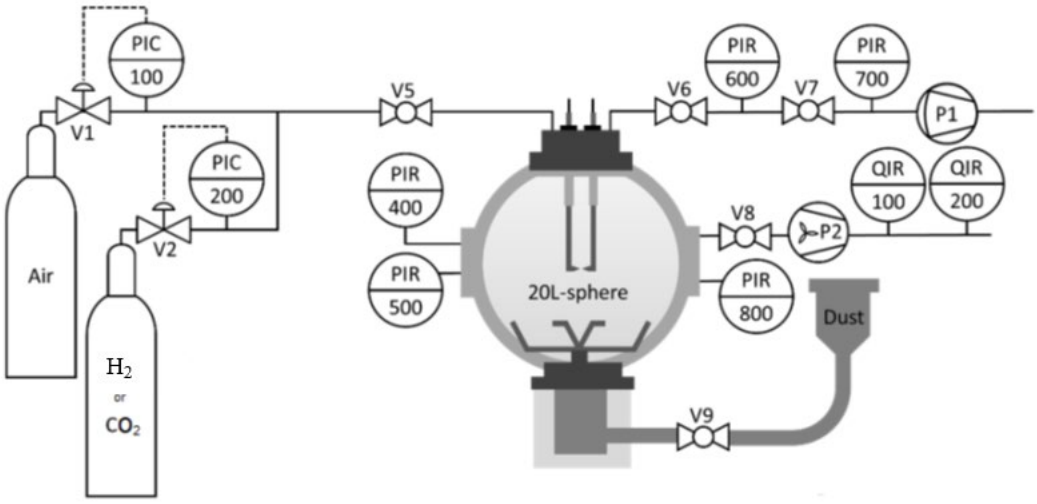

Figure 1:*20L-sphere with modification for hybrid mixtures* (Spitzer et al., 2022)

The sphere was evacuated to a pressure of 200 mbar before each test. Then the vessel was filled with the partial pressure of hydrogen (20 mbar or 50 mbar for a concentration of 2 mol% or 5 mol% respectively) and filled with compressed air until a pressure of 400 mbar. At the start of the test, the dust was injected from the dust inlet chamber with compressed dry air by opening a fast-acting valve through a rebound nozzle. The ignition delay time (tv) is 60ms. In each test, the pressure in the 20 L sphere was 400 ± 2 mbar before dust injection. The pressure development was recorded with two piezo-electric pressure sensors.

Figure 2 shows a typical pressure–time profile in an explosion test, where (dP/dt), P_{ex} is obtained for a specific concentration of pure dust or gas or a combination of both. P_{max} is the maximum value of P_{ex}. K_{St} and K_G are the maximum values of $(dP/dt)_{ex}$ at varying dust or gas

concentrations. Ignition delay t_v influences the degree of turbulence (Popa et al., 2021). The method to determine MEC and Kst of activated carbon of three different fractions was (ASTM, 2021; EN 14034, 2011). The explosion experiment for hybrid materials followed (DIN/TS 31018-1, 2023)

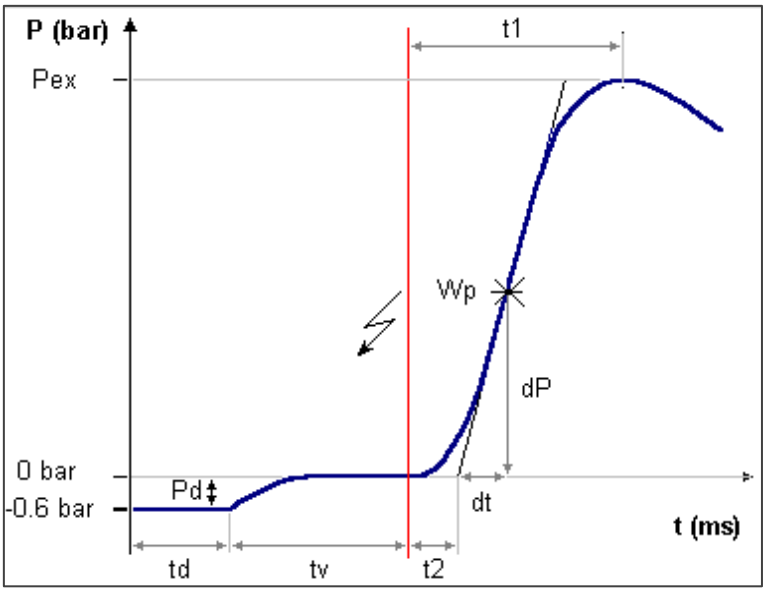

Figure 2: *Typical pressure/time - diagram* (Popa et al., 2021)

3. Results and discussion

a. Dust explosion

Activated carbon dust explosion characteristics have been widely studied. Activated Granular Carbon for this study was procured from Norit Netherlands (Norit Rox 0.8). This carbon material is milled in a rotary sieve mill, sieve 200 µm, 18000rpm and 3 sieve fractions are used for different characterization using the (HORIBA laser scattering particle size analyser, LA950) laser diffraction method. In our experiments, the LEL of activated carbon has been tested for three fractions as shown below.

Table 1: *LEL of the dust only*

Fraction	**Median value d_{10} µm**	**Median value d_{50} µm**	**Median value d_{90} µm**	**LEL g/m³**
Sieved < 45 µm	6.1	11.1	21.1	70
Sieved 45-71 µm	7.7	46.9	84.4	140
Sieved 71-125 µm	66.1	95.2	122.3	200

b. Hybrid explosion

Hydrogen: 99.9% pure. The concentration of gas Cgas (mol% or vol%) is calculated for the preparation of a hybrid mixture.

$$C_{gas} = \frac{P_{gas}}{(PV+PIPR-PIPD)} - Deviation_{conc} \quad (4)$$

The sum of the partial fraction of gas, partial vacuum, pre-ignition pressure rise and post-ignition drop is taken as the concentration of H_2 for each Mol fraction. These tests are performed without the mix of dust. The partial vacuum before opening the fast-acting valve is

0.4 bar. The Preigniton pressure rise from the dust container was 0.63 bar. The difference was observed ±0,2 Mol-% for each concentration of H_2.

The explosion behaviour of studied hybrid mixtures has been shown in below table 2.

Table 2:*LEL, P_{max}, dp/dt and K_{st} of Hybrid mixture AC and H_2*

	0 mol% H_2				**2 mol% H_2**				**5 mol% H_2**			
Sieved fraction	**LEL**	**Pmax**	**dP/dt_max**	**Kst**	**LEL**	**Pmax**	**dp/dt$_{max}$**	**Kst**	**LEL**	**Pmax**	**dP/dt_max**	**Kst**
	g/m³	**barg**	**bar/s**	**bar m/s**	**g/m³**	**barg**	**bar/s**	**bar m/s**	**g/m³**	**barg**	**bar/s**	**bar m/s**
< 45 µm	70	6.5	167	45	40	7.1	180	49		7.2	241	66
45-71 µm	140	6.0	124	34	50	6.8	150	41		6.9	214	58
71-125 µm	200	6.0	60	16	70	6.6	145	39		6.8	179	49

Using the results from the above table a graph has been developed in Figure 3. The x-axis is H_2 Mol% and y – the y-axis is activated carbon MEC in g/m^3.

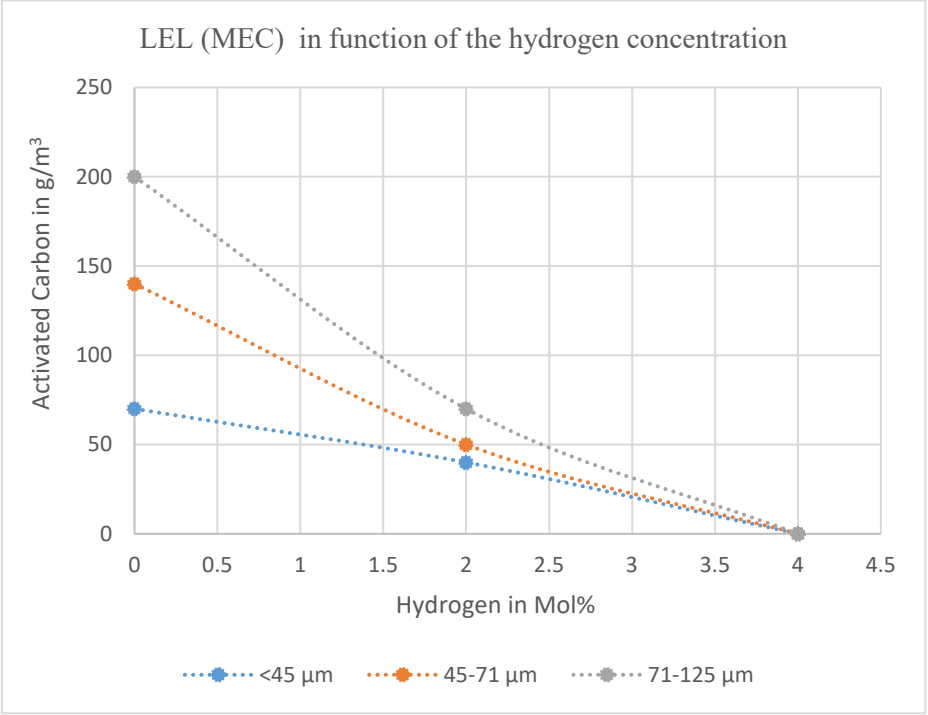

Figure 3. *Explosion tests for hybrid mixtures*

c. *Comparison*

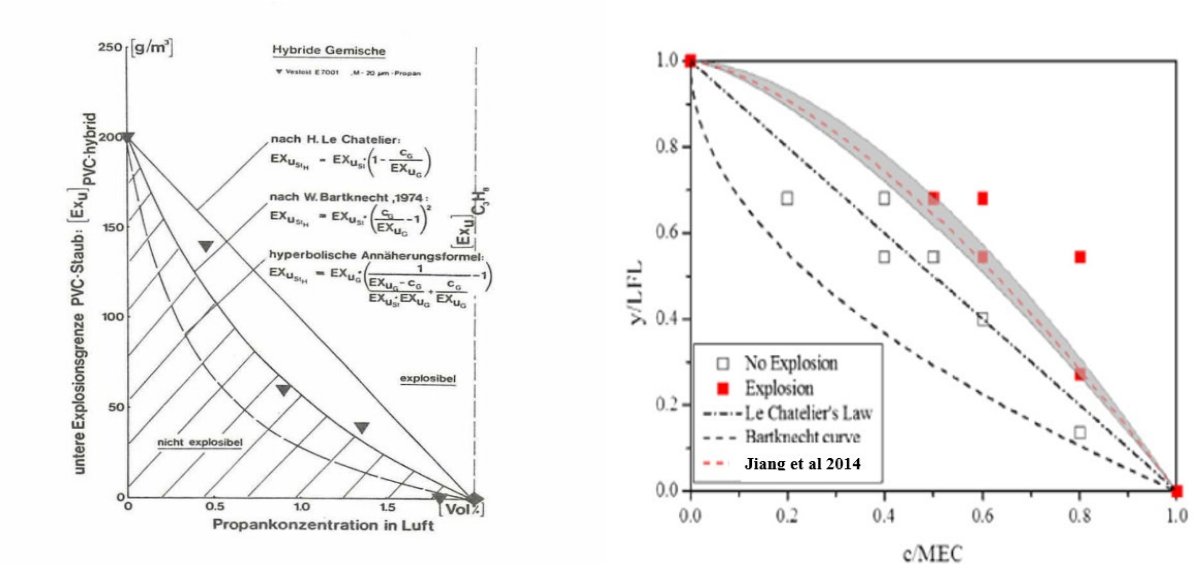

Figure 4:*Pellmont- super Bartknecht vs Le Chatelier- line vs Jiaojun Jiang* (Jiang et al., 2014; Pellmont, 1979)

The Lower Explosible Limit (LEL) for gases or Minimum Explosible Concentration (MEC) for dust represents the threshold concentration of fuel within an air mixture, below which the self-sustained propagation of a flame cannot transpire. Understanding these thresholds is crucial for the prevention and mitigation of risks associated with explosions involving gas, dust, or hybrid mixtures. By discerning these limits, it becomes possible to establish safeguards within systems to ensure that concentrations remain below the critical threshold, thereby minimizing the potential for explosion incidents (Addai et al., 2016). For hybrid mixtures, Glassman (1996), Bartknecht et al. (1981) and Jiang et al. (2014) have already proposed a model to predict LEL for hybrid mixtures as discussed in equations (1, 2 and 3). However, (Cashdollar, 1996) and (Addai et al., 2015) observed deviations from these models for different gas and dust mixtures. It is noticed from Figure 5, Figure 6, and Figure 7 that the deviations of (Jiang et al., 2014) are massive from the original work as the fact the LEL of gases are derived from the literature data for testing conditions and the K_G of gases is determined under turbulence and different ignitors. Hence, a different approach has been suggested in this work to predict the LEL of a hybrid mixture for finer dust fractions, which falls right below the Le Chatelier line and closer to the Bartknecht curve.

Figures,5, 6 and 7 show the test results of the LEL-determination of AC dust fractions < 45 µm, 45-71µm and 71-121 µm with 2 mol% H_2 mixtures and comparisons of previous models as per Figure 4 vs newly proposed methods to predict the LEL.

It can be seen from Figures 6 and 7 that the LEL from the two coarser fractions lies below the linear correlation of Le Chatelier or a super effect is observed. The LEL from the finest fraction (< 45 µm) lies above the linear correlation of Le Chatelier, see Figure 6. It can be concluded that the correlation proposed by (Jiang et al., 2014), see equation 3, cannot be applied to these hybrid mixtures because this prediction lies far from the correlation of Le Chatelier because of the low K_{st}/K_G ratio (with K_G = 550 bar m/s, reference (NFPA, 2007). Also, the LEL for the gas component is taken from other literature and it is supposed, that the turbulence that is inherent when testing hybrid mixtures would have extinguished the ignition source that was used in the work of (Spitzer, 2023) page 68 ff.

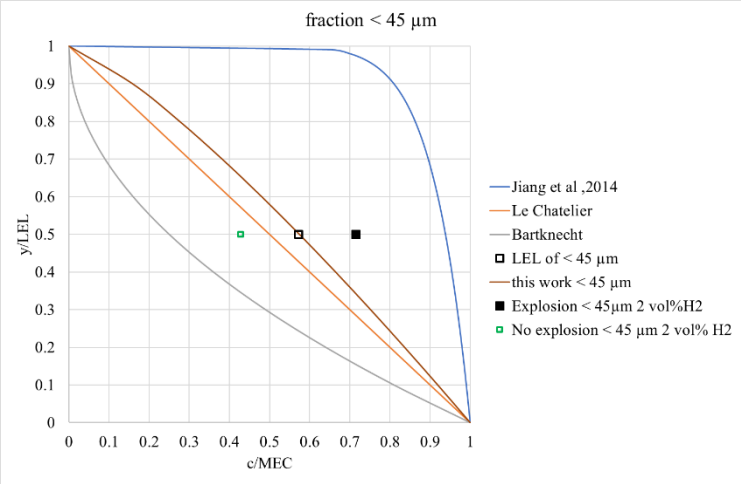

Figure 5: *Comparison between the previous models and this work with H_2 and fractions <45µm (y/LEL is the fuel or hydrogen concentration divided by the lower flammability limit of hydrogen in the air (LEL = 4 mol%) and c/MEC is the dust concentration divided by the MEC dust concentration of that fraction in the air)*

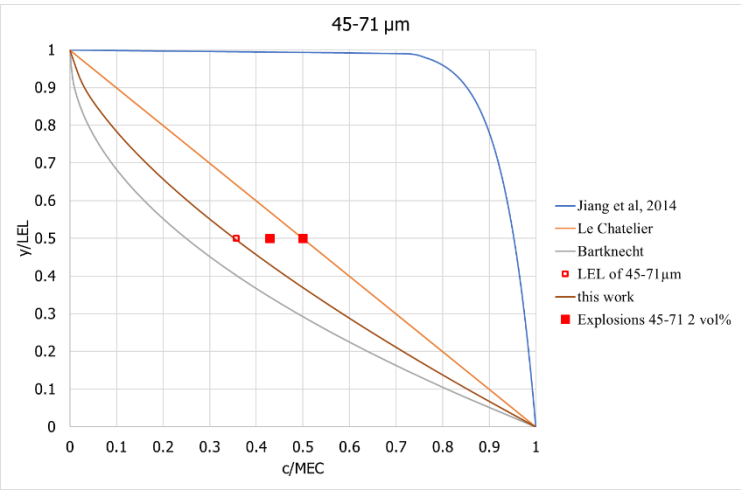

Figure 6: *Comparison between the previous models and this work with H_2 and the fraction 45-71µm*

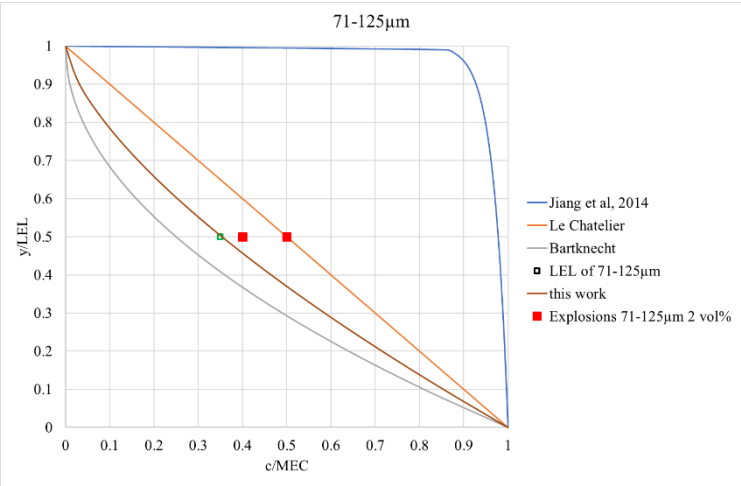

Figure 7: *Comparison between the previous models and this work with H_2 and the fraction 71-121µm*

4. Conclusions

The simplest hybrid mixture containing only two atoms, carbon and hydrogen, was investigated on its lower explosion limit. The carbon was milled and sieved to obtain three different particle sizes. For the combination of coarse dust adding 2 mol% of hydrogen (1/2 LEL of it) reduced the LEL to less than half compared to the dust alone, so a "super-effect" was observed. This is similar to the findings by Bartknecht and Pellmont whose predictions fell below the LeChatelier linear approach.

Finer dust fractions had a lower LEL but the LEL of the hybrid mixture was not equally dropping and was closer to the Le Chatelier curve. The correlation of Jiang et al. (2014) couldn't be applied as the test conditions for the hybrid were different to the literature gas value conditions referred to establish the prediction.

The finest dust fraction together with the hybrid mixture and the LEL of the hydrogen alone were in accordance with the linear approach by Le Chatelier. So the confusion about the different behaviours of hybrid mixtures as well as the different equations for the curves are actually a result of the particle size distribution of the dust sample.

Equations exceeding the Le Chatelier line took literature values for one component tested under different conditions. Testing them under the same conditions (turbulence and ignition source) might have resulted in similar results.

Acknowledgement

The authors gratefully acknowledge the financial contribution of the Fike Corporation to complete the experimental tests.

Bibliography

Abuswer, M. A. (2012). *A quantitative risk management framework for dust and hybrid mixture explosions*. Dalhousie University Halifax.

Addai, E. K., Gabel, D., & Krause, U. (2015). Lower explosion limit of hybrid mixtures of burnable gas and dust. *Journal of Loss Prevention in the Process Industries*, *36*, 497–504.

Addai, Emmanuel. K., Gabel, D., & Ulrich, K. (2016). Models to Estimate the Lower Explosion Limits of Dusts, Gases and Hybrid Mixtures. *AIDIC*, *48*.

Almerinda Di Benedetto, Paola Russo, R Sanchirico, & Valeria Di Sarli. (2013). CFD simulations of turbulent fluid flow and dust dispersion in the 20 liter explosion vessel. *AIChE Journal*, *59*(7), 2485–2496.

Amyotte, P. R., & Eckhoff, R. K. (2010). Dust explosion causation, prevention and mitigation: An overview. *Journal of Chemical Health and Safety*, *17*(1), 15–28.

Amyotte, P. R., Mintz, K. J., Pegg, M. J., & Sun, Y. H. (1993). The ignitability of coal dust-air and methane-coal dust-air mixtures. *Fuel*, *72*(5), 671–679.

ASTM. (2021). ASTM 1226-12a: Standard Test Method for Explosibility of Dust Clouds. *ASTM International*.

Bartknecht, W., Burg, H., & Almond, T. (1981). *Explosions-course, prevention, protection.*

Cashdollar, K. L. (1996). Coal dust explosibility. *Journal of Loss Prevention in the Process Industries*, *9*(1), 65–76.

Cashdollar, K. L., Hertzberg, M., Sapko, M. J., & Weiss, E. S. (1987). Laboratory and mine dust explosion research at the Bureau of Mines. *ASTM International*.

Denkevits, A. (2007). Explosibility of hydrogen–graphite dust hybrid mixtures. *Journal of Loss Prevention in the Process Industries*, *20*(4–6), 698–707.

DIN/TS 31018-1. (2023). *Determination methods for safety-related parameters of explosion protection for hybrid mixtures of substances - Part 1: Gases*.

Dufaud, O., Perrin, L., Traore, M., Chazelet, S., & Thomas, D. (2009). Explosions of vapour/dust hybrid mixtures: A particular class. *Powder Technology*, *190*(1–2), 269–273.

Eckhoff, R. K. (2005). Current status and expected future trends in dust explosion research. *Journal of Loss Prevention in the Process Industries*, *18*(4–6), 225–237.

EN 14034. (2011). *Determination of explosion characteristics of dust clouds*.

Garcia-Agreda, A., Di Benedetto, A., Russo, P., Salzano, E., & Sanchirico, R. (2011). Dust/gas mixtures explosion regimes. *Powder Technology*, *205*(1–3), 81–86.

Glassman, I. (1996). Combustion. In *Combustion (3rd,Ed)* (3rd ed.).

Jiang, J., Liu, Y., & Mannan, M. S. (2014). A correlation of the lower flammability limit for hybrid mixtures. *Journal of Loss Prevention in the Process Industries*, *32*, 120–126.

NFPA. (2007). Standard on Explosion Protection by Deflagration Venting. *NFPA*.

Pellmont, G. (1979). *Explosions- und Zündverhalten von hybriden Gemischen aus brennbaren Stäuben und Brenngasen*.

Popa, C. M., Nan, S. M., Părăian, M., Jurca, A., & Păun, F. (2021). Aspects of laboratory tests for the determination of the minimum ignition energy of the fuel / dust mixture. *MATEC Web of Conferences*, *342*, 04004.

Prugh, R. W. (2008). The relationship between flash point and LFL with application to hybrid mixtures. *Process Safety Progress*, *27*(2), 156–163.

Spitzer, S. H. (2023). *Influence of the ignition source on the safety characteristics of hybrid mixtures*.

Spitzer, S. H., Askar, E., Hecht, K. J., Gabel, D., Zakel, S., & Krietsch, A. (2022). Requirements for a Hybrid Dust-Gas-Standard: Influence of the Mixing Procedure on Safety Characteristics of Hybrid Mixtures. *Fire*, *5*(4), 113.

Effect of pipe diameter and volume ratio on dust explosion in interconnected vessels

Zongling Zhang [a], Haipeng Jiang [a], Yi Sun [a] & Wei Gao [a*]

[a] State Key Laboratory of Fine Chemicals, Department of Chemical Machinery and Safety Engineering, Dalian University of Technology, Dalian 116024, China

E-mail: gaoweidlut@dlut.edu.cn

Abstract

The explosion process of 150 nm polymethyl methacrylate (PMMA) dust in the interconnected vessels was studied through numerical simulations, which supported the safety protection of the powder-related industry. The simulation results are verified by the overpressure and the flame propagation velocity. The simulation results are in excellent agreement with the experimental results and have high reliability. The results show that with the expansion in the pipe diameter, the turbulent velocity in the primary vessel decreases while the precompression increases. And with the growth of the volume ratio, the maximum explosion overpressure decreases first and then mounts. For industrial explosion-proof design, it should be avoided to use pipe diameters for the most dangerous conditions. The existence of an optimal volume ratio is the optimal choice for explosion-proof designs. This study provides support for an in-depth understanding of the evolution mechanism of pressure-piling in interconnected vessels and contributes effective methods for designing equipment with explosion risk.

Keywords: *dust explosions, interconnected vessels, nano-sized PMMA, computational fluid dynamics*

1. Introduction

In modern industrial production, dust explosions have always seriously threatened personal safety and equipment, resulting in many catastrophic accident consequences (Blair, 2007). In particular, as the frequency of use of nanomaterials increases, their smaller particle sizes will increase the likelihood and power of accidents. Many studies have shown that the minimum ignition energy and minimum ignition temperature of nano-sized dust are significantly reduced compared to microscale dust particles (Azhagurajan et al., 2012; Blair, 2007; Bouillard et al., 2010; Vignes et al., 2012). (Wu et al., 2010) pointed out that a reduction in the size of the nano-sized particles reduced the minimum explosive concentration of dust. In addition to increased blast susceptibility, nano-sized dust exhibits elevated explosin intensity. (Escot Bocanegra et al., 2010) and (Krietsch et al., 2021) noted that the burning velocity of micro-sized particles flame is lower than that of nano-sized particles. (Zhang et al., 2019) and (Li et al., 2016) showed that the smaller dust particle size would make the particle combustion more complete. The dust particle size had a significant effect on the explosion kinetic characteristics. The maximum explosion pressure and maximum pressure rise rate gradually increased with the decrease in dust particle size. (Tan et al., 2020) also proved that the explosion intensity of nano-sized dust is higher by studying the explosion characteristics of coal dust with different particle sizes. (Gao et al., 2016) pointed out that such enhanced explosion intensity was more prominent at low dust concentrations. Therefore, studying nano-sized dust explosions is integral to preventing dust explosion accidents and avoiding abnormally serious accidents that exceed expectations.

Industrial dust explosion prevention aims to obtain the intensity and sensitivity parameters of dust explosions through experiments (Siwek, 1996). At present, the most widely used experimental devices are the 1.2 L Hartmann tube (Danzi et al., 2023; Whitmore, 1992), the 1 m^3 spherical device (Chatrathi, 1994; Sattar et al., 2014), and the 20 L spherical device (Boilard et al., 2013; Hossain et

al., 2014; Iarossi et al., 2013). The experimental parameters obtained in this experimental device are widely used in the design guidance of industrial explosion-proof equipment. However, different containers and piping systems are connected in actual industrial production to form a complex interconnected structure. In the event of an explosion, the accelerating flames and increased turbulence levels inside will significantly increase the overpressure (Holbrow et al., 1999; Reding et al., 2020; Zhuang et al., 2020). (Singh et al., 1994) and (Willacy et al., 2006) conducted an explosion experiment with a connected vessel and found that the explosion was several times stronger than that in a single vessel. Even the detonation phenomenon could be observed. (Lunn et al., 1996) and (Holbrow et al., 1996) pointed out that the degree of precompression and the maximum explosion overpressure in the interconnected vessels were significantly affected by the volume ratio and pipe diameter. An increase in the volume ratio and a decrease in the pipe diameter would lead to a raised explosion overpressure. However, when the diameter of the pipe was reduced to a specific value, the explosion could not be propagated along the pipe to another vessel. (Kosinski et al., 2005a, 2005b, 2006) also demonstrated through numerical simulations that smaller pipe diameters limit the propagation of explosions. (Pang et al., 2022) studied the propagation process of dust explosion in a dry dust collector, and the results showed that the explosion propagation of dust in the pipeline with a complex structure showed an accelerated combustion process and a violent pressure shock. (Di Benedetto et al., 2010) used CFD to study the explosion process in the interconnected vessels with different volume ratios, which further explained the mechanism of the pressure piling phenomenon. The simulation results agreed with the experimental results, and the increase in the volume ratio significantly enhanced the pre-compression level in the second container. As a result, current design methods underestimate the explosion intensity in industrial connectivity vessels, risking device failure. The dynamics and the accident consequences of the dust explosion in the interconnected vessels still need to be further studied.

Due to the limitations of experimental equipment and measurement techniques, computational fluid dynamics (CFD) has been widely used to study the overpressure (Radandt et al., 2001; Skjold et al., 2014), turbulence (Di Benedetto et al., 2015; Di Sarli et al., 2015), flame propagation process (Cao et al., 2014), dust dispersion process (Islas et al., 2023), and protection system design of dust explosion (Polanczyk et al., 2013). (Ogle et al., 1988) and (Bind et al., 2010) simulated the dust explosion in the 20 L sphere device by establishing a mathematical model of turbulent dust explosion with multiple scales. The results showed that the proposed method could effectively predict the characteristic parameters of the dust explosion. (Khan et al., 2024) also used the CFD method to study the explosion severity of coal mining samples in the 20 L sphere and pointed out that velocity vectors obtained by simulation had high reliability. In response to the enormous demand for computing power in CFD, FLACS-DustEx simplified the dust explosion process (Abg Shamsuddin et al., 2023). Due to the trade-off between accuracy and computational efficiency, the FLACS-DustEx could be applied to industrial-scale research and design guidance relatively simply. (Tascón et al., 2015) noted that the FLACS-DustEx simulation results were similar to EN14491 and NFPA68. The reliability of the kinetic characterization of dust explosion processes using CFD is demonstrated. (Tascón et al., 2017) used FLACS-DustEx to simulate the explosion venting of dust in a 5 m3 container, and the results were in good agreement with the experiment. The possibility of this procedure to extend the scope of effectiveness of the current exhaust standard is noted. (Reding et al., 2020) used the same procedure to evaluate the effects of flame jet ignition and pressure piling in interconnected vessels on maximum explosion overpressure and minimum venting area of organic dust explosions. It is recommended that simulation programs can be applied to system designs outside the standard range.

This research studied the nano-sized PMMA dust explosion in the interconnected vessels using numerical simulation methods. The reliability of computational fluid dynamics tools was verified by comparing them with the experimental results. The simulation program captured turbulence changes and overpressure contours that the experiment could not obtain. This is helpful in explaining the pressure piling phenomenon in the interconnected vessels and provides theoretical support for the

quantification of dynamic characteristics and safety protection design of dust explosion in industrial manufacture.

2. Methodology

2.1. Experimental apparatus and materials

The experimental data used for comparison were previously reported studies (Zhang et al., 2024). The dust explosion test was carried out in the interconnected vessels, which consisted of two spherical devices with a volume of 20 L and 120 L connected by pipes. The length of the pipe was 2 m, and the diameter was 40 mm, 80 mm, and 125 mm. In addition, the experimental system includes the dust dispersion part, the ignition part, the timing control part, and the data acquisition part.

Due to its regular particle size distribution and acceptable combustion performance, organic dust polymethyl methacrylate (PMMA) was selected. A detailed description has been given in previous studies (Zhang et al., 2024).

2.2. Simulations

2.2.1. FLACS-DustEx model

The simulation was performed using the Dust Explosion module embedded in FLCAS 21.1. Based on the finite volume method, the program constructs a cube mesh on the cartesian coordinate system, solving the equilibrium equations of mass, momentum, enthalpy, and chemical composition. The tensor form of the conservation equation is as follows (Tascón et al., 2017):

$$\frac{\partial}{\partial t}\left(\beta_v \rho\right)+\frac{\partial}{\partial x_i}\left(\beta_i \rho u_i\right)=0 \tag{1}$$

$$\frac{\partial}{\partial t}\left(\beta_v \rho u_i\right)+\frac{\partial}{\partial x_j}\left(\beta_j \rho u_j u_i\right)=-\beta_v \frac{\partial p}{\partial x_i}+\frac{\partial}{\partial x_j}\beta_j \tau_{ij}+\beta_v \rho g_i+R_i \tag{2}$$

$$\frac{\partial}{\partial t}\left(\beta_v \rho h\right)+\frac{\partial}{\partial x_j}\left(\beta_j u_j \rho h\right)=-\frac{\partial}{\partial x_j}\left(\beta_j J_{h,j}\right)+\beta_v \frac{Dp}{Dt}+\beta_v S_h \tag{3}$$

$$\frac{\partial}{\partial t}\left(\beta_v \rho m_j\right)+\frac{\partial}{\partial x_i}\left(\beta_i \rho u_i m_j\right)=-\frac{\partial}{\partial x_i}\left(\beta_i J_{j,i}\right)+R_j \tag{4}$$

The κ-ε turbulence model is adopted:

$$\frac{\partial}{\partial t}\left(\beta_v \rho k\right)+\frac{\partial}{\partial x_j}\left(\beta_j \rho u_j k-\beta_j \frac{\mu_{eff}}{\sigma_k}\frac{\partial k}{\partial x_j}\right)=G-\beta_v \rho \varepsilon \tag{5}$$

$$\frac{\partial}{\partial t}\left(\beta_v \rho \varepsilon\right)+\frac{\partial}{\partial x_j}\left(\beta_j \rho u_j \varepsilon-\frac{\mu_{eff}}{\sigma_\varepsilon}\frac{\partial k}{\partial x_j}\right)=C_1 G\frac{\varepsilon}{k}-C_2 \beta_v \rho \frac{\varepsilon^2}{k} \tag{6}$$

2.2.2 Combustion model

The combustion model within FLACS consists of a flame model and a combustion velocity model. The default flame model is the β model (Skjold, 2007), and the flame thickness is usually three mesh elements. The equation for the flame model is:

$$\frac{\partial}{\partial t}\left(\beta_v \rho Y_{fuel}\right)+\frac{\partial}{\partial t}\left(\beta_j \rho u_j Y_{fuel}\right)=\frac{\partial}{\partial x_j}\left(\beta_j \rho D\frac{\partial Y_{fuel}}{\partial x_j}\right)+R_F \tag{7}$$

The turbulent burning velocity is defined by an empirical model:

$$S_t = 15.1 S_l^{0.784} u_{rms}^{'\ 0.412} L^{0.196} \quad (8)$$

The acquirement of the laminar burning velocity S_L and ratio of the reactive fuel λ needs to be experimented with the 20 L sphere facility and estimated based on the obtained pressure curve.

2.2.3. Geometry and meshing

The geometry used for the simulation is shown in Fig. 1. The internal diameters of the spheres are 0.62 m and 0.34 m, respectively. The internal diameters of the pipes are 0.04 m, 0.08 m, and 0.13 m (used to simulate 0.125 m due to the limitation of the minimum size of the grid), respectively. The wall thickness of 0.1 m is selected to ensure accurate identification of the wall. The distributed porosity method avoids the detailed meshes required for complex structures in large scenes and the unacceptable computation time. The porosity of each grid element can vary from 0 to 1, where 0 represents a completely open channel, and 1 represents an impassable solid wall. The tensile mesh of 0.01 m*0.02 m*0.01 m is adopted. The maximum tensile coefficient is astricted as 1.2, and the maximum mesh size is limited to 0.02 m*0.04 m*0.02 m.

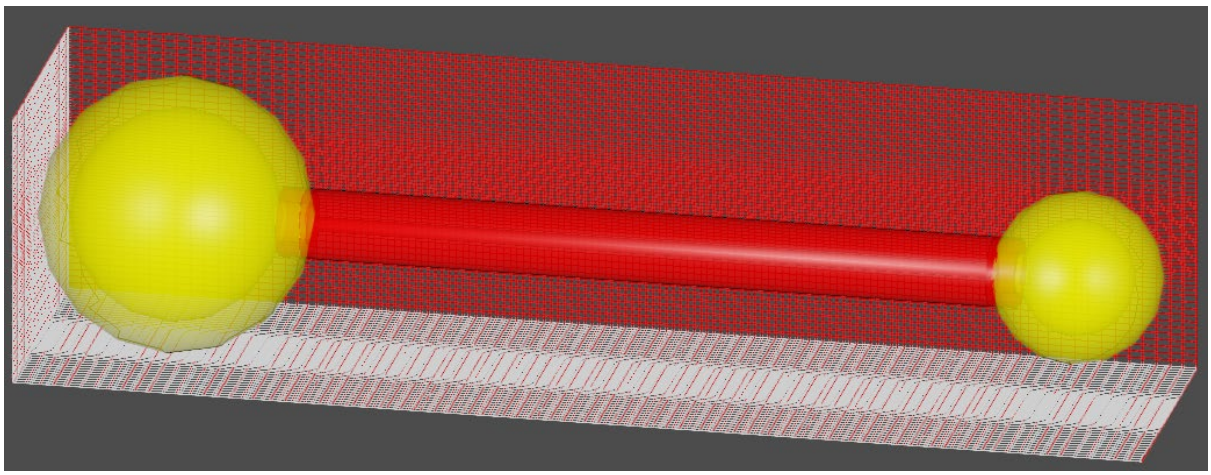

Fig. 1. *The geometry and meshing of the interconnected vessels*

3. Results

3.1. Reliability verification

The comparison between the experimental and simulated results with the volume ratio of 6 is shown in Fig. 2. Fig.2 (a) and (b) show the evolution curves of the overpressure at different positions inside the interconnected vessels with the pipe diameter of 80 mm over time. The numerical results reproduce the three stages of dust explosion overpressure in the interconnected vessels. In the first stage, the pressure rises after ignition in the primary vessel, and the first peak occurs. In the second stage, the pressure rises after ignition in the primary vessel, and the first peak occurs. The flame front enters the pipe, and the pressure in the pipe and the second vessel rises slowly while the pressure of the primary vessel decreases due to the outflow of the medium and the change of the position of the flame front. In the second stage, the jet flame outside the pipe ignites the combustible dust cloud in the second vessel, and the pressure in the primary vessel, the connected pipe, and the second vessel rises rapidly to reach the overpressure peak. In the third stage, the reflection of the pressure wave in the interconnected vessels causes an oscillation of the overpressure curve. The numerically calculated differential pressure curve agrees with the experimentally measured overpressure curve, which can effectively reproduce the complex hydrodynamic process of dust explosion in the connected container.

Fig. 2 (c) and (d) show the flame propagation velocity inside the connected pipe with pipe diameters of 80 mm and 125 mm, respectively. The red square represents the experimental measurement result, which is the average velocity recorded by the photoelectric sensor at different positions, and the blue ball represents the numerical calculation result, which is the average velocity recorded by the

detection points at different positions. It can be found that regardless of whether the pipe diameter is 80mm or 125mm, the flame always accelerates the propagation within the pipe. The numerical calculation and experimental results are basically consistent with the numerical size, and the accelerated propagation process of dust explosion in the connected container can be reproduced.

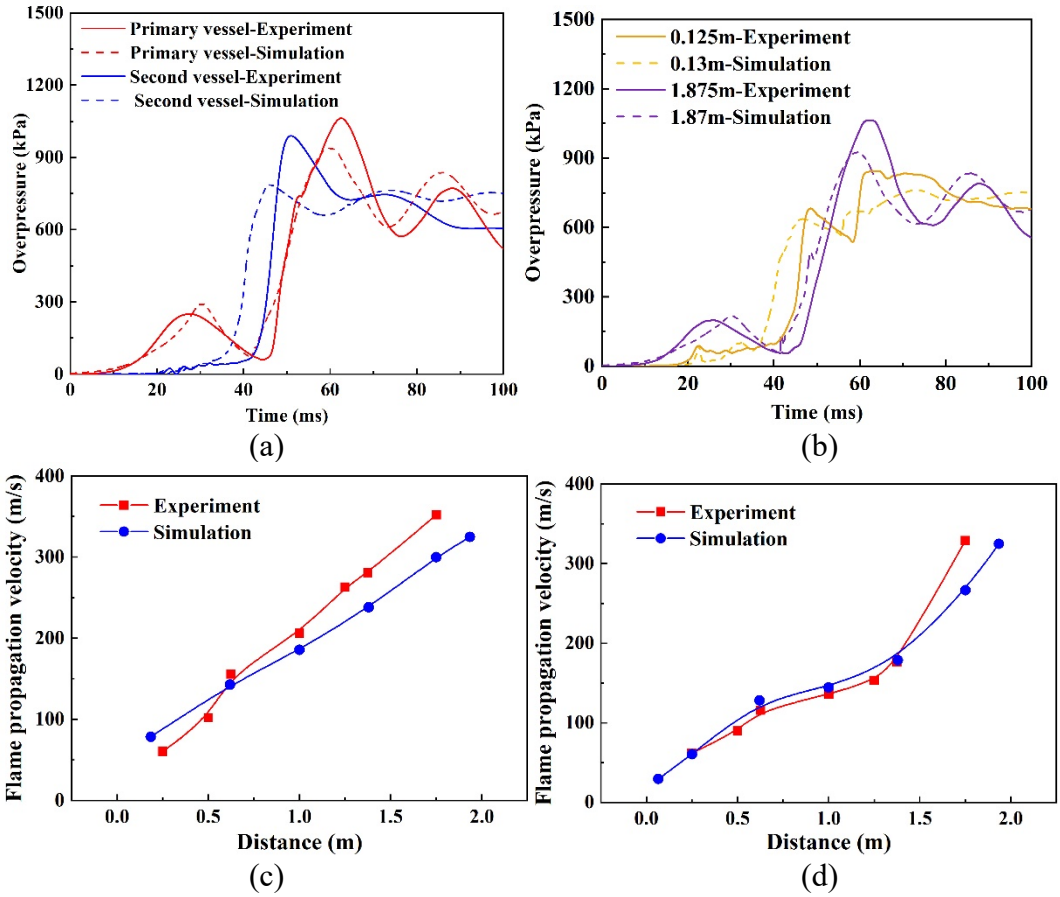

Fig. 2. *Comparison of experimental and simulation results. (a) The overpressure in primary vessel and second vessel with D=80 mm. (b) The overpressure in pipe with D=80 mm. (c) The flame propagation velocity with D=80 mm. (d) The flame propagation velocity with D=125 mm*

3.2. Effect of the pipe diameter

The pressure piling phenomenon in the interconnected vessels is strongly dependent on the jet flame flowing from the pipe, the pre-compression in the second vessel before the dust cloud is ignited, and the turbulence in the combustion area. The change in the pipe diameter significantly changes the cross-sectional area of the jet flame and is manifested as a significant change in energy. In addition, the flow rate of the medium from the primary vessel is positively correlated with the pipe diameter.

Fig. 3 shows the flame development process with the pipe diameter of 80 mm, and 125 mm when the volume ratio of 1/6. As shown in the figure, the dust explosion in the interconnected vessels mainly undergoes the following process. Firstly, the dust cloud in the primary vessel is ignited, and the flame front expands to the surroundings in a spherical shape. The flame propagation speed is slower at this stage. Immediately after the flame enters the pipeline, the flame deformation leads to an increase in the burning area and the acceleration of the combustion speed. The continuous acceleration of the flame in the pipeline and the high-energy flame ejected from the pipeline ignite the combustible dust cloud in the second vessel. Due to the pre-compression and turbulence, the explosion in the second vessel develops rapidly.

The simulated flame successfully ignites the dust cloud in the second vessel with the pipe diameter of 40 mm, while it is not ignited in the experiment. Because the heat transfer of the wall surface is ignored and the minimum size of the mesh is limited by 0.01 m, it is not recommended to use this procedure for analysis when the pipe diameter is too small. The jet flames with pipe diameters of 80 mm and 125 mm entered the second vessel almost simultaneously, causing a rapid combustion of the dust cloud, accompanied by violent vortices.

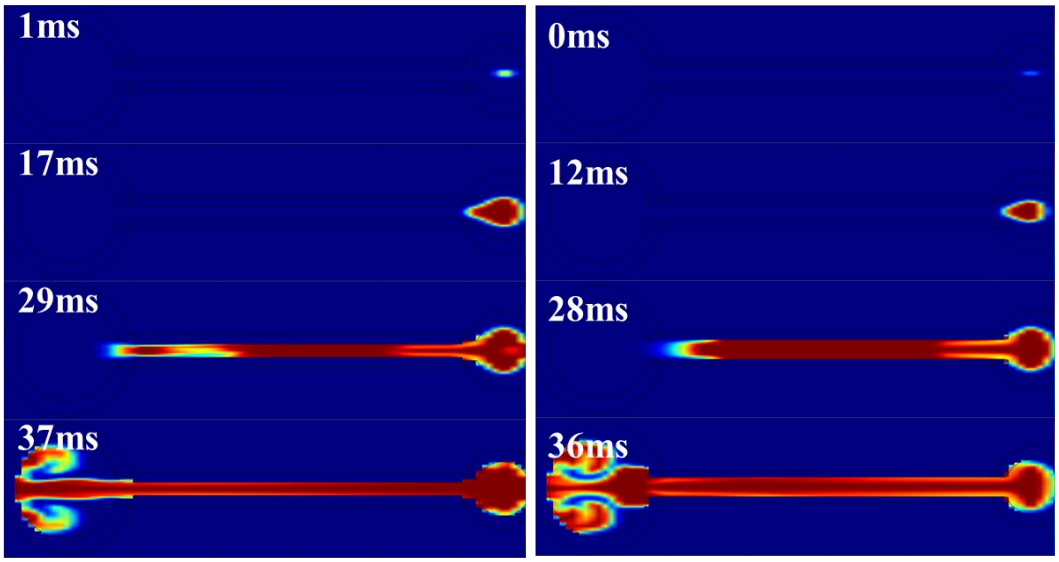

(a) (b)

Fig. 3. *The flame development process with the pipe diameter of 80 mm and 125 mm. (a) D=80 mm. (b) D=125 mm*

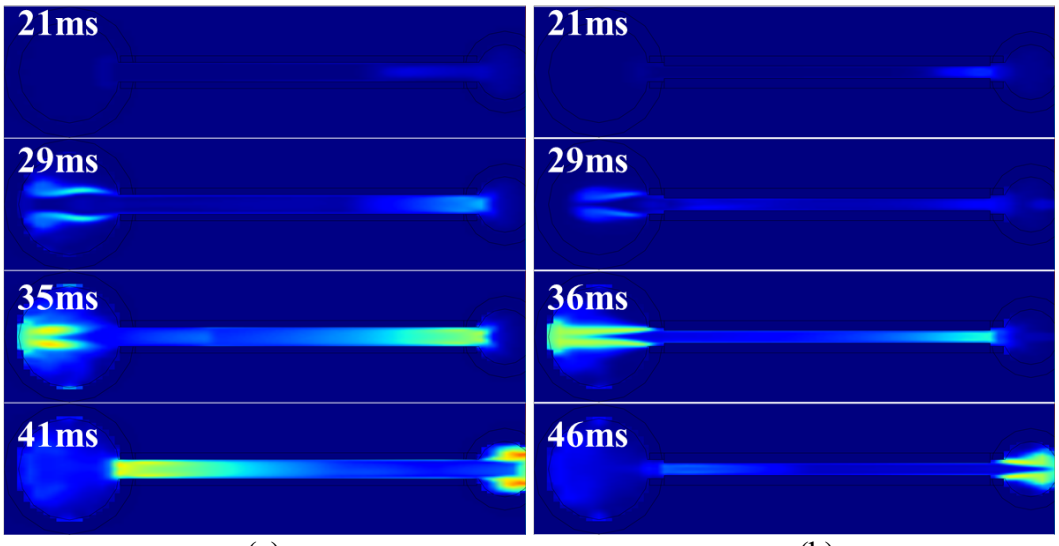

(a) (b)

Fig. 4. *The turbulent velocity change process with the pipe diameter of 80 mm and 125 mm. (a) D=80 mm. (b) D=125 mm*

Fig. 4 shows the change process of the turbulent velocity with the pipe diameter of 40 mm, 80 mm, and 125 mm when the volume ratio is 1/6. As shown in the figure, the turbulent velocity gradient is concentrated at the pipe inlet and in front of the flame front during flame propagation. Before 28 ms, there is already a significant turbulence velocity in the second vessel, proving that the dust cloud is already under the increased turbulence level before the flame enters the second vessel. With the further diffusion of the flame, the turbulence in the second vessel is gradually intensified, and the turbulence velocity exceeds 110 m/s at a maximum time. At 39 ms, due to the high instantaneous

pressure in the second vessel, reverse flow (from left to right) occurs due to the differential pressure. The turbulence velocity in the primary vessel significantly increased as a result. In addition, it can be found that the turbulence velocity increases to a certain extent as the pipe diameter decreases from 125 mm to 40 mm.

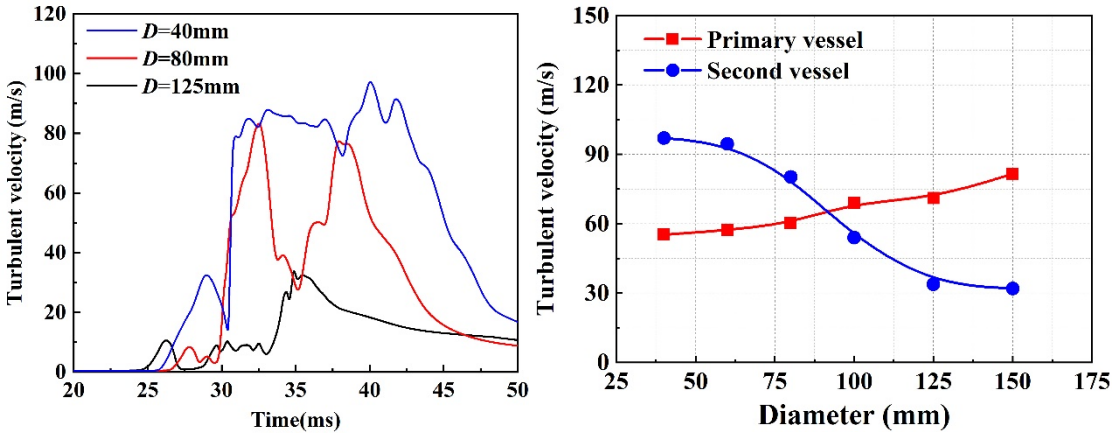

(a) (b)

Fig. 5. *The turbulent velocity at the center of the primary and second vessels. (a) The curve of turbulent velocity in the second vessel with time. (b) The variation of the maximum turbulent velocity in the primary and second vessels with the pipe diameter*

In order to clearly illustrate the variation of turbulent velocity with pipe diameter, Fig. 5 exhibits the turbulent velocity at the center of the primary and second vessels. Fig. 5 (a) shows the variation of turbulent velocity in the second vessel with time, and Fig. 5 (b) shows the variation of the maximum turbulent velocity in the primary and second vessels with the pipe diameter. The multimodal structure of turbulent velocity is due to the reflection of the jet flame at the wall. It can be found that with the increase of the pipe diameter, the decrease of the pressure difference between the primary and second vessels leads to a significant attenuation of the turbulent velocity in the second vessel during the initial stage of the explosion. However, the turbulent velocity in the primary vessel shows an upward trend, which can be attributed to the limitation of the gas flow rate by the small pipe diameter.

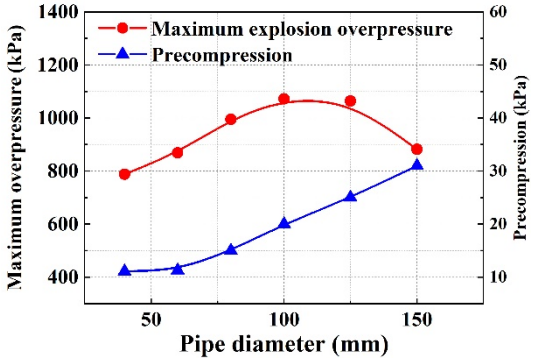

Fig. 6. *The precompression and maximum explosion overpressure in the interconnected vessel with the pipe diameter*

Fig. 6 shows the variation of precompression and maximum explosion overpressure of nano-PMMA dust explosion in the interconnected vessels with different pipe diameters. It can be seen that as the pipe diameter increases, the precompression in the second vessel is constantly rising. The mass flow rate along the pipe is positively correlated with the pipe diameter (Chippett, 1984):

$$\frac{\mathrm{d}m}{\mathrm{d}t}=\frac{AP_1}{T^{1/2}}\cdot\left\{\frac{2\gamma}{R(\gamma-1)}\left[\left(\frac{2}{\gamma+1}\right)^{\frac{2}{\gamma-1}}-\left(\frac{2}{\gamma+1}\right)^{\frac{\gamma+1}{\gamma-1}}\right]\right\}^{1/2} \tag{9}$$

Although the precompression is constantly augmenting, the maximum explosion overpressure appears at the pipe diameter of around 100 mm and then begins to decrease. This confirms that the pressure piling phenomenon is influenced by the combination of jet flame, turbulence, and precompression. Although the diameter of the jet flame and the precompression overpressure increase with the diameter of the pipe, the turbulence velocity in the second vessel keeps failing inversely. This antagonism leads to the presence of a definable pipe diameter that maximizes the explosion overpressure. Therefore, for industrial explosion-proof design, it should be avoided to use pipe diameters for the most dangerous conditions.

3.3. Effect of the volume ratio

Fig. 7 illustrates the flame development process with the volume ratio of 1/6 and 6 when the pipe diameter is 80 mm. It can be found that the explosion in the interconnected vessel ends later when the volume ratio is 6, compared with the volume ratio of 1/6. This is because the ignition center is far away from the pipe inlet in the 120 L spherical vessel, and the flame has been in spherical development for a long time. At this stage, the acceleration of the flame is mainly dependent on flame instability, such as the Landau-Darrieus and Kelvin-Helmholtz instabilities. The increase in combustion velocity is much slower than that of stretching and turbulence in the pipe.

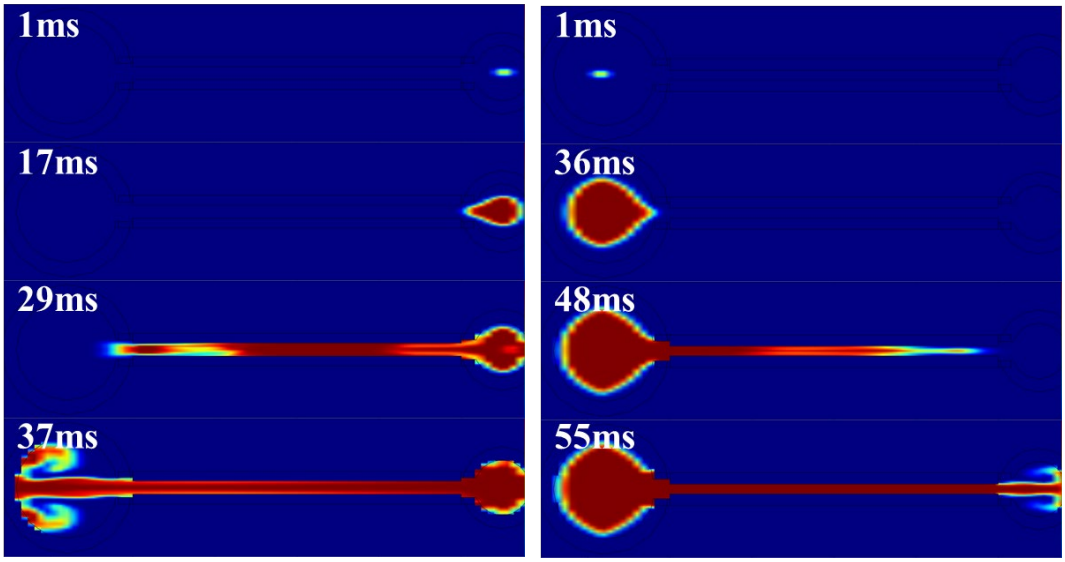

(a) (b)

Fig. 7. *The flame development process with the pipe diameter of 80 mm. (a) Volume ratio=1/6. (b) Volume ratio=6*

The turbulent velocity at the center of the primary vessel and the second vessel with different volume ratios are shown in Fig. 8. The connected pipe diameter is 80 mm, and the dimensions of the primary vessel and the second vessel are listed in Table 1. The results show that regardless of whether the volume of the primary is 20 L or 120 L, the turbulence velocity in the second vessel decreases with the increase of the volume ratio. It is conceivable that this reduction will not be endless. Changes in vessel volume can significantly affect the magnitude and distribution of turbulence velocity. Although the volume ratio of No. 4 and No. 5 is 1, the turbulent velocity in the second vessel with a volume of 120 L is much greater than that at a volume of 20 L.

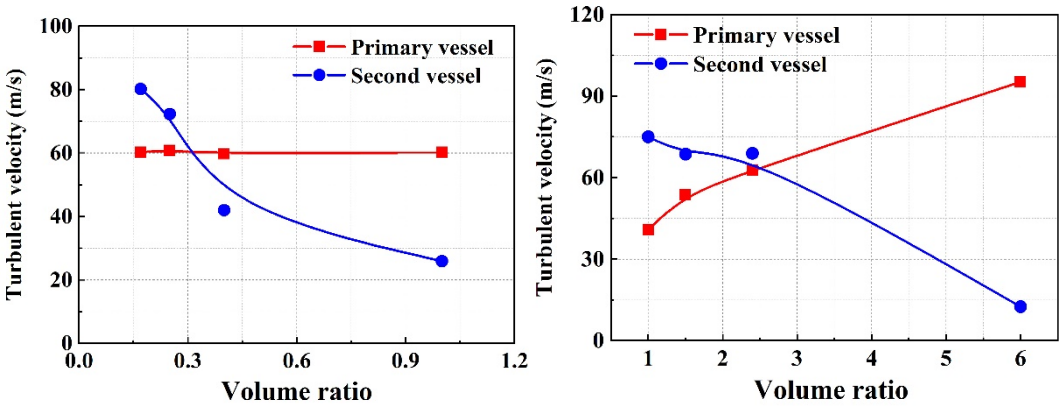

Fig. 8. *The turbulent velocity at the center of the primary and second vessels with different volume ratio. (a) Ignition in the 20 L spherical device. (b) Ignition in the 120 L spherical device*

Table 1*. Specific settings with different volume ratios*

No.	Volume ratio	Volume of the primary vessel	Volume of the second vessel
1	1/6	20 L	120 L
2	0.25	20 L	80 L
3	0.4	20 L	50 L
4	1	20 L	20 L

No.	Volume ratio	Volume of the primary vessel	Volume of the second vessel
5	1	120 L	120 L
6	1.5	120 L	80 L
7	2.4	120 L	50 L
8	6	120 L	20 L

Fig. 9 illustrates the precompression and maximum explosion overpressure in the interconnected vessels as a function of the volume ratio. The influence mechanism of volume ratio on precompression is that the kinetic energy is converted into pressure potential energy after the compressible medium of different masses enters the second vessel. As the volume ratio increases, the mass entering the vessel increases, and the precompression will increase without limitation. It is worth noting that when the volume ratio is less than 1, the maximum explosion pressure appears in the primary vessel. However, when the volume ratio is greater than 1, the maximum explosion pressure appears in the second vessel. Therefore, when the volume ratio is greater than 1, the maximum explosion pressure maintains an upward trend with the continuous increase of the precompression and turbulence velocity in the primary vessel. When the volume ratio is less than 1, the degree of precompression in the second vessel gradually decreases with the increase of the volume ratio. It is observed that the minimum explosion overpressure occurs near the volume ratio of 0.4. Therefore, the existence of an optimal volume ratio is the optimal choice for explosion-proof designs.

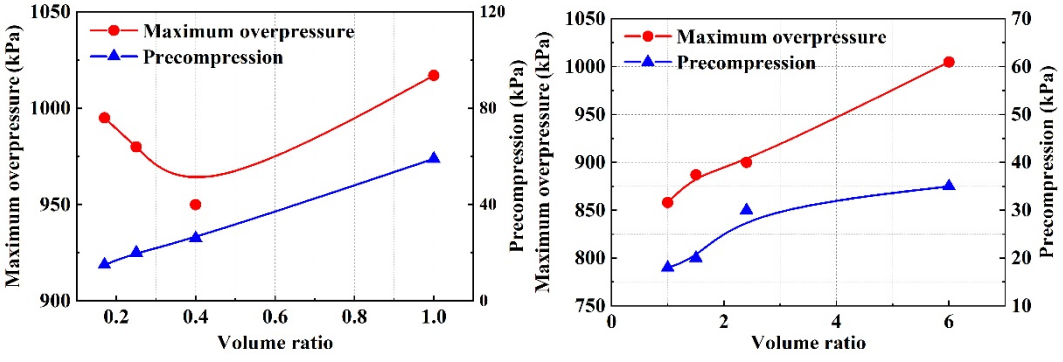

Fig. 9. *The precompression and maximum explosion overpressure in the interconnected vessel with different volume ratio. (a) Ignition in the 20 L spherical device. (b) Ignition in the 120 L spherical device*

4. Conclusions

In this study, Flacs-DustEX was used to simulate the explosion process of 150 nm PMMA dust in the interconnected vessels. The simulation results further explain the dynamic phenomena in the previous experimental studies, analyzing the laws outside the scope of the experimental conditions. The results show that:

(1) The simulation results can excellently reproduce the overpressure evolution at different stages of dust explosion in the interconnected vessels and the flame acceleration behavior in the pipe. The overpressure and flame velocity are basically consistent with the experimental result.

(2) With the expansion in the pipe diameter, the turbulent velocity in the primary vessel decreases while the precompression increases. This antagonism causes the maximum explosion overpressure to rise to a peak and then decrease continuously. For industrial explosion-proof design, it should be avoided to use pipe diameters for the most dangerous conditions.

(3) With the growth of the volume ratio, the maximum explosion overpressure decreases first and then mounts. The existence of an optimal volume ratio is the optimal choice for explosion-proof designs.

Acknowledgements

The authors appreciate the financial support by the National Key R&D Program of China (No. 2022YFC3080700), National Natural Science Foundation of China (No. 52374185), and the Central Guidance on Local Science and Technology Development Fund of Liaoning Province (No. 2023JH6/100100048).

References

Abg Shamsuddin, D. S. N., Mohd Fekeri, A. F., Muchtar, A., Khan, F., Khor, B. C., Lim, B. H., Rosli M. I., Takriff, M. S., 2023. Computational fluid dynamics modelling approaches of gas explosion in the chemical process industry: A review. Process Safety and Environmental Protection. 170, 112-138.

Azhagurajan, A., Selvakumar, N., & Yasin, M. M., 2012. Minimum ignition energy for micro and nano flash powders. Process Safety Progress. 31, 19-23.

Bind, V. K., Roy, S., & Rajagopal, C., 2010. CFD modelling of dust explosions: Rapid combustion in a 20 L apparatus. The Canadian Journal of Chemical Engineering. 89, 663-670.

Blair, A. S., 2007. Dust explosion incidents and regulations in the United States. Journal of Loss Prevention in the Process Industries. 20, 523-529.

Boilard, S. P., Amyotte, P. R., Khan, F. I., Dastidar, A. G., & Eckhoff, R. K., 2013. Explosibility of micron- and nano-size titanium powders. Journal of Loss Prevention in the Process Industries. 26, 1646-1654.

Bouillard, J., Vignes, A., Dufaud, O., Perrin, L., & Thomas, D., 2010. Ignition and explosion risks of nanopowders. J Hazard Mater. 181, 873-880.

Cao, W., Gao, W., Peng, Y., Liang, J., Pan, F., & Xu, S., 2014. Experimental and numerical study on flame propagation behaviors in coal dust explosions. Powder Technology. 266, 456-462.

Chatrathi, K., 1994. Dust and hybrid explosibility in 1 m^3 spherical chamber. Process Safety Progress. 13, 183-189.

Chippett, S., 1984. Modeling of vented deflagrations. Combustion and Flame. 55, 127-140.

Danzi, E., Dufaud, O., Franchini, F., Pietraccini, M., & Marmo, L., 2023. Study of dust cloud behaviour in the modified Hartmann tube using the image subtraction method (ISM). Journal of Loss Prevention in the Process Industries. 82, 104997.

Di Benedetto, A., Russo, P., Sanchirico, R., & Di Sarli, V., 2015. A fan-equipped reactor for dust explosion tests. AIChE Journal. 61, 1572-1580.

Di Benedetto, A., & Salzano, E., 2010. CFD simulation of pressure piling. Journal of Loss Prevention in the Process Industries. 23, 498-506.

Di Sarli, V., Sanchirico, R., Russo, P., & Di Benedetto, A., 2015. CFD modeling and simulation of turbulent fluid flow and dust dispersion in the 20-L explosion vessel equipped with the perforated annular nozzle. Journal of Loss Prevention in the Process Industries. 38, 204-213.

Escot Bocanegra, P., Davidenko, D., Sarou-Kanian, V., Chauveau, C., & Gökalp, I., 2010. Experimental and numerical studies on the burning of aluminum micro and nanoparticle clouds in air. Experimental Thermal and Fluid Science. 34, 299-307.

Gao, W., Li, J., Li, Y., Yan, X., Yu, J., & Zhang, X., 2016. Explosion characteristics of nano-PMMA particles. Combustion, Explosion, and Shock Waves. 52, 117-123.

Holbrow, P., Andrews, S., & Lunn, G. A., 1996. Dust explosions in interconnected vented vessels. Journal of Loss Prevention in the Process Industries. 9, 91-103.

Holbrow, P., Lunn, G. A., & Tyldesley, A., 1999. Dust explosion protection in linked vessels: guidance for containment and venting. Journal of Loss Prevention in the Process Industries. 12, 227-234.

Hossain, M. N., Amyotte, P., Abuswer, M., Dastidar, A., Khan, F., Eckhoff, R., & Chunmiao, Y., 2014. Influence of liquid and vapourized solvents on explosibility of pharmaceutical excipient dusts. PROCESS SAFETY PROGRESS. 33, 374-379.

Iarossi, I., Amyotte, P. R., Khan, F. I., Marmo, L., Dastidar, A. G., & Eckhoff, R. K., 2013. Explosibility of polyamide and polyester fibers. Journal of Loss Prevention in the Process Industries. 26, 1627-1633.

Islas, A., Fernández, A. R., Betegón, C., Martínez-Pañeda, E., & Pandal, A., 2023. Biomass dust explosions: CFD simulations and venting experiments in a 1 m3 silo. Process Safety and Environmental Protection. 176, 1048-1062.

Khan, A. M., Mohalik, N. K., Ray, S. K., Mishra, D., Pandey, J. K., & Mandal, S., 2024. Multiphase CFD Simulation of Coal Dust Dispersion and Explosion in a 20 L Explosion Chamber. Paper presented at the Recent Advances in Industrial Machines and Mechanisms, Singapore.

Kosinski, P., & Hoffmann, A. C., 2005a. Dust explosions in connected vessels: Mathematical modelling. Powder Technology. 155, 108-116.

Kosinski, P., & Hoffmann, A. C., 2005b. Mathematical modelling of dust explosions in interconnected vessels. Nonlinear Analysis: Theory, Methods & Applications. 63, e1087-e1096.

Kosinski, P., & Hoffmann, A. C., 2006. An investigation of the consequences of primary dust explosions in interconnected vessels. J Hazard Mater. 137, 752-761.

Krietsch, A., Reyes Rodriguez, M., Kristen, A., Kadoke, D., Abbas, Z., & Krause, U., 2021. Ignition temperatures and flame velocities of metallic nanomaterials. Journal of Loss Prevention in the Process Industries. 71, 104482.

Li, Q., Wang, K., Zheng, Y., Ruan, M., Mei, X., & Lin, B., 2016. Experimental research of particle size and size dispersity on the explosibility characteristics of coal dust. Powder Technology. 292, 290-297.

Lunn, G. A., Holbrow, P., Andrews, S., & Gummer, J., 1996. Dust explosions in totally enclosed interconnected vessel systems. Journal of Loss Prevention in the Process Industries. 9, 45-58.

Ogle, R. A., Beddow, J. K., Chen, L. D., & Butler, P. B., 1988. AN INVESTIGATION OF ALUMINUM DUST EXPLOSIONS. Combustion Science and Technology. 61, 75-99.

Pang, L., Cao, J., Xiao, Q., Yang, K., & Shi, L., 2022. Explosion propagation in a dust removal pipeline under dust collector explosion. Journal of Loss Prevention in the Process Industries. 74,

Polanczyk, A., Wawrzyniak, P., & Zbicinski, I., 2013. CFD Analysis of Dust Explosion Relief System in the Counter-Current Industrial Spray Drying Tower. Drying Technology. 31, 881-890.

Radandt, S., Shi, J., Vogl, A., Deng, X. F., & Zhong, S. J., 2001. Cornstarch explosion experiments and modeling in vessels ranged by height/diameter ratios. Journal of Loss Prevention in the Process Industries. 14, 495-502.

Reding, N. S., & Shiflett, M. B., 2020. Consequence prediction for dust explosions involving interconnected vessels using computational fluid dynamics modeling. Journal of Loss Prevention in the Process Industries. 65, 104149.

Sattar, H., Andrews, G. E., Phylaktou, H. N., & Gibbs, B. M., 2014. Turbulent Flames Speeds and Laminar Burning Velocities of Dusts using the ISO 1 m^3 dust explosion method. Paper presented at the cisap6: 6th international conference on safety & environment in process & power industry.

Singh, J., & Inst Chem, E., 1994. Gas-explosions in inter-connected vessels - pressure piling. Paper presented at the hazards xii - European advances in process safety.

Siwek, R., 1996. Determination of technical safety indices and factors influencing hazard evaluation of dusts. Journal of Loss Prevention in the Process Industries. 9, 21-31.

Skjold, T., 2007. Review of the DESC project. Journal of Loss Prevention in the Process Industries. 20, 291-302.

Skjold, T., Castellanos, D., Olsen, K. L., & Eckhoff, R. K., 2014. Experimental and numerical investigation of constant volume dust and gas explosions in a 3.6-m flame acceleration tube. Journal of Loss Prevention in the Process Industries. 30, 164-176.

Tan, B., Shao, Z., Xu, B., Wei, H., & Wang, T., 2020. Analysis of explosion pressure and residual gas characteristics of micro-nano coal dust in confined space. Journal of Loss Prevention in the Process Industries. 64, 104056.

Tascón, A., & Aguado, P. J., 2015. CFD simulations to study parameters affecting dust explosion venting in silos. Powder Technology. 272, 132-141.

Tascón, A., & Aguado, P. J., 2017. Simulations of vented dust explosions in a 5 m3 vessel. Powder Technology. 321, 409-418.

Vignes, A., Muñoz, F., Bouillard, J., Dufaud, O., Perrin, L., Laurent, A., & Thomas, D., 2012. Risk assessment of the ignitability and explosivity of aluminum nanopowders. Process Safety and Environmental Protection. 90, 304-310.

Whitmore, M. W., 1992. Prediction of dust cloud minimum ignition energy for organic dusts from modified hartmann tube data. Journal of Loss Prevention in the Process Industries. 5, 305-309.

Willacy, S. K., Phylaktou, H. N., Andrews, G. E., & Mkpadi, M. C., 2006. Detonation of Hydrogen in a Partially Filled Interconnecting Vessel Following an Initial Period of Pressure Piling. Combustion Science and Technology. 178, 1911-1926.

Wu, H. C., Ou, H. J., Peng, D., Jr., Hsiao, H. C., Gau, C. Y., & Shih, T.-S., 2010. Dust Explosion Characteristics of Agglomerated 35 nm and 100 nm Aluminum Particles. International Journal of Chemical Engineering. 2010, 1-6.

Zhang, J., Sun, L., Nie, F., & Zhou, H., 2019. Effects of particle size distribution on the explosion severity of coal dust. Energy Sources, Part A: Recovery, Utilization, and Environmental Effects. 43, 2077-2087.

Zhang, Z., Gao, W., Jiang, H., Zheng, G., & Bai, Q., 2024. Explosion mechanism of nano-sized dust cloud in interconnected vessels. Combustion and Flame. 259, 113135.

Zhuang, C., Wang, Z., Zhang, K., Lu, Y., Shao, J., & Dou, Z., 2020. Explosion suppression of porous materials in a pipe-connected spherical vessel. Journal of Loss Prevention in the Process Industries. 65, 104106.

Reactivity and Dynamics of Hybrid-Mixture Explosions at Large Scales

Lorenz R. Boeck, C. Regis L. Bauwens & Sergey B. Dorofeev

FM Global, Research Division
Norwood, MA, USA

E-mail: lorenz.boeck@fmglobal.com

Abstract

Hybrid mixtures pose severe explosion hazards in industries such as mining, power generation, chemical, pharmaceutical, agriculture and food, and other manufacturing. Developing risk assessment methods and explosion prevention/mitigation solutions requires knowledge of explosion sensitivity and severity parameters for these mixtures, and an understanding of explosion dynamics at realistic industrial scales. This work presents the results of novel hybrid-mixture explosion experiments conducted in an 8-m^3 vessel and discusses reactivity parameters including maximum explosion pressure, deflagration index, and turbulent burning velocity. Experimental results show how the hybrid-mixture composition significantly affects explosion dynamics and demonstrate that conventional reactivity parameters, especially the deflagration index K, are inadequate to fully capture these effects.

Keywords: *hybrid explosions, large-scale experiments*

Nomenclature

Symbol	Description	Units
A	Area	(m^2)
K	Deflagration index	(bar·m/s)
m	Mass	(kg)
P	Pressure	(bar-g)
S	Burning velocity	(m/s)
t	Time	(s)
u	Velocity	(m/s)
V	Volume	(m^3)
X	Volumetric concentration	(-)
γ	Ratio of heat capacities	(-)
Π	Nondimensional pressure	(-)
ρ	Density	(kg/m^3)
σ	Expansion ratio	(-)
Superscripts		
‘	Turbulent fluctuation	
Subscripts		
0	Initial condition	
b	Burned	
eff	Effective	
f	Flame	
max	Maximum	
rms	Root-mean-square	
t	Turbulent	
u	Unburned	

1. Introduction

Reactive mixtures of flammable gases/vapors with combustible dusts and oxidizer, referred to as hybrid mixtures, pose severe explosion hazards in industries such as mining, power generation, chemical, pharmaceutical, agriculture and food, and other manufacturing (Eckhoff, 2003; Bartknecht, 2012). These hazards may exist within process equipment, for example where a combustible dust is suspended and mixed with a vaporized solvent, or in larger enclosures and rooms, such as in mines where coal dust and methane gas may both participate in a potential explosion. Developing risk assessment methods and explosion prevention/mitigation solutions requires knowledge of explosion sensitivity and severity parameters for hybrid mixtures, and an understanding of explosion dynamics at realistic industrial scales.

The explosion severity of hybrid mixtures is typically characterized by standardized test equipment such as 20-L or 1-m^3 spheres that are modified to introduce a flammable gas/vapor in addition to the combustible dust (*e.g.*, ASTM E1226, 2019). Test results are reported in terms of conventional reactivity parameters, including the deflagration index, $K_{}$, and the maximum explosion pressure, P_{max}. Scientific studies have adopted similar methodologies and have been mostly limited to small (*e.g.*, 20-L) or intermediate-scale (*e.g.*, 1-m^3) test volumes. These studies have produced critical scientific insight, for example regarding the relative impact of gas/vapor and dust concentrations on mixture reactivity (*e.g.*, Chatrathi, 1994; Dufaud et al., 2007; Amyotte et al., 2009; Addai et al. 2020) and explosion regimes of hybrid mixtures (Garcia-Agreda et al., 2011; Sanchirico et al., 2011; Cloney et al., 2017).

The goal of this work is to examine the reactivity and dynamics of hybrid mixtures under conditions that reflect industrial applications more closely than tests conducted at small or intermediate scales. It is well known that small test volumes, such as 20-L spheres, can bias the explosion characteristics of combustible dusts compared to larger volumes (Proust, 2007). Most critically, conventional reactivity parameters obtained at small scales may not always provide robust predictions of explosion severity at industrial scales (Eckhoff, 2015). Characterizing the reactivity of hybrid mixtures therefore requires a careful experimental approach that includes an evaluation of potential biases due to the choice of test apparatus and procedure, as well as the parameters used to quantify reactivity. Ultimately, these reactivity parameters need to enable robust predictions of potential explosion severity in industrial applications.

A large-scale setup was developed at FM Global to conduct explosion tests with hybrid mixtures at large scales. For this work, a series of tests with cornstarch-propane-air mixtures were performed and analyzed in terms of conventional reactivity parameters, *i.e.*, K and P_{max}. Finally, effective turbulent burning velocities are inferred from pressure histories to describe flame propagation over the course of an explosion and provide insight into the large-scale dynamics of hybrid-mixture explosions.

2. Methodology

2.1 Experimental setup and procedure

The experiments presented in this work were performed in an 8-m^3 explosion test vessel at the FM Global Research Campus in West Glocester, RI, USA. The vessel, see Figure 1, was equipped with four injectors, each comprising a 150-L air cannon, a dust container, a fast-acting valve that isolates the injector from the vessel shortly before ignition, and a hemispherical perforated injection nozzle

inside the vessel. This system can be used to perform dust, gas, or hybrid-mixture explosions. The following procedure was used to conduct a test:

(1) The specified quantity of dust was loaded into the dust containers, (2) the vessel was flushed with dry air, (3) the vessel was supplied with the required amount of gaseous fuel to achieve the final target concentration, (4) the vessel was mixed using a circulation pump, and (5) the mixture composition was verified using gas sampling. Subsequently, (6) all air cannons were pressurized with dry air to 8.27 bar-g, and (7) the vessel was partially evacuated to 0.48 bar-a. (8) All air cannons were fired to inject dust along with air, returning the vessel pressure to 1 bar-a, and (9) ignition was triggered after an ignition delay of 0.65 s for this study.

Since air addition during injection dilutes the gaseous fuel-air mixture, the initial mixture (pre-injection) contained a pre-determined fuel concentration that exceeded the desired final concentration. Preliminary testing and gas sampling showed that, following air injection, the final fuel concentration was achieved with an uncertainty of ±0.1% by volume.

The initial test series examined hybrid mixtures composed of propane (C_3H_8) and cornstarch dust (CS). Propane was instrument-grade, with a minimum purity of 99.5%. The cornstarch dust was tested in accordance with ASTM E1226 (2019), yielding a K_{St} value between 155–166 bar·m/s and P_{max} between 7.9–8.1 bar-g, at an optimum concentration of 750 g/m^3. The dust was dried prior to testing to a maximum moisture content of 1% by weight. Experiments were conducted over a range of gas concentrations with pure C_3H_8-air mixtures (0 g/m^3 CS), mixtures of C_3H_8 with a low concentration of CS (100 g/m^3 CS), and C_3H_8 with optimum concentration of CS (750 g/m^3 CS). Two experiments were performed at each condition. The vessel pressure during the explosion, P, was measured using three redundant Kistler 4260A transducers.

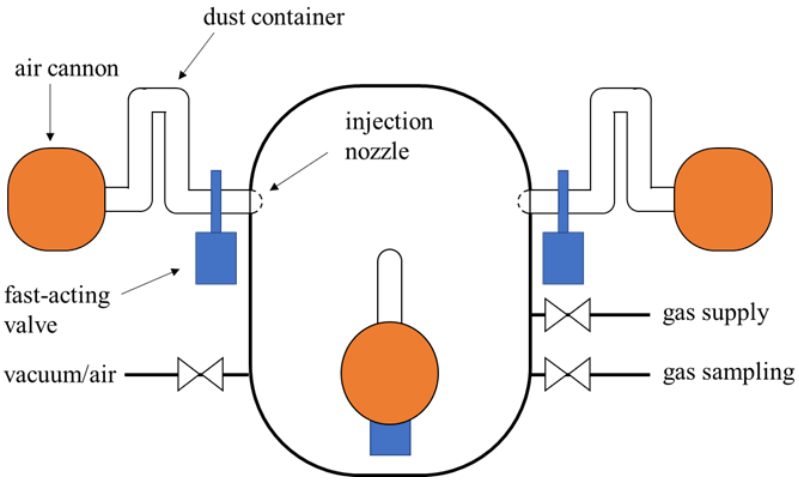

Fig. 1. *Schematic of the 8-m^3 explosion vessel with gas supply and dust injection systems*

2.2 Initial turbulence

The injection system creates turbulence inside the vessel that decays over time, and the turbulence intensity at the time of ignition can be adjusted by varying the delay between the start of injection and ignition. To correlate turbulence intensity and ignition delay time, turbulence measurements were taken using a bidirectional velocity probe (McCaffrey and Heskestad, 1976) located at the center of the vessel, with both horizontal and vertical probe orientations. Only air was injected (no dust was loaded into the dust containers) in these tests, with air cannons charged to 8.27 bar-g and the vessel

evacuated to 0.48 bar-a. Turbulence intensity is expressed in terms of fluctuation velocity u'_{rms}, according to the Reynolds decomposition for turbulent flow,

$$u(x,y,z,t) = \overline{u(x,y,z)} + u'_{\mathrm{rms}}(x,y,z,t)\,, \tag{1}$$

where u and $\bar{u}$ are the instantaneous and average flow velocities at a location (x, y, z), respectively. Equation (1) is evaluated in 50-ms intervals centered around the times of interest shown in Figure 2. The resulting values of u'_{rms} only show a weak dependence (about ±3%) on the length of the time interval used to evaluate Equation (1) in a range of 20–80 ms.

Figure 2 shows the measurements of u'_{rms} over a period of 0.5–0.8 s after the beginning of injection, where turbulence decay can be approximated as

$$u'_{\mathrm{rms}} = 10^{0.94-0.50t}\,. \tag{2}$$

No systematic differences are observed between horizontal and vertical probe orientations, indicating isotropic turbulence at the probe location. The test-to-test variability of u'_{rms} measurements seen in Figure 2 may reflect the combined variability of local turbulence intensity and the measurement uncertainty. Future efforts may consider the use of non-intrusive methods for characterizing initial turbulence, such as LDA (Laser-Doppler Anemometry) or PIV (Particle-Image Velocimetry), to validate the present measurements and further examine the uniformity of turbulence intensity throughout the vessel.

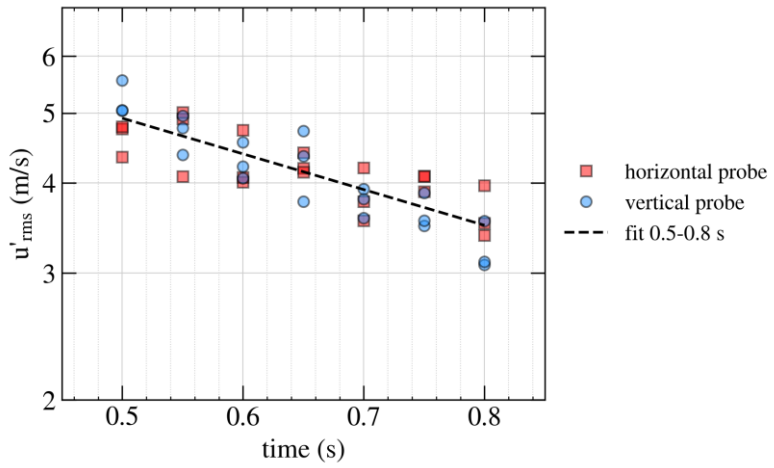

Fig. 2. *Turbulent fluctuation velocity u'_{rms} as a function of time, where t = 0 s signifies the beginning of injection*

2.3 Data interpretation

Explosion pressure histories were analyzed to determine the effective deflagration index, $K_{\mathrm{eff}} = (\mathrm{d}P/\mathrm{d}t)_{\max} V^{1/3}$, and the maximum explosion pressure, $P_{\max}$. Furthermore, a spherical-flame model was used to infer effective turbulent burning velocities, S_{eff}, from the pressure recordings. This model assumes point ignition and considers mass balances for unburned (subscript u) and burned (subscript b) gas in a closed vessel with volume V,

$$\frac{dm_{\mathrm{u}}}{dt} = -S_{\mathrm{eff}}\rho_{\mathrm{u}}A_{\mathrm{f}};\ \frac{dm_{\mathrm{b}}}{dt} = S_{\mathrm{eff}}\rho_{\mathrm{u}}A_{\mathrm{f}};\ V = \frac{m_{\mathrm{b}}}{\rho_{\mathrm{b}}} + \frac{m_{\mathrm{u}}}{\rho_{\mathrm{u}}}, \tag{3}$$

where the unburned and burned gas densities are obtained from

$$\rho_u = \rho_0 \left(\frac{P}{P_0}\right)^{1/1.4} ; \rho_b = \rho_0 \left(\frac{P}{P_{max}}\right)^{1/\gamma^*}. \quad (4)$$

The effective isentropic exponent for burned gas, γ^*, is given by

$$\gamma^* = \frac{\log (P_0/P_{max})}{\log (1/\sigma_0)}, \quad (5)$$

using the initial expansion ratio, σ_0, which can be taken from equilibrium calculations or estimated as $\sigma_0 \approx (P_{max}–P_0)/P_0$, where P_{max} and P_0 are the maximum explosion pressure and initial pressure, respectively. The effective turbulent burning velocity, S_{eff}, is optimized such that the experimental pressure history is reproduced at minimum root-mean-square error within a defined pressure range. Figure 3 shows an example where the experimental pressure history (red curve) is approximated using the spherical-flame model (dashed black line) by optimizing the fit across an optimization region of 0.005 bar-g < P-P_0 < 0.18 bar-g.

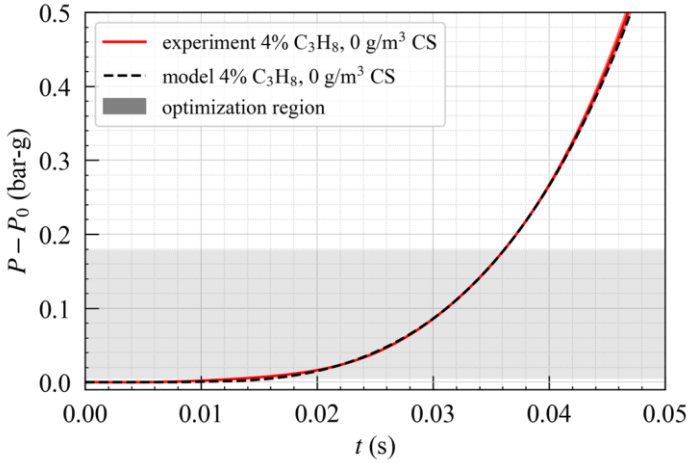

Fig. 3. *Example of fit between experimental pressure history (red curve) and spherical-flame model (black dashed line)*

3. Results

The experimental results will be presented in terms of conventional reactivity parameters, *i.e.*, deflagration index and maximum explosion pressure, Section 3.1; pressure histories and profiles of rate of pressure rise, Section 3.2; and effective turbulent burning velocity, Section 3.3.

3.1 Conventional reactivity parameters

Parameters commonly used to characterize the reactivity of combustible dusts and hybrid mixtures for explosion protection purposes include the deflagration index, K, and the maximum explosion pressure, P_{max}. These parameters were determined for the large-scale experiments conducted in the present work and are summarized in Figure 4, as a function of volumetric C_3H_8 concentration, X_{C3H8}. The deflagration index is referred to as the "effective" deflagration index, K_{eff}, since experiments were conducted in a non-standard experimental setup.

Pure CS at 750 g/m^3 exhibits $K_{eff} \approx 200$ bar·m/s, and a moderate increase in K_{eff} occurs with increasing X_{C3H8}, peaking at X_{C3H8} = 3% and 253–285 bar·m/s and decreasing toward higher X_{C3H8}. Experiments at 100 g/m^3 CS show a strong increase in K_{eff} with increasing X_{C3H8}, from 30–34 bar·m/s at X_{C3H8} = 0% to 407–459 bar·m/s at X_{C3H8} = 5%. Mixtures with 100 g/m^3 CS exceed the deflagration indices of pure gas mixtures across the range of tested X_{C3H8}. At 5% C_3H_8 + 100 g/m^3 CS, where the overall

highest values of K_{eff} occur, K_{eff} exceeds the value for pure gas by 9%. These results indicate that the high reactivity of this hybrid mixture is primarily driven by the gas component with a comparably small contribution from the dust.

Figure 4, right panel, summarizes P_{max} values. At 750 g/m^3 CS, addition of C_3H_8 leads to a decrease in P_{max}, whereas at 100 g/m^3 CS, addition of C_3H_8 increases P_{max}. Likewise, P_{max} increases for pure gas mixtures with increasing X_{C3H8}. The peak value of P_{max} occurs at 0% C_3H_8 + 750 g/m^3 CS.

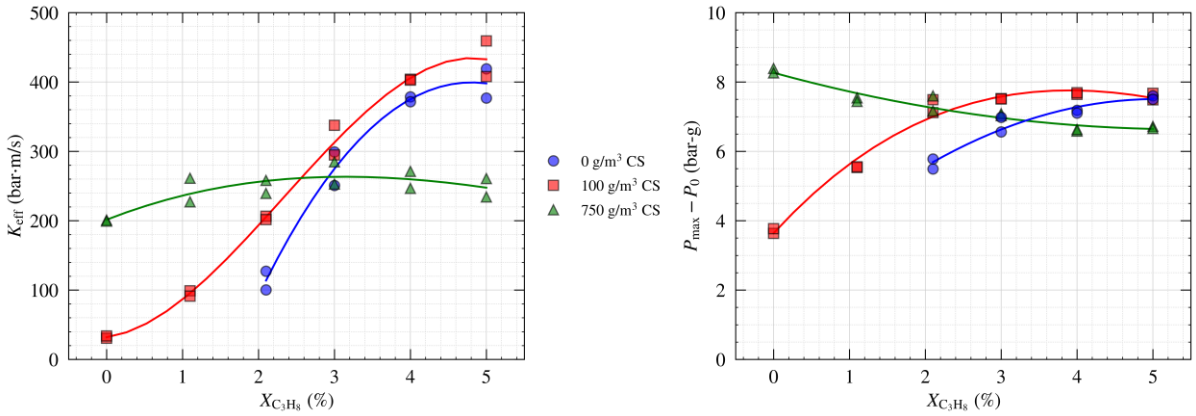

Fig. 4. *Experimental results for deflagration index K (left panel) and maximum explosion pressure P_{max} (right panel)*

3.2 Pressure histories and profiles of rate of pressure rise

It is well understood that the deflagration index K alone does not fully capture the dynamics of an explosion, as it only describes the maximum rate of pressure rise at one specific instant, while failing to characterize how the rate of pressure rise varies throughout the entire course of an explosion (Bauwens et al., 2020). In order to examine explosion dynamics more comprehensively, pressure histories are analyzed next. Figure 5 shows selected pressure histories as a function of time, left column, and profiles of rate of pressure rise, dP/dt, as a function of dimensionless pressure, $\Pi = (P–P_0)/(P_{max}–P_0)$, right column. In each figure, shaded areas represent the spread between two repeated tests conducted at each condition, and solid lines represent their average.

For mixtures with 4% or 5% C_3H_8, the earlier analysis of K_{eff} suggested that the addition of a low concentration of dust may increase reactivity compared to the pure gas mixture, *cf.* Figure 4. Interestingly, pressure histories, see left column of Figure 5, show a different overall trend and suggest that pressure rises earlier/faster for pure gas. As the $P = f(t)$ depiction can be biased by time shifts due to variations in early flame development, plots of $dP/dt = f(\Pi)$ provide more unbiased information, see right column of Figure 5. For 4% C_3H_8, the rate of pressure rise early on ($\Pi \leq 0.45$) is comparable between 4% C_3H_8 and 4% C_3H_8 + 100 g/m^3 CS, whereas later on ($\Pi > 0.45$), combustion rates of the hybrid mixture are higher. The higher rate of pressure rise in the hybrid mixture late in the process produces the higher value of K_{eff} seen in Figure 4. For 5% C_3H_8, rates of pressure rise are higher early on ($\Pi \leq 0.4$) in 5% C_3H_8 compared to 5% C_3H_8 + 100 g/m^3 CS, whereas later on ($\Pi > 0.4$), the trend reverses. Results for K_{eff} alone would suggest a higher overall reactivity of hybrid mixtures of C_3H_8 + 100 g/m^3 CS compared to C_3H_8 at all investigated X_{C3H8}. In particular, K_{eff} results would indicate that the most reactive investigated mixture is composed of 5% C_3H_8 + 100 g/m^3 CS. By contrast, more detailed analyses of pressure histories, and especially profiles of $dP/dt = f(\Pi)$, reveal that the investigated hybrid mixtures are not universally more reactive than pure gas mixtures, but a more nuanced interpretation is needed: the observed differences in K_{eff} are due to differences in the

evolution of burning rate in the late stages of the explosion, whereas pure gas mixtures may burn faster than hybrid mixtures early in the process.

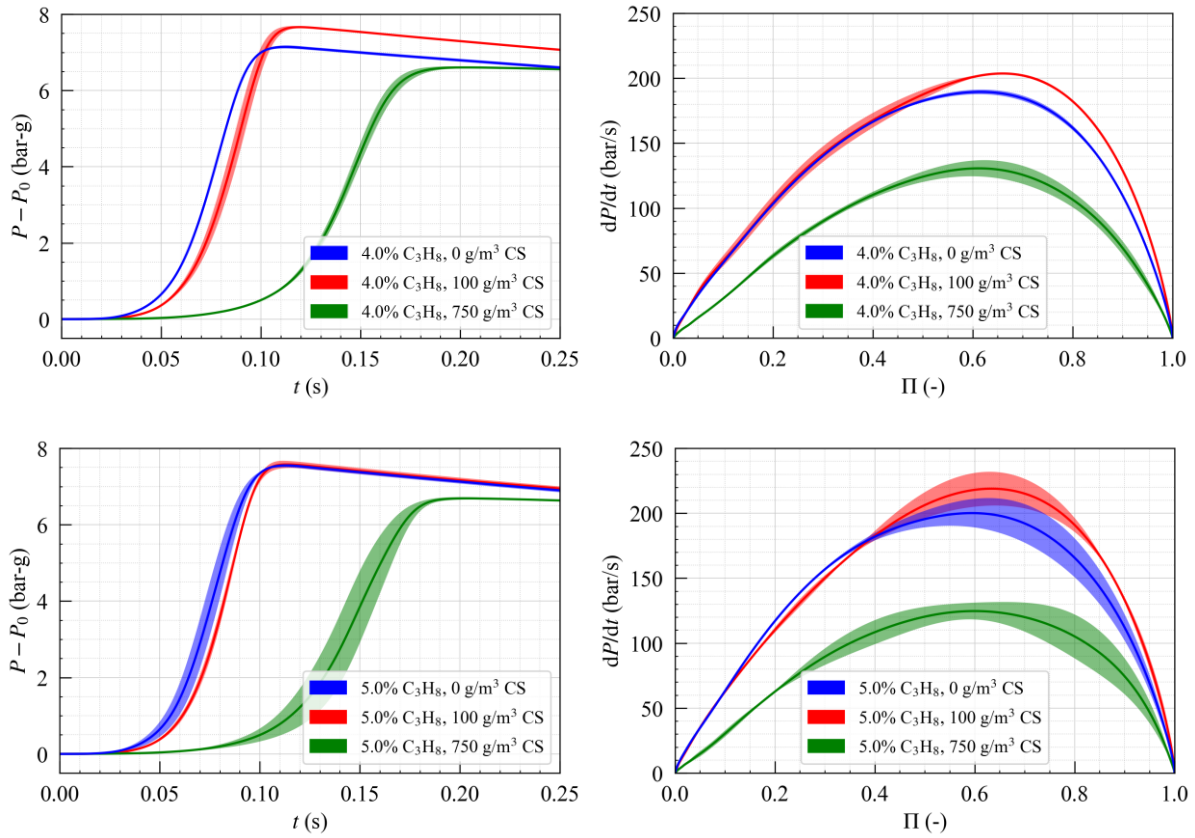

Fig. 5. *Experimental results for pressure histories (left column) and profiles of rate of pressure rise [right column; Π = (P–P0)/(Pmax–P0)] for mixtures containing 4% C3H8 (top row) and 5% C3H8 (bottom row)*

3.3 Effective turbulent burning velocities

To further evaluate the early phase of flame propagation, in contrast to the late phase characterized by K, effective turbulent burning velocities S_{eff} were inferred from the experiments as described in Section 2.3 and are presented in Figure 6. The fit between spherical-flame model and experiments was optimized across a range of Π in intervals of 0.1, where values close to zero and one represent early and late combustion, respectively. It is important to note that S_{eff} should not be expected to be constant throughout the course of flame propagation in a closed vessel due to effects of turbulence and flame instability, finite flame thickness, precompression of reactants, and heat loss to the vessel walls and flame quenching.

At X_{C3H8} = 2.1%, the highest peak values of S_{eff} occur in CS at its optimum concentration of 750 g/m^3, followed by 2.1% C_3H_8 + 100 g/m^3 CS and 2.1% C_3H_8 (0 g/m^3 CS). Only immediately after ignition, 2.1% C_3H_8 + 100 g/m^3 CS shows higher S_{eff} than 2.1% C_3H_8 + 750 g/m^3 CS, which indicates slower flame development from the ignition kernel in the latter mixture. At X_{C3H8} = 3.0%, peak values of S_{eff} are similar between all three mixtures. Initial flame development is again delayed in 3.0% C_3H_8 + 750 g/m^3 CS. At X_{C3H8} = 4.0%, peak values of S_{eff} in the pure gas mixture exceed values in the hybrid mixtures across the displayed range of Π. At the highest investigated C_3H_8 concentration, X_{C3H8} = 5.0%, values of S_{eff} are slightly higher or similar in 5.0% C_3H_8 (0 g/m^3 CS) compared to 5.0% C_3H_8 + 100 g/m^3 CS at Π ≤ 0.4. At Π > 0.4, where S_{eff} shows a relative decay after passing its peak value,

5.0% C_3H_8 + 100 g/m^3 CS maintains higher S_{eff} compared to 5.0% C_3H_8 (0 g/m^3 CS), supporting the late peak in dP/dt in this mixture, *cf*. Figure 5.

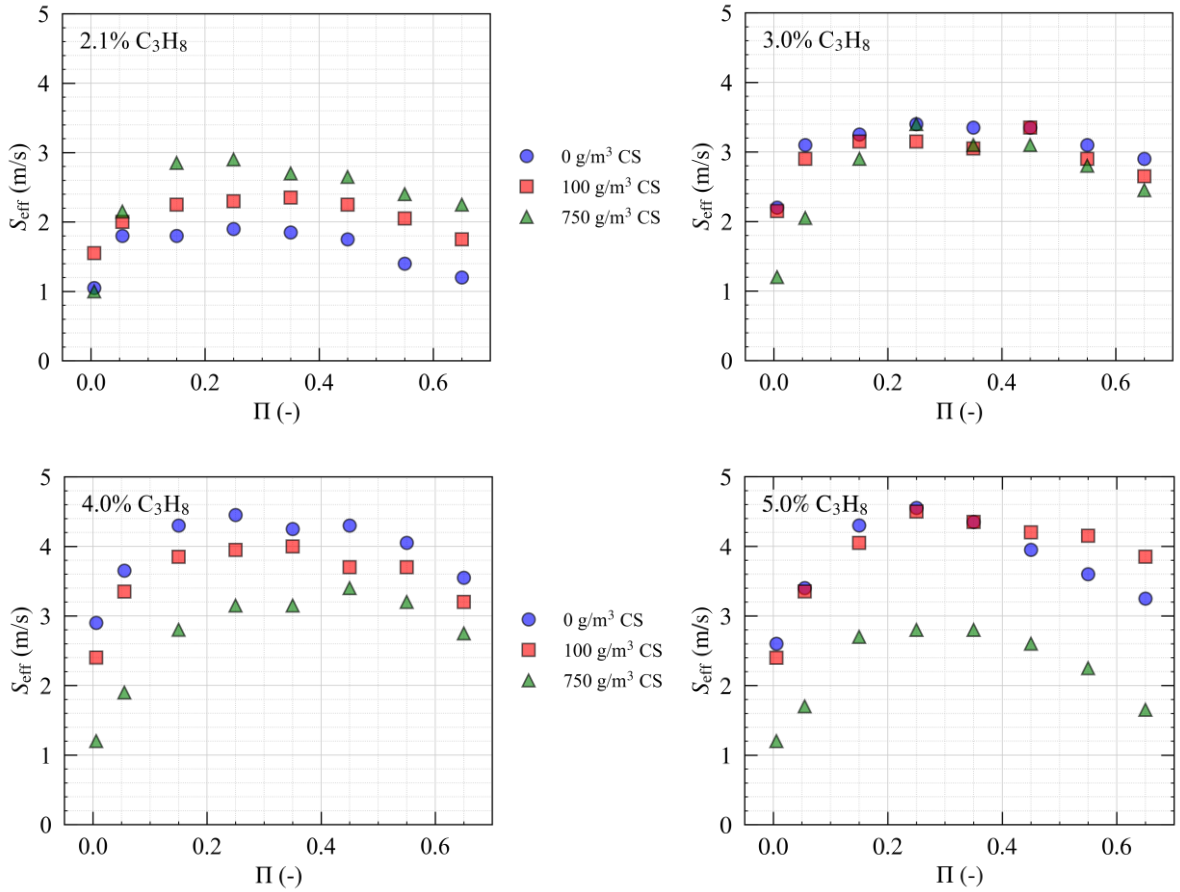

Fig. 6. *Effective turbulent burning velocities inferred from experimental pressure histories using a spherical-flame model, as a function of* $\Pi = (P–P_0)/(P_{max}–P_0)$

4. Discussion

Combining the results from K_{eff}, P_{max}, P = f(t), dP/dt = f(Π), and S_{eff} analyses provides new insight into the dynamics of hybrid-mixture explosions at large scales, compared to pure gas or dust explosions. Several aspects are highlighted:

- Among all experiments conducted in this work, the highest deflagration indices K were observed in mixtures with near-stoichiometric gas composition (4–5% C_3H_8) and low dust concentration (100 g/m^3 CS), see Figure 4. This observation is consistent with small-scale studies, reviewed recently by Spitzer et al. (2023) and mostly performed in 20-L spheres, which have suggested that hybrid mixtures with low dust concentrations may present a worst-case explosion hazard, exceeding the K values of pure gas mixtures. Several mechanisms have been proposed to potentially explain this apparent reactivity enhancement, including enhanced turbulence generated by typical experimental apparatuses when dust is injected compared to gas alone (Spitzer et al., 2023; Banhegyi et al., 1983); flame wrinkling caused by dust particles (Spitzer et al., 2023); and effects of radiative pre-heating of dust ahead of the flame (Spitzer et al., 2023; Ivanov et al., 2015). In the present experiments, the apparent enhancement in K for hybrid mixtures of 4–5% C_3H_8 + 100 g/m^3 CS is produced specifically due to faster combustion at late times, when pressure is high (Π > 0.4). At early times (low Π), by contrast, combustion is comparable or slower than in pure gas mixtures, suggesting

that the investigated hybrid mixtures are not inherently more reactive than the pure gas mixtures, but the apparent enhancement in K is a result of effects taking place when the flame is large and interacts with the vessel walls. Increased turbulence, flame wrinkling, or continuous radiative pre-heating would lead to uniformly faster combustion also at low Π; hence, these mechanisms do not appear to be responsible for the apparent enhancement in K in the present experiments. Modifications of burning rate or heat transfer at high Π, when flame-wall interactions limit the overall rate of combustion in the vessel and the resulting maximum rate of pressure rise, may explain the differences observed at late times. Additional fundamental research is needed to further examine these phenomena.

- The composition of hybrid mixtures affects not only their conventional reactivity parameters K and P_{max}, but also their detailed large-scale explosion dynamics. K alone, indeed, can be a misleading metric when describing reactivity as it only considers the late phase of an explosion and, most critically, does not characterize the incipient phase when industrial explosion mitigation systems operate. For example, explosion suppression and isolation systems must detect an explosion shortly after ignition, typically at overpressures less than 0.1 bar-g, and achieve mitigation before pressure exceeds the strength of the protected vessel or the flame can pass an isolation barrier, rendering it ineffective.
- From an applied perspective, the observed differences in reactivity between the most reactive hybrid and pure gas mixtures are relatively small, suggesting that the gas explosion mainly drives the hazard with a relatively small contribution from the dust. Pure gas mixtures showed similar or higher reactivities especially during the early phase of an explosion. While these observations provide important insight that may inform future improvements of risk assessment, engineering recommendations, and mitigation design, additional work is needed to generalize conclusions for a wider range of hybrid mixtures.

5. Conclusions

This study presented large-scale experiments on hybrid-mixture explosions that provide detailed insight into explosion dynamics at realistic industrial scales. The results show how the hybrid-mixture composition affects explosion dynamics and demonstrate that conventional reactivity parameters, especially the deflagration index K, are inadequate to fully capture these effects. In particular, if the deflagration index K alone was used to specify reactivity, it would identify mixtures with low dust concentrations and near-stoichiometric gas concentrations as the most reactive mixtures, posing the most severe explosion hazards. Examinations of the entire explosion process, however, revealed that these mixtures are not universally more reactive. In fact, they showed similar or lower rates of pressure rise and turbulent burning velocities than pure gas mixtures during the early combustion process, a critical time when mitigation systems typically operate and mitigate the effects of an explosion. It is only at late times when combustion rates exceeded those of pure gas mixtures, which was ultimately responsible for the higher deflagration indices. These results indicate the need of developing a more differentiated characterization of hybrid-mixture explosion dynamics, which could improve risk assessment, engineering recommendations, and mitigation design for hybrid mixtures.

References

Addai, E. K., Aljaroudi, A., Abbas, Z., Amyotte, P., Addo, A., Krause, U., 2020. Investigation of the explosion severity of multiphase hybrid mixtures. Process Safety Progress, 39, e12139.

Amyotte, P., Lindsay, M., Domaratzki, R., Marchand, N., Di Benedetto, A., Russo, P., 2010. Prevention and mitigation of dust and hybrid mixture explosions. Process Safey Progress, 29, 17-21.

ASTM E1226-29 Standard test method for explosibility of dust clouds. ASTM International, West Conshohocken, PA, 2019.

Banhegyi, M., Egyedi, J., 1983. Method for determining the explosive limits of a mixture of coal dust, methane, and inert matter. International Conference of Safety in Mines Research Institutes, Sheffield, UK.

Bartknecht, W., 2012. Explosions: course, prevention, protection. Springer Science & Business Media.

Bauwens, C.R., Boeck, L.R., Dorofeev, S.B., 2020. A simple dust combustion model for characterizing reactivity in large-scale experiments. 13th ISHPMIE, Braunschweig, Germany

Chatrathi, K., 1994. Dust and hybrid explosibility in a 1 m^3 spherical chamber. Process Safety Progress, 3, 183-189.

Cloney, C.T., Ripley, R.C., Pegg, M.J., Amyotte, P.R., 2017. Evaluating regime diagrams for closed volume hybrid explosions. Journal of Loss Prevention in the Process Industries, 49, 12-918.

Dufaud, O., Perrin, M., Traore, M., Chazelet, S., Thomas, D., 2007. Hybrid mixtures explosions: When vapours met dusts. IChemE Symposium Series No. 153.

Eckhoff, R. K., 2003. Dust explosions in the process industries. Gulf Professional Publishing.

Eckhoff, R.K., 2015. Scaling of dust explosion violence from laboratory scale to full industrial scale – A challenging case history from the past. Journal of Loss Prevention in the Process Industries, 36, 271-280.

Garcia-Agreda, A., Di Benedetto, A., Russo, P., Salzano, E., Sanchirico, R., 2011. Dust/gas mixtures explosion regimes. Powder Technology, 205, 81-86.

Ivanov, M.F., Kiverin, A.D., Liberman, M.A., 2015. Ignition of deflagration and detonation ahead of the flame due to radiative preheating of suspended micro particles. Combustion and Flame, 162, 3612-3621.

McCaffrey, B. J., Heskestadt, G., 1976. A robust bidirectional low-velocity probe for flame and fire application. Combustion and Flame, 26, 125-127.

Proust, C., Accorsi, A., Dupont, L., 2007. Measuring the violence of dust explosions with the “20 L sphere” and with the standard “ISO 1 m3 vessel”: Systematic comparison and analysis of the discrepancies. Journal of Loss Prevention in the Process Industries, 20, 599-606.

Sanchirico, R., Di Benedetto, A., Garcia-Agreda, A., Russo, P., 2011. Study of the severity of hybrid mixture explosions and comparison to pure dust-air and vapour-air explosions. Journal of Loss Prevention in the Process Industries, 24, 648-655.

Spitzer, S.H., Askar, E., Hecht, K.J., Gabel, D., Geoerg, P., Krause, U., Dufaud, O., Krietsch, A., 2023. The maximum rate of pressure rise of hybrid mixtures. Journal of Loss Prevention in the Process Industries, 86, 105178.

Experimental investigation of hybrid aluminium dust-methane-air mixture

Chayma EL GADHA, Stéphane BERNARD & Mame WILLIAM-LOUIS

PRISME Laboratory EA 4229, IUT de Bourges, University of Orleans, INSA-CVL, France

chayma.el-gadha@univ-orleans.fr

stephane.bernard@univ-orleans.fr

mame.william-louis@univ-orleans.fr

Aluminum particles are currently widely used in propulsion system, as the oxidation of aluminum metal is characterized by a significant release of heat. Indeed, the combustion of aluminum particles has been the subject of numerous studies due to its widespread use, notably in solid rockets to increase the thrust of aerobic rocket engines and reduce the oscillatory instabilities in the combustion of hydrocarbon fuels. Here, the process of ignition and combustion of methane with the addition of aluminum particles was investigated.

On the other hand, hybrid mixtures of methane/aluminum dust are highly sensitive to ignition, which also represents a safety constraint for industrial production, since hybrid explosions can still be initiated even if the concentration of gas and dust is below to their lower explosive limit (LEL).

In a first part, severity parameters representing the overpressure and the rate of pressure rise of hybrid methane/aluminum dust explosions are experimentally investigated in this paper. Experiments were carried out in the modified 20L sphere, in order to introduce the gas. Aluminum dust with a median diameter of 21.36 µm was mixed with methane at a concentration of 0% to 15%. The results of the hybrid mixtures were compared to the severity parameters of pure aluminum dust and pure methane gas, in order to understand the effect of adding methane fractions to aluminum dust and conversely. The explosion tests show that the addition of flammable gas to dust increases the maximum explosion pressure and the maximum rate of pressure rise. However, the increase in the maximum rate of pressure rise was more pronounced than the explosion pressure one. The findings also showed that the explosive limits of methane were affected by the addition of aluminum dust.
In a second part, flame temperatures and ignition delays of hybrid mixture methane/aluminum dust were determined. It has been shown that the addition of aluminum dust particles is a promising way of improving methane combustion performance by decreasing ignition delay.

Keywords: *Methane/aluminum dust, Hybrid explosion, Ignition delays, Flame temperature*

Introduction

The combustion of aluminum particles is of practical importance and has been extensively studied due to its widespread use in solid rockets to increase engine specific impulse. Because of the difficulty of stabilizing aluminum flames, some applications opt for hybrid flames, to prevent oscillatory instabilities in combustion. This work is focused on the explosibility of hybrid aluminum/methane mixture. Methane was chosen due to its well-established explosive properties and extensive utilization in researching hybrid mixtures involving dust from various sources.

Several studies have examined the combustion behavior of aluminum particles in different atmospheres in the past, but there are still open questions regarding the phenomena involved. Soo et al., 2013 seeded methane- air flames with progressively increasing concentrations of aluminum particles. They noted that the aluminum particles have different combustion behaviour depending on the atmosphere. They observed a gas diffusion flame around the aluminum particles and high concentrations of aluminum vapor in the space around the particles when they burn in air. Nevertheless, in a methane/air flame, the concentration of aluminum vapor surrounding the particles was lower and no diffusion microflame was formed, demonstrating that the combustion process is kinetically controlled. The authors explained that the formation of the secondary aluminum dust flame coupled to the primary methane flame was manifested by a rapid increase in the luminosity and temperature of the flame when a critical value of the aluminum concentration is reached.

Further evidence of the double front flame structure was obtained in the work carried out by Palecka et al., 2015. The authors experimentally measured quenching of laminar combustion of a methane-aluminum particles in different dust concentrations. Experiments were performed with freely propagating flames in a 48 mm-inner diameter Pyrex glass tube At concentrations below 400 g/m^3, the aluminum flame decoupled from the methane flame and quenched while the methane flame still propagated. At concentrations above 400 g/m^3, only a coupled aluminum–methane flame could be observed to propagate, and demonstrated a weaker dependence of the quenching distance on aluminum concentration.

Denkevits and Hoess, 2015 were interested in the explosibility of aluminum/H_2 in a Siwek sphere. The mixture were ignited by a weak electric spark. The authors found that the addition of hydrogen can improve the explosion intensity of aluminum dust. They noted that Al/H_2 mixtures have a higher pressure rise rate than each of the fuels separately. The authors also pointed out that at lower hybrid fuel concentrations, a hydrogen explosion is initiated, followed by an aluminum dust explosion. As concentration increases, the two-phase explosion regime becomes a single-phase regime in which the two fuel explode together. In this regime, the two fuels are in competition for oxygen, as the concentration of dust increases, the proportion of O_2 consumed increases.

Vickery et al., 2017 investigated the flame propagation of hybrid aluminum-methane-oxidizer mixture at constant pressure in 30 cm diameter transparent latex ballons. Dust dispersion and the spherical flame propagation process were recorded using high-speed cameras. The results revealed that, at low concentrations, aluminum behaves like an inert additive, contributing mainly to increase the heat capacity of the mixture. This results in lower flame temperature and reduces combustion rates. Above a critical concentration, the metal particles react with the hydrocarbon combustion products to form a flame front that couples thermally with the methane flame, resulting in a stabilisation of the combustion rate as the aluminium concentration increases. They conclude that at low concentrations in mixtures with and without excess oxygen, the aluminum particles react with free oxygen to burn in the diffusion limited combustion mode.

Recently, a study has been carried out by Jeanjean et al., 2024 on aluminum/methane-air hybrid flames in a laminar Bunsen-type burner. Direct observations of flame luminosity and local temperature fields were analysed. For all methane concentrations, the flame can be divided into three distinct reaction zones. Firstly, there is a premixed flame zone where methane and a part of the

aluminum particles burn together. Next, there's an external diffusion flame zone where the unconsumed aluminum reacts with the surrounding air. And finally, there's a reaction zone in the downstream plume, where the unconsumed aluminum reacts with the CO_2/H_2O produced. When the methane burns off almost all the oxygen injected into the premixed flame, the aluminum reacts mainly in the external diffusion flame.

Unfortunately, until now, there has not been an examination of the combustion and explosion of hybrid aluminum-methane mixture in the unsteady regime in the 20L sphere. Therefore, the present aims to explore the combustion behavior of hybrid aluminum-methane mixture.

This paper is organized as follows. First, the experimental set-up and powder characterization are presented. Second, the severity parameters for pure aluminum dust and methane gas are determined and then for hybrid aluminum-methane mixture. Third the ignition delays time and flame temperatures are established to understand the effect of methane addition on aluminum combustion.

1. Experimental setup

1.1. Experimental apparatus

As advised by the international standard EN 14034-series 1,2,3:2011, the experimental device used in this study is the 20-liter explosion sphere, with the exception of the ignition system. Consistent with the previous research El Gadha et al., 2023, the 20L sphere is mainly composed of an explosion chamber, dust storage container connected with the chamber through a dust outlet valve (Kühner AG). The valve is controlled by an electric arc generator. The ignition and injection delays can be adjusted as desired. The data acquisition system for monitoring flame propagation includes a Kistler 701A pressure sensor with a pressure range of 0 to 20 bar which is coupled with a 5011 charge amplifier and the pressure signals are retrieved via a digital oscilloscope as shown in Fig.1. An OceanOptics HR 2000+ spectrometer is used to acquire spectra in the 200-1100 nm spectral range with a spectral resolution of about 0.9 nm for observation of AlO molecular bands. Data from this spectrometer are analysed to determine the flame temperature.

The explosion experiments were first carried out for pure aluminum dust Al, for pure methane CH_4, and then for Al/CH_4. To study the explosions of hybrid mixtures, it was necessary to modify the 20L sphere to include methane. An electronic pressure transducer was added to prepare the gas mixture in the sphere using the partial pressure method.

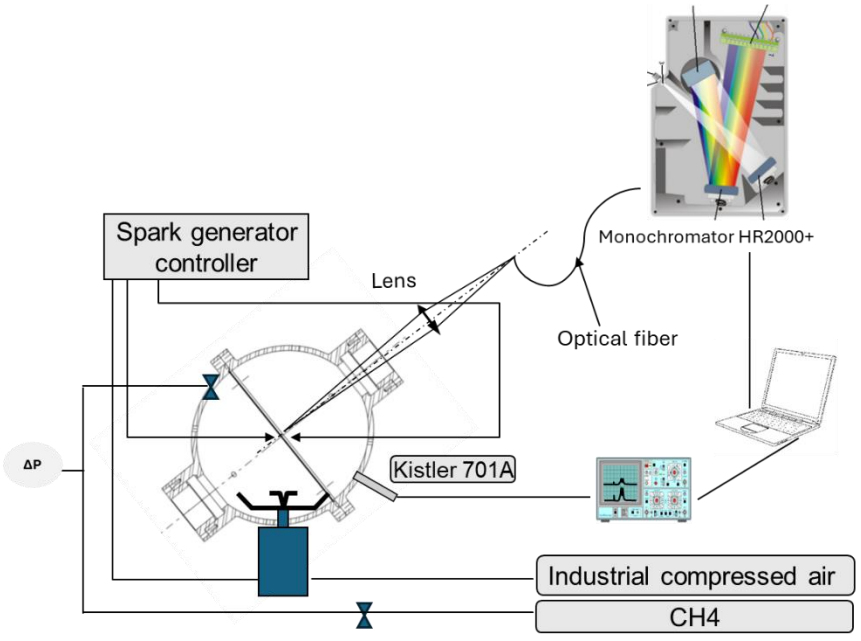

Fig. 1. Modified 20L sphere

Parameter	*Value*
Spark current intensity, A	4
Spark energy, J	66
Spark duration, ms	200
Spark power, W	330
Electrode gap, mm	4
Electrode shape	Conical (°40)

Table 1. Ignition conditions in the 20L spherical bomb

1.2. Experimental materials and test procedures

The tests were conducted, first, on pure aluminum with a median diameter D_{50}=21.36 µm obtained from the distribution using a laser diffraction technique (Malvern instrument), as shown in Fig.2. The surface morphology of aluminum particles was also observed by scanning electron microscopy (SEM) as shown in Fig.2.

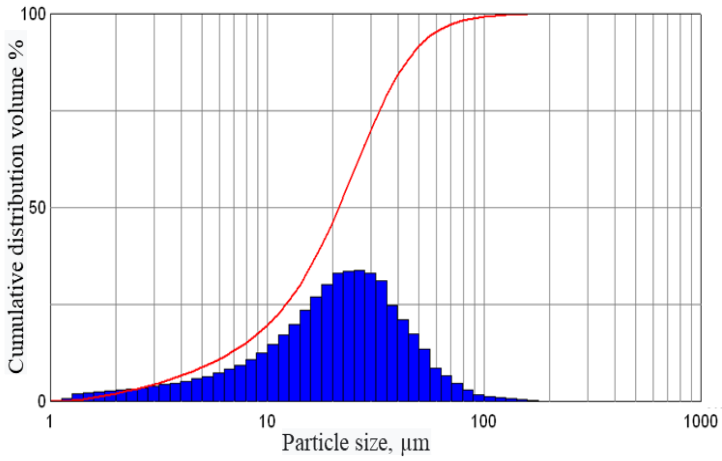

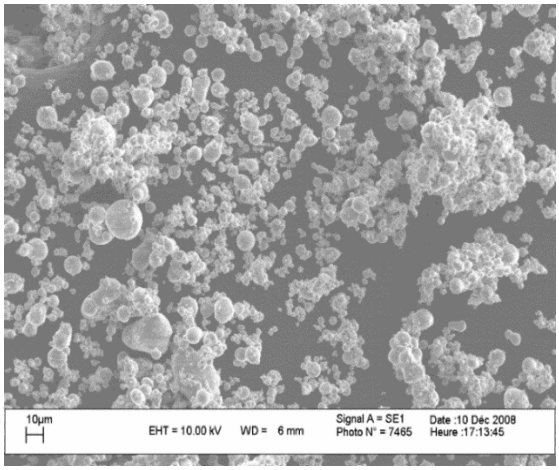

$D_V(10)$	$D_V(90)$	$D_V(50)$
5.6 µm	47.45 µm	21.36 µm

Fig. 2. Particle size distribution of aluminium dust(left) and SEM photograph (right)

Before experiments, the aluminum powder was dried for about 24 h at the temperature of 80 °C for the removal of adsorbed moisture. The amount of aluminum dust varies depending on the experiment. The dust is introduced into the storage container which is then filled with air at a pressure of 12 bars in order to disperse the dust into the explosion vessel. The decision to use 12 bars as the dispersion pressure is based on the optimum conditions for there to be enough particles in the middle to be effectively dispersed in the 20L sphere using the electric igniter. However, when the pressure is increased to 20 bar, segregation occurs, with particles tending to separate or segregate rather than being uniformly dispersed. Then, the chamber is evacuated to 0.4 bar and the aluminum dust is dispersed into the chamber. An explosion is obtained through the electrical ignition source, the maximum explosion overpressure P_{max} and the maximum rate of pressure rise $(dP/dt)_{max}$ are recorded via the traditional Kistler 701A pressure sensor.

Subsequently, methane was used as a gaseous fuel. This choice was motivated by methane's low reactivity compared to other combustible gases and its limited flammability range. Furthermore, in order to validate our experimental results, scientific literature provided comparative references. High purity (>99.95%) bottled methane (CH_4) was used for the gas explosion experiments and its introduction into the explosion chamber and control were facilitated by regulation of the gas's partial pressure. For example, when using methane concentrations of 5 vol % and 15 vol %, the partial pressures of methane were 0.05 bar and 0.15 bar respectively, and the evacuation pressures were 0.35 bar and 0.25 bar respectively.

For Al/CH_4/Air hybrid mixtures, the testing procedure follows the same principle as described in the previous paragraph.

1.3. Flame temperature measurement

The emission spectrum of the AlO molecule is observed to determine the flame temperature of aluminum powders. The AlO molecule is an intermediate species in combustion and is formed in the flame. This molecule therefore has a temperature very close to that of the flame.

From the spectral data of the AlO molecule, the spectra of this molecule are simulated as a function of temperature. Thus, and using the approach outlined by Pellerin et al., 1996, it is possible to determine the temperature of the measured AlO spectrum.

The primary emission band $A^2\Sigma^+ - X^2\Sigma^+$ of AlO spectra, typically at 483.6 nm, is considered. Using LTESpec software, Sankhe et al., 2019 simulated spectral luminance within the range of 460 to 540 nm is analyzed at temperatures of 2700, 2900, and 3000 K. The simulated spectra are used in this study.

2. Results and discussion

To understand the explosion behavior of hybrid mixture Al/CH4/Air, it was necessary to determine first the explosion severity parameters P_{max}, maximum overpressure and $(\frac{dP}{dt})_{max}$, maximum rate of pressure rise of pure aluminum dust and then pure CH_4 in the 20L apparatus.

2.1. The methane gas explosibility

Explosion experiments were carried out by varying the methane concentration in the range 5.3%-12 % $_{v/v}$. As seen in Fig.3, the maximum explosion overpressure increases as the concentration increases until it reaches a maximum, then decreases. The maximum overpressure P_{max} is 6.5 bar obtained at a concentration of 10% $_{v/v}$ CH_4. Literature data reported by Garcia-Agreda, 2010 and Spitzer et al., 2022 are also presented. The P_{max} obtained by Garcia-Agreda, 2010 is about 7.075 bars. This slight difference could be due to injection conditions, as the injection pressure in her study is 21 bars whereas in our experiments it is 12 bars. Spitzer et al., 2022 recorded a P_{max}=7.3 bars. Nevertheless, this variation can be attributed to the utilization of pyrotechnic igniters with an energy of 1 kJ each.

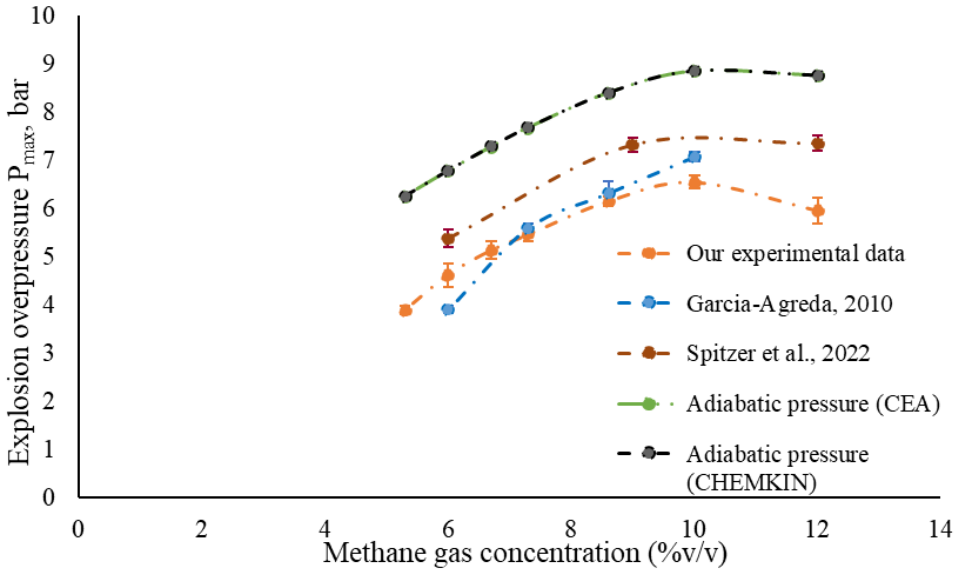

Fig. 3. Evolution of the explosion overpressure as a function of methane concentration

For the rate of pressure rise, the maximum value $(\frac{dP}{dt})_{max}$ = 1227 bar /s, is reached at a concentration of 10% $_{v/v}$ CH_4. Garcia-Agreda, 2010 obtained $(\frac{dP}{dt})_{max}$=1214 bar/s at the same concentration of 10% $_{v/v}$ CH_4. In the research conducted by Spitzer et al., 2022, they noted a higher rate of pressure rise than obtained in our experiments, $(\frac{dP}{dt})_{max}$=1418 bar/s as shown in Fig.4.

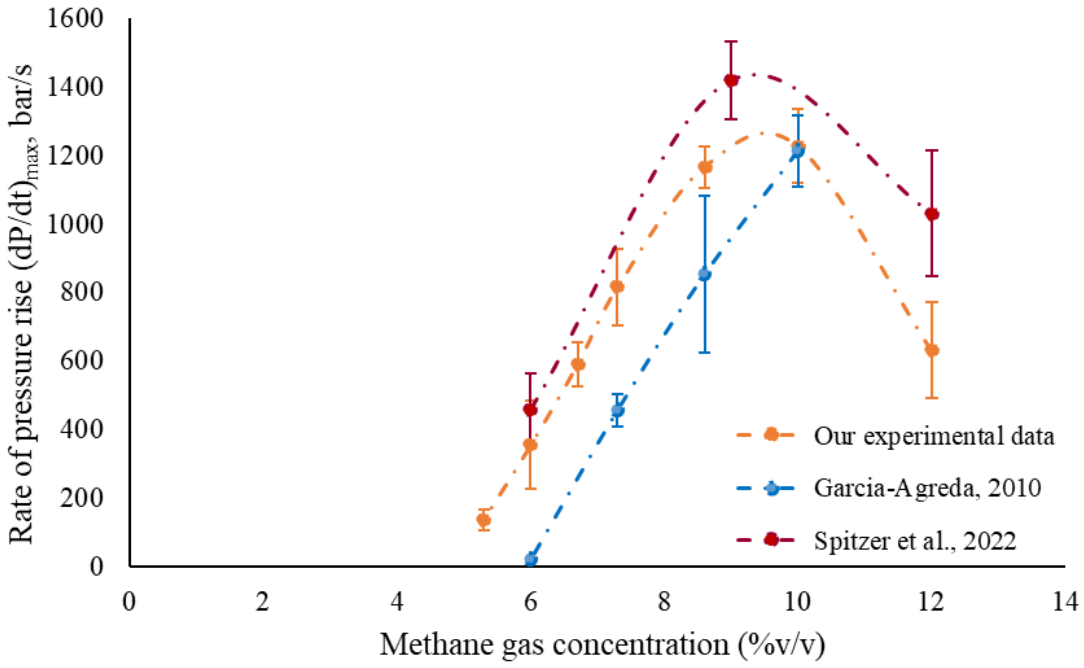

Fig. 4. Evolution of the rate of pressure rise as a function of methane concentration

2.2. The aluminum dust explosibility

The explosion severity of aluminum was studied for concentration between 200 and 1500 g/m^3.To ensure result consistency, three runs were performed for each concentration. The experimental results

of the maximum explosion pressure are illustrated versus the dust concentration in Fig.5. The explosion overpressure increases with dust concentration, reaches its maximum P_{max}= 7.74 bars at 1000g/m^3 and then decreases slightly. Millogo et al., 2020 noted P_{max} values ranging from 8 to 9 bars for aluminum powder with a median diameter D_{50}=20 µm and from 7 to 8 bars for aluminium powder with a median diameter D_{50}=35 µm. For smaller aluminum particles size with mean diameter ranging from 7 to 17µm, Lomba et al., 2015 reported a maximum overpressure P_{max} of 8 to 9 bars.

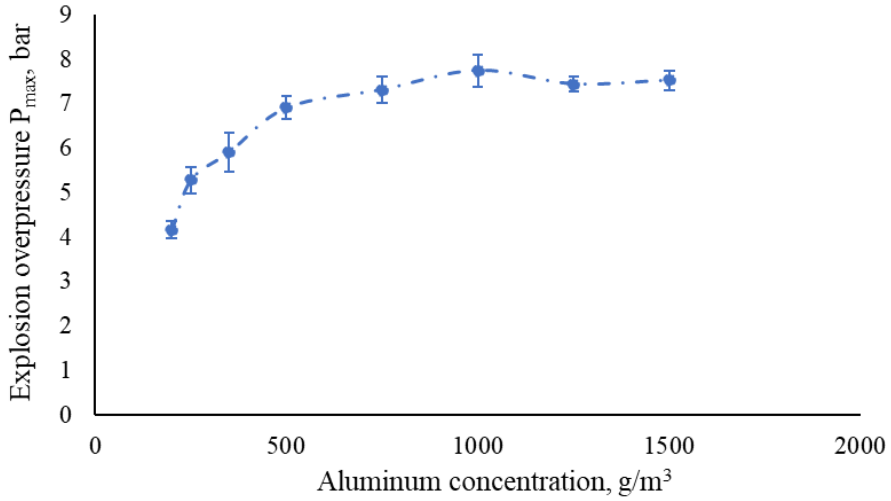

Fig. 5. Evolution of the explosion overpressure as a function of aluminum concentration

Fig.6. shows the maximum rate of pressure rise, the highest rate of pressure rise $(\frac{dP}{dt})_{max}$ obtained was at 1165 bar/s. Comparing our results with the literature, Millogo et al., 2020 noted a maximum pressure rise $(\frac{dP}{dt})_{max}$=1372 bar/s obtained at a concentration of 1200 g/m^{3}for aluminum particles with D_{50}=35 µm. However, in the study conducted by Dufaud et al., 2010, the authors noted a higher pressure rise rate $(\frac{dP}{dt})_{max}$=1456 bar/s for aluminum particles with an average diameter of 11 µm. The reason for this result is that the rate of pressure rise, $\frac{dP}{dt}$, increases as the particle size decreases. This means that the reaction speed is higher for particles with a larger specific surface area. In addition, in our study and that of Millogo et al., 2020, the results were obtained with an electric ignitor, whereas in the study conducted by Dufaud et al., 2010, tests have been performed with two pyrotechnic ignitors of 5 kJ each.

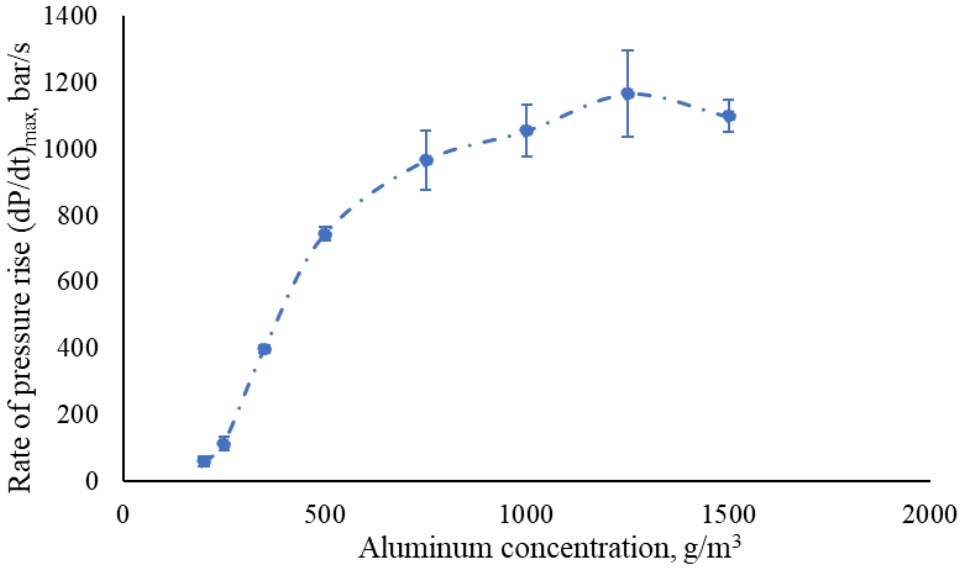

Fig. 6. Evolution of the rate of pressure rise as a function of aluminum concentration

2.3. Explosion behavior of aluminum/methane/air mixtures

Experiments with aluminum/methane/air mixtures were carried out to investigate the effect of methane addition, first, on the explosivity of aluminum dust clouds. The severity parameters of Al/CH_4/Air mixtures were determined for aluminum concentrations ranging from 250 g/m^3 to 750 g/m^3 , while initially maintaining a methane volume content of 3% as illustrated in Fig.7 and Fig.8. The maximum overpressure P_{max}=7.73 bars was obtained at a concentration of C_{Al}=350g/m^3 +3% of methane. This value is higher than the maximum overpressure obtained with pure aluminum dust P_{max}=5.9 at the same concentration 350g/m^3 of aluminum and considering that pure methane at 3% does not ignite (below the lower explosion limit, LEL, the methane is non-flammable). Consequently, the main component involved in the hybrid explosion reaction is the aluminum dust and the explosion overpressure is still mainly caused by the explosion of the aluminum dust. Above 350 g/m^3, the P_{max} of the hybrid mixture decreases. This can be explained by the cooling effect due to the presence of unburnt dust particles . Rates of pressure rise of the hybrid mixture were also seen to accelerate by at least 3.2 and 1.5 times greater than of the aluminum alone even though the percentage of CH_4 did not exceed its LEL which is about 5%$_{v/v}$. As shown in Fig.8., the maximum rate of pressure rise of the hybrid mixture $(\frac{dP}{dt})_{max}$=864.3 bar/s, this value still lower than the maximum rate of pressure rise of methane alone (1227bar/s at 10%$_{v/v}$ of CH_4). This is consistent with literature results as Wang et al., 2020 studied the severity parameters of coal/methane mixture. The results showed that the maximum value of the pressure rise rate of the hybrid mixture remains lower than that of gas alone.

In fact, the maximum value of $(\frac{dP}{dt})_{max}$ is obtained C_{Al}=500g/m^3. Below this concentration, the presence of methane in the aluminum cloud makes the dust more severe and reactive. At C_{Al}= 250g/m^3 for example, the aluminum alone has a very low rate of pressure rise $(\frac{dP}{dt})_{max}$ =114 bar/s, adding a small amount of 3% of methane activates the explosive reaction and increases the rate of pressure rise to $(\frac{dP}{dt})_{max}$= 372 bar/s. These results are consistent with previous studies which have

shown that the addition of flammable gases into the dust suspension system will increase the explosion severity compared with pure dust suspension (Song et al., 2019; Zhao et al., 2020).

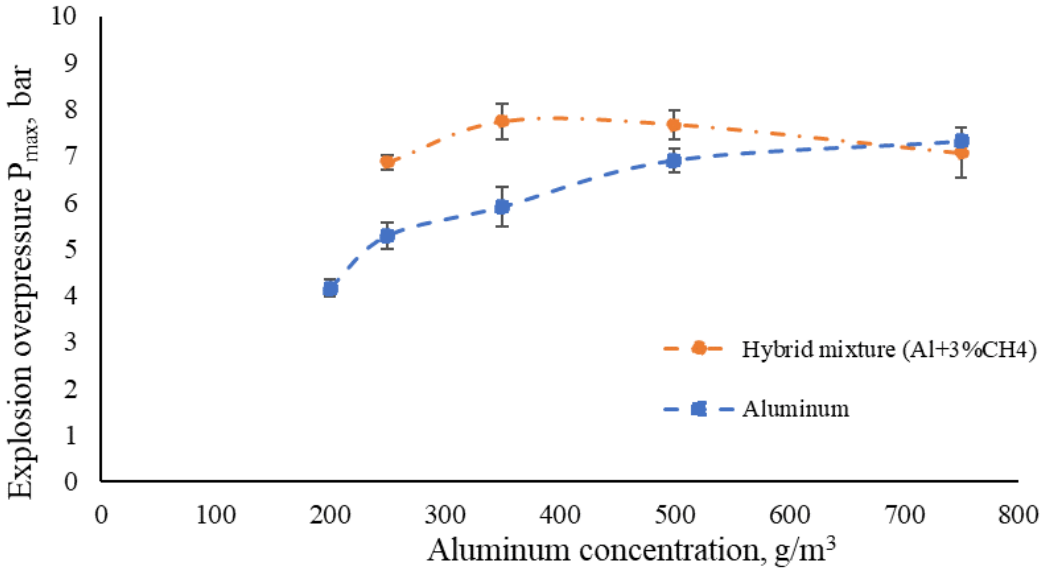

Fig. 7. Evolution of the explosion overpressure of aluminum dust with 3% CH_4

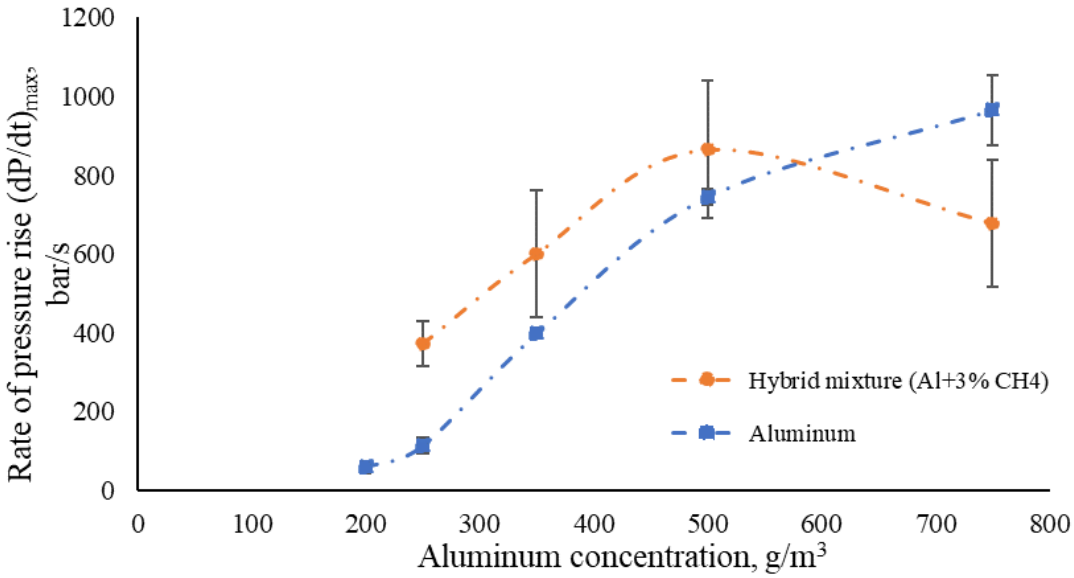

Fig. 8. . Evolution of the rate of pressure rise of aluminum dust with 3% CH_4

Subsequently, to evaluate the influence of the addition of aluminum on methane combustion, methane concentrations ranging from 4.3 % to 12% were studied while maintaining aluminum concentration at C_{Al}=350g/m^3. As can bee seen in Fig.9 and Fig.10, the P_{max} and $(\frac{dP}{dt})_{max}$ of the hybrid mixture at each methane concentration is higher than that of pure methane at the same concentration. At 4.3% methane alone, the mixture did not ignite. However, when 350g/m^3 of aluminum dust was added, the mixture became explosive. This means that the addition of aluminum fractions has changed the lower explosive limit for methane.

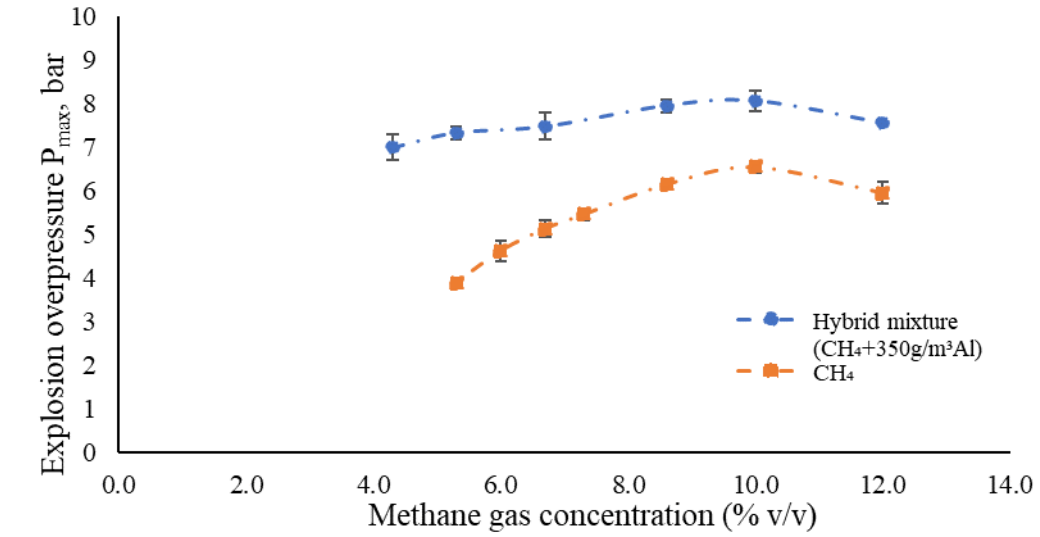

Fig. 9. Evolution of the explosion overpressure of methane with aluminum dust 350g/m^3

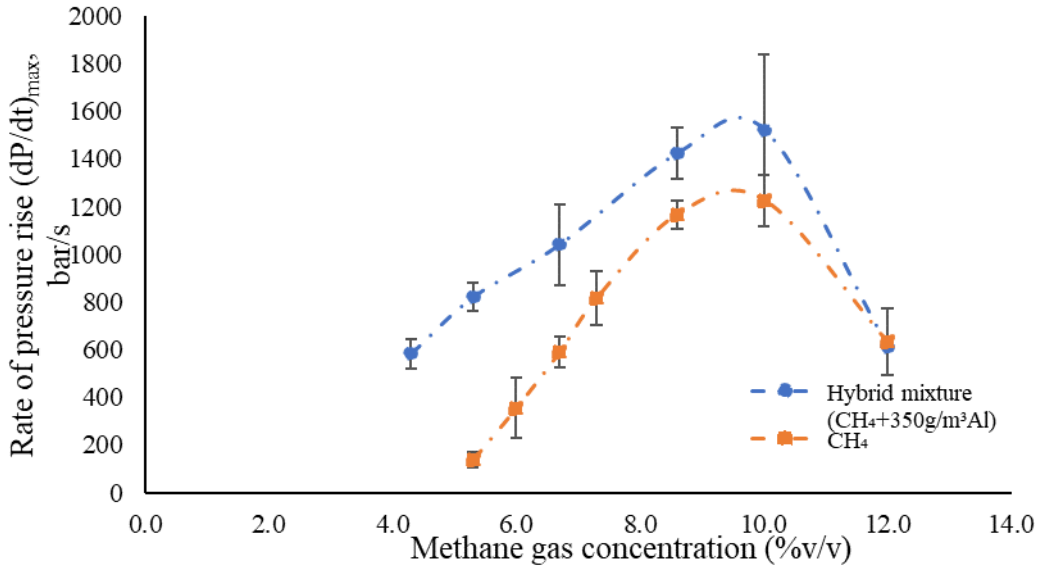

Fig. 10. Evolution of the rate of pressure rise of methane with aluminum dust 350g/m^3

2.4. Ignition delay time

Investigating the interaction between the spark and the powder in suspension, the determination of the ignition delay proves to be a highly relevant parameter. The ignition delay time t_i is defined as the time between the beginning of the ignition and the beginning of the 1% increase in overpressure.

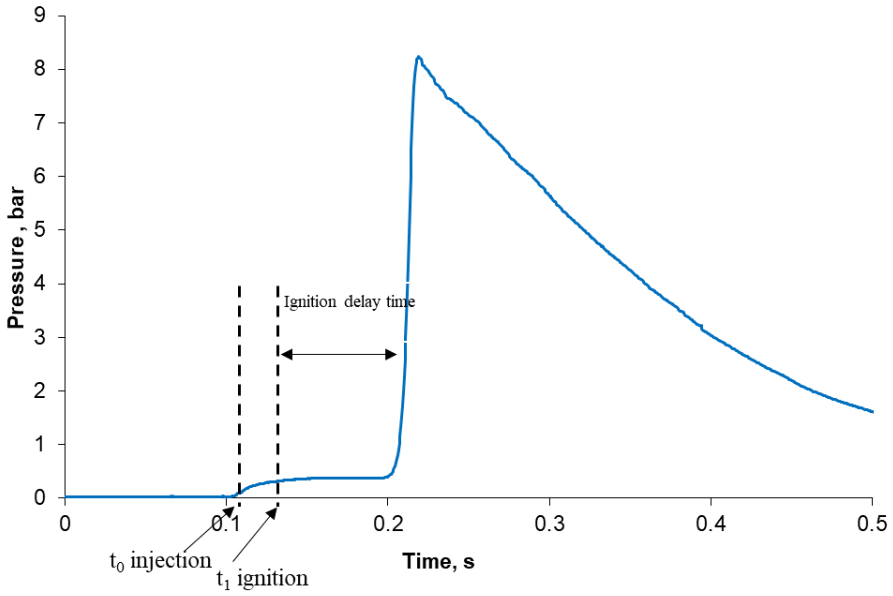

Fig. 11. Evolution of the explosion pressure with time

According to the maximum pressure rise rate of dust and hybrid mixture explosion, the ignition delay time t_i of Al , Al+ 3% CH_4 and CH_4 + 350g/m^3 aluminum were obtained. As shown in Fig.12, t_i of aluminum decreases with increasing dust concentration. At low concentrations, the increase in ignition delay can be attributed to the quantity of burning particles, which hinders the transfer of heat to the surrounding particles. At C_{Al}=250g/m^3, the ignition delay t_i=113 ms, with adding 3% of CH_4 to this concentration, t_i decreases to t_i=86ms. So, adding CH_4 reduces ignition delay significantly at low concentrations of aluminum. However, for hybrid mixture (Al+ 3% CH_4), the ignition delay is almost constant at 86 ms over the range of concentration tested.

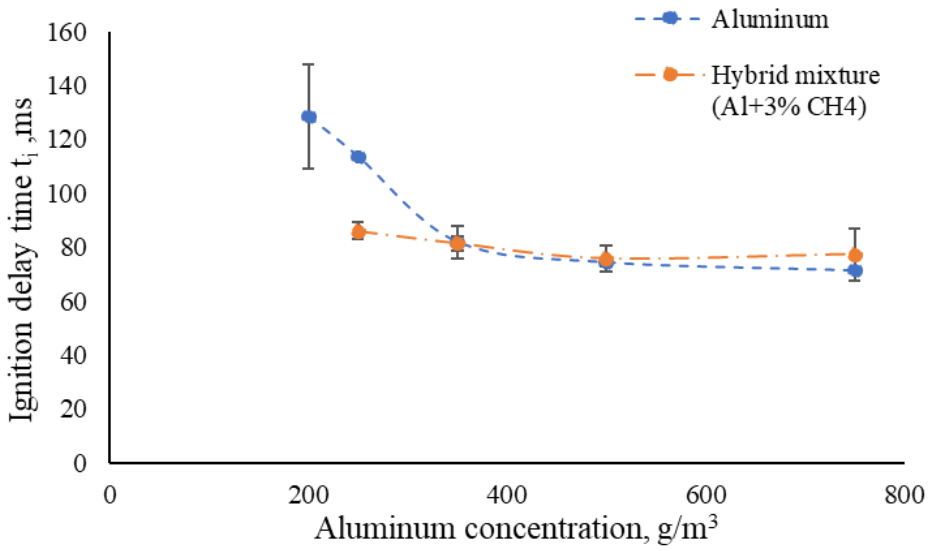

Fig. 12. Comparison of ignition delay time of Al and Al + 3% CH_4

For pure methane, the ignition delay decreases with increasing methane concentration (Fig.13). The effect of adding a concentration of 350g/m^3 aluminum to the methane significantly reduced the ignition delay (t_i=162ms to t_i=79ms) at 5.3%v/v of methane gas. This is due to the fact that the heat released by the combustion of methane increases the temperature of the gas. Aluminum particles

easily absorb the heat of the gas and ignite more easily and rapidly, shortening the ignition delay. According to the experimental results of the study conducted by Yu et al., 2021, the addition of hydrogen can significantly affect the ignition delay time and the flame propagation velocity of hydrogen/aluminum mixture.

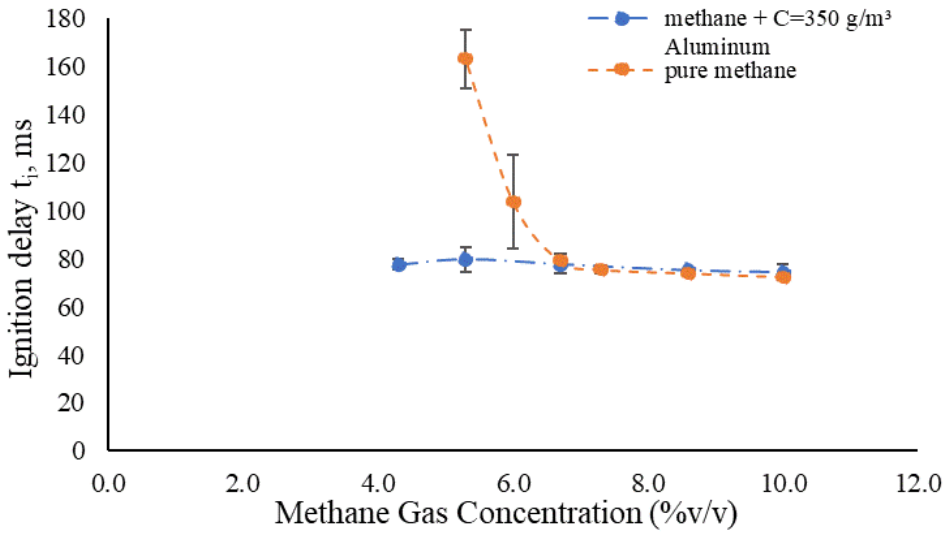

Fig. 13. Comparison of ignition delay time of CH_4 and CH_4+350g/m^3 Aluminum

2.5. Flame temperature

Flame temperatures are determined for pure aluminum, first, at 250, 350, 500, 750, 1000, 1250 and 1500 g/m^3. The temperatures measurements plotted are the average temperatures of at least three shots (Fig.14). Error bars represent standard deviation calculated for at least three repetitions in the same conditions. Temperatures vary from 2832 to 2665 K by increasing the aluminum concentration from 250 to 1500 g/m^3. As the concentration increases, the temperature decreases slightly. This can be explained by the cooling effect of the radiation and the diffusion heat to unburnt dust particles in excess. The temperature values obtained are closed to the boiling temperature of aluminum (2791K at 1atm). Glumac et al., 2005 measured the emission and absorption spectroscopy of AlO and obtained temperatures of 3000~ 3200K. Goroshin et al., 2007 obtained T_{flame}= 3250K for aluminum dust with an average particle size of d_{32}=5.6 µm, in a burner. One explanation for our temperatures being lower than the literature is that the formation of a saturated solution of Al-O decreases the boiling point of Al and thus reduces the overall flame temperature for particles burning with a vapor-phase flame. This is described in detail in the study carried out by Dreizin, 2000.

For hybrid mixture (Al +3% CH_4), Flame temperatures decrease slightly with the addition of methane. The temperatures vary between 2777 and 2613K. This can be explained by the fact that the luminous intensity decreases with the addition of the hydrocarbon because less aluminum burns due to the lack of oxygen and therefore, the aluminum oxidizes relatively slowly in the products of the methane.

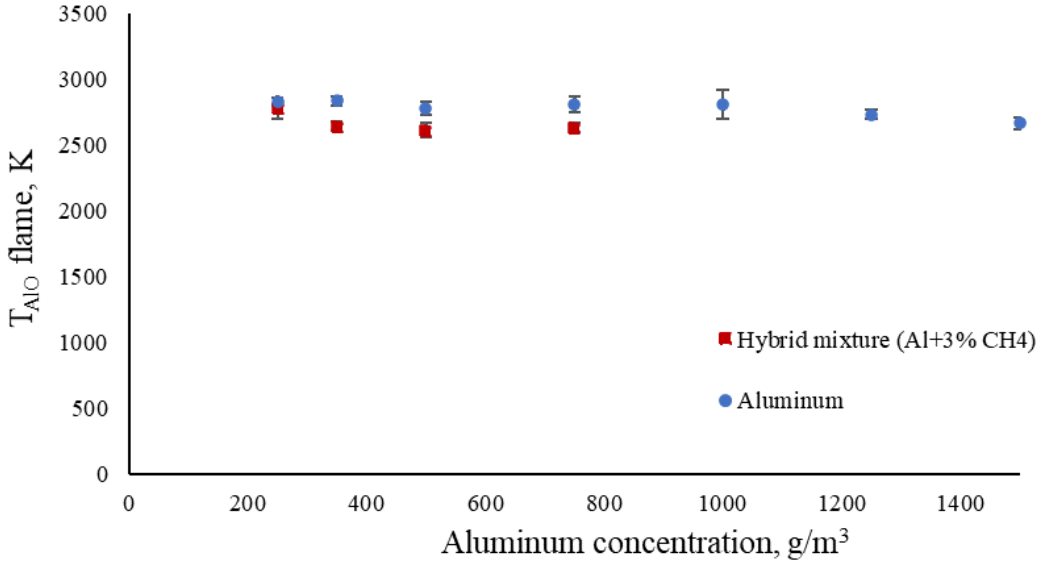

Fig. 14. Flame temperature of aluminum and hybrid mixture (Al+ 3% CH_4)

3. Conclusions

In this work, firstly, the explosion overpressure and the rate of pressure rise of hybrid aluminum dust-methane-air mixture were studied in the 20L sphere. The addition of CH_4 had a significant effect on the severity parameters of aluminum dust. The maximum overpressure of 350 g/m^3 of aluminum dust is P_{max}=5.9 bar, with the addition of 3% CH_4, the maximum overpressure increases to Pmax=7.73 bar. It was also shown that the rate of pressure rise of the hybrid mixture (Al+3% CH_4) accelerated by at least 3.2 and 1.5 times those of aluminum dust alone. The maximum pressure rise rate of the hybrid mixture obtained $(\frac{dP}{dt})_{max}$=864.3 bar/s, this value still lower than the pressure rise rate of methane alone (1227 bar/s at 10%$_{v/v}$ of CH_4). This was followed by tests to evaluate the effect of the addition of aluminum dust on methane severity parameters. It was found that the P_{max} and $(\frac{dP}{dt})_{max}$ of the hybrid mixture at each methane concentration are higher than those of pure methane at the same concentration. Furthermore, the addition of aluminum dust has been shown to modify the lower explosive limit of methane. In a second part, the ignition delay and flame temperatures were determined for the hybrid mixture. The results showed that the addition of methane significantly reduced the ignition delay of the mixture at low concentration of aluminum. Regarding the flame temperatures of the mixture, the addition of methane slightly decreases flame temperatures. Adding additional tests would be relevant to better understand the influence of the introduction of methane on the temperature of the flames.

Further work with different methane concentrations is planned to elucidate the combustion kinetics of hybrid aluminum dust-methane-air mixture.

Acknowledgements

This work was funded by the project Chaire Industrielle ACXEME supported by the French Agence Nationale de la Recherche (ANR), in France, under reference ACXEME - ANR-19-CHIN-0004.

References

Denkevits, A., Hoess, B., 2015. Hybrid H2/Al dust explosions in Siwek sphere. J. Loss Prev. Process Ind. 36, 509–521. https://doi.org/10.1016/j.jlp.2015.03.024

Dreizin, E.L., 2000. Phase changes in metal combustion. Prog. Energy Combust. Sci. 26, 57–78. https://doi.org/10.1016/S0360-1285(99)00010-6

Dufaud, O., Traoré, M., Perrin, L., Chazelet, S., Thomas, D., 2010. Experimental investigation and modelling of aluminum dusts explosions in the 20 L sphere. J. Loss Prev. Process Ind. 23, 226–236. https://doi.org/10.1016/j.jlp.2009.07.019

El Gadha, C., Bernard, S., William-Louis, M., 2023. A comparative study between two ignition sources: Electric igniter versus pyrotechnic igniter. J. Loss Prev. Process Ind. 83, 105091. https://doi.org/10.1016/j.jlp.2023.105091

Garcia-Agreda, A., 2010. Study of hybrid mixture explosions (PhD thesis,). Univerità Degli Studi di Napoli Federico II.

Glumac, N., Krier, H., Bazyn, T., Eyer, R., 2005. TEMPERATURE MEASUREMENTS OF ALUMINUM PARTICLES BURNING IN CARBON DIOXIDE. Combust. Sci. Technol. 177, 485–511. https://doi.org/10.1080/00102200590909030

Goroshin, S., Mamen, J., Higgins, A., Bazyn, T., Glumac, N., Krier, H., 2007. Emission spectroscopy of flame fronts in aluminum suspensions. Proc. Combust. Inst. 31, 2011–2019. https://doi.org/10.1016/j.proci.2006.07.175

Jeanjean, S., Bertsch, J., Legros, G., Chauveau, C., Halter, F., 2024. Thermal structure of an aluminum-methane/air hybrid flame. Exp. Therm. Fluid Sci. 153, 111130. https://doi.org/10.1016/j.expthermflusci.2023.111130

Lomba, R., Halter, F., Chauveau, C., Bernard, S., Gillard, P., Mounaim-Rousselle, C., Tahtouh, T., Guezet, O., 2015. Experimental characterization of combustion regimes for micron-sized aluminum powders, in: 53rd AIAA Aerospace Sciences Meeting. Presented at the 53rd AIAA Aerospace Sciences Meeting, American Institute of Aeronautics and Astronautics, Kissimmee, Florida. https://doi.org/10.2514/6.2015-0925

Millogo, M., Bernard, S., Gillard, P., 2020. Combustion characteristics of pure aluminum and aluminum alloys powders. J. Loss Prev. Process Ind. 68, 104270. https://doi.org/10.1016/j.jlp.2020.104270

Palecka, J., Julien, P., Goroshin, S., Bergthorson, J.M., Frost, D.L., Higgins, A.J., 2015. Quenching distance of flames in hybrid methane–aluminum mixtures. Proc. Combust. Inst. 35, 2463–2470. https://doi.org/10.1016/j.proci.2014.06.116

Pellerin, S., Cormier, J.M., Richard, F., Musiol, K., Chapelle, J., 1996. A spectroscopic diagnostic method using UV OH band spectrum. J. Phys. Appl. Phys. 29, 726–739. https://doi.org/10.1088/0022-3727/29/3/034

Sankhe, M., Bernard, S., Pellerin, S., Gillard, P., Wartel, M., 2019. Pyrometric and Spectroscopic Measurements of Temperatures of Metallic Dust Combustion Ignited by Characterized Spark Discharge in a Hartmann Tube. IEEE Trans. Plasma Sci. 47, 488–499. https://doi.org/10.1109/TPS.2018.2883543

Song, S., Cheng, Y., Meng, X., Ma, H., Dai, H., Kan, J., Shen, Z., 2019. Hybrid CH4/coal dust explosions in a 20-L spherical vessel. Process Saf. Environ. Prot. 122, 281–287. https://doi.org/10.1016/j.psep.2018.12.023

Soo, M., Julien, P., Goroshin, S., Bergthorson, J.M., Frost, D.L., 2013. Stabilized flames in hybrid aluminum-methane-air mixtures. Proc. Combust. Inst. 34, 2213–2220. https://doi.org/10.1016/j.proci.2012.05.044

Spitzer, S.H., Askar, E., Hecht, K.J., Gabel, D., Zakel, S., Krietsch, A., 2022. Requirements for a Hybrid Dust-Gas-Standard: Influence of the Mixing Procedure on Safety Characteristics of Hybrid Mixtures. Fire 5, 113. https://doi.org/10.3390/fire5040113

Vickery, J., Julien, P., Goroshin, S., Bergthorson, J.M., Frost, D.L., 2017. Propagation of isobaric spherical flames in hybrid aluminum-methane fuel mixtures. J. Loss Prev. Process Ind. 49, 472–480. https://doi.org/10.1016/j.jlp.2017.05.027

Wang, Y., Qi, Y., Gan, X., Pei, B., Wen, X., Ji, W., 2020. Influences of coal dust components on the explosibility of hybrid mixtures of methane and coal dust. J. Loss Prev. Process Ind. 67, 104222. https://doi.org/10.1016/j.jlp.2020.104222

Yu, X., Yu, J., Wang, C., Lv, X., Wang, Y., Hou, Y., Yan, X., 2021. Experimental study on the overpressure and flame propagation of hybrid hydrogen/aluminum dust explosions in a square closed vessel. Fuel 285, 119222. https://doi.org/10.1016/j.fuel.2020.119222

Zhao, P., Tan, X., Schmidt, M., Wei, A., Huang, W., Qian, X., Wu, D., 2020. Minimum explosion concentration of coal dusts in air with small amount of CH4/H2/CO under 10-kJ ignition energy conditions. Fuel 260, 116401. https://doi.org/10.1016/j.fuel.2019.116401

Validation of a new standard for safety characteristics of hybrid mixtures: HYBRID II

Stefan H. Spitzer [b,j], Wojciech Adamus[c], Enis Askar[b], Alexander Benke[b], Sebastian D'Hyon[d], Zdzislaw Dyduch[c], Olivier Dufaud[m], Friederike Flemming[e], Nicole Gehle[e], Michael Hohenberger[h], Vojtech Jankuj[o], Wang Jian[i,l], Arne Krietsch[j], Miroslav Mynarz[o], Frederik Norman[a], David Osborne[k], Maria Prodan[g], Nelly Sandsta[n], Adrian Toman[c], Trygve Skjold[n], Jan Skrinsky[o], Alexis Vignes[f], Matthijs van Wingerden[n] and Shenjung Zhong[i,l]

[a]Adinex NV, Noorderwijk, Belgium
[b] BAM, Berlin, Germany
[c]Experimental Mine "Barbara" of Central Mining Institute, Mikołów, Poland
[d]GCG Health Safety & Hygiene, Brisbane, Australia
[e]IBEXU, Freiberg, Germany
[f]INERIS, Verneuil-en-Halatte, France
[g]INSEMEX, Petrosani, Romania
[h]Montanuniversität Leoben, Leoben, Austria
[i]Northeastern University, Shenyang, P. R. China
[j]PTB, Brunswick, Germany
[k]Simtars Sponcom, Redbank, Australia
[l]Suzhou EnvSafe Test Co. Ltd, Suzhou, P. R. China
[m]Université de Lorraine, Nancy, France
[n]University of Bergen, Bergen, Norway
[o]VSB — Technical University of Ostrava, Ostrava, Czech Republic

E-mail: stefan.spitzer@ptb.de

Abstract

Safety characteristics are used for the safe operation of processes. In a first step it is checked whether the used component is combustible and if yes in which quantities respectively in which concentration if mixed with air (explosive region) determining the lower and the upper explosion limit. If it can't be guaranteed, that the process is run outside the explosive region, constructive measures may be undertaken, as for technical processes it is often assumed that an ignition source is available. For constructive explosions protection measures, explosion characteristics are determined, namely the maximum explosion pressure (p_{max}) and the maximum rate of pressure rise $(dp/dt)_{max}$.

Safety characteristics of single-phase components (solid, liquid or gas) can be determined according to standards that were developed 40 years ago and are continuously improved. For hybrid mixtures containing a flammable gas and a combustible dust there has been an approach in the 80[s] but it has never been improved nor applied ever since (ISO6184-3). A new approach by four German research facilities and the German Institute for standardization (DIN) with the aim of developing a new standard was launched in 2019. In 2022 the key findings led to a first international round robin test with eleven participating facilities from seven countries (Spitzer et al. (2023)). The dust component was corn starch, as gas component methane was chosen.

To have a stronger data basis before finalizing and publishing the new standard, a second round robin test was initiated with hydrogen as gas component and lycopodium as dust. The dust was provided by Otto-von-Guericke University of Magdeburg (OvGU) and tested and sent by the German National Metrology Institute (PTB) to the participating facilities.

The paper will summarize the findings and their influence on the new standard.

Keywords: *hybrid mixtures, safety characteristics, industrial explosions, round robin tests*

1. Introduction

Hybrid mixtures gain more and more attention in the field of process safety. While they were mostly discussed with regards to colliery explosions and in coating and spray-drying processes they are found in several other specialized novel production steps and fields. The following list shows examples of diverse processes in which hybrid mixtures might occur:

- Coal or aluminum dust accidentally added to hydrogen in fusion reactors due to abrasion (Denkevits (2007), Denkevits and Hoess (2015))
- Hexane and soy flour combined in the production of soy oil (Cheng and Rosentrater (2017))
- Metals and hydrogen for “metal hydride” hydrogen storage (Cheng et al. (2019))
- Dust from cork trees and fumes from very volatile glue in cork manufacturers or vineyards (Pilao et al. (2006))
- For the recycling of metal oxides with hydrogen when utilizing the metals as energy carriers (Bergthorson (2018)) or within the production process of steel (Spreitzer and Schenk (2019))
- In a waste processing plant a pre-shredder became stuck by phenolic resin-impregnated paper waste between the cavities of the missing cutting blades. The heating induced by the friction initiated the formation of gas of the combustible volatile components of the phenolic resin and which lowered the minimum ignition energy of the dust in the air by the formation of a hybrid mixture (ZEMA (1994))

While there are several standards for the determination of safety characteristics very few of them have a possibility for the evaluation and validation (Cesana (2019)). Especially the very dynamic test method for the determination of safety characteristics of dusts and the adaption to hybrid mixtures depends on so many experimental parameters (Spitzer et al. (2023)) that some kind of validation method is necessary to obtain comparable results from one facility to another.

In this second international round robin test the key findings from the first one were implemented and attention on them emphasized. In parallel, a German pre-standard was passed during the testing period (DIN/TS 31018) and will be forwarded to the international standardizing committees in Europe (CEN) and worldwide (ISO). The following fourteen institutions from ten countries participated (see also Figure 1):

- Adinex NV, Noorderwijk, Belgium
- Bundesanstalt für Materialforschung und -prüfung (BAM), Berlin, Germany
- CEET - VSB — Technical University of Ostrava, Ostrava, Czech Republic
- Experimental Mine “Barbara” of Central Mining Institute, Mikołów, Poland
- FBI - VSB — Technical University of Ostrava, Ostrava, Czech Republic
- IBEXU, Freiberg, Germany
- INERIS, Verneuil-en-Halatte, France
- INSEMEX, Petrosani, Romania
- Montanuniversität Leoben, Leoben, Austria
- Northeastern University, Shenyang, P. R. China
- Simtars Sponcom, Redbank, Australia
- Suzhou EnvSafe Test Co. Ltd, Suzhou, P. R. China
- Université de Lorraine, Nancy, France
- University of Bergen, Bergen, Norway

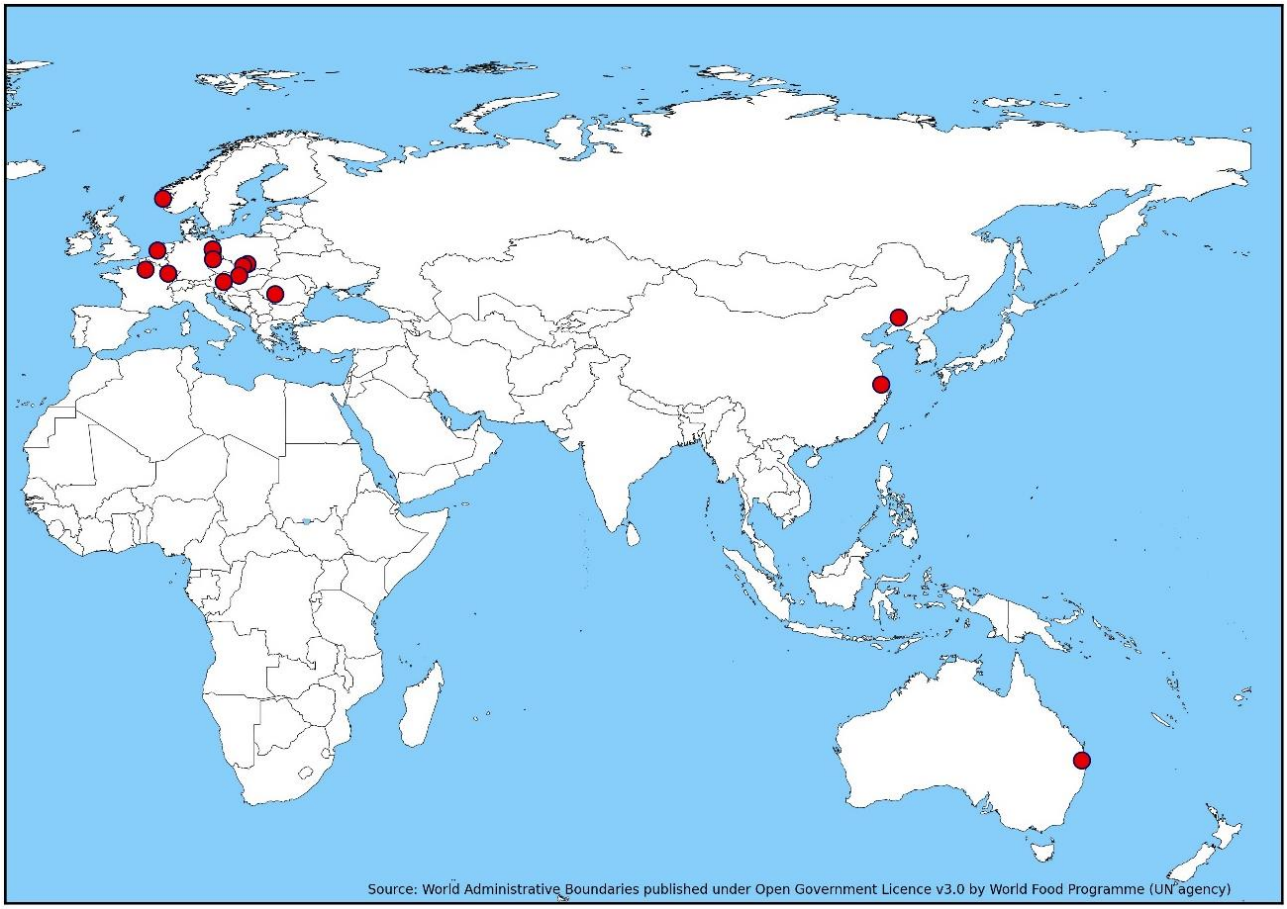

Figure 1: Map with participating facilities worldwide

2. Methods and Materials

For the second round robin test lycopodium was chosen as dust component that shall be checked on the usual concentrations according to the dust-standards (ASTM E1226, EN14034-1, EN14034-2, EN14034-3). As gas hydrogen was picked and should be checked together with the dust at the admixtures of 0 mol% (dust only), 2 mol%, and 10 mol%.

The lycopodium was stored for several years to ensure that no volatile organic components would evaporate while sending or during the testing period. As gas component for the hybrid mixture testing hydrogen was picked with a fraction of 2 mol% in air (= 1/2 lower explosion limit) and 10 mol%. The Lycopodium was tested for its particle size distribution using a laser-diffractometer Mastersizer 3000 (Malvern Panalytical, Worcestershire, United Kingdom). The moisture content was also checked before each dispatch by using a moisture analyzer Sartorius MA35 (Sartorius GmbH, Goettingen, Germany) to ensure, that the sample has not changed.

The test procedure consists of three steps, two pre-tests and the actual test series. The first pre-test is the determination of the leakage-rate of the test vessel. If the test-vessel has a leakage-rate this affects the gas concentration and with that leads to the determination of false safety characteristics. Because of the connecting tubes and valves a low leakage-rate of less than 1 mbar/min seems to be acceptable regarding the precision while still being feasible to implement.

The second pre-test is the validation of the gas amount. Gas is introduced into the test vessel with the partial pressure method to 400 mbar absolute. Then the injection from the dust container with pressurized air is activated using no dust and no ignition source. Afterwards, the gas-air mixture is pumped to a gas analyzing system to determine the real gas amount and to calculate the deviation from the aimed concentration. This test was conducted three times for both 2 mol% and 10 mol% of hydrogen and if the mean deviation was above 0.2 mol% the partial pressure had to be adjusted and the tests had to be repeated.

Eventually the actual tests were conducted with two times 1 kJ chemical igniters as ignition sources. All experimental parameters and their limitations as well as the three-step-procedure may also be found in DIN / TS 31018-1.[1]

In the upcoming standard the values for p_{max} will not be corrected anymore, since it might be crossed out in the upcoming dust standards as well (Jankuj et al. (2024)). Here they are still calculated with the following two equations:

$$p_{max} = 0.775 * p_{max,20L}^{1.15} \text{ [bar g]} \quad \text{if the determined value is above 5.5 bar g} \quad (1)$$

$$p_{max} = \frac{5.5*(p_{max,20L}-0.32)}{5.18} \text{ [bar g]} \quad \text{if the determined values is below 5.5 bar g} \quad (2)$$

Clear statements about the scattering of results for safety characteristics are scarce, especially the confusion about scattering within a facility or deviations between several facilities and the absence of reference materials for dusts make it difficult to assess this problem. However, the following statements about variations (scattering or deviation) might give an overview of what is expected and accepted in the community and might help for interpretation of the results:

- The results of p_{max} for dusts must not deviate by more than 5 % from the results previously obtained with the reference dust (deviation within a facility; EN14034-1)

- The p_{max} results for dusts must not deviate by more than 10% from the results previously obtained by another laboratory (deviation between several facilities, EN14034-1)

- The results of $(dp/dt)_{max}$ should not deviate by more than 30 % for values below 50 bar/s, 20 % for values between 50 bar/s and 100 bar/s, 12 % for values between 100 bar/s and 200 bar/s and 10 % for values above 200 bar/s from the results previously obtained with the reference dust (deviation within a facility) or from the results obtained by another facility (EN 14034-2)

- Typical scattering within a facility of the data obtained with the 20L-sphere for dusts with a (dp/dt) between 100 and 250 bar*m/s is 3 % for p_{max} and 10 % for $(dp/dt)_{max}$ (Proust et al. (2007))

[1] The SOP will be uploaded separately as appendix to this paper.

- Duplicate measurements (scattering) for dusts should agree within 5 % for p_{max} within a facility (ASTM E1226))

- Duplicate measurements for dusts at different laboratories (deviation) should agree within 10 % for p_{max} (ASTM E1226))

- Duplicate measurements (scattering) for dusts should agree to within 30 % at K_{St} = 50 bar·m/s, 20 % at K_{St} = 100 bar·m/s, and within 10 % at K_{St} = 300 bar·m/s (ASTM E1226))

- Duplicate measurements for dusts at different laboratories (deviation) should agree to within 30 % at K_{St} = 50 bar·m/s, within 20 % at K_{St} = 100 bar·m/s, and within 10 % at K_{St} = 300 bar·m/s (ASTM E1226))

3. Results and Discussion

As a basis, all facilities tested the dust alone in the 20L-sphere. This way a possible contamination or change of the dust sample was excluded. The results for the maximum explosion pressure p_{max} for the lycopodium are shown in Figure 2.

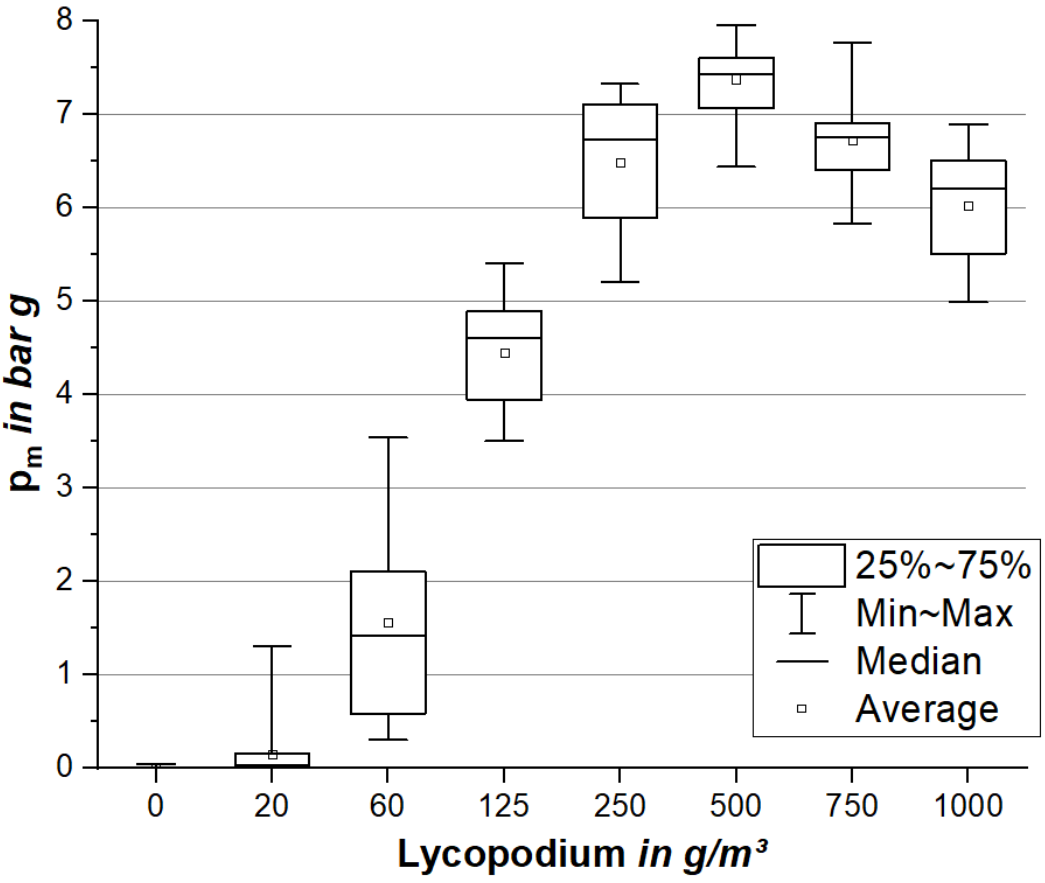

Figure 2: Explosion pressure of lycopodium without hydrogen

The determined values for the maximum rate of pressure rise $(dp/dt)_{max}$ are shown in Figure 3.

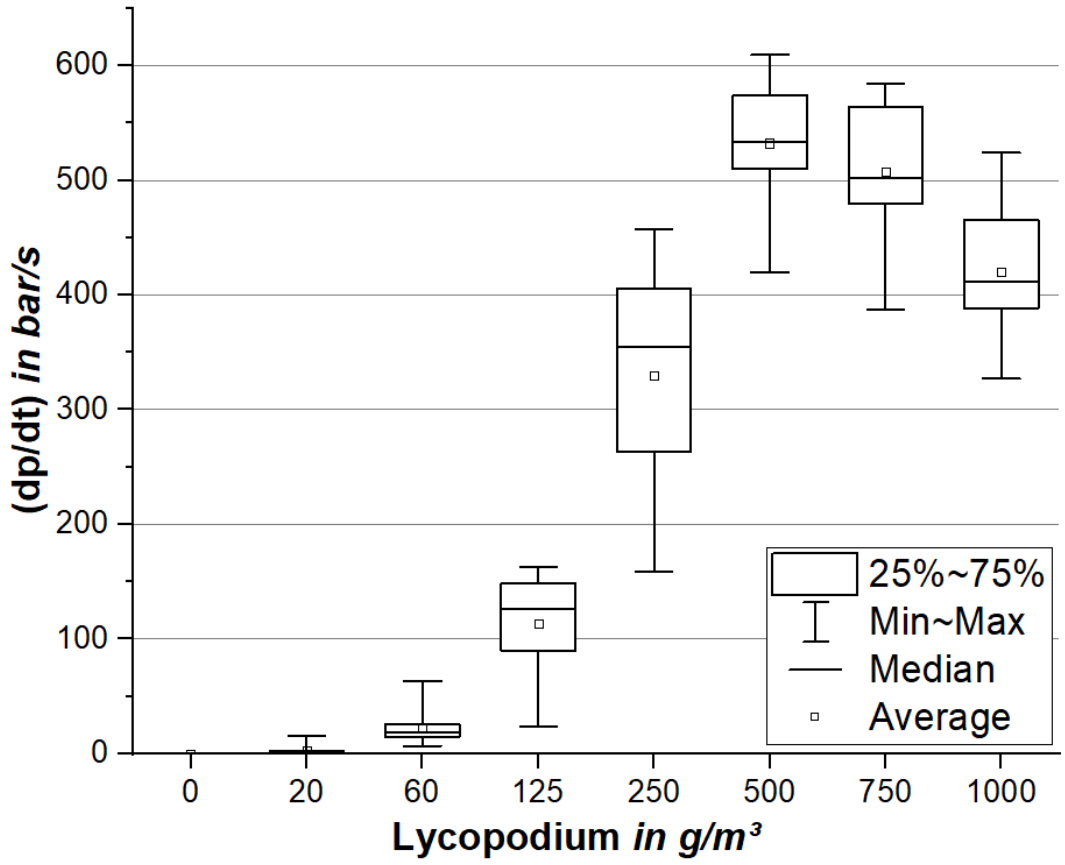

Figure 3: Rate of pressure rise of lycopodium without hydrogen

The measured values for the lower explosion limit (in US standards it is called MEC for minimum explosible concentration (ASTM E1226)) vary between 0 g/m³ (20 g/m³ already exceeded the threshold of 0.5 bar g, lower concentrations were not tested) and 60 g/m³. The reason for this wide range might be a "smearing" of dust after testing higher concentrations and left unburned dust in some dead volume of the tubing and connections of the 20L-sphere causing the concentration to be higher, than the stated one. One shall keep in mind, that a concentration of 20 g/m³ is equal to 0.4 g of dust in the 20L-sphere. However, the values for p_{max} are with ± 13.5 % slightly above the usual scattering of ± 10 %. The values for $(dp/dt)_{max}$ fit with ± 12.8 % in the allowed range of ± 20 % for this safety characteristic.

The determined values for the hybrid mixtures containing 2 mol% of hydrogen are displayed in Figure 4 and Figure 5. The values for the LEL showed again a high variation: While one facility already detected an explosion at 2 mol% without dust, three facilities detected no explosion with 20 g/m³ lycopodium and 2 mol%.

The results for p_{max} show a scattering of ± 13.7 % that is slightly higher compared to the tests with dust alone. The value for $(dp/dt)_{max}$ and K_H are with ± 18.7 % again within an acceptable range.

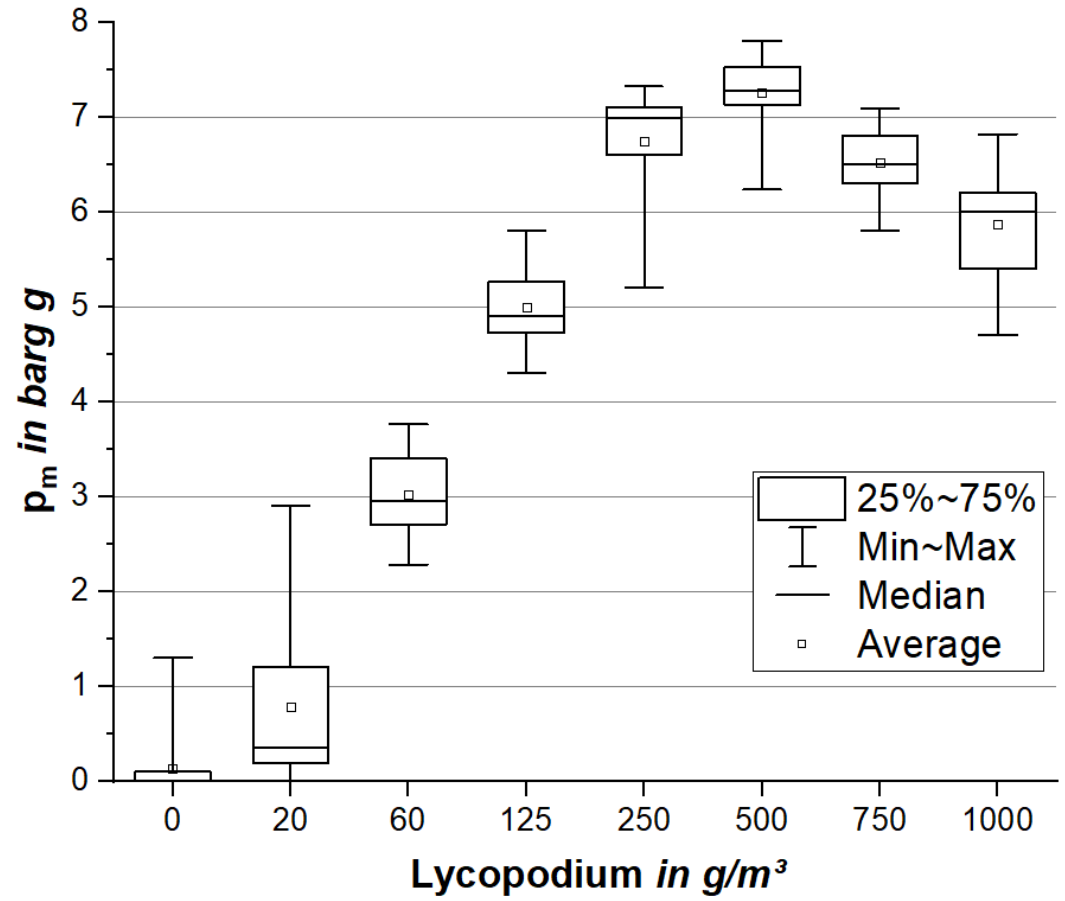

Figure 4: Explosion pressure of the hybrid mixture containing 2 mol% hydrogen

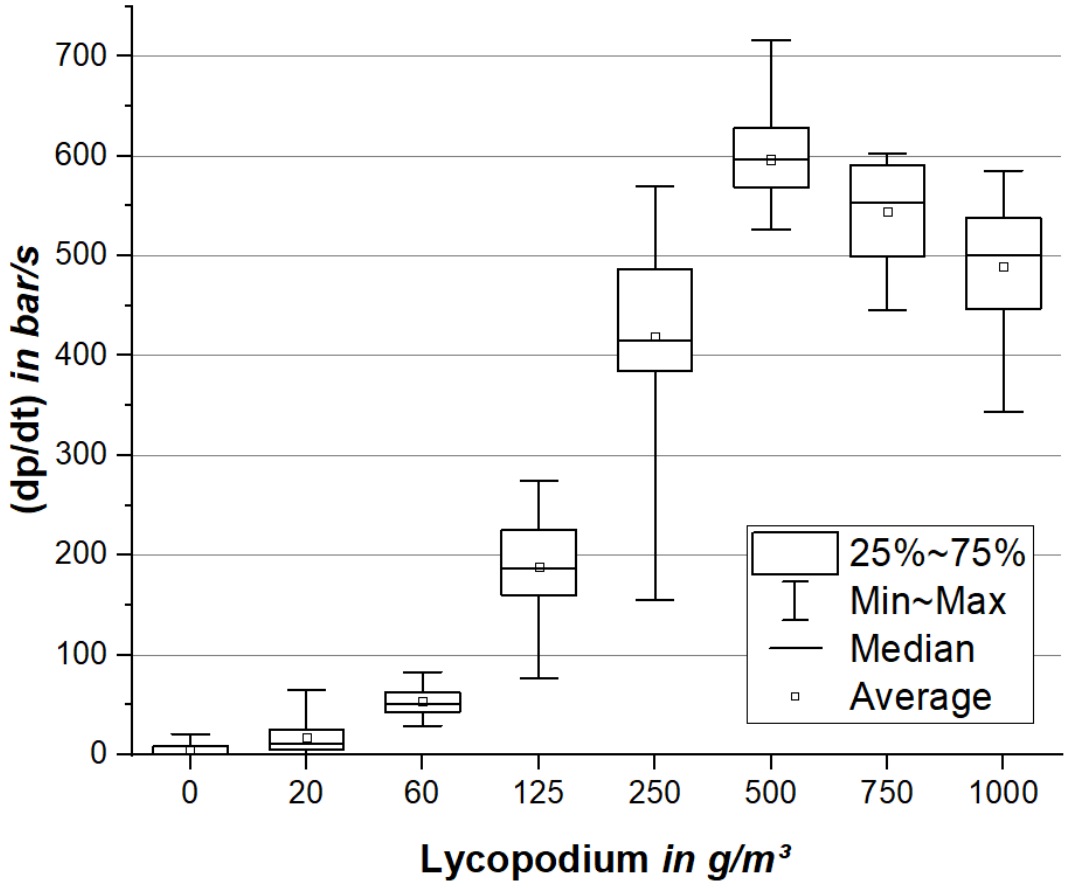

Figure 5: Rate of pressure rise for the hybrid mixture containing 2 mol% hydrogen

The results for the hybrid mixture containing 10 mol% hydrogen are displayed in Figure 6 and Figure 7. Since 10 mol% of hydrogen are already inside the explosion region, no LEL was observed.

The results for p_{max} show a scattering of ± 10 % that is even lower compared to the tests with dust alone. The value for $(dp/dt)_{max}$ and K_H are with ± 27 % above the acceptable range. However, excluding one facility the deviation would be ± 18 % so this might be an outlier.

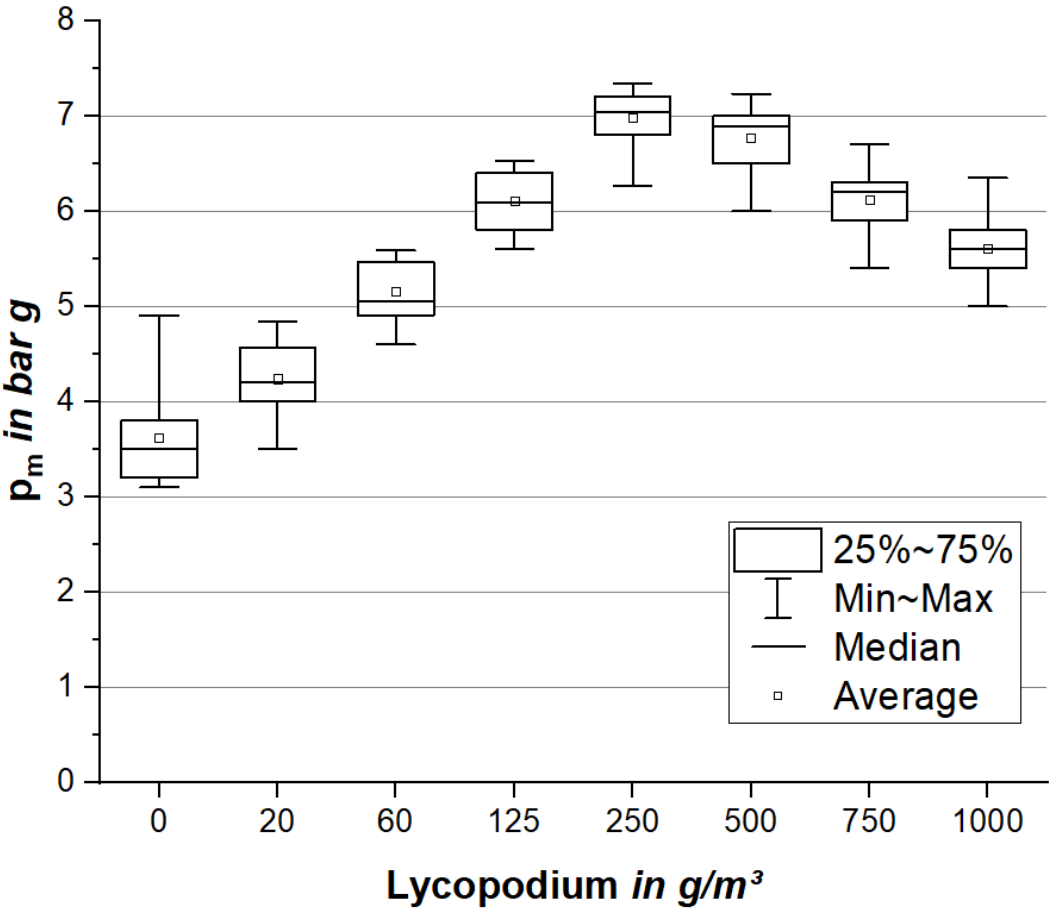

Figure 6: Explosion pressure for the hybrid mixture containing 10 mol% hydrogen

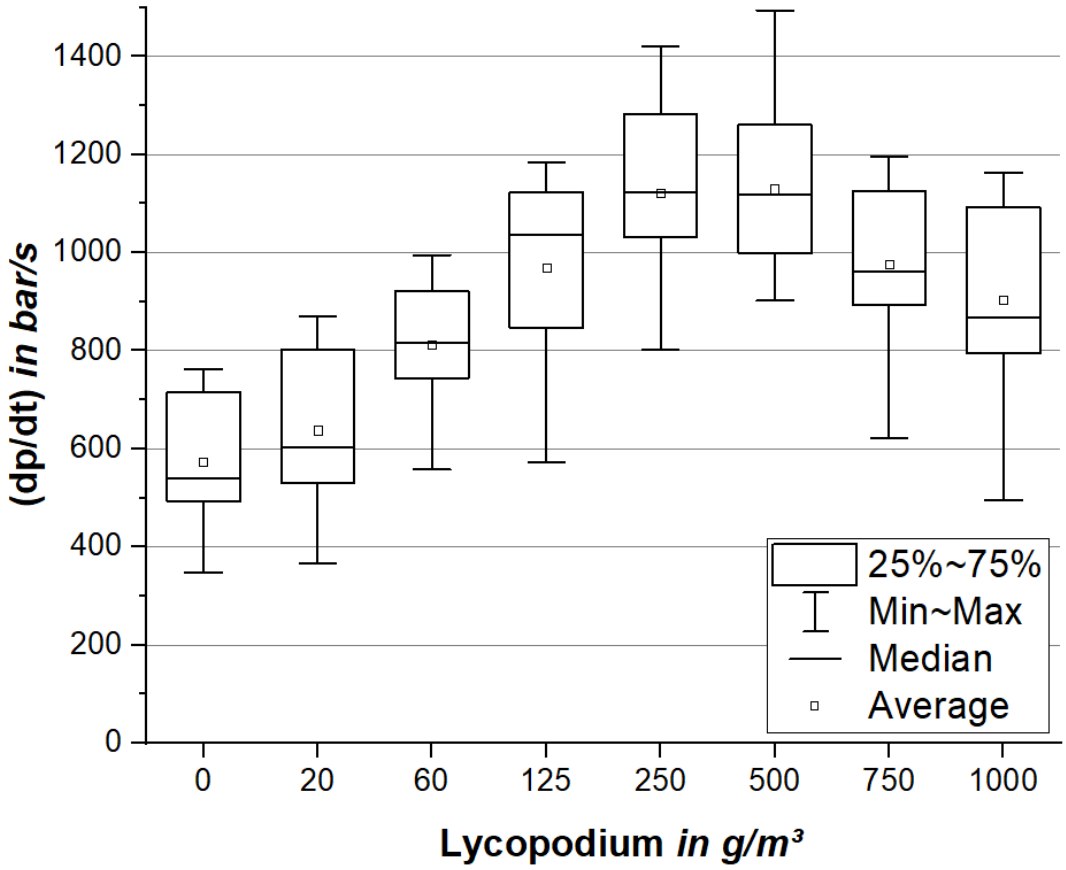

Figure 7: Rate of pressure rise for the hybrid mixture containing 10 mol% hydrogen

The overall results are displayed in table 1.

***Table 1**. Maximum explosion pressure, maximum rate of pressure rise and K_H-values for lycopodium and the hybrid mixtures*

Sample	**p_{max}**	**$(dp/dt)_{max}$**	**K_H**
	in bar g	***in bar/s***	***in bar*m/s***
Lycopodium	7.4 ± 1.0 (±13.5 %)	551 ± 71	150 ±19
Lycopodium + 2 mol% H_2	7.3 ± 1.0 (±13.7 %)	603 ± 113	164±31
Lycopodium + 10 mol% H_2	7.0 ± 0.7 (±10.0 %)	1174 ±320	319±87

4. Conclusions

A round robin test on hybrid dust-gas-mixtures was conducted by fourteen facilities in ten countries worldwide. To obtain a better data basis a different type of dust and gas like in the first round robin test was used.

The deviations for the maximum explosion pressure p_{max} and the maximum rate of pressure rise $(dp/dt)_{max}$ were with 13.7% and 27 % slightly higher to the expected deviations testing dust alone, even though this procedure has more experimental parameters. This is only possible, if the variation of the experimental parameters is narrowed and if the gas concentration is validated before conducting the tests.

By checking the leakage-rate of the explosion vessel and the gas concentration and by applying the standard procedure in this adopted way it may be possible in the future to reproduce scientific data and by that creating a data base for hybrid mixtures like the existing ones for gases and dusts.

Acknowledgements

The authors gratefully acknowledge the provision of the dust from Dieter Gabel (OvGU, Magdeburg, Germany) and the drawing of the map from Paul Geoerg (VFDB eV, Münster, Germany).

References

ASTM E1226a, 2012. Standard Test Method for Explosibility of Dust Clouds. Standard. American Society for Testing and Materials (ASTM). doi: 10.1520/E1226-19

Bergthorson, J. M. Recyclable metal fuels for clean and compact zero-carbon power. Progress in Energy and Combustion Science, 2018. doi: 10.1016/j.pecs.2018.05.001

EN14034-1, 2011. Determination of explosion characteristics of dust clouds - Part 1: determination of the maximum explosion pressure pmax of dust clouds. Standard. Comité Européen de Normalisation (CEN). doi: 10.31030/1709463

EN14034-2, 2011. Determination of explosion characteristics of dust clouds - Part 2: determination of the maximum rate of explosion pressure rise (dp/dt)max of dust clouds. Standard. Comité Européen de Normalisation (CEN). doi: 10.31030/1709464

EN14034-3, 2011. Determination of explosion characteristics of dust clouds - Part 3: determination of the lower explosion limit LEL of dust clouds. Standard. Comité Européen de Normalisation (CEN). doi: 10.31030/1709465

Cesana C., Eiche M., Schwaninger M., 2019, Quality Management in the Determination of Safety Characteristics, Chemical Engineering Transactions, 77, 985-990 doi:10.3303/CET1977165

Cheng, M.-H. and Rosentrater, K. A. Economic feasibility analysis of soybean oil production by hexane extraction. Industrial Crops & Products, 2017. doi:1 0.1016/j.indcrop.2017.07.036

Cheng, Y.-F., Song, S.-X., Ma, H.-H., Su, J., Han, T.-F., Shen, Z.-W., and Meng, X.-R. Hybrid H2/Ti dust explosion hazards during the production of metal hydride TiH2 in a closed vessel. International Journal of Hydrogen Energy, 2019. doi: 10.1016/j.ijhydene.2019.02.189

Denkevits, A. Explosibility of hydrogen–graphite dust hybrid mixtures. Journal of Loss Prevention in the Process Industries, 20(4):698–707, 2007. doi: 10.1016/j.jlp.2007.04.033.

Denkevits, A. and Hoess, B. Hybrid H2/Al dust explosions in Siwek sphere. Journal of Loss Prevention in the Process Industries, 36:509–521, 2015. doi: 10.1016/j.jlp.2015.03.024

DIN/TS 31018-1:2023-10 – Draft, Determination methods for safety-related parameters of explosion protection for hybrid mixtures of substances - Part 1: Gases, doi:10.31030/3447022

ISO6184-3:1985. Explosion protection systems — Part 3: Determination of explosion indices of fuel/air mixtures other than dust/air and gas/air mixtures

Jankuj, V., Skrinsky, J., Krietsch, A., Schmidt, M., Krause, U., Kuracina, R., Szabova, Z., Spitzer, S. Simplifying standards, opening restrictions Part I: The influence of the test vessel volume on the maximum explosion pressure of dusts. 2024 – 15th International Symposium on Hazards, Prevention and Mitigation of Industrial Explosions (ISHPMIE)

Pilao, R., Ramalho, E., and Pinho, C. Explosibility of cork dust in methane/air mixtures. Journal of Loss Prevention in the Process Industries, 19(1):17–23, 2006. doi: 10.1016/j.jlp.2005.05.001

Proust, Ch., Accorsi, A., Dupont, L. Measuring the violence of dust explosions with the ‘‘20 l sphere’’ and with the standard ‘‘ISO 1 m3 vessel’’ Systematic comparison and analysis of the discrepancies. Journal of Loss Prevention in the Process Industries, 20 :599–606, 2007. doi:10.1016/j.jlp.2007.04.032

Spitzer, S. H., Askar, E., Benke, A., Cloney, C., D’Hyon, S., Dufaud, O., Dyduch, Z., Gabel, D., Geoerg, P., Heilmann, V., Jankuj, V., Jian, W., Krause, U., Krietsch, A., Mynarz, M., Norman, F., Skrinsky, J., Taveau, J., Vignes, A., Zakel, S. & Zhong, S. (2023). 1st international round robin test on safety characteristics of hybrid mixtures. *Journal of Loss Prevention in the Process Industries*, Volume 81, 104947

Spitzer, S.H. A. Krietsch, V. Jankuj, Experimental Parameter Study and Inherent Scattering of Safety Characteristics of Dusts, Chemical Engineering Transactions. 104 (2023) 1-6. doi:10.3303/CET23104001.

Spreitzer, D. and Schenk, J. Reduction of Iron Oxides with Hydrogen. steel research international, 2019. doi: 10.1002/srin.201900108

ZEMA. 1994-07-09 Explosion eines Staub- / Luftgemisches mit Folgebrand. Resopal, 1994

Ignition of hybrid mixtures by brush discharges

Sabine Zakel, Nikhil Tanwar, Michael Hau, Michael Beyer & Carola Schierding

Physikalisch-Technische Bundesanstalt (PTB), Braunschweig, Germany

E-Mail: *Sabine.Zakel@ptb.de*

Abstract

Brush discharges are recognized for their inability to ignite combustible dust mixtures when combined with air. However, they possess the potential to ignite flammable gas mixtures. Experiments conducted thus far have reached a maximum equivalent energy of 4 mJ. The question now arises, at what composition can hybrid mixtures of dusts and gases be ignited by brush discharges? In the case of gases alone, the transferred ignition charges are like those, used to determine the minimum ignition energy. Given that even small admixtures of gases significantly reduce the minimum ignition energy of dusts, it is plausible that brush discharge may exhibit a similar effect. In this study, experiments are presented which serve to develop an ignition apparatus in which direct ignition tests are carried out on hybrid mixtures with brush discharge. To achieve this, a charging/discharging mechanism and appropriate measurement techniques were established based on a high voltage source and back charging of the insulating plate. Additionally, the hybrid mixtures will be calibrated based on their Minimum Ignition Energy (MIE), which will be measured using a modified MIKE 3 apparatus. Furthermore, the mechanism of dust dispersion will be investigated, as low turbulence is advantageous for achieving minimum ignition energy values. For this purpose, the whirling up as well as dropping of dust will be compared. An optical analysis system was set up and tested for this purpose.

Keywords: *brush discharge, hybrid mixture, equivalent energy, transferred charge*

1. Introduction

Explosive hybrid mixtures frequently occur in industries as a mixture of combustible dusts and flammable gases or solvent vapors in air. Processes such as introducing powders into prefilled solvents, spray drying, and granulation exemplify these scenarios. For this reason, the safety characteristics of hybrid mixtures were under special investigation throughout the years (Hesener, 2016) (Spitzer, 2023) (Heilmann, 2024) (Wu, 2023). Measures to prevent explosions typically involve mitigating ignition sources, but mitigating brush discharges, which occur during dust processing, poses challenges. They directly occur between a charged surface (e.g. polymer surface) and a grounded object acting as electrode in the near distance. For this reason, the affected processes are often carried out in an inert nitrogen atmosphere to mitigate risks. Regarding the costs, a more differentiated design of the safety measures resulting from the incendivity of brush discharges in hybrid mixtures is desirable. While dust alone is not ignitable by brush discharge, the addition of even small quantities of flammable gases might shift the mixture into the explosive range. This is why the determination of a limit value for the gas or vapor content that can either be used generally or individually for a defined hybrid system would be most useful. A detailed study of the brush discharge itself might lead to an additional correlation between transferred charge and incendivity. This idea was directly transferred to this study from the “industry meets science session” of 14th ISHPMIE which took place at Braunschweig, Germany in 2022.

1.1. Brush discharge

In the context of discharging electrostatic energy, various forms can influence the ignition of gas-air mixtures (Lüttgens, 1988). The electrostatic discharge can basically be categorized as an arc discharge (spark discharge) or as a pre-discharge. In the case of pre-discharge, a distinction is usually made

between corona and brush discharges. It's worth noting that brush discharges are not exclusive to highly charged insulating plastic surfaces. Whenever a conductive electrode is grounded and placed in an electric field with high field strength, brush discharges are anticipated. The electric field can be created, for example, by a highly charged insulating liquid or suspension, a droplet mist, a layer of insulating bulk material or a dust cloud (Glor, 2000).

A frequently occurring arrangement for producing artificial brush discharge is a highly charged insulator surface, which is approached by a conductive spherical electrode which is connected to earth (Figure 1). If the electrode with a radius of curvature greater than a few millimeters is placed in the electric field which is close to the breakdown field strength, the breakdown field strength can be reached locally due to the field distortion on the electrode surface. This results in a gas discharge that starts at the location of the highest field strength on the electrode surface and ends somewhere in space because of the decreasing field. Space can also mean the insulator surface, but not a second electrode. Starting from the surface of the electrode, a discharge channel is formed which branches out finely after a few millimeters (Gibson, 1965) (Lüttgens, 1988) (Glor, 2000).

With brush discharge, only a limited part of the surface is discharged. The discharged charge quantity in a three-dimensional representation forms the shape of a cone with the base of the discharge at the center. Approximations have been made to describe the discharge cone and discharge current pulse as functions of the initial parameters (Müller, 2004).

There are many parameters influencing the process of brush discharge and the variation in its power densities over time and space: on the one hand it is the ability of the surface to accumulate charge and on the other hand there are the properties of the gas phase that fills the gap. Furthermore, the distance and the shape of the grounded electrode play a significant role. Ambient temperature and humidity strongly influence the charging of a surface and the surrounding climate should therefore be controlled and monitored during testing. The size of the insulating surface decides whether enough charge can accumulate. The surface charge density (surface potential), the material (dielectric constant) and the thickness are just as important as cleanliness and evenness. If insulating materials are in direct contact with an earthed, conductive plate on the back, surface charge densities that are orders of magnitude higher are possible. Additionally, multiple discharge events may occur as the spherical electrode approaches continuously.

In practice, a surface is mostly charged tribological via contact with a different material followed by separation (Lüttgens, 1988). This kind of tribological charging occurs when breaking up a substance (crushing, spraying, atomizing) or when substances flow along walls. High charges can also occur when lifting chargeable plates from a conductive or non-conductive surface or when rubbing such plates. In the case of frictional loading, charges are transferred between two bodies in contact. Alternatively, insulating surfaces can be charged by spraying electrodes using a negative high-voltage needle electrode or a multi-needle electrode (fakir electrode) for homogeneous loading of larger surfaces. Once the isolating surface is loaded, degradation of the charge density over time depends on the disc material. With a grounded, conductive plate on the back, after a ten-minute waiting period, the surface potential on PTFE is only 0.21% below the initial value, while for PVC it is 6.1% less, and for POM it is <50% (Müller, 2004). This makes PTFE the preferred insulating material for brush discharge experiments."

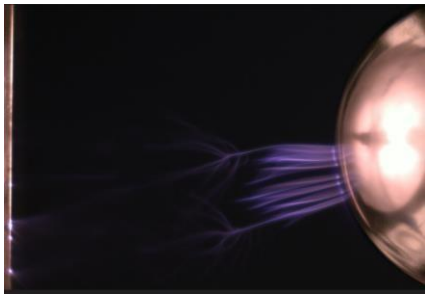

Fig. 1. *Brush discharge of a charged flat surface (left side) by the curved surface of a grounded electrode.*

1.2. Incendivity of brush discharge

Brush discharges are recognized for their inability to ignite combustible dust mixtures when combined with air. However, vapor/air mixtures can be ignited by this type of ignition source within a small ignition-sensitive concentration range (Gibson, 1965) (Langer, 2011). Notably, this range does not align with the explosion range determined in explosion limit measurements according to standards. For instance, Figure 2 illustrates that, for methane, only mixtures containing at least 7.5% by volume can be ignited, while the lower explosion limit (LEL) specified in standard EN 1839 (2017) is 4.2% by volume for methane (Chemsafe, 2024). For hybrid mixtures, the common rule, that below 20 % of the LEL the gas or vapour does not affect the hybrid mixture (TRGS 722, 2021), appears to be exaggerated in this context for the incendivity of brush discharges. However, valid experimental results are lacking. As the influence of vapours on the MIE of dust is very strong (Pellmont, 1979), this could be also applied to brush discharges.

Gibson (1965) demonstrated a correlation between the incendivity of brush discharges and the amount of transferred electrical charge. Negative charging was found to be far more incendiary than positive charging. Gibson (1988) delved deeper into this concept, aiming to distinguish between discharge types and their ignition potential under various atmospheric conditions. Their experiments involved testing discharges from charged polyethylene surfaces in flammable gas-air and solvent- vapor-air mixtures. Key findings highlighted the direct relationship between charge transfer and incendivity, with spatial and temporal factors influencing the assessment.

Von Pidoll (2002) found nearly the same levels of transferred charge for the incendivity of a spark (calculated from MIE) and the charge transfer from a surface area just below the safety threshold leading to a brush discharge in gases (Heidelberg, 1988). The therein cited threshold values from the now withdrawn IEC 60079 for the brush discharges were derived from literature on measurements with electrostatic spray guns. It was noted that, compared to MIE, transferred charge is less dependent on voltage and distance.

Langer (2011) determined the transferred charge in real ignition experiments to verify the thresholds specified in ISO 80079-36 (2016), which had not been confirmed by brush discharge experiments before (Table 1). A wide series of experiments on the incendivity of brush discharges was performed with the testing gases for explosion groups IIA (propane), IIB (ethylene), and IIC (hydrogen). The experimental setup forms the basis for the experiments reported in this study (Figure 3). At the beginning of the experiment, the flammable gas/air-mixture was introduced to the glass cross. Then the insulating plate at the bottom of the glass cross was charged with the help of the fakir electrode (- 70 kV) which was removed afterwards. Brush discharge was initiated by slowly lowering the spherical electrode until a single discharge was detected by the Coulombmeter at the top. The transferred charge necessary to ignite the gas mixtures in the experiments is detailed in Table 1. The results confirm the threshold values specified in the standards.

Several studies were performed to get dust cloud ignition with brush discharge. Schwenzfeuer and Glor made significant efforts in this regard, but successful ignition of dust clouds at the point of discharge was elusive. Sulphur was the only dust to be ignited (Schwenzfeuer, 1993) under artificial conditions when the discharge zone was separated from the dust ignition zone and the brush discharge was transformed into a spark discharge beforehand. Nevertheless, in industrial situations, the formation of a brush discharge is inhibited by the presence of a dust cloud and of course the conditions of a spark discharge are not comparable to the brush discharge. Hybrid mixtures were also ignited with the aid of that setup (Schwenzfeuer, 2001). No ignition was obtained at the point of discharge, even for hybrid mixtures. This suggests that not only the energy of the discharge influences ignition, but also the presence of the dust cloud. One reason for ignition failure is the observed reduction in the charge transfer due to the presence of the dust cloud at the region of the brush discharge (Schwenzfeuer, 2005). To address this issue, back-charging of the insulating plate was also explored by Schwenzfeuer (1997). Brush discharges were generated by the pneumatic transport of polymeric granules through insulating pipes. Insulating surface from polyethylene of 0.6 mm thickness. Discharge and the ignition tests were conducted externally to reduce turbulence.

A dust cloud produced with the help of a pulsed low pressure air stream via mushroom nozzle. It was found by the authors that the quantity of charge build-up on the insulating surface was too low to build up brush discharge (Schwenzfeuer, 2001)

Larsen (2001) succeeded to ignite Sulphur with brush discharges only under enhanced oxygen concentrations larger than 50 % by volume in the gas phase with an ignition probability of 1 %. In his setup (Figure 4), the isolating plate was charged from the front, the fakir electrode was then removed, and the dust cloud blown into the explosion chamber as the electrode approaches.

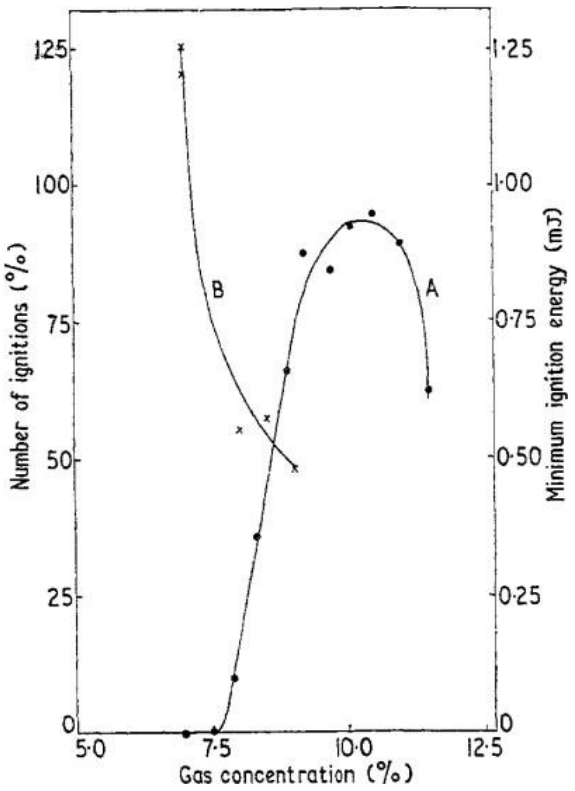

Fig. 2. *Incendivity of sparks from polyethylene. A: ignition probability plotted against methane concentration. B: minimum ignition energy from capacitive spark (Gibson, 1965)*

Table 1*. Results of gas testing at volume fraction (φ) by Langer (2011)*

Gas	**φ in %**	**Ignition probability brush discharge**	**Transferred charge in brush discharge nC**	**MIE (Pidoll, 2002) nC**	**Limiting value IEC 80079-36**
Hydrogen	22	29/82	22.7	12	IIC (10 nC)
Ethene	8	27/184	31.5	32	IIB (30 nC)
Propane	5.2	27/606	93.4	70	IIA (60 nC)

1.1. Measurement of transferred charge and equivalent energy

Different methods might address single or multiple brush discharge detection and transferred charge measurement. Single discharge events can be simply measured using a hand-coulombmeter, which triggers the first event and displays the digital reading of the transferred charge. For the scenarios involving, a high-frequency shunt resistor connected to an oscilloscope offers a practical and effective means of studying discharge characteristics (von Pidoll, 2002). The transferred charge (Q_b) of an isolated single event can be determined via the measured discharge current pulse (i_b) by forming the integral of the oscilloscope reading (u_b) over time (t) divided by the resistance of the shunt (R_{sh}):

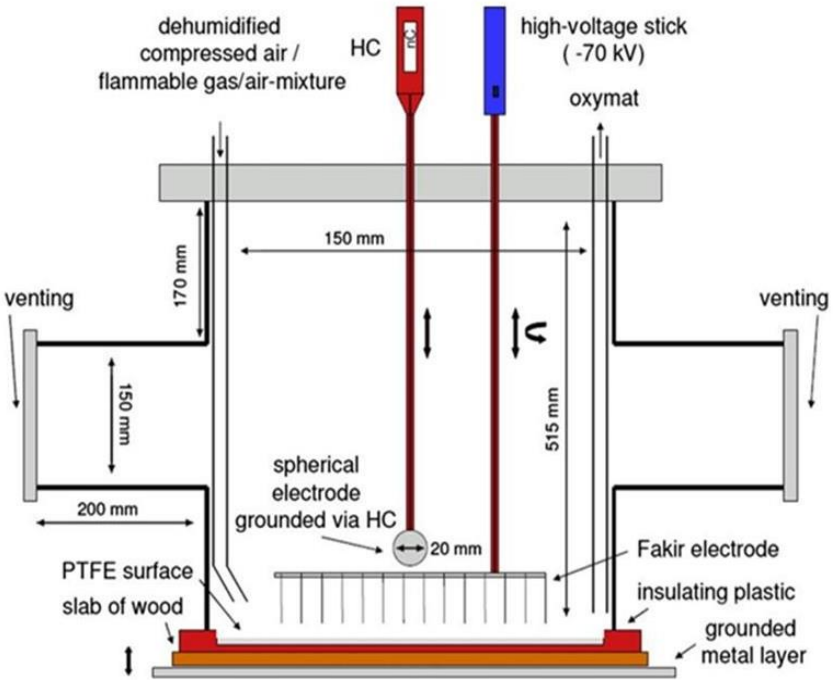

Fig. 3. *Setup according to Langer (2011) in which a glass cross of 15.7 l volume and a PTFE disc of 1.6 mm thickness were used to produce brush discharge that ignites gases.*

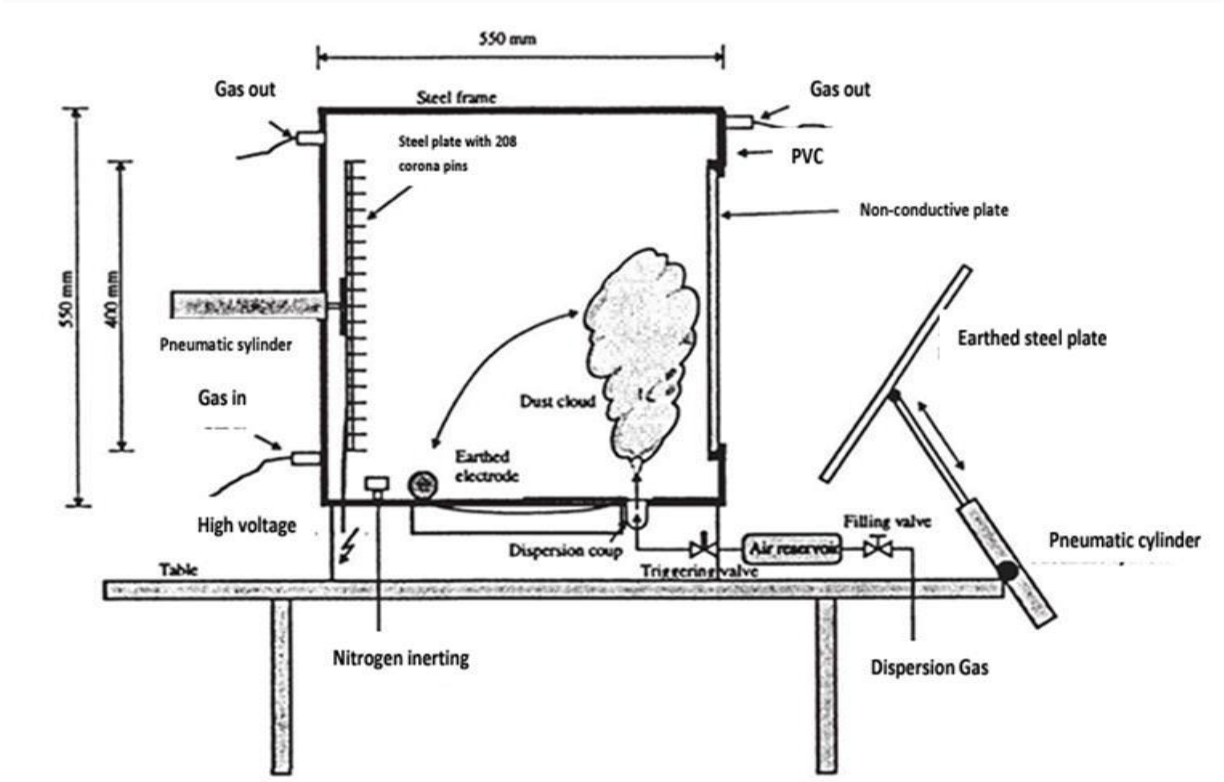

Fig. 4. *Setup for igniting dust clouds according to Larsen (2001). The plate diameter was 300 mm and the thickness 8 mm. The spherical electrode had a diameter of 40 mm*

$$Q_b = \int i_b(t)dt = \frac{1}{R_{sh}} \int u_b(t)dt \qquad \text{(eq. 1)}$$

Chowdhury (2012) developed a setup to measure uncertainties in recording charge transfer during brush discharge. Their experiments with nickel-coated copper spheres and PTFE samples revealed insights into probe design and sample positioning, highlighting the importance of understanding charge losses and spatial distribution for accurate measurements. Wamsley (2011) emphasized the relationship between charges disc radii, charge collection efficiency, and breakdown voltage.

The equivalent energy and the transferred charge are two distinct approaches to quantify the incendivity of brush discharges. The concept of equivalent energy considers that the ignition capability of different discharge forms varies (Glor, 2000). In the case of spark discharge, which is substantially different from brush discharge, it was initially assumed that the entire energy stored in the capacitor is converted in the arc and is available for ignition. In contrast to that, only part of the stored energy is converted to act as ignition source in the brush discharge. Brush discharge last longer than spark discharge and only the narrow part near the electrode where the spark channel forms contribute to ignition. The energy that goes into ignition is therefore not directly accessible. As a quantitative approach the concept of equivalent energy was introduced to brush discharge by Gibson (1965). It represents the amount of energy that, when converted into an electrical spark discharge under defined conditions, has the same ignition capability as the individual brush discharge.

The amount of energy in an electrical spark discharge, that just has ignition capability under optimized conditions is the minimum ignition energy (MIE). It is a property of the individual substance mixture. If the mixture can be ignited by a brush discharge, this discharge has at least an energy content of the MIE. The MIE of gases and vapors is generally lower than that of dusts, making it easier to ignite gases with brush discharges than dusts. For gases the MIE is minimal in a quiescent mixture. Nevertheless, it is well-known that MIE is not a perfect point ignition source and has some experimental limitations. Jaines (2008) compared MIKE 3 and Hartmann tube apparatuses. MIKE 3 demonstrated superior sensitivity, attributed to factors such as dust dispersion method, turbulence levels, and ignition delay. Addition of inductance in capacitive circuits facilitated slower energy release, contributing to lower recorded MIE values. Randberg and Eckhoff highlighted the limitations of independent dust dispersion and spark triggering methods in MIE tests, advocating for synchronization between dust dispersion and ignition triggers for more representative results.

The reported values for equivalent energies of brush discharges at which ignition occurs depend on the setup and are typically a few millijoule (Gibson, 1965). The highest value reported, 3.6 mJ was obtained by Glor (1981) with an electrode of 35 mm radius on a polyethylene disc of 10 mm thickness within an area of 0.13 m^2 area, using propane/air and 30 vol% nitrogen. From this investigation the established maximum equivalent energy of a brush discharge of 4 mJ emerged. Although this lies in the region of the MIE of several dusts, no dust ignitions could be observed with brush discharges.

The aim of this study is to determine the boundary conditions for the design of an apparatus that can be used to directly ignite hybrid mixtures of dusts and gases by means of a brush discharge. The MIE of the test mixtures should be measured either in the same apparatus or separately. The transferred charge of both, brush discharge and spark are to be measured in combination with hybrid mixture testing. The study is furthermore concerned with the controlled dispersion of the dust in the presence of gas and with the triggering of the brush discharge to the time of minimum turbulence. To this end, the experience with dusts or gases reported in the literature was collected and fundamental tests were carried out.

2. Experiments

The Langer glass cross, previously utilized at PTB in 2011 was repurposed for this study to compare the transferred charge to the already determined levels in different gas mixtures (Langer, 2011). It has been rotated 90° to bring the insulating surface into a vertical position on the right-hand side. This adjustment facilitates charging the surface either from inside the vessel (front charging) or from outside (back charging) and most importantly, it would also prevent the deposition of dust during ignition experiments.

2.2. Front charging and back charging

In most of the studies on the ignition capability of brush discharges published to date, the insulating surface was charged from the side that was exposed to the ignitable mixture. A grounded metallic backing could be applied to the rear side, for long-term charge retention with increased charge density. This method, referred to as front charging, involves removing the fakir electrode after charging and replacing it with the spherical discharge electrode (Figure 5).

Alternatively, brush discharges can be produced on the front side of an insulating surface when charged from the back side (Schwenzfeuer, 1997). For ignition tests with dusts and hybrid mixtures, back charging from outside the explosion vessel offers advantages. It eliminates the need to move the charging fakir electrode inside the ignition vessel, reducing the risk of electrode damage during ignition. Additionally, it provides more flexibility in determining the discharge time, as charging can be initiated and halted from the outside as needed. However, this method may result in less stable charge binding over time due to the absence of metallic backing. Additionally, the spherical electrode can either be put in place before charging or it can be moved towards the plate during the charging process. Experiments were carried out, in which the loading fakir electrode was mounted outside the glass cross at one millimeter distance to the insulating plate. A second fakir electrode originally mounted inside the glass cross was grounded and used to discharge and refresh the surface from inside before each experiment.

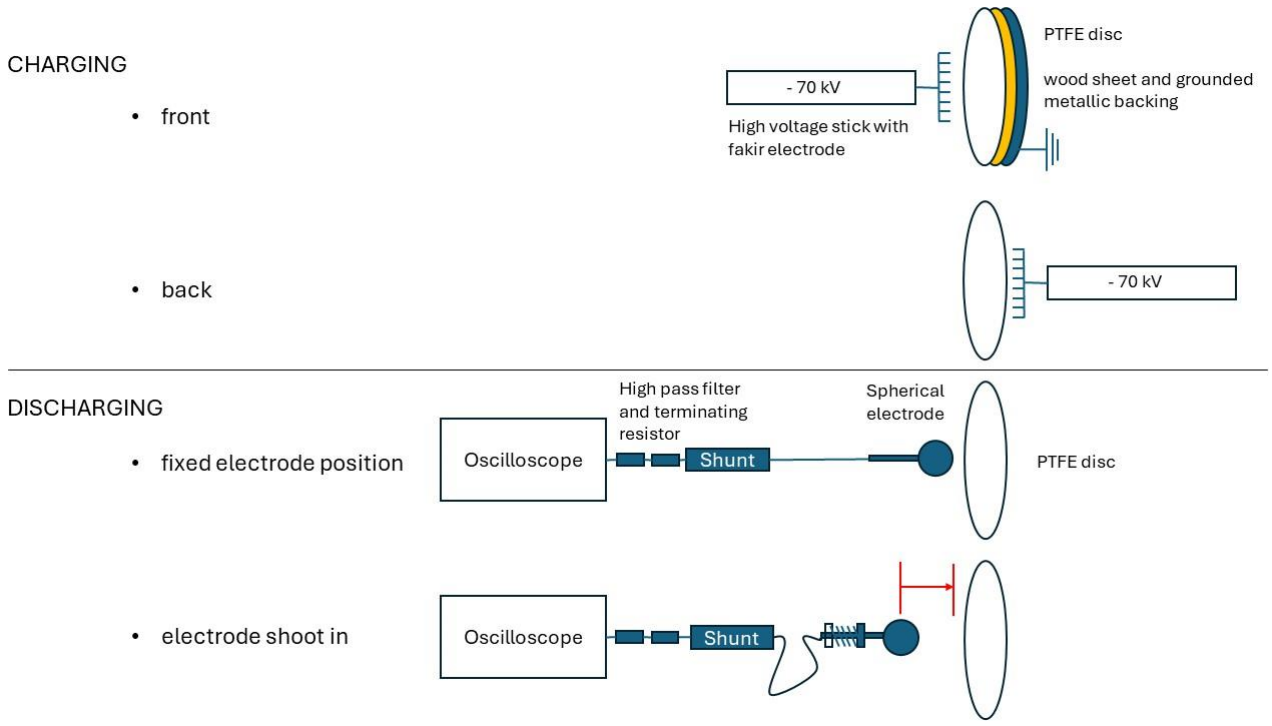

Fig.5. *Front charging from inside glass cross with metallic backing and wood disc of 10 mm thickness, back charging from outside, and discharge with fixed spherical electrode at the front or electrode shoot in.*

2.3. Discharge with fixed or moving spherical electrode

To measure the transferred charge, either a hand-held Coulombmeter with an accuracy of at least 10 % or a coaxial shunt resistance were utilized. The shunt resistance (0.25 **Ω**) requires calibration before and after the brush discharge experiments due to its sensitivity to mechanical stress. A calibrated LCR meter was used to determine the resistance of the shunts after 1 h of pre-warming. Subsequently, clips, tips and bottom of the shunt were carefully cleaned with ethanol and allowed to dry. A frequency sweep ranging from 20 Hz to 3 MHz, with a step size 4 MHz, was conducted to measure the impedance as a function of frequency.

To ensure proper shunt measurement, specific conditions must be met, as outlined in the enquiry stage of IEC 60079-0: Ed 8 Draft 7_2023-03 V1, currently is a committee draft for vote and might be published as IEC international standard within the next month. The shunt used for measurement should be designed coaxially with at least three parallel and symmetrically arranged resistors. It should be equipped with a ball electrode having (25 ± 5) mm in diameter and have a resistance determined with an accuracy of ≤ 2,5 % and shall be indicated to the third decimal place. Furthermore, it should have an earth cable attached to the outside of the shunt leading directly to the earth potential of the equipotential bonding bar of the test facility (Figure 6). The system consisting of shunt and double shielded coaxial cable shall ensure a limit frequency of ≥ 500 MHz. The oscilloscope used for measurement shall record the measurements with ≥ 1 GS/s and a bandwidth of ≥ 300 MHz and have a DC amplification with an uncertainty of ≤ 2 %. The stability of the time base shall be of ≤ 20 ppm related to a time interval of 1 ms; have a zero integral forming a value of < 1,5 nVs and record the total discharge on the screen of the oscilloscope. The entire measurement system for recording the discharge should be aligned to 50 Ohm.

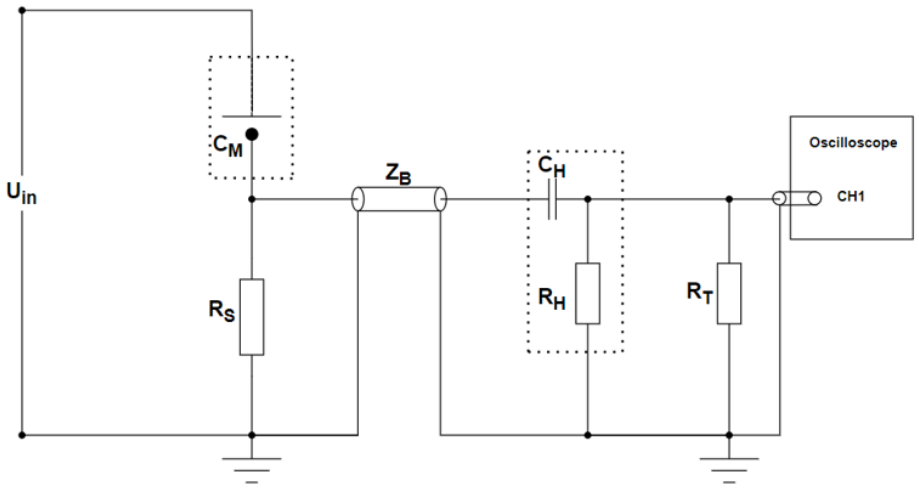

U_{in} - Input Direct Voltage

C_M - Capacitance of Measuring Setup

R_s – Resistance of Shunt

Z_B – Impedance of the BNC Cable

C_H – Capacitance of High Pass

R_H – Resistance of High Pass

R_T – Terminal Resistance

Fig.6. *Setup for measuring transferred charge of brush discharge between sample and electrode with a shunt resistor, high pass filter and termination resistor.*

2.4. Dust dropping

A glass tube of 10 cm diameter and 50 cm length was used for the dust dropping experiments. A dust dropping setup consisting of a mesh sieve with small vibrating motor was mounted to the tube lid (Figure 7). Videos were taken with a high-speed camera of 1000 fps using a laser sheet of 450 nm with a pulse duration of 10 µs for illumination. Processing of individual video frames was done by using python coding. Three different algorithms were adopted (positive difference method, delta frame, initial difference method) aiming to eliminate the background brightness and light reflections. Dried corn starch (< 8 % humidity, 2.5 g per test) was used in the experiments.

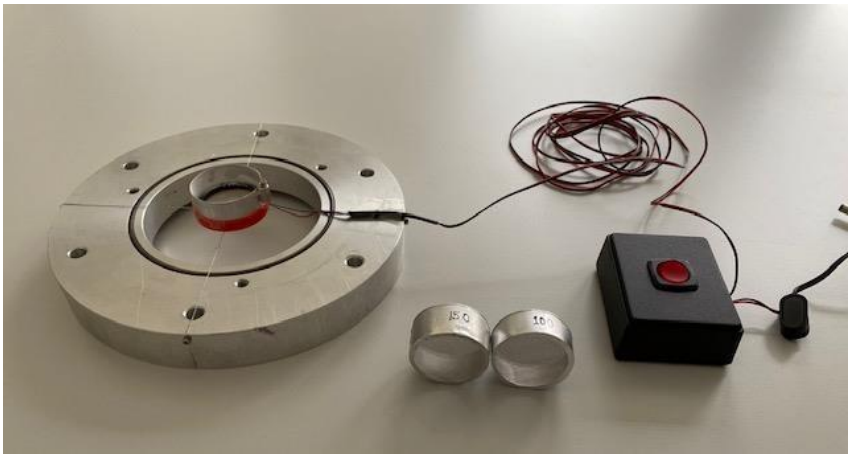

Fig. 7. *Dust dropping setup with small motor mounted to the tube lid.*

2.5. Equivalent Energy

A MIKE 3 apparatus is modified for the measurement of hybrid mixtures according to Han (2018). Therefore, it is necessary to purge the glass tube with premixed gas/air-mixture (Figure 8). The dust is then blown inside with a pressure blast of premixed gas/air-mixture.

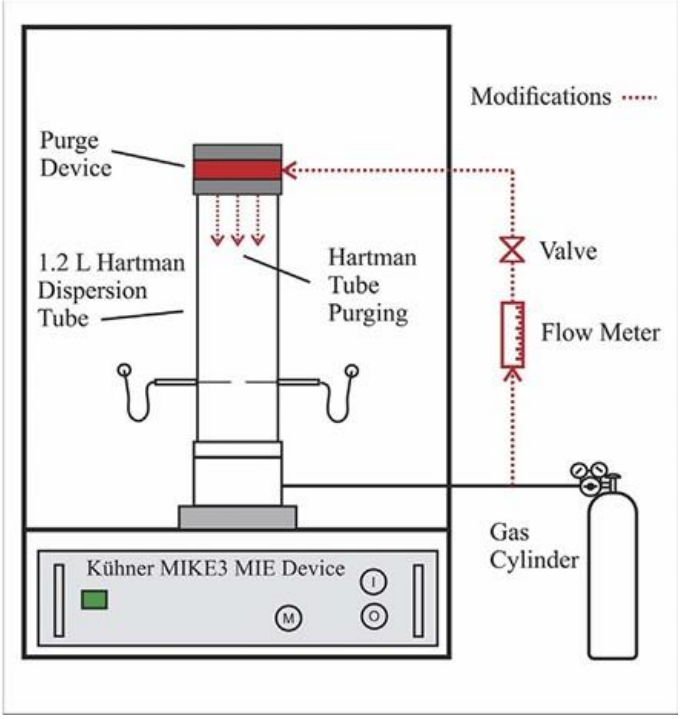

Fig. 8. *Modified MIE setup according to Han (2018).*

MIE of hybrid mixtures were measured this way before and it was found out, that they can be calculated according to figure 9 from the MIE of the dust itself and the minimum value for the gas under turbulence (Pellmont, 1979). If now a mixture is just ignited with a certain brush discharge, one can derive the equivalent energy of the brush discharge and possibly draw conclusions about other gases.

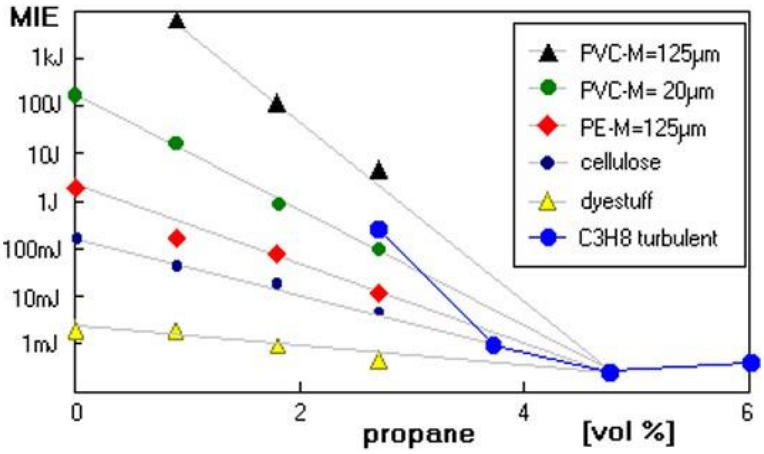

Fig. 9. *Semi-logarithmic plot of MIE versus added propane content in hybrid mixtures (Cesana AG, 2023).*

3. Results and Discussion

A MIKE 3 was modified to measure MIE of hybrid mixtures for equivalent energy measurements. Furthermore, experiments with dust dropping were carried out to establish homogenous dust clouds and optical analysis. Experiments with brush discharges were performed going stepwise from outside the glass cross to the inside and from front charging to back charging. Moreover, the feasibility of fixed or moving position of the spherical electrode was tested with back charging. Special focus was laid on whether proper shunt measurements were possible in each step of the modification to get transferred charge values.

3.1. Front charging

A front charge/discharge experiment was carried out with a 1.1 mm thick PTFE disc of 25 mm diameter loaded for 5 s with a -70 kV fakir electrode. A 0.25 mΩ coaxial shunt, connected to the oscilloscope with or without a specially configured high pass filter and a termination resistance was approached slowly to detect a single discharge event. The spherical electrode attached directly to the shunt was 25 mm. The result is given if figure 10 (left). An enhancement in signal was detected using the high pass filter and terminal resistance configuration and this was kept throughout the rest of the study. Highest equivalent energies of brush discharges were obtained with spherical electrodes of 35 mm diameter (Glor, 1981). In Langer´s experiments at PTB the diameter of the electrode was 20 mm. To ensure comparability between the old and new PTB measurements a 20 mm spherical electrode was selected, and a comparison measurement was conducted with an electrode diameter of 25 mm. No significant difference between both diameters was observed regarding shape and transferred charge. Considering gas/dust mixtures, the 20 mm sphere was retained for the remainder of the study as the equivalent energy of hybrid mixtures might not need to be as high. Coaxial shunts of different resistance value were also tested (figure 10, right). Since the 0.25 Ω shunt yielded the optimal signal, it was employed throughout the study.

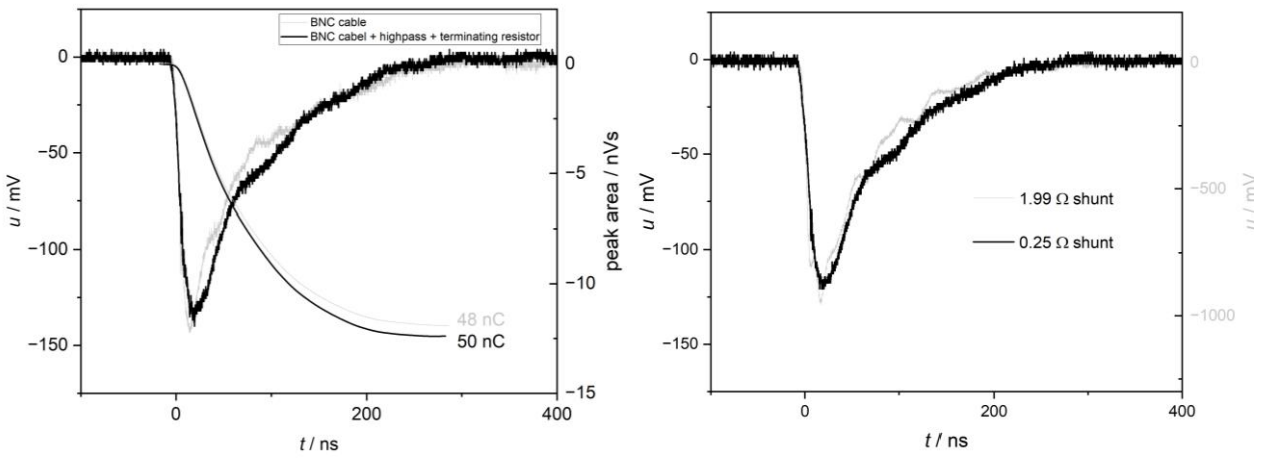

Fig. 10. *Single brush discharge with and without high pass and termination resistance (left) and with different coaxial shunts (right)*

Experiments were also carried out, in which the spherical electrode was brought to a safe distance of no discharge after the front charging process. It was then shoot in by spring force over a distance of 20 mm and the transferred charge was measured with a Coulombmeter according to the Langer setup. The results are given in figure 11. At 3 mm distance of the metallic backing, the start position at 35 mm is not free of spontaneous discharge. Nevertheless, the transferred charges can be as high as 280 nC. When the distance of the metallic backing is increased, no more spontaneous discharge occurred and the transferred charge during the 40 ms propelling phase reduced. This trend persisted even with further increase in the distance from the metallic backing.

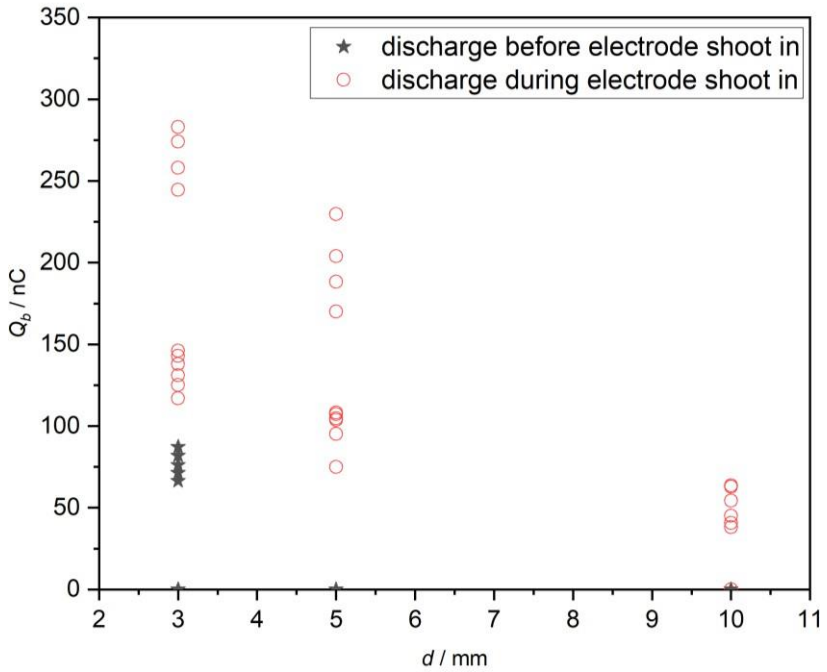

Fig. 11. *Transferred charge as a function of the distance of the wood/metallic backing stack from the insulating PTFE disc during electrode shoot in. The start position of the spherical electrode is 35 mm away from the PTFE disc while the stop position is 15 mm away.*

3.2. Back charging

In the next step, the fakir electrode was positioned on the back side of the PTFE disc at a distance of 1 mm. Initially, the entire set-up was assembled outside the glass cross, and the experiments performed in the lab under controlled humidity and temperature set at 20 °C. Before each experiment. The PTFE disc had to be discharged from both sides, front and back. Discharge to the spherical electrode at a distance of 20 mm occurred within the first second after the high voltage stick was turned on. As can be seen from figure 12, the transferred charge of 28 nC was found to be less compared to front charging, but thicker plate resulted more charge transfer. Therefore, 2 mm PTFE disc was utilized throughout the rest of this study.

When changing to positive polarity of the high voltage by using a different high voltage stick, the polarity of the discharge also changes as shown in figure 13 (left). Nevertheless, the signal is much smaller and as it is known that negative discharge is more incentive, negative high voltage was used.

When mounting the disc and shunt to the glass cross, there is an additional antenna signal detected, that might be triggered by the brush discharge (Figure 13, right). It is assumed, that this signal originates from the spark discharge of the fakir electrode pins, likely due to the uneven distribution of pins, causing irregularities in the discharge patters. This issue can be addressed by employing direct plate charging: a metallic plate is in contact with the insulating PTFE plate and is charged via cable with the high voltage stick.

1.1. Gas ignition experiments

Ignition in the glass cross was carried out with direct plate charging in back charging configuration. The high voltage stick (-70 kV) was connected to the metal plate with a cable of 1.5 m length. The spherical electrode was fixed inside the glass cross 15 mm from the front side of the PTFE plate. A mixture of 8 vol% ethylene in air was introduced to the glass cross and let come to rest. When the switch of the high voltage stick was turned on, ignition of the gas-mixture occurred within a maximum of two seconds. A single or multiple discharge was detected at the oscilloscope. In the experiments all single discharges with a transferred charge of more than 34 nC caused an ignition, the weaker charges with less than 30 nC did not. This result is in very good agreement with the experiments of Langer (2011) who found 31.5 nC as the ignition-limit. When reducing the distance to 10 mm, more multiple discharge events occur with smaller charge transfer (Figure 14). A series of them was able to ignite the mixture even though the first discharge event transferred only 20 nC. Nevertheless, this event sums up with the following events to a total of 37 nC. Further experiments will be carried out to determine the igniting transferred charge as a function of concentration regarding the statistical ignition probability, the number of discharge events and their distance in time.

1.2. Dust dropping experiments and adoption to MIKE 3

Danzi (2023) revealed insights into particle behavior, turbulence levels, and distribution patterns in the MIKE3. While dust dispersion through blasting offered advantages in breaking down agglomerates, high turbulence levels posed challenges for MIE testing. Consequently, dust dropping will be performed and compared in MIKE 3 and the future brush discharge setup. Corn starch was dropped through the glass tube simply by opening a ball valve of 2 cm diameter (Figure 15). Big lumps were observed, and the picture was partly overexposed. To improve dust dropping to be homogeneous, top feeding to the tube using a small vibration motor attached to side of a sieve mounting was installed. Different sieve sizes were tested. A combination of a 200 µm sieve on top of a 100 µm sieve turned out to yield best results concerning homogeneity of the dust cloud.

2. Conclusions

Experiments are presented which serve to develop an ignition apparatus in which direct ignition tests are carried out on hybrid mixtures with brush discharge. To this end, a charging/discharging mechanism and suitable measurement technique was established based on a high voltage source and back charging of the insulating plate. This is a promising alternative to the devices previously presented in the literature, in which the charge was not sufficient to ignite the dust, or the dust cloud had a negative effect on the charge. Furthermore, the high-voltage source can either remain switched on permanently to supply additional charge or be switched off before discharging. Multiple discharges can be detected using shunt measurement technology. The discharge can now be triggered either with a fixed spherical electrode and switching on the high voltage stick or with approaching the spherical electrode with a shoot in mechanism. In addition, the hybrid mixtures will be calibrated based on their MIE which will be measured with a modified MIKE 3 apparatus. Furthermore, the mechanism of dust dispersion is to be determined, as low turbulence is advantageous to get minimum values of ignition energy, and the presence of dust can cause problems in provoking discharge. An optical analysis system was set up and tested for this purpose. Ignition experiments with gases will be the next step before dust will be introduced either under turbulence from the bottom or with low turbulence dust dropping.

Acknowledgements

The authors gratefully acknowledge the financial contribution from BG RCI (raw materials and chemical industry trade association) in Heidelberg, Germany. Furthermore, we thank Enrico Danzi for advice in optical analysis of the dust dropping experiments and Jürgen Franke for discussion about adopting dust dropping to MIKE 3 and brush discharge experiments. The MIKE 3 device was kindly provided by BASF SE.

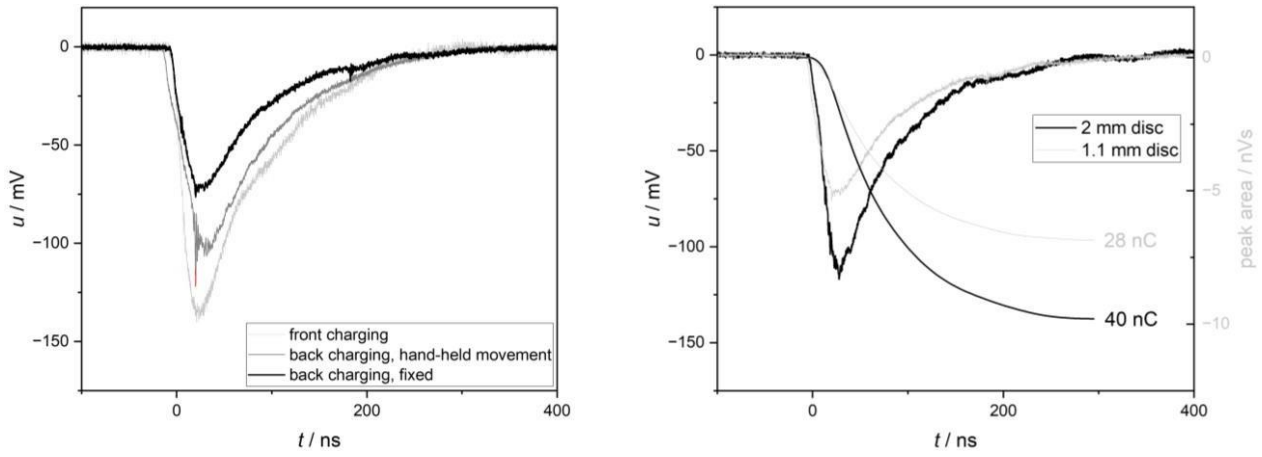

Fig. 12. *Left: Comparison of discharge after front or back charging with the hand-held spherical electrode approaching or at a fixed at a distance of 12 mm from the insulating disc. Right: Comparison of discharges after back charging from PTFE disc of different thickness.*

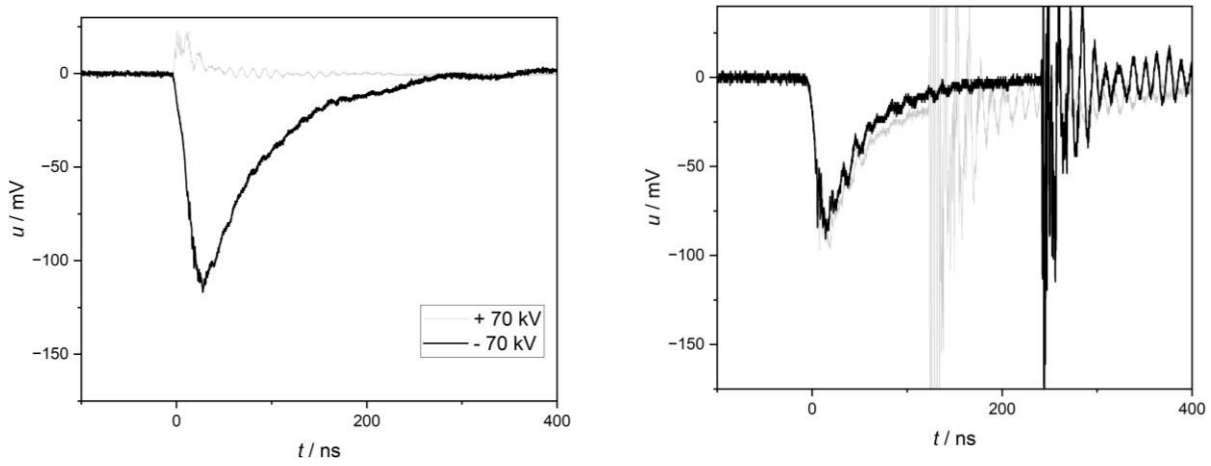

Fig. 13. *Left: Comparison of discharge after back charging with positive or negative charge. Right: Discharge measurement inside glass cross.*

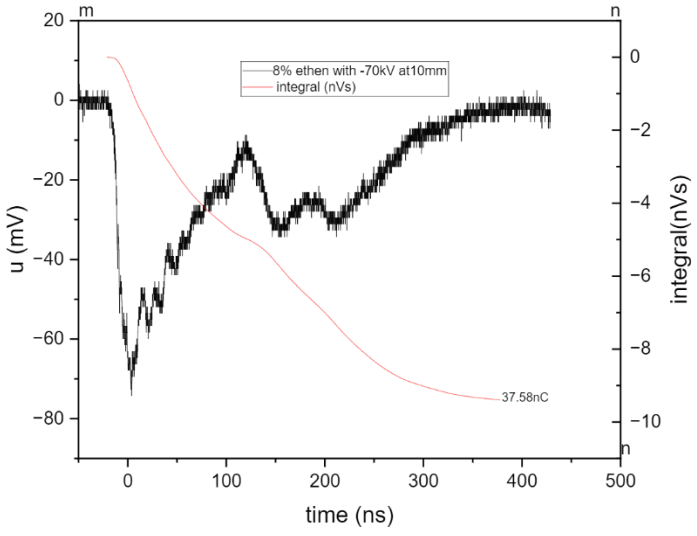

Fig. 14. *Series of discharges causing ignition in an 8 vol% ethene/air-mixture.*

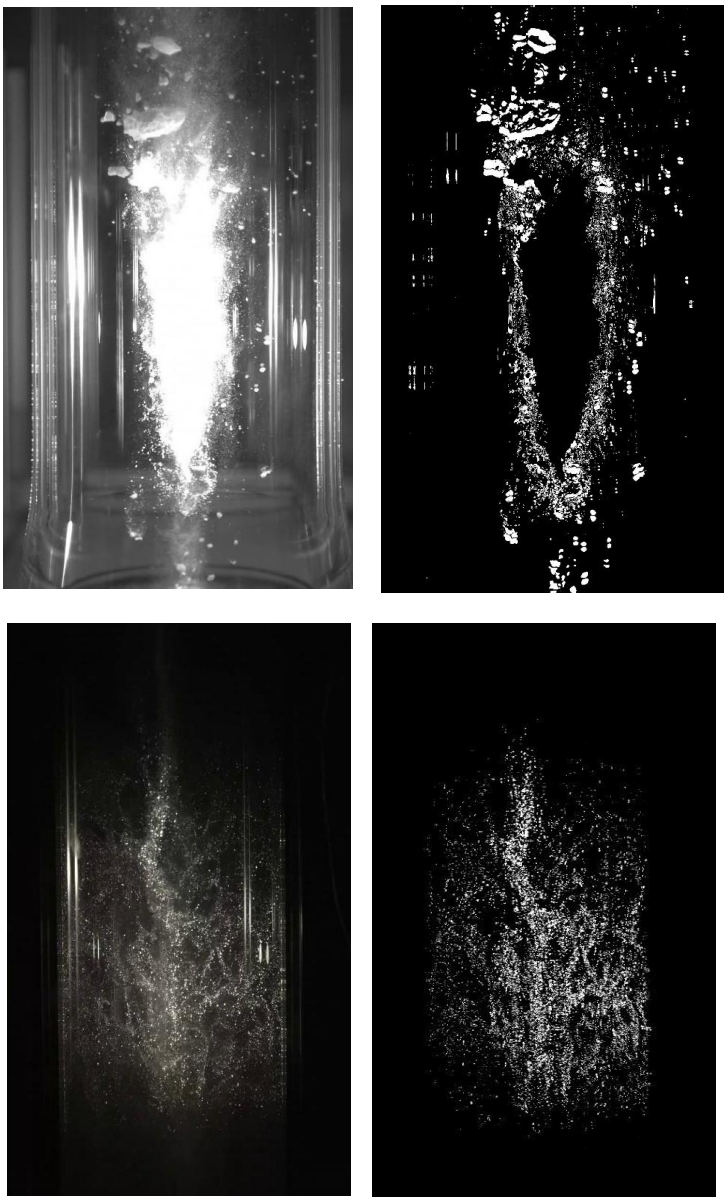

Fig. 15. *Original single video fame (left) and processed picture (right) for the analysis of particle density. The upper frame was taken without motor setup and the lower with a combination of two meshes.*

References

Cesana AG, 2023. Mike 3 manual, page 6, https://www.cesana-ag.ch/download/B022_075.pdf

Chemsafe, 2024. Database for safety charcteristics in explosion protection (Version 08/23), www.chemsafe.ptb.de, UTI: 5000-001-001/20111005, date of access: 11th May 2024

Chowdhury, K., von Pidoll, U., 2012. Experimental investigation on the measurement deviations in recording brush discharges from insulating surfaces by Coulombmeters. Journal of Electrostatics 70, 4, 347-355.

Danzi, E., Dufaud, O., Franchini, F., Pietraccini, M., Marmo, L., 2023. Study of dust cloud behaviour in the modified Hartmann tube using the image subtraction method (ISM). Journal of Loss Prevention in the Process Industries 82, 104997

EN 1839, 2017. Determination of the explosion limits and the limiting oxygen concentration for flammable gases and vapours. Tube Method, Beuth Verlag, Berlin

Gibson, N., F. C. Lloyd., 1965. Incendivity of discharges from electrostatically charged plastics. British Journal of Applied Physics 16, 11, 1619

Gibson, N., Harper, D.J., 1988. Parameters for assessing electrostatic risk from non- conductors- a discussion. Journal of Electrostatics, 21, 27-36

Glor, M., 1981. Ignition of gas/air mixtures by discharges between electrostatically charged plastic surfaces and metallic electrodes. Journal of Electrostatics, 10, 327-332

Glor, M., in Steen, H., Behrend, E., 2000. Handbuch des Explosionsschutzes. Wiley-VCH, Weinheim, New York

Glor, M., Schwenzfeuer, K.., 2005. Direct ignition tests with brush discharges. Journal of Electrostatics, 63, 463-468

Han, H. Chaudhari, P., Bagaria, P. Mashiga, C., 2018. Novel method for hybrid gas-dust cloud ignition using a modified standard minimum ignition energy device. Journal of Loss Prevention in the Process Industries, 52, 108-112.

Heidelberg, E., 1988. Test and Judgement of ignition hazards caused by electrostatic spray guns and charged surfaces without the use of explosive mixtures. Journal of Electrostatics, 21, 1-17

Heilmann, V. et al., 2024, European round robin on safety characteristics of hybrid mixtures from vapors and dusts, Journal of Loss Prevention in the Process Industries, 88, 1-5

Hesener, U., Beck, M., 2016, Forschungsbericht Sicherheitstechnische Kenngrößen von hybriden Gemischen vom 31.03.2016, DEKRA-EXAM, https://www.bgrci.de/exinfode/ex-schutz-wissen/aktuelle-forschung/sicherheitstechnische-kenngroessen-von-hybriden-gemischen

ISO 80079-36:2016, Explosive atmospheres - Part 36: Non-electrical equipment for explosive atmospheres - Basic method and requirements; German version EN ISO 80079-36:2016, Beuth Verlag, Berlin

Jaines, A., Chaineaux, J., Carson, D., Le Lore, P.A., 2008. MIKE 3 versus HARTMANN apparatus: Comparison of measured minimum ignition energy (MIE). Journal of Hazardous Materials, 152, 32-39

Langer, T., Beyer, M., von Pidoll, U., 2008. Messtechnische Charakterisierung elektrostatischer Entladungen. Technisches Messen, 75,9

Langer, T., Möckel, D., Beyer, M., 2011. Transferred charge of brush discharges in

explosive gas atmospheres- A verification of the ignition threshold limits. Journal of Electrostatics 69, 200-205

Larsen, O., Hagen, J.H., van Wingerden, K., 2001. Ignition of dust clouds by brush discharges in oxygen enriched atmospheres. Journal of Loss Prevention in the Process Industries 14, 111-122

Lüttgens, G., Blum, C., Künzig, H., Schüler, G. Linberg, K., 1988. Statische Elektrizität begreifen-beherrschen-anwenden, 4. Edition, Expert Verlag

Müller, L., 2004. Untersuchung und Modellierung elektrostatischer Entladungen (ESD) von elektrisch isolierenden Oberflächen. Dissertation Universität Stuttgart, Institut für Energieübertragung und Hochspannungstechnik

Pellmont, G., 1979. Explosions- und Zündverhalten von hybriden Gemischen aus brennbaren Stäuben und Brenngasen, Dissertation, ETH Zürich

Schwenzfeuer, K., Glor, M., 1993. Tests to determine the ignition of dust by brush discharges. Journal of Electrostatics, 30, 115-122

Schwenzfeuer, K., Glor, M., 1997. A new apparatus for ignition tests with brush discharges. Journal of Electrostatics 40 & 41, 383-388

Schwenzfeuer, K., Glor, M., 2001. Ignition tests with brush discharges. Journal of Electrostatics 51-52, 402-408

Schwenzfeuer, K., Glor, M., 2005. Direct ignition tests with brush discharges. Journal of Electrostatics, 63, 463-468

Spitzer, S. et al., 2023. The maximum rate of pressure rise of hybrid mixtures, Journal of Loss Prevention in the Process Industries, 86

Spitzer, S. et al, 2023. 1st International round robin test on safety characteristics of hybrid mixtures, Journal of Loss Prevention in the Process Industries, 81, 1-6

TRGS 722, 2021. Technische Regel für Gefahrstoffe: Vermeidung oder Einschränkung gefährlicher explosionsfähiger Gemische, Gemeinsames Ministerialblatt GMBI, Ausgabe Februar 2021

von Pidoll, U., Brozostek, E., Froechtenigt, H.-R., 2002. Determining the incendivity of electrostatic discharges without explosive gas mixture. IEEE Transactions on Industry Applications, 40,6, 1467-1475

Walmsley, H., 2011. Induced-charge errors in charge-transfer measurement: Calculations for sparks and additional brush-discharge geometries. Journal of Electrostatics, 69,79-86

Wu, D. et al., 2023. A review on hybrid mixture explosions: Safety parameters, explosion regimes and criteria, flame characteristics, Journal of Loss Prevention in the Process Industries, 82, 1 – 24

Pre-normative study for the limiting oxygen concentration of hybrid dust-gas-mixtures

Arne Krietsch [a], Martin Schmidt [b], Ernesto Salzano [c], Ulrich Krause [d] & Stefan H. Spitzer [a,b,e]

[a] Physikalisch-Technische Bundesanstalt (PTB), Braunschweig, Germany
[b] Bundesanstalt für Materialforschung und -prüfung (BAM), Berlin, Germany
[c] University of Bologna, Bologna, Italy
[d] Otto-von-Guericke-Universität, Magdeburg, Germany
[e]Eifi-Tech, Schwäbisch-Gmünd, Germany

E-mail: arne.krietsch@ptb.de

Abstract

To inert processes that involve combustible dusts or gases, the oxygen concentration in the surrounding atmosphere can be reduced under a certain level, below which no combustion can propagate, the so-called limiting oxygen concentration (LOC). The LOC is a widely used safety characteristic in the process industries. There are standardized test methods for dusts and gases but not for their mixtures though both are present in some processes. To assess this gap of knowledge a standardized test method was developed with special focus on the mixture preparation and the ignition source to obtain reproducible results for hybrid dust/gas-mixtures.

Keywords: *hybrid mixtures, limiting oxygen concentration, explosion protection, ignition sources*

1. Introduction

Safety characteristics are used to prevent combustible substances to cause harm to apparatuses or facilities. Beside the lower explosion limit, reducing the amount of combustible substance under a certain threshold level, the surrounding atmosphere can be inerted by reducing the oxygen concentration fully or partially. While full inertization is used in laboratory scales in industrial scales a partial inertization is often realized below a certain threshold value under which no combustion occurs anymore (an explanation on the molecular basis can be seen in **Figure 1**).

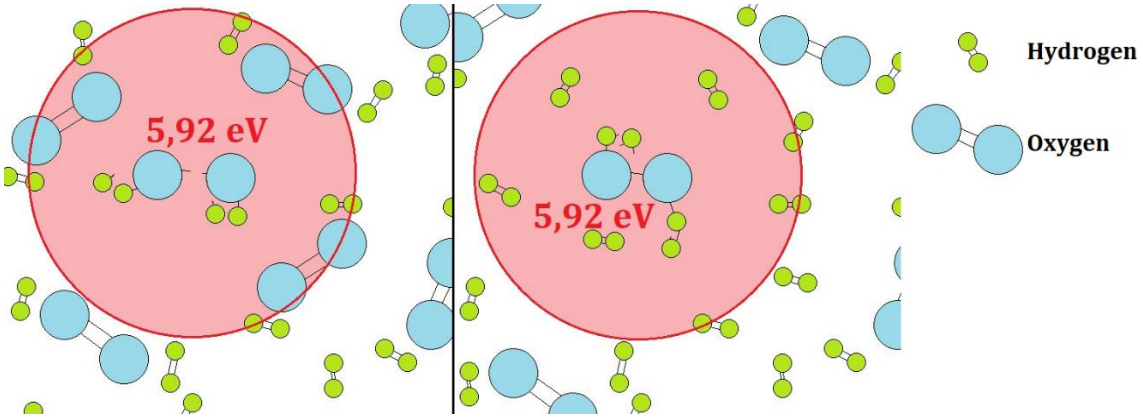

***Figure 1**: Limiting oxygen concentration for hydrogen and air (taken from Spitzer (2023))*

On the left side enough reactants of both are inside the combustion zone of one core reaction. On the right side there is not enough oxygen, and no chain reaction goes off. The reddish circle is the impact zone of the initial reaction, which releases an energy of 5.92 eV per mol oxygen with two

moles hydrogen. Within this zone the energy is sufficient to trigger a new core reaction. For better visibility nitrogen is not displayed.

In the European standard for dusts the limiting oxygen concentration it is defined as "...the maximum concentration of oxygen of a dust/air/inert gas mixture at which dust explosions cannot occur. The measurement of the limiting oxygen concentration forms the basis for explosion protection by „inerting“." (EN 14034-4, 2011). The European standard for gases and vapors describes it equally as "...the highest mole fraction of oxygen in a mixture of a flammable substance with air and inert gas at which an explosion is not yet triggered." (EN 1839, 2017), while the American standard describes it briefly as "...the oxygen (oxidant) concentration at the limit of flammability for the worst case (most flammable) fuel concentration." (ASTM 2079, 2000). LOC values of various gases, vapors and dusts are listed in table 1.

Table 1. *Limiting oxygen concentrations of selected dusts, gases and vapors*

Substance	**Gas/Vapor/Dust**	**LOC in mol %**	**Source**
Hydrogen	Gas	5.1	PTB-BAM, 2024
Methane	Gas	11	PTB-BAM, 2024
Propane	Gas	9	PTB-BAM, 2024
Butane	Gas	10.5	PTB-BAM, 2024
Methanol	Vapor	8.1	PTB-BAM, 2024
Ethanol	Vapor	8.5	PTB-BAM, 2024
Isopropanol	Vapor	8.7	PTB-BAM, 2024
Wood	Dust	10	Beck et al., 1997
Pea flour	Dust	15	Beck et al., 1997

There are standards for the determination of the LOC for dusts and gases but not for their mixtures. This article describes the difficulties that arise testing these so-called hybrid mixtures, provides a standardized test method and presents data that was obtained with this method for methane, corn starch and their mixture.

2. Experimental

A major difference in the determination methods for combustible dusts and gases is that gases are usually ignited under quiescent conditions without turbulence. To determine the explosion characteristics of combustible dusts, they must be dispersed in air, which means that a precisely defined degree of turbulence must prevail. In order to be able to analyze hybrid mixtures of combustible gases and dusts, these must also be ignited at a defined level of turbulence. It is therefore advisable to carry out the experiments in the standardized test apparatus for dusts. The so-called 20L-sphere and the 1 m³ apparatus are usually used for this purpose (e.g. ASTM E1226, 2019 and EN 14034-1, 2011). The test method for dusts in the 20-L sphere was adapted accordingly to be able to determine the LOC of hybrid mixtures. **Figure 2** illustrates the adapted test setup. For oxygen concentrations below 13 mol% the dust container was filled with compressed nitrogen instead of air.

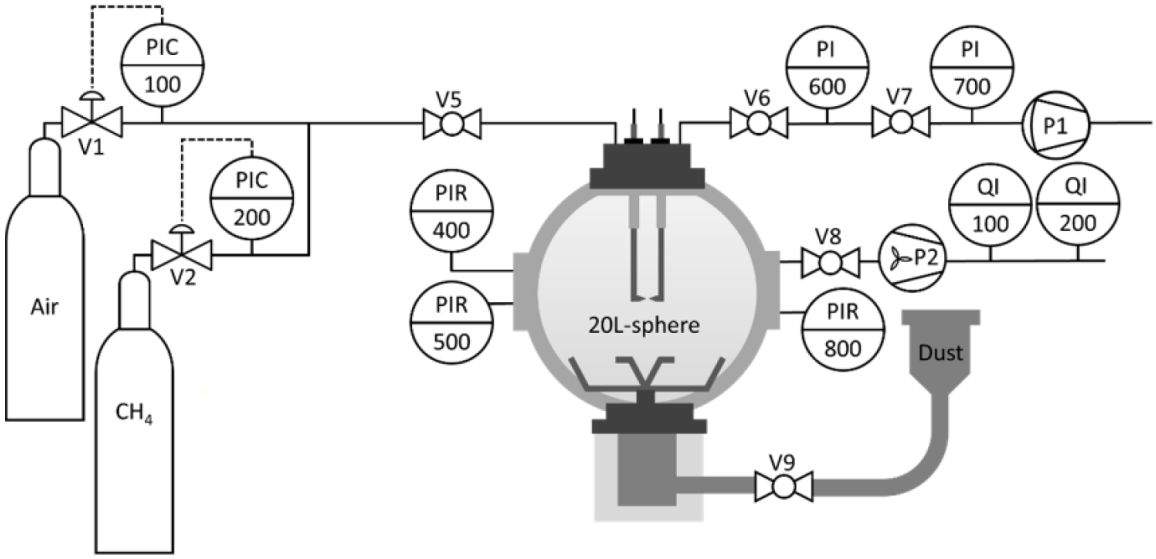

***Figure 2**: 20L-sphere with adaptions for hybrid mixture testing (Spitzer et. al., 2022b)*

2.1 Leakage rate

To ensure that the fuel gas concentration in the test volume can be adjusted precisely, the test apparatus must be as leak-proof as possible. Therefore, in a first step, the explosion chamber was evacuated below 5 mbar, the chamber closed, and the pressure rise recorded (**Figure 3**). The division of the leakage by the time is the leakage rate. With a typical time for mixture preparation of three to five minutes, the influence of the leakage-rate that was measured in the sphere on the accuracy of the gas mixtures can be neglected. After three minutes the detected pressure rise was 0.3 mbar leading to an error of the gas concentration of 0.03 mol%. Considering the great effort to achieve low leakage-rates in the 20L-sphere that was designed for dust-testing, the maximum permissible value of 1 mbar per minute was chosen for the standard operating procedure (DIN/TS 31018-1, 2023) and the round robin test contributing to the overall uncertainty of the mixture composition by 0.5 mol%. If the tests are always conducted in the same way and in a comparable time this deviation is systematic and can therefore be adjusted.

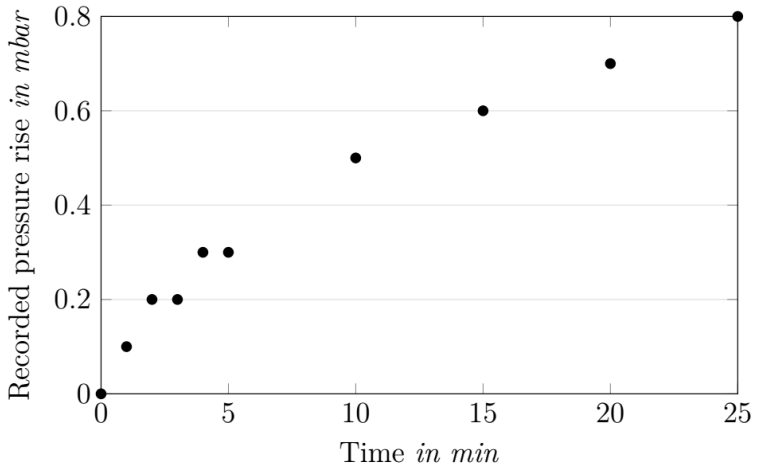

***Figure 3**: Pressure over time inside the 20L-sphere (initial pressure set to 0)*

2.2 Influence of pre-ignition pressure rise (PIPR) and post-injection pressure drop (PIPD)

When investigating hybrid dust/gas mixtures, it is particularly important to establish the exact fuel gas concentration in the explosion chamber. Spitzer et al (2022a) have shown that mixing using the partial pressure method may lead to inaccurate fuel gas concentrations. In the worst-case scenario, this could possibly result in an incorrect limiting oxygen concentration, that does not lead to successful inerting. The pressure inside the 20L-sphere before injection of the dust, the difference between the pressure in the sphere at the time of ignition and before injection of the dust (or Pre-ignition pressure rise, PIPR) and the subsequent pressure drop (post injection pressure drop, PIPD), that occurs due to thermodynamic equilibration by dissipation of the heat induced previously by adiabatic compression inside the sphere have to be taken into account for calculating the amount of flammable gas correctly in case of hybrid mixtures and to obtain robust and reproducible results for the determination of safety characteristics. According to the American Standard (ASTM E1226, 2019) a pressure before injection of 0.4 bar a and a pressure at the ignition moment between 0.94 bar a and 1.06 bar a are demanded for the tests but no accuracy of the pressure measuring system is mentioned. According to the EN 14034 series a pressure before injection of 0.4 bar a and an accuracy of the pressure measuring system of ± 0.1 bar is suitable resulting in a pressure before injection of the dust of 0.3 bar a to 0.5 bar a (EN 14034 part 1-4, 2011). It should be clear, that the explosion overpressure will increase with increasing PIPR, which is mainly due to the higher initial pressure at the moment of ignition in the 20L-sphere, even though conditions might be within the acceptable range, that is mentioned in the standards.

If hybrid mixtures are tested, variations of the PIPR additionally have a strong influence on the accuracy of the gas mixture, if the mixing is conducted inside the chamber (and not conducted with premixed gases), what is usually the case. Therefore, the allowed variations should be narrowed and the PIPR should be stated with all test results.

In addition, according to Spitzer et al. (2022a) the PIPR has an influence on the so-called post injection pressure drop PIPD, which increases with higher initial pressures. Why is this the case and what does the PIPD mean? In accordance to the standard procedures the whole mixture should have 1 bar a (ASTM E1226, 2019) or 1.013 bar a (EN 14034-1, 2011) after the fast injection of the combustible substance or mixture via pressurized air from the storage container and the pressure is recorded. Normally the ignition takes place shortly after the opening of the valve and this pressure shortly before ignition is usually taken as the initial pressure p_I and used for the calculation of the flammable gas fraction. However, the temperature rise due to the compression is not considered in the standard procedures. Especially, in case of hybrid mixtures, if this initial pressure is used for calculating the amount of flammable gas according to the partial pressures, this leads to wrong results. The effect of adiabatic compression is not mentioned in any standard and has not been found in research articles so far. Poletaev (2021) observed the temperature increase when air is added to the test vessel and Cashdollar (1996) observed the temperature increase while and decrease after the injection process.

For determining the safety characteristics of hybrid mixtures greater variations in the concentration of the flammable gas have an influence on the test result, so it is necessary to reduce this variation to an acceptable level. For this purpose, the PIPR and PIPD should be measured precisely, and test gas fractions were calculated according to following equation 1, with p_{Gas} [bar] being the partial pressure

of the flammable gas, PV the Partial Vacuum before injection of the dust (0.400 bara ± 0.002 bar) and a pre-ignition pressure rise (PIPR) of 0.64 bar ± 0.01 bar:

$$c_{Gas} = \frac{p_{Gas}}{(PV+PIPR-PIPD)} - Deviation_{Average} \quad (1)$$

It is also advisable to measure the gas concentration after injection (without ignition) to ensure that the exact gas concentration is produced. Only then should explosion tests be carried out with the corresponding concentration. Equation (1) was used for both, the oxygen concentration and the flammable gas and both were determined before the test series. The initial amount of air inside the dust container is covered by the "$Deviation_{Average}$"-term in the equation and was in our case 0.7 mol%

2.4 Characterization of tested corn starch

Corn starch and methane were selected to validate the test method for determining the LOC of hybrid dust/gas mixtures. This is because both components have a very similar LOC. The LOC of the analyzed corn starch is 12 mol% with nitrogen as inert gas, while the LOC of methane is 11 mol%. In this way, it should also be investigated whether the LOC of hybrid mixtures can lead to overlapping and therefore more critical values in comparison to the single components.

The particle size distribution of a dust sample has a significant influence on the explosion behavior. For this reason, the particle size was measured with a MALVERN Mastersizer 2000 before the start of the tests. This optical measuring method is based on measuring the scattering of the light by diffraction of a laser beam. The results are illustrated in **Figure 4**.

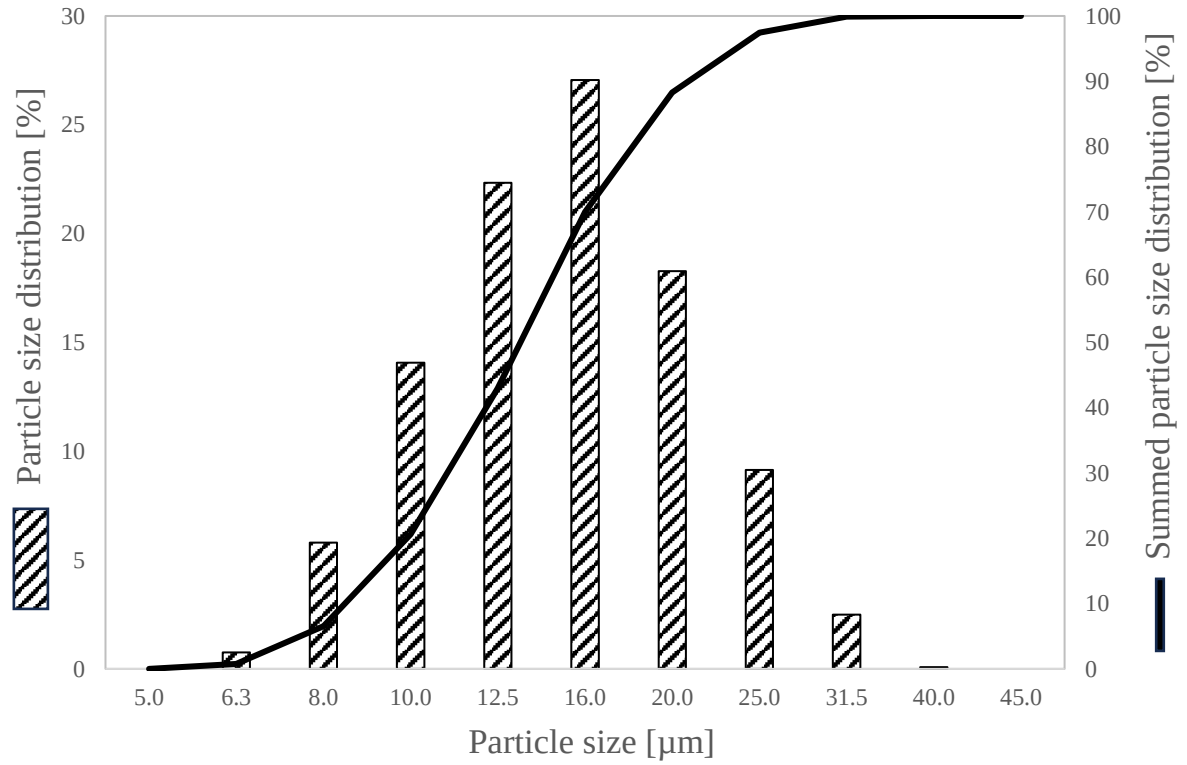

***Figure 4**: Particle size distribution of tested corn starch*

In addition to the particle size, the moisture content of a sample can also have an influence on the explosion behavior. For this reason, the moisture content was measured weekly during the test period to rule out changes and to ensure comparability of the measurement results. The tests were carried out with a Sartorius MA 35 moisture analyzer (see **Figure 4** left side). The corn starch was dried for 15 minutes at a temperature of 115 °C and the weight loss between the starting weight and the weight at the end of the measurement is then calculated. The water contents and particle size distributions (if they were determined) are shown per week in **Figure 4** (right side). The water content remained relatively constant over all weeks between approx. 7.2-7.9 weight % and the particle size distribution also showed very little variation (median between 13.1-13.9 µm). From this it can be concluded that the essential properties of the dust sample remained very constant over the entire test period.

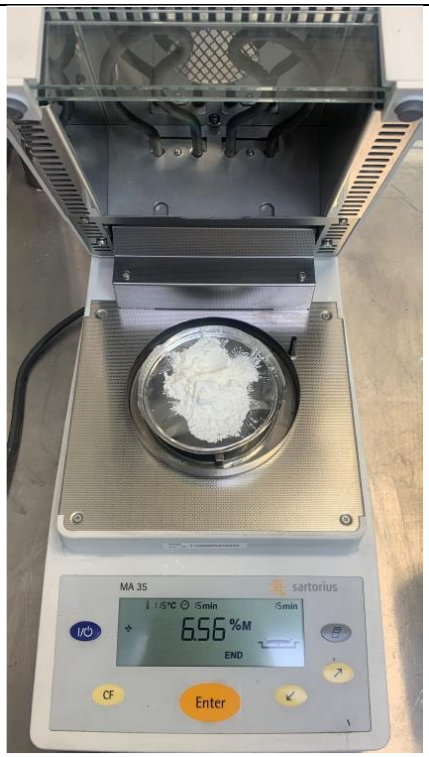

	moisture content [weight-%]	median particle diameter [µm]
week 1	7.7	13.8
week 2	7.43	-
week 3	7.56	13.9
week 4	7.46	13.9
week 5	7.5	13.8
week 6	7.23	13.3
week 7	7.94	13.3
week 8	7.55	13.3
week 9	7.35	-
week 10	7.31	13.6
week 11	7.19	-
week 12	7.37	-
week 13	7.28	13.1
week 14	7.28	13.1
week 15	7.23	13.6

***Figure 5**: Moisture analyser (left) and moisture content and median particle size over time of tested corn starch (right)*

3. Results and discussion

The following chapter presents the results of the experiments with the test setup and the adopted operating procedure. Firstly, it was important to investigate the influence of the degree of turbulence and the ignition energy on the LOC of methane. In a second step, the limiting oxygen concentration of the dust and the hybrid dust/air mixtures were then analyzed. For this purpose, a few per cent methane was added to the dust.

3.1 Influence of turbulence on the limiting oxygen concentration of methane

The ignition source and energy did not affect the determined limiting oxygen concentration of methane when tested under quiescent conditions. However, under turbulent conditions that are normally present when hybrid mixtures are tested, the measured LOC-value increased from 11 mol% determined at quiescent conditions to 13 mol% with an ignition energy of 20 J, even at 14 and 15 mol% only every third respectively two of three tests showed an ignition (**Figure 6**, left side). The

determined LOC might lead to unsafe safety measures since inerting is typically applied with the LOC minus a safety margin of three mol% as described e.g. in the German TRGS 722 (2021). Increasing the ignition energy from 20 J to 200 J, the determined value of the LOC decreased from 14 mol% to about 12 mol% under turbulence. This is closer to the literature value of 10.7 mol% but the deviation is still on the unsafe side (**Figure 6**, right side).

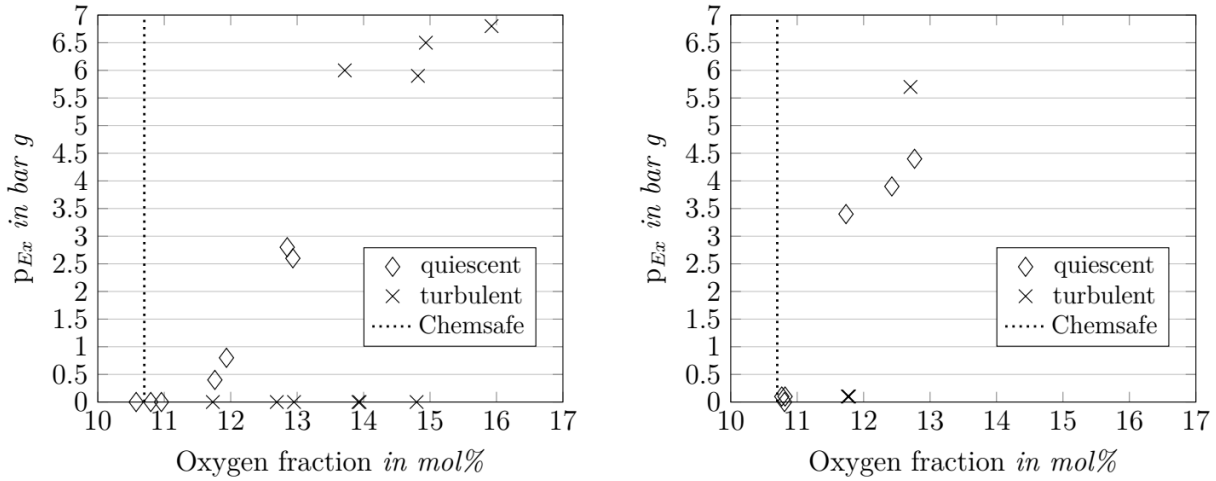

***Figure 6**: Explosion overpressures for stoichiometric methane-mixtures with different oxygen concentrations with 20 J (left) and 200 J (right) ignition energy*

A further increase of the ignition energy to 2 kJ led to the same value for the LOC under turbulent conditions of 10.7 mol% (or with 11 mol% close to that) as found in the literature determined according to the standard procedure for gases (EN 1839, 2017) under quiescent conditions and with an ignition energy of 20 J (see **Figure 7**, left side). Under quiescent conditions the ignition criterion (pressure rise) was just reached at an oxygen fraction of 10.8 mol% and clearly exceeded when the oxygen fraction was further increased by 1 mol%. Using the exploding wire with 2 kJ the explosion pressure was clearly increased, if the oxygen fraction was increased from 11 mol% to 12 mol% allowing a clear distinction between "ignition" and "non-ignition" for both quiescent and turbulent conditions. With the chemical igniters the LOC was as well 11 mol% with a pressure rise exceeding the ignition criterion at 12 mol% for turbulent conditions. However, the increase of the explosion pressure with increasing oxygen fraction is so flat that the distinction between "ignition" and "non-ignition" is difficult and that small changes in the experimental parameters might have resulted in unsafe values. A clear ignition with an explosion pressure clearly exceeding the ignition criterion of 0.5 bar g was not detected under turbulent conditions until 14 mol% (**Figure 7**, right side). Interestingly this is also the case for the quiescent mixture in which even the 20 J gave a clear rise at 12 mol%. This might be a result of the fact, that the chemical igniters consume oxygen and with that are influenced if the oxygen amount is decreased. This was demonstrated by carrying out tests with chemical igniters without dust in the 20L-sphere and then measuring the oxygen concentration in the explosion chamber. A slightly lower oxygen content was measured. It is true that the chemical detonators contain barium peroxide. However, the amount of barium peroxide does not appear to fully compensate for the oxygen required to burn the igniters.

In both, **Figure 6** and **Figure 7**, the methane concentration is half the oxygen concentration (stoichiometric mixture) and the plotted value of 10.7 mol% is taken from the Chemsafe database (PTB-BAM, 2024).

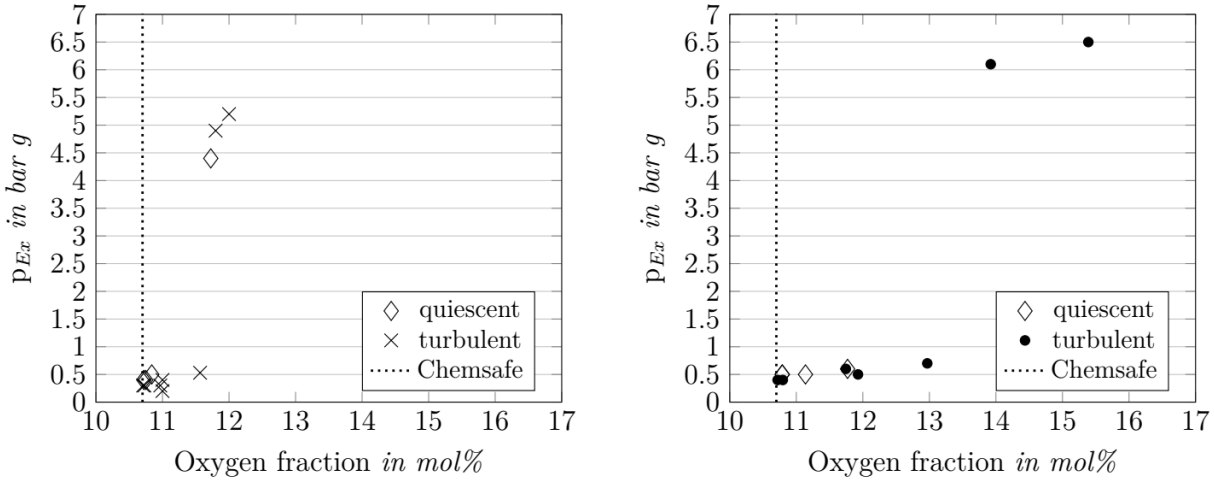

***Figure 7**: Explosion overpressure for stoichiometric methane-mixtures with different oxygen concentrations with 2 kJ ignition energy and exploding wires (left) and chemical igniters (right) as ignition source*

3.2 Influence of the ignition energy on the LOC of hybrid mixtures

The limiting oxygen concentration of the corn starch was determined according to the European standard (EN 14034-4, 2011) and in addition with different ignition sources and energies. Following dust concentrations have been tested: 125 g/m3, 250 g/m3, 500 g/m3 and 750 g/m3. The results are presented in Table 2. It can be seen clearly that the ignition energy should not be reduced below 2000 J for dusts when determining the limiting oxygen concentration since this would lead to conclusions on the unsafe side.

Table 2. Limiting oxygen concentration of corn starch with different ignition sources and energies

Ignition source	Ignition energy [J]	LOC [mol%]	LOC with 1 mol% CH_4 [mol%]	LOC with 3 mol% CH_4 [mol%]
Chemical Igniter	2000	12	12	11
Exploding wire	2000	11	11	11
Exploding wire	200	13	13	13
Exploding wire	20	17	16	14

However, the influence of the addition of 1 mol% and 3 mol% of methane was tested with the result, that the lowest ignition energy of 20 J did ignite at a closer value to the ones determined with high ignition energies, still being unsafe and not applicable. The determined value for 200 J and 2 kJ for the exploding wire did not change for all tested dust concentrations. The determined value for the chemical igniters is slightly lower and at the same level as the exploding wire with 2 kJ. This result shows that the introduced SOP can be used for hybrid mixtures and provides reliable, reproducible, and comparable results.

The connection to the test methods for single-phase substances is given as well. The ignition energy should be higher than the ones that are used for gases under quiescent conditions. An ignition energy of two times 1 kJ delivers the best results and especially for the LOC the exploding wire has the advantage of a clearly detectable pressure rise inside the explosion region (**Figure 7**).

5. Conclusions

The limiting oxygen concentration of a hybrid dust/gas-mixture consisting of corn starch and methane was investigated. The gas mixture was validated before the actual tests according to an existing standardized test method for the determination of other safety characteristics of hybrid mixtures. A special focus was also on the ignition source and energy to obtain reproducible results.

The key points are summarized in the following:

i) The ignition energy of 2 x 1 kJ is suitable for the tests, lower ignition energies shall not be used because of the extinguishing effect of the high level of turbulence that lead to unsafe safety characteristics

ii) The gas concentrations shall be checked and validated before starting the tests. Potential leakages of the sphere or other influencing factors may lead to false concentrations and with that to false safety characteristics

iii) Exploding wires are the better solution for the determination of the LOC since chemical igniters consume oxygen and with that lead to lower explosion pressures that may not exceed the threshold level of 0.5 bar g

iv) Because of the scattering of this dynamic test/mixing method, concentration steps of less than 0.5 to 1 mol% are not realizable and with that shall not be stated for hybrid mixtures

v) If the gas and the dust component have comparable LOCs, their combination has the same LOC since no “super-effect” (like the Bartknecht-curve for the LEL of hybrid mixtures (Bartknecht, (1981))) was observed

Acknowledgements

The authors would like to thank Alexander Benke for setting up the test equipment and Amir Reza Delalat and Sohail Irshad for their help conducting the tests in the 20L-sphere.

References

ASTM E1226, 2019. Standard Test Method for Explosibility of Dust Clouds. American Society for Testing and Materials.

ASTM 2079, 2000. Standard Test Methods for Limiting Oxygen (Oxidant) Concentration in Gases and Vapors. American Society for Testing and Materials.

Bartknecht, W., (1981) Explosions, course, prevention, protection. Springer-Verlag

Beck, H.; Glienke, N.; Möhlmann, C., 1997. Brenn- und Explosionskenngrössen von Stäuben. Technical report, Berufsgenossenschaftliches Institut für Arbeitssicherheit BIA.

Cashdollar, K. L., 1996. Coal dust explosibility. Journal of Loss Prevention in the Process Industries, 1996. DOI: 10.1016/0950-4230(95)00050-X.

DIN/TS 31018-1, 2023. Determination methods for safety-related parameters of explosion protection for hybrid mixtures of substances - Part 1: Gases.

EN 14034-1, 2011. Determination of explosion characteristics of dust clouds - part 1: Determination of the maximum explosion pressure p_{max} of dust clouds. CEN

EN 14034-2, 2011. Determination of explosion characteristics of dust clouds – part 2: Determination of the maximum rate of explosion pressure rise $(dp/dt)_{max}$ of dust clouds. CEN.

EN 14034-3, 2011. Determination of explosion characteristics of dust clouds – part 3: Determination of the lower explosion limit LEL of dust clouds. CEN

EN 14034-4, 2011. Determination of explosion characteristics of dust clouds - Part 4: Determination of the limiting oxygen concentration LOC of dust clouds. CEN.

EN 1839, 2017. Determination of the explosion limits and the limiting oxygen concentration (LOC) for flammable gases and vapours.

Poletaev, N. L., 2021. A change in the air temperature inside a 20-liter chamber when air is added from the receiver. Pozharovzryvobezopasnost/Fire and Explosion Safety, 2021.

PTB-BAM, 2024. Chemsafe online database (March 2024). https://chemsafe.ptb.de

Spitzer, S. H., Askar, E., Benke, A., Janovsky, B., Krause, U., and Krietsch, A., 2022a. Influence of pre-ignition pressure rise on safety characteristics of dusts and hybrid mixtures. FUEL, DOI: 10.1016/j.fuel.2021.122495.

Spitzer, S., Askar, E., Hecht, K. J., Gabel, D., Zakel, S., and Krietsch, A., 2022b. Requirements for a Hybrid Dust-Gas-Standard - Influence of the Mixing Procedure on Safety Characteristics of Hybrid Mixtures. fire, 5(4). DOI: 10.3390/fire5040113

Spitzer, S., 2023. Influence of the ignition source on the safety characteristics of hybrid dust-gas mixtures. Dissertation, Otto-von-Guericke University Magdeburg. DOI: 10.25673/111748

TRGS 722, 2021. Vermeidung oder Einschränkung gefährlicher explosionsfähiger Gemische. Ausschuss für Gefahrstoffe (AGS). 2021.

Research on Fire Test of Liquid Hydrogen Dewar Storage Tank

Yi Sun, Wei Gao*

State Key Laboratory of Fine Chemicals, Department of Chemical Machinery and Safety Engineering, Dalian University of Technology, Dalian 116024, PR China

E-mail: *gaoweidlut@dlut.edu.cn*

Abstract

In this paper, 1000L liquid hydrogen Dewar storage tank fire test was carried out to investigate the state of the internal pressure in response to an external propane fire, the change in the tank state and the temperature of the hydrogen in the tank when the safety valve was activated. The results show that: as shown in Figure 1. The shell of the storage tank collapses inwardly after being burned by the fire and is tightly adhered to the inner liner; and the hydrogen in the tank was warmed up to 135K to 141K when the internal pressure is close to the start-up pressure of the safety valve (1.5MPa). Parameters related to the fire test of 500L and 1000L tanks were compared. The detailed parameters of the two tests are shown in Table 1.

Table 1. *Comparison of fire tests conditions between 500L and 1000L liquid hydrogen storage tanks*

Tank Volume/L	Filling Level/%	LH2 Capacity/L	Total Burning Time/min	Maximum Pressure /MPa	Whether the tank is deformed
500L	50%	250	33	1.14	No
1000L	20%	200	10.85	1.4846	Yes

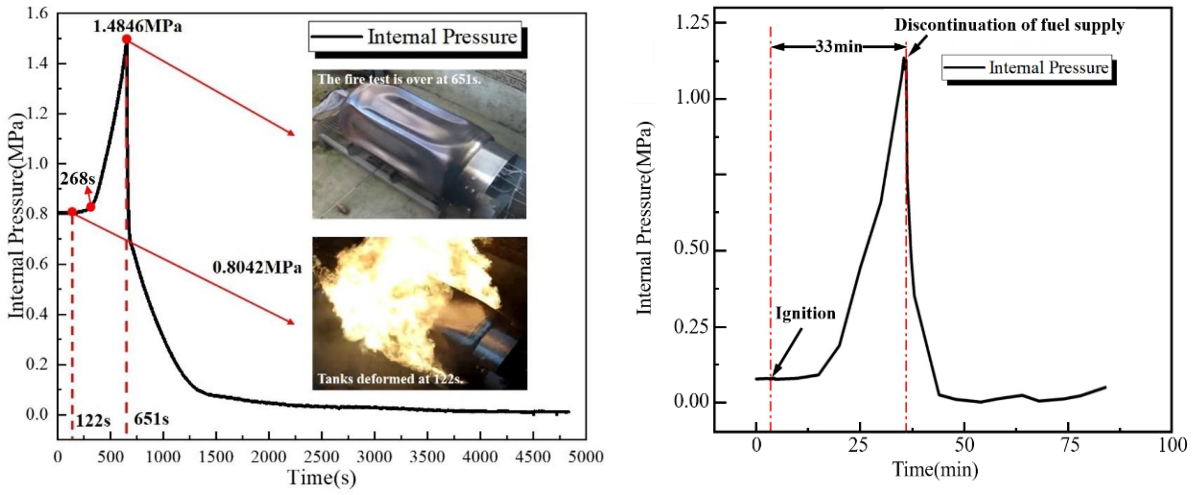

(a) Pressure changes in 1000L tanks

(b) Pressure changes in 500L tanks

Fig.1. *Two liquid hydrogen tank pressure change curves*

Keywords: *Liquid hydrogen storage tank, fire test; pressure response*

1. Introduction

Hydrogen as a fuel with high energy density (McAllister et al., 2011) has a heat of combustion of 121,061 kJ/kg compared to other common fuels such as gasoline with a heat of combustion of 44,467 kJ/kg, methane with a heat of combustion of 50,054 kJ/kg and ethanol with a heat of combustion of 27,006 kJ/kg. The heat of combustion of hydrogen is the highest among common fuels. When hydrogen is used to provide electricity for hydrogen-energy vehicles, the only products are water and heat(Fumey et al., 2018; Maggio et al., 2019). The cleanliness and high energy density of hydrogen can reverse the world's dependence on fossil fuels and move towards the use of clean and renewable energy sources. Hydrogen can be prepared from a wide range of raw materials, either by separating hydrogen from low-carbon hydrocarbons through separation technology or by electrolysis of water. As clean, renewable energy sources such as solar and wind power become more widely used, hydrogen can be produced by electrolysing water to produce hydrogen from its residual energy, greatly reducing pollutant emissions from the production process.

Hydrogen liquefaction is one of the most important methods to increase the density of hydrogen (71.279 kg/m^3 at 20K) (Landucci et al., 2008; NIST, 2019) and is widely used in the process of hydrogen storage and transport. In the liquefaction process, a catalyst is required and a large amount of energy is expended to convert all of the ortho-hydrogen (75% of ortho-hydrogen in conventional hydrogen) into para-hydrogen (Edeskuty and Stewart, 1996; Zhuzhgov et al., 2018). In order to avoid too rapid evaporation of liquid hydrogen, liquid hydrogen is usually stored in double-walled Dewar storage tanks with thermal insulation (Barthelemy et al., 2017). These Dewar storage tanks usually consist of having three layers from the outside to the inside, with the first layer being the external storage tank, the second layer being the thermal insulation layer (evacuated and filled with a combination of insulating materials), and the third layer being the inner tank where the liquid hydrogen is stored (van Wingerden Kees et al., 2022). The insulation in the thermal barrier is usually perlite and the multilayer insulation (MLI), which isolates the external convective heat transfer and thermal radiation from entering the inner tank (Peschka, 1992). Transporting and storing liquid hydrogen in Dewar's tanks can increase the efficiency of energy transport and reduce losses during transport.

Hydrogen is a flammable and explosive colourless substance with a wide range of explosive limits. The safe utilisation of hydrogen is a very important issue when applying it to industries such as automotive and transport. The utilisation of hydrogen raises the demand for risk handling, and an emerging technology often creates new risks due to people's lack of experience and knowledge (Jovanović and Baloš, 2013). For example, the occurrence of a BLEVE phenomenon in a tank filled with liquid hydrogen due to an external shock is an extremely serious accident (Rigas and Sklavounos, 2005).The occurrence of a BLEVE usually results in the formation of overpressure shocks, projectiles, and fireballs, and a number of scholars have already studied all three phenomena (Birk et al., 2007, 2006; Eyssette et al., 2021; Hemmatian et al., 2016; Laboureur et al., 2015).After the occurrence of BLEVE, a large amount of low-temperature liquid hydrogen will be spilled into the external environment with the rupture of the storage tank, and a huge overpressure is generated by the compression of surrounding air due to the flashing effect of liquid hydrogen. The volume of liquid hydrogen flash vapour instantly expands to 800 times, and with the air to form a huge premixed gas cloud (Center for Chemical Process Safety, 2010). The cloud is very easy to form an explosion or even explosion under the ignition of external fire and sparks, which poses a great threat to the safety of people's lives and properties. Tanks can fail and rupture due to a variety of external impacts, including flame impact, external impact, safety valve failure and so on. Among them, fire impact is the most common external impact. The flame impact is the most common external impact, including jet fire, oil pool fire, etc., whose high temperature will reduce the mechanical strength of the tank wall, prompting the evaporation of the material inside the tank to increase the pressure (Paltrinieri et al., 2009), triggering the rupture of the tank. However, the study of the liquid hydrogen BELVE accident is rarely mentioned in the literature. One test has been carried out by Pehr et al (1996) who carried out the liquid hydrogen tank test at BMW, observing overpressure, debris and fireball

phenomena. Wingerden et al. (2022) who carried out three times in the BAM 1m^3 double-walled liquid hydrogen storage tank fire test, obtained the tank heating process of the pressure, gas-liquid and temperature change curves, and the maximum overpressure was measured to be 0.13 bar at 22.5m and 0.1 bar at 26.4 m, respectively. Hansen et al (2020) in the Integrated Design for Demonstration of Efficient Liquefaction of Hydrogen project (IDEALHY) compared the similarities and differences between the BLEVE phenomenon in liquid hydrogen storage tanks and LNG storage tanks. Ustolin et al (2020) et al. in the Safe Hydrogen Fuel Handling and Use for Efficient Implementation project (SH2IFT) investigated the BLEVE phenomenon in liquid hydrogen storage tanks by means of experiments and modelling. Ustolin et al (2022) simulated the pressure changes in liquid hydrogen storage tanks exposed to fire using CFD methods, and the results showed that the simulation results matched well with the experimental results.

The purpose of this paper is to study the changes in internal pressure of 1000L liquid hydrogen Dewar tank during the fire process, and to provide data support for the subsequent study of the liquid hydrogen tank failure criterion and other elements.

2. Experiments

The fire test of the liquid hydrogen Dewar storage tank was conducted at Research Institute of China Academy of Aerospace Science and Technology Corporation sixth 101th in Beijing. The test site in the institute is a 5m×5m×3m (Length × Width × Height) deep pit shown as Figure 2, which is specially used to carry out experiments related to the performance testing of cryogenic tanks, eliminating the influence of ambient wind on the fire.

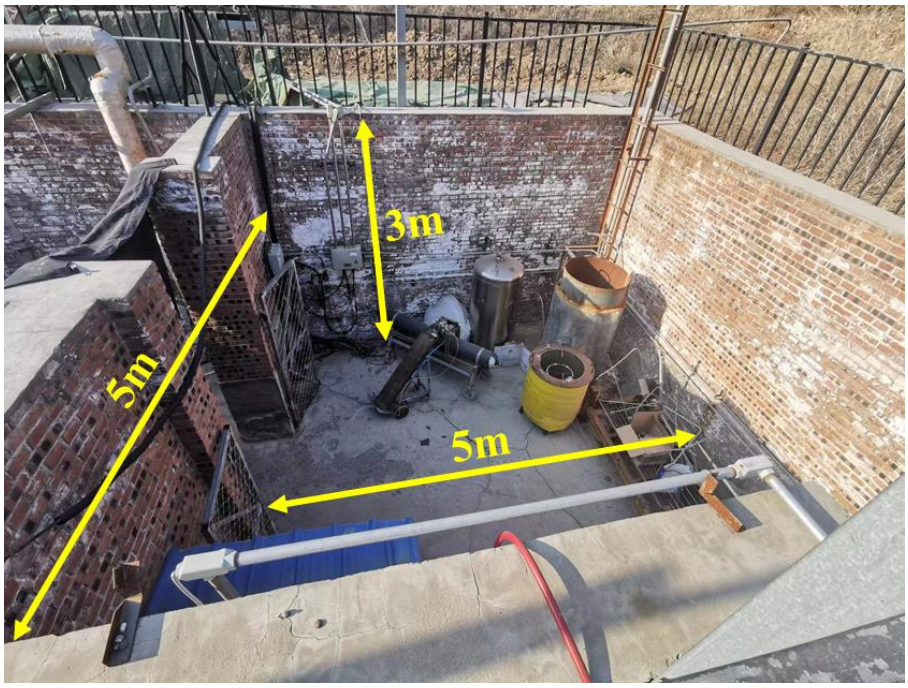

Fig.2. *1000L liquid hydrogen storage tank fire test site*

2.1. Test tank

The test tank with a nominal volume of 1,000L liquid hydrogen Dewar tank complies with China's management system standards GB/T19001-2016 and ISO9001:2015. The test tank is a horizontal tank consisting of an outer shell, the vacuum layer and an inner vessel. The insulation layer adopts high vacuum multi-layer insulation, winding more than 140 layers of P-type insulation paper (thickness less than 60mm) around the outer side of the inner vessel and the pressure of the vacuum

layer is 1×10^{-3}Pa. The materials of the outer shell and inner vessel of the test tank were both 316 stainless steel, which conformed to the requirements of the standard ASTM A240-05. The design wall thickness of both the tank shell and the head was 4 mm. In addition, the inner vessel was filled with LN2 to measure the static evaporation rate which was less than 1.0 %/d. Table 2 summarizes all relevant parameters of the tank. Furthermore, a pressure transducer P0 was installed in the gas phase region of the inner vessel to detect the pressurization pattern of the inner vessel during the fire test. Other piping components such as safety valves are arranged as shown in Figure 3. To prevent the propane fire from damaging the safety valve, a metal protective cover is welded to one end of the liquid hydrogen storage tank inlet.

Table 2. *Liquid hydrogen storage tank specifications*

Specification	**Property**
Nominal capacity (L)	1000
Length (m)	2.351（end to end）
Outer diameter of inner vessel diameter (m)	0.858
Outer diameter of outer shell diameter (m)	1.058
Interlayer leak (Pa • m^3/S)	≤5×10^{-9}
Leak disinflate speed rate (Pa • m^3/S)	≤6×10^{-7}

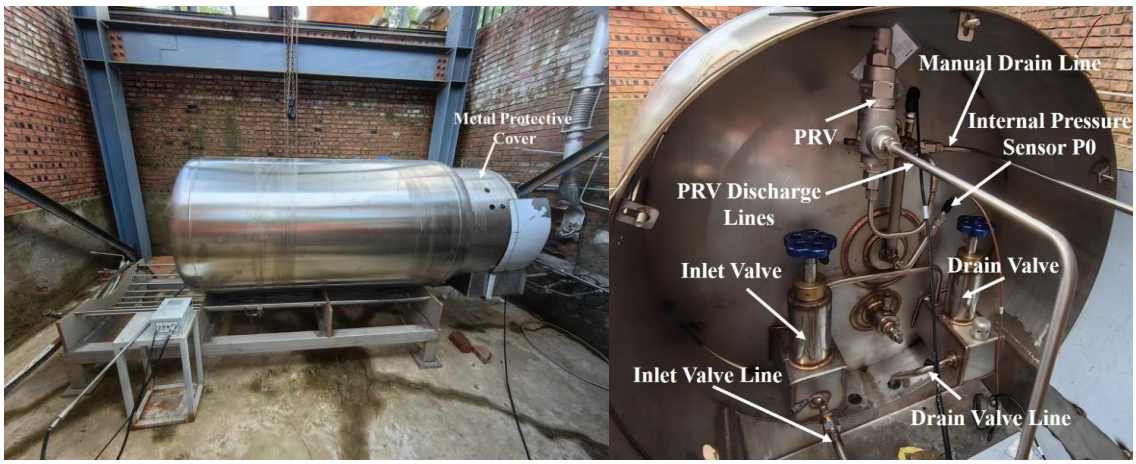

Fig.3. *1000L Liquid Hydrogen Storage Tank General and Component Drawing*

2.2. Fire system design

A gas burner fueled by propane gas was used as the fire source. In this way, the fire can be conveniently controlled and the fire properties can keep stable. The burner was 2.53 m long and 1 m wide as shown in Figure 4. The propane burner is divided into three sections, each section is equipped with 21 heating pipes, and a valve is installed between two adjacent sections to achieve independent heating of each section. The detailed parameters are shown in Figure 4.

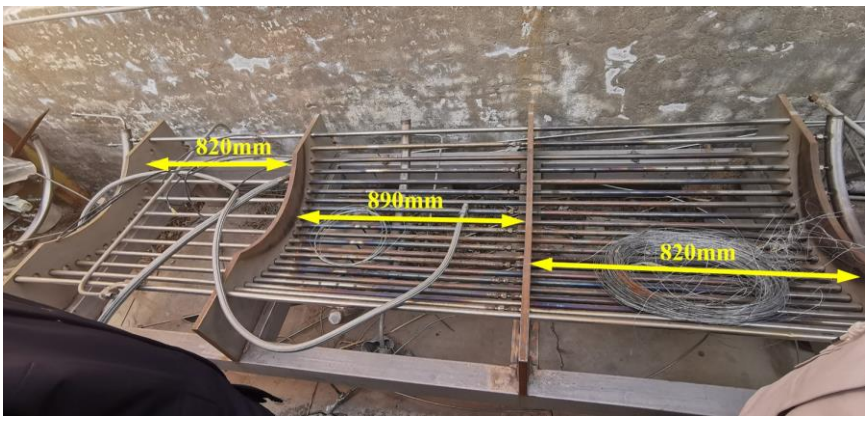

Fig.4. *Propane burner*

2.3. Instrumentation

Arrange 4 pressure sensors P1~P4 and 5 K-type armored thermocouples T0~T4 at the discharge guide pipe of the storage tank. The sensor arrangement is shown in Figure 5. Pressure sensors and thermocouples are used to measure the temperature and pressure parameters of two phases at the time of discharge, and can be used to calculate pipeline flow resistance and discharge flow rate. Many storage tank fire tests arrange thermocouples in the gas and liquid phases inside the tank to study the thermal stratification phenomenon of the liquid phase during the fire process. However, for such tanks with double walls, this plan is hard to realize because arranging multiple thermocouples or pressure sensors in the inner vessel will inevitably cause damage to all three layers particularly the vacuum layer, which will in turn cause the tank to rupture and explode. Therefore, in this test, only the pressure sensor P0 for measuring the pressure of the internal pressure was deployed.

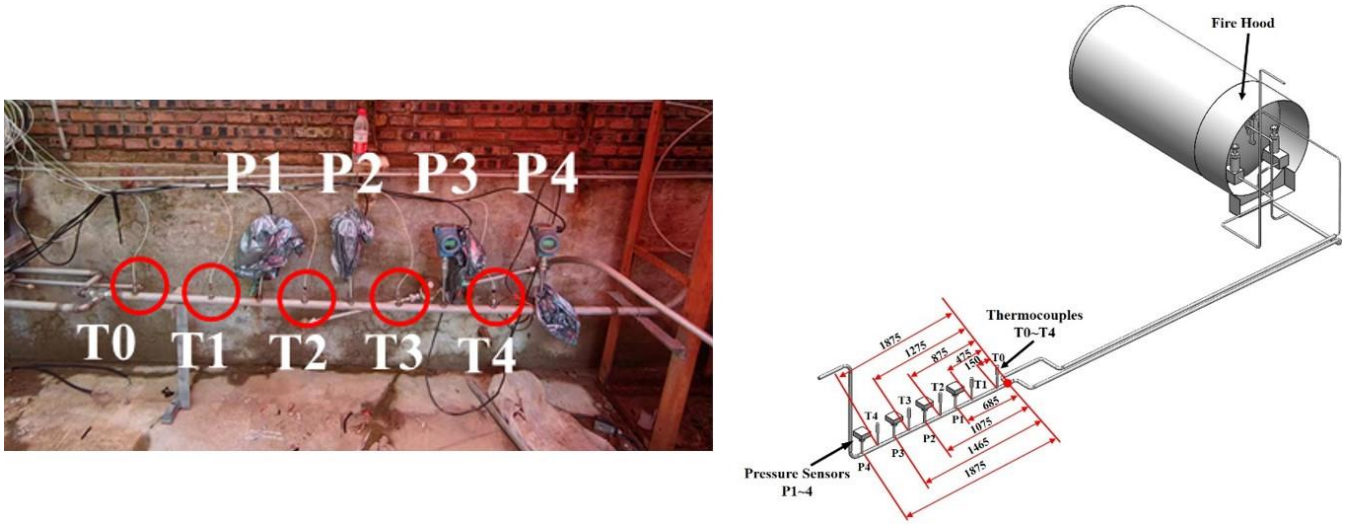

Fig.5. *Location of thermocouples and pressure sensors*

2.4. Propane test

The 1000 L tank was filled with 200 L of liquid hydrogen or 20% filling rate. It can be assumed that the heat released by the fire is radiated to the external environment in addition to a small part of the heat, most of the rest of the heat are transferred to the tank. In order to prevent the tank from failing and exploding and damaging the test site, a manual release was completed when the internal pressure approached 1.5 MPa. Figure 6 illustrates the three states of the storage tank throughout the fire process.

During the fire process, the outer wall of the tank was severely deformed, collapsing and pressing against the inner wall.

(a) Status of tanks before fire *(b) Tank status at time of fire*

(c) Status of tanks after fire

Fig.6. *Changes in the state of storage tanks when subjected to fire*

2.5. Fire condition

The temperatures measured by the two thermocouples T5 and T7 located at the bottom of the tank and tank wall temperature thermocouple T6 are shown in Figure 7. The temperature can be converted to a constant value by weighted averaging the temperatures. Therefore, temperatures of T5 ~ T7 can be 1127 K, 901 K, 862 K. Thermocouple T7 is measured by the tank wall temperature change, can be equivalent to the shell wall temperature into a constant temperature T_{wall} = 589 ℃. Formula (1) is used to calculate the heat flux which is 5.42kW/m^2.

$$q = \varepsilon_w \sigma \left(T_{fire}^4 - T_{wall}^4 \right) \tag{1}$$

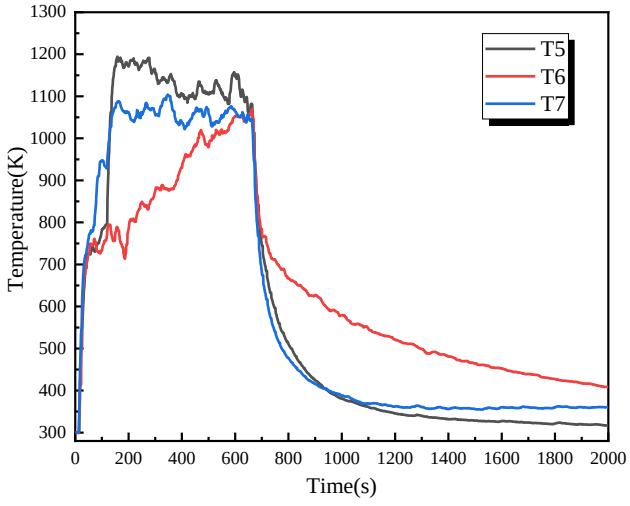

Fig.7. *Propane heater flame temperature*

3. Results and discussion

3.1. Results

The whole fire process lasted 651s (10.9min), then the PRV was opened manually, and the pressure of the tank was 1.4846MPa at the time of release while the internal pressure of the tank was 0.8032MPa at the beginning of the test. The shell was concave inward at 122s and the deformation lasted for about 1min. The reason for the deformation of the tank may be that the heat significantly reduces the strength of the outer wall and the support structure between out shell and inner vessel which leads to collapse under the atmospheric pressure. Due to the shell and the distance between the inner wall is reduced, the shell of the inner vessel of the supposed heat transfer intensity becomes larger, but through the Figure 8 can be seen in the 122s after the collapse of the tank, the rate of pressure rise did not have a significant increase. It shows that relative to the insulation layer, the insulation layer plays a major role in thermal insulation. the insulation layer has two main roles: a) to prevent direct contact between the shell and the wall of the inner liner, and b) to reduce the thermal radiation flux from the shell to the inner liner.

As shown in Figure 8 (a), the pressure response of the storage tank consists of a smooth pressure phase and a rapid pressure rise phase when it is subjected to fire impact. The internal pressure increases abruptly when the test is carried out to 268s, corresponding to Figure 8 (b), the pressure increase rate at 268s shows an increasing trend. The pressure curve after 268s is an externally convex monotonic curve, corresponding to Figure 8 (b) the rate of pressure rise is always positive. 268s is the cut-off time for the pressure rise, because before 268s, the heat mainly enters into the inner wall from the outer wall through radiation heat transfer and heat conduction slowly. And then the liquid hydrogen absorbs the heat and evaporates into a gas, which leads to a rapid increase of the inner pressure. 413s can be regarded as the evaporation of the liquid hydrogen, and then the tendency to increase the pressure rise rate is slowed down.

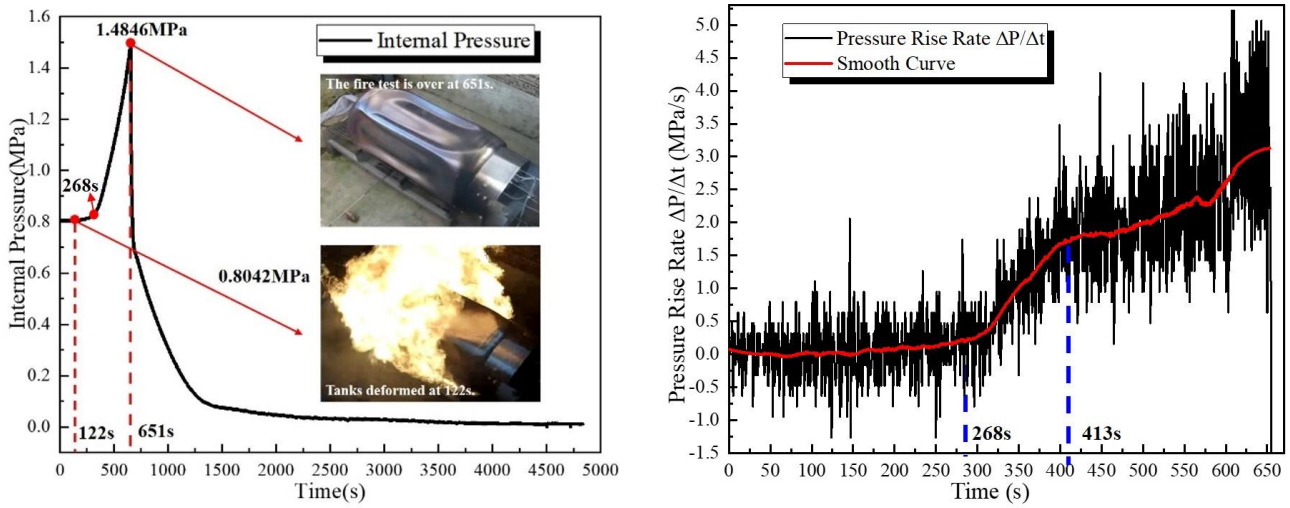

(a) Pressure change curve *(b) Pressure rise rate curve*

Fig.8. *Pressure change and pressure rise rate curve of 1000L tanks*

As shown in Figure 9 (a), the temperature measured by T3 thermocouple on the relief pipeline has a large deviation meaning T3 was damaged because of the low temperature. The temperature trend measured by the rest of the thermocouples is more or less the same, and reaches the lowest point of 141 K in 1095 s. It can be assumed that during the whole period of the fire test, the liquid hydrogen

is warmed up from 20 K to 141 K. Therefore, the substance in the relief pipeline is all hydrogen gas. Figure 9 (b) shows that after the tank discharged, the safety valve opens the instantaneous release of high-pressure hydrogen on the pipeline to form a high-pressure impact, and the maximum pressure is 0.0829MPa. Figure 9 (b) also shows that the relationship among the pressure of P1 ~ P4 is P1> P2> P3> P4. This is because the pressure is reduced by the pressure resistance during the flow.

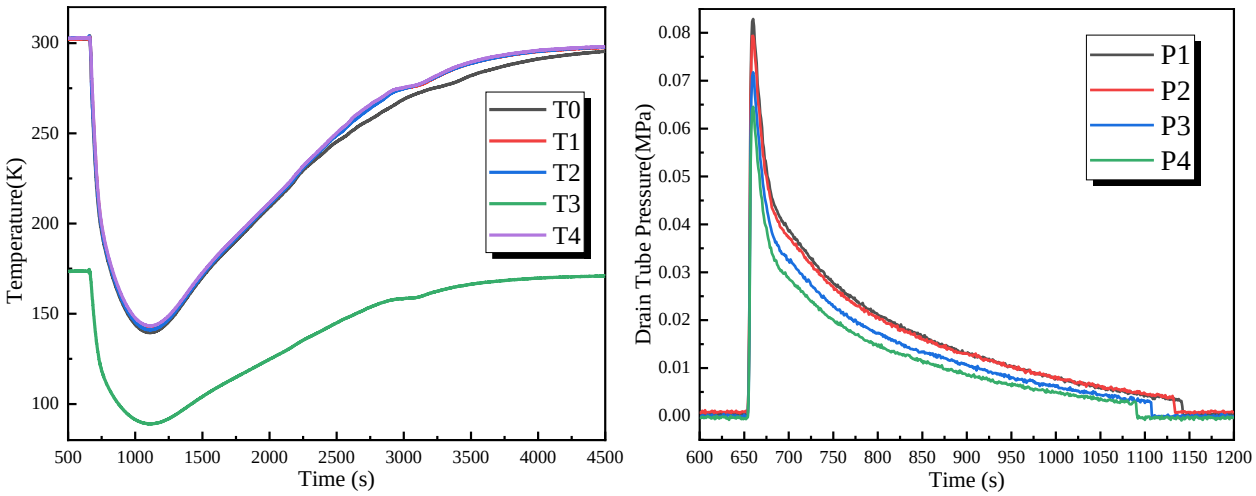

(a) Temperature profile of the released substance *(b) Pressure change in drain tube*

Fig.9. *Temperature and pressure diagram of the substance in the drain pipe*

3.2. Comparison of 500L and 1000L tank fire tests

The results of the fire test of 1000L liquid hydrogen storage tank are compared with some of the data of the fire test of 500L liquid hydrogen storage tank (filled with 250L of liquid hydrogen or 50% filling rate) conducted previously. The test process is shown in Figure 10. The whole process lasted 33 min and the fire temperature was kept between 650 K and 850 K. The initial pressure inside the tank was 0.11 MPa at the beginning and the internal pressure reached 1.14 MPa when the heating was stopped shown in Figure 11. A comparison of more parameters is shown in Table 3. The 500L tank was not deformed by the heat, which may be related to the low flame temperature. More tests need to be done to obtain data for targeted comparisons to obtain more instructive conclusions.

Fig.10. *500L liquid hydrogen storage tank fire test*

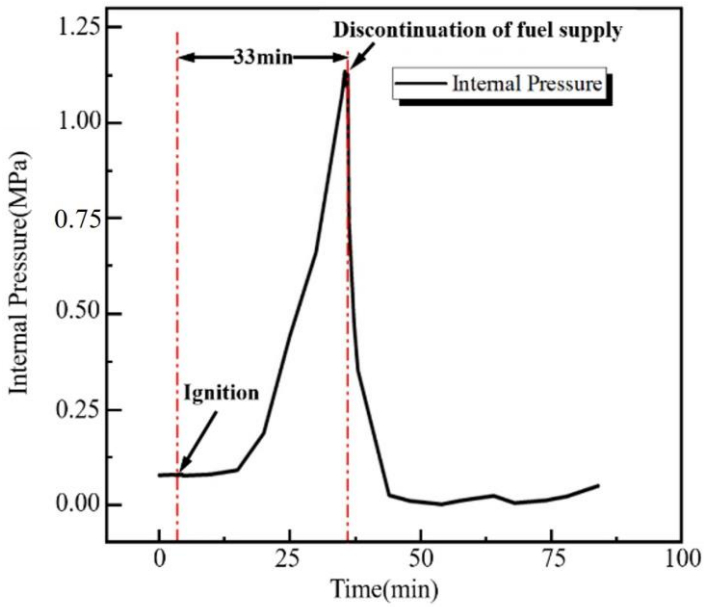

Fig.11. *Pressure changes in 500L tanks*

Table 4. *Comparison of fire tests conditions between 500L and 1000L liquid hydrogen storage tanks*

Tank Volume/L	Filling Level/%	LH2 Capacity/L	Total Burning Time/min	Maximum Pressure /MPa	Whether the tank is deformed
500L	50%	250	33	1.14	No
1000L	20%	200	10.85	1.4846	Yes

4. Conclusions

In this paper, fire test was carried out using a 1000 L liquid hydrogen Dewar tank with an industrial filling rate of 20%. A heater was used to generate a cover fire capable of wrapping the entire tank at temperatures between 1000K and 1200K. The tank internal pressure reached a maximum pressure of 1.4846 MPa after 651 s, and a manual release was subsequently performed to ensure the integrity of the test site. The lowest temperature of gas in the relief pipe was 141K and the maximum relief pressure was about 85kPa. The test data was compared with the data related to the 500L tank fire test.

Acknowledgements

The authors appreciate the financial support by the National Key R&D Program of China (No. 2021YFB4000902).

References

Barthelemy, H., Weber, M., Barbier, F., 2017. Hydrogen storage: Recent improvements and industrial perspectives. International Journal of Hydrogen Energy 42, 7254–7262.

Birk, A.M., Davison, C., Cunningham, M., 2007. Blast overpressures from medium scale BLEVE tests. Journal of Loss Prevention in the Process Industries 20, 194–206.

Birk, A.M., Poirier, D., Davison, C., 2006. On the response of 500gal propane tanks to a 25% engulfing fire. Journal of Loss Prevention in the Process Industries 19, 527–541.

Center for Chemical Process Safety, 2010. Guidelines for Vapor Cloud Explosion, Pressure Vessel Burst, BLEVE, and Flash Fire Hazards, 1st ed. Wiley.

Edeskuty, F.J., Stewart, W.F., 1996. Safety in the Handling of Cryogenic Fluids. Springer US, Boston, MA.

Eyssette, R., Heymes, F., Birk, A.M., 2021. Ground loading from BLEVE through small scale experiments: Experiments and results. Process Safety and Environmental Protection 148, 1098–1109.

Fumey, B., Buetler, T., Vogt, U.F., 2018. Ultra-low NOx emissions from catalytic hydrogen combustion. Applied Energy 213, 334–342.

Hansen, O.R., 2020. Liquid hydrogen releases show dense gas behavior. International Journal of Hydrogen Energy 45, 1343–1358.

Hemmatian, B., Planas, E., Casal, J., 2016. On BLEVE definition, the significance of superheat limit temperature (Tsl) and LNG BLEVE's. Journal of Loss Prevention in the Process Industries 40, 81.

Jovanović, A.S., Baloš, D., 2013. iNTeg-Risk project: concept and first results. Journal of Risk Research 16, 275–291.

Laboureur, D., Birk, A.M., Buchlin, J.M., Rambaud, P., Aprin, L., Heymes, F., Osmont, A., 2015. A closer look at BLEVE overpressure. Process Safety and Environmental Protection 95, 159–171.

Landucci, G., Tugnoli, A., Cozzani, V., 2008. Inherent safety key performance indicators for hydrogen storage systems. Journal of Hazardous Materials 159, 554–566.

Maggio, G., Nicita, A., Squadrito, G., 2019. How the hydrogen production from RES could change energy and fuel markets: A review of recent literature. International Journal of Hydrogen Energy 44, 11371–11384.

McAllister, S., Chen, J.-Y., Fernandez-Pello, A.C., 2011. Fundamentals of Combustion Processes, Mechanical Engineering Series. Springer New York, New York, NY.

Naryshkin, D.G., 2013. Possibilities of cloud educational technologies in the study of physical chemistry. CTE Workshop Proc. 1, 154–155.

Paltrinieri, N., Landucci, G., Molag, M., Bonvicini, S., Spadoni, G., Cozzani, V., 2009. Risk reduction in road and rail LPG transportation by passive fire protection. Journal of Hazardous Materials 167, 332–344.

Pehr, K., 1996. Aspects of safety and acceptance of LH2 tank systems in passenger cars*1. International Journal of Hydrogen Energy 21, 387–395.

Peschka, W., 1992. Liquid Hydrogen - Fuel of the Future, first ed. Springer Vienna, Vienna.

Rigas, F., Sklavounos, S., 2005. Evaluation of hazards associated with hydrogen storage facilities. International Journal of Hydrogen Energy 30, 1501–1510.

Ustolin, F., Paltrinieri, N., Landucci, G., 2020. An innovative and comprehensive approach for the consequence analysis of liquid hydrogen vessel explosions. Journal of Loss Prevention in the Process Industries 68, 104323.

Ustolin Federico, Scarponi Giordano Emrys, Iannaccone Tommaso, Cozzani Valerio, Paltrinieri Nicola, 2022. Cryogenic Hydrogen Storage Tanks Exposed to Fires: a CFD study. Chemical Engineering Transactions 90, 535–540.

van Wingerden Kees, Kluge Martin, Habib Abdel Karim, Ustolin Federico, Paltrinieri Nicola, 2022. Medium-scale tests to investigate the possibility and effects of BLEVEs of storage vessels containing liquified hydrogen. Chemical Engineering Transactions 90, 547–552.

Zhuzhgov, A.V., Krivoruchko, O.P., Isupova, L.A., Mart'yanov, O.N., Parmon, V.N., 2018. Low-Temperature Conversion of ortho-Hydrogen into Liquid para-Hydrogen: Process and Catalysts. Review. Catal. Ind. 10, 9–19.

Experimental Investigation of Dust Explosion Risks in Black Mass from Lithium-Ion Battery (LIB) Recycling Plants

Chen Huang [a], Andrei Lipatnikov [b], Cecilia Lövström [a]

[a] Division of Safety and Transport, RISE Research Institutes of Sweden, Sven Hultins Plats 5, SE-412 58 Gothenburg, Sweden

E-mail: chen.huang@ri.se

[b] Chalmers University of Technology, Department of Mechanics and Maritime Sciences, SE-412 96, Gothenburg, Sweden

Abstract

Four black mass samples from different LIB recycling plants are experimentally investigated. The microscope images, particle size distribution, water content and organic carbonates are analysed. Dust explosion experiments are performed in a 20-L vessel. Parameters including dust concentration, ignition energy, ignition timing, dust injection pressure are varied. Results show that a 10-kJ ignition energy cannot generate high explosion overpressure, whereas an ignition energy of 20-kJ yields an explosion overpressure above 6 bar for black mass sample C at a concentration of 300 g/m^3. More research into combustible dust of black mass is needed to ensure a safe and cost-effective LIB recycling process.

Keywords: *Dust explosion, lithium-ion battery, LIB, recycling, black mass, particle size distribution, water content, organic solvent, process safety.*

Introduction

The Lithium-ion battery (LIB) is one of the most promising technologies to decarbonize different energy sectors. At the same time, growing number of LIBs in various applications presents a serious waste-management challenge at the end-of-life (EoL). In the pre-process prior to the hydrometallurgical process, there are many steps that involve handling of combustible dust, such as in the conveyer belt, mill, drying equipment, dust collector, etc. Several articles highlighted the dust explosion risks during battery recycling, e.g., for graphite dust (Kim et al. 2021, Yi et al. 2021, Yu et al. 2021, Ali et al. 2022). For instance, an explosion occurred at an old battery recycling plant of CATL with a capacity of 15 000 ton/year for battery ternary precursors on January 7th, 2021. It was unclear if the explosion was directly related to combustible dust. However, according to the recycling firm, the explosion was caused by waste aluminium foil caught fire in a garbage dump. The blast generated a mushroom cloud in the sky that could be seen from several kilometres away. The incident led to one fatality and 20 injuries (Argus 2021, Independent 2021). Another incident is that a 25-year-old man was seriously injured during an explosion at a battery factory north Sweden on November 4th, 2023. The explosion occurred during a maintenance of a cleaning equipment. The injured person was reported passed away on December 15th, 2023. The investigation showed that the explosion was related to aluminium dust (Gunnars 2024).

Furthermore, a report highlighted dust explosion risks associated with black mass which contains elemental lithium and organic carbonates (Sattar et al. 2023). The black mass is the main product of European LIB recyclers. It is created after crushing LIBs at EoL and contains mainly material consisting of the shredded cathodes and anodes of the batteries. It may also contain small amounts of

copper, aluminium, iron, lithium hexafluorophosphate ($LiPF_6$), electrolyte, separator, etc. There is no standard of composition of black mass, which varies widely due to the use of different recycling processes and the feed materials. There is little knowledge about the dust explosion risks associated with black mass during LIB recycling process. This paper (i) reports preliminary dust explosion data obtained in experiments with black mass associated with Nickel-Cobalt-Manganese (NCM) battery chemistry and (ii) discusses some future research needs.

1. Black mass dust samples

Four types of black mass material were provided by two LIB recycling firms. These samples were obtained in mechanical processes using LIBs associated with NCM chemistry. In the following, the samples are named A, B, C, and D. The first three samples were provided by one LIB recycling factory and sample D was given by another LIB recycling facility. Before explosion tests, certain material properties were measured, as reported in next subsections.

1.1. Microscope images

Black mass was investigated using a microscope. The obtained microscope images show that samples A, B and C from one LIB recycling plant contain larger pieces of particles, probably copper and aluminum foil, when compared to sample D; see Figure 1. Moreover, sample D shows obvious agglomeration, which is not very well observed for samples A, B and C.

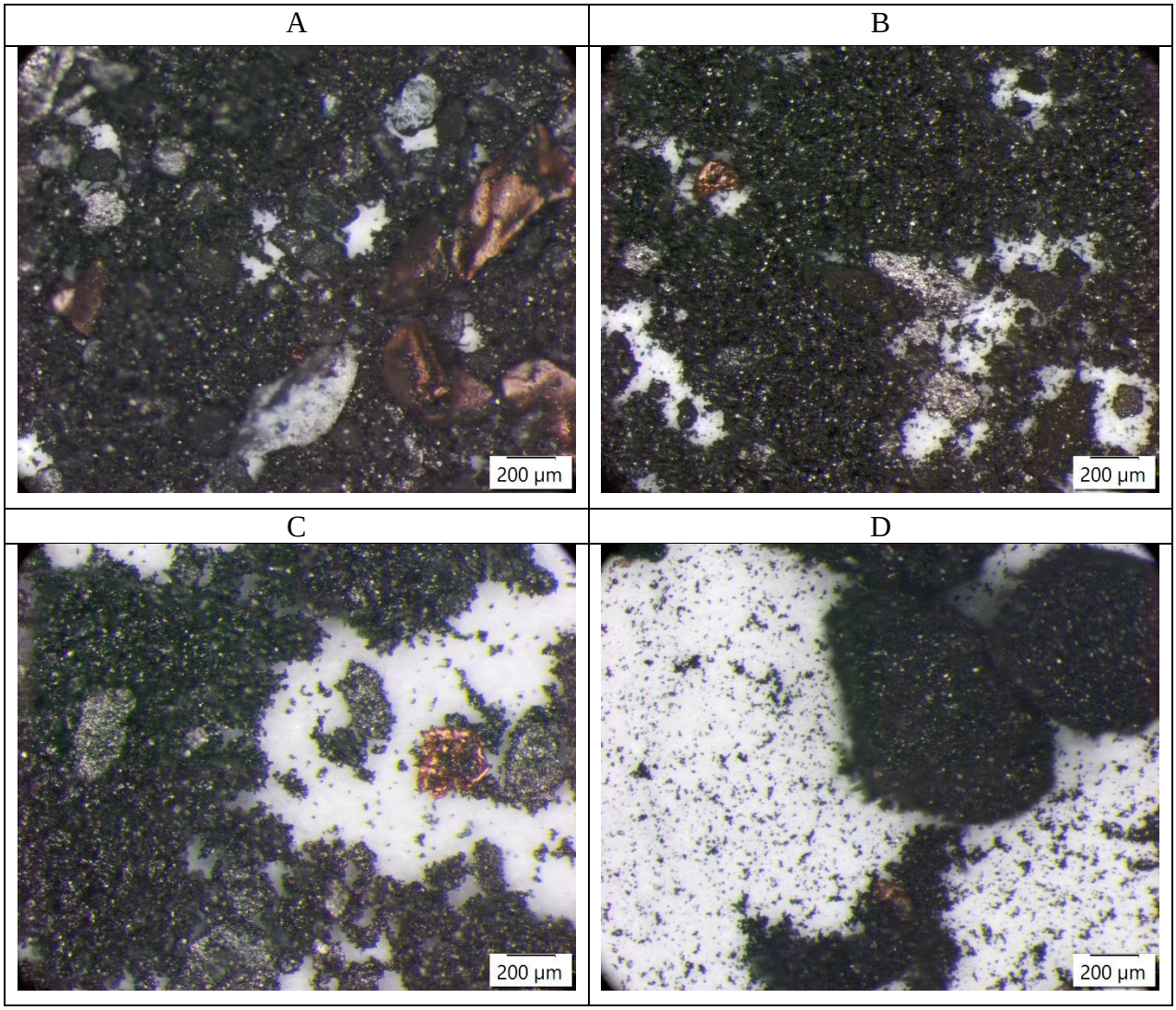

Fig. 1. *Microscope images of samples A, B, C, and D.*

1.2. Particle size distribution and water content

Particle size distributions were measured using a sieve shaker manufactured by Retsch of series AS200 control, equipped with sieve mesh sizes of 20, 32, 63, 75, 125, 180, 250, 350, 500, 600, 710, 800, 1000 μm and a sieve frame diameter of 200 mm. The sieves were arranged in a stack, with the coarsest sieve at the top and finest sieve at the bottom. The top sieve was filled with approximately one third of the volume with the powder material. When shaking the material in a 3-dimensional direction, particles larger than a sieve mesh size remained on the sieve.

The material weights on the sieves were then measured, and a particle size distribution was determined. The sieve shaker operated for 5 minutes with an interval operation of 10 seconds and a shaking amplitude of 1.6 mm. The test results obtained using a total material mass of about 100 g are shown in Figure 2. In addition, to quantify particle size distributions for different samples, several particle size parameters are reported in Table 1. Here, D_{10}, D_{50}, and D_{90} represent the particle diameters associated with 10%, 50%, and 90%, respectively, of the total particle mass, e.g., the mass of particles smaller than D_{10} is equal to 10% of the total mass. Moreover, the following parameter

$$\sigma_d = \frac{D_{90} - D_{10}}{D_{50}} \tag{1}$$

represents the span of a particle size distribution.

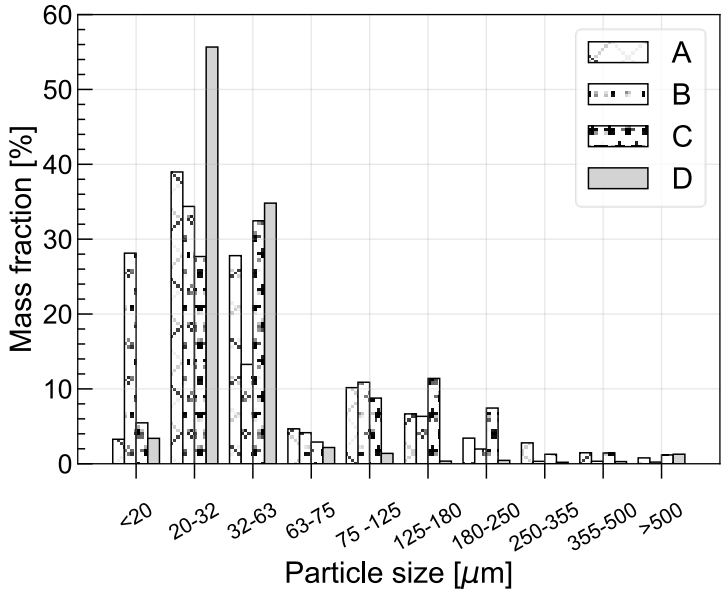

Fig. 2. *Comparison of particle size distributions of four black mass samples.*

In addition, Table 1 reports the water content (weight) determined using a Karl-Fischer Titration method.

***Table 1**. Characteristics of particle size distributions and water contents.*

Parameters	Sample A	Sample B	Sample C	Sample D
D_{10} [μm]	12.76	3.55	12.62	11.90
D_{50} [μm]	32.00	20.18	37.16	23.40
D_{90} [μm]	140.40	97.67	163.66	45.11
σ_d [-]	3.99	4.66	4.06	1.42
water content [-]	0.70%	0.36%	0.19%	0.36%

1.3. Organic solvents in black mass

Electrolytes used in LIB cells consist of organic solvents, such as various carbonates, and salts dissolved in the solvents (Wang et al. 2019). The organic solvents, constituting approximately 10 % of the cell mass, may ignite and burn in the presence of air (Ribière et al. 2012). The organic solvents may exist in black mass as impurities and may influence the dust explosion characteristics. Therefore, it is necessary to quantify the content of organic carbonates in the black mass.

Two distinct analytical approaches were employed. Initially, the black mass underwent extraction using dichloromethane (DCM) and was subsequently subjected to Gas Chromatograph Mass Spectrometer (GCMS) analysis. The second method utilized Head Space (HS)-GCMS, where the black mass underwent heating within the HS-vial for an hour at 150°C prior to analyzing the gas content above the material. The results obtained via GCMS are presented here due to its superior quantitative capabilities compared to the HS-GCMS method. Concurrently, HS-GCMS served as a supplementary technique for qualitative analysis, particularly in identifying volatile compounds within the black mass. Among the identified organic carbonates, ethylene carbonate ($C_3H_4O_3$) predominated, with minor traces of other compounds observed; refer to Table 2. Notably, Sample C yielded no detectable carbonates using the current methodologies.

***Table 2**. The content (weight %) of Semi Volatile Organic Compounds (SVOC) in black mass determined by GCMS method.*

Chemical	Sample A	Sample B	Sample C	Sample D
Ethylene carbonate [-]	2.99 %	0.014 %	-	3.00 %
Ethane-1,2-diyl diisobutyl decarbonate [-]	0.07 %	-	-	-
Ethylene glycol [-]	-	0.14 %	-	-
Propylene glycol [-]	-	0.08 %	-	-
N-Methyl-2-pyrrolidone [-]	-	0.07 %	-	-
Triphenyl phosphate [-]	-	-	-	0.12 %
4-(tert-Butyl)phenyl diphenyl phosphate [-]	-	-	-	0.12 %

2. Experimental setups

The dust explosion experiments were conducted in a 20 L vessel manufactured by Anko, as and sketched in Figure 3. First, a vacuum pressure of -0.6 bar gauge was created by evacuating air from the spherical vessel. Second, the dust sample was loaded into a pressurized container at 20 bar

gauge. Third, the dust was injected into the spherical chamber via a fast-actuating valve and a rebound V-shape nozzle. After the dust injection, a relatively homogenous dust-air cloud was formed and the pressure within the vessel stabilized at approximately 1 atm. Fourth, pyrotechnical igniters were employed to ignite the dust cloud after a variable ignition delay time, i.e., time interval between the dust injection and ignition. Fifth, the pressure curve $P(t)$ was recorded using dynamic pressure sensors. Finally, the rate of pressure rise was calculated by differentiating $P(t)$.

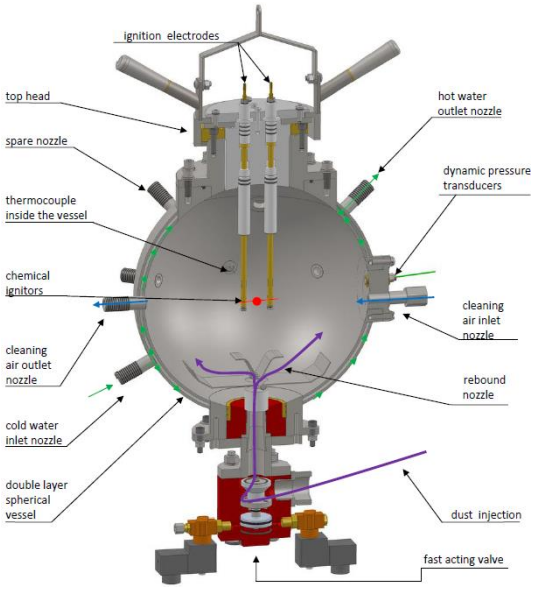

***Fig. 3**. 20-litre spherical vessel (Anko 2017).*

3. Results and discussion

Different parameters were varied to study black mass dust explosion, as summarized in Table 3. A total number of 72 experiments were performed in the 20-L vessel.

***Table 3**. Summarize of parameters and their variation range*

Parameters	**Variation range**
Material	A, B, C, D
Dust concentration [g/m3]	100, 125, 200, 300 400, 500, 600, 750, 1500, 2500
Ignition energy [kJ]	2, 10, 20, 30
Ignition delay [ms]	50, 60, 70 80
Injection pressure [barg]	19.6, 20, 20.4

Figure 4 shows a typical pressure-curve $P(t)$ and its derivative dP/dt in the case of successful ignition of a dust cloud. The focus of the following discussion will be placed on (a) the maximum explosion overpressure $P_{\max}$ and (b) the deflagration index, $K_{St} = (dP/dt)_{\max}V^{1/3}$, which is proportional to the maximum pressure growth rate $(dP/dt)_{\max}$, show in filled black-grey circles in Figures 4 (a) and 4 (b), respectively.

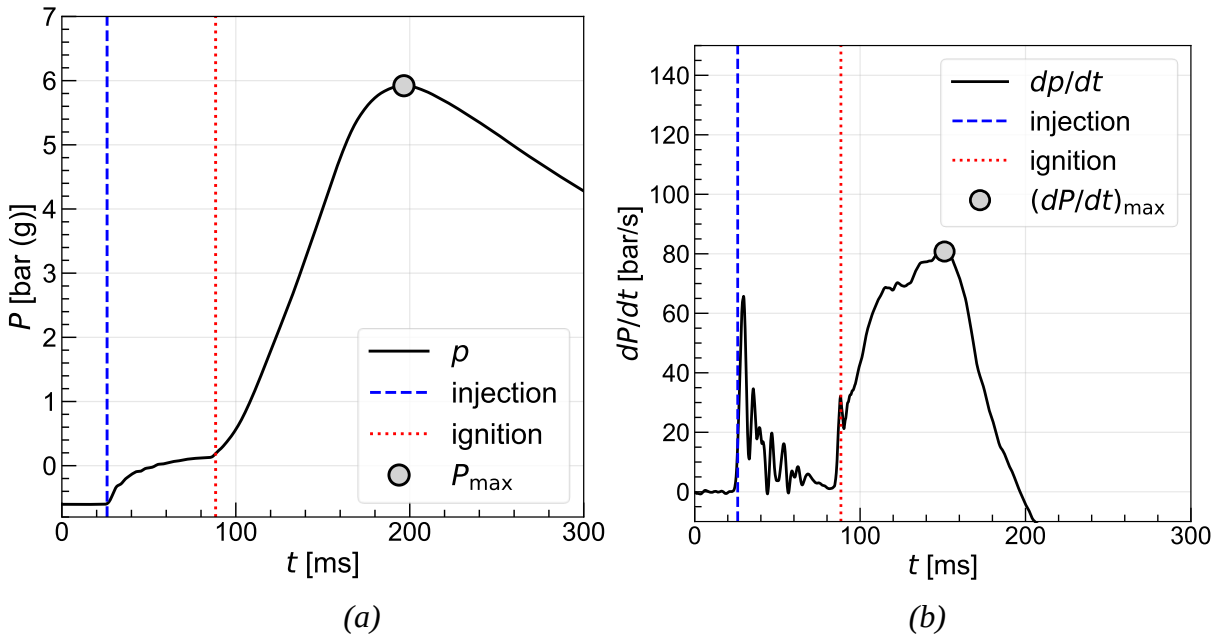

Fig. 4. *Explosion overpressure (a) and pressure rise rate (b) versus time for black mass sample C. Dust concentration is equal to 300 g/m^3. Ignition energy is equal to 20 kJ. Dust injection timing and the ignition timing are marked in blue dashed line and red dotted line, respectively.*

Black circles in Figure 5 (a) show that black mass dust explosion experiments with the 10 kJ ignitor have yielded an overpressure around 1 bar for all studied samples, thus, indicating weak explosion process. On the contrary, the 20 kJ ignitor is able to initiate sufficiently intense combustion of black mass, which yields a relatively high explosion overpressure; see red squares in Figure 5 (a), with dependence of the maximum explosion overpressure on dust concentration being typically of a parabolic shape. However, a further increase in the ignition energy weakly affects $P_{\max}$ for sample C, cf. red squares and blue diamonds. Dependence of the deflagration index K_{St} on dust concentration also has a parabolic shape when using the 20 kJ ignitor; see Figure 5 (b). However, there are large fluctuations in deflagration index for the 30 kJ ignitor. These fluctuations could be attributed to random variations in the dust cloud characteristics at the ignition instant and call for repeating each measurement several times.

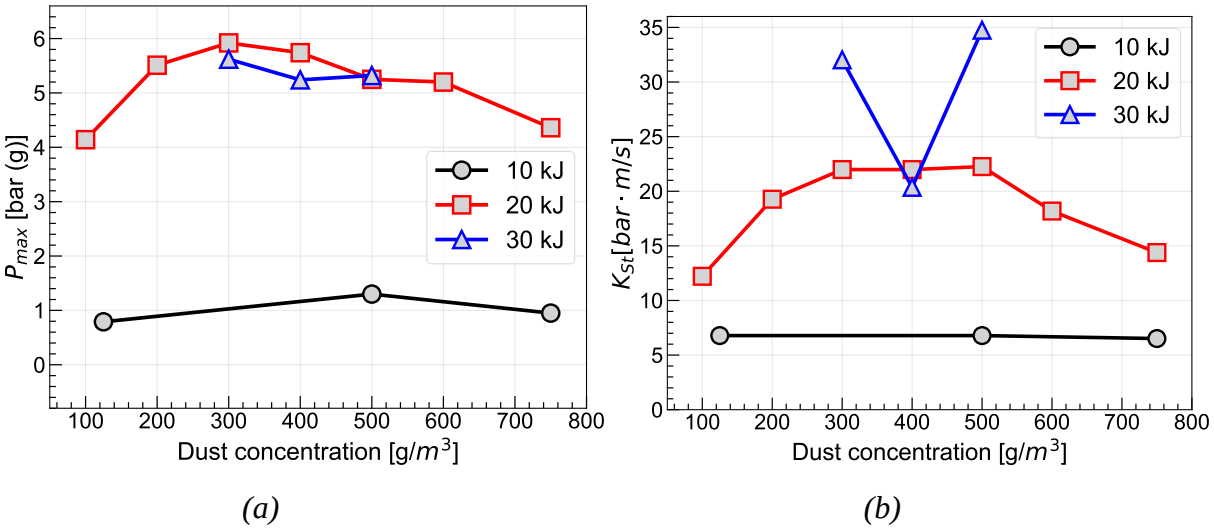

Fig. 5. *Maximum explosion overpressure (a) and deflagration index (b) versus concentration of black mass sample C at different ignition energies.*

Figure 6 reports the repeated dust explosion measurements for dust sample C at a concentration of 300 g/m^3 with an ignition energy of 20 kJ. The mean values for $P_{\max}$ and K_{St} are 5.89 bar (g) and

19 bar·ms^{-1} respectively. The standard derivation of K_{St} is higher compared to $P_{\max}$, c.f. 2.05 and 0.14.

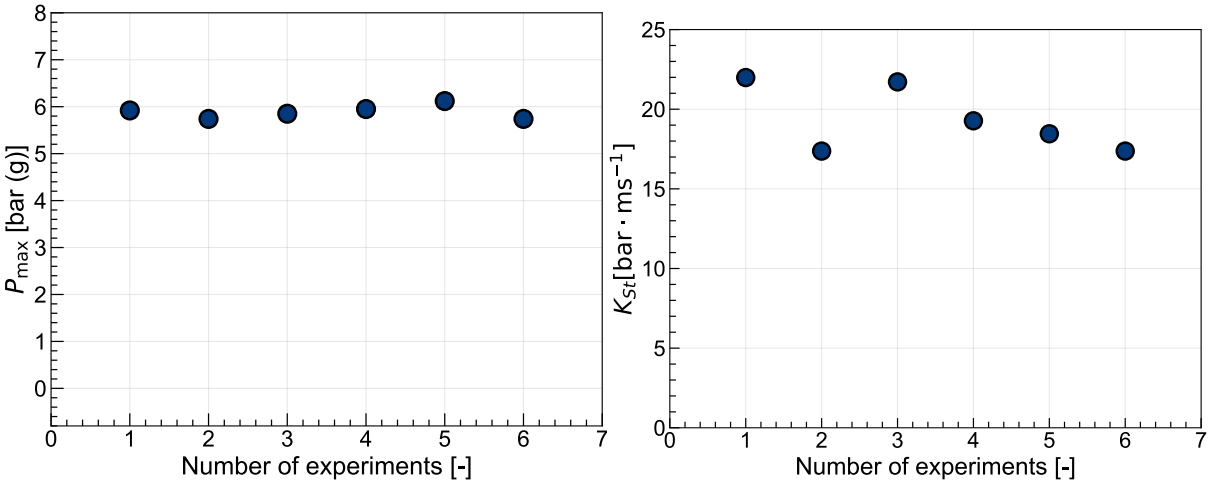

(a) *(b)*

Fig. 6. *Repeated dust explosion experiments for dust sample C at a concentration of 300 g/m^3 with an ignition energy of 20 kJ.*

Comparison of maximum explosion overpressures for different samples at a dust concentration of 500 g/m^3 and an ignition energy of 20 kJ is shown in Figure 7. Samples B and C generate $P_{\max}$ higher than 4.5 bar, whereas samples A and D yields a lower $P_{\max}$. Further research is required to explain the reasons. At a first glance, the differences could be attributed to different water contents; see Table 1, which shows that sample A has a relatively higher water contents compared to other samples. Alternatively, the difference could be due to different compositions of the black mass samples, because they came from different process plants with different compositions.

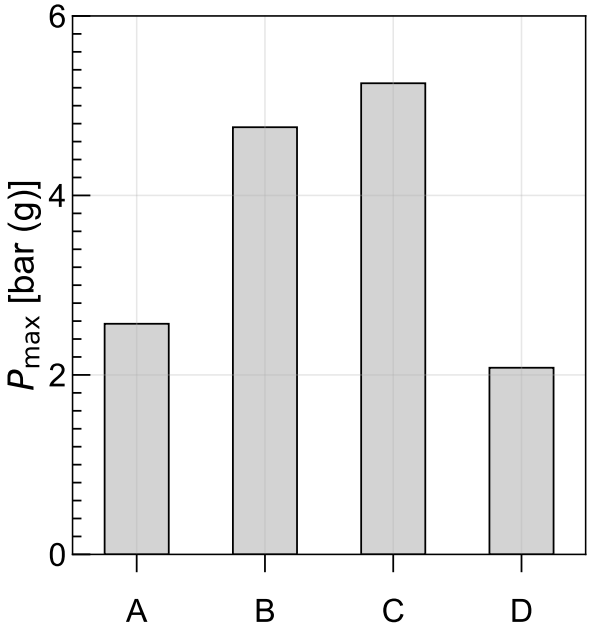

Fig. 7. *Maximum explosion overpressures measured for different black mass samples at the dust concentration of 500 g/m^3 and ignition energy of 20 kJ.*

The effect of ignition delay time on $P_{\max}$ is shown in Figure 8. The ignition delay time controls the dust distribution and turbulence characteristics in the vessel at ignition instant. For black mass powders B and C and ignition energy of 10 kJ, the highest $P_{\max}$ (but still low) was measured at ignition delay time of 70 ms, see black circles and red squares in Figure 8 (a). Note this delay time is

longer than recommended standard value of 60 ms. However, this standard delay time yields the largest P_{max} in the case of a higher ignition energy and intense dust combustion, see blue and violet triangles, which show results obtained from samples C and D, respectively, using ignition energy of 20 kJ and 30 kJ, respectively. Deflagration index is also largest in these two cases, see Figure 8 (b).

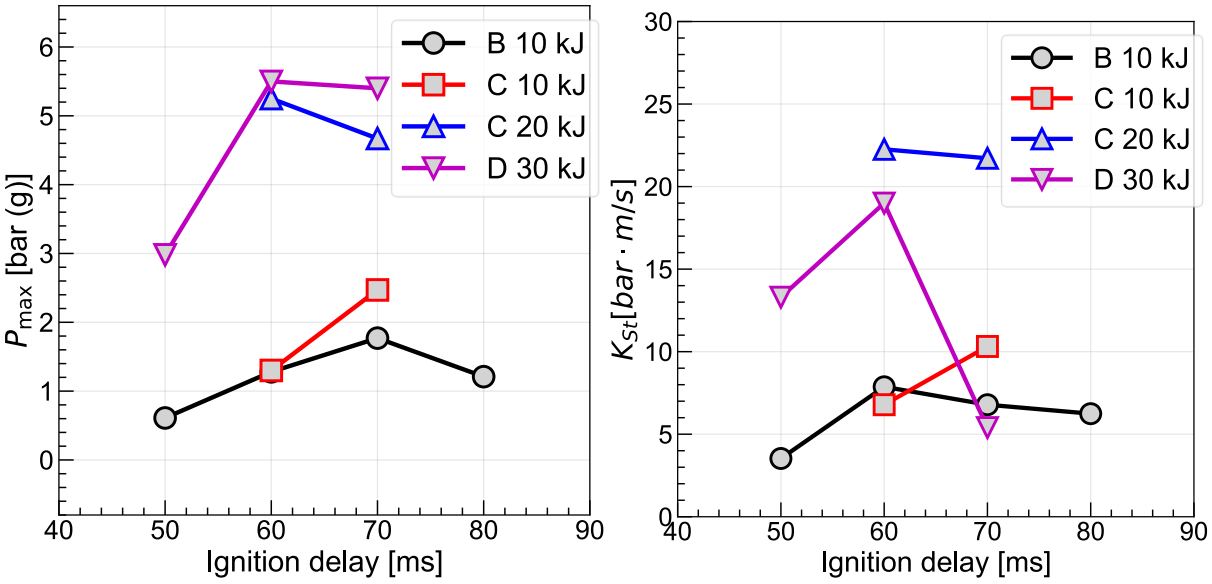

(a) *(b)*

Fig. 8. *Effect of ignition delay time on the maximum explosion overpressure (a) and deflagration index (b) for black mass samples B, C and D with various ignition energies.*

Maximum explosion overpressures measured using black mass sample C and varying the dust injection pressure are reported in Figure 9. P_{max} increases linearly with the injection pressure.

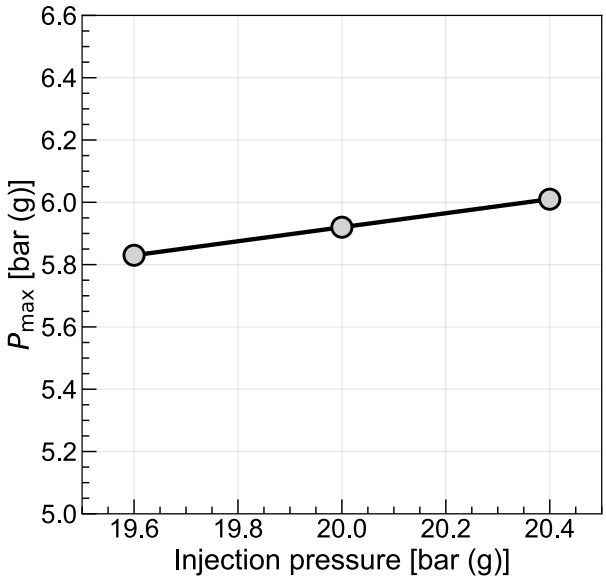

Fig. 9. *Maximum explosion overpressures measured for black mass C at the dust concentration of 300 g/m^3 and an ignition energy of 20 kJ.*

4. Conclusions

Four black mass samples from different LIB recycling plants were analysed to obtain dust sample microscope images, particle size distributions, water contents and organic solvents. Subsequently, dust explosion experiments were performed in a 20-L vessel by varying the dust concentration, ignition energy, ignition timing, and dust injection pressure. Results show that an ignition energy of

10 kJ is not sufficient to generate a high explosion overpressure, whereas an ignition energy of 20 kJ can yield an explosion overpressure above 6 bar for black mass sample C at a concentration of 300 g/m^3. So high ignition energy could be released during hot work like welding or fire. More research into dust explosion risks of black mass is needed to ensure a safe and cost-effective LIB recycling industry.

Acknowledgements

The Swedish Energy Agency is greatly acknowledged through SafeDust ReLIB project (number P2023-00060), a pre-study on dust explosion risks for LIB Recycling. The authors would like to acknowledge the support of Northvolt Revolt AB and Stena Recycling International AB for providing samples and for valuable discussions. Nathália Vieceli, Zari Musavi, Björn Hall, and Mengqiao Di are greatly acknowledged. Nijaz Smajovic, Leena Andersson, and Abdelrahman Ismail are acknowledged for their measurements of particle size distribution, water content and organic solvents. Michael Magnusson and Sven-Gunnar Gustafsson are acknowledged for their support in performing risk analysis for dust explosion experiments. Patrik Nilsson, Peter Lindqvist are acknowledged for their measurements of dust explosions in 20-L vessel.

References

Ali, H., Khan, H.A., Pecht, M., 2022. Preprocessing of spent lithium-ion batteries for recycling: Need, methods, and trends. Renew. Sustain. Energy Rev., 168, 112809.

Anko, 2017, 20-Liter sphere apparatus for determination of explosive characterises of dust clouds.

Argus, (2021). Explosion hits CATL battery precursors plant in China, accessed 28 November 2023, https://www.argusmedia.com/en/news/2175179-explosion-hits-catl-battery-precursors-plant-in-china.

Gunnars L., (2024). En dammexplosion i veckan – ändå missar företagen risken, accessed May 3rd, 2024, https://tidningenelektrikern.se/2024/04/29/en-dammexplosion-i-veckan-anda-missar-foretagen-risken/

Independent, (2021). Explosion at Chinese battery recycling plant kills one and injures 20, accessed November 28th , 2023, https://www.independent.co.uk/news/world/asia/explosion-blast-china-battery-fire-hunan-b1784643.html.

Kim, S., Bang, J., Yoo, J., Shin, Y., Bae, J., Jeong, J., Kim, K., Dong, P., Kwon, K., 2021. A comprehensive review on the pretreatment process in lithium-ion battery recycling. J. Clean. Prod. 294, 126329.

Ribière, P., Grugeon, S., Morcrette, M., Boyanov, S., Laruelle, S., Marlair, G., 2012, Investigation on the fire-induced hazards of Li-ion battery cells by fire calorimetry. Energy Environ. Sci., 5(1), 5271-5280.

Sattar, A., Cooper, L., Dowson, M., Greenwood, D., 2023, Health and safety considerations in Lithium-ion Battery Recycling.

Wang, Q., Mao, B., Stoliarov, S. I., Sun, J., 2019, A review of lithium ion battery failure mechanisms and fire prevention strategies. Prog. Energy Combust. Sci., 73, 95-131.

Yi, C., Zhou, L., Wu, X., Sun, W., Yi, L., Yang, Y., 2021. Technology for recycling and regenerating graphite from spent lithium-ion batteries. Chin. J. Chem. Eng., 39, 37-50.

Yu, D., Huang, Z., Makuza, B., Guo, X., Tian, Q., 2021. Pretreatment options for the recycling of spent lithium-ion batteries: A comprehensive review. Miner. Eng., 173, 107218.

Polymer dust explosion part II: Experimental tests

Enrico Danzi[b], Maria Portarapillo [a], Luca Marmo[b] & Almerinda Di Benedetto [a]

[a] Department of Chemical, Materials and Production Engineering, University of Naples Federico II, P.le V. Tecchio 80,
80125, Naples, Italy
[b] Dipartimento di Scienza Applicata e Tecnologia-Politecnico di Torino, C.so Duca degli Abruzzi 21, 10129, Torino, Italy

E-mail: maria.portarapillo@unina.it

Abstract

This paper follows the previous "Polymer dust explosion part I," which provides an overview of the literature on polymer dust explosion.

In this work, several dust samples were tested according to standard dust explosibility tests: explosibility, cloud and layer Minimum Ignition Temperature (MIT_C and MIT_L), Minimum Ignition Energy (*MIE)*, Maximum pressure rise p_{max}, maximum rate of pressure rise, *dp/dt*, and Lower explosibility limit (*LEL)*.

More tests, such as Fourier-transform infrared (FTIR), were also used to characterize the samples further and detect relevant features like chemical composition and particle size distribution (PSD). Additional characteristics were also studied through optical and electronic microscopy imaging (SEM) and moisture determination.

More than 90% of samples exhibited explosibility behavior and must be considered "explosible". Non-explosible samples were flocculent dusts that were almost impossible to disperse in the testing equipment or were high nitrogen-content samples.

A rank of explosion severity (namely in terms of maximum pressure rise and k_{St}) was drawn from the results. Generally, polyolefins exhibit more severe explosible properties than dust composed of more complex molecules (resins or polyesters). Particle size and morphology were relevant in determining more severe parameters. The greatest value was exhibited by PS/PPE dust mixture collected from a recycling plant: this revealed information on the likely synergistic effect of different polymers in the mixture and the potential hazard of different plastic industry sectors. Significative comparisons may be made between the present results and past literature studies. The explosibility ranking should be used as a reference for safety consultants in dust hazard analysis.

Keywords: *dust explosion, polymers, explosibility parameters*

Introduction

Plastics, as a generic term, are commonly referred to by the great public as something intrinsically flammable or suspected of fire hazards and flame propagation if involved in a fire. Polymers are likely explosible in the form of powder material of micrometric particles when suspended in a cloud confined in an enclosure and in the presence of an adequate ignition source. Most polymers are shaped in powder to be further processed by the plastic industry into final products: the plastic industry has been aware of dust explosion hazards for several years.

This work is conceived as the second part of a "polymer dust explosion" review, presenting experimental laboratory testing results on industrial samples obtained from the plastic industry and its affiliated sectors (recycling, finishing, waste disposal). While the first part (Marmo et al., 2024).

presented statistics and case histories, the deflagration parameters of various polymer-based dust are reported here and compared with relevant literature data, among those identified in Table 1.

While most literature studies are focused on specific polymer-based dust, this paper presents the results of commercial tests on real dust. Almost all samples are mixtures collected at industrial plant abatement systems, where different dust streams rather than pure polymer dust may be collected. This feature allowed us to trace a more comprehensive analysis of the actual industrial dust explosion risk, as collecting systems such as baghouse filters or cyclones serving different process lines necessarily include a mixture of different materials.

The "pure powder" results extracted from the literature are used to compare the influence of mixing polymers on explosibility behavior (see Table 1).

1 Overview of literature studies

The most referenced work in this field is the paper from the US Bureau of Mines (Jacobson et al., 1962), which presented a comprehensive collection of experimental tests performed on 241 dusts (comprising plastics, resins, and rubbers). Later, Echkoff, R. K. (2003) summarized the results of different authors. Echkoff's book presented a section where peculiar aspects of polyester and epoxy resins used in electrostatic powder coating processes are presented.

Many recent papers contain results of dust explosion tests performed on pure plastic powders. The most relevant are listed in **Table 1**, where the polymer studied and the parameters measured are indicated.

***Table 1**. Recent literature studies on polymer dust explosions.*

Reference	Dust polymer investigated	Measured Parameters
Ji et al., (2018)	Polyethylene	K_{St}, Pmax
Gan et al., (2018)	Polyethylene	MEC
Cashdollar (2000)	Polyethylene	MEC
Addo et al., (2019)	Polyethylene	K_{St}, Pmax, MIT, MIE MEC,
Pang et al., (2019)	Polyethylene	K_{St}, Pmax
Mittal et al., (1996)	Polyethylene	MIT
Yang et al., (2019, a)	Polypropylene	K_{St}, Pmax, MIE, MEC, MIT
Myers & Ibarreta (2009).	Phenolic resin	K_{St}, Pmax, MIE, MEC, LIT
Iarossi et al., 2013	Polyamide, polyester fibres	K_{St}, Pmax, MIE, MEC
Marmo & Cavallero (2008)	Polyamide, polyester fibres	K_{St}, Pmax, MIE, MEC
Portarapillo et al., 2020	Polyamide, polyester fibres	K_{St}, Pmax, MIE
Yang et al., (2019, b)	Styrene-acrylonitrile copolymer	K_{St}, Pmax, MIE, MEC
Kao & Duh, (2002)	ABS	K_{St}, Pmax, MIE, MEC
Jiang et al., (2018)	Polystyrene	K_{St}, Pmax, MIE, MEC
Nifuku et al., (2006)	Polyurethane	K_{St}, Pmax, MIE, MEC
Li et al., (2017)	Rubber	K_{St}, Pmax, MIE, MEC
Zhang et al., (2020)	Polymethylmethacrylate	K_{St}, Pmax
Krock et al., (2012)	PVC	K_{St}, Pmax

2 Experiments

This paper presents the results of commercial tests carried out at the Polytechnic of Turin's powder explosion laboratory. The materials tested were delivered by customers as part of the dust explosion risk analysis process. The samples were picked up at various stages of the manufacturing process. Most samples were collected at bag filters or other dust collector devices located downstream of suction plants.

2.1 Sample characterization

Materials tested were characterized for their chemical nature, particle size, moisture content, and origin. Since relevant studies have demonstrated these parameters' role over ignition sensitivity and dust deflagration parameters, the same approach has been followed here, as in Marmo et al. (2017) and Marmo et al. (2018). The origin of samples, which means the collection location, the dust source, and the industrial sector, is considered a relevant factor in identifying potential high-risk processes or operations in the plastic manufacturing chain.

Most of the samples originated from the waste handling or dust abatement system of industrial operations involving plastics. The resulting material is a powdered sample whose particle size and morphology depend on the different processes and operations involved.

The most significant factors influencing polymer dust flammability are:

- Particle size distribution and shape
- Resin chemical structure.
- Presence of additives
- Copolymerization
- Synergistic effects between different polymers

All samples are characterized according to the methods indicated in Table 2.

2.2 Methods

Samples chemical nature has been determined with a FTIR analysis to focus on functional groups. A Nexus FTIR spectrometer equipped with a DTGS KBr detector (neutralized triglycine sulfate with potassium bromide windows) was used for this purpose. FTIR absorption spectra were recorded in the 4000-400 cm^{-1} range and with 2 cm^{-1} spectral resolution. All samples were prepared by mixing 200 mg KBr and 1 mg dried sample powder and pressing the mixture to form a pellet of 13 mm diameter. The spectrum of each sample was corrected for that of blank KBr.

It is important to emphasize that the FTIR technique is not the best choice for polymer mixtures. In fact, the interaction between the pure substances can make it challenging to interpret the peaks contained in the spectra, which can result in a combination of vibrations of similar bonds or cause shifts from the usual wave numbers. In addition, FTIR can only identify the species present in larger quantities in the mixture without being able to identify species present in trace amounts. Nevertheless, the method is reliable for identifying the main polymer matrix in the samples; further detailed analysis of the chemical nature could be achieved via TGA-IR coupled techniques.

Particle size distribution was measured through preliminary mechanical sieving with different sieve mesh (ASTM 500 is reported here as a reference value). A more detailed characterization was obtained by Laser diffractometry analysis performed using laser granulometry (Malvern Mastersizer

E1000) with a dry powder feeder unit (Scirocco, 2000M model). The measurement range is 0.01–1000 µm. The procedure was adapted from ISO 13320:2009.
Sample flammability was determined according to the ISO/IEC80079-20-2:2016 method. The procedure implies submitting the material to an ignition attempt first in the modified Hartmann tube using a continuous arc and then a glowing wire. If no ignition is observed, the sample is submitted to an ignition attempt in the 20-litre sphere with 2*1kJ igniters or, alternatively, in the GG furnace at 1000°C.
The maximum pressure (*Pmax*) and deflagration index (k_{ST}) were measured in the 20 l Siwek sphere according to UNI EN 14034-1:2011. Sobbe chemical igniters (2 * 5 kJ) were used.
The lower explosion concentration (LEL) was measured in the 20 l Siwek sphere according to UNI EN 14034-3:2011. Sobbe chemical igniters (2 * 1 kJ) were used.
The minimum ignition energy (MIE) was determined using a MIKE 3 device (Kuhner, CH), according to the UNI EN 13821:2004 standard. The delay time used was generally 60 ms.
The cloud ignition temperature (MIT_C) was determined in a Godbert Greenwald furnace according to ISO/IEC80079-20-2:2016. Several tests were conducted at different sample amounts and pressure dispersion (generally, 0.3- 0.5 bar). Autoignition is detected after 10 consecutive attempts with no ignition.
MIT_L was measured using a hot-place testing device (Chilworth Technologies, model 5 mm-LIT-H, serial number J303161A) equipped with a 5 high ring. The measurement procedure was defined according to ISO/IEC80079-20-2:2016.

Table 2: Characterization tests and standards.

Parameter	**Standard/Methodology**	**Unit of measure**
Moisture	ISO 562:2010	Weight %
PSD by Sieving	Internal laboratory procedure	Weight %
PSD by Laser diffraction	ISO 13320:2009	Weight percentiles
Chemical nature	FTIR analysis	Spectra
Flammability	ISO 80079	-
Pmax and Kst	UNI EN 14034-1 e 2:2011	bar, bar/m s
MIE	UNI EN 13821:2004	mJ
LEL	UNI EN 14034-3:2011	g/m^3
MITc	ISO/IEC80079-20-2:2016	°K
MIT_L	ISO/IEC80079-20-2:2016	°K

2.3 Experimental procedure

Each material was tested “as received” unless its physical or morphological features were unfit for analytical determination. In general, the only pretreatment consisted of eliminating the coarsest fraction (> 2000 mm) by sieving since coarse particles get stuck in the ignition devices of the GG furnace and the 20-liter sphere. Samples were not dried before testing to provide a reliable picture of in-field dust behavior.
All measures were determined according to the current standards listed in Table 2.

3 Results and discussion

The sample origin is represented in Fig. 1. The distribution should not be intended as a statistical representation of the industrial sector interested in polymer dust presence. It is likely a picture referred to the north of Italy.

3.1 Characterization results

First, particle size distribution and flammability according to ISO 80079 were determined. The results are summarized in Fig. 1 and Table 3.

As identified in previous work (Marmo et al., 2017), the tenth percentile (d_{10}) is reported here as the more significant size parameter in influencing dust explosibility for k_{St} and *Pmax* determination.

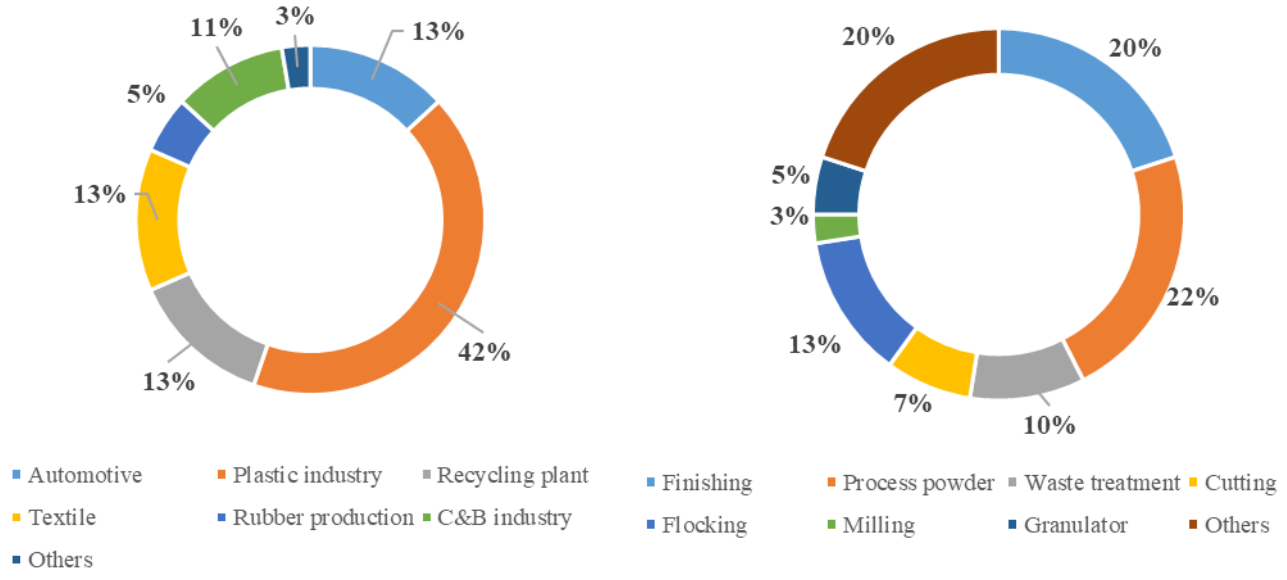

Fig. 1: Samples origin by industrial sector and operations involved.

Almost half of the samples have a d_{10} very small, less than 50 um, which may potentially imply a high sensitivity to ignition. The finest samples are two PVC final products, while other relatively smaller samples are those identified as "finishing" material, i.e., samples derived from mechanical operations and collected into some abatement system. Coarser samples, with a smaller than 500 um-weight fraction (say Y_{M500}) relatively low (less than 20%), are likely less susceptible to ignition and demonstrated low values of explosibility parameters in the experimental tests. Y_{M500} lower than 10% is typical of fibrous samples, such as XPS derived from cutting operation (i.e. sample XXXI), which present a coarse particle distribution and blade-like shape particles. Despite their fibrous nature, nylon flock samples (XV to XIX) have small particle sizes (Y_{M500}=100%). At the same time, their PSD is not measurable by laser granulometry, which is suitable for spherical shape particles but not for particles with a high length-to-diameter ratio). In that case, the dimensions shown in Table 3 are the "equivalent diameter", as calculated by Portarapillo et al. (2022).

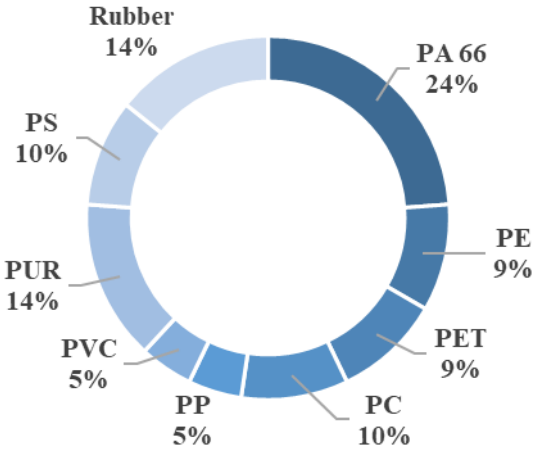

Fig. 2: Samples nature distribution by polymer identified by FTIR analysis.

As expected, almost all the materials were flammable according to standards. Although the ISO 80079 test does not allow to drive any conclusion about the actual flammability attitude of the sample (it must be considered a go/no-go test), one can assume qualitatively that those samples that ignite at the Hartman test (continuous arc or glowing wire) are more reactive than samples that ignite only in the GG furnace or in the 20-liter sphere. Most of the samples studied ignited in the Hartmann tube (30/39). Only 2 samples over 39 were not flammable. This result confirms the relevant reactivity of polymer dust.

***Table 3**. Sample characterization.*

Sample	Chemical nature	PSD				Moisture	Flammability (ISO 80079)	Sector	Operations
		Y_{M500}	d_{10}	d_{50}	d_{90}				
I.	PVB	-	36.5	170.8	489.8	11.1	Y (Electric arc)	Automotive	Finishing
II.	Cellophane	-	54.6	194.0	523.6		Y (Electric arc)	Plastic industry	Waste treatment
III.	PET	98.4	18.1	51.5	129.0	0.8	Y (Electric arc)	Recycling plant	Fines collecting
IV.	PC	74.4	63.5	260.4	618.3	<0.1	Y (Electric arc)	Plastic industry	Waste treatment
V.	PC	77.8	45.2	272.1	653.4		Y (Electric arc)	Plastic industry	Waste treatment
VI.	PS/PSVC		-	-	-	-	Y (Electric arc)	Plastic industry	Granulator
VII.	PP	39.3	100.6	287.2	622.1		Y (Electric arc)	Plastic industry	Waste treatment
VIII.	PC	52.3	11.1	210.3	573.9	0.3	Y (Electric arc)	Plastic industry	Milling/filter
IX.	PS/PPE	97.3	1.8	9.7	41.4	0.2	Y (Electric arc)	Plastic industry	Granulator
X.	PU/PC	99.5	3.9	11.5	36.1	0.8	Y (Electric arc)	Automotive plant	Finishing
XI.	P(S-MMA)	98.5	3.7	11.7	37.6	0.7	Y (Electric arc)	Automotive plant	Finishing
XII.	PS	48.6	177.2	355.8	688.2	0.3	Y (G-G furnace)	Shoe manufacturing	Finishing
XIII.	PP	6.6	97.6	323.9	680.1	0.8	Y (Electric arc)	Waste treatment	Milling
XIV.	Polyether urethane	11.6	94.5	288.2	595.5	0.7	Y (G-G furnace)	Building industry	Waste treatment/cutting
XV.	PA6,6	100	87*	-	-	-	Y (Electric arc)	Textile	Flocking
XVI.	PA6,6	100	115*	-	-	-	Y (Electric arc)	Textile	Flocking
XVII.	PA6,6	100	144*	-	-	-	Y (Electric arc)	Textile	Flocking

VIII.	PA6,6	100	189*	-	-	-	Y (Glowing wire)	Textile	Flocking
XIX.	PA6,6	100	64*	-	-	-	Y (Glowing wire)	Textile	Flocking
XX.	PE	33.8	15.5	167.6	535.8	0.6	Y (Electric arc)	Plastic industry	Process
XXI.	NBR	76,3	36.5	137.6	461.8	0.1	Y (Electric arc)	Rubber production	Waste treatment
XXII.	PUR	14,5	161.9	371.7	717.7	0.6	Y (Glowing wire)	Automotive	Waste treatment
XIII.	PUR	84,2	39.6	101.0	314.2	0.6	Y (Electric arc)	Automotive	Waste treatment
XIV.	PVC	100	0.88	13.6	41.5	0.2	Y (G-G furnace)	Plastic industry	Process
XXV.	PVC/PVA	98,8	0.71	2.1	7.5	0.2	Y (G-G furnace)	Plastic industry	Process
XVI.	Rubber (ACR/B)	74,4	43.9	140.2	359.7	0.2	Y (Glowing wire)	Rubber production	Finishing
XVII.	PET	8,5	ND	ND	ND	0.3	N*	Plastic industry	Finishing
VIII.	PS	69	159.5	364.1	694.3	0.2	Y (Glowing wire)	Plastic industry	Finishing
XIX.	EPS	90	56.9	248.7	620.3	0.4	Y (Electric arc)	Recycling	Densifier
XXX.	XPS	7.2	ND	ND	ND	1.6	N*	Recycling	Cutting
XXI.	PVA	99,4	32.7	106.9	231.5	0.5	Y (Electric arc)	Building industry	Process
XXII.	PVA	100	36.8	84.4	167.2	0.3	Y (Electric arc)	Building industry	Process
XIII.	PVA	100	31.9	104.8	215.5	0.8	Y (Electric arc)	Building industry	Process
XIV.	PP	93.8	19.3	64.2	202.8	<0.1	Y (Electric arc)	Plastic industry	Finishing
XXV.	PET	50.8	142.5	344.0	674.6	0.3	Y (Glowing wire)	Recycling	Cutting
XVI.	PET	99.2	119.6	230.0	405.6	0.3	Y (20L)	Recycling	Planing mill
XVII.	PVC	100	127.4	174.4	238.5	2.8	Y (Glowing wire)	Plastic industry	Process
VIII.	EPS	97.4	15.5	48.7	136.5	0.2	Y (Electric arc)	Plastic industry	Process
XIX.	HDPE	56.4	81.2	265.6	595.0	<0.1	Y (Glowing wire)	Plastic industry	Process

3.2 Deflagration parameters

Flammable samples were submitted to measure the deflagrating parameters (**Table 4**). Customers requested the results presented here. For this reason, only some samples were submitted to complete characterization, i.e., *kst, Pmax, MIT$_C$, MIE*, and *MIT$_L$* measurement. Nevertheless, all samples were included in this work as it aims to present the broadest possible range of dust materials obtained from the plastic manufacturing chain.

***Table 4**. Explosibility properties.*

Sample	*MITc*, °C	*MIT$_L$*, °C	*MIE*, mJ	*LEL*, g/m^3	*k$_{St}$*, bar m/s	*Pmax*, bar
I	530	-	440	100	68	7
II	470	-	79	50	86	6.8
III	510	-	26	50	143	6.3
IV	580	Melts*	440	200	-	-
V	PC	-	62	62.5	-	-
VI	480	-	1.9	-	-	-
VII	460	>400	-	-	-	-

Sample	*MITc*, °C	*MIT*$_L$, °C	*MIE*, mJ	*LEL*, g/m^3	k_{St}, bar m/s	*Pmax*, bar
VIII	610	-	540	-	187	7.2
IX	480	-	-	40	281	8.0
X	510	-	-	-	-	-
XI	440	-	4	60	205	6.5
XII	>1000	-	>1000	-	25.8	5.5
XIII	550	-	ND	-	14	4.4
XIV	550	-	740	-	61.9	4.9
XV	-	-	471	-	42.6	4.8
XVI	-	-	>1000	-	30	6.4
XVII	-	-	>1000	-	22	6.6
XVIII	-	-	>1000	-	11	5.2
XIX	540		228	-	68	7.0
XX	-		240	-	-	-
XXI	-	-	-	-	69.6	6.4
XXXI	490	310	-	-	23.5	4.4
XXXII	480	330	-	-	31.1	4.7
XXXIII	530	>400	-	-	25.3	4.6
XXXVII	-	-	>1000	-	7.9	4.0
XXXVIII	-	-	14	-	106.2	5.8
XXXIX	-	-	>1000	-	20.2	4.6

The following figures give an overview of the influence of some variables on the explosion parameters. The most influential variable is d_{10}, which significantly affects the k_{st} (Fig. 3, Fig. 4). Neither the dust origin (Fig. 3) nor its chemical nature (Fig. 4) affects the k_{st} as significantly as d_{10} does. d_{10} seems to be a good predictor of k_{st}.

As expected, finer samples demonstrated higher k_{st}. At the same time, a sort of "plateau" is seen for d_{10} larger than about 100 um: it seems that coarser particles do not affect the sample's explosibility, whose k_{st} value is generally lower than 50 bar m/s.

The samples' origin may affect the PSD, namely the d_{10}. So, an indirect effect of the sample origin on the k_{st} is observed in Fig. 3, where samples deriving from "finishing" and "recycling" operations are grouped towards the low d_{10}—high k_{st} region. Process powders tested, except for flocking samples, are less reactive in light of their higher d_{10}. Fig. 4 shows the chemical nature of the samples. Although not clearly indicated, PVA, PVB, and PVC powders are generally less reactive than others.
Acrylates and styrene-based samples exhibited the highest value of k_{st}, both in this study and in the literature (Fig. 4 and Fig. 5).

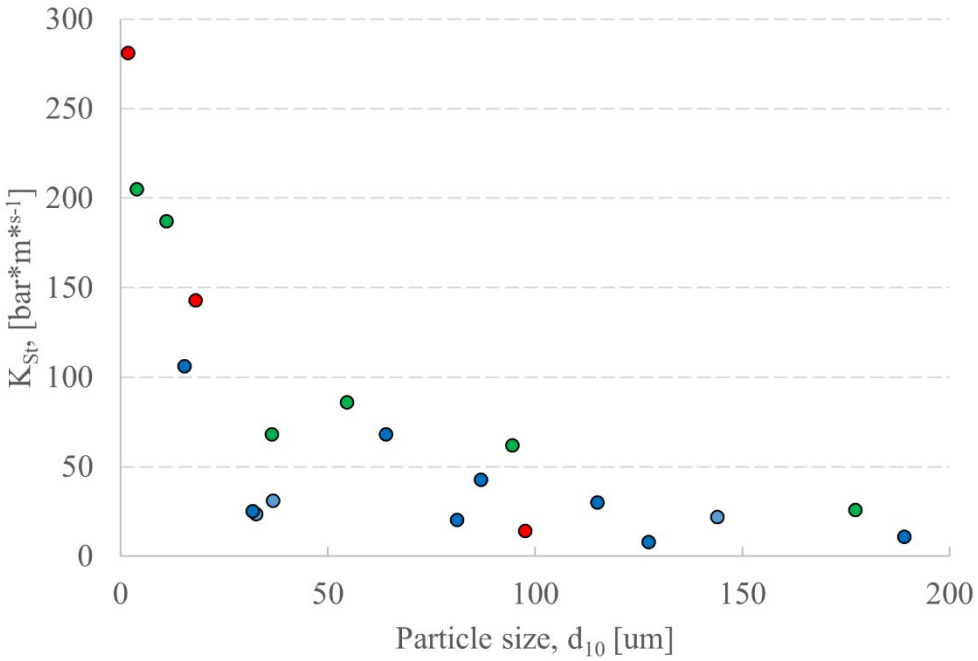

Fig. 3: Experimental values of k_{St} versus d_{10}. Red dots: Recycling/waste treatment; blue: process powder; green: finishing operations.

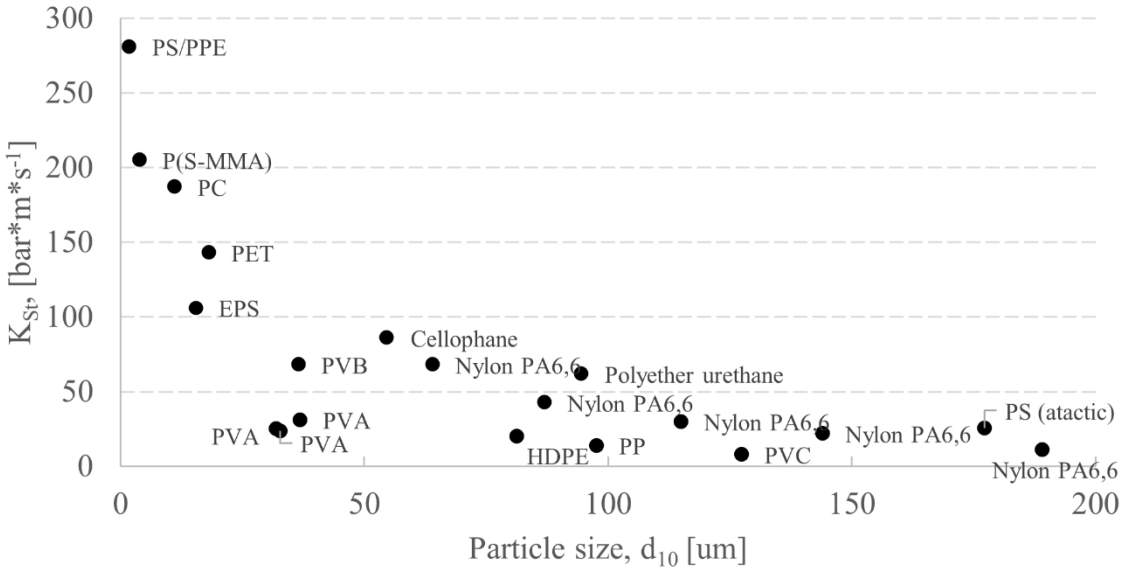

Fig. 4: Experimental values of k_{St} vs. d_{10} versus the polymer nature (this work)

Fig. 5 shows some literature data taken from the papers in **Table 1**, plotted versus d_{10}. These data show the same trend as those obtained in this work. Also, the order of magnitude of the k_{st} is about the same.

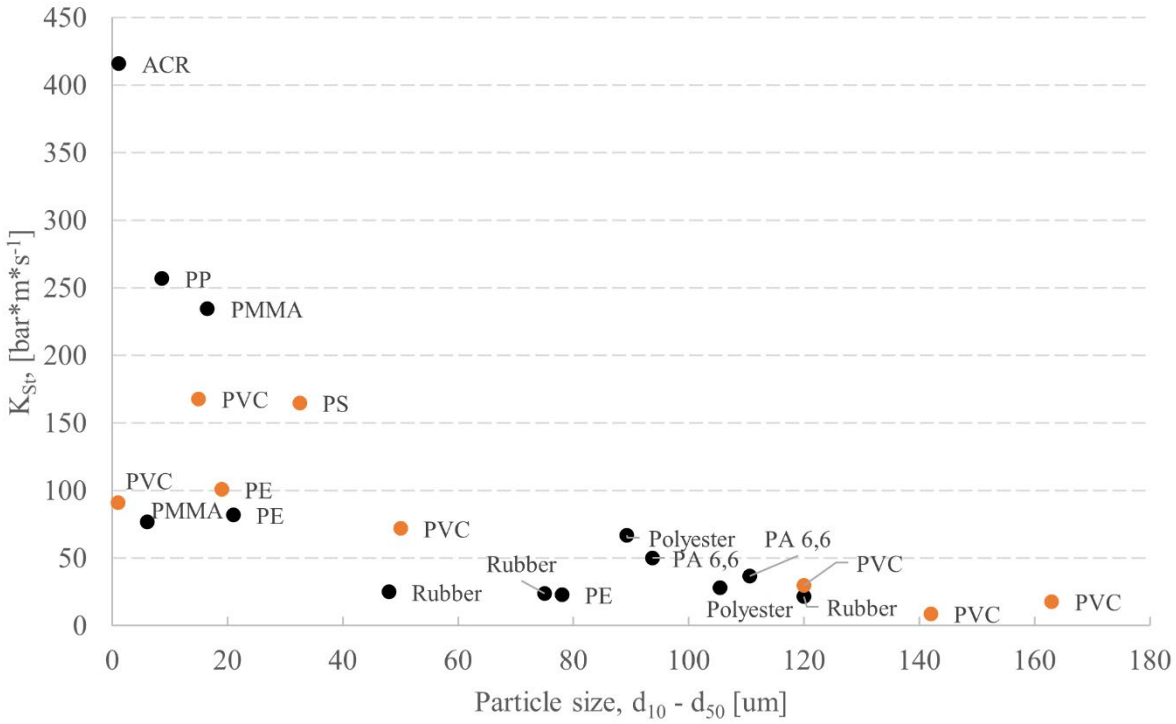

Fig. 5: Experimental values from the literature vs polymer nature. Black dots refer to d_{10}, while orange to d_{50}.

k_{st} values appear below a maximum value, which depends on d_{10} in inverse proportion, such as a hyperbola.

Fig. 6 shows the dependence of MIE on d_{10}. As expected, MIE increases almost linearly with d_{10}. When the latter exceeds approximately 100 µm, the MIE exceeds 1000 mJ and goes beyond the measuring range of the MIKE 3. In this case, the data are somewhat sparse. The effect of the material type is likely to be quite significant.

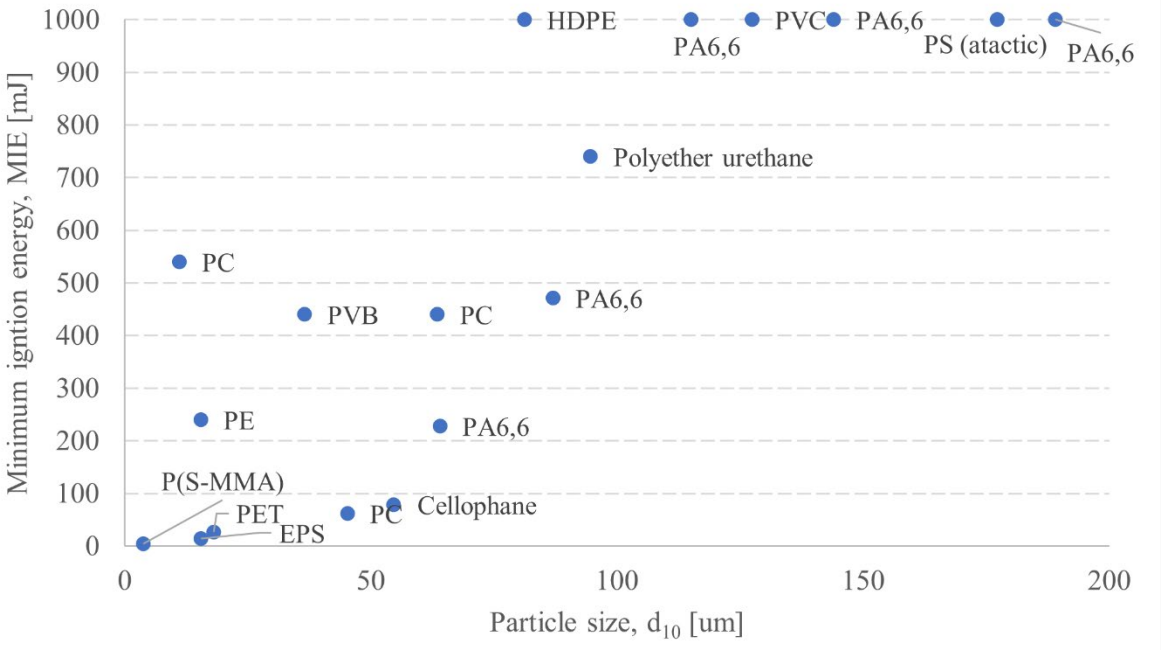

Fig. 6: Experimental values of MIE vs. d_{10} according to polymer nature (this work)

4 Conclusions

This study aims to give an overview of the explosiveness of powders from the polymer processing chain, including dust representative of the whole spectra from raw material to the recycling of plastic products.

Thirty-nine samples collected at manufacturing sites were subjected to explosivity testing and characterization of the deflagrating parameters. The results were compared with current data from the literature on polymer powders.

In line with the literature data, the results obtained here show that particle size is essential in determining sample explosivity. In particular, d_{10} is an excellent predictor of the maximum k_{st} value that can be expected. An inversely proportional relation between k_{st} and d_{10} is observed, approximately according to a hyperbola.

The d_{10} also affects *MIE*. An increase in d_{10} causes an increase in *MIE*. When d_{10} exceeds 100 μm, *MIE* generally exceeds 1000 mJ. The effect of d_{10} is less on the *Pmax* value.

Chemical nature has a moderate effect. Polystyrene, polyacrylate, and polycarbonate appear to be the most reactive materials.

MIT of plastic samples investigated is in a narrow range around 400° and 600°C, lowest values are obtained from acrylates, P(S-MMA). Moreover, the *MIT* of polymer dust also did not rely entirely on PSD or other variables measured in this work.

In synthesis, d_{10} seems to be a good predictor of the explosion hazard posed by the dust. Risk analysts may benefit from d_{10} measurement to prioritize the dust to be submitted to further determination of the explosible parameters.

References

Centrella, L., Portarapillo, M., Luciani, G., Sanchirico, R., & di Benedetto, A. (2020). Synergistic behavior of flammable dust mixtures: A novel classification. Journal of Hazardous Materials, 397, 122784. https://doi.org/10.1016/j.jhazmat.2020.122784

Danzi, E., Marmo, L., Portarapillo, M., Sanchirico, R., Di Benedetto, A.: "Waste and Recycling of plastics: dust explosion risk evaluation", pp. 462 - 473. In: "Proceedings of the 14th International Symposium on Hazards, Prevention and Mitigation of Industrial Explosions (ISHPMIE 2022)", Braunschweig, Germany, 2022. DOI: 10.7795/810.20221124

Iarossi, I., Amyotte, P. R., Khan, F. I., Marmo, L., Dastidar, A. G., & Eckhoff, R. K. (2013). Explosibility of polyamide and polyester fibers. Journal of Loss Prevention in the Process Industries, 26(6), 1627–1633. https://doi.org/10.1016/j.jlp.2013.07.015

ISO/IEC 80079-20-2:2016, Explosive atmospheres Part 20-2: Material characteristics—Combustible dusts test methods.

Jacobson, M., Nagy, J., and Cooper, A. R. (1962). Explosibility of dusts used in the plastic industry. U.S. Dept. of Interior, Bureau of Mines.

Jiang, Y., Pan, Y., Guan, J., Yao, J., Jiang, J., & Wang, Q. (2018). Experimental studies on thermal analysis and explosion characteristics of superfine polystyrene powders. Journal of Thermal Analysis and Calorimetry, 131(2), 1471–1481. https://doi.org/10.1007/s10973-017-6656-y

Kao, C. S., & Duh, Y. S. (2002). Accident investigation of an ABS plant. Journal of Loss Prevention in the Process Industries, 15(3), 223–232. https://doi.org/10.1016/S0950-4230(01)00068-7

Krock, R., Halprin, L. P., De La Cruz, P., Keller, H., & Washington, D. C. (2012). Osha's combustible dust national emphasis program and combustibility characteristics testing of pvc resins and pvc dusts.

Li, Y., Liu, F., Zhang, Q., Yu, Y., Shu, C. M., & Jiang, J. (2017). Explosion characteristics of micron-size conveyor rubber dust. Journal of Loss Prevention in the Process Industries, 45, 173–181. https://doi.org/10.1016/j.jlp.2016.12.005

Marmo, L., & Cavallero, D. (2008). Minimum ignition energy of nylon fibres. Journal of Loss Prevention in the Process Industries, 21(5), 512–517. https://doi.org/10.1016/j.jlp.2008.04.003

Marmo, L., Riccio, D., & Danzi, E. (2017). Explosibility of metallic waste dusts. Process Safety and Environmental Protection, 107, 69–80. https://doi.org/10.1016/j.psep.2017.01.011

Marmo, L., Sanchirico, R., di Benedetto, A., di Sarli, V., Riccio, D., & Danzi, E. (2018). Study of the explosible properties of textile dusts. Journal of Loss Prevention in the Process Industries, 54(March), 110–122. https://doi.org/10.1016/j.jlp.2018.03.003

Marmo L., Danzi E., Di Benedetto A., Portarapillo M., Polymer dust explosion part I: literature review and case studies, presented at the 15th International Symposium on Hazards, Prevention and Mitigation of Industrial Explosions (ISHPMIE 2024)"

Mittal, M., & Guha, B. K. (1996). Study of Ignition Temperature of a Polyethylene Dust Cloud. Fire and Materials, 20(2), 97–105. https://doi.org/10.1002/(SICI)1099-1018(199603)20:2<97::AID-FAM568>3.0.CO;2-L

Myers, T., & Ibarreta, A. (2009). Investigation of the Jahn Foundry and CTA Acoustics dust explosions: similarities and differences. Journal of Loss Prevention in the Process Industries, 22(6), 740–745. https://doi.org/10.1016/j.jlp.2009.08.016

Nifuku, M., Tsujita, H., Fujino, K., Takaichi, K., Barre, C., Paya, E., … Sochet, I. (2006). Ignitability assessment of shredder dusts of refrigerator and the prevention of the dust explosion. In Journal of Loss Prevention in the Process Industries (Vol. 19, pp. 181–186). https://doi.org/10.1016/j.jlp.2005.04.007

Portarapillo, M., Danzi, E., Guida, G., Luciani, G., Marmo, L., Sanchirico, R., & di Benedetto, A. (2022). On the flammable behavior of non-traditional dusts : dimensionless numbers evaluation traditional dusts : dimensionless numbers evaluation for nylon 6,6 short fibers. Journal of Loss Prevention in the Process Industries.

UNI. EN 13821: 2004. Potentially explosive atmospheres—Explosion prevention and protection − Determination of minimum ignition energy of dust/air mixtures.

UNI. EN 14034-1: 2011 Determination of Explosion Characteristics Of Dust Clouds, Part 1 to 3

Yang, J., Li, Y., Yu, Y., Zhang, Q., Zheng, L., Suo, Y., & Jiang, J. (2019). Experimental investigation of the inerting effect of CO2 on explosion characteristics of micron-size Acrylate Copolymer dust. Journal of Loss Prevention in the Process Industries, 62. https://doi.org/10.1016/j.jlp.2019.103979

Yang, J., Yu, Y., Li, Y., Zhang, Q., Zheng, L., Luo, T., Suo, Y., & Jiang, J. (2019). Inerting effects of ammonium polyphosphate on explosion characteristics of polypropylene dust. Process Safety and Environmental Protection, 130, 221–230. https://doi.org/10.1016/j.psep.2019.08.015

Zhang, X., Gao, W., Yu, J., Zhang, Y., Zhang, J., Huang, X., & Chen, J. (2020). Effect of flame propagation regime on pressure evolution of nano and micron PMMA dust explosions. Journal of Loss Prevention in the Process Industries, 63. https://doi.org/10.1016/j.jlp.2019.104037

Towards the LES of large-scale explosions: study of a larger-than-laboratory-scale H_2/air vented explosion

Francis Adrian Meziat Ramirez[a,b], Omar Dounia[a], Thomas Jaravel[a], Quentin Douasbin[a] & Olivier Vermorel[a]

[a] CERFACS, 42 Avenue G. Coriolis, Toulouse Cedex 01 31057, France
[b] Air Liquide, Paris Innovation Campus, 1 Chemin de la Porte des Loges, Les Loges-en-Josas, 78354, France

E-mail: *meziat@cerfacs.fr*

Abstract

The growth in the use of hydrogen raises safety issues, in particular the increased likelihood of vapour cloud explosions arising from leaks in confined environments. In this context, predictive means of studying explosions in confined and vented geometries are needed. Widespread methods in the industry rely on Unsteady Reynolds Averaged Navier-Stokes (URANS) simulations, for their robustness and low computational cost. These approaches are strongly reliant on their constituting models, as they do not resolve the turbulent scales of these reactive, highly-turbulent phenomena. With the rise of computational power and through cost-optimisation techniques, such as Adaptive Mesh Refinement (AMR), it is now possible to use Large Eddy Simulation (LES) for the assessment of complex, larger-than-laboratory-scale explosions. This study shows the application of LES to a hydrogen/air vented explosion, with a total fluid volume of 43 m^3 (Daubech et al., 2013). The results demonstrate that LES can be used as a predictive tool at a reasonable cost, even in larger-scale scenarios, provided the experimental setup to be reproduced is correctly characterised. In particular, the results highlight the critical impact on flame acceleration of small-scale geometric elements inside the chamber, that are usually overlooked. A physical analysis of the explosion shows that, while the internal chamber overpressure is piloted by the enhanced combustion in the vicinity of the small-scale obstacles, the overpressure recorded at the exterior of the chamber is mainly piloted by the rapid flame acceleration due to the flow contraction at the vent. Finally, AMR allows to obtain results as precise as with a uniformly fine, static mesh, while saving 58% of the computational cost. Thus, the present LES allows for a detailed characterisation of the key physical mechanisms driving the overpressure generation, in a configuration relevant for industrial applications and for a reasonable computational cost.

Keywords: *Vented Explosion, Safety, Hydrogen, Large Eddy Simulation, Adaptive Mesh Refinement*

Introduction

With the rising importance of hydrogen in the industrial context, the prediction and assessment of explosion hazards becomes of key importance for the safe and reliable deployment of a wide range of applications. In particular, vapour cloud explosions arising from leaks of hydrogen in confined environments are of great interest for the process industry. In this context, vents are often used as a mitigation tool to limit the overpressure generated during an accidental explosion. Vented explosions have been studied extensively, for instance by Tolias and Venetsanos (2018) and the references therein. The studied phenomenon of interest is the so-called external explosion: the combustion of the unburnt mixture that has been evacuated through the vent, forming an external turbulent cloud with strong recirculating motions. The mechanisms of the flame acceleration (FA) process inside the vented chamber and the external explosion are at the origin of the external overpressure generated in these scenarios. In the case of hydrogen, some of the most relevant experimental configurations in the literature are: the 1 m^3 configuration from Karlsruhe Institute of Technology (KIT) (Kuznetsov et al., 2015), the 4 m^3 setup from the DIMITRHY project at INERIS (Daubech et al., 2013) and the 64 m^3 test rig from FM Global (Bauwens et al., 2008, Chao et al., 2011). Given the cost and complexity of such experiments, these have also been studied through Computational Fluid Dynamics simulations, especially through URANS, even leading to benchmark comparison exercises (Tolias and Venetsanos,

2018, Tolias et al., 2018, Vyazmina et al., 2019). LES resolves the larger turbulent structures in the flow and, by construction, yields a more precise description of the physics at the expense of a higher computational cost. It has already been used to study the KIT and FM Global configurations (Tolias and Venetsanos, 2018, Bauwens et al., 2011). However, this higher-fidelity simulation approach has never been applied to an in-depth analysis of the stoichiometric mixtures of the DIMITRHY configuration (Vyazmina et al., 2016, 2019).

The present study focuses on LES of a close-to-stoichiometric hydrogen-air deflagration in the DIMITRHY vented explosion chamber (Daubech et al., 2013). As accurate LES require to resolve structures down to a reasonably fine scale, it can be more sensitive to the presence of small-scale, turbulence-generating obstacles. Therefore, the question of the representation of small-scale obstacles present in the DIMITRHY enclosure and not considered in previous studies (Vyazmina et al., 2016, 2019) is assessed. The LES methodology is, thus, validated on a larger-than-laboratory-scale explosion scenario and detailed numerical diagnostics are used to understand the complete deflagration process and the overpressure-generating mechanisms. In addition, AMR is applied to reduce the computational cost for the present high-fidelity simulation and to evaluate the potential gains.

The DIMITRHY explosion configuration is presented in Section 1. The simulation setup is introduced in Section 2. Finally, the simulation results are analysed in Section 3, with special focus on the impact of the correct representation of the geometry (Section 3.1) and the computational cost reduction from the use of AMR (Section 3.2) .

1 Experimental setup

The experimental setup is illustrated in Fig. 1. It corresponds to a $4\,m^3$ enclosure where Daubech et al. (2013) performed vented explosions of hydrogen/air mixtures, in the framework of the DIMITRHY project. The reader is referred to Daubech et al. (2013) for more information. The configuration con-

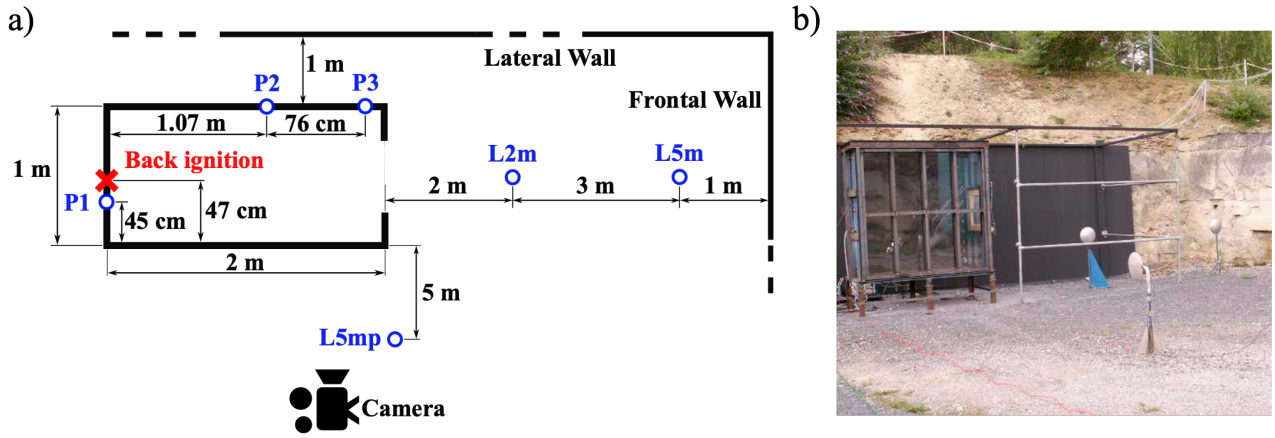

***Fig. 1**: (a) Schematic of the experimental setup (top view) with the location of the pressure probes (circles) and (b) picture with lateral view (adapted from Daubech et al. (2013))*

sists of a $2\,m \times 2\,m \times 1\,m$ chamber with a square-shaped vent, filled with a homogeneously premixed hydrogen/air flammable mixture. The vent, placed at the center of one side of the chamber, is covered by a thin plastic sheet, held in place by magnets. One side of the vented chamber is made of a transparent PMMA plate to allow for the visualisation of the explosion. The unburnt mixture is seeded with NH_4Cl particles to visualise the shape of the ejected unburnt mixture cloud. The explosion is ignited by an electrical spark. The chamber is placed outdoors, above the ground, and is partially surrounded by natural walls: a lateral wall to the side of the chamber, and a wall on the front of the vent (Fig. 1). Taking into account the volume of the chamber ($4\,m^3$), plus the 3 m-radius hemisphere in front of the vent where the external explosion takes place, the explosion takes up a total volume of $43\,m^3$. In this study, the experimental operating condition selected corresponds to a 28.7% hydrogen mixture ($\phi = 0.96$), with a $0.49\,m^2$ vent and ignition at the chamber wall opposed to the vent (so-

called back ignition). This is the strongest and fastest explosion among the experimental database, with significantly higher maximal overpressures than the operating conditions studied in the literature (Vyazmina et al., 2016, 2019). The available experimental data consists of pressure measurements at 6 piezoresistive pressure probes inside and outside the chamber (see Fig. 1), plus video recordings from a high-speed camera system. In this paper, only experimental pressure signals from probes P2, L2m and L5m will be used in the comparison with the simulation results, since they are the most significant in the assessment of the explosion physics.

Several sources of incertitude are identified in the experimental setup. The enclosure is not airtight, suffering from leaks as the hydrogen is fed into the chamber and during the explosion. However the leaks during the explosion are estimated to be negligible with respect to the flow though the vent. There is only one explosion recorded at every operating point, lacking any assessment of repeatability. The walls and the geometrical elements inside the chamber are not characterised or described in the available publications or technical reports.

2 Computational setup

The simulations are performed using the massively parallel solver AVBP (Gicquel et al., 2011). It is a time-explicit, cell-vertex/finite element code, that solves the multispecies, compressible Navier-Stokes equations on unstructured meshes. A centered continuous Taylor–Galerkin scheme, third-order in space and fourth-order in time (TTG4A (Colin and Rudgyard, 2000)) is used. A selective filter is applied on the pressure field (Schmitt, 2020) to detect shocks and apply second order artificial diffusion to handle the associated stiff gradients. The subgrid scale turbulence is modelled by the WALE model (Nicoud and Ducros, 1999). The mesh resolution is homogeneous and set to 2 cm, inside the 43 m^3 encompassing the interior of the chamber plus the external explosion region. Outside the 43 m^3 volume, the mesh is progressively coarsened following a maximal growth ratio of 20%, until the domain boundaries are reached. This results in a total of 32.7 million tetrahedral elements (of which 30.5 million are contained in the 43 m^3 volume).

Regarding Boundary Conditions (BC), isothermal walls are employed to model the chamber walls, with the temperature being set at the ambient initial value $T_{\text{wall}} = 300\,\text{K}$. A law-of-the-wall approach (Schmitt et al., 2007) is employed as the mesh resolution is not sufficient to resolve the turbulent boundary layers induced by the high velocity flow during the explosion. Both the ground and the natural, surrounding walls are explicitly modelled as slip wall BC. In fact, Vyazmina et al. (2019) show that capturing the reflection of the compression waves on such surfaces is key to recover the correct overpressure levels outside the chamber. The other BC, that are used to model the atmosphere, are set as non-reflective pressure outlets at atmospheric conditions ($p_0 = 1\,\text{bar}$), using the NSCBC formalism (Poinsot and Lele, 1992).

The combustion modelling associates the DTFLES (Legier et al., 2000) approach, which artificially thickens the flame front to resolve it on the computational mesh, with the efficiency function from Charlette et al. (2002), to account for the loss of wrinkling at the subgrid scale due to the artificial flame thickening. A resolution of five cells in the thickened flame thickness is ensured.

The simulation is initialised with a quiescent, homogeneous hydrogen/air mixture ($\phi = 0.96$) inside the chamber and with quiescent air outside. The explosion is initiated through a hemispherical, 20 cm-radius, kernel of burnt gases, centered at the position of the spark ignition in the experiments (see Fig. 1a). The transition from fresh to burnt gases is done by mapping the species, density and temperature profiles of a 1-D planar and premixed flame, computed with the chemical kinetics solver Cantera (Goodwin et al., 2017).

Regarding chemistry, a unitary Lewis, single-step and four species chemical scheme is used: $H_2 + 0.5\,(O_2 + 3.76\,N_2) \rightarrow H_2O + 1.88\,N_2$. The fuel consumption is computed following an Arrhenius law where the parameters have been fitted so that a reference laminar flame speed ($s_L^0 = 2.13\,\text{m/s}$) is recovered. It corresponds to the flame speed predicted by the complex sub-mechanism for hydrogen combustion from the University of San Diego (UCSD, 2016), at the initial conditions of the deflagration ($\phi = 0.96$, $T_u^0 = 300\,\text{K}$ and $p_0 = 1\,\text{bar}$). The corresponding adiabatic temperature ($T_b^0 = 2460\,\text{K}$)

is close that of the reference scheme. As the mixture is close to stoichiometry, thermodiffusive effects are not expected to be significant and do not require further modelling.

3 Results and discussion

3.1 Vented explosion physics: impact of small-scale geometric elements

In this section, the impact of small-scale geometric elements present inside the vented chamber is assessed. These are structural components of the enclosure and comprise: the protruding beams used to reinforce the transparent PMMA plate, V-shaped protrusions used to place removable obstacles and three horizontal bars that span across the chamber and hold the enclosure together during the explosion (see Fig. 2b). These horizontal bars are located in the direct trajectory of the explosion and have a strong potential of FA through the generation of turbulence in their wake (Ciccarelli and Dorofeev, 2008). These small-scale elements (of the order of the cm) are sometimes overlooked as details, deemed to play a minor role in the explosion process as long as they do not provide a significant blockage ratio. Here, the blockage ratio provided by these small-scale obstacles is of 14.5%. In previous simulation studies, using URANS methods (Vyazmina et al., 2019), they are not represented in the geometry, as they are of the order of the grid size (or even smaller). This approach is reproduced in the present work, by the use of a first, simplified geometry (see Fig. 2a). Then, the results are compared with a simulation on a detailed geometry, containing the small-scale geometrical elements (see Fig. 2c).

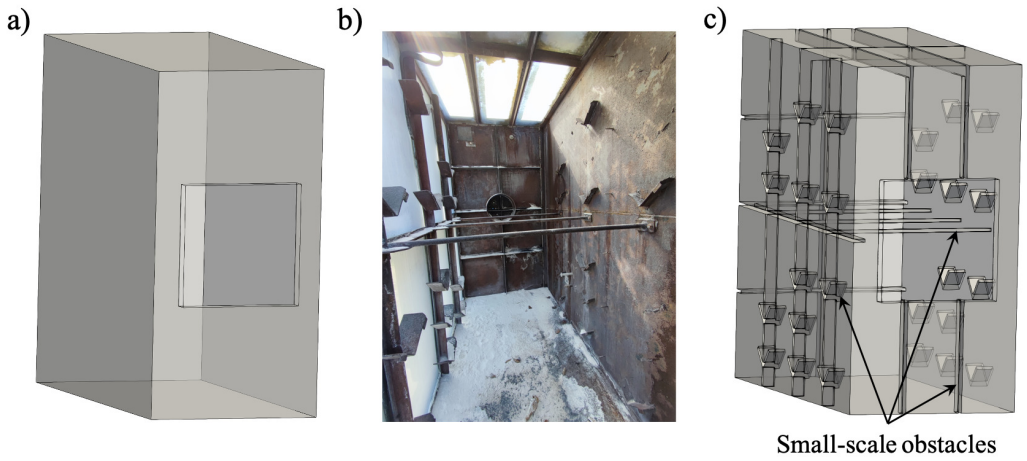

Fig. 2*: (a) Simplified geometry, (b) picture of the solid obstacles inside the chamber and (c) associated detailed geometry.*

The comparison between simulation and experimental pressure signals for both geometries is shown in Fig. 3. All LES temporal signals are shifted in time, by the same Δt_{shift}. Its value is chosen to match the sharp pressure increase found in probe L2m, for the detailed geometry. This shift accounts for the simplified ignition procedure used in LES. In the case of the simplified geometry, a clear underprediction of the overpressure inside the chamber is obtained (P2, Fig. 3a). A peak overpressure of around 1 bar is expected, whereas around 0.25 bar is found. Even so, the peak overpressure captured in the exterior of the chamber by the LES is reasonably close to the experimental values (L2m and L5m, Fig. 3b and c). For the detailed geometry, all three overpressure signals are very close to the experimental measurements, both in terms of maximal values and shape of the signals. Only a slight overprediction of around 0.1 bar is observed for L2m and L5m.

In Fig. 4a, the absolute flame speed is evaluated and compared with the experiment. In the LES, the flame front is identified through a hydrogen mass fraction isocontour. Then, the position (in the X axis) of the most advanced point of the flame (so-called flame tip) is followed over time at every time-step ($\sim 0.5\,\mu$s). Its absolute speed (in the laboratory reference frame) s_{tip} is obtained by numerical differentiation using a Butterworth filter with a cut-off frequency of 100 Hz. For the experiments, the

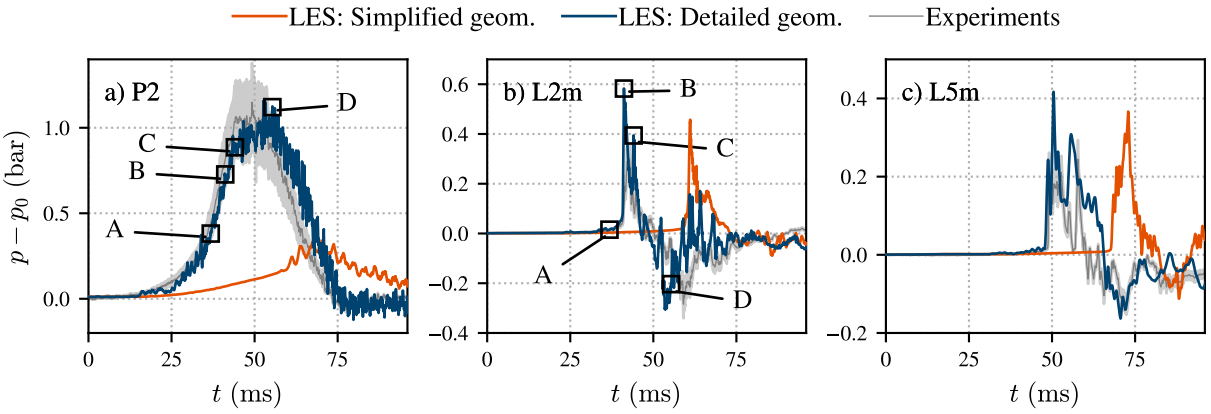

***Fig. 3**: Temporal evolution of the overpressure at probes P2, L2m and L5m (see Fig. 1a for their exact position). Comparison between LES (simplified and detailed geometries) and experiments. A 20% uncertainty on the experimental pressure signals is displayed, following results from Duclos (2019). The time instants shown in Fig. 6 are indicated on the signals from P2 and L2m (A to D).*

position of the flame tip is manually estimated using the high-speed images, recorded at 3000 FPS. The flame speed signal is obtained following the same differentiation and filtering procedure, with a cut-off frequency of 28 Hz. Since only one explosion was recorded, a rough estimation of the experimental uncertainty was obtained by performing the manual extraction of the data five times and calculating the 95% confidence interval based on the variance of the flame speed data. The comparison of LES and experimental data reveals a good agreement for the detailed geometry and an overall underprediction of the absolute flame speed for the simplified geometry, which seems coherent with the overpressure results at P2 (Fig. 3a). For the simplified geometry, the flame speed evolution is linear inside the chamber, following the acceleration imposed by the geometrical confinement. As the flame reaches the vent, a sharp flame speed increase is observed. This has been widely observed in the literature (see, for instance (Ciccarelli and Dorofeev, 2008)) and can be explained by the flow contraction (FC) at the vent, which creates a high flow velocity region that aspirates the flame front. FC is a very strong FA mechanism that produces almost exponential acceleration in the immediate vicinity of the section-restricting obstacle (here, the vent) and also impacts the flame surface and shape. The maximum flame speed levels for the simplified geometry are of $s_{\text{tip}} = 320\,\text{m/s}$, reached at the exterior of the chamber, at around $X_{\text{tip}} = 2.5\,\text{m}$. In the case of the detailed geometry, the flame undergoes successive accelerations at each of the three horizontal bars inside the chamber, showing a higher flame speed than the simplified case. When reaching the vent, the flame in the detailed geometry is 150 m/s faster than the flame in the simplified geometry. The maximum flame speed levels for the detailed geometry are of $s_{\text{tip}} = 470\,\text{m/s}$, falling within the experimental uncertainty ranging from 330 to 580 m/s.

To complement the analysis, Fig. 4b shows the evolution of the volume-averaged heat release rate over the domain $\overline{H}_{\text{RR}}$, for the LES. Both the resolved and total $\overline{H}_{\text{RR}}$ are shown. An increase of resolved $\overline{H}_{\text{RR}}$ mainly accounts for an increase in overall flame surface. The pre-heat of the fresh gases from compression can also slightly affect the resolved $\overline{H}_{\text{RR}}$ but significantly less. The increase in total $\overline{H}_{\text{RR}}$ on the other hand, accounts for the local, subgrid-scale contribution to fuel consumption. For the simplified geometry, all $\overline{H}_{\text{RR}}$ is resolved (the flame remains laminar) until the flame exits the chamber, where the heat release rate rises by one order of magnitude, mainly through the subgrid contribution. In the case of the detailed geometry, the resolved $\overline{H}_{\text{RR}}$ is systematically higher, with the total $\overline{H}_{\text{RR}}$ suddenly increasing after the flame crosses each one of the three horizontal bars. For both geometries, total $\overline{H}_{\text{RR}}$ peaks at around $X_{\text{tip}} = 3.5\,\text{m}$, which is 1 m after the peak in absolute flame speed.

The aforementioned trends can be related with the deflagration dynamics through the visualisation of the evolution of the flame front presented in Fig. 5. Both geometries seem to qualitatively capture

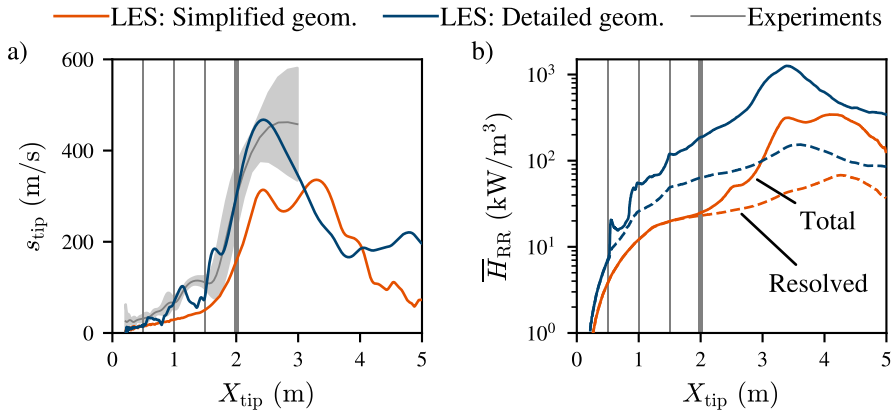

***Fig. 4**: Evolution with respect to the flame tip position (in the X axis) of the (a) absolute flame tip speed and (b) volume-averaged heat release rate. The flame speed of the LES is compared with an approximate experimental uncertainty envelope evaluated from high-speed video recordings (a). Both the resolved (dotted line) and total (dashed line) mean heat release rates are shown for LES (b). The positions of the three solid bars inside the chamber are indicated by vertical lines. The vent is located at $X_{tip} = 2\,m$.*

the FA through the vent and the external explosion. After ignition, a hemisphere of hot products grows and elongates following the aspect ratio of the chamber (Fig. 5a to c). The flame surface increases and the flame accelerates due to the geometric confinement and the burnt gases expansion. For the simplified geometry, no flame interaction with turbulence takes place inside the chamber, as no obstacles are present. The flame remains laminar and with a constant level of heat release along its surface while propagating inside the chamber. Meanwhile, in the detailed geometry, the flame front interacts with the obstacle-generated turbulence (Ciccarelli and Dorofeev, 2008) as it propagates. The progressively more turbulent flame surface is deformed by the presence of the obstacles, burning locally more intensely. This is reflected on the total $\overline{H}_{RR}$, as seen in Fig. 4b. These local accelerations through resolved or subgrid flame surface generation result in an overall increase of the absolute flame speed, being at the origin of the successive accelerations at each of the three horizontal bars seen in Fig. 4a. For both cases, when reaching the vent, the flame front is aspirated by the higher velocities created by FC. This creates the acceleration and the elongation of the flame tip (Fig. 5d and e). Finally, the flame tip interacts with the highly rotational turbulent flow of the recirculating region out of the vent, which intensifies combustion, mainly through the subgrid efficiency function (as seen in Fig. 4b). This creates the external explosion as the flame expands and consumes all the unburnt reactants ejected from the chamber (Fig. 5f).

The previous analysis reveals that the correct representation of the small-scale obstacles present inside the chamber is critical to the correct reproduction of the deflagration by the LES: said obstacles create turbulence in their wake, which increases flame surface and local reaction rate through the activation of the subgrid combustion efficiency function. This provides a supplementary FA mechanism that results in higher heat release rate and absolute flame speed levels all along the explosion, promoting higher overpressures inside the chamber. Even so, external overpressure signals seem to be much less sensitive to the presence of the obstacles. To investigate this, the compression waves responsible for the recorded overpressure at L2m (Fig. 3a) are analysed through a numerical schlieren visualisation, at relevant time instants, in Fig. 6. As the flame accelerates inside the chamber due to the confinement and the presence of obstacles, the unburnt mixture is compressed (Fig. 6a and A instant in Fig. 3). Part of the unburnt mixture is ejected and small, weak compression waves are emitted. This is not at the origin of the external overpressure peaks (L2m and L5m in Fig. 3). It is the strong FC-induced flame acceleration undergone as the flame exits the vent that generates the strong compression waves responsible of the first peak in L2m (Fig. 6b and B instant in Fig. 3). The secondary peak in L2m corresponds to the reflection of the compression wave off the ground (Fig. 6c and C instant in Fig. 3).

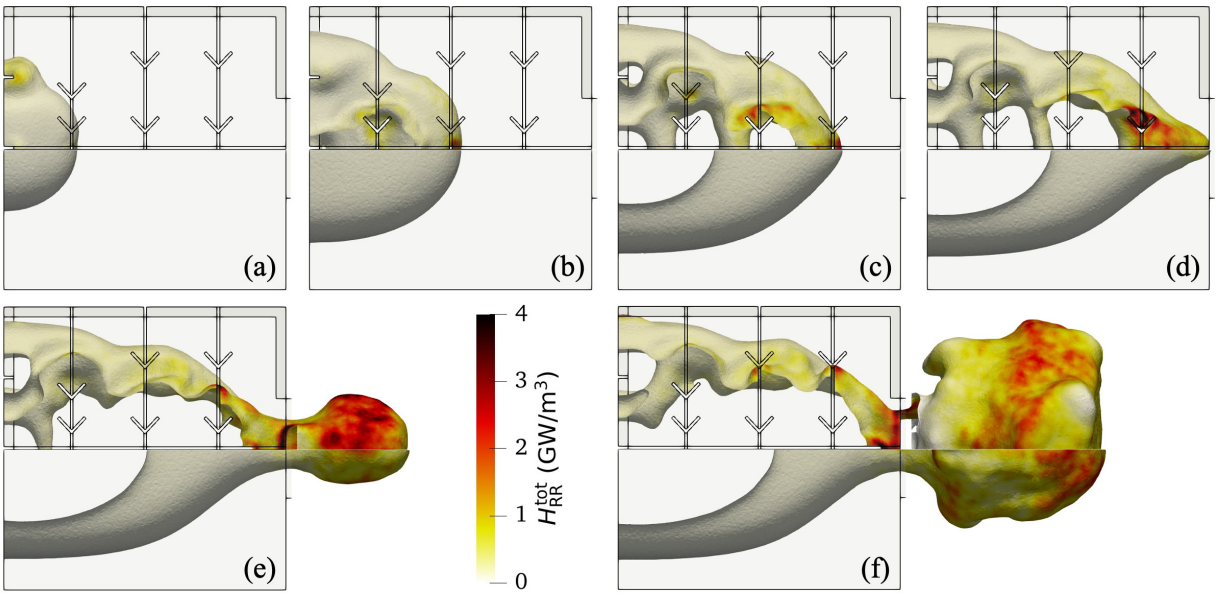

Fig. 5*: Visualisation of the flame front coloured by heat release rate for the detailed (top half) and simplified (bottom half) geometries, at six selected time instants.*

After that, the pressure stops rising inside the chamber following the deceleration of the flame front (P2 in Fig. 3a). Finally, the pressure inside the chamber is maintained as the compressed burnt gases try to escape. The flow is chocked as the pressure ratio across the vent is $p_0^{\text{in}}/p^{\text{out}} \approx 2$. The compressed burnt gases feed a supersonic jet, which creates a high velocity, low pressure flow. This causes the negative overpressures observed in L2m (Fig. 6d and D instant in Fig. 3). In addition, Fig. 6 also allows to visually compare the shape and evolution of the ejected unburnt gases cloud with the high-speed images. Although the images are overexposed towards the end of the explosion, which makes it difficult to identify the flame front, a good agreement between LES and experiments is observed. This further validates the LES approach, showing its added value as a way to explore, in detail, the physics of the vented explosion.

3.2 Adaptive Mesh Refinement and computational cost reduction

In this section, the Turbulent Flame Propagation-Adaptive Mesh Refinement method (TFP-AMR) (Vanbersel et al., 2024) is used to reduce the computational cost of the LES, which is often the limiting factor for its application to larger-than-laboratory-scale explosion scenarios. The TFP-AMR method has been applied and validated on several gas explosion configurations with varying mixtures, geometry and scale (Vanbersel et al., 2024, 2023). With this methodology, the unstructured, tetrahedral mesh is adapted on-the-fly, automatically setting a user-selected fine mesh resolution in regions containing the physical phenomena of interest: the flame front and the resolved vortical structures. The resolution is selected to match the fine resolution of the static mesh, used as reference (here $\Delta_x^{\text{fine}} = 2\,\text{cm}$). The physical phenomena of interest are detected with dedicated sensors, which define the quantities of interest (QoI) for AMR. Outside said regions of interest, a user-selected coarse mesh resolution is applied, allowing for a significant reduction in the computational cost (here $\Delta_x^{\text{coarse}} = 8\,\text{cm}$ is used). A transition following a maximal growth ratio of 20% is ensured between fine and coarse mesh regions. This is illustrated for the present configuration in Fig. 7b: while the static mesh (named STATIC, top half) is fine everywhere in the chamber and in the region where the external explosion takes place, the AMR mesh (bottom half) is only fine in the flame front and in the vortical, turbulent regions created downstream of the vent. Figure 7a displays a comparison of the flow fields between AMR and STATIC simulations. The flame and flow physics of the STATIC simulation are perfectly reproduced by AMR. The flame front shows almost identical shapes and coherent levels of heat release rate. The instantaneous vorticity fields, which are the product of the complete time-history of the explosion,

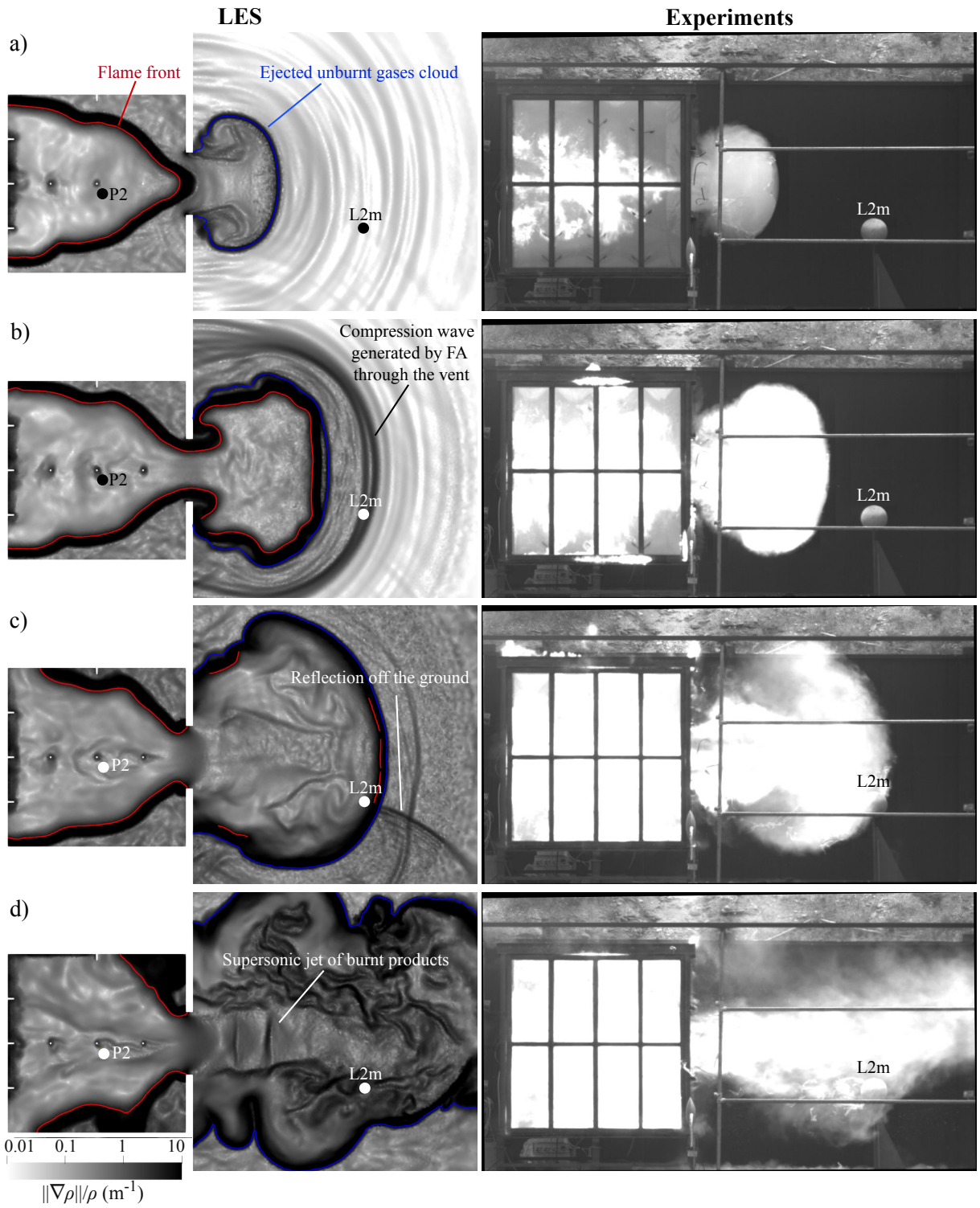

***Fig. 6**: Comparison of the explosion visualisation from LES results on the detailed geometry (left) and experimental high-speed recordings (right). For the LES, a numerical schlieren is shown on a cut across the ignition kernel's center. A hydrogen mass fraction isocontour (red line) indicates the position of the flame and an oxygen mass fraction isocontour (blue line) indicates the limit of the ejected flammable cloud. The position of probes P2 and L2m is indicated and the four selected time instants are reported on the corresponding pressure signals in Fig. 3. (For interpretation of the references to colour in this figure legend, the reader is referred to the web version of this article.)*

match nicely.

As a final validation of the TFP-AMR method on the present configuration, STATIC and AMR cases

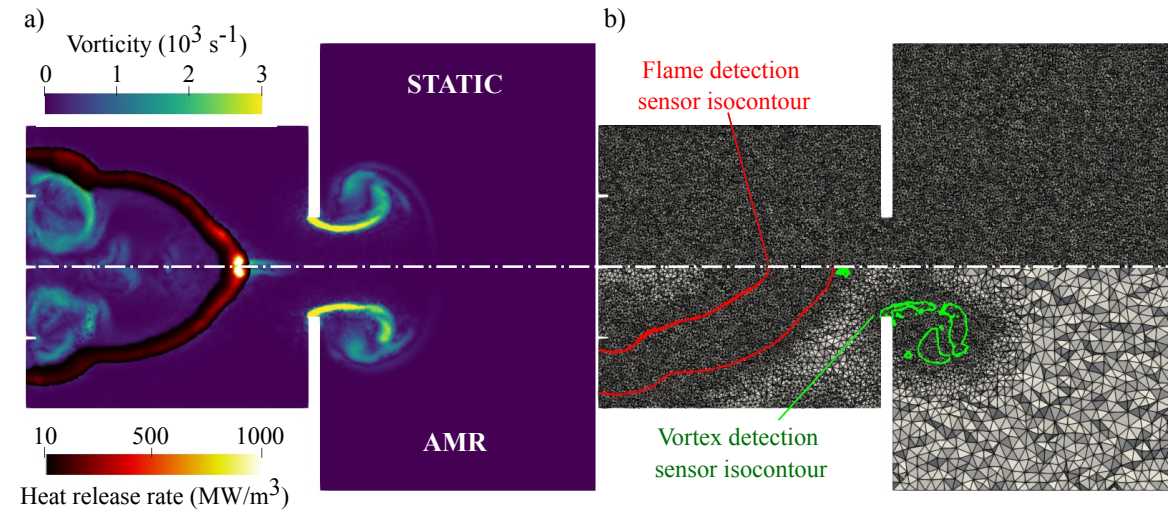

***Fig. 7**: Comparison of STATIC (top half) and AMR (bottom half) LES on a cut across the ignition kernel's center. Both LES display identical regions of the flow and are mirrored around the horizontal axis. (a) Heat release rate at the flame front plus vorticity magnitude contours. (b) Visualisation of the mesh with flame (red) and vortex (green) detection sensor isocontours for the AMR case. (For interpretation of the references to colour in this figure legend, the reader is referred to the web version of this article.)*

are compared through the temporal evolution of the overpressure signals at the probes, the flame tip absolute speed and the volume-averaged heat release rate along the explosion propagation, in Figs. 8 and 9. For the overpressure signals of Fig. 8, the same temporal shift Δt_{shift} is used for both LES. The results show very good agreement between both simulations, which is especially challenging as the signals are not filtered and have have a tendency to be noisy in highly compressible scenarios such as the present explosion. This also shows that the LES is capable of correctly propagating the compression waves and conserving their amplitude, even on the coarse regions of the mesh. Regarding the

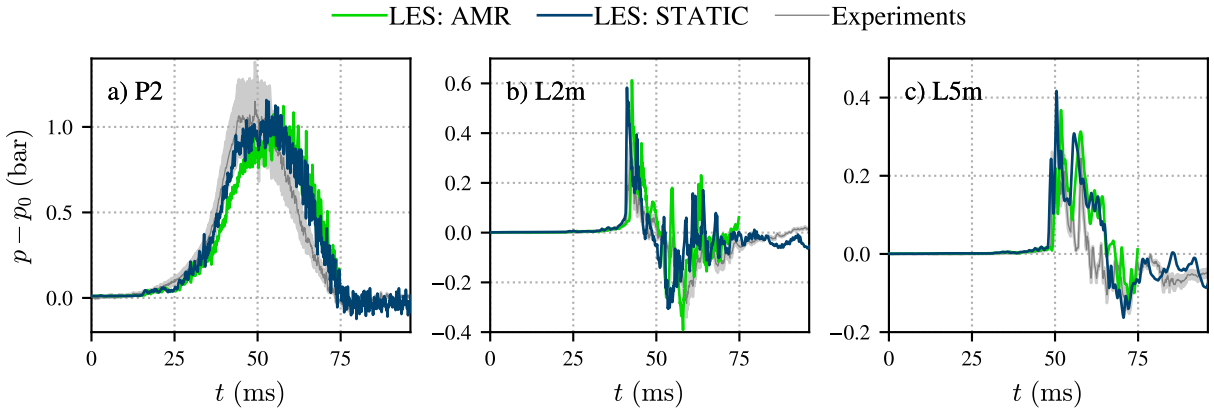

***Fig. 8**: Temporal evolution of the overpressure at probes P2, L2m and L5m. Comparison between LES on the static, reference mesh (STATIC) and dynamically adapted mesh (AMR).*

absolute flame velocity and heat release rate of Fig. 9, a perfect agreement is found between STATIC and AMR simulations.

The previous analysis shows the capability of the TFP-AMR method to recover precise results on yet another explosion configuration. Regarding the computational cost, the total cost of the AMR simulation is 9.25 khCPUcore, running overnight on 540 Intel Skylake (Xeon Gold 6140) processors. This represents a 58% reduction of the cost with respect to the STATIC simulation on the static mesh, with the same Δ_x^{fine}. The cost of the mesh adaptations is around 13% of the total computational cost

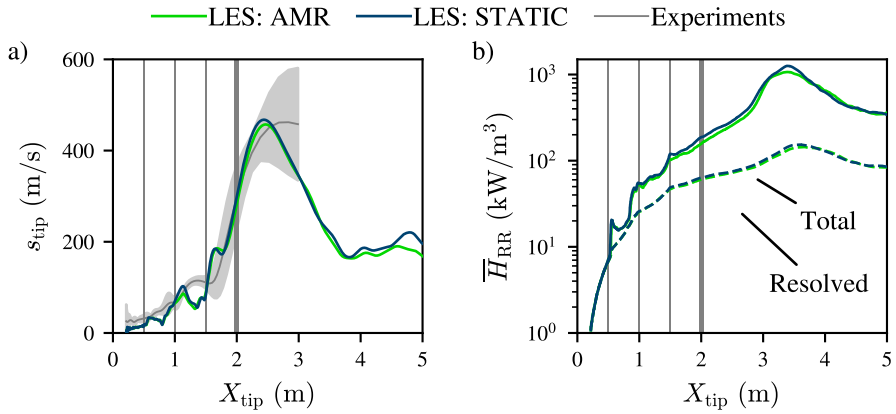

***Fig. 9**: Evolution with respect to the flame tip position (in the X axis) of the (a) absolute flame tip speed and (b) volume-averaged heat release rate. Comparison between LES on the static, reference mesh (STATIC) and dynamically adapted mesh (AMR).*

of the AMR simulation, for a total of 116 mesh adaptations along the simulation. To better interpret the cost gains, it is key to highlight that the computational cost reduction from the use of AMR (with respect to a static mesh with the same Δ_x^{fine}) is proportional to the ratio between the fine and coarse mesh sizes $\Delta_x^{\text{coarse}}/\Delta_x^{\text{fine}}$. However, the maximum gain is limited by the average fraction of fluid volume that is occupied by the physical quantities of interest $\overline{V}_{\text{QoI}}$. In practice, this implies that it is only reasonable to expect very high gains from AMR in configurations where the physical quantities of interest are very localised in the fluid volume, such as deflagrations in long channels (see (Vanbersel et al., 2023) where gains up to 88% were obtained). For instance, in the present configuration, the physical quantities of interest occupy, on average during the explosion, $\overline{V}_{\text{QoI}} = 17\%$ of the fluid volume. This means that a computational cost reduction of 83% would be the maximum attainable, and only for very large values of $\Delta_x^{\text{coarse}}/\Delta_x^{\text{fine}}$ (versus $\Delta_x^{\text{coarse}}/\Delta_x^{\text{fine}} = 4$ here). Of course, $\overline{V}_{\text{QoI}}$ and the fraction of the cost taken by the mesh adaptations may also be dependent on the fine mesh resolution. It is, thus, difficult to precisely predict the AMR gains for a given configuration, although $\overline{V}_{\text{QoI}}$ provides an educated estimate.

4 Conclusions

Regarding the physics of the vented explosion, the driving mechanisms of overpressure-generation are successfully identified and the phenomenon of external explosion is reproduced, through the present LES methodology. The pressure rise inside the chamber is driven by the flame acceleration due to geometrical confinement and to the interaction with the small-obstacle-generated turbulence. The highest flame acceleration rate is induced by the flow contraction at the vent. This sudden acceleration drives the generation of the strong compression waves responsible for the external overpressure. The presence of the ground and the surrounding walls is required to account for the reflections of said pressure waves, which impact the external overpressure signals measured. Finally, after the external explosion, a pressurised hot mixture of burnt products is trapped inside the chamber and creates a supersonic jet in front of the vent.

Small-scale geometrical elements, overlooked as details in previous publications and technical reports, have a critical impact on the flame acceleration. Since LES uses resolved quantities as inputs to the models, a minimal resolution of the flow is required. This implies that a good characterisation of the geometry, initial conditions and boundary conditions in the experiments is imperative for a predictive use of high-fidelity approaches. Therefore, more precise and repeatable safety experiments are needed to go further in the validation of high-fidelity simulation applied to highly complex, large-scale explosions. In addition, the TFP-AMR method is validated for the simulation of vented explosions, providing results as precise as with a homogeneously fine, static mesh and with a total computational cost reduction of 58%. The present example shows that the LES methodology is able to correctly

reproduce the detailed physics of a vented explosion of the scale of tens of cubic meters, for a reasonable computational cost of 9.25 khCPUcore (which corresponds to 17 h of computational runtime on 540 processors), given that sufficient experimental characterisation of the setup is performed.

Acknowledgements

The authors thank TotalEnergies, GRTgaz and Air Liquide for their financial support in the framework of the LEFEX project and ANRT for the funding through CIFRE-2021-1379. This work was performed using HPC resources from GENCI-IDRIS (Grant 2024-A0152B10157). The authors thank J. Daubech and INERIS for providing the experimental data and for the welcoming, fruitful discussions. The authors also thank L. Bernard, S. Jallais and B. Labegorre for their valuable help.

References

Bauwens, C. R., Chaffee, J., Dorofeev, S. (2008). *Experimental and numerical study of methane-air deflagrations in a vented enclosure*. Proceedings of the Ninth International Symposium on Fire Safety Science, pages 1043–1054.

Bauwens, C. R., Chaffee, J., Dorofeev, S. B. (2011). *Vented explosion overpressures from combustion of hydrogen and hydrocarbon mixtures*. International Journal of Hydrogen Energy, 36:2329–2336.

Chao, J., Bauwens, C. R., Dorofeev, S. B. (2011). *An analysis of peak overpressures in vented gaseous explosions*. Proceedings of the Combustion Institute, 33:2367–2374.

Charlette, F., Meneveau, C., Veynante, D. (2002). *A power-law flame wrinkling model for LES of premixed turbulent combustion part i: non-dynamic formulation and initial tests*. Combustion and Flame, 131:159–180.

Ciccarelli, G., Dorofeev, S. (2008). *Flame acceleration and transition to detonation in ducts*. Progress in Energy and Combustion Science, 34:499–550.

Colin, O., Rudgyard, M. (2000). *Development of high-order taylor-galerkin schemes for LES*. Journal of Computational Physics, 162:338–371.

Daubech, J., Proust, C., Gentilhomme, O., Jamois, C., Mathieu, L. (2013). *Hydrogen-air vented explosions: new experimental data*. Proc. of 5th ICHS, pages 37–49.

Duclos, A. (2019). *Development of phenomenological and risk assessment models of explosion for the emerging hydrogen-energy industry*. Ph.D. thesis, Universite de Technologie de Compiegne.

Gicquel, L. Y. M., Gourdain, N., Boussuge, J. F., Deniau, H., Staffelbach, G., Wolf, P., Poinsot, T. (2011). *Calcul parallèle haute performance des écoulements en géométries complexes*. Comptes Rendus - Mecanique, 339:104–124.

Goodwin, D. G., Moffat, H. K., Speth, R. L. (2017). *Cantera: An object-oriented software toolkit for chemical kinetics, thermodynamics, and transport processes*.

Kuznetsov, M., Friedrich, A., Stern, G., Kotchourko, N., Jallais, S., L'Hostis, B. (2015). *Medium-scale experiments on vented hydrogen deflagration*. Journal of Loss Prevention in the Process Industries, 36:416–428.

Legier, J. P., Poinsot, T., Veynante, D. (2000). *Dynamically thickened flame LES model for premixed and non-premixed turbulent combustion*. Proceedings of the Summer Program, Centre for Turbulence Research, pages 157–168.

Nicoud, F., Ducros, F. (1999). *Subgrid-scale stress modelling based on the square of the velocity gradient tensor*. Flow, Turbulence and Combustion, 62:183–200.

Poinsot, T., Lele, S. K. (1992). *Boundary conditions for direct simulations of compressible viscous flows*. Journal of Computational Physics, 101:104–129. ISSN 10902716. doi:10.1016/0021-9991(92)90046-2.

Schmitt, T. (2020). *Large-eddy simulations of the mascotte test cases operating at supercritical pressure*. Flow, Turbulence and Combustion, 105:159–189.

Schmitt, P., Poinsot, T., Schuermans, B., Geigle, K. P. (2007). *Large-eddy simulation and experimental study of heat transfer, nitric oxide emissions and combustion instability in a swirled turbulent*

high-pressure burner. Journal of Fluid Mechanics, 570:17–46.

Tolias, I. C., Stewart, J. R., Newton, A., Keenan, J., Makarov, D., Hoyes, J. R., Molkov, V., Venetsanos, A. G. (2018). *Numerical simulations of vented hydrogen deflagration in a medium-scale enclosure*. Journal of Loss Prevention in the Process Industries, 52:125–139.

Tolias, I. C., Venetsanos, A. G. (2018). *An improved CFD model for vented deflagration simulations – analysis of a medium-scale hydrogen experiment*. International Journal of Hydrogen Energy, 43:23568–23584.

UCSD (2016). *Chemical-kinetic mechanisms for combustion applications*.

Vanbersel, B., Meziat Ramirez, F. A., Mohanamuraly, P., Staffelbach, G., Jaravel, T., Douasbin, Q., Dounia, O., Vermorel, O. (2024). *A systematic adaptive mesh refinement method for large eddy simulation of turbulent flame propagation*. Flow, Turbulence and Combustion.

Vanbersel, B., Meziat Ramirez, F. A., Vermorel, O., Jaravel, T., Douasbin, Q., Dounia, O. (2023). *Large eddy simulations of a hydrogen-air explosion in an obstructed chamber using adaptive mesh refinement*. 10th International Conference on Hydrogen Safety.

Vyazmina, E., Jallais, S., Krumenacker, L., Tripathi, A., Mahon, A., Commanay, J., Kudriakov, S., Studer, E., Vuillez, T. (2016). *CFD benchmark on vented explosion of hydrogen / air mixtures: best practices and recommendations*. Congrès Lambda Mu 20 de Maîtrise des Risques et de Sûreté de Fonctionnement.

Vyazmina, E., Jallais, S., Krumenacker, L., Tripathi, A., Mahon, A., Commanay, J., Kudriakov, S., Studer, E., Vuillez, T., Rosset, F. (2019). *Vented explosion of hydrogen/air mixture: An intercomparison benchmark exercise*. International Journal of Hydrogen Energy, 44:8914–8926.

CFD modelling of premixed flame propagation of cornstarch dust in the 20 L sphere

Alain Islas[a], Adrián Pandal[a], Maria Portarapillo[b*], Roberto Sanchirico[c] and Almerinda Di Benedetto[b]

[a] Department of Energy, University of Oviedo - 33203 Gijón, Asturias, Spain
[b] Department of Chemical, Materials, and Production Engineering, University of Naples Federico II, P.le V. Tecchio 80, 80125 Naples, Italy
[c] Istituto di Scienze e Tecnologie per l'Energia e la Mobilità Sostenibili (STEMS), Consiglio Nazionale delle Ricerche (CNR), Piazzale Tecchio 80, 80125, Napoli, Italy

E-mail: maria.portarapillo@unina.it

Abstract

The development of CFD simulations for dust explosions poses a major challenge when it comes to finding a suitable combustion model for air/dust mixtures. On the one hand, particle-based Lagrangian models provide a comprehensive description of the thermochemical conversion of fuels, but they often require a large number of computational packages, making them expensive and impractical for most industrial scenarios. In contrast, premixed combustion models assume that an air/dust mixture can be represented by a single homogeneous fluid in which the chemical reactions take place mainly in the homogeneous gas phase. These models are particularly suitable for the simulation of biomass dust explosions, since biomass flames are dominated by the rapid release and combustion of volatile gases. This paper presents a novel CFD model for premixed dust explosions based on OpenFOAM that incorporates a novel correlation for the laminar flame speed of the air/dust mixture based on Mallard-Le Chatelier theory. The model is validated with literature data from cornstarch dust explosions in the 20L bomb.

Keywords: *Dust explosions; Cornstarch; Flame propagation; Premixed combustion; CFD simulations*

1. Introduction

Despite more than two centuries of progress in industrial safety, dust explosions continue to pose a significant risk to workers and property. These explosions can occur when the conditions of the explosion pentagon are met, namely the presence of combustible dust, an ignition source, oxygen, confinement and dispersion of the dust particles. Various measures can be taken to minimise the risk of dust explosions, including explosion suppression and isolation systems and vent panels. However, effective design of these systems requires a detailed understanding of the explosiveness of dust clouds in real industrial environments. Conducting experiments in real industrial environments can be prohibitively expensive and logistically difficult, which has led to the development of laboratory-scale testing equipment. The 20-litre Siwek sphere enables the determination of the explosion pressure P_{ex} and the deflagration index K_{St}, i.e. the maximum rate of pressure rise, normalised to the volume of the combustion chamber. These parameters can be transferred to conditions that are representative of large-scale explosions using the cubic root law. The precise determination of these parameters is crucial for the development of effective strategies to mitigate explosions.

A decisive factor influencing the severity of dust explosions is the type of flame propagation, which depends on the chemical composition of the dust cloud. Combustion can occur by heterogeneous reactions controlled by oxygen diffusion and/or by homogeneous reactions dominated by the rate of

degassing and combustion of volatile gases (Di Benedetto and Russo, 2007). For example, the combustion of coal particles is primarily driven by heterogeneous reactions (coal oxidation or gasification), while the combustion of biomass particles is dominated by the devolatilization and homogeneous gas phase reactions due to the high release of volatile substances.

Unsteady flame propagation, turbulence and particle sedimentation arising during dust explosions are strictly related, and to perform consequence analysis, advanced CFD models are a real breakthrough. The development of CFD models for dust explosions poses a major challenge when it comes to finding a suitable combustion model for air/dust mixtures. Particle-based Lagrangian models may provide a comprehensive description of the thermochemical conversion of fuels when couple to detailed combustion models. In a previous work, Islas et al. (2022) used an open-source CFD code (OpenFOAM) to simulate the dispersion and the combustion of combustible dust in a 20 L container ((Islas et al., 2023, 2022a, 2022b)). To represent the combustion of Pellets Asturias and Cupressus Funebris dusts, the model includes, in addition to the equation of the gas phase and for the particle tracking, also equations for the combustion in the homogeneous phase, the radiation model, the drying and devolatilization model and the surface reaction equations.

However, this approach has high computational cost and it is mostly impractical for industrial scenarios (Islas et al., 2022a). The trade-off could be a CFD model based on the Eulerian approach coupled to premixed combustion models . In this case, the air/dust mixture is modelled as a homogeneous fluid in which the chemical reactions take place in the homogeneous gas phase. These models are particularly suitable for the simulation of biomass dust explosions since biomass flames are controlled by the combustion of volatile gases, produced by biomass pyrolysis. This work presents a CFD model of premixed dust explosions in which the combustion sub-model is based on the use of a novel correlation for the laminar burning velocity of the air/dust mixture inspired by the Mallard-Le Chatelier theory (Portarapillo et al., 2023). CFD model has been developed by means of the open-source CFD code OpenFOAM 8. The developed model has been validated by comparing the results with literature data of cornstarch explosions in the 20 L bomb and the effect of the stoichiometric concentration of the dust and pre-ignition turbulence level was investigated.

2. Numerical modeling

2.1. Gas-phase governing equations

To simulate dust explosions, the 3D transient form of the Reynolds-Averaged Navier Stokes (RANS) equations were solved. The equations that apply to the gas phase consist of the equations for mass, momentum and energy transport. The mass transport is:

$$\frac{\partial \bar{\rho}}{\partial t} + \frac{\partial}{\partial x_i}(\bar{\rho}\tilde{u}_i) = 0 \quad (1)$$

Where $\bar{\rho}$ is the Reynolds-averaged density, t is the time, x_i is the direction and $\tilde{u}_i$ is the density-weighted time averaged or Favre-averaged velocity.
The momentum transport equation is:

$$\frac{\partial(\bar{\rho}\tilde{u}_i)}{\partial t} + \frac{\partial}{\partial x_j}\left(\bar{\rho}\tilde{u}_i\tilde{u}_j\right) = \frac{\partial \bar{p}}{\partial x_j} + \frac{\partial \bar{\tau}^{ij}}{\partial x_j} + \frac{\partial}{\partial x_j}\left(-\bar{\rho}\widetilde{u_i' u_j'}\right) \quad (2)$$

Where $\bar{\tau}^{ij}$ are the viscous stresses composed by the linear and volumetric rate of deformation and $\bar{\rho}\widetilde{u_i' u_j'}$ are addressed by invoking the Boussinesq hypothesis. Due to its robustness for industrial applications, we chose the standard k-ε model to close the Reynolds stress tensor (Launder and Spalding, 1983). The transport equations of k and ε are:

$$\frac{\partial(\bar{\rho}k)}{\partial t}+\frac{\partial}{\partial x_i}(\bar{\rho}\tilde{u}_i k)-\frac{\partial}{\partial x_i}\left[\bar{\rho}\left(\mu+\frac{\mu_t}{\sigma_k}\right)\frac{\partial k}{\partial x_i}\right]=\bar{\rho}P_k-k\left(\frac{2}{3}\bar{\rho}\frac{\partial\tilde{u}_i}{\partial x_i}+\frac{\bar{\rho}\varepsilon}{k}\right) \quad (3)$$

$$\frac{\partial(\bar{\rho}\varepsilon)}{\partial t}+\frac{\partial}{\partial x_i}(\bar{\rho}\tilde{u}_i \varepsilon)-\frac{\partial}{\partial x_i}\left[\bar{\rho}\left(\mu+\frac{\mu_t}{\sigma_k}\right)\frac{\partial \varepsilon}{\partial x_i}\right]=\frac{C_1\bar{\rho}P_k\varepsilon}{k}-\varepsilon\left[\left(\frac{2}{3}C_1-C_3\right)\bar{\rho}\frac{\partial\tilde{u}_i}{\partial x_i}+\frac{C_2\bar{\rho}\varepsilon}{k}\right] \quad (4)$$

An energy transport equation is solved for both the total mixture and the unburned gases:

$$\frac{\partial(\bar{\rho}\tilde{h}_0)}{\partial t}+\frac{\partial}{\partial x_i}\left(\bar{\rho}\tilde{u}_i\tilde{h}_0\right)=\frac{\partial\bar{p}}{\partial t}+\frac{\partial}{\partial x_i}\left[\bar{\rho}\left(\alpha+\frac{\nu_t}{Pr_t}\right)\frac{\partial\tilde{h}_a}{\partial x_i}\right] \quad (5)$$

$$\frac{\partial(\bar{\rho}\tilde{h}_{0,u})}{\partial t}+\frac{\bar{\rho}}{\bar{\rho}_u}\frac{\partial}{\partial x_i}\left(\bar{\rho}\tilde{u}_i\tilde{h}_{0,u}\right)=\frac{\bar{\rho}}{\bar{\rho}_u}\frac{\partial\bar{p}}{\partial t}+\frac{\partial}{\partial x_i}\left[\bar{\rho}\left(\alpha+\frac{\nu_t}{Pr_t}\right)\frac{\partial\tilde{h}_{a,u}}{\partial x_i}\right] \quad (6)$$

Where $\tilde{h}_0=\tilde{h}_a+\frac{\tilde{u}_i^2}{2}$ is the total mixture enthalpy (absolute enthalpy plus kinetic energy), $\tilde{h}_{0,u}=\tilde{h}_{a,u}+\frac{\tilde{u}_i^2}{2}$ is the total enthalpy of the unburned gases, α is the laminar thermal diffusivity, and Pr_t is the turbulent Prandlt number. The absolute enthalpy of either the mixture or the unburned gases, are at the same time, the sum of the corresponding sensible and chemical enthalpies.

2.2. Premixed combustion model

For premixed flames, combustion chemistry can be reduced to a single one-step, irreversible global reaction. In this work, the propagation of the flame front is modelled by the assumption of a unity turbulent Lewis number (i.e., the turbulent mass diffusivity and turbulent thermal diffusivity are identical) and the solution of a transport equation for the regression variable *b*:

$$\frac{\partial(\bar{\rho}b)}{\partial t}+\frac{\partial}{\partial x_i}(\bar{\rho}\tilde{u}_i b)=\frac{\partial}{\partial x_i}\left[\bar{\rho}\left(\alpha+\frac{\nu_t}{Sc_t}\right)\frac{\partial b}{\partial x_i}\right]-\bar{\dot{\omega}}_b+\omega_{ign} \quad (7)$$

where Sc_t is the turbulent Schmidt number, $\bar{\dot{\omega}}_b$ is the reaction rate, ω_{ign} is the ignition source term (Poinsot and Veynante, 2005; Veynante and Vervisch, 2002). The reaction rate $\bar{\dot{\omega}}_b$ and the regression variable *b* are expressed as:

$$\bar{\dot{\omega}}_b=\bar{\rho}_u S_u \Xi\left|\frac{\partial b}{\partial x_i}\right| \quad (8)$$

$$b=1-c=1-\frac{T-T_u}{T_b-T_u}=\frac{T-T_b}{T_u-T_b} \quad (9)$$

Where $\Xi=\frac{S_t}{S_u}$ is the turbulent-to-laminar burning velocity ratio, $\bar{\rho}_u$ is the density of the unburned gases, where T, T_u, and T_b are the temperatures of the mixture, the unburned and the burnt gases, respectively, *c* is the progress variable.

2.3. Ignition model

An initial distribution of the regress variable is required to start the flame propagation process. This task is carried out with a simplified deposition model (Gianetti et al., 2023). Starting from an initial flame kernel diameter d_{ign} and an ignition duration Δt_{ign}, an ignition source term is imposed in the cells for which the distance from the ignition core is less than $d_{ign}/2$. The ignition source is expressed as:

$$\omega_{ign} = \frac{S_{tr}\rho_u V_{ign}}{\Delta t_{ign} b} \quad (10)$$

where S_{tr} is a user-defined strength coefficient and V_{ign} is the volume of the ignition cells. With the deposition model, the CFD solver can explicitly calculate the formation of the initial kernel. The spark discharge is simulated by depositing the total spark energy in a spherical volume with a diameter of 1 cm in the geometric centre of the 20 L sphere. The spherical volume in which the spark energy is deposited, is transported by the local mean flow. In our work, to reflect the diminishing rate of pressure rise as the quantity of ignitable dust increases, we assumed that S_{tr} scaled linearly with dust concentration.

2.4. Laminar and turbulent burning velocity

The laminar flame speed S_u was calculated with Portarapillo et al. (2023) correlation (Portarapillo et al., 2023), which is applicable to dust-air mixtures whose combustion is dominated by volatile flames. The theoretical derivation is based on a three-layers model (Glassman and Yetter, 2008) and is represented by the following equation:

$$S_u = \frac{\rho_{dev} S_l Cp_{gas,II}(T_{ign} - VP)}{\rho_{dust+air}(Cp_{dust+air}(VP-25)+\Delta H_{dev})} \quad (11)$$

Where ΔH_{dev} is the devolatilization heat, ρ_{dev} is the density of unburnt gases, S_l is the laminar burning velocity of the gaseous mixture with air, $Cp_{gas,II}$ is the specific heat of the unburnt gases, T_{ign} is the autoignition temperature of the generated gases, VP is the volatile point of the dust, $\rho_{dust+air}$ is the particles density mixed with air, $Cp_{dust+air}$ is the specific heat of the combustible dust mixed with air. The turbulent flame speed is modeled using the Zimont approach (Zimont et al., 1998). The model assumes that there is a small-scale turbulence in the laminar flame that is in equilibrium, which leads to an expression for the turbulent burning velocity that is based solely on large-scale turbulent parameters. The model is only valid if the smallest turbulent eddies in the flow, the so-called Kolmogorov scales, are smaller than the flame thickness and enter the flame zone, which is referred to as the thin reaction zone.

2.5. Stoichiometry of combustion

The physical and chemical processes that lead to the spread of dust flames can vary in intensity depending on the fuel concentration. The stoichiometric air-fuel ratio on a mass basis AFR_{stoich} was determined using the following formula by Andrews and Phylaktou (Andrews and Phylaktou, 2010; Saeed et al., 2022, 2016):

$$AFR_{stoich} = \frac{1}{0.232}\left(\frac{8}{3}\cdot C + 8\cdot H - O\right) kg_{air}/kg_{fuel} \quad (12)$$

Where C, H and O represent the mass fraction of carbon, hydrogen and oxygen in the ultimate analysis (**Table 1**). The AFR_{stoich} for cornstarch is 5.211 kg_{air}/kg_{fuel}, which is converted to C_{St} = 230.27 g/m^3. This stoichiometric dust concentration is in excellent agreement with other values from the literature reported by Dahoe (2000), Lee et al. (1992) and Mazurkiewicz et al. (1993) (Dahoe, 2000; Lee et al., 1992; Mazurkiewicz et al., 1993).

The equivalence ratio ϕ is defined as the actual dust concentration C of a particular mixture divided by the dust concentration at stoichiometric conditions. It is used to indicate whether a combustible dust mixture is fuel lean (ϕ < 1), fuel rich (ϕ > 1) or stoichiometric (ϕ = 1). The thermophysical properties of the unburnt and burnt mixtures were calculated as a function of temperature using the open-source library Cantera. For the 1D chemistry calculations, we applied the GRI 3.0 reaction mechanism to the volatile gases of corn starch experimentally measured by Mazurkiewicz

(Mazurkiewicz et al., 1993). We then fitted these thermophysical properties to the NIST JANAF format with 7 polynomial coefficients.

Table 1. *Ultimate and proximate analyses of cornstarch dust.*

Samples	**Values**
Fixed carbon (wt. %ar)	12.04
Volatile (wt. %ar)	67
Moisture (wt. %ar)	18.59
Ash (wt. %ar)	2.37
C (wt. %daf)	46.92
H (wt. %daf)	5.40
O (wt. %daf)	47.42
N (wt. %daf)	0.20
S (wt. %daf)	0.06

2.6. Model setup

Computational domains are shown in **Fig. 1**. The first geometry, reported in **Fig. 1a**, was used for the simulations with uniform turbulence level while the second (**Fig. 1b**) represents the actual configuration of the 20 L vessel (including canister and feeding tube) and was used to consider the actual pre-ignition turbulence level established in the sphere after the dust injection. The simulated domains consist of a three-dimensional mesh of 1.18 million and 1.6 million hexahedral and tetrahedral elements, respectively. The average cell length is 2.5 mm with a minimum orthogonal quality of 0.60. It was created manually using ANSYS ICEM meshing software and then converted to OpenFOAM format for simulation purposes.

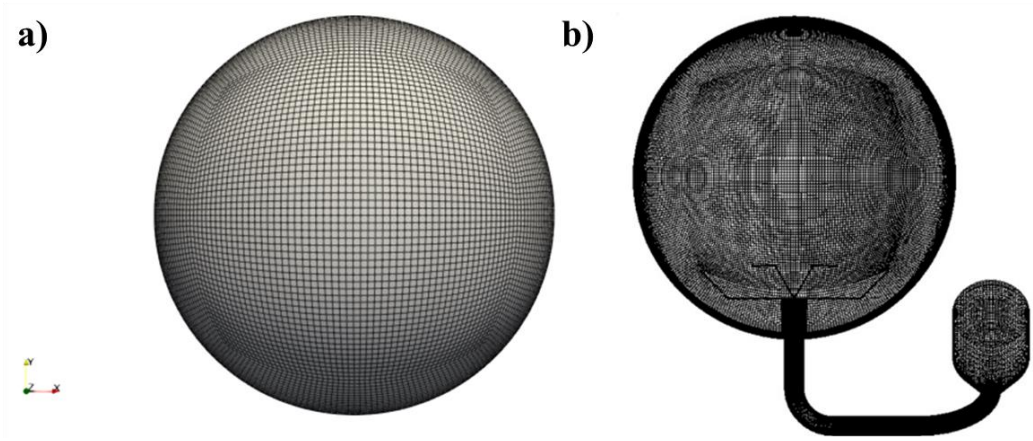

Fig. 1. *Computational grids*

The governing equations were solved using the finite volume method in OpenFOAM. The coupling of pressure and velocity was carried out using the iterative PIMPLE algorithm. This included one corrector step and two outer corrector steps. The governing equations were discretized with second order schemes, with upwind boundary and non-orthogonal correction for the convective and diffusive terms, respectively. The gradients were evaluated with a linear scheme with central differentiation, while the unsteady discretization was treated with the second-order Crank-Nicolson scheme and a

blending factor of 0.9. The time step was automatically adjusted using an adaptive time step method controlled by a Courant number Co = 0.2. The boundary and initial conditions of the simulation are provided in **Table 2**.

Table 2. *Boundary and initial conditions case set-up.*

	Uniform turbulence		Variable turbulence	
Variable	**Boundary condition**	**Initial value**	**Boundary condition**	**Initial value**
U	No slip	0 m/s	No slip	0 m/s
T	externalWallHeatFluxTemperature	293 K h = 118 W/m2 K	externalWallHeatFluxTemperature	293 K h = 118 W/m2 K
k	kqRWallFunction	u'=2 m/s*	kqRWallFunction	mapped
ε	epsilonWallFunction	u'=2 m/s*	epsilonWallFunction	mapped
O_2/N_2	zeroGradient	0.23/0.77 (%w)	zeroGradient	0.23/0.77 (%w)
p_{sphere}	zeroGradient	1 bar	zeroGradient	0.4 bar
$p_{canister}$	-	-	zeroGradient	21 bar

**k* was calculated considering isotropic turbulence and the integral length scale used for the calculation of ε equal to the 7% of the pipe/nozzle

3. Results and discussion

3.1. Effect of stoichiometric concentration

The first effect considered is that of the stoichiometric concentration. In fact, many authors agree that in the case of cornstarch, the stoichiometric concentration was found to be 230 g/m^3 (Dahoe, 2000; Lee et al., 1992; Mazurkiewicz et al., 1993), while Ogle et al. (2016) measured a concentration of 298 g/m^3 (Ogle, 2016). This concentration has a direct effect on the equivalence ratio and therefore on the combustion reaction itself. The results obtained from the simulations in terms of pressure trends as a function of time were compared with the only experimental data available in the literature (Dahoe, 2000) and reported in **Fig. 2**. This shows that the stoichiometric concentration has no effect on the rate of pressure rise, but does change the maximum explosion pressure. As can be seen, the rate of pressure rise on which the deflagration index depends is perfectly represented by the model, while the largest differences are found in the maximum pressure.

At 250 g/m^3, the behavior is best represented by the simulation performed with C_{stoic} = 230 g/m^3 while for intermediate concentrations the simulations identify a range in which the experimental data fall. In contrast, the concentration at C_{stoic} = 298 g/m^3 overestimates the richer condition (625 g/ m^3). Although the fit is not fully optimized in terms of maximum pressure, it is important to emphasize the strength of the result obtained. It is worth remembering that these results were obtained without solving equations related to the solid phase, so the phenomenon is directly considered as a premixed flame consisting of air and the gases produced by the devolatilization of the dust, leading to great consequences from the point of view of simplicity of the model and lower computational costs.

Fig. 3 shows the explosion pressures trend as a function of dust concentration for cornstarch air mixtures as obtained by the CFD model in the case of C_{stoic} = 230 g/m^3 (a) and C_{stoic} = 298 g/m^3 (b), compared with experimental data available in the literature (Dahoe, 2000). As can be seen, the monotonically decreasing trend of the maximum pressure in the concentration range 250-625 g/m^3 is clearly captured by the C_{stoic} case of 230 g/m^3. Regarding the values, a maximum deviation of pressure values from those evaluated with the model of 10% is detected in the case of C_{stoic} = 298 g/m^3 and 8% equal to the most shared value in the scientific literature (Dahoe, 2000; Lee et al., 1992; Mazurkiewicz et al., 1993). Results are also reported in terms of deflagration index in **Table 3** and as

can be seen in the case of C_{stoic} of 230 g/m^3, the agreement with the experimental data are always very good (deviation<15%).

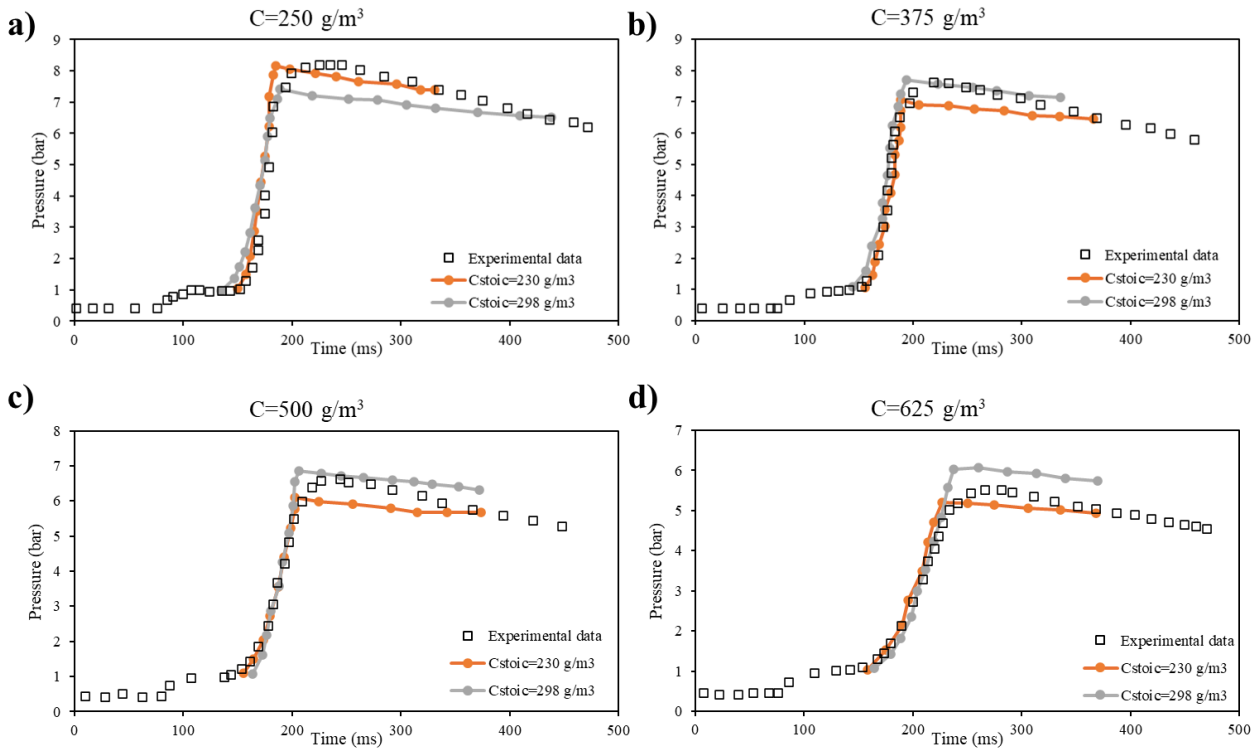

Fig. 2. *Explosion curves for cornstarch air mixtures as obtained by the CFD model in the case of C_{stoic} = 230 g/m^3 (orange line) and C_{stoic} = 298 g/m^3 (grey line), in the case of dust concentration at 250 (a), 375 (b), 500 (c) and 625 (d) g/m^3, compared with experimental data available in the literature* (Dahoe, 2000).

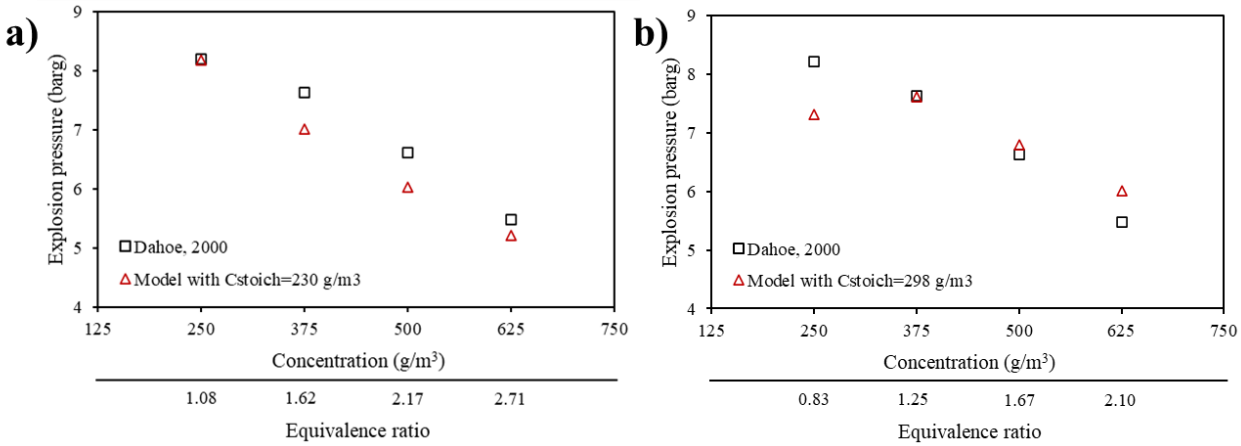

Fig. 3. *Explosion pressures as a function of dust concentration for cornstarch air mixtures as obtained by the CFD model in the case of C_{stoic} = 230 g/m^3 (a) and C_{stoic} = 298 g/m^3 (b), compared with experimental data available in the literature* (Dahoe, 2000). *The equivalence ratio is also reported as secondary X-axis.*

Table 3. *Summary of the results obtained in the simulations concerning the effect of stoichiometric concentration and pre-itnition turbulence in terms of explosion pressure, maximum rate of pressure rise and deflagration index.*

		P_{ex} (bar)	$(dP/dt)_{max}$ (bar/s)	K_{St} (bar m/s)
250 g/m³	**Experimental**	8.2	478	131
	Model C_{stoic}=230 g/m³	8.2	408	112
	Model C_{stoic}=298 g/m³	7.4	336	92
	Uniform turbulence	8.2	408	112
	Variable turbulence	8.2	410	113
375 g/m³	**Experimental**	7.6	681	187
	Model C_{stoic}=230 g/m³	7.1	708	194
	Model C_{stoic}=298 g/m³	7.7	353	97
	Uniform turbulence	7.1	708	194
	Variable turbulence	6.9	681	113
500 g/m³	**Experimental**	6.6	157	43
	Model C_{stoic}=230 g/m³	6.0	147	40
	Model C_{stoic}=298 g/m³	6.8	371	100
	Uniform turbulence	6.0	147	40
	Variable turbulence	6.0	162	44
625 g/m³	**Experimental**	5.5	94	26
	Model C_{stoic}=230 g/m³	5.2	132	36
	Model C_{stoic}=298 g/m³	6.1	134	36
	Uniform turbulence	5.2	132	36
	Variable turbulence	5.2	93	26

3.2. Effect of turbulence level

CFD simulations were performed with geometry b in **Fig. 1** in the case of a cornstarch dispersion of 50 microns at different dust concentrations to obtain the turbulence distribution before ignition typical of the ignition time. The results obtained from simulations with geometry b are shown in **Fig. 4** in terms of turbulent kinetic energy maps in the center x-y plane that vary with the concentration of supplied dust, which as can be seen has a perturbing influence on the momentum field, as found in previous works (Di Benedetto et al., 2013; Di Sarli et al., 2014). As usually found, there is a large variability in turbulence level from the center to the wall, with a maximum at 85 m^2/s^2 near the ignition site. It is also possible to visualize a different turbulence field depending on the analyzed concentration, a direct consequence of the fact that the simulations were performed taking into account the influence of the fluid on the particle motion and vice versa (two-way coupling considering the classification by (Elghobashi, 1994)). As for the simulations performed with a uniform turbulence level, a velocity fluctuation value u'=2 m/s was chosen, corresponding to the light blue zone in **Fig. 4**. The results obtained from the simulations in terms of pressure trends as a function of time were compared with the only experimental data available in the literature (Dahoe, 2000) and reported in **Fig. 5**. The non-uniform initial turbulence fields modifies the rate of pressure rise and simultaneously plays no effect on the maximum pressure, as reported in

Table 3. For the cornstarch dust studied here, sometimes this is negligible (leanest concentrations) while on other occasions, it has a noticeable impact (richest concentration). It is noting, that in our model the flame propagation is modeled as a premixed flame in which the fuel is homogeneous. As a result, the effect of non uniform dust concentration due to sedimentation and/or dispersion interacting with the turbulent flow is not taken into account. Therefore, a higher turbulence level only causes an increase in the rate of flame propagation. Contrarily, in the real experiment, turbulence certainly changes the dispersion of dust and thus the fuel accumulation zones. Future work will be developed to also simulate the effect of dust distribution on the phenomena occurring in the heterogeneous phase (dust heating, oxygen diffusion, dust devolatilization).

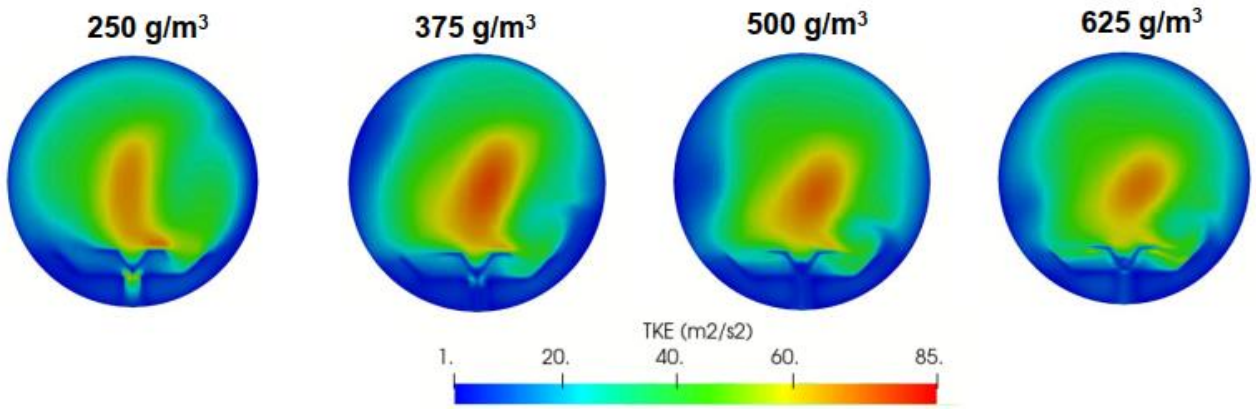

Fig. 4. *Turbulent kinetic energy map in the center x-y plane as a function of dust concentration for cornstarch air mixtures as obtained by the CFD model in the case of C = 250,375, 500 and 625 g/m^3.*

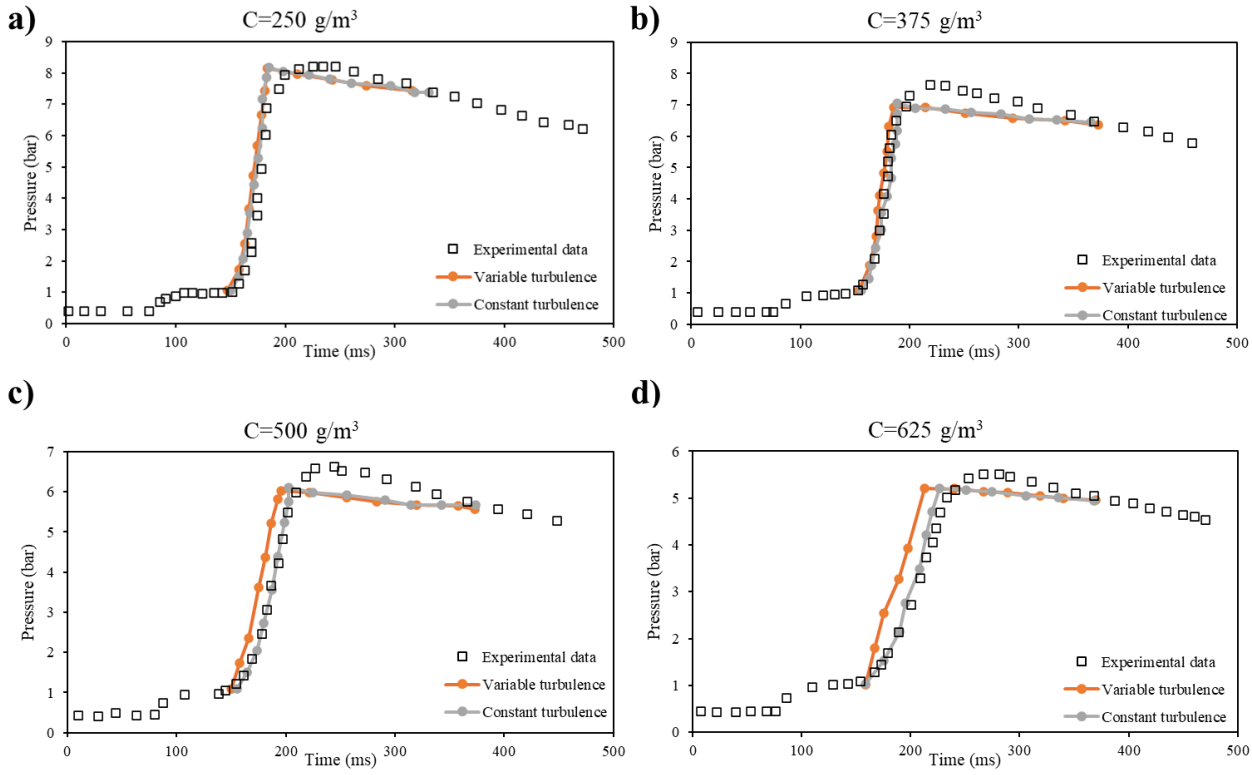

Fig. 5. *Explosion curves for cornstarch air mixtures as obtained by the CFD model in the case of variable turbulence (orange line) and constant turbulence (grey line), in the case of dust concentration at 250 (a),*

375 (b), 500 (c) and 625 (d) g/m^3, compared with experimental data available in the literature (Dahoe, 2000).

4. Conclusions

The study presents a new CFD model for the simulation of dust explosions, as a premixed gas explosion not considering solid-phase equations, which is particularly applicable to scenarios dominated by the combustion of volatile gases, such as biomass dust explosions. This model offers a balance between computational cost and accuracy, making it suitable for industrial applications. For these cases, the average simulation time was just 6-8 hours, using mesh of ~1M elements and 32 cores. For similar cases with Lagrangian modeling and same mesh/processors,, the solution time was around 10 days. The developed CFD model, based on OpenFOAM, was validated against literature data on cornstarch dust explosions in a 20-liter bomb. The validation process demonstrated the model ability to accurately predict key parameters such as explosion pressures and pressure rise rates. The study examined the effect of stoichiometric concentration on explosion characteristics, highlighting the influence on maximum explosion pressure while demonstrating no significant influence on pressure rise rates. This insight is crucial for understanding and predicting the behavior of dust explosions under different conditions. The analysis of turbulence levels before ignition revealed their disruptive influence on the momentum field, which affects the rate of flame propagation. Simulation results showed that higher turbulence levels led to higher pressure rise rates, emphasizing the importance of considering turbulence effects when modeling dust explosions. Overall, the developed CFD model provides a promising approach for simulating dust explosions, providing valuable insights for improving industrial safety measures and designing effective explosion prevention strategies.

Acknowledgement

The authors acknowledge Mr. Andrea Bizzarro for his excellent technical support.

References

Andrews, G.E., Phylaktou, H.N., 2010. Explosion safety. Handbook of Combustion.

Dahoe, A.E., 2000. Dust explosions: a study of flame propagation. TU Delft.

Di Benedetto, A., Russo, P., 2007. Thermo-kinetic modelling of dust explosions. J. Loss Prev. Process Ind. 20, 303–309. https://doi.org/10.1016/j.jlp.2007.04.001

Di Benedetto, A., Russo, P., Sanchirico, R., Di Sarli, V., 2013. CFD Simulations of Turbulent Fluid Flow and Dust Dispersion in the 20 Liter Explosion Vessel. AIChE 59, 2485–2496. https://doi.org/10.1002/aic

Di Sarli, V., Russo, P., Sanchirico, R., Di Benedetto, A., 2014. CFD simulations of dust dispersion in the 20 L vessel: Effect of nominal dust concentration. J. Loss Prev. Process Ind. 27, 8–12. https://doi.org/10.1016/j.jlp.2013.10.015

Elghobashi, S., 1994. On predicting particle-laden turbulent flows. Appl. Sci. Res. 52, 309–329. https://doi.org/10.1007/BF00936835

Gianetti, G.G., Lucchini, T., D'Errico, G., Onorati, A., Soltic, P., 2023. Development and Validation of a CFD Combustion Model for Natural Gas Engines Operating with Different Piston Bowls. Energies 16, 1–23. https://doi.org/10.3390/en16020971

Glassman, I., Yetter, R.A., 2008. Combustion-Fourth edition. Elsevier.

Islas, A., Fernández, A.R., Betegón, C., Martínez-Pañeda, E., Pandal, A., 2023. Biomass dust explosions: CFD simulations and venting experiments in a 1 m3 silo. Process Saf. Environ.

Prot. 176, 1048–1062. https://doi.org/10.1016/j.psep.2023.06.074
Islas, A., Fernández, A.R., Betegón, C., Martínez-Pañeda, E., Pandal, A., 2022a. Computational assessment of biomass dust explosions in the 20L sphere. Process Saf. Environ. Prot. 165, 791–814. https://doi.org/10.1016/j.psep.2022.07.029
Islas, A., Rodríguez-Fernández, A., Betegón, C., Martínez-Pañeda, E., Pandal, A., 2022b. CFD simulations of turbulent dust dispersion in the 20 L vessel using OpenFOAM. Powder Technol. 397. https://doi.org/10.1016/j.powtec.2021.117033
Launder, B.E., Spalding, D.B., 1983. the Numerical Computation of Turbulent Flows, Numerical Prediction of Flow, Heat Transfer, Turbulence and Combustion. Pergamon Press, Ltd. https://doi.org/10.1016/b978-0-08-030937-8.50016-7
Lee, J.H.S., Zhang, F., Knystautas, R., 1992. Propagation mechanisms of combustion waves in dust-air mixtures. Powder Technol. 71, 153–162. https://doi.org/10.1016/0032-5910(92)80004-G
Mazurkiewicz, J., Jarosinski, J., Wolanski, P., 1993. Investigations of burning properties of cornstarch dust-air flame. Arch. Combust. 13.
Ogle, R.A., 2016. Dust Explosion Dynamics, Dust Explosion Dynamics. https://doi.org/10.1016/c2014-0-03833-6
Poinsot, T., Veynante, D., 2005. Theoretical and numerical combustion - Second edition. Edwards.
Portarapillo, M., Sanchirico, R., Luciani, G., Di Benedetto, A., 2023. Flame propagation of combustible dusts: A Mallard-Le Chatelier inspired model. Combust. Flame 251. https://doi.org/10.1016/j.combustflame.2023.112737
Saeed, M.A., Niedzwiecki, L., Arshad, M.Y., Skrinsky, J., Andrews, G.E., Phylaktou, H.N., 2022. Combustion and Explosion Characteristics of Pulverised Wood, Valorized with Mild Pyrolysis in Pilot Scale Installation, Using the Modified ISO 1 m3 Dust Explosion Vessel. Appl. Sci. 12. https://doi.org/10.3390/app122412928
Saeed, M.A., Slatter, D.M., Andrews, G.E., Phylaktou, H.N., Gibbs, B.M., 2016. The burning velocity of pulverised biomass: The influence of particle size. Chem. Eng. Trans. 53, 31–36. https://doi.org/10.3303/CET1653006
Veynante, D., Vervisch, L., 2002. Turbulent combustion modeling. Prog. Energy Combust. Sci. 28, 193–266. https://doi.org/10.1016/S0360-1285(01)00017-X
Zimont, V., Polifke, W., Bettelini, M., Weisenstein, W., 1998. An efficient computational model for premixed turbulent combustion at high reynolds numbers based on a turbulent flame speed closure. Proc. ASME Turbo Expo 120, 526–532. https://doi.org/10.1115/97-GT-395

Full and Laboratory Scale Tests for the Assessment of Transient Thermal Effects from ignited Natural Gas Pipeline Ruptures

Cowling N. [a,b]*, Phylaktou H. [b]*, Allason D. [a], Andrews G.E. [b]

[a] DNV, Loughborough, Leicestershire, LE11 3GR, UK.

[b] University of Leeds, Leeds, LS2 9JT, UK

E-mail: nick.cowling@dnvgl.com, h.n.phylaktou@leeds.ac.uk

Abstract

Despite the relative safety of natural gas transmission pipelines, the continuing occurrence of rupture incidents, poses significant risks of property damage, environmental harm, and human casualties. This paper presents a study on the thermal hazards of natural gas pipeline ruptures, with a focus on the development of small-scale testing methodologies. It encompasses both large-scale rupture tests, involving a 1.2-meter diameter pipeline with a 90-ton gas release, and innovative laboratory-scale experiments. The aim was to enhance the understanding of transient thermal radiation development and material responses to it, in pipeline rupture-and-ignition scenarios. A novel laboratory setup, based on the bench-scale cone calorimeter, was developed, demonstrating a high correlation on the transient thermal impulse with the large-scale tests. This setup facilitated the investigation of various materials, including plastics and cellulosic substances, under different heat flux conditions, thereby improving the prediction of ignition risks for common materials. Furthermore, the study expanded the application of the thermal dose concept, traditionally used for human exposure, to assess material responses such as smoke onset, piloted ignition, and spontaneous ignition. Empirical correlations derived from these tests, with a coefficient of determination of 0.88, provide robust statistical validation. The versatility of the laboratory setup was further demonstrated in evaluating material behaviour under variable and transient heat flux conditions, suggesting its applicability in diverse scenarios like deflagrations and military applications.

Keywords: Transient Thermal Effects, Gas Pipeline Rapture, Lab-Scale Testing

1. Introduction

Data from the European Gas pipeline Incident data Group (EGIG, 2020) illustrates the heightened risks associated with natural gas pipeline ruptures. Fatality rates from ruptures are significantly higher at 0.69%, compared to 0% for pinhole/crack leaks and 0.08% for holes, emphasizing the severe risk ruptures pose to human life. In Europe, there's an average of 1.82 rupture incidents per year, with a frequency of 0.013 ruptures per 1000 km per year from 2015 to 2019. Conversely, in America, the average was 13.4 incidents per year based on 67 ruptures during the same period (PHMSA, 2022). Despite advancements in pipeline technology and safety practices, these incidents underscore the persistent risk and potential for significant property and environmental damage.

The data also highlights the growing concern over pipeline safety as residential and commercial developments encroach on pipeline routes, elevating the importance of strategic planning by pipeline operators to mitigate the risks associated with thermal radiation hazards from ruptures. The fireball scenario occurs when there is immediate ignition of a release that results in thermal radiation levels of up to 70 kW/m^2 at 200m (Cowling et al, 2019).

A key aspect in determining the acceptability of a natural gas pipeline at a particular location is the response of buildings. Currently, the response of the built environment in the UK is determined by reference the ignition of wood under a steady-state heat flux (Bilo and Kinsmann, 1997), without consideration given to the duration of the exposure. The methodology for assessing harm to the built environment differs from the approach used to evaluate harm to individuals. The latter is based on a combination of thermal radiation level and the duration of exposure. Though variability is recognised in this approach, an inquiry into the conservatism of employing fixed radiation levels is justified as it could lead to safe but more cost effective risk reduction strategies.

Given the rarity yet severe impact of large-scale underground natural gas pipeline ruptures, which can cause extensive damage and loss of life, there exists a critical gap in comprehensive data to fully understand these phenomena. This scarcity of data stems from the high costs and complexities associated with conducting large-scale tests and has led to a conservative approach in the implementation of safety measures.

Recognising the potential of lab-scale tests to offer reliable, scalable insights at a fraction of the cost and complexity, the research focused on leveraging controlled environments to simulate these catastrophic events. The laboratory setup aimed to replicate the thermal effects observed during the fireball phase of ruptures, providing a novel avenue for data collection and analysis.

This study focused on four objectives:

1. Quantifying thermal radiation flux peak values, durations, and profiles in fireballs from ignited large-scale gas pipeline releases.
2. Creating a laboratory setup to mimic the transient thermal exposure from the large-scale experiments.
3. Examining material responses to short-term (up to 12 seconds) variable heat flux exposure using this setup.
4. Assessing the feasibility of establishing thermal dose limits and empirical correlations for materials near gas pipelines, similar to limits for human vulnerability.

2. Methodology

2.1. Large Scale

The fracture propagation facility at DNV's Spadeadam Test Site was used to carry the fracture of a 48-inch (1219 mm) diameter test pipe. A full description of how the tests were carried out has been described by Cowling et al (2019). The thermal radiation resulting from the tests was measured using an array of Medtherm wide angle radiometers (total field of view of 150^{o}) distributed around the test area. In one of the tests, a peak thermal radiation level of over 70 kW/m^2 at 200 m was observed (see Fig. 1). It took 6 seconds to reach this thermal radiation level. At 750 m it took over 20 seconds for the thermal radiation level to fall below 1 kW/m^2. The fireball mushroomed from the release point and was observed to be tilted by the prevailing wind direction (295°, 7.6 m/s). Thus, the peak thermal radiation level was observed on the eastern radiometer. As a peak of 35 kW/m^2 observed on the western radiometer also located 200 m form the release point, the thermal radiation field was found to be asymmetrical.

2.2. Laboratory Scale

The large scale experiments only provided a limited opportunity to investigate the response of materials to a short duration thermal radiation and were expensive to carry out. Using the thermal radiation data from the large scale tests, the cone calorimeter at University of Leeds was adapted to expose samples to the equivalent thermal radiation exposure at laboratory scale. This adaptation enabled swift testing under controlled conditions, offering supplementary data to enhance the findings from large-scale tests and to explore additional scenarios.

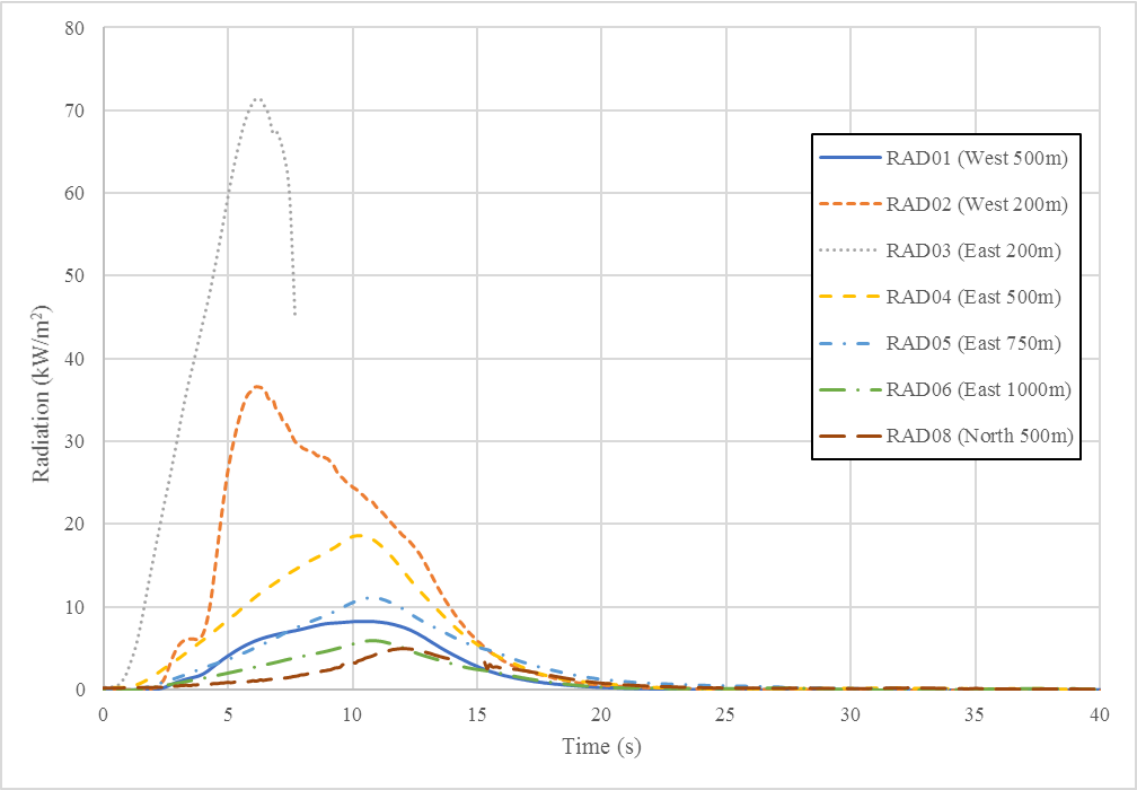

Fig. 1. *Thermal Radiation Measurements from Test 1(Cowling et al, 2019)*

2.2.1. University of Leeds Cone Calorimeter

The University of Leeds cone calorimeter was purchased from FTT (Fire Testing Technology Ltd.). The standard cone calorimeter, is a popular bench scale tool in fire flammability testing of materials. It utilises a truncated conical radiant heater (electrical coil) that applies a controlled heat flux, typically from 0 to 100 kW m^{-2}, to a standardized sample size, usually 100 mm x 100 mm (5 to 50 mm thick) mounted at a fixed distance below the heater. The standard calorimeter's key features include, measuring critical heat fluxes for ignition, the time to ignition when exposed to fixed heat flux, the heat release rate, which is determined by analysing oxygen consumption during combustion, monitoring the mass loss rate during burning using a load cell. It also quantifies smoke production via optical systems, allowing for analysis of smoke yield and obscuration. At the start of a test the pyrolyzing gases produced can be allowed to auto ignite, or can be exposed to an ignition source such as repeating spark or a pilot flame. The time to ignition is an important measurement performed by the system. Additionally, the calorimeter conducts gas analysis, examining the combustion by-products and efficiency. Figure 2 shows the main components of the standard cone calorimeter.

2.2.2. Adapted Cone Calorimeter

In this study, the standard cone calorimeter setup underwent significant modifications, utilising only selected measurements. The aim was to mimic the transient heat flux profile observed in large-scale tests on ground targets as accurately as possible. With the calorimeter set at 930°C, it delivers a steady heat flux of 70 kW/m² to a sample placed 12.5 mm beneath the heating element, matching the highest heat flux recorded in large-scale experiments. To simulate the varying heat exposure from an expanding fireball and its subsequent decline, the original fixed sample holder was replaced with an actuator. This actuator moves vertically, carrying the sample from a lower starting point to the closest point beneath the heater and back, in a single continuous palindromic movement. This process subjects the sample to increasing heat as it ascends and decreasing heat as it descends.

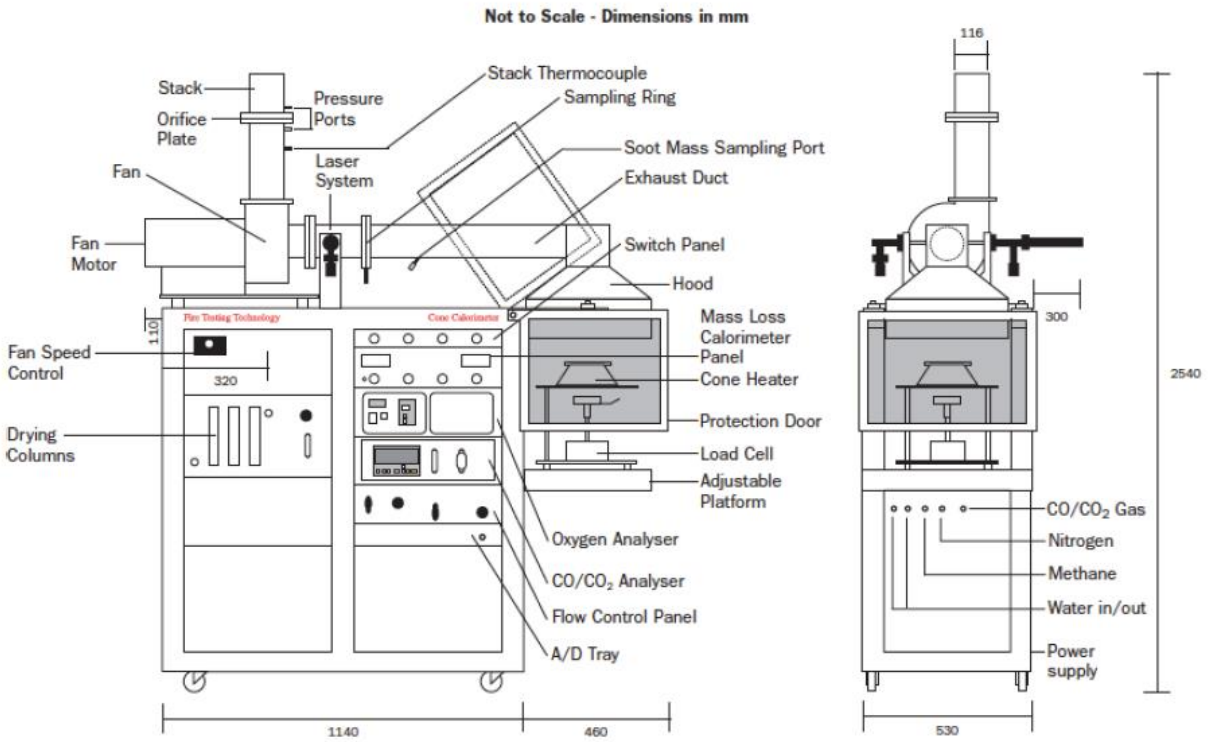

Fig. 2. *Schematic of a standard FTT cone calorimeter. Reproduced from Twilley, W. H. et al (1988)*

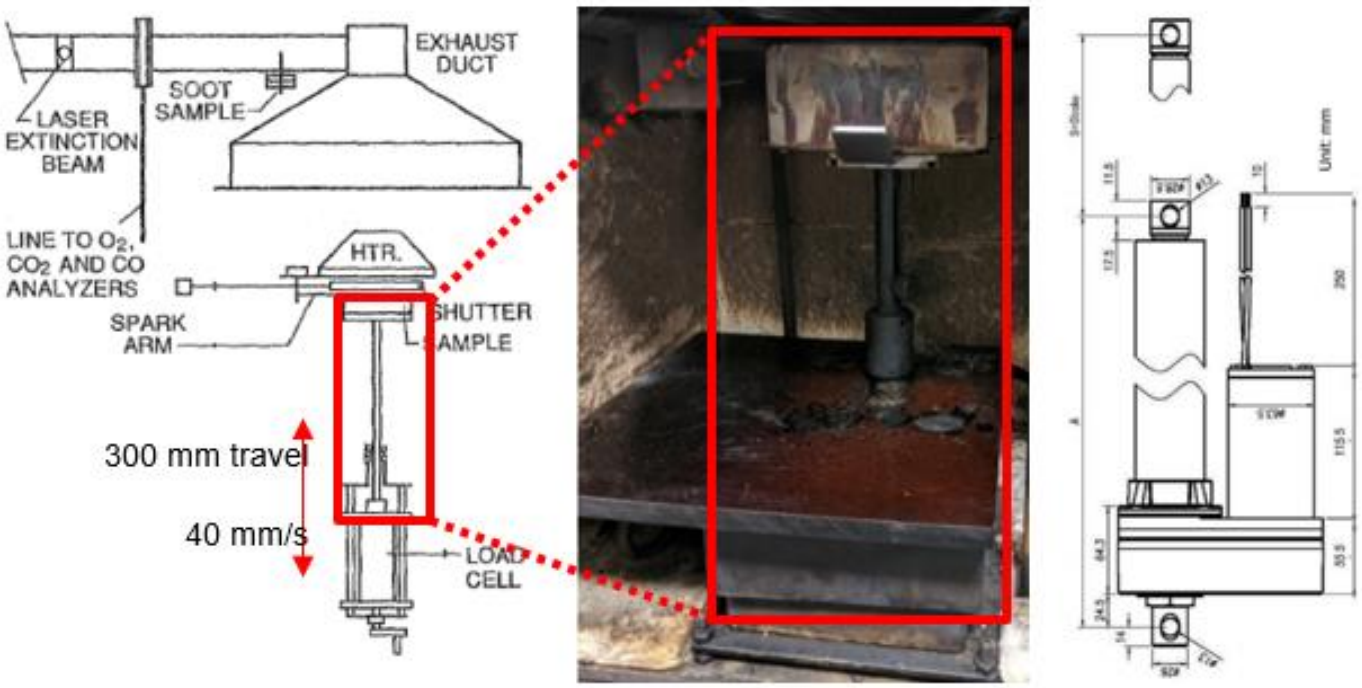

Fig. 3. *Schematic of a standard setup with the load cell element that was replaced with an actuator for the laboratory scale experiments.*

The travel distance and speed of the actuator arm was based on theoretical modelling of the incident heat flux using view factor relationships and determined to require a travel distance of 240 mm and speed of 40 mm s^{-1} (based on a travel time of 6 seconds). The actuator was installed on the cone calorimeter (see Fig. 4) so the sample holder was located 252.5 mm from the heating element at its furthest and 12.5 mm at its closest (see Fig. 5). The proposed setup differs from Maluk et al (2016) which utilises a sample located vertically as opposed to the horizontal orientation in the current work.

Fig. 4. *Photo of the revised setup with the load cell element replaced with an actuator for the laboratory scale experiments*

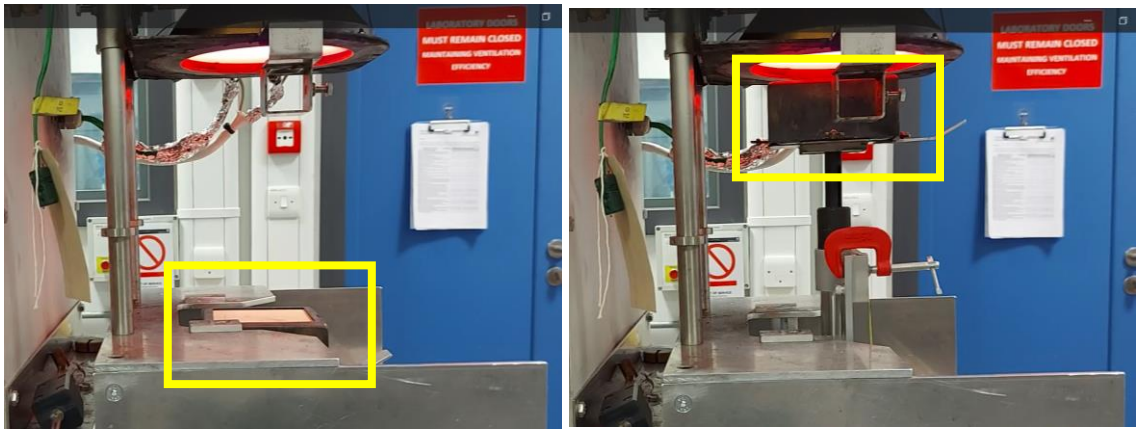

Fig. 5. *Photo of the revised setup with the sample at the base on the left and at the top on the right 6 seconds later*

2.2.3. Validation of adapted Cone Calorimeter setup against large scale test data

To validate that the laboratory scale setup samples received comparable thermal radiation fluxes at different distances from the cone, a plot of distance from the cone against measured thermal radiation fluxes with equivalent large scale experimental data readings is shown in Fig.6. Note that the effect of lower fluxes incident on more distant targets in large scale tests is simulated in the lab scale by having a lower cone heater temperature and hence a lower maximum heat flux the sample is at top of its travel. Also, for the full scale tests the x-axis in Fig. 6 is effectively an equivalent time axis.

The corresponding correlation data between the lab and full scale test are shown in Fig. 7. The coefficient of determination for all 3 cases is in excess of 0.9 demonstrating the laboratory accurately replicates the large scale test data.

In Fig. 6, the curve represents the target in its ascending path which experiences an increasing heat flux which will be the mirror image of the curve shown in Fig. 6, which is demonstrated in Fig.8 in its full form and against time rather than distance from the cone. The area under the curve is the cumulative thermal dose.

The thermal dose exposure was calculated by multiplying the thermal radiation by the time of exposure (carried out at least 1 second time steps to account for the change in thermal radiation). For the calculation of thermal dose, the mid-point between two thermal radiation readings was used as shown in Fig.8. A similar procedure was used for the full scale tests.

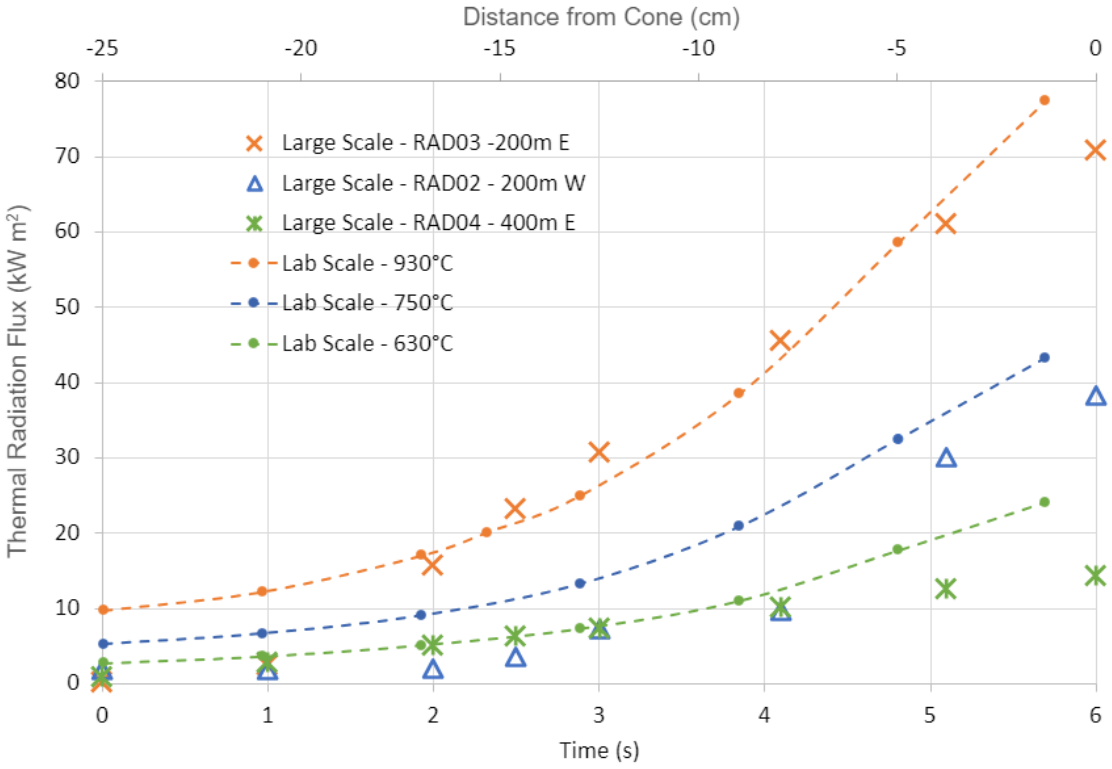

Fig. 6. Laboratory thermal fluxes at different maximum values and distances from the cone, with equivalent large scale test data (versus equivalent time)

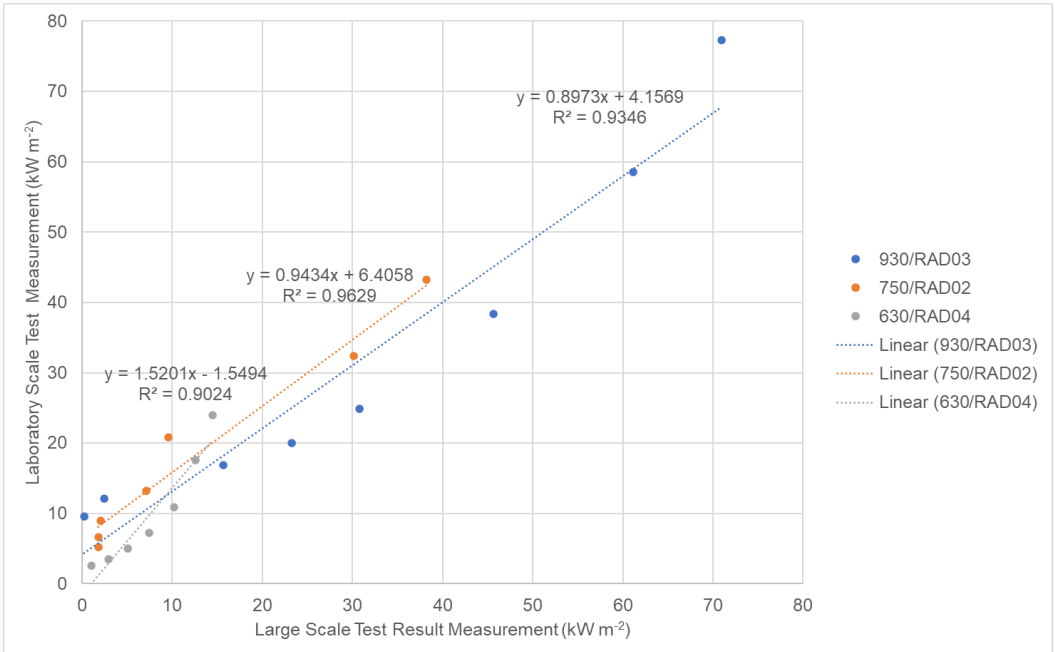

Fig. 7. *Evaluation of measured laboratory scale thermal radiations fluxes for different temperature settings against large test data*

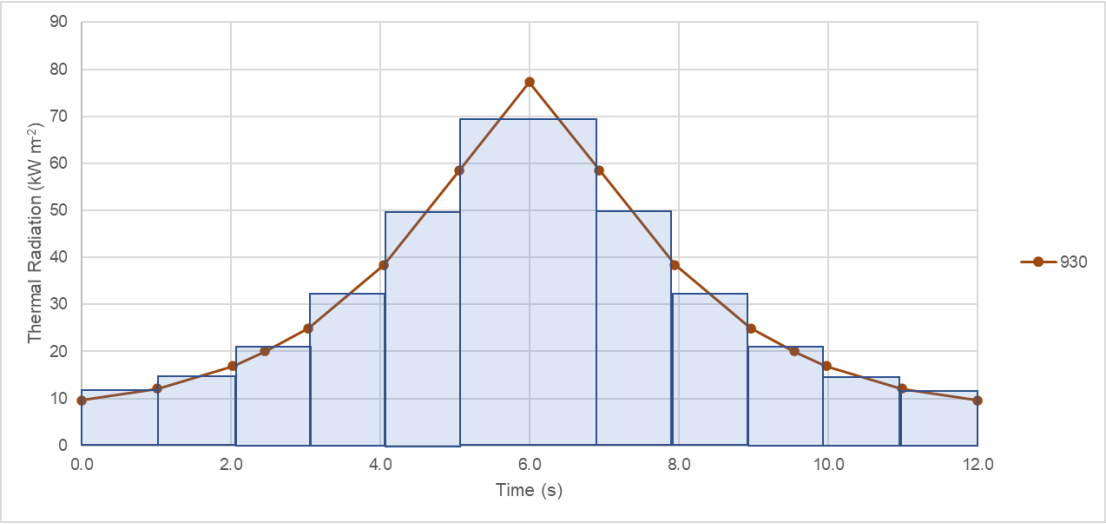

Fig. 8. *Full transient heat flux curve as function time from the laboratory scale experiments, for a cone temperature setting of 930°C. The area under the curve is effectively the thermal dose and the plot shows a calculation procedure that was used.*

The cumulative thermal dose at the 930°C temperature setting (78 kW m^{-2} at 12.5 mm from the cone), during the ascending phase was compared with the cumulative thermal dose the large scale test data during the fireball growing phase using the radiometer which recorded the highest heat flux (see **Fig**.1), radiometer RAD03 with a maximum around 70 kW m^{-2}. The coefficient of determination from this graph shown in Fig. 9 is 0.97, demonstrating that the laboratory scale transient set up replicates well the large scale transient data.

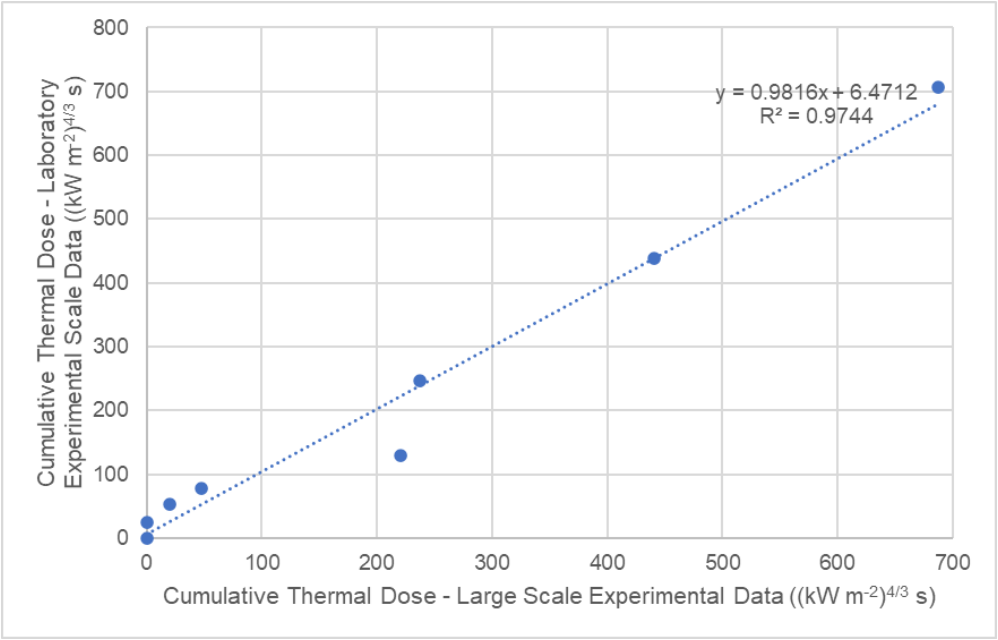

Fig.9*.Cumulative thermal dose – Laboratory (930°C) vs large scale (RAD03) thermal dose data over a time period of 6 seconds*

At this point a quick comparison to the Heat-Transfer Rate Inducing System (H-TRIS) Test Method (Maluk et al, 2016) is appropriate. HTRIS uses a similar in approach but it is a completely new dedicated equipment set up, intended at larger target specimens and over longer timescales. In brief the H-TRIS equipment include a gas fired radiant panel array with dimensions of 0.2m x 0.4m, mounted on a linear motion system for controlling the distance between the radiant panels and the test specimen which has similar dimensions to the radiant panel. The method proposed here utilises

the existing established technology of the cone calorimeter which allows all the measurements normally performed with the cone calorimeter (critical heat fluxes, ignition timing, heat release rate, smoke density, gas analysis and toxic yields) to be applied to a transient heating event with minimal modifications and cost.

2.2.4. Laboratory test procedures

The materials tested using the laboratory scale equipment generally focused on thermally thin items. Primarily the mass loss rate and evidence of the damage sustained (including ignition) was recorded for all tests. Materials which underwent transient tests included paper, cardboard, polyethylene sheets (0.2 mm, 0.5 mm and 1 mm thick), plastic drainpipe (black), Perspex, foam, grass, cotton, painted plywood (grey and yellow) and polystyrene.

To compare transient thermal doses with the laboratory scale setup, steady-state tests were conducted using 1 mm, 0.5 mm, and 0.2 mm polyethylene sheets, along with cardboard and paper of thicknesses shown in Table 1. For the purposes of this paper the transient and steady state tests of only these materials are reported.

Samples were weighed before and after tests. For the laboratory scale tests, a set of Criacr Digital Pocket Scales were used. The scales were capable of measuring up to 500 g, with a resolution of 0.01 grams and were calibrated using certified mass weights between 2 and 200 g.

The bulk thickness of samples was measured using a set of digital Vernier callipers with certified calibration. The callipers were capable of measuring distance up to 150 mm, with a resolution of 0.01 mm. The density of the samples was calculated from measurements of the mass and volume of the samples. Importantly for cardboard, measurements were taken of the top layer only after separation from the corrugated internal spacing layer. The density used in the analysis is based on the average density of all samples for each material.

Other properties of the test materials such as specific heat capacity and thermal conductivity were taken from the literature as reported in Table 2. If the actual values for the samples tested were significantly different from the literature values this would introduce a consistent bias in the comparison between actual and expected behaviour. None was detected.

In the steady state tests the top face of the sample was positioned at 12.5 mm from the face of the cone heater. The incident heat flux was at a constant value (at 20, 35, 45, 55 and 65 kWm^{-2}). In the transient tests the cone temperature setting was ranged from 700 to 930°C corresponding to maximum heat fluxes 33 to 78 65 kWm^{-2} at 12.5 mm from the cone heater.

In each test the time to visible smoke evolution and either spontaneous or piloted ignition was recorded. To help with the determination of the timings of these events, all tests were recorded with a Canon Power shot SX610 HS, high-definition camera. The camera was positioned on a tripod at a fixed position in all tests and was used to get the timings of significant events as flaming ignition and appearance of visible smoke. The timing had a resolution of 0.01 s.

At each condition at least 3 repeat tests were performed (total number of tests just over 200 for the data presented here) reduced to average values at each condition. There was a significant scatter of the ignition (and other event) timings and this is evident in the test results presented later. This is typical of ignition timing measurements in the literature.

The cumulative thermal dose required to cause ignition was calculated based on the relationship proposed by Eisenberg (1975) (based on a 4/3 exponent) as shown below. As described in the results this was later simplified to a linear product of flux and time as it was found to correlate the results better.

$$L = \dot{q}^{\frac{4}{3}} t \qquad \textit{(Equation 1)}$$

Where: L = Thermal dose units (TDU) ((kW m^{-2})$^{4/3}$ s)
$\ddot{q}$ = Thermal radiation flux (kW m^{-2})
t = Time (s) to ignition (or smoke appearance)

3. Results and discussion

The thermal dose required to cause ignition in the steady state tests have been compared with the results for the transient tests in Table 1, columns 3 and 4.

***Table 1**. Comparison of thermal dose required under different test conditions*

Material (thickness in mm)	Steady State Exposure		Transient - Thermal Dose required for spontaneous ignition (kW m^{-2})$^{4/3}$ s)
	Thermal Dose required for piloted ignition (kW m^{-2})$^{4/3}$ s)	Thermal Dose required for spontaneous ignition ((kW m^{-2})$^{4/3}$ s)	
Card (0.29)	644 - 2468	1019 - 2316	591 – 729
Paper (0.19)	146 - 705	271 - 651	392 - 685
Polyethylene (0.2)	732 – 1233*	996 – 2988*	591 - 971
Polyethylene (0.5)	1866 - 2511	2330 – 5064*	No ignition
Polyethylene (1.0)	4472 - 7285	5381 – 6510*	No ignition
* No ignition at 20 kW m^{-2}			

The calculations above have utilised Equation 1 without alteration, i.e. maintaining the 4/3 exponent. Similar trends are obtained when using an exponent of 1. Based on the method employed by Eisenberg (1975), it was anticipated that the thermal dose required for ignition should remain consistent regardless of a steady state or transient exposure. Therefore, other parameters other than thermal radiation flux and duration of exposure affect ignition. Although, there was no ignition of the 0.5 or 1 mm polyethylene samples during the transient tests the results suggest that transient exposures require lower thermal doses compared to steady-state tests. This is unexpected and a possible explanation might be that in the transient tests the piston movement of the sample might be pushing the volatiles ahead of it increasing thus their concentration to ignitable levels earlier than in the fixed sample position case. This needs further investigation.

To enable a robust statistical analysis to be carried, the video records were examined to identify the first time that visible smoke was observed. This was achieved by examining the frame by frame video records. This point has been utilized as it is predicted to be the point at which the temperature at the surface is in the range of 200-260°C (Drysdale, 2011). This is particularly relevant as hemicellulose begins to release smoke at this temperature (for cardboard and paper samples). The surface temperature at the point of ignition is assumed to be 300°C (Quintiere, 2006).

Microsoft Excel was used to carry out multivariate linear regression analysis of the results. Multivariate linear regression analysis is a statistical technique that uses more than one independent variable to predict the outcome of a dependent variable. To carry out the analysis, the thermal dose was assumed to be function of density, thermal conductivity, specific heat capacity and thickness. The form of the equation used was:

$$L = Constant.\rho^{p_1}.h^{p_2}.c_s^{p_3}.l_t^{p_4} \qquad \textit{(Equation 2)}$$

As Equation 2 is a non-linear power correlation, this equation was transformed into a linear from by taking the natural logs as shown in Equation 3.

$$ln(L) = ln(Constant) + p_1\, ln(\rho) + p_2\, ln(h) + p_3\, ln(c_s) + p_4 ln(l_t) \qquad \textit{(Equation 3)}$$

In Equation 3, ln(constant) is the intercept, ln(L) is the dependent variable and p1 to p4 are the coefficients to be determined. The values used for density, thermal conductivity, specific heat capacity and thickness are shown in Table 2.

***Table 2**. Properties used for the materials tested*

Material	Density, ρ (kg m^{-3})	Thermal Conductivity, k (W m^{-1} K^{-1})	Specific heat capacity, c_s (J kg^{-1} K^{-1}) (Drysdale, 2011)	Thickness, l_t (mm)
Paper (Cellulose)	398.67	0.039 (Zhao et al, 2011)	1.3	0.19
Cardboard	720.68	0.039 (Zhao et al, 2011)	1.3	0.32
Polyethylene	478.82	0.4 (Drysdale, 2011)	2.1	0.20
Polyethylene	1074.76	0.4 (Drysdale, 2011)	2.1	0.50
Polyethylene	1307.28	0.4 (Drysdale, 2011)	2.1	1.00

As part of the analysis the 4/3 exponent (in Equation 1) was initially varied and it was observed that an exponent of 1 yielded a more favourable coefficient of determination. A lower exponent shows the built environment is less sensitive to the thermal radiation flux than for human exposure.

To provide assurance in the derived coefficients a range of statistical tests were carried out. The standard error shows a percentage variability or uncertainty associated with the sample estimate of a population parameter. The values calculated above are reasonable with respect to standard error. The t stat is how many standard errors a sample estimate is from a proposed value. P values are used with t stat to determine the statistical significance, with lower values indicating that derived results are unlikely to have occurred by chance alone.

One unsatisfactory result was a zero value for the specific heat capacity coefficient. Investigation into different specific heat capacity values for paper and card yields a relatively high coefficient (~3) for the specific heat capacity. It is postulated that this due to similar specific heat values (no significant variation) for the materials used in this research. Therefore the analysis without this coefficient was re-run with the results shown in Fig. 10 and Table 3.

The results in bulk followed expected trends. As density, thermal conductivity, and thickness increase, the thermal dose necessary for production of smoke also rises. This is illustrated by Fig. , which shows thermal dose ascending for paper (purple circle) and cardboard (yellow circle). The same trend is also shown for 0.2 mm (red circle), 0.5 mm (green circle) and 1 mm plastics. It is however noted that for 1 mm plastics there appears to be a greater spread of data. Whilst this is typical of this type of experimental work, it should be noted that some of the thermal properties of the materials used in the present work are based on typical literature values rather than actual measurements which introduces a source of error and uncertainty in the current indicative correlations. This will be addressed in future work by careful quantification of all the relevant parameters for the materials tested.

The statistical analyses, coupled with a coefficient of determination of 0.88, provide confidence that the relationship between the thermal properties of a material and the dosage required for ignition is

accurate. While additional testing on a broader range of materials is necessary, this research supports that refinements in the criteria for assessing whether a material would ignite is warranted.

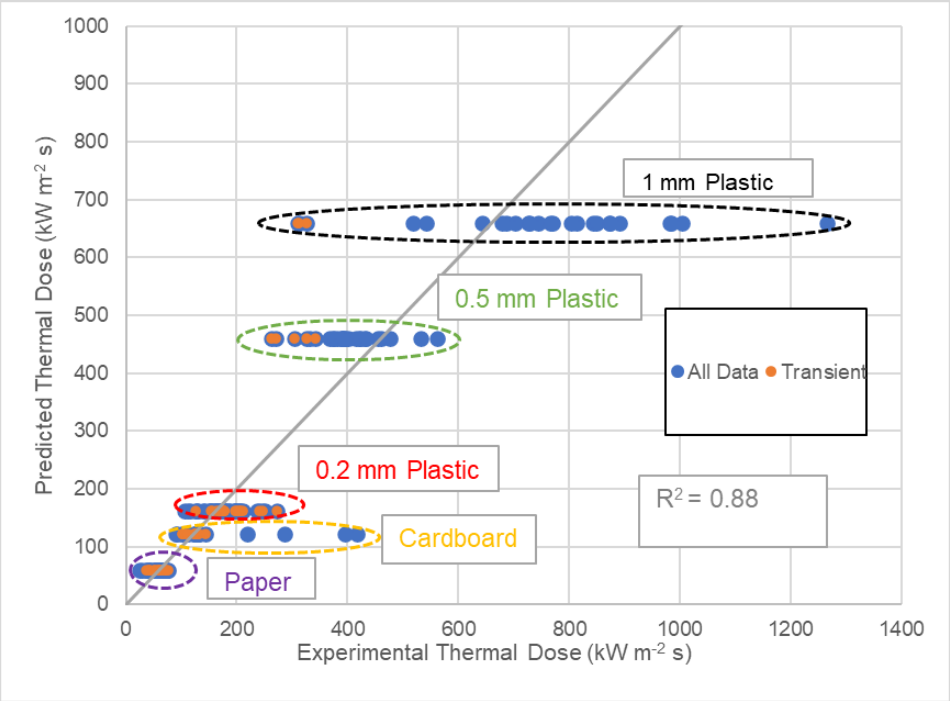

Fig. 10. *Results of multivariate regression analysis for smoke observations with 3 coefficients*

Table 3*. Statistical tests of the fit for data in Fig.*

Parameter	Coefficient	Standard Error	t Stat	P-value
Intercept	-0.65	1.58	-0.41	0.68
p_1 (Density)	1.04	0.22	4.80	4.0×10^{-6}
p_2 (Thermal conductivity)	0.34	0.03	12.69	5.6×10^{-25}
p_4 (Thickness)	0.22	0.16	1.44	0.15

Using the coefficients in Table 3, the correlation in Equation 3 is therefore:

$$ln(L) = ln(-0.65) + 1.04\,ln(\rho) + 0.34\,ln(h) + 0.22ln(l_t) \qquad \textit{(Equation 4)}$$

Using this relationship gives thermal doses for the onset of smoke as shown in Table 4.

Table 4*. Calculated thermal doses for the onset of smoke*

Material	Thickness, l_t (mm)	Calculated Thermal Dose, L (kW m^{-2} s)
Paper (Cellulose)	0.19	60
Cardboard	0.32	122
Polyethylene	0.20	162
Polyethylene	0.50	461
Polyethylene	1.00	660

4. Conclusions

The newly developed experimental laboratory scale setup successfully replicated fireball exposure and permitted materials to be subjected to controlled transient heat fluxes. When comparing the laboratory scale thermal dose exposure with the large scale experimental data, a coefficient greater than 0.9 was obtained demonstrating that the laboratory scale setup accurately replicates the large scale tests.

In this study, the investigation focused on the thermal dose linked to both spontaneous and piloted ignition across various materials. The application of the Biot number did not yield definitive results. Steady-state tests were carried out to enable comparisons with the thermal dose needed for ignition in transient tests. It became evident that different thermal doses were necessary to induce ignition. The analysis of the Biot number, coupled with these findings, underscored the need to consider other parameters in the study.

In addition to the data on pilot and spontaneous ignition, video records were scrutinized to pinpoint the initial appearance of smoke during the tests. This facilitated a statistical analysis of three sets of data, with physical properties of the materials tested included. This approach proved successful, with a correlation for predicting ignition across limited set of materials that had a coefficient of 0.88. Application of the derived correlation with respect to the built environment highlighted that the current approach is conservative.

Beyond fireballs, the laboratory setup could be used to research other applications, by adjusting the speed of the sample's rise or fall of a sample for example. Applications of interest in this context include the assessment of material responses to detonations, real fires and military scenarios that would otherwise be costly to replicate at large scale.

References

Bilo, M. and Kinsman, R, 1997. Thermal radiation criteria used in pipeline risk assessmente. Pipes & Pipelines.

Cowling N., Phylaktou H., Allason D., Andrews G.E, 2019. Thermal Radiation Hazards from Gas Pipeline Rupture Fireballs, : Proceedings of the Ninth International Seminar on Fire and Explosion Hazards. Vol. 2. Ninth International Seminar on Fire and Explosion Hazards

Drysdale, D., 2011. An Introduction to Fire Dynamics. 3rd Edition, Wiley.

Eisenberg, N., 1975. Vulnerability Model. A Simulation System for Assessing Damage Resulting from Marine Spills, Department of Transportation.

EGIG, 2020. 11th EGIG Report. Retrieved February 6, 2023, from https://www.egig.eu/reports/$60/$61

Maluk, C, Bisby, L, Krajcovic, M & Torero, JL 2016. A Heat-Transfer Rate Inducing System (H-TRIS) Test Method', Fire Safety Journal. https://doi.org/10.1016/j.firesaf.2016.05.001

PHMSA, 2022. All Reported Incident 20 Year Trend. [Online] [Cited: 7 February 2023.] https://www.phmsa.dot.gov/data-and-statistics/pipeline/pipeline-incident-20-year-trends

Quintiere, J. G, 2006, Fundamentals of fire phoenomena, Wiley.

Twilley, W. H., Babrauskas, V. and Gaithersburg, M. D, 1988. User's guide for the cone calorimeter, National Bureau of Standards.

Zhao, J., Du, F., Zhou, X., Cui, W., Wang, X., Zhu, H., Xie, X. and Mai, Y.,.2011. Thermal conductive and electrical properties of polyurethane/hyperbranched poly(urea-urethane)-grafted multi-walled carbon nanotube composites. Wuhan : Composites Part B: Engineering. Vol. 42.

Incident Investigation of Hydrogen Explosion and Fire in a Residue Desulfurization Process

Ting-Chia Kao [a], Yuan-Chen Lin [a], Hui-Ning Yang [a], Hsiao-Yun Tsai [a,b] & Jenq-Renn Chen [a,b]

[a] Southern Center of Emergency Response of Toxic Chemical Substance (SERT), National Kaohsiung University of Science and Technology (NKUST), Kaohsiung, Taiwan
[b] Department of Safety, Health and Environmental Engineering, National Kaohsiung University of Science and Technology (NKUST), Kaohsiung, Taiwan

E-mail: jrc@nkust.edu.tw

Abstract

A large explosion and fire occurred on October 27 2022 in a residue desulfurization (RDS) process in a refinery in Kaohsiung, Taiwan. The incident occurred during pressurization of the RDS reactors and downstream coolers by hydrogen. The incident led to significant damages to the downstream coolers and some part of the RDS reactors. Detailed incident investigation was carried out. A reactor effluent air cooler (REAC) in the downstream of RDS reactors was found to be ruptured in the rectangular header box. With security videos, process DCS data, leak and dispersion modelling, and actual damage on the process, it is possible to reproduce the leak rate, size of the initial fire ball and damages done to the process. Recommendations are made to prevent and mitigate any future incident from the RDS process.

Keywords: *residue desulfurization, sulfide stress cracking, hydrogen leak, hydrogen fire and explosion.*

Introduction

Residue desulfurization (RDS) is a high-pressure catalytic hydrotreating process that produce low sulfur fuel oil or feedstock for residuum fluid catalytic cracking (RFCC) unit. Sulfur in the residue is catalytic converted into hydrogen sulfide at elevated pressure and temperature. The feeds for RDS are atmospheric and vacuum residue from crude oil distillation. The technology of the incident RDS unit was licensed from Chevron Lummus Global (CLG) which is the major source of RDS licensing worldwide.

Desulfurization and catalytic cracking are major parts of refinery technology to produce low sulfur and high value fuel oil and since 1950. These technologies all had similar corrosion experiences that eventually were identified as being associated with the presence of hydrogen sulfide (H_2S) and ammonia (NH_3), and their reaction product ammonium bisulfide (NH_4HS), in the reactor effluents. The corrosion leads to equipment rupture and severe fire and explosion (API, 2002). The causes and prevention measures through selection of corrosive resistant alloy have been subjected to extensive studies.

In this work, we report a large explosion and fire occurred on October 27 2022 in a RDS process in a refinery in Kaohsiung, Taiwan. The incident occurred during pre-startup pressurization of the RDS reactors and downstream coolers by hydrogen. The incident led to significant damages to the downstream coolers and some part of the RDS reactors. NKUST SERT team was involved in the incident investigation aiming at proposing recommendations for preventing future incidents. Special emphasis was placed not only the cause of the incident but also on the consequence analysis of the leak. A reactor effluent air cooler (REAC) in the downstream of RDS reactors was found to be ruptured in the rectangular header box. With security videos, process DCS data, leak and dispersion

modelling, and actual damage on the process, it is possible to reproduce the leak rate, size of the initial fire ball and damages done to the process. The rupture led to a large hydrogen leak that spontaneously ignited with very small delay ignition time (<3s), and created a fire ball with a size of around 83 m and very small overpressure.

1. On-scene incident investigation

1.1. Events before the incident

The incident RDS unit was under regular maintenance before the incident. Various equipment, including the E-3004A/B reactor effluent air coolers (REAC), were isolated and pressure tested. On October 13, the RDS unit was ready for pressurization and dry of catalyst by nitrogen. Upon drying was completed on October 20, temperature was reduced to 160°C and hydrogen was fed into the system to replace nitrogen. By October 23 17:15, system pressure reached 5.5 MPa and hydrogen concentration above 88%, a small leak was fund on one of the plug in E-3004A/B outlet. The leak cannot be sealed by tightening and thus the system hydrogen was depressurized and replaced by nitrogen. The plug leak was sealed by welding on October 25 and pressurization resumed. By October 27 19:50, pressure reached 12.35 MPa and hydrogen concentration was above 88%. Pressurization was then continued and by 22:34 a large fire occurred near the area below E3004 A/B unit. The fire lasted about four hours causing extensive damage to the RDS unit.

1.2. The damage of the RDS unit

Figure 1 shows the damage on RDS reactors which had sign of flash fire as far as R-3002. The damage on REAC E-3004A was however more extensive as shown in Figure 2. Tube bundle of the E-3004A was bended as well its forced draft fan unit was detached and destroyed while E-3004B and its fan unit remained intact. There was extensive damage on the steel structure and pipeline beneath the REAC. The REAC is a special type of heat exchanger that use forced air flow to cool down the process fluid in the tube side. Unlike typical shell-and-tube heat exchangers, there is no shell around the tubes and tubes are arranged and fitted to rectangular header boxes. Each tube is also finned in the outer surface to maximize the heat transfer. Each E-3004 unit has a total of 138 tubes with tube length of 9.136 m and internal diameter of 22.1 mm.

Fig. 1. *Photo of damage on RDS reactors*

Fig. 2. *Photo of damage on E-3004A/B REAC and nearby steel structure and pipeline*

Upon the E-3004A/B was removed from the site as shown in Figure 3, a large crack was found on the outlet side of the rectangular header box of E-3004A as shown in Figure 4. The crack measured to around 1.2 m in length and the maximum opening width was around 6 cm. There were also several tubes ruptured but the number of tubes ruptured was limited. It is unlikely that the tube rupture was the cause of the leak but the leak size should be consistent with the consequence analysis. The both header boxes of E-3004A were cut out for internal inspection. There were four stiffening plates inside the rectangular header box. Fig. 5 showed the photo of cut-out of E-3004A outlet side header box. One of the stiffening plates was completed detached from the box while the remaining three plates had at least one side weld cracked.

Fig. 3. *Photo of damage on E3004 A/B REAC*

Fig. 4. *Photo of the crack on E-3004A outlet header box and ruptured tubes*

Fig. 5. *Photo of cut-out of E-3004A outlet side header box*

1.3. Process data from DCS

Pressure and temperature data were recorded in DCS system. These data were retrieved for analysis. Figure 6 and 7 show the simplified flow diagram and temperature/pressure data of the RDS unit. Any leak from the process will lead to pressure drop monotonically in all upstream and downstream sensors. As shown in Figure 7, both pressure data for R-3004 and R-3005 dropped to zero after the incident indicating a broken data connection. Pressure drop rate is higher at PI-0028/D-3002 than those at PI-0047/D-3003. Thus, the leak should occur closer to D-3003. Temperature data were however scattered. All data at T-0181/E-3002 and upstream were roughly the same after the incident, except that T-0171 experienced a spike around 270 s after the incident. TI-0193 actually increased and approached to the temperature of its upstream indicating a loss or reduced cooling. TI-0194/TI-0195 both dropped to zero after incident which indicate broken data connection. Further downstream at TI-0203A dropped close to ambient temperature. Isentropic expansion leading to rapid cooling occurred mostly near the crack. On the other hand, the leak will result an increased flow which will also reduce cooling in the upstream of the leak. Thus, the leak should take place at down stream of TI-0193/E-3003A/B, and possibly near TI-0194/TI-0195 for E-3004A/B. This is consistent with the fact of the split in E-3004A outlet header box which is located right between TI-0193 and TI-0194. These data will be used for validation for possible leak rate and consequence analysis.

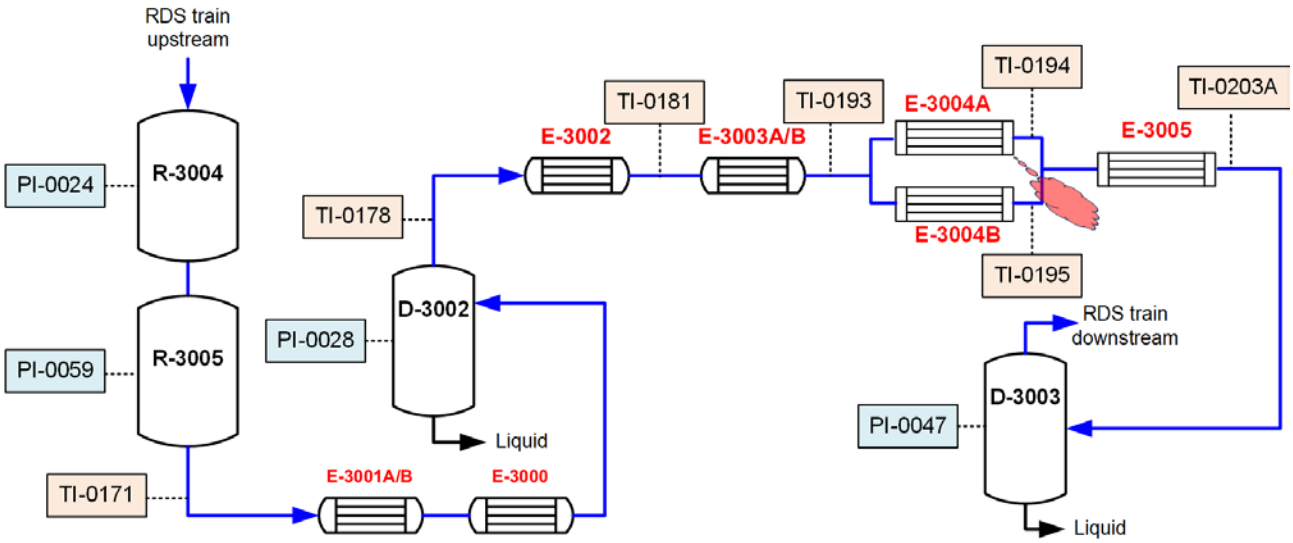

Fig. 6. *Simplified process flow diagram of RDS units*

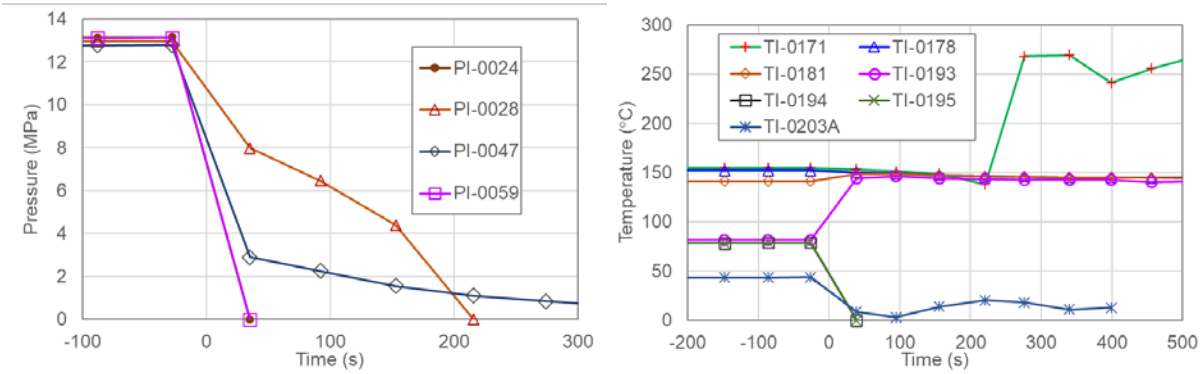

Fig. 7. *Temperature and pressure data of RDS units*

1.4. Video data

Although there were many surveillance video cameras in the plant, none of them catch the instant of the leak and fire. On the other hand, an elevated camera on top of a stack in another plant 3 km away from the incident site captured the whole event as shown in Figure 8. The fire ball looks completely engulfed the whole plant, yet Fig. 1 showed that the actual flame impingement was limited to within the RDS units. Thus, it is difficult to evaluate the fire ball size based on this video. There was however a camera in a unit next to the RDS captured fire ball a few seconds after the initial leak as shown in Figure 9. Based on the distance of the two distillation columns that bracket the fire ball, it is possible to estimate the fire ball size at 22:40:13 was about 25 m. Thus, the fire ball size for the remote video at same time should bear the same size, and the largest fire ball diameter can be estimated accordingly to be approximately 85 m in Figure 9. The light damage on the inlet pipe to R-3002 shown in Fig. 1 is about 45 m away from E-3004 which is roughly consistent with the radius of the observed fire ball. The fire ball size will be useful for validate the leak and its consequence analysis.

Fig. 8. *Video clips of the leak and fire taken from camera 3 km away*

Fig. 9. *Estimation of initial fire ball size based on comparison of video clips*

2. Consequence analysis

2.1. Release modelling

Owing to the complexity of the RDS unit, it will be difficult to perform detail release modelling based on exact process configuration. Instead, the RDS unit is simplified into a single vessel with equivalent volume of all vessels from R-3000 to D-3002. Volume of connecting piping as well as vessel/reactor internal structure/catalyst are neglected. The equivalent volume is estimated to be 2,053.9 m^3. The simplified vessel is assumed to have pressure and temperature of 12.97 MPa and 152.11°C, respectively, which are the lowest values of RDS unit before the incident. The hole size is assumed to be a circular orifice with area of 0.036 m^2 which is the area of the triangular crack measured to 1.2 m in length and 0.06 m in height. For simplicity, the fluid is assumed to be 100% gaseous hydrogen.

ALOHA (Areal Locations of Hazardous Atmospheres) is the hazard modeling program developed by National Oceanic and Atmospheric Administration (NOAA) (Jones et al., 2013). ALOHA can model toxic and flammable gas clouds, BLEVEs (Boiling Liquid Expanding Vapor Explosions), jet fires, pool fires, and vapor cloud explosions, all for single component chemical. Although ALOHA is a simplified, macroscopic model, its extensive range of chemical data and

For the release modeling of the single vessel hydrogen leak, ALOHA first determines whether gas flow will be sonic (choked) or subsonic (unchoked) and calculate the respective flow rate. The estimated rate of gas release drops over time as the tank pressure is expected to drop as gas exits the tank. Adiabatic expansion is also taking into account to cool the tank contents and further reducing the pressure. Figure 10 shows the comparison of calculated leak rate against pressure data. The calculated leak rate matches quite well the pressure data at PI-0028/D-3002 which is upstream of the leak. PI-0047/D-3003 showed a lower pressure as it was located at downstream of the leak and thus detached from the main RDS unit. Peak leak rate is estimated to be 8670 kg/min.

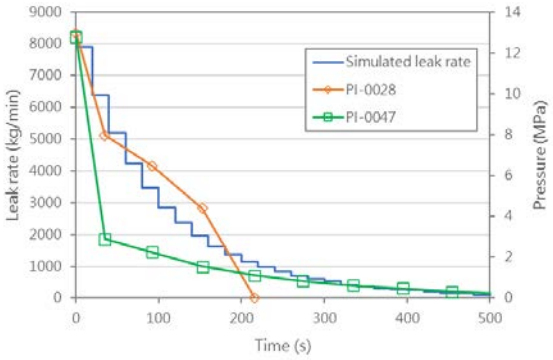

Fig. 10. *Comparison of calculated leak rate against pressure data*

2.2. Fire and explosion modelling

The damage in Fig. 1 suggests that the release resulted in a flash fire rather than explosion and overpressure. Flame affected as far as 41 m from the leak. Thus, the present fire and explosion modelling aims to reproduce the results to uncover the precise release consequence. For pressurized release, ALOHA can model gas clouds, jet fires, and vapor cloud explosions (VCE). The difference lies in the ignition time. VCE is possible only for ignition delay 3 s or more. For a full VCE with all possible ignition times, the overpressure of 8 psi capable of destructing building extends more than 800 m as shown in Fig. 11. This is clearly inconsistent with the actual damage. For 3 seconds delayed ignition, the overpressure of 8 psi is limited to a short range of 11 m. This is a more plausible scenario as structure damage was limited to the area near E-3004A as shown in Figure 2.

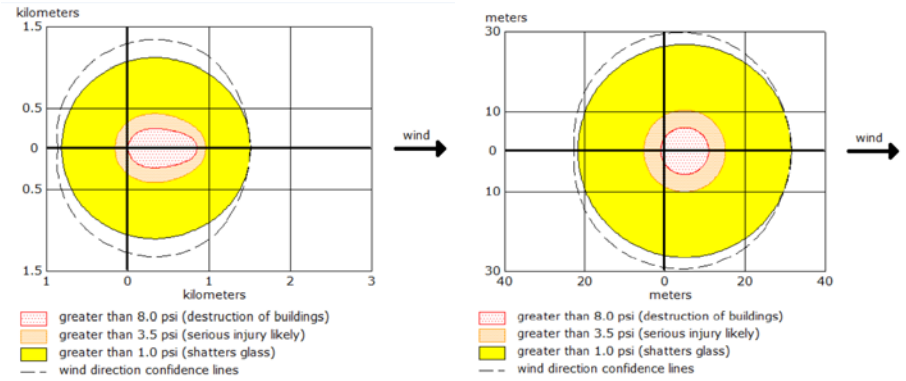

Fig. 11. *Overpressure from VCE modelling. Left: full VCE with for all possible ignition times. Right: VCE with 3 s ignition delay*

For jet fire modelling, the range of thermal radiation of 15.77 kW/m^2 extends to 82 m as showing in Fig. 12. The 15.77 kW/m^2 is the thermal radiation level on structure for sizing flare stack height (API, 1997) as is considered a safe radiation level for structure. At 41 m, the thermal radiation peaks at 61.3 kW/m^2 but decays rapidly. Effect of thermal radiation from fire is depending not only on the radiation level but also on the radiation time. Although exact analysis requires further studies but the observed limited range of thermal radiation damage plus no sign of overpressure damage suggest that the leak resulted in spontaneous ignition and jet fire. It is well known that pressurized releases of hydrogen into air may lead to spontaneous ignition (Dryer et al., 2007; Golub et al., 2007). The spontaneous ignition is a result of shock heating to cause autoignition of mixtures formed with hydrogen and air, as well as a critical volume of the mixture that is capable of undergoing flame spreading. To achieve spontaneous ignition, it requires a proper combination of downstream geometry and sufficiently high failure pressure. Dryer et al. (2007) reported a critical value of 2.27 MPa for spontaneous ignition. The current RDS pressure was well abve the critical value and thus spontenous ignition was likely which resulted in jet fire instead of VCE.

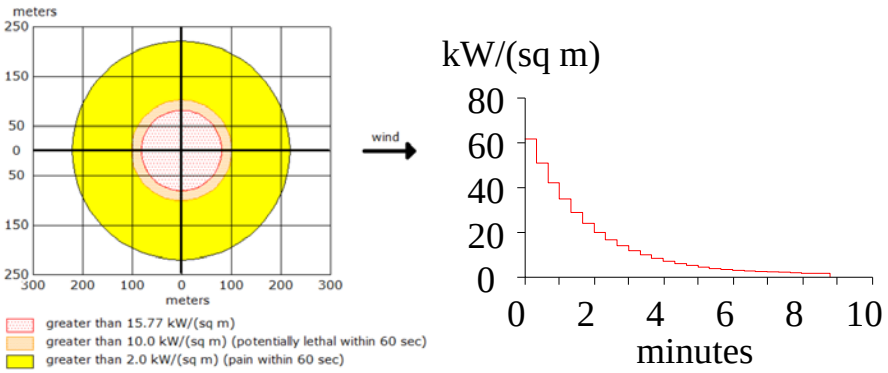

Fig. 12. *Left: range of thermal radiation from jet fire modelling. Right: thermal radiation level at 41 m*

2.3. Analysis of subsequent fire

Figure 10 suggests that the hydorgen in the RDS unit should be released completely in less than 10 min time. Nevertheless, the fire continued for about four hours. As VCE was excluded as the main cause of damage, the continued fire after emptying the RDS units was investigated.

The video camera showed quite different fire behaviors after the initial hydrogen jet fire in Figure 9. Figure 13 left clip showed pecular bright flame and sparkles on 22:48 which lasted for around 5 min. The flame later turn into light orange color and heavy smoke as shown in the right clip of Figure 13. The sparkle was found to be the burning of aluminum fins on E-3004 tube exterior surface. It is likely that the bending and rupture of tube bundle occurred and the fins were burnt and proppelled out from the tube. The later stage fire with heavy smoke was confirmed to be rupture of fuel pipe and flare header that located beneath the E-3004 which contained vented fuel oil and other waste gases. The fire was put off eventually by shutting off the waste gas into the flare system. The rupture was a direct result of flame impingement on the piping and structure. Unfortunately, there is no sprinkler system to protect the area from fire impingement. The extent of the damage could be far smaller should the RDS area is protected properly with fire proofing insulation and sprinkler system.

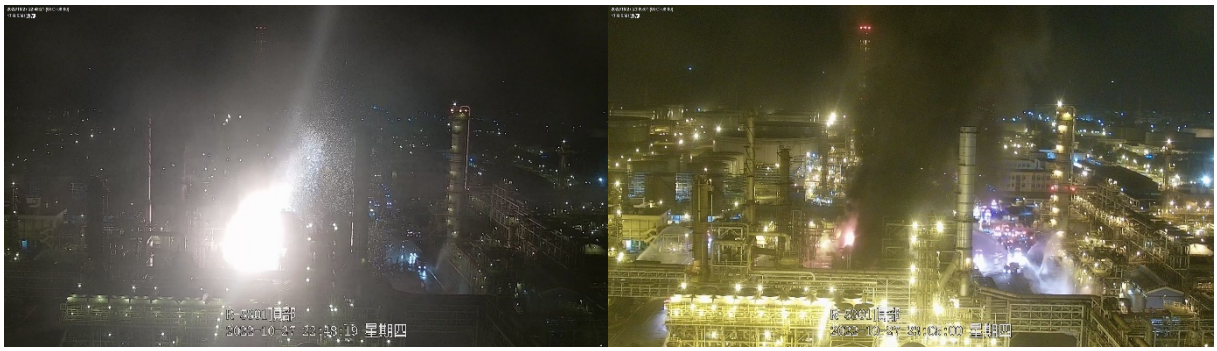

Fig. 13. *Left: bright flame and sparkles on 22:48. Right: light orange flame and heavy smoke on 23:05*

3. Cause of leak

Corrosion has been a major issue for all RDS unit due to the presence of sulfur. Lower grade steel performs poorly in this service and duplex stainless steel 2205 has been proposed for better corrosion resistance. These stainless steels typically have an annealed structure that is generally half ferrite and half austenite. However, special welding requirement and inspection are required (API, 2015). In particular, proper phase balance of ferrite and austenite in weld deposits and heat affected zones is a critical concern during welding and should be verified by ferrite measurements done on the weld procedure qualification samples.

Inspection of the ruptured header box as shown in Figure 5 revealed that the stiffener plates inside the box were welded poorly with significant numbers of welding defects, including imbalanced ferrite. Sulfur was also found on the cracked welding surface. It is concluded that the failure was caused by

sulfide stress cracking (SSC). In combining with the stringent welding requirement of duplex stainless steel and the tight space inside the header box, it is not a surprise to find that REACs made of duplex stainless steel have contributed to many fires and explosions in the RDS processes around the world (Lin and Risse, 2013; API, 2002; He et al., 2016; Volfson, 2018).

Recommendations are made to either replace the duplex stainless steel by Alloy 825 or perform strict inspections and analyses of the welding of duplex stainless steel. In addition, visual inspection of all existing duplex REACs through the tube plug holes should be done to uncover any major welding defect and premature cracking of the stiffener plates inside the header box.

4. Conclusions and recommendations

Contrary to typical heat exchangers, reactor effluent air-coolers for RDS unit bear special risks as any crack would leak into air directly. Numerous lessons can be learnt from the present investigation. The following recommendations are given:

- Welding and inspection of the duplex stainless steel header box should follow strictly the requirement given in relevant guidelines such as API (2015).
- Existing duplex REAC should be checked to prevent similar incident from occurring. Inspection of the stiffening plate welding is possible through the use of endoscope inserting into the plug holes.
- When the RDS system contained primarily hydrogen, fire instead of VCE was the major cause of damage as the leaked hydrogen was subjected to shock-induced ignition.
- Proper fire protection measures such as sprinkler system and fire proofing insulation should be taken to mitigate the damage from fire.
- It is possible to assess the leak location from DCS pressure and temperature data. Proper isolation instead of completely blowdown of the RDS system can minimize the impact of the leak should the exact leak location can be assessed in early stage of the incident.

Acknowledgements

The authors gratefully acknowledge the financial supports from Taiwan CPC Co.

References

Americal Petroleum Institute (API), 1997. Guide for Pressure-Relieving and Depressuring Systems, 4th Ed., API RP 521.

Americal Petroleum Institute (API), 2002. A Study of Corrosion in Hydroprocess Reactor Effluent Air Cooler Systems, API Publication 932-A, Septermber.

American Petroleum Institute (API), 2015. Use of Duplex Stainless Steels in the Oil Refining Industry, API Technical Report 938-C, 3rd ed., February.

Dryer, F. L., Chaos, M., Zhao, Z., Stein, J. N., Alpert, J. Y., & Homer, C. J., 2007. Spontaneous ignition of pressurized releases of hydrogen and natural gas into air, Combustion Science and Technology, 179, 663–694.

Ghosal. S., 2014. Failure Analysis of Reactor Effluent Air Cooler (REAC) in Hydrocracker Unit. NACE International, Corrosion 2014-3730.

Golub, V. V., Baklanov, D. I., Bazhenova, T. V., Bragin, M. V., Golovastov, S. V., Ivanov, M. F., Volodin, V. V., 2007. Shock-induced ignition of hydrogen gas during accidental or technical opening of high-pressure tanks, Journal of Loss Prevention in the Process Industries, 20, 439–446.

He, M., Lippold, J., Alexandrov, B., Penso, J., 2016. Evaluation of the Susceptibility of Duplex Stainless Steel 2205 to Hydrogen Assisted Cracking in REAC Systems, ASME 2016 Pressure Vessels and Piping Conference, Vancouver, British Columbia, Canada, July 17–21.

Jones, R., W. Lehr, D. Simecek-Beatty, R. Michael Reynolds. 2013. ALOHA® (Areal Locations of Hazardous Atmospheres) 5.4.4: Technical Documentation. U. S. Dept. of Commerce, NOAA Technical Memorandum NOS OR&R 43. Seattle, WA: Emergency Response Division, NOAA. 96 pp.

Lin, E., Risse, P., 2013. Reactor effluent air cooler safety through design, Revamps, 1-3, 2013.

Volfson, B., 2018. Failure Analysis of a High Pressure Air Cooled Heat Exchanger, Proceedings of the ASME 2018 Pressure Vessels and Piping Conference PVP2018, Prague, Czech Republic, July 15-20.

Safety characteristics of hybrid mixtures: Applications related to the replacement of coal by hydrogen as reducing agent in the processing of metal ore

Nelly Sandstå [a], Matthijs van Wingerden [a] & Trygve Skjold [a]

[a] University of Bergen, Department of Physics and Technology, Bergen, Norway

E-mail: nelly.sandsta@student.uib.no

Abstract

Replacing coal with green hydrogen as reducing agent in metal and steel production is considered a viable solution for reducing the global emissions of carbon dioxide. At the same time, it is of vital importance to evaluate the implications for safety when hydrogen is introduced in industrial processes. Explosive atmospheres encountered in the processing of metal ore may contain both flammable gases and combustible dusts.

This paper describes an experimental investigation of safety characteristics of hybrid mixtures composed of hydrogen, air, and representative dusts from the processing of the titanium-iron oxide mineral ilmenite. The approach adopted entails the measurement of the maximum explosion pressure P_{max} and the maximum rate of pressure rise $(dP/dt)_{max}$ of hybrid explosions in a 20-litre explosions vessel, following the procedure prescribed for a recent round robin study.

The results demonstrate that 2 vol.% of hydrogen in air, i.e. significantly below the lower explosible limit (LEL), can have pronounced effect on P_{max} and $(dP/dt)_{max}$ for the hybrid mixtures. For hybrid mixtures with hydrogen concentrations exceeding LEL, the maximum rate of pressure rise is dominated by the high reactivity of hydrogen, whereas the higher energy release per mole of oxygen for titanium has a pronounced effect on P_{max}.

Keywords: *hybrid mixtures, hybrid explosions, hydrogen, ilmenite, iron, titanium*

1. Introduction

Humankind consumes fossil fuels at an increasing rate, and the release of carbon dioxide on a massive scale continues to drive climate change. According to Olabi *et al.* (2022), the process industry is responsible for almost one-fifth of the global greenhouse gas emissions. Sectors that consume large amounts of fossil materials as fuel or feedstock, such as cement, steel, glass, and petrochemicals, are particularly challenging to decarbonise (Lamb *et al.*, 2021).

Hydrogen is a carbon-free energy carrier that can be produced from renewable energy sources, and hydrogen can also replace coal as reducing agent in industrial processes. However, hydrogen-air mixtures are highly flammable, easily ignitable, and have a propensity for deflagration-to-detonation-transition (DDT). This represents a significant challenge for risk assessments and safety.

Although there has been renewed interest in hybrid explosions in recent years (Wu *et al.*, 2023), there is limited information in the public domain on the safety characteristics of flammable mixtures of hydrogen and dusts from intermediate or end products encountered in the production of metals.

This paper presents an experimental study of hybrid mixtures composed of hydrogen and representative dusts encountered in the processing of the titanium-iron oxide mineral ilmenite ($FeTiO_3$), as well as pure titanium. The approach adopted entails the measurement of the maximum explosion pressure P_{max} and the maximum rate of pressure rise $(dP/dt)_{max}$ of hybrid explosions in a 20-litre explosions vessel, following the procedure described by Spitzer *et al.* (2023).

1.1. Hybrid explosions

1.1.1. Definition

Bartknecht (1993) limited the definition of hybrid explosions to mixtures of air, flammable gas, and combustible dust where the gas concentration is below its lower explosion limit (LEL). A more general definition includes all mixtures of flammable gases and combustible dusts, regardless of their respective concentrations (Addai *et al.*, 2015).

A hybrid mixture can support flame propagation even if the individual concentrations of its components are below the LEL for the flammable gas and below the minimum explosible concentration (MEC) for the combustible dust.

1.1.2. Previous work on hybrid explosions with non-metal dusts

Denkevits (2007) studied hybrid explosions with hydrogen and fine graphite dust in a 20-litre vessel. At low concentrations, the explosion pressures developed in two stages: a fast hydrogen explosion, followed by an additional increase in pressure from the combustion of the dust.

Khalil (2013) observed higher deflagration severity indices for hybrid mixture of hydrogen and activated carbon compared to pure gaseous mixtures with the same concentration of hydrogen.

Kosinski *et al*. (2013) studied hybrid mixtures of carbon black and propane in a 20-litre vessel. The addition of carbon black to lean gaseous mixtures increased the explosion pressure.

Wang *et al*. (2020a) observed that the addition of methane (<LEL) decreased the MEC for different types of coal dust. The decrease was more significant for coal dust with high volatile content.

Ji *et al*. (2022) studied different hybrid mixtures over a wide range of concentrations in a standard 20-litre spherical explosion vessel. The addition of flammable gases (<LEL) to dust clouds increased P_{max} and $(dP/dt)_{max}$. However, both P_{max} and $(dP/dt)_{max}$ were lower for hybrid mixtures compared to pure gaseous mixtures (>LEL).

Wu *et al*. (2023) presented a comprehensive review of safety characteristics, explosion regimes/criteria, and flame characteristics of hybrid mixture explosions.

1.1.3. Previous work on hybrid explosions with metal dusts

Cardillo and Anthony (1978) studied hybrid mixtures of propane-air and iron. The MEC of iron was reduced from 200 to 100 g m^{-3} when 1 vol.% propane was added to the mixture.

Skjold (2013) observed two-stage pressure development in hybrid explosions in a 20-litre vessel for certain combinations of hydrogen and silicon concentrations in hybrid mixtures.

Denkevits and Hoess (2015) studied hybrid mixtures of hydrogen and aluminium particles in a 20-litre vessel. Both P_{max} and $(dP/dt)_{max}$ were higher for the hybrid mixtures, compared to pure gaseous mixtures and dust clouds. For low concentrations (<LEL/MEC), the explosion pressures developed in two stages.

Wang *et al*. (2020b) studied the explosion characteristics of aluminium powder in different mixed gas environments. They observed a secondary pressure peak for hybrid mixtures of hydrogen, oxygen, and aluminium dust with excessive amounts of aluminium powder in the 20-litre vessel.

Ji *et al*. (2023) observed flame propagation in hybrid mixtures of hydrogen and magnesium dust in an open-ended duct. Both the maximum pressure and the maximum rate of pressure rise increased significantly when the hydrogen concentration surpassed 10 vol.%.

2. Materials and methods

This section describes the materials used, the experimental apparatus, and the experimental procedures.

2.1. Materials

Three of the four dusts used in this study were provided by INEOS Tyssedal, a metallurgical conversion plant that produces titanium dioxide slag and high purity pig iron from ilmenite ($FeTiO_3$). The company intends to replace coal with hydrogen as reducing agent, and the three dusts selected for testing were ilmenite and two by-products from the pre-reduction process: magnetic fines, and non-magnetic fines.

The test matrix was complemented with titanium dust from Chemetall ("Titaniummetallpulver S"). The available sample originated from a study of minimum ignition energy (Randeberg, 2006).

Compressed hydrogen was supplied from a 50-litre bottle (Hydrogen 5.0 Ultra, >99.999 vol.% H_2).

Table 2.1 summarises the results from particle size measurements with a Malvern Mastersizer 3000. $d_{v,0.1}$, $d_{v,0.5}$, and $d_{v,0.9}$ are standard percentile readings, meaning that the particle size within the corresponding percentage is below the stated size. $d_{4,3}$ is the volume moment mean.

Table 2.1: Particle size distribution characteristics for the samples investigated.

Sample	**$d_{v,0.1}$ (μm)**	**$d_{v,0.5}$ (μm)**	**$d_{v,0.9}$ (μm)**	**$d_{4,3}$ (μm)**
Ilmenite	0.04	1.87	14.2	6.8
Magnetic fines	1.13	4.48	17.8	8.2
Non-magnetic fines	0.11	8.72	28.1	12.1
Titanium	10.70	23.2	44.2	26.3

2.2. Apparatus

The experiments were conducted in a 20-litre explosion vessel of the USBM type (Figure 2.1), fitted with the control and dispersion system from the standard 20-litre Siwek sphere (Skjold, 2003).

Digital pressure indicators of type DPI 705 measured the initial pressures in the vessel and in the dust reservoir. The standard KSEP 332 unit from Kuhner triggered dust injection and ignition and collected pressure data measured with piezoelectric pressure transducers and charge amplifiers from Kistler (Cesana & Siwek, n.d.). Figure 2.2 shows a typical pressure-time history from a test in a constant volume explosion vessel, where:

P_{ex} is the maximum explosion overpressure measured in a specific test – P_m is the corrected maximum explosion overpressure, adjusted for the effect of heat losses and the pressure generated by the chemical ignitors, and P_{max} is the average value of the three highest P_m values measured over a wide range of fuel concentrations.

$(dP/dt)_m$ is the maximum rate of pressure rise measured in a specific test – $(dP/dt)_{max}$ is the average value of the three highest $(dP/dt)_m$ values measured over a wide range of concentrations, and the K_{St} value is $(dP/dt)_{max}$ normalised by the cube root of the vessel volume V_v: $K_{St} = (dP/dt)_{max}\, V_v^{1/3}$.

Figure 2.1: The 20-litre explosion vessel.

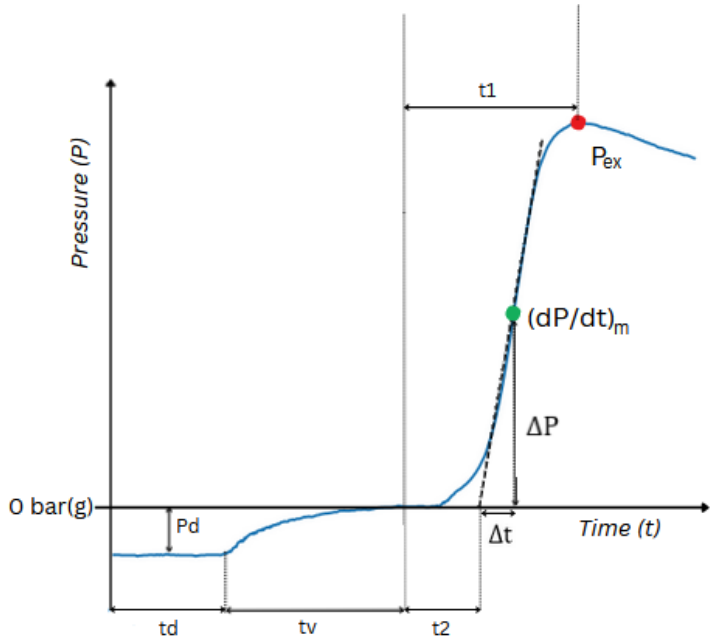

Figure 2.2: Typical pressure-time curve from an explosion in the 20-litre vessel.

2.3. Experimental procedure

The determination of P_{max} and $(dP/dt)_{max}$ for dust clouds followed the standard procedure for the 20-litre vessel (Cesana & Siwek, n.d.), with 2 × 5 kJ chemical igniters as the ignition source.

The testing of gaseous and hybrid mixtures followed the procedure prescribed for the recent round robin tests for safety characteristics of hybrid mixtures (Spitzer *et al.*, 2023), with 2 × 1 kJ chemical igniters as the ignition source.

3. Results and discussion

This section presents and discusses the results obtained for the four dusts mentioned in section 2.1.

3.1. Ilmenite

Ilmenite is an oxide, and hence not combustible. This was confirmed in the experiments. Ilmenite did however exhibit a quenching effect on hydrogen explosions. A change in colour, from the dark grey mineral injected into the vessel, to an orange residue deposited on surfaces inside the vessel after explosion tests, indicated that ilmenite reacted chemically. A likely reaction can be the reduction of ilmenite with hydrogen (Zhao and Shadman, 1991; Sabat *et al.*, 2014; Sargeant *et al.*, 2020):

$$FeTiO_3\ (s) + H_2\ (g) \rightarrow Fe\ (s) + TiO_2\ (s) + H_2O\ (g)$$

The iron produced in this reaction may explain why the residue was conducting, resulting in short-circuiting of the insulated holders for the chemical igniters inside the vessel after tests.

3.2. Magnetic fines

Magnetic fines consist of crushed metallised pellets, and like ilmenite, this material was also non-reactive, apart from a certain quenching effect on hydrogen explosions.

3.3. Non-magnetic fines

Non-magnetic fines comprise of fine coke and non-metallic dust, and the results from standard dust explosion testing using 10 kJ ignition energy showed some reactivity. Here non-magnetic fines had a maximum explosion pressure of 6.77 bar(g), and a maximum rate of pressure rise of 147.3 bar s^{-1}, corresponding to a K_{St} value of 40 bar m s^{-1}.

Figure 3.1 summarises the results for non-magnetic fines using 2 kJ ignition energy, with and without hydrogen. The tests with 0 vol.% hydrogen (blue symbols), exhibited a peak explosion pressure of 0.4 bar(g), and a peak rate of pressure rise of 40 bar s^{-1}. Compared with the standard dust testing, the impact of ignition energy on the explosion indices of non-magnetic fines is significant.

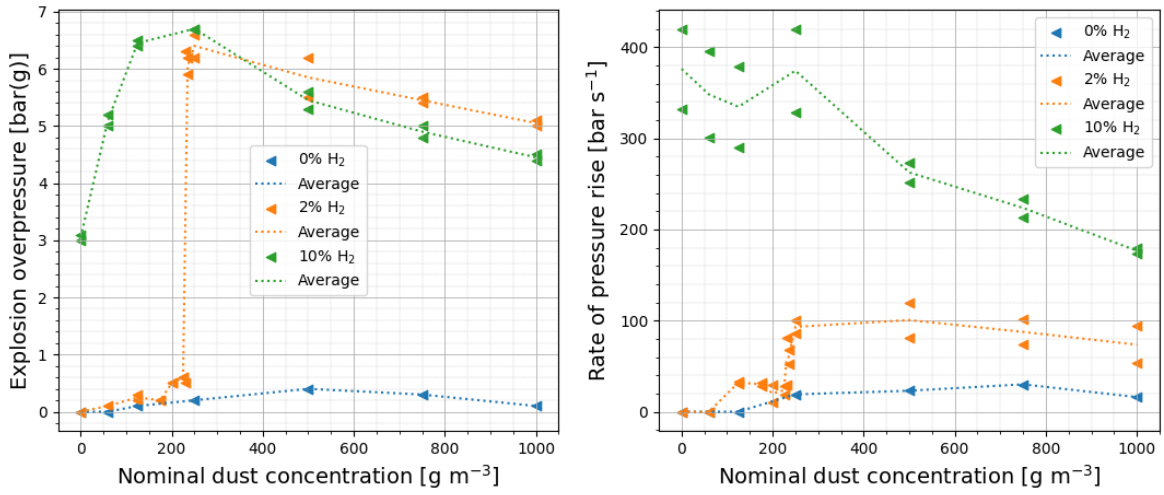

Figure 3.1: Explosion overpressure (left) and rate of pressure rise (right) as a functions of nominal dust concentration for non-magnetic fines, for 0, 2, and 10 vol.% hydrogen in air, using 2 kJ ignition energy.

For hybrid mixtures with only 2 vol.% hydrogen, i.e. 50% of LEL for pure hydrogen-air mixtures, both P_m and $(dP/dt)_m$ increased rapidly when the concentration of non-magnetic fines reached a critical concentration of about 230-235 g m^{-3} (orange symbols). Figure 3.1 shows that the explosion pressure increased from 0.6 to 6.4 bar(g), and the rate of pressure rise increased from 20 to almost 100 bar s^{-1}. For nominal dust concentrations exceeding 250 g m^{-3}, the explosion pressure declines

linearly, whereas the rate of pressure rise increases slightly up to about 500-600 g m^{-3} and declines slowly for higher concentrations.

For hybrid mixtures with 10 vol.% hydrogen (green symbols), the highest explosion pressure of 6.6 bar(g) is reached for a nominal dust concentration of 250 g m^{-3}. This is more than twice the pressure obtained for 10 vol.% hydrogen in air without dust. For higher dust concentrations, the P_m values decline below the values obtained for hybrid mixtures with 2 vol.% hydrogen. This is reasonable, since an increase from 2 to 10 vol.% hydrogen in the hybrid mixture implies that there is less oxygen available for the combustion of the dust particles. The development of $(dP/dt)_m$ for dust concentrations up to 250 g m^{-3} is more complex, and there is significant spread in the results. For higher dust concentrations, there is a near linear decrease in the maximum rate of pressure rise.

Figure 3.2 shows selected pressure-time curves from the tests with non-magnetic fines summarised in Figure 3.1, for mixtures with 2 vol% hydrogen (left) and 10 vol.% hydrogen (right). The curves for the flammable hydrogen-air mixtures with added dust on the right show the typical behaviour of a two-stage combustion process.

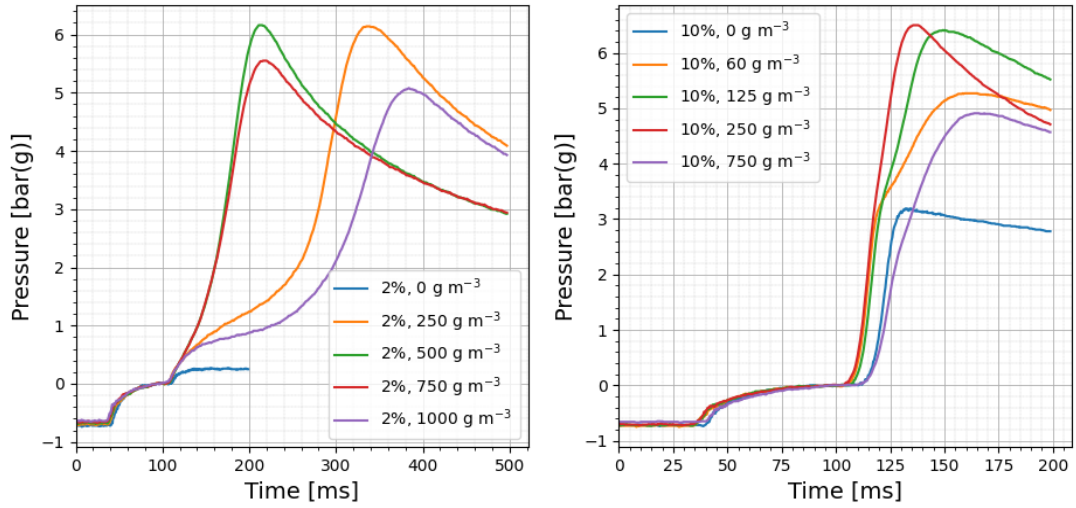

Figure 3.2: Pressure-time histories for explosions with non-magnetic fines, with and without hydrogen, using 2 kJ ignition energy.

3.4. Titanium

The results from the standard dust explosion testing of the titanium dust using 10 kJ ignition energy indicate P_{max} and $(dP/dt)_{max}$ values of at least 6.36 bar(g) and 454 bar s^{-1}, respectively, corresponding to a K_{St} value of 123 bar m s^{-1}. The number of tests that could be performed was limited by the size of the available dust sample, and it was not possible to determine maximum values for all mixture compositions since the experimental apparatus could not generate dust clouds with higher concentrations than 1000 g m^{-3}.

Figure 3.3 summarises the results from the hybrid tests for titanium dust using 2 kJ ignition energy, with and without added hydrogen. The tests with 0 vol. % hydrogen (blue symbols) indicate peak P_m and $(dP/dt)_m$ values of 5.9 bar(g) and 460 bar s^{-1}, respectively. The P_m and $(dP/dt)_m$ values obtained for hybrid mixtures with 2 vol.% hydrogen are quite similar to the results obtained for those with 0 vol.% hydrogen. For hybrid mixtures with 10 vol.% hydrogen, the explosion pressures are significantly higher, especially for nominal dust concentrations up to about 250 g m^{-3}, and the flammable hydrogen-air mixture has a pronounced effect on $(dP/dt)_m$ over the entire range of concentrations.

Figure 3.4 shows selected pressure-time histories from the hybrid tests with titanium summarised in Figure 3.3, for nominal dust concentrations of 500 g m^{-3} (left) and 1000 g m^{-3} (right). Unlike the

results for non-magnetic fines in Figure 3.2, there is no indication of a two-stage combustion process for these hybrid mixtures. There is, however, a significant increase in both P_m and $(dP/dt)_m$ for the tests with 10 vol.% hydrogen.

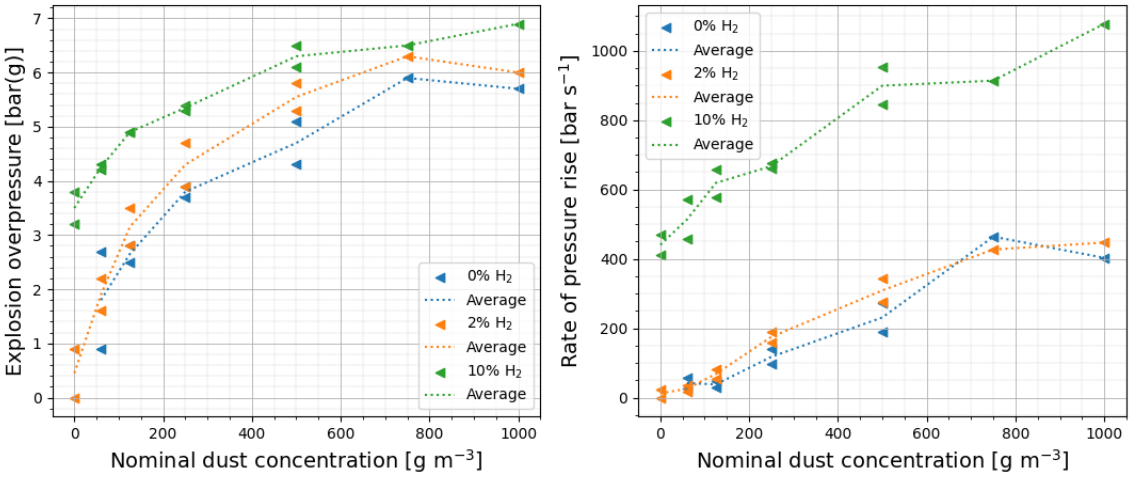

Figure 3.3: Explosion overpressure (left) and rate of pressure rise (right) as a functions of nominal dust concentrations for titanium, for 0, 2, and 10 vol.% hydrogen in air, using 2 kJ ignition energy.

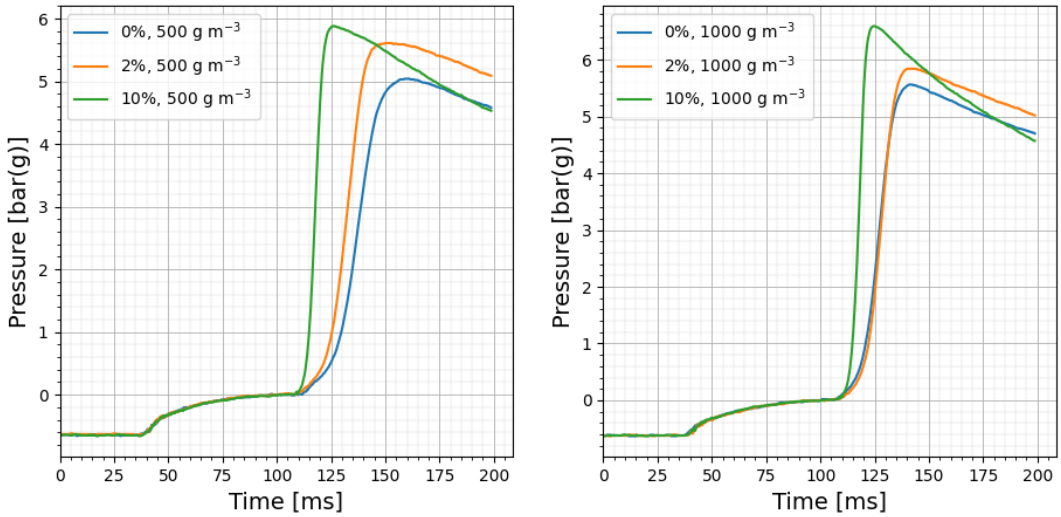

Figure 3.4: Pressure-time histories for explosions with titanium dust, with and without hydrogen, using 2 kJ ignition energy.

3.5. Overall discussion

The higher explosion pressures obtained for hybrid mixtures, compared to gaseous mixtures and dust clouds, are consistent with previous studies (Denkevits, 2007; Kosinski *et al.*, 2013; Denkevits and Hoess, 2015). The significant increase in $(dP/dt)_m$ for hybrid mixtures with 10 vol% hydrogen, i.e. flammable hydrogen-air mixtures with added dust, also seems reasonable given the extreme reactivity of hydrogen relative to most other fuels.

Non-magnetic fines are comprised of fine coke and non-metallic dust from the reduction of ilmenite by coal. Hence, the energy content and explosion characteristics of this dust are likely to be comparable to that of carbon. Carbon exhibits a heat of combustion per mole oxygen consumed of 394 kJ. For titanium and hydrogen, the corresponding values are 945 kJ and 484 kJ, respectively. The significant difference in the energy that can be released during explosions in closed vessels between

non-magnetic fines and titanium dust can explain why the addition of hydrogen had a more pronounced effect on the explosion pressure for non-magnetic fines, compared to titanium.

Concerning the prospect of replacing coal with hydrogen as reducing agent in the processing of metal ore, the dramatic increase in both P_m and $(dP/dt)_m$ for hybrid explosions with non-magnetic fines and only 2 vol.% hydrogen is of particular concern from a safety perspective.

4. Conclusions and suggestions for further work

This study was motivated by the possibility of replacing coal with green hydrogen as reducing agent in the processing of metal ore. The approach adopted entailed an experimental investigation of hybrid explosions in a 20-litre explosions vessel.

The main conclusions can be summarised as follows:

- The addition of a low concentration of hydrogen, significantly below LEL, can have a dramatic effect on both P_{max} and $(dP/dt)_{max}$ for a combustible dust with low reactivity.
- For hybrid mixtures with hydrogen concentrations exceeding LEL, the maximum rate of pressure rise is dominated by the high reactivity of hydrogen.
- The high energy release per mole of oxygen for titanium has a pronounced effect on P_{max}.

Suggestions for further work include:

- Investigating additional hydrogen concentrations – the number of tests that could be performed in the present study was limited by the availability of chemical igniters.
- Additional testing of hybrid explosions with metals, including titanium and iron – the number of tests that could be performed with titanium in the present study was limited by the sample size, and iron dust was not available.

Acknowledgements

The authors gratefully acknowledge the support from the Research Council of Norway (RCN) under grant agreement number 326281 for the project *Safe Hydrogen Implementation: Pre-normative research for Ships* (SH2IPS), the support from INEOS Tyssedal, and the support from the focus area *Climate and Energy Transition* at the University of Bergen.

References

Addai, E. K., Gabel, D., & Krause, U. (2015). Lower explosion limit of hybrid mixtures of burnable gas and dust. *Journal of Loss Prevention in the Process Industries, 36*, 497–504. https://doi.org/https://doi.org/10.1016/j.jlp.2015.02.014

Bartknecht, W. (1993). Explosionsschutz - grundlagen und andwendung. *Springer-Verlag*.

Cardillo, P., & Anthony, E. (1978). The flammability limits of hybrid gas and dust systems. *La Rivista del Combustibili*, XXXII, 390–395.

Cesana, C., & Siwek, R. (n.d.) *Manual for 20-l-apparatus.* TÜV SÜD Schweiz AG and Cesana AG. Switzerland. https://www.cesana-ag.ch/download/B000_071.pdf

Denkevits, A. (2007). Explosibility of hydrogen–graphite dust hybrid mixtures. *Journal of Loss Prevention in the Process Industries, 20* (4), 698–707. https://doi.org/https://doi.org/10.1016/j.jlp.2007.04.033

Denkevits, A., & Hoess, B. (2015). Hybrid H_2/Al dust explosions in Siwek sphere. *Journal of Loss Prevention in the Process Industries, 36*, 509–521. https://doi.org/https://doi.org/10.1016/j.jlp.2015.03.024

Eckhoff, R. (2016). *Explosion hazards in the process industries*. Elsevier Inc

Ji, W., Wang, Y., Yang, J., He, J., Lu, C., Wen, X., & Wang, Y. (2023). Explosion overpressure behaviour and flame propagation characteristics in hybrid explosions of hydrogen and magnesium dust. *Fuel, 332*, 125801. https://doi.org/https://doi.org/10.1016/j.fuel.2022.125801

Ji, W.-t., Gan, X.-y., Li, L., Li, Z., Wen, X.-p., & Wang, Y. (2022). Prediction of the explosion severity of hybrid mixtures. *Powder Technology, 400*, 117273. https://doi.org/https://doi.org/10.1016/j.powtec.2022.117273

Khalil, Y. (2013). Experimental investigation of the complex deflagration phenomena of hybrid mixtures of activated carbon dust/hydrogen/air. *Journal of Loss Prevention in the Process Industries, 26* (6), 1027–1038. https://doi.org/https://doi.org/10.1016/j.jlp.2013.03.006

Kosinski, P., Nyheim, R., Asokan, V., & Skjold, T. (2013). Explosions of carbon black and propane hybrid mixtures. *Journal of Loss Prevention in the Process Industries, 26* (1), 45–51. https://doi.org/https://doi.org/10.1016/j.jlp.2012.09.004

Lamb, W. F., Wiedmann, T., Pongratz, J., Andrew, R., Crippa, M., Olivier, J. G. J., Wiedenhofer, D., Mattioli, G., Khourdajie, A. A., House, J., Pachauri, S., Figueroa, M., Saheb, Y., Slade, R., Hubacek, K., Sun, L., Ribeiro, S. K., Khennas, S., de la Rue du Can, S., Chapungu, L., Davis, S. J., Bashmakov, I., Dai, H., Dhakal, S., Tan, X., Geng, Y., Gu, B. & Minx, J. (2021). A review of trends and drivers of greenhouse gas emissions by sector from 1990 to 2018. *Environmental Research Letters, 16 (7)*, 073005. https://doi.org/10.1088/1748-9326/abee4e

Olabi, A.G., Wilberforce, T., Elsaid, K., Sayed, E.T., Maghrabie, H.M. & Abdelkareem, M.A. (2022). Large scale application of carbon capture to process industries – A review. *Journal of Cleaner Production*, 36, 132300. https://doi.org/10.1016/j.jclepro.2022.132300

Randeberg, E. (2006). Electric spark ignition of sensitive dust clouds in the sub 1 mJ range. PhD dissertation, University of Bergen. https://hdl.handle.net/1956/1868

Sabat, K.C., Rajput, P., Paramguru, R.K., Bhoi, B., & Mishra, B.K. (2014). Reduction of oxide minerals by hydrogen plasma: An overview. *Plasma Chemistry and Plasma Processing*, 34, 1–23. https://doi.org/10.1007/s11090-013-9484-2

Sargeant, H.M. Abernethy, F.A.J. Barber, S.J. Wright, I.P. Anand, M. Sheridan, S., & Morse, A. (2020). Hydrogen reduction of ilmenite: Towards an in situ resource utilization demonstration on the surface of the Moon, Planetary and Space Science, 180, 104751. https://doi.org/10.1016/j.pss.2019.104751

Skjold, T. (2003). *Selected aspect of turbulence and combustion in 20-litre explosion vessels.* Master thesis, University of Bergen. https://hdl.handle.net/1956/1631

Skjold, T. (2013). An experimental investigation of flame propagation in clouds of silicon dust dispersed in air, hydrogen-air mixtures, and hybrid Si-H_2-air mixtures. 24 ICDERS, Taipei, 28 July - 2 August 2013. http://www.icders.org/ICDERS2013/abstracts/ICDERS2013-0182.pdf

Spitzer, E.H., Askar, E., Benke, A., Cloney, C., D'Hyon, S., Dufaud, O., Dyduch, Z., Gabel, D., Geoerg, P. Heilmann, V., Jankuj, V., Jian, W, Krause, U., Krietsch, A., Mynarz, M., Norman, F., Skrinsky, J., Taveau, J., Vignes, A., Zakel, S. & Zhong, S. (2023). 1st international round robin test on safety characteristics of hybrid mixtures. *Journal of Loss Prevention in the Process Industries*, 81: 104947. https://doi.org/10.1016/j.jlp.2022.104947

Wang, X., Wang, Z., Ni, L., Zhu, M., & Liu, C. (2020b). Explosion characteristics of aluminum powder in different mixed gas environments. *Powder Technology, 369*, 53–71. https://doi.org/https://doi.org/10.1016/j.powtec.2020.04.056

Wang, Y., Qi, Y., Gan, X., Pei, B., Wen, X., & Ji, W. (2020a). Influences of coal dust components on the explosibility of hybrid mixtures of methane and coal dust. *Journal of Loss Prevention in the Process Industries, 67*, 104222. https://doi.org/https://doi.org/10.1016/j.jlp.2020.104222

Wu, D., Zhao, P., Spitzer, S.H., Krietsch, A., Amyotte, P. & Krause, U. (2023). A review on hybrid mixture explosions: Safety parameters, explosion regimes and criteria, flame characteristics. *Journal of Loss Prevention in the Process Industries*, 82: 104969. https://doi.org/10.1016/j.jlp.2022.104969

Zhao, Y. & Shadman, F. (1991). Reduction of ilmenite with hydrogen. Industrial & Engineering Chemistry Research, 30, 2080-2087. https://pubs.acs.org/doi/pdf/10.1021/ie00057a005

Hybrid Mixture Explosions in an Industrial Polymer Production Process

Anton Schrader [a], Katherine Axani [b], Mohammad Alauddin [a], Alison Scott [a], Chris Cloney [a,c] & Paul Amyotte [a]

[a] Dalhousie University, Halifax, Canada
[b] Imperial Oil Limited, Sarnia, Canada
[c] DustEx Research, Halifax, Canada

E-mail: *antonschrader@dal.ca*

Abstract

This paper presents research on the explosibility of industrial high-density polyethylene (HDPE) dust. Experiments were conducted to investigate the explosion behaviour of the HDPE dust as well as of HDPE/ethylene hybrid mixtures. The dust explosion results further emphasize the importance of avoidance of accumulation of fine particles, as finer samples had lower explosion likelihood and higher explosion severity parameters. Hybrid mixture explosion data is presented in the form of explosion regime diagrams, which will be made accessible to process operators and designers to promote the inherently safer transfer of polymer particles. Finally, inherently safer approaches to dust explosion prevention and mitigation in relation to the results of this study have been discussed.

Keywords: *hybrid mixtures, industrial explosions, dust explosions, inherently safer design*

1. Introduction

The objective of this work is to apply the principles of inherently safer design to the prevention of polyethylene explosions. Avoidance of the formation of fine-size dust clouds and hybrid mixtures (combustible dust and flammable gas) is emphasized by means of experimentally determined explosion regime diagrams. Explosion boundaries for inherently safer transfer of polymer particles will thus be made available to process designers and operators. The fundamental behaviour of hybrid mixture explosions is well established and has been studied by numerous research groups for several decades. This work seeks to expand on this previous work through explosion regime diagrams tailored to process operators to enhance their understanding of the potential consequences of hazardous conditions and to better select prevention and mitigation measures.

The system studied in this project consists of high-density polyethylene (HDPE) dust samples and ethylene gas. The materials were selected based on their applicability to fluidized-bed catalytic reactors. The experimental work for this project was divided into two parts: dust-testing and hybrid mixture testing. Modeling is planned using the results of the hybrid mixture work to better understand the behaviour of the system in the synergistic explosion region.

High-density polyethylene dust samples were received from Imperial Oil Limited in Sarnia, Canada. Experimental work was conducted at Dalhousie University in the Dust Explosions Laboratory. The dust explosion parameters investigated in this project are (i) maximum explosion pressure, P_{max}, (ii) maximum rate of pressure rise, $(dP/dt)_{max}$, (iii) size-normalized maximum rate of pressure rise, K_{St}, (iv) minimum explosible concentration, MEC, (v) minimum ignition energy, MIE, and (vi) minimum ignition temperature, MIT. Parameters (i-iv) were tested using the Siwek 20-L explosion chamber, while MIE and MIT were tested in the MIKE 3 apparatus and BAM oven, respectively.

1.1. Hybrid Mixture Explosions

Hybrid mixtures have been the subject of extensive research and scrutiny over the last few decades, largely due to the relatively low amount of understanding about their mechanics. A major finding in the area was the occurrence of explosions at concentrations less than the respective lower explosibility limits of the components, as seen in many works (e.g., Abuswer et al., 2013; Amyotte et al., 2008; Cloney et al., 2017). One approach taken to quantify and express the effects of the admixture of gas to dust explosions was the development of explosion regime diagrams (Garcia-Agreda et al., 2011; Sanchirico et al., 2011). In these diagrams, the dust and gas concentrations are tested at ratios of their lower explosibility limits. The diagrams can be divided into four main regions, namely the dust-driven, gas-driven, dual-fuel, and synergistic regions (Garcia-Agreda et al., 2011; Sanchirico et al., 2011). These regions are summarized in Fig. 1.

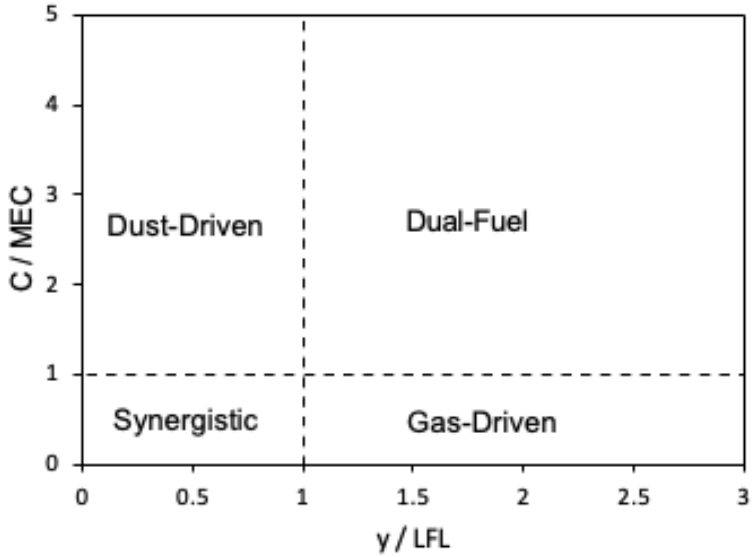

Fig. 1. *Explosion regions in the explosion regime diagram, where C is the concentration of dust (g/m^3), MEC is the minimum explosible concentration (g/m^3), y is the gas concentration (%), and LFL is the lower flammability limit of the gas (%)*

Some work has been completed toward the creation of models to predict the behaviour in the synergistic region. Two of the simplest models developed were the Bartknecht model in 1981 and Le Chatelier's model, which was proposed by Glassmann in 1996 (Addai et al., 2015). Since then, many models have been proposed but there has yet to be a universally accepted model for all hybrid systems (Ji et al., 2022).

1.2. Polyethylene Explosions

Polyethylene dust has been shown to be explosible in a large number of studies performed across the world, in part due to the versatility and wide-scale usage of the polymer (Amyotte et al., 2009; Cheng et al., 2022; Gan et al., 2018). There have also been numerous incidents that have been caused by polyethylene dust, with one notable incident being the explosion at West Pharmaceuticals in Kingston, North Carolina, which resulted in six fatalities, 38 injuries, and the destruction of the facility (Sugar Dust Explosion and Fire, 2009). In a previous research grant awarded by Imperial Oil Limited (IOL) to Dalhousie University, polyethylene dust-based hybrid mixtures were tested, using ethylene, propane, and hexane as the gases. The findings were published by Amyotte et al. in 2008 and 2009 and are summarized below:

- A decrease in particle size leads to an increase in dust explosibility
    - Minimum explosible concentration decreases (MEC)

  - Maximum rate of pressure rise increases ($(dP/dt)_{max}$)
  - No impact on maximum explosion pressure (P_{max})
- The addition of hydrocarbon gas increases explosibility
  - Explosions possible under MEC of dust and LFL of gas
  - Maximum rate of pressure rise increases ($(dP/dt)_{max}$)
  - No impact on maximum explosion pressure (P_{max})
  - Leaner dust mixtures have higher values for both $(dP/dt)_{max}$ and P_{max}

The current study takes these concepts and applies them to the explosion regime diagrams, which will also be used to analyze the behaviour of hybrid mixtures present at the Imperial Oil facility in Sarnia, Canada.

2. Experiments

The materials, apparatus, and methods used in this project are described in this section.

2.1. Materials

High-density polyethylene dust samples were received from Imperial Oil Limited in Sarnia, Canada. Two separate samples were received: one coarse sample (CS) and one fine sample (FS). The coarse sample was tested as received (CS1) and after being sieved using a US-35 screen (CS2). Finally, one commercial fine polyethylene sample (CM), purchased from Sigma-Aldrich, was used as well. The samples were characterized using Malvern light scattering particle size analysis at the Dalhousie Minerals Engineering Centre, the results of which can be seen in Table 1.

Table 1. *Results of particle size analysis*

Sample	Sample ID	D(10)[a] [µm]	D(50)[b] [µm]	D(90)[c] [µm]
Coarse Sample (as-received)	CS1	380	777	1650
Coarse Sample (<500 µm)	CS2	171	322	534
Fine Sample	FS	37	177	477
Commercial Sample	CM	23	42	70

[a] D(10) denotes the diameter > 10% of particles
[b] D(50) denotes the diameter > 50% of particles
[c] D(90) denotes the diameter > 90% of particles

Ethylene gas and compressed air were both purchased from Linde Canada. The ethylene gas was analytical grade and had a purity of 99.9%. The lower flammability limit of ethylene is 2.75%. The compressed air had an oxygen concentration of 20.9% +/- 0.1% with nitrogen as a balance gas.

2.2. Apparatus

The experiments for the determination of P_{max}, K_{St}, and MEC were performed in a Siwek 20-L explosion chamber. The pressure leak rate of the chamber was minimized prior to experiments through equipment maintenance to a rate of approximately 1 mm Hg/hr. P_{max} and K_{St} were determined using ASTM E1226-19, *Standard Test Method for Explosibility of Dust Clouds*, while MEC was

determined using ASTM E1515-14(2022), *Standard Test Method for Minimum Explosible Concentration of Combustible Dusts*. It should be noted that for MEC, the ignition energy used for all experiments was 2.5 kJ. Testing for MIE was performed in a MIKE 3 apparatus. These tests were performed in accordance with ASTM E2019-03(2019), *Standard Test Method for Minimum Ignition Energy of a Dust Cloud in Air*. Finally, MIT was determined using the BAM oven; tests were conducted in accordance with ASTM E1491-06(2019), *Standard Test Method for Minimum Autoignition Temperature of Dust Clouds*. Equipment schematics for dust testing can be found in related works and previous work by the Dalhousie Dust Explosion Research group.

For the hybrid mixture work, ethylene gas was added to the secondary gas inlet line of the Siwek 20-L chamber. A flashback arrestor was added to the inlet gas line as a safety precaution. For the hybrid mixture experiments, gas is added to the evacuated explosion chamber to the desired concentration using the partial pressures method. The concentration of gas in the chamber will be validated by extracting the preignition explosion chamber gas through a septum and analyzing the gas using gas chromatography at Dalhousie University.

Note that no hybrid mixture work will be conducted in the MIKE 3 apparatus and the BAM oven due to the difficulty of the reconfiguration required. This is outside the scope of the current research.

2.3. Hybrid Mixture Experimental Protocol

To create the explosion regime diagrams, an experimental protocol was developed to fully explore the explosion behaviour of the hybrid systems. The emphasis of the experimental design was placed on the synergistic region, as it is in this region that the occurrence of explosions is often unexpected. The behaviour will be compared to existing models. In the synergistic region, a 5^2 full factorial experiment was designed, meaning that two different parameters, in this case, the dust and gas ratios, will be tested at five levels. This will allow for the observation of the explosion behaviour while simultaneously minimizing the number of trials required. In the dual-fuel, gas-driven, and dust-driven explosion regions, the dust and gas ratios will be tested at three levels, or a 3^2 full factorial experiment in each region. Every data point will be taken in triplicate (based on ASTM E1226-19). The full experimental test protocol can be seen in Fig. 2, where each data point represents one set of concentrations at which a test will be conducted.

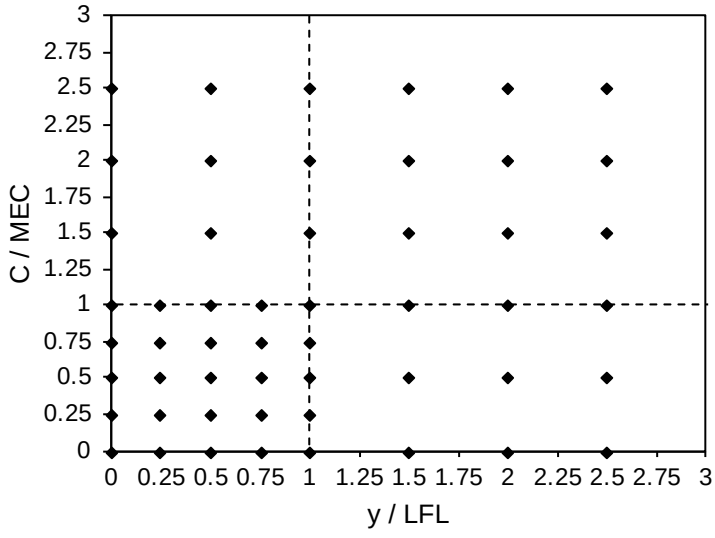

Fig. 2. *Experimental design for hybrid mixture testing*

3. Results and Discussion

In this section, the experimental results to date are presented and discussed. Experimental work is ongoing.

3.1. Dust Explosion Results

The first portion of the experimental work performed in this study was the dust explosion parameter testing of the HPDE dust. As previously mentioned, three samples from IOL and one commercial sample were tested for P_{max}, $(dP/dt)_{max}$, K_{St}, MEC, MIE, and MIT using the respective ASTM standards. The results of P_m and $(dP/dt)_m$ for all dust samples are presented in Figs. 3 and 4. Results for P_{max} and K_{St}, MEC, MIE, and MIT are presented in Tables 2-5, respectively.

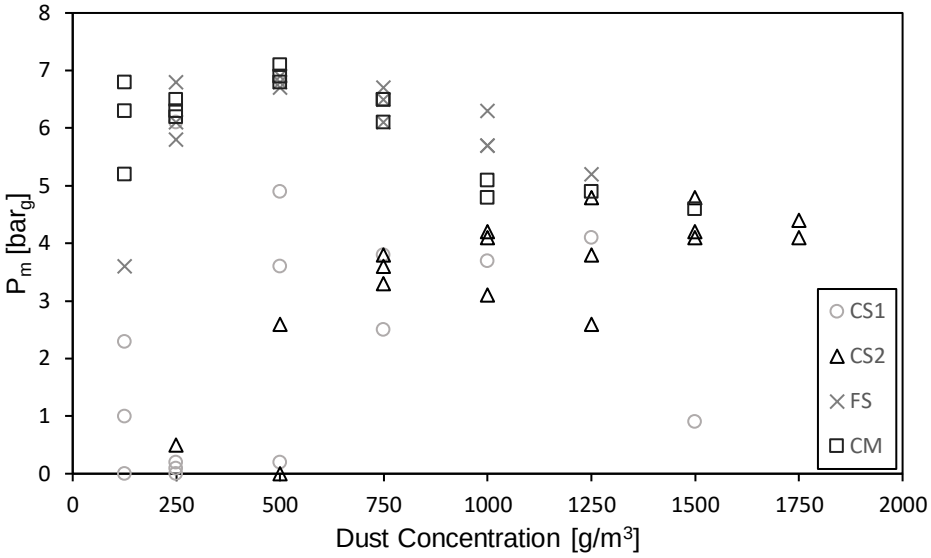

Fig. 3. *Results for P_m of HDPE dust samples*

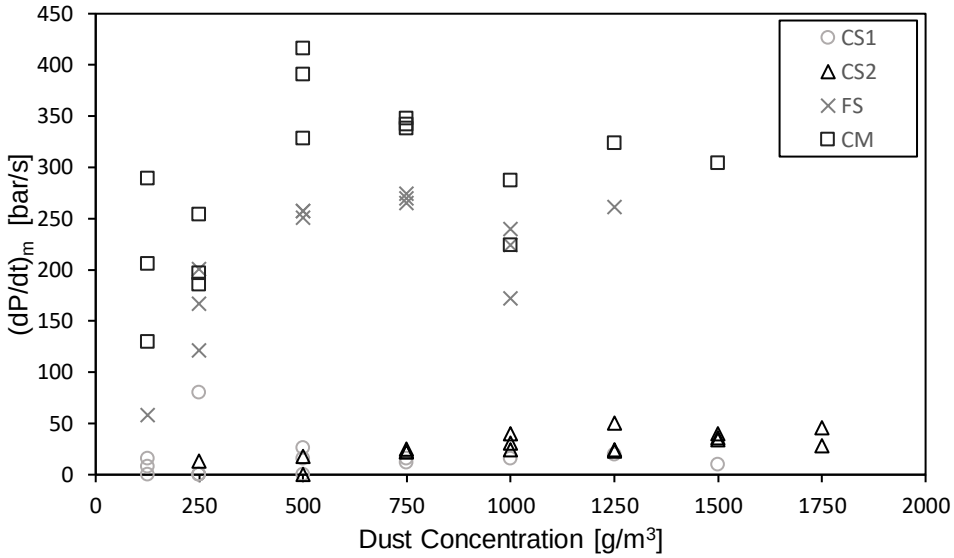

Fig. 4. *Results for $(dP/dt)_m$ for all HDPE samples*

***Table 2**. P_{max}, $(dP/dt)_{max}$, and K_{St} of HDPE dust samples*

Sample	P_{max} [bar]	$(dP/dt)_{max}$ [bar / s]	K_{St} [bar m / s]
CS1	N/A [a]	N/A[a]	N/A[a]
CS2	4.4	40	11
FS	6.8	270	73
CM	6.9	382	104

[a] CS1 exploded inconsistently as a result of the large particle size distribution, meaning that P_{max}, $(dP/dt)_{max}$, and K_{St} lose their meaning

***Table 3.** MEC results for all HPDE dust samples*

Sample ID	MEC [g m^{-3}]
CS1	>1000
CS2	750-1000
FS	50
CM	40

***Table 4.** MIE results for all HDPE dust samples*

Sample ID	MIE without inductance (H = 0 mH) [mJ]	MIE with inductance (H = 1 mH) [mJ]	Es without inductance (H = 0 mH) [mJ]	Es with inductance (H = 1 mH) [mJ]
CS1	>1000	>1000	N/A[a]	N/A[a]
CS2	>1000	>1000	N/A[a]	N/A[a]
FS	300 < MIE < 1000	10 < MIE < 30	360	24
CM	100 < MIE < 300	10 < MIE < 30	140	21

[a] E_S could not be calculated for CS1 and CS2 as the sample did not ignite at any ignition energy as a result of their large particle size

***Table 5.** MIT results for all HDPE dust samples*

Sample ID	MIT [°C]
CS1	450
CS2	450
FS	430
CM	430

The results of the testing from this work very much fall into the same trends based on the relative particle size as observed by Amyotte et al. (2008). In the current study, it was observed that a reduction in particle size has a greater effect on the rate of pressure rise in an HDPE dust explosion while having a lesser effect on maximum explosion pressure. This trend is observable in Fig. 4, where there is a significant difference between the different samples. Here, CM (D_{50} = 42 µm) has the highest values of $(dP/dt)_m$, followed then by FS (D_{50} = 177 µm). CS1 and CS2 (D_{50} = 777 and 322

µm, respectively) have dP/dt values that are nearly a factor of 10 lower, which is expected based on their large particle sizes. In Fig. 3, it can be seen that CM and FS had the highest values for P_m, but the values for all samples are much more similar than their $(dP/dt)_m$ values. The same trend was observed for the calculated values for P_{max} and K_{St}, which can be found in Table 5. One note for these values is that the P_{max} and K_{St} for CS1 could not be determined as a result of the inconsistent nature of the explosions at this particle size. Finally, the MEC of the samples also showed a reduction as a function of particle size. The two coarse samples required very high concentrations to ignite, while the two finer samples (FS and CM) were found to be explosible at concentrations of 50 and 40 g/m^3, respectively. This is also consistent with the findings of Amyotte et. al. (2008).

The MIE and MIT values determined in the current study follow a trend similar to that seen in another study by our research group, conducted by Addo (2018). Both in the current study and in this previous study, the MIE of the samples with a large particle size could not be determined using the MIKE 3 apparatus and was found to be greater than 1 J, with and without inductance. However, the fine samples that were tested were found to have measurable ignition energies. The sample with the smallest average particle size (CM) was found to have the lowest ignition energy without inductance, while both fine HPDE samples (FS and CM) were found to have an ignition energy between 10 and 30 mJ with inductance. These results are similar to the previous work conducted in our research group, with one notable difference being that the MIE of the CM without inductance was found to be lower in the previous study. However, this occurred at a high concentration and delay time in the previous study, and could not be replicated in the current study. The MIT results were not greatly influenced by the particle size, with the coarse samples having an MIT of 450 ºC and the finer samples igniting at 430 ºC.

3.2. Hybrid Mixture Results

Initial hybrid mixture experiments have been performed as a proof-of-concept study. In these experiments, the gas and dust concentrations as a ratio to their lower explosibility limits were varied to show the behaviour of explosions in each of the regions on the explosion regime diagram. Single-component explosions were also conducted above and below the lower explosibility limits to further validate the experimental procedure. The HDPE sample used for the preliminary experiment was CM, based on particle size and available dust quantity. Recall that the MEC of this dust was found to be 50 g/m^3, while the LFL of ethylene is 2.75%. The P_m, $(dP/dt)_m$, and K_m results of this work are summarized in Table 6. Note that the size-normalized maximum rate of pressure rise, K_m, is calculated by multiplying $(dP/dt)_m$ by the cube root of the vessel volume, which is 20 L for this work.

Table 6. *Preliminary hybrid mixture results*

y/LFL	C/MEC	P_m [bar]	$(dP/dt)_m$ [bar s^{-1}]	K_m [bar m s^{-1}]
0	0.75	0	0	0
0	2	1.7	19	6
0.68	0	0	0	0
0.68	0.75	4.1	56	17
0.68	2	5.7	146	45
1.89	0	7.9	2132	662
1.89	0.75	7.4	1716	533
1.89	2	7.9	2004	623

Using the preliminary data, it is possible to create a basic version of the explosion regime diagram, which is pictured in Fig. 5. The behaviour of the explosions in this diagram is as expected, based on the behaviour of the hybrid mixtures used in the work of both Garcia-Agreda et al. (2011) and

Sanchirico et al. (2011). No single component explosions at concentrations less than their respective lower explosibility limits were observed, while explosions did occur at concentrations higher than the limits. Again, this was expected. The maximum explosion pressure and maximum rate of pressure rise of the pure gas explosions were found to be significantly higher than those of pure dust explosions. The same is true for the explosions in the dust- and gas-driven regions, where the gas-driven explosions had higher P_{max}, $(dP/dt)_m$, and K_m values than the dust-driven explosions. In the dual-fuel explosion, the same maximum explosion pressure as observed in the pure gas explosion was reached, but the maximum rate of pressure change was reduced. This behaviour has also been observed in other hybrid mixture explosion work to date. These results further emphasize the recommendations from previous hybrid mixture research to apply the necessary measures to prevent the formation of hybrid mixtures in a process. These recommendations follow the inherently safer design principle of moderation, while it may not be possible to completely eliminate flammable gas from a system, gas concentration can possibly be maintained below the LFL.

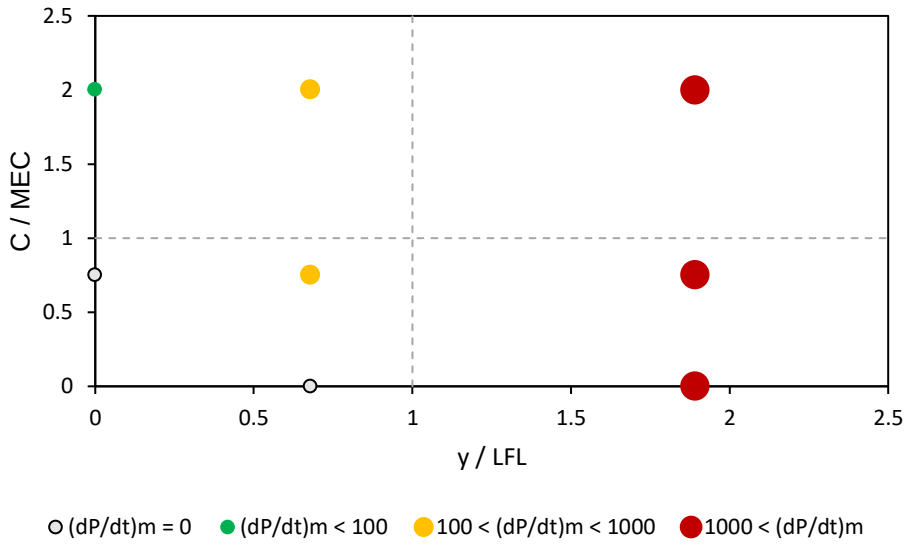

Fig. 5. *Preliminary explosion regime diagram*

Further hybrid mixture explosion research is ongoing and will include performing full explosion regime diagrams for all HDPE dust samples. The results of these experiments will be communicated in future correspondence from the authors.

3.3. Inherently Safer Approaches to Dust Explosion Prevention and Mitigation

This section presents how inherently safer design (ISD), a proactive approach where safety is built into the process rather than being added on, can help reduce dust explosions. The application of the ISD principles of minimization, substitution, moderation, and simplification to dust explosion prevention and mitigation is shown in Table 7.

Minimization of fuel loadings, the use of less hazardous materials, and simplification of dust handling equipment are somewhat intuitive. In the moderation principle of ISD, a material is processed under less severe operating conditions or in a less hazardous form. Common strategies for controlling dust explosions from the perspective of the moderation principle include increasing dust particle size, preventing the formation of hybrid mixtures of explosible dust and flammable gases, altering dust composition by admixture of solid inertants, and handling dust beyond its explosible limit (e.g., using dense-phase pneumatic transport).

The increased particle size distribution of combustible dust results in a reduction in maximum explosion pressure, a significant reduction in the rate of pressure rise, and an increased value of MEC. Figs. 3 and 4 and Table 2 show the variation of dust explosibility of different samples exhibiting the reduced explosibility of the larger particles as expected. The moderation effect of larger particles can be attributed to decreased surface area and reactivity of dust, as discussed in several studies (Amyotte et al., 2007; Amyotte et al., 2009; Cashdollar, 2000; Castellanos et al., 2014; Dufaud et al., 2010).

Preventing the formation of hybrid mixtures is crucial in moderating dust explosions. The preliminary results of this work are a reminder of how the addition of ethylene significantly increases maximum explosion pressure and maximum rate of pressure rise as discussed in Section 3.2. These results further emphasize the recommendations from previous hybrid mixture work from our research group to apply the necessary measures to prevent the formation of hybrid mixtures (Amyotte et al., 2007, 2010; Cloney et al., 2019).

Table 7*. Inherently safer approaches to dust explosion prevention and mitigation*

Inherently safer strategy	**Description**	**Examples**
Minimization	Reducing the quantity of hazardous materials in the absence of safer alternatives	Minimization of fuel loadings Evacuation/prevention of flammable gas
Substitution	Replacing a hazardous material with a safer option	Substitution of less hazardous dust if possible
Moderation	Using a hazardous material under the least hazardous conditions	Increasing the dust particle size Avoiding the formation of hybrid mixtures of explosible dusts and flammable gases Altering the composition of a dust by admixture of solid inertants Processing and handling dust above the material's upper explosible limit (e.g., dense-phase pneumatic transport)
Simplification	Eliminating process complexity to provide fewer opportunities for error and equipment failure	Using robust equipment for bulk-solids and dust handling

Adding inert materials to combustible dust mixtures can lower the likelihood of an explosion by increasing MIE and MIT (Addai et al., 2016; Bu et al., 2020; Janès et al., 2014; Yu et al., 2018). Mixing inert dust with combustible dust in sufficient amounts can moderate dust explosions by removing the heat needed for combustion or by having a rate-limiting effect in combustion reactions (Amyotte et al., 2009). The moderation effect of admixture of solid inertants is feasible when the combustible dust is a waste by-product but difficult to employ when the combustible dust is the actual

value-added product (Amyotte & Khan, 2021) as in this case of HDPE. Also, inerting requires a certain minimum concentration to be effective. Adding insufficient solid inertants can cause the suppressant-enhanced explosion parameter (SEEP) phenomenon, leading to increased explosion pressure (Amyotte, 2013; A. Dastidar & Amyotte, 2002; Jiang et al., 2019). Dust explosions can also be moderated by processing dust beyond the explosible limit, like through the use of dense-phase pneumatic transport.

While ISD can significantly reduce risk in a dust explosion scenario, it does not eliminate all risks associated with dust storage, handling, and processing. A hierarchical approach to preventing and mitigating dust explosions based on ISD, passive, active, and procedural safety has been outlined by Amyotte (2013).

3.3. Modeling Work

Following the completion of the ongoing hybrid mixture explosion experiments, the behaviour of the explosions in the synergistic explosion region will be modeled using existing models.

4. Conclusion

This study has investigated the explosion behaviour of industrial HPDE dust, both in dust explosion settings and in hybrid mixtures. It was found that the finer polyethylene samples had lower explosion likelihood parameters and higher explosion severity parameters (as expected). A preliminary explosion regime diagram was used to quantify the effects of the admixture of ethylene gas on the dust. Further explosion regime diagrams will be made available for process designers and operators to promote the inherently safer transfer of polymer particles.

Acknowledgements

The authors gratefully acknowledge the financial support from Imperial Oil Limited in the form of an Imperial Research Grant.

References

Abuswer, M., Amyotte, P. R., & Khan, F. (2013). A quantitative risk management framework for dust and hybrid mixture explosions. *Journal of Loss Prevention in the Process Industries*, *26*(2), 283–289.

Addai, E. K., Gabel, D., & Krause, U. (2015). Explosion characteristics of three component hybrid mixtures. *Process Safety and Environmental Protection*, *98*, 72–81.

Addai, E. K., Gabel, D., & Krause, U. (2016). Experimental investigations of the minimum ignition energy and the minimum ignition temperature of inert and combustible dust cloud mixtures. *Journal of Hazardous Materials*. *307*, 302-311.

Addo, A., Dastidar, A. G., Taveau, J. R., Morrison, L. S., Khan, F. I., & Amyotte, P. R. (2019). Niacin, lycopodium and polyethylene powder explosibility in 20-L and 1-m3 test chambers. *Journal of Loss Prevention in the Process Industries*, *62*, 103937.

Amyotte, P. R. (2013). *An introduction to dust explosions: Understanding the myths and realities of dust explosions for a safer workplace*. Butterworth-Heinemann.

Amyotte, P. R., & Khan, F. (2021). The role of inherently safer design in process safety. *The Canadian Journal of Chemical Engineering*, *99*(4), 853–871.

Amyotte, P. R., Khan, F. I., & Kletz, T. A. (2009). Inherently safer design activities over the past decade. *Institution of Chemical Engineers Symposium Series*, *155*, 736–743.

Amyotte, P. R., Lindsay, M., Domaratzki, R., Marchand, N., Di Benedetto, A., & Russo, P. (2009). Prevention and Mitigation of Polyethylene and Hydrocarbon/Polyethylene Explosions. *Paper 7D*, 541–556.

Amyotte, P. R., Lindsay, M., Domaratzki, R., Marchand, N., Di Benedetto, A., & Russo, P. (2010). Prevention and mitigation of dust and hybrid mixture explosions. *Process Safety Progress*, *29*(1), 17-21.

Amyotte, P. R., Marchand, N., Di Benedetto, A., & Russo, P. (2008). *Influence of Particle Size and Ethylene Admixture on Polyethylene Dust Explosions*. *3*, 103–112.

Amyotte, P. R., Pegg, M. J., Khan, F., Nifuku, M., & Yingxin, T. (2007). Moderation of dust explosions. *Journal of Loss Prevention in the Process Industries*, *20*(4–6), 675–687.

Bu, Y., Amyotte, P. R., Yuan, W., Yuan, C., & Li, G. (2020). Moderation of Al dust explosions by micro- and nano-sized Al2O3 powder. *Journal of Hazardous Materials*, *381*(August 2019), 120968.

Cashdollar, K. L. (2000). Overview of dust explosibility characteristics. *Journal of Loss Prevention in the Process Industries*, *13*(3), 183–199.

Castellanos, D., Carreto-Vasquez, V., Mashuga, C. V., Trottier, R., & Mannan, M. (2014). The effect of particle size polydispersity on the explosibility characteristics of aluminum dust. *Powder Technology*, *254*, 331–337.

Cheng, Y.-C., Chang, S.-C., & Shu, C.-M. (2022). Effects of volatile organic compounds on the explosion characteristics of polyethylene dust. *Process Safety and Environmental Protection*, *168*, 114–122.

Cloney, C. T., Ripley, R. C., Pegg, M. J., & Amyotte, P. R. (2017). Evaluating regime diagrams for closed volume hybrid explosions. *Journal of Loss Prevention in the Process Industries*, *49*, 912–918.

Cloney, C. T., Ripley, R. C., Pegg, M. J., Khan, F. I., & Amyotte, P. R. (2019). Role of particle diameter in the lower flammability limits of hybrid mixtures containing coal dust and methane gas. *Journal of Loss Prevention in the Process Industries*, *61*, 206–212.

Dastidar, A. G., & Amyotte, P. R. (2002). Determination of minimum inerting concentrations for combustible dusts in a laboratory-scale chamber. *Process Safety and Environmental Protection*, *80*(6), 287–297.

Dufaud, O., Traoré, M., Perrin, L., Chazelet, S., & Thomas, D. (2010). Experimental investigation and modelling of aluminum dusts explosions in the 20 L sphere. *Journal of Loss Prevention in the Process Industries*, *23*(2), 226–236.

Gan, B., Li, B., Jiang, H., Zhang, D., Bi, M., & Gao, W. (2018). Ethylene/polyethylene hybrid explosions: Part 1. Effects of ethylene concentrations on flame propagations. *Journal of Loss Prevention in the Process Industries*, *54*, 93–102.

Garcia-Agreda, A., Di Benedetto, A., Russo, P., Salzano, E., & Sanchirico, R. (2011). Dust/gas mixtures explosion regimes. *Powder Technology*, *205*(1), 81–86.

Janès, A., Vignes, A., Dufaud, O., & Carson, D. (2014). Experimental investigation of the influence of inert solids on ignition sensitivity of organic powders. *Process Safety and Environmental Protection*, *92*(4), 311–323.

Ji, W., Wang, Y., Yang, J., He, J., Wen, X., & Wang, Y. (2022). Methods to predict variations of lower explosion limit associated with hybrid mixtures of flammable gas and dust. *Fuel*, *310*, 122138.

Jiang, H., Bi, M., Li, B., Zhang, D., & Gao, W. (2019). Inhibition evaluation of ABC powder in aluminum dust explosion. *Journal of Hazardous Materials*, *361*, 273-282.

Sanchirico, R., Di Benedetto, A., Garcia-Agreda, A., & Russo, P. (2011). Study of the severity of hybrid mixture explosions and comparison to pure dust–air and vapour–air explosions. *Journal of Loss Prevention in the Process Industries*, *24*(5), 648–655.

Sugar Dust Explosion and Fire (Investigation Report 2008-05-I-GA). (2009). U.S. Chemical Safety and Hazard Investigation Board.

Yu, Y., Li, Y., Zhang, Q., Ni, W., & Jiang, J. (2018). Experimental investigation of the inerting effect of crystalline II type Ammonium Polyphosphate on explosion characteristics of micron-size Acrylates Copolymer dust. *Journal of Hazardous Materials*, *344*, 558–565.

Simplifying standards, opening restrictions Part I: The influence of the test vessel volume on the maximum explosion pressure of dusts

Vojtech Jankuj[a], Jan Sktrinky[a], Arne Krietsch[b], Martin Schmidt[c], Ulrich Krause[d], Richard Kuracina[e], Zuzana Szabová[e] & Stefan H. Spitzer[b,c,f*]

[a] Faculty of Safety Engineering VSB - TUO, Ostrava, Czech Republic
[b] Physikalisch Technische Bundesanstalt, Braunschweig, Germany
[c] Bundesanstalt für Materialforschung und – prüfung, Berlin, Germany
[d] Otto von Guericke University, Magdeburg, Germany
[e] Slovak University of Technology, Trnava, Slovakia
[f] EIfI-Tech, Schwaebisch-Gmuend, Germany

E-mail: vojtech.jankuj@vsb.cz, s.spitzer@eifi-tech.eu

Abstract

Explosion characteristics are widely used in the process industries to determine the potential hazard of the used substances. In the American and in the European standards for the determination of the maximum explosion pressure of dusts, the measured pressure is corrected if the tests are conducted in the 20L-sphere. This correction formula increases the measured values if they are above 5.5 bar g. It also causes, that the only two volumes for testing that are used are the standard 1m³ and the 20L-sphere because the measured value might have to be corrected.

In this article explosion tests were performed with four different dusts, lycopodium, lignite, aluminum and nitrocellulose, in four different vessel-sizes, 20 liters, 250 liters 365 liters and 1000 liters to investigate the influence of the vessel size.

Keywords: *Dust explosion, Upscaling, Safety Characteristics*

1. Introduction

The maximum explosion pressure p_{max} is an often-used safety characteristic, that is determined experimentally for gases and dusts. The common test vessels for dusts have an inner volume of one cubic meter (1000 liters) and 20 liters, the so called 20L-sphere. Normally the values from the 20L-sphere are corrected with equation 1 (if the measured value is above 5.5 bar g) because it was observed in the past, that the measured values are lower, than the ones determined in the 1m³ (Figure 1)

$$P_m = 0.775 * P_{ex}^{1.15} \quad (1)$$

with P_m being the corrected explosion pressure and P_{ex} the measured one, both for the 20L-sphere. In the European standard it is stated, that "Due to cooling effects a correction shall be made according to the … equation" stated above (EN 14034-1). In the American standard it is stated "To obtain results equivalent to the 1-m^3 vessel, [the measured] P_{ex} value may be corrected." And that "numerous correlation tests between the 1-m³ vessel and the 20-L sphere have shown that the following equation may be utilized for this correction." (ASTM-E-1226a)

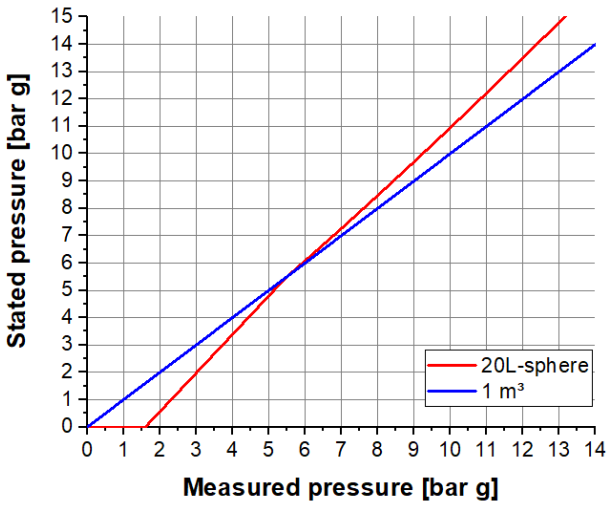

Fig. 1 *Stated pressure against measured pressure for the 20L-sphere and the 1m³ according to EN 14034 Part 1 and ASTM-E-1226a*

Since this correction is often automatically done by the measurement software the comparison of literature values is difficult. In practice, since the data basis seems to only be existent for the 1m³ and the 20L-sphere, all other volumes are excluded from the standardized determination of the explosion pressure of dusts.

Taking a closer look at the two testing procedures, one can see that the beginning pressure in the 1m³ at the moment of ignition is a slight overpressure of 1.1 bar abs to 1.2 bar abs since one or two dust chambers with an inner volume of 5.4 liter pressurized to 21 bar abs are used to inject the dust into the test vessel that is at ambient pressure before injection. The 20L-sphere has a beginning pressure of 0.4 bar abs before injection, the dust chamber has an inner volume of 0.6 liter, and it is also pressurized to 21 bar abs. After the injection process the pressure at the moment of ignition is 1 bar abs in theory but due to clogging or simply because the dust takes away some of the volume of the dust chamber, the pressure is often lower. Additionally, the whole process is much faster than for the 1m³ and the thermodynamic effects cause a higher measured beginning pressure, than it would normally be in thermal equilibrium (Spitzer et al., 2022). Also, due to friction inside the injection system and other experimental parameters, the beginning pressure is unintentionally varied, causing a high scattering of the determined safety characteristics.

In earlier research on scale dependence of dust explosions using different test vessel sizes (especially the 20L-sphere and the standard 1m³), the focus was often on other safety characteristics like the flammability limits (Cashdollar et al., 1992; Going et al., 2000) the deflagration index, the so called K_{St}-value or rate of pressure rise, the flame velocity (Pu, 2007) and not on the maximum explosion pressure. Even though Proust et al. (2007) list a number of 15 different dusts of which the p_{max} was determined in the 20L-sphere and the 1m³, the main focus of the article is the deflagration index and little information is given on the experimental parameters.

Skavland (2018) investigated the explosion pressure and rate of pressure rise of the standard 20L-sphere and a non-spherical 500-liter test vessel. The correction equation (1) was applied, and the explosion pressures determined with the 20L-sphere were slightly higher. On Page D.1 it can be seen that the beginning pressure with a PIPR (here called “Pd”) of 0.56 bar would be lower than ambient, considering the pressure drop around 0.9 bar abs. A beginning pressure closer to 1 bar abs might have resulted in uncorrected values closer to the ones measured in the 500-liter sphere.

In an article from Skrinsky (2018) about the influence of the test vessel size on the maximum explosion pressure of propanol it can be seen that, if the beginning pressures are comparable, the corrected explosion pressures of the 20L-sphere exceed the ones measured in the 1m³.

The research that was closest to the one presented here is from Lucas (1994) who compared the two standard vessels from the western world (20L-sphere and 1m³) to the ones formerly used in the German Democratic Republic with an internal volume of 56 liters and 380 liters. Though this might look close to the presented work, the goal of this work was to compare the existing procedures with different beginning pressures and different other experimental parameters, and thus the recorded pressures varied and were all 1,5 bar lower in case of the 54-liter vessel and 10 % lower in case of the 380-liter vessel. With that direct comparison of the data was not possible. In the paper, correction methods and equations for comparison are presented.

It has been known and investigated before, that as the initial pressure increases, there is a proportional increase of the maximum explosion pressure of the dust-air mixture but the requirements for the standards were not adjusted afterwards (Pilao (2006); Glarner (1983); Hertzberg (1986); Lazaro (2000); Li (2013)). It has also been known and investigated, that the fast compression inside the 20L-sphere causes an increase in temperature (Poleatev (2021) vessel size close to 20 L; Cashdollar (1996)) and with that in pressure but the conclusion has not been drawn before, that this might lead to biased explosion pressures.

2. Materials and methods

2.1. 20L-sphere

Three dusts samples were measured on moisture content (heated up to 115 °C and weight measured before and after 15 min) and the maximum explosion pressure was determined according to EN 14034-1 and ASTM-E-1226a in the 20L sphere. The beginning pressure was kept very narrow at 400 mbar ± 1 mbar and the weights were measured with an accuracy of ± 82 mg. The pre-ignition pressure rise was also chosen in a narrowed and, due to the thermodynamic effects, slightly increased range of 0.61 bar to 0.7 bar to decrease its impact on the test results (Spitzer et al., 2022). First, the dusts were tested with the typical concentrations stated in the standards for the determination of their safety characteristics. After the determination of the concentration with the highest explosion pressures these concentrations were tested again four times with 2 x 1 kJ and four times with 2 x 5 kJ chemical igniters. The values determined with 2 x 5 kJ are displayed with and without the correction equation (1), the values determined with 2 kJ are displayed without correction.

2.2. 250L-sphere

The 250L-sphere is an original explosion chamber with an internal volume of 250 L developed by the Faculty of Safety Engineering, VSB-Technical University of Ostrava. The device is designed for the measurements of explosion characteristics of flammable dusts (Lepík et al., (2014a)), gases and vapors (Lepík et al., (2014b)) and also their combinations (Serafin et al., (2012)) according to EN 14034. The explosion chamber consists of two stainless steel symmetrical hemispheres, where the lower one is static and the upper one is used for opening and closing of the explosion chamber due to their connection to a movable frame. Both parts of the chamber are locked during the test by hydraulically controlled blocks. The chamber is equipped with valves for adjusting the composition and internal pressure, including the exhaust of emissions. The stirrer and the plug-in hot plate should be placed in the lower part of the chamber. The chamber should be heated up and change the initiate condition. The ignition source is placed in the sphere center, where the contacts for initiation are attached to construction. There should be used different types of ignitors such as a pyrotechnical, exploding wire, etc. The other specific part of the 250L explosion chamber should be seen on the Figure 2. For the purpose of these experimental measurement the rebound nozzle was use as the dispersion device, but the equipment is adjustable for different types of dispersion. The volume of the dust container is 5 dm³ and it is pressurized up to 20 bar before the test. The explosion chamber

is evacuated to 0,6 bar. The ignition source is activated after predefined time and the data are recorded with the pressure sensors (Kistler) and analyze via converter to connected PC.

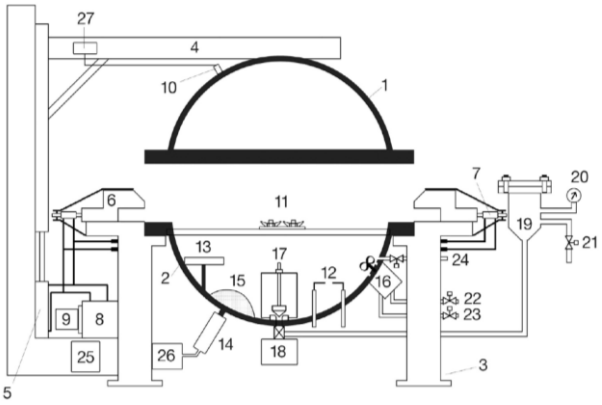

Fig. 2. *Diagram of the test apparatus VA 250 (Serafin et al., (2013). 1. Upper hemisphere; 2. Lower hemisphere; 3.Lower frame construction; 4. Movable frame construction; 5. Hydraulic piston for chamber opening; 6. Closing blocks; 7. Hydraulic piston for closing blocks; 8. Hydraulic unit; 9. Motor of hydraulic unit; 10. Pressure sensor; 11. Contacts for initiation of igniters; 12. High voltage electrodes; 13. Plug-in hot plate; 14. Pneumatic valve of air pump; 15. Covering sieve; 16. Stirrer; 17. Adjustable dispersion device; 18. Pneumatic valve for dispersion; 19. Container for sample being dispersed; 20. Manometer; 21. Electromagnetic valve; 22. Electromagnetic valve e GAS 1; 23. Electromagneticvalve e GAS 2; 24. Electromagnetic depressurizing valve; 25. Electronics of explosion test apparatus; 26. Air pump motor; 27. Electric signal converter*

2.3. 365L-sphere

The KV 150M2 is a spherical steel explosion chamber with an internal diameter of 90 cm (radius: 45 cm) and an internal volume of 365 liter (Figure 3). The dust dispersion is achieved by a dispersing system with a compressed air tank (volume 6.5 liter; pressure 15 bar). The air is blown on a sample placed on a dispersing plate through an air flow reverser. Figure 4 shows a cross section of the disperser. The ignition of the dispersed dust is ensured by two pyrotechnic igniters placed in the center of the sphere with an ignition energy of 5 kJ each. The activation of the igniters after dispersing the dust sample is ensured by the control system after an ignition delay time of 350 ms (for the development and validation of the experimental parameters see Kuracina et. al. (2021)) . The pressure changes during the explosion of the dispersed dust are recorded by piezoresistive pressure transducers (Keller, 23SX series). The response speed of the pressure transducer (working overpressure 0–16 bar) is 6 000/s. The recording speed during the measurement was 5 000/s with a 16-bit resolution. The overpressure at the moment of ignition was 0.021 bar for compensating the thermodynamic effects.

For the measurement of the aluminum sample (for better dispersion of the sample due to its properties - bulk density, clustering of particles) the disperser was supplemented with a hemispherical sieve with a mesh size of 1.5 mm.

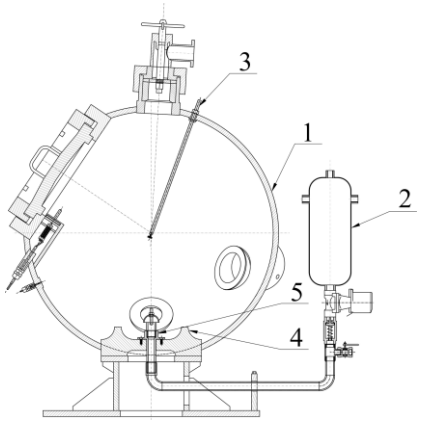

Fig. 3. *Cross-section of KV 150M2 explosion chamber (1 – spherical chamber, 2 – dust container, 3 – electrodes for ignition source, 4 – dispersing plate, 5 + 6 – disperser)*

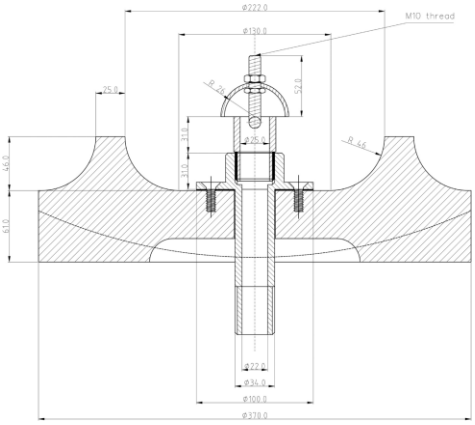

Fig. 4. *Cross section of disperser, taken from Kuracina et al. (2023)*

2.4. 1 m³ chamber CA 1M3

This chamber is a spherical vessel with an internal diameter of 124 cm (radius: 62 cm) and a capacity of 1 m3 (Figure 5). The vessel is equipped with an opening with a diameter of 80 cm and provided with a lockable door. The material of the chamber and components comply with the standards for the use of equipment for experiments at atmospheric initial pressure and an initial temperature in the range between 15 °C and 200 °C.

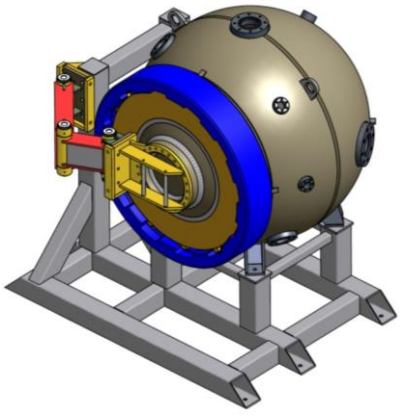

Fig. 5. *CAD-model of the CA 1M3*

The dispersion system consists of a dust reservoir with a capacity of 5.5 liters. The reservoir is designed for operating pressures up to 31 bar abs. A rapid-reaction pneumatic ball valve with an opening time of less than 50 ms is attached to the conical bottom of the container. The CA 1M3 explosion chamber is equipped with the Siemens Simatic 1215 PLC connected to a PC as a user

interface. As an ignition source two chemical igniters with an energy of 5 kJ each were used. After weighing, the dust was introduced into the dust reservoir. The vessel was evacuated to 0.9 bar abs and the dust reservoir was then pressurized with air at 20 bar to disperse the dust into the explosion chamber. The PLC initiates the dispersion and, with a predefined ignition delay time of 600 ms, activates the ignition source and the explosion pressure is then recorded (Janovský (2019)).

2.5. Dust samples and testing procedure

Three dusts, lycopodium, lignite and aluminum, were measured on moisture content and the maximum explosion pressure was determined according to EN 14034-1 and ASTM-E-1226a in the 20L-sphere. Afterwards the dust samples were sealed and sent to three test facilities having test vessels with volumes of 250 liters, 365 liters and 1000 liters and they were tested four times on the concentration where the maximum explosion pressure occurred in the 20L-sphere.

Nitrocellulose was also tested at a concentration of 750 g/m³. This dust was chosen since it can combust without air and with that, the explosion pressure can be set to a given value. In our case we needed a pressure between 10 bar g and 15 bar g. Because it is not possible to convey nitrocellulose properly through the rebound nozzle an alternative type of nozzle was used for the tests in the 20L-sphere, the so called Janovsky-nozzle (Figure 6).

Fig. 6. *Picture of the Janovsky-nozzle, taken from Janovsky et. al. (2024)*

The specifications of the test vessels are stated in Janovsky et al. (2024).

Table 1. *Specifications of the different test vessels*

	20L-sphere	250L-sphere	365L-sphere	1m³
Inner volume in *l*	20	250	365	1000
Ignition delay time in *ms*	60	420	350	600
Igniters	chemical	chemical	chemical	chemical
Ignition energy in *kJ*	2 x 1 and 2 x 5	2 x 5	2 x 5	2 x 5
Lycopodium in *g*	10	125	182.5	500
Lignite *g*	10	125	182.5	500
Radius (i. e. ignition source to wall) in *cm*	17	39	44	62
Volume/Surface in *cm*	5.6	13.0	14.8	20.7

Pressure before injection in *bar abs*	0.4	0.56	0.8	0.9
Pre-ignition pressure rise in *bar*	0.64±0.04	0.44±0.03	0.2±0.01	0.1±0.01

3. Results and discussion

The moisture content of the aluminum was 0.09 wt%, from the lycopodium 3.5 wt% and from the lignite 16 wt%, tested shortly before the dispatch to the testing facilities. The moisture content of the nitrocellulose was approximately 1 wt% after drying. However, it caught fire in the moisture analyzer after a third of the measuring time.

The results of the explosion tests with lycopodium at a concentration of 500 g/m³ are shown in Figure 7.

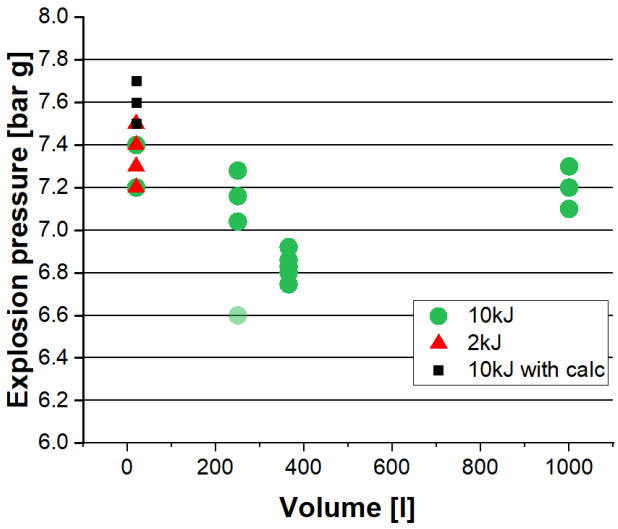

Fig. 7. *Explosion pressure of Lycopodium with a concentration of 500 g/m³, light green point at 250 l had an increased ignition delay time of 520 ms*

The differences between the averaged measured values determined in the different vessel sizes are with 7.3 bar g (20L-sphere), 7.2 bar g (250L-sphere, just the upper three points), 6.8 bar g (365L-sphere) and 7.2 bar g (1m³) comparably low. Also, replacing the standard 5 kJ chemical igniters by the smaller 1 kJ chemical igniters in the 20L-sphere did not change the measured value significantly (less than 50 mbar on average). Applying the standard correction equation, the values measured in the 20L-sphere are a little further apart from the other two. It would lead thereby to slightly conservative safety measures, even though the difference is with 0.3 bar not critical.

The results of the explosion tests with lignite at a concentration of 500 g/m³ are shown in Figure 8.

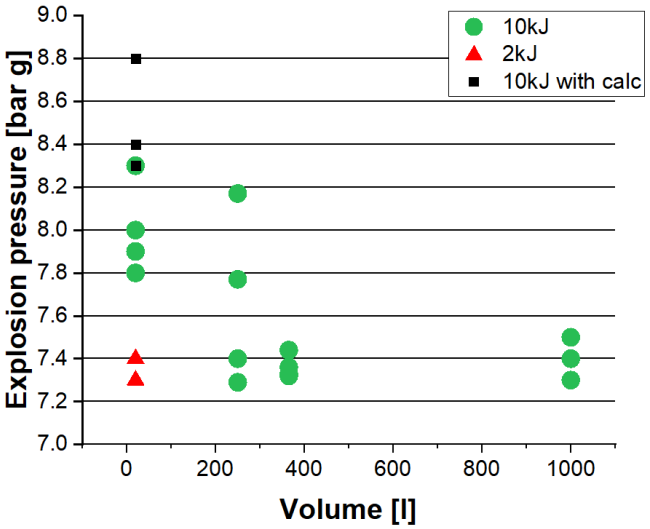

Fig. 8. *Explosion pressure of lignite at a concentration of 500 g/m³*

The average values from the different vessel sizes are with 8 bar g (20L-sphere), 7.7 bar g (250L-sphere), 7.4 bar g (365L-sphere) and 7.4 bar g (1m³) also quite close, but again the 20L-sphere gives slightly higher values. A further correction to 8.5 bar g instead of 7.4 bar g may cause overpriced safety measures and should be avoided. Replacing the standard 5 kJ igniters in the 20L-sphere with 1 kJ igniters lowered the measured values and were even closer to the other two volumes. The reduction of the ignition energy in the 20L-sphere has been recommended before by other researchers to match the values of the 1m³ (Going et al. (2000), Chawla et al. (1996)).

The third dust sample was a coarse aluminum dust. The injection process in the 20L-sphere did not cause any troubles and values between 8.0 bar g and 8.6 bar g were measured with 2 x 1 kJ igniters (between 8.0 bar g and 9.0 bar g with 2 x 5 kJ). In the 1m³ the injection process is probably too long and some of the dust fell to the ground. When the test chamber was opened some aluminum was still glowing and may not have combusted (see Figure 9). The measured values were with 4.0 bar g, 4.6 bar g and twice 4.9 bar g significantly lower.

Fig. 9. *1m³ after the explosion tests with aluminum. One can clearly see the still glowing aluminum on the bottom*

In the 365L-sphere it was not possible to distribute the aluminum dust with the distribution system displayed in Figure 4 because it was too heavy/dense to be conveyed in the short time span. A different system was built and used for these tests. The results were with 6.3 bar g, 9.2 bar g and 9.4 bar g closer to the ones measured in the 20L-sphere but the distribution system was destroyed and had to be replaced after each test (Figure 10). Also, with more than 3 bar the values are spreading too far for a clear statement on the behavior. Only three tests were performed in the 365L-sphere with the aluminum due to a lack of sieves for the distribution system.

Fig. 10. *Distribution system of the 365L-sphere before (with sieve) and after the explosion test (sieve completely burned) with aluminum*

The values obtained with the nitrocellulose are displayed in Figure 11. With more than 1.5 bar difference it is clearly visible, that the correction is not necessary when compared to the other volumes.

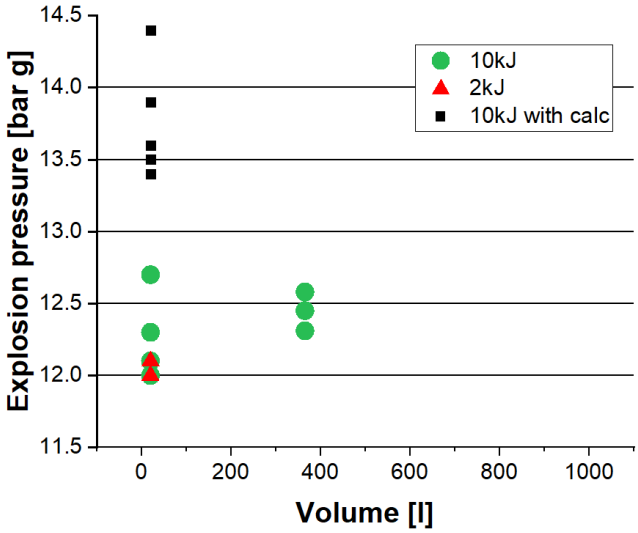

Fig. 11. *Explosion pressure of nitrocellulose at a concentration of 750 g/m³*

That the different obtained values from the 20L-sphere and the 1m³ are not due to heat loss is mentioned in one of Bartknecht's books (Bartknecht, (1989)), where it is stated that the "…results obtained in the 1-m³ vessel are based on a starting pressure of pi = 0.1 bar (1.1 bar absolute). This is

inherent to the dust investigation procedure. For the above-mentioned correlation … , these results have to be corrected to a pressure of 1.0 bar (absolute)."

With these investigations it can be said that the correction equation might be an artefact of the 1m³ and it shall not be applied on the values determined with the 20L-sphere. It shall also be taken into account, that the pressure inside the 20L-sphere is dropping after the compression and should with that be slightly higher as pointed out by Spitzer et al., (2022).

Though these tests were performed with accuracy and under different conditions, further tests with more test vessel sizes and other dusts will be performed in the near future. This way, it is hoped, that the correction equation is soon neglected from the standards for a better comparison with data determined with other test vessels and with the data for gases and vapors.

4. Conclusions

The maximum explosion pressure for three different dusts was tested in three different volumes at otherwise equivalent conditions. The measured pressures were the same within a reasonable range and no increasing or decreasing trend was observed for the different vessel sizes.

The existing correction equation from the dust standards for the determination of the maximum explosion pressure may be neglected since the origin may be an artifact of the dust testing procedure in the 1m³. This way, the comparison of dust explosion data from different vessel sizes and also from dusts to vapors and gases may be simplified in the future.

Also, the dust standard would be simplified, and other testing volumes would be suitable for further testing.

Acknowledgements

The authors would like to thank Zdzislaw Dyduch for providing them with the quote from W. Bartknecht. Part of this research (measured on the KV-150M2 chamber) was supported by the Slovak Research and Development Agency under the Contract No. APVV-21-0187

References

ASTM E 1226 – 12a (2012) - Standard Test Method for Explosibility of Dust Clouds

Bartknecht, W., 1989. Dust Explosions. Springer Berlin Heidelberg. doi: 10.1007/978-3-642-73945-3

Cashdollar, K., L., Weiss, E., S., Greninger, N., B., Chatrathi, K., 1992. Laboratory and Large-Scale Dust Explosion Research, Plant/Operations Progress, Vol. 11, No. 4

Cashdollar, K., L., 1996. Coal dust explosibility, Journal of Loss Prevention in the Process Industries, Volume 9, Issue 1, doi: 10.1016/0950-4230(95)00050-X

Chawla, N., Amyotte, P. R., and Pegg, M. J. A comparison of experimental methods to determine the minimum explosible concentration of dusts. FUEL, 75(6):654–658, 1996. doi: 10.1016/0016-2361(96)00006-3.

EN 14034-1 (2011) - Determination of explosion characteristics of dust clouds – Part 1: Determination of the maximum explosion pressure pmax of dust clouds

Glarner, T., 1983. Temperatureinfluss auf das Explosions- und Zündverhalten brennbarer Stäube, PhD Thesis, ETH Zürich

Going, J., E., Chatrathi, K., Cashdollar, K., L., 2000. Flammability limit measurements for dusts in 20-L and 1-m3 vessels, Journal of Loss Prevention in the Process Industries, Volume 13, Issues 3–5, Pages 209-219, doi: 10.1016/S0950-4230(99)00043-1

Hertzberg, M., Cashdollar, K., L., Zlochower, . A., I., 1986. Flammability limit measurements for dusts and gases - ignition energy requirements and pressure dependencies, 21st Symposium (International) on Combustion, doi: 10.1016/S0082-0784(88)80258-3

Janovsky, B., Skrinsky, J., Cupak, J., Veres, J., 2019. Coal dust, Lycopodium and niacin used in hybrid mixtures with methane and hydrogen in 1 m3 and 20 l chambers, Journal of Loss Prevention in the Process Industries, Volume 62, 103945, doi: 10.1016/j.jlp.2019.103945.

Janovsky, B., Pandal, A., Rodríguez, M., V., Schmidt, M., Dahoe, A., Danzi, E., Dufaud, O., Spitzer, S., H., 2024. Investigations on different distribution systems for dusts inside the 20L-sphere

Kuracina, R., Szabová, Z., Bachratý, M., Mynarz, M., Škvarka, M., 2021. A new 365-litre dust explosion chamber: Design and testing, Powder Technology, Volume 386, Pages 420-427, doi: 10.1016/j.powtec.2021.03.061

Kuracina, R., Szabová, Z., Kosár, L., Sahul, M., 2023. Study into influence of different types of igniters on the explosion parameters of dispersed nitrocellulose powder, Journal of Loss Prevention in the Process Industries, Volume 83, doi: 10.1016/j.jlp.2023.105017

Lazaro, C., E., Torrent, G., 2000. Experimental research on explosibility at high initial pressures of combustible dusts, Journal of Loss Prevention in the Process Industries, Volume 13, Issue 3-5

Lepik, P., Havelkova, J., Mynarz, M., & Serafin, J. 2014a. The effect of dust grain size on lower explosive limit, minimum ignition energy and minimum ignition temperature. 21st International Congress of Chemical and Process Engineering, CHISA 2014 and 17th Conference on Process Integration, Modelling and Optimisation for Energy Saving and Pollution Reduction, PRES 2014, 4, 2392.

Lepik, P., Mynarz, M., Serafin, J., & Bernatik, A. 2014b. Explosion limits of industrial spirit and their affecting by temperature. Process Safety Progress, 33(4), 380–384. https://doi.org/10.1002/PRS.11675

Li, Y., Xu, H., Wang, X., 2013. Experimental study on the influence of initial pressure on explosion of methane-coal dust mixtures, Procedia Engineering, doi: 10.1016/j.proeng.2013.08.151

Lucas, J., 1994 Explosionsfähige Staub/Luft-Gemische, Technische Überwachung, Volume 35, Issue 2, Pages 61-68

Pilao, R., Ramalho, E., Pinho, C., 2006. Overall characterization of cork dust explosion. Journal of Loss Prevention in the Process Industries. Doi: 10.1016/j.jhazmat.2005.10.015

Poletaev, N., L., 2021. A change in the air temperature inside a 20-liter chamber when air is added from the receiver, Pozharovzryvobezopasnost/Fire and Explosion Safety

Proust, Ch., Accorsi, A., Dupont, L., 2007. Measuring the violence of dust explosions with the “20l sphere” and with the standard “ISO 1m3 vessel”: Systematic comparison and analysis of the discrepancies, Journal of Loss Prevention in the Process Industries, Volume 20, Issues 4–6, Pages 599-606, doi: 10.1016/j.jlp.2007.04.032

Pu, Y., K., Jia,F., Wang, S., F., Skjold, T., 2007. Determination of the maximum effective burning velocity of dust–air mixtures in constant volume combustion, Journal of Loss Prevention in the Process Industries, Volume 20, Issues 4–6, Pages 462-469, doi: 10.1016/j.jlp.2007.04.036

Serafín, J., Mynarz, M., Konderla, I., Bebčák, A., & Lepík, P., 2012. Study of Influence of Combustible Gas on Explosion Parameters of Black Coal Dust. 29. https://doi.org/10.3303/CET1229160

Serafín, J., Bebcak, A., Bernatik, A., Lepik, P., Mynarz, M., Pitt, M. 2013. The influence of air flow on maximum explosion characteristics of dusteair mixtures, Journal of Loss Prevention in the Process Industries. Volume 26, Pages 209-2014, doi: 10.1016/j.jlp.2012.11.002

Skavland, C., E., 2018. Pressure Development in Dust Explosions - An experimental study in the 20-liter Siwek sphere and a 0.5 m3 non-standardized vessel, Master's Thesis, University of Bergen

Skrinsky, J., 2018. Influence of Temperature and Vessel Volume on Explosion Characteristics of Propanol/Air Mixtures in Closed Spherical Vessels, CHEMICAL ENGINEERING TRANSACTIONS, doi: 10.3303/CET1870226

Spitzer, S., H., Askar, E., Benke, A., Janovsky, B., Krause, U., Krietsch, A., 2022. Influence of pre-ignition pressure rise on safety characteristics of dusts and hybrid mixtures, Fuel, Volume 311, 122495, doi: 10.1016/j.fuel.2021.122495

Preconditioning of the dust and fluid in a 20 L chamber during ignition by chemical ignitor

Romana Friedrichova [a], Jan Karl [a], Bretislav Janovsky [b]

[a] Technical Institute of Fire Protection, Prague, Czech Republic
[b] University of Pardubice, Pardubice, Czech Republic

E-mail: *jan.karl@hzscr.cz*

Abstract

Dust explosion prevention and the mitigation of the consequences thereof require measurement of dust explosion parameters. Testing methods are defined by European and American Standards producing results in explosion chambers of a 1 m^3 standard volume and, alternatively, 20 L. However, the results are influenced by some processes which are neglected by the Standards, perhaps because it is believed that their effect is small in a 1 m^3. But their effect becomes significant in a smaller 20 L chamber. Preconditioning of the system caused by dust dispersion itself and ignitor's flame is one such problem.

The aim of this work is to go deeper into the physical and chemical processes caused by dust preheating after an ignitor's action. Analytical methods such as STA, GC/MS and FTIR analysed the composition of the atmosphere after exposure of lycopodium dust, as a natural material, to certain temperatures up to 550 °C in air and nitrogen. In the second step, gas samples were taken from the 20 L chamber after dispersion of lycopodium and ignition by two 5 kJ pyrotechnical ignitors.

Depending on the temperature and atmosphere, various concentrations of CO, CO_2, H_2O, NO_x, organic compounds were measured. It seems that the dispersed dust decomposes into mostly CO and CO_2 in area near the ignitors even in an atmosphere where the oxygen concentration is lower than 2 % by volume. The concentrations of other organic compounds were very low, including mostly methane, ethylene and acetaldehyde. The dispersed dust behaves as a heat sink which does not allow large dust modification of the whole dust cloud by the flame generated by ignitor's action prior to dust flame arrival.

Keywords: *dust explosion, pyrotechnic ignitor, dust preconditioning, decomposition*

Introduction

Both dust explosion prevention and the mitigation of the consequences thereof require measurement of dust explosion parameters. Testing methods defined by Standards (EN 14034-1,2, 2011; ASTM E1226, 2012) require dust cloud testing in explosion chambers of standard size of 1 m^3 and alternatively 20 L. However, the results are influenced by some processes which are neglected by the Standards probably due to their small effect in 1m^3. Their effect became significant in a smaller 20L chamber.

Problems with initial conditions and conditions at the time of ignition activation were discussed by Spitzer et al. (2022), who found out that the dispersion of the dust causes compression of the gas inside the chamber and a temperature increase to 45 °C at the time of ignition activation which decrease measured maximum explosion pressure. A much greater problem is the influence of the pyrotechnical ignitors' action known as overdriven ignition. A few authors have evaluated the

influence of ignition energy on explosion parameters (Ajrash et al., 2016; Cieliński et al., 2020; Clouthier et al., 2019; Di Benedeto et al., 2012; Kuai et al., 2011, 2013; Kuna et al., 2024; Rodgers et al., 2011; Spitzer et al., 2022; Thomas et al., 2013), minimum explosive concentration (Cashdollar et al., 1993; Going et al., 2000; Hertzberg et al., 1986), dust inerting concentration (Dastidar et al., 2001, 2002) and limiting oxygen concentration (Addai et al., 2019). But only a few were interested in the effect of pyrotechnic mixture burning on the atmosphere inside the chamber, including the tested dust. One of them is Cloney et al. (2013) with their CFD finite volume 1D simulations of ignitor´s action and its effect on the dispersed dust. They found that small particles of polyethylene (10 – 30 μm) at thermal equilibrium have a temperature of between 120 and 130 °C.

Taveau et al. (2017) was the other author, focusing on the explosible system in a 20 L chamber after pyrotechnic ignitor explosion. He hypothesised in his paper that: "*It is likely that the strong preheating created by the pyrotechnical igniter(s) affects the dust prior to flame arrival, causing partial reaction and the formation of a more reactive hybrid mixture, consisting of a turbulent flammable gas (or vapour) and dust. We proposed to call this phenomenon an igniter-induced hybrid.*"

The aim of this work is to go a bit deeper into the physical and chemical processes caused by natural dust preheating after an ignitor's action by analysis of gas and solid lycopodium clavatum post-explosion products. Dust clouds were generated in an inert atmosphere. Such a test should show what happens in the chamber after the ignitors' explosion when the flame is not propagating through the dust cloud.

Analysis of post-explosion products after dust explosion is not a completely new topic. Most of the effort was put in studies of coal dust explosion products, specifically in China. Geng et al. (2009) used Fourier transform infrared (FTIR) spectrometry for Australian lignites-carboxyl group and aromaticity analysis. He et al. (2017) applied FTIR and Raman spectroscopy for functional group analysis in various coals. Li et al. (2020) conducted an SEM–EDS analysis of post-explosion solid residues together with TGA/DTG analysis. Their gaseous products were studied by gas chromatography. Lin et al. (2019a) investigated the properties of different functional groups and the FTIR structural parameters of a coal sample and the solid residue by FTIR spectra, the use of the same method was published in Lin et al. (2019b). FTIR and gas chromatography were applied also by Nie et al. (2021) in their study on gas and solid residues of coal dust. Qian et al. (2023) employed a gas chromatographic analyser in his coal dust explosion tests. However, a paper originating in the USA can also be found (Cashdollar et al., 2007). Marmo et al. (2011) used X-Ray diffraction to highlight the decomposition of sodium carbonate, whereas Li et al. (2018) used the same method for pre- and post-explosion products of coals in 20 L chamber. Analysis of lycopodium is of the most interest, and it was found by Bidabadi et al. (2013, 2015) in a paper focused on lycopodium dust flame. They used the assumption that 90 % of lycopodium converts to methane gas when it is pyrolyzed and the rest is char in their calculations. They mentioned Derivative Thermogravimetry (DTG) analysis of a Thermogravimetry (TG) diagram of lycopodium published in Han et al. (2000). Mostafavi et al. (2015) published their results obtained from tests with lycopodium thermogravimetry. They analysed the kinetics of reactions of lycopodium particles in a nitrogen environment and also in an oxidising environment by simultaneous thermal analysis (STA) in TG-DTA. Lycopodium elemental composition was also analysed.

1. Experiments

Two types of tests were conducted. A lycopodium clavatum sample was measured in an analytical laboratory during the first phase. Analytical methods such as STA, GC/MS, FTIR and Elemental analysis CHNS were chosen according to a literature survey for analysis of atmosphere composition after exposure of lycopodium dust as a natural material. Samples were exposed to certain temperatures up to 500 °C and, in some cases, even higher in both air and nitrogen atmospheres. In

the second step, the atmospheric composition was measured in the 20 L chamber after dispersions of lycopodium dust in nitrogen atmosphere and ignition by two 5 kJ Sobbe pyrotechnical ignitors.

To determine the composition of the explosion gases, the infrared spectroscopy method (FTIR) was used, by means of which the concentration of gas mixtures was continuously determined. The Matrix MG2 infrared spectrometer and the OPUS GA measurement software were used for the measurements. The measurements were taken in a heated gas cell and with a stable gas flow through the cell. The concentration of selected gases was determined. Determination of the elemental composition of lycopodium was carried out by the method of elemental analysis, which allows determination of the content of elements C, H, N and S. A Thermo Finnigan FLASH EA 1112 Series CHNS/O Analyzer was used for the determination of elemental composition. An oven designed for determining the ignition and autoignition temperatures of solid materials in a gaseous atmosphere was used (according to the standard ČSN 64 0149:1978 "Determination of the flammability of materials" and ISO 871:2006 "Plastics – Determination of ignition temperature using a hot-air furnace") for estimating the behaviour of lycopodium during higher temperatures. The flue gases after decomposition/burning were led through a heated sampling line into an FTIR heated gas cell. The behaviour of lycopodium during gradual heating in a gaseous atmosphere was studied using the method of simultaneous thermal analysis. This thermal analysis technique combines thermogravimetric analysis (TGA) and differential scanning calorimetry (DSC). TGA quantifies the sample weight changes, DSC quantifies the heat flow of a sample over a temperature range. The STA 449 F1 Jupiter instrument was used for the measurements.

The explosion tests were carried out in the 20 L explosion chamber CA 20L by OZM Research according to EN 14034-1,2, (2011) and described in Janovsky et al. (2019). It is a stainless steel (1.4435) double-walled vessel of spherical shape with an internal diameter of 336 mm. The vessel is provided with an opening of an inside diameter of 148 mm. The chamber is shown in Figure 1. A rebound nozzle was used for the dispersion of the dust. Dynamic pressure was measured by a pair of piezoelectric pressure sensors type 112B05 by PCB with a sampling rate of 50 kS/s/channel. The automatic procedure was controlled by a Siemens Simatic 1215, connected to the PC interface. The ignition delay time was set to 60 ms.

***Fig.** 1. The 20 dm^3 explosion chamber CA 20L by OZM Research.*

Spores of natural herd lycopodium clavatum and talc dust, a common silicate mineral with the chemical formula $Mg_3Si_4O_{10}(OH)_2$, were used for the tests. Granulometric distribution was measured by laser diffraction on a Malvern Mastersizer 3000. Moisture content of both samples was

measured using a Kern type DBS60-3 moisture analyser. Results of the measurements are shown in Table 1.

***Table** 1. Granulometric distribution of dusts used*

Parameter	Lycopodium	Talc
Diameter at 10 % (μm)	21.5	8.8
Diameter at 50 % (μm)	30.5	41.1
Diameter at 90 % (μm)	43.7	95.6
Specific Surface Area (m²/kg)	172.9	281.7
Moisture (% by mass)	5.1	0.4

Chemical composition of lycopodium was determined by elemental analysis showing that the material used consisted of 66.24 % of C, 9.24 % of H, 24.40 % of O and 0.12 % of N.

Lycopodium was also tested according to an old, but still valid, Czech Standard ČSN 64 0149. The sample spontaneously ignited (no external ignition source) when the temperature of the air flowing around the sample was 390 ± 5 °C.

For standard dust explosion testing, chemical ignitors by Fr. Sobbe GmbH are used all around the world and therefore a pair of their 5 kJ chemical ignitors were used. The Standard EN 14034-1,2 (2011) defines the pyrotechnic mixture as mixture of 40 % Zr, 30 % $Ba(NO_3)_2$ and 30 % BaO_2.

1.1 Lycopodium in analytical laboratory

The lycopodium sample was characterised in TGA first in both air and nitrogen atmosphere to get overview about the response of the dust to heating and differences in behaviour of the sample in oxidizing and inert atmosphere. Sample weights ranged from 12.2 to 14.4 mg. The samples were heated from 20 °C to 600 °C at a rate of 10 °C/min and a gas flow rate of 50 mL/min.

First, the flash point of lycopodium in the testing crucible was determined under Czech standard ČSN 64 0149. Then the Setchkin method was slightly modified in the manner of sample insertion. The standard method requires introduction of the sample in a crucible (cup) into the oven, but dust in the crucible does not represent the behaviour of dust particles in dispersion. However, a few initial tests with dust in a crucible and an air atmosphere were performed. The mass of the sample varied between 2 and 3 g. The flow rate of the air was 1 L/min and the heating rate of the oven was 30 (10) °C/min. The samples were exposed to various temperatures ranging from 150 °C up to 220 °C and concentration of CO, CO_2, NO, SO_2 and CO_2 were measured by TESTO analyser.

To have conditions closer to the situation in the explosion chamber, dust was slotted into the Setchkin's oven warmed up to a specified temperature through a small chimney on the top producing dust dispersion inside. Measurement accuracy was increased by connecting the FTIR unit to the gas outlet line from the Setchkin oven. Tests at temperatures from 200 to 600 °C were conducted under both air and nitrogen atmospheres. Then a sample ranging in weight from 0.12 – 0.15 g was slotted into the oven. CO_2, CO, H_2O, HBr, HCl, HF, HCN, NO, NO_2, SO_2. CH_4, C_2H_2, acetaldehyde, acetic acid and NH_3 concentrations were monitored in the gas outflow from the oven each 6 s. The flow rate of the air or nitrogen through FTIR gas cell was 2 L/min. The FTIR unit is unfortunately not able to detect hydrogen. The same tests were performed for lycopodium, which was dried before the test.

1.2 Lycopodium and talc in 20 L chamber

The second phase of measurement was performed in 20 L chamber made by OZM Research according to EN 14034-1,2 (2011). Two standard 5 kJ igniters by Sobbe were ignited in an air atmosphere and then in a nitrogen atmosphere where the concentration of the oxygen was below

2 % by volume. The concentration of the remaining oxygen was given by ultimate vacuum of the vacuum pump used and the air remaining in the dust reservoir after insertion of the dust. Samples of the gas atmosphere were taken by diaphragm pump with flow rate of 1 L/min to FTIR instrument for analysis.

The series where talc, as an inert dust, were used followed. Sufficient results for lycopodium dust explosion parameters testing are produced when lycopodium is tested in concentrations of 125, 250, 500 and 750 g/m^3. The same concentrations of talc were therefore prepared and exposed to two 5 kJ igniters by Sobbe. Talc tests were performed under air atmosphere. Lycopodium was dispersed into the nitrogen atmosphere in the last series of the test. The concentration of the oxygen was below 2% by vol. again. Concentrations of lycopodium tested were 125, 250, 500 and 750 g/m^3. Atmospheric composition after each test was analysed with the FTIR instrument again and solid residue samples were taken for elemental analysis.

2. Results and discussion

2.1 Lycopodium in analytical laboratory

TGA/DSC analysis of pure lycopodium in air and nitrogen were done first. TGA results show two active zones as published by Mostafavi et al. (2015) in oxygen atmosphere (probably air). They found the first maximum rate of mass reduction in the range of 300-400 °C while the second peak were lying between 500–600 °C. Results of our TGA measurements in an air atmosphere presented in Figure 2 show also two similar active zones, but the temperature intervals are shifted to lower temperatures. The same measurement shown in Figure 3 was done in nitrogen atmosphere.

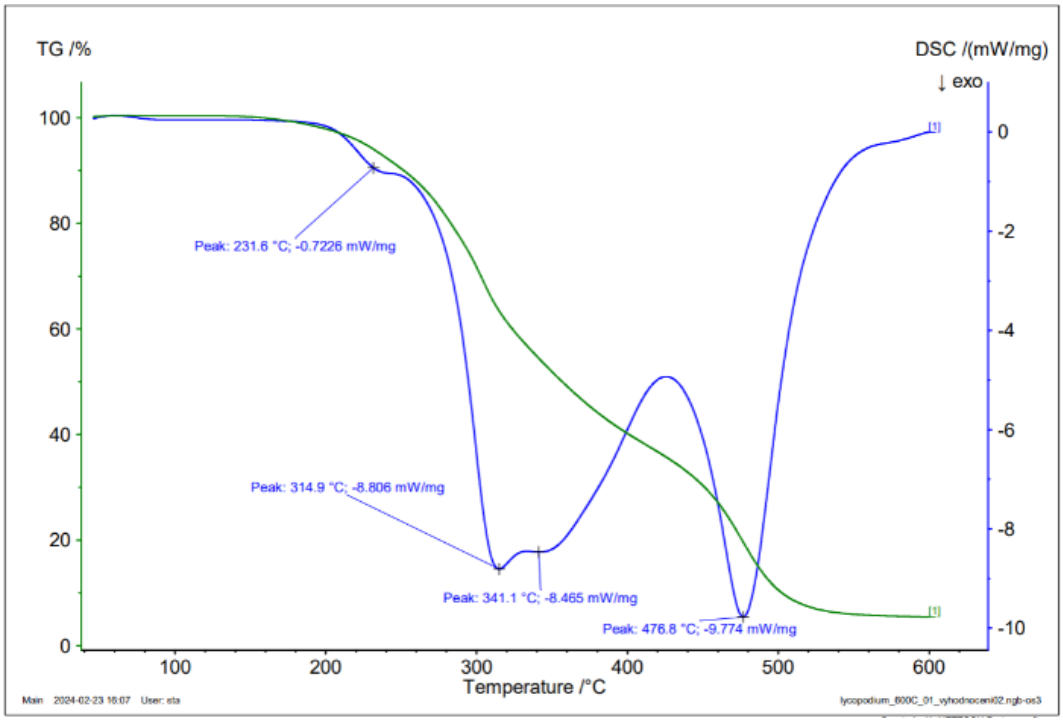

***Fig.** 2. TGA and DSC curves from lycopodium testing measured in air atmosphere*

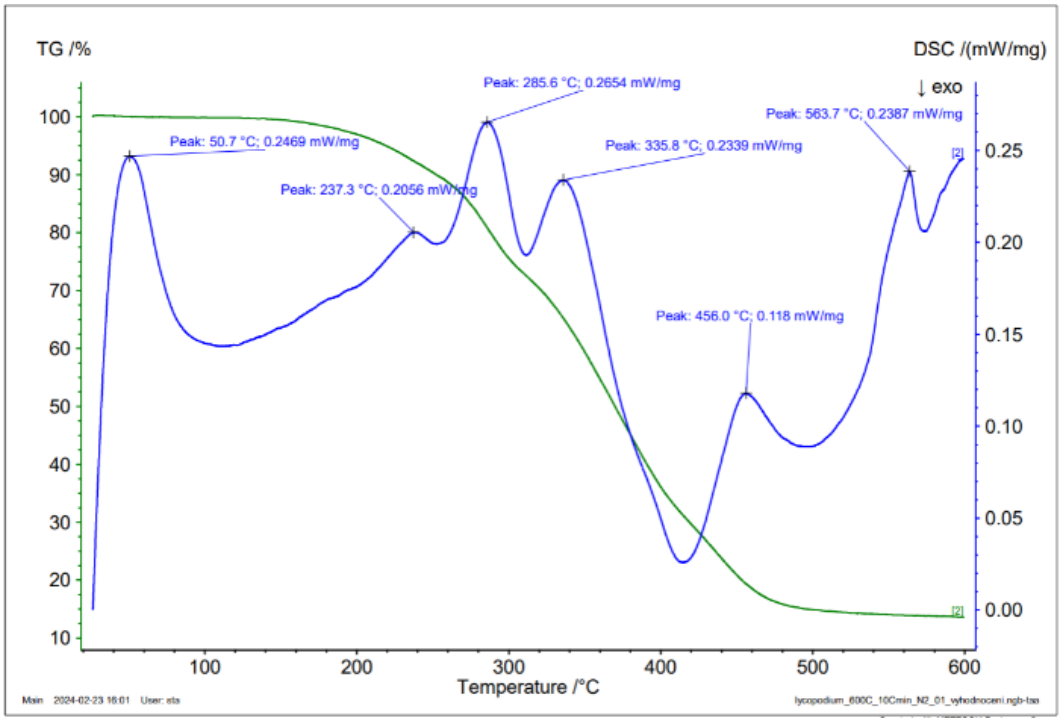

Fig. 3. *TGA and DSC curves from lycopodium testing measured in nitrogen atmosphere*

The first maximum rate of mass reduction occurs in the range of 250 and 350 °C while the second one occurs in the interval between 450 and 520 °C. However, the DSC curve (air atmosphere) shows three zones where the rate of energy release increases. The first zone, where small amount of energy release occurs between 200 and 245 °C, corresponding with endo-peak of 237 °C under nitrogen atmosphere, transiting in a very intensive energy release up to 315 °C. Reacting material in this range is characterised by a maximum production rate with maximum at 286° C at endo-curve for nitrogen atmosphere. Subsequently, the energy release in the air atmosphere slowed down up to 415 °C with a small peak at 341 °C corresponding with endo-peak 336 °C under nitrogen atmosphere. This slowing down transforms to another fast energy production in air, reaching maximum at 477 °C with the maximum rate of flammable material production at 456 °C under nitrogen atmosphere. After reaching this temperature, the rate of energy release decreases to almost zero line at temperature 560 °C. DSC curve correlates well with the TGA curve, having peaks at the same temperatures as the maximum rate of mass reduction rates at TGA curves.

Mostafavi et al. (2015) attributed the mass reduction in the first active zone only to the pyrolysis process, whereas they supposed the mass reduction in the second active zone is due to both the pyrolysis and combustion of solid particles. The DSC curve measured in an air atmosphere shows huge energy release in the temperature zone similar to the first active zone by Mostafavi et al. (2015). It seems that gas/vapour products of pyrolysis directly oxidise in that zone, increasing the local temperature and intensifying the pyrolysis process.

TGA/DSC measurement is very good tool for monitoring of sample reaction on exposure to increasing temperature of the environment, however, does not correspond to conditions in a real dust cloud. Modified Setchkin's method, where the sample of the dust is slot into the chamber from the top, is much closer to real dust cloud conditions. Results of FTIR measurements of CO, CO_2, acetaldehyde, CO_2 and water concentrations in the oven are shown in the Figure 4.

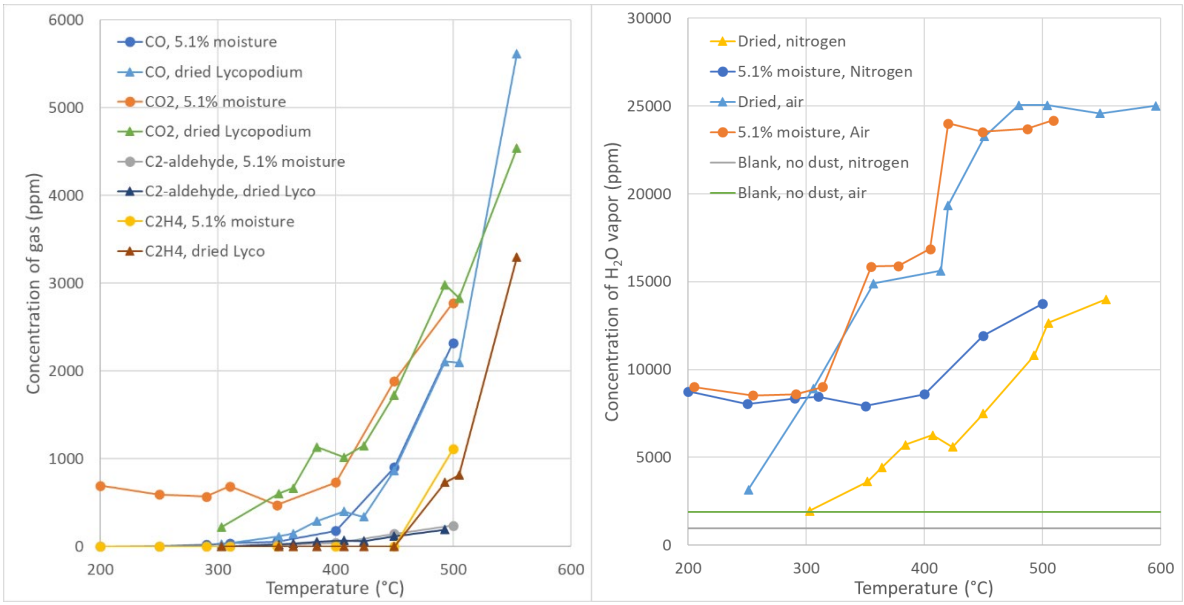

***Fig.** 4. Concentration of the decomposition products measured in the Setchkin apparatus; left graph: concentrations measured in nitrogen atmosphere; right graph: concentration of water vapor measured in both air and nitrogen atmosphere.*

Setchkin measurements show that production of the main reaction products (CO, CO_2 and water) starts at temperatures between 250 and 280 °C, which corresponds well with the beginning of the first intensive heat production zone with a peak at 315 °C at the DSC curve (air atmosphere). The concentration of all products increases continuously with increasing oven temperature. The concentration of the acetaldehyde was very small, and its sign appeared at 400 °C. C_2H_4 appeared from a temperature 500 °C. Bidabadi et al. (2013) cited in the paper his older works where he assumed that methane gas is the only product of the lycopodium pyrolysis. The presented measurements do not support his assumption used for his calculations. Methane was first detected at temperatures above 550 °C in nitrogen atmosphere. Surprisingly, methane was detected in gas products in tests under an air atmosphere at temperatures at and above 450 °C where burning of lycopodium particles were observed.

Figure 4 also shows the influence of the moisture content. Comparison of water vapour concentration between moist and dried samples of lycopodium is plotted on the right-hand graph of Figure 4. The moist sample shows a high concentration of water vapour already at a temperature 200 °C, confirming complete water evaporation at a temperature below that. The concentration of water vapour for moist sample starts increasing above 315 °C under an air atmosphere in contrast with dried lycopodium where the concentration of water vapour starts increasing already at a temperature of 250 °C, reaching the same values with moist lycopodium at about 310 °C. It seems that water vapour evaporated from the moist sample inhibits the reactions producing water in the first heat producing zone found at DSC record. The curves for water vapour concentration in a nitrogen atmosphere shows the same effect of moisture evaporated, but the nitrogen inhibits the reactions producing water until 400 °C in case of a moist sample, whereas the dried sample shows a water concentration increase starting at 300 °C. It seems that nitrogen has a similar effect as water vapour from moist sample in an air atmosphere. But a moist sample together with nitrogen inhibits water producing reactions up to 350 °C. Figure 4 shows nice agreement with the DSC record at a temperature interval 341 and 415 °C where heat production decreases. Setchkin measurements show stagnation in water production by reactions in this interval under an air atmosphere. Both samples under nitrogen atmosphere also did not increase water concentration in this interval. A very similar effect can be seen in the case of CO_2 production under nitrogen atmosphere. The relaxation in CO_2 production for a dried sample starts at 357 °C continuing up to 420 °C. The moist sample started CO_2 production above 400 °C. The production of CO by the dried sample copies the

production of CO_2. Small concentrations of acetaldehyde were measured in tests with both samples in nitrogen above 350 °C. The first concentration of ethylene was measured at 500 °C where the DSC curve shows a decreasing rate of heat production in the interval of temperatures higher than 477 °C.

2.2 Lycopodium and talc in 20 L chamber

The main aim of the work was evaluation of the chemical ignitors effect on lycopodium clavatum. The results of FTIR measurements of atmosphere composition after ignitors´ action in an atmosphere with an oxygen concentration reduced below 2 % by volume are written in Table 2 and shown in Figure 5.

***Table** 2. Results of measurements by FTIR, L means lycopodium, N_2 means measurement under atmosphere with oxygen concentration less than 2 % by vol.*

Substance	2x 5 kJ	2x 5 kJ, N_2	LN2-125	LN2-250	LN2-500	LN2-750
CO (ppm)	64	6	4591	5652	7766	7490
CO_2 (ppm)	2683	257	1382	1383	1247	1344
H_2O (ppm)	5998	574	4977	5840	8056	11231
HBr (ppm)	0	0	0	0	0	0
HCl (ppm)	0	0	0	0	0	0
HCN (ppm)	0	0	0	0	0	0
HF (ppm)	0	0	0	0	0	0
NO (ppm)	573	55	182	124	130	181
NO_2 (ppm)	35	0	0	0	0	0
SO_2 (ppm)	0	0	0	0	0	0
Acetaldehyde (ppm)	0	0	34	62	83	83
Acetic acid (ppm)	0	0	0	0	0	0
C_2H_4 (ppm)	0	0	702	1238	1589	1693
Methane (ppm)	0	0	478	848	1117	1176
NH_3 (ppm)	0	0	0	0	0	0

It is seen that the main flammable product formed by ignitor flame is CO followed by C_2H_4 and methane. The sample used were not dried and therefore a significant concentration of water vapour was recorded. An almost constant concentration of CO_2 depending on the amount of dust dispersed confirms the very low oxygen concentration in the atmosphere.

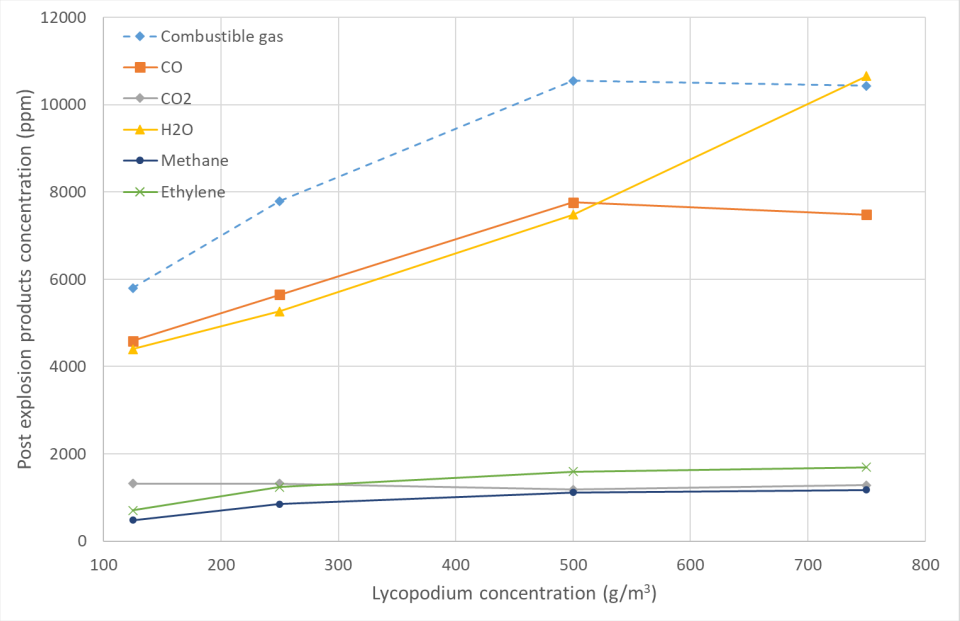

***Fig.** 5. Concentration of the post explosion products in dependence on lycopodium concentration, oxygen concentration was less than 2 % by vol.*

Concentrations of all measured species increase with increasing dust concentration which was the expected result, but only water vapour concentration increases almost linearly. Concentrations of flammable products slow down their increase with increasing dust concentration. Water vapour is mostly given by the evaporation of the moisture under temperatures lower than 200 °C according to Setchkin's results. But water vapour produced by lycopodium decomposition starts at 300 °C and therefore water vapour production does not slow down with dust concentration.

Taveau et al. (2017) and Kuna et al. (2024) presented pictures of fireball formation after ignitor activation. The fireballs showed can easily fill the whole 20 L chamber. Taveau et al. (2017) stated that mean temperature increases inside the 20 L vessel can be 350 K, and locally much greater with the maximum in the centre of the vessel. He also presented photos of the flame by fast IR camera originally published by Scheid et al. (2013) who separated the flame into two temperature zones 2000 – 650 °C and 650 – 200 °C. It is therefore evident that the temperature in the chamber is stratified with the maximum in the centre and the temperature approaching ambient temperature near the wall.

Using Setchkin's results it is possible to deduce the extent of ignitors´ fireball effect on a dust cloud according to the concentration of measured gases. The water vapour production region (limiting temperature lower than 200 °C) is larger than the regions for production of the other products and increase almost linearly with increasing dust concentration. CO production starts at more than 300 °C, C_2H_4 needs temperature near 500 °C to be produced and methane production starts at 550 °C in a nitrogen atmosphere. Increasing the lycopodium concentration should increase production of these species if the temperature stratification inside the chamber does not change with increasing dust concentration, but this was not observed. Concentration of these three gases did not increase linearly and increase slowed down with increasing dust concentration. It could be caused by a local decrease in dust concentration due to a pressure wave generated by the ignitors' explosion and/or by a decrease in ignitors fireball size due to dust mass.

The dust cloud behaves as a heat sink in the chamber. Increasing dust concentration decreases maximum pressure generated by the ignitors as shown in Figure 6. First only talc was used as an inert dust merely to show how the mass of the dust influences the conditions in the chamber after ignitor action. Then the same amount of lycopodium was used but dispersed and ignited under a nitrogen atmosphere.

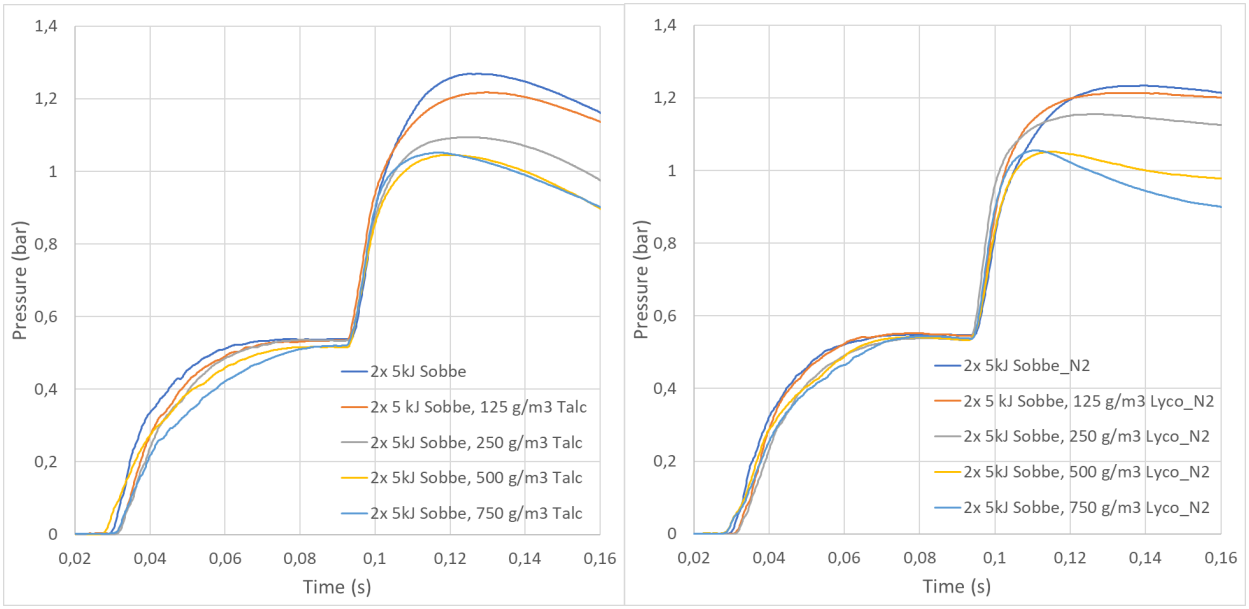

***Fig.** 6. Pressure records for tests with Talc and pressure records for tests with lycopodium in atmosphere where oxygen concentration was less than 2 % by vol.*

The maximum overpressure generated decreases with increasing dust concentration from 0.73 bar to 0.53 bar for talc in air and 0.51 bar for lycopodium in nitrogen. The same overpressures were generated with 500 and 750 g/m^3 concentration of both talc and lycopodium. Some differences could be seen in the shape of the curves produced by talc and lycopodium, which could be caused by the production of small volumes of gas produced by lycopodium decomposition in the fireball near the centre and also by the moist evaporation after. While the effect is negligible, it could show the contribution of the decomposition products generated only in the "hot" zone of the ignitors' fireball. Significant preconditioning of the lycopodium cloud, as the natural material, was not confirmed, because lycopodium decomposition products did not measurably increase the overpressure after the ignitors´ action compared to ignition in a talc cloud.

3. Conclusions

Analytical methods such as STA, GC/MS and FTIR analysed composition of the atmosphere after exposure of lycopodium dust, as a natural material, to certain temperatures up to 550 °C in air and nitrogen in the Setchkin apparatus. Those measurements showed dependence of each measured substance appearance on the temperature of the atmosphere in comparison to FTIR measurements of decomposition products in a 20 L chamber. In the second step, gas samples were taken from the 20 L chamber after dispersion of lycopodium and ignition by two 5 kJ pyrotechnical ignitors. Depending on the temperature and atmosphere, various concentrations of CO, CO_2, H_2O, NO_x, and organic compounds were measured. It seems that dust dispersed decomposes to mostly CO and CO_2 even in an atmosphere where the oxygen concentration is lower than 2 % by volume. The concentrations of other organic compounds were very low, including mostly ethylene and acetaldehyde, confirming that higher temperatures act on a dust cloud only near the centre of the 20 L sphere. The temperature in the rest of the chamber volume is less than 200 °C, which is not enough to pyrolyse the lycopodium. The dispersed dust behaves as a heat sink which does not allow large dust modification/precondition in the whole dust cloud by the flame generated by ignitors' action prior to dust flame arrival. It shows that the lycopodium cloud, as the natural material, is not significantly preconditioned, and therefore the ignitors induced hybrid mixtures which are not produced in case of lycopodium.

Acknowledgements

The authors gratefully acknowledge the lending of their CA20L explosion chamber from the Czech company OZM Research Ltd. Hrochuv Tynec.

We would like to express our gratitude to the Ministry of the Interior of the Czech Republic for their institutional support, which made this article possible. Without their financial and organisational contribution, this research would not have been feasible.

References

Addai, E., K., Clouthier, M., Amyotte, P., Safdar, M., Krause, U., 2019. Experimental investigation of limiting oxygen concentration of hybrid mixtures. Journal of Loss Prevention in the Process Industries, 57, 120–130.

Ajrash, M., J., Zanganeh, J., Moghtaderi, B., 2016. Methane-coal dust hybrid fuel explosion properties in a large-scale cylindrical explosion chamber. Journal of Loss Prevention in the Process Industries, 40, 317-328.

ASTM International, 2019. ASTM E1226-19, Standard Test Method for Explosibility of Dust Clouds. ASTM International, West Conshohocken, PA www.astm.org.

Bidabadi, M., Mostafavi, S., A., Dizaji, H., B., Dizaji, F., F., 2013. Lycopodium dust flame characteristics considering char yield. Scientia Iranica B, 20(6), 1781-1791.

Bidabadi, M., Dizaji, H., B., Dizaji, F., F., Mostafavi, S., A., 2015. A parametric study of lycopodium dust flame. J Eng Math, 92: 147–165.

Cashdollar, K., L., Chatrathi, K., 1993. Minimum Explosible Dust Concentration Measured in 20-L and 1-M^3 Chambers. Combustion Science and Technology, 87, 1-6, pp. 157-171.

Cashdollar, K., L., Weiss, E., S., Montgomery, T., G., Going, J., E., 2007. Post-explosion observations of experimental mine and laboratory coal dust explosions. Journal of Loss Prevention in the Process Industries, 20, 607–615.

Celiński, M., Borucka, M., Gloc, M., Gajek, A., Sałasińska, K., 2020. Determination of explosion characteristics, fire behavior and thermal degradation products of aspartame. Fire Safety Journal 117, 103208.

Cloney, C.T., Ripley, R.C., Amyotte, P.R., Khan, F.I. (2013) Quantifying the effect of strong ignition sources on particle preconditioning and distribution in the 20-L chamber. Journal of Loss Prevention in the Process Industries, 26: 1574–1582.

Clouthier, M., P., Taveau, J., R., Dastidar, A., G., Morrison, L., S., Zalosh, R., G., Ripley, R., C., Khan, F., I., Amyotte, P., R., 2019. Iron and aluminum powder explosibility in 20-L and 1-m^3 chambers. Journal of Loss Prevention in the Process Industries, 62, 103927.

Dastidar, A., G., Amyotte, P., R., Going, J., E., Chatrathi, K., 2001. Inerting of coal dust explosions in laboratory- and intermediate-scale chambers. Fuel, 80, 1593-1602.

Dastidar, A., G., Amyotte, P., R., 2002. Determination of minimum inerting concentrations for combustible dusts in a laboratory-scale chamber. Trans IChemE, Vol 80, Part B

Di Benedetto, A., Garcia-Agreda, A., Russo, P., Sanchirico, R., 2012. Combined Effect of Ignition Energy and Initial Turbulence on the Explosion Behavior of Lean Gas/Dust-Air Mixtures. Ind. Eng. Chem. Res., 51, 7663–7670.

EN 14034-1 (2011) - Determination of explosion characteristics of dust clouds – Part 1: Determination of the maximum explosion pressure p_{max} of dust clouds. CEN, the European Committee for Standardization.

EN 14034-2 (2011) - Determination of explosion characteristics of dust clouds – Part 2: Determination of the maximum rate of explosion pressure rise $(dp/dt)_{max}$ of dust clouds. CEN, the European Committee for Standardization.

Geng, W., Nakajima, T., Takanashi, H., Ohki, A., 2009. Analysis of carboxyl group in coal and coal aromaticity by Fourier transform infrared (FT-IR) spectrometry. Fuel 88, 139–144.

Going, J., E., Chatrathi, K., Cashdollar, K., L., 2000. Flammability limit measurements for dusts in 20-L and 1-m^3 vessels. Journal of Loss Prevention in the Process Industries, 13, 209–219.

Han, OS,, Yashima, M,, Matsuda, T,, Matsui, H,, Miyake, A,, Ogawa, T., 2000. Behavior of flames propagating through lycopodium dust clouds in a vertical duct. Journal of Loss Prevention in the Process Industries 13:449–457

He, X., Liu, X., Nie, B., Song, D., 2017. FTIR and Raman spectroscopy characterization of functional groups in various rank coals. Fuel, 206, 555–563.

Hertzberg, M., Cashdollar, K., L., Zlochower, I., A., 1986. Flammability limit measurements for dusts and Gases: Ignition energy requirements and pressure dependences. Twenty-first Symposium (International) on Combustion, The Combustion Institute, pp. 303-313.

Janovsky, B., Skrinsky, J., Cupak, J., Veres, J., 2019. Coal dust, Lycopodium and niacin used in hybrid mixtures with methane and hydrogen in 1 m3 and 20 l chambers. Journal of Loss Prevention in the Process Industries, 62, 103945

Kuai, N., Li, J., Chen, Z.,, Huang, W., Yuan, J., Xu, W., 2011. Experiment-based investigations of magnesium dust explosion characteristics. Journal of Loss Prevention in the Process Industries, 24 302-313.

Kuai, N., Huang, W., Du, B., Yuan, J., Li, L., Gan, Y, Tan, J., 2013. Experiment-based investigations on the effect of ignition energy on dust explosion behaviors. Journal of Loss Prevention in the Process Industries, 26, 869-877.

Kukfisz, B., Dowbysz, A., Samsonowicz, M., Markowska, D., Maranda, A., 2023. Comparative Analysis of Fire and Explosion Properties of Lycopodium Powder. Energies, 16, 6121.

Kuna, P., Janovsky, B., Pelikan, V., 2024. Effect of energy and design of ignitor on dust explosion characteristics. Fuel, 358, Part B, 130339

Li, Q., Tao, Q., Yuan, C., Zheng, Y., Zhang, G, Liu, J., 2018. Investigation on the structure evolution of pre and post explosion of coal dust using X-ray diffraction. International Journal of Heat and Mass Transfer, 120, 1162–1172.

Li, H., Deng, J., Chen, X., Shu, C-M., Kuo, C-H, Zhai, X., Wang, Q., Hu, X., 2020. Qualitative and quantitative characterization for explosion severity and gaseous–solid residues during methane–coal particle hybrid explosions: An approach to estimating the safety degree for underground coal mines. Process Safety and Environmental Protection, 141, 150–166.

Lin, S, Liu, Z., Qian, J., Li, X., 2019. Comparison on the explosivity of coal dust and of its explosion solid residues to assess the severity of re-explosion. Fuel, 251, 438–446.

Lin, S, Liu, Z., Zhao, E., Qian, J., 2019. A study on the FTIR spectra of pre- and post-explosion coal dust to evaluate the effect of functional groups on dust explosion. Process Safety and Environmental Protection, 130(4).

Liu, Z., Li, X., Qian, J., Lin, S, Zhang, S., 2017. A Study of the Characteristics of gaseous and Solid Residues after Coal Dust Explosions. Combustion Science and Technology, 189(9), 1639-1658.

Marmo, L., Fois, G., M., Luzzi, R., 2011. The effect of mixing combustible and inert dust on the minimum ignition energy. Sci. Tech. Energetic Materials, 72(5).

Mostafavi, S., A., Salavati, S., Dizaji, H., B., Bidabadi, M., 2015. Pyrolysis and combustion kinetics of lycopodium particles in thermogravimetric analysis. J. Cent. South Univ., 22: 3409−3417.

Nie, B., Gong, J., Yang, L., Peng, C., Fan, Y., Zhang, L., 2021. Experimental Analysis on Gas and Solid Residues of Pre- and Post-explosion Coal Dust. Energy Fuels, 35, 1727−1740.

Qian, J., Liu, Z., Liu, H., Hong, S., Liu, G., 2018. Characterization of the Products of Explosions of Varying Concentrations of Coal Dust. Combustion Science and Technology, DOI: 10.1080/00102202.2018.1519806.

Qian, J., Liu, Z., Lin, S., Liu, H., Ali, M., Kim, W., 2023. Re-explosion hazard potential of solid residues and gaseous products of coal dust explosion. Advanced Powder Technology, 34, 104129.

Rodgers, S., A., Ural, E., A., 2011. Practical Issues with Marginally Explosible Dusts—Evaluating the Real Hazard. Process Safety Progress, 30(3).

Scheid, M., Klippel, A., Tschirschwitz, R., Schröder, V., Zirker, S., Kusche, C., 2013. New ignition source “exploding wire” for the determination of explosion characteristics of combustible dusts in the 20-l sphere. 9th Global Congress on Process Safety, American Institute of Chemical Engineers, San Antonio, Texas.

Slatter, D., J., F., Sattar, H., Medina, C., H., Andrews, G., E., Phylaktou, H., N., Gibbs, B., M., 2015. Biomass explosion testing: Accounting for the post-test residue and implications on the results. Journal of Loss Prevention in the Process Industries, 36, 318-325.

Spitzer, S., H., Askar, E., Benke, A., Janovsky, B., Krause, U., Krietsch, A., 2022. Influence of pre-ignition pressure rise on safety characteristics of dusts and hybrid mixtures. Fuel, 311, 122495.

Taveau, J.R., Going, J.E., Hochgreb, S., Lemkowitz, S.M., Roekaerts, D.J.E.M. (2017). Igniter-induced hybrids in the 20-l sphere. *Journal of Loss Prevention in the Process Industries*, 49: 348–356.

Thomas, J., K., Kirby, D., C., Going, J., E., 2013. Explosibility of a Urea Dust Sample. Process Safety Progress,.32(2).

Flame propagation of aluminum dust clouds under microgravity conditions

Wookyung Kim [a], Rinrin Saeki [a], Ritsu Dobashi [b,c], Takuma Endo [a], Kazunori Kuwana [c], Toshio Mogi [b], Minhyeok Lee [b], Shigetoshi Yazaki [d], Masato Mikami [e], Yuji Nakamura [f] & Takehiko Ishikawa [g]

[a] Hiroshima University, Higashi-Hiroshima, Japan
[b] The University of Tokyo, Tokyo, Japan
[c] Tokyo University of Science, Noda, Japan
[d] Meiji University, Kawasaki, Japan
[e] Yamaguchi University, Ube, Japan
[f] Toyohashi University of Technology, Toyohashi, Japan
[g] Japan Aerospace Exploration Agency, Tsukuba, Japan

E-mail: kimwk@hiroshima-u.ac.jp

Abstract

Dust explosions pose serious risks in industrial environments, necessitating a thorough understanding of their behavior and mechanisms for effective safety measures. Microgravity environments offer unique conditions to study dust explosions, isolating gravitational effects and revealing fundamental combustion processes. Previous research has explored various aspects of dust explosions under microgravity conditions, demonstrating the impact of factors like particle size, concentration, and ignition delay on flame characteristics. Our study builds upon this research by conducting microgravity experiments and numerical simulations to investigate particle behavior and flame propagation dynamics. We find that under microgravity conditions, flame behavior tends to become more discrete with larger particle sizes or lower concentrations, a phenomenon supported by numerical simulations. Additionally, we observe the importance of particle size and heat conduction rate in determining flame characteristics, with larger particles and slower heat conduction leading to more discrete flame propagation. The comparison between experimental and numerical results highlights the unique insights provided by microgravity experiments, particularly regarding the observation of discrete flame behavior. Overall, our study underscores the vital role of microgravity experiments in advancing our understanding of dust explosions and enhancing safety practices in industrial settings.

Keywords: *dust explosion, flame, aluminum, microgravity*

1. Introduction

Dust explosions present significant hazards across various industrial environments, highlighting the necessity to comprehend their behavior and mechanisms for implementing effective safety and prevention measures. Microgravity environments offer unique opportunities to investigate dust explosions by isolating gravitational effects and unveiling fundamental combustion processes (Nomura et al. 2000; Mikami et al. 2019). Previous research in microgravity has extensively explored various aspects of dust explosions, revealing insights into flame characteristics influenced by factors such as particle size, concentration, and ignition delay (Ballal 1983; Bozier and Veyssière 2006; Tang et al., 2009; Bozier and Veyssière 2010; Goroshin et al., 2011; Tang et al., 2011; Palecka et al., 2020). Notably, microgravity experiments conducted at JASMIC by Japanese researchers have provided invaluable contributions to our understanding of dust explosion behavior (Kobayashi et al., 1994; Hanai et al., 1999).

Despite the invaluable insights gained from microgravity experiments, monitoring particle behavior during combustion remains challenging due to payload limitations inherent in microgravity environments. To address this challenge, there is a pressing need to conduct combustion experiments in reduced flow fields while simultaneously visualizing unburned particles. This integrated approach promises a comprehensive understanding of dust explosion dynamics under microgravity conditions.

In this study, we aim to address these challenges by measuring fuel particle speeds and evaluating interparticle distances both critical factors influencing flame propagation. Our experiment seeks to confirm the minimal change in interparticle distance, which is vital for effective flame propagation. Despite the progress made in microgravity research on dust explosions, further investigation is warranted to comprehensively understand underlying mechanisms and optimize safety measures.

Therefore, the objective of this study is to conduct microgravity experiments and numerical simulations to elucidate dust explosion behavior and mechanisms, with a focus on flame propagation and temperature distribution. By integrating experimental observations with numerical models, this research aims to provide valuable insights into fundamental aspects of dust explosions and inform safety practices in industrial settings.

2. Microgravity experiments

2.1 COSMOTORRE 2.5 second drop tower test

An experimental apparatus was developed to conduct microgravity experiments on dust explosions at the 50 m drop tower COSMOTORRE, operated by the Hokkaido Aerospace Science and Technology Incubation Center (HASTIC), as depicted in Fig. 1 (a). The 2.5-second microgravity test time in the drop tower is achieved by allowing the experimental capsule to freefall. The microgravity experimental apparatus was assembled within the payload size of ϕ 500 mm × 1050 mm to facilitate microgravity experiments. In this study, combustion experiments were conducted in an explosion tube with inner dimensions of W30 mm × D30 mm × H250 mm. Figure 1 (a) illustrates the camera angles, where two high-speed video cameras (Photon FASTCAM Mini AX100, monochrome and color) recorded simultaneously. A dichroic mirror was installed to separate wavelengths into green and red, enabling a simultaneous visualization system to capture both unburned particles and flame propagation behavior. The color camera visualized aluminum luminous flames, while the monochrome camera captured dispersed particles illuminated by a laser light sheet. A band-pass filter, for particle visualization at 532 nm, was attached to the monochrome camera. The color camera utilized a long pass filter to exclude short wavelengths, allowing observation of only flame propagation behavior. The time sequence of each microgravity experiment was controlled by a programmable controller during capsule dropping. When capsule dropping commenced ($t = -2$ s), the powder was dispersed by compressed air at 120 kPa from an air tank (0.835 L) for 1 second. A 15 kV electric discharge was applied between tungsten rods with a diameter of 2 mm, with an ignition delay of 1 second after dispersion ended. Thus, ignition timing was defined as t=0 s. The ignition point (x =0 mm, y =0 mm) was 50 mm above the bottom of the explosion tube. In this study, micron-sized aluminum powders (Sauter Mean Diameter (SMD) of d_{32}= 20, 32, 46 µm), procured from Toyo Aluminium K.K., were used. The powder was loaded into a dispersion system before capsule dropping. The dispersion system automatically initiated powder dispersion into the tube when capsule dropping commenced. Suspended particle clouds were ignited by spark discharging between tungsten rods with ϕ = 2 mm. Further details of the dispersion and control system were provided in (Kim et al., 2021).

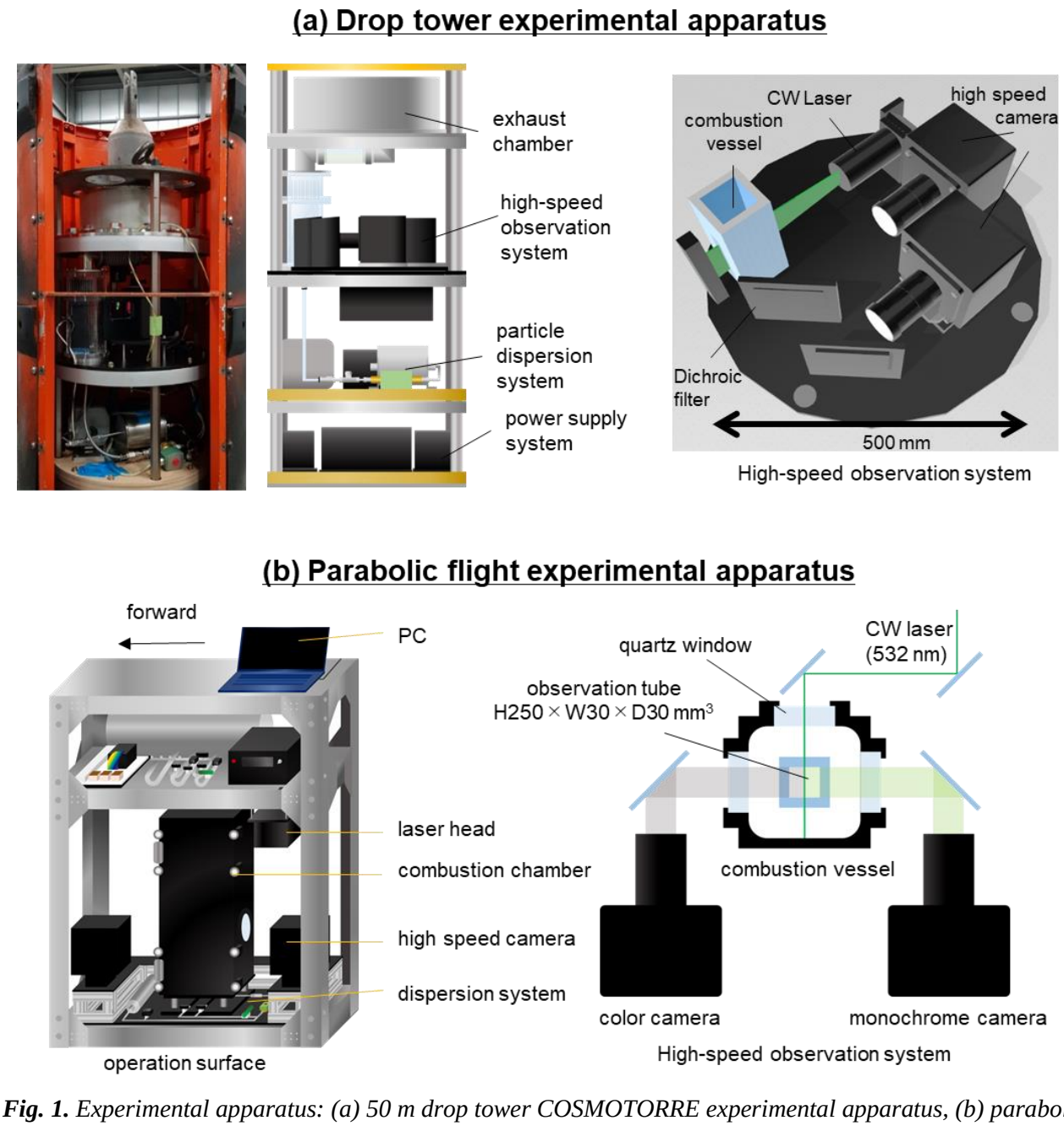

Fig. 1. *Experimental apparatus: (a) 50 m drop tower COSMOTORRE experimental apparatus, (b) parabolic flight experimental apparatus on MU 300*

2.2 Parabolic flight test by MU-300

The microgravity experimental apparatus was developed in accordance with the safety requirements for parabolic flights aboard the MU300 aircraft operated by Diamond Air Service, Inc. (DAS). These flights provided repeated sessions of 20 seconds of microgravity. Experimental systems were mounted on the MU300 experimental shelf measuring W600 mm × D450 mm × H900 mm, as depicted in Figure 1 (b). The same observation tube used in the drop tower was utilized, with spare tubes available next to the experimental shelf for each experiment. The top of the tube featured a semi-open-end structure consisting of stainless mesh and connected to the exhaust chamber, which contained combustible particles in the tube while preventing pressure increases during combustion experiments. This structure assumed that flame propagation only occurred inside the observation tube. The observation tube was enclosed by an aluminum combustion chamber with three quartz windows meeting the regulations for aircraft combustion experiments. At the start of each microgravity experiment, aluminum powder was dispersed into the tube using a 120 kPa compressed air flow for

2 seconds. Eight seconds after the particle dispersion ended, aluminum dust was ignited by a 15 kV electric discharge. The simultaneous observation system surrounded the combustion chamber and began recording 2 seconds before the ignition timing. Two high-speed cameras, FASTCAM AX100 (Photron), observed aluminum dust illuminated by a laser sheet and flame propagation simultaneously at 3000 frames per second.

3. Results and discussion

3.1 Dust clouds in a microgravity environment

To assess the velocity of aluminum particles affecting combustion experiments, Particle Image Velocimetry (PIV) was conducted using high-speed images of particles illuminated by a 1 mm thick laser light sheet. Figure 2 displays the flow fields of aluminum particles (d_{32}= 20 μm) prior to ignition timing in both drop tower and parabolic flight experiments. Based on the observation coordinates, the three-dimensional particle speed u can be estimated as the Root Mean Square (RMS) value by substituting u_z, which corresponds to the depth direction in the laser sheet, assuming that the thickness of the laser sheet is sufficiently thin. The results of the drop tower test showed a significant increase in the value of u during the dispersion process, followed by a rapid decrease after the dispersion of particles ended, as depicted in Fig. 3 (a). These trends in particle speed were reproducible in other experimental tests. Despite the decrease in velocity, the particles still moved at a reduced speed, and their movement did not reach a quasi-steady flow state during the drop tower tests. The results regarding particle velocity from drop tower tests suggest that long-term microgravity environments are necessary to accurately estimate flame propagation behaviors near the minimum explosible concentration.

The results from parabolic flight tests demonstrated that the effect of dispersion flow on particle behavior decreases during an 8-second ignition time delay, and the vectors in a flow field indicate that dispersed particles remain suspended in a reduced-gravity environment. Although the particle velocity becomes slower, the distribution of particle velocity appears to be non-uniform, ranging from several mm/s to 1 cm/s due to the effects of g-jitter in all directions during a parabolic flight experiment using an aircraft. The measured mean particle velocity is slower than 3.9 cm/s, the terminal velocity of 20 μm aluminum particles estimated by Stokes' law, as shown in Fig. 3 (b).

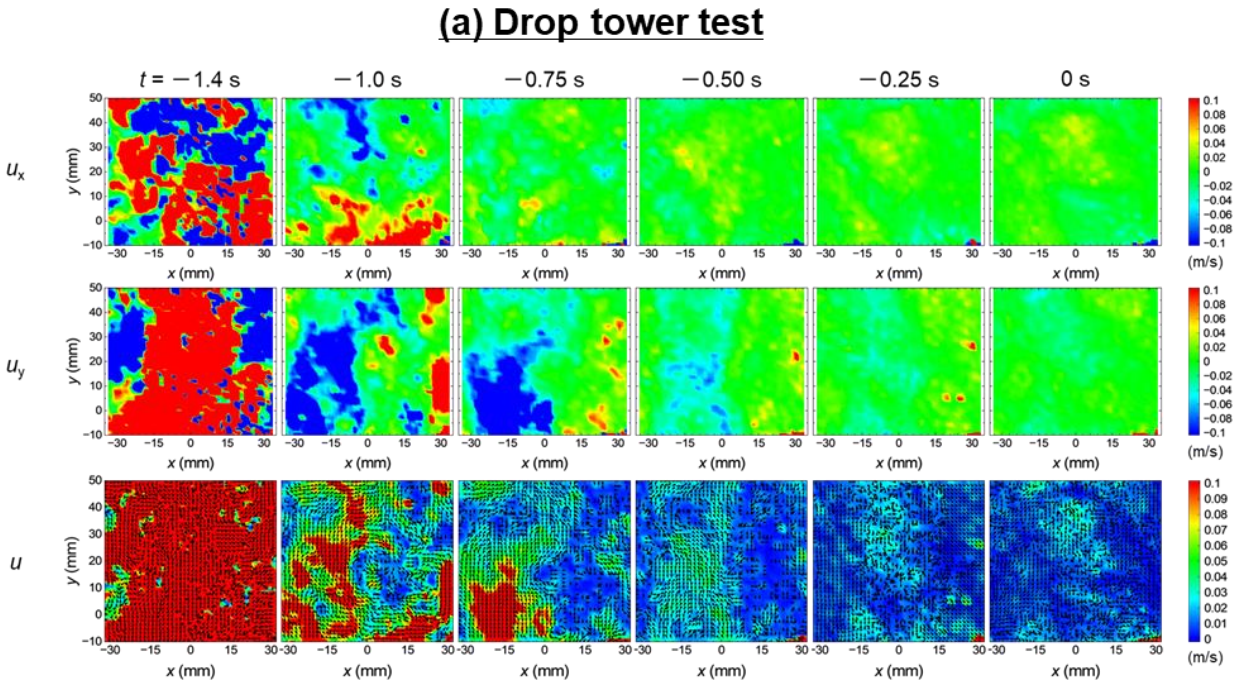

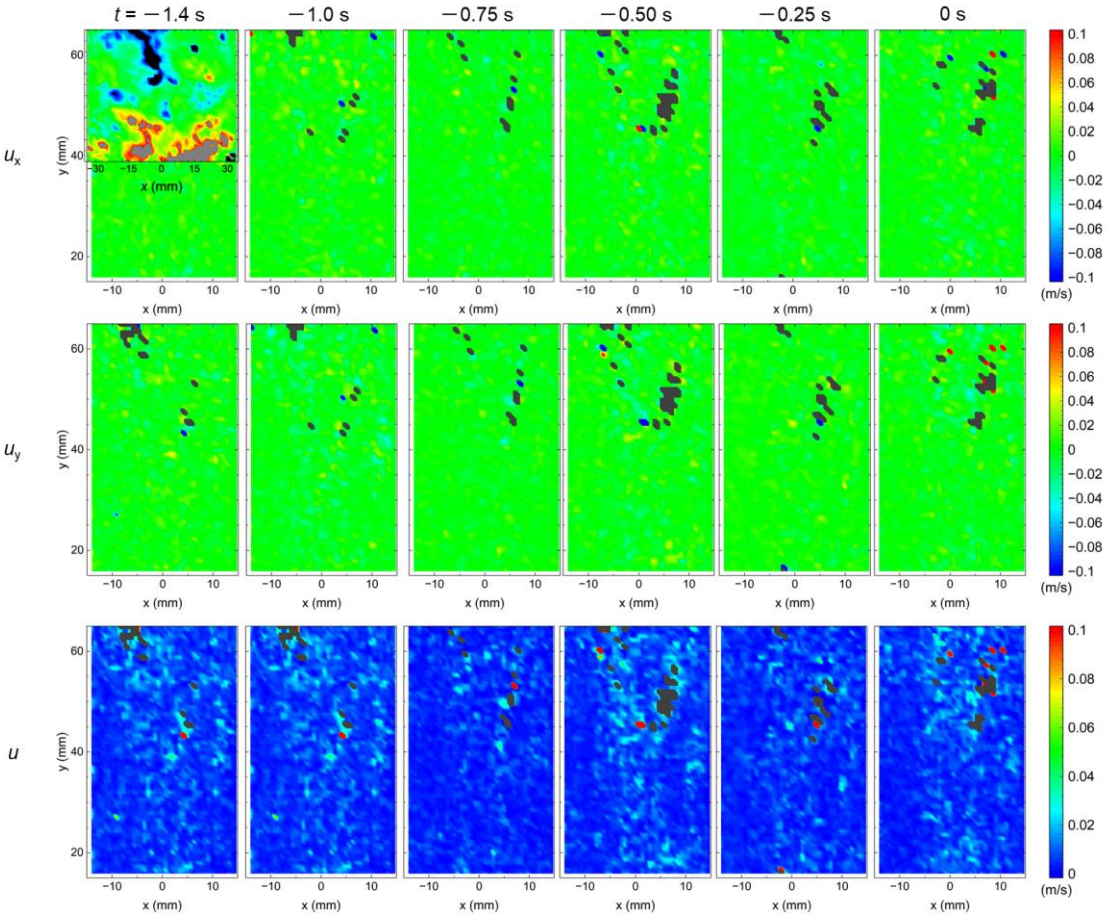

Fig. 2. *PIV images of dust speed before ignition timing.*

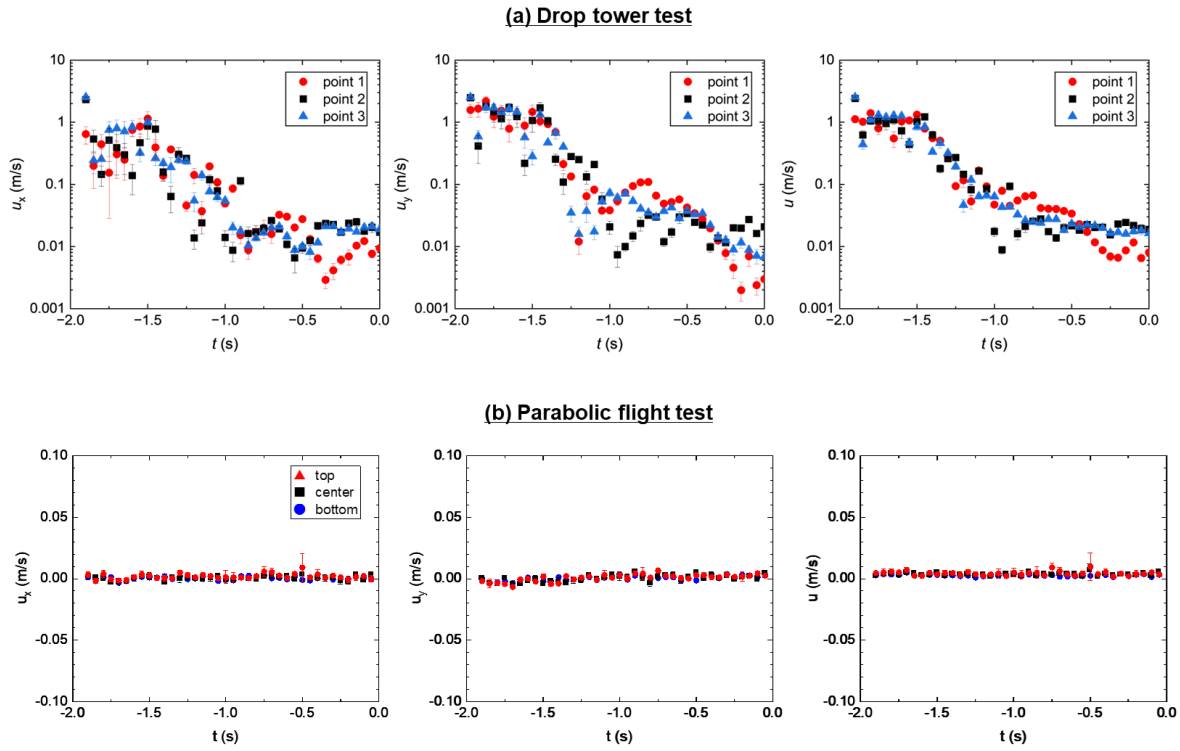

Fig. 3. *Time histories of dust speed before ignition timing*

The images of dust concentration distribution before ignition timing are shown in Fig. 4. In this study, value of dust concentration was calculated as:

$$C = \frac{\pi d_{\mathrm{p}}^3 \rho_{\mathrm{p}} n}{6AD} \tag{1}$$

where d_{p} is the particle size ρ_{p}, is the particle density, n is the number of particles in measurement volume, A is the measurement area, D is the thickness of the laser sheet. The value of dust concentration remained ununiform even after the particle dispersion ended, however the value fluctuations gradually decreased. In particular, the aluminum dust in parabolic flight tests continued to be suspended in air, and dust concentration indicated a minor change during ignition time delay. The risk of dust explosion lasts in a microgravity environment because the particle sedimentation does not occur.

The distribution of aluminum dust concentration was plotted in Figure 5. Error bars illustrate the standard deviation of the instantaneous observation area. After the end of particle dispersion, the average value of dust concentration remains almost constant. This result also suggests that the likelihood of a dust explosion persists once a combustible dust cloud is formed in a microgravity environment. The values of dust concentration for three regions were not the same, indicating that dust concentration should not be defined by the average value.

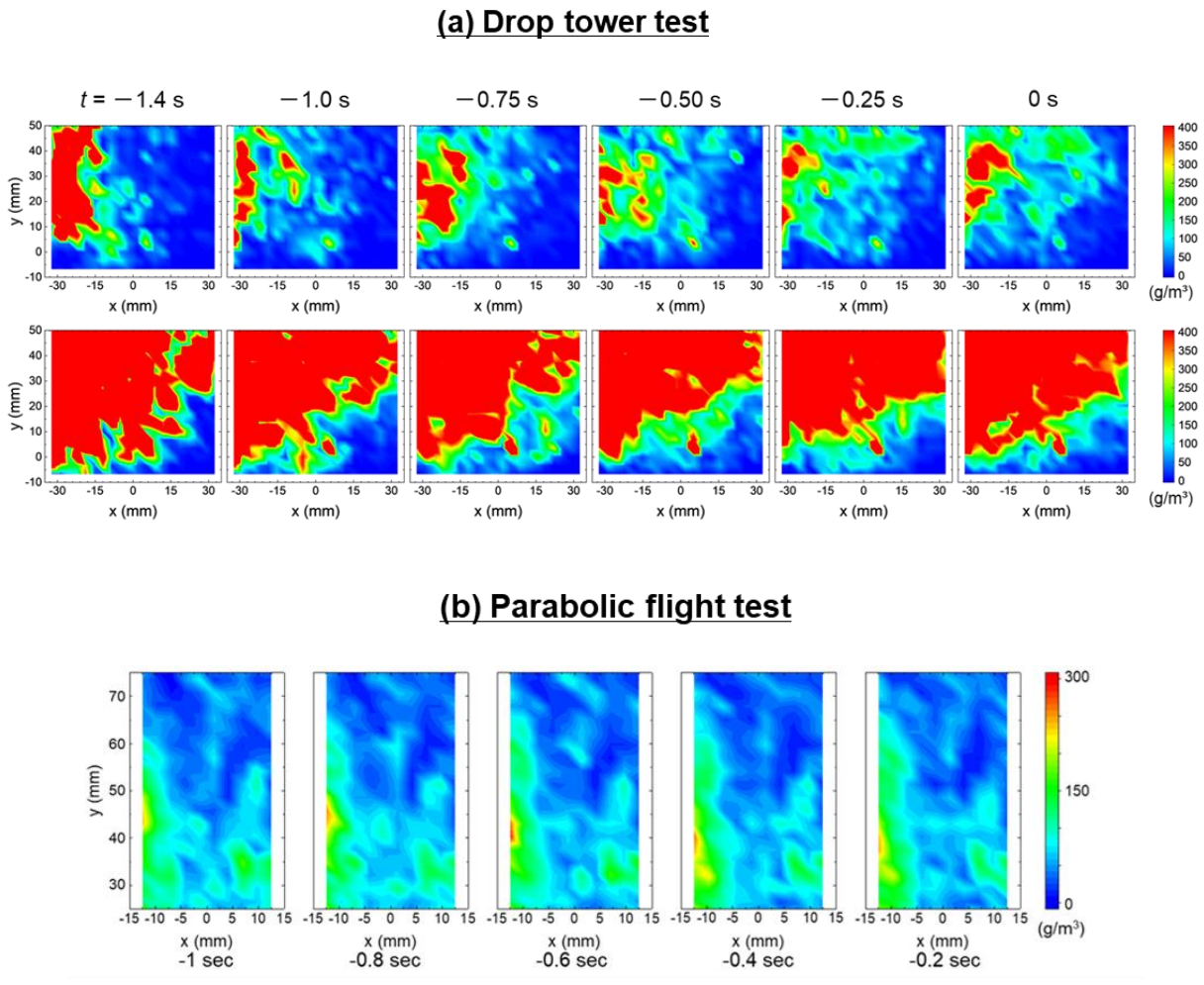

Fig. 4. *PIV images of dust concentration before ignition timing*

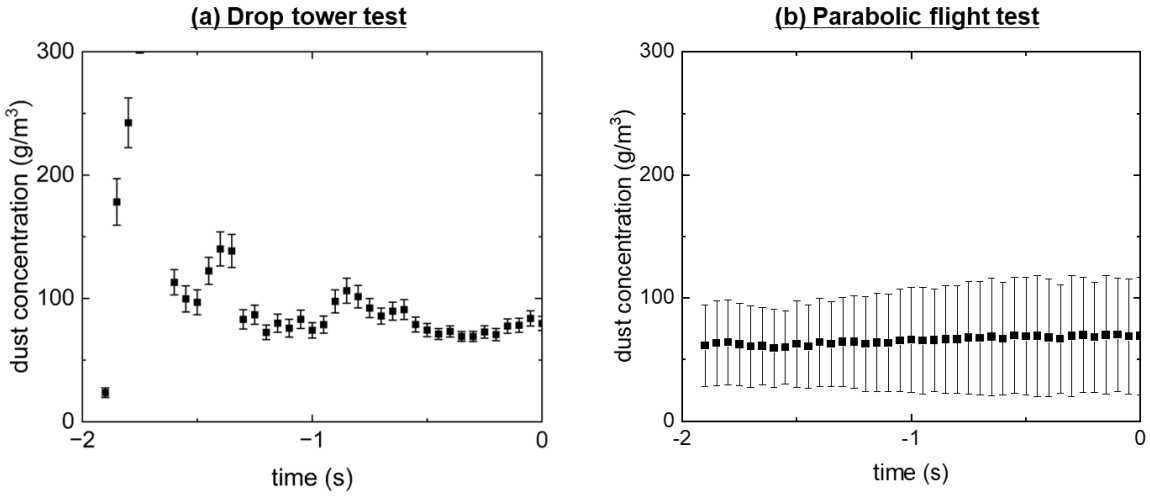

Fig. 5. *Time histories of dust concentration before ignition timing*

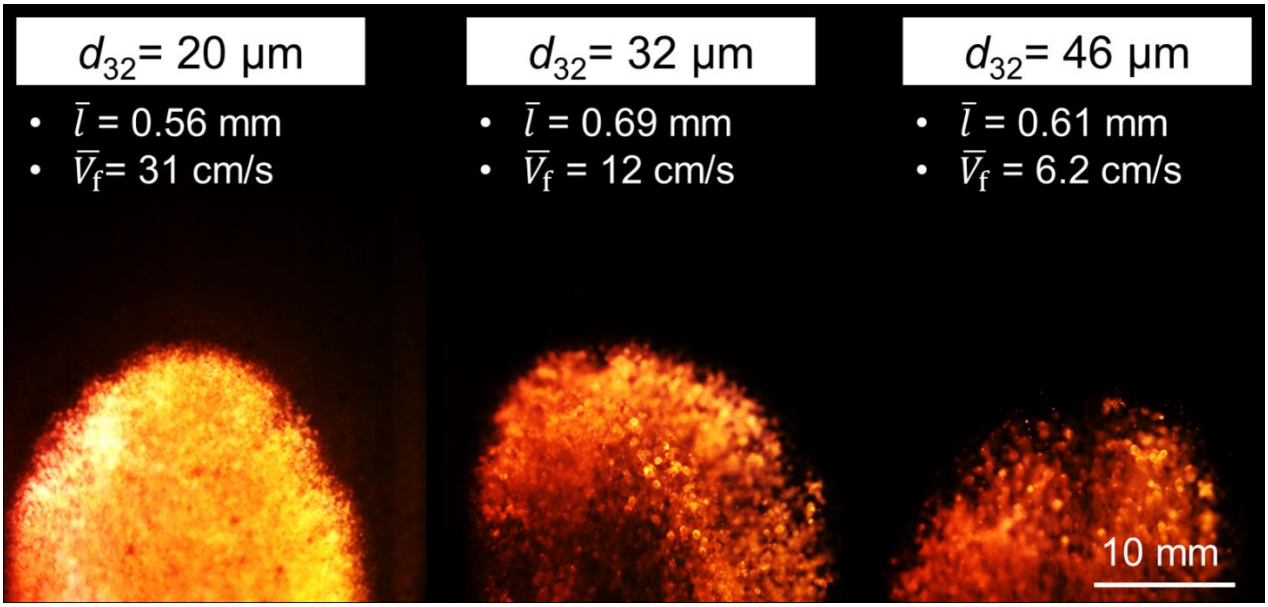

Fig. 6. *Effect of particle size on aluminum laminar flame propagation*

3.2 Laminar flame propagation in a microgravity environment

The flame propagation behaviors of the aluminum powders were observed, as depicted in Fig. 6. The flame speed $\bar{V}_f$ increased with a decrease in particle size. While a continuous flame was observed in the flame front of 20 μm aluminum dust, partially discontinuous flames were captured as the particle size increased. Specifically, the flame propagation for 46 μm aluminum powder indicated discrete flames compared to the 20 μm aluminum powders, with spot flames and dark zones clearly observed. These intriguing characteristics of flame front behaviors, revealed by the results of the microgravity test, can be discussed in terms of the discreteness parameter χ. This parameter is defined as the ratio of the combustion time of a single aluminum particle t_c to the characteristic heat diffusion time between adjacent particles t_d.

$$\chi = \frac{t_c}{t_d} = \frac{t_c \alpha}{l^2} \tag{2}$$

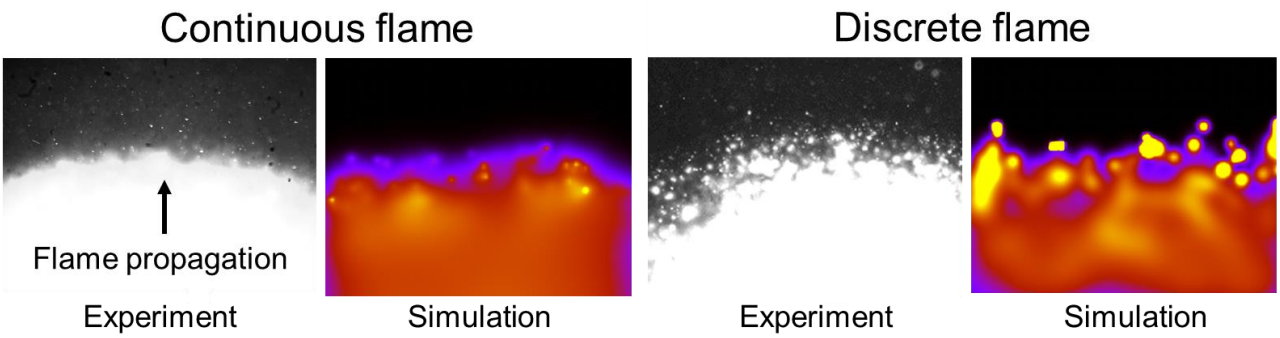

Fig. 7. *Comparison between the continuous and discrete flames*

where α represents the thermal diffusivity, l denotes the average particle distance. The heat diffusion time between adjacent particles is proportional to the square of the l. Since the value of l is proportional to the particle diameter d_p, the interparticle heat diffusion time is also proportional to the square of the particle diameter (d_p^2). It is known that for a single aluminum particle with a micron diameter (>10 μm), the combustion time t_c is proportional to $d_p^{1.8}$ (Bouillard et al., 2010; Kim et al., 2023). Therefore, the effect of the heat diffusion time is more significant for aluminum powders with larger particle sizes. The results demonstrate that the flame propagation behavior tends to become discrete as the particle size increases. Additionally, for the 20 μm aluminum powders, a discrete flame front near the minimum explosible concentration was observed, while a continuous flame front at rich dust concentration was captured, as shown in Fig. 7.

The results from microgravity experiments were compared with those of numerical simulations where the combustion wave propagates through heat conduction between particles in random particle configurations (Lam et al., 2017; Lam et al., 2020; Kuwana et al., 2023). In these calculations, the source term in the heat conduction equation is expressed as the summation of delta functions. Herein, $\theta = (T - T_\mathrm{u})/(T_\mathrm{b} - T_\mathrm{u})$ represents the dimensionless temperature. Assuming each particle to be a point heat source releasing heat from the dimensionless ignition time $\tau_{\mathrm{ign},i}$ to reaction time τ_c, the solution to the three-dimensional heat conduction equation can be expressed using the Green's function as follows (Kuwana et al., 2023):

$$\theta(\boldsymbol{X},\tau) = \sum_i \frac{1}{4\pi\tau_\mathrm{c}|\boldsymbol{X}-\boldsymbol{X}_{\mathrm{p},i}|}\left[\mathrm{erfc}\frac{|\boldsymbol{X}-\boldsymbol{X}_{\mathrm{p},i}|}{\sqrt{4(\tau-\tau_{\mathrm{ign},i})}} - \mathrm{erfc}\frac{|\boldsymbol{X}-\boldsymbol{X}_{\mathrm{p},i}|}{\sqrt{4(\tau-\tau_{\mathrm{ign},i}-\tau_\mathrm{c})}}\right] \quad (3)$$

where $\boldsymbol{X}$ represents the laboratory coordinate system, and $\boldsymbol{X}_{\mathrm{p},i}$ denotes the position of particle i. In the case where the reaction is infinitely fast ($\tau_\mathrm{c} = 0$), the temperature near the particles immediately after ignition significantly exceeds the adiabatic combustion temperature, and the influence of discrete heat sources on the temperature distribution is prominently observed. This phenomenon cannot be represented by a continuum model. On the contrary, in the case of $\tau_\mathrm{c} = 1$, where heat conduction is relatively rapid, the extent of local temperature increase, often described as the roughness of the temperature distribution, diminishes, aligning more closely with the temperature distribution anticipated by the continuum model. Figure 7 shows the comparison of continuous and discrete flames between experimental and numerical images. It is evident that as the particle size increases or the concentration decreases, the flame becomes more discrete. Microgravity experiments are extremely useful for observing the behavior and mechanisms of the discrete flame due to its slow propagation speed.

4. Conclusions

In conclusion, our microgravity experiments and numerical simulations have provided valuable insights into the behavior and mechanisms of dust explosions, focusing on particle behavior and flame propagation dynamics. Our findings demonstrate that in microgravity conditions, flame behavior tends to become more discrete as particle size increases or concentration decreases. This observation was corroborated by numerical simulations, highlighting the importance of microgravity environments in studying such phenomena. Moreover, our experiments underscored the significance of particle size and heat conduction rate in shaping flame characteristics, with larger particles and slower heat conduction resulting in more discrete flame propagation. The comparison between experimental and numerical outcomes emphasized the unique insights offered by microgravity experiments, particularly in observing discrete flame behavior. Overall, our study underscores the crucial role of microgravity experiments in advancing our understanding of dust explosions and associated combustion processes.

Acknowledgements

This work was partially supported by JSPS KAKENHI Grant Numbers JP21K14379, JP21H04593, 23KK0270, 22J23064, the light metal educational foundation, the iwatani naoki foundation, the electric technology research foundation of chugoku, Hiroshima carbon circular project, and the front-loading research project of the Japan Aerospace Exploration Agency (JAXA), Institute of Space and Astronautical Science (ISAS) in Japan.

References

Ballal, D. R. 1983. 'Flame Propagation through Dust Clouds of Carbon, Coal, Aluminum and Magnesium in an Environment of Zero Gravity', *Proceedings of the Royal Society of London Series a-Mathematical Physical and Engineering Sciences*, 385: 21-&.

Bouillard, J., Vignes, A., Dufaud, O., Perrin, L., and Thomas. D., 2010. 'Ignition and explosion risks of nanopowders', *J Hazard Mater*, 181: 873-80.

Bozier, O., and Veyssière. B., 2006. 'Influence of suspension generation on dust explosion parameters', *Combustion Science and Technology*, 178: 1927-55.

Bozier, O., and Veyssière. B., 2010. 'Study of the Mechanisms of Dust Suspension Generation in a Closed Vessel Under Microgravity Conditions', *Microgravity Science and Technology*, 22: 233-48.

Goroshin, S., Tang, F. D., Higgins, A. J., and Lee. J. H. S., 2011. 'Laminar dust flames in a reduced-gravity environment', *Acta Astronautica*, 68: 656-66.

Hanai, H., Ueki, M., Maruta, K., Kobayashi, H., Hasegawa, S., and Niioka. T., 1999. 'A lean flammability limit of polymethylmethacrylate particle-cloud in microgravity', *Combustion and Flame*, 118: 359-69.

Kim, W., Sakei, R., Dobashi R., Endo, T., Kuwana, K., Mogi, T., Lee, M., Mikami, M., and Nakamura, Y., 2021. 'Research on Risk of Dust Explosions in Microgravity for Lunar and Planetary Exploration', *International Journal of Microgravity Science and Application*, 38: 380204.

Kim, W., Sakei, R., Ueno, Y., Johzaki, T., Endo, T., and Choi, K., 2023. 'Effect of particle size on the minimum ignition energy of aluminum powders', *Powder Technology*, 415: 118190.

Kobayashi, H., Ono, N., Okuyama, Y., and Nioka. T., 1994. 'Flame propagation experiment of PMMA particle cloud in a microgravity environment', *Symposium (International) on Combustion*, 25: 1693-99.

Kuwana, K., S. Yazaki, W. Kim, T. Mogi, and R. Dobashi. 2023. 'Gravity Effects on the Minimum Explosive Concentrations in 1-D Dust Explosion', *Combustion Science and Technology*, 195: 1622-36.

Lam, F., Mi, X. C., and Higgins. A. J., 2017. 'Front roughening of flames in discrete media', *Physical Review E*, 96.

Lam, F., Mi, X. C., and Higgins. A. J., 2020. 'Dimensional scaling of flame propagation in discrete particulate clouds', *Combustion Theory and Modelling*, 24: 486-509.

Mikami, M., Yoshida, Y., Seo, T., Moriue, O., Sakashita, T., Kikuchi, M., and Kan. Y., 2019. 'Recent Accomplishment of "Group Combustion" Experiments aboard Kibo on ISS', *International Journal of Microgravity Science and Application*, 36.

Nomura, H., Koyama, M., Miyamoto, H., Ujiie, Y., Sato, J., Kono, M., and Yoda. S, .2000. 'Microgravity experiments of flame propagation in ethanol droplet-vapor-air mixture', *Proceedings of the Combustion Institute*, 28: 999-1005.

Palecka, J., Goroshin, S., Higgins, A. J., Shoshin, Y., Goey, P., Angilella, J. R., Oltmann, H., Stein, A., Schmitz, B., Verga, A., Vincent-Bonnieu, S., Sillekens, W., and Bergthorson. J. M., 2020. 'Percolating Reaction-Diffusion Waves (PERWAVES)-Sounding rocket combustion experiments', *Acta Astronautica*, 177: 639-51.

Tang, F. D., Goroshin, S., and Higgins. A. J., 2011. 'Modes of particle combustion in iron dust flames', *Proceedings of the Combustion Institute*, 33: 1975-82.

Tang, F. D., Goroshin, S., Higgins, A., and Lee. J., 2009. 'Flame propagation and quenching in iron dust clouds', *Proceedings of the Combustion Institute*, 32: 1905-12.

Effect of initial pressure, temperature, and water vapor concentration on ignitability of hydrogen oxygen mixture

Seiji Tokumitsu [a], Toshio Mogi [a] & Ritsu Dobashi [a]

[a] University of Tokyo, Tokyo, Japan

E-mail: tokumitsu-seiji1641@g.ecc.u-tokyo.ac.jp

Abstract

Most of the studies on the ignitability of mixtures of hydrogen and pure oxygen, which are expected for accidents involving the formation of hydrogen and oxygen mixtures, have been conducted under atmospheric pressure or positive pressure, and most of the studies on the ignitability under reduced pressure have been on self-ignition, so there have been few studies on the hazard of external ignition. In this study, we attempted to analyse the ignitability of hydrogen-oxygen mixtures and three-component mixture containing water vapor under reduced pressure, and the effect of water vapor on ignitability. Using an ignition determination based on pressure change according to ASTM standards, the LEL was found to be larger for smaller initial pressure and smaller for smaller initial temperature. Regarding flame spread behaviours when ignited at ultra dilute concentrations near LEL, it was confirmed that flame spread velocity tends to increase with lower pressure. Flame propagation speed decreased with the addition of water vapor, and the range of pressure increase at ignition tended to be smaller. This tendency was more pronounced for larger concentrations of water vapor in the gas phase.

Keywords: *hydrogen, lower explosion limit, industrial explosion*

Introduction

As the demand for hydrogen energy increases, more and more systems in various industrial areas are expected to form hydrogen-oxygen mixtures. Hydrogen-oxygen mixtures have a high ignition hazard due to their wide explosion range and very low minimum ignition energy. There are many previous studies on the ignitability of hydrogen-oxygen mixtures.

Auto-ignition properties at theoretical mixing ratios have been studied by detailed simulations of elementary reaction processes and actual measurements (Liang et al., 2018). In particular, it has been found that H2O has a greater inhibitory effect than the reactants H2 and O2 and the inert substances N2 and Ar, especially with regard to the third-body effect that affects the ignition limit (Michael et al., 2002). It is also known that the reaction rate of each elementary reaction is affected by pressure (Shimizu et al., 2011).

For ignition of hydrogen-oxygen mixtures by an external energy source, there are studies on the explosion range and on the propagation of the flame when ignited. Most of the measurements of the explosion range are based on the visual standard method of flame propagation (Coward et al., 1914), and the lower explosion limit of hydrogen-oxygen mixtures in the standard state is about 4% (Jones et al., 1937) (Clusius et al., 1936) when measured by upward propagation and about 9~10% (Clusius et al., 1936) (Drop et al., 1935) when measured by downward propagation. In the case of ignition by hot wire, it has been found that the ignition delay varies depending on the amount of energy of the hot wire used and the ambient pressure (Rubstow, 2020). It is also known that premixed flame propagation after ignition is affected by pressure (Bradley et al., 1998) (Qin et al., 2000).

As mentioned above, most of the existing studies on ignition hazards due to external energy sources have been conducted under standard conditions or under high pressure, such as in engines, and there are few studies under reduced pressure. However, with the expansion of the use of fuel cells and photocatalysts (Nishiyama et al., 2021), it is expected that hydrogen will be used at high elevations and under lower than standard atmospheric pressure. Therefore, knowledge of the explosion hazard of hydrogen gas under reduced pressure is required. The purpose of this study is to obtain knowledge on the ignition hazard of hydrogen-oxygen mixtures under reduced pressure, such as the lower explosive limit and flame spread, with a view to operating under various conditions in the future.

1. Experiments

This study was divided into two experiments, one for Dry, a two-component system of hydrogen oxygen, and one for Wet, a three-component system of hydrogen oxygen vapor.

The experimental apparatus is shown in Figure 1. The combustion chamber is a stainless steel pseudo-spherical vessel with an outer diameter of 114 mm, an inner diameter of 104 mm, and a height of 100 mm, with a 30 mm diameter circular vent in the center of the vessel ceiling for safety reasons. The temperature and pressure inside the vessel were measured by temperature and pressure sensors mounted on the vessel ceiling, respectively, and were recorded and displayed every 0.1 second by a data logger. Pressure changes during ignition were recorded at 100 μs intervals. The electrode was a 5 mm diameter tungsten electrode and a 15 kV, 20 mA discharge with a neon transformer was continued for 0.3 s. The discharge duration was controlled by a pulse generator. The discharge duration was controlled by a pulse generator.

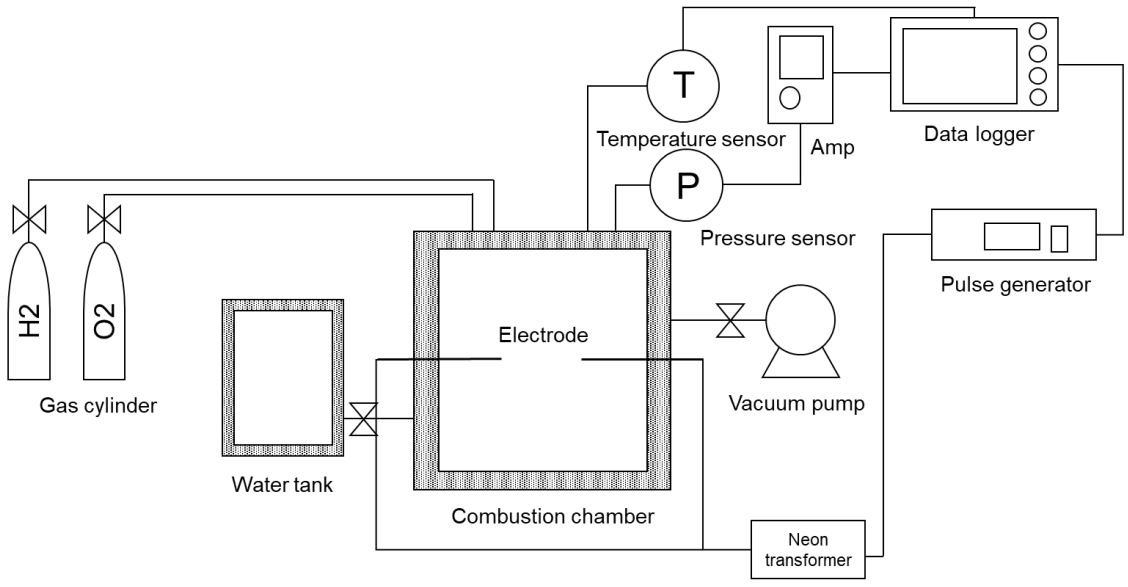

Fig.1. *Overall schematic view of the experimental apparatus*

1.1. Ignition experiment of hydrogen-oxygen mixture in Dry conditions

In Dry conditions, a vacuum pump was used to create a vacuum in the chamber, and then hydrogen gas, oxygen gas, were added at the partial pressures necessary to achieve the desired mixed composition. Each gas was added to the chamber at a flow rate of 100 cc/min ~ 150 cc/min, and after all gases flowed in, the chamber was left for at least 3-4 minutes to create a well-mixed stationary system (Cashdollar., 2000) before ignition. The pressure and temperature at ignition were at the desired conditions.

1.2. Ignition experiment of hydrogen-oxygen-water vapor mixture in Wet conditions

In Wet conditions, the chamber was evacuated by a vacuum pump, the water supply valve was opened, the liquid was supplied to a sufficiently small thickness that it did not affect the container volume to the chamber from the water tank, it was left to reach saturation vapor pressure at the set temperature, and then hydrogen gas and oxygen gas was added and ignited following the same procedure as in the dry condition.

The experiment first measured the lower explosive limit (LEL) of hydrogen-oxygen binary systems at two temperatures, 20°C and 60°C under Dry conditions, at pressures of 100 kPa, 60 kPa, 40 kPa, and 20 kPa, to confirm the effects of temperature and pressure on the LEL. The system was then ignited at other pressures at the same concentration as the largest LEL value to confirm the effect of pressure on the rate of combustion near the lower limit. Ignition at each LEL concentration was then attempted under Wet conditions to confirm the effect of water vapor on the ignitability of the hydrogen oxygen mixture.

2. Results and discussion

2.1. Ignition experiment of hydrogen-oxygen mixture in Dry conditions

Since the ASTM standard (American Society for Testing and Materials., 2015) considers a pressure increase of 10% or more of the initial pressure at ignition as flame propagation, the LEL in this experimental system was determined by the following equation (1).

$$LEL = \frac{1}{2}(L_1 + L_2) \tag{1}$$

where L_1 is the maximum hydrogen concentration at which the pressure increase was less than 10% of the initial pressure, and L_2 is the minimum hydrogen concentration at which the pressure increase exceeded 10%.

Note that this experiment includes an error in concentration corresponding to the 0.25% error range of the pressure sensor because the concentration in the chamber was adjusted using the partial pressure method (Cashdollar., 2000).

The results of these measurements under each condition are shown in Figure 2 below.

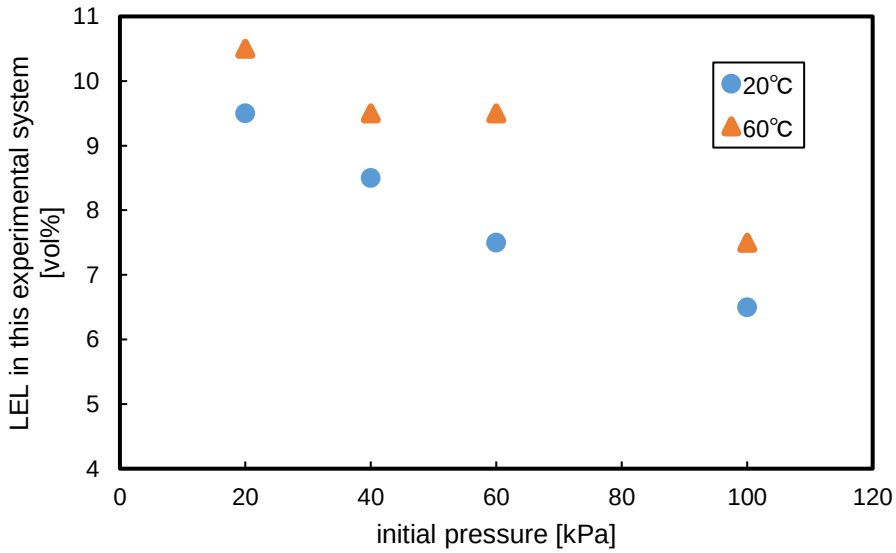

Fig. 2. *LEL measurement results for each initial pressure and temperature in this experimental system*

The LEL in this experimental system was found to be larger at pressure below atmospheric pressure for smaller initial pressures and larger for larger initial temperatures. The LEL of the hydrogen-oxygen mixture in the standard state is about 4% (Jones et al., 1937) (Clusius et al., 1936) when measured by upward propagation on a visual basis and about 9~10% (Clusius et al., 1936) (Drop et al., 1935) when measured on a downward propagation basis, while it was about 6.5% on a pressure basis in this experimental system.

Regarding the fact that the LEL increased with decreasing initial pressure, while previous studies at positive pressure showed a tendency for the LEL to decrease with decreasing initial pressure (Nuckolls., 1920), the opposite tendency was observed in this experiment at negative pressure. As for the effect of pressure on flame spread, since the effect of radiation heat loss increases with increasing pressure (Law., 1992), the higher the pressure, the harder the flame is to spread, which means that the LEL should also be larger.

The influence of initial temperature on flame propagation has been demonstrated by a number of theoretical calculations and experiments. In general, many studies have shown that for many combustible materials, the higher the initial temperature, the smaller the LEL (Kondo et al., 2011) (Zhang et al., 2022).

It is known that the results of LEL measurements under standard conditions differ between visual and pressure standards (Cashdollar, 2000). Therefore, the effects of initial pressure and initial temperature on the LEL in pressure-based measurements may also give different results than in visual-based measurements. In judging LEL by visual inspection, the smaller the unburned gas pressure or the higher the unburned gas temperature, the more easily the flame propagates due to enhanced molecular diffusion, and thus the LEL is considered to be smaller. On the other hand, when pressure increase is used as the criterion, as in this experiment, the probability of collision between active molecules in the chamber before ignition, i.e., the concentration of active molecules, is considered to have a greater effect than the speed of molecular diffusion.

The flame propagation when ignition occurs at ultra dilute concentrations near the lower boundary is then analyzed in detail. The pressure history at the time of ignition is compared with a mixture of 10 vol% hydrogen and 90% oxygen, in which ignition was confirmed under all conditions at every 10 kPa from 10 kPa to 50 kPa at 50°C. The pressure history is extracted from the output value of the data logger every 5 ms and smoothed by a polynomial fitting method with an 11-point average. Figure 3 shows that ignition occurs at t = 100 ms, and the pressure change ΔP from the initial pressure is taken on the vertical axis.

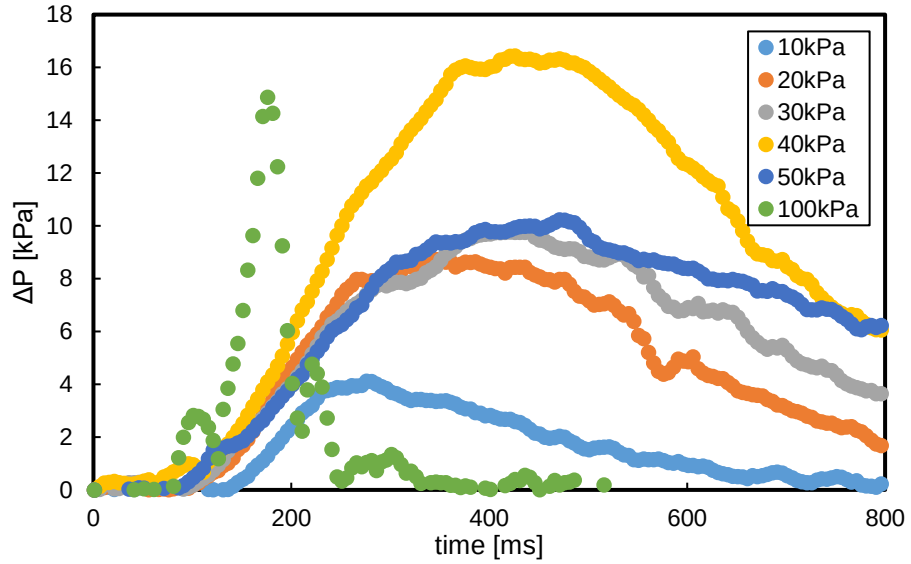

Fig. 3. *Pressure history at ignition of mixture at 50°C, 10% hydrogen 90% oxygen*

With the exception of the initial pressure conditions of 100 kPa and 40 kPa, the larger the initial pressure, the larger the pressure rise range and the longer the time to reach the maximum pressure. The reason for the larger pressure rise at higher pressures is thought to be that the concentration of active molecules before ignition increases in proportion to the initial pressure, as described above. The fact that the maximum pressure is reached in about 200 ms at 100 kPa is due to the fact that the chamber pressure exceeds the atmospheric pressure due to the explosion, and therefore, the maximum pressure is reached in about 200 ms. This is thought to be due to the fact that the chamber pressure exceeded the atmospheric pressure due to the explosion, and the vent on the ceiling of the vessel was released for safety reasons, allowing air to flow into the chamber.

The laminar flame speed [m/s] was calculated from the pressure history at the concentration near the lower boundary when the flame ignited under each condition. The following equation (2) is applicable to a spherically propagating flame in a quasi-spherical vessel of constant volume (Law., 2010), and was also used in this study.

$$\frac{s_b}{R} = \left[3\gamma \left(1 - \frac{\rho_{b,0}}{\rho_{u,0}} \right)^{\frac{1}{3}} \tilde{p}^{\left(1+\frac{1}{\gamma}\right)} \left(1 - \tilde{p}^{\frac{-1}{\gamma}} \right)^{\frac{2}{3}} \right]^{-1} \frac{d\tilde{p}}{dt} \tag{2}$$

where R, γ, $\rho_{b,0}$, $\rho_{u,0}$, and $\tilde{p}(=\frac{p}{p_0})$ are the vessel bottom radius, specific heat ratio, existing gas density, initial unburned gas density, and dimensionless pressure (ratio of pressure at time t to initial pressure), respectively. The predicted thermophysical properties and adiabatic laminar flame speed for each condition were calculated by Cantera (Goodwin et al., 2009). These comparisons are shown in Table 1.

Table.1. *Measured and predicted average laminar flame speed at each pressure*

Initial Pressure p_0 [kPa]	Average laminar flame speed (experiment) $\bar{s_b}$ [m/s]	Average laminar flame speed (Cantera) $\bar{s_b}$ [m/s]
10	0.385	0.0671
20	0.197	0.0364
30	0.182	0.0226
40	0.100	0.0146
50	0.132	0.00917
100	0.351	0.00283

As shown in Table 1, the combustion velocity of the hydrogen-oxygen mixture in this experimental system was about one order of magnitude greater than the value calculated by Cantera, but both qualitative trends of greater combustion velocity at lower pressures were generally consistent with previous studies (Kumar., 1985). There are two possible reasons why the experimental values were larger than the calculated values. The first is the acceleration caused by the discharge. Spherical flame propagation by spark discharge generally goes through three states: ignition affected, quasi-steady state, and chamber affected, followed by a decrease in burning speed (Kelley et al., 2009). In this experiment, since the discharge was from 100 ms to 400 ms in Figure 3, when propagation is considered to have been sustained, the state of being subject to the ignition affected was maintained, and the combustion velocity is considered to have increased by that amount. The second reason is that the flame propagation may not have been spherical. Flame propagation of hydrogen-oxygen mixtures at an ultra-dilute concentration near the LEL under atmospheric pressure is assumed to be spherical (Tarrazo et al., 2012), but under reduced pressure, the flame propagation becomes likely mushroom-shaped or flattened, which may be due to acceleration caused by instability, unlike the spherical assumption of equation (2)

2.2. Ignition experiment of hydrogen-oxygen-water vapor mixture in Wet conditions

The results of the Wet experiments are shown in Table 2, where Wet is the saturated vapor pressure at each condition and Dry is the concentration near the LEL at each temperature and pressure for ignition as a comparison. Since the saturated vapor concentration in the gas phase is strongly affected by temperature, we also attempted ignition at 80 °C and 60 kPa to confirm the temperature dependence in detail.

***Table 2**. Difference in flame spread between Dry and Wet at each initial pressure and temperature*

Initial Temperature [°C]	Initial Pressure [kPa]	Hydrogen concentration [vol%]	Water vapor concentration [vol%]	Pressure change [kPa]	Average laminar flame speed [m/s]
20	60	8.0	0(Dry)	8.63	0.0901
		8.0	3.9(Wet)	8.51	0.0753
60	40	10.0	0(Dry)	5.29	0.0706
		10.0	50(Wet)	2.73	0.0541
	60	10.0	0(Dry)	11.8	0.0812
		10.0	33.3(Wet)	8.89	0.0733
80	60	11.0	0(Dry)	6.13	0.0728
		11.0	79(Wet)	2.14	0.0654

It is known from previous studies on hydrogen-air premixed flame propagation (Katsumi et al., 2021) that the addition of water vapor reduces the flame velocity. The same tendency was confirmed for the hydrogen-oxygen mixture in this experimental system. Based on previous studies, it is also considered that water vapor has the effect of accelerating the cessation reaction from a kinetic point of view (Michael et al., 2002), and from a hydrodynamic point of view, the radiation heat loss is larger (Shimizu et al., 2011), which makes it harder to propagate and reduces the pressure increase range. Table 2 shows that ΔP is smaller in the Wet case than in the Dry case for each condition, and that the degree of decrease is also larger the greater the water vapor concentration in the gas phase. Thus, the dilution effect of water vapor addition was confirmed.

3. Conclusions

In this study, in order to investigate the effects of initial pressure, initial temperature, and water vapor on the ignition hazard of hydrogen-oxygen mixtures under pressure below atmospheric pressure by an external energy source, experiments on the lower explosive limit and flame propagation were conducted and the following results were obtained.

The LEL under negative pressure tended to be larger at lower initial pressure and higher initial temperature. This is a different trend from the existing results under positive pressure and may be due

to the difference between the visual flame spread judgment and the pressure-based judgment or may indicate a new influence of initial pressure and temperature on the LEL.

The flame spread behaviours when ignited at ultra dilute concentrations near the LEL tended to increase with decreasing pressure, which was qualitatively consistent with previous studies under positive pressure and with Cantera calculation.

In the Wet experiment, the addition of water vapor decreased the flame spread rate and tended to reduce the pressure increase range. This suggests the influence of water vapor on flame spread, which may be due to chemical kinetics and hydrodynamic factors.

These results suggest that the influence of water vapor as well as pressure and temperature should be considered when evaluating the safety of hydrogen-oxygen mixtures under negative pressure. It was also suggested that flame propagation judgments based on visual and pressure criteria may yield different results in the evaluation of these effects and should be used differently for different purposes. Future studies should include more detailed safety assessments through experiments under a wider range of conditions.

References

American Society for Testing and Materials., 2015, Standard Test Method for Concentration Limits of Flammability of Chemicals (Vapors and Gases)

Bradley, D., Hicks, R., Lawes, M., Sheppard, C, G, W., Woolley, R., 1998, The Measurement of Laminar Burning Velocities and Markstein Numbers for Iso-octane–Air and Iso-octane–n-Heptane–Air Mixtures at Elevated Temperatures and Pressures in an Explosion Bomb, Combust. Flame, 115, 126-144

Cashdollar, K, L., 2000, Flammability of methane, propane, and hydrogen gases, Journal of Loss Prevention in the Process Industries, 13, 327-340

Clusius, H, K., Gutschmidt, H.,1936, FLAMMEN VON LEICHTEM UND SCHWEREM WASSERSTOFF, Zeitschrift für Elektrochemie und angewandte physikalische Chemie, 42, 498

Coward, H, F., Cooper, C., Jacobs, J., 1914, CIV.—The ignition of some gaseous mixtures by the electric discharge**,** J. Chem. Sci, 105, 1096-1093

Drop, J., 1935, Explosion Regions At Reduced Pressure. First Communication: Pressure Limits in the System H2 - O2 - N2, Rec. trav. Chim, 54, 671-679

Goodwin, D, G., Moffat, H, K., Speth, R, L., 2009, Cantera: An object-oriented software toolkit for chemical kinetics, thermodynamics, and transport processes, Caltech, Pasadena, CA, Available at https:// zenodo.org/record/48735#.XcRdfpJKj _ 8

Jones, G, W., Hooker, A, B., Coggeshall, E, J., 1937, Behavior of flame safety lamps in mine atmospheres deficient in oxygen, U.S. Bur. Min. Rept. Invest

Katsumi, T., Yoshida, Y., Nakagawa, R., Yazawa, S., Kumada, M., Sato, D., Aung, T. T., 2021, The effects of addition of carbon dioxide and water vapor on the dynamic behavior of spherically expanding hydrogen/air premixed flames, Journal of Thermal Science and Technology, 16, 1-13

Kelley, A, P., Law, C, K., 2009, Nonlinear effects in the extraction of laminar flame speeds from expanding spherical flames, Combustion and Flame, 156, 1844-1851

Kumar, R, K., 1985, Flammability limits of hydrogen-oxygen-diluent mixtures, Journal of Fire Sciences, 3, 245-262

Law, C, K., Egolfopoulos, F, N., 1992, A unified chain-thermal theory of fundamental flammability limits, Twenty-Fourth Symposium (International) on (Combustion/The Combustion Institute), 137-14

Law, C, K., 2010, Combustion Physics, Cambridge University Press, Cambridge UK, 271

Liang, W., Law, C, K., 2018, An analysis of the explosion limits of hydrogen/oxygen mixtures with nonlinear chain reactions, Phys. Chem. Chem Phys., 20, 742-751

Nishiyama, H., Yamada, T., Nakabayashi, M., Maehara, Y., Yamaguchi, M., Kuromiya, Y., Nagatsuma, Y., Tokudome, H., Akiyama, S., Watanabe, T., Narushima, R., Okunaka, S., Shibata, N., Takata, T., Hisatomi, T., Domen, K., 2021, Photocatalytic solar hydrogen production from water on a 100-m2 scale, Nature, 598, 304-318

Nuckolls, A, H., 1920, Explosive limits of mixtures of hydrogen and oxygen under pressure, Rept. Underwriter's Labo

Qin, X., Kobayashi, H, Niioka, T., 2000, Laminar burning velocity of hydrogen–air premixed flames at elevated pressure, Experi. Therm. Fluid Sci., 21, 58-63

Rubstow, N, M., 2020, Ignition of hydrogen-oxygen and stoichiometric hydrogen-methane-oxygen mixtures on hot wires at low pressure, Mendeleev Commun, 30, 241-243

Shimizu, K., Hibi, A., Koshi, M., 2011, Updated Kinetic Mechanism for High-Pressure Hydrogen Combustion, Journal of Propulsion and Power, 27, 383-395

Tarrazo, E, F., Sanchez, A, L., Linan, A., Williams, F, A., 2012, Flammability conditions for ultra-lean hydrogen premixed combustion based on flame-ball analyses, International Journal of Hydrogen Energy, 37, 1813-1825

Zhang, K., Luo, T., Li, Y., 2022, Effect of ignition, initial pressure and temperature on the lower flammability limit of hydrogen/air mixture, International Journal of Hydrogen Energy, 47, 15107-15119

Study of the Suppression Mechanisms of Heptafluoropropane and Carbon Dioxide Mixtures on Hydrogen-air Explosions

Baisheng Nie, Mengying Zhang, Li Chang*

State Key Laboratory of Coal Mine Disaster Dynamics and Control, School of Resources and Safety Engineering, Chongqing University, Chongqing 400044, China

E-mail: lchang@cqu.edu.cn

Abstract

Hydrogen energy is widely recognized as a promising alternative to fossil fuels, while hydrogen explosions can present a considerable industrial hazard due to their low ignition energy and wide explosion limit. This study investigates the inhibition mechanisms of hydrogen-air explosion by heptafluoropropane (CF_3CHFCF_3, 0 - 6%) and CO_2 (0 - 20%) mixtures. It was observed that as the concentrations of CF_3CHFCF_3 and CO_2 increased, there were distinctive decreases in both the laminar burning velocity and pressure build-up. The suppressant mixture of 4% CF_3CHFCF_3 and 10% CO_2 resulted in a decrease of 92.88% in $(dp/dt)_{max}$ and 48.4% in P_{max} compared to the baseline case (stoichiometric H_2-air explosion). The hydrogen-air mixture became non-ignitable within 6% CF_3CHFCF_3 and 15% CO_2. Furthermore, a chemical kinetic analysis was performed, which showed that the introduction of new fundamental reactions into the hydrogen-air explosion caused the increased suppression effect. The dehydrogenation reactions (R1466, R1475) of CF_3CHFCF_3 increased significantly with the increase of CF_3CHFCF_3 concentration. The inhibition of the combustion rate by R861 was the greatest when the CF_3CHFCF_3 concentration was increased to 6%. The results of the study provide new insights into the prevention and control of hydrogen explosions, which could promote the safe use of hydrogen energy.

Keywords: *Hydrogen; Explosion suppression; CF_3CHFCF_3; Kinetic mechanism.*

Introduction

Hydrogen energy is widely regarded as a promising clean and renewable energy source, while it presents a higher explosive hazard than conventional hydrocarbons due to its low ignition energy, wide flammability range, and high combustion rate (Dutta, 2014; Faghih et al., 2016). Currently, the focus of explosion suppression for hydrogen mixtures is on inert gases, fine water mist and powder suppressants (Gong et al., 2023; Wen et al., 2019; Zhang et al., 2023). There is a growing interest in researching more economical, efficient, and environmentally friendly hydrogen explosion suppressants.

Heptafluoropropane (CF_3CHFCF_3) as a new environmentally friendly halon substitute with low ozone depletion potential, low global warming potential, low toxicity and good dispersibility, is widely used in the field of hydrocarbon fuel flare suppression (Babushok et al., 2012). Liang et al. (2024) found that the increase in the lower flammability limit of hydrogen combustion with C_3F_7H is significantly higher than with N_2 and CO_2. However, the critical inhibition concentration under lean conditions was found to be N_2>CO_2>C_3F_7H. Zhang et al. (2021) studies the suppression effects of on hydrogen/methane/air flames and observed different effects depending on the hydrogen concentration resulting in enhancement or inhibition. The study by Fan et al. (2022) on the inhibitory effects of CF_3CHFCF_3 on hydrogen explosions at different equivalence ratios showed that low concentrations of CF_3CHFCF_3 enhanced the explosion of lean hydrogen-air mixtures (Φ =0.8 and 1.0), but inhibited the explosion of rich mixtures (Φ =1.3 and 1.6).

In addition, many scholars applied numerical simulations to study the inhibition, pyrolysis, combustion mechanisms of CF_3CHFCF_3 (Duncan et al., 2010; Peterson and Francisco, 2002). Hynes et al. (1999) investigated the addition of 1.0 and 3.2 mol% CF_3CHFCF_3 to lean hydrogen flames and showed that the inhibitory effect is mainly achieved by the reaction of fluorides with H radicals to form HF and other less reactive intermediates. Mi et al. (2024) found that the chain transfer reactions R333 ($C_3F_7H \Rightarrow CF_3 + CF_3CHF$) and R343 ($C_3F_7 + O_2 \Rightarrow C_3F_7O_2$) have a significant effect on the inhibition of hydrogen-methane deflagration. The products of the pyrolysis of CF_3CHFCF_3, such as HF, CO, and CO_2, might be the main reasons for the increase of the explosion pressure in the system at later stages. Kinetic simulations by Wang et al. (2024) found that the initial consumption of H and OH radicals by CF_3CHFCF_3 was crucial in inhibiting hydrogen combustion, with subsequent processes influenced by the physical and chemical interactions of the products.

Previous research has shown that CF_3CHFCF_3 has excellent suppression performance but also pointed out the potential risk of increased explosion overpressure and pressure rise rate due to its exothermic reaction process (Shang et al., 2024, 2022; Yang et al., 2023). Some studies have shown that mixing CF_3CHFCF_3 with inert gases can enhance the inhibition on methane-air mixture, effectively reducing the explosion reaction rate and improving suppression effects (Cao et al., 2021; Li， Yiming). However, the study on the impact of CF_3CHFCF_3 and inert gas mixtures on hydrogen explosions is very limited. This study investigates the suppression effects of various concentration combinations of CF_3CHFCF_3 (0 - 6%) and CO_2 (0 - 20%) on the stoichiometric hydrogen-air mixture through experiments and simulations. The analysis of the hydrogen combustion and explosion process consider both flame propagation characteristics and explosion intensity. Theoretical studies based on CHEMKIN-PRO is conducted to understand the impact of using CF_3CHFCF_3 and CO_2 mixture suppressants on flame structure and laminar burning velocity of premixed gas flames.

1. Experimental setup

Figure 1 shows the schematic of the experimental setup. The experiment utilized a stainless-steel rectangular duct measuring 140x140x1000mm. The duct featured three evenly distributed circular observation windows, each with a diameter of 110mm, located on the side of the duct. The distance between the windows was 360mm. The ignition electrode is positioned at the center window on the left-hand side. The electrodes were triggered using an ignition control module (HY180). Ignition was initiated by a 50ms duration electric spark between the platinum electrodes. The flame propagation process was captured on a monochrome high-speed camera (Revealer X213) equipped with a Zeiss 35mm/F2.0 prime lens. The camera was set to record at a rate of 8000 frames per second (fps). The exposure was kept constant throughout the experiments for flame brightness analysis. The pressure-time curve was obtained by a high frequency pressure sensor located in the center of the rectangular pipe (ZXP660, range: 0 - 2MPa). The sampling rate of the pressure transducer was 5kHz.

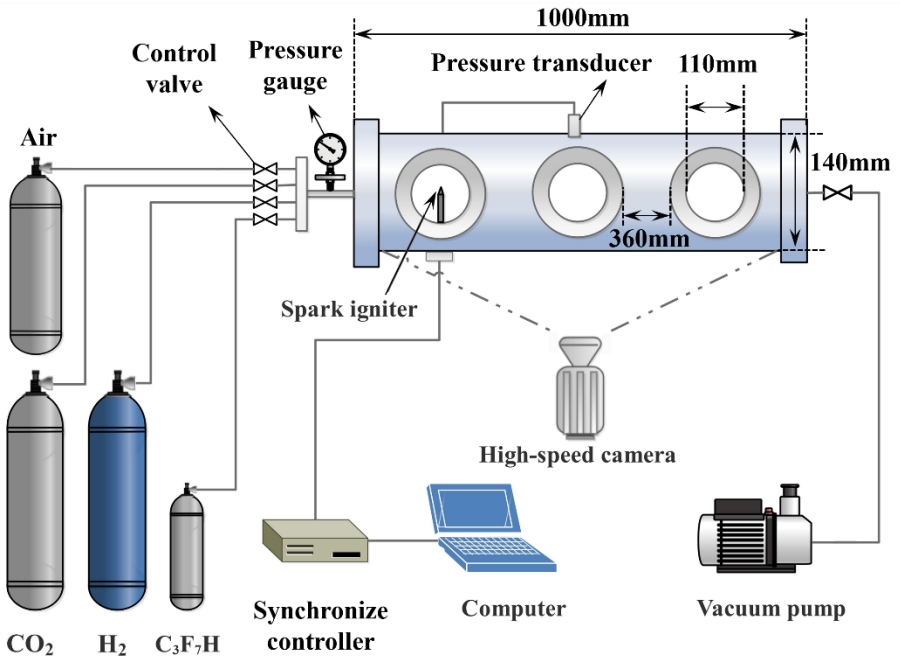

Fig. 1. *Schematic of the experimental setup.*

All experiments in this work were carried out at ambient temperature and pressure. The Dalton partial pressure method was used to configure the gas mixture. Before conducting each experiment, the vacuum pump was used to evacuate the explosion duct. Specified volume fractions of H_2 (stoichiometric H_2/air ratio), CF_3CHFCF_3 (0 - 6%) and CO_2 (0 - 20%) suppressants were sequentially added using fine-adjustable valves, followed by filling air to the ambient pressure (Fig. 1). The baseline case was a pure H_2-air mixture at stoichiometric. CF_3CHFCF_3 at volume ratios of 0, 1, 2, 4, and 6% were mixed respectively with CO_2 at volume ratios of 0, 5, 10, 15 and 20%. The equivalent ratio, Φ of H_2-air was kept constant at 1. To achieve homogeneous mixing

of the reactants, the mixture was ignited after standing for 10 minutes. The pressure transducer and high-speed camera recordings were synchronized with the electrode trigger, and the results of each experiment were stored by in the PC after ignition. Each experimental configuration was repeated three times.

2. Results and discussion

3.1 Flame behaviour

Figure 2 shows the flame evolution of the H_2-air premixed flame propagating through the three observation windows (Fig. 1) under different concentrations of suppressant mixtures. In all cases, the first two observation windows are observed in the flame structure from "spherical" to "finger-shaped" process, which matches with works by (Xiao et al., 2012). Increasing the concentration of suppressants slows down the spherical and finger-shaped flames, reducing their brightness. The time for the flame to reach the center of the observation window was 7.3ms for the baseline, and that was extended to 33.1, 13.1 and 98.8ms by using 4% CF_3CHFCF_3, 10% CO_2 and 4% CF_3CHFCF_3-10% CO_2 mixtures respectively.

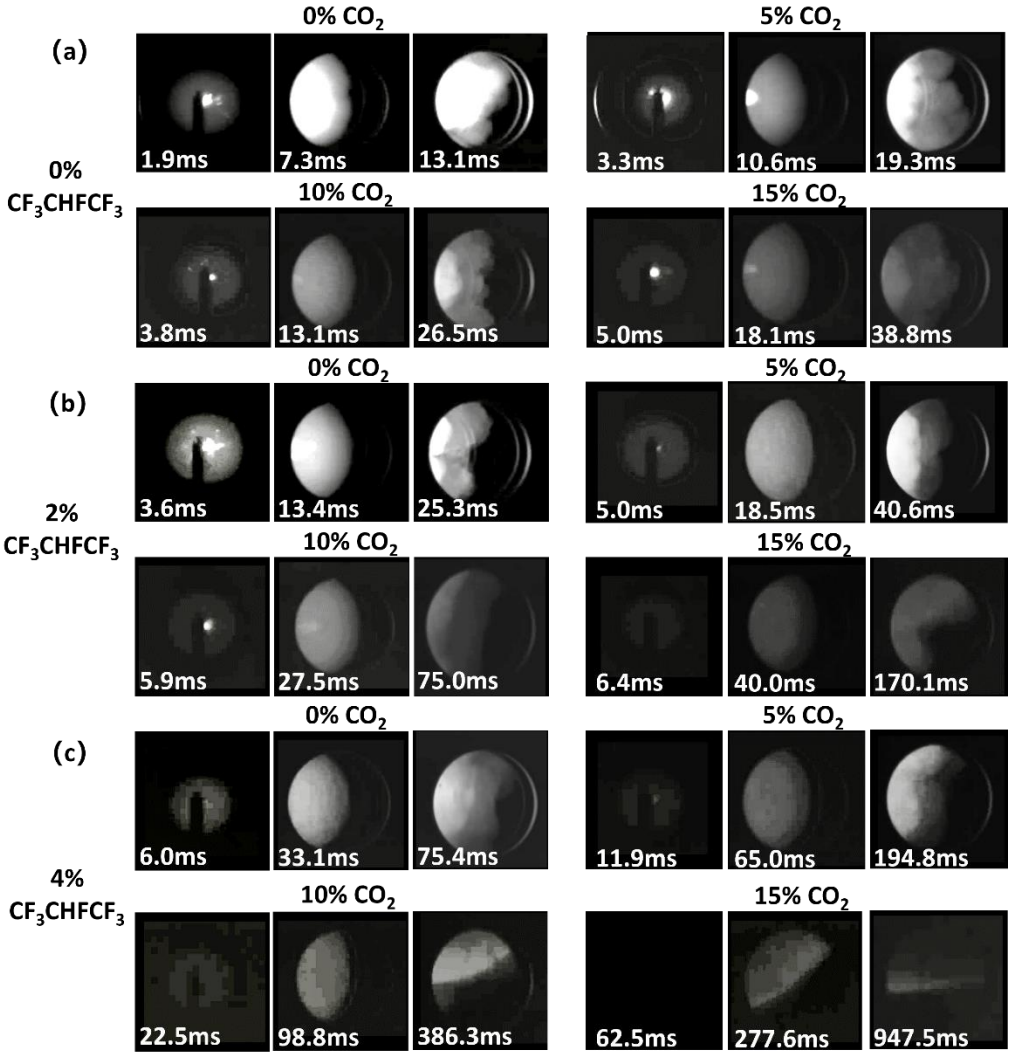

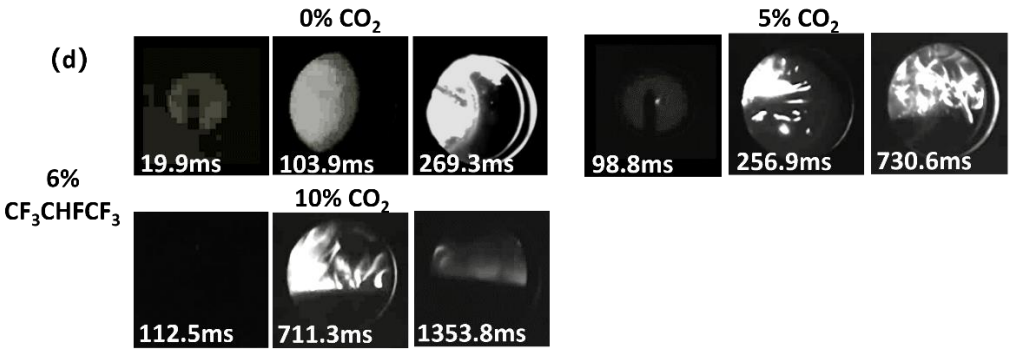

Fig. 2. *Flame Snapshots in three observation windows with CF_3CHFCF_3 and CO_2 concentrations varying from 0-6% and 0-15%. (a) 0% CF_3CHFCF_3. (b) 2% CF_3CHFCF_3. (c) 4% CF_3CHFCF_3. (d) 6% CF_3CHFCF_3.*

Furthermore, different concentrations of CF_3CHFCF_3 noticeable affected the flame shape in the third observation window. 2% CF_3CHFCF_3 concentration cases are observed with a folded flame front or tulip-shaped flame phenomenon (Fig. 1b). Whereas, at CF_3CHFCF_3=4%, 6% the flame front propagated in a near-planar shape (Fig. 1c). Meanwhile, the flame uplift and instability phenomena were observed towards the end of flame propagation. Such as the 6% CF_3CHFCF_3-10% CO_2 case, where the spherical flame exhibited an upward trend during the pre-laminar flame propagation phase. This was due to the higher density of the suppressant and the resulting buoyancy instability (Fig. 1d). As the CO_2 concentration increased to 15%, the flame extinguishing limit is reached. It should be noted that a bright spotted flame was generated at the flame front for 6% CF_3CHFCF_3 cases. This is because of the thermal decomposition of CF_3CHFCF_3 that producing fluorides, which also involves cyclization and polymerization of large molecule fluorides and results in the formation of droplets and soot (Shebeko et al., 2000; Yang et al., 2023).

3.2 Explosion pressure

Figure 3 shows the suppression effects of varying concentrations of CF_3CHFCF_3-CO_2 mixtures on the maximum explosion overpressure P_{max}, time to maximum pressure t_{max}, and maximum pressure rise rate $(dp/dt)_{max}$ of hydrogen. It was found that where was a slight upward trend (increase from 0.729MPa to 0.766MPa compared to baseline) in the P_{max} when 0 - 2% CF_3CHFCF_3 was added without CO_2, and a similar effect was observed in related studies (Gao et al., 2021; Osorio et al., 2017). This was because of the heat release during the reaction of CF_3CHFCF_3. P_{max} is significantly reduced (from 0.729MPa baseline to 0.621MPa and 0.458MPa) as the concentration of CF_3CHFCF_3 increases to 4% and 6%, the effect of free radicals consuming OH and O reactive radicals overwhelms, which caused a decrease in the heat release of the reaction (Das et al., 2024). When using CF_3CHFCF_3-CO_2 mixtures, the suppressants presented inhibitory effects on the P_{max} under all conditions, and the reach to t_{max} was prolonged (Fig. 3a). And the suppression effect was significant 2% and 4% concentrations of CF_3CHFCF_3 were mixed with CO_2. Compared to the baseline, P_{max}

decreased by only 11.7% when 10% CO_2 was used. When 4% CF_3CHFCF_3-10% CO_2 was used, P_{max} decreased by 48.4%. This is due to the trapping of radicals by fluorine-containing radicals at higher concentrations of CF_3CHFCF_3 and the dilution and cooling effect of CO_2.

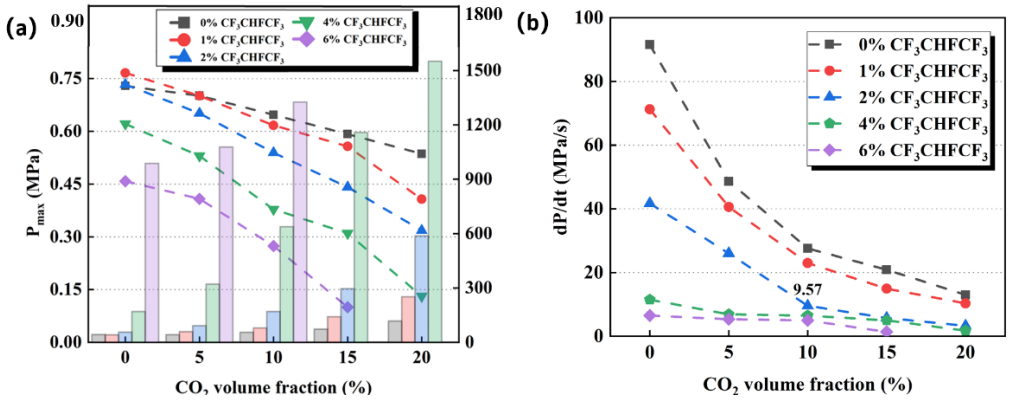

Fig. 3. *Pressures of CF_3CHFCF_3-CO_2 suppression on H_2 explosion. (a) maximum explosion overpressure and time to maximum pressure. (b) maximum pressure rise rate.*

Figure 3b shows the variation of $(dp/dt)_{max}$ under the suppression effect of different concentrations of CF_3CHFCF_3 and CO_2 mixtures. In the closed duct, the late shock wave and flame interaction lead to flame oscillation and rapid changes in the pressure rise rate. The $(dp/dt)_{max}$ of the combustion system in the pre-laminar flame stage is used to characterise the explosion intensity of the hydrogen-air-inhibitor mixture system. Compared to the P_{max} trends shown in Figure 3a, $(dp/dt)_{max}$ decreases rapidly with low concentrations of CF_3CHFCF_3. In addition, 2% CF_3CHFCF_3-10% CO_2 case has $(dp/dt)_{max}$ of 10.72MPa/s, which is a decrease of 88.29% compared to the baseline. Further increasing concentration of CF_3CHFCF_3 or CO_2 on has limited suppression effects on $(dp/dt)_{max}$, such that 2% CF_3CHFCF_3-15% CO_2 and 4% CF_3CHFCF_3-10% CO_2 conditions $(dp/dt)_{max}$ are 93.72% and 92.88% lower compared to the baseline. When the concentration of CF_3CHFCF_3 is more than 4%, the effect of adding CO_2 on $(dp/dt)_{max}$ becomes unnoticeable.

3.3 Laminar burning velocity

The spherical flame propagation method is used to calculate the experimental laminar burning velocity for flames in the pre-pressure stage of combustion (Faghih and Chen, 2016). The laminar burning velocity is approximated by the following expression,

$$S_L = \frac{\rho_b dR}{\rho_u dt}, \tag{1}$$

where R is the instantaneous flame radius, t is the time elapsed since the spark ignited. ρ_b and ρ_u are the densities of the burned and unburned gases at equilibrium respectively and are obtained using CHEMKIN-PRO. S_L is the experimental laminar

burning velocity of the mixture at the initial temperature and pressure.

PREMIX model in CHEMKIN-PRO is used to simulate the laminar burning velocity. The initial conditions were set according to the experimental conditions, considering the average transport properties of the mixture and the Soret effect (Shang et al., 2022). The computational threshold length was set to 4 cm to allow full coverage of the free-spreading flame. The integrated reaction consists of three sub-mechanisms: the hydrocarbon-air combustion dynamics mechanism USC Mech Version II from Wang et al (2007); and updated HFC mechanisms: including the NIST C_1-C_3 HFC and the William's C_3F_7H reaction mechanisms (Babushok et al., 2015; Burgess et al., 1995; Linteris et al., 2012; Williams et al., 2000).

Figure 4 shows the effects of CF_3CHFCF_3 and CO_2 on the laminar burning velocity. For 0% CF_3CHFCF_3 cases, the laminar burning velocity decreased linearly with the CO_2 concentration. For CF_3CHFCF_3-CO_2 cases, the decrease in laminar burning velocity decreases with increasing CO_2 concentration when the CF_3CHFCF_3 concentration is fixed, and this trend becomes more evident at higher CF_3CHFCF_3 concentrations. Great agreements were achieved between the results predicted by this model and the experimental measurements with R^2 of 0.98.

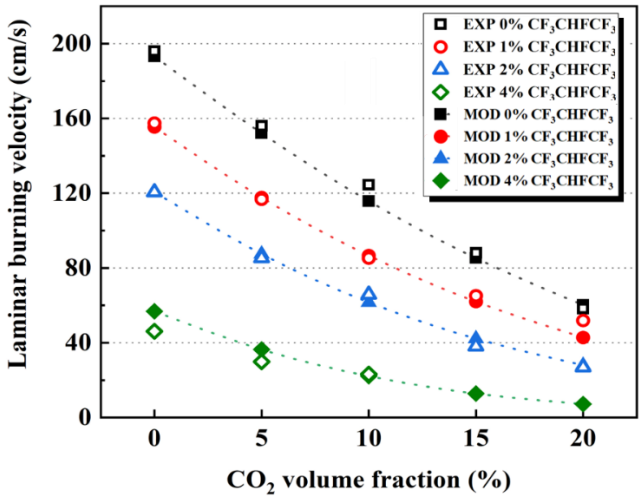

Fig. 4. *Effects of CF_3CHFCF_3 and CO_2 on the laminar burning velocity.*

3.4 Suppression mechanisms

Figure 5 shows the laminar flame structure of premixed H_2-air flame ($\Phi = 1$, T_0 =298 K, P_0 =1 bar). From the substance distribution, O_2 was more thoroughly consumed in the case of adding CF_3CHFCF_3, reflecting the influence of HFCs as an additional fuel in lean mixtures (Shebeko et al., 2000). In the 2% CF_3CHFCF_3-10% CO_2 case, the production of H_2O is higher than that of HF and is produced before HF, whereas in the 6% CF_3CHFCF_3-10% CO_2 condition, the production of H_2O is much lower than that of HF and is produced later than H_2O. In addition, as the concentration of CF_3CHFCF_3

increases to 4 and 6%, the reaction zone enlarges significantly, and the laminar burning velocity is greatly reduced. The H radicals originally involved in the formation of H_2O were transferred to HF. The formation of H_2O, the combustion product of hydrogen, was suppressed, leading to a gradual increase in the yield of the product HF. The adiabatic combustion temperature of H_2-air without the addition of the suppressant is high at 2350 K. The addition of the suppressant causes a decrease in the reaction temperature of the combustion system. In Figure 5d, e, and f, the flame temperatures can be reduced by 320 K, 480K and 640K, respectively, compared to those without suppressant, indicating that the cooperative use of CF_3CHFCF_3-CO_2 can effectively reduce the flame temperature and thus control the combustion.

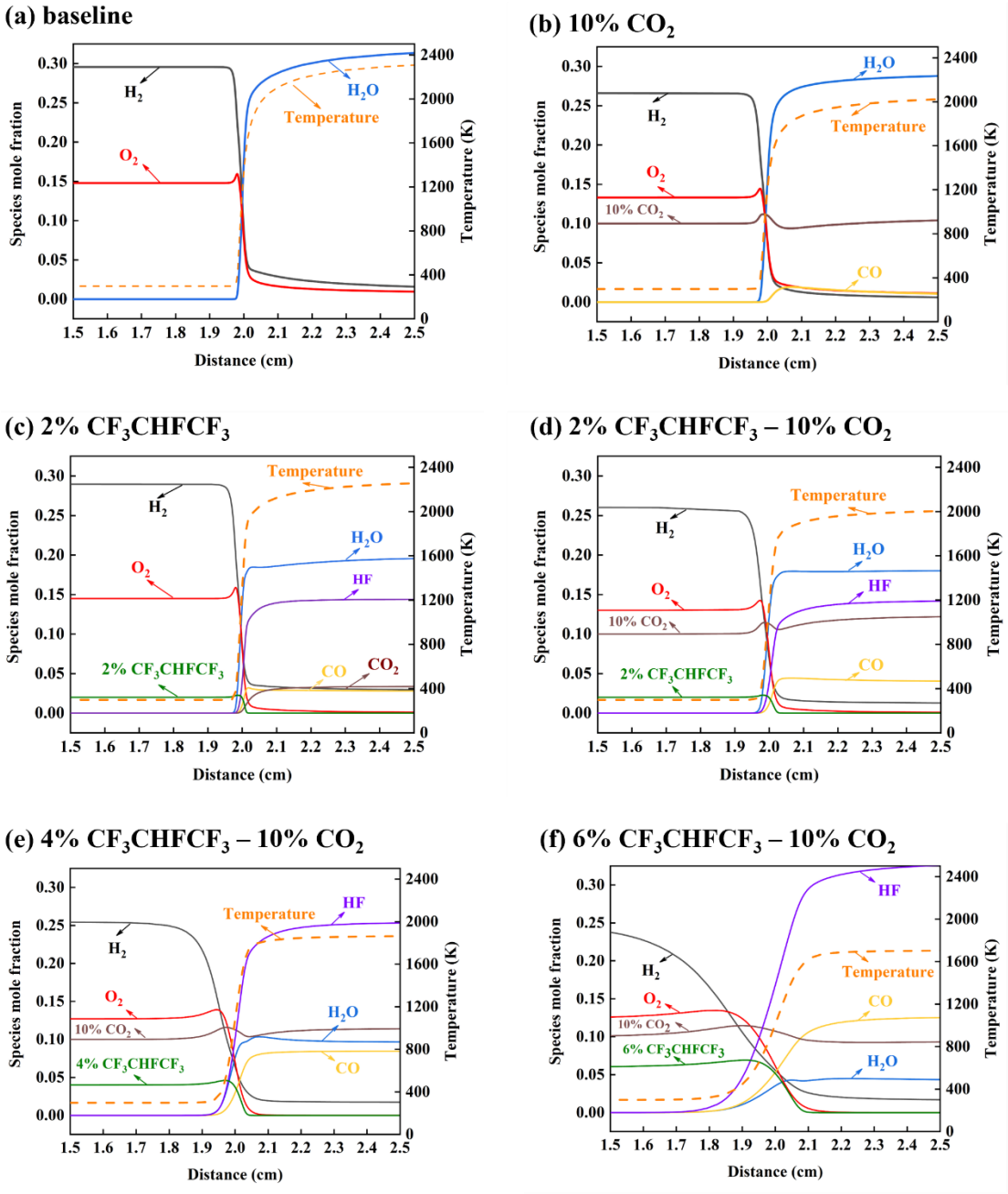

Fig. 5. *Effects of CF_3CHFCF_3 and CO_2 on the laminar flame structure.*

Figure 6 shows the sensitivity coefficients of the primary elementary reactions for the laminar burning velocity with a mixture of 10% CO_2 and 0, 2, 4, 6% CF_3CHFCF_3. Positive and negative coefficients represent enhancement and inhibition of the laminar burning velocity. Compared to the baseline, the addition of CF_3CHFCF_3-CO_2 mixture leads to new reactions that suppresses hydrogen-air explosions. Reactions R830 and R1010 show increasing inhibition with increasing HFP concentration. The dehydrogenation reactions of CF_3CHFCF_3 with O and OH to form CF_3CHFCF_3 (R1466, R1475) noticeably affect the combustion process, indicating that the addition of CF_3CHFCF_3-CO_2 mixture effectively consumes the H, O and OH active radicals. This leads to interrupting the hydrogen-oxygen chain reaction and reducing the reaction activity, and finally causing decrease of the laminar burning speed. In addition, the sensitivity coefficient of R937 is negative when the CF_3CHFCF_3 concentration is below 6% and turns positive when it is above 6%. The negative sensitivity coefficient of R861 increases rapidly at 6% CF_3CHFCF_3, showing the most effective concentration in reducing the risk of combustion explosion in the system (Li et al., 2019).

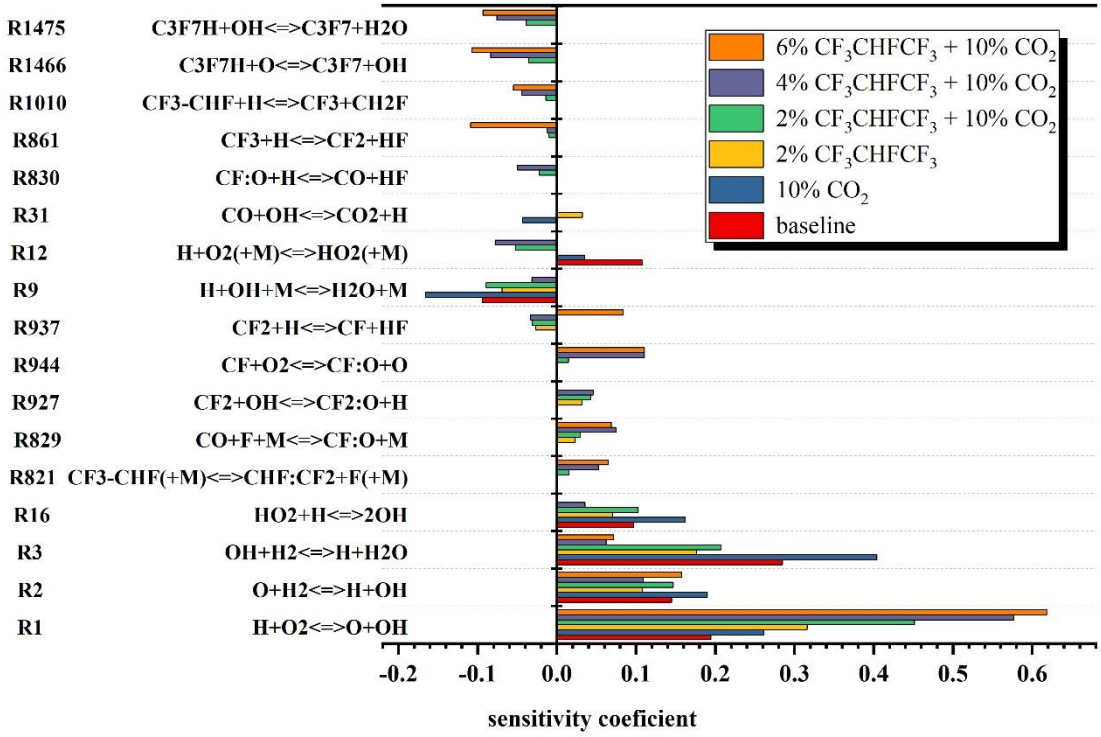

Fig. 6. *Effects of CF_3CHFCF_3 and CO_2 on sensitivity coefficient of hydrogen-air mixtures.*

Furthermore, when CF_3CHFCF_3 and CO_2 mixture are used, the chemical inhibition effect of CO_2 became less apparent. In previously work (Li et al., 2018), it was found that CO_2 was able to suppress the exothermic reaction by competing for the H radical through the reaction (CO + OH ↔ CO_2 + H), which reduced the laminar burning velocity of the flame. This is confirmed by the negative sensitivity coefficient in R31 of 10% CO_2 case (Fig. 6). However, when 2% CF_3CHFCF_3 is used, the chemical conversion of CO_2 is increased thereby facilitating the reaction. In CF_3CHFCF_3-CO2

mixture cases, the sensitivity coefficient becomes ineligible, which means the unwanted reaction enhancement by CF_3CHFCF_3 is effectively seized by the addition of CO_2. On the other hand, CO_2 absorbs the heat released by the combustion thus reducing the system temperature and performs as a dilutant that reducing the collision probability of the reactant molecules. Moreover, CO_2 undergoes ternary collision reactions (e.g. R9, R12) with high energy radicals such as H, OH, turning active radicals into stabilized molecules, by which the reaction rate decreases.

3. Conclusions

This paper studies the effects of CF_3CHFCF_3 and CO_2 mixtures in varying concentrations on the H_2-air explosion at the equivalence ratio and investigates the relating chemical kinetic mechanisms. The gas mixture presents noticeable suppression performance reducing the explosion pressure and the flame propagation speed. The additional CO_2 mixed with low concentration CF_3CHFCF_3 ($<4\%$) counteracted the exotherm reaction of CF_3CHFCF_3, achieving the decrease of P_{max} and $(dP/dt)_{max}$ up to 48.4% and 93.72% respectively compared to the baseline. A mixture of 6% CF_3CHFCF_3-15% CO_2 reached the quench limit of premixed gases at stoichiometric ratio. Furthermore, CF_3CHFCF_3- CO_2 mixture was found to present both physical and chemical suppression effects on H_2-air explosion, mainly because of CF_3CHFCF_3 consuming reactive radicals, cutting off the hydrogen-oxygen chain reactions. The concentration of CF_3CHFCF_3 has a significant effect on the reaction rate when combined suppressants are used. Dehydrogenation of CF_3CHFCF_3 (R1466, R1475) and defluorination of CF_3 become more important to reduce the combustion rate at higher CF_3CHFCF_3 concentrations. In low CF_3CHFCF_3 concentrations, the mixing of CO_2 effectively reduces the sensitivity coefficient of R31. In addition, it enhances the heat absorption and dilution effects, and acts as a third body in the chain reaction (R9, R12), suppressing the reaction rate and thus reducing the explosion intensity.

Acknowledgements

The authors gratefully acknowledge the financial contribution from the National Natural Science Foundation of China (Grant No. 52204205), Chongqing Overseas Scholar Entrepreneurship and Innovation Support Program (Grant No. cx2022037), Chongqing Technology Innovation and Application Development Specialized Key Projects (Grant No. CSTB2023TIAD-KPX0089).

References

Babushok, V.I., Linteris, G.T., Burgess, D.R., Baker, P.T., 2015. Hydrocarbon flame inhibition by C3H2F3Br (2-BTP). Combust. Flame 162, 1104–1112.

Babushok, V.I., Linteris, G.T., Meier, O.C., 2012. Combustion properties of halogenated fire suppressants. Combust. Flame 159, 3569–3575.

Burgess, D.R., Zachariah, M.R., Tsang, W., Westmoreland, P.R., 1995.

Thermochemical and chemical kinetic data for fluorinated hydrocarbons. Prog. Energy Combust. Sci. 21, 453–529.

Cao, X., Lu, Y., Jiang, J., Wang, Z., Wei, H., Li, Yiming, Li, Yongjun, Lin, C., 2021. Experimental study on explosion inhibition by heptafluoropropane and its synergy with inert gas. J. Loss Prev. Process Ind. 71, 104440.

Das, S.K., Swami, V. V., Joshi, G.N., Kulkarni, P.S., 2024. Inhibition of hydrogen-air mixtures by using chemical vapor additives. J. Loss Prev. Process Ind. 87, 105225.

Duncan, J.R., Roach, M.S., Stiles, B.S., Holmes, B.E., 2010. Unimolecular rate constant and threshold energy for the HF elimination from chemically activated CF3CHFCF3. J. Phys. Chem. A 114, 6996–7002.

Dutta, S., 2014. A review on production, storage of hydrogen and its utilization as an energy resource. J. Ind. Eng. Chem. 20, 1148–1156.

Faghih, M., Chen, Z., 2016. The constant-volume propagating spherical flame method for laminar flame speed measurement. Sci. Bull. 61, 1296–1310.

Faghih, M., Gou, X., Chen, Z., 2016. The explosion characteristics of methane, hydrogen and their mixtures: A computational study. J. Loss Prev. Process Ind. 40, 131–138.

Fan, R., Wang, Z., Guo, W., Lu, Y., 2022. Experimental and theoretical study on the suppression effect of CF3CHFCF3 (FM-200) on hydrogen-air explosion. Int. J. Hydrogen Energy 47, 13191–13198.

Gao, M., Bi, M., Ye, L., Li, Y., Jiang, H., Yang, M., Yan, C., Gao, W., 2021. Suppression of hydrogen-air explosions by hydrofluorocarbons. Process Saf. Environ. Prot. 145, 378–387.

Gong, H., Guan, W., Dong, C., Ren, C., 2023. Analysis of research trends on hydrogen explosion by bibliometric approach. Environ. Sci. Pollut. Res. 30, 102653–102672.

Hai Wang, Xiaoqing You, Ameya V. Joshi, Scott G. Davis, Alexander Laskin, Fokion Egolfopoulos & Chung K. Law, USC Mech Version II. High-Temperature Combustion Reaction Model of H2/CO/C1-C4 Compounds. http://ignis.usc.edu/USC_Mech_II.htm, May 2007.

Hynes, R.G., Mackie, J.C., Masri, A.R., 1999. Shock-tube study of the pyrolysis of the halon replacement molecule CF3CHFCF3. J. Phys. Chem. A 103, 54–61.

Li，Yiming. Experimental study of suppressing the methane/air explosion by heptafluoropropane. Dalian University of Technology.

Li, G., Zhou, M., Zhang, Z., Liang, J., Ding, H., 2018. Experimental and kinetic studies of the effect of CO2 dilution on laminar premixed n-heptane/air flames. Fuel 227, 355–366.

Li, Y., Bi, M., Yan, C., Liu, Q., Zhou, Y., Gao, W., 2019. Inerting effect of carbon dioxide on confined hydrogen explosion. Int. J. Hydrogen Energy 44, 22620–

22631.

Liang, H., Wang, T., Luo, Z., Yu, J., Yi, W., Cheng, F., Zhao, J., Yan, X., Deng, J., Shi, J., 2024. Investigation on the lower flammability limit and critical inhibition concentration of hydrogen under the influence of inhibitors. Fuel 356, 129595.

Linteris, G.T., Burgess, D.R., Takahashi, F., Katta, V.R., Chelliah, H.K., Meier, O., 2012. Stirred reactor calculations to understand unwanted combustion enhancement by potential halon replacements. Combust. Flame 159, 1016–1025.

Mi, H., Shao, P., Luo, N., Wang, S., Wang, Y., Jiang, X., Wang, W., Duan, Y., Shu, C.M., 2024. Determination of CF3CHFCF3 suppression effects on premixed hydrogen-methane deflagration via experiment and simulation. Fuel 358, 130190.

Osorio, C., Morones, A., Hargis, J.W., Petersen, E.L., Mannan, M.S., 2017. Effect of C2HF5 and C3HF7 on methane and propane ignition and laminar flame speed: Experimental and numerical evaluation. J. Loss Prev. Process Ind. 48, 21–31.

Peterson, S.D., Francisco, J.S., 2002. Theoretical study of the thermal decomposition pathways of 2-H heptafluoropropane. J. Phys. Chem. A 106, 3106–3113.

Sazali, N., 2020. Emerging technologies by hydrogen: A review. Int. J. Hydrogen Energy 45, 18753–18771.

Shang, S., Bi, M., Gao, W., 2024. Investigation on synergistic suppression of hydrogen explosion behaviors by ethylene and carbon dioxide. J. Loss Prev. Process Ind. 87, 105214.

Shang, S., Bi, M., Zhang, Z., Li, Y., Gao, Z., Zhang, C., Li, X., Zhang, K., Gao, W., 2022. Synergistic effects of isobutene and carbon dioxide on suppressing hydrogen-air explosions. Int. J. Hydrogen Energy 47, 25433–25442.

Shebeko, Y.N., Azatyan, V. V., Bolodian, I.A., Navzenya, V.Y., Kopylov, S.N., Shebeko, D.Y., Zamishevski, E.D., 2000. The influence of fluorinated hydrocarbons on the combustion of gaseous mixtures in a closed vessel. Combust. Flame 121, 542–547.

Wang, F., Ye, L., Zhang, L., Bi, Y., Cong, H., Gao, W., Bi, M., 2024. A kinetic study of the inhibition mechanism of HFC-227ea on hydrogen combustion. Combust. Flame 260, 113262.

Wen, X., Wang, M., Su, T., Zhang, S., Pan, R., Ji, W., 2019. Suppression effects of ultrafine water mist on hydrogen/methane mixture explosion in an obstructed chamber. Int. J. Hydrogen Energy 44, 32332–32342.

Williams, B.A., L'Espérance, D.M., Fleming, J.W., 2000. Intermediate species profiles in low-pressure methane/oxygen flames inhibited by 2-H heptafluoropropane: Comparison of experimental data with kinetic modeling. Combust. Flame 120, 160–172.

Xiao, H., Makarov, D., Sun, J., Molkov, V., 2012. Experimental and numerical investigation of premixed flame propagation with distorted tulip shape in a

closed duct. Combust. Flame 159, 1523–1538.

Yang, K., Chen, S., Ji, H., Xing, Z., Hao, Y., Zheng, K., Jiang, J., 2023. Experimental study on the coupling effect of heptafluoropropane and obstacles with different slits on the methane-air explosion. Energy 269, 126798.

Zhang, Siyu, Wen, X., Guo, Z., Zhang, Sumei, Ji, W., 2023. Effect of N2 and CO2 on explosion behavior of hydrogen-air mixtures in non-premixed state. Fire Saf. J. 138, 103790.

Zhang, X., Yang, Z., Huang, X., Wang, X., Pan, Y., Zhou, X., 2021. Combustion enhancement and inhibition of hydrogen-doped methane flame by HFC-227ea. Int. J. Hydrogen Energy 46, 21704–21714.

Pressure Dynamics from Head-on Reflections of High-Speed Combustion Waves: from Fast Flames to Detonations

Hongxia Yang[a], Willstrong Rakotoarison[a] & Matei Radulescu[a]

[a] University of Ottawa, Ottawa, Canada

E-mail: *hyang6@uottawa.ca*

Abstract

We systematically investigated the reflected pressures and time-resolved impulses of a range of combustion waves, spanning from fast flames to detonations, through a comprehensive suite of experiments and simulations. The experiments were performed in a shock tube using an H_2/O_2 mixture. High-speed schlieren visualization and pressure measurements, revealed that the highest impulses were achieved with reflected fast flames when DDT (Deflagration to Detonation Transition) occurred in the shock-compressed gases within the detonation initiation timescale. They were followed, in order of importance, by the reflected pressure generated by quasi-detonations/detonations and fast flames with no ignition. The one-dimensional reactive Euler equations with a simplified two-step combustion model, were adopted to simulate the reflection of high-speed combustion waves at different states: choked flame, super fast flame and unsupported CJ (Chapman-Jouguet) detonation waves in a fixed channel. The simulation results show that the peak pressure in order of sequence depends on the incoming shock speed. Within reaction timescales, the largest impulse is caused by the super fast flame reflection. While at timescales greater than 0.1 times the initial acoustic timescale, the large pressure and impulse are attributed to the unsupported detonation reflection.

Keywords: head-on reflection, fast flame, detonation, pressure dynamics, 2-step combustion model

1 Introduction

The reflected pressure and impulse generated by high-speed combustion waves interacting normal to a wall are of importance in various applications such as internal combustion engines, explosion safety, and propulsion. Depending on the mixture sensitivity, there is a continuous spectrum of wave speeds of high-speed deflagrations (or fast flames), quasi-detonations, and detonations, ranging from close to the sound speed of the combustion product to the CJ detonation speed. The overpressures generated by these waves range from 10 to 35 times the initial pressure. Previous studies have suggested that DDT events may generate larger loadings than propagating detonations or deflagrations, as established anecdotally by many groups (e.g., Liang and Shepherd (2007)). Additionally, the possibility of DDT in the pre-compressed gas (Rakotoarison et al. (2019, 2020), Oran and Gamezo (2007)) from reflections of high speed deflagrations can result in even higher pressures on the timescale of autoignition (Studer et al. (2022)). However, it's important to note that the level of overpressure and impulse is not solely determined by the characteristics of the combustion wave itself. Rather, it also depends significantly on the timescale of the interaction between the combustion wave and the end wall. This underscores the necessity of evaluating pressure and impulse across various timescales to ensure the safe design of explosion-proof walls.

The present study presents a comprehensive suite of experiments and simulations to establish the mechanisms and conditions controlling the reflected pressures and time resolved impulse of reflected combustion waves ranging from fast flames to detonation waves. Four distinct sets of experiments with simultaneous visualization and pressure measurements are performed in a lean H_2/O_2 mixture. The time histories of pressure and impulse resulting from reflected detonations are compared with those of attenuated detonations obtained by initially passing the detonation through a diverging sec-

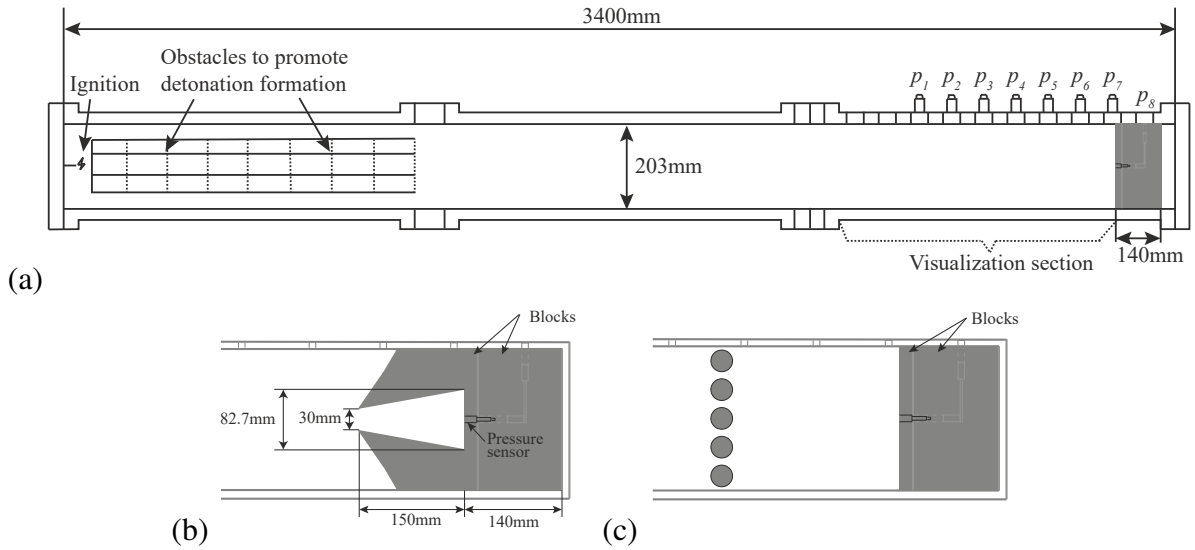

Fig. 1*: Schematic of the experimental setup: (a) the smooth shock tube configuration, (b) the diverging ramps in the test section and (c) the obstacles with a blockage ratio of 75% and a distance of 250 mm or 500 mm from the center to the end wall.*

tion, which serves to attenuate the lead shock and further decouple the reaction zone (Xiao and Radulescu (2020), Khasainov et al. (2005)). High speed deflagrations are generated by guiding a detonation wave through a column of cylinders, generating a decoupled shock-flame complex following the methodology outlined in previous works (Rakotoarison et al. (2019, 2020), Saif et al. (2017)). The strength and separation distance between the flame and shock are regulated by controlling the distance over which they propagate.

One-dimensional (1D) Euler simulations with a simplified two-step combustion model have been conducted to investigate choked flame, super fast flame, and unsupported detonation wave reflection within a fixed channel. The different wave speeds represent gases with different reactivities. The high-speed deflagration waves were represented by a 1D shock followed by a reaction front in the model. In the case of the choked flame configuration, the flame was characterized as a discontinuity, corresponding to a CJ deflagration, with the particle velocity set to zero to meet the end wall boundary condition. The super fast flame was defined to have a precursor shock propagating at a higher speed than the choked flame, followed by a CJ deflagration. An expansion wave was introduced between the end wall and the CJ deflagration to satisfy the boundary condition. The unsupported detonation wave was modeled by a ZND profile followed by a Taylor expansion wave, which was controlled by the channel configuration. These simulations serve to elucidate the dynamics of the pressure and impulse under wave reflection across different timescales.

2 Experimental details

The experiments were conducted in a shock tube with dimensions of 3400 mm $\times$ 19.1 mm $\times$ 203.2 mm, as shown in figure 1. The mixture of H_2/O_2 at an equivalence ratio of 0.5 was ignited by capacitor discharge. Mesh wires were inserted in the initiation section to promote the formation of detonations. Eight high frequency piezoelectric PCB pressure sensors were mounted flush on the top wall (p1-p7) and the end wall (p8) of the shock tube to collect pressure signals. The pressure signals were sampled at a rate of 1.538 MHz, and low-pass filtered at 100 kHz. Three different configurations were adopted in the test section: the smooth shock tube, the diverging channel and the shock tube with a column of equally spaced obstacles. The latter two geometries serve to decouple or attenuate the detonation to a fast flame of interest. The diverging channel was formed by a pair of smooth ramps. The entrance of the channel was chosen to be of the same order as the detonation cell size, the area increase to 2.8 times the initial value over a distance of 5 times the entrance. The column of equally spaced obstacles

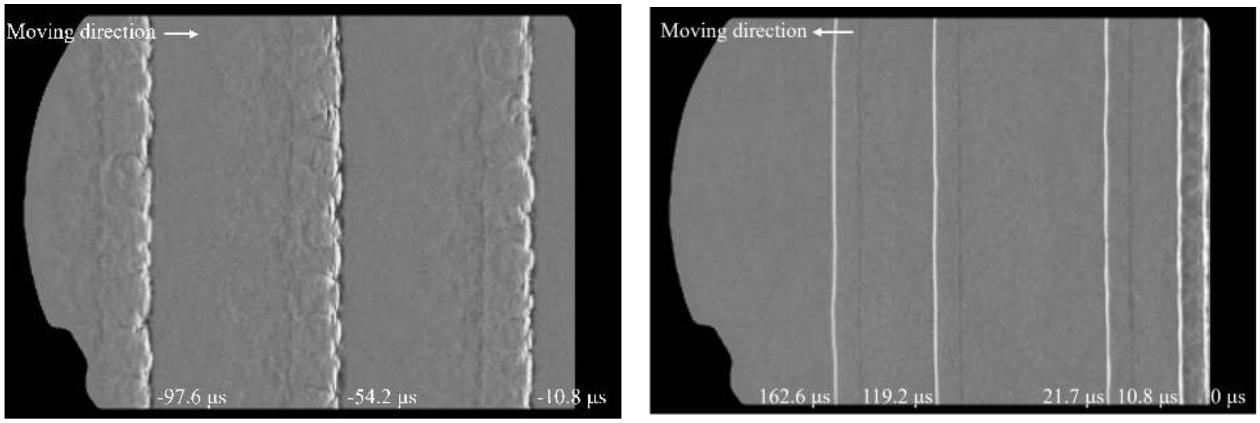

(a) Before reflection *(b) After reflection*

***Fig. 2**: Schlieren image sequence of detonation propagation and reflection from the end wall.*

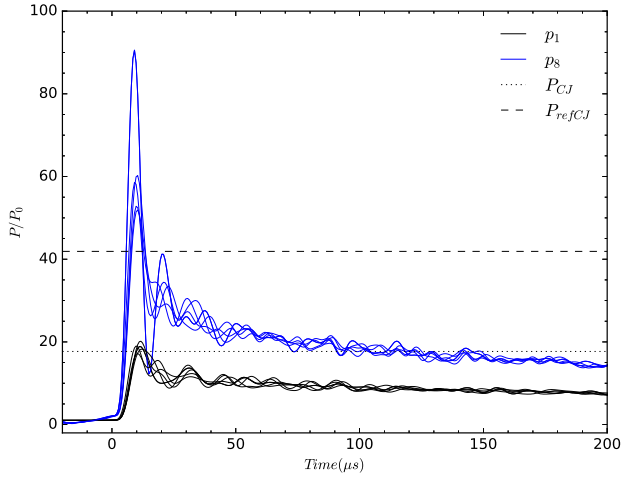

***Fig. 3**: Pressure profiles recorded at p1 and p8 locations for all 5 detonation tests.*

has a blockage ratio of 75% and was placed at a distance of 250 mm or 500 mm from the end wall. At least five repeated experiments were performed for each configuration.

For each experiment, the shock tube was evacuated to a pressure less than 80 Pa. Then, the mixture was filled into the shock tube. The gases were prepared in mixing tanks by the method of partial pressure and were left to mix for more than 24 hours. The initial pressure of the test mixtures was kept constant at 8.9 kPa for all tests, unless otherwise mentioned. The ambient temperature was 294 K. A pair of glass windows was installed at the test section in order to visualize the phenomenon using the Z-type Schlieren system with a field of view of 317.5 mm in diameter. The image sequence was recorded using a high-speed camera (Phantom v1210). The frame rate was 77481 to 92,219 frames per second (fps) with a resolution of 384 $\times$ 240, and the exposure time was set to 0.468 μs.

3 Experimental Results

3.1 Detonation reflection in a smooth channel

Figure 2 shows an example of the detailed evolution of the detonation reflection in the smooth channel. The detonation propagates from left to right with approximately 10 cells, corresponding to a cell size of 20 mm. The local speed of the detonation wave varies within 5% of D_{CJ}, indicating the state of the detonation wave is close to the ideal state and the loss to the channel wall is negligible. As shown in Fig. 3, the peak pressure of the incident detonation is close to the CJ detonation pressure (P_{CJ}), which

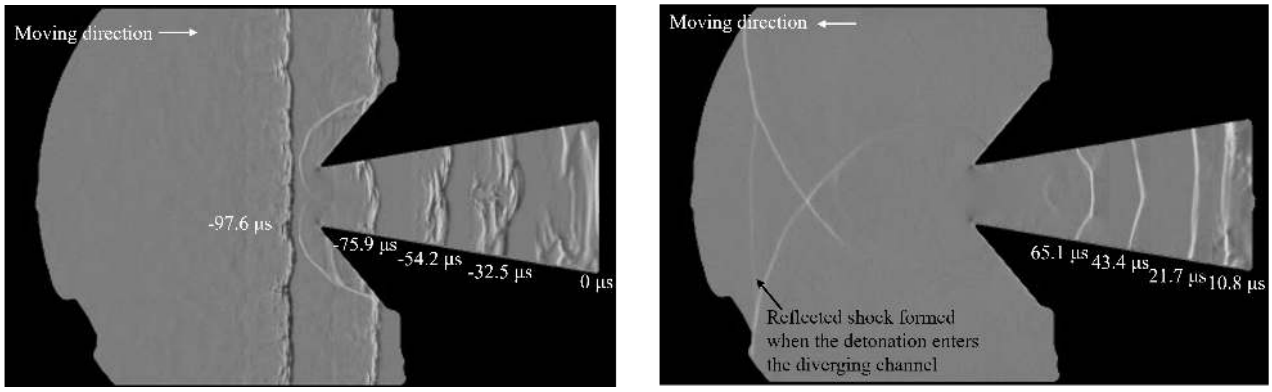

(a) Before reflection *(b) After reflection*

***Fig. 4**: Schlieren image sequence of quasi-detonation propagation and reflection from the end wall in the diverging channel.*

is evaluated using the SDToolbox (Lawson and Shepherd (2019)) with the San Diego thermodynamic database UCSD (2016). A clear oscillation in pressure profile is observed in the products, which matches closely the spacing between transverse waves divided by the sound speed in the products. The pressure traces also indicate a slowly decaying signal, due to the loss to the channel wall and the Taylor wave trailing the detonation wave.

Upon reaching the end wall, the detonation immediately burned out all the reactive mixture within in one frame and reflected as an inert shock propagating backwards to the left. The peak pressure at the end wall is about 20% to 115% larger than reflected pressure for detonation at CJ state (P_{refCJ}), which is caused by the immediate burning of the reactant upon reflection. The stochasticity in peak pressure is associated with the sample rate of the pressure signals as compared to the reaction time of the gas behind the reflected shock, as well as the detonation cellular structure and the proximity of the pressure sensor to the triple point collision and Mach stem formation, which generate the largest pressures. The pressure then went through two distinct decreasing stages, similar to the incident detonation pressure profile. Within 200 μs, the pressure asymptotes to below P_{CJ}.

3.2 Reflection of attenuated detonations in the diverging channel

The attenuated detonations were generated by directing the well-established detonation wave into a diverging channel formed by a pair of smooth ramps. Figure 4 illustrates the detailed detonation attenuation and reflection. The detonation wave enters the diverging channel with two triple points. As it propagates further inside the channel, the detonation decays to a quasi-detonation with a thickened front due to the channel expansion. The generation of unreacted gas pocket can also be found at the back of the detonation. The wave speed decays to approximately 1400 m/s, which is 0.63 D_{CJ}, upon reaching the end wall. The reflected shock transmits through the unburned gas and consumes all the unreacted gas within less than 21.7 μs, corresponding to the time interval between three frames of the high speed video.

Figure 7a shows the pressure profile resulting from the attenuated detonation reflection at the end wall. Despite propagating at a much lower speed, the quasi-detonation reflection generates a comparable, and possibly larger, pressure loading at the end wall. The large overpressure quickly decreases to P_{CJ} within 20 μs after reflection and remains nearly constant thereafter.

3.3 Reflection of high speed deflagrations with detonation re-initiation

Figure 5 shows the propagation and reflection of the high-speed deflagration resulting from passing a detonation through the obstacles placed 250 mm from the end wall. After traversing the obstacles,

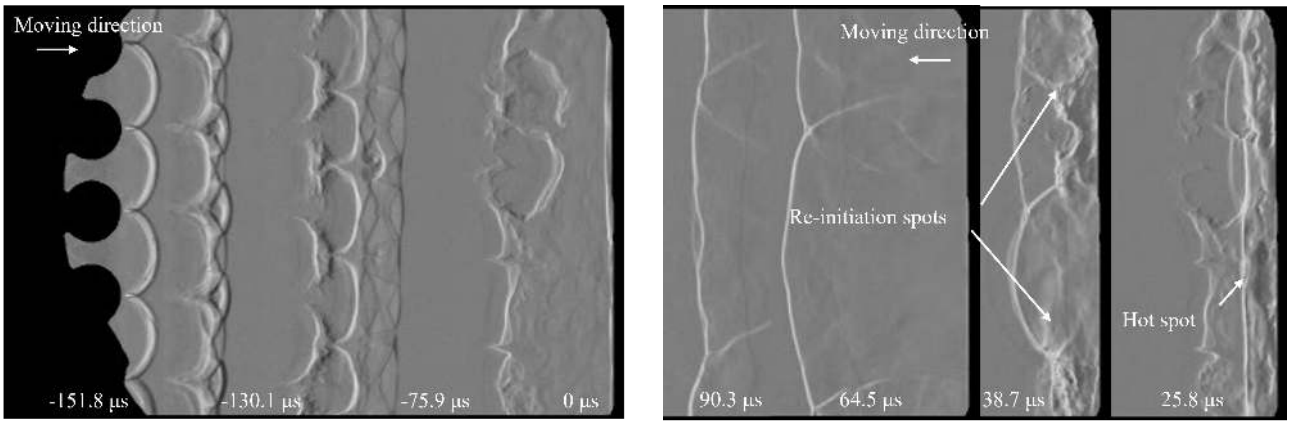

(a) Before reflection *(b) After reflection*

***Fig. 5**: Schlieren image sequence of high-speed deflagration propagation and reflection from the end wall with detonation re-initiation.*

the detonation wave front gradually thickened, forming a shock-flame complex. The speed of the fast flame continuously decreases to about 1232 m/s (0.55 D_{CJ}) when the incident shock reaches the end wall. Following the reflection of the leading shock, an auto-ignition hot spot emerges at about one-third of the channel's height from the bottom wall. At 38.5 μs, the two re-initiation spots become more evident. These re-initiated spots then burn out the reactant and propagate to the left as an inert shock. It's worth noting that the location of the re-initiation spot is random, depending on the wave structure during the reflection, and this randomness can be reflected in the pressure plot, as depicted in Fig. 7a. The time taken to reach the peak pressure in all five experiments conducted differs by 30 μs. Depending on the location of the re-initiation, the measured pressure peak can differ by about 50 times the initial pressure. Moreover, the overall peak pressure is higher than the reflection pressure caused by both the detonation and the attenuated detonation.

3.4 Reflection of high speed deflagrations with no re-initiation

Figures 6 and 7a depict the results obtained from experiments conducted in the shock tube with obstacles positioned 500 mm from the end wall. In this configuration, the distance between the leading shock and the flame is much larger than that observed in the 250 mm case, where the shock-flame complex reached the end wall. The leading shock speed decays to approximately 1050 m/s (0.47 D_{CJ}) upon reaching the end wall. Subsequently, it reflects as an inert shock and interacts with the incoming flame. This interaction results in an increase in the flame surface area, albeit without detonation re-initiation. The peak pressure at the end wall is approximately 30 times the initial pressure, and it continues to decrease as the reflected shock propagates further to the left.

3.5 Comparison of the pressure and impulse profiles for different combustion waves reflection

A summary of the pressures and average impulses for all the configurations considered is presented in Fig. 7. The impulse was calculated for each case as $I = \int_0^t (P(t) - P_0)\,\mathrm{d}t$ and then averaged over the 5 repeated experiments. The pressure and impulse increase for the direct detonation reflection and attenuated detonation reflection in the diverging channel show no significant differences within the first 20 μs, although the pressure at the end wall for the diverging channel quickly decreases to below the CJ detonation pressure, whereas the end wall pressure for the direct detonation reflection case remains larger than the CJ detonation pressure.

The pressures and impulses for the fast flame reflections remain smaller than the other cases until the detonation re-initiation occur. For the cases with successful re-initiation, the impulse is larger than

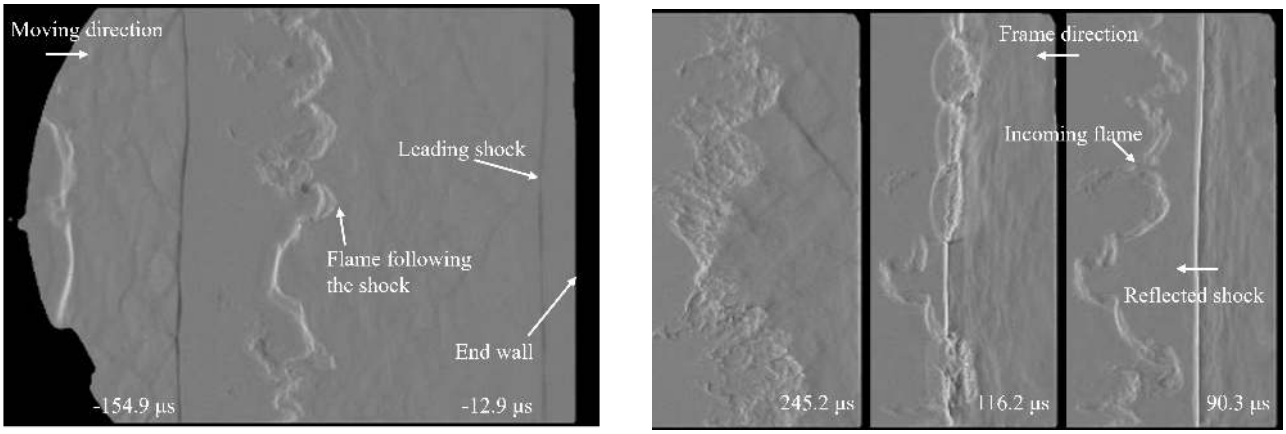

(a) Before reflection *(b) After reflection*

***Fig. 6**: Schlieren image sequence of high-speed deflagration propagation and reflection from the end wall with no re-initiation.*

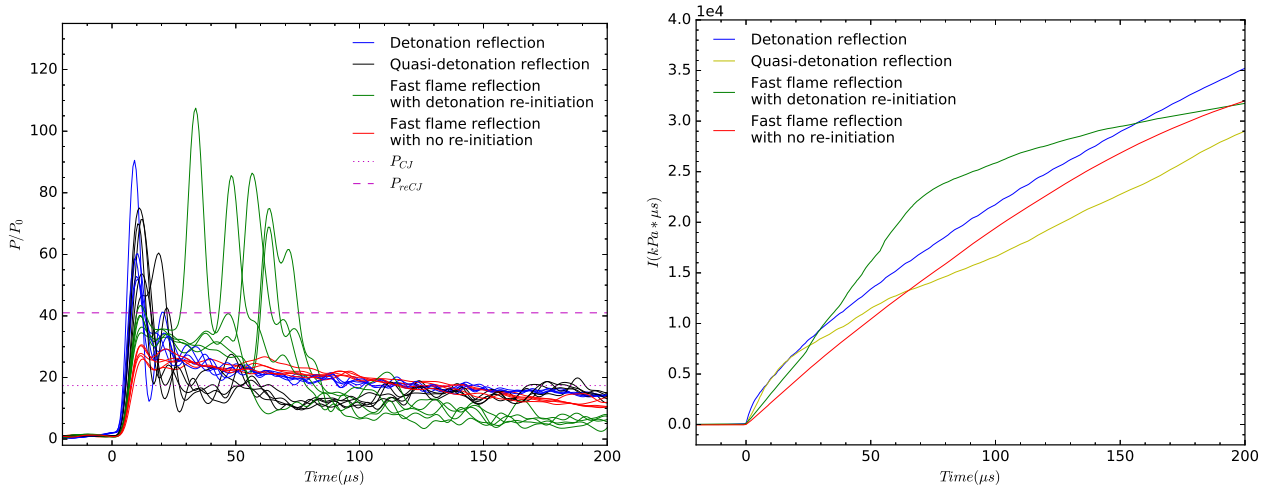

***Fig. 7**: (a) Pressure profile and (b) averaged impulses at the end wall for all combustion waves considered. Time 0 corresponds to the time when the shock reached the pressure sensor.*

for the detonation reflection in the smooth channel or attenuated detonation diverging channel. For the failed re-initiation cases, obtained with obstacles placed 500 mm from the end wall, the increase rate of the impulse is nearly constant and remains smaller than the rest. The results thus clearly show that the largest pressure and impulse are obtained for initially weaker shock flame complexes with internal DDT or strong ignition.

4 Numerical method and physical model

In experiments, the highest levels of pressure and impulses were obtained within the detonation initiation timescale. Additionally, the velocity of high-speed deflagration waves is not steady before reaching the end wall. It is thus challenging to assess the level of pressure and impulses evolution for different wave reflections at later times. To address this issue, we developed a system of 1D simulations for choked flame, super fast flame and unsupported detonation in a channel with a fixed length, as depicted in Figures 8 and 9. In these simulations, we assume uniform states across the leading shock and a constant speed of flame propagation. Furthermore, the activation energy, heat release, and specific heat ratio are held constant. The problem was addressed using the reactive Euler equations with a two-step combustion model, which allows individual control of the induction and reaction zone.

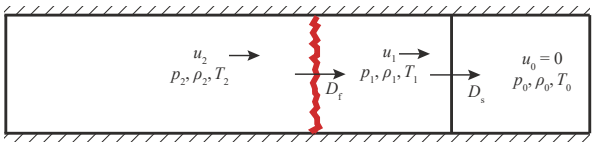

***Fig. 8**: Sketch of a propagating flame following a precursor shock in a smooth tube.*

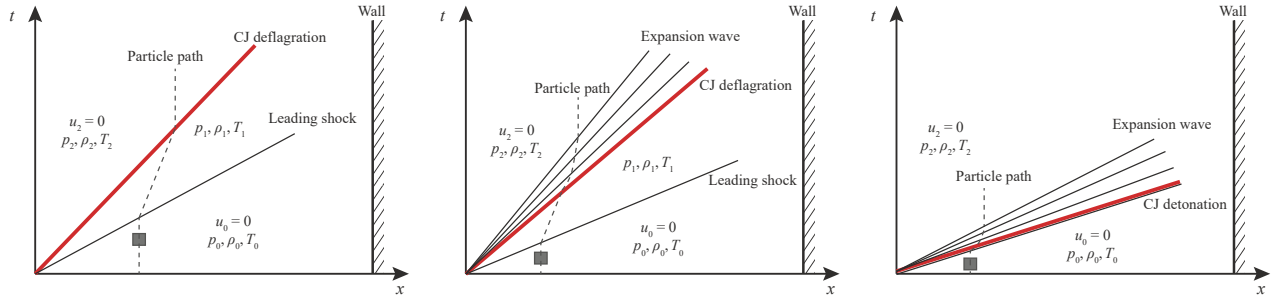

(a) Choked flame *(b) Sueper fast flame* *(c) Unsupported CJ detonation*

***Fig. 9**: Space-time diagram sketches illustrating the cases studied in the current paper.*

The 1D reactive Euler equations, specifically the equations of mass, momentum, and energy conservation in the reactive fluid, can be found in Sharpe (2002). These equations were solved using a finite-volume in-house code developed by Sam Falle at the University of Leeds, using a second-order accurate Godunov exact Riemann solver (Falle et al. (1993)) with adaptive mesh refinement. In the two-step combustion model, the transport equations of the induction and reaction variables can be written as

$$\begin{aligned} \frac{D\lambda_i}{Dt} &= [1-\mathscr{H}(\lambda_i)]k_i \exp(-\frac{Ea}{RT}), \\ \frac{D\lambda_r}{Dt} &= \mathscr{H}(\lambda_i)k_r(1-\lambda_r)^{\nu}, \end{aligned} \tag{1}$$

where ν is the reaction order, λ_i is the induction progress variable, taking a value of 0 in the reactants and 1 at the end of the induction zone; λ_r the reaction progress variable, with a value of 0 in the unburned zone and 1 in the burned products. $\mathscr{H}(\lambda_i)$ is the Heaviside function, assuming a value of 1 when $\lambda_i \geq 1$, and 0 for $\lambda_i < 1$, used to disable the progress of λ_i at the end of the induction zone. k_i and k_r are rate constants.

The input parameters for the combustion model are given in Table 1. For simplicity, they were calibrated from the detailed chemistry using the SDToolbox (Lawson and Shepherd (2019)) with the San Diego thermodynamic database UCSD (2016). γ is the post-shock specific heat ratio of the CJ detonation, while the heat release Q was determined from the perfect gas relation recovering the correct CJ detonation Mach number. The effective activation energy Ea was evaluated from the logarithmic derivative of the ignition delay with respect to the inverse of post-shock temperature. The rate constant k_i was obtained from Eq. 1 for the ignition delay time of the CJ detonation, while k_r was determined by $\frac{1}{t_r}\frac{c_p T}{Q}$, where c_p is the constant pressure heat capacity. ν was found by fitting the detailed chemistry ZND structure.

The leading shock Mach numbers and flame properties for the 3 types of combustion waves illustrated

***Table 1**: The calibrated parameters for the 2-step model from the detailed chemistry.*

γ	E_a/RT_0	Q/RT_0	k_i	k_r	ν
1.3158	25.29	20.35	133083719	1123457	1.1

***Table 2**: The calibrated non-dimensional parameters for the 2-step model from the detailed chemistry.*

	Choked flame	Super fast flame	Unsupported detonation
M_s	2.75	3.15	4.96
M_f	0.28	0.3	/

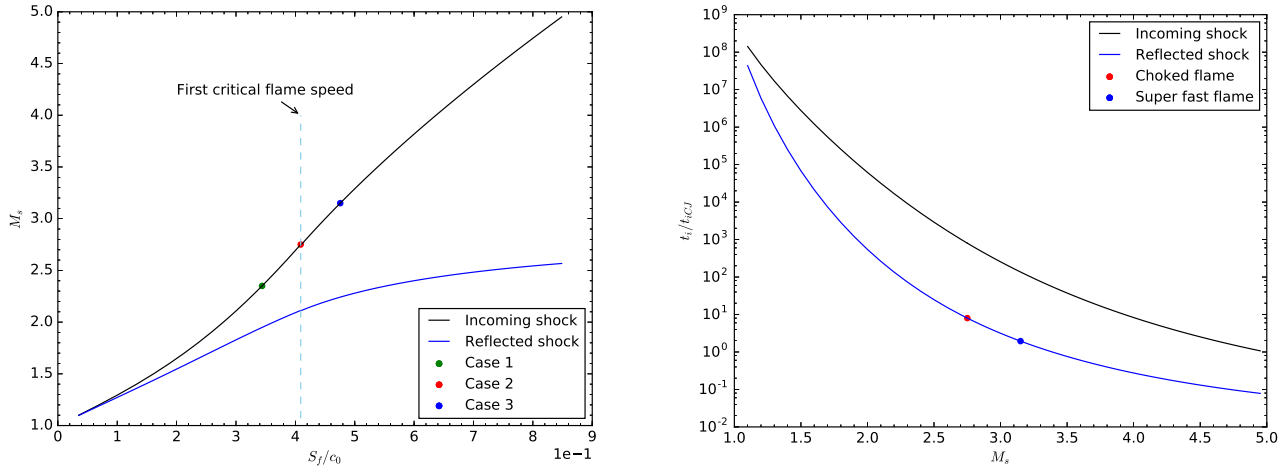

(a) *(b)*

***Fig. 10**: (a) Precursor shock speed for different values of burning velocity, (b) The ignition delay time vs. precursor shock Mach number in the current combustion model.*

in Fig. 9 are detailed in Table 2 and Fig. 10. These parameters were derived by solving the jump equations across the shock and the flame using the perfect gas relations, under the assumption that the shock-flame complex propagates in a closed channel. As shown in Fig. 10, as the flame burning velocity increases, both the precursor shock and the reflected shock Mach number rise. Consequently, the autoignition delay time for the gas at the post-shock state decreases. When the flame burning velocity increases to the first critical flame speed, the flame is at CJ deflagration state. If the flame burning velocity exceeds the first critical flame speed, it continues to be in the CJ deflagration state, which is the maximal steady speed permissible. Accordingly, an expected expansion wave forms between the reaction front and the end wall.

For simplicity, the simulations of high-speed deflagrations reflection were divided into two parts. Firstly, we started the simulation from the point where the leading shock had reflected from the end wall. In the second part, the CJ deflagration was modeled as a discontinuity to interact with the reflected shock. The distance between the flame and the leading shock depends on the wave velocity and the length of the channel. A base grid of 400 grid points per x_i, where $x_i = t_i \times \sqrt{P_{rs}/\rho_{rs}}$ with P_{rs} and ρ_{rs} representing the pressure and density at the post-reflected shock state, was utilized, along with up to 5 levels of grid refinement. For the simulation of the unsupported detonation, the ZND profile followed by a Taylor wave corresponding to the channel configuration was directly placed at the end wall. A base grid of 1/2 grid points per induction zone length, along with 5 level of grid refinement levels, were used. A fixed channel length L of 0.5 m was considered, unless otherwise specified, and a reflective boundary condition was imposed at the boundary.

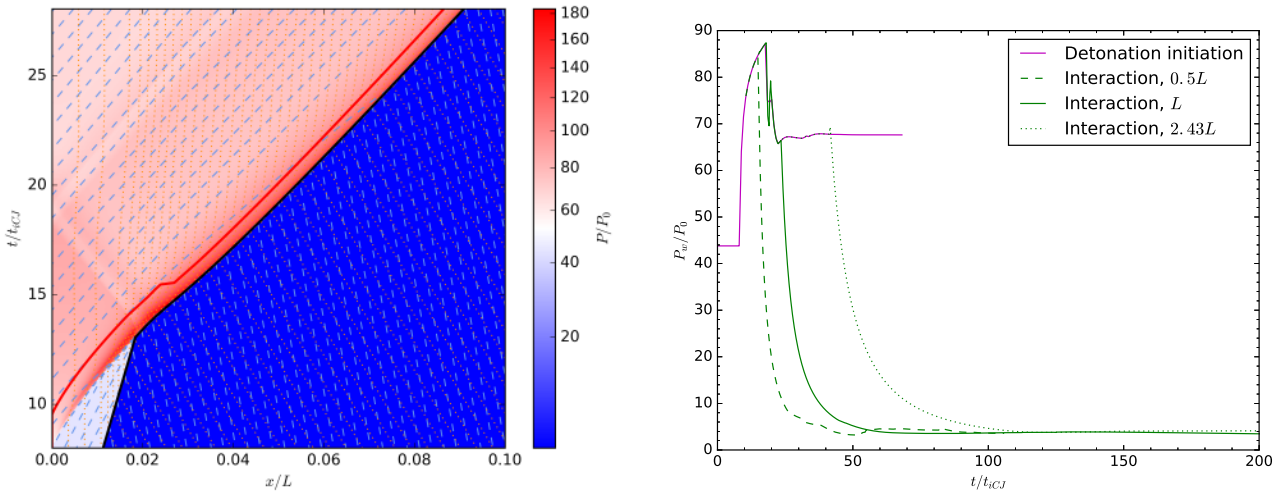

(a) *(b)*

***Fig. 11**: (a) Characteristic space-time on top of the pressure profile to illustrate the initiation induced by the shock reflection for choked flame reflection; the orange dotted lines represent the particle path; the light blue lines are the C^+ characteristics; the black line is the main shock front; the red line indicates the 99% of the consumption of reactant. (b) End-wall pressure evolution. Time 0 represents the time the shock reached the end wall.*

5 Numerical results

5.1 Reflection of choked flame with $M_s = 2.75$

5.1.1 Flow evolution during detonation initiation

The flow field evolution of the detonation initiation and the pressure at the end wall due to the leading shock reflection of the choked flame are shown in Fig. 11. The space-time diagram in Fig. 11 illustrates also the evolution of the particle paths, C^+ characteristics, the shock trajectory and the flame marked by the 99% of the consumption of reactant. The pressure at the end wall undergoes four distinct stages during the detonation initiation. The reaction starts at 8.0 t_{iCJ}, resulting in the formation of a detonation wave. As the detonation wave propagates away, a Taylor expansion fan forms between the detonation and the end wall, as evidenced by the increasing distance between the red line and the first C^+ characteristic behind it. Concurrently with detonation formation, the end wall pressure rapidly increases. The detonation wave reaches the leading shock at 13 t_{iCJ}, forming a forward-facing detonation followed by a Taylor expansion and a series of backwards-facing waves. These waves, which are similar to the waves formed during the longitudinal oscillation in a square-wave detonation (Fickett and Davis (2000)), in order of time sequence are an expansion wave resulting from the two inert shock interaction, a compression wave formed due to the shorter ignition time of the particles at the contact surface formed during the interaction of the two shocks, and lastly, an expansion wave established when the old reaction front reached the newly formed reaction zone. The backward-facing waves reach the end wall at 18 t_{iCJ}, marking the end of the increase in end wall pressure at 83 P_0. The reflection of the expansion wave leads to a sharp decrease in end-wall pressure. Subsequently, the end-wall pressure gradually increases as the compression wave reflects back from the wall. Finally, the last part of the expansion wave further lowers the end wall pressure. In the last stage, the secondarily formed detonation becomes steady, and the pressure at the end wall remains constant.

5.1.2 Flow evolution for detonation-CJ deflagration interaction

The space-time diagrams in Fig. 12 show the flow field evolution of the interaction between the initiated detonation wave with the CJ deflagration discontinuity. At 15.9 t_{iCJ}, the detonation interacts with

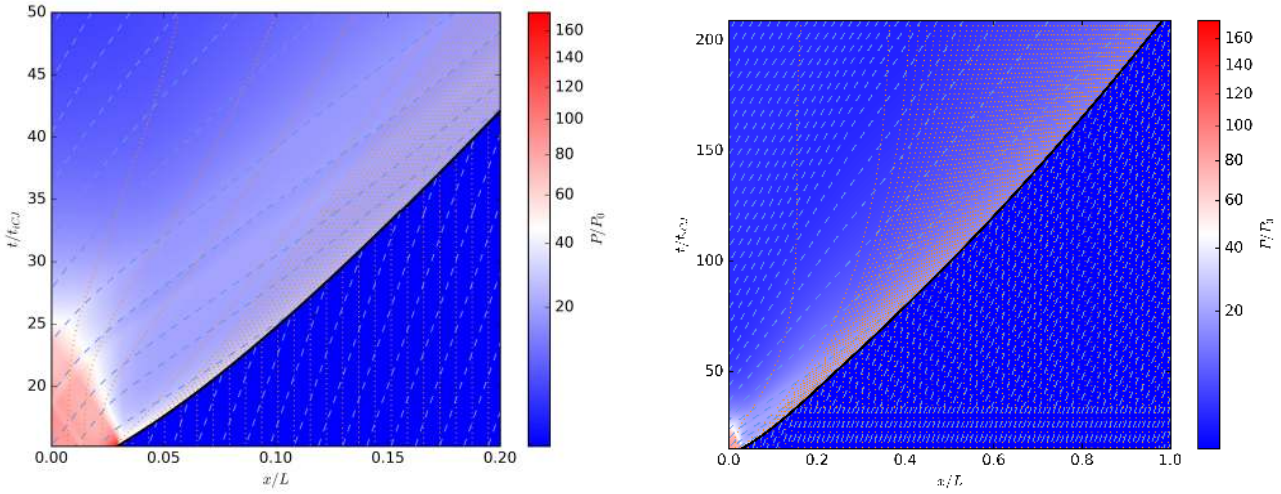

(a) (b)

***Fig. 12**: (a) Zoomed-in and (b) Overall characteristic space-time on top of the pressure profile to illustrate the flow field of the detonation-choked flame interaction.*

the flame, resulting in a transmitted shock in the burned gas, a backward-traveling expansion wave, and a contact surface in between. Subsequently, the expansion wave interacts with the end wall-reflected waves and reaches the end wall at 19 t_{iCJ}, before the series of backwards-facing waves fully reflect from the end wall. This leads to a sudden increase in the end wall pressure, as depicted in Fig. 11b. The pressure at the end wall then decreases further until the tail of the expansion waves eventually leaves the end wall at 60 t_{iCJ}, reducing the end wall pressure to 4 P_0. The reflected expansion wave then propagates to catch up with the transmitted shock.

To investigate the impact of channel length, two additional configurations were examined with lengths of 0.5 L and 2.43 L, representing the interactions of the CJ deflagration and the detonation before and after the second detonation fully develops. Fig. 11b compares the pressure profiles at the end wall for all three configurations. The peak pressure and the overall pressure evolution are similar across all three cases. However, in a longer channel, the distance between the leading shock and the flame is larger, resulting in the prolonged duration of high pressure.

5.2 Reflection of super fast flame with $M_s = 3.15$ followed by an expansion wave

The space-time diagram in Fig. 13a illustrates the flow field evolution of the detonation initiation due to the reflection of the $M_s = 3.15$ shock. The reaction starts at 3.3 t_{iCJ}, resulting in the formation of a forward facing compression wave. This compression wave heats the gas behind it and eventually forms a detonation wave at 4.2 t_{iCJ}. The initiation of the detonation generates a weak shock wave propagating backwards. During this stage, there is a sharp increase in pressure at the end wall. The weak shock reaches the end wall at 4.7 t_{iCJ} and reflects back, causing a further increase in end wall pressure to 122 P_0, as shown in Fig. 14. Subsequently, the detonation catches up with the compression wave and the reflected shock at 5.2 t_{iCJ} and 5.7 t_{iCJ}, respectively. Both interactions lead to the formation of a transmitted detonation and a series of backwards-facing waves. These backward facing waves reach the end wall at 8 t_{iCJ}, initiating a decrease in end wall pressure.

The transmitted detonation then interacts with the flame at 8.29 t_{iCJ}. The space-time diagram in Fig. 13b shows the flow field evolution of the interaction between the detonation wave and the CJ deflagration, followed by an expansion wave. This interaction results in a transmitted shock followed by an expansion wave, as well as a backward-traveling expansion wave. Subsequently, the expansion wave interacts with the end wall at 13.2 t_{iCJ} and eventually reflects back to the right at approximately 50 t_{iCJ}. The pressure at the end wall then remains constant at the same final pressure as in the choked

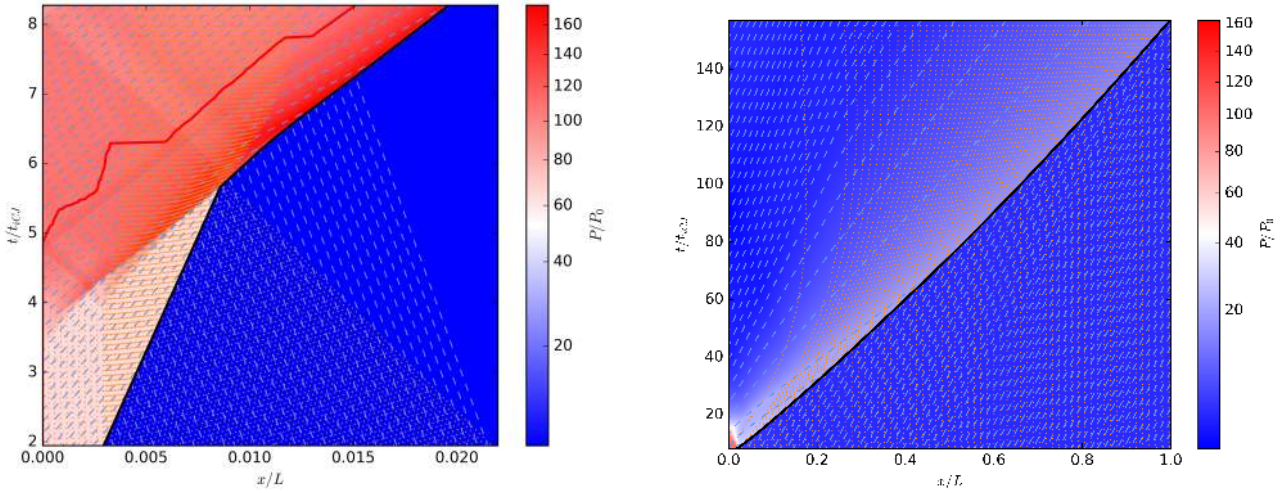

(a) *(b)*

***Fig. 13**: Characteristic space-time on top of the pressure profile to illustrate the (a) initiation induced by the shock reflection, and (b) interaction between the detonation wave and the CJ deflagration followed by an expansion wave, same legend as for Fig. 11a.*

flame reflection.

5.3 Unsupported detonation reflection

The the pressure plot in Fig. 15 and the space-time diagram in Fig. 16 depict the flow field evolution of the unsupported detonation reflection. The reflection of the leading shock quickly leads to an increase in end wall pressure to 220 P_0 in 0.1 t_{iCJ}, equivalent to one time step in the current simulation. This peak pressure corresponds to the constant volume combustion of the gas at the post-shock state of the incoming shock. However, it's important to note that variations in the time step size can lead to corresponding changes in the peak pressure, resulting in smaller or larger values. The reflected shock then traverses the reaction zone and the Taylor wave, resulting in a transmitted shock and a backward-facing expansion wave. As the shock moves further away, the end wall pressure sharply decreases. The reflected detonation wave burns out 99% the reactant at 3.6 t_{iCJ}, at which point the pressure at the end wall corresponds to the reflected CJ detonation pressure. The pressure remains constant until the backward-facing expansion wave reaches the end wall at 11.5 t_{iCJ}. The reflection of the expansion wave leads to further decay of the end wall pressure until the tail of the backwards-facing wave finally reaches the end wall at about 175 t_{iCJ}, resulting in a end wall pressure of 5.6 P_0.

5.4 Comparison of the pressure and impulse profiles for different combustion waves reflection

A summary of the end wall pressures and impulses for the three cases considered in the simulation is presented in Fig. 17. Note that the parameters in Fig. 17 are normalized by the initial pressure P_0 and initial acoustic timescale $t_{c0} = L/c_0$, where c_0 is the sound speed in the initial state. The peak pressure, in order of sequence, depends on the incoming shock speed. The highest impulse was achieved for the super fast flame reflection before 0.09 t_{c0}, followed by the choked flame and the unsupported detonation reflection. By 0.07 t_{c0}, the end wall pressure decays to the final pressure for the two cases of high-speed deflagration reflection, while for the unsupported detonation reflection case, it continues to decay due to the long Taylor wave. The final pressure for all three cases is the same. However, the impulse caused by the unsupported detonation reflection is significantly larger than the rest from 0.1 t_{c0}.

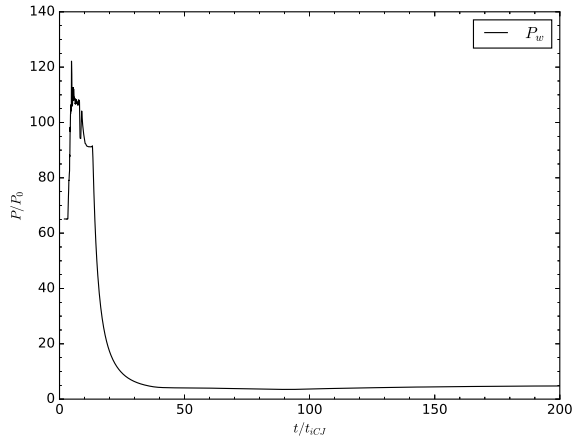

***Fig. 14**: End-wall pressure evolution as a function of time for super fast flame reflection.*

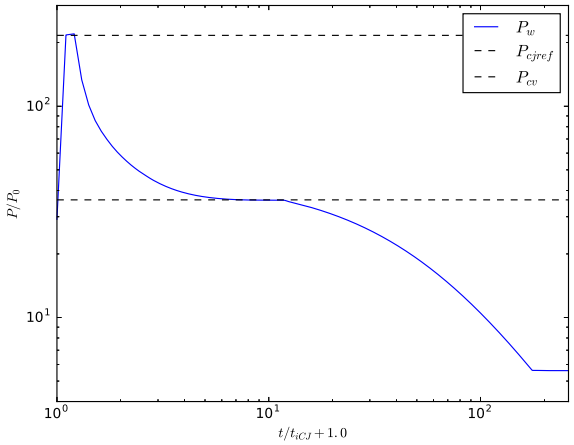

***Fig. 15**: End-wall pressure evolution as a function of time for unsupported detonation reflection.*

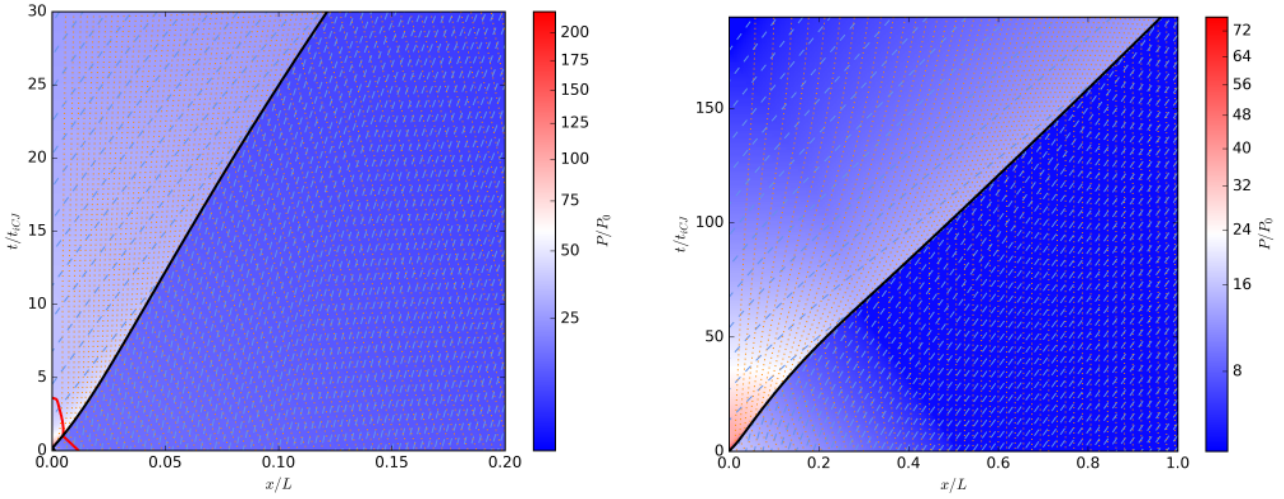

(a) *(b)*

***Fig. 16**: (a) Zoomed-in and (b) Overall characteristic space-time on top of the pressure profile to illustrate the unsupported detonation reflection, same legend as for Fig. 11a.*

6 Conclusions

In conclusion, we have conducted experiments and 1D numerical simulations of the head-on reflection of detonation waves, attenuated quasi-detonations and high speed deflagrations normal to a wall. Both the experiments and simulation results show that the largest impulse arises from the reflection of high-speed deflagration due to the initiation of detonation in the post-reflected gas within the detonation re-initiation timescale. The simulation results for different combustion waves demonstrate that the peak pressure varies depending on the incoming shock speed. However, the peak pressure is also influenced by the sample rate of pressure signals, potentially resulting in different orders. This explains why, in experiments, the highest overpressures and impulses were achieved with the re-initiation of detonation formed by shock reflection during the head-on reflection of high-speed deflagration. Following this, in order of importance, are quasi-detonations, detonations, and shock flame without re-ignition. At times larger than 0.1 t_{c0}, both the high pressure and impulse originate from the unsupported detonation reflection. These findings provide clarification and theoretical prediction for the dynamics of the end wall pressure resulting from the different combustion waves.

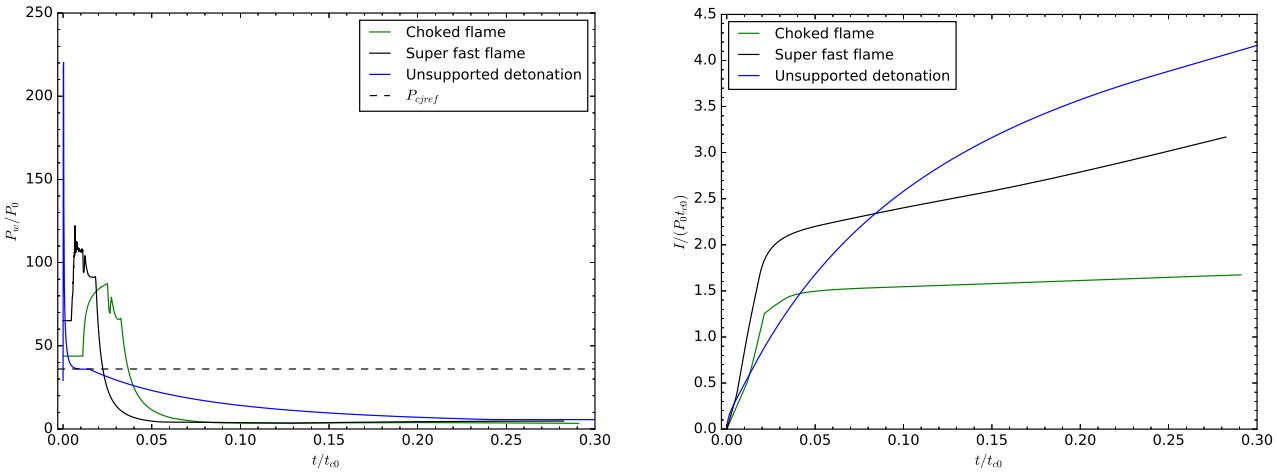

(a) *(b)*

***Fig. 17**: Comparison of the (a) pressure and (b) impulse evolution at the end wall for all 3 cases considered in the simulation.*

Acknowledgements

The authors wish to thank Z. Liang from Canadian Nuclear Laboratorie and E. Studer and S. Koudriakov from Université Paris-Saclay CEA for the sponsorship and useful discussions.

References

Falle, S., Giddings, J., Morton, K., Baines, M. (1993). *Numerical Methods for Fluid Dynamics 4*. Clarendon Press, Oxford.

Fickett, W., Davis, W. C. (2000). *Detonation: Theory and experiment*. Courier Corporation.

Khasainov, B., Presles, H.-N., Desbordes, D., Demontis, P., Vidal, P. (2005). *Detonation diffraction from circular tubes to cones*. Shock Waves, 14(3):187–192.

Lawson, J., Shepherd, J. (2019). *Shock and detonation toolbox installation instructions*. California Institute of Technology, Pasadena, CA.

Liang, Z., Shepherd, J. (2007). *Explosion testing of nested can containment system*. Part I: Planar Gap, Explosion Dynamics Laboratory Report FM2007, 1.

Meyer, J., Oppenheim, A. (1971). *On the shock-induced ignition of explosive gases*. Symposium (International) on Combustion, 13(1):1153–1164. ISSN 0082-0784. doi:https://doi.org/10.1016/S0082-0784(71)80112-1. Thirteenth symposium (International) on Combustion.

Ng, H. D., Ju, Y., Lee, J. H. (2007). *Assessment of detonation hazards in high-pressure hydrogen storage from chemical sensitivity analysis*. International Journal of Hydrogen Energy, 32(1):93–99.

Oran, E. S., Gamezo, V. N. (2007). *Origins of the deflagration-to-detonation transition in gas-phase combustion*. Combustion and Flame, 148(1-2):4–47.

Rakotoarison, W., Maxwell, B., Pekalski, A., Radulescu, M. I. (2019). *Mechanism of flame acceleration and detonation transition from the interaction of a supersonic turbulent flame with an obstruction: Experiments in low pressure propane–oxygen mixtures*. Proceedings of the Combustion Institute, 37(3):3713–3721.

Rakotoarison, W., Pekalski, A., Radulescu, M. I. (2020). *Detonation transition criteria from the interaction of supersonic shock-flame complexes with different shaped obstacles*. Journal of Loss Prevention in the Process Industries, 64:103963.

Saif, M., Wang, W., Pekalski, A., Levin, M., Radulescu, M. I. (2017). *Chapman–jouguet deflagrations and their transition to detonation*. Proceedings of the Combustion Institute, 36(2):2771–2779.

Sharpe, G. J. (2002). *Shock-induced ignition for a two-step chain-branching kinetics model*. Physics of Fluids, 14(12):4372–4388. doi:10.1063/1.1518693.

Studer, E., Koudriakov, S., Fernando, D. (2022). *Detailed examination of deformations induced by internal hydrogen explosions: open questions*. CEA, Personal Communication to M. Radulescu.

UCSD (2016). *Chemical-kinetic mechanisms for combustion applications, San Diego Mechanism web page, Mechanical and Aerospace Engineering (Combustion Research)*.

Xiao, Q., Radulescu, M. I. (2020). *Dynamics of hydrogen–oxygen–argon cellular detonations with a constant mean lateral strain rate*. Combustion and Flame, 215:437–457.

Pressure Dynamics Resulting from Head-On Reflection of Detonation

Farzane Zangene[a], Hongxia Yang[a] & Matei Radulescu[a]

[a] Department of Mechanical Engineering, University of Ottawa , Ottawa, ON K1N6N5, Canada

E-mail: *fzang055@uottawa.ca*

Abstract

In this study, the pressure evolution resulting from the head-on reflection of detonation waves as the reflected shock travels through the reaction zone is investigated. Detailed experiments on detonation reflection were conducted, and the transient dynamics were monitored using pressure transducers and high-speed Schlieren videos. This allowed us to resolve the inner structure of the reflection dynamics and the sequence of events controlling the overall pressure evolution within the reaction time scale. The experiments were performed using mixtures of $CH_4/2O_2$ and $2H_2/O_2/7Ar$, spanning the degree of cellular regularity of detonations in reactive gases. It was found that for regular mixtures characterized by a long reaction zone structure, the simple one-dimensional ZND model is sufficiently accurate to predict the pressure evolution of the reflection. This was further confirmed through a comparison of experiments with both two-dimensional and one-dimensional simulations, employing a previously introduced model that accounts for boundary layer losses. For irregular detonation waves in which the reaction zone significantly departs from the steady ZND model, we propose a new model that accounts for the hydrodynamics thickness of the detonation. The hydrodynamic thickness was found to be approximately one cell width, λ, in both mixtures investigated. Using this knowledge, a simplified one-step combustion model tailored to the global structure of the reaction zone is introduced. This model employs one-dimensional reactive Euler equations, assuming constant volume combustion upon reflection, thus constructing the pressure evolution of the reflected detonation in irregular structure detonations. The results demonstrated that the end-wall pressure evolution resulting from the reflection of high-speed detonation can be reliably predicted using the simple proposed model.

Keywords: detonation reflection experiments, reaction zone length, pressure evolution, numerical modelling

1 Introduction

When a detonation wave propagates inside a closed vessel and reaches the end wall, it produces a reflected shock wave that travels back into the tube. This shock wave serves to bring the gas behind the detonation to a state of rest. The over-pressures produced by these waves depend significantly on the regularity of the incoming detonation, the configuration of the vessel and the angle of the reflection often resulting in very high pressure spikes (Shepherd et al., 1991). This increased pressure near the wave reflection region is of great interest in safety analyses, as it can have significant implications for operational safety. While extensive efforts have been made to study various aspects of the phenomena (Shepherd et al., 1991, Karnesky, 2010, Damazo, 2013, Damazo and Shepherd, 2017), there is a lack of detailed insights into the structure of detonation and its reflection with sufficient time resolution in the scales of the reaction zone time.

This paper presents an experimental and numerical investigation of detonation behavior prior to reflection and the subsequent reflected wave in $2H_2/O_2/7Ar$ and $CH_4/2O_2$ mixtures exhibiting both regular and irregular cellular structures. First, detailed experiments were conducted to visualize the detonation propagation inside a narrow channel and its reflection from the end wall. Then, the pressure dynamics were quantified using pressure transducers as the detonation wave traversed the channel and the reflected shocks passed through the reaction zone of the preceding detonation wave. For the regular mixture of $2H_2/O_2/7Ar$, a previously proposed model is employed to account for boundary layer losses to reproduce the reflection dynamics and wave structure through both 2D and 1D simulations (Xiao et al., 2021, Zangene et al., 2022). However, for irregular structure detonation waves in the

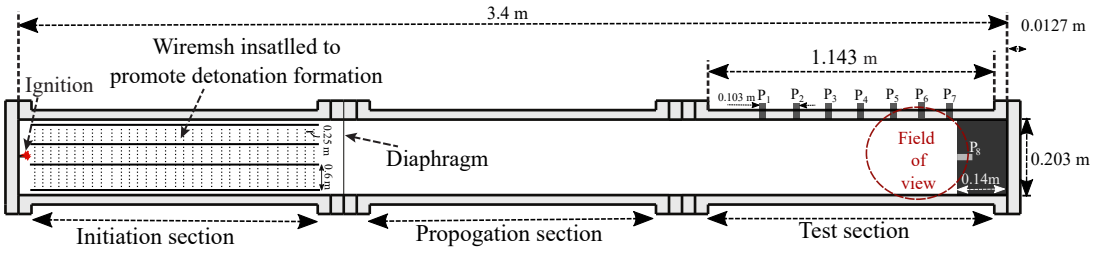

***Fig. 1**: Schematic of the shock tube used in the experiment.*

***Table 1**: The experimental test gases and their properties.*

Mixture	p_0 [kPa]	χ	D_{CJ}	p_{CJ} [kPa]	$p_{CJ,Reflected}$ [kPa]
$2H_2/O_2/7Ar$	4	0.73	1602	64	155
$CH_4/2O_2$	6	522	2267	162	405

$CH_4/2O_2$ mixture, a simplified one-step combustion model fitted to the overall structure of the detonation hydrodynamic thickness was introduced, where the reaction zone deviates significantly from steady ZND model predictions (Lee and Radulescu, 2005). This model utilizes one-dimensional reactive Euler equations, assuming constant volume combustion upon reflection, thereby calculating the pressure evolution of the reflected detonation in irregular structure detonations.

2 Experiments

2.1 Experimental set-up

The experiments were performed in a 3.4-m-long shock tube, with 0.019-m-thickness and 0.203-m-height. The schematic illustrating the experimental set-up is shown in Fig. 1. Mesh wires were placed in the initial section of the shock tube to ensure the formation of detonation within this segment. Subsequently, the detonation propagated through the second section to reach a steady propagation speed before entering the third test section. A rectangular object, composed of polyvinyl chloride, was placed at the end of the test section to serve as a wall. Additional details regarding the experimental set-up can be found in a previous work (Bhattacharjee, 2013).

The two mixtures studied were a stoichiometric mixture of methane-oxygen ($CH_4/2O_2$) and a stoichiometric mixture of hydrogen-oxygen diluted with argon ($2H_2/O_2/7Ar$). The selection of these two mixtures was based on their significant differences in cellular regularity. As shown in Table 1, the detonation stability parameter χ, (Radulescu, 2003), varies widely between the two selected mixtures. The Chapman-Jouguet (CJ) detonation speed, D_{CJ}, pressure, p_{CJ} and reflected pressure, $p_{CJ,Reflected}$, are calculated using the Shock and Detonation Toolbox (SDToolbox) (Williams, 2014) and Sandiego mechanism (SanDiego, 2016). We varied the initial pressure, p_0, of the test gas to create a single large detonation cell, enhancing the visibility of the reflection process. Since the mixture of $2H_2/O_2/7Ar$ has low reactive sensitivity, a more reactive driver gas of stoichiometric ethylene-oxygen (i.e., $C_2H_4/3O_2$) was used in the initiation section, which was separated from the propagation section with a thin aluminum foil diaphragm. Preliminary tests were conducted to prevent an excessively driven detonation wave in the test section resulting from the high-pressure driver gas. The minimum pressure required to initiate detonation waves was identified. Throughout all experiments, a constant ratio of 2.4 between the driver gas and the test gas was maintained as a reference for filling the shock tube. All experiments reported were conducted at an initial temperature of 293 K. To guarantee the results reliability and reproducibility, the experiments were conducted twelve times under identical conditions in the $2H_2/O_2/7Ar$ mixture and thirteen times in the $CH_4/2O_2$ mixture.

Each mixture was prepared in a separate mixing tank by the method of partial pressures and was then

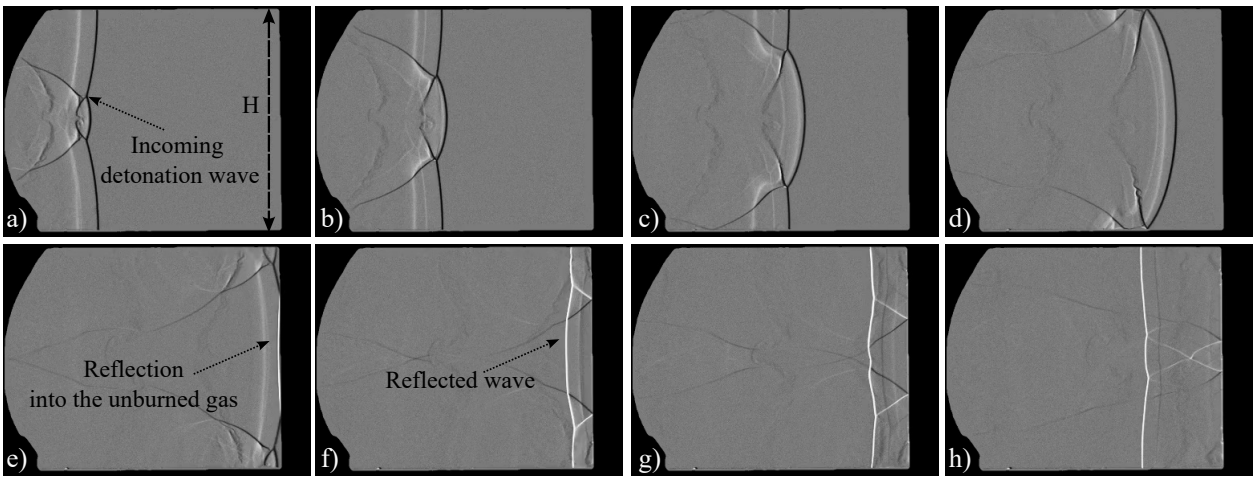

***Fig. 2**: Schlieren images of the incident detonation and the reflected shock wave in the mixture of $2H_2/O_2/7Ar$ at $p_0 = 4$ kPa. H is the channel height of 0.203 m.*

***Table 2**: Detonation average propagation speed and cell width measured from the experiments.*

Mixture	p_0 [kPa]	λ [m]	**D** [m/s]	$t_\Delta = \frac{\lambda}{D}$ [µs]
$2H_2/O_2/7Ar$	4	0.203	1285±40	158±5
$CH_4/2O_2$	6	0.10±0.022	2096±91	47±10

left to mix for more than 24 hours. Monitoring of the mixing process was done using an Omega PX409-015AV pressure transducer with the accuracy of ± 0.08%. The shock tube was evacuated to a pressure below 80 Pa before filling it with the gas. The initial ignition of the premixed combustible mixture was achieved using a high voltage igniter (HVI) that was custom designed and built (Bhattacharjee, 2013). The HVI utilized a capacitor discharge method for ignition. In all experiments, the capacitor was charged to a voltage of around 25 kV.

A linear arrangement of two 113B24 piezoelectric PCB pressure sensors, followed by five 113B27 sensors, was evenly distributed along the top wall of the shock tube. This setup was used to capture pressure signals from the detonation before reflection. Additionally, for the investigation of detonation reflection, one 113B24 piezoelectric PCB pressure sensor was inserted into the center of the end wall to measure the over-pressure resulting from the reflection. The sensors resonate at 500kHz, while the pressure signals during the experiments were recorded at a rate of 1.5 MHz. All pressure gauges used in the experiments have a diameter of 5.5-mm and a maximum error of 1.3%, as determined from the calibration data. The signal conditioners used for these pressure sensors are the PCB Piezotronics model 482C05 and 482C16. To improve the quality of the pressure signals and minimize noise, a filtering process was applied to the raw data using a cut-off frequency of 250 kHz. This frequency selection aimed to preserve crucial information regarding the smallest spatial scales observed in the detonation structure during the experiments. Furthermore, the propagation process was visualized by utilizing the classical Z-type Schlieren technique with the Phantom v1210 camera at 77108 frames per second (about 12.9 μs for each interval). The Schlieren visualization was implemented with a vertical knife-edge utilizing a light source of 360 W, with the exposure time set to 0.44 μs and the frame resolution kept at 384×288 px^2.

2.2 Experimental results

The propagation of the incident detonation and its reflection from the end wall in the regular cellular structure mixture of hydrogen-oxygen-argon is shown in Fig. 2. The detonation propagates from left

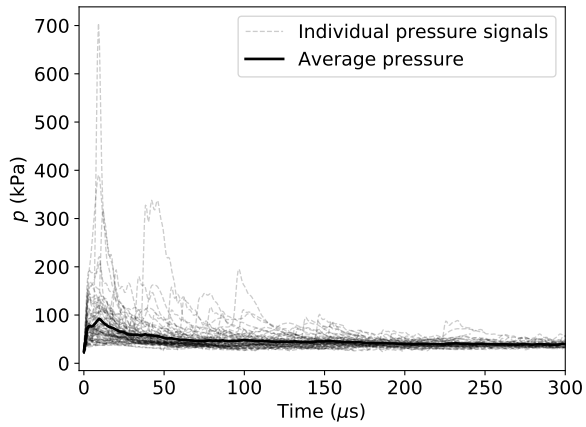

(a) Experimental results from 72 pressure sensors.

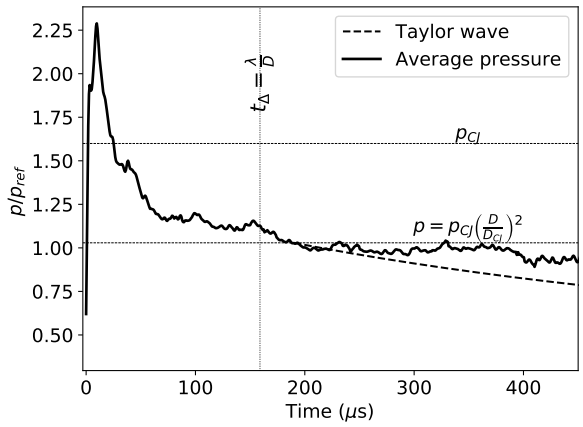

(b) Scaled average pressure.

***Fig. 3**: Temporal evolution of the incoming detonation wave pressure measured on the top wall in the mixture of $2H_2/O_2/7Ar$ at $p_0 = 4$ kPa.*

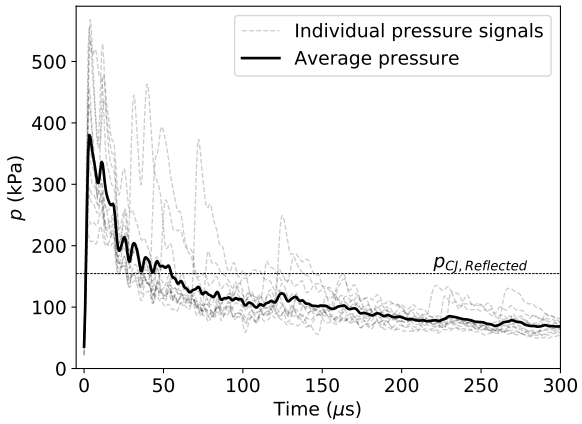

***Fig. 4**: Temporal evolution of the reflected wave pressure measured on the end wall in $2H_2/O_2/7Ar$ mixture at $p_0 = 4$ kPa.*

to right, as depicted in Fig. 2 (a, b, c and d). The detonation front has a single large cell, displaying a notably regular pattern characteristic of this mixture with long reaction zone length. Immediately following the head on reflection of the detonation from the end wall, as shown in Fig. 2 (e, f, g and h), the shock rapidly consumes all the unburned gases. Subsequently, it continues to propagate from right to left, into the reaction zone of the preceding incoming detonation wave.

The global propagation speed, D, of the detonation wave across the entire test section was determined by pressure sensors using the time-of-arrival method, as detailed in Table 2. The reported cell width, λ, is the average obtained from Schlieren images. The speed and cell size measurements are the average value of the repeated experiments. The value of the time corresponding to one cell behind the detonation, which indicates the potential location of the sonic surface, $t_\Delta = \frac{\lambda}{D}$, is also presented in Table 2. The standard deviation of the propagation speed and cell width measured in repeated experiments is included. Figure 3a depicts the 72 pressure signals recorded by pressure sensors on the top wall following the passage of the detonation wave, with the average pressure indicated by the solid line. The signal in the plot has been shifted so that zero time on the plot corresponds to the time of detonation arrival. While the peak of the average pressure reaches approximately 100 kPa, certain sensors recorded peaks as high as 700 kPa. The high peaks might arise from the stronger part of the detonation front passing or from a transverse wave detected by the sensor.

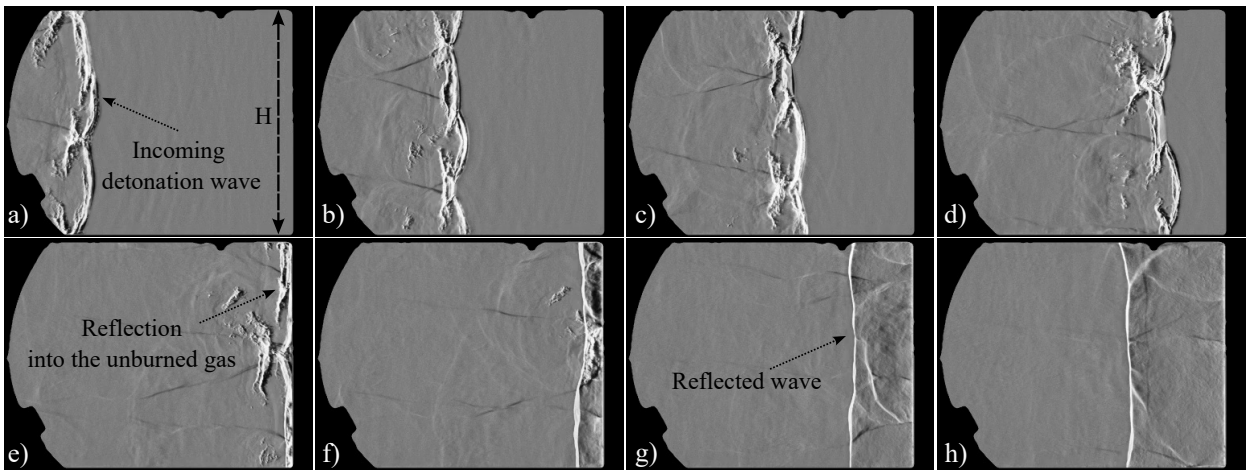

***Fig. 5**: Schlieren images of the incident detonation and the reflected shock wave in the mixture of $CH_4/2O_2$ at $p_0 = 6$ kPa. H is the channel height of 0.203 m.*

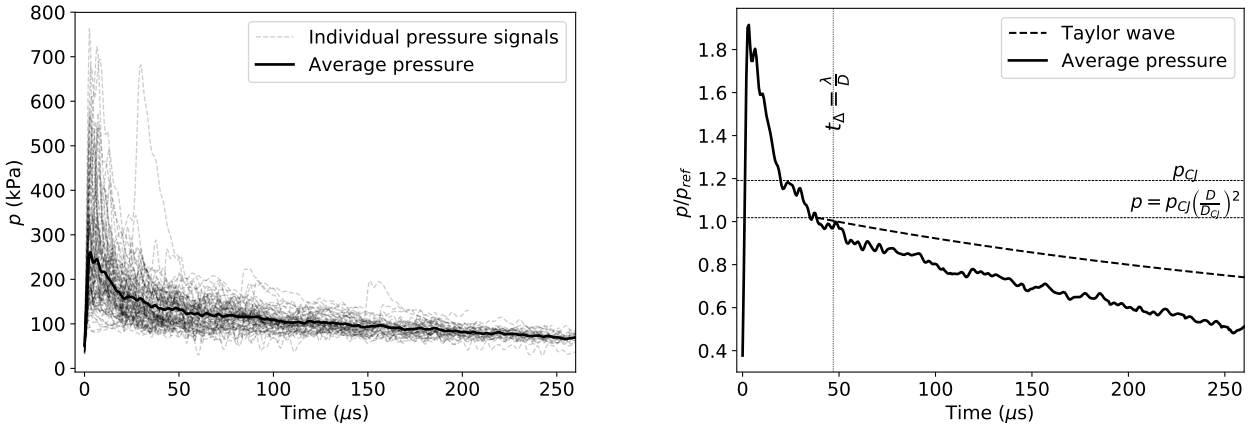

(a) Experimental results from 78 pressure sensors.

(b) Scaled average pressure signal.

***Fig. 6**: Temporal evolution of the incoming detonation wave pressure measured on the top wall in $CH_4/2O_2$ mixture at $p_0 = 6$ kPa.*

Using the strong detonation solution, the pressure at CJ state is given by $p = \frac{\rho_0 \cdot D^2}{\gamma+1}$ (Lee, 2008). In this equation, D, ρ_0 and γ denote the experimentally measured detonation speed, the density at the initial state and the specific heat ratio at equilibrium state derived from the equilibrium sound speed, respectively. This pressure serves as the reference pressure, p_{ref}, in Fig. 3b for normalizing the pressure signals observed during the experiments. In scenarios with detonations experiencing heat losses, the equilibrium pressure tends to decrease compared to p_{CJ}. Utilizing conservation laws for mass and momentum in a strong detonation case, one can derive the pressure at the sonic surface as $p = p_{CJ} * (\frac{D}{D_{CJ}})^2$, with D denoting the average velocity obtained from the experiments. Figure 3b illustrates a rapid pressure increase after the detonation passage and a subsequent decline within the hydrodynamic thickness, leading the signal towards a plateau pressure. The point where the line representing calculated equilibrium pressure with losses intersects with the pressure plot is around 190 μs, suggesting a potential time for the sonic surface. This time corresponds approximately to the time calculated from experimental values for one cell $t_\Delta = 158$ μs. The profile of the Taylor expansion wave following the detonation is calculated at the position where the detonation wave has traveled from the ignition point to the first pressure gauge ($x_{traveled} = 2.6$ m)(Law, 2006). The reduction in pressure observed in the experimental data is smaller than that calculated from the expansion wave. This difference can be caused by the presence of the driver gas in these experiments, which continues

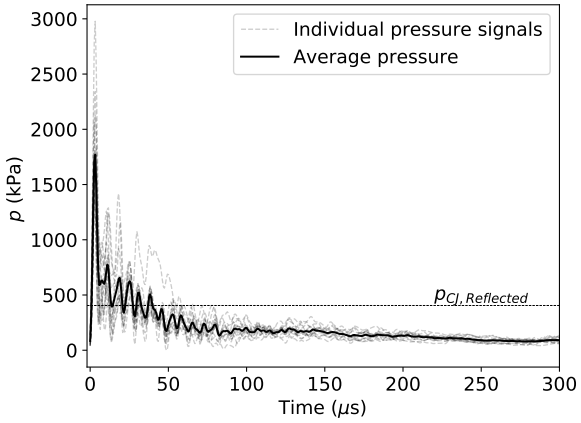

***Fig. 7**: Temporal evolution of the reflected wave pressure measured on the end wall in $CH_4/2O_2$ mixture at $p_0 = 6$ kPa.*

to affect the propagation of the detonation. Following the detonation reflection from the end wall, the rapid ignition of the gas within the induction zone causes the pressure to surge to three times the peak average pressure of the incoming detonation, as depicted in Fig. 4. Subsequently, as it traverses the long reaction zone, the pressure decreases below the reflected wave pressure $P_{CJ,Reflected}$. The plot captures the oscillation and envelope of these signals as they gradually decay over time across 12 repeated experiments.

The Schlieren images in Fig. 5 illustrate the propagation of the detonation and its subsequent reflection in methane-oxygen mixture. In contrast to the laminar reaction front seen in hydrogen-oxygen-argon mixture, the reaction front here is turbulent, with unreacted gas pockets trailing behind.

Figure 6a displays the pressure dynamics of the incoming detonation from 78 sensors, alongside the average pressure. Notably, the peak pressure exceeds twice the average peak pressure seen in hydrogen-oxygen-argon mixture, reaching oscillations up to 750 kPa that swiftly decay toward a plateau. As shown in Fig. 6b, the time when the pressure crosses the sonic surface is about 47 μs, which closely matches the time of one cell measured in experiments, refer to Table 2. The decrease in pressure observed in the experiment exceeds that predicted by the Taylor wave calculation, which can be attributed to the presence of heat losses in the experiment.

The pressure dynamics as the reflected shocks traverse through the reaction zone of the detonation wave are depicted in Fig. 7. Various signals in the plot correspond to 13 repeated experiments conducted under identical conditions. The peak average pressure of the reflected detonation reaches up to 7 times higher than the average pressure of the incoming detonation and gradually decreases toward a plateau below the CJ pressure of the reflected wave.

3 Numerical Simulations

3.1 Modelling the reflection of the regular cellular structure detonation wave

A quasi-2D model is employed to simulate boundary layer losses of a detonation in a thin channel, as discussed elsewhere (Xiao et al., 2021, Zangene et al., 2022). The governing equations, reactive inviscid Euler equations, were solved using a second-order-accurate exact Godunov solver with Adaptive Mesh Refinement (AMR). The code utilized is the MG code, developed by S. Falle at the University of Leeds (Falle, 1991). In line with a previous (Xiao et al., 2021) mesh study under similar conditions, the numerical resolution adopted 5 levels of mesh refinement, with coarsest and finest grid sizes of 1/2 Δ_i (induction zone length) and 1/16 Δ_i, respectively.

The computational domain height remained constant at the experimental height of 0.203 m, equivalent to 72 Δ_i for $p_0 = 4.1$ kPa in the $2H_2/O_2/7Ar$ mixture. The domain length was set to 1500 Δ_i. The

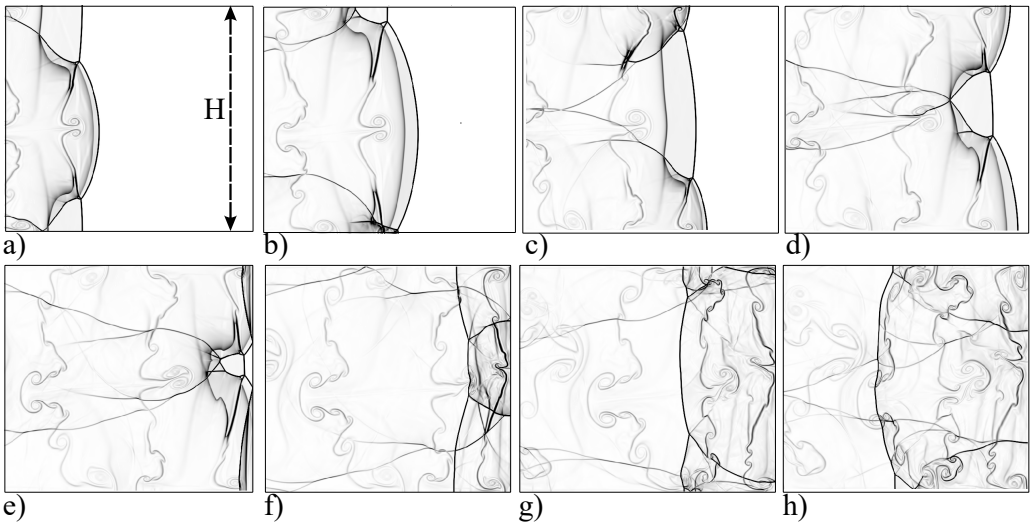

***Fig. 8**: The gradient of the density of the incoming detonation and reflected wave from the quasi-2D simulation in 2H2/O2/7Ar mixture at $p_0 = 4$ kPa. H is the channel height of 0.203 m.*

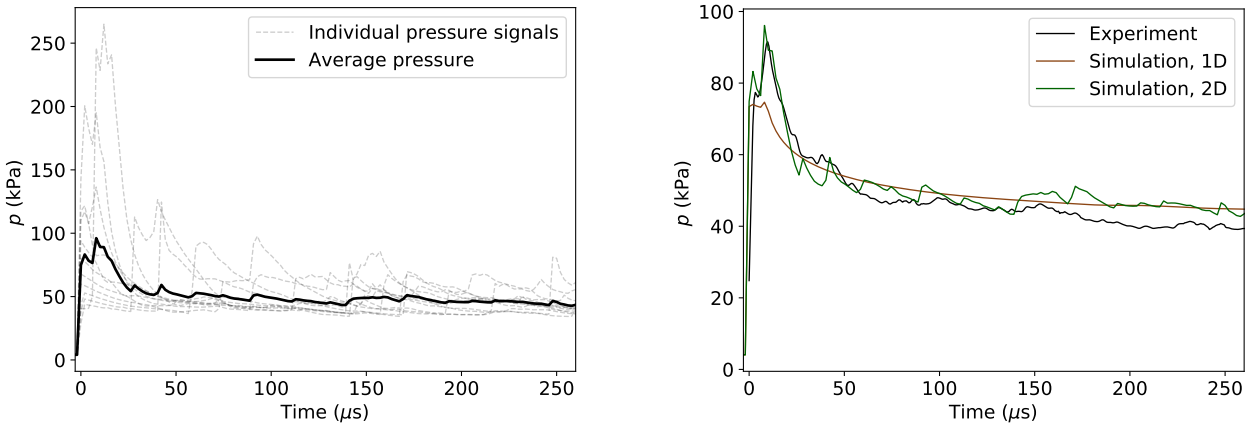

(a) 2D Simulation results from 12 locations.

(b) Average pressure comparison.

***Fig. 9**: Temporal evolution of the incoming detonation wave pressure measured on the top wall in $2H_2/O_2/7Ar$ mixture at $p_0 = 4$ kPa.*

detonation propagated from left to right, with reflective boundary conditions applied to the top, bottom, and right ends, and zero-gradient boundary conditions applied to the left end. The computations were initiated using a ZND profile positioned 300 Δ_i from the left boundary. We utilized a two-step chemistry model that includes a thermally neutral induction zone and an exothermic reaction zone to model the combustion.

Figure 8 illustrates that the density gradient from the quasi-2D simulation accurately replicates the experimentally observed qualitative characteristics of the detonation structure before and after reflection from the end wall. This simulation effectively captures the cellular dynamics and cell size, indicating the reliability of the proposed quasi-2D formulation and the two-step chemistry model in simulating real detonations. Similar simulations are also conducted in one dimension.

The average velocity deficit of detonation propagation measured in one cell in the two-dimensional simulation ($D/D_{CJ} = 0.82$) and the one-dimensional simulation (0.83) is in good agreement with the global velocity measured from the experiments (0.8). To analyze the pressure dynamics before the detonation wave reflects, we extracted pressure signals from 12 locations across one cell in the 2D numerical simulation, recorded at a frequency of 500 kHz. Figure 9a presents these pressure

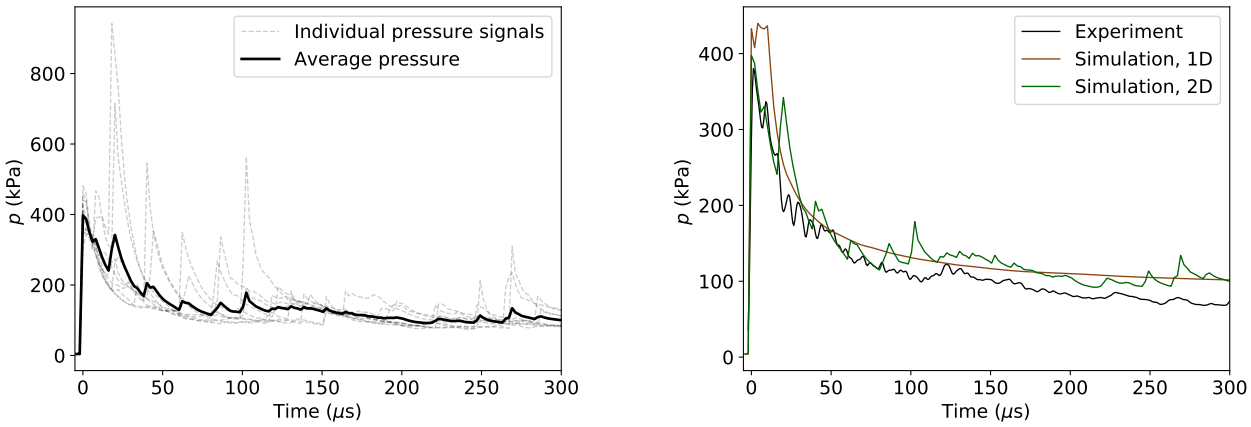

(a) 2D Simulation results from 9 locations.

(b) Average pressure comparison.

***Fig. 10**: Temporal evolution of the reflected wave pressure measured on the end wall in $2H_2/O_2/7Ar$ mixture at $p_0 = 4$ kPa*

signals alongside the average pressure across one detonation cell. Remarkably, the average pressure measured from the simulation closely matches the experimental data, capturing both peak pressure and decay rate towards the plateau as shown in Fig. 9b. The 1D simulation also predicts a similar trend in pressure evolution. After 158 µs, which marks the end of one cell, the experimental signal drops slightly more. This decrease can be ascribed to heat losses and Taylor waves following the detonation.

In repeated experiments, we consistently observed that the detonation wave impacted the pressure sensor on the middle of the end wall every time, but with varying parts of the cell, such as the Mach shock or incident shock. This variability resulted in different overpressures. To ensure a meaningful comparison with experiments, we selected nine evenly distributed locations from the top to the bottom of the end wall. This approach allows us to capture the overpressure resulting from the reflection of the detonation from different parts of the cell in our simulation results. The pressure signals from these 9 locations on the end wall of the simulation are extracted over time, and all the signals, along with the average, are presented in Fig. 10a. As shown previously with the signals from the repeated experiments, all the oscillations decay over time, and the average tends towards a plateau. A similar good agreement between the numerics and experiments is observed when examining Fig. 10b. The 2D simulation closely predicts the oscillation and decay rate of the experiments, with the experimental pressure dropping more over time. Although the 1D simulation does not predict the oscillation due to the cellular structure of the detonation, it still predicts the overall decay rate of pressure very well.

3.2 Modelling the reflection of the irregular cellular structure detonation

For irregular detonation waves where the reaction zone deviates significantly from the steady ZND model (Lee and Radulescu, 2005), we utilize a fitted 1D global structure to model the experimentally observed structure of the detonation. Based on our experiments, we found that the average hydrodynamic thickness in the methane-oxygen mixture aligns closely with one detonation cell width. Therefore, we modify the pressure profile of the detonation before reflection to reach the CJ state within this single cell thickness, as illustrated in Fig. 11a. After reflection, we consider constant volume combustion within the gas, using the conditions of the von Neumann state (vn) of the incoming detonation, as illustrated in Fig. 11b. The reflected shock will propagate back into the reaction zone of the preceding detonation. The governing equations utilized are the one-dimensional reactive Euler

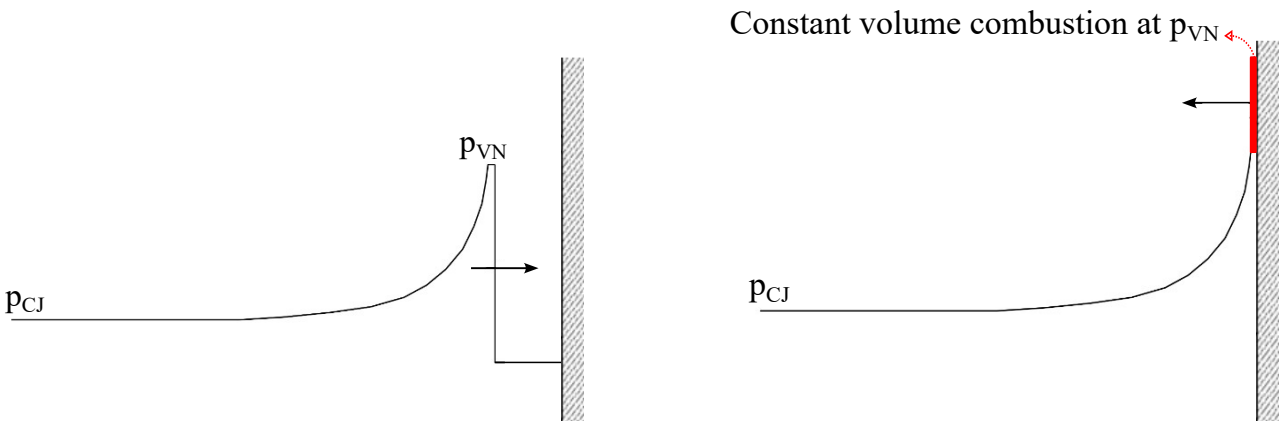

(a) Pressure profile of the incoming detonation. *(b) Pressure profile at the time of the reflection.*

***Fig. 11**: Sketch of the proposed one-dimensional model in $CH_4/2O_2$ mixture at $p_0 = 6$ kPa.*

***Table 3**: Thermo-chemical properties and model parameters for one-dimensional detonation reflection simulation at T_0=293 K.*

Mixture	p_0 (kPa)	γ_{VN}	$\frac{Q}{RT_0}$	k_r	ν	Δ_i (m)
$CH_4/2O_2$	6	1.17	62	3	1	0.0087

equations, outlined as follows:

$$\frac{\partial \rho}{\partial t} + \frac{\partial \rho u}{\partial x} = 0 \tag{1}$$

$$\frac{\partial \rho u}{\partial t} + \frac{\partial \rho u u}{\partial x} + \frac{\partial p}{\partial x} = 0 \tag{2}$$

$$\frac{\partial \rho E}{\partial t} + \frac{\partial (\rho E + p)u}{\partial x} = Q\frac{D\rho\lambda_r}{Dt} \tag{3}$$

Where ρ, $\mathbf{u}$, p, Y and λ_r represent density, velocity vector, pressure, mass fraction of the product and the reaction progress variable, respectively. The total energy is defined as $E = \frac{p}{\rho(\gamma-1)} + \frac{\mathbf{u}^2}{2}$. The global heat release Q was determined to accurately reproduce the CJ Mach number, M_{CJ}, as specified for a perfect gas (Lee, 2008).

$$\frac{Q}{RT_0} = \frac{\gamma}{2(\gamma^2-1)}(M_{cj} - \frac{1}{M_{cj}})^2. \tag{4}$$

In the above equation, R represents the universal gas constant and γ denotes the isentropic index calculated in the post-shock state. The transport equation of the one-step reaction variable employed in the model can be written as:

$$\frac{\partial \rho\lambda_r}{\partial t} + \frac{\partial \rho u\lambda_r}{\partial x} = k_r\rho(1-\lambda_r)^\nu \tag{5}$$

In this context, k_r is the rate constants and ν indicates the reaction order. Table 3 lists the values utilized in the simulation. In this table, k_r is a dimensionless value obtained through non-dimensionalization with respect to the initial state.

Our experiments in the methane-oxygen mixture revealed that the reaction zone spans approximately one detonation cell length, $\lambda_{Experiemnt} = 0.10$ m. By adjusting the value of k_r, we can align the reaction zone thickness with the observed hydrodynamic thickness of $\lambda = 12\Delta_i$. Figure 12a shows the fitted pressure profile of the incoming detonation used in the simulation at the time of reflection. A two-

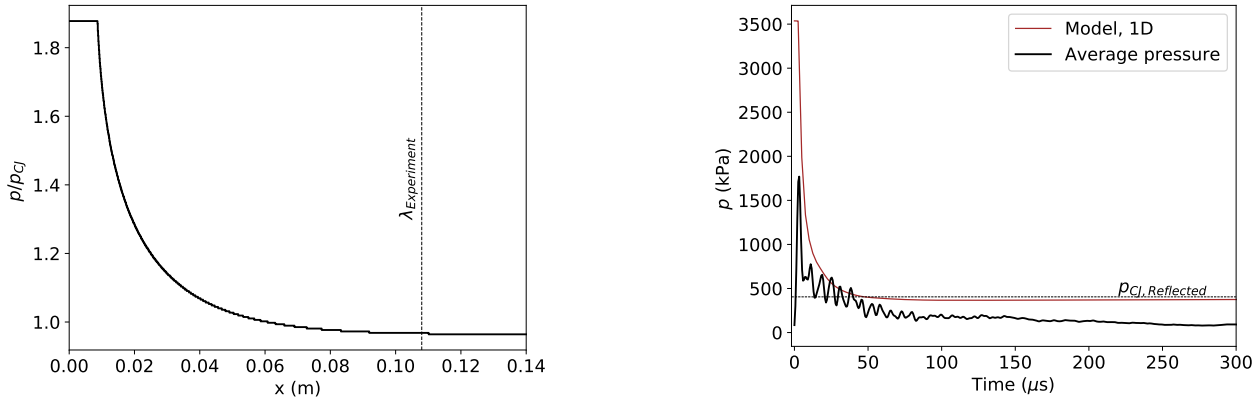

(a) ZND pressure profile of the detonation.

(b) Reflected pressure from the end wall.

***Fig. 12**: a) Fitted 1D global structure of the detonation and b) the reflected pressure evolution with time in comparison with experiment in $CH_4/2O_2$ mixture at $p_0 = 6$ kPa.*

step chain-branching reaction model is employed to describe the ZND profile of the detonation before reflection. The solver utilized for the numerical simulation is identical to the one described for the regular mixture simulations. The numerical resolution employed five levels of mesh refinement, with the coarsest grid size being $\frac{1}{4}\Delta_i$ and the finest grid size being $\frac{1}{64}\Delta_i$.

Figure 12b presents the outcome of the 1D simulation, showing pressure-time traces of the reflected wave from the simulation, captured at the end wall. The frequency of collecting data from the simulation is 500 kHz. The model accurately captures the decay rate observed in the experiments until reaching the sonic surface, 47 µs. Beyond this point, both signals converge toward a plateau. However, the experimental pressure continues to decline, due to Taylor expansion waves and heat dissipation.

4 Conclusions

The present work showed the detailed dynamics of the structure and pressure evolution resulting from head-on reflection of detonation waves on the time scales of the reaction zone structure. Experiments show, after the reflection, very rapid ignition of the gas inside the induction zone followed by a shock passing through the long reaction zone. For the regular mixture of $2H_2/O_2/7Ar$ with a notably thinner induction zone compared to the reaction zone, both 2D and 1D models align well with experimental observations within the reaction zone length. However, the equilibrium pressure observed in experiments falls below that measured in simulations.

We further show that for the irregular cellular structure detonations a simple 1D model fitted to match experimentally measured hydrodynamics thickness can predict the experimental pressure traces closely. In both mixtures, the pressure traces observed in experiments shows a plateau at pressures lower than the reflected P_{CJ}. This could be attributed to expansion waves and heat losses in the experiments, factors not considered in the modeling.

Acknowledgements

The authors would like to express their appreciation to Z. Liang from the Canadian Nuclear Laboratories (CNL), and E. Studer and S. Koudriakov from Université Paris-Saclay, the French Alternative Energies and Atomic Energy Commission (CEA), for their sponsorship and valuable discussions.

References

Bhattacharjee, R. (2013). *Experimental investigation of detonation reinitiation mechanisms following a Mach reflection of a quenched detonation*. University of Ottawa, Master Thesis.

Damazo, J. S. (2013). *Planar reflection of gaseous detonations*. California Institute of Technology.

Damazo, J., Shepherd, J. E. (2017). *Observations on the normal reflection of gaseous detonations*. Shock Waves, 27(5):795–810.

Falle, S. (1991). *Selfsimilar jets*. Monthly Notices of the Royal Astronomical Society.

Karnesky, J. A. (2010). *Detonation induced strain in tubes*. Ph.D. thesis, California Institute of Technology.

Law, C. (2006). *Law. combustion physics*. New York.

Lee, J. (2008). *The Detonation Phenomenon*. Cambridge University Press.

Lee, J., Radulescu, M. (2005). *On the hydrodynamic thickness of cellular detonations*. Combustion, Explosion and Shock Waves, 41:745–765.

Radulescu, M. (2003). *The propagation and failure mechanism of gaseous detonations: experiments in porous-walled tubes*. McGill University, Ph.D. thesis.

SanDiego, . (2016). *Chemical mechanism: Combustion research group at uc san diego*.

Shepherd, J., Teodorcyzk, A., Knystautas, R., Lee, J. (1991). *Shock waves produced by reflected detonations*. Progress in Astronautics and Aeronautics, 134:244–264.

Williams, F. (2014). *Chemical mechanism: combustion research group at uc san diego*.

Xiao, Q., Sow, A., Maxwell, B., Radulescu, M. (2021). *Effect of boundary layer losses on 2D detonation cellular structures*. Proceedings of the Combustion Institute, 38:3641–3649.

Zangene, F., Sow, A., Radulescu, M. (2022). *Predictability of hydrogen-based mixtures detonations in thin channels: new experiments and improvements in the quasi-two-dimensional model*. in: Proceedings of the Twenty-eighth, ICDERS, Naples.

Requirements for Passive Fire Protection concerning blast resistance

Karthik Nagendra, Neil Wickham, Robin Wade

AkzoNobel, Newcastle upon Tyne, United Kingdom

E-mail: Karthik.Nagendra@akzonobel.com

Abstract

Passive fire protection (PFP) is specified and applied to structural steel and divisions to prevent steel temperatures rising to the point of failure in a fire and the integrity and adhesion of the PFP is critical to its effectiveness as an insulator. Although thermal loading from accidental events is the primary driver behind PFP design, there are many other factors and loads to consider when specifying PFP.

Blast loads due to an accidental explosion are one such factor and are often overlooked when specifying PFP, despite the potential risk. A hydrocarbon leak may cause congestion allowing for a gas cloud build-up and subsequent ignition. Thus, since a blast explosion will generally precede a fire, resilience of the PFP system must be ensured. Additionally, response criteria for structural steelwork subjected to blast loads are typically expressed in terms of ductility ratios and/or support rotations (in contrast to material stress limits used for satisfying requirements in operational design considerations), where ductility ratio is the maximum deflection divided by the deflection at yield, and the support rotation is as defined. In conventional construction, for which PFP systems are typically tested, rotations are generally limited to less than 0.25-0.5˚. However, in situations where the structure is required to provide protection from a single event, like an explosion, acceptable ductility ratios can vary from 1-20˚.

At time of writing, there is no test standard in place to verify PFP resilience to blast, leaving manufacturers to verify conformance via potentially unsuitable means, such as through small-scale material tests like the Static Bend Test. Consequentially, AkzoNobel have carried out large-scale blast tests on representative steel specimens (plate girders, stiffened plates and corrugated panels) to induce deformations pertaining to Low, Medium, and High Component Response Level as defined by Table 5.B.1.B of *ASCE Design of Blast Resistant Buildings, 2nd Edition, 2010*. Upon completion of blast tests, both qualitative and quantitative assessments have been undertaken. The qualitative assessment determines PFP integrity in terms of crack initiation and associated dimensions, delamination, and/or detachment, whereas the quantitative assessment determines this through fire testing (by comparing insulation performance versus type approvals). Further, finite element (FE) modelling utilizing Abaqus software has been carried out to explore modelling approaches as a viable alternative to full scale blast testing.

Results from both the qualitative and quantitative assessment have demonstrated PFP resilience for Low and Medium component response levels. When considering the ASCE definition for High component response, it is concluded that PFP resilience is not practicable for this deformation severity. Also, the FE models have shown good agreement with the blasted specimens and will be further developed in due course.

Keywords: *structural steel, fire, explosion, blast, passive fire protection, resilience*

Introduction

In structural design, blast loading is considered an accidental load and the overpressure from explosions is usually the primary destructive feature. Structures are designed to resist blast loads with or without plastic deformation as long as collapse does not occur. Structural response to blast loading is dependent upon both the peak pressure and blast impulse duration. Certain structural members are more sensitive to blast pressure, while other types of members are more sensitive to blast impulse duration. In particular, fire events and explosion events often occur sequentially wherein loads imposed by each result in a cumulative impact.

In the case of a hydrocarbon fluid leak, an explosion may proceed a fire event if congestion allows for a buildup of vapor clouds which ultimately ignite. Passive fire protection (PFP) is specified and applied to structural steel and divisions to prevent steel temperatures from rising to the point of failure in a fire event. *American Petroleum Institute Recommended Practice 2FB* (API, 2006) recognises the need to analyse the effects of such a combined event which is imperative for materials like PFP where fire protection of critical structural elements is expected after being previously subjected to blast loading. The integrity and adhesion of PFP is critical to its effectiveness at insulating structural elements in a fire.

Structural response criteria for blast loading are typically expressed in terms of ductility ratios (μ) and joint rotations (θ). Ductility ratio is defined as the ratio of permanent deflection and elastic deflection while joint rotation refers to the angle of rotation of the member from end connection. Structural blast-resistant design typically follows the guidance within the ASCE document for the Design of Blast Resistant Buildings in Petrochemical Facilities (ASCE, 2010). The guidance given within Table 5.B.1.A in ASCE document is presented in terms of overall building damage level in Table 1.

***Table 1**. Building damage levels (ASCE, 2010)*

Damage level	Building damage level description
Low	Localized component damage. Building can be used; however, repairs are required to restore integrity of structural envelope. Total cost of repairs is moderate
Medium	Widespread component damage. Building should not be occupied until repaired. Total cost of repairs is significant
High	Key components may have lost structural integrity and building collapse due to environmental conditions (i.e. wind, snow, rain) may occur. Building should not be occupied. Total cost of repairs approaches replacement cost of building

In an ideal design, a blast-resilient building will absorb some of the blast energy through minor plastic deformation of some components while still maintaining the structural envelope. In order to achieve this, individual building components are typically designed to achieve response levels between ‘low’ and ‘medium’, depending on their function as described in table 5.B.1.B of the ASCE document. Limit values, which the blast specimens in this test program were compared against, are taken from table 5.B.2 in the ASCE document (ASCE, 2010) and summarised in Table 2.

Table 2. *Component response criteria (ASCE, 2010)*

Component	Low Response		Medium Response		High Response	
	Ductility ratio (μ)	**Joint rotation (θ)**	**Ductility ratio (μ)**	**Joint rotation (θ)**	**Ductility ratio (μ)**	**Joint rotation (θ)**
Steel primary members (with compression)	1.5	1	2	1.5	3	2
Steel primary members (without compression)	1.5	1	3	2	6	4
Steel plates	5	3	10	6	20	12

It would not be practical to specify the application of PFP on structural steel that would need to be replaced if subjected to a 'high' response design level blast event as the compromised structural integrity of the building would pre-empt any concerns about the condition of the fireproofing. However, it is incumbent upon both the engineer and fireproofing manufacturer to demonstrate that the fireproofing can withstand design level blast events without significant loss in integrity and fire performance.

Historical methods of assessing PFP integrity following an explosion resulted in no permanent deformation occurring during the test and thus, PFP performance at 'low' or 'medium' design damage levels are not explored.

There are currently no formal test standards published that address PFP resilience to blast conditions. Therefore, International Paint worked with DNV to conduct a large-scale gas explosion testing on a range of representative structural elements to simulate realistic damage levels (low and medium) used in blast-resistant design.

1. Experiment

International Paint worked with DNV to conduct the blast testing program at Spadeadam facility in the UK. Two distinct test specimens, a corrugated plate, and a plate girder were selected in order to capture blast response on real world structures. The performance criteria against which PFP should be judged are twofold: qualitative and quantitative. The qualitative assessment establishes PFP integrity following explosion testing of structures achieving various response levels. These qualitative criteria are defined in terms of crack initiation and associated dimensions, delamination, and/or detachment. The quantitative assessment of whether the PFP is apposite following an explosion will be achieved through fire testing to compare insulation performance versus a control sample.

1.1. Explosion chamber

A total of eight natural gas explosion tests were conducted using a 786 m^3 (12mx8mx8m) section of the Large Explosion Chamber (LEC) designed and built by DNV as shown in Fig 1. Computational Fluid Dynamics (CFD) was used to determine the loads on the walls, roof panels and the specimens placed outside the vent at the north end of the chamber. To increase the magnitude of the overpressures generated in the LEC, two congestion modules (3 m^3) were placed close to the ignition point within the chamber.

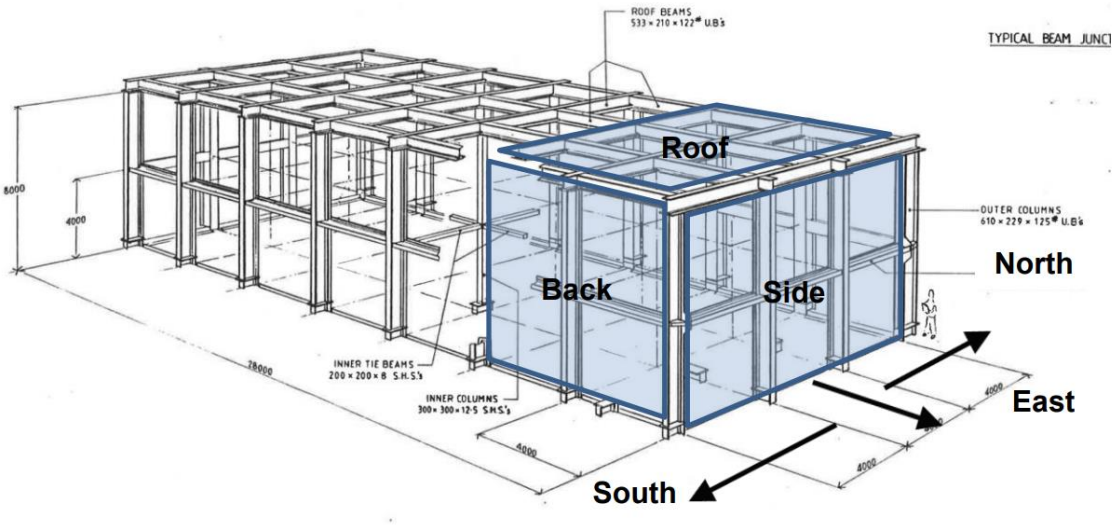

***Fig 1**. Steel framework used for Large Explosion Chamber (LEC) with blast chamber shaded*

1.2. Overpressure

The blast magnitudes measured align with the values in Table 2.1 of the ASCE document (ASCE, 2010) which is based on historic atomic bomb testing (70-1000 mbar) and also with API 2FB Table C.6.3.1-1 (API, 2006) which is based on safety case studies (500-3000 mbar). The first experiment (Test 1) was a commissioning test conducted at gas concentrations lower than stoichiometric equivalent to examine rig and instrumentation functionality as well as calibration without fully loading the specimens.

The subsequent four tests (Test 2 to 5) were at stoichiometric concentration but did not deliver the expected blast severity. This is speculated to be a result of chamber moisture content, restricted air movement and poor-quality mixing of fuel gas and air. In order to reach peak blast loads, the spark ignition location was moved closer to the back (south wall) in line with the congestion modules. As a result, test 6 to 8 delivered the required explosion severity. Table 3 provides a summary of the pressure measurements for all the tests. The overpressure data shown in Fig 2 has been time shifted to group all eight tests together and also to accommodate the delay in chemical fuse heads from initiating the explosions. However, similarities can still be observed with Test 2 and 5 along with Test 6, 7 and 8. This establishes the repeatability of the test setup.

***Table 3**. Summary of pressure measurements of all tests*

Test number	Maximum Pressure (mbar)	Rise Time (ms)	Duration (ms)
Test 1	456	139.3	262
Test 2	1227	96	243
Test 3	1364	112.9	225
Test 4	1093	129.7	311
Test 5	1399	106.0	217
Test 6	1844	99.2	199
Test 7	2248	101.0	207
Test 8	1558	108.4	242

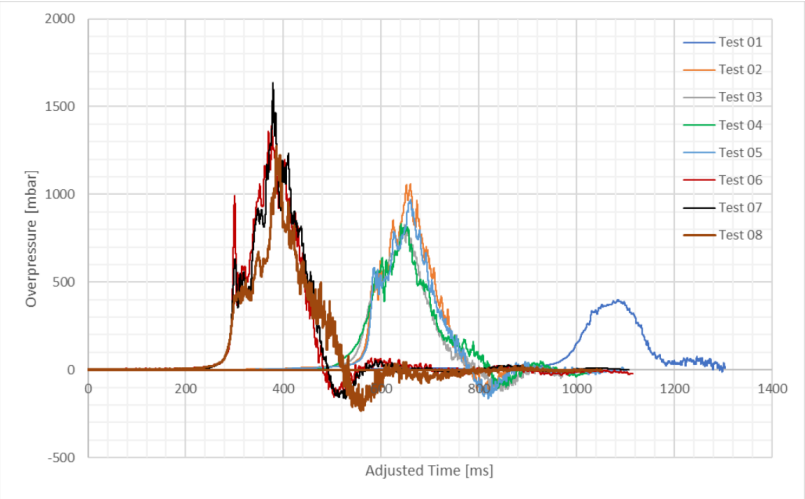

Fig 2. *Representative overpressure profiles from Test 1 to 8 with adjusted timing*

1.3. Passive Fire Protection coating

PFP coatings are used in the industry to provide thermal insulation to steel structures in the event of a fire. Two epoxy intumescent coatings (EPFP1 and EPFP2) have been supplied by International Paint for the purposes of this study and are high performance for protection against cryogenic spills, hydrocarbon pool fires and jet fires. The Dry Film Thickness (DFT) of coating prescribed to all specimens are based on 120-minute duration Hydrocarbon pool fire or 60-minute duration Jet fire protection, based on type approval data.

1.4. Specimens

The study considered two distinct specimen types to understand blast response on real world steel structures; plate girders i.e. primary structure and corrugated panels i.e. blast walls. These were chosen to align with the ASCE document criteria for 'steel plates' and 'steel primary frame members without significant compression loads. The steel used conforms to S275 grade and the resulting material properties.

1.4.1. Plate girders

Two plate girders, of a representative length used in typical designs of oil and gas facilities were tested in this study where the first plate girder (PG1) was oriented to be bent about its weaker minor axis and the second plate girder (PG2) about its stronger major axis: both spanning perpendicular to the blast as shown in Fig 3.

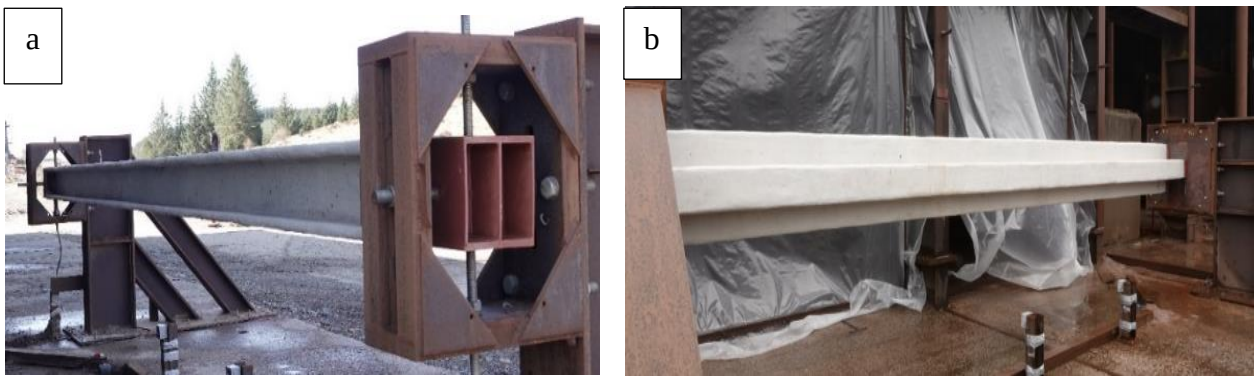

Fig 3*. Plate Girders: PG1 oriented in minor axis (a), PG2 oriented in major axis (b)*

The girders were supported on two stands to provide only a 'simply supported' boundary condition and were positioned outside the vent of the explosion chamber where they were exposed to a combination of pressure and drag loading from the flow through the vent. PG1 was designed and fabricated with a flange width of 300 mm, depth of 290 mm, and span of 8 m.

PG2 was designed as an asymmetrical plate girder with a depth of 300 mm, and span of 8m. A large explosion-facing flange of 575 mm width was fabricated to attract more load onto the specimen, necessary now that major axis bending was the primary structural phenomenon. The flange was also reinforced with 20 mm stiffeners at 400 mm centres. Its design was governed by the predicted blast load and the targeted blast response.

1.4.2. Corrugated Panels

The corrugated panels tested, shown in Fig 4, were 3000 mm x 3000 mm x 8 mm thick steel crimped plate with a height and width of 3 m x 3 m, designed and manufactured by MECHTOOL. Panels spanned top to bottom only and were also 'simply supported'. The coating was applied to the blast-exposed face only since compressive and tensile strains could develop in the coating in this configuration alone, due to the presence of the corrugations.

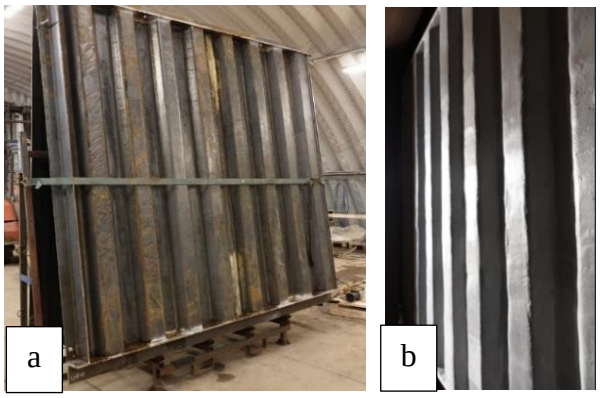

***Fig 4**. Corrugated panel: Prior to application with EPFP1 (a), Coated with EPFP1 on the blast- exposed side (b)*

2. Blast test results and coating response

The response or damage level of the structural steel specimens was measured following the series of explosion tests performed on the specimens mentioned in 1.4. Structural steel response levels were determined by evaluating pressure measurements taken inside and outside the explosion chamber, strain measurements from the test specimens, displacement measurements, and calculated joint rotation angles. The level of response as per Table 1 was defined in accordance with the criteria given within the ASCE document (ASCE, 2010). The performance of the epoxy intumescent coating was then evaluated both qualitatively and quantitatively.

2.1. Corrugated panels

Corrugated panels CP1 and CP2, which were coated on the blast-exposed side with EPFP1 and EPFP2 respectively, were determined to have reached medium response. The explosion caused some permanent bending of the corrugated panels, which was measured at 20 mm (CP1) and 40 mm (CP2). No defects were present on the coating of CP1 post-test whereas CP2 coating suffered hairline cracking. Fig 5 shows the permanent deflection of the panels post-test.

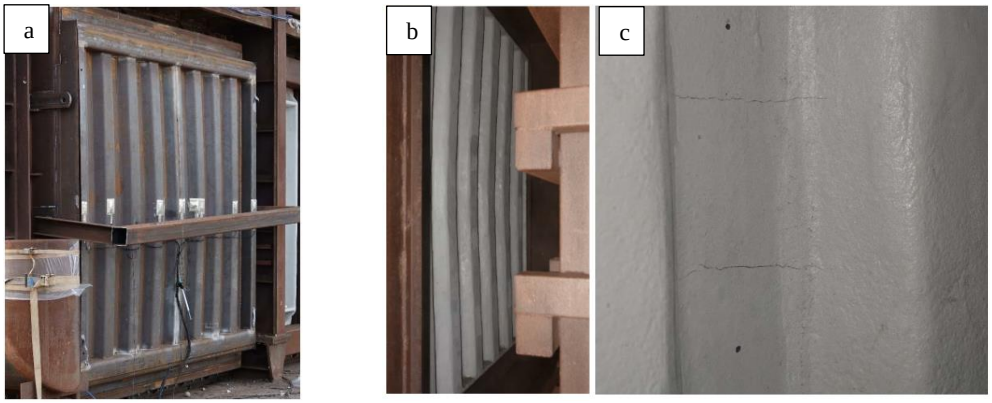

***Fig 5**. Corrugated panels post-test. Back face deflection on CP1 (a), CP2 Deflection of blast facing side (b) and hairline cracking of PFP on tensile side (c)*

2.2. Plate Girders

Plate girder PG1, which was coated with EPFP1 and subjected to blast loading about its minor axis, was determined to have reached medium response. The plate girder was plastically deformed after the end of the test, as shown in Fig 6. The permanent deflection in the centre was measured with string line and tape measure to be 40 mm. No damage to the EPFP1 coating was observed.

Plate girder PG2, which was coated with EPFP1 and subjected to blast loading about its major axis, was determined to have also reached medium response. The asymmetric girder in Test 8 experienced 70 mm permanent deflection and some cracks were found on the tensile face side of the neutral axis on both the web and the flange, as shown in Fig 6. Visual inspection of the cracks indicated that they are thin in nature and don't appear to have impacted adhesion of EPFP1.

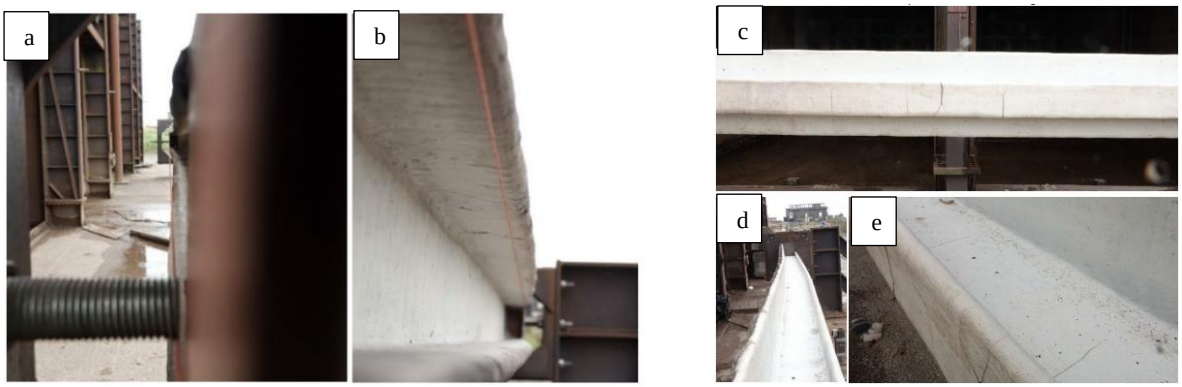

***Fig 6.** Plate girders post-test. Bending on exposed face (a) and bending on tensile face of PG1 (b), Bending of PG2 (d) and crack formation on unexposed flange (c and e)*

2.3. Results summary

A detailed summary of the blast test results is provided here in Table 4.

***Table 4.** Blast test results summary*

Specimen	Test number	Product	Joint rotation (θ)	Damage levels	Coating description
CP1	Test 8	EPFP1	4.5°	Medium	No damage
CP2	Test 7	EPFP2	3.5°	Medium	Hairline cracking
PG1	Test 1 to 6	EPFP1	1.2°	Medium	No damage
PG2	Test 8	EPFP1	1.5°	Medium	Minor cracking on tensile side

2.4. Jet fire testing of blast specimens

The results from the blast testing on PG2 and CP2 showcased small, defected areas of PFP coating. Therefore, fire testing of these specimens' post-blast was undertaken to compare the performance of defected coatings to the expected performance of PFP from type approvals (PG2) or a control (CP2), in order to assess the effect of cracking on PFP product performance. In doing so, a series of Jet fire tests were conducted in accordance with ISO22899-1 standard (ISO, 2007). The Jet fire tests were conducted for 120 minutes throughout.

Plate girder (PG2) was tested as a 1-sided protected scenario considered on the narrower lower flange which contained cracking. Thermocouples (TC) were arranged as per the test standard and included additional measurements at the cracks. Fire tests showed no appreciable loss in performance for corrected data as shown in Fig 7.

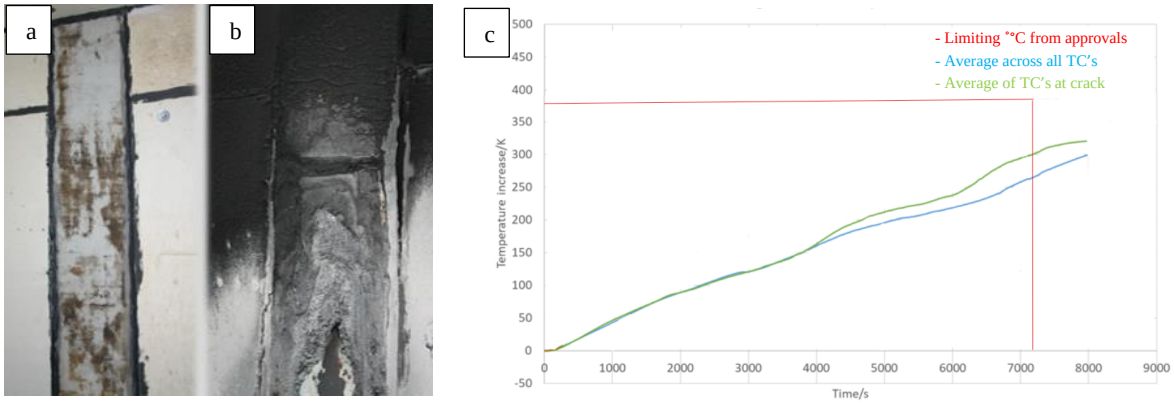

Fig 7*. Jest fire test of specimen PG2. (a) PG2 pre-Jet fire test (b) Char formation of PFP post Jet fire test. (c) Temperature-time curve of PG2 thermocouples showcasing negligible reduction in PFP performance.*

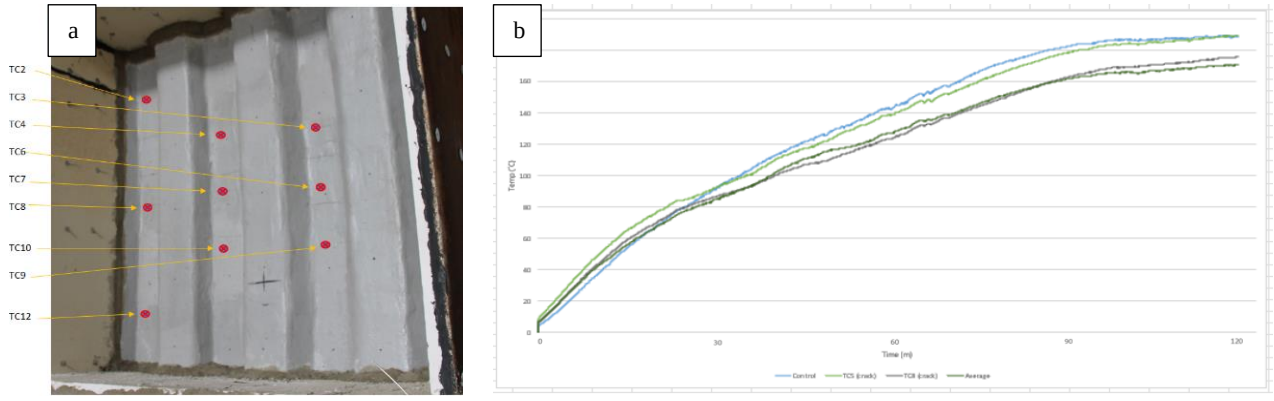

Fig 8*. Jet fire test of specimen CP2. (a) Thermocouple arrangement on coating side including at the cracked regions, (b) Time-temperature curve of CP2 thermocouples showcasing negligible reduction in PFP performance*

Corrugated panel (CP2) was tested as per the standard with additional thermocouples beneath the cracks. Fire test data was used to compare the thermocouple temperatures at regions with and without crack as shown in Fig 8. The results were also compared against data from jet fire testing of non-blast panels of a similar specification, albeit with corrections made to account for differences in steel plate thickness and coating DFT. The jet fire test data showed no appreciable loss in the performance post-blast scenario.

2.5. Explicit finite element modelling

International Paint outsourced the finite element (FE) modelling of three blast test scenarios to Dassault Systems to simulate the testing configuration, deflection as well as the PFP cracking on Simulia/Abaqus package. If good correlation was observed, the PFP response to realistic blast scenarios can be simulated and therefore predicted for project-specific details from modelling approaches verified against full scale testing. This would also avoid the need for impractical and expensive future large scale blast testing. Steel material properties as per S275 grade were utilised with ultimate tensile strength of 476 MPa at 32% strain and yield strength (F_y) of 297Mpa as per mill test certification. PFP properties, were utilised as per the testing conducted by a third-party independent laboratory where nominal stress-strain curves were converted to true stress-strain format for simulation. Blast overpressure and drag data from pressure transducers were simplified to obtain peak amplitude and create a nominal pressure-time curve.

A progressive damage model is used to define material damage and failure in FE modelling. The strength and stiffness of material reduces as the damage variable increases. Once an element reaches 95% of failure displacement it is referred to as a fully damaged element and represented as a crack. Fig 9 shows crack formation in CP2 created using this methodology which agrees with test results.

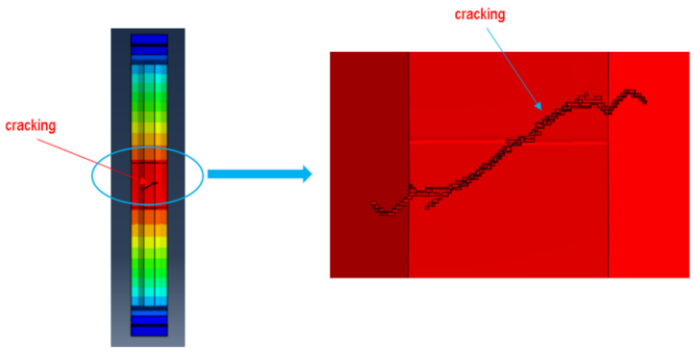

***Fig 9**. Simulation of coating damage as observed in testing of specimen CP2*

A 'perfect' geometry model with no imperfection has been assumed and designed for PG2 which is coated with a 'real' layer of PFP to simulate the imperfections that exist in real world applications. Geometric imperfection within the coating is introduced by removing individual mesh elements from the flange tips (tensile end) and by shifting the nodes on the surface to create shallow grooves which mimic discontinuity on the top surface of PFP coating. This 'imperfection' in turn reduces the damage initiation value required to induce crack formation. Thus at 20% damage initiation value, a single crack appears as shown in Fig 10.

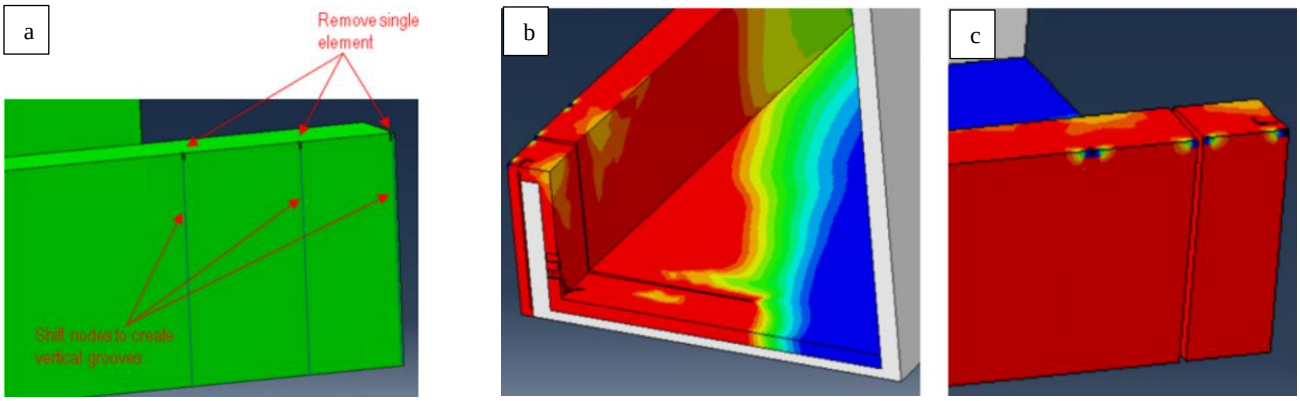

***Fig 10**. Inducing coating imperfection in PG2 (a) Crack formation at 20% damage initiation value (b-c)*

From the results of the simulation, it is evident that the modelling is in very good agreement with the deflection calculations as well as coating damage. The summary of the results from the simulation are provided in Table 5.

Table 5. *Simulia/Abaqus finite element modelling results*

Model	Test deflection	Simulation deflection	Test cracking	Simulation cracking
PG2	70mm	70.15mm	Cracking	No cracking unless coating made 'imperfect'
CP1	20mm	18.4mm	No cracking	No cracking
CP2	40mm	38mm	Hairline cracking	Single crack

3. Discussion and conclusions

International paint have undertaken eight natural gas explosion tests to verify the resilience of PFP on steel test specimens. The design of blast test was carried out to ensure representative specimens were subjected to large scale blasts with subsequent plastic deformations. Industry guidance and relevant applicable design standards have been considered in achieving this.

The results of these tests have shown that no significant damage has occurred to the PFP coating on the blast exposed side of the specimens. Rather, since the majority of the cracks found are concentrated towards the tensile part of the sections, it is clear that induced tensile strains are most critical to PFP survivability. The primary performance affecting parameters of PFP such as debonding, primer level detachment and large cracks have not been observed in any of the test scenarios. It is also important to note that even after subsequent blast loads (Test 1-6), specimen PG1 showed no signs of damage on its coating.

Subsequent fire tests on blasted specimens have demonstrated that the presence of defects within the coating did not adversely impact on insulation performance when subjected to the ISO22899-1 jet fire test for 120-minute duration (ISO, 2007). Further, the thermocouples placed behind the cracks in the PFP showed no significant increase in steel temperature. The results highlight the integrity of the epoxy passive fire protection tested to withstand low and medium level structural response scenarios.

Simulia/Abaqus finite element modelling has shown good agreement with test results and shows promise as a viable alternate approach to large scale blast testing in assessing PFP performance under blast. Further modelling work and sensitivity analyses have been planned to characterise the epoxy passive fire protection non-linear response and failure point. A further investigation on FE modelling using Extended Finite Element Methodology (XFEM) has been planned to assess 'micro-crack' propagation through the thickness of the PFP.

The testing has provided a great insight into the effectiveness of large-scale blast testing and its requirement in understanding the behaviour of intumescent PFP coatings in synergistic blast and fire loads. The understanding and information gained is intended to give insight and context in the development of the new ISO draft standards for testing PFP coated steel work subject to blast.

4. References

API, 2006. *American Petroleum Institure Recommended Practice 2FB, First edition.* Washington DC: API.

ASCE, 2010. *Design of Blast-Resistant Buildings in Petrochemical Facilities, Second Edition.* Virginia: ASCE.

ISO, 2007. *International Standard Organisation (ISO) 22899-1, First edition.* Geneva: ISO.

Delayed ignition of high-pressure hydrogen releases – experiments and engineering models

Vincent Blanchetière [a], Adam Armstrong [b], Yanshu Wang [a], Romain Jambut [a], Brian Wilkins [b], Nicolas Salaün [b]

[a] GRTgaz, Villeneuve-la-Garenne, France
[b] GEXCON AS, Bergen, Norway

E-mail: vincent.blanchetiere@grtgaz.com

Abstract

Before operating its first hydrogen transmission pipelines, GRTgaz is developing methods and engineering models for risk assessment and consequences analysis. In this framework, GRTgaz decided in 2022 to launch an experimental campaign to understand the consequences of delayed ignition of high-pressure pure hydrogen releases, in open field. The tests also included ignited releases of methane-hydrogen mixture, with 2% and 20% of hydrogen. GRTgaz was associated with Storengy to fund this campaign performed by Gexcon AS. The tests took place at the test facility of Gexcon in Sotra island, close to Bergen (Norway).

The campaign was divided in two test series. The phase 1 aimed at characterising gas concentration in the release axis to provide validation data for simple models and to facilitate the positioning of igniter for the explosion tests, in phase 2. In this second phase, the releases were ignited by chemical devices or electrical sparks, located in the axis at different equivalence ratio. The release system designed by Gexcon enabled to perform 40 barg releases through calibrated orifices of 4 and 6 mm. In total, 15 tests were performed for the first phase with unignited releases and 29 explosion tests for the second phase. All tests are steady-state horizontal releases.

The test results provide comprehensive data to better understand hydrogen jet explosion and challenge engineering models. The maximal overpressures were well above the blind predictions, with records over 650 mbar close to ignition region, where about 200 mbar were expected. High-speed videos showed a tremendous acceleration around the ignition source that cause these intense overpressures coupled with very short-duration positive pulses. These results tend to indicate that the overpressure is produced in a limited volume compared to the flammable plume.

Then, simulations with the PERSEE+ software are compared to the experiments. Dispersion results are in good agreement with the recorded concentration with a relative deviation around +/- 30%. For overpressures, the prediction in the far field is also acceptable, whereas effects in the near field are often underpredicted. The article finally discusses about improvement of engineering models to estimate consequences of a delayed ignition of high-pressure hydrogen releases.

Keywords: *hydrogen, jet release, unconfined explosion, consequences analysis*

Introduction

Through the ratification of the Paris agreement on climate change, the international community under the United Nations has set up a series of challenging environmental goals to transform the global economy as to limit the impact of our power generation, production methods and consumption patterns on the climate system. This implies for the energy sector to change drastically its business

Classification GRTgaz : Public [ ] Interne [X] Restreint [ ] Secret [ ]

model and technologies towards a decarbonised system to ensure the growing population to benefit from an affordable and reliable energy while reducing the greenhouse gases emissions.

With the goals to move the society to a low carbon economy, the use of hydrogen as a new energy carrier appears more and more relevant for new types of industries and for the decarbonation of historical industries relying on a hydrocarbon-based economy, such as energy providers or gas network operators. GRTgaz is one of the main gas network operators in Europe with a 33 700km long natural gas network. To address these new challenges, GRTgaz is upgrading its network for the new gases such as hydrogen. GRTgaz has joined forces with other European energy infrastructure operators to create the European Hydrogen Backbone (EHB) initiative, which aims to accelerate Europe's decarbonisation journey by defining the future hydrogen network based on existing and new pipelines. Strong investments are underway to operate 31 500 km of hydrogen pipelines prior to 2030.

Storengy, as the first natural gas storage operator in Europe, is developing new underground storages to support hydrogen development in Europe. The development of storage facilities in salt caverns will enable to balance hydrogen production and consumption needs and manage the intermittent nature of renewable energies and provide tools for flexibility and optimisation of electricity grids.

Converting existing natural gas installations to hydrogen implies to address some major issues to ensure a safe design and operations such as material compatibility, hazardous area classification, operating philosophies, gas quality, safety, etc. GRTgaz and Storengy are supported by the GRTgaz Research and Innovation Center for Energy (RICE) in addressing these topics by carrying Research & Development work in its different laboratories such as the FenHYx platform or the Jupiter 1000 power to gas demonstrator. RICE has also developed numerous partnerships with external test fields and experts to conduct various types of experiments.

In this context, GRTgaz and Storengy have decided in 2022 to conduct dispersion an explosion tests for high pressure hydrogen releases in open field. For these medium-scale tests, RICE has chosen the test facility of Gexcon AS in Sotra island, close to Bergen (Norway). The main objectives of these tests are to estimate the overpressures generated by the delayed ignition of a hydrogen turbulent jet release, and to better understand the explosion mechanism. RICE acquired a good knowledge of this phenomenon for natural gas release thanks to experimental campaigns at medium (Sail et al., 2014) and large-scale (Hisken et al., 2021). These tests demonstrated that, for natural gas, ignition in the turbulent core of the flammable plume generates non negligible overpressures even without congestion or confinement. However, these explosion effects are limited compared to thermal effects of the subsequent jet fire.

The higher reactivity of hydrogen compared to natural gas implies more severe flame acceleration and higher explosion effects, which will be no longer negligible compared to thermal effects, including without congestion or confinement. Past experiments performed by INERIS (Daubech et al., 2015) or DNV (Miller et al., 2015) with medium and large hydrogen releases highlighted the dependency of maximal overpressure with ignition location and the intensity of jet explosion, with measured overpressures above 0.4barg. Based on these experimental works, engineering methods have been proposed (Jallais et al., 2017) to predict safety distances for hydrogen jet explosion in open field.

The tests performed by Gexcon in Sotra provides numerous validation data to assess the engineering method and to understand this particular type of hydrogen explosion.

Classification GRTgaz : Public [ ] Interne [X] Restreint [ ] Secret [ ]

1. Experimental set-up

1.1. Release configuration

The explosion experiments were performed using a dedicated jet release system, where the gas is supplied through a pressurized manifold via 6 skids of 12 bottles (Figure 1). Each bottle contained about 50 litres of hydrogen, with an initial pressure around 180 to 200 barg. The gas supply manifold and connected equipment was protected from the release by a concrete barrier.

Fig. 1. *Overview photograph of the gas supply manifold system, showing the gas supply skids, their high-pressure hosing (red hoses), the pneumatically actuated ball valves (circled in green) and Coriolis flow meter (circled in red).*

The pressurized manifold had an internal diameter of 100mm, and a length of approximately 6m, and fed the test gas through a DN25 piping system to the release nozzle. Two calibrated circular nozzles were used to generate 4mm and 6mm diameter releases (Figure 2).

Fig. 2. *Photograph of the 4mm-diameter nozzle used to mimic small puncture.*

Classification GRTgaz : Public [ ] Interne [X] Restreint [ ] Secret [ ]

Pressure was monitored in the manifold and at the nozzle with both an analogue pressure gauge as well as a 0-100 barg pressure transducer. Temperature in the manifold was also monitored with a 1.5 mm diameter steel-mantled K-type thermocouple.

Gas flowrate was monitored after the manifold and a reduction down to DN25 where a Coriolis flow meter was connected. The Coriolis flow meter is a Endress+Hauser Promass F 300 with a range of 0-100 g/s for pure hydrogen, and a low-flow signal cut-off for flows below 1% of the full range.

Downstream from the Coriolis flow meter there was a DN25 actuated valve which acted as the main gas release on/off valve as it isolated the manifold from the release nozzle. A flexible hose (DN25) was used after the main on/off valve for height adjustment of the final 6 m long DN25 pipe including the nozzle on the tip.

Prior to a test, the manifold was pressurized from one of the skids to slightly above the intended test pressure. When the test began, the valve supplying the nozzle was opened, and then 500ms later all the valves going to the skids were opened. This way, the release system provided a constant mass flow rate for the duration of the tests, about 20s for the dispersion tests and 15s for the explosion tests.

1.2. Gas concentration measurement system

The first part of the campaign aimed at measuring the gas concentration in the jet axis to locate the ignition source at the chosen initial concentration.

To get a good understanding of the concentration gradient of the fuel during a given release, 8 sampling locations were used along the jet release axis, although additional locations are also monitored for some of the tests for diagnostic purposes leading to a dataset with up to 10 sampling locations. All the locations were monitored using galvanic cell oxygen sensors to measure the oxygen content at the sampling location, which was then used to calculate the concentration of the test gas at the location. At two of the locations, the concentration was also measured by a binary gas analyzer for results verification, and also to ensure that the oxygen to fuel calculation from the galvanic cells was working at an acceptable level.

To take the samples, a copper tube had one end suspended at the sampling location, which was then connected to a measuring chamber, which then was connected by nylon hosing to a vacuum pump. The gas sampling rate was approximately 500 ml/s at each location. Since the sample measuring chamber had an internal volume that must be filled, as well as all of the connected hosing, both a delay in initial response, as well as a delay in full value signal was present. Extensive pre-testing references were carried out to determine these values, so that the gas cloud releases were held as short as possible to conserve fuel. It was found that a 20 second release would be sufficient to reach a steady state value for all the locations, accounting for both the delayed initial sampling time, exchange time within the sample measuring chamber, and the gas diffusion time within the galvanic cell itself.

For locations with higher gas concentrations, this set-up led to a dataset with an extended period of steady state gas concentration. For locations with lower gas concentrations, in far field, this set-up led to a dataset where the steady state gas concentration is reached for only a second or two before the release shutdown.

1.3. Ignition system

During the explosions testing, two different ignition sources were used, one being chemical based, and the other electrical. The chemical ignitor used was a 100 J pyrotechnical ignitor produced by Fr. Sobbe, model EBBOS ChZ. This ignitor produced a flame “ball”, about 10cm diameter, directly in front of the ignitor itself, with the casing acting as a shaped charge. The electrical ignitor used was a Danfoss EBI4, which produced an oscillating spark at 50 Hz, with a voltage of 15 kV. The sparks generated last for 10 ms, followed by a period of no spark for 10 ms, followed by a 10 ms spark, and

Classification GRTgaz : Public [ ] Interne [X] Restreint [ ] Secret [ ]

so on until deactivated. The sparks were produced between two steel electrodes with a spark gap of approximately 5mm.

1.4. Blast pressure measurement system

The blast pressures were measured by eight 0-1600mbara piezoresistive pressure sensors, with 20 kHz acquisition rate. The sensors were placed outside the plume, in different orientations relative to the release and ignition location. Initially, all the plates were positioned perpendicular to both the ground and the jet axis, or the anticipated ignition location. However, after experiencing stronger than expected blast pressures, it was determined that some of the blast sensors were likely experiencing significant amounts of stagnation pressure on the face of the blast plate and were therefore rotated to face upwards such that they were still perpendicular to the release, but then parallel with the ground, as shown in Figure 3, and therefore less susceptible stagnation pressures.

***Fig. 3.**: Photograph of the sensor layout and the orientation of the blast pressure plates*

2. Results and discussions

2.1. Release characteristics

The release system designed by Gexcon enabled to reach a plateau with constant mass flow rate, for all the 10 dispersion tests (301 to 310) and 20 explosions tests (401 to 420) performed with pure hydrogen. The control of the mass flow rate is essential to get reliable concentrations values with the oxygen meters and to ignite well-characterised releases.

For test 310, which is a 4mm release, the mass flow rate measured by the Coriolis flowmeter was 32g/s (Figure 4). The nozzle exit pressure was measured at 42.6barg. As illustrated here, the system of skids and manifold was sufficient to provide a steady controlled release rate. The only limitation experienced for this system was the reproducibility of the nozzle exit pressure. With a targeted pressure of 40barg for all tests, the standard deviation is about 2.6bars, i.e. 6.5% of the full value. It implies a slight variability of results for repeated tests induced by release pressure difference.

Classification GRTgaz : Public [ ] Interne [X] Restreint [ ] Secret [ ]

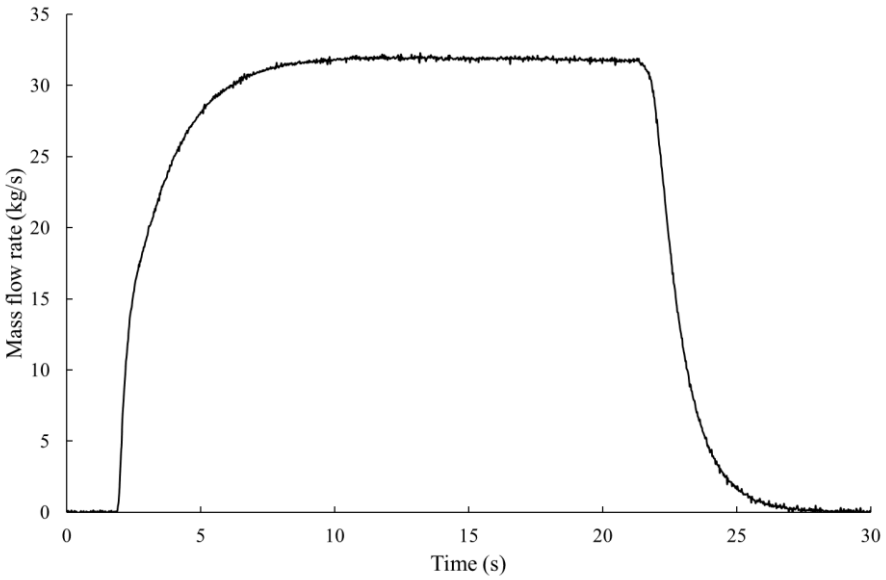

***Fig. 4.**: Mass flow rate curve for test 310*

2.2. Dispersion tests

The campaign included 10 dispersion tests with two release diameters, 4 and 6mm, and three release heights, 0.1, 0.2 and 1m above a flat concrete ground.

For test 310, the sampling tubes are located at 0.15m, 0.3m, 0.45m, 0.6m, 0.75m, 0.9m, 1.5m and 2m in the jet axis (Figure 5). The concentration values are averaged over one second, i.e. over the last 50 consecutives values.

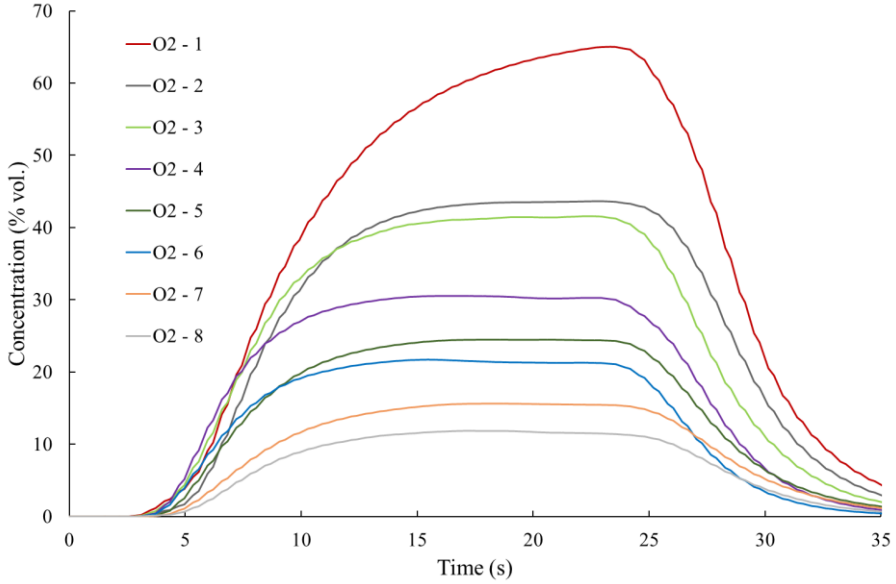

***Fig. 5.**: Concentration deduced with the oxygen meters for test 310*

The concentration profile based on maximal values approximatively follows a 1/x decay, where x is the distance to the nozzle in the release axis (Figure 6).

Classification GRTgaz : Public [ ] Interne [X] Restreint [ ] Secret [ ]

The following similarity law (Schefer et al., 2008) is proposed to calculate the mass fraction decay in the centreline (Y_{cl}) for hydrogen jet releases:

$$Y_{cl} = \frac{d\left(\rho_j/\rho_a\right)^{1/2}}{0.208(x-4d)}$$

where d is the nozzle diameter (m), ρ_j is the jet density at the nozzle (kg/m^3), ρ_a is the ambient air density (kg/m^3).

This relation enables a quick and simple evaluation of the hydrogen concentration compared to engineering tools or CFD simulations. For risk assessment studies, GRTgaz uses an in-house engineering software called PERSEE+. Initially, developed for natural gas and LNG releases, PERSEE+ is continuously improved especially to include hydrogen releases, since 2018. PERSEE+ integrates two different dispersion models. Model 1 is a top-hat dispersion model. The centreline concentration is estimated by considering mass, momentum, and energy conservation (Ooms, 1972). The radial concentration is given by gaussian profiles. Model 2 is an integral model for predicting the dispersion of a turbulent jet in a crossflow (Cleaver et al., 1990).

For test 310, engineering models are more accurate than the similarity law (Figure 6). In this case, the similarity law overestimates the concentration. At 2m from the nozzle, the relative deviation with the measured concentration reaches +34%. Daubech et al. (2015) showed a better agreement of the similarity law proposed by Schefer et al. for dispersion tests with a higher release rate, approximatively 250g/s.

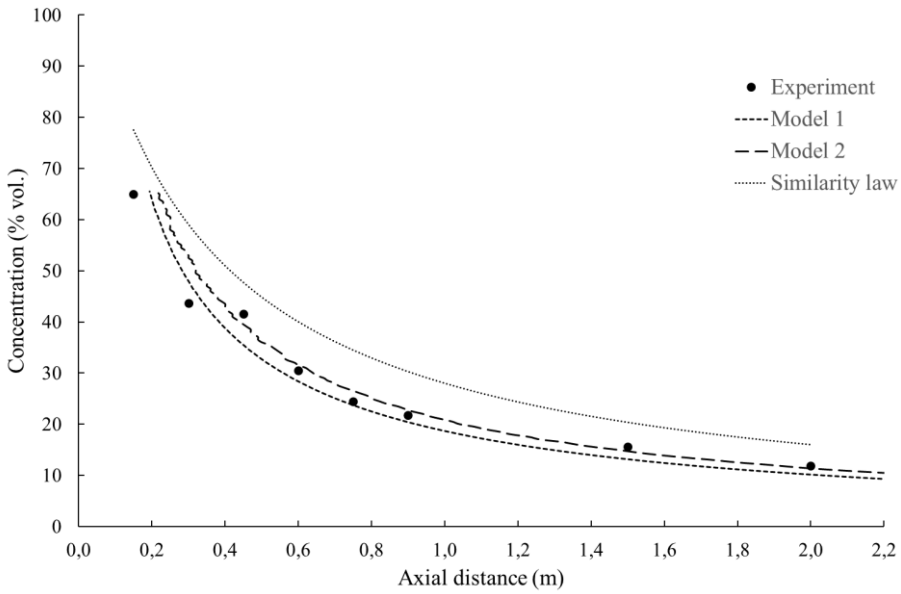

***Fig. 5.**: Comparison of similarity law and engineering models for centreline concentration decay measured for test 310*

For test 310, Model 1 is slightly less accurate than Model 2. This trend is confirmed when comparing with the measured concentrations for all the dispersion tests (Figure 7). By definition, Model 1 is not fully adapted for test releases close to the ground (0.1 and 0.2m high) since ground interaction is not taken into account. Model 2 seems particularly accurate for both releases with or without ground impingement.

Classification GRTgaz : Public [ ] Interne [X] Restreint [ ] Secret [ ]

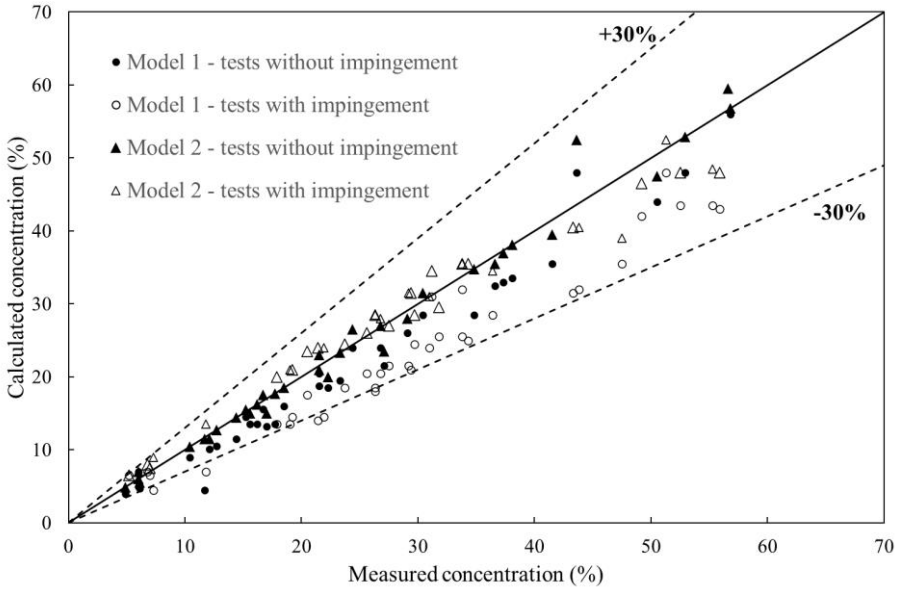

***Fig. 7.**: Comparison of engineering models with the measured concentration during the 10 dispersion tests*

2.3. Explosion tests

The campaign included 20 explosion tests with the same two release diameters, 4 and 6mm, and three release heights, 0.1, 0.2 and 1m. Three ignition locations were considered for releases at 1m high. Based on the dispersion tests, the igniters were located at the following centreline concentration: 50%, 45%, 30% vol. For the 4mm diameter releases, the ignition point at 50% is replaced by an ignition at 60%. For the releases at 0.1 and 0.2 m high, the igniters are only located at 50%. All tests were repeated twice, at least.

For the pure hydrogen tests, the blast pressure data was only post-processed with a baseline offset applied to convert the measured absolute pressure to a relative overpressure. As such, pre-ignition atmospheric conditions are represented as an average of 0 mbarg, and therefore any measured overpressures are relative to atmospheric conditions. There was no filtering of any kind. The default filter used by Gexcon was disabled, since for the preliminary tests, it tends to filter out the blast pressure, due to the very short duration of the peak (Figure 8).

The Figure 8 gives the overpressure signals for the 8 pressure sensors used for the explosion test 408. The position of the sensors for test 408 are given (Table 1) in considering the origin of the cartesian coordinate system at the nozzle, where Z is the vertical axis and X the release axis. The hydrogen plume is ignited by an electrical spark located at 0.5m in the release axis.

***Table 1.**: Position of the pressure sensors for the explosion test 408*

Sensors	P1	P2	P3	P4	P5	P6	P7	P8
X (m)	0.25	0.5	1	1.5	1.5	1.5	1.5	1.5
Y (m)	0.5	0.5	0.5	0.5	0.75	1	1.5	2
Z (m)	0	0	0	0	0	0	0	0

Classification GRTgaz : Public [ ] Interne [X] Restreint [ ] Secret [ ]

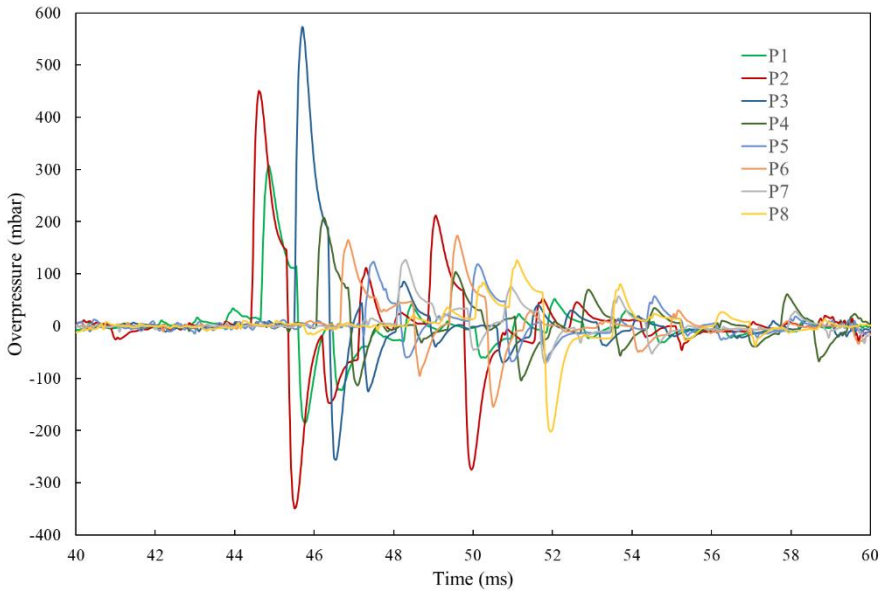

***Fig. 8.**: Overpressure results for explosion test 408*

The maximal overpressure observed for the test 408 is 573 mbar (57.3 kPa), measured by the P3 sensor. The maximal impulse is 30 Pa.s, also measured at P3. This very low impulse is explained by a very short duration of the first positive peak, approximately 1ms. According to the criteria given by Merx et al. (1992) for survival after lung damage, impact of the head or after impact of the whole body, these pressure and impulse values would not be sufficient to cause significant impact for human being. For a peak pressure of 573 mbar, the maximal impulse to be in a safe zone is about 3000 Pa.s for both impact of the head and impact of the whole body (Figure 9).

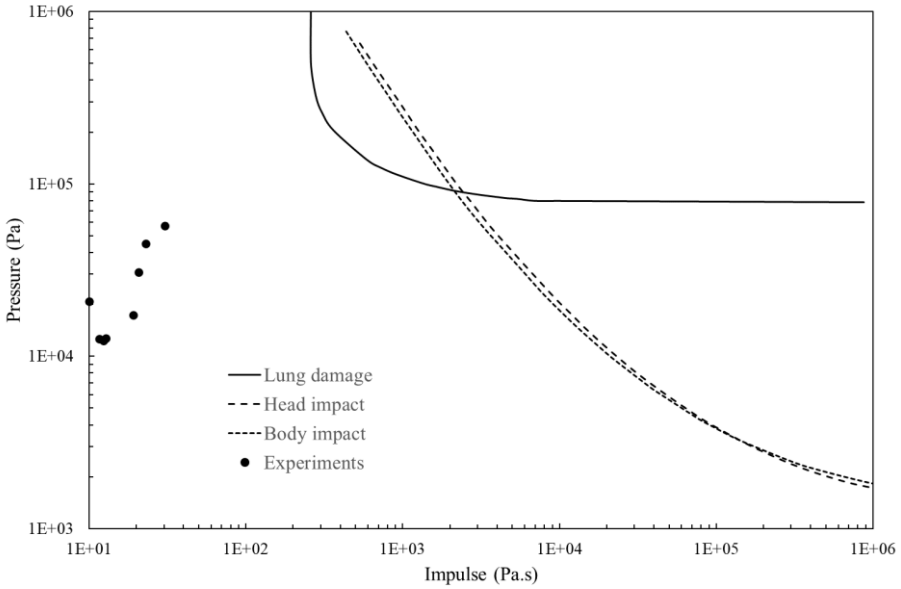

***Fig. 9.**: Comparison of measured pressure-impulse with lower limit defined for effects on human being.*

The high-speed camera captured 4000 images per second. The image processing was particularly challenging due to the low visibility of the hydrogen flame and the fluctuation of natural light. The test with the chemical ignitor facilitated the image processing. For test 403, similar to test 410 but with a chemical ignitor, the first images after ignition shows a quasi-spherical development of the flame front (Figure 10).

Classification GRTgaz : Public [ ] Interne [X] Restreint [ ] Secret [ ]

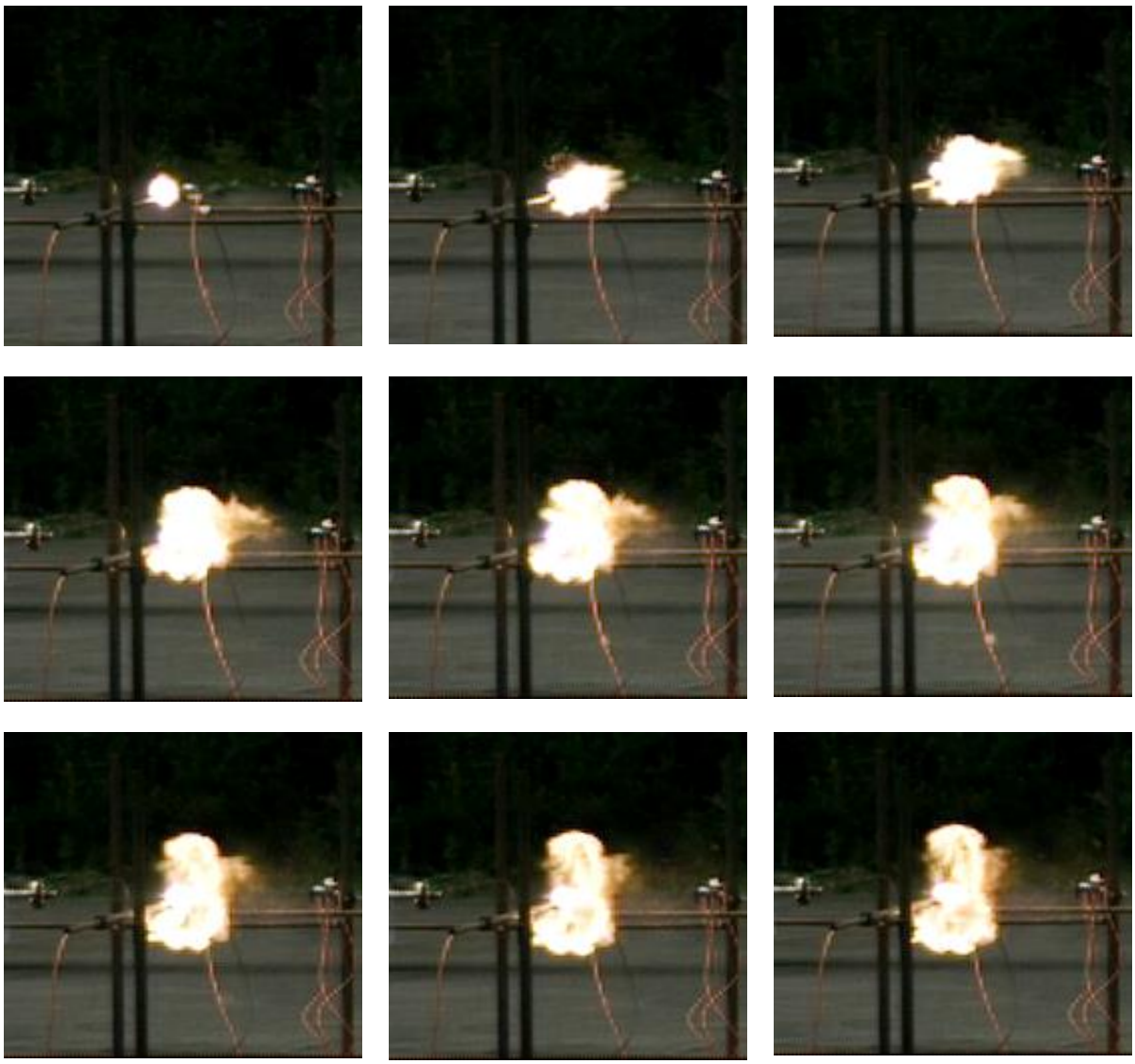

***Fig. 10.**: Consecutive images immediately after the ignition of the release for test 403.*

The post-processing of these images shows a quicker expansion of the flame front in the release axis compared to the radial direction (Figure 11). In both directions, the flame front follows a first phase of quick expansion, up to 470 m/s in axial direction and 120 m/s in radial direction, followed by a slower propagation. The gas flow velocity in the jet axis probably explains the quicker flame front propagation in the release axis compared to the radial propagation. For test 403, the gas flow velocity at the ignition point was estimated with PERSEE+ (model 1) at 278m/s.

The first phase of the flame propagation might correspond to the jet explosion whereas, the second might be the jet fire development. The "explosion" phase last about 1.5ms in the axial direction which is consistent with the duration of the pressure peak measured for both tests 403 and 408. These results suggest that only a very limited part of the flammable mass contribute to the overpressure generation. A similar behaviour has been observed for ignition of methane high-pressure release (Sail et al., 2014).

Classification GRTgaz : Public [ ] Interne [X] Restreint [ ] Secret [ ]

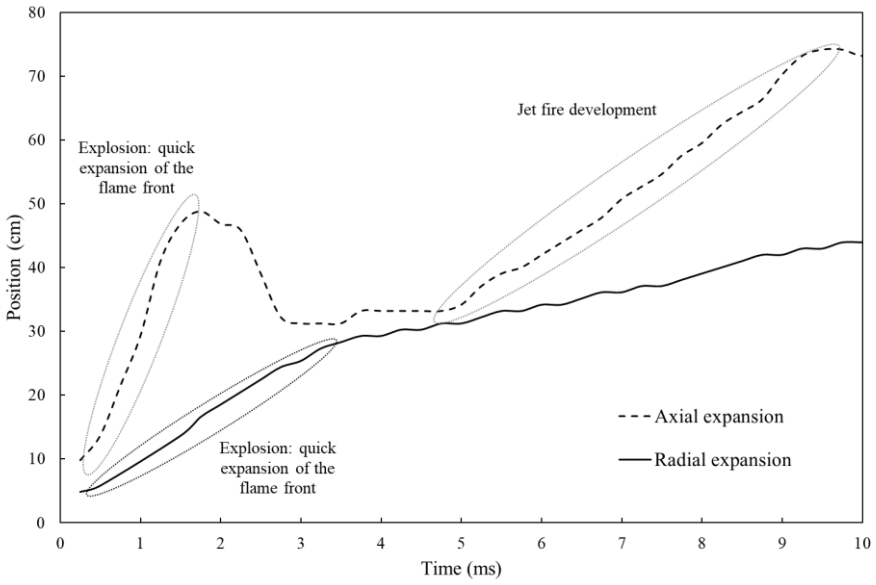

***Fig. 11.**: Position of the front flame from the ignitor in radial and axial direction for test 403*

To predict safety distances, Jallais et al. (2017) proposed an engineering method with a more conservative approach, i.e. in considering the entire mass of hydrogen between 10 and 75% vol. inside the plume when the ignition occurs. Jallais et al. (2017) also recommends TNO Multi-Energy index depending on the release rate and the hydrogen concentration at the ignition source (Table 2).

***Table 2.**: Recommended TNO Multi-Energy index by Jallais et al. (2017)*

Ignition concentration	Index 4	Index 5	Index 6
30% vol.	Below 0.5kg/s	0.5 to 1kg/s	1 to 10kg/s
55-65 %vol.	Below 0.1kg/s	0.1 to 1kg/s	1 to 10kg/s

Previously, Daubech et al. (2016) proposed an empirical curve of the dependency of maximal overpressure with mass flow rate, which enables to derive thresholds for the use of the TNO Multi-Energy index (Table 3). For a free jet, Daubech et al. (2016) suggests using this severity index in considering the fuel mass contained in the largest inscribed sphere along the flammable plume (4 to 75%).

***Table 3.**: TNO Multi-Energy index defined from Daubech et al. (2016)*

Ignition concentration	Index 5	Index 6	Index 7
Undefined	Below 0.45kg/s	0.45 to 10.9kg/s	from 108kg/s

GRTgaz implemented in PERSEE+ a hybrid solution, which considers the hydrogen mass between 10 and 75% (Jallais et al. 2017) and the thresholds given by Daubech et al. (2016). The comparison of this methodology and the overpressure results gives a satisfactory agreement in far field, to assess safety distances for human being (Figure 12). The overpressure thresholds defined in the French regulation are 20, 50, 140 and 200mbar, respectively for undirect hurts, irreversible hurts, first lethal effects, and significant lethal effects. For the free hydrogen releases and the measured overpressures

Classification GRTgaz : Public [ ] Interne [X] Restreint [ ] Secret [ ]

in the range of 20 to 200 mbar, the relative deviations are between -30% and + 30% for 44% of the calculated values and between -50% and +100%, i.e. a deviation by a factor 2, for 74% of the results.

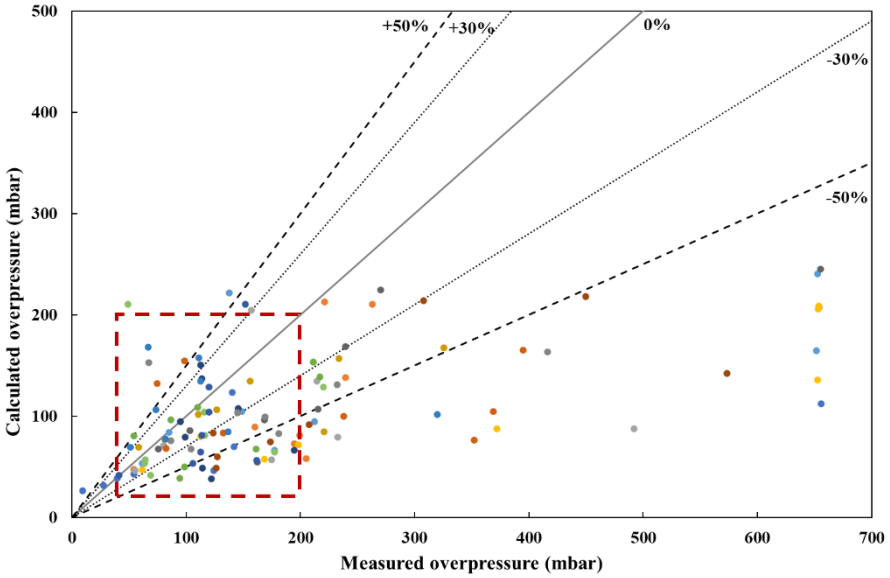

***Fig. 12.**: Comparison of engineering model based on TNO Multi-Energy with the measured overpressures.*

In the near field, the calculation method appears less accurate and underpredicts the overpressure for most of the values. It indicates that a different method should be used for near field prediction and application dealing with potential structural damages or domino effects.

Originally, GRTgaz developed for methane jet explosion a 1D model to calculate flame propagation and overpressure field, described by Sail et al. (2014). This approach uses an empirical correlation to estimate the turbulent burning velocity (S_T)$S_T = A \cdot u'^b \cdot {S_L}^c \cdot \upsilon^d \cdot {L_t}^e$ or $S_T = A \cdot u'^b \cdot {S_L}^c \cdot \upsilon^d \cdot {L_t}^e + S_L$. For this comparison, after testing different correlations from Dorefeev et al. (2007), Bradley et al. (1987) and Omer at al. (1990), the following relation of Bray et al. (1990) was selected:

$$S_T = 0.96\, u'^{0.912}\; S_L^{0.284} \left(\frac{L_t}{\upsilon}\right)^{0.196} + S_L$$

where *u'* is the root-mean-square of the turbulent velocity fluctuations (m.s^{-1}), S_L the laminar burning velocity (m.s^{-1}), L_t the turbulent length scale (m) and υ the cinematic viscosity of fluid (m².s^{-1}). The instantaneous flame front velocity is then deduced by $V_F = \sigma \cdot S_T$, where σ is the ratio between the density of burnt gas and unburnt gas.

Finally, based on incompressible assumption, the overpressure over time around the ignition point is estimated, according to Deshaies et al. (1981)

$$\Delta p(r,t) = \frac{\rho_0}{r}\left(1-\frac{1}{\sigma}\right)\left[2r_F(\tau)\left(\frac{dr_F(\tau)}{dt}\right)^2 + r_F^2(\tau)\left(\frac{d^2r_F(\tau)}{dt^2}\right)\right]$$

where r_F is the flame radius, r the distance from the ignition point in the radial direction, t the duration, ρ_0 the air density, and $\tau = 1-r/c_0$ where c_0 is the sonic velocity in air. The model allows to calculate and display the overpressure over time for each point of interest. This model is theoretically limited to incompressible cases, and thus to low Mach numbers ($M_f < 0.35$), corresponding to maximum flame speed around 120 to 150 m/s.

Classification GRTgaz : Public [ ] Interne [X] Restreint [ ] Secret [ ]

With this method extrapolated to hydrogen, PERSEE+ gives overpressures slightly lower than the previous method based on the TNO Multi-Energy method (Figure 13). The overall accuracy is relatively similar for the measured overpressures in the range of 20 to 200 mbar. The relative deviations are between -30% and + 30% for 40% of the calculated values and between -50% and +100% for 61% of the results. Above 200mbar, the underpredicting trend observed for the TNO Multi-Energy method is also observed with this second method.

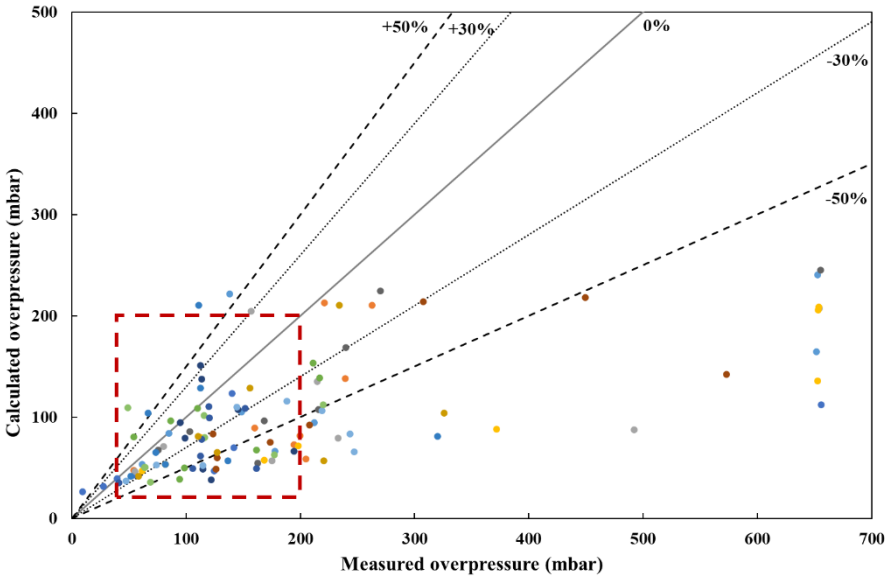

***Fig. 12.**: Comparison of engineering model based on the Bray correlation with the measured overpressures.*

The main interest of this method is the possibility to consider the effect of ignition location and the more realistic description of the explosion development. However, this approach shall be improved to solve the axial propagation of the flame front, instead of the radial propagation only. The incompressible assumption shall be ideally revised but might be challenging to overcome. Finally, a more refined way to estimate the turbulent burning velocity, considering the Lewis number effect, would also be more appropriate for hydrogen.

3. Conclusions

Thanks to the experimental set-up designed and operated by Gexcon, 10 dispersion tests and 20 explosion tests were performed, providing valuable data to characterise hydrogen jet explosions in open field and to validate engineering models used for consequence analysis.

For this experimental campaign, the engineering models for dispersion modelling shows a very good agreement with experiments. The relative deviation is lower than +/- 30%, which is a satisfactory result for simple models.

The explosion tests showed the potential intensity of hydrogen jet explosion in open field, with overpressures above 0.65 bar despite the limited size of the flammable plumes. These overpressures are apparently produced by the flame propagation in the vicinity of the ignition source, and not by the propagation in the whole flammable plume. This limited flammable mass involved in the explosion would explain the very short peak pressure duration, compared to other vapour cloud explosions. Consequently, the use of the maximum overpressure for consequence analysis might overestimate the explosion effects. Thresholds based on pressure-impulse are probably more appropriate for this specific kind of explosion. The comparison of the engineering models for explosion effects shows a good agreement with overpressure measurements below 200mbar.

Classification GRTgaz : Public [ ] Interne [X] Restreint [ ] Secret [ ]

However, in near field, the models tend to underpredict the peak pressures. These models should be revised for the assessment of domino effects and structural damages.

Acknowledgements

The authors gratefully acknowledge the financial contribution from Storengy and GRTgaz and the technical support of Gexcon teams.

References

Abdel Gayed, R.G., Bradldey, D., Lawes, M., 1987. Turbulent burning velocities: a general correlation in terms of straining rates, Proc. R. Soc. Lond. 414.

Bray, K.N.C., (1990), Studies of the Turbulent Burning Velocity. Proc. R. Soc. Lond. A 431:315-335.

Cleaver, R.P., Edwards, P.D., 1990, Comparison of an integral model for predicting the dispersion of a turbulent jet in a crossflow with experimental data, Journal of Loss Prevention in the Process Industries, Vol. 3.

Daubech, J., Hebrard, J., Jallais, S., Vyazmina, E., Jamois, D., Verbecke, F., 2015, Un-ignited and ignited high pressure hydrogen releases: Concentration - turbulence mapping and overpressure effects, Journal of Loss Prevention in the Process Industries, Vol. 36.

Daubech, J., Prats, F., Leprette, E., Merlier, F., Duplantier, S., 2016, Formalisation du savoir et des outils dans le domaine des risques majeurs - Les explosions non confinées de gaz et de vapeurs - Ω UVCE.

Dorofeev, S., Evaluation of safety distances related to unconfined hydrogen explosions, Int. J. Hydrog. Energy 32.

Hisken, H., Mauri, L., Atanga, G., Lucas, M., Van Wingerden, K., Skjold, T., Quillatre, P., Dutertre, A., Marteau, T., Pekalski, A., Jenney, L., Allason, D., Johnson, M., Leprette, E., Jamois, D., Hébrard, J., Proust, C., 2021, Assessing the influence of real releases on explosions: selected results from large-scale experiments, Journal of Loss Prevention in the Process Industries, Vol. 72.

Jallais, S., Vyazmina, E., Miller, Thomas, K., 2017, Hydrogen Jet Vapor Cloud Explosion: A Model for Predicting Blast Size and Application to Risk Assessment, Proceedings of the 13th Global Congress on Process Safety.

Merx, W.P.M., 1992, Methods for the determination of possible damage to people and objects resulting from releases of hazardous materials, CPR16E, Chapter 3

Miller, D., Eastwood, C., Thomas, K., 2015, Hydrogen Jet Vapor Cloud Explosion: Test Data and Comparison with Predictions, Proceedings of the 11th Global Congress on Process Safety.

Omer, L., 1990. Turbulent premixed flame propagation models for different combustion regimes, 23rd Symposium on Combustion/The Combustion institute: 743-750

Ooms, G., 1972, A new method for the calculation of the plume path of gases emitted by a stack, Atmospheric Environment, Vol. 6.

Sail, J., Blanchetiere, V., Geniaut, B., Osman, K., Daubech, J., Jamois, D., Hébrard, J., 2014, Review of knowledge and recent works on the influence of initial turbulence in methane explosion, proceedings of the international symposium on hazards, prevention, and mitigation of industrial explosions (X ISHPMIE).

Classification GRTgaz : Public [ ] Interne [X] Restreint [ ] Secret [ ]

Schefer, R., Houf, W., Williams, T., 2008. Investigation of small-scale unintended releases of hydrogen : momentum-dominated regime, Int. J. Hydrog. Energy 33.

Classification GRTgaz : Public [ ] Interne [X] Restreint [ ] Secret [ ]

Investigation of the thermal radiation from hydrogen jet flames

Christopher Bernardy [a], Abdel Karim Habib [a], Martin Kluge [a], Bernd Schalau [a], Hanjo Kant [a], Marcel Schulze [a], Alessandro Orchini [b]

[a] Bundesanstalt für Materialforschung und -prüfung (BAM), Berlin

[b] Chair of Nonlinear Thermo-Fluid Mechanics, Technical University of Berlin

E-Mail: Christopher.bernardy@bam.de

Abstract

For industrial applications dealing with hydrogen, the definition of safety distances and the assessment of possible hazards emanating from releases is mandatory. Since hydrogen is usually stored and transported under pressure, one scenario to be considered is the momentum driven release of hydrogen from a leakage with subsequent ignition. In this scenario, the emitted heat radiation from the resulting jet flame to the surroundings has to be determined to define adequate safety distances.

For hydrocarbon flames, different jet flame models are available to assess the hazards resulting from an ignited jet release. Since hydrogen flames differ from hydrocarbon flames in their combustion behavior, it has to be checked if these models are also applicable for hydrogen.

To evaluate the accuracy of these models for hydrogen jet flames, tests at real-scale are carried out at the BAM Test Site for Technical Safety (BAM-TTS). Herein, the flame geometry and the heat radiation at defined locations in the surroundings are recorded for varying release parameters such as leakage diameter (currently up to 30 mm), release pressure (currently up to max. 250 bar) and mass flow (up to max. 0.5 kg/s). The challenge here is the characterization of the flame geometry in an open environment and its impact on the thermal radiation. Existing heat radiation data from the literature are mostly based on unsteady outflow conditions. For a better comparability with the steady state jet flame models, the experiments presented here are focused on ensuring a constant mass flow over the release duration to obtain a (quasi) stationary jet flame. In addition, stationary outflow tests with hydrocarbons (methane) were also carried out, which are intended to serve as reference tests for checking flame models based on hydrocarbon data.

Keywords: *hydrogen, release, jet flame, thermal radiation*

1. Introduction

In order to reduce global CO_2 emissions, hydrogen is becoming increasingly important as an energy carrier. Due to the enormous demand for hydrogen, the focus is shifting to safe production, transportation and storage. As hydrogen is usually transported and stored under pressure, one potential scenario is the momentum driven release of hydrogen from a leakage with subsequent ignition. The resulting high momentum driven hydrogen flame is called diffusion hydrogen jet flame. To assess the impact and hazards, the resulting jet flame must be characterized in terms of the flame geometry and emitted heat radiation. As a result, safety regulations can be derived from the knowledge gained.

Various models already exist in the literature which describe the flame geometry and emitted heat radiation of jet flames. Most of the models currently used are based on studies by Becker and Liang (Becker, 1978) and Kalghatgi (Kalghatgi, 1984), who did fundamental research on the flame geometry of jet diffusion flames. They established dependencies on the release diameter, mass flow,

Reynolds number and the resulting flame length. Based on this, Chamberlain (Chamberlain, 1987) and Johnson et al. (Johnson et al., 1994) developed model approaches taking wind influence into account.

In addition to characterizing the flame geometry, the influence of the thermal radiation emitted into the environment was also considered here. In Chamberlain's investigations for vertical outlet conditions, mainly low momentum hydrocarbon jet flames were measured. For a horizontal release of hydrocarbon jet flames Johnson et al. (Johnson et al., 1994) carried out experiments taking into account the influence of buoyancy. Miller (Miller, 2017) extended these models to outlet angles of 45° and used weighted point sources on the flame centreline in contrast to (Johnson et al., 1994) and (Chamberlain, 1987) who used cone shaped surface emitter sources.

The models mentioned are mainly based on a large number of experimental investigations of hydrocarbon flames such as methane, ethane, propane and natural gas. For hydrogen, Molkov et al. (Molkov et al., 2009; Molkov & Saffers, 2013) developed their own approaches in which the flame lengths can be described using empirical formulas. These approaches were developed on the basis of experiments with hydrogen jet flames by Kalghatgi (Kalghatgi, 1984), Shevyakov et al. (Shevyakov & Komov, 1977), Schefer et al. (Schefer et al., 2006), Proust et al. (Proust et al., 2011), Mogi et al. (Mogi et al., 2005) and Studer et al. (Studer et al., 2009). Other studies have investigated influences such as the curvature of the flame geometry due to the buoyancy effect on horizontal jet flames (Ekoto et al., 2014). To quantify the thermal radiation emitted by a hydrogen jet flame into the environment, various approaches were developed in the work of Molina et al. (Molina et al., 2007), Houf et al. (Houf & Schefer, 2007; Houf et al., 2009), Schefer et al. (Schefer et al., 2006; Schefer et al., 2007; Schefer et al., 2009) and Proust et al. (Proust et al., 2011).

Most of the documented experimental data was obtained under transient outflow conditions (Hall et al., 2017; Proust et al., 2011; Schefer et al., 2006). Due to the decreasing pressure and mass flow during the release, the resulting jet flames do not have stationary outflow conditions. Experimental investigations with constant, stationary, outflow conditions have mainly been carried out on a laboratory scale only (Choudhuri & Gollahalli, 2003; Imamura et al., 2008; Kalghatgi, 1984; Mogi et al., 2005). A validation of existing (stationary) jet flame models for real-scale hydrogen releases is therefore currently only possible to a limited extent.

In order to close this gap, experimental investigations of real-scale hydrogen jet flames under stationary outflow conditions were carried out at the Test Site for Technical Safety at the Bundesanstalt für Materialforschung und -prüfung (BAM-TTS). The purpose of the investigations is to characterize the flame geometry and the emitted heat radiation. Furthermore, the generated data are used to evaluate existing jet flame models with regard to their suitability for hydrogen jet flames.

2. Experiments

2.1 Experimental Setup

To ensure a constant mass flow over several minutes, the test setup is supplied from 6 bundles with 12 hydrogen bottles each. These 6 bundles contain a total of m=90 kg of hydrogen at a pressure level of p=300 bar, so that an average test duration of t = 120 s per test can be realized. The mass flow is adjusted via a control valve in conjunction with three orifices (d=1,6 mm, 3,3 mm, 7,7 mm) and recorded using a Coriolis mass flow meter (Rheonik Coriolis RHE28).

The three orifice diameters were used to allow for a same outlet mass flow at different pressure stages, enabling an optimal utilization of the gas storage. The test rig is designed for the release of hydrogen with mass flows of up to $\dot{m}$=0,5 kg/s and pressure levels of up to p=1000 bar. Pressure and temperature are measured at several points along the pipe section and at the outlet (cf. Figure 1).

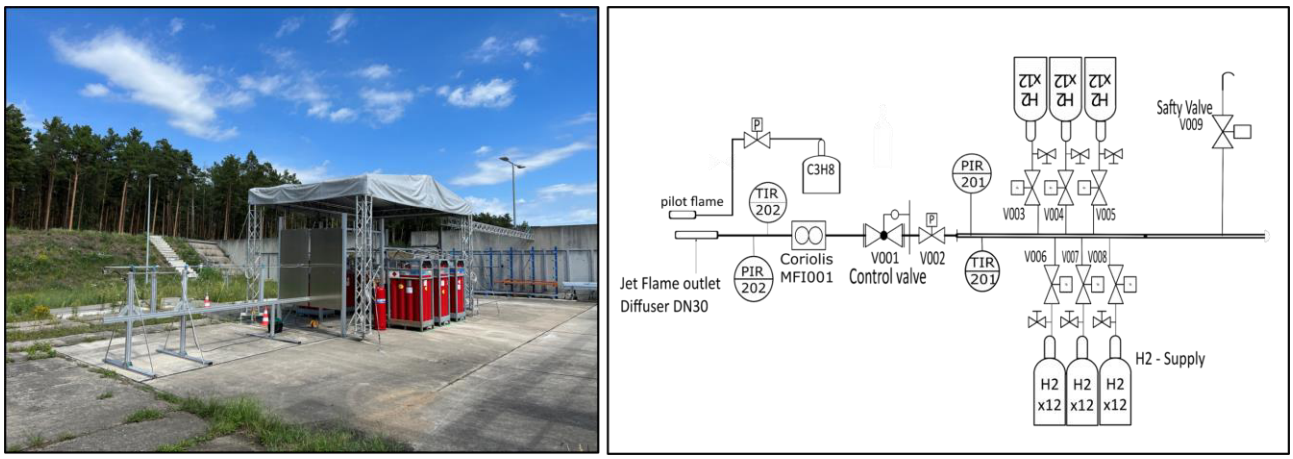

Figure 1: Test stand at the BAM TTS Size of test rig 18 m x 5 m x 4 m (Length x Width x Height) (left) and flow chart of the test stand with used monitoring equipment (right)

The flame geometry is determined using infrared (IR) cameras. Two infrared camera systems (a FLIR SC4000 with cooled IR sensor wavelength spectrum λ=1,5 µm - 5 µm and a recording frequency of f=200 Hz, and a FLIR E96 with λ=7,5 µm - 14 µm and a recording frequency of f=30 Hz) are directed at the flame from two different angles. Four thermal radiation sensors (bolometers - Medtherm Series 64) are used to measure the thermal radiation emitted by the jet flame into the surroundings.

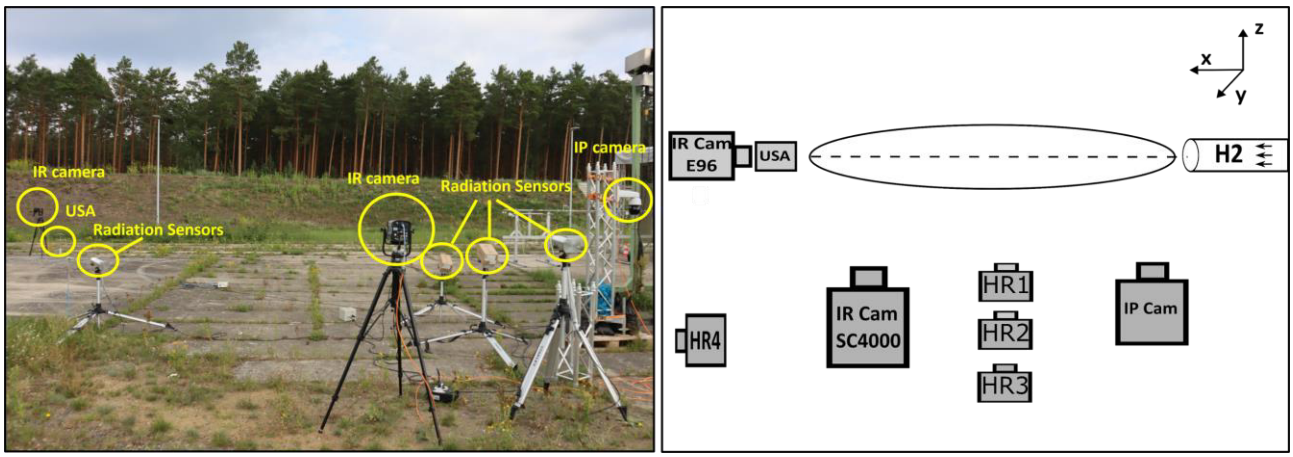

Figure 2: Measuring equipment in open field at the test area (left) and schematic illustration of the positions of the measuring equipment (right)

Three of these bolometers (cf. Figure 2 – Heat Radiation (HR) sensors) are positioned at different distances from the flame. The fourth is used to measure the background radiation of the environment (cf. Figure 2). This background radiation is subtracted as an offset from the measured thermal radiation of the three bolometers, which are aligned with the flame. The thermal radiation sensors have a spectrum of λ= 0,5 µm – 14,5 µm, a maximum frequency of f=100 Hz and are designed for a maximum irradiance of 2,25 kW/m². Each sensor has a view angle of 150°.

All three sensors directed at the flame are inclined vertically with increasing distance at angles of γ=14,4° $(HR1)$; 10,4°$(HR2)$; 4,3°$(HR3)$. A swivelling 360° IP camera (BASCOM – 1 Dom System Plus) is installed for additional test monitoring. An overview of the position of cameras and heat radiation sensors placed at the test areas is listed in Table 1.

Table 1: Overview of the positions (distance measured to the outlet) of the thermal radiation sensors and cameras (cf. Figure 2)

Position	IR Cam E96	IR Cam SC4000	IP Cam	HR1	HR2	HR3	HR4
x in m	15	4,5	3,5	4,05	4,05	4,05	8,5
y in m	0	12,32	7	8,23	10,32	12,31	11
z in m	1,6	1,65	1,8	0,74	1,04	1,34	0,74

An ultra-sonic anemometer (USA - Metek type USA-1 Scientific) is used to record the wind field. The gas mixture is ignited by a propane pilot flame at the outlet with a piezoelectric high-voltage ignition. The pilot flame is switched off immediately after ignition of the jet.

2.2 Experimental Program

To date, a total of 128 jet flame tests have been carried out. Of these, 50 were tests with pure hydrogen and 78 tests with pure methane. The methane tests in particular should serve as a "reference", since the available flame models in the literature are largely based on data from tests with hydrocarbons. Furthermore, all tests were carried out with a horizontal outlet. Only test series in which there was no headwind were used for the evaluation.

Preliminary tests showed that, for methane, there is no stable burning flame if the outlet velocity is too high (small outlet diameter, d=4 mm orifice, $\dot{m}$ >0,043 kg/s, T=20 °C). For this reason, a pipe (l=1 m) with an internal diameter of d=30 mm was placed at the outlet to serve as a diffuser (Figure 3). This made it possible to reduce the exit momentum and adapt the turbulent flame speed to the outlet velocity, allowing for a stable burning flame over the entire mass flow range from $\dot{m}$=0,005 kg/s to $\dot{m}$=0,2 kg/s.

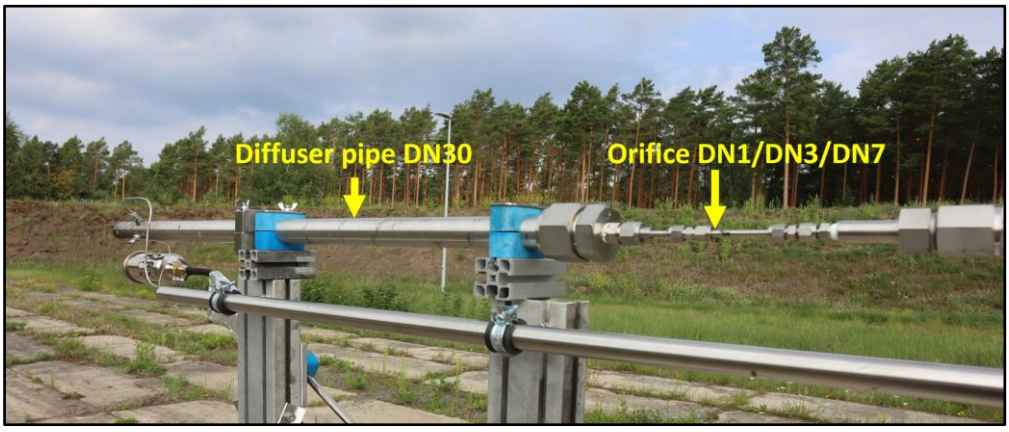

Figure 3: Diffuser pipe DN30 (l=1 m) attached on orifice DN1/DN3/DN7 (l=0,2 m)

3. Results and discussion

The focus of the experiments is the investigation the flame geometry and the emitted thermal radiation. The procedure used here is illustrated in the following example. Figure 4 shows a snapshot of a hydrogen jet flame (outlet diameter of d=30 mm, outlet mass flow $\dot{m}$=0,172 kg/s, T=20 °C) in the visible and IR range. From Figure 4 it can be seen that hydrogen jet flames do not emit any radiation in the visible wavelength range. This could be observed not only in all hydrogen experiments, but also in the experiments carried out here with methane. The flame geometry can therefore only be determined using an IR camera, which requires the specification of a temperature range and an emissivity.

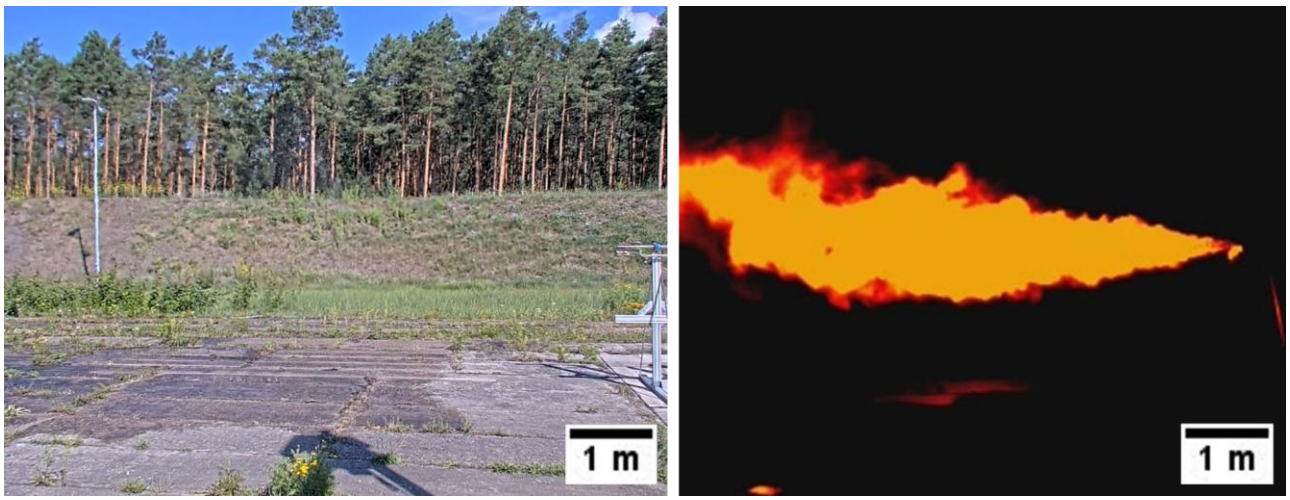

Figure 4: Comparison of the Diffusion Hydrogen Jet Flame monitored with IP Cam (left) and IR-Cam (right)

The emissivity ε of IR absorbing gases depends on many parameters such as the species concentration, the layer thickness, the temperature of the flame, the ambient pressure and the wavelength (Gore et al., 1987; Hottel et al., 1936) and is much more complex compared to measurements on solids.

Furthermore, a jet flame is a diffusion flame that does not have a homogeneous species distribution across the layer thickness and is additionally influenced by the wind speed, direction and turbulence (Coelho, 2012). For the IR measurements, the emissivity was set to ε=1 and a temperature range of T=850 °C to T=2000 °C was used.

To determine the flame geometry, an algorithm was developed that averages each individual frame from the IR image over the duration of the experiment. With a recording frequency of f=200 Hz and a test duration of t=120 s, this results in averaging over 24000 frames. Figure 5 shows exemplarily the averaging procedure and result.

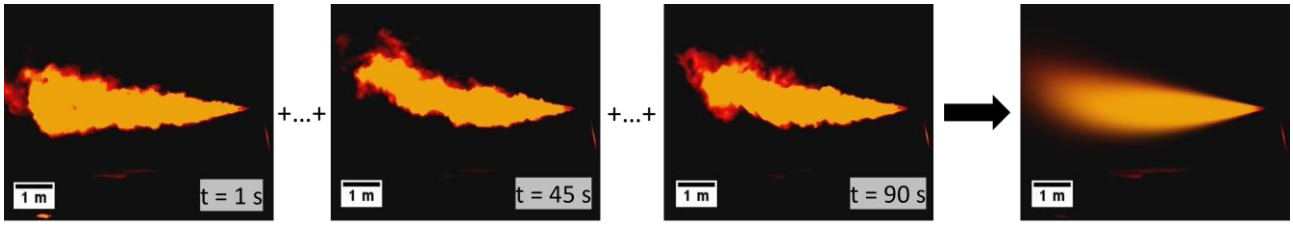

Figure 5: Numerical calculation and determination of mean flame shape over test duration

All flame parameters (flame length, mean diameter and view factor) are calculated on the basis of the generated time-averaged (stationary) flame geometry.

The flame shape (contour) is then defined via a RBG value, manually specified so that only the flame surface and no reflections from the test apparatus or the floor are visible in the image. The experimental non-dimensional flame lengths and diameters are shown in Figure 6.

The comparison of the flame geometry of hydrogen and methane in Figure 6 shows that hydrogen flames are longer and thinner compared to methane flames, which are more compressed (shorter with wider diameters). In a mass-specific comparison, this is due to the difference in density and consequently higher outlet velocity. Due to the lower density, a higher volume flow and consequently a greater outlet momentum are available with the same mass flow for hydrogen. This allows the hydrogen jet flame to spread more easily into the surrounding medium, resulting in longer flames.

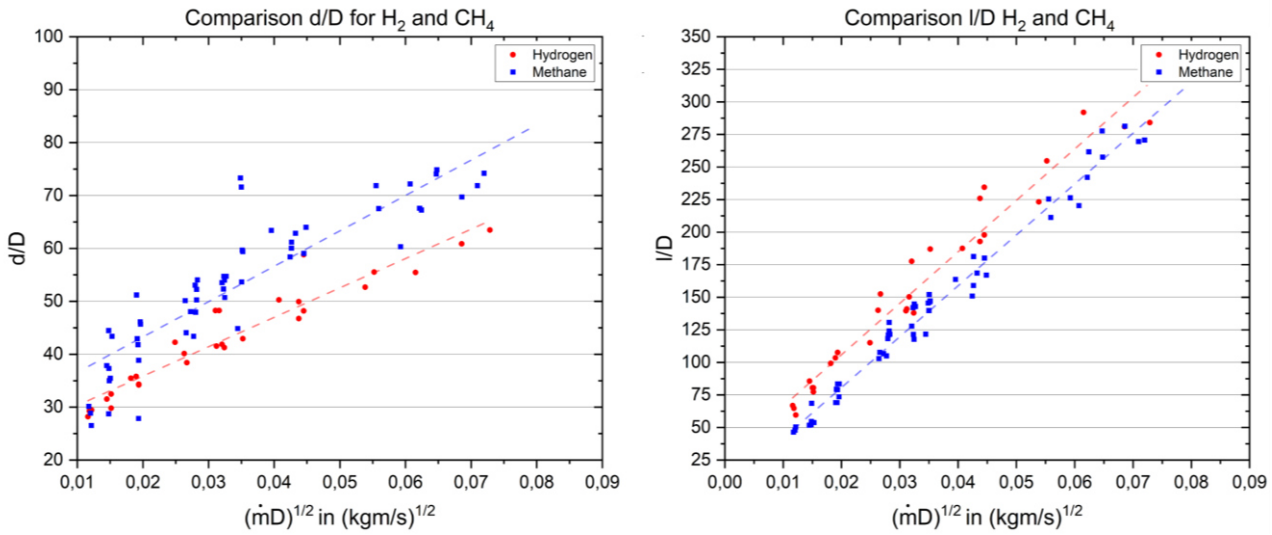

Figure 6: Comparison of hydrogen and methane regarding to non-dimensional parameter flame diameter/outlet diameter (d/D) over nominated parameter mass flow/outlet diameter $(\dot{m}D)^{1/2}$ *(left) and non-dimensional parameter of flame length/outlet diameter (l/D) over nominated parameter mass flow/outlet diameter* $(\dot{m}D)^{1/2}$

From the geometric data of the flame and the heat radiation intensity Q_{rad_Sensor} in W/m² measured by the bolometers (cf. Figure 7), the SEP of the flame can be determined using Eq. 1

$$\mathrm{SEP} = \frac{\mathrm{Q_{rad\_Sensor}}}{\tau_{1\_2}\ \varphi_{1\_2}} \qquad \text{Eq. 1}$$

with the view factor φ_{1_2} (unitless) and the transmittance τ_{1_2} (unitless) of the air are required (index "1_2" refers to the path between emitter "1" and receiver "2").

The transmittance τ of the air was calculated according to Wayne et al. using Eq. 2 (Wayne, 1991).

$$\tau_{1\_2} = 1{,}006 - 0{,}01171(\log_{10}X_{H2O}) - 0{,}02368(\log_{10}X_{H2O})^2 - 0{,}03188(\log_{10}X_{CO2}) + 0{,}001164(\log_{10}X_{CO2})^2$$

Eq. 2

$$\text{with} \quad X_{H2O} = \frac{R_H L S_{mm} 2{,}88651 * 10^2}{T} \quad \text{and} \quad X_{CO2} = \frac{273L}{T}$$

where $\boldsymbol{\tau_{1\_2}}$ is the transmittance (unitless), $\boldsymbol{X_{H2O}}$ parameter for water vapor in the atmosphere (unitless), $\boldsymbol{X_{CO2}}$ parameter for CO_2 in the atmosphere (unitless), $\boldsymbol{R_H}$ relative humidity (unitless), L the path length between emitter and absorber (in m), $\boldsymbol{S_{mm}}$ vapor pressure of water (in mmHg) and T the air temperature (in K).

The view factor φ_{1_2} is calculated numerically, based on the determined flame geometry (cf. Figure 5, right). Assuming a radially symmetrical flame, the flame geometry is divided into vertical slices with the width of one pixel of the IR image. The view factor is calculated as a function of the distance of the slice from the bolometer according to the relationships given in (VDI, 2010). The overall view factor of the flame is then calculated from the sum of the individual view factors of each section. Thus, the SEP of the flame can be determined from the temporal average of the measured thermal radiation of the individual bolometers. Ideally, the SEP values of the flame calculated from the different bolometer signals should be identical. Under atmospheric conditions, this is only achieved within a certain accuracy limit, but with satisfactory agreement.

Figure 7 shows a comparison of the SEP values determined from the measurements for methane and hydrogen. A trend can be seen here that hydrogen jet flames have higher SEPs than methane jet flames. For methane, SEPs in the range of 7 kW/m² - 9,5 kW/m² and for hydrogen SEPs between 10 kW/m² - 15 kW/m² were determined.

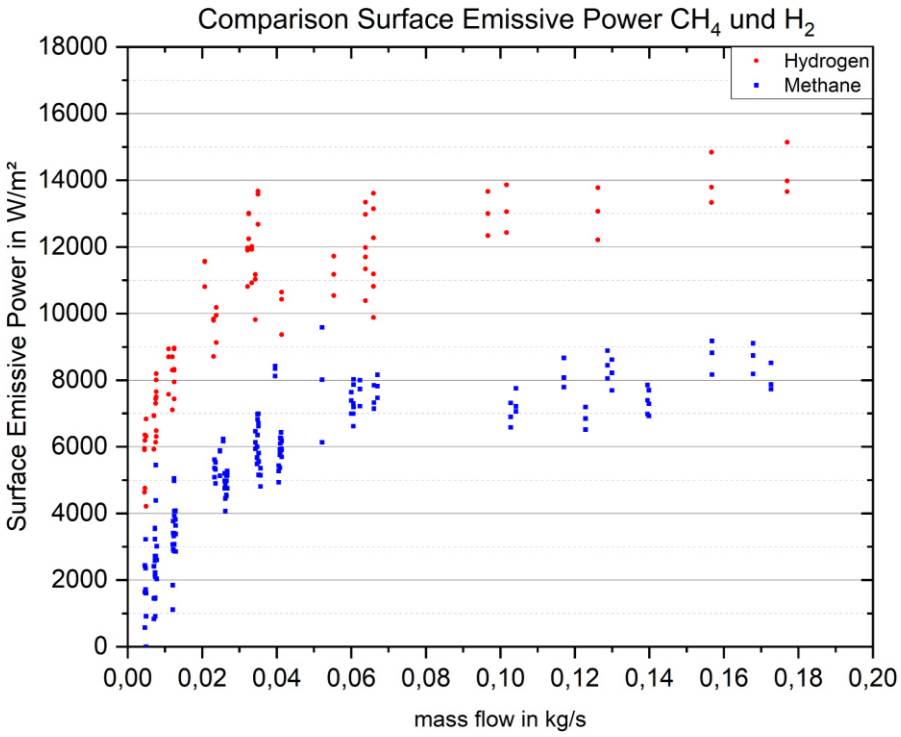

Figure 7: Comparison of Surface Emissive Power for hydrogen and methane drawn over mass flow

In the literature (Chamberlain, 1987; Fishburne & Pergament, 1979; Mogi et al., 2005; Proust et al., 2011; Schefer et al., 2006; Schefer et al., 2007) the radiant heat fraction of the flame is derived from the measured heat radiation of the flame and the total energy (heat release rate) produced during combustion which can be calculated from Eq. 3:

$$Q_{Combustion} = \dot{m}\Delta H_c \qquad \text{Eq. 3}$$

with the mass flow ($\dot{m}$) and the lower heating value (ΔH_c). The lower heating value is ΔH_{c_H2} =120 MJ/kg for hydrogen and ΔH_{c_CH4} =50,3 MJ/kg for methane (Uwe Riedel, 2018).

The radiative fraction can only be calculated indirectly via the measured thermal radiation and the flame area. Here, x_{rad} is calculated according to Eq. 4, where A_{flame} is the flame area. The product of x_{rad} and ΔH_c can be understood as the radiant heat energy that is converted into thermal radiation during combustion.

$$x_{rad} = \frac{SEP_{exp}\, A_{Flame}}{\dot{m}\Delta H_c} \qquad \text{Eq. 4}$$

For methane, radiant heat fractions in the range of x_{rad_CH4}=0,08-0,25 (Chamberlain, 1987; Houf & Schefer, 2007; Johnson et al., 1994; Schefer et al., 2006) and for hydrogen of x_{rad_H2}=0,03-0,13 (Choudhuri & Gollahalli, 2003; Houf & Schefer, 2007; Miller, 2017; Schefer et al., 2006; Schefer et al., 2007; Studer et al., 2009) are given in the literature.

With reference to Eq. 4, the radiant heat fractions for hydrogen and methane can be calculated. A comparison of the results for methane and hydrogen is shown in Figure 8. The determined radiant heat fraction shows lower values for hydrogen than for methane. This is consistent with the results found in the literature above. The graph for hydrogen shows a maximum value of x_{rad_H2}=0,08 and decreases to a minimum value of x_{rad_H2}=0,04 as the mass flow increases. For methane, with increasing mass flow a value up to x_{rad_CH4}=0,1 can be observed. Subsequently, as for hydrogen, a decrease in the radiation fraction can be seen to a value of x_{rad_CH4}=0,06. The phenomenon that the radiant heat fraction decreases with increasing mass flow and thus increasing exit velocity can also be found in the literature (Chamberlain, 1987; Miller, 2017). The reason for this is the change in the ratio of combustion energy, which is converted into convection instead of radiation depending on the exit velocity.

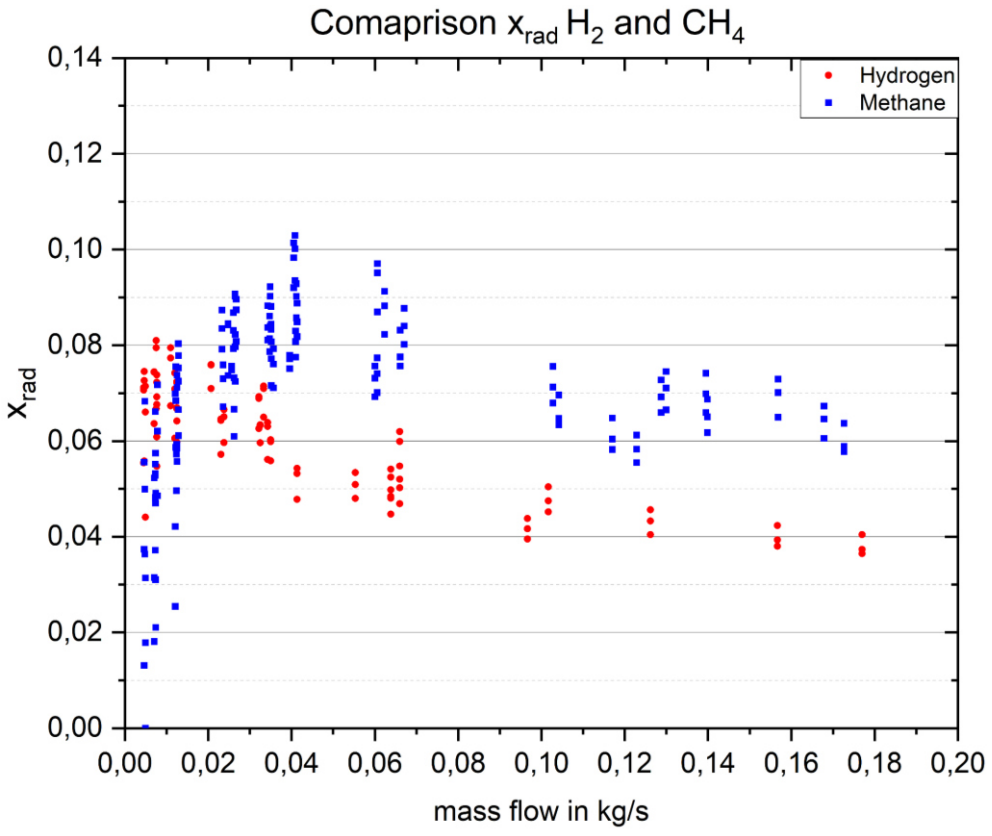

Figure 8: Comparison of heat fraction for hydrogen and methane over mass flow

Moreover, it can be seen that the radiant heat fraction values for hydrogen are within the range observed in the literature (see above). The values for methane are at the lower range of the values measured in the literature.

This could be due to the fact that mainly visible (luminous) methane flames have been examined in the literature. In contrast, in the present work only non-visible (non-luminous) flames have occurred so far. Studies on the differences between luminous and non-luminous flames with regard to thermal radiation have only been examined sporadically in the literature. One of the early investigations performed by (Hottel et al., 1936; Sherman, 1934) with natural gas showed a lower thermal radiation for non-luminous flames in comparison to luminous flames due to differences in the radical species and emissivity of the flame.

4. Conclusion

From the test results presented here, initial findings regarding flame geometry and heat radiation have been made.

1. Hydrogen jet flames have a longer and thinner flame than methane jet flames for the same mass flow.

2. Hydrogen jet flames show higher thermal radiation values for the same mass flow rate compared to methane jet flames.

3. The radiant heat fractions of the hydrogen jet flames determined so far correspond to the values given in the literature, whereas those for methane are significantly lower than the values given in the literature (rather at the lower limit), which may be due to the non-luminescence of the flames in this work.

Outlook: The difference of heat radiation between luminous and non-luminous flames will be investigated further as well as releases with different outlet angles and outlet diameters. The results obtained will be used to check the applicability and accuracy of jet flames models and, if necessary, the further development of these.

References

Becker, H. A. L., B. . (1978). Visible Length of free turbulent diffusion flames. *Combustion and Flame*, *32*, 115-117.

Chamberlain, G. A. (1987). Developments in design methods for predicting thermal radiation from flares. *65:4*.

Choudhuri, A. R., & Gollahalli, S. R. (2003). Characteristics of hydrogen–hydrocarbon composite fuel turbulent jet flames. *International Journal of Hydrogen Energy*, *28*(4), 445-454. https://doi.org/https://doi.org/10.1016/S0360-3199(02)00063-0

Coelho, P. J. (2012). The role of turbulent fluctuations on radiative emission in hydrogen and hydrogen-enriched methane flames. *International Journal of Hydrogen Energy*, *37*(17), 12741-12750. https://doi.org/https://doi.org/10.1016/j.ijhydene.2012.05.159

Ekoto, I. W., Ruggles, A. J., Creitz, L. W., & Li, J. X. (2014). Updated jet flame radiation modeling with buoyancy corrections. *International Journal of Hydrogen Energy*, *39*(35), 20570-20577. https://doi.org/https://doi.org/10.1016/j.ijhydene.2014.03.235

Fishburne, E. S., & Pergament, H. S. (1979). The dynamics and radiant intensity of large hydrogen flames. *Symposium (International) on Combustion*, *17*(1), 1063-1073. https://doi.org/https://doi.org/10.1016/S0082-0784(79)80102-2

Gore, J. P., Jeng, S. M., & Faeth, G. M. (1987). Spectral and Total Radiation Properties of Turbulent Hydrogen/Air Diffusion Flames. *Journal of Heat Transfer*, *109*(1), 165-171. https://doi.org/https://doi.org/10.1115/1.3248038

Hall, J. E., Hooker, P., O'Sullivan, L., Angers, B., Hourri, A., & Bernard, P. (2017). Flammability profiles associated with high-pressure hydrogen jets released in close proximity to surfaces. *International Journal of Hydrogen Energy*, *42*(11), 7413-7421. https://doi.org/https://doi.org/10.1016/j.ijhydene.2016.05.113

Hottel, H. C., Meyer, F. W., & Stewart, I. (1936). Temperature in Industrial Furnaces: Interpretation and Use to Measure Radiant Heat Flux. *Industrial & Engineering Chemistry*, *28*(6), 708-710. https://doi.org/https://doi.org/10.1021/ie50318a023

Houf, W., & Schefer, R. (2007). Predicting radiative heat fluxes and flammability envelopes from unintended releases of hydrogen. *International Journal of Hydrogen Energy*, *32*(1), 136-151. https://doi.org/https://doi.org/10.1016/j.ijhydene.2006.04.009

Houf, W. G., Evans, G. H., & Schefer, R. W. (2009). Analysis of jet flames and unignited jets from unintended releases of hydrogen. *International Journal of Hydrogen Energy*, *34*(14), 5961-5969. https://doi.org/https://doi.org/10.1016/j.ijhydene.2009.01.054

Imamura, T., Hamada, S., Mogi, T., Wada, Y., Horiguchi, S., Miyake, A., & Ogawa, T. (2008). Experimental investigation on the thermal properties of hydrogen jet flame and hot currents in the downstream region. *International Journal of Hydrogen Energy*, *33*(13), 3426-3435. https://doi.org/https://doi.org/10.1016/j.ijhydene.2008.03.063

Johnson, A., Brightwell, H., & Carsley, A. (1994). A model for predicting the thermal radiation hazards from large-scale horizontally released natural gas jet fires. *Process Safety and Environmental Protection*, *72*, 157-166.

Kalghatgi, G. (1984). Lift-off Heights and Visible Lengths of Vertical Turbulent Jet Diffusion Flames in Still Air. *COMBUSTION SCIENCE AND TECHNOLOGY*, *41*(No. 1-2), 17-29. https://doi.org/https://www.tandfonline.com/doi/abs/10.1080/00102208408923819

Miller, D. (2017). New model for predicting thermal radiation from flares and high pressure jet fires for hydrogen and syngas. *Process Safety Progress*, *36*(3), 237-251. https://doi.org/ https://doi.org/10.1002/prs.11867

Mogi, T., Nishida, H., & Horiguchi, S. (2005). Flame Characteristics of high-pressure hydrogen gas jet.

Molina, A., Schefer, R., & Houf, W. G. (2007). Radiative fraction and optical thickness in large-scale hydrogen-jet fires. *Proceedings of The Combustion Institute*, *31*, 2565-2572. https://doi.org/https://doi.org/10.1016/j.proci.2006.08.060

Molkov, V., Makarov, D., & Bragin, M. (2009). Physics and modelling of under-expanded jets and hydrogen dispersion in atmosphere. *Physics of Extreme State of Matter 2009*, 143-145.

Molkov, V., & Saffers, J.-B. (2013). Hydrogen jet flames. *International Journal of Hydrogen Energy*, *38*(19), 8141-8158. https://doi.org/https://doi.org/10.1016/j.ijhydene.2012.08.106

Proust, C., Jamois, D., & Studer, E. (2011). High pressure hydrogen fires. *International Journal of Hydrogen Energy*, *36*(3), 2367-2373. https://doi.org/https://doi.org/10.1016/j.ijhydene.2010.04.055

Schefer, R. W., Houf, W. G., Bourne, B., & Colton, J. (2006). Spatial and radiative properties of an open-flame hydrogen plume. *International Journal of Hydrogen Energy*, *31*(10), 1332-1340. https://doi.org/https://doi.org/10.1016/j.ijhydene.2005.11.020

Schefer, R. W., Houf, W. G., Williams, T. C., Bourne, B., & Colton, J. (2007). Characterization of high-pressure, underexpanded hydrogen-jet flames. *International Journal of Hydrogen Energy*, *32*(12), 2081-2093. https://doi.org/https://doi.org/10.1016/j.ijhydene.2006.08.037

Schefer, R. W., Kulatilaka, W. D., Patterson, B. D., & Settersten, T. B. (2009). Visible emission of hydrogen flames. *Combustion and Flame*, *156*(6), 1234-1241. https://doi.org/https://doi.org/10.1016/j.combustflame.2009.01.011

Sherman, R. (1934). Radiation from luminous and non-luminous Natural-Gas Flames. *Trans. ASME. Feb 1934, 56(2): 177-185*. https://doi.org/https://doi.org/10.1115/1.4019691

Shevyakov, G. G., & Komov, V. F. (1977). Effect of noncombustible admixtures on length of an axisymmetric on-port turbulent diffusion flame. *Combustion, Explosion and Shock Waves*, *13*(5), 563-566. https://doi.org/https://doi.org/10.1007/BF00742209

Studer, E., Jamois, D., Jallais, S., Leroy, G., Hebrard, J., & Blanchetière, V. (2009). Properties of large-scale methane/hydrogen jet fires. *International Journal of Hydrogen Energy*, *34*(23), 9611-9619. https://doi.org/https://doi.org/10.1016/j.ijhydene.2009.09.024

Uwe Riedel, C. S., Jürgen Warnatz, Jürgen Wolfrum. (2018). *Grundlagen der Verbrennung: Wärmefreisetzung und adiabatische Flammentemperaturen*. De Gruyter. https://doi.org/10.1515/physiko.5.152

VDI. (2010). *VDI Heat Atlas*. Springer Berlin Heidelberg. https://books.google.de/books?id=0t-HrUf1aHEC

Wayne, F. D. (1991). An economical formula for calculating atmospheric infrared transmissivities. *Shell Research Ltd. , Thornton Research Center, UK 1991*. https://doi.org/https://doi.org/10.1016/0950-4230(91)80012-J

Laminar burning velocity of Lithium-ion battery vent gas during thermal runaway

Sofia Ubaldi & Paola Russo

Department of Chemical Engineering Materials Environment, Sapienza University of Rome, Rome, Italy

E-mail: *paola.russo@uniroma1.it*

Abstract

In the energy storage and transportation sectors, the use of lithium-ion (LIB) battery technology is growing rapidly. However, the potential for fire and explosion raises safety concerns. Thermal runaway (TR) events can occur in LIBs, releasing flammable gases and posing fire and explosion risks. However, there are limited data available on the flammability characteristics of gases released during a thermal failure event. This paper evaluates an important safety characteristic, the laminar burning velocity (S_u), using experimental data and modelling approach to assess the influence of cell chemistry on LIB behaviour. Commercial cylindrical cells with various chemistries, i.e., Lithium Nickel Cobalt Aluminium Oxide (NCA) and Lithium Nickel Manganese Cobalt Oxide (NMC), were tested at 100 % SoC. The gas released from the cell was analysed by heating the cell at a constant heating rate of 5 °C/min in a laboratory scale apparatus equipped with an on-line FT-IR spectrometer coupled with a mass spectrometer for continuous gas analysis. H_2, CH_4, CO, CO_2, HF and vapours of electrolyte compounds, such as dimethyl carbonate (DMC), diethyl carbonate (DEC) and ethylene carbonate (EC), were the main components of the battery vent gas (BVG) produced during TR. S_u was calculated using the 1-D laminar premixed flame model in the CHEMKIN software. Due to the continuous monitoring of the released gas, different compositions of the BVG were considered for the S_u calculation. Depending on the cell chemistry, the most critical BVG composition is released during the TR phase (NCA) or during the venting phase (NMC). The main reason of this behaviour is related to the H_2 emission. Finally, the effect of temperature reached during the TR on the Su was evaluated, so the simulations were carried out at 25 °C, 150 °C, 300 °C, and 500 °C at 1 atm.

Keywords: *Lithium-ion batteries, LIBs, thermal abuse, battery vent gas, BVG, laminar burning velocity, Su, premixed flame, CHEMKIN.*

Introduction

The internal composition, structure and the main advantages of lithium-ion batteries (LIBs) have been extensively investigated and explained in numerous papers (Park, 2012). LIBs are defined by their nominal voltage range, indicated by the state of charge (SoC), and their geometry, which can vary between cylindrical, coin, prismatic, or pouch shapes. The chemical composition of internal components, such as the anode and cathode active materials or the electrolyte, is the main chemical property (Park, 2012). Commercial chemical compositions currently available for the cathode include Lithium Nickel Cobalt Aluminium Oxide (NCA), Lithium Iron Phosphate (LFP), Lithium Nickel Manganese Cobalt Oxide (NMC), and Lithium Cobalt Oxide (LCO). For the anode the two possibilities are graphite and Lithium Titanate Oxide (LTO). The prevailing organic carbonates used for the electrolyte are the dimethyl carbonate (DMC), diethyl carbonate (DEC), and ethylene carbonate (EC). The safety operating windows for the use of Li-ion cells are defined by their physical-chemical properties, expressed in terms of temperature and voltage (Zhang et al., 2018). Li-ion cells can be subject to internal or external abuse, classified as electrical, mechanical or thermal, outside of this range (Lu et al., 2013). Abuse leads to degradation of the internal components, resulting in

subsequential reactions between the products. This degradation causes an increase in internal pressure and temperature, which leads to venting and ultimately to thermal runaway (TR) (Lu et al., 2013).

The physical and chemical properties of the Li-ion cell and the type of abuse to which the device is subjected strictly correlate with the TR properties and the relative products, such as gases, solids, and liquids (Lopez et al., 2015; Ubaldi et al., 2023). The most significant product emitted during abuse is gas. According to the literature review, the gas produced during TR is mainly composed of: H_2, CO, CO_2, CH_4, fluorinated compounds, such as HF (Andersson et al., 2016; Ubaldi et al., 2023), and vapours of electrolyte solvents, such as DMC, EC, and DEC (Diaz et al., 2019; Ubaldi et al., 2023). The correlation of the gas species and their relative amounts with the state of charge (SoC) and cell type, is summarised in Table 1. It presents the composition of battery vent gas (BVG) as reported in various literature works obtained by thermal abuse tests on cylindrical (18650) Li-ion cells.

Table 1: *Gas composition of Li-ion 18650 cells subjected to thermal abuse tests*

Cell	Feed	SoC (%)	H_2 (%)	CO_2 (%)	CO (%)	CH_4 (%)	C_2H_2 (%)	C_2H_4 (%)	C_2H_6 (%)	Reference
NCA	N_2	100	25.6	20.0	44.7	7.0	n.r.	2.1	0.6	Golubkov et al., 2015
NCA	N_2	50	17.5	33.8	39.9	5.2	n.r.	3.2	0.4	Golubkov et al., 2015
LFP	N_2	50	20.8	66.2	4.8	1.6	n.r.	6.6	n.r.	Golubkov et al., 2015
LFP	N_2	100	29.4	48.3	9.1	5.4	n.r.	7.2	0.5	Golubkov et al., 2015
LCO/NMC	N_2	100	10.0	24.9	27.6	8.6	n.r.	7.7	1.2	Golubkov et al., 2014
NMC	N_2	100	30.8	41.2	13.0	6.8	n.r.	8.2	n.r.	Golubkov et al., 2014
LFP	N_2	100	30.9	53.0	4.8	4.1	n.r.	6.8.	0.3	Golubkov et al., 2014
LCO	Inert	50	38.3	39.9	4.5	7.1	n.r.	6.9	3.4	Somandepalli et al., 2014
LCO	Inert	100	30.7	33.2	25.3	7.0	n.r.	2.5	1.3	Somandepalli et al., 2014
LTO	Air	100	8.4	37.6	5.3	1.2	0.001	1.38	0.40	Yuan et al., 2020
NMC	Air	100	12.4	13.2	30.3	10.5	0.003	0.10	0.16	Yuan et al., 2020
NMC	Air	100	12.5	19.9	28.1	12.9	0.003	0.16	0.21	Yuan et al., 2020

n.r.: not reported.

The composition of BVG has been measured in various experimental conditions, such as the type of feed gas and equipment used (i.e., accelerating rate calorimeter (ARC) or reactor chamber), using different instruments, such as the GC or FT-IR (Essl et al., 2020; Peng et al., 2020; Larsson et al., 2016). However, it is common to report only the average concentration of the gas. Table 1 shows that the main species emitted are H_2, CO_2, CO and CH_4. The ratio between these species varies depending on the SoC and the chemical composition of the electrodes. The H_2 percentage is the lowest for LTO (8.4 % at 100 % SoC), and ranges between 10 % (LCO/NMC at 100 % SoC) and 38.3 % (LCO at 50 % SoC). The higher amount of CO was emitted by the NCA (44.7 % at 100 % SoC) and NMC (30.3 % at 100 % SoC) cells, while the highest percentage of CO_2 (66.2 % at 50 % SoC and 53.0 mol % at 100 % SoC) was emitted by LFP cell. The papers considered do not provide information on the electrolyte and fluorinated compounds that are released during the TR. These species present in the BVG can contribute to the flammability and/or toxicity of the gas. Regarding gas toxicity, it is discussed in the literature that HF and CO can reach the Immediately Dangerous to Life and Health (IDLH) by NIOSH (Peng et al., 2020; Ubaldi et al., 2023).

Regarding the flammability, gases that are vented may ignite either inside or outside the battery (accumulating into a module), depending on various conditions such as gas temperature, pressure, gas flow speed, gas mixture composition, and convection as it enters the air outside the battery. To assess the fire and explosion risk of BVG, it is important to evaluate key gas properties such as the lower flammability limit (LFL), laminar burning velocity (S_u), and the maximum explosion overpressure. S_u is a fundamental combustion property and a crucial parameter for understanding flame propagation, gas explosions, and combustion reaction mechanisms (Henriksen et al., 2021).

Experiments and one-dimensional (1D) modelling are the two main methods for obtaining S_u. The measurements are conducted using various methods. The simulations use chemical kinetic mechanisms to calculate S_u. The accuracy of the simulations depends on the size, stiffness, and numerical setup of the mechanism.

There has been a recent increase in concern for the safety of LiBs, but only a small number of published works are focused on the laminar burning velocity evaluation. Some modelling works (Baird et al., 2020; Fernandes et al., 2018) are based on experimental data from other authors, but their analyses are limited using chemical mechanisms with restricted capacity. Henriksen et al. (2021), examined the laminar burning velocities of typical Li-ion vent gas mixtures, but did not consider carbonates and fluorinated compounds. Their motivation was to produce gas mixtures that are representative and suitable for well-defined experimental and modelling studies. However, fluorinated species can affect the S_u and explosion characteristics, as shown by Gao et al. (2021) in their study on explosion suppression of hydrogen explosions. The S_u value for BVG was found to depend on both the SoC and the chemical composition of the cell. According to Baird et al. (2020), the laminar burning velocity increases with an increase in the SoC. Henriksen et al. (2021) found that the NCA had a higher maximum value (1.0 m/s) compared to the LCO (0.6 m/s) and to the LFP cell (0.3 m/s). The observed behaviour can be explained by the composition of the BVG, which contains a higher amount of H_2 and a lower amount of CO_2 in the case of NCA cell with respect to the other cells. The maximum velocity observed is consistently around an equivalent ratio of 1.0 regardless of the type of cell and the SoC.

In this framework, this work comprises experimental and modelling studies. Firstly, thermal abuse tests were conducted on Li-ion cells to identify the components and to measure the concentration of emitted gas. The tests refer to 18650 Li-ion cells with two different chemistries namely NCA and NMC, both at the same state of charge (SoC) of 100 %. An analysis system combining an FT-IR spectrometer with a mass spectrometer was used to obtain information on a wider range of gas components. The evaluated compounds included H_2, CO, CO_2, CH_4, and fluorinated compounds such as HF, as well as vapours of electrolyte solvents, specifically DMC, EC, and DEC. Subsequently, S_u was calculated using the composition data obtained from the experiments. The S_u was evaluated by 1-D premixed laminar flame model using the CHEMKIN Premix module. According to Nilsson et al. (2023), a chemical kinetic mechanism that incorporates common hydrocarbon compounds in vent gases (i.e. three carbonates, and several fluorinated compounds) was constructed. This mechanism is validated and used to increase understanding of the combustion characteristics of Li-ion battery vent gas mixtures including all classes of molecular components that are common in Li-ion battery vent gases. The calculation of S_u was carried out by considering the various compositions of the released species during different phases of the thermal abuse test, including venting, TR, and the entire event.

1. Experimental

Thermal abuse tests were conducted on 18650 Li-ion cells with different chemical composition of cathode to evaluate the thermal behaviour, in terms of temperature, pressure and BVG.

1.1. Li-ion cells

In Table 2 are reported the cylindrical Li-ion cells, 18650, considered in this study with their chemical composition. The cells were identified with an identification code (Id-cell) which indicates the cathode active material. NCA cells have a minimum voltage of 2.75 V, and a maximum of 4.20 V and a rated capacity 3.25 Ah. NMC cells have a minimum voltage of 2.50 V a maximum of 4.20 V, and a rated capacity 2.85 Ah. Before tests, a standard cycling procedure consisting of five charge-discharge cycles for the formation of the solid electrolyte interface (SEI) was carried out on the cells using the Battery Test System BaSyTec CTS (Thasar, Italy). The cells were charged at the maximum SoC (100 %), setting the maximum voltage according to the specifications reported in Table 2.

Table 2: *Li-ion 18650 cells under investigation*

Id-cell	Anode material	Cathode material	SoC - Voltage
NCA	Graphite (C)	Lithium nickel cobalt aluminium oxide (NCA)	100 % - 4.20 V
NMC	Graphite (C)	Lithium nickel manganese cobalt oxide (NMC)	100 % - 4.20 V

1.2. Laboratory setup and conditions

Thermal abuse tests were carried out in a laboratory-built reactor with an inlet airflow of 500 NmL/min over a temperature range of 20 to 400 °C. The heating rate was 5 °C/min, applied by an electrical oven (PID controlled). When the TR condition was reached, the oven was switched off. Two thermocouples, TC_1 and TC_2, were placed on the cell surface to monitor the cell temperature and a pressure transducer was placed in the reactor to monitoring pressure changes.

An online FT-IR spectrometer (Spectrum 3, Perkin Elmer) was connected to the reactor outlet to continuously monitor the emitted gases. To avoid condensation, the transfer line and the FT-IR cell are heated up to 180°C. The spectra were collected with a resolution of 4 cm^{-1} in the spectral range between 4500 cm^{-1} and 650 cm^{-1}, using a scan/spectrum of 8 and detected by a MCT detector. Identification and quantification were achieved using standard spectra and calibration lines, obtained through SpectrumQuant software (Perkin Elmer). Furthermore, a Quantitative Gas Analyser (QGA) mass spectrometer from Hiden Analytical with a sampling interval of 10 s was used.
The characteristics of the reactor, acquisition, and quantification procedure are more comprehensively described in a previous study (Ubaldi et al., 2023).

2. S_u Calculation

A 1-D flame propagation model was used to evaluate the laminar burning velocity (S_u) for different BVG compositions at various stages of thermal abuse. The study considered four BVG compositions: i) venting, from the start of venting to the onset of the TR, ii) TR, from the start of venting to the peak temperature, iii) maximum, corresponding to the peak temperature, and iv) global, for the entire event. The study simulated the homogeneous combustion of the BVG using a detailed reaction mechanism. The CHEMKIN PREMIX module implemented this mechanism to calculate the laminar burning velocity based on the BVG composition.

2.1. Chemical kinetics model

None of the chemical kinetics models in the open literature include all the different types of fuels present in the Li-ion BVG. The chemistry set proposed by Nilsson et al. (2023) includes the kinetics mechanism for the following species: DMC (proposed by Alexandrino et al., 2018), DEC (proposed by Sun et al., 2017), F-compounds (proposed by Linteris et al., 2020), C_1-C_2 (proposed by Metcalfe et al., 2013), and H_2 (proposed by Kéromnès et al., 2013). In addition to these species, the EC chemistry set proposed by Takahashi et al. (2022) was also considered. All of the kinetics mechanisms considered were validated with experimental trends of the separate components by their respective authors. Nilsson et al. (2023) confirmed that the proposed mechanism it is suitable for modelling typical Li-ion battery gas mixture compositions.

2.2. Modelling approach

The 1-D laminar premixed flame has been modelled by combining the chemical reaction mechanism (kinetics), thermal properties, and transport properties. To describe all the species present in the BVG obtained from the experimental thermal abuse tests, this study uses a new combination of the chemistry set proposed in section 2.1. The code adopts a hybrid time-integration/Newton- iteration technique to solve the steady-state mass, species, and energy conservation equations. Mixture-averaged formulas were used to evaluate the transport properties. The ambient was auto-populate

with air, all species were considered as fuel mixture with the exception of HF which was included as added species. Initial and boundary conditions were assigned to define the problem environment. For simulations, curvature and gradient parameters were set both to 0.2, respectively, resulting in a grid of 300 points. For an accurate solutions 3 continuations were considered with decreasing curvature and gradient parameters (0.8, 0.5, and 0.2). The unburned mixture's inlet velocity was set to 40.0 cm/s. The unburned mixture was assigned at different temperatures (i.e., 25 °C, 150 °C, 300 °C, and 500 °C), at 1 atm of pressure, and a specific composition at the inlet boundary. At the exit boundary, it was specified that all gradients vanish.

3. Results and discussion

3.1. Thermal abuse tests

Figure 1 shows the temperature profile, monitored by thermocouples TC_1 and TC_2 placed on the surface of the cell, and the inner reactor pressure profile indicating the venting, onset of TR and the maximum peak, reached during the thermal abuse tests on NCA (Figure 1a) and NMC (Figure 1b).

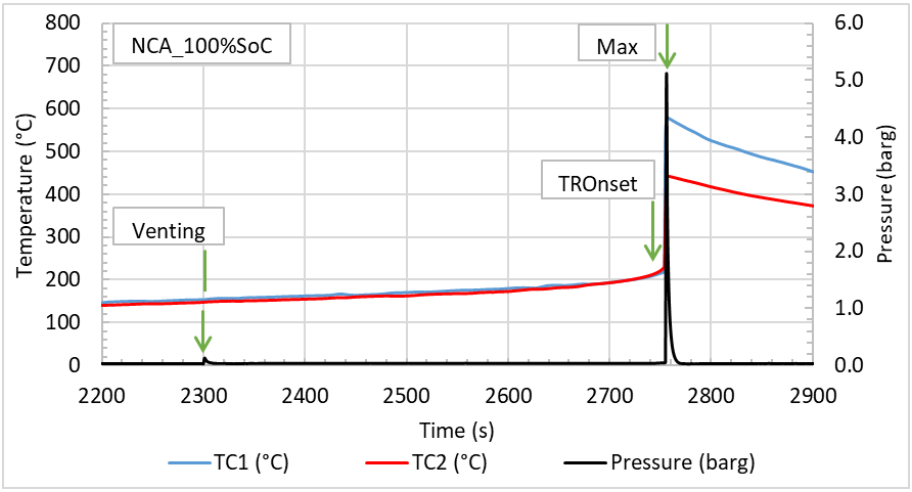

a)

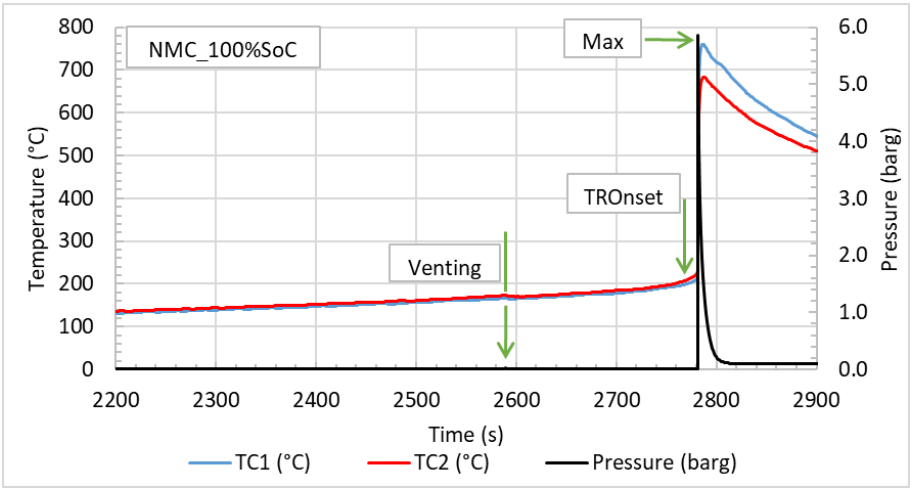

b)

Fig. 1. *Temperature and pressure profile for thermal abuse tests on: (a) NCA; (b) NMC*

These data allowed for the determination of the maximum temperature reached on the cell surface and the pressure resulting from gas release. Figure 1 shows that the maximum peak for both parameters occurred simultaneously during the thermal abuse tests. Table 3 summarises the results in terms of time (s), the temperature on the cell surface, which is the average between TC_1 and TC_2, and the pressure inside the reactor during the key events, such as venting, TR onset, and maximum peak

for the thermal abuse test of both cells. The TRonset is defined as the point at which the temperature's increase rate exceeds 10 °C/min (Doughty et al., 2012). The first difference between the two cells is between the venting temperatures. Specifically, for NCA the venting starts at 150 °C, while for NMC at higher temperature, 169 °C. The most significant difference is observed in the maximum temperature values reached, with NCA reaching around 510 °C and NMC exceeding 720 °C. The maximum pressure values are not significantly different, with both cells reaching maximum values over 5 barg.

Table 3: *Time (s), temperature (°C) and pressure (barg) relative to the key events of the thermal abuse tests*

Id-cell	$T_{venting}$ (°C)	$P_{venting}$ (barg)	$T_{TRonset}$(°C)	$P_{TRonset}$ (barg)	T_{Max} (°C)	P_{Max} (barg)
NCA	150	0.125	204	0.037	511	5.071
NMC	169	0.017	202	0.007	721	5.858

The maximum temperatures measured in this work were compared with those reported in the literature. Golubkov et al. (2014, 2015) reported a maximum temperature of 911 °C for NCA and 678 °C for NMC, while Yuan et al. (2020) reported a maximum temperature of 917 °C for NMC. It should be noted that differences in cell characteristics (e.g., chemistry and voltage), equipment (e.g., reactor, ARC), and experimental conditions (e.g., feed gas and heating rate) can significantly affect the resulting maximum temperature. The description of the cathode composition alone is insufficient to fully define the cell's characteristics. The chemical composition of the anode and electrolyte can also vary depending on the type of solvents used (i.e., DEC, DMC, and EC) and their relative ratios. The technical safety data sheet typically does not include this information. In addition, the voltage range may vary depending on the final use of the cell. Therefore, a SoC level of 100 % does not necessarily correspond to the same voltage value.

Regarding the gas emission profile, the concentrations of H_2, CO, CO_2, CH_4, EC, DMC, and HF along the entire thermal abuse test are reported in Figure 2 (a,b) for NCA and (c,d) for NMC. Figure 2 displays concentration profiles that replicate the events observed during the thermal abuse tests in Figure 1. For both cells, CO, CO_2 and H_2 reach a maximum peak of around 10^5 ppmv, while CH_4 of the order of 0.5 x10^5 ppmv (Figure 2b). The other species related to the electrolyte (i.e., DMC, DEC, EC, and HF) reach a maximum peak value of around 10^3 ppmv (Figure 2a). The main difference between the two cells is the emission of H_2. In the case of NCA, the release of H_2 is mainly observed around the maximum temperature (Figure 2b). However, in the case of NMC, the release starts earlier and is significant in correspondence with the TR onset (figure 2d).

The mole fractions and the relative volume (in NmL) of the gas for the different phases, namely venting, TR, and global (as defined in Section 2), are provided in Table 4. In addition, the composition of the gas at the maximum temperature is reported.

Table 4: *Mole fractions of the gas species and relative volume (NmL) emitted during the thermal abuse test phases: venting; TR; Max; Global*

Id-cell	Phase	H_2	CH_4	CO	CO_2	HF	DMC	EC	DEC	Volume (NmL)
NCA	Venting	0.014	0.002	0.664	0.304	0.007	0.009	< 0.001	n.d.	$1.61*10^3$
NCA	TR	0.087	0.015	0.556	0.331	0.004	0.006	< 0.001	n.d.	$2.79*10^3$
NCA	Max	0.376	0.044	0.307	0.271	< 0.001	0.001	0.001	n.d.	
NCA	Global	0.236	0.042	0.315	0.395	0.010	0.002	< 0.001	n.d.	$1.51*10^4$
NMC	Venting	0.839	0.026	0.043	0.074	0.018	0.001	n.d.	n.d.	$1.83*10^2$
NMC	TR	0.395	0.043	0.243	0.302	0.015	< 0.001	0.002	n.d.	$6.83*10^2$
NMC	Max	0.356	0.058	0.325	0.257	0.004	n.d.	0.001	n.d.	
NMC	Global	0.407	0.039	0.140	0.392	0.010	< 0.001	0.012	n.d.	$3.12*10^4$

n.d.: not detected.

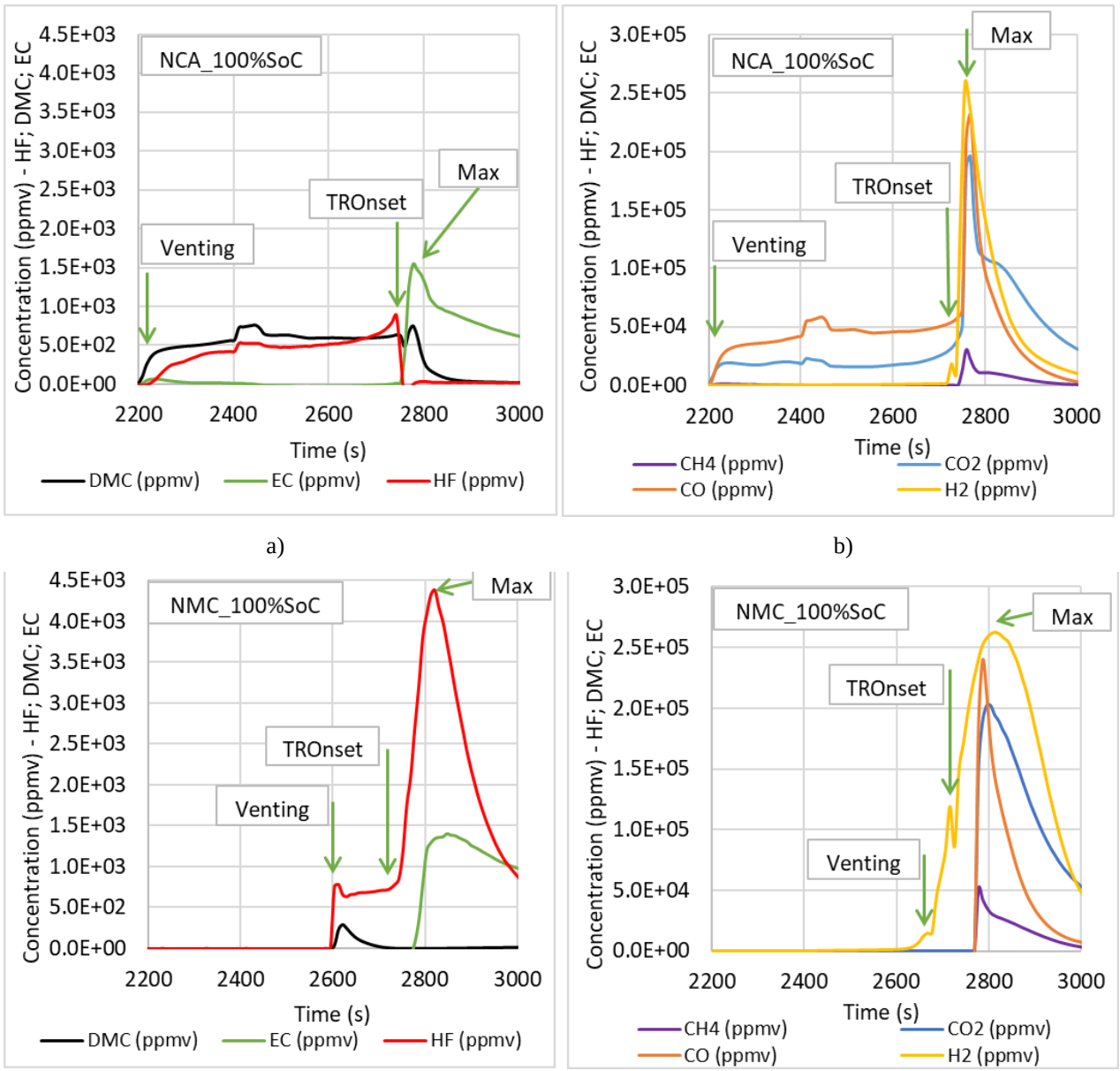

Fig. 2. *Gas emissions profile for: (a, b) NCA; (c, d) NMC*

According to the analysis presented in Figure 2b, the primary distinction in concentration of emitted species across phases is primary distinguished by H_2. During the entire thermal abuse test, for NCA, the percentage of H_2 measured was 23.6 %, which is mainly released during the TR phase (with a maximum of 37.6%) while is not observed during the venting phase. Similar behaviour is observed for CH_4, but the maximum concentration is 4.4%. During the venting phase, CO, CO_2, and HF appear, and their concentration remain constant (Figure 2a). However, during the TR phase the concentration of CO e CO_2 increases (with a maximum of 30.7 and 27.1%,respectively) while HF completely disappears at the maximum peak. Additionally, among the species attributable to the electrolyte, DMC is detected throughout the entire test, while EC is only detected during the TR phase. However, their percentage values are always below 1.0 %. In contrast, the emissions from the NMC exhibit a different trend. During the venting phase, the H_2 percentage is higher (83.9 %) than the TR phase (39.5 %). This because significant concentrations of CH_4, CO, and CO_2 are only observed during the TR. Regarding the species attributable to the electrolyte, DMC appears only during the venting phase, while EC appears only during the TR, but the concentrations are always below 1.2%. This different behaviour is due to the different boiling temperature of the two components (90 °C for DMC and 244

°C for EC), and considering that the onset of TR is measured at surface temperature higher than 200°C.

The volume of gas emitted during the different phases of the thermal abuse test, as shown in Table 4 is another important parameter to consider. The data reveal that NCA and NMC release respectively 15.1- 31.2 NL of gas globally. For NCA, the volume of gas released during both the venting and TR phases is around 2 NL, while for NMC is around 0.2 NL for venting and 0.7 L for TR. This difference is attributed to the H_2, CO and CO_2 emissions from NCA that appear already during the venting phase.

3.2. Laminar burning velocity of BVG

The S_u vs equivalence ratio (ER) plot calculated for the four BVG compositions corresponding to the different phases of thermal abuse test (venting, TR, max, and global) for NCA are shown in Figure 3. S_u refers to initial conditions of 25 °C and 1 atm.

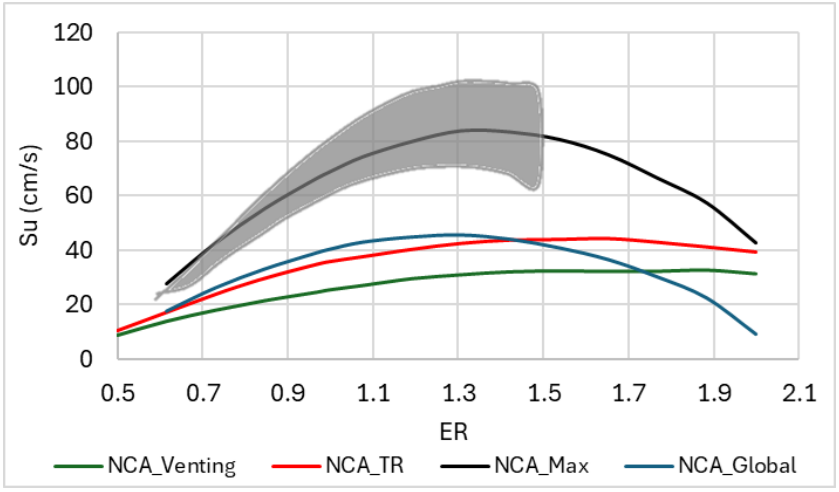

Fig. 3. *S_u as a function of the ER calculated for BVG from NCA (100% SoC) compared to literature data (Baird et al., 2020) (grey area).*

Figure 3 illustrates that the highest S_u value is achieved by considering the composition of the BVG at the maximum (83.7 cm/s), followed by the global composition during the entire event (45.5 cm/s), then that of the TR (44.4 cm/s), and finally the BVG composition of the venting phase (32.5 cm/s). These behaviours are correlated with the different mole fractions of H_2. The molar fraction of H_2 is highest at the maximum and decreases during other phases of the thermal abuse test, where the presence of other species, especially CO_2, reduces S_u values. Furthermore, a distinct bell-shaped curve is observed for S_u, between 0.5 and 2.0 ER, for the global composition of BVG and at the maximum, while venting and TR BVG do not exhibit this pattern. The width of the bell-shaped curve is related to the lower flammability of the gas emitted in the initial phases.

Figure 4 displays the S_u vs equivalence ratio plot obtained for BVG from NMC.

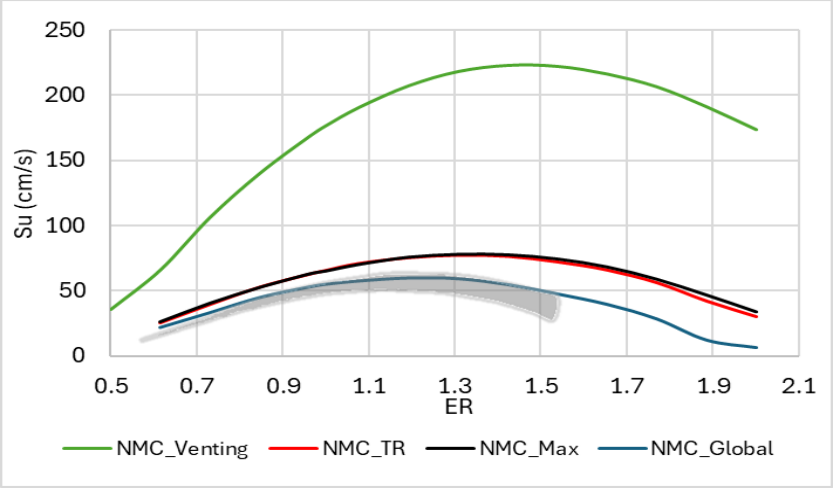

Fig. 4. *S_u as a function of the ER, calculated for BVG from NMC (100 % SoC) compared to literature data (Baird et al., 2020) (grey area).*

The figure shows the effect of H_2 on S_u values. As previously noted, a higher percentage of this species was quantified during the early phase of the thermal abuse test, venting, which explains why S_u obtained for the BVG in this phase is significantly higher than the others (222.6 cm/s venting, 77.2 cm/s TR, 77.8 cm/s max, and 59.9 cm/s global). The decrease in values during subsequent phases is due to an increase in CO_2 and a decrease in H_2 concentration. It is also observed that the maximum S_u is shifted to gas compositions with lower oxygen content (higher ER) compared to NCA. The high reactivity of these oxygen-depleted flames is due to the combustion chemistry being driven by H atoms instead of OH radicals, which dominate at higher oxygen levels.

Baird et al. (2020) calculated the variability of S_u, in the range of 0.6 - 1.5 ER, for different cathode chemistries (NCA, LFP, LCO, and NMC), at 100% SoC. For each chemistry, they used the different gas species concentrations noted in the literature (refer to Table 1 for NCA and NMC). Subsequently, for each concentration found in the literature, they calculated a curve of laminar burning velocity versus equivalence ratio. Figure 3 compares the range of variability calculated by Baird (grey area) with the S_u obtained in the present work for NCA, while Figure 4 shows the same comparison for NMC.

Despite variations in the changes in laminar burning velocity associated with individual experiments, these figures clearly demonstrate a difference in the S_u for different chemistries at the same SOC. Specifically, NCA exhibits a higher maximum S_u (105 cm/s) compared to NMC (62.8 cm/s). The range of variability differs between NCA and NMC, with NCA having a wider range and NMC having a narrower range. When comparing the values reported by Baird et al. (2020) with the S_u curves obtained in the present study for NCA, it is evident that only the S_u calculated for BVG at the maximum peak falls within the range, while the other curves are lower. In contrast, for NMC, only the curve relative to the global BVG is included in the range, while the other curves are higher. From these comparisons, it is clear that previous literature studies have typically focused on the average concentration of BVG throughout the event. However, it is important to note that the species do not emerge simultaneously, but rather at different times and with varying compositions.

In addition, BVG at these various compositions are not released at room temperature but rather at higher temperatures, as indicated in Table 3. To evaluate the effect of temperature, S_u was calculated at different initial temperatures (i.e., 25 °C, 150 °C, 300 °C, and 500 °C) and at constant pressure (1 atm). The maximum S_u value obtained for the four BVGs as function of temperature is shown in Figure 5.

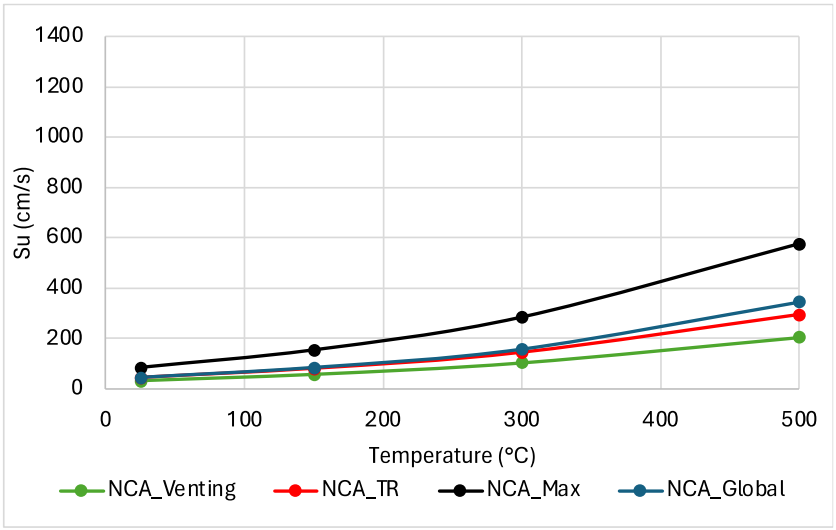

(a)

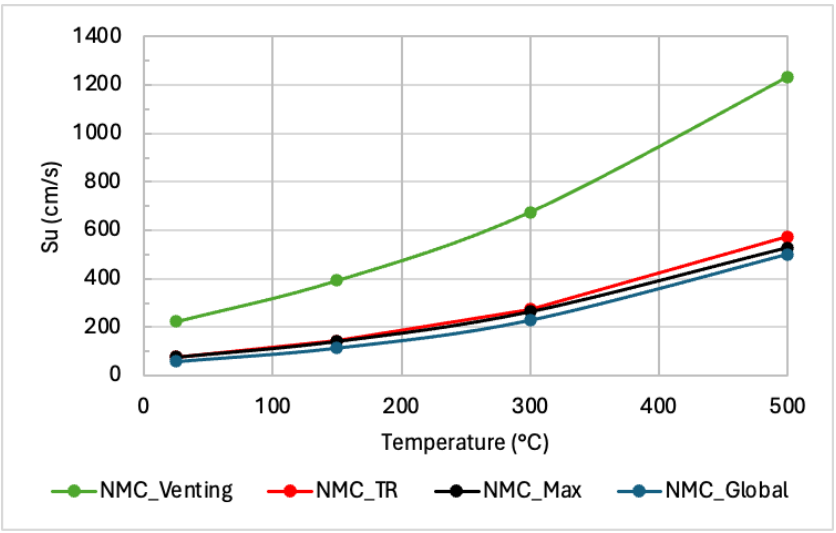

(b)

Fig. 5. *Effect of temperature on maximum S_u calculated for BVG from NCA (a) and NMC (b) (100 % SoC).*

Figure 6 shows that an increase in temperature led to an increase in S_u value considering for the different BVG compositions. A significant difference is observed when comparing the two cell chemistries. In the range of temperatures investigated, the maximum S_u value reached for NCA is 576 cm/s for the BVG at maximum peak, while the highest S_u for NMC was 1234 cm/s for the BVG during the venting phase. The increase in S_u in relation to the increase in temperature is due to the greater flammability of the species present in the mixture at higher temperature values.

These evaluations can have practical applications in the design of mitigation strategies for thermal runaway of LIBs. Firstly, they help to properly design a vent valve that can control the moment of rupture at a suitable temperature, and then to dilute the flammable gases to an extreme lean zone possibly using inert gases. In addition, LIBs can be designed with containment structures or placed in areas where any vented gases can be safely isolated, minimizing explosion hazards.

4. Conclusions

The risk posed by the flammability properties of the substances emitted during the thermal runaway of Li-ion cells is evaluated in this study. The laminar burning velocity of the emitted gas is evaluated using experimental data of BVG composition obtained from thermal abuse tests in air on various Li-ion cells (i.e., NCA, and NMC) at 100 % SoC are used to evaluate. The kinetic model used for the

calculation includes all relevant gas component types necessary for predicting both hydrocarbon combustion and the formation of toxic fluorinated compounds.

The results of thermal abuse tests indicate that the cell's chemistry affect the maximum temperature reached during the event (511 °C NCA vs 721 °C NMC). Furthermore, the emitted BVG compositions vary across different phases of the event.

During a thermal event in a NCA cell, the first vent emits gas mixtures with high CO and CO_2 contents, which burn slowly. The highest S_u for NCA cells is achieved with the gas mixture emitted at the maximum temperature, where the highest concentration of H_2 is present. On the contrary, during the venting phase, NMC cells release BVG with a high concentration of H_2, resulting in the highest S_u value in the initial part of the event.

The impact of the temperature was evaluated by considering typical temperatures of the BVG, ranging from 150-500 °C. As expected, the S_u values increased as the temperature increases, while maintaining correlation between the data.

Acknowledgements

This study was carried out within the MOST – Sustainable Mobility Center and received funding from the European Union Next-GenerationEU (PIANO NAZIONALE DI RIPRESA E RESILIENZA (PNRR) – MISSIONE 4 COMPONENTE 2, INVESTIMENTO 1.4 – D.D. 1033 17/06/2022, CN00000023). This manuscript reflects only the authors' views and opinions, neither the European Union nor the European Commission can be considered responsible for them.

References

Alexandrino, K., A., Alzueta, M.U. & Curran, H.J. (2018). An Experimental and Modeling Study of the Ignition of Dimethyl Carbonate in Shock Tubes and Rapid Compression Machine. *Combustion and Flame*, 188: 212–26.

Andersson, P., Blomqvist, P., Lorén, A. & Larsson F. (2016). Using Fourier Transform Infrared Spectroscopy to Determine Toxic Gases in Fires with Lithium-Ion Batteries: FTIR to Determine Toxic Gases. *Fire and Materials*, 40(8): 999–1015.

Baird, A.R., Archibald, E.J., Marr, K.C. & Ezekoye, O.A. (2020). Explosion Hazards from Lithium-Ion Battery Vent Gas. *Journal of Power Sources*, 446: 227257.

Diaz, F., Wang, Y., Weyhe, R. & Friedrich B. (2019). Gas Generation Measurement and Evaluation during Mechanical Processing and Thermal Treatment of Spent Li-Ion Batteries. *Waste Management* 84: 102–11.

Doughty, D.H. & Roth, E.P. (2012). A General Discussion of Li Ion Battery Safety. *Electrochemical Society Interface*, 21(37): 8.

Essl, C., Golubkov, A.W., Gasser, E., Nachtnebel, M., Zankel, A., Ewert, E. & Fuchs, A. (2020). Comprehensive Hazard Analysis of Failing Automotive Lithium-Ion Batteries in Overtemperature Experiments. *Batteries*, 6(2): 30.

Gao, M., Bi, M., Ye, L., Li, Y., Jiang, H., Yang, M., Yan, C. & Gao, W. (2021). Suppression of hydrogen-air explosions by hydrofluorocarbons. *Process Saf. Environ. Protect.*, 145: 378-387,

Golubkov, A.W., Fuchs, D., Wagner, J., Wiltsche, H., Stangl, C., Fauler, G., Voitic, G., Thaler, A. & Hacker, V. (2014). Thermal-Runaway Experiments on Consumer Li-Ion Batteries with Metal-Oxide and Olivin-Type Cathodes. *RSC Adv.*, 4(7): 3633–42.

Golubkov, A.W., Scheikl, S., Planteu, R., Voitic, G., Wiltsche, H., Stangl, C., Fauler, G., Thaler, A. & Hacker, V. (2015). Thermal Runaway of Commercial 18650 Li-Ion Batteries with LFP and NCA Cathodes – Impact of State of Charge and Overcharge. *RSC Advances*, 5(70): 57171–86.

Henriksen, M., Vaagsaether, K., Lundberg, J., Forseth, S. & Bjerketvedt, D. (2021). Laminar Burning Velocity of Gases Vented from Failed Li-Ion Batteries. *Journal of Power Sources*, 506: 230141.

Kéromnès, A., Metcalfe, W.K., Heufer, K.A., Donohoe, N., Das, A.K., Sung, C.-J., Herzler, J., Naumann, C., Griebel., P., Mathieu, O., Krejci, M.C., Petersen, E.L., Pitz, W.J. & Curran, H.J. (2013). An Experimental and Detailed Chemical Kinetic Modeling Study of Hydrogen and Syngas Mixture Oxidation at Elevated Pressures. *Combustion and Flame*, 160(6): 995–1011.
Larsson, F., Andersson, P. & Mellander, B.E. (2016). Lithium-Ion Battery Aspects on Fires in Electrified Vehicles on the Basis of Experimental Abuse Tests. *Batteries*, 2(2): 9.
Linteris, G. & Babushok, V. (2020). Laminar Burning Velocity Predictions for C1 and C2 Hydrofluorocarbon Refrigerants with Air. *Journal of Fluorine Chemistry*, 230: 109324.
Lopez, C.F., Jeevarajan, J.A. & Mukherjee, P.P. (2015). Characterization of Lithium-Ion Battery Thermal Abuse Behavior Using Experimental and Computational Analysis. *Journal of The Electrochemical Society*, 162(10): A2163–73.
Lu, L., Han, X., Li, J., Hua, J. & Ouyang M. (2013). A Review on the Key Issues for Lithium-Ion Battery Management in Electric Vehicles. *Journal of Power Sources*, 226: 272–88.
Metcalfe, W.K., Burke, S.M., Ahmed, S.S. & Curran, H.J. (2013). A Hierarchical and Comparative Kinetic Modeling Study of C 1 − C 2 Hydrocarbon and Oxygenated Fuels. *International Journal of Chemical Kinetics*, 45(10): 638–75.
Nilsson, E.Jk., Brackmann, C. & Tidblad, A.A. (2023). Evaluation of Combustion Properties of Vent Gases from Li-Ion Batteries. *Journal of Power Sources*, 585: 233638.
Park, J.K. (2012). *Principles and Applications of Lithium Secondary Batteries*. Weinheim, Germany: Wiley-VCH.
Peng, Y., Yang, L., Ju, X., Liao, B., Ye, K., Li, L., Cao B. & Ni, Y. (2020). A Comprehensive Investigation on the Thermal and Toxic Hazards of Large Format Lithium-Ion Batteries with LiFePO4 Cathode. *Journal of Hazardous Materials*, 381: 120916.
Somandepalli, V., Marr, K. & Horn, Q. (2014). Quantification of combustion hazards of thermal runaway failures in lithium-ion batteries. *SAE Int. J. Altern. Powertrains*, 3: 98-104.
Sun, W., Huang, C., Tao, T., Zhang, F., Li, W., Hansen, N. & Yang, B. (2017). Exploring the High-Temperature Kinetics of Diethyl Carbonate (DEC) under Pyrolysis and Flame Conditions. *Combustion and Flame*, 181: 71–81.
"Table of IDLH Values | NIOSH | CDC.". Accessed September 4th, 2023. Available online: https://www.cdc.gov/niosh/idlh/intridl4.html.
Takahashi, S., Kanayama, K., Morikura, S., Nakamura, H., Tezuka, T. & Maruta, K. (2022). Study on Oxidation and Pyrolysis of Carbonate Esters Using a Micro Flow Reactor with a Controlled Temperature Profile. Part II: Chemical Kinetic Modeling of Ethyl Methyl Carbonate. *Combustion and Flame*, 238: 111878.
Ubaldi, S., Conti, M., Marra, F. & Russo, P. (2023). Identification of Key Events and Emissions during Thermal Abuse Testing on NCA 18650 Cells. *Energies*, 16(7): 3250.
Ubaldi, S. & Russo, P. (2023). Comparison Between 18650 Lithium-ion Cells of Different Composition Subjected to Thermal Abuse. *Chemical Engineering Transactions*, 104: 49-54.
Yuan, L., Dubaniewicz, T., Zlochower, I., Thomas, R. & Rayyan, N. (2020). Experimental Study on Thermal Runaway and Vented Gases of Lithium-Ion Cells. *Process Safety and Environmental Protection*, 144: 186–92.
Zhang, R., Xia, B., Li, B., Cao, L., Lai, Y., Zheng, W., Wang, H. & Wang, W. (2018). State of the Art of Lithium-Ion Battery SOC Estimation for Electrical Vehicles. *Energies*, 11(7): 1820.

Critical Peclet numbers for the onset of the intrinsic instabilities of Lithium-ion battery thermal runaway vent gas in air

Akihiro Ueda [a], Tomoyuki Johzaki [a], Takuma Endo [a], Yangkyun Kim [b] & Wookyung Kim [a]

[a] Hiroshima University, Higashi-Hiroshima, Japan
[b] Korea Institute of Civil Engineering and Building Technology, Hwaseong, Korea

E-mail: kimwk@hiroshima-u.ac.jp

Abstract

Lithium-ion batteries have garnered attention as alternative energy carriers to fossil fuels. However, this battery releases vent gas containing flammable gases during thermal runaway. Vent gas is mainly composed of hydrogen, carbon monoxide, carbon dioxide, methane, and ethylene, which can be explosive when mixed with atmospheric air. And it is well known that when the magnitude of the explosion is increased, all flames accelerate due to the intrinsic instabilities. Therefore, in our study, we measured the critical flame radius of the vent gas under elevated pressure using a constant volume chamber and Schlieren method. The flame acceleration behavior was observed and the values of unstretched laminar burning velocity, critical Péclet number and the Markstein number for vent gas mixtures with changing the mole fraction of H_2 and CO in the vent gas were obtained experimentally. Experimental results show that diffusive-thermal instability has a significant effect on the onset of acceleration of vent gas flames and enhancement or suppression of diffusive-thermal instability by increasing the H_2 fraction depends on the ratio of H_2 to CO in the vent gas.

Keywords: *Gas Explosion, Lithium-ion battery, vent gas, flame acceleration, Diffusive-thermal Instability*

1. Introduction

Lithium-ion batteries have been used in various electronic devices in recent years due to their advantage of high energy density. However, if they are misused, short-circuited, or overcharged, an exothermic reaction can occur in the battery, leading to thermal runaway. Understanding the process of thermal runaway in lithium-ion batteries is crucial for safety (Meng et al., 2023; Yuan et al., 2022; Golubkov et al., 2014; Belharouak et al., 2006; Bang et al., 2006; Golubkov et al., 2015; Doughty et al., 2005; Abraham et al., 2006). During thermal runaway, lithium-ion batteries release vent gases, which contain flammable gases. The vent gases generated can cause lithium-ion batteries to ignite or rupture. Fires resulting from lithium-ion batteries pose major safety hazards that necessitate effective mitigation measures. Previous studies have shown that the composition of the vent gas varies depending on the state of charge of the lithium-ion battery (Golubkov et al., 2014; Golubkov et al., 2015). The main components of the vent gas are H_2, CO, CO_2, and some hydrocarbons such as CH_4 and C_2H_4. The trend of the composition ratio of the vent gases is that the CO_2 concentration decreases and the H_2 and CO concentrations increase with increasing the state of charge. If the vent gas explodes after mixing with the atmosphere, it is expected to cause significant damage to the surrounding area. In addition, as the magnitude of the explosion is increased, it is necessary to take into account the flame acceleration phenomenon due to intrinsic instabilities. The onset of flame acceleration is particularly affected by Darrieus-Landau and diffusive-thermal instability. Darrieus-Landau instability appears in all premixed flames because of the thermal expansion of the gas during combustion. Conversely, diffusive-thermal instability is caused by the difference between the mass

and thermal diffusion coefficients and it is evaluated using the Lewis number, Le, which is the ratio of the mixture thermal diffusivity and mass diffusivity of the limiting reactant in relation to the inert reactant. Previous studies (Dobashi et al., 2011; Dorofeev, 2011; Kim et al., 2014; Kim et al., 2015) have reported that the prediction of blast wave, which is the main cause of damage in an explosion, can be underestimated if the acceleration of the flame is not considered. Therefore, it is important to estimate the onset of flame acceleration in order to predict the damage caused by an explosion. In this study, we experimentally investigated the laminar burning velocity and onset of flame acceleration of vent gases in lithium-ion batteries under high pressure conditions. We also evaluated the effect of vent gas composition on the onset of flame acceleration.

2. *Experimental set-up*

Experimental set-up is shown in Fig.1. This set-up consists of a high-pressure constant volume vessel with a total volume of 0.79 L, a spark ignition system, gas feeding system and a Schlieren imaging system with a high-speed camera. The high-pressure chamber is equipped with two 70 mm diameter acrylic windows to observe the inside of the vessel. In the experiment, the chamber was evacuated with a vacuum pump and filled with the H_2-CO-CO_2-CH_4-C_2H_4-Air mixture according to the partial pressure of each gas. The pressure inside the vessel was measured using a pressure gauge with a resolution of 0.25 kPa. After that, the chamber was left for about 20 minutes after filling all the gases to allow the gases to mix by diffusion and to make the mixture in the chamber homogeneous. After that, the mixture was ignited by a spark generated in the center of the vessel by a pair of electrodes equipped on both sides of the vessel and linked to a high-voltage source. The flame propagation behaviors inside the chamber visualized by the Schlieren imaging system, consisting of a light source, a pair of concave mirrors with a diameter of 300 mm, and a knife edge, were captured by a high-speed camera (Photron FASTCAM AX-100) with an exposure time of 10 μs and frame rate of 10,000 fps.

The equivalence ratio of the H_2-CO-CO_2-CH_4-C_2H_4-Air mixture is given by the following equation.

$$\phi = \frac{F/A}{(F/A)_{\mathrm{st}}} = \frac{\left(n_{\mathrm{H_2}} + n_{\mathrm{CO}} + n_{\mathrm{CH_4}} + n_{\mathrm{C_2H_4}}\right)/n_{\mathrm{O_2}}}{\left\{\left(n_{\mathrm{H_2}} + n_{\mathrm{CO}} + n_{\mathrm{CH_4}} + n_{\mathrm{C_2H_4}}\right)/n_{\mathrm{O_2}}\right\}_{\mathrm{st}}} \tag{1}$$

where n_{i} is the mole number of each gas.

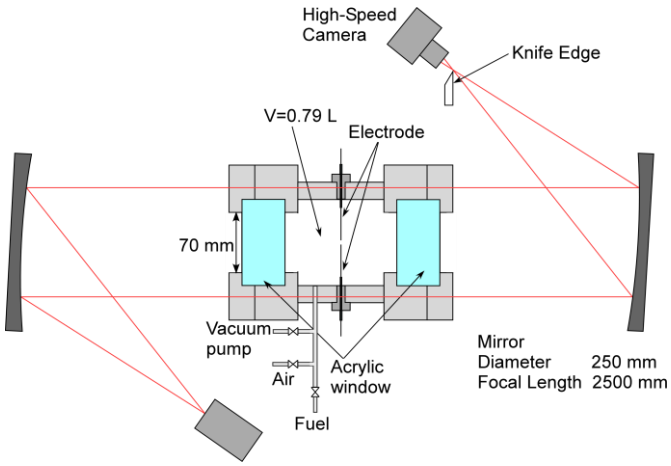

Fig. 1. *Schematic of experimental set-up*

***Table 1**. The volumetric fraction of fuel gas*

x_{H_2}	H_2 (%)	CO (%)	CO_2 (%)	CH_4 (%)	C_2H_4 (%)
0.25	20	60	10	5	5
0.5	40	40	10	5	5
0.75	60	20	10	5	5

In this study, to evaluate the onset of flame acceleration of vent gas generated by lithium-ion batteries, the composition of the fuel gas was determined based on the composition of vent gas reported in previous studies (Golubkov et al., 2015; Baird et al., 2020). According to the calculations of Baird et al., 2020, the laminar burning velocity of the vent gas is the fastest when the cathode material is $Li_x(Ni_{0.80}Co_{0.15}Al_{0.05})O_2$ (NCA) compared to other cathode materials. Lammer, M. et al., 2017 reported that when the cathode material is NCA, the concentration of CO_2 in the vent gas composition was about 10%, and approximately 80% of the vent gas composition consisted of H_2 and CO. For this reason, in this study, we focused on the ratio of hydrogen and carbon monoxide in the vent gas because these gases are the main fuels of vent gas. Therefore, the composition ratio of CO_2, CH_4 and C_2H_4 in the fuel were set to 10%, 5%, and 5% for all experimental conditions, respectively. And the index x_{H_2} was introduced to evaluate the ratio of hydrogen and carbon monoxide in the fuel as following:

$$x_{H_2} = \frac{n_{H_2}}{n_{H_2} + n_{CO}} \tag{2}$$

The compositions of the fuel gas used in this experiment are shown in Table 1. The initial pressure was 0.5 MPa and the initial temperature of the mixture was approximately 298 K. Also, the values of ϕ and x_{H_2} were varied in the range of 0.8 to 1.6 and 0.25, 0.5 and 0.75 for all experimental conditions. Furthermore, to evaluate the flame thickness, the combustion under the experimental conditions was simulated by numerical analysis of a one-dimensional planar flame model using Ansys Chemkin-Pro with Aramco Mech1.3 (Metcalfe et al., 2013) chemical kinetic models. In this study, the flame thickness δ was estimated from temperature profile as following:

$$\delta = \frac{T_{ad} - T_u}{(dT/dx)_{max}} \tag{3}$$

where T_{ad} is the adiabatic flame temperature, T_u is the initial temperature of unburned gas and $(dT/dx)_{max}$ is the maximum temperature gradient.

3. Result and discussion

3.1. Derivation of unstretched laminar burning velocity

Figure 2 shows the images of flame propagation behavior at different gas composition taken in this experiment. In this study, wrinkled flame was observed under all experimental conditions. To analyze the flame images taken in this experiment, ImageJ Fiji software was used in this study. The edges of flame front in the Schlieren images were detected using Sobel filter. After that, the number of pixels corresponding to the flame area was determined by filling in the flame edge. Flame area A was estimated by converting the number of pixels to the actual scale, and flame radius r was obtained

from the flame area as $r = \sqrt{A/\pi}$. The flame speed S_n was determined by time differentiation of the values of r. The flame stretch rate κ is the rate of change in flame surface area over time and is estimated as $\kappa = (1/A)\,\mathrm{d}A/\mathrm{d}t = (2/r)\,\mathrm{d}r/\mathrm{d}t = (2/r)S_n$. The relationships between the flame speed and flame stretch rate at different gas composition were shown in Fig.3. A linear relationship between the flame speed and fame stretch rate was observed, and flame propagated at a constant speed relative to the flame stretch rate up to a certain flame stretch rate. After the certain flame stretch rate, flame acceleration was happened. Therefore, in this study, the flame radius corresponding to the flame stretch rate at which flame acceleration occurs was defined as the critical flame radius r_c. And the unstretched laminar flame speed S_n^0 was obtained by fitting the part of the flame propagating at a constant velocity without acceleration. Previous studies suggested a linear relationship between flame speed S_n and stretch rate κ as follows:

$$S_n^0 - S_n = L_b\kappa \tag{2}$$

where S_n^0 is the unstretched laminar flame speed, L_b is the proportionality constant which is known as the burned gas Markstein length (Paul, 1985; Law and Sung, 2000). In the present experiments, equation (2) was only applied when the flame radius was greater than 5 mm and less than 20 mm. Flames with radii less than 5 mm and greater than 20 mm were discarded because of the effect of ignition energy and wall effect, respectively. Then, the unstretched laminar burning velocity S_u^0 was derived by dividing the unstretched laminar flame speed S_n^0 by expansion ratio σ as follows:

$$S_u^0 = \frac{\rho_b}{\rho_u}S_n^0 = \frac{S_n^0}{\sigma} \tag{3}$$

where ρ_u is the unburned gas density at T_u and ρ_b is the burned gas density at T_{ad}.

Figure 4 shows the unstretched laminar burning velocity as a function of equivalence ratio at different gas composition. The unstretched laminar burning velocity increased with increasing hydrogen fraction in the gas mixture. Table 2 summarizes the test conditions and major experimental and numerical results.

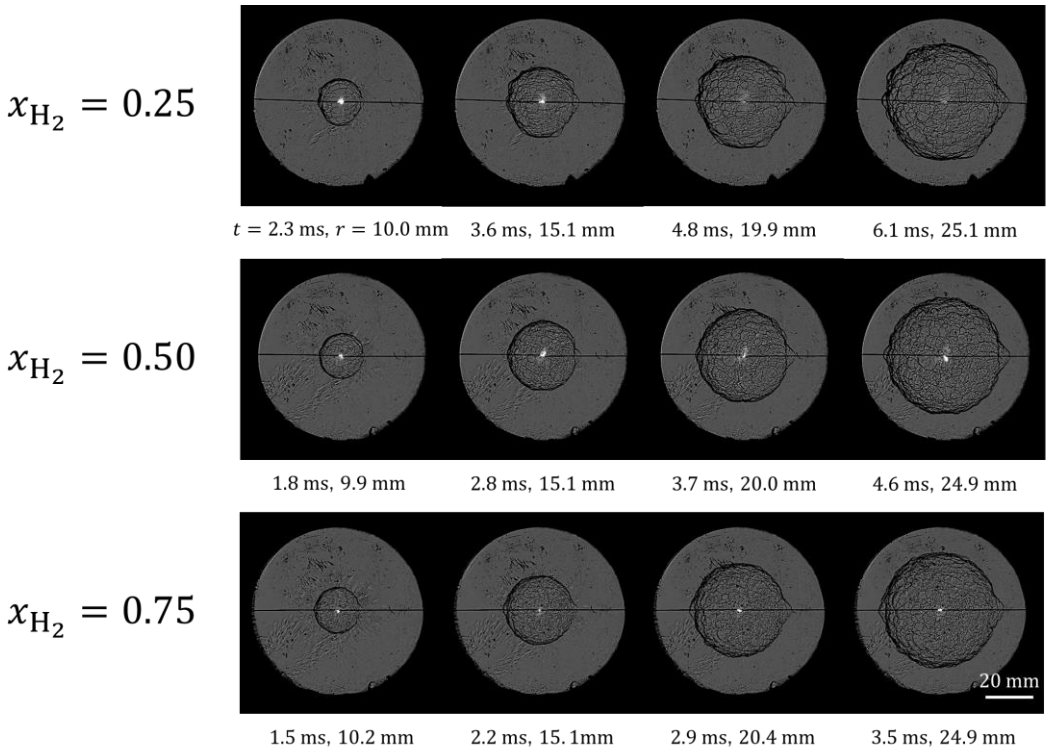

Fig. 2. *Spherical flame propagation images at* $\phi = 1.0$

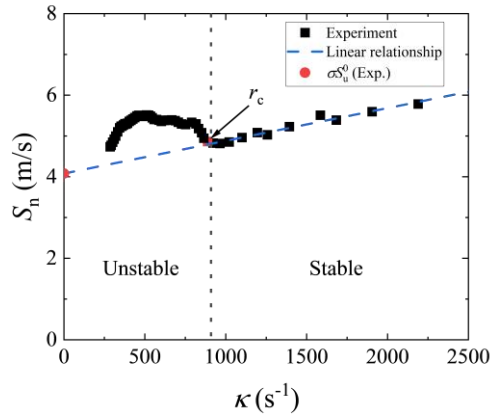

Fig. 3. *Flame speed as a function of equivalence ratio ($x_{H_2} = 0.50, \phi = 1.0$)*

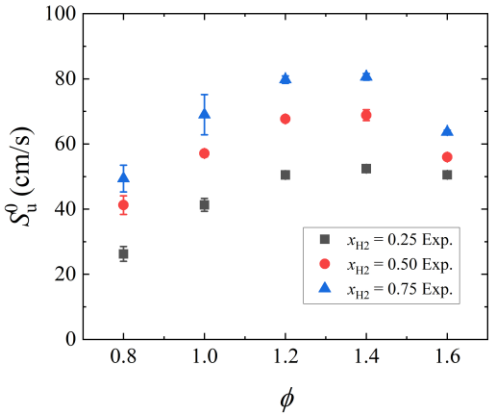

Fig. 4. *Unstretched laminar burning velocity as a function of equivalence ratio*

Table 2*. Summary of test conditions and results*

x_{H_2}	ϕ	S_u^0 [cm/s]	r_c [mm]	L_b [mm]	δ [mm]
0.25	0.8	26.2±2.3	10.3	-0.71±0.26	0.114
	1.0	41.3±2.0	8.9	-0.72±0.12	0.0932
	1.2	50.5±0.7	10.1	-0.34±0.46	0.0800
	1.4	52.4±0.8	9.1	-0.41±0.48	0.0735
	1.6	50.5±0.4	-	-0.21±0.42	0.0760
0.50	0.8	41.2±2.8	10.	-0.40±0.24	0.0982
	1.0	57.1±1.0	11.0	-0.80±0.05	0.0806
	1.2	67.7±0.9	8.8	-0.61±0.04	0.0702
	1.4	68.8±1.7	13.3	-0.46±0.09	0.0666
	1.6	56.0±0.6	-	-0.45±0.06	0.0744
0.75	0.8	49.4±4.1	6.9	-0.70±0.14	0.0855
	1.0	69.0±6.2	8.3	-0.83±0.23	0.0712
	1.2	79.8±1.1	9.4	-0.50±0.03	0.0633
	1.4	80.5±1.0	-	0.02±0.06	0.0627
	1.6	63.6±0.6	-	0.01±0.05	0.0779

3.2. Comparison with different gas composition on Pe_c and Ma_b

The critical Peclet number calculated from critical flame radius measured experimentally as a function of equivalence ratio are shown in Fig.5. When the x_{H_2} is 0.25 and 0.50, flame acceleration was not observed within the observation area of this experiment at $\phi = 1.6$. Also, when the x_{H_2} is 0.75, flame acceleration was not observed at $\phi = 1.4$ and 1.6. For all mixtures, the values of critical Peclet number tended to increase with increasing equivalence ratios at all x_{H_2}. Previous studies show that onset of flame acceleration is mainly influenced by the diffusive-thermal instability (Bradley et al., 1998; Bradley et al., 2007; Gu et al., 2000; Ueda et al., 2023; Tanaka et al., 2024). To evaluate the effect of the diffusive-thermal instability, burned Markstein number $Ma_b = L_b/\delta$ was obtained experimentally from the linear relationship between flame speed S_n and stretch rate κ. The values of Ma_b as a function of equivalence ratio are shown in Fig. 6. Figure 6 shows that for all gas compositions, Ma_b showed a decreasing trend with increasing ϕ from 0.8 to 1.0. In contrast, the values of Ma_b were increased with increasing ϕ from 1.0 to 1.6. It suggests the flame of vent gas-air mixture is most unstable at $\phi = 1$ in terms of diffusive-thermal instability. In terms of the effect of the composition ratio of hydrogen in the fuel mixture, Ma_b decreased with increasing x_{H_2} from 0.25 to 0.50. In contrast, Ma_b increased with increasing x_{H_2} from 0.50 to 0.75. This non-monotonic trend in Ma_b due to hydrogen addition has been similarly reported in previous studies of hydrogen-hydrocarbon mixtures and hydrogen-ammonia mixtures (Ichikawa et al., 2015; Okafor et al., 2014). Furthermore, the values of Ma_b were negative over a wide range of ϕ for all gas compositions. This means that the propagation flame of vent gas consisting of H_2-CO-CO_2-CH_4-C_2H_4 is strongly affected

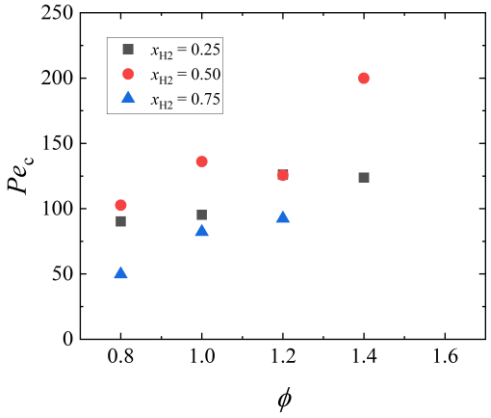

Fig. 5. *Critical Peclet number as a function of equivalence ratio*

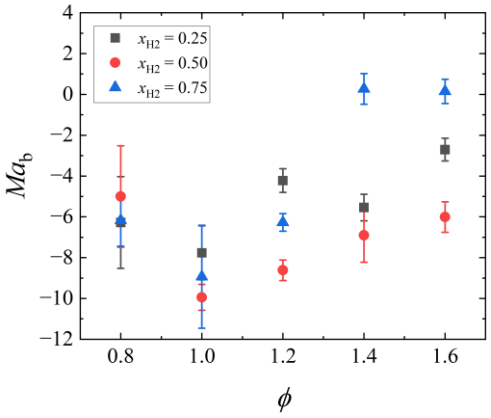

Fig. 6. *Markstein number as a function of equivalence ratio*

by diffusive-thermal instability. From the analysis of Bechtold and Matalon (Bechtold and Matalon, 1987), Ma_{b} is expressed as a function of $Ze(Le_{\mathrm{eff}}-1)$ where Ze is the Zeld'vich number and Le_{eff} is the effective Lewis number. Therefore, in this study, the change in the value of $Ze(Le_{\mathrm{eff}}-1)$ due to the change in the ϕ and the $x_{\mathrm{H_2}}$ was computationally determined and evaluated. The Zeld'vich number Ze is obtained from the equation for temperature reported by Müller et al. (Müller et al., 1997) as follows:

$$Ze = 4\frac{T_{\mathrm{ad}}-T_{\mathrm{u}}}{T_{\mathrm{ad}}-T^{0}} \tag{4}$$

where T^0 is the inner layer flame temperature at the point of maximum temperature gradient. To calculate the values of Le for multifuel mixtures, in this study, diffusion-based formulation reported by Dinkelacker et al., 2011 was adopted. Firstly, mass diffusion coefficient,$D_{\mathrm{i,mix}}$, were calculated assuming that the fuel-air mixture consisted only of fuel i and air at the same ratio as the composition ratio in the vent gas in the following equation:

$$D_{\mathrm{i,mix}} = \left(1-Y_{\mathrm{i,mix}}\right)\left(\sum_{\substack{\mathrm{s}=1\\ \mathrm{s}\neq\mathrm{i}}}^{\mathrm{N}}\frac{\chi_{\mathrm{s}}}{D_{\mathrm{i,s}}}\right)^{-1} \tag{5}$$

where $Y_{\mathrm{i,mix}}$ is the mass fraction of fuel i in the fuel i-air mixture and χ_{s} is the mole fraction of each species, s, in the mixture. The diffusion coefficient of oxidizer was defined as the diffusion coefficient of oxygen for overall vent gas-air mixtures. Thermal diffusivity, α, also calculated from the thermal properties of unburned vent gas-air mixtures. Then, the Lewis number for multifuel mixtures, Le_{fuel}, was calculated by diffusion-based formulation as follows:

$$Le_{\mathrm{fuel}} = \frac{\alpha}{\sum_{\mathrm{i}=1}^{\mathrm{fuel}}\chi_{\mathrm{i}}D_{\mathrm{i,mix}}} \tag{6}$$

Finally, effective Lewis number of vent gas-air mixture, Le_{eff}, was calculated by eq. (7):

$$Le_{\mathrm{eff}} = 1+\frac{(Le_{\mathrm{exc}}-1)+A_1(Le_{\mathrm{def}}-1)}{1+A_1} \tag{7}$$

where Le_{exc} and Le_{def} are the Lewis number of the excessive and deficient reactant, respectively. The parameter A_1 is calculated as follows:

$$A_1 = \begin{cases} 1+Ze(1/\phi-1) & (\phi<1) \\ 1+Ze(\phi-1) & (\phi\geq 1) \end{cases} \tag{8}$$

Figure 7 shows the $Ze(Le_{\mathrm{eff}}-1)$ of each gas composition as a function of ϕ. In the range of $0.8 \leq \phi \leq 1$, the $Ze(Le_{\mathrm{eff}}-1)$ is decreased with increasing the ϕ. While in the range of $1.0 \leq \phi \leq 1.6$, the $Ze(Le_{\mathrm{eff}}-1)$ is increased with increasing the ϕ. The trend of the variation of $Ze(Le_{\mathrm{eff}}-1)$ with the ϕ is in good agreement with the trend of Ma_{b} determined from the experiment. In terms of the effect of the composition ratio of hydrogen in the fuel mixture, $Ze(Le_{\mathrm{eff}}-1)$ decreased with increasing $x_{\mathrm{H_2}}$ from 0.25 to 0.50. In contrast, $Ze(Le_{\mathrm{eff}}-1)$ increased with increasing $x_{\mathrm{H_2}}$ from 0.50 to 0.75. This trend also in good agreement with the trend of Ma_{b}. The reason is that H_2 has a higher mass diffusion coefficient than CO, so the increase in the hydrogen fraction increases the mass diffusion coefficient of the fuel mixture and Le_{eff} is decreased and diffusive-thermal instability is enhanced in the range of $0.25 \leq x_{\mathrm{H_2}} \leq 0.50$. On the other hand, H_2 has a higher thermal diffusivity than CO, so in the range of $0.5 \leq x_{\mathrm{H_2}} \leq 0.75$, Le_{eff} increases and diffusive-thermal instability is suppressed because the increase in thermal diffusivity due to the increased hydrogen fraction is greater than the increase in mass diffusion coefficient. The suppression of instability by increasing the hydrogen fraction results in the no flame acceleration observed under $x_{\mathrm{H_2}} = 0.75$ at a smaller ϕ than for other $x_{\mathrm{H_2}}$, as shown in Fig.5. The above results show that the diffusive-thermal instability is

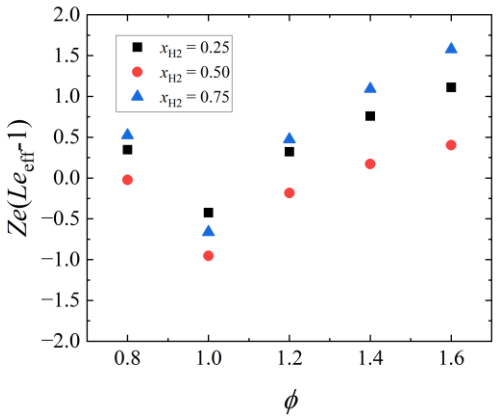

Fig. 7. *Variation of* $Ze\left(Le_{eff}-1\right)$ *with equivalence ratio*

enhanced by an increase in the H_2 mole fraction in the vent gas when the composition ratio of hydrogen is smaller than that of CO, while the instability is suppressed by an increase in the H_2 mole fraction in the vent gas when the composition ratio of hydrogen is larger than that of CO in the vent gas with the composition assumed in this study.

4. Conclusions

In this study, critical Peclet numbers for the onset of flame acceleration due to the intrinsic instabilities of lithium-ion battery thermal runaway vent gas in air investigated experimentally. The values of S_{u}^{0}, Pe_{c} and Ma_{b} were obtained from the spherically propagating flame at elevated pressure with changing the mole fraction of H_2 and CO in the fuel mixture, $x_{\mathrm{H_2}}$. The values of S_{u}^{0} were increased with increasing $x_{\mathrm{H_2}}$. For all mixtures, the values of critical Peclet number tended to increase with increasing equivalence ratios at all $x_{\mathrm{H_2}}$. However, when the $x_{\mathrm{H_2}}$ is 0.25 and 0.50, flame acceleration was not observed within the observation area of this study at $\phi = 1.6$. Also, when the $x_{\mathrm{H_2}}$ is 0.75, flame acceleration was not observed at $\phi = 1.4$ and 1.6. The experimental values of Ma_{b} were negative over a wide range of ϕ for all gas compositions. This means that the propagation flame of vent gas consisting of H_2-CO-CO_2-CH_4-C_2H_4 is strongly affected by diffusive-thermal instability. From the calculation results of $Ze(Le_{\mathrm{eff}}-1)$, the values of $Ze(Le_{\mathrm{eff}}-1)$ decreased with increasing $x_{\mathrm{H_2}}$ from 0.25 to 0.50. In contrast, $Ze(Le_{\mathrm{eff}}-1)$ increased with increasing $x_{\mathrm{H_2}}$ from 0.50 to 0.75. This trend also in good agreement with the trend of Ma_{b}.It was suggested that diffusive-thermal instability is enhanced by an increase in the H_2 mole fraction in the vent gas when the composition ratio of hydrogen is smaller than that of CO, while the instability is suppressed by an increase in the H_2 mole fraction in the vent gas when the composition ratio of hydrogen is larger than that of CO in the vent gas with the composition assumed in this study.

References

Abraham, D. P., Roth, E. P., Kostecki, R., McCarthy, K., MacLaren, S., Doughty, D. H., 2006. Diagnostic Examination of Thermally Abused High-Power Lithium-Ion Cells. J. Power Sources, 161, 648-657.

Baird, A. R., Archibald, E. J., Marr, K. C., Ezekoye, O. A., 2020. Explosion Hazards from Lithium-Ion Battery Vent Gas. J. Power Sources, 446, 227257.

Bang, H. J., Joachin, H., Yang, H., Amine, K., Prakash, J., 2006. Contribution of the Structural Changes of LiNi0.8Co0.15Al0.05O2 Cathodes on the Exothermic Reactions in Li-Ion Cells. J. Electrochem. Soc., 153, A731.

Bechtold, J. K., Matalon, M., 1987. Hydrodynamic And Diffusion Effects on The Stability of Spherically Expanding Flames. Combust. Flame., 67, 77-90.

Belharouak, I., Lu, W., Vissers, D., Amine, K., 2006. Safety Characteristics of Li(Ni0.8Co0.15Al0.05)O2 and Li(Ni1/3Co1/3Mn1/3)O2. Electrochem. commun., 8, 329-335.

Bradley, D., Hicks, R. A., Lawes, M., Sheppard, C. G. W., Woolley, R. ,1998. The Measurement of Laminar Burning Velocities and Markstein Numbers for Iso-octane–Air and Iso-octane–n-Heptane–Air Mixtures at Elevated Temperatures and Pressures in an Explosion Bomb. Combust. Flame., 115, 126-144.

Bradley, D., Lawes, M., Liu, K., Verhelst, S., Woolley, R. ,2007. Laminar Burning Velocities of Lean Hydrogen–Air Mixtures at Pressures up to 1.0 Mpa. Combust. Flame., 149, 162-172.

Dinkelacker, F., Manickam, B., Muppala, S. P. R., 2011. Modelling and Simulation of Lean Premixed Turbulent Methane/Hydrogen/Air Flames with an Effective Lewis Number Approach. Combust. Flame., 158, 1742-1749.

Dobashi, R., Kawamura, S., Kuwana, K., Nakayama, Y., 2011. Consequence Analysis of Blast Wave from Accidental Gas Explosions. Proc. Combust. Inst., 33, 2295-2301.

Dorofeev, S. B., 2011. Flame Acceleration and Explosion Safety Applications. Proc. Combust. Inst., 33, 2161-2175.

Doughty, D. H., Roth, E. P., Crafts, C. C., Nagasubramanian, G., Henriksen, G., Amine, K. ,2005. Effects of Additives on Thermal Stability of Li Ion Cells. J. Power Sources, 146, 116-120.

Golubkov, A. W., Fuchs, D., Wagner, J., Wiltsche, H., Stangl, C., Fauler, G., Voitic, G., Thaler, A., Hacker, V., 2014. Thermal-Runaway Experiments on Consumer Li-Ion Batteries with Metal-Oxide and Olivin-Type Cathodes [10.1039/C3RA45748F]. RSC Adv., 4, 3633-3642.

Golubkov, A. W., Scheikl, S., Planteu, R., Voitic, G., Wiltsche, H., Stangl, C., Fauler, G., Thaler, A., Hacker, V., 2015. Thermal Runaway of Commercial 18650 Li-Ion Batteries with LFP and NCA Cathodes – Impact of State of Charge and Overcharge [10.1039/C5RA05897J]. RSC Adv., 5, 57171-57186.

Gu, X. J., Haq, M. Z., Lawes, M., Woolley, R., 2000. Laminar Burning Velocity and Markstein Lengths of Methane–Air Mixtures. Combust. Flame., 121, 41-58.

Ichikawa, A., Hayakawa, A., Kitagawa, Y., Kunkuma Amila Somarathne, K. D., Kudo, T., Kobayashi, H., 2015. Laminar Burning Velocity snd Markstein Length of Ammonia/Hydrogen/Air Premixed Flames at Elevated Pressures. Int. J. Hydrogen Energy, 40, 9570-9578.

Kim, W. K., Mogi, T., Dobashi, R., 2014. Effect Of Propagation Behaviour of Expanding Spherical Flames on the Blast Wave Generated During Unconfined Gas Explosions. Fuel, 128, 396-403.

Kim, W. K., Mogi, T., Kuwana, K., Dobashi, R., 2015. Prediction Model for Self-Similar Propagation and Blast Wave Generation of Premixed Flames. Int. J. Hydrogen Energy, 40, 11087-11092.

Lammer, M., Königseder, A. Hacker, V., 2017. Holistic methodology for characterisation of the thermally induced failure of commercially available 18650 lithium ion cells, RSC Adv., 7, 24425–24429.

Law, C. K., Sung, C. J., 2000. Structure, Aerodynamics, and Geometry of Premixed Flamelets. Prog. Energy Combust. Sci., 26, 459-505.

Müller, U. C., Bollig, M., Peters, N., 1997. Approximations for Burning Velocities and Markstein Numbers for Lean Hydrocarbon and Methanol Flames. Combust. Flame., 108, 349-356.

Meng, D., Wang, X., Chen, M., Wang, J., 2023. Effects Of Environmental Temperature on the Thermal Runaway of Lithium-Ion Batteries During Charging Process. J. Loss Prev. Process Ind., 83, 105084.

Metcalfe, W. K., Burke, S. M., Ahmed, S. S., Curran, H. J., 2013. A Hierarchical and Comparative Kinetic Modeling Study of C1 − C2 Hydrocarbon and Oxygenated Fuels. Int. J. Chem. Kinet., 45, 638-675.

Okafor, E. C., Hayakawa, A., Nagano, Y., Kitagawa, T., 2014. Effects of Hydrogen Concentration on Premixed Laminar Flames of Hydrogen–Methane–Air. Int. J. Hydrogen Energy, 39, 2409-2417.

Paul, C., 1985. Dynamic Behavior of Premixed Flame Fronts in Laminar and Turbulent Flows. Prog. Energy Combust. Sci, 11, 1-59.

Tanaka, K., Ueda, A., Kim, Y., Kim, W., 2024. Cellular Instabilities of Outwardly Propagating Spherical Hydrogen-Oxygen Flames Using a Soap Bubble Method. Process Saf. Environ. Prot., 183, 645-652.

Ueda, A., Tanaka, K., Kim, Y., Kim, W., 2023. Onset of Flame Acceleration in Propane–Oxygen Mixtures. J. Energy Inst., 110, 101335.

Yuan, W., Liang, D., Chu, Y., Wang, Q., 2022. Aging Effect Delays Overcharge-Induced Thermal Runaway of Lithium-Ion Batteries. J. Loss Prev. Process Ind., 79, 104830.

ISHPMIE 2024
Napoli, Italy

15th INTERNATIONAL SYMPOSIUM ON HAZARDS, PREVENTION AND MITIGATION OF INDUSTRIAL EXPLOSIONS